# Encyclopedia of Nanoscience and Nanotechnology

Volume 5 Number 1 2004

# Magnetostrictive Nanomaterials for Sensors

Keat G. Ong, Craig A. Grimes

*The Pennsylvania State University, University Park, Pennsylvania, USA*

## CONTENTS

## 1. INTRODUCTION

Amorphous ferromagnetic glasses are noncrystallized ferromagnetic alloys free from defects such as grain boundaries, precipitates, or phase segregation [1, 2]. The amorphous structure of these materials gives rise to unique magnetic and mechanical properties, such as high mechanical strength [3], large magnetoelastic coupling, large magnetostriction [4], and the so-called giant magnetoimpedance effect (GMI) [5], which make them suitable for various sensor applications. The large magnetostriction allows the permeability of the materials to significantly change with applied stress and also causes the ferromagnetic glasses to exhibit a strong mechanical vibration when excited by a time-varying magnetic field. The high degree of magnetoelastic coupling allows efficient conversion between mechanical and electrical energies [6], so the response of the ferromagnetic glasses can be remotely detected by measuring the magnetic flux change. Furthermore, the GMI effect, wherein the electrical impedance of a ferromagnetic glass significantly changes with applied magnetic field, allows them to be used as ultrasensitive magnetic field sensors. Since there are few defects in the amorphous glass to restrict magnetic domain wall motion, magnetically soft ferromagnetic glasses have properties useful in sensor design including low coercivity, low hysteresis loss, and high permeability. The soft magnetic properties increase the performance and the stability of ferromagnetic glass-based sensors by allowing them to have good reversibility with little hysteresis in response to applied mechanical stresses and magnetic fields.

Ferromagnetic glasses are fabricated by rapid quenching techniques (e.g., melt-spinning) to prevent crystallization. Material properties are largely dependent upon the alloy composition, generally a combination of transition metals, rare-earth metals, and glass-forming metalloids. The lack of long-range order in the amorphous glasses eliminates the crystalline anisotropy energy, rendering them magnetically soft. However, inhomogeneous cooling of the alloy melt creates internal stresses that increase stress anisotropy energy. Since the amorphous nanostructure of these materials allows atomic rearrangement at a temperature far below crystallization, the stress anisotropy can be removed by relaxing the materials with low-field annealing at a moderate temperature. Alternatively, depending upon the application an anisotropy field can be introduced in a ferromagnetic glass by annealing under applied stress or magnetic field at moderate temperatures [7–9]. For certain amorphous alloys, annealing can be preformed above the crystallization temperature (500–900 °C) to create nanocrystalline structures of 10–20 nm in size for enhancing the soft magnetic properties of the materials [10].

Although there are many types of ferromagnetic glasses with a range of mechanical and magnetic properties, as dependent upon the composition and annealing history, the most generally useful type of ferromagnetic glass for sensor applications is magnetically soft transition-metalloid-based alloys with a high Fe or Co content. For example Fe-rich alloys have magnetostriction constants as high as $\lambda_S \approx 10^{-5}$, and magnetoelastic couplings as high as 0.98, while Co-rich transition-metalloid alloys have low magnetostriction on the order of $10^{-7}$. Rare-earth amorphous alloys, which exhibit large magnetostriction as high as $10^{-4}$, are useful as transducers since a small applied field can causes a large change in the material dimensions. Some of the commercially available ferromagnetic glasses [11] for sensor applications are the Fe-rich Metglas 2605SC ($Fe_{81}B_{13.5}Si_{3.5}C_2$) and 2826MB ($Fe_{40}Ni_{38}Mo_4B_{18}$) that have a magnetostriction coefficient

on the order of $10^{-5}$ and a high magnetoelastic coupling coefficient, and the Vitrovac amorphous alloys that have a near zero magnetostriction and excellent soft magnetic properties ($B_S = 0.55$ T, $\mu_{max} = 10^5$).

Ferromagnetic glasses were initially used as the sensing materials for induction-based sensors to measure stress/strain and torque [12], magnetic field [13], and displacement [14] since their permeability varies with applied stress and field. These sensors, usually composed of solenoids loaded with ferromagnetic glass cores, are simple in design, stable over a wide range of temperature, and have a good linearity and low hysteresis.

Ferromagnetic glasses are also used as field and stress sensors based on the GMI effect. The GMI magnetic sensors are highly sensitive, with maximum impedance variation reaching 400%. Ferromagnetic glasses have been used to construct magnetostrictive delay lines (MDL) for the measurement of stress, torque, and displacement [15–22]. The MDL sensor is usually a long ferromagnetic glass wire or ribbon surrounded with an excitation coil at one end and a sensing coil at the opposite end. An acoustic wave is excited by passing a voltage pulse to the excitation coil and is captured by a sensing coil as an induced voltage. The parameters of interest, such as stress, torque, and weight, are determined from the attenuation of the acoustic wave, which is obtained by normalizing the measured voltage amplitude to the excitation voltage amplitude.

Magnetoelastic resonant sensors, which are based on the change in the magnetoelastic resonant frequency of a ferromagnetic glass ribbon in response to applied stress and field, have become popular in the past decade due to their remote-query capability, simple design, and low cost. These sensors have been used to measure pressure [23], liquid viscosity and density [24], liquid flow velocity [25], temperature [26], and thin-film elasticity [27]. Magnetoelastic resonance chemical and gas sensors have also been built by applying a layer of mass-changing chemically responsive material, the mass loading of which changes the mechanical resonant frequency of the sensor, as does the elasticity of the applied coating [28–33].

Ferromagnetic glass thin films are also used as the active layer of a magnetic surface acoustic wave (MSAW) sensor [34]. Due to the stress and field dependencies in the ferromagnetic glass, the MSAW sensor can be used to measure stress, magnetic field, or displacement. Recently, a viscosity sensor [35] was built based on the spontaneous mechanical rotation of a large magnetostrictive ferromagnetic glass wire when subjected to an ac magnetic field.

## 2. PRINCIPLES OF MAGNETISM

In this section the fundamental principles of magnetism and magnetic materials are reviewed. It begins by introducing the concept and origin of magnetic fields and fluxes, followed by a discussion on the constitutive relations and some basic magnetism principles, such as Faraday's induction law, Lorentz's force equation, and Maxwell's equations. Different types of magnetic materials are then introduced. Intrinsic properties of ferromagnetic materials, such as magnetic domains, anisotropy, and magnetization processes, are detailed.

## 2.1. Origin of Magnetic Fields

Although a magnetic compass was apparently used over 4000 years ago [see for example T. C. Lucretius, *On The Nature of the Universe* ($\approx$100 B.C.), translated by R. Latham, Penguin Books, New York, 1992], the mechanism and principles of magnetism were not put to paper until 1819, when Oersted [36] discovered that an electric current produces a magnetic field, resulting in the modern field of magnetism. The reader requiring greater knowledge on the subject of magnetism is encouraged to seek one or more of the many excellent books extensively dealing with the topic of magnetism that have been published over the past 50 years [37–43].

### 2.1.1. Magnetic Dipoles and Moments

Magnetic fields originate from electrical charges in motion, be they electrical currents (free moving electrons) flowing in a conductor, or the orbital motions of electrons (the so-called "Amperian currents"). Since magnetic fields are generated by electrical currents, the basic unit of the magnetic field, $H$, is amperes per meter (A/m). It is common to treat magnetic fields as lines of force that originate and terminate from magnetic poles or magnetic charges, just like those in an electrostatic system. However, magnetic poles exist as opposing dipoles—there are no magnetic monopoles. Figure 1 is a simple illustration of the magnetic fields generated by a permanent magnet, represented by the lines of force originated from the north (N) pole and terminated at the south (S) pole; the field lines form a closed loop inside the magnet from the S to N pole.

Similar to electrical charges, physically separating two magnetic poles generates a force. For two magnetic poles separated by a distance $l$ the force between them is quantified by the Coulomb magnetic moment $p_m$ given in volt-second-meters (V · s · m) as

$$p_m = Q_m l \tag{1}$$

where $Q_m$ is the Coulomb magnetic pole strength, in Webers (Wb) or volt-seconds (V · s), which depends on the magnetic properties of the materials. Under a homogeneous $H$ field,
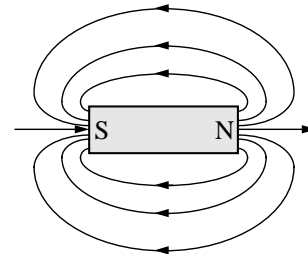


**Figure 1.** Magnetic field represented by lines of force originating from the N pole and terminated at the S pole.

the magnetic moment experiences a torque $T$:

$$T = p_m \times H \qquad (2)$$

Equation (2) describes the fundamental principle of the first magnetic sensor, the compass; earth's magnetic generates a torque on the needle shaped compass magnet and orients it parallel to the direction of earth's field along a north–south direction.

### 2.1.2. Magnetic Fields around Current-Carrying Conductors

A current-carrying conductor consists of moving electrical charges that generate a magnetic field. The fundamental principle that describes the generation of magnetic fields by an electrical current is the Biot–Savart law, an empirical equation discovered in 1820. According to the Biot–Savart law, the field contributed by a segment of current-carrying conductor with length $\delta l$ is

$$\delta H = \frac{I \delta l \times u}{4\pi r^2} \qquad (3)$$

where $I$ is the current in the conductor segment, $u$ is the unit vector of the current direction, and $\delta H$ is the contribution to the magnetic field at $r$ due to the current element $I \delta l$.

Figure 2 illustrates the generation of magnetic fields with conduction currents. A flowing current in a conductor loop generates a magnetic field $H$ passing through the loop, while a current in a straight wire generates a circumferential field around the wire. The direction of the $H$ field is given by the right-hand rule as illustrated in Figure 2.

Although the Biot–Savart law provides great understanding on how electrical currents generate magnetic fields, it can only be solved analytically when the current conductor contains high symmetry and the observation point is at the symmetry axis. For example, the field generated by a long straight wire at a distance $r$ is given as $H = I/2\pi r$, the field along the axis of an $N$-turn solenoid with length $l$ is $H = NI/l$, and the field along the $z$-axis of a circular loop of diameter $d$ that is centered on the $xy$-plane is $H = Id^2(d^2 + 4z^2)^{-3/2}$.

## 2.2. Magnetic Principles

This section shows the connection between magnetic fields and fluxes in vacuum and in magnetic materials. This section also introduces the fundamental magnetic principles that describe the relations between magnetic and electric
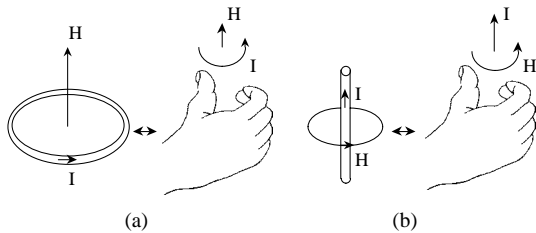


**Figure 2.** A flowing current in a loop or a straight wire generates a magnetic field $H$, the direction of which is given by the right-hand rule.

quantities, such as Ampere's law [44] and Faraday's law [45]. Lorentz's force equation, which links magnetic fluxes to force and torque, is also discussed in this section.

### 2.2.1. Magnetic Constitutive Relations

In the MKS unit system, the vacuum magnetic flux density $B$, in Webers per meter$^2$ (Wb/m$^2$) or volt-seconds per meter$^2$ (V · s/m$^2$), is related to $H$ as

$$B = \mu_0 H \qquad (4)$$

where $\mu_0$ is the free space magnetic permeability that has a value of $4\pi \times 10^{-7}$ Wb/A · m. When a magnetic field passes through a magnetic material, the magnetic dipoles in the material tend to align with the applied field. This phenomenon is called magnetization, and the intensity of magnetization is generally represented by $M$ having the same unit basis as $H$. The direction and intensity of the magnetization depend on the material: for nonmagnetic materials the value is close to zero, but for ferromagnetic materials the number can reach $10^6$ (see Section 2.4). The magnetization process effectively increases the density of magnetic fields in the magnetic material, so the flux density inside the material becomes

$$B = \mu_0(H + M) \qquad (5)$$

To simplify Eq. (5) so the flux $B$ only depends on the applied field $H$, the magnetic permeability $\mu$ (in Wb/A · m) and the relative permeability $\mu_r$ (unitless) are introduced as

$$B = \mu H = \mu_r \mu_0 H \qquad (6)$$

Comparing Eqs. (5) and (6), the permeability $\mu$ can be expressed as

$$\mu = \mu_0(1 + M/H) = \mu_0(1 + \chi) \qquad (7)$$

The ratio of magnetization to applied field $M/H$ is defined as the relative magnetic susceptibility $\chi$ (unitless). Most magnetic materials used for engineering applications are ferromagnetic materials with large magnetization $M$. As a result, the susceptibility and relative permeability are often treated as approximately equal ($\mu_r \approx \chi$).

At high frequency, many materials dissipate field energies as the field passes through them. To compensate for the field dissipation, the relative complex permeability $\mu_r^*$ is used,

$$\mu_r^* = \mu_r' - j\mu_r'' \qquad (8)$$

where the real part represents the magnetization and the imaginary part represents the energy loss. For anisotropic materials where the permeability varies with directions, $\mu_r^*$ is replaced by the relative complex permeability tensor $\bar{\mu}_r^* = \bar{\mu}_r' - j\bar{\mu}_r''$.

### 2.2.2. Ampere's Circuital Law

Consider a long circular conductor carrying a current $I$. By the Biot–Savart law, the magnetic field integrated along a circular path outside the conductor with radius $r$ can be

expressed as

$$\oint_c H \cdot dl = \frac{I}{2\pi r} \oint_c dl = I \tag{9}$$

Replacing the current $I$ with the current density $J_c$ in the conductor, Eq. (9) becomes

$$\oint_c H \cdot dl = \int_s J_c \cdot ds \tag{10}$$

Equation (10) is the Ampere's circuital law, which states the line integral of $H$ around a closed path is equal to the total current crossing any surface bounded by the line integral path.

### 2.2.3. Faraday's Induction Law

According to Faraday's induction law, an electromotive force (emf) will be induced in a closed-path electrical circuit if there is a change of magnetic flux linking to the circuit. In equation form, Faraday's law is expressed as

$$\text{emf} = -A\frac{dB}{dt} \tag{11}$$

where $A$ is the surface area, and $B$ is the magnetic flux. The negative sign in the equation is a result of Lenz's law, which states the direction of the induced voltage is such that the induced flux opposes the incident flux. Faraday's induction law is demonstrated in Figure 3 with a moving bar magnet and a closed loop. The movement of the permanent magnet results in a change in the magnetic flux linking to the loop, causing an induction voltage in the loop with a sense that would produce a current whose magnetic field opposes the flux change. Faraday's induction law is important for induction and search coil sensors, which detect magnetic fields by the induction voltage.

### 2.2.4. Lorentz's Force in Magnetic Fields

According to Lorentz's force equation, an electric charge $q_e$ traveling at a velocity $v$ inside flux $B$ experiences a force $F$ perpendicular to $B$ and $v$:

$$F = q_e(v \times B) \tag{12}$$

For a current $I$ flowing in a closed loop of area $A$, a torque $T$ appears on the conductor according to the Lorentz's force:

$$T = IA \times B \tag{13}$$
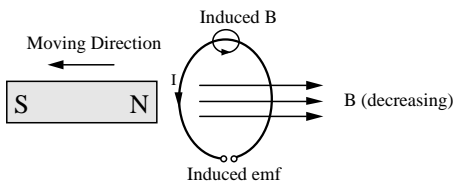


**Figure 3.** Illustration of Faraday's induction law. The decrease in the magnetic flux creates an induced emf, which produces a current $I$ that in turn generates an induced flux opposing to the initial change.

The term $IA$ is defined as the magnetic moment $\mu_m$. Note the similarity between the magnetic moment $\mu_m$ and the Coulomb magnetic moment $p_m$ in Eq. (13) and Eq. (2), respectively. In vacuum, they are scaled by the free space permeability $\mu_0$. Equation (13), similar to Eq. (2), describes the operational principle of electrical motors that generate rotational motion by passing a current within a magnetic field.

### 2.2.5. Maxwell's Equations

Maxwell combined the observations discovered by Ampere, Faraday, and Gauss into a final form for governing electric and magnetic fields, charges, and currents [46]. These equations, known as the Maxwell's equations, are useful for understanding magnetism and electromagnetism. In differential form, Maxwell's equations can be written as

$$\nabla \times E = -\frac{\partial B}{\partial t} \tag{14}$$

$$\nabla \times H = J_C + \frac{\partial D}{\partial t} \tag{15}$$

$$\nabla \cdot D = \rho_{es} \tag{16}$$

$$\nabla \cdot B = 0 \tag{17}$$

where $J_c$ is the conduction current and $\rho_{es}$ is the surface charge density. A more familiar form of Faraday's induction law can be obtained from Eq. (14) by integrating over an open surface $S$ bounded by a curve $C$ and applying Stoke's theorem on the left-hand side as

$$\oint_c E \cdot dl = -\frac{\partial}{\partial t} \int_s B \cdot ds \tag{18}$$

Equation (18) is essentially identical to (11) because emf is defined as $\int E \cdot dl$. Applying Stokes' theorem on Eq. (15) yields

$$\oint_c H \cdot dl = \int_s J_c \cdot ds + \frac{\partial}{\partial t} \int_s B \cdot ds \tag{19}$$

Equation (19) is identical to Ampere's law except for the second term on the right-hand side, which is the displacement current added by Maxwell to complete Ampere's law under ac conditions. Equations (16) and (17) are Gauss' electric and magnetic field laws, which state that electrical charges can operate as sources or sinks, originating or terminating electric flux, while magnetic flux forms closed loops with no known sources and sinks.

## 2.3. Types of Magnetism

All materials exhibit unique magnetization behavior and from the magnetization profiles can be categorized. Among the categories, diamagnetic and paramagnetic materials are considered as "weak magnetic" materials because the magnetization is relatively small, $\mu \approx \mu_0$ and $\chi \approx 0$ (although there are exceptions such as superconductors that exhibit a perfect diamagnetism, $\chi \approx -1$). Ferromagnetic and ferrimagnetic materials exhibit large magnetization with applied field; for some ferromagnetic materials $\mu_r$ can reach $\approx 10^6$.

### 2.3.1. Diamagnetism

All materials exhibit diamagnetism; however, the effect of diamagnetism is small and often shadowed by other magnetic effects. A diamagnetic material has the ability to "repel" magnetic fields, with the flux density in diamagnetic materials actually being less than in vacuum. Classically, diamagnetism is explained by the reduction of the electron velocity due to an external magnetic field. To understand diamagnetism, first consider an atom with an electron moving clockwise in an orbit perpendicular to an applied field. Since the electron carries an electrical charge, the orbital motion of the electron is equivalent to a current on a conductor loop. By Faraday's law, the increase in the applied field generates an induction current on the loop to produce an opposing field. For an orbiting electron the opposing field is generated by decreasing the electron velocity. Now consider another electron orbit adjacent to this orbit, with its plane parallel to the first one but the electron moving counterclockwise. In the absence of an external applied field, the moments of these two electrons cancel each other, yielding zero net moment. As the applied field increases, both orbits produce a magnetic moment opposing the applied field. The classical explanation for diamagnetism is illustrated in Figure 4.

For a diamagnetic material with $Z$ electrons per atom, $N$ atoms per cubic meter, and at effective equilibrium distance of $2r$, the susceptibility $\chi$ is given by

$$\chi = -\mu_0 N \frac{q_e^2 Z \langle r^2 \rangle}{6 m_e} \tag{20}$$

where $q_e$ is the electron charge and $m_e$ is the electron mass. For most diamagnetic materials, the value of $\chi$ is very small, about $10^{-5}$. As a result, diamagnetic materials have almost no effect on magnetic fields under most conditions, and they are commonly used as materials that do not disturb magnetic fields. Examples of diamagnetic materials are noble gases such as helium, neon, and argon, diatomic gases such as hydrogen and nitrogen, ionic solids such as sodium chloride (NaCl), and almost all organic compounds. Many metals also exhibit diamagnetic properties, for example, copper, zinc, silver, cadmium, gold, mercury, lead, and bismuth.

Superconductors exhibit the most unusual diamagnetic behavior. Superconductors are typically metals such as lead and tantalum, or compounds such as $Nb_3Sn$. At normal operating temperatures these materials are either diamagnetic or paramagnetic. However, when they are cooled to
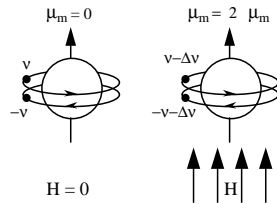
a critical temperature, they repel all magnetic flux by generating a thin layer of nondissipating surface currents. This effect is known as the Meissner effect. Ideally, superconductors have a perfect diamagnetism, which is $\chi = -1$. Superconductors such as lead and tantalum exhibit perfect diamagnetism. Superconductive diamagnetic materials are the key elements for superconducting quantum interference device field sensors.

### 2.3.2. Paramagnetism

Paramagnetic materials are composed of atoms or molecules that have a net magnetic moment because the spin and orbital moments of electrons do not completely cancel out. In the absence of applied fields, the magnetic moments are oriented randomly and thus macroscopically the net moment of a paramagnetic material is zero. When a magnetic field is applied on the material, the magnetic moments tend to align with the field. However, thermal agitation in the atoms or molecules opposes this tendency and tries to keep the moments in random states. This will result in a partial alignment of the magnetic moments; thus a small positive susceptibility is observed in paramagnetic materials. Increasing temperature increases the thermal energy in the atoms or molecules and therefore reduces the susceptibility.

In general, the magnetization $M$ in a paramagnetic material is nonlinear, which can be given by the Langevin function $L$ with $s = \mu_m B / k_B T$ as

$$M = N\mu_m \frac{s(e^s + e^{-s}) - (e^s - e^{-s})}{(e^s - e^{-s})} = N\mu_m L(s) \tag{21}$$

where $\mu_m$ is the magnetic moment of each atom, $T$ is the temperature, $k_B$ is the Boltzmann constant ($k_B = 5.38 \times 10^{-23}$), and $N$ is the number of atoms. In room temperature ($T \approx 300$ K) and at a moderate field $B \approx 1$ T, which is the operation condition for most technical applications, $s \approx 0$ and Eq. (21) becomes

$$\chi = \frac{\mu_m^2 N \mu_0}{3 k_B T} = \frac{C}{T} \tag{22}$$

Equations (21) and (22) are the results from classical Langevin paramagnetism [47]. The paramagnetic behavior can also be predicted using quantum mechanic theorems, and the results are identical to Eq. (22) for moderate fields at room temperature. The typical value for $\chi$ is generally on the magnitude of $10^{-3}$. Examples of paramagnetic substances are diatomic gases such as oxygen and nitric oxide, polyatomic gases such as $NO_2$ and $ClO_2$, and metals such as aluminum, titanium, platinum, palladium, magnesium, molybdenum, and vanadium.

### 2.3.3. Ferromagnetism and Ferrimagnetism

Ferromagnetic and ferrimagnetic materials are perhaps the most useful materials for technical applications. Like paramagnetic materials, each molecule in the ferro- and ferrimagnetic materials contains a net magnetic moment. However, because of the existence of a strong molecular field that aids the applied field in the magnetization process, the susceptibility of ferro- and ferrimagnetic materials is much larger than paramagnetic materials, ranging from $10^2$ to $10^6$. Even



**Figure 4.** In the absence of an external field, the orbital motions of two electrons with velocity $v$ and $-v$ create two opposing moments, resulting in zero net moment. When a field is applied, additional moments, $\Delta\mu_m$, are created at both atoms due to the change in the electron velocity. These two moments add up to reduce the applied field.

under zero applied field, the atomic moments of ferromagnetic materials are oriented in parallel due to the strong molecular field (in quantum magnetism, it is the exchange energy that causes the alignment of the moments), causing a large spontaneous magnetization. The moments of antiferromagnetic alloys are oriented in antiparallel, resulting in a zero net moment in the absence of an orienting magnetic field. Ferrimagnetic materials are composed of antiparallel atomic moments that do not completely cancel out. The moment alignments in ferro-, antiferro-, and ferrimagnetic materials are shown in Figure 5.

Due to the strong molecular field, ferro- and ferrimagnetic materials are self-saturating, or "spontaneously magnetized" in the absence of an external field. However, it is still easy to find a ferro- or ferrimagnetic sample in the unmagnetized state. This is because ferro- and ferrimagnetic contain many small regions, called "domains," which are spontaneously magnetized to saturation $M_s$ but oriented at different directions to minimize the energy potential within the material. The $M_s$ in these domains cancel each other, yielding zero macroscopic magnetization. When an external field is applied, these domains align with the field, and a large magnetization is observed. A permanent magnet sample consists of domains that do not cancel out macroscopically due to the crystal structure, applied stress, or mechanical defects. Section 2.5 details the domains and magnetization processes in ferro- and ferrimagnetic materials.

Magnetization in ferromagnetic magnetic materials is a critical function of temperature. The spontaneous magnetization below the Curie temperature $T_\theta$ of a ferromagnetic material is given by

$$M_s = N\mu_m \tanh\left(\mu_0\mu_m \frac{H + \mu_0\gamma M_s}{k_B T}\right) \tag{23}$$

where $\gamma$ is the Weiss constant. At $T_\theta$, the thermal energy $k_B T_c$ is equal to the molecular exchange energy, and this makes $M_s$ zero. All ferromagnetic materials become paramagnetic above $T_\theta$, and the susceptibility above $T_\theta$ is given by Curie–Weiss law [48] as

$$\chi = \mu_0 \frac{\mu_m N}{3k_B(T - T_\theta)} \tag{24}$$

Equation (24) is actually an extension of the Curie law in Eq. (22). Figure 6 depicts the transition of a material from ferromagnetism to paramagnetism with increasing temperature. At low temperature, the material exhibits strong ferromagnetism with a large magnetization $M_{s0}$. As the temperature increases, the saturation magnetization decreases and becomes zero at $T_\theta$. Above $T_\theta$, the susceptibility of the material decreases with temperature following the profile given by Eq. (24).
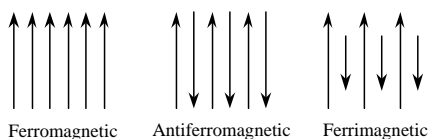


**Figure 5.** The atomic moment alignment of the ferromagnetic, antiferromagnetic, and ferrimagnetic materials.
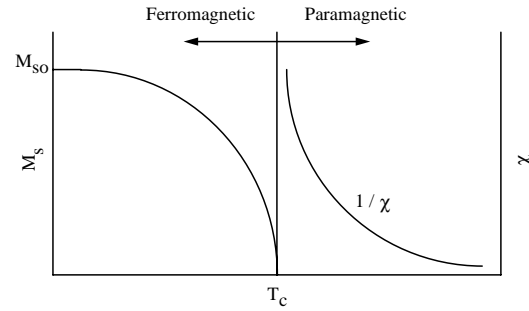


**Figure 6.** The transition of a material from ferromagnetic state to paramagnetic. The material is ferromagnetic below $T_\theta$, but becomes paramagnetic above $T_\theta$ according to the Curie–Weiss law.

Quantum theory explains ferromagnetism on the basis of exchange forces, which are caused by the exchange orbit of two adjacent electrons from two atoms. The exchange energy $E_{ex}$ is given as

$$E_{ex} = -2J_{ex}s_1 \cdot s_2 \tag{25}$$

where $s_1$ and $s_2$ are the spins of two adjacent electrons, and $J_{ex}$ is the exchange integral. Since the moments of ferromagnetic materials are parallel (i.e., $s_1$ and $s_2$ have the same sign), $J_{ex}$ must also be positive for a ferromagnet to minimize $E_{ex}$. The same argument goes for antiferromagnetic, where $J_{ex}$ must be negative. Figure 7, known as the Bethe–Slater curve [49, 50], shows that the exchange integral varies with the ratio of the atomic distance to the $3d$-shell distance, $r_a/r_{3d}$. The curve shows that ferromagnetism only appears in some metals such as Fe, Co, and Ni because their $r_a/r_{3d}$ ratios correspond to positive $J_{ex}$. Following a similar argument, ferromagnetic materials can be created by alloying two or more nonferromagnetic materials by changing in the effective $r_a/r_{3d}$. Examples of ferromagnetic alloys are manganese–aluminum–chromium, manganese–copper–tin, and all rare-earth magnets. Although later Herring and others [51] showed that this method of determining ferromagnetism is unreliable, the Bethe–Slater curve still provides insights on the origin of ferromagnetism.

## 2.4. Anisotropy

Due to defects, shape, and crystallographic structure, the applied field required for magnetizing a magnetic material commonly varies with the direction of the applied field
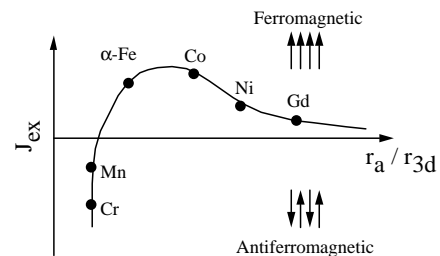


**Figure 7.** Bethe–Slater curve shows that the exchange integral varies with the ratio of the atomic distance to the $3d$-shell distance.

relative to the direction of the magnetization vector within the material. The minimum field needed to magnetize a sample is for a field parallel to the magnetization vector direction. Conversely, the maximum field needed to magnetize a sample is when the applied field is perpendicular to the easy axis, the so-called hard axis. This phenomenon is called anisotropy, and there are three major causes of anisotropy: magnetocrystalline anisotropy, shape anisotropy, and magnetostriction anisotropy. Anisotropy determines the magnetic hardness of materials and is usually controlled for enhancing the magnetic materials as needed for specific applications.

### 2.4.1. Magnetocrystalline Anisotropy

The electron orbits of a crystalline magnetic material, such as iron, are fixed on certain crystallographic directions due to a strong orbit–lattice coupling. When an external field is applied the electron orbits tend to reorient. However, the strong orbit–lattice coupling force creates a resistance that hinders the reorientation of the electron orbits. The energy needed to overcome this orbit–lattice coupling is equal to the energy needed to rotate the electron spin away from the easy direction, which is known as the crystalline anisotropy energy $u_a$.

The anisotropy of a magnetic material is generally represented by an energy function that describes the equilibrium orientation of the magnetization under different fields, stresses, temperatures, etc. The easiest way to approximate the energy function is by applying a power series expansion on a set of directional basis functions. The anisotropy energy function for the simplest geometry, the hexagonal uniaxial structure, is expressed as

$$u_a = K_0 + K_1 \sin^2 \theta + K_2 \sin^4 \theta + \cdots \qquad (26)$$

where $\theta$ is the angle between $M_s$ and the main axis of the uniaxial structure. In Eq. (26), $K_0$ has no meaning for anisotropy properties because it is directional independent. The first term $K_1$ describes the shape of the energy function, where $K_1 > 0$ means an oblate spheroid and $K_1 < 0$ a prolate spheroid. An example of material having this geometry is cobalt, which at room temperature has

$$K_1 = 4.1 \times 10^5 \text{ J/m}^3 \qquad K_2 = 5.5 \times 10^5 \text{ J/m}^3 \qquad \text{cobalt}$$

The energy function of cobalt, plotted in Figure 8a, indicates that in the absence of an applied field, the magnetization seeks the lowest energy orientation, namely, along the $z$-axis.

The anisotropy of a magnetic material is also commonly defined by a fictitious anisotropy field $H_k$, which for the simplified case of a uniaxial structure is given by

$$H_k = \frac{2K_1}{M_s} \qquad (27)$$

The energy function for a cubic system can be written as

$$u_a = K_0 + K_1\left(\alpha_1^2\alpha_2^2 + \alpha_2^2\alpha_3^2 + \alpha_3^2\alpha_1^2\right) + K_2\left(\alpha_1^2\alpha_2^2\alpha_3^2\right) + \cdots \qquad (28)$$

where $\alpha_1$, $\alpha_2$, and $\alpha_3$ are the directional cosines of the magnetization along the main coordinate axes ($\alpha_i = M_i/M_s$).
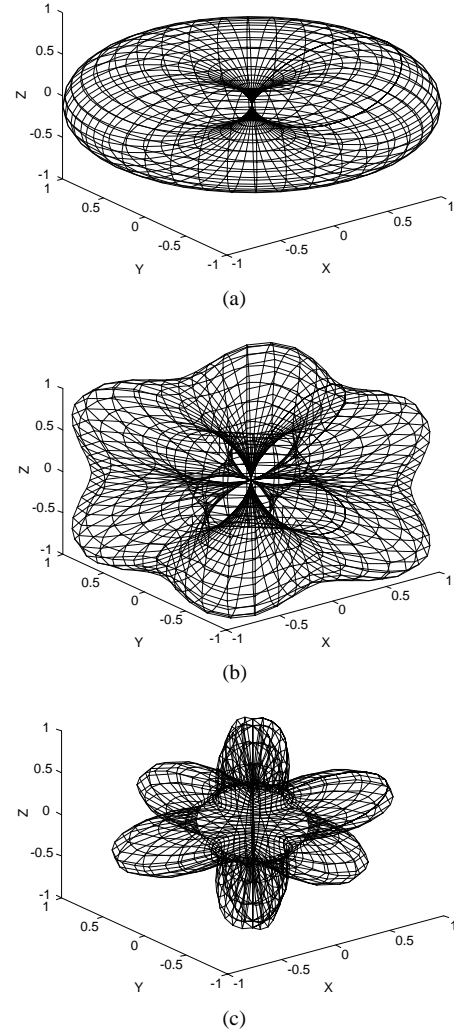


**Figure 8.** Anisotropy energy for (a) uniaxial cobalt, (b) fcc iron, and (c) bcc nickel. The length of the radius at the surface of the wire frame defines the anisotropy energy in that direction.

The anisotropy constants at room temperature for the face-centered cubic (fcc) iron and body-centered cubic (bcc) nickel are

$$K_1 = 4.8 \times 10^4 \text{ J/m}^3 \qquad K_2 = -5.0 \times 10^4 \text{ J/m}^3 \qquad \text{iron}$$

$$K_1 = -4.5 \times 10^3 \text{ J/m}^3 \qquad K_2 = -2.3 \times 10^3 \text{ J/m}^3 \qquad \text{nickel}$$

Figure 8b and c shows the energy plots of, respectively, iron and nickel. For iron and nickel the change in the sign of $K_1$ changes the number of easy directions (the nulls in the energy patterns). Iron has six easy directions and hence three easy axes, while nickel has eight easy directions and four easy axes. Cobalt has a uniaxial anisotropy that results in an omnidirectional energy pattern with one easy axis.

Notice how the sign of $K_1$ inverses the anisotropy pattern in Figures 8b and c by turning nulls into peaks and vise versa. At the point when $K_1$ changes sign ($K_1 = 0$), the anisotropy pattern becomes spherical (no anisotropy or $H_k = 0$). By alloying iron and nickel that have opposite signs

in $K_1$, $H_k$ can become very small, allowing easy magnetization at every direction. A good low $H_k$ alloy is the permalloy (NiFe) material (see Section 2.6 for details).

Figure 9 plots the magnetization $M_s$ in iron, nickel, and cobalt as a function of applied $H$ field. As shown in the plot, the materials have the lowest saturation fields when the applied field is along the easy axis, which is $\langle 100 \rangle$ for iron, $\langle 111 \rangle$ for nickel, and $\langle 001 \rangle$ or the $\|c$-axis for cobalt.

### 2.4.2. Shape Anisotropy and Demagnetizing Fields

A magnetized material is composed of small magnetic dipoles. As illustrated in Figure 10, these dipoles cancel out within the material body, but not on the surface. The surface dipoles create a demagnetizing field $H_d$, which is proportional but antiparallel to the magnetization $M$,

$$H_d = -N_d M \tag{29}$$

where $N_d$ is the demagnetizing factor, $N_d = (N_a, N_b, N_c)$, defined over a general ellipsoid with axes $a$, $b$, and $c$. The field inside the material $H_i$ is the sum of the applied $H$ field and the demagnetizing field:

$$H_i = H + H_d \tag{30}$$

The energy density of the demagnetizing field, $u_d$, of a general ellipsoid is given as

$$u_d = \frac{\mu_0 M_s^2}{2} \left( N_a \alpha_1^2 + N_b \alpha_2^2 + N_c \alpha_3^2 \right) \tag{31}$$

where $\alpha_1$, $\alpha_2$, and $\alpha_3$ are the directional cosines of the magnetization with respect to the ellipsoid axes $a$, $b$, and $c$. Generally, the demagnetizing field is larger along a shorter direction. The demagnetizing factor for a long rod parallel to the $a$-axis is $N_a \approx 1/2$ and $N_b \approx N_c \approx (\ln 2r - 1)/r^2$, for a thin disc centered on the $bc$-plane is $N_a \approx 1$ and $N_b = N_c \approx 0$, and for a sphere is $N_d = 1/3$. By choosing an appropriate



**(a)**



**(b)**



**(c)**
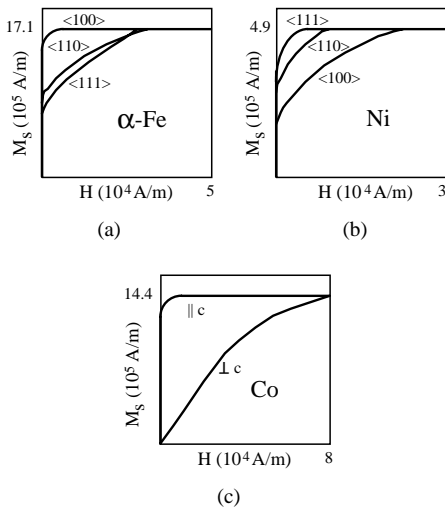
**Figure 9.** The magnetization of (a) iron, (b) nickel, and (c) cobalt at different crystalline axes.
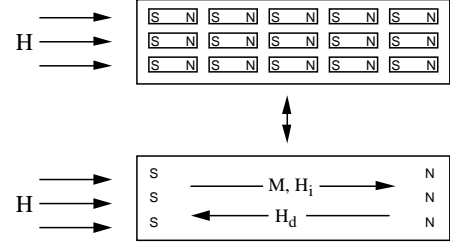


**Figure 10.** The magnetized sample is composed of nano/microscopic dipoles. The dipoles cancel out within the sample, but the surface dipoles remain, creating a demagnetizing field.

shape, $u_d$ can become much larger than the magnetocrystalline anisotropy energy $u_a$, thus providing an easy way to control the direction of the anisotropy without worrying about the crystal structure of the material.

### 2.4.3. Magnetostriction Anisotropy

Many magnetic materials exhibit the magnetostriction effect, a phenomenon that elongates the material dimension parallel to the applied magnetic field and shortens the dimension perpendicular to the field, or vice versa. Not all materials exhibit the isotropic magnetostriction effect; for example, magnetization of an iron crystal in its $\langle 100 \rangle$ direction causes an elongation along $\langle 100 \rangle$ but magnetizing in the $\langle 111 \rangle$ direction causes an contraction along the $\langle 111 \rangle$ direction. The anisotropic magnetostriction effect, or the magnetostriction anisotropy, couples with the magnetocrystalline anisotropy, so the total energy function $u$ of a cubic material becomes

$$
\begin{aligned}
u &= u_a + u_{me} + u_{el} \\
&= K_0 + K_1 \left( \alpha_1^2 \alpha_2^2 + \alpha_2^2 \alpha_3^2 + \alpha_3^2 \alpha_1^2 \right) + K_2 \alpha_1^2 \alpha_2^2 \alpha_3^2 + \cdots \\
&\quad + B_1 \left( \alpha_1^2 e_{xx} + \alpha_2^2 e_{yy} + \alpha_3^2 e_{zz} \right) \\
&\quad + B_2 \left( \alpha_1^2 \alpha_2^2 e_{xx} + \alpha_2^2 \alpha_3^2 e_{yy} + \alpha_3^2 \alpha_1^2 e_{zz} \right) \\
&\quad + c_{11}/2 (e_{xx} + e_{yy} + e_{zz}) + c_{11}(e_{xx}e_{yy} + e_{yy}e_{zz} + e_{zz}e_{xx}) \\
&\quad + c_{44}/2 (e_{xy}^2 + e_{yz}^2 + e_{zx}^2) + \text{const} \times e_{ij}
\end{aligned} \tag{32}
$$

where $u_a$ is the anisotropy energy shown in Eq. (28), $u_{me}$ is the magnetoelastic energy, $u_{el}$ is the pure elastic energy, $B$ is the magnetoelastic coefficient that relates the coupling between the strain $e_{ij}$ and the magnetization direction given by $\alpha_i$, and the $c$ terms in the $u_{el}$ are the elastic coefficients. The strain or magnetostriction $\lambda = \Delta l / l$ is derived form Eq. (32) as

$$
\begin{aligned}
\lambda &= \frac{3}{2} \lambda_{100} \left( \alpha_1^2 \beta_1^2 + \alpha_2^2 \beta_2^2 + \alpha_3^2 \beta_3^2 \right) \\
&\quad + 3\lambda_{111} \left( \alpha_1 \alpha_2 \beta_1 \beta_2 + \alpha_2 \alpha_3 \beta_2 \beta_3 + \alpha_3 \alpha_1 \beta_3 \beta_1 \right)
\end{aligned} \tag{33}
$$

where $\beta$ gives the direction of the measured strain, and $\lambda_{100}$ and $\lambda_{111}$ are the saturation magnetostriction along the crystallography axes $\langle 100 \rangle$ and $\langle 111 \rangle$ given by

$$\lambda_{100} = -\frac{2}{3} \frac{B_1}{c_{11} - c_{12}} \qquad \lambda_{111} = -\frac{1}{3} \frac{B_2}{c_{44}} \tag{34}$$

For an isotropic polycrystalline material, the isotropic saturation magnetostriction $\lambda_S$ is

$$\lambda_S = \frac{2}{5}\lambda_{100} + \frac{3}{5}\lambda_{111} \qquad (35)$$

For an isotropic material where $\lambda_{100} = \lambda_{111} = \lambda_s$, the relative length change is dependent only on the angle $\theta$ between the measured strain and the magnetization:

$$\lambda = \frac{3}{2}\left(\cos^2\theta - \frac{1}{3}\right) \qquad (36)$$

## 2.5. Magnetic Domains and Magnetization Process

This section explains the formation of magnetic domains in ferromagnetic materials, and the motion of domain walls that is responsible for dynamic magnetization processes. This section also presents the magnetization curve of ferromagnetic materials and some common parameters that characterize ferromagnetic materials.

### 2.5.1. Domains and Domain Walls

In the absence of an external field, the magnetic moments inside a ferromagnetic material are self-segregated into different domains of 10–100 $\mu$m in size to reduce the fringing fields so the potential energy in the material is minimized. Within each domain, the magnetic moments are all oriented in parallel due to the strong exchange force. Figure 11 illustrates the formation of magnetic domains in the absence of an external field. The magnetic sample starts out with two opposing domains and gradually splits into more domains to reduce the fringing fields until reaching a pattern for which the a minimum potential energy level is reached. Since the domains in the sample are opposing each other, the net moment is zero and the sample is unmagnetized. In some cases, due to crystalline structures, defects, and stresses, these domains do not align such that the moments cancel each other, and the sample is said to have a net spontaneous magnetization.

When the sample is subjected to an external field, it magnetizes along the direction of the field. To explain the magnetization process, first consider the sample shown in Figure 12, which has only two opposing domains, Domains
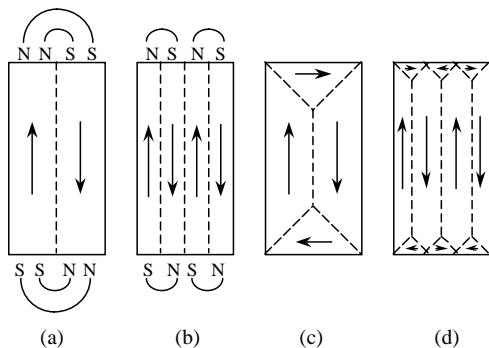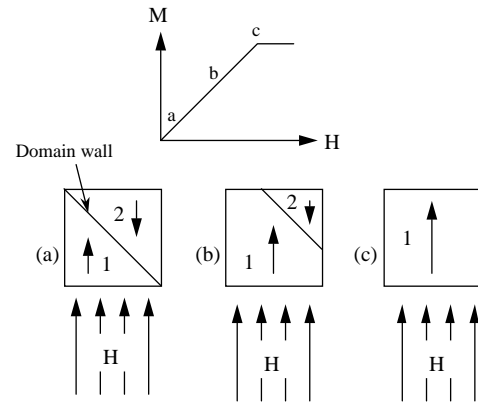


**Figure 12.** Illustration of the magnetization process. Initially the two opposing domains are equal in size, so the net moment is zero. As the external field increases, the domain wall moves toward Domain 2, resulting in an increase in the net moment. Eventually, only Domain 1 remains, and increasing field will have no effect on the magnetization.

1 and 2, separated by a boundary known as the domain wall or the Bloch wall. In the absence of an applied field, these two domains are oriented antiparallel so the net moment is zero. When an external field is applied, the size of Domain 1 increases, and the domain wall moves toward Domain 2. The change in domain size creates a net magnetic moment parallel to the field direction. Eventually, Domain 1 dominates the whole sample, and further increases in the magnitude of the applied field no longer increase the net magnetic moment. The sample is referred to as being in saturation. If the sample is free from structural defects and stress, the magnetization will return to zero when the applied field is removed; this type of material is classified as "magnetically soft."

In the case of nonideal materials with imperfections such as grain boundaries and precipitates, the magnetization will be irreversible due to the pinning of domain walls at the defects. Figure 13 illustrates the irreversible magnetization due to imperfections (represented by the black dots). The domain wall is initially pinned on the defects, so further field energy is needed to force the wall to jump over the defects until it is pinned again. The jump, known as the Barkhausen jump, dissipates energy due to spin relaxation and microscopic eddy currents. As a result, the domain wall motion will be different dependent upon whether the applied field is increasing or decreasing; hence the sample demonstrates hysteresis (history dependent) in its magnetization. Magnetically hard materials exhibit large hysteresis.



**Figure 11.** The change of the domain pattern from two domains to an optimized pattern where the total energy is lowest.



**Figure 13.** Illustration of domain wall (dashed line) pinning at defects (black dots). The process from (a) to (b) is reversible, but the process from (b) to (c) is not.

The domain wall, separating regions (domains) having different magnetization directions, has a width that depends upon the anisotropy and exchange energies of the materials. To understand and determine the width of the domain wall of a given sample, first consider a hypothetical scenario where the change in direction between two adjacent domains is abrupt (i.e., the domain wall is infinitesimally thin as shown in Fig. 14). The sample has an easy direction along the $\pm z$ direction, which means the anisotropy energy is smallest when the domains are parallel or antiparallel along the $z$ direction. However, the exchange energy in a ferromagnet is minimal only when the moments are in parallel. Therefore, the domain wall in Figure 14 has a minimum anisotropy energy but a large exchange energy. To minimize the exchange energy, the direction of the moments must change gradually within the domain walls so the angle between two consecutive moments is less than 180° see Fig. 15). However, this will increase the anisotropy energy because some domains are no longer aligned along the easy axis. As a result, there are two competing energies trying to minimize the total energy: the anisotropy energy that tries to reduce the width of the domain wall, and the exchange energy that tries to widen the wall. The actual thickness of the domain wall $\delta$ is determined when these two competing effects are minimum. For a cubic sample with length $a$, $\delta$ is given by

$$\delta = \sqrt{\frac{J_{ex}S^2\pi^2}{Ka}} \qquad (37)$$

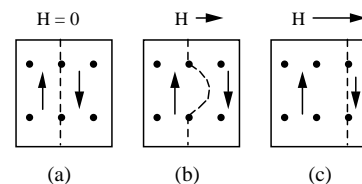where $K$ is the anisotropy constant, $J_{ex}$ is the exchange integral, and $S$ is the electron spin. The details of determining $\delta$ are given in Cullity [37]. Generally, the domain wall is about 10–100 nm wide.

The magnetization of fine magnetic particles is explained by single-domain rotation. When an external field is applied to a single-domain particle, the $M_s$ vector of the particle rotates toward the field direction from its easy axis, working against the anisotropy field.

### 2.5.2. Magnetization Curve

As indicated in Section 2.2, the magnetic flux $B$ and field $H$ are scaled by the permeability $\mu$; similarly the magnetization $M$ and field $H$ are scaled by the susceptibility $\chi$. For ferro- and ferrimagnetic materials, $\mu$ and $\chi$ are not constants; instead they are nonlinear functions that depend on the previous state of magnetization (hysteresis). Figure 16 is a plot of $B$ and $\mu_0 M$ versus $H$, known as the *BH* or *MH* loop, where $\mu$ and $\chi$ are the tangents of the curve at different operating $H$. Note that from Figure 16, the *BH* and
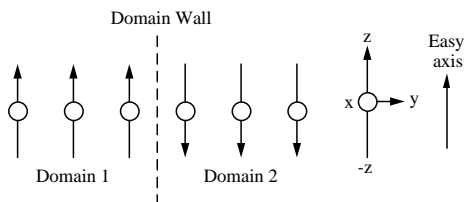


**Figure 15.** To minimize the exchange energy associated with the infinitely thin domain wall of Figure 35, the directions of the moments (represented by the arrows) change gradually so the angle between two consecutive moments is less than 180°.

*MH* curves are offset by the vacuum induction $\mu_0 H$. For most ferro- and ferrimagnetic materials, the susceptibility is much larger than 1, so the *BH* and *MH* loops are commonly considered the same.

The *BH* loop begins with an initial curve, which is obtained by applying a field on a demagnetized sample. As the field increases, the sample magnetizes through reversible domain wall movement including irreversible Barkhausen jumps until reaching the saturation magnetization $B_S$. As the $H$ field reduces to zero, the magnetization does not reduce to zero but remains at the remanence $B_r$ due to the irreversible rotation of the magnetization vectors within the material. The magnetization becomes zero only when $H$ reaches to the coercive field $H = -H_c$. As the $H$ field continues to decrease, the sample will saturate at $-B_S$. When the $H$ field increases again, the *MH* curve reaches $B_r$, $H_c$, and $B_S$ sequentially. Note that the *BH* loop will not go back to the origin. To reset the *BH* loop to the origin the sample needs to be demagnetized by either annealing the sample over $T_c$ or by applying a time-varying amplitude-decaying ac field. Annealing over $T_c$ is the best way to erase all magnetic memory of the sample; however, the process may also alter the mechanical properties of the material. Applying a decaying ac field is the most common way because it is easy to implement and imposes no permanent physical damage, but it yields no random distribution of the domain magnetization



**Figure 14.** A hypothetical infinitely thin domain wall separating two domains with a 180° difference in direction.



**Figure 16.** *MH* and *BH* hysteresis loops. The remanence, saturation magnetization, and coercive force are shown.

over the easy axis. An improvement for the decaying-field demagnetization is to rotate the sample (or the field) while undergoing a demagnetizing field that yields a more random domain distribution.

Although the *MH* loop or *BH* loop provides a complete picture on the magnetization, numerical permeability values are more convenient for general engineering applications. A material can have many different permeability values depending upon which part of the *BH* loop the material is at (biasing field magnitude). A commonly used value is the initial permeability

$$\mu_i = \lim_{\substack{H \to 0 \\ B \to 0}} \frac{B}{H} \tag{38}$$

which is the tangent line at the origin of the initial *BH* curve, the maximum permeability

$$\mu_{\max} = \left. \frac{B}{H} \right|_{\max} \tag{39}$$

which is the tangent line of the $B(H)$ curve at $B = 0$, the reverse permeability

$$\mu_{\mathrm{rev}} = \lim_{\Delta H \to 0} \left. \frac{\Delta B}{\Delta H} \right|_{B_t, H_t} \tag{40}$$

which is the limit of the superposition permeability of a small ac field on the operating point $H_t$, $B_t$, and the differential permeability

$$\mu_{\mathrm{diff}} = \frac{dB}{dH} \tag{41}$$

which is the derivative of the $B(H)$ curve.

For an anisotropic material, the magnetization curve varies when the field is applied from different directions. As a result, many magnetic materials, especially thin films, are categorized with two *BH* loops, one measured along the easy axis and the other along the hard axis. Figure 17a illustrates the *BH* loop measured along the easy and hard axes. Notice that along the hard axis, a larger applied field is needed to saturate the material. The anisotropy field $H_k$ can also be determined from the hard axis by measuring the linearized minor loop and extrapolating the linear line until it reaches saturation $B_S$ (see Fig. 17b).

## 2.6. Magnetic Materials

Strong magnetic materials such as ferro- and ferrimagnetic alloys that exhibit large magnetization are by far the most useful materials and are commonly categorized by the coercive force $H_c$. Generally, materials with $H_c < 1000$ A/m are considered magnetically soft, materials with $H_c$ between 1 and 30 kA/m are semihard, and materials with $H_c > 30$ kA/m are considered hard (for calibration, earth's magnetic field is approximately 50 A/m at the pole, 25 A/m at equator). This section includes an overview of magnetically soft and hard ferromagnetic materials, as well as magnetoelastic and magnetostrictive materials (soft magnetic materials that react magnetomechanically with stress).
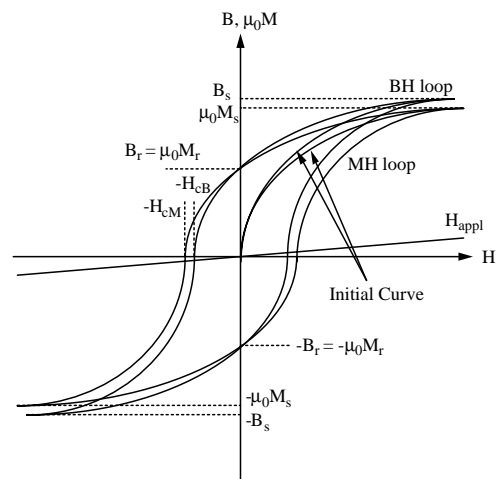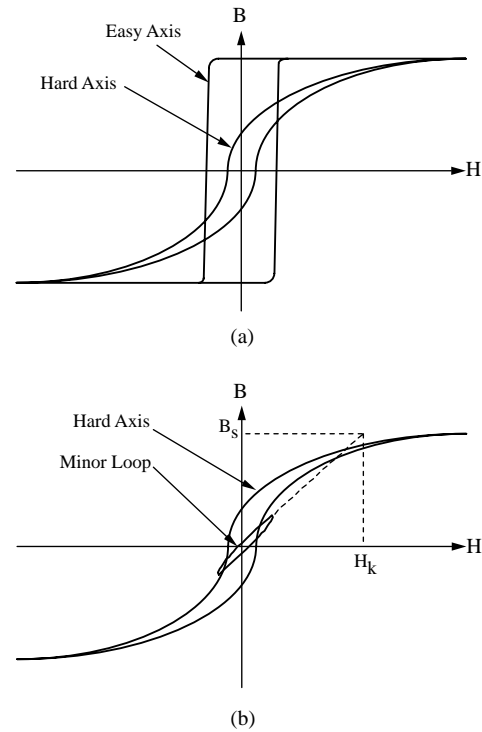


**Figure 17.** (a) The *BH* loop measured along the easy and hard axes. (b) The anisotropy field $H_k$ can be determined by extrapolating the small-signal linearized minor loop.

### 2.6.1. Soft Magnetic Materials

Magnetically soft materials have a low coercivity and high permeability, which result from the low crystalline and strain anisotropy energies. The low anisotropy energy minimizes the domain wall energy, allowing the rotation of domain wall with minimum energy loss when subjected to an external field. Due to reversible magnetization and a correspondingly low hysteresis loss, soft magnetic materials are largely used in field sensors, power transformers, induction motors, etc. Soft magnetic materials include various crystalline ferrites, as well as nanocrystalline and amorphous alloys. Some common magnetically soft materials and their $B_S$, $H_c$, and $\mu_{\max}$ are listed in Table 1.

Metallic crystals without impurities are good soft magnetic materials. For example, pure iron, which has a small magnetocrystalline anisotropy of $K_1 = -4.8 \times 10^4$ J/m$^3$, has a relatively large saturation flux density of 2.15 T and a $\mu_{\max}$ of 5000. The low anisotropy energy in pure iron allows domain wall movement with little resistance, hence the low coercivity and high permeability. Other good magnetically soft crystalline materials are iron–nickel (FeNi) alloys such as Permalloy, Supermalloy, Mumetal®, cobalt–iron (CoFe) alloys, silicon steels (SiFe), and Sendust (FeAlSi).

Amorphous ferromagnetic alloys produced by rapid quenching do not exhibit long-range order, resulting in zero magnetocrystalline anisotropy; generally a cooling rate of approximately $10^5$ °C/s is needed to achieve such materials. Amorphous magnetic materials have a higher electrical resistance (120–200 $\mu\Omega$) compared to crystalline magnetic

**Table 1.** A list of common magnetically soft materials with their saturation magnetization, coercive force, and maximum permeability.

| Material | Composition | $B_S$ (T) | $H_c$ (A/m) | $\mu_{max}$ |
|---|---|---|---|---|
| Iron[e] | $Fe_{99.8}$ | 2.15 | 80 | 5000 |
| Cobalt[e] | $Co_{99.8}$ | 5.79 | 800 | 250 |
| Nickel[e] | $Ni_{99.8}$ | 0.61 | 60 | 600 |
| Silicon steel[a, e] | $Fe_{96}Si_4$ | 5.97 | 40 | 7000 |
| Sendust[e] | $Fe_{85}Si_{10}Al_5$ | 5.00 | 4 | 120,000 |
| Hiperco[e] | $Fe_{64}Co_{35}Cr_{0.5}$ | 2.42 | 80 | 10,000 |
| Permalloy[e] | $Fe_{22}Ni_{78}$ | 5.08 | 4 | 100,000 |
| Permendur[e] | $Fe_{50}Co_{50}$ | 2.45 | 160 | 5000 |
| Supermendur[e] | $Fe_{49}Co_{49}V_2$ | 2.40 | 16 | 60,000 |
| Mumetal 3[e] | $Fe_{17}Ni_{76}Cu_5Cr_2$ | 0.90 | 0.8 | 100,000 |
| Supermalloy[e] | $Fe_{16}Ni_{79}Mo_5$ | 0.79 | 0.16 | 1,000,000 |
| Ferroxcube 3F3[b, f] | $Mn–Zn–Fe_2O_3$ | 0.50 | 15 | 1800 |
| Manifer 230[c, f] | $Ni–Zn–Fe_2O_3$ | 0.35 | 8 | 150 |
| Metglas 2605SC[d, g] | $Fe_{81}Ni_{13.5}Si_{3.5}C_2$ | 0.55 | 10 | 300,000 |

[a] Nonoriented.
[b] At 100 kHz.
[c] At 100 MHz.
[d] Annealed.
[e] Crystalline.
[f] Soft ferrite.
[g] Amorphous.

materials (30–50 $\mu\Omega$), making them a better choice for high frequency and high power applications due to reduced eddy currents. Amorphous alloys are widely used as field and stress sensors and high-power distribution transformers. Typically these glasses are composed of metals such as iron, cobalt, and nickel. To stabilize the alloys in an amorphous state metalloids such as silicon, boron, and molybdenum are added. Amorphous glasses of the transition metals (Zr, Nb, Hf), or rare-earth metals (Tb, Dy, Er, Gd) can also be made; however, the addition of rare-earth metals increases the magnetic anisotropy. Due to the presence of the glass-forming metalloids the saturation magnetizations of amorphous alloys are lower than their crystalline counterparts.

As-cast amorphous alloys typically contain large stress anisotropies, which reduce the soft magnetic properties of the materials. In practice, amorphous alloys are relaxed by low-temperature annealing to remove the internal stress. When used as stress sensors, amorphous alloys are annealed under magnetic field to create an anisotropy to increase the stress sensitivity.

Nanocrystalline grains of 10–15 nm can be formed in the amorphous alloys by annealing them at their crystallization temperature ($\sim$450–550 °C). These nanostructured alloys have excellent soft magnetic properties with the permeability on the order of $10^5$, and a low hysteresis loss. However, due to the increase of phase segregation and precipitation, these nanocrystalline materials are mechanically brittle making them difficult to handle.

Soft ferrites are generally composed of 70% of iron oxide $Fe_2O_3$ and 30% of metal oxides such as zinc oxide and nickel oxide. Although ferrites are relatively inexpensive to fabricate the low magnetization ($\sim$0.5 T) limits their applications. However, ferrites have high resistivity and therefore can be used at higher frequencies.

### 2.6.2. Hard Magnetic Materials

Magnetically hard materials are categorized by their large coercive force ($10^4$–$10^6$ A/m) that makes them hard to magnetize and a large remanence that allows them to exhibit significant spontaneous magnetization in zero applied field. Magnetically hard materials encompass permanent magnets, magnetic data storage, and sensors. A common way to characterize hard magnetic materials is to determine the maximum $B$-$H$ energy product, $(BH)_{max}$. Figure 18 illustrates how to determine $(BH)_{max}$ from the second quadrant of a $BH$ loop.

Hard magnetic materials are made so that they have a large number of grain boundaries that act to pin the magnetization vector in a given direction. Early magnets were iron-based, such as magnetite ($Fe_3O_4$) and iron carbon magnets ($Fe_3C$). These were replaced by tungsten, Co–Mo, and Co–Cr steels with larger coercive force and magnetization during the 1940s. Another magnet widely used since the 1930s was the Alnico ($Fe_2NiAl$) magnet, which has subsequently been phased out by the rare-earth–transition metal magnets. Examples are $SmCo_5$, $R_2Co_7$, and $Sm_2(CoFe)_{17}$. These magnets have coercive fields of 0.8–2.4 MA/m and an energy product reaching a few hundred kJ/m$^3$; common permanent magnets are listed in Table 2.

### 2.6.3. Magnetoelastic and Magnetostrictive Materials

The most common magnetoelastic materials are the rare-earth intermetallic compounds and amorphous magnetically soft ferromagnetic glasses. Crystalline rare-earth intermetallic compounds, such as Terfenol-D ($Tb_{0.3}Dy_{0.7}Fe_{5.95}$), have a magnetostriction on the order of $10^{-3}$, a magnetoelastic coupling of $k = 0.7$, and a low compliance. As a result, such materials are useful actuators for a range of applications including sonar transducers. Other examples of rare-earth compounds are GdCo and GdFe. Amorphous ferromagnetic alloys with high iron content exhibit magnetostrictions on the order of $10^{-5}$ and a magnetoelastic coupling close to 1 after annealing. Amorphous ferromagnetic alloys, such as $Fe_{81}B_{13.5}Si_{3.5}C_2$, have a low anisotropy field ($H_k = 70$ A/m), which allows the rotation of magnetization and accompanying magnetostrictive strain with low applied fields and stresses, resulting in a high magnetoelastic coupling. Ferromagnetic glasses are widely used as stress/strain sensors and field sensors and as cores of power transformers. Some
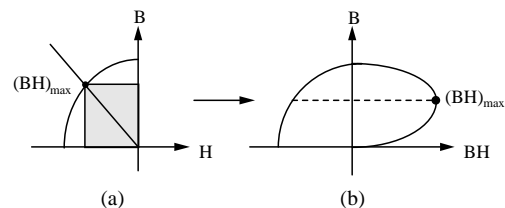


**Figure 18.** (a) Second quadrant of a $BH$ loop. The location of the $(BH)_{max}$ corresponds to a rectangular area where the product of $BH$ is maximal. (b) The $(BH)_{max}$ can be determined by plotting $B$ versus $BH$ and determining the maximum of the curve along the $x$-axis.

**Table 2.** A list of common magnetically hard materials with their remanence, coercive force, and energy product.

| Material | Composition | $B_r$ (T) | $H_c$ (kA/m) | $(BH)_{max}$ (kJ/m³) |
|---|---|---|---|---|
| Iron carbon | $Fe_3C$ | 5.24 | 4 | 4 |
| Tungsten steel | $Fe_{92}W_8$ | 2 | 7 | 8 |
| Alnico 5 | $Fe_{50}Co_{25}Ni_{15}Al_8Cu_2$ | 5.2 | 50 | 42 |
| Fe–Cr–Co | Fe–Cr–Co | 5.6 | 65 | 80 |
| Hexagonal ferrites | isotropic $BaO$–$Fe_2O_3$ | 0.22 | 145 | 9 |
| Co–rare earth | $SmCo_5$ (aligned) | 5.0 | 2900 | 200 |
| Fe–rare earth | $Fe_{14}Nd_2B$ (aligned) | 5.6 | 1600 | 350 |

common magnetoelastic materials, along with their saturation magnetization, magnetostriction, and magnetoelastic coupling coefficients, are listed in Table 3.

# 3. FERROMAGNETIC GLASS PREPARATION AND PROPERTIES

This section describes some fabrication processes, properties, and methods of enhancing the properties of the ferromagnetic glass alloys.

## 3.1. Preparation of Ferromagnetic Glasses

Ferromagnetic glasses are commonly fabricated using melt quenching methods such as melt-spinning [52] and atomic condensation techniques such as electrodeposition [53, 54] and sputtering [55]. The key to successfully fabricating a ferromagnetic glass is rapid removal of heat from the melt, to preclude crystallization in the alloy. In most cases, cooling rates of $10^5$ °C/s are needed. Most of the magnetically soft ferromagnetic glasses are based on $3d$ transition metals (T) with glass forming metalloids (M) such as boron, carbon, silicon, or phosphors to stabilize the amorphous state. The composition of transition-metalloid-based alloys, $T_{1-x}M_x$, is usually in the range of $15 < x < 30$ at% such as $Fe_{80}B_{20}$, $Fe_{40}Ni_{40}P_{14}B_6$, and $Co_{74}Fe_5B_{18}Si_3$. The late transition metals (TL = Fe, Co, Ni) can also be stabilized in an amorphous state by alloying with early transition metals (Zr, Nb, Hf), forming $TE_{1-x}TL_x$, with $x$ in the range 5–15 at% such as $Co_{90}Zr_{10}$. Ferromagnetic glasses are also built by alloying transition metals (TL = Fe, Ni, Co) with rare-earth metals (R = Tb, Dy, Er, Gd), forming $R_{1-x}TL_x$ with $x$ typically 10–25 at%. Among these ferromagnetic glasses, the

**Table 3.** A list of magnetoelastic materials and their saturation magnetization, magnetostriction, and magnetoelastic coupling coefficient.

| Material | Composition | $B_S$ (T) | $\lambda_S$ (ppm) | $k_{max}$ |
|---|---|---|---|---|
| Metglas 2605SC[a] | $Fe_{81}B_{13.5}Si_{3.5}C_2$ | 5.61 | 30 | 0.98 |
| Metglas 2826MB[a] | $Fe_{40}Ni_{38}Mo_4B_{18}$ | 0.88 | 12 | 0.5 |
| Ferromagnetic glass[a] | $Fe_{4.5}Co_{68.15}Si_{12.5}B_{15}$ | 0.7 | −0.1 | — |
| Ferromagnetic glass[a] | $Co_{72.5}Si_{12.5}B_{15}$ | 0.5 | −1 | — |
| Terfenol-D[b] | $Tb_{0.3}Dy_{0.7}Fe_{5.95}$ | 5.2 | 1500 | 0.75 |

[a] Amorphous.
[b] Crystalline.

transition-metalloid-based alloys have the most useful properties for sensor applications, such as high magnetostrictive and magnetoelastic coupling coefficient and low magnetic anisotropy. Although transition-rare-earth-based amorphous alloys such as TbDyFe and TbCo have a lower magnetoelastic coupling coefficient, of ∼0.5–0.7, they have the largest known values of magnetostriction on the order of $10^{-4}$ [56, 57].

## 3.2. Summary of Physical and Magnetic Properties of Ferromagnetic Glasses

As-cast ferromagnetic glasses are flexible, with Young's moduli of around 100 GPa, about 20–30% lower than their crystalline counterparts [58]. As-cast ferromagnetic glasses also exhibit high mechanical strength and ductility. For example, the tensile strength of as-cast Metglas 2605SC and 2826MB alloys is approximately 1000 to 1700 MPa, and for as-cast FC20 alloys ($Fe_{93.3}Si_{2.9}C_{3.4}B_{0.4}$) it can reach to 3400 MPa. However, annealing processes, although improving the soft magnetic properties by creating nanocrystalline structures, can destroy the mechanical properties and render these materials brittle by increasing precipitation and phase segregation. In general, the tensile strength and Vicker's hardness of the ferromagnetic glasses show a small increase at low temperature annealing but decrease significantly when the annealing temperature reaches the crystallization temperature $T_c$ [59]. Nanocrystalline alloys, produced by annealing ferromagnetic glasses at temperatures at or above $T_c$, have a lower mechanical strength compared to their amorphous counterparts.

Ferromagnetic glasses contain localized random anisotropies, which act like the crystalline anisotropy but on the scale of few nanometers. The strength and direction of the localized anisotropy vary with position, resulting in zero macroscopic crystalline anisotropy (although most ferromagnetic glasses still contain stress anisotropy as a result of the fabrication process). Ferromagnetic glasses made of transition metals and metalloids have weak coupling between the local anisotropies; as a result they are magnetically soft and can be easily magnetized. However, rare-earth-based ferromagnetic glasses have strong localized coupling forces; hence saturation magnetization is much harder to achieve, and the materials are magnetically harder to a significant degree. Common magnetically soft ferromagnetic glasses have magnetic susceptibilities on the order of $10^5$, saturation magnetizations of about 1 T, and compared to their crystalline counterparts low hysteresis loss. Annealed and nanocrystalline ferromagnetic glasses have a higher susceptibility due to the reduction of stress anisotropy energy.

The electrical resistivity of ferromagnetic glasses are generally one order of magnitude higher than their crystalline counterparts, with typical values of 100–200 $\mu\Omega \cdot$ cm. The high resistivity significantly reduces eddy currents making the ferromagnetic glasses more suitable for high frequency applications.

Note that the values given above are those of common materials, as generally fabricated and used; properties can be altered by changing alloy composition and performing annealing, as will be detailed in Section 3.3. In addition to

these properties, ferromagnetic glasses also exhibit attractive properties for sensor applications such as magnetoelastic and magnetostriction effects, magnetoelastic resonance, and the GMI effect, which will be explained in the following sections.

### 3.2.1. Magnetoelastic and Magnetostriction Effects

Most ferromagnetic glasses exhibit magnetostriction, a phenomenon where the dimensions of an object change when subjected to the influence of an external magnetic field. Magnetostriction is generally quantified with the saturation magnetostriction $\lambda_S$, which is defined as the ratio of the change in length $\Delta l/l$ at magnetic saturation. Although it is well known that the magnetostriction of a ferromagnetic glass varies with alloy composition, predicting the effects of alloy composition on the magnetostriction is still difficult, and most existing theoretical models are only applicable to specific binary or ternary alloys. In general, rare-earth-based alloys exhibit the highest magnetostriction with $\lambda_S \approx 10^{-4}$, followed by Fe-rich alloys with $\lambda_S \approx 10^{-5}$, while Co-rich alloys have a low magnetostriction of $\lambda_S \approx 10^{-7}$. Magnetostriction also depends upon applied stress, structural relaxation [60, 61], and fabrication parameters [56, 62]. Generally, $\lambda_S$ increases when ferromagnetic glasses are relaxed under low field annealing but decreases when the annealing temperature is beyond the crystallization temperature.

The magnetoelastic effect, which describes the coupling between the elastic energy and magnetic energy, is usually quantified by the magnetoelastic coupling coefficient $k$, defined as the ratio of the coupled elastic-magnetic energy to the pure elastic and magnetic energies. Magnetoelastic and magnetostriction are related but not necessarily proportional to each other due to the influence of other parameters such as applied stress. For example, rare-earth-based alloys have a very high $\lambda_S$, but their magnetoelastic coupling is lower than the Fe-rich alloys, which have a lower $\lambda_S$.

The most common model for understanding the effects of applied stress and field on the susceptibility, magnetoelastic coupling, and the Young's modulus of a ferromagnetic ferromagnetic glass ribbon is shown in Figure 19. The model considers a ribbon-shaped ferromagnetic glass having a widthwise magnetic easy axis and a uniaxial anisotropy with an energy contribution of $K_U \cos\theta$ per unit volume. In the absence of an applied field and applied stress the magnetization in the domains aligns across the width of the ribbon. When a longitudinal field $H$ and stress $\sigma$ are applied
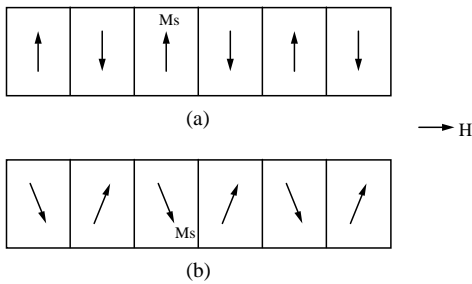


**Figure 19.** (a) Magnetic domain of a transverse-field annealed ferromagnetic glass ribbon at (a) zero bias field ($H = 0$) and (b) $0 < H < H_k$.

the magnetization rotates from the width toward the length direction (see Fig. 19), yielding a magnetostrictive strain $\varepsilon$ given by [63]

$$\varepsilon = \frac{\sigma}{E_M} + \frac{3\lambda_S}{2}\left(\frac{H^2}{H_k^2} - \frac{1}{3}\right) \qquad H < H_k \qquad (42)$$

where $E_M$ is the Young's modulus at a constant magnetization, and the anisotropy field $H_k$ is given by

$$H_k = \frac{2K_U - 3\lambda_S\sigma}{M_s} \qquad (43)$$

where $M_s$ is the saturation magnetization. The susceptibility $\chi$ is related to the applied strain as

$$\chi = \frac{M_s^2}{2K_U - 3\lambda_S\sigma} \qquad (44)$$

From Eq. (44), the sensitivity of the susceptibility toward applied stress is given by

$$\frac{d\chi}{d\sigma} = \frac{M_s^2}{(2K_U - 3\lambda_S\sigma)^2}3\lambda_S \qquad (45)$$

It is clear that the sensitivity of the susceptibility increases with higher $\lambda_S$ and a lower $K_U$. The magnetoelastic coupling factor $k$ can be related to the parameters already derived as

$$k = \left(1 + \frac{M_s H_k^3}{9E_M\lambda_S^2 H^2}\right)^{-1/2} \qquad H < H_k \qquad (46)$$

Equation (46) shows that a high magnetoelastic coupling requires a high $\lambda_S$ and $E_M$ and a low $H_k$. For applications based on changes in the elastic modulus, for example a strain sensor, the parameter of interest is the fractional difference between the elastic modulus at constant magnetization $E_M$ and the modulus at constant field $E_H$, or the so-called $\Delta E$ effect, which is given by

$$\frac{\Delta E}{E_M} = \frac{E_M - E_H}{E_M} = \frac{9\lambda_S^2 E_H H^2}{M_s H_k^3} = k^2 \qquad H < H_k \qquad (47)$$

### 3.2.2. Magnetoelastic Resonance

A magnetoelastic ribbon- or wire-shaped glass exhibits a resonance when excited by a time-varying magnetic field. For a magnetoelastic glass ribbon with its length parallel to the $x$-axis of a rectangular coordinate system, excited by an $x$-directed ac magnetic field, the ribbon exhibits a vibration that can be described with the equation of motion as [28]

$$\rho_s \frac{\partial^2 u_x}{\partial t^2} = \frac{E_H}{1 - \sigma_p^2} \frac{\partial^2 u_x}{\partial x^2} \qquad (48)$$

where $u_x$ is the displacement in the $x$-direction, $\rho_s$ is the density of the ferromagnetic glass ribbon, and $\sigma_p$ is Poisson's ratio. Although the ribbon exhibits vibrations at almost every frequency, the vibrations are most pronounced at the resonant frequencies [64, 65]

$$f_n = \frac{1}{L}\sqrt{\frac{E_H}{\rho_s(1 - s^2)}} \qquad (49)$$

where $L$ is the length of the ribbon. For most sensor applications, only the first harmonic ($n = 1$) is considered due to its significantly higher amplitude. The frequency response of a 37.5 mm $\times$ 12.5 mm $\times$ 28 $\mu$m as-cast Metglas 2826MB ribbon is plotted in Figure 20.

### 3.2.3. Giant Magnetoimpedance Effect

Giant magnetoimpedance is a phenomenon that significantly changes the radio-frequency electrical impedance of a magnetic conductor with a small variation of magnetic field. Ferromagnetic glasses, especially Co-based alloys with near zero magnetostriction ($\approx 10^{-7}$), display excellent GMI effects, which makes them suitable for the measurement of magnetic fields in the range of few Oersteds. The GMI effect in amorphous wires is due to the change of skin depth in response to external fields. The change in external dc field changes the transverse permeability of the wire (due to the domain wall motion), which leads to the change of the skin depth since skin depth is a function of permeability [66]. Since the ac current in a wire flows within a region near the wire surface (skin depth effect), the change in skin depth will change the wire impedance. The GMI effect depends on the anisotropy of the wire: for a wire with axial anisotropy, the impedance is highest at zero-applied field and decreases monotonically with applied field, whereas for a wire with circumferential anisotropy the maximum occurs at $H_k$ [67]. Most rapid-quenched amorphous wires have circumferential anisotropy due to the heat dissipation along the radial direction during the fabrication process.

To measure the GMI effect, generally a ferromagnetic glass wire is connected to an ac current source and voltmeter, and the impedance is determined from the ratio of the measured voltage to the applied current. The sensitivity of the GMI in a ferromagnetic glass is largely dependent upon the frequency of the driving current and the magnitude of the transverse permeability in the glass. For a circular ferromagnetic glass wire, the impedance measured across the length is given by [68]

$$Z = \frac{a}{2\sqrt{2\rho_e}} \left( R_{dc} + j\frac{\rho L}{\pi a^2} \right) (\omega \mu_\theta)^{1/2} \qquad (50)$$
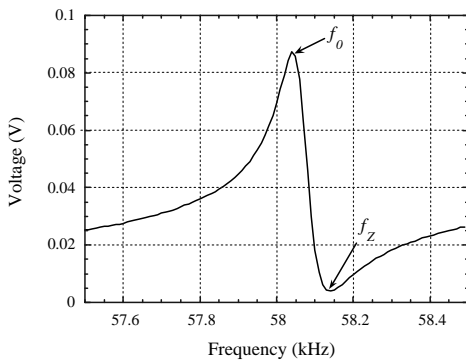


**Figure 20.** The frequency response of a 37.5 mm $\times$ 12.5 mm $\times$ 28 $\mu$m as-cast Metglas 2826MB ribbon. The resonant frequency $f_0$ is the maximal of the frequency spectrum and antiresonant frequency $f_a$ is the minimal.

where $j$ indicates a complex number, $\omega$ is the radian frequency of the driving current, $a$ is the radius of the wire, $\rho_e$ is the resistivity of the ferromagnetic glass, $R_{dc}$ is the dc resistance, and $\mu_\theta$ is the circumferential permeability. Besides wires, ferromagnetic glass ribbons are also common since ribbon structures can be easily incorporated in MEMS devices. The impedance measured across the length of an amorphous ribbon is given by [69]

$$Z = \frac{(1 - j)L}{4w} (2\rho_e \omega \mu_t)^{1/2} \qquad (51)$$

where $w$ and $L$ are respectively the width and length of the ribbon, and $\mu_t$ is the transverse permeability of the ferromagnetic glass.

The GMI effect is usually expressed as a function of applied field as the GMI ratio, GMI%, which is defined as

$$\text{GMI\%} = \frac{Z(H_{appl}) - Z(H_{max})}{Z(H_{max})} \qquad (52)$$

where $Z$ is the impedance, and $H_{appl}$ and $H_{max}$ are respectively the applied and saturation magnetic fields. The GMI% for ferromagnetic glasses is relatively high, normally in the range between 100% and 500%, depending upon the ferromagnetic glass composition, heat treatment, dc bias current, and the design of the sensor.

### 3.3. Tailoring of Ferromagnetic Glasses for Sensor Applications

This section describes methods to control the mechanical and magnetic properties of ferromagnetic glasses.

### 3.3.1. Effects of Alloy Compositions on the Ferromagnetic Glass Properties

The magnetomechanical properties of ferromagnetic glasses, such as magnetostrictive and magnetoelastic coupling, magnetic hardness, hysteresis losses, and anisotropy are all dependent upon alloy composition. Although there are no general theories for predicting the effects of alloy composition on the properties of the ferromagnetic glasses, several models have been developed to describe the effects of alloy composition on Fe-rich and Co-rich ferromagnetic glasses [70]. In general, Fe-rich transition-metalloid-based alloys can have substantial magnetostriction constants and high magnetoelastic couplings because they have low anisotropy energy $K_U$ and low anisotropy field $H_k$, which permit the rotation of the magnetization and accompanying magnetostrictive strain with low applied fields or stresses. For example, Metglas 2605SC, which has a high magnetostriction of $3 \times 10^{-5}$ and magnetoelastic coupling of 0.98 has relatively low $K_U$ and $H_k$ of 38 J/m and 370 A/m, respectively. Rare-earth-based alloys have a larger magnetostriction but are also magnetically harder than Fe-based alloys; for example nanocrystalline TbDyFe has a large magnetostriction of $3.5 \times 10^{-4}$ and a $H_k$ of 2400 A/m.

Addition of glass-forming metalloids, such as B, Si, Mo, and C, generally increases the mechanical strength but reduces the magnetic and magnetoelastic properties of the ferromagnetic glasses. It is found that the induced

anisotropy constant $K_U$ of Fe-rich alloys increases strongly with the presence of additional transition elements such as Ni or Co [63]. This is the reason the magnetoelastic coupling of the 2826MB $Fe_{40}Ni_{38}Mo_4B_{18}$ ($k \approx 0.5$) is inferior compared to the 2605SC $Fe_{81}B_{13.5}Si_{3.5}C_2$ ($k = 0.98$).

### 3.3.2. Control of Magnetoelastic Coupling via Annealing

The model in Section 3.2.1 indicates that a widthwise magnetic domain distribution and a low uniform $H_k$ are required for achieving a high magnetoelastic coupling $k$. However, in an as-cast ferromagnetic glass ribbon the surface defects and irregularities create localized stresses and cause an inhomogeneous $K_U$ distribution on the ribbon, leading to variations in the direction and amplitude of localized magnetic domains and $H_k$, and in turn reduce the magnetoelastic coupling. Lower magnetoelastic coupling leads to a smaller $\Delta E$ effect and lower stress sensitivity. It is thus necessary to remove the internal stresses and orient the magnetic domains widthwise without including significant crystallization.

Transverse field annealing is the most common method used to remove internal stresses in ferromagnetic glasses thereby increasing $\lambda_S$ and $k$. Extensive investigations have been conducted to analyze the effects of annealing temperature and time on $\lambda_S$, $k$, and the permeability $\mu$ of various ferromagnetic glasses. The results are unanimous [8, 9, 60, 64, 71–76]; $\lambda_S$, $k$, and $\mu$ increase under transverse-field annealing at temperatures below $T_c$ ($\approx$450–500 °C) but decrease above $T_c$. For materials with a broad alloy spectrum, the reduction of $\lambda_S$, $k$, and $\mu$ can happen at temperatures far below $T_c$ at around 300 °C. Certain ferromagnetic glasses such as TbDyFeNb and FeZrBCu are nanocrystallized when annealed at $T_c$. Nanocrystalline alloys are magnetically softer, having larger values of $\mu$ and $k$, but are generally mechanically brittle. Inversely coupled to the permeability $\mu$, annealing under stress and field can lower $H_k$. According to Eq. (43), $H_k$ is proportional to the term ($K_U - 3/2\lambda_S\sigma$); thus by choosing an appropriate stress $\sigma$ one can set the term to zero and obtain a low $H_k$.

### 3.3.3. Controlling the GMI Effect

Equations (51) and (52) show that the impedance of the ferromagnetic glasses increases with the factor $\sqrt{\omega\mu_{t,\theta}}$ for both ferromagnetic glass wires and ribbons. Hence one can increase the sensitivity of a GMI sensor by increasing the operating frequency. In addition, it is also found that the transverse and circumferential permeabilities are dependent upon the amplitude of the driving current, applied stress, and annealing temperature.

The effect of ac frequency on the GMI% was studied by Knobel et al. [77] and Ovari et al. [78], and they found the GMI% generally increases with frequency. However, depending upon the types of ferromagnetic glasses and annealing conditions, the GMI% decreases when the frequency is beyond 1–200 MHz due to the domain wall damping that causes permeability relaxation at very high frequencies [66]. The amplitudes of the dc bias and ac currents and the internal stress of the ferromagnetic glass have also been found to influence the sensitivity of the GMI%

[79, 80]. However, these parameters interact with each other and also depend on the alloy composition of the ferromagnetic glass. Extensive investigations on the annealing effect on the GMI% have been reported [5, 79, 81–83]. The effect of annealing on GMI is similar to that on magnetoelastic coupling, which is that the increase in annealing temperature increases the GMI%. However, the GMI% drops as the annealing temperature reaches the crystallization temperature of the ferromagnetic glass, which is around 500–600 °C. Recently, Brunetti et al. [84] improved the sensitivity of the GMI sensors by 600% by coating a glass layer on a $Fe_{73.5}Cu_3Nb_1Si_{13.5}B_9$ ferromagnetic glass microwire. Cobeno et al. [85] also altered the sensitivity of the GMI% by applying a tensile stress on a glass-coated $Co_{68.5}Mn_{6.5}Si_{10}B_{15}$ ferromagnetic glass microwire, and they found the maximum improvement for the GMI% occurs at around 60 MPa.

## 4. SENSOR APPLICATIONS

Section 4.1 demonstrates the applications of ferromagnetic glasses in induction-based sensors for measuring field, stress, torque, and displacement. Section 4.2 shows application of ferromagnetic glass wires as magnetoimpedance sensors. Section 4.3 illustrates how ferromagnetic glass wires are used to construct magnetostrictive delay lines for the measurement of stress, torque, and displacement. Magnetoelastic resonant sensors, which are used to measure pressure, liquid flow and density/viscosity, temperature, elasticity, and chemical concentration, are presented in Section 4.4. Section 4.5 demonstrates the uses of ferromagnetic glasses as the sensing elements of MSAW sensors and magnetomechanical-rotation-based sensors.

### 4.1. Induction-Based Sensors with Ferromagnetic Glass Cores

Ferromagnetic glasses were widely used in the 1980s as the permeability/susceptibility-changing ferromagnetic glass cores for the induction-based sensors. Since the inductance of the coil is proportional to the susceptibility of its core material, changes in the ferromagnetic glass susceptibility can be determined from the change of the coil inductance. It is also common to use a pair of excitation and sensing coils, where the excitation coil excites the ferromagnetic glass with an ac magnetic field, and the susceptibility of the ferromagnetic glass is determined from the amplitude of the induced voltage recorded by the sensing coil.

### 4.1.1. Measurement of Stress/Strain

As indicated in Eqs. (44) and (47), the susceptibility and elasticity of the ferromagnetic glasses are strongly dependent upon the applied stress and field. As a result, stresses and strains are readily monitored by measuring the susceptibility of the ferromagnetic glass with an inductive coil. As shown in Figure 21, the inverse susceptibility of the ferromagnetic glass $1/\chi$ shows good linearity with applied stress [12]. For ferromagnetic glasses with positive magnetostriction $1/\chi$ is inversely proportional to $\sigma$ until reaching the demagnetization factor $N$, where $1/\chi$ becomes independent
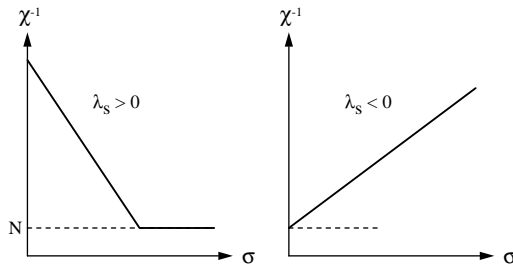
**Figure 21.** The inverse susceptibility of a ferromagnetic glass: $1/\chi$ linearity decreases with applied stress when the ferromagnetic glass has a positive magnetostriction but linearly increases when the ferromagnetic glass magnetostriction is negative.

of $\sigma$. For negative $\lambda_S$, $1/\chi$ is directly proportional to $\sigma$ starting from $N$. To directly compare the sensitivity of a ferromagnetic glass sensor to semiconductor based stress sensors, the figure of merit for the ferromagnetic glass sensors is derived as [12, 13]

$$F = \frac{\Delta\chi/\chi_0}{\Delta\varepsilon} \approx \frac{3\lambda_S E_M}{2K_U} \tag{53}$$

Metglas alloy 2605SC has been widely used for stress sensing due to its high magnetoelastic coupling coefficient, 0.98 after transverse field annealing, and high magnetostriction of $3 \times 10^{-5}$. The figures of merit of 2605SC Metglas sensors have been calculated to be in the range of $10^5$ [12], three orders of magnitude greater than semiconductor strain gauges. Different experimental configurations were designed to measure the susceptibility shift of the ferromagnetic glass sensors for tensile, compressive, and torsion stresses. Figure 22a is a basic tensile stress sensor designed by Mitchell et al. [86] and later improved by Barandiaran and Gutierrez [87] by connecting the output to a bridge circuit for eliminating the background signal and enhancing the sensitivity of the sensor. The susceptibility of the setup in Figure 22a has a linear response to tensile stress. Figure 22b is an improved toroid-shape sensor designed by Mohri and Korekoda [88] and Meydan et al. [89]. The four terminals in the setup in Figure 22b are connected in a bridge configuration so the signal is zero in an unstressed case, but positive to tensile stress and negative to compressive stress. A stress sensor designed for compressive stress is illustrated in Figure 22c, where the sensor is stretched by a spring, and
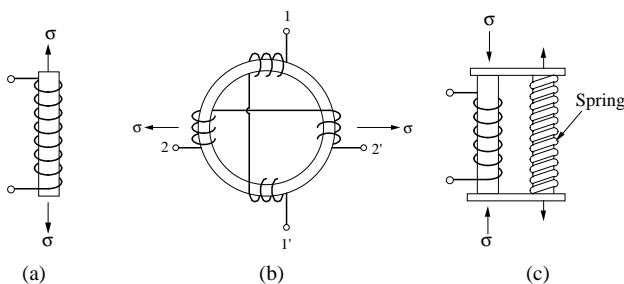
the actual stress experienced by the sensor is reduced when compressive stress is exerted [13].

Another application based on ferromagnetic glass stress sensors is the shock detection system proposed by Mohri and Takeuchi [90]. The shock sensor is essentially a stress sensor surrounded by an excitation coil and a sensing coil. When a shock is applied to the sensor, it causes a sudden change in the ferromagnetic glass permeability, which will be captured by the sensing coil as a voltage spike.

### 4.1.2. Torque Measurement

Figure 23a illustrates a novel torque sensor comprised of two ferromagnetic glass strips attached at an angle of 45° to the shaft surrounded by an excitation coil and two series-connected sensing coils. In the absence of torque, the symmetrical configurations of the two ferromagnetic glass strips and the two sensing coils eliminate the background signal. When torque is applied, the ferromagnetic glass strips are stressed or compressed, destroying the symmetry of the magnetic field pattern and causing an induction voltage at the sensing coils. A sensitivity of 1.4 V/N·m at 20 kHz has been reported [91].

Another ferromagnetic glass-based torque sensor is a four-arm orthogonal yoke design shown in Figure 23b [92]. There is no output signal in the absence of torque due to the symmetrical magnetic field pattern on the ferromagnetic glass shaft. However, when a torque is applied at the ends of the shaft, due to the changes in the magnetic field pattern, a signal will appear in the sensing coil at the secondary yoke if an ac field is excited at the primary yoke.

### 4.1.3. Measurement of Magnetic Flux

Due to their high susceptibility and low hysteresis loss ferromagnetic glasses are widely used as the cores of magnetoinductance sensors to measure magnetic flux. Most ferromagnetic glasses used for flux sensing are composed of Co-rich alloys, which have a near-zero magnetostriction ($10^{-7}$). Moldovanu and co-workers [93, 94] designed
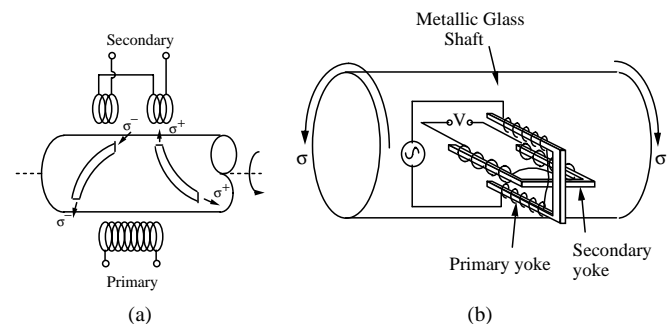


**Figure 23.** (a) A coaxial torque sensor consisting of two ferromagnetic glass ribbons. In the absence of torque, the sensing coil receives no signal due to the symmetrical configurations of the two ferromagnetic glasses. When a torque is applied to the shaft, the ferromagnetic glasses are compressed or stretched, destroying the symmetry of the magnetic field pattern and causing an induction voltage at the sensing coil. (b) A torque sensor based on a four-arm orthogonal yoke design, where a signal will appear in the secondary coil if a torque is applied to the ferromagnetic glass shaft and an ac source is excited at the primary coil.



**Figure 22.** (a) A ferromagnetic glass ribbon used to measure tensile stress. (b) A ferromagnetic glass toroid used to measure tensile and compressive stresses. (c) A ferromagnetic glass sensor used to measure compressive stress.

an induction-based magnetic flux sensor by inserting two $Co_{68.25}Fe_{4.5}Si_{12.25}B_{15}$ ferromagnetic glass ribbons inside a sensing coil and an excitation coil. When an external magnetic flux is applied on the ferromagnetic glasses, it changes the apparent permeability of the ferromagnetic glasses and in turn changes the voltage received by the sensing coil. The sensitivity of the sensor is highest when the magnetic flux is parallel to the basal axis of the coil since the coil intercept maximum flux at this orientation. The output voltage of the sensor is linear with magnetic flux with sensitivity between 4.5 and 5.5 $\mu$V/nT, and for fields greater than 100 nT it is independent of temperature variation within 20–70 °C. Using the same principle, Nielsen and co-workers [95, 96] also designed a flux sensor based on Vitrovac 6025 alloys, with a sensitivity of 5–10 $\mu$V/nT; Ghatak and Mitra [97] designed a flux sensor based on CoFeCrSiB with a sensitivity of 3 $\mu$V/nT.

### 4.1.4. Displacement Sensors

Ferromagnetic glasses are also used to measure the object displacement [13]. As shown in Figure 24a, when the location of the magnet changes, so does the magnetic field exerted on the ferromagnetic glass sensing element. Hence, the displacement of the object can be determined from the changes of the ferromagnetic glass permeability. Alternatively, the object of interest can be attached to the end of the ribbon. As the object moves away from the sensor, it pulls the ferromagnetic glass ribbon and changes the applied stress, in turn altering the ribbon susceptibility (see Figure 24b). Using this principle, Mohri [14] came up with a displacement sensor that can detect a displacement of approximately 1 $\mu$m.

### 4.2. Giant Magnetoimpedance/ Stress-Impedance Sensors

The basic design of a GMI sensor is illustrated in Figure 25. The two ends of a ferromagnetic glass wire are connected to a dc-biased ac current source and a voltmeter, and the
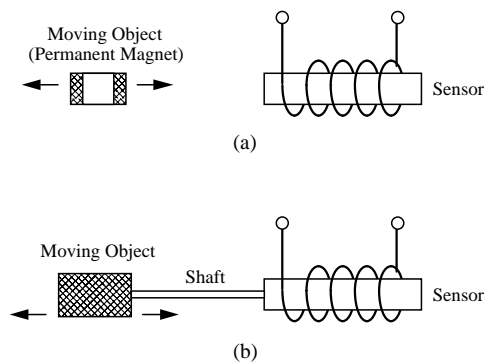


**Figure 24.** (a) A displacement sensor using a permanent magnet as a marker. The displacement of the magnet changes the dc bias field on the ferromagnetic glass, which in turn changes the permeability. (b) A displacement sensor where the object of interest is attached to the end of a ferromagnetic glass ribbon. As the object moves, it pulls the ferromagnetic glass, creating a stress on the ferromagnetic glass and changing the permeability.
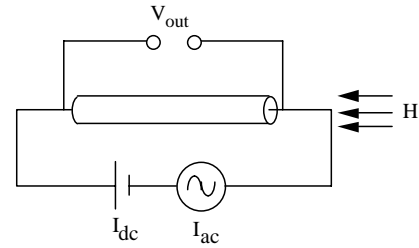


**Figure 25.** A magnetoimpedance sensor. The two ends of a ferromagnetic glass ribbon are connected to a dc-biased ac current source and the voltage across the two ends is measured.

impedance of the ferromagnetic glass $Z$ is determined by taking the ratio of the measured voltage to the applied current. A typical response of a GMI sensor using a circumferential anisotropic amorphous wire is illustrated in Figure 26, where it shows the GMI% increases rapidly with applied magnetic field $H$ when $H$ is smaller than $H_k$ but decreases with $H$ for $H > H_k$.

### 4.2.1. Giant Magnetoimpedance Sensors Based on Ferromagnetic Glasses

Utilizing the GMI effect, ferromagnetic glass wires are widely used as magnetometers for detecting magnetic field in the range of few Oersteds (a few hundred A/m). Some commonly used ferromagnetic glass alloys for GMI sensors are $Fe_{4.35}Co_{68.15}Si_{12.5}B_{15}$ and $Co_{72.5}Si_{12.5}B_{15}$ [98], $Co_{68.5}Mn_{6.5}Si_{10}B_{15}$ [85], and $Fe_{73.5}Cu_1Nb_3Si_{13.5}B_9$ [5].

To increase the sensitivity, linearity, and signal-to-noise ratio of the GMI sensors, usually the ferromagnetic glass wires are connected to oscillator circuits, such as the Colpitts oscillator [68, 99] and the double Hartley oscillator [100]. Figure 27a is a Colpitts oscillator that utilizes the resonance of the inductance of the ferromagnetic glass and the capacitance $C_1$ and $C_2$ to create an ac signal to excite the ferromagnetic glass. This design allows the GMI% of the ferromagnetic glass to increase several times at frequencies of $\approx$100 MHz. Since the oscillator output roughly follows the GMI curve, this sensor design provides nonlinear results similar to the curve shown in Figure 26. By applying a longitudinal bias field, Bushida et al. [68] were able to shift the curve in Figure 26 horizontally and allowed the ferromagnetic glass to operate linearly over the range of interest.
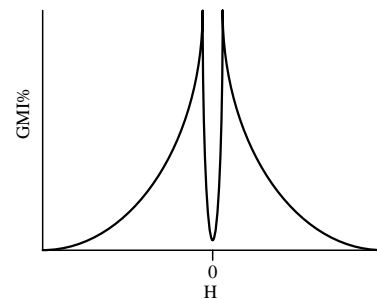


**Figure 26.** A typical response of a magnetoimpedance sensor. The GMI ratio increases rapidly at low magnetic field $H$ until reaching the anisotropy field of the ferromagnetic glass, whereupon the GMI ratio starts falling off with increasing $H$.

An oscillator circuit that provides linear output, the double Hartley oscillator, is shown in Figure 27b [100, 101]. For this design, two identical ferromagnetic glasses biased by two opposing magnetic fields $H_b$ are needed. As shown in Figure 28, the output of this sensor is almost linear in the range of $-H_b < H < H_b$. In Bushida's design [100], for example, the sensitivity of the GMI% can reach to $10^{-6}$ Oe at $\pm 1$ Oe (80 A/m) full scale for an ac field. The biasing fields $H_b$, however, require small solenoids wound around the ferromagnetic glasses, which is a major restriction for sensor miniaturization. By using twisted amorphous wires with dc bias currents, Kitoh and co-workers [98] were able to avoid using solenoids and yet retain the linear characteristic for a limited range of magnetic field.

### 4.2.2. Stress-Impedance Sensors Based on Ferromagnetic Glasses

When a tensile stress is applied to a near-zero magnetostriction ferromagnetic glass it changes the saturation magnetostriction coefficient, causing a variation in the ferromagnetic glass permeability and in turn the impedance. Utilizing this stress-impedance (SI) effect, a stress sensor was constructed by passing a high-frequency current through a $Co_{66.3}Fe_{3.7}Si_{12}B_{18}$ ferromagnetic glass ribbon (10 cm × 0.8 mm × 18 $\mu$m) and measuring the voltage across the wire [102]. The impedance of the ferromagnetic glass is found to be linearly decreasing with applied stress, and the impedance change is about 10% over the range of zero to 500 MPa. Based on the SI effect, ferromagnetic glasses were incorporated into multivibrator circuits for the detection of blood vessel pulsation [103, 104]. Ferromagnetic glasses have also been used to measure liquid flow rate [105], with the stress associated with flow over the surface of the sensor changing its electrical impedance.



(a)



(b)
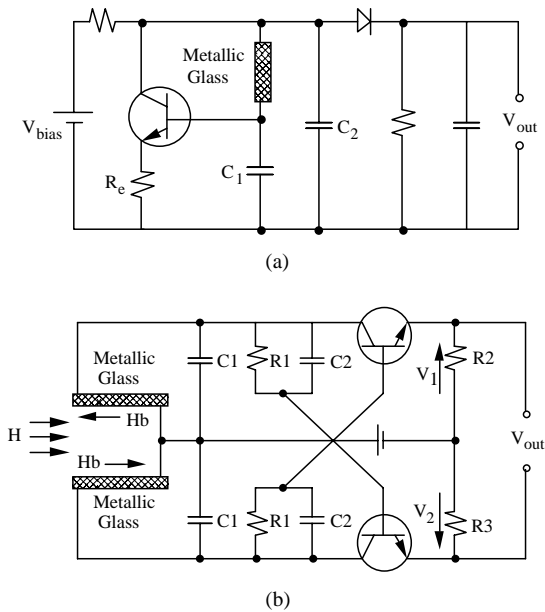
**Figure 27.** A magnetoimpedance sensor connected to (a) a Colpitts oscillator and (b) a double Hartley oscillator. Although more complicated in design, the double Hartley oscillator provides better linearity in output voltage.
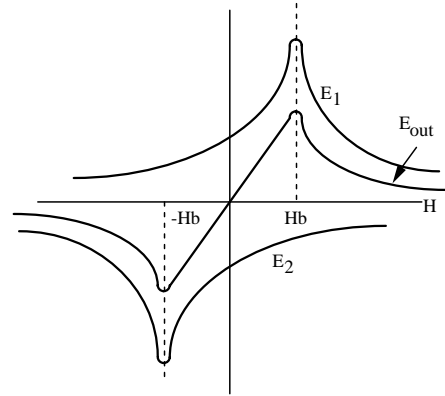


**Figure 28.** The output of the double Hartley oscillator, where $V_{out}$ is linear when the applied field is smaller than the bias field.

## 4.3. Magnetostrictive Delay Line Sensors

Ferromagnetic glasses, in particular Fe-rich alloys, are widely used to construct magnetostrictive delay lines since they have a large magnetoelastic coupling, which allows efficient energy conversion between magnetic fields and acoustic waves. The basic arrangement of the MDL is illustrated in Figure 29: A current pulse is first sent to the excitation coil to generate an ac magnetic field, and an elastic wave is created and propagated along the MDL due to the magnetostrictive effect. As the elastic wave propagates to the other end of the MDL, it generates an induction voltage at the sensing coil due to the inverse magnetostrictive effect. The parameter of interest, such as force, which is applied between the source and receiver, dissipates the elastic energy of the propagating acoustic wave and in turn attenuates the induction voltage received at the sensing coil. By taking the ratio of the received voltage to the excitation voltage, the attenuation of the elastic wave can be determined and used to measure the applied force. Bias fields are usually applied at the excitation and receiving regions to enhance the magnetostrictive effect of the ferromagnetic glass.

### 4.3.1. MDL Stress and Torque Sensors

Hristoforou and Reilly [17] designed a simple MDL force sensor using a Metglas 2605SC ribbon. The sensor is similar to that shown in Figure 29, but with the excitation coil
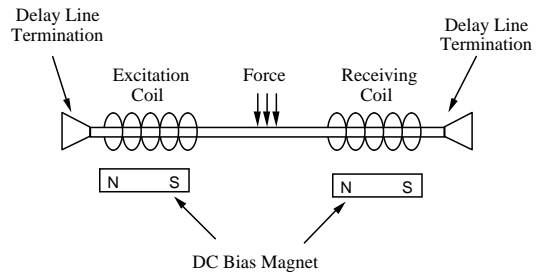


**Figure 29.** The basic arrangement of a magnetoelastic delay line. An elastic wave is generated by the excitation coil and propagated along the MDL due to the magnetostrictive effect. As the elastic wave propagates to the other end of the MDL, it causes an induction voltage at the sensing coil by the inverse magnetostrictive effect.

replaced by a conductor line carrying a voltage pulse. Experimental results show the MDL force sensor can detect a small force of 0.01 N, and the force dependency follows an exponential profile up to 0.35 N.

Chiriac et al. [34] and Hristoforou et al. [18] also designed a stress and torque sensor based on the MDL. The sensor, illustrated in Figure 30, consists of a FeSiB ferromagnetic glass wire with its top end fixed and bottom end loaded with a mass or torque. An excitation coil is placed near the top end of the wire to generate an acoustic wave, and a sensing coil is placed at the bottom end to convert the propagating acoustic wave to an induced voltage. Two bias coils are used to generate the required biasing field for enhancing the magnetostrictive effect of the ferromagnetic glass. The attenuation of the acoustic wave, which is due to the mass load or torque, is recorded as the reduction in the measured induced voltage. Their experimental results show the as-cast ferromagnetic glass sensor has a linear response toward force and a monotonic but nonlinear response toward torque. They also found that annealing the ferromagnetic glass at 300 °C, which increases the magnetoelastic coupling and magnetostriction, increases the sensitivity but reduces the linearity of the sensor response. Recently, Hristoforou and co-workers [19] and Chiriac et al. [34] simplified the design of their MDL stress/torque sensor by using overlapping sensing and excitation coils. Since both ends of the ferromagnetic glass wire are bound, the acoustic wave generated by the excitation coil will be reflected from the ends back to the sensing coil. The response of the overlapping coil design is almost identical to the original design.

A stress sensor designed for measuring thin film thickness using the MDL arrangement was developed by Hristoforou and co-workers [20]. The sensor, shown in Figure 31, consists of two ferromagnetic glasses at the ends of a rectangular glass substrate. An acoustic wave is generated by one of the ferromagnetic glasses and propagates along the substrate. When the acoustic wave reaches the other ferromagnetic glass, an induced voltage proportional to the amplitude
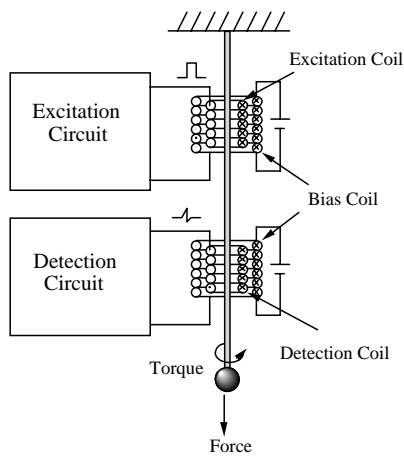


**Figure 30.** A MDL stress and torque sensor. The sensor is composed of a ferromagnetic glass wire with one of its ends fixed and the other loaded with a mass or applied torque. An excitation coil is placed near the top of the wire to generate an acoustic wave, and a sensing coil is placed at the bottom end to convert the propagating acoustic wave to an induced voltage.
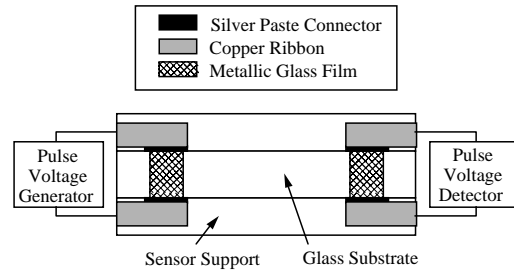


**Figure 31.** A MDL stress sensor consisting of two ferromagnetic glasses at the ends of a rectangular substrate. An acoustic wave is generated by one of the ferromagnetic glasses, the signal propagates along the glass substrate at a speed dependent upon coating thickness, and it is captured by the other ferromagnetic glass.

of the acoustic wave is generated. Since the acoustic wave attenuation is directly proportional to the mass load on the glass substrate the thin film thickness can be determined by measuring the amplitude of the induced voltage.

### 4.3.2. MDL Displacement and Vibration Sensors

Using the MDL setup, ferromagnetic glasses are also used to measure the displacement of an object by attaching the object to a ferromagnetic glass ribbon, or attaching the moving object with a marker magnet. The displacement sensor designed by Germano et al. [22], similar to that shown in Figure 30, consists of a long ferromagnetic glass ribbon surrounding by an excitation coil and a receiving coil; the object of interest is attached to the end of the ribbon. As the object moves away from the sensor, it pulls the ferromagnetic glass ribbon and changes the applied stress, altering the attenuation of the acoustic wave and in turn changing the voltage received by the receiving coil. Germano used $Fe_{40}Ni_{40}P_{14}B_6$, $Fe_{80}B_{14}Si_6$, and $Fe_{82}B_{12}Si_4C_2$ in their experiment, and they found that $Fe_{40}Ni_{40}P_{14}B_6$ has the best linearity compared to the others, which is due to the linear stress dependency on the magnetostriction for that material. Another MDL displacement sensor by Germano and Lanotte [21] consists of a ferromagnetic glass ribbon surrounded by a pair of excitation and detection coils, but the moving object is a permanent magnet. When the permanent magnet changes position, the dc magnetic field experienced by the ferromagnetic glass ribbon changes, changing the ribbon susceptibility and the acoustic wave attenuation.

The displacement sensor developed by Chariac and Marinescu [16] consists of a long ferromagnetic glass with an excitation coil at one end; see Figure 32. The ferromagnetic glass is set to resonance so a standing wave is generated along the sensor. A mobile pick-up coil is then moved along the length of the sensor. Since the sensor experiences a standing wave vibration, the voltage recorded by the pick-up coil $V$ will be in the form of $V(x) = V_0 \sin(\pi x/L)$, where $x$ is the displacement, $L$ is the sensor length, and $V_0$ is a constant depending on the sensor setup; the displacement $x$ is determined from the measured voltage $V$.

Due to its high sensitivity and fast response, the MDL displacement sensor is also used to detect small vibrations. Ausanio and co-workers [106] have successfully illustrated
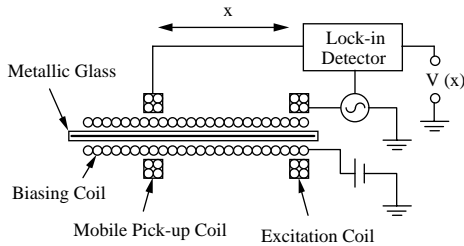
**Figure 32.** A displacement sensor consisting of a ferromagnetic glass set to resonance so a standing wave is generated along the sensor. A mobile pick-up coil is then moved along the length of the sensor, and the displacement $x$ is determined from the measured voltage $V$.

the detection of a vibrating steel ribbon by placing a MDL displacement sensor near the ribbon. The vibration of the steel ribbon changes the magnetic flux distribution around the ferromagnetic glass, and in turn changes the susceptibility of the ferromagnetic glass and the output voltage from the sensing coil.

## 4.4. Magnetoelastic Resonant Sensors

Magnetoelastic resonant sensors operate by monitoring the changes in the magnetoelastic resonant frequency of a ferromagnetic glass ribbon in response to changing stress and field. Generally, magnetoelastic resonant sensors are made of Fe-rich ferromagnetic glasses because they have a high magnetostriction coefficient, which allows them to exhibit pronounced mechanical vibrations, when excited by an ac magnetic field, and high magnetoelastic coupling, which allows efficient conversion between magnetic energy and elastic energy.

To determine the resonant frequency of a ferromagnetic glass ribbon, an ac magnetic field is first generated from an excitation coil to vibrate the ribbon. The frequency response of the sensor in vibration is then recorded as an induced voltage at the sensing coil. The excitation and detection of the sensor can be performed in the frequency domain, where a function generator produces a frequency-varying sinusoidal wave at the excitation coil, and the voltage across the sensing coil is measured as a function of frequency (see Fig. 33). The sensor can also be excited and detected in
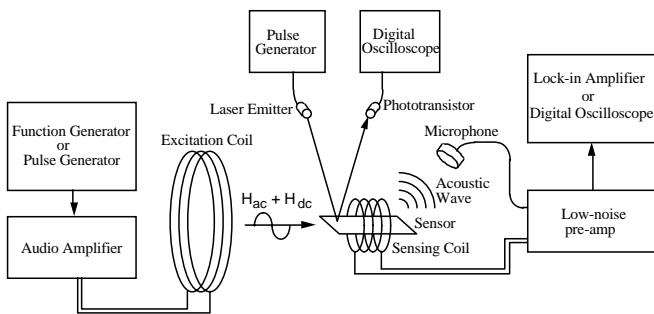


**Figure 33.** Magnetoelastic ferromagnetic glass sensors can be interrogated magnetically, acoustically, or optically. Magnetically the sensor is excited by an excitation coil and is detected by a sensing coil, while acoustically it is detected by a microphone in air or hydrophone in liquids. A laser emitter and a phototransistor are used to interrogate the sensor optically.

the time domain, where a pulse generator produces a magnetic pulse, and a digital oscilloscope is used to capture the transient time-dependent response of the sensor. The time-domain signal is then converted to the frequency domain using fast Fourier transform, from which the resonant frequency is determined.

Recently, Jain et al. [107] proposed the detection of the resonant frequency of the magnetoelastic resonant sensors acoustically with a microphone. The advantage of acoustic detection is the longer detection range; up to 1 m has been reported. In addition to the acoustical detection method, the sensor can be detected optically by shining a laser beam on the sensor surface [108]. The vibration of the sensor modulates the intensity of the laser beam reflected off the vibrating surface, and the changes in intensity are detected by a phototransistor as a change in voltage that can be monitored electronically. The advantage of the optical detection method is the large detection range; up to few meters have been reported. However, the optical detection method requires precise sensor alignment. The magnetic, acoustic, and optical detection methods are illustrated in Figure 33.

### 4.4.1. Pressure Measurement

A magnetoelastic resonant sensor for measuring atmospheric pressure was developed by Grimes et al. [109] using an as-cast Metglas 2826MB ribbon. The variation of the atmospheric pressure changes the vibrational modes of a stressed sensor in turn changing the resonant frequency. Experimental results show that the Metglas 2826MB sensor is linearly dependent upon atmospheric pressure over the range of 0 to 80 psi (550 kPa), with a resonant frequency shift of 5 Hz/psi (0.73 Hz/kPa). Recently Kouzoudis and Grimes [110] showed that the sensitivity of the pressure sensor could be increased by prestressing the sensor through dimpling, curving, or folding the sensor. The curving of the sensor causes a vibration in the basal plane of the sensor in addition to the longitudinal vibration. Since the surface area on the basal plane is at least three orders larger than the cross section of a typical sensor ribbon, the basal plane vibration significantly increases the sensor interactions with air, leading to a large increase in sensitivity.

### 4.4.2. Monitoring of Liquid Flow Rate

A ferromagnetic glass ribbon can also be used to measure liquid flow rates since laminar flowing liquid creates a stress, which is proportional to the flow rate, on the sensor surface and causes changes in the magnetoelastic resonant frequency of the ribbon. A magnetoelastic resonant sensor for fluid-flow measurement was fabricated using a Metglas 2826MB ribbon by Kouzoudis and Grimes [24]. The sensor length is placed parallel to the flow direction of the liquid. When the liquid flow is laminar, the stress on the sensor surface follows a parabolic profile, resulting in a quadratic decrease in the resonant frequency. However, when the flow turns to turbulence, the applied stress is not uniform over the sensor surface, causing the resonant frequency to shift upward.

### 4.4.3. Simultaneous Measurement of Liquid Viscosity and Density

When a ferromagnetic glass ribbon is immersed in a liquid, the shear wave created in the liquid due to the ribbon vibration generates a damping force opposing the oscillations of the ribbon and changes the resonant frequency and the quality factor of the ribbon. For a flat ferromagnetic glass ribbon with perfect surface smoothness immersing in a liquid, the resonant frequency shift $\Delta f$ is given by [24]

$$\Delta f = \frac{\sqrt{\pi f_0}}{2\pi \rho_s d} (\eta_l \rho_l)^{1/2} \tag{54}$$

where $f_0$ is the resonant frequency of the ferromagnetic glass ribbon in the air, $\rho_s$ and $d$ are the density and thickness of the ribbon, and $\eta_l$ and $\rho_l$ are the liquid viscosity and density. In Eq. (54), $\eta_l$ and $\rho_l$ are inseparable; thus measurement of $\eta_l$ and $\rho_l$ with a smooth ribbon is impossible. However, due to surface roughness, the liquid trapped in the ferromagnetic glass surface pores will act like a mass loading instead of a damping force. To compensate for the mass loading effect, Eq. (54) is modified as

$$\Delta f = \frac{\sqrt{\pi f_0}}{2\pi \rho_s d} (\eta_l \rho_l)^{1/2} - \frac{\rho_l \Delta V f_0}{2M} \tag{55}$$

where $\Delta V$ is the volume of liquid trapped by the surface roughness of the ribbon, and $M$ is the mass of the ribbon. From Eq. (55) the liquid density and viscosity can be separated by using two ferromagnetic glass ribbons with different surface roughnesses, indicated by subscripts 1 and 2, and finding the difference of the two resonant frequencies as

$$\Delta f_2 - \Delta f_1 = \rho_l \frac{(\Delta V_1 - \Delta V_2) f_0}{2M} \tag{56}$$

Figure 34a illustrates the measurement of liquid density using two 30 mm × 3 mm × 30 $\mu$m Metglas 2826MB ribbons, one coated with $TiO_2$ on both sides and the other uncoated. Figure 34b shows that the frequency shift difference between the two ferromagnetic glass ribbons is linearly proportional to the liquid density.

For highly viscous liquid, the damping force generated by the liquid becomes too large for the ferromagnetic glass to exhibit a detectable resonance. In practice, highly viscous liquids can be measured by dipping a small fraction of the ferromagnetic glass ribbon into the liquid [111]. Experimental results [111] show that the sensitivity of the ferromagnetic glass increases as the immersion depth increases, up to the point where the damping force in the liquid becomes too large for the ferromagnetic glass ribbon to resonate. The effect of surface roughness for mechanically oscillating sensors on liquid property measurements is described in detail by Jain and Grimes in [112].

### 4.4.4. Elasticity Measurement

The elasticity of a thin-film coating can also be determined by monitoring the shifts in the resonant frequency of a coated ferromagnetic glass ribbon. The ratio between the resonant frequency of a ribbon coated with the material of
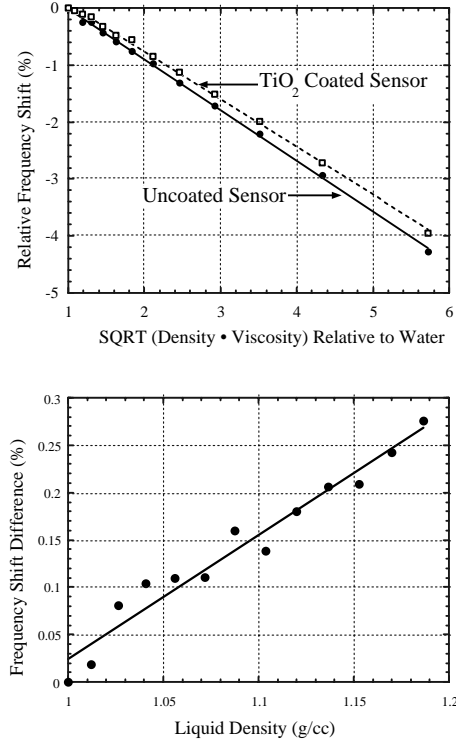


**Figure 34.** (a) Relative frequency shifts vs (density × viscosity)$^{1/2}$ of an uncoated sensor and a $TiO_2$-coated sensor. (b) The difference between the frequency shifts of a $TiO_2$-coated and an uncoated sensors vs the liquid density.

interest $f_t$ and the resonant frequency of an uncoated ribbon $f_0$ can be shown as [27]

$$\left(\frac{f_t}{f_0}\right)^2 = (1 - \beta^2)\frac{m_0}{m_t} + \beta^2 \tag{57}$$

where $m_0$ and $m_t$ are respectively the mass of the uncoated and coated ribbons, and $\beta$ is

$$\beta = \sqrt{\frac{E_c \rho_s}{E_S \rho_c}} \tag{58}$$

where $E_S$ and $E_C$ are respectively the Young's moduli of the ferromagnetic glass and the coating, and $\rho_s$ and $\rho_c$ are respectively the mass density of the ferromagnetic glass and the coating. To determine the elasticity of the coating, the mass and resonant frequency of the uncoated ribbon are first measured. A uniform coating is then applied and the resonant frequency and mass are determined. The process is repeated $N$ times until sufficient data points are collected. The value of $\beta$ can then determined by applying a least-square fit on the collected data using Eq. (57) as

$$\beta^2 = \frac{\sum_{i=1}^{N} \left(\left(\frac{f_t^i}{f_0}\right)^2 - \frac{m_0}{m_t^i}\right)\left(1 - \frac{m_0}{m_t^i}\right)}{\sum_{i=1}^{N} \left(1 - \frac{m_0}{m_t^i}\right)^2} \tag{59}$$

The parameters $E_S$, $\rho_s$, and $\rho_c$ are measured before the experiment. By substituting the calculated $\beta$ into Eq. (58), the Young's modulus of the material of interest $E_C$ is
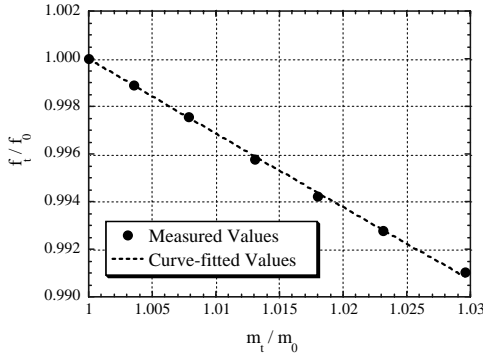
**Figure 35.** The relative resonant frequency of the ferromagnetic glass decreases linearly with the relative mass of sliver coating. A least square fit (dashed line) is used to calculate the Young's modulus of the silver.



**Figure 36.** The resonant frequency shifts of a ferromagnetic glass sensor vs temperature and bias field $H$. The highest positive temperature dependency happens at $H = 9.9$ Oe (790 A/m), highest negative temperature dependency at $H = 16.51$ Oe (1.32 kA/m), and zero-temperature dependency at $H = 7.01$ Oe (560 A/m).

determined. Figure 35 plots the frequency shift of a silver-coated sensor as a function of coating mass. The data points were fitted with Eq. (59) and $E_S$ of silver is determined as 74.8 GN/m², only 1.6% different from the theoretical value. Experiments for calculating the Young's moduli of aluminum, polyurethane paint, and acrylic paint have been conducted by Schmidt and Grimes [27], and the errors are all less than 2% of the theoretical values.

### 4.4.5. Temperature Measurement

Ferromagnetic glasses are also used for monitoring ambient temperature. Temperature influences mechanical properties such as material elasticity (at constant magnetization) $E_M$ and magnetic properties such as $\lambda_S$, $M_s$, and $H_k$. For an unloaded ferromagnetic glass ribbon, the resonant frequency is dependent upon the temperature $T$ and applied bias field $H$ as [26]

$$f_0(T, H) = \frac{1}{2L(T)} \sqrt{\frac{E_M(T)}{\rho_s}} \left( 1 + \frac{9\lambda_S^2(T)H^2 E_M(T)}{M_s(T)H_k^3(T)} \right)^{-1/2} \tag{60}$$

As indicated in Eq. (60), the resonant frequency shift of the ferromagnetic glass ribbon can be positive or negative, large or small, depending upon the material properties of the sensor and the applied field. For a temperature sensor, an appropriate $H$ field can be applied to the ribbon to yield an optimum temperature sensitivity, while for other sensor applications the value of $H$ must be chosen so that the ribbon has a minimum temperature dependency. The temperature

dependency of a 3 cm × 1.27 cm × 30 $\mu$m 2826MB Metglas ribbon is plotted in Figure 36 for varying $H$. From the plot, the maximum positive temperature dependency happens at $H = 9.9$ Oe (790 A/m), maximum negative temperature dependency happens at $H = 16.51$ Oe (1.32 kA/m), and zero-temperature dependency can be achieved at $H = 7.01$ Oe (560 A/m).

### 4.4.6. Chemical Monitoring

By applying a mass-changing chemically responsive layer (CRL), magnetoelastic ferromagnetic glass sensors have been used to monitor chemical analyte concentrations including glucose, carbon dioxide ($CO_2$), ammonia ($NH_3$), and pH. Table 4 lists various magnetoelastic chemical and gas sensors that have been built and tested.

Generally, the mass change for these CRLs is small, so the resonant frequency shift $\Delta f$ is linear,

$$\Delta f = -f_0 \frac{\Delta m}{2m_t} \tag{61}$$

where $\Delta m$ is the change of mass and $m_t$ is the total mass of the sensor and the coating. Figure 37 shows that the resonant frequency of the $CO_2$ sensor, based on acrylamide and isooctylacrylate coating, decreases linearly with the $CO_2$ percentage. Figure 37 also shows that the sensitivity of the sensor increases with the coating thickness until 20 $\mu$m, where the mass load is too large for the sensor to resonate.

**Table 4.** Magnetoelastic sensors are used to monitor humidity, $CO_2$, $NH_3$, pH, and glucose based on the mass change of the chemical responsive layers.

| Sensor | Chemical responsive layer | Maximum $\Delta f$ | Range | Stability | Ref. |
|---|---|---|---|---|---|
| $CO_2$ | acrylamide + isooctylacrylate | −5.6 Hz/vol% | 0–50 vol% | stable | [31] |
| $NH_3$ | poly(acrylic acid-co-isooctylacrylate) | −14 Hz/log(vol%) | 0–100 vol% | stable | [33] |
| pH | acrylic acid (20 mol%) + iso-octylacrylate (80 mol%) | −333 Hz/pH | 5.5–8.5 pH | stable | [32] |
| Glucose | PVA and a co-polymer made of DMAA, BMA, DMAPAA, MAAPBA | −13 Hz/(mg/L) | 0–100 mg/L | dissolves after four cycles | [28] |
| Humidity | titanium dioxide alumina | −1.2 Hz/% RH | 2–98% RH | stable | [29] |
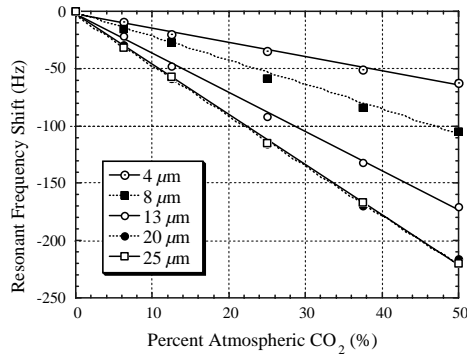
**Figure 37.** A ferromagnetic glass $CO_2$ sensor; the $CO_2$ sensitive coating is synthesized from acrylamide and isooctylacrylate [31].

## 4.5. Ferromagnetic Glass Sensors Based on Other Principles

### 4.5.1. Magneto-Surface-Acoustic-Wave Sensors

Chiriac and co-workers [113] proposed the fabrication of a magneto-surface-acoustic-wave sensor based on the ferromagnetic glass $Fe_{70}B_{15}Si_{15}$ thin film and $(Fe_{70}B_{15}Si_{15}/SiO_2)$ multilayer as the active layer. The design of a MSAW is illustrated in Figure 38, where an acoustic wave is generated using an interdigital transmitter and is received with another interdigital receiver. The ferromagnetic glass active layer is sputtered on the substrate. When a force or magnetic field is applied on the ferromagnetic glass layer, it changes the internal stresses within the ferromagnetic glass, which in turn changes the velocity of the acoustic wave that travels across the ferromagnetic glass layer. As a result, by monitoring the amplitude of the received voltage at the interdigital receiver, the MSAW can be used to measure magnetic field, stress, and pressure.

### 4.5.2. Ferromagnetic Glass Sensors Based on Magnetomechanical Rotation

A viscosity sensor [35] has been reported by Vazquez and co-workers based on a gyromagnetic effect: a spontaneous mechanical rotation of a large magnetostrictive ferromagnetic glass wire when subjected to an ac magnetic field having a frequency of the order of kHz, applied along the
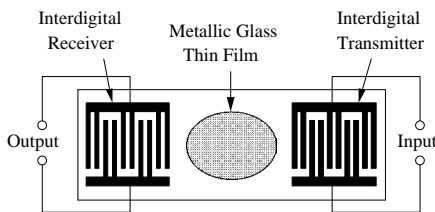


**Figure 38.** A magneto-surface-acoustic wave sensor based on the ferromagnetic glass thin film. An acoustic wave is generated using an interdigital transmitter and is received with an interdigital receiver. The ferromagnetic glass active layer is sputtered between the transmitter and the receiver on the substrate.
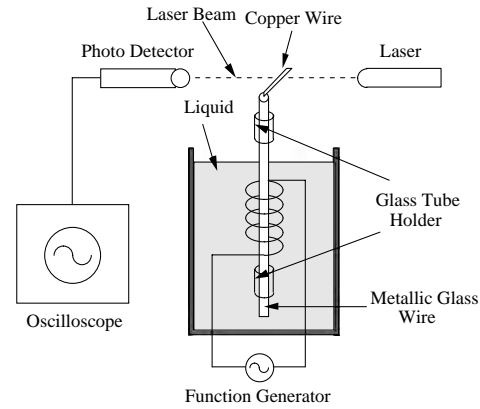


**Figure 39.** A viscosity sensor based on the spontaneous mechanical rotation of a large magnetostrictive ferromagnetic glass. When the ferromagnetic glass wire is subjected to an ac magnetic field, it rotates and the copper wire attached to it will modulate the laser beam enabling rotation frequency to be determined. The rotation frequency of the ferromagnetic glass wire decreases linearly with increasing viscosity, as highly viscous liquid creates more friction on the wire surface.

wire axis [114, 115]. Although the exact origin of the spontaneous rotation is still unclear, it is widely believed this phenomenon is connected to the conversion of the magnetoelastic standing wave energy to the mechanical rotation energy at magnetoelastic resonance [116]. As illustrated in Figure 39, the ferromagnetic glass wire is vertically supported by two short glass tubes while immersing in the liquid of interest. A copper wire is perpendicularly connected to the top end of the wire, so when the ferromagnetic glass rotates the copper wire can block a laser beam thereby determining angle. Vazquez experimented on FeSiB and CoSiB, and they found that the rotation frequencies of both ferromagnetic glasses are dependent upon the magnitude and frequency of the ac magnetic field. However, FeSiB is more suitable for viscosity measurement because it has a higher rotation frequency, which reduces the experimental error because more averages can be taken for a given time period. Results show that the rotation frequency of the ferromagnetic glass wire decreases linearly with increasing viscosity, since the viscosity of the liquid creates a frictional force on the wire surface that slows the rotation.

## 5. SUMMARY

The properties of ferromagnetic glasses and their applications as useful sensors have been reported. Ferromagnetic glasses are suitable for sensor applications due to their changing susceptibility, impedance, and magnetoelastic resonant frequency in response to various parameters including stress/strain, temperature, and magnetic field. Ferromagnetic glasses are fabricated by rapid quenching from a melt to prevent the formation of crystalline structure. Alloy compositions in the ferromagnetic glasses play an important role on the properties of the materials. Generally, Fe-rich and rare-earth-based amorphous alloys have a large magnetostriction, while Co-rich alloys have a small or zero magnetostriction. To control the desired properties, as-cast

ferromagnetic glasses are generally annealed under applied transverse field or stress. For example it has been found that transverse field annealing can improve the magnetoelastic coupling and magnetostriction of Metglas 2605SC to 0.98 and $3 \times 10^{-5}$, respectively.

One of the most common applications of ferromagnetic glasses is in the cores of induction-based sensors for the measurement of stress/strain, torque, magnetic field, and displacement. Although there are many different designs available, the operational principle is based on the changing susceptibility of the materials with applied stress and field. It is found that the sensitivity of a ferromagnetic glass stress sensor can be three orders higher than a standard semiconductor stress sensor. Ferromagnetic glasses are also used as displacement sensors by attaching a small magnet on a moving object, or directly attaching the moving object on a ferromagnetic glass.

Ferromagnetic glasses are widely used as the sensing elements of magnetoimpedance sensors. The magnetoimpedance sensors based on ferromagnetic glasses are suitable for the detection of small magnetic field; up to $10^{-6}$ Oe within 1 Oe (80 A/m) full scale has been reported. By constructing magnetostrictive delay lines using ferromagnetic glass wires, parameters such as stress, torque, and displacement have been measured. In addition, ferromagnetic glasses are also used as the active layer of a magneto-surface-acoustic-wave sensor. A viscosity sensor based on the spontaneous rotation of a ferromagnetic glass wire under an ac excitation field has also been built and successfully tested.

Magnetoelastic resonant sensors, which operate by monitoring the changes in the magnetoelastic resonant frequency, are commonly made of high magnetostrictive ferromagnetic glass alloys. Magnetoelastic resonant sensors are used to track the variation in atmospheric pressure and the liquid flow rate since these parameters apply a stress on the surface of the ferromagnetic glasses that changes the resonant frequency. Magnetoelastic resonant sensors have also been used for simultaneous measurement of liquid viscosity and density by using two ribbons with different surface roughness because the resonant frequency depends upon the viscosity and density of the liquid, as well as the surface roughness of the ribbon. In addition, magnetoelastic resonant sensors can also be used to measure the elasticity of an applied coating of known mass. A temperature sensor was also fabricated from a Metglas 2826MB ribbon, the sensitivity of which is controllable by the applied dc magnetic biasing field. In combination with a mass-changing chemical responsive layer the magnetoelastic resonant sensors have been used to measure chemical analyte concentrations such as pH, glucose, carbon dioxide, ammonia, and humidity. For small mass loading, the resonant frequency shifts down linearly with increasing mass. The advantage of this type of chemical sensor is its remote query capability making it ideally suited for applications requiring *in-situ* and *in vivo* monitoring.

## LIST OF SYMBOLS

| | |
|---|---|
| $a$ | radius of the ferromagnetic glass wire |
| $B_r$ | remanence |
| $B_s$ | saturation induction |
| $C$ | Curie constant |
| $d$ | thickness of the ferromagnetic glass ribbon |
| $D$ | electric flux density |
| $E_C$ | Young's modulus of the ferromagnetic glass coating at a constant applied field |
| $E_{ex}$ | exchange energy |
| $E_H, E_S$ | Young's modulus of the ferromagnetic glass ribbon at a constant applied field |
| $E_M$ | Young's modulus of the ferromagnetic glass ribbon at a constant magnetization |
| $F$ | figure of merit |
| $f_n$ | $n$th harmonic resonant frequency of a vibrating ferromagnetic glass sensor |
| $f_t$ | resonant frequency of a ferromagnetic glass ribbon after applying a thin coating |
| GMI% | giant magnetoimpedance ratio |
| $H, H_{appl}$ | applied magnetic field |
| $H_c$ | coercive force |
| $H_i$ | internal magnetic field |
| $H_k$ | anisotropy field |
| $H_d$ | demagnetizing field |
| $H_{max}$ | saturation magnetic field |
| $I$ | electric current |
| $j$ | complex number |
| $J_c$ | conduction current |
| $J_{ex}$ | exchange integral |
| $k$ | effective magnetoelastic coupling |
| $k_B$ | Boltzmann constant |
| $K$ | anisotropy constant |
| $K_U$ | anisotropy energy |
| $L$ | length of the ferromagnetic glass sensor |
| $m_0$ | mass of the ferromagnetic glass sensor |
| $m_t$ | mass of the ferromagnetic glass sensor after applying a thin coating |
| $M$ | magnetization |
| $M_s$ | saturation magnetization |
| $N, N_d$ | demagnetization factor |
| $p_m$ | Coulomb magnetic moment |
| $q_e$ | electric charge |
| $Q_m$ | Coulomb magnetic pole strength |
| $R_{dc}$ | dc electrical resistance |
| $s$ | electron spin |
| $T$ | temperature, torque |
| $T_\theta$ | Curie temperature |
| $T_c$ | crystallization temperature |
| $u_a$ | anisotropy energy |
| $u_{el}$ | elastic energy |
| $u_{m\ell}$ | magnetoelastic energy |
| $u_x$ | displacement of a vibrating ferromagnetic glass sensor |
| $V, V_1, V_2$ | measured voltage across the length of the ferromagnetic glass sensor |
| $w$ | width of the ferromagnetic glass ribbon |
| $Z$ | electrical impedance |
| $\chi$ | magnetic susceptibility |
| $\chi_0$ | magnetic susceptibility of a ferromagnetic glass sensor at zero applied stress |
| $\Delta\chi$ | change of magnetic susceptibility |
| $\Delta E$ | the $\Delta E$ effect, defined as the fractional difference between $E_M$ and $E_H$ |
| $\Delta\varepsilon$ | change of applied strain |

| | |
|---|---|
| $\Delta f$ | resonant frequency shift |
| $\Delta m$ | variation of mass |
| $\Delta V$ | volume of the liquid trapped in the ferromagnetic glass surface |
| $\alpha$ | directional cosines of magnetization |
| $\delta$ | domain wall thickness |
| $\varepsilon$ | magnetostrictive strain |
| $\gamma$ | Weiss constant |
| $\eta_l$ | liquid viscosity |
| $\lambda_S$ | magnetostriction constant |
| $\mu$ | magnetic permeability |
| $\mu_0$ | magnetic permeability in vacuum |
| $\mu_m$ | magnetic moment |
| $\mu_r$ | relative magnetic permeability |
| $\mu_t$ | transverse permeability of the ferromagnetic glass ribbon |
| $\mu_\theta$ | circumferential permeability of the ferromagnetic glass wire |
| $\upsilon$ | velocity |
| $\rho_c$ | density of the coating material of the ferromagnetic glass sensor |
| $\rho_e$ | electrical resistivity |
| $\rho_{es}$ | surface charge density |
| $\rho_s$ | density of the ferromagnetic glass sensor |
| $\rho_l$ | liquid density |
| $\sigma$ | applied stress |
| $\sigma_p$ | Poisson's ratio |
| $\omega$ | radian frequency |

## GLOSSARY

**Giant magnetoimpedance** a phenomenon that significantly changes the radio-frequency electrical impedance of a magnetic conductor with a small variation of magnetic field.

**Magnetoelastic** the coupling between the elastic energy and magnetic energy in a magnetostrictive material.

**Magnetostriction** deformation of a ferromagnetic material when subjected to the influence of an external magnetic field.

$\Delta E$ **effect** variation in the elastic modulus of a magnetoelastic material when exposed to different magnetic fields.

## ACKNOWLEDGMENTS

## REFERENCES

1. P. Duwez and S. Lin, *J. Appl. Phys.* 38, 4096 (1967).
2. S. Mader and S. Nowick, *Appl. Phys. Lett.* 7, 57 (1965).
3. A. Inoue, *Mater. Sci. Eng. A* 304–306, 1 (2001).
4. T. J. de Lacheisserie, *J. Magn. Magn. Mater.* 25, 251 (1982).
5. M. Knobel, J. Schoenmaker, J. P. Sinnecker, T. Sato, R. Grossinger, and W. Hofstetter, *Mater. Sci. Eng. A* 226–228, 546 (1997).
6. R. C. O'Handley, "Modern Magnetic Materials: Principles and Applications." Wiley, New York, 2000.
7. M. Brouha and J. van der Borst, *J. Appl. Phys.* 50, 7594 (1979).
8. C. Modzelewski, H. T. Savage L. T. Kabacoff, and A. E. Clark, *IEEE Trans. Magn.* MAG-17, 2837 (1981).
9. M. H. Price and K. J. Overshott, *J. IEEE Trans. Magn.* MAG-19, 1931 (1983).
10. A. Makino, T. Hatanai, and Y. Naitoh, *IEEE Trans. Magn.* 33, 3793 (1997).
11. Honeywell, 101 Columbia Road, Morristown, NJ 07962 USA, http://www.honeywell.com; Vacuumschmelze Gmbh & Co. KG, Grüner Weg 37, D-63450 Hanau, Germany, http://www.vacuumschmelze.com.
12. M. L. Spano, K. B. Hathaway, and H. T. Savage, *J. Appl. Phys.* 53, 2667 (1982).
13. A. Hernando, M. Vazquez, and J. M. Barandiaran, *J. Phys. E* 21, 1129 (1988).
14. K. Mohri, *IEEE Trans. Magn.* MAG-20, 942 (1984).
15. H. Chiriac, E. Hristoforou, M. Neagu, I. Darie, and G. Lionis. *Sens. Actuators A* 59, 79 (1997).
16. H. Chiriac and C. S. Marinescu, *Sens. Actuators A* 81, 174 (2000).
17. H. Hristoforou and R. E. Reilly, *IEEE Trans. Magn.* 28, 1974 (1992).
18. E. Hristoforou, H. Chiriac, and M. Neagu, *IEEE Trans. Magn.* 32, 4953 (1996).
19. E. Hristoforou, H. Chiriac, M. Neagu, and I. Darie, *Sens. Actuators A* 68, 307 (1998).
20. E. Hristoforou, H. Chiriac, and J. N. Avaritsiotis, *Sens. Actuators* 76, 156 (1999).
21. R. Germano and L. Lanotte, *Sens. Actuators A* 59, 337 (1997).
22. R. Germano, G. Ausanio, V. Iannotti, L. Lanotte, and C. Luponio, *Sens. Actuators* 81, 134 (2000).
23. D. Kouzoudis and C. A. Grimes, *J. Smart. Mater. Struct.* 9, 885 (2000).
24. C. A. Grimes, D. Kouzoudis, and C. Mungle, *Rev. Sci. Instrum.* 71, 3822 (2000).
25. D. Kouzoudis and C. A. Grimes, *J. Appl. Phys.* 87, 6301 (2000).
26. C. Mungle, C. A. Grimes, and W. R. Dreschel, *Sensors Actuators A* 101, 143 (2002).
27. S. Schmidt and C. A. Grimes, *IEEE Trans. Magn.* 37, 2731 (2001).
28. C. A. Grimes, K. G. Ong, K. Loiselle, P. G. Stoyanov, D. Kouzoudis, Y. Liu, C. Tong, and F. Tefiku, *Smart Mater. Struct.* 8, 639 (1999).
29. C. A. Grimes, D. Kouzoudis, E. C. Dickey, D. Qian, M. A. Anderson, R. Shahidian, M. Lindsey, and L. Green, *J. Appl. Phys.* 87, 5341 (2000).
30. C. A. Grimes, Q. Cai, K. G. Ong, and K. Loiselle, *Proc. SPIE* 4097, 123 (2000).
31. Q. Y. Cai, A. Cammers-Goodwin, and C. A. Grimes, *J. Environ. Monit.* 2, 556 (2000).
32. Q. Y. Cai and C. A. Grimes, *Sens. Actuators B* 71, 112 (2000).
33. Q. Y. Cai, M. K. Jain, and C. A. Grimes, *Sens. Actuators B* 77, 614 (2001).
34. H. Chiriac, E. Hristoforou, M. Neagu, and F. Borza, *Sens. Actuators A* 91, 223 (2001).
35. M. Vazquez, *Sens. Actuators A* 91, 112 (2001).
36. H. C. Oersted, *Ann. Philos.* 16 (1820).
37. B. D. Cullity, "Introduction to Magnetic Materials." Addison–Wesley, Reading, MA, 1972.
38. R. M. Bozorth, "Ferromagnetism." Van Nostrand, New York, 1951.
39. E. Kneller, "Ferromagnetism." Springer, Berlin, 1962.
40. J. A. Stratton, "Electromagnetic Theory." McGraw-Hill, New York, 1941.
41. S. Chikazumi, "Physics of Magnetism." Wiley, New York, 1964.
42. A. H. Morrish, "The Physical Principles of Magnetism." Wiley, New York, 1965.
43. J. Smit and H. P. J. Wijn, "Ferrites." Wiley, New York, 1959.
44. A. M. Ampere, "Theorie Mathematique des Phenomenes Electro-dynamiques Uniquement Diduite de l'Experience." Reprinted by Blanchard, Paris, 1958.
45. M. Faraday, *Philos. Trans. Roy. Soc. London Ser. A* 136 (1846).

46. J. C. Maxwell, "A Treatise on Electricity and Magnetism." Clarendon Press, Oxford, 1873.
47. P. Langevin, *Ann. Chem. Phys.* 5, 70 (1905).
48. P. Weiss, *Compt. Rend.* 143, 1136 (1906).
49. H. Bethe and D. Handb, *J. Phys.* 24, 595 (1933).
50. J. C. Slater, *Phys. Rev.* 35, 509 (1930).
51. C. Herring, *Rev. Mod. Phys.* 34, 63A (1962).
52. H. Lieberman and C. D. Graham, *IEEE Trans. Magn.* 12, 921 (1976).
53. T. Yamasaki, P. Schobmacher, K. Ehrlich, and Y. Ogino, *Nanostruct. Mater.* 10, 375 (1998).
54. M. Donton, H. Cesiulis, and Z. Stojek, *Electrochim. Acta* 45, 3389 (2000).
55. S. H. Lim, *IEEE Trans. Magn.* 33, 3940 (1997).
56. A. Speliotis, O. Kalogirou, N. Vouroutzis, and D. Niarchos, *J. Magn. Magn. Mater.* 187, 17 (1998).
57. J. Betz, K. Mackay, and D. J. Givord, *J. Magn. Magn. Mater.* 207, 180 (1999).
58. G. Knuyt and L. de Schepper, *J. Phys. F* 16, 1989 (1986).
59. A. Inoue and X. M. Wang, *Acta Mater.* 48, 1383 (2000).
60. Z. Kaczkowski, G. Vlasak, P. Duhaj, and P. J. Ruuskanen, *J. Magn. Magn. Mater.* 185, 112 (1998).
61. L. Lanotte, G. Ausanio, and V. Iannotti, *J. Magn. Magn. Mater.* 97, 865 (1999).
62. V. Haslar, L. Kraus, D. Janickovic, P. Svec, and P. Duhaj, *Mater. Sci. Eng. A* 226–228, 331 (1997).
63. J. D. Livingston, *Phys. Status Solidi A* 48, 591 (1982).
64. P. Anderson III, *J. Appl. Phys.* 53, 8101 (1982).
65. M. A. Mitchell, J. R. Cullen, R. Abbundi, A. Clark, and H. Savage, *J. Appl. Phys.* 50, 1627 (1979).
66. M. Vazquez, *J. Magn. Magn. Mater.* 226–230, 693 (2001).
67. N. A. Usov, A. S. Antonov, and A. Lagar'kov, *J. Magn. Magn. Mater.* 185, 159 (1998).
68. K. Bushida, K. Mohri, and T. Uchiyama, *IEEE Trans. Magn.* 31, 3134 (1995).
69. F. Machado and S. M. Rezende, *J. Appl. Phys.* 79, 6558 (1996).
70. H. K. Lachowicz and H. J. Szymczak, *J. Magn. Magn. Mater.* 41, 327 (1984).
71. S. Atalay, H. I. Adiguzel, and O. Kamer, *Mater. Sci. Eng. A* 304–306, 459 (2001).
72. P. Minguez, H. A. Davies, I. Todd, M. R. Gibbs, A. Garcia-Arribas, and J. J. Gutierrez, *J. Non-Cryst. Solids* 287, 428 (2001).
73. O. V. Nielsen, *IEEE Trans. Magn.* MAG-21, 2008 (1985).
74. M. Vazquez, E. Ascasibar, A. Hernando, and O. V. Nielsen, *J. Magn. Magn. Mater.* 66, 37 (1987).
75. J. Gonzalez, M. Vazquez, J. M. Barandiaran, V. Madurga, and A. Hernando, *J. Magn. Magn. Mater.* 68, 151 (1987).
76. V. Soyka, L. Kraus, K. Zaveta, and K. Jurek, *J. Magn. Magn. Mater.* 196–197, 262 (1999).
77. M. Knobel, H. Chiriac, J. P. Sinnecker, S. Marinescu, and T. A. Ovari, *Sens. Actuators A* 59, 256 (1997).
78. T. A. Ovari, H. Chiriac, and C. S. Marinescu, *Sens. Actuators A* 91, 207 (2001).
79. P. Allia, M. Coisson, A. Stantero, P. Tiberto, F. Vinai, G. Ausanio, and L. Lanotte, *Sens. Actuators A* 91, 1999 (2001).
80. K. Kawashima, I. Ogasawara, S. Ueno, and K. Mohri, *IEEE Trans. Magn.* 35, 3610 (1999).
81. Y. Takemura, *IEEE Trans. Magn.* 32, 4947 (1996).
82. J. A. Moya, *J. Magn. Magn. Mater.* 203, 117 (1999); J. He, H. Q. Guo, B. Shen, K.Y. He, and H. Zhang, *Mater. Sci Eng. A* 304–306, 988 (2001).
83. H. R. Hilzinger, *IEEE Trans. Magn.* MAG-21, 2020 (1985).
84. L. Brunetti, M. Coisson, P. Tiberto, and F. Vinai, H. Chiriac, and F. Borza, *Sens. Actuators A* 91, 203 (2001).
85. A. Cobeno, A. Zhukov, J. Blanco, V. Larin, and J. Gonzalez, *Sens. Actuators A* 91, 95 (2001).
86. E. E. Mitchell, R. DeMoyer, and J. Vranish, *IEEE Trans. Ind. Electron.* IE-33, 166 (1986).
87. J. M. Barandiaran and J. Gutierrez, *Sens. Actuators A* 58, 38 (1997).
88. K. Mohri and S. Korekoda, *IEEE Trans. Magn.* MAG-14, 1071 (1978).
89. T. Meydan, M. G. Blundell, and K. J. Overshott, *IEEE Trans. Magn.* MAG-17, 3376 (1981).
90. K. Mohri and S. Takeuchi, *IEEE Trans. Magn.* MAG-17, 3379 (1981).
91. K. Harada, I. Sasada, T. Kawajiri, and A. Inoue, *IEEE Trans. Magn.* MAG-18, 1767 (1982).
92. I. Sasada, A. Hiroike, and K. Harada, *IEEE Trans. Magn.* MAG-20, 951 (1984).
93. A. Moldovanu, H. Chiriac, M. Macoviciuc, E. Diaconu, C. Ioan, and M. Tomut, *Sens. Actuators A* 59, 105 (1997).
94. A. Moldovanu, H. Chiriac, C. Moldovanu, M. Macoviciuc, and C. Ioan, *Sens. Actuators* 81, 189 (2000).
95. O. V. Nielsen, J. Gutierrez, B. Hernando, and H. T. Savage, *IEEE Trans. Magn.* MAG-26, 276 (1990).
96. O. V. Nielsen, J. R. Petersen, F. Primdahl, P. Brauer, and P. Ripka, *Meas. Sci. Technol.* 6, 1099 (1995).
97. S. K. Ghatak and A. Mitra, *J. Magn. Magn. Mater.* 103, 81 (1992).
98. T. Kitoh, K. Mohri, and T. Uchiyama, *IEEE Trans. Magn.* 31, 3137 (1995).
99. T. Uchiyama, *IEEE Trans. Magn.* 31, 3182 (1995).
100. K. Bushida, K. Mohri, T. Kanno, D. Katoh, and A. Kobayashi, *IEEE Trans. Magn.* 32, 4944 (1996).
101. K. Inada, K. Mohri, and K. Inuzuka, *IEEE Trans. Magn.* 30, 4623 (1994).
102. M. Tejedor, *Sens. Actuators* 81, 98 (2000).
103. D. Kusumoto, L. P. Shen, Y. Naruse, K. Mohri, and T. Uchiyama, *IEEE Trans. Magn.* 35, 4115 (1999).
104. K. Mohri, T. Uchiyama, L. Shen, C. Cai, and L. Panina, *Sens. Actuators A* 91, 85 (2001).
105. E. Hristoforou, I. MN. Avaritsiotis, and H. Chiriac, *Sens. Actuators A* 59, 94 (1997).
106. G. Ausanio, V. Iannotti, C. Luponio, L. Lanotte, R. Germano, A. D'Agostino, M. Inverno, and R. Sorrention, *Sens. Actuators A* 91, 123 (2001).
107. M. K. Jain, S. Schmidt, and C. A. Grimes, *Appl. Acoustics* 62, 1001 (2001).
108. M. K. Jain, S. Schmidt, C. Mungle, K. Loiselle, and C. A. Grimes, *IEEE Trans. Magn.* 37, 2767 (2001).
109. C. A. Grimes, P. G. Stoyanov, D. Kouzoudis, and K. G. Ong, *Rev. Sci. Instrum.* 70, 4711 (1999).
110. C. A. Grimes and D. Kouzoudis, *Sens. Actuators* 84, 205 (2000).
111. K. Loiselle and C. A. Grimes, *Rev. Sci. Instrum.* 71, 1441 (2000).
112. M. K. Jain and C. A. Grimes, *Sens. Actuators A* 100, 63 (2002).
113. H. Chiriac, M. Pletea, and E. Hristoforou, *Sens. Actuators A* 91, 107 (2001).
114. H. Chiriac, C. Marinescu, and T. Ovari, *IEEE Trans. Magn.* 33, 3349 (1997).
115. F. J. Castano, M. Vazquez, D. Chen, M. Tena, C. Prados, R. Pina, A. Hernando, and G. Rivero, *Appl. Phys. Lett.* 75, 2117 (1999).
116. F. J. Castano, M. Vazquez, T. A. Ovari, D. Chen, and A. Hernando, *IEEE Trans. Magn.* 36, 2791 (2000).

# Magnetotransport in Nanogranular Materials

## Jinke Tang

*University of New Orleans, New Orleans, Louisiana, USA*

## CONTENTS

## 1. INTRODUCTION

Granular systems consist of granules of one phase embedded in the matrix of a second phase. The grain boundaries sometimes act as the second phase separating the grains. One or both phases can be conducting. In the case when both are conducting, electron transport is dominated by the scattering. Tunneling between metallic grains becomes the main transport mechanism when the second phase is an insulator. The transport in these types of granular systems exhibits so-called giant magnetoresistance (GMR) and tunneling magnetoresistance (TMR) if the particles are magnetic [1–9]. GMR and TMR in layered and granular thin films have revealed a host of fascinating physics of spin-dependent electron transport. They have also had an enormous impact on the information technology and electronics industries.

One of the primary potential applications of GMR and TMR materials is as the sensor element in magnetoresistance (MR) read heads and magnetic memories. In recent years, the traditional inductive heads in magnetic recording devices have steadily been replaced by magnetoresistance heads for several reasons: Magnetoresistive elements provide a velocity-independent signal, a more durable and robust recorded signal, and greater sensitivity and lower noise than inductive elements. Among magnetoresistive heads, GMR/TMR heads exhibit superior properties to permalloys due to their much-enhanced MR values. These spin-dependent transport materials also have potential application in nonvolatile memories. Magnetic random access memory (MRAM), an integrated magnetic memory technology that uses magnetic storage and magnetoresistive reading with semiconductor support circuits, is currently being developed based on GMR/TMR technologies. Other advantages of a GMR/TMR memory cell include high density, high speed, and low power consumption [10]. In the following, some of the important issues of the spin-dependent transport in granular systems are discussed.

## 2. GRANULAR GIANT MAGNETORESISTANCE

Granular magnetic materials, where magnetic metallic particles are embedded in a nonmagnetic metallic host, show remarkable negative giant magnetoresistance (GMR). Granular GMR was first found in Cu–Co granular systems by Berkowitz et al. and Xiao et al. in 1992 [3, 4] after the discovery of GMR in Fe/Cr multilayers in 1988 [1]. The equilibrium solubility of Co in Cu is extremely small. But an extended solid solution can be formed in Cu–Co thin films. By thermally annealing the solid-solution films, Co nanoparticles precipitate out of the Cu matrix. The sizes of the magnetic Co nanoparticles embedded in the Cu matrix range from a few to a few tens of nanometers and can be controlled by the annealing temperature or parameters used during the deposition of the films.

Such granular systems can be prepared by a number of other nonequilibrium techniques. Methods that have been demonstrated to effectively produce granular GMR materials include mechanical milling [11–13], melt spinning [14–17], spinodal decomposition [18, 19], electrodeposition [20], Joule heating [21–23], pulsed laser deposition [24], low-energy cluster beam deposition [25], ion beam co-sputtering [26], gas flow condensation [27], and ion implantation [28].

Besides Cu–Co mentioned previously, Ag–Co, Cu–Fe(Ni), and Ag–Fe(Ni) have all been shown to exhibit granular

GMR when magnetic granules of Co or Fe(Ni) are embedded in a Cu or Ag matrix [29–36]. Similar systems such as Mg–Fe films and Cr–Fe bulk alloys also show negative GMR [37, 38]. In addition, GMR was observed in a macroscopic ferrimagnet Co–TbN, where magnetic TbN particles precipitate in a Co matrix [39]. However, this last example may be an exception. Studies conducted so far indicate that GMR is probably exclusive to the transition metal system. The strong itinerant nature of 3d electrons, which is distinctively different from that of 4f electrons, plays an important role in determining the GMR. There has been no report of GMR in a granular system where insulating magnetic particles are embedded in a nonmagnetic metallic matrix, although this is possible in theory, considering the large contribution to the GMR from the interface scattering.

The correlation among the microstructure, magnetic, and magnetotransport properties has been extensively investigated [40–48]. The dependence of GMR on particle size, particle morphology, particle concentration, and chemical composition has been obtained. Some of the key characteristics of granular GMR are worth mentioning here. The magnitude of the MR depends on the volume fraction of the magnetic particles and their sizes. GMR is only observed when the volume fraction of the magnetic particles is below the percolation limit. The maximum MR occurs near a volume fraction of 20–30%. The optimum particle size for GMR lies in the range of a few nanometers. These magnetic particles are single domain and are superparamagnetic at high temperatures. Both the low-temperature blocked state and the high-temperature superparamagnetic state exhibit a GMR effect of similar characteristics because the electron relaxation time is much shorter than the superparamagnetic relaxation time. For GMR to occur, the sizes of the magnetic particles should be comparable to or smaller than the electron mean free path. The GMR is enhanced if the electron mean free path is increased or if the interparticle distance is reduced. Large magnetoresistance ratios, $\Delta R/R = (R_H - R_0)/R_0$, have been found (20–30% at room temperature and up to 60–70% at low temperatures). The values are similar to those found in multilayered films. Another important feature of GMR is that the negative MR is isotropic, independent of the orientation of the applied field relative to the current and film plane. This contrasts with the anisotropic magnetoresistance (AMR) of a ferromagnet, where the magnitude and sign are different for current parallel or perpendicular to the applied field. It also differs from the GMR of multilayered films, where the orientation dependence originates from the shape anisotropy of the magnetic films.

The GMR effect in granular materials arises from spin-dependent scattering due to dissimilar scattering of conduction electrons from majority and minority bands by magnetic particles with different magnetization directions [49–61]. The angular distribution of magnetization of such scattering centers can be varied by an external magnetic field, and the minimum resistance is usually achieved for their parallel alignment in a sufficiently strong field. In the case of multilayered systems, the GMR effect is controlled by the relative magnetization directions in the neighboring magnetic layers separated by a nonmagnetic spacer. The maximum resistance of such systems is realized by the antiparallel arrangement of the layers. Both the interfaces between the magnetic and nonmagnetic layers and the bulk of the magnetic layers are considered to contribute to the spin-dependent scattering although studies show an enhanced contribution of interface scattering to the total resistance. In granular materials, magnetic grains with initially randomly oriented magnetization directions play the role of scattering centers, and the ordering of their directions in a magnetic field results in a decrease in the overall resistance of the material. The magnitude of the spin-dependent scattering is dependent on the orientation of the electron spin relative to the magnetization of the magnetic particles.

Theoretical studies on GMR in multilayers have been reported in several papers [55–61]. Both quasiclassical treatment [55, 56] based on the Boltzmann equation and quantum treatment [57, 58] based on the Kubo formula have been approached. While there has been some controversy about the applicability of the quasiclassical approach to metallic multilayers, Camblong and Levy [60], in their nonlocal linear transport theory, found a direct connection between the two approaches. Their study lends support to the quasiclassical approach and shows the enhanced contribution of interface scattering to the total resistivity. Zhang and Levy took into account the correlations in the scattering from the ordering of impurities due to interdiffusion across the interfaces and found that the constructive interference between scattering amplitudes produces enhanced spin-dependent scattering from the interface between magnetic and nonmagnetic metals [61]. The importance of interface scattering has been emphasized in a number of experimental studies [51, 62, 63]. Fullerton et al. [51] reported an experimental study on Fe–Cr supperlattices that clearly shows that the GMR is enhanced by the presence of interfacial roughness. Itoh et al. [63] ascribe the microscopic origin of the GMR in metallic supperlattices to the spin-dependent random exchange potential caused by roughness of the interfaces.

The origin of GMR in granular systems has been studied by a number of theoretical groups [64–78]. In granular systems, the space distribution of the magnetic field, the electron spin diffusion process, and the spin transitions are much more complex than in multilayered systems. However, the dependence of $\Delta R/R$ on the particle size [79] suggests that magnetic scattering at the interfaces is responsible for the GMR in granular systems. Zhang and Levy have calculated the ensemble-averaged conductivity in terms of the average scattering in the medium and came to the very significant conclusion that GMR arises from spin-dependent scattering primarily at the interfaces [80]. The temperature dependence of the GMR has been attributed to spin-mixing scattering and reduced magnetization as a result of spin-wave excitations in the magnetic granules [81–83]. The effects of magnetic coupling between the granules on the GMR have also been extensively studied [84–89].

Since GMR is the result of the alignment of magnetic granules by an external magnetic field, which reduces the spin-dependent scattering of the system, a general observation is GMR $\propto (M/M_S)^2 = \langle \cos \theta \rangle^2$, where $M$ is the global magnetization, $M_S$ the saturation magnetization, $\theta$ the angle

between the magnetic moment of a granule and the external field, and $\langle \cos \theta \rangle$ the average value of $\cos \theta$ [4]. This angular dependence has been explained by Zhang and co-workers [58, 80, 90] and Asano et al. [91] based on the spin-dependent scattering at the granule–matrix interfaces.

That GMR is related to the *relative orientations* of the magnetic granules is a generally accepted concept and is experimentally demonstrated in trilayer or multilayered magnetic films, where the GMR varies linearly with the cosine of the relative angle between the moments of the magnetic layers [92–99]. For a granular system of random distribution, it can be easily shown that $\langle \cos \phi_{ij} \rangle = \langle \cos \theta \rangle^2$, where $\phi_{ij}$ is the relative angle between the magnetic axes of uncorrelated magnetic granules. Pogorelov et al. [100] have shown, using the microscopic theory of granular GMR, that the spin-dependent conductance in granular systems can be sensitive to the short-range magnetic order in addition to the long-range order and that GMR should be linearly proportional to an extra term $\langle \cos \phi_{ij} \rangle$. It is of interest to measure directly the resistance as a function of the relative orientation of the magnetic granules; however, controlling the relative angle between magnetic moments is difficult in granular systems. Dai and Tang have designed an experiment in which one can statistically adjust the relative angle $\phi$ between the magnetic moments of different granules in $Cu_{80}Co_{20}$ [101]. The moments of the granules are mostly aligned in the same direction by field cooling to low temperature in a high magnetic field. A small field applied at an angle relative to the cooling field rotates the moments of a portion of the granules that have small particle size and coercivity. It is found that the GMR varies linearly with $\cos \phi$. This behavior disappears if the sample is cooled in zero fields, or if the rotating field is too large or too small, or if the measuring temperature is higher than the blocking temperature. The results show that the GMR in granular structures has the same linear dependence as found in layered films and confirm the existing theories and recent microscopic models of granular GMR suggesting a crucial role of the relative orientations of the magnetic granules in determining the spin-dependent scattering.

## 3. TUNNELING MAGNETORESISTANCE

The large TMR found in the ferromagnet–insulator–ferromagnet (FM–I–FM) structure is due to the spin-dependent tunneling of electrons across the barrier [5–9]. It has attracted much attention partly because of the interesting problem of "spin tunneling" involved in such systems. It is now possible to reliably deposit tunnel junctions between ferromagnetic materials that show consistent TMR. Most of the tunnel barriers are made of $Al_2O_3$, although other materials are also used [102]. The field-dependent tunneling resistance arises from the tunneling probability, which depends on the density of states at the Fermi levels of the electrodes on either side of the barrier for a given spin channel. An applied field reorients the magnetic electrodes, thus changing the tunneling resistance. The essential features of the observed TMR can be explained by the models proposed by Julliere [5], Slonczewski [6], and others, although successful models are still needed to incorporate both the true band structure in the presence of the interfaces and the

dependence of the tunneling current on the barrier height and thickness [7]. In addition, spin-independent tunneling due to the presence of impurities in the barrier has been considered [103, 104].

Figure 1 shows a schematic view of the tunneling process between two magnetic electrodes involving spin-up and spin-down channels when a voltage is applied. The upper panel represents the situation when the two magnetic electrodes are aligned parallel to each other, and the lower panel represents the situation when the two electrodes are antiparallel. The total conductance of the magnetic tunnel junction is the sum of the two channels: one for spin-up electrons and the other for spin-down electrons. The conductance of each channel is proportional to the product of the densities of states at the Fermi level of the two electrodes. For parallel orientation of the magnetization of the two electrodes, the conductance $G_{\parallel}$ is proportional to $N_{1\uparrow}N_{2\uparrow} + N_{1\downarrow}N_{2\downarrow}$, where $N_{1\uparrow}$ is the density of states at the Fermi level of the first electrode for the spin-up channel. The meanings for the other symbols are self-explanatory. For antiparallel orientation, the conductance $G_{\uparrow\downarrow}$ is proportional to $N_{1\uparrow}N_{2\downarrow} + N_{1\downarrow}N_{2\uparrow}$. The difference between $G_{\parallel}$ and $G_{\uparrow\downarrow}$ is the change in conductance due to the reorientation of the two electrodes. It can be shown easily [5] that the magnetoresistance $\Delta R/R$ depends on the effective polarization of the tunneling electrons in a simple way

$$\Delta R/R = 2P_1 P_2/(1 + P_1 P_2) \qquad (1)$$

where $P_1$ and $P_2$ are the spin polarization ratios of the effective tunneling density of states in the two FM electrodes, $P_i = (N_{i\uparrow} - N_{i\downarrow})/(N_{i\uparrow} + N_{i\downarrow})$. Most of the magnetic tunnel junctions include a thin layer, for example, CoFe, between the NiFe electrode and the barrier to enhance the effects on the spin polarization of the tunneling electron. CoFe is used because it has a higher spin polarization than NiFe, but the latter is magnetically softer, which is suitable
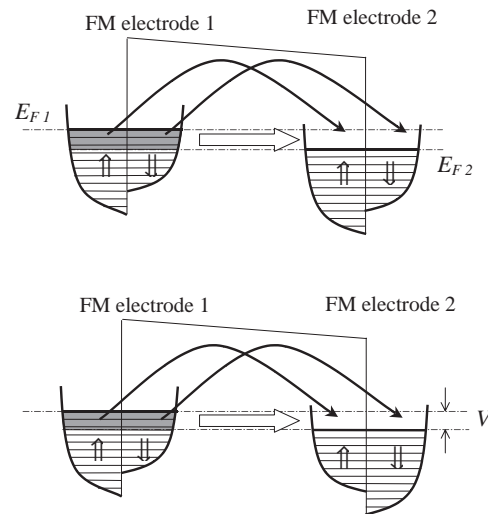


**Figure 1.** Schematic view of the tunneling process between two magnetic electrodes involving spin-up and spin-down channels when a voltage is applied. Upper panel, parallel alignment of the two electrodes; lower panel, antiparallel alignment.

for a free layer. An extremely large $\Delta R/R$ is expected when both electrodes are made of half-metallic materials in which the electrons are 100% spin polarized ($P_1 = P_2 = 1$). Examples of half-metallic materials include $CrO_2$, $Fe_3O_4$, $La_{0.7}Sr_{0.3}MnO_3$ perovskites and some of the Heusler alloys [105–110]. The half-metallicity of $CrO_2$, for example, has been demonstrated experimentally with a superconducting point contact experiment [111, 112] and vacuum tunneling measurement [113].

The principal advantage of a tunneling device is that the sense signal path does not have to carry a high current to get a large signal, and hence the settling time for the sense line voltage is eliminated, which offers potential for still faster read memory than those using conventional GMR structures. In addition, because of the tunneling device's high resistance, the signal levels could be sufficiently high to make simple direct sensing possible. The ability of using current-perpendicular-to-plane (CPP) geometry in a tunneling device eliminates several drawbacks associated with the current-in-plane (CIP) geometry such as shunting, channeling, and diffusive surface scattering. One added attractive feature of TMR devices is that the saturation field can be smaller than the GMR multilayers or spin valves.

TMR in granular materials originates from the tunneling of electrons from one grain to an adjacent grain across a barrier separating the two. It has been shown in a number of systems. It was first reported by Helman and Abeles in 1976 in a system where fine Ni grains (50 Å) are dispersed in $SiO_2$, which exhibits a large negative magnetoresistance [114]. Recent studies on granular TMR have been inspired by the TMR observed in simple tunnel junctions. Large negative and isotropic magnetoresistance was found in reactively sputtered Co–(Al, Si)–O and Fe–Mg–O thin films. The films have a two-phase nanostructure consisting of Co (Fe)–rich metallic magnetic grains and $Al_2O_3$ (or $SiO_2$/MgO) narrow intergrains [115]. Granular TMR and its characteristics have been investigated and reported in a number of similar systems where metallic magnetic nanoparticles are embedded in an insulating matrix [116–128].

Due to its half-metallic nature, very large TMR values have been reported in $CrO_2$ cold-pressed powders and polycrystalline thin films. A TMR ratio of 15%–50% can be reached [108, 109, 129]. The tunnel barrier here is a native surface layer of $Cr_2O_3$ surrounding the $CrO_2$ particles [130]. The TMR in these $CrO_2$ systems is well understood as the spin-dependent tunneling between the particles (in powder compacts) or grains (in films) across a grain boundary barrier, which is thus termed spin-dependent intergranular tunneling (Fig. 2). Magnetite ($Fe_3O_4$) is
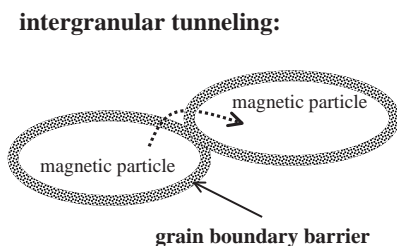
another very interesting half-metallic material besides $CrO_2$. Interesting magnetotransport properties have been reported in $Fe_3O_4$ powders and thin films, which are associated with the intergranular spin-dependent tunneling of electrons across the grain boundaries [107]. The magnetoresistance of $La_{0.67}Sr_{0.33}MnO_3$ polycrystalline ceramics [131] and $La_{0.67}Ca_{0.33}MnO_3$ and $La_{0.67}Sr_{0.33}MnO_3$ polycrystalline films [132] exhibits a sharp drop at low magnetic fields followed by a linear dependence at higher fields. The sharp drop has been attributed to spin-polarized tunneling between misaligned grains.

The switching field (the magnetic field at which a significant MR ratio has been reached) of systems of random grain orientation is quite large ($>1$ T), which is much higher than that required for most applications. The value of the switching field corresponds to the external field at which the magnetic moments of particles (grains) are reversed. Random orientation of moments causes the overall switching field to become much larger than the coercivity along the easy axis of a needle-shaped single particle. This problem can be solved by finding a way to align the $CrO_2$ single-crystal particles to the same orientation. The switching field can then be reduced theoretically to the coercive field of a single particle along its easy axis.

Since the magnetic moments of the needle-shaped $CrO_2$ single-crystal particles are along the easy axes ($c$ axes), the particles can be reoriented by applying a strong magnetic field. The aligned needle-shaped $CrO_2$ particles show very interesting MR characteristics with two well-separated peaks, similar to that of a single magnetic tunneling junction, as shown in Figure 3 [133]. Compared to the cold-pressed powders in which the particles have random orientations, the junction-like MR of the aligned powders is about 41%



**Figure 2.** Schematic view of intergranular tunneling.
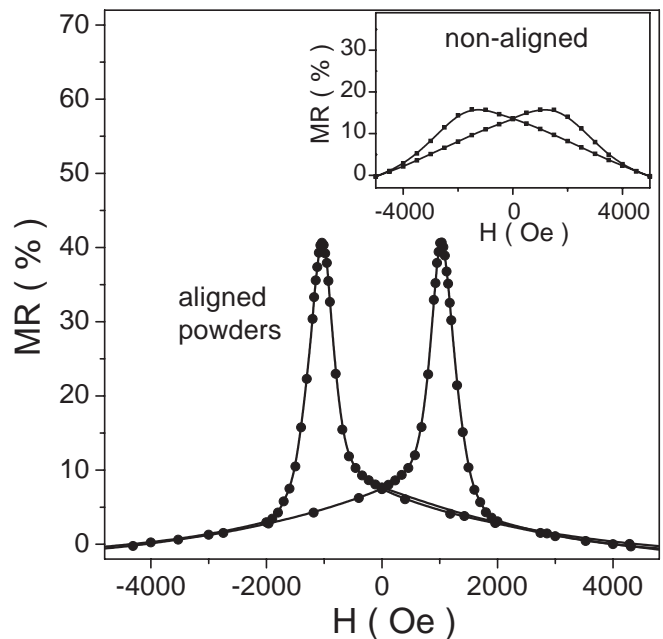


**Figure 3.** TMR of the aligned powders of $CrO_2$ at $T = 5$ K. Inset shows the MR of cold-pressed powders with random orientation over the same field range. Reprinted with permission from [133], J. Dai and J. Tang, *Phys. Rev. B* 63, 054434 (2001). © (2001), American Physical Society.

at $T = 5$ K, and the switching field significantly decreases to about $\pm 1000$ Oe. Notice that the resistance change is less than 5% for the random-oriented pressed powders over the same range of magnetic field (Fig. 3, inset). By using an alignment technique, a much larger MR ratio can be reached over a low field range (0–$\pm 1000$ Oe), which shows a much better switching behavior than that of the randomly oriented powder compacts.

Particle interface and grain boundaries play a very important role in the spin-dependent transport of half-metallic systems. The large TMR found in the cold-pressed and field-aligned $CrO_2$ nanoparticles is due to spin-dependent tunneling across the particle interface. Understanding the microstructure, composition, impurity level, and so on, of this barrier layer is important to further improve the TMR effect for practical purposes.

It has been suggested that the barriers in the granular $CrO_2$ systems are made of a native $Cr_2O_3$ layer on the surface of $CrO_2$ [109, 129, 134] since $Cr_2O_3$ is the most stable phase of $CrO_x$ [109, 135]. There has also been speculation that the surface layer is made of amorphous $CrO_2$ [135, 136] or even compounds such as CrOOH [137]. Experiments conducted recently provide direct evidence that the native surface layer of $Cr_2O_3$ is the tunnel barrier in $CrO_2$ granular systems [130]. Using transmission electron microscopy (TEM), a native oxide layer 1–3 nm thick has been directly observed on the surface of the $CrO_2$ single-crystal particles. X-ray photoelectron spectroscopy (XPS) results suggest that $Cr^{3+}$, not $Cr^{4+}$ as in $CrO_2$, dominates in the near surface region ($\sim$10 monolayers) of the $CrO_2$ particles. Combined TEM and X-ray diffraction slow-scan data indicate that the 1- to 3-nm-thick surface layer on the $CrO_2$ particles is not $CrO_2$ but $Cr_2O_3$ and confirm that the $Cr_2O_3$ layer is the tunnel barrier in the intergranular tunneling in $CrO_2$ systems.

$Cr_2O_3$ is an ideal and natural barrier material in granular $CrO_2$ systems due to its chemical stability and dense and uniform morphology. It is known that $CrO_2$ can be transformed into $Cr_2O_3$ by heating. The intergranular TMR ratio increases [129] after introducing more $Cr_2O_3$ into the $CrO_2$ particle interface by annealing. This may be due to either the increase in the thickness of the $Cr_2O_3$ surface layer or the precipitation of more $Cr_2O_3$ in the interface region. It may also be correlated to an improvement in the quality of the $Cr_2O_3$ barrier by heating. Detailed analysis of the effects of thermal annealing on the barrier quality is still lacking.

An unsolved problem of the TMR in $CrO_2$ half-metallic systems is the decrease in the TMR ratio with increasing temperature [138, 139]. It is usually reduced to less than 3% in $CrO_2$ systems and less than 7% for $Fe_3O_4$ at room temperature. Several mechanisms have been suggested to explain the temperature dependence of the TMR of the magnetic tunnel junctions. Coey et al. [129] suggested the existence of spin-flip processes introduced by the excitation of antiferromagnetic magnons in the interface layer or maybe the weakly exchange coupled $Cr^{3+}$ ions at the interfaces. The study of Watts et al. [140] showed the two-band magnetotransport in $CrO_2$ films and suggested a temperature-dependent spin-flip scattering corresponding to the temperature dependence of carrier mobilities and MR. It is also possible that the MR is reduced by the suppression of spin polarization $P$ at high temperature due to thermally excited surface spin waves [141]. Itoh et al. [142] presented a double-exchange model showing that $P$ decreases with increasing temperature; their calculated results also indicated that the MR can still be large considering the decrease in $P$. Guinea suggested that bulk magnon-assisted tunneling also reduces the MR [143]. Davis et al. have found that the magnetic band structure change due to Fermi smearing can be sufficient to account for the temperature dependence of the TMR in Co/I/Co junctions [144] although the temperature dependence in such junctions is much more gradual than that in $CrO_2$. To explain the rapid decrease in the MR with temperature in $CrO_2$ systems, one needs to take into account the hopping conductance via localized states in the barrier [141]. The suppression of MR at high temperature is found to be mainly due to the rapid increase in the spin-independent hopping channel with increasing temperature as will be discussed later although other mechanisms mentioned previously should still be considered.

## 4. COULOMB BLOCKADE

When an electron tunnels into a small particle or grain, it gives rise to an interesting phenomenon, Coulomb blockade (Fig. 2). Adding the electron to the particle increases the energy of the system by a charging term $E_c = e^2/2C$, where $e$ is the charge of the electron and $C$ the capacitance of the particle. The charging energy becomes large when the particle is very small. Tunneling is blocked unless the charging energy is overcome by thermal energy or applied bias voltage. The charging effect of the particles leads to single-electron tunneling represented by the Coulomb blockade of electric current below a threshold voltage and Coulomb staircase at higher voltages.

The conductance of intergranular tunneling is proportional to the tunneling matrix element $\exp[-2\chi s]$, where $s$ is the separation between the particles and $\chi = (2m\Phi/\hbar^2)^{1/2}$ ($m$ and $\Phi$ are the effective mass and barrier height, respectively) [145], and the population of a single particle $\exp[-E_c/2k_BT]$. The conductance is thus given by

$$G \propto \exp[-2\chi s - E_c/(2k_BT)] \qquad (2)$$

Sheng et al. [146] have made an assumption, when averaging over the distribution for particle size and separation, that the ratio of particle separation and particle size is constant. That is, $sE_c$ is a constant and $s\chi E_c = C$. Tunneling occurs mainly between particles with an optimum charging energy $E_c^0 = 2(Ck_BT)^{1/2}$ such that the conductance in (2) is maximized. The final temperature dependence of the conductance is given by

$$G \propto \exp[-2(C/k_BT)^{1/2}] \qquad (3)$$

The preceding temperature dependence has been observed in a wide range of granular systems where intergranular tunneling is at play. When the particles involved are magnetic, the tunneling is spin dependent and the conductance depends also on the global magnetization of the sample and the spin polarization of the magnetic particles. The

spin-dependent intergranular tunneling conductance $G_{SDT}$ as a function of temperature is then given by [147–149]

$$G_{SDT} = G_0(1 + P^2 m^2) \exp\left[-2(C/k_B T)^{1/2}\right] \quad (4)$$

where $P$ is the spin polarization, $m = M/Ms$ is the relative magnetization, and $G_0$ is a constant.

Coulomb blockade has been shown to enhance the TMR in granular systems at low temperatures due to amplified co-tunneling, where coherent tunneling through a double junction via a virtual intermediate state is energetically favorable [150–152]. Independent tunneling through the same double junction is, on the other hand, suppressed due to Coulomb blockade. Because the total resistance is proportional to the product of the junction resistance in the former case and proportional to the sum of the junction resistance in the latter, the TMR is enhanced when co-tunneling dominates. Other models have been proposed to explain the effects of Coulomb blockade on the TMR [153, 154]. Recent studies show oscillatory TMR behavior associated with the Coulomb staircase, which is based on the interplay of spin-dependent tunneling and single-electron tunneling [155–157].

The temperature dependence of the intergranular tunneling conductance of a cold-pressed $CrO_2$ nanoparticle compact is shown in Figure 4. Also shown is that of a sample annealed at high temperature so that it contains a substantial amount of $Cr_2O_3$. It is seen that the intergranular tunneling conductance follows a linear relationship between $\ln G$ and $1/T^{1/2}$ at low temperature ($<50$ K) and thus obeys the expression given in (4) for intergranular tunneling. This implies that intergranular tunneling is the major contribution to the conductance at low temperature [158].

When the temperature increases, the conductance becomes much greater than the intergranular tunneling given in (4), which indicates that another conduction channel becomes involved and plays a major role at high temperature. It is found that the additional conductance follows a power law of temperature, which is consistent with electron inelastic hopping through the localized states due to imperfections, impurities, and defects in the tunnel barrier.
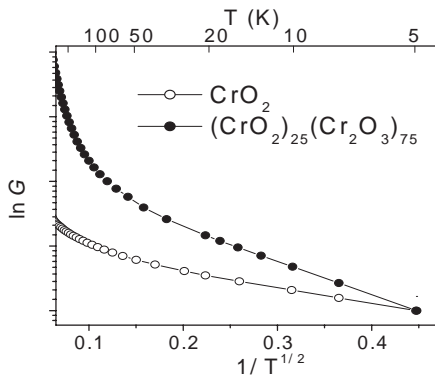
This channel is a spin-independent conducting channel since the electron flips its spin when it hops through the localized states.

It is known [159, 160] that the inelastic hopping conductance can be expressed as $G_{SI} \propto T^\gamma$, where $\gamma = N - [2/(N+1)]$ and $N$ is the number of localized states the electron hops through. A higher temperature, a higher level of impurity, and a thicker barrier can result in a higher order of inelastic hopping (greater $\gamma$). The total conductance $G$ of a powder compact is given by [158]

$$G = G_{SDT} + G_{SI} = C_1 \exp\left[-2(C/k_B T)^{1/2}\right] + C_2 T^\gamma \quad (5)$$

The experimental data on the $CrO_2$ powder compact and theoretical fits using (5) are shown in Figure 5. It is found the hopping conductance is dominated by the second-order hopping ($T^{1.33}$). The $I–V$ curves measured at room temperature also suggest the corresponding power law behavior [158]. As the temperature increases, the hopping channel becomes important. This spin-independent inelastic hopping conductance should be one of the main reasons for the rapid decrease in MR with increasing temperature [158, 161]. It is desirable to increase the TMR at room temperature by controlling the inelastic hopping conductance. As mentioned before, the suppression of TMR at high temperature may have more than one cause. The decrease in surface spin polarization, Fermi smearing, surface antiferromagnetic magnons, and bulk magnon-assisted tunneling also contribute to the decrease. Each mechanism has its own characteristic temperature and bias dependence. For example, surface spin polarization and bulk magnon-assisted tunneling both give $T^{3/2}$ dependence, but the former does not give rise to nonlinear $I–V$ characteristics [143]. Surface antiferromagnetic magnons, on the other hand, give rise to the $T^2$ and $V^2$ behaviors.

## 5. DOMAIN WALL RESISTANCE

The resistance due to domain walls has been controversial and not well understood although a large number of studies were devoted to the subject [162–166]. In fact, both positive



**Figure 4.** Temperature dependence of the conductance showing $G \propto \exp[-2(C/k_B T)^{1/2}]$ at low temperature for $CrO_2$ and $(CrO_2)_{25}(Cr_2O_3)_{75}$. Reprinted with permission from [158], J. Dai and J. Tang, *Phys. Rev. B* 63, 064410 (2001). © (2001), American Physical Society.
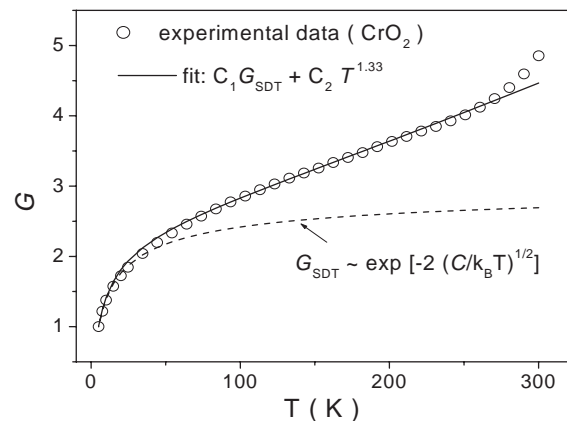


**Figure 5.** Experimental data fit with (5). As the temperature increases, a spin-independent channel, which follows a power law, becomes dominant. Reprinted with permission from [158], J. Dai and J. Tang, *Phys. Rev. B* 63, 064410 (2001). © (2001), American Physical Society.

and negative domain wall resistances have been reported and their origins are still being explored. One difficulty associated with the measurement of the domain wall resistance is the fact that it is always accompanied by anisotropic magnetoresistance and both are sensitive to the domain structure. One particular aspect of the domain wall resistance is analogous to GMR in magnetic multilayered films. As an electron passes from one domain to an adjacent one with different magnetic orientation, the effect resembles that of a GMR trilayer. However, the domain wall is usually too thick to exhibit large magnetoresistance because the electrons lose their spin memory before traveling through the domain wall. Attention has been paid to controlling the domain wall size to within several nanometers. A domain wall can be trapped in a structure of nanometer size, thus limiting the wall thickness. Recent reports have shown that two nanosized ferromagnetic tips contacting each other perpendicularly can have a large MR effect. An MR ratio of 300–3000% in Ni nanocontacts has been observed [167, 168]. $Fe_3O_4$ is especially interesting in light of very recent studies [169], in which 500% and larger MR is observed and attributed to transport of spin-polarized electrons through a narrow domain wall in a nanocontact of $Fe_3O_4$. Little is known about the connection, if any, between the negative MR and the existence of antiphase boundaries found in $Fe_3O_4$. It has been argued that the antiphase boundaries may become immobile magnetic domain walls [170]. It is of interest to study the MR due to pinned domain walls as their thickness can become smaller than the spin diffusion length and give large MR [167]. It is still a challenge to find a way to precisely fabricate patterned ferromagnetic nanocontact arrays to realize narrow domain wall thickness on, for example, Si chips.

# 6. MAGNETOTRANSPORT IN GRANULAR MATERIALS OF TWO-DIMENSIONAL WEAK LOCALIZATION

We have discussed the magnetoresistance of granular materials where at least one component is magnetic. However, interesting magnetotransport behaviors are not exclusive to such systems. Negative magnetoresistance (NMR) has been predicted by the weak localization theory in two-dimensional (2D) systems [171, 172], indicating that the localization effect could be destroyed when a magnetic field perpendicular to the film plane is applied. Previous experiments on metallic films [173–179] have shown NMR in a perpendicular field due to the suppression of the weak localization. It is known that the low-dimension effects become significant when the thickness of a sample is less than the Thouless length $L_T = (2l_{el}l_{in})^{1/2}$, where $l_{el}$ and $l_{in}$ are the elastic and inelastic scattering lengths, respectively. When the Landau orbital size $(\hbar c/eH)^{1/2}$ becomes close to $L_T$, the localization effect will be suppressed by applying a perpendicular magnetic field. The threshold field is given by

$$H_c^\perp = \hbar c/2el_{el}l_{in} \tag{6}$$

and the change in conductance is given by

$$\Delta\sigma_\perp = -\frac{e^2}{2\pi^2\hbar}\left[\ln\left(\frac{\hbar c}{2eHl_{el}l_{in}}\right) - \psi\left(\frac{1}{2} + \frac{\hbar c}{2eHl_{el}l_{in}}\right)\right] \tag{7}$$

where $\psi$ is the digamma function and $H$ is the perpendicular field. In the case of heavy metals, which have strong spin-orbit scattering, for example, in Au–Cu films [173, 175, 180], the MR may change sign.

Scaling theory suggests that there is no NMR in a strictly 2D system when the field is applied parallel to the film. In 1984, Altshuler and Aronov [181] predicted that, due to the finite thickness of a thin film, there is a negative magnetoresistance in the parallel field (NMR$_\parallel$). The magnetoresistance in a parallel field is given by

$$\Delta\sigma_\parallel = \frac{e^2}{2\pi^2\hbar}\ln\left(\frac{t^2L_T^2}{12L_H^4} + 1\right) \tag{8}$$

where $t$ is the film thickness and $L_H = (\hbar c/eH)^{1/2}$ is the Landau orbit size. One sees that the NMR$_\parallel$ will become 0 when the thickness $t = 0$. Equation (8) can be understood considering this is an orbit effect and the NMR$_\parallel$ does not vanish until the film thickness equals 0. No significant parallel field NMR$_\parallel$ has been observed in previous experiments on homogeneous metallic films. According to [179], this is because of the following

$$\Delta\sigma_\parallel/\Delta\sigma_\perp = 2t^2/L_T^2 \ll 1 \tag{9}$$

where one can see that the NMR$_\parallel$ is generally very small for ultrathin films. For a parallel field, the characteristic field strength is much stronger [181] than the field applied perpendicular to the film plane

$$H_C^\parallel \approx \frac{\hbar c}{et\sqrt{l_{el}l_{in}}} \tag{10}$$

The localization effect of highly inhomogeneous 2D systems of granular films has only been studied to a limited extent. Bergmann [175] has pointed out that weak localization may still exist in these systems. Unique MR effects have been reported in granular island-like ultrathin nonmagnetic Cu films [182]. The NMR has been observed in both perpendicular ($H_\perp$) and parallel ($H_\parallel$) magnetic fields. A large NMR$_\perp$ in a perpendicular field has been found which follows $\ln H$ in high field as suggested in (7). A large NMR$_\parallel$ is observed and is close to the prediction given by [181]. The large NMR$_\parallel$ is due to the island-like granular structure, and it has not been previously observed in homogeneous Cu films [173–175]. The Thouless length $L_T$ and effective Landau orbit size $L_H$ can be statistically reduced by the granular structure. Since the ratio of $\Delta\sigma_\parallel/\Delta\sigma_\perp$ is determined by $2t^2/L_T^2$, a reduction in $L_T^2$ leads to a relatively increased $\Delta\sigma_\parallel$. This provides a good explanation as to why the NMR$_\parallel$ has been observed in granular Cu samples but not in previous experiments on homogeneous Cu films. That island-like geometry leads to relatively large NMR$_\parallel$ is also consistent with the experimental results by Komori et al. [180], which has shown a large NMR$_\parallel$ in highly inhomogeneous Cu–Cu oxide mixture films although the mechanism was not explicitly given. Compared to the homogeneous films, it is seen that the Thouless length and electron orbit size are affected by the geometry of the granular structure.

## 7. SUMMARY

It has become increasingly evident that the spin degree of freedom of electrons, in addition to the charge, will become an integrated part of semiconductor-based electronics. Spin-dependent transport forms the backbone of such technology. Some GMR- and TMR-based devices have already found applications as field sensors and nonvolatile magnetic memories, MRAMs. Although it is not clear at present whether GMR and TMR in granular systems will be technologically competitive with their counterparts in multilayered films, the study of these phenomena has led to interesting discoveries and better understanding of the physics involved. As one explores magnetotransport in granular systems, one finds the fascinating physics of spin-dependent scattering and spin-dependent tunneling, which are the basis for GMR and TMR. Readers are referred to some of the excellent review articles for a more thorough discussion of these subjects [183–187]. Magnetic tunnel junctions made of half-metals, whose spin polarization is close to 100%, are expected to play a major role in the future materials of spin-dependent tunneling because of their large magnetoresistance. Although not discussed at length in this review, the interplay between spin-dependent tunneling and Coulomb blockade is intriguing. Since the sizes of the particles we deal with here are in the nanometer range, blockade due to charging of the particles when an electron tunnels into them becomes an important factor in determining the transport. Some of the recent research interests in this area are single-electron tunneling and the interplay between magnetotransport and the Coulomb staircase. The exact nature of the domain wall resistance is still being explored, yet it has shown one of the largest magnetoresistances to date when the domain wall thickness is appropriately controlled. Equally interesting is the magnetotransport in nonmagnetic granular systems. An example is presented in the last part of the review. Many challenges lie ahead. It is desirable to be able to control the particle sizes within a very small distribution and model realistically the spin-dependent scattering in granular GMR systems. It is also challenging to deal with the issue of the temperature dependence of the TMR in some of the half-metallic systems. To make the granular systems more technologically relevant, the switching field needs to be further reduced. The prospect for research in granular transport is promising. With the advances in nanotechnology and the ability to make granular materials of patterned structure, exciting discoveries and possible new applications of spin-dependent transport in granular systems can be expected.

## GLOSSARY

**Coulomb blockade** Blockade of the conduction of electrons due to the Coulomb charging energy associated with the small size of the grains and particles.

**Giant magnetoresistance (GMR)** Large magnetoresistance due to scattering of the conduction electrons by magnetic nanoparticles or layers in films.

**Half-metal** A magnetic material that is metallic for one spin direction but has a gap at the Fermi level for the other spin direction.

**Magnetic random access memory (MRAM)** An integrated magnetic memory that uses magnetic storage and magnetoresistive reading with semiconductor support circuits.

**Spin polarization** The percentage of extra electrons having majority spins.

**Tunneling magnetoresistance (TMR)** Magnetoresistance due to electron tunneling between two magnetic electrodes across a nonmagnetic barrier.

## REFERENCES

1. M. N. Baibich, J. M. Broto, A. Fert, F. Nguyen van Dau, F. Petroff, P. Etienne, G. Creuzet, A. Friederich, and J. Chazeles, *Phys. Rev. Lett.* 61, 2472 (1988).
2. S. S. P. Parkin, R. Bhadra, and K. P. Roche, *Phys. Rev. Lett.* 66, 2152 (1991).
3. A. E. Berkowitz, J. R. Mitchell, M. J. Carey, A. P. Young, S. Zhang, F. E. Spada, F. T. Parker, A. Hutten, and G. Thomas, *Phys. Rev. Lett.* 68, 3745 (1992).
4. J. Q. Xiao, J. S. Jiang, and C. L. Chien, *Phys. Rev. Lett.* 68, 3749 (1992)
5. M. Julliere, *Phys. Lett. A* 54, 225 (1975).
6. J. C. Slonczewski, *Phys. Rev. B* 39, 6995 (1989).
7. J. M. Maclaren, X. G. Zhang, and W. H. Bulter, *Phys. Rev. B* 56, 11827 (1997).
8. J. S. Moodera, L. R. Kinder, T. M. Wong, and R. Meservey, *Phys. Rev. Lett.* 74, 3273 (1995).
9. J. S. Moodera and L. R. Kinder, *J. Appl. Phys.* 79, 4724 (1996).
10. J. Dai, J. Tang, S. T. Hsu, and W. Pan, *J. Nanosci. Nanotechnol.* 2, 281 (2002).
11. S. S. Saxena, J. Tang, Y. S. Lee, and C. J. O'Connor, *J. Appl. Phys.* 76, 6820 (1994).
12. K. Ounadjela, A. Herr, R. Poinsot, J. M. D. Coey, A. Fagan, C. R. Staddon, D. Daniel, J. F. Gregg, S. M. Thompson, K. O'Grady, and S. Grieves, *J. Appl. Phys.* 75, 6921 (1994).
13. J. S. Jiang, J. Pearson, D. Hinks, and S. D. Bader, *J. Appl. Phys.* 82, 4435 (1997).
14. J. Wecker, R. von Helmolt, L. Schultz, and K. Samwer, *Appl. Phys. Lett.* 62, 1985 (1993).
15. M. Rubinstein, V. G. Harris, B. N. Das, and N. C. Koon, *Phys. Rev. B* 50, 12550 (1994).
16. B. J. Hickey, M. A. Howson, S. O. Musa, and N. Wiser, *Phys. Rev. B* 51, 667 (1995).
17. C. S. Martins, H. R. Rechenberg, and F. P. Missell, *J. Appl. Phys.* 83, 7001 (1998).
18. L. H. Chen, S. Jin, T. H. Tiefel, S. H. Chang, M. Eibschutz, and R. Ramesh, *Phys. Rev. B* 49, 9194 (1994).
19. J. Tang, K.-Y. Wang, L. Spinu, H. Srikanth, P. J. Schilling, and N. Moelders, *J. Magn. Magn. Mater.* 249, 73 (2002).
20. T. Cohen-Hyams, W. D. Kaplan, D. Aurbach, Y. S. Cohen, and J. Yahalom, *J. Electrochem. Soc.* 150, C28 (2003).
21. F. C. S. da Silva, E. F. Ferrari, and M. Knobel, *J. Appl. Phys.* 84, 5366 (1998).
22. P. Allia, M. Knobel, P. Tiberto, and F. Vinai, *Phys. Rev. B* 52, 15398 (1995).
23. R. H. Yu, X. X. Zhang, J. Tejada, J. Zhu, M. Knobel, P. Tiberto, P. Allia, and F. Vinai, *J. Appl. Phys.* 78, 5062 (1995).
24. W. Zhang, I. W. Boyd, N. S. Cohen, Q. T. Bui, Q. A. Pankhurst, M. Elliott, and W. Herrenden-Harkerand, *J. Appl. Phys.* 81, 5211 (1997).
25. F. Parent, J. Tuaillon, L. B. Stern, V. Dupuis, B. Prevel, A. Perez, P. Melinon, G. Guiraud, R. Morel, A. Barthélémy, and A. Fert, *Phys. Rev. B* 55, 3683 (1997).
26. H. Sang, N. Xu, J. H. Du, G. Ni, S. Y. Zhang, and Y. W. Du, *Phys. Rev. B* 53, 15023 (1996).

27. L. Dimesso and H. Hahn, *J. Appl. Phys.* 84, 953 (1998).
28. J. C. Soares, L. M. Redondo, C. M. de Jesus, J. G. Marques, M. F. da Silva, M. M. Pereira de Azevedo, J. A. Mendes, M. S. Rogalski, and J. B. Sousa, *J. Vac. Sci. Technol. A* 16, 1812 (1998).
29. A. Tsoukatos, H. Wan, G. C. Hadjipanayis, and Z. G. Li, *Appl. Phys. Lett.* 61, 3059 (1992).
30. K. R. Coffey, T. L. Hylton, M. A. Parker, and J. K. Howard, *Appl. Phys. Lett.* 63, 1579 (1993).
31. T. A. Rabedeau, M. F. Toney, R. F. Marks, S. S. P. Parkin, R. F. C. Farrow, and G. R. Harp, *Phys. Rev. B* 48, 16810 (1993).
32. R. J. Gambino, T. R. McGuire, J. M. E. Harper, and C. Cabral, Jr., *J. Appl. Phys.* 75, 6909 (1994).
33. N. Thangaraj, C. Echer, K. M. Krishnan, R. F. C. Farrow, R. F. Marks, and S. S. P. Parkin, *J. Appl. Phys.* 75, 6900 (1994).
34. P. Panissod, M. Malinowska, E. Jedryka, M. Wojcik, S. Nadolski, M. Knobel, and J. E. Schmidt, *Phys. Rev. B* 63, 014408 (2001).
35. A. Milner, A. Gerber, B. Groisman, M. Karpovsky, and A. Gladkikh, *Phys. Rev. Lett.* 76, 475 (1996).
36. F. Badía, A. Labarta, X. Batlle, and M. L. Watson, *J. Appl. Phys.* 76, 6481 (1994).
37. K. Pettit, E. Kita, K. Araga, A. Tasaki, and M. B. Salamon, *J. Appl. Phys.* 75, 6918 (1994).
38. U. Brüx, T. Schneider, M. Acet, and E. F. Wassermann, *Phys. Rev. B* 52, 3042 (1995).
39. T. W. Kim, R. J. Gambino, and T. R. McGuire, *J. Appl. Phys.* 89, 7299 (2001).
40. J. He, Z. D. Zhang, J. P. Liu, and D. J. Sellmyer, *Appl. Phys. Lett.* 80, 1779 (2002).
41. A. Tsoukatos, D. V. Dimitrov, A. S. Murthy, and G. C. Hadjipanayis, *J. Appl. Phys.* 76, 6799 (1994).
42. D. J. Kubinski and H. Holloway, *J. Appl. Phys.* 77, 2508 (1995).
43. A. García Prieto, M. L. Fdez-Gubieda, C. Meneghini, and A. García-Arribas, *J. Appl. Phys.* 91, 8596 (2002).
44. M. B. Stearns and Y. Cheng, *J. Appl. Phys.* 75, 6894 (1994).
45. W. Wang, F. Zhu, J. Weng, J. Xiao, and W. Lai, *Appl. Phys. Lett.* 72, 1118 (1998).
46. D. J. Kubinski and H. Holloway, *J. Appl. Phys.* 77, 2010 (1995).
47. K. Ounadjela, S. M. Thompson, J. F. Gregg, A. Azizi, M. Gester, and J. P. Deville, *Phys. Rev. B* 54, 12252 (1996).
48. H. Vrenken, B. J. Kooi, and J. Th. M. De Hosson, *J. Appl. Phys.* 89, 3381 (2001).
49. F. Petroff, A. Barthelemy, D. H. Mosca, D. K. Lottis, A. Fert, P. A. Schroeder, W. P. Pratt, Jr., R. Loloee, and S. Lequien, *Phys. Rev. B* 44, 5355 (1991).
50. W. P. Pratt, Jr., S. F. Lee, J. M. Slaughter, R. Loloee, P. A. Schroeder, and J. Bass, *Phys. Rev. Lett.* 66, 3060 (1991).
51. E. E. Fullerton, D. M. Kelly, J. Guimpel, I. K. Schuller, and Y. Bruynseraede, *Phys. Rev. Lett.* 68, 859 (1992).
52. L. M. Falicov, D. T. Pierce, S. D. Bader, R. Gronsky, K. B. Hathaway, H. J. Hopster, D. N. Lambeth, S. S. P. Parkin, G. Prinz, M. Salamon, I. K. Schuller, and R. H. Victora, *J. Mater. Res.* 5, 1299 (1990).
53. R. L. White, *IEEE Trans. Magn.* 28, 2482 (1992).
54. S. S. P. Parkin, Z. G. Li, and D. J. Smith, *Appl. Phys. Lett.* 58, 2710 (1991).
55. R. E. Camley and J. Barnas, *Phys. Rev. Lett.* 63, 664 (1989).
56. A. Barthelemy and A. Fert, *Phys. Rev. B* 43, 13124 (1991).
57. P. M. Levy and S. Zhang, *Phys. Rev. Lett.* 65, 1643 (1990).
58. S. Zhang, P. M. Levy, and A. Fert, *Phys. Rev. B* 45, 8689 (1992).
59. R. E. Camley and R. L. Stamps, *J. Phys.: Condens. Matter* 5, 3727 (1993).
60. E. Camblong and P. M. Levy, *Phys. Rev. Lett.* 69, 2835 (1992).
61. S. Zhang and P. M. Levy, *Phys. Rev. Lett.* 77, 916 (1996).
62. S. S. P. Parkin, R. F. Marks, and R. F. C. Farrow, "Proceedings of the 13th International Colloquium on Magnetic Films and Surfaces," 1991.
63. H. Itoh, J. Inoue, and S. Maekawa, *Phys. Rev. B* 47, 5809 (1993).
64. S. Zhang, *Appl. Phys. Lett.* 61, 1855 (1992).
65. M. R. Parker, J. A. Barnard, D. Seale, and A. Waknis, *J. Appl. Phys.* 73, 5512 (1993).
66. L. Sheng, H. Y. Teng, and D. Y. Xing, *Phys. Rev. B* 58, 6428 (1998).
67. D. Kechrakos and K. N. Trohidou, *J. Appl. Phys.* 89, 7293 (2001).
68. E. F. Ferrari, F. C. S. da Silva, and M. Knobel, *Phys. Rev. B* 59, 8412 (1999).
69. R. Yang, W. Zhang, and W. J. Song, *J. Appl. Phys.* 84, 2044 (1998).
70. R. Y. Gu, L. Sheng, D. Y. Xing, Z. D. Wang, and J. M. Dong, *Phys. Rev. B* 53, 11685 (1996).
71. L. Sheng, Z. D. Wang, D. Y. Xing, and J.-X. Zhu, *Phys. Rev. B* 53, 8203 (1996).
72. C. Xiao, J. Yang, K. Deng, and K. Wang, *Phys. Rev. B* 55, 3677 (1997).
73. L. Xing and Y.-C. Chang, *Phys. Rev. B* 48, 4156 (1993).
74. L. Sheng, D. Y. Xing, Z. D. Wang, and J. Dong, *Phys. Rev. B* 55, 5908 (1997).
75. P.-B. Zhao and F.-C. Pu, *Phys. Rev. B* 51, 11603 (1995).
76. J. F. Gregg, W. Allen, S. M. Thompson, M. L. Watson, and G. A. Gehring, *J. Appl. Phys.* 79, 5593 (1996).
77. E. F. Ferrari, F. C. S. da Silva, and M. Knobel, *Phys. Rev. B* 56, 6086 (1997).
78. M. Rubinstein, *Phys. Rev. B* 50, 3830 (1994).
79. P. Xiong, G. Xiao, J. Q. Wang, J. Q. Xiao, J. S. Jiang, and C. L. Chien, *Phys. Rev. Lett.* 69, 3220 (1992).
80. S. Zhang and P. M. Levy, *J. Appl. Phys.* 73, 5315 (1993).
81. A. Gerber, A. Milner, I. Ya. Korenblit, M. Karpovsky, A. Gladkikh, and A. Sulpice, *Phys. Rev. B* 57, 13667 (1998).
82. R. H. Yu, J. Zhu, X. X. Zhang, and J. Tejada, *J. Appl. Phys.* 83, 3134 (1998).
83. J.-Q. Wang and G. Xiao, *Phys. Rev. B* 50, 3423 (1994).
84. J. Viana Lopes, J. M. B. Lopes dos Santos, and Yu. G. Pogorelov, *Phys. Rev. B* 66, 064416 (2002).
85. L. G. Pereira and M. N. Baibich, *AIP Conf. Proc.* 378, 492 (1996).
86. M. El-Hilo, R. W. Chantrell, and K. O'Grady, *J. Appl. Phys.* 84, 5114 (1998).
87. D. Kechrakos and K. N. Trohidou, *Phys. Rev. B* 62, 3941 (2000).
88. D. Altbir, J. d'Albuquerque e Castro, and P. Vargas, *Phys. Rev. B* 54, R6823 (1996).
89. M. El-Hilo, K. O'Grady, and R. W. Chantrell, *J. Appl. Phys.* 76, 6811 (1994).
90. H. Camblong, S. Zhang, and P. M. Levy, *Phys. Rev. B* 51, 16052 (1995).
91. Y. Asano, A. Oguri, J. Inoue, and S. Maekawa, *Phys. Rev. B* 49, 12831 (1994).
92. P. Dauguet, P. Gandit, J. Chaussy, S. F. Lee, A. Fert, and P. Holody, *Phys. Rev. B* 54, 1083 (1996).
93. B. Dieny, V. S. Speriosu, S. S. P. Parkin, B. A. Gurney, D. R. Wilhoit, and D. Mauri, *Phys. Rev. B* 43, 1297 (1991).
94. B. Dieny, C. Cowache, A. Nossov, P. Dauguet, J. Chaussy, and P. Gandit, *J. Appl. Phys.* 79, 6370 (1996).
95. A. Chaiken, G. A. Prinz, and J. J. Krebs, *J. Appl. Phys.* 67, 4892, (1990).
96. S. Mao, M. Plumer, A. Mack, Z. Yang, and E. Murdock, *J. Appl. Phys.* 85, 5033 (1999).
97. M. Xu and Z. Mai, *Phys. Rev. B* 60, 9224 (1999).
98. J. Barnas, O. Baksalary, and A. Fert, *Phys. Rev. B* 56, 6079 (1997).
99. A. V. Vedyaev, O. A. Kotel'nikova, N. G. Pugach, and M. G. Chshiev, *Phys. Solid State* 41, 1665 (1999).
100. Y. G. Pogorelov, M. M. P. de Azevedo, and J. B. Sousa, *Phys. Rev. B* 58, 425 (1998).
101. J. Dai and J. Tang, *Appl. Phys. Lett.* 76, 3968 (2000).
102. C. L. Platt, B. Dieny, and A. E. Berkowitz, *Appl. Phys. Lett.* 69, 2291 (1996).
103. A. M. Bratkovsky, *Phys. Rev. B* 56, 2344 (1997); A. M. Bratkovsky, *Appl. Phys. Lett.* 72, 2334 (1998).
104. C. T. Tanaka and J. S. Moodera, *J. Appl. Phys.* 79, 6265 (1996).

*105.* K. Ghosh, S. B. Ogale, S. P. Pai, M. Robson, E. Li, I. Jin, Z. Dong, R. L. Greene, R. Ramesh, T. Venkatesan, and M. Johnson, *Appl. Phys. Lett.* 73, 689 (1998).

*106.* H. van Leuken and R. A. de Groot, *Phys. Rev. B* 51, 7176 (1995).

*107.* J. M. D. Coey, A. E. Berkowitz, L. Balcells, F. F. Putris, and F. T. Parker, *Appl. Phys. Lett.* 72, 734 (1998).

*108.* H. Y. Hwang and S.-W. Cheong, *Science* 278, 1607 (1997).

*109.* S. S. Manoharan, D. Elefant, G. Reiss, and J. B. Goodenough, *Appl. Phys. Lett.* 72, 984 (1998).

*110.* C. L. Platt, B. Dieny, and A. E. Berkowitz, *J. Appl. Phys.* 81, 5523 (1997).

*111.* R. J. Soulen, J. M. Byers, M. S. Osofsky, B. Nadgorny, T. Ambrose, S. F. Cheng, P. R. Broussard, C. T. Tanaka, J. Nowak, J. S. Moodera, A. Barry, and J. M. D. Coey, *Science* 282, 85 (1998).

*112.* Y. Ji, G. J. Strijkers, F. Y. Yang, C. L. Chien, J. M. Byers, A. Anguelouch, G. Xiao, and A. Gupta, *Phys. Rev. Lett.* 86, 5585 (2001).

*113.* R. Wiesendanper, H. J. Guntherodt, G. Guntherodt, R. J. Gambino, and R. Ruf, *Phys. Rev. Lett.* 65, 247 (1990).

*114.* J. S. Helman and B. Abeles, *Phys. Rev. Lett.* 37, 1429 (1976).

*115.* H. Fujimori, S. Mitani, and S. Ohnuma, *J. Appl. Phys.* 79, 4733, (1996).

*116.* K. Ono, C. Yasui, H. Yanagihara, T. Koyano, K. Ota, and E. Kita, *Jpn. J. Appl. Phys., Part 1* 41, 97 (2002).

*117.* B. Hackenbroich, H. Zare-Kolsaraki, and H. Micklitz, *Appl. Phys. Lett.* 81, 514 (2002).

*118.* T. Furubayashi and I. Nakatani, *J. Appl. Phys.* 79, 6258 (1996).

*119.* K. Inomata, H. Ogiwara, Y. Saito, K. Yusu, and K. Ichihara, *Jpn. J. Appl. Phys., Part 2* 36, L1380 (1997).

*120.* S. Honda, T. Okada, M. Nawate, and M. Tokumoto, *Phys. Rev. B* 56, 14566 (1997).

*121.* Q. Y. Xu, G. Ni, H. Sang, and Y. W. Du, *J. Appl. Phys.* 87, 3421, (2000).

*122.* Y.-H. Huang, J.-H. Hsu, J. W. Chen, and C.-R. Chang, *Appl. Phys. Lett.* 72, 2171 (1998).

*123.* A. Y. Vovk, J.-Q. Wang, W. Zhou, J. He, A. M. Pogoriliy, O. V. Shypil, A. F. Kravets, and H. R. Khan, *J. Appl. Phys.* 91, 10017, (2002).

*124.* T. Zhu, Y. J. Wang, H. W. Zhao, J. G. Zhao, and W. S. Zhan, *J. Appl. Phys.* 89, 6877 (2001).

*125.* S. Sankar, A. E. Berkowitz, and D. J. Smith, *Phys. Rev. B* 62, 14273 (2000).

*126.* D. K. Petrov, L. Krusin-Elbaum, J. Z. Sun, C. Feild, and P. R. Duncombe, *Appl. Phys. Lett.* 75, 995 (1999).

*127.* M. A. S. Boff, J. Geshev, J. E. Schmidt, W. H. Flores, A. B. Antunes, M. A. Gusmão, and S. R. Teixeira, *J. Appl. Phys.* 91, 9909 (2002).

*128.* D. L. Peng, K. Sumiyama, T. J. Konno, T. Hihara, and S. Yamamuro, *Phys. Rev. B* 60, 2093 (1999).

*129.* J. M. D. Coey, A. E. Berkowitz, L. Balcells, and F. F. Putris, *Phys. Rev. Lett.* 80, 3815 (1998).

*130.* J. Dai, J. Tang, H. Xu, L. Spinu, W. Wang, K.-Y. Wang, A. Kumbhar, M. Li, and U. Diebold, *Appl. Phys. Lett.* 77, 2840 (2000).

*131.* H. Y. Hwang, S.-W. Cheong, N. P. Ong, and B. Batlogg, *Phys. Rev. Lett.* 77, 2041 (1996).

*132.* A. Gupta, G. Q. Gong, G. Xiao, P. R. Duncombe, P. Lecoeur, P. Trouilloud, Y. Y. Wang, V. P. Dravid, and J. Z. Sun, *Phys. Rev. B* 54, R15629 (1996).

*133.* J. Dai and J. Tang, *Phys. Rev. B* 63, 054434 (2001).

*134.* A. Barry, J. M. D. Coey, and M. Viret, *J. Phys: Condens. Matter* 12, L173 (2000).

*135.* K. P. Kamper, W. Schmitt, and G. Guntherodt, *Phys. Rev. Lett.* 59, 2788 (1987).

*136.* N. Heiman and N. S. Kazama, *J. Appl. Phys.* 50, 7633 (1979).

*137.* M. Essig, M. W. Muller, and E. Schwab, *IEEE Trans. Magn.* 26, 69 (1990).

*138.* S. Mitani, K. Takanashi, K. Yakushiji, and H. Fujimori, *J. Appl. Phys.* 83, 6524 (1998).

*139.* G. J. Strijkers, H. J. M. Swagten, B. Rulkens, R. H. J. N. Bitter, W. J. M. de Jonge, P. J. H. Bloemen, and K. M. Schep, *J. Appl. Phys.* 84, 2749 (1998).

*140.* S. M. Watts, S. Wirth, S. V. Molnar, A. Barry, and J. M. D. Coey, *Phys. Rev. B* 61, 9621 (2000).

*141.* C. H. Shang, J. Nowak, R. Jansen, and J. S. Moodera, *Phys. Rev. B* 58, 2917 (1998).

*142.* H. Itoh, T. Ohsawa, and J. Inoue, *Phys. Rev. Lett.* 84, 2501 (2000).

*143.* F. Guinea, *Phys. Rev. B* 58, 9212 (1998).

*144.* A. H. Davis, J. M. MacLaren, and P. LeClair, *J. Appl. Phys.* 89, 7567 (2001).

*145.* J. G. Simmons, *J. Appl. Phys.* 34, 1793 (1963).

*146.* P. Sheng, B. Abeles, and Y. Arie, *Phys. Rev. Lett.* 31, 44 (1973).

*147.* S. Mitani, S. Takahashi, K. Takanashi, K. Yakushiji, S. Maekawa, and H. Fujimori, *Phys. Rev. Lett.* 81, 2799 (1998).

*148.* J. Inoue and S. Maekawa, *Phys. Rev. B* 53, 11927 (1996).

*149.* T. Zhu and Y. J. Wang, *Phys. Rev. B* 60, 11918 (1999).

*150.* S. Takahashi and S. Maekawa, *Phys. Rev. Lett.* 80, 1758 (1998).

*151.* S. Ju and Z.-Y. Li, *J. Appl. Phys.* 92, 5281 (2002).

*152.* F. Fettar, S.-F. Lee, F. Petroff, A. Vaures, P. Holody, L. F. Schelp, and A. Fert, *Phys. Rev. B* 65, 174415 (2002).

*153.* M. B. A. Jalil, *J. Appl. Phys.* 91, 7628 (2002).

*154.* M. García-Hernández, F. Guinea, A. de Andrés, J. L. Martínez, C. Prieto, and L. Vázquez, *Phys. Rev. B* 61, 9549 (2000).

*155.* K. Yakushiji, S. Mitani, K. Takanashi, and H. Fujimori, *J. Appl. Phys.* 91, 7038 (2002).

*156.* H. Imamura, *Phys. Rev. B* 61, 46 (2000).

*157.* K. Yakushiji, S. Mitani, K. Takanashi, S. Takahashi, and S. Maekawa, H. Imamura, and H. Fujimori, *Appl. Phys. Lett.* 78, 515 (2001).

*158.* J. Dai and J. Tang, *Phys. Rev. B* 63, 064410 (2001).

*159.* L. I. Glazman and K. A. Matveev, *Zh. Eksp. Teor. Fiz.* 94, 332, (1988) [*Sov. Phys. JEPT* 67, 1276 (1988)].

*160.* Y. Xu, D. Ephron, and M. R. Beasley, *Phys. Rev. B* 52, 2843 (1995).

*161.* L. V. Lutsev, Yu. E. Kalinin, A. V. Sitnikov, and O. V. Stogne, *Phys. Solid State* 44, 1889 (2002).

*162.* A. D. Kent, U. Rûdiger, J. Yu, L. Thomas, and S. S. P. Parkin, *J. Appl. Phys.* 85, 5243 (1999).

*163.* G. R. Taylor, A. Isin, and R. V. Coleman, *Phys. Rev.* 165, 621 (1968).

*164.* P. M. Levy and S. Zhang, *Phys. Rev. Lett.* 79, 5110 (1997).

*165.* J. F. Gregg, W. Allen, K. Ounadjela, M. Viret, M. Hehn, S. M. Thompson, and J. M. D. Coey, *Phys. Rev. Lett.* 77, 1580 (1996).

*166.* M. Viret, D. Vignoles, D. Cole, J. M. D. Coey, W. Allen, D. S. Daniel, and J. F. Gregg, *Phys. Rev. B* 53, 8464 (1996).

*167.* G. Tatara, Y.-W. Zhao, M. Muñoz, and N. García, *Phys. Rev. Lett.* 83, 2030 (1999).

*168.* H. D. Chopra and S. Z. Hua, *Phys. Rev. B* 66, 020403(R) (2002).

*169.* J. J. Versluijs, M. A. Bari, and J. M. D. Coey, *Phys. Rev. Lett.* 87, 026601 (2001).

*170.* D. T. Margulies, F. T. Parker, M. L. Rudee, F. E. Spada, J. N. Chapman, P. R. Aitchison, and A. E. Berkowitz, *Phys. Rev. Lett.* 79, 5162 (1997).

*171.* B. L. Altshuler, D. Khmel'nitzkii, A. I. Larkin, and P. A. Lee, *Phys. Rev. B* 22, 5142 (1980).

*172.* S. Hikami, A. I. Larkin, and Y. Nagaoka, *Prog. Theor. Phys.* 63, 707 (1980).

*173.* C. Van Hesendonck, L. Van den Dries, Y. Bruynseraede, and G. Deutscher, *Phys. Rev. B* 25, 5090 (1982).

*174.* L. Van den Dries, C. Van Haesendonck, Y. Bruyn-seraede, and G. Deutscher, *Phys. Rev. Lett.* 46, 565 (1981).

*175.* G. Bergmann, *Phys. Rep.* 1, 107 (1984).

*176.* R. S. Markiewicz and L. A. Harris, *Phys. Rev. Lett.* 46, 1149 (1981).

177. N. Giordano and M. A. Pennington, *Phys. Rev. B* 47, 9693 (1993).
178. S. Hsu and J. M. Valles, *Phys. Rev. B* 74, 2331 (1995).
179. R. S. Markiewicz and C. J. Rollins, *Phys. Rev. B* 29, 735 (1984).
180. F. Komori, S. Kobayashi, and W. Sasaki, *J. Phys. Soc. Jpn.* 51, 3136 (1982).
181. B. L. Altshuler and A. G. Aronov, *Zh. Eksp. Teor. Fiz. Pis'ma Red.* 33, 515 (1981) [*JETP Lett.* 33, 499 (1981)].
182. J. Dai and J. Tang, *J. Appl. Phys.* 92, 6047 (2002).
183. C. L. Chien, *Annu. Rev. Mater. Sci.* 25, 129 (1995).
184. S. S. P. Parkin, *Annu. Rev. Mater. Sci.* 25, 357 (1995).
185. J. S. Moodera, J. Nassar, and G Mathon, *Annu. Rev. Mater. Sci.* 29, 381 (1999).
186. J. M. D. Coey, *J. Appl. Phys.* 85, 5576 (1999).
187. M. Ziese, *Rep. Prog. Phys.* 65, 143 (2002).

# Manganite Nanocomposites

## B. K. Chaudhuri

*Indian Association for the Cultivation of Science, Kolkata, India; and National Sun Yat Sen University, Taiwan, Republic of China*

## Aritra Banerjee, Sudipta Pal

*Indian Association for the Cultivation of Science, Kolkata, India*

## CONTENTS

## 1. INTRODUCTION

Colossal magnetoresistive manganites exhibit large decrease in resistivity under the application of an external magnetic field. Transport, magnetic, and thermal properties are also strongly magnetic field-dependent. Owing to this high field-dependent behavior, the manganite samples are technologically important [1] for making memory and switching devices. The magnetoresistance ratio ($MR = -(\rho_H - \rho_0)/\rho_0$, $\rho_H$ and $\rho_0$ are, respectively, resistivity in presence of a magnetic field H and at zero magnetic field) is an important parameter for the colossal magnetoresistive (CMR) materials. The values of MR may be as high as 10,000% or more [1]. The magnetic field dependence of resistance of such a high magnitude has not been observed in any other bulk metallic system where low-temperature magnetoresistance arises from the field-dependent electronic mean free path. Here resistivity change in presence of magnetic field [2] is usually limited to a few percent. On the other hand, multilayer metallic thin films show relatively large sensitivity to magnetic fields [3]. The giant magnetoresistance (GMR)

effect in these films is largely due to the spin-valve effect between spin-polarized metals. Spin-valve devices have been used in magnetic storage devices for several years in the form of magnetoresistive read heads. Though the physical behavior of the GMR materials is well understood, the technological challenges for the production of smaller-faster-better sensors are limited, which draws attention of the researcher in the field of CMR materials over the last couple of years [4–7].

### 1.1. Colossal Magnetoresistive Manganites

Recently, it has been recognized that some perovskite oxides (divalent doped lanthanum and rare-earth manganites and some related oxides of Ruddlesden–Popper series [8]) possess large negative magnetoresistance or colossal magnetoresistance (CMR). These materials undergo phase transition from the paramagnetic (PM) insulating (semiconducting) phase to the ferromagnetic (FM) metallic phase below the corresponding Curie temperature. In these perovskite oxides, metal-insulator transition (MIT) temperature ($T_p$) and Curie point ($T_c$) coincide [9] and CMR materials also show temperature-dependent anomalies in their various physical parameters like thermoelectric power [10–12], Hall effect [13, 14], heat capacity [15, 16], thermal conductivity [17], etc. around $T_p$. Well-prepared samples show giant negative magnetoresistive effect near $T_p$ or $T_c$ [4–6, 18]. This phenomenon was first noticed in 1950 after the well-known work of van Santen and Jonker [19, 20] on single crystals. Magnetoresistance and other transport properties were well presented in 1954 by Volger [9]. However, the microscopic mechanism governing the transport property in CMR materials is still not clear. The details about the progress of development and explanation of transport and other properties of these types of manganite systems are available from the excellent review of Dagatto et al. [21].

Manganese compounds of composition $AMnO_3$ (A = La, Ca, Ba, Sr, Pb, Nd, Pr) crystallize in the cubic perovskite structure and they are known as manganites. In these manganite samples, commonly called CMR materials, mixed valence of Mn was considered for attributing double exchange mechanism by Zener [21]. Depending on the composition, they show a variety of magnetic and electronic phenomena, including ferromagnetic, antiferromagnetic, charge, and orbital orderings. If A site is partially occupied by two different atoms, one trivalent (for example, La) and one divalent (say Ca), then both the valence states of manganese, viz. $Mn^{3+}$ and $Mn^{4+}$, coexist in the samples. These compounds show different interesting physical properties as the temperature, doping concentrations, particle size, etc. are changed. The different phase transitions (metal-insulator transition, ferromagnetic-antiferromagnetic transition, charge ordering, orbital and spin degree of freedom, order-disorder transition, etc.) displayed by the mixed valence manganite are also sensitive to external parameters such as pressure, magnetic field, etc. It is important to note that other than manganites [22], a number of oxides such as pyrochlores like $Tl_2Mn_2O_7$ [23], double-layered perovskite oxide like $La_{2.2x}Sr_{1-2x}Mn_2O_7$ [24], $La_{2.2x}Ca_{1-2x}Mn_2O_7$ [25], perovskite related structure $CaCu_3Mn_4O_{12}$ [26], also show CMR behavior.

For various technological applications in the field of magnetic memory devices, magnetic sensors, etc. (discussed later), these oxides have already been found to be important. The most effective perovskite materials, having large magnetoresistive property around $T_p$, are the divalent element (like Sr, Pb, Ba, Ca) doped $LaMnO_3$ [1, 4–7] type systems.

## 1.2. CMR Manganites: The Role of Grain Size

As mentioned earlier, colossal magnetoresistance (CMR) effect has been the subject of current interest because of its potentiality in practical applications [4–6, 27]. However, the properties of the CMR materials are found to be highly particle-size-dependent as discussed later. Depending on the origin, the CMR effect is of two types. The intrinsic CMR effect [4, 18, 28], observed in perovskite manganites like $La_{1-x}(Sr, Ca, Pb)_xMnO_3$ ($0.0 \leq x \leq 0.5$), is restricted to the vicinity of $T_p$ and to high magnetic field of several Tesla. Whereas extrinsic CMR effect, like grain boundary magnetoresistance (GBMR) [29], observed at moderately low fields ($B \leq 0.1$ T) and in wide temperature range down to low temperature, is more appropriate for device applications. The GBMR has been observed in polycrystalline bulk materials [11, 30–33] thin films [34–36], and bicrystal manganite films [37–39]. GBMR is usually interpreted in terms of spin-polarized tunneling through electronic barriers in the grain boundaries [30–39] and/or grain boundary scattering [31, 32, 34]. It appears that the existence of grain boundary (GB) plays a major role in CMR mechanism, particularly from the technological point of view. Due to the GB effect, the low field sensitivity of magnetic and transport properties in these materials is found to be enhanced. Here emerges the importance of grain-size-dependent study of the properties of CMR manganites. The variation of grain size in polycrystalline samples affects the grain boundary

scattering/tunneling, which in turn largely influences different physical properties, particularly the MR behavior of the samples.

Mahesh et al. [31] first reported the grain size effect on the magnetic field-dependent transport properties of a polycrystalline $La_{0.7}Ca_{0.3}MnO_3$ sample. While comparing the grain-size-dependent physical properties, it is always ensured that $Mn^{4+}$ content, a crucial factor in determining the magnetic and transport properties, remained constant for samples of different grain sizes. The resistivity ($\rho$) of the CMR sample was found to increase with decrease of grain size. Again, the magnetoresistance ratio at lowest temperature (4.2 K), and around $T_c$, decreases with increasing particle size. The corresponding peak near the Curie temperature was also found to be broadened with decrease of grain size, whereas the value of MR near the peak did not show a significant change with the variation of particle size. It was further observed [31] that at the lowest temperature (well below $T_p$), MR is considerably higher in the sample of smaller particle size, while MR values in single-crystal and epitaxially grown films were very small around the temperature range well below $T_p$. This observation implies that a substantial part of the MR at low temperatures arises from grain boundaries. Recently it has also been demonstrated [32] to show the effect of particle size on the magnetic field-dependent transport properties like resistivity and thermoelectric power of the $La_{0.5}Pb_{0.5}MnO_3$ type samples. The particle sizes of these samples were varied from 102 to 229 nm, and it was observed that grain size of the sample increases with increasing annealing time and temperature. This observation also supports the finding of Mahesh et al. [31]. Moreover, grain size has comparatively little effect on Seebeck coefficient (S) since heat flow from grain to grain is additive in nature. It is to be noted that not only the resistivity data but also the transport mechanism governing the resistivity data is influenced by the variation of grain size [32, 40]. Recently it was reported that grain size also influences the Hall coefficient of these samples [41]. Thus it can be clearly concluded that particle size largely influences the transport properties of the CMR manganites [32, 41, 42]. In another effort, Hossain et al. [33] studied the magnetic and magnetoresistive properties of grain-size-dependent polycrystalline $La_{0.67}Ca_{0.33}MnO_{3-\delta}$ samples (average grain size varying from 3.3 to 3.4 $\mu$m). They showed that Curie temperature $T_c$ is independent of grain size, but the variation of the saturation magnetization with change of grain size appreciably depends on the magnetic history. At lower temperature around 20 K and at 8 T magnetic field, the magnetization was found to decrease as grain size increases. An appropriate linear variation of resistivity and magnetoresistance with grain size allowed the authors [33] to estimate the intrinsic magnetoresistance and also to separate the grain and grain boundary resistivity contributions. It is noteworthy to mention that while studying the variations of resistivity, giant magnetoresistance, and thermopower for the La-Sr-Mn-O type of samples with particle size, ferromagnetic transition temperature of the samples did not vary appreciably [11] with particle size. However, the corresponding metal-insulator transition temperatures ($T_p$ values) were largely influenced by the change of particle size of the sample.

A more direct comparison of MR and field-dependent magnetization values of single-crystal and bulk polycrystalline $La_{2/3}Sr_{1/3}MnO_3$ samples, in the low-temperature ferromagnetic metallic state, has been made by Hwang et al. [30]. Both single-crystal and the polycrystalline samples showed sharp drop of $\rho$ at $T_c$. However, low-temperature resistivity of the polycrystalline sample was found to be significantly higher than that of the single crystals. They further demonstrated [30] that the intrinsic MR in single crystal was due to suppression of spin fluctuation. On the other hand, magnetoresistance in the polycrystalline samples exhibited two distinct regions: large MR at low fields dominated by spin-polarized tunneling between grains, and the high-field MR which was found to be temperature independent. It was found [30] that MR values in polycrystalline samples are dominated by transport across the grain boundaries. MR is also extremely sensitive to the applied magnetic field [30]. In another work, Gupta and Sun [29] made detailed study on the role of grain boundary in the MR of manganites by comparing the properties of epitaxial and polycrystalline films of $La_{0.67}D_{0.33}MnO_{3-\delta}$ (D = Ca, Sr, or vacancies). The mean grain sizes of different polycrystalline manganite samples studied by Gupta and Sun were 3, 14, and 24 $\mu$m. These authors observed that the MR values of epitaxial films showed a sharp peak near $T_c$ with a very small value at low temperatures. On the other hand, the polycrystalline films showed large MR values over a wide range of temperature even at low-temperature (5 K). Based on the results of polycrystalline films, they suggested [29] that the low-field MR was the consequence of spin-dependent scattering of polarized electrons at the grain boundary, which served as pinning centers for magnetic domain walls [29, 32].

Continuous effort is being made to reduce the grain size less than 10 nm and to study grain size effect on different physical properties. This is because of the fact that grain size in the nanometer range modifies the grain boundary scattering/tunneling substantially [43–48]. Zhang et al. studied the grain-size- (nanometer range) dependent magnetic properties of granular $La_{0.85}Sr_{0.15}MnO_z$. They associated magnetoresistance of the system to a tunneling behavior of grain surface. This is, however, not an intrinsic crystal effect [43]. These authors also studied [45] magnetization, heat capacity, structural distortion, and magnetoresistance of nanometer ($\sim$150 nm) size perovskite sample (viz. $La_{0.82}Sr_{0.18}MnO_3$). Their studies demonstrated that in such systems the interfacial tunneling plays an important role in the electronic and transport properties. The interfacial tunneling again depends on the difference of the magnetic moments between the cores and the surfaces of the grains but not on the magnetic moments of the neighboring grains [45]. In a recent work, Hueso et al. showed how CMR could be tuned in $La_{0.67}Ca_{0.33}MnO_3$ by changing grain size. Below a certain particle size ($\sim$150 nm), CMR disappeared, but large intergrain MR remained well above $T_c$. This was explained on the basis of single magnetic domain like behavior of the samples consisting of nanoparticle grains [44]. Very recently, Hueso et al. [48] prepared samples of particle diameter ranging from 60 to 500 nm by sol–gel method. They studied magnetocaloric effect (MCE) and FM to PM phase transition in the $La_{2/3}Ca_{1/3}MnO_{3-\delta}$ system. It was observed that for the samples with larger particles, the transition from the ferromagnetic to the paramagnetic state is of first order in nature. On the other hand, for the samples having smaller particles ($\sim$60 nm or less), the corresponding transition becomes a second-order type [48]. Above-mentioned grain-size-dependent interesting results obtained from the study of different physical properties of CMR manganites are important from a fundamental as well as technological (magnetoresistive devices) point of view.

## 1.3. CMR Manganite Nanocomposites

In the previous section we have discussed the role of grain boundary (GB) scattering in modifying the low-field extrinsic magnetoresistance. To increase the low-field tunneling magnetoresistance in manganites, it is important to enhance the electronic barriers in the GB by controlled doping at the intergranular regions. Recently, it was reported that introduction of a second phase, usually a nonmagnetic or an antiferromagnetic insulator, into the ferromagnetic manganite matrix would lead to an improvement of MR [49–53]. This interesting result encouraged scientists worldwide to study CMR composites [54, 55]. In recent years, several groups have tried to merge the high degree of spin-polarization present in manganites with advantages of a heterogeneous granular structure [55–57]. The extrinsic phase which modifies the GB of ferromagnetic manganites is mainly insulator [51, 55, 57]. Enhanced room-temperature magnetoresistance has also been found in glass composites [50]. Especially near the percolation threshold [55], the mixture of a metallic ferromagnetic manganite with an insulator (F/I) shows an enhancement of magnetoresistance. The properties of the above-mentioned composites can be modified by increasing the grain surface. So efforts are still going on to reduce the particle size in the nanometer scale. The other form of nanocomposite is CMR nanoparticle dispersed in insulating/dielectric matrix [56], where superparamagnetic behavior of the nanoparticles was observed both for the antiferromagnetic and ferromagnetic phases at low-temperature. Precipitation of CMR materials like La-Pb-Mn-O in nonmagnetic $B_2O_3$-$P_2O_5$ glass matrix has also been attempted [58].

Apart from the F/I composite system just discussed, this review also focuses on a different type of CMR composite of manganite/nonmagnetic metal. This system is emerging as a separate class of composites of current interest [59]. These new composites show increase of conductivity with nonmagnetic metal doping, and though the low-temperature MR does not change significantly, the MR around room temperature enhances for a typical concentration of the external phase (nonmagnetic metal). This property can have promising practical applications in switching and memory devices.

## 2. SYNTHESIS OF COLOSSAL MAGNETORESISTANCE (CMR) NANOCOMPOSITES

Composites can be prepared in different ways. For making these composites, the insulating material chosen should be inert to the manganites in which they are inserted and insulator should also easily form nano-grade particles in

the manganite matrix. Conventional methods of preparing CMR materials can also be employed for synthesizing CMR composite [27, 51] with other oxides (magnetic or nonmagnetic). Magnetic nanoparticles, a widely studied material (with metal oxides grain size <10 nm), can be easily formed in an insulating/dielectric matrix by several methods such as sputtering, pulsed laser deposition, ion implementation, etc. But there is no such report on the preparation of CMR nanocomposites using those methods. We shall discuss in the following the preparation techniques of different types of CMR composites of nanometer order as reported so far. The composites of manganite/manganite ($La_{0.7}Sr_{0.3}MnO_3/Sm_{0.7}Sr_{0.3}MnO_3$), manganite/insulator ($La_{0.7}Sr_{0.3}MnO_3/MgO$, $La_{2/3}Sr_{1/3}MnO_3/CeO_2$, $La_{2/3}Ca_{1/3}MnO_3/Al_2O_3$, or $La_{2/3}Ca_{1/3}MnO_3:xSiO_2$), manganite-glass ($La_{0.7}Sr_{0.3}MnO_3$-borosilicate glass), and manganite/nonmagnetic-metal ($La_{0.7}Pb_{0.3}MnO_3/Ag$) are the main focus in this review due to their promising features and interesting physical properties (see Table 1).

## 2.1. Solid-State Reaction Method

It is observed that for preparing nanocomposite of nonmagnetic, insulating, and/or glass particle in ferromagnetic manganite matrix, solid-state reaction method, with low-temperature sintering, is a useful one. The efficiency of these composites depends on how the insulating component is dispersed around the grain boundaries of the ceramic. Bulk polycrystalline $La_{0.7}Pb_{0.3}MnO_3$ + x wt % Ag (LPMO/Ag) (x = 0–20) composites have been prepared at relatively lower sintering temperature (900 °C) to keep the grain size smaller [59]. For the preparation of the composite, high-purity (99.99%) $La_2O_3$, PbO, $Mn(CH_3COO)_3$, and $AgNO_3$ powders were mixed in stoichiometric ratio. The powder was preheated at a temperature of 500 °C for 6 hr. Then it was sintered at 800 °C for 24 hr and at

900 °C for 24 hr with intermediate grindings. The pelletized samples were finally sintered at 800 °C for 12 hr and then slowly furnace cooled to room temperature. The whole system becomes a composite with nonmagnetic Ag dispersed in ferromagnetic $La_{0.7}Pb_{0.3}MnO_3$. The average grain size of the CMR samples varied between ~17 and 20 nm. $La_{1-x}Ca_xMnO_3/SrTiO_3$ and $La_{2/3}Sr_{1/3}MnO_3/CeO_2$ (LSMO/$CeO_2$) composites were made by using high-temperature flash sintering process [54, 55]. Presynthesized LSMO and $CeO_2$ powdered samples were mixed by ball-milling in an agate mortar, and the resulting powder was sintered simultaneously by using a rapid heating process up to 1100 °C for 10 min, followed by a cooling process at about 500 °C/hr [55]. But for the preparation of $La_{1-x}Ca_xMnO_3/SrTiO_3$ nanocomposite system, high-temperature sintering at 1600 °C for about 1 hr has been used [54]. The manganite/alumina nanocrystalline composite was also prepared by solid-state reaction method [51]. However, the sol–gel method, discussed in Section 2.2, was used to synthesize the pre-prepared $La_{0.67}Ca_{0.33}MnO_3$ (LCMO) sample.

## 2.2. Sol–Gel Method

The sol–gel method is a very useful tool for the preparation of nanocomposites of CMR materials. $La_{0.7}Sr_{0.3}MnO_3/Sm_{0.7}Sr_{0.3}MnO_3$ (LSMO/SSMO) nanocomposite was prepared by this method, with inorganic nitrates as starting materials [52]. Ethylene-tetra-diamine-acetic acid (ETDA) was used as complexing agent. SSMO powder was prepared first and this powder was then mixed with La-Sr-Mn-O precursor gel. The mixed solution was calcined at 800 °C. Das et al. [57] also used low-temperature sol–gel processing to prepare LCMO/$xSiO_2$ nanocomposites. Since $Si^{4+}$ ion of silica is unlikely to enter the perovskite structure of LCMO due to its strong preference for tetrahedral coordination, the authors preferred the sol–gel method for

**Table 1.** Different types of manganite nanocomposites.

| CMR manganite nanocomposite system | | | | |
| --- | --- | --- | --- | --- |
| Base matrix (manganite) | Impurity phase or second phase | Synthesized by | Magnetization property | Magnetoresistance property |
| $La_{0.7}Sr_{0.3}MnO_3$ | paramagnetic insulator at RT ($Sm_{0.7}Sr_{0.3}MnO_3$) | sol–gel reaction [52] | The value of magnetization decreases with increase of the second phase. | The value of low field and low temperature magnetoresistance enhances and shows a maximum for a particular concentration of the second phase. |
| $La_{0.7}Sr_{0.3}MnO_3$ | nonmagnetic insulator as 1. MgO 2. $CeO_2$ 3. borosilicate glass | 1. aerosol deposition technique [60] 2. solid-state reaction [55] 3. solid-state reaction | | |
| $La_{2/3}Ca_{1/3}MnO_3$ | nonmagnetic insulator as 1. $Al_2O_3$ 2. $SiO_2$ 3. $SrTiO_3$ | 1. solid-state reaction [51] 2. sol–gel reaction [57] 3. solid-state reaction [54] | | |
| $La_{0.7}Pb_{0.3}MnO_3$ | nonmagnetic metal as Ag | solid-state reaction [59] | | |

synthesizing the sample in contrast to flash sintering method used in $LCMO/SrTiO_2$ and $LSMO/CeO_2$ discussed earlier [54, 55]. In case of $LCMO/SrTiO_2$ and $LSMO/CeO_2$ prepared by solid-state reaction method, the possibility of entering $Ce^{4+}$, $Sr^{2+}$, or $Ti^{4+}$ ion into the LCMO or LSMO could not be ruled out. However, in the case of $LCMO/xSiO_2$ type nanocomposites, prepared by sol–gel method, $Si^{4+}$ can either form a chemical compound with other ions retaining the $SiO_4$ tetrahedra intact or precipitate as $SiO_2$ at grain boundaries of the LCMO phase [57].

## 2.3. Aerosol Deposition Technique

Koster et al. [53] used metal organic aerosol deposition technique (MAD) to grow the films of $La_{0.7}Sr_{0.3}MnO_3/MgO$ (LSMO/MgO) composite. Precursors, acetylacetonates of the corresponding metals, taken at the respective ratios, were dissolved into dimethylformamide and then sprayed as an aerosol in the substrate $Al_2O_3$, heated to 700–750 °C. The details about the aerosol deposition technique can be obtained from the published work of Moshnyaga et al. [60], where the authors discussed the method of synthesis of $La_{0.67}Ca_{0.33}MnO_3$ and $La_{0.67}Sr_{0.33}MnO_3$ thin films by MAD technique.

## 2.4. Other Methods

The $La_{0.7}Sr_{0.3}MnO_3$ (LSMO)-glass composites were grown through solid-state-reaction route, but in the final stage the sample was quenched rapidly from high temperature to room temperature [50]. The rapid cooling was essential to avoid crystallization of the glass. The glass used for this purpose was borosilicate glass with the following composition: $SiO_2$ (80.5%), $B_2O_3$ (12.9%), $Na_2O$ (3.8%), $Al_2O_3$ (2.2%), and $K_2O$ (0.6%). The composites were prepared through standard solid-state-reaction method by mixing appropriate amount of pre-prepared LSMO and borosilicate glass. The mixture was compressed and heated at 3 °C/min up to 300 °C and subsequently heated at 10 °C/min up to 800 °C. The sample was kept at 800 °C for 10 min and subsequently quenched to room temperature. The details regarding the synthesis can be obtained elsewhere [50]. Further, Mondal and Chaudhuri [58] also employed this technique using bismuth phosphate glass to precipitate $La_{0.5}Pb_{0.5}MnO_3$ nanocomposites. These composites show giant dielectric constants.

## 3. PHYSICAL PROPERTIES OF CMR COMPOSITES

### 3.1. Microstructure

X-ray diffraction patterns of the ferromagnetic/insulator manganite composites show that the reflection of the peaks of respective perovskite manganite and insulating phases do not shift, which indicates that no reaction has occurred between the two subsystems. This is clearly observable from the XRD patterns of $LCMO/Al_2O_3$ and $LSMO/CeO_2$ composite systems [51, 55]. The thin film of $(La_{0.7}Sr_{0.3}MnO_3)_{1-x}/(MgO)_x$ composite also showed similar behavior [53]. The grain size can be estimated using

Scherer's formula, viz. $S = k\lambda/\beta\cos\theta$, where $k$ is a constant depending on the grain shape, $\lambda$ is the wavelength of the radiation used, and $\beta$ is the full width at half maxima (FWHM) of the respective XRD peak [61, 62]. It is to be noted that the manganite/manganite composite system like LSMO/SSMO is actually a F/I system at room temperature. Here, SSMO is not in ferromagnetic phase at higher temperature ($T_c \sim 63$ K). The XRD pattern indicates the coexistence of two peaks, and the intensity of a particular peak increases with SSMO concentration [52]. The more direct evidence of the coexistence of two phases comes from the SEM cross-section micrograph, where two different types of crystallites can be identified [51, 52]. Again, Koster et al. [53] studied the microstructure by high-resolution transmission electron micrograph (HRTEM) in cross-section geometry and observed a GB with an ultra thin (about 3 nm) MgO layer between two neighboring LSMO grains, which was further confirmed by chemical mapping performed by energy filtered TEM (EFTEM).

Figure 1 shows the XRD pattern of a typical LPMO/Ag composite. Other than perovskite peaks, some extra peaks of Ag appear, confirming the composite nature of the sample. From the XRD pattern, using Scherer formula [61], sizes of the LPMO grains ($\sim$17 nm) and Ag grains ($\sim$20 nm) were estimated independently. It was observed that the size of the perovskite grains does not change significantly with
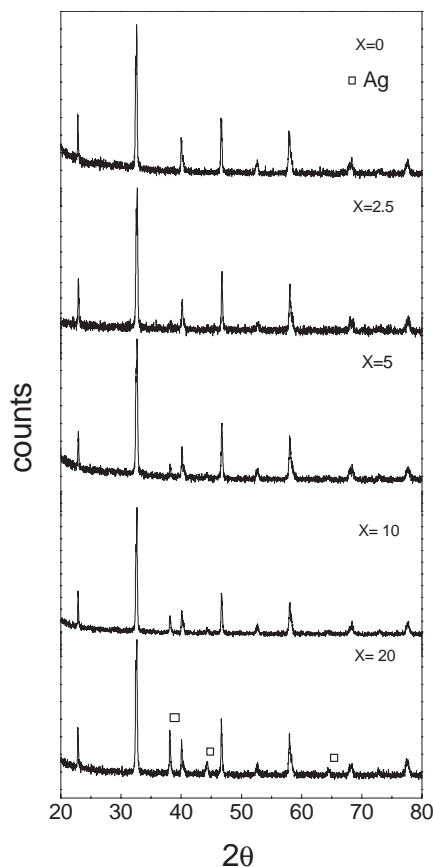


**Figure 1.** X-ray diffraction patterns of $La_{0.7}Pb_{0.3}MnO_3 + x$ wt % Ag with x = 0, 2.5, 5, 10, 20 wt %, respectively. The peaks due to Ag are marked with □.

Ag doping. The elemental mapping of Ag (Fig. 2) indicates the homogeneous distribution of Ag particles in the sample. The shape and size of the composite have been investigated by means of scanning electron microscopy (SEM) (Fig. 3). Similar to the result discussed earlier, the evidence for the coexistence of the two phases is also reflected from the SEM picture. Two different types of crystallites can be clearly identified from the SEM micrographs. The brighter regions indicate Ag grains, which are embedded into LPMO matrix.

## 3.2. Resistivity and Magnetoresistance

### 3.2.1. Manganite/Insulator Composite System

Insulating materials like MgO, $Al_2O_3$, $CeO_2$, $SiO_2$, and also borosilicate and other glasses have already been used to prepare CMR composites. The resistivity and magnetoresistance of the nanocomposites like LSMO/MgO, LSMO/CeO$_2$, LCMO/Al$_2$O$_3$, LCMO/SiO$_2$, LSMO/glass, etc. reported in the literature are discussed here. Temperature-dependent magnetotransport properties of such composites behave in a similar fashion as that of the pure material. The resistivity is found to increase with the increase of insulating material. In LCMO/Al$_2$O$_3$ nanocomposite, for example, the metal-insulator transition is completely suppressed for Al$_2$O$_3$ doping concentration higher than 8% (Fig. 4) [51]. It has been suggested that this increase of resistivity and disappearance of metal-insulator transition are primarily due to the increase of the electron scattering with the alumina grains in the microstructure. In the resistivity data, a percolation point, beyond which resistivity increases significantly, was observed [51]. The MR values of the $(1 − x)$LCMO/$x$Al$_2$O$_3$ system with different values of concentration x have been shown in Figure 5. It is observed that around x = 10%, MR value is a maximum. Hueso et al. were able to increase (∼three times) the intergranular MR around the percolation threshold, which for both the LCMO/Al$_2$O$_3$ and LCMO/SiO$_2$ composite system is around 10% of alumina and SiO$_2$ doping [51, 57]. It is a common feature of all the granular material to have an optimal doping region of the external phase [54, 55]. Similarly, in the LSMO/CeO$_2$ composite, the percolation threshold is around 80% of CeO$_2$ doping, beyond which the resistivity becomes extremely large ($>10^6$ ohm-cm) [55]. For the



**Figure 3.** SEM photograph of LPMO/10 wt % Ag composite sample. The brighter regions indicate Ag clusters. Pores and empty regions are also observable.

LCMO/$x$SiO$_2$ sample, $\rho$-T curve shows two peaks. The MR at 1 T magnetic field shows a sharp peak at T$_c$ and a minimum just below T$_c$ similar to those reported in several polycrystalline LCMO composites [57]. The sharp peak near T$_c$ is attributed to the CMR effect inside grains comprising pure manganite LCMO phase, while the broad peak below T$_c$ is attributed to the scattering at the grain boundary, which also accounts for the observed low-temperature MR value. Moreover, in LSMO/MgO and LSMO/CeO$_2$ films, metal-insulator-like transition (observed broad peak in the normalized resistivity curve [55]) appears with the increase of external insulating phase, that is, MgO [53] or CeO$_2$ [55]. It is due to the fact that at high temperature, the "bad" interparticle contacts significantly contribute to the intergranular regime and thus resistivity decreases in these composites. The field sensitivity of magnetoresistance, that is, $d$MR/$d$H in $x$LSMO/$(1 − x)$CeO$_2$ has been observed to be five times larger than that of the pure metallic LSMO sample both at low-temperature and near the percolation threshold [55]. Gupta et al. showed that the room-temperature low-field MR values could be enhanced by diluting the CMR sample with appropriate glassy materials [50]. They observed an enhancement of the low-field (<200 Oe) MR at room



**Figure 2.** (a) Elemental mapping of Ag in a typical sample La$_{0.7}$Pb$_{0.3}$MnO$_3$ + 10 wt % Ag showing uniform distribution of Ag cluster between perovskite grains. (b) SEM of the same sample is given for reference of scale.
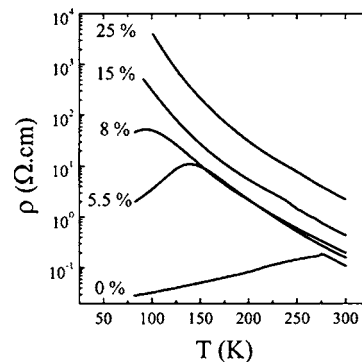


**Figure 4.** Temperature dependence of resistivity for different percentages of LCMO/Al$_2$O$_3$. Metal-insulator transition temperature drops, and is also suppressed by alumina contribution. Reprinted with permission from [51], L. E. Hueso et al., *J. Appl. Phys.* 89, 1746 (2001). © 2001, American Institute of Physics.
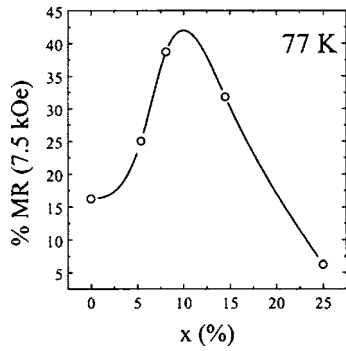
**Figure 5.** Magnetoresistance (MR) at T = 77 K vs alumina percentage. The optimum doping value for MR enhancement is around 10%. Reprinted with permission from [51], L. E. Hueso et al., *J. Appl. Phys.* 89, 1746 (2001). © 2001, American Institute of Physics.



**Figure 6.** Temperature dependence of magnetoresistance (MR) ratio obtained at 5 T for $(LSMO)_{1-x}(SSMO)_x$ with x = 0, 0.2, 0.4, 0.6, 0.7, and 1; the inset shows MR as a function of x at 200 and 293 K. Reprinted with permission from [52], C. H. Yan et al., *J. Appl. Phys.* 91, 7406 (2002). © 2002, American Institute of Physics.

temperature for the optimal doping of 25 wt % of borosilicate glass in $La_{0.7}Sr_{0.3}MnO_3$-glass composites. The glass, separating the grain boundaries, acts as barrier for spin-polarized tunneling, thereby enhancing the low-field magnetoresistance [50].

### 3.2.2. $La_{0.7}Sr_{0.3}MnO_3/Sm_{0.7}Sr_{0.3}MnO_3$ Composite System

The microstructure of this bulk polycrystalline composite system consists of two phases as discussed earlier. In $(LSMO)_{1-x}/(SSMO)_x$ composite, SSMO is a half-metallic ferromagnet just like LSMO, but its Curie temperature $T_c$ is much lower than that of LSMO. SSMO is a paramagnetic insulator above 63 K [63]. So, at higher temperature, LSMO/SSMO is actually a F/I composite. Resistivity of the composite increases with increasing SSMO concentration (x) and metal-insulator transition temperature also shifts to lower temperature similar to that of a F/I composite discussed earlier. Figure 6 displays the corresponding MR as a function of temperature under a magnetic field of 5 T for the samples with x = 0, 0.2, 0.4, 0.6, 0.7, and 1. The MR values increase with x and are found to show a maximum for the sample with x = 0.6 at 293 K (see the inset of Fig. 6). Enhancement of low-temperature MR arises mainly due to tunneling within LSMO grain boundaries and additional grain boundary effects introduced by SSMO particle.

### 3.2.3. $La_{0.7}Pb_{0.3}MnO_3/Ag$ Composite System

Figure 7 represents temperature variation of resistivity of a typical Ag-containing composite for different concentrations of Ag. The resistivity peak at $T_p$ of the Ag-free sample that is, undoped LPMO, is observed at 235 K, which is lower than that of the previously reported value (~320 K) [64]. This is due to smaller grain size (~17 nm) of the present sample. When the grain size is small enough, spin-dependent tunneling dominates in the transport properties, so the resistivity peak for $La_{0.7}Pb_{0.3}MnO_3$ (x = 0 wt % of Ag) occurs far below the corresponding Curie temperature [59]. The resistivity of the samples decreases with the addition of silver and $T_p$ shifts to higher temperature region. Ag addition actually
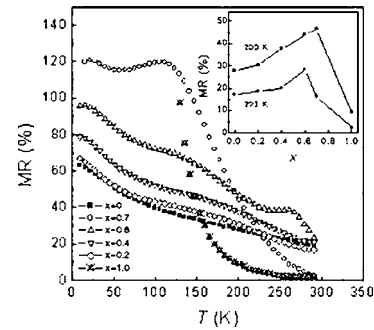
increases the grain boundary contact, which results in the decrease of scattering at grain boundary, thereby increasing conductivity.

Since the grain size does not vary appreciably in the samples, we believe that oxygen concentration in the grains is one of the key factors that lead to the observed increase in conductivity. However, crystal structure has been examined to observe the variation of oxygen content in this system. The crystal structure of $La_{0.7}Pb_{0.3}MnO_3$ (without Ag) is found to be hexagonal (space group $R\bar{3}C$) with lattice constants $a = 5.5167$ Å and $c = 13.4048$ Å. It has been observed that with increase of Ag content in LPMO, the value of $c$-axis lattice parameter decreases. Previous results on Ag + La-Ca-Mn-O films [65] and also on the bulk materials have established the correlation between the $c$-axis lattice parameter and oxygen stoichiometry, where increase in oxygen content was found to reduce the $c$-axis lattice parameter.
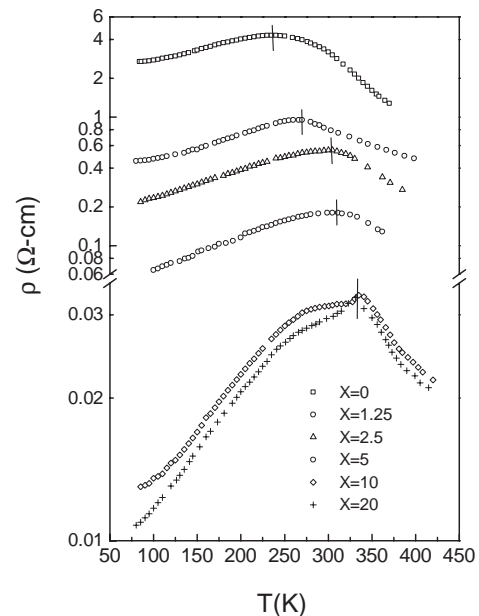


**Figure 7.** Thermal variation of resistivity ($\rho$) of $La_{0.7}Pb_{0.3}MnO_3$ + x wt % Ag (x = 0, 1.25, 2.5, 5, 10, 20 wt %) showing metal-insulator transitions for all the samples. Transition temperature is marked with straight line.

From Figure 8, it is observed that magnetoresistance ratio of the sample also decreases with increasing Ag concentration, which indicates that magnetic order is less in the Ag-containing samples than in the Ag-free LPMO sample. However, near room temperature, the value of MR reaches a maximum value for x = 5 wt % Ag. From a practical point of view, such an enhancement of the MR value around room temperature is very important.

## 4. TRANSPORT MECHANISM

Temperature-dependent resistivity behavior in the ferromagnetic manganite/insulator composite is often explained by two-channel models, that is, two resistances in parallel, weighting each one with a different fitting factor [50, 51, 55]

$$\frac{1}{\rho(T)} = \frac{A}{\rho_c} + \frac{B}{\rho_i} \tag{1}$$

where $\rho_c$ indicates the resistivity inside the conducting manganite grain and $\rho_i$ represents an insulating channel created by the extra electron scattering with insulating region. $A$, $B$ are the normalized section fraction for the conducting and the insulating channel, respectively, and $A = 1 - B$. $\rho_i$ can be expressed as $\exp(E/kT)$, which represents a semiconductor like resistivity. Though the fits to the experimental results with Eq. (1) are found to be satisfactory [51], this simple model does not, however, exactly fit the data of all the samples, suggesting the importance of further development of the model.

On the other hand, the LPMO/Ag nanocomposite is quite different in its transport behavior. Here the observed temperature-dependent conductivity behavior has been explained on the basis of polaron hopping mechanism in the high-temperature phase and the corresponding low-temperature metallic phase with different scattering mechanisms [32, 66, 67]. It has been discussed earlier that grain

boundary scattering is less in LPMO/Ag nanocomposite system compared to that of the pure LPMO oxide. So with the addition of Ag, spin-related intrinsic scattering becomes prominent due to the reduction of grain boundary scattering. In this regard, LPMO/Ag system is different from other nanocomposite systems mentioned [50, 55], where addition of external insulating phase increases the extrinsic grain boundary scattering, resulting in an enhancement of grain boundary magnetoresistance. The temperature-dependent conductivity in this system has been discussed with different models applicable in different temperature ranges. It is observed from the resistivity curves (Fig. 5) that above and below the MIT temperature ($T_p$), different kinds of transport mechanisms are followed by this system. The conductivity data in the high-temperature semiconducting region (i.e., above $T_p$) followed "small polaron" hopping conduction mechanism of Mott [40, 68]. According to this model, the expression for conductivity is given by the relation

$$\sigma(T) = \sigma_0 \exp(-E_p/kT) \tag{2}$$

where $E_p$ is activation energy of the polaron. In Figure 9, a plot of $\ln \sigma T$ versus $1000/T$ is shown which indicates Arrhenius behavior of conductivity ($\sigma$). With increase of Ag content in the samples, activation energy $E_p$ (estimated from Eq. (1)) decreases and attains a minimum value with Ag concentration at around 10 wt %. Intergranular connectivity is improved by Ag addition, which causes the activation energy to decrease. Here we must note that activation energy also decreases with the application of magnetic field, which can be explained on the basis of alignment of magnetic spins and hence increase of conductivity.

In the low-temperature regime ($T < T_p$), conductivity data of all the samples showed metallic behavior. The experimental data in this temperature range have been fitted with the existing theoretical expressions [66, 67] to find the best model fitting the conductivity data for the present composite system as well as to find the nature of different types of interaction (electron-electron, electron-magnon, or electron-phonon) governing the transport mechanism in
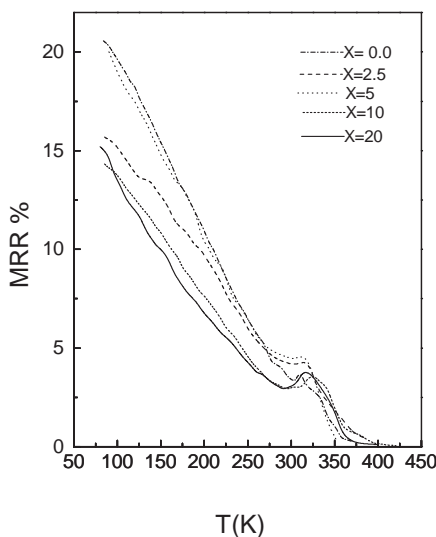


**Figure 8.** Magnetoresistance ratio (MRR = $-(\rho_{1.5} - \rho_0)/\rho_0$) as a function of temperature for the samples $La_{0.7}Pb_{0.3}MnO_3$ + x wt % Ag with x = 0, 2.5, 5, 10, 20. All samples show peak around 320 K arises due to magnetic ordering between $Mn^{3+}$ and $Mn^{4+}$.
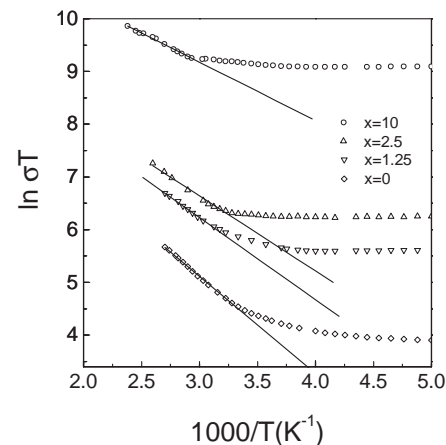


**Figure 9.** Variation of $\ln \sigma T$ as a function of inverse temperature $1000/T$ for $La_{0.7}Pb_{0.3}MnO_3$ + x wt % Ag (x = 0, 1.25, 2.5, 5, 10, 20) above the respective MIT temperatures. Solid lines indicate the best fit of the experimental data with Eq. 1.

the low-temperature metallic phase. The resistance versus temperature curves of the samples, in the low-temperature $(T < T_p)$ region where magnetization $M(T)$ behavior indicates that the local ferromagnetic order is almost complete, well fit with the expression

$$\rho = \rho_\alpha + \rho_m T^m \qquad (3)$$

where the temperature-independent part $\rho_\alpha$ is due to domain, grain boundary, and other temperature-independent scattering mechanism. The term $\rho_{2.5}T^{2.5}$ (for $m = 2.5$ in Eq. (3)) arises due to electron-magnon scattering process [32, 66, 69]. When $m = 2$ (Eq. (3)), the term $\rho_2 T^2$ [66, 68, 70] corresponds to the electron-electron scattering. It has been attempted to fit the low-temperature data $(T < T_p)$ with both the expressions as shown in Figure 10. Interestingly, it has been observed that the experimental conductivity data of all the samples in this system cannot be fitted with a single expression ($\rho = \rho_\alpha + \rho_2 T^2$ or $\rho = \rho_\alpha + \rho_{2.5}T^{2.5}$). It was found that for higher silver doped composites (i.e., $x \geq 5$ wt % Ag), low-temperature data are well fitted with the equation $\rho = \rho_\alpha + \rho_2 T^2$. Whereas for lower Ag ($x = 0, 1.25, 2.5$ wt %) doped samples, the corresponding conductivity data is well fitted with the $T^{2.5}$ term. The $T^{2.5}$ term indicates the signature of electron-magnon scattering in the low-temperature range. So it can be said that the scattering phenomenon changes from electron-magnon to electron-electron with the decrease of resistivity (or with the increase of Ag content in the composites) in low-temperature phase (below $T_p$).

## 5. MAGNETIZATION

### 5.1. Manganite/Insulator and La$_{0.7}$Sr$_{0.3}$MnO$_3$/ Sm$_{0.7}$Sr$_{0.3}$MnO$_3$ Composite System

Since magnetization (M) is closely related to magnetoresistance, the study of magnetization is also very important for a deeper understanding of the transport mechanism. The magnetic hysteresis loops for samples (LSMO)$_{1-x}$(SSMO)$_x$ with $x = 0, 0.5$, and 1 at 300 K (Fig. 11) indicate that LSMO is ferromagnetic and SSMO is paramagnetic. Magnetization of the sample with $x = 0.5$ is much smaller than the average M value of LSMO and SSMO [52]. This demonstrates that the ferromagnetic order is weakened and the magnetic disorder is enhanced in the sample with $x = 0.5$. So it has been suggested that the magnetic disorder caused by the addition of SSMO should be responsible for the enhancement of MR in the high temperature range. Curie temperatures in these composites do not change appreciably with doping of external phase in the manganites. However, there is a decrease in saturation magnetization due to the presence of nonmagnetic external phase [51–57]. The magnetic contribution is reduced proportionately with the corresponding increased amount of nonmagnetic insulator percentage in the composite. Similar magnetic behavior is also obtained for the other CMR nanocomposites discussed earlier. For the sample LCMO/SiO$_2$, Das et al. [57] reported that the decrease of saturation magnetization is actually due to the presence of insulating Ca$_2$La$_8$(SiO$_4$)$_6$O$_2$ phase, which is formed since SiO$_2$ partially reacts with LCMO. From the
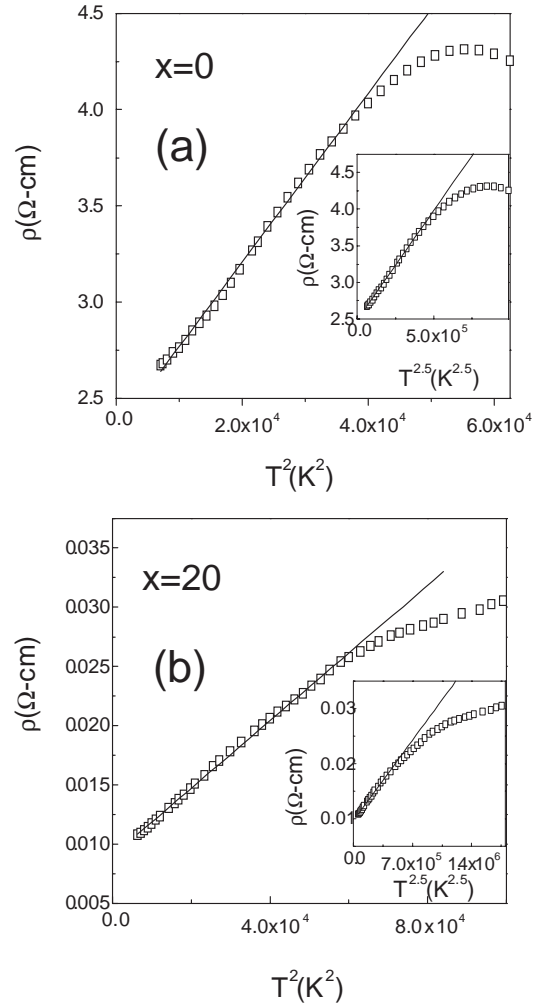


**Figure 10.** Low-temperature resistivity data of two typical samples La$_{0.7}$Pb$_{0.3}$MnO$_3$ + x wt % Ag (for x = 0, 20) fitted with the expression $\rho_\alpha + \rho_2 T^2$ and $\rho_\alpha + \rho_{2.5}T^{2.5}$ (Eq. (2)). Solid lines indicate the best fit of the experimental data. The straight lines show the first expression fits better for the samples with x = 20 wt %.
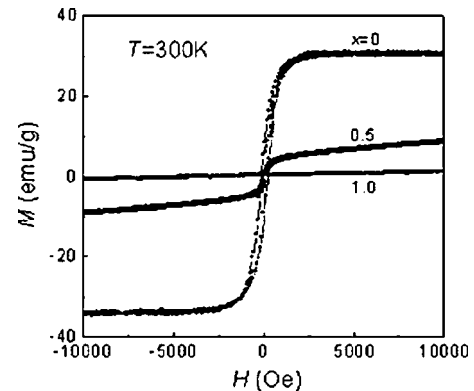


**Figure 11.** Magnetic hysteresis loops for (LSMO)$_{1-x}$(SSMO)$_x$ composite with x = 0, 0.5, and 1 at 300 K. Reprinted with permission from [52], C. H. Yan et al., *J. Appl. Phys.* 91, 7406 (2002). © 2002, American Institute of Physics.
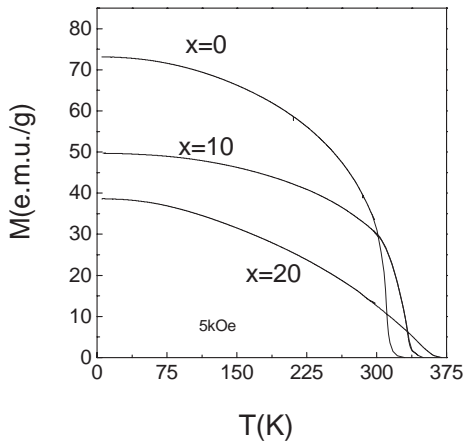
**Figure 12.** Thermal variation of d.c. magnetization of (LPMO/x Ag) composite with x = 0, 10, 20 wt %, respectively, in presence of magnetic field B = 5 kOe.

thermal variation of magnetization curves of LCMO/SrTiO$_3$ and LCMO/SiO$_2$ composites, a small upturn is observed around 50 K [54, 57], which was explained on the basis of local microscopic magnetic inhomogeneities arising from the variation in the Mn oxidation state [71] or due to the presence of MnO$_2$ phase [72]. Das et al. also explained this small upturn of the LCMO/SiO$_2$ system considering the presence of Ca$_2$La$_8$(SiO$_4$)$_6$O$_2$ impurity phase [57].

## 5.2. La$_{0.7}$Pb$_{0.3}$MnO$_3$/Ag Composite System

Figure 12 shows the temperature variation of magnetization at 5 kOe for the LPMO/x wt % Ag (x = 0, 10, 20) samples. The Curie temperature T$_c$ of these samples increases with increase of Ag content (viz. T$_c$ ∼ 317, ∼341, and ∼361 K, respectively, for x = 0, 10, and 20 wt % observed from high-temperature magnetic measurement). In the Ag composite system, it is reasonable to assume that Ag particles form clusters. This is also indicated from the SEM study. Since Ag content is increasing, the connectivity between two FMM (ferromagnetic metallic) regions increases. This indicates magnetic homogeneity in the samples improves significantly with addition of Ag. With increase of temperature, FMM regions decrease due to spin disorder. But because of the presence of Ag, the connectivity exists. With further increase of temperature, FMM regions become so small that connectivity between different FMM regions is lost and then it becomes paramagnetic (semiconducting). Therefore, it is reasonable to argue that with increasing Ag concentration, T$_c$ increases. Furthermore, it had also been observed that the saturation magnetization decreases with increase of Ag content owing to the precipitation of the nonmagnetic Ag when the concentration exceeds ∼5 wt% [59].

## 6. APPLICATIONS

Though it is still in the rudimentary state, the CMR manganite nanocomposite is a promising candidate for technological applications. In Section 1.2, we discussed in length that low field grain boundary magnetoresistance is more appropriate

for device applications. The presence of grain boundary in the nanocomposites plays a major role in CMR mechanism, particularly for enhancing the low-field sensitivity of CMR manganites [30–39].

Continuous effort to reduce the grain size is being made by the researchers, since nanometer-range grain size modifies the grain boundary/tunneling substantially [43–48]. Here emerges the important role of CMR manganite nanocomposites. Controlled doping of nonmagnetic, insulating materials into the GB of ferromagnetic manganite matrix would lead to an improved low field MR and make manganite nanocomposites a suitable candidate for technological applications. Recently Sun et al. constructed a device consisting of a pillar composed of two layers of ferromagnetic manganite separated by a SrTiO$_3$ spacer [73]. This prototype device, beside showing large resistivity changes in low fields, also demonstrates how it could be possible to use films of ferromagnetic manganites as electronic spin polarizers and analyzers [73]. Large MR is, however, only one useful property for device applications. Future work, for example, on the issues involving power consumption, noise, and compatibility with established fabrication methods [74] is to be done.

## 7. CONCLUSION

The nanocomposite of CMR materials with other external phase like nonmagnetic insulator or metallic phase shows large improvement of the extrinsic magnetoresistance, which promises large potential for their applications from a technological standpoint. These results focus on the new possibilities to improve the performance of the colossal magnetoresistive devices. In the manganite/nonmagnetic-metal (viz. Ag) nanocomposites, improvement in grain boundary scattering and hence MR around room temperature has been observed. Magnetoresistance can be greatly enhanced on ferromagnetic/insulator (F/I) manganite composites near the percolation threshold. Large variation of physical properties is observed in the transport and magnetic properties of the composites at cryogenic temperature, though near room temperature the corresponding effects are very small. For magnetic read head application, for example, the low field MR effect should be larger. Moreover, the preparation of very small grain size (∼2–3 nm) CMR composite is a challenging current problem. However, recent development on CMR nanocomposites is still in the early stage. It is just a beginning of the long emerging prospect of CMR nanocomposites in the field of technological applications for which more smaller and uniform-size nanoparticles are required. Research in this direction would be potentially rewarding in terms of new physics and novel devices using CMR nanocomposites. Theoretical understanding of the transport and magnetic properties, phase separation behavior of CMR composites, etc. is also not yet complete. Study of spin dynamics of CMR nanocomposites is an important field of fundamental research. In the near future, CMR nanoparticles stabilized by chemical materials are expected to open a new field of interdisciplinary research for physicists, chemists, biologists, and engineers.

# GLOSSARY

**Colossal magnetoresistance (CMR)**   A huge decrease in resistance with the application of magnetic field.

**Magnon**   Quantized spin wave.

**Perovskite oxides**   Structures having of combination of face centered cubic (fcc) and body centered cubic (bcc) lattice. For example, oxides of structure $ABO_3$ (A = element with larger radius, B = element smaller with radius), where A lies at the corner, B at the center and O at the face of the cubic structure.

**Phonon**   Quantized lattice wave.

**Polaron**   Formed mainly in an insulator, the combination of the localized electron and its strained field.

**Pyrocholore**   A group of rare minerals found in pegmatitic granites, syenites and carbonatites. For example, PYRO-CHOLORE GROUP $(Ce, Ca, Y)_2(Nb, Ta)_2O_6(OH, F)$ Isometric.

# ACKNOWLEDGMENTS

# REFERENCES

1. C. N. R. Rao and B. Raveau Eds., "Colossal Magnetoresistance, Charge Ordering, and Related Properties of Manganese Oxides." World Scientific, Singapore, 1998.
2. J. M. Ziman, "Electrons and Phonons: The Theory of Transport Phenomena in Solids." Clarendon Press, Oxford, 1962.
3. S. P. P. Parkin, *Ann. Rev. Matter. Sci.* 25, 357 (1995).
4. R. von Helmolt, J. Wecker, B. Holzapfel, L. Schultz, and K. Samwer, *Phys. Rev. Lett.* 71, 2331 (1993).
5. K. Chahara, T. Ohno, M. Kasai, and Y. Kozono, *Appl. Phys. Lett.* 63, 1990 (1993).
6. S. Jin, M. McCormack, T. H. Tiefel, and R. Ramesh, *J. Appl. Phys.* 76, 6929 (1994).
7. M. B. Salamon and M. Jaime, *Rev. Mod. Phys.* 73, 583 (2001).
8. S. Ruddlesden and P. Popper, *Acta Crystallogr.* 11, 541 (1958).
9. J. Volger, *Physica* 20, 49 (1954).
10. M. Jaime, M. B. Salamon, K. Pettit, M. Rubinstien, R. E. Treece, J. S. Horwitz, and D. B. Chirsey, *Appl. Phys. Lett.* 68, 1576 (1996).
11. R. Mahendiran, R. Mahesh, A. K. Raychaudhuri, and C. N. R. Rao, *Solid State Commun.* 99, 149 (1996).
12. A. Asamitsu, Y. Moritomo, and Y. Tokura, *Phys. Rev. B* 53, R2952 (1996).
13. M. Jaime, H. T. Hardner, M. B. Salamon, M. Rubinstein, P. Dorsey, and D. Emin, *Phys. Rev. Lett.* 78, 951 (1997).
14. P. Matl et al., *Phys. Rev. B* 57, 10248 (1998).
15. B. F. Woofield, M. L. Wilson, and J. M. Byers, *Phys. Rev. Lett.* 78, 3201 (1997).
16. J. M. D. Coey, M. Viret, L. Ranno, and K. Ounadjela, *Phys. Rev. Lett.* 75, 3910 (1995).
17. W. D. Visser, A. P. Ramirez, and M. A. Subramanian, *Phys. Rev. Lett.* 78, 3971 (1997).
18. S. Jin, T. H. Tiefel, M. McCormack, R. A. Fastnacht, R. Ramesh, and J. H. Chen, *Science* 264, 413 (1994).
19. G. H. Jonker and J. H. van Santen, *Physica* 16, 337 (1950).
20. J. H. van Santen and G. H. Jonker, *Physica* 16, 599 (1950).
21. E. Dagatto, T. Hotta, and A. Moreo, *Phys. Rep.* 344, 1 (2001).
22. A. K. Raychaudhuri, "Frontiers in Materials Science," Vol. 1. Allied Publishers Pvt. Limited, New Delhi, 2002.
23. Y. Shimakawa et al., *Nature* 379, 53 (1997).
24. Y. Moritomo, A. Asamitsu, H. Kuwahara, and Y. Tokura, *Nature* 380, 141 (1996).
25. H. Asano, J. Hayakawa, and M. Matsui, *Appl. Phys. Lett.* 68, 3638 (1996).
26. Z. Zeng, M. Greenblatt, M. A. Subramanian, and M. Croft, *Phys. Rev. Lett.* 82, 3164 (1999).
27. J. M. D. Coey, M. Viret, and S. Von Molnar, *Adv. Phys.* 48, 271 (1999).
28. J. W. Feng, C. Ye, and L. P. Hwang, *Phys. Rev. B* 61, 12271 (2000).
29. A. Gupta and J. Z. Sun, *J. Magn. Magn. Mater.* 200, 24 (1999).
30. H. Y. Hwang, S.-W. Cheong, N. P. Ong, and B. Batlogg, *Phys. Rev. Lett.* 77, 2041 (1996).
31. R. Mahesh, R. Mahendiran, A. K. Raychaudhuri, and C. N. R. Rao, *Appl. Phys. Lett.* 68, 2291 (1996).
32. A. Banerjee, S. Pal, S. Bhattacharya, and B. K. Chaudhuri, *J. Appl. Phys.* 91, 5125 (2002).
33. A. K. M. Akhter Hossain et al., *J. Magn. Magn. Mater.* 192, 263 (1999).
34. A. Gupta et al., *Phys. Rev. B* 54, R15629 (1996).
35. R. Shreekala et al., *Appl. Phys. Lett.* 71, 282 (1997).
36. X. W. Li et al., *Appl. Phys. Lett.* 71, 1124 (1997).
37. K. Steenbeck, T. Eick, K. Kirsch, K. O'Donnell, and E. Steinbeiß, *Appl. Phys. Lett.* 71, 968 (1997).
38. N. D. Mathur et al., *Nature* 387, 266 (1997).
39. K. Steenbeck, T. Eick, K. Kirsch, H.-G. Schmidt, and E. Steinbeiß, *Appl. Phys. Lett.* 73, 2506 (1998).
40. N. F. Mott and E. A. Davis, in "Electronics Process in Non Crystalline Materials." Clarendon, Oxford, 1971.
41. A. Banerjee et al., "Hall effect measurement of Pb and Cr doped $LaMnO_3$ manganites and grain size effect on Hall coefficient," unpublished.
42. A. Banerjee, S. Pal, and B. K. Chaudhuri, *Mat. Res. Soc. Symp. Proc.* 718, D7.25.1 (2002).
43. N. Zhang, W. Ding, W. Zhong, W. Yang, and Y. Deu, *J. Phys.: Condens. Matter* 9, 4281 (1997).
44. L. E. Hueso, J. Rivas, F. Rivadulla, and M. A. Lopea-Quintela, *J. Appl. Phys.* 86, 3881 (1999).
45. N. Zhang and W. Wang, *Mod. Phys. Lett. B* 13, 399 (1999).
46. A. I. Shames et al., *J. Magn. Magn. Mater.* 203, 259 (1999).
47. Z. H. Wang et al., *J. Appl. Phys.* 87, 5582 (2000).
48. L. E. Hueso, P. Sande, D. R. Miguens, J. Rivas, F. Rivadulla, and M. A. Lopea-Quintela, *J. Appl. Phys.* 91, 9943 (2002).
49. J. M. Liu et al., *Appl. Phys. Lett.* 74, 2286 (2000).
50. S. Gupta, R. Ranjit, C. Mitra, P. Raychaudhuri, and R. Pinto, *Appl. Phys. Lett.* 78, 362 (2001).
51. L. E. Hueso, J. Rivas, F. Rivadulla, and M. A. Lopea-Quintela, *J. Appl. Phys.* 89, 1746 (2001).
52. C. H. Yan et al., *J. Appl. Phys.* 91, 7406 (2002).
53. S. A. Koster et al., *Appl. Phys. Lett.* 81, 1648 (2002).
54. D. K. Petrov, L. Krusin-Elbaum, J. Z. Sun, C. Feild, and P. R. Duncombe, *Appl. Phys. Lett.* 75, 995 (1999).
55. L. Balcells, A. E. Carrillo, B. Martínez, and J. Fontcuberta, *Appl. Phys. Lett.* 74, 4014 (1999).
56. T. Tajari, S. Maruoka, H. Deguchi, S. Takagi, M. Mito, Y. Ishida, and S. Kohiki, preprint.
57. D. Das, P. Chaudhuri, R. N. Das, C. M. Srivastava, A. K. Nigam, and D. Bahadur, *J. Magn. Magn. Mater.* 238, 178 (2002).
58. U. Mondal and B. K. Chaudhuri, Thesis, Jadavpur University, 2002.
59. S. Pal, A. Banerjee, and B. K. Chaudhuri, "Proceedings of the ICTMC-13," 2002.

*60.* V. Moshnyaga, I. Khoroshun, A. Sidorenko, P. Petrenko, A. Weidinger, M. Zeitler, B. Rauschenbach, R. Tidecks, and K. Samwer, *Appl. Phys. Lett.* 74, 2842 (1999).

*61.* A. Guinier, "Theory et Technique de la Radiocrystallographie," 3rd ed., p. 482. Dunod, Paris, 1964.

*62.* A. Taylor, "X-ray Metallography," p. 674. Willey, New York, 1961.

*63.* R. M. Thomas, L. Ranno, and J. M. D. Coey, *J. Appl. Phys.* 81, 5763 (1997).

*64.* R. Mahendran, R. Mahesh, A. K. Raychaudhuri, and C. N. R. Rao, *J. Phys. D: Appl. Phys.* 28, 1743 (1995).

*65.* R. Shreekala, M. Rajeswari, S. P. Pai, S. E. Lofland, V. Smolyaninova, K. Ghosh, S. B. Ogale, S. M. Bhagat, M. J. Downes, R. L. Greene, R. Ramesh, and T. Venkatesan, *Appl. Phys. Lett.* 74, 2857 (1999).

*66.* A. Banerjee, S. Pal, and B. K. Chaudhuri, *J. Chem. Phys.* 115, 1550 (2001).

*67.* A. Banerjee, S. Pal, S. Bhattacharya, B. K. Chaudhuri, and H. D. Yang, *Phys. Rev. B* 64, 104428 (2001).

*68.* N. F. Mott, in "Metal-Insulator Transitions." Taylor and Francis, London, 1974.

*69.* L. Pi, L. Zheng, and Y. Zhang, *Phys. Rev. B* 61, 8917 (2000).

*70.* A. Milner, A. Gerber, B. Groisman, et al., *Phys. Rev. Lett.* 76, 475 (1996).

*71.* H. L. Ju and H. Sohn, *J. Magn. Magn. Mater.* 167, 200 (1997).

*72.* J. R. Gebhardt, S. Roy, and N. Ali, *J. Appl. Phys.* 85, 5390 (1999).

*73.* J. Z. Sun et al., *Appl. Phys. Lett.* 69, 3266 (1996).

*74.* A. P. Ramirez, *J. Phys.: Condens. Matter* 9, 8171 (1997).

# Mechanical Behavior of Nanomaterials

A. Li Bassi, C. E. Bottani

*Politecnico di Milano, Italy*

## CONTENTS

## 1. INTRODUCTION

Nanocrystalline and nanostructured materials have recently stimulated a great interest both in the scientific and in the technology community, due to the possibility of a tailoring of their properties via structural control at the atomic and supra-atomic level. The change in physical, thermodynamic, electronic, optical properties (and many others), when matter is confined in building blocks whose size is of the order of tens of nanometers or less, suggests the great potentiality that nanomaterials offer for many envisaged applications.

In particular, significant effects of the nanoscale reduction on the mechanical behavior of nanophase materials have been observed since the beginning of the nanoscience era (see, e.g., [1] and references therein for a broad bibliography of recent experimental work in this field).

If we consider nanocrystalline materials, we can see that grain boundaries and interphases can comprise up to 50% of the volume fraction, when the grain size is reduced to 5 nm. Moreover, dislocations are seldom seen inside these grains, particularly when the grain size is in the lower range of the nanometer scale. The porosity level can also be significant, and in the absence of agglomeration, the pore size is smaller than or equal to grain size. Microcrystalline materials already have a mechanical behavior which is grain-size dependent; it is no surprise that all these characteristics may have an even more considerable effect on the bulk material effective mechanical behavior when the grain size

is nanometric, that is, on hardness, ductility, grain boundary migration, and sliding. In general, microstructural features including grain size, grain shape, pore distribution, flaws, surface condition, impurity level, and crystal defects all affect mechanical properties.

More generally, nanostructured materials (not necessary nanocrystalline) possess original mechanical behaviors.

Among the peculiar mechanical properties that were first observed for nanostructured materials we mention:

- elastic moduli were found to be 30–50% lower than in conventional grain-size materials;
- very high hardness and strength, with hardness values for nanocrystalline pure metals ($\sim$10 nm grain size) up to seven times higher than those of conventional coarse-grained ($>$1 $\mu$m) metals; in general, tensile and compressive strengths in nearly all materials show anomalously high values at the nanometer scale;
- ultrahigh hardness has also been measured in nanoscale multilayers made of metallic or ceramic materials;
- a negative Hall–Petch slope, that is, decreasing hardness with decreasing grain size in the nanoscale grain-size regime;
- ductility (possibly superplastic behavior?) at low temperatures in brittle ceramics or intermetallics with nanoscale grain size, probably due to diffusional deformation mechanisms, though the real attribution of this behavior is being debated.

While some of these early observations have been verified, some have been found to be due to artifacts introduced by defects or to the different structures induced by the particular growing procedure.

It also often results that the measured mechanical properties in nanostructured materials depend on the degree of porosity: this is especially true in materials obtained by nanopowder sintering. Metals can be easily compacted and sintered, while ceramic powders are more difficult to densify. The porosity level in a ceramic can be as high as 60%, while it is about 20% in metals (the best obtainable porosity level in a compacted metallic nanomaterial is about 5%, and 15–25% in ceramics). It has been observed that strength and hardness increase approximately linearly with the density of the compact. During pressure sintering, below 10 nm

the pore curvature dominates the driving force for densification, while at about 100 nm, the magnitude of the applied pressure is more important. In the intermediate range both effects are significant, and this implies that a threshold stress (inversely related to the grain size and necessary to create additional surface area by grain boundary sliding) has to be overcome before the densification rate can be increased. Anyway, a detailed analysis of the effect of porosity and defects on the mechanical properties at these scales is currently missing.

In the following, after a brief introduction concerning general definitions of elastic and mechanical properties, the peculiar aspects of the mechanical behavior of nanomaterials will be discussed together with some examples.

## 2. MECHANICAL PROPERTIES: GENERAL DEFINITIONS

### 2.1. Stress, Strain, and Elastic Constants

As for all other physical properties, the mechanical response of materials depends on the scale at which it is measured. For three-dimensional (3D) compact materials (e.g., diamond), when the characteristic observation length scale is much bigger than the typical interatomic distance, the mechanical behavior is conveniently modeled by standard continuum mechanics based on contact interactions (e.g., local elasticity). Yet for special materials with a complex mesostructure or nanostructure this approach is not appropriate. For instance, nanocrystalline materials, nanostructured materials or multilayers, carbon aerogels, and some types of cluster-assembled carbon films belong to this category.

Polycrystalline or multiphase solids, though their properties are influenced and determined by their local microstructure, can be characterized by macroscopic elastic parameters such as the bulk modulus $B$ and the shear modulus $\mu$. Such materials are elastically isotropic at the macro scale and two parameters are often sufficient to describe their behavior (though physicists are traditionally more interested in anisotropic single crystals). In order to describe the kinematics of the deformation process (see [2] also for the following treatment), let a vector field $\mathbf{r}$ span all points within the material volume $V$ in an undeformed thermodynamic equilibrium state at temperature $T$. If now a material deformation is produced, the old (undeformed) material positions are mapped into the new ones as $\mathbf{r}' = \mathbf{r} + \mathbf{u}(\mathbf{r})$ by the displacement vector field $\mathbf{u}(\mathbf{r})$, describing both deformations (volume and shape variations) and rigid rotations. In the small strain regime, the symmetric part of the gradient of the displacement vector field $\mathbf{u}(\mathbf{r})$ is the *strain tensor* $\varepsilon_{rs}$

$$\varepsilon_{rs} = Sym(\nabla\mathbf{u}) = \frac{1}{2}\left(\frac{\partial u_r}{\partial x_s} + \frac{\partial u_s}{\partial x_r}\right) \tag{1}$$

This tensor describes how infinitesimal cubic volume elements $dV = dx\,dy\,dz$ can change their volume and their shape. The diagonal components of the strain tensor represent tensile strains (e.g., $\varepsilon_{xx} = (dx' - dx)/dx$), while the off-diagonal components represent shear deformations. More precisely, assuming in the following a summation from 1 to 3

over repeated vector and tensor suffixes, the relative volume variation $(dV' - dV)/dV$ is equal to $\varepsilon_{ll}$, the *trace* of $\varepsilon_{rs}$. $\varepsilon_{ll}$ is either a pure dilation ($\varepsilon_{ll} > 0$) or a pure hydrostatic compression ($\varepsilon_{ll} < 0$). Instead, $e_{ik} = \varepsilon_{ik} - \frac{1}{3}\delta_{ik}\varepsilon_{ll}$ is a pure shear strain (a *strain deviator*, where $\delta_{ik}$ is the unit tensor); in fact $e_{ll} = 0$, proving that $e_{ik}$ is a pure shear. In the undeformed state the angle, for instance, $\alpha_{xy}$, between $d\mathbf{x}$ and $d\mathbf{y}$ is 90°. After a shear deformation the angle is reduced by an amount $\delta\alpha_{xy} = \gamma_{xy} = 2\varepsilon_{xy} = 2e_{xy}$. Any deformation can be conceived as the sum of a pure shear and a dilation (or compression) as it is evident from the identity $\varepsilon_{ik} = e_{ik} + \frac{1}{3}\delta_{ik}\varepsilon_{ll}$.

Provided the produced strains are small and reversible, a generalized Hooke's law describes the linear elastic material response

$$\sigma_{ik} = c_{ikrs}\varepsilon_{rs} \tag{2}$$

In the above equation $\sigma_{ik}$ is the *stress tensor*. $\sigma_{ik}$ is the $k$-component of the force per unit area acting on a face of a cubic element whose outgoing normal is the unit vector of the $i$—th cartesian axis. The diagonal components represent tractions, while the off-diagonal components represent shear stresses. The elastic material properties are embodied in the fourth-rank tensor $c_{ikrs}$, the *elastic constant tensor* with $3^4 = 81$ elements. Because of the symmetry of $\sigma_{ik}$ and $\varepsilon_{ik}$, the number of independent components of $c_{ikrs}$ diminishes to 36. This number is further lowered to 21 by energetic considerations. Using then Voigt's contraction scheme

$$i, k \text{ or } r, s \quad 11 \quad 22 \quad 33 \quad 23 \text{ or } 32 \quad 13 \text{ or } 31 \quad 12 \text{ or } 21$$
$$\alpha \text{ or } \beta \quad\;\; 1 \quad\;\; 2 \quad\;\; 3 \quad\quad 4 \quad\quad\;\; 5 \quad\quad\;\; 6$$

Eq. (2) can be given a simpler *matrix* form

$$\sigma_\alpha = c_{\alpha\beta}\varepsilon_\beta \tag{3}$$

where the elastic constant $6 \times 6$ matrix $c_{\alpha\beta}$ is symmetric.

The material symmetry produces further reduction. In the case of cubic crystals, for instance, the independent constants are 3 and only 2 in an isotropic material, as anticipated. In the simplest case of isotropic elasticity, Eq. (3) becomes

$$\begin{pmatrix} \sigma_1 \\ \sigma_2 \\ \sigma_3 \\ \sigma_4 \\ \sigma_5 \\ \sigma_6 \end{pmatrix} = \begin{pmatrix} B+4\mu/3 & B-2\mu/3 & B-2\mu/3 & 0 & 0 & 0 \\ B-2\mu/3 & B+4\mu/3 & B-2\mu/3 & 0 & 0 & 0 \\ B-2\mu/3 & B-2\mu/3 & B+4\mu/3 & 0 & 0 & 0 \\ 0 & 0 & 0 & 2\mu & 0 & 0 \\ 0 & 0 & 0 & 0 & 2\mu & 0 \\ 0 & 0 & 0 & 0 & 0 & 2\mu \end{pmatrix} \begin{pmatrix} \varepsilon_1 \\ \varepsilon_2 \\ \varepsilon_3 \\ \varepsilon_4 \\ \varepsilon_5 \\ \varepsilon_6 \end{pmatrix} \tag{4}$$

The last three components of the *column vectors* stand for pure shear stresses and strains respectively, while the first three components involve length and volume variations. In engineering two different elastic constants, namely the Young's modulus $E$ and the Poisson's ratio $\nu$, are usually introduced. If a uniaxial stress $\sigma_{xx} = \sigma_1 = \sigma$ is applied (with all other $\sigma_i = 0$), only strains $\varepsilon_{xx} = \varepsilon_1 = \varepsilon$, $\varepsilon_{yy} = \varepsilon_2$, and $\varepsilon_{zz} = \varepsilon_3 = \varepsilon_2$ are nonzero. Then $E$ is defined as $\sigma/\varepsilon$ and $\nu$ as $-\varepsilon_2/\varepsilon = -\varepsilon_3/\varepsilon$. Since there are only two independent

elastic constants, $E$ and $\nu$ can be obtained from $B$ and $\mu$ by the following formulae

$$E = \frac{9B\mu}{3B + \mu} \qquad (5)$$

$$\nu = \frac{3B - 2\mu}{2(3B + \mu)} \qquad (6)$$

The meaning of bulk modulus $B$ appears clearly in *hydrostatic pressure conditions*: $\sigma_1 = \sigma_2 = \sigma_3 = -p$ and $\sigma_4 = \sigma_5 = \sigma_6 = 0$. In this case $\varepsilon_1 = \varepsilon_2 = \varepsilon_3 = -p/3B$ and $\varepsilon_4 = \varepsilon_5 = \varepsilon_6 = 0$. Thus the relative volume variation $\varepsilon_{kk} = \varepsilon_1 + \varepsilon_2 + \varepsilon_3 = -p/B$.

Since $\mu$ too is always positive, $\nu$ can vary between $-1$ (when $B = 0$) and $\frac{1}{2}$ (when $\mu = 0$). In practice there are no homogeneous materials known for which $\nu < 0$.

In the case of simple shear, for example, $\sigma_4 = \tau$ and all other $\sigma_i = 0$, then $\varepsilon_4 = \tau/2\mu$ and all other $\varepsilon_i = 0$. If one introduces the angular shear strain measure $\gamma_4 = 2\varepsilon_4 = \gamma$, the last equation reads $\gamma = \tau/\mu$, which illustrates the physical meaning of $\mu$.

## 2.2. Hardness and Yield Stress

The stress-strain *tensile* curve of a particular sample is measured in terms of the elongation produced by a tensile stress (typically one plots the stress $\sigma$ versus the strain $\varepsilon$). Two regions can be distinguished in such a curve:

- *elastic* deformation (completely reversible deformation), from which one can get information about the elastic constants and the strain moduli;
- *plastic* deformation (irreversible deformation), which occurs above the *yield stress*.

The collection of sufficient volumes of material is the main problem in tensile strength testing. The limit at which deformation becomes permanent is conventionally taken as 0.2% of the strain, and the corresponding stress is defined as the *yield stress* ($\sigma_y$). Other important parameters which can be evaluated are the total strain to fracture, the stress level at which the sample fails, or the fracture stress. Another important aspect to be considered when materials are subjected to deformation or stress cycles is work hardening (i.e., the material becomes stronger after yielding).

In nanomaterials, as well as in thin films or multilayers, an investigation of the near-surface hardness can be performed by using an indentation load-depth sensing apparatus, that is, a nanoindenter, which directly measures the load on a triangular pyramidal diamond indenter tip as a function of its in-depth displacement from the surface. Hardness is related to the size of the footprint left on the material surface by the diamond indenter, for a given load and a given load time, and can be determined from the load data using the relationship

$$H = L(h)/A(h) \qquad (7)$$

where $L(h)$ is the measured load and $A(h)$ is the projected area of the indenter (footprint) as a function of the plastic depth $h$. Measurements are usually made at a constant load rate (e.g., of the order of about 20 mN/s) to a typical nominal depth, which can for instance be about $\frac{1}{10}$ of the film thickness; several indents are usually made on the same sample and the data are averaged. The actual depth includes the plastic depth and the elastic recovery as the tip is removed, and from this assumption a more detailed analysis can be performed (see, e.g., [3]). Thus, in general, the indentation process can be quite complex. Also hardness or stress-strain experiments under constant load or constant strain-rate conditions can be performed, as a function of time and temperature: this provides the possibility of obtaining information about the creep behavior. In monitoring hardness of thin nanometric layers on a substrate, problems may arise when the substrate is harder than the film. Then, the measured properties can be very sensitive to the presence of the substrate and can be influenced by the value of the substrate hardness [4].

We here recall that super- and ultrahard materials are defined as those with hardness $\gtrsim 40$ and 60 GPa, respectively. The only super- and ultrahard materials available as single crystals are cubic boron nitride (c-BN, $H \approx 48$ GPa) and diamond ($H \approx 70$–90 GPa).

## 2.3. Ductility

*Ductility* can be defined as the ability of a material to change shape without fracturing. Different quantities can be measured which are related to this property, for example, the relative percent elongation due to uniform plastic flow before a mechanical instability or fracture occurs, or the corresponding relative (percent) reduction in area. By analogy with conventional polycrystalline materials, it can be predicted that in nanocrystals ductility should be enhanced. In particular, the grain-size reduction should result in an increase in ductility, as well as a strengthening of the material.

From a quantitative point of view, ductility (or brittleness, which is the property opposite to ductility) can be defined in terms of the strain-rate sensitivity $m$, which is the exponent in the equation

$$\sigma = k(d\varepsilon/dt)^m \qquad (8)$$

(where $k$ is a proper constant), and can vary from 0 (perfectly brittle material) to 1 (perfectly ductile material).

## 3. MECHANICAL PROPERTIES IN NANOMATERIALS AND NANOSTRUCTURES

### 3.1. Elastic Properties

Among early observations of the atypical mechanical behavior of materials possessing an ultrafine grain structure was the reduction of the elastic constants, in comparison with the corresponding coarse-grained materials; this reduction was often of the order of 20–30%. The first measurements of the elastic constants and in particular of the Young's modulus $E$ of nanocrystalline materials were performed with samples prepared by the inert gas condensation method.

One of the first proposed explanations [5, 6] was that elastic moduli of the grain boundary regions are much smaller

than the corresponding moduli of the grain bulk region. In terms of the linear theory of elasticity established for polycrystalline materials, the elastic constants are then expected to be reduced by a fraction determined by the volume fraction of the grain boundaries

$$C^{-1} = (1 - \alpha)C_0^{-1} + \alpha C_{gr}^{-1} \tag{9}$$

where $C_0$ is the grain bulk modulus, $C_{gr}$ is the grain boundary modulus, $\alpha \approx 3\Delta d/d$ is its relative volume fraction, where $d$ is the grain size and $\Delta d$ is the grain boundary width. This should lead to significant changes only for sizes about or below 10 nm. However, an anomalous elastic modulus reduction was observed also for greater sizes, up to $d = 200$ nm. Other theories have thus been developed. For instance, some of explanations are based on the theory of inelasticity and on the inelastic effects caused by the peculiar structural state of the grain boundary region.

Nowadays, the results documented in the literature regarding the variation of the elastic modulus $E$ with grain size are, at least, conflicting [7]. Most results actually indicate a reduction in $E$, but some experiments suggest on the contrary that no change of the elastic modulus can be attributed to the reduced size. Many authors have thus assumed a grain-size dependence of the elastic constants (e.g., reduction of shear modulus $G$ due to increased interaction distance in the interface region [8] and reduction of $E$ due to increased spacing between atoms in the grain boundary [9]); but, in contrast, other authors attribute the observed reduction to porosity and assume $E$ of the material itself to be independent of the grain size, or even to increase with decreasing size [3] (as reported for high-density nanocrystalline gold in [10]).

The reduction in the Young's modulus may be the result of an enhancement of the stress intensity factor from pores in the material. For instance, the Young's modulus of pore-free, electrodeposited nanophase NiP has been measured to be comparable to that of the corresponding coarse-grained material [11]. It was suggested by Krstic and co-workers [12] that the presence of extrinsic defects (e.g., pores and cracks) was responsible for the low values of $E$ in nanomaterials compacted from powders. Other studies used a phase mixture model consisting of a mixture of crystalline phase, intercrystalline phases, and pores [7], and the result was that the calculated elastic modulus of nanocrystalline materials should in effect decrease with a decrease in the grain size, this effect being anyhow relevant only for sizes below 10 nm. The effect of porosity, however, is predicted to be greater than the grain-size effect. Molecular dynamics studies seem to confirm these conclusions.

Subsequent works on porosity-free materials have supported these conclusions, and it is now believed that the intrinsic elastic moduli of nanostructured materials are essentially the same as those of conventional grain-size materials, at least until the grain size becomes very small, for example, <5 nm; at this size the number of atoms associated with grain boundaries and triple junctions becomes very large. Thus, for most nanostructured materials (grain size > 10 nm), the elastic moduli do not represent peculiar or unique properties.

It must be here observed that many studies about the mechanical behavior of nanomaterials reflect the influence of sample imperfections, given the difficulty of making high-quality samples with such a small grain size. Moreover, most studies limit their investigation to microhardness measurements, because of the usually small sample size which renders stress-strain curve measurements difficult, and do not investigate the value of the elastic constants.

## 3.2. Hardness and Strength

The hardness and the strength of conventional grain-size materials (grain diameter $d > 1~\mu$m) have been known to be a function of the grain size for a long time. For ductile polycrystalline materials a semiempirical relationship, called the *Hall–Petch* equation, has been found to express the grain-size dependence of the flow stress at any plastic strain, up to ductile fracture. In terms of yield stress, this expression can be written as

$$\sigma_y = \sigma_0 + kd^{-1/2} \tag{10}$$

where $\sigma_y$ is the yield stress, $\sigma_0$ is a friction stress opposing to dislocation motion, $k$ is a constant, and $d$ is the grain diameter. The same behavior has been found to hold for hardness

$$H = H_0 + kd^{-1/2} \tag{11}$$

In order to explain these empirical observations, several models have been proposed, which involve either dislocation pileups at grain boundaries or grain boundary dislocation networks acting as dislocation sources. In all cases the Hall–Petch effect is related to the phenomena of dislocation generation and dislocation motion in materials that exhibit plastic deformation.

From an experimental point of view, in general, pure *nanophase metals* turn out to be harder by a factor from 2 to 7 than the coarse-grained counterpart at room temperature (and this is apparently independent of the nanometal synthesis method). For instance, nanophase Cu ($d = 6$ nm) shows a hardness five times greater than bulk Cu ($d = 50~\mu$m). The yield stress of nanophase Pd ($d = 7$ nm) is five times greater than that in the corresponding bulk metal ($d = 100~\mu$m). This anomalous behavior substantially derives from the difficulty in creating dislocations and from the existence of barriers to dislocation motion.

Generally speaking, the mechanical behavior is mainly determined by the type of bonding in the materials. Metals, with highly delocalized bonds, are ductile and thus usually soft; ionic solids are more difficult to deform (due to charge neutrality); covalent solids have strong localized bonds, so that ceramics and intermetallics are subject to brittle fracture. In a crystalline structure, dislocations can be introduced and atomic planes can slide over one another. In the nanophase, both these behaviors are altered. In nanophase metals the hardness increases with decreasing grain size because defects and dislocations are required for deformation to occur, and they are almost absent in nanostructured materials, although regenerative sources of dislocations exist. In other words, the dislocations needed for easy deformation are frozen and new ones are prevented from forming in nanomaterials.

We must here observe that most of the mechanical investigations on nanocrystalline materials refer to hardness, although also tensile test data have been reported. We can say that the overall trend indicates an increase in hardness as the grain-size drops. However, stress-strain curves on small tensile samples show little change of the yield stress. Several recent reviews have summarized the mechanical behavior of nanostructured materials in terms of hardness and yield stress [13–15]. It appears evident that as the grain size is reduced down to the nanoscale regime (<100 nm), hardness typically increases with decreasing grain size and can reach values up to several times greater for pure nanocrystalline metals (10 nm grain size) than for coarse-grained (>1 $\mu$m) metals. However, at the smallest nanocrystal grain sizes (<20 nm), different experiments have evidenced different behaviors for the dependence of hardness on grain size. All the following behaviors were found by different researchers [14, 15]

- positive slope ("normal" Hall–Petch behavior), often with a decreasing gradient at some critical size (see Figs. 1 and 2);
- essentially no dependence (almost zero slope);
- in some cases, a negative slope (sometimes below a critical size).

The negative (or inverse) Hall–Petch effect for very small grain sizes has been discussed. For instance, in the case of intermetallics, at large grain sizes $H$ increases with decreasing $d$, but often decreases or saturates below a critical size, thus showing a transitional behavior. Some nanocrystalline thin films with a grain size $\leq 6$ nm were also found to exhibit a negative Hall–Petch behavior. This behavior was often found in nanocrystalline samples that have been annealed in order to increase the average crystal grain size and make measurements at different sizes. It is possible that thermally treating nanophase samples in the as-produced condition, which results in structural changes such as densification, stress relief, phase transformations, or grain boundary structural changes, may lead to the observed negative Hall–Petch behavior [16]. When annealing or a higher consolidation temperature is adopted in order to increase the
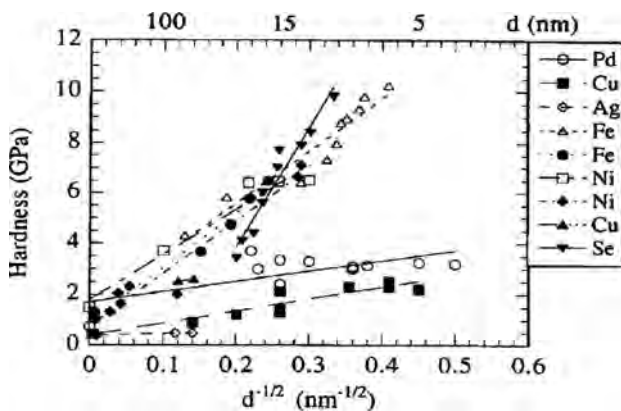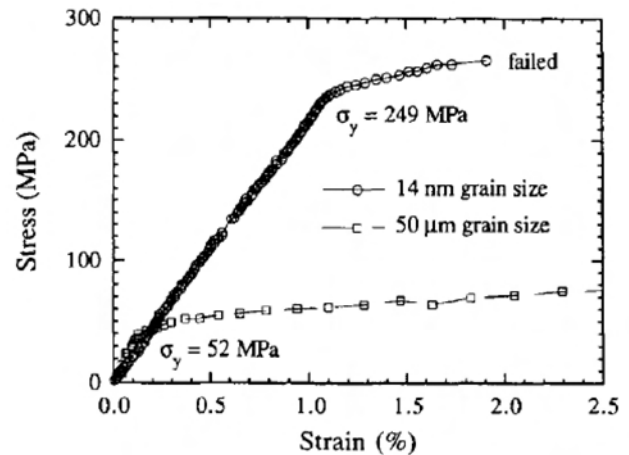


**Figure 2.** Stress-strain curves for nanophase and annealed coarse-grained Pd. Reprinted with permission from [18], R. W. Siegel and G. E. Fougere, *Nanostruct. Mater.* 6, 205 (1995). © 1995, Elsevier Science.

grain size, the size and density of flaws can decrease and the internal stresses in the obtained material can change. Then, also these effects have to be considered together with the change in grain size. In fact, only a few cases of negative Hall–Petch behavior have been reported for as-produced nanocrystalline samples with a broad range of grain sizes (e.g., electrodeposited nanocrystalline alloys and devitrified nanocrystalline alloys [17]), that is, for samples in which the change in the grain size is not accompanied by possible structural defects or stress changes.

Although in many cases the observed negative Hall–Petch slopes are due to artifacts of the specimen preparation methods, it is also possible that conventional dislocation-based deformations are not operable in nanocrystalline materials at the smallest grain sizes ($\leq 30$ nm). At these sizes, theoretically, mobile dislocations are unlikely to occur; in fact, they were not observed in *in-situ* TEM deformation experiments [16]. In any case, it is clear that the hardness, strength, and deformation behavior of nanocrystalline materials, although unique, are not yet well understood.

We have already said that in nanophase materials, in the grain-size range where the hardness increases monotonically, this happens because the defects and dislocations required for deformation to occur are almost totally absent. However, in defect-free conventional grain-sized materials there are also dislocation sources, which are regenerative sources of dislocations. The critical stress required to activate, for instance, Frank–Read sources is $\sigma_{cr} = K(\mu b/L)$, where $K \approx 1$ (=0.5 for edge dislocations and =1.5 for screw dislocations), $b$ is the Burgers vector, and $L$ is the distance between pinning points [18]. In nanomaterials, the grain size can be identified with the limiting value for $L$. Thus, in very small particles $\sigma_{cr}$ actually exceeds the conventional yield stress for the material. We can simply put it by saying that in nanostructured materials the dislocations needed for deformation are frozen, and new ones are prevented from forming.

Also the *plastic* deformation behavior and in particular the yield stress have been investigated [7]. It is well established that coarse-grained materials exhibit a constant



**Figure 1.** Room-temperature hardness versus grain size for nanophase metals compared with the hardness of their coarse-grained counterparts (values near origin). Reprinted with permission from [18], R. W. Siegel and G. E. Fougere, *Nanostruct. Mater.* 6, 205 (1995). © 1995, Elsevier Science.

Hall–Petch gradient $d\sigma/d(d^{-1/2})$ (see Eq. (10)); again, three types of behavior have been observed in the case of nanostructured materials: positive Hall–Petch gradient (corresponding to what is observed in coarse-grained materials), decreasing gradient at smaller sizes, and a negative gradient below some critical size.

In summary, the Hall–Petch equation, which relates the yield stress or the hardness to the inverse square root of the grain size, predicts great increases in the material strength with grain refinement [19]. On the other hand, theory indicates that the high volume fraction of interfacial regions leads to increased deformation by grain boundary sliding in metals with grain size in the low end of the nanocrystalline range. The Hall–Petch relationship is usually explained in terms of dislocation pileups at grain boundaries, and it should break down at sizes such that a grain cannot support a pileup. Great efforts have been recently devoted to the use of molecular dynamics simulations of deformations in the nanophase, in order to verify and explain these predictions. Still many questions remain open (see, e.g., [20]).

Again, as in the case of the attempted explanation of the anomalously low values of the elastic constants, most models of nanocrystalline matter describe the mechanical behavior in a defect-free material, while real materials actually contain pores, flaws, trapped gases, and impurities and they are better described by a wide distribution of grain sizes. Moreover, one of the main practical problems, especially in the case of nanoceramics, is represented by the difficulty of making specimens that are both fully dense and large enough to perform traditional measurements and mechanical tests.

## 3.3. Tensile and Compressive Response, Ductility and Creep, Superplasticity

Again, the starting point in the discussion of these properties is the already well-known strong effect that grain size has on the ductility and toughness of conventional grain-size ($>1\ \mu$m) materials. For example, the ductile-brittle transition temperature in conventional mild steel can be lowered by about 40 °C by reducing the grain size by a factor of 5. We here recall that the brittleness can be defined in terms of the strain-rate sensitivity $m$, that is, the exponent in the equation

$$\sigma = k(d\varepsilon/dt)^m \qquad (12)$$

and can vary from 0 (perfectly brittle) to 1 (perfectly ductile).

A significant enhancement of ductility has been observed also for nanosize crystalline samples, and in some cases, the term *superplasticity* has been employed to indicate the manifestation of an exceptional ductile behavior when the grain size is reduced in the nanometer range, that is, the manifestation of an exceptionally enhanced strain to failure. We can define superplasticity as the capability of polycrystalline materials to exhibit very large tensile deformations without showing fracture, or necking. Elongations in the range 100–1000% are considered to be the typical defining feature of this phenomenon, with respect to conventional behavior, with elongations of the order of some percent. Superplasticity is usually observed only above a certain critical temperature in the materials that present this behavior also when

coarse-grained, and these "activation" temperatures are usually higher than 0.5 $T_M$, where $T_M$ is the melting temperature. When the grain size is decreased, it is found that the threshold temperature can be lowered; at the same time, an increase in the strain rate for the occurrence of superplasticity is observed. When these behaviors were first reported, it was believed that creep rates could be enhanced by many orders of magnitude by simply reducing the grain size below 100 nm, and that superplastic behavior could be observed also in nanocrystalline materials at temperatures much lower than 0.5 $T_M$. Subsequent creep experiments have not fully confirmed this prediction, and instead the observed creep rates are comparable to or lower than those measured in coarse-grained samples of the same material at temperatures <0.5 $T_M$.

However, there is some evidence of a superplastic behavior enhancement in nanocrystalline materials at temperatures >0.5 $T_M$, and, as we have said, superplasticity has been observed at lower temperatures and at higher strain rates in nanocrystalline materials than in coarse-grained materials. In any case, it must be observed that tensile superplasticity is limited to materials that already exhibit superplasticity for coarser grain sizes (1–10 $\mu$m). For example, for zirconia ($ZrO_2$) and titania ($TiO_2$), $m = 0.02$ at 300 K for $d = 100$ nm (with reference to Eq. (12)), but $m$ increases almost exponentially below 50 nm for both the oxides [13].

Superplastic behavior has been observed [21] in some alloys, for example, in nanocrystalline Pb(62%)Sn at 0.64 $T_M$ and in nanocrystalline Zn(22%)Al at 0.52–0.60 $T_M$; however, it was also observed [22] in 200-nm nanocrystalline Ti (190% elongation, $m = 0.32$) at 0.42 $T_M$, that is, a temperature 50 °C lower than for 10-$\mu$m grain size Ti. The flow stress for the 200-nm Ti at 550 °C was 90 MPa, compared to 120 MPa for 10-$\mu$m Ti at 600 °C. A heavily deformed Ti alloy with an initial grain size of about 20 nm could be elongated by 600% at 500 °C. The same alloy, but with a grain size in the micrometer range, exhibits superplasticity only in the temperature range 900–950 °C; otherwise typical elongations are extremely limited (0–2%).

In contrast with oxides and alloys, single-phase nanostructured metals usually exhibit high strength and hardness but brittle behavior at low temperatures (<0.5 $T_M$). So far there is no evidence of superplasticity behavior in tension for nanomaterials prepared by powder metallurgical methods. Experimental results on the ductility of single-phase nanocrystalline materials indicate little ductility in tension for grain sizes less than about 25 nm, and this is true both for materials that are ductile when coarse-grained (e.g., elemental metals) and materials that are brittle when coarse-grained. Tensile creep measurements on nanophase metals have been performed at room temperature for Cu, Ni, and Pd, which exhibited a logarithmic stress-strain behavior as a function of time, apparently resulting from dislocation activity or grain boundary sliding. The plastic strain rate increases with decreasing grain size [19] (while it is usually roughly constant for sizes >10 nm). This suggests that in nanophase metals no damage accumulation is happening, which is a characteristic of superplasticity.

In some metals, for example, in Cu, ductile behavior is observed in compression, with yield strengths about twice those observed in tension. The limited ductility exhibited

by single-phase nanometals can be attributed, as already explained, to the difficulty in creating and moving dislocations at the smallest grain sizes, but may as well depend on the fact that the results of these measurements are sensitive to a significant presence of flaws and porosity (and in fact annealing after consolidation has resulted in an improved ductility and strength of nanomaterials subjected to tension). This could also be the reason for the asymmetry observed when comparing the results obtained in compression or in tension tests, respectively; in addition, the nature of the deformation process in terms of *shear banding* (see Section 3.6) may also be important.

Also for intermetallics or ceramics, experiments concerning a possible increase in ductility by grain-size reduction are contradictory.

Compressive creep tests of nanophase *intermetallic* materials have instead confirmed the enhanced plasticity and compressive strength behavior for this class of materials. Also hardness tests at elevated temperatures can be used to study compressive creep behavior of nanomaterials. In this case a nanoindenter is usually employed as a static tool, but if loading times are increased, while the load is kept constant (at a given temperature), the indentation size can be monitored and this can provide information about the dynamic compressive behavior. At low temperatures, for instance, nanophase TiAl showed little change in hardness until the temperature rose to the point that thermally activated deformation by diffusional creep started.

Many studies have been devoted in particular to ceramics and nanoceramics (see, e.g., [23, 24]). Early observations of ductile behavior of brittle nanoceramics at low temperatures suggested that brittle ceramics or intermetallics might exhibit ductility with nanoscale grain structures, but many more recent results seem to contradict what was previously predicted. An apparent plastic behavior in compression was observed in nanocrystalline $CaF_2$ at 80 °C and $TiO_2$ at 180 °C [24]. Nanocrystalline ceramics are considered interesting because they have, with respect to conventional ceramics, a lower sintering temperature (e.g., ~600 °C for titania) and an enhanced strain to failure. Most of the data currently available on the stress-strain behavior of nanoceramics is from small compression specimens, while tensile behavior has never been quantified in detail.

Most ceramics tested in compression at room temperature usually exhibit brittle behavior. Instead, in nano-intermetallic $Fe_{28}Al_2Cr$, whose yield strength is about 10 times greater than for its coarse-grained (75 $\mu$m) counterpart, a compressive strain of about 1.4 could be obtained at room temperature. In general, in nanoceramics, creep processes have been observed at lower temperatures than in coarse-grained ceramics. As usual, porosity and imperfections in the as-prepared nanocrystalline material affect the testing, but it has been found that when the porosity is lower than 20%, the creep rate in compression of ceramic powder compacts is only weakly dependent on the porosity degree.

The results of studies on two-phase nanostructured materials suggest that the combination of high hardness/strength and toughness/ductility may be possible in multiphase nanostructured materials. Many of Al-, Mg-, and Ni-based alloys with a nanoscale structure consist of nanocrystallites in an amorphous matrix. Some Al-rich alloys contain nanoscale

particles surrounded by crystalline face-centered cubic Al. These multiphase nanostructured alloys possess extremely high strength coupled with some ductility [25]. Ductility is high in compression, but uniform elongation in tension is limited. This behavior is analogous to that exhibited by ductile amorphous alloys. These results again suggest the possibility of the development of nanostructured multiphase composites that combine extremely high hardness and strength with toughness and ductility. Such materials could in principle be useful for many applications where they may be employed as unique structural materials.

Let us discuss the characteristics of creep mechanisms in nanostructured materials. Since creep is primarily controlled by diffusion, it is expected to occur quickly in nanophase materials because of the large volume fraction of grain boundaries and the short diffusion distances. Diffusion along grain interfaces is very rapid, and mechanisms similar to those that drive sintering and neck formation at room temperature in nanophase metals may enhance also the creep rates in these materials. Creep rates may also be influenced by the level of porosity in nanophase samples, since free surfaces tend to increase diffusion rates relative to grain boundary rates.

The possible enhanced ductility in nanophase ceramics can find an explanation in terms of the so-called *Ashby–Verral* model, which is based on the principle of grain boundary sliding with diffusional flow. If a compressive stress is applied to a system of equiaxed grains, there is a diffusional flow in the boundary regions. This can lead to a change in the external shape, but the grains remain equiaxed and maintain their size and orientation, sliding over one another by diffusional accommodation at the interfaces. The reason why this mechanism should be activated when the grain size is decreased in ceramics is that sliding would occur if, when a crack is opened at an interface, diffusion can contribute to fill it. In small grains, the number of atomic rearrangements required for healing is possible in real time during the sliding, while it would take long times in conventional grain-sized materials.

Karch et al. [24] also attributed ductility to enhanced diffusional creep providing the plasticity, where conventional grain-size materials would fail in the elastic regime. Their model relates the strain rate (or creep rate) to grain boundary diffusion

$$\frac{d\varepsilon}{dt} = \frac{B\sigma\Omega\Delta D_b}{d^3 kT} \tag{13}$$

where $\sigma$ is the applied stress, $\Omega$ is the atomic volume, $d$ is the grain size, $k$ is the Boltzmann constant, $T$ is the temperature, $B$ is a constant, and $D_b$ is the grain boundary diffusion coefficient. Going from a grain size of 1 $\mu$m down to 10 nm should increase $d\varepsilon/dt$ by $10^6$ or more if $D_b$ is significantly larger for nanomaterials. However, their results obtained for nanocrystalline $CaF_2$ at 80 °C and $TiO_2$ at 180 °C have not been reproduced, and it is believed that the porous nature of these samples was responsible for the apparent ductile behavior. Recent creep measurements of nanocrystalline Cu, Pd, and Al-Zr at low temperatures [26] found creep rates comparable to or lower than the corresponding coarse-grained material rates. One possible explanation is that the observed low creep rates are caused by the

high fraction of low-energy grain boundaries in conjunction with the limitation in dislocation activity due to the small grain sizes.

In summary, exceptional ductility due to diffusional creep in nanocrystalline brittle ceramics or intermetallics at temperatures significantly less than 0.5 $T_M$ has not been realized, while effective enhanced ductility has been obtained at somewhat higher temperatures, and an improvement of creep properties can be seen in terms of a lower "activation" temperature for superplasticity and a higher strain-rate regime. Experimental results and interpretations are still in contrast and not very clear, so that it can be said that the real effect of the nanostructure on these properties has not been fully understood.

It must be underlined that grain boundaries, in this kind of materials, are in a nonequilibrium configuration, and even in a material with a fixed grain size a wide range of properties can be obtained and measured depending on the sample preparation (and on the measurement procedure); also the presence of metastable phases may be important for the comprehension of the ductile and plastic properties of nanomaterials. This suggests that control of mechanical properties through grain boundary engineering is possible.

## 3.4. Fracture and Toughness

In practical applications of (e.g., structural) materials, a significant limitation is often represented by the fracture strength of the material, and not by the yield strength. A material can yield and with this mechanism sustain itself against an imposed stress. This is possible because of the behavior of microstructures like dislocations and grain boundaries, which prolongs plasticity. However, a material possessing an elevated strength can also fail suddenly in a brittle way, with little plasticity (and this is a serious problem for real applications).

The results and comprehension concerning the fracture properties of nanostructured materials have so far been very limited and, as usual, influenced by the presence of porosity [27]. Some bending tests [27] of compacted NiP showed that by decreasing the grain size an enhancement of the fracture stress and of the strain-to-fracture can be realized. High-resolution electron microscopy of *in-situ* fracture of nanophase Au and Au/Si composite films on Al substrates showed a strong dependence of the fracture behavior on the grain size. For microstructured materials, improvements in toughness and a lower brittle-to-ductile transition temperature are obtained by decreasing the grain size, but the same behavior has still to be proved for nanomaterials. In a study of intermetallic TiAl (grain size in the range 100 nm–70 $\mu$m), the toughness was found to decrease with decreasing grain size, as intragranular cracking gave way to intergranular fracture, but there are no studies in the more significant range 5–100 nm.

Mechanical failure, which limits ductility, can be viewed as a competition between dislocations and nucleation or propagation of cracks, depending on the grain size. (In small grains, crack propagation can be more difficult.) However, the large increase in yield stress (hardness) observed in nanomaterials suggests that the fracture stress can be lower than the yield stress and therefore result in a reduced ductility.

## 3.5. Fatigue and Wear

Fatigue has not been extensively studied in nanostructured materials [27]. The high cycle fatigue behavior of bulk specimens of nano-Ni produced by electrodeposition (in the grain-size range 50–100 nm) has been reported to be very similar to that of the conventional material [27]. No quantitative data on the fatigue life and fatigue crack growth rate are available for any nanomaterial.

A summary of the wear behavior analysis of nanomaterials (bulk cutting tool materials and surface coatings) has been performed by Morris [28]. Hardness was found to be generally greater than in the conventional corresponding material, but toughness was found to be independent of hardness; abrasive wear resistance and sliding wear resistance were very high; tool life increased significantly when the grain size was below 300 nm. (This property has already been exploited in industry for the manufacture of tools with complex cutting edge shapes.) There is currently no complete explanation for the wear behavior of nanostructured materials. An analysis of friction and wear for nanolaminated Ti-TiN and Al-Al$_2$O$_3$ composites was performed by Northwood and Alpas [29], and the friction coefficient and the wear rate were found to decrease with thickness.

## 3.6. Observations

Some generalizations can be made about the deformation mechanisms in nanostructured materials. Dislocation activity dominates for temperatures $<0.5$ $T_M$, when the grain size is in the range 50–100 nm. Then, as grain size decreases, dislocation activity also decreases. The lack of dislocations in grains whose size is below 50 nm is the result of the *image forces* that act on dislocations near surfaces or interfaces.

The lack of dislocations in confined spaces, such as single-crystal whiskers, has been known for many years. Also the creation of new dislocations is more difficult as the grain size reaches the low end of the nanoscale, since stresses needed to activate dislocation sources, as the Frank–Read source, are inversely proportional to the distance between dislocation pinning points, so that these activation stresses can reach the theoretical shear stress of a dislocation-free crystal (this happens roughly at a grain size of ∼2 nm, i.e., when the grain size limits the distance between pinning points). Thus, other mechanisms, such as grain boundary sliding or grain rotation accompanied by short-range diffusion healing events [14], may control the deformation behavior at this scale.

Another comment is necessary for the observation of examples of deformation by *shear banding* for some nanocrystalline materials, where deformation in compression proceeds by intense localized shear banding. In these cases the stress-strain curves exhibit essentially elastic–perfectly plastic behavior; that is, no measurable strain hardening was observed. Shear banding is also the deformation mode observed in amorphous metallic alloys and in amorphous polymers. This suggests an evident similarity between deformation mechanisms in nanocrystalline materials and in amorphous materials, even though not all tensile data on nanocrystalline materials exhibit a lack of strain hardening. In general, amorphous materials exhibit many of the

phenomenological characteristics of deformation in nano-materials, that is, shear banding, asymmetry between tensile and compressive behavior, and perfectly plastic behavior. Unfortunately, deformation mechanisms are not completely understood in amorphous materials either.

# 4. SPECIAL NANOSTRUCTURES

## 4.1. Nanocomposite Materials and Dispersions

The benefits of introducing precipitates of nanometric size (1–100 nm) in a conventional material are well known [27] (this is called *precipitation hardening*). Well-established structural materials (tempered steel and age-hardened aluminum alloys) contain nanoscale features in order to achieve better mechanical properties. For instance, when nanosize Mo (5–20 vol.%) is dispersed in micrometer-sized $Al_2O_3$, considerable improvements in hardness, fracture strength, and toughness are obtained, though each property has a different behavior as a function of composition. The hardness of $Al_2O_3$-, MgO-, and $Si_3N_4$-based nanocomposites was found to increase with decreasing grain size and with increasing SiC content (the hardness change being in agreement with the rule of mixtures). By introducing nano-structured SiC dispersions (200 nm) in a matrix of $Al_2O_3$, the fracture strength can be increased by a factor of 3 and also the high-temperature mechanical properties are enhanced. The decrease in hardness with increasing temperature is significantly less in nanocomposite $Al_2O_3/SiC$ than in monolithic $Al_2O_3$. The tensile strength and elongation to fracture in Mg-Zn-La alloys containing Mg nanoparticles (5–10 nm; interparticle distance 3–10 nm) are considerably greater than in amorphous Mg-Zn-La alloys of similar compositions, and the main reason is that the nanoparticles suppress homogeneous shear. By introducing nanoscale multifilaments of $Nb_3Sn$ in $Cu$-$Nb_3Sn$ composites, unique combinations of superconducting and mechanical properties can be obtained. Some controversy exists about the super-modulus effect reported in thin layers containing granular metal particles.

A particular class of nanocomposites is represented by polymer nanocomposites. The reinforcement of polymers with a second phase, organic or inorganic, in order to obtain a polymer composite is commonly employed in the production of modern plastics. Polymer nanocomposites [30–32] represent an alternative and an improvement with respect to conventional polymer composites. A doubling in tensile modulus and strength has been demonstrated for some nanocomposites, and the heat-distortion temperature can be increased by up to 100 °C. Moreover, polymer nanocomposites can be much lighter than conventional polymer composites.

The key point for the mechanical properties of polymer nanocomposites is that uniform dispersions of nanosized particles (nanoelements) can lead to an ultralarge interfacial area between the constituents per volume of material (up to 700 $m^2/cm^3$, e.g., for dispersions of silicates in polymers). An interface limits the number of conformations that polymer molecules can adopt, and this affects the mechanical behavior (see [30] for details). The influence of an interface is

related to some fundamental lengths: the size of a nanoelement, its aspect ratio (e.g., length/transverse dimension), the interelement distance, and the length scale of the adjacent matrix, which for polymers is of the order of the radius of gyration of a chain (5–10 nm). In a polymer nanocomposite the interfacial region becomes the dominant bulk phase (see Fig. 3).

The inclusion of elastomeric nanoparticles in polypropylene and the subsequent effect on the resulting elastic properties has also been studied, and it has shown the possibility of combining good toughness and stiffness properties in this nanocomposite material [33].

## 4.2. Nanotubes

Single-walled carbon nanotubes (SWNTs) can be thought of as obtained by warping a single graphitic layer to form a seamless cylindrical object [34]. Beyond possessing unique electronic properties, depending on the symmetry, or chirality, of the carbon lattice, nanotubes attract today an enormous attention also because they are expected to be very strong and have high elastic moduli [35, 36], and it is now possible to grow multiwalled or single-walled nanotube microarrays or patterns with a desired geometry and alignment. In 1996 Thomas Ebbesen estimated Young's modulus of a carbon nanotube by measuring the vibrations of the free end of a nanotube clamped at the other end with a TEM, and more recently Young's modulus has been estimated by observing their bending with an atomic force microscope [37]. The estimates (up to 1.25 TPa) were consistent with the exceptionally high values of Young's modulus measured for a graphene sheet, that is, about 1 TPa. Single-walled carbon nanotubes are also expected to be very strong and to resist fracture under extension. Moreover, molecular dynamics simulations indicate that the nanotube should regain its original shape when the stress distorting it is removed.

The expected very high strength-to-weight ratio of SWNTs has stimulated an enormous interest in view of applications as reinforcement fibers in composite materials, high-strength cables, actuators, etc. [34, 38–40]. Elastic properties of SWNTs, and acoustic vibrational modes in carbon nanotubes, have been calculated both by *ab initio* calculation (lattice dynamics, e.g., [41]) and by continuum models [42]. Acoustic vibrational properties are strictly related to elastic properties of SWNTs, and these (e.g., Young's modulus)
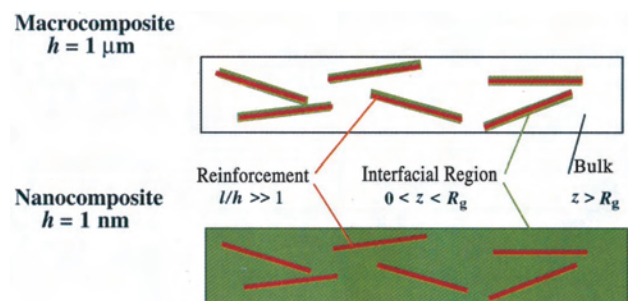


**Figure 3.** Schematic picture of a polymer nanocomposite. Reprinted with permission from [30], R. A. Vaia and E. P. Giannelis, *MRS Bull.* 26, 395 (2001). © 2001, Materials Research Society.

have been estimated by observing their bending with AFM [37] or, as we have said, their freestanding room-temperture bending vibrations with TEM [40, 43]. With these methods problems arise from the lack of precision in determining the SWNT diameter, length, temperature, and vibrational frequency, and the tendency of SWNTs to form bundles complicates the analysis. Nevertheless, a Young's modulus of the order of $E = 1.25$ TPa was found. Moreover, different theoretical approaches have been proposed to model a SWNT with an elastic continuum model, or by *ab initio* calculations, and the predicted Young's moduli are scattered over a large interval. It is still a matter of speculation whether the curvature modifies the original properties of the graphene sheet, since the Young's modulus of SWNTs appears to be systematically higher than the in-plane elastic modulus of graphite, and no precise comparison could be made between SWNTs and MWNTs (see, e.g., [44]). The higher value of their Young's modulus could be attributed to an increased strength due to the wrapping [43] (stiffening of the graphite sheets is predicted for a radius lower than 0.5 nm).

Brillouin scattering (see Section 5.2.2) has been used to measure longitudinal acoustic modes in SWNTs [45, 46], and from the measurement of their frequencies, it was possible to estimate the two-dimensional Young's modulus for the nanotube walls, $E_{2D} = 110$ N/m. This value is of the same order of magnitude as the C-C atomic force constant computed for a graphite plane. If one considers the thickness of a graphite layer, this corresponds to a Young's modulus for an ideal isolated graphitic plane of the order of 1 TPa. This measurement was made possible by the preparation of a sample of pure oriented and almost noninteracting SWNTs. This measurement allows an estimate of the in-plane elastic properties (2D Young's modulus) of the tube walls, and thus of a curved graphitic sheet, which is in agreement with reported computations; with samples possessing a more defined geometry, the proposed method would in principle allow a more precise measurement of SWNT elastic constants. In the case of SWNTs, the 2D Young's modulus is the only unambiguously defined elastic property of the material constituting the tube. In fact, in the rod model previously used in the literature, the 3D Young's modulus is an effective elastic property embodying uncertain geometrical parameters. In these aligned SWNT bundles, only vibrational modes propagating along the tubes were detected (and not perpendicularly to the tube direction), thus confirming that the lateral cohesion between tubes is poor (thus hindering the propagation of effective modes transverse to the bundle orientation) and that the high strength of the material is highly anisotropic. This limitation must be taken into account when considering these structures for mechanical applications as reinforcing high-performance fibers.

## 4.3. Multilayers

Nanolayered materials also exhibit interesting structural and mechanical behaviors [47, 48]. Physical vapor deposition permits to choose among elements, alloys, and compounds as layer constituents. The interface area density is usually very high, so that interface effects dominate the multilayer properties, and this can lead to unusually large strains and to the realization of metastable structures. The interest in the

mechanical properties of nanolayered materials arises from the fact that plastic deformation can be confined to small volumes by controlling both the frequency and the magnitude of obstacles to dislocation motion. The assumptions used to model mechanical behaviors at the small scales may not be valid at the nanometer scale even if this confinement is limited to one dimension (perpendicular to the film plane), and the result is that there is a critical layer thickness below which improvement in strength does not occur [49], similarly to what happens in nanocrystal grains. Usually, metals are employed for the deposition of superlattices with improved mechanical properties (see, e.g., [47, 48, 50, 51] and references therein): TiN/NbN multilayers reach a hardness value of 50 GPa [52], while hardness of single TiN or NbN films is around 20 GPa. Mo/NbN, W/NbN, Fe/Pt, Ag/Cr, Cu/Ag, Al/Ti are just some examples of metal superlattices.

Almost all thin films deposited on a substrate are normally in a state of stress if no film treatment is performed (e.g., annealing) [50]. While the structure of the films can be measured by X-ray diffraction (for the atomic order and crystalline structure; in particular, grazing angle incidence X-ray scattering, GIXS, is a nondestructive powerful tool to characterize epitaxially grown films) or X-ray reflectivity (for density, layering period, roughness, and interface roughness determination), double-crystal diffraction topography can be used to make precise thin-film stress measurements. The substrate itself is in principle strained. The film stress may curve the substrate. The difference in the curvature of the substrate before and after deposition can be measured and the stress in the film can be computed using the *Stoney equation*

$$\sigma = E_s d^2 (1/R - 1/R_0)/6(1 - \nu_s)t \qquad (14)$$

where $\sigma$ is the film stress, $E_s$ and $\nu_s$ are Young's modulus and Poisson's ratio of the substrate, $d$ is the substrate thickness, $t$ is the film thickness, $R$ is the radius of curvature of the substrate after deposition, and $R_0$ is that radius before deposition.

Stress may have different origins and can be principally of three types: coherency stress, thermal stress, and intrinsic (or growth) stress.

Coherency stress results when a thin film is lattice matched to a substrate that has an equilibrium in-plane lattice parameter different from the film.

Thermal stress is generated when a film-substrate system experiences a change in temperature, and the film and the substrate have different thermal-expansion coefficients. If a film is deposited at temperature $T_1$ and then heated or cooled at a temperature $T_2$, there will be a thermal stress

$$\sigma_{th} = -E\Delta\alpha(T_2 - T_1)/(1 - \nu) \qquad (15)$$

where $\Delta\alpha$ is the difference in the thermal expansion coefficients of the film and substrate. Intrinsic stresses are stresses generated during film growth.

A superlattice constituted by layers made of elements with similar structures, but with a mismatch in the lattice constant, exhibits interfaces with different degrees of structural coherency. Superlattice layers may be coherently strained with respect to each other (e.g., for small values of the

thicknesses and small degrees of mismatch); otherwise the mismatch can be relaxed by the introduction of interfacial misfit dislocations (e.g., for large thicknesses and mismatch). The critical thickness at which strain relaxation is favored can be predicted (a formalism has been developed by Matthews and Blakeslee). The balance between misfit dislocation energy and the strain energy can predict the observed strain relaxation.

As far as elastic properties are concerned, early observations reported a very large ($>100\%$) enhancement of the elastic moduli in multilayers. This phenomenon was named the *supermodulus* effect. Recent works have shown that these were artifacts or anomalies, and only a 10% enhancement in the elastic moduli appears to be real.

The quantity that is most easily measurable in thin films or multilayers is the hardness $H$, which can be related in a typical simple plasticity model to the yield $\sigma_y$ strength of a material by the relation $H \approx 3\sigma_y$. Hardness, measured, for example, by nanoindentation, has been studied in many systems as a function of the bilayer period (both in epitaxial and polycrystalline multilayer systems). In any case, in general it can be said that all systems show a decrease in hardness as the bilayer period increases above roughly 4 nm (and this decrease has been interpreted in terms of the Hall–Petch behavior, see Eq. (11), as for nanocrystalline materials). Also, in some systems hardness decreases as the period decreases below 1–2 nm. More recent works have instead focused on the plastic properties of superlattices.

Some of the possible explanations for hardening in multilayers and superlattices involve structure barrier strengthening, coherency stress strengthening, misfit dislocation density strengthening, but the dominant mechanism seems to be the effect of the dislocation image force associated with a discontinuity in the elastic modulus at the interfaces. Moreover, at larger bilayer periods, dislocation pileup and bowing processes occur.

In 1970, Koehler [53] suggested that a strong solid could be obtained by layering materials with the same structure but much different shear moduli, since plastic flow would be inhibited by the stresses on dislocations in the softer layers. He also suggested that in order to obtain a strong material, the layers should be thin enough to prevent the operation of dislocation sources. The result of his analysis was that the stress required to operate a dislocation source is roughly inversely proportional to the layer thickness, if this is in the nanometer range.

As we have already stated, the hardness behavior has also been interpreted in the framework of the well-known Hall–Petch behavior for nanocrystalline materials. Here we recall that the repulsive force of like dislocations piling up at a barrier results in a yield strength given by $\sigma_y = \sigma_0 + k_{HP}/\sqrt{d}$.

Applied to the hardness of multilayers, we might expect the hardness to follow the same law as a function of the bilayer period (replacing the grain size)

$$H = H_0 + \frac{k'_{HP}}{\sqrt{\Lambda}} \quad (16)$$

where it can be shown that [47] $H_0 \approx 3\sigma_0$ and $k'_{HP} \approx 3\sqrt{2}k_{HP}$ (assuming $d = \Lambda/2$), and where $\Lambda$ is the bilayer period. A
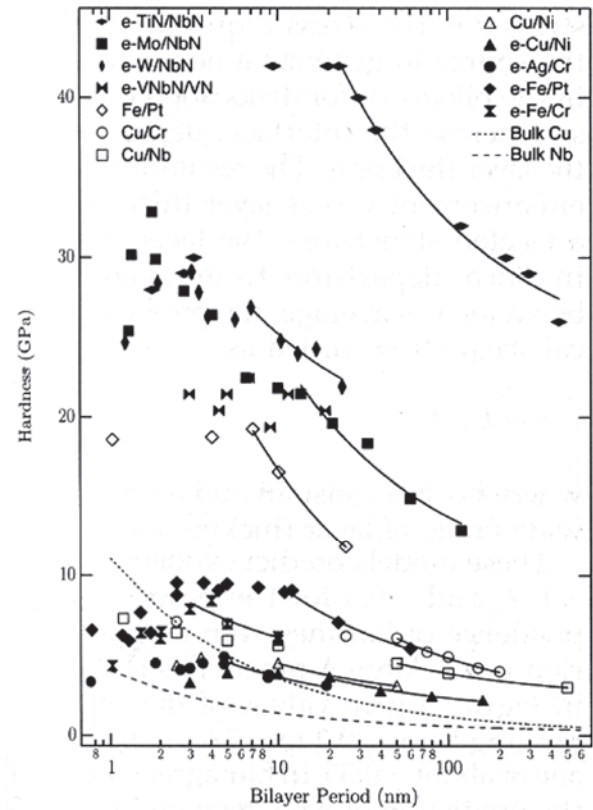


**Figure 4.** Plot of hardness versus bilayer period for several multiplayer systems. Their behavior is often well described by a Hall–Petch equation (solid lines). Reprinted with permission from [47], B. M. Clemens et al., *MRS Bull.* 24, 20 (1999). © 1999, Materials Research Society.

plot of hardness versus $1/\sqrt{\Lambda}$ is usually linearly fitted to obtain a typical Hall–Petch plot (see Fig. 4).

Anderson and Li [54] developed a model which considers dislocation sources and interaction of the resulting dislocation pileup with interfaces. The stress required to operate the source increases as the number of dislocations present in the pileup increases. The result is a double pileup of screw dislocations. The critical shear stress $\tau$ is the stress required either for the source to generate a new dislocation in the pileup or for dislocation transmission across the interface, depending on layer thickness. On average, the predicted critical shear stress varies as

$$\tau = k_{AL}\Lambda^{-p} \quad (17)$$

where $k_{AL}$ is a constant and $p \approx 0.3$ over a wide range of layer thicknesses.

The three models illustrated (Koehler, Hall–Petch, and Anderson–Li) predict exponents of $-1$, $-\frac{1}{2}$, $-0.3$ for the power dependence of hardness versus bilayer period in a large $\Lambda$ range. Fits to existing data suggest possible values between $-0.2$ and $-0.6$ [47].

Hall–Petch strengthening is observed as dislocations pileup provides the force required to pass dislocations from layer to layer. As the bilayer period decreases, this becomes increasingly difficult and the image force barrier for dislocation motion between layers becomes the strength-limit mechanism. This results in a deviation from the Hall–Petch

behavior. In all cases, the resistance to dislocation motion in the individual layers must be overcome for dislocation motion to occur. Hence the observed hardness will be the sum of the stress required to overcome this resistance plus the weaker of the other mechanisms.

Also the plastic behavior of multilayers has been investigated by some researchers, by means of tensile tests in order to overcome problems related to the nanoindentation measurement, and the yield stress was found to increase with decreasing bilayer period $\Lambda$ (e.g., from ∼500 to 700 MPa going from 90 to 10 nm in an Al/Ti system [51]).

Anderson et al. [49] present a detailed analysis of dislocation-based deformation mechanisms in metallic nanolaminates. They observe that (e.g., in Ni/Cu superlattices) the tensile yield stress increases with decreasing bilayer period only down to a thickness of roughly 20 nm (for which the yield stress is maximum), then the yield stress decreases. The material is coherent when $\Lambda < 8$ nm, while the barrier strength increases progressively as $\Lambda$ increases. The maximum in the strength coincides with the presence of just one dislocation in a layer. Strength then falls at values of $\Lambda$ higher than 20 nm because of stress amplification at the head of successively longer pileups (see Fig. 5). We refer the reader to [49] for the details of the analysis.

## 5. EXPERIMENTAL TECHNIQUES

The standard technique for the measurement of hardness in nanostructured materials and thin films or multilayers is nanoindentation, which has been described before. We here mention other interesting and recent techniques for the analysis of elastic and mechanical properties, which have been demonstrated suitable especially when applied to nanostructured materials.

### 5.1. Atomic Force Microscopy

The atomic force microscope (AFM), or scanning force microscope (SFM), was invented in 1986 by Binnig, Quate, and Gerber. Like all other scanning probe microscopes, the



**Figure 5.** Tensile yield stress in a Ni/Cu superlattice as a function of the bilayer period. Below 8 nm the layer is coherent; for a thickness of 20 nm just one dislocation is present in the layer. Reprinted with permission from [49], P. M. Anderson et al., *MRS Bull.* 24, 27 (1999). © 1999, Materials Research Society.

AFM utilizes a sharp probe moving over the surface of a sample in a raster scan. In the case of the AFM, the probe is a tip on the end of a cantilever which bends in response to the force between the tip and the sample.

The first AFM used a scanning tunnelling microscope at the end of the cantilever to detect the bending of the lever, but now most AFMs employ an optical lever technique. As the cantilever flexes, the light from a laser is reflected onto a split photodiode. By measuring the difference signal, changes in the bending of the cantilever can be measured. Since the cantilever obeys Hooke's law for small displacements, the interaction force between the tip and the sample can be found.

The movement of the tip or sample is performed by an extremely precise positioning device made from piezoelectric ceramics, most often in the form of a tube scanner. The scanner is capable of sub-angstrom resolution in x-, y-, and z-directions. The z-axis is conventionally perpendicular to the sample.

Different operational modes can be chosen; for example, contact, noncontact, and intermittent-contact AFMs are used for measuring the morphology or topography of a sample surface.

Anyway, other modes are possible [55]. Lateral force microscopy (LFM) measures lateral deflections (twisting) of the cantilever that arise from forces on the cantilever parallel to the plane of the sample surface. LFM studies are useful for imaging variations in surface friction that can arise from inhomogeneities in the material surface. As the cantilever is scanned over the specimen surface (with the cantilever now scanning with its long axis perpendicular to the fast scan direction), variations in friction between the tip and sample will cause the tip to slick/slip during its scan, resulting in twisting of the cantilever.

Force modulation microscopy (FMM) is an extension of AFM imaging that includes characterization of a sample's mechanical properties. In FMM mode, the AFM tip is scanned in contact with the sample, and the z feedback loop maintains a constant cantilever deflection (as for constant-force mode AFM). The amplitude of the resulting cantilever modulation varies according to the elastic properties of the sample. Phase detection microscopy (PDM), or phase imaging, is another technique used to map variations in surface properties such as elasticity, adhesion, and friction. It refers to the monitoring of the phase lag between the signal that drives the cantilever to oscillate and the cantilever oscillation output signal. Changes in the phase lag reflect changes in the mechanical properties of the sample surface. In order to monitor local elasticity, atomic force acoustic microscopy (AFAM) can be used [56]: the sample is insonified by ultrasonic waves or the cantilever is oscillated at ultrasonic frequencies; in contact with the sample, the resonances of the cantilever-tip system are measured and the local stiffness can be measured.

In general, scanning probe microscopy (SPM) can also find a nonstandard application in the field of nanolithography: normally an SPM is used to image a surface without damaging it in any way. However, either an AFM or STM can be used to modify the surface deliberately, by applying either excessive force with an AFM, or by a thermomechanical process, or by applying high-field pulses with an STM,
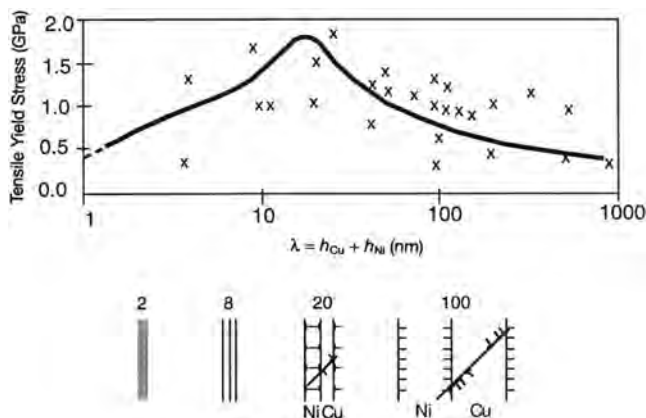
in order to realize precise nanometer-scale patterns on a surface.

Scanning probe microscopies are also being more and more often employed for single-molecule and single-atom positioning, by simply dragging these nanometric objects around the surface with the aid of the SPM tip. Otherwise, by applying a voltage difference between the tip and the atom or molecule, it is possible to "stick" the object to the tip and move it in a new position with sub-nanometric precision.

The possibility of modulating the force exerted by the tip onto the surface allows one to use an AFM as a precise scanning nanoindenter (see, e.g., [55, 57]), so that the reaction of the surface or of a molecule, or nanotube, to an applied pressure can be monitored. Nanowear studies can be performed by exploiting the same principles, for example, by scratching the surface with the tip while applying a constant force (i.e., a constant cantilever deflection).

By combining atomic manipulation and nanomechanical characterization, for instance, an AFM was used (as already discussed) to measure the Young's modulus of a carbon nanotube [37], by first positioning it in a proper suspended configuration, and then by bending the tube with a fixed force and measuring the tube deflection.

## 5.2. Elastic Properties: The Measurement of Surface Acoustic Waves

A bare substrate can support bulk acoustic waves and, at the external surface, also surface acoustic waves (SAWs) [58]. SAWs are characterized by a wavevector $\mathbf{q}_\parallel$ parallel to the surface and by a displacement field confined in the neighborhood of the surface. The Rayleigh wave (RW), the prototype of SAWs, has a velocity $v_R$ independent of the wavelength and a displacement field which decays exponentially with depth, the decay length being the same as the wavelength $\lambda_\parallel = 2\pi/q_\parallel$. When a layer of thickness $h$ is deposited onto the substrate, it modifies the spectrum of SAWs (i.e., their dispersion relation) [59]. A "thick" film ($q_\parallel h > 1$) can act as an acoustic waveguide: the dispersion relation can include several branches, whose velocities depend on the wavelength $\lambda_\parallel$ through the product $q_\parallel h$. A "thin" film ($q_\parallel h \lesssim 1$) only modifies the behavior of the RW, resulting in a modified Rayleigh wave (MRW), whose velocity is a function of $q_\parallel h$. Most of the displacement field is in the substrate, but close to the surface, where the wave amplitude and energy density are maximum, so that the MRW propagates in the film and senses the film properties. When $q_\parallel h$ increases the decay depth decreases, and the MRW becomes more confined in the film and more sensitive to its properties. The values of the Rayleigh velocities of the film $v_{R(film)}$ and the substrate $v_{R(subs)}$ determine two different behaviors: in the fast films case ($v_{R(film)} > v_{R(subs)}$), the MRW velocity is an increasing function of $q_\parallel$, while in the slow films case ($v_{R(film)} < v_{R(subs)}$), it is a decreasing function of $q_\parallel$. It must be remembered that acoustically fast means stiff and/or light, acoustically slow means soft and/or heavy.

### 5.2.1. Laser-Induced Surface Acoustic Waves

Frequency spectra of acoustic waves can be measured either exciting the waves, by piezoelectric excitation in quantitative acoustic microscopy [60] or by laser pulses in laser

acoustic methods (see below) [61, 62], or exploiting the thermally excited waves, in Brillouin scattering experiments [63]. In acoustic microscopy, a piezoelectric transducer is coupled, through an acoustic lens and a contact fluid, to the specimen surface: the transducer excites and detects the waves. In laser acoustic methods, waves are excited by laser pulses and the displacement of the specimen surface is sensed, after a propagation path of a few millimeters, by either a piezoelectric transducer or an interferometric set-up.

At the mesoscopic scale short laser pulses can excite broadband surface waves in solids [64]. The absorbed laser radiation leads to localized heating and thermoelastic expansion at the solid surface, which generates a traveling 2D surface wave. The smallest laser-excited SAW wavelength is a few micrometers; such wavelengths correspond to frequencies components approaching 1 GHz and limit the SAW pulse length to the nanosecond range. In principle, SAW pulses with shorter wavelengths may be obtained using near-field optics to overcome the diffraction limit of light. Propagating SAW pulses can be detected, without contacting the surface, also by using CW lasers.

In particular, the laser-acoustic technique has proved an efficient method for testing hard and superhard thin films [62]. It yields the Young's modulus, that essentially determines the mechanical strength, fracture toughness, and adhesion. The technique, being based on surface acoustic waves, is very sensitive to surface thin films. As explained before, SAWs in layered systems show dispersion, that is, the film modifies the phase velocity of the wave with respect to the bare substrate case, and this velocity can be measured very accurately. These dispersive oscillatory waveforms contain specific information about the mechanical and elastic properties of the layer and substrate material. Monitoring the pulse profiles at two distances from the excitation source allows the frequency dependence of the phase velocity to be determined (i.e., the dispersion relation).

For a homogeneous and isotropic material, with Young's modulus $E$, Poisson's ratio $\nu$ and density $\rho$, the phase velocity $v_s$ is

$$v_s = \frac{0.87 + 1.12\nu}{1 + \nu} \sqrt{\frac{E}{2\rho(1 + \nu)}} \qquad (18)$$

A film whose properties differ from those of the substrate varies the effective elastic properties in the vicinity of the surface, and therefore also the propagation velocity is varied.

From an experimental point of view, short laser pulses (down to 0.5 ns) are focused by a cylindrical lens onto the surface of the sample and generate wide-band surface wave impulses. The SAW impulses are then detected, for example, by a wide-band piezoelectric transducer. The dispersion curve can then be determined ($v_s$ as a function of frequency). Comparisons have been made with microindentation and membrane displacement test, and confirm the utility and precision of this technique [61].

The amount of information that can be extracted from the signal spectrum depends on the thickness of the film and the minimum wavelength of the pulse. If the ratio of the thickness $d$ to the minimum wavelength $\lambda$ is $d/\lambda < 0.1$, only one film property, such as the Young's modulus, can

be determined by fitting the linear dispersion to theory; for $d/\lambda > 1$, generating nonlinear dispersion, two or even three film properties, such as the density and Poisson's ratio, may be accessible.

An important property that can be studied with this technique is also the mechanical strength. Except for a few materials, the theoretical strength may be orders of magnitude higher than the measured value. With laser-excited nonlinear SAW pulses, it is possible to generate steep shocks with stresses that exceed the mechanical strength of covalent brittle materials such as silicon. These stresses lead to transient fracture by impulsive loading. The influence of rapidly rising stress pulses of very short duration on the dynamics of fracture is currently not well understood. Nonlinear SAW pulses provide a new tool to study transient fracture dynamics without seed cracks.

### 5.2.2. Brillouin Scattering

A very powerful, nondestructive, and sensitive technique for the characterization of elastic properties of materials, and in particular for thin films or multilayers, but also for nanostructured materials, is Brillouin spectroscopy. Brillouin light scattering is the inelastic scattering of an incident optical wave field by thermally excited elastic waves (usually called acoustic phonons). Since the advent of lasers, Brillouin scattering has received considerable interest for the characterization of elastic and optoelastic bulk and surface properties of materials.

Due to the small frequencies of acoustic phonons for small wavevectors, the Brillouin lines are separated by small frequency shifts, of the order of less than 1 cm$^{-1}$, from the elastic line. For this reason it is not possible to use a grating monochromator as for Raman scattering, but rather a Fabry–Perot interferometer must be used. In terms of the corpuscular theory of light, first-order Brillouin scattering corresponds to an inelastic collision of a photon with an acoustic phonon. As for Raman scattering, the photon either loses a quantum of vibrational energy (Stokes line) or acquires such a quantum (anti-Stokes line). For a complete presentation of Brillouin scattering theory the reader is referred to [63, 65, 66].

Brillouin scattering by SAWs is called surface Brillouin scattering (SBS). The measurement is intrinsically contactless and local. Since spontaneous Brillouin scattering relies on thermally excited acoustic waves, interaction occurs with waves having an amplitude much smaller than that of the waves excited in the other techniques cited before, implying that Brillouin scattering measurements are more time consuming. However, the acoustic wavelengths probed in a Brillouin scattering experiment can be significantly smaller than those probed by other techniques: this gives Brillouin scattering a unique potential in terms of spatial resolution, particularly relevant in the case of ultrathin films.

In the case of thin or ultrathin films, this technique proves really powerful. The velocities of surface acoustic waves can be measured by Brillouin spectroscopy. If independent measurements of film thickness and mass density are available, the elastic constants can be derived from the measured acoustic velocities. Such measurements can be performed, for example, by X-ray reflectivity (see, e.g., [67]). Combining Brillouin scattering and X-ray reflectivity measurements

of thickness and density, the elastic constants of films have been measured for film thicknesses ranging from hundreds to tens of nanometers. It has been demonstrated that it is possible to extend the limits of the sensitivity of both the X-ray and Brillouin scattering techniques, in order to characterize films down to a few nanometers thick.

### 5.2.3. Surface Brillouin Spectroscopy

In the bulk of a material, the interaction between acoustic waves and electromagnetic waves occurs by the elasto-optic effect, that is, the dynamical modulation of the electrical susceptibility by the strain field of the acoustic wave. At a surface, interaction also occurs by the ripple effect, that is, the dynamical modulation of the surface geometry due to the acoustic wave. The ripple mechanism is the only one in metallic materials, and is however typically dominant in SBS, since the strain field of SAWs is confined in the vicinity of the surface.

In a Brillouin scattering measurement, a monochromatic laser beam of wavelength $\lambda_0$, circular frequency $\Omega_i$, and wavevector $\mathbf{k}_i$ ($|\mathbf{k}_i| = 2\pi/\lambda_0$) is focused onto the specimen, and scattered light of wavevector $\mathbf{k}_s$ is collected along a given direction. The scattering geometry selects the exchanged wavevector, that is, the acoustic wavevector $\mathbf{q}$ being probed

$$\mathbf{q} = \pm(\mathbf{k}_s - \mathbf{k}_i) \qquad (19)$$

the $-$ and $+$ signs referring to Stokes and anti-Stokes events, respectively. The wavevectors $\mathbf{k}_i$ and $\mathbf{k}_s$ have essentially the same modulus, and the relative difference is at most twice the ratio of the acoustic velocity to the light velocity. The spectrum of the scattered light is dominated by the elastically scattered light at the incident circular frequency $\Omega_i$. If light is inelastically scattered by an acoustic wave of velocity $v$, the spectrum also contains a doublet at frequencies

$$\Omega_s = \Omega_i \pm \omega \qquad (20)$$

the $-$ and $+$ signs referring again to Stokes and anti-Stokes events, respectively; the frequency shift $\omega = v\mathbf{q}$ immediately gives the acoustic velocity.

In SBS only the wavevector component parallel to the surface is conserved: Eq. (19) takes the form

$$\mathbf{q}_\| = \pm(\mathbf{k}_s - \mathbf{k}_i)_\| \qquad (21)$$

and the SAW velocity $v = \omega/q_\|$ is obtained. In SBS the backscattering configuration is often adopted because it maximizes $q_\|$, and because it allows a simpler set-up, since the same lens is exploited to focus and to collect. In backscattering with incidence angle $\theta$, the nominal exchanged wavevector is $q_\| = (4\pi/\lambda_0)\sin\theta$. This means that SAWs are probed having wavelength $\lambda_\| = \lambda_0/(2\sin\theta)$ and, although $\theta$ seldom exceeds 70°, acoustic wavelengths are probed down to about $\lambda_0/2$. With visible light this means that wavelengths $\lambda_\|$ below 300 nm can be probed. They are completely determined by the scattering geometry alone, and with common values of material properties they correspond to SAW frequencies up to above 20 GHz. This gives SBS its unique sensitivity to submicrometric films; with other techniques the frequency rather than the wavelength is determined by the experimental set-up, and the frequencies typically lie in the tens to

hundreds of megahertz range. A dispersion relation $v(q_\parallel)$ is obtained varying the incidence angle $\theta$. Measurements are performed at a set of incidence angles $\theta^i$ obtaining a set of measured circular frequencies $\omega_m^i$ and a set of measured velocities $v_m^i = v_m(q_\parallel^i) = \omega_m^i/q_\parallel^i$.

### 5.2.4. Derivation of the Elastic Constants

From the measured acoustic velocities the elastic properties of materials can be derived. Both bulk acoustic waves [68] and SAWs [69] have been exploited. The velocities of the SAWs in layered structures, and namely for a single film on a substrate, can be computed by the continuum elastodynamics equations as a function of the material properties of both the film and the substrate, of the film thickness, and of the wavevector. In particular, materials are characterized by the mass density $\rho$ and the elements $C_{ij}$ of the elastic constants tensor, and the computed velocities $v_c$ are obtained as $v_c = v_c([\rho, C_{ij}]_{substrate}, [\rho, C_{ij}]_{film}, t, \mathbf{q}_\parallel)$ [70]. The continuum elastodynamics equations are appropriate when the wavelength is much larger than interatomic distances. It must be remembered that the acoustic wavelengths probed by SBS are of hundreds of nanometers and safely fulfill the above condition.

The computation of SAW velocities as functions of physical parameters, that is, the solution of the direct problem, allows to solve the inverse problem, that is, the derivation of physical properties from measured SAW velocities, by fitting the computed velocities $v_c$ to the measured ones $v_m$. The substrate properties are assumed to be known; if the film thickness and mass density can be independently measured, typically by X-ray reflectivity, the only unknown properties remain the film elastic constants $[C_{ij}]_{film}$, which are then obtained by fitting the computed velocities to those measured by SBS.

For elastically isotropic films, such as nanocrystalline or amorphous films, two independent quantities are sufficient to fully determine the whole matrix $[C_{ij}]_{film}$. These quantities are typically taken as any couple among $C_{11}$ and $C_{44}$, Young's modulus $E$, shear modulus $G$ (in this case $G = C_{44}$), bulk modulus $B$, and Poisson's ratio $\nu$. They are subjected to limitations like $G > E/3$ or $\nu \le 0.5$ arising from the physical requirement that the elastic strain energy be definite positive. It has been shown that the $(E, G)$ couple is the most appropriate for the solution of the inverse problem. The computed velocities are therefore obtained as $v_c^i(E, G)$, and the $(E, G)$ values are obtained by the generalized least square estimator $GLS$

$$GLS = \sum_i \frac{(v_m^i - v_c^i(E, G))^2}{(\sigma_m^i)^2} \qquad (22)$$

where the $\sigma_m^i$ are the variances associated to the $v_m^i$ values. $GLS$ gives both the most probable values of the elastic constants $(\bar{E}, \bar{G})$, that is, the point of the $(E, G)$ plane at which the $GLS$ is minimum, and, by the $F$ distribution (the Fisher function), the confidence intervals at any given confidence level [71].

Not all the $(E, G)$ plane is physically meaningful: the region at $G < E/3$ corresponds to $\nu > 0.5$, which means thermodynamic instability, while the region at $G > E/2$ corresponds to $\nu < 0$, which does not mean thermodynamic

instability but is almost never observed. The analysis of data is therefore supplemented by physical plausibility criteria. For instance, it is assumed that the tetrahedral amorphous carbon films have a positive Poisson ratio $\nu$ and a bulk modulus $B$ lower than that of diamond ($B_{diamond} = 445$ GPa), and only the part of the confidence region which complies with these two limitations is taken as the outcome of the measurements.

We mention here one of the possible applications of Brillouin scattering to the characterization of the mechanical properties of nanometer-thick films. Protective hard tetrahedral carbon coatings of thickness down to 2 nm are needed to maintain the increasing trend of storage density in magnetic hard disks and reach the 100 Gbit/in$^2$ target [72]. The thinner the protective carbon coating, the closer the reading head can approach the magnetic part of the disk and thus the smaller the size of the bits and the higher the bit density. For films having a thickness in the nanometer range, the measurement of the elastic properties is critical. Indentation techniques become very sensitive to the substrate properties, in the sense that often, if little care is taken in the measurement, substrate properties are measured. Acoustic waves provide a clean way to measure the elastic properties, and the velocities of surface acoustic waves can be measured by surface Brillouin scattering. If independent measurements of film thickness and mass density are available (and they have been done for ta-C films with X-ray reflectivity), the elastic constants can be derived from the measured acoustic velocities. It has been shown that the limits of these techniques can be pushed to the sub-10-nm range [73, 74]. An average density of 2.8 g/cm$^3$ was measured down to 2–3 nm thickness, while the average elastic constants of the ultra-thin layers were found to increase steeply with thickness, being comparable with those of thicker films already from 8-nm-thick films. Anyway, even the thinnest 2.2-nm film has a Young's modulus of at least $\sim$100 GPa.

Brillouin scattering has also been used to characterize nanostructured films obtained by the assembly of carbon clusters. This case can show how complex the study of the mechanical properties of a nanostructured assembled material can be, when it is not simply a nanocrystalline sample or a more or less compacted powder. Particularly challenging is instead the attempt of getting and interpreting Brillouin spectra of cluster-assembled films with a rough surface and/or a granular or porous structure.

The mechanical properties of carbon nanostructures have received considerable interest [40, 75]. In particular, the use of carbon clusters and nanotubes as building blocks for the synthesis of nanocrystalline and composite materials with unusual elastic properties has been suggested theoretically and several experiments to identify possible synthetic routes have been reported [75–77].

Experimental characterization and theoretical modelization of cluster-assembled materials have to face the problem of cluster coalescence and of their organization in structures spanning length scales from the nanometer up to the micrometer. The different structures in which the precursor clusters are organized need experimental probes sensitive to the different length scales typical of intracluster and intercluster interactions. For carbon-based materials Raman spectroscopy can be used for a characterization at a nanometer

scale. In order to study the organization of clusters at a scale of hundreds of nanometers, which is the typical scale of thermally excited long-wavelength acoustic phonons, Brillouin light scattering has been used by Bottani et al. [78]. The extraction of the elastic properties of low-density cluster-assembled carbon films from the spectroscopic data can be based only partially on what is known in the case of *good* films and a complete theory is still lacking. Bulk and surface Brillouin scattering signals have been obtained from films characterized by a complex structure from the atomic to the hundreds of nanometers level, showing that this technique can be used also for nanostructured materials with irregular surfaces. Bulk and shear modulus of the material have been determined giving information on the acoustic properties at a mesoscopic scale. This allows to infer the nature of the bonding between the carbon aggregates.

In particular, thick cluster-assembled carbon films (thickness $\geq 0.8$ $\mu$m) and thin films (thickness $\simeq 0.1$ $\mu$m) have been examined [79]. In thick films only damped bulk acoustic phonons with a typical wavelength $\lambda_{ph}$ of the order of 170 nm have been detected, giving rise to coherent Brillouin scattering of laser light. This indicates that for a length $d \geq \lambda_{ph}$ the films can be modeled as a continuum with translational invariance and *effective* elastic constants although structural disorder at smaller scales scatters the phonons significantly. The presence of a rather strong central peak in the spectra could be ascribed to nonpropagating (overdamped), or confined vibrational excitations within the films, probably connected with different characteristic correlation lengths less than $d$. The most damped bulk acoustic phonons could be coupled to the confined modes by a relaxation mechanism. The films own a high degree of surface roughness and multiscale granularity: this leads to considerable broadening of the phonon peaks and to the presence of an intense elastic background. This strong elastic and quasi-elastic bulk signal impeded the measurement of surface phonons which could be almost overdamped if not already replaced by surface fractons or by localized cluster modes. Instead, in thinner films surface peaks were detected (see Fig. 6). The *effective* elastic constants of the films were

obtained. The shear modulus and the bulk modulus turned out to be respectively $\mu \simeq 4.0$ GPa and $B \simeq 3.67$ GPa, corresponding to a Poisson's ratio $\nu$ of about 0.10.

The numerical value of $\mu$ is in the range of the $C_{44}$ elastic constant of hexagonal crystalline graphite ($C_{44} = 2 \approx 5$ GPa) and equals the value of its shear modulus along the C-axis. Yet the film material is not elastically identical to nanocrystalline graphite; in fact, the values of $B$ (and, consequently, $\nu$) are significantly different. These experiments have demonstrated the possibility of using Brillouin spectroscopy as a tool for the characterization of the elastic properties of thin films owning a disordered granular structure in a range from atomic dimensions up to hundreds of nanometers. This opens interesting perspectives for the study of the mechanical and elastic properties of nanocrystalline materials.

## 6. APPLICATIONS

Nanostructured materials or reinforced materials including special nanostructures, as well as hard thin films or multilayers, are of course extremely interesting in view of a number of applications as structural materials or reinforcement fibers, hard protective coatings, or high-resistance components in special devices such as MEMS (micro-electromechanical systems), NEMS (nano-electromechanical systems), magnetic media, X-ray optical elements (e.g., multilayers), etc.

Metals, alloys, intermetallics, and ceramics show improved or peculiar mechanical properties when a modulation of the nanoscale structure is induced (e.g., by sintering and compaction of nanopowders), as we have seen, and therefore bulk nanocrystalline materials are studied since they may become the basis of new structural materials for construction or hybrid structures. For example, a new and simple process to obtain nanostructured bulk low-carbon steel with superior mechanical properties (e.g., higher tensile strength) has been reported [80]. The inclusion of nanoparticles in a matrix (nanodispersions, e.g., in steel or alloys) also improves mechanical properties and thus nanoparticle precipitation represents a different route for the realization of innovative nanostructured construction materials or structures. It is possible to tailor the shape of these inclusions, and obtain extremely light materials with high degrees of stiffness and strength by including in the matrix more or less aligned rods or plates (nanocomposites, e.g., polymer nanocomposites). Also fibers can attain significant enhancement in their mechanical properties by the size reduction of their constituents (nanofibers). As far as nanocomposites and nanofibers are concerned, carbon nanotubes, possessing an extremely high Young's modulus, and polymers reinforced with nanoplates of a second phase attract today much attention, as discussed before.

Hard nanocoatings are currently being employed for protection of surfaces (e.g., razor blades, but especially magnetic hard disks). In particular, diamond-like (tetrahedrally bonded) amorphous carbon is used for covering of magnetic disks, since it is possible to deposit layers down to a thickness of a few nanometers, which enormously increases the information storage density (up to 100 Gbit/in$^2$) on the disk [81], due to the possibility of approaching the reading tip more closely to the magnetic surface. Indeed, a combination
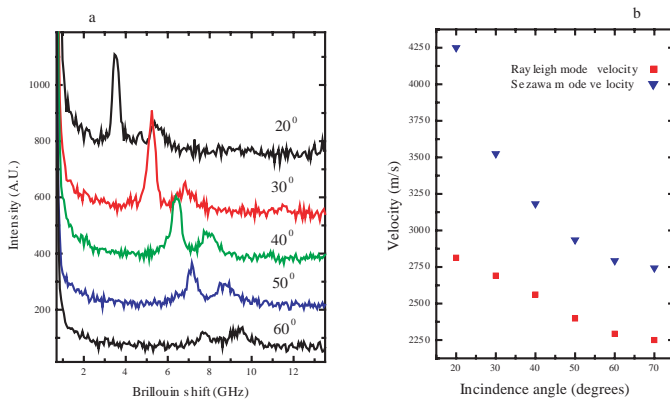


**Figure 6.** (a) Brillouin spectra from cluster-assembled carbon films as a function of incidence angle. Two peaks are visible, corresponding to a surface Rayleigh mode and to a Sezawa mode (guided mode in the film). (b) Dispersion relation for the velocity of the Rayleigh and Sezawa peaks in the same sample.

of the layer (coating) geometry and of an internal nano-structuring can greatly improve the mechanical properties (hardness, wear resistance, toughness) of protective materials (e.g., see [82] for a study of the mechanical behavior of nanostructured WC–Co coatings). Other materials are used for coating of other surfaces, for example, mirrors, glasses, where good and improved mechanical properties (hardness, anti-wear properties) have to be combined with other characteristics (e.g., transparency, lubrication, i.e., low friction, thermal barrier properties, self-cleaning properties, e.g., for the development of self-cleaning surfaces, but also catalysis, UV filtering, etc.). In these cases, the nanometric limitation to the layer thickness can be coupled with the intrinsic nanostructure of the deposited (e.g., cluster-assembled) material, for example, for gas sensing and catalysis applications. Another field is represented by functional active coatings that must at the same time possess good mechanical and wear properties (e.g., for solar cells, or sensors). Multilayers, or superlattices, are employed for their special magnetic properties in magnetic devices, or for X-ray optical elements, and mechanical properties are obviously important.

A new frontier is represented by NEMS. MEMS and NEMS represent a marriage between semiconductor processing and mechanical engineering at a very small scale (e.g., by nanolithography). They are based on the measurement of forces by means of structures with particular modes of vibrations and elastic constants (deflections, vibrations), coupled with transducers for optical and electrical signals. MEMS already find applications in many sectors (optical elements, micromirrors, motion or acceleration micro- or nanosensors, e.g., for the deployment of airbags) and NEMS are the natural evolution of the process of miniaturization, since the reduction in the weight (i.e., of the inertia) of these devices greatly improves their sensitivity, and their intrinsically low energy consumption [83, 84]. Of course the mechanical properties of these structures are extremely important; silicon is usually used since it benefits from the established know-how of semiconductor processing, but also nanostructured materials, such as SiC, nanotubes, or ultrananocrystalline diamond (whose mechanical properties are substantially indistinguishable from those of diamond [85, 86]) for the fabrication of freestanding cantilevers with submicrometric feature resolution. These hard materials (Si, SiC, ultrananocrystalline diamond, but also SWNTs) also find application for the fabrication of AFM submicrometric hard probes (nanotips).

# 7. CONCLUSIONS

What is known about the mechanical properties of nanophase materials, though still limited, allows one to draw some general conclusions. We refer the reader, for a review of interpretations of the mechanical behavior of nanomaterials, to [1, 3, 18]. First, dislocation activity still dominates the mechanical behavior of pure nanophase metals. However, the dislocation activity seems to decrease with decreasing grain size due to the decreased availability of dislocations and ability to create new dislocations in nanometer grains. The absence of mobile dislocations in nanophase grains has been documented experimentally and is the result of the

long known and well-understood *image forces* that act on dislocations near surfaces and thus, particularly, in confined media. The difficulty in creating new dislocations in confined crystallites was already known also from investigations in single-crystal whiskers. The minimum stress required to activate a dislocation source (e.g., a Frank–Read source) is inversely proportional to the distance between dislocation pinning points, and this stress will increase with decreasing grain size (limitation of the maximum distance between pinning points). When the grain size reaches 1–2 nm (the limit size is also dependent on the value of the shear modulus), the theoretical yield stress of a dislocation-free metal may be approached. Thus, it appears that the increasing hardness and strength observed in pure nanophase metals with decreasing grain size is simply a result of diminishing dislocation activity.

For nanophase intermetallic materials the situation is more complicated, since other phenomena are involved, such as the grain-size dependence of the phase stability. However, their mechanical behavior in the higher end of the nanophase regime is often similar to that of pure metals.

Nevertheless, many of these hard, strongly bound materials exhibit a clear transition from hardening behavior to softening behavior with decreasing grain size. This increased ductility appears to be related to an increase in grain boundary sliding with decreasing grain size as evidenced by stress-strain and creep measurements. The mechanical response of these intermetallics thus appears to be transitional between that of pure nanophase metals at larger grain sizes and that of nanophase ceramics at smaller grain sizes. Grain boundary sliding, with short-range diffusion-assisted healing events, dominates the deformation behavior of strongly bound and conventionally brittle materials in the nanoscale regime.

These observations suggest a qualitative interpretation, proposed by Siegel [18], and shown in Figure 7, for the understanding of the mechanical properties of nanomaterials. With decreasing grain size, the frequency of dislocation activity decreases and that of grain boundary sliding increases. The dominating effect depends on the grain-size regime, the type of material, and the nature of bonding. Metals with nondirectional bonding fall at the left of Figure 7
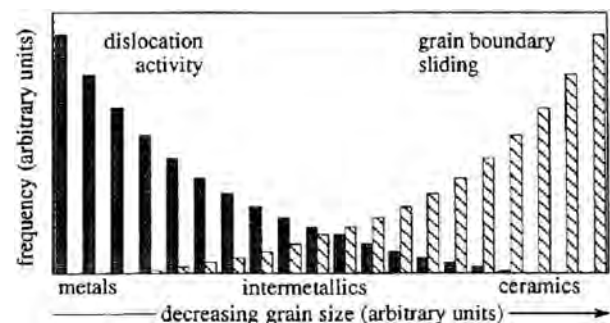


**Figure 7.** Schematic framework for the grain-size dependence of dislocation activity and grain boundary sliding contributions to the deformation behavior of the various classes of nanophase materials. The nature of its interatomic bonding determines the appropriate location for a particular material. Reprinted with permission from [18], R. W. Siegel and G. E. Fougere, *Nanostruct. Mater.* 6, 205 (1995). © 1995, Elsevier Science.

and those with more covalent bonding fall in the transitional region where decreasing dislocation activity yields to increasing grain boundary sliding; nanophase ceramics with their strong ionic or covalent bonding lie in the region to the right dominated by grain boundary sliding.

In addition to nanostructured and nanocrystalline materials, we finally recall the extreme interest recently shown by the nanotechnology community in the peculiar properties of special single nanostructures, among which carbon nanotubes are the most promising. Their unique electronic and mechanical properties, and the increasing possibility of controlling their deposition (alignment, manipulation of single nanotubes, patterning), have attracted much attention for a wide range of applications, from single nanotransistors, nanotube field emission flat panel displays, to reinforcement of fibers or structural building materials.

## GLOSSARY

**Carbon nanotube**   Carbon cylindrical nano-object; it can be thought as formed by warping a single graphitic layer into a cylindrical object with diameter in the nm range.

**Cluster-assembled materials**   Materials synthesized by deposition of clusters (i.e., particles composed by up to thousands of atoms, they represent an intermediate step between molecules and bulk materials).

**Composite material**   A material with distinct interfaces separating the components, created to obtain properties that cannot be achieved by any of the components acting alone.

**Creep**   Time-dependent strain produced in materials following a change in loading conditions.

**Ductility**   Ability of a material to change shape without fracturing (i.e., to experience significant plastic deformation before fracturing).

**Elastic constants**   Elements of the elastic constant tensor, which relates the stress tensor and the strain tensor in the linear (elastic) regime.

**Fatigue strength**   Resistance of a material to failure under cyclic loading.

**Hall–Petch relationship**   Equation expressing dependence of yield stress or hardness on the inverse square-root of the grain size in micro- and nanocrystalline materials.

**Hardness**   Resistance to penetration of a diamond indenter under standardized conditions. It is related to the material strength, and also to its wear (abrasion) resistance.

**Multilayers**   Thin films constituted by alternating nanolayers of different (usually two) elements or materials; also called *superlattices*.

**Nanomaterials, nanostructured materials**   Materials whose properties (compositional, chemical, morphological, structural, mechanical, electronic, vibrational, etc.) are related to characteristic lengths in the $\approx$1–100 nm range. Related terms are *nanocrystalline materials, nanocomposites, nanoparticles, nanotubes, nanowires*.

**Plastic deformation**   Irreversible (permanent) deformation, following the elastic deformation regime, occurring for high values of stress.

**Poisson's ratio**   $\nu$, ratio between longitudinal elongation and transverse contraction in uniaxial testing.

**Sbear modulus**   $\mu$ (or $G$), proportionality coefficient between stress and strain in pure shear. It can be derived from the Young's modulus using the relationship $E/[2(1 + \nu)]$.

**Strain tensor**   Tensor describing changes in length of a body in some direction relative to an undistorted length (not necessarily the same), i.e. describing how infinitesimal cubic volume elements change volume and shape in a material subject to deformation.

**Stress tensor**   Tensor describing forces per unit area acting on a face of an infinitesimal cubic element subject to external actions.

**Superplasticity**   Exceptional ductile behaviour (exceptionally enhanced strain to failure, with elongations in the range 100–1000%).

**Yield stress**   Threshold stress beyond which deformation is irreversible (plastic).

**Young's modulus**   $E$, proportionality coefficient between stress and strain for small deformations in uniaxial tensile testing (elastic regime).

## REFERENCES

 1. H. Kung and T. Foecke (Guest Eds.), *MRS Bull.* 24, 14 (1999).
 2. C. E. Bottani, in "Nanostructured Carbon for Advanced Applications" (G. Benedek, Ed.). Kluwer Academic, Dordrecht, 2001.
 3. S. Veprek and A. S. Argon, *J. Vac. Sci. Technol. B* 20, 650 (2002).
 4. R. Saha and W. D. Nix, *Acta Mater.* 50, 23 (2002).
 5. H. Gleiter, *Progr. Mat. Sci.* 33, 224 (1989).
 6. Y. M. Soifer and N. P. Kobelev, *Nanostruct. Mater.* 6, 647 (1995).
 7. H. S. Kim and M. B. Bush, *Nanostruct. Mater.* 11, 361 (1999).
 8. M. Weller, J. Diehl, and E.-E. Schaefer, *Philos. Mag.* A63, 527 (1991).
 9. D. Chen, *Mater. Sci. Eng.* A190, 193 (1995).
10. H. Tanimoto, S. Sakai, and H. Mizubayashi, *Nanostruct. Mater.* 12, 751 (1999).
11. L. Wong, D. Ostrander, U. Erb, G. Palumbo, and K. T. Aust, in "Nanophases and Nanocrystalline Structures" (R. D. Shull and J. M. Sanchez, Eds.). Materials Research Society, Warrendale, PA, 1994.
12. V. Krstic, U. Erb, and G. Palumbo, *Scr. Metall. Mater.* 29, 1501 (1993).
13. R. W. Siegel, *Analusis Mag.* 24, M10 (1996).
14. R. W. Siegel, *Mater. Sci. Forum* 235–238, 851 (1997).
15. J. R. Weertman and R. S. Averback, in "Nanomaterials: Synthesis, Properties, and Applications" (A. S. Edlestein and R. C. Cammarata, Eds.). Institute of Physics Publishers, Bristol, 1996.
16. R. W. Siegel and G. E. Fougere, in "Nanophase Materials" (G. C. Hadjipanayis and R. W. Siegel, Eds.). Kluwer Academic, Dordrecht, 1994.
17. H. Alves, M. Ferreira, U. Koster, and B. Muller, *Mater. Sci. Forum* 225–227, 769 (1996).
18. R. W. Siegel and G. E. Fougere, *Nanostruct. Mater.* 6, 205 (1995).
19. J. R. Weertman, D. Farkas, K. Hemker, H. Kung, M. Mayo, R. Mitra, and H. Van Swygenhoven, *MRS Bull.* 24, 44 (1999).
20. J. R. Weertman, *Mater. Sci. Forum* 386–388, 519 (2002).
21. R. S. Mishra, R. Z. Valiev, and A. K. Mukherjee, *Nanostruct. Mater.* 9, 473 (1997).
22. G. A. Salishekev, O. R. Valiakhmetov, V. A. Valitov, and S. K. Mukhtarov, *Mater. Sci. Forum* 170–172, 121 (1994).
23. H. J. Höfler, R. Tao, L. Kim, R. S. Averback, and C. J. Altstetter, *Nanostruct. Mater.* 6, 901 (1995).
24. J. Karch, R. Birringer, and H. Gleiter, *Nature* 330, 556 (1987).

25. C. C. Koch, D. G. Morris, K. Lu, and A. Inoue, *MRS Bull.* 24, 54 (1999).
26. P. G. Sanders, M. Rittner, E. Kiedaisch, J. R. Weertman, H. Kung, and Y. C. Lu, *Nanostruct. Mater.* 9, 433 (1997).
27. K. A. Padmanabhan, *Mater. Sci. Eng. A* 304–306, 200 (2001).
28. D. G. Morris, "Mechanical Behaviour of Nanostructured Materials," Mater. Sci. Foundations 2, p. 1. Trans. Tech. Publ., Aedermannsdorf, Switzerland, 1998.
29. D. O. Northwood and A. T. Alpas, *Nanostruct. Mater.* 10, 777 (1998).
30. R. A. Vaia and E. P. Giannelis, *MRS Bull.* 26, 395 (2001).
31. R. A. Vaia and R. Krishnamoorti, Eds., "Polymer Nanocomposites." American Chemical Society, Washington, DC, 2001.
32. T. J. Pinnivaia and G. W. Beal, Eds., "Polymer-Clay Nanocomposites." John Wiley & Sons, New York, 2001.
33. M. Zhang, Y. Liu, X. Zhang, J. Gao, F. Huang, Z. Song, G. Wei, and J. Qiao, *Polymer* 43, 5133 (2002).
34. M. S. Dresselhaus, G. Dresselhaus, and P. C. Eklund, "Science of Fullerenes and Carbon Nanotubes." Academic Press, New York, 1996.
35. J. P. Salvetat-Delmotte and A. Rubio, *Carbon* 40, 1729 (2002).
36. J. Bernholc, D. Brenner, M. B. Nardelli, V. Meunier, and C. Roland, *Ann. Rev. Mater. Res.* 32, 347 (2002).
37. J.-P. Salvetat, G. A. D. Briggs, J.-M. Bonard, R. R. Bacsa, A. J. Kulik, T. Stöckli, N. A. Burnham, and L. Forró, *Phys. Rev. Lett.* 82, 944 (1999).
38. R. H. Baughman, C. Cui, A. A. Zakhidov, Z. Iqbal, J. N. Barisci, G. M. Spinks, G. G. Wallace, A. Mazzoldi, D. De Rossi, A. G. Rinzler, O. Jaschinski, S. Roth, and M. Kertesz, *Science* 284, 1340 (1999).
39. J. P. Lu, *Phys. Rev. Lett.* 79, 1297 (1997).
40. M. M. J. Treacy, T. W. Ebbesen, and J. M. Gibson, *Nature* 381, 678 (1996).
41. V. N. Popov, V. E. Van Doren, and M. Balkanski, *Solid State Commun.* 114, 395 (2000).
42. D. Kahn, K. W. Kim, and M. A. Stroscio, *J. Appl. Phys.* 89, 5107 (2001).
43. A. Krishnan, E. Dujardin, T. W. Ebbesen, P. N. Yianilos, and M. M. J. Treacy, *Phys. Rev. B* 58, 14013 (1998).
44. E. W. Wong, P. E. Sheehan, and C. M. Lieber, *Science* 277, 1971 (1997).
45. C. E. Bottani, A. Li Bassi, M. G. Beghi, A. Podestà, P. Milani, A. Zakhidov, R. Baughman, D. A. Walters, and R. E. Smalley, *Phys. Rev. B* 67, 155407 (2003).
46. A. Li Bassi, M. G. Beghi, C. S. Casari, C. E. Bottani, A. Podestà, P. Milani, A. Zakhidov, R. Baughman, D. A. Walters, and R. E. Smalley, *Diamond Relat. Mater.* 12, 806 (2003).
47. B. M. Clemens, H. Kung, and S. A. Barnett, *MRS Bull.* 24, 20 (1999).
48. D. Josell and F. Spaepen, *MRS Bull.* 24, 39 (1999).
49. P. M. Anderson, T. Foecke, and P. M. Hazzledine, *MRS Bull.* 24, 27 (1999).
50. R. C. Cammarata, J. C. Bilello, A. Lindsay Greer, K. Sieradzki, and S. M. Yalisove, *MRS Bull.* 24, 34 (1999).
51. D. Josell, D. van Heerden, D. Shechtman, and D. Read, *Nanostruct. Mater.* 12, 405 (1999).
52. M. Shinn, L. Hultman, and S. A. Barnett, *J. Mater. Res.* 7, 901 (1992).
53. J. S. Koehler, *Phys. Rev. B* 2, 547 (1970).
54. P. M. Anderson and C. Li, *Nanostruct. Mater.* 5, 349 (1995).
55. K. Miyahara, N. Nagashima, T. Ohmura, and S. Matsuoka, *Nanostruct. Mater.* 12, 1049 (1999).
56. E. Kester, U. Rabe, L. Presmanes, Ph. Tailhades, and W. Arnold, *Nanostruct. Mater.* 12, 779 (1999).
57. D. DeVecchio and B. Bhushan, *Rev. Sci. Instrum.* 68, 4498 (1997).
58. G. W. Farnell, in "Physical Acoustics" (W. P. Mason and R. N Thurston, Eds.), Vol. 6, pp. 109–166. Academic Press, New York, 1970.
59. G. W. Farnell and E. L. Adler, in "Physical Acoustics" (W. P. Mason and R. N. Thurston, Eds.), Vol. 9, pp. 35–127. Academic Press, New York, 1972.
60. P. Zinin, in "Handbook of Elastic Properties of Solids, Liquids and Gases" (M. Levy et al., Eds.), Vol. 1, pp. 187–226. Academic Press/Harcourt Publishers Ltd., Sidcup, UK, 2000.
61. D. Schneider, B. Schultrich, H.-J. Scheibe, H. Ziegele, and M. Griepentrog, *Thin Solid Films* 332, 157 (1998).
62. D. Schneider, T. Witke, T. Schwarz, B. Schoneich, and B. Schultrich, *Surf. Coat. Technol.* 126, 136 (2000).
63. J. R. Sandercock, in "Light Scattering in Solids III" (M. Cardona and G. Guntherodt, Eds.). Springer–Verlag, Berlin, 1982.
64. P. Hess, *Phys. Today*, p. 42 (March 2002).
65. M. Cardona, in "Light Scattering in Solids," Vols. I and II. Springer-Verlag, Berlin, 1982.
66. P. Milani and C. E. Bottani, in "Handbook of Nanostructured Materials and Nanotechnology." Academic Press, New York, 1998.
67. B. Lengeler, in "X-ray Absorption and Reflection in the Hard X-Ray Range" (M. Campagna and K. Rosei, Eds.). North-Holland, Amsterdam, 1990.
68. M. Grimsditch, in "Handbook of Elastic Properties of Solids, Liquids and Gases" (M. Levy et al., Eds.), Vol. 1, pp. 331–347. Academic Press/Harcourt Publishers Ltd., Sidcup, UK, 2000.
69. J. D. Comins, in "Handbook of Elastic Properties of Solids, Liquids, and Gases" (M. Levy et al., Eds.), Vol. 1, pp. 349–378. Academic Press/Harcourt Publishers Ltd., Sidcup, UK, 2000.
70. A. Amici, M. G. Beghi, and C. E. Bottani, *Comput. Mater. Sci.* 17, 404 (2000).
71. M. G. Beghi, C. E. Bottani, and R. Pastorelli, in "Mechanical Properties of Structural Films," ASTM STP 1413 (C. Muhlstein and S. B. Brown, Eds.). American Society for Testing Materials, Philadelphia, PA, 2001.
72. J. Robertson, *Thin Solid Films* 383, 81 (2001).
73. M. G. Beghi, A. C. Ferrari, K. B. K. Teo, J. Robertson, C. E. Bottani, A. Libassi, and B. K. Tanner, *Appl. Phys. Lett.* 81, 3804 (2002).
74. M. G. Beghi, A. C. Ferrari, C. E. Bottani, A. Libassi, B. K. Tanner, K. B. K. Teo, and J. Robertson, *Diamond Relat. Mater.* 11, 1062 (2002).
75. G. A. J. Amaratunga, M. Chowalla, C. J. Kiely, I. Alexandrou, R. Aharonov, and R. M. Devenish, *Nature* 383, 321 (1996).
76. P. Melinon, V. Paillard, V. Dupuis, A. Perez, P. Jensen, A. Hoareau, J. P. Perez, J. Tuaillon, M. Broyer, J. L. Vialle, M. Pellarin, B. Baguenard, and J. Lerme, *Int. J. Mod. Phys. B* 9, 339 (1995).
77. P. Milani, M. Ferretti, P. Piseri, C. Bottani, A. Ferrari, A. Li Bassi, G. Guizzetti, and M. Patrini, *J. Appl. Phys.* 82, 5793 (1997).
78. C. E. Bottani, A. C. Ferrari, A. Li Bassi, P. Milani, M. Ferretti, and P. Piseri, *Carbon* 36, 535 (1998).
79. C. Casari, A. Li Bassi, C. E. Bottani, P. Piseri, E. Barborini, and P. Milani, *Phys. Rev. B* 64, 085417 (2001).
80. N. Tsuji, R. Ueji, Y. Minamino, and Y. Saito, *Scr. Mater.* 46, 305 (2002).
81. P. R. Goglia, J. Berkowitz, J. Hoehn, A. Xidis, and L. Stover, *Diamond Relat. Mater.* 10, 271 (2001).
82. J. He and J. M. Schoenung, *Surf. Coat. Technol.* 157, 72 (2002).
83. M. L. Roukes, *Phys. World*, p. 25 (February 2001).
84. M. L. Roukes, in "Tech. Digest. Solid State Sensor and Actuator Workshop," 2000.
85. D. M. Gruen, *MRS Bull.* 26, 771 (2001).
86. J. Philip, P. Hess, T. Feygelson, J. E. Butler, S. Chattopadhyay, K. H. Chen, and L. C. Chen, *J. Appl. Phys.* 93, 2164 (2003).

# Mechanical Molecular Nanodevices

Laura Frankfort, Xiange Zheng, Karl Sohlberg

*Drexel University, Philadelphia, Pennysylvania, USA*

## CONTENTS

## 1. INTRODUCTION

Nanotechnology promises engineered devices constructed from just one or a few molecules, a technology with a potentially staggering impact. Applications are envisioned in medicine, molecular electronics based information processing systems, and information gathering and monitoring for defense, space science, and other extreme environments. Richard Feynman first speculated about the possibility of making machines from molecules in his historic address on December 29, 1959 entitled, "There's Plenty of Room at the Bottom," where he challenged all to try to maneuver matter one atom at a time [1]. Beginning in the early 1980s, K. Drexler was one of the first to bring the idea of nanodevices to public attention with his publications, which contained foresight into the future of nanotechnology [2, 3]. Since then our abilities to design and construct artificial molecular machines have been aided by a number of major breakthroughs in physics, chemistry, and biology.

Molecular analogs to macroscopic mechanical devices are currently being discovered at a remarkable pace. These molecules have all the essential features of macroscopic devices but with individual molecules serving as the components. In all probability, simple molecular devices will eventually be combined to form molecular and nanosystems that will resemble macroscopic machines. Broken down into the key features, a macroscopic machine consists of a power source (fuel) and work of a repetitive and often cyclic nature [4]. Molecular machines possess these same key features.

Currently there are two techniques being researched by which to construct such devices [5, 6]. The first and most popular of these methods is self-assembly. In self-assembly, the molecules move randomly and explore many possible orientations. Given sufficient time, a preferred arrangement will be adopted if it is more stable (the lowest energy conformation). Biological functions display the most sophisticated and effective examples of self-assembly [7]. The second method, positional assembly or template-directed assembly, is commonly found at the macroscopic level, but has yet to see widespread use for molecular and nanosystems. In positional assembly, some force keeps the parts/molecules positioned at or near a particular location. Deliberately moving the parts/molecules into close proximity with one another and linking them together achieves assembly. Recently it has been possible to construct a large range of molecular machines. These include abacuses, bearings, brakes, motors, rotors, ratchets, shuttles, sockets, and switches.

In systems where millions of molecular devices are utilized, the issue of heat dissipation will need to be taken into account [8, 9]. Knowing the amount of heat a single device emits will put a limit on the number of devices that could be combined on a substrate. By taking into consideration the thermal challenges of such systems, there will still be a considerable improvement over current technologies, but far below what could be achieved if considerations for heat dissipation did not need to be made [9].

In Section 2, realized examples of mechanical molecular devices are reviewed. In Section 3, we review theoretical and computational studies of both proposed and realized molecular and nanodevices. The focus is on molecular systems that have demonstrably "device like" character.

## 2. MOLECULAR ANALOGS OF MECHANICAL DEVICES

### 2.1. Molecular Switches

One class of molecules that has gained significant popularity over the past few years as a result of their ability to function as molecular shuttles is the rotaxanes and catenanes. These molecules are assemblies of two or more molecules that are mechanically linked but chemically independent and

can be formed by means of self-assembly [10]. Some rotaxanes and catenanes have been synthesized that serve as prototypes for artificial molecular machines because the relative motion of their components can be shuttled, hence evoking images of a nanoscale switch. Such devices are of considerable interest because they are thought to foreshadow the development of molecular-scale information processing systems [11]. A typical rotaxane system consists of a cyclic component threaded by a dumbbell shaped component (see Fig. 1). Rotaxanes are related to but topologically different from catenanes, which consist of two or more interlocked rings. If the macrocyclic component of a rotaxane (or catenane) can be induced to move from one initially favored "station" to a second "station" as a result of some external stimulus, then a very basic molecular switch has been produced. (Effectively the external stimulus is changing the preferential binding site.) This property, in which relative movement of their ring- and/or dumbbell-shaped components may be induced to switch between stable rest states with an external stimulus, endows the rotaxane (or catenane) with device-like character.

The existence of interlocked molecules was first described as early as 1912 by Willstatter [12]. However, due to the topologically complex structural features associated with rotaxanes and catenanes, their syntheses posed a significant challenge and only at the beginning of the 1960s were synthetic routes to such systems clearly stated by Frisch and Wasserman [12–16].

### 2.1.1. Rotaxanes

Several different schemes have now been reported for producing a rotaxane that undergoes shuttling action in response to an external stimulus. In 1991 one of the first functional molecular shuttles produced in reasonable yields was reported by Anelli and co-workers [11]. It is a [2] rotaxane containing a linear dumbbell-shaped component, possessing two $\pi$-electron rich hydroquinone rings separated by a polyether chain, and terminated by two bulky triisopropylsilyl groups as stoppers. A cyclic tetracationic cyclophane threaded onto the dumbbell component completes the system. The tetracationic cyclophane component shuttles back and forth between the two hydroquinone rings. This molecular shuttle was proposed as a prototype in designing more intricate systems in which different "stations" were inserted
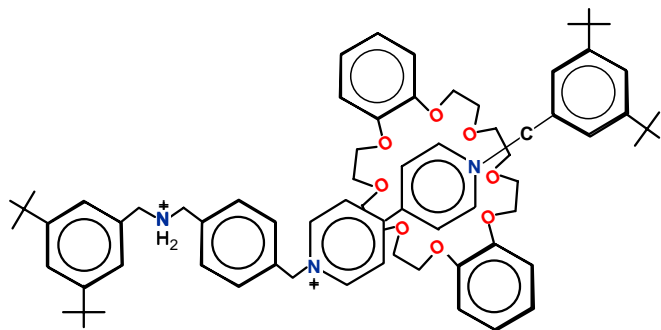
onto the dumbbell component. These different "stations" would act to desymmetrize the system so that they could be addressed selectively by chemical, electrochemical, or photochemical means. Examples of more advanced rotaxane systems are described below.

Indeed both rotaxanes and catenanes can be designed and constructed with chemically, electrochemically, and/or photochemically active recognition sites introduced into one of their two interlocked components. Chemical controls, including for example systems whose switching properties are pH dependent, present a straightforward method for controlling molecular machines. However, such a system will require addition of fresh reactants or "fuel" to power the machine, which in turn will generate waste products that must be removed from the system [17]. This will undoubtedly cause limitations in the design of molecular machines based on such inputs. Electrochemical and photochemical inputs can "fuel" a molecular machine without the associated formation of waste as found in those machines that are chemically induced [17]. Photochemical means used for switching purposes are generally photoinduced redox reactions and photoisomerization, while electrochemically controlled systems make use of redox reactions.

***Chemically Induced Switching***  A chemically controllable molecular shuttle has been produced in which a [2] rotaxane is composed of a dibenzo[24]crown-[8] macrocycle and a dumbbell-shaped component that contains a dialkylammonium center and a 4,4′-bipyridinium unit [18]. Since the hydrogen bonding interactions between the macrocycle and the ammonium center are much stronger than the charge transfer interaction of the macrocycle with the bipyridinium unit, the stable conformation is that in which the macrocycle surrounds the ammonium station. Upon deprotonation of the system, displacement of the macrocycle to the bipyridinium unit is obtained where its ring becomes involved in weak donor/acceptor interactions. The system is shown schematically in Figure 2. The switching process is fully reversible and its mechanical movements can be induced by an acid/base stimulus.

Another acid-base controllable molecular shuttle in which the rotaxane bears a fluorescent and redox-active anthracene stopper unit in addition to a dialkylammonium center ($NH_2^+$) and a bipyridinium unit ($Bpym^{2+}$) has been reported by Ashton et al. [19]. Upon addition of an appropriate base, the $NH_2^+$ is deprotonated and the crown ether switches from the NH center to the $Bpym^{2+}$. Treatment with acid restores the $NH_2^+$ center and reverses the processes. Using the anthracene stopper, it is possible to monitor the switching process by means of electrochemical and photophysical
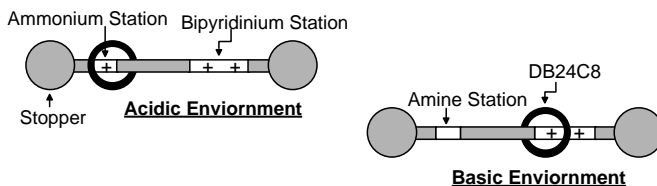


**Figure 1.** A schematic of a typical rotaxane system is shown above. In this system protonation/deprotonation of the ammonium station induces the shuttling action of the crown ether [18].



**Figure 2.** A schematic showing the relative positioning of the ring component with respect to the shaft component of a rotaxane as a result of its pH-dependency as described by Martinez-Diaz et al. [18].

techniques due to its absorption, luminescence, and redox properties.

A pH-switchable bistable [2] rotaxane that is kinetically controlled (therefore allowing the second state to be maintained after removal of the stimulus) has been reported by Lee et al. [20]. The [2] rotaxane consists of cucurbituril as the macrocycle, one protonated diaminobutane unit as the initial station, two pyridinium groups as linkers, two hexamethylene units as subsequent stations, and two terminal viologen groups. Previously all systems that had been reported to display switching properties were found to be in thermodynamic equilibrium. Therefore once the stimulus is removed, the system reverts back to its initial state. This system however has a high activation barrier and upon removal of the stimulus the reverse process is extremely slow, taking weeks to achieve the initial state of the system. Upon heating, however, the macrocycle shuttles back quickly and completely to its initial location. This feature is promising because in functional devices it may be impractical to maintain different chemical environments for each switched state. This type of system will allow the second state to be "locked in" and could be useful in designing "safeguarded" molecular switches [20].

***Electrochemically Induced Switching*** A rotaxane system described by Bissell et al. [21] has been shown to exhibit electrochemical switching. The dumbbell-shaped component of this system contains two recognition sites, one a benzidine and the other a biphenol unit. This system exhibits translation isomerism with the macrocycle located preferentially on the benzidine unit, the more $\pi$-electron rich station. However, electrochemical oxidation of the benzidine unit converts it to the monocationic radical state, and as a result of the repulsive electrostatic interactions, the macrocycle with its four formal positive charges moves to the biphenol unit. This redox system is completely reversible upon electrochemical reduction.

***Photochemically Induced Switching*** An example of a molecular shuttle shown to exhibit relative translation of the ring and shaft induced by photoexcitation with a laser pulse was reported by Brouwer et al. [22]. In this device, the stoppers on the two ends of the chain component are succinamide (*succ*) and 3,6-di-tert-butyl-1,8-naphthalimide (*ni*) units, respectively, which are separated by a $C_{12}$ alkyl spacer and serve as two potential H-bonding stations. The chain is encircled by a benzylic amide crown ether ring molecule named 1,4,7,14,20-hexaaza-2,6,15,19-tetraoxo-3,5,9,12,16,18,22,25-tetrabenzocyclohexacosane, which can be induced to change its position and shuttle between the *succ* and *ni* stations on the linear chain. The succinamide (*succ*) station on one end of the shaft component is an excellent macrocyclic ring binding site in the ground state. Meanwhile, naphathalimide on the other end is a poor H-bond acceptor [23] in the neutral ground state, and the rotaxane adopts the *succ*-co-conformation. The H-bond-accepting affinity [23] of naphathalimide is greatly enhanced when the shaft is reduced to the anionic state, which may be induced photochemically by a nanosecond laser pulse. It has been observed experimentally that after photoexcitation, the *ni* chromophone on the shaft undergoes an intersystem crossing to the triplet (T) state in high yield [22]. An electron donor can induce the formation of a contact radical ion pair by reduction of the triplet, which enables the shuttling of the macrocyclic ring component down the shaft from its original succinamide station to the reduced naphthalimide unit where ring binding is preferred in the reduced state.

Another photochemically induced switchable rotaxane system has been reported by Murakami et al. [24]. It consists of an $\alpha$-cyclodextrin macrocycle, an azobenzene chain molecule, and 2,4-dinitrobenzne units as stoppers. The macrocycle on this rotaxane systems moves between the azobenzene unit and a methylene spacer upon alternating photoirradiation with UV and visible light. The shuttle is forced to change position with respect to the shaft by conformational isomerization of the shaft.

### 2.1.2. Catenanes

Numerous schemes have also been reported in which catenanes undergo shuttling action in much the same manner as the rotaxanes. The first reported syntheses of catenanes, topologically fascinating molecules consisting of two or more interlocked rings, came in the 1960s [12]. During the subsequent three decades catenanes have received increasing attention. One of the first template directed synthesis of a positively charged [2] catenane was reported by Ashton et al. [25]. This [2] catenane demonstrated a highly efficient one-step template directed synthesis and dynamic $^1H$ NMR spectroscopic behavior.

Around the same time, terminology for these structures was evolving. A catenate is a transition metal complex whose organic backbone consists of interlocked coordinating rings [26]. A catenand is a demetalated catenate; this structure was identified and the name proposed by Dietrich-Buchecker et al. [27] when studying a technique of synthesis based on a template effect around a metal ion leading to a metallocatenane as an intermediate. The catenand obtained after demetalation of a catenate contains interlocked rings characteristic of a catenane.

***Chemically Induced Switching*** A switchable hybrid [2] catenane in which two template concepts were combined has been reported by Amabilino et al. [28]. This has resulted in a molecular system whose properties are governed by either of the two template binding modes. In this case the combination of transition metal ion chelating units and $\pi$-electron donor-acceptor complexes was chosen. In this [2] catenate one ring contains a 2,9-diphenyl-1,10-phenanthroline (**dpp**) ligand and a 1,5-dixoynaphthalene unit and the other ring contains a **dpp** ligand and two bipyridinium units. This molecule possesses two different coordination sites: 1) coordination of Cu(I) by the two dpp ligands and 2) a donor-acceptor interaction between the 1,5-dioxynaphthalene unit and the two bipyridinium units (see Fig. 3). The coordination recognition site is stronger, and so the stable conformer is that in which the Cu(I) ion is complexed by the two **dpp** ligands. Removal of the Cu(I) ion however, forces the molecule to undergo a topological change in which it maximizes the noncovalent bonding interactions present in the demetalated system and affords the [2] catenand. Additionally the [2] catenand exhibits pH dependency. In the presence of acid, the formation of the protonated species occurs
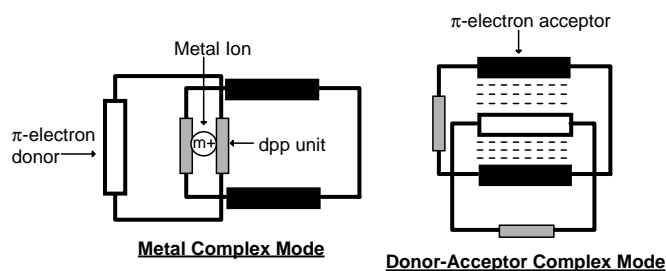
**Figure 3.** A schematic of the two coordination sites in the [2] catenate/[2] catenand described by Amabilino et al. [28].

such that the H$^+$ ion is imbedded between the two **dpp** ligands, forcing a considerable change in the geometry of the molecule. Subsequent treatment with base regenerates the [2] catenand in which the donor-acceptor interactions dictate the relative positioning of the rings with respect to each other.

***Electrochemically Induced Switching*** One candidate for electrochemical switching is a [2] catenane in which a dissymmetric tetracationic cyclophane containing two different recognition sites (a bipyridinium unit and a trans-bis(pyridinium)ethylene unit) is interlocked with the symmetrical macrocyclic polyether ring, bis(p-phenylene)-34-crown-10 (**BPP34C10**) [29]. The bipyridinium unit resides inside the cavity of the **BPP34C10** component as a result of its high $\pi$-accepting ability. The first one-electron reduction occurs preferentially at the "inside" bipyridinium unit, yielding the radical cation, which is due to its much impaired $\pi$-accepting ability, undergoes circumrotation of the charged component through the **BBP34C10** ring, wherein the trans-bis(pyridinium) ethylene unit (the now better $\pi$-acceptor) is located inside the cavity of the crown ether. On oxidation, the species loses an electron and the circumrotation process is completed, returning the [2] catenane to its original geometry.

Another dissymmetric catenane in which the ring motions can also be driven by electrochemical means was reported by Livoreil et al. [30]. A copper catenate, a copper complex whose organic backbone is a [2] catenane and is able to adjust its coordination geometry to the oxidation state of the metal by changing the respective positions of its rings, was generated. The catenate consists of two different rings. The first rings is a 2,9-diphenyl-1,10-phenanthroline (dpp) unit. The second ring comprises a dpp moiety and a terdentate ligand, 2,2′:6′,2″-terpyridine (terpy). Both units are linked by three methylene groups. This catenate is able to adopt two geometries, each stabilizing preferentially a different oxidation state of the metal center. Oxidation or reduction generates a metastable complex, which rearranges to adopt the coordination mode best fitting the new oxidation state of the metal center. After oxidation of Cu$^I$N$_4$, the catenate undergoes a linkage isomerization, transforming the metastable complex Cu$^{II}$N$_4$ into the more favorable Cu$^{II}$N$_5$. Addition of hydrazine monohydrate or ascorbic acid triggers the reverse process, giving the starting complex, Cu$^I$N$_4$.

***Photochemically Induced Switching*** The co-conformational motion associated with the copper [2] catenate reported by Livoreil et al. [30] can also be induced

photochemically. Upon irradiation of a solution of the copper [2] catenate in MeCN in the presence of *p*-nitrobenzylbromide, the Cu$^I$-based chromophoric unit is excited to a metal-to-ligand charged transfer excited state. Electron transfer from the photoexcited copper [2] catenate with *p*-nitrobenzylbromide follows, which generates a pseudo-tetrahedral Cu$^{II}$ ion that forms a more stable pentacoordinated geometry. Upon addition of ascorbic acid, the pentacoordinated Cu$^{II}$ center is reduced to a tetracoordinated Cu$^I$ ion.

### 2.1.3. Related Molecular Structures

***Molecular Abacus*** An abacus is a manual computing device that consists of a frame holding parallel rods strung with movable beads, which serve as counters. When comparing this structure with that of a rotaxane, it is easy to see the correlation between the two. For this reason rotaxanes have begun to form the basis for molecular level abacuses. One example is provided by Ashton et al. [31] The [2] rotaxane is composed of a $\pi$-electron-donating macrocyclic polyether bis-*p*-phenylene-34-crown-10 and a dumbbell-shaped component that contains (1) a Ru$^{II}$ polypyridine complexes as one of its stoppers in the form of a photoactive unit, (2) a *p*-terphenyl-type ring system as a rigid spacer, (3) a 4,4′-bipyridinium unit and a 3,3′-dimethyl-4,4′-bipyridinium unit as $\pi$-electron accepting stations, and (4) a tetraarylmethane group as the second stopper. The ring component or "counter" can be induced by light excitation to move between two different recognition sites or "stations" on the dumbbell-shaped component.

A more complex molecular abacus is described by Shigekawa et al. [32] where an $\alpha$-CyD molecule on a polyrotaxane was able to be manipulated with an STM to move. It was possible for Shigekawa's group to initiate and terminate shuttle movement at a predetermined time, control the direction of the movement, and read the shuttle position. The movement was in a linear fashion along the dumbbell-shaped component of the polyrotaxane and performed without disturbing any of the other $\alpha$-CyDs that were present. Additionally they found it possible to move a pair of adjacent $\alpha$-CyDs simultaneously. The two $\alpha$-CyDs were reversibly manipulated while keeping their mutual positioning intact.

***Molecular Piston Cylinder*** A pseudorotaxane is essentially a rotaxane in which at least one of the terminal stoppers has been eliminated, making it possible to remove the macrocycle from the linear component. These systems may be viewed as molecular examples of a piston-cylinder since they undergo assembly and disassembly reminiscent of the movement of a piston in a cylinder (in which the macrocycle is the cylinder and the linear rod is the piston). An example was reported by Ashton et al. [33] who were able to incorporate a "light-fueled" motor into a pseudorotaxane and show that it behaves as a light-driven molecular machine in the form of a piston-cylinder through light-induced assembly and disassembly of the pseudorotaxane.

A similar system was described by Ishow et al. in which they report a molecular plug/socket in the form of a pseudorotaxane [34]. The molecular plug and socket system was generated using crown ethers that incorporate a binaphthyl

unit and a wire-like compound bearing an anthracenyl unit. The pH-dependency of the system controls the plug in/plug out motion of the system. The possibility of association (controlled by $H^+$ bonding between the ammonium unit and the crown ether oxygens) of these systems is strongly affected by the size of the crown ether and the bulkiness of the wire-like component.

***Synthetic Molecular Muscle*** Jimenez et al. [35] have found it possible to construct a unimolecular linear array capable of undergoing contraction and stretching. This molecule is composed of a rotaxane dimer. The stretching and contracting of the molecule is activated by a chemical stimulus. The molecular assembly was designed to mimic real muscles in which two filaments glide along one another. Both filaments move along one another but stay together as a result of the interlocked nature of the system. The doubly threaded compound reported can bind simultaneously to two metal centers, either in a four-coordinate or a five-coordinate geometry. The four-coordinate geometry corresponds to an extended state and the five-coordinate to a contracted state. From CPK model estimations, the length of the compound goes from 65 angstroms in the five-coordinate geometry to 83 angstroms in the four-coordinate geometry, a 128% change.

***Entropy-Driven Molecules*** Hanke and Metzler [36] have proposed a new type of mechanical molecule based on systems of similar topological nature to rotaxanes and catenanes. Typically, in molecules including rotaxanes and catenanes the Gibbs free energy, $F$,

$$F = U - TS \tag{1}$$

is minimized by variations in $U$, the internal energy. The proposed molecules rely on the minimization of the Gibbs free energy by variations in the entropy, $S$, while the energies and chemical bonds (internal energy $U$) are left unchanged. The entropy functional units can be specifically controlled by external parameters such as temperature, light, or electromagnetic fields. Functional behavior such as controlled transition from linear chain to ring polymer, swelling/de-swelling, switching, and molecular motion could be achieved. One such example provided describes a polymer ring along which a number of slip links are placed. Within each of the fringe loops, additional sliding rings are placed. If the sliding rings are immobile, the central loop consumes almost the entire length of the polymer. However, if the sliding rings are free to move, large fringe loops are entropically favored and the central loop will be drastically smaller.
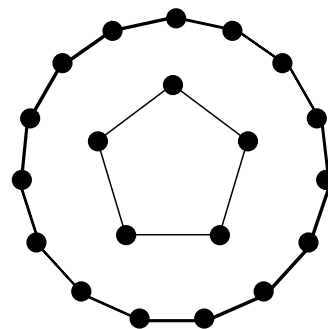
## 2.2. Molecular Bearings

Bearings are an essential component in many macroscopic machines and are expected to hold equal importance in many molecular machines and devices. However, constructing a molecular bearing has proven difficult [37]. While friction in the conventional sense is not a problem it may still be the case that the bearing has certain preferred locations as a result of variations in the energy of the system upon rotation of the shaft with respect to the sleeve. Ultimately this could cause the bearing to stick in certain preferred positions determined by the lowest energy conformation of the system. Merkle [37] has proven theoretically, however, that bearings with short periods (A short period is created if the shaft and sleeve are made with $m$-fold and $n$-fold symmetry, respectively, by selecting $m$ and $n$ so that the greatest common divisor of $m$ and $n$ is small.) will usually have small barriers separating one minimum from the next, and that this can be achieved by paying attention to symmetries of the shaft and sleeve (see Fig. 4). Molecular mechanics models of such bearings have shown that potential energy as a function of rotational position is very nearly flat. Therefore, the barriers of rotation will be small, thereby reducing any "stickiness" in the system.

More recently the Gimzewski et al. have demonstrated how rotor molecules surrounded by molecules that form supramolecular bearings could be constructed [38]. This was achieved by depositing hexa-*tert*-butyl decacyclene molecules on copper surfaces under ultra-high vacuum. This molecule has a structure that is twisted into the shape of a propeller with six blades because of steric interactions among its hydrogen atoms. When coverage of the copper surface is just short of a monolayer, some of these molecules can function as rotors if a loosely packed collar of identical molecules that act as a supramolecular bearing surrounds them. Interaction of the rotor molecule with its bearing causes rotation, and the driving force is the thermal energy in the system. Manipulating the rotor with the tip of a scanning tunneling microscope can induce rotation.

## 2.3. Molecular Brakes

Another fundamental component of macroscopic machine is the brake. The automobile provides an excellent example in which brakes are essential components of the machine. They could well be equally critical in molecular machines. Brakes are designed to halt or control the speed of rotary motion. Kelly et al. reported a molecular analog to the brake [39]. The system is constructed of a triptycene wheel and a brake as seen in Figure 5. Triptycene is a rigid molecular unit with three blades composed of benzene rings and is reminiscent of a gear. Initial attempts to construct a molecular brake from such a molecule instead provided a system that acted more "like a playing card on a bicycle tire" [39]. However, it was found that upon addition of a metal (in this case $Hg^{2+}$), the brake is activated and the spinning of the wheel is



**Figure 4.** A schematic end-on view of a molecular bearing in which the shaft possesses 5-fold symmetry and the sleeve 15-fold symmetry.
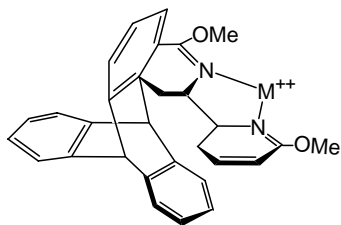
**Figure 5.** A molecular analog to the brake constructed of a triptycene wheel, as reported by Kelly et al. [39].



**Figure 6.** A triptycenocrown ether, which constitutes a molecular gearing system that displays dynamic "rope-skipping" behavior [46]. The system has been synthesized with various chemical groups at the position marked X (O, S, NH, $CH_2$, $SiH_2$, $C_2H_2$).

halted. Treatment of the $Hg^{2+}$ complex with EDTA removes the $Hg^{2+}$ and releases the brake allowing the wheel to spin rapidly.

An alternative device was constructed in which the photochemical switching process of the donor-acceptor substituted helical alkene could be blocked completely by protonation of the N, N-dimethylamine donor unit [40]. Protonation of the amine group results in an acceptor-acceptor substituted lower half, and as a result the photochemical switching is blocked. Deprotonation restores the donor amine group, and the switching process is once again functional. The reversible protonation constitutes a brake effect, as by simple de(protonation) the on mode and off mode are addressed.

Yet another device that acts to control the speed of motion of a molecular rotor can also be considered a brake [41]. This device consists of a thioxanthene-based switch and a biaryl rotor. Photoisomerization from the *cis* conformation to the *trans* conformation moves the upper naphthalene unit away from the rotor, resulting in a decrease in steric hindrance and, one might expect, an increased propeller speed. The reverse was found, however, since in the *cis*-isomer the naphthalene unit easily bends away to allow passage of the rotor. In the case of the *trans*-isomer, the methyl substituents of the rotor interfere with the methylene groups of the upper part and therefore hinder the speed of the rotor. It was concluded from this study that the rate of motion of a rotor can be controlled by *cis-trans* isomerization.

## 2.4. Molecular Gearing Systems

Molecular gearing systems were among the first successful examples of rotary mechanical devices engineered and synthesized using conventional chemistry. The major efforts aimed at synthesizing molecular gears have been focused on triptycene derivatives. The use of triptycenes as molecular gears started during the 1970s with a significant body of the research being done by Mislow and Iwamura [42–44]. The simplest triptycene gears, however, were constructed by Oki [45] using two triptycene derivatives connected by an appropriate bridge.

More recent work has been done using triptycenes by Gakh et al. [46]. The simplest molecular systems that mimic bevel gears were constructed from two triptycene "gearing" fragments connected by an appropriate bridge. In other systems described, a crown ether bridge connects two ends of principle axis of the triptycene as seen in Figure 6. The "fan blades" of the triptycene gear pass through the ring of the
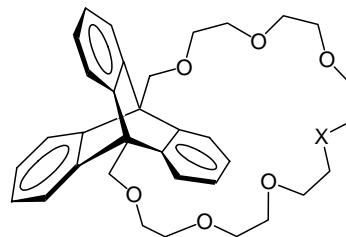
crown ether. The findings of this study indicate that not all synthesized triptycenocrown ethers display dynamic behavior, that is, the expected "rope-skipping" does not occur in all of the studied systems. This was often the case in systems with small crown ether bridges. It was anticipated that complexation of a guest by the crown ether would control the "rope-skipping" rotation [46], and indeed a small effect was observed for certain guests. Systems in which complexation would have greater control over rotation await further development.

### 2.4.1. Molecular Ratchets

Ratchets are devices that allow motion in only one direction. Generally they consist of three components: 1) the ratchet wheel, 2) the pawl, which acts to prevent rotation of the wheel in the wrong direction, and 3) the spring, which holds the pawl in place. Kelly et al. sought to translate these macroscopic properties of the ratchet to the molecular scale using triptycene as a wheel and helicenes as the pawl and spring components [47, 48]. The synthesis of triptycyl [4]helicene successfully incorporated the essential components of a simple ratchet into a single molecule (see Figure 5). It was demonstrated experimentally, however, that the molecular ratchet described rotates bidirectionally rather that unidirectionally. Rotation in both the clockwise and counter-clockwise direction requires the same amount of energy and therefore dictates an equal potential to rotate in either direction.

### 2.4.2. Molecular Rotors

Unidirectional motion was finally achieved by both Kelly et al. [49] and Koumura et al. [50] in another example of a molecular device, a molecular rotor. The system identified by Kelly et al. [49] is reminiscent of the unsuccessful molecular ratchet [47, 48] described by that same group in which the rate of rotation was controlled by a conformational change. The system consists of a three-blade triptycene and a [4]helicene connected by a single bond, and was found to exhibit unidirectional motion [49]. However when this system is thermally stimulated, rotation of the triptycene occurs in both the clockwise and anticlockwise directions to an equal extent. The unidirectional rotation results from the asymmetric skew of the helicene and the use of a monosubstituted triptycene, which results in non-identical energy surfaces for clockwise and counter-clockwise rotation.

The first system designed by Koumura et al. [51] is a rotor consisting of helical alkenes in which unidirectional rotation around a central carbon-carbon double bond occurs. The structure of the rotor is (3R,3′R)-(P,P)-*trans*-1,1′,2,2′,3,3′,4,4′-octahydro-3,3′-dimethyl-4,4′-biphenanthrylidene and consists of two identical halves connected by the central carbon-carbon double bond (see Fig. 7). Irradiation with ultraviolet light causes rotation about the central bond. The cycle may be regarded as four distinct states (at each of the isomerization steps) in an optical molecular switch, each achieved using the appropriate temperature and wavelength of light. If the appropriate temperature and wavelength are achieved, it is possible to induce a continuous unidirectional rotation.

More recently Koumura et al. [50] have reported a second-generation molecular rotor, which contains a chiral 2-methyl-2,3-dihydrothiopyran "upper half" and a thioxanthene "lower half." The upper naphthothiopyran unit has been found to undergo 360 degrees of rotation with respect to the lower portion of the system. At the appropriate wavelength and temperature, rotation is continuous and unidirectional. This rotor containing distinct upper and lower halves has been found to exhibit unidirectional rotation with the addition of a single stereogenic center.

Another example of rotary motion was reported by Bedard and Moore [52] in which they describe a molecular turnstile. The turnstile consists of a hexa(phenylacetylene) macrocyclic frame with a diethynylarene bridge. The bridging unit should exhibit rotation about its axis and act as the spindle of the turnstile. Hinderance to rotation about the spindle axis is almost entirely due to steric interactions between groups attached to the spindle and the macrocycle framework.

## 2.5. Molecular Piston

Components where internal cylinders are repeatedly moved back and forth inside the outer cylinders such as pistons or syringes also play an important role in macroscopic machines. Yu et al. [53] have succeeded in creating an equivalent molecular system consisting of multiwalled carbon nanotubes (MWCNTs) as seen in Figure 8. Both a stick-slip motion and a smooth pullout motion were observed in both of the MWCNTs studied. The data and analysis suggest that theoretical modeling will shed further light on the systems. The studies reported were the first to observe the sliding of nested shells in MWCNTs.

## 2.6. Molecular Barrow

A molecular barrow consisting of two front wheels, two rear legs, and a central board to work on a Cu(100) surface has been reported by Joachim et al. [54]. The barrow



**Figure 8.** Multiwalled carbon nanotubes (MWCNTs) exhibit movement that is similar to a bearing or piston/cylinder system.

is specifically designed to be guided by the tip of an STM and therefore to act as an individual nanoscale molecular machine. A tetracene unit was selected as the molecular board, and triptycene molecules were used for the two front wheels with a triple bond per wheel to ensure structural stability of the front axle. The rear legs are *tert*-butyl phenyl groups, which display efficiency for STM manipulation. All the pieces of the molecular equipment are covalently bonded together, resulting in a single molecule as seen in Figure 9. Unfortunately the wheels do not rotate and instead slide along the surface upon STM manipulation. One reason is that the Cu(100) surface corrugation is not large enough for the wings of wheels to find some friction to engage their rotation. A new structure was proposed in which there were two ratchet groups on the central board; however, the task remains to synthesize the proposed structure and manipulate it with STM. Uses for this molecular



**Figure 7.** A molecular rotor designed by Kourmura et al. [50].
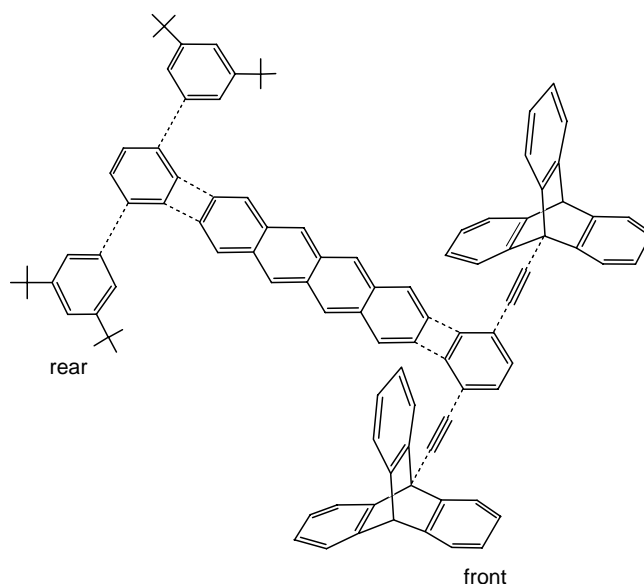


**Figure 9.** A molecular barrow as reported by Joachim et al. [54].

machine could include the reconstruction of an atomic surface or the building of an atomic wire.

## 2.7. Molecular Motors

Recently, attempts at designing the first molecular motor have been made by Kelly et al. [55, 56]. The task is still incomplete, but the group reports that progress has been made. The motor is based on a molecular ratchet that the group reported previously (see Figure 5) [47–49]. The motor would work by trapping the molecule in an excited state, at which point it has a new "low energy" position closer in energy to the peak of the potential energy surface (see Fig. 10). Random thermal energy will eventually elevate the molecule from the new "low energy" position to the peak, which it can descend on the other side corresponding to unidirectional rotation. Trapping the molecule in the excited state is achieved by a 60 degree rotation followed by urethane formation that traps molecule in an energetically excited conformation around the triptycene/helicene bond. The next step will be to achieve repeated rotation controlled selectively at the appropriate time. Much work remains to be done before this and similar systems rival that of their biological and mechanical counterparts.

# 3. THEORETICAL STUDIES OF MECHANICAL MOLECULES AND NANO-DEVICES

Needed for the large-scale commercialization of nanomachines is a process equivalent to design engineering. Toward this end, there has been an increasing effort to identify simulation techniques for molecular and nanodevices. Molecular modeling is desirable in order to circumvent the need for time-consuming and expensive fabrication of numerous prototype systems. It is expected to provide a shortcut to functional molecular devices by enabling the screening of proposed designs and modifications based on predicated performance.

There are several technical challenges that must be met in order for a theoretical/computational treatment of a molecular or nanosystem to be successful. The most important concern is that the method gives reliable information. While the quantitative accuracy may vary, the method must correctly predict the fundamental aspects of the system. The second problem is that the method must be sufficiently efficient to allow a reasonable number of prospective designs
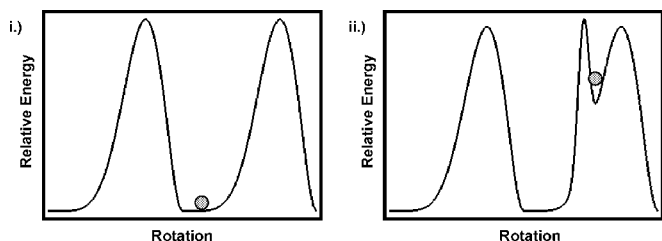


**Figure 10.** Upon formation of urethane there is an increase in the periodicity of hindered rotation, and as a result the molecule is trapped in an excited state affording a new "low energy" position that is now higher in energy.

to be screened within a reasonable time frame. While "reasonable" carries significant latitude, it must be acknowledged that if the time required is too long, or the required computational facilities too expensive, the modeling process will not serve as a useful design tool. Finally, perhaps the greatest challenge is that the method accommodates the wide variety of chemical and physical properties at play in nanosystems.

In the theoretical description of molecular devices, five key issues are identified:

1. Molecular device conformational isomerism
2. Molecular recognition
3. Skeletal vibrations and oscillations
4. Multicomponent dynamics
5. Manifestations of quantum mechanics

All five areas have been targeted in theoretical and computational studies. These studies often offer insight that was previously unknown and can be used to design more powerful and useful nanodevices.

## 3.1. Applications of Methods and Techniques

There exist three broad categories of theoretical methods for investigating static molecular properties. In approximate order of increasing complexity, they are the molecular mechanics (MM) methods, semi-empirical methods, and *ab initio* methods.

While MM methods are fast and readily allow energy minimizations and searching through large configurational spaces, they typically have some important limitations. For example, MM methods incorporate electronic structure effects only *implicitly* through empirical parameters. It is becoming increasingly evident that simultaneous simulation of mechanical and electronic properties is critical in molecular device modeling [57, 58]. At the other extreme, *ab initio* methods incorporate electronic structure effects *explicitly* and can in principle provide sufficient accuracy, but in practice extensive computational resources are required to treat even the smallest systems [59, 60]. Semi-empirical (SE) electronic structure methodology represents a compromise between these two extremes. SE methods treat only the valence electrons explicitly, and parameterize the computation of certain difficult-to-evaluate integrals for greatly increased computational efficiency. Techniques from all three categories have found application in the theoretical and computational description of molecular devices, with different techniques being most applicable to different key issues.

### 3.1.1. Molecular Device Conformational Isomerism

In a macroscopic machine there are typically two or more stable rest states [61]. For example, a valve may be open or shut, and a selector switch may take any of several positions. The analogous states of a molecular device are stable molecular conformations. The ability to design a molecular device entails the ability to predict these stable conformations.

Grabuleda and Jaime [62] have applied molecular mechanics methods to model the switching processes observed in

[2] rotaxanes. The MM3 and MM3* force fields were chosen, which they noted model nonbonded interactions reasonably well. The molecular mechanics studies on the series of rotaxanes chosen show that electrostatic and van der Waals terms are the major factors controlling the energy minima. This conclusion is probably generally true for large macrocycles containing highly electronegative atoms [63]. The simulation of the behavior of the rotaxanes as molecular devices at thermal equilibrium using the MM3 force field agrees with the experimental results for the preferred location of the translational isomers only when the dielectric constant has been changed to simulate solvent effects. Complementary computations were carried out using the MM3* force field, which showed less reliable and sometimes wrong behavior in the prediction of stability between isomers [62].

Calculations and statistical analyses of X-ray crystal structures were carried out by Biscarini et al. [64] on mechanically interlocked molecules, including rotaxanes and catenanes. The MM3 model [65–67] was used (as implemented in the TINKER package). They reported that they were able to reproduce experimentally determined rotational barriers and steric energies in these types of interlocked molecules [64].

Ceroni et al. [68] reported a comparative investigation of the electrochemistry of a benzylic amide [2] catenane and its topologically trivial subcomponents. They proposed that the redox behavior of the catenane can be understood in terms of the electrochemistry of smaller molecular fragments and simple molecular orbital considerations. Semiempirical quantum chemical (MNDO) calculations were performed on both neutral and doubly charged catenane species, and analyzed with electrochemical data from experiments. The electrochemical study and theoretical considerations suggest that the reductive behavior of the catenane is governed predominantly by the amide carbonyl groups. The quantum chemical calculations and the electrochemical behavior suggest that an electrochemically induced reaction in the catenane connects and disconnects the two interlocked macrocycles. The formation of a C—C bond between two reduced carbonyl groups, which arises from the close proximity brought on by macrocyclic ring rotation of the catenane, prevents further macrocyclic ring circumrotation. This could provide a useful means of switching "on" and "off" the dynamics of such interlocked macrocycles.

A computational investigation on several unsymmetrical [2] catenanes was carried out by Raymo et al. [69] with empirical force field and *ab initio* quantum mechanical calculations, for the purpose of understanding the factors governing the equilibrium proportions of the translational isomers and the nature of the $\pi$-$\pi$ stacking interactions associated with these systems. Monte Carlo conformational searches [70] were carried out individually on each of those catenane complexes and their separate components, which were constructed with the program Macromodel 5.0 [71] and energy minimized with the AMBER force field [72] and the GB/SA solvation model for $H_2O$, as implemented in Macromodel 5.0. Single point *ab initio* calculations were performed in vacuum at the HF/6-31G** level using the program Spartan 4.1 [73] to determine the electrostatic potential [74], (*Ep*), calculated on the surface of the aromatic units and the energies of the highest occupied molecular orbitals

(HOMO), $E_{HOMO}$. In their *ab initio* single point calculations [69], the tetracationic cyclophane component was removed from the global minima of the complexes obtained from the Monte Carlo conformational searches, and the polyether substituents attached to the aromatic units of the guests were replaced by methoxy groups without modifying the dihedral angles around the Ar—O bonds. The factors governing the translational isomerism are reported to be (i) the differences between the solvation energies of the two translational isomers and (ii) the differences between the binding energies of the corresponding supramolecular complexes, which are controlled by electrostatic interactions. The relative populations of the translational isomers observed in solution presumably arise from a competition between these two factors.

Results reported by Kelly et al. [48] for a proposed "molecular ratchet" and studies of conformational isomerism in bacteriorhodopsin, a potential candidate for protein-based molecular memory [75], suggest that semi-empirical electronic structure methods are a suitable choice for investigating molecular device systems.

As previously discussed, Murakami et al. have synthesized and characterized a novel two-component functional nanosystem, a light-driven molecular shuttle [24]. For example, Sohlberg et al. carried out a semi-empirical investigation [76] of the light-driven molecular shuttle of Murakami et al. [24]. The results of the semi-empirical calculations agree well with the experimental results as obtained by Murakami et al. [24]. As an isolated molecule the rotaxane shaft shows two-fold symmetry, but in both rotaxane conformers the symmetry is broken. The loss of symmetry upon inclusion into the cyclodextrin was also found experimentally [24]. The *cis* conformer was found to be energetically more stable, in accord with the experimental findings of Murakami et al. [24] who report a 2:1 preponderance of the *cis* conformer (67% vs. 33%) at 278 K. In the rotaxane *trans* conformer, the shaft is very nearly centered in the cyclodextrin cavity, as Murakami et al. [24] inferred from induced circular dichroism spectra. In the *cis* conformer, the shaft is off-center. This is presumably the source of the shuttling action described by Murakami et al. [24]. Additionally the *cis* conformer of the rotaxane structure displays a kink in the shaft, and therefore the conformational isomerism from *trans* to *cis* (or vice versa) involves significant structural transformation. Finally it was found that the barrier to conformational isomerization is $\geq 11$ kcal/mol. The significant structural transformation and large energy barrier account for the observed very slow rate of isomerization at room temperature [24].

More recently Frankfort and Sohlberg have reported semi-empirical electronic structure calculations for a switchable rotaxane that was demonstrated experimentally by Martinez-Diaz et al. [18] (reviewed above) and have shown that these calculations capture the essential "device-like" character of the system [77]. It has been established experimentally that the mobile component of this rotaxane system, DB24C8, resides initially on the dialkylammonium station and that it is possible to deprotonate the $NH_2^+$ center with base and "drive" the ring to the bipyridinium station [18]. AM1 semi-empirical calculations were able to replicate this feature [77]. Unlike some other methods, AM1 has

been found to be qualitatively acceptable for intermolecular hydrogen bonding [78], the dominant interaction between the macrocycle and the shaft in this rotaxane.

A starting structure of the rotaxane molecule was constructed from its principle subcomponents [77]. There are three subcomponent structures: the ring, shaft, and stopper. The ring is a crown-ether, dibenzo [24] crown-8; the shaft contains a dialkylammonium center, a stopper (3,5-di-tert-butylbenzyl), and a bipyridinium unit; and the stopper is 3,5-di-tert-butylbenzyl bromide. Low energy conformations were identified for each subcomponent and optimized using the AM1 semi-empirical method. The rotaxane was then assembled from the optimized subcomponents by computationally mimicking the $S_N2$ mechanism by which it is synthesized. The computations showed that internal energy of the system decreases during construction. Given that association of the shaft and macrocycle is most probably entropically unfavorable, an accompanying decrease in internal energy is presumably necessary for a practical synthetic mechanism.

After construction, the shuttling action of the [2] rotaxane was tracked by correlating the energy of the system to the position of the ring in both the protonated and *de*protonated states [77]. For both the protonated and *de*protonated species, 95 separate trial structures of the rotaxane were fully optimized at the AM1 level of theory. To generate these trial structures, the initial rotaxane structure (from the $S_N2$-mimicking construction) was modified by translating and rotating the ring about the shaft. For the fully assembled rotaxane in the protonated state, the heavily dominant structure places the ring around the dialkylammonium station. This structure accounts for 64% of the total population at 300 K; the second and third lowest energy structures constitute essentially all of the remaining 36%. The most highly populated structure is representative of all three since they are essentially the same, the only difference being slight translation of the macrocycle around the dialkylammonium center. Upon *de*protonation the ring is driven to the opposite side of the shaft where the bipyridinium station is located. The calculations identify three deprotonated structures that compose 86% of the population at 300 K. In all of these structures the ring is oriented asymmetrically around the bipyridinium station. The bipyridinium station contains a nitrogen atom on either end. The macrocycle associates with either of these two nitrogen atoms rather than symmetrically positioned between the two. This asymmetric positioning around the bipyridinium station in the *de*protonated state is in agreement with the experimental results based on proton NMR [18]. As shown by the energetic data for the structures, the addition of the proton to the dibenzylamine station is energetically favorable, which is also in accordance with experimental results. The calculations further show that relatively little structural change in the shaft accompanies the shuttling action. In agreement with experimental findings [18], the semi-empirical AM1 calculations predict that the DB24C8 ring resides initially on the $NH_2^+$, and upon *de*protonation with a base, the preference of the ring location changes, at which point it shuttles to the bipyridinium station. Another aspect of these calculations was an indication that once the shaft was *de*protonated the ring could not be made to approach the NH center closer than approximately 4 angstroms. Trial structures with ring-NH separations shorter than this distance either optimized to structures with the ring pushed beyond 4 angstroms or failed to converge entirely. This characteristic of the system suggests that the shuttling action performed by the ring is relatively strong. Such calculations may be useful for *a priori* predictions of the effect of proposed structural modifications on the shuttling action and therefore serve as a screening tool for selection of future synthetic targets [77].

Zheng and Sohlberg [79] have demonstrated, on an experimentally realized example, a procedure for modeling a photo-induced, redox-switchable, rotaxane-based molecular device that captures the features critical to its device-like character. The system consists of a benzylic amide macrocycle mechanically locked onto a thread featuring two potential hydrogen bonding stations, a succinamide (*succ*) site and a 3,6-di-tert-butyl-1,8-naphthalimide (*ni*) unit separated by a $C_{12}$ alkyl spacer. The system (previously described in detail) exhibits extremely fast and fully reversible shuttling motion.

The computational procedure includes conformational searching over the full torsional space of the rotaxane. This is followed by single-point semi-empirical calculations for all co-conformations in their neutral singlet, triplet, and anionic doublet states, and statistical analysis to correlate the structural features with energy in each state. The conformational searching was performed based on all torsional bonds of the two component molecules and generated more than $10^4$ co-conformations. The observed correlation was checked by repeating the analysis after full geometry optimizations on a subset of co-conformations ($\sim$1%). The overall procedure accurately captures the structural and switching characteristics of the physical system.

Based on calculations of single point energy and radius of gyration for 10,118 rotaxane structures, it was found that co-conformations with ring binding at the *succ* site predominate in the low energy regime for singlet and triplet species, with preference for the shaft component being extended [79]. Doublet species prefer to take on co-conformations with ring binding at the *ni* site in low energy structures, with coiled and extended shaft conformations being energetically. Zheng and Sohlberg [79] obtained effectively the same results by geometrical optimizations of a subset of co-conformations. These results are in excellent agreement with previous experimental observations [22]. Therefore, they proposed that the structure versus energy profile produced in the less expensive way, by using systematic conformational searching followed by semi-empirical single point energy calculations and correlating the structural features to energy, is consistent with what would be obtained if each structure were fully optimized. They suggest that instead of carrying out full structural optimizations at the semi-empirical level for each trial structure, the use of single point calculations is sufficient to obtain the profile of structural features versus energy, as long as the trial structures generated from the systematic conformational search are "chemically reasonable."

The systems described above provide strong evidence that semi-empirical calculations are capable of predictions of molecular device bistability that are consistent with measured properties and can provide considerable insight into functional nanosystems.

### 3.1.2. Molecular Recognition

Molecular recognition is a key issue in successful molecular device architecture [61]. Molecular recognition directs the self-assembly [7, 80] from the individual device components and subcomponents. Obviously, one critical key to molecular device design is a modeling tool that properly predicts molecular recognition.

In simple terms, molecular recognition is highly specific intermolecular interactions. Molecular recognition technology has a history of successful applications for ion separations [81–85], starting from the first reports of cation [86] and anion [87] inclusion compounds. This technology has led to the development of commercial ion separation systems [88]. Molecular recognition for the self-assembly of molecular device components is obviously more complicated than ion recognition. Nevertheless, owing to the availability of extensive experimental data, recognition serves as an excellent testing ground for molecular recognition modeling tools. Sohlberg and Tarbet have shown that when used to compute the energetics of certain ion exchange reactions, semi-empirical electronic structure methods reliably predict selectivites in the binding affinity of numerous anion receptors for atomic anions [89].

In 1994 Ricketts et al. [90] reported one of the first attempts at modeling interlocked molecules using molecular mechanics. They argued that the time would come when structural complexity and size would render current analysis techniques such as $^1$H NMR and X-ray crystallography less effective and more difficult to apply. They proposed a technique that uses molecular mechanics methods together with semi-empirical molecular orbital calculations. Ricketts et al. were able to predict structures of inclusion complexes in agreement with those obtained using X-ray crystallographic methods [90]. Noncovalent bonding interactions were reproduced using this technique and binding energies were found to follow the same trend as those determined experimentally. This is a common theme in the theoretical and computational description of molecular and nanodevices. The salient features are captured in trends, so computations of qualitative reliability are of considerable value.

Raymo et al. [91] have also used a molecular mechanics technique in order to study a system of interlocked molecules. These calculations were motivated by the study of a slippage approach to self-assembly in a series of [n] rotaxanes, each consisting of a bipyridinium-based backbone, encircled by one or more dioxyarene-based macrocyclic components. Systematic variations in the $R$ group attached to one of the phenyl rings of the tetraarylmethane-based stopper was found to greatly affect the yields. When certain $R$ groups are used no rotaxane was isolated leading to the observed "all-or-nothing" substituents effect. A computational study was undertaken in order to explain this substituents effect. The study revealed two main energy barriers for the slipping-off of the macrocycle over the stoppers. The trend in calculated energy barriers was in good agreement with experimental yields of the corresponding rotaxanes and the abrupt substituent effect was found to be a result of steric hindrance. This is an excellent example of theory and computation yielding qualitative trends that lead to insight that allows for targeted synthesis, accelerating the development process.

Due to the extensive computational resources needed to treat even the smallest systems using *ab initio* techniques, few studies of molecular devices have been undertaken in which *ab initio* is the primary means computation. Dobrowolski and Mazurek [92] reported *ab initio* calculations of the qualitative theoretical $^{13}$C NMR chemical shifts ($\delta$) of model carbyne catenanes and knots including $C_{10}C_{30}$ and $C_{20}C_{30}$ (Hopf links). They found that the chemical shift ($\delta$) tends to alternate along the catenane or a knot branch, and the $\delta$ fluctuation is associated with the redistribution of $C\equiv C$ triple bond $\pi$ electrons, which arises from the repulsion between catenane components or knot branches. Repulsion polarizes the $\pi$ electrons so that a carbon atom located closer to the perturbation is deshielded and one placed further away is more shielded.

One study performed by Raymo et al. [93] investigated the magnitude of [C—H···O] hydrogen bonding, which is typically the dominant intercomponent interaction. The investigations were carried out on complexes containing the following components: N-methylpyridinium cation, dimethyl ether, and the dimethyl phosphate anion. The quantum mechanical investigation studies the interactions between charged and uncharged systems, in which the main non-bonded contacts involve [C—H] bonds on electron-deficient species and oxygen atoms on electron-rich species. The results provide quantitative measures of the large stabilization energies that arise from [C—H···O] contacts in charged systems. These attractions are responsible for the self-assembly of bipyridinium based catenanes and rotaxanes.

Pioneering investigations of the mechanisms by which mechanically interlocked components move with respect to each other in benzylic amide catenanes, have been reported by Leigh et al. [94]. It was reported that the interlocked macrocycle dynamics are governed by a delicate balance of steric effects, intermacrocyclic arrays of hydrogen bonds, $\pi$-$\pi$ stacking, and "T herringbone-type interactions." T herringbone-type interactions are phenyl-phenyl interactions in the geometry of a distorted "T." It was found that a cascade of hydrogen-bond ruptures and formations occur during circumrotation and that these are accompanied by a series of cooperative conformational and co-conformational rearrangements that help to stabilize the energy of the molecule. The polarity of the environment was also reported to play a role in determining the interring dynamics.

### 3.1.3. Skeletal Vibrations

Previous simulations of the behavior of nanocomponents have revealed one common theme: the rigidity of a component is key to its proper performance. For example, Tuzun et al. simulated the flow of rare gas atoms inside carbon nanotubes [95] and found that the rigidity of the tube has a profound effect on the fluid flow. The performance of nanobearings has also been shown to depend critically on their rigidity [96]. Excessively large vibrational motion imposes drag on the rotational motion. Nanogears exhibit similar characteristics [97]. Clearly, successful nanomachine engineering will depend on the ability to reliably anticipate vibrational properties [98].

In the just-mentioned studies [95–97], and indeed in the vast majority of nanosystem simulations to date, the vibrational properties were computed with fully atomistic

numerical classical trajectories, which follow the molecular dynamics [99]. Molecular Dynamics (MD) methods solve Newton's equation of motion for some or all of the atoms in the system, typically based on an empirical functional form of the interatomic potential energy function. The method generates a series of time-correlated points from a suitable starting set of coordinates and velocities by a series of finite time steps [100]. Since small time steps must be used for integrating Newton's equation, (Typically a time step one order of magnitude smaller than the period of the highest frequency vibrational mode of the system is required for good energy conservation in the numerical determination of the classical trajectory.) considerable computer time is required for the simulation of a short period of molecular motion. In spite of the steady geometric increase in computer speeds over time, routine analysis of the dynamics of nanosystems by fully atomistic numerical classical trajectories is impractical. Admittedly, simulations of systems containing thousands of atoms are common, and even one million atom systems are now accessible, but such simulations are computationally demanding. Large-scale simulations have their place in fundamental research and in detailed final design work, but clearly the fully atomistic numerical classical trajectory is not an ideal design tool. In addition to the cost issue, they also ignore possible quantum effects.

An alternate approach, which focuses on the overall mechanical behavior of the structure and not on local details dependent on just a few atoms, is to employ continuum methods. Because the dynamical behavior of nanomachines will be governed predominantly by the gross movements of their components, it seems reasonable to assume that reliable predictions about the performance of nanosystems might be achieved through the uses of equations from the theory of elastic solids. Continuum methods have been successfully applied to numerous modes of nanotubes, including longitudinal stretching, circumferential breathing, torsional twisting, and transverse flexing [101]. Extensions to damped systems [102, 103] and systems with size dependent elastic moduli [104, 105] have also been reported. Popov et al. [106] have shown how to accurately estimate the elastic moduli through the application of a lattice-dynamical model.

### 3.1.4. Multicomponent Dynamics

Another important aspect of the design of a complex multi-component molecular device is the prediction of its dynamical behavior. Molecular device dynamics is most often studied with MD methods.

Another application of MD techniques is to search for low energy configurations of the system. Based on the ergodic hypothesis, if one assumes that the system can be modeled as a set of oscillators of incommensurate frequencies, a dynamical trajectory will eventually (given sufficient time) sample all of the energetically accessible configuration space. One problem with this method is that in order to sample the whole potential energy surface, an impractically long simulation time is necessary. Typically only the local area around the starting point is sampled [107]. In the event of commensurate vibrational frequencies, resonances occur and the ergodic hypothesis breaks down. Another difficulty with MD

techniques is that they neglect to take into consideration the quantum mechanical aspects of the system, which are of fundamental importance [108, 109]. Despite these shortcomings, MD methods have been employed with considerable success in the study of molecular and nanodevices.

Several studies have been undertaken in which MD simulations are used. Grabuleda and Jaime [62] have performed MD simulations in conjunction with the MM calculations reported in their study of translational isomerism in [2] rotaxanes mentioned previously. The reason for this was to avoid certain limitations of the molecular mechanics simulations. As described in the previous paragraph, molecular dynamics simulations in theory allow more extensive sampling of the phase space. These MD computations show qualitative agreement with the MM computations in the estimation of the shuttling barrier. Additionally, the MD computations provided information regarding [C—H•••O] hydrogen-bonding interactions throughout the shuttling process.

Leigh et al. have demonstrated the application of inelastic neutron scattering (INS) spectroscopy in combination with MD simulations to investigate the dynamics of catenane systems [110]. Since INS depends on the vibrational dynamics, it is a valuable tool for the investigation of the dynamical properties of complicated molecular systems. The accurate simulation of INS spectra provides a description of the atomic motions. Leigh et al. [110] noted that owing to its very large incoherent scattering length, hydrogen dominates the INS response of organic molecules. Inelastic neutron scattering spectra is therefore able to monitor the amount of motion of the hydrogen atoms, which is a crucial aspect of benzylic amide catenanes since they form a number of inter-ring or intramolecular and intermolecular hydrogen bonds. Leigh et al. reported molecular dynamics (MD) simulations of two benzylic amide [2] catenanes [110] with a model that was successfully used before [111, 112]. The Tinker program [113–115] and the MM3 force field [65–67] were employed for the calculations.

Another such simulation was performed by Caciuffo et al. [116]. The simulations were based on calculation of the normal modes of the isolated catenane and therefore included neither anharmonic nor crystal effects. These studies demonstrated that the combination of INS spectroscopy and MD can be used to discriminate between different proposed structures in large interlocked molecular systems, and that this combination of techniques is particularly well suited to access the strength of intramolecular and intermolecular hydrogen bonds that are the crucial interactions that govern the dynamics of such systems.

Tuzun et al. [117] have described a molecular motor based on a nanobearing on which molecular dynamics were carried out to simulate the rotation of the sleeve about the shaft upon laser excitation. The shaft consists of concentric carbon nanotubes with positively and negatively charged species bonded to atoms on one end of the ring. It was found that when the laser field is applied, the shaft with the attached charges tends to crimp (or uncrimp). This laser-induced periodic motion, along with the electric field, propels the shaft over the rotational energy barrier. If the end of the shaft crimps too severely, however, frictional braking occurs. A wide range of operating parameters, such as

laser frequency and power, molecular bearing sizes, and the positions of the charges within the molecular bearing, were searched for stable unidirectional rotations of the inner bearing tube. For a single applied laser field under all investigated operating conditions, the bearing would rotate in one direction and then rotate in the opposite direction. Using two applied laser fields the duration of unidirectional rotation was increased, and an attempt to find the optimal set of operating parameters with a neutral net simulator was made. It was concluded from this study that the use of laser excitation on nanocomponents might be a practical method for introducing controlled motion into nanomachines.

Srivastava has reported similar results in which he investigated rotational dynamics of carbon nanotubes under a single applied laser field [118]. An intrinsic frequency of the nanotube oscillations was defined for a given laser field strength and location of charges in the body. If the laser field frequency is much less than the intrinsic frequency, of the nanotubes, the motor shows rotational oscillations in both directions. When the laser field frequency is of the same order of magnitude as the intrinsic frequency, a quasiresonance between the nanotube oscillations and the laser field oscillations is present. If the phases of the two oscillations are also properly matched, unidirectional rotation of the nanotubes is possible.

Vacek and Michl describe a computer simulation of molecular propellers mounted on a square grid using molecular dynamics methods [119]. The propellers consist of a chiral complex of Re(I) with two phenanthroline-type ligands providing two blade areas oriented at about 45 degrees to the propeller axis and at about 90 degrees to each other. The computational procedure consisted of geometry optimization of a suitable molecular structure and subsequently a series of MD calculations on the grid-propeller combination in a stream of gas approaching the grid perpendicularly from the side opposite to that on which the propeller was mounted. Constraints were introduced in order to prevent the stream of gas from sweeping the propeller downstream. All of the runs showed one of two classes of behavior. Immediately after the gas flow was turned on, the propeller suffered a period of confused motion, vibrating and rotating randomly. After a period of picoseconds it either settled into a smooth rotational motion or it continued the initial random behavior. Inspection of the propeller shape during the simulation revealed considerable bending of the axle, acting more as a pendulum than a propeller, this lack of rigidity being the most obvious weakness of the system. As a result of the simulations conducted, it was found that there is a region of gas flow parameters for which the propellers will work in the sense of producing a fairly regular motion in the steady state (achieved after approximately 20–50 ps). From this study, a more stable propeller can be proposed in which the axle is fixed at both ends in order to prevent the pendulum-like motion. This is an excellent example of the type of iterative refinement of design that can be facilitated with theoretical and computational simulations.

More recently, Vacek and Michl carried out a similar study in which a grid-mounted dipolar rotor is mounted on a square grid and driven in vacuum by a rotating electric field [120]. Prior to simulation, the molecular structures were optimized. Initial velocities were assigned, and various starting geometries and velocity distributions were used in order to widely sample the operational envelope of the system. They anticipated five regimes of behavior (synchronous, asynchronous, random driven, random thermal, and hindered rotor) dictated by the relative importance of 1) random thermal forces described by $kT$, 2) the strength of maximum rotor-field interaction, 3) the friction constant $\eta$ that describes the break-off drag torque, and 4) the rotational barrier height $W$. Four of the five regimes were studied. The MD simulations provided a detailed view of the friction and thermal motion on the rotor.

In addition to rotors, several nanoscale ratcheting mechanisms have been proposed [48, 121–123], and the development of nanomachines incorporating such elements will obviously require design models capable of describing their dynamical behavior.

By analogy to macroscopic systems, it can be intuited that the dynamical performance of nanomachines will be governed predominantly by the gross movements of their components, and not by the details of the motion of the individual atoms. This observation suggests that accurate predictions about the performance of nanosystems can be achieved through the use of the rigid body approximation. The rigid body approximation has been tested on a prototypical nanosystem [124].

A nanobearing might consist of a pair of nested carbon nanotubes [37] with the outer tube (sleeve) held in place but the inner tube (shaft) held in position by the assemblage of the nanomachine only in the longitudinal ($z$) direction. In this configuration, the shaft is free to translate and rotate in the $x$-$y$ plane, but is restricted to maintain its $z$-position. As a prototype of such a system, a rigorously planar model was considered. It consists of a single atomic layer (slice perpendicular to the $z$-axis) from such a pair of nested nanotubes. This model, while synthetically unachievable, bears striking similarities to actual molecular rotors [38] and contains the essentials of the dynamics of a nanobearing. The two components (the shaft and the sleeve) are treated as rigid bodies. The configuration of the system is completely described with three independent variables: the $x$ and $y$ positions of the center of mass (COM) of the shaft, and the angular orientation of the shaft in the $x$-$y$ plane, $\phi$. It was found that for certain initial conditions, the dynamics of this model is quasiperiodic, but for other initial conditions the motion is chaotic. For optimum performance it is desirable to operate the bearing in the quasi-periodic regime because therein it will rotate without dissipating rotational kinetic energy into other modes over time as intimated by Feynman [1] (super-rotation). It can be seen that in order to ensure stable quasiperiodic dynamics, the bulk of the total system energy must be tied up in spin of the shaft. This is exactly the sort of insight needed for successful nanodevice design: How do gross movements of the components affect system performance?

In a rigid body simulation, it is necessary to specify the orientation of the body as well as its position. The specification of the location of a rigid body in space requires three coordinates. The specification of the orientation of that body requires another three parameters. In a typical analytical representation of the orientation of a rigid body, these three orientation parameters are typically taken to be the Euler angles [125]. A dynamical simulation of the motion of the

rigid body then requires solving the equations of motion not only for the coordinates of the center of mass of the body, but also those for the Euler angles. Unfortunately, the equations of motion for the Euler angles are inappropriate for use in numerical simulations because they become singular for certain orientations of the body. A solution to this problem is found in the use of the quaternion parameters to specify the orientation of the body [126]. The quaternion parameters contain just one redundant variable and have the advantage that the equations of motion expressed in quaternions are everywhere nonsingular [127]. This formulation of the dynamical equations of motion has been successfully employed in several rigid body simulations of nanosystems [124, 128].

### 3.1.5. Quantum Mechanical Considerations in Nanosystem Dynamics

In the prototype molecular bearing model just reviewed [124], the motion involves three independent degrees of freedom that are not analytically separable. In cases of high spin (of the shaft), however, the spin of the bearing shaft is essentially decoupled from the motion of its center of mass. The quantum state of the spin of the bearing shaft can then be given, to an excellent approximation, by applying the quantum condition for a rigid rotor. For a rotor of momenta of inertia, $I_s$, the allowed quantum eigenenergies are given by

$$E_s = S(S+1)/2I_s \tag{2}$$

where $S$ is a non-negative integer, the quantum number corresponding to the spin of the bearing shaft, and $E_s$ is the energy in spin.

The two remaining modes are due to the motion of the center of mass (COM) and correspond approximately to vibration in the radial displacement of the COM from its equilibrium position, and precession of the COM about this equilibrium. There is a radial coordinate $r = (x^2 + y^2)^{1/2}$ corresponding to the vibrational motion and an angular coordinate $\theta = \tan^{-1}(y/x)$ corresponding to the precession. The angular momentum conjugate to the precession coordinate $\theta$ can be quantized with the semiclassical methods.

The above analysis can provide insights available only when quantum mechanical considerations are taken into account. For example, from the analysis it can be seen that in the general case the level spacing of the spin eigenstates will be different from that of the precessional eigenstates. This means that there will be very low propensity for quantum transitions involving the exchange of angular momentum between the spin and precessional modes. A transition, which conserves total energy, will not conserve total angular momentum and vice versa. Any quantum transition will as a necessity involve yet an additional mode to maintain energy conservation. Simultaneous multistate and multiquantum transitions are typically low probability events.

Leigh et al. reported a low-dimensional quantum-mechanical modeling description of circumrotation in benzylic amide [2] catenanes [129]. They found that by appropriate fitting of parameters in the analytic potential form to match the symmetry and energy properties of the system, they were able to reproduce rate constants and barriers similar to those determined by temperature-dependent nuclear magnetic resonance experiments. The calculation of the rates of circumrotation was accomplished by employing transition state theory (TST) in the harmonic approximation. Related low-dimensional quantum-mechanical modeling of molecular shuttling in a rotaxane has also been reported by Leigh et al. [130]. A one-dimensional quartic potential is used to describe the variation in potential with shuttle movement along the shaft of a rotaxane. This is a double-well potential, each well corresponding to one of two ring-binding stations on the shaft separated by a potential barrier. The coefficients on the quadratic and quartic terms in the potential are adjusted to reproduce the observed shuttling rate at 298 K. The model yields considerable insight into the contributions of quantum effects to the shuttling dynamics. For example, it is found that energies slightly in excess of the barrier correspond to a high quantum number eigenstate, which implies that the probability distribution approaches the classical limit. This means that at these energies the shuttle may be found with greatest probability in the vicinity of the barrier, settling into one of the ring-binding stations with high probability only at energies far below that of the barrier.

Quantum mechanical effects are also manifest in electronic degrees of freedom. Brouwer et al. [131] suggest that for materials science applications, the properties of interest to catenanes are likely to be electronic and vibro-electronic. Such properties require a theoretical model that explicitly includes electronic degrees of freedom. They reported a study of the electronic states of a benzylic amide [2] catenane through a combination of experimental and theoretical techniques. Semiempirical quantum chemical calculations were carried out with the CNDO/S method [132, 133] and showed partial delocalization of the electronic states over the many chromophores of the catenane.

Manifestations of the quantum mechanical nature of matter are quite important in nanosystems [109, 124]. Semiempirical techniques may be used effectively for electronic properties, being sufficiently efficient for application to quite large molecular systems, while still retaining an explicit description of the (valence) electronic degrees of freedom. The application of semiclassical methods to nanosystems can provide key insights into dynamical properties [124].

## 4. CONCLUSIONS

The past decade has seen rapid advances in the field of mechanical molecular and nanodevices. A wide array of devices, based on diverse chemistry, has now been reported. Most successful synthetic schemes have employed self-assembly, with relatively few using positional assembly. The former is almost certainly more practical for mass production, given that self-assembly can be carried out in mole quantities.

The theoretical and computational description of mechanical molecular devices has seen successful application for techniques from four broad classes of methods: molecular mechanics, semi-empirical quantum mechanics, *ab initio* quantum mechanics, and molecular dynamics. Examples

of theory-directed synthesis and theory-accelerated design refinement are starting to emerge.

## GLOSSARY

**Carbon nanotubes** A cylindrical arrangement of carbon atoms with a diameter in the nanometer range. Often described as a sheet of graphite rolled up and joined along opposite edges.

**Catenane** An assembly of two or more ring molecules that are chemically independent, but mechanically linked, as in interlocked rings.

**Molecular device** A molecule or an assembly of a few molecules that can be made to carry out a specific task by responding to an external stimulus. Molecular devices may perform electrical or mechanical tasks (or both).

**Molecular machine** A machine, the principle components of which are individual molecules.

**Multiwalled carbon nanotube** Nested carbon nanotubes.

**Nanodevice** A machine or circuit with characteristic length in the nanometer range.

**Pseudorotaxane** A *rotaxane* that lacks one or both bulky terminal groups and therefore may spontaneously unthread.

**Rotaxane** An assembly of two or more chemically independent molecules in which a long chain molecule is encircled by one or more rings. The chain component is terminated on both ends with bulky functional groups to prevent unthreading of the ring(s).

**Self-assembly** The spontaneous organization of molecules into a complex structure.

**Template-directed assembly** Deliberately moving device components (molecules) into close proximity with one another and linking them together to achieve assembly.

## ACKNOWLEDGMENTS

## REFERENCES

1. R. P. Feynman, *Eng. and Sci.* 23, 22 (1960).
2. K. E. Drexler, *Proc. Nat. Acad. Sci. USA* 78, 5275 (1981).
3. K. E. Drexler, "Engines of Creation," Doubleday, New York, 1986.
4. J. F. Stoddart, *Acc. Chem. Res.* 34, 410 (2001).
5. R. C. Merkle, *Nanotechnology* 17, 271 (1999).
6. R. C. Merkle, *Nanotechnology* 11, 89 (2000).
7. E. C. Constable and D. Smith, *Chem. Br.* 31, 33 (1995).
8. J. M. Tour, M. Kozaki, and J. M. Seminario, *J. Am. Chem. Soc.* 120, 6480 (1998).
9. M. A. Reed and J. M. Tour, *Sci. Am.* 282, 86 (2000).
10. F. M. Raymo and J. F. Stoddart, *Chem. Rev.* 99, 1643 (1999).
11. P. L. Anelli, N. Spencer, and J. F. Stoddart, *J. Am. Chem. Soc.* 113, 5131 (1991).
12. G. Schill, Ed., "Organic Chemisty, A Series of Monographs," Academic Press, New York, 1971.
13. E. Wasserman, *J. Am. Chem. Soc.* 82, 4433 (1960).
14. G. Schill and A. Luttringhaus, *Angew. Chem., Int. Ed. Engl.* 3, 546 (1964).
15. I. T. Harrison and S. J. Harrison, *J. Am. Chem. Soc.* 89, 5723 (1967).
16. G. Schill and H. Zollenkopf, *Liebigs Ann. Chem.* 721, 53 (1969).
17. R. Ballardini, V. Balzani, A. Credi, M. T. Gandolfi, and M. Venturi, *Acc. Chem. Res.* 34, 445 (2001).
18. M.-V. Martinez-Diaz, N. Spencer, and J. F. Stoddart, *Angew. Chem., Int. Ed. Engl.* 36, 1904 (1997).
19. P. R. Ashton, R. Ballardini, V. Balzani, I. Baxter, A. Credi, M. C. T. Fyfe, M. T. Gandolfi, M. Gomez-Lopez, M.-V. Martinez-Diaz, A. Piersanti, N. Spencer, J. F. Stoddart, M. Venturi, A. J. P. White, and D. J. Williams, *J. Am. Chem. Soc.* 120, 11932 (1998).
20. J. W. Lee, K. Kim, and K. Kim, *Chem. Commun.*, 1042 (2001).
21. R. A. Bissell, E. Cordova, A. E. Kaifer, and J. F. Stoddart, *Nature* 369, 133 (1994).
22. A. M. Brouwer, C. Forchot, F. G. Gatti, D. A. Leigh, L. Mottier, F. Paolucci, S. Roffia, and G. W. H. Wurpel, *Science* 291, 2124 (2001).
23. A. Niemz and V. M. Rotello, *Acc. Chem. Res.* 32, 44 (1999).
24. H. Murakami, A. Kawabuchi, K. Kotoo, M. Kunitake, and N. Nakashima, *J. Am. Chem. Soc.* 119, 7605 (1997).
25. P. R. Ashton, T. T. Goodnow, A. E. Kaifer, M. V. Reddington, A. M. Z. Slawin, N. Spencer, J. F. Stoddart, C. Vicent, and D. J. Williams, *Angew. Chem., Int. Ed. Engl.* 28, 1396 (1989).
26. A. Livoreil, C. O. Deitrich-Buchecker, and J.-P. Sauvage, *J. Am. Chem. Soc.* 116, 9399 (1994).
27. C. O. Dietrich-Buchecker and J.-P. Sauvage, *J. Am. Chem. Soc.* 106, 3043 (1984).
28. D. B. Amabilino, C. O. Dietrich-Buchecker, A. Livoreil, L. Perez-Garcia, J.-P. Sauvage, and J. F. Stoddart, *J. Am. Chem. Soc.* 118, 3905 (1996).
29. P. R. Ashton, R. Ballardini, V. Balzani, M. T. Gandolfi, D. J.-F. Marquis, L. Perez-Garcia, L. Prodi, J. F. Stoddart, and M. Venturi, *J. Chem. Soc. Commun.* 177 (1994).
30. A. Livoreil, J.-P. Sauvage, N. Armaroli, V. Balzani, L. Flamigni, and B. Ventura, *J. Am. Chem. Soc.* 119, 12114 (1997).
31. P. R. Ashton, R. Ballardini, V. Balzani, A. Credi, K. R. Dress, E. Ishow, C. J. Kleverlaan, O. Kocian, J. A. Preece, N. Spencer, J. F. Stoddart, M. Venturi, and S. Wenger, *Chem.—Eur. J.* 6, 3558 (2000).
32. H. Shigekawa, K. Miyake, J. Sumaoka, A. Harada, and M. Komiyama, *J. Am. Chem. Soc.* 122, 5411 (2000).
33. P. R. Ashton, V. Balzani, O. Kocian, L. Prodi, N. Spencer, and J. F. Stoddart, *J. Am. Chem. Soc.* 120, 11190 (1998).
34. E. Ishow, A. Credi, V. Balzani, F. Spadola, and L. Mandolini, *Chem.—Eur. J.* 5, 984 (1999).
35. M. C. Jimenez, C. Dietrich-Buchecker, and J.-P. Sauvage, *Angew. Chem., Int. Ed.* 39, 3284 (2000).
36. A. Hanke and R. Metzler, *arXiv:cond-mat/0205539* 1 (2002).
37. R. C. Merkle, *Nanotechnology* 4, 86 (1993).
38. J. K. Gimzewski, C. Joachim, R. R. Schlittler, V. Langlais, H. Tang, and I. Johannsen, *Science* 281, 531 (1998).
39. T. R. Kelly, M. C. Bowyer, K. V. Bhaskar, D. Bebbington, A. Garcia, F. Lang, M. H. Kim, and M. P. Jette, *J. Am. Chem. Soc.* 116, 3657 (1994).
40. N. P. M. Huck and B. L. Feringa, *J. Chem. Soc., Chem. Commun.* 11, 1095 (1995).
41. A. M. Schoevaars, W. Kruizinga, R. W. J. Zijlstra, N. Veldman, A. L. Spek, and B. L. Feringa, *J. Org. Chem.* 62, 4943 (1997).
42. N. Koga, Y. Kawada, and H. Iwamura, *J. Am. Chem. Soc.* 105, 5498 (1983).
43. N. Koga, Y. Kawada, and H. Iwamura, *Tetrahedron* 42, 1679 (1986).
44. H. Iwamura and K. Mislow, *Acc. Chem. Res.* 21, 127 (1988).
45. M. Oki, *Angew. Chem., Int. Ed. Engl.* 15, 87 (1976).

46. A. A. Gakh, R. A. Sachleben, and J. C. Bryan, *CHEMTECH* 27, 26 (1997).
47. T. R. Kelly, J. P. Sestelo, and I. Tellitu, *J. Org. Chem.* 63, 3655 (1998).
48. T. R. Kelly, I. Tellitu, and J. P. Sestelo, *Angew. Chem., Int. Ed. Engl.* 36, 1866 (1997).
49. T. R. Kelly, H. D. Silva, and R. A. Silva, *Nature* 401, 150 (1999).
50. N. Koumura, E. M. Geertsema, A. Meetsma, and B. L. Feringa, *J. Am. Chem. Soc.* 122, 12005 (2000).
51. N. Koumura, R. W. J. Zijlstra, R. A. v. Delden, N. Harada, and B. L. Feringa, *Nature* 401, 152 (1999).
52. T. C. Bedard and J. S. Moore, *J. Am. Chem. Soc.* 117, 10662 (1995).
53. M.-F. Yu, B. I. Yakobson, and R. S. Ruoff, *J. Phys. Chem. B* 104, 8764 (2000).
54. C. Joachim, H. Tang, R. Moresco, G. Rapenne, and G. Meyer, *Nanotechnology* 13, 330 (2002).
55. T. R. Kelly, *Acc. Chem. Res.* 34, 514 (2001).
56. T. R. Kelly, R. A. Silva, H. D. Silva, S. Jasmin, and Y. Zhao, *J. Am. Chem. Soc.* 122, 6935 (2000).
57. Mikrajuddun, K. Okuyama, and F. G. Shi, *Phys. Rev. B* 61, 8224 (2000).
58. in "Nanotechnology Research Directions: IWGN Workshop Report Vision for Nanotechnology Research and Development in the Next Decade," (M. C. Roco, S. Williams, and P. Alivisatos, Eds.), WTEC, Loyola College in Maryland, 1999.
59. D. Glendening and D. Feller, *J. Phys. Chem.* 99, 3060 (1995).
60. E. D. Glendening, D. Feller, and M. A. Thompson, *J. Am. Chem. Soc.* 116, 10657 (1994).
61. B. Yurke, A. J. Turberfield, A. P. Mills, F. C. Simmel, and J. L. Neumann, *Nature* 506, 605 (2000).
62. X. Grabuleda and C. Jaime, *J. Org. Chem.* 63, 9635 (1998).
63. R. B. Shirts and L. D. Stolworthy, *J. Inclusion Phenom. Mol. Recognit. Chem.* 20, 297 (1994).
64. F. Biscarini, M. Cavallini, D. A. Leigh, S. Leon, S. J. Teat, J. K. Wong, and F. Zerbetto, *J. Am. Chem. Soc.* 124, 225 (2002).
65. N. L. Allinger, Y. H. Yuh, and J. H. Lii, *J. Am. Chem. Soc.* 111, 8551 (1989).
66. J. H. Lii and N. L. Allinger, *J. Am. Chem. Soc.* 111, 8566 (1989).
67. J. H. Lii and N. L. Allinger, *J. Am. Chem. Soc.* 111, 8576 (1989).
68. P. Ceroni, D. A. Leigh, L. Mottier, F. Paolucci, S. Roffia, D. Tetard, and F. Zerbetto, *J. Phys. Chem. B* 103, 10171 (1999).
69. F. M. Raymo, K. N. Houk, and J. F. Stoddart, *J. Org. Chem.* 63, 6523 (1998).
70. G. Chang, W. C. Guida, and W. C. Still, *J. Am. Chem. Soc.* 111, 4379 (1989).
71. F. Mahamadi, N. G. K. Richards, W. C. Guida, R. Liskamp, M. Lipton, D. Caufield, G. Chang, T. Hendrickson, and W. C. Still, *J. Comput. Chem.* 11, 440 (1990).
72. S. J. Weiner, P. A. Kollman, D. A. Case, V. C. Singh, G. Ghio, G. Alagona, J. S. Profeta, and P. Weiner, *J. Am. Chem. Soc.* 106, 765 (1984).
73. Spartan V 4.1, Wavefunction, INC., Irvine, CA.
74. P. Polister and J. S. Murray, Eds., VCH, New York, 1991.
75. R. R. Birge, D. S. K. Govender, K. C. Izgi, and E. H. L. Tan, *J. Phys. Chem.* 100, 9990 (1996).
76. K. Sohlberg, B. G. Sumpter, and D. W. Noid, *J. Mol. Struct. (Theochem)* 491, 281 (1999).
77. L. Frankfort and K. Sohlberg, *J. Mol. Struct. (Theochem)* in press (2002).
78. G. Buemi, F. Zuccarello, and A. Raudino, *J. Mol. Struct. (Theochem)* 164, 379 (1988).
79. X. Zheng and K. Sohlberg, *J. Phys. Chem. A*, submitted.
80. S. R. Whaley, D. S. Englich, E. L. Hu, P. F. Barbara, and A. M. Belcher, *Nature* 405, 665 (2000).
81. R. M. Izatt, J. S. Bradshaw, S. A. Nielsen, J. D. Lamb, J. J. Christensen, and D. Sen, *Chem. Rev.* 85, 271 (1985).
82. R. M. Izatt, K. Pawlak, J. S. Bradshaw, and R. L. Bruening, *Chem. Rev.* 91, 1721 (1991).
83. H. An, J. S. Bradshaw, and R. M. Izatt, *Chem. Rev.* 92, 543 (1992).
84. D. E. Kaufmann and A. Otten, *Angew. Chem., Int. Ed. Engl.* 33, 1832 (1994).
85. F. P. Schmidtchen and M. Berger, *Chem. Rev.* 97, 1609 (1997).
86. C. J. Pedersen, *J. Am. Chem. Soc.* 89, 7017 (1967).
87. C. H. Park and H. E. Simmons, *J. Am. Chem. Soc.* 90, 2431 (1968).
88. J. S. Bradshaw, R. M. Izatt, R. L. Bruening, and J. J. Christensen. U.S. Patent, #4,943,375, 1990.
89. K. Sohlberg and B. Tarbet, *J. Inclusion Phenom.* 23, 203 (1995).
90. H. G. Ricketts, J. F. Stoddart, and M. M. Hann, in "Computational Approaches in Supramolecular Chemistry" (G. Wipff, Ed.), p. 377, Kluwer Academic Publishers, Dordrecht, Netherlands, 1994.
91. F. M. Raymo, K. N. Houk, and J. F. Stoddart, *J. Am. Chem. Soc.* 120, 9318 (1998).
92. J. C. Dobrowolski and A. P. Mazurek, *Chem. Phys. Lett.* 348, 60 (2001).
93. F. M. Raymo, M. D. Bartberger, K. N. Houk, and J. F. Stoddart, *J. Mol. Struct. (Theochem)* 123, 9264 (2001).
94. D. A. Leigh, A. Murphy, J. P. Smart, M. S. Deleuze, and F. Zerbetto, *J. Am. Chem. Soc.* 120, 6458 (1998).
95. R. E. Tuzun, D. W. Noid, and B. G. Sumpter, *Nanotechnology* 7, 241 (1997).
96. R. E. Tuzun, D. W. Noid, and B. G. Sumpter, *Nanotechnology* 6, 64 (1995).
97. J. Han, A. Globus, R. Jaffe, and G. Deardorff, *Nanotechnology* 8, 95 (1997).
98. K. E. Drexler, "Nanosystems: Molecular Machinery, Manufacturing, and Computation," John Wiley, New York, 1992.
99. R. N. Porter, *Ann. Rev. Phys. Chem.* 25, 317 (1974).
100. F. Jensen, "Introduction to Computational Chemistry," John Wiley & Sons, Chichester, U.K. 1999.
101. K. Sohlberg, B. G. Sumpter, R. E. Tuzun, and D. W. Noid, *Nanotechnology* 9, 30 (1998).
102. R. Lifshitz and M. L. Roukes, *Phys. Rev. B.* 61, 5600 (2000).
103. S. Rast, C. Wattinger, U. Gysin, and E. Meyer, *Rev. Sci. Instrum.* 71, 2772 (2000).
104. V. B. Shenoy and R. E. Miller, *Phys. Rev. Lett.* 80, 742 (1998).
105. V. B. Shenoy and L. B. Freund, Vol. 2002, Los Alamos National Laboratory, Preprint Archive, 2002.
106. V. N. Popov, V. E. V. Doren, and M. Balkanski, *Phys. Rev. B* 61, 3078 (2000).
107. R. E. Tuzun, D. W. Noid, and B. G. Sumpter, *Computers Math. Applic.* 35, 93 (1998).
108. R. E. Tuzun, B. G. Sumpter, and D. W. Noid, *Macromol. Theory Simul.* 7, 203 (1998).
109. D. W. Noid, R. E. Tuzun, and B. G. Sumpter, *Nanotechnology* 8, 119 (1997).
110. D. A. Leigh, S. F. Parker, D. Timpel, and F. Zerbetto, *J. Chem. Phys.* 114, 5006 (2001).
111. A. J. Ramirez-Cuesta, P. C. H. Mitchell, S. Parker, and P. M. Rodger, *Phys. Chem.* 1, 5711 (1999).
112. A. J. Ramirez-Cuesta, P. C. H. Mitchell, A. P. Wilkinson, S. F. Parker, and P. M. Rodger, *Chem. Commun.* 2653 (1998).
113. M. J. Dudek and J. W. Ponder, *J. Comput. Chem.* 16, 791 (1995).
114. C. E. Kundrot, J. W. Ponder, and F. M. Richards, *J. Comput. Chem.* 12, 402 (1991).
115. J. W. Ponder, *J. Comput. Chem.* 8, 1016 (1987).
116. R. Caciuffo, A. D. Esposti, M. S. Deleuze, D. A. Leigh, A. Murphy, B. Paci, S. F. Parker, and F. Zerbetto, *J. Chem. Phys.* 109, 11094 (1998).
117. R. E. Tuzun, D. W. Noid, and B. G. Sumpter, *Nanotechnology* 6, 52 (1995).
118. D. Srivastava, *Nanotechnology* 8, 186 (1997).
119. J. Vacek and J. Michl, *New J. Chem.* 21, 1259 (1997).

120. J. Vacek and J. Michl, in "Proc. Natl. Acad. Sci. U.S.A." 98, 5481 (2001).
121. M. Porto, M. Urbakh, and J. Klaafter, *Phys. Rev. Lett.* 84, 6058 (2000).
122. A. V. Zolotaryuk, P. L. Christiansen, B. Norden, A. V. Savin, and Y. Zolotaryuk, *Phys. Rev. E* 61, 3256 (2000).
123. C. Kettner, P. Reimann, P. Hanggi, and F. Muller, *Phys. Rev. E* 61, 312 (2000).
124. K. Sohlberg, R. E. Tuzun, B. G. Sumpter, and D. W. Noid, *Nanotechnology* 8, 103 (1997).
125. H. Goldstein, "Classical Mechanics," Addison-Wesley, Reading, MA. 1980.
126. D. J. Evans and S. Murad, *Mol. Phys.* 34, 327 (1977).
127. M. P. Allen and D. J. Tildesley, "Computer Simulation of Liquids," Clarendon Press, Oxford, 1987.
128. R. E. Tuzun, K. Sohlberg, D. W. Noid, and B. G. Sumpter, *Nanotechnology* 9, 37 (1998).
129. D. A. Leigh, A. Troisi, and F. Zerbetto, *Chem.—Eur. J.* 7, 1450 (2001).
130. D. A. Leigh, A. Troisi, and F. Zerbetto, *Angew. Chem., Int. Ed.* 39, 350 (2000).
131. A. M. Brower, W. J. Buma, R. Caudano, M. Fanti, C. A. Fustin, D. A. Leigh, A. Murphy, P. Rudolf, F. Zerbetto, and J. M. Zwier, *Chem. Phys.* 238, 421 (1998).
132. J. D. Bene and H. H. Jaffe, *J. Chem. Phys.* 48, 1807 (1968).
133. K. Nishimoto and N. Mataga, *J. Phys. Chem.* 13, 140 (1957).

# Mechanical Processing
# for Nanomaterials

## E. Gaffet

*UMR 5060 CNRS/UTBM, Belfort Cedex, France*

## G. Le Caër

*UMR CNRS 6626, Université de Rennes I, Rennes Cedex, France*

## CONTENTS

## 1. INTRODUCTION

In Lilliput, Gulliver noted that "there are some laws and customs in this Empire very peculiar" [1], an observation which might apply to nanophased materials too. Nanophased materials behave indeed differently from their macroscopic counterparts because their characteristic sizes are smaller than the characteristic length scales of physical phenomena occurring in bulk materials. Hereafter, we shall focus on consolidated nanomaterials or on powdered materials, named "nanostructured materials" (NSMs) [2, 3], whose particle sizes are large as compared to the mean crystallite size which is required to be lower than 100 nm, a conventional limit usual for structural materials. Materials whose grain size ranges between 100 nm and 1 $\mu$m are commonly named ultrafine grained materials.

Nanostructured materials are bulk solids with a nanometer-scale microstructure "in which the chemical composition, the atomic arrangement and/or the size of the building blocks (e.g. crystallites) forming the solid vary on a length scale of a few nanometers throughout the bulk" [2]. Nanostructured materials have then a significant fraction of atoms residing in defect environments (grain boundaries, interfaces, interphases, triple junctions). The volume fraction associated with grain boundaries is for instance $\sim$20% for a grain boundary thickness of $\sim$0.7 nm [4] and a grain size of 10 nm. Metastable nanostructured and ultrafine grained materials are produced by a large variety of methods. In this chapter, we shall concentrate on processes based on the deformation behavior of materials, more particularly on high-energy ball-milling [5–14], notable methods being the processing of bulk materials using severe plastic deformation methods [15] and the codeformation of multilayers by cold-rolling [16–20] which consists of successive rolling and folding steps. We finally mention mechanofusion, a process used for producing coated powders in specially designed mills [21].

Sophisticated methods most often spring to mind when thinking of means of mixing and combining elements in the solid state down to the atomic scale at moderate temperatures. Surprisingly, milling, a technique which was and still is mainly used for reducing the sizes of particles of various materials, is a possible method for this purpose. High-energy ball-milling offers indeed supplementary degrees of freedom in the choice of possible routes for synthesizing new materials and appears further as an attractive method of synthesis in view of its potential for large scale production. For a period of about 30 years, milling has indeed been a method of synthesis of advanced materials. Mechanical alloying (MA) [5–14], which is basically a dry and high-energy milling process, is a powerful technique for synthesizing all kinds of materials from initial mixtures made of powders with different chemical compositions: extended solid solutions,

alloys of immiscible elements, synthesis of alloys made from elements with widely different melting points, quasicrystals, amorphous phases, all sorts of compounds and composites. Moreover, it is amusing that the repeated fracturing and rewelding processes of powder particles, which occur in a mill, mix elements in a way reminiscent of chaotic transformations of the "baker" type. The synthesized materials, often with nonequilibrium structures, include, among others, crystalline materials with nanometer-sized grains, with a typical average size of ca. 10 nm. Besides materials synthesis, high-energy ball-milling is a way of modifying the conditions in which chemical reactions usually take place either by changing the reactivity of as-milled solids (mechanical activation [10–14]—increase of reaction rates, lowering of reaction temperatures of ground powders)—or by inducing chemical reactions during milling (mechanochemistry [10–14]). It is, furthermore, a way of inducing phase transformations in starting powders whose particles have all the same chemical composition: amorphization or polymorphic transformations of compounds, disordering of ordered alloys [12–14], etc., Mechanical alloying and grinding of materials are complex processes which depend on many factors, for instance on physical and chemical parameters such as the precise dynamical conditions, temperature, nature of the grinding atmosphere, chemical composition of the powder mixtures, chemical nature of the grinding tools, etc. This may partly explain why the theoretical problem of predicting nonequilibrium phase transitions under milling is still in debate.

High-energy ball-milling, which has been described in broad outline, is the central theme of this chapter. Its interest stems from a fortunate combination of technical simplicity and of complexity both of phenomena occurring during grinding and of mechanosynthesized materials. A fair and exhaustive review of all published contributions to the field of mechanical alloying and of mechanical milling would require thousands of pages (more than three papers are now published every day) and would discourage even those used to tackle frightening creatures. We decided thus to select topics which appear important in our eyes, to a large extent based on our own results, and to refer readers to networks, databases, journals, and complementary review papers devoted to mechanical alloying for more information [22–35]. By that choice, we run the risk not to "render unto Caesar that which is Caesar's" as it is further often difficult to find who is Caesar and what is really "that which is Caesar's," the literature sometimes being misleading on who did what first. Some 19th century papers on mechanochemistry have for instance been dug up only recently by Takacs (private communication). Further, many Russian (and some French, Japanese, etc.) papers on mechanical alloying and on mechanical grinding written in the 1960s and 1970s were (some probably are still) ignored, among others because the journals in which they were published were (and are) not very accessible. We apologize in advance to the authors who might think that they have not been given the credit they deserve for their work.

This chapter first describes some general characteristics and some applications of high-energy ball-milling. After having evoked some basic features of high-energy ball-milling

(Section 2), we shall present a few selected examples to illustrate the flexible use of these means of mechanochemical synthesis, in short mechanosynthesis, to transform and to synthesize materials, notably nanophased materials.

Phase transformations induced by milling in oxides (Section 3), mechanically activated annealing of transition metal silicides, mechanically activated self-heat-sustaining reactions (MASHS) of intermetallic compounds (FeAl, $NbAl_3$, $FeSi_2$, $MoSi_2$, $Cu_3Si$) (Section 4), and the synthesis route from mechanosynthesized powders to consolidated alumina–(Fe,Ti) composites (Section 5) will be discussed. Some investigations aimed at understanding the physical mechanisms at work during mechanosynthesis, particularly in systems for which thermal and mechanical energy compete, are finally considered in Section 6 (order–disorder) and in Section 7 (unmixing–mixing) respectively.

As mentioned, the main purposes of this chapter were to focus on particular features of mechanosynthesis/mechanical activation and to point out the strong advantages of such powder processings in terms of very versatile powder processings. Some formerly published reviews will kindly complete the given text [22–35]. Up to date references may also be found on the website of the Réseau Français de Mécanosynthèse [36].

## 2. TYPICAL INGREDIENTS OF HIGH-ENERGY BALL-MILLING

### 2.1. Milling Equipment and Experimental Conditions

Experiments are performed in various types of high-energy mills including for instance attrition mills (milling results from the stirring action of a rotating impeller with arms, horizontal in Fig. 1, which produces a relative movement between balls and powders), planetary mills, and vibratory mills [37] (Fig. 1).

### 2.1.1. Various Milling Machines

Planetary mills, for example, Fritsch commercial mills P5 or P7, or mills G5 and G7 designed by Gaffet et al. [37] (in which the rotation speeds of the vials $\omega$ and of the disc $\Omega$ can be varied independently; mill G5 is now sold by Fristch under the name "vario planetary mill P4"), vibratory mills
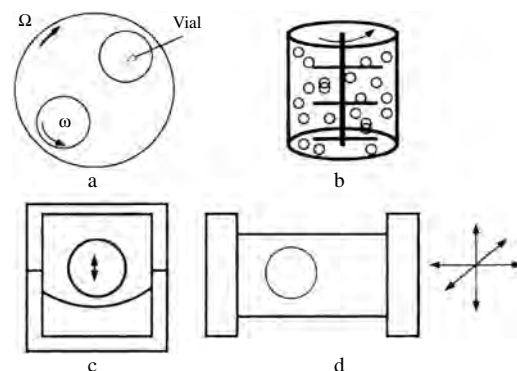


**Figure 1.** Various types of mills.

(e.g., Spex 8000), and mills with control by an external magnetic field (designed by Calka and Radlinski [38]) are the most widely used in laboratories.

In a planetary ball mill (Fig. 1a), a rotating disc bears vials which rotate in opposite directions. Both rotation speeds are of the order of some hundreds rpm (the maximum rotation speeds $\omega_m$ and $\Omega_m$ are 1000 rpm for the mills G5 and G7).

In a vibratory mill like the Spex 8000 mill, the vial is shaken at a frequency of $\sim$20 Hz in three orthogonal directions. The impact speed of balls is of the order of some m/s [39] and shock frequencies are about some hundreds of Hz.

### 2.1.2. Milling Media

Powders of the materials to be ground are introduced in the required proportions in a vial together with balls. Surface-active organic agents may be added to the powders to optimize the balance between welding and fracturing (see next section). They may give rise to a detrimental contamination of the ground powders by carbon.

The vial is generally sealed in a glovebox in various atmospheres (argon, nitrogen, air, etc.) or in vacuum. Nitrogen may, however, react with ground powders to form interstitial solid solutions or nitrides. Balls and vials are usually made of hardened steel, tungsten carbide, zirconia, etc.

Besides the previous experimental conditions, other important experimental parameters include the number of balls which depends on the mill and on the vial volume, the powder to ball mass ratio which is typically of the order of 1/5 to 1/50, the minimum time which is needed to reach a final stationary state, and the milling temperature which may be for instance conveniently varied in some vibratory mills [39–41].

The milling duration depends among others on the type of mill used, milling intensity, which sets for instance the rotation speeds $\omega$ and $\Omega$ in a planetary mill, milling mode (friction or direct shock), and milling temperature. It amounts typically to some tens of hours for most high-energy ball mills. Le Brun et al. [42] have modeled the MA process in planetary mills as a function of $\omega/\Omega$. They conclude that most commercial mills operate in a mode which involves friction on the inner wall of the vial and not impact.

## 2.2. Process Description

Figure 2 compares the typical average powers, in eV/at.s., involved in various processes applied to solid materials (the actual distribution of the injected power among atoms would have to be considered for more detailed comparisons) [37]. Ball-milling is seen to cover a convenient range of injected powers.

In the MA process of ductile powder mixtures of A and B, particles are trapped between colliding balls or between ball and vial and are subjected to a severe plastic deformation, which exceeds their mechanical strength, accompanied by a temperature rise. During collisions, powder particles are subjected to high stresses (of the order of 200 MPa for steel balls in a Spex mill) for times of the order of milliseconds [43]. The waiting period between such efficient trapping events is typically of the order of tens to hundreds of seconds [44, 45]. Particles are repeatedly flattened, fractured, and welded. Fracture and welding are the two basic events which produce a permanent exchange of matter
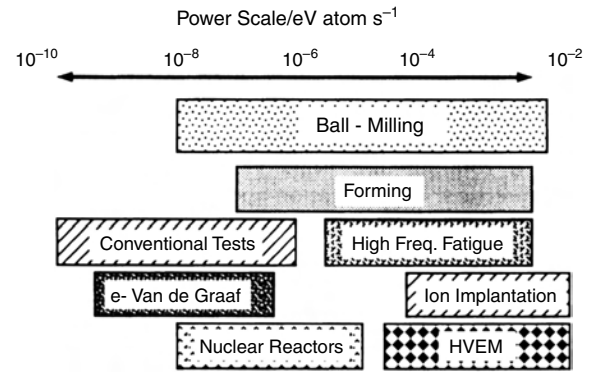


**Figure 2.** Typical average injected powers (expressed, in eV/at) for various processes.

between particles and ensure mixing of the various elements of ground powders.

A layered structure of A and B is thus formed and progressively refined and convoluted. Five typical stages of evolution of ductile powder mixtures are shown in Figure 3. A balance between coalescence and fragmentation is achieved during MA which leads to a rather stable average particle size. The mixture of constituents finally becomes homogeneous and the elements are mixed on an atomic scale.

In the case of brittle materials [46] the temperature rise of the powder surface plays a major role and thermal activation is required for MA to occur. In the latter case, a granular-type microstructure is observed. The temperature rise $\Delta T$ of metallic powders during MA is believed to be less than 300 K [46].

Mechanical alloying of mixtures of powders of pure elements or of powders of already partially combined elements has to be distinguished from grinding of materials whose chemical composition remains the same during milling but whose structure is expected to evolve. They may lead to distinct end products whose nature depends on the various parameters of such synthesis and transformation processes (i.e., as previously mentioned, the powder to ball mass ratio, the milling duration, the milling temperature).

Kinematic analyses have considered average shock energies, average shock frequencies [47], or ball momenta [41] to define dynamical parameters characterizing a milling
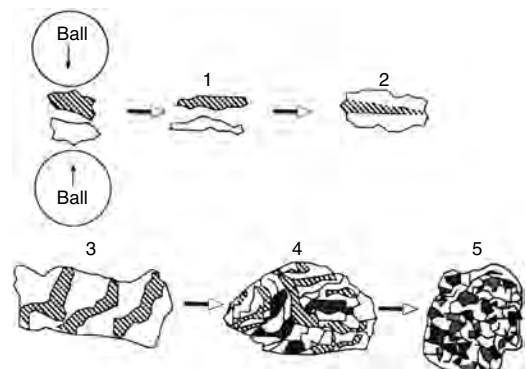


**Figure 3.** Steps of powder evolution during mechanical alloying.

experiment which are expected to be relevant for most mills. They lead to the definition of dynamical phase diagrams which describe, for a given milling temperature, the various phases which may be expected to form from an initial powder mixture according to the milling conditions.

## 2.3. Milling Machine Modelling

Various methods have been used to model the motion of balls inside mills, including analytical ones or a discrete element method [48]. They will be discussed in the next sections.

### 2.3.1. Planetary Milling Machines

From an historical point of view, the work of Joisel [49] is worth being mentioned as the first attempt (to the best of our knowledge) to study the shock kinematics of a "satellite milling machine," named in French "Broyeur à Satellites," and to design a "broyeur à satellites" working in a continuous way. Considering milling as a suitable way to comminute powders, the work was focused on the determination of the milling parameters which optimize shock energy. Fifty years ago, computers were not in current use as they are today. The various parameters were therefore determined geometrically and the theoretical predictions were checked experimentally using a specifically designed planetary mill. The specific powder area was measured as a function of the milling parameters.

Some industrial developments of such a mill can be found in a paper of Bradley et al. [50]. This paper reported some industrial developments related to a centrifugal mill. Such a three-tube vertically operated centrifugal mill was installed at Durban Roodepoort Deep in 1971. The weight of the mill rotor assembly, containing three satellite tubes, was 0.7 tons. The total ball charge was approximately of 70 kg. At 11 Hz, the apparatus drew 150 kW, equivalent to a very high power density in the mill of 2 MW per ton of balls.

The main aspect in terms of industrial development was the fact that the results of tests to date suggested that for mill powers up to 500 kW, it should be possible to construct a mill having a mass about one-tenth that of an equivalent convential mill (i.e., horizontal ball mill).

In such a centrifugal mill, it is shown that the power drawn is given approximatively by

$$\text{Power} \propto D^3 \times L \times G \times N^3 |R|$$

where $D$ is the inside tube diameter, $L$ is the inside tube length, $G$ is the gyration diameter, $N$ is the speed of rotation of the assembly, and $|R|$ is the absolute value of sun to planetary gear ratio.

**Ball Kinematics**   Many works have aimed to study the trajectories and the impact velocities of grinding bodies in planetary mills.

**Influence of the Ratio of the Planetary Wheel Speed to the Satellite Speed**   Schilz et al. [51, 52] have shown that the crucial role in milling performance is played, from a macroscopical point of view, by the geometry of the mill and by the ratio of the angular velocities of the planetary and

of the system wheel. Indeed, under the assumption of single particle movements, the trajectories and thus the impact energies of mass particles depend only on the ratio of planetary and system wheel radii and on the ratio of their angular velocities. In the case of the brittle–brittle Si–Ge system, the frequency ratio has to be set to achieve the maximum normal impact energy (i.e., to a value of $-2.5$), whereas for the ductile–brittle $Mg_2Si$ system, a higher frequency ratio is desirable. One related observation of the solid state mechanism which is mentioned by Schilz et al. is the fact that the alloy formation occurs via solid-state diffusion for the Si–Ge system whereas in the case of $Mg_2Si$ or $Mg_2(Si,Sn)$, alloying occurs on the surfaces of Mg particles.

For the ductile–brittle Mg–Si system [53], the efficiency of the planetary ball mill was found to be mostly influenced by the ratio of the angular velocity of the planetary wheel to that of the system wheel and the amount of load. It was demonstrated that a ratio of angular velocities of at least 3 (i.e., $\omega/\Omega$ is necessary to compensate the reduction of efficiency due to slip. Such a ratio has been found to lead to a separation of the milling balls from the vial wall and to a higher energy transfer into the powder.

The effect of rotational direction and rotation-to-revolution speed ratio in planetary ball milling has been studied by Mio et al. [54].

The discrete element method was used to calculate the effects on the specific impact energy of balls, of the rotational direction of a pot in a planetary ball mill, and of the rotation speed to the rotation speed of the disc.

The main conclusions of this work can be summarized as follows: The rotation of the satellites and of the disc in opposite directions rather than in the same direction can enhance the impact energy of balls up to large energies.

Specific attention has been paid to the *in-situ* study of the mechanically injected power during mechanosynthesis [55]. Magini et al. [55] have, for instance, clearly shown that the power consumption due to the milling action can be revealed by suitable electrical power measurements. In the case of single path cumulative reaction, the only factor governing the progress of the reaction is thus found to be the energy consumption during milling. Modifiyng the milling parameters but absorbing the same energy will lead to the same end product.

- The specific impact energy of balls increases with an increasing rotation-to-revolution speed ratio, but it falls about the critical speed ratio due to rolling motion.
- It is important to keep the milling conditions at the critical speed ratio for effective milling. The critical speed ratio can be estimated according to

$$r_c = ((R/l_c) - 1)^{-1/2}$$

where with $l_c$ is the distance from the rotating shaft to the centroïd of the ball that contacts with the mill wall, $R$ is the revolution radius, and $r_c =$ ratio of rotation-to-revolution speeds.

Based on the work undertaken by Mishra [56] studying the ball charge dynamics in a planetary mill, the coefficient of friction has been found to play an important role in the analysis of the charge. It is shown that the charge tends to

loosen when the coefficient of friction is high. Also, there is an increase in high-energy impacts with an increase in the coefficient of friction.

Based on a kinematic modeling of the planetary ball mill developed by Abdellaoui and Gaffet [47, 57], the kinematic equations giving the velocity and the acceleration of a ball in the vial have been determined. Theoretical and experimental dynamical phase diagrams for ball-milled $Ni_{10}Zr_7$ were obtained and comparisons of the calculated to some experimental results show that neither the shock energy nor the shock frequency, separately taken into account, governs the end product but only the injected shock power is responsible for the ball-milled end product.

***Effect of Filled Vial Fraction*** Based on computer simulation analyses of the milling process in a planetary ball mill carried out by by Shelekhov et al. [58], the nature of ball motion in a vial of a planetary ball mill was concluded to depend strongly on the filled fraction. When it reaches 55%, a transition takes place from a motion of balls in aggregation to the effect of their spread on the vial wall. This effect is accompanied by an abrupt decay of energy dissipation and temperature.

An increase of the ball size at a given filled fraction in most cases results in an increase of energy dissipation and temperature. By varying the filling factor, it is possible to modify the character of action on the materials from abrasion to shock strain.

### 2.3.2. Vibratory Milling Machine (*Shaker*)

Shulin et al. have focused attention on the impact dynamics of a vibration rod mill [59]. A mathematical model of the vibration system is determined by the principal and subharmonic impacts of the grinding media which consist of balls or of rods made of various materials. An impact acts on the system not only as an excitation, but also as damping. The changing rate of the impact mass is proportional to the exciting frequency.

### 2.3.3. Tumbling Milling Machine

Several works have been devoted to the determination of the motions of balls or barrels in tumbling milling machines [60–62].

Considering the work of Raasch [60], if the grinding bodies are small in comparison to the mill shell diameter, it is reasonable to consider their motion as that of point masses. Such a point mass $P$ is subjected to two forces, a gravity force $Fg$,

$$Fg = mg$$

and a centrifugal force $Fc$,

$$Fc = mR\omega^2$$

where $R$ is the mill shell radius and $\omega$ is its rotation speed.

At the point of projection (defined by an angle so-called hereafter $\alpha_0$), the radial component corresponding to the sum of the two forces has to be equal to zero. That is,

$$mR\omega^2 - mg \cos \alpha_0 = 0$$

leading to

$$\cos \alpha_0 = R\omega^2/g$$

As mentioned by Raasch, for grinding bodies located on different radii $R$, different angles of projection $\alpha_0$ are obtained. The locus of the points is a semicircle of diameter

$$y_c = g/\omega^2$$

that is, a semicircle, which is known as the Davis circle.

Considering such a circle, a critical value of the speed rotation, $\omega_c$, is reached when the outermost layer of grinding bodies is no longer projected. For example, with

$$R = D/2 \quad \text{and} \quad \alpha_0 = 0$$

it gives

$$\omega_c = (2g/D)^{-1/2}$$

As discussed by Raasch [60], it should be stressed that a precise theory of the grinding body motion in a conventional ball mill does not exist. The simplest theory is suitable to describe such motion when the mill filling is cataracting (i.e., in the case of moderate fractional mill fillings and relatively high rotation speed). In the case of larger fractional fillings and lower speeds, the mill filling is essentially rolling in itself. Such a behavior cannot be described by any of the existing theories, as claimed by Raasch [60].

It has been shown experimentally that the grinding effect of a conventional ball mill in dry milling of hard products is greatest if the ratio of rotational speed $n$ to its critical value $n_k$ is chosen as approximately $n/n_k = 0.76$, corresponding to an angle of projection $\alpha_0 = 54.7°$ for the outermost layer of grinding bodies.

A method for simulating the three-dimensional motion of balls under the presence of a powder in a tumbling ball mill has been developed by Kano et al. [63]. The method is based on the particle element method and a coefficient of friction of colliding balls is the key to simulate the motion under powder filling. Such a model has been applied to four kinds of samples (i.e., glass beads, silica, aluminum hydroxide, and kaolinite powders).

Based on video recorder observations of the movement of the balls without and with powders, the actual movement of the grinding media has been found to depend on the kind of sample. The variation of the movements can be calculated by the given method by choosing a suitable coefficient of friction for each sample. The one for kaolinite (the largest one) has been found to be four times larger than that in grinding without powder.

The notion of critical rotation speed for ball-milling using a tumbling machine has been considered by Watanabe [64].

Based on some previous observations made in 1957 by Rose and Sullivan, the following events may be observed as the rotation speed increases: distinct avalanche, continuous avalanche, cascading motion, cataracting motion, and centrifugal motion. In this final stage, the outermost layer balls are placed stationarily with respect to the inner wall of the vial, the corresponding rotation speed being called the critical rotation speed.

Based on the results of the discussed work, it has been shown that the critical rotation speed significantly depends on ball-containing fraction in jars and approaches a value asymptotically as the ball-containing fraction approaches one. This asymptotic value is equal to the traditional critical rotation speed. The effect of individual rotation of the ball of the jar is significantly small to centrifugal motion.

## 2.4. Effective Mechanical Energy Transfer/Shock Events

In the earliest 1990s, Maurice and Courtney reported on the physics of mechanical alloying [65]. Based on their idea, the mechanical alloying process has been modeled on the basis of a perturbed Hertzian impact. The powder particles are presumed to only mildly alter the elastic collision between the grinding media.

Specific aspects of the developed model [66] (consider a porous powder cylinder impacted between colliding work-pieces having a relative collision velocity) depend on the choice of the milling machine. The cylinder radius and the duration of impact are defined by the Hertzian impact theory. Two milling machines have been considered, a Spex milll and an attritor.

In the case of the attritor, the average ball velocity has been estimated to be 2/3 the maximum velocity (i.e., 0.53 m/s). For the Spex shaker mill, the value of the ball speed has been determined as being equal to 3.9 m/s. The ball speed for a horizontal ball mill has been given as ranging from 4.4 to 6.3 m/s for commercial drums varying from 1 to 2 m in diameter.

Ten years later, from the analysis by Chattopadhyay et al. [67], it emerges that the role of velocity components of the ball at the instant of its impact on the vial wall warrants proper consideration, because the tangential force determines the lower bound of the vial-to-disc speed ratio conducive for effective transfer of impact energy to the powder charge in the mill. A comparison of the experimental results of grain size reduction during milling of an elemental Fe and Cu all powder mixture with the similar predictions of the given analysis demonstrates that elastic properties of the balls and vials play an important role in determining the rate of structural refinement during ball-milling.

Szymanski and Labaye [68] have investigated the energy dissipation in the dynamics of a bouncing ball based on a one-dimensional model consisting of a rigid wall, a vibrating plate, and an object moving horizontally between the wall and the plate. The dynamics of such a model has been studied on both numerical and experimental approaches. Three types of behaviors have been observed:

(1) high energy periodic modes which exhibit period doubling routes to chaotic solutions with nearly unchanged energy characteristics,
(2) short period chattering and locking in which a small amount of energy is dissipated,
(3) chaotic or long-period modes.

The first type is called resonant, the others nonresonant. A remarkable gain of shock power is observed in the simulation as well as in the experimental approach when the system enters into a resonant mode.

A nanocomposite mechanical approach has been proposed by Rahouadj and Gaffet [69] to investigate the shock transfer. Such a model is based on the nanostructural aspect of the ball-milled materials and therefore on the transfer of a macroscopic mechanical power (induced by the milling ball) to the materials exhibiting nanometer size structures.

The latter are assumed to consist of rheological assemblies (serial and parallel features). Such a mechanical approach based on the cyclic loading response allows one to understand the effective saturation of the phase transition which may be introduced by mechanical alloying or ball milling.

The main results are as follows:

(1) The energy which is dissipated at each shock drastically decreases as a function of the number of shocks. By assuming that the microstructural transformation $M \Rightarrow nM$ depends on this transfered mechanical energy, the probability of transformation has been found to become maximum during the first shocks.
(2) The parallel model reveals a qualitative occurrence of internal stresses from the first shocks. The amplitude of theses stresses tends to decrease as a function of the number of shocks.

The investigation of the effect of powder on the impact characteristics between a ball and a plate using free falling experiments has been developed by Huang et al. [70]. Based on the results of such a study of the effects of milling conditions, including impact velocity, ball size, and powder thickness, on the coefficient of restitution and impact force, it is noted that the powder has a significant influence on the impact process due to its porous structure. Such an effect has been demonstrated using a modified Kelvin model. When the powder thickness is increased, the buffer effect of the powder is enhanced, thus resulting in a decrease of the magnitude of the impact force and an increase of the impact duration.

The second main point of this work has been to show that the impact force is a relevant parameter for characterizing the impact event due to its sensitivity to the milling conditions.

Another interesting feature occurring during milling is fracturing which may occur at contact surfaces subjected to normal and tangential loads. Such a feature has been investigated by Shah and Wong [71].

The partial-slip situation increases both tensile and shear stresses even though the contact is subject to the same forces and shows the importance of the friction coefficient at the contact. During unloading of the tangential force, the location of maximum tensile stress moves away from the trailing edge toward the center and may be responsible for surface damage during cyclic loading. The critical fracture load required for the development of a hertzian crack system is reduced significantly by the tangential load application. The spacing, which is the inverse of surface fracture density, reduces with applied loads and also with friction coefficient.

Some other investigations have been performed to study the energy transfer. Local modeling of a collision event, coupled with a classical thermodynamic assessment of the $Fe_2O_3$–$Fe_3O_4$ system, was used by Zdujic et al. [72] to rationalize the experimental results. It is proposed that

the mechanochemical reactions proceed at the moment of impact by a process of energization and freezing of highly localized sites of a short lifetime. Excitation on a time scale of $10^{-5}$ s corresponds to a temperature rise of the order $(1–2) \times 10^3$ K. Decay of the excited state occurs rapidly at a mean cooling rate higher than $10^6$ K/s.

### 2.4.1. Milling Induced Vial Heating (Milling Temperature)

In the case of experimental work performed by Xu et al. [73] studying the deformation-assisted decomposition of an unstable $Fe_{50}Cu_{50}$ solid solution during low energy ball-milling, the experimental results are interpreted in terms of an effective-temperature model which has been adapted from former models applied to irradiated alloys.

The Fe–Cu system has been selected as a model alloy to examine the transformation kinetics and steady state during ball-milling.

The precipitation kinetics has been determined to be significantly enhanced by milling-induced deformation, despite the reduced driving force due to the homogenizing effect of the deformation.

In contrast to irradiated materials, the ballistic interdiffusion coefficient has been found to be strongly dependent on microstructure in the case of ball-milled materials. Such a behavior results in a time dependent effective temperature, leading to a nonmonotonic decomposition behavior.

The ball temperatures during mechanical alloying in planetary mills have been investigated by Kwon et al. [74]. The temperature rise during milling is mainly due to ball-to-ball, ball-to-powder, ball-to-vial wall collisions, and frictions. An implementation to take into account is the exothermic contribution of the reaction involving the component powders which have been introduced in the vials.

The influence of the ball temperature on the MA process was demonstrated in the case of the $Mg_{67}Ni_{33}$ and $Ni_{50}Al_{50}$ powder blends. Based on a calorimetric technique, the temperature of balls has been estimated during mechanical alloying in a planetary ball mill. The major comment from Kwon et al. is that the temperature distribution during mechanical alloying is more complicated than a simple overall temperature in the vial and local temperatures due to the collisions. An essential difference has been found between the ball temperature and the vial wall one, except for cryomilling. The ball temperatures have been found to increase with increasing milling power and ball diameter. A decrease has been observed when increasing the total surface of the balls, heat conductivity, and gas pressure in the vials. A specific high temperature rise up to 600 °C has been determined in the case in which compact milled powder layers are formed on the ball surface and on the vial wall. In the case of free powders, a decrease of the ball temperature has been observed.

### 2.5. Particle Evolution during Milling/Macroscopic Model

A model, based on the modified isoconcentration contour migration, has been developed by Pabi et al. [75] to predict the kinetics of diffusive intermixing in a mechanically alloyed binary miscible system. The as-discussed model takes into account the variation of the diffusion coefficient with composition, and an interface shift induced both by the species interdiffusion and the mechanical deformation. Based on a comparison with the experimental investigation of the ball-milling induced behavior for the Cu–Ni and Cu–Zn systems, it has been shown that the effective mass transport which is operative during mechanical alloying reaches a rate intermediate between that for volume and grain boundary diffusion.

The use of an effective temperature, $T_{eff}$, for such a diffusive alloying is proposed. $T_{eff}$ has been found not to depend on the localized temperature rise at the point of ball-to-powder impact but rather on the alloy composition, being related to the liquidus of the studied mechanically alloyed systems.

To determine the correlation of size reduction rate of inorganic materials with impact energy of balls in planetary ball-milling, room-temperature planetary ball-milling of four kinds of powder materials has been selected based on the grindabililty (i.e., talc, gibbsite, limestone, and quartz).

It has been found by Kano et al. [76] that the size reduction rate ($K_p$) of each material is proportional to the specific impact energy of the balls.

The specific impact energy is defined as

$$E_w = (n^* \times m \times v_r^{*2})/(2 \times W)$$

where $n^*$ is the number of collisions of a ball against another ball or vial wall per second, $V_r$ is the relative speed of the balls, and $W$ is the weight of powder put in the vial.

$K_p$ is expressed by $AE_w$, where $A$ is a proportional constant, inversely proportional to net work index, which is calculated by substituting $E_w$ instead of the required energy in Bond's equation.

Several empirical energy laws on communition have been proposed and one of them is known to be the third theory proposed by Bond [77], given by

$$W_b = 10W_i\big(1/P_{80}^{1/2} - 1/F_{80}^{1/2}\big)$$

where $P_{80}$ and $F_{80}$ are the 80% product and feed size respectively. $W_b$ is the energy required to reduce the particle size from $F_{80}$ to $P_{80}$ and $W_i$ is the work index.

Many papers have described the particle size distribution of powder during mechanical alloying and communition [78, 79]. Harris et al. [80] compared different models of mechanical alloying.

Five potential models describing the particle size distribution of powder during the mechanical alloying process were analyzed. Such models are based on Smoluchowski's coagulation–fragmentation equations and use a range of size dependent aggregation and fragmentation rates.

The first model (model 1) is the simplest one, having no size dependence. The aggregation and fragmentation rates are constant. As mentioned by Harris et al. [80], such a model is very similar to the one previously developed by Aikin and Courtney [81].

Models 2 and 5 generalize model 1, using aggregation rates that are size dependent while maintaining a size-independent fragmentation rate. In model 2, the aggregation rate is proportional to the sum of the sizes of particles or

equivalently the size of the agglomerate formed. In model 5, the rate is supposed to depend on the product of the sizes of the particles before combination.

Models 3 and 4 also use size-dependent aggregation rates, but introduce size-dependent fragmentation as well.

The rates used in models 2 and 3 increase more slowly with size, suggesting that smaller particles will aggregate more readily than larger ones when involved in collision.

Models 4 and 5 are unsuccessful because they predict that some proportion of the material will form infinitely large particles early in the process. Such models are better suited for materials that aggregate readily during milling.

A discrete event molecular dynamics simulation engine was developed to investigate the collision rate and energy transfer of shaker ball mills [82]. The input parameters of the model include geometry of the cylinder, filling ratios, and ball characteristics. It has been shown that the end product distribution of the particle radius is almost independent of the initial particle radius (i.e., the milling rate is significantly higher for larger particles). It has also been observed that the milling rate is independent of the amount of materials put into the mill.

Based on a nonlinear elastoplastic model for collisions between solid particles, the average impact duration, force, geometry, the normal and tangential velocities, and normal and tangential stresses have been calculated [83, 84].

Such results of the given approach were used to determine the $t - p\, T$ conditions of mechanochemical processes in grinding machines (pressure and temperature pulses in the contact area of particles). The results of their investigations show that the physicochemical effect of mechanochemical reactors is due to brief pressure ($10^9$–$10^{10}$ Pa) and temperature pulses. The largest temperature pulses (up to $10^3$ K) are associated with dry friction. For micronic particles, the characteristic length and time of the process are $10^{-8}$ m and $10^{-8}$ to $10^{-9}$ s.

In some work performed by Gonzalez et al. [85], the particle size has been found to not depend on intensity but on milling time for all the investigated mill configuration conditions. The elastic and plastic energies are exponentially dependent on the impact frequency and this has a marked effect on the efficiency of alloy formation. In addition, the change of the milling frequency has been found to allow a control of the time for alloy formation in the case of the Fe–Al system, ball-milled using a Spex machine.

## 2.6. Local Effect/Microscopic Model

In a recent paper, Tian and Atzmon have studied the kinetics of microstructure evolution in nanocrystalline Fe powder during mechanical milling [86]. A phenomenological model has been proposed based on the assumption of simultaneous grain refinement and grain growth. The weak temperature dependence of the grain-growth term is consistent with nonequilibrium vacancy production. Based on the results of such an approach, it has been shown that the efficiency for refinement and vacancy production decreases with increasing vibration amplitude.

Nevertheless, the main conclusion of the aforementioned paper is that the detailed mechanisms of grain refinement and growth need to be explored to better understand the formation of nanocrystalline materials during ball milling. In the next, selected contributions will be discussed.

The model developed by Schwarz [87] is based on dislocation kinetics and the diffusion of solutes along the dislocation cores. Such a developed model is based on jerky dislocation kinetics (i.e., short gliding times separated by long waiting times) and solute diffusion along dislocation cores during the waiting times.

During MA, the dislocations act as solute-pumping stations which introduce solutes into crystalline lattices even in the presence of a chemical energy barrier. In response, the solutes diffuse into the dislocation cores and populate the cores forming linear solute chains. When the dislocations are mechanically forced to move, they leave behind rows of substitutional solutes in an otherwise perfect lattice. Therefore, the lattice is locally left in a state of high supersaturation. Such a mechanism is named dislocation solute pumping.

As discussed by Pochet et al. [88], two main features have been investigated: atomistic scale modeling of coherent phase transformation and evidence of milling enhanced precipitation. Atomistic modeling reveals unique features of the microstructure in crystallites under milling: depending on the conditions of the latter, stationary microstructures are stabilized, at variance with thermal equilibrium. These microstructures are characterized by a stationary coherency length. In the case of a positive heat of mixing, the latter length has been found to continuously evolve with the shear frequency and temperature.

In the ordering case, the amount and geometry of the chemical disorder introduced by each shearing event, as well as the number of injected vacancies, are found to have important consequences on phase stability in such dynamical systems. Dynamical transitions between microstructures are observed rather than transition between phases. Such an atomistic model has been applied to the Ni–Ge system.

Pochet et al. [89] have explained that phase transformation under ball-milling can be addressed from the theoritical point of view, as transitions between stationary states of a driven alloy: shear induces some sort of disorder which is annealed by thermal diffusion, between two shearing events. This type of problem has been modeled in great detail in the context of irradiation effects on phase stability of alloys.

Depending on the milling temperature and intensity, it has been found in the case of the Fe–Al system that the crystallites are either in an ordered state with the B2 structure or disordered as body-centered cubic (bcc) solid solution (A2). In the ordered state, the degree of order has been observed to reach a steady state value, depending in a reversible way on both the temperature and the milling intensity: the higher the intensity or lower the temperature, the lower the steady degree of order.

As predicted by their model, the order–disorder transition which is of second order at equilibrium can become of first order under appropriate milling conditions.

Such a driven alloy theory has also been used for the precipitation–dissolution reaction under ball-milling. From atomistic Monte Carlo simulations, it is noted that stationary mesoscopic microstructures can be stabilized and that their characteristic length scales can be adjusted by tuning the milling conditions.

In a complementary work, Wu et al. [90] have studied the forced mixing and nanoscale decomposition in ball-milled Cu–Ag characterized by atom probe field ion microscopy (APFIM). Statistical analyses of the atom probe field ion microscopy yield the degree of mixing induced by ball-milling in the Ag–Cu system (equiatomic composition). Atomic composition has been determined as a function of the length scale. These results have been compared with the ones obtained from kinetic Monte Carlo simulations. The model one is a kinetic Monte Carlo algorithm with competing dynamics. In these simulations, thermally activated vacancy migration promotes phase separation of an $A_{50}B_{50}$ binary alloy, which consists of immiscible elements distributed on a face-centered cubic (fcc) rigid lattice, whereas shears, produced at a controlled frequency along randomly selected glide systems of the fcc lattice, homogenize the composition field.

The experimental investigations provide direct confirmation of the near random mixing obtained for the 85 K milling and of the nanoscale decomposition for the 453 K milling. APFIM also evidences the presence of long-range composition heterogeneities, at scales larger than 10 nm, for all the studied temperatures (i.e., 85, 315, and 453 K). A comparison of the observed features has been found to stress the merits of such simulations but also their limitations.

Based on a different approach, Badmos and Bhadeshia [91] have investigated the evolution of solutions by the way of a thermodynamic analysis of mechanical alloying.

To analyze the various mechanisms occurring during the mechanical alloying process, the purpose of the work is to examine the way in which a solution is created by continuously refining a mixture of powder particles composed of pure elements, from a purely thermodynamic point of view.

Based on the results of such a model, it is predicted that solution formation by mechanical alloying of solid components cannot occur unless there is a gain in coherency as the particles become small. In complement, the formation of a metastable state prior to the achievement of full solution may be achieved when the component atoms prefer like neighbors.

Strain-induced structural changes and chemical reactions have been investigated from thermomechanical and kinetic models by Levitas et al. [92]. Strain induced chemical reactions are experimentally observed in shear bands for both Ti–Si and Nb–Si mixtures. One of the aims of the discussed paper is to find, theoretically, whether there are possible macroscopic mechanisms of intensification of the observed chemical reactions due to plastic shear in the solid state.

The class of structural change (SC) without stable local temperature state is treated. The SCs are considered as a process of variation of the transformation deformation gradient in an infinitesimal final volume from the initial to final value which is accompanied by a jump in all thermomechanical properties. The kinetics of a thermal SC can be described in terms of applied stresses, deformations, and temperature, rather than real time. A thermodynamically consistent kinetic theory of thermally activated SC is suggested. A specific approach has been developed considering the time of structural change in some transforming volume instead of known approaches describing kinetics in terms of rate of phase volume fraction change. The former is consistent with

the standard method of nonequilibrium thermodynamics which relates conjugate force and rate in the expression for dissipation rate. The discussed model leads to the threshold-type generalizaton of Arrhenius-type kinetics in which the actual activation energy includes the driving force, dissipative threshold, and surface energy. By introducing such an effective temperature, it has been taken into account that temperature can vary significantly during SC.

Some years ago, Gilman [93] suggested that elastic shear strain can accelerate the chemical reactions by lowering the highest occupied bonding molecular orbital/lowest unoccupied antibonding molecular orbital energy gap.

Another major effect of energy/power threshold is the capability to initiate self-propagating high temperature synthesis during milling. Attention has been paid the synthesis and formation mechanisms of molybdenum silicide by mechanical alloying [94].

The milling energy was calculated using a collision model and the milling energy maps were attained. Results showed that when the effective extensive factory is above 1.06 J/g s, the formation mechanism of $MoSi_2$ by mechanical alloying is a self-propagating high-temperature synthesis one. Otherwise, when it is below 0.917 J/g s, the formation mechanism of $MoSi_2$ is a diffusion solution.

# 3. GRINDING OF ELEMENTAL POWDERS

## 3.1. Introduction

Ball-milling of elemental powders has been thoroughly investigated in various conditions of energy transfer to identify the mechanisms by which materials deform to produce nanometer-sized grains, characterize the intergranular and intragranular defects of nanograined ground powders, and measure the resulting changes in properties with respect to those of coarse-grained elements, for instance mechanical, magnetic, hydrogen storage capacity [95–126]. Notable examples are bcc metals (Cr, Fe, Nb, Mo, W), fcc metals (Al, Ni, Cu, Rh, Pd, Ag, Ir), hexagonal close-packed metals (Mg, Ti, Co, Zn, Zr, Ru, Hf) [95–136], semiconductors Si, Ge, and graphite [137–146].

In most cases, the crystallographic structure of the starting element remains unchanged when grain size decreases down to an average size $d$ of ca. 10 nm, the typical size reached in classical high-energy laboratory mills. Phase transformations may, however, take place; for instance bcc Nb has been reported to be transformed into fcc Nb [130] while Si, Ge, Se, and graphite are partially or totally amorphized [137–146]. To establish the very nature of the observed structural transformations, it is, however, essential to analyze the possible consequences of the unavoidable contamination of ground elements. During milling, impurities may indeed be incorporated in the starting elements from solids constituting the milling tools (ex: hardened steel, tungsten carbide, zirconia, etc.), from gazes of the milling atmosphere (argon, nitrogen, hydrogen, air, etc.), or from elements physi- or chemisorbed on starting powder particles. Contamination may further occur during air exposure of as-milled powders. For instance, the uptake of argon, oxygen, nitrogen, and iron and their consequences on the formation

of disordered phases at grain boundaries or on the formation of nitrides has been been followed during milling of molybdenum in various atmospheres [136]. Finally, mechanical characteristics of powders may change significantly during milling because of the grain size decrease (Hall–Petch relation for example). The flow stress of ground and consolidated Fe powders with a grain size of $\sim$80 nm is for instance about twice that of coarse-grained Fe at strain rates of $\sim$$10^3$–$10^4$/s [147] which are typical of the compression rates of particles trapped during milling between colliding bodies. More importantly, such changes cause a decrease of the energy transferred from balls to powders [148].

## 3.2. Grain Size Reduction

Ball-milled crystalline materials have grain sizes generally in the range from $\sim$5 to $\sim$30 nm. Most often, for instance in metallic materials, the average size of as-milled powder particles is, however, not in the nm range but typically micronic or submicronic as a result of a steady-state equilibrium between fracture and welding. Every powder particle includes many nanograins, $\sim$$10^6$ grains/$(\mu m)^3$, and may thus be considered as a textureless polycrystal with a large density of grain boundaries. Brittle or ductile elements may, however, exhibit particle size distributions which are shifted significantly downward or upward respectively. Such shifts reflect the modifications of the aforementioned steady-state equilibrium. A predominance of cold-welding over fracture results for instance in the formation of millimeter-sized hollow particles, up to 10 mm in diameter, which contain themselves smaller particles (Russian Doll effect) when "grinding" a copper powder with a micronic average particle size [100]. Milling particles of Al and of Zn with a starting size of 50 $\mu$m similarly yields millimeter-sized particles [133].

At high strain rates, the deformation of the starting coarse-grained particles is localized in shear bands which contain a high density of dislocations. The subsequent recombination of dislocations to form a nanosized cellular structure with small-angle grain boundaries, which are in turn replaced by higher angle grain boundaries through grain rotation, is a proposed scenario for the development of a nanocrystalline microstructure [101, 102, 107]. The fragmentation and the reorientation of crystal volumes at the nanometer level may occur through the generation and interaction of partial wedge disclinations which have been observed in ball-milled bcc Fe by high-resolution transmission electron microscopy [127]. In fcc Cu, twinning is the preferred mode of deformation when the average grain size becomes smaller than some critical value [117]. The crystallite size of ball-milled metals decreases rapidly with milling time but reaches a saturation value with prolonged grinding. A balance between the defect structure produced by plastic deformation and its rate of recovery by thermal processes explains the latter. A phenomenological model based on the assumption of simultaneous grain refinement and grain growth was for instance applied to low-energy ball-milling of Fe, evidencing further the role of nonequilibrium vacancy production [114]. Oscillatory variation of the hardness with milling time is observed in cryomilled nanocrystalline Zn [134]. Large variations in the dislocation density and grain-size distribution occur during cryomilling as a result of recrystallization which takes place in larger grains when the dislocation density due to strain-hardening reaches a critical level. Similarly, the reduction of grain size of ball-milled Mg down to 42 nm occurs by twinning and retwinning within the grains developing subgrain boundaries. The relatively large minimum grain size obtained for ground Mg as compared to other metals and the associated low internal strain value are due to the occurrence of recovery processes during milling of this low melting temperature metal [135].

The stationary grain size reached during milling, from $\sim$25 nm for Al and Ag to $\sim$6 nm for Pd, scales inversely with the melting temperature when the latter is below $\sim$1800 K [98, 107]. For higher melting temperatures, it appears that $d$(fcc) $< d$(bcc) $< d$(hcp) independently of the mill energy [107]. The grain size is most often derived from X-ray diffraction patterns whose line broadening further yields strain values which depend on $d$ and have typical values of some 0.1%.

## 3.3. Defects

### 3.3.1. Grain Boundaries

Nanostructured materials (NSMs) have a significant fraction of atoms residing in defect environments. The volume fraction associated with grain boundaries (GBs) is for instance $\sim$20% for a grain boundary thickness of $\sim$0.7 nm, as found from computer-generated $n$-Ni [149], and a grain size of 10 nm. For grain sizes less than $\sim$10 nm, the volume fraction of triple junctions becomes significant and may influence some properties, for instance the mechanical properties. The understanding of the structure of grain boundaries and of the nature of intragranular defects in nanostructured materials benefits from high-resolution electron microscopy experiments and from computer simulations. Molecular dynamics is currently used for investigating the nature of grain boundaries in nanostructured materials which is still in dispute between the defenders of amorphous models [150, 151] and those who conclude that they are similar to grain boundaries of coarse-grained materials [152, 153].

From transmission electron microscopy (TEM) observations, Li et al. [117] conclude that most grain boundaries in NSMs prepared by nanocrystallization of amorphous alloys, inert-gas condensation, *in-situ* consolidation, and mechanical alloying are similar to grain boundaries in coarse-grained materials. Grain boundaries with a disordered structure are frequently observed in samples prepared by the last two methods [117]. The structure of grain boundaries might, however, change when thinning samples for TEM observations [153]. Measurements of bulk properties are thus of great interest to provide additional information on interface structure. The self-diffusivity of consolidated $n$-Fe and of $n$-Pd is for instance measured to be close to that expected for conventional grain boundary diffusion from the extrapolation of high-temperature data ($\sim$$10^{-20}$ m$^2$/s for $n$-Fe with $d \sim 20$ nm at 500 K) [154]. Kolobov et al. [155] investigated recently the diffusion of copper deposited on the surface of coarse-grained cg-Ni ($d \sim 20$ $\mu$m), of ultrafine uf-Ni ($d = 300$ nm) prepared by equal channel angular extrusion, and on the surface of $n$-Ni prepared by electrodeposition ($d = 30$ nm). The Cu diffusivity, which is $4.3 \times 10^{-19}$, $9.6 \times 10^{-15}$, and $3.8 \times 10^{-17}$ m$^2$/s for cg-Ni, uf-Ni, and $n$-Ni at 423 K, is not found

to be faster for the smallest grain size. The higher diffusivity in $n$-Ni than in $gc$-Ni is attributed to triple junctions. Copper diffusion is concluded to be primarily determined by the GB structure and not by the volume fraction of interfaces. Not surprisingly, the "structure" of grain boundaries in a given NSM depends on the nonequilibrium method used to synthesize it and in turn influences its properties. Significant changes of strength and of ductility occur for instance when going from electrodeposited $n$-Cu with low-angle grain boundaries to $n$-Cu with high-angle ones, both with $d \sim$ 20 nm [156, 157]. The formation of a work-hardened layer along the grain boundaries, which is expected to depend on the GB structure, modifies the mechanical characteristics of NSMs [158]. A phenomenological model which represents then NSMs as composite materials exhibits an inverse Hall–Petch behavior [159] and a trend to strain localization with a limited ductility when $d$ decreases [158]. High-energy GB configurations, with their associated high densities of GB defects and dislocations, are argued to induce large microstrains in their vicinity [160]. An overall microstrain release occurs without grain growth by annealing of $n$-Cu synthesized by magnetron sputtering and reflects changes of the GB microstructure. It is accompanied by a decrease of the linear thermal expansion coefficient $\alpha$ from 16.6(2) $10^{-6}$ to 15.0(2) $10^{-6}$ K$^{-1}$ (80 K $\leq T \leq$ 290 K) when the strain decreases from 0.24% to 0.14% [160]. A similar decrease of $\alpha$, associated with GB relaxation, was found during milling of Fe [126]. Finally, an enhanced thermal stability of NSMs has been predicted theoretically as a consequence of the redistribution of the excess volume of grain boundaries during grain growth [161] and has been verified quantitatively for ball-milled $n$-Fe between 750 K and 960 K [162].

### 3.3.2. Intragranular Defects

Recent TEM observations led to the conclusion that grains of NSMs prepared by the *in-situ* inert gas condensation and consolidation method or by nanocrystallization of bulk amorphous alloys are defect-free while grains of mechanically alloyed NSMs contain dislocations in their interior or at the GBs and twins [117]. The density of dislocations is $\sim 5 \times 10^{15}$ m$^{-2}$ in $n$-Cu (cfc) with $d$ between $\sim$15 nm and $\sim$30 nm, $\sim 5 \times 10^{15}$ m$^{-2}$ in milled $n$-Ti (hcp) with $d \sim 9 \pm 3$ nm and $\sim 10^{16}$ m$^{-2}$ for milled $n$-Fe (bcc) with $d = 8$ nm, that is $\sim$1 dislocation with a length of $\sim$10 nm per grain [126, 131]. These dislocation segments are in any case too short to be glissile and to be involved in plastic deformation. Nanovoids are observed by TEM in local regions of various NSMs [117]. Pores are often considered as major artifacts from two-step synthesis methods which involve a final consolidation stage to prepare bulk samples from powders in order to reach the highest possible density while avoiding a significant coarsening of nanosized grains [163]. The free volume in $n$-Ni, synthesized by different techniques, inert gas condensation (two steps), electrodeposition, and high-pressure torsion (one step), has been very recently studied by TEM and positron lifetime spectroscopy [164]. Experimental results show the presence of nanovoids of 12–25 vacancies which can be located inside the grains, in the GBs, or in the triple junctions. Even in the fully dense samples, 1–2 nm sized pores as well as smaller nanovoids were observed suggesting

that these nanovoids are actually intrinsic defects of nanostructured materials [164].

The enthalpy stored in a ball-milled metal, with its high density of grain boundaries and intragranular defects, is a large fraction, typically $\sim$20%, of the enthalpy of melting which is not achieved in materials processed with conventional cold working methods [95, 98, 106, 107, 111]. The stored elastic energy associated with disclination defects has recently been suggested to be partly responsible for the high enthalpy found for ball-milled Fe (15% of the enthalpy of melting [95]) [127]. Finally, the stored enthalpy was found to decrease during milling of Fe because of a GB relaxation process taking place during the stage of the steady-state grain size [126].

## 3.4. Grinding of Transition Metals, Notably of Fe

### 3.4.1. Experimental Results and Difficulties

Besides its theoretical and applied importance either as a metal or in combination with all kinds of elements to form alloys and compounds, iron is further an almost unavoidable element in ball-milled materials when they are ground with steel tools. All these reasons explain that milling of elemental iron has been and is still of widespread interest [95, 103, 106, 108–115, 117–126]. The difference in the interfacial energies of $\alpha$-Fe and of $\gamma$-Fe might favor fcc $n$-Fe over bcc $n$-Fe at room temperature when the grain size is sufficiently small [128]. A bcc $\to$ fcc transformation was recently reported to occur in ground elemental Nb when $d$ becomes smaller than 10 nm [130]. A significant amount of contamination by C, N, and Fe was, however, found. These elements were assumed to remain mostly dissolved in the final fcc Nb phase [130]. It would be worth examining if such solute elements may influence the fcc $\to$ bcc transformation.

Because of its interest in cemented carbides, the cobalt cubic to hexagonal transformation produced by wet milling of WC and Co was studied by Kimmel [165]. The extent of the transformation was reported to depend on both milling intensity and initial carbide particle size. The allotropic transformation induced by dry ball-milling of cobalt was also investigated [166–170]. After milling for a few hours, Cardellini and Mazzone [166] observed that the hcp phase transforms to a disordered phase composed of an essentially random stacking of close-packed planes. They further concluded that prolonged milling does not affect the stability of this phase up to the point where iron contamination induces the transition to the fcc structure. As emphasized by Mazzone [167], the progressive contamination arising from the steel milling tools can result in a stabilization of the fcc phase for iron concentrations of only a few at% as shown by the equilibrium Fe–Co phase diagram. The allotropic transformation of hcp Co to fcc Co, which occurs in all cases by heating the ground powders at sufficiently high temperatures, seems to be related to the amount of disorder present in the stacking sequence of close-packed planes. A similar study was later performed by Huang et al. [168–170] whose results were reported to be in broad agreement with those of Cardellini and Mazzone. Besides contamination effects, they stressed the importance of the milling intensity which

controls the rate and level at which defects accumulate. Sort et al. [171] have shown similarly that a large amount of stacking faults is accumulated in cobalt during ball-milling. They did not obtain a pure fcc phase, even after increasing the milling time and/or the milling intensity. The final state was concluded to resemble a random hcp–fcc stacking sequence rather than two well separated phases.

Similarly, the characterization of the contamination of iron during ball-milling is essential to reach firm conclusions about the occurrence of phase transformation as iron is easily combined during milling and/or during subsequent exposure to air [111] or/and annealing with many elements, notably with oxygen, carbon, and nitrogen. The possible formation of a magnetically ordered fcc Fe phase in milled and annealed $\alpha$-Fe [108] is indeed the subject of much controversy [117, 118] among other things because its reported transition temperature (about 500 K) and hyperfine magnetic field (21 T at room temperature) are very close to those of easily formed cementite $Fe_3C$ (485 K and 20.8 T, respectively). Classical fcc $\gamma$-Fe has a complex antiferromagnetic structure with a transition temperature at about 67 K but its magnetic properties can be drastically different according to its lattice parameter [123]. The determination of the isomer shift of the discussed phase would certainly be of great help to distinguish between these two phases. The use of zirconia milling tools, without magnetic contaminants and without risks of carbide formation at grain boundaries, might be of further interest in such studies.

The inclusion of nitrogen in Fe by enhanced diffusion along GBs during ball-milling or during subsequent exposure to air must be further considered. It was, for instance, responsible for the formation of $Fe_4N$ during heating of $n$-Fe ball-milled in vacuum [111]. When milling Fe powders in nitrogen with a Szegvari-type attrition mill, infused nitrogen is located at GBs and in layers along GBs transforming the bcc lattice to a body-centered-tetragonal (bct) lattice [110, 116]. As the concentration of interstitial nitrogen increases, this outer bct shell of grains forces the inner bcc phase to expand [116]. Milling of iron in nitrogen with a Uni-Ball-Mill was concluded from X-ray diffraction patterns to result in a bcc phase containing ~4 at% N. Further, $^{57}$Fe Mössbauer spectra show evidence of significant contributions from Fe atoms perturbed by N atoms in contrast with spectra recorded for Fe milled in vacuum or in helium [105]. Milling Fe in a continuous flow of nitrogen produces even iron nitrides with significantly higher nitrogen contents (up to $Fe_2N$) [172].

Finally, a nanostructured surface layer of a thickness of ~15 $\mu$m was formed on a Fe plate by means of "surface mechanical attrition," a technique which is a combination of milling and of shot peening in which the bulk Fe sample is simply part of a wall of the vial [129]. High strains with a high strain rate are both found to be necessary for the formation of nanocrystallites during plastic deformation of the iron plate.

### 3.4.2. Some Properties of Ground Metals

High-pressure X-ray diffraction experiments were recently performed to obtain the equation of state of $n$-Fe ($d = 10$ nm) up to 46 GPa [125]. Nanocrystalline bcc Fe

transforms into $\varepsilon$-Fe when compressed to 10.9 GPa while $\varepsilon$-Fe transforms back to bcc Fe at a pressure lower than 7.6 GPa, both transformations taking likely place at lower pressures than the corresponding transformations in coarse-grained Fe. Chen et al. [125] conclude that the equations of state do not differ within experimental uncertainty for $n$-Fe and for cg-Fe.

Bulk moduli and Young's moduli of ground nanocrystalline metals (Fe, Cu, Ni) were measured to be the same as those of coarse-grained metals for grain sizes larger than ~10 nm [104, 115]. A Young's modulus decrease of ~5% when compared with that of cg-Fe is measured for ground $n$-Fe with $d = 7$ nm [104]. Molecular dynamics simulations yield similar conclusions for Young's moduli of $n$-Ni and of $n$-Cu with $d > \sim$10 nm. Young's modulus is found to decrease when $d$ decreases below ~5 nm, being for instance reduced by about 25% of the bulk value for $d = 3.4$ nm in $n$-Ni [173, 174]. An opposite variation, namely an increasing bulk modulus with a decreasing grain size, was, however, measured for ground $n$-Ni [115]. The vibrational densities of states (VDOS) have also been determined for $n$-Fe and $n$-Ni with $d$ around 15 nm [120, 121]. In comparison with reference coarse-grained samples measured in the same conditions, the nanocrystalline specimens exhibit a slight increase in the population of low-frequency modes and a distinct broadening of the transverse and longitudinal phonon peaks. The former feature has been related to the presence of interface modes and the latter to reduced phonon lifetimes due to the nanometer scale of crystallites. The VDOSs of bulk $n$-Ni and $n$-Cu model samples, with $d$ between 5 and 12 nm, were calculated recently from molecular-dynamics simulations [175]. The density of states is shown to be enhanced at low and high phonon energies, with a power-law behavior of the low-frequency grain-boundary VDOS possibly due to a reduced dimensionality effect. The enhancement of the VDOS at low and high energies, which increases with decreasing grain size, is found to be mainly caused by the high number of grain-boundary atoms [175].

Recent investigations [122, 124] failed to detect changes of Mössbauer spectra and room-temperature magnetic properties when ball-milling Fe down to grain sizes of ~10 nm. A similar result was found for $n$-Ni [103]. The low-temperature magnetic behavior of ball-milled $n$-Fe has been investigated recently [112]. A transition from a high-temperature ferromagnetic state to a low-temperature disordered regime was attributed to structurally disordered GBs.

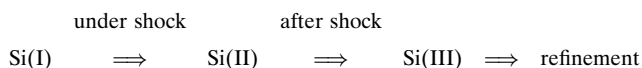## 3.5. Amorphization of Elements Si, Ge, Se, C

### 3.5.1. Si, Ge, Ge–Si Amorphization Induced by Milling

The crystal to amorphous phase transformation depends on the ability of the crystalline phase formed by mechanical alloying or mechanical milling to sustain or not a nanostructured state. In other words, the grain size of systems which possibly amorphize are expected to be close to a critical germination size. A transformation from a crystalline phase to an amorphous phase was first reported to

occur for various elements or alloys with a diamond-type cubic structure such as Si [137], Ge [176], GeSi [177], and GaAs [178].

Mechanical milling (Si, Ge, GaAs) and/or mechanical alloying (GeSi) leads to a refinement of the grain size. Two critical grain sizes are found experimentally: the first, $d_1$ (in the range of 20 to 30 nm for ball-milled silicon or germanium), is the grain size below which the lattice expands significantly (up to 0.2% and 0.4% in the case of ball-milled silicon and germanium respectively) and the second, $d_2$ (8 and 4 nm for Si and Ge respectively), $d_2 < d_1$, is the grain size below which the crytal to amorphous phase transition takes place. The size $d_1$ has been proposed to be the size below which the surface energy becomes larger than that of the volume. Lattice expansion is a way to compensate for this energy difference while keeping constant the total number of atoms (isolated grain hypothesis). Such a mechanism cannot be effective at any size smaller than $d_1$ and a new mechanism, namely a crystal to amorphous phase transformation, must operate below a second critical value $d_2$. The problem which remains open is that of the refinement mechanism that allows crystals to decrease so strongly in size.

Gaffet and Harmelin [137], following a suggestion of Swain (CSIRO, Sidney, Australia), proposed a mechanism to explain the Si amorphization,

$$\text{Si(I)} \underset{\text{under shock}}{\Longrightarrow} \text{Si(II)} \underset{\text{after shock}}{\Longrightarrow} \text{Si(III)} \Longrightarrow \text{refinement}$$

with Si(I), Si(II), and Si(III) exhibiting different structures, namely the diamond cubic (initial state), $\beta$-Sn, and bcc structures respectively. Such Si(II) and Si(III) structures are indeed observed in high-pressure experiments. The Si(I) → Si(II) phase transition occurs when silicon is compressed during mechanical shocks up to 11.3 GPa, leading to a relative volume decrease of 22%. During pressure release, Si(II) transforms into Si(III) at 7.5 GPa. The Si(III) volume per atom is equal to 92% of that of Si(I). The volume increase from Si(II) to Si(III) induces mechanical strains, leading to a breakage of the material and thus to grain refinement.

Further works performed in particular by Shen et al. have confirmed the crystal to amorphous phase transition induced by ball-milling [138, 179]. Two amorphous phase and nanocrystalline Si were produced by ball-milling of polycrystalline elemental Si. The nanocrystalline component contains some defects such as dislocations, twins, and stacking faults which are typical defects of conventional coarse-grained polycrystalline materials. The estimated volumic fraction of amorphous Si is about 15% while the average size of nanocrystalline grains is about 8 nm. Oxygen-free amorphous elemental Si can be obtained by ball-milling. The distribution of amorphous Si and the size of nanosized Si crystallites is heterogeneous in the milled powder. The amorphous Si is concentrated near the surface of milled particles while the grain size of nanocrystalline Si ranges from 3 to 20 nm. Two possible amorphization mechanisms (i.e., pressure-induced amorphization and crystallite-refinement-induced amorphization) are proposed for the amorphization of Si induced by ball-milling.

Such an amorphization of silicon induced by mechanical treatment has recently been investigated by Strelestkii et al. [180, 181]. The mechanical treatment of silicon in an inert atmosphere is accompanied by the formation of two populations (coarse and fine) of nanoparticles along with the formation of an amorphous phase. It may be concluded that the decrease of grain size below the critical value of about 4 nm is accompanied by the amorphization of silicon. The amount of amorphous phase for the maximum injected energy (500 kJ/g) exceeds 40%.

Particular attention has been paid to the cathodoluminescence of mechanically milled silicon [182]. Nanocrystalline silicon has been produced by ball-milling of silicon single crystals. The milled powder shows cathodoluminescence in the visible and near-infrared ranges. The main visible band appears at about 1.61–1.64 eV and is attributed to the presence of nanocrystals. An intense infrared band, which is not systematically observed in nanocrystalline silicon structures, appears in milled silicon at the same energy (0.8 eV) as the well-known dislocation luminescence band of silicon. It is suggested that this emission arises from the high density of extended defects generated during the milling treatment.

### 3.5.2. Se, Ge–Se Amorphization Induced by Ball-Milling

Experiments show evidence that mechanical attrition can induce complete crystallization of an amorphous solid and complete amorphization of a nanocrystalline phase as shown in the case of Se [142]. The induced MA phase transformation has been found to be closely related to the initial microstructure of the processed materials. Depending on the starting materials, MA may either (i) raise the excess energy of the milled sample by accumulating various microdefects or (ii) lower the total excess energy by activating a phase transformation to a more stable state (such as crystallization).

Some calorimetric experiments [140] have shown that during cryogenic temperature milling, amorphization is faster than at ambient temperature. The experimental results have been interpreted as a crystal to amorphous phase transition driven by defects created by frequent mechanical deformation.

X-ray diffraction investigations and thermal analyses have revealed that the amorphization onset corresponds to a critical size and a drop in microstrain [143]. During the major amorphization process, the remaining crystallite size remains unchanged with a constant lattice expansion. The amorphization kinetic was explained in terms of a crystallite destabilization model rather than by the classical shell kinetic model.

The interpretation of the latter authors has been questioned by Caro and Van Swygenhoven from computer simulations [149]. For these amorphous Se-annealed samples, a correct account of GB area and energy balance in the nanocrystalline phase yields a grain boundary width of 2.5 nm and a grain boundary energy of 0.4 J/m$^2$. The GB width is significantly larger than in simulated nanocrystalline nickel. A description which does not correctly take into

account the finite width of the GB leads thus to an apparent decrease of the GB energy with decreasing grain size.

Nasu et al. [183] analyzed the structure of amorphous Ge–Se prepared by mechanical milling. The amorphization process and the short-range-order structure of amorphous $GeSe_2$, $Ge_3Se_4$, and $Ge_4Se_5$ prepared by mechanical milling was investigated. $GeSe_2$ becomes amorphous in a shorter milling time. A much longer time is needed to amorphize Ge-enriched alloys such as $Ge_4Se_5$. Amorphous $GeSe_2$ and $Ge_3Se_2$ prepared by mechanical milling exhibit a local order similar to the corresponding amorphous phases prepared by liquid quenching, that is, the covalent 4(Ge)–2(Se) folded structure. The amorphous $Ge_4Se_5$ (which cannot be obtained by liquid quenching) also has the 4–2 folded structure, although its composition is nearer to GeSe.

Such a crystalline–amorphous transition of Ge–Se alloys by mechanical grinding has been also investigated by Tani et al. [184]. The mechanisms for amorphization of Se are suggested to be based on the distortion between helical chains connected by van der Waals forces. Monoclinic $GeSe_2$ is amorphized by disordering between the connected tetrahedra. The tetrahedral unit of $GeSe_2$ by mechanical grinding is distorted with wide distributions. $GeSe_2$ is completely amorphized after 4 hours of grinding, and Se after 30 hours for the given milling conditions. The difference has been considered an indication that disordering between the connected tetrahedral units in monoclinic $GeSe_2$ is induced more easily than it is between chains in trigonal Se.

### 3.5.3. Graphite Amorphization Induced by Ball-Milling

Huang investigated by high resolution TEM and electron energy loss spectroscopy the defect structure and the amorphous-like graphite induced by ball milling [185]. The deformation structures and the amorphization kinetics of graphite were clearly revealed in that way. Basal plane stacking disorder, cleavage, delamination cracks, misorientation bands, and low angle (0002) twist boundaries are observed. The basal plane stacking disorder is probably produced by a simultaneous shearing. Other defects such as a number of half Frank loops or interstitial loops, and bending and buckling of the basal planes, are also observed. Frequent shearing of (0002) planes acting in parallel with the increase of the Frank loop density finally leads to the breakage of the hexagonal network at a very fine scale until an amorphous-like structure results. The amorphous-like phase comprises highly curled flakes with $L_a$ less than 5 nm and $L_c$ less than 2 nm and it exhibits an $sp^2$ hybridization. The amorphization kinetics has been found to correspond to a defect-controlled process.

Welham and Williams have also studied extended milling of graphite and activated carbon [186]. Graphite and activated carbon were ball-milled under vacuum for up to 1000 hours. The graphite became amorphous, with no evidence of recrystallization after heating up to 1200 °C. There was little change in the structure of the activated carbon. Heating the two milled samples under argon showed that they absorbed substantial gas amounts, over 30% of their mass in some cases. The onset temperature of oxidation of graphite and activated carbon is decreased by ball-milling for extended times. The greatest decrease in ignition temperature for graphite was concomitant with the largest increase in noncrystalline carbon indicating the role of disordered carbon in enhancing the oxidation. Indeed, graphite milled for 1000 hours showed reactivity similar to that of activated carbon.

The structural disorder and phase transformation produced by ball-milling in graphite was also investigated by Shen et al. [144]. It was shown that nanocrystalline graphite with a crystallite size of about 2 nm is formed after 8 hours of ball-milling. Further milling produces a mixture of nanocrystalline and amorphous phases. Relatively large structural disorder is induced in the ball-milled graphite as revealed by X-ray diffraction (XRD) and Raman scattering experiments. Furthermore, the nanocrystalline graphite is relatively stable when compared with some nanocrystalline metals.

Salver-Disma et al. have performed transmission electron microscopy studies of carbon materials prepared by mechanical milling [187]. Mechanical grinding has been observed to generate an increasing amount of disordered carbon at a rate depending on the type of grinding mode used (shear- or shock-type modes). When the shock-type grinding is used, the triperiodic structure and the lamellar microtexture of graphite completely break down to give microporous and turbostratic carbons made of misoriented basic structural units. Graphite grinding permits the elaboration of disordered carbons. The involved mechanism differs from a simple reverse graphitization, since not only the structure but also the microtexture is strongly modified by the grinding. After heat treatment at 2800 °C, the graphite organization is not recovered, and a mesoporous turbostatic carbon is mainly obtained. Shear grinding has been found to be less effective since remnants of graphitic carbon are still present within the disordered carbon.
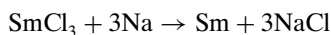
In order to achieve lithium intercalation, such a milling process has been performed in graphite and soft carbons [188, 189]. The effects of mechanical grinding on the morphology and electrochemical performance of graphite and soft carbon powders with respect to lithium insertion were studied. The morphology of the milled graphite powders was found to depend strongly upon the nature of the interactions (i.e., impact or shear shock modes) generated by two kinds of mixer mills used. For the same milling time, crystallite size was smallest and the density of defects highest for graphitic powders that were ball-milled using impact interactions. For each grinding mode (shear of impact shock modes), the resulting ball-milled carboneceous powders were found to be totally independent of the nature of the precursor used (graphite, carbon, coke) and/or of its morphology (layers, microbeads, and fibers).

In complement, the effect of liquid media during milling of graphite has been investigated by Janot and Guerard [190]. Ball-milling of graphite in the presence of a liquid leads to very thin, well-crystallized, and anisometric particles. In the presence of water, the graphite particles are covered by gamma $Fe_2O_3$ (maghemite) formed by the oxidation of the ferrous alloy coming from the milling tools. In the presence of $n$-dodecane, well-crystallized and highly

anisotropic particles of graphite can be synthesized, exhibiting promising features as anodic materials for lithium-ion batteries.

## 3.6. Elemental Nanoparticles Dispersed in a Matrix

We describe finally two uses of ball-milling which do not involve a unique element right from the start but end up with a nanosized dispersion of an element inside a matrix. Attractive nanograined metals are indeed also obtained from chemical reactions which take place between ground reactants at temperatures and at rates at which they would normally not occur. Some reactions, for instance the mechanochemical reduction of $SmCl_3$,

$$SmCl_3 + 3Na \rightarrow Sm + 3NaCl$$

which would never occur at elevated temperatures due to unfavorable thermodynamical conditions, are even rendered possible. Mechanochemical reactions may thus be put to work to prepare dispersions of nanometric elemental particles ($\sim$10 nm and smaller) within matrices, for instance within sodium chloride [191–196] which is dissolved afterward and within alumina [197, 198]. Redox or displacement reactions like

$$\text{oxide or chloride of } A + B \rightarrow \text{oxide or chloride of } B + A$$

(for instance, A = Ti, V, Cr, Fe, Ni, Cu, Zn, Zr, Ta, Gd, Er, Sm, B = Na, Mg, Al, Si, Ca, Ti, Ni) have been used recently to prepare ultrafine magnetic metal powders with promising applications (recording media, ferrofluids, nanocomposite magnets), quantum dots, cermets, etc. Ball-milling of Al-10 wt% M blends made up of pure immiscible elements M and Al (M = In, Sn, Bi, Cd, Pb) has been used to disperse elemental nanoparticles of M in an Al matrix to investigate the size dependence of their melting temperatures [199–201]. The particle size was controlled simply by varying the milling time. Both the melting point $T_m(d)$ and the latent heat of fusion decrease linearly with $1/d$ [199]. For nanoparticles embedded in a matrix, the melting behavior is controlled not only by the particle size but also by the nature of particle/matrix interfaces. In the case of M = In, for instance, the semicoherent In/Al interfaces formed in melt-spun samples are associated with superheating of particles whose melting temperature increases with $1/d$ [$T_m(\infty) - T_m(10 \text{ nm}) \sim -27$ K]. By contrast, the melting temperature decreases with $1/d$ for the incoherent In/Al interfaces formed during ball-milling [$T_m(\infty) - T_m(10 \text{ nm}) \sim +23$ K] [201].

To conclude, ball-milling is a simple technique of preparation of nanograined elements. The follow-up of ground elements tells much about the physics of ball-milling. Once characterized with care, ground crystalline elements allow further investigation of the size dependence of all kinds of properties. Some properties are found to be largely determined by the actual grain size distributions of NSMs and not by their sole mean size $d$ which may sometimes constitute just a rough representation of a broad distribution. Such distributions may then be tailored to improve the properties of NSMs by combining the advantages of nanograined materials with those of coarse-grained materials. Most NSMs are often extremely hard and brittle, for instance with a low tensile ductility at room temperature with an elongation to failure less than 5% in the absence of strain hardening. A thermomechanical treatment that results in a bimodal grain size distribution, with micrometer-sized grains embedded inside a matrix of nanocrystalline and ultrafine grains ($d < 300$ nm), was applied to copper [202]. This heterogeneous microstructure of copper imparts both high strength and high tensile ductility (a yield strength of about 350 MPa and an overall uniform elongation of $\sim$30% are measured at room temperature). To toughen nanostructured materials, microstructures combining both nanometer sized phases and micrometer sized ductile crystalline phases were recently engineered [203]. An *in-situ*-formed nanostructured matrix/ductile dendritic phase composite microstructure was prepared in Ti-base alloys (ex: $Ti_{60}Cu_{14}Ni_{12}Sn_4Ta_{10}$) by using well-controlled solidification conditions [203]. Deformation occurs partially through dislocation movement in dendrites and partially through a shear-banding mechanism in the nanostructured matrix. The dendrites act as obstacles to the propagation of shear bands by isolating them in small, discrete interdendritic regions. In a compression test at room temperature, the $Ti_{60}Cu_{14}Ni_{12}Sn_4Ta_{10}$ composite exhibits a yield strength of 1.3 GPa, an ultimate stress of 2.4 GPa, and a 14.5% plastic strain [203].

## 4. MECHANICAL ACTIVATION

### 4.1. Mechanical Activation of Self-Heat-Sustaining Reaction

#### 4.1.1. Nanostructured Porous Materials Synthesis

Combustion synthesis or self-heat-sustaining (SHS) reactions provides a suitable method for producing advanced materials, such as ceramics, composites, and intermetallics. The SHS process offers advantages with respect to process economy and simplicity. The basis of such a synthesis method relies on the ability of highly exothermic reactions to be self-sustaining and therefore energetically efficient.

If a very exothermic reaction between solids or solid and liquid reactants is locally initiated, it may generate enough heat to ensure the propagation of a transformation front leading to an end product involving all the initial amounts of the elemental components. Such a process is characterized by a fast moving combustion front (1–100 mm/s) and a self-generating heat which leads to a sharp increase of temperature, sometimes up to several thousands of K/s. The temperature reached inside the reaction front has been found to be effective to volatilize low boiling point impurities, helping by the way to produce purer end products than those obtained by some more conventional techniques.

Furthermore, if the temperature variation after the end product formation is kept under control, no chemical macrosegregation occurs.

The new version of the SHS process introducing a first mechanically activation step (before the ignition of the SHS reaction), that is, the so-called MASHS process, was first proposed by Gaffet in 1995 for the synthesis of the nanocrystalline FeAl compound [201].

Such a MASHS process has been successfully used to obtain various nanocrystalline compounds such as FeAl [202–206], $MoSi_2$ [207, 208], $FeSi_2$ [209, 210], $Cu_3Si$ [211–213], and $NbAl_3$ [214–217].

Such a mechanical activation effect on the combustion synthesis of $NbAl_3$ has been recently investigated by Neto and da Rocha [218]. As milling time is increased, the ignition temperature is decreased to temperatures below the melting point of aluminum, going from 850 to 500 °C. Also a variation in the reaction evolution is observed, changing from two stage to single stage reaction.

Uenishi et al. [219] have succeeded in the synthesis of nanostructured titanium aluminides and their composites formed by combustion synthesis of mechanically alloyed powders. Application of MA and $TiB_2$ addition was confirmed to be effective for the suppression of grain growth as well as for the nanostructure synthesis caused by the subsequent heat treatment, but it made the sintering conditions harder for full densification.

Such a combustion synthesis of ball-milled powders has been applied to the fabrication of a thick intermetallic compound $Al_3Ti$ layer on metal substrate [220]. A thick intermetallic compound $Al_3Ti$ layer was formed on a Cu or Ti substrate by a coating process involving combustion synthesis of a ball-milled Al–Ti powder mixture. This layer has almost the same wear property and hardness as that of a cast $Al_3Ti$.

The influence of premechanical alloying on the self-propagating high temperature synthesis has been investigated in the case of difficult to initiate reactions, that is, $Ni_3Si$ [221]. Self-propagating high temperature synthesis of $Ni_3Si$ is difficult, if not totally impossible, without mechanical alloying. The propagation rate of the reaction is influenced by MA. The ignition became easier as the reactivity increased due to MA. Increasing reactivity lowered the threshold temperature where reaction starts and therefore decreased the need for preheating.

The combustion synthesis of mechanically activated powders in the Ti–Si system has been found to be strongly modified [222]. Reactivity in the system Ti–Si was investigated as a function of milling. The reduction of the particle size as a consequence of the milling process has been found to stabilize the combustion propagation for the Ti:Si $= 1:2$ composition and to increase the front temperature and velocity for the Ti:Si $= 5:3$ composition. These compositions were found to produce single phases. Two different steps are proposed for the interaction: solid state interaction at the reaction front followed by the solid–liquid homogeneization step in the postfront region. The first step has been observed to be influenced by milling, while the second shows no such dependence.

The combustion synthesis of an alpha′ AlFeSi intermetallic has been investigated by Murali et al. [223]. The speed of ball-milling has been found to be an important parameter in the combustion synthesis of intermetallics from elemental powders. Synthesis of a monophase alpha′ from

its stoichiometric mixture is possible when ball-milled at 22 rpm. At higher milling speeds (100, 200, 380 rpm), synthesis is incomplete.

### 4.1.2. MASHS Process in-situ Study

In order to control the SHS as well as MASHS and MAFA-PAS (see Section 4.2.1) reactions, a better understanding of the initial conditions controlling the ignition step is requested, since the initial conditions are the easiest ones, if not the only parameters allowing control of the reaction.

Many different characterizations have been used in order to obtain such information. Until recently, it has been difficult to investigate these reactions by conventional techniques due to the high temperatures involved and the fast rates of combustion. Conventional techniques do not permit the study of the intimate mechanisms which are involved during such exothermic reactions, such as the role of the liquid formation and the existence of transitory phase and other parameters which may induce changes of the texture or nature of the end product.

Recently, real time *in-situ* investigations of structural change and chemical dynamics occurring in the combustion area have been made possible by the use of synchrotron radiation. Our group consortium involving several laboratories from Dijon (UMR 5613 CNRS, Univ. Bourgogne, F. Bernard), Belfort (UMR 5060 CNRS, UTBM), Villetaneuse (LIMHP, D. Vrel), and Orsay (LURE, M. Gailhanou, D. Thiaudière) have developed a specific tool suitable to study the SHS reaction by time resolved X-ray diffraction coupled to 2D surface temperature recording with an infrared camera, under synchrotron radiation flux (see Figs. 3 and 4) [224, 225].
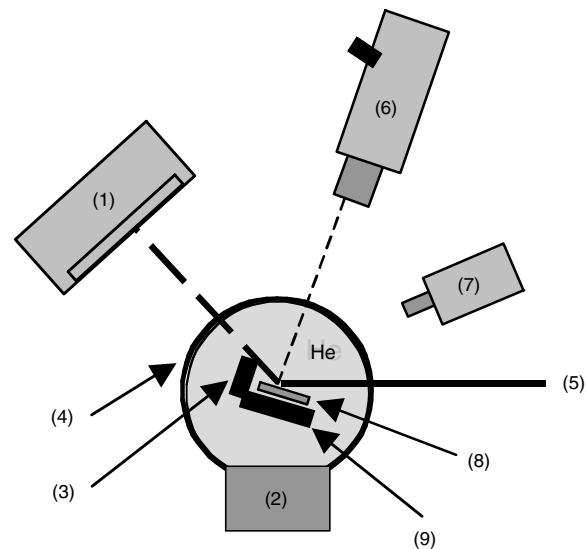


**Figure 4.** Synchrotron TRXRD apparatus for *in-situ* MASHS characterization: (1) X-ray fast detector (using 80° two theta), (2) reaction chamber under controlled He atmosphere, (3) vertical heating elements, (4) Mylar window, (5) synchrotron radiation, (6) infrared camera, (7) video camera, (8) sample ($1.5 \times 1 \times 0.5$ cm$^3$), (9) horizontal heating elements.

## 4.2. Mechanical Activation of Sintering Processes

Full attention has been paid to the synthesis of dense nanometric $MoSi_2$ through mechanical and field activation. To achieve such an objective, mechanically activated powder metallurgy processing has been developed.

### 4.2.1. Mechanically Activated Field Activated Pressure Assisted Synthesis (Nanostructured Fully Dense Homogeneous Materials)

Some years ago, the simultaneous effect of an electrical field combined with an applied pressure during the combustion was found by Munir (Univ. Davis, California, USA) as a suitable method to produce dense intermetallics compounds in a one-step process.

Such a process has been called field-activated pressure assisted synthesis (FAPAS) (see Fig. 5).

The application of the FAPAS process to mechanically activated powders has been found to be a new way to produce dense nanostructured materials (the so-called MAFAPAS process) [226]. The feasibility of this new approach for the simultaneous synthesis and densification of nanomaterials has been successfully demonstrated for the synthesis of FeAl [227], $MoSi_2$ [228], and $NbAl_3$ [229] compounds.

This new process combining electric field activation and the imposition of pressure from mechanically activated powder mixtures is demonstrated as a means to simultaneously synthesize and densify nanostructured materials in one step.

The mechanically activated powder mixtures were first cold compacted into well-adjusted cylindrical graphite dies using a uniaxial charge (from 0 to 200 MPa). The relative density of the green samples ranged from 50 to 65%. The graphite die containing the cold compacted mixture was placed inside the FAPAS reaction chamber, evacuated, and back-filled with argon (quality U) to minimize oxidation phenomena.

Then, mechanically activated reactant powders were subjected to a uniaxial pressure (0–110 MPa) while a high level electric current (0–1750 A) is passed through the die (see Fig. 6 for typical experiment set). Under these conditions, a reaction is initiated and completed within a
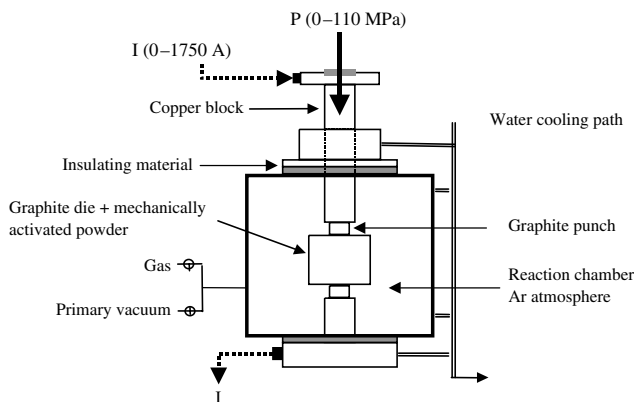


**Figure 5.** The FAPAS apparatus.
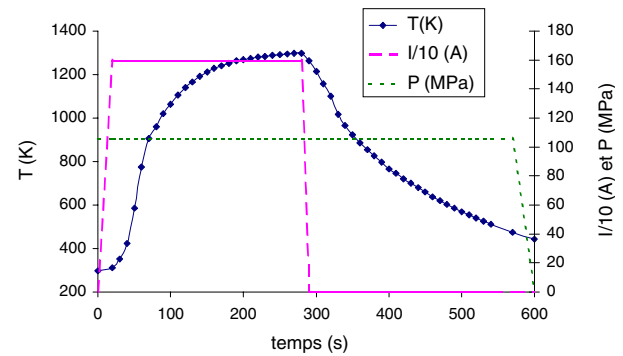


**Figure 6.** Typical combination of current intensity and uniaxial pressure during a FAPAS synthesis. The induced temperature is also shown.

short period of time (2–6 min). Temperature was measured on the external surface of the die by means of a K-type thermocouple.

The densified MAFAPAS end-products specimens were disks of 20 mm in diameter and about 2 to 5 mm height.

The relative density evaluated by weight and geometric measurements, the crystallite size determined from X-ray line profile analysis, and chemical composition are presented in Table 1.

The various tested end products were found to be nanocrystalline compounds corresponding to the expected phases with little or absolutely no secondary phases.

### 4.2.2. Mechanically Activated Spark Plasma Sintering Monolithic Compounds

In a work by Orru et al. [230], powders of Mo and Si, milled separately or co-milled in a planetary ball mill, were reacted in a spark plasma synthesis (SPS) apparatus under different electric current conditions. Milled powders reacted faster and required less current than unmilled powders. Mixtures of powders which were milled separatedly (to nanometric size) have been found to lead to the formation of micrometric alpha $MoSi_2$. Similar results were obtained for samples co-milled to produce nanometric reactants which did not contain detectable amounts of the end product phase. When products were formed during milling, they contain both the alpha and beta $MoSi_2$ phases. The product after the SPS reaction was nanometric $MoSi_2$ with a crystallite size of 140 nm.

In complement of the reported work, the effect of phase transformation during high energy milling on field activated synthesis of dense $MoSi_2$ has been investigated by Sannia et al. [231]. The effect of mechanical activation through high-energy ball-milling of reactant powders on the subsequent synthesis of $MoSi_2$ by field activation was investigated. The initiation of the synthesis reaction required a

**Table 1.** Relative density, crystallite size, and phases obtained in each system.

| System | Density | Size | Phases |
|---|---|---|---|
| Fe/Al [227] | 98 to 99.5% | 32–90 nm | $Fe_{0.515}Al_{0.485}$ |
| Nb/3Al [229] | 85–96% | 57–150 nm | $NbAl_3$, $Al_2O_3$ |
| Mo/2Si [228] | 82 to 93% | 58–75 nm | $MoSi_2$ |

threshold power level (equivalent to the level of the current, according to the authors), with the threshold decreasing with increased milling time. However, the initiation time increased when milling resulted in the formation of a significant amount of the product phase, with the increase being markedly significant at low power levels.

The characterizations of NiAl intermetallic produced by mechanical alloying and consolidated by spark plasma sintering have been realized by Coreno-Alonso et al. [232]. Elemental powder mixtures were milled for times shorter than those required for the formation of the NiAl intermetallic, then subsequently hot consolidated by spark plasma sintering. Such a fabrication process has been demonstrated to produce consolidated nanocrystalline NiAl specimens having densification levels up to 91–93% and maximum microhardness values of about 609–661 VHN.

***Nanocomposites*** The synthesis of Cu dispersed $Al_2O_3$ nanocomposites by high-energy ball-milling and pulsed electric current sintering was studied by Kim et al. [233]. The nanocomposite powders with crystallite size of about 25 nm were successfully synthesized by a high-energy ball-milling process. The composites sintered at 1250 °C for 5 min showed a relative density above 97% and enhanced fracture toughness of 4.51 MPa $m^{1/2}$.

Microstructural observation of the sintered composites revealed that the nanosized Cu particles were uniformly distributed and situated on the grain boundaries of $Al_2O_3$ matrix.

Dense nanocrystalline $TiB_2$–$TiC$ composites have been formed by field activaton from high-energy ball-milled reactants [234]. Elemental powders (Ti,C,B) were milled in a planetary mill to produce nanometric powders without product formation. No significant amount of any of the two product phases was found to be formed until after 3 hours of milling. The as-milled powders were reacted under the influence of a high current (ac current 1800 A) and a uniaxial pressure (30 MPa, 3 min). Dense (up to 98.6%) nanocomposites were formed. The crystallite sizes of $TiB_2$ and $TiC$ in the dense composite formed from powders milled for 10 h were 71.4 and 62.5 nm, respectively. The microhardness of this composite was 20.6 GPa.

El-Eskandarany et al. [235] have succeeded in the synthesis of nanocomposite WC/MgO powders by mechanical solid state reduction and subsequent plasma-activated sintering. A mixture of elemental Mg, $WO_3$, and C powders is milled under an argon gas atmosphere at room temperature, using high-energy ball-milling. A nanocomposite powder of WC/MgO (17.6 at% MgO) was obtained after milling. Plasma-activated sintering was applied to consolidate this end product into a fully dense bulk sample. The consolidation step does not lead to extensive grain growth and the compact sample consists of nanoscale grains of MgO (2.5 nm in diameter) embedded into the matrix of WC. This as-fabricated nanocomposite combines high values of hardness (about 15 GPa) and fracture toughness (14 MPa $m^{1/2}$).

***Composites*** In order to produce alumina–Cr and –Nb composites, attrition-milled Nb–50 vol% $Al_2O_3$ and Cr–50 vol% $Al_2O_3$ have been densified from 1310 to 1450 °C in about 10 min using the SPS process applying 45 MPa of pressure [236]. The milling intensity as conducted on the

metal–$Al_2O_3$ powders has been found to play a fundamental role determining not only the degree of densification but also the final nature of the composites thus processed. The longer milling time has been found to lead to a material exhibiting a finer microstructure. The maximum fracture strength developed in these composites has been achieved at 1380 °C sintering, reaching 825 MPa for the Nb–$Al_2O_3$ materials.

Murakami et al. [237] have studied the microstructure, the mechanical properties, and the oxidation behavior of powder compacts of the Nb–Si–B system prepared by spark plasma sintering. The microstructure, mechanical properties, and oxidation resistance of spark-plasma sintered compacts with eight different compositions in the $Nb_5Si_3$–$NbB_2$–$NbSi_2$ triangle were investigated. Compacts were prepared via three different routes, that is, (i) blending elemental powders in a rotational ball mill and sintering blended powders, (ii) mechanically alloying elemental powders and sintering mechanically alloyed powders, and (iii) presintering blended elemental powders, milling presintered compacts, and sintering presintered and milled powders. The most homogeneous and the least oxygen contamined compacts were obtained via the third route.

### 4.2.3. Mechanically Activated Sintering

The influence of milling process on sintering zirconia alloys has been studied by Farne et al. [238]. Innovative milling processes such as mechanofusion (MF) and MA were introduced on powder prepared from traditional oxides and from pyrolytic precursors. All the sintered products appeared largely porous, above all the samples prepared by MF processing. These products seem to exhibit promising features for the all cases where a high surface area can be requested (i.e., gas sensors).

The dilatometric analysis on the sintering behavior of nanocrystalline W–Cu prepared by mechanical alloying has been investigated by Ryu et al. [239]. Dilatometry showed that the shrinkage behavior of nanocrystalline mechanically alloyed W–30 wt% Cu powder was quite different from that of simple mixed powder with coarse grains. The shrinkage of simple mixed W–Cu powder increased steeply at the Cu melting point. Nanocrystalline powders have been shown to exhibit a shrinkage behavior in two stages, which was strongly dependent on the heating rate, and the temperature at which the sintering shrinkage started to be accelerated was considerably below the Cu melting point due to the enhanced densification in solid phase. Such a feature was attributed to the coupling effect of the sintering occuring inside individual powders and the sintering between powder particles.

## 4.3. Mechanical Activation of Annealing-Induced Reactions

### 4.3.1. Metallic Compound Formation

In the case of silicide synthesis by direct mechanical alloying, it has to be noticed that a high contamination is detected. Some ways to solve such a problem may be found by the addition of a solvent. In the early 1990s, an alternative to this problem has been proposed by Gaffet et al. [240–243],

the so-called mechanically activated annealing processing (M2AP, called in French "Elaboration par Recuit Activé Mécaniquement" or ERAM).

Such a solid state method, combining short duration mechanical alloying and low temperature annealing, has been successfully applied to the synthesis of $FeSi_2$ [240, 241], $MoSi_2$ [242], and $WSi_2$ [243]. Starting from a mixture of elemental powders, the first M2AP step corresponding to the short duration mechanical alloying leads to the formation of micrometer powders in which nanoscale 3D polyinterfaces of the elemental components have been formed. The true solid-state reaction leading to the end product phases occurred during the annealing. The effect of the milling conditions on the grain sizes as well as the residual stresses has been reported to modify the phase transformation kinetics induced by low temperature isothermal annealing starting from pre-short-duration mechanically alloyed elementary components.

Therefore, according to such experimental results, M2AP is a very suitable powder metallurgy process allowing the direct driving of the solid-state reaction occurring for example during the reactive sintering process.

More than that, M2AP has been found to be a very suitable method to produce nanocrystalline $MoSi_2$ phase. Indeed, the first mechanical M2AP step leads to an activation of the three-dimensional elementary distribution which reacts 400 °C below the temperature of the classical processes (i.e., 800 instead of 1200 °C).

$Mg_2Si$ (as a negative electrode material for lithium-ion batteries) was synthesized [244] by mechanically activated annealing and evaluated as a negative electrode materials. Such an annealing processing was achieved at 600 °C and the structural investigation has been found to prove that the silicon is the host phase for alloy formation.

In the case of solid-state reactions in nanometer scaled diffusion couples prepared using high-energy ball-milling, it has been shown by Zhang and Ying [245] that when the size of the diffusion couples is reduced and the atomic diffusivity is enhanced through prolonged milling, the temperatures for activating the solid-state reactions decrease significantly. It has been noticed that in the case of the Al–Ti and Cu–Al systems, the phases which have been formed during heating the mechanically prepared nanometer scaled diffusion couples are the same as those formed during mechanical alloying and during low-temperature annealing of multilayer thin films prepared by using sputtering.

### 4.3.2. Ceramic Phase Formation

Ren et al. have studied the preparation of nanostructured TiN powder via an integrated mechanical and thermal activation [246]. $TiO_2$ and graphite are used as starting materials and the carbothermic reduction and the simultaneous nitriding reaction are enhanced by high-energy milling prior to reactions. It is found that under the same nitridation condition, 100% TiN is formed for $TiO_2$ and graphite powder mixtures with high-energy milling, whereas no TiN is obtained for powder mixtures without milling.

Based on the same approach, the synthesis of nanostructured TiC via carbothermic reduction enhanced by mechanical activation has been achieved by Ren et al. [247].

The set of experiments has demonstrated that carbothermic reduction of $TiO_2$ by graphite from TiC can be greatly enhanced by mechanical activation. In comparison with the current industrial carbothermic reduction, temperatures for a complete reduction of $TiO_2$ to TiC have been reduced by 500 °C and at the same time, the reduction time shortened to 1–2 hours by high-energy milling the reactants for 2 hours at ambient temperature. TiC powder formed through mechanically activated synthesis is submicrometer sized with nanostructures.

The solid state synthesis of strontium oxoferrates from the mechanically activated system $SrCO_3$–$Fe_2O_3$ has been investigated by Berbenni and Marini [248]. The starting chemicals $SrCO_3$ and $Fe_2O_3$ have been dry milled in a high-energy planetary milling machine. It has been found that the $SrFe_{12}O_{19}$ phase is produced from mechanically activated mixture at temperatures lower (800 °C) than in the conventional solid state route.

The mechanical activation conditions of the $Fe_2O_3$ and $V_2O_3$ mixture powders in order to obtain a nanometric vanadium spinel ferrite have been studied by Nivoix et al. [249]. Co milling of iron and vanadium oxides allows one to obtain an intimate oxide mixture at a nanoscale, similar to coprecipitates elaborated by soft chemistry. Reduction of such a mixture in the same temperature and oxygen partial pressure conditions (500 °C and $10^{-25}$ Pa) as the soft chemistry products lead to a nanometric vanadium ferrite with the only spinel phase.

The kinetics of the thermal decomposition of mechanically activated pyrite and nonactivated pyrite was studied by Hu et al. [250] using the Friedman method. It is found that the mechanical activation of the original materials brings about a change in the surface structure of pyrite, which results in activated pyrite's transformation into metastable pyrite in the course of mechanical activation. The metastable pyrite is more liable undergo to thermal decomposition than nonactivated pyrite.

Various works have paid attention to the synthesis of Ba-based compounds. The effect of mechanical milling on the solid state reactions in the barium oxalate–iron (III) oxide system has been studied by Berbenni et al. [251]. The effect of mechanical activation on the formation of barium hexaferrite ($BaFe_{12}O_{19}$) from barium oxalate and hematite has been investigated. Thermogravimetric analysis shows that mechanical activation of $BaC_2O_4$–$6Fe_2O_3$ mixtures results in the mass loss being complete at about 600 °C, that is, well below the temperature where $BaCO_3$ (the more common barium precursor) spontaneous decomposition is complete ($T > 850$ °C). Such a noticeable temperature lowering is a consequence of the high-energy milling enhancing the formation of $BaFe_2O_4$.

A ternary mixture $BaCO_3$–$Al_2O_3$–$SiO_2$ was mechanically activated for different lengths of time [252]. The obtained data show that reaction rate increases with prolonged activation time, under the same conditions of thermal treatment ranging from 750 to 1200 °C. Formation of hexacelsian via a series of solid state reactions involving Ba silicates was favored with increasing activation time. Direct formation of monoclinic celsian has been found to be retarded with prolonged activation.

BaAl$_2$O$_4$/aluminum bearing composites have been synthesized [253] via the low temperature oxidation of Ba–Al precursors. Ba–Al powder mixtures were prepared via high-energy vibratory milling, then unixially pressed into bar-shaped samples which were then exposed to heat treatment in pure flowing oxygen at temperatures up to 640 °C. Oxidation at 300 °C resulted in the formation of barium peroxides (BaO$_2$). Heat treatment at 550 °C leads to the consumption of BaO$_2$ and of some aluminum to yield to BaAl$_2$O$_4$ and Al$_4$Ba. The oxidation of Al$_4$Ba at 640 °C has been found to produce additional BaAl$_2$O$_4$.

The fast synthesis of YBa$_2$Cu$_3$O$_z$ superconductor at low temperatures of its orthorhombic modification existence using mechanically activated and densified two-powder precursors has been investigated by Goodilin et al. [254]. Mechanically activated and densified two-powder precursors yield reproducibly an YBa$_2$Cu$_3$O$_z$ phase when using internal oxygenation of soft chemistry produced Cu$_2$O by YBa$_2$O$_{3.5}$ (containing BaO$_2$) in their mixture (Y:Ba:Cu = 1:2:3) mechanically activated in a planetary mill and warmly compacted at 250 °C into a dense pellet.

A "mild" mechanochemical synthesis based on mechanical activation of highly reactive compounds in the grinders (solid acids and bases, hydrated oxides, acidic or basic salts, crystallohydrates) has been used for the preparation of cordierite [255]. Mechanical activation accelerates the mixing and mass transfer processes at an atomic level. Sometimes, this treatment suffices to complete thermodynamically favorable reactions. However, in the majority of cases, the amorphous phases are formed and a subsequent thermal treatment is necessary at temperatures which are 200–300 °C lower than that of common thermal synthesis.

### 4.3.3. Nanotubes/Nano"cage" Synthesis

Mechanically activated solid state reaction has been found to be a suitable method for the production of carbon and boron nitride nanotubes [256]. Both carbon and boron nitride nanotubes have been produced by first ball-milling of graphite and boron nitride powders at room temperature and then by isothermal annealing at temperatures less than 1500 °C. Ball milling has been found to create the nuclei for nanotubes and the subsequent isothermal annealing is responsible for nanotube growth.

The investigation [257] of morphological and structural changes during high-energy ball-milling and thermal annealing of the mixtures soot–iron and soot–nickel demonstrated that the activation is accompanied by the formation of nanosized metal particles (10–50 nm) distributed over the amorphous carbon matrix. Prolonged mechanical activation of the amorphous soot iron has been found to lead to the formation of nanosized cementite Fe$_3$C compound. Morphological characteristics of the annealed, mechanically activated soot–metal samples depend on the time of the mechanical activation step. Annealing after short-time mechanical activation has been demonstrated to cause a crystallization of the amorphous carbon as onionlike graphite–metal structures. Annealing of the soot–metal samples after mechanical treatment for more than 5 min leads to the formation of metal nanoparticles (40–50 nm) encapsulated by graphite. The longer the preliminary mechanical activation, the smaller the size of encapsulated particles.

## 5. MECHANOCHEMISTRY

Mechanochemical processing is broadly the use of mechanical energy to cause reactions, which normally require elevated temperatures, to occur at ambient temperatures. For example reduction reactions which are normally carried out at temperatures close to 1000 °C can be achieved at ambient temperatures through the mechanochemical process [258, 259].

Normally the reaction products formed by the process are ultrafine powders with a wide distribution of particle size ranging from a few nanometers to micrometers [260].

In a paper entitled "Recent development of materials design through a mechanochemical route," Senna [261] wrote a critical overview of the principle and practice of modern mechanochemical processes for the preparation and design of high-value-added materials. The importance of the low coordination states and effects of symmetry disturbance of crystal and ligand fields are emphasized. Several successful examples of applications are displayed, such as inorganic complexes for electronic and construction materials, bioceramic materials, and metal organic coordination compounds.

Starting from the binary system, Ca(OH)$_2$–SiO$_2$, it was shown that a proton from a surface silanol group transfers to an OH group of Ca(OH)$_2$, a so-called mechanochemical dehydration, leaving a bridging bond, Ca–O–Si [262]. Similar reactions lead to heterobridging bonds or heterometaloxane bonds when two dissimilar metal atoms, Me(I) and Me(II), are connected by an oxygen atom serving as a hinge. Several conditions must be associated for such a reaction mechanism to occur. One is the state of the low coordination number of atoms. The coordination number of Ca in Ca(OH)$_2$ is equal to 6 in the crystal bulk but it may decrease to 5, 4, or even 3, not only for atoms located on surfaces (edge or corner atoms) but, more importantly, due to various lattice defects. The second condition, not less important, is the loss of crystal field symmetry.

Knowing that bridging bond formation is a consequence of a redox reaction between two metal oxides or hydroxides, it has been applied to complex oxide syntheses such as that of perovskite compounds Pb(Mg$_{1/3}$Nb$_{2/3}$)O$_3$. The same principle has been applied to complex oxides other than perovskites, for example, the formation of MgTiO$_3$ starting from Mg(OH)$_2$ and TiO$_2$·H$_2$O hydrogel [263, 264] or of Sr$_{0.6}$FeO$_4$ from Sr(OH)$_2$ and alpha-FeOOH.

Another field of successful applications is the synthesis of rapid hardening agents for cement which are necessary for emergency construction and for shortening construction time. It has been realised via a mechanochemical activation. When Al(OH)$_3$ was milled by an agitation mill and subsequently mixed with Ca(OH)$_2$ in equimolar proportions, the mixture served as an excellent hardener [265].

## 5.1. Formation of Ultrafine Oxide Nanoparticles

Various ultrafine particles have been reported to be prepared by a combination of mechanochemical and thermal processes. Several examples are described.

One is the synthesis of pure $ZrO_2$ by mechanochemical reaction of $ZrCl_4$ with MgO, as given by $ZrCl_4 + 2MgO \rightarrow ZrO_2 + 2MgCl_2$. The degree of interparticle agglomeration was found to be significantly reduced by postmilling heat treatments and also by the use of alcohol wash solvents [266].

The solid-state reduction of haematite (alpha-$Fe_2O_3$) with carbon mainly to nanocrystalline wüstite by room-temperature dry ball-milling was investigated by Matteazzi and Le Caër [267]. In addition to wüstite, a small amount of nanocrystalline magnetite is also formed, possibly by a disproportionation reaction of wüstite.

In some cases, the chemical reaction has been found to not occur during milling but during a postmilling annealing step. The formation of alumina via the reaction

$$2AlCl_3 + 3CaO \rightarrow Al_2O_3 + CaCl_2$$
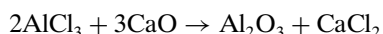
does not occur during mechanical milling. Annealing at 150–200 °C leads to the formation of $AlCaCl_5$. $CaCl_2$ was found to form by annealing at temperatures higher than 300 °C, indicating the formation of alumina. After washing to remove the chloride, the samples were found to consist of gamma alumina nanoparticles (10–20 nm). This phase, which is metastable at room temperature, transforms into alpha alumina during annealing at 1250 °C [268].

Such a feature is also the case for the mechanochemical synthesis of ultrafine $ZrO_2$ powders [269].

They are obtained by a subsequent annealing of ground powders at 300–400 °C, according to the expected milling induced reaction

$$ZrCl_4 + 2CaO \rightarrow ZrO_2 + 2CaCl_2 \qquad (\Delta G = -440 \text{ kJ})$$
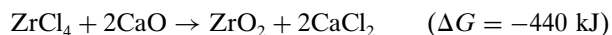
In fact, the absence of diffraction peaks for the $ZrCl_4$ phase just after milling suggests that amorphization occurs during milling, leading to an embedding of separated CaO crystallites in an amorphous $ZrCl_4$ matrix. After annealing, the $ZrO_2$ nanophase is dispersed in a $CaCl_2$ matrix which can then be dissolved in methanol.

The same behavior is observed in the case of hematite powders synthesized by mechanochemical processing [270] according to the following chemical reactions:
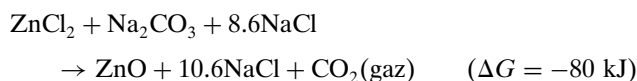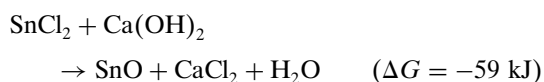
$$2FeCl_3 + 3CaO \rightarrow Fe_2O_3 + 3CaCl_2 \quad (\Delta G = -508 \text{ kJ})$$
$$2FeCl_3 + 3Ca(OH)_2 \rightarrow Fe_2O_3 + 3CaCl_2$$
$$+ 3H_2O \quad (\Delta G = -341 \text{ kJ})$$
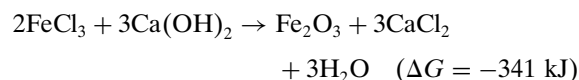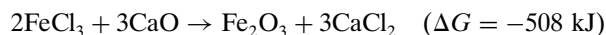
The diffraction pattern for the as-milled powder indicates that CaO remained unreacted during milling. Annealing at 50 and 100 °C did not result in any changes of the as-milled mixture. After annealing at 150 °C, X-ray diffraction peaks associated with the $CaCl_2$ and $Fe_2O_3$ phases were observed indicating that the reaction has occurred. A methanol washing was used to remove the $CaCl_2$ phase. The $Fe_2O_3$ powder exhibits particle sizes ranging from 100 to 500 nm. Dilution of the starting materials with $CaCl_2$ resulted in the reduction of the $Fe_2O_3$ particle size down to 10–30 nm.

Milling of a starting mixture which contains $Ca(OH)_2$ results in the formation of FeOOH. Annealing at temperatures below 150 °C did not lead to any significant changes in the XRD patterns. Annealings above 200 °C are needed to form crystalline $CaCl_2$ and hematite $Fe_2O_3$, due to dehydration of FeOOH. The hematite particle size ranges between 20 and 50 nm.

The synthesis of ultrafine (Sn, Zn, Ce) oxides by mechanochemical reaction and subsequent calcinations was studied [271]. A simple washing process has been found to remove the by-product phase, resulting in the production of nanopowders of $SnO_2$, ZnO, and $CeO_2$ with mean particle size of 40, 28, and 10 nm, respectively:

$$SnCl_2 + Ca(OH)_2$$
$$\rightarrow SnO + CaCl_2 + H_2O \qquad (\Delta G = -59 \text{ kJ})$$
$$ZnCl_2 + Na_2CO_3 + 8.6NaCl$$
$$\rightarrow ZnO + 10.6NaCl + CO_2(\text{gaz}) \qquad (\Delta G = -80 \text{ kJ})$$
$$CeCl_3 + 3NaOH$$
$$\rightarrow Ce(OH)_3 + 3NaCl \qquad (\Delta G = -345 \text{ kJ})$$
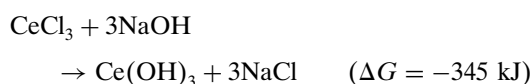
To prevent the occurrence of a combustion reaction, 12 moles of NaCl diluent were added to the starting mixture yielding the reaction

$$CeCl_3 + 3NaOH + 12NaCl \rightarrow Ce(OH)_3 + 15NaCl$$
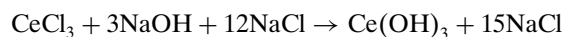
which takes place progressively instead. In the cases of the $SnCl_2$ and $CeCl_3$ initial chlorides, such reactions lead to the hydroxide phase formation during milling. The removal of $H_2O$ and the final oxidation step occur on heating ground powders above 100 °C in air. With the $ZnCl_2/Na_2CO_3$ reaction, the $ZnCO_3$ phase is stable at room temperature and calcinations above 200 °C were required to form ZnO.
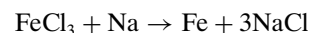
## 5.2. Formation of Ultrafine Metallic Nanoparticles

Mechanochemical synthesis has been successfully applied to the synthesis of ultrafine metallic powders.

### 5.2.1. Na Reducing Agent

Such a method has been applied to the production of ultrafine Fe powders [272].

The formation of Fe is due to the reduction of $FeCl_3$ by Na via the reaction

$$FeCl_3 + Na \rightarrow Fe + 3NaCl$$

An important requirement for the formation of nanoscale particles is that the volume fraction of the by-product phase has to be sufficient to prevent the particle agglomeration resulting in an increase of the crystallite size.

In the case of ultrafine Cu particles prepared by the mechanochemical process [273], the milling induced solid state displacement reaction is
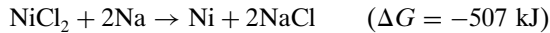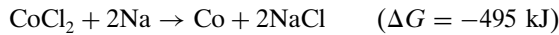
$$CuCl_2 + 2Na \rightarrow Cu + 2NaCl$$
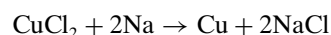
Depending on the reaction modes (continuous or combustion ones), two distinct morphologies of Cu particles have been observed; Cu particles with sizes uniformly distributed

in the range 20–50 nm are formed by a steady state reaction during mechanical milling, whereas larger particles were observed in the combustion reaction case.

McCormick et al. showed such an addition of Na to metal chlorides [274] to produce ultrafine Co and Ni particles, with particle sizes of 10–20 nm, according to the following reactions:

$$CoCl_2 + 2Na \rightarrow Co + 2NaCl \quad (\Delta G = -495 \text{ kJ})$$

$$NiCl_2 + 2Na \rightarrow Ni + 2NaCl \quad (\Delta G = -507 \text{ kJ})$$

The formation of ultrafine particles requires again the volume fraction of the metallic phase being formed to be small relative to that of the by-product phases and combustion during milling must be avoided to prevent particle coarsening.

### 5.2.2. Mg Reducing Agent

Instead of using Na as reactant, a solid state displacement reaction between $NiCl_2$ and Mg, induced by mechanical milling [275], was employed for the production of fine Ni powders. The end product was leached with dilute HCl to obtain the nickel powder with sizes ranging between about 10 to 500 nm. It has been observed that unlike the results on reduction reaction in ZnO/Ti and CuO/Fe systems, interruption during milling of $NiCl_2$/Mg prolongs the start of ignition. A critical combination of intimate mixing of the reactants with freshly formed surfaces, structural strains, and a milling induced temperature rise is necessary for the ignition to take place.

Such a Mg reactant chemical reaction has also been used for the reduction of tantalum chloride by magnesium during reaction milling [276]. The reaction used is

$$2TaCl_5 + 5Mg \rightarrow 2Ta + 5MgCl_2 \quad (\Delta G = -356 \text{ kcal})$$

The vial temperature, which was measured during milling, indicated that the *in-situ* mechanochemical reaction which has been found to occur is a combustion one. Crystalline Ta and $MgCl_2$ were identified immediately after the combustion (corresponding to an abrupt increase of the vial temperature) while further milling led to chloride amorphization. The ball mass has an important effect on the conditions required for combustion to occur.

A mechanochemical reduction of nickel oxide by graphite has been tested to produce ultrafine Ni [277]. Milling at ambient temperature did not result in the reduction of nickel oxide to nickel. However, milling significantly decreased the critical reaction temperature for the reduction, from 1350 K for the unmilled sample to 650 K for samples milled for 12 hours or longer. Reduction of NiO to Ni occurred during milling at elevated temperatures. The extent of the reaction during milling at elevated temperatures was dependent on the partial pressure of $CO_2$ in the sealed vial.

Ultrafine Mo particles can be produced as a result of the slow burning transition into detonation in the $MoS_2$–Mg mixture [see N. G. Danielian et al. *Mod. Phys. Lett. B* 5, 1301 (1991)] according to the following reaction:

$$MoS_2 + 2Mg \rightarrow 2MgS + Mo$$
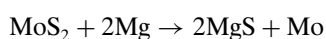
The mechanical treatment of the reactant mixture results in a considerable decrease of the ignition temperature and in a strong increase of the burning speed.

To close this section about the description of the mechanochemical synthesis of ultrafine metallic particles, we notice that similar methods can be used to prepare nanostructured intermetallic compounds [278].

The basis for the synthesis of Ti–Al alloys is the coreduction reaction induced mechanically:

$$6TiCl_4 + 2AlCl_3 + 7CaH_2 + 8Mg \rightarrow 2Ti_3Al(H)$$
$$+ 7CaCl_2 + 8MgCl_2$$
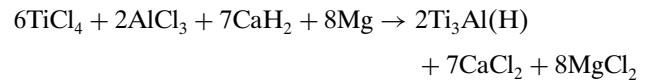
The reaction product after leaching is $Ti_3Al(H)$ with hydrogen in interstitial sites of the $Ti_3Al$ structure. The use of $CaH_2$ as a reducing agent in the given example results in the formation of $Ti_3Al(H)$ which is more passive to oxidation than $Ti_3Al$.

Nanocrystalline TiC was synthesized by the displacement reaction

$$TiCl_4 + 2CaC_2 \rightarrow TiC + 2CaCl_2 + 3C$$
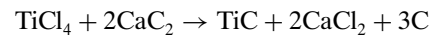
The reaction has also been modified to avoid the formation of free carbon, by the addition of Mg:

$$2TiCl_4 + CaC_2 + 3Mg \rightarrow 2TiC + CaCl_2 + 3MgCl_2$$
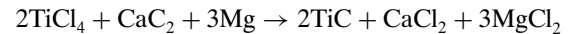
### 5.2.3. Si, Fe Reducing Agents

The mechanochemical synthesis of refined Ag and Zn composite powders starting from oxides using Si and Fe as reducing agents was reported by de la Torre et al. [279]. $Ag_2O$ and ZnO powders were reduced by a mechanochemical process using Si and Fe as reducing agents.
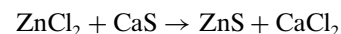
A number of advantages are conferred to the end products Ag–$SiO_2$, Ag–$Fe_2O_3$, Zn–$SiO_2$, and ZnO–$Fe_2O_3$ submicrometric composite products prepared in that way. The active oxides, with nanometer-sized tailored particles, are for instance homogeneously dispersed into the reduced metal matrix.

## 5.3. Formation of Semiconductor Nanoparticles

Mechanochemical synthesis has been applied to the large scale preparation of ultrafine Si nanoparticles by ball-milling [280]. Si nanoparticles were synthesized by ball-milling of mixtures of graphite and of $SiO_2$ powders followed by subsequent annealing at 150 °C.

## 5.4. Sulphide Reduction or Production

Mechanical milling [281] of $ZnCl_2$ and CaS mixtures resulted in the formation of 500 nm ZnS particles containing aggregates of 12 nm crystallites according to the following reactions:

$$ZnCl_2 + CaS \rightarrow ZnS + CaCl_2$$

$$ZnCl_2 + CaS + 3.6CaCl_2 \rightarrow ZnS + 4.6CaCl_2$$

$$ZnCl_2 + CaS + 8.2CaCl_2 \rightarrow ZnS + 9.2CaCl_2$$

The addition of 71 vol% $CaCl_2$ as a diluent to the reactants resulted in the formation of separated 16 nm particles of ZnS. Using mechanically alloyed CaS (10–50 nm particle size) enabled the synthesis of isolated ZnS particles 7–9 nm in size.

Such a method is claimed to be applicable for the production of nanoparticles of other II–VI semiconductors, of ternary II–VI semiconductors such as CdHgSe and CdSTe, or of heavily doped semiconductors such as Zn(Mn)S as well as that of metal sulphide compounds.

Solid-state room temperature reduction and exchange reactions of metal (M) sulphides (FeS, $WS_2$, $MoS_2$, $Cu_2S$, CoS, PbS, ZnS) [282] were driven by ball-milling of powder mixtures of a sulphide and of either a reductant (R = Al, Mn, Fe, Si) or an exchange compound (CaO).

Milling results in a complete reduction of the metal sulphide and in the formation of nanocomposites made of M and R sulphide. Exchange reactions with CaO show the formation of M oxide–CaS nanocomposites:

$$MS + R \rightarrow RS + M$$

$$MS + CaO \rightarrow CaS + MO$$
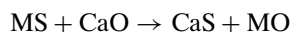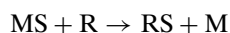
Iron sulphides were for instance reduced by aluminum, manganese, and silicon, copper sulphides by aluminum and iron, and cobalt, lead, and zinc sulphides by aluminum. Exchange reactions took place for iron, tungsten, and molybdenum sulphides.
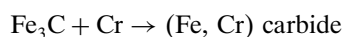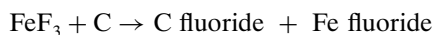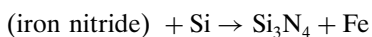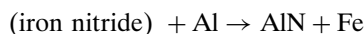
## 5.5. Nanocomposite Formation

### 5.5.1. Magnetic Nanocomposites

Magnetic nanocomposites [283] of small iron particles embedded in nonmagnetic zinc oxide have been prepared by ball-milling (Spex machine) via *in-situ* displacement reactions:

$$Fe_3O_4 + 4Zn \rightarrow 3Fe + 4ZnO$$
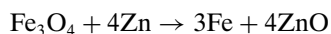
The final particle size is about 9 nm as estimated from X-ray diffraction line broadening. The end product is a semi-hard magnetic material exhibiting a significant volume fraction of superparamagnetic Fe particles.

Solid-state room temperature exchange reactions of iron nitride, fluoride, and cementite $Fe_3C$ with silicon or aluminum, carbon, and chromium respectively were investigated [284] according to

$$(\text{iron nitride}) + Al \rightarrow AlN + Fe$$

$$(\text{iron nitride}) + Si \rightarrow Si_3N_4 + Fe$$

$$FeF_3 + C \rightarrow C \text{ fluoride } + \text{ Fe fluoride}$$

$$Fe_3C + Cr \rightarrow (Fe, Cr) \text{ carbide}$$

A partial transfer of nitrogen from iron nitride to aluminum and silicon, with the formation of aluminum and silicon nitrides, was evidenced. Partial transfer of fluorine was obtained too by reaction milling. A mixed, largely amorphous (Fe,Cr) C alloy was formed. The as-milled powders have small crystallite sizes (10–20 nm) and may

thus be considered as nanocomposites composed of AlN–$Fe_{2.5}N$–(FeAl) alloy, $Si_3N_4$–$Fe_{2.5}N$–(FeSi) alloy, $FeF_3$–$FeF_2$–$FeF_3(H_2O)_{0.33}$–$CF_n$–$(CF_{1.1})_n$ and (Fe,Cr)carbide–(Fe,Cr)C amorphous alloy.

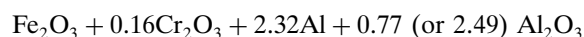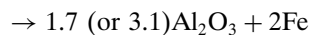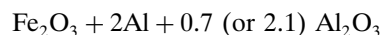### 5.5.2. Synthesis of Nanocermets (Oxide–Metal Nanocomposites)

Metal–matrix composites (MMCs) have been of interest for several decades. Several methods have been developed to incorporate large volume fractions of oxides, carbides, borides, and other particles into metallic matrices. The mechanical alloying technology has been used to produce strengthened MMCs with oxide dispersions and controlled fine microstructures. Derived from mechanical alloying, the mechanochemical process is suited for the formation of complex precursor oxides for advanced materials technology applications. Schaffer and McCormick [285] reported the direct synthesis of metallic Cu by milling mixtures made of its oxide and of various reducing elements such as Al, Ca, Ti, Mg, Mn, Fe, and Ni.

### 5.5.3. Alumina–Metal Nanocomposites

Nanometer sized alpha-$Al_2O_3$–M composites (M = Fe, V, Cr, Mn, Co, Ni, Cu, Zn, Nb, Mo, W, Si, Fe alloys) were synthesized by solid-state reduction reactions occurring during room-temperature ball-milling of mixtures of a metal oxide ($M_xO_y$) and aluminum ($Al_{2y/3}$) [286, 287].

The sizes of both alumina and metal crystallites obtained in that way are close to 10 nm for powders processed in a vibratory mill (24 hours). In a planetary mill, nanocrystalline phases have crystallite sizes about 2–3 times larger after milling for about one hour with a smaller powder-to-ball ratio.

Nanocomposite powders [(Fe or Fe–Cr alloy)/alpha alumina (75 and 85 vol%)] were prepared [288] by room temperature high-energy milling powder mixtures of haematite (and chromium oxide) with aluminum and alumina in a high-capacity mill according to the following reactions:

$$Fe_2O_3 + 2Al + 0.7 \text{ (or 2.1) } Al_2O_3$$
$$\rightarrow 1.7 \text{ (or 3.1)}Al_2O_3 + 2Fe$$

$$Fe_2O_3 + 0.16Cr_2O_3 + 2.32Al + 0.77 \text{ (or 2.49) } Al_2O_3$$
$$\rightarrow 1.93 \text{ (or 3.65) } Al_2O_3 + 2Fe + 0.32Cr$$

Both the metallic and ceramic phases have crystallite sizes smaller than 15 nm for all the investigated compositions. A spinel oxide, hercynite, $FeAl_2O_4$, is formed during the reduction reaction and is retained in small amounts in the final powders. In the Fe–Cr/$Al_2O_3$ composite, the metallic matrix has a lower Cr content than expected as a significant amount of Cr is dissolved in alumina.

The solid-state reduction of $Fe_2O_3$ (haematite) by ball-milling with Al or Mg has been investigated by Nasu et al. [289] according to the following equations:

$$Fe_2O_3 + 2Al \rightarrow 2Fe + Al_2O_3$$

$$Fe_2O_3 + 3Mg \rightarrow 2Fe + 3MgO$$
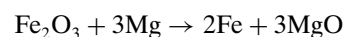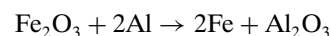
A partial substitution of Fe by Al in the alpha-Fe lattice has been revealed by Mössbauer analyses.

For the second reaction, the reduction of $Fe_2O_3$ results in the formation of alpha-Fe, MgO, and an unknown compound (presumably a wustite-like $Fe_{1-x}Mg_xO$ compound).

Takacs has studied the reduction of magnetite by aluminum by the way of a displacement reaction induced by mechanical alloying [290]. An explosive solid-state reaction occurs in a wide composition range as revealed by the sudden temperature rise of the grinding media. The reduction of $Fe_3O_4$ to Fe by metallic Al is consistent with the following reaction:

$$3Fe_3O_4 + 8Al \rightarrow 9Fe + 4Al_2O_3$$
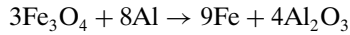
Off–stoichiometry lengthens the incipient stage of the reaction and changes the reaction products. A slight reduction of the amount of Al results in the formation of hercynite, $FeAl_2O_4$, instead of $Al_2O_3$; an excess of Al suppresses the formation of the metastable gamma-$Al_2O_3$ phase and of $FeAl_2O_4$ and results in a disordered bcc alpha-FeAl solid solution and alpha-$Al_2O_3$.

Shengqi et al. have investigated the solid-state reaction of the Al/CuO couple by high-energy ball-milling [291]. A sole reduction occurs for an Al content of 20 wt%. When the amount of Al exceeds 20 wt%, along with the reduction leading to the formation of alumina, a synthesis reaction occurs simultaneously. As the amount of Al increases, the reaction products are $Cu_9Al_4$, $CuAl_2$, or a Al(Cu) solid solution, respectively.

### 5.5.4. Silica–Metal Nanocomposite Formation

The reduction induced by ball-milling of hematite ($Fe_2O_3$) by silicon takes place through the formation of intermediate phases containing divalent iron [292].

The phases are oxides (magnetite and wüstite) and silicates (fayalite and iron silicate glass). In the stoichiometric conditions, the reduction is not fully achieved leading to an end product consisting of alpha-Fe and divalent iron in a silicate glass. In the case of an $Fe_2O_3$ excess in the starting powder mixture, the final product is also composed of fayalite and magnetite.

On the basis of the intermediate compounds which were characterized by Mössbauer spectrometry, during the evolution of the reaction, the following steps have been proposed to describe the oxygen transfer:

(1)  $2Fe_2O_3 + Si \rightarrow 4FeO + SiO_2$
     $FeO + Fe_2O_3 \rightarrow Fe_3O_4$

(2)  $2FeO + SiO_2 \rightarrow Fe_2SiO_4$
     $xFeO + SiO_2 \rightarrow Fe_xSiO_{2+x}$
     $FeO + Si \rightarrow Fe + SiO_2$

(3)  $Fe_3O_4 + 2Si \rightarrow 3Fe + 2SiO_2$
     $Fe_xSiO_{2+x} + x/2 \rightarrow xFe + x/2SiO_2$

Corrias et al. have prepared Ni–silica, Cu–silica [293], and Fe–silica [294] nanocomposites by ball-milling according to the following reactions:

$$2NiO + Si \rightarrow 2Ni + SiO_2$$

$$2CuO + Si \rightarrow 2Cu + SiO_2$$
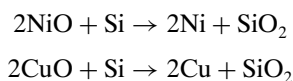
In the first reaction, oxygen is directly transferred from NiO to Si which is completely oxidized into silica, while the stoichiometric quantity of NiO is reduced to Ni. The sizes of the Ni crystallites are in the nanometer range. Similar milling processing conditions, which have applied to mixtures containing CuO, give rise to the formation of Cu(I) intermediate products.

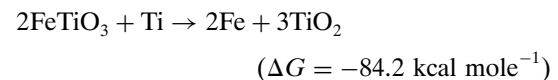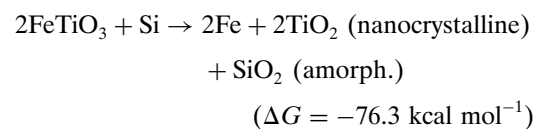### 5.5.5. Other Nanocomposite Formation

In a study of the dynamics of planetary ball mills, Dallimore and McCormick have investigated the CuO/Ni displacement reaction milling kinetic [295]. A two-dimensional, discrete element method software (so-called DEM simulation) has been developed to predict ball motion in a planetary ball mill. Various models have been assessed to simulate actual milling impacts. They have been used to study the relevant parameters of the kinetics of the CuO/Ni displacement reaction propagated under these conditions. It was concluded that the distribution of the impact energies does not significantly affect reaction propagation over the range of the investigated speeds.

The structural evolution of rod-milled $Cu_2O$ and Ti powders during mechanical solid-state reactions has been studied by El-Eskandarany [296]. Cuprous oxide is reduced to metallic copper by elemental titanium in such processing conditions. The end product is a mixture of nanocrystalline Cu and $TiO_2$ powders with an average crystallite size of 7 nm.
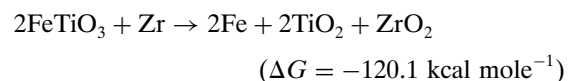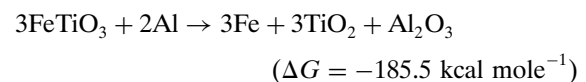
### 5.5.6. Reduction of Minerals: The Case of Ilmenite

The mechanochemical reactions of ilmenite with different additives have been investigated by several authors.

Chen et al. [297] have reported the reactions with Si and Ti. The results can be summarised as follows:

$$2FeTiO_3 + Si \rightarrow 2Fe + 2TiO_2 \text{ (nanocrystalline)}$$
$$+ SiO_2 \text{ (amorph.)}$$
$$(\Delta G = -76.3 \text{ kcal mol}^{-1})$$
$$2FeTiO_3 + Ti \rightarrow 2Fe + 3TiO_2$$
$$(\Delta G = -84.2 \text{ kcal mole}^{-1})$$

The reactions with Al and Zr differ from the previous ones as they result in the formation of a mixture of alpha-Fe and of a multinary amorphous phases. Therefore, ball-milling induces not only reduction/oxidation reactions but also new chemical reactions:

$$3FeTiO_3 + 2Al \rightarrow 3Fe + 3TiO_2 + Al_2O_3$$
$$(\Delta G = -185.5 \text{ kcal mole}^{-1})$$
$$2FeTiO_3 + Zr \rightarrow 2Fe + 2TiO_2 + ZrO_2$$
$$(\Delta G = -120.1 \text{ kcal mole}^{-1})$$

Mechanically induced chemical reactions between $FeTiO_3$ and Si [298] lead to the formation of elemental iron, $TiO_2$,

and metal silicides, depending on the Si content. The products are increasingly reduced as the molar ratio of silicon to ilmenite increases from 1:2 to 2:1. The reaction has been found to lead to the formation of $TiO_2$ and elemental iron. Further reduction of the $TiO_2$ to $Ti_nO_{2n-1}$ phases then occurred in parallel with iron silicide formation. The final stage is the reduction of the $Ti_nO_{2n-1}$ phase to titanium silicide. Under a high intensity impact, the reaction proceeds more rapidly than under low intensity impact.

Milling of a mixture of ilmenite and aluminum [299] leads to reaction within the mill forming $TiAl_3$, $Fe_4Al_{13}$, $Al_2O_3$. The same reaction occurs in unmilled powders after heating to a temperature higher than 850 °C for 1 h.

To increase the efficiency of the preceeding reduction process, the carbothermic reactions were extensively investigated [300].
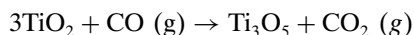
The chemical reactions that occur during the reduction process can be conveniently separated into a solid-state reduction (typically from 860 to 1000 °C),

$$FeTiO_3 + C \rightarrow Fe + TiO_2 + CO \quad (gas)$$
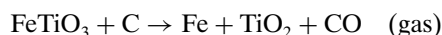
a gaseous reduction (typically above 1000 °C),

$$FeTiO_3 + CO\ (g) \rightarrow TiO_2 + Fe + CO_2\ (g)$$
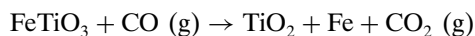
and a reduction of rutile (typically above 1200 °C),

$$3TiO_2 + CO\ (g) \rightarrow Ti_3O_5 + CO_2\ (g)$$

After ball-milling of a carbon–ilmenite mixture at room temperature, ilmenite was found to be reduced to rutile and alpha iron during subsequent low temperature annealing. The reduction temperature and the reduction kinetics for production of this intermediate reduction state ($TiO_2$) depend critically on the milling conditions:

(1) With increasing milling time, the reduction temperature decreases and the reaction rate increases.
(2) High milling intensity also leads to a lowering of the annealing temperature for the main reduction step to rutile.

A parametric study of the mechanically activated carbothermic reduction of ilmenite has been performed by Welham [301]. As reported by Welham, ilmenite ($FeTiO_3$) is the primary global source of titanium dioxide which is commonly used as a whitening agent in paper manufacture and as a pigment in paint manufacture:

$$FeTiO_3 + C \rightarrow Fe + TiO_2 + CO$$
$$C + CO_2 \rightarrow 2CO$$
$$FeTiO_3 + CO \rightarrow Fe + TiO_2 + CO_2$$
$$nTiO_2 + CO \rightarrow Ti_nO_{2n-1} + CO_2$$
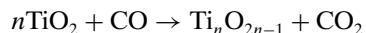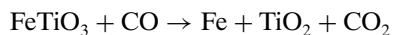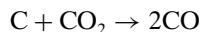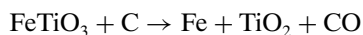
The separation of iron from titanium has been enhanced by milling ilmenite and coal powder together prior to annealing. The subsequent solubility of iron was maximized when the fraction of the elemental iron after annealing was at a maximum. On the other hand, titanium solubility was minimized when rutile was the predominant titanium product.

The leaching step is much faster than conventional processing, primarily due to the much finer particle size. No elemental iron could be detected by X-ray diffraction after leaching. Leaching indicated that the reduction of rutile was detrimental to iron removal and led to increased titanium dissolution.

### 5.5.7. Reduction of Minerals: The Case of Bastnaesite

A nonthermal process for extracting rare earths from bastnaesite by means of mechanochemical treatment has been developed by Zhang and Saito [302]. Bastnaesite ($ReCO_3F$, Re = rare earths) is one of the most important resources containing rare earth elements such as La and Ce. There are several hydrometallurgical methods for extracting them from bastnaesite. They can be classified into two process methodologies: one is the acidic method using $H_2SO_4$ solution; the other the alkali method using NaOH. In the former, bastnaesite is dissolved in a concentrated acid solution which is heated to 473 K to form rare earth sulfates. Another method is the dissolution of bastnaesite in acid solution after roasting at 1073 K. In this case, the initial material is decomposed into oxide forms $Re_2O_3$. One of them, $Ce_2O_3$, is oxidized to $CeO_2$ which is hard to dissolve in the acid solution. Therefore acid leaching is used for separating soluble rare earths from $CeO_2$.

In contrast, several investigations using the alkali method have been reported. One is the decomposition of bastnaesite by a 45% NaOH solution heated at near the boiling point. Another involves the decomposition of minerals by a NaOH solution in an autoclave or by a molten NaOH medium. In any case, high temperature treatments are needed to extract the rare earths from bastnaesite. Therefore an alternative process operated at relatively low temperature and mild conditions would be desirable:

$$LaCO_3F + 3NaOH \rightarrow La(OH)_3 + Na_2CO_3 + NaF$$
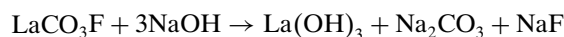
Extraction of the rare earth elements such as La, Ce, Pr, Nd, Sm included in bastnaesite was attempted with NaOH powder using a planetary mill.

(1) Milling of the mixture composed of bastnaesite and NaOH powders permits the formation of rare earth hydroxides and Na compounds. The $Ce(OH)_3$ and $Pr(OH)_3$ so formed are changed into the respective oxides in the high oxidation state during and after the milling operation.
(2) The rare earth hydroxides/oxides can be separated from the Na compounds by washing with distilled water at room temperature. Most of the carbonates and 75% of the fluorides are removed from the milled mixture by the washing operation.
(3) The rare earth oxides are dissolved by either $H_2SO_4$ or HCl solutions at room temperature. Controlling the concentration of the $H_2SO_4$ solution is a key to the preferential extraction of La, Nd, Sm from Ce and Pr in the leaching stage. In addition, milling of the mixture composed of bastnaesite and NaOH powders plays a significant role in achieving a high yield of rare earth elements in the leaching of the washed sample.

# 6. ORDER–DISORDER TRANSFORMATIONS AND BALL-MILLING

## 6.1. Introduction

Order–disorder transformations, which have played a major role in the development of modern physical metallurgy, attract still a great deal of attention both for theoretical reasons and for their applications as high-temperature structural materials [303–307]. Further, recent potential applications of ordered alloys are based on peculiar combinations of magnetic, transport, and structural properties which are strongly dependent on chemical order (among others [308–311] and references therein). Notable examples are Heusler alloys such as $Co_2MnGe$, $Co_2MnSi$, or $Ni_2MnIn$ for spin-sensitive electronic devices which include magnetic memory and hard disk read-heads, or $Ni_2MnGa$ for actuators and sensors because giant deformations can be induced by an externally applied magnetic field to which the alloy responds much faster than to heating or cooling. Another notable ordered alloy is $Fe_{65}Co_{35}$, which has the largest room-temperature magnetization, but it is a soft magnet. A way to enhance the properties of permanent magnets is through "exchange coupling" between a hard material and a soft material with a large magnetization. Models show that the soft phase must have grains of about 10 nm diameter and that the hard phase too must have nanosized grains ([312] and references therein). An ideal exchange-coupled magnet, consisting of aligned grains of $Sm_2Fe_{17}N_3$ and of $Fe_{65}Co_{35}$, is expected to reach an energy product of about 125 MGOe [313]. For both applied and fundamental aspects, it is thus necessary to characterize and master the state of order of alloys, in particular for the more demanding class of nanostructured materials for which there are prospects of improved properties with respect to those of their classical counterparts and expectations of extended fields of applications.

Ordered intermetallics are usually found in rather narrow compositional ranges around simply expressed stoichiometric compositions which reflect the underlying existence of superlattices which are few in number. Reversibly ordered alloys have their critical ordering temperature $T_C$ which is lower than their melting temperature $T_m$ (examples are $L1_2$ $Cu_3Au$, $DO_3$ $Fe_3Al$, $DO_{19}$ $Ti_3Al$, $L1_0$ $CuAu$, B2 FeCo, B2 CuZn). By contrast, permanently ordered alloys have only a virtual ordering temperature $T_C$ as it is higher than $T_m$ (examples are $L1_2$ $Ni_3Al$, B2 NiAl, $L1_0$ TiAl) [303, 304]. Reversibly ordered alloys are the sole alloys which can in principle be retained in a disordered nonequilibrium state at temperatures lower than $T_C$ by a heat treatment followed by a quench. As discussed by Cahn [303, 304] thermal treatments of the latter alloys falls into three categories: (1) alloys which are easily disordered or ordered by slow cooling, (2) alloys in which the self-diffusivity is so high that disordering is difficult at normal quenching rates, and (3) alloys in which the self-diffusivity is so low that it is difficult to order them even by very slow cooling. Other methods may be used to drive order–disorder transformations, notably irradiation [35, 314]. As reviewed (and modeled) by Martin and Bellon [35], two contradictory processes compete under

irradiation for establishing a steady-state configuration, on the one hand a chemical disordering proportional to the irradiation flux, on the other hand a reordering promoted by thermally activated point defects at a rate proprotional to the product of their concentration, their jump frequency, and their temperature-dependent driving force for ordering. The eventual steady-state configurations achieved by such alloys depend on the "forcing" conditions. Dynamical equilibrium phase diagrams have been determined theoretically and experimentally [35].

Plastic deformation is also a means of changing the state of order of alloys which was and is still used to prepare and investigate structures far from equilibrium. The changes of magnetic properties of B2 $Fe_{1-x}Al_x$ $(0.30 \leq x \leq 0.40)$ alloys during compression testing were for instance studied recently [315]. A technique to plastically deform particles is simply ball-milling and the focus will be hereafter on its effect on order–disorder transformations. Earlier works are about the influence of grinding on the magnetic properties and on the hyperfine magnetic properties [nuclear magnetic resonance (NMR), Mössbauer spectroscopy] of B2 FeAl [316] and of $L2_1$ Heusler alloys $X_2MnY$ (X = Ni, Cu, Pd, Y = Al, In, Sn, Sb) [317, 318] (Fig. 7). The crushing of some Heusler alloys to prepare powdered samples was indeed observed to change drastically their magnetic properties, for instance reducing the saturation magnetization to about one-third of its value, increasing the NMR signal intensity, and generating satellite lines in $Pd_2MnSn$ [318, 319]. These investigations were thus motivated by the need to eliminate the defects produced by cold-work (dislocations, antiphase boundaries, atomic disorder) by annealing treatments. More recent studies of ball-milling of ordered alloys are still aimed at characterizing ground alloys with nanometer-sized grains and their reordering kinetics if disordered but the determination of steady states "under" milling has become central to that research field [35, 314].

The studies of ball-milled ordered alloys typically show a large accumulation of defects during milling which can drive phase transformations such as amorphization [320–322]. The reverse transformation, disordering a B2-ordered $Fe_{60}Al_{40}$ nanocrystalline alloy during high-energy ball-milling, has also been studied recently [323]. We shall first describe a study of mechanical milling of $X_2MnSn$ Heusler alloys to emphasize the possibility that thermally induced disorder differs from mechanically induced disorder. Then, we will describe an example of reordering of disordered nanocrystalline FeV alloys by low-temperature annealing.
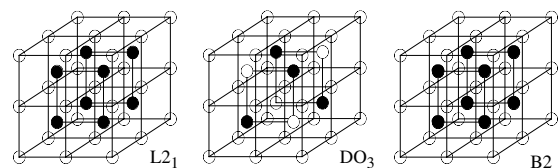


**Figure 7.** The ordered structures: $L2_1$, $D0_3$, and B2, shown on an underlying lattice of eight bcc unit cells. In the $L2_1$ structure of $X_2MnSn$, the X atoms occupy the white sites, the Mn occupy the gray, and the Sn occupy the black.

## 6.2. Disordering of Ordered Alloys by Ball-Milling: The Example of X₂MnSn Heusler Alloys

Heusler alloys X$_2$YZ, more particularly X$_2$MnSn alloys in which Mn atoms carry a magnetic moment of more than 3 $\mu_B$, are excellent candidates for evidencing such behavior. Their structure is indeed reasonably simple (Fig. 7) and their magnetic (and hyperfine magnetic) properties are well documented (see [324–331] among others). The L2$_1$ structure may contain two types of antiphase boundaries (APBs) with fault vectors of $a/4\langle 111\rangle$ (B2 APBs) and $a/2\langle 100\rangle$ (L2$_1$ APBs) respectively, where $a$ is the lattice parameter [317, 318]. First and second nearest-neighbor Mn atoms are altered in the APBs with the formation of first nearest-neighbor Mn–Mn pairs in L2$_1$ APBs and of second nearest-neighbor Mn–Mn pairs in B2 APBs. As the magnetic properties are strongly dependent on the interactions between Mn atoms, a difference in the nature of thermal APBs and of APBs formed during plastic deformation may produce large magnetic differences between thermally and mechanically disordered alloys. The effect of cold work simply produced by crushing samples with a pestle in an agate mortar varies indeed considerably from one Heusler alloy to another [316–319]. A significant reduction of saturation magnetization, by about 60%, with cold work is for instance observed to occur in Pd$_2$MnSn [317–319] and is attributed to a high density of B2 antiphase boundaries created by plastic deformation [317, 318]. By contrast, crushing is supposed to bring about only L2$_1$ APBs in Pd$_2$MnSb because the reduction of magnetization is very small for that alloy [318]. The Heusler alloys Cu$_2$MnSn [332] and Cu$_2$MnAl [333] were found to be unstable when milled for short and for long times respectively.

The disorder induced thermally in Ni$_2$MnSn was compared to the disorder induced by ball-milling using neutron diffraction and [119]Sn Mössbauer spectrometry [332]. As-cast Ni$_2$MnSn alloys were annealed under low-pressure argon at a temperature $T_a$ ($T_a$ = 773, 973, 1023, 1073, 1173, 1273 K) for 1 month and were quenched into water. Samples were milled under an argon atmosphere in a Fritsch P7 planetary mill for different times from 0.5 to 20 h with different powder-to-ball weight ratios, $R$, from 1/15 to 1/50. The magnetic properties (Fig. 8) and the hyperfine magnetic field distributions $P(H)$, where $P(H)\Delta H$ is the fraction of [119]Sn atoms whose hyperfine magnetic field is between $H$ and $H + \Delta H$ (Fig. 9), of as-milled samples differ strongly from those of samples quenched from high temperatures. The Curie temperature $T_c$ decreases sligthly from 343(3) to 333(3) K when $T_a$ increases from 773 to 1073 K. The magnetization curves of all as-quenched samples are similar to those of Figure 8 (left). In contrast, Figure 8 (right) shows that drastic changes of the magnetic structure take place in ground samples. As-milled Ni$_2$MnSn, which remains of the L2$_1$ type with a tendency toward B2 type of order, has a disordered magnetic structure while as-quenched samples remain basically ferromagnetic [332]. Further, neutron diffraction patterns indicated that the disorder retained by quenching from $T_a$ is similar to the disorder measured by *in-situ* diffraction experiments at temperatures identical or
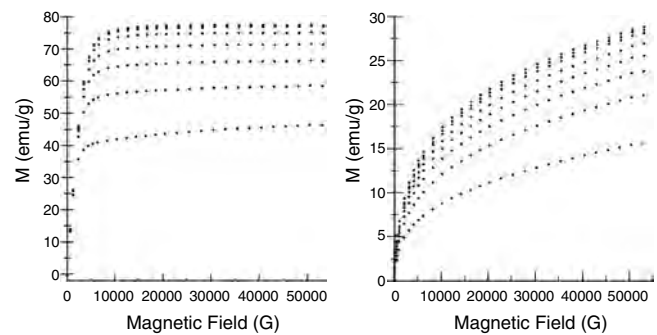


**Figure 8.** Magnetization curves at 5, 30, 50, 100, 150, 200, 250, 300 K (from top to bottom) of Ni$_2$MnSn quenched from 1273 K (left) and ground (right) (note the difference in scales).

close to $T_a$. High-temperature neutron diffraction measurements at 1080, 1180, and 1265 K show that the structure of Ni$_2$MnSn is still of the L2$_1$ type above 980 K and not of the B2 type as proposed in the literature [334]. Moreover, the lattice parameter of as-quenched samples decreases regularly from 0.6045(1) to 0.6015(2) nm for 973 K = $T_a$ = 1273 K while it is 0.6022 nm for the ground sample.

Figure 9 shows the [119]Sn Mössbauer spectra at 80 K of as-quenched samples and the associated hyperfine magnetic field distributions $P(H)$. The 119 Sn hyperfine magnetic field distributions of as-quenched samples at 80 K have two characteristics: a main peak near 90 kG, the sole contribution expected for a perfectly ordered alloy, and a broad
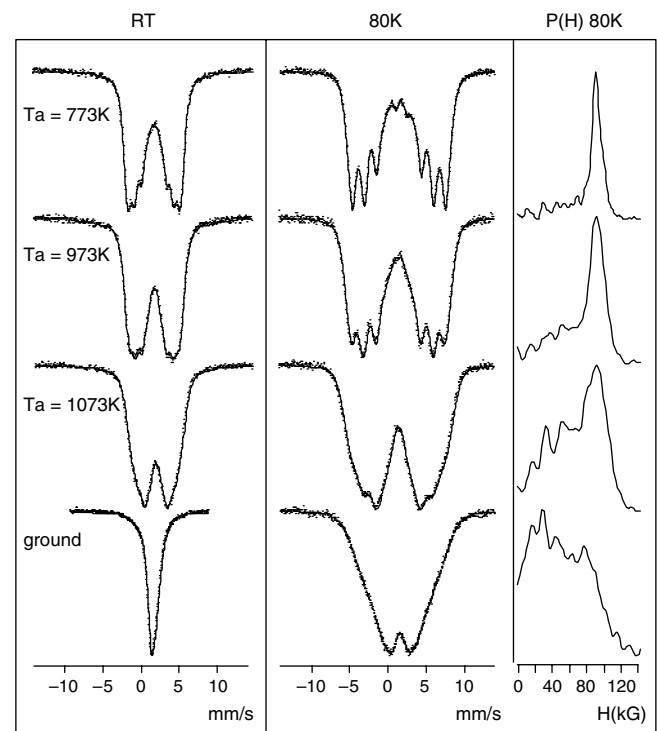


**Figure 9.** [119]Sn Mössbauer spectra at room temperature and at 80 K of Ni$_2$MnSn either quenched from $T_a$ or ground and hyperfine magnetic field distributions $P(H)$ associated with the spectra recorded at 80 K.

low-field tail (Fig. 9) [332]. The increase of the weight of the latter contribution with $T_a$ reflects the greater chemical disorder retained by quenching from higher $T_a$. This increase reflects the greater chemical disorder retained by quenching from higher $T_a$. The main peak of $P(H)$ remains at the same position for all $T_a$. In contrast, spectra from the as-milled samples differ strongly from those of as-quenched samples with broad, almost featureless, field distributions without a main peak near 90 kG. The mean field at 5 K was found to be reduced from 92 kG for perfect order to 69 kG for $T_a = 1273$ K and to 55 kG for ground samples milled long enough to be in a steady state. Hyperfine properties show thus that the magnetic disorder in ground samples differs from the magnetic disorder in as-quenched samples in agreement with magnetic measurements. These results suggest that in the as-milled samples there is a broad distribution in both magnitudes of Mn moments and angles between them. Changes of magnetic (and hyperfine magnetic) properties combined with the strong reduction of the intensity of the (111) superlattice neutron diffraction line in milled samples confirm that disorder induced by the shear deformation of grinding differs from the disorder induced by temperature. Therefore, it appears impossible to find an annealing temperature that can provide as-quenched $Ni_2MnSn$ samples with the same chemical disorder as for milled samples. These conclusions appear to be consistent with the preferential formation of $L2_1$ APBs and of B2 APBs in annealed alloys and in as-milled alloys respectively. Similar differences between thermal and mechanical disorder were found for $Co_2MnSn$ alloys [332]. Doubt is thus cast upon the universal validity of phase diagrams of ground ordered alloys which consider that mechanical energy and thermal energy have identical effects.

## 6.3. Reordering of Ground Disordered Alloys

The high density of defects of materials disordered by milling, especially vacancies and grain boundaries, enhance the kinetics of ordering, enabling studies at lower temperatures and more practical times than in coarse-grained quenched alloys. For example, a metastable B2 phase has been prepared in Fe–V alloys with equiatomic compositions by quenching from above ~1500 K and annealing the unstable bcc phase for a few hours at 870 K [335–337], or for a few days at temperatures between 700 and 800 K [337]. Annealing for only 8 h at 723 K is needed to reach the steady state of B2 order for as-milled bcc $Fe_{0.53}V_{0.47}$ [338].

The study of ordering in nanocrystalline alloys is itself a topic of widespread current interest. The formation of B2, $L1_2$, and $D0_3$ order in several nanocrystalline alloys has been reported, including Ti–Al, Fe–Al, Fe–Si, Fe–Co, Ni–Al, and Cu–Au, sometimes with ternary additions [339–358]. These studies have emphasized various aspects of defects and diffusion in nanostructured alloys, with comparison to coarse-grained materials. A number of features seem common to the reordering of chemically disordered nanocrystalline materials, in spite of differences in their methods of synthesis (e.g., ball-milling [339–340, 344, 346–349, 352–353, 355], plastic deformation [356], gas-phase condensation with compaction [350, 351], sputtering [345], ion irradiation

[357]), microstructures (isolated clusters [345] or more typically micrometer-sized particles composed of nanometer-sized grains), and ordered structures. Reordering can occur at low temperatures and involves only few jumps of nonequilibrium vacancies that were not promptly annihilated at sinks [346, 350–353, 356–358]. Grain boundaries probably prevent order from propagating from one grain to another [344, 348]. It is less clear if chemical disorder exists near grain boundaries or antiphase boundaries.

A curious feature of ordered nanocrystals is that the steady-state value of the long-range order (LRO) parameter is generally lower than that of bulk samples [345, 348–351]. For example, the relative long-range order parameter of $Fe_{0.53}Al_{0.47}$ synthesized by gas-phase condensation and high-pressure compaction, annealed at 800 K and below, stabilizes at 0.8 instead of increasing to 1.0 [350, 351]. Recent studies lead to the conclusion that this suppressed order parameter is not intrinsic to the nanocrystalline structure but that it is a kinetic effect associated with low temperatures of annealing. The example of the ordering of ground nearly equiatomic Fe–V alloys is described.

## 6.4. Ordering of Nearly Equiatomic Nanostructured Fe–V Alloys

The equilibrium Fe–V phase diagram shows complete mutual solubility of Fe and V in a bcc $\alpha$-phase at high temperatures and shows a $\sigma$-phase below ~1500 K in the central part of the diagram. Owing to the slow kinetics of the $\alpha \rightarrow \sigma$ transformation, as also found for nearly equiatomic Fe–Cr alloys, the $\sigma$-phase formation can be bypassed kinetically, and a disordered bcc phase can be obtained at low temperatures by rapid cooling [335]. A chemical ordering transformation into an ordered B2 phase can then occur on the bcc lattice during annealing at low temperatures [336, 337]. For example, a metastable B2 phase has been prepared in Fe–V alloys with equiatomic compositions by quenching from above ~1500 K, and annealing the unstable $\alpha$-phase for a few hours at 870 K, or for a few days at temperatures between 700 and 800 K [335]. Although the B2 phase does not appear on the equilibrium phase diagram, a metastable Fe–V phase diagram for the A2 and B2 phases, without $\sigma$-phase, has been theoretically calculated [336].

Nanocrystalline nearly equiatomic bcc Fe–V alloys can be synthesized by mechanical alloying for instance [337] and then ordered by annealing at low temperatures [338]. The values of the LRO parameter $S$ are most reliable for the lower annealing temperatures, where enhanced kinetics in nanocrystalline materials allow steady state to be reached in reasonable times. The high density of grain boundaries in nanocrystals promotes the formation of $\sigma$-phase at higher temperatures. Although the formation of $\sigma$-phase is relatively sluggish, it is indeed much faster in these nanocrystalline Fe–V alloys than in coarse-grained Fe–V. In a conventional coarse-grained $Fe_{0.50}V_{0.50}$ alloy annealed for 120 h at 873 K, $\sigma$-phase forms only near free surfaces, and negligibly in the bulk [338]. A $Fe_{0.53}V_{0.47}$ alloy annealed for 100 h at 873 K is fully transformed into $\sigma$-phase while only 30 min suffice at 973 K. In contrast, the metastable steady state of $Fe_{0.53}V_{0.47}$ is in the B2 single-phase region between 700 and 873 K [338]. The LRO parameter, $S$,

of a B2 $Fe_{1-x}V_x$ alloy is $S = 2([Fe]_{Fe-1+x})$, where $[X]_Y$ $(X, Y = Fe, V)$ is the concentration of atomic species X on sublattice Y, where the designation Y for the sublattice refers to its majority species. The LRO parameter reaches its minimum value, $S = 0$, when the alloy is fully disordered while its maximum value is $S_m = 1 - 2|\Delta x|$, where $\Delta x = x - 0.5$, for a negligible concentration of vacancies.

Figure 10 presents the LRO parameter measured by neutron diffractometry as a function of annealing time at 723 K and other temperatures. At 723 K, $S$ increases rapidly at first and reaches a plateau between 8 and 24 h. The very small size of the ordered domains in the as-milled $Fe_{0.53}V_{0.47}$ is comparable to the 2.5 nm domain size reported for ball-milled B2 FeAl [352]. At 723 K, the ordered domain size increases with annealing time and matches the crystallite size after some hundreds of hours. Figure 11 compares the steady-state experimental values of the LRO parameter, $S$, as a function of $T/T_c$, along with LRO calculated by the cluster variation method, and from the classical Bragg–Williams model [338]. The experimental LRO parameters, $\sim0.80$, are smaller than the values expected for equilibrium. The measured steady-state LRO parameters for different V contents were found to be consistent with the aforementioned metastable Fe–V phase diagram [338]. The previous LRO parameters are close to those reported for nanocrystalline materials reordered at low temperature [350, 351]. The thermal stability of disordered mechanosynthesized $Ni_{40}Al_{40}T_{20}$ (T = Cr, Fe) was recently investigated [359]. The highest value of the long-range order parameter in mechanosynthesized NiAl was measured to be about 0.75 during reordering at 873 K. Grain growth was found to slow down once the order parameter reaches a steady value at any annealing temperature for the investigated alloys. Preliminary investigations indicate that reordering of disordered $Ni_2MnSn$ occurs already by annealing at 523 K for times as short as 5 hours [360].

The kinetics and mechanisms of chemical ordering could be altered by the nanocrystalline nature of the material. Any material with a $\sim7$ nm grain size has indeed a high density of grain boundaries. An even higher density of antiphase boundaries exists in these materials, since the
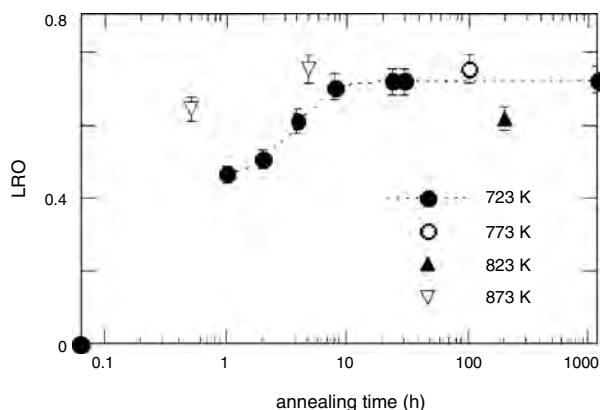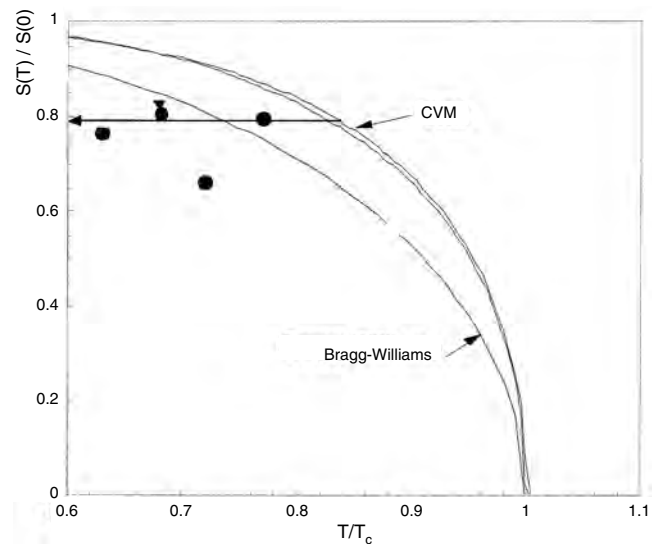


**Figure 11.** Reduced long-range order parameter of $Fe_{1-x}V_x$ as a function of $T/T_c$ calculated with the CVM model and the Bragg–Williams model. Full circles are experimental values of the steady state values for $x = 0.47$ and full triangle are for $x = 0.39$. Reprinted with permission from [338], T. Ziller et al., *Phys. Rev. B* 65, 024204 (2002). © 2002, American Physical Society.

domain sizes are only 2–3 nm in the early stages of ordering. Monte Carlo simulations of ordering with a vacancy mechanism at low temperatures have revealed a high density of antisite defects once ordered domain formation is complete [361–363]. The high antisite population is quite different from the clean ordered domains during ordering by interchanges of atom pairs, for example, even when the domain structures are comparable [361]. Antiphase domain boundaries serve as traps for vacancies [361], reducing their effectiveness in annealing out the antisite atoms, and the motion of the APBs is not always conservative. This transient population of antisite atoms is responsible for a slow coarsening regime at low temperature [363]. Once the APBs are eliminated, the last antisite atoms are removed slowly [361–363]. Mössbauer spectroscopy proved useful to quantify the fraction of antisite Fe atoms in partially ordered FeV alloys and to evidence the role of antisite defects [338]. The fraction of antisite atoms was shown to decrease when $S$ increases at early annealing times. A further reduction of the latter fraction was measured when nanocrystals are single domains without APBs. The steady-state LRO parameter is smaller than the equilibrium value because of residual antisite defects that do not anneal out on the time scale of the experiments. The LRO parameters in these Fe–V alloys were not sensitive to grain growth. Little change in $S$ (about 0.7) was for instance observed at 723 K when most grain growth occurred [338]. The elimination of antisite defects requires some longer range diffusion, which is very slow in ordered domains at low temperatures. The kinetics at the later stages of annealing may also be suppressed by a low vacancy concentration. At the higher temperature of 873 K, however, once the domain size grows to the crystal size, $S$ then increases from 0.64 to 0.75, which is close to the value expected in thermodynamic metastable equilibrium (Fig. 11) [338].



**Figure 10.** Long-range order parameter at room temperature of as-milled $Fe_{0.53}V_{0.47}$ as a function of annealing time at different temperatures. Reprinted with permission from [338], T. Ziller et al., *Phys. Rev. B* 65, 024204 (2002). © 2002, American Physical Society.

In summary, reordering results first from the elimination of antiphase boundaries and second from the removal of the last antisite defects which is very slow in ordered domains at low temperatures. Thermal reordering takes place prior to recrystallization, and in a temperature range similar to the milling temperature [364]. The reduction of the steady-state value of the long-range order parameter is due to a kinetic effect associated with the low temperatures of annealing.

Besides their historical and practical importance [303–307], order–disorder transformations play an important role in the understanding of the physics of mechanical alloying. Some of the most convincing proof of the very existence of dynamical equilibrium under milling is for example provided by ground FeAl alloys [314, 358, 364] which further show that initially disordered alloys may reorder under milling if the pertinent parameters, a dynamical parameter and the milling temperature, are adequately chosen. As briefly described for Heusler alloys and as emphasized by Martin et al. [314, 358, 364], the destruction of long-range order is a result of the plastic shear of grains (e.g., one dislocation gliding along its slip plane leaves a planar stacking fault behind). Alternatively, one pair of jogged dislocations on a single slip plane leaves behind a tube of stacking faults, etc. Moreover, shear induced vacancies enhance the atomic mobility and hence speed up the reordering process in the time interval between two collisions. These mechanically induced "ballistic jumps" occur in a collective manner along the shear planes. As suggested by computer simulations, these space and time correlations of ballistic jumps might result in original microstructures [364].

# 7. ALLOYING BY HIGH-ENERGY BALL-MILLING (SUPERSATURATED SOLID SOLUTIONS)

## 7.1. Introduction

The fundamental problems of the mechanisms of mixing of elements by milling and of the resulting formation of phases such as extended solid solutions, in particular in binary metallic systems of elements which have limited solid solubilities or are immiscible in equilibrium, intermetallic compounds, amorphous phases, or the two-phase coexistence in alloys for certain concentration ranges are still thoroughly investigated. Some examples are Cr–Sn, Fe–Cr, Fe–Cu, Fe–Sn, Fe–Ta, Co–Cu, Ni–Cu, Ni–Ag, Cu–Ta, Ag–Cu [365–392]. The interest in the characterization and modeling of supersaturated solid solutions formed in a large number of systems with positive heats of mixing is obviously not restricted to mechanosynthesized materials but extends to materials produced by all kinds of methods [393–398].

To reach sound conclusions about their actual structures on a nanometer scale (are they compositionally homogeneous or decomposed?), techniques which yield both global information and local information on ground powders must be combined. In that way, it is possible to follow not only the average properties of powder particles but also their fluctuations in the whole sample both during milling and in as-milled materials. Single-phase structures have been, for instance, obtained by mechanical alloying in a broad concentration range in the archetypal Fe–Cu system, for example,

fcc Cu(Fe) solid solution for iron contents lower than 45 at% and bcc Fe(Cu) solid solution for iron contents higher than 55 at% [15–17, 23–27].

In between, the two phases coexist [379, 381]. However, some results of Mössbauer spectrometry and atom probe investigations indicate that these solid solutions are chemically heterogeneous on a nanometer scale [379, 381, 389–391]. In a recent work on nanocrystalline $Fe_yCu_{1-y}$ ($0.141 \leq y \leq 0.450$) alloys produced by ball-milling [390], Fernandez et al. used a small-angle X-ray scattering technique to conclude that the synthesized alloys are heterogeneous on a nanometer scale since composition fluctuations were detected inside nanocrystalline grains. Wanderka et al. [389] investigated the microstructure and composition on the nanometer scale of mechanically alloyed $Cu_{50}Fe_{50}$ with a tomographic atom probe. They concluded that samples contain nanometer-sized regions with strongly varying composition. Further, supersaturated solid solutions formed deep inside a miscibility gap through rapid quenching or solid state routes may have decomposition features on the scale of a few nanometers as shown recently for sputtered fcc Ag–Cu solid solutions [397] or for mechanically alloyed $Fe_{30}Cr_{70}$ alloys [392] and for milled as-cast $Fe_{30}Cr_{70}$ alloys as will be further discussed.

In the following, we denote as $p-A_xB_y$ the initial mixture of powders of element A and of powders of element B in the atomic ratio $x:y$.

## 7.2. Composition Fluctuations during Mechanical Alloying: Two Notable Times

Given milling conditions, $t_m$ is defined as the current milling time and the synthesis time $t_f$ as the *minimum* time needed to enter a stationary state in which all kinds of powder characteristics remain unchanged when milling for $t_m \geq t_f$ (hardness, magnetic properties, average grain sizes, crystallographic structures, etc.).

Besides the synthesis time, $t_f$, a second characteristic milling time $t_{cm}$ was considered and termed "chemical mixing time" [399], $t_{cm} \leq t_f$. To define it, let us consider for instance a binary mixture of elemental powders with a mean composition $A_{1-x}B_x$ (Fig. 12). Powder particles are initially either pure A or pure B. The time $t_{cm}$ is then the *minimum* milling time at which *all powder particles* have essentially the final chemical composition $A_{1-x}B_x$. The particle scale is relevant because $t_{cm}$ can be measured, for instance using a microprobe [399], and because it is the shortest possible synthesis time, $t_f \geq t_{cm}$. Even if they have the expected composition, powder particles may be made up of various phases whose structures and compositions may still evolve for $t_{cm} \leq t_m \leq t_f$ (Fig. 12). For $t_m \leq t_{cm}$, mixing occurs simultaneously at different scales with a broad distribution of characteristics from particle to particle. Both $t_f$ and $t_{cm}$ were obtained, as will be described, for $Fe_{1-x}T_x$ elemental powder mixtures ground in a planetary ball mill, with $x = 0.50, 0.70, 0.72$ for T = V, Cr, and Mn respectively [399]. The synthesis time depends strongly on the considered Fe–T alloy while chemical mixing times were estimated to be similar whatever the element $T$, $t_{cm} \approx 3$–4 h, in the milling conditions described in [399] (planetary ball mill Fritsch Pulverisette 7 with a powder-to-ball weight ratio of 1/20).
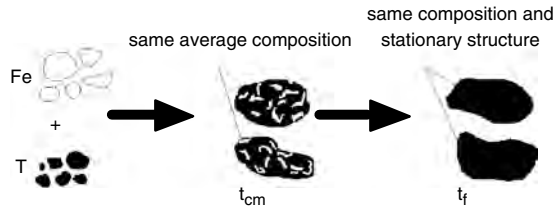
**Figure 12.** Two characteristic times, the chemical mixing time $t_{cm}$ and the synthesis time $t_f$, illustrated for milling of Fe–T elemental powder mixtures.

### 7.2.1. Simple Method to Estimate the Chemical Mixing Time

To estimate the chemical mixing time $t_{cm}$ of A and B, a powder mixture p-$A_{1-x}B_x$ is ground for a time $t_m$ and the A content $x(i, t_m)$ of every powder particle ($i = 1, \ldots, N$) is imagined to be measured with standard methods. The fluctuation of the A content from particle to particle at time $t_m$ is then conveniently characterized by a standard deviation $\sigma(t_m)$ of the distribution of composition found in that way:

$$\sigma^2(t_m) = \frac{1}{N} \sum_{i=1}^{N} (x(i, t_m) - x)^2)$$

The chemical mixing time $t_{cm}$ is thus the shortest milling time for which $\sigma(t_{cm}) \approx 0$ in the considered experimental conditions. For instance, microprobe analyses performed on about 20–30 powder particles for samples of p-$Fe_{1-x}T_x$ (T = V, Cr, Mn) ground for $t_m$ yield a good estimate of $\sigma(t_m)$ (Fig. 13) [399]. The milling time dependence of the fluctuation $\sigma(t_m)$ appears to be well approximated by an exponential decrease in the case of some Fe–T binary systems,

$$\sigma(t_m) = \sigma(0) \exp\left(-\frac{t_m}{\tau_{cm}}\right) \qquad (1)$$

with a time constant $\tau_{cm}$. Time constants $\tau_{cm} = 39$ ($\pm3$) min, $\tau_{cm} = 55$ ($\pm5$) min, and $\tau_{cm} = 66$ ($\pm3$) min were obtained for T = V, Cr, Mn respectively. The times for which $\sigma \approx 0$ are then found to be similar, $t_{cm} \approx 4\tau_m \approx 3$–4 h, and for all alloys in the given milling conditions. The times, $\approx4$ h, needed to observe a stationary hardness and stationary shapes of hyperfine magnetic field distributions for T = V, Cr were found to both be of the order of $t_{cm}$. Figure 13 further shows the milling time dependence of the relative fraction
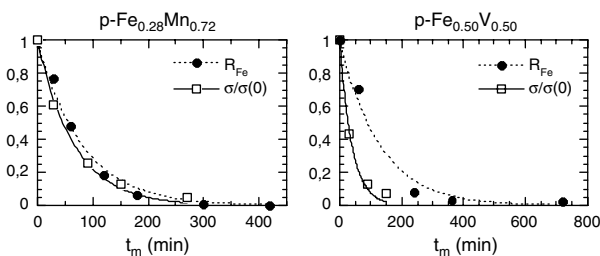


**Figure 13.** Milling time dependences of $\sigma(t_m)/\sigma(0)$ [and of $R_{Fe}(t_m)$ obtained from Mössbauer spectra] for p-$Fe_{0.28}Mn_{0.72}$ (left) and p-$Fe_{0.50}V_{0.50}$ (right).

$R_{Fe}(t_m)$ of Fe atoms which give rise to the "$\alpha$-Fe" contribution in Mössbauer spectra of p-$Fe_{0.50}V_{0.50}$. $R_{Fe}(t_m)$ clearly shows that the chemical mixing time $t_{cm}$ is much less than the synthesis time $t_f$ for this alloy. The typical chemical mixing times estimated in these experiments are not short as compared to the synthesis times (more than about 50%) and must be borne in mind when characterizing ground powders which have not yet reached a stationary dynamical state.

The importance of the chemical mixing time was evidenced too in a recent investigation of the mechanical alloying of Fe–Ge alloys [400]. For p-$Fe_{0.75}Ge_{0.25}$, mechanical alloying was indeed found to occur in two steps: for $t_m < t_{cm} \approx 4$ h, the mixture of Fe and Ge refines down to a nanometer scale with the formation of solute supersaturated regions near interfaces, possibly by a dislocation pumping solute mechanism. The latter process consists of repeated sequences of solute diffusion in dislocation cores, pinning and depinning due to stresses applied during shocks. An homogenization process occurs for longer milling times [400].

The time $t_f$ needed to reach a final stationary state is obtained to be of the order of $\approx8$–10 h for V and Cr, a time much larger than $t_{cm}$, while it is of the order of $t_{cm}$, being $\approx5$–6 h, for Mn. The long synthesis times reflect the fundamental role of competing mechanisms in the establishment of dynamical stationary states with a trend to unmixing in nearly equiatomic Fe–Cr and a trend to ordering in nearly equiatomic Fe–V alloys. By contrast Fe and Mn tend to mix, as shown by the large equilibrium solubility of Fe in Mn.

### 7.3. Composition Fluctuations in Mechanosynthesized Materials: The Example of p-$Fe_{0.30}Cr_{0.70}$

A considerable amount of theoretical and experimental work has been devoted to coarse-grained Fe–Cr alloys, a binary system which exhibits among others a wide miscibility gap, stable or metastable, below about 1000 K [400]. Mechanical alloying of p-$Fe_{1-x}Cr_x$ alloys has been thoroughly investigated for the whole range of $x$ [392, 399, 401, 410]. Homogeneous solid solutions and an amorphous phase, for $x \sim 0.70$ [403–405], were reported to be the dynamical equilibrium phases according to the composition and the milling conditions. However, recent investigations [409] demonstrate the favorable role of oxygen on the amorphous phase formation, particularly for contents larger than $\sim1.5$ wt%. Conclusions about the formation of homogeneous Fe–Cr solid solutions with nanosized grains were most often obtained from room-temperature (RT) Mössbauer spectra because heterogeneities can hardly be detected from broadened X-ray diffraction patterns of ground powders. Magnetization and magnetoresistance measurements [408] led, however, the reconsideration of the conclusions drawn from RT Mössbauer spectra about the formation of a solid solution in p-$Fe_{0.30}Cr_{0.70}$ alloys milled in classical experimental conditions (Fritsch Pulverisette 7 planetary ball mill with steel vial and seven balls with a powder-to-ball weight ratio $R = 1/22$ and a disc rotation speed $\Omega = 640$ rpm [392]) by evidencing the existence of composition fluctuations, whose amplitude $\Delta x$ is $\sim0.1$, on a scale of a few nanometers inside grains [392, 399, 408]. As described, the average chemical

compositions of all particles of ground powders are essentially the same for $t_m > \approx 3$–4 h in these milling conditions.

## 7.4. Steady State Structure of Milled $Fe_{0.30}Cr_{0.70}$

Detailed magnetic characterizations of $Fe_{0.34}Cr_{0.66}$ synthesized by high-energy ball-milling from p-$Fe_{0.30}Cr_{0.70}$ initial mixtures of chromium and iron powders are reported in [392]. They evidence the existence of a dominant superparamagnetic contribution from Fe-rich clusters at 400 K above the Curie temperature of the classical homogeneous alloy with the same composition, $T_c < \approx 380$ K [411]. X-ray diffraction patterns, transmission electron microscopy, and Mössbauer spectra at 7 K show no evidence of the formation of an amorphous phase which is known to be nonmagnetic at least down to 5 K. This indicates that oxygen contained in the starting powders does not play a significant role in the steady state achieved in these experimental conditions, as further confirmed by the results of chemical anlayses and of annealing experiments. The final ground $Fe_{0.34}Cr_{0.66}$ alloys were concluded to have complex structures with intragranular composition fluctuations of $\approx 0.1$ in amplitude at a scale of a few nm (of the order of 2–4 nm) which reflect the strong trend of Fe and Cr toward segregation. To show that the latter microstructure is a true dynamical equilibrium state, an as-cast $Fe_{0.30}Cr_{0.70}$ alloy was ball-milled in the same milling conditions as those used previously for mechanically alloyed powders of elemental Fe and Cr. Advantage was taken from a brittle–ductile transition located between room-temperature and liquid–nitrogen temperature to obtain coarse powder particles from a bulk as-cast alloy. The incorporation of steel from milling tools into ground powders was found to be negligible in such experimental conditions. The magnetic moment at 5 K is for instance 1.8 $\mu_B$/Fe atom for the as-cast alloy [412], in perfect agreement with the moment measured by Fischer et al. [411]. The reduced contamination explains why the Fe content is smaller in milled as-cast alloys than in alloys which were mechanosynthesized from elemental $Fe_{0.30}Cr_{0.70}$ mixtures. Magnetic susceptibilities (Fig. 14) were measured with a commercial susceptometer between 5 and 350 K with an ac field of 2 Oe at four frequencies ranging from 10 Hz to 10 kHz. The experimental results were similar for all investigated frequencies. When $T$ decreases, the ac susceptibility $\chi(T)$ of the as-cast alloy (Fig. 14) exhibits a broad transition around $\approx 290$ K, reaches a maximum at $\approx 200$ K and then decreases when $T$ decreases down to 5 K. These characteristics reflect the influence of short-range order, namely a strong tendency to clustering [411], on magnetic properties as clearly shown by the effect of annealing on Fe–Cr alloys with compositions similar to those investigated by Delcroix et al. [412]. The ac susceptibility of the mechanosynthesized alloy exhibits a clear ferromagnetic transition at $\approx 170$ K, the Curie temperature of an alloy with a Cr content $x \approx 0.75$. Then it reaches a maximum at $\approx 150$ K and decreases when $T$ decreases down to 50 K. It decreases more markedly below 50 K, as expected from the reentrant transition from a ferromagnetic phase to a cluster-glass-like state for $x \approx 0.75$ [392]. The susceptibility of the as-cast alloy milled for 4 h 30 (Fig. 14) is very close to that of the MA alloy with
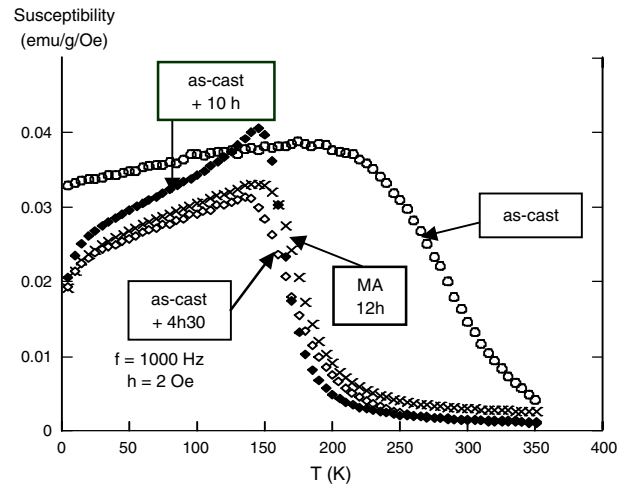


**Figure 14.** Ac susceptibility of $Fe_{0.30}Cr_{0.70}$ (1) mechanically alloyed (crosses, MA, $t_m = 12$ h), (2) as-cast (empty circles), (3) and as-cast and milled for various times (empty diamonds: $t_m = 4$ h 30, solid diamonds: $t_m = 10$ h).

a small temperature shift likely due to the composition difference. Finally, the susceptibility of the alloy ground for 10 h shows a transition at the same temperature as the alloy ground for 4 h 30, but it is more abrupt for the former alloy. This suggests that the distribution of Fe contents in Fe-rich clusters become narrower with milling time. As discussed in [392], the overall behavior of $\chi(T)$ of as-milled samples is dominated by the contribution of Cr-rich zones. It complements the information drawn from high-temperature magnetization which is dominated by superparamagnetic Fe-rich clusters.

In summary, both mechanically ground and mechanically alloyed $Fe_{0.30}Cr_{0.70}$ alloys exhibit similar stationary microstructures with intragranular composition fluctuations of $\approx 0.1$ in amplitude at a scale of a few nm. They differ from those found for a macroscopic phase separation. These results reinforce the conclusion of a recent study of $Ag_{0.50}Cu_{0.50}$ alloys [397] about the likely phase separation on ultrafine scales that escaped detection in many alloys obtained inside miscibility gaps which are often believed to be homogeneous. He et al. further question the reliability of diffraction methods to determine the true level of supersaturation or the homogeneity of a solid solution (see also [413]).

To conclude, the characterization of composition fluctuations is essential for a thorough description of the mechanical alloying process and of mechanosynthesized materials.

## 8. CONCLUSION

Investigations performed for a period of about 20 years provide realistic ideas about the actual potentialities of synthesis methods which involve mechanical energy and about the problems they raise. Mechanosynthesis is a promising synthesis method for all kinds of nanomaterials, often with original features, and a step in the preparation of consolidated materials with improved properties. Milling must no more be kept in mind as the sole millenial method of

powder processing but it must considered nowadays as being also a modern technique, mechanosynthesis, of preparation and transformation of materials which turns progressively simple mills into true "mechanoreactors" [414]. For both applied and fundamental aspects, it is necessary to characterize and master the "microstructures" of the demanding class of nanostructured materials for which there are expectations of improved properties and of promising applications. Besides the chemical engineering and materials synthesis aspects mentioned, the physical understanding of mechanosynthesis still requires detailed investigations particularly in systems for which thermal and mechanical energy compete (order–disorder, unmixing–mixing) to drive milled materials to dynamical stationary states far from equilibrium with original microstructural features. Mechanosynthesized nanostructured materials belong to a larger family whose properties still remain to be characterized and understood. For instance, how do such materials plastically deform when there is no apparent activity of dislocations? Which are the characteristics of phase separation in nanostructured materials?

As already mentioned, important aspects of mechanosynthesis of nanostructured materials have not been covered in this chapter. This is the case for instance for computer simulations of mechanical alloying which provide already some information about original morphologies that may be formed thanks to competing interactions between elements to be mixed [35] but, as emphasized by Martin, a safe modeling of the shearing event itself is still lacking [314]. This is further the case for the synthesis of all kinds of compounds (intermetallic compounds, "Xides" where X stands for bor, carb, nitr, alumin, phosph, silic, etc., and metallic glasses) but many of them are prepared in a straightforward way simply by grinding elemental powder mixtures. Further, applications of nanostructured materials often require them to be processed in a temperature range in which they may undergo grain growth and thus risk losing their specific properties. Lund and Schuh [415–416] explored recently driven alloy systems (irradiation, mechanical alloying, severe plastic deformation) to test the assumption according to which only completely random configurations are dynamically stable in the limit where ballistic effects are dominant. Their molecular simulations of driven binary alloys suggest that complex ordered or segregated structures may evolve even in the absence of thermally activated diffusion [415]. They have indeed found that binary alloys can mix, demix, and even order under an external driving force at $T = 0$ K. Lund and Schuh emphasize that atoms would have a microscopic degree of freedom to select their preferred nearest neighbors, whenever there is a force enabling their motion, in systems with local stresses due to either an atomic size mismatch or a high density of crystalline defects. In the latter systems, the formation of preferred bonds would result from subatomic translations since there is no fixed lattice site for a given atom.

"Micromégas," the hero of the Voltaire's *Conte philosophique* which echoes Swift's *Gulliver's Travels*, imagines an animal "not quite one 600,000th of an inch in height" [417] ("qui aurait à peu près la six-cent millième partie d'un pouce en hauteur"), that is, an animal whose height is about 40 nm. Micromégas seems thus to be the right giant we

need to close this chapter on mechanical alloying and nanostructured materials, a class of materials in which widely different scales are linked too [417]:

> "Quel plaisir sentit Micromégas en voyant remuer ces petites machines, en examinant tous leurs tours, en les suivant dans toutes leurs opérations!"
>
> "What pleasure Micromégas felt in watching the movements of those little machines, in examining all their feats, in following all their operations!"

# GLOSSARY

**Ball milling (BM)**  A process consisting of mechanical mixing of powders based on prealloyed components (as example intermetallic phases, ceramic compounds).

**Combustion**  A reaction which is found to liberate quasi-instantaneously its exothermic energy.

**Field activated pressure assisted sintering (FAPAS)**  Compared to a classical sintering process under pressure, a current is applied in order to assist the sintering. A current exhibiting a high intensity (up to 8,000 A) under low voltage (10 V) is applied.

**Grinding**  Mechanical processing leading to a decrease in the crystallite grain size. The initial material is pure element or alone compound.

**Mechanical activated annealing processing (M2AP)**  Before an annealing treatment, a former mechanical step is introduced leading to a mechanical activation of the powders.

**Mechanical activated self-heat-sustaining (MASHS)**  For SHS (see SHS terms), before igniting SHS reaction, a first step is performed consisting of short duration mechanical alloying of elementary component. The duration is enough to generate a 3D nanoscale distribution of the elementary component inside each micrometer powder grain.

**Mechanical activation processing (MA processing)**  Before powder metallurgy processing (i.e., sintering, densification, reactive sintering), a step consisting of a short duration mechanical alloying is performed.

**Mechanical alloying (MA)**  A process consisting of a mechanical mixing at the nanoscale of elementary components. A long duration of such a mechanical process is expected to lead to the formation a stationary end product constituted by definite compounds.

**Mechanochemistry**  Processing involving mechanical treatment in order to achieve chemical reactions.

**Milling**  A mechanical processing for treatment of powders. Introduction of a component helping the milling is defined as wet milling. Without such an additive, it is the so-called dry milling.

**Nanocomposites**  Dense materials composed of various materials. One of the latter has a nanoscale dimension.

**Nanoparticles**  Isolated particles whose diameters are well below 100 nm, classically less than 10 nm.

**Self-heat-sustaining (reaction) (SHS)**  An exothermic reaction between two elementary components exhibiting enough energy to be self-sustaining (i.e., without the need for an external energy source).

**Solid state reaction**    Reaction occurring below the melting point of any elementary component or compounds.

**Spark plasma sintering**    A process leading to bulk materials by a sintering step using pulse electric discharge. Due to the high intensity of the current, plasma may occur between the various powder grains.

**Thermomechanical treatment**    A treatment of materials combining thermal effect and mechanical solications, both being successive or simultaneously performed.

**Ultrafine (particles)**    Particles which are isolated each from each other and exhibiting a nanometer scale (less than 100 nm).

## REFERENCES

1. J. Swift, "Gulliver's Travels," Ch. 6 (1726). http://www.on-line. literature.com/swift/gulliver/.
2. H. Gleiter, *Acta Mater.* 48, 1 (2000).
3. R. W. Cahn, "The Coming of Materials Science." Pergamon, Amsterdam, 2001.
4. A. Caro and H. Van Swygenhoven, *Phys. Rev. B* 63, 134101 (2001).
5. J. S. Benjamin, *Metall. Trans.* 1, 2943 (1970).
6. J. S. Benjamin, *Sci. Amer.* 234, 40 (1976); *Mater. Sci. Forum* 88–90, 1 (1992).
7. R. L. White, Ph.D. Dissertation, Stanford University, 1979.
8. C. C. Koch, O. B. Kavin, C. G. Mckamey, and J. O. Scarbrough, *Appl. Phys. Lett.* 43, 1017 (1983).
9. J. J. De Barbadillo, *Key Eng. Mater.* 77–78, 187 (1993).
10. V. V. Boldyrev, N. Z. Lyakhov, Yu. T. Pavlyukhin, E. V. Boldyreva, E. Yu. Ivanov, and E. G. Avvakumov, *Sov. Sci. Rev. B. Chem.* 14, 105 (1990).
11. E. Gaffet, F. Bernard, J. C. Niepce, F. Charlot, C. Gras, G. Le Caër, J. L. Guichard, P. Delcroix, A. Mocellin, and O. Tillement, *J. Mater. Chem.* 9, 305 (1999).
12. B. S. Murty and S. Ranganathan, *Int. Mater. Rev.* 43, 101 (1998).
13. C. Suryanarayana, *Progr. Mater. Sci.* 46, 1 (2001).
14. L. Takacs, *Progr. Mater. Sci.* 47, 355 (2002).
15. R. Z. Valiev, R. K. Islamgaliev, and I. V. Alexandrov, *Progr. Mater. Sci.* 45, 103 (2000).
16. M. Atzmon, K. M. Unruh, and W. L. Johnson, *J. Appl. Phys.* 58, 3865 (1985).
17. F. Bordeaux and A. R. Yavari, *J. Appl. Phys.* 67, 2385 (1990).
18. L. Battezzati, P. Pappalepore, F. Durbiano, and I. Gallino, *Acta Mater.* 47, 1901 (1999).
19. H. J. Fecht, *Scripta Mater.* 44, 1719 (2001).
20. Y. Watanabe, K. N. Ishihara, and P. H. Shingu, *Scripta Mater.* 44, 1853 (2001).
21. A. Csanády, A Csordás-Pintér, L. Varga, L. Tóth, and G. Vincze, *J. Phys. I France* 6, 925 (1996).
22. C. Suryanarayana, E. Ivanov, and V. V. Boldyrev, *Mater. Sci. Eng. A* 304–306, 151 (2001).
23. L. Takacs, *Progr. Mater. Sci.* 47, 355 (2002).
24. B. S. Murty and S. Ranganathan, *Int. Mater. Rev.* 43, 101 (1998).
25. F. Bernard and E. Gaffet, *Int. J. Self Propagating High Temp. Synthesis* 10, 109 (2001).
26. E. Gaffet, N. Malhouroux, and M. Abdellaoui, *J. All. Comp.* 194, 339 (1993).
27. L. Lü and M. O. Lai, Kluwer Academic, Dordrecht, 1998.
28. R. Z. Valiev, R. K. Islamgaliev, and I. V. Alexandrov, *Progr. Mater. Sci.* 45, 103 (2000).
29. F. H. Froes, O. N. Senkov, and E. G. Baburaj, *Mater. Sci. Eng. A* 301, 44 (2001).
30. C. Suryanarayana, Cambridge International Science, England, 1995.
31. G. Le Caër (Issue Ed.), Special Issue, *Ann. Chim.* 22, 341 (1997).
32. R. Z. Valiev (Issue Ed.), *Ann. Chim./Sci. Mater.* 21, 369 (1996).
33. E. M. Gutman, World Scientific, Singapore, 1994.
34. P. Y. Butyagin, *Russian Chem. Rev.* 63, 965 (1994).
35. G. Martin and P. Bellon, *Solid State Phys.* 50, 189 (1996).
36. http://www.bls.fr/amatech/Sciences/Mecanosynthese/mecanosynthese.htm
37. E. Gaffet, M. Abdellaoui, and N. Malhouroux-Gaffet, *Mater. Trans. JIM* 36, 198 (1995).
38. A. Calka and A. P. Radlinski, *Mater. Sci. Eng. A* 134, 1350 (1991).
39. D. Basset, P. Matteazzi, and F. Miani, *Mater. Sci. Eng. A* 174, 71 (1994).
40. P. Pochet, E. Tominez, L. Chaffron, and G. Martin, *Phys. Rev. B* 52, 4006 (1995).
41. Y. Chen, M. Bibole, R. Le Hazif, and G. Martin, *Phys. Rev. B* 48, 14 (1993).
42. P. Lebrun, L. Froyen, and L. Delaey, *Mater. Sci. Eng. A* 161, 75 (1993).
43. R. B. Schwarz, *Mater. Sci. Eng.* 97, 71 (1988).
44. T. H. Courtney, *Mater. Trans. JIM* 36, 110 (1995).
45. T. H. Courtney and D. Maurice, *Scripta Mater.* 34, 5 (1996).
46. R. M. Davis, B. McDermott, and C. C. Koch, *Metall. Trans. A* 19, 2867 (1988).
47. M. Abdellaoui and E. Gaffet, *Acta Metall. Mater.* 43, 1087 (1995).
48. B. K. Mishra and C. V. R. Murty, *Powder Technol.* 115, 290 (2001).
49. A. Joisel, *Rev. Mater. Construction* 493, 234 (1952).
50. A. A. Bradley, A. J. Freemantle, and P. J. D. Lloyd, *J. South African Inst. Mining Metall.* 10, 78 (1975).
51. J. Schilz, M. Riffel, K. Pixius, and H.-J. Meyer, *Powder Technol.* 105, 149 (1999).
52. J. Schilz, *Mater. Trans. JIM* 39, 1152 (1998).
53. M. Riffel and J. Schilz, *J. Mater. Sci.* 33, 3427 (1998).
54. H. Mio, J. Kano, F. Saito, and K. Kaneko, *Mater. Sci. Eng. A* 332, 75 (2002).
55. M. Magini, C. Colella, A. Iasonna, and F. Padella, *Acta Mater.* 46, 2841 (1998).
56. B. K. Mishra, *Kona* 13, 151 (1995).
57. M. Abdellaoui and E. Gaffet, *J. All. Comp.* 209, 351 (1994).
58. E. V. Shelekhov, V. V. Tcherdyntsev, L. Yu, S. D. Kaloshin, and I. A. Tomilin, *J. Metast. Nanocryst. Mater.* 8, 603 (2000).
59. W. Shulin, Y. Xianqi, and L. Juguang, "Integrating Dynamics, Condition Monitoring and Control for the 21st Century" (Starr, Leung, Wright, and Sandoz, Eds.), pp. 465–470. Rotterdam, 1999.
60. J. Raasch, *Chem. Eng. Technol.* 15, 245 (1992).
61. M. Abdellaoui and E. Gaffet, *Acta Mater.* 44, 725 (1996).
62. H. Watanabe, *Powder Technol.* 104, 95 (1999).
63. J. Kano, N. Chujo, and F. Saito, *Adv. Powder Technol.* 8, 39 (1997).
64. H. Watanabe, *Powder Technol.* 104, 95 (1999).
65. D. R. Maurice and T. H. Courtney, *Metall. Trans. A* 21, 289 (1990).
66. T. H. Courtney and D. R. Maurice, "Solid State Powder Processing" (A. H. Clauer and J. J. de Barbadillo, Eds.), Vol. 3. The Minerals, Metals and Materials Society, 1990.
67. P. P. Chattopadhyay, I. Manna, S. Talapatra, and S. K. Pabi, *Mater. Chem. Phys.* 68, 85 (2001).
68. K. Szymanski and Y. Labaye, *Phys. Rev. E* 59, 2863 (1999).
69. R. Rahouadj and E. Gaffet, *Mater. Sci. Forum* 225–227, 249 (1996).
70. H. Huang, M. P. Dallimore, J. Pan, and P. G. McCormick, *Mater. Sci. Eng. A* 241, 38 (1998).
71. K. R. Shah and T.-F. Wong, *Int. J. Rock Mech. Min. Sci.* 34, 727 (1997).
72. M. Zdujic, C. Jovlekic, Lj. Karanovic, M. Mitric, D. Poletti, and D. Skala, *Mater. Sci. Eng. A* 245, 109 (1998).
73. J. Xu, G. S. Collins, L. S. J. Peng, and M. Atzmon, *Acta Mater.* 47, 1241 (1999).
74. Y.-S. Kwon, K. B. Gerasimov, and S.-K. Yoon, *J. All. Comp.*, in press.
75. S. K. Pabi, D. Das, T. K. Mahapatra, and I. Manna, *Acta Mater.* 46, 3501 (1998).

76. J. Kano, H. Mio, and S. Saito, *J. Chem. Eng. Japan* 32, 445 (1999).
77. F. C. Bond, *Mining Eng.* 4, 484 (1952).
78. E. P. Zemskov, *Powder Technol.* 102, 71 (1999).
79. V. Buchholtz, J. A. Freund, and T. Pöschel, *Europ. Phys. J.*, in press.
80. J. R. Harris, J. A. D. Wattis, and J. V. Wood, *Acta Mater.* 49, 3991 (2001).
81. B. J. M. Aikin and T. H. Courtney, *Mater. Sci. Eng. A* 147, 229 (1993).
82. D. Gavrilov, O. Vinogradov, and W. J. D. Shaw, *Powder Technol.* 101, 63 (1999).
83. F. Kh. Urakaev and V. V. Boldyrev, *Inorganic Mater.* 35, 189 (1999).
84. F. Kh. Urakaev and V. V. Boldyrev, *Inorganic Mater.* 35, 405 (1999).
85. G. Gonzalez, L. D'Angelo, J. Ochoa, B. Lara, and E. Rodriguez, *Mater. Sci. Forum* 386–388, 159 (2002).
86. H. H. Tian and M. Atzmon, *Acta Mater.* 47, 1255 (1999).
87. R. B. Schwarz, *Mater. Sci. Forum* 269–272, 665 (1998).
88. P. Pochet, P. Bellon, L. Boulanger, L. Chaffron, and G. Martin, *Mater. Sci. Forum* 269–272, 655 (1998).
89. P. Pochet, P. Bellon, L. Chaffron, and G. Martin, *Mater. Sci. Forum* 225–227, 207 (1996).
90. F. Wu, P. Bellon, A. J. Melmed, and T. A. Lusby, *Acta Mater.* 49, 453 (2001).
91. A. Y. Badmos and H. K. D. H. Bhadeshia, *Metall. Mater. Trans. A* 28, 2189 (1997).
92. V. I. Levitas, V. F. Nesterenko, and M. A. Meyers, *Acta Mater.* 46, 5929 (1998).
93. J. J. Gilman, *Philos. Mag. B* 71, 1057 (1995).
94. H. Zhang and X. Liu, *Int. J. Refractory Metals Hard Mater.* 19, 203 (2001).
95. H. J. Fecht, E. Hellstern, and W. L. Johnson, *Metall. Trans. A* 21, 2333 (1990).
96. J. S. C. Jang and C. C. Koch, *Scripta Metall. Mater.* 24, 1599 (1990).
97. P. Le Brun, E. Gaffet, L. Froyen, and L. Delaey, *Scripta Metall. Mater.* 26, 1743 (1992).
98. J. Eckert, J. C. Holzer, C. E. Krill III, and W. L. Johnson, *J. Mater. Res.* 7, 1751 (1992).
99. T. Tanaka, S. Nasu, B. Huang, K. N. Ishihara, and P. H. Shingu, *Nucl. Instrum. Methods B* 76, 195 (1993).
100. A. M. Harris, G. B. Schaffer, and N. W. Page, *J. Mater. Sci. Lett.* 12, 1103 (1993).
101. H. J. Fecht, *Nanostruct. Mater.* 6, 33 (1995).
102. A. Benghalem and D. J. Morris, *Acta Metall. Mater.* 42, 4071 (1995).
103. L. Daroczi, D. L. Becke, G. Posgay, and M. Kis-Varga, *Nanostruct. Mater.* 6, 981 (1995).
104. T. D. Shen, C. C Koch, T. Y. Tsui, and G. M. Pharr, *J. Mater. Res.* 10, 2892 (1995).
105. S. J. Campbell and W. A. Kaczmarek, in "Mössbauer Spectroscopy Applied to Magnetism and Materials Science" (G. J. Long and F. Grandjean, Eds.), Vol. 2, p. 273. Plenum, New York, 1996.
106. D. Oleszak and P. H. Shingu, *J. Appl. Phys.* 79, 2975 (1996).
107. C. C. Koch, *Nanostruct. Mater.* 9, 13 (1997).
108. E. Bonetti, E. G. Campari, L. Pasquini, and E. Sampaolesi, *J. Appl. Phys.* 84, 4219 (1998).
109. L. Del Bianco, C. Ballesteros, J. M. Rojo, and A. Hernando, *Phys. Rev. Lett.* 81, 4500 (1998).
110. J. Rawers, D. Cook, and T. Kim, *Mater. Sci. Eng. A* 248, 212 (1998).
111. A. Révész and J. Lendvai, *Nanostruct. Mater.* 10, 13 (1998).
112. E. Bonetti, L. Del Bianco, D. Fiorani, D. Rinaldi, R. Caciuffo, and A. Hernando, *Phys. Rev. Lett.* 83, 2829 (1999).
113. A. Hernando, *J. Phys.: Condens. Matter* 11, 9455 (1999).
114. H. H. Tian and M. Atzmon, *Acta Mater.* 47, 1255 (1999).
115. E. Gaffet, C. Meunier, S. Vives, and J. P. Itié, *J. Metastable Nanocryst. Mater.* 2–6, 587 (1999).
116. J. Rawers and D. Cook, *Nanostruct. Mater.* 11, 331 (1999).
117. D. X. Li, D. H. Ping, J. Y. Huang, Y. D. Yu, and H. Q. Ye, *Micron* 31, 581 (2000).
118. J. Balogh, D. Kaptas, T. Kemeny, I. Vincze, and G. Radnoczi, *Phys. Rev. Lett.* 82, 4150 (1999).
119. L. Del-Bianco, C. Ballesteros, J. M. Rojo, and A. Hernando, *Phys. Rev. Lett.* 82, 4151 (1999).
120. B. Fultz, J. L. Robertson, T. A. Stephens, L. J. Nagel, and S. Spooner, *J. Appl. Phys.* 79, 8318 (1996).
121. E. Bonetti, L. Pasquini, E. Sampaolesi, A. Deriu, and G. Cicognani, *J. Appl. Phys.* 88, 4571 (2000).
122. J. Balogh, L. Bujdoso, D. Kaptas, T. Kemeny, I. Vincze, S. Szabo, and D. L. Beke, *Phys. Rev. B* 61, 4109 (2000).
123. A. Hernando, *J. Phys.: Condens. Matter* 11, 9455 (1999); A. Hernando and A. Gonzalez, *J. Non-Cryst. Solids* 287, 256 (2001).
124. E. P. Elsukov, G. A. Dorofeev, A. I. Ul'yanov, A. V. Zagainov, and A. N. Maratkanova, *Phys. Metals Metallography* (*Russia*) 91, 258 (2001).
125. B. Chen, D. Penwell, M. B. Kruger, A. F. Yue, and B. Fultz, *J. Appl. Phys.* 89, 4794 (2001).
126. Y. H. Zhao, H. W. Sheng, and K. Lu, *Acta Mater.* 49, 365 (2001).
127. M. Murayama, J. M. Howe, H. Hidaka, and S. Takaki, *Science* 295, 2433 (2002).
128. Q. Meng, N. Zhou, Y. Rong, S. Chen, and T. Y. Hsu (Xu Zuyao), *Acta Mater.* 50, 4563 (2002).
129. N. R. Tao, Z. B. Wang, W. P. Tong, M. L. Sui, J. Lu, and K. Lu, *Acta Mater.* 50, 4603 (2002).
130. P. P. Chatterjee, S. K. Pabi, and I. Manna, *J. Appl. Phys.* 86, 5912 (1999).
131. P. Chatterjee and S. P. Sen Gupta, *Philos. Mag. A* 81, 49 (2001).
132. X. Zhang, H. Wang, J. Narayan, and C. C. Koch, *Acta Mater.* 49, 1319 (2001).
133. X. Zhang, H. Wang, M. Kassem, J. Narayan, and C. C. Koch, *Scripta Mater.* 46, 661 (2002).
134. X. Zhang, H. Wang, R. O. Scattergood, J. Narayan, C. C. Koch, A. V. Sergueeva, and A. K. Mukherjee, *Acta Mater.* 50, 3995 (2002).
135. S. Hwang, C. Nishimura, and P. G. McCormick, *Mater. Sci. Eng. A* 318, 22 (2001).
136. I. Lucks, P. Lamparter, and E. J. Mittemeijer, *Acta Mater.* 49, 2419 (2001).
137. E. Gaffet and M. Harmelin, *J. Less-Common Met.* 157, 201 (1990).
138. T. D. Shen, C. C. Koch, T. L. McCormick, R. J. Nemanich, J. Y. Huang, and J. G. Huang, *J. Mater. Res.* 10, 139 (1995).
139. J. Y. Huang, H. Yasuda, and H. Mori, *Philos. Mag. Lett.* 79, 305 (1999).
140. G. J. Fan, F. Q. Guo, Z. Q. Hu, M. X. Quan, and K. Lu, *Phys. Rev. B* 55, 11010 (1997).
141. F. Q. Guo and K. Lu, *Phys. Rev. B* 57, 10414 (1998).
142. F. Q. Guo and K. Lu, *Philos. Mag. Lett.* 77, 181 (1998).
143. Y. H. Zhao, Z. H. Jin, and K. Lu, *Philos. Mag. Lett.* 79, 747 (1999).
144. T. D. Shen, W. Q. Ge, K. Y. Wang, M. X. Quan, J. T. Wang, W. D. Wei, and C. C. Koch, *Nanostruct. Mater.* 7, 393 (1996).
145. S. Orimo, G. Majer, T. Fukunaga, A. Züttel, L. Schlapbach, and H. Fujii, *Appl. Phys. Lett.* 75, 3093 (1999).
146. X. H. Chen, H. S. Yang, G. T. Wu, M. Wang, F. M. Deng, X. B. Zhang, J. C. Peng, and W. Z. Li, *J. Cryst. Growth* 218, 57 (2000).
147.
148. D. Choulier, R. Rahouadj, and E. Gaffet, *Ann. Chim. Sci. Mater.* 22, 351 (1997).
149. A. Caro and H. Van Swygenhoven, *Phys. Rev. B* 63, 134101 (2001).
150. P. Keblinski, D. Wolf, S. R. Phillpot, and H. Gleiter, *Scripta Mater.* 41, 631 (1999).
151. D. Wolf, *Current Opinion Solid State Mater. Sci.* 5, 435 (2001).
152. H. Van Swygenhoven, D. Farkas, and A. Caro, *Phys. Rev. B* 62, 831 (2000).
153. H. Van Swygenhoven, *Science* 296, 2386 (2002).
154. H. E. Schaefer, K. Reimann, W. Straub, R. Phillipp, H. Tanimoto, U. Brossmann, and R. Würschum, *Mater. Sci. Eng. A* 286, 24 (2000).

*155.* Yu. R. Kobolov, G. P. Grabovetskaya, M. B. Ivanov, A. P. Zhilyaev, and R. Z. Valiev, *Scripta Mater.* 44, 873 (2001).

*156.* D. Jia, K. T. Ramesh, E. Ma, L. Lu, and K. Lu, *Scripta Mater.* 45, 613 (2001).

*157.* S. R. Agnew, B. R. Elliott, C. J. Youngdahl, K. J. Hemker, and J. R. Weertman, *Mater. Sci. Eng.* 285, 391 (2000).

*158.* H. H. Fu, D. J. Benson, and M. A. Meyers, *Acta Mater.* 49, 2567 (2001).

*159.* E. Arzt, *Acta Mater.* 46, 5611 (1998).

*160.* L. H. Qian, S. C. Wang, Y. Z. Zhao, and K. Lu, *Acta Mater.* 50, 3425 (2002).

*161.* Y. Estrin, G. Gottstein, E. Rabkin, and L. S. Shvindlerman, *Scripta Mater.* 43, 141 (2000).

*162.* C. E. Krill III, L. Helfen, D. Michels, H. Natter, A. Fitch, O. Masson, and R. Birringer, *Phys. Rev. Lett.* 86, 842 (2001).

*163.* C. C. Koch, *J. Metastable Nanocryst. Mater.* 18, 9 (2003).

*164.* S. Van Petegem, F. Dalla Torre, D. Segers, and H. Van Swygenhoven, *Scripta Mater.* 48, 17 (2003).

*165.* E. R. Kimmel, *Int. J. Refract. Hard Met.* 2, 84 (1983).

*166.* F. Cardellini and G. Mazzone, *Philos. Mag. A* 67, 1289 (1993).

*167.* G. Mazzone, *Appl. Phys. Lett.* 67, 1944 (1995).

*168.* J. Y. Huang, Y. K. Wu, and H. Q. Ye, *Appl. Phys. Lett.* 66, 308 (1995).

*169.* J. Y. Huang, Y. K. Wu, and H. Q. Ye, *Appl. Phys. Lett.* 67, 1945 (1995).

*170.* J. Y. Huang, Y. K. Wu, and H. Q. Ye, *Acta Mater.* 44, 1201 (1996).

*171.* J. Sort, N. M. Mateescu, J. Nogués, S. Suriñach, and M. D. Baró, *J. Metastable Nanocryst. Mater.* 12, 126 (2002).

*172.* M. S. El-Eskandarany, K. Sumiyama, K. Aoki, and K. Suzuki, *Mater. Sci. Forum* 88–90, 801 (1992).

*173.* H. Van Swygenhoven, M. Spaczer, A. Caro, and D. Farkas, *Acta Mater.* 47, 3117 (1999).

*174.* J. Schiotz, T. Vegge, F. D. Di Tolla, and K. W. Jacobsen, *Phys. Rev. B* 60, 11971 (1999).

*175.* P. M. Derlet, R. Meyer, L. J. Lewis, U. Stuhr, and H. Van Swygenhoven, *Phys. Rev. Lett.* 20, 205501 (2001).

*176.* E. Gaffet, *Mater. Sci. Eng. A* 136, 161 (1991).

*177.* E. Gaffet, F. Faudot, and M. Harmelin, *Mater. Sci. Eng. A* 149, 85 (1991).

*178.* E. Gaffet and J. P. Gaspard, *J. Phys. Suppl. Coll. C* 4, 205 (1990).

*179.* T. D. Shen, I. Shmagin, C. C. Koch, R. M. Kolbas, Y. Fahmy, L. Bergman, R. J. Nemanich, M. T. McClure, Z. Sitar, and M. X. Quan, *Phys. Rev. B* 55, 7615 (1997).

*180.* A. N. Streleskii, A. V. Leonov, and P. Yu Butyagin, *Coll. J.* 63, 630 (2001).

*181.* A. N. Strelestkii, A. V. Leonov, I. V. Beresteskaya, S. S. Mudretsova, A. F. Majorova, and P. Ju. Butyagin, *Mater. Sci. Forum* 386–388, 187 (2002).

*182.* C. Diaz-Guerra, A. Montone, J. Piqueras, and F. Cardellini, *Semicond. Sci. Technol.* 17, 77 (2002).

*183.* T. Nasu, F. Araki, O. Uemura, T. Usuki, Y. Kameda, S. Takahashi, and K. Tokumitsu, *J. Metast. Nanocryt. Mater.* 10, 203 (2001).

*184.* Y. Tani, Y. Shirakawa, A. Shimosaka, and J. Hidaka, *J. Non-Cryst. Solids* 293–295, 779 (2001).

*185.* J. Y. Huang, *Acta Mater.* 47, 1801 (1999).

*186.* N. J. Welham and J. S. Williams, *Carbon* 36, 1309 (1998).

*187.* F. Salver-Disma, J.-M. Tarascon, C. Clinard, and J.-N. Rouzaud, *Carbon* 37, 1941 (1999).

*188.* F. Disma, L. Aymard, L. Dupont, and J.-M. Tarascon, *J. Electrochem. Soc.* 143, 3959 (1996).

*189.* F. Salver-Disma, C. Lenain, B. Beaudoin, L. Aymard, and J.-M. Tarascon, *Solid State Ionics* 98, 145 (1997).

*190.* R. Janot and D. Guerard, *Carbon*, in press.

*191.* G. B. Schaffer and P. G. McCormick, *Mater. Sci. Forum* 88–90, 779 (1992).

*192.* G. B. Schaffer and P. G. McCormick, *Appl. Phys. Lett.* 55, 45 (1989).

*193.* P. G. McCormick, *Mater. Trans. JIM* 36, 228 (1995).

*194.* J. Ding, T. Tsuzuki, P. G. McCormick, and R. Street, *Mater. Trans. JIM* 36, 228 (1995).

*195.* T. Tsuzuki and P. G. McCormick, *Appl. Phys. A* 65, 607 (1997).

*196.* J. Ding, T. Tsuzuki, and P. G. McCormick, *J. Mater. Sci.* 34, 5293 (1999).

*197.* P. Matteazzi and G. Le Caër, *J. Am. Ceram. Soc.* 75, 2749 (1992).

*198.* L. Takacs, *Progr. Mater. Sci.* 47, 355 (2002).

*199.* H. W. Sheng, K. Lu, and E. Ma, *Acta Mater.* 46, 5195 (1998).

*200.* K. Chattopadhyay and R. Goswami, *Progr. Mater. Sci.* 42, 287 (1997).

*201.* K. Lu and Z. H. Jin, *Current Opinion Solid State Mater. Sci.* 5, 39 (2001).

*202.* Y. Wang, M. Chen, F. Zhou, and E. Ma, *Nature* 419, 912 (2002).

*203.* G. He, J. Eckert, W. Löser, and L. Schultz, *Nature Mater.* 2, 33 (2003).

*201.* M. Zeghmati, E. Duverger, and E. Gaffet, in "Proc. CANCAM 95" (B. Tabarrock and S. Dost, Eds.), *Cong. Canad. Mécan. Appl.* 2, 952 (1995).

*202.* F. Charlot, E. Gaffet, B. Zeghmati, F. Bernard, and J.-C. Niepce, *Mater. Sci. Eng. A* 262, 279 (1999).

*203.* F. Bernard, F. Charlot, E. Gaffet, and J. C. Niepce, *Int. J. Self Prop. High Temp. Synth.* 7, 233 (1998).

*204.* F. Charlot, E. Gaffet, F. Bernard, Ch Gras, and J. C. Niepce, *Mater. Sci. Forum* 312–314, 287 (1999).

*205.* F. Charlot, F. Bernard, D. Klein, E. Gaffet, and J.-C. Niepce, *Acta Mater.* 47, 619 (1999).

*206.* F. Charlot, C. Gras, M. Grammond, F. Bernard, E. Gaffet, and J. C. Niepce, *J. Phys. Suppl. Coll.* IV, 497 (1998).

*207.* Ch Gras, D. Vrel, E. Gaffet, and F. Bernard, *J. All. Comp.* 314, 240 (2001).

*208.* Ch. Gras, F. Charlot, F. Bernard, E. Gaffet, and J. C. Niepce, *Acta Mater.* 47, 2113 (1999).

*209.* Ch. Gras, N. Bernsten, F. Bernard, and E. Gaffet, *Intermetallics* 10, 271 (2002).

*210.* Ch. Gras, E. Gaffet, F. Bernard, and J. C. Niepce, *Mater. Sci. Eng. A* 264, 94 (1999).

*211.* H. Shouha, E. Gaffet, F. Bernard, and J. C. Niepce, *J. Mater. Sci.* 35, 3221 (2000).

*212.* F. Bernard, H. Souha, and E. Gaffet, *Mater. Sci. Eng. A* 284, 301 (2000).

*213.* H. Shouha, F. Bernard, E. Gaffet, and B. Gillot, *Thermochem. Acta* 351, 71 (2000).

*214.* V. Gauthier, F. Bernard, E. Gaffet, D. Vrel, and J. P. Larpin, *Intermetallics* 10, 377 (2002).

*215.* V. Gauthier, F. Bernard, E. Gaffet, C. Josse, and J. P. Larpin, *Mater. Sci. Eng. A* 272, 334 (1999).

*216.* V. Gauthier, C. Josse, F. Bernard, E. Gaffet, and J.-P. Larpin, *Mater. Sci. Eng. A* 265, 117 (1999).

*217.* V. Gauthier, J. P. Larpin, M. Vilasi, F. Bernard, and E. Gaffet, *Mater. Sci. Forum* 369–372, 793 (2001).

*218.* R. M. L. Neto and C. J. da Rocha, *Key Eng. Mater.* 189–191, 567 (2001).

*219.* K. Uenishi, T. Matsubara, M. Kambara, and K. F. Kobayashi, *Scripta Mater.* 44, 2093 (2001).

*220.* T. Matsubara, K. Uenishi, and K. F. Kobayashi, *Mater. Trans. JIM* 41, 631 (2000).

*221.* J. Lagerbom, T. Tiainen, M. Lehtonen, and P. Lintula, *J. Mater. Sci.* 34, 1477 (1999).

*222.* F. Maglia, U. Anselmi-Tamburini, G. Cocco, M. Monagheddu, N. Bertolino, and Z. A. Munir, *J. Mater. Res.* 16, 1074 (2001).

*223.* S. Murali, T. Sritharan, and P. Hing, *Int. J. Powder Metall.* 37, 67 (2001).

*224.* D. Vrel, N. Girodon-Boulandet, S. Paris, J.-F. Mazué, E. Couqueberg, M. Gailhanou, D. Thiaudière, E. Gaffet, and F. Bernard, *Rev. Sci. Instrum.* 73, 422 (2002).

225. F. Bernard, E. Gaffet, M. Gramond, M. Gailhanou, and J. C. Gachon, *J. Synchrotron Radiation* 7, 27 (2000).

226. Z. A. Munir, F. Charlot, F. Bernard, and E. Gaffet, One Step Synthesis and Consolidation of Nanophase Materials, U.S. Patent 6, 200, 515, 2001.

227. F. Charlot, E. Gaffet, F. Bernard, and Z. A. Munir, *J. Amer. Ceram. Soc.* 84, 910 (2001).

228. Ch. Gras, F. Bernard, F. Charlot, E. Gaffet, and Z. A. Munir, *J. Mater. Res.* 13, 542 (2002).

229. V. Gauthier, F. Bernard, E. Gaffet, Z. Munir, and J.-P. Larpin, *Intermetallics* 9, 571 (2001).

230. R. Orru, J. Woolmann, G. Cao, and Z. A. Munir, *J. Mater. Res.* 16, 1439 (2001).

231. M. Sannia, R. Orru, J. E. Garay, G. Cao, and Z. A. Munir, *Mater. Sci. Eng.*, in press.

232. O. Coreno-Alonso, J. G. Cabanas-Moreno, J. J. Cruz-Riverra, H. A. Calderon, M. Umemoto, K. Tschiya, S. Quintana-Molina, and C. Falcony, *J. Metast. Nanocryst. Mater.* 8, 635 (2000).

233. Y. D. Kim, S.-T. Oh, K. H. Min, H. Jeon, and I.-H. Moon, *Scripta Mater.* 44, 293 (2001).

234. J. W. Lee, Z. A. Munir, and M. Ohyanagi, *Mater. Sci. Eng. A* 325, 221 (2002).

235. M.-S. El-Eskandarany, M. Omori, T. J. Konno, K. Sumiyama, T. Hirai, and K. Suzuki, *Metall. Mater. Trans. A* 32, 157 (2001).

236. S. D. de la Torre, D. E. Garcia, N. Claussen, R. Janssen, Y. Nishikawa, H. Miyamoto, R. Martinez-Sanchez, A. Garcia-L., and D. Rios-Jara, *Mater. Sci. Forum* 386–388, 299 (2002).

237. T. Murakami, C. N. Xu, A. Kitahara, M. Kawahara, Y. Takahashi, H. Inui, and M. Yamaguchi, *Intermetallics* 7, 1043 (1999).

238. G. Farne, F. G. Ricciardiello, L. K. Podda, and D. Minichelli, *J. Europ. Ceram. Soc.* 19, 347 (1999).

239. S. S. Ryu, Y. D. Kim, and I. H. Moon, *J. All. Comp.* 335, 233 (2002).

240. E. Gaffet, N. Malhouroux, and M. Abdellaoui, *J. All. Comp.* 194, 339 (1993).

241. N. Malhouroux-Gaffet and E. Gaffet, *J. All. Comp.* 198, 143 (1993).

242. E. Gaffet and N. Malhouroux-Gaffet, *J. All. Comp.* 205, 27 (1994).

243. E. Gaffet, N. Malhouroux-Gaffet, M. Abdellaoui, and A. Malchère, *Rev. Métal.* 757 (1994).

244. G. A. Roberts, E. J. Cairns, and J. A. Reimer, *J. Power Sources*, in press.

245. D. L. Zhang and D. Y. Ying, *Mater. Sci. Eng. A* 301, 90 (2001).

246. R. Ren, Z. Yang, and L. L. Shaw, *Mater. Sci. Eng. A* 286, 65 (2000).

247. R.-M. Ren, Z.-G. Yng, and L. L. Shaw, *Scripta Mater.* 38, 735 (1998).

248. V. Berbenni and A. Marini, *Mater. Res. Bull.* 37, 221 (2002).

249. V. Nivoix, F. Bernard, E. Gaffet, P. Perriat, and B. Gillot, *Powder Technol.* 105, 155 (1999).

250. H. Hu, Q. Chen, Z. Yin, P. Zhang, J. Zou, and H. Che, *Thermochim. Acta* 389, 79 (2002).

251. V. Berbenni, A. Marini, N. J. Welham, P. Galinetto, and M. C. Mozzati, *J. Europ. Ceram. Soc.* 23, 179 (2003).

252. S. Boskovic, D. Kosanovic, Dj. Bahloul-Hourlier, P. Thomas, and S. J. Kiss, *J. All. Comp.* 290, 230 (1999).

253. R. Citak, K. A. Rogers, and K. H. Sandhage, *J. Amer. Ceram. Soc.* 82, 237 (1999).

254. E. A. Goodilin, D. Pyoryshkov, A. V. Knot'ko, V. V. Lennikov, N. N. Oleynikov, and Y. D. Tretyakov, *Physica C* 349, 278 (2001).

255. E. G. Avvakumov, E. T. Devyatkina, N. V. Kosova, O. A. Kirichenko, N. Z. Lyakhov, and A. A. Gusev, *Kinetics Catal.* 39, 663 (1998).

256. Y. Chen, L. T. Chadderton, J. S. Williams, and J. FitzGerald, *J. Metast. Nanocryst. Mater.* 8, 63 (2000).

257. B. Bokhonov and M. Korchagin, *J. All. Comp.* 333, 308 (2002).

258. P. G. McCormick and F. H. Froes, *JOM* 50, 61 (1998).

259. E. G. Baburaj, O. N. Senkov, and F. H. Froes, Reduction of Metal Oxides through Mechanochemical Processing, U.S. Patent Pending 60/074693, 1998.

260. F. H. Froes, O. N. Senkov, and E. G. Baburaj, *Mater. Sci. Technol.* 17, 119 (2001).

261. M. Senna, *Int. J. Inorganic Mater.* 3, 509 (2001).

262. T. Watanabe, T. Isobe, and M. Senna, *J. Solid State Chem.* 130, 284 (1997).

263. K. Hamada, T. Isobe, and M. Senna, *J. Mater. Sci. Lett.* 15, 603 (1996).

264. JG Baek, T. Isobe, and M. Senna, *Solid State Ionics* 90, 269 (1996).

265. M. Kitamura, M. Kamitani, and M. Senna, *J. Amer. Ceram. Soc.* 83, 523 (2000).

266. A. C. Dodd, K. Raviprasad, and P. G. McCormick, *Scripta Mater.* 44, 689 (2001).

267. P. Matteazzi and G. Le Caër, *Mater. Sci. Eng. A* 149, 135 (1991).

268. J. Ding, T. Tsuzuki, and P. G. McCormick, *J. Am. Ceram. Soc.* 79, 2956 (1996).

269. J. Ding, T. Tsuzuki, and P. G. McCormick, *Nanostruct. Mater.* 8, 75 (1997).

270. J. Ding, T. Tsuzuki, and P. G. McCormick, *Nanostruct. Mater.* 8, 739 (1997).

271. Tsuzuki and McCormick, *Mater. Sci. Forum* 343–346, 383 (2000).

272. J. Ding, W. F. Miao, P. G. McCormick, and R. Street, *Appl. Phys. Lett.* 67, 3804 (1995).

273. J. Ding, T. Tsuzuki, P. G. McCormick, and R. Street, *J. All. Comp.* 234, L1 (1996).

274. J. Ding, T. Tsuzuki, P. G. McCormick, and R. W. Streep, *J. Phys. D* 29, 2365 (1996).

275. E. G. Baburaj, K. T. Hubert, and F. H. Froes, *J. All. Comp.* 25, 146 (1997).

276. H. Yang and P. G. Mc Cormick, *J. Mater. Sci. Lett.* 12, 1088 (1993).

277. H. Yang and P. G. McCormick, *Metall. Mater. Trans. B* 29, 449 (1998).

278. F. H. Froes, O. N. Senkiv, and E. G. Baburaj, *Mater. Sci. Technol.* 17, 119 (2001).

279. S. D. de la Torre, K. N. Ishihara, P. H. Shingu, D. Rios-Jara, and H. Miyamoto, *Proc. Innovative Processing/Synthesis: Ceramics Glasses Composites* 2, 287 (1999).

280. C. Lam, Y. F. Zhang, Y. H. Tang, C. S. Lee, I. Bello, and S. T. Lee, *J. Cryst. Growth* 220, 466 (2000).

281. T. Tsuzuki, J. Ding, and P. G. McCormick, *Physica B* 239, 378 (1997).

282. P. Matteazzi and G. Le Caër, *Mater. Sci. Eng. A* 156, 229 (1992).

283. L. Takacs and M. Pardavi-Horvath, *J. Appl. Phys.* 75, 5864 (1994).

284. P. Matteazzi and G. Le Caer, *J. All. Comp.* 187, 305 (1992).

285. G. B. Schaffer and P. G. Mc Cormick, *Mater. Sci. For.* 88–90, 779 (1990).

286. P. Matteazzi and G. Le Caër, *J. Amer. Ceram. Soc.* 75, 2749 (1992).

287. P. Matteazzi, G. Le Caër, and A. Mocellin, *Ceram. Int.* 23, 39 (1997).

288. P. Matteazzi and M. Alcalà, *Mater. Sci. Eng. A* 230, 161 (1997).

289. T. Nasu, K. Tokumitsu, K. Miyazawa, A. L. Greer, and K. Suzuki, *J. Metast. Nanocryst. Mater.* 2–6, 185 (1999).

290. L. Takacs, *Mater. Lett.* 13, 119 (1992).

291. S. Xi, X. Qu , M. Ma, J. Zhou, Zheng, and X. Wang, *J. All. Comp.* 268, 211 (1998).

292. G. Concas, F. Congiu, A. Corrias, C. Muntoni, G. Paschina, and D. Zedda, *Z. Naturforsch.* 51, 915 (1996).

293. A. Corrias, G. Paschina, and P. Sirigu, *J. Non-Cryst. Solids* 232–234, 358 (1998).

294. A. Corrias, G. Ennas, A. Musinu, G. Paschina, and D. Zedda, *J. Mater. Res.* 12, 2767 (1997).

295. M. P. Dallimore and P. G. McCormick, *Mater Trans JIM* (1996).

296. M. S. El-Eskandarany, *Mater. Trans. JIM* 36, 182 (1995).

297. Y. Chen, J. S. Williams, and B. Ninham, *Colloids Surfaces A* 129–130, 61 (1997).

*298.* N. J. Welham, *J. All. Comp.* 274, 303 (1998).

*299.* N. J. Welham, *J. All. Comp.* 270, 228 (1998).

*300.* Y. Chen, T. Hwang, M. Marsh, and J. S. Williams, *Metall. Mater. Trans. A* 28, 1115 (1997).

*301.* N. J. Welham, *Minerals Eng.* 9, 1189 (1996).

*302.* Q. Zhang and F. Saito, *Hydrometallurgy* 47, 231 (1998).

*303.* R. W. Cahn, *Mater. Sci. Forum* 179–181, 53 (1995).

*304.* R. W. Cahn, in "Physics of New Materials" (F. E. Fujita, Ed.), 2nd updated ed., p. 179. Springer, Berlin, 1998.

*305.* C. T. Liu and K. S. Kumar, *JOM* 45, 38 (1993).

*306.* K. S. Kumar and C. T. Liu, *JOM* 45, 28 (1993).

*307.* Y. W. Kim, *JOM* 46, 30 (1994).

*308.* K. A. Kylian and R. H. Victora, *J. Appl. Phys.* 87, 7064 (2000).

*309.* S. Picozzi, A. Continenza, and A. J. Freeman, *IEEE Trans. Mag.* 38, 2895 (2002).

*310.* B. Ravel, M. P. Raphael, V. G. Harris, and O. Huang, *Phys. Rev. B* 65, 184431 (2002).

*311.* T. Kakeshita and K. Ullakko, *MRS Bull.* 27, 105 (2002).

*312.* D. J. Sellmyer, *Nature* 420, 374 (2002).

*313.* R. Skomski and J. M. D. Coey, *Phys. Rev. B* 48, 15812 (1993).

*314.* G. Martin, *Current Opinion Solid State Mater. Sci.* 3, 552 (1998).

*315.* S. Takahashi, X. G. Li, and A. Chiba, *J. Phys.: Condens. Matter* 8, 11243 (1996).

*316.* G. P. Hufman and R. M. Fisher, *J. Appl. Phys.* 38, 735 (1967).

*317.* A. J. Lapworth and J. P. Jakubovics, *Philos. Mag.* 29, 253 (1974).

*318.* T. Shinohara, K. Sasaki, H. Yamanchi, H. Watanabe, H. Sekizawa, and T. Okada, *J. Phys. Soc. Japan* 50, 2904 (1981).

*319.* J. Schaf, K. Le Dang, P. Veillet, and I. A. Campbell, *J. Phys. F* 13, 1311 (1983).

*320.* E. P. Elsukov, V. A. Barinov, V. R. Galakhov, E. E. Yurchikov, and A. E. Ermakov, *Phys. Metals Metallograph.* 55, 119 (1983).

*321.* H. Bakker, G. F. Zhou, and H. Yang, *Progr. Mater. Sci.* 39, 159 (1995).

*322.* C. C. Koch and J. D. Whittenberger, *Intermetallics* 4, 339 (1996).

*323.* D. Negri, A. R. Yavari, and A. Deriu, *Acta Mater.* 47, 4545 (1999).

*324.* P. J. Webster, *Contemp. Phys.* 10, 559 (1969).

*325.* J. S. Brooks and J. M. Williams, *J. Phys. F* 4, 2033 (1974).

*326.* C. C. M. Campbell, *J. Phys. F* 5, 1931 (1975).

*327.* J. C. Suits, *Phys. Rev. B* 14, 4131 (1976).

*328.* Le Dang Khoi, P. Veillet, and I. A. Campbell, *J. Phys. F* 8, 1827 (1978).

*329.* Y. Watanabe, Y. Murakami, and S. Kachi, *J. Japan Inst. Metals* 45, 551 (1981).

*330.* R. A. Dunlap, R. H. March, and G. Stroink, *Can. J. Phys.* 59, 1577 (1981).

*331.* A. Ayuela, J. Enkovaara, K. Ullakko, and R. M. Nieminen, *J. Phys.: Condens. Matter* 11, 2017 (1999).

*332.* G. Le Caër, P. Delcroix, B. Malaman, R. Welter, B. Fultz, and E. Ressouche, *Mater. Sci. Forum* 235–238, 583 (1997).

*333.* J. S. Robinson, P. G. McCormick, and R. Street, *J. Phys.: Condens. Matter* 7, 4259 (1995).

*334.* E. Wachtel, F. Henninger, and B. Predel, *J. Magn. Magn. Mater.* 38, 305 (1983).

*335.* J. I. Seki, M. Hagiwara, and T. Suzuki, *J. Mater. Sci.* 14, 2404 (1979).

*336.* R. J. Chandross and D. P. Shoemaker, *J. Phys. Soc. Jpn. Suppl. B-III* 17, 16 (1962).

*337.* J. M. Sanchez, M. C. Cadeville, V. Pierron-Bohnes, and G. Inden, *Phys. Rev. B* 54, 8958 (1996).

*338.* T. Ziller, G. Le Caër, O. Isnard, P. Cénédèse, and B. Fultz, *Phys. Rev. B* 65, 024204 (2002).

*339.* A. R. Yavari, *Acta Metall. Mater.* 41, 1391 (1993).

*340.* C. Bansal, Z. Q. Gao, L. B. Hong, and B. Fultz, *J. Appl. Phys.* 76, 5961 (1994).

*341.* Z. Q. Gao and B. Fultz, *Hyp. Interact.* 94, 2213 (1994); 94, 2361 (1994).

*342.* Z. Q. Gao and B. Fultz, *Nanostruct. Mater.* 4, 939 (1994).

*343.* C. Bansal, Z. Q. Gao, and B. Fultz, *Nanostruct. Mater.* 5, 327 (1995).

*344.* F. Cardellini, V. Contini, and G. Mazzone, *Scripta Metall. Mater.* 32, 641 (1995).

*345.* U. Herr, M. Pollack, D. L. Olynick, J. M. Gibson, and R. S. Averback, *Mater. Res. Soc. Symp. Proc.* 398, 575 (1996).

*346.* P. Scherrer, C. Dimitropoulos, F. Borsa, and S. Rubini, *Phys. Rev. B* 57, 10462 (1998).

*347.* A. Hernando, X. Amils, J. Nogués, S. Surinach, M. D. Baro, and M. R. Ibarra, *Phys. Rev. B* 58, R11864 (1998).

*348.* S. Gialanella, X. Amils, M. D. Barò, P. Delcroix, G. Le Caër, L. Lutteroti, and S. Surinach, *Acta Mater.* 46, 3305 (1998).

*349.* R. A. Varin, J. Bystrzycki, and A. Calka, *Intermetallics* 7, 785 (1999); 7, 917 (1999).

*350.* K. Reimann and H. E. Schaefer, *Nanostruct. Mater.* 12, 633 (1999).

*351.* H. E. Schaefer, K. Reimann, W. Straub, R. Phillipp, H. Tanimoto, U. Brossmann, and R. Würschum, *Mater. Sci. Eng. A* 286, 24 (2000).

*352.* X. Amils, J. Nogués, S. Surinach, M. D. Baro, M. A. Munoz-Morris, and D. G. Morris, *Intermetallics* 8, 805 (2000).

*353.* L. Pasquini, A. A. Rempel, R. Würschum, K. Reimann, M. A. Müller, B. Fultz, and H. E. Schaefer, *Phys. Rev. B* 63, 134114 (2001).

*354.* S. Sarkar and C. Bansal, *Acta Mater.* 49, 1789 (2001).

*355.* D. G. Morris, X. Amils, S. Surinach, M. D. Baro, and M. A. Munoz-Morris, *Mater. Sci. Forum* 360–362, 195 (2001).

*356.* K. Reimann, H. J. Fecht, and H. E. Schaefer, *Scripta Mater.* 44, 1999 (2001).

*357.* J. C. Evert and G. Schmitz, *Eur. Phys. J. B* 17, 391 (2000).

*358.* P. Pochet, E. Tominez, L. Chaffron, and G. Martin, *Phys. Rev. B* 52, 4006 (1995).

*359.* J. Joardar, S. K. Pabi, H. J. Fecht, and B. S. Murty, *Philos. Mag. Lett.* 82, 469 (2002).

*360.* E. A. Leonova, P. Delcroix, G. Le Caër, S. D. Kaloshkin, and Yu. V. Baldokhin, in "Ninth International Symposium on Metastable Mechanically Alloyed and Nanocrystalline Materials," ISMANAM 2002, 8–12 September 2002, Seoul, South Korea, *J. Metastable Nanocryst. Mater.*, in press.

*361.* B. Fultz, *J. Chem. Phys.* 88, 3227 (1988).

*362.* B. Fultz and L. Anthony, *Philos. Mag. Lett.* 59, 237 (1989).

*363.* D. Le Floc'h, P. Bellon, and M. Athènes, *Phys. Rev. B* 62, 3142 (2000).

*364.* L. Chaffron, Y. Le Bouar, and G. Martin, *C.R. Acad. Sci. Paris Ser. IV* 2, 749 (2001).

*365.* A. R. Yavari, P. J. Desre, and R. Benameur, *Phys. Rev. Lett.* 68, 2235 (1992).

*366.* C. Gente, M. Oehring, and R. Bormann, *Phys. Rev. B* 48, 13244 (1993).

*367.* J. Xu, U. Herr, T. Klassen, and R. S. Averback, *J. Appl. Phys.* 79, 3935 (1996).

*368.* L. B. Hong and B. Fultz, *J. Appl. Phys.* 79, 3946 (1996).

*369.* G. Mazzone and M. Vittori Antisari, *Phys. Rev. B* 54, 441 (1996).

*370.* T. Klassen, U. Herr, and R. S. Averback, *Acta Mater.* 45, 2921 (1997).

*371.* J. Y. Huang, Y. D. Yu, Y. K. Wu, D. X. Li, and H. Q. Ye, *Acta Mater.* 45, 113 (1997).

*372.* J. Xu, J. H. He, and E. Ma, *Metall. Mater. Trans. A* 28A, 3935 (1997).

*373.* E. P. Yelsukov, E. V. Voronina, G. N. Konygin, V. A. Barinov, S. K. Godovikov, G. A. Dorofeev, and A. V. Zagainov, *J. Magn. Magn. Mater.* 166, 334 (1997).

*374.* G. Martin and P. Bellon, *Metall. Sci. Techn.* 9, 61 (1991); *Solid State Phys.* 50, 189 (1997).

*375.* R. Bormann, *Mater. Sci. Eng. A* 226–228, 268 (1998).

*376.* G. Martin, *Current Opinion Solid State Mater. Sci.* 3, 552 (1998).

*377.* M. Zhu, X. Z. Che, Z. X. Li, J. K. L. Lai, and M. Qi, *J. Mater. Sci.* 33, 5873 (1998).

378. J. Rüsing, V. Naundorf, N. Wanderka, and H. Wollenberger, *Ultramicroscopy* 73, 267 (1998).
379. L. B. Hong and B. Fultz, *Acta Mater.* 46, 2937 (1999).
380. J. Xu, G. S. Collins, L. S. J. Peng, and M. Atzmon, *Acta Mater.* 47, 1241 (1999).
381. P. J. Schilling, J. H. He, R. C. Tittsworth, and E. Ma, *Acta Mater.* 47, 2525 (1999).
382. E. Gaffet, F. Faudot, and M. Harmelin, *J. Alloys Comp.* 194, 23 (1993).
383. S. Zghal, M. J. Hÿtch, J. P. Chevalier, R. Twesten, F. Wu, and P. Bellon, *Acta Mater.* 50, 4695 (2002).
384. S. Zghal, R. Twesten, F. Wu, and P. Bellon, *Acta Mater.* 50, 4711 (2002).
385. U. Czubayko, N. Wanderka, V. Naundorf, V. A. Ivchenko, A. Ye. Yermakov, M. A. Uimin, and H. Wollenberger, *Mater. Sci. Eng. A* 327, 54 (2002).
386. H. W. Sheng, G. Wilde, and E. Ma, *Acta Mater.* 50, 4711 (2002).
387. J. Z. Jiang, C. Gente, and R. Bormann, *Mater. Sci. Eng. A* 242, 268 (1998).
388. P. Crespo and A. Hernando, *Recent Res. Devel. Nanostruct.* 1, 63 (1999).
389. N. Wanderka, U. Czubayko, V. Naundorf, V. A. Ivchenko, A. Ye. Yermakov, M. A. Uimin, and H. Wollenberger, *Ultramicroscopy* 89, 189 (2001).
390. M. B. Fernandez van Raap, L. M. Socolovsky, F. H. Sanchez, and I. L. Torriani, *J. Phys.: Condens. Matter* 14, 857 (2002).
391. S. D. Kaloshkin, I. A. Tomilin, G. A. Andrianov, U. V. Baldokhin, and E. V. Shelekhov, *Mater. Sci. Forum* 235–238, 565 (1997).
392. P. Delcroix, T. Ziller, C. Bellouard, and G. Le Caër, *Mater. Sci. Forum* 360–362, 329 (2001).
393. J. H. He, H. W. Sheng, P. J. Schilling, C. L. Chien, and E. Ma, *Phys. Rev. Lett.* 86, 2826 (2001).
394. J. H. He and E. Ma, *Phys. Rev. B* 64, 144206 (2001).
395. H. R. Gong, L. T. Kong, W. S. Lai, and B. X. Liu, *Phys. Rev. B* 66, 104204 (2002).
396. H. W. Sheng, J. H. He, and E. Ma, *Phys. Rev. B* 65, 184203 (2002).
397. J. H. He, H. W. Sheng, J. S. Lin, P. J. Schilling, R. C. Tittsworth, and E. Ma, *Phys. Rev. Lett.* 89, 125507 (2002).
398. R. Enrique, F. Wu, and P. Bellon, *Surface Coat. Technol.* 150, 1 (2002).
399. G. Le Caër, T. Ziller, P. Delcroix, and C. Bellouard, *Hyp. Interact.* 130, 45 (2000).
400. A. F. Cabrera and F. H. Sanchez, *Phys. Rev. B* 65, 094202 (2002).
401. J. S. Benjamin and T. E. Volin, *Metall. Trans.* 5, 1929 (1974).
402. H. Kuwano, H. Ouyang, and B. Fultz, *Mater. Sci. Forum* 88–90, 561 (1992).
403. S. K. Xia, E. Baggio-Saitovitch, F. C. Rizzo Assunção, and V. A. Pena Rodriguez, *J. Phys.: Condens. Matter* 5, 2729 (1993).
404. T. Koyano, T. Takizawa, T. Fukunaga, U. Mizutani, S. Kamizuru, E. Kita, and A. Tasaki, *J. Appl. Phys.* 73, 429 (1993).
405. S. K. Xia, F. C. Rizzo Assunçao, and E. Baggio-Saitovitch, *Mater. Sci. Forum* 225–227, 459 (1996).
406. G. Le Caër, P. Delcroix, T. D. Shen, and B. Malaman, *Phys. Rev. B* 54, 12775 (1996).
407. G. Le Caër, P. Delcroix, and J. Foct, *Mater. Sci. Forum* 269–272, 409 (1998).
408. C. Bellouard, G. Le Caër, and P. Delcroix, *Mater. Sci. Forum* 343–346, 819 (1998).
409. C. Lemoine, A. Fnidiki, D. Lemarchand, and J. Teillet, *J. Phys.: Condens. Matter* 11, 8341 (1999); C. Lemoine, Ph.D. Thesis, Université de Rouen, 2000.
410. B. F. O. Costa, G. Le Caër, and B. Luyssaert, *J. Alloys Comp.* 350, 36 (2003).
411. S. F. Fischer, S. N. Kaul, and H. Kronmüller, *Phys. Rev. B* 65, 064443 (2002).
412. P. Delcroix, C. Bellouard, and G. Le Caër, in preparation.
413. C. Michaelsen, *Philos. Mag. A* 72, 813 (1995).
414. H. Heegn, *Chem. Ing. Tech.* 73, 1529 (2001).
415. A. C. Lund and C. A. Schuh, *Phys. Rev. Lett.* 91, 235505 (2003).
416. A. C. Lund and C. A. Schuh, *Appl. Phys. Lett.* 82, 2017 (2003).
417. http://wondersmith.com/scifi/micro.htm

# Mechanical Properties of Nanostructured Materials

## S.-P. Hannula, J. Koskinen

*VTT Industrial Systems, Finland*

## E. Haimi

*Helsinki University of Technology, Finland*

## R. Nowak

*Helsinki University of Technology, Finland, and
Hiroshima University, Kagamiyama, Japan*

## CONTENTS

## 1. INTRODUCTION

In recent years a wide range of nanostructured materials has been introduced. These novel materials are produced in various forms such as nanopowders, nanostructured particulates, fibers, tubes, thin films, as well as bulk by using a number of processing routes. Nanostructured materials have many interesting properties. These include a number of useful mechanical properties related to strength, hardness, elastic properties, toughness, plasticity, etc. In this chapter these properties are described and discussed in detail with a reference to existing or potential practical applications.

Distinction of different forms of nanostructured materials may be made by their dimensionality [1, 2]. Nanostructural materials may exist in (i) zero-dimensional atomic clusters (all three dimensions in nanoscale), (ii) one- or two-dimensional multilayers or filamentary structures (one or two dimensions in nanoscale, one or two in macroscale), and (iii) bulk (all dimensions in macroscale) with three-dimensional nanocrystalline grains (see Fig. 1).

There is a variety of processes suitable for producing nanocrystalline materials. Bulky nanocrystalline materials may be produced, for example, by electrodeposition, severe plastic deformation (SPD) of preforms, or by using various powder metallurgical routes to consolidate nanopowders or powders with nanocrystalline structure produced by, for example, mechanical alloying (MA). The bulk form of these materials includes electrodeposited sheets, equal channel angular pressed (ECAP) rods, ball-milled and consolidated pellets, composite films produced by a variety of deposition techniques, etc. It should be noted that their properties are related not only to their nanostructure, but also to the processing method by which they are produced, because the detailed microstructural features may differ after various processing routes even at the same nominal composition and grain size. These microstructural features include type of grain boundaries, grain shape, crystal defects, pores
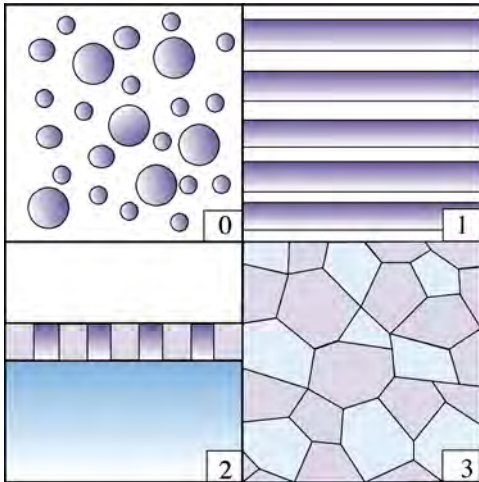
**Figure 1.** Schematic illustration of various nanomaterials having a different number of dimensions [1, 2]; zero-dimensional powder, one-dimensional thin deposited layer, surface coating with nanostructure in two-dimensions, and three-dimensional bulk nanomaterial.

and their distribution, other flaws, impurities, and surface condition.

Mechanical testing of nanocrystalline materials is generally different from that used for their coarse-grained counterparts because the amount of nanocrystalline material is in many cases so small that conventional test methods with large bulk samples cannot be used. Therefore, methods using small amounts of material have often been used instead of conventional testing. Results have been obtained either by modified traditional testing methods or by specially designed tests that probe materials with small dimension, such as instrumented nanoindentation. Most of the data that exist are from the nanostructured thin films or bulk materials processed by powder metallurgy (PM) techniques or by severe plastic deformation (SPD). These data are not always as reliable as those obtained from conventional bulk samples. Further elaboration of results is also subject to uncertainty because the determination of the grain size in nanoscale is more tedious and subject to larger experimental errors than in materials with conventional grain sizes.

Nevertheless, it has been shown that nanocrystalline materials have special mechanical properties. Typically the strength of crystalline materials is increased with decreasing grain size and materials with small grain size often exhibit also superplastic behavior. Nanocrystallinity may also have a positive influence on fatigue properties of metals and toughness of ceramic materials. Ductility, however, may also be decreased due to increased tendency to flow localization, but hardness and wear properties of materials and coatings can be improved.

There are several recent reviews on mechanical properties of nanocrystalline materials (e.g., [3–5], to mention a few) and the reader is referred also to them for a more thorough review of different particular subjects. In this chapter, we wish to give a collective view on various current developments related to mechanical properties of nanocrystalline materials.

# 2. THEORETICAL BACKGROUND OF MECHANICAL PROPERTIES

The main feature distinguishing nanomaterials from conventional materials is the large fraction of atoms located in the grain/interphase boundaries. Grains are typically equiaxed with a narrow and lognormal size distribution and dislocations are seldom seen inside the grains. Those that are seen are typically in sessile configurations [6]. Level of various defects arising from processing may be present in significant amounts and they all influence the mechanical properties. Even in nominally fully dense nanocrystalline materials there are 1- to 2-nm-sized pores and smaller nanovoids [7]. Two divergent views exist on the nature of grain boundaries in nanomaterials. According to the classic interpretation, the nature of grain boundaries in nanomaterials is no different from the nature of grain boundaries in coarse-grained materials [8]. However, based on a more recent study by computer simulation, it has been suggested that in nanomaterials a long-range periodicity does not exist, the grain boundary energy and width distributions are narrower and the grain boundaries wider than in bicrystals, and that the grain boundaries are an isotropic, cement-like phase different from glasses or bicrystals [9]. The grain boundary structure results in enhanced solute solubilities and enhanced diffusion as well as a different thermodynamic behavior [10]. Therefore, retention of nanocrystallinity at elevated temperatures either during processing or in service is quite difficult.

## 2.1. Scale Dependence of Strength and Elastic Properties

### 2.1.1. Dependence of Strength (and Hardness) on the Grain Size

It has been known for a long time that refining the grain size of materials increases their strength, that is, the yield and flow stress as well as stress to rupture. The theoretical background for increasing strength with decreasing crystalline size lies in the theory for dislocation slip in crystalline materials. This tendency has been explained by using three different models, that is, the pile-up model, the work-hardening model, and the composite model; see, for example, the review of Lasalmonie and Strudel [11]. In nanocrystalline materials the conventional dislocation mechanisms cease to be operational. As the size of a Frank–Read dislocation source cannot exceed the size of a grain, such sources become inoperable with decreasing grain size under typical loads. Recent simulations on nanocrystalline Al have also demonstrated that the nucleation of complete dislocations at the grain boundary becomes impossible as the grain size becomes smaller than the so-called splitting distance of the dislocation [12].

The grain size ($d$) dependence of the yield strength ($\sigma_y$) with materials of conventional grain size in the micrometer range typically follows an expression of the type

$$\sigma_y = \sigma_0 + k/d^{1/2} \qquad (1)$$

where $\sigma_0$ is the friction stress and $k$ is a material-dependent constant. This relation is known as the Hall–Petch relation

originally proposed by Hall [13] and Petch [14]. However, this relation has been found to break in nanometer-scale materials. At fine grain sizes (in the submicron range), the slope becomes lower and at ultrafine grain sizes, $k$ may become negative [15–17]. The latter occurs when the grain size decreases to the range of few tens of nanometers although in some cases increase in flow stress has been reported down to the grain size of 10 nm [18, 19].

Several models have been proposed to explain the inverse Hall–Petch relation, that is, grain boundary deformation mode effect [20], triple junction volume effect [21], size-dependent line tension effect [22, 23] composite model [24, 25], and that of Takeuchi [26]. All the models incorporate a softening mechanism at fine grain sizes. Wang et al. [27] have been able to explain the different deviations from the Hall–Petch relation at different grain sizes by describing the material as a composite consisting of four different phases (crystal, grain boundary, triple line junctions, and quadruple node phases) with different strengths and relative volume fractions. Due to four fitting parameters, this model is capable of describing any kind of strength variations with grain size. However, it does not provide a physical explanation for the operational mechanisms.

One plausible physical explanation for the softening is grain boundary sliding and rotation, which can explain both the accelerated deformation rates and the softening at the finest grain sizes and the hardening at larger grain sizes. This explanation is decribed by Padmanathan and co-workers [28–31]. According to their model, the deviation from the Hall–Petch behavior, which eventually leads to the inverse Hall–Petch behavior, can be attributed to competition between the grain boundary sliding controlled process and dislocation dominated deformation. These mechanisms are independent and the one that in particular conditions of grain size, alloying, temperature, and strain rate requires lower stress to operate will be the favored mode of deformation. In general, when the deformation is dislocation controlled, the grain refinement increases the stress required, and when the grain boundary sliding is the dominant mechanism, the grain refinement will decrease the stress to deformation.

The latter explanation is finding support from the atomistic modeling of deformation in nanocrystalline materials. Recent molecular-dynamics simulations have revealed an inverse Hall–Petch behavior for very small grain sizes attributed to grain boundary (GB) sliding [32–35]. The simulation of nanoindentation in 5- and 12-nm nanocrystalline gold has shown that GBs act as a sink for partial dislocations emitted under the indenter and there is a collective motion of grains pointing towards the presence of GB sliding; that is, grain boundaries for a number of grains that are randomly oriented may straighten and slide collectively. Neighboring grains may rotate and form also larger grains [36, 37]. This mechanism supposedly works without diffusion accommodation and has been criticized by Yamakov et al. [12], who claim observation of GB sliding does not rule out the diffusion-assisted creep mechanisms even at room temperature.

One should also note that the experimental results are influenced by the detailed GB structure of the nanostructured materials, which in turn is dependent on the particular method with which the materials have been produced. For instance, despite the similar grain size, the deformation behavior of Cu produced by ECAP is significantly different in the as-pressed state than after a short anneal at 473 K, which results in recovery of the defect structure at grain boundaries and a sharp decrease of internal stresses [5]. This means that in addition to the mean grain size, the defect density at grain boundaries influences the strength properties of nanostructured materials. See Figure 2.

### 2.1.2. Elastic and Anelastic Properties of Nanocrystalline Materials

There are very few theoretical considerations related to the elasticity of nanocrystalline materials. Some early experimental results have prompted ideas on elastic properties being dependent on the volume fraction of lower-density grain boundary phase in relation to the bulk phase [39]. Later, however, the experimental results [40, 41] have, according to Morris [2], quite convincingly showed that the grain size refinement does not play any obvious role in modifying Young's modulus, shear modulus, or bulk modulus, but the observed reduction is inherited from the quality (porosity content) of the processed material.

On the other hand, detailed studies of nanostructured copper samples processed by equal channel angular (ECA) pressing have been carried out by using ultrasound method [42]. According to this study, the values of elastic moduli in nanocrystalline copper were lower by 10–15% as compared to coarse-grained copper. The explanation was based on the differences of elastic properties of near grain boundary regions and grain interiors. The change in elastic values of nanostructured copper could be explained if it was assumed that the elastic modulus of the near grain boundary regions is 15–17% of the value of the elastic modulus of the coarse-grained copper. Reduction of elastic modulus in ECA pressed copper and copper composites has also been obtained in other studies [43–45]. Some new modeling results support the decreasing of elastic modulus values at very small grain sizes. However, this is realized in a substantial level only at grain sizes below 10 nm [46].

Internal friction studies are used to study the deviation of the material from Hooke's law and its anelastic behavior. Internal friction studies show that the damping for nanocrystalline materials is significantly higher than in coarse-grained
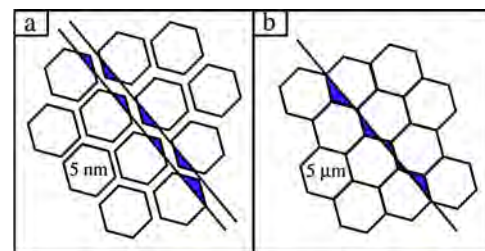


**Figure 2.** Schematic illustration in two dimensions of grain arrangements in a nanocrystalline (a) and conventional polycrystalline (b) material. Forming of a mesoscopic planar interface can occur if atoms in the darker regions rearrange [38]. Rearrangement is favored in the nanocrystalline material because of the three orders of magnitude smaller thickness of the critical region.

materials. For example, studies on ECA pressed copper have revealed that damping in nanocrystalline material is higher by a factor of 4–5 than in coarse-grained material processed by annealing at high temperatures and even higher by a factor of 2–3 as compared to the level of damping in gray cast iron ($50 \times 10^{-4}$), typically used as a reference for damping [40, 47]. Previous studies have also shown that the onset of the intense growth of internal friction is significantly lower (by 120 K) in nanocrystalline materials than in coarse-grained materials. Similar results have been obtained for the nanocrystalline copper obtained by consolidating mechanically milled powders by hot isostatic pressing [48]. Furthermore, it has been noticed that the dislocation-associated peak typically present in coarse-grained materials at low temperatures is absent, indicating that there are only few mobile dislocations in nanocrystalline materials.

The internal friction curve of nanocrystalline ECA copper has a strong maximum of the so-called grain boundary peak at 475 K associated with the intensification of grain boundary sliding in the material. According to Valiev et al. [4], these anomalies are associated not only with small grain sizes but also with specific structure connected with nonequilibrium grain boundaries formed in ECA processed material and their transformation from nonequilibrium grain boundaries to equilibrium grain boundaries.

Internal friction studies have been performed also in other nanocrystalline materials, such as Pd [49], Al [50–52], Au [53], and Fe [54]. In general, a damping peak superimposed on a background increasing with temperature is observed. Furthermore, some additional peaks may be observed related to, for example, grain boundary impurities and films [49].

### 2.1.3. Fatigue of Nanocrystalline Materials

In fatigue (cyclic loading), material undergoes reversed deformation which results in accumulation of damage and finally fracture. Cyclic deformation produces typically at some advanced stage microstructural features, that is, dislocation cells that are typical of the plastic strain amplitude in question. The relaxed dislocation cell structure that develops during fatigue testing is typically in the half-micron level. In nanostructured materials, it may therefore be expected that the continuous deformation will lead to cyclic softening and an extensive growth of crystal structure. Data obtained on low cycle fatigue of nanocrystalline ECA processed copper seems to support this idea [55–58].

On the other hand, it has been shown that the fatigue behavior of nanocrystalline Ni produced by electrodeposition is exactly similar to that of conventional Ni [59] and in another study that the formation of nanostructures by severe plastic deformation results in a significant increase in fatigue strength and life [3]. These contradictory results may at least partly be explained by the differences in the details of the nanostructures. Hashimoto et al. [60] have studied the fatigue response of different types of nanostructures produced by ECA. At a constant plastic amplitude fatigue, the material having a rather homogeneous nanocrystalline structure showed cyclic hardening while the material having a banded structure with elongated grains and fragments of low angle boundaries showed cyclic softening. Similarly, significant changes in the anelastic response of materials having

nominally the same grain size have been observed [53]. The extent of Bauschinger effect in nanocrystalline ECA pressed copper was found to increase substantially in a short low-temperature annealing, which did not alter the grain size but recovered the grain boundary structure. These results demonstrate the significant influence of the type of nanostructure on the cyclic response.

After the early studies, the cyclic response of nanocrystalline materials has been a subject of growing interest and several investigations on different materials have been carried out [61–67]. As a conclusion from these studies, ECA-produced copper and 5056 Al-Mg alloy exhibit notable improvement of fatigue properties in load-controlled cycling while under constant strain amplitude they last considerably shorter than their coarse-grained counterparts. On the other hand, ECA pressed titanium shows no cyclic softening or degradation in strain-controlled cyclic loading [58]. Based on these studies, Vinogradov et al. have proposed a one-parameter dislocation-based model to describe the experimental results. According to this model the cyclic saturation stress at high strains takes the form

$$\tau_s = \tau_o + \alpha\mu b/(Ly)^{1/2} \qquad (2)$$

where $\tau_o$ is the minimum stress for the dislocations to move, $\alpha$ is a geometrical factor of the order of 0.5, $\mu$ is the shear modulus, $L$ is the slip path of the dislocations with a Burgers vector $b$, and $y$ is the so-called annihilation length. This simple relation seems to be applicable both for an aluminum alloy [64] and for titanium [61]. Most of the characteristic features of the fatigue behavior of ultrafine grain size materials can be understood based on the ordinary dislocation kinetic, dislocation hardening, and Hall–Petch hardening. On the other hand, the susceptibility of the ECA pressed materials to strain localization limits their tensile and fatigue ductility and in practice to a large extent determines the fatigue performance. However, there still exists very little information on the fatigue behavior of nanocrystalline materials in the range of few nanometers up to few tens of nanometers.

### 2.1.4. Creep of Nanocrystalline Materials

In creep, the material gradually undergoes straining under the load which may be well below the loads causing macroscopic deformation, for example, in tension. It is well known that creep may be ascribed to a number of different deformation processes, which typically operate more or less in parallel under given conditions. Under particular conditions of stress and temperature, it may be possible to identify a single process responsible for the measured creep rate. At very low stresses and small grain sizes, vacancies rather than dislocations are generally held responsible for the observed creep rate. Two models, Nabarro–Herring creep and Coble creep, can be used to account for plastic flow under those circumstances [5]. Nabarro–Herring creep involves the vacancy diffusion through the grain volume and Coble creep involves vacancy diffusion along grain boundaries. Nabarro–Herring creep has an inverse square dependence and Coble creep has an inverse cubic dependence of grain size with creep rate. Coble creep predominates over Nabarro–Herring creep at low homologous temperatures

and very small normalized grain sizes. A number of studies have been designed to study the low-temperature creep in nanocrystalline materials since, for example, in nanocrystalline copper the diffusivity at room temperature has been reported to be orders of magnitude higher than the grain boundary diffusivity of regular polycrystalline copper [68]. Such high diffusivities have been proposed to be responsible for the additional modes of deformation which may contribute to softening at fine grain sizes [15].

The studies on creep behavior of nanostructural materials have established that they typically exhibit very high creep rates. The behavior has typically been explained in terms of grain boundary diffusional creep in combination with triple point diffusion [69–71], but as Mohammed and Li [5] have pointed out, some of the characteristics reported, such as instantaneous strain and primary creep with decreasing creep rate [72, 73], are not typical of diffusional creep. Although a number of studies on creep of nanocrystalline materials have already been conducted, the full picture of creep deformation is still somewhat unclear. However, it may be concluded that the creep properties of nanocrystalline materials are very sensitive to their microstructure. Therefore two nanocrystalline materials with the same nominal composition and structure may exhibit different deformation behavior. A current review on the subject is given by Mohammed and Li [5].

## 2.2. Plasticity of Nanocrystalline Materials

Plasticity of nanocrystalline materials is of interest from both theoretical and practical points of view. The practical aspects are related both to the ease of producing complicated forms by plastic deformation as well as to the service performance of these materials. As discussed in the previous section, the susceptibility of, for example, fine-grained ECA pressed materials to strain localization limits their tensile and fatigue ductility and in practice to a large extent determines their fatigue performance. On the other hand, the increasing relative amount of atoms at grain boundaries and grain junctions with decreasing grain size results in enhanced diffusion rates in nanocrystalline materials as compared to standard polycrystalline materials.

### 2.2.1. Ductility of Nanocrystalline Materials

The ductility of nanocrystalline materials can be examined by tensile testing. In a tensile test ductility is related to the elongation at fracture or the reduction of area (at necking) at fracture. A classical approach to theoretical consideration of the ductility of nanomaterials is that of Morris [2], who uses the so-called Considére construction to describe the respective importance of stress level and work-hardening rate in controlling the geometric instability responsible for the onset of necking. Generally, a high work-hardening rate will result in large strain at the instability while a low work-hardening rate, typical of nanomaterials, will result in a small strain to failure or in extreme case no strain at all.

However, the stability of flow and consequently the degree of ductility of a (ductile) material in tensile test depends, in addition to its strain hardening, also on strain rate hardening characteristics (see, e.g., Hart [74]). As both of these characteristics may differ from those of the coarse

(or conventional) grain size materials, it is expected that the ductility of nanostructural materials differ from that of their coarse-grained counterparts.

A more complete treatment of the conditions for necking would include the strain rate sensitivity of the flow stress of nanostructural materials, which as already mentioned, typically also is different from that of coarse-grained materials. Hart [74] has shown that the instability in tensile test is determined by the equation

$$\gamma + m \geq 1 \tag{3}$$

where $\gamma$ is the strain-hardening rate and $m$ is the strain rate sensitivity of the flow stress. Since for metals $m$ is generally less than unity (in fact, generally much less than unity), the strain-hardening exponent $\gamma$ must be clearly greater than zero for the flow to be stable. As nanocrystalline metals show only little strain hardening in tension, their tensile strain at the flow at necking often remains small.

### 2.2.2. Superplasticity

Many materials are known to exhibit superplasticity in proper conditions. In the superplastic state, elongations of several hundred or even more than one thousand percent are obtained. Typical attributes to superplastic deformation are a proper temperature–strain rate regime (typically temperature around $0.5$–$0.6T_m$, where $T_m$ is the melting point of the material, and strain rates around $10^{-3}$–$10^{-4}$ s$^{-1}$), a small grain size (typically less than 10 $\mu$m), and a relatively stable microstructure of the material during deformation [75, 76]. It is possible to describe superplasticity by a constitutive equation of the form

$$\dot{\varepsilon} = A(DGb/KT)(b/d)^p(\sigma/E)^n \tag{4}$$

where $\dot{\varepsilon}$ is the strain rate, $A$ is a constant, $D$ is the coefficient of grain boundary diffusion, $G$ is the shear modulus, $b$ is the Burgers vector, $K$ is the Boltzmann constant, $T$ is the temperature, $d$ is the grain size, $p$ is the grain size exponent (usually equal to 2), $\sigma$ is the flow stress, $E$ is Young's modulus, and $n$ is the stress exponent. This law would predict the decrease of the temperature or increase in strain rate regime with decreasing grain size where superplasticity occurs. A closer examination of this relation shows that the slow strain rates associated with superplasticity in the conventional materials having a grain size around 1 $\mu$m could be accelerated by several orders of magnitude or correspondingly the temperature may be decreased even by several hundreds of degrees. The superplasticity in nanocrystalline materials is therefore of special interest as it would extend the phenomenon to lower temperatures or higher strain rates, thus opening new technological opportunities.

One of the requirements in order to technologically utilize the low-temperature or high strain rate superplasticity of nanomaterials is to control the grain growth during processing. During superplastic deformation both static and dynamic grain growth may occur. The static grain growth can be described by [3]

$$D_s^N - D_0^N = kt \tag{5}$$

where $D_s$ is the grain size after temperature exposure, $D_0$ is the grain size at the beginning of temperature exposure, $N$ is the grain size exponent (2 in pure materials near the melting point and 3–4 in many practical cases), $k$ is a rate constant with an Arrhenius dependence ($k = k_0 \exp(Q/RT)$), and $t$ is time. Because of the processing time needed for superplastic forming, static grain growth is always a concern. However, dynamic grain growth is in practice much more severe than static grain growth. Dynamic grain growth occurs because of the applied strain and may cause the grain size to grow severalfold during forming even at low temperatures. The increment of grain growth solely of dynamic origin ($\Delta D_d$) is independent of time and temperature and may be described by [3]

$$\Delta D_d = D_f - D_s = c\varepsilon \qquad (6)$$

where $D_f$ is the grain size after forming, $D_s$ is the grain size before forming, $c$ is a material constant, and $\varepsilon$ is the strain in forming. Because of the grain growth (both static and dynamic), deformation becomes increasingly difficult with increasing strain.

So far superplasticity has been demonstrated at elevated temperatures for several nanocrystalline metal and ceramic systems. The major systems investigated so far include several Al-Ni-Mm alloys [77, 78], Ti, Al, or Mg-based SPD alloys [79–82], boron doped $Ni_3Al$-alloy [83, 84], Y-TZP [85–88], $TiO_2$ [89–91], and $MgO \cdot Al_2O_3$ spinels [92]. Evidence of superplasticity in ceramic nanomaterials has mainly been obtained by other than tensile testing, that is, compressive testing, hardness testing, or bulge testing, because of difficulties in producing fully dense nanocrystalline specimens of adequate size for tensile testing.

Large ductility in compression is not necessarily an evidence of superplasticity since neck instability and cavitation failure are absent in compressive deformation [93]. An example of excellent compressive properties but poor tensile behavior is that of Fe-28Al-2Cr alloy [94]. It was possible to deform this to a strain of >1.4 in compression, whereas no tensile ductility was observed. The flow stress in compression (2.1 GPa) was considerably higher than the tensile fracture stress (0.65 GPa). Tensile superplasticity of nanocrystalline materials has been studied more extensively over the last years since the first evidence of tensile superplasticity was reported [95] in 1993.

According to studies so far, superplasticity of nanomaterials occurs most likely as a result of grain boundary sliding and some diffusional accommodation without visible dislocation activity in the grains. In order to limit the grain growth, both solute and second-phase additions have been used to pin the grain boundaries with a mixed success [96, 97].

## 2.3. Fracture Toughness of Nanocrystalline Materials

Fracture toughness of the material is related to the ability of the material to sustain the creation and propagation to failure of local flaws and cracks. During loading the pre-existing subcritical flaws or cracks will grow as some localized straining will take place ahead of the flaw. When the critical size is reached, a catastrophic failure will take place. Fracture

toughness of nanocrystalline materials may be quite different from that of bulk materials. [Chan [98] assumed that the fracture toughness and the yield stress remain constant, but that the starting flaw size is decreased as the grain size is decreased the critical stress to be imposed for a flaw to grow will increase.] As a result, the strain to failure will be increased as the grain size is reduced. A dramatic increase in fracture strain will occur as the grain size reaches a characteristic value for the material (combination of fracture toughness and yield stress). Of course, then the flaw size has to decrease with grain size (which may not always be the case). Other assumptions must also be valid for the theory to work; that is, the critical stress intensity factor at the point of catastrophic failure should be constant and independent of grain size, and the plastic properties including yielding must be independent of grain size. Morris [2] has criticized especially the last assumption and refined the analysis of Chan by adapting the classical Hall–Petch relationship (Eq. (1)) to describe the dependence of yield strength on grain size. He arrived at the following critical crack length ($c$) at the failure point for a material of toughness $K_c$ when a stress equal to the yield stress is applied:

$$c = 1/\pi[K_c/(\sigma_0 + kd^{-n})]^2 \qquad (7)$$

where $\sigma_0$ is the friction stress, $k$ is a material-dependent constant, and $d$ is the grain size. This equation gives a possibility to examine whether the material tends to become more or less brittle as the grain size changes for a material at a given fracture toughness level. Using this equation Morris and Morris [99, 100] have shown that the critical flaw size is only slightly and subtly different from the change of grain size, and in the absence of any change in the intrinsic property of fracture toughness, the critical flaw size and the grain size change in a closely correlated manner. Based on the analysis, Morris and Morris conclude that it is impossible to tell whether the nanocrystalline state will offer any improved ductility/failure characteristics. A complete analysis on the subject can be found in [98] with the further refinements in [2].

# 3. MODELING OF MECHANICAL PROPERTIES OF NANOSTRUCTURED MATERIALS

Mechanical behavior of nanostructured materials is frequently investigated using various simulation techniques, due to difficulties associated with *in-situ* observation of deformed nanostructured material components. Hence, the modeling by finite element method, molecular dynamics, or atomistic calculations enables us to conclude on the phenomena that govern the mechanical response of these particular solids, and in consequence, to conclude on their mechanical properties. Since the cross-sectional dimensions of nanostructured components or entire material approach the scale of interatomic distances (it is already possible to fabricate the 1- to 5-unit-cells-thick ceramic plates [101] or $SiO_2/SiC$ nanorods with 100 atoms across [102, 103]), their size challenges the classical approach used in continuum mechanics, and as a result, the scale effects cannot be ruled

out in the modeling. This makes it difficult to perform the simulation of deformation of nanostructures, which is based in the classical continuum approach.

Furthermore, it should be noted that all the above listed methods of modeling are used to simulate also nanoindentation testing, the probing technique which is frequently used to test nanostructured materials. The FEM-based analysis of the contact problems is already well developed, while molecular dynamics and atomistic simulations have recently gained common interest (refer to the next section).

## 3.1. Finite Element Method

Despite the drawbacks of the traditional mechanical approach, finite element simulation of the deformation and fracture of nanostructures is widely used. It appears, however, in this area of research as a hybrid method supplemented by either empirical atomistic models such as this used by Robertson et al. [104] to study uniaxial tensile and compressive response of carbon nanotubes, or multiscale robust simulation of surface deformation (see, e.g., [105]) that allowed the authors to conclude on the microscopic aspects of phase transformation in silicon while investigating different interatomic potentials and various finite element meshes. In the latter approach the constitutive response of the material is obtained from atomistic calculations, which contrasts standard FEM methodology that employs empirical-phenomenological rule.

Moreover, the recent comparison of finite element modeling and artificial neural network (ANN) appears quite beneficial for nanostructured materials and contacts in nanoscale. This type of approach allowed Muliana et al. [106] to resolve the long-persisting dilemma concerning the nanoindentation deformation of hard films/multilayer structure deposited on soft substrate—something already investigated by Myers et al. [107] and Nowak et al. [108, 109]. The ANN models have demonstrated excellent predictive capability for indentation of nonlinear materials.

FEM modeling on the mechanical behavior of nanostructures proved to be efficient when one tackles the problems associated directly with application of a new structure. The proper example is here mechanical analysis of micromechanical clips for optical fibers, offered recently by Lu et al. [110], that targets the performance and reliability of new silicon nitride fiber-clips [111, 112] which might make the production and assembly process of full integrated optoelectronic systems cheap and reliable. Consequently, Lu et al. [110] used FEM to determine stress fields near the corner of the clip/substrate system and developed theoretical models to predict its failure.

Furthermore, the finite element simulation has become widely used in studying deformation phenomena in microscale and in new mechanical processing oriented towards nanotechnology. The FEM-assisted analysis of anomalous surface deformation of sapphire [113], stress and cracks in nanostrip casting process [114], tribology in nanomanufacturing and nanopowders for solid lubrication [115], nanomechanical properties of cutting tools for nanomanufacturing [116], material removal during submicroscale polishing [117], estimation of nanoscale zone in corroded surface ceramic layers [118], and cohesive strength of thin films [119], serve as selected examples of the present trend in research. These studies are again followed by FEM-aided nanoindentation exploration of mechanical response of microsprings and microcantilevers—the subject being in the center of interest for microfabrication [120].

## 3.2. Molecular Dynamics and Atomistic Simulation

Given the recently used direct machining of material surface to fabricate nanostructured components, it became necessary to achieve better understanding of such processes as adhesion, cutting, or surface deformation at atomistic level, where continuum mechanics cannot be applied. Hence, the molecular dynamic (MD) simulation method that allows one to study the behavior of atoms during short time interactions appears as a proper tool to model indentation, friction, adhesion, fracture, and ultraprecise cutting on the atomic scale [121]. In particular, nanoindentation is the area of research in which MD simulation was already exercised for several years, since the nanoscale contact problem falls clearly beyond the frames of continuum mechanics.

The studies of this kind made use of realistic many-body interatomic potentials to obtain information concerning the way in which the defects are created under the tip as well as the fate of individual atoms. This provides a new insight into such phenomena as pressure-induced phase transformations, elastic to plastic transition, or amorphization of the tested material, as demonstrated in the case of nanoindentation of silicon structure [121–124], as well as FCC and BCC crystalline lattices in contact with a rigid [125] or atomistic modeled [126] tip.

The above-mentioned conventional MD studies were followed by *ab initio* quantum mechanical approach [127] and local strain diagnostics [128] that provided a complete picture of atomic distribution near elastic contact and clarified origins of plastic deformation and amorphization in nanoindented silicon, respectively. Furthermore, the similar classical two-dimensional MD analysis applied to nanocutting process by Zhang and Tanaka [129] and Shimizu et al. [130] was improved in terms of a three-dimensional approach offered by Fang and Weng [131], who used canonical MD ensemble corresponding to their copper crystal processed with the diamond pin tool.

It should be emphasized at this stage that the MD approach to nanoindentation or nanocutting reviewed in this section are in fact nothing other than hybrid FEM-MD methods which we discussed in the previous section [104, 105]. In contrast to this combined approach, the atomistic simulation represented here by the work of Astala et al. [127] has different character and provides better insight into atomistic processes, despite the fact that the size of the simulated cluster is considerably smaller than the experimental contact area (the common problem for the atomistic numerical models of this kind).

The excellent example of the atomistic simulation of elastic properties of nanostructured materials was given by Miller and Shenoy [132] who used direct simulation of nanoscale structures using embedded atom method for FCC lattice and Stillinger–Weber potentials for diamond structures. Their size-dependent modeling of effective stiffness

properties $D$ of nanosized elements such as plates and beams led to the general formulation of the deviation of elastic property from that defined by conventional mechanics $D_c$ [132]:

$$\frac{D - D_C}{D_C} = \alpha \frac{S}{E} \frac{1}{h} \qquad (8)$$

where $\alpha$ defines nondimensional constant that is function of geometry, $S$ stands for surface elastic constant, $E$ is elastic modulus of bulk material, and $h$ denotes length—the size of the structure. The authors found that $S/E$ parameter sets the scale at which the effect of the free surface becomes significant [132]. They verified their simulated results by both uniaxial loading and pure bending of small-size plates and bars.

For the sake of completeness of the present review, one should mention interesting modeling of dendrimers for nanoapplication [133] as well as recent numerical approach to phase transitions in nanoscopic layered systems [134]. Moreover, the detailed review of the status and perspectives of nanoscale device modeling was presented by Macucci et al. [135] who targeted development of nanoelectronic devices and quantitative predictive capabilities.

### 3.3. Simulation of Nanotribology

Tribology describes phenomena on the contacting surfaces of materials in motion related to each other. The interactions at the contacting surfaces are closely related to atomic and molecular size effects, that is, nanosize effects. The MD simulation methods have successfully been used to describe a number of such phenomena [136]. However, most realistic tribological systems are of such complexity, including surface topography variations, impurities, and lubricants, that the present computers are capable to simulate tribology only partially [137]. When using empirical interatomic potentials, it is possible to simulate relatively large systems containing millions of atoms. MD methods have been used, for example, to simulate the elastohydrodynamic contact of real rough surfaces in the presence of hydrocarbon lubricants [138].

FEM modeling of sliding contact surfaces has been carried out by taking into account realistic asperity textures of the surfaces. Dimensions down to 100 nm have been assessed in the simulations of the contact area and coefficient of friction [139, 140]. Molecular dynamic simulation of contacting surfaces has been done mostly to simulate an indentation to a solid surface. Recently simulations of indentation of an ideal rigid tip to Al have taken into account the melting of material [136]. Common phenomena in the indentation simulation, such as local melting and dislocation nucleation, were observed. The effect of Al orientation and temperature were investigated. The results provided information on nanoscale phenomena present in such processes as wear in engine piston rings and metal forming.

Modeling of stress distributions related to crack initiation and delamination of thin films has been investigated [141]. Simulations have also been used to design coated surfaces with multilayer and gradient structure with high adhesion and crack growth inhibition [142]. Recently, FEM modeling

has been used successfully to simulate the contact scratch testing experiment in order to experimentally determine the fracture toughness of the coated surface [143].

## 4. EXPERIMENTAL METHODS DESIGNED FOR PROBING OF MECHANICAL PROPERTIES OF NANOSTRUCTURED MATERIALS

Many of the traditional methods used for testing of mechanical properties of materials may be used also for nanomaterials provided that adequate amount of material is available. However, in a number of occasions that is not possible. Then other methods must be used. Among them instrumented nanoindentation is the most important and will be described in detail here. Other methods are also briefly discussed.

### 4.1. Instrumented Nanoindentation

#### 4.1.1. Principle and Equipment

Conventional hardness measurement is insufficient to estimate the properties of, for example, thin nanostructured films, because of its low accuracy in the low-load indentation region that is due to limitations of the resolution of the optical systems attached to the hardness testers of conventional type. The development of the testing equipment has enabled the users to continuously monitor the load experienced by the indenter and the depth of penetration. This made it possible to overcome the limitations of the optical system and allowed us to derive new information on the complex mechanical behavior of materials deformed in a very small area. Thus, the nanoindentation appears as a unique method for studying the mechanical properties of solids with a tiny volume.

The idea of depth-sensing indentation measurements was already realized for the first time more than two decades ago [144], while the first nanoindentation testers were designed ten years later [145–148]. Further, the pioneering results of ultra low-load indentation reported by Pethica et al. [146] resulted in a rapid development of this new area of research that recently has found its important application in a case of nanostructured materials.

The nanoindentation experiments achieved a "new level," owing to the new phenomena available for study as a consequence of recent developments in this particular research equipment. This has stimulated an urgent need for a general theory of indentation-induced deformation, which would yield a sound basis for interpreting experimental results. Considerable effort has already been undertaken to analyze the data of depth-sensing tests and to relate them to the observed phenomena [146, 148–152].

The significant progress has been achieved in this area through numerical modeling based on the finite element method [113, 153, 154]. However, the critical issue of this approach lies in the formulation of the pertinent constitutive equations as well as in the difficulty in estimating the elastic/plastic stress-state in the vicinity of the contact. The only case solved analytically is the pure elastic contact of spherical (Hertzian indentation [155, 156]) and axisymmetric

sharp indenters (cone indentation—Boussinesq stress field [157]).

Nanoindentation devices which allow us to use loads as low as fraction of millinewtons have recently been developed in response to an increasing number of requirements for the mechanical testing of crystalline thin films designed for electronics. Some commercial instruments operate automatically after initial setup and measure independently force and displacement experienced by the indenter tip. The successful examination of nanomaterials is in a part due to the selected tester. Indeed, the precision of measurements is of primary importance when one deals with new, advanced materials, which have never been characterized so far.

Indentation techniques may be broadly classified according to the shape of the indenter used in experiments. It was found that sharp indenters, for example, the Berkovich pyramid, are useful in the investigation of mechanical properties in the smallest possible region, while the spherical tip is recommended for crystalline material with remarkable anisotropy.

### 4.1.2. Determination of Elastic Modulus

Hertzian theory [156] of contact between two nonrigid bodies yields the relationship between their Young's moduli:

$$\frac{1}{E_{\text{eff}}} = \frac{1 - \nu_1^2}{E_1} + \frac{1 - \nu_2^2}{E_2} \tag{9}$$

where $E_{\text{eff}}$ is the effective elastic modulus, which can be obtained from load-depth indentation results. Hence, one is able to determine the elastic modulus of the tested solid ($E_1$) based on the indentation data.

However, the contact of a sharp indenter into a solid surface inevitably involves plastic deformation, which makes it difficult to model the process and analyze the experimental data. Since an analytical solution of the elastic/plastic contact problem is not available [157], and the elastic contact between axisymmetric punches and isotropic and anisotropic half-spaces has been the subject of thorough investigations (see, e.g., [158–160]), most researchers assume elastic punch contact as suitable for modeling elastic/plastic surface deformation. Consequently, Bulychev et al. [161] proved that the relationship between stiffness $S$, effective elastic modulus $E_{\text{eff}}$, and the projected area of the contact $A$:

$$S = \frac{2\sqrt{A}}{\sqrt{\pi}} E_{\text{eff}} \tag{10}$$

holds for cylindrical, conical, and spherical indenters. The above universal formula seems to be valid for all indenter shapes being a body of revolution of a smooth function, as proved by King [162].

Oliver and Pharr [163] proposed the method of analyzing indentation data obtained with sharp indenter, while taking advantage of the punch contact problem. The authors assumed that, during the unloading cycle, the deformation of the tested solid is entirely elastic, and they applied the relationships derived for elastic contact of an axisymmetric punch, along with the approach by Doerner and Nix [149]. The latter is based on the assumption that a considerable

part of the unloading $P - h$ curve possesses a linear character, which makes the equations derived for punch problem [refer to Eqs. (9) and (10)] to hold when one considers the indentation unloading. The assumptions by Doerner and Nix, followed by Pharr and Oliver, require contact area to remain unchangeable during the indentation cycle. Doerner and Nix [149] argued that the residual indentation depth $h_r$ (see Fig. 3a) is affected by elastic recovery within the contact and it cannot be used to determine the contact area. In order to estimate the size of the plastic contact region and residual plastic depth $h_p$, the authors suggested subtraction of the elastic contribution from the maximum indentation depth $h_{\text{max}}$. Consequently, the elastically recovered depth $h_e$ can be obtained in the form

$$h_e = h_{\text{max}} - h_p = \frac{P_{\text{max}}}{S} \tag{11}$$
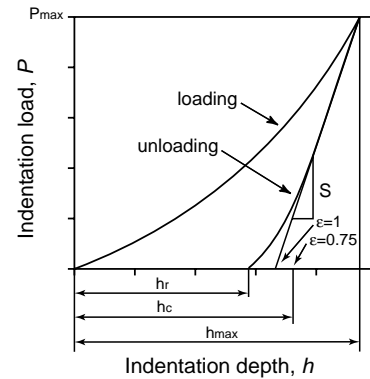
while the elastic modulus of the examined solid $E_1$ [Eq. (9)] may be calculated using the relationship

$$\frac{1 - \nu_1^2}{E_1} = \frac{1}{E_{\text{eff}}} - \frac{1 - \nu_2^2}{E_2} = \frac{2}{S\sqrt{\pi}}\sqrt{A} - \frac{1 - \nu_2^2}{E_2} \tag{12}$$

where $S$ defines the slope of the unloading curve ($S = dP/dh$), $P_{\text{max}}$ is the maximum load, and $A$ is the contact area.
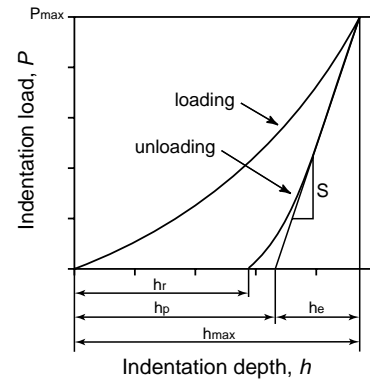


**Figure 3.** (a) Schematic of the indentation load–displacement curve with the parameters used in the Doerner and Nix analysis. (b) Schematic of the indentation load–displacement curve with the parameters used in the Oliver and Pharr analysis.

The Oliver–Pharr analysis of depth-sensing indentation [150, 163] approximates the unloading curve by a power-law relationship:

$$P = B \cdot (h - h_f)^m \qquad (13)$$

where $h_f$ is the residual displacement after unloading determined by the curve fitting with $B$ and $m$ values as fitting parameters. Oliver and Pharr stated that the depth at the contact $h_c$ (see Fig. 3b) appears to be dependent on the initial unloading slope $S$ as well as the maximum penetration depth $h_{max}$. The discussed dependence yields the simple relationship for the $h_c$ parameter:

$$h_c = h_{max} - \varepsilon \cdot \frac{P_{max}}{S} \qquad (14)$$

where $\varepsilon$-value equals 1, 0.75, and 0.73 for a flat punch, the Berkovich tip, and cone-shaped indenter, respectively.

The essential point of the Oliver and Pharr analysis [163] is the evaluation of the shape function $A = f(d_c)$, which expresses the relation between the projected contact area $A$ and its distance $d_c$ from the indenter tip. The method employs the $P - h$ data obtained for a model-specimen for which the authors developed a simple empirical calibration procedure which avoids the imaging of indents. As a result, Oliver and Pharr found the value of effective elastic modulus $E_{eff}$ using the following equation [163]:

$$E_{eff} = \frac{\sqrt{\pi}}{2\beta} \frac{S}{\sqrt{A}} \qquad (15)$$

where $\beta$ depends on the geometry of the indenter and equals 1.034 for the Berkovich tip.

It should be emphasized that the method by Oliver and Pharr [163] is perhaps the most widely used nowadays to routinely analyze the data obtained by means of various nanoindentation systems.

The measurement of Young's modulus proposed by Field and Swain for the spherical indenter employs stepwise indentation with multiple partial unloading [164–166]. The stress field is well-defined in the solid deformed by an axisymmetric tip, whose radius may be selected to control the depth of penetration [164–167]. Furthermore, the indentation with multiple partial unloading produced data which allowed Field and Swain to separate the elastic and plastic components of indentation (Fig. 4) and, in a consequence, to estimate the elastic modulus at each step of the penetration. The above-mentioned fact is of great importance for the application of the method, since such a separation is essential for extracting information relating to material properties [166].

Taking advantage of the basic relationship between force $P$ and the depth of the elastic penetration for a spherical indenter which was derived originally by Hertz [155, 156], and reviewed by Johnson [157], Field and Swain were able to derive a simple formula for calculating the elastic modulus $E_{eff}$ [165]:

$$E_{eff} = \frac{0.75 \cdot P}{a \cdot (h_t - h_r)} \qquad (16)$$

where $h_t - h_r$ denotes the elastic depth recovery.
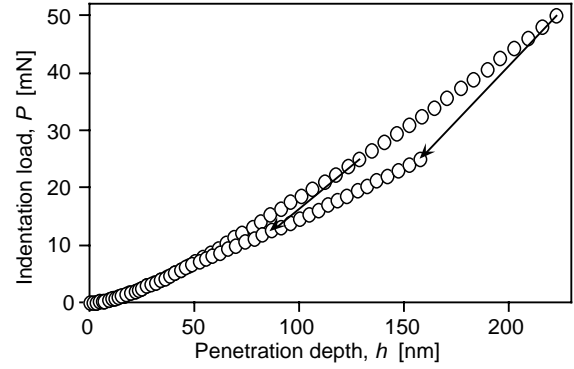


**Figure 4.** Typical load–partial-unload force-displacement data obtained for an elastic/plastic material.

The stepwise indentation allowed the authors a near-continuous assessment of the effective Young's modulus with the depth of penetration.

Hainsworth et al. [168] noticed that the unloading cycle hardly fits the existing models by Oliver and Pharr [163, 169] or Field and Swain [165, 170], and proposed the original method of Young's modulus evaluation by using the loading part of an indentation cycle. Hainsworth et al. [168] concluded that the information on elastic and plastic properties of a tested solid may be obtained by analysis of the loading curve that follows the quadratic relationship. They found the simple relationship between the contact radius $a$, indentation load $P$, and hardness $H$:

$$a = \sqrt{\frac{P}{H}} \qquad (17)$$

Further, following the approach by Loubet et al. [171], Hainsworth et al. [168] derived the power-law dependence between indentation load and depth:

$$P = K_m h^2 \qquad (18)$$

where

$$K_m = E \cdot \left( \phi \cdot \sqrt{\frac{E}{H}} + \psi \cdot \sqrt{\frac{H}{E}} \right)^{-2} \qquad (19)$$

The empirically determined $\phi$ and $\psi$ values depend on the indenter geometry, while $E$ stands for Young's modulus of the material. They verified Eq. (18) for a number of materials with widely varying $E/H$ ratio (steel, bronze, copper, iron, silicon crystals, as well as TiN and $CN_x$ thin films) and concluded that the $P - h^2$ relationship holds for $\phi = 0.194$ and $\psi = 0930$ [168].

In sum, Hainsworth et al. [168] predicted the shape of the loading indentation curves which allows us to determine the commensurate value of Young's modulus $E$ of the indented material in the case when hardness $H$ is known.

Taljat et al. [172] investigated the unloading cycle of a ball-indentation process by the FEM analysis with the stress-strain curve of the indented material used as independent variable (input) in FEM calculations. They defined Young's modulus of the indented solid as a functional dependence on

a normalized unloading slope $S_u$ and the estimate of deformation $d/D$ (ratio of the diameter of the impression and indenter) [172]:

$$E = f\left(S_u, \frac{d}{D}\right) = \left[C_1\left(\frac{d}{D}\right)^{C'}\right] \cdot S_u \qquad (20)$$

where $C_1$ and $C'$ constants were determined using FEM analysis. The authors estimated the indenter deformation employing an analytical solution for the displacement of the center of the contact circle and subtracted it from the total indenter compliance—the correction essential in the calculation of elastic modulus [172].

The complete study of elastic loading and elastic/plastic unloading of a spherical indenter was accomplished by Gerberich et al. [173]. Their method of Young's modulus evaluation suits the requirements of ultra low-load experiments and was scrutinized for numerous materials [173]. The original analysis of the elastic displacement above ($h_1$) and below ($h_2$) the contact line (refer to Fig. 5) by Gerberich et al. [173] contrasts the elastic analysis by Field and Swain [166] who assumed the simplified relationship $h_1 = h_2$.

The solution of elastic and rigid plastic contact problems with the boundary conditions allowed the authors to determine elastic displacements ($h_E$, $h_t$), contact radius ($a$), the total indentation load ($P$), that led to the expression which describes the unloading curve, and consequently, the effective modulus $E_{\text{eff}}$ [173]:

$$E_{\text{eff}} = \frac{3 \cdot R \cdot P}{4 \cdot \left[\left(2 - \frac{h_E^{\max}}{h_t^{\max}}\right) \cdot Rh_E - \left(1 - \frac{h_E^{\max}}{2h_t^{\max}}\right) \cdot h_E^2\right]^{1/2}} \qquad (21)$$

where $R$ is a radius of the spherical indenter. Hence, Gerberich et al. [173] were the first to provide a complete method of estimating the elastic modulus of an indented material. It has been demonstrated that accurate simulation of elasticity may be in special cases elaborated to yield even compositional differences in the nanolayer composites [174].

### 4.1.3. Determination of Hardness

The physical importance of hardness $H$—denoted according to Meyer's concept—lies in the relationship between the $H$-value and the fundamental physical parameters such as yield strength $\sigma_Y$ or Young's modulus $E$. Despite being
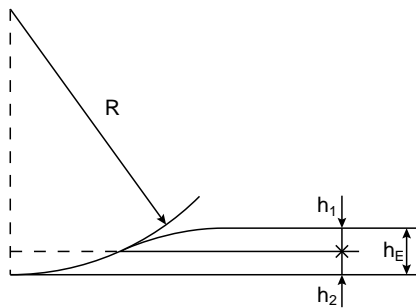


**Figure 5.** The geometry of elastic penetration of spherical indenter into a solid surface. Model by Gerberich et al. [173].

widely used by engineers, hardness appears to be an ill-defined parameter which does not describe a single material property, as criticized by Söderlund and Rowcliffe [175]. The measured hardness is affected by indentation-induced cracking, densification, strain hardening, and creep, and it depends on Young's modulus $E$, yield strength $\sigma_Y$, toughness $K_{\text{IC}}$, work-hardening exponent $n$, stress-dependent creep rate $\varepsilon^c$, as well as the applied maximum indentation load $P_{\max}$. With the advent of nanostructured materials and nanoindentation instruments, confusion arose as to how to determine the hardness parameter from the monitored displacement of the indenter. Starting with the pioneering work by Oliver et al. [176], efforts were being made to settle the characteristic contact area $A'$ at each step of the penetration, and consequently to determine Meyer's hardness as

$$H = P/A' \qquad (22)$$

As a result, the estimation of the depth–hardness profile became the standard procedure in the commercially available nanodepth-sensing indentation instruments.

Furthermore, the original definition of hardness $\boldsymbol{H}$, which appears a load-independent parameter, was introduced by Sakai and Nowak [177]. In contrast to the other approaches, $\boldsymbol{H}$ is a physical parameter defined on the basis of the energy consumed for the irreversible deformation of an indented material.

Doerner and Nix [149] considered the hardness as the average pressure under the acting indenter. They proposed the subtraction of the elastic contribution $h_e$ from indentation depth $h$ measured during a depth-sensing test, in order to evaluate the level of hardness. Further, they have shown that plastic indentation depth $h_p$ may be determined by extrapolating to zero load the line which is fit tangent to the unloading $P - h$ curve (see Fig. 3). Doerner and Nix were well aware of the drawbacks of their assumption of a perfect shape of a pyramidal indenter [149]. They also admitted that the estimation of the influence of the strain rate on the obtained results was beyond the resolution of the proposed method.

Since the main difficulty associated with evaluation of the level of hardness lies in the estimation of the projected area $A'$ of permanent indentation [refer to Eq. (22)], Pharr, Oliver, and co-workers determined the empirically assessed shape of indenter at the contact depth $h_c$ $A = f(d_c)$ [150, 163]. The $f(d_c)$ function can be assessed from the depth-sensing indentation data which allow us to evaluate the relationship between the area $A$ and the contact depth $h_c$. The shape-function derived for a perfect Berkovich geometry,

$$f(d_c) = 24.56d_c^2 \qquad (23)$$

was used by Oliver and Pharr as a first estimate of the contact area [150], while to determine a realistic shape of the indenter, they used a standard specimen [150, 163, 169]. They carried out numerous indentations under various maximum loads $P_{\max}$ in fused quartz or fused silica materials with well-defined isotropic properties, and the fitting procedure was applied several times in an iteration method to achieve suitable accuracy [163]. Once the $f(d_c)$ function was determined, it was possible to evaluate the hardness from the

indentation results according to Eq. (22). Recently, Pharr and associates have provided us with a new insight into hardness analysis by investigating the influence of pileup on the hardness of the indented solid [169].

Since the direct measurement of the contact area is usually impossible, the FEM simulation is effectively used to determine hardness. Numerical simulation allows us nowadays to conclude on a variety of mechanical parameters, such as contact stiffness, the effective elastic modulus, and yield strength, and may be used to predict the actual surface profile or the shape of the plastic zone created directly under an acting indenter. All these advantages, combined with the high computational capabilities that are readily available today, have caused interest in FEM-aided analysis of indentation data particularly in the case of unknown materials or nanostructures.

Hill, Storåkers, and co-workers derived general expressions for the influence of the Brinell head-shape on the load and surface deformation by solving a class of boundary-value problems in elasticity [178, 179]. They also applied a novel FEM procedure to the deformation theory of plasticity [178, 180, 181]. Numerical simulations were performed for the elastoplastic homogeneous half-space, indented to a fixed depth by a smooth rigid ball. The solid was deformed according to the power-law hardening rigid-plastic model.

Hill et al. determined the distribution of contact pressure, the profile of the deformed surface, and the contours of representative strain. Further, Storåkers and Larsson derived the universal relationship for hardness at creep applicable in the case of the Boussinesq and Brinell indentation [180]:

$$\frac{P}{\pi \alpha^2} = \alpha \cdot \sigma_c \left\{ \left( \frac{\beta}{(2n+1)D} \right)^2 \left( \frac{P}{\pi \alpha \sigma_c} \right) t^{-2} \right\}^{1/(2n+1)} \quad (24)$$

where $a$ is the contact radius under the ball indenter of diameter $D$, $t$ denotes time, $\alpha$ and $\beta$ are constants and $\sigma_c$, $n$ are material parameters defined by the stress-strain ($\sigma - \varepsilon$) creep law given by Norton [182].

The studies by Storåkers, Hill, Larsson, and associates proved that the indentation-deformation occurs in the low-strain-hardening materials close to the indenter [178–181], which indicates the necessity to contract the mesh to a smaller size during subsequent stages of the simulation.

FEM analysis of sharp indentation was first performed by Bhattacharya and Nix [183] and subsequently, by Lursen and Simo [154]. The authors performed their calculations for an axisymmetric cone of equal volume with a pyramid shape indenter in order to reduce computer time necessary for calculations.

Bhattacharya and Nix provided the computer-simulation study of the frictionless penetration process of perfectly rigid tip as well as completely adhesive indentation contact using incremental elastoplasticity [153]. The authors applied constitutive equations of an elastic-plastic von Mises type with no strain hardening and with a linear, isotropic strain hardening. The mesh used in FEM procedure was fine right under the tip (four node elements, 0.02 $\mu$m thick) which made it possible to estimate the radius of the contact area, the parameter being essential to determining the hardness value. The authors extended their considerations to the various combinations of hard/soft thin films and substrates [183]

and their report introduces the evaluation of the thin-film hardness.

Hence, Bhattacharya and Nix were the first to demonstrate the successful simulation of the ultra-low-load indentation using the finite element method with simple constitutive data.

Following the pioneering research by Bhattacharya and Nix [153, 183], Lursen and Simo presented a detailed numerical simulation of surface deformation of elastic/power-law plastic materials [154]. The work addressed axisymmetric cone indentation into bulk aluminum and silicon as well as thin films of various degrees of thickness. They emphasized numerical evaluation of the contact area and the surface profile near impression.

Recently, Nowak et al. had applied the FEM simulation of the penetration by an axisymmetric indenter into the multilayer system to explain the surprising difference in the hardness of virgin and ion-treated, 50- to 300-nm thin HfN films [109]. The FEM calculations allowed them to conclude that bombardment with highly energetic ions (MeV energy range) results in formation of the amorphous silicon interlayer located under the top-film.

The axisymmetric approximation of the pyramidal tip is hardly acceptable in the case of anisotropic materials. Thus, the three-dimensional (3D) FEM analysis of a sharp indentation has become highly required.

The first attempt to perform a 3D finite element simulation of indentation by Wang and Bangert [184] was soon followed by a complete analysis of the Vickers indentation by Giannakopoulos et al. [185]. The latter formulated the problem as the penetration of a rigid indenter into a homogeneous, isotropic, rate-independent body. It was assumed that Hook's law and the Prandl–Reuss equations govern the elastic and elastoplastic behavior of the deformed material, respectively [185].

The small strain formulation, elastic analysis by Giannakopoulos et al. allowed them to conclude on the parabolic relationship between the indentation load $P$ and depth $h$ at the loading cycle, and to determine hardness as the average contact pressure $p_{av}$, while the deformation was found to be directly dependent on indentation depth [185]. Elastoplastic examination of the loading process led to the evaluation of the effect of the pileup and yield stress on the Vickers hardness $HV$ ($p_{av} = HV$). This resulted in the universal formula for the Vickers hardness:

$$p_{av} = C \cdot \sigma_u \left( 1 + \frac{\sigma_v}{\sigma_u} \right) \cdot \left( 1 + \ln \frac{E \cdot \tan 22°}{3\sigma_y} \right) \cdot \left( 1 - \frac{u_{2\,max}}{h} \right)$$
$$(25)$$

where $C$ is constant, $u_{2\,max}$ defines the maximum positive surface displacement caused by material pileup, while $\sigma_u$ and $\sigma_Y$ stand for the ultimate stress and yield stress, respectively.

Calculations of steady-state hydrostatic stress and Mises effective stress profiles for materials with and without strain hardening, indicate that strain hardening suppresses pileup at the contact boundary [185]. The maximum tensile principal stress at loading, predicted in the vicinity of indenter tip, helped the authors to localize the region in which the fracture is likely to be initiated.

Pursuing their successful FEM-added study of the Vickers indentation [185, 186], the authors provided a common analysis of the deformation induced around a triangular indenter of Berkovich type which is mostly used in nanoindentation testers [187]. Larsson et al. [187] found that the $P - h$ relationship for a triangular tip is again parabolic, when the indentation is simulated using either an elastic or an elastoplastic approach.

Corresponding formulae denoting the average contact pressure under a Berkovich indenter (the estimation of the Berkovich hardness) were also derived for elastic [Eq. (26)] and elastoplastic [Eq. (27)] cases [187]:

$$p_{av} = 0.2201 \cdot (1 - 0.21\nu - 0.01\nu^2 - 0.41\nu^3) \cdot \frac{E}{1 - \nu^2} \quad (26)$$

$$p_{av} = 0.245 \cdot \sigma_y \left(1 + \frac{\sigma_u}{\sigma_y}\right) \cdot \left(1 + \ln \frac{E \cdot \tan 24.7°}{3\sigma_y}\right) \quad (27)$$

This accounts for the pileup effect and provides the universal formula for Berkovich hardness.

The complete 3D FEM analysis of sharp indentation into pressure-sensitive materials was offered by Giannakopoulos and Larsson in 1997 [188], who introduced pressure sensitivity of the studied material according to the classic model of pressure-sensitive flow, proposed by Drucker and Prager for ideal soils [189].

The results obtained using such an incremental elastoplastic law comprised the solution of complete load-unload cycles, the determination of the contact area, evaluation of the average contact pressure, local mechanical fields (the Mises effective stress), and their singularities near the tip and edges of the indenter. A large plastic strain and small elastic strain approach, as well as high and low, linearly isotropic strain-hardening effects were considered. It was found that the relationship between the indentation load $P$ and depth $h$ is parabolic, similar to earlier FEM-aided studies by Giannakopoulos and Larsson [185, 187]:

$$P = -\int \sigma_{2j} N_j d\Gamma_c = Ch^2 \quad (28)$$

where $\Gamma_c$ denotes the actual contact area, $N_j$ stands for an inward vector normal to the surface within the contact area, and $C$ is constant. The calculations proved that the total energy $U_r$ spent for indentation depends on the maximum indentation load to power 3/2:

$$U_r = \int_0^{h_{max}} Pdh = \frac{P_{max}^{3/2}}{3C^{1/2}} \quad (29)$$

The general formula for the average contact pressure $p_{av}$ (equivalent to the Meyer hardness) derived for pressure-sensitive materials reads

$$p_{av} = 0.77 \cdot \frac{3(1 + q)(\sigma_y + qp_0)}{3 + q}$$
$$\cdot \left(\frac{(3 + q)E}{3(1 + \nu)(\sigma_y + qp_0)}\right)^{2q/(3(1+q))} - (\sigma_y + qp_0) \quad (30)$$

where $q = 3a_0/(3 - a_0)$, while $a_0$ is the material constant that measures pressure sensitivity and $p_0$ is a far-field hydrostatic compression.

The recent FEM simulations resulted in the general theory of indentation of piezoelectric solids [190] and clarified the evolution of the surface residual stress and deformation field in compositionally graded materials [191, 192]. Furthermore, the research is coming closer to the requirements imposed by the structure of nanomaterials targeting small-scale structures. In the latter case the FEM analysis which works yet for thin multilayered systems [107–109, 193] must be replaced by atomistic simulations (see, e.g., [124, 194]) or hybrid methods which combine advantages of FEM and elements of molecular dynamics calculations (refer to [105]). Another trend observed nowadays is improvement of FEM analysis by employing artificial neural network within the code [106].

All of this indicates that, despite unavoidable simplifications, the finite element calculations proved to be quite useful when studying the mechanics of indentation. Without the FEM approach, several complicated problems which concern surface deformation of solids would be still unsolved.

A new concept of hardness, based on the amount of energy irreversibly consumed to create a unit volume of indentation impression in a perfectly plastic material, was proposed by Sakai and Nowak in 1992 [177], while its complete version was published by Sakai in 1993 [195]. The propounded theory—the energy principle of indentation (EPI)—is quite revolutionary in the traditional engineering field of hardness testing, where all the definitions have only been made on an empirical basis. Although not as popular as the approach by Oliver and Pharr [163], the EPI method has been widely recognized.

Starting with the idea of hardness being a measure of the material resistance against plastic deformation induced by a rigid indenter, the EPI approach is based on the assumption that hardness should be directly related to the energy $U_r$ expended for irreversible deformation of the tested solid [177, 195]. The above-mentioned energy can be readily determined from depth-sensing indentation data $(P - h)$, since it is represented by the area bound by loading and unloading curves (see Fig. 6). In the case of the perfectly elastic contact, the energy $U_r$ equals zero (see Fig. 6a), while it attains the maximum value for the indentation in perfectly plastic material (Fig. 6b). Usually one deals with a combined response typical for elastoplastic contact (Fig. 6c).

Taking advantage of the determined shape of the $P - h$ function, it was possible for Sakai and Nowak to calculate the
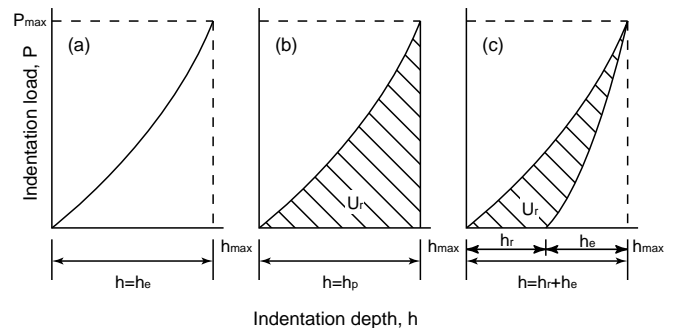


**Figure 6.** Typical loading–unloading indentation curves for the perfectly elastic (a), plastic (b), and elastic-plastic material which exhibits an appreciable elastic recovery (c).

energy expended for an irreversible indentation deformation of the tested solid [177, 195]. In the case of an elastic-plastic material illustrated in Figure 6c, the $U_r$ energy was obtained through integrating $P(h)$ function with respect to $h$:

$$U_r = \int_0^{h_{\max}} P_L(h)\, dh - \int_{h_r}^{h_{\max}} P_{UL}(h)\, dh \qquad (31)$$

where $P_L(h)$ and $P_{UL}(h)$ stand for loading and unloading $P - h$ functions. Furthermore, Sakai and Nowak derived the relationship between $U_r$ and the applied maximum load $P_{\max}$, which in turn allows us to determine $H$ from the plotted $U_r - P_{\max}^{3/2}$ experimental data in a relatively easy way [177]:

$$U_r = (3 \cdot \sqrt{\alpha_0} \cdot \tan\psi)^{-1} \cdot H^{-1/2} \cdot P_{\max}^{3/2} = C \cdot P_{\max}^{3/2} \qquad (32)$$

Indeed, when one determines the slope $C$ of the linear function $U_r - P_{\max}^{3/2}$ measured for several maximum loads $P_{\max}^{3/2}$, it is possible to estimate the value of the true hardness $H$, given the determined shape of a sharp indenter (geometry described by the angle $\alpha_0$ and $\psi$). It is worth emphasizing that the hardness $H$ is a physically well-based parameter which appears to be load-independent, in contrast to the conventionally measured hardness $H$.

### 4.1.4. Determination of Creep, Stress Relaxation, and Other Attributes to Local Plasticity

Indentation experiments can also be used to study the deformation mechanisms of nanocrystalline materials. They offer convenient means to determine, for example, the strain rate sensitivity of the material. Strain rate sensitivity $m$ is the slope of a plot of log applied stress versus log strain rate, that is, the inverse of the stress exponent $n$ in Eq. (4). The effective strain rate $\dot{\varepsilon}_{\text{eff}}$ is obtained from

$$\dot{\varepsilon}_{\text{eff}} = \dot{x}_p / \sqrt{A} \qquad (33)$$

where $A = A(x_p)$ is projected contact area and $x_p$ is the plastic depth beneath the indenter.

In order to determine the rate sensitivity of hardness (stress) by indentation tests, various approaches can be used, for example, indentation creep, rate change, or load relaxation experiments [148, 196]. In an indentation load relaxation experiment, the indenter is pushed into the specimen surface until a predetermined load is reached; then the depth is held fixed, allowing the load to relax as elastic displacement due to the specimen and load-train is gradually traded for plastic penetration. In the indentation creep experiment, the indenter is pushed into the specimen surface at a fixed rate of displacement until a predetermined load is reached; then the load is held constant, allowing the penetration depth to increase with time while the penetration is monitored. In an indentation creep test, the load slightly decreases as the projected area increases during the test, in contrast to a tensile creep test with a constant load, where the stress gradually increases with decreasing cross-sectional area of the test specimen. In the indentation rate change experiments, the indenter is pushed into the sample surface at a fixed rate of displacement until a predetermined load, upon which the indenter is partially unloaded, then reloaded at a second rate of displacement.

## 4.2. Atomic Force Microscopy and Measurement of Mechanical Properties

In the previous section we elaborated about the nanoindentation technique being frequently the most suitable tool to examine mechanical properties of multilayered and nanostructured materials. The method proved effective independent of crystallinity of the probed material; that is, it works equally well for crystalline structures [197–199] and amorphized [200, 201] surfaces.

Another powerful tool to study nanostructured materials is the atomic force microscope (AFM), which can be used both to image the details of the structure and to determine the mechanical properties of the investigated surface.

The crucial part of the AFM is a cantilever with the microfabricated tip which remains in contact with the investigated surface. The deflection of the tip, which is made of silicon or silicon nitride, may be very precisely measured by using optical lever, interferometric, or electronic tunneling method [202]. Consequently, one may acquire force-distance curves that are analogous to the discussed $P - h$ indentation curves with accuracy as high as 2.5 nm and 0.01 nm for lateral and vertical dimensions, respectively. The contact force can be estimated with a resolution of 1 pN [202].

It is worth emphasizing here, after an excellent review of the subject by Cappella and Dieter [202], that AFM force-displacement curve is not recording of tip-sample interaction, contrary to nanoindentation plots. However, this curve results from tip-surface interaction and the elastic force of cantilever. The measurement allows us to determine the elastoplastic properties. One should keep in mind, however, that the AFM experiment is in a much finer scale than the nanoindentation method.

The AFM evaluation of elastoplastic response of the surface is continuously improving. A proper example could be here a new scanning Moiré method, which allowed to determine in-plane deformation by AFM [203], while the detailed thermal fluctuation measurement allowed Catlege et al. [204] to conclude on the spring constant of cantilevers used in AFM.

Furthermore, Kracke and Damaschke [205] recently used a scanning force microscope to measure nanohardness and nanoelasticity of thin gold films. Due to advantages offered by this particular method, the authors were able to estimate properties of single gold island formed during film formation.

In sum, the AFM measurement of mechanical properties of nanostructured materials must be considered as one of the most powerful methods available nowadays for investigating the nanomaterials.

## 4.3. Methods for Exploring Nanotribological Properties

Most tribological contacts occur at the asperities of the surface. The nanoscale tribological events have been investigated successfully with the help of the recent development

of proximity probes and tip-based microscopes and surface force apparatus with the help of computational techniques simulating the tip contact. The concept of nanotribology has been introduced in association with experimental and theoretical investigations of interfacial processes on atomic and molecular scales, which occur during adhesion, friction, scratching, wear, nanoindentation, and thin-film lubrication at sliding surfaces [206]. The main tools at present are surface force apparatus (SFA), scanning tunneling microscope (STM), atomic force microscope (AFM), and friction force microscope (FFM). The comparison of the operating parameters of these methods is shown in Table 1.

### 4.3.1. Wear Tests for Nanostructured Materials

The magnetic media are constantly in development of higher data storage capacity which demands the reduction of the coating thickness on the media [207]. Of importance in terms of the tribological properties are the 5- to 10-nm-thick protective layer of diamond-like carbon (DLC) and the 0.5- to 2-nm thick perfluoropolyether lubricant layer. As an example, AFM has been used to investigate the wear evolution of a magnetic disc coated with DLC. On nanoscale it was observed that the wear is not uniform and initiates at nanoscratches [208]. AFM wear tests have been used to evaluate the wear resistance of the ultrathin DLC coatings prepared by varying the deposition parameters [207]. The surface defects present at the nanoscratches act as initiation sites for wear. FFM has been used to indicate any imperfections and variation of the coating thickness on the magnetic disk. AFM has also been used to compare the tribological properties of DLC coatings by varying the deposition method and coating thickness (from 2.5 to 20 nm). The 20-nm-thick coatings had the highest wear resistance [209].

### 4.3.2. Determination of Friction in Nanostructured Materials

FFM provides the means to map the surface of material on nanoscale. FFM method has been used to investigate the properties of nanostructured carbon coatings (ns-C) [210]. It was found that the friction varied depending on the individual carbon nanocluster and the overall friction behavior was dependent on the parameters of the cluster beam.

## 5. MECHANICAL PROPERTIES OF NANOSTRUCTURED MATERIALS

### 5.1. Nanoparticles, Nanotubes, and Nanofibers

#### 5.1.1. Nanoparticles with Various Aspect Ratios

Nanoscale particles (spheres, rods, wires) can be fabricated with a variety of different methods and the methods have been applied to a multitude of materials. Generally, mechanical properties of individual nanoparticles, irrespective of their morphology, become near to ideal properties of flawless single crystals. This is due to the size effects associated to characteristic lengths of mechanical properties of materials as discussed previously. However, the large proportional number of surface atoms has an additional effect.

Proportion of surface atoms to bulk atoms has been suggested to produce size dependency in elastic properties of nanosized particles. The size dependency has been modeled using continuum mechanics [132]. An important length scale in the phenomena was identified to be the ratio of the surface elastic modulus to the elastic modulus of the bulk of the material. Typically, the size dependency starts to be significant in particle sizes of a few nanometers depending on material.

The strength of small wires (whiskers) has been observed to approach the theoretical cohesive strength of solid matter already in submicrometer size range [211]. The theoretical cohesive strength lies in the range of 0.03 to 0.17 times the modulus of elasticity. In case of metallic nanowires, the exceptionally high strength has been confirmed experimentally in studies of nanometer-size gold contacts using scanning tunneling microscope [212, 213]. For comparison, gold is the softest of all metals in larger dimensions.

Mechanical properties of nanoparticles have been contrasted here with bulk properties of materials. However, structural forms of nanoparticles that are characteristic of the nanometer scale only, such as fullerenes and nanotubes, are also observed.

#### 5.1.2. Nanotubes

Nanotubes are large macromolecules similar to a sheet of graphite rolled into a cylinder and capped with half fullerene at both ends. Essentially, they are one-dimensional

**Table 1.** Comparison of typical operating parameters in SFA, STM, and AFM/FFM used for micro/nanotribological studies [206].

| Operating parameter | SFA | STM[a] | AFM/FFM |
|---|---|---|---|
| Radius of mating surface/tip | ~10 mm | 5–100 nm | 5–100 nm |
| Radius of contact area | 10–40 $\mu$m | N/A | 0.05–0.5 nm |
| Normal load | 10–100 mN | N/A | <0.1–500 nN |
| Sliding velocity | 0.001–100 $\mu$m/s | 0.02–2 $\mu$m/s (scan size ~ 1 nm × 1 nm to 125 $\mu$m × 125 $\mu$m; scan rate < 1–122 Hz) | 0.02–2 $\mu$m/s (scan size ~ 1 nm × 1 nm to 125 $\mu$m × 125 $\mu$m; scan rate < 1–122 Hz) |
| Sample limitations | Typically atomically smooth, optically transparent mica; opaque ceramic, smooth surfaces can also be used | Electrically conducting samples | None |

[a] Can only be used for atomic-scale imaging.

nanostructures having nanometer scale diameter, and length ranging from nanometers to millimeters. Since the discovery of carbon nanotubes in 1991 [214], two kind of tubes have been found: single-walled carbon nanotubes (SWNTs) with only one cylinder of an atomic layer, and multiwalled carbon nanotubes (MWNTs), with cylinders inside each other. The atomic structure of nanotubes is described in terms of the tube chirality, which is defined by pair of integers $(n, m)$ expressing the chiral vector. The chiral vector can be understood as a description of how the hexagonal sheets have been "rolled." According to the atomic structure, nanotubes can be grouped into three categories: armchair $(n = m)$, zigzag $(n = 0$ or $m = 0)$, and chiral (any other $n$ and $m$) [215]. An additional feature of carbon nanotubes is that the carbon SWNTs tend to self-assemble into "ropes," which consist of hundreds of SWNTs in a two-dimensional triangular lattice [216]. Besides the carbon, materials such as BN, $BC_3$, $BC_2N$, $WS_2$, and $MoS_2$ have been discovered to form nanotubes. It has been suggested that all compounds having layered structures in the bulk are likely to form nanotubes [217–219].

There is a growing body of evidence indicating that nanotubes have exceptional mechanical properties. Theoretical calculations based on in-plane C—C bond in graphite, which is one of the strongest chemical bonds known in nature, indicate that nanotubes are very strong materials having axial elastic modulus in TPa range [220–223]. The first Young's modulus measurement of carbon MWNTs was performed utilizing amplitude of their intrinsic thermal vibration. This transmission electron microscopy study gave an axial Young's modulus of 1.8 TPa as an average of 11 samples [224]. Carbon SWNTs have been studied with the same technique yielding an average axial Young's modulus of 1.25 TPa [225]. Another technique to measure Young's modulus of nanotubes is based on bending anchored samples with AFM. With this technique, the results of 1.28 TPa [226] and 0.81 TPa [227] have been reported for carbon MWNTs. As expected, all the values are close to the value of in-plane modulus of graphite sheet, which indicates that chirality and tube diameter of nanotubes have only minor influence on axial elastic properties. The studies of carbon SWNT ropes show that also they are high axial modulus fibers (∼1 TPa) [228, 229]. In case of other materials than carbon, the vibration amplitude technique has been used for determining the properties of BN MWNTs giving the axial Young's modulus of 1.22 TPa [230]. Recently, tight-binding calculations of axial Young's modulus for C, BN, $BC_3$, $BC_2N$, and $C_3N_4$ nanotubes with various chirality have been published. For the exact values, the original reference should be consulted [231].

Theoretical analysis predicts that nanotubes can sustain extreme strains in tension without breaking [232, 233]. Tensile strengths of individual carbon MWNTs have been measured with "nanostressing stage" located within a scanning electron microscope. The measured tensile strengths of the outermost layer of MWNTs ranged from 11 to 63 GPa [234]. The values are high compared to conventional fibers but not as high as expected. Carbon SWNT ropes have been studied with the same technique, resulting in tensile strength on the perimeter of the rope ranging from 13 to 52 GPa [235].

The hollow structure and closed topology of nanotubes produce extraordinary mechanical response in bending. It has been shown that carbon MWNTs can be bent repeatedly through large angles without failure [236]. In fact, deformations such as buckling can be fully reversible. Combination of experimental and theoretical work has shown that the bending angle up to 110° does not produce any damage in atomic arrangement, despite the formation of complex kink shapes [237]. The first direct bending strength measurement of large-diameter carbon MWNTs was performed with AFM. The average value of bending strength in the point of elastic buckling was 14.2 GPa [226]. The ability of carbon nanotubes to sustain load elastically at large bending angles enables them to store or absorb considerable energy.

As far as property variations are concerned, the synthesis method of carbon nanotubes has been reported to affect their mechanical properties. The carbon MWNTs synthesized by arc-discharge method have much higher bending strength than those produced by catalytic decomposition of hydrocarbons. The difference in the results is explained by presence of defects in the latter nanotubes [227].

In literature reports on mechanical properties of individual nanotubes, most authors use estimated tube wall thickness for defining Young's modulus and tensile strength. Obviously, if the total occupied cross-sectional area is used, the values would be much lower. Propably the most impressive mechanical property of nanotubes is their specific strength, because of the low weight. Consequently, nanotubes are expected to be useful structural reinforcement in high-performance light-weight composites.

## 5.2. Layered Materials

### 5.2.1. Multilayered Materials

The multilayer coatings are a means to produce tailored surfaces. The multilayer coatings optimization with optimum mechanical properties has been reviewed by several authors [238, 239]. Holleck and Schier [239] have reviewed the mechanical properties and design principles of multilayer coatings. The multilayer coating may be classified into coatings with (1) a limited number of single layers in order to combine the different properties of the individual materials used; (2) a high number of non-isostructural coatings, where the amount of interface volume as sites for energy dissipation is important; (3) superlattice coatings, where isostructural single-layer materials with similar chemical bonding, atomic radii, and lattice distance and with layer thickness similar to the lattice dimensions are used. Superlattice coatings have been reported to have higher hardness as expected to result from the individual layers following the rule of mixture, for example, in TiN/(V, Nb)N coatings [240].

One trend in development of coatings is to increase the surface hardness. Coatings are usually divided into two groups: (1) hard coatings having a hardness up to 40 GPa, and (2) superhard coatings having a hardness over 40 GPa. Compared to a large number of hard materials, there are only a few superhard materials, that is, cubic boron nitride (c-BN), amorphous diamond-like carbon (DLC), amorphous carbon nitride (a-CN x), and polycrystalline diamond. Superlattice coatings are one means to obtain also superhardness.

Superlattice coatings are nanometer-scale multilayers composed of two different alternating layers with a superlattice period, that is, the bilayer thickness of two materials, ranging from 5 to 10 nm. The bilayers of these superlattices can be metal layers, nitrides, carbides, or oxides of different materials or a combination of one layer made of nitride, carbide, or oxide of one metal and the second layer made of another metal. According to the composition of the bilayer, superlattice coatings can be divided into five groups: (1) metal superlattices, (2) nitride superlattices, (3) carbide superlattices, (4) oxide superlattices, and (5) nitride, carbide, or oxide/metal superlattices [241]. Single crystal superlattice coatings have been reported to have hardness values in the range of 45 to 56 GPa (e.g., TiN/VN 56 GPa, TiN/CN$_x$ 20–50 GPa). The nitride/metal multilayers are less hard but more ductile (e.g., TiN/Ti). The toughness of the coating increases the adhesion of the coating to its substrate, giving a fundamental advantage to the coating.

A typical hard multilayer is the sputter deposited nitride film, for example, CrN/TiN, AlN/TiN. The hardness is a result of dislocation blocking and the metastable phases in the nanolayered structure. For example, AlN normally forms in a hexagonal structure, but when the deposited layer thickness is less than 2 nm, a cubic rock-salt structure of AlN is resulted corresponding to about a 50% increase of the film hardness. Hard metastable CrCu nanocomposite coatings have also been reported [242].

When using the layer thickness as a parameter similar to grain size, Hall–Petch relation (see Eq. (1)) was observed in the hardness and abrasive wear experiments. Ti/TiN multilayer coatings have wear resistance similar to TiN coating (1 N, alumina ball 25% RH, 5 m/s) [243]. The Hall–Petch relation in tensile strength has been observed also for polycrystalline silicon coatings [244].

Multilayered films have higher elasticity and hardness and better tribological properties as compared to the constituent layer materials alone [245], for example, in case PECVD is used to coat nanostructured Si:H and SiC:H multilayers. These multilayers have been proposed for various applications as protective coatings because of their properties (hard, tough, corrosion resistant, and high-temperature tolerant) [246, 247].

Properties of amorphous hydrogenated carbon (a-C:H) films are strongly dependent on the deposition parameters. By cyclically alternating the deposition parameters, a nanolayered coating may be produced. Thus nanoscaled multilayer films with modulated layer properties may be grown by using computer-controlled PACVD methods [248]. The wear resistance, for example, is optimal with both high and low elastic modulus layers when the single layer thickness is 12–14 nm. When Ti is incorporated, a hard coating suitable for bone implants, providing enhanced bone ingrowth and reducing bone resorption, can be produced.

The toughness of the TiC-metal multilayered film was observed to be better than that of the monolytic films, whereas the value of hardness depends on the choice of metal [249]. The optimum hardness and toughness values were obtained with TiC-Fe multilayer with modulation thickness of about 6–8 nm.

The abrasive wear resistance of multilayer coating of Cr-CrN has been modeled by Berger et al. [250]. The theory is based on a physical model for how the microscale abrasion mechanisms result in the macroscopic abrasive wear resistance of multilayer coatings. The model results in a linear rule of mixtures for the wear resistances of the two interlayers plus that of a wear-resistant supported zone, that is, the transition zone from Cr to CrN. Despite its simple rule of mixtures, the model agrees very well with the experimental results.

### 5.2.2. Design Rules for Multilayered Materials

The important parameters in designing multilayered materials are the lamellae thickness and bond type of the materials. Holleck suggested the use of multilayers of different ceramic materials, such as TiC and TiB$_2$, selected on the basis of their dominant bonding mechanism, that is, metallic, covalent, or ionic [251]. Multilayer coatings are a practical method to produce coatings of covalent bonded materials such as AlN, BN, SiC, or B$_4$C, since those materials, as single-layer coatings to metallic substrates, have a low adhesion [239]. On the other hand, covalent bonded materials adhere well to metallic hard materials such as TiC and TiN. Thus it is possible to introduce the hard covalent layer as interlayers into the multilayer coating. Holleck has also demonstrated improvements in hardness, indentation toughness, adhesion, and wear performance under optimized layer thickness conditions. For example, high values of hardness at elevated temperature (800 °C) have been reported for multilayer coatings with B$_4$C, BN and AlN interlayers embedded into TiN/TiC multilayer coatings. Also TiC-C nanocomposite coatings have shown promising tribological properties [252].

The properties of the interface play an important role in determining the mechanical properties of multilayer coatings. The properties of the interface are determined by the various deposition parameters used, but they depend also on the layer materials. The interface is typically a diffuse layer with a thickness varying from 1 to 3 nm. The total volume of the interface region depends on the thickness of individual interface region and the layers. Thus the interface volume may vary widely from only a few percent to almost 100%. The different toughening mechanisms are a result of the fine-grained microstructure, crack deflection, reduced stress concentration, nanoplasticity of the interfaces, and periodical stress and strain fields [239, 253, 254].

Leyland and Matthews [255] have reviewed the significance of H/E ratio of the coatings to the tribological behavior of the surface. Based on the contact mechanical models, it is determined that a high H/E value is beneficial in obtaining a wear-resistant surface with optimal properties of elastic strain to failure, critical yield pressure for plastic deformation, and fracture toughness. In practical applications it is advantageous to have a closely matched strain behavior between coating and substrate. Multilayer and nanocomposite coatings particularly with functional gradient properties have been investigated to optimize this effect. The coatings studied include Ti-B-N/Ti-B-C [256–263] and Ti-Al-B-N [264–268] nanocomposite coatings. For the CrN ceramic nitride and also for the metallic Cr+10 at. % nitrogen, the H/E value is about 0.05. By adding copper (<5 at. %) in

the Cr-Cu-N system at low nitrogen content (<10 at. %), it is possible to obtain high hardness values (H 20–25 GPa) while keeping the H value low (H 280 GPa). Thus the H/E value is increased up to 0.09 [269]. In conclusion, optimal H/E values may be obtained by using metallic nanocomposite coatings based on binary mixtures of a transition metal with another, low-miscibility, metal. It is required that the transition-metal component can be strengthened by solution hardening with interstitial elements (such as B, C, N), without creating a high-modulus ceramic phase [255].

The multilayer coatings provide three means to combine material properties: combination of several materials (multilayers), metastable materials, and graded structures. The tailored multilayer coating of Ti-TiC-DLC and $CN_x$ with excellent tribological properties has been demonstrated by Voevodin [142]. Graded nanoscale layer or interlayer designs have been used to reduce stresses of the films [270, 271].

### 5.2.3. Nanocrystalline Coatings

Nanocrystalline alloy films may be grown from, for example, NiCr (80/20 wt. %) and TiSi (90/10 at. %) [272]. Crystal size less than 100 nm results if the plasma parameters (ion energy, ion/neutral arrival rate, temperature) are such that sufficient crystal nucleation takes place and also grain growth is not too rapid. In addition, alloy species must have more than 15% difference in atomic radius and a large negative enthalpy of formation.

Veprek et al. have proposed a simple concept for the design of superhard coating material [273, 274]: (1) one has to use ternary or quaternary systems, which show strong segregation into two binary compounds, (2) low-temperature deposition should be applied in order to avoid interdiffusion in heterostructures, (3) one should use one amorphous phase in order to avoid lattice misfit, and (4) use nanometer range size crystalline material, the grains of which do not contain dislocations. Experimentally these design rules have been verified in a superhard nc-TiN/a-Si$_3$N4/na-TiSi$_2$ coating produced by PACVD [275]. Up to 100 GPa hardness values were obtained when about 10-nm TiN crystals are separated by roughly a nanolayer of Si$_3$N$_4$, with TiSi$_2$ precipitates at the interfaces. Respectively, nanocrystalline TiN/a-BN coating prepared by plasma CVD was reported to have a hardness of 45–50 GPa [276]. The very high hardness values obtained by indentation measurements are also explained by the small size of the critical flaw on the surface. This is due to self-organizing of the stable nanostructure during the coating process [277].

### 5.3. Monolithic Bulk Materials

### 5.3.1. Strength and Ductility of Nanocrystalline Metals

The grain size refinement of metallic materials has been a subject of intensive research over the recent years, since in principle grain size refinement is a strengthening method that does not increase the material cost. Many of the studies on the mechanical behavior of the nanocrystalline metals have provided data that are largely a reflection of the influence of sample imperfections. This is implied by the

large scatter of individual experiments, but also as regards data trends observed between different studies. Therefore, it has been very difficult to make decisive conclusions on the strength increase or softening at smallest grain sizes of nanocrystalline metals. However, tensile testing using a microtensile tester [278] has shown that substantial increase in strength for nanocrystalline Cu can be achieved. Samples with 26-nm nominal grain size have over 850 MPa in tensile fracture stress, and for nanocrystalline nickel with the grain size of 21 nm, strength values over 2.1 GPa in compression were reported, this being within an order of magnitude of theoretical strength for nickel [279].

Because the fabrication techniques have greatly limited the availability of reliable tensile test data on nanostructural materials, the most convincing results so far have been obtained by hardness tests. Siegel [280] has collected data on various materials which show convincingly the hardening independently of the method of synthesis. The pure nanocrystalline materials can be 2–7 times harder than their coarse-grained counterparts [280, 286]. In Figure 7, dependence of hardness on grain size/layer thickness for different classes of nanocrystalline materials is given.

The behavior at the smallest grain sizes (<20 nm) varies from hardening to softening. A negative Hall–Petch relationship (softening) is found, for example, in copper and palladium [15].

Nanostructured materials with a grain size of 20–40 nm fabricated by gas condensation or ball-milling and subsequent consolidation have been found to exhibit low
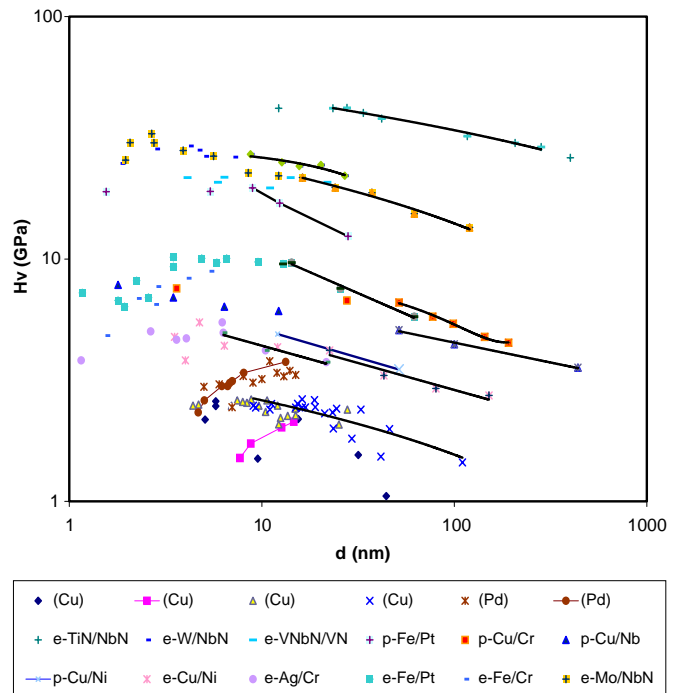


**Figure 7.** Dependence of hardness on grain size/layer thickness for different classes of nanocrystalline materials. Examples are given for metallic (Cu [17, 220, 282, 287] and Pb [220, 282]) and layered nanocomposites (TiN/NbN [288], VNbN/VN [289], Fe/Pt [290–292], Cu/Cr [293], Cu/Nb [293], Cu/Ni [293, 294], Ag/Cr [295], Fe/Cr [291, 292], Mo/NbN [296], and W/NbN [296]).

tensile ductility [2, 279]. This is manifested by a strong tendency of these materials to strain localization in a tensile test. In some cases annealing after consolidation and/or polishing has been found to increase the strength and ductility of nanomaterials in tension [6]. In the latter study Young's modulus of fully dense nanomaterials was comparable to that of the coarse-grained counterpart, but decreased two- to sixfold when pores and flaws were present.

It is not yet well understood whether the brittle behavior is an intrinsic feature of nanocrystalline materials, or whether it is caused by processing difficulties such as imperfect consolidation of nanocrystalline powders. Most of the experimental results so far indicate little ductility in tension for grain sizes below 25 nm [297, 298] for materials which are ductile when coarse-grained. A summary of the reported results on tensile ductility is given in Figure 8.

While in many cases the low ductility may be attributed to the flaws and inhomogeneities of the microstructure dependent on the method of preparation, it seems that the deformation mechanisms related to the lack of strain hardening are also important factors contributing to mechanical instability and localized deformation already at low strains. In this respect the deformation and fracture behavior of nanocrystalline materials resemble that of amorphous metals.

In compression the behavior may be different. Lu et al. [307] have reported that nanocrystalline copper having a mean grain size of 20 nm may be cold-rolled up to 5100% strain without cracking, and further cold-rolling was still possible. Such extreme extensibility has not been observed in conventional copper, which typically cracks already after extensions of about 800%.

Metallic nanostructured materials with the highest thermal stability are so far based on aluminum [308, 309]. Considerable improvements in strength have been obtained,
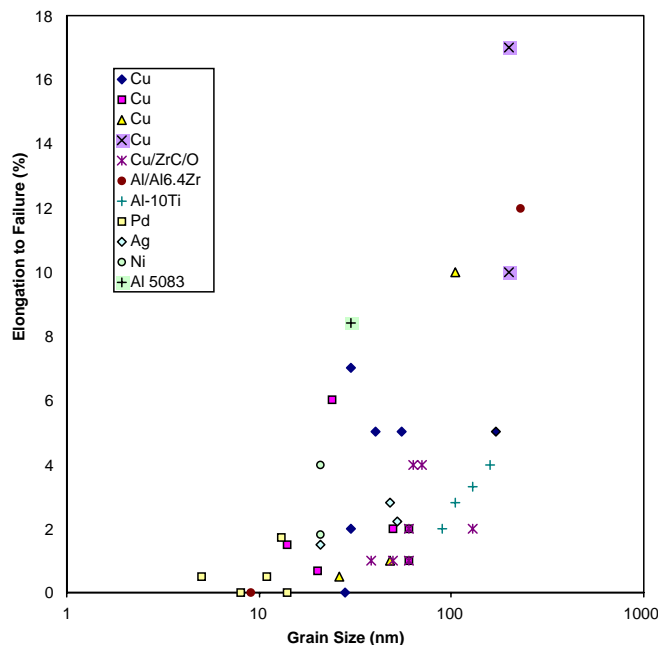
for example, with a nanostructured version of spray-atomized 5083 Al alloy as compared to the commercial grade [310]. The alloy having a grain size of about 30 nm was found to have a 30% increase in yield strength and ultimate strength over the strongest commercially available form of 5083 Al with no decrease in tensile ductility.

Also wear properties of nanocrystalline metals are expected to be better than those of their coarse-grained counterparts because of the generally higher hardness of nanocrystalline metals. The few studies on wear of metallic nanocrystalline materials seem to confirm this. Takagi and co-workers [311, 312] have studied the wear properties of nanocrystalline aluminum alloys and their composites and noticed improvement of sliding wear properties both at room temperature and elevated temperature (473 K). Thermally sprayed nanostructured Co-Cr coatings have also been developed in order to diminish wear in prosthesis [313].

### 5.3.2. Creep and Superplasticity of Nanocrystalline Metals

Pure metals usually do not exhibit superplastic behavior due to the low stability of their microstructure to thermally induced changes at the elevated temperatures needed for the superplasticity to occur. This applies also to nanocrystalline metals, which are often unstable even at room temperature. Therefore, superplastic behavior is usually encountered in alloys, which are stable enough at the relevant temperatures [75, 76, 314, 315].

A summary of the studies on creep and superplasticity of nanocrystalline metallic and intermetallic materials is presented in Table 2. Neither of the two models, that is, Nabarro–Herring creep and Coble creep, described earlier can be used to fully account for plastic flow under the reported circumstances. In general, it seems that the strain rate sensitivity is increased as the grain size is decreased independent of the particular deformation mechanisms (range of *n*). It is clear that at low temperatures the Coble creep does not account for the creep behavior. Also, it is typical that the activation energy for deformation is higher than than of the grain boundary diffusivity. It may also be concluded that the creep properties of nanocrystalline materials are very sensitive to their microstructure. Therefore two nanocrystalline materials with same nominal composition and structure may exhibit different deformation behavior.

Based on the experimental findings, it is clear that tensile superplasticity occurs at higher strain rates and lower temperatures in nanocrystalline materials than in their coarse-grained counterparts. However, it is not possible to obtain low-temperature superplasticity in pure metals in which grain sizes are less than 100 nm; the superplastic flow at low temperatures is neutralized by the onset of significant grain growth at the same temperature range [5].

### 5.3.3. Single-Phase Ceramics

Ceramics are inherently brittle materials. In most structural ceramics, deformation rarely involves dislocation movement at low temperatures with exception of severe multiaxial compressive stress-state situations. In Figure 9 the grain



**Figure 8.** Tensile elongation to failure vs. grain size for several metals and alloys [220, 299–306].

**Table 2.** Summary of studies on creep and superplasticity in nanocrystalline metallic and intermetallic materials.[a]

| Materials | Processing | Grain size (nm) | $T$ (K) | $n$ | $Q$ (kJ/mol) | $e_f$ | Test mode | Ref. |
|---|---|---|---|---|---|---|---|---|
| Pd | IGC | 7–10 | RT | — | — | — | tension | [316] |
| Cu, Pd | IGC | 50 | RT | — | — | — | tension | [220] |
| Ni-P | AC | 28 | 543–573 | 1.2 | 68.5 | — | tension | [72, 73] |
| Ni-P | AC | 257 | 573–648 | 2.5 | 106 | — | tension | [72, 73] |
| Al-Ni-Mm-Zr | HPGA | 80 | 873 | 2 | — | — | tension | [77] |
| Ti-Al-Cr | BM | 25–50 | 1023–1223 | 6 | — | — | compression | [317] |
| Fe-B-Si | AC | 27 | 733–763 | 1.2 | 144 | — | tension | [69] |
| Fe-B-Si | AC | 250 | 733–763 | 2.0 | 193 | — | tension | [69] |
| $Ni_{80}P_{20}$ | AC | 28 | 543–573 | 1.2 | 68.5 | — | tension | [70] |
| $Ni_{80}P_{20}$ | AC | 28 | 543–573 | 1.2 | 68.5 | — | tension | [70] |
| Ni | ED | 6, 20, 40 | RT | 1.2, 2, 5.3 | — | — | tension | [21] |
| Cu, Pd, Al-Zr | IGC | 10–55 | 0.24–0.64 $T_m$ | — | — | — | tension | [318] |
| Zn-22Al | TS | 37 | 393 | 3 | — | — | tension | [93] |
| Pb-62Sn | TS | 32 | RT | 2 | — | 300% | tension | [95] |
| $Ni_3Al$ | TS | 50 | 923–998 | — | — | 560% | tension | [83] |
| $Ni_3Al$ | TS | 70 | 923 | — | — | 300% | tension | [81] |
| Cu-Nb | SD | 3.5–430 | RT | 34-59 | | | indentation | [319] |
| Ni | ED | 20 | 553–693 | | | >200% | tension | [320] |
| Al 1420 | SPD | 100 | 523–623 | | | | tension | [320] |
| $Ni_3Al$ | SPD | 50 | 923–998 | | | 350% | tension | [320] |
| Al-4%Mg | HIP/E | 300 | 573 | 8 | | | tension | [321] |
| Cu | ED | 30 | 293–323 | 1 | 0.72 eV | | tension | [322] |
| Ni | ED | 30 | 290, 373 | 1.1, 6.5 | | | | [323] |
| Cu | ED | 20 | RT | | | 5000% | cold-rolling | [324] |
| Cu-TiC | HIP/BM/HR | 55, 67, 70, 100 | 330–900 | 11 | 70–110 | | indentation | [325] |
| Ti-6Al-4V | TS-SPD | 30–50 | 898 | 5.2 | 312 | 140% | tension | [82] |
| Al-3.8%AlN | HP/E | | 823 | 3 | | | tension | [326] |
| Cu | CR | 30 | 293–323 | 2 | 0.82 | | tension | [327] |
| NI₃AL | TS-SPD | 85–100 | 873–923 | 2.6 | — | | tension | [84] |

[a] IGC: inert gas condensation, ED: electrodeposition, HIP: hot isostatic pressing, HP: hot pressing, E: extruded, SPD: severe plastic deformation, TCHPGA: high pressure gas atomization, AC: amorphous crystallization, BM: ball-milling, TS: torsion straining, HR: hot rolling; SD: sputter deposition, CR: cold-rolling, E: extrusion, $e_f$: elongation to failure, $T_m$: melting temperature.

size dependence of dislocation processes and grain boundary sliding has been schematically compared in cases of ceramics and other materials reflecting differences in interatomic bonding. From the point of view of mechanical
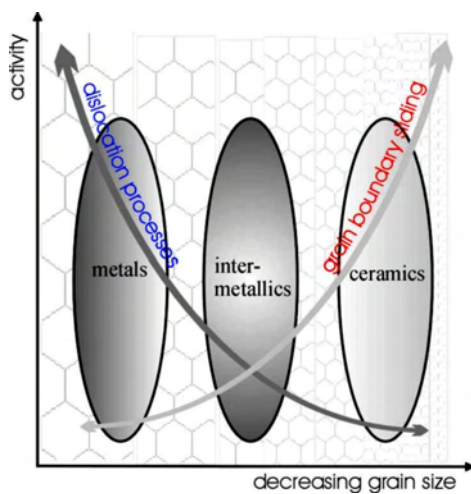


**Figure 9.** Grain size dependence of dislocation processes and grain boundary sliding compared in cases of ceramics and other materials. The interatomic bonding determines the location of a particular material in the framework. Temperature is a factor determining the activity of the processes and influences also the relative importance of the two processes. This is not shown in the figure.

properties, the scientific interest in nanophase ceramics is predominantly motivated by the prospects for superplastic deformation. Furthermore, structural reliability in single-phase ceramics is associated with microstructural uniformity, which is usually better in the case of finer grain sizes. The promise of room-temperature ductility in nominally brittle single-phase ceramics with nanometer-range grain size has not been realized. Recent tests, where macroscopic, dense nanocrystalline specimens have been used, have not shown enhanced ductility at room temperature [3].

Superplasticity is phenomenologically defined as the ability of a material to exhibit exceptionally large tensile elongation during loading. The resulting deformation is often in hundreds of percent also for ceramics. This is highly significant, since ceramics are usually formed into shapes before firing and in case of tight dimensional requirements they have to be machined after the firing. There are two basic types of superplasticity, which are termed transformation and structural superplasticity. Only structural superplasticity is associated to nanostructure of materials and is discussed here. General requirements for structural superplasticity are small, stable grain size and relatively high homologous processing temperature. An additional requirement, relevant for superplastic behavior in ceramic materials, is lack of intergranular brittleness. The superplastic flow derives from diffusion-controlled processes at grain boundaries, which has been discussed earlier.

The first clear demonstration of superplastic behavior in single-phase ceramic materials with sub-micrometer grain size occurred in 1986 when Wakai et al. reported tensile elongations of over 100% in an yttria-stabilized tetragonal zirconia [328]. There are earlier reports on enhanced plastic deformation capability of ceramics in compressive loading. However, this is not a best test for superplastic flow, since it ignores to a large extent the effect of possible intergranular brittleness. As a grain boundary effect, also the presence of second phase at grain boundaries has to be considered not only in case of ceramic composites, but in the case of other ceramics as well. Introduction of glassy phases at grain boundaries has been shown to produce superplastic behavior. It is common to refer to ceramics as single-phase materials even though, due to very low solubility limits, they may contain thin glassy layers at their grain boundaries.

A majority of investigations on structural superplasticity in ceramics have concentrated on ytria-stabilized tetragonal zirconia. Other single-phase ceramics which have been found to be superplastic include alumina and hydroxyapatite. Polyphase ceramics have not been discussed here. The grain size of ceramics with superplasticity is less than 1 $\mu$m, which is smaller than in case of metals. Typical processing temperatures are at or above 0.5 $T_m$, where $T_m$ means absolute melting temperature. Applicable strain rates for superplastic deformation in ceramics are close to $10^{-4}$ sec$^{-1}$, which is an order of magnitude slower than for metals. Unlike in metals, tensile ductilities do not correlate well with strain-rate sensitivity in superplastic ceramics, because in practice, grain boundary decohesion always limits tensile ductility. A major concern in superplastic processing of ceramics is suppression of dynamic grain growth, which has led to utilization of additives that segregate on grain boundaries. Several reviews that summarize data on superplasticity of ceramics in case of sub-micrometer grain sizes have been published [329–334].

An examination of phenomenological relationship between factors affecting superplasticity indicates that the slow strain rates in ceramic superplasticity could be accelerated by orders of magnitude if the grain size were reduced sufficiently to true nanostructure range ($< 100$ nm). Equivalently, finer grain sizes lead to the same strain rates at lower temperatures. Both effects have been tentatively demonstrated in nanocrystalline ceramics [3]. However, this has been achieved nearly without exception by using compressive loading and small specimen sizes due to sample fabrication difficulties. To author's knowledge, only tensile test results have been reported for nanocrystalline 5 mol % ytria-stabilized zirconia with 75 nm grain size [335]. It was demonstrated that 70% engineering strain could be obtained at 1403 K processing temperature (0.46 $T_m$).

## 5.4. Nanocrystalline Composites

Nanocomposite materials can be defined as composites of more than one Gibbsian solid phase where at least one of the phases has dimensions in the nanometer range [336]. The solid phases may be in amorphous, semicrystalline, or crystalline state. The nanocomposite materials may be divided into four categories: intragranular, intergranular, hybrid, and nano/nano composites [337], where

the nanophase material locates at the interface, within the matrix (large) crystals, or in both of them, respectively. The nano/nano composite consists of two phases with grain sizes not more than 100 nm (Fig. 10).

### 5.4.1. Metal Matrix Nanocomposites

Nanocomposites incorporating mainly nanostructured ceramic particles or fibers in a metallic nanocrystalline matrix have been studied quite intensively over the last years. Among them are the nanostructured WC-Co composites that are being developed for tool applications. Chemical methods have been developed for producing premixed powders at the nanoscale level [338, 339]. To inhibit the grain growth of WC, sintering is carried out in a liquid state and small amount of grain growth inhibitors, such as VC, are added. According to Jia et al. [340], the hardness of nanocrystalline WC-Co is considerably higher than that of conventional WC-Co composite. This is not only a result of nanocrystalline structure but also due to the simultaneous alloy strengthening of the binder phase itself. Corresponding developments have been carried out in coating technologies by thermal spray both in plasma and HVOF spraying [335, 341].

Other metal-ceramic nanocomposite systems have also been studied including duplex Ni-TaC [342], Cu-Al$_2$O$_3$ [343], and NiCr-Cr$_3$C$_2$, [344, 345]. The Ni-TaC system is interesting because hardness values (12 GPa) comparable to WC-Co cermets are obtained with a much lower carbide content than in the latter material. The strength of Cu-0.5% Al$_2$O$_3$ material is not much different from that of pure nanocrystalline copper, but the apparent activation energy for creep is significantly higher than in the pure nanocrystalline copper. NiCr-Cr$_3$C$_2$ system has been developed primarily for coating applications where an increase of about 20% has been obtained as compared to commercial coatings. A recent review on the latest developments is in [345].

It has been proposed that incorporation of nanotubes instead of carbon fibers as reinforcing elements into plastic, ceramic, and metallic matrixes can potentially provide structural materials with dramatically improved modulus and strength [345]. Preliminary investigations on the synthesis of carbon-nanotube-metal-matrix composites with different
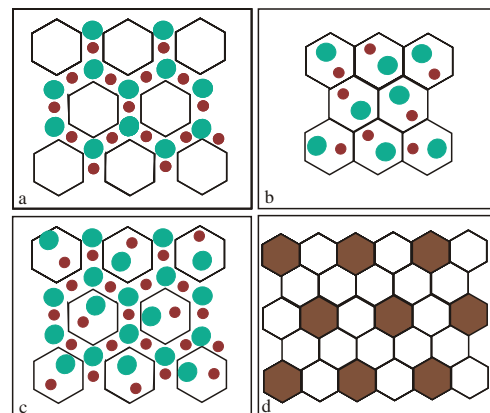


**Figure 10.** The classification of nanocomposites: (a) inter-type, (b) intra-type, (c) hybrid-type, (d) nano/nano-type [337].

techniques and different systems have been carried out by Laurent et al. [346], Kuzumaki et al. [347], Wu et al. [348], and Chen et al. [349]. However, only limited data are available at the moment on the mechanical properties of these novel composites, those showing so far only marginal improvements in the mechanical properties of the composites [345].

### 5.4.2. Ceramic Matrix Nanocomposites

According to Sternitzke, the different classes of ceramic nanocomposites are structural ceramics (e.g., $Al_2O_3$/SiC, $Si_3N_4$/SiC, MgO/SiC, Mullite/SiC) [350–352], low-temperature sol–gel derived, [353–357], glass ceramics, glass/metal (photosensitive glasses) [358–360], nanocomposite films (e.g., lead zinconate titanate (PZT)/nickel) [361], entrapment-type (e.g., zeolite/metallic or zeolite/organic complexes) [362], layered ceramics (e.g., pillared clays) [363], metal/ceramics (e.g., Fe-Cr/$Al_2O_3$, Ni/$Al_2O_3$) [364–366], and organoceramic (e.g., polymeric matrix/$PbTiO_3$) [367, 368].

In order to enhance the mechanical strength of the brittle ceramic materials, there are two approaches: increase fracture toughness by reduction of the critical flaw size or design ceramics with high flaw-tolerance [369]. The former approach includes development of the processing technologies to reduce the processing flaws [370]. In the latter case fracture toughness can be reached by introducing energy-dissipating components such as whiskers and platelets of particles into the ceramic microstructure [371–373]. These reinforcements deflect the crack or serve as bridging elements which hinder the further opening of the crack. One may include metallic particles which absorb energy by plastic deformation [253, 374]. A second phase which undergoes a phase transformation with a volume expansion initiated by the stress field of a propagating crack, has also been investigated [375]. The effect of these mechanisms responsible of the toughening of the nanocomposite ceramics has been reviewed by Sternitzke [336], Reimanis [376], and Bhaduri and Bhaduri [377]. Common observations are that the mechanical properties are very sensitive to the processing method of the nanocomposite and it is not always clear how the microstructure dictates the properties. However, there is a very large scatter of the reported strength values by numerous research groups [376]. At low temperature the $Al_2O_3$/SiC intragranular nanocomposites have been reported to have strength values up to 1000 MPa [378]. The fracture behavior changed to a transcrystalline mode. This resulted in a reduced wear rate and improved resistance against surface damage, due to grain boundary strengthening caused by SiC nanoinclusions [379, 380]. The effect on the toughness is marginal. On the other hand, $Al_2O_3$/$ZrO_2$ nano/nano composite has a low hardness but a high toughness (8–10 $K_{IC}$(MPa m$^{1/2}$) [381].

At high temperatures the benefits of the nanocomposites are more pronounced. The $Si_3N_4$/SiC nanocomposites show improved strength compared to $Si_3N_4$ in high temperatures [349, 382, 383]. $Si_3N_4$/30 vol. % SiC maintains the strength of about 1080 MPa up to 1400 °C temperature whereas the strength of $Si_3N_4$ is greatly reduced. Niihara and co-workers [384, 385] reported improved tensile creep at 1400 °C and

200 MPa stress in tension; monolithic $Si_3N_4$ failed after 0.4 h at 0.3% strain while the composite did not fail for 1000 h and at 1.5% strain. The nanophase SiC improved also the creep resistance of these materials with up to a threefold reduction in the steady-state creep rate [386, 387]. This is attributed to the SiC nanoparticles bridging the interface and reducing grain boundary sliding. In summary, the nanocomposite ceramics show improved fracture toughness and strength as compared to their single-phase counterparts, and the strength of the nanocomposites is equivalent to or better than the composites reinforced with a coarse second phase [375, 388].

Carbon nanotube composites offer a future potential to combine ceramic materials with the exceptional properties of CNT such as mechanical strength and electronic properties. CNT-metal-ceramic (CNT-Co-MgO and CNT-FeCo-$MgAl_2O_4$) composites have been developed by Peigney et al. [392].

Composites with about 2–6 wt. % of CNT had electrical conductivity in the range of 0.2 to 4.0 S cm$^{-1}$. Pull-out of the CNT was observed near the fracture surface but no macroscopic mechanical reinforcement was demonstrated. A 10% improvement in strength and fracture toughness of nano-SiC composite with 10 wt. % of CNT has been reported [390, 391]. The CNT composites have been reviewed by Thostenson et al. [392].

A summary of the mechanical properties of nanocrystalline materials is presented in Table 3.

## 6. APPLICATION OF NANOMATERIALS RELEVANT TO MECHANICAL PROPERTIES

Most of the applications of nanocrystalline materials so far have been introduced due to other than mechanical properties. In many applications, however, mechanical properties are of great importance even though the nanomaterial may not be directly applied for structural or mechanical purposes. Such applications may be found, for example, within electronics and sensor technology, where the nanomaterials are used because of their electrical, optical, or other functional properties. These materials have to withstand also stresses built up during processing or in use.

However, applications which are primarily induced because of the novel mechanical properties of nanocrystalline materials exist, and many more are under intensive study. Main hindrances for the development of structural applications of nanostructural materials lay in the difficulties in processing of the materials; either the processing technologies are not developed well enough yet or they are too expensive to justify the use of nanostructural materials. In the following, some examples of the existing and potential applications are reviewed.

### 6.1. Coating Applications

### 6.1.1. Applications Requiring Wear Resistance and Controlled Friction Properties

The development of materials to be used in more demanding conditions is typically solved by development of coatings. On the other hand, layered nanomaterial structures are

**Table 3.** Selected examples of nanomaterials and their mechanical properties at room temperature.

| Material | Grain size (nm) | Elastic modulus (GPa) | Ultimate strength (MPa) | Strain at Fracture (%) | Hardness (GPa) | Toughness (MPa m$^{1/2}$) | Ref. |
|---|---|---|---|---|---|---|---|
| Metals and intermetallics | | | | | | | |
| Fe | <100 | | 1190 (compression) | 19 | | | [393] |
| Fe | 5 | | | | 10 | | [280] |
| Cu | 10–22 | 108–116 | 340–480 | 1.6–2.4 | 2.2–2.6 | | [394, 282, 297] |
| Pd | 13–47 | 117–123 | | 2.6–4 | 3.2–3.7 | | [280, 394, 297] |
| Cr | 130 | | | | 6.0 | | [285] |
| Ni | 21 | | 1.82–2.04 | 2.6–4.0 | 5.5.–6.0 | | [305] |
| 5083 Al | 25–35 | | 462 | 8.4 | | | [306] |
| FeAl | 30–40 | | 2350 (compression) | | | 6–11 | [395] |
| NiTi | 20–30 | | 2650 | 5 | | | [396] |
| TiAl-X X = Cr, Mn, or Fe | 30 | | 2500 | | | | [397] |
| Nanocomposites | | | | | | | |
| Al$_2$O$_3$-SiC | | | 355–1.017 | | — | 3.25–4.70 | [378] |
| | | | 760–1.000 | | 19.1–21.2 | 2.7–3.6 | [378] |
| | | | | | — | 3–4.8 | [398] |
| | | | ~732 | | — | | [399] |
| Y-TZP-Al$_2$O$_3$-SiC | | | — | | 16–20 | ~4.7 | [400] |
| MgO-SiC | | | 340–700 | | — | 1.7–4.0 | [401] |
| | | | | | — | 1–4 | [378] |
| Si$_3$N$_4$-SiC | | | ~1.300 | | — | 6–7.5 | [402] |
| | | | | | 15–17.8 | 6–6.8 | [403] |
| | | | — | | 14–18.8 | 5.4–5.8 | [404] |
| | | | 1.100–1.550 | | | — | |
| | | | 577–875 | | 15–19 | 5.4–5.8 | [405] |
| | | | 505–520 | | — | 1.9–3.8 (R.T.) | |
| SiC-Si$_3$N$_4$ | | | 640 | | — | 6.6 | [406] |
| Si-C-N | | | 622–1.063 (R.T.) | | 17–21 | 4.4–5.9 | |
| | | | 807 (1.000 °C) | | — | — | [407] |
| | | | 700 (1.300 °C) | | | | [408] |
| | | | 800–1.000 | | — | — | |
| Al$_2$O$_3$-ZrO$_2$ | | | — | | ~4 | 8–10 | [402] |
| 3Y-TZP-Mo | | | ~2100 | | — | ~11.4 | [381] |
| Al$_2$O$_3$-W | | | — | | 16.3–19.6 | 3.34–4.63 | [409] |
| 70% Zr2(Cu, Pd) + 30% Zr60Cu20Pd10Al10 | 5–10 | 62.5 | 1900 | | 6 | | [410] |
| | | | | | | | [297] |
| Carbon nanotubes | | | | | | | |
| CNT | | 1800 | | | | | [224] |
| CNT | | 1250 | | | | | [225] |
| CNT | | 1280 | | | | | [226] |
| CNT | | | 11,000–63,000 | | | | [234] |

the means to enhance and tailor the coating properties to be used in, for example, such applications as gas turbines (thermal barrier coatings), bearings [411], tooling [412–416], optical [417], and magnetic recording media [207].

Thin-film growing methods often provide the means to grow layered coatings. This allows to design the properties of the coating in order to tailor the material surface. The idea is to introduce gradient structures, avoid sharp interfaces of different materials, and prevent the local stresses needed for crack initiation and growth. In macroscopic applications, tool coatings subjected to high stresses are an example of coatings. On the other hand, only very thin layers may be used as protective coatings for magnetic recording discs. In the following, some examples of multilayer films related to applications are described.

Multilayer Ti-TiN protective tool coating forms a superlattice, where the individual Ti and TiN layers are textured [002] and [111], respectively. The wear resistance of the multilayer film was best when the period thickness was 2.5 nm and when the Ti/TiN interface was pure [243]. Multilayered films have higher elasticity, hardness, and tribological

properties as compared to the constituent layer materials alone [245].

Complicated nanolayered films with gradient structure and nanocomposites including self-lubricating bearing or tooling materials such as $WS_2$ and diamond–like carbon (DLC) have been prepared with a hybrid technology combining laser ablation and magnetron sputtering [418, 419]. A self-adapting functional tribological layer formation was obtained: when sliding in humid air DLC forms a graphite-like layer and in vacuum a hexagonal $WS_2$ tribolayer is formed, both providing a COF below 0.1. Multilayered coatings have been developed also towards gradient structures in order to tailor the surface properties [420–424]. This enhances the adhesion of the protective coating used for wear protection in general.

Gell [425] has reviewed the potential use of nanocrystalline materials in gas turbine industry. In order to increase the operating temperature for better efficiency of gas turbines, the development of thermal barrier coatings is the single most important factor. Nanocrystalline coatings offer better thermal shock resistance, lower thermal conductivity, and better wear resistance than their conventional counterparts and therefore are especially interesting for use in this application. Consequently, strong effort has been made to develop nanocrystalline powders and their plasma spraying [426–436]. The developed alumina-titania coatings show superior wear resistance, adhesion, toughness, and spallation resistance and have been qualified by the U.S. Navy for use in a number of shipboard and submarine applications.

## 6.2. Structural Applications

### 6.2.1. Applications of Nanocrystalline Superplasticity

The increased rate of forming or the lower temperatures related to the superplastic deformation of nanocrystalline materials would make superplasticity more industrially accessible, extending its possible limits of use. With nanocrystalline metals, superplastic deformation may be possible to extend to such rapid and large-scale forming processes as forging. It has been demonstrated, for example, that it is possible to forge an 8- cm-long connecting rod from an extruded blank of an Al-alloy having a grain size of 80 nm in less than one second [77]. Forming experiments have also been carried out with nanocrystalline ceramics. It has been demonstrated that it is possible exactly to replicate die surfaces [90] and form cylinders of, for example, $TiO_2$ [89] and 3Y-TZP [85, 86].

In conclusion, experiences with forming of superplastic materials suggest that they may potentially be used especially in near-net shape processes. However, it has been claimed that the application of nanocrystalline materials would be limited to niche applications because other concurrent developments in control of superplasticity will increase the competitiveness of traditional superplastic materials [3]. It is speculated that nanocrystalline superplasticity will have an advantage over traditional superplastic materials when material chemistry may not be changed because of the nature of the application [e.g., in electronic applications] or when high strength after forming is demanded.

Another area of applications to superplastic materials is that of diffusion bonding. It has been shown that the use of a superplastic intermediate layer in diffusion bonding of non-superplastic stainless steel dramatically improves the properties of the joint especially if the mating surfaces are rough [437]. Nanocrystalline intermediate layers may thus offer possibility to reduce the processing time or temperature.

It has also been shown that nanocrystalline ceramics can be used for direct bonding of ceramic materials to each other. Superplasticity allows the mating surfaces to adapt better to surface asperities. The superplastic ceramic may also be in the form of an interlayer as in the case of metals. This interlayer may also be used to accommodate stresses in thermally mismatched structures as in metal-ceram joints and metal-ceram coating systems. When the compound is heated, a superplastic interlayer or coating could accommodate larger thermal mismatch strains than conventional interlayers or coatings without cracking by the processes of superplastic flow and stress relaxation [438].

Superplasticity may also be utilized in the processing of nanocrystalline ceramics themselves. Nanocrystalline ceramics are difficult to produce by pressureless sintering routes typically used for conventional ceramics, but they may be produced by sinter-forging, which uses the superplasticity of the material itself by closing pores with the aid of plastic flow [439]. It has also been demonstrated that nanocrystalline-based fiber-reinforced composites are denser, and because of significantly lower consolidation temperature, there is no damage to the fiber and no reaction occurs between the fiber and the matrix [440] as compared to conventional high-temperature processing. Also combustion synthesis can be realized at a lower temperature as shown by Uenishi et al. [441] for processing of $Al_3Ti$ from mechanically alloyed powders.

### 6.2.2. Application of Nanostructural Bulk Materials for Improved Strength and Ductility

Higher strength of nanocrystalline materials may be utilized in several potential applications, when processing of the materials is adequately developed. Gell [425] has reviewed the potential use of nanocrystalline materials in gas turbine industry. The highest pay-off applications are related to the improved engine performance which, in addition to higher operating temperature mentioned above, can be realized by higher motor speed. This requires the development of main shaft bearing materials and has led to the development of nanocrystalline M50 steel [442–444].

Also the need for tools with improved hardness/toughness properties has prompted interest in the development of nanostructured tool steels and improved properties have been demonstrated [445]. Similarly, development of WC-Co nanocomposites has been driven by the aim of obtaining cutting tools and hard metal coatings with superior properties as compared to their traditional counterparts. These materials are already starting to have commercial impact and are used in the manufacture of machine tools, drill bits, and wear parts [446]. Tools made of cemented carbide nanocomposites have enhanced hardness, fracture toughness, and wear resistance compared to their conventional counterparts.

Currently, nanocrystalline titanium is considered to be a potential material for medical implants. In order to obtain adequate strength, titanium alloys (mainly Ti-6Al-4V) are used, for example, for hip prostheses. Development of nanocrystalline pure titanium for such an application would allow the alloying content to be decreased for increased biocompatibility [447].

High-strength titanium alloys are also a subject of increasing interest for other applications where high strength is needed. For example, Zhernakov et al. [448] have demonstrated that both the static and the fatigue strength of commercially pure titanium fasteners and threaded articles can be substantially increased by ECA processing, producing a nanocrystalline grain structure.

An interesting technology for near-net shape forming of ceramic nanocrystalline materials is that of plasma spraying on a mandrel [449], which is afterwards removed. Both the mandrel and the plasma gun are computer controlled, allowing fabrication of complex shapes from nanocrystalline aluminum oxide. The fabrication of tapered alumina rings for space-based lightweight X-ray mirror shells with a smooth inside finish was demonstrated.

Nanocrystalline ceramics have also been considered for orthopaedic and dental implants of the future. Nanomaterials with improved mechanical properties could then replace some of the conventional biomaterials and could be tailored to meet clinical requirements associated with anatomical differences or patient age [450].

Incorporation of nanotubes instead of carbon fibers as reinforcing elements into plastic, ceramic, and metallic matrixes can potentially provide structural materials with dramatically improved modulus and strength. At the same time other functions such as electromagnetic shielding may be realized [451]. The focus of much of the research in nanotube-based composites has been on polymer-matrix materials, but the unique properties of carbon nanotubes can also be exploited in ceramic- or metal-matrix composites. So far the realized improvements in ceramic- and metal-matrix composites have been marginal and real applications are still awaiting. On the other hand, many improvements have taken place in use of nanoparticles as filler materials in polymers. These include fillers in dental polymers to improve their performance, for example, wear resistance or stiffness as in polymer-layered silicate nanocomposites. The detailed developments in this area are beyond the scope of the present review. Those interested can find more information on dental fillers, for example, in [452] and on polymer-layered silicate nanocomposites in [453].

Applications of nanocrystalline metallic materials have been limited because of low ductility in tension [454–456]. However, results of Lu et al. [307] on cold-rolling of nanocrystalline copper have opened up interesting views for developing novel processing for some metallic materials utilizing the nanocrystalline structure. It seems that the traditional deformation-annealing technique routinely used may be much simplified by using nanocrystalline metals as starting materials. With proper post-heat treatments, the microstructure may be easily controlled so that desired properties in the final product can be achieved.

## 6.3. Special Applications

The conductivity of CNT-ceramic composites has been applied for electric components and components in fuel injection applications to avoid risks related to static electricity [343, 387].

Low-Z nanocomposite ceramic materials (SiC, C-SiC, Si-SiC) have been shown to have high erosion resistance in high radiation and heat load conditions. This implies the application potential as a plasma facing material in fusion reactors [457, 458].

Carbon nanotube scanning probe tips for atomic probe microscopes are commercially available. Resolution of these microscopes depends on the sharpness of their probe tips, which deteriorate with operating time. The mechanical robustness of nanotubes dramatically increases probe life in comparison to conventional probe tips [459].

## 7. SUMMARY

In recent years a wide range of nanostructured materials has been introduced. These novel materials are produced in various forms such as nanopowders, nanostructured particulates, fibers, tubes, thin films as well as bulk by using a number of processing routes. Already the early theoretical predictions have shown that nanomaterials may have interesting mechanical properties in addition to their interesting functional properties. The bulk form of these materials includes electrodeposited sheets, equal channel angular pressed rods, ball-milled and consolidated pellets, composite films produced by a variety of deposition techniques, etc. Among the most interesting mechanical properties are, for example, their strength, hardness, elastic properties, toughness, and superplasticity.

In summary, it can be concluded that the elasticity of nanocrystalline materials is roughly the same as that of conventional materials unless the grain size is very small (<5 nm). In those cases the modeling results indicate that the elasticity is increased. The hardness and yield stress are steadily increased as the grain size is decreased until the grain size is below 20 nm. At smaller grain sizes the behavior varies dependent on the material system. For example, in pure Cu and Pd, softening is noticed. Some evidence exists that this is caused by the formation of collective grain boundary glide planes. High ductility predicted for the nanocrystalline ceramics and intermetallics at low temperatures has not been confirmed and the tensile ductility of metals has been found to decrease with decreasing grain size. Superplasticity has been observed at lower temperatures and higher strain rates in some nanocrystalline materials as compared to their coarse-grained counterparts. Some mechanical property related applications already exist while others are being developed. Due to the difficulties in producing bulk nanocrystalline materials, it is expected that nanocrystalline coatings will be first more widely applied.

## GLOSSARY

**Finite element method (FEM)** Method in which the domain to be analyzed is divided into elements, and then the displacement field within each element is interpolated

in terms of displacements at given points (nodes) around the element boundary.

**Molecular dynamics simulation (MD simulation)** Computer simulation of the molecular structure and motions of a system in response to external conditions.

**Nanoindentation** The method of testing the mechanical properties in near-surface region. The registration of load exerted on the diamond tip penetrating the surface and indentation depth make it possible to conclude on elastic and plastic properties of surface region or thin film.

**Nanotubes** Large macromolecules similar to a sheet of graphite rolled into a cylinder and capped with half fullerene at both ends.

**Neural networks** Mathematical models inspired by the neural circuit network of the human brain.

**Physical vapor deposition (PVD)** Thin-film vacuum coating method where the properties of the growing film are partly governed by the kinetic energy of the vapor species.

**Plasma assisted vapor deposition (PACVD)** Thin-film growing method, where the glow discharge plasma is used to enhance the growth of the film.

**Superlattice** Layered structure, which is composed of ultrathin layers of different materials providing new electronic and mechanical properties.

**Superplasticity** Ability of a material to exhibit exceptionally large tensile elongation during loading.

**Tribology** The science of rubbing surfaces, study of friction, lubrication, and wear.

# REFERENCES

1. R. W. Siegel, *Nanostruct. Mater.* 4, 121 (1994).
2. D. G. Morris, in "Mechanical Behavior of Nanostructured Materials." Trans. Tech. Publ. 85, Switzerland, 1998.
3. M. J. Mayo, *Nanostruct. Mater.* 9, 717 (1997).
4. R. Z. Valiev, R. K. Islamgaliev, and I. V. Alexandrov, *Prog. Mater. Sci.* 45, 103 (1999).
5. F. A. Mohammed and Y. Li, *Mater. Sci. Eng. A* 298, 1 (2001).
6. K. A. Padmanabhan, *Mater. Sci. Eng. A* 304–306, 200 (2001).
7. S. Van Petegem, F. Dalla Torre, D. Segers, and H. Van Swygenhoven, *Scr. Mater.* 48, 17 (2003).
8. W. Siegel, *Mater. Sci. Eng. A* 168, 189 (1993).
9. S. R. Phillpot, D. Wolf, and H. Gleiter, *J. Appl. Phys.* 78, 847 (1995).
10. R. W. Siegel, "Superplasticity of Metals, Ceramics and Intermetallics," MRS Symposium, Vol. 196, p. 59. Materials Research Society, Pittsburgh, PA, 1990.
11. Lasalmonie and Strudel, *J. Mater. Sci.* 1837 (1986).
12. V. Yamakov, D. Wolf, M. Salazar, S. R. Phillpot, and H. Gleiter, *Acta Mater.* 49, 2713 (2001).
13. E. O. Hall, *Proc. Phys. Soc. (London) B* 64, 747 (1951).
14. N. J. Petch, *J. Iron Steel Inst.* 174, 25 (1953).
15. A. H. Chokshi, A. Rosen, J. Karch, and H. Gleiter, *Scr. Metall. Mater.* 23, 1679 (1989).
16. K. Lu, W. D. Wei, and J. T. Wang, *Scr. Metall. Mater.* 24, 2319 (1990).
17. G. E. Fougere, J. R. Weertman, R. W. Siegel, and S. Kim, *Scr. Metall. Mater.* 26, 1879 (1992).
18. G. D. Hughes, S. D. Smith, C. S. Pande, H. R. Johnson, and R. W. Armstrong, *Scr. Metall. Mater.* 20, 93 (1983).
19. J. S. C. Jang and C. C. Koch, *Scr. Metall. Mater.* 24, 1599 (1990).
20. T. G. Nieh and J. Wadsworth, *Scr. Metall. Mater.* 25, 955 (1991).
21. N. Wang, Z. Wang, K. Aust, and U. Erb, *Acta Metall. Mater.* 31, 47 (1995).
22. R. O. Scattergood and C. C. Koch, *Scr. Metall. Mater.* 27, 1195 (1992).
23. J. Lian, B. Baudelet, and A. A. Nazarov, *Mater. Sci. Eng. A* 172, 23 (1993).
24. V. G. Gryazov, M. Yu. Gutkin, A. E. Romanov, and L. I. Trusov, *J. Mater. Sci.* 38, 4359 (1993).
25. R. A. Masumura, P. M. Hazzledine, and C. S. Pande, *Acta Mater.* 46, 4527 (1998).
26. S. Takeuchi, *Scr. Metall. Mater.* 44, 1483 (2001).
27. N. Wang, Z. Wang, K. Aust, and U. Erb, *Acta Metall. Mater.* 43, 519 (1995).
28. K. A Padmanathan, R. Nitsche, and H. Hahn, "Proceedings of the 4th European Conference on Advanced Materials and Processes," 1995, p. 289.
29. H. Hahn and K. A. Padmanathan, *Nanostruct. Mater.* 6, 191 (1995).
30. H. Hahn and K. A. Padmanathan, *Philos. Mag. B* 76, 559 (1997).
31. H. Hahn, P. Mondal, and K. A. Padmanathan, *Nanostruct. Mater.* 9, 603 (1997).
32. J. Schiøtz, F. D. Di Tolla, and K. W. Jacobsen, *Nature* 39, 561 (1998).
33. H. Van Swygenhofen and A. Caro, *Phys. Rev. B* 58, 11246 (1998).
34. J. Shotz, F. D. Di Tolla, and K. W. Jacobsen, *Phys. Rev. B* 60, 11971 (1999).
35. H. Van Swygenhofen, M. Spaczer, A. Caro, and D. Farkas, *Phys. Rev. B* 60, 22 (1999).
36. S. Van Petegem, D. Segers, H. Van Swygenhoven, F. Dalla Torre, and J. Kuriplach, "Proceedings of the 2nd Workshop on Nanomaterials: Fundamentals and Applications," 2002, p. 3-4.10.
37. D. Fleichtinger, P. M. Derlet, and H. Van Swygenhoven, "Proceedings of the 2nd Workshop on Nanomaterials: Fundamentals and Applications," 2002, p. 3-4.10.
38. H. Hahn, P. Mondal, and K. A. Padmanathan, *Nanostruct. Mater.* 9, 603 (1997).
39. H. Gleiter, *Prog. Mater. Sci.* 33, 223 (1989).
40. G. E. Fougere, L. Riester, M. Ferber, J. R. Weertman, and R. W. Siegel, *Mater. Sci. Eng. A* 204, 1 (1995).
41. M. Hoffman and R. Birringer, *Acta Mater.* 44, 2729 (1996).
42. N. A. Akhmadeev, N. P. Kobelev, R. R. Mulyukov, Y. M. Shaefer, and R. Z. Valiev, *Acta Metall. Mater.* 41, 1041 (1993).
43. R. Molyukov, M. Weller, R. Z. Valiev, Th. Gessmann, and H. E. Schaefer, *Nanostruct. Mater.* 6, 577 (1995).
44. A. B. Lebedev, Yu Burenkov, S. A. Pulnev, V. V. Vetrov, and V. I. Kopylov, *J. de Physique IV* C8, 365 (1996).
45. A. B. Lebedev, S. A. Pulnev, V. I. Kopylov, Y. Burenkov, and V. V. Vetrov, *Scr. Mater.* 35, 1077 (1996).
46. J. Shiøtz, T. Vegge, F. D. Di Tolla, and K. W. Jacobsen, in "Modelling of Structure and Mechanics of Materials from Microscale to Product" (J. V. Carstensen, T. Leffers, T. Lorenzen, O. B. Pedersen, B. F. Sørensen and G. Winther, Eds.), p. 133. Risø National Laboratory, Roskilde, Denmark, 1998.
47. A. B. Lebedev, Yu A. Burenkov, V. I. Kopylov, A. E. Romanov, and V. G. Gryaznovhil. *Mag. Lett.* 73, 241 (1996).
48. W. N. Weins, J. D. Makinson, R. J. De Angelis, and S. C. Axtell, *Nanostruct. Mater.* 9, 509 (1997).
49. M. Weller, J. Diehl, and H. E. Schafer, *Philos. Mag. A* 63, 527 (1991).
50. E. Bonetti and G. Valdre, *Philos. Mag. B* 68, 967 (1993).
51. A. Al Sadi, E. Bonetti, P. Mattioli, and G. Valdre, *J. Alloys Comp.* 211/212, 489 (1994).
52. B. Cai, Q. P. Kong, P. Chui, H. T. Cong, and X. K. Sun, *Scr. Mater.* 44, 1043 (2001).
53. S. Okuda, F. Tang, H. Tanimoto, and Y. Iwamoto, *J. Alloys Comp.* 211/212, 494 (1994).
54. E. Bonetti, L. D. Bianco, L. Pasquini, and E. Sampaolesi, *Nanostruct. Mater.* 10, 741 (1998).

55. S. R. Agnew and J. R. Weertman, *Mater. Sci. Eng. A* 244, 145 (1998).
56. A. Vinogradov, Y. Kaneko, K. Kitagawa, S. Hashimoto, V. V. Stolyarov, and R. Z. Valiev, *Scr. Mater.* 36, 1345 (1997).
57. A. B. Whitney, P. G. Sanders, J. R. Weertman, and J. A. Eastman, *Scr. Metall. Mater.* 33, 2025 (1995).
58. A. B. Whitney, P. G. Sanders, J. R. Weertman, and J. A. Eastman, *Int. J. Fatigue* 19, 265 (1997).
59. G. Palumbo, F. Gonzales, A. M. Brennenstuhl, U. Erb, W. Shmayada, and P. C. Lichtenberger, *Nanostruct. Mater.* 9, 737 (1997).
60. S. Hashimoto, Y. Kaneko, K. Kitagawa, A. Vinogradov, and R. Z. Valiev, *Proc. Int. Conf. ISMANAM* 10, (1998).
61. A. Yu Vinogradov, V. V. Stolyarov, S. Hasimoto, and R. Z. Valiev, *Mat. Sci. Eng. A* 318, 163 (2001).
62. H. Mughrabi, in NATO Science Series, Vol. 3/80, 241, "Investigations and Applications of Severe Plastic Deformation" (T. C. Lowe and R. Z. Valiev, Eds.), Kluwers Publishers, Dordrecht, 2000.
63. A. Vinogradov, S. Nagasaki, V. Patlan, K. Kitagawa, and M. Kawazoe, *Nanostruct. Mater.* 11, 925 (1999).
64. V. Patlan, A. Vinogradov, K. Higashi, and K. Kitagawa, *Mater. Sci. Eng. A* 300, 171 (2001).
65. S. R. Agnew, A. Yu. Vinogradov, S. Hashimoto, and J. R. Weertman, *J. Electr. Mater.* 28, 1038 (1999).
66. A. Vinogradov, H. Miyamoto, T. Mimaki, and S. Hashimoto, *Ann. Chim. Sci. Mat.* 27, 65 (2002).
67. A. Vinogradov, V. Patlan, Y. Suzuki, K. Kitagawa, and V. I. Kopylov, *Acta Mater.* 50, 1639 (2002).
68. S. Schumacher, R. Birringer, R. Strauss, and H. Gleiter, *Acta Metall.* 37, 2485 (1989).
69. M. L. Xiao and Q. P. Kong, *Scr. Mater.* 36, 299 (1997).
70. Q. P. Kong and M. L. Xiao, *Mater. Sci. Eng. A* 234–236, 91 (1997).
71. B. Cai, Q. P. Kong, L. Lu, and K. Lu, *Scr. Mater.* 41, 755 (1999).
72. D. L. Wang, Q. P. Kong, and J. P. Shui, *Scr. Metall. Mater.* 31, 47 (1994).
73. J. Deng, D. L. Wang, Q. P. Kong, and J. P. Shui, *Scr. Metall. Mater.* 26, 349 (1995).
74. E. W. Hart, *Acta Met.* 23, 351 (1967).
75. O. A. Kaibyshev, "Superplasticity in Metals, Intermetallics and Ceramics." Springer, Frankfurt, 1992.
76. T. G. Nieh, J. Wadsworth, and O. G. Sherby, in "Superplasticity in Metals and Ceramics," p. 290. Cambridge Univ. Press, Cambridge, 1997.
77. K. Taketani, A. Uoya, K. Ohtera, T. Uehara, K. Higashi, A. Inoue, and T. Masumoto, *J. Mater. Sci.* 29, 6513 (1994).
78. K. Higashi, in "Superplasticity in Advanced Materials" (T. G. Langdon, Ed.), ICSAM-94, p. 131. Trans. Tech, Aedermansdorf, Switzerland, 1994.
79. R. Z. Valiev, *Mater. Sci. Eng. A* 137, 35 (1991).
80. R. Z. Valiev, A. V. Korznikov, and R. R. Mulyukov, *Mater. Sci. Eng. A* 168, 141 (1993).
81. R. Z. Valiev, R. K. Islamgaliev, V. V. Stolyarov, R. S. Mishra, and A. K. Mukherjee, *Mater. Sci. Forum* 969, 269 (1998).
82. R. S. Mishra, V. V. Stolyarov, C. Echer, R. Z. Valiev, and A. K. Mukherjee, *Mater. Sci. Eng. A* 298, 44 (2001).
83. R. S. Mishra, R. Z. Valiev, S. X. McFadden, and A. K. Mukherjee, *Mater. Sci. Eng. A* 252, 174 (1998).
84. S. X. McFadden, R. Z. Valiev, and A. K. Mukherjee, *Mater. Sci. Eng. A* 319–321, 849 (2001).
85. M. Ciftcioglu and M. J. Mayo, *MRS Symp. Proc.* 196, 77 (1990).
86. G. B. Prabhu and D. L Bourell, *Scr. Met. Mater.* 33, 761 (1995).
87. M. M. R. Boutz et al., *J. Eur. Ceram. Soc.* 13 (1994).
88. M. J. Mayo, in "Superplasticity in Advanced Materials," (S. Hori, M. Tokizane, and N. Furushiro, Eds.), p. 541. Japan Society for Research on Superplasticity, Osaka, 1991.
89. H. Hahn and R. S. Averback, *J. Am. Ceram. Soc.* 74, 2918 (1991).
90. J. Karch and R. Birringer, *Ceram. Intl.* 16, 291 (1990).
91. Z. Cui and H. Hahn, *Nanostruct. Mater.* 1, 419 (1992).
92. R. Lappalainen and R. Raj, *Acta Metall. Mater.* 39, 3125 (1991).
93. R. S. Mishra, R. Z. Valiev, and A. K. Mukherjee, *Nanostruct. Mater.* 9, 473 (1997).
94. M. Jain and T. Christman, *Acta Metall. Mater.* 42, 1901 (1994).
95. G. A Salishchev, O. R. Valiakmetov, and R. M. Galeyev, *J. Mater. Sci.* 28, 2898 (1993).
96. H. Hahn, R. S. Averback, H. J. Höfler, and J. Logas, *MRS Symp. Proc.* 206, 569 (1991).
97. R. S. Averback, H. J. Höfler, and R. Tao, *Mater. Sci. Eng. A* 166, 169 (1993).
98. K. S. Chan, *Scr. Metall. Mater.* 24, 1725 (1990).
99. D. G. Morris and M. A Morris, *Scr. Mater.* 34, 45 (1996).
100. D. G. Morris and M. A Morris, in "Synthesis and Properties of Mechanically Alloyed and Nanocrystalline Materials" (D. Fiorani and M. Magini, Eds.), Vols. 235–238, p. 861. Trans. Tec. Pubs. Ueticon-Zürich, 1997.
101. P. E. Sheehan and C. M. Lieber, *Science* 272, 1158 (1996).
102. B. I. Jakobson and R. Smalley, *Am. Sci.* 85, 324 (1997).
103. M. Terrones, N. Grobert, W. Hsu, Y. Zhu, W. Hu, H. Terrones, J. Hare, H. Kroto, and D. Walton, *Mater. Res. Soc. Bull.* 24, 43 (1999).
104. D. H. Robertson, D. W. Brenner, and J. Mintmire, *Phys. Rev. B* 45, 12592 (1992).
105. G. S. Smith, E. B. Tadmor, N. Bernstein, and E. Kaxiras, *Acta Mater.* 49, 4089 (2001).
106. A. Muliana, R. Steward, R. M. Haj-Ali, and A. Saxena, *Metal. Mater. Trans.* 33A, 1939 (2002).
107. S. M. Myers, J. A. Knapp, D. Follstaedt, and M. T. Dugger, *J. Appl. Phys.* 83, 1256 (1998).
108. R. Nowak, F. Yoshida, J. Morgiel, and B. Major, *J. Appl. Phys.* 85, 841 (1999).
109. R. Nowak, C. L. Li, T. Okada, and F. Yoshida, *Nucl. Instr. Meth. Phys. Res. B* 148, 110 (1999).
110. T. J. Lu, D. F. Moore, and M. H. Chia, *J. Micromech. Microeng.* 12, 168 (2002).
111. R. M. Bostock, J. D. Collier, R.-J. E. Jansen, R. Jones, D. F. Moore, and J. E. Townsend, *J. Micromech. Microeng.* 8, 343 (1998).
112. J.-S. Liu and T. J. Lu, *J. Micromech. Microeng.* 11, 195 (2001).
113. R. Nowak, T. Manninen, C. L. Li, K. Heiskanen, S.-P. Hannula, V. K. Lindroos, T. Soga, and F. Yoshida, *JSME Int. J.* 46, 265 (2003).
114. D.-Y. Ju and H.-Y. Zhao, *JSME/ASME Int. Conf. Mater. Proc. Jap. Soc. Mechan. Eng. Tokyo* 1, 204 (2002).
115. B. Bushan, Ed., "Modern Tribology Handbook." CRC Press, Boca Raton, FL, 2001.
116. K. Virwani, D. K. Sood, W. F. Schmidt, A. Malshe, E. A. Stach, and A. M. Minor, *JSME/ASME Int. Conf. Mater. Proc. Jap. Soc. Mechan. Eng. Tokyo* 1, 285 (2002).
117. J. Luo and D. A. Dornfield, *IEEE Trans. Semiconductor MFG.* 14, 112 (2001).
118. M. Futakawa, I. Wakui, and M. Eto, *J. Eur. Ceram. Soc.* 20, 1135 (2000).
119. N. Naka, K. Yamamoto, Y. Isono, T. Tanaka, and N. Terayama, *J. Jap. Soc. Mech. Eng. A* 66, 698 (2000).
120. M. W. Seto, B. Dick, and M. J. Brett, *J. Micromech. Microeng.* 11, 582 (2001).
121. U. Landman, W. D. Luedtke, N. A. Burnham, and R. J. Colton, *Science* 248, 454 (1990).
122. A. Bedun, S. Ciraci, and I. P. Batra, *Phys. Rev. B* 57, 2468 (1998).
123. L. C. Zhang and H. Tanaka, *JSME Int. A* 42, 546 (1999).
124. W. C. D. Cheong and L. C. Zhang, *Nanotechnol.* 11, 173 (2000).
125. D. Christopher, R. Smith, and A. Richter, *Nanotechnol.* 12, 372 (2001).
126. D. Christopher, R. Smith, and A. Richter, *Nucl. Instr. Meth. Phys. Res. B* 180, 117 (2001).

*127.* R. Astala, M. Kaukonen, R. M. Nieminen, and T. Heine, *Phys. Rev. B* 61, 2973 (2000).

*128.* A. Gannepalli and S. K. Mallapraganda, *Nanotechnol.* 12, 250 (2001).

*129.* L. C. Zhang and H. Tanaka, *Wear* 211, 44 (1997).

*130.* J. Shimizu, H. Eda, M. Yoritsune, and E. Ohmura, *Nanotechnol.* 9, 118 (1998).

*131.* T.-H. Fang and C.-I. Weng, *Nanotechnol.* 11, 148 (2000).

*132.* R. E. Miller and V. B. Shenoy, *Nanotechnol.* 11, 139 (2000).

*133.* T. Cagin, G. Wang, R. Martin, N. Breen, and W. A. Goddard, *Nanotechnol.* 11, 77 (2000).

*134.* M. Marques and J. A. Gonzalo, *Nanotechnol.* 12, 143 (2001).

*135.* M. Macucci, G. Iannacone, J. Martorell, D. W. L. Sprung, A. Schenk, I. Yakimienko, K.-F. Berggren, K. Stokbro, and N. Gippius, *Nanotechnol.* 12, 136 (2001).

*136.* H. Yu, J. B. Adams, and L. G. Hector, Jr., *Modelling Simul. Mater. Sci. Eng.* 10, 319 (2002).

*137.* H. Spikes, *Tribology Int.* 34, 789 (2001).

*138.* C. D. Elcoate, H. P. Evans, T. G. Hughes, and R. W. Snidle, "Proceedings of the Leeds–Lyon Symposium, Lubrication at the Frontier, 1998," 1999, p. 16372.

*139.* R. Grüebler, H. Sprenger, and J. Reissner, *J. Mater. Process. Tech.* 103, 80 (2000).

*140.* F. Klocke, T. Beck, S. Hoppe, T. Krieg, N. Müller, T. Nöthe, H.-W. Raedt, and K. Sweeney, *J. Mater. Process. Tech.* 120, 450 (2002).

*141.* A. V. Olver, S. J. Cole, and R. S. Sayles, "Proceedings of the 19th Leeds–Lyon Symposium on Tribology, Thin Films in Tribology," 1993.

*142.* A. A. Voevodin, S. D. Walck, and J. S. Zabinski, *Wear* 203, 516 (1997).

*143.* K. Holmberg, A. Laukka, H. Ronkainen, K. Wallin, and S. Varjus, *Wear* (2003) to be published.

*144.* R. W. Armstrong and W. H. Robinson, *N. Z. J. Sci.* 17, 429 (1974).

*145.* D. Newey, M. A. Wilkins, and H. M. Pollock, *J. Phys. E. Sci. Instrum.* 15, 1655 (1982).

*146.* J. B. Pethica, R. Hutchings, and W. C. Oliver, *Philos. Mag. A* 48, 593 (1983).

*147.* P. E. Wierenga and A. J. J. Franken, *J. Appl. Phys.* 55, 4244 (1984).

*148.* S.-P. Hannula, D. Stone, and C.-Y. Li, *Mat. Res. Soc. Symp. Proc.* 40, 217 (1985).

*149.* M. F. Doerner and W. D. Nix, *J. Mater. Res.* 1, 601 (1986).

*150.* G. M. Pharr, W. C. Oliver, and F. R. Brotzen, *J. Mater. Res.* 7, 613 (1992).

*151.* C. W. Shih, M. Yang, and J. C. M. Li, *J. Mater. Res.* 6, 2623 (1992).

*152.* M. F. Tambwe, D. S. Stone, J.-P. Hirvonen, I. Suni, and S.-P. Hannula, *Scr. Mater.* 37, 1421 (1997).

*153.* A. K. Bhattacharya and W. D. Nix, *Int. J. Solids Structures* 24, 881 (1988).

*154.* T. A. Lursen and J. C. Simo, *J. Mater. Res.* 7, 618 (1992).

*155.* H. Hertz, *J. Reine und angewandte Mathematik* 92, 156 (1882).

*156.* H. R. Hertz, "Miscellaneous Papers." Macmillan, London, 1986.

*157.* K. L. Johnson, "Contact Mechanics." Cambridge Univ. Press, Cambridge, 1985.

*158.* J. R. Turner, *Int. J. Solids Structures* 16, 409 (1980).

*159.* V. I. Fabrikant, *Trans. ASME* 53, 798 (1986).

*160.* H. Fan and L. M. Keer, *Trans. ASME* 61, 250 (1994).

*161.* S. L. Bulychev, V. P. Alekhin, M. K. Shorshorov, A. P. Ternovski, and G. D. Shmyrev, *Int. Lab.* 41, 1409 (1975).

*162.* R. B. King, *Int. J. Solids Structures* 23, 1657 (1987).

*163.* W. C. Oliver and G. M. Pharr, *J. Mater. Res.* 7, 1564 (1992).

*164.* T. J. Bell, A. Bendelli, J. S. Field, M. V. Swain, and E. G. Twaite, *Metrologia* 28, 463 (1992).

*165.* J. S. Field and M. V. Swain, *J. Mater. Res.* 8, 297 (1993).

*166.* J. S. Field and M. V. Swain, *J. Mater. Res.* 10, 101 (1995).

*167.* E. R. Weppelmann and M. V. Swain, *Thin Solid Films* 286, 111 (1996).

*168.* S. V. Hainsworth, H. W. Chandler, and T. F. Page, *J. Mater. Res.* 8, 1987 (1996).

*169.* G. M. Pharr, *Mater. Sci. Eng. A* 253, 151 (1998).

*170.* M. V. Swain, *Mater. Sci. Eng. A* 253, 160 (1998).

*171.* J. L. Loubet, J. M. Georges, and G. Meille, in "Microindentation Techniques in Materials Science and Engineering" (P. J. Blau and B. R. Lawn, Eds.), p. 72. American Society for Testing and Materials, Philadelphia, PA, 1986.

*172.* B. Taljat, T. Zacharia, and F. M. Haggag, *J. Mater. Res.* 4, 965 (1997).

*173.* W. W. Gerberich, W. Yu, D. E. Kramer, A. Strojny, D. F. Bahr, E. T. Lilleodden, and J. Nelson, *J. Mater. Res.* 13, 421 (1998).

*174.*

*175.* E. Söderlund and D. J. Rowcliffe, *J. Hard Mater.* 5, 149 (1994).

*176.* W. C. Oliver, R. Hutchings, and J. B. Pethica, in "ASTM STP" (P. J. Blau and B. R. Lawn, Eds.), p. 90. American Society for Testing and Materials Philadelphia, PA, 1986.

*177.* M. Sakai and R. Nowak, in "Ceramics Adding the Value (M. J. Bannister, Ed.), AUSTCERAM 92, p. 922. CSIRO Publications, Sydney, 1992.

*178.* R. Hill, B. Storåkers, and A. B. Zdunek, *Proc. Roy. Soc. Lond. A* 423, 301 (1989).

*179.* R. Hill and B. Storåkers, in "Elasticity: Mechanical Methods and Applications" (G. Eason and R. W. Ogden, Eds.), p. 199. Ellis Horwood, Chichester, 1990.

*180.* B. Storåkers, and P. L. Larsson, *J. Mech. Phys. Solids* 42, 307 (1994).

*181.* S. Biwa and B. Storåkers, Analysis of Fully Plastic Brinell Indentation, Report 168, Dept. Solid Mechanics, The Royal Institute of Technology, Stockholm, 1994.

*182.* F. H. Norton, "Creep of Steel in High Temperatures." McGraw-Hill, New York, 1929.

*183.* A. K. Bhattacharya and W. D. Nix, *Int. J. Solids Structures* 24, 1287 (1988).

*184.* H. Wang and H. Bangert, *Mater. Sci. Eng. A* 163, 43 (1993).

*185.* A. Giannakopoulos, P. L. Larsson, and R. Vestergaard, *Int. J. Solids. Structures* 5, 149 (1994).

*186.* K. Zeng and D. J. Rowcliffe, *Acta Metall. Mater.* 43, 1935 (1995).

*187.* P. L. Larsson, A. Giannakopoulos, E. Söderlund, D. J. Rowcliffe, and R. Vestergaard, *Int. J. Solids Struct.* 33, 221 (1996).

*188.* A. Giannakopoulos and P. L. Larsson, *Mech. Mater.* 25, 1 (1997).

*189.* D. C. Drucker and W. Prager, *Q. Appl. Math.* 10, 157 (1952).

*190.* A. E. Giannakopoulos and S. Suresh, *Acta Mater.* 46, 2153 (1999).

*191.* S. Suresh, A. E. Giannakopoulos, and J. Alcala, *Acta Mater.* 45, 1307 (1997).

*192.* S. Suresh and A. E. Giannakopoulos, *Acta Mater.* 46, 5755 (1998).

*193.* J. A. Knapp, D. M. Follstaedt, S. M. Myers, J. C. Barbour, and T. A. Friedmann, *J. Appl. Phys.* 85, 1460 (1999).

*194.* C. J. Kelchner, S. J. Plimpton, and J. C. Hamilton, *Phys Rev. B* 58, 11085 (1998).

*195.* M. Sakai, *Acta Metall. Mater.* 41, 1751 (1993).

*196.* D. Stone and K. B. Yoder, *J. Mat. Res.* 9, 2524 (1994).

*197.* R. Nowak, T. Sekino, S. Maruno, and K. Niihara, *Appl. Phys. Lett.* 68, 1063 (1996).

*198.* R. Nowak, T. Sekino, and K. Niihara, *Philos. Mag. A* 74, 171 (1996).

*199.* R. Nowak, M. Pessa, M. Suganuma, M. Leszczynski, I. Grzegory, S. Porowski, and F. Yoshida, *Appl. Phys. Lett.* 75, 2070 (1999).

*200.* R. Nowak and M. Sakai, *Oyo Buturi (Applied Physics Forum)* 65, 1262 (1996) (in Japanese).

*201.* R. Nowak, C. L. Li, and M. V. Swain, *Mater. Sci. Eng. A* 253, 167 (1998).

*202.* B. Cappella and G. Dieter, *Surf. Sci Rep.* 34, 1 (1999).

*203.* H. Xie, S. Kishimoto, A. Asundi, C. Gin, N. Shinya, and B. K. A. Ngoi, *Nanotechnol.* 11, 24 (2000).

*204.* S. A. Catlege, P. T. Spencer, and Y. K. Vohra, *Appl. Phys. Lett.* 77, 3568 (2000).

205. B. Kracke and B. Damaschke, *Appl. Phys. Lett.* 77, 361 (2000).
206. B. Bhushan, *Wear* 225–229, 465 (1999).
207. A. K. Menon and B. K. Gupta, *Nanostruct. Mater.* 11, 965 (1999).
208. B. Bhushan, V. N. Koinkar, and J. Ruan, *J. Eng. Tribol.* 208, 17 (1994).
209. S. Sundararajan and B. Bhushan, *Wear*, 225–229, 678 (1999).
210. R. Buzio, E. Gnecco, C. Boragno, and U. Valbusa, *Carbon* 40, 883 (2002).
211. A. P. Levitt, "Whisker Technology," p. 478. Wiley, New York, 1970.
212. A. Stalder and U. Durig, *Appl. Phys. Lett.* 68, 637 (1996).
213. N. Agrait, G. Rubio, and S. Vieira, *Phys. Rev Lett.* 74, 3995 (1995).
214. S. Iijima, *Nature* 318, 56 (1991).
215. M. S. Dresselhaus, G. Dresselhaus, and R. Saito, *Carbon* 33, 883 (1995).
216. A. Tess, R. Lee, P. Nikolaev, H. Dai, P. Petet, J. Robert, C. Xu, Y. H. Lee, S. G. Kim, A. G. Rinzler, D. T. Colbert, G. E. Scuseria, D. Tomanek, J. E. Fisher, and R. E. Smalley, *Science* 273, 483 (1996).
217. L. Vaccarini, C. Goze, L. Henrard, E. Hernandez, P. Bernier, and A. Rubio, *Carbon* 38, 1681 (2000).
218. T. Oku, T. Hirano, M. Kuno, T. Kusunose, K. Niihara, and K. Suganuma, *Mater. Sci. Eng. B* 74, 206 (2000).
219. P. Fairley, *Chemical Week* 163, 23 (2001).
220. G. W. Nieman, J. R. Weertman, and R. W. Siegel, *J. Mater. Res.* 6, 1012 (1991).
221. G. Overney, W. Zhong, and D. Tomanek, *Z. Physik D* 27, 93 (1993).
222. B. I. Yakobson, C. I. Brabec, and J. Bernhole, *Phys. Rev. Lett.* 76, 2511 (1996).
223. A. Peigney, Ch. Laurent, E. Flahaut, R. R. Bacsa, and A. Rousset, *Carbon* 39, 507 (2001).
224. M. M. J. Treacy, T. W. Ebbesen, and J. M. Gibson, *Nature* 381, 678 (1996).
225. A. Krishnan, E. Dujardin, T. W. Ebbesen, P. N. Yianilos, and M. M. J. Treacy, *Phys. Rev. B* 58, 14013 (1998).
226. E. W. Wong, P. E. Sheehan, and C. M. Lieber, *Science* 277, 1971 (1997).
227. J.-P. Salvetat, J.-M. Bonard, N. H. Thomson, A. J. Kulik, L. Forro, W. Benoit, and L. Zuppiroli, *Appl. Phys. A* 69, 255 (1999).
228. J.-P. Salvetat, G. A. D. Briggs, J.-M. Bonard, R. R. Bacsa, A. J. Kulik, T. Stöckli, N. A. Burnham, and L. Forro, *Phys. Rev. Lett.* 82, 944 (1999).
229. D. A. Walters, L. M. Ericson, M. J. Casavant, J. Liu, D. T. Colbert, K. A. Smith, and R. E. Smalley, *Appl. Phys. Lett.* 74, 3803 (1999).
230. N. G. Chopra and A. Zettl, *Solid State Commun.* 105, 297 (1998).
231. E. Hernandes, C. Goze, P. Bernier, and A. Rubio, *Appl. Phys. A* 68, 287 (1999).
232. M. B. Nardelli, B. I. Yakobson, and J. Bernholc, *Phys. Rev. B* 57, R4277 (1998).
233. Q. Zhao, M. B. Nardelli, and J. Bernholc, *Phys. Rev. B* 65, 144105 (2002).
234. M.-F. Yu, O. Lourie, M. J. Dyer, K. Moloni, T. F. Kelly, and R. S. Ruoff, *Science* 287, 639 (2000).
235. M.-F. Yu, B. S. Files, S. Arepalli, and R. S. Ruoff, *Phys. Rev. Lett.* 84, 5552 (2000).
236. M. R. Falvo, G. J. Clary, R. M. Taylor, V. Chi, F. P. Brooks Jr., S. Washburn, and R. Superfine, *Nature* 389, 582 (1997).
237. S. Iijima, C. Brabec, A. Maiti, and J. Bernholc, *J. Chem. Phys.* 104, 2089 (1996).
238. K. Holmberg, A. Matthews, and H. Ronkainen, *Tribol. Int.* 31, 107 (1998).
239. H. Holleck and V. Schier, *Surf. Coat. Technol.* 76–77, 328 (1995).
240. X. Chu and S. A. Barnett. *J. Appl. Phys.* 77, 4403 (1995).
241. J. Musil, *Surf. Coat. Technol.* 125, 322 (2000).
242. M. A. Baker, P. J. Kench, M. C. Joseph, C. Tsotsos, A. Leyland, and A. Matthews, *Surf. Coat. Technol.* (2002), in press.
243. C. Sant, M. Ben Daia, P. Aubert, S. Labdi, and P. Houdy, *Surf. Coat. Technol.* 127, 167 (2000).
244. J. Koskinen, J. E. Steinwall, R. Soave, and H. H. Johnson, *J. Micromech. Microeng.* 3, 1 (1993).
245. E. Bertran, E. Martínez, G. Viera, J. Farjas, and P. Roura, *Diamond Rel. Mater.* 10, 1115 (2001).
246. E. Bertran, G. Viera, E. Martínez, J. Esteve, Y. Maniette, J. Farjas, and P. Roura, *Thin Solid Films* 377, 495 (2000).
247. H. Leiste, U. Dambacher, S. Ulrich, and H. Holleck, *Surf. Coat. Technol.* 116, 313 (1999).
248. R. Hauert, L. Knoblauch-Meyer, G. Francz, A. Schroeder, and E. Wintermantel, *Surf. Coat. Technol.* 120–121, 291 (1999).
249. J. L. He, W. Z. Li, H. D. Li, and C. H. Liu, *Surf. Coat. Technol.* 103–104, 276 (1998).
250. M. Berger, U. Wiklund, M. Eriksson, H. Engqvist, and S. Jacobson, *Surf. Coat. Technol.* 116–119, 1138 (1999).
251. H. Holleck, *Surf. Eng.* 7, 137 (1991).
252. M. Stuber, H. Leiste, S. Ulrich, H. Holleck, and D. Schild, *Surf. Coat. Technol.* 150, 218 (2002).
253. S.-T. Oh, M. Sando, and K. Niihara, *J Mater. Sci.* 36, 817 (2001).
254. J. Patscheider, T. Zehnder, and M. Diserens, *Surf. Coat. Technol.* 146–147, 201 (2001).
255. A. Leyland and A. Matthews, *Wear* 246, 1 (2000).
256. C. Rebholz, A. Leyland, J. M. Schneider, A. A. Voevodin, and A. Matthews, *Surf. Coat. Technol.* 120–121, 412 (1999).
257. H. Holleck, *J. Vasc. Sci. Technol. A* 4, 2661 (1986).
258. H. Holleck and H. Schulz, *Surf. Coat. Technol.* 36, 707 (1988).
259. C. Mitterer, M. Rauter, and P. Rödhammer, *Surf. Coat. Technol.* 41, 351 (1990).
260. H. Ronkainen, I. Nieminen, K. Holmberg, A. Leyland, K. S. Fancey, A. Matthews, B. Matthes, and E. Broszeit, *Mater. Sci. Eng. A* 140, 602 (1991).
261. H. Ronkainen, I. Nieminen, K. Holmberg, A. Leyland, A. Matthews, B. Matthes, and E. Broszeit, *Surf. Coat. Technol.* 49, 468 (1992).
262. W. Gissler, *Surf. Coat. Technol.* 68, 556 (1994).
263. P. Mitterer, F. Losbichler, P. Hofer, P. N. Warbichler, W. Gibson, and W. Gissler, *Vacuum* 50, 313 (1998).
264. C. Rebholz, H. Ziegele, A. Leyland, and A. Matthews, *J. Vasc. Sci. Technol. A* 16, 2851 (1998).
265. C. Rebholz, J. M. Schneider, A. A. Voevodin, J. Steinebrunner, C. Charitidis, S. Logothetidis, A. Leyland, and A. Matthews, *Surf. Coat. Technol.* 113, 126 (1999).
266. C. Rebholz, A. Leyland, and A. Matthews, *Thin Solid Films* 343–344, 242 (1999).
267. C. Rebholz, A. Leyland, P. Larour, C. Charitidis, S. Logothetidis, and A. Matthews, *Surf. Coat. Technol.* 116–119, 648 (1999).
268. C. Rebholz, A. Leyland, D. Schneider, B. Schultrich, C. Charitidis, S. Logothetidis, and A. Matthews, *Thin Solid Films*, to be published.
269. C. Rebholz, H. Ziegele, A. Leyland, and A. Matthews, *Surf. Coat. Technol.* 115, 222 (1999).
270. J. Koskinen, J.-P. Hirvonen, S.-P. Hannula, K. Pischow, H. Kattelus, and I. Suni, *Diamond Rel. Mater.* 3, 1107 (1994).
271. M. Stüber, S. Ulrich, H. Leiste, A. Kratzsch, and H. Holleck, *Surf. Coat. Technol.* 116–119, 591 (1999).
272. J. F. Musil, *J. Regent, Vac. Sci. Tech. A* 16, 3301 (1998).
273. S. Veperk and R. Reiprich, *Thin Solid Films* 128, 64 (1995).
274. S. Veprek and M. Jilek, *Vacuum* 67, 443 (2002).
275. S. Veprek, A. Niederhofer, K. Moto, T. Bolom, H.-D. Männling, P. Nesladek, G. Dollinger, and A. Bergmaier, *Surf. Coat. Technol.* 133, 152 (2000).
276. P. Karvankova, M. G. J. Veprek-Heijman, O. Zindulka, A. Bergmaier, and S. Veprek, *Surf. Coat. Technol.*, to be published.
277. S. Veprek and A. S. Argon, *Surf. Coat. Technol.* 146, 175 (2001).
278. W. N. Sharpe, Jr. and R. O. Fowler, *ASTM STP 1204, Am. Soc. Test. Mater.* 386 (1993).

279. J. R. Weertman, D. Farkas, K. Hemker, H. Kung, M. Mayo, R. Mitra, and H. Van Swygenhoven, *MRS Bull.* 24, 44 (1999).

280. R. W. Siegel, *Mater. Sci. Forum* 235–238, 851 (1997).

281. X. K. Sun, H. T. Cong, M. Sun, and M. C. Yang, *Metall. Mater. Trans.* 31A, 1017 (2000).

282. A. H. Choksi, A. Rosen, J. Karch, and H. Gleiter, *Scr. Metall.* 23, 1679 (1989).

283. D. G. Sanders, J. A. Eastman, and J. R. Weertman, *Acta Mater.* 26, 1879 (1997).

284. C. J. Youngdahl, P. G. Sanders, J. A. Eastman, and J. R. Weertman, *Scr. Mater.* 37, 809 (1997).

285. V. Provenzano, R. Valiev, D. G. Rickerby, and G. Valdre, *Nanostruct. Mater.* 12, 1103 (1999).

286. F. Dalla Torre, H. Van Swygenhoven, and M. Victoria, *Acta Mater.* 50, 3957 (2002).

287. D. G. Sanders, J. A. Eastman, and J. R. Weertman, *Acta Mater.* 45, 4019 (1997).

288. M. Shinn, L. Hultman, and S. A. Barnett, *J. Mater. Res.* 7, 901 (1992).

289. M. Shinn and S. A. Barnett, *Appl. Phys. Lett.* 64, 61 (1994).

290. B. J. Daniels, W. D. Nix, and B. M. Clements, in "Structure and Properties of Multilayered Thin Films" (T. D. Nguyen, B. M. Lairson, B. M. Clements, S.-C. Shin, and K. Sato, Eds.), Mater. Res. Soc. Symp. Proc. 382, p. 315. Materials Research Society, Pittsburgh, PA, 1995.

291. B. J. Daniels, W. D. Nix, and B. M. Clements, in "Polycrystalline Thin Films—Structure, Texture, Properties and Applications" (K. Barmak, M. A. Parker, J. A. Floro, R. Sinclair, and D. A. Smith, Eds.), Mater. Res. Soc. Symp. Proc. 343, p. 549. Materials Research Society, Pittsburgh, PA, 1994.

292. B. J. Daniels, W. D. Nix, and B. M. Clements, *Thin Solid Films* 253, 218 (1994).

293. A. Misra, M. Verdier, Y.-C. Lu, H. Kung, T. E. Mitchell, M. A. Nastasi, and J. D. Embury, *Scr. Mater.* 39, 555 (1998).

294. M. Verdier, M. Niewczas, J. D. Embury, M. A. Nastasi, and H. Kung, in "Fundamentals of Nanoindentation and Nanotribology" (S. Baker, N. Burnham, W. Gerberich, and N. Moody, Eds.), Mater. Res. Soc. Symp. Proc. 522. Materials Research Society, Warrendale, PA, 1998.

295. G. R. English, G. F. Simenson, B. M. Clements, and W. D. Nix, in "Thin Films: Stresses and Mechanical Properties V" (S. P. Barker, C. A. Ross, P. H. Townsend, C. A. Volkert, and P. Børgesen, Eds.), Mater. Res. Soc. Symp. Proc. 356, p. 363. Materials Research Society, Pittsburgh, PA, 1995.

296. A. Madan, Y.-Y. Wang, S. A. Barnett, C. Engstrom, H. Ljungcrantz, L. Hultman, and M. Grimsditch, *J. Appl. Phys.* 84, 776 (1998).

297. C. C. Koch, D. G. Morris, K. Lu, and A. Inoue, *MRS Bull.* 24, 54 (1999).

298. C. Koch, "Nanostructure Science Technology NSTC Report Worldwide Status and Trends," p. 93. Kluwer Academic, Dordrecht, 1999.

299. J. A. Eastman, M. Choudry, M. N. Rittner, C. J. Youngdahl, M. Dollar, J. R. Weertman, R. J. DiMelfi, and L. J. Thompson, in "Chemistry and Physics of Nanostructures and Related Non-Equilibrium Materials" (E. Ma, B. Fultz, R. Shull, J. Morral, and P. Nash, Eds.), p. 173. The Minerals, Metals & Materials Society, Warrendale, PA, 1997.

300. V. Y. Gertsman, M. Hoffmann, H. Gleiter, and R. Birringer, *Acta Metall. Mater.* 42, 3539 (1994).

301. B. Günther, A. Baalman, and H. Weiss, in "Physical Phenomena in Granular Materials" (G. D. Cody, T. H. Geballe, and P. Sheng, Eds.), Mater. Res. Soc. Symp. Proc. 195, p. 611. Materials Research Society, Pittsburgh, PA, 1990.

302. P. Sheng, Mater. Res. Soc. Symp. Proc. 195, p. 611. Materials Research Society, Pittsburgh, PA, 1990.

303. P. G. Sanders, J. A. Eastman, and J. R. Weertman, in "Processing and Properties of Nanocrystalline Materials" (C. Suryanarayana, J. Singh, and F. H. Froes, Eds.), p. 379. The Minerals, Metals & Materials Society, Warrendale, PA, 1996.

304. D. G. Morris and M. A. Morris, *Acta Metall. Mater.* 39, 1763 (1991).

305. F. Dalla Torre, H. Van Swygenhoven, and M. Victoria, *Acta Mater.* 50, 3957 (2002).

306. V. L. Tellkamp and E. Lavernia, *Nanostruct. Mater.* 12, 249 (1999).

307. L. Lu, M. L. Sui, and K. Lu, *Science* 287, 1463 (2000).

308. R. Z. Perez, B. Huang, and E. J. Lavernia, *Nanostruct. Mater.* 7, 565 (1996).

309. Q. R. Hayes, V. Tellkamp, and E. Lavernia, *Scr. Mater.* 7, 743 (1999).

310. V. L. Tellkamp and E. Lavernia, *Nanostruct. Mater.* 12, 249 (1999).

311. H. Ohta, H. Iwata, M. Takagi, T. Imura, Y. Kawamura, and A. Inoue, in "Proceedings of the 4th Special Symposium on Advanced Materials, 1998, p. 95.

312. M. Takagi, H. Ohta, T. Imura, Y. Kawamura, and A. Inoue, *Scr. Mater.* 44, 2145 (2001).

313. M. L. Lau, E. Strock, A. Fabel, C. J. Lavernia, and E. J. Lavernia, *Nanostruct. Mater.* 10, 723 (1998).

314. V. Provenzano and R. L. Holtz, *Mater. Sci. Eng. A* 204, 125 (1995).

315. R. K. Islamgaliev, R. Z. Valiev, R. S. Mishra, and A. K. Mukherjee, *Mater. Sci. Eng. A* 304–306 (2001).

316. G. W. Nieman, J. R. Weertman, and R. W. Siegel, *Scr. Metall. Mater.* 24, 145 (1991).

317. R. S. Mishra, A. K. Mukherjee, D. K. Mukhopadhyay, C. Suryanarayana, and F. H. Froes, *Scr. Mater.* 34, 1765 (1996).

318. P. G. Sanders, M. Rittner, E. Kiedaisch, J. R. Weertman, H. Kung, and Y. C. Lu, *Nanostruct. Mater.* 9, 433 (1997).

319. M. F. Tambwe, D. Stone, A. J. Griffin, H. Kung, Y. C. Lu, and M. Nastasi, *J. Mater. Res.* 14, 407 (1999).

320. S. X. McFadden, R. S. Mishra, R. Z. Valiev, and A. P. Zhilyaev, *Nature* 398, 684 (1999).

321. Q. R. Hayes, V. Tellkamp, and E. Lavernia, *Scr. Mater.* 7, 743 (1999).

322. B. Cai, Q. P. Kong, L. Lu, and K. Lu, *Mater. Sci. Eng. A* 286, 188 (2000).

323. W. M. Yin, S. H. Whang, R. Mirshams, and C. H. Xiao, *Mater. Sci. Eng. A* 301, 18 (2001).

324. L. Lu, M. L. Sui, and K. Lu, *Science* 287, 1463 (2000).

325. B. L. Shen, T. Itoi, T. Yamasaki, and Y. Ogino, *Scr. Mater.* 42, 893 (2000).

326. C. Goujon and P. Goeuriot, *Mater. Sci. Eng. A* 315, 180 (2001).

327. B. Cai, Q. P. Kong, P. Cui, L. Lu, and K. Lu, *Scr. Mater.* 45, 1407 (2001).

328. F. Wakai, S. Sakaguchi, and Y. Matsuno, *Adv. Ceram. Mater.* 1, 259 (1986).

329. K. S. Chan, *Scr. Metall. Mater.* 24, 1725 (1990).

330. Y. Maehara and T. G. Langdon, *J. Mat. Sci.* 25, 2275 (1990).

331. T. G. Langdon, *JOM* 42, 8 (1990).

332. M. Jimenez-Melendo, A. Dominguezs-Rodriques, and A. Bravo-Leon, *J. Am. Ceram. Soc.* 81, 2761 (1998).

333. I.-W. Chen and L. A. Xue, *J. Am. Ceram. Soc.* 73, 2585 (1990).

334. U. Betz and H. Hahn, *Nanostruct. Mater.* 12, 911 (1999).

335. U. Betz, K. A. Padmanabhan, and H. Hahn, *J. Mater. Sci.* 36, 5811 (2001).

336. M. Sternitzke, *J. Eur. Ceram. Soc.* 17, 1061 (1997).

337. K. Niihara, *J. Ceram. Soc. Jpn.* 99, 974 (1991).

338. B. H. Kear and P. R. Strutt, *Nanostruct. Mater.* 6, 227 (1995).

339. R. W. Siegel and B. Kear, Nanotechnology Research Directions: IWGN Workshop Report, Loyola College, Baltimore, 1999, p. 97.

340. K. Jia, T. E. Fischer, and B. Gallois, *Nanostruct. Mater.* 10, 875 (1998).

341. J. He, M. Ice, S. Dallek, and E. J. Lavernia, *Metall. Mater. Trans.* 31A, 541 (2000).

*342.* J. R. Wilde and A. L. Greer, *Mater. Sci. Eng. A* 304–306, 932 (2001).

*343.* R. K. Islamgaliev, W. Buchgraber, Y. R. Kolobov, N. M. Amirkhanov, A. V. Sergueeva, K. V. Ivanov, and G. P. Grabovetskaya, *Mater. Sci. Eng. A* 319–321, 872 (2001).

*344.* J. He, M. Ice, and E. J. Lavernia, *Nanostruct. Mater.* 10, 1271 (1998).

*345.* E. Flahaut, A. Peigney, Ch. Laurent, Ch. Marlière, F. Chastel, and A. Rousset, *Acta Mater.* 48, 3803 (2000).

*346.* Ch. Laurent, A. Peigney, O. Dumortier, and A. Rousset, *J. Eur. Ceram. Soc.* 19, 2005 (1998).

*347.* T. Kuzumaki, K. Miyazawa, H. Ichinose, and K. Ito, *J. Mater. Res.* 13, 2445 (1998).

*348.* C. L. Wu, B. Q. Wei, R. Z. Ma, J. Liang, X. K. Ma, and D. H. Wu, *Carbon* 37, 855 (1999).

*349.* X. Chen, J. Xia, J. Peng, W. Li, and S. Xie, *Comp. Sci. Tech.* 60, 301 (2000).

*350.* K. Niihara and A. Nakahira, *Ceram. Soc. Jpn.* 99, 404 (1991).

*351.* K. Izaki, K. Hakkei, K. Ando, T. Kawakami, and K. Niihara, in "Ultrastructure Processing of Advanced Ceramics" (J. M. MacKenzie and D. R. Ulrich, Eds.), p. 891. John Wiley & Sons, New York, 1988.

*352.* K. Niihara and A. Nakahira, "Proceedings of the 3rd International Symposium Ceramics Materials Comp. Eng.," 1988, p. 919.

*353.* R. Roy, R. A. Roy, and D. M. Roy, *Mater. Lett.* 4, 323 (1986).

*354.* R. Roy, *Ceram. Microstructures* 86, 25 (1987).

*355.* S. Komarneni, *J. Mater. Chem.* 2, 1219 (1992).

*356.* K. E. Gonsalves, T. D. Xiao, and G.-M. Chow, *ACS Symp. Ser.* 572, 195 (1994).

*357.* P. Colomban and L. Mazerolles, *J. Mater. Sci.* 26, 3503 (1991).

*358.* W. H. Armistead and S. D. Stookey, *Science* 144, 150 (1964).

*359.* D. Chakravorty, *Bull. Mater. Sci.* 15, 411 (1992).

*360.* R. E. Newnham, "Third Euro, Ceramics" (P. Durán and J. F. Fernández, Eds.), Vol. 2, pp. 1–9. Faenza Editrice Ibérica, Spain, 1993.

*361.* T. K. Kundu and D. Chakravorty, *Appl. Phys. Lett.* 66, 3576 (1995).

*362.* S. Özkar, G. A. Ozin, and R. A. Prokopowicz, *Chem. Mater.* 4, 1380 (1992).

*363.* S. Yamanaka, *Ceram. Bull.* 70, 1056 (1991).

*364.* C. Laurent, J. J. Demai, A. Rousset, K. R. Kannan, and C. N. R. Rao, *J. Mater. Res.* 9, 229 (1994).

*365.* E. Breval, G. Dodds, and C. G. Pantano, *Mater. Res. Bull.* 20, 1191 (1985).

*366.* A. F. Zimmerman, G. Palumbo, K. T. Aust, and U. Erb, *Mater. Sci. Eng. A* 328, 137 (2002).

*367.* H. Krug and H. Schmidt, *New J. Chem.* 18, 1125 (1994).

*368.* P. B. Messersmith and S. I. Stupp, *Chem. Mater.* 7, 454 (1995).

*369.* R. W. Davidge, "Mechanical Behaviour of Ceramics." Cambridge Univ. Press, Cambridge, 1979.

*370.* F. F. Lange, *J. Am. Ceram. Soc.* 72, 3 (1989).

*371.* F. F. Lange, *J. Am. Ceram. Soc.* 56, 445 (1973).

*372.* P. F. Becher, *J. Am. Ceram. Soc.* 72, 255 (1991).

*373.* M. Harmer, H. M. Chan, and G. A. Miller, *J. Am. Ceram. Soc.* 75, 1715 (1992).

*374.* L. S. Sigl, P. A. Mataga, B. J. Dalgleish, R. M. McMeeking, and A. G. Evans, *Acta Metall.* 36, 945 (1983).

*375.* D. J. Green, *J. Am. Ceram. Soc.* 65, 610 (1982).

*376.* I. E. Reimanis, *Mater. Sci. Eng. A* 237, 159 (1997).

*377.* S. Bhaduri and S. B. Bhaduri, *JOM* 44 (1998).

*378.* K. Niihara and A. Nakahira, *Ann. Chim. Fr.* 16, 479 (1991).

*379.* L. Gao, H. Z. Wang, J. S. Hong, H. Miyamoto, K. Miyamoto, Y. Nishikawa, and S. D. D. L. Torre, *J. Eur. Ceram. Soc.* 19, 609 (1999).

*380.* M. Sternitzke, E. Dupas, P. Twigg, and B. Derby, *Acta Mater.* 45, 3963 (1997).

*381.* S. Bhaduri, S. B. Bhaduri, and E. Zhou, *J. Mater. Res.* 13, 156 (1998).

*382.* I. E. Reimanis, *Composites B* 30, 647 (1999).

*383.* A. W. Weimer and R. K. Bordia, *Composites B* 30, 647 (1999).

*384.* T. Hirano and K. Niihara, *Mater. Lett.* 22, 249 (1995).

*385.* K. Niihara, K. Suganuma, A. Nakahira, and K. Izaki, *J. Mater. Sci. Lett.* 9, 589 (1990).

*386.* A. Rendtel, H. Hubner, and M. Herrmann, "Fourth Euro, Ceramics" (A. Bellosi, Ed.), Vol. 4, p. 225. Gruppo Editoriale Faenza Editrice S.p.A. Faenza, 1995.

*387.* A. Rendtel, H. Hubner, M. Herrmann, and C. Schber, *J. Am. Ceram. Soc.* 81, 1109 (1998).

*388.* S. Bhaduri and S. D. Bhaduri, *Ceram. Int.* 28, 153 (2002).

*389.* A. Peigney, E. Flahaut, Ch. Laurent, F. Chastel, and A. Rousset, *Chem. Phys. Lett.* 352, 20 (2002).

*390.* R. Z. Ma, J. Wu, B.-Q. Wei, J. Liang, and D. H. Wu, *J. Mater. Sci.* 33, 5243 (1998).

*391.* A. Peigney, Ch. Laurent, E. Flahaut, and A. Rousset, *Ceram. Int.* 26, 677 (2000).

*392.* E. T. Thostenson, Z. Ren, and T.-W. Chou, *Comp. Sci. Tech.* 61, 1899 (2001).

*393.* D. P. Harvey II, R. Kalyanaraman, and T. S. Sudarshan, *Mater. Sci. Technol.* 18, 959 (2002).

*394.* D. G. Sanders, J. A. Eastman, and J. R. Weertman, *Acta Mater.* 26, 1879 (1997).

*395.* M. A. Morris-Munoz, A. Dodge, and D. G. Morris, *Nanostruct. Mater.* 11, 873 (1999).

*396.* A. V. Sergueva, C. Song, R. Z. Valiev, and A. K. Mukherjee, *Mater. Sci. Eng. A* 339, 159 (2003).

*397.* H. A. Calderon, V. Garibay-Febles, M. Umemoto, and M. Yamaguchi, *Mater. Sci. Eng A* 329–331, 196 (2002).

*398.* J. Zhao, L. C. Stearn, M. P. Harmer, H. M. Chan, G. A. Miller, and R. E. Cook, *J. Am. Ceram. Soc.* 76, 503 (1993).

*399.* K. Niihara and A. Nakahira, in "Avdanced Structure of Inorganic Composites" (P. Vincenzini, Ed.), p. 637. Elsevier Science, Netherlands, 1990.

*400.* C. N. Walker, C. E. Borsa, and R. J. Brook, *Br. Ceram. Proc.* 53, 249 (1994).

*401.* K. Niihara, N. Unal, and A. Nakahira, *J. Mater. Sci.* 29, 164 (1994).

*402.* K. Niihara and A. Nakahira, *Proc. First Japan Int. SAMPE Symp.* 1120 (1989).

*403.* T. Hirano and K. Niihara, *Mat. Lett.* 22, 249 (1995).

*404.* K. Niihara et al., *Ceram. Trans.* 42, 207 (1994).

*405.* H. Hirano and K. Niihara, *Mater. Lett.* 26, 285 (1996).

*406.* G. Pezzotti and M. Sakai, *J. Am. Ceram. Soc.* 77, 3039 (1994).

*407.* A. Bellosi, *Mat. Sci. Forum* 195, 79 (1995).

*408.* A. Bellosi, *Mat. Sci. Forum* 195, 79 (1995).

*409.* M. Nawa, K. Yamazaki, T. Sekino, and K. Niihara, *J. Mat. Sci.* 31, 2849 (1996).

*410.* T. Sekino, A. Nakahira, M. Nawa, and K. Niihara, *Kona* 10, 192 (1992).

*411.* E. Santner, *TriboTest* 7, 155 (2000).

*412.* M. Gell, *Mater. Sci. Eng. A* 204, 246 (1995).

*413.* M. A. Baker, S. Klose, C. Rebholz, A. Leyland, and A. Matthews, *Surf. Coat. Technol.* 151–152, 338 (2002).

*414.* M. A. Baker, C. Rebholz, A. Leyland, and A. Matthews, *Vacuum* 67, 471 (2002).

*415.* P. Holubar, M. Jilek, and M. Sima, *Surf. Coat. Technol.* 133–134, 145 (2000).

*416.* H. Jensen, G. Sorensen, I. Mannike, F. Muktepavela, and J. Sobota, *Surf. Coat. Technol.* 116–119, 1070 (1999).

*417.* S. Seal and N. B. Dahotre, *JOM* 54, 20 (2002).

*418.* A. A. Voevodin, S. D. Walck, and J. S. Zabinski, *Surf. Coat. Technol.* 116–119, 36 (1999).

*419.* K. Miyoshi, B. Polchuck, K. W. Street, J. S. Zabinski, J. H. Sanders, A. A. Voevodin, and R. L. C. Wu, *Wear* 225–229, 65 (1999).

*420.* J. Vetter, W. Burgmer, H. G. Dederichs, and A. J. Perry, *Surf. Coat. Technol.* 61, 209 (1993).

*421.* A. A. Voevodin and J. S. Zabinski, *Diamond Rel. Mater.* 7, 463 (1998).

422. W. J. Yang, J. Won, K. H. Auh, C. L. and K. Niihara, *J. Mater. Sci. Lett.* 19, 1649 (2000).

423. P. J. Fallon, V. S. Veerasamy, C. A. Davis, J. Robetson, G. A. J. Amaratunga, W. I. Milne, and J. Koskinen, *Phys. Rev. B* 48, 15 (1993).

424. J.-P. Hirvonen, J. Koskinen, M. Kaukonen, R. Nieminen, and H.-J. Scheibe, *J. Appl. Phys.* 81, 7248 (1997).

425. M. Gell, *Mater. Sci. Eng. A* 204, 246 (1995).

426. P. G. Klemens and M. Gell, *Mater. Sci. Eng. A* 245, 143 (1998).

427. M. Gell, E. H. Jordan, Y. H. Sohn, D. Goberman, L. Shaw, and T. D. Xiao, *Surf. Coat. Technol.* 146–147, 48 (2001).

428. Y. H. Sohn, J. H. Kim, E. H. Jordan, and M. Gell, *Surf. Coat. Technol.* 146–147, 70 (2001).

429. Y. H. Sohn, K. Vaidyanathan, M. Ronski, E. H. Jordan, and M. Gell, *Surf. Coat. Technol.* 146–147, 102 (2001).

430. N. P. Padture, K. W. Schlichting, T. Bhatia, A. Ozturk, B. Cetegen, E. H. Jordan, M. Gell, S. Jiang, T. D. Xiao, P. R. Strutt, E. Garcia, P. Miranzo, and M. I. Osendi, *Acta Mater.* 49, 2251 (2001).

431. E. H. Jordan, M. Gell, Y. H. Sohn, D. Goberman, L. Shaw, S. Jiang, M. Wang, T. D. Xiao, Y. Wang, and P. Strutt, *Mater. Sci. Eng. A* 301, 80 (2001).

432. D. Goberman, Y. H. Sohn, L. Shaw, E. Jordan, and M. Gell, *Acta Mater.* 50, 1141 (2002).

433. L. L. Shaw, D. Goberman, R. Ren, M. Gell, S. Jiang, Y. Wang, T. D. Xiao, and P. R. Strutt, *Surf. Coat. Technol.* 130, 1 (2000).

434. X. Jiang, E. H. Jordan, L. Shaw, and M. Gell, *J. Mat. Sci. Technol.* 18, 287 (2002).

435. J. He and J. M. Schoenung, *Mat. Sci. Eng. A* 336, 274 (2002).

436. B. H. Kear, Z. Kalman, R. K. Sadangi, G. Skandan, J. Colaizzi, and W. E. Mayo, *J. Thermal Spray Technol.* 9, 483 (2000).

437. M. S. Yeh and T. H. Chuang, *Scr. Metall. Mater.* 33, 1277 (1995).

438. T. H. Cross and M. J. Mayo, *Nanostruct. Mater.* 3, 163 (1994).

439. D. C. Hague and M. J. Mayo, *Mater. Sci. Eng. A* 204, 83 (1995).

440. S. Bose, *Mater. Sci. Eng. A* 196, 105 (1995).

441. K. Uenishi, T. Matsubara, T. Shibutani, and K. F. Koboyashi, *Intermetall.* 10, 105 (2002).

442. K. E. Gonsalves, S. P. Rangarajan, C. C. Law, A. Garcia-Ruiz, and G. M. Chow, *Nanostruct. Mater.* 9 (1997).

443. K. E. Gonsalves, H. Li, R. Perez, P. Santiago, and M. Jose-Yacaman, *Coord. Chem. Rev.* 206–207, 607 (2000).

444. M. L. Lau, H. G. Jiang, R. J. Perez, J. Juarez-Islas, and E. J. Lavernia, *Nanostruct. Mater.* 9, 157 (1997).

445. P. Matteazzi and F. Wolf, *Mater. Sci. Eng. A* 248, 19 (1998).

446. Y. Lu and P. K. Liaw, *JOM* 53, 31 (2001).

447. L. Zeipper, E. Schafler, B. Mingler, H. P. Karnthaler, M. Zehetbauer, and G. Korb, "Proceedings of the 2nd Workshop on Nanomaterials: Fundamentals and Applications," 2002, P2.2.

448. V. S. Zhernakov, V. V. Latysh, V. V. Stolyarov, A. I. Zharikov, and R. Z. Valiev, *Scr. Mater.* 44, 1771 (2001).

449. A. Agarwal, T. McKechnie and S. Seal, *JOM* 54, 42 (2002).

450. T. J. Webster, R. W. Siegel, and R. Biozios, *Nanostruct. Mater.* 12, 983 (1999).

451. P. Glatkowski, P. Mack, J. L. Conroy, J. W. Piche, and P. Winsor, U.S. Patent 6, 265, 466, 2002.

452. N. Moszner and U. Salz, *Prog. Polym. Sci.* 226, 535 (2001).

453. M. Alexandre and P. Dubois, *Mater. Sci. Eng.* 28, 1 (2000).

454. D. G. Morris, in "Mechanical behavior of nanostructured materials." Mater. Sci. Found. 2, Trans. Tech. Publ. 61. Switzerland, 1998.

455. A. Korznikov, Z. Pakiela, and K. J. Kurzydlowski, *Scr. Mater.* 45, 309 (2001).

456. G. Korznikova, A. Korznikov, Z. Pakiela, and K. J. Kurzydlowski, *Mater. Chem. Phys.* 81, 401 (2003).

457. R. Vaßen, A. Kaiser, and D. Stöver, *J. Nucl. Mater.* 233, 708 (1996).

458. M. Rose, G. Gorzawski, G. Miehe, A. G. Balogh, and H. Hahn, *Nanostruct. Mater.* 6, 731 (1995).

459. R. H. Baugham, A. A. Zakhidov, and W. A. deHeer, *Science* 297, 787 (2002).

# MEMS-Based Nanotechnology

## H. V. Jansen, N. R. Tas, J. W. Berenschot

*University of Twente, Enschede, The Netherlands*

## CONTENTS

## 1. MEMS-BASED NANOTECHNOLOGY

"Imagine working machines so small that it is imperceptible to the human eye and with gears no bigger than a dust particle. Visualize fluidic channels having a diameter of less than a thousand of atoms where most living cells cannot enter. Think about these systems being batch fabricated tens of thousands at a time, at a cost of only a few cents each. Fancy a realm where the world of design is turned upside down, and the seemingly impossible suddenly becomes easy; a place where gravity and inertia are no longer important, but the effects of atomic forces and surface science dominate. You are now in the microdomain, a world occupied by an explosive new technology known as microtechnology [6]."

### 1.1. Integrated Circuit Technology

The field of microtechnology is a logical follow-up to microelectronics. The advent of solid-state microelectronics dates from the invention of the bipolar transistor effect by Bardeen, Brattain, and Shockley in Bell Laboratories in 1947 (Fig. 1). The technology progressed during the early 1950s, using germanium as the semiconductor material. However, germanium proved unsuitable in certain applications and silicon became a practical substitute. Nowadays, silicon has almost fully supplanted germanium as a material for solid-state device fabrication.

In time, the size of the silicon transistor decreased and integrated circuits (ICs) came onto the market with resolution in the nanometer range. The silicon IC is surely one of the wonders of our age and has changed virtually every aspect of our lives. The hallmark of the IC technology (ICT) has been the ability to fabricate tens of millions of individual components on a silicon chip with an area of a few square cm using lithographic techniques (Fig. 2). As time has progressed, chip complexity increased at an exponential rate, primarily because of the constant shrinking of device geometries, improved manufacturing practice, basic discoveries, and clever inventions enabling specific functions to be implemented in new ways. This rapid advance in the number of transistors per chip and growth in the functionality of microelectronic circuits is truly phenomenal and has lead to ICs with continuously increasing capability and performance and has enabled information age.

In ICT, pattern transfer from partially transparent masks onto a substrate is accomplished almost exclusively via photolithography. It involves three sequential steps as illustrated in Figure 3:

- application of photoresist, which is a photosensitive emulsion layer, on top of a substrate;
- optical ultraviolet exposure to print the image from the mask onto the resist;
- immersion in an aqueous developer solution to dissolve the exposed resist and render visible the latent image.

### 1.2. Microsystem Technology

Due to the good mechanical characteristics of silicon, ICT appeared to be useful for the fabrication of a variety of structures. This new field became known as micromechanics and some typical examples of this field are found in Figure 4a–c. Almost at the same time other disciplines emerged like micro-optics (Fig. 4d) and microchemics (Fig. 4e, f). The integration of all these groups of microspecializations is nowadays known as micro system technology (MST). MST has become a fundamental tool for the fabrication of microtechnological devices and, in general, miniature sensors and actuators. Micromachining techniques include first the basic processing steps of ICT, namely, film
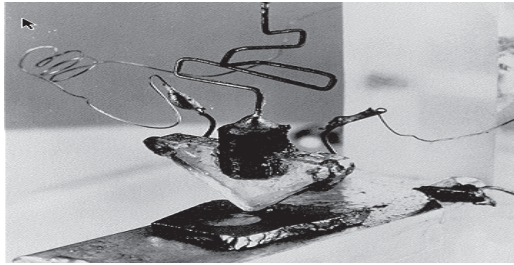
**Figure 1.** First transistor invented in the Bell laboratories.

formation, lithography, and film etching. In addition, they incorporate special micromachining processes which allow for the sculpturing of three-dimensional (3D) microstructures. Silicon micromachining can be subdivided into two main categories: bulk and surface micromachining. Bulk micromaching refers to the realization of structures out of the single-crystal silicon wafer. Devices fabricated with surface micromachining techniques are located on the wafer surface and consist most often of a stack of thin films between 100 nm and 10 $\mu$m thick. A typical surface micromachining process sequence for the cessation of a simple freestanding aluminum bridge is illustrated in Figure 5.

Within the field of MST, a group of systems has been paid special attention in the past decades: microelectromechanical systems (MEMS). This is due to its integratability with respect to ICT. The name "MEMS" should have been used for electromechanical transducers only, but especially in the United States the name MEMS became used in a much broader sense. Nowadays, it includes non-electromechanical devices also, such as optical switches or lab-on-chips. Nevertheless, in Europe most people still give these products the more logical name of microsystems, and the technology to create such devices is then called microsystem technology. So, in fact, a MEMS is just a specific MST product. In Japan, commonly, MST is called micromachining (MM). This might be caused by their opinion that the MEMS/MST products are created by fine mechanical techniques, if only a little smaller. This philosophy has resulted in a tendency to downscale fine mechanical equipment such as microdrills, spark erosion, and lasers in Japan, as opposed to the fine-tuning of IC equipment in the United States and Europe. But whatever people call these microtechniques, MM, MEMS, or MST, the results are—not rarely—astonishing and will influence the future of mankind one way or another.
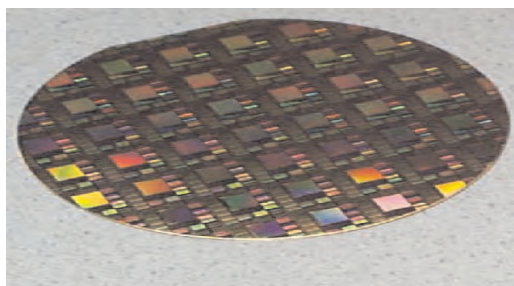


**Figure 2.** Integrated circuits on a wafer.



1. Spin-coat a layer of photoresist.

2. Illuminate the resist through a mask.

3. Develop the resist.
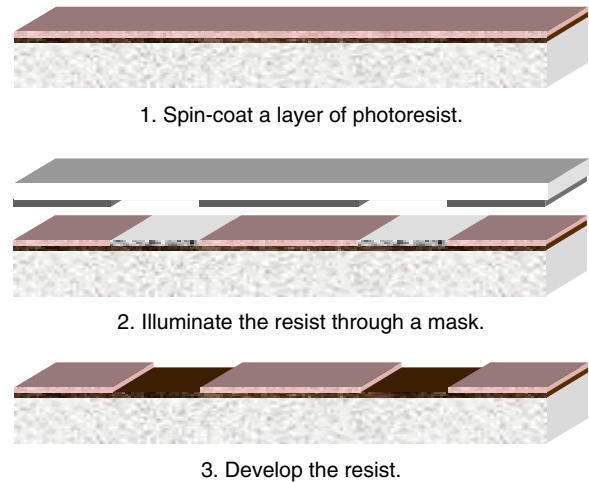
**Figure 3.** Basic lithographic process.

Generally, the resulting structures from the MST process are relatively flat, and the urge for spatial structures for a stiffer construction stimulated the activities with respect to microstructuring by means of different methods. In addition, the brittleness of silicon and the need for materials with specific properties (e.g., optical properties) stimulated the microstructuring of different materials as well. The development of the so-called LIGA technology has given a stimulus with respect to high aspect ratio structuring of different materials. The materials range from metals such as
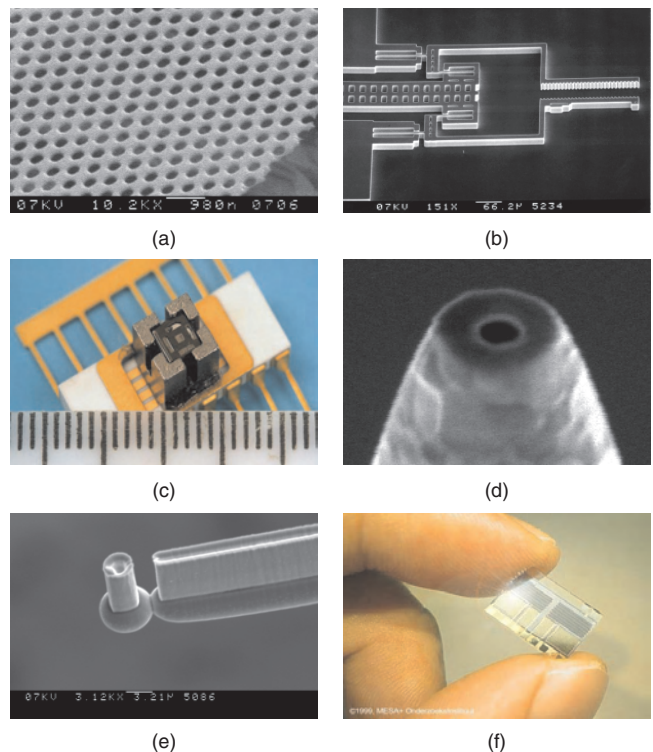


**Figure 4.** Typical products of microsystem technology. (a) Microsieve. (b) Microgripper. (c) Three-dimensional accelerometer. (d) Optical tip. (e) Micropipette. (f) Fluid dosing system.
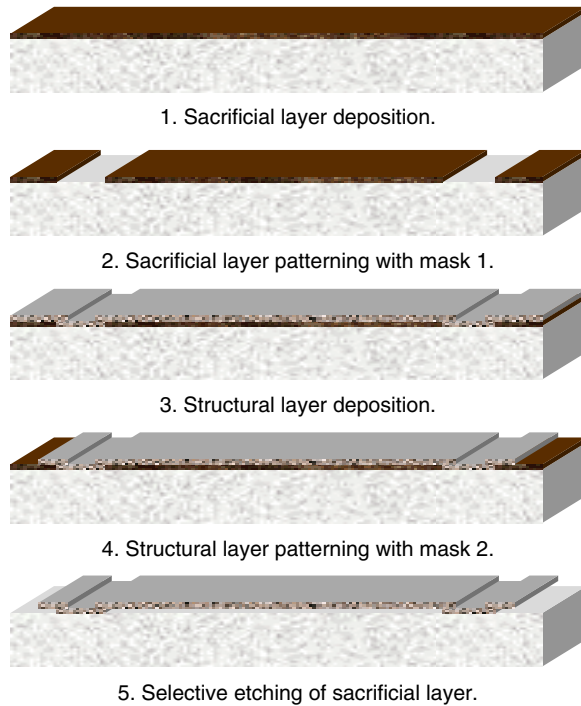
**Figure 5.** Basic micromachining process.

nickel and gold and alloys such as nickel iron up to polymers such as poly-oxy-methylene, poly-methyl-methacrylate, polysterene, polycarbonate, and others. However, the use of synchrotron radiation and the resulting complicated fabrication of the mask make LIGA technology economically less attractive and more time consuming. Therefore, a variety of alternatives has been developed, such as ultraviolet (UV) "SU-8" lithography, laser ablation, microdrilling, ion milling, and spark erosion. Also, the innovations in dry etching enabled the fabrication of micromolds in silicon. This micromold can subsequently be electroplated resulting in a metal micromold.

So the field of MST explores the science of miniaturization. A question asking for a more specific definition is certain to generate a broad collection of replies, with few common characteristics other than "miniature." But such apparent divergence in the responses merely reflects the diversity of application this technology enables, rather than a lack of harmony. MST is simultaneously a toolbox, a physical product, and a methodology all in one:

- It is a portfolio of techniques and processes to design and create miniature systems.
- It is a physical product often specialized and unique to a final application. One can seldom buy a generic MST product at the neighborhood electronics store.
- MST is a way of making things. These "things" merge the functions of sensing and actuation with computation and communication to locally control physical parameters at the microscale, yet cause effects at much grander scales.

Although a universal definition is lacking, MST products possess a number of distinctive features. They are miniature *embedded* systems involving one or many *micromachined*

components or structures. Miniaturization methods and materials include micromachining in or on top of single crystal silicon and other materials based on planar lithographic techniques (known from the semiconductor industry) as well as more traditional materials and nonlithographic miniaturization options (known from fine mechanical engineering). All these techniques are specifically enhanced or modified for creating small three-dimensional structures with dimensions ranging from subcentimeters to submicrometers, involving electronics, sensors, actuators, or other microcomponents, and microsystems. In this way, MST products *enable* higher level functions, although in and of themselves their utility may be limited. A micromachined pressure sensor in one's hand is useless, but under the hood it controls the fuel–air mixture of the car engine. They often *integrate* smaller functions into one package for greater utility, for example, merging an acceleration sensor with electronic circuits for self-diagnostics. They can also bring *cost benefits*, directly through low unit pricing or indirectly by cutting service and maintenance costs.

MST is a relatively new technology which exploits the existing microelectronics infrastructure to create complex machines on a chip with micrometer feature sizes. These machines can have many functions, including on-chip sensing, communication, and actuation. So the next step in the silicon revolution will be different, and more important than simply packing more transistors onto the silicon. It might be the incorporation of new types of functionality onto the chip; structures that will enable the chip to not only sense but to act and communicate as well. This enables the creation of "intelligent" microsystems which know where they are and what is going on around them. This revolution will be enabled by MST and everyday we are finding more applications. MST focuses on a variety of defense and commercial applications (Table 1), applications ranging from inertial sensors for large scale commercial applications to locking mechanisms for weapon systems. Recent studies have estimated the market for intelligent micromachine-based systems to be around 100 Billion Euro/year.

Although the vast majority of today's MST products are best categorized as components or subsystems, the emphasis in MST technology is on the "systems" aspect. True microsystems may still be a few years away, but their development and evolution rely on the success of today's components, especially as these components are integrated to perform functions ever increasing in complexity. Building microsystems is an evolutionary process. We spent the last 30 years learning how to build micromachined components. Only recently have we begun to learn about their seamless integration into subsystems, and ultimately into complete microsystems.

One notable example is the evolution of crash sensors for airbag safety systems. Early sensors were merely mechanical switches. They later evolved into micromechanical sensors that directly measured acceleration. The current generation of devices integrates electronic circuitry with a mechanical sensor to provide self-diagnostics and a digital output. It is anticipated that the next generation of devices will also incorporate the entire airbag deployment circuitry that decides whether to inflate the airbag. As the technology matures, the airbag crash sensor may be integrated one

**Table 1.** R&D fields and topics in microtechnology.

| Commercial applications | Military applications |
| --- | --- |
| Mass data storage systems | low-power, high-density mass data storage devices |
| Miniature biochemical analytical instruments | miniature fluidic systems for early detection of biochemical warfare |
| Cardiac management systems (e.g., pacemakers, catheters) | integrated fluidic systems for miniature propellant and combustion control |
| Drug delivery systems (e.g., insulin, analgesics) | inertial systems for munitions guidance and personal navigation |
| Neurological disorders (e.g., neurostimulation) | weapons safting, arming, and fuzzing |
| Engine and propulsion control | head- and night-display systems |
| Automotive safety, braking and suspension systems | active, conformable surfaces for distributed aerodynamic control aircraft |
| Telecommunication optical fiber components and switches | distributed unattended sensors for asset tracking, environmental and security surveillance |
| Invasive and noninvasive biomedical sensors | embedded sensors and actuators for condition-based maintenance |
| Distributed sensors for condition-based maintenance and monitoring structural health | integrated micro-opto-mechanical components for identify-friend-or-foe systems |
| Distributed control of aerodynamic and hydrodynamic systems | electromechanical signal processing for small and low-power wireless communication |
| Electromechanical signal processing | |

day with micromachined yaw-rate and other inertial sensors to form a complete microsystem responsible for passenger safety and vehicle stability. But examples of future microsystems are not limited to automotive applications. Efforts to develop micromachined components for the control of fluids are just beginning to bear fruit. These could lead one day to the integration of micropumps with microvalves and reservoirs to build new miniature drug delivery systems.

## 1.3. Nanosystem Technology

The area of nanotechnology is one step beyond microtechnology and can be defined as: *The area of science and technology where dimensions in the range of 100 nm play a critical role*. The term "nano" stands for "one billionth" and is inspired by the ancient Greek word "nanos," meaning dwarf. But nanotechnology is everything but a dwarf technology. It encompasses precision engineering as well as the lithographic technology known from the microtechnology, but also chemical and biochemical synthesis and biomedical multiplication techniques in areas as diverse as semiconductor electronics, scanning probe microscopy analysis, microsystems or MEMS, telecommunication, information technology, protein duplication, gene therapy, and drug delivery.

Nanotechnology has created of new world of terminology, a kind of "nanodictionary." For example, two fundamental different approaches in nanotechnology are graphically termed "top-down" and "bottom-up." Top-down refers to making miniature (or "nanoture") structures by lithographic printing and nonlithographic machining techniques, the basic techniques for manufacturing microelectronics and microsystems. Bottom-up, or molecular engineering (such as self-assembled films), applies to building organic or inorganic structures atom-by-atom, or molecule-by-molecule, and having its origin in the chemical and biochemical industry. A recent dramatic breakthrough that may herald the beginning of the bottom-up nanotechnology has been the discovery of spinning molecular structures. These may open the door to realizing the holy grail of power generation and

controllable motion at the molecular level, with huge applications for medicine and information technology. Clearly, a prime feature of nanotechnology is that it is the one area of research and development which is truly multidisciplinary. Research at the nanoscale is unified by the need to share knowledge, tools, and techniques, as well as information on the physics affecting atomic and molecular interactions in this new realm. Materials scientists, mechanical and electronic engineers, and medical researchers are now forming teams with biologists, physicists, chemists, and even mathematicians. For sure, nanotechnology is the technical underpinning of the microelectronic and microsystem technologies and they will likely all advance together.

Recently, the necessity to establish a fundamental plan for nanotechnology was discovered. For example, in mid 2001, the National Science and Technology Advisory Board of Korea established a national master plan for nanotechnology to invest 1.4 billion Euros within 10 years. The plan contains three axes of national activities: research and development, Education and Training, and Facility and Infrastructure. The R&D program generally focuses on four fields (Table 2): nanoprocesses, nanostructures, nanofunctions, and nanosystems. The Nanoprocesses include processing methods in the nanometer regime, such as chemical synthesis, evaporation, lithography, and plasma etching. Nanostructures consist of one-, two-, or three-dimensional nanostructures, such as multinanolayers, nanotubes, quantum dots, and photonic crystals. Nanofunctions place focus on the creation of properties and functionalities of nanocomponents and nanocompounds, such as highstrength or highendurance, electron/light emission, information storage, molecule detection, particle separation, nonlinear optics, and thermal isolation. Nanosystems contain nanosensors, nanoactuators, nanodevices, and nanosystems, such as single-electron devices, photonic waveguides, molecular systems, biochips, biomotors, solar/fuel cells, and NEMS (nanoelectromechanical systems).

Despite the importance of bottom-up molecular engineering, this chapter emphasizes the top-down strategies leaning on the MST. This means that also a related and very relevant subject likely to become "hot nanonews" in the near future

**Table 2.** R&D fields and topics in nanotechnology.

| Field | Area | Topic |
|---|---|---|
| Nanoprocesses | bottom-up | self-assembly, self-duplication, photosynthesis, chemical synthesis, bioanalogic process |
| | top-down | physical vapor deposition, chemical vapor deposition, forming, evaporation–condensation, thermal growing, arc, plasma, alloying, crushing, sol–gel, chemical deposition, printing, patterning, lithography, molding, deformation, etching, chemical mechanical polishing, electrochemical etching |
| Nanostructures | one dimension | quantum well, nanolayer, nanosurface, multinanolayers |
| | two dimensions | quantum line, nanotube, nanowire |
| | three dimensions | quantum dot, nanopowder, self-assembled, polymeric, bulk (porous), photonic crystal |
| | others | ER/MR fluids, compound chemicals |
| Nanofunctions | property | strength, hardness, toughness, friction/loss, elasticity, isolation, endurance |
| | functionality | single electron, electron/light emission, spectroscopy, nonlinear optics, spin storage, information storage, molecule recognition/detection, detection, membrane, transport, particle separation, electro-osmotic flow, process enhancement, combustion |
| Nanosystems | sensors | single-electron devices, molecule detector, bolometer |
| | actuators | spintronic, molecular engine, biomotor, NEMS |
| | transducers | NEMS, solar/fuel cells, LED, Laser |
| | devices | photonic waveguide, super capacitor, nano-CMOS, DNA chip, biochip, bioanalogical |

is missing in this chapter, that is, the combination of top-down with bottom-up strategies or a "nanolink." Moreover, the most prominent printing technology in the semiconductor manufacturing facilities—projection lithography—is treated only briefly. This is because progress in this area is self-sustained, as microelectronics will evolve in a natural way into nanoelectronics. For example, it is expected that sub-50 nm projection lithography using extreme UV (EUV) will produce the next generation nanoelectronics within 5 years and 15 nm EUV projection printing has already been demonstrated.

Nevertheless, enough issues remain to be found in this chapter and the drive to establish off-the-road printing techniques is found in the need for rapid prototyping techniques orders in magnitudes cheaper than the equipment needed for EUV projection printing (typically 10 million Euros investments per tool). Moreover, some very useful methods have been proposed recently to improve the resolution of state-of-the-art printing techniques, not depending on the specific underlying printing method. For example, a new add-on technology for existing lithography—the so-called sidewall patterning technology—is able to enhance the resolution of the existing lithography by a factor of two or more without the need for new expensive equipment. Using this technique, sub-50 nm printing on top of 2 $\mu$m projection lithography has been demonstrated.

In "MEMS-based nanotechnology," the tools available from the MST will be treated and classified. The goal is to familiarize the reader with most of the established MST tools, directions, materials, and jargon in order to facilitate a confident choice of fabrication method for a particular problem. By combining the tools in a subsequent order, systems can be realized with the sub-100 nm critical dimensions,

that is, the regime of nanosystem technology (NST). Basically, this chapter is a comprehensive incomplete overview of MST with respect to methods and materials. In particular, the lithography-based ICT is treated as it covers almost the entire MST. In subsequent sections, the following technology issues are discussed; wafer fabrication, film formation, lithography, film etching, and micromachining. Film formation means the deposition or growth of a (thin) film without the direct intent to create a pattern. Film etching is the process of the removal of film or substrate material again without the specific intent to directly form a pattern. Lithography on the other hand is meant to shape a film with a pattern formed by a printing mask or writing stylus. Micromachining is the set of design and fabrication tools that precisely machine and form miniature structures and elements at a scale well below the limits of our human perceptive faculties, the microscale.

Important to notice in a micromachining process flow is the repetitive emergence of these steps; this is schematically shown in Figure 6. Therefore, the arrangement of this section is determined by this schematic. Every section will end with "Conclusion and Nanoperspective" in which some closing remarks will be given with respect to the applicability of the given techniques in nanotechnology. For more details concerning the microfabrication technology, the reader is encouraged to read excellent "standard" works such as [1–7].

*Silicon VLSI Technology* by James Plummer, *VLSI Technology*, edited by S. Sze, *Fundamentals of Microfabrication* by Marc Madou, *The MEMS Handbook* by Mohammed Gad-el-Hak, *Silicon Micromachining* by Miko Elwenspoek and Henri Jansen, *Nanotechnology* by A. ten Wolde, and *Handbook of Microlithography, Micromachining, and Microfabrication* by P. Rai-Choudhury.
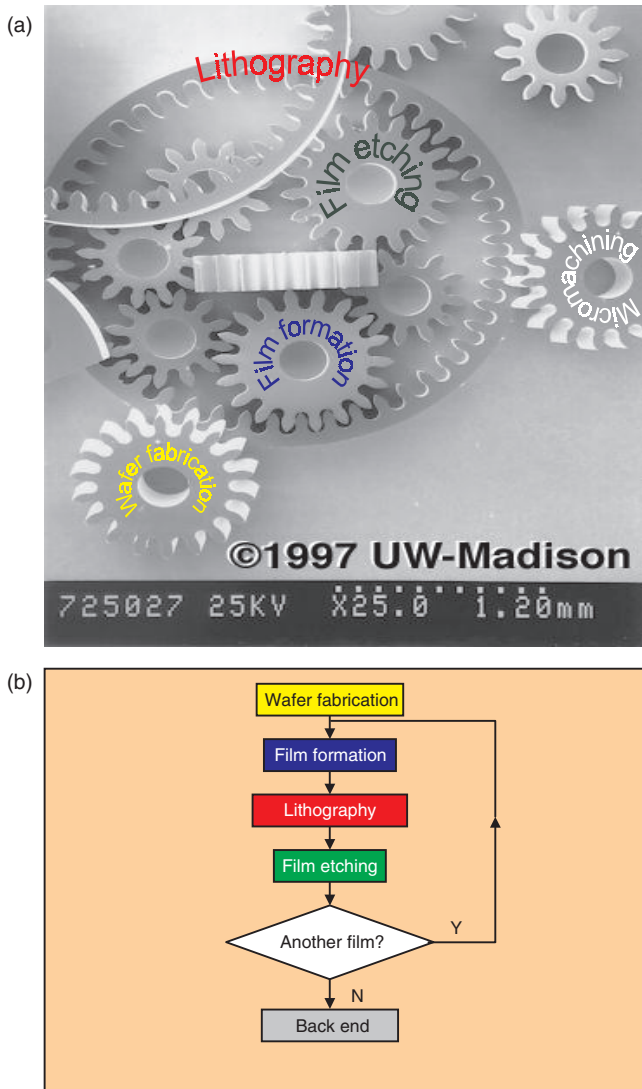
**Figure 6.** (a) Arrangement of sections in this Chapter. (b) An abstract representation of a typical process flow found in micromachining.

## 2. WAFER FABRICATION

Before a device fabrication process is actually started we have to select an appropriate wafer. The wafer can be silicon when device integration with electronics is requested, gallium-arsenide for laser applications, quartz for radio-frequency (rf) devices, or borosilicate glass for electro-osmotic flow devices. Due to the small feature sizes, the lithographic process is quite sensitive to dust particles. Therefore, this section appropriately introduces the chapter by informing where to process wafers, discussing different types of wafers, and how to clean the wafer sufficiently.

### 2.1. Cleanroom

A MEMS fabrication facility requires a clean processing room, especially in the area used for lithography (Figs. 7 and 8). The need for such a cleanroom arises because dust particles in the air can settle on wafers and lithographic masks and can cause defects in the devices that result in



**Figure 7.** MESA+ outside the cleanroom.

failure. For example, a dust particle incorporated into a growing oxide film can result in device failure due to an unintended low breakdown voltage. The situation is even more critical in the lithographic area. When dust particles adhere to the surface of a photomask, they behave as opaque patterns on the mask, and these patterns will be transferred to the underlying layers along with the circuit patterns on the mask. Therefore, in a cleanroom, the total number of dust particles per unit volume must be tightly controlled along with temperature and humidity. Classifications of cleanrooms are established by the number of particles that are one micrometer or larger in a cubic foot of space per minute; Class $= [\wp] * (\wp)^2$, where $\wp$ represents the size of the particle in micrometers and $[\wp]$ is the number of those particles per cubic foot per minute. So a class 100 cleanroom is one which has a 1 $\mu$m diameter dust count of 100 particles/min ft$^3$. And in a class 1 cleanroom only one such a particle can be found per minute in the same volume, which is about a million times less than that of ordinary room air. Clearly, due to the ever-shrinking sizes of electronic and mechanical components, the cleanroom condition is getting more stringent too. For example, going from 500 toward 50 nm lithography, needs a 100 times cleaner environment to achieve the same defect density; a class 0.01



**Figure 8.** MESA+ inside the cleanroom.

is needed instead of class 1. But cleaner environments are much more difficult to construct and more expensive to maintain. Therefore, minienvironments such as cluster tools are becoming more and more mandatory to perpetrate state-of-the-art nanotechnology.

## 2.2. Wafer Selection

Almost every MEMS is processed on top of a wafer; therefore, a wafer must be chosen to start. In general this means specifying wafer material (e.g., silicon, germanium, quartz, Pyrex glass, or silicon carbide), conductivity type ($n$ or $p$), resistivity (doping level), crystal orientation ($\langle 100 \rangle$, $\langle 111 \rangle$, ...), wafer size, and a number of other parameters having to do with flatness, trace impurity levels, and so on. The major choices in the IC technology are the type, resistivity, and orientation of a silicon wafer. In MEMS this is mainly wafer material, flatness, and orientation. (The importance of orientation is found when discussing wet anisotropic etching more in detail in Section 5.3.3, and that of flatness when discussing wafer bonding in Section 3.7.10). The choice of the substrate material (wafer) is given by considering the application for which the device will be used. Important criteria are mechanical strength, chemical inertness, optical transparency, radio-frequency losses, and so on. Three classes of materials are found in MEMS technology: single-crystal, polycrystal, and amorphous wafer materials.

Being a semiconductor, the chemical binding between single-crystal silicon (SCS) atoms is covalent. Covalent-binding potentials are strongly anisotropic and they have a deep minimum. This is in great contrast to metal-binding potentials, and consequently, crystal dislocations are much more movable in metals than in semiconductor or insulator materials. Therefore, metals are ductile and semiconductors or glasses are brittle. SCS can be made almost perfect—virtually without any defects or impurities in the crystal lattice and no dislocation lines in the silicon lattice that are able to move at room temperature (Fig. 9).
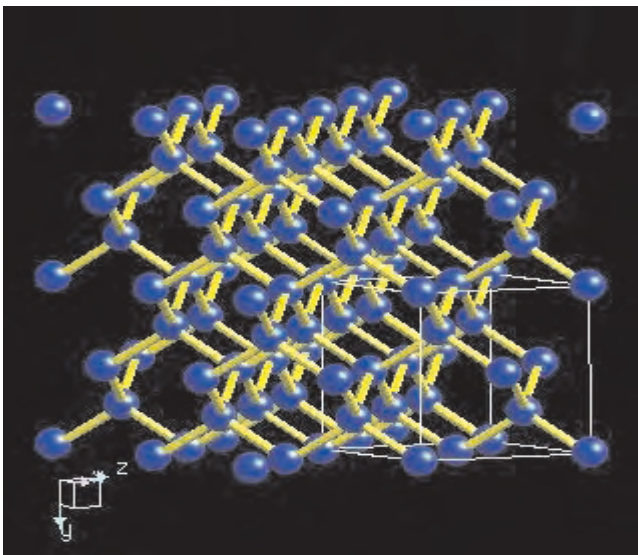
Therefore, SCS can only be deformed elastically (i.e. without any plastic deferability and no mechanical hysteresis). This pure elastic behavior makes SCS a material of strength comparable to amorphous stainless steel and mechanically superior to any metal in many applications. However, the introduction of a dislocation line immediately causes a crack in the brittle SCS and it will break while the ductile metals can stand a much larger strain than SCS. Mechanical engineers often try to avoid the use of brittle materials for very obvious reasons. But ductile materials are easily plastically deformed, meaning that these materials are subject to mechanical hysteresis.

Important and well-known materials for high-speed rotating micromachines, such as Si and SiC, are superior to the materials commonly used in macromachines like steel, titanium, and nickel-based superalloys. Micromechanical structures have been shown to be able to reach yield strengths above 10 GPa, with average strengths around 7 GPa. However, since the materials are brittle, the probability of fracture has to be taken into account, using Weibull statistics. This is also the reason brittle materials are not used in large machines, although often superior in miniaturized machines (i.e., for too large machines the probability of fracture becomes unacceptable). An additional material consideration is that thermal shock increases with length scale. Thus, materials that have high temperature capabilities but are not considered high temperature structural ceramics due to their susceptibility to thermal shock are viable at the millimeter and below length scales. These materials, like aluminum and sapphire, have not been much concerned for micromachining.

Although single-crystal silicon is still the number one in use for many MEMS applications, new materials emerge having special properties. Single-crystal gallium-arsenide (GaAs) has electro-optical properties and is therefore found in laser applications. Single-crystal quartz has piezoelectric properties, which is of use in resonating devices. The arrangement of silicon atoms in quartz is similar to that of SCS, but in quartz there is an oxygen atom between each pair of Si atoms (Fig. 10). In this figure, the heart of a tetrahedral contains a Si atom surrounded by four O atoms. The O atoms connect the tetrahedrals at the corners. Moreover, its chemical inertness makes it suitable for biological and/or chemical applications. For the same reason, amorphous stainless steel is becoming increasingly



**Figure 9.** Single-crystal silicon. Reprinted with permission from www. webelements.com.
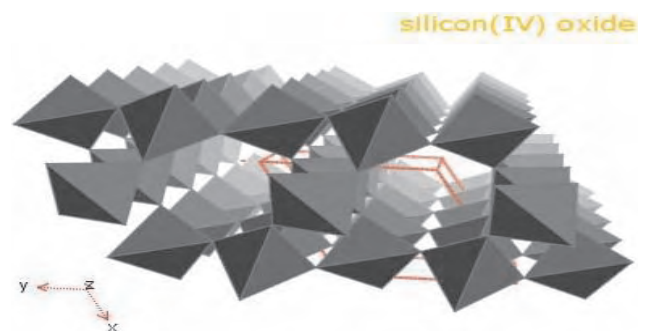


**Figure 10.** A piece of beta quartz. Reprinted with permission from www.webelements.com.

popular. The amorphous alkali glasses (e.g., Pyrex) have high ionic mobility at relatively low process temperatures. This makes Pyrex wafers suitable for wafer-bonding purposes. For on-chip radio-frequency applications, high-resistivity substrates are of prime importance. Although chromium-doped GaAs or quartz does satisfy this basic requirement, there are much cheaper solutions such as alkali-free glass (e.g., AF45™ from Schott). Other, less frequently found wafer materials are synthetic polymers (e.g., polycarbonate), alumina ($Al_2O_3$), graphite (C), and silicon carbide (SiC). When low-budget devices are requested, plastic wafers for single-use devices are increasingly found. The future could show the use of biodegradable organic wafers for medical applications.

In recent years the growth and development of semiconductor devices in the electronics industry has been nothing less than remarkable. In an electrical goods store nowadays, there are very few items that do not comprise semiconductors. Some people, however, are unaware that the most important prerequisite material for semiconductor technology is high purity silicon, a very sensitive and chemically reactive substance, easily fragmented through mishandling. Due to the dominant position of SCS, the next section will describe the production of SCS more in detail. This procedure is roughly the same for all the other wafer materials, although normally less high-tech (e.g., amorphous materials).

## 2.3. Single-Crystal Semiconductor Wafer Production

The starting material to produce SCS is silicon dioxide (or silica), which is chemically processed to form high-purity polycrystalline silicon (abbreviated: polysilicon) from which single crystals (or monocrystals) are grown (Fig. 11). The single-crystal ingots are grinded to define the diameter of the material and sawed (sliced) into wafers. Finally, these afers are lapped, etched, and polished to provide smooth, specular surfaces on which or from which microdevices will be made. In the subsequent sections, the just mentioned processing steps will be described in more detail.
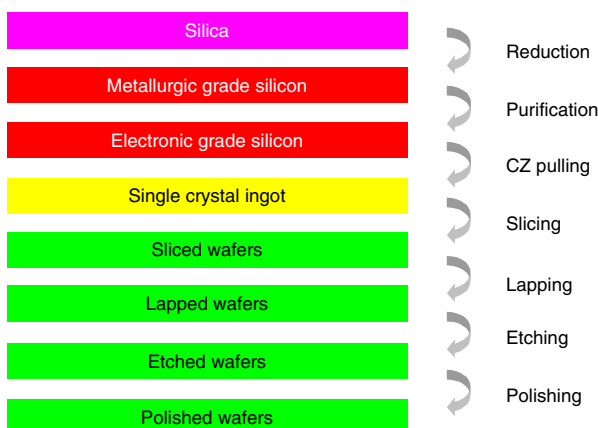
### 2.3.1. Polycrystalline Silicon (Polysilicon) Rod Production

The starting material for silicon is a relatively pure form of sand ($SiO_2$) called quartzite. This is placed in a furnace with various forms of carbon (coal, coke, and wood chips). While a number of reactions take place in the furnace, the overall reaction is

$$SiC + SiO_2 \rightarrow Si + SiO^\uparrow + CO^\uparrow$$
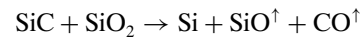
This process produces metallurgic-grade silicon (MGS) with a purity of about 98%. Next, the silicon is pulverized (Fig. 12) and treated with hydrogen chloride (HCl) to form trichlorosilane ($SiHCl_3$). The $SiHCl_3$ is a liquid at room temperature. Fractional distillation of the liquid removes the unwanted impurities. The purified $SiHCl_3$ is then used in a hydrogen reduction reaction to prepare the electronic-grade silicon (EGS). The resulting purified polysilicon is grown on the surface of an electrically heated silicon rod, which serves as the nucleation point for the deposition of silicon (Fig. 13):

$$Si_{bulk} + SiHCl_3 + H_2 = Si_{bulk} - Si + x * HCl$$
$$+ (3 - x)/2 * (H_2 + Cl_2)$$
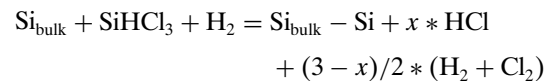
The resulting substance is then cleaned and etched with fluoronitric acid ($HNO_3 + HF$) to obtain a more than adequate surface for the next step. Pure EGS generally has impurity concentrations in the parts-per-billion range. Polycrystalline EGS is the raw material used to prepare SCS.

### 2.3.2. Single-Crystal Silicon Ingot Production

In general, semiconductor-grade devices cannot be fabricated directly from polysilicon without it first being converted into a single-crystal ingot form. Silicon single-crystal ingots are usually produced by either the Czochralski (CZ) method or the Float Zone (FZ) method.

***CZ Single Crystal*** Virtually all the silicon crystals and wafers for the IC and MEMS industry are prepared by the CZ technique. The CZ technique for silicon crystal growth uses an apparatus called a puller. In the crystal-growing process, polysilicon is placed in a quartz crucible (Fig. 14) and the furnace is heated with a graphite resistor element above



**Figure 11.** SCS manufacturing process.
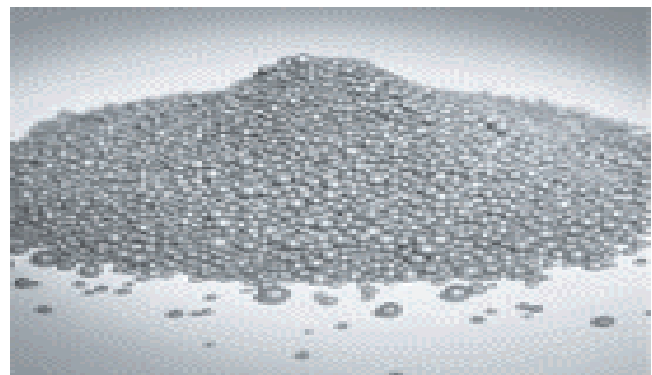


**Figure 12.** Pulverized MGS. Reprinted with permission from http://www.memc.com/.
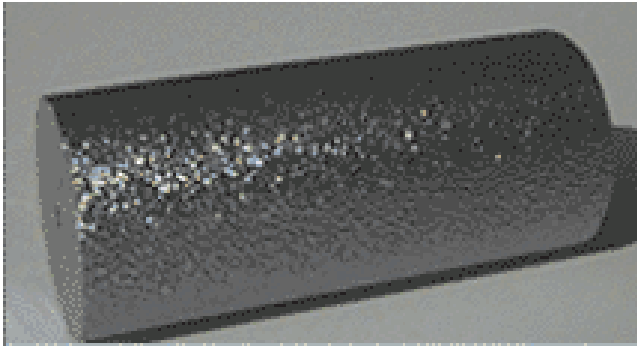
**Figure 13.** Polycrystalline silicon rod.

the melting temperature of silicon (i.e., 1420 °C) in an inert gas atmosphere. A suitable oriented seed crystal (e.g., ⟨111⟩) is suspended over the crucible in a seed holder and the seed is inserted into the melt. Part of it melts, but the tip of the remaining seed crystal still touches the liquid surface. It is then slowly withdrawn (pulled) while rotating with a typical pull rate of a few millimeters per minute (Figs. 15 and 17). The surface tension between the seed and the molten silicon causes a small amount of the liquid to rise with the seed and cool into a single-crystalline ingot (Fig. 16) with the same orientation as the seed and with a specified diameter. In crystal growth, a known amount of dopant is added to the melt to obtain a desired doping concentration. For silicon, boron (p-type Si) and phosphorus (n-type Si) are the most common dopants.

***FZ Single Crystal*** The float zone process can be used to grow silicon that has a lower contamination level than that obtained by the CZ technique. In the FZ process, a high-purity polysilicon rod with a seed crystal at the bottom is placed in an inert atmosphere and held in a vertical position which is rotated. During the operation, a small zone of the crystal is kept molten by a radio-frequency heater, which is moved from the seed upward so that this floating zone traverses the length of the rod (Figs. 18 and 19). The molten silicon is retained by surface tension between the melting and growing solid-silicon faces. As the zone moves upward, a single crystal freezes at the zone's retreating end and grows



**Figure 15.** Schematic view of CZ furnace. Reprinted with permission from http://www.memc.com/.

as an extension of the seed crystal until the entire polysilicon rod has been converted to a single crystal.

The FZ technique can be used to purify a single-crystal rod (i.e., to remove impurities), because the impurities have difficulties in passing the molten zone. There is a substantial reduction of impurity concentration in the rod after each pass. Multiple passes can be performed on a rod much more easily than a crystal can be grown, cropped off the end region, and regrown from the melt. Therefore, the FZ process is ideally suited for crystal purification. Because of this purification, materials with higher resistivities can be obtained from the FZ process than from the CZ process. Furthermore, since no crucible is used in the



**Figure 14.** Polysilicon in crucible.
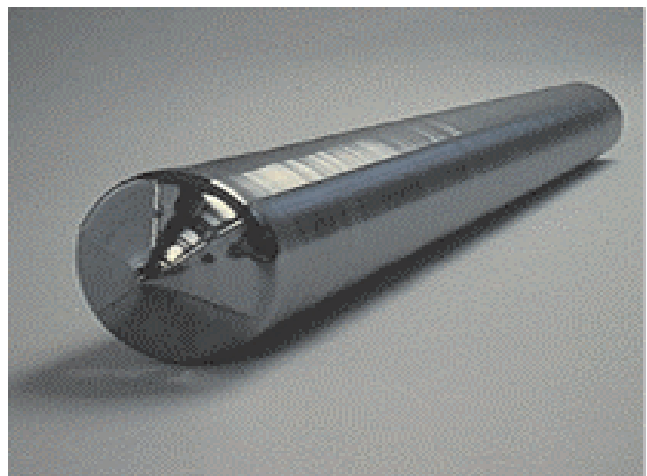


**Figure 16.** SCS ingot.
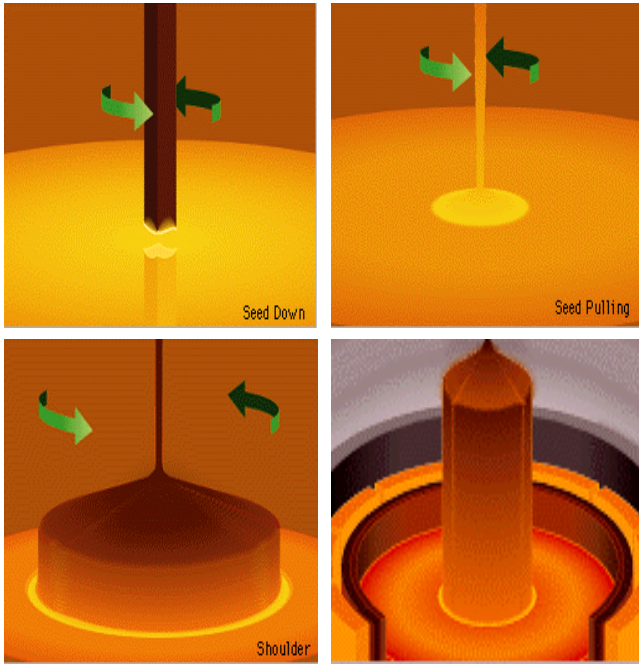
**Figure 17.** Process of single-crystal pulling and growing. Reprinted with permission from http://www.memc.com/.



**Figure 19.** Schematic view of FZ furnace. Reprinted with permission from http://www.memc.com/.

FZ process, there is no oxygen contamination from the crucible (as with CZ growth). At the present time, FZ crystals are used mainly for high-power, high-voltage devices and rf devices, where high-resistivity wafer materials are required.

As the wafer diameter size increased, there was a corresponding higher incidence of crystals with lineage defects. Thus, the FZ method compared to the CZ method was more difficult with larger diameters and proved to be extremely unstable and unpredictable. Even the slightest vibration often meant that the whole process would fail. Compared to the CZ method, the FZ method brought a reduced yield and lower electric power efficiency. Finally, with the introduction of the 100 mm diameter single-crystalline technology, the FZ method almost vanished.

### 2.3.3. Ingot Grinding

After a crystal is grown, the first shaping operation is to remove the seed (to be reused) and the other end of the ingot. The next operation is to grind the surface so that the diameter of the material is defined. After that, one or more flat regions are ground along the length of the ingot. These regions, or flats, mark the specific crystal orientation of the ingot and the conductivity type of the material. The most common wafer orientations in SCS manufacturing are shown in Figure 20: $\langle 100 \rangle$, $\langle 011 \rangle$, and $\langle 111 \rangle$ wafers (this subject will be treated in more detail in Section 5.3.3). The largest flat, the primary flat, allows a mechanical locator in automatic processing equipment to position the wafer and to orient the devices relative to the crystal in a specific manner. Other smaller flats, the secondary flats, are ground to identify orientation and conductivity type of the crystal. Once these



**Figure 18.** FZ crystal growth.
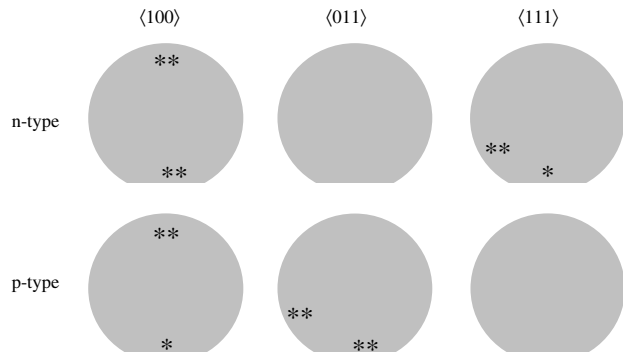


**Figure 20.** Most common Si wafers in microtechnology. * = primary flat, ** = secondary flat.

operations have been done, the ingot is ready to be sliced by a diamond saw into wafers.

### 2.3.4. Wafer Slicing

Slicing determines four wafer parameters: surface orientation (e.g., $\langle 111 \rangle$), thickness (depending on wafer diameter, e.g., 700 micrometers), taper (i.e., wafer-thickness variation from one end to another), and wafer bow (i.e., surface curvature of the wafer, measured from the center of the wafer to its edge). Wafer slicing can be done either with an outer saw (Fig. 21), an inner saw, or a wire saw. However, in most cases the traditional outer saw is not used anymore due to kerfs of the blade and irregularities in shape. Also, with increasing ingot diameter, gradually "bowing" became a serious problem for the inner saw technique that was affecting production rate. Therefore, in 1994 wire saws were introduced.

In a few cases, customers demand nonstandard crystal orientation (i.e., not $\langle 100 \rangle$, $\langle 110 \rangle$, or $\langle 111 \rangle$). In such cases, the SCS ingot is sawed under a specified angle creating elliptical-shaped wafers instead of the usual circular-shaped wafers. Due to the off-the-road procedure, normally the wafers are much more expensive (Fig. 22).

### 2.3.5. Wafer-Edge Profiling

After the sawing process, the individual slices have sharp, fragile edges. These edges must be rounded or "profiled" in order to provide strength to the wafer (Fig. 23). Profiling will ultimately prevent chipping or breakage in subsequent internal processing and during device fabrication. Without edge profiling, the wafer is susceptible to edge fractures.

### 2.3.6. Wafer Lapping

In order to increase symmetry and remove surface roughness from saw cuts and process damage, the sliced wafer is now mechanically lapped. That is, both sides of the wafer are lapped using a mixture of abrasive alumna ($Al_2O_3$) powder and glycerine, which is fed through a chute onto two conversely rotating base plates (Fig. 24). Wafers are simultaneously revolving separately and within an orbiting carrier, which creates four-way rotation and produces a very smooth finished product (i.e., a typical flatness uniformity within 2 micrometers). This lapping style has remained more or less unchanged from 1962 until the present.



**Figure 22.** Sliced wafers.

### 2.3.7. Wafer Etching

The surface of the lapped wafers should be cleaned (etched) to remove any remaining microcracks or surface damage introduced by the alumna abrasive in the previous lap stage. Etching is done chemically using a corrosive mixture of nitric acid and glacial acetic acid solution (Fig. 25). This acidic surface dissolving technique is preferred in Japan over the more caustic U.S. etching method, which uses a sodium hydroxide (NaOH) base solution.

### 2.3.8. Wafer Polishing

The final step of wafer fabrication is chemical–mechanical polishing (CMP). This method is currently employed and involves both mechanical and chemical polishing mechanisms. Its purpose is to provide a smooth, specular surface where device features can be defined by lithographic processes (see Section 4) or to improve bondability (refer to Section 3.7.10). Wafers are fixed to a hard ceramic base plate using a wax bonding method. These are then lowered against a synthetic-leather-made polishing pad, attached to a metal plate and buffed to a state of minimum roughness with a solution of silica powder, which is dissolved in deionized water and controlled at a pH 10–11 with sodium hydroxide alkaline solvent (Fig. 26). This method improves parallelism, creates the surface mirror, and removes any remaining surface roughness (Fig. 27). The combined effect of the mechanical and chemical approach also ensures that there is no additional damage during the process.



**Figure 21.** Schematic view of slicing machine. Reprinted with permission from http://www.memc.com/.
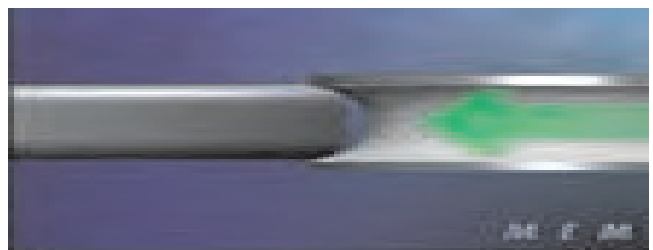


**Figure 23.** Edge profiling. Reprinted with permission from http://www.memc.com/.
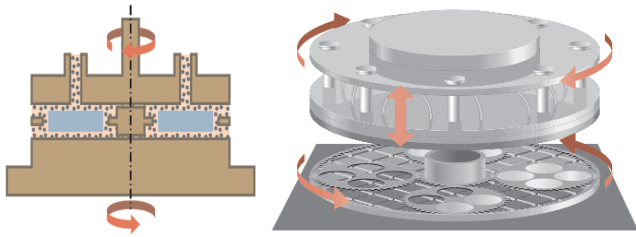
**Figure 24.** Schematic view of lapping machine. Reprinted with permission from http://www.memc.com/.

### 2.3.9. Wafer Cleaning

Using the latest cleaning and inspection technologies, the final stages of SCS manufacturing can all be carried out with no handling or contamination. This means that each wafer arrives in perfect condition ready for immediate use by the end user. In each of these areas, there is considerable ongoing research that we will briefly describe in this section. Typically, the cleaning procedure of SCS consists of three steps: (1) First, the wafer is oxidized and (organic) particles are removed. (2) Next, the oxide is removed and (inorganic) particles are liberated and removed from the surface. (3) Finally, the surface is replaced by super clean new natural oxides, which grow on the surface.

***RCA Cleaning***    The RCA cleaning method was developed by the American Corporation RCA in 1970 and instantly adopted by silicon wafer producers worldwide. The process had three steps, beginning with the SC-1 solution, which is comprised of ammonia, hydrogen peroxide, and water, to remove organic impurities and particles from the wafer surface. Next, natural oxides and metal impurities are removed with hydrofluoric acid solution. Then, finally, the SC-2 solution, a mixture of hydrochloric acid and hydrogen peroxide, is put onto the now bare surface and the surface is oxidized. Even now the RCA method is used although concentrations, temperatures, and time adjustments differ among companies, as do the chemical recycling processes and the option to use ultrasonic waves. In general, the number of particles on the surface of the final product does not exceed 10 with diameters larger than 0.16 $\mu$m particles, with the density of surface metal ions at less than $10^{10}$ atoms/cm$^2$. Yet nanotechnology inspires one to investigate improved methods to decrease particle contamination. For example, hydrogen peroxide ($H_2O_2$) is unstable at the temperatures used in the SC-1 and SC-2 solutions and decomposes into $H_2O$
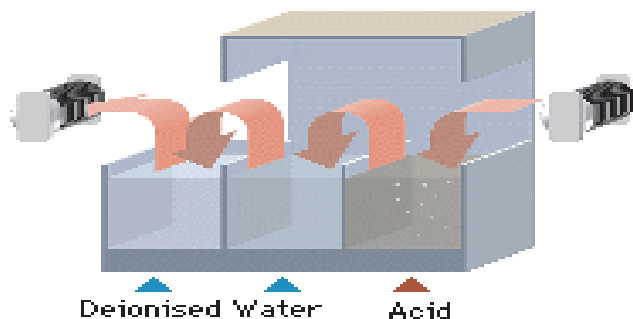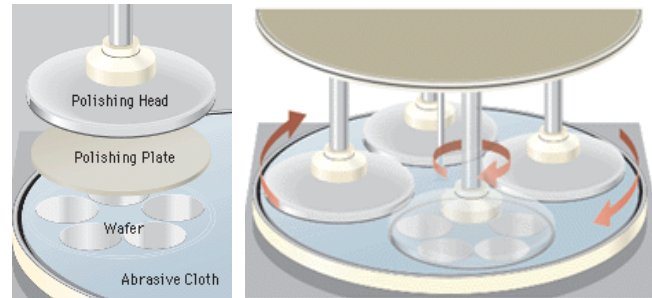


**Figure 26.** Schematic view of polishing machine. Reprinted with permission from http://www.memc.com/.

and $O_2$. In the SC-1 solution, if the concentration of $H_2O_2$ drops too much, the $NH_4OH$ will attack silicon.

***Ozonized Cleaning***    A number of replacement cleaning procedures have been proposed. A particularly interesting procedure is to use ozonized ultrapure water. The process is all at room temperature, uses far fewer chemicals than the standard RCA clean, and is claimed to be as effective in cleaning wafers. A strong oxidant (ozon, $O_3$) is used to oxidize organics and metals. Megasonic agitation is used to loosen particles that may have adhered to the wafers. The final steps involve an HF etch of the surface. This strips away the chemical oxide that naturally grows as part of the cleaning procedure. The silicon surface atoms are left with dangling (incomplete) bonds which are highly reactive and which form hydrogen bonds with H atoms from the HF solution [2, 3]. The hydrogen-passivated surface that results is ready for immediate further processing, such as film deposition. There are some concerns with using a final HF step for wafers whose next processing step is oxidation. The hydrogen-passivated silicon {100} surface is roughened by the H passivation process and may lead to poorer quality thin oxides grown on these surfaces. In addition, the hydrogen-passivated surface is very sensitive to ambient effects between the time the cleaning ends and the next process step begins, so special care may have to be taken in transporting and handling such wafers. Of course, as in the case of RCA cleaning, one could opt for an additional ozon-oxidation step to form a clean and stable surface oxide.

***Dry Cleaning***    There has also been considerable recent work on "dry" cleaning procedures including vapors, plasmas, sputtering, and photochemically enhanced cleaning



**Figure 25.** Wafer cleaning.
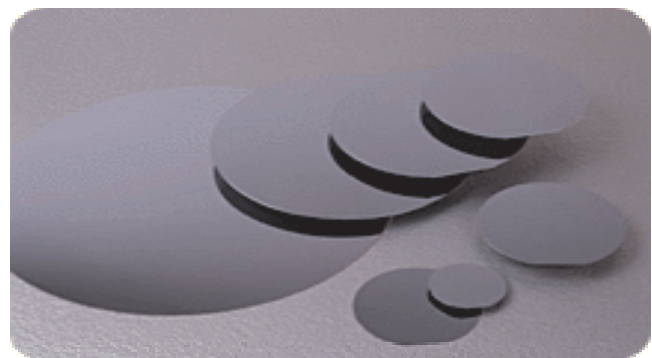


**Figure 27.** Polished SCS wafers.

in which UV energy is used to help break surface bonds and release contaminants on the wafer surface. This work has been motivated both by the environmental issues associated with wet chemistries and the increasing use of cluster tools in IC manufacturing. In these tools, multiple-process steps, often on single wafers, are performed in a single machine by moving wafers from one chamber to another. There is great interest in accomplishing the cleaning process in one of these chambers because wafers would then move directly to the process step under well-controlled ambient conditions, minimizing contamination between cleaning and the next step.

### 2.3.10. Wafer Inspection

A real crystal (such as a silicon wafer) differs from the ideal crystal in important ways. It is finite; thus, surface atoms are incompletely bonded. Furthermore, it has defects, which strongly influence the electrical, mechanical, chemical, and optical properties of the semiconductor. There are four categories of defects: point defects (i.e., incorporated foreign atoms into the semiconductor lattice or missing silicon atoms), line defects (i.e., an extra plane of atoms in the lattice, also known as edge dislocation), area defects (represents a large area discontinuity in the lattice such as twins and grainboundaries), and volume defects (i.e., precipitates of impurities or dopant atoms). Point defects are particularly important subjects in the kinetics of diffusion and oxidation processes. All these topics can be found in specific literature [1]. The oxygen and carbon concentrations are substantially higher in CZ crystals than in FZ crystals due to the dissolution of the silica crucible (for oxygen) and transport to the melt from the graphite susceptor during crystal growth. Typical carbon and oxygen concentrations range from $10^{16}$ to about $10^{17}$ atoms/cm$^3$ and low $10^{17}$ to $10^{18}$ atoms/cm$^3$, respectively (the atomic density of silicon is $5 \times 10^{22}$ atoms/cm$^3$). Carbon in silicon occupies substitutional lattice sites and its presence aids the formation of defects. Oxygen, however, has both deleterious and beneficial effects. It can act as a donor, distorting the resistivity of the crystal. On the other hand, oxygen in an interstitial lattice site can increase the yield strength of silicon. In addition, the precipitates of oxygen due to the solubility effect can be used for gettering (see next section). It is possible to obtain silicon crystals that are virtually free of dislocations (500 dislocation/cm$^2$ or less). In spite of this, high-resistivity silicon is very difficult to achieve and is limited to ca. $10^4$ $\Omega$ cm. To obtain high-resistivity crystals, gallium arsenide can be doped with chromium to give a starting resistivity of $10^9 \Omega$ cm. Another option to increase the resistivity is to start with an insulating material like quartz crystal, which is, of course, not a semiconductor.

### 2.3.11. Postwafer Production

Previously, wafer manufacturers only produced up to the polished-wafer stage while device manufacturers (the "customer") would continue from these stages. However, as market prices came down and demand for ICs increased, the competition for high performance wafers for semiconductors became more and more intense. In reaction to this pressure and as a result of the increase in technical

know-how, product lines were expanded to include epitaxial (EPI) wafers, diffused wafers, and silicon-on-insulator (SOI) wafers. Moreover, oxygen donors (silicon and oxygen compounds) cause incorrect resistivity values during the intentional doping process and must be annihilated using a continuous wafer heat treatment called wafer gettering. Gettering is a general term meaning a process that removes harmful defects or impurities such as iron and copper from the wafer surface by diffusing a contaminant into the substance. When the wafer is subjected to high-temperature treatment (e.g., 1050 °C in $N_2$), oxygen evaporates from the surface. This lowers the oxygen content near the surface, so that precipitation of oxygen does not occur there. The treatment creates a defect-free zone. Additional thermal cycles can be used to promote the formation of oxygen precipitates in the interior of the wafer for gettering of impurities. They are then cooled again at a similar high speed to prevent regeneration of the doner. As the silicon matrix is very stable, excess oxygen will precipitate to form irregular fields and thereby create free space in which the impurities can be trapped. In 1988, polysilicon chemical vapor deposition (CVD) was introduced as an effective gettering source. Polycrystal could be placed at the backside of the silicon wafer to attract impurities into the irregular space.

***EPI Wafer*** In 1963, EPI wafers entered the world market. It is a technology closely related to crystal pulling from a melt and it involves the deposition of a single-crystal semiconductor layer upon a single-crystal semiconductor substrate, so that the lattice of the newly formed film duplicates that of the substrate (Fig. 28). This is called epitaxy, from the Greek words epi (meaning "on") and taxis (meaning "arrangement"). Epitaxial processes are differentiated from the melt pulling process in that the epitaxial layer can be deposited at a temperature substantially below the melting point. If the film is of the same material as the substrate, the process is called homoepitaxy, epitaxy, or simply epi. If the deposit is made on a chemically different substrate, usually of closely matched lattice spacing and thermal expansion, the process is termed heteroepitaxy. The key reason for EPI growth is to create an extremely pure layer with different, usually lower, concentration of electrically active dopant to the substrate. The dopant in the film can be n- or p-type and is independent of the substrate doping. The three types of epitaxial film formation processes currently employed are vapor-phase (VPE), liquid-phase (LPE), and molecular beam epitaxy (MBE) as can be found in Section 3.7. Depending on the device to be made, the EPI
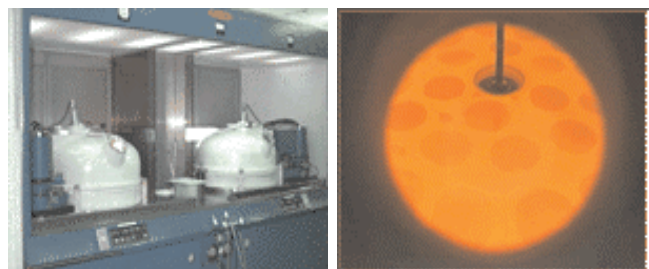


**Figure 28.** Vertical EPI reactor.

layer must meet a set of specifications for thickness, electrically active dopant concentration, defect density, and contamination. The gas used in this process is highly toxic and inflammable. One heteroepitaxy application is the deposition of silicon on sapphire ($Al_2O_3$) or "SOS." Mono-, di-, trichlorosilane, or silicon tetrachloride, and hydrogen are the source gases, which are combined with either diborane or phosphine gas to act as dopant atoms. In the period 1972–73, vertical and horizontal style reactor models were developed, along with cylindrical style, single wafer style reactors, and reduced pressure reactors, in response to customer demand.

***SOI Wafer*** Silicon devices have problems with inherent parasitic capacitances due to the relatively low maximum resistivity. One way to circumvent the problem is to fabricate silicon devices on an insulating substrate. The initial approach was to grow silicon epitaxially on a substrate of sapphire (called SOS). A more recent approach is the silicon-on-insulator process. SOI wafers have an oxide film under the active wafer top layer (Fig. 29). This allows for high speed operation of ICs with a minimum latch-up or punch-through and makes them especially good for memory devices such as next generation DRAMs and SRAMs. Moreover, it is believed that more and more microstructures will exploit SOI wafers. For example, crystalline layers of a predetermined thickness on a thin $SiO_2$ layer afford well-controlled suspended membranes. There are a few approaches to create a SOI wafer: SOI, BESOI, SIMOX, and Smart Cut®.

In the first method, a silicon wafer is oxidized and processed to give a flat surface with a pattern of exposed silicon area within the surrounding oxide. The surface is then coated with silicon to a thickness of 0.5 to 1 $\mu$m. However, only amorphous or polycrystalline silicon is formed on the almost entire amorphous $SiO_2$ substrate; therefore, a strip heat source can be used to recrystallize the deposited silicon into SCS. The heat source melts the polysilicon through to the substrate and the substrate acts as a seed to the molten silicon. As the heat source is moved laterally, SCS is grown laterally over the oxide-covered regions. Capping the molten zone with silicon dioxide and silicon nitride layers will improve the zone's thermal stability.

Recently the bonded BESOI (backside etched SOI) wafer has become widely used with the negligible thickness variation in the active layer of these wafers. After oxidizing a silicon wafer, the wafer is bonded with a second silicon wafer.
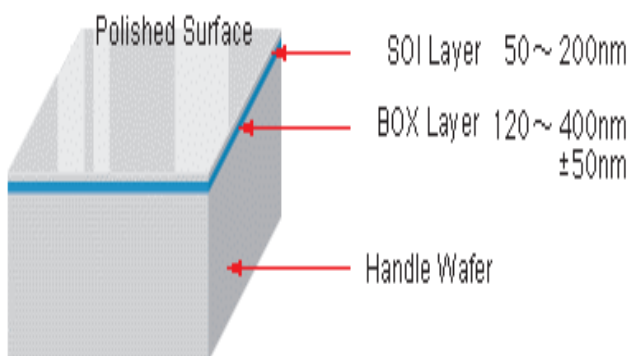
The stack is immersed in a silicon etch solution in which one of the silicon wafers is almost entirely removed. Only a thin SCS layer (between a few micrometers up to wafer thickness) is left to form the active layer.

The third method is SIMOX, which is an abbreviation for separation by implanted oxygen. It is a method of oxide film implantation beneath the surface of a SCS wafer, which results in a similar finished product to SOI wafers but with a completely different manufacturing process.

A fourth method, "Smart Cut®," is based on the technical principles of thermal oxidation, ion implantation, wafer bonding, and atomic level splitting (Fig. 30). Its key feature, hydrogen implantation, irreversibly weakens the silicon crystal at the desired depth. This acts as an atomic scalpel to lift off a thin layer of silicon, bonded on a base wafer of your choice. For example, a very thin perfect monocrystalline silicon layer is transferred onto a silicon support wafer, which has been covered first with an insulating layer of silicon dioxide. The resulting SOI wafer is now ready for the microchip manufacturing process. A key advantage of Smart Cut® compared to other SOI approaches is that it relies on existing standard microelectronic manufacturing equipment. As a result, this innovative technology is the only industrial process in use today that enables high-volume production of SOI wafers. This technology offers unique flexibility, in terms of wafer diameter, SOI and buried oxide layer thickness, and uniformities.

***Diffused Wafer*** In 1970, diffused wafers were developed. The structure of a diffused wafer is similar to an EPI wafer although it has a thicker active layer and both sides of the



**Figure 29.** Sample structure of SOI product.
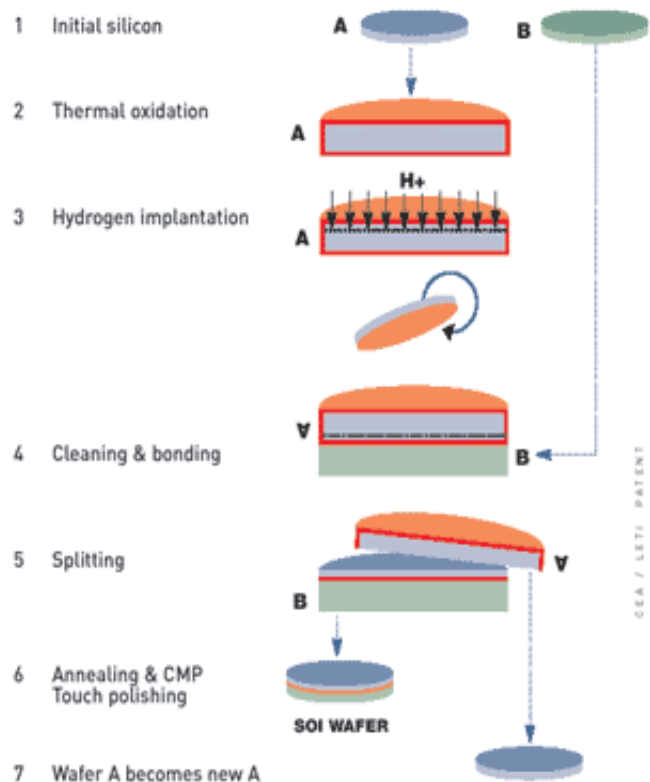


**Figure 30.** Smart Cut® SOI wafer production.

lapped or etched wafers have been diffused with either phosphorus or boron (Fig. 31). They are mainly used in power transistor devices.

In some applications a very homogeneous distribution of dopants is required. To obtain this, we use a float zone silicon slice that has an average doping concentration well below the required amount. The slice is then irradiated with thermal neutrons. This process gives rise to fractional transmutation of silicon into phosphorous and dopes the silicon $n$-type. Because the penetration depth of neutrons in silicon is about 100 cm, doping is very uniform throughout the slice.

## 2.4. Single-Crystal Quartz Wafer Production

Quartz in some respects presents us with an even more ideal substrate material than silicon because of its nearly temperature-independent thermal expansion coefficient. A variety of quartz micromachined piezoelectric devices are on the market such as electronic filters, resonators, and wristwatch tuning forks.

Natural quartz has been replaced by alpha quartz grown in large single crystals using a hydrothermal process. It is not at all like the growing of single-crystal silicon. It occurs at 350 °C in a sealed vessel usually called an autoclave. Two growth methods are used. One uses sodium carbonate as a mineralizer; the pressure in the autoclave is about 60 atmospheres. The other uses sodium hydroxide where the pressure is about 125 atmospheres. Most likely, crystal would be needed to be made to the requested specifications of size, thickness, angle tolerance, surface finish, etc. All planes can be made up to the physical size of available stones. For the $\langle 100 \rangle = Y$–cut wafer, the $Y$ axis is normal to major face, for the $\langle 110 \rangle = X$–cut, the $X$ axis is normal to major face. The $\langle 111 \rangle$-oriented quartz wafer is not a standard wafer.

## 2.5. Amorphous Float Glass Wafer Production

Float glass offers the quality of plate glass combined with the lower production cost traditionally associated with sheet glass manufacturing. Float glass is virtually distortion and defect free, making it ideal for various premium-glazing applications in buildings and homes or for automotive glass along with hundreds of other glass fabrications. Float glass manufacturing is not unlike the manufacturing of commodities like steel or plastic. Each of the processes requires raw materials to be weighed, mixed, melted at high temperatures, formed into continuous ribbons, cooled, and cut into a size that fits its use. Float glass manufacturing is described in the following.

### 2.5.1. Charging the Raw Materials

Float glass is made from a combination of several ingredients such as sand, soda ash, dolomite, limestone, salt cake, and cullet (Fig. 32). The raw materials are kept in different silos. After being weighed separately they are mixed and then poured into the charging hopper along with the cullet (crushed scrap glass).

### 2.5.2. Melting in the Furnace

The raw materials are melted in the furnace at a temperature of 1550 °C produced by powerful fuel-oil and/or gas burners. As it melts, the mixture vitrifies and flows slowly down inside the furnace, undergoing a process known as "fining." During this process, the molten glass is kept at a high temperature for several hours, enabling bubbles of air trapped within it to escape.

### 2.5.3. Floating on a Tin Bath

From the working end of the melting furnace, the glass flows through the canal area and then into the float furnace (tin bath or float bath) onto molten tin. The molten glass forms a continuous ribbon that floats on the molten tin with a thickness that can range from 2 to 12 mm. The float furnace atmosphere is controlled using a mixture of nitrogen and hydrogen gas to prevent the tin from oxidizing. From one end of the bath to the other, the temperature of the glass and of the tin gradually drops from 1100 to 600 °C allowing the glass to become flat and parallel. Top rollers on either side draw out the glass mechanically to give it the required thickness and width.

### 2.5.4. Annealing

The glass emerges from the tin bath in the form of a continuous strip. This is led by way of a roller conveyor to an annealing tunnel, known as a "lehr." Here, the glass is gradually cooled in a controlled way, in order to ensure perfect flatness and eliminate any internal mechanical stresses, which could cause breakage. The glass comes out of the lehr at ambient temperature, ready for cutting.
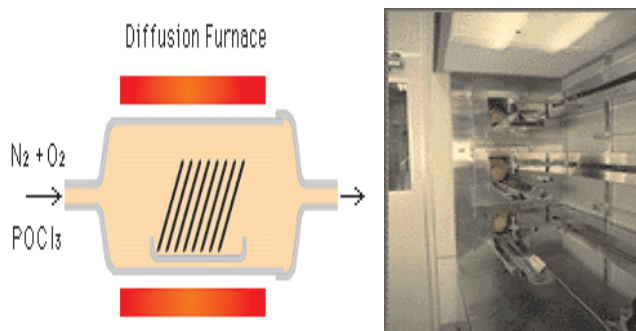


**Figure 31.** Schematic view of a diffusion furnace.



**Figure 32.** Raw materials.

### *2.5.5. Cutting*

The cooled glass ribbon exits the lehr and is conveyed to the cutting area by a system of rollers and drives linked to the lehr drive system. The glass is scored with carbide cutting wheels, parallel and perpendicular to the ribbon travel, into sizes that meet the plant's customer requirements. The scored glass ribbon is then separated into lites for packaging for transfer to the wareroom for storage or shipment to the customer.

## 2.6. Wafer Cleaning

After selecting a wafer and in between different wafer processing steps, the device manufacturer should clean the wafers to remove traces of dust. This cleaning procedure may be identical to the silicon wafer production facility cleaning procedures (Section 2.3.9.) but normally is less severe in MST facilities. However, in NST it might be necessary to perform a full three-step cleaning process. Standard cleaning often consists of fuming (70%) nitric acid to remove organic dust and boiling nitric acid to remove metallic particles. Because standard cleaning is an oxidizing agent, silicon wafers will be coated with a thin native oxide. This oxide is sometimes beneficial to improve adhesion of resist, which is applied during the lithography. When this oxide is unintended, the cleaning can be ended with a short dip of the wafer in HF to remove the oxide.

## 2.7. Conclusion and Nanoperspective

In this chapter, a typical fabrication process of SCS substrates has been treated. Polished wafers, as raw materials for ICs and other devices, are made from single-crystal ingots that have been precisely cut and chemically polished. First, silicon ingots are sliced into wafers using a diamond saw or wire saw. The resulting sliced wafers are then lapped mechanically to remove any surface roughness. The surface of the lapped wafers is then etched in an acidic solution to remove any remaining process damage. Finally the etched wafers become polished wafers after surface polishing. The next beautiful virtual reality movies show how the silicon wafer production process is accomplished (Table 3). When the semiconductor behavior is not requested or even is a disadvantage (as in the case of rf components or chemical applications), float glass offers the same ultraflat wafer surface as currently available for single crystalline material, but for a much lower price. This can become crucial to enable the widespread introduction of microcomponents in the near future. The most prominent part of the float glass production process is the tin bath, which removes almost any surface irregularity.

The goals for the nanofuture are fairly clear—cleaner environments in which to process wafers, better cleaning procedures that remove particles and trace contaminants more reliably, and better gettering procedures for eliminating contaminants from device regions of wafers. Traditionally, semiconductor manufacturing facilities have used the approach of providing cleanrooms in which to manufacture the chips. While this has been very successful, it is in some sense a wasteful approach because the volume of the cleanroom is far larger than the wafers that are being processed.
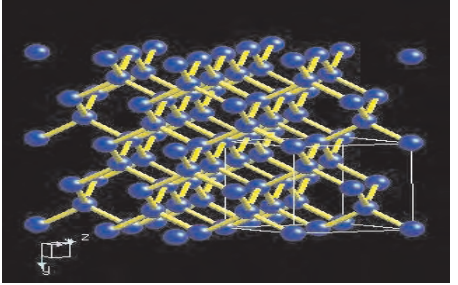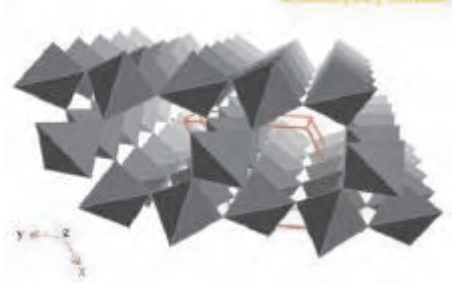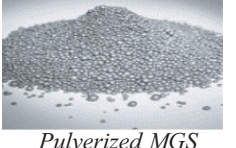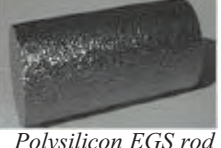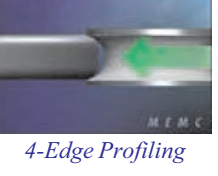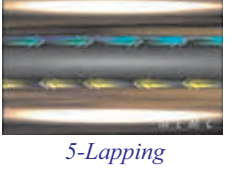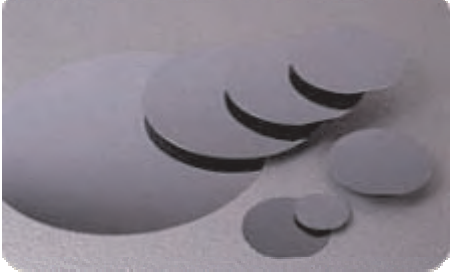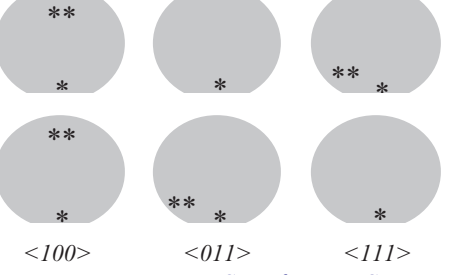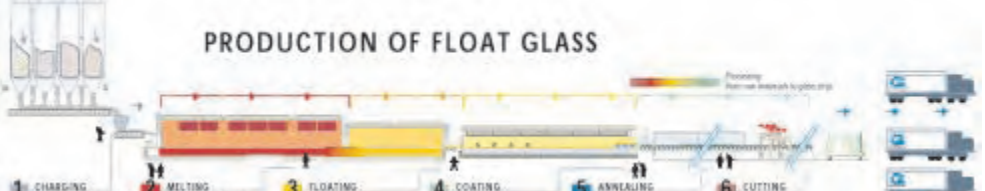
There are approaches to minimizing the actual volume of "cleanroom" which must be maintained. These approaches keep the wafers in sealed minienvironments in which they are transported from one machine or process to another. An alternative approach is to combine equipment to a single cluster tool. The wafer in such a system is transported from one module to the other with the help of a central robotic-arm system. Economics may play a significant role in determining how extensively such minienvironments are used in the "nanofuture," since the costs associated with constructing and operating large ultra-clean-rooms are very large. Gettering methods have remained relatively unchanged for the past decade. It is likely that intrinsic gettering will dominate the "nanofuture" because with smaller devices, thermal budgets for processing will have to decrease. Moreover, with decreasing size, the effect of local inhomogeneous doping becomes critical with respect to device performance. Therefore, tighter controls on oxygen concentration in CZ wafers will be required and may reintroduce FZ wafers.

Although the history of silicon production for semiconductor devices dates back only 30 years, it has become the most pervasive technology of the 20th century. As we move into the 21st century there will be no reprieve for manufacturers as revolutionary applications for ICs in areas such as supercomputers are continually researched and developed to support the so-called information age. All around the world large investment is being made into the more efficient, lower cost mass memory components for future generations. And in terms of machinery, the catch up race between new manufacturing technology and the development of corresponding evaluating equipment has clearly become a neverending game of cat and mouse as each in turn surpasses the other.

## 3. FILM FORMATION

After a substrate or wafer has been selected, the next step generally is to form a thin solid film (or layer) on top of the substrate. The material of this film is chosen such that it reflects the specific task of the microdevice to be constructed. Film formation generally means the *deposition* of a new layer on top of a substrate. *Growth* of a film, as in oxidation of a silicon wafer, differs from straight deposition due to the consumption of the substrate (sub)surface material while forming the film. The film can be formed on the substrate—physically or chemically—from a gas state, liquid state, or solid state. Gas-phase film formation methods are of key importance in microtechnology and are found schematically in Figure 33. The mechanism for physical film deposition (Fig. 33a) is quite straightforward: the reactants are transported to the surface and adsorb. Physical film growth (Fig. 33b) is possible due to the subsurface implantation of high-velocity particles—most often ionic species. The chemical film deposition (Fig. 33c) involves three essential steps, which are identical to chemical film etching—only the direction of transport is reversed: the reactants are transported to the surface (e.g., ionic) and adsorb. Then surface reactions occur (e.g., thermally activated). Finally the products from the surface are desorbed and transported away from the surface (e.g., by dissolving). Finally, in chemical film growth (Fig. 33d) the reactants adsorb first, and then they diffuse into the substrate and react. Basic requirements

**Table 3.** Schematic overview of wafer production methods.



| | | |
|---|---|---|
| **Material**<br><br>Reprinted with permission from<br><br>www.webelements.com | *Single crystal silicon* | *Single crystal silicon dioxide(beta quartz)* |
| **Silicon purification** | *Pulverized MGS*  *Polysilicon EGS rod* | *PolySi incrusible*  *SCS ingot* |
| **Single-crystal semiconductor**<br><br>Reprinted with permission from<br><br>www.memc.com | *1-Crystal Pulling*  *2-Rod Grinding*  *5-Lapping*  *6-Polishing*  *Polished SCS wafers* | *3-Wire Cutting*  *4-Edge Profiling*  *7-Laser Inspection*  *8-Epitaxy*  *<100>*  *<011>*  *<111>*<br>*Most common Si-wafers in MST.*<br>*\* = primary flat, \*\* = secondary flat* |
| **Amorphous float-glass**<br><br>Reprinted with permission from<br><br>www.ajzonca.tripod.com | PRODUCTION OF FLOAT GLASS | |

for a good formation process are that the reactants must be able to be transported to the wafer surface, and the products—if any—must be transported away easily. The latter means that soluble, gaseous, or volatile products are needed in film formation.

The choice of film material and film formation method is very important because it influences the material proper-ties, such as film conductivity, structure, stress, and adhesion, which determine the device characteristics in the end. Depending on the film formation method, layer thickness will be influenced by the topography of the underlying substrate, that is, the step coverage is influenced by the film formation method. Moreover, the deposited film might mix (alloy) with the underlying layer due to
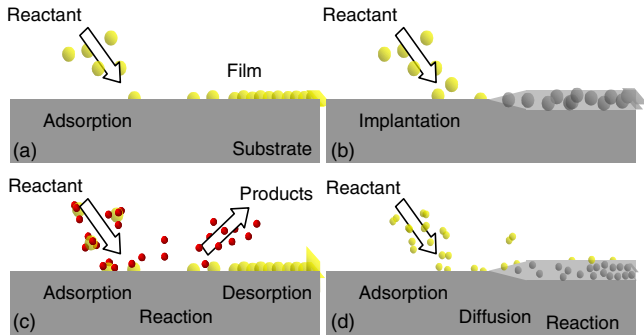
**Figure 33.** Schematics of a film formation processes from the gas phase. (a) Physical vapor deposition. (b) Physical vapor growth. (c) Chemical vapor deposition. (d) Chemical vapor growth.

temperature-controlled diffusive mass transport, which might degrade device performance in time (device drifting). The film formation process should be uniform, should be safe to use, and should cause minimal damage to structures on the chip. The process should be clean, with low particulate production and little film contamination, and should be cost effective. Finally, when a film is formed, device features generally are defined by lithographic and etch processes; therefore, each film must both perform its intended function and be compatible with overall processing sequence. That is, the film must withstand the required chemical treatment and thermal cycle while its structure remains stable. Unarguably, many parameters, such as temperature and reactant composition, will influence the formation rate depending on the mechanism involved and surface impurities sometimes play an important role and might produce unreliable results

(film delamination). This makes film formation a very difficult subject. The subdivision of film formation methods into gas, liquid, and solid states is so important that most sections have been organized in this way. The scope of this chapter is to give a short description of each of the subjects described and to emphasize those most important for microtechnology. Principles of the underlying physical and chemical phenomena are explained. In the final section, typical layers formed with these techniques will be treated, such as silicon oxide and aluminum.

## 3.1. Film Materials and Their Use

Film formation processes span a wide range of materials from inorganic to organic. Besides the typical metallic elements (e.g., Al, Cu or Au) and alloys (e.g., Ni–Fe or Pb–Sn), a plethora of exotic compounds are used to construct micromachines ranging from enzyme layers to shape memory alloys (e.g., Ni–Ti), piezoelectrics (e.g., ZnO), and superconductive materials (e.g., $YBa_2Cu_3O_{7-x}$). In Table 4, the elements are listed in the well-known periodic table. Information about a specific element and its compounds can be found by clicking on the element.

Films can be classified into three groups: conductors (e.g., metal films), semiconductors (e.g., silicon films), and insulators (e.g., dielectric films). These films can be either amorphous (e.g., glass), polycrystalline (e.g., polysilicon), or monocrystalline (e.g., epitaxial silicon). Conducting films are used for electrical interconnection, Ohmic contact to $n^+$- and $p^+$-layers, rectifying metal–semiconductor contact, catalytic and seed layers, or as electrode material in electrostatically driven devices. Semiconducting films are used

**Table 4.** Elements with their characteristics and compounds.



*Source:* Reprinted with permission from www.webelements.com.

as a conductive material for multilevel metallization, electronic material, or as a structural layer to create free moving MEMS structures. Insulating layers such as deposited silicon oxide and silicon nitride are used for isolation between conducting layers, for etching, diffusion, and ion implantation masks, for capping doped films to prevent loss of dopants, as a sacrificial layer in surface micromachining, and for passivation to protect devices from impurities, moisture, and scratches.

## 3.2. Film Stress and Strain

Stresses and strains that develop in interconnect layers and structures can greatly affect their physical integrity and long-term stability. For instance, excessive compressive or tensile stress results in failures such as cracking, blistering, and loss of adhesion (delamination or peeling), shape problems such as bending, shrinking, curling, or buckling of structures, as well as reliability problems such as void and hillock formation and long term shifts in material properties. Further, the resonance frequency of typical micromachined structures such as doubly supported (clamped–clamped) beams increases with increasing tensile stress. Also, the deflection of a diaphragm as a result of an applied pressure decreases with increasing tensile stress in the diaphragm material. If the diaphragm is used, for example, in a capacitive microphone, this leads to a reduced sensitivity. Therefore, a proper understanding of the residual stress state of the formed film is of prime importance to the MST design engineer.

Let us start with a typical example of film stress: the growth of a silica ($SiO_2$) film on top of a silicon substrate. It occurs when an oxygen atom is inserted between two silicon atoms at elevated temperatures in an oxygen or steam ambient (furnace). The Si–Si separation then increases from 2.35 to 3.08 Å [170], which implies isotropic expansion of 31%. Therefore, the oxidation of silicon induces a drastic expansion of the silicon lattice. The expansion of the layer is free in the direction toward the surface of the silica film (the $z$-direction in Fig. 34), but strained parallel to it. As a result, this anisotropic expansion induces a compressive stress $\sigma$ parallel to the surface:

$$\sigma = \sigma_{xx} = \sigma_{yy} \qquad \sigma_{zz} = \sigma_{zx} = \sigma_{zy} = \sigma_{xy} = 0 \qquad (1)$$

A direct consequence of this built-in compressive stress, $\sigma_f$, in the silica thin film (the subscript $f$ standing for film) is that the substrate itself will build up a compensating tensile
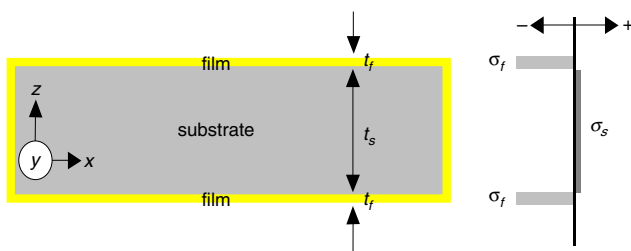
stress, $\sigma_s$, to balance forces ($\Sigma F = 0$, no translation occurs). So if a film with thickness $t_f$ is formed on both sides of a substrate with thickness $t_s$ (Fig. 34), then $\Sigma F = \sigma_f t_f + \sigma_s t_s + \sigma_f t_f = 0$ or

$$\sigma_s = -2m \, \sigma_f \qquad (2)$$

$$m = t_f / t_s \qquad (3)$$

For example, 250 nm of silica film with an assumed compressive stress of $\sigma_f = 300$ MPa, thermally grown on both sides of a 500 $\mu$m thick silicon substrate wafer, will result in a tensile stress of $\sigma_s = 300$ kPa in the silicon substrate. With the help of Hooke's law and the expression for the fractional change in length, the stretching is calculated (this relative change in length $\Delta l$ with respect to the original length $l$ is called the strain $\varepsilon$) [43]:

$$\acute{Y} = Y/(1 - \nu_s) \qquad (4)$$

$$\varepsilon = \sigma / \acute{Y} \qquad (5)$$

$$\Delta l = \varepsilon l \qquad (6)$$

Here, Poisson's ratio (see Table 5 [171]) $\nu_s$ is the lateral contraction per unit width divided by the longitudinal extension per unit length and the Young's modulus (or the modulus of elasticity) $Y$ refers to longitudinal strain with respect to the axial (or normal) stress when the load is applied in the $x$-direction and the $y$- and $z$-directions are not constraint (i.e., a beam under stress). $\acute{Y} = Y/(1 - \nu_s)$ refers to a *surface* under stress to account for the boundary condition that only the $z$-direction is free to move. Other frequently found moduli having different boundary conditions are the bulk, rigidity, and shear modulus. The bulk modulus refers to the ratio of pressure to the decrease in volume—this is the inverse of compressibility. The rigidity modulus refers to the change of shape produced by a tangential stress and the shear modulus to the deformation caused by shear or parallel stresses.

Using Eqs. (1)–(6), it is shown that a silicon substrate will be stretched for almost 200 nm along its diameter of 100 mm when a layer of 250 nm silica is grown. This means that if one transfers two times the same mask pattern to a silicon substrate—the first time just before oxidation and the second time directly after—that the pattern will not correspond anymore. Likewise, a 250 nm thick stoichiometric LPCVD silicon nitride film having a tensile stress of ca. 1000 MPa will compress the silicon wafer by almost 700 nm.

Evidently, tuning the residual stress (or strain) in a thin film formation process in the first place necessitates methods to measure the residual film stress. However, before this subject about stress diagnostics will be given, the two most common kinds of residual stresses in thin films will be



**Figure 34.** Tensile substrate stress to balance for the compressive film stress.

**Table 5.** Young's modulus $Y$ [GPa] and Position's ratio at 300 K.

| | | | | | |
|---|---|---|---|---|---|
| $Si_3N_4$ | 400 | 0.27 | quartz–glass | 70 | 0.17 |
| Si-rich $SiN_x$ | 270 | 0.27 | $SiO_2$ | 70 | 0.17 |
| Si⟨100⟩ | 140 | 0.22 | AF45–glass | 66 | 0.17 |
| Si⟨110⟩ | 170 | 0.22 | stainless-steel | 220 | 0.33 |
| Si⟨111⟩ | 180 | 0.22 | aluminum | 70 | 0.33 |

considered: thermal and intrinsic stresses. Due to the difference in thermal–mechanical properties between the film and substrate, thermal stress is usually unavoidable. Intrinsic stress is generated during film formation and is strongly dependent on process conditions. These stresses are causing, for example, structural buckling or even film fracture and the stress gradient in a single layer causing, for example, structural bending or curling.

### 3.2.1. Thermal Stress

A common source of stress in thin films is caused by differences in thermal expansion between two layers, which are tightly connected. Thermal expansion, $\alpha$, is the change in dimension of a material as its temperature is altered and depends on the material, crystal orientation, and temperature [173]. It is usually expressed as a fractional change in length per unit temperature change:

$$\varepsilon = \Delta l / l = \alpha \Delta T \tag{7}$$

Table 6 shows the thermal expansion of some materials common in microtechnology. The identical thermal expansion of Kovar steel with Pyrex glass is not a coincidence. By altering the steel composition, this expansion has been adjusted with respect to that of Pyrex to prevent high interfacial stresses—and therefore delamination or blistering—between these materials during thermal cycles in the fabrication process. It should be noted that the thermal expansion normally increases with temperature [173]. For example, for silicon this dependency is best fitted with the formula [67]

$$\alpha_{Si}(T) = 3{,}725 * [1 - \exp\{-0{,}00588 * (T - 124)\}]$$
$$+ 0{,}0005548 * T \quad [\mu m/mK] \tag{8}$$

With this expression, the total strain is calculated with

$$\varepsilon = \Delta l / l = \int_{To}^{T1} \alpha(T) \, dT \tag{9}$$

As found in Figure 35, the thermal expansion of silicon varies from about zero at 130 K to 4.5 $\mu$m/mK at 1400 K. It has an average value of about 3.9 $\mu$m/mK between room temperature and 1300 K. Likewise, silica and silicon-nitride have an average value of 0.8 and 3.2 $\mu$m/mK respectively between room temperature and 1300 K. Next, the influence of a change in temperature on a stack of layers, which are often found in microfabrication, will be treated mathematically. In the first case the growth of a thin film on both sides of a substrate, typically for CVD processes, is studied. The second case shows the result of a deposited thin film at only one side of the substrate as usually found in PVD processes or after stripping only one side after a CVD process.

**Table 6.** Thermal expansion $\alpha[\mu m/mK]$ at 300 K.

| Quartz-glass | 0.5 | Pyrex-glass | 2.6 |
|---|---|---|---|
| Si₃N₄ | 0.8 | AF45-glass | 4.5 |
| Silicon | 2.6 | stainless-steel | 17.0 |
| Kovar-steel | 2.6 | aluminum | 25.0 |
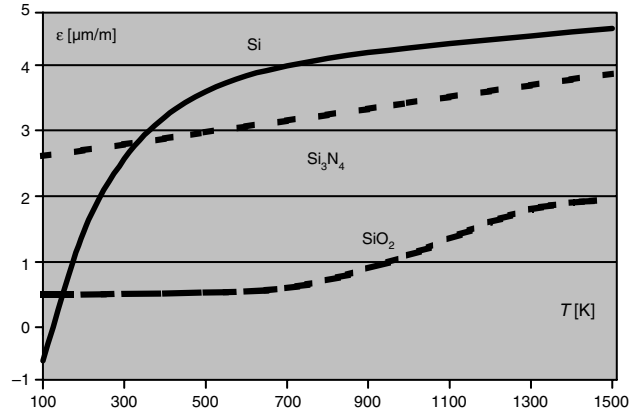


**Figure 35.** The thermal expansion of silicon compounds as a function of the temperature.

**Double-Side Film Formation** In many processes in microtechnology a layer is formed on both sides of a substrate material at elevated temperature. After cooling down toward room temperature, stress will occur. In this section the magnitude of this stress is calculated. As a typical example, the thermal oxidation of a silicon wafer at 1100 °C is taken (Fig. 36). At this temperature, the amorphous silica film with thickness $t_f$ is viscoelastic and there are no stresses in both the materials [173, 180]. However, when the temperature is lowered to 1000 °C, the silica film hardens out and stresses start to develop between the silica film and silicon substrate due to the difference in thermal expansion. Let the length of the film and substrate at $T_h$=1000 °C be $l_h$. Then, after cooling down to room temperature $T_c$, the film and substrate material would like to shrink to $l_{fc}$ and $l_{sc}$, respectively (in this case, the silicon wants to shrink more than the silica):

$$l_{fc} = l_h(1 + \alpha_f \Delta T) \tag{10}$$

$$l_{sc} = l_h(1 + \alpha_s \Delta T) \tag{11}$$

However, as the film and substrate are tightly connected, the length of the stack will be $l_c$, which is somewhere in between $l_{fc}$ and $l_{sc}$. Therefore, the film will have a strain $\varepsilon_{fc} = (l_c - l_{fc})/l_{fc}$ and, identically, the substrate will have a
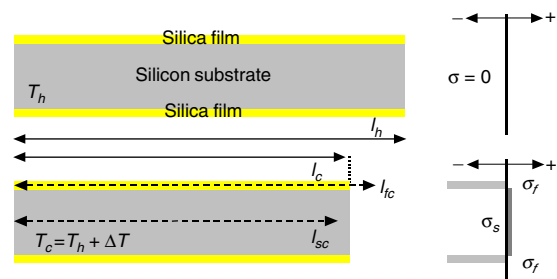


**Figure 36.** Thermal stress caused by a double-side silica film covering a silicon substrate.

strain $\varepsilon_{sc} = (l_c - l_{sc})/l_{sc}$. Due to these strains, stresses will develop:

$$\sigma_{fc} = \acute{Y}_f \, \varepsilon_{fc} = \acute{Y}_f(l_c - l_{fc})/l_{fc} \qquad (12)$$

$$\sigma_{sc} = \acute{Y}_s \, \varepsilon_{sc} = \acute{Y}_s(l_c - l_{sc})/l_{sc} \qquad (13)$$

From Eqs. (12) and (13), $l_c$ is eliminated and Eqs. (10) and (11) are used to arrive at

$$\alpha_{sf}\Delta T \acute{Y}_s \acute{Y}_f = (1 + \alpha_f \Delta T)\acute{Y}_s \sigma_{fc} - (1 + \alpha_s \Delta T)\acute{Y}_f \sigma_{sc} \qquad (14)$$

with $\alpha_{sf} = (\alpha_s - \alpha_f)$. In general, $\alpha \Delta T \ll 1$, and therefore

$$\alpha_{sf} \, \Delta T \, \acute{Y}_s \, \acute{Y}_f = \acute{Y}_s \, \sigma_{fc} - \acute{Y}_f \, \sigma_{sc} \qquad (15)$$

There is no translation of the stack ($\Sigma F = 0$). Thus $\sigma_{sc} = -2\sigma_{fc} \, t_f/t_s$,

$$\sigma_{fc} = \alpha_{sf} \, \Delta T \, \acute{Y}_f / (1 + 2mn) \qquad (16)$$

$$\sigma_{sc} = -2m \, \sigma_{fc} \qquad (17)$$

With $m = t_f/t_s$ and $n = \acute{Y}_f/\acute{Y}_s$. In most situations, $2mn \ll 1$ and therefore

$$\sigma_{fc} = \alpha_{sf} \, \Delta T \, \acute{Y}_f \qquad (18)$$

$$\sigma_{sc} = -2m \, \sigma_{fc} \qquad (19)$$

When Eq. (18) is used for the thermal oxidation of a silicon wafer at a temperature above 1000 °C, the calculated compressive stress in the silica thin film is about 280 MPa, which is indeed close to the measured value of 300 MPa [168]. Of course, both the thermal expansion and Young's modulus depend on temperature and we should have used instead

$$\sigma_{fc} = \int_{Th}^{Tc} \alpha_{sf}(T) \, \acute{Y}_f(T) \, dT \qquad (20)$$

***Single-Side Film Formation*** On many occasions a thin film exists at only one side of a substrate wafer. As an instructive example, the stress distribution inside the thermally grown silica film of the former section is taken after the bottom film is removed (Fig. 37). When the silica-silicon stack is at an elevated temperature $T_h = 1000$ °C, no stresses between the materials will occur and the structure appears straight (Fig. 37a). After cooling down to $T_c$ = room temperature, the silica film will develop a compressive film stress with approximately the same value as in case of the double-side silica film. However, due to the nonsymmetric stress, the structure will bend and the substrate will develop stress proportional to its position along the $z$-direction (Fig. 37b). To be able to predict the stresses inside the stack and the wafer curvature, the structure is best understood by considering it as a bimorph. In the bimaterial laminated plate theory, the bending is calculated by considering the so-called neutral zones $l_{fc}$ and $l_{sc}$. These are zones—one zone for each of the materials—in which no stresses exist and the zones lay not necessarily inside the layer (Fig. 37c),

$$l_{fc} = l_h(1 + \alpha_f \Delta T) = (\rho + t_n)\varphi \qquad (21)$$

$$l_{sc} = l_h(1 + \alpha_s \Delta T) = \rho \varphi \qquad (22)$$
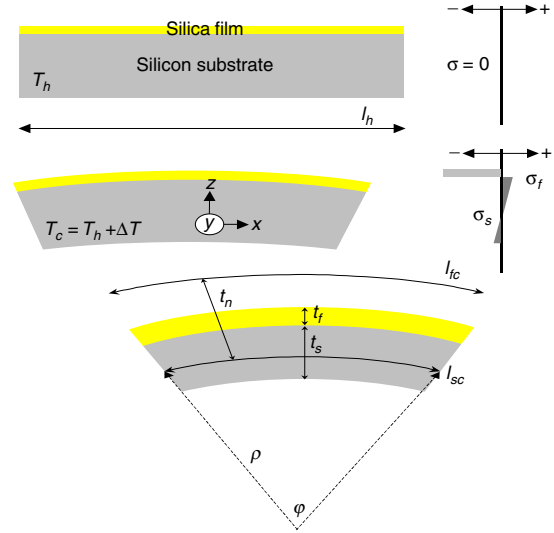


**Figure 37.** Thermal stress caused by a single-side silica film covering a silicon substrate (a), Leads to stresses and bending of the silica-silicon stack (b). Parameters to determine film stress (c).

in which $t_n$ is used to represent the distance between the two neutral zones and $\rho$ is the radius of curvature. From these equations, the angle $\varphi$ is eliminated and the radius of curvature is found:

$$\rho = t_n(1 + \alpha_s \Delta T)/\alpha_{fs} \, \Delta T \sim t_n/\alpha_{fs} \, \Delta T \qquad (23)$$

The distance between the neutral zones is found after a tedious but straightforward calculation with the help of two conditions: there is no translation and the bending of the stack is stable. $\Sigma F = \Sigma M = 0$,

$$t_n/t = 2/3 + (m^2 n - 1)^2/6mn(m + 1)^2 \qquad (24)$$

with $t = t_f + t_s$, $m = t_f/t_s$, and $n = \acute{Y}_f/\acute{Y}_s$. When $m \ll 1$ and $mn \ll 1$, as usually is the case, then

$$t_n/t \sim 1/6mn \qquad (25)$$

$$\rho \sim t/6mn \, \alpha_{fs} \, \Delta T \qquad (26)$$

Again using Hooke's law and the expression for the fractional change in length we find the stress at the surface of both materials and at their interface,

$$Surface: \quad \sigma_{fc} = \acute{Y}_f \alpha_{sf} \Delta T[-am + b]/c \sim +\acute{Y}_f \alpha_{sf} \Delta T \quad (27)$$

$$Interface: \quad \sigma_{fc} = \acute{Y}_f \alpha_{sf} \Delta T[+am + b]/c \qquad (28)$$

$$Interface: \quad \sigma_{sc} = \acute{Y}_f \alpha_{sf} \Delta T[-a - bmn]/c \sim -4m \, \sigma_{fc} \quad (29)$$

$$Surface: \quad \sigma_{sc} = \acute{Y}_f \alpha_{sf} \Delta T[+a - bmn]/c \sim +2m \, \sigma_{fc} \quad (30)$$

with $a = 3mn(m + 1)$, $b = m^3 n + 1$, $c = 9mn(m + 1)^2 + (m^2 n - 1)^2$. Notice the difference between Eq. (19) and Eq. (29).

### 3.2.2. Intrinsic Stress

Another type of stress in films is called "intrinsic" stress. This is the stress present after deposition, at the deposition temperature. There are several mechanisms that might be responsible for the generation of intrinsic stress. Typical examples include incorporation of atoms (e.g., residual gases, precipitation inclusion, or energetic ion bombardment), chemical reaction as in thermal oxidation [171, 172, 181], recrystallization, dislocation rearrangements, lattice mismatch between film and substrate, excess vacancy annihilation, grain boundary relaxation, and phase transformations. As many of these effects are strongly temperature dependent, the residual intrinsic stress is sturdily influenced by postannealing steps. Therefore, if the deposition has been performed at an elevated temperature, the residual stress measured at room temperature afterward would include contributions from both the intrinsic stress and the thermal stress and the influence of thermal annealing should be considered.

As a typical example, a single-side PECVD silica film is taken [168]. Since these films are deposited at low temperature (e.g., 300–400 °C), lack of surface diffusivities of molecules may lead to considerable porosity. As a consequence, the films contain a significant concentration of hydrogen in the range of 3–5%, which makes an important contribution on the intrinsic compressive stress, bowing the wafer with the film on the convex surface. This compressive intrinsic stress can be lowered by out gassing the incorporated hydrogen at temperatures typically around 500 °C for 1 hour in nitrogen ambient—the process of densification (Fig. 38a). Thermal stress develops in thin films when high temperatures are involved and can be reached on purpose (annealing steps) or "unintentionally" (extra LPCVD film formation steps). Therefore, in order to understand the behavior of intrinsic stress, the thermal stress component must be subtracted from the measured residual stress. For simplicity, thermal stress can be estimated based on the assumption of constant material properties: $\sigma_{fc} = \alpha_{sf}\Delta T \acute{Y}_f$ [Eq. (18)]. Figure 38b shows a typical example of the decomposition of residual stress in a single-side PECVD silica film deposited at 300 °C, where the thermal stress is assumed to be zero. Apparently, the variation of stress with temperature is due to two superimposed effects: a constant linear thermal stress component, and a time and temperature dependent nonlinear irreversible intrinsic stress component. It should
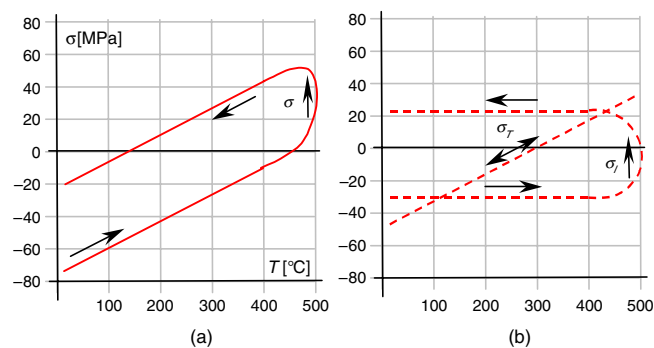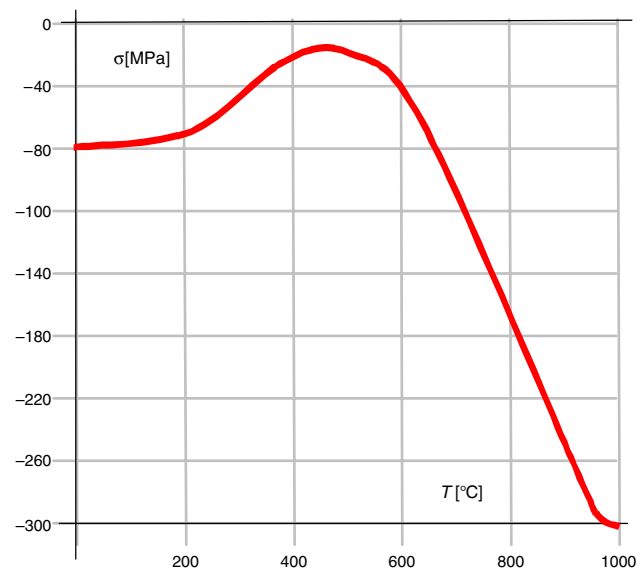
be noted that the room temperature residual stress might be identical for a longer anneal step at a lower temperature to that for a shorter anneal step at a higher temperature. In the end it is in the first place, the hydrogen content influencing the intrinsic stress.

As temperature increases, residual gases are driven out due to the increase in chemical potential. In addition, the surface diffusivities of solid structure are also enhanced. Shrinkage then occurs in order to reduce the surface energy, and room temperature tensile intrinsic stress is generated. The tendency toward shrinkage is retained as temperature increases and the hydrogen content drops to below 0.2% at temperatures higher than 750 °C. However, as the temperature further increases silica films become viscoelastic and residual stress is gradually relieved by material flow [180]. As a result, the room temperature residual stress in silica films becomes again strongly compressive when cooled from very high densification temperature exceeding 750 °C (Fig. 39). Finally, silica films become stress-free at temperatures higher than about 900 °C and the residual stress becomes solely thermal stress.

### 3.2.3. Stress Gradient

Bending of even a single-layer structure can be caused by the existence of a stress gradient and is typically observed when releasing the structural layer in surface micromachining (Fig. 40). For example, during the deposition of a layer of aluminum, it is possible that the substrate heats up due to the impact and slowly increases in temperature during deposition. This means that the initial atomic layers have been deposited at a lower temperature than the final atomic layers. Therefore, after the film has been deposited a built-in thermal stress gradient will form causing bending of the structure. Another example is found in doping silicon. Inhomogeneous doping will result in an inhomogeneous internal stress gradient. Also, the formation and growth of grains in polycrystalline films as found in most metallic films will



**Figure 39.** Room temperature residual stress as function of the anneal temperature.



**Figure 38.** Residual film stress during a 500 °C anneal (a). Decomposition of residual stress into thermal and intrinsic stress (b).

**Figure 40.** Stress gradient in a single layer.

cause a stress gradient. For the formation of nanofilms it is important to realize that the initial layers ($<10$ nm) vary considerably in stress due to the mismatch with the underlying lattice of the substrate [183]. If the temperature during formation of a film with thickness $t_f$ increases with $\Delta T_{\text{form}}$, then the radius of curvature will be

$$\rho = t_f/(\alpha_f \Delta T_{\text{form}}) \tag{31}$$

### 3.2.4. Film Fracture

The ability to deposit films is limited by residual stress, which can result in substrate distortion or cracking of the film or even of the substrate. These stress problems tend to increase with thickness and annealing temperature and are a prime limitation to the deposition of very thick thin films. The excessive wafer-bow after densification causes difficulties for subsequent lithographic processing. Moreover, since wafer curvature (in case of single-side film formation processes) and film cracking both seriously impact process integrity and device reliability, it is important to elucidate the factors contributing to residual stresses in thin films and optimize the film formation process so as to reduce wafer curvature and to avoid film cracking. The critical annealing temperature at which cracking occurs can be predicted using mixed mode fracture mechanics as will be briefly treated in this section. Finally, some engineering solutions will be discussed to overcome fracture.

It is well known that film cracking only occurs when the film experiences a tensile stress. For example, since the thermal expansion of a silica film is less than that of silicon, cooling from the deposition temperature leads to compressive stresses in the silica film and will not result in failure. However, since the critical stress for shear flow in Si at 1000 °C is about 3.4 MPa, it is entirely plausible to see plastic deformation of silicon beneath discontinuities in growing $SiO_2$ layers (near the edges of windows, etc.) [181, 185]. The fracture mechanics of thin films has been analyzed by Hutchinson and Suo [167] and Zhang et al. [168]. The strain energy release rate $G_f$ [J/m$^2$] for a crack propagating in a thin film is given by

$$G_f = Z t_f \sigma_f^2 / \acute{Y}_f \tag{32}$$

$Z$ is a dimensionless parameter which depends on the particular cracking pattern. For example, short microcracks at the surface are often initiated from the edge and arrested by the interface. Sometimes the film exhibits long channelling cracks and a connected channel network surrounding islands of the intact film. For the microcracks $Z \sim 4$ and for the long cracks $Z \sim 2$. Fracture occurs when $G_f$ exceeds the intrinsic fracture energy $G_{\text{frac}}$ of the film material: $G_f > G_{\text{frac}}$. Using Eqs. (18) and (31) and $\sigma = \sigma_T + \sigma_I$ ($\sigma_I$ is the intrinsic stress at a certain temperature), the critical temperature

for fracture $T_{\text{frac}}$ can thus be expressed as a function of film thickness $t_f$:

$$T_{\text{frac}} > T_0 - (\sigma_I/\acute{Y}_f \alpha_{sf}) + \sqrt{(G_{\text{frac}}/Z\acute{Y}_f t_f \alpha_{sf}^2)} \tag{33}$$

Apparently, $T_{\text{frac}}$ decreases with increasing intrinsic tensile film stress, increasing difference in thermal expansion between the substrate and film $\alpha_{sf}$, and the square root of the film thickness.

### 3.2.5. Stress and Strain Diagnostics

Several methods have been developed to measure residual film stress, for instance wafer curvature, load-deflection technique (bulge method), dynamic methods relying on the shift of the resonant frequency in atomic force microscope (AFM) cantilevers, and *in-situ* micromachined stress and strain diagnostics.

*Wafer Curvature* A common way to measure stress in a film is by measuring how much a substrate bends after the film is deposited or processed (i.e., wafer curvature). In the absence of any movement restraints, the structure in Figure 41 will bend in order to balance the force moments caused by the stresses. For the top film in compressive stress (it wants to expand more than the bottom layer), as is the case in this example, the entire structure will bend with the edges downward relative to the middle. The amount of bending is dependent on the internal mechanical properties of the film and substrate (specifically Young's modulus and Poisson's ratio), the thickness, and the stresses in the film and substrate. By measuring the amount of bending, and knowing the film thickness and mechanical constraints, one can extract the stress in the film. If we assume that the film thickness is much smaller than the thickness of the substrate and that the film is in an isotropic biaxial stress state (i.e., $\sigma_z = 0$ and $\sigma_x = \sigma_y$), then the biaxial stress in the film $\sigma_f(=\sigma_x = \sigma_y)$ as derived from Eqs. (26) and (27) equals [178, 179]

$$\sigma_f = \frac{\acute{Y}_s}{6} \frac{t_s^2}{\rho t_f} = \frac{4}{3} \frac{Y_s}{(1 - \nu_s)} \frac{t_s^2 \delta}{D^2 t_f} \tag{34}$$

Here $Y_s$ is Young's modulus of the substrate, $\nu_s$ is Poisson's ratio for the substrate (typically $\nu_s = 1/4$), $t_s$ is the substrate thickness, $\rho$ is the radius of curvature (i.e., a measure of
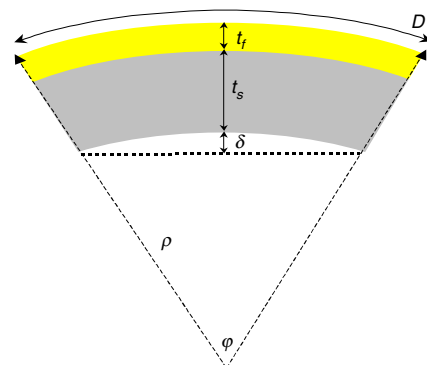


**Figure 41.** Wafer curvature.

the bending), and $t_f$ is the film thickness. Alternatively, the deflection $\delta (\sim D^2/8\rho$ using simple goniometric considerations) at the center of a surface scan over a distance $D$ is a measure for the residual stress. In practice, the deflection or curvature is measured before and after the film is deposited (or before and after the film is processed in some way), since the wafer might not be flat to start with. Thus $1/\rho$ would be given by $(1/\rho_{\text{final}} - 1/\rho_{\text{initial}})$. The difference in curvature is then related to the stress induced by depositing or processing the film.

***Micromachined Diagnostics*** Specific freely suspended (freestanding) micromachined structures are often realized which, because of their sensitivity to residual stress, are useful for making *in-situ* measurements of residual stress. For instance, average compressive strain can be measured by determining the critical buckling length of clamped–clamped beams (Fig. 42a). For this, an array of clamped–clamped beams with stepwise increasing length is realized. The transition length between buckling and nonbuckling provides information on the residual compressive stress in the film. However, when the thin film exhibits a stress gradient in the normal direction, the buckling load is often decreased enormously. Tensile stress can be measured by a series of ring and beam structures, which are constrained to the substrate at two points (Fig. 42b). Tensile stress in the film results in a compressive load on the beam as shown. Curvature of a cantilever (single-supported) beam is a measure for the stress gradient in the direction of the film thickness (Fig. 42c). Other stress-diagnostic structures are so-called $T$ and $H$, diamond, and push–pull structures, and rotating pointers with or without Vernier gauges (Fig. 42d).

## 3.3. Film Adhesion

Film adhesion is an important property to be considered in film formation. Due to insufficient adhesion, freshly applied films can locally detach or even delaminate from the substrate. Evidently, this delamination is undesirable and proper surface modification is needed to promote correct film attachment to the substrate. Sometimes the adhesion can be improved simply by cleaning the substrate surface, but these solvents usually remove only oils and greases, leaving more tenacious materials such as surface oxides, which may prevent interdiffusion and thus adhesion. For films
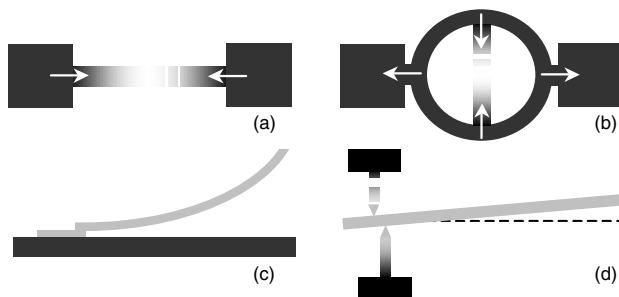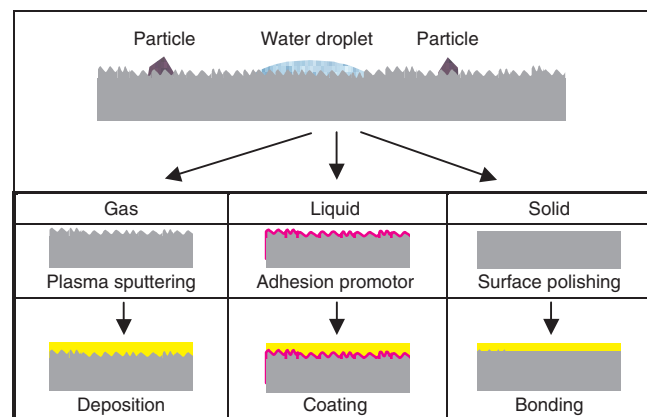
formed from the gas phase, the adhesion is generally promoted by including plasma presputtering, which removes the surface oxide, before forming the new layer (Fig. 43). In case of liquid-phase film formation, (chemical) surface modifiers are coated prior to the new film being formed. In case of solid-phase-formed films, surface properties such as roughness are important and, therefore, the substrate is commonly polished before the next layer is formed.

## 3.4. Film Step Coverage, Planarization, and Capping

In general, before forming a new thin film, the surface of a substrate will have a complex topography (Fig. 44). Trenches and patterned layers from earlier process steps will cover the surface. Conventional methods experience difficulty in depositing metals or oxides conformal on such stepped surfaces. In many cases, more film tends to build on top surfaces than into trenches or at their sidewalls, showing a pronounced tendency for narrow spaces to be covered before completely filled, creating voids. Step coverage relates the surface topography of a deposited or grown film to the previous wafer irregularities. Films formed from the gas phase differ from films from the liquid phase in what kind of forces control the layer thickness along these surface steps. The same accounts for films deposited from the solid phase. For gas-phase-formed films, the layer thickness largely depends on the phenomena from the individual atoms such as gas-phase collisions and surface migration. In the case of liquid-phase-formed films, bulk properties of the deposited film are more important such as gravitational forces, surface tension, and wettability. To improve step coverage an option is to etch back a formed layer using polymer or spin-on-glass (SOG) with subsequent plasma etching or CMP.
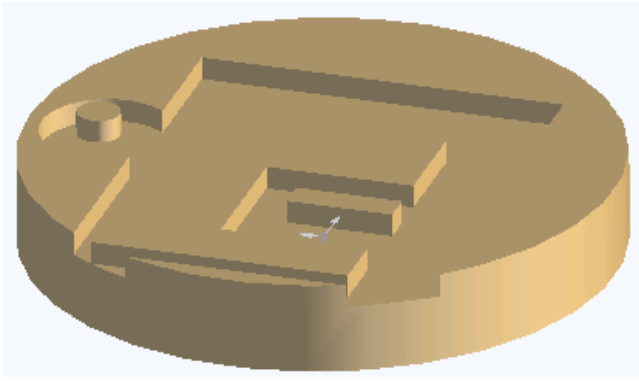
### 3.4.1. Gas-Phase Film Formation

In this overview, the term step coverage is used when the film is formed out of the gas phase. The layer thickness along the step largely depends on the trajectory of the individual particle in the gas phase and on the substrate surface before coming at rest. In the gas phase we have to consider the mean free path between collisions of the particle before reaching the substrate surface. Then, when a particle



**Figure 42.** Stress and strain diagnostics: (a) Clamped–clamped beam to measure compressive stress. (b) Ring and beam to measure tensile stress. (c) Cantilever beam to measure stress gradient. (d) Pointer beam to measure tensile or compressive strain.



**Figure 43.** Surface treatment to improve adhesion.

**Figure 44.** Processed wafer surface during MEMS processing.

has reached the surface, the required reaction analysis is the same, regardless of the formation method. In the ideal, or conformal, step coverage film, the thickness is uniform along all surfaces of the step (Fig. 45). This conformal coverage is due to the rapid migration of reactants after adsorption on the step surface and before a bond is established with the underlying substrate.

The molecular phenomena at the surface to be considered include thermally activated processes such as sticking coefficient, surface adsorption, surface diffusion, surface reaction, desorption, and film or crystal growth. A process controlling step coverage and trench filling issues is that of desorption of reacting species before any reaction can occur. This is related to the sticking probability and becomes important in low-pressure systems, since the desorbed species redeposit elsewhere such as the sidewall of a trench or contact hole. In CVD processes the emission and redeposition process may occur quite readily, corresponding to a low sticking coefficient, and can lead to better coverage. Surface migration or diffusion can also occur on a more long-range scale on nonflat topographies due to surface curvature and surface energy reduction considerations. This can affect coverage and filling in a similar manner to sticking probability. Surface migration is increasing with the kinetic energy of the adsorbed species and, therefore, a higher temperature will normally improve step coverage. High-temperature CVD deposited polysilicon and silicon nitride, and thermally grown silicon oxide, often show conformal step coverage. In physical vapor deposition (PVD), the sticking probability of the depositing species is usually very close to one, meaning that they stick where they hit and there is little or no redeposition of material to other regions. Surface diffusion is also very slow at low temperatures. In addition, there is also no resputtering of material in evaporation systems, as in the case of PECVD or sputter PVD, due to ion bombardment.
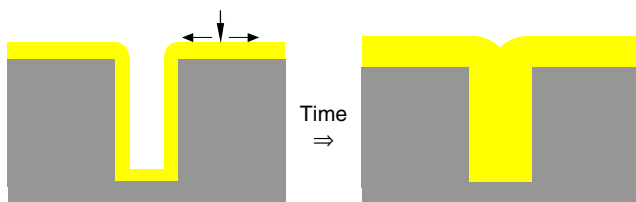
All these issues lead to very poor step coverage. Clearly, heating the substrate during deposition may improve step coverage.

At lower temperatures, the surface migration is minimal and gas-phase collisions determine step coverage. Two major categories can be distinguished: low-pressure direct line-of-sight impingement methods and high-pressure diffusive–convective mass transfer techniques.

At the lower pressures employed in a PVD reactor, the vaporized material encounters few intermolecular collisions while travelling to the substrate. Modeling of deposition rates is a relatively straightforward geometrical line-of-sight exercise in this case. Figure 46 shows an example of a nonconformal step coverage, which results when reactants travel almost without intermolecular gas-phase collisions and adsorb and react without significant surface migration. In this instance the deposition rate is proportional to the arrival angle of the gas molecules. Reactants arriving along the top horizontal surface come from many different angles and $\phi_1$, the arrival angle, varies in two dimensions from 0 to 180° while reactants arriving at the top of a vertical wall have an arrival angle $\phi_2$ that varies from 0 to 90°. Thus the film thickness on the top surface is double that of a corner wall. Further down the wall, $\phi_3$ is related to the width of the opening, and the film thickness is proportional to $\phi_3 \approx$ arctan $(W/H)$ where $H$ is the distance from the top surface and $W$ is the width of the opening. This type of step coverage is thin along the vertical walls, with a possible crack at the bottom of the step caused by self-shadowing. Most evaporated or sputtered metal films have step coverage similar to this. As will be found in the section concerning resist lithography this type of step coverage can be used for lift-off pattern transfer.

In the case of a CVD reactor, the diffusive–convective transport to the substrate due to the higher pressures used involves many intermolecular collisions (except for deep trenches smaller in dimension than the mean free path between collisions). Accordingly, mass and heat transfer modeling of deposition rates becomes more complex. In Figure 47, the mean free path is too short to reach the bottom and there is little surface migration. In such cases, the film thickness is directly proportional to the range of feasible angles of arrival, $\phi$, of the depositing species. The arrival angle at a planar surface is $\phi_1 = 180°$. At the top of a vertical step, the arrival rate is nonzero over a range of $\phi_2 = 270°$; the resultant film thickness is 270/180, or 1.5 times greater than for the planar case. At the bottom corner of a



**Figure 45.** Ideal (conformal) step coverage. Rapid surface migration.
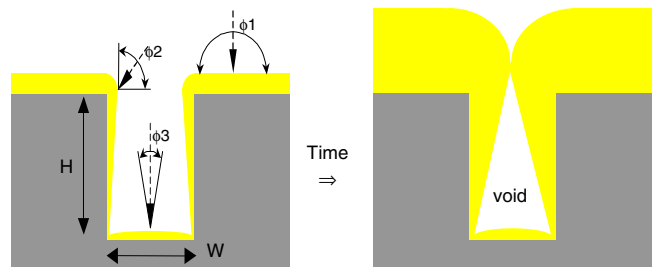


**Figure 46.** Non-conformal step coverage. Little surface migration and large mean free path.
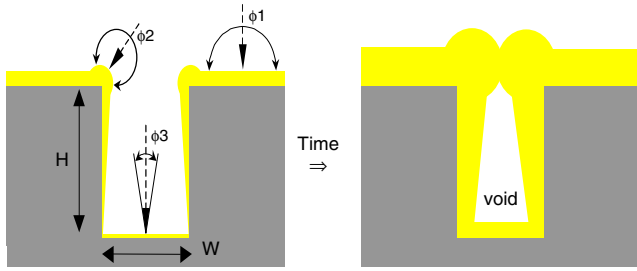
**Figure 47.** Nonconformal step coverage. Little surface migration and small mean free path.

trench the arrival angle is only 90°, and the film thickness is 90/180, or one-half that of the planar case. The CVD profile of Figure 47, where the mean free path is short compared to the trench dimensions and there is no surface migration, reflects the 90, 180, 270 arrival angles. The thick cusp at the top of the step and the thin crevice at the bottom combine to give a reentrant shape that is particularly difficult to cover with PVD material in a subsequent process step. Gas depletion effects also are observed along the trench walls. Low-temperature plasma-deposited silicon oxide and silicon nitride are typical examples of this kind of step coverage.

### 3.4.2. Liquid-Phase Film Formation

For films formed from a liquid solution, bulk properties of the film and substrate determine the step coverage of the formed layer. Important phenomena to consider are surface free energy, wettability, and viscosity and include inertia effects caused by fast rotation in a spindle as in spin coating. In general, the term planarization is used in such cases. In the ideal case, the deposited film will perfectly fill any surface irregularity and forms a flat surface as shown in Figure 48. This result is then called full or ideal planarization.

When planarization is not ideal, the term degree-of-planarization (DOP) is used, defined as DOP = $(1 - [T_{plan}/T_{step}])$ as shown in Figure 49. A smoothing liquid should exhibit two properties, that is, filling in gaps and flattening of a film's top surface. Currently, polyimides and BCB polymers are able to planarize large pitch geometry to a 95% level with a single coat. Reluctance to expand the use of polyimide as an insulating material at this point is linked to its poor barrier properties toward moisture and ions. It is important to notice that the DOP depends on the dimension of a trench; a small but deep trench ($T_{plan1}$ in Fig. 49) is much easier to planarize than a wide trench ($T_{plan2}$). Clearly,
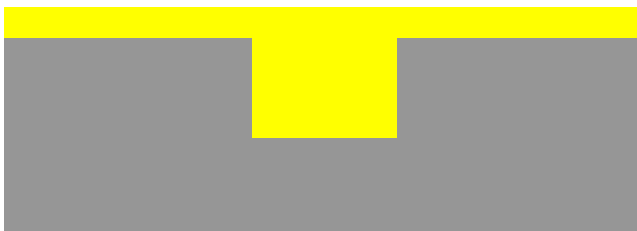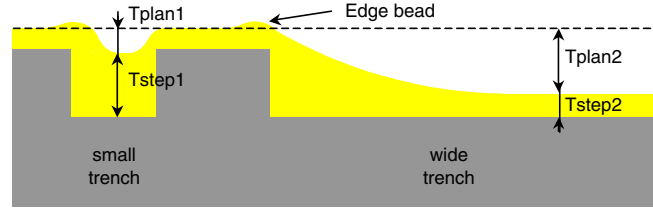


**Figure 49.** Degree of planarization (DOP).

the thickness of the coating at the bottom of the trenches far away from the edges of structures will be identical to the thickness of the coating on top of the structures, again far away from edges. Another phenomenon (typically observed during spin-coating) is the forming of so-called edge bead at the edges of structures (including the edge of the wafer). It is caused by the influence of centrifugal forces on the surface tension forces.

### 3.4.3. Solid-Phase Film Formation

When a film is formed from the solid phase, such as the placement of a foil—by way of lamination or bonding—on top of a structured surface, bulk properties of the solid film, such as the modulus of elasticity and stress relaxation, determine the step coverage. In such cases, film capping can be used as a measure to describe the step coverage. In the ideal case, the film will nicely stretch along the valleys forming a straight bridge or membrane cap as found in Figure 50. This result is then called ideal capping. In general, a thicker film is much more difficult to deform than a thin film. Therefore, thick films such as bonded wafers on top of patterned substrates look like the perfect capping.

In general, the newly formed film will cap trenches and holes and, therefore, gas inclusion (including vacuum inclusion) cannot be prevented. The difference in pressure between the capped volume and the environment will cause bending of the film as shown in Figure 51. Film stress caused by differences in (thermal) extension between the substrate and the film will have the same effect. For example, when the film is under compressive stress, the film might buckle and deform as indicated in Figure 51. When the film creates a tensile stress with respect to the underlying substrate, the film will nicely stretch across the valley and will have an almost perfect capping.

### 3.5. Film Mixing/Alloying

Bimetallic systems exhibit eutectic characteristics; that is, the addition of either component lowers the system's melting point below that of either metal. For example, in the



**Figure 48.** Ideal planarization.
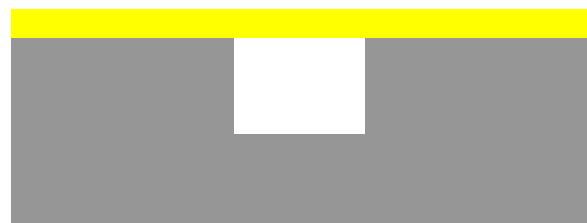


**Figure 50.** Ideal capping.

**Figure 51.** Film deformation.

Al–Si system the minimum melting temperature, called the eutectic temperature, is 577 °C, corresponding to an 11.3% Si–88.7% Al composition. The melting points of pure aluminum and pure silicon are 660 and 1412 °C respectively. Because of the eutectic characteristics, during aluminum deposition the temperature on the silicon substrate must be limited to less than 577 °C. Hence, wherever aluminum contacts silicon, the silicon will dissolve into the aluminum during annealing. For example, the solubility $S$ of silicon in aluminum is 0.25 wt% at 400 °C and $S = 0.8$ wt% at 500 °C. The opposite, that is, the dissolving of aluminum into silicon, will also occur but is only pronounced at temperatures close to the melting point of silicon. The amount of silicon dissolved will depend not only on the solubility at the annealing temperature but also on the volume of aluminum to be saturated with silicon. Consider a long aluminum metal line with a thickness $H$ and a width of $W$ in contact with an area of $WZ$ of silicon. After an annealing time $t$, the silicon will diffuse a distance of approximately $\sqrt{(Dt)}$ along the aluminum line from the edge of the contact, where $D$ is the diffusion coefficient given by $0.04 \exp(-0.92/kT)$ for silicon diffusion in deposited aluminum films. Assuming that this length of aluminum is completely saturated with silicon, the depth to which silicon will be consumed is

$$b \sim 2(H/Z)S\sqrt{(Dt)} \qquad (35)$$

The diffusion coefficient of silicon in aluminum at 500 °C is about $D = 2 \times 10^{-8}$ cm$^2$/s and $S = 0.8$ wt%. Therefore, after a time $t = 30$ min, $\sqrt{(Dt)}$ is 60 $\mu$m. When $Z = 1$ $\mu$m and $H = 1$ $\mu$m, aluminum will fill a depth of ca. 1 $\mu$m from which silicon is consumed. In a practical situation, the dissolution of silicon does not take place uniformly but rather at only a few points. Therefore, the effective area is less than the actual contact area. Hence $b$ is much larger. In such situations spikes are formed at only a few points where aluminum is penetrating the silicon. One way to minimize the aluminum spiking is to add silicon to the aluminum by co-evaporation until the amount of silicon contained by the alloy satisfies the solubility requirement. Another option is to form a layer in between the two mixing layers (i.e., a barrier layer such as tantalum or titanium).

## 3.6. Film Structure

Thin films are formed to establish specific electrical, mechanical, or chemical properties. It is well known that these properties may be quite different from those of the bulk, particularly if the film thickness is very small. These "anomalous" properties are due to the peculiar (nano)structure of the film. This structure—in turn—is dictated by processes which occur during film formation. So the film formation method, the film thickness, and the resulting film structure greatly affect the film properties. The film structure is characterized by crystallographic orientation, texture, defects, crystal size, and morphology. Evidently, many parameters will affect the film structure such as the energy and direction of the incoming particles, its binding energy to the substrate and to each other, the temperature of the substrate, surface mobility, substrate surface morphology (crystalline, amorphous, rough, etc.), deposition rate, and the presence of "alien" particles. The surface morphology of surfaces can be subdivided into three types: monocrystalline, polycrystalline, and amorphous as shown in Figure 52. In crystalline solids (Fig. 52a), the atoms are neatly stacked and this order extends to macroscopic dimensions. Polycrystalline films are different and can be either microstructured or nanostructured (Fig. 52b). Microstructured films show structural variation (morphology) on a micrometer scale. In nanostructured films (also called nanophase films), this variation has decreased to nanoscale dimensions. Finally, amorphous films (Fig. 52c) exhibit short-range order only—the average distance between neighboring atoms or molecules corresponds to the film density. Because the nanoscale lies in between the microscopic and the atomic scale, it is also referred to as the mesoscopic domain (meso = Greek for middle).

The first (initial) formed monolayers of a film often determine the resulting film structure and therefore, in general, two stages are distinguished in film formation: the initial stage (nucleation, island, and coalescence) and actual stage
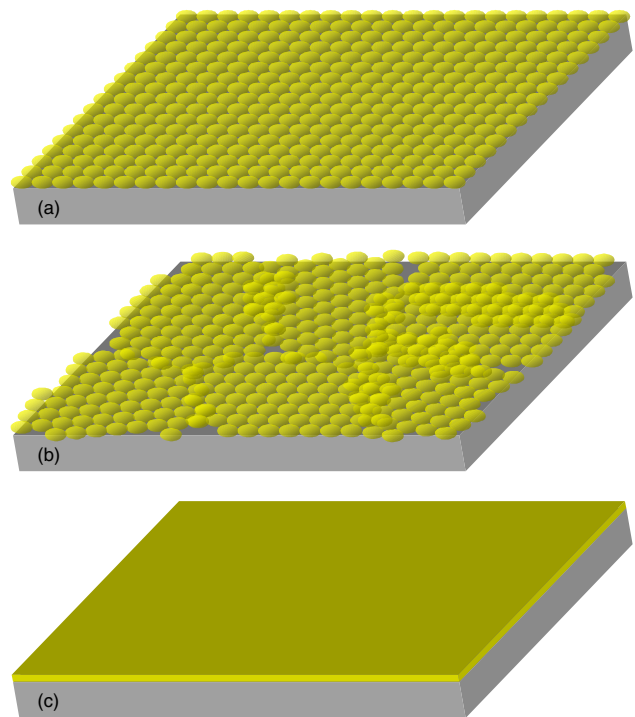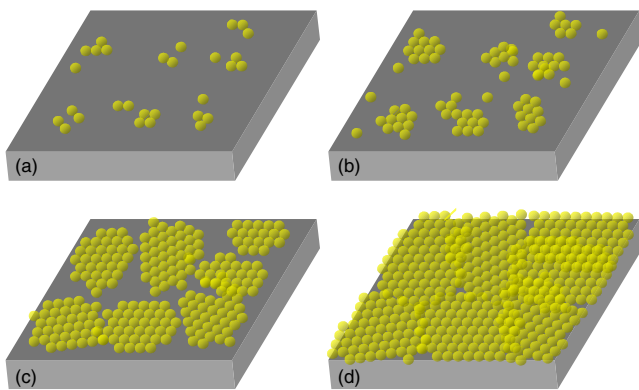


**Figure 52.** Film structure. (a) Monocrystalline. (b) Polycrystalline. (c) Amorphous.

as shown in Figure 53. During the initial stage, chemical and physical properties of the substrate, and interaction between substrate and particles (atoms or molecules) arriving, play an important role. The process of nucleation (Fig. 53a) can be briefly described as follows: incoming particles collide with the substrate surface, adsorb, migrate (up to 50 nm or more), collide with each other, cluster, and show a stable condensate when a specific critical dimension is reached. Energetically, the surface of a (crystalline) substrate surface is like an egg carton, with each of the depressions constituting a temporary resting point or adsorption site for the depositing and migrating atoms. At each "hop," the atom will either jump over the barrier into an adjacent site or might reevaporate (a measure for this is the sticking probability). After a time, the atom will either evaporate from the surface or will join another migrating atom to form a doublet, which is less mobile and more stable than a single atom. The change of forming a doublet will depend on the single atom density and hence on the arrival rate and sticking probability. In time, the doublets will be joined with other atoms to form triplets, quadruplets, and so on. This leads to the formation of quasi-stable islands, each containing tens or hundreds of atoms at a density of $10^{10}/cm^2$ (i.e., one island every 100 nm). Growth of the islands is three-dimensional, but the growth parallel to the substrate is greater than that normal to it. This is probably because deposition occurs largely by the surface diffusion of monomers on the substrate, rather than by direct impingement from the vapor phase. During the next phase of the initial stage (Fig. 53b), the islands grow in size rather than in number. Each island is usually single crystal or contains just a few crystals. Eventually, the islands grow large enough to touch—this is the agglomeration or coalescence stage (Fig. 53c). Coalescence proceeds until the film reaches continuity (Fig. 53d), but this may occur in some cases until the film is several tens of nm in average thickness. During the initial formation, the film typically consists of hills and valleys. The initial phase is known well and experimentally observed with for example, transmission electron microscopy and it appears that the islands often display liquidlike behaviour during coalescence. There are often crystallographic reorientations as a result of competition between the structures of the coalescing islands.



**Figure 53.** Film deposition stages. (a) Nucleation stage. (b) Island stage. (c) Coalescence stage. (d) Actual stage.

On a monocrystalline substrate, the islands orientations may be determined by the substrate structure so that nucleation and coalescence lead to a single crystal film. This is the phenomenon of epitaxy. If surface atoms are mobile, they have a greater opportunity of finding low energy positions, consistent with the crystal lattice. Mobility is enhanced by increased substrate temperature, but since it also takes time to find an energetically favorable lattice position, crystal formation is also encouraged by low deposition rates. Hence, on single crystal substrates, for each deposition rate there will be a temperature, the epitaxial temperature $T_{epi}$, above which single crystal films can be formed. Obviously, on a polycrystalline substrate the orientation of the resulting film is polycrystalline too, but on an amorphous substrate the surface lattice will be random and the initial deposition will favor the ⟨111⟩-orientation due to the higher packing density. The same mechanisms hold as in single crystal formation so that high substrate temperature and low deposition rate lead to large grains and low density of crystal defects.

After an initial layer—covering the substrate—has formed, actual formation begins, during which only interaction occurs between particles of the film material. Important parameters are the energy of the particles arriving at the film surface, energy absorption at the time of collision, chemical and physical interaction between adatoms and film surface, pressure, and temperature. These parameters determine, to a great extent, the morphology (overall shape of the film and the geometry of crystallites or amorphous structures inside the film) and texture (orientation of crystallites). The structure of the film is found to be extremely sensitive to deposition conditions. For example, high-energetic electron or ion bombardment either prior to or during deposition is found to encourage film continuity and reduce epitaxial temperatures. Several mechanisms can cause the formation of oriented layers. If the lattice constants of substrate and film material approximately match each other, epitaxial deposition can occur and even if they do not match, oriented deposition is often observed. Increase of orientation during actual deposition is based on different deposition rates of the crystal planes. Starting from random crystal orientation in the initial layer, crystals with the fastest depositing crystal plane parallel to the substrate, such as the (111)-plane, "survive" at the cost of the others. This phenomenon is also known as "survival of the fastest" and implies a related increase of crystal orientation and grain size with film thickness (taperwise film formation). Even when the film is initially well oriented, taperwise film formation might occur due to thermodynamically driven coalescence of crystallites (grain-boundary movement).

In general, the morphology of the film is greatly affected by the temperature of the substrate $T_s$ and the melting temperature $T_m$ of the film material. There is a trend with increasing temperature for the morphology to change from amorphous to fine-grained polycrystalline to polycrystalline to monocrystalline. When $T_s < 0.3T_m$, called zone I, amorphous or porous layers with rough surfaces are formed due to low adatom mobility (slow surface diffusion) and shadowing. When $0.3T_m < T_s < 0.45T_m$ (i.e., zone II), adatom mobility is high enough to overcome the shadow effect and deposition is controlled by surface diffusion, resulting in more dense layers with small columnar grains. When

$0.45 T_m < T_s < T_{epi}$, zone III, due to bulk diffusion, smaller grains coalesce to form larger, not necessarily columnar, grains. Finally when $T_s > T_{epi}$, epitaxial layers might form at single-crystalline substrate surfaces because grains and boundaries vanish. Homogeneous gas-phase reactions might incorporate nanosized particles into a film during deposition, altering the film morphology. The impact of fast moving particles from the gas phase alters film morphology even further. For example, due to collisions with argon ions (in plasma enhanced deposition), the energy of the particles arriving at the surface decreases with argon pressure, leaving less energy for surface diffusion. Besides, at high pressures, adsorbed argon limits adatom mobility. Therefore, the transition temperatures between zone I and II increase with pressure. The transition temperature between zone II and III is independent of pressure, since this transition is determined by bulk diffusion.

## 3.7. Film-Formation Methods

Considerations in selecting a film formation process are, for example, the substrate temperature and morphology, film deposition rate, uniformity, structure, stress and adhesion, electrical and mechanical properties, and chemical composition and inertness of the films. In general, for the deposition of thin films used in microelectronics, low-pressure gas-phase processes are preferred over the older conventional chemical liquid-phase methods such as electroplating, because deposition from an aqueous solution often produces poorer quality films. On the other hand, electrochemical deposition is gaining renewed interest with microstructures because of their emerging importance to replication of photoresist molds. As listed in Table 7, thin films can be formed by various methods and are conveniently divided into deposition or growth from the gas phase, liquid phase, and solid phase. The methods include chemical vapor deposition, physical vapor deposition, chemical vapor growth (CVG), and physical vapor growth (PVG). The most common CVD processes are low-pressure CVD, atmospheric-pressure CVD, VPE, plasma-enhanced CVD, metal-organic CVD, and pyrolysis. Well-known PVD processes are evaporation, laser ablation, plasma sputter deposition, MBE, cluster beam, and ion plating. The vapor growth group has only a few members; thermal oxidation and diffusion (both CVG) and ion implantation (PVG). Liquid-phase film formation methods, involving thin and thick organic materials, are of extreme importance to the construction of chemical and biological sensors. Except for liquid-phase epitaxy and self-assembling monolayers (SAMs), most chemical liquid deposition (CLD) processes are electrochemically driven, such as electroplating, immersion plating, and electroless plating. Physical liquid deposition (PLD) processes are all kinds of coating techniques such as spinning, dipping, spraying, painting, casting, and melting. There is only one practical electrochemical liquid growth (ECLG) method: anodization. The solid-phase film formation is important in packaging and the development of encapsulated mechanical structures. We can distinguish between physical solid deposition (PSD) methods (including direct, anodic, adhesive, eutectic, and compression bonding) and chemical solid growth (CSG) methods (solid-source diffusion such as doping).

### 3.7.1. Chemical Vapor Deposition

During chemical vapor deposition, the constituents of a vapor phase, often diluted with an inert carrier gas, are introduced into a reaction chamber and adsorbed on a heated surface. The adatoms undergo migration and film-forming reactions to form the desired film. In CVD, the diffusive–convective transport to the substrate involves many intermolecular collisions. Therefore, the reactions forming a solid material do not always occur on or close to the heated substrate (heterogeneous reactions) but can also occur in the gas phase (homogeneous reactions). As homogeneous

**Table 7.** Film formation methods.

| State | Technique | Example | State | Technique | Example |
|-------|-----------|---------|-------|-----------|---------|
| Gas | (V)LP CVD | W | liquid | electroplating ECLD | Cu |
| Gas | AP CVD | $SiO_2$ | liquid | immersion plating ECLD | Zn→Cu |
| Gas | VPE/AP CVD | epi | liquid | electroless plating ECLD | Au |
| Gas | (HD)PE CVD | SiN | liquid | LPE CLD | epi |
| Gas | MO CVD | Al | liquid | SAM CLD | softlitho |
| Gas | pyrolysis CVD | Si | liquid | spin and dip coating PLD | Resist |
| Gas | evaporation PVD | Al(Cu) | liquid | spray and paint coating PLD | Wires |
| Gas | laser ablation PVD | | liquid | cast and melt coating PLD | lithography |
| Gas | sputtering PVD | Pt | liquid | anodization ECLG | $Ta_2O_5$ |
| Gas | MBE PVD | epi | solid | direct bonding PSD | Si/Si |
| Gas | cluster beam PVD | | solid | anodic bonding PSD | Si/Pyrex |
| Gas | ion plating PVD | | solid | adhesive bonding PSD | Si/Riston |
| Gas | thermal CVG | | solid | eutectic bonding PSD | Si/Au |
| Gas | diffusion CVG | B | solid | compression bonding PSD | Au/au |
| Gas | ion implantation PVG | B, epi | solid | solid-source diffusion CSG | doping |

reactions lead to gas-phase cluster deposition and result in poor adhesion, low density, and high defect films (pinholes), heterogeneous reactions are preferred. The most favorable end-product of a CVD reaction is a stoichiometric-correct film. Several activation barriers need to be surmounted to arrive at this stoichiometric film. Some energy source, such as thermal, photons, electron or ion bombardment, is required to achieve this. The CVD method is very versatile and can create amorphous, polycrystalline, uniaxially oriented polycrystalline, and epitaxial layers with a high degree of purity and control. Figure 54 illustrates the various transport and reaction processes underlying CVD with the numbers representing the following:

1. mass transport of reactant gases and diluents in the bulk gas flow region to the deposition zone
2. homogeneous gas-phase reactions leading to film precursors and by-products
3. mass transport of film precursors and reactants to the substrate surface
4. adsorption of film precursors and reactants on the substrate surface
5. heterogeneous surface reactions of adatoms occurring selectively on the heated surface
6. surface migration of film formers to the deposit sites
7. incorporation of film constituents into the depositing film, that is, nucleation (island formation)
8. desorption of by-products of the surface reactions
9. mass transport of by-products in the bulk gas flow region away from the deposition zone

A full treatment of the kinetics of CVD processes would involve all the steps in Figure 54. However, it is often sufficient to consider the fluxes for the mass transport (i.e., diffusion) and surface reactions processes only and equate them under steady state conditions.

**Diffusion-Controlled Processes** The mass transport in the gas phase takes place through diffusion proportional to the diffusivity of the gas $D$ and the concentration gradient $\Delta c$ across the boundary layer that separates the bulk flow (source) and substrate surface (sink). The flux of deposited material is found with the help of Fick's first law: $\phi = D\, dc/dx = D(3\Delta c/2L)\sqrt{R_e}$, where $L$ stands for the length

of the plate being deposited on and $R_e$ is Reynolds number which is proportional to the gas flow velocity $U$ and inversely proportional to the source gas molecular weight $M$. According to this equation, the film deposition rate $DR$ should depend on the square root of $U$ and be inversely proportional to the square root of $M$. Therefore, $DR(U)/DR_{Uo} = \sqrt{[U/U_o]}$, where the constant $DR_{Uo}$ represents the deposition rate at velocity $U_o$. Taking the logarithm of both sides we arrive at

$$\log[DR(U)/DR_{Uo}] = \log\left[\sqrt{(U/U_o)}\,\right]$$
$$= 1/2\ \log[U/U_o] \qquad (36)$$

**Thermally Activated Processes** The surface-reaction processes can be modeled by a thermally activated phenomenon—as shown in Figure 55, left—proceeding at a rate $DR(T) = DR_\infty \exp(-E_a/kT)$, where $DR_\infty$ is the maximum deposition rate (also called the frequency factor) at $T \Rightarrow \infty$, $E_a$ is the activation energy (J), $T$ is the temperature (K), and the Boltzmann's constant $k = 1.38 \times 10^{-23}$ J/K. Many times it is more convenient to express the activation energy in electronvolts (1 eV $= 1.60 \times 10^{-19}$ J). In such cases, we take $k = 86 \times 10^{-6}$ eV/K. Identically, when the activation energy is expressed in J/mol, we write $DR(T) = DR_\infty \times \exp(-E_a/RT)$, with the molar gas constant $R = 8.3$ J/molK. Replacing $E_a/k$ ($E_a$ in J) or $E_a/R$ ($E_a$ in J/mol) with $T_a$ we find: $DR(T)/DR_\infty = \exp(-T_a/T)$. $T_a$ is the activation temperature, the temperature $T$ at which the rate $DR$ is $\exp(-1) \sim 0.37$ times the maximum value $DR_\infty$. For
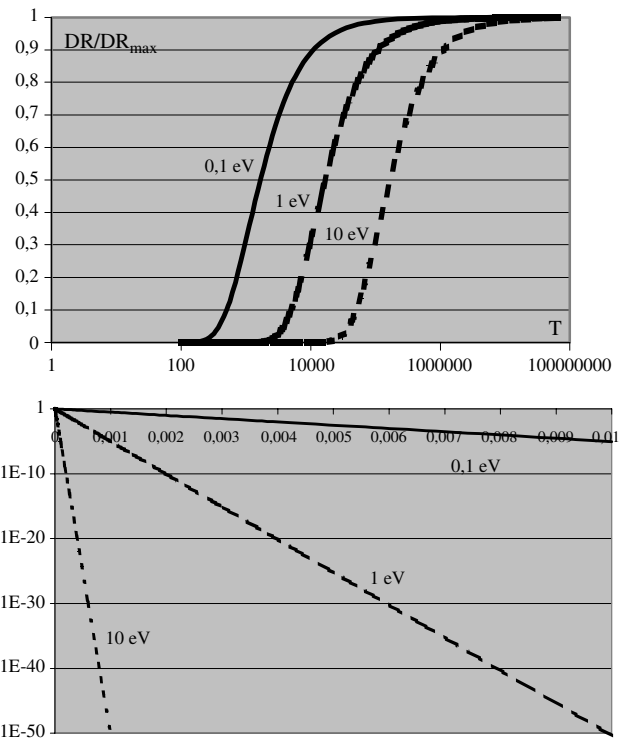


**Figure 55.** Temperature-controlled processes. Left: Relative rate $DR/DR_\infty$ versus temperature $T$ for various activation energies. Right: Arrhenius plot of the same function [i.e., $\log(DR/DR_\infty)$ versus reciprocal temperature $1/T$].



**Figure 54.** Schematic of a CVD process.

example, an activation energy of 1 eV resembles an activation temperature of 11,604 K. Taking the logarithm of both sides we arrive at the Arrhenius equation:

$$\ln[DR(T)/DR_\infty] = 2.30 * \log[DR(T)/DR_\infty] = -T_a/T \quad (37)$$

So if $\ln[DR(T)/DR_\infty]$ is plotted against the reciprocal temperature $1/T$, a straight line is found with slope $-T_a$ and from this slope the activation energy of the rate determining surface process can be deduced (Fig. 55, right). When the temperature changes from $T_1$ to $T_2$,

$$\log[DR(T_1)/DR(T_2)] = (T_a/2.3) * (1/T_2 - 1/T_1) \quad (38)$$

For example, when the activation temperature is 11,604 K ($E_a = 1$ eV) and the temperature changes from $T_1 = 100$ K to $T_2 =$ infinite (i.e., the reciprocal temperature $1/T$ changes from 0.01 toward zero), then we compute $\log[DR(T_1)/DR(T_2)] = (11604/2.3) * (-0.01) = -50$ (Fig. 55, right). For small changes in temperature ($T_1 \sim T_2$) we arrive at $1/T_2 - 1/T_1 = (T_1 - T_2)/T_1*T_2 \sim (T_1 - T_2)/T^2$ [i.e., $d(1/T) = -d(T)/T^2$]. So

$$T_a = T^2 * 2.3 * \log[DR(T_1)/DR(T_2)]/(T_2 - T_1) \quad (39)$$

Assume a process near room temperature (300 K) where the deposition rate doubles with an increase in temperature of 9 K. Then $T_a = (300)^2 * 2.3 * \log[2]/9 = 10,000 * 2.3 * 0.3 = 6900$ K is calculated and thus the activation energy is $6900/11,604 \sim 0.6$ eV. At room temperature, the thermal energy $kT = 0.026$ eV and, therefore, processes having an activation energy $E_a < 0.02$ eV will nearly depend on temperature above room temperature because the thermionic deposition rate is almost saturated. Saying it differently, processes which are almost independent of temperature are indicative for processes having small activation energy.

***Diffusion and Thermionic Processes***   In general, the deposition rate will depend on both the mass-transport and the surface-reaction processes. At high flow rates, the growth rate reaches a maximum and then becomes independent of flow. In this regime, the surface-reaction rate controls the deposition, no matter how high the flow rate is increased. This regime is referred to as surface-reaction limited deposition. On the other hand, at high temperatures, the reaction rate cannot proceed any faster than the rate at which the reactant gases are supplied to the substrate by mass transport, no matter how high the temperature is raised. This situation is referred to as mass-transport (or diffusion) limited deposition. These two limiting cases are analogous to the CVG oxidation cases (see Section 3.7.3), but the deposition rate in both regimes is now linear with time; neither is parabolic. In the intermediate region where both the mass-transport and the reaction rate are important it is possible to arrive at the deposition rate by combining the flow-rate and reaction rate dependent equations so that the smaller of the two dominates (two processes acting in series):

$$DR(T, U) = DR(T) * DR(U)/[DR(T) + DR(U)] \quad (40)$$

$$DR(T, U)/DR_\infty = \exp(-T_a/T) * \sqrt{(U/U_o)}$$
$$/[(DR_\infty/DR_{Uo}) \exp(-T_a/T)$$
$$+ \sqrt{(U/U_o)}] \quad (41)$$

$$2.3 * \log[DR(T, U)/DR_\infty] = (-T_a/T) + 1/2 \ln(U/U_o)$$
$$- \ln[(DR_\infty/DR_{Uo}) \exp(-T_a/T)$$
$$+ \sqrt{(U/U_o)}] \quad (42)$$

The resulting deposition rate behaves as shown in Figure 56. The transition region is located where $DR(T) = DR(U)$, that is, at $T_{trans} = T_a/[\ln(DR_\infty/DR_{Uo}) + 1/2 \ln(U_o/U)]$.

Thin films deposited by CVD may be doped during the deposition process. This is common for oxides, polysilicon, and epitaxial silicon. The dopant is introduced at the same time as the silicon tetrachloride during epitaxial growth. Gaseous diborane ($B_2H_6$) is used as the *p*-type dopant, while phosphine ($PH_3$) and arsine ($AsH_3$) are used as *n*-type dopants. Gas mixtures are ordinarily used with hydrogen as the diluent to allow reasonable control of flow rates for the desired doping concentrations. CVD can be used to deposit compounds, such as $SiO_2$ and $Si_3N_4$, as well as elements. However alloys, such as Al(2%Cu), are much more difficult. The problem is usually that separate reactions are required for each constituent (Al and Cu in our example) and it is difficult to avoid unwanted reactions between the different reactant species, or precursors. In addition, it is hard to control the exact composition of the alloy, because unlike compounds where limited compositions result (very close to 2:1 oxygen-to-silicon in $SiO_2$), a wide range of alloy compositions are possible. PVD methods are usually better suited for alloy deposition. The most common CVD processes will be treated next: APCVD and LPCVD, VPE, PECVD and HDPECVD, and pyrolysis. Other, less common, approaches such as VLPCVD very low pressure CVD and MOCVD metal-organic chemical-vapor deposition, which uses metal-organic compounds to grow a film, will not be discussed in detail.

***APCVD vs LPCVD***   The thermal energy is the sole driving force in high temperature CVD reactors such as APCVD (atmospheric-pressure CVD) and LPCVD (low-pressure CVD). In a hot-wall LPCVD reactor, a quartz tube is heated by a three-zone furnace and gas is introduced at one end
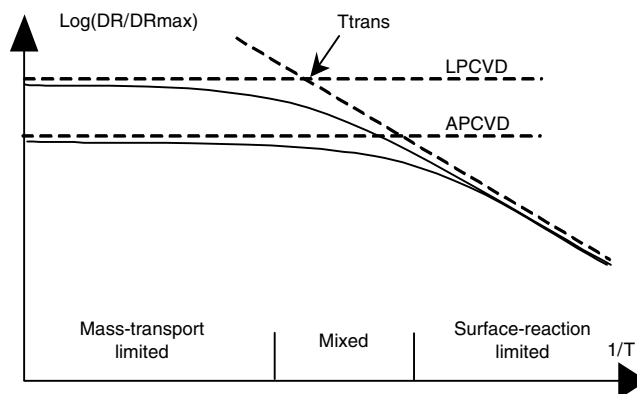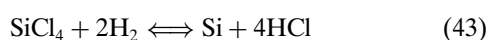


**Figure 56.** Arrhenius plot for a CVD process.

and pumped out at the opposite end. The quartz tube wall is hot because it is adjacent to the furnace. Typical reaction chamber pressures vary from 30 to 250 Pa (0.25 to 2 Torr) and temperatures are normally 300 to 900 °C. Among the benefits of this reactor are that it deposits films with excellent uniformity and large throughput. However, the gases used may be toxic, corrosive, or flammable. The APCVD reactor is similar to resistance heated hot-wall oxidation furnace except that different gases are used at the gas inlet. In contrast, in a cold-wall APCVD reactor such as the epitaxial reactor, the wafers are heated by using a graphite susceptor, which is heated by rf induction.

A direct practical application of the possible rate-limiting processes is the way substrates are stacked in LPCVD vs APCVD reactors. In a LPCVD reactor, the diffusion of the gas species is increased by a factor 1000 over that in APCVD due to the difference in pressure, resulting in a one order of magnitude increase in the transport of reactants to the substrate. The rate-limiting step becomes the surface reaction. This is an important result because it is easier to achieve a uniform temperature distribution than a uniform arrival of gas species across a wafer surface. Therefore, deposition is more uniform at higher flow and lower temperature settings. LPCVD reactors enable wafers to be stacked vertically at very close spacing as the rate of arrivals of reactants is less important. Polysilicon is usually deposited at lower temperatures in LPCVD systems and in the surface-reaction regime. Here the gas-phase processes are not important (so that stacking of wafers is possible), but the deposition is very temperature sensitive. On the other hand, APCVD, operating in the mass-transport-limited regime, must be designed such that all locations on the wafer and all wafers are supplied with an equal flux of reactant species. In this case the wafers often are placed horizontally.

***VPE-APCVD*** Among various epitaxial processes, vapor phase epitaxy is by far the most important. Epitaxial Si deposition has traditionally been done at higher temperatures (typically in APCVD systems) to ensure that all the Si atoms being deposited are incorporated into lattice sites in order to obtain a single-crystal thin film. This means that epitaxial Si in these systems is deposited in the mass transport regime where gas-phase processes are important. The epitaxial process offers an important means of controlling the doping profiles so that device and circuit performance can be optimized. For example, a semiconductor layer with a relatively low doping concentration can be grown epitaxially upon a substrate, which contains the same type of dopant in a much higher concentration (e.g., *n*-type silicon on a $n^+$-silicon substrate or undoped layer on top of a silicon wafer). In this way the series resistance associated with the substrate can be substantially reduced. Many device structures, especially for microwave and photonic devices, can be made on top of such so-called epi-wafers. Four silicon sources have been used for VPE-APCVD growth: silicon tetrachloride ($SiCl_4$, reacting at 1200 °C), trichlorosilane ($SiHCl_3$, 1150 °C), dichlorosilane ($SiH_2Cl_2$, 1100 °C), and silane ($SiH_4$, 1000 °C). The overall reaction of $SiCl_4$, the most widely used source, that results in the deposition of silicon layers is

$$SiCl_4 + 2H_2 \Longleftrightarrow Si + 4HCl \qquad (43)$$

An additional competing reaction is taking place that results in etching:

$$SiCl_4 + Si \Longleftrightarrow 2SiCl_2 \qquad (44)$$
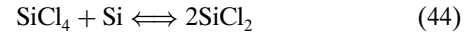
As a result, if the silicon tetrachloride concentration is too high or if the carrier gas entering the reactor contains HCl, etching with speeds up to 5 $\mu$m/min rather than deposition of silicon will take place. Actually, this etching operation is used for *in-situ* cleaning of the silicon wafer prior to epitaxial growth.

***Pyrolysis LPCVD*** Very-low-temperature CVD will become more important as microdevices incorporate materials (e.g., aluminum or polymers) not able to withstand high post-temperatures. For example, a low-pressure reactor operated between 600 and 650 °C is used to deposit polysilicon by pyrolyzing silane according to

$$SiH_4 \rightarrow Si + 2H_2 \qquad (45)$$

***MOCVD*** To improve step coverage, sometimes metals can be deposited by MOCVD using metal-organic compounds such as tri-isobutyl aluminum:

$$2[(CH_3)_2CHCH_2]_3Al \rightarrow 2Al + 3H_2 + \text{by-products} \qquad (46)$$
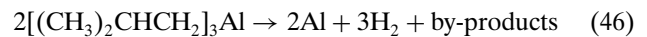
***PECVD and HDPECVD*** Sometimes there are restrictions on the temperature that the substrate can be exposed to when depositing a film. The most obvious example is when depositing a silicon dioxide when an aluminum layer is already in place. The melting point of Al is 660 °C, and any subsequent processing temperature must be less then about 450 °C. Another example is the use of the lift-off technique where the resin should withstand the deposition temperature. Finally, phase transitions may occur at temperatures substantially lower than the melting temperature of the layer deposited (such as between amorphous silicon and polysilicon or eutectic alloying).

For lower temperature deposition, an additional energy source is needed, as found in PECVD (plasma-enhanced CVD). PECVD is an energy-enhanced CVD method, because plasma energy is added to the thermal energy of a conventional CVD system. The parallel-plate PECVD consists of a cylindrical glass or aluminum chamber sealed with aluminum endplates (Fig. 57). Inside are two parallel aluminum electrodes. Wafers are placed on the lower electrode (anode), which is heated between 100 and 400 °C by
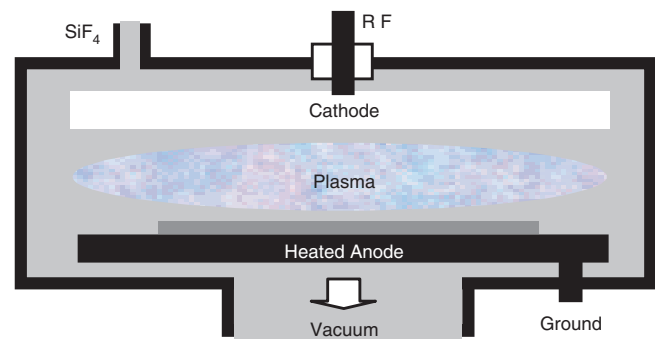


**Figure 57.** Thin film PECVD reactor.

resistance heaters. Process gas flows through the discharge from outlets located along the circumference of the lower electrode. An rf voltage is applied to the upper electrode, while the lower electrode is grounded. The rf voltage causes a plasma discharge between the electrodes. In the plasma, interactions with the high-energy electrons cause the reactant gases to dissociate and ionize into a variety of species. Most species are extremely reactive, such as $SiH_3$ in deposition and F in etching, and are absorbed onto the wafer surface, migrate, interact, rearrange, and chemically recombine to form the film. The net result is that the deposition can occur at much lower temperatures. However, its throughput is low, especially for large-diameter wafers, and the wafers may become contaminated if loosely adhering deposits fall on them (flaking).

The reactions and processes that occur in a PECVD system are complicated and difficult to predict. The complexity of the plasma reactions can lead to nonstoichiometric compositions of films (e.g., Si-rich $SiO_2$), as well as the incorporation of $H_2$ or $N_2$ by-products into the film. This can result in outgassing, peeling, or cracking of the film during subsequent processing. Film density and stress may also vary, depending on the conditions of the deposition. PECVD can result in fairly good coverage and filling of nonplanar topography (such as TEOS $SiO_2$ deposition: Section 3.8.2), better than what might be expected at these low temperatures, probably due to surface emission and redeposition events caused by ion bombardment.

HDPECVD utilizes a very high-density plasma and a separate rf bias applied on the substrate to obtain very good filling of narrow gaps. It is used primarily for silicon dioxide depositions. The high-density source can be generated by a variety of sources such as inductively coupled plasma (ICP) and results in a dense film at low temperatures and with a very low chamber pressure in the 1–10 mTorr range. Sputtering—the knocking off of atoms from a solid by incident ions when the solid is electrically biased—occurs preferentially on sloped surfaces rather than on vertical or horizontal surfaces. This simultaneous sputtering of the film during its deposition can result in planarized and void-free films.

***Other CVD Systems*** Most of the low-temperature methods use energy-enhanced CVD techniques (e.g., a focused electron beam) to deposit dielectric films between 25 and 300 °C. An other energy-enhanced CVD method uses UV radiation to form vapor phase reactants that enhance the deposition rates. Silicon dioxide films have been deposited at a rate of 15 nm/min at temperatures as low as 50 °C by means of UV radiation.

### 3.7.2. Physical Vapor Deposition

Rather than relying on chemical reactions to produce the reacting species to form the film as in CVD, PVD methods use mainly physical processes to deposit films. PVD is more versatile than CVD, allowing for the deposition of almost any material. PVD is done under vacuum using, either the evaporation of a solid or molten source or by using energetic gaseous ions in a plasma to knock off—or sputter/dislodge—the atoms from a source target. These atoms or molecules then travel through a vacuum or a very

low-pressure gas phase, impinge on the wafers, and condense on the surface to form the film. The key distinguishing attribute of a PVD reactor is that the deposition of the material onto the substrate is a line-of-sight impingement-type deposition.

In an evaporation system, the vacuum chamber is evacuated by a roughing pump from atmospheric pressure to a pressure of about 15 Pa, followed by high-vacuum pumping to reduce the pressure to $10^{-3}$ Pa ($\sim 10^{-5}$ Torr) or lower. System cleanliness is required to reduce the pump-down period. To remove a major source of trapped atmospheric gas, all interior film buildup must be removed. To ensure uniform thickness of the deposited film, appropriate mechanical motion of the substrate of evaporation similar to that of the planetary system can be employed to expose the substrate to the same average number of evaporated atoms.

During film sputter deposition, approximately 1 Pa argon pressure is needed. Sequential deposition of different films is possible if several sources are available in the chamber. Using multiple sources also facilitates co-evaporation or co-sputtering to produce compounds, alloy films, or multilayer depositions, where Ti and Al layers may be deposited one after the other in the chamber without breaking vacuum. Similar cleanliness precautions as in the case of evaporation should be observed for sputter deposition.

Compounds such as silica are much harder to evaporate in the right composition as alloys with single-source sputter systems. The composition of the vapor phase is usually not the same as the source compound, and chemical reactions and molecular changes often occur as the material is evaporated. Sputter deposition generally does a much better job in depositing compositionally uniform films of both alloys and compounds. This is because the sputter rates of elements are usually much closer to each other than their vapor pressures are. In addition, because sputtering occurs just from the top surface of the target and little mixing from the layers below takes place (as opposed to evaporation where the mixing in the melt wipes out any concentration gradients), a steady-state condition soon develops. Initially, the element with the higher sputter rate does preferentially sputter off more from the surface. This leaves the top surface enriched with the element of the lower sputter yield. But now more of the element with the lower sputter yield is knocked off since the surface region is enriched with that element; a steady-state is achieved.

PVD reactors may use a solid, liquid, or vapor raw material in a variety of source configurations. The magnetron in some sputtering systems operates at voltages an order of magnitude below the e-beam source voltage and thus generates less penetrating radiation. In sputtering, the source is not heated to high temperatures and the vapor pressure of the source is not a consideration as in vacuum–evaporation. Other PVD techniques, very useful in the deposition of complex compound materials for example, e.g. nanotechnology, are MBE and laser ablation deposition. Ion-plating and cluster deposition are based on a combination of evaporation and plasma ionization and offer some of the advantages inherent to both techniques.

***Evaporation PVD*** Thermal evaporation represents one of the oldest ($\sim 100$ years!) thin-film deposition techniques. Evaporation is based on the boiling off or sublimation of

a heated material onto a substrate in a vacuum. The substances used most frequently for thin-film formation by evaporation are elements or simple compounds whose vapor pressure exceeds 1 mTorr for temperatures below 2000 °C and typically deposit at a rate from 50 to 1000 nm/min. Three common techniques are used to evaporate materials: electron-beam (e-beam) evaporation, resistance-heated evaporation, and rf induction-heated evaporation.

In an electron-beam evaporation, the most popular evaporation system, a thermionic filament supplies the electron current to the beam and the electrons are accelerated by an electric field (3 to 20 kV) to strike the surface of a charge (e.g., aluminum) which melts locally (Fig. 58). To prevent impurities from the filament reaching the charge that is placed in a recess in a water-cooled copper hearth, a magnetic field bends the e-beam path thus screening the impurities. Moreover, the metal forms its own crucible and the contact with the hearth is too cool for physical or chemical reactions, resulting in minimal source-contamination problems. Very high deposition rates on the order of 1 $\mu$m/min are possible in this system depending upon source-to-substrate distance. E-beam heaters can achieve high temperatures so that a wide range of materials can be evaporated such as aluminum and its alloys, silicon, palladium, titanium, molybdenum, platinum, tungsten, etc. and several dielectrics such as silicon dioxide. A disadvantage of the e-beam process is the generation of X-rays by the e-beam. This ionizing radiation can penetrate the surface layers of the devices, causing damage such as the creation of oxide-trapped charges. Therefore, subsequent annealing is required to remove such damage. The X-ray damage may

be avoided by using a focused, high-power laser beam (see section on laser ablation).

In a resistance-heated source, a refractory metal (i.e., a metal such as tungsten with a high melting point) is coiled into a filament or formed into a containment structure and a small piece of material (e.g., aluminum) is placed. Resistance-heated evaporation is simple and inexpensive and produces no ionizing radiation. Its disadvantages are possible contamination from the heater filament and limited film thickness because of the small charge than in the case of electron-beam evaporation. Moreover, resistance heaters cannot achieve temperatures as high as e-beam heaters so that a smaller range of materials can be evaporated. For example, refractory metals such as platinum, molybdenum, tantalum, and tungsten do not easily heat to the temperatures required to reach a sufficient vapor pressure.

In some cases an evaporation source is heated by rf induction with frequencies of several hundred kilohertz. In rf induction heating, a water-cooled rf coupling coil surrounds a crucible with the material to be evaporated. Usually boron nitride is used to form the crucible. Again there is no radiation problem and contamination may occur.

Evaporation registers a low energy impact on the substrate ($\sim$0.1 eV); that is, no surface damage results except when using e-beam evaporation. As a result of the low-energy impact, adhesion is generally poor in evaporation and delamination might occur. The problem of delamination can be diminished when incorporating an *in-situ* plasma treatment or depositing an additional adhesion layer such as Cr, Ta, or Ti prior to the evaporation. The plasma is able to remove surface contaminants such as water and can activate the surface to improve adhesion.

There is a need for a good vacuum; even at a pressure of $10^{-5}$ Torr, five contaminating monolayers per second arrive at the substrate and might react. (Note: The number of atoms per unit area corresponding to a 3 Å thick monolayer for a metal is about $10^{15}$/cm$^2$.) Especially, water vapor and oxygen gas may cause the formation of oxygen impurities. On the other hand, when one wants to form the oxides of the deposited metals, evaporation is performed in a low-pressure oxygen atmosphere. When oxygen is added one refers to reactive evaporation. The oxygen supply comes from a jet directed at the substrate during deposition. To obtain the correct stoichiometry the deposition needs to take place on a heated substrate.

If a high vacuum is established, most atoms/molecules will deposit on the substrate without suffering intervening collisions with other gas molecules. This results in a line-of-sight deposition. The fraction of particles scattered by collisions with atoms of residual gas is proportional to $1 - \exp(-d/\lambda)$ where $d$ is the distance between source and substrate (see Fig. 59) and $\lambda$ is the mean free path between collisions of the particles. At 0.01 mTorr the mean free path in air hovers about 5 m. The source-to-wafer distance must be smaller than the mean free path of the residual gas. Typically, this distance is 25 to 70 cm. The arrival rate $A$ at distance $d$ from a small evaporation source follows the cosine law of deposition: $A \sim \cos \beta / d^2$ where $\beta$ is the angle between the normal to the substrate and the radial vector joining the source to the arrival point being considered. The straight-line deposition of evaporant leads to difficulties in obtaining
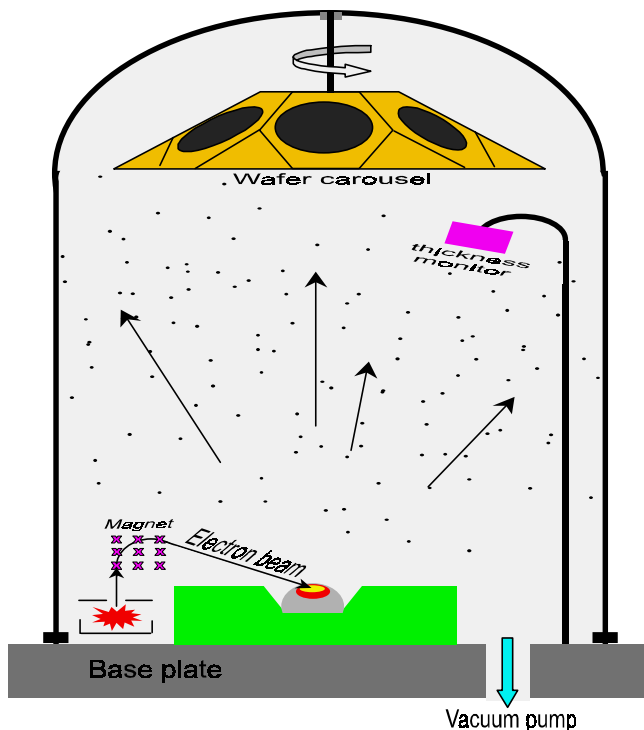


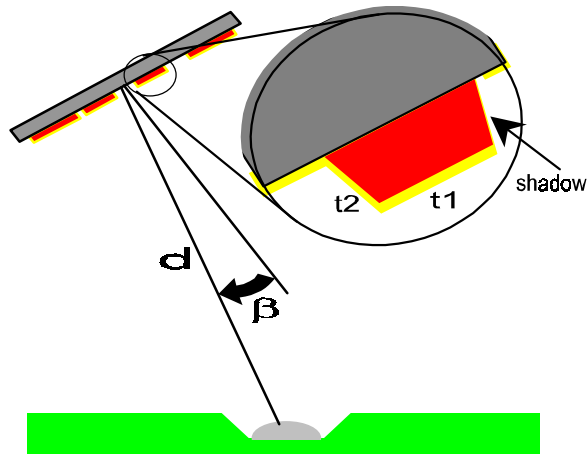**Figure 58.** Thin film deposition by evaporation.

**Figure 59.** Shadowing in evaporation.

a continuous coating over topographical steps on a wafer, a problem known as shadowing. This is of particular concern in microdevices where high aspect ratio features are requested. Figure 59 illustrates the problem. Since the thickness of the deposited film $t$ is proportional to $\cos \beta$ (in case of no surface migration of the deposit), the ratio of the film thickness is given as $t_1/t_2 = \cos \beta_1 / \cos \beta_2$. In case of a steep wall, the ratio can be 10 or more. The thinner section $t_2$ is susceptible to cracking at the extreme ends of the interval. Rotating the wafers in a planetary motion does help to widen the range of arrival angles but shadowing still occurs. To overcome the nonconformal deposition, the substrate can be heated during deposition (300 to 400 °C) to increase the surface mobility of the arriving atoms or the wafers can be rotated individually so that the angle $\beta$ varies during deposition. Nevertheless, a nonconformal step coverage is beneficial when considering the so-called lift-off technique (see Section on lithography).

***Laser Ablation PVD*** Laser ablation deposition uses intense laser radiation to erode a target and deposit the eroded material onto a substrate. A high-energy focused laser beam avoids the X-ray damage to the substrate encountered with e-beam evaporation. A high-energy excimer laser pulse coming from, for example, a KrF laser at 248 nm with a pulse energy in the focus of 2 J/cm$^2$ is directed onto the material to be deposited. The energy of the very short wavelength radiation is absorbed in the upper surface of the target, resulting in an extreme temperature flash, evaporating a small amount of material. This material, partially ionized in the laser-induced plasma, is deposited onto a substrate almost without decomposition. This technique is particularly useful when dealing with complex compounds, as in the case of the deposition of high temperature superconductor films, for example, $YBa_2Cu_3O_{7-x}$. Pulsed laser deposition faithfully replicates the atomic ratios present in the hot isostatically pressed target disc onto the thin film coating. Achieving complex stoichiometries presents more difficulties than with any other deposition technology. Approximately 10,000 pulses (pulse length of 20 ns and a repetition rate of 15 pulses per second) are needed to achieve a film thickness of 100 nm (i.e., approximately 10 nm/min). Normally, the laser deposited films are amorphous. The energy necessary

to crystallize the film comes from heating the substrate (700 to 900 °C) and from the energy transferred from the intense laser beam to the substrate via atomic clusters. Because of the small source size, laser ablation is not useful for large-scale coatings but is very useful in forming ultrathin layers for nanoapplications.

***Sputter PVD*** Sputtering is preferred over evaporation in many applications due to a wider choice of materials to work with, better step coverage, and better adhesion to the substrate. Several sputter systems exist such as dc, reactive, rf, and magnetron sputtering as will be explained next.

Figure 60 illustrates schematically a dc sputter deposition system. In the sputter system an inert gas is fed into the reactor at low pressure. A voltage is applied across two electrodes and plasma is created. The top electrode, the cathode or "target" where a negative dc voltage is applied, is actually the source material to be deposited, a plate of aluminum for example. The bottom electrode—the anode where the wafers are located—is another metal plate and is grounded. The positive ions from the plasma source, usually $Ar^+$, are accelerated through the potential gradient where they bombard the target. Through momentum transfer, atoms near the surface of the target material become volatile and are transported as a vapor to the substrate. At the substrate the film forms through deposition (the vapor condenses). Since the target acts as an electrode in the dc mode of sputter deposition, the target of source material must be conductive. Therefore, Al, W, Ti, silicides and other metallic components can be sputtered this way. Sometimes sputtering of the wafer is desirable—for example to improve adhesion. In such cases, a negative bias is applied to the wafer electrode. Positive argon ions from the plasma will now be accelerated to the wafer and sputter off atoms, thus removing any contaminants or native oxides. In addition it will improve adhesion due to the creation of surface dangling bonds by the ion impact.

In reactive sputtering, a reactive gas is introduced in the reactor in addition to the argon plasma, and the compound is formed by the elements of that gas combining with the sputtered material. For example, TiN can be deposited by sputtering Ti in the presence of nitrogen. dc sputtering is not suitable for insulator deposition. Therefore, in radio frequency sputtering an rf voltage source is used to couple capacitively through the insulating target, so that conducting electrodes are not necessary. In magnetron sputtering, magnets are used to increase the ionization efficiency of the plasma. Electrons originating at the cathode are trapped in a
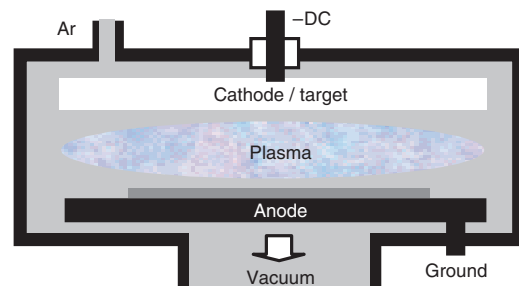


**Figure 60.** Thin film deposition by dc sputtering.

spiral motion and confined by the magnetic fields until they collide with an argon atom. This can speed up the deposition 10 to 100 times faster than without magnets.

Having a larger target and higher gas phase pressure than evaporation means that the arrival angles of the atoms at the wafer surface are more widely distributed which generally improves step coverage. Also, the number of resputtered atoms on the wafer surface is higher for sputtering due to the bombardment of energetic particles, which increases the arrival angle distribution even more. In some cases, though, we actually want to narrow the arrival distribution—for example when filling a deep via with metal. This can be achieved using collimated and ionized sputtering systems. In collimated sputtering, a plate with holes is placed between the target and the wafer. The collimator acts as a physical filter to low-angle sputtered atoms. In ionized sputtering an rf antenna is used instead to direct ionized atoms toward the substrate and increasing directionality. Another way is applying bias to the substrate, which allows a minimal sputter etching concurrently with the deposition. In this way, sharp edges of the deposit are reduced during the sputter deposition due to the angle-dependent sputter yield. Surfaces with pointed and sloped features are removed more easily than horizontal or vertical surfaces. Not only does this help planarize the film, but overhang that can develop when depositing into a trench or hole is preferentially sputtered away, allowing for a better filling of the hole. Another factor may be that the resputtered atoms allow for some redeposition on sidewalls. By increasing the ion energy, the resputtering and redeposition of the atoms can be increased, resulting in better sidewall coverage. Another option for improved hole filling is to do the deposition and etching sequentially, as opposed to simultaneously. This can be done in a cluster tool with separate chambers for each process or using a plasma system, which allows both sputter deposition and etching such as in downstream cascade arc plasma (Section 5.3).

Deposition rates depend on source-to-substrate distance and can be as high as 1 $\mu$m/min for aluminum and its alloys. A typical sputter yield (i.e., ejected atoms per incident ion) is between 0.1 and 10 atoms/ion and is a function of ion energy and their direction. Below the so-called threshold energy, the ions have not enough energy to break the metallic bonds and subsequently the sputter yield is very low. The yield increases rapidly from the threshold energy level, which is usually in the range of 10 to 100 eV for common metals (e.g., 13 eV for Al, 15 eV for Pd, and 34 eV for Pt). To minimize the energy required to eject an atom from the target, the process uses ion energy within the range for which the sputter yield is about one atom per ion. Ion energies in the range of 0.5 to 3 keV typically are used for dc sputter deposition as nuclear collisions are predominant in this range. At ion bombardment energies in the range of 10 keV to 1 MeV, the sputter yield reaches a maximum and then gradually declines in value as a result of deep ion implantation. Average ejection energies of ions from the target range between 10 and 100 eV. At those energies, the incident ion can penetrate a substrate one to two atomic layers into the surface on which it lands. As a result, the adhesion of sputtered films is superior to films deposited by other methods. An ion coming in at low, glancing angle will not be as successful at dislodging an atom, with the ion itself being

reflected off the surface (specular reflection). At the other extreme, ions arriving normal to the surface will push a surface atom further into the target but not necessary sputter it off. The sputter yield peaks at some angles less than 90°, just as is the case in ion beam etching (Section 5.3). The angles that the sputtered atoms leave the surface of the targets are usually found to be diffusely distributed, with an ideal cosine-emitted angle distribution.

### Molecular-Beam PVD (Epitaxial Crystal Deposition)
Molecular-beam epitaxy is a PVD epitaxial process involving the reaction under ultrahigh vacuum conditions ($<10^{-10}$ Torr). In MBE, the heated single-crystal (400 to 800 °C) is placed in the path of streams of atoms from heated cells that contain the material of interest. These atomic streams impinge, in a line-of-sight fashion, on the surface-creating layers with a structure controlled by crystal structure of the surface, the thermodynamics of the constituents, and the sample temperature. MBE can achieve precise control in both chemical compositions and doping profiles. Single-crystal multilayer structures with dimensions of the order of atomic layers can be made using MBE. The deposition rate of MBE is very low (i.e., about 20 nm/min), which accounts for the ultrahigh vacuum needed to obtain high-purity epilayers. Because MBE uses an evaporation method, the basic kinetic theory of gases in a vacuum system has to be considered. We will not go into detail, but as an example: at room temperature and at a pressure of 1 Torr it takes 2 $\mu$s to form a monolayer of oxygen. At $10^{-6}$ Torr this is 2 s and at $10^{-10}$ Torr it becomes 6 hr. Therefore, in order to avoid oxygen contamination it is of paramount importance to maintain ultrahigh vacuum conditions. Fast-acting shutters control the deposition. A few atomic layers of material lie between every shutter action. This becomes important when an ultrasharp profile is called for. The low deposition rate gives the operator better control over the film thickness. MBE has several potential advantages over CVD epitaxy (i.e., VPE); for example, the relatively low growth temperatures reduce diffusion and autodoping effects. Novel structures such as quantum devices and superlattices can be made. The limitations to consider lie in volume manufacturing and costs. The ultrahigh vacuum requirements make operation very expensive.

### Cluster-Beam PVD
When applying cluster-beam technology, ionized atom clusters (100 to 1000 atoms) are deposited on a substrate in a high vacuum ($10^{-5}$ to $10^{-7}$ Torr). Those atom clusters typically carry one elementary charge per cluster and therefore achieve the same energy in an electrical field as a single ion would. To make these atom clusters, a special evaporation cell must be used. The heating of the evaporant in an evaporation cell with a small opening causes adiabatic expansion, from more than 100 to $10^{-7}$ mbar, of the vapor upon exiting that cell. The expansion causes a sudden cooling, inducing the formation of atom clusters. These clusters are then partially ionized by an electron bombardment from a heated filament. Low energy neutral clusters (0.1 eV) and somewhat higher energy ionized clusters (a few eV) arrive at the surface where they flatten and form a film of excellent adhesion and purity, with a relatively low

number of defects. Cluster-beam epitaxy is possible at temperatures as low as 250 °C, and no charge buildup occurs when depositing on an insulator.

***Ion Plating PVD***   In ion plating, evaporation of a material is combined with ionization of the atom flux by an electron filament or plasma. The addition of a gas (e.g., nitrogen) to the reactor enables one to make new compounds (such as TiN) on the substrate surface with the gas reacting with the ionizing atoms from the evaporation source (Ti). Because of the high kinetic energy of the impacting ions, a very well adhering, dense TiN film with extraordinary low friction coefficient and high hardness coefficient (Vickers hardness of 50,000) forms. Because of the thermal nature of the process, very high deposition rates can be achieved.

### 3.7.3. Chemical Vapor Growth

Chemical and physical vapor growth are processes where the substrate material is transformed into a layer with different properties. Within this group, thermal oxidation is of prime importance in IC technology where thermally grown field and gate oxides can provide the highest quality oxides having the lowest interface trap densities. Diffusion and ion implantation are two key processes which are used to introduce controlled amounts of dopants into semiconductors. They are used to dope selectively the semiconductor substrate to produce either an *n*-type or *p*-type region. Both diffusion and ion implantation are used for fabricating microsystems because these processes generally complement each other. For example, diffusion is used to form deep subsurface doping profiles, whereas ion implantation is used to form shallow junctions.

***Thermal***   Semiconductors can be oxidized (or nitrided) by various methods. These include thermal oxidation, electrochemical anodization (see section on chemical liquid growth), and plasma reaction. Among these methods thermal oxidation is by far the most important for silicon devices. Silicon dioxide formed by thermal oxidation of silicon is used as a common insulating layer, as a mask, and as a sacrificial material. The oxidation temperature is generally in the range of 900 to 1200 °C and takes place in a furnace (Fig. 61). Because a silicon surface has a high affinity for oxygen, an oxide layer rapidly forms when silicon is exposed to an oxidizing ambient. The chemical reactions describing the thermal oxidation of silicon in oxygen or water vapor are given:

$$\text{Dry oxidation:} \quad \text{Si(s)} + \text{O}_2\text{(g)} \rightarrow \text{SiO}_2\text{(s)} \quad \text{(47a)}$$
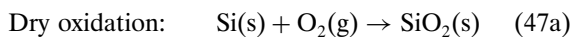


**Figure 61.** Thermal oxidation furnace.

$$\text{Wet oxidation:} \quad \text{Si(s)} + 2\text{H}_2\text{O(g)} \rightarrow \text{SiO}_2\text{(s)} + \text{H}_2\text{(g)} \quad \text{(47b)}$$
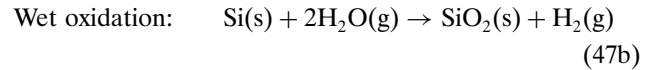
The basic process involves shared valence electrons between silicon and oxygen; the silicon–oxygen bond structure is covalent. The basic structural unit of thermally grown silicon dioxide is a silicon ion surrounded tetrahedrally by four oxygen ions (Fig. 36). These tetrahedra are joined together at their corners by oxygen bridges in a variety of ways to form the various phases or structures of silicon dioxide (also called silica). Silica has several crystalline structures (e.g., quartz) and an amorphous structure. When silicon is thermally oxidized, the silicon dioxide structure is amorphous. Typically amorphous silica, with a formula weight $M = 60.1$, has a density of 2.21 g/cm$^3$, as compared to 2.65 g/cm$^3$ for quartz and 2.33 g/cm$^3$ for silicon ($M = 28.1$). The relatively open structure of the amorphous structure accounts for the lower density and allows a variety of impurities (such as sodium) to enter and diffuse readily through the silicon dioxide layer. Both types of thermal oxidation are carried out in a quartz tube. An oxide thickness of a few tenths of a micrometer is used most frequently, with a few micrometers being the practical upper limit for conventional thermal oxides, although layers thicker than 10 micrometers have been fabricated.

During the course of the oxidation process, the Si–SiO$_2$ interface moves into the silicon. Its volume expands and based on the densities and molecular weights of Si and SiO$_2$; we can calculate that for growth of an oxide of thickness $d$, a layer of silicon with a thickness of $(28.1/60.1) * (2.21/2.33) * d = 0.44d$ is consumed. This relationship holds importance for calculating step heights that form in silicon microstructures. The oxidation proceeds by gas-phase transport of oxidant to the surface, the diffusion of the oxidizing species through the oxide to the Si–SiO$_2$ interface, and the oxidation reaction itself. In the early stage of growth in dry oxidation, there is a large compressive stress in the oxide layer because the (volume) expansion is restricted laterally by the substrate underneath the growing film. Such stress reduces the oxygen diffusion coefficient in the oxide. Especially sharp silicon corners will develop large stresses and therefore these places will create a lag in oxidation. This effect is effectively used in the manufacturing of ultrasharp needles for scanning probe microscopy. As the oxide becomes thicker, the stress will be reduced due to the viscous flow of silica and the diffusion coefficient will approach its stress-free value. When the temperature is ramped down from, say 1000 °C, to room temperature after finishing the oxidation, the growing film will develop again a high compressive stress (∼300 MPa), but now it is caused by the difference in thermal expansion coefficient between silicon and silica as found in Section 2.2. Due to this oxide films with a certain critical thickness (in the order of a few micrometers) might start to delaminate from the substrate after cooling down if the ramping is too fast.

Using simple kinetics of thermal oxidation of silicon, it can be shown that the oxide thickness $x$ after an oxidizing time $t$ is given by the Deal–Grove equation [177],

$$x^2 + Ax = B(t + t_o) \quad \text{(48)}$$

where $t_o$ represents a shift to account for the initial oxide layer at $t = 0$. $A$ is a function of the surface reaction rate constant for oxidation $k$ and the diffusion constant of the oxidizing species in silica $D$ ($A = 2D/k$). $B$ is a measure of the diffusion process of the oxidizing species through the silica ($B = 2DC_0/C_1$). For small values of $x$ ($x \ll A$), this equation reduces to a linear law:

$$x = (B/A)(t + t_o) = k(C_0/C_1)(t + t_o) \qquad (49)$$

And for large values of $x$ ($x \gg A$), it reduces to a parabolic law:

$$x^2 = Bt = 2D(C_0/C_1)t \qquad (50)$$

Thus, during the early stage of oxide growth, when surface reaction is the rate-limiting factor, the oxide thickness varies linearly with time. For this reason, the term $B/A$ is referred to as the linear rate constant. As the oxide layer becomes thicker, the oxidant must diffuse through the oxide layer to react at the silicon–silica interface and the reaction becomes diffusion-limited. The oxide growth then becomes proportional to the square root of the oxidizing time, which results in a parabolic growth rate. Therefore, the term $B$ is referred to as the parabolic rate constant.

The temperature dependence of the linear rate constant $B/A$ varies as $\exp(-E_a/kT)$, where the activation energy $E_a$ found experimentally is about 2 eV for both dry and wet oxidations. This closely agrees with the energy required to break silicon–silicon bonds, that is, 1.83 eV. The temperature dependence of the parabolic rate constant $B$, which can also be described by $\exp(-E_a/kT)$, is different for dry and wet oxidation. The activation energy $E_a$ is 1.24 eV for dry oxidation, which is comparable to that for oxygen diffusion in fused silica (1.18 eV). The corresponding value for wet oxidation, 0.71 eV, compares favorably with the value of 0.79 eV for the activation energy of diffusion of water in fused silica [176]. Oxidation in high-pressure steam can produce substantial acceleration in the growth rate because the parabolic rate constant $B$ is proportional to the partial pressure of the oxidizing species in the gas phase. High-pressure oxidation offers the advantage of low-temperature processing at growth rates comparable to high-temperature, 1 atm conditions. Because wet oxidation occurs at a substantially greater rate than dry oxidation, any unintentional moisture accelerates the dry oxidation. Also, the common dopant elements, when present in silicon at high concentration levels, can enhance the oxidation behavior. The dopant impurities are redistributed at the growing Si–SiO$_2$ interface (i.e., the dopant segregates either into the silicon or into the oxide). The redistribution of the impurity at the interface influences the oxidation behavior. The quality of thermal silica depends heavily on its growth method. Dry oxidation in pure oxygen produces a better quality oxide than steam oxidation. Such a thermal oxide is stoichiometric, has a high density, and is basically pinhole free. Wet oxidation in steam water causes a loosening effect on the silica, making it more prone to impurity diffusion.

Experiments have indicated that the oxidation kinetics is a function of the crystallographic orientation of the silicon surface [169, 171]. The linear rate constant is related to the interface reaction kinetics and depends on the rate at which oxide atoms are incorporated into the silicon lattice with lattice constant $a = 0.543$ nm and $a^{-2} \sim 3.39 \times 10^{14}$ atoms/cm$^2$. This might depend on the silicon surface atom concentration, which is orientation dependent, $\{011\}:\{111\}:\{100\} = 2a^{-2}(\sqrt{2} : 2\sqrt{3}/3 : 1) \sim 1.41 : 1.15 : 1$, or the available bond density, which is also orientation dependent, $\{011\}:\{111\}:\{100\} = 2a^{-2}(\sqrt{2} : 2\sqrt{3}/3 : 2) \sim 1.41 : 1.15 : 2$. However, the experimental linear oxidation rate for silicon surfaces follows the sequence $\{011\} > \{111\} > \{311\} > \{511\} > \{100\}$, which resembles the surface atom concentration orientation dependency. For example, after 16 hours of oxidation at 800 °C of $\langle 011 \rangle$-, $\langle 111 \rangle$-, and $\langle 100 \rangle$-oriented wafers, 300 nm oxide grows on the $\langle 011 \rangle$-wafer, 280 nm Oxide on the $\langle 111 \rangle$-wafer, and 200 nm oxide on the $\langle 100 \rangle$-wafer, revealing a ratio of $\{011\}:\{111\}:\{100\} = 1.5 : 1.4 : 1$. So, because the density of silicon atoms on the $\{011\}$-plane is larger than that on the $\{111\}$ and $\{100\}$-plane, the linear rate constant for $\langle 011 \rangle$-silicon is also larger and oxidation proceeds faster in the initial growing process where the growing proceeds still linearly with time. The parabolic rate constant is independent of crystal orientation. This independence is expected, because it is a measure of the diffusion process of the oxidizing species through a random network layer of amorphous silica.

Addition of chlorine-containing chemicals during oxidation increases the dielectric breakdown strength and the rate of oxidation and improves the threshold voltage of many electronic devices However, too high concentrations of halogens at high temperatures can pit the silicon surface. In general, the quality of the silicon–silica interface fails to be of importance in the MEMS field unlike the IC industry. One notable exception being the ion sensitive field effect transistor (ISFET).

Understanding the stress associated with a film is important because high stress levels can contribute to wafer warpage, film cracking, and defect formation in the underlying silicon. Room temperature measurements following thermal oxidation of silicon show the film to be in a state of compression on the surface. Film stress values of 700 MPa are reported, with the stress attributed to the difference in thermal expansion for Si and SiO$_2$ (thermal stress) and stress resulting from the change in volume between silicon and its oxide (intrinsic oxidation stress). For more details on all the subjects described above, see [1]. Evidently, such stresses are of prime concern when dealing with extremely small structures as found in nanotechnology where natural oxides are major contributions to the total thickness of structures such as nanocantilevers.

***Diffusion*** Until the early 1970s, selective doping was done mainly by diffusion at elevated temperatures. In this method the dopant atoms are placed on or near the surface of the semiconductor wafer by deposition from gas phase of the dopant or by using doped-oxide sources. The dopant distribution is determined mainly by the temperature and diffusion time.

Diffusion of impurities is typically done by placing semiconductor wafers in a furnace and passing an inert gas that contains the desired dopant through it. The furnace and gas flow arrangements are similar to those used in thermal oxidation. The temperature usually ranges between 800 and

1200 °C for silicon. For diffusion in silicon, boron is the most popular dopant introducing a *p*-type impurity, while arsenic and phosphorous are used extensively as *n*-type dopants. These three elements are highly soluble in silicon as they have solubilities above $5 \times 10^{20}/\text{cm}^3$ (i.e., 1% of the silicon density!) in the diffusion temperature range. These dopants can be introduced in several ways, including solid sources (e.g., BN for boron, $As_2O_3$ for arsenic, and $P_2O_5$ for phosphorous), liquid sources ($BBr_3$, $AsCl_3$, and $POCl_3$), and gaseous sources ($B_2H_6$, $AsH_3$, and $PH_3$). Usually, the source material is transported to the semiconductor surface by an inert carrier gas (e.g., nitrogen) and is then reduced at the surface.

The diffusitivities of commonly used doping impurities (e.g., As, B, and P) are considerably smaller in silicon dioxide and silicon nitride than in silicon. Therefore silicon dioxide can be used as an effective mask against impurities. If we etch windows in the oxide and use the remaining oxide as a mask, we can incorporate dopant impurities into a silicon substrate in selective areas. For silicon dioxide, the diffusion process can be described as occurring in two steps. During the first step, the dopant impurities react with silicon dioxide to form a silicate glass. As the process continues, the thickness of the silicate glass increases until the entire silicon dioxide layer is converted into a silicate glass (e.g., phosphosilicate glass). After the glass forms, the second step begins. The dopant impurity diffuses through the glass; upon reaching the glass–silicon interface, it enters and diffuses into the silicon. During the first step, silicon dioxide is completely effective in masking the silicon against dopant impurities in the gas phase. Therefore, the thickness of silicon dioxide required for masking is determined by the rate of formation of the glass, which in turn is determined by the diffusion of the diffusant into the silicon dioxide. Because it has a higher diffusitivity in silicon dioxide, phosphorous requires thicker masking layers (between 20 and 80 times thicker) than boron. Silicon nitride is even more effective as a diffusion barrier than silicon dioxide. Therefore much thinner layers of silicon nitride are sufficient to effectively block dopants.

Dopant impurities near the silicon surface will be redistributed during thermal oxidation. The redistribution depends on several factors. When two solid phases are brought together, an impurity in one solid will redistribute between the two solids until it reaches equilibrium. The ratio of the equilibrium concentration of the impurity in the silicon to that in the silicon dioxide is called the segregation coefficient $k$. For $k < 1$, the oxide takes up the impurity and for $k > 1$ it rejects the impurity. An example is phosphorous, with $k$ approximately equal to 10.

### 3.7.4. Physical Vapor Growth

Ion implantation is the introduction of energetic, charged particles into a substrate such as silicon. The practical use of ion implantation in semiconductor technology has been mainly to change the electrical properties of the substrate or to form a buried oxide layer for SIMOX wafers (see Section 2.3.11).

***Ion Implantation*** Since the early 1970s, many doping operations have been performed by ion implantation. In this process the dopant ions (e.g., $B^+$ and $As^+$) are implanted into the semiconductor by means of a high-energy ion beam. Typical ion energies are between 30 and 300 keV, and typical ion doses vary from $10^{11}$ to $10^{16}$ ions/cm$^2$. The high-energy ion beam passes through vertical and horizontal scanners and is implanted into the semiconductor substrate. The energetic ions lose their energy through collisions with electrons and nuclei in the substrate and finally come to rest. Due to the kinetic energy of the impinging ions, the doping concentration has a peak inside the semiconductor and the profile of the dopant distribution is determined mainly by the ion mass and the implanted-ion energy. The advantages of the ion implantation process are precise control of the total amount of dopants, improved reproducibility of impurity levels, and lower temperature processing.

For heavy ions, the energy loss is primarily due to nuclear collisions; therefore substantial lattice disorder (damage) occurs. When the displaced atoms per unit volume approach the atomic density of the semiconductor, the material becomes amorphous. For 100-keV arsenic ions, the dose required to make amorphous silicon is $6 \times 10^{13}/\text{cm}^2$. Much of the energy loss for light ions (e.g., $B^+$ in silicon) is due to electronic collisions, which do not cause lattice damage. The ions lose their energies as they penetrate deeper into the substrate. Eventually, the ion energy is reduced sufficiently for nuclear stopping to become dominant. Therefore, most of the lattice disorder occurs near the final ion position at a depth up to a few hundreds of nm.

***Solid-Phase Epitaxy*** Because of the damaged region that results from ion implantation, semiconductor parameters such as mobility and lifetime are severely degraded. In addition, most of the ions implanted are not located in substitutional sites. To activate the implanted ions and to restore mobility and other material parameters, we must anneal the semiconductor at an appropriate combination of time and temperature in a furnace. For boron implantation, higher annealing temperatures are needed for higher doses. For phosphorus at lower doses, the annealing behavior is similar to that for boron. However, when the dose is greater than $10^{15}/\text{cm}^2$, the annealing temperature drops to about 600 °C. This phenomenon is related to the solid-phase epitaxy process. At such high doses, the silicon surface layer becomes amorphous. The single-crystal semiconductor underneath the amorphous layer serves as a seeding area for recrystallization of the amorphous layer. The epitaxial-growth rate along the $\langle 100 \rangle$-direction is 10 nm/min at 500 °C and 50 nm/min at 600 °C, with activation energy at 2.4 eV. Therefore, a 500 nm amorphous layer can be restored in a few minutes. During the solid-phase epitaxial process, the impurity dopant atoms are incorporated into the lattice sites along with the host atoms; thus, full activation can be obtained at relatively low temperatures. Note that a thin layer of damaged silicon on top of a silicon dioxide layer will not be repaired due to the missing subsurface single-crystal seeding area.

In order to achieve low temperature recrystallization for boron implantation, we can implant inert ions into silicon to form an amorphous layer. The silicon can then be annealed at low temperatures (600 °C) by the solid-phase epitaxy process to remove the implanted damage from the dopant ions. Another possibility to restore the crystal lattice without the

need of a furnace is to use electron-beam annealing or laser-beam annealing. With low-temperature e-beam annealing we can activate the dopant fully with minimal redistribution, while the high-temperature furnace annealing substantially broadens the profile.

### 3.7.5. Chemical Liquid Deposition

In the IC industry one tends to avoid wet chemistry when a dry deposition method presents itself, but MEMS needs are forcing reconsideration of electrochemical techniques as a viable solution. In micromachining, electrochemical liquid deposition (ECLD) is used to make structural microelements from a wide variety of metals, metal alloys, and even composite materials. Moreover, ECLD enables the metal replication of high-aspect-ratio resist molds while maintaining the highest fidelity. A chemical liquid deposition method that has been developed for copper is electrolytic plating. This can be done with the use of external electrodes and applied current. Applying an external voltage is generally referred to as electroplating. Deposition without an applied field is called electrodeless or electroless deposition and, when the substrate surface is replaced by a deposit, the process is called immersion plating. These processes are used commonly in printed circuit board manufacturing and on-chip interconnect fabrication. While the electroless method has received a lot of attention in recent years, mostly due to its selectivity deposition capabilities, the electroplating method has become the current method of choice for copper deposition in integrated circuits.

***Electroplating***   In electroplating, the wafers are mounted on a cathode and immersed into a plating solution that contains metallic ions ($M^{2+}$ such as $Ni^{2+}$ or $Cu^{2+}$) as shown in Figure 62. An inert anode, made of graphite (or platinum), for example, is also immersed into the solution. A voltage is applied between the two electrodes and the current drives the metal ions (or cations) toward the wafer at the cathode, forming, for example, nickel on the surface. The negative anions are attracted to the positive anode, which picks up electrons forming $Cl_2$, according to the electrochemical reaction

$$\text{Red:} \quad M^{2+} + 2e^- \rightarrow M \quad \text{(reduction at cathode)} \quad (51)$$

$$\text{Ox:} \quad 2Cl^- \rightarrow Cl_2 + 2e^- \quad \text{(oxidation at anode)} \quad (52)$$
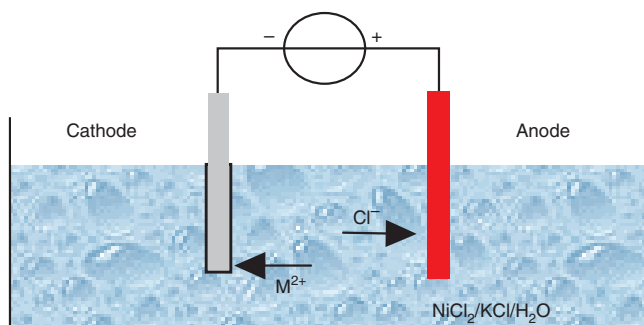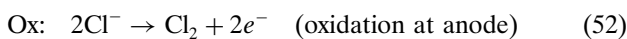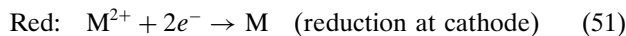


**Figure 62.** Electroplating set-up.

A thin seed layer, Au (or Cu), is often deposited first over the wafer so that electrical contacts can be made to the surface of the wafer and so that nickel is electroplated over the entire wafer surface. This seed layer formation can be done by PVD or CVD techniques.
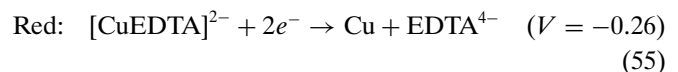
Excellent filling can be achieved with electroplating and is enhanced by using "leveling" agents or additives into the solution. These chemicals inhibit the deposition. They preferentially adsorb on the top surfaces of the topography rather than on the bottom of trenches or vias due to diffusion limitations. The top surfaces and corners then receive less deposition than the bottoms of trenches, resulting in excellent filling ability. Low resistivity and high deposition rate can be achieved with electroplating. Important process parameters are pH, current density, temperature, agitation, and solution composition.

***Immersion Plating***   Simple metal displacement reactions where the surface of a less noble metal such as zinc immersed in a copper sulphate solution gets replaced by a copper surface feature the simplest example of electrochemical deposition, known as immersion plating. No external potential is applied, and both anodic and cathodic partial reactions occur on the same electrode surface. Zinc gives off two electrons and goes into solution while copper ions receive two electrons and deposit as a metal:

$$\text{Red:} \quad Cu^{2+} + 2e^- \rightarrow Cu \quad (53)$$

$$\text{Ox:} \quad Zn \rightarrow Zn^{2+} + 2e^- \quad (54)$$
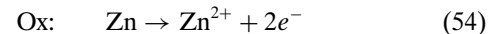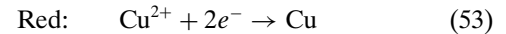
The surface of the zinc substrate becomes a mosaic of anodic (zinc) and cathodic (copper) sites, which could have nano-applications. The displacement process is continuous until the entire surface is covered with copper. At this point, oxidation (dissolution) of the zinc anode virtually stops and copper deposition ceases. The process only proceeds slowly by way of diffusion of copper and zinc ions through the copper deposit and is quite identical in time-dependent growth behavior with the thermal oxidation process. Deposits range up to 3 micrometers thick.

***Electroless Plating***   Electroless deposition involves the formation of thick metallic films from electrolytic solution without the use of external electrodes (as in electroplating) and without the dissolution of the substrate (as in immersion plating). In order to achieve this, it is essential that a sustainable oxidation reaction be employed. Simultaneous oxidation–reduction reactions between two half-reactions occur to deposit the film from solution. By this method, both blanket and selective films of good quality, low resistivity, and good filling properties can be obtained. In a typical process, the solution contains formaldehyde (HCOH) as a reducing agent and CuEDTA as the oxidizing agent and source of copper. The two half-reactions with their redox potentials in this pH = 12 solution are:

$$\text{Red:} \quad [CuEDTA]^{2-} + 2e^- \rightarrow Cu + EDTA^{4-} \quad (V = -0.26)$$
$$(55)$$

$$\text{Ox:} \quad 2HCOH + 4OH^- \rightarrow 2HCOO^- + 2H_2O + H_2 + 2e^-$$
$$(V = 0.32) \quad (56)$$
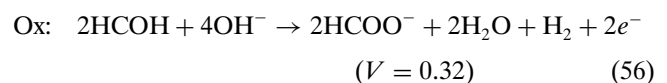
The hydroxide ion is commonly produced from sodium or potassium hydroxide. The net potential is positive so that the combined reaction to deposit copper is thermodynamically favorable. In parallel to the oxidation reaction, more or less severe hydrogen reduction goes on, which might upset the quality of the deposit. Stabilizers (i.e., catalytic poisons such as thiourea and $Pb^{2+}$) are needed as the solutions are thermodynamically unstable; deposition might start spontaneously onto the container walls. In addition, buffers, accelerators (exaltants), and complexing and surfactant agents are commonly added to the solution. In order for the copper to be deposited, a thin seeding layer is required to catalyze the electroless process. These are often Pd, Au, or Cu layers, CVD or PVD deposited. Alternatively, the wafer surface is activated by dipping it into $SnCl_2/HCl$ or $PdCl_2/HCl$. For selective electroless deposition, the seed layers should only be in the locations where the copper deposit is desired. This can be done by selectively etching the seed layer itself or using lift-off techniques. A problem with the electroless method has to do with contamination. The seed layer materials can all act as deep-level traps in underlying silicon. Of more concern are the alkali ions needed for the highly basic solution. Sodium and potassium ions can drift in silica and alter the electrical properties of the device; therefore tetra-methyl-ammonium-hydroxide $[N(C_2H_5)_4OH]$, or TMAH, is often used instead. Electroless plating is an inexpensive technique enabling plating of conductors (such as nickel, copper, cobalt, platinum, or gold). Metal alloys, such as nickel–boron or palladium–nickel, can be produced by co-deposition.

***Liquid Phase Epitaxy***   This is the growth of epitaxial layers on crystalline substrates by direct precipitation from the liquid phase. LPE is suited only to deposit thin epi layers because it has a slow deposition rate. It is also found to be useful to grow multilayered structures in which precise doping and composition controls are required.

***SAM***   Self-assembled monolayers are indispensable for many nanoprocesses. SAMs are close-packed monolayers of molecules—just like a soap molecule—with a head attached to the underlying substrate and a tail pointing upward. The composition of the head depends on the substrate it has to be connected with: typically a silane head (SiOH or SiCl) for silicon substrates and a thiol head (SH) for gold substrates. The tail can have a varying composition and functionality and is typically between 4 and 10 carbon atoms in length (i.e., a few nm). Deposition of SAMs is a simple method to modify surface wetting properties of a variety of substrate materials. Because SAMs are close-packed, they are virtually pinhole free. Moreover, they are self-assembled and thus the thickness is highly controllable. Finally, due to the "free-to-choose" tail composition, the properties of a surface can be varied almost without any constriction.

For example, hexamethyl disiloxane is a SAM used as an intermediate layer to promote adhesion of resist film to silicon-based substrates. Another example, by controlling the water content in the solvent, SAMs of trichlorosilanes can be formed on silica substrates in a short period of time. The photochemistry of the 2-nitrobenzyl group can be used for photocleavable SAMs. Ultraviolet irradiation through masks placed on top of SAM-modified surfaces leads to the production of hydrophilic carboxylate groups in the irradiated regions leaving the nonirradiated regions hydrophobic. Once photopatterned, aqueous solutions can be confined to the irradiated hydrophilic regions, which results in surface-directed flow devices. Another important group has applications in biochemistry. These are SAMs having a "proteinphilic," which can be very specific for certain enzymes. SAMs are also found in lithographs as seen in Section 4.2.3.

### 3.7.6. Physical Liquid Deposition

In physical liquid deposition, an amount of liquid is deposited (coated) first on a substrate and then it is hardened to form a solid film. Several methods exist such as dipping, spraying, painting, casting, or melting as will be treated in this section.

***Spinning***   Spin coating has been optimized for deposition of thin layers of polymer on round and nearly ideally flat surface silicon wafers. For example in photoresist spinning, the wafer is held on a vacuum spindle, and $\sim 1$ cm$^3$ of liquid resist is applied to the center of the wafer. The wafer is then rapidly accelerated up to a constant rotational speed (generally in the range 1000 to 10,000 rpm), which is maintained for about 30 s to give a uniform film. During spinning, the centrifugal forces push the excess solution over the edge of the wafer, and the residue on the wafer remains due to surface tension. The thickness of the resulting resist film is given by $t_{Res} \sim \rho\alpha/\sqrt{\omega}$ with $\rho$ the liquid viscosity, $\alpha$ the percent solid content in the resist, and $\omega$ the spin speed. In this way films down to 10 nm and up to several tens of micrometer can be formed.

***Dipping***   In dip coating, a substrate is dipped into a solution containing a polymer and a solvent. After evaporation of the solvent, a thin layer forms on the surface. To obtain pinhole-free layers, the dipping is repeated several times interspersed with drying periods. Unlike spin coating, dip coating allows us to coat 3D surfaces such as wires uniformly. Thermoplastic and thermosetting coatings are formed by dipping a heated part into a container of resin particles set in motion by a stream of low-pressure air (fluidized-solid bed). Dip coating of a substrate in a dissolved polymer typifies the simplest method to apply an organic layer to a substrate.

***Spraying***   Spray coating may involve liquids, gases, or solids. Spray coating of a liquid involves pressurization by compressed air or pushing liquid mechanically through tiny orifices. Vapors are carried in an inert dry vapor carrier. In the case of a solid, a powdered plastic resin is melted and blown through a flame-shrouded nozzle. In electrostatic spraying a negatively charged plastic powder is spray gunned onto grounded conductive parts.

***Painting***   In some applications, it can be practical to introduce a given amount of material using a brush. Clearly, this technique is not microsystem-compatible and therefore only seldom used. Nevertheless, this process is suited in packaging where sometimes only very specific spots should be covered by a film.

***Casting*** Casting is based on the application of a given amount of dissolved material on a surface and letting the solvent evaporate. A rim structure is fashioned around the substrate, providing a "flat beaker" for the solution. This method provides a more uniform and a more reproducible layer than dip coating.

***Melting*** Melting is a technique similar to casting. Identically, it uses a dummy container to confine a liquid. The liquid is formed by melting granules of material, often a metal or polymer, in a nitrogen-purged furnace. In the liquid phase, a layer forms having a very high degree of planarization. After cooling down, the container is removed leaving a metallic layer on top of the substrate. Clearly, when using metal melting, the container should withstand the temperature. Alloying of the metallic layer with the container material (contamination) is a factor of concern.

### 3.7.7. Chemical Liquid Growth

In order to avoid the necessity of heating substrates to high temperatures as in the case for chemical vapor growth, it is possible to enhance oxidation by immersing parent metals in a chemical oxidizing liquid medium. In most cases this is the oxidation of a metal film in an electrolytic cell. The medium may be aqueous, nonaqueous, or a fused salt.

***Anodization*** Anodization is a widely used technique for obtaining amorphous, highly insulating, pinhole-free, and low-stress (due to the low temperature film growth) films and there is a very large commercial usage of these in electronic capacitors. Anodization is an oxidation process performed in an electrolytic cell as schematically shown in Figure 63 with an applied voltage ranging from 20 to 600 V. The material to be anodized becomes the anode (+) while a noble metal or graphite is made the cathode (−). When electric current is passed, the surface of the anode material is converted to an oxide having protective, insulating, or other properties. (At the cathode, the only important reaction is $H_2$ evolution.) The oxygen required originates from the electrolyte used and the coating progresses from the solution side inward, toward the metal, so that the last-formed oxide is adjacent to the metal. Depending on the solubility of the anodic reaction products, an insoluble layer (e.g., an oxide film) results or in the case of a soluble reaction product, the electrode etches. For example, if the primary oxidizing agent is water, the resulting oxides generally are porous, whereas organic electrolytes may lead to very dense oxides providing excellent passivation.
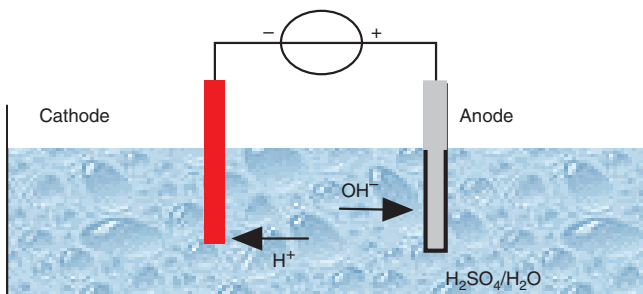
So anodic oxide coatings may be of two main types. One is the so-called barrier layer, which forms when the anodizing electrolyte has little capacity for dissolving the oxide. These coatings are essentially nonporous and their thickness is limited to about 1–2 nm/V applied. This thickness represents the distance through which ions can penetrate the oxide under the influence of the applied potential. Once this limiting thickness is reached, it is an effective barrier to further ionic or electronic flow. The current drops from a typical few tens of mA/cm$^2$ to a low leakage value and oxide formation stops. Scanning electron microscope (SEM) studies reveal the presence of close-packed cells of amorphous oxide. Their size is a function of the anodizing voltage and is typically around 100 nm. The oxide film, which forms on, for example, tantalum during anodic oxidation, is a product of the following electrochemical reaction.

$$\text{Red:} \qquad 10H^+ + 10e^- \rightarrow 5H_2 \qquad (57)$$

$$\text{Ox:} \qquad 2Ta + 10OH^- \rightarrow Ta_2O_5 + 5H_2O + 10e^- \qquad (58)$$
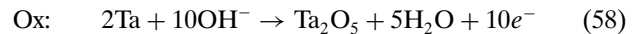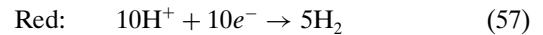
The rate-controlling process is the ion migration within the oxide film. At high fields the current density during the anodization depends exponentially on the field strength, and the rate of oxide growth is proportional to the density of the current. Since the current efficiency is about 100%, Faraday's law can be used for determining the amount of oxide formed from the quantity of electricity passed through the electrolytic cell. Figure 64 shows the behavior of voltage and current with time during anodization. The oxide formation usually consists of a constant current phase until a preselected voltage is reached. During this phase the oxide increases at a constant rate, according to the increase in potential, necessary to maintain the current. After the requested voltage is reached, the anodization continues until the ion current has decreased to a sufficiently low level of about 1% of its original value. This is to increase film uniformity and to remove pinholes. For example, at a current density of 1 mA/cm$^2$, the growth rate of tantalum pentoxide is about 0.57 nm/s. At this current density the measured voltage rise is 0.33 V/s, resulting in a growth constant of 1.73 nm/V for the formation. If this process continues until the voltage has risen to, for example, 100 V, the oxide thickness will be 173 nm.
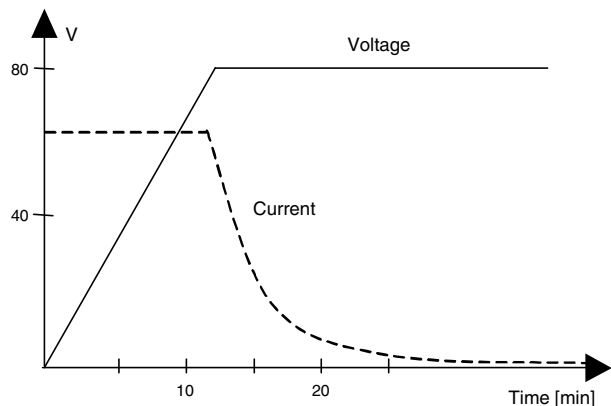


**Figure 63.** Anodization setup.



**Figure 64.** Anodization steps: constant current–constant voltage.

When the electrolyte has appreciable solvent action on the oxide, the barrier layer does not reach its limiting thickness; current continues to flow, resulting in a porous oxide structure. Porous coatings may be quite thick—up to several tens of micrometers—but a thin barrier oxide layer always remains at the metal–oxide interface.

As in the case of thermal growth, only a limited number of materials form coherent oxides in anodization. These include the valve metals (Al, Ta, Nb, Zr, and Hf), either alone or as alloys within the group, Group IV and Group III–V semiconductors, and materials such as Bi, W, TaN, SiC, Sb, Y, Ti, Mg, Zn, Cu, Ag, Cd, and steel. The rate of formation of the oxide is a function of the current density and the final oxide thickness is limited to the voltage applied to the electrolytic cell. Asymptotic growth curves are obtained, as was the case for thermal growth. For the case of aluminum an anodization constant of approximately 1.3 nm/V and for tantalum 1.7 nm/V is found. The disadvantage of using a constant voltage approach is that the initial growth stages of anodization require very high current densities, and one way around this difficulty is to anodize initially using a constant current rather than a constant voltage. The limiting condition of the thickness of the film is the breakdown under high voltages, and in the case of aluminum and tantalum this occurs at oxide thicknesses of 1.5 and 1.1 $\mu$m respectively. Other factors can, however, limit the thickness to values less than those quoted, and in particular the purity of the substrate and composition of the electrolyte are important.

Although anodizing processes are used for many metals, aluminum is by far the most important. The mechanism of anodic oxidation is not completely understood. Faraday's law predicts that for each Faraday of electricity passed, ca. 9 grams of aluminum would react, forming 17 grams of alumna, for a "coating ratio" $[Al_2O_3]/2[Al] = 1.89$. This ratio is never observed; it seldom exceeds about 1.60. Although many electrolytes have been suggested and used for anodization of aluminum, $H_2SO_4$ is the most widely employed. Concentrations are from 12 to 25 wt%. For special effects or attainment of special properties, chromic acid anodic coatings are opaque, limited to about 10 micrometers in thickness. They are used as a base for paints or adhesive bonding. Phosphoric acid anodizing has been used as a basis for plating on aluminum, though it has been superseded by zincate.

Tantalum pentoxide films have been extensively studied for use in electronic devices. The high dielectric constants of these films make them very attractive as storage capacitors. Studies of tantalum films doped with 2–7 at% nitrogen demonstrated that the reliability and leak current characteristics of tantalum pentoxide capacitors obtained by anodization can be improved.

The anodic oxidation of titanium is important in the use of platinum-plated titanium anodes, because even through pores in the platinum coating, the titanium oxidizes anodically and resists the action of the electrolyte involved.

Oxidation of silicon never led to a commercially acceptable process, mainly because the interface state density at the $SiO_2/Si$ interface is prohibitively high for semiconductor applications. Instead, anodization of silicon in a highly concentrated HF solution (excellent etchant for the anodic oxidation product $SiO_2$) may lead to porous silicon and very

high aspect ratio pores, with diameters ranging from 2 nm to several micrometers. The growth rate and degree of porosity of the silicon can be controlled by the current density. More on this subject is found in Section 5.3.3.

### 3.7.8. Physical Liquid Growth

There is no practical process known.

### 3.7.9. Chemical Solid Deposition

There is no practical process known.

### 3.7.10. Physical Solid Deposition

Wafer bonding has been a subject of interest for many years and a wide variety of bonding techniques have been reported, such as direct, plasma, anodic, adhesive (polymer, glass, or solder), eutectic, and compression bonding (thermocompression or ultrasonic). The basic principle of bonding is that two solid materials fuse and adhere to each other if they are brought in sufficiently close contact. The cohesion of atoms and molecules in a solid material as well as those between two different solid materials is ensured by a number of basic bond types, which are covalent, metallic, ionic, or van der Waals. All these are bond types and based on Coulombic forces resulting from the attraction of opposing electrical charges. Covalent and van der Waals bonds are the dominating bonding mechanisms and the atoms of two opposing surfaces must be less than 0.5 nm apart because these forces do not extend further than this distance. On the other hand, direct Coulombic forces can reach up to a distance of several micrometers and are dominant whenever charging occurs. This charging is due to macroscopically adsorbing or desorbing electrons. These direct Coulombic forces become negligible when water molecules are present at the interface, which partly neutralizes the charge on the surface. This overview is taken from the thesis of Frank Niklaus, "Adhesive Wafer Bonding for Microelectronic and Microelectromechanical Systems." In this section, we are mainly concerned with wafer bonding in which two full wafers should join. Two other applications, wire bonding and bump bonding, are mostly found in packaging applications and are not treated here. Bonding can be performed between two identical wafers or two dissimilar wafers. In the latter case, high bonding temperatures might cause pronounced shear stresses at the bonding interface preventing a correct bond. In such cases, the composition of one of the wafer materials is often adapted for thermal matching. For example, materials which are fit to become bondable with silicon are Pyrex glass and Kovar steel.

***Direct Bonding*** Direct bonding is also referred to as fusion bonding or thermal bonding. In direct bonding two wafers are contacted without the assistance of any significant pressure, electrical fields, or intermediate layers. It relies on the tendency for very smooth and flat surfaces to adhere to each other. It typically involves wafer surface preparation and cleaning, room temperature contacting of the wafers, and an annealing step to increase the bond strength. Direct bonding can be applied to identical wafers (e.g., silicon-to-silicon annealing between 600 and 1200 °C) and even dissimilar materials such as silicon-to-glass (annealing between 400

and 600 °C). Direct bonding usually leads to strong bonds and is widely used in SOI technology.

**Plasma Bonding**  In this technique, the surfaces to be bonded are exposed to (oxygen) plasma for, for example, 30 seconds, dipped in deionized water, and then placed together. After 24 hr at room temperature, the surface energy is deemed sufficiently high (>1 J/m$^2$) to establish a bond.

**Anodic Bonding**  The terms electrostatic bonding and field assisted bonding are also commonly used for this bonding technique. Anodic bonding is based on joining conducting material (e.g., silicon) and a material with ion conductivity (e.g., alkali-containing glass such as Pyrex). Two contacted wafers are heated to 180–500 °C to mobilize the ions while a voltage of 200–1500 V is applied. The voltage creates a large electric field that pulls the wafer surfaces into intimate contact and fuses them together. Due to the high force of attraction that is created by the electric field, anodic bonding is more tolerant to surface roughness than direct bonding. It is also possible to anodically bond two wafers with intermediate layers like glass, aluminum, silicon nitride or polysilicon. Anodic bonding usually leads to strong and hermetic bonds and is widely used for microsensor fabrication and for hermetic sealing of micromachined devices.

**Adhesive Bonding**  Adhesive bonding uses organic (polymer) or inorganic (ceramics or solders) intermediate layers to create a bond between two wafers. The adhesive material deforms and flows so it can make sufficiently close contact with the wafer surface to create a bond. The adhesive layer is deposited on one or both of the wafers, for example, by spin coating, spraying, screen-printing, extrusion, sedimentation, PVD, CVD, plating, or laminating. The wafers are brought into intimate contact and the intermediate adhesive layer is cured, typically by applying heat or UV radiation and pressure. The exact bonding procedure depends very much on the adhesive material used. The advantage of adhesive bonding, as compared to anodic and direct bonding, is the ability to join various wafer materials. It does not require assisting electric fields, the intermediate bonding material is not very susceptible to particles and structure at the wafer surfaces, and, moreover, it is carried out at moderate temperatures, which minimizes bond interface shear stresses. Adhesive wafer bonding requires no special wafer surface treatments such as planarization making it a low-cost bonding process. The process and materials employed determine the hermeticity and controllability of the cavity ambient.

A huge variety of organic adhesives (mainly polymers) with different chemistries and material properties are available. The bonding temperatures for polymer adhesives vary between room temperature and 450 °C making the process CMOS compatible. However, hermetical sealing is limited due to the intermediate polymer material used. A typical polymer bonding is using benzocyclobutene (BCB), a commercially available polymer from Dow Chemical. BCB is selected for its minimal outgassing, low moisture uptake, liquidlike behavior during bonding, high resistivity, chemical resistance, low processing temperatures (<250 °C), and ease of processing.

Ceramic adhesives are mostly based on oxides or silicates. For example, melting glass bonding is a variation on adhesive polymer bonding in which an inorganic glass layer (glass or glass frit) is used as the intermediate bonding material. The glass deforms or reflows during heating and makes sufficiently close contact with the wafer surfaces to create a bond between them. Two different types of glasses are available: devitrifying glasses and vitreous glasses. Devitrifying glasses are thermosetting materials which crystallize during the heating process. The melting point of these glasses is permanently increased after the curing process. Vitreous glasses are thermoplastic materials, which melt and flow at the same melting temperature each time they are thermally processed. Glasses with curing temperatures between 400 and 1100 °C are available. The advantage of glass adhesive bonding over organic adhesive bonding is that glass adhesive is able to achieve hermetic bonds (to be used in packaging of microsystems).

In solder (adhesive) bonding, layers of metal or metal-alloy based solders are used to bond wafers. The metal layers can be applied by, for example, PVD, CVD, or plating. The solder reflows during heating and wets both wafer surfaces, which causes intimate contact and bonding of the surfaces. A popular solder material is lead–tin (Pb–Sn) solder that melts at a temperature below 250 °C. Gold–tin and copper–tin solders are also suitable solder materials. Most solder-bonding processes use flux to remove oxides from the metal surfaces. If oxides are present at the metal surfaces, they can prevent wetting of the surfaces with the liquid solder, which causes poor bonding. Using *in-situ* vacuum metal deposition and bonding may prevent the development of such oxides. Like the ceramic intermediate layer, solder is able to create a hermetic sealing. Solder bonding is widely used to create electrical contacts in flip-chip bonding.

**Eutectic Bonding**  Eutectic bonding is a variation of solder bonding in which the low melting temperatures of certain alloys are used to bond two wafers. This effect is used to join two wafers with dissimilar surface materials. When the wafers are brought into intimate contact (eventually with an additional heating and high pressure applied), diffusion mechanisms between the surface materials cause the creation of an alloy at the bond interface. The alloy has a lower melting temperature than the individual materials. Thus, the melting occurs only in an extremely thin layer directly at the bond interface. The most commonly used material combination is silicon (melting point–mp—is 1414 °C) and gold (mp = 1064 °C) with a eutectic temperature of 363 °C. Also, other combinations such as lead (mp = 328 °C) and tin (mp = 232 °C) have been used. Eutectic bonding can result in strong and hermetic bonds at low temperatures and is often used for packaging microsystems. The disadvantage of eutectic bonding is the difficulty to obtain complete bonding over large areas due to native oxides at the material surfaces. This problem can be minimized by *in-situ* vacuum metal deposition and prebonding.

**Compression Bonding**  This bonding is also referred to as solid-state welding. In this bonding scheme two surfaces, of which at least one is usually a metal layer, are brought into close contact by applying a high pressure. The pressure (continues hydraulic or instantaneous explosive) causes

plastic deformation of the metal, which results in intimate contact and bonding between opposing surfaces. The application of heat improves the resulting bond quality (thermocompression bonding). Instead of directly heating the bond interface, the heat can also be supplied by ultrasonic energy—the process of ultrasonic bonding. The application of ultrasonic energy has the advantage that native oxides, particles, and surface nonuniformities at the bond interface are removed by scrubbing the surfaces at the bond interface. Common materials for compression bonding are Au to Au, Al to Au, Al to Al, and Al to glass. Typical bonding parameters for Au to Au bonding are pressures of about 300 MPa and temperatures of about 500 °C. The disadvantage is that huge net forces are required when bonding larger wafer areas. Thus, compression-bonding schemes are mainly used in wire bonding and in bump bonding schemes in which only very small areas are bonded.

### 3.7.11. Chemical Solid Growth

In some cases it is possible to apply first a solid film on a substrate. This film is subsequently used to diffuse atoms into the substrate layer beneath it, generally at elevated temperatures. A typical example is the formation of a boron or phosphor glass on top of a silicon wafer. During an annealing step, boron or phosphor atoms diffuse from the glass into the silicon due to the concentration gradient. After this "drive-in" step, the remaining (and depleted) oxide layer is removed in an etching process. Another example is the creation of a silicate film after the indiffusion of metal atoms into silicon or glass (Au or Al).

### 3.7.12. Physical Solid Growth

There is no practical process known.

### 3.8. Film Formation Examples

Different types of equipment used for the formation of thin films were discussed in the previous section. In this section the techniques used today to form specific thin films will be briefly described (see also pp. 556–571 in Plummer for epi-Si, poly-Si, $SiN_x$, $SiO_x$, Al, Ti, TiW, W, $TiSi_2$, $WSi_2$, TiN, and Cu). Table 8 provides a summary of some materials together with their formation techniques and a typical function of the film.

### 3.8.1. Silicon

Using CVD silicon as the gate electrode in MOS devices is considered a significant development in MOS circuit technology. One important reason is that silicon surpasses aluminum for electrode reliability. The silicon is clearly

**Table 8.** MEMS materials, formation method, and typical application.

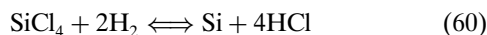| Material | Formation technique | Function |
|---|---|---|
| Al | evaporation, sputtering, PECVD | conductor, microstructure |
| Ti | evaporation, sputtering, PECVD | conductor, adhesion layer |
| Cr | evaporation, sputtering, electroplating | adhesion layer |
| Au | evaporation, sputtering, electroless, electroplating | protective layer |
| Cu | evaporation, sputtering, electroless, electroplating | conductor |
| Mo | sputtering | conductor |
| Pd | sputtering | adhesion layer, gas selective membrane |
| Pt | sputtering | interdiffusion barrier |
| Ni | evaporation, sputtering, electroplating | microstructure |
| W | LPCVD, sputtering | conductor |
| Al–Si–Cu | evaporation, sputtering | electrical conductor |
| Ni–Cr | evaporation, sputtering | resistor |
| Permalloy | sputtering | magnetoresistor, thermistor |
| Ti–Ni | sputtering | shape memory alloy |
| $Al_2O_3$ | CVD, sputtering, anodization | insulator |
| $InO_x$ | sputtering | semiconductor |
| $Ta_2O_5$ | CVD, sputtering, anodization | insulator, dielectric |
| Tin oxide | sputtering | semiconductor |
| ZnO | sputtering | insulator, piezoelectric |
| TaN | sputtering | resistor |
| TiN | MOCVD, sputtering | |
| Epitaxial Si | LPCVD, APCVD, PVD, CLD | high-resistivity semiconductor |
| Alpha-Si–H | CVD, PECVD, sputtering | semiconductor |
| Polysilicon | CVD, PECVD, sputtering | conductor, microstructure |
| Silicides | CVD, PECVD, sputtering, diffusion | conductor |
| $n/p$ Type Si | implantation, diffusion | semiconductor, etch stop |
| Porous Si | anodization | porous membrane, LED |
| $SiO_2$ | oxidation, sputtering, anodization, CVD | (thermal) isolation, masking, encapsulation |
| $SiN_x$ | LPCVD, PECVD, nitridation | (thermal) isolation, masking, encapsulation |
| Hydrogel | silk screen | electrolyte |
| Photoresist | coating | mask, planarization, pattern transfer |
| Polyimide | coating | insulator, planarization, microstructure |

superior, especially for thinner oxides, due to spiking of aluminum. Additional uses include manufacture of conductors, high-value resistors, and sacrificial layer material.

A low-pressure reactor operated between 600 and 650 °C is used to deposit polysilicon by pyrolyzing silane according to

$$SiH_4 \rightarrow Si + 2H_2 \tag{59}$$

Of the two most common low-pressure processes, one operates at a pressure of 0.2 to 1.0 Torr using 100% silane, while the other process involves a diluted mixture of 20 to 30% silane in nitrogen at the same total pressure. Both processes can deposit polysilicon with high throughput and with good uniformity (i.e., thickness within 5%). At low silane partial pressure, the deposition rate is proportional to the silane pressure almost not depending on the temperature. At higher concentrations, saturation of the deposition rate occurs and the process becomes temperature controlled. Deposition at reduced pressure is generally limited to temperatures between 600 and 650 °C. In the temperature range, the deposition rate varies as $\exp(-E_a/kT)$, where the activation energy $E_a$ is 1.7 eV, which is essentially independent of the total pressure in the reactor. At higher temperatures, gas phase reactions that result in a rough, loosely adhering deposit become significant and silane depletion will occur, causing poor uniformity. At temperatures much lower than 600 °C, the deposition rate is too slow to be practical. Process parameters that affect the polysilicon structure are deposition temperature, dopants, and the heat cycle applied following the deposition step. While the initial deposited film appears amorphous when deposition occurs below 600 °C, a columnar structure results when polysilicon is deposited at a temperature of 600 to 650 °C. This structure is comprised of polycrystalline grains ranging in size from 30 to 300 nm, at a preferred orientation of $\langle 110 \rangle$. When phosphorus is diffused at 950 °C, the structure changes to crystallite, and grain size increases to an average of between 0.5 and 1.0 $\mu$m. When temperature is increased to 1050 °C during annealing, the grains reach a final size of 1 to 3 $\mu$m. Polysilicon can be doped by diffusion, or the addition of dopant gases during deposition, which is referred to as *in-situ* doping. The implantation method is most commonly used because of its lower processing temperatures.

An atmospheric-pressure reactor is used to deposit episilicon. Four silicon sources have been used for VPE-APCVD growth: silicon tetrachloride ($SiCl_4$, reacting at 1200 °C), trichlorosilane ($SiHCl_3$, 1150 °C), dichlorosilane ($SiH_2Cl_2$, 1100 °C), and silane ($SiH_4$, 1000 °C). The overall reaction of $SiCl_4$, the most widely used source, that results in the deposition of silicon layers is

$$SiCl_4 + 2H_2 \Longleftrightarrow Si + 4HCl \tag{60}$$

An additional competing reaction is taking place that results in etching,

$$SiCl_4 + Si \Longleftrightarrow 2SiCl_2 \tag{61}$$

As a result, if the silicon tetrachloride concentration is too high or if the carrier gas entering the reactor contains HCl, etching with speeds up to 5 $\mu$m/min rather than deposition

of silicon will take place. Actually, this etching operation is used for *in-situ* cleaning of the silicon wafer prior to epitaxial growth.

### 3.8.2. Silicon Oxide

In Section 3.7.3, the formation of silicon dioxide by way of thermal oxidation has already been discussed sufficiently. Although it is possible to evaporate, sputter, anodize, and even spin-coat silicon oxide layers, this section focuses on some CVD techniques. CVD oxides are used to complement the thermal oxides: A layer of undoped silicon dioxide is used to insulate multilevel metallization, to mask ion implantation and diffusion, and to increase the thickness of thermally grown field oxides. Short of using an ellipsometer to determine the oxide thickness, the silicon oxide thickness color table comes in handy (Table 9). Phosphorus-doped silicon dioxide (P-glass) is used both as an insulator between metal layers and as a final passivation layer over devices. Oxides doped with phosphorus, arsenic, or boron are used occasionally as diffusion sources.

Most of the ultra-low-temperature methods use energy-enhanced CVD techniques (e.g., a focused electron beam) to deposit dielectric films between 25 and 300 °C. PECVD processes utilize a plasma to overcome the chemical inertness at low temperature. As a result, many radicals and intermediate species still exist after reaction. Another energy-enhanced CVD method uses UV radiation to form vapor phase reactants that enhance the deposition rates. Silicon dioxide films have been deposited at a rate of 15 nm/min at temperatures as low as 50 °C by means of UV radiation. Sometimes it is convenient to use PVD deposition. Compounds such as silica are much harder to evaporate in the right composition as alloys with single-source sputter systems. The composition of the vapor phase is usually not the same as the source compound, and chemical reactions and molecular changes often occur as the material is evaporated. Sputter deposition generally does a much better job in depositing compositionally uniform films of both alloys and compounds.

For low-temperature deposition (300 to 500 °C), the films are formed by reacting silane, dopant, and oxygen. The

**Table 9.** Oxide thickness (nm) color table.



| Color | | | | |
|---|---|---|---|---|
| Grey | 10 | | | |
| Tan | 30 | | | |
| Brown | 50 | | | |
| Blue | 80 | | | |
| Violet | 100 | 280 | 460 | 650 |
| Blue | 150 | 300 | 490 | 680 |
| Green | 180 | 330 | 520 | 720 |
| Yellow | 210 | 370 | 560 | 750 |
| Orange | 220 | 400 | 600 | |
| Red | 250 | 440 | 620 | |

chemical reactions for phosphorus-doped oxides at 450 °C are

$$SiH_4 + O_2 \rightarrow SiO_2 + 2H_2 \tag{62}$$

$$4PH_3 + 5O_2 \rightarrow 2P_2O_5 + 6H_2 \tag{63}$$
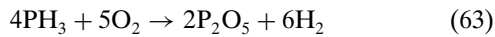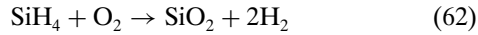
The deposition process can be performed in an APCVD or LPCVD reactor. The low deposition temperature of the silane–oxygen reaction makes it a suitable process when films must be deposited over a layer of aluminum.

For intermediate-temperature CVD (500 to 800 °C), silicon dioxide can be formed by decomposing tetra-ethyl-ortho-silicate, $Si(OC_2H_5)_4$, in an LPCVD reactor. The compound, abbreviated TEOS, is vaporized from a liquid source and decomposes at 700 °C as follows:

$$Si(OC_2H_5)_4 \rightarrow SiO_2 + \text{by-products} \tag{64}$$
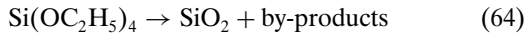
While the intermediate temperature required for the reaction prevents its use over aluminum or polymers, it is suitable for polysilicon gates requiring a uniform insulating layer with good step coverage. Residual stresses can be tuned with for example, the deposition temperature or pressure and can be below 100 MPa tensile. The oxides can be doped by adding small amounts of the dopant hydrides (phosphines, arsine, or diborane) similar to the process in epitaxial growth.

For high-temperature deposition (700–900 °C), silicon dioxide is formed by reacting, for example, 30 sccm dichlorosilane, $SiCl_2H_2$, with 90 sccm nitrous oxide at reduced pressure (~500 mTorr):

$$SiCl_2H_2 + 2N_2O \rightarrow SiO_2 + 2N_2 + 2HCl \tag{65}$$
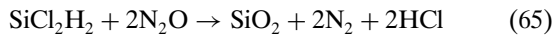
This deposition at a rate of ca. 1 nm/min (and a refractive index of $\eta = 1.45$) gives excellent film uniformity and is sometimes used to deposit layers over polysilicon.

In general, there is a direct correlation between deposition temperature and film quality. The lower densities occur in films deposited below 500 °C. Heating deposited silicon dioxide at temperatures between 600 and 1000 °C causes densification, during which the oxide thickness decreases while the density increases to 2.2 g/cm$^3$. At higher temperatures, deposited films are structurally similar to silicon dioxide that has been thermally grown and the compressive stress rises to ca. 300 MPa and the refractive index to the usual 1.46 (at a wavelength of 633 nm). Oxides with lower indices are porous, such as the oxide from the silane–oxygen deposition. The porous nature of the oxide also is responsible for the lower dielectric strength. Dichlorosilane- and TEOS-oxide give a nearly conformal coverage due to rapid surface migration. However, during silane–oxide deposition, no surface migration takes place and the step coverage is determined by the arrival angle. A smooth topography is usually required for the deposited silicon dioxide that is used as an insulator between metal layers. If the oxide used to cover the lower metal is concave, circuit failure may result from an opening that may occur in the upper metal layer during deposition. Because P-glass deposited at low temperatures becomes soft and flows upon heating, it provides a smooth surface and is often used to insulate adjacent

metal layers. This process is called P-glass-flow. P-glass-flow depends on annealing time, temperature, phosphorus concentration, and annealing ambient. The etch rates of oxides in a hydrofluoric acid solution depend on deposition temperature, annealing history, and doping concentration. Usually, higher quality oxides are etched at lower rates.

Although silicon nitride is a much better diffusion barrier, silicon dioxide performs well as a mask against diffusion of the common dopants in silicon; the diffusion coefficient $D$ of boron at 900 °C in silica is $2.2 \times 10^{-19}$ cm$^2$/sec compared to $4.4 \times 10^{-16}$ in silicon; for phosphorous, $D$ equals $9.3 \times 10^{-19}$ cm$^2$/sec in silica compared to $7.7 \times 10^{-15}$ in silicon. For many other elements, silica forms a poor diffusion barrier. The amorphous oxide has a more open structure than crystalline quartz; only 43% of the space is occupied. Consequently, a wide variety of impurities (especially alkali ions such as sodium and potassium) can readily diffuse through amorphous silica. Diffusion through the open silica structure happens especially fast when the oxide is hydrated. One of the reasons for the poor performance of silicon dioxide-based ISFETs in aqueous solutions can be traced back to the simple observation that silica in water behaves like a sponge for ions. This is why, in such devices, silica is often topped off with the excellent ionic barrier material $Si_3N_4$. The use of silica as a diffusion mask often stems from convenience; silica is easy to grow, whereas one cannot put silicon nitride that easily onto silicon.

### 3.8.3. Silicon Nitride

Thin films of silicon nitride are of special interest for microtechnology. These films can be used for passivating devices, because they serve as good moisture barriers, prevent sodium diffusion, and provide excellent scratch protection. The films also can be used as masks for selective oxidation of silicon ("LOCOS"), because silicon nitride oxidizes very slowly. Another application is the use as an etching mask for wet chemical KOH etching and the use as a construction material in microsensors or in X-ray masks. Silicon nitride films can be deposited in a low-temperature (300 °C) PECVD process or an intermediate-temperature (750 °C) low-pressure (below 1 Torr) LPCVD process. The films deposited by PECVD are not stoichiometric and have low density (2.4 to 2.8 g/cm$^3$). Because of the low deposition temperature, these films can be deposited over the completely fabricated devices and serve as their final passivation. The LPCVD films deposited at ca. 800 °C and 200 mT have stresses ranging from low tensile (<300 MPa) for nonstoichiometric (silicon-rich) films up to high tensile (~1000 MPa) for stoichiometric ($Si_3N_4$) films with high density (2.9 to 3.1 g/cm$^3$).

In the PECVD process, silicon nitride is formed at 300 °C inside a radial-flow parallel-plate reactor either by reacting silane and ammonia in argon plasma or by reacting silane in a nitrogen discharge.

$$SiH_4 + NH_3 \rightarrow SiNH + 3H_2 \tag{66}$$

$$2SiH_4 + N_2 \rightarrow 2SiNH + 3H_2 \tag{67}$$
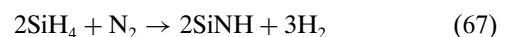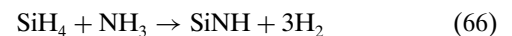
The products depend strongly on deposition conditions but the deposition rate generally increases with increasing temperature, power input, and reactant gas pressure. Large concentrations of hydrogen are contained in PECVD films. The plasma nitride film (SiN) used in semiconductor processing generally contains 20 to 25 at% hydrogen. Films with low tensile stress ($\sim 2$ GPa) can be prepared. Film resistivities range from $10^5$ to $10^{21}$ $\Omega$ cm depending on silicon-to-nitrogen ratio, while dielectric strengths are between 0.1 and 0.6 V/nm.

In the LPCVD process, for example, 30 sccm dichlorosilane (DCS) and 90 sccm ammonia react at reduced pressure ($\sim 300$ mTorr) to deposit silicon nitride at temperatures between 700 and 900 °C with good film uniformity, conformal step coverage, low speed (ca. 7 nm/min, $\eta = 2.00$), high wafer throughput, and often combined with the high temperature silicon oxide LPCVD. The reaction is

$$3SiCl_2H_2 + 4NH_3 \rightarrow Si_3N_4 + 6HCl + 6H_2 \qquad (68)$$
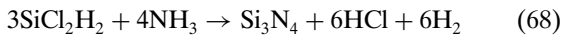
The activation energy for deposition is about 1.8 eV. It is found that—in decreasing order of importance—the gas flow ratio of Si and N containing precursors, temperature, and pressure are the most relevant parameters determining the electrical, mechanical, and optical properties of the films and the deposition rate and uniformity in film properties across a wafer. Standard processes as used in the IC industry employ an excess of ammonia, resulting in a nearly stoichiometric $Si_3N_4$ film. The LPCVD nitride is an amorphous dielectric with a dielectric constant of 6, containing up to 8 at% hydrogen. The resistivity at room temperature is about $10^{16}$ $\Omega$ cm, its dielectric strength is 1 V/nm, and the etch rate in buffered HF is less than 1 nm/min. The film's very high tensile stress of approximately 1 GPa makes films thicker than 200 nm sensitive for cracking and, therefore, the films are less suitable as a construction material. Stress reduction—and even stress reversal from tension to compression—can be accomplished when an excess of DCS is used. In such cases, silicon-rich layers (ending in polysilicon) will form with large variations in the optical refractive index, mechanical stress, and electrical resistivity. The deposition rate increases with increasing total pressure or dichlorosilane partial pressure and decreases with an increasing ammonia-to-dichlorosilane ratio.

### 3.8.4. Multilayer Silicon Compounds

The LPCVD reactor operating with dichlorosilane vapor is well suited to deposit a stack of alternating layers of, for example, silicon, silicon oxide, and silicon nitride by introducing alternatively additional amounts of hydrogen, nitrous oxide, and ammonia respectively. It is even possible to smoothly vary from stoichiometric silicon nitride to silicon-rich silicon nitride and back by smoothly varying the mass flow of ammonia during deposition. It is possible to deposit silicon oxynitride by simultaneously introducing both ammonia and nitrous oxide. In order to deposit a stack of alternating nanolayers it is important to notice that the mass flow controllers (MFCs) should be well controlled. Especially, the initialization of the MFC is a point of concern. Figure 65 shows a time diagram of the MFC flows of DCS, ammonia,
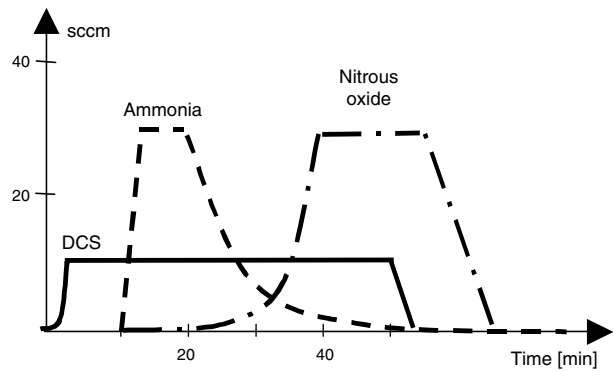


**Figure 65.** Multilayer LPCVD deposition.

and nitrous oxide of a freely chosen silicon compound nanostack using LPCVD at 800 °C and 300 mTorr. The stack starts with the growth of a 10 nm thin layer of polysilicon at 10 sccm DCS flow. Then 30 sccm ammonia is introduced to deposit 10 nm stoichiometric silicon nitride. After closing the ammonia flow and introducing nitrous oxide slowly, subsequently silicon-rich nitride, silicon oxynitride, silicon-rich oxide, and 10 nm of silica form. Finally, after closing the DCS flow, the nitrous oxide continues flowing to passivate the stack with pure silica.

### 3.8.5. Silicides

Silicides such as $TiSi_2$ and $TaSi_2$ have reasonably low resistivity ($<50$ $\mu\Omega$ cm) and are generally compatible with MEMS processing. These silicides remain stable during contact with polysilicon. Silicides may be formed in several ways; depositing a refractory metal film on (poly)silicon and sintering the structure, co-deposition the metal and silicon in a PVD system, or forming the silicide by CVD. All silicides can withstand much higher processing temperatures than aluminum. Of course, the eutectic temperature will limit the maximum process temperature of the silicide in contact with silicon.

### 3.8.6. Aluminum

Aluminum and its alloys are used extensively for metallization in microsystems, because of its low resistivity (i.e., 2.7 $\mu\Omega$ cm for Al and up to 3.5 $\mu\Omega$ cm for its alloys). Aluminum also adheres well to silicon dioxide. However, the use of aluminum creates problems such as spiking and electromigration. To improve the characteristics of pure aluminum, other materials are added, such as silicon (to prevent spiking) or copper (to prevent electromigration or hillocking).

Most often, aluminum is deposited in PVD systems. Resistance-heated evaporation is difficult with Al because during heating the surface of the aluminum melt is readily oxidized due to impurities deriving from the reactor or from the crucible. Instead, e-beam evaporation is used to break the surface oxide layer. Residual film stresses differ a lot but typically range between a few MPa up to several tens of MPa strongly depending on the deposition temperature.

To improve step coverage, aluminum can be deposited by MOCVD using metal-organic compounds such as tri-isobutyl aluminum:

$$2[(CH_3)_2CHCH_2]_3Al \rightarrow 2Al + 3H_2 + \text{by-products} \qquad (69)$$

As devices become smaller, the corresponding current density becomes larger. High current densities can cause device failure due to electromigration. The term electromigration refers to the transport of mass in metals under the influence of current. It occurs by the transfer of momentum from the electrons to the positive metal ions. When a high current passes through thin metal conductors, metal ions in some regions will pile up and voids will form in other regions. The pileup can short-circuit adjacent conductors while the voids can result in an open circuit. The electromigration resistance of aluminum film conductors can be increased by alloying with copper (e.g., Al with 0.5% Cu) or encapsulating the conductor in a dielectric.

### 3.8.7. Other Metals

CVD is attractive for metallization because it offers coatings of conformal nature with good step coverage and large throughput. The basic setup is the same as that used for deposition of dielectrics and polysilicon. CVD is capable of producing conformal step coverage over a wide range of topographical profiles often with lower electrical resistivity than that from PVD, which also suffers from the effects of shadowing and poor step coverage. One of the major applications of CVD metal deposition has been in the area of refractory-metal deposition. For example, tungsten's low electrical resistivity (5.3 $\mu\Omega$ cm) and its refractory nature make it a desirable metal for use in microfabrication. The following two chemical equations show both the pyrolysis and the reduction of tungsten:

$$WF_6 \rightarrow W + 3F_2 \tag{70}$$

$$WF_6 + 3H_2 \rightarrow W + 6HF \tag{71}$$
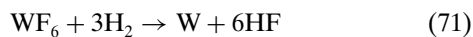
Many other metals such as molybdenum, tantalum, and titanium are of interest for microdevice applications. These metals can be deposited by hydrogen reduction in a LPCVD reactor having the overall reaction

$$2MCl_5 + 5H_2 \rightarrow 2M + 10HCl \tag{72}$$
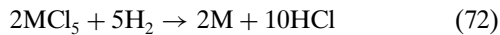
where M stands for the aforementioned metals.

### 3.9. Conclusion and Nanoperspective

Developing near-term commercially viable products is of vital importance for the development of the nanofield. Near-term opportunities of nanomaterials lie in functional nanomaterials such as tougher and harder cutting tools, the superplasticity of ceramics during processing, high performance parts for the aerospace and the building industry, energy and filter technologies (novel solar cells and water purification), the automobile industry, optical and catalytic applications, and sensors. On a longer term, and dependent on the developments in the electronic industry, (opto)electronic applications of nanomaterials such as photonics may find a big market. Interdisciplinary cooperation in research and development is important for the realization of scientific breakthroughs and for new products such as hybrid coatings or nanoelectronic devices. Currently, the preparation technology of nanomaterials plays an important role in state-of-the-art science and dedicated scientific journals and conferences have appeared already. Fundamental physics and chemistry, as well as materials science and engineering, are involved in advancing the level of understanding and handling atomic arrangement and hence properties of nanomaterials. The nanoscale offers many opportunities for materials and devices with new properties that vary greatly in origin, composition, production method, properties, and price. It is hard to predict which of them will play a role in products based on nanotechnology, but the main challenges along the path to new commercially viable (MEMS-based) nanomaterials can be summarized as:

- *Fundamental physics:* Understanding nanomaterial formation and composition and the critical role of surfaces, interfaces, defects, and particulates is important.
- *Fabrication:* Reproducible and uniform production of nanomaterials is necessary.
- *Characterization:* Nanoscale resolution microscopes are essential tools for characterization.
- *Economics:* Cost-efficiency and scaleable production of nanomaterials is requested.

Nanomaterials can be divided into nanofilms, nanoparticles, and nanostructured films. In MEMS-based film formation, as described in this chapter, the formation of a film with a thickness between 1 and 100 nm is defined as a nanofilm or nanolayer. In nanofilms particles should be avoided. Particles might create pinholes and shorts, which influence the electrical, chemical, and mechanical strength of the layer. However, the formation of individual nanoparticles (i.e., a particle between 1 and 100 nm in diameter) can be beneficial in quantum devices and other applications. When such nanoparticles are "collected" or incorporated in an overall framework (thin film), it is called a nanostructured film. All these nanomaterials exhibit new or improved properties compared to the corresponding bulk material. This makes them attractive for applications such as quantum dot lasers, (electro)luminescent devices, novel solar cells, gas sensors, resistors and varistors, conductive and capacitive films, high-temperature superconductors, and thermoelectric, optical, and magnetic films. Both nanoparticles and nanostructured films were not treated in this chapter in detail but are likely to become very important in future nanotechnology. Therefore, some brief remarks will be given here.

**Nanofilms** In order to form a nanofilm accurately it is important to have a process which is able to deposit or grow the film in such a way that the thickness, composition, and structure are guaranteed within certain specifications. In such cases film formation processes which are sensitive to particle creation (such as homogeneous gas phase reaction in CVD or dusty plasmas) and processes with high film-formation speed are avoided. Typical processes able to form nanolayers are LPCVD, MBE, laser ablation deposition, thermal and chemical oxidation, anodization, spin coating, and SAMs. The growth of ultrathin silica films follows different kinetics than "thick" films. For example, the thickness and growth rate of native oxides (<1 nm) strongly depend on surface preparation and the environmental conditions regarding exposure and seem to form layer-by-layer [184]. It is thus very difficult to prepare a native oxide of a

certain quality. Chemical oxides (1–3 nm) are more stable than native oxides and are produced in strongly oxidizing agents such as $HNO_3$, $H_2O_2$, or just water. This renders silicon more or less inert to further oxidation by air even up to about 600 °C. Growth of ultrathin thermal oxides (1–10 nm) at temperatures above 600 °C is influenced by the nature of oxidants for the surface reaction such as the presence of O or $O_2$, or by the stress present, or by the transport through micropores. In this regime the growth is linear with time although for the initial layers growth is repressed by high internal stresses [172, 183]. On the other hand for "ordinary" thermal oxides (>10 nm), the growth is parabolic with time because only the diffusion of the oxidant through the growing film is controlling the rate. At temperatures above about 1200 °C, silicon reacts with nitrogen, $N_2$, in the air as well as oxygen, to form the silicon nitrides SiN and $Si_3N_4$. The forming of large-scale single crystal nanofilms on top of amorphous layers might be difficult. Although preshaping the substrate (with a repetition smaller than the domain size) might induce single crystal formation, the accuracy of the lithography could prohibit this option. The surface condition will have a major influence on the properties of nanofilms. For example, condensed water, organic "dirt," or trapped ionic species will alter the initial film formation process and, therefore, the film adhesion, morphology, and structure. The growth of natural oxides is increasingly important due to stress considerations as the dimensions of freestanding structures are getting smaller and smaller. A short overview of these subjects, as found in this section, is depicted in Table 10.

***Nanoparticles*** At present, many ways exist to synthesize nanoparticles, such as mechanical ball milling and gas-phase synthesis (such as dusty plasmas and CVDs). In the latter case, the particles are collected as a powder or deposited on a substrate. If the particles have dimensions comparable to the wavelength of the electrons, phonons, magnons, etc. inside the material, quantum mechanical effects predominate. A particle becomes a quantum dot and quantum confinement leads to a change in the density of states. The macroscopic properties (electronic, optical, electrical, magnetic, chemical, and mechanical) of materials can thus be affected substantially by small changes in the nanoparticle. It is important to realize that many aspects of nanoparticles in liquids have been (and are being) studied in colloid science. Due to their large surface-to-volume ratio, nanoparticles are very reactive. The particles tend to both agglomerate and oxidize, which causes substantial handling problem.

***Nanostructured Films*** Examples of nanostructured films are nanoporous, nanocrystalline, nanocomposite, and hybrid films. Nanoporous films have nanosized pores, nanocrystalline material consists of many crystalline domains, and nanocomposite film contains two or more phase-separated components with morphology of spheres, cylinders, or networks with nanodimensions. Nanohybrid films are constructed from a combination of polymeric organic components and inorganic or ceramic components that are chemically interconnected on a molecular level. Both the size of the nanostructure and the scale of order within
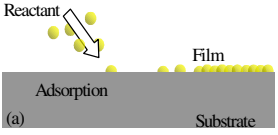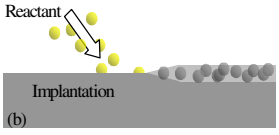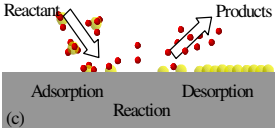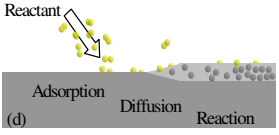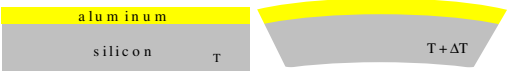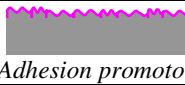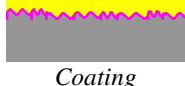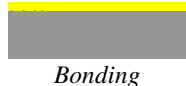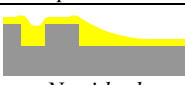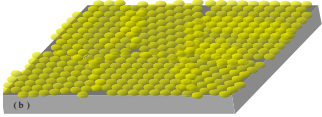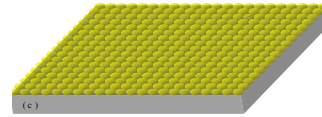
them affect the film properties and they often exhibit properties that are drastically different from those of conventional films. In many cases, this is a result of the large fraction of grain boundaries—the boundaries between the nanoparticles in the film—and hence by the percentage of surface atoms. This surface can border on the embedding matrix, on a nanoparticle, on air, or on vacuum in case of a pore or defect. Due to this, film properties become governed by surface properties. The size range of 1 to 100 nm implies a number of atoms per particle varying from several to ten million or more. For the smallest sizes, the surface-to-volume ratio becomes very large. For instance, for close-packed spheres the percentage of surface atoms is about 80% for a 50-atom particle and is still 20% for a 2000-atom particle. A very instructive example is glass. Although generally classified as an amorphous material, glass is in fact a nanostructured material. The nanoparticle is the silicon ion surrounded tetrahedrally by four oxygen ions. These tetrahedral are joined together at their corners by oxygen bridges in a variety of ways to form varies phases or structures of silica with very different properties. This nanostructure might explain the viscoelastic behavior of glass occurring even at relatively low temperature and is responsible for the spongelike behaviour of glass for water with ionic species such as sodium [170]. Mixing the silicon oxide with, for example, boron oxide creates a glass with thermoelectric properties and there are many more examples where the mixing of the silica nanoparticles with other ceramic nanoparticles or (alkali) ions influences the behavior of the glass drastically.
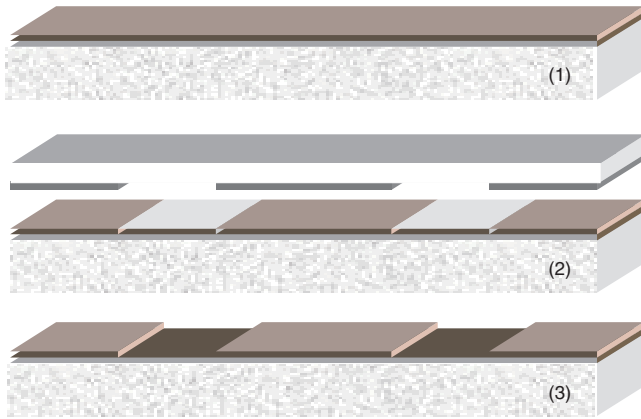
## 4. LITHOGRAPHY

A thin film deposited on the wafer surface is usually not interesting enough to form a microdevice. The thin film should be shaped to leave the desired pattern of the film on the wafer surface. For this purpose lithography has been introduced. Words such as printing, writing, and lithography have more or less the same meaning in daily life. However, in order to create a consistent terminology, in this section we will subdivide lithography into two independent techniques, printing and writing.

"Lithography" is Greek for "to write" [gráphein] with a "stone" [lithos]. A lithograph, for people interested in art, is a less expensive picture made by impressing in turn several flat, embossed slabs, each covered with greasy ink of a particular color, onto a piece of stout paper. In this way, many "originals" can be made from the same slab. The various colors must be accurately aligned with respect to one another within some registration tolerance to produce the effect intended by the artist who carved or etched the slabs. However, nowadays the term lithography has a somewhat broader meaning and includes not only mechanical impressing techniques. For example, the ability to print patterns using optical techniques with submicrometer features and to place those patterns on a substrate with better than 0.1 micrometer precision is what makes today's microcomponents (including microelectronics and microsystems) possible. The concept is simple as found in Fig. 66). (1) A radiation-sensitive resist is spun onto a substrate forming a thin layer on the surface. (2) The resist is then selectively exposed, by shining radiation (photons, electrons, or

**Table 10.** Schematic overview of film formation methods and phenomena.



| | Deposition | | Growth | |
|---|---|---|---|---|
| **Formation** | *Physical* — Reactant, Film, Adsorption, (a), Substrate | | *Physical* — Reactant, Implantation, (b) | |
| | *Chemical* — Reactant, Products, Adsorption, Desorption, (c), Reaction | | *Chemical* — Reactant, Adsorption, (d), Diffusion, Reaction | |
| **Stress** | *Bimorph thermal stress.* — aluminum, silicon, T, T + ΔT | | *Monomorph intrinsic stress gradient.* | |
| **Adhesion** | **Gas-phase** | **Liquid-phase** | **Solid-phase** | |
| | *Plasma sputtering* | *Adhesion promotor* | *Surface polishing* | |
| | *Deposition* | *Coating* | *Bonding* | |
| **Step coverage** | **Gas-phase** | **Liquid-phase** | **Solid-phase** | |
| | *Ideal step coverage* | *Ideal planarization* | *Ideal capping* | |
| | *Nonideal* | *Nonideal* | *Nonideal* | |
| | *Amorphous* (a) | *Polycrystalline* (b) | *Monocrystalline* (c) | |

| **Methods** | Deposition | Growth | Deposition | Growth | Deposition | Growth |
|---|---|---|---|---|---|---|
| | (V)LPCVD<br>APCVD<br>APCVD-VPE<br>MOCVD<br>(HD)PECVD | Thermal oxidation<br>Therm. nitridation<br>Diffusion | Electroplating<br>Immersion plating<br>Electroless plating<br>LPE<br>SAM | Anodization | | Solid-source diff. |
| | Evaporation<br>Laser ablation<br>Sputtering<br>MBE<br>Cluster beam<br>Ion plating | Ion implantation | Spin coating<br>Dip coating<br>Spray coating<br>Painting<br>Casting<br>Melt coating | | Direct bonding<br>Anodic bonding<br>Adhesive bonding<br>Eutectic bonding<br>Compression b. | |

**Figure 66.** Basic lithographic process. (1) Spin-coat a layer of photoresist. (2) Illuminate the resist through a mask. (3) Develop the resist.

ions) through a mask, which contains the pattern information for the particular layer being fabricated. That is, the mask is partly transparent and partly opaque to form this pattern. (3) The resist is then developed which completes the pattern transfer from the mask to the substrate. Therefore, the optical lithography used in the microcomponent industry is related to the imprinting lithography of the art world. The artist corresponds to the chip designer and the slabs are masks for the various thin film levels. The press corresponds to the exposure system, which also aligns it to a completed level. The ink may be compared with the radiation-sensitive resist and the paper can represent the substrate onto which the patterns will be transferred. Due to the fact that the method is identical with the planographic printing technique, in this section it will be defined as *print lithography*. So, although historically lithography was synonymous with stone writing, nowadays the word is best translated into printing instead of writing. As should be clear by now, to be able to perform print lithography, a mask is needed. For the fabrication of this mask we need calligraphy.

"Calligraphy" is Greek for "beautiful writing." It is a skilled penmanship practiced as a fine art. In the East calligraphy has been consistently practiced as a major aesthetic expression. In China, from the 5th century BC, when it was first used, calligraphy has always been considered equal, or even superior, to painting. Nowadays, calligraphy is a very basic step in cleanroom facilities. For example, the making of a mask, needed for print lithography, is done by transferring a pattern into a radiation sensitive resist layer while writing with a narrow beam. Due to the use of the narrow beam of electrons, ions, photons, or even a liquid to write a pattern on or in a substrate (including a resist film) we will define this technique as *write lithography*. Although the term write lithography seems to be a pleonasm, the author believes that it is a necessary amalgamation to discern it from print lithography. The pattern is normally transferred using a computer aided design (CAD) controlled *XY*-stage and, therefore, the writing process is relatively slow compared to print lithography. Therefore, the writing process is nowadays restricted to small-scale specialities and mask making for print lithography.

So writing (of a mask) and printing (with a mask) are two independent but indispensable techniques to perform lithography in present microcomponent development. Print lithography uses a broad beam exposure tool together with a mask to replicate a pattern in one flash and the pattern on this mask is usually fabricated with the help of narrow beam write lithography. Nevertheless, today's lithographic equipment consists of impressive machinery that is used to repeatedly image a pattern of a mask onto a silicon wafer, which is best specified as a combination of both printing and writing. This process is known as *stepper lithography*: the process of writing a replicating pattern with the help of a "stepper mask" in an *XY* fashion several times. Stepper lithography is not only used to produce a pattern directly on a wafer surface, but it can also be used to create a mask, which is then used in print lithography to replicate a pattern on a wafer.

The use of an intermediate resist layer to transfer a pattern is not strictly necessary (see section on resist lithography). It is possible to directly print or write with, for example, an ion beam into a layer without the help of resist. Although this normally lowers the selectivity between different layers (the physical nature of the ion beam is normally quite material insensitive), it increases the resolution enormously (radiation scattering in resist limits the resolution typically by a factor of two). This issue becomes increasingly important in sub-100 nm lithography (i.e., nanolithography) and will be treated in the section on direct lithography.

While the concept of lithography is simple, the actual implementation is very expensive and very complex, primarily because of the demands placed on this process. The performance of a lithographic process is determined by parameters such as resolution, depth of focus, exposure field, registration, throughput, defect density, and resist material. The *resolution* (Res) is the minimum feature dimension that can be transferred with high fidelity to a film on a wafer. It is basically determined by the wavelength of the radiation employed, according to Rayleigh's criterion: $\text{Res} = k_1 \lambda / NA$—the separation of two barely resolved point sources. Here $k_1$ is a system-dependent constant (typically around 0.5), $\lambda$ is the wavelength of the lithographic system, and NA ($= \sin \alpha$) is the numerical aperture, which indicates the radiation acceptance angle of the system. Meanwhile, the *depth of focus* (DOF) of this image changes with the wavelength and NA according to $\text{DOF} = k_2 \lambda / NA^2$, with $k_2 (\sim 0.5)$ an imaging constant depending for instance on the coherence of the source and on the resist. This shows that the resolution can be improved by either reducing the wavelength or increasing NA. However, the DOF degrades much more rapidly by increasing NA than by decreasing $\lambda$ and a reasonable DOF is needed to expose wafers with certain topography with height variations patterned in previous manufacturing steps. This explains the trend toward shorter wavelengths in lithography. *Exposure field* requirements result from ever-increasing chip sizes and the need to expose at least one full chip with each exposure. *Registration* (i.e., alignment or placement accuracy) is a measure of how accurately patterns on successive masks can be aligned with respect to previously defined patterns on the wafer. It remains at about one-third of the minimum feature size for each generation of technology. *Throughput* is

the number of wafers that can be exposed per hour for a given mask level and is directly determined by the kind of exposure tool used. Wafer exposure tools today cost about 10 million Euro and must be capable of printing on the order of 1 wafer per minute in order to meet cost objectives. *Defect density* or yield translates directly into yield loss and therefore higher costs for the finished chips. Defects introduced during the lithographic process are a significant contributor to final chip yield. Another important subject is the *resist material* itself (in case of resist lithography), which is a radiation-sensitive compound. Here the primary issues are sensitivity, contrast, tone, etch resistance, etch selectivity with respect to underlying layers, profile (3D), step coverage, resolution, and ruggedness. Sensitivity is a key characteristic and it determines the resist's efficiency in responding to a given amount of radiation.

In order to facilitate a confident choice to perform nano-lithography, sections on write lithography, print lithography, stepper lithography, and alternative and related lithography will be treated in succession.

## 4.1. Write Lithography

The overall write lithography (or writing) process is conceptually illustrated in Figure 67. The patterns that comprise the various layers in a microsystem are designed using CAD systems. Today these systems contain many advanced capabilities that greatly improve the efficiency of designing microcomponents having practically any shape. As already is the case for IC design, we envision libraries of previous designs that are known to work and are available, from which basic functions can be cut and pasted into new (more complex) designs. Software tools are used to help route the connections between functional blocks. Additional tools check the design to make sure that there are no violations of design rules. And finally, system-level simulation tools are available to predict the performance of the new design. Once the design is complete and ready to transfer to the fabrication facility, the information for each mask level is transferred to a machine that is either an electron, ion, or laser



**Figure 67.** Schematic of write lithography.

beam pattern generator (Fig. 67). These machines raster this narrow (focused) beam in an *XY* pattern across the substrate (wafer or mask blank) with the beam blanked on and off as necessary to generate the appropriate pattern. Generally the beam size is on the order of 0.1–0.5 micrometer. It is perhaps obvious that the e-beam (or ion beam) system could be used directly to write images on a wafer simply putting the electron sensitive resist on the wafer rather than on the mask. The reason this is not done in high-volume manufacturing is simply because the wafer throughput would be too slow. Typical e-beam pattern generators would require tens of minutes to expose a full wafer. This is much slower than optical steppers that typically have throughputs on the order of 1 wafer per minute.

In case the pattern generator is used to create a mask (to be used in print lithography), the mask itself is usually a fused silica plate covered with a thin layer (ca. 80 nm) of chromium and a layer of resist. A thin antireflection coating (10–15 nm) is also often used between the chrome and the resist to prevent reflections from the chrome layer, which can degrade pattern resolution. The beam exposes the resist which is then developed and used as an etch mask to transfer the mask pattern into the chrome. The chrome layer is usually wet etched. Once the chrome is etched, the resist is removed. The fused silica substrate has a highly polished surface so that light is not scattered as it passes through the mask and has a small thermal expansion coefficient so that mask dimensions are stable over small temperature changes. It is also obviously important that the silica has high transparency at the wavelength of radiation used in the wafer exposure system. In optical lithography, this is becoming more difficult to achieve in practice as the exposing wavelength moves deeper into the ultraviolet region to achieve higher resolution. Even though the mask material (basically $SiO_2$) has a large bandgap, trace impurities in the glass can degrade optical transparency because they can absorb light at these short wavelengths.

### 4.1.1. Electron Beam Writing

Electron beam writing (EBW) uses an electron gun for patterning. The gun is a device that can generate a beam of electrons with a suitable current density; a tungsten thermionic-emission cathode or single-crystal lanthanum boride ($LaB_6$) can be used for the electron gun. Condenser lenses are used to focus the electron beam to a spot size of 1–100 nm in diameter. Beam-blanking plates (to turn the electron beam on and off) and beam deflection coils are computer-controlled and operated at high rates (MHz) to direct the focused electron beam to any location in the scan field on the substrate. Because the scan field (typically 1 cm) is much smaller than the substrate diameter, a precision mechanical stage is used to position the substrate to be patterned. EBW offers higher resolution than optical lithography because of the small wavelength of the 10–50 keV electrons. The ultimate resolution of EBW is not limited by diffraction (the wavelength is of the order of $10^{-13}$ m, which is much smaller than atomic sizes), but by electron scattering in the resist (in case of resist lithography) and by the various aberrations of the electron optics. Due to its flexibility in creating patterns, EBW is widely used in research or small
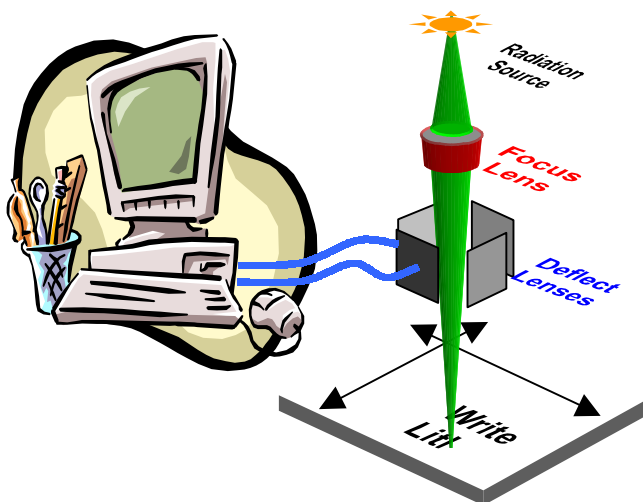
volume production specialities, and it is the primary technique for mask fabrication. Electron resists are polymers. The behavior of an electron resist is similar to that of a photoresist; that is, a chemical or physical change is induced in the resist by radiation. This change allows the resist to be patterned. Common positive electron resists are poly(methyl methacrylate), called PMMA, and poly(butene-1 sulfone). Positive electron resists have resolutions of 0.1 micrometer or better. Poly(glycidyl methacrylate-co-ethyl acrylate), called COP, is a common negative electron resist. COP, like a negative photoresist, also swells during development so the resolutions are limited to about 1 micrometer.

To minimize the resolution limitation caused by the resist, it is possible to use an electron beam to directly deposit a layer from a precursor gas or to write directly into a layer (e.g., Teflon). Evaluation of practical parameters suggests that typical best resolution that may be expected is around 5 nm.

### 4.1.2. Ion Beam Writing

Ion beam writing (IBW) is important when the minimum feature dimension is reduced to about 0.2 micrometer and below. IBW can be operated in a shallow writing mode using PMMA as an ion beam resist. It can achieve higher resolution than optical, X-ray, or electron beam lithographic techniques because ions have a higher mass and therefore scatter less than electrons. In addition, resists are more sensitive to ions than to electrons.

Focused ion beam etching (FIBE) does not employ resist for pattern definition. It directly sputters material or directly deposits material from a focused ion beam. FIBE is mainly used for mask repair and offers patterned-doping and oxidation capability and very high resolution (10 nm). Ion implantation can also be used to do resistless pattern generation. One example is the etch rate enhancement in silicon dioxide when it is implanted with various ions. The etch rate is doubled when $10^{14}/cm^2$ argon ions are implanted. Thus, oxide layers can be patterned without any resist. Another example is the modification of the oxidation rate of implanted silicon. After silicon ions are implanted into the silicon substrate, followed by thermal oxidation, the thickness of silicon dioxide increases in the implanted area. On the other hand, nitrogen implantation into silicon retards the oxidation rate of the implanted area (a kind of LOCOS). These interesting effects of ion implantation are potentially very useful in the fabrication of submicrometer devices.

### 4.1.3. Mechanical Beam Writing

Recently, it has become clear that a scanning probe microscope, where a sharp probe moves within a distance of the order of 1 nm from a surface, not only allows to image this surface down to the atomic level but also allows one to modify it in a controlled way down to the nanometer level. Many techniques for scanning probe lithography (SPL) have been presented in literature.

On conducting surfaces, the scanning tunneling microscope (STM) tip can serve as a very-low-voltage electron source for the exposure of thin electron-sensitive resist layers, avoiding most of the resolution-limiting aspects of conventional electron beam lithography. Alternatively, by giving short voltage pulses, one can deposit small amounts of the tip material on the substrate via field evaporation or, after passivation with hydrogen atoms (using, e.g., hydrofluoric acid), one can locally depassivate and oxidize a surface such as silicon. At ultrahigh vacuum and low temperature (4 K), it is even possible to manipulate individual atoms or molecules on a conducting surface—by sliding atoms to exactly controlled positions, a structure can be built atom by atom, and one could even construct artificial molecules (i.e., "mechanosynthesis"). Nice examples can be found on the IBM website. In contrast to STM, the AFM can be used to pattern both conducting and nonconducting surfaces, but usually not with atomic resolution. The very controlled mechanical contact between the sharp tip and the surface allows one to etch small grooves in a soft layer or even to induce atomic scale modification.

The lithographic techniques discussed in the rest of this section do not provide the ultimate resolution that SPL can offer but are competitive down to 5 nm, and SPL is probably essential when resolution at the molecular scale is required. Currently, SPL suffers from a poor reproducibility at the nanometer level in most cases, and from a very low processing speed (throughput), which hampers a fast introduction in commercial production processes. A possible route toward mass production of nanoscale devices may rely on the fabrication of many probes in parallel or ultrafast scanning speeds. These contain large areas with arrays of nanotips and these multitips would then write a limited part of the nanocircuit in parallel. Recently, has become possible to write and read data using a polycarbonate sample and tips in parallel with integrated resistors that locally heat the tip.

### 4.1.4. Photon Beam Writing

With a laser source, it is possible to write a pattern on a surface directly by scanning the micrometer-sized laser beam over the surface most often in the presence of the suitable reactive gases. By adjusting the focal point of the laser continuously, it is even possible to grow three-dimensional microstructures such as fibers and springs in a wide variety of materials such as boron, carbon, tungsten, silicon, SiC, $SiN_x$, etc. Alternatively, a scanning near-field optical microscope might be useful to optically write very locally with a scanning probe a pattern: the process of scanning near-field optical writing.

### 4.2. Print Lithography

Figure 68 illustrates the steps of transfer of patterns with the help of print lithography (or printing). As an example, we will take optical lithography because it is the main lithographic technique. In our example, a pattern from a mask is transferred onto a silicon wafer that has a radiation-sensitive resist, for example, on top of an insulating $SiO_2$ layer formed on its surface. Resist is applied by dropping the solution on the wafer and rotating the wafer on a spinning wheel. After the spinning step, the wafer is given a pre-exposure baking (typically 80 to 100 °C) to remove the solvent from the resist film and to improve resist adhesion to the wafer. The wafer is aligned with respect to the mask in an optical lithographic system and the resist is exposed to ultraviolet
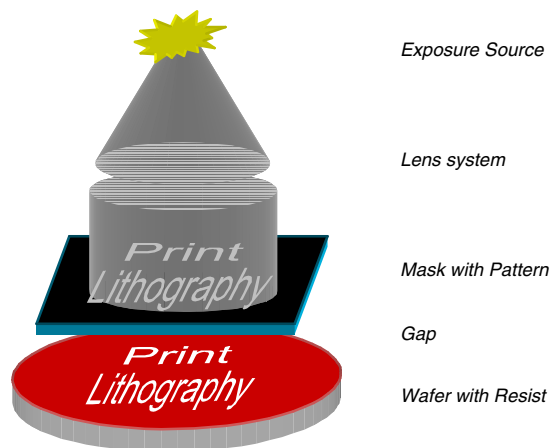
Exposure Source

Lens system

Mask with Pattern

Gap

Wafer with Resist

**Figure 68.** Schematic overview of print lithography.

light. The exposed (positive) resist is dissolved in the developer, which is usually done by spraying the wafer with the developer solution. The wafer is then rinsed and dried. After development, a postexposure baking (at 100 to 180 °C) may be required to increase the adhesion of the resist to the substrate. The wafer is then put in an ambient that etches the exposed insulating layer but does not attack the resist (e.g., buffered hydrofluoric acid is a typical $SiO_2$ etchant). Finally, the resist is stripped (e.g., using solvent, or plasma oxidation), leaving behind an insulator image that is the same as the opaque image on the mask. The insulator image can be used as a mask for subsequent processing. For example, emerging the patterned silicon wafer into a potassium hydroxide solution will etch the exposed silicon, but not the area covered by the insulator. This subject is more extensively described in Section 5 on film etching. The complete microchip is fabricated by applying the next layer and aligning the next mask in the sequence to the previous pattern and repeating the lithographic transfer process.

### 4.2.1. Electron Beam Printing

To increase the wafer throughput of EBW, different schemes have been developed. For example, the SCALPEL technique (scattering with angular limitation projection electron beam lithography) is a way to circumvent the sequential writing. In SCALPEL, a 100 nm thin silicon nitride membrane with a 50 nm tungsten pattern is uniformly illuminated by a parallel beam of electrons. Electrons passing through transparent areas (silicon nitride only) move virtually straight on, are focused by a magnetic lens, and pass through a back-focal-plane aperture to illuminate the wafer. Electrons passing through a tungsten scattering area form divergent beams that are largely blocked by the aperture and hence image contrast is obtained. In this way a 4:1 demagnified image of the mask is produced at the wafer plane. SCALPEL uses a scattering mask rather than absorbing mask, which is susceptible to heating at a limited acceleration voltage. An additional advantage over optical lithography is that the entire electron beam can be deflected by magnetic fields and each image is effectively assembled from many small pieces using a stepper approach. Patterns of 80 nm wide holes are possible and the ultimate resolution is about 35 nm.

### 4.2.2. Ion Beam Printing

Ion beam printing (IBP) is typically performed with hydrogen or helium ions. The image construction requires several complementary stencil masks. The machine exposes one image field (die) at a time and steps from die to die (i.e., stepper lithography). The electrostatic lens system operates at a 4:1 demagnification. Presently, the resolution of IBP is around 180 nm, a resolution which can also be obtained with advanced optical lithography in a much cheaper way. However, IBP has proven to print structures well below 100 nm. In the end, IBP is expected to be the cheapest solution for 50 nm resolution. The main risk factors are the stencil mask fabrication, the design of the ion imaging system, the demonstration of a good blur versus throughput, and the stitching of complementary masks.

### 4.2.3. Mechanical Printing

The technique of mechanical printing is quite versatile. For example, microcontact printing, or stamping, is a method of producing submicrometer details in nanometer thick monolayers, which are SAMs and self-ordening layers only one molecule thick. A related but essentially different method is imprinting in which a mold is pressed into a polymer film on a substrate. Another technique is molding in which the polymer is poured into a mold.

**Stamping**   In stamping, a flexible rubber stamp is used to apply small quantities of a specially selected reagent solution as "ink" onto a surface. Since only the top of the pattern will contact the substrate, these are the only regions where the reagent can react with the substrate. The stamp is created using a master (e.g., a silicon wafer with a resist pattern). A silicon rubber is molded on the master and peeled off, thus forming the stamp. Typically, a SAM is used as ink (see also Section 3.7.5). SAMs offer chemically selective processes at surfaces and interfaces. A typical example of a SAM is the formation of a 2 nm thick thiol monolayer on gold, silver, or copper. Stable SAMs are only formed when reagent, substrate, and reaction conditions are carefully selected. For example, the substrate should be without contaminants and a long hydrocarbon chain in the reagent is needed to obtain a well-ordered monolayer. The height and width of the pattern on the stamp are crucial for a reproducible printing process. If the stamp structures are too high, too narrow, or too close, they might collapse under the pressure during stamping. If they are too low or spaced too far apart, extra (unwanted) contacts of the stamp with the surface are the result. Typically, lateral details of 20 nm up to 150 micrometers are possible and the height of the structures varies between 0.6 and 4 micrometers depending on the pattern. Due to the flexibility of the stamp, curved surfaces can also be printed.

**Imprinting**   The essence of imprinting is that a reusable mold is pressed hard into a thin thermoplastic polymer film, so that polymeric material is pushed away from the imprinted regions. The tiny patterns are created on the surface of a material using a "pattern transfer element" or mold that has a three-dimensional structure formed onto its surface. These pattern-transfer elements are always made from an elastomer—a polymer network that deforms under the

influence of a force and regains its shape when the force is released. This elasticity is why these techniques are also called "soft" lithography. The achievable critical dimensions depend only on the mold dimensions that can be prepared with one of the techniques found in this chapter.

***Molding*** The essence of molding is identical with imprinting and is normally used to duplicate high-aspect-ratio structures. One of the following molding techniques is suitable: injection molding or compression molding. During reaction injection molding, the polymer components (e.g., polyurethane or PMMA) are mixed shortly before injection into a mold and the polymerization takes place in the mold itself. Thermoplastic injection molding means heating the polymer (e.g., PVC, ABS, or PMMA) above the glass transition temperature and introducing it in a more or less viscous form into the mold, where it hardens by cooling. Compression molding or hot embossing means heating the mold material above its glass transition temperature and patterning it in vacuum by impression of the molding tool. Hot embossing is typically performed at a pressure of 4 bar and a temperature of 200 °C. The embossing pressure should be sufficiently high to provide filling of the mold insert. High-aspect-ratio metal structures can be molded and demolded with polymers quite easily, as long as a polymer with a small adhesive power and rubber-elastic properties, such as silicone rubber, is used. However, those plastics have low shape stability and would not be adequate. Shape-preserving polymers on the other hand, after hardening, require a mold with extremely smooth inner surfaces to prevent form-locking between the mold and the hardened polymer. A mold release agent may be required for demolding.

### 4.2.4. Screen Printing

Screen printing includes silk screening and has special applications in the printing industry. Silk-screen printing is a form of stencil printing (i.e., printing where the ink is applied to the back of the image carrier and pushed through porous or open areas).

### 4.2.5. Optical Printing

Optical lithography comprises the formation of images with visible or near-UV radiation ($\lambda = 300$–380 nm) in a resist (e.g., Novolac) using shadow or projection printing. Shadow printing may be employed where the gap between mask and wafer is small. In case of projection printing, some sort of image-forming system (e.g., a 4:1 demagnification lens) is interposed between mask and wafer. The linewidth limit of optical printing lies near 0.4 $\mu$m, although 0.2 $\mu$m features may eventually be printed under carefully controlled conditions. Optical printing spans almost the entire current lithographic processing and will continue to occupy the primary position for the foreseeable future.

***Shadow Printing*** Shadow printing is a general name for contact printing and proximity printing. In shadow printing, the minimum linewidth that can be printed is roughly $l_{\min} \approx \sqrt{(\lambda g)}$ when $\lambda$ is the wavelength of the exposure radiation and $g$ is the gap between the mask and the wafer and includes the thickness of the resist. For $\lambda = 0.4$ micrometer and $g = 50$ micrometers, the minimum linewidth is

4.5 micrometers. If we reduce $\lambda$ to 0.25 micrometer (i.e., inside the deep-UV spectral region) and $g$ to 15 micrometers, $l_{\min}$ becomes 2 micrometers. Thus, there is an advantage in reducing both $g$ and $\lambda$. However, for a given distance $g$, any dust particle with a diameter larger than $g$ potentially can cause mask damage.

In contact printing a typically chromium or emulsion covered photomask is pressed against the resist-covered wafer and exposed by light of wavelength near 400 nm. Depending on the contact pressure between mask and substrate, we can distinguish between hard contact (with pressures in the range of 0.05 to 0.3 atm), soft contact (no additional pressure), and vacuum contact. With an Hg source the strong lines at 436, 405, and 365 nm provide exposure flux. The intimate contact between resists and mask provides high resolution ($<1\ \mu$m linewidth). However, a dust particle or a speck of silicon dust on the wafer can be imbedded into the mask when the mask makes contact with the wafer. The imbedded particle causes permanent damage to the mask and results in (pattern transfer) defects in the wafer with each succeeding exposure. Moreover, because of spatial nonuniformity of the contact, resolution may vary considerably across the wafer (Newton rings). To provide better contact over the whole wafer, a thin (0.2 mm) flexible mask has been used; 0.4 $\mu$m lines have been formed in a 1 $\mu$m resist. Loss of resolution can be reduced by use of $Fe_2O_3$ or $Cr_2O_3$–Cr masks ($Cr_2O_3$ means that the chromium is covered with a thin chromium oxide layer to reduce reflectivity), which have much lower reflectivity than chromium and reduce scattered light under the opaque parts of the mask. The contact printing produces defects in both the mask and the wafer so that the mask may have to be discarded after a short period of use. Defects include pinholes in the chromium film, scratches, intrusions, and star fractures. Mask defect densities increase typically with 3 defects/cm$^2$ after every exposure. Contact printing nevertheless continues to be widely used.

Proximity printing has the advantage of longer mask life because there is no contact between the mask and the wafer. It is similar to the contact printing method except that there is a small gap. Typical separations between mask and wafer are in the range of 20 to 50 micrometers. The small gap, however, results in optical diffraction at feature edges on the photomask (i.e., when light passes by the edges of an opaque mask feature, fringes are formed, and some light penetrates into the shadow region) and the resolution is degraded to the 2- to 5-micrometer range. Linewidth control is in general more difficult in proximity printing than in contact printing. Linewidth is influenced by variations in light intensity, mask–wafer gap, and resist properties.

***Projection Printing*** To avoid the mask damage problem associated with shadow printing, projection printing exposure tools have been developed to project an image of the mask patterns onto a resist-coated wafer with higher resolution than proximity printing together with large separation of many centimeters between mask and wafer. There are two types of projection printers with respect to the image forming system used: reflective and refractive. In reflective optics, a curved lamp source illuminates an arc on the mask, and this arc is imaged onto the wafer with unity magnification. In this arrangement only a small zone of the spherical

primary mirror is used, providing nearly diffraction-limited imaging. Mask and wafer are swept through the arc to form an image of the whole mask. The other printers use refractive optics: high quality lenses with many elements. They project a 5 times reduced image onto the wafer. To increase resolution, only a small portion of the mask is exposed at a time. The small image area is scanned or stepped over the wafer to cover the entire wafer surface (see the section on stepper lithography).

Usually the mask is fabricated with pattern dimensions 4X to 5X larger than the features actually desired on the wafer because the wafer exposure system reduces the image by the same factor. Demagnification in the wafer exposure system makes the mask easier to fabricate and easier to check for imperfections. Once the mask is checked, it is usually protected from later contamination by dust particles with a thin transparent membrane (pellicle) stretched over a metal frame above the chrome side of the mask. Pellicles are usually made from nitrocellulose a few micrometers thick. Since the pellicles are offset from the mask, dust particles that fall on the pellicle during use will be out of focus on the wafer and therefore will usually not print. Typically the pellicle might be mounted a few mm above the mask. Since the DOF of modern exposure systems is only a few micrometers, dust particles as large as 100 micrometers will not print on the wafer during exposure.

### 4.2.6. Deep Ultraviolet Printing

Deep ultraviolet printing (DUVP) with wavelength between 200 and 300 nm is basically identical to optical printing. However, the UV line at 365 nm of the Hg source is in the process of being replaced by a Xe–Hg source with an enhanced output in the 200–300 nm spectral region. Alternatively, a krypton fluoride laser radiating at a wavelength of 248 nm is possible. This improves the resolution and the DOF sufficiently to enable imaging of features down to 200 and 600 nm respectively. Further gain is possible by utilizing an argon fluoride excimer laser operating at 193 nm or a fluoride laser radiating at 157 nm as the next DUVP sources. The most favorable resists nowadays are based on a polyhydroxy-styrene backbone and a photoacid generator and PMMA. DUV exposure tools today are capable of 80 nm registration, a throughput of ca. 1 wafer per minute, and defect densities of roughly 50 particles per layer/$m^2$ @ 40 nm defect size. Quartz or alumina mask substrates must be used to pass these shorter wavelengths, since the usual borosilicate glass strongly absorbs wavelength less than 300 nm.

### 4.2.7. Extreme Ultraviolet Printing

To extend the ongoing technological trends to wavelengths below 100 nm, processes of a short-wavelength imaging method are explored, which includes "reduction optics" analogs to optical projection printing. Such a reduction scheme with the ability of making diffraction-limited images would take full advantage of the short wavelength. The method, initially called soft X-ray projection lithography but later named extreme-ultraviolet printing (EUVP with wavelength between 4 and 200 nm), uses reflecting optics and masks with special multilayer coatings. The preferred wavelength in EUVP is 13 nm, just below an absorption edge

of silicon, which is one of the components in the multilayer reflective coating. The EUV radiation requires optical elements fabricated with a surface accuracy and roughness in the subnanometer range. The optimal radiation source in EUVP is commonly believed to be a laser-produced plasma source, although compact synchrotron sources are also an option. A laser-plasma is created by focusing the laser onto a metal target. The plasma thus produced emits an intense burst of photons, including the desired EUV. Before EUVP can be successful, a method must be developed to mitigate pollution by plasma debris created by the focused laser beam.

### 4.2.8. X-ray Printing

Röntgen or X-ray printing (XRP) uses a one-to-one shadow printing method similar to optical proximity printing, because for this wavelength no suitable optics is available. The soft X-ray wavelength (0.4 to 4 nm) is much shorter than that of the ultraviolet light (4 to 400 nm) used for optical, DUV, and EUV lithography. Diffraction effects are reduced and resolution is improved by reducing the wavelength; however, optical materials become opaque because of the fundamental absorption and mask materials might become transparent. For an X-ray wavelength of 0.5 nm and a gap of 40 micrometers, the minimum line width obtained is less than 0.2 micrometer. XRP required the development of an application-specific X-ray source, for which so-called compact synchrotron radiation sources are currently employed. These bright sources are basically scaled down versions of the large synchrotron facilities used for fundamental research. Although costly ($\sim$25 MEuro), one synchrotron source can have several exposure beam lines and serve up to 20 wafer steppers. The utilization of the cheaper and smaller laser plasma X-ray sources turned out to be limited, due to their pointlike source nature. In another XRP system, a 25 keV, 5 kW electron beam is incident upon a palladium target that emits X-rays with a wavelength of 0.44 nm. The X-rays pass through a beryllium window into a helium-filled chamber (air is a strong X-ray absorber) to illuminate a mask, which casts shadows into a resist-covered wafer. Materials useful for the absorptive and transmissive parts of the mask, the atmosphere in the exposure chamber, and the resist are in large part determined by the absorption spectra of these materials in the X-ray region. Over a wide range of wavelength the absorption coefficient of an elemental material of density $\rho$ and atomic number $Z$ is proportional to $\rho Z^4 \lambda^3$. As $\lambda$ increases, the proportionality constant decreases in step-function fashion at the "absorption-edge" wavelengths corresponding to the ionization energies of the inner electrons of the $K$, $L$, and other shells. An X-ray mask consists of an absorber on a transmissive membrane substrate. Of the heavy metals with larger $\rho Z^4$ absorbers, gold has been widely used because it is easily patterned. In general, in order to have large enough absorption, the gold metal is considerably thicker (600 nm) than chromium layers used in optical printing.

Electron beam resists can be used as X-ray resists. This is because when an X-ray photon is absorbed by an atom, the atom goes to an excited state with the emission of an

electron. The excited atom returns to its ground state by emitting an X-ray having a different wavelength than the incident X-ray. This X-ray is absorbed by another atom and the process repeats. Since all the processes result in the emission of electrons, a resist film under X-ray irradiation is equivalent to one being irradiated by a large number of secondary electrons from any of the processes. One of the most attractive X-ray resists is dichloropropyl acrylate (DCOPA) and glycidyl methacrylate-co-ethyl acrylate, because it has a very low threshold ($\sim$10 mJ/cm$^2$). Structures well below 100 nm have been reproduced faithfully in various laboratories. The domain of dimensions down to 70 nm can be covered using traditional (optimized) masks, and 30 nm lines were achieved using phase-shifting techniques (see section on phase-shift lithography). XRP has the advantage of being insensible to particle or dust contamination, explained by the large penetration power of the X-rays used. The XRP does not take advantage of the short wavelength due to the lack of suitable optics. In contrast to optical lithography, in which a resolution comparable to the wavelength of the light can be obtained, the (Fresnel) diffraction over the finite gap between mask and wafer limits the resolution to about 100 nm, whereas the physical limit for an imaging system would be several nanometers. In principle the practical resolution could be improved by reducing the gap, but the delicate mask requires a minimal distance (about 10 micrometers) to protect it from damage due to dust particles. Occasionally, alternative X-ray schemes involving novel types of optics are proposed. For instance, a scheme involving "zone plate arrays" has been devised to focus parts of the beam through MEMS shutters onto the surface. This would allow 25 nm resolutions. The question remains if the technique is suitable for commercial mass manufacturing. Due to the one-to-one reproduction method, the mask features should be made to at least the same tolerance as the final structure, while the support membrane cannot be thicker than a few micrometers to ensure sufficient transmission and contrast. Consequently, X-ray masks are delicate and costly.

### 4.2.9. Holographic Printing

In holographic printing, a holographically constructed photomask replaces the standard photomask. In the recording or construction phase of the hologram, one uses the interference of two mutually coherent beams: an object beam and a reference beam. A well collimated, flood laser (object beam) passes through the photomask and is diffracted by the mask features. This signal beam contains the amplitude and phase information of the photomask. When this diffracted object beam passes through the holographic recording layer, it interacts with another beam, the reference beam, to create the interference pattern. The reference beam converts the amplitude and phase information into intensity information, which is stored in the photosensitive holographic resist polymer as variations in the refractive index. Pattern printing or image reconstruction is accomplished by scanning a collimated laser illumination beam—the phase conjugate of the reference beam—to create the hologram. By interaction with the recorded hologram, the latter beam generates an image of the original photomask at precisely its original position in space. When a photoresist-coated substrate

resides in this plane, a copy of the original mask can be printed. The image is only diffraction limited, and because the holographic mask and the wafer can be very close, a high numerical aperture—and thus a very good resolution down to 300 nm—is possible.

### 4.3. Stepper Lithography

There are two basic types of wafer stepper machines, which are routinely used to produce structures as small as 250 nm in a layer of resist on the wafer surface and utilizing reducing projection printing with complex lens systems: "step-and-repeat" and "step-and-scan." In step-and-repeat lithography, the complete pattern of a circuit (die) is imaged at once and then the wafer is moved ("stepped") and the next die is imaged. In step-and-scan lithography, each die is imaged line-by-line by synchronized movements or "scanning" of the mask and the wafer.

A typical step-and-repeat system is illustrated in Figure 69. Radiation from a high-intensity source is collimated and passed through the mask. Each transparent area on the mask transmits the radiation, which is then collected and focused by a second lens system. This second lens system also serves to reduce the image size by 4X–5X. The field of view of such systems is typically only a few cm on a side. Therefore, the wafer is physically moved to the next exposure field and the process repeated so these systems are commonly called step-and-repeat tools or simply steppers.

In step-and-scan lithography, a narrow slit of radiation is produced by the source system and the mask and wafer are simultaneously scanned mechanically so that the mask image is scanned line-by-line across the wafer. Note that in systems of this type, the mechanical system must scan the mask 4X–5X times faster than the wafer, corresponding to the optical reduction factor. Scanners greatly increase the field size up to the limit of the mask dimension, at least in the scanning direction.
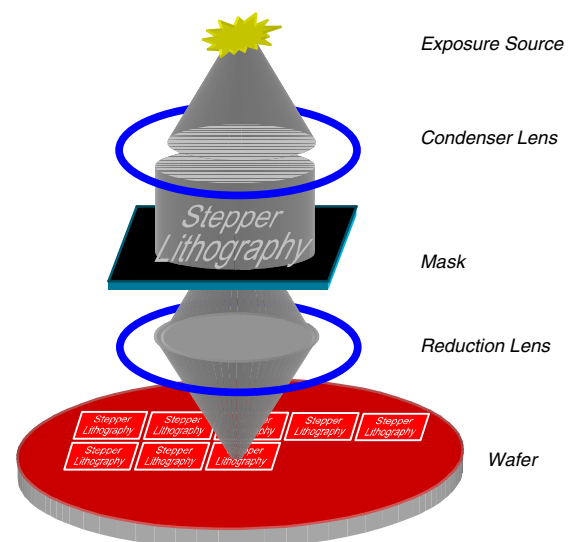


**Figure 69.** Schematic overview of stepper lithography.

## 4.4. Alternative and Related Lithography

Resolution enhancement techniques based on the use of the phase of light, such as the use of laser interference, atomic laser interference, stereo techniques, phase-shifting masks which improve contrast and thus resolution, or mask illumination improvements, are increasingly being employed to extend the scope of optical lithography to its limits. Additionally, add-on techniques are found such as edge lithography and combinatorial techniques, which "combine" two or more of the other lithographic techniques to enhance throughput. Optical lithographers expect that the optical techniques will ultimately enable a resolution of 120 nm using argon fluoride lasers. For wavelengths below 120 nm, no optical materials are transparent and the development of diffraction-limited lenses is improbable. Nevertheless, it has recently been shown that it is possible to fabricate 40 nm lines using optical lithography with 193 nm wavelength in combination with a technique called top surface imaging. But the inherent physical limitations become more and more evident.

Several technologies that potentially could be used for nanolithography are described. Independent of the lithography used—write, print, or stepper lithography—the exact lithographic process scheme can be altered to improve certain aspects. The next processes are related to lithography, "resist lithography," "direct lithography" as opposed to resist lithography, "lift-off lithography" which is a complementary method to resist lithography, "trilevel lithography" which is able to enhance resolution for patterned surfaces, and "LIGA."

### 4.4.1. Laser Interference Lithography

In laser interference lithography (LIL), the interference pattern of two intersecting laser beams is used to expose a thin resist. Of course, one can only create gratings (and arrays by multiple exposure), but the grating period can be as small as half the laser wavelength. In case of an argon fluoride eximer laser radiating at 193 nm this would produce 100 nm patterns. This is smaller than what is achievable by conventional photolithography and complete wafers can be exposed in a matter of minutes. This gives this technique a big advantage over for instance electron-beam lithography, if gratings or arrays are the only patterns needed (e.g., data storage media). Patterns with an even smaller periodicity are possible using special period doubling techniques. For example, in achromatic LIL, an interference pattern is produced by diffraction of incoherent (achromatic) light on two identical parallel gratings, which produces an interference pattern with half the periodicity of the gratings. By this technique 100 nm patterns have been realized using gratings with 200 nm periodicity.

### 4.4.2. Atom Lithography

Recently, atom lithography (AL) has emerged as a promising method of massively parallel patterning with nanometer-scale resolution. In AL, a beam of atoms is projected onto a surface through a laser interference pattern. AL relies on fundamental interaction processes between atoms and photons. An atom moving in a near-resonant laser field exhibits

a dipole force, which can be derived from an optical potential, which, to the first approximation, is linear in the light intensity. Atoms moving in such an optical potential tend to oscillate around their minima. The focusing of atoms can be qualitatively understood from the analogy with the focusing property of a lens with a parabolic refractive index profile in conventional optics. The period of the resulting structure is equal to half of the wavelength. Because the dipole potential is weak compared to typical transversal thermal kinetic energies of atoms, the atomic beam needs to be collimated before focusing. This cannot be met by mechanical collimation, since it would result in a high loss of flux. Therefore, optical collimation methods based on the dissipative light forces on atoms are used such as Doppler cooling schemes. The diffraction limit of this approach is lower than that of optical lithography, down to a few nm, due to the short de Broglie wavelength (Planck's constant over the atomic momentum) of thermal atoms. By using atoms that stick well on surfaces, AL can be applied to write structures directly onto substrates. On the other hand, metastable rare gases or chemically aggressive atoms can be used to pattern surfaces in an indirect way: the pattern is first imaged on a special resist and then transferred to the substrate using other methods, such as selective etching.

### 4.4.3. Stereolithography

In stereolithography light exposure solidifies a special liquid resin into a desired shape. The liquid resin is kept either in the free surface or in the fixed surface mode. The latter has a resin container with a transparent window plate for exposure. The solidification always happens at the stable window/resin interface. An elevator is pulled over the thickness of one additional layer above the window for each new exposure. In the case of free surface, solidification occurs at the resin/air interface and more care needs to be taken to avoid waves or a slant of the liquid surface. A 3D structure can be made of a UV polymer by exposing the polymer with a set of 2D cross-sectional shapes (masks) of the final structure or the sliced shapes can be written directly from a CAD-controlled (laser) beam. In this way a complicated 3D shape can be constructed by stacking thin films of hardened polymer layer upon layer. The position accuracy for the 5 micrometers in diameter laser beam spot is 1 micrometer in the $z$-axis and 250 nm in the $x$- and $y$-directions. The plastic shapes made by stereolithography may be used as a cast for electroplating metals or for other materials, which can be molded into the polymer structures.

### 4.4.4. Phase-Shift Lithography

The use of phase-shifting masks allows further improvement of the photolithographic resolution at a given wavelength and numerical aperture by carefully controlling light diffraction using constructive and destructive interference. Using these masks, one controls both amplitude and phase of the light and, in particular, one arranges the mask so that with opposite phase emerges from adjoining mask features. In that case, destructive interference can be used to cancel some of the image-spreading effects of diffraction. In Figure 70 we illustrate the effect for three nearby mask apertures; a conventional transmission mask is added
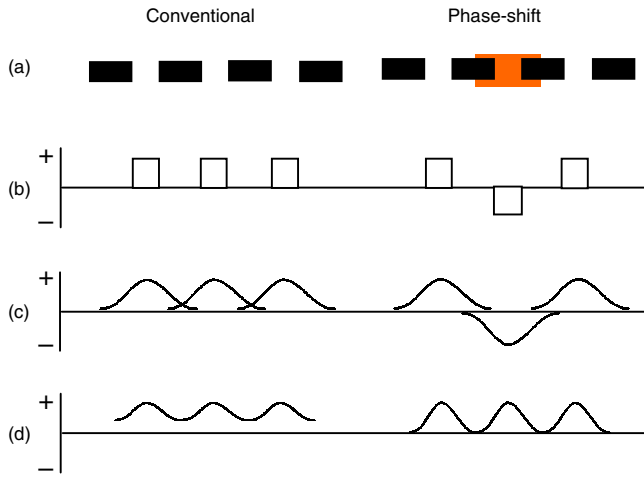
**Figure 70.** Schematic overview of phase-shift lithography. (a) Conventional and phase-shift transmission mask. (b) Light amplitude distribution on a mask. (c) Light amplitude distribution on a wafer. (d) Light intensity distribution on a wafer.

for comparison. The amplitude profile at the plane of the classical mask consists of three square-cornered features with positive amplitude. The amplitude at the wafer level is broadened and rounded but does not change sign. With a phase-shifting mask, a shifter layer results in a reversal of the phase of the light at the mask. As the photoresist only shows sensitivity toward the intensity of the light and not the sign, the three bright features develop identically and the areas where the light of opposite phases causes destructive interference form very dark contrast lines. Phase-shifting masks can easily improve resolution by a factor of two.

### 4.4.5. Edge Lithography

Edge lithography is a form of lithography in which the edges of the original pattern become the features of the final pattern (see Fig. 71). It is an add-on technology for existing lithography in which the sidewalls of prefabricated steps are used to produce truly 2D and 3D nanoscale structures. The resolution of these nanopatterns is basically controlled only by the thickness of the deposited film and the accuracy of this thickness is believed to be controllable down to the atomic level. This gives this technique a big advantage over, for instance, traditional lithography, employing visible and
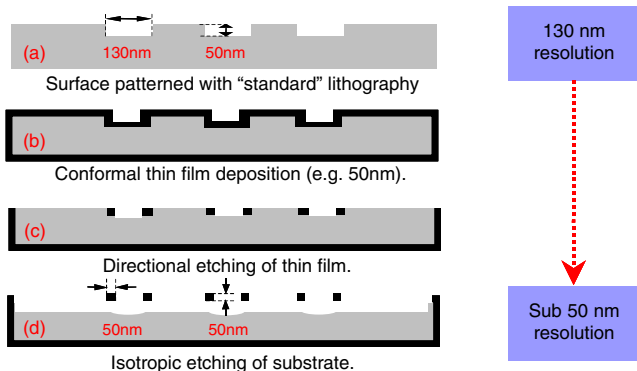


**Figure 71.** Schematic overview of edge lithography.

ultraviolet light, which is confronted with a serious barrier due to far-field limitation of the wavelength of light. Edge lithography is an add-on technology (it uses the pattern of a different lithographic process) that might be comparable to the best in the world. This technology can even be enhanced by incorporation of standard microsystem technologies to enable connection ports with the macroworld.

### 4.4.6. Hybrid Lithography

In order to improve resolution and keeping throughput high, sometimes write lithography is combined with print lithography. For example, the combination of imprinting with scanning probe lithography for the mold preparation may possibly provide an important breakthrough for a low-cost mass preparation of nanometer scale devices. At this point, the local oxidation of semiconductor or metal surfaces seems to offer the most reliable method to produce the required molds. It is important to note that the scanning probe microscopes can at the same time also be used to inspect the mold quality down to atomic scale. As a second example, the use of electron-sensitive deep UV resists opens up the possibility to expose the same resist layer both in a deep UV stepper and an electron-beam writer before development—the so-called "mix-and-match" technology. In this way, large surface areas are being exposed with medium-to-low resolution by the fast stepper, whereas the high-resolution details are being exposed by the accurate but slowly scanning writer. The overall result is an on-average acceptable replication time with higher resolution details in the most critical areas. Another example is the combination of SAMs with surfaces having a pre-etched regular pattern. Some SAMs have the tendency to form hexagonal patterns with a periodicity as small as 20 nm and have a high resistance against plasma etching. This can be used to form nanopatterned surfaces in a one-step film-formation and film-etching process. However, the regularity of these patterns (domains) extends over a few 100 nm only, which limits the application of this technique. The regularity can be improved by using prepatterned surfaces smaller than the size of the domains to extend the nanoregularity into the microdomain. Other examples, and without going into more detail, are to combine LIL with edge lithography, to combine "micro" lithography with "nano" e-beam or ion-beam, or to create first a photonic crystal by LIL and then machine waveguides inside the photonic crystal.

### 4.4.7. Resist Lithography

In resist lithography, a chemically amplified resist is composed of a polymer with groups reactive to protons and a photoacid generator. A photoacid generator is a chemical compound supplying a proton upon irradiation. This proton catalyzes reactions at the polymer, resulting in solubility differences between the exposed and unexposed regions. In resist lithography, a wafer is placed in a cleanroom, which typically is illuminated with yellow light, since photoresists are not sensitive to wavelength greater than 0.5 micrometer. Typical resists today are carbon-based organic materials, such as Novolacs, that have been engineered for optimum performance in micro- and nanotechnology. Radiation-sensitive resists can be classified as positive and negative

tone resist, depending on how they respond to radiation. A negative tone resist on exposure to radiation becomes less soluble in a developer solution, while a positive tone resist becomes more soluble. The net result is that the patterns or images formed in the positive resist are the same as those on the mask. For the negative resist, they are the inverse.

Commercial negative resists consist of two parts: a chemically inert polyisoprene rubber, which is the film-forming component, and a photoactive agent. The photoactive agent on exposure to light reacts with the rubber to form cross-links between rubber molecules, making the rubber less soluble in an organic developer solvent. The reactive species formed during the exposure can react with oxygen and be rendered ineffective for cross-linking. Therefore the resist is usually exposed in a nitrogen atmosphere. The developer solvent dissolves the unexposed resist. One major drawback of a negative photoresist is that in the development process the exposed resist swells by absorbing developer solvent as the un-cross-linked molecules are dissolved. The swelling distorts the pattern features and limits resolution to 2 to 3 times the initial film thickness. However, the swelling is an advantage when the so-called lift-off lithography is used (see next section).

Positive resists consist of three components: a base resin, a photoactive compound, and an organic solvent. Prior to exposure, the photosensitive compound is insoluble in the developer solution. The photoactive compound is a dissolution inhibitor. When it is destroyed by exposure to light, the resin becomes more soluble in an aqueous developer solution and upon development the exposed areas are removed. The unexposed regions do not swell much in the developer solution, so higher resolution is possible with positive resists. The sensitivity of most standard resists peaks in the 300 to 400 nm spectral range. Photoresists are being developed for exposure at shorter wavelengths where higher resolution is possible. A few such deep UV resists, sensitive for $\lambda < 250$ nm, are PMMA and polybutene sulfone. At these shorter wavelengths, the radiation quantum is large enough to produce scission (breakage) of the molecular chain.

Besides the wet-developed methods described, dry-developed resist chemistry forms another important strategy toward nanolithography. An important advantage of dry development is that the swelling found in wet development is prevented. In one approach, plasma-polymerized methylsilane is transformed by deep UV radiation in the presence of oxygen into a poly-methyl-siloxane. By subsequent plasma development with chlorine, and a plasma treatment with oxygen to transfer the poly-methyl-siloxane into silicon oxide, images with sub-180 nm features can be transferred.

With respect to step coverage we have to note that lithographic process latitude can become severely limited, even for a perfectly planarized topography. Resist films crossing over steps have their local thickness altered; thinning occurs over high features and pile-up in low-lying regions. During exposure the thin resist region may get overexposed and the thick resist region underexposed. Moreover, resist pile-up at step corners may exhibit standing wave effects, leading to reduction of resolution. Reflective notching on buried topographical features and the swelling of negative tone resist during development could decrease resolution even further. Practical DOF should encompass device topography, resist

thickness, wafer flatness, focus, and tilt errors in order for the projected image to remain sharp over the whole wafer.

The light intensity, which is effective in exposing a volume element of resist at a certain height above the substrate, depends on the reflectivity of the substrate, the thickness of the resist, and the convolution of the absorption spectrum of the resist with the spectrum of the incident light. The refractive index of most resists is about 1.6, leading to an optical mismatch at the air/resist interface. If the substrate is highly reflective, the interference pattern of standing waves that are set up has a node at the substrate and a peak amplitude that depends on resist thickness. This variation in peak intensity with resist thickness becomes less with decreasing substrate reflectivity and increasing absorption by the resist. Since resist thickness varies at a step in substrate topology, the resulting difference in effective exposure leads to size variations in the resist image. To circumvent this problem, various trilevel lithographic techniques have been used (see next section). Because of the high resolution of positive resists, the standing wave patterns are often well resolved, and the resulting corrugations are seen in the resist edge profile. The edge of a feature in developed resist occurs at the position where the product of light intensity and exposure time equals the resist threshold dose: typically around 10 mJ/cm$^2$.

Other properties of resists, being quite important, are good adhesion to the substrate and resistance to wet and dry etch processes. In general, the commercially available optical resists are compatible with such processes. The unwanted variation of feature size in the resist image is due to many effects, some related to resist properties (e.g., scattering) and resist processing (e.g., reflections) and others to the exposure tool (e.g., coherence).

### 4.4.8. Direct Lithography

Although lithography normally uses an intermediate radiation-sensitive resist layer to transfer a pattern into or onto a film or substrate (i.e., the process known as *resist lithography*), to enhance resolution it might be beneficial to directly transfer a pattern into or onto the film without the use of a resist film (i.e., the technique called *direct lithography*). This enhancement—by a factor of two or even more—is possible because scattering of the exposure flux in the resist and swelling of the resist during development are prevented. For example, it is possible to directly write a pattern in a substrate with a laser, ion, or electron beam, as already found in the sections about beam writing, or it is possible to equip an SEM with high-precision linear and rotary positioning stages inside the vacuum chamber and to construct a metal shape and even a vacuum ball by controlling the stage position and the electron beam direction. This transfer technique is known as *direct write lithography*. Alternatively, the beam could enhance a CVD process to deposit, for example, a dielectric layer only beneath the regions defined by the focused beam. The gases in the reaction chamber are decomposed locally by the focused energy source, and localized film deposition occurs by a pyrolysis or photolysis process. The focused energy sources are also potentially useful to deposit metal films in selected areas to repair devices and a chemical modification of the substrate surface is caused by the beam which could result in etching.

Although direct write lithography can be found already in many applications such as mask fabrication, write lithography has the disadvantage of being "a series technology" making it a rather slow process and "batch-process repellent." But the use of a focused beam is not necessary. By pressing a fused silica mask with etched cavities tidily on top of a H-terminated silicon substrate and meanwhile exposing the stack with UV light, it is possible to oxidize or etch the silicon locally: the process of *direct print lithography*. For example, when $O_2$ molecules are enclosed in the cavities, during exposure with UV light, the molecules are cracked into O-atoms and react with the silicon surface (Fig. 72). The process is self-terminating because only a limited amount of oxygen is present in the cavity and the silicon surface has a well-defined number of reactive sites. Moreover, the wavelength of the UV source does not determine the pattern resolution as long as it is able to create reactive species. Alternatively, it might be possible to deposit a metal-organic compound when the correct wavelength can be found. This is the process of local oxidation or local MOCVD.

A somewhat different approach is the use of radiation-etchable substrate material. For example, photoetchable glass is a very promising material for the production of components for a wide variety of microsystems. The glass is illuminated with 310 nm radiation and an energy density of ca. 2 J/cm$^2$, which is sufficient to structure a 1 mm thick wafer. After exposure to ultraviolet radiation and subsequent heat treatment (1 hour at 500 °C), these glasses will partially crystallize. The crystalline phase is lithium silicate, which is 20 times more soluble in hydrofluoric acid than the surrounding unexposed amorphous glass. High aspect ratio microstructures (up to 20) can be realized by using slightly modified semiconductor equipment and relatively low fabrication costs are achievable already in small-scale production. A typical photoetchable glass is FOTURAN of Schott and similar glasses are produced by Corning (FOTOFORM) and Hoya (PEG3).

### 4.4.9. Lift-off Lithography

A related pattern transfer process to the conventional resist lithography is the lift-off technique. It uses the shadowing by surface topography of the resist layer as will be clarified next. For example, a positive resist can be used to form a resist pattern on a substrate (Fig. 73b). The film (e.g., aluminum) is deposited over the resist and the substrate, where the film thickness must be smaller than that of the resist. Those portions of the film on the resist are removed by
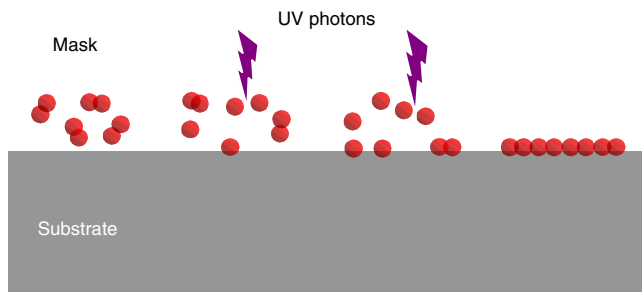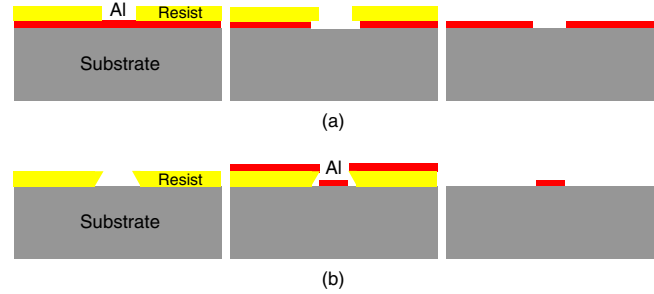
**Figure 73.** Schematic of resist pattern transfer. (a) Conventional lithography. (b) Lift-off lithography.

selectively dissolving the resist layer in an appropriate liquid etchant (e.g., aceton) so that the overlying film is lifted off and removed. This process leaves only material on the sites where no resist was present after resist development. The lift-off technique is capable of high-resolution pattern transfer. This is because in case of conventional resist lithography, the underlying film has to be etched in a subsequent process step. This etching generally produces underetch and roughness of the film edges (for example, the different crystals of polycrystalline material such as aluminum etch with a different speed).

Because of the finite size of, for example, an electron beam evaporator (with diameter $d_{evap}$), and a finite resist thickness $t_{res}$, a penumbral effect results. The penumbral blur $d$ on the edge of the resist image is $d = d_{evap}t_{res}/L$ where $L$ is the distance from the source to the wafer. If $d_{evap} = 2.5$ cm, $t_{res} = 2$ micrometers, and $L = 50$ cm, the penumbral blur is of the order of 0.1 micrometer. In case of sputter equipment, $d_{sput} = 25$ cm and $L = 5$ cm and the blur is of the order of 10 micrometers. This is why sputter equipment is in general not suited for the lift-off technique. Another geometrical effect is the lateral magnification error, due to the finite resist thickness and the nonvertical incidence of the evaporated material. The projected images of the resist mask are shifted laterally by an amount $d = rt_{res}/L$ where $r$ is the radial distance from the center of the wafer. The shift is zero at the center of the wafer but increases linearly toward the wafer edge. For a 10 cm (4 inch) wafer, the shift can be as large as 1 micrometer. Lift-off procedures have many appearances. In Figure 74 we singled out the schematic for deposition of a buried conductor. The process can be followed by an electroless deposition.

### 4.4.10. Trilevel Lithography

To minimize step coverage problems on patterned surfaces, trilevel lithography might be beneficial. In this technique, first a polymeric layer with a sufficient planarization effect
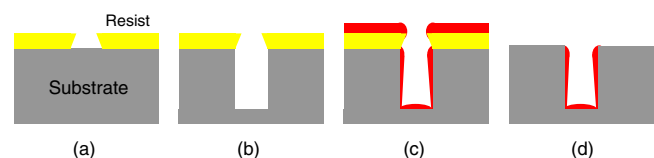
**Figure 74.** Schematic of a buried conductor process. (a) Pattern lift-off resist. (b) Etch substrate. (c) Deposit PVD metal. (d) Lift-off.

**Figure 72.** Direct print lithography.

is coated on top of the irregular surface (Fig. 75). On top of this polymer a thin layer of, for example, aluminum is deposited and photoresist is applied and patterned in the usual way. After the aluminum has been etched, the planarization polymer is dry etched with oxygen plasma.

## 4.5. Conclusion and Nanoperspective

This section has shown that there are numerous ways to achieve nanostructures of surfaces using lithography and new developments in lithography will largely determine which direction the ICT and MST will take the coming years. Top-down nanofabrication involves other techniques as well, such as etching and forming, but the lithography process will play a key role because it defines the critical dimensions of the structures (with the exception of the edge lithography) that are finally the basis for operation of the circuits to their ultimate specifications. Therefore, different lithography techniques have been discussed extensively in this chapter and we have tried to define the optimum lithography for the near future, which may be different for NST than for MST or ICT. Whereas finer linewidths are the main quest in NST and standardized materials in the ICT, MST seeks high features and high aspect ratios and the introduction of new materials. For example, wafer topography poses a significant challenge for the lithographic definition of "high rise" structures typical for MST.

The main characteristics of the most prominent lithography techniques discussed in this section are listed in Tables 11 and 12. The listed resolutions have been obtained or are considered achievable (bracketed). The techniques labelled "option" are candidates for the mass manufacturing of chips with features below 100 nm. Various other approaches are still in the "research" phase but may be applicable in the future. Writing lithography is too slow for the mass manufacturing of chips, but it is a very useful tool for mask fabrication and special low-volume application. However, a possible route toward mass production of nanoscale devices may rely on the fabrication of many mechanical probes in parallel. In the end, the choice will depend on the critical factors and the application rather than on the achievable resolution.

Fabrication of the newest generations of semiconductor devices continuously imposes higher demands on lithography. Most likely, optical lithography will be the system of choice for many years to come because of its relative simplicity, convenience, and reasonable high throughput.
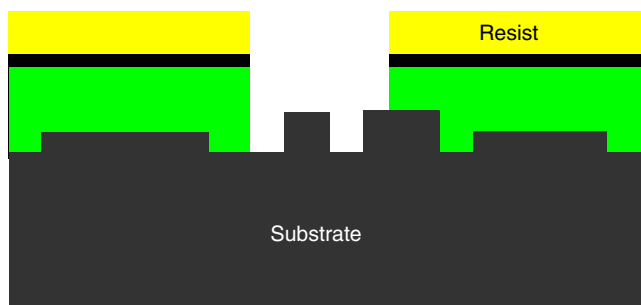


**Figure 75.** Trilevel lithography.

It will continue to improve with wavelength approaching 120 nm using 193 nm UV radiation. But, although optical lithography is the most prominent lithographic tool, it is not likely that it will be extendible to the sub-100 nm generation. Development of nanotechnology makes it necessary to replace the current lithography technology by higher resolution replication techniques. Beyond that limit several options exist including the use of ions, electrons, and short wavelength photons and potential candidates to replace optical lithography include EUV, X-ray, e-beam direct write, and projection e-beam, each of which is being explored in a variety of approaches. Each method has its limitations: diffraction effects in optical lithography, proximity effects in electron beam lithography, mask fabrication complexities in X-ray lithography, and beam deflection difficulties in ion beam lithography.

Most methods have found their one special place in the lithographic process; electron beam lithography is used to generate the mask set with the help of CAD programs where high resolution is essential, the masks are checked and eventually repaired with the help of ion beam lithography because only ions are energetic enough to repair (i.e., etch or deposit) the mask locally, and finally the mask set is used in mask or stepper lithography to manufacture chips with large throughput. EUV is currently the most likely "winner" in stepper lithography and sub-50 nm EUV is already foreseen to become operational before 2008 and 15 nm resolution has already been demonstrated. Custom circuits, masks, and experimental devices for which high throughput is not needed will continue to be patterned by scanning electron-beam systems. In these applications, fine definition, good overlay, flexibility, and quick turnaround are requested.

In microtechnology, many mask levels are involved but it is not necessary to use the same lithographic methods for all levels. Even within the same level we might combine lithographic methods. This hybrid lithographic approach can take advantage of the unique features of each lithographic process to maximize throughput with a certain requested resolution. Also, the transition from microtechnology toward nanotechnology requires the introduction of totally new production techniques. Besides self-organization of molecular structures on microstructured surfaces, nanoscale patterning of surfaces with SPL may play an important role for achieving this transition. SPL allows one to prepare the individual devices which are needed to evaluate the downscaling of existing devices or to develop totally new quantum devices. When combined with a parallel processing technique such as imprinting—or alternatively, if integrated arrays of probes can be developed—SPL may even allow the mass production of nanoscale devices. Finally, SPL is suited to interconnect, modify, and repair nanostructures during inspection.

Typically, the lithographic process uses a temporally, intermediate, resist layer to transfer a pattern. Resist lithography is the process of transferring patterns of geometric shapes on a mask to a thin layer of radiation-sensitive material (called resist) covering the surface of a wafer. These patterns define the various regions in microdevices such as anchor points for cantilevers, implantation regions, contact windows, and bonding-pad areas. In general, the resist patterns defined by the lithographic process are not permanent

**Table 11.** Schematic overview of lithographic methods and phenomena.



| Basic lithographic process | | |
|---|---|---|
| (1) | (2) | (3) |
| *Spin-coat a layer of photoresist.* | *Illuminate the resist through a mask.* | *Develop the resist* |
| *Write lithography (writing)* | *Print lithography (printing)* | *Stepper lithography* |
| **Parameters:** Resolution, DOF, exposure field, registration, throughput, defect density, resist material (sensitivity, contrast, tone, etch resistance, etch selectivity, step coverage, resolution, and ruggedness) | | |
| **Alternatives lithographic methods:** LIL, atom, and stereo. **Related lithographic methods:** direct, lift-off, trilevel, phase-shift, edge, LIGA and hybrid. | | |

elements of the final device but only replicas of device features. Due to scattering of the energetic particles of the exposure system in the resist layer, resist lithography is generally much less accurate than direct lithography. But it is still the prime technique because of higher selectivity and throughput than possible with direct lithography. To produce device features, these resist patterns must be transferred once more into the underlying layers comprising the device. The pattern transfer is accomplished by an etching process which selectively removes unmasked portions of a layer. This etching process is considered in the next section.

## 5. FILM ETCHING

In general, a lithographically patterned resist layer by itself is not interesting enough for micro- or nanotechnology. Other materials—such as the substrate itself or deposited layers or films—are needed having specific patterns, such as wires, vias, or channels, and with appropriate characteristics such as electrical isolation or conductivity, chemical resistance, or mechanical strength. Resist patterns, formed in the lithographic process, can be transferred to such materials by physical or chemical etching techniques as shown in Figure 76. The mechanism for physical etching

(Fig. 76a) is straightforward; the reactants—usually ionic species—approach the substrate with high velocity where they erode the surface due to impulse transfer. However, chemical etching (Fig. 76b) involves three essential steps, which are quite identical to chemical film formation—only the direction of transport is reversed. The reactants are transported to the reacting surface (e.g., by diffusion) and adsorb, then reactions occur at the surface (e.g., electrochemical), and finally the products from the surface are desorbed and transported away from the surface (e.g., again by diffusion). Basic requirements for a good etch process are that the reactants used for the etching must be able to be transported to the wafer surface, and the products of the etch process must be transported away easily. The latter means that soluble, gaseous, or volatile products are produced in etching. The etch process should be uniform, should be safe to use, and should cause minimal damage to structures on the chip. Finally, the etching process should be clean, with low particulate production and little film contamination, and should be cost effective. Unarguably, many parameters, such as temperature and etchant composition, will influence the etch rate depending on the etch mechanism involved and surface and bulk impurities most often play an important role and might produce unreliable results. This makes etching a very difficult subject. In this

**Table 12.** Comparison of lithographic techniques.

| Technique | Resolution | Critical factor | Status | Remark |
|---|---|---|---|---|
| **WRITING** | | | | |
| Electron | 5 (1) | speed | tool | |
| Ion | 10 (1) | speed | tool | FIBE |
| Mechanical | 0.1 | speed | option | SPL, parallel beams possible |
| Photon | 200 | speed | tool | |
| **PRINTING** | | | | |
| Electron | 80 (35) | mask, blur, stitching | option | SCALPEL, promising |
| Ion | 100 (35) | mask, optics, stitching | option | relatively cheap |
| Mechanical | 50 (20) | limited patterns, wear | research | |
| Screen | | | | |
| Optical | 400 (200) | resolution | tool | |
| Deep UV | 130 (70) | optical imaging | development | pushing the limit |
| Extreme UV | 100 (35) | mask, optics, source | option | promising |
| X-ray | 70 (25) | mask, optics, source | option | no mask commercialisation |
| Holographic | 300 (---) | | | |
| **STEPPING** | | | | |
| | 250 (200) | resolution | tool | |
| **ALTERNATIVE** | | | | |
| LIL | 150 (75) | | research | |
| Atom | 80 (20) | limited patterns | research | |
| Stereo | 5000 (1000) | | research | |
| Phase-shift | halves | | option | |
| Edge | 50 (1) | add-on process | research | poor man's nanoprocess |

chapter the major film-etching methods will be described and two basic concepts that should be considered in all etch techniques—profile and selectivity.

## 5.1. Etch Profile

The profile of an etched film is a direct consequence of the etch directionality. Etch directionality is a measure of the relative etch rates in different directions, usually normal versus lateral. We can distinguish between four special

cases of material etching: isotropic etching, and orientation-dependent-, tapered-, and vertical-anisotropic etching. The isotropic etch profile is shown in Figure 77a. Ideal isotropic etching occurs in pure chemical processes where etch rates are the same in all directions (i.e., the underetch equals the etch depth). The etch profile would approach a perfect semicircle, forming an ideal isotropic profile. For example, amorphous materials of uniform composition etch isotropically in chemical processes. A special case of anisotropic (i.e., nonisotropic) etching is found when etching monocrystalline material in Figure 77b. For example, silicon is generally etching faster in the $\langle 110 \rangle$ and $\langle 100 \rangle$ direction than in the $\langle 111 \rangle$ direction in many alkaline-based etch solutions. This kind of profile is called the orientation-dependent profile. Physical "bombardment-driven" processes usually give rise to tapered profiles as shown in Figure 77c. Finally, when
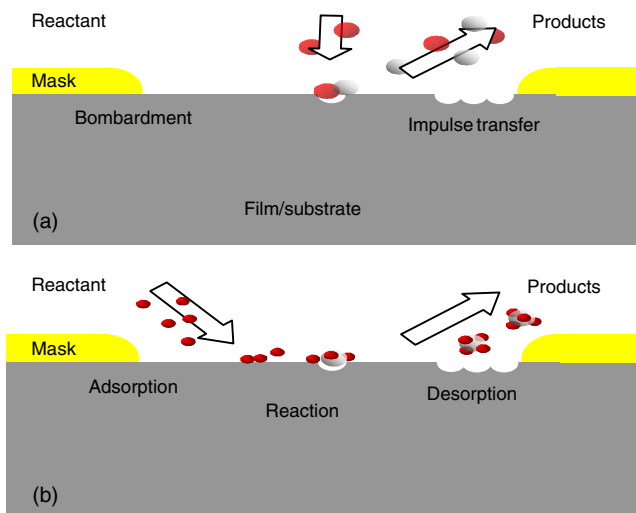


**Figure 76.** Processes involved in film etching. (a) Physical. (b) Chemical.
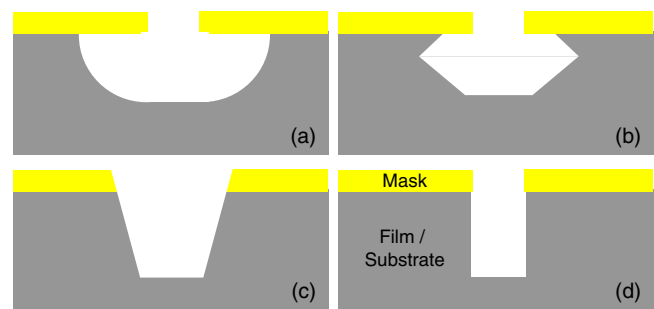


**Figure 77.** Ideal etch profiles: (a) Isotropic. (b) Crystal-dependent anisotropic. (c) Tapered anisotropic. (d) Vertical anisotropic.

combining both chemical and physical processes (i.e., synergistic), vertical etching is possible. The ideal vertical etch profile in Figure 77d has perfectly straight sidewalls exactly under the edge of the mask and the etching under the mask approaches zero.

Mostly, the profile is in between one of the ideal profiles, where the normal etching proceeds faster than the lateral one, as illustrated in Figure 78. The amount of undercutting of the mask leads to nonvertical sidewalls in the film. On the one hand, the more chemical an etch process is, the more selective (see next section) and the more isotropic it generally is. The exception to this are those which are sensitive to crystallographic orientation. On the other hand, the more physical an etch process is, the more tapered and the less selective it generally is.

The ideal vertical profile is seldom found in pure physical processes and tapering (or facetting) is found instead. Two prime reasons for tapered profiles are the mask erosion and the angular dependence of the etch rate (or sputter yield $S$, i.e., the number of atoms removed per incoming ion). Figure 79 is a generalization of the angular dependence effect due to ion impact. Sputter ejection due to normal ion incidence (in the angular sense) requires 180° reversal of the momentum; this is not very likely and accounts for the low yield of the sputter process at normal incidence. As the angle of incidence ($\theta$) increases, so does the sputter yield, again for momentum considerations. This is accompanied by the sputter ejection angular distribution becoming pronounced in the direction of specular reflection. Ultimately the yield goes to zero at 90° incidence, resulting in a maximum yield at $\theta = \theta_m$ somewhat between 0° and 90° depending on the target material, and the ion identity and energy. This angular dependence has several consequences. For example, the polymeric materials used for photoresist tend to sputter rather easily and also degrade under ion bombardment. Sometimes heating of the resist induced by the ion impact or glow causes resist reflow, so that its profile changes. These effects combine to make resist masks prone to etch back and causing tapering during physical etching. The phenomenon of anisotropic tapering, which is illustrated in Figure 80, usually starts on corners, which always have some rounding and therefore present a variety of incidence angles to the incoming ions. A facet will develop for the plane which has the highest etch rate ($\theta = \theta_m$ in Fig. 79), as the more slowly etching planes are consumed. The effect is then transferred to the film but at a different angle corresponding to $\theta_m$ for the film material and the difference in etch rate between the mask and the film. Due to the formation of a tapered-anisotropic profile—or just tapered profile—and because the mask itself is also etched, the final dimension of the opening in the mask will be greater than the initial dimension (Fig. 80d). Consequently, the influence



**Figure 79.** Variation of sputter yield with angle of incidence (with respect to the target normal).

of the mask on the etch profile of the film can be quite pronounced and depends on its initial thickness and profile.

A vertical profile is often desired in an etch process because it maintains lithographically defined feature sizes as they are transferred by etching into underlying films. However, vertical structures that result from vertical etching may also cause problems in subsequent processing. Depositing another layer on top of a structure with vertical steps may cause step coverage problems, as discussed in the section on film formation. Less steep steps, obtained with less vertical etching, would make it easier to obtain good step coverage and would allow easier filling in later formed layers. Because of shrinking feature sizes, however, modern fabrication methods tend to employ vertical etching with little undercutting and use formation techniques that achieve good filling and step coverage even for near-vertical structures. To obtain the perfect vertical profile, usually the synergetic action of both chemical and physical etching is necessary as will be shown in the section on synergistic etching.

## 5.2. Etch Selectivity

Etch selectivity is the ratio of the etch rates of the different materials in an etch process. When the etch rates of the mask and the underlying substrate are near zero, while the etch rate of the thin film is appreciable, then the etch selectivity of the film with respect to both the mask and the substrate is high. Selectivity in the range of 25 or higher is usually considered reasonable. Different materials have
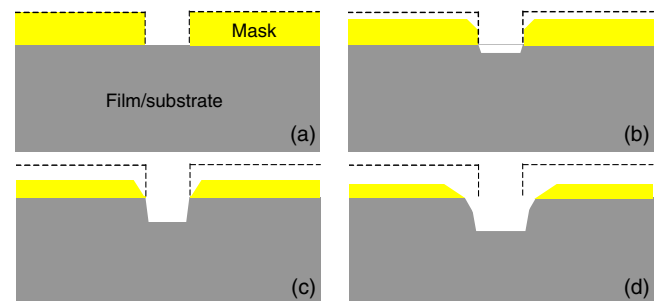


**Figure 78.** Etch directionality.



**Figure 80.** A tapered profile in physical etching: (a) The mask cross-section prior to etching. (b) The onset of facet formation in the mask. (c) The mask facet intersects the original substrate surface plane. (d) The facet propagates laterally in the film thereby exposing additional film to physical etching and consequent facetting.

different etch rates usually because of the chemical effects involved with etching, as opposed to the physical effects. Therefore, chemical reactions can be very selective whereas physical processes tend to be similar for most materials.

In many cases, resist is not enough as a masking layer to transfer a pattern into the underlying material, and generally an intermediate layer is needed. These intermediate masks stand up better to certain etching conditions (i.e., having a higher selectivity) than resist and are often called hard masks. Of course, these hard masks themselves must be selectively etched usually with lithographically defined resist as the soft-masking layer. In Figure 81 a typical procedure to pattern a silicon substrate in an alkaline solution (e.g., KOH) is shown. Resist is attacked in KOH solutions and therefore an intermediate silicon dioxide layer is used. (a) First the oxide is formed (e.g., thermally grown) and coated with a resist pattern. (b) Subsequently, the oxide is (isotropically) etched in an acidic solution (e.g., HF) with the help of the resist pattern (resist can fairly withstand most acidic solutions). (c) Finally, after the resist is removed, the oxide is used as a KOH resistant hard mask to (anisotropically) etch the silicon.

Achieving good selectivity and vertical etching at the same time is important and sometimes quite difficult—with the exception of crystal-dependent etching—for a number of reasons. These reasons are indicated with numbers in Figure 82, where a thin film on top of a substrate is etched. (1) The edge rate of the mask is usually nonzero, and the mask itself is etched. The selectivity for the material to be etched with respect to the mask determines how thick the mask material must be so that the mask is not completely removed during the etching process. Moreover, the mask itself is not perfectly rectangular with rounded top corners and sloped sides due to, for example, postbake procedures of resist (to improve etch selectivity of the resist with respect to the film to be etched). This effect will widen the trench opening during etching (see also Fig. 80). (2) The film structure is an important issue to be considered in film etching. For example, a pinhole will etch the film at places not intended by the designer. (3) Bad adhesion—many times in conjunction with film stress—might curl the mask from the film at the etching corners of structures and might even lift off the whole mask during etching. (4) All etch processes generally employ some amount of overetching in order to ensure that the desired etching process has gone to completion. For example, differences in thickness or etch rate of the thin film between wafer center and wafer edge make extra etch time necessary (typically 10% of the total time). Thus underlying films or the substrate are normally subjected to the etchant for some period of time toward the end of the etch period. The selectivity for the material
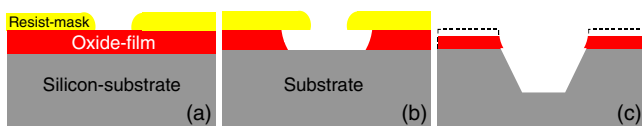


**Figure 81.** Typical etch procedure: (a) Resist patterning (first pattern transfer with developer). (b) Silicon dioxide etching (second pattern transfer with HF). (c) Silicon etching (third pattern transfer with KOH).
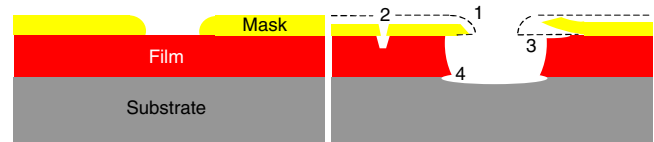


**Figure 82.** Real etch profile.

being etched with respect to the underlying material determines how much etching of the underlying materials occurs. Clearly, if the substrate beneath the thin film is attacked by the etchant, then the profile of the film will be affected even further.
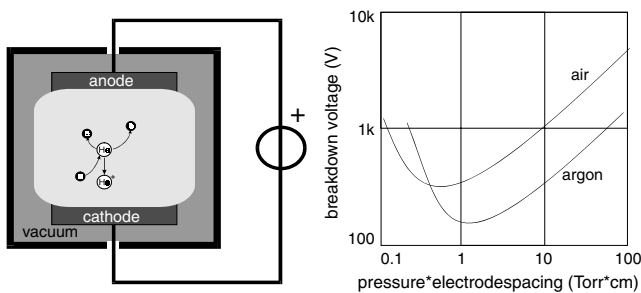
## 5.3. Film-Etching Methods

Etching can be done either in a plasma- or gas-phase ("dry etching"), liquid-phase ("wet etching"), or solid-phase "abrasive etching" environment. Wet etching involves the use of liquid etchants and is most often a purely chemical process. The wafers are usually immersed in the etchant or spray-etched (e.g., developer solutions) and etching proceeds by dissolution of a material in a solvent or by conversion of a material into a soluble compound, which subsequently dissolves in the etching medium. In the early days of the industry, wet etching was used exclusively. It was a well-established, simple, and inexpensive technology with a high selectivity possible between the masking material and the thin film to be etched due to the chemical nature of the process. Eventually, however, the need for smaller linewidths and more vertical structures required new techniques such as plasma etching. Plasma etching involves the use of reactive etchants from a discharge. Here the etching usually takes place by a combination of chemical and physical processes and forms gaseous or volatile products. The creation of plasma is not always necessary. For example, silicon is etched with $XeF_2$ gas and silicon oxide etches readily in HF vapors. This type of dry etching is beneficial in manufacturing devices where plasma damage would distort the device performance drastically. Solid-phase etching such as powder blasting is not often found in microstructuring. It is a pure physical process and involves the bombardment of particles (typically a few tens of $\mu$m in diameter), which removes material due to physical momentum transfer.

Film etching generally means the complete local removal of a film as given in by the mask pattern on top of the film. However, in some cases the film is not removed but only changes structure. A well-known example of the latter process is the etch formation of porous silicon from single-crystal silicon. This subdivision of film etching into film removal and porous film formation is quite identical with the subdivision of film formation into film deposition and film growing. Therefore this section is organized in more or less the same way as the section on film-formation—it is split into plasma-phase, gas-phase, liquid-phase, and solid-phase etching. Nevertheless, mostly the plasma etching is treated due to its prominent position in current microsystem manufacturing.

### 5.3.1. Plasma-Phase Etching

While wet chemical etching was successfully used in the early days of integrated circuit manufacturing, it has been largely replaced by plasma, or dry, etching due to two main reasons. The first reason is that very reactive chemical species are produced in plasma, which can often etch more vigorously than species in a nonplasma environment. The second reason is that vertical etching—to minimize underetching—is possible with plasma etch systems. This allows smaller and more tightly packed structures. The vertical etching is due to the presence of ionic species in the plasma and the electric fields that direct them normal (i.e., vertical) to the equipotential wafer surface. One of the first widespread uses of plasma etching was in the early 1970s to etch PECVD silicon nitride. Boiling phosphoric acid was commonly used, but this etchant often lifted off photoresist masks so that a mask of silicon oxide had to be used, requiring its own masking and etching steps. It was found that by using $CF_4/O_2$ gas mixture in a plasma atmosphere, atomic fluorine is produced which can etch the nitride film much more easily. In addition, a photoresist mask is not lifted off in this process, making the process simpler and more reliable.

***Principle of Plasma Etching***   The principle of plasma-assisted etching is simple; use a gas glow discharge to dissociate and ionize relatively stable molecules forming chemically reactive and ionic species, and choose the chemistry such that these species react with the solid to be etched to form volatile or gaseous products. Electrical discharges have commonly been used to generate plasma in the laboratory using a glass tube in which two metal electrodes are installed (Fig. 83). The plasma is accomplished by evacuating the discharge tube to a pressure range between $10^{-5}$ to $10^{-3}$ atmosphere and applying a voltage between the two electrodes. As the voltage gradually increases, only a very small electrical current flows. However, when the voltage has reached a few hundred volts, electric current through the tube shows an abrupt increase, and the tube begins to emit visible orange–red light. This condition in the discharge tube is called plasma and is caused by the relaxation of excited particles, which are created by electron impact. The gas becomes electrically conductive due to ionization; the process is also caused by electron impact in which an atom

is fragmented into an ion while liberating an extra electron. Because the extra electrons formed by ionization will also convert electrical energy into kinetic energy—which will produce even more electrons—the electrical fields are quite effective in creating plasma. Generally in such plasma, positively charged ions and negatively charged electrons drift in opposite direction according to the electrical field. The moment when the strength of the electrical field is high enough to increase the number of electrons rapidly is called breakdown, and at this moment the gas ashes and becomes a plasma. This moment depends on the pressure and it is expressed with the help of the so-called Paschen curve, which also is found in Figure 83. Typically, the electrode separation is 10 cm and the gas is turned into plasma at pressures ranging from 10 mTorr up to 1 Torr. At higher pressures, the electrons make too many collisions to be able to gain enough energy necessary for ionization, and only the lower excitation processes take place without an increase in electrons. At the lower pressures, the electrons do not make any collisions with gas particles and they will hit the anode with high energy, again without an increase in electrons.

Wafers are most frequently located directly in the plasma, separated from it only by the natural boundaries of the sheath, where they are bombarded by all of the energetic species of the discharge. These include positive and negative ions, electrons, photons created by electron bombardment of surfaces or from decaying excited atoms or radicals, short-lived radicals, and hot and metastable atoms. It is possible to protect the wafers from some of these particles by appropriate shields or by removing the wafers from the region where the plasma is created. So, while increasing the distance between the sample and the plasma, particles which deteriorate the etch process can be filtered out. In this way it is possible to operate at much lower pressures than when the sample would be mounted directly in the plasma glow region. Therefore, an important classification is to distinguish between a contact plasma, where the sample is in direct contact with the plasma, and a remote plasma, where the sample is located at a distance from the plasma (Fig. 84). In contact plasma etching, samples will be bombarded by all kinds of plasma particles. Members of this important group are the barrel reactors and planar reactors. In barrel etchers or volume-loaded reactors, wafers are simply stacked in a notched quartz support stand that is inserted into a reactor without any attempt to specify the directions of the exciting fields. The planar reactor group can be split up into



**Figure 83.** A direct current (dc) plasma reactor showing ionization by electrons accelerated by the electric field between two electrodes (i.e., anode and cathode) together with the Paschen curve showing the breakdown voltage of a gas between the two electrodes separated by a distance $d$ at a pressure $p$; 1 atm $\sim$ 1 bar $= 10^5$ Pa $\sim$ 760 Torr.
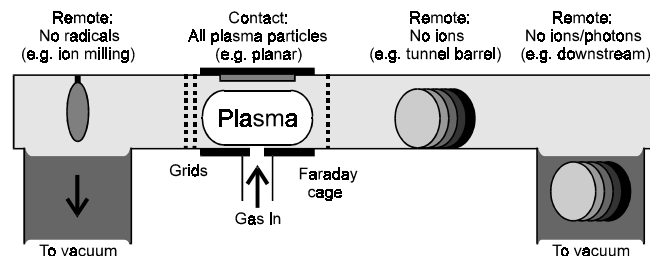


**Figure 84.** Plasma etching at different distances between the plasma and the sample to filter out specific particles from reaching the surface of the sample: Contact and remote plasma etching.

(1) diode reactors with horizontal target plates for single-wafer processing, (2) triodes with an extra electrode used for increased ion bombardment, and (3) hexodes designed for batch processing in which the vertically arranged cathode has the shape of a hexagon surrounded by the cylindrical chamber walls forming the anode. A disadvantage of the contact plasma reactors is that the flux of all the impinging species at the sample surface is difficult to control. A way to improve this is by way of the remote plasma reactors, such as the tunnel-barrel and downstream reactors, which exclude the ionic species by way of a Faraday cage, and ion mill reactors, which subtract the ions from the plasma by way of high-voltage driven grids.

*CCP Reactor* Plasma, such as can be obtained by a dc glow discharge, can also be generated at low pressure (1 mTorr–1 Torr) by a rf discharge with powers of several tens up to hundreds of watts. A basic capacitively coupled plasma (CCP) reactor—currently the most important configuration—is illustrated in Figure 85. The reactor is also known as a plan-parallel plate, planar or diode reactor, and is similar to the PECVD and sputter PVD systems shown earlier (Section 3.7). The energy is supplied by an rf generator—usually operating at 13.56 MHz—and a voltage bias develops between the plasma and the electrodes. This is due to the difference in mobility of the electrons and the ions. Initially, the more mobile electrons are lost to the electrodes at a faster rate than the slower ions. This results in the plasma being biased positively with respect to the electrodes. In CCP reactors, the degree of ionization is typically only $10^{-4}$, so the gas consists mostly of neutral but excited species. A characteristic of this plasma is the lack of thermal equilibrium between the electron temperature and the gas temperature. The rf field is able to effectively convert electrical energy into kinetic energy for the electrons only. In turn, the electrons convert their kinetic energy into inelastic energy for the neutrals to produce ions, radicals, and excited species or they bounce with the neutrals elastically without energy transfer. Thus, the mean neutral velocity is not changed a lot. Hence, this type of plasma is called a nonequilibrium plasma or cold plasma.

For a symmetric CCP reactor (equal electrode areas), the voltage distribution that develops is shown by the solid curve in Figure 86. The sheaths are the regions next to
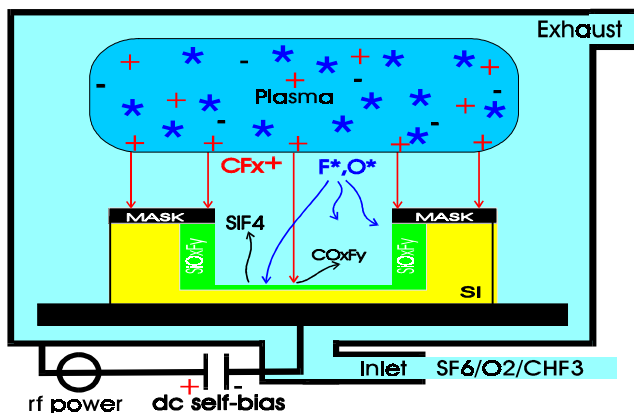


**Figure 85.** A capacitively coupled plasma (CCP) reactor.
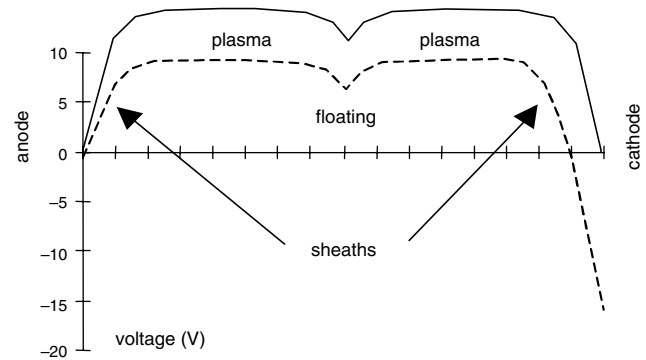


**Figure 86.** Potentials inside a CCP reactor.

each electrode where the voltage drops occur. The sheaths form to slow down the electron loss so that it is equal to the ion loss per rf cycle and so that the average current to the electrodes is zero. Whereas the heavy ions respond to the average sheath voltage, the light electrons respond to the instantaneous rf voltage. During most of the rf cycle, the electrons are turned back at the sheath edge, resulting in the sheaths—on the average—being depleted of electrons. This depletion of electrons in the sheath results in the sheath being dark because of the lack of electron/atom collisions and subsequent relaxation by light emission. In the bulk of the plasma, both ionization and excitation events occur, the latter producing the characteristic glow of the plasma. The lack of electrons in the sheath also increases the impedance of the sheath compared to the plasma bulk resulting in the main voltage drop being across the sheaths. If one of the electrodes is made much smaller in area, then the voltage distribution becomes asymmetric with a much larger voltage drop occurring from the plasma to the smaller electrode in order to maintain current continuity throughout the system, as shown by the dashed curve in Figure 86. At low pressure, these reactors develop still higher potentials and bias. The external circuit usually has a blocking capacitor (Fig. 85) so that the negative dc self-bias voltage will appear between the small electrode and the ground (the rf power generator would otherwise shorten the bias voltage).

*ICP, ECR, MIE and Arc Reactors* In the CCP reactors as discussed thus far, the rf generator is capacitively coupled with the plasma. This means that, in order to create high-density plasma, the rf power and thus the dc bias will be high. To lower the bias while keeping the plasma density high it is possible to use an inductively coupled plasma, electron cyclotron resonance (ECR), or magnetron ion etching (MIE) reactor. Unlike the CCP reactors, ICP reactors make use of an inductive coupling in which the electric fields are generated by a coil wrapped around the discharge chamber. These systems commonly operate at a frequency of 13.56 MHz, with powers of several hundreds to thousands of watts. The chamber is typically made of Pyrex, quartz, or alumna. The inductive coupling has the advantage above capacitive coupling that there will be no large or high-voltage sheaths present in the chamber, and as a result no sputtering of the wall. Therefore, these reactors are often used for fast isotropic etching. In ECR, a discharge is produced by microwave excitation (commonly 2.45 GHz).

When a magnetic field of $B = 875$ Gauss is applied, resonance between the cyclotron motion of the electrons in the magnetic and microwave field occurs. Electrons at resonance efficiently convert microwave energy into dissociation of gas species at pressures much lower than possible in CCP or ICP reactors. In MIE, magnetic fields from magnets are used to enhance ionization by confining a discharge. Arrangements similar to those used for magnetron sputtering have been incorporated into etching hardware. Magnetic field lines parallel and electric field lines normal to the cathode surface (self-bias) confine electrons on cycloidal trajectories near the cathode. The probability of an electron undergoing collisions with gas phase species is thus enhanced, and the ion/neutral ratio can be 50 times greater in MIE reactors than in CCP reactors. The mobility of electrons toward the cathode is decreased because of this confinement, causing the self-bias to be lower than conventional CCP. A large flux of low-energy ions is thus produced in MIE reactors at low pressure, whereas in CCP reactors a small flux of high-energy ions is produced for the same input power. There are more types of plasmas, such as thermal arc plasmas, which are used for fusing metal and are generated at near atmospheric pressure or above, microwave multipolar plasma reactors equipped with confinement magnets which surround the etching chamber and use ECR sources, distributed ECR reactors, rf driven double cathode etchers, hallow cathode systems, and magnetically controlled reactive ion (MCRIE) etchers, to name only a few.

*Kaufman Reactors*   In 1961 H. R. Kaufman invented the ion source. In the first instance, the source was used as an ion thruster for space propulsion, but later on it was used for milling (i.e., etching) purposes too. It can generate a collimated ion beam from a wide choice of gas species. The low-pressure (<1 mTorr), line-of-sight nature of beam techniques prevents ion scattering and redeposition of sputtered material due to gas-phase collisions. This possibility of separately controlling ion energy and flux provides a flexibility of directional bombardment not available in other plasma processes. Because it is difficult to start plasma at such low pressure, it is created in a remote, small, higher pressure chamber (Fig. 87). In this so-called Kaufman-source chamber, a high density of electrons is created by way of a heated cathode wire. These electrons are forced to the anode by way of an external voltage source (ca. 40 V). Moreover, their lifetime is increased with the help of permanent magnets surrounding the chamber. The ions are extracted from this plasma with electrostatically controlled grids (up to 1000 V and more) and are directed to the substrate to be etched.
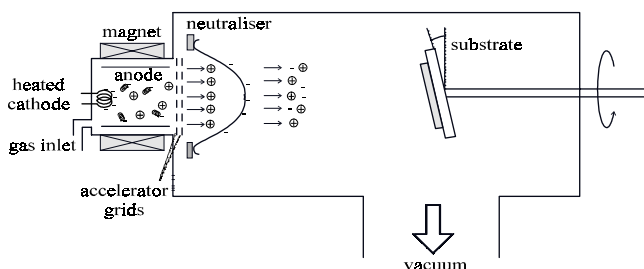


**Figure 87.** Basic schematic for ion beam etching.

A neutralizer is used to prevent charging of the (insulating) substrate, which could cause a nondesirable deflection of incoming ions.

In the previous sections, a few important plasma reactor systems have been treated. These systems can be used for film formation and film etching. As a typical example, the processes which take place in a planar CCP reactor (Fig. 85) are now given:

- *Generation:* An rf generator is used to supply energy for a discharge. This glow discharge is used to generate from a suitable feed gas (e.g., $SF_6$ for Si etching) by electron-impact dissociation/ionization the gas-phase etching environment, which consists of neutrals, electrons, photons, radicals (F), and positive ($SF_5^+$) and negative ($F^-$) ions.

- *Dc-bias formation:* The sample or wafer is placed on an rf driven capacitively coupled electrode. Since the electron mobility is much greater than the ion mobility, after ignition of the plasma the electrode acquires a negative charge with respect to the plasma glow region resulting in the creation of the so-called dc self-bias voltage.

- *Diffusion/forced convection:* The transport of reactive intermediates from the bulk of the plasma to the wafer occurs by diffusion. Positive ions from the glow region are forced to the wafer by way of the dc self-bias and will assist the etching.

- *Adsorption:* Reactive radicals adsorb on the wafer surface. This step can be strongly enhanced by concurrent ion bombardment, which serves to produce "active sites" since it aids in the removal of, for example, an $SiO_xF_y$ layer, which otherwise passivates the surface.

- *Reaction:* A reaction between the adsorbed species and the wafer must take place. In the case of fluorine-based etching of silicon, chemical reactions between the F atoms and the surface spontaneously produce either volatile species, $SiF_4$, or their precursors, $SiF_x$ ($x < 4$). However, in Cl-based etching, Cl atoms are known to adsorb readily on Si surfaces, but the spontaneous etch rate is very slow. Ion bombardment makes it possible for adsorbed Cl atoms to attack the backbones of Si more efficiently and form a volatile $SiCl_4$ molecule. This mechanism is called ion-induced etching.

- *Desorption:* The desorption of the reaction product into the gas phase requires that the reaction product is volatile; thus it should have a high vapor pressure at the substrate temperature. Additionally, there should be no deposited blocking film at the surface. The removal of these films can be greatly accelerated by ion bombardment via sputtering. This mechanism is known as ion-inhibitor etching.

- *Exhaust:* The desorbed species diffuse from the etching surface into the bulk of the plasma and should be pumped out; otherwise plasma-induced dissociation of product molecules will occur and redeposition can take place.

Thus, the two main types of species involved in plasma etching are the reactive neutral chemical species (radicals) and the "physical" ions. It is the free radicals and sometimes other species such as $Cl_2$ or $XeF_2$-, which are primarily responsible for the chemical component in plasma

etch processes creating isotropic or crystal-oriented profiles. It is the ions that are responsible for the physical component creating tapered profiles. Plasma etch systems can be designed such that either the radicals (i.e., chemical plasma etching) or the ions (i.e., physical plasma etching) dominate. The radicals and ions can also work together in a synergistic manner; this is called ion-enhanced or synergistic plasma etching creating various profiles including the ideal vertical profile while maintaining an acceptable degree of selectivity. In Figure 88 the results of the interaction between ionic and radical species with a surface facing plasma are shown, that is, (a) the chemical radical etching (RE), which uses predominantly radicals but not depending on the crystallography, (b) the synergetic ion beam assisted orientation-dependent etching, which depends on crystallography, (c) the synergetic ion beam assisted radical etching (IBARE), which uses both radicals and ions, and (d) the physical sputter etching (SE) or ion beam etching (IBE), which uses only ions. Generally, IBE shows only positively tapered profiles, low selectivity, and low etch rates, whereas RE gives rise to isotropic profiles, high etch rates, and high selectivity.
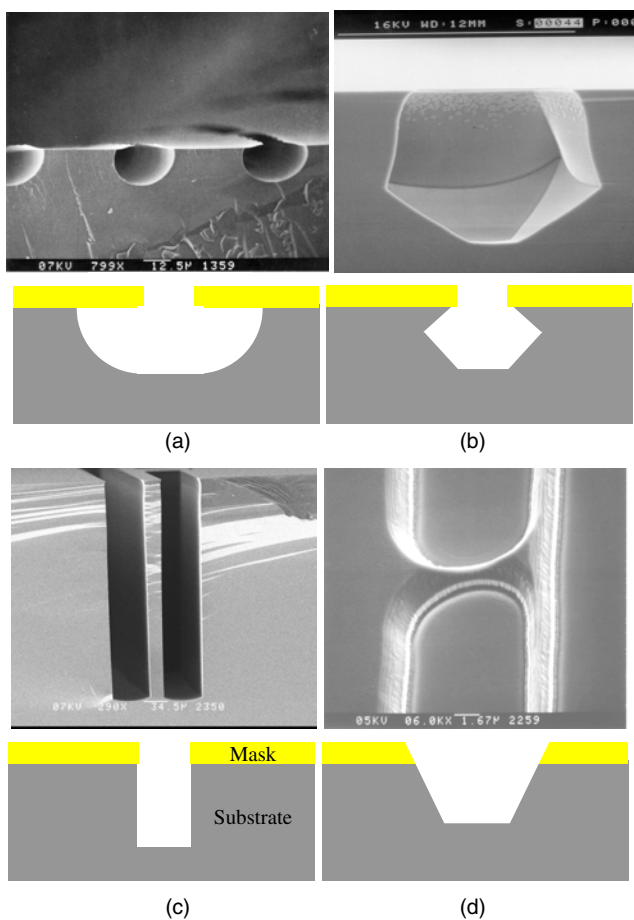


**Figure 88.** Typical products of the four basic mechanisms of dry plasma etching: (a) Chemical radical etching (isotropic RE). (b) Synergetic ion beam assisted orientation-dependent etching (anisotropic IBA-ODE). (c) Synergetic ion beam assisted radical etching (anisotropic vertical IBARE or RIE). (d) Physical sputter etching or ion beam etching (anisotropic taper IBE).

IBARE enables the achievement of profile control due to the synergetic combination of physical sputtering with chemical activity of reactive species with high etch rates and high selectivity. Next, each of these etching mechanisms will be described more in detail.

***Chemical Plasma Etching*** Radical etching is characterized by almost entirely chemical etching and a minimum of ion bombardment (Fig. 88a). Unfortunately, these chemical plasma systems are also called plasma etchers (PE). Of course, the IBARE and IBE systems are plasma etchers as well. Typical reactor types for RE include the barrel etchers (no ions) and downstream etchers (no ions and photons) in which, generally, the plasma is excited using microwaves (Fig. 84). Such systems are often used for photoresist stripping and other applications where high selectivity and low radiation damage are key requirements and where the isotropic nature of the etching is not a problem or even an advantage (think about plasma-assisted releasing in surface micromachining; Section 6.2). Sometimes symmetrical planar CCP reactors are used. Because of the equal area of both electrodes, there is no bias created between the two electrodes. When the pressure in the reactor is high (say 1 Torr), then the plasma potential and bombardment of ions will be low. Generally, it is more convenient to use an asymmetrical system in which the rf powered electrode (where the wafers are situated) is large relative to the grounded surface area. This is the so-called PE mode. In these cases the plasma potential will be high with respect to the grounded electrode but will almost equal the target electrode potential. Hence, no highly energetic ion bombardment will occur at the substrates. Unfortunately, the wafer can easily be contaminated by material sputtered off the grounded counterelectrode. As a matter of fact, this mode is often found in sputter deposition reactors! Because the grounded surface is more negatively charged than the target electrode, this type of system is also referred to as an "anode-loaded PE system," as opposed to the cathode-loaded IBARE systems for synergistic plasma etching.

***Physical Plasma Etching*** It is often hardly possible to etch a specific substrate material because there is no chemical etchant available. In these cases the patterning is fulfilled by sputtering the layer with a directed energetic ion flux (Fig. 88d). When the ion bombardment takes place at higher pressures in contact with the plasma, it is called sputter etching. In contradiction, at low pressures in remote plasmas, it is known as ion milling or ion beam etching. In SE, a sample is mounted on top of the cathode electrode of, for example, a CCP reactor (Fig. 85). The sample is in contact with the plasma where it is bombarded by highly energetic ions (e.g., $Ar^+$ from the plasma glow region), which pass the plasma sheath region. In sputter processes, radicals and photons are not important enough to influence the overall etch rate, and the ions control the etch rate by way of their impact on the sample surface. However, due to the relatively high pressure, redeposition is often found because of gaseous particles, just sputtered from the surface, which are reflected back from the plasma due to collisions with plasma particles. Moreover, due to collisions of the ions with plasma particles while passing the sheath (i.e., ion scattering), the impact angle of the ions with respect to the surface

is not fully normal anymore, resulting in an undercut. The collisional problems of SE are less pronounced in IBE systems (Fig. 87). This is because the operating pressure in IBE can be much lower (<0.1 mTorr) and, thus, there is less chance of sputtered material (from the target or more importantly from the mask or target support) colliding in the gas phase and being backscattered onto the target. Nevertheless, sputtered material from the mask or the target will be redeposited directly and is responsible for the typical phenomenon of "ears" in IBE (Fig. 89). In IBE, the ions are accelerated toward the sample with the help of a high-voltage source. Because pure physical etching is a slow process, typically 1–30 nm/min, sometimes an extra reactive feed gas is led into the reactor. Such processes are known as chemical-assisted (reactive) ion beam etching (CAIBE, RIBE, and CARIBE). In RIBE, and more in particular CAIBE, it is possible to manipulate important parameters in plasma-assisted etching (e.g., temperature and electron or photon impact). For this reason, basic studies of the surface science aspects of plasma etching were initiated using CAIBE at the beginning of the 1980s in laboratories all over the world.

***Synergistic Plasma Etching*** In applications where, besides radicals, ion bombardment is required, planar reactors can be employed (Figs. 88c and 85). As for the chemical plasma etching, the name for this synergistic plasma etching system is not always straightforward. Trade jargon often refers to low-pressure asymmetric planar reactors as reactive ion etchers, distinguishing higher pressure operation (>100 mTorr) with the term plasma etchers. Of course plasma etching is taking place in both regimes and ions are almost never the primary etchants. We prefer the name of ion beam assisted radical etching instead of reactive ion etching. In IBARE it is difficult to independently control the temperature and fluxes of species. This is one of the reasons for the lack of consistency in the reports concerning the fluorine-based IBARE of silicon. Nevertheless, IBARE is the most important plasma techniques in use today. Popular types of IBARE systems are the planar reactors. As in the case of the radical etch equipment, planar reactors for IBARE processes can be either symmetric, where the cathode area equals the anode area, or asymmetric, where these areas are different in size. In symmetrical low-pressure systems, the plasma potential is high and both electrodes are bombarded by energetic ions. Due to the zero bias caused by the equal electrode areas, this type of etcher is often confused with real RE (i.e., no bombardment). More commonly, in asymmetrical systems, the wafer-loaded rf-powered electrode is small relative to the grounded surface area. These systems are characterized by a low plasma potential (10–50 V) and a large bias on the



**Figure 89.** Resputtering of material in physical plasma etching.

rf-driven electrode (10–1000 V), which increases ion energy and improves the directionality of the etch process. Because of the low plasma potential, relatively little sputter contamination from the grounded surface occurs. Nevertheless, due to the sometimes large bias voltage created in these systems, one should be aware of resputtered mask material toward the etching regions. Because the target electrode is more negatively charged than the grounded surface, this type of system is also referred to as a "cathode-loaded IBARE system," as opposed the anode-loaded PE systems for chemical plasma etching.

An important credit of IBARE is its ability to achieve etch directionality. Etch directionality is due to directed energy input into an etching reaction at a surface and can be accomplished by neutral, ion, electron, or photon bombardment of a surface exposed to a chemical etchant. In the case of IBARE, the achievement of etch directionality is due to energetic ion bombardment. An important clarifying experiment is the exposure of a silicon surface to a well-defined dosage of chemical etchants, $XeF_2$, and energetic ions, argon. It is found that the etch rate obtained for a silicon surface exposed to both particle fluxes simultaneously is much greater than the sum of the etch rates for exposure to the ion beam and chemical etchant separately. Ion-enhanced, ion-assisted, or synergistic plasma etching can be divided in two main groups: ion-induced (reaction controlled etching) and ion-inhibitor (desorption controlled etching) etching.

***Ion-Induced Etching*** Ion-induced etching is used when the surface of the substrate is not reacting spontaneously, such as in the chlorine–silicon, fluorine–silica, or oxygen–polymer system. Ions do modify the surface reactions in one or another way and make it possible for radicals to react with the substrate. Depending on the particular etchant substrate under consideration, a different ion-induced mechanism may be dominant. For instance, it appears that the lattice damage model is important for the oxygen–polymer and chlorine–silicon systems but not for the fluorine–silicon system. Lattice damage produced by ion bombardment increases the reaction rate of etchant species with the substrate relative to undamaged material. For example, when an organic compound like a polymer is exposed to reactive oxygen, the radicals may react spontaneously with the backbones of the long-stretched nonvolatile molecules. However, it is difficult for the oxygen to break such molecules into smaller volatile pieces and thus the etch rate is low. Therefore, an extra energetic ion beam may help to crack these big molecules and will increase the etch rate, because now the oxygen will remove the smaller parts. In Figure 90, typical results of this technique are shown: the directional etching of a polymer and silica with the help of an IBARE system. Note that when the temperature is increased above the so-called glass temperature of the polymer, the reaction of the polymer with the oxygen may become spontaneous, (i.e., no ion bombardment is needed anymore), and the profile will become isotropic. This is not an IBARE process anymore, but a thermally assisted radical etching process.
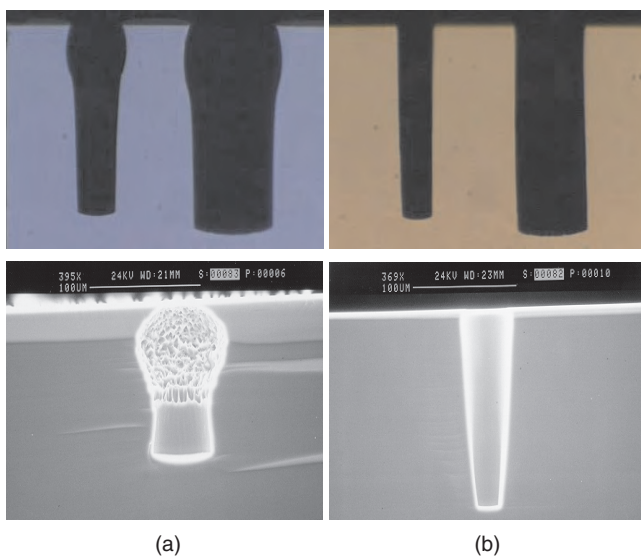
***Ion-Inhibitor Etching*** In ion-inhibitor etching, the substrate is etched spontaneously and therefore an inhibiting layer is needed to achieve directionality. Sidewalls of trenches
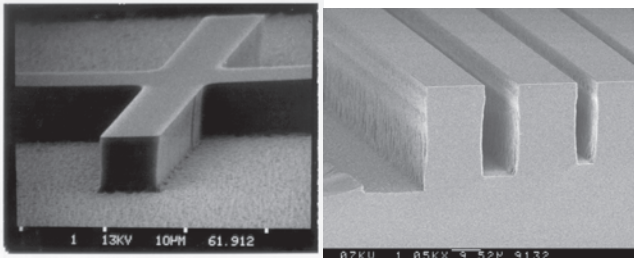
**Figure 90.** Ion-induced etching in an IBARE reactor: (a) Oxygen-based polymer etching ($O_2$ resist). (b) Fluorine-based silica (glass) etching ($SF_6$–$SiO_2$).

are not exposed to ion bombardment and will be covered by the film. However, the bottom of the trench is exposed to ion bombardment and thus free from this deposit and etching can proceed. The passivating layer can be grown by (1) inserting gases which act as a silicon oxidant forming siliconoxy-halogens, as shown in Figure 91, (2) inserting gases which act as polymer precursors forming carbon–halogens, (3) eroding and redepositioning mask material such as metal–halogens, or (4) freezing the normally volatile reaction products of silicon with radicals at the trench walls, such as silicon–halogens. The deposition of a polymeric carbon–halogen film has the disadvantage that this film is thermally less stable than an inorganic silicon–oxyhalogen film. The freezing of reaction products uses expensive cryogenic coolers, and the redeposition of mask material is not acceptable because areas which should stay clean are also contaminated (Fig. 89). Because the passivating film is very thin, the incoming ions should not be highly energetic, so the mask to silicon selectivity will be very high and the substrate damage will be low. Also, because of the low energy of the ions, trenching and faceting (typical IBE problems) are not found, and it is very easy to change

the direction of the impinging ions, thus changing the etched profile (as will be shown in the following). It is exactly these characteristics which make the ion-inhibitor etching such a popular plasma technique.

Because of their high etch rates, normally hydrogen- and halogen-based (i.e., F, Cl, and Br) plasmas are used for the IBARE of silicon and the etch products are volatile $SiH_4$, $SiF_4$, $SiCl_4$, and $SiBr_4$. Whereas F-based plasmas are generally used for isotropic etching, Cl- and Br-based plasmas such as $Cl_2$ are primarily used to achieve anisotropic etch profiles due to ion-induced etching. The latter gases are particularly hazardous ($Br_2$ or Cl compounds) and special precautions are recommended. Therefore, F-based mixes, such as $SF_6/O_2$, are often preferred. In $SF_6/O_2$-based silicon etching in conventional CCP reactors, trenches (up to 200 $\mu$m) with high aspect ratios (up to 10) can be etched at high etch rates (up to several $\mu$m/min) and low ion energies (15–90 eV). The $SF_6/O_2$ mix primarily dissociates in $SF_5$ (little $SF_4$), F, and O radicals. Directionality is achieved by the forming of a passivating $Si_xO_yF_z$ film, which is removed by ion impact at horizontal surfaces but remains at vertical surfaces. In Figure 92 SEM images of Si trenches using various percentages of $O_2$ are displayed. The horizontal etching depends on the thickness of the passivating $Si_xO_yF_z$ layer and the F-atom density trying to etch the Si by penetrating this layer. The thickness of the $Si_xO_yF_z$ layer is a function of, for example, the O-atom density, the ion impact, and the local temperature. The F-atom density is a function of, for example, the $SF_6$ flow, power, and (micro)loading.

*Dual Source Reactors* A disadvantage of CCP systems is that the etch rate is directly controlled by the rf power supply which, in turn, directly controls the bias voltage and, therefore, the ion energy and mask selectivity. Clearly, a



**Figure 91.** Ion-inhibitor etching in an IBARE reactor. Fluorine-based silicon etching ($SF_6/O_2$–Si) using $Si_xO_yF_z$ as inhibitor: (a) Typical nonoptimized profiles. (b) Profiles after proper tuning of the chemistry.



30%          25%

20%
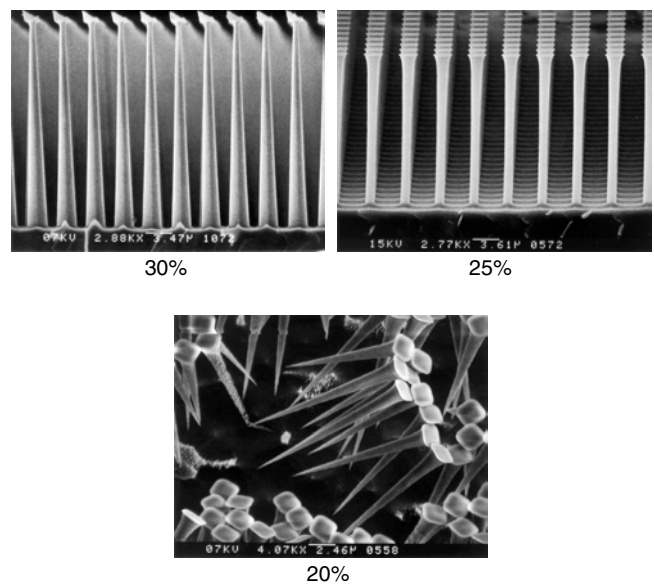
**Figure 92.** The effect of oxygen addition in an $SF_6/O_2$ plasma. With decreasing oxygen content, the thickness of the inhibiting layer decreases and therefore the profile changes from positive to negative: 30% oxygen content resulting in positive-tapered needles, 25% oxygen content resulting in vertical pillars, 20% oxygen content resulting in negative-tapered nails.

low ion-energy prevents substrate damage (electronics) and mask erosion and makes it easy to change the profile of the trench. For this reason it would be convenient to have independent control of the bias voltage with respect to the rf power. Currently, plasma systems are available aiming especially at the micro- and nanoengineering market, which fulfill this demand and come with double powered plasma sources. One is an ICP or ECR source to create a high radical and ion density (i.e. high-density plasma) into a quartz dome. The other is a CCP or dc source to direct the ions from the plasma glow region toward the wafer surface with a specific ion energy controlled by the dc self-bias as developed by the CCP source. In this way it is possible to control independently the energy flux of radicals and ionic species. High etch rates, needed for production of single-wafer etch in microsystem technology, usually require substantially higher power density than batch systems. Special techniques are necessary to handle the resultant thermal loads and enhanced helium backside cooling may require hardware features like wafer clamping (mechanically or electrostatically) and special gas control features to permit adding high-pressure gas behind the wafer, so-called helium chucks. In all cases, coolant fluids need to be circulated to the electrodes in sufficient quantities to remove the heat created by the discharge. Electrode temperatures from $-150$ to $300\,°C$ may be needed for different processes. In addition, it is desirable to control the temperature of all electrodes, because they may affect process performance, so refrigerated cooling systems are common. To control the anisotropy, different ion-inhibitor schemes are in use. A few systems are using cryogenic wafer cooling for profile control and an $SF_6/O_2$-based chemistry for a high etch rate. Others have incorporated the Bosch patent in their system to control the anisotropy (Fig. 93).

*Cryogenic Reactors*    Etching at extremely low substrate temperatures, down to $-150\,°C$, has gained more and more interest in the past years. Advantages seem to be a better control of the undercut during directional etching and an increased selectivity with respect to polymer mask materials. Commonly in CCP reactors, the substrate is cooled by circulating a coolant through the platen on which the substrate rests. However, this technique is insufficient for cryogenic cooling, because the heat transfer between the wafer and the platen is inadequate at such low temperatures and at the pressures normally used for plasma etching. Therefore, helium backside cooling is generally utilized. After optimization of the cryogenic system, etch rates of silicon up
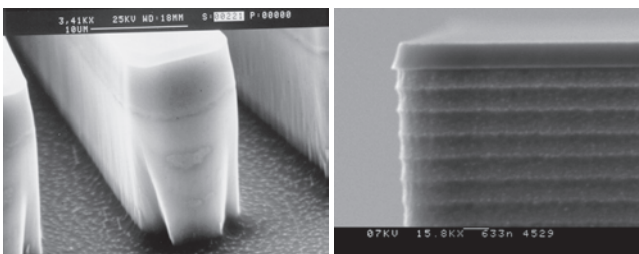
to 15 $\mu$m/min can be obtained at relatively high pressure (4 Pa = 30 mTorr) and ICP power (2 kW) while keeping the anisotropy high (Fig. 93a). At the same time, the erosion rates of thermal silicon dioxide and ordinary photoresist (Shipley S1805) are as low as 7 nm/min (i.e., selectivity up to 2000). Increasing the pressure to 20 Pa, the selectivity increases to 10,000. The high etch rate and high selectivity are especially important in case of microengineering, where wafer through etching with the help of plasmas will become a standard in the near future. In case of nanoengineering, however, profile control is the main concern. To prevent undercut in such cases, in particular bottling due to a broad ion angular distribution, the pressure should be sufficiently low. The best results were found at pressures down to 0.2 Pa = $1\frac{1}{2}$ mTorr and at a low ICP power of 350 W to prevent a too strong mask erosion caused by the low pressure. The silicon etch rate decreased to 1 $\mu$m/min and the erosion rate of the oxide and resist were both approximately 20 nm/min giving a selectivity of 50.

A remarkable effect is observed when the normally isotropic etch chemistry is operated at cryogenic temperatures ($-150\,°C$) with little additional ion bombardment (low bias and plasma potentials—i.e., high pressure). The etch rate turns out to be dependent on the crystallographic structure of the silicon; that is, orientation-dependent etching (ODE) is found. Figure 88b clearly shows the {111} planes probably created due to the difference in activation energy of the crystal orientation (More about this subject is found in Section 5.3.3). Figure 94 shows two related phenomena. The originally circular masks (both opening and dot) have turned into squares! The sidewalls are found to be {110} planes. So the etching at extremely low temperature changes from ion bombardment anisotropy into ion-enhanced crystal anisotropy.

*Bosch Reactors*    In some cases it is possible to switch a plasma chemistry continuously between the isotropic etching with a highly reactive gas (e.g., $SF_6$) and the directional deposition of an inhibiting layer (e.g., $C_4F_8$). Figure 95 shows the basic idea behind this Bosch patent. During the etching of trenches, an intrinsic roughness at the sidewalls is developed (Fig. 93b). This roughness is caused by the isotropic etch and depends on the frequency in which the equipment is switched between etching and depositing and is in the order of the etched depth during one isotropic etch run. However, the etch and deposit runs are using different gases, so the switch frequency is limited by the time



**Figure 93.** Dual-source high-speed etch processes. (a) Cryo process, $SF_6/O_2$ continuous. (b) Bosch process, $SF_6/C_4F_8$ cycle.
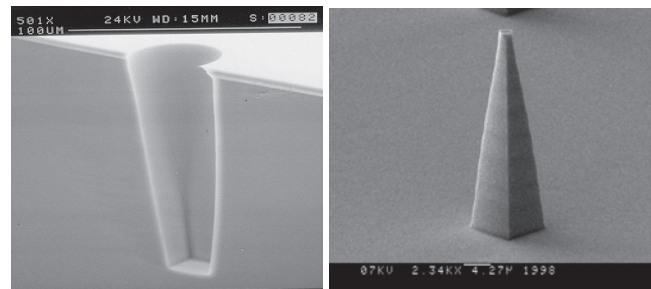


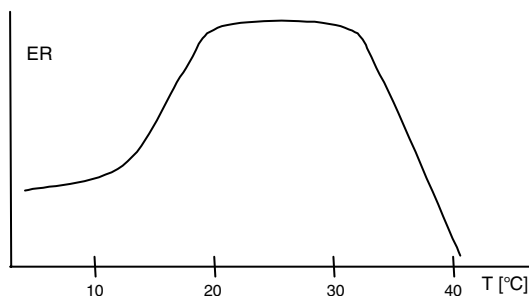**Figure 94.** Ion-enhanced ODE forming {110}-planes- at cryogenic temperature.
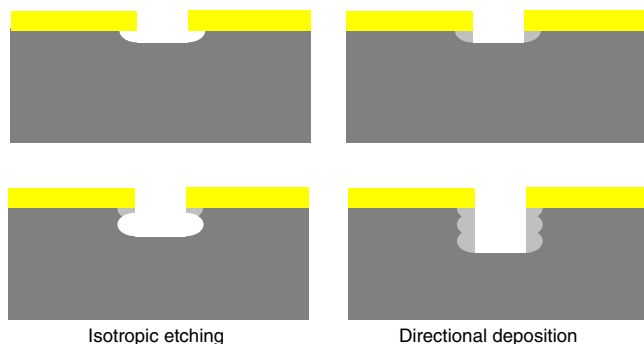
Figure 95. Pulsed plasma etching. After an isotropic etching always a directional deposition follows.



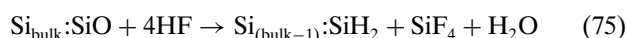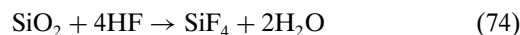Figure 96. Vapor HF $SiO_2$. Etch rate versus temperature.

needed to change the reactor volume between these two gas chemistries: the residence time. Another method to control the directionality is to switch the frequency or power and leave the gases undisturbed. This is feasible because plasma deposition rates are depending on the ion energy. So at high power or low excitation frequency, the reactor is in the etch mode. In contrast, at low power or high frequency, the reactor switches over to deposition. The advantage of this method is the higher switch frequency possible with respect to gas switching.

### 5.3.2. Gas-Phase Etching

Major limitations of wet chemical etching of silicon (dioxide) with hydrofluoric acid (HF) include the necessity for a subsequent rinse and dry step after each etch step, which is critical when dealing with fragile structures. Moreover, the hydrophobic silicon surface strongly attracts particles and other bath contaminations. Another drawback is the inability of wet chemicals to penetrate small geometries with high aspect ratios due to surface tension. Moreover, as wafer size continues to increase beyond 300 mm, single wafer processing becomes a necessity and the clustering ability of dry cleaning or etching processes becomes advantageous. It has been known that the $HF/H_2O$ mixture in the vapor state etches silicon dioxide. In vapor HF or VHF, a vapor from an aqueous solution is delivered to an oxidized surface via carrier gas (Ar or $N_2$) and a condensed phase on the wafer surface is formed to initiate etching. The VHF etch rate peaks between 20 and 30 °C and drops to zero at temperatures above 40 °C, where the condensed phase cannot be maintained (Fig. 96). In VHF etching, first the $HF/H_2O$ is introduced onto the oxide surface. When the partial pressures of HF and $H_2O$ are sufficient, a condensed film forms on the oxide surface. This film is analogous to a thin wet HF layer on the oxide. Etching of the oxide occurs after the aqueous film is present forming $H_2SiF_6$ acid [Eq. (73)] with some liberation of $SiF_4$ [Eq. (74)]. After the oxide is completely removed, the wafer surface becomes hydrophobic, while leaving the silicon surface H-passivated [Eq. (75)]. Reactant species and products desorb from the surface but $H_2SiF_6$ is not a readily volatile species. Therefore, a high-temperature anneal (>100 °C) might be necessary [Eq. (76)]:

$$SiO_2 + 6HF \rightarrow 2H^+ + SiF_6^{2-} + 2H_2O \qquad (73)$$

$$SiO_2 + 4HF \rightarrow SiF_4 + 2H_2O \qquad (74)$$

$$Si_{bulk}:SiO + 4HF \rightarrow Si_{(bulk-1)}:SiH_2 + SiF_4 + H_2O \qquad (75)$$

$$H_2SiF_6 \rightarrow SiF_4 + 2HF \qquad (76)$$
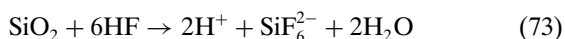
VHF is now a proven technique for removal of native, thermal, and chemical oxides. Given the chemical activity of VHF, the chambers of the various available systems range from Teflon, to SiC, to dense alumna, to stainless steel. Processing pressures range from 10 Torr to atmosphere. The HF is delivered with anhydrous HF gas, or by bubbling a carrier gas through an HF containing solution. Water or IPA is supplied to the chamber via the bubbler or a vaporizer.

Gas-phase silicon etching without the use of a plasma discharge usually contains halide atoms, typically fluorine or chlorine, which form volatile etch products such as $SiF_4$, $SiF_2$, or $SiCl_4$. Silicon can be etched in several fluorine-containing gases, including $XeF_2$, $BrF_3$, $IF_5$, and $F_2$, as well as $HF + H_2O + O_3$, at room temperature and etching in these gases is isotropic (at cryogenic temperatures the etch might show crystal-dependent behavior). Commercial $XeF_2$ etchers are available with adequate gas delivery, which can etch silicon at 0.3 to over 10 $\mu$m/min but etched surfaces tend to be rough. $XeF_2$ etching of silicon has the unusual characteristic of etching more slowly as the temperature rises above room temperature, presumably due to decreased precursor surface coverage. Because the reaction is exothermic, the etch rate may be slowed with time as the substrate is self-heated unless cooling elements are in place. $XeF_2$ is supplied in crystalline form and has a vapor pressure at room temperature of about 4 Torr. It can be masked with photoresist, $SiO_2$, $Si_3N_4$, or Al. Because native oxide can block $XeF_2$–silicon etching, it should first be removed (vapor or wet HF dip). An undissociated molecule $F_2$ etches silicon, but many orders of magnitude slower than $XeF_2$. Therefore high-temperature gas-phase etching (from 220 °C for $F_2$ gas up to 1500 °C for $Cl_2$ gas) is useful for *in-situ* removal of a surface layer of silicon (and native oxide) prior to epitaxial silicon growth to reduce the density of defects such as stacking faults. The $HCl/H_2$ system results in ODE (see Section 5.3.3) forming {111}-plane family facets in openings defined by $SiO_2$ or $Si_3N_4$ windows. A different silicon-etch technique uses a jet from a $SF_6$ gas thermally decomposed at very high temperature (2000–3200 °C).

### 5.3.3. *Liquid-Phase Etching*

The first etchants used in microtechnology were simple wet chemical etchants which were developed for all steps in the fabrication process. By spraying or immersing the wafers into baths of liquid chemicals, the exposed films could be etched away, leaving unetched those regions of the film that were masked with resist or other films. The limiting steps in wet etch processes are usually the chemical reactions in which the etch species react with the film, forming the soluble or gaseous products. Most wet chemical etches result in isotropic profiles—isotropic chemical etching (ICE)—but when etching single-crystalline material, ODE is often found. Wet etches can be very selective because they often depend on chemistry rather than physical processes. The exception for this is the spraying of a high-velocity "water jet," sometimes enriched with powder, which removes material due to physical impact. Moreover, when applying a voltage between the liquid and the substrate, i.e. electrochemical etching (ECE), it is possible to manipulate the etch result and create non-isotropic profile.

***Isotropic Chemical Etching***   A common wet ICE of silicon dioxide is HF acid. It removes (native) oxide while changing HF acid into hexafluoride ($H_2SiF_6$) acid:

$$SiO_2 + 6HF \rightarrow 2H^+ + SiF_6^{2-} + 2H_2O \qquad (77)$$
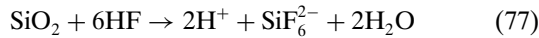
As an example, 50% HF etches $SiO_2$ at a rate of ca. 2 $\mu$m/min, silicon-rich nitride at ca. 4 nm/min, and silicon at a speed of 0.01 nm/min. Buffering agents are often added to the etch solution to keep the etchants at strength over use and time. For example, ammonium fluoride ($NH_4F$) is added to HF to help prevent depletion of the fluoride ions in the oxide etch. This is called "buffered HF" or BHF. The addition of ammonium fluoride also decreases the etch rate of resist and helps to minimize lifting of the resist during oxide etching.

In some cases the ICE occurs in two steps by first oxidizing the surface of the film or material and then dissolving the oxide. For example, a common etchant for isotropic silicon etching is a mixture of nitric acid ($HNO_3$), HF, and water. The nitric acid oxidizes the surface of the silicon [Eq. (78)] followed by dissolving the oxidation product by HF [Eq. (79)]. Alternatively, oxidants such as oxygen (dissolved in water) or peroxide ($H_2O_2$) can be used:

$$Si + 2HNO_3 \rightarrow SiO_2 + 2HNO_2 \qquad (78)$$

$$SiO_2 + 6HF \rightarrow 2H^+ + SiF_6^{2-} + 2H_2O \qquad (79)$$
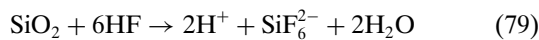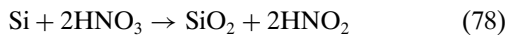
Acetic acid, $CH_3COOH$, is often added to the nitric/hydrofluoric acid mix to limit the dissociation of the nitric acid (undissociated $HNO_3$ is the primary oxidant) and to improve wetting and therefore smoother etched surfaces. Any combination of these reagents is commonly referred to as "HNA" for hydrofluoric-nitric-acetic. The etch rate in HNA peaks at over 200 $\mu$m/min at a concentration in the ratio of 2:1:0 (no added diluent). For a range of HNA solutions (e.g., in a ratio of 1:3:8), the silicon etch rate is reduced by more than an order of magnitude for doping levels (whether *n*- or *p*-type) below $10^{17}$/cm$^3$. This is related to the charge-carrier concentration available for charge transfer as part of the reaction. At low HF and high $HNO_3$ concentrations, the etch surface is usually smooth, but the etch rate drops with use as HF is consumed. These etchants can be masked with photoresist, silicon nitride, or gold. At low $HNO_3$ concentrations, the etch rate is limited by the oxidation step—which is a function of crystal orientation, defects, and doping—and therefore, the orientation-dependent etching is found. Etching, however, tends to be difficult to initiate but is aided by a catalyst such as $NaNO_3$. HNA etches are not used as much commercially as alkaline etches due to difficulty of controlling the etch rate but are useful in rounding sharp corners in microstructures to reduce stress concentration. Aside from the HNA system, several HF-based solutions (e.g., concentrated HF and BHF) have been used to etch silicon very slowly.
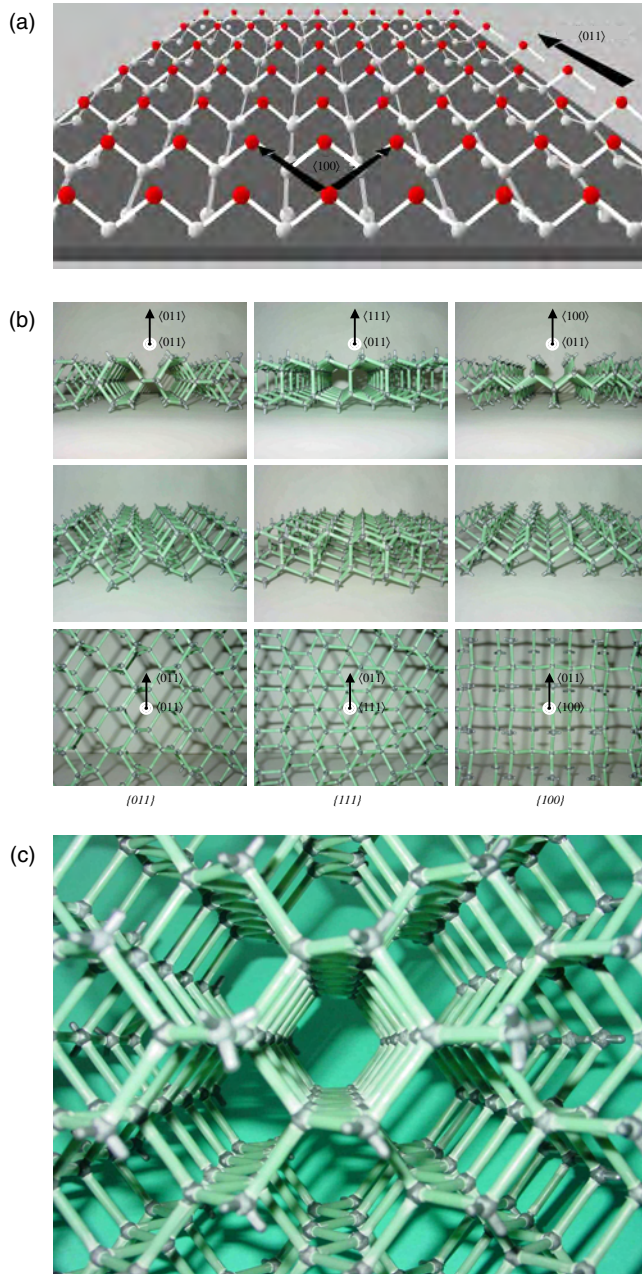
***Crystal-Dependent Anisotropic Etching***   Wet ODEs are aqueous alkaline solutions that anisotropically etch SCS at rates that vary with crystallographic direction. ODEs etch rapidly in $\langle 110 \rangle$, $\langle 100 \rangle$, and some higher-order crystal directions, effectively terminating at {111} planes as the etch rate drops by over an order of magnitude. The rate of ODE is limited under most conditions by the surface reaction rate rather than mass transport, resulting in more uniform etching than isotropic HNA etchants. Slower etching is observed, however, in the centers of larger exposed areas and deep grooves in $\langle 110 \rangle$ silicon and stratification of etchant concentration has been observed in some unstirred solutions, resulting in etch-rate variation with depth in a solution. In this section some typical ODEs will be discussed. However, before continuing, some definitions concerning the crystal structure will be discussed.

The periodic arrangement of atoms in a crystal is called the lattice. The unit cell in a lattice is a segment representative of the entire lattice. For each unit cell, basis vectors ([100], [010], and [001]) can be defined such that if that cell is translated by integral multiples of these vectors, one arrives at a new unit cell identical to the original. In case of silicon, a simple (face-centred) cubic crystal unit cell is sufficient to describe the silicon lattice with a dimension of 0.543 nm. To identify a plane or a direction, a set of integers *h*, *k*, and *l* called the Miller indices are used. For a specific crystal face, the resulting set of numbers is written down as the (*hkl*) plane and the vector perpendicular with this plane is the [*hkl*] direction. The family of faces which bear like relationships to the crystallographic axes—for example, the planes (001) and (010)—are all equivalent and they are marked as the set of {100} planes. Identically, the family of identical directions—such as [110] and [101]—is marked as $\langle 011 \rangle$ orientations. When ordering silicon wafers, the crystal orientation must be specified. The most common orientations used in microelectronics are the $\langle 100 \rangle$- and $\langle 111 \rangle$ orientation and in micromachining, $\langle 011 \rangle$ orientation is used as well. As found in the section on wafer fabrication, some standards have been formed to identify the crystal orientation with respect to the wafer flat. For example, on a $\langle 100 \rangle$-oriented wafer (commonly just called a $\langle 100 \rangle$ wafer), the {011} plane is often made evident by a flat segment, also called an orientation flat. The precision on the flat typically is about a few degrees. Unfortunately, the standard for the

⟨011⟩ wafer flat is not generally accepted but often parallels a {111} plane. However, it is possible to find the crystal orientation by breaking or cleaving the wafer. If properly done, the wafer will break along one of the {011} planes in case of ⟨100⟩ wafers. In Figure 97a, a "close-up" of the {100} plane in a silicon crystal is shown. In Figure 97b some pictures of a plastic model of three important crystal are shown taken under different angles.

The order of directional etch rates varies considerably with conditions and etchant. A representative order from



(a)

(b)

(c)

fastest to slowest etching planes is {411}, {011}, {311}, {144}, {211}, {100}, {133}, {122}, and {111}. Etch-rate ratios for the primary directions ⟨011⟩:⟨100⟩:⟨111⟩ range from 20:12:1 up to 400:200:1. These ratios are found by using a so-called wagon wheel oxide pattern on top of a silicon wafer. Figure 98 shows such a mask and the "etch-flower" pattern emerging on a wagon-wheel-masked ⟨100⟩ wafer. When {111} planes meet at concave corners of a mask, etching effectively halts. At convex ("sharp") corners, however, undercutting of the mask occurs, with the fastest undercutting planes being {411}. Shaping the undercutting of masks by adding mask structures to convex corners (known as corner compensation) will slow down these corners from etching.

To explain the difference in etch rate ratio between the different oriented planes—it usually follows the sequence {011} > {100} > {111}—some models were proposed based on the reaction kinetics of the collection of surface atoms. For example, the {111} planes present a higher density of surface atoms per $cm^2$ to the etchant than the {100} planes. Due to the subsequent increase in shielding by surface-bonded OH or oxygen, the etch rate would become slower. However, the {011} planes have an even higher density. Another suggestion is that the etch rate correlates with available density of surface bonds, the surface with the highest bond density etching faster. However, the available bond densities follow the sequence 1.41:2:1.15 for the {011}:{100}:{111} surfaces. Alternatively, the {111} planes oxidize faster during etching and, therefore, they are better protected against etching. However, now the oxidation rate follows the sequence {011} > {111} > {100}. In a more consistent model based on the reaction kinetics of the individual surface atoms, it is assumed that the anisotropy is due to differences in activation energy, backbond geometry, and reaction probability. For example, the available bonds per silicon surface atom follow the sequence 1:2:1 for the {011}:{100}:{111} planes, but the backbonds follows the sequence 1:2:3 (the ⟨011⟩ wafer has two in-plane bonds per silicon atom). So, in order to liberate a single silicon atom from a {111} surface, three backbonds have to be broken at the same time and for a {100} surface only two backbonds. If the change that one backbond is broken would be, for example, 1%, then the change that two backbonds are broken at the same time will be 100 times smaller, and for three backbonds this change is still 100 times smaller. This difference will be even larger because occupied bonds will lower the bond energy of the backbonds left.

In the silicon crystal {111} planes form an octahedron and the orientation of the silicon defines how the octahedron is located in the wafer (with respect to the wafer

**Figure 97.** (a) Silicon crystal lattice showing the {100} plane. The silicon atoms at the surface (red-dark) have two bonds available for etching. (b) Silicon crystal lattice showing the various planes. Top: cross section. Middle: birth view. Bottom: top view. (c) Silicon crystal lattice looking into a ⟨110⟩ direction.
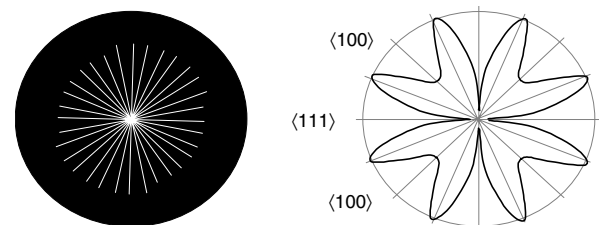


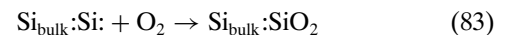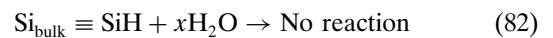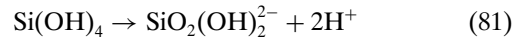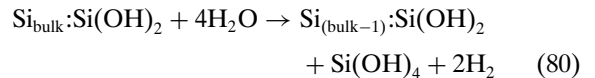**Figure 98.** Lateral underetch rates as a function of orientation.

flats), and therefore the shapes which can be achieved by ODE. Figure 99 shows the octahedron of {111} planes and the way in which it is positioned in $\langle 011 \rangle$, $\langle 111 \rangle$, and $\langle 100 \rangle$ SCS wafers. In the most common application of ODE, a {100}-silicon surface is etched through a rectangular mask window whose sides are parallel to $\langle 011 \rangle$ directions (Fig. 100a). The etch proceeds downward until {111} planes are reached, forming a V-shaped pit in which the {111} planes intersect the {100} surface at a 54.7° angle. However, with silicon wafers this angle will vary slightly as the etch rate of the {111} planes is nonzero and the alignment of the wafer surface and wafer flat with crystal direction is rarely perfect. In such cases, undercutting of the mask is observed as shown in Figure 100b. When the sides of the rectangular are parallel to $\langle 100 \rangle$ directions, the etch process is not halted by the {111} planes (Fig. 100c). In such cases $\langle 100 \rangle$ planes—having a local etch rate minimum—will develop and undercutting of the mask is found with the same amount as the etch depth. Alternatively, high aspect ratio trenches with vertical sidewalls (90° angle)—and V-grooves which intersect the {011} surface at a 35.3° angle—can be formed in a {011} surface using a parallelogram-shaped mask window with sides parallel to $\langle 111 \rangle$ directions (Fig. 99).

*KOH Etching*   Alkali hydroxides such as KOH, NaOH, and LiOH in water etch silicon at about the same rate for the same molarity—almost independent of the cation. KOH is the most popular ODE, having been in industrial use for decades. It can produce a fast etch rate of several micrometers per minute at 100 °C. In the hydroxide etching of silicon both hydroxide ($OH^-$) and $H_2O$ are involved, which explains the initial increase in etch rate with KOH concentration (up to 18% by weight at 80 °C), followed by a decrease at higher KOH (and therefore lower $H_2O$) concentration. Although the reaction kinetics is quite unclear a very
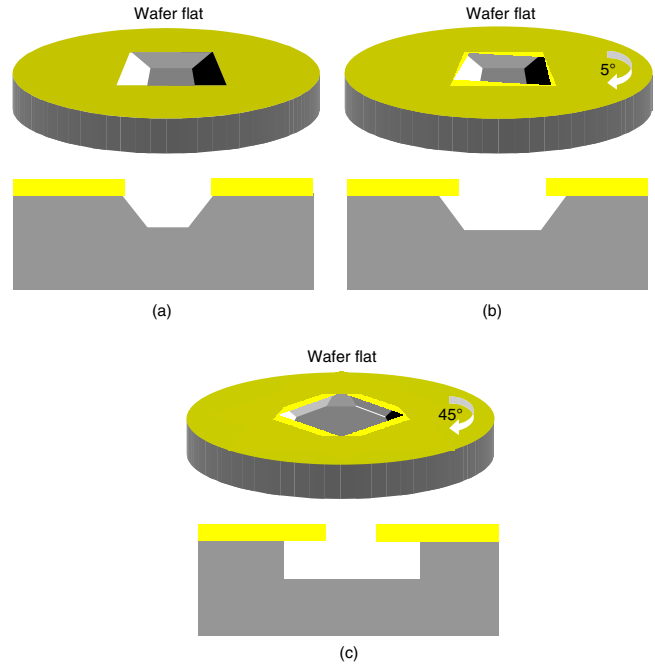


**Figure 100.** Influence of mask rotation on the etch profiles in $\langle 100 \rangle$ silicon ODE: (a) Etch stop on {111} planes intersecting the surface at a 54.7° angle. (b) Influence of small rotation (5°) of the mask with respect to the wafer surface. (c) Influence of 45° rotation. Etch stop on {100} planes caused by the local etch minimum of the {100} plane.
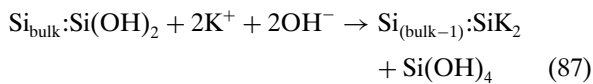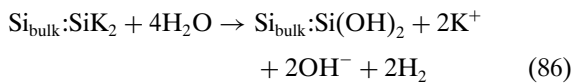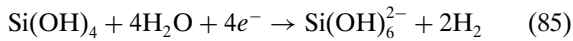
basic reaction is the etching of silicon in pure water from which the oxygen molecules has been removed. The $\langle 100 \rangle$ surface is terminated by OH molecules, which enables etching [Eq. (80)] and the reaction product $Si(OH)_4$ is removed by diffusion. For pH values above 12 the product dissolves [Eq. (81)]. If this production is too fast, for solutions with a high water concentration, this product leads to the formation of a $SiO_2$-like complex (white residue). In contradiction, it has been found with infrared spectroscopy that $\langle 111 \rangle$ silicon is terminated by H-atoms, which effectively blocks etching [Eq. (82)]. In the presence of oxygen, both surfaces immediately oxidize and block further etching [Eq. (83)]:

$$Si_{bulk}:Si(OH)_2 + 4H_2O \rightarrow Si_{(bulk-1)}:Si(OH)_2$$
$$+ Si(OH)_4 + 2H_2 \quad (80)$$

$$Si(OH)_4 \rightarrow SiO_2(OH)_2^{2-} + 2H^+ \quad (81)$$

$$Si_{bulk} \equiv SiH + xH_2O \rightarrow \text{No reaction} \quad (82)$$

$$Si_{bulk}:Si: + O_2 \rightarrow Si_{bulk}:SiO_2 \quad (83)$$

The etch mechanism in strong basic solutions is still quite unclear and one model needs silicate production [Eqs. (84) and (85)]. Another possible mechanism involves the catalytic action of the alkali ion [Eqs. (86) and (87)] and could explain the (small) difference in etch behaviour for different types of alkali ions but the silicon–potassium intermediate is doubtful:

$$Si_{bulk}:Si(OH)_2 + 4OH^- \rightarrow Si_{(bulk-1)}:Si(OH)_2$$
$$+ Si(OH)_4 + 4e^- \quad (84)$$
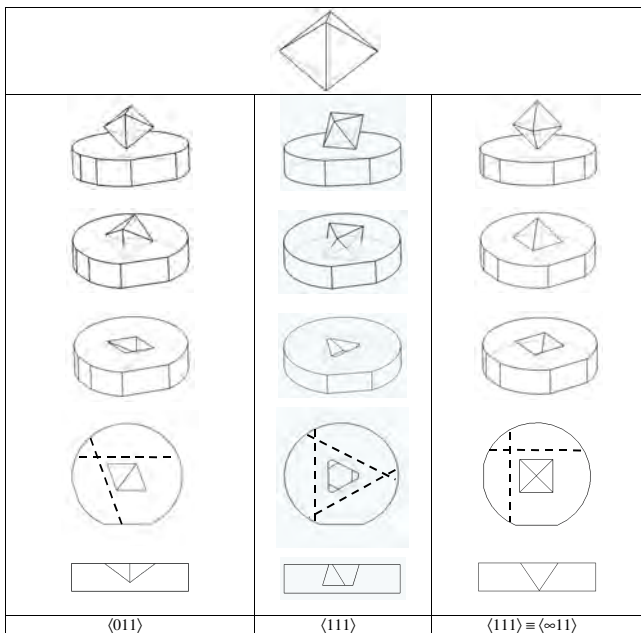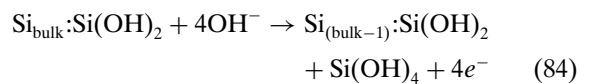


**Figure 99.** Position of the octahedron limited by {111} planes in differently oriented silicon wafers. The bold dashed lines in the lower figures indicate the plane along which the wafer will break.

| $\langle 011 \rangle$ | $\langle 111 \rangle$ | $\langle 111 \rangle \equiv \langle \infty 11 \rangle$ |

$$Si(OH)_4 + 4H_2O + 4e^- \rightarrow Si(OH)_6^{2-} + 2H_2 \quad (85)$$

$$Si_{bulk}:SiK_2 + 4H_2O \rightarrow Si_{bulk}:Si(OH)_2 + 2K^+$$
$$+ 2OH^- + 2H_2 \quad (86)$$

$$Si_{bulk}:Si(OH)_2 + 2K^+ + 2OH^- \rightarrow Si_{(bulk-1)}:SiK_2$$
$$+ Si(OH)_4 \quad (87)$$

Etch-surface smoothness tends to improve as the concentration is increased, especially above 30% KOH. The concentration of maximum etch rate is therefore usually not used because of the rough surfaces and because of the formation of insoluble residues below 15% KOH. A concentration of 30% KOH by weight at 80 °C is a representative etch. Higher temperatures give a faster etch, with an activation energy $E_A$ of 0.595 eV used in the curve-fit equation (where the concentrations are in mol/liter). The density and molecular weight of KOH are 2.055 g/cm$^3$ and 56.11 g/mol, respectively (and 1.00 g/cm$^3$ and 18.02 g/mol for water):

KOH-{100}silicon etch rate

$$= 413[H_2O]^4[KOH]^{1/4} \exp(-E_A/kT)\mu m/min \quad (88)$$

KOH etching has several disadvantages. Hydrogen gas bubbles are evolved during etching which can locally block the transport of reactants to the surface, increasing roughness, and can also damage delicate microstructures. All of the alkali hydroxides, of course, contain alkali ions, which are not compatible with MOS circuitry (and therefore not allowed in many semiconductor facilities). Also of concern for on-chip circuitry, KOH etches aluminum. KOH–silicon etching can be masked by, for example, gold, silicon nitride, and silicon dioxide for short etches due to a non-negligible oxide etch rate (several nm/min). Photoresist is rapidly removed. Boron doping can be used as an etch stop for KOH concentrations below 10%; it is not as effective as in ethylenediamine (EDP) etching. Adding isopropyl alcohol to KOH solutions reduces convex-corner undercutting and also improves uniformity but slows etching by about 20% and lowers the {100}:{111} etch-rate ratio.

*EDP Etching*   EDP in water, sometimes with the addition of pyrazine, is a classic ODE that exhibits etch rates roughly half those of KOH. EDP and water are the primary etchants. EDP has the preferable properties over KOH of halting etching at boron etch stops more effectively, leaving generally smooth surfaces, having a much better selectivity over silicon dioxide, and not containing alkali ions. Because the etch rate of silicon dioxide is so low, native oxide should be removed just before EDP etching. EDP is not used as much as KOH, however, because it is considered to be too toxic and ages quickly with oxygen exposure, giving a faster etch rate and turning the solution opaque.

*TMAH Etching*   Several quaternary ammonium hydroxides—tetramethylammonium hydroxide ($N(C_2H_5)_4 \cdot OH$), or TMAH, tetraethylammonium hydroxide (TEAH), choline (each in water)—came into use for ODE in the early 1990s. TMAH has the advantage over KOH of etching silicon dioxide very slowly, not containing alkali ions, and not attacking aluminum when properly "doped," all of which make TMAH

IC compatible. It has the advantage over EDP of not being considered as toxic. TMAH solutions, however, have a lower etch-rate ratio of {011}:{100}:{111} planes of—typically—60:20:1, and etch silicon about half the rate of KOH at the same concentration and temperature, and tend to yield rougher surfaces. The maximum {100} etch rate is at 2% by weight for TMAH and 20% for TEAH over the temperature range of 60–90 °C. Smooth surfaces are obtained above 20% TMAH. The {100}:{111} etch-rate ratio rises continuously as the TMAH concentration is reduced. By adding 1–2 mol/l of $NH_4HPO_4$ acid and/or dissolving 2–4 mol/l of silicon in a 20% TMAH solution, the pH can be raised sufficiently to reduce the etch rate of aluminum by several orders of magnitude. TMAH with several percent surfactant (30 wt% polyoxythene alkyl phenyl ether) added has the unusual property of etching ⟨100⟩ directions faster than ⟨110⟩ directions, leaving {110} planes exposed after short etches.

*Hydrazine Etching*   Hydrazine and water is an ODE that has been used to a limited degree, because it is toxic and is explosive. It has maximum practical etch rate similar to KOH, stops etching on oxide and heavy *p*-type doping, and can be masked by most metals (but not Al), but has a lower {100}:{111} selectivity than KOH.

*Other ODEs*   Gallic acid + etanolamine + pyrazine + water is found to be most useful. It has etch rates similar to KOH, stops on heavily boron-doped regions better than EDP, etches silicon dioxide slowly, does not contain alkali ions, and is nontoxic. $NH_4OH$ has also been used but was slower than KOH and resulted in rough surfaces. The addition of $H_2O_2$ gave smoother surfaces and faster etch rates. Preferential etches are used to delineate crystal defects such as dislocations or stacking faults and are sometimes sensitive to orientation. All of these etches use a two-step etch process similar to the HNA etchants—silicon is first oxidized and then the resulting oxidized material is etched by HF. A few preferential etches use $HNO_3$ as an oxidizing agent such as the dash etch ($HF_{49\%}/HNO_{3\,70\%}/CH_3COOH_{100\%} = 1/3/10$), which etches ⟨100⟩ silicon at a rate of 130 nm/min and has a {100}:{111} etch-rate ratio of 26:1.

***Electrochemical Anisotropic Etching***   Electrically conducting or semiconducting materials are sometimes etched by application of an external voltage: the process of electrochemical etching. ECE is considerably more complicated than other techniques but can yield results not otherwise attainable. The etch rate and selectivity can be controlled by the potential and/or the current density applied. Electropolishing of metals is a good example of this technique, but a more instructive example is the ECE of silicon (Fig. 101). The silicon substrate is immersed in highly concentrated hydrofluoric acid and a voltage is applied between the silicon and a platinum counterelectrode. Etching can be divided into two types: cathodic and anodic. In the cathodic overpotential, where the silicon is negatively biased, neither *n*- nor *p*-type silicon dissolves into the electrolyte. On the other hand—when anodic overpotential is applied—in both *n*- and *p*-type silicon electronic holes trigger the ECE reaction of silicon dissolution. Since the electronic hole is the majority carrier in *p*-type silicon, there is minor difference between the anodic *I–V* curves of the substrate
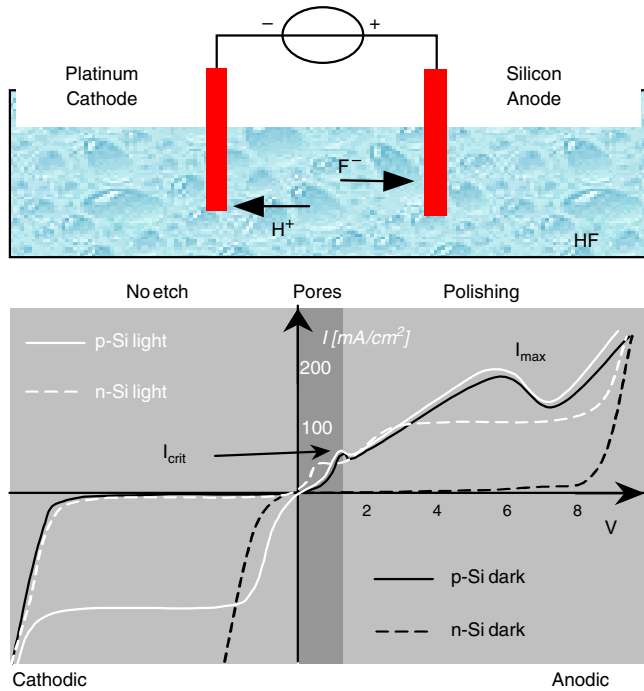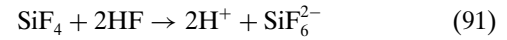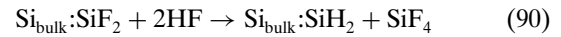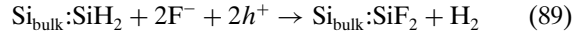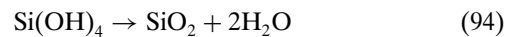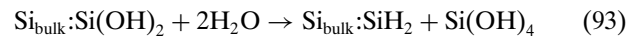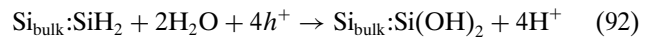
**Figure 101.** Basic ECE setup.

with and without illumination and the curves present two peaks, characterized by $I_{crit}$ and $I_{max}$. In case of $n$-type silicon, the electronic hole is the minority carrier and the $I$–$V$ curves with and without illumination are now completely different. In the case of intense illumination of the silicon substrate with photons having energy larger than the bandgap of silicon, electron–hole pairs are generated and the $I$–$V$ curve of $n$-type silicon is roughly similar to that of $p$-type silicon. In the ECE for $n$-type silicon in the dark at a lower overpotential, virtually no reaction takes place but—if the overpotential is greater than breakdown energy—electronic holes are generated and electropolishing occurs.

There are two regions for anodic silicon dissolution. One is porous silicon formation, which occurs at a lower overpotential and at a current below $I_{crit}$, consuming two electronic holes. The other is electropolishing, which uses four electronic holes to dissolve silicon via silicon dioxide and occurs at currents above $I_{crit}$. The first peak in the $I$–$V$ curve shown in Figure 101 (roughly at 1 V and 50 mA/cm$^2$) marks this change from the potential range where the etching results in the formation of porous silicon (charge-supply-limited) to the potential range where polishing occurs (mass-transport-limited). First the chemical reaction of porous silicon formation is given. Silicon, which is immersed in the HF electrolyte, is terminated by hydrogen. The silicon consumes two electronic holes (coming from the inside of the substrate to the surface) and reacts with two F$^-$ ions to become SiF$_2$ with the emission of a hydrogen bubble, H$_2$ [Eq. (89)]. The silicon backbond between silicon atoms is weakened due to large electronegatives of fluorine. Therefore, SiF$_2$ reacts with 2HF and becomes SiF$_4$ [Eq. (90)]. At this stage the silicon atom has been removed from the substrate. SiF$_4$ reacts with 2HF and

becomes H$_2$SiF$_6$. This product is easy to solve in HF as SiF$_6^{2-}$ [Eq. (91)]:

$$Si_{bulk}:SiH_2 + 2F^- + 2h^+ \rightarrow Si_{bulk}:SiF_2 + H_2 \quad (89)$$

$$Si_{bulk}:SiF_2 + 2HF \rightarrow Si_{bulk}:SiH_2 + SiF_4 \quad (90)$$

$$SiF_4 + 2HF \rightarrow 2H^+ + SiF_6^{2-} \quad (91)$$

On the other hand, four electronic holes are consumed by electropolishing, and in the course of silicon dissolution, silicon dioxide is formed. Finally, silicon dioxide dissolves in HF as SiF$_6^{2-}$. During this chemical reaction, hydrogen bubbles are not evolved:

$$Si_{bulk}:SiH_2 + 2H_2O + 4h^+ \rightarrow Si_{bulk}:Si(OH)_2 + 4H^+ \quad (92)$$

$$Si_{bulk}:Si(OH)_2 + 2H_2O \rightarrow Si_{bulk}:SiH_2 + Si(OH)_4 \quad (93)$$

$$Si(OH)_4 \rightarrow SiO_2 + 2H_2O \quad (94)$$

$$SiO_2 + 6HF \rightarrow SiF_6^{2-} + 2H^+ + 2H_2O \quad (95)$$

The porous film delaminates and bright electropolishing occurs at current densities above $I_{max}$. With dissolution of chemical reactants, HF is depleted at the electrode surface and a charge of holes builds up at the interface. Hills on the surface dissolve faster than depressions because the current density is higher on high spots. As a result, the surface becomes smoother (i.e., electropolishing takes place). So the basic technique to make porous silicon is by electrochemical etching in hydrofluoric acid. This technique produces a three-dimensional silicon nanostructure with a very high aspect ratio (depth/width or height/width) above 250 in a single step, which cannot be achieved by the other conventional silicon etching techniques. It also leads to all types of new devices from quantum structures, permeable membranes, photoluminescent and electroluminescent devices, to a basis for making thick silicon dioxide or silicon nitride films. Porous silicon is classified by the pore diameter: pores with a diameter of less than 2 nm are called—how inconvenient—microporous silicon, and those with a diameter of between 2 and 20 nm are mesoporous silicon. These two types of silicon have pores which are highly interconnected and which form network structures (Fig. 102a). Thus etched structures cannot be controlled precisely. Porous silicon with pore diameters larger than 20 nm is called macroporous silicon. The location of the macropores can be controlled by small initial pits to EC etching as proposed by Lehman and is applied, for example, to make photonic crystals and large 3D capacitors (Fig. 102b). Porosity varies with the current density and HF concentration and might follow crystallographic orientation. Porous silicon is highly reactive, oxidizes, and etches at a very high rate.

ODEs also slow or stop etching at heavily doped $p$-type regions ($>2 \times 10^{19}$/cm$^3$ boron). At intermediate steps in the EC reaction, four free electrons are generated that reside in the silicon near the etch surface before being exchanged. $p$-Type doping reduces this surface supply of electrons. The drop in etch rate varies with etchant. While $p+$-silicon is used as an etch stop without the application of an external bias, it is possible to etch through a $p$-type layer and stop on $n$-type silicon with the use of an EC etch stop by protecting
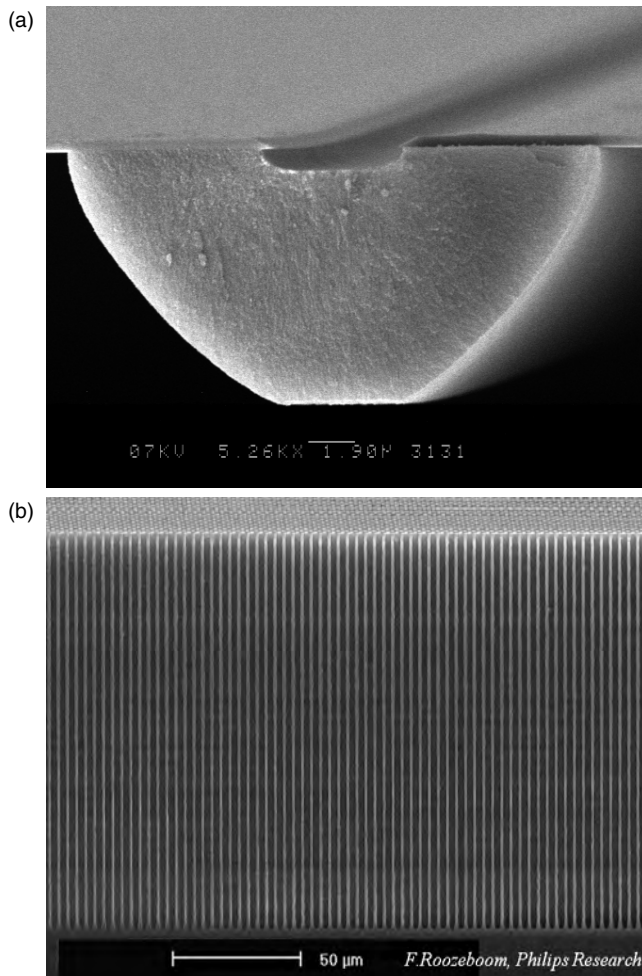
Figure 102. Porous silicon patterns. (a) Irregular. (b) Regular. Figure courtesy of Fred Roozeboom, Philips Research.

the *n*-type silicon from the solution (e.g., layer of silicon nitride) and reverse-biasing the *p–n* diode that is formed. Electrodeless EC etching can also be performed by way of generating a potential from gold contacting both the *n*-type silicon and the etchant.

### 5.3.4. Solid-Phase Etching

Chemical–mechanical polishing is used in wafer preparation when a relatively defect-free and smooth surface is required. The combination of slow liquid chemical surface etching with gentle mechanical abrasion to continuously remove products from the etching reaction can result in a high-quality surface polish. More details about wafer polishing can be found in Section 2.3.8.

The development of flat panel displays in the 1990s caused powder blasting to be developed to an accurate machining tool. Powder blasting is an old technique in which a particle jet is directed toward a target for mechanical material removal. The particles (typically 30 micrometers in size) are accelerated toward the target with a high-pressure airflow through a circular nozzle with a diameter of 1.5 mm. The particles hit the target with a speed up to 300 m/s (depending on the air pressure and the particle size) in

a ventilated box. A lateral movement ensures an evenly eroded surface while a patterned mask covers the target. Powder blasting can be used to erode any type of brittle material such as glass, silicon, and ceramics. Ductile metals and elastomers have high resistance against powder blasting, which allows them to be used as mask materials. Due to the large particle sizes, powder blasting is not suitable in conjunction with high-resolution lithography. Powder blasting creates rough surfaces and is not suitable to selectively remove material for, for example, surface micromachining since it attacks all brittle materials; it is a truly bulk micromachining technique. Figure 103 shows a typical example of an etch-trough hole in a silicon substrate to enable fluid from a "macro" tube to be connected with micromachined channels.
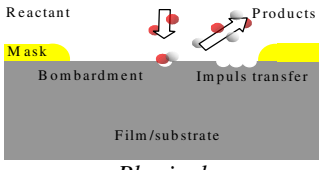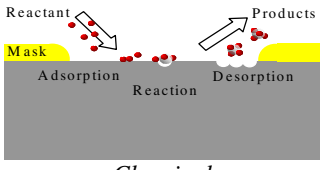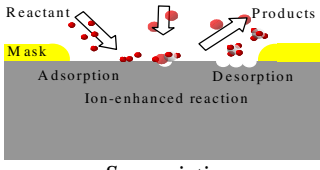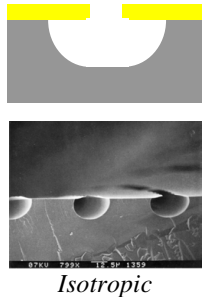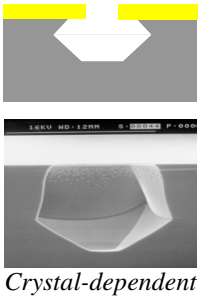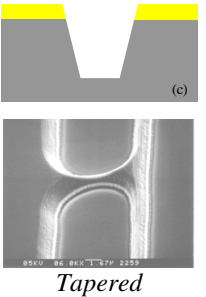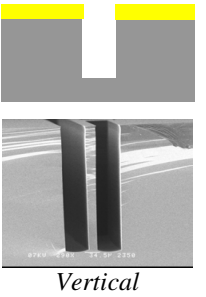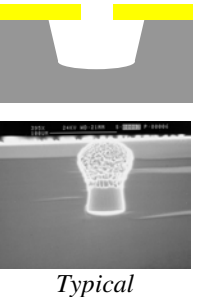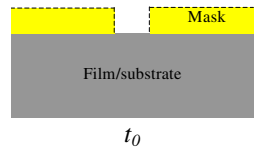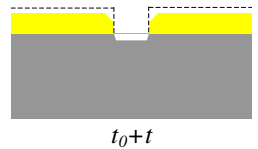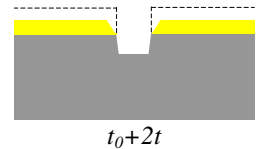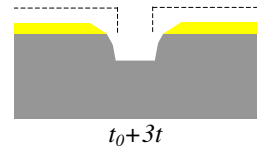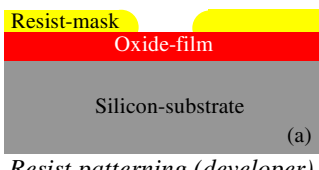
### 5.4. Conclusion and Nanoperspective

Table 13 summarizes this section with a schematic overview of film etching methods and phenomena in micromachining. In etching nanostructures, several aspects are different from micromanufacturing. In case of microelectronic devices, the etch depth is typically less than 1 micrometer and therefore moderate—but accurate—etch rates are requested to ensure a precise etch depth and a smooth surface finish. On the other hand, in case of micromechanical devices, many times high etch rates are needed and nonstandard materials are used to construct high aspect ratio devices with specific properties (e.g., piezoelectric or electro-optic systems). In nanotechnology where the surface interactions play a dominant role, etch processes of different materials having a low etch rate (typically a few nm per minute or slower to control the etch depth using a time stop) and leaving a clean surface finish are of prime concern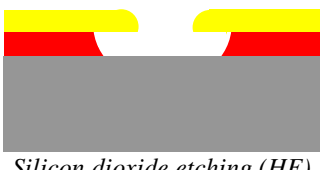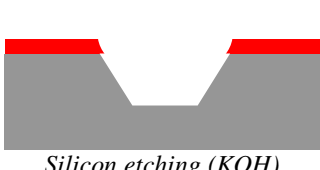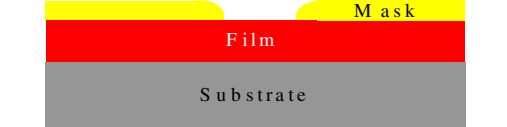. So, with respect to nanomachining, the etch rate of the film is not as demanding as in case of microtechnology and the etch depth is fairly identical with semiconductor manufacturing. In addition, the materials from micromachining are requested. Etching nanometer instead of micrometer structures does not significantly alter the etch result, as long as layer thickness are scaled down with lateral dimensions: a process yielding a 5 micrometer deep trench at 1 micrometer width—at best—cannot be
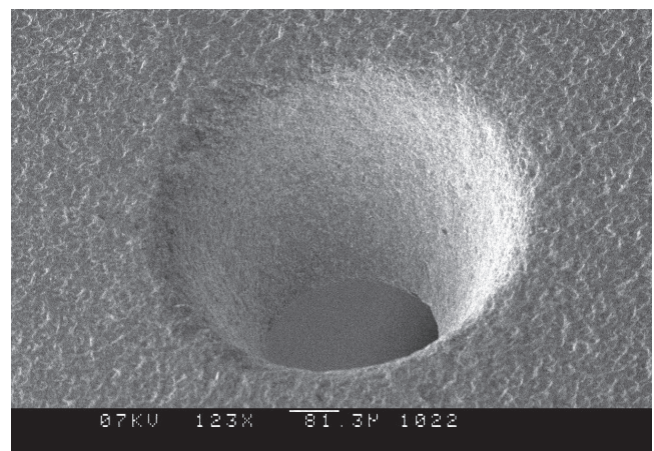


Figure 103. Etch through hole by way of powder blasting.

**Table 13.** Schematic overview of film etching methods and phenomena.



| Etching | Physical | Chemical | Synergistic |
|---|---|---|---|
| Profile | *Isotropic* — *Crystal-dependent* — *Tapered* — *Vertical* — *Typical* | | |
| Facetting | $t_0$ — $t_0+t$ — $t_0+2t$ — $t_0+3t$ | | |
| Selectivity | *Resist patterning (developer)* — *Silicon dioxide etching (HF)* — *Silicon etching (KOH)* | | |
| Real | Mask / Film / Substrate | | |

| | Plasma-phase | Gas-phase | Liquid-phase | Solid-phase |
|---|---|---|---|---|
| Method | CCP ICP ECR MIE Cascade Kaufman | | ICE ODE ECE | CMP Powder |

expected to do better than 50 nm depth at 10 nm width. Therefore, in nanotechnology the etching should fulfill the following characteristics:

(i) It should be slow enough to ensure a precise etch-depth in the film.
(ii) It should leave an "atomic-level" smooth surface.
(iii) It should be able to shape diverse materials.

The control in etch depth and surface finish of all kinds of materials can be achieved with two different techniques (Fig. 104). In the first method (Fig. 104a), the substrate or

film is shaped directly with a low-speed etch recipe. The main task is to find a process having the ability to etch slow enough to be able to etch only a few atomic layers up to several tens of nanometers. Additionally, the surface should be smooth enough to ensure proper functioning of the finished product. In the second approach (Fig. 103b), first a film is formed on top of the substrate with a well-defined thickness. After this, it is selectively etched with a chemical that stops accurately when the underlying substrate is reached. So, in the first approach, the film etching is critical whereas in the second approach the film formation defines
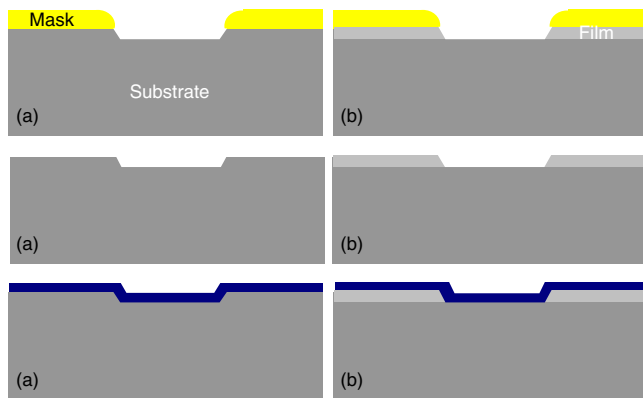
**Figure 104.** Typical accurate etch procedures: (a) Accurate etching. (b) Accurate film formation and selective etching.

the surface topography. In both cases, the nanostep can be covered eventually with an additional (nonstandard) layer having specific characteristics (Fig. 104, bottom).

The successful application of etching to new materials in the nanoscale regime mainly depends on the ability to find a chemistry which yields volatile etch products only. The most straightforward way to control etch depth and surface finish is the use of wet chemicals, which are easy to dilute to lower the etch rate. For example, a standard TMAH-based etchant for photoresist (OPD developer) etches silicon approximately at a speed of 3 nm/min at room temperature and a 1% HF solution etches silicon dioxide roughly at 5 nm/min. Clearly, we have to bear this in mind when processing silicon wafers in the lithography step and native oxide should be included to protect the silicon during resist development. Also, it is a well-known effect that silicon etches in oxygen-free water, so rinsing steps in demiwater without controlling the oxygen atmosphere might produce unexpected results.

In microtechnology, low-pressure plasma reactors are much more demanding in terms of pumping equipment and wafer cooling than conventional systems, because moderate gas flows at these low pressures demand very high pumping speeds. However, in nanotechnology the etch rate is not as stringent as in microtechnology and, therefore, ultralow vacuum etch equipment such as ion beam etching ($p <$ 0.1 mTorr) reactors or dual source systems ($p <$ 10 mTorr) equipped with conventional pumping systems are of interest. IBE is a slow and clean plasma process enabling atomic level etches with smooth surface finish. However, the physical nature of the process generally creates tapered profiles, which might be a disadvantage for some applications. With dual-source plasma etchers, the profile can be altered and vertical etching is possible. However, the etch rate is normally too fast to be useful for nanoetch applications. Nevertheless, it might be possible to slow down the etch process by optimizing the equipment. Vertical etching is easier to achieve in low-pressure reactors because of a high ion-to-neutral flux ratio and the reduced probability of ion-neutral collisions in the sheath region at low pressure. Wafer cooling is a critical issue because of significant ion bombardment and low-pressure operation. Backside helium cooling using a wafer clamp or an electrostatic chuck is necessary in order to control the etching process. Process integration is

introduced to effectively integrate plasma etch systems into the overall fabrication sequence (e.g., by connecting deposition and etching chambers by clean, evacuated transport chambers, i.e., cluster tools).

Finally, if proper etch chemistries are unknown, other structuring procedures should be investigated such as ultrathin photoresist layers or films formed using stamping, implantation, plating, or lift-off lithography.

## 6. MICROMACHINING

Micromachining is the underlying foundation of MST fabrication; it is the tool of MST to make high performance microdevices and is suitable for the creation of a range of transducers including pressure sensors, accelerometers, gyros, thermal flow sensors, optical and rf switches, and bio/chemical devices [21–41, 99–127, 631–795]. Furthermore, a great number of conferences are held showing the popularity of MST [79–98]. Of course, material properties play a crucial role in the success of a micromachined device and detailed studies are found in literature [42–78, 145–186]. Arguably, the birth of the first micromachined components dates back many decades, but it was the well-established integrated circuit industry that indirectly played an indispensable role in fostering an environment suitable for the development and growth of micromachining technologies [1–20, 128–144]. Therefore, in order to make these three-dimensional structures—often freestanding and on top of a substrate—a specific sequence of lithographically based techniques such as film formation, lithography, and film etching techniques is required as schematically shown in Figure 105 and which have been treated more extensively in the first sections. These techniques, useful in micro- and nanomachining, have been greatly improved as device dimensions have been reduced and can be boiled down to four basic concepts: bulk, surface, mold, and bond micromachining. In bulk micromachining features are formed out of the bulk of substrate material. In contrast, surface micromachined features are built up—layer by layer—on top
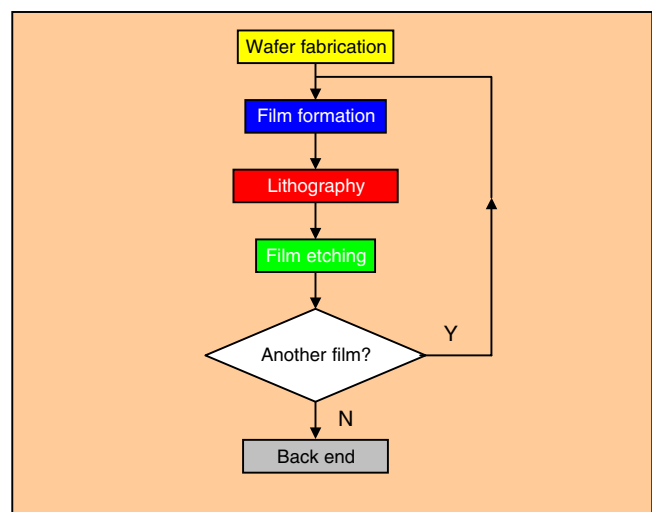


**Figure 105.** An abstract representation of a typical process flow found in micromachining.

of the surface of a substrate. In mold micromachining, a (metal) structure serves as a mold insert to form many plastic replicas. The advantage of mold micromachining is the economically favorable replication characteristic, but truly three-dimensional structures are not possible with replicating. In many cases, the micromachining process is ended with a bonding step to seal the device. However, in bond micromachining, the structure is formed at the interface of two patterned wafers, which enables *in-situ* sealing of the device. In the following sections these basic technologies will be discussed.

## 6.1. Bulk Micromachining

Bulk micromachining is one of the earliest processes in the field of microsystem technology [187–276]. While there are many different types of bulk micromachining, the basic concept is to create features out of a substrate. In general, a silicon, SOI, or glass wafer serves as the substrate material and the structures are created by way of removing (etching) the parts of the wafer that are not wanted, leaving the desired structure behind. Typically, this is done through a sequence of photopatterning steps on the surface of a silicon substrate followed by wet or dry etching of the silicon. Wet orientation dependent etching with alkaline solutions such as potassium hydroxide is often used to create thin membranes with sensor elements on top of it. Dry vertical etching with plasma environments ($SF_6/O_2$) or xenon difluoride ($XeF_2$) gases are found to construct high aspect ratio freestanding actuator elements. Since these two methods have their own advantages and disadvantages, the bulk etching technique should be chosen according to which application is requested such as sensors or actuators.

Figure 106 shows two basic process sequences for a flow sensor fabricated by wet bulk micromachining using ODE of silicon. In this thermal flow sensor, a platinum resistor is heated up, and an airflow removes heat from the resistor. The flow rate can be measured by the change in resistance. In order to improve the sensitivity of the sensor, the resistor is formed on a thin silicon nitride membrane, which is thermally isolated from the silicon substrate. In the first step, silicon nitride is formed on both sides of a silicon wafer and patterned. Next, platinum is deposited and patterned on the frontside to make resistive elements. Finally, the
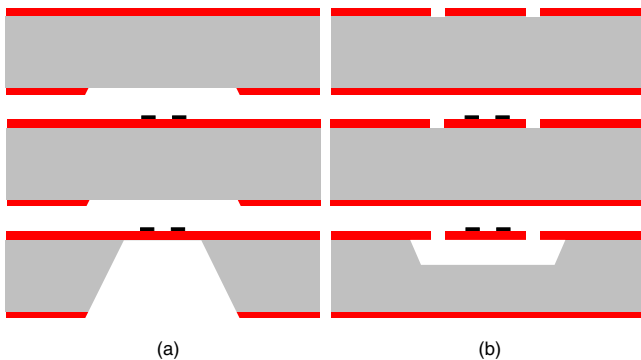
membrane is fabricated by removing the silicon by alkaline etching with the silicon nitride used as a hard mask. A disadvantage of the method depicted in Figure 106a is that double-sided alignment is necessary to align the patterns at the backside with those at the frontside. This complicates the lithographic equipment. This problem can be solved when micromachining from one side only as shown in Figure 106b. However, the mask design to construct a freestanding structure is somewhat more complicated due to blocking {111} planes.

Figure 107a shows an example of a thin structured membrane (photo taken from the backside), fabricated with the help of through-the-wafer wet etching. Figure 107b shows a so-called shadow mask to be used as a technique to pattern irregular surfaces. Figure 107c shows a force sensor bridging a flow channel, which is wet bulk micromachined from a single side.

Bulk micromaching using wet alkaline ODE solutions has many advantages. The equipment is cheap and a high throughput can be obtained due to a batch process. Also, the etching stops on a crystal plane, such as the {111} plane and, thus, the etched surface is smooth and lateral dimensions are well defined. On the other hand, the silicon structural shape is also restricted by the crystal {111} planes. Moreover, the stopping plane is slanted with respect to the surface of the substrate, as is shown in Figure 106, and therefore the membrane area on the surface is smaller than the open area of the masking material on the other side of the wafer. This results in relatively large chips. Furthermore, misalignment between the crystal orientation and the mask in lithography (Fig. 100) or due to misorientation of the wafer flat can lead to an error in the etched dimension. Therefore, a pretreatment is necessary to ascertain the crystal orientation precisely (Fig. 98). To enable dimensional control and to realize more complicated structures, plasma-etching
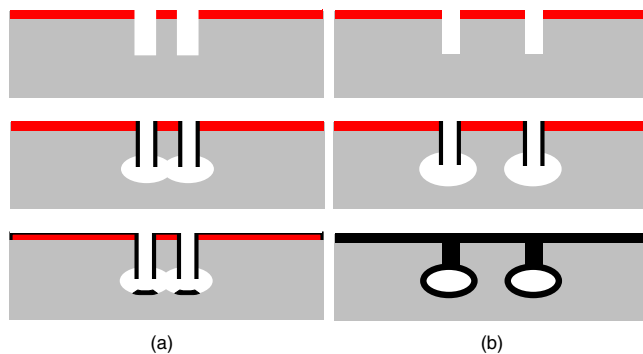


(a)

(b)

(c)
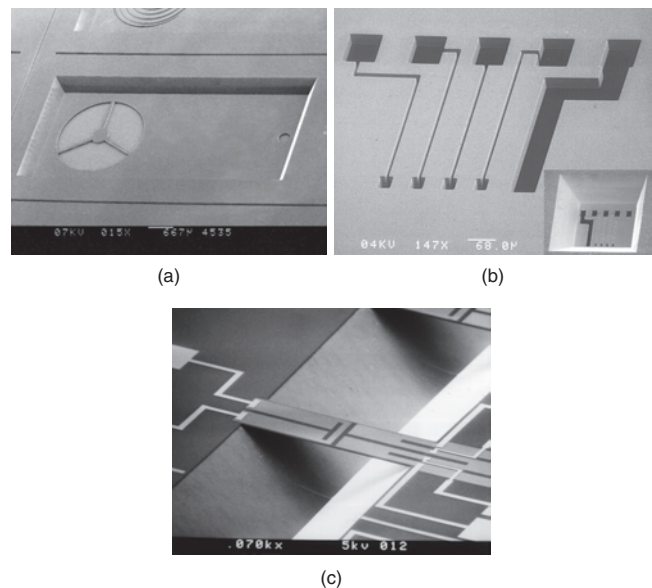
**Figure 107.** Some typical structures created by means of wet ODE bulk micromachining: (a, b) Double-sided lithography. (c) Single-side lithography.



(a)

(b)

**Figure 106.** Typical schemes for wet ODE bulk micromachining: (a) Double-side litho. (b) Single-side litho.
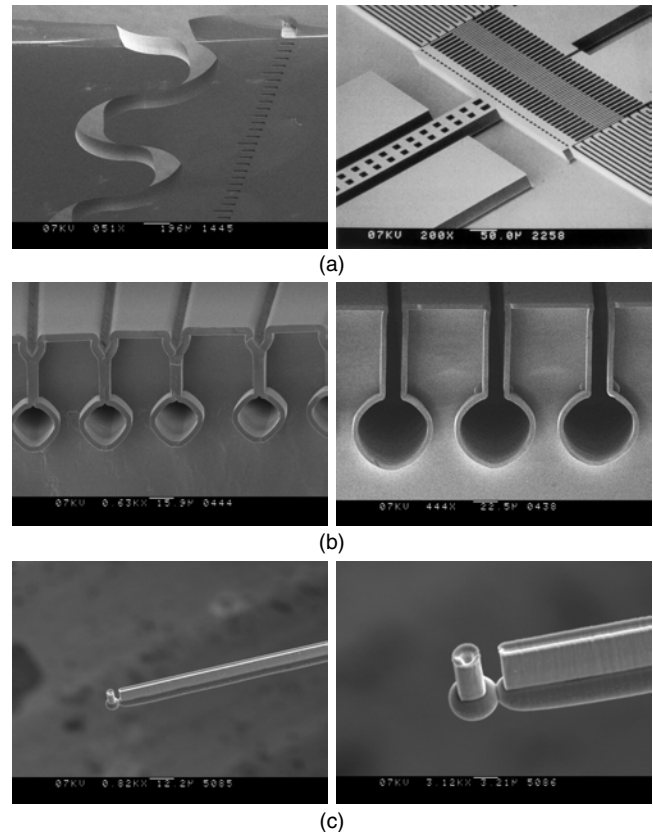
techniques have been developed. This technique generally does not depend on crystal orientation and, therefore, high aspect ratio structures are possible. In Figure 108a, freestanding single-crystal structures of silicon are fabricated by combining anisotropic and isotropic dry etching. First, trenches are etched using vertical plasma etching. Next, a passivation layer is deposited on the etched surface and subsequently removed on the bottom using directional plasma etching after which an isotropic plasma etch follows. Finally, a metallic layer is deposited to enable electrical contacting of the freestanding structure as shown in Figure 108a. Alternatively, if the trenches etched in the first step are narrow enough, it is possible to seal the trench with a uniform film. In this way, subsurface or buried channels are created as shown in Figure 108b. Figure 109 shows a comb-drive actuator fabricated with the help of dry bulk micromachining and some buried channels.

It is possible to explore the ODE of silicon when using specific mask designs or to combine it with plasma etching to extend the range of microdevices possible with bulk micromachining. In Figure 110 just three of the many possible examples are shown. In Figure 110a, full advantage is taken from the development of {111} planes during ODE of silicon to construct thin single-crystal silicon blades. In the first step, silicon nitride is formed on both sides of a silicon wafer and patterned. Next, the silicon is anisotropically etched. The etch process continues until etched trenches from both sides meet in the middle the wafer and the initially stable {111} planes are broken. Finally, the etching will halt at some other {111} planes, which are stable due to the silicon nitride mask restriction. In Figure 110b, dry and wet etching is combined to achieve needles with various shapes. Such needles can subsequently be plated to form a nickel mold to make many single-use plastic replicas useful in medical instrumentation (drug delivery and invasive penetration). A third example (found in Fig. 110c) is the construction of special fluidic channels with atomically smooth walls. It is primarily a question of smart thinking, and not of the limitation of bulk micromachining, which limits the range of devices possible.

Figure 111a shows how {111} plates can be etched to form a kind of silicon "fan" or a single-crystal valve. Combining both wet and dry bulk micromachining increases the range of structures possible even further. For example, in


Figure 109. Some typical structures created by means of dry plasma bulk micromachining: (a) Single-crystal silicon freestanding structures. (b) Open and closed buried channels. (c) Micropipette.

Figure 111b, a beautiful example of a needle structure created using wet bulk micromachining and stopping on {111} planes is shown. The last example, found in Figure 111c, is the construction of microchannels with extremely smooth walls and micropipettes for fluid injection.

## 6.2. Surface Micromachining

Surface micromachining is a technique to make freestanding structures on the surface of a wafer by the successive deposition, photopatterning, and etching of a sacrificial layer and a structural layer [277–450]. Figure 112 shows the basic process flow. First, a film—the sacrificial layer—is formed on top of a wafer and patterned to make anchors where the freestanding structures will be fixed to the substrate. The


Figure 108. Typical schemes for dry plasma bulk micromachining: (a) Single-crystal structures. (b) Buried channels.
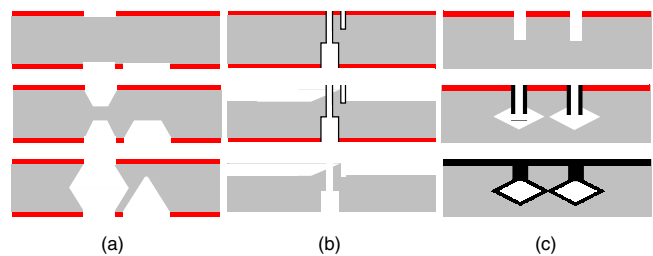

Figure 110. Special schemes for bulk micromachining: (a) Single-crystal blades. (b) Single-crystal needles. (c) Buried channels.
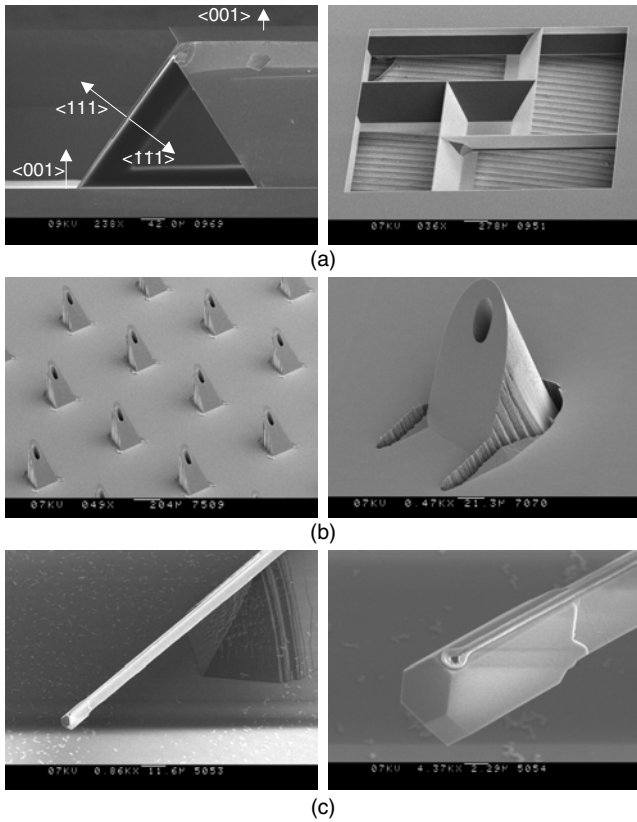
**Figure 111.** Some special structures created by means of bulk micromachining: (a) {111} plates after special ODE. (b) Microneedles after combining ODE and plasma etching. (c) Micropipette as in (b).

sacrificial film serves as a spacer layer between the structural layer and the substrate. Next, another layer—the structural layer—is formed and patterned with, for example, irrigation holes, thus providing access to the sacrificial layer. Finally, the sacrificial layer is etched away, leaving the structural
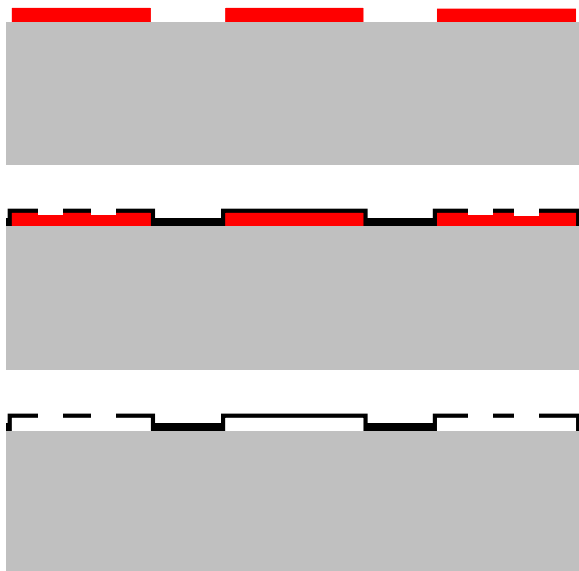


**Figure 112.** Typical scheme for surface micromachining.

levels free to move and operate. Eventually, small access holes to speed up sacrificial layer etching and large holes to allow for, for example, fluid exchange in fluidic applications are etched and the small holes can be reclosed using a conformal deposited layer. Typically in surface micromachining, polycrystalline silicon (polysilicon) is used as the structural material, and silicon dioxide is used as the sacrificial material. At the end of the process, wafers are immerged in wet hydrofluoric acid, which removes the silicon dioxide layers, leaving the polysilicon and single-crystal silicon substrate untouched. Figure 113 (top) gives some typical examples of this technique.

A key process sequence in surface micromachining is "sacrificial layer etching," the process o etch selectively the sacrificial layer underlying the structural layer. A notorious problem in this process is the release of stress in the structural layer when the underlying sacrificial layer is removed, which causes deformation in the released microstructure. To avoid this, it is necessary to measure the strain and a controlled deposition process is required. Another problem in this process is bubble and rinse-damage of the surface micromachined structures (due to drag forces during wafer handling in liquids) and the phenomenon of sticking or stiction (i.e., the permanent attachment of slender structures to the underlying substrate after drying). To avoid this damage, it is possible to use other structural/sacrificial material combinations, such as a structural metal layer in which a sacrificial resist layer is removed in dry oxygen plasma. Figure 113 (bottom) shows some golden mirrors, surface micromachined with this combination. Such a device could
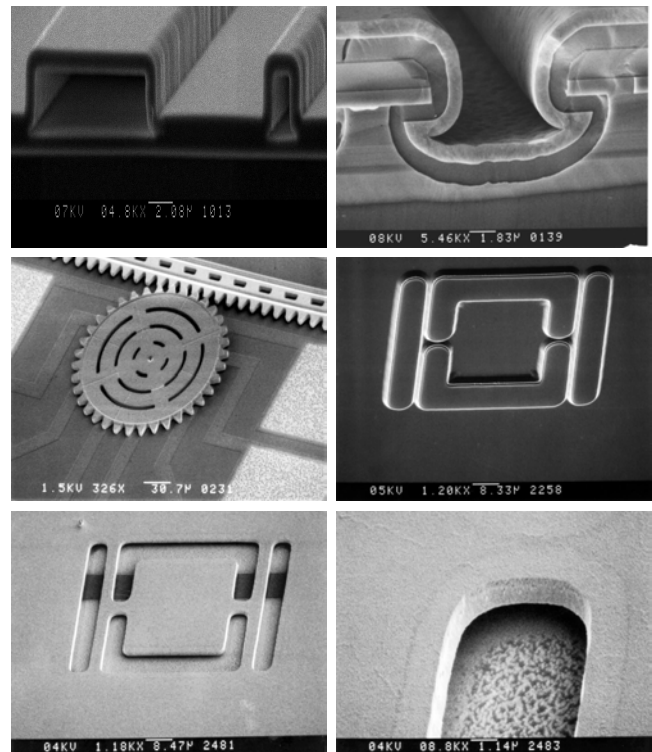


**Figure 113.** Some typical structures created by means of surface micromachining. Top: Polysilicon structures with silicon dioxide as sacrificial layer. Bottom: Gold structures with photoresist as a sacrificial layer.

be useful to measure rf power along a transmission line by way of monitoring the deflection of the mirror.

## 6.3. Mold Micromachining

Although a variety of three-dimensional structures have been fabricated in silicon and silicon nitride such as nozzles, diaphragms, bridges, and beams, inexpensive fabrication processes for microstructuring of different materials are desirable as well. For certain applications the availability of such materials is a necess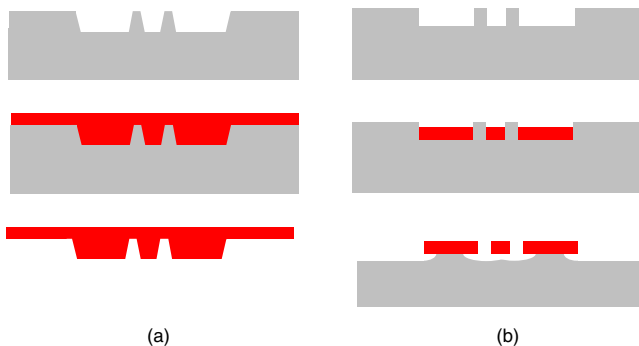ity, as in the case of optical devices or single-use plastic devices useful in surgery. This is accomplished with mold micromachining, which forms mechanical features by first creating a mold [451–464]. This mold, which is in the shape of the desired structure, is filled with a structural material and then the mold can be etched away or removed to leave the desired device as shown in Figure 114a. Alternatively, the mold can be filled with an electroplated material such as nickel and then the mold is partially etched away as shown in Figure 114b to form a freestanding metal structure.

Recently, many mold technologies have been developed that are compatible with the traditional semiconductor infrastructure. For example, in dry etching, electroplating, and molding, structures with variable tapering and high aspect ratios can be fabricated in silicon. The silicon is etched with, for example, a plasma system and can be used either directly for molding (described in the section on lithography) or indirectly by first electroplating a metal mold and subsequent molding with this metal structure. The advantage of direct molding with silicon is that the fabrication process of a polymer structure is reduced to silicon etching and molding, facilitating fast prototyping of plastic microstructures. However, the difference of the thermal expansion coefficient of polymer and silicon is larger with respect to, for example, nickel. Therefore, higher shear forces are created when releasing the structure. In order to shape the silicon mold, $SF_6/O_2$ plasma allows elegant control of the tapering as shown in Figure 115. High aspect ratio vertical or slightly positive tapered profiles are feasible, as has been mentioned before in Section 5.3.1 and the roughness of the silicon is well below 100 nm, which facilitates separating the mold from the mold insert (i.e., demolding).
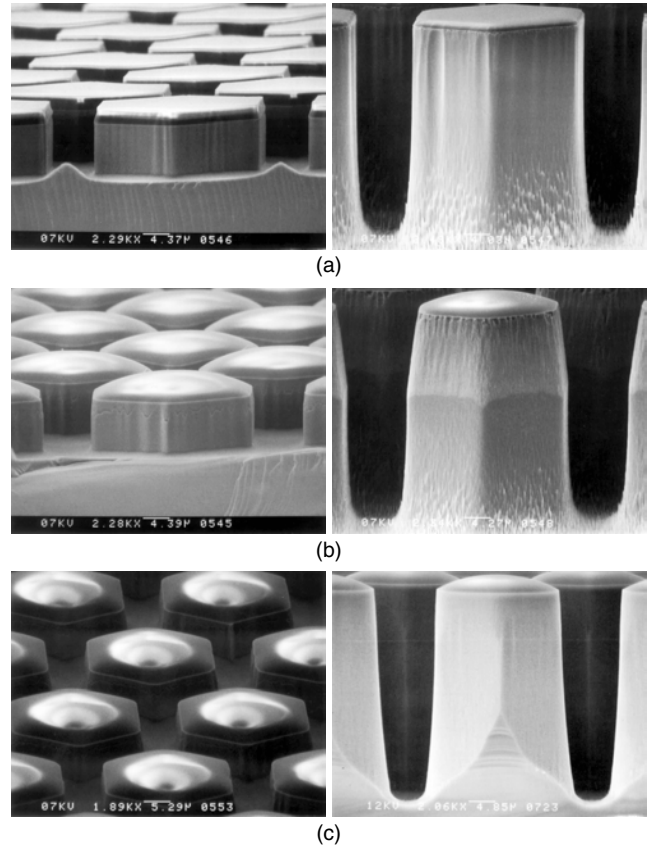


Figure 115. Optimization of the $SF_6/O_2$ plasma chemistry and mask profile to facilitate demolding. For explanation see text.

When silicon structures are etched in a $SF_6/O_2$ plasma system with a highly selective mask, purely straight sidewalls or a positive tapering usually correlate with roughness (so-called "grass") in the valleys of the trenches. In Figure 115a this grass is clearly visible. This grass can be prevented by settling the plasma process into a chemistry where a slightly negative tapering occurs. However, this negative tapering, like the grass, is undesirable for most molding purposes because it is difficult to demold such a structure without destroying (parts of) the feature. Therefore, in molding applications, a slightly positive tapering without grass is highly preferable. In order to achieve this, it is possible to use a slowly withdrawing mask to create a positive sidewall angle, although the plasma etch process itself is settled to create a otherwise slightly negative tapering to prevent roughness. In Figure 115, features are etched with photoresist as a mask. In Figure 115a, the profile is shown after 10 (top) and 20 minutes (bottom) of silicon etching with photoresist baked at 90 °C and the plasma system settled with a gas mixture where a slightly positive taper occurs. The resist has an almost straight slope, which does not facilitate a withdrawing of the mask during plasma etching and roughness is observed. On the other hand, Figure 115b shows the profile using the same plasma setting but now the resist is baked at 130 °C in order to spread (reflow) the resist a little, forming a spherical-like resist pattern. Due to the low selectivity of the resist with respect to the silicon plasma etching and the positive slope of the



Figure 114. Typical schemes for mold micromachining. (a) Replicating. (b) Electroplating.

resist, the mask will repeal during etching and a much more positive tapered profile is transferred into the silicon while preserving the same amount of grass. It is observed that the withdrawing resist has its up influence halfway the structure height, creating a much more positive taper. Now when this process is optimized, it is possible to create features with smooth and positive tapered profiles, as found in the Figure 115c. This is achieved by giving the resist a bake at 130 °C and a pre-etch in an oxygen plasma to remove any remaining vertical slope in the resist and settling the plasma at a recipe, which normally would result in negative tapering but—due to the withdrawing of the positive-sloped mask—the profile becomes slightly positive tapered too. In Figure 116 a glass structure is shown before (a) and after (b) demolding. An important consideration is the prevention of gas inclusions as observed in Figure 116b.

In recent years there has been considerable interest in high aspect ratio processing. The most famous technology to accomplish this is the LIGA technology. LIGA is an acronym for the German words lithography (lithographie), electroforming (galvanic), and molding (abformung). In the LIGA process, masks are created containing the shape of the desired structure. Then, a synchrotron radiation source of 2 Å wavelength is used to expose a thick PMMA resist layer. The irradiated area of the resist is then dissolved with a developer. Subsequent electroplating copper or nickel into the resist pattern and dissolving the remaining resist leaves the mold insert for molding as shown in Fig. 116c. While the LIGA technology enables the fabrication of high-aspect-ratio micromachines and creates extremely precisely dimensioned devices, the technology is limited in that it requires a high-energy synchrotron radiation source. Such a source is not part of the standard semiconductor infrastructure, making this technology not widely available and therefore economically less attractive.
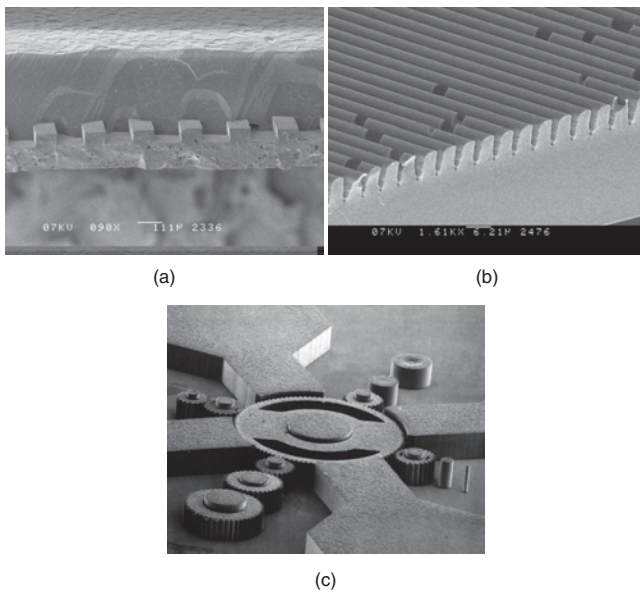
## 6.4. Bond Micromachining

Bond micromachining is a two-wafer process in which a structure is formed at the interface of two bonded wafers [465–630]. Figure 117 shows the basic scheme and it is very straightforward; trenches are etched in one of the wafers and bonded with another wafer to seal the trench. Two variations are possible. In the first method (top), the substrate itself is etched. In the second approach (bottom), first a film is formed on top of the substrate with a well-defined thickness and, then, it is etched with a chemical that stops when the underlying substrate is reached. Alternatively, the cavities can be made accessible by way of through-wafer holes in one or both of the wafers.

In Figure 118a an example of the first method is found. First, a silicon wafer is etched to a depth of 50 nm. Then, a 1% HF dip and an additional Piranha step are performed to clean the silicon surface and to grow a well controlled layer of native oxide on the silicon surface. Finally, the wafer is fusion bonded (2 hours at 1100 °C) to a second silicon wafer. The high temperature needed in silicon-to-silicon fusion bonding can be prevented by using different bonding schemes as described in the section on film formation such as anodic or adhesive bonding. For example, the same etched silicon wafer is also bondable (4 hour annealing at 400 °C) with a borofloat glass wafer as shown in Figure 118b. This annealing temperature of the silicon-to-glass bond is sufficiently low to prevent plastic deformation of the glass (and thereby possibly closing of the nanochannels) and interference of the bonding process with previous micromachining steps. Finally, in Figure 118c an example is found of the second approach. A silicon wafer with a patterned 10 nm thin oxide film is bonded with a second silicon wafer. Other bonding candidates are two patterned borofloat wafers, two oxidized silicon wafers, or wafers coated with for example, a BCB polymer.

The range of structures possible with bond micromachining can be increased enormously when one of the two wafers—a "capping wafer"—is dissolved in the process sequence. Figure 119 (top) shows such an "extended"
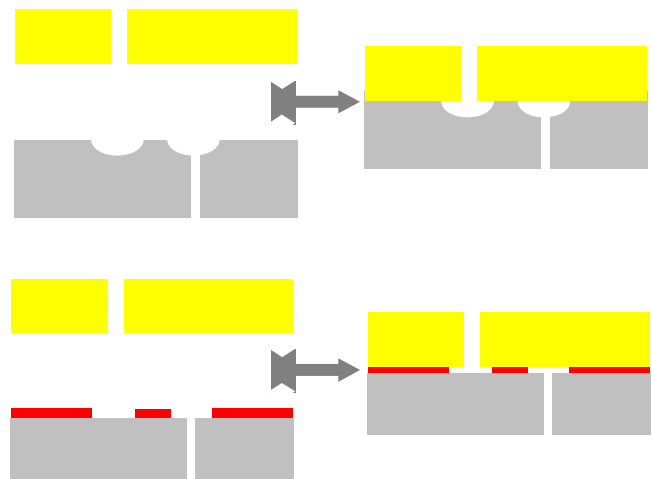


**Figure 116.** Some typical structures created by means of mold micromachining. (a) Silicon mold with deposited glass. (b) Glass structure after demolding. Nickle LIGA structure after demolding.



**Figure 117.** Typical scheme for bond micromachining. Top: Substrate etching. Bottom: Film etching.
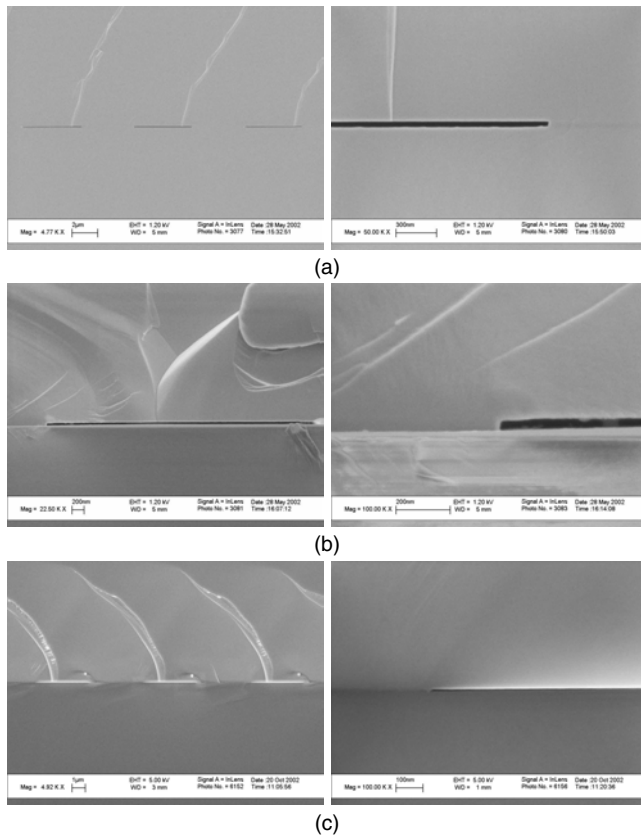
Figure 118. Some typical structures created at the interface of two wafers by means of bond micromachining: (a) 50 nm nanochannel Si–Si bond, (b) Si–glass bond, (c) 10 nm nanochannel $(Si + SiO_2)$-to-Si bond.

scheme. In the first step, trenches are etched in the capping wafer and covered with a conformal capping film. Then, the wafer is bonded with a structure wafer, which forms channels in between both wafers. Finally, the capping wafer is dissolved to make the capped structures accessible for measuring or further processing. Alternatively, the trenches can be etched in the structure wafer as shown in Figure 119 (bottom), in order to leave a flat wafer surface after wafer dissolving. This enables easier further lithographic processing. Figure 120 gives some typical examples of this "dissolved-wafer" bond micromachining technique.

In addition, the structure wafer and capping layer can be patterned on one or both sides with additional patterned (metal) layers for sensing (e.g., flow) or actuation (e.g., switch) purposes. In this way, it is possible to integrate
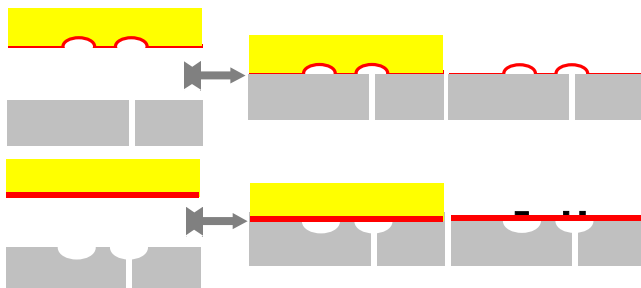


Figure 119. Extended schemes for bond micromachining.
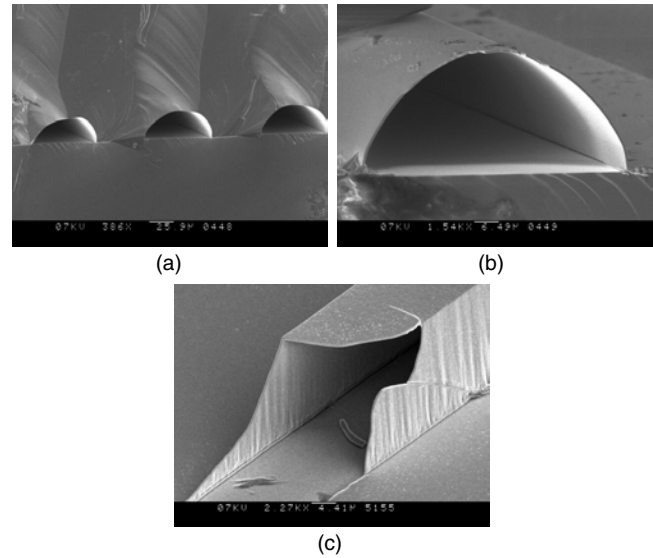


Figure 120. Some typical structures created by means of bond micromachining. (a) Enclosed microchannels after silicon-to-silicon wafer bonding. (b) Idem after wafer dissolving. (c) Silicon nitride channels. Figure courtesy of Stefan Schlautmann.

electrodes on top of a channel wall for sensing purposes. Figure 121 shows an artist impression of such "smart" channels. Many variations on this scheme are imaginable such as the use of an additional wafer, which "encapsulates" the encapsulated structures, and so on. Therefore, bond micromachining is an excellent technique to construct nano- or microchannels for many fluidic or rf-MEMS applications. Moreover, the technique exhibits an *in-situ* sealing of structures. A disadvantage is that in bond micromachining surfaces should be reasonably smooth to ensure a successful bond.

## 6.5. Conclusion and Nanoperspective

The four most important micromachining techniques as discussed in this section are summarized; bulk, surface, mold, and bond micromachining. In order to sculpture nanostructures (i.e., nanomachining), several aspects are different from micromanufacturing, especially in relation to etching techniques. In Table 14 the four basic micromachining techniques to construct 1D nanostructures are summarized. While using clever design rules in micromachining, it is possible to realize truly nanostructures (at least
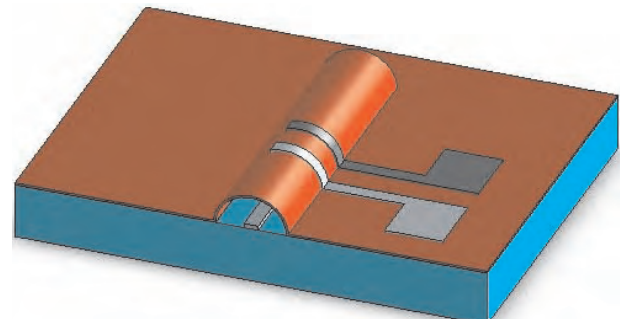


Figure 121. Smart scheme for bond micromachining.

**Table 14.** Schematic overview of micromachining techniques to create 1D nanostructures (in short: nanostructures).
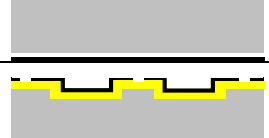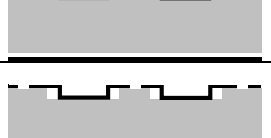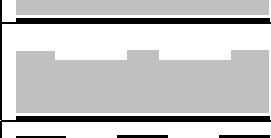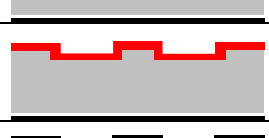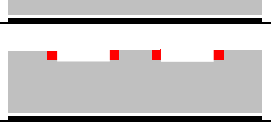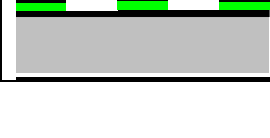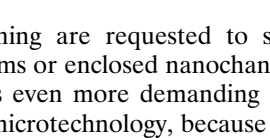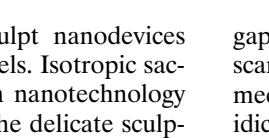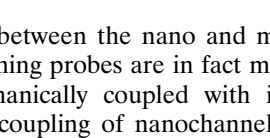
| | Step 1 | Step 2 | Step 3 | Remarks |
|---|---|---|---|---|
| **Bulk** | | | | *double-side wet* |
| | | | | *single-side wet* |
| | | | | *dry* |
| | | | | *buried channel* |
| **Surface** | | | | *sticking* |
| **Mold** | | | | *replica* |
| | | | | *plate* |
| **Bond** | | | | *substrate etching* |
| | | | | *film etching* |
| | | | | *extended scheme* |
| | | | | *smart channels* |

two dimensions below the 100 nm) without using expensive sub-100 nm lithography. In order to fabricate such 2D nanostructures (or nanonanostructures) in Table 15 a few "nanonanoschemes" are outlined based on the edge lithography. Finally, the fabrication of nanostructures is one thing, but how does one connect these structures with the macroworld (i.e., packaging) and how does one control them?

**Nanomachining** In *bulk micromachining*, many times the substrate is etched some tens of micrometers in depth—and in some cases even through the wafer—to make high-aspect-ratio structural parts (generally with the help of plasma systems) or thin membranes (using wet etches). Therefore, there is a strong demand for high-speed directional etch processes. Moreover, in order to construct *in-situ* freestanding microstructures, high-speed isotropic etch processes are requested as well. On the other hand, in case of bulk nanomachining, the etch depth is fairly identical to semiconductor manufacturing and, thus, typically less than 1 micrometer. Therefore moderate—but accurate—etch rates are requested to ensure a precise etch depth and a smooth surface finish. In *surface nanomachining*, isotropic sacrificial layer etching techniques from

**Table 15.** Schematic overview of micromachining techniques to create 2D nanostructures (in short: nanonanostructures).

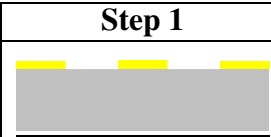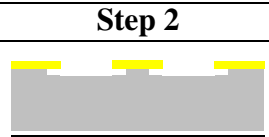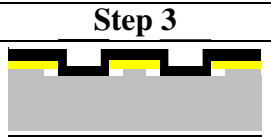| | Step 1 | Step 2 | Step 3 | Remarks |
|---|---|---|---|---|
| Channel | | | | *substrate etching* |
| | | | | *film etching* |
| | | | | *film growing* |
| | | | | *film sticking* |
| Beam | | | | *vertical etching* |
| | | | | *lateral growing* |

the micromachining are requested to sculpt nanodevices such as nanobeams or enclosed nanochannels. Isotropic sacrificial etching is even more demanding in nanotechnology with respect to microtechnology, because the delicate sculptured nanostructures are more easy to damage due to drag forces during wafer handling in wet chemicals and the probability of sticking of slender nanostructures during drying after wet etching. To avoid damage of sculptured nanostructures or sticking of the nanostructures, dry release techniques are favorable. In *mold micromachining*, lithography seems to be the most prominent step and advances will probably take place in soft lithography and related technologies. *Bond micromachining* seems to be well suited for nanomachining, at least where it concerns the manufacturing of 1D nanochannels as was found in Figure 118.

***Nanonanomachining*** In order to construct nanodevices with at least two dimensions in the nanometer range, it is still possible to use micromachining techniques (i.e., without the use of expensive nanolithographic techniques). In Table 15 a few basic schemes are found to fabricate nanonanochannels or nanonanobeams.

***Nanopackaging*** System packaging is much more difficult and complex than electronics packaging and will frequently be the prime determinant in success or failure. This is because system packaging is customer specific and not only embraces electronic connections but also fluidic and mechanical coupling. For nanotechnology, it is essential to have a direct control of matter—either between two nano-objects or between a micro (or macro) object and a nano-object. In the bottom-up molecular engineering strategies, this is certainly a nontrivial issue. However, top-down microtechnology seems to be ideally suited to perform this task and seems to be a logical technique to bridge the

gap between the nano and macro world. For example, the scanning probes are in fact micromachined microcantilevers mechanically coupled with integrated nanotips. The fluidic coupling of nanochannels with the outer world is not very well known, but in fact not at all troublesome. Currently, already a few options exist to connect microchannels with the macrochannels (e.g., http://www.upchurch.com/). The only problem left to solve is how to couple the nanochannels with microchannels or reservoirs. An option is to first machine nanochannels in a wafer. This is followed by machining microchannels in the same wafer. The through-wafer holes are constructed (powder blasted) in a second wafer. Finally, the wafers are bonded to seal the channels. Figure 122 shows an artist's impression and pictures of such a system.
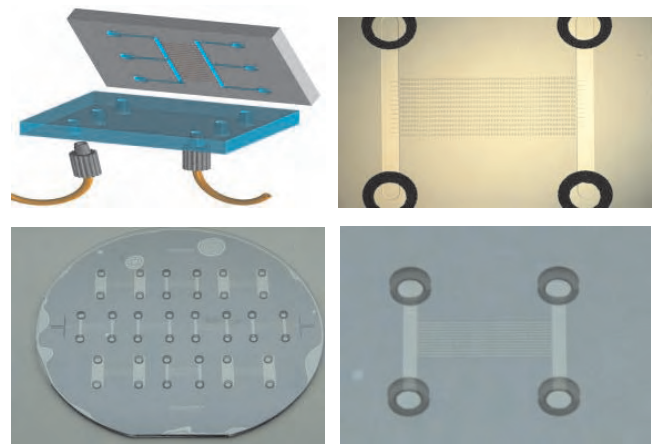


**Figure 122.** Artist's impression and pictures of a fluidic packaging system to connect nanochannels with macrocapillaries.

## ABBREVATIONS

**AFM**   Atomic-force microscopy.

**AL**   Atom lithography.

**APCVD**   Atmospheric-pressure CVD.

**CAIBE**   Chemical-assisted IBE.

**CARIBE**   Chemical-assisted RIBE.

**CCP**   Capacitively coupled plasma.

**CLD**   Chemical liquid deposition.

**CLG**   Chemical liquid growth.

**CMP**   Chemical–mechanical polishing.

**CSG**   Chemical solid growth.

**CVD**   Chemical vapor deposition.

**CVG**   Chemical vapor growth.

**CZ**   Czochralski.

**DC**   Direct current.

**DOF**   Depth of focus.

**DOP**   Degree of planarization.

**DPL**   Direct print lithography.

**DUVP**   Deep-UV printing.

**EBP**   Electron-beam printing.

**EBW**   Electron-beam writing.

**ECE**   Electrochemical etching.

**ECR**   Electron cyclotron resonance.

**EL**   Edge lithography.

**EPI**   Epitaxial.

**EUVP**   Extreme-UV printing.

**FIBE**   Focussed IBE.

**FZ**   Float zone.

**HC**   Hallow cathode.

**IBARE**   Ion-beam assisted radical etching.

**IBE**   Ion-beam etching.

**IBP**   Ion-beam printing.

**IBW**   Ion-beam writing.

**ICE**   Isotropic chemical etching.

**ICP**   Inductively coupled plasma.

**ICT**   Integrated circuit technology.

**LIL**   Laser-interference lithography.

**LPCVD**   Low-pressure CVD.

**LPE**   Liquid-phase epitaxy.

**MBE**   Molecular-beam epitaxy.

**MCRIE**   Magnetically controlled RIE.

**MEMS**   Microelectromechanical systems.

**MESA**   Microelectronics sensors and actuators.

**MIE**   Magnetron ion etching.

**MM**   Micromachining.

**MOCVD**   Metal-organic CVD.

**MST**   Microsystem technology.

**NEMS**   Nanoelectromechanical systems.

**NST**   Nanosystem technology.

**ODE**   Orientation-dependent etching.

**PE**   Plasma etching.

**PECVD**   Plasma-enhanced CVD.

**PLD**   Physical liquid deposition.

**PVD**   Physical vapor deposition.

**PVG**   Physical vapor growth.

**PSD**   Physical solid deposition.

**RF**   Radio frequency.

**RIBE**   Reactive IBE.

**RIE**   Reactive ion etching.

**SAM**   Self-assembled monolayer.

**SCALPEL**   Scattering with angular limitation projection electron-beam lithography.

**SCS**   Single crystal silicon.

**SE**   Sputter etching.

**SNOM**   Scanning near-field optical microscopy.

**SNOW**   Scanning near-field optical writing.

**SOI**   Silicon on insulator.

**SOG**   Spin-on-glass.

**SPE**   Solid-phase epitaxy.

**SPL**   Scanning-probe lithography.

**STM**   Scanning tunnel microscopy.

**TARE**   Thermal-assisted radical etching.

**UV**   Ultraviolet.

**VPE**   Vapor-phase epitaxy.

**XRP**   X-ray printing.

## GLOSSARY

**Adhesive bonding**   A bonding method, which uses organic (polymer) or inorganic (ceramic) intermediate layers. The adhesive material deforms and flows so it can make sufficient close contact with the wafer surface to promote adhesion.

**Amorphous film**   A material showing short-range (atomic) order and only the average distance between neighboring atoms or molecules can be used to the determine film density.

**Anodic bonding**   A bonding method based on joining a conducting material and a material with ion conductivity, such as Pyrex, by applying a high voltage at sufficient high temperature to mobilize the ions.

**Anodization**   A film deposition method for obtaining amorphous, highly-insulating, pinhole-free and low-stress films. It is an oxidation process performed in an electrolytic cell and using a voltage source. When electric current is passed, the substrate surface at the positive electrode is converted to an oxide.

**Atmospheric pressure chemical vapour deposition**   A chemical vapour deposition technique performed at atmospheric pressure to increase deposition rate.

**Atomic-force microscopy**   A way to image surface forces to the nanometer level by moving a sharp tip within a distance of the order of 1 nm from the surface.

**Atom lithography**   An alternative technique of print lithography with nanometer-scale resolution in which a beam of atoms is projected onto a surface through a laser interference pattern.

**Bond micromachining** A micromachining technique in which features are formed at the interface of two patterned wafers meanwhile enabling *in-situ* sealing of a device.

**Bottom-up nanotechnology** The area of nano system technology, which applies to building organic or inorganic structures atom-by-atom, or molecule-by-molecule, and having its origin in the (bio)chemical industry.

**Bulk micromachining** A micromachining technique in which features are formed out of the bulk of substrate material.

**Capacitively-coupled plasma** A form of plasma making use of a capacitively coupling in which electric fields are generated by two isolated platens at both sides of a discharge chamber. These systems commonly operate at a frequency of 13.56 MHz and powers up to several hundreds of watts.

**Casting** A film deposition method where a rim structure is fashioned around the substrate, providing a "flat beaker" for the drying solution.

**Chemical deposition** A form of film deposition that involves three essential steps, which are identical to chemical film etching except the direction of transport is reversed: the reactants are transported to the surface and adsorb, then surface reactions occur, finally the products are desorbed and transported away from the surface while leaving the desired film.

**Chemical etching** A film etching process involving three essential steps, the reactants are transported to the reacting surface and adsorb, then reactions occur at the surface, and finally the products from the surface are desorbed and transported away from the surface. It usually results in an isotropic or orientation-dependent profile.

**Chemical growth** A form of film growth in which reactants adsorb first at a substrate surface and then they diffuse into the substrate and react.

**Chemical vapour deposition** A film deposition method where the constituents of a vapour phase, often diluted with an inert carrier gas, are introduced into a reaction chamber and adsorbed on a heated surface. The adatoms undergo migration and film-forming reactions to form the desired film.

**Cleanroom** A facility to perform micro- and nano-technology where the total number of dust particles per unit volume is minimized and tightly controlled along with temperature and humidity in order to maximize device yield.

**Cluster beam deposition** A film deposition method where ionized atom clusters are deposited in a high vacuum.

**Compression bonding** A bonding method where the two surfaces are brought in close contact by applying high pressure (continuous hydraulic or instantaneous explosive). It is sometimes called solid-state welding.

**Czochralski technique** A wafer fabrication technique to enable single crystal growth by pulling a single crystal seed from a melt and forming a single crystal ingot. Afterward, the seed is removed to be reused. See also float zone.

**Deep ultraviolet printing** A kind of print lithography, basically identical with optical lithography, in which an image is transferred in a resist through a mask using deep-ultraviolet radiation ($\lambda = 200–300$ nm).

**Defect density** A measure in lithography, which translates directly transfer mistakes into loss.

**Depth of focus** The maximum feature height in lithography that can be transferred with high fidelity to a film or substrate.

**Dip coating** A film deposition method where a substrate is dipped into a solution containing a polymer and a solvent. After evaporation of the solvent on a hotplate, a thin layer is formed.

**Direct bonding** A bonding method, which relies on the tendency for very smooth and flat surfaces to adhere to each other, it is also known as fusion bonding.

**Direct lithography** A form of lithography in which a pattern is transferred without the use of an intermediate resist layer in order to enhance resolution.

**Dry etching** A form of etching without using any liquids. It is usually synonymous for plasma-phase etching, but includes the less common gas-phase and solid-phase etching too. Due to the physical nature of dry etching it enables smaller linewidth and more vertical profiles than possible in wet etching, but usually lacks high selectivity.

**Edge lithography** An alternative form of print lithography in which the edges of the original pattern become the features of the final pattern.

**Electrochemical etching** A film etching process in which an electrically (semi)conducting material is etched by application of an external voltage. The etch rate and selectivity can be controlled by the potential or the current density applied. Electroless electrochemical etching is possible by way of generating a potential from e.g., gold contacting both the material and the etchant.

**Electroless plating** A film deposition method related to electroplating and also using an electrolytic solution but without the need for external electrodes.

**Electron beam printing** A kind of print lithography in which a wide parallel beam of electrons is forced through a thin film (silicon nitride) mask containing a (tungsten) pattern, which selectively scatters the electrons for the pattern transfer.

**Electron beam writing** A kind of write lithography in which an electron gun is used for the patterning.

**Electroplating** A film deposition method where the substrate is immersed into a liquid plating solution that contains metal ions. A voltage is applied between the substrate and a counter electrode forcing the metal ions toward the wafer forming a metal deposit.

**Epitaxial deposition** A technology involving the deposition of a single crystal layer upon a single crystal substrate so, that the lattice of the newly formed film duplicates that of the substrate.

**Etch directionality** A measure of the relative etch rate in different directions, usually normal versus lateral.

**Etch profile** The profile or shape of an etched film as a direct consequence of the etch directionality.

**Etch selectivity** The ratio of the etch rate of different materials in an etch process.

**Eutectic bonding**   A bonding method like the solder bonding where the eutectic property of metal alloy is used to lower the melting temperature.

**Evaporation**   A film deposition method based on the boiling off or sublimation of a heated material onto a substrate in a high vacuum.

**Exposure field**   The maximum exposure area in lithography. The requirements result from ever-increasing chip sizes and the need to expose at least one full chip with each exposure.

**Extreme ultraviolet printing**   A kind of print lithography in which an image is transferred in a resist with atomically smooth reflecting optics and through a mask with multilayer coatings using extreme-ultraviolet or soft X-ray radiation ($\lambda = 4$–$200$ nm).

**Film adhesion**   An important film property to be considered in film formation. Due to insufficient adhesion, freshly applied films can locally detach or even delaminate from the surface.

**Film deposition**   A form of film formation in which a new layer is deposited on top of a substrate surface.

**Film etching**   The process of transferring a pattern from one layer into another one. It is one of the basic steps in a micromachining process flow.

**Film formation**   The collection of techniques to form a layer on top of or into a substrate. It is one of the basic steps in a micromachining process flow.

**Film growing**   A form of film formation in which substrate surface material is consumed while forming a layer with different properties.

**Film step coverage**   Film property, which relates the surface topography of a deposited or grown film to the previous wafer irregularities.

**Film stress**   Film property showing the emergence of film tension during film formation, which can greatly affect physical integrity and long-term stability and might result in failures such as cracking, blistering, and loss of adhesion (delamination or peeling), shape problems such as bending, shrinking, curling, or buckling of structures, as well as reliability problems such as void and hillock formation and long-term shifts in material properties due to creep.

**Film uniformity**   Global film property, which relates the changes of other film properties across the wafer surface.

**Float glass**   The production of atomically smooth glass by flowing glass into a float furnace onto molten tin (tin bath).

**Float zone technique**   Wafer fabrication technique to purify a single crystal ingot using a moving molten zone. See also Czochralski.

**Focused ion beam etching**   A form of ion beam etching in which the ion beam is focused to a single spot.

**Gas-phase etching**   A form of dry etching using solely gaseous reactants.

**Gas-phase formation**   The formation of a film out of the vapour or gas phase.

**Holographic printing**   A kind of print lithography in which a laser reference is used to interfere with a holographically constructed mask to form a hologram to transfer a pattern.

**Hybrid lithography**   A form of lithography combining two or more of the other lithographic techniques to improve resolution and keeping throughput high.

**Immersion plating**   A film deposition method where a metal displacement reaction occurs between relatively noble metal ions in a solution and less noble metal ions at a wafer surface forming a surface layer of noble metal.

**Imprinting**   A kind of mechanical printing in which a reusable mould is pressed hard into a thin thermoplastic polymer film so that polymeric material is pushed away from the imprinted regions.

**Inductively-coupled plasma**   A form of plasma making use of an inductively coupling where magnetic fields are generated by a coil wrapped around the discharge chamber. These systems commonly operate with powers of several hundreds to thousands of watts. The inductive coupling has the advantage above capacitive coupling that there will be no large or high-voltage sheaths present in the chamber, and as a result, no sputtering of the wall.

**Ingot grinding**   The machining of the single crystal silicon ingot to define the wafer diameter and one or more flat regions along the length of the ingot to mark the specific orientation.

**Integrated circuit technology**   The ability to fabricate tens of millions of individual semiconductor components on a silicon chip with an area of a few square cm using lithographic techniques.

**Intrinsic stress**   A form of film stress caused by several mechanisms such as incorporation of atoms (e.g., residual gases, precipitation inclusion, or energetic ion bombardment), chemical reaction as in thermal oxidation, recrystallization, dislocation rearrangements, lattice mismatch between film and substrate, excess vacancy annihilation, grain boundary relaxation, or phase transformations.

**Ion beam assisted radical etching**   A form of plasma etching, which makes use of the synergetical action of both radicals and ionic species.

**Ion beam etching**   A form of plasma etching in which a broad collimated ion beam is produced in a remote plasma reactor. The possibility of separately controlling ion energy and flux at very low pressure provides a flexibility of directional bombardment not available in other plasma processes, but limits selectivity severely.

**Ion beam printing**   Print lithography in which a wide parallel beam of ions is directed through a set of stencil masks for the patterning.

**Ion beam writing**   Write lithography in which a focused ion beam is used for the patterning.

**Ion implantation**   Film growth method where a dopant is implanted into a material by means of a high-energy ion beam.

**Ion plating**   Film deposition method where the evaporation of a material is combined with ionization of the atom flux by an electron filament or plasma.

**Isotropic profile**   A typical result of chemical etching where the etch rate is the same in all directions, i.e., the under etch equals the etch depth.

**Laser ablation**  A film deposition method, which uses intense laser radiation to erode a target and subsequently deposits the eroded material onto a substrate.

**Laser-interference lithography**  An alternative technique of print lithography in which the interference pattern of two intersecting laser beams is used to expose a resist layer.

**Lift-off lithography**  A form of resist lithography, which uses the shadowing by surface topography of a resist pattern. The film to be patterned is deposited after a resist pattern is applied—and not before as is the case in conventional resist lithography—and subsequently selectively removed by dissolving the resist with the film on top of it leaving the inverse pattern on top of the substrate.

**Liquid-phase etching**  A form of wet etching in which wafers are immersed in an etchant and etching proceeds by dissolution of a material in a solvent or by conversion of a material into a soluble compound, which subsequently dissolves in the etching medium.

**Liquid-phase formation**  The formation of a film out of the liquid phase.

**Lithography**  A technique used in the micro- and nanotechnology to shape (pattern) a thin film or substrate. It is one of the basic steps in a micromachining process flow.

**Low pressure chemical vapour deposition**  A chemical vapour deposition technique at low pressure to increase film uniformity.

**Mechanical beam writing**  Write lithography in which a sharp atomic-force microscopy probe is used for the patterning.

**Mechanical printing**  Print lithography in which a stamp or mould is used for patterning.

**Melting**  Film deposition method just like casting but now the liquid is formed by melted granules of material in a nitrogen-purged furnace.

**Micro system technology**  A portfolio of techniques and processes usually having its foundation in the integrated circuit technology to design and create miniature systems. It is suitable for the creation of a range of transducers including pressure and flow sensors, accelerometers, gyros, optical, and radio frequency switches, and (bio)chemical devices. These systems merge the functions of sensing and actuation with computation and communication to locally control physical parameters at the microscale, yet cause effects at much grander scales.

**Molecular beam epitaxy**  Film deposition method involving the reaction under ultrahigh vacuum conditions.

**Molding**  Mechanical printing used for high-aspect-ratio structures in which a polymeric film is poured into a mold where it hardens.

**Mould micromachining**  A micromachining technique in which a (metal) structure serves as a mold insert to form many (plastic) replicas.

**Nanosystem technology**  The area of science and technology where dimensions in the range of 100 nm play a critical role. It encompasses precision engineering as well as lithographic technology, but also (bio)chemical synthesis and biomedical multiplication techniques in areas as diverse as semiconductor electronics, scanning probe microscopy analysis, microsystems, telecommunication, information technology, protein duplication, gene therapy, and drug delivery.

**Optical printing**  Print lithography in which an image is transferred in a photosensitive resist through a mask using visible ($\lambda = 380$–$780$ nm) or near-ultraviolet radiation ($\lambda = 300$–$380$ nm).

**Orientation-dependent profile**  A specific result of chemical etching found when etching single crystal material where the etch rate depends on the crystallographic direction.

**Phase-shift lithography**  An alternative technique of print lithography which controls both amplitude and phase of the light to enable destructive interference to cancel some of the image spreading effects of diffraction generally found in optical printing.

**Photon beam writing**  Write lithography in which a laser or optical beam is used for the patterning.

**Physical deposition**  A form of film deposition in which reactants are transported to a surface and adsorb.

**Physical etching**  Film etching process in which reactants, usually ionic species, approach a substrate with high velocity where they erode the surface due to impulse transfer. It usually results in a tapered profile.

**Physical growth**  A form of film growth possible due to sub-surface implantation of high-velocity particles—most often ionic species.

**Plasma bonding**  A bonding method where the surfaces to be bonded are first treated with plasma.

**Plasma enhanced chemical vapour deposition**  A chemical vapour deposition technique using an additional plasma source to lower the deposition temperature.

**Plasma-phase etching**  A form of dry etching which involves the use of very reactive species or etchants from a discharge. It usually takes place by a combination of chemical (radicals) and physical (ionic) processes and forms gaseous or volatile products. Vertical profiles are possible due to the presence of ionic species in the plasma and the electric fields that direct them normal (i.e. vertical) to the wafer surface.

**Poly crystal film**  A material having a collection of single crystals with different orientations and showing structural variation (morphology) on a micron scale (microstructured films) or decrease to nanoscale dimensions (nanostructured films).

**Print lithography**  A parallel lithographic technique in which an intermediate radiation-sensitive resist is selectively exposed by shining radiation through a mask, which contains the pattern information for the particular layer being fabricated.

**Projection printing**  Optical printing in which an image-forming system (e.g., a 4:1 demagnification lens) is interposed between the mask and wafer with large separation of many centimeters to avoid mask damage associated with shadow printing.

**Pyrex**  A material often used for bonding purposes in the microsystem technology due to its identical coefficient of thermal expansion with respect to silicon.

**Registration**   A measure in lithography of how accurately patterns on successive masks can be aligned with respect to previously defined patterns on a substrate.

**Resist lithography**   A form of lithography in which a chemically amplified resist is used composed of a photoacid proton generator and a polymer with groups reactive to protons. The photoacid generator is a chemical compound supplying a proton upon irradiation. This proton catalyses reactions at the polymer, resulting in solubility differences between the exposed and unexposed regions.

**Resolution**   The minimum lateral feature dimension in lithography that can be transferred with high fidelity to a film or substrate.

**Scanning near-field optical microscopy**   A way to image a surface to the nanometer level by moving a sharp optical fiber tip within a distance of the order of a few nm from the surface.

**Scanning tunnel microscopy**   A way to image surface conduction to the atomic level by moving a sharp tip within a distance of the order of 1 nm from the surface.

**Screen printing**   A kind of print lithography in which ink is applied to the back of an image carrier or stencil and pushed through porous or open areas.

**Self-assembled monolayer**   A film deposition method of a close-packed monolayer of molecules—just like soap molecules—with a (polar) head attached to the underlying substrate and a (non-polar) tail pointing upwards.

**Shadow printing**   A kind of optical printing in which the gap between the mask and the resist is zero (contact printing) or near zero (proximity printing).

**Silicon**   The most dominant element in integrated circuit technology.

**Silicon-on-insulator wafer**   Wafers having an oxide film under the electronically active single crystal top later.

**Single crystal film**   A material having a perfect arrangement of atoms, a lattice virtually without defects or impurities and this order extends to macroscopic dimensions.

**Single crystal ingot**   A single crystal rod having electronic grade purity.

**Single crystal seed**   A piece of single crystal material used to initialise crystal growth in the Czochralski technique.

**Solder bonding**   An adhesive bonding method using a temporally molten metal as the adhesive.

**Solid-phase etching**   A pure physical etch process, which involves the bombardment of particles (typically a few tens of micrometer in diameter), that remove material due to physical momentum transfer.

**Solid-phase formation**   The formation of a film out of the solid phase.

**Spin coating**   A film deposition method where a substrate is held on a vacuum spindle and a droplet of liquid (resist) is applied to the center of the wafer. The wafer is then rapidly accelerated up to a constant rotational speed to give a uniform film.

**Spraying**   A film deposition method on a substrate involving pressurization by compressed air or pushing liquid mechanically through tiny orifices forming a spray.

**Sputter deposition**   A film deposition method in which positive ions from a plasma source, usually Ar+, are accelerated to bombard a target and subsequently deposits the bombarded material onto a substrate.

**Sputter etching**   A form of plasma etching making use of the ionic species in the plasma only. Like ion beam etching it is a purely physical process but the pressure during etching is much higher.

**Sputter yield**   The number of atoms removed per incoming ion in physical etching.

**Stamping**   A kind of mechanical printing in which a flexible (rubber) stamp is used to apply selectively small quantities of a specially selected reagent solution as ink onto a surface.

**Stepper lithography**   A lithographic technique combining both writing and reduction projection printing to enhance throughput.

**Stereo lithography**   An alternative technique of write lithography where a resist is hardened into a 3 dimensional shape by way of two intersecting scanning laser beams.

**Surface micromachining**   A micromachining technique in which features are built up layer-by-layer on top of a surface or substrate.

**Synergetical etching**   A film etching process involving both physical as well as chemical etching. It preferably results in a vertical-anisotropic profile.

**Tapered profile**   A common result of physical etching resulting in facets caused by mask erosion and the angle dependency of the etch rate or sputter yield.

**Thermal bonding**   A bonding method, just like direct bonding but using a high-temperature annealing step to improve adhesion.

**Thermal diffusion**   A film growth method where a dopant is driven into a material at high temperature.

**Thermal oxidation**   A film growth method where a material is oxidized at high temperature.

**Thermal stress**   A form of film stress caused by differences in thermal expansion between two layers, which are tightly connected.

**Throughput**   The number of wafers that can be exposed per hour for a given mask level.

**Top-down nanotechnology**   The area of nanosystem technology, which refers to making miniature (or "nanoture") structures by lithographic printing and non-lithographic machining techniques.

**Tri-level lithography**   A form of lithography to minimize step coverage problems on patterned surfaces.

**Vertical-anisotropic profile**   A typical result of synergetical etching having perfectly straight sidewalls exactly under the edge of the masking layer and the etching under the mask approaches zero. A vertical profile is often desired in an etch process because it maintains lithographically defined feature sizes as they are transferred by etching into underlying films.

**Wafer bonding**   A deposition method where two solid materials fuse and adhere to each other if they are brought in sufficient close contact. The cohesion of atoms and molecules between the two (different) materials is ensured by a number of basic bond types and based on Coulombic forces, which are covalent, metallic, ionic, or Van der Waals.

**Wafer edge profiling** The rounding of sharp, fragile edges of wafers in order to provide strength to the wafer after wafer slicing.

**Wafer etching** A process following wafer lapping to remove remaining microcracks or surface damage introduced by the alumna abrasive in the previous lap-stage.

**Wafer fabrication** The first basic step in a micromachining process flow. It generally means the preparation of an atomically smooth and particle free surface.

**Wafer lapping** A wafer fabrication process following wafer edge profiling to increase symmetry and remove surface roughness from saw cuts and process damage using a mixture of alumna powder and glycerine.

**Wafer orientation flat** Regions in a wafer to mark the specific crystal orientation and conductivity type of the material.

**Wafer polishing** A technique following wafer etching to provide an atomically smooth, specular surface where device features can be defined by lithographic processes or to improve bondability.

**Wafer slicing** The machining of the single crystal ingot into wafers using a saw after ingot grinding.

**Wet etching** A form of etching that involves the use of liquid etchants and is often a pure chemical process. It is a well-established, simple, and inexpensive technology with a possible high selectivity between the mask material and the thin film to be etched due to the chemical nature of the process.

**Write lithography** A serial lithographic technique in which a narrow (focused) beam or probe is scanned in a XY-pattern across a substrate to transfer a pattern.

**X-ray printing** A kind of print lithography in which an image is transferred through a mask in a resist using X-ray radiation ($\lambda = 0.4$–4 nm). It uses a one-to-one method, similar to optical shadow printing, because for this wavelength no suitable optics is available.

# REFERENCES

## Books

### Microtechnology

1. J. D. Plummer, M. Deal, and P. B. Griffin, "Silicon VLSI Technology." Prentice Hall, Upper Saddle River, NJ, 2000.
2. S. M. Sze, "VLSI Technology." McGraw–Hill, Boston, 1988.
3. M. Elwenspoek and H. V. Jansen, "Silicon Micromachining." Cambridge Univ. Press, Cambridge, UK, 1998.
4. M. J. Madou, "Fundamentals of Microfabrication." CRC Press, Boca Raton, FL, 1997.
5. M. Gad-el-Hak, "The MEMS Handbook." CRC Press, Baco Raton, FL, 2002.
6. P. Rai-Choudhury, "Handbook of Microlithography, Micromachinimng, and Microfabrication," Vol. 1. SPIE Press, Bellingham, WA, 1997.
7. P. Rai-Choudhury, "Handbook of Microlithography, Micromachining, and Microfabrication," Vol. 2. SPIE Press, Bellingham, WA, 1997.
8. G. Klein Lebbink, Microsystem Technolgy—Exploring Opportunities: STT 56, The Hague, 1994.
9. A. Heuberger, "Mikromechanik." Springer-Verlag, Heidelberg, 1989.
10. S. Büttgenbach, "Mikromechanik." Teubner Studienbücher, Stuttgart, 1991.
11. W. Menz and P. Bley, "Mikrosystemtechnik für Ingenieure." Wiley–VCH, Weinhem, 1993.
12. Q.-Y. Tong and U. Gösele, "Semiconductor Wafer Bonding: Science and Technology." Wiley, 1998.
13. "Industrial Adhesives Handhook." Casco Nobel, Fredensborg, Denmark, 1992.
14. R. R. Tummala, E. J. Rymaszewski, and A. G. KIopfenstein, "Microelectronics packaging handbook," Part 1, 2nd ed. Chapman & Hall, New York, 1997.
15. J. P. Colinge, "Silicon-on-Insulator Technology: Materials to VLSI," 2nd ed. Kluwer Academic, Boston, 1997.
16. S. Cristoloveanu and S. S. Li, "Electrical Characterization of Silicon-on-Insulator Materials and Devices." Kluwer Academic, Boston, 1995.
17. J. L. Vossen and W. Kern, "Thin Film Processes." Academic Press, Orlando, 1978.
18. T. Sugano, "Applications of Plasma Processes in VLSI Technology." Wiley, New York, 1985.
19. S. M. Rossnagel, J. J. Cuomo, and W. D. Westwood, "Handbook of Plasma Processing Technology." Noyes, Park Ridge, NJ, 1990.
20. R. d'Agostino, "Plasma Deposition, Treatment, and Etching of Polymers." Academic Press, Boston, 1990.

### Micromachined Transducers

21. G. T. A. Kovacs, "Micromachined Transducer Sourcebook." WCB/McGraw–Hill, Boston, 1998.
22. M.-H. Bao, "Micro Mechanical Transducers: Pressure Sensors, Accelerometers and Gyroscopes," Handbook of Sens. Actuators Series, Vol. 8 Elsevier, Amsterdam, 2000.
23. R. S. Muller, "Microactuators." IEEE, New York, 1999.
24. M. Tabib-Azar, "Microactuators: Electrical, Magnetic, Thermal, Optical, Mechanical, Chemical and Smart Structures by 1998." Kluwer Academic, Dordrecht, 1998.
25. R. S. Muller, R. T. Howe, S. T. Senturia, R. L. Smith, and R. M. White, "Microsensors." IEEE, New York, 1991.
26. J. W. Gardner, "Microsensors." Wiley, Chichester, UK, 1994.
27. R. S. Muller, R. T. Howe, S. D. Senturia, R. L. Smith, and R. M. White, "Microsensors." IEEE Press, New York, 1991.
28. S. M. Sze, "Semiconductor Sensors." Wiley, New York, 1994.
29. L. Ristic, "Sensor Technology and Devices." Artech House, Boston, 1994.
30. W. Göpel, J. Hesse, and J. N. Zemel, "Sensors a Comprehensive Survey: Fundamentals and General Aspects," Vol. 1. Wiley–VCH, New York, 1989.
31. W. Göpel, J. Hesse, and J. N. Zemel, "Sensors a Comprehensive Survey: Chemical and Biochemical Sensors," Vol. 2/3. Wiley–VCH, New York, 1991.
32. W. Göpel, J. Hesse, and J. N. Zemel, "Sensors a Comprehensive Survey: Thermal Sensors," Vol. 4. Wiley–VCH, New York, 1990.
33. W. Göpel, J. Hesse, and J. N. Zemel, "Sensors a Comprehensive Survey: Magnetic Sensors," Vol. 5. Wiley–VCH, New York, 1990.
34. W. Göpel, J. Hesse, and J. N. Zemel, "Sensors a Comprehensive Survey: Optical Sensors," Vol. 6. Wiley–VCH, New York, 1991.
35. W. Göpel, J. Hesse, and J. N. Zemel, "Sensors a Comprehensive Survey: Mechanical Sensors," Vol. 7. Wiley–VCH, New York, 1993.
36. W. Göpel, J. Hesse, and J. N. Zemel, "Sensors a Comprehensive Survey: Cumulative Index and Selected Topics," Vol. 8 Wiley–VCH, New York, 1997.
37. V. K. Varadan, K. J. Vinoy, and K. A. Jose, "RF MEMS and Their Applications." Wiley, Chichester, UK, 2003.
38. H. J. De Los Santos, "Introduction to Microelectromechanical (MEM) Microwave Systems." Artech House, Boston, 1999.

### *Nanotechnology*

39. A. ten Wolde, "Nanotechnology—Towards a Molecular Construction Kit." STT 60, The Hague, 1998.
40. K. E. Drexler, "Nanosystems." Wiley, 1992.
41. K. E. Drexler, "Engines of Creation—The Coming Area of Nanotechnology." Anchor Books, New York, 1986.

### *Material Properties*

42. D. R. Lide, "Handbook of Chemistry and Physics," 74th ed. CRC Press, Boca Raton, 1994.
43. S. Timoshenko, "Strength of Materials, Part I—Elementary Theory and Problems," 3rd SI ed. Van Nostrand, New York, 1955.
44. J. M. Gere and S. P. Timoshenko, "Mechanics of Materials," 3rd ed. Chapman & Hall, London, 1991.
45. R. C. Hibbeler, "Engineering Mechanics—Mechanics of Materials," 3rd ed. Prentice Hall, New Jersey, 1997.
46. R. A. Higgins, "Properties of Engineering Materials." Industrial Press, New York, 1994.
47. T. L. Anderson, "Fracture Mechanics: Fundamentals and Applications," 2nd ed. CRC Press, Boca Raton, 1995.
48. W. M. Alvino, "Plastics For Electronics: Materials, Properties, and Design." McGraw–Hill, New York, 1995.
49. H. R. Huff and R. R. Burgess, "Semiconductor Silicon," Softbound Proceedings Series. The Electrochemical Society, Princeton, 1973.
50. T. I. Kamins, "Polycrystalline Silicon." Kluwer, New York, 1989.
51. F. Shimura, "Semiconductors and Semimetals: Oxygen in Silicon," Vol. 42 Academic Press, San Diego, 1994.
52. R. H. Doremus, "Glass Science." Wiley, New York, 1994.
53. P. Heller, J. Vervest, and H. Wilbrink, "Vademecum voor de glastechniek." Kluwer, Deventer, 1992.
54. INSPEC, "Properties of Indium Phosphide," EMIS Datareviews Series No. 06. Short Run Press Ltd., Exeter, 1991.
55. S. Adachi, "Properties of Aluminum Gallium Arsenide," EMIS Datareviews Series No. 07. Short Run Press Ltd., Exeter, 1993.
56. P. K. Bhattacharya, "Properties of Lattice-Matched and Strained Indium Gallium Arsenide," EMIS Datareviews Series No. 08. Short Run Press Ltd., Exeter, 1993.
57. P. Capper, "Properties of Narrow Gap Cadmium-Based Compounds," EMIS Datareviews Series No. 10. Short Run Press Ltd., Exeter, 1994.
58. J. Edgar, "Properties of Group III Nitrides," EMIS Datareviews Series No. 11. Short Run Press Ltd., Exeter, 1994.
59. E. Kasper, "Properties of Strained and Relaxed Silicon Germanium," EMIS Datareviews Series No. 12. Short Run Press Ltd., Exeter, 1995.
60. G. L. Harris, "Properties of Silicon Carbide," EMIS Datareviews Series No. 13. Short Run Press Ltd., Exeter, 1995.
61. K. Maex and M. van Rossum, "Properties of Metal Silicides," EMIS Datareviews Series No. 14. Short Run Press Ltd., Exeter, 1995.
62. P. Bhattacharya, "Properties of III–V Quantum Wells and Superlattices," EMIS Datareviews Series No. 15. Short Run Press Ltd., Exeter, 1996.
63. M. R. Brozel and G. E. Stillman, "Properties of Gallium Arsenide," 3rd ed. EMIS Datareviews Series No. 16. Short Run Press Ltd., Exeter, 1996.
64. R. Bhargava, "Properties of Wide Bandgap II–VI Semiconductors," EMIS Datareviews Series No. 17. Short Run Press Ltd., Exeter, 1996.
65. L. Canham, "Properties of Porous Silicon," EMIS Datareviews Series No. 18. Short Run Press Ltd., Exeter, 1997.
66. T. M. Searle, "Properties of Amorphous Silicon and Its Alloys," EMIS Datareviews Series No. 19. Short Run Press Ltd., Exeter, 1998.
67. R. Hull, "Properties of Crystalline Silicon," EMIS Datareviews Series No. 20, Short Run Press Ltd., Exeter, 1999.
68. T. P. Pearsall, "Properties, Processing and Applications of Indium Phosphide," EMIS Datareviews Series No. 21. Short Run Press Ltd., Exeter, 2000.
69. D. W. Hewak, "Properties, Processing and Applications of Glass and Rare Earth-Doped Glasses for Optical Fibres," EMIS Datareviews Series No. 22. Short Run Press Ltd., Exeter, 1998.
70. J. Edgar, S. Strite, I. Akasaki, H. Amano, and C. Wetzel, "Properties, Processing and Applications of Gallium Nitride and Related Semiconductors," EMIS Datareviews Series No. 23. Short Run Press Ltd., Exeter, 1999.
71. E. Kasper and K. Lyutovich, "Properties of Silicon Germanium and SiGe:carbon," EMIS Datareviews Series No. 24. Short Run Press Ltd., Exeter, 2000.
72. D. A. Dunmur, A. Fukuda, and G. R. Luckhurst, "Physical Properties of Liquid Crystals: Nematics," EMIS Datareviews Series No. 25. Short Run Press Ltd., Exeter, 2001.
73. M. H. Nazare and A. J. Neves, "Properties, Growth and Applications of Diamond," EMIS Datareviews Series No. 26. Short Run Press Ltd., Exeter, 2001.
74. K. K. Wong, "Properties of Lithium Niobate," EMIS Datareviews Series No. 28. Short Run Press Ltd., Exeter, 2002.
75. S. R. P. Silva, "Properties of Amorphous Carbon," EMIS Datareviews Series No. 29. Short Run Press Ltd., Exeter, 2002.
76. D. Dawson, "History of Tribology." Longman, London, 1979.
77. B. Bhushan, "Tribology Issues and Opportunities in MEMS." Kluwer Academic, Dordrecht, 1997.
78. B. Bhushan, "Micro/nanotribology and Its Applications." Kluwer Academic, Dordrecht, 1996.

## Relevant Conferences

### *Microtechnology*

79. Micro Electro Mechanical Systems, "Proceedings of IEEE MEMS." Institute of Electrical and Electronics Engineers, Salem/Danvers, MA, annual.
80. Micro-Electro-Mechanical Systems, "Microfabrication and Micro(-electro-)mechanical Systems," International Mechanical Engineering Congress and Exposition, ASME, NY, annual.
81. Micro System Technologies, "International Conference on Micro Electro, Opto, Mechanic Systems and Components" (H. Reichl, Ed.), Springer-Verlag, Berlin, annual.
82. EIPBN, "International Conference on Electron, Ion, and Photon Beam Technology and Nanofabrication," annual.
83. Transducers, "International Conference on Solid-State Sens. Actuators," biannual.
84. Eurosensors, "European Conference on Solid-State Transducers and Microsystems." Elsevier, Amsterdam, annual.
85. *Sens. Actuators A* (physical), "Proceedings of Eurosensors." Elsevier, Amsterdam, annual.
86. *Sens. Actuators B* (chemical), "Proceedings of Eurosensors." Elsevier, Amsterdam, annual.
87. "European workshop on electrochemical processing of semiconductors." 1993.
88. Micromechanics Europe, "Workshop on Micromachining, Micromechanics and Microsystems." MME, annual.
89. "IEEE Solid-State Sensors Workshop." IEEE, Salem/Danvers, MA, annual.
90. "IEEE Solid-State Sensor and Actuator Workshop." IEEE, Salem/Danvers, MA, biannual.
91. "Conference on New Actuators" (H. Borgmann, Ed.). Messe Bremen GMBH, Bremen, Germany, biannual.
92. "Proceedings of the Sensor Technology Conference." Kluwer Academic, Dordrecht, annual.

93. "Semiconductor Wafer Honding: International Symposium on Wafer Bonding Science, Technology, and Applications" (Gösele, Ed.). The Electrochemical Society, Pennington, NJ, biannual.

94. Micro Total Analysis Systems, "Proceedings of the μTAS Symposium" (A. van den Berg, Ed.). Kluwer Academic, Dordrecht, biannual.

95. "Micromachined Devices and Components," *Proc. SPIE* (1994–).

96. The Leeds–Lyon Symposium, "Symposium on Tribology." Elsevier, Amsterdam, annual.

97. Micro- and Nano-engineering, "Proceedings of the International Conference on MNE." Elsevier, Amsterdam, annual.

98. NanoTech, "European Conference on Micro & Nanoscale Technologies for the Biosciences," annual.

## Theses

### *Microtechnology*

99. K. J. M. Eijkel, A Thin-Film Magnetoresistive Angle Detector, Ph.D. Dissertation (Thesis), University of Twente, Enschede, the Netherlands, 1988.

100. F. C. M. van de Pol, A Pump Based on Micro-engineering Techniques, Ph.D. Dissertation (Thesis), University of Twente, Enschede, The Netherlands, 1989.

101. F. R. Blom, Resonant Silicon Beam Force Sensor, Ph.D. Dissertation (Thesis), University of Twente, Enschede, The Netherlands, 1989.

102. S. Bouwstra, Resonating Microbridge Mass Flow Sensor, Ph.D. Dissertation (Thesis), University of Amsterdam, Amsterdam, The Netherlands, 1990.

103. T. S. J. Lammerink, Optical Operation of Micro-mechanical Resonator Sensors, Ph.D. Dissertation (Thesis), University of Twente, Enschede, The Netherlands, 1990.

104. G. J. M. Krijnen, All-Optical Switching in Nonlinear Integrated Optic Devices, Ph.D. Dissertation (Thesis), University of Twente, Enschede, The Netherlands, 1992.

105. J. Elders, Laser-Induced Chemical Vapor Deposition of Titanium Diboride, Ph.D. Dissertation (Thesis), University of Twente, Enschede, The Netherlands, 1992.

106. R. J. Wiegerink, Analysis and Synthesis of MOS Translinear Circuits, Ph.D. Dissertation (Thesis), University of Twente, Enschede, The Netherlands, 1992.

107. H. A. C. Tilmans, Micro-mechanical Sensors Using Encapsulated Built-in Resonant Strain Gauges, Ph.D. Dissertation (Thesis), University of Twente, Enschede, The Netherlands, 1993.

108. C. J. van Mullem, Micromachined Silicon Integrated Resonant Sensors, Ph.D. Dissertation (Thesis), University of Twente, Enschede, The Netherlands, 1993.

109. A. Prak, Silicon Resonant Sensors: Operation and Response, Ph.D. Dissertation (Thesis), University of Twente, Enschede, The Netherlands, 1993.

110. V. L. Spiering, Package Stress Reduction for Micromechanical Sensors: Application in a Pressure Sensor, Ph.D. Dissertation (Thesis), University of Twente, Enschede, The Netherlands, 1994.

111. G.-J. Burger, A Slider Motion Monitoring System, Ph.D. Dissertation (Thesis), University of Twente, Enschede, The Netherlands, 1995.

112. H. V. Jansen, Plasma Etching in Microtechnology, Ph.D. Dissertation (Thesis), University of Twente, Enschede, The Netherlands, 1996.

113. R. Legtenberg, Electrostatic Actuators Fabricated by Surface Micromachining Techniques, Ph.D. Dissertation (Thesis), University of Twente, Enschede, The Netherlands, 1996.

114. H.-E. de Bree, The Microflown, Ph.D. Dissertation (Thesis), University of Twente, Enschede, The Netherlands, 1997.

115. J. C. C. van Kuijk, Numerical Modelling of Flows in Micro Mechanical Devices, Ph.D. Dissertation (Thesis), University of Twente, Enschede, The Netherlands, 1997.

116. C. R. Neagu, A Medical Microactuator Based on an Electrochemical Principle, Ph.D. Dissertation (Thesis), University of Twente, Enschede, The Netherlands, 1998.

117. C.-Q. Gui, Direct Wafer Bonding with Chemical Mechanical Polishing, Ph.D. Dissertation (Thesis), University of Twente, Enschede, The Netherlands, 1998.

118. R. W. Tjerkstra, Isotropic Etching of Silicon in Fluoride Containing Solutions as a Tool for Micromachining, Ph.D. Dissertation (Thesis), University of Twente, Enschede, The Netherlands, 1999.

119. R. E. Oosterbroek, Modelling, Design and Realization of Microfluidic Components, Ph.D. Dissertation (Thesis), University of Twente, Enschede, The Netherlands, 1999.

120. N. R. Tas, Electrostatic Micro Walkers: Micro Electromechanics and Micro Tribology, Ph.D. Dissertation (Thesis), University of Twente, Enschede, The Netherlands, 2000.

121. S. Kuiper, Development and Applications of Microsieves, Ph.D. Dissertation (Thesis), University of Twente, Enschede, The Netherlands, 2000.

122. A. F. Zwijze, Micro-machined High Capacity Silicon Load Cells, Ph.D. Dissertation (Thesis), University of Twente, Enschede, The Netherlands, 2000.

123. A. J. Njdam, Anisotropic Wet-Chemical Etching of Silicon: Pits, Peaks, Principles, Pyramids and Particles, Ph.D. Dissertation (Thesis), University of Twente, Enschede, The Netherlands, 2001.

124. J. F. Burger, Cryogenic Microcooling, Ph.D. Dissertation (Thesis), University of Twente, Enschede, The Netherlands, 2001.

125. H. Wensink, Fabrication of Microstructures by Powder Blasting, Ph.D. Dissertation (Thesis), University of Twente, Enschede, The Netherlands, 2002.

126. J. J. J. van Baar, Distributed Thermal Micro Sensors for Fluid Flow, Ph.D. Dissertation (Thesis), University of Twente, Enschede, The Netherlands, 2002.

127. M. T. Blom, On-chip Separation and Sensing Systems for Hydrodynamic Chromatography, Ph.D. Dissertation (Thesis), University of Twente, Enschede, The Netherlands, 2002.

## Papers (Journals & Proceedings)

### *Microtechnology*

128. R. P. Feynman, *J. Microelectromech. Syst.* 1, 60 (1992).

129. R. P. Feynman, *J. Microelectromech Syst.* 2, 4 (1993).

130. S. D. Senturia, Feynman revisited, in "Proceedings IEEE Micro Electro Mechanical Systems," 1994, pp. 309–312.

131. R. S. Muller, From IC's to microstructures: materials and technologies, in "Proceedings IEEE Micro Robots and Teleoperators Workshop," 1987, pp. 1–5.

132. T. Hayashi, Micromechanism and their characteristics, in "Proceedings IEEE Micro Electro Mechanical Systems," 1994, pp. 39–44.

133. G. Tschulena, Micromechanics business opportunities, in "Proceedings 3rd Int. Conf. on Micro Electro, Opto, Mechanic Systems and Components," 1992, pp. 51–57.

134. R. S. Muller, *Sens. Actuators A* 21–23, 1 (1990).

135. K. D. Wise, Integrated microelectromechanical systems: A perspective on MEMS in the 90s, in "Proceedings IEEE Micro Electro Mechanical Systems," 1991, pp. 33–38.

136. M. Mehregany, *IEEE Circuits Devices Mag.* 9, 14 (1993).

137. W. S. N. Trimmer, *Sens. Actuators* 19, 267 (1989).

138. H. Fujita and K. Gabriel, New opportunities for micro actuators, in "Proceedings 6th Int. Conf. Solid-State Sens. Actuators (Transducers '91)," 1991, pp. 14–20.

139. W. Benecke, Silicon microactuators: Activation mechanisms and scaling problems, in "Proceedings 6th Int. Conf. Solid-State Sens. Actuators (Transducers '91)," 1991, pp. 46–50.

140. P. Dario, R. Valleggi, M. C. Carrozza, M. C. Montesi, and M. Cocco, *J. Micromech. Microeng.* 2, 141 (1992).

141. H. Fujita, *Microsystem Technol.* 1, 93 (1995).
142. R. T. Howe, Resonant microsensors, in "Proceedings 4th Int. Conf. Solid-State Sens. Actuators, Transducers '87," 1987, pp. 843–848.
143. W. Benecke, *Microelectron. Eng.* 11, 73 (1990).
144. B. Hök, Micromechanics and micromachining of semiconductor sensors, *Acta Polytech. Scand. Eng. Ser. E* 163, 65 (1988).

**Material Properties**

145. R. I. Pratt, G. C. Johnson, and R. T. Howe, Micromechanical structures for thin-film characterization, in "Proceedings 6th Int. Conf. Solid-State Sens. Actuators, Transducers'91," 1991, pp. 205–208.
146. S. D. Senturia, Microfabricated structures for the measurement of mechanical properties and adhesion of thin films, in "Transducers'87," 1987, p. 11.
147. K. E. Petersen, *Proc. IEEE* 70, 420 (1982).
148. P. A. Krulevitch, Micromechanical Investigations of Silicon and Ni–Ti–Cu Thin Films, Ph.D. Dissertation (Thesis), Dept. of Mechanical Engineering, University of California at Berkeley, 1994.
149. M. Biebl, G. T. Mulhem, and R. T. Howe, *In-situ* phosphorus doped polysilicon for integrated MEMS, in "Proceedings 8th Int. Conf. Solid-State Sens. Actuators, Transducers '95," 1995, pp. 198–201.
150. R. T. Howe and R. S. Muller, *Sens. Actuators* 4, 447 (1983).
151. H. Guckel, D. W. Buros, H. A. C. Tilmans, D. W. DeRoo, and C. R. Rutigliano, Mechanical properties of fine-grained polysilicon: The repeatability issue, "Proceedings IEEE Solid-State Sensor and Actuator Workshop," 1988, pp. 96–99.
152. W. N. Sharpe, B. Yuan, and R. Vaidyanathan, Measurements of Young's modulus, Poisson's ratio, and tensile strength of polysilicon, in "Proceedings IEEE Micro Electro Mechanical Systems Workshop," 1997, pp. 424–429.
153. Y. C. Tai and R. S. Muller, Measurement of Young's modulus on microfabricated structures using a surface profiler, in "Proceedings IEEE Micro Electro Mechanical Systems Workshop," 1990, pp. 147–152.
154. M. Biebl, G. Brandl, and R. T. Howe, Young's modulus of *in-situ* phosphorus doped polysilicon, in "Proceedings 8th Int. Conf. Solid-State Sens. Actuators, Transducers'95," 1995, pp. 80–83.
155. D. Maier-Schneider, J. Maibach, E. Obermeier, and D. Schneider, *J. Micromech. Microeng.* 5, 121 (1995).
156. H. Guckel, T. Randazzo, and D. W. Buros, *J. Appl. Phys.* 57, 1675 (1985).
157. R. T. Howe and R. S. Muller, *J. Appl. Phys.* 54, 4674 (1983).
158. P. Krulevitch, G. C. Johnson, and R. T. Howe, Stress and microstructure in phosphorus doped poly-crystalline silicon, in "Proceedings Materials Research Society Symp.," 1992, Vol. 276, pp. 79–84.
159. P. Krulevitch, G. C. Johnson, and R. T. Howe, Stress in undoped LPCVD polycrystalline silicon, in "Proceedings 6th Int. Conf. Solid-State Sens. Actuators, Transducers'91," 1991, pp. 949–952.
160. P. Krulevitch and G. C. Johnson, Stress gradients in thin films used in micro-electro-mechanical systems, in "Proceedings ASME Winter Ann. Meeting," 1993, Vol. DSC-46, pp. 89–95.
161. B. Chou, J.-S. Shie, and C.-N. Chen, *IEEE Electron Device Lett.* 18, 599 (1997).
162. C. Mastrangelo, Y.-C. Tai, and R. S. Muller, Thermophysical properties of low-residual stress, silicon-rich, LPCVD silicon nitride films, *Sens. Actuators A* 21–23, 856 (1990).
163. S. J. Cunningham, W. Suwito, and D. T. Read, Tensile testing of epitaxial silicon films, in "Proceedings 8th Int. Conf. Solid-State Sens. Actuators, Transducers'95," 1995, pp. 96–99.
164. W. Suwito, M. L. Dunn, and S. J. Cunningham, Strength and fracture of micromachined silicon structures, in "Proceedings ASME Winter Annual Meeting," 1997, Vol. DSC-62, pp. 99–104.
165. D. Mirfendereski and A. Der Kiureghian, Probabilistic analysis of micro-fabricated multicrystalline beams, in "Proceedings 6th Int. Conf. Structural Safety and Reliability," Rotterdam, The Netherlands, 1994, pp. 361–367.
166. A. Singh, Internal Process Characterization Study, Berkeley Sensor and Actuator Center, Univ. of California at Berkeley, 1997.
167. Z. Hutchinson and W. Suo, *Adv. Appl. Mech.* 29, 63 (1991).
168. X. Zhang, K.-S. Chen, R. Ghoddsi, A. A. Ayon, and S. M. Spearing, *Sens. Actuators A* 91, 373 (2001).
169. E. A. Lewis and E. A. Irene, *J. Electrochem. Soc.* 134, 2332 (1987).
170. N. F. Mott, *Philos. Mag. B* 55, 117 (1987).
171. E. A. Irene, *Philos. Mag. B* 55, 131 (1987).
172. G. Ghibaudo, *Philos. Mag. B* 55, 147 (1987).
173. B. Leroy, *Philos. Mag. B* 55, 159 (1987).
174. A. M. Stoneham, C. R. M. Grovenor, and A. Cerezo, *Philos. Mag. B* 55, 201 (1987).
175. J. P. Hagon, A. M. Stoneham, and M. Jaros, *Philos. Mag. B* 55, 211 (1987).
176. J. P. Hagon, A. M. Stoneham, and M. Jaros, *Philos. Mag. B* 55, 225 (1987).
177. B. E. Deal and A. S. Grove, *J. Appl. Phys.* 36, 3770 (1965).
178. K. S. Pister and S. B. Dong *Proceedings Am. Soc. Civil Eng.* 85, 1 (1959).
179. G. G. Stoney, *Proc. Roy. Soc. London Ser. A* 82, 172 (1909).
180. E. P. EerNisse, *Appl. Phys. Lett.* 30, 290 (1977).
181. E. P. EerNisse, *Appl. Phys. Lett.* 35, 8 (1979).
182. S. M. Hu, *J. Appl. Phys.*, 70, R53 (1991).
183. E. Kobeda and E. A. Irene, *J. Vac. Sci. Technol. B* 6, 574 (1988).
184. T. Yasaka, M. Takakura, S. Miyazaki, and M. Hirose, *Mater. Res. Soc. Symp. Proc.* 222 (1991).
185. J. Fruhauf, E. Gardner, and E. Jansch, *J. Micromech. Microeng.* 9, 305 (1999).
186. J.-Y. Yen and J.-G. Hwu, *Appl. Phys. Lett.* 76, 1834 (2000).

**Bulk Micromachining**

*Dry Plasma Etching*

187. G. T. A. Kovacs, N. I. Maluf, and K. E. Petersen, *Proc. IEEE* 86, 1536 (1998).
188. M. J. de Boer, R. W. Tjerkstra, J. W. Berenschot, H. V. Jansen, G. J. Burger, J. G. E. Gardeniers, M. C. Elwenspoek, and A. van den Berg, *J. Microelectromech. Syst.* 9 (2000).
189. H. V. Jansen, H. Gardeniers, M. J. de Boer, M. C. Elwenspoek, and J. H. J. Fluitman, *J. Micromech. Microeng.* 6, 14 (1996).
190. Z. L. Zhang and N. C. MacDonald, *J. Micromech. Microeng.* 2, 31 (1992).
191. K. A. Shaw, Z. L. Zhang, and N. C. MacDonald, *Sens. Actuators A* 40, 63 (1994).
192. D. Zhang, Z. Li, T. Li, and G. Wu, *J. Micromech. Microeng. J* 1, 13 (2001).
193. W. Hofrnann and N. C. MacDonald, Fabrication of multiple-level electrically isolated high-aspect-ratio single crystal silicon microstructures, in "Proceedings IEEE Micro Electro Mechanical Systems Workshop," 1997, pp. 460–464.
194. Y. X. Li, P. J. French, P. M. Sarro, and R. F. Wolffenbuttel, Fabrication of a single crystalline silicon capacitive lateral accelerometer using micromachining based on single step plasma etching, in "Proceedings IEEE Micro Electro Mechanical Systems," 1995, pp. 398–403.
195. M. de Boer, H. Jansen, and M. Elwenspoek, The black silicon method 5: A study of the fabrication of movable structures for MEMS, in "Proceedings 8th Int. Conf. Solid-State Sens. Actuators, Transducers '95," 1995, Vol. 1, pp. 565–568.
196. C. G. Keller and R. T. Howe, Hexsil tweezers for teleoperated microassembly, in "MEMS'97," 1997, pp. 72–77.
197. U. Sridhar, C. H. Lau, Y. B. Miao, K. S. Tan, P. D. Foo, and L. J. Liu, Single crystal silicon microstructures using trench isolation, in "Transducers'97," 1999, pp. 258–261.
198. F. Ayazi and K. Najafi, *Sens. Actuators A* 87, 46 (2000).
199. G. Ensell, *J. Micromech. Microeng.* 5, 1 (1995).

200. A. Selvakumar and K. Najafi, High-density vertical comb array microactuators fabricated using a novel bulk/polysilicon trench refill technology, in "Proceedings Solid-state Sensor and Actuator Workshop," 1994, pp. 138–141.

201. C. Keller and M. Ferrari, Milli-scale polysilicon structures, in "Proceedings IEEE Solid-State Sens. Actuators Workshop," 1994, pp. 132–137.

202. T. J. Brosnihan, J. M. Bustillo, A. P. Pisano, and R. T. Howe, Embedded interconnect and electrical isolation for high-aspect-ratio, SOl inertial instruments, in "Proceedings 9th Int. Conf. Solid-State Sens. Actuators, Transducers '97," 1997, pp. 637–640.

203. J. Bhardwaj, H. Ashraf, and A. McQuarrie, Dry silicon etching for MEMS, in "Proceedings Symp. Microstructures and Microfabricated Systems," 1997.

204. H. Baltes, Microtransducers by industrial IC technology and micromachining, in "Proceedings 10th Sensor Symposium," 1991, pp. 17–24.

205. C. Linder, T. Tschan, and N. F. de Rooij, Deep dry etching techniques as a new IC-compatible tool for silicon micromachining, in "Transducers '91," 1991, pp. 524–527.

206. S. Aachboun and P. Ranson, J. Vac. Sci. Technol. A 17, 2270 (1999).

207. I. W. Rangelow, Vacuum 62, 279 (2001).

208. W.-C. Tian and S. W. Pang, J. Vac. Sci. Technol. B 19, 433 (2001).

209. S. Franssila, J. Kiihamaki, and J. Karttunen, Microsyst. Technol. 6, 141 (2000).

210. H. V. Jansen, M. J. de Boer, H. Wensink, B. Kloeck, and M. C. Elwenspoek, The Black Silicon Method 8: A study of the performance of etching silicon using SF6/O2-based chemistry with cryogenical wafer cooling and a high density ICP source, in "Microelectronic Engineering Conference, MNE'97," 1997.

211. M. J. de Boer, J. G. E. Gardeniers, H. V. Jansen, E. Smulders, M.-J. Gilde, G. Roelofs, J. N. Sasserath, and M. C. Elwenspoek, J. Microelectromech. Syst. 11 (2002).

212. S. Aachboun, P. Ranson, C. Hilbert, and M. Boufnichel, J. Vac. Sci. Technol. A 18, 1848 (2000).

213. K. W. Kok, W. J. Yoo, K. Sooriakumar, J. S. Pan, and E. Y. Lee, J. Vac. Sci. Technol. B 20, 1878 (2002).

214. M. McNie, D. King, C. Vizard, A. Holmes, and K. W. Lee, Microsyst. Tech. 6, 184 (2000).

215. H. V. Jansen, M. J. de Boer, R. Legtenberg, and M. C. Elwenspoek, J. Micromech. Microeng. 5, 115 (1996).

216. H. V. Jansen, M. J. de Boer, J. Burger, R. Legtenberg, and M. C. Elwenspoek, Microelectron. Eng. 27, 475 (1995).

217. H. V. Jansen, M. J. de Boer, B. Otter, and M. C. Elwenspoek, BSM 4: The fabrication of three-dimensional structures in silicon with high aspect ratios for scanning probe microscopy and other applications, in "Micro Electro Mechanical Systems MEMS '95," 1995, pp. 88–93.

218. H. V. Jansen, M. J. de Boer, and M. C. Elwenspoek, BSM 6: High aspect ratio trench etching for MEMS applications, in "Micro Electrical Mechanical Systems MEMS '96," 1996, pp. 250–257.

219. H. V. Jansen, M. J. de Boer, R. Wiegerink, N. R. Tas, E. Smulders, C. R. Neagu, and M. C. Elwenspoek, Microelectron. Eng. 35, 45 (1997).

220. J. Kiihamaki and S. Franssila, J. Vac. Sci. Technol. A 17, 2280 (1999).

221. K. P. Giapis and G. S. Hwang, Thin Solid Films 374, 175 (2000).

222. K. Nishikawa, H. Ootera, S. Tomohisa, and T. Oomori, Thin Solid Films 374, 190 (2000).

223. A. A. Ayon, K. Ishihara, R. A. Braff, H. H. Sawin, and M. A. Schmidt, J. Vac. Sci. Technol. A 17, 2274 (1999).

224. J. Kiihamaki, J. Vac. Sci. Technol. A 18, 1385 (2000).

225. B. Volland, F. Shi, P. Hudek, H. Heerlein, and I. W. Rangelow, J. Vac. Sci. Technol. B 17, 2768 (1999).

226. T. Zijlstra, E. van der Drift, M. J. A. de Dood, E. Snoeks, and A. Polman, J. Vac. Sci. Technol. B 17, 2734 (1999).

227. Z. Zhu and C. Liu, J. Microelectromech. Syst. 9, 252 (2000).

228. J. Voigt, B. Reinker, I. W. Rangelow, G. Mariotto, I. Shvets, P. Guethner, and H. Loschner, J. Vac. Sci. Technol. B 17, 2764 (1999).

229. A. K. Paul, A. K. Dimri, and R. P. Bajpai, Vacuum 68, 191 (2003).

230. D. Moser, O. Brand, and H. A. Baltes, CMOS compatible thermally excited oxide beam resonator with aluminum mirror, in "Transducers '91," 1991, Technical digest, pp. 547–550.

231. O. Brand, H. Baltes, and U. Baldenweg, J. Micromech. Microeng. 2, 208 (1992).

232. H. Baltes, D. Moser, T. Boltshauser, R. Lenggenhager, O. Brand, and D. Jaeggi, Micromech. Sensors Actuators Syst. DSC-32, 61 (1991).

233. D. Moser, R. Lenggenhager, and H. Baltes, Sens. Actuators A 27, 577 (1991).

234. T. Boltshauser, M. Schónholzer, O. Brand, and H. Baltes, J. Micromech. Microeng. 2, 205 (1992).

235. S. Bouwstra, R. Legtenberg, H. A. C. Tilmans, and M. Elwenspoek, Sens. Actuators A 21–33, 332 (1990).

236. C. Mastrangelo, Thermal Applications of Microbridges, Ph.D. dissertation, Univ. of California, Berkeley, 1991.

237. B. W. Chui, T. W. Kenny, H. J. Mamin, B. D. Terris, and D. Rugar, A novel dual-axial AFM cantilever with independent piezoresistive sensors for simultaneous detection of lateral and vertical forces, DSC-Vol. 62/HTD-Vol. 354, MEMS-ASME (1997), p. 55.

238. E. Hoffinan, B. Warneke, E. Kruglick, J. Weigold, and K. S. J. Pister, 3D structures and piezoresistive sensors in standard CMOS, in "Proceedings IEEE Micro Electro Mechanical Systems Workshop," 1995, p. 228.

239. N. C. MacDonald, Nanomechanisms and tips for microinstruments, in "Proceedings 7th Int. Cont. Solid-State Sens. Actuators, Transducers' 93," 1993, p. 8.

240. B. P. van Drieenhuizen, N. I. Maluf, I. E. Opris, and G. T. Kovacs, Force-balanced accelerometer with mG resolution, fabricated using silicon fusion bonding and deep reactive ion etching, in "Proceedings 9th Int. Conf. Solid-State Sens. Actuators, Transducers'97," 1997, pp. 1229–1230.

241. L. C. SpangIer and C. J. Kemp, ISAAC-Integrated silicon automotive accelerometer, in "Proceedings 8th Int. Conf. Solid-State Sens. Actuators, Transducers'95," 1995, pp. 585–588.

242. C. Song, Commercial vision of silicon based inertial sensors, in "Proceedings 9th Int. Conf. Solid-State Sens. Actuators, Transducers'97," 1995, pp. 839–842.

243. F. Ayazi and K. Najafi, J. Microelectromech. Syst. 10 (2001).

244. K. S. Lebouitz, R. T. Howe, and A. P. Pisano, Permeable polysilicon microsheIl etch-access windows, in "Proceedings 8th Int. Conf. Solid-State Sens. Actuators," Transducers '95, 1995, pp. 224–227.

### Wet Orientation dependent etching

245. H. Seidel, The mechanism of anisotropic, electrochemical silicon etching in alkaline solutions, "IEEE Solid-State Sensor and Actuator Workshop," 1990, Technical digest, pp. 86–91.

246. B. Kloeck, S. D. Collins, R. L. Smith, and N. F. de Rooij, IEEE Trans. Electron Devices 36, 663 (1989).

247. H. Seidel, The mechanism of anisotropic silicon etching and its relevance for micromachining, in "Proceedings Int. Conf. Solid-State Sens. Actuators (Transducers '87)," 1987, pp. 120–125.

248. Y. Bäcklund and L. Rosengren, J. Micromech. Microeng. 2, 75 (1992).

249. J. Hsieh and W. Fang, J. Micromech. Microeng. 12, 574 (2002).

250. S. Park, B. Kim, J. Kim, S. Paik, B.-D. Choi, I. Jung, K. Chun, and D.-I. D. Cho, J. Micromech. Microeng. 12, 650 (2002).

251. S. Lee, S. Park, and D. Cho, Jpn. J. Appl. Phys. 38, 2699 (1999).

252. H. Fukidome and M. Matsumura, Jpn. J. Appl. Phys. 38, L1085 (1999).

253. G. Schropfer, M. de Labachelerie, and C. R. Tellier, Microsyst. Technol. 5, 194 (1999).

*254.* E. D. Palik, J. Glembocki, I. Heard, P. S. Burno, and L. Tenerz, *J. Appl. Phys.* 70, 3291 (1991).

*255.* J. T. L. Thong, P. Luo, W. K. Choi, and S. C. Tan, *J. Micromech. Microeng.* 11, 61 (2001).

*256.* H. Omi and T. Ogino, *Thin Solid Films* 380, 15 (2000).

*257.* J. A. Dziuban, Microwave enhanced fast anisotropic etching of monocrystalline silicon, *Sens. Actuators* 85, 133 (2000).

*258.* James D. Patterson, Micro-Mechanical Voltage Tunable Fabry-Perot Filters Formed in (111) Silicon, NASA Technical Paper 3702, 1997.

*259.* T. Fukuda, *J. Vac. Sci. Technol. A* 17, 2800 (1999).

*260.* D. J. Sadler, M. J. Garter, C. H. Ahn, S. Koh, and A. L. Cook, *J. Micromech. Microeng.* 7, 263 (1997).

*261.* T. Takami, S. Ishidzuka, Y. Igari, H. Range, and I. Kusunoki, *Thin Solid Films* 376, 89 (2000).

*262.* I. Zubel and M. Kramkowska, *Sens. Actuators A* 101, 255 (2002).

*263.* S. Bütefisch, A. Schoft, and S. Büttgenbach, *J. Microelectromech. Syst.* 9, 551 (2000).

*264.* A. Holke and H. T. Henderson, *J. Micromech. Microeng.* 9, 51 (1999).

*265.* T. Baum and D. J. Schiffrin, *J. Micromech. Microeng.* 7, 338 (1997).

*266.* J. Chen, L. Liu, Z. Li, Z. Tan, Q. Jiang, H. Fang, Y. Xu, and Y. Liu, *Sens. Actuators A* 96, 152 (2002).

*267.* H. Namatsu, M. Nagase, K. Kurihara, K. Iwadate, T. Furuta, and K. Murase, *J. Vac. Sci. Technol. B* 13, 1473 (1995).

*268.* F. S.-S. Chien, C.-L. Wu, Y.-C. Chou, T. T. Chen, and S. Gwo, *Appl. Phys. Lett.* 75, 2429 (1999).

*269.* M. Manimaran, T. Tada, and T. Kanayama, *Mater. Lett.* 48, 151 (2001).

*270.* G. Yan, P. C. H. Chan, I.-M. Hsing, R. K. Sharma, J. K. O. Sin, and Y. Wang, *Sens. Actuators A* 89, 135 (2001).

*271.* K. Sato, M. Shikida, T. Yamashiro, K. Asaumi, Y. Iriye, and M. Yamamoto, *Sens. Actuators* 73, 131 (1999).

*272.* P. M. Sarro, D. Brida, W. v. d. Vlist, and S. Brida, *Sens. Actuators* 85, 340 (2000).

*273.* C. M. A. Ashruf, P. J. French, P. M. Sarro, R. Kazinczi, X. H. Xia, and J. J. Kelly, *J. Micromech. Microeng.* 10, 505 (2000).

*274.* K. Sakaino and S. Adachi, *Sens. Actuators A* 88, 71 (2001).

*275.* Y. Nemirovsky and A. El-Bahar, *Sens. Actuators* 75, 205 (1999).

*276.* F.-G. Tseng and K.-C. Chang, A precision alignment method to ⟨100⟩ direction on (110) silicon wafer, in "Proceedings of 2001 ASME International Mechanical Engineering Congress and Exposition," 2001, pp. 1–4

### Surface micromachining

*277.* H. C. Nathanson, W. E. Newell, R. A. Wickstrom, and J. R. Davis, Jr., *IEEE Trans. Electron Dev.* 14, 117 (1967).

*278.* C. Linder, L. Paratte, M.-A. Gretillat, V. P. Jaecklin, and N. F. De Rooij, *J. Micromech. Microeng.* 2, 122 (1992).

*279.* R. T. Howe, Recent advances in surface micromachining—A review, in "13th Sensor Symposium IEE of Japan," 1995.

*280.* J. M. Bustillo, R. T. Howe, and R. S. Muller, *Proc. IEEE* 86, 1552 (1998).

*281.* R. S. Payne, S. Sherman, S. Lewis, and R. T. Howe, Surface micromachining: From vision to reality to vision, in "Proceedings IEEE Int. Solid-State Circuits Conf.," 1995, pp. 164–165.

*282.* R. T. Howe, Surface micromachining for microsensors and microactuators, *J. Vac. Sci. Technol. B* 6, 1809 (1988).

*283.* M. Mehregany and Y.-C. Tai, *J. Micromech. Microeng.* 1, 73 (1991).

*284.* L.-S. Fan, Y.-C. Tai, and R. S. Muller, *IEEE Trans. Electron Dev.* 35, 724 (1998).

*285.* M. Mehregany, K. J. Gabriel, and W. S. N. Trimmer, *IEEE Trans. Electron Dev.* 35, 719 (1988).

*286.* J. M. Bustillo, G. K. Fedder, C. T.-C. Nguyen, and R. T. Howe, *Microsystem Technol.* 1, 30 (1994).

*287.* C. Linder and de N. F. Rooij, *Sens. Actuators A* 21–23, 1053 (1990).

*288.* H. Guckel, J. J. Sniegowski, T. R. Christenson, and F. Raissi, *Sens. Actuators A* 21–23, 346 (1990).

*289.* P. J. French, *Sens. Actuators A* 99, 3 (2002).

*290.* A. Kovacs and A. Stoffel, Process optimization of free-standing polysilicon microstructures, in "Micromechanics Europe '92," 1992, Workshop digest, pp. 114–117.

*291.* R. T. Howe and R. S. Muller, *J. Electrochem. Soc.* 130, 1420 (1983).

*292.* R. T. Howe, Polycrystalline silicon microstructures, in "Micromachining and Micropackaging of Transducers," pp. 169–187. Elsevier, Amsterdam, 1985.

*293.* H. Guckel and D. W. Burns, Planar processed polysilicon-sealed cavities for micromechanical sensors, in "IEDM 1984," 1984, pp. 223–225.

*294.* H. Guckel, D. W. Burns, C. R. Rutigliano, D. K. Showers, and J. Uglow, Fine grained polysilicon and its applications to planar pressure transducers, in "Proceedings 4th Int. Conf. Solid-State Sens. Actuators, Transducers '87," 1987, pp. 277–282.

*295.* H. Guckel, *Sens. Actuators A* 28, 133 (1991).

*296.* M. Kandler, J. Eichholz, Y. Manoli, and W. Mokwa, CMOS compatible capacitive pressure sensor with read-out electronics, in "Proceedings 1st Int. Conf. Micro Electro. Opto. Mech. Syst. Comp., Micro System Technologies '90," 1990, pp. 574–580.

*297.* M. Kandler, Y. Manoli, W. Mokwa, E. Spiegel, and H. A. Vogt, Miniature single chip pressure and temperature sensor, in "Micromechanics Europe '92," 1992, Workshop Digest, pp. 183–186.

*298.* B. Halg, *IEEE Trans. Electron Dev.* 37, 2230 (1990).

*299.* S. Sugiyama, K. Shimaoka, and O. Tabata, Surface micromachined micro-diaphragm pressure sensors, in "Transducers '91," Technical digest, 1991, pp. 188–191.

*300.* P. R. Scheeper, W. Olthuis, and P. Bergveld, Fabrication of a subminiature silicon condenser microphone using the sacrificial technology, in "Transducers '91," Technical digest, 1991, pp. 408–411.

*301.* H. Baltes, Microtransducers by industrial IC technologies and micromachining, in "IEEE Japan 10th Sensor Symp.," Technical digest, 1991, pp. 17–23.

*302.* R. A. Brennen, M. G. Lim, A. P. Pisano, and A. T. Chou, Large displacement linear actuator, "IEEE Solid State and Actuator Workshop," 1990, Technical digest, pp. 135–139.

*303.* N. Takeshima, K. J. Gabriel, M. Ozaki, J. Takahashi, H. Horiguchi, and H. Fujita, Electrostatic parallelogram actuators, in "Transducers '91," 1991, Technical digest, pp. 63–66.

*304.* W. C. Tang, T. H. Nguyen, and R. T. Howe, Laterally driven polysilicon resonant microstructures, in "IEEE Micro Electro Mech. Syst. Workshop," 1989, Technical digest, pp. 53–59.

*305.* C. J. Kim, A. P. Pisano, R. S. Muller, and M. G. Lim, Polysilicon microgripper, in "IEEE Solid-State Sensor and Actuator Workshop," 1990, Technical digest, pp. 48–51.

*306.* T. Hirano, T. Furuhata, K. J. Gabriel, and H. Fujita, *J. MEMS 1*, 52 (1992).

*307.* V. P. Jaecklin, C. Linder, N. F. de Rooij, and J. M. Moret, Micromechanical comb actuators with low driving voltage, in "Actuator '92," 1992, Technical digest.

*308.* V. P. Jaecklin, C. Linder, N. F. de Rooij, J. M. Moret, R. Bischof, and F. Rudolf, Novel polysilicon comb-actuators for *xy*-stages, in "IEEE Micro Electro Mech. Syst. Workshop," 1992, Technical digest, pp. 147–149.

*309.* S. F. Bart, T. A. Lober, R. T. Howe, J. H. Lang, and M. F. Schlecht, *Sens. Actuators* 14, 269 (1988).

*310.* L. Paratte, G.-A. Racine, N. F. de Rooij, and E. Bornand, *Sens. Actuators* 27, 597 (1991).

*311.* Y.-C. Tai, L.-S. Fan, and R. S. Muller, IC-processed micromotors: design, technology and testing, in "Proceedings 2nd Workshop Micro Electro Mech. Syst.," 1989, pp. 1–6.

*312.* L. S. Tavrow, S. F. Bart, and J. H. Lang, Operational characteristics of microfabricated electric motors, "Transducers '91," 1991, Technical digest, pp. 877–881.

*313.* M. Mehregany, S. M. Phillips, E. T. Hsu, and J. H. Lang, Operation of harmonic side-drive micromotors studied through gear

ratio measurements, in "Transducers '91," 1991, Technical digest, pp. 59–62.

314. L. Paratte, G.-A. Racine, N. F. de Rooij, and E. Bornand, A novel comb-drive electrostatic stepper motor, in "Transducers '91," 1991, Technical digest, pp. 886–889.

315. L. Paratte, G.-A. Racine, N. F. de Rooij, and E. Bornand, A rigid ring electrostatic harmonic wobble motor with axial field, in "Transducers '91," 1991, Technical digest, pp. 886–889.

316. K. E. Petersen, *IBM J. Res. Develop.* 23, 376 (1979).

317. H. V. Allen, Silicon based micromechanical switches or industrial applications, in "IEEE Proceedings Micro Robots Teleop. Workshop," 1987.

318. W. Benecke and W. Riethmuller, Applications or silicon-microactuators based on bimorph structures, in "IEEE Micro Electro Mech. Syst. Workshop," 1989, Technical digest, pp. 116–120.

319. R. M. Langdon, *J. Phys. E* 18, 103 (1985).

320. R. A. Buser and N. F. de Rooij, *Sens. Actuators A* 21–23, 323 (1990).

321. R. T. Howe and R. S. Muller, *IEEE Trans. Elecctron Dev.* 33, 499 (1986).

322. J. J. Sniegowski, H. Guckel, and T. R. Christenson, Performance characteristics of second generation polysilicon resonating beam rorce transducers, in "IEEE Solid-State Sensor and Actuator Workshop," 1990, Technical digest, pp. 9–12.

323. C. Linder, E. Zimmermann, and N. F. de Rooij, Capacitive polysilicon resonator with MOS detection circuit, *Sens. Actuators A* 25–27, 591 (1991).

324. E. Obermeier and H. Reichl, *NTG Fachberichte Band* 79, 49 (1982).

325. E. Obermeier, Polysilicon layers lead to a new generation of pressure sensors, in "Proceedings 3rd Int. Conf. Solid-State Sens. Actuators," Transducers '85, 1985, pp. 527–536.

326. C. Linder, M. Grétillat, and N. F. de Rooij, *Microelectron. Eng.* 15, 411 (1991).

327. S. Shoji and M. Esashi, Micro-pump or integrated chemical analyzing systems, in "IEE Japan 7th Sensor Symp.," 1988, Technical digest, pp. 217–220.

328. J. T. Kung and H.-S. Lee, An integrated air-gap-capacitor process for sensor applications, in "Proceedings 3rd Int. Conf. Solid-State Sens. Actuators, Transducers '85," 1985, pp. 1010–1013.

329. J. Brugger, R. A. Buser, and N. F. de Rooij, *J. Micromech. Microeng.* 2, 218 (1992).

330. H. Guckel and D. W. Burns, A technology for integrated transducers, in "Proceedings Int. Conf. Solid-State Sens. Actuators, Transducers '85," 1985, pp. 90–92.

331. R. S. Muller, Microdynamics, in "Proceedings 5th Int. Conf. Solid-State Sens. Actuators, Transducers '89," 1989, pp. 1–8.

332. L. S. Fan, Y. C. Tai, and R. S. Muller, *IEEE Trans. El. Dev.* 35, 724 (1988).

333. L.-S. Fan, Y.-C. Tai, and R. S. Muller, Pin joints, gears, springs, cranks and other novel micromechanical structures, in "Proceedings 4th Int. Conf. Salid-State Sens. Actuators, Transducers '87," 1987, pp. 849–856.

334. T. A. Lober and R. T. Howe, Surface-micromachining processes for electrostatic microactuator fabrication, in "Proceedings IEEE Solid-State Sens. Actuators Workshop," 1988, pp. 59–62.

335. K. S. J. Pister, M. W. Judy, S. R. Burgett, and R. S. Fearing, *Sens. Actuators A* 33, 249 (1992).

336. T. Roessig, A. P. Pisano, and R. T. Howe, *DSC* 57-2, 871 (1995).

337. T. Tsuchiya, O. Tabata, J. Sakata, and Y. Taga, *J. Microelectromech. Syst.* 7, 106 (1998).

338. R. L. Alley, G. J. Cuan, R. T. Howe, and K. Komvopoulos, The effect of release-etch processing on surface microstructure stiction, in "Solid-state Sensors and Actuator workshop," 1992, pp. 202–207.

339. R. Legtenberg, H. A. C. Tilmans, J. Elders, and M. Elwenspoek, *Sens. Actuators A* 41–43, 230 (1994).

340. C.-J. Kim, J. Y. Kim, and B. Sridharan, *Sens. Actuators A* 64, 17 (1998).

341. T. Abe, W. C. Messner, and M. L. Reed, *J. Microelectromech. Syst.* 4, 66 (1995).

342. C. H. Mastrangelo and C. H. Hsu, *J. Microelectromech. Syst.* 2, 33 (1993).

343. C. H. Mastrangelo and C. H. Hsu, *J. Microelectromech. Syst.* 2, 44 (1993).

344. C. T.-C. Nguyen, MEMS for wireless communications, in "Proceedings IEEE Micro Electra Mechanical Systems Workshop," 1998, pp. 1–7.

345. R. T. Howe, Silicon micromachining for resonator fabrication, in "Proceedings IEEE Frequency Control Symp.," 1994, pp. 2–7.

346. K. Dutta et al., Integrated micromotor concepts, in "Proceedings Int. Conf. Microelectronic Circuits and System Theory," 1970, pp. 36–37.

347. IC-processed electrostatic micromotors, in "Proceedings IEEE Int. Electron Devices Meeting," 1988, pp. 666–669.

348. K. J. Gabriel, W. S. N. Trimmer, and M. Mehregany, Micro gears and turbines etched from silicon, in "Proceedings 4th Int. Conf. Solid-State Sens. Actuators, Transducers '87," 1987, pp. 857–860.

349. Y.-C. Tai and R. S. Muller, *Sens. Actuators* 20, 48 (1989).

350. M. Mehregany, P. Nagarkar, S. D. Senturia, and J. H. Lang, Operation of microfabricated harmonic and ordinary side-drive motors, in "Proceedings IEEE Micro Electro Mechanical Systems," 1990, pp. 1–8.

351. R. T. Howe and R. S. Muller, Polycrystalline silicon micromechanical beams, in "Proceedings Electrochemical Society Spring Meeting," 1982, pp. 184–185.

352. R. T. Howe and R. S. Muller *J. Electrochem. Soc.* 130, 1420 (1983).

353. *IEEE Trans. Electron Devices* ED-33, 499 (1986).

354. K. Deng, H. Miyajima, V. R. Dhuler, M. Mehregany, S. W. Smith, F. L. Merat, and S. Furukawa, Polysilicon micromotors for optical scanner applications, in "Proceedings Solid-State Sensor and Actuator Workshop," 1994, pp. 234–239.

355. R. S. Muller and K. Y. Lau, *Proc. IEEE* 86, 1705 (1998).

356. L.-S. Fan, Y.-C. Tai, and R. S. Muller, *IEEE Trans. Electron Devices* 35, 724 (1988).

357. W. C. Tang, T.-C. H. Nguyen, M. W. Judy, and R. T. Howe, *Sens. Actuators A* 21–23, 328 (1990).

358. A. P. Lee, D. J. Nikkel, Jr., and A. P. Pisano, Polysilicon linear vibromotors, in "Proceedings 7th Int. Conf. Sens. Actuators," 1993, pp. 46–47.

359. K. S. J. Pister, M. W. Judy, S. R. Burgett, and R. S. Fearing, *Sens. Actuators A* 33, 249 (1992).

360. J. M. Bustillo, G. K. Fedder, C. T.-C. Nguyen, and R. T. Howe, *Microsyst. Technol.* 1, 30 (1994).

361. R. T. Howe, B. E. Boser, and A. P. Pisano, *Sens. Actuators A* 56, 167 (1996).

362. T. A. Core, W. K. Tsang, and S. J. Sherman, *Solid State Technol.* 36, 39 (1993).

363. R. A. Wood, C. J. Han, and P. W. Kruse, Integrated uncooled infrared detector arrays, in "Proceedings IEEE Solid-State Sensor and Actuator Workshop," 1992, pp. 132–135.

364. B. E. Cole C.-J. Han, R. E. Hlgashl, J. Rldley, J. Holmen, J. Anderson, D. Nielsen, H. Marsh, K. Newstrom, C. Zins, P. Wilson, and K. Beaudoin, 512 × 512 infrared scene projector array for low-background simulations, in "Proceedings Solid-State Sensor and Actuator Workshop," 1994, pp. 7–12.

365. L. Hombeck, Current status of the digital micromirror device (DMD) for projection television applications, in "Proceedings IEEE Int. Electron Devices Meeting," 1993, pp. 381–384.

366. R. T. Howe, Polysilicon integrated microsystems: Technology and applications, in "Proceedings 8th Int. Cont. Solid-State Sens. Actuators, Transducers '95," 1995, pp. 43–46.

367. W. C. Tang, T.-C. H. Nguyen, and R. T. Howe, *Sens. Actuators* 20, 25 (1989).

368. W. C. Tang, Electrostatic Comb Drive for Resonant Sensor and Actuator Applications, Ph.D. Dissertation (Thesis), Univ. of California, 1990.

369. J. J. Sniegowski, MEMS: A new approach to micro-optics, in "MOEMS'97," 1997, pp. 209–214.

370. J. J. Sniegowski and M. S. Rodgers, Multi-layer enhancement to polysilicon surface-micromachining technology, in "IEEE IEDM," 1997, pp. 903–906.

371. L. SpangIer and C. J. Kemp, *Proc. SPIE* 2722, 135 (1996).

372. J. H. Smith, S. Montague, J. J. Sniegowski, J. R. Murray et al., Embedded micromechanical devices for the monolithic integration of MEMS with CMOS, "Proceedings IEDM," 1995, pp. 609–612.

373. R. D. Nasby, J. J. Sniegowski, J. H. Smith, S. Montague, C. C. Barron, W. P. Eaton, P. J. McWhorter, D. L. Hetherington, C. A. Apblett, and J. G. Fleming, Application of chemical-mechanical polishing to planarization of surface-micromachined devices, in "Proceedings IEEE Solid-State Sensor and Actuator Workshop," pp. 48–50.

374. J. H. Smith, S. Montague, and J. J. Sniegowski, *Proc. SPIE* 2639, 64 (1995).

375. R. T. Howe and R. S. Muller, Integrated resonant-microbridge vapor sensor, in "Proceedings IEEE IEDM," 1984, pp. 213–216.

376. R. T. Howe, PolycrystalIine silicon microstructure, in "Micromachining and Micropackaging of Transducers" (C. D. Fung et al., Eds.), pp. 169–187. Elsevier, Amsterdam, 1985.

377. M. A. Lemkin, M. A. Ortiz, N. Wongkomet, and B. E. Boser, A 3-axis surface micromachined Sigma Delta accelerometer, in "IEEE Int. Solid-State Circuits Conf.," Dig. Tech. Papers, 1997, Vol. 40, pp. 202–203.

378. C. Hierold, A. Hildebrandt, U. Naher, T. Scheiter et al., A pure CMOS surface micromachined integrated accelerometer, in "Proceedings 9th IEEE MEMS Workshop," 1996, pp. 174–179.

379. K. H.-L. Chau, S. R. Lewis, Y. Zhao, R. T. Howe et al., An integrated forced-balanced capacitive accelerometer for low-*g* applications, in "Proceedings 8th Int. Conf. Solid-State Sens. Actuators, Transducers '95," 1995, pp. 593–596.

380. P. Lange, M. Kirsten, W. RiethmulIer, B. Wenk et al., Thick polycrystaline silicon for surface micromechanical applications: Deposition, structuring and mechanical characterization, in "Proceedings 8th Int. Conf. Solid-State Sens. Actuators, Transducers '95," 1995, pp. 202–205.

381. M. Lutz, W. Golderer, J. Gerstenmeier, J. Marek, B. Mainhofer, S. Mahler, H. Munzel, and U. Bischof, A precision yaw rate sensor in silicon micromachining, in "Proceedings 9th Int. Conf. Solid-State Sens. Actuators, Transducers'97," 1995, pp. 847–850.

382. M. Offenberg, F. Lamer, B. Elsner, H. Munzel et al., Novel process for a monolithic integrated accelerometer, "Proceedings 8th Int. Conf. Solid-State Sens. Actuators, Transducers'95," 1995, pp. 589–592.

383. H. Guckel, J. J. Sniegowski, T. R. Christenson, and F. Raissi, *Sens. Actuators A* 21–23, 346 (1990).

384. H. Guckel, C. Rypstat, M. Nesnidal, J. D. Zook, D. W. Burns, and D. K. Arch, Polysilicon resonant microbeam technology for high performance sensor applications, in "Proceedings IEEE Solid-State Sensor and Actuator Workshop," 1992, pp. 153–156.

385. U. Srinivasan, M. R. Houston, R. T. Howe, and R. Maboudian, Self-assembled fluorocarbon films for enhanced stiction reduction, in "Proceedings 9th Int. Conf. Solid-State Sens. Actuator Transducers '97," 1997, pp. 1399–1402.

386. C. Lu, M. Lemkin, and B. E. Boser, A monolithic surface micromachined accelerometer with digital output, in "Proceedings IEEE Int. Solid-State Circuits Conf.," 1995, pp. 160–161.

387. T. Juneau, Micromachined Dual Input Axis Rate Gyroscope, Ph.D. Dissertation, Univ. of California, 1997.

388. D. W. Burns, J. D. Zook, R. D. Homing, and W. R. Herb, A digital pressure sensor based on resonant microbeams, in "Proceedings Solid-State Sensor and Actuator Workshop," 1994, pp. 221–224.

389. G. K. Fedder, J. C. Chang, and R. T. Howe, Thermal assembly of polysilicon microactuators with narrow-gap electrostatic comb drive, in "Proceedings IEEE Solid-State Sensor and Actuator Workshop," 1992, pp. 63–68.

390. G. K. Fedder, Simulation of Microelectromechanical Systems, Ph.D. dissertation, Univ. of California, 1994.

391. K. Tanaka, Y. Mochida, S. Sugimoto, K. Moriya, T. Hasegawa, K. Atsuchi, and K. Ohwada, A micromachined vibrating gyroscope, in "Proceedings IEEE Micro Electro Mechanical Systems Workshop," 1995, pp. 278–281.

392. M. W. Putty and K. Najafi, A micromachining vibrating ring gyroscope, in "Proceedings Solid-State Sensor and Actuator Workshop," 1994, pp. 213–220.

393. K. B. Lee and Y.-H. Cho, A triangular frequency-tuning comb array, in "Proceedings ASME Int. Mechanical Engineering Congress and Exposition," 1997, Vol. DSC-62/HTD-354, pp. 127–131.

394. S. J. Sherman, W. K. Tsang, T. A. Core, and D. E. Quinn, A low cost monolithic accelerometer, in "Proceedings IEEE Symp. VLSI Technology," Seattle, WA, pp. 34–35.

395. L. Ristic, R. Gutteridge, B. Dunn, D. Mietus, and P. Bennett, Surface micromachined polysilicon accelerometer, in "Proceedings IEEE Solid-State Sensor and Actuator Workshop," 1992, pp. 118–122.

396. D. J. Monk, D. S. Soane, and R. T. Howe, *Thin Solid Films* 232, 1 (1993).

397. D. J. Monk, D. S. Soane, and R. T. Howe, *J. Electrochem. Soc*. 141, 264 (1994).

398. T. moue and H. Osatake, *Arch. Bistol. Cytol.* 51, 53.

399. N. Takeshima, K. J. Gabriel, M. Ozaki, J. Takahashi, H. Horiguchi, and H. Fujita, Electrostatic parallelogram actuators, in "Proceedings 6th Int. Conf. Solid-State Sens. Actuators, Transducers '91," 1991, pp. 63–66.

400. H. Guckel, J. J. Sniegowski, T. R. Christenson, S. Mohney, and T. F. Kelley, *Sens. Actuators* 20, 117 (1989).

401. G. T. Mulhem, D. S. Soane, and R. T. Howe, Supercritical carbon dioxide drying of microstructures, in "Proceedings 7th Int. Conf. Solid-State Sens. Actuators, Transducers '93," 1993, pp. 296–299.

402. T. Abe, w. C. Messner, and M. L. Reed, Effective methods to prevent stiction during post-release-etch processing, in "Proceedings IEEE Micro Electro Mechanical Systems Workshop," 1995, pp. 94–99.

403. K. Deng, R. J. Collins, M. Mehregany, and C. N. Sukkenik, Performance impact of monolayer coating of polysilicon micromotors, in "Proceedings IEEE Micro Electro Mechanical Systems Workshop," 1995, pp. 368–373.

404. L. Lin, K. M. McNair, R. T. Howe, and A. P. Pisano, Vacuum-encapsulated lateral microresonators, in "7th Int. Conf. Solid-State Sens. Actuators, Transducers '93," 1993, pp. 270–273.

405. T. Yoshida, T. Kudo, S. Kato, S. Miyazaki, S. Kiyono, and K. Ikeda, Strain sensitive resonant gate transistor, in "Proceedings IEEE Micro Electro Mechanical Systems Workshop," 1995, pp. 316–321.

406. M. W. Judy and R. T. Howe, Polysilicon hollow beam lateral resonators, in "Proceedings IEEE Micro Electro Mechanical Systems Workshop," 1993, pp. 265–271.

407. D. J. Monk, P. Krulevitch, R. T. Howe, and G. C. Johnson, *Mater. Res. Soc. Symp. Proc.* 308, 641.

408. R. Maboudian and R. T. Howe, *Tribol. Lett*. 3, 215 (1997).

409. *Vac. Sci. Technol. B* 15, 1 (1997).

410. R. L. Alley, R. T. Howe, and K. Komvopoulos, The effect of release-etch processing on surface microstructure stiction, in "Proceedings IEEE Solid-State Sensor and Actuator Workshop," 1992, pp. 202–207.

411. R. L. Alley, P. Mai, K. Komvopoulos, and R. T. Howe, Surface roughness modification of interfacial contacts in polysilicon microstructures, in "Proceedings 7th Int. Conf. Solid-State Sens. Actuators, Transducers'93," 1993, pp. 288–291.

412. M. R. Houston, R. Maboudian, and R. T. Howe, Ammonium fluoride surface treatments for reducing in-use stiction in polysilicon microstructures, in "Proceedings 8th Int. Conf. Solid-State Sens. Actuators, Transducers '95," 1995, pp. 210–213.

413. Y. Yee, K. Chun, and J. D. Lee, Polysilicon surface modification technique to reduce sticking of micro-structures, in "Proceedings 8th Int. Conf. Solid-State Sens. Actuators, Transducers '95," 1995, pp. 206–209.

414. F. Kozlowski, N. Lindmair, T. Scheiter, C. Hierold, and W. Lang, A novel metbod to avoid sticking of surface micromachined structures, in "Proceedings 8th Int. Conf. Solid-State Sens. Actuators, Transducers '95," 1995, pp. 220–223.

415. M. R. Houston, R. Maboudian, and R. T. Howe, Self-assembled monolayer films as durable anti-stiction coatings for polysilicon microstructures, in "Proceedings IEEE Solid-State Sensor and Actuator Workshop," 1996, pp. 42–47.

416. Diamond-like carbon for silicon passivation in micromechanical devices, in "Materials Research Society Spring Meeting," 1995.

417. J. H. Lee, Y. I. Lee, W. I. Jang, C. S. Lee, and H. J. Yoo, Gas-phase etching of sacrificial oxides using an hydrous HF and CH30H, in "Proceedings 10th IEEE Micro Electro Mechanical Systems Workshop," 1997, pp. 448–452.

418. S. A. Henck, *Tribol. Lett*. 3, 239 (1997).

419. S. Tatic-Lucic, P. Jaramillo, J. Bustillo, S. Cunningham, and L. Starr, Application of the statistical analysis on the evaluation of anti-stiction methods for micromechanical devices, in "Proceedings 11th Eur. Conf. Solid State Transducers, Eurosensors Xl," 1997, pp. 297–300.

420. J. Y. Kim and C.-J. Kim, Comparative study of various release methods for polysilicon surface micromachining, in "Proceedings IEEE Micro Electro Mechanical Systems Workshop," 1997, pp. 442–447.

421. C.-J. Kim, J. Y. Kim, and B. Sridharan, *Sens. Actuators A* 64, 17 (1998).

422. M. Houston, Surface Treatments for Adhesion Reduction in Polysilicon Micromechanical Devices, Ph.D. dissertation, Univ. of California, 1996.

423. K. S. J. Pister, M. W. Judy, S. R. Burgett, and R. S. Fearing, Microfabricated hinges: 1 mm vertical features with surface micromachining, in "Proceedings 6th Int. Conf. Solid-State Sens. Actuators, Transducers'91," 1991, pp. 647–650.

424. K. Suzuki, I. Shimoyama, H. Miura, and Y. Ezura, Creation of an insect-based microrobot with an external skeleton and elastic joints, in "Proceedings IEEE Micro Electro Mechanical Systems Workshop," 1992, pp. 190–195.

425. L. Y. Lin, S. S. Lee, M. C. Wu, and K. S. J. Pister, Micromachined integrated optics for free space interconnection, in "Proceedings IEEE Micro Electro Mechanical Systems Workshop," 1995, pp. 77–82.

426. M. J. Danernan, N. C. Tien, O. Solgaard, A. P. Plsano, K. Y. Lau, and R. S. Muller, Linear microvibromotor for positioning of optical components, in "Proceedings IEEE Micro Electro Mechanical Systems Workshop," 1995, pp. 55–60.

427. C. G. Keller and R. T. Howe, Hexsil tweezers for teleoperated micro-assembly, in "Proceedings IEEE Micro Electro Mechanical Systems Workshop," 1997, pp. 72–77.

428. L. J. Hornbeck, Deformable-mirror spatiallight modulators, in "Spatial Light Modulators and Applications lII, SPIE Critical Reviews," 1989, Vol. 1150, pp. 86–102.

429. L. A. Yoder, The state of the art in projection display, in Digital Light Processing, Texas lnstruments-DLP product literature, 1996.

430. D. Young and B. Boser, A micromachined variable capacitor for monolithic low-noise VCO's, in "Proceedings IEEE Solid-State Sensor and Actuator Workshop," 1996, pp. 86–89.

431. L.-Y. Chen, E. P. Santos, and N. C. MacDonald, An isolation technology for joined MEMS, in "Proceedings IEEE Micro Electro Mechanical Systems Workshop," 1993, pp. 189–194.

432. N. C. MacDonald, S. G. Adams, A. A. Ayon, K. F. Bohringer et al., Micromachined microdevices and microinstrurnents, *Microelectron. Eng.* 30, 563 (1996).

433. C. H. Ahn, M. G. Allen, W. Trimrner, Y.-N. Jun et al., A fully integrated micromachined magnetic particle separator, *J. Microelectromech. Syst.* 5, 151 (1996).

434. C. Storment, D. A. Borkholder, V. Westerlind, J. W. Suh et al. Flexible, dry-released process for aluminum electrostaticactuators, *J. Microelectromech. Syst.* 3, 90 (1994).

435. C. H. Mastrangelo and G. S. Saloka, A dry-release method based on polymer columns for micro-structure fabrication, in "Proceedings IEEE Micro Electro Mechanical Systems Workshop," 1993, pp. 77–81.

436. P. F. Man, B. P. Gogoi, and C. H. Mastrangelo, *J. Microelectromech. Syst.* 6, 25 (1997).

437. O. Solgaard, F. S. A. Sandejas, and D. M. Bloom, *Opt. Lett*. 17, 688 (1992).

438. M. Seikemoto, H. Yoshihara, and T. Ohkubo, *J. Vac. Sci. Technol*. 21, 1017 (1982).

439. G. K. Fedder, S. Santhanam, M. L. Reed, S. C. Eagle et al., *Sens. Actuators A*, 57, 103 (1996).

440. B. Wameke, E. Hoffrnan, and K. S. J. Pister, *Proc. SPIE* 2642, 95 (1995).

441. O. Paul, D. Westberg, M. Homung, V. Ziebart, and H. Baltes, Sacrificial aluminum etching for CMOS microstructures, in "Proceedings IEEE Micro Electro Mechanical Systems Workshop," 1997, pp. 523–528.

442. L. J. Hombeck et al., Digital micromirror device-commercialization of a massively parallel MEMS technology, in "Proceedings ASME Int. Mechanical Engineering Congress and Exposition," 1997, Vol. DSC-62/HTD-354, pp. 3–8.

443. K. Ikeda et al., Silicon pressure sensor with resonant strain gages built into diaphragm, in "7th Sensor Symp." 1988, pp. 55–58.

444. H. Guckel, J. J. Sniegowski, T. R. Christenson, and R. Raissi, *Sens. Actuators A* 21–23, 346 (1990).

445. C. G. Keller and R. T. Howe, Hexsil bimorphs for vertical actuation, in "Proceedings 8th Int. Conf. Solid-State Sens. Actuators, Transducers '95," 1995, pp. 99–102.

446. M. B. Cohn, C.-J. Kim, and A. P. Pisano, Self-assembling electrical networks: An application of micromachining technology, in "Proceedings 6th Int. Conf. Solid-State Sens. Actuators, Transducers '91," 1991, pp. 490–493.

447. H.-J. J. Yeh and J. S. Smith, Fluidic self-assembly of microstructures and its application to the integration of GaAs on Si, in "Proceedings IEEE Micro Electro Mechanical Systems Workshop," 1994, pp. 279–284.

448. A. K. Verma, M. A. Hadley, and J. S. Smith, Fluidic self-assembly of silicon microstructures, in "Proceedings 45th Electronic Components and Technology Conf.," 1995.

449. A. Terfort, N. Bowden, and G. M. Whitesides, *Nature* 386, 162 (1997).

450. C. H. Ahn, Y. J. Kim, and M. G. Allen, A planar variable reluctance magnetic micromotor with fully integrated stator and wrapped coils, in "Proceedings IEEE Micro Electro Mechanical I Systems Workshop," 1993, pp. 1–6.

### Mould Micromachining

451. E. W. Becker, W. Ehrfeld et al., Herstellung von Mikrostrukturen mit großem Aspektverhältnis und großer Strukturhöhe durch Röntgentiefenlithografie mit Synchrotronstrahlung, Galvanoformung und Kunststoffabformung (LIGA-Verfahren), Kernforschungszentrum Karlsruhe, KfK-bericht 3995, 1985.

452. W. Ehrfeld, P. Bley, F. Götz, P Hagmann, A. Maner, J. Mohr, H. O. Moser, D. Münchmeyer, W. Schelb, D. Schmodt, and E. W. Becker, Fabrication of Microstructures Using the LIGA Process. IEEE Press, New York, 1987.

453. H. Guckel, T. Christenson, and K. Skrobis, *J. Micromech. Microeng.* 2, 225 (1992).

454. A. Rogner, J. Eicher, D. Münchmeyer, R. P. Peters, and J. Mohr, *J. Micromech. Microeng.* 2, 133 (1992).

455. J. Mohr, P. Bley, M. Strohrmann, and U. Wallrabe, *J. of Micromec. Microeng.* 2, 234 (1992).

456. B. Löchel, A. Maciossek, M. König, H. J. Quenzer, and B. Wagner, Electroplated electromagnetic components for actuators, in "Proceedings 4th Int. Conf. and Exhibition on Micro Electro, Opto, Mechanical Systems and Components (Actuator '94)," 1994, pp. 109–113.

457. A. B. Frazier and M. G. Allen, High aspect ratio electroplated microstructures using a photosensitive polyimide process, in "Proceedings IEEE Micro Electro Mechanical Systems," 1992, pp. 87–92.

458. A. B. Frazier and M. G. Allen, *J. Microelectromec. Syst.* 2, 87 (1993).

459. H. Lorentz, L. Paratte, R. Luthier, N. F. de Rooij, and P. Renaud, Low-cost technology for multilayer electroplated parts using laminated dry film resist, in "Proceedings 8th Int. Conf. on Solid-State Sens. Actuators (Transducers '95)," 1995, Vol. 1, pp. 569–572.

460. S. C. Chang, M. W. Putty, and D. B. Hicks, The formation of electroplating molds by reactive ion etching, "Proceedings 8th Int. Conf. Solid-State Sens. Actuators (Transducers '95)," 1995, Vol. 1, pp. 577–580.

461. S. Roy and M. Mehregany, Fabrication of electrostatic nickel microrelays by nickel surface micromachining, in "Proceedings IEEE Micro Electro Mechanical Systems," 1995, pp. 353–357.

462. J. Elders, H. V. Jansen, M. C. Elwenspoek, and W. Ehrfeld, DEEMO: A new technology for the fabrication of microstructures, in "Proceedings IEEE Micro Electro Mechanical Systems," 1995, pp. 238–243.

463. C. G. Keller and R. T. Howe, Nickel-filled HexSil thermally actuated tweezer, in "Proceedings 8th Int. Conf. Solid-State Sens. Actuators, Transducers '95," 1995, pp. 376–379.

464. Q. Shi, S.-C. Chang, M. W. Putty, and D. B. Hicks, Characterization of electroformed nickel microstructures, *Proc. SPIE* 2639, 191 (1995).

## Bond Micromachining

### General

465. Lord Rayleigh, *Proc. Phys. Soc. A* 156, 326 (1936).

466. W. P. Maszara, Semiconductor wafer bonding: An overview, in "Proceedings 1st Int. Symp. Semiconductor Wafer Bonding," 1992, p. 3.

467. S. Bengtsson, *J. Electron. Mater.* 21, 669 (1992).

468. Q.-Y. Tong and U. Gosele, *Mater. Chem. Phys.* 37, 101 (1994).

469. U. Gosele, H. StenzeI, M. Reiche, T. Martini, H. Steinkirchner, and Q.-Y. Tong, *Solid State Phenom.* 47/48, 33 (1996).

470. R. Stengl, T. Tan, and U. Gösele, *Jpn. J. Appl. Phys.* 28, 1735 (1989).

471. Z. H. Zhu, F. E. Ejeckam, Y. Qian, J. Zhang, Z. Zhang, G. L. Christenson, and Y. H. Lo, *IEEE Sel. Top. Quantum Electron.* 3, 927 (1997).

472. W. H. Ko, J. T. Suminto, and G. J. Yeh, Bonding techniques for microsensors, in "Micromachining and Micropackaging of Transducers," pp. 41–62. Elsevier, Amsterdam, 1985.

473. S. Schulze, Silicon bonding in microsystem technology, in "Proceedings NEXUS Workshop IMSAS," 1996.

474. M. A. Schmidt, *Proc. IEEE* 86, 1575 (1998).

475. F. S. d'Aragona and L. Ristic, "Sensor Technology and Devices" (L. Ristic, Ed.), p. 157. Artech House, Boston, 1994.

476. A. Hanneborg, Silicon wafer bonding techniques for assembly of micromechanical elements, in "Proceedings of IEEE Workshop on MEMS," 1991, pp. 92–98.

477. Y. Gianchandani and K. Najafi, Micron-sized, high aspect ratio bulk silicon micromechanical devices, in "Proceedings IEEE Micro Electro Mechanical Systems," 1992, pp. 208–213.

478. W. H. Juan and S. W. Pang, A novel etch-diffusion process for fabricating high aspect ratio Si microstructures, in "Proceedings 8th Int. Conf. Solid-State Sens. Actuators, Transducers '95," 1995, Vol. 1, pp. 560–563.

479. U. Gösele, J. Haisma, M. Schmidt, and T. Abe (Eds.), "Proceedings of the 1st International Symposium on Semiconductor Wafer Bonding: Science, Technology and Applications," Vol. 92-7. The Electrochemical Society, Pennigton, NJ, 1992.

480. H. Baumgart, C. Hunt, M. Schmidt, and T. Abe (Eds.), "Proceedings of the 2nd International Symposium on Semiconductor Wafer Bonding: Science, Technology and Applications," Vol. 93-29. The Electrochemical Society, 1993.

481. H. Baumgart, C. Hunt, S. Iyer, U. Gosele, and T. Abe (Eds.), "Proceedings of the 3rd International Symposium on Semiconductor Wafer Bonding: Science, Technology and Applications," Vol. 95-7. The Electrochemical Society, Pennington, NJ, 1995.

482. U. Gösele, H. Baumgart, T. Abe, C. Hunt, and S. Iyer (Eds.), "Proceedings of the 4th International Symposium on Semiconductor Wafer Bonding: Science, Technology and Applications," Vol. 97-36. The Electrochemical Society, Pennington, NJ, 1998.

483. B. Muller and A. Stoffel, *J. Micromech. Microeng.* 1, 161 (1991).

484. H. J. Quenzer and W. Benecke, *Sensors Actuators A* 32, 340 (1992).

485. K. Ljunberg, Ph.D. Dissertation (Thesis), University of Uppsala, 1995.

486. Y. Bäcklund, K. Hermannsson, and L. Smith, *J. Electrochem. Soc.* 139, 2299 (1992).

487. G. Kissinger and W. Kissinger, *Sensors Actuators A* 36, 149 (1993).

488. W. P. Maszara, B.-L. Liang, A. Yamada, G. A. Rozgonyi, H. Baumgart, and A. J. R. de Kock, *J. Appl. Phys.* 69, 257 (1991).

489. H. Dannenberg, *J. Appl. Polymer Sci.* 5, 125 (1961).

490. H. S. Jeong and R. C. White, *J. Vac. Sci. Technol. A* 11, 1373 (1993).

491. C. Gui, M. Elwenspoek, N. R. Tas, and J. G. E. Gardeniers, The surface adhesion parameter: a measure for wafer bondability, in "Proceedings IEEE MEMS Workshop," 1999, pp. 290–295.

492. K. N. Q. Fuller and D. Tabor, *Proc. Roy. Soc. London A* 345, 327 (1975).

493. M. B. Cohn, Y. Liang, R. T. Howe, and A. P. Pisano, Wafer-to-wafer transfer of microstructures for vacuum packaging, "Proceedings IEEE Solid-State Sensor and Actuator Workshop," 1996, pp. 32–35.

494. M. Esashi, *Microsyst. Technol.* 1, 2 (1994).

495. R. L. Smith and S. D. Collins, Micromachined packaging for chemical microsensors, *J. Trans. Elec. Dev.* 35, 787 (1988).

496. T. Corman, Vacuum-Sealed and Gas-Filled Micromachined Devices, Ph.D. Dissertation (Thesis), Royal Inst. of Technol. (KTH), Stockholm, Sweden, 1999.

497. S. A. Audet and K. M. Edenfeld, Integrated sensor wafer-level packaging, in "Proceedings Transducers," 1997, pp. 287–289.

498. J. Kim, M. Chiao, and L. Lin, Ultrasonic bonding of In/Au and AI/Al for hermetic sealing of MEMS packaging, in "Proceedings MEMS," 2002, pp. 415–418.

499. R. K. Traeger, Hermeticity of polymeric lid sealant, in "Proceedings Electronic Components Conference," 1976, pp. 361–367.

500. B. Rogers, M. J. Berry, I. Turlik, P. Garrou, and D. Castillo, *Proc. SPIE* 2105, 187 (1993).

501. B. P. Chinoy, *Trans. Components Packaging Manuf. Technol. C* 20, 199 (1997).

502. A. J. G. Strandjord et al., Photosensitive benzocyclobutene for stress-buffer and passivation applications, in "Proceedings

IEEE Electronic Components and Technology Conference," 1997, pp. 1260–1268.

503. C. Reyerse, S. Kanev, and E. Meusel, Technical challenges of precision wafer bonding in controlled environments, in "Proceedings Symposium on Semiconductor Wafer Bonding: Physics and Applications," 1995, pp. 174–183.

504. A. R. Mirza, Wafer-level packaging technology for MEMS, in "Proceedings Thermal and Thermomechanical Phenomena in Electronic Systems," 2000, pp. 113–119.

505. A. R. Mirza, One micron precision, wafer-level aligned bonding for interconnect, MEMS and packaging applications, in "Proceedings IEEE Electronic Components and Technology Conference," 2000, pp. 676–680.

506. K. Winchester, S. M. R. Spaargaren, and J. M. Dell, *Proc. SPIE* 3892, 142 (1999).

507. V. Milanovic, M. Maharbiz, A. Singh, B. Wameke, N. Zhou, H. K. Chan, and K. S. J. Pister, Microrelays for batch transfer integration in RF systems, in "Proceedings MEMS," 2000, pp. 787–792.

508. E.-H. Yang and D. V. Wiberg, A new wafer-level membrane transfer technique for MEMS deformable mirrors, in "Proceedings MEMS," 2001, pp. 80–83.

509. R. Aigner, K.-G. Oppermann, H. Kapels, and S. Kolb, Cavity-inicromachining technology: Zero-package solution for inertial sensors, in "Proceedings Transducers," 2001, Vol. 1, pp. 186–189.

510. M. Bartek, J. A. Foerster, and R. F. Wolffenbuttel, *Sens. Actuators A* 61, 364 (1997).

511. B. E. Cole, R. E. Higashi, J. A. Ridley, and R. A. Wood, *Proc. SPIE* 4369, 235 (2001).

512. M. Kada and L. Smith, Advancements in stacked chip scale packaging (S-CSP), provides system-in-a-package functionality for wireless and handheld applications, in "Proceedings Pan Pacific Microelectronics Symposium," 2000, pp. 246–251.

513. M. A. Michalicek and V. M. Bright, Flip-chip fabrication of advanced microinirror arrays, in "Proceedings MEMS," 2001, pp. 313–316.

514. T. S. McLaren and Y.-C. Lee, Modeling and evaluation criterion for thermocompression flip-chip bonding, in *J. IEEE Transactions Adv. Packaging* 23, 652 (2000).

515. K. W. Oh and C. H. Ahn, Development of an innovative flip-chip bonding technique using micromachined conductive polymer bumps, in "Proceedings Solid-State Sensor and Actuator Workshop," 1998, pp. 170–173.

516. K. F. Harsh, W. Zhang, V. M. Bright, and Y. C. Lee, Flip-chip assembly for Si-base RF MEMS, in "Proceedings MEMS," 1999, pp. 273–278.

## Direct

517. J. Haisma, G. A. C. M. Spierings, U. K. P. Biermann, and A. A. van Gorkum, *Appl. Opt.* 33, 1154 (1994).

518. Y. Bäcklund, K. Ljungberg, and A. Söderbärg, *J. Micromech. Microeng.* 2, 158 (1992).

519. L. G. Sun, J. Zhan, Q. Y. Tong, S. J. Xie, Y. M. Caim, and S. J. Lu, *J. Phys. Colloq. C* 49, 79 (1988).

520. M. Shimbo, *J. Inst. Electron Inf. Commun. Eng.* 70, 593 (1987).

521. M. Shimbo, K. Furukawa, K. Fukuda, and K. Tanzawa, *J. Appl. Phys.* 60, 2987 (1986).

522. C. Harendt, B. Höfflinger, H.-G. Graf, and E. Penteker, *Sens. Actuators A* 25–27, 87 (1991).

523. S. Bengtson and O. Engström, *J. Appl. Phys.* 66, 1231 (1989).

524. S. Sanchez, C. Gui, and M. Elwenspoek, *J. Micromech. Microeng.* 7, 111 (1997).

525. Special issue on direct Bonding, *Philips J. Res.* 49, 1 (1995).

526. K. Kwon and S. Park, *S&A A* 66, 250 (1998).

527. J. Bagdahn, M. Petzold, M. Reiche, and K. Gutjahr, *Electrochem. Soc. Proc.* 97-36, 291 (1998).

528. C. Gui, M. Elwenspoek, N. R. Tas, and J. G. E. Gardeniers, *J. Appl. Phys.* 85, 7448 (1999).

529. C.-Q. Gui, Direct Wafer Bonding with Chemical Mechanical Polishing: Applications in Sens. Actuators, Ph.D. Dissertation (Thesis), University of Twente, Enschede, The Netherlands, 1998.

## Plasma

530. A. Weinert, P. Amirfeiz, and S. Bengtsson, *Sens. Actuators A* 92, 214 (2000).

531. P. Amirfeiz, S. Bengtsson, M. Bergh, E. Zanghelline, and L. Borjesson, *J. Electrochem. Soc.* 147, 2693 (2000).

532. M. Bring, A. Sanz-Velasco, H. Rodjegard, and P. Enoksson, *J. Micromech. Microeng.* 13, S51 (2003).

## Fusion

533. C. Harendt, H. G. Graf, B. Hofflinger, and E. Penteker, *J. Micromech. Microeng.* 2, 113 (1992).

534. Z. X. Xiao, G. Y. Wu, Z. H. Li, G. B. Zhang, Y. L. Hao, and Y. Y. Wang, *Sens. Actuators A* 72, 46 (1999).

535. B. P. van Drieenhuizen, N. I. Maluf, I. E. Opris, and G. T. A. Kovacs, Force-balanced accelerometer with mG resolution, fabricated using silicon fusion bonding and deep reactive ion etching, in "Proceedings 9th Int. Conf. Solid-State Sens. Actuators, Transducers '97," 1997, pp. 1229–1230.

536. P. W. Barth, *Sens. Actuators A* 23, 919 (1990).

537. E. H. Klaassen, K. Petersen, M. Noworolski, J. Logan, N. I. Maluf, J. Brown, C. Storment, W. McCulley, and G. T. A. Kovacs, Silicon fusion bonding and deep reactive ion etching; a new technology for microstructures, in "Proceedings 8th Int. Conf. Solid-State Sens. Actuators, Transducers '95," 1995, Vol. 1, pp. 556–559.

538. P. W. Barth, *Sens. Actuators A* 23, 919 (1990).

539. K. Petersen, P. W. Barth, J. Poydock, J. Brown, J. Mallon, Jr., and J. Bryzek, Silicon fusion bonding for pressure sensors, in "IEEE Solid State Sensor and Actuator Workshop," 1988, pp. 144–147.

540. L. A. Field and R. S. Muller, *Sens. Actuators A* 23, 935 (1990).

541. Z. L. Liau and D. E. Mull, *Appl. Phys. Lett.* 56, 737 (1990).

542. C. Gni, H. Albers, J. G. E. Gardeniers, M. Elwenspoek, and P. V. Lambeck, *Microsyst. Tech.* 3, 122 (1997).

543. L. A. Field and R. S. Muller, *Sens. Actuators A* 23, 935 (1990).

544. J. M. McNamara and J. S. Raby, Wafer bonding using low temperature melting glass, in "Proceedings IEEE SOSISOI Technology Workshop," 1988, p. 14.

545. A. Weinert, P. Amirfeiz, and S. Bengtsson, *Sens. Actuators A* 92, 214 (2001).

546. A. Sanz-Velasco, The RDGT Integration of Micromechanics and Electronics by Plasma Assisted Wafer Bonding, Ph.D. Dissertation (Thesis), Chalmers University of Technology, Goreborg, Sweden, 2002.

## Anodic

547. G. Wallis and D. I. Pomerantz, *J. Appl. Phys.* 40, 3946 (1969).

548. H. Henmi, S. Shoji, Y. Shoji, K. Yoshimi et al., Vacuum packaging for microsensors by glass-silicon anodic bonding, in "Proceedings 7th Int. Conf. Solid-State Sens. Actuators, Transducers'93," 1993.

549. A. Hanneborg, M. Nese, and P. Ohlckers, Silicon-to-silicon anodic bonding, in "Proceedings 2nd Europ. workshop on micromachining, micromechanics and Microsystems, MME '90," 1990, pp. 100–107.

550. M. Nese and A. Hanneborg, *Sens. Actuators A* 37–38, 61 (1993).

551. A. Hanneborg, M. Nese, H. Jacobsen, and R. Holm, *J. Micromech. Microeng.* 2, 117 (1992).

552. R. Legtenberg, S. Bouwstra, and M. Elwenspoek, *J. Micromech. Microeng.* 1, 157 (1991).

553. T. R. Anthony, *J. Appl. Phys.* 54, 2419 (1983).

554. A. D. Brooks and R. P. Donovan, *J. Electrochem. Soc.* 119, 545 (1972).

555. M. Esashi, A. Nakano, S. Shoji, and H. Hebiguchi, *Sensors Actuators A* 21–23, 931 (1990).

556. J. W. Berenschot, J. G. E. Gardeniers, T. S. J. Lammerink, and M. Elwenspoek, *Sensors Actuators A* 41–42, 338 (1994).

557. E. Obermeier, Anodic wafer bonding, in "Proceedings of the 3rd International Symposium on Semiconductor Wafer Bonding; Science, Technology and Applications," Vol. 95-7, pp. 212–220. The Electrochemical Society, Pennington, NJ, 1995.

558. A. Cozrna and B. Puers, *J. Micromech. Microeng.* 5, 98 (1995).

559. U. Kreissig, S. Grigull, K. Lange, P. Nitzsche, and B. Schmidt, *Nucl. Instrum. Methods B* 674 (1998).

560. M. Harz and W. Brickner, *Eletrochem. Soc. Proc.* 95-8, 315 (1995).

561. F. Pigeon, B. Biasse, and M. Zussy, *Elec. Lett.* 31, 792 (1995).

562. J. A. Plaza, J. Esteve, and E. Lora-Tamayo, Non-destructive *in-situ* test for anodic bonding, in "Proceedings Eurosensors X," 1996, pp. 176–180.

563. J. A. Plaza, J. Esteve, and E. Lora-Tamayo, *Sens. Actuators A* 67, 181 (1998).

564. J. A. Plaza, E. González, J. Esteve, M. M. Visser, D. T. Wang, and A. Hanneborg, *Electrochem. Solid-State Lett.* 3, 392 (2000).

565. S. Johansson, K. Gustafsson, and J.-A. Schweitz, *Sens. Mater.* 3, 143 (1988).

566. S. Johansson, K. Gustafsson, and J.-A. Schweitz, *Sens. Mater.* 4, 209 (1988).

567. D. Y. Sim, T. Kurabayashi, and M. Esashi, *J. Micromech. Microeng.* 6, 266 (1996).

568. S. E. Vargo, A. A. Green, J. Mueller, D. P. Bame, and R. H. Reinicke, *Proc. SPIE*.

569. T. T. Veenstra, J. W. Berenschot, J. G. E. Gardeniers, R. G. P. Sanders, M. Elwenspoek, and A. van den Berg, *J. Electrochem. Soc.* 148, G68 (2001).

*Solder/Eutectic*

570. A. Singh, D. A. Horsley, M. B. Cohn, A. P. Pisano, and R. T. Howe, Batch transfer of microstructures using flip-chip solder bump bonding, in "Proceedings 9th Int. Conf. Solid-State Sens. Actuators, Transducers'97," 1997, pp. 265–268.

571. S. E. Shoaf and A. D. Feinerman, *J. Vac. Sci. Technol. A* 12, 19 (1994).

572. C. den Besten, R. E. G. van Hal, J. Munoz, and P. Bergveld, Polymer bonding of micromachined silicon structures, in "Proceedings IEEE Workshop on MEMS," 1992, p. 104.

573. V. L. Spiering, J. W. Berenschot, M. Elwenspoek, and J. H. J. Fluitman, *J. Microelectromec. Syst.* 4, 151 (1995).

574. V. L. Spiering, Package Stress Reduction for Micromechanical Sensors: Application in a Pressure Sensor, Ph.D. Dissertation (Thesis), University of Twente, The Netherlands, 1994.

575. A. A. Shores, Thermoplastic films for adhesive bonding: Hybrid microcircuit substrates, in "Proceedings Electronic Components Conference," 1989, pp. 891–895.

576. C. den Besten, R. E. G. van Hal, J. Munoz, and P. Bergveld, Polymer bonding of micro-machined silicon structures, in "Proceedings MEMS," 1992, pp. 104–109.

577. W. P. Eaton, S. H. Risbud, and R. L. Smith, *App. Phys. Lett.* 65, 439 (1994).

578. S. K. Malik, R. Srinath, R. A. Pearson, R. Kodnani, J. Dzwilefsky, and A. Call, *Proc. SPIE* 2649, 130 (1995).

579. G. A. C. M. Spierings, J. Haisma, and F. J. H. M. van der Kruis, *Philips J. Res.* 49, 139 (1995).

580. V. L. Spiering, J. W. Berenschot, M. Elwenspoek, and J. H. J. Fluitman, *J. Microelectromech. Syst.* 4, 151 (1995).

581. P. Arquint, P. D. van der Wal, B. H. van der Schoot, and N. F. de Rooij, Flexible polysiloxane interconnection between two substrates for microsystem assembly, in "Proceedings Transducers," 1995, pp. 263–264.

582. E. Booth, C. E. Hunt, W. E. Brown, and R. J. Stover, Low temperature adhesion bonding methods, in "Proceedings Semiconductor Wafer Bonding: Science. Technology and Applications," 1995, Vol. 95-7, pp. 201–211.

583. M. V. Weckwerth, J. A. Simmons, N. E. Harff, M. E. Sherwin, M. A. Blount, W. E. Baca, and H. C. Chui, *Superlattices Microstruct.* 20, 56l (1996).

584. M. O. Horo, J. O. Neil, E. Peeters, and S. Vandebroek, Micro electro mechanical system technology for commercial thermal inkjet document output products, in "Proceedings Eurosensors," 1996, pp. 431–435.

585. A. B. Frazier, Low temperature IC-compatible wafer-to-wafer bonding with embedded micro channels for integrated sensing systems, in "Proceedings Midwest Symposium on Circuits and Systems," 1996, pp. 505–508.

586. S. Matsuo, T. Nakahara, K. Tateno, and T. Kurokawa, *IEEE Photon. Technol. Lett.* 8, 1507 (1996).

587. S. Matsuo, K. Tateno, T. Nakahara, and T. Kurokawa, *Electron. Lett.* 33, 1148 (1997).

588. S. Van der Groen, M. Rosmeulen, P. Jansen, K. Baert, and L. Deferm, CMOS compatible wafer scale adhesive bonding for circuit transfer, in "Proceedings Transducers," 1997, pp. 629–632.

589. S. Van der Groen, M. Rosmeulen, K. Baert, P. Jansen, and L. Deferm, *J. Micromech, Microeng.* 7, 108 (1997).

590. I. B. Kang, M. Manda, A. Hariz, N. D. Samaan, and M. R. Haskard, Polymer bonding technique for silicon micromoulds, in "Proceedings Australian Microelectronics Conference," 1997, pp. 129–133.

591. R. Dekker, P. Baltus, M. Van Deurzen, W. van der Einden, H. Maas, and A. Wagemans, An ultra low-power RF bipolar technology on glass, in "Proceedings International Electron Devices meeting," 1997, pp. 92l–923.

592. E. Booth, C. E. Hunt, W. E. Brown, and R. J. Stover, Backside imaging CCD using bonded and etched back silicon on epoxy, in "Proceedings Semiconductor Wafer Bonding: Science, Technology and Applications," 1998, Vol. 97-36, pp. 584–591.

593. R. Dekker, M. H. W. A. van Deurzen, W. T. A. van der Einden, H. G. R. Maas, and A. G. Wagemans, A low-cost substrate transfer technology for fully integrated transceivers, in "Proceedings Bipolar/BiCMOS Circuits and Technology Meeting," 1998, pp. 132–135.

594. G. Klink and B. Hillerich, *Proc. SPIE* 3514, 50 (1998).

595. S. R. Sakamoto, C. Ozturk, Y. T. Byun, J. Ko, and N. Dagil, *IEEE Photon. Technol. Lett.* 10, 985 (1998).

596. B. Ilic, P. Neuzil, T. Stanczyk, D. Czaplewski, and G. J. Maclay, *Electrochem. Solid-State Lett.* 2, 86 (1999).

597. B. H. Jo and D. J. Beebe, *Proc. SPIE* 3877, 222 (1999).

598. I. K. Glasgow, D. J. Beebe, and V. E. White, *J. Sensors Mat.* 11, 269 (1999).

599. H. Nguyen, P. Patterson, H. Toshiyoshi, and M. C. Wu, A substrate-independent wafer transfer technique for surface-micromachined devices, "Proceedings MEMS," 2000, pp. 628–632.

600. A. Han, K. W. Oh, S. Bhansali, H. T. Henderson, and C. H. Ahn, A low temperature biochemically compatible bonding technique using fluoropolymers for biochemical microfluidic systems, in "Proceedings MEMS," 2000, pp. 414–418.

601. T.-K. A. Chou and K. Najafi, 3D MEMS Fabrication using low-temperature wafer bonding with benzocyclobutene (BCB), in "Proceedings Transducers," 2001, pp. 1570–1573.

602. R. J. Jackman, T. M. Floyd, R. Ghodssi, M. A. Schrnidt, and K. F. Jensen, *J. Micromech. Microeng.* 11, 263 (2001).

603. J. C. Selby, M. A. Shannon, K. Xu, and J. Economy, *J. Micromech. Microeng.* 11, 672 (2001).

604. P. P. Absil, J. V. Hryniewicz, B. E. Little, F. G. Johnson, K. J. Ritter, and P.-T. Ho, *IEEE Photon. Technol. Lett.* 13, 49 (2001).

605. G.-D. J. Su, H. Toshiyoshi, and M. C. Wu, *IEEE Photon. Technol. Lett.* 13, 606 (2001).

606. A. Jourdain, P. de Moor, S. Parnidighantam, and H. A. C. TiImans, Investigations of the hermeticity of BCB-sealed cavities for housing (RF-)MEMS devices, in "Proceedings MEMS," 2002, pp. 677–680.

607. K. W. Oh, A. Han, S. Bhansali, and C. H. Ahn, *J. of Micromech. Microeng*. 12, 187 (2002).

608. C. Jansson, U. Ringh, K. C. Liddiard, and N. Robinson, *Proc. SPIE* 3698, 264 (1999).

609. A. Bayrashev and B. Ziaie, Silicon wafer bonding with an insulator interlayer using RF dielectric heating, in "Proceedings MEMS," 2002, pp. 419–422.

610. Y.-K. Park, H.-W. Park, D.-J. Lee, J.-H. Park, I.-S. Song, C.-W. Kim, C.-M. Song, Y.-H. Lee, C.-J. Kim, and B.-K. Ju, A novel low-loss wafer-level packaging of the RF-MEMS devices, in "Proceedings MEMS," 2002, pp. 681–684.

611. I. T. Matsumoto, M. Satoh, K. Sakuma, H. Kurino, N. Miyakawa, H. Itani, and M. Koyanagi, *Jpn. J. of App. Phys*. 37, 1217 (1998).

### SOI

612. K. Mitani and U. Gosele, *J. Electron. Mater*. 21, 669 (1992).

613. W. P. Maszara, *J. Electrochem. Soc*. 138, 341 (1991).

614. W. P. Maszara, G. Goetz, A. Caviglia, and J. B. McKitterick, *J. Appl. Phys*. 64, 4943 (1988).

615. A. Benitez, J. Esteve, and J. Bausells, Bulk silicon micro electromechanical devices fabricated from commercial BESOI substrates, in "Proceedings IEEE Micro Electro Mechanical Systems," 1995, pp. 404–407.

616. J. B. Lasky, S. R. Stiffler, F. R. White, and J. R. Abernathy, Silicon-on-insulator (SOI) by bonding and etch-back, in "Proceedings of the IEEE International Electronic Device Meeting," 1985, pp. 684–687.

617. J. B. Lasky, *Appl. Phys. Lett*. 48, 78 (1986).

618. K. Izumi, M. Doken, and H. Ariyoshi, *Electron Lett*. 14, 593 (1978).

619. J. Haisma, B. A. C. M. Spierings, U. K. P. Biermann, and J. A. Pals, *Jpn. J. Appl. Phys*. 28, 1426 (1989).

620. M. Bruel, *Electron. Lett*. 31, 1201 (1995).

621. M. Bruel, B. Aspar, and A J. Auberton-Herve, *Jpn. J. Appl. Phys*. 36, 1636 (1997).

622. E. Jalaguier, B. Aspar, S. Pocas, J. F. Michaud, M. Zussy, A. M. Papon, and M. Bruel, *Electron. Lett*. 34, 408 (1998).

623. Q.-Y. Tong, K. Gutjahr, S. Hopfe, U. Gosele, and T. H. Lee, *Appl. Phys. Lett*. 70, 1390 (1997).

624. L. Di Cioccio, Y. Le Tiec, F. Letertre, C. Jaussaud, and M. Bruel, *Electron. Lett*. 32, 1144 (1996).

625. J. W. Matthews and A. E. Blakeslee, *J. Cryst. Growth* 26, 118 (1974).

626. J. Woltersdorf and E. Pippel, *Thin Solid Films* 116, 77 (1984).

627. L. B. Freund and W. D. Nix, *Appl. Phys. Lett*. 69, 173 (1996).

628. D. Teng and Y. H. Lo, *Appl. Phys. Lett*. 62, 43 (1993).

629. F. E. Ejeckam, Y. H. Lo, S. Subramanian, H. Q. Hou, and B. E. Hammon, *Appl. Phys. Lett*. 70, 1685 (1997).

630. F. E. Ejeckam, M. Seaford, Z. H. Zhu, J. Zhang, Y. H. Lo, Q. Hou, and B. E. Hammons, *Appl. Phys. Lett*. 71, 776 (1997).

631. T. Y. Tan and U. Gösele, *Appl. Phys. A* 64, 631 (1997).

## Micromachined Transducers

632. S. Shoji and M. Esashi, Bonding and assembling methods for realising a microTAS, in "Proceedings microTAS," 1995, pp. 165–179.

633. I. F. A. Kish, *Proc. IEEE* 85, 1752 (1997).

634. G. Ocvirk, E. Verpoorte, A. Manz, M. Grasserbauer, and H. M. Widmer, *Anal. Methods Instr*. 2, 74 (1995).

635. S. Hannoe, I. Sugimoto, and T. Katoh, "Proceedings MicroTAS," 1998, pp. 145–148.

636. B. He, F. Regnier, Microfabricated liquid chromatography columns based on colocated monolith support structures, in "Proceedings microTAS", 1998, pp. 451–455.

637. N. J. Mourlas, D. Jaeggi, A. F. Flannery, B. L. Gray, B. P. van Drieënhuizen, C. W. Storment, N. I. Maluf, and G. T. A. Kovacs, *Sens. Actuators A* 77, 57 (1999).

638. O. Leistiko and P. F. Jensen, Integrated bio/chemical microsystems employing optical detection: A cytometer, in "Proceedings MicroTAS," 1998, pp. 291–294.

639. N. H. Bings, C. Wang, C. D. Skinner, C. L. Colyer, P. Thibault, and D. J. Harrison, *Anal. Chem*. 71, 3292 (1999).

640. T. J. Yao, S. Lee, W. Fang, and Y. C. Tai, Micromachined rubber O-ring microfluidic coupiers, in "Proceedings MEMS," 2000, pp. 624–627.

641. A. Puntambekar and C. H. Ahn, Self-aligning microfluidic interconnects with low dead volume, in "Proceedings MicroTAS," 2000, pp. 323–326.

642. E. Chmela, M. T. Blom, J. G. E. Gardeniers, A. van den Berg, and R. Tijssen, *Anal. Chem*. 74, 3470 (2002).

643. R. E. Oosterbroek, T. S. J. Lammerink, J. W. Berenschot, G. J. M. Krijnen, M. C. Elwenspoek, and A. van den Berg, *Sens. Actuators A* 77, 167 (1999).

644. J. E. Gragg, W. E. McCulley, W. B. Newton, and C. E. Denington, Compensation and calibration of a monolithic four terminal silicon pressure tranducer, in "Proceedings of IEEE Solid State Sensor and Actuator Workshop," 1984, pp. 21–27.

645. Y. Bäcklund, L. Rosengren, B. Hök, and B. Svedberg, *Sens. Actuators A* 21–23, 58 (1990).

646. G. J. Veldhuis, C. Gui, T. Nauta, T. M. Koster, J. W. Berenschot, P. V. Lambeck, J. G. E. Gardeniers, and M. Elwenspoek, *Opt. Lett*. 23, 1532 (1998).

647. G. A. Antypas and J. Edgecumbe, *Appl. Phys. Lett.* 26, 371 (1975).

### Piezoelectric Actuators

648. H. T. G. van Lintel, F. C. M. van de Pol, and S. Bouwstra, *Sens. Actuators* 15, 153 (1988).

649. W. P. Robbins, D. L. Polla, T. Tamagawa, D. E. Glumac, and J. W. Judy, Linear motion microactuators using piezoelectric thin films, in "Proceedings Int. Conf. on Solid-State Sens. Actuators," 1991, pp. 55–58.

650. A. M. Flynn, L. S. Tavrow, S. F. Bart, R. A. Brooks, D. J. Ehrlich, K. R. Udayakumar, and L. E. Cross, *J. Microelectromec. Syst*. 1, 44 (1992).

651. D. E. Brei and J. Blechschmidt, *J. Microelectromech. Syst*. 1, 106 (1992).

652. T. Yasuda, I. Shimoyama, and H. Miura, Microrobot actuated by a vibrating energy field, in "Proceedings 7th Int. Conf. Solid-State Sens. Actuators," 1993, pp. 42–45.

653. G. A. Racine, R. Luthier, and N. F. de Rooij, Hybrid ultrasonic micromachined motors, in "Proceedings IEEE Micro Electro Mechanical Systems," 1993, pp. 128–132.

654. H. Toshiyoshi, H. Fujita, T. Kawai, and T. Ueda, Piezoelectrically operated actuators by quartz micromachining for optical application, in "Proceedings IEEE Micro Electro Mechanical Systems," 1993, pp. 133–142.

655. P. Schiller and D. L. Polla, Integrated piezoelectric microactuators based on PZT thin films, in "Proceedings 7th Int. Conf. Solid-State Sens. Actuators," 1993, pp. 154–157.

656. P. Dario, M. C. Carrozza, N. Gracew, and B. Magnani, A piezoelectric micropump realized by stereolithography, in "4th Int. Conf. on New Actuators," 1994, pp. 42–45.

657. H. Toshiyoshi, D. Kobayashi, H. Fujita, and T. Ueda, A piezoelectric pseudo-static actuator for large displacement under ac voltage operation, in "Proceedings 8th Int. Conf. Solid-State Sens. Actuators," 1995, Vol. 1, pp. 389–392.

658. P. Muralt, A. Kholkin, M. Kohli, T. Maeder, K. G. Brooks, R. Luthier, and N. Setter, Fabrication and characterization of PZT films for micromotors, in "Proceedings 8th Int. Conf. Solid-State Sens. Actuators," 1995, Vol. 1, pp. 397–400.

659. M. Sakata, S. Wakabayashi, H. Totani, M. Ikeda, H. Goto, M. Takeuchi, and T. Yada, Basic characteristics of a piezoelectric buckling type of actuator, in "Proceedings 8th Int. Conf. Solid-State Sens. Actuators," 1995, Vol. 1, pp. 422–425.

660. M. Mescher, T. Abe, B. Brunett, H. Metla, E. Schlesinger, and M. L. Reed, Piezoelectric lead zirconate titanate actuator films for microelectromechanical systems applications, in "Proceedings IEEE Micro Electro Mechanical Systems," 1995, pp. 261–266.

661. K. Yanagisawa, A. Tago, T. Ohkubo, and H. Kuwano, Magnetic micro-actuator, in "Proceedings IEEE Micro Electro Mechanical Systems," 1991, pp. 120–124.

### Electrostatic Actuators

662. H. Fujita and A. Omodaka, *IEEE Trans. El. Devices* 35, 731 (1988).

663. W. C. Tang, T. C. H. Nguyen, M. W. Judy, and R. T. Howe, Electrostatic-comb drive of lateral polysilicon resonators, in "Proceedings 5th Int. Conf. Solid-State Sens. Actuators," 1989, pp. 328–331.

664. Y. C. Tai, L. S. Fan, and R. S. Muller, IC-processed micro-motors: design, technology and testing, in "Proceedings IEEE Micro Electro Mechanical Systems," 1989, pp. 1–6.

665. R. Jebens, W. Trimmer, and J. Walker, *Sens. Actuators* 20, 65 (1989).

666. M. Mehregany, S. F. Bart, L. S. Tavrow, J. H. Lang, S. D. Senturia, and M. F. Schlecht, A study of three microfabricated variable-capacitance motors, in "Proceedings 5th Int. Conf. Solid-State Sens. Actuators," 1989, pp. 173–179.

667. L. S. Tavrow, S. F. Bart, J. H. Lang, and M. F. Schlecht, A LOCOS process for an electrostatic microfabricated motor, in "Proceedings 5th Int. Conf. Solid-State Sens. Actuators," 1989, pp. 893–898.

668. R. Mahadevan, K. J. Gabriel, and Mehregany, Application of electric microactuators to silicon micromechanics, in "Proceedings 5th Int. Conf. Solid-State Sens. Actuators," 1989, pp. 219–225.

669. R. A. Brennen, M. G. Lim, A. P. Pisano, and A. T. Chou, Large displacement linear actuator, in "Proceedings IEEE Solid-State Sens. Actuators Workshop," 1990, pp. 135–139.

670. S. Egawa and T. Higuchi, Multi-layered electrostatic film actuator, in "Proceedings IEEE Micro Electro Mechanical Systems," 1990, pp. 166–171.

671. K. S. J. Pister, R. S. Fearing, and R. T. Howe, A planar air levitated electrostatic actuator system, in "Proceedings IEEE Micro Electro Mechanical Systems," 1990, pp. 67–71.

672. W. C. Tang, M. G. Lim, and R. T. Howe, Electrostatically balanced comb drive for controlled levitation, in "Proceedings IEEE Solid-State Sens. Actuators Workshop," 1990, pp. 23–27.

673. R. A. Brennen, A. P. Pisano, and W. C. Tang, Multiple mode micromechanical resonators, in "Proceedings IEEE Micro Electro Mechanical Systems," 1990, pp. 9–14.

674. S. Nakagawa, S. Shoji, and M. Esashi, Micromachined silicon microvalve, in "Proceedings IEEE Micro Electro Mechanical Systems," 1990, pp. 95–98.

675. P. L. Bergstrom, T. Tamagawa, and D. L. Polla, Design and fabrication of micromechanical logic elements, in "Proceedings IEEE Micro Electro Mechanical Systems," 1990, pp. 15–20.

676. M. Mehregany, S. M. Philips, E. T. Hsu, and J. H. Lang, Operation of harmonic side-drive micromotors studied through gear ratio measurements, in "Proceedings 6th Int. Conf. Solid-State Sens. Actuators," 1991, pp. 59–62.

677. L. S. Tavrow, S. F Bart, and J. H. Lang, Operational characteristics of microfabricated electric motors, in "Proceedings 6th Int. Conf. Solid-State Sens. Actuators," 1991, pp. 877–881.

678. N. Takeshima, K. J. Gabriel, M. Ozaki, J. Takahasji, H. Horiguchi, and H. Fujita, Electrostatic parallelogram actuators, in "Proceedings 6th Int. Conf. Solid-State Sens. Actuators," 1991, pp. 63–66.

679. P. Gunther, *Sens. Actuators A* 32, 357 (1992).

680. K. J. Gabriel, O. Tabata, K. Shimaoka, S. Sugiyama, and H. Fujita, Surface-normal electrostatic/pneumatic actuator, in "Proceedings IEEE Micro Electro Mechanical Systems," 1992, pp. 128–132.

681. U. Breng, T. Gessner, C. Kaufmann, R. Kienscherf, and J. Markert, *J. Micromech. Microeng.* 2, 256 (1992).

681. V. P. Jaecklin, C. Linder, N. F. de Rooy, and J. M. Moret, *J. Micromech. Microeng.* 2, 250 (1992).

682. T. Hirano, T. Furuhata, K. J. Gabriel, and H. Fujita, *J. Micromech. Syst.* 1, 52 (1992).

683. K. Sato and M. Shikida, Electrostatic film actuator with large vertical displacement, in "Proceedings IEEE Micro Electro Mech. Syst.," 1992, pp. 1–5.

684. C. J. Kim, A. P. Pisano, and R. S. Muller, *J. Micromech. Syst.* 1, 31 (1992).

685. J. Branebjerg and P. Gravesen, A new electrostatic actuator providing improved stroke length and force, in "Proceedings IEEE Micro Electro Mech. Syst.," 1992, pp. 6–11.

686. A. P. Lee and A. P. Pisano, *J. Micromech. Syst.* 1, 70 (1992).

687. W. C. Tang, M. G. Lim, and R. T. Howe, *J. Micromech. Syst.* 1, 170 (1992).

688. U. Breng, C. Kaufmann, R. Kiehnscherf, J. Markert, and M. Rauch, Electrostatic micromechanic actuators, in "3rd Int. Conf. on New Actuators," 1992, pp. 177–182.

689. V. P. Jaecklin, C. Linder, N. F. de Rooij, J. M. Moret, R. Bischot, and F. Rudolf, Novel polysilicon comb actuators for *xy*-stages, in "Proceedings IEEE Micro Electro Mechanical Systems," 1992, pp. 147–149.

690. N. Tirole, D. Hauden, P. Blind, M. Froelicher, and L. Gaudriot, *J. Micromech. Microeng.* 3, 155 (1993).

691. M. Yamaguchi, S. Kawamura, K. Minami, and M. Esashi, Distributed electrostatic micro actuator, in "Proceedings IEEE Micro Electro Mechanical Systems," 1993, pp. 18–23.

692. V. P. Jaecklin, C. Linder, and N. F. de Rooij, *Sens. Actuators A* 39, 83 (1993).

693. T. Akiyama and K. Shono, *J. Micromech. Syst.* 2, 106 (1993).

694. T. Niino, S. Egawa, and T. Higuchi, High-power and high-efficiency electrostatic actuator, in "Proceedings IEEE Micro Electro Mechanical Sytems," 1993, pp. 236–241.

695. T. Hirano, T. Furuhata, and H. Fujita, Dry released Nickel micromotors and their friction characteristics, in "Proceedings 7th Int. Conf. Solid-State Sens. Actuators," 1993, pp. 80–83.

696. L. Y. Chen, E. J. P. Santos, and N. C. MacDonald, Serial-parallel isolated capacitive microactuators, in "Proceedings 7th Int. Conf. Solid-State Sens. Actuators," 1993, pp. 84–87.

697. G. Fuhr and B. Wagner, Surface-charge induction micromotors with two aluminum rotors isolated by $SiO_2$, in "Proceedings 7th Int. Conf. Solid-State Sens. Actuators," 1993, pp. 88–92.

698. A. P. Lee, A. P. Pisano, and D. J. Nikkel, Polysilicon linear microvibromotors, in "Proceedings 7th Int. Conf. Solid-State Sens. Actuators," 1993, pp. 46–49.

699. T. Matsubara, M. Yamaguchi, K. Minami, and M. Esashi, Stepping electrostatic microactuator, in "Proceedings 7th Int. Conf. Solid-State Sens. Actuators," 1993, pp. 50–53.

700. V. P. Jaecklin, C. Linder, N. F. deRooij, J. M. Moret, and R. Vuilleumier, Optical microshutters and torsional micromirrors for ligth modulator arrays, in "Proceedings IEEE Micro Electro Mechanical Systems," 1993, pp. 124–127.

701. V. P. Jaecklin, C. Linder, J. Brugger, and N. F. deRooij, Mechanical and optical properties of surface micromachined torsional mirrors in silicon, polysilicon and aluminum, in "Proceedings 7th Int. Conf. Solid-State Sens. Actuators," 1993, pp. 958–961.

702. K. Aratani, P. J. French, P. M. Sarro, R. F. Wolffenbuttel, and S. Middelhoek, Surface micromachined tunable interferometer array, in "Proceedings 7th Int. Conf. Solid-State Sens. Actuators," 1993, pp. 678–681.

703. J. B. Sampsell, The digital micromirror device and its application to projection displays, in "Proceedings 7th Int. Conf. Solid-State Sens. Actuators," 1993, pp. 24–27.

704. E. Obermeier, J. Lin, and V. Schlichting, Design and Fabrication of an electrostatically driven micro-shutter, in "Proceedings 7th Int. Conf. Solid-State Sens. Actuators," 1993, pp. 132–137.

705. O. Tabata, R. Asahi, N. Fujitsuka, M. Kimura, and S. Sugiyama, Electrostatic driven optical chopper using SOI, in "Proceedings 7th Int. Conf. Solid-State Sens. Actuators," 1993, pp. 124–127.

706. J. Bernstein, A. T. King, A. Kourepenis, P. Maciel, and M. Weinberg, A micromachined comb-drive tuning fork rate gyroscope, in "Proceedings IEEE Micro Electro Mechanical Systems," 1993, pp. 143–148.

707. J. W. Judy, T. Tamagawa, and D. L. Polla, Surface-machined micromechanical membrane pump, in "Proceedings IEEE Micro Electro Mechanical Systems," 1993, pp. 182–186.

708. S. M. Bobbio, M. D. Kellam, B. W. Dudley, S. Goodwin-Johansson, S. K. Jones, J. D. Jacobson, F. M. Tranjan, and T. D. DuBois, Integrated force arrays, in "Proceedings IEEE Micro Electro Mechanical Systems," 1993, pp. 149–154.

709. J. Schimkat, L. Kiesewetter, H. J. Gevatter, F. Arndt, A. Steckenborn, and H. F. Schlaak, Moving wedge actuator: An electrostatic actuator for use in microrelay, in "Proceedings 4th Int. Conf. Exh. Micro-, Electro-, Opto-, Mechanical. Syst. and Comp.," 1994, pp. 989–996.

710. H. Guckel, T. R. Christenson, T. Earles, K. J. Skrobis, and J. Klein, Processing and design considerations for high force output-large throw electrostatic, linear micro actuators, in "4th Int. Conf. New Actuators," 1994, pp. 105–108.

711. H. Kalb, B. Kowanz, W. Bacher, J. Mohr, and R. Ruprecht, Electrostatically driven linear stepping motor in LIGA technique, in "4th Int. Conf. New Actuators," 1994, pp. 83–85.

712. K. Deng and M. Mehregany, Outer-rotor polysilicon wobble micromotors, in "Proceedings IEEE Micro Electro Mechanical Systems," 1994, pp. 269–272.

713. K. Deng, H. Miyajima, V. H. Dhuler, M. Mehregany, S. W. Smith, F. L. Merit, and S. Furukawa, The development of polysilicon micromotors for optical scanner applications, in "Proceedings IEEE Solid-State Sens. Actuators Workshop," 1994, pp. 234–238.

714. R. B. Apte, F. S. A. Sandejas, W. C. Banyai, and D. M. Bloom, Deformable grating light valves for high resolution displays, in "Proceedings IEEE Solid-State Sens. Actuators Workshop," 1994, pp. 1–6.

715. P. Y. Chen and R. S. Muller, Microchopper-modulated IR microlamp, in "Proceedings IEEE Solid-State Sens. Actuators Workshop," 1994, pp. 239–242.

716. C. W. Stroment, D. A. Borkholder, V. A. Westerlind, J. W. Suh, N. I. Maluf, and G. T. A. Kovacs, Dry-released process for aluminum electrostatic actuators, in "Proceedings Solid-State Sensor and Actuator Workshop," 1994, pp. 95–98.

717. M. Fischer, H. Graaf, and W. von Münch, *Sens. Actuators A* 44, 83 (1994).

718. R. Zengerle, S. Kluge, M. Richter, and A. Richter, A bidirectional silicon micropump, "Proceedings IEEE Micro Electro Mechanical Systems," 1995, pp. 19–24.

719. A. A. Yasseen, S. W. Smith, M. Mehregany, and F. L. Merat, Diffraction grating scanners using polysilicon micromotors, "Proceedings IEEE Micro Electro Mechanical Systems," 1995, pp. 175–180.

720. P. F. Indermuhle, V. P. Jaecklin, J. Brugger, C. Linder, N. F. De Rooij, and M. Binggeli, *Sens. Actuators A* 47, 562 (1995).

721. A. Selvakumar, K. Najafi, W. H. Juan, and S. Pang, Vertical comb array microactuators, in "Proceedings IEEE Micro Electro Mechanical Systems," 1995, pp. 43–47.

722. T. Akiyama and H. Fujita, A quantitative analysis of scratch drive actuator using buckling motion, in "Proceedings IEEE Micro Electro Mechanical Systems," 1995, pp. 310–315.

723. P. Rangsten, L. Smith, L. Rosengren, and B. Hök, Electrostatically excited diaphragm driven as a loudspeaker, in "Proceedings 8th Int. Conf. Solid-State Sens. Actuators," 1995, Vol. 1, pp. 430–433.

724. L. S. Fan, S. Woodman, T. C. Reiley, H. H. Zappe, and T. Furuhata, Batch fabrication of mechanical platforms for high density data storage, in "Proceedings 8th Int. Conf. Solid-State Sens. Actuators," 1995, Vol. 1, pp. 434–437.

725. S. G. Adams, F. M. Bertsch, K. A. Shaw, P. G. Hartwell, N. C. MacDonald, and F. C. Moon, Capacitance based tunable microme-chanical resonators, in "Proceedings 8th Int. Conf. Solid-State Sens. Actuators," 1995, Vol. 1, pp. 438–441.

726. M. T. A. Saif and N. C. MacDonald, A milli Newton micro loading device, in "Proceedings 8th Int. Conf. Solid-State Sens. Actuators," 1995, Vol. 2, pp. 60–63.

727. J. Drake, H. Jerman, B. Lutze, and M. Stuber, An electrostatically actuated micro-relay, "Proceedings 8th Int. Conf. Solid-State Sens. Actuators," 1995, Vol. 2, pp. 380–383.

728. J. J. Yao and M. F. Chang, A surface micromachined miniature switch for telecommunications applications with signal frequencies from DC up to 4 GHz, in "Proceedings 8th Int. Conf. Solid-State Sens. Actuators," 1995, Vol. 2, pp. 384–387.

729. J. J. Sniegowski and C. Smith, An application of mechanical leverage to microactuation, in "Proceedings 8th Int. Conf. Solid-State Sens. Actuators," 1995, Vol. 1, pp. 364–367.

730. E. J. Garcia and J. J. Sniegowski, Surface micromachined micro-engine as the driver for micromechanical gears, in "Proceedings 8th Int. Conf. Solid-State Sens. Actuators," 1995, Vol. 2, pp. 365–368.

731. R. Legtenberg, E. Berenschot, M. Elwenspoek, and J. Fluitman, Electrostatic curved electrode actuators, in "Proceedings IEEE Micro Electro Mechanical Systems," 1995, pp. 37–42.

732. R. Legtenberg, E. Berenschot, T. Lammerink, and M. Elwenspoek, An electrostatic axial gap wobble motor, in "Proceedings 8th Int. Conf. Solid-State Sens. Actuators," 1995, Vol. 2, pp. 404–407.

733. R. Legtenberg, A. W. Groeneveld, and M. Elwenspoek, Towards position control of electrostatic comb drives, in "Proceedings 6th European workshop on Micromachining, Micromechanics and Microsystems," 1995, pp. 124–127.

### Electromagnetic Actuators

734. B. Wagner, M. Kreutzer, and W. benecke, Electromagnetic microactuators with multiple degrees of freedom, in "Proceedings 6th Int. Conf. Solid-State Sens. Actuators," 1991, pp. 614–617.

735. B. Wagner, W. Benecke, G. Engelmann, and J. Simon, *Sens. Actuators A* 32, 598 (1992).

736. C. H. Ahn and M. G. Allen, A fully integrated surface micromachined magnetic microactuator with a multilevel meander magnetic core, *J. Micromech. Syst.* 2, 15 (1993).

737. K. Yanagisawa, H. Kuwano, and A. Tago, An electromagnetivally driven microvalve, in "Proceedings 7th Int. Conf. Solid-State Sens. Actuators," 1993, pp. 102–105.

738. H. Guckel, T. R. Christenson, K. J. Skrobis, T. S. Jung, J. Klein, K. V. Hartojo, and I. Widjaja, A first functional current excited planar rotational magnetic micromotor, in "Proceedings IEEE Micro Electro Mechanical Systems," 1993, pp. 7–11.

739. C. H. Ahn and M. G. Allen, *J. Micromech. Microeng.* 3, 37 (1993).

740. D. Bosch, B. Heimhofer, G. Muck, H. Seidel, U. Thumser, and W. Welser, *Sens. Actuators A* 37–38, 684 (1993).

741. C. Liu, T Tsao, Y. C. Tai, and C. M. Ho, Surface micromachined magnetic actuators, in "Proceedings IEEE Micro Electro Mechanical Systems," 1994, pp. 57–62.

742. H. Guckel, T. Christenson, T. Earles, K. Skrobis, D. Zook, and T. Ohnstein, Electromagnetic, spring constrained linear actuator with large throw, in "4th Int. Conf. on New Actuators," 1994, pp. 52–55.

743. B. Lochel, A. Maciossek, H. J. Quenzer, B. Wagner, and G. Engelmann, *Sens. Actuators A* 46, 98 (1995).

744. K. I. Arai, W. Sugawara, and T. Honda, Magnetic small flying machines, in "Proceedings 8th Int. Conf. Solid-State Sens. Actuators," 1995, Vol. 1, pp. 316–319.

745. B. Rogge, J. Schultz, J. Mohr, A. Thommes, and W. Menz, Fully batch fabricated magnetic microactuators using a two layer LIGA process, in "Proceedings 8th Int. Conf. Solid-State Sens. Actuators," 1995, Vol. 1, pp. 320–321.

746. H. Guckel, T. Earles, J. Klein, D. Zook, and T. Ohnstein, Electromagnetic linear actuators with inductive position sensing for micro

relay, micro valve and precision positioning applications, in "Proceedings 8th Int. Conf. Solid-State Sens. Actuators," 1995, Vol. 1, pp. 324–327.

747. J. W. Judy and R. S. Muller, Magnetic microactuation of torsional polysilicon structures, in "Proceedings 8th Int. Conf. Solid-State Sens. Actuators," 1995, Vol. 1, pp. 332–335.

748. C. H. Ahn and M. G. Allen, Fluid micropumps based on rotary magnetic actuators, in "Proceedings IEEE Micro Electro Mechanical Systems," 1995, pp. 408–412.

### Electrostatic Versus Electromagnetic Actuators

749. H. Fujita and A. Omodaka, Electrostatic actuators for micromechatronics, in "Proceedings IEEE Micro Robots and Teleoperators Workshop," 1987.

750. J. H. Lang and S. F. Bart, Towards the design of successful electric micromotors, in "Proceedings IEEE Solid-State Sens. Actuators Workshop," 1988, pp. 127–130.

751. S. F. Bart, T. A. Lober, R. T. Howe, J. H. Lang, and M. F. Schlecht, *Sens. Actuators* 14, 269 (1988).

752. R. H. Price, J. E. Wood, and S. C. Jacobsen, *Sens. Actuators* 20, 107 (1989).

753. I. J. Busch-Vishniac, *Sens. Actuators A* 33, 207 (1992).

### Giant Magnetostrictive Alloy Actuators

754. T. Fukuda, H. Hosokai, H. Ohyama, H. Hashimoto, and F. Arai, Giant magnetostrictive alloy (GMA) applications to micro mobile robot as a micro actuator without power supply cables, in "Proceedings IEEE Micro Electro Mechanical Systems," 1991, pp. 210–215.

755. T. Honda, K. I. Arai, and M. Yamaguchi, Fabrication of actuators using magnetostrictive thin films, in "Proceedings IEEE Micro Electro Mechanical Systems," 1994, pp. 51–56.

756. E. Quandt and K. Seemann, Fabrication of giant magnetostrictive thin film actuators, in "Proceedings IEEE Micro Electro Mechanical Systems," 1995, pp. 273–277.

### Mechanochemical Actuators

757. T. Nagakura, K. Ishihara, T. Furukawa, K. Masuda, and T. Tsuda, Auto-regulated medical pump without energy supply, in "Proceedings 8th Int. Conf. Solid-State Sens. Actuators," 1995, Vol. 2, pp. 287–290.

### Electrochemical Actuators

758. M. W. Hamberg, C. Neagu, J. G. E. Gardeniers, D. J. Ijntema, and M. C. Elwenspoek, An electrochemical microactuator, in "Proceedings IEEE Micro Electro Mechanical Systems," 1995, pp. 106–110.

### Fluid Activated Actuators

759. L. A. Field, R. M. White, and A. P Pisano, Fluid-powered rotary gears and micro-flow channels, in "Proceedings 6th Int. Conf. Solid-State Sens. Actuators," 1991, pp. 1033–1036.

760. Y. Ikei, A. Koga, H. Morkiawa, and Y. Okawa, Fluid driven microactuator with feedback mechanism, in "Proceedings IEEE Micro Electro Mechanical Systems," 1993, pp. 213–218.

761. S. Konishi and H. Fujita, A conveyance system using air flow based on the concept of distributed micro motion systems, in "Proceedings 7th Int. Conf. Solid-State Sens. Actuators," 1993, pp. 28–31.

762. D. Y. Sim, T. Kurabayashi, and M. Esashi, Backable silicon pneumatic microvalve, in "Proceedings 8th Int. Conf. Solid-State Sens. Actuators," 1995, Vol. 2, pp. 280–283.

763. C. Vieider, O. Öhman, and H. Elderstig, A pneumatically actuated micro valve with a silicone rubber membrane for integration with fluid handling systems, in "Proceedings 8th Int. Conf. Solid-State Sens. Actuators," 1995, Vol. 2, pp. 284–286.

764. T. S. J. Lammerink, N. R. Tas, J. W. Berenschot, M. C. Elwenspoek, and J. H. J. Fluitman, Micromachined hydraulic astable multivibrator, in "Proceedings IEEE Micro Electro Mechanical Systems," 1995, pp. 13–18.

### Thermopneumatic and Phase Change Actuators

765. F. C. M. van de Pol, H. T. G. van Lintel, M. Elwenspoek, and J. H. J. Fluitman, *Sens. Actuators A* 21, 198 (1990).

766. L. Lin, A. P. Pisano, and A. P. Lee, Microbubble powered actuator, in "Proceedings 6th Int. Conf. Solid-State Sens. Actuators," 1991, pp. 1041–1044.

767. J. J. Sniegowski, A microactuation mechanism based on liquid-vapor surface tension, in "Proceedings 6th Int. Conf. Solid-State Sens. Actuators," 1991, pp. 1041–1044.

768. T. S. J. Lammerink, M. Elwenspoek, and J. H. J. Fluitman, Integrated micro-liquid dosing system, in "Proceedings IEEE Micro Electro Mechanical Systems," 1993, pp. 254–259.

769. M. J. Zdeblick, R. Anderson, J. Jankowski, B. Kline-Schoder, L. Cristel, R. Miles, and W. Weber, Thermopneumatically actuated microvalves and integrated electro-fluidic circuits, in "4th Int. Conf. on New Actuators," 1994, pp. 56–60.

770. J. Fahrenberg, D. Maas, W. Menz, and W. K. Schomburg, Active microvalve system manufactured by the LIGA process, in "4th Int. Conf. on New Actuators," 1994, pp. 71–74.

771. B. Büstgens, W. Bacher, W. Bier, R. Ehnes, D. Maas, R. Ruprecht, W. K. Schomburg, and L. Keydel, Micromembrane pump manufactured by molding, in "4th Int. Conf. on New Actuators," 1994, pp. 86–90.

772. J. Chen and K. D. Wise, A high-resolution silicon monolithic nozzle array for inkjet printing, in "Proceedings 8th Int. Conf. Solid-State Sens. Actuators," 1995, Vol. 2, pp. 321–324.

773. P. Krause, E. Obermeier, and W. Wehl, Backshooter-A new smart micromachined single-chip inkjet print head, in "Proceedings 8th Int. Conf. Solid-State Sens. Actuators," 1995, Vol. 2, pp. 325–328.

774. P. L. Bergstrom, J. Ji, Y. N. Liu, M. Kaviany, and K. D. Wise, *J. Micromech. Syst.* 4, 10 (1995).

### Thermal Actuators

775. W. Benecke and W. Riethmuller, Applications of silicon microactuators based on bimorph structures, in "Proceedings IEEE Micro Electro Mechanical Systems," 1989, pp. 116–120.

776. M. Parameswaran, L. Ristic, K. Chau, A. M. Robinson, and W. Allegretto, CMOS electrothermal microactuators, in "Proceedings IEEE Micro Electro Mechanical Systems," 1990, pp. 128–131.

777. Q. Dong, W. Benecke, and H. Schliwinski, *Microelectron. Eng.* 15, 415 (1991).

778. M. Ataka, A. Omodaka, N. Takeshima, and H. Fujita, *J. Micromech. Syst.* 2, 146 (1993).

779. B. Rashidian and M. G. Allen, Electrothermal microactuators based on dielectric loss heating, in "Proceedings IEEE Micro Electro Mechanical Systems," 1993, pp. 24–29.

780. W. H. Chu, M. Mehregany, and R. L. Mullen, *J. Micromech. Microeng.* 3, 4 (1993).

781. T. Lisec, S. Hoerschelmann, H. J. Quenzer, and B. Wagner, A fast switching silicon valve for pneumatic control systems, in "4th Int. Conf. on New Actuators," 1994, pp. 30–33.

782. H. Matoba and T. Ishikawa, A bistable snapping microactuator, in "Proceedings IEEE Micro Electro Mechanical Systems," 1994, pp. 45–50.

783. P. W. Barth, Silicon microvalves for gas flow control, in "Proceedings 8th Int. Conf. Solid-State Sens. Actuators," Vol. 2, 1995, pp. 276–279.

784. H. J. Quenzer, A. Maciossek, B. Wagner, and H. Pott, Surface micromachined metallic microactuator with buckling characteristics, in "Proceedings 8th Int. Conf. Solid-State Sens. Actuators," 1995, Vol. 1, pp. 128–131.

785. J. Franz, H. Baumann, and H. P. Trah, A silicon microvalve with integrated flow sensor, "Proceedings 8th Int. Conf. Solid-State Sens. Actuators," 1995, Vol. 2, pp. 313–316.

786. C. G. Keller and R. T. Howe, Nickel-filled HEXSIL thermally actuated tweezers, in "Proceedings 8th Int. Conf. Solid-State Sens. Actuators," 1995, Vol. 2. pp. 376–379.

### Memory Alloy Actuators

787. M. Bergamasco, P. Dario, and F. Salsedo, *Sens. Actuators A* 21, 253 (1990).

788. A. D. Johnson, *J. Micromech. Microeng*. 1, 34 (1991) .

789. S. Miyazaki and K. Momura, Development of perfect shape memory effect in sputter-deposited Ti-Ni thin films, in "Proceedings IEEE Micro Electro Mechanical Systems," 1994, pp. 176–181.

790. A. P. Lee, D. R. Ciarlo, P. A. Krulevitch, S. Lehew, J. Trevino, and M. A. Northrup, A practical microgripper by fine alignment, eutectic bonding and SMA actuation, in "Proceedings 8th Int. Conf. Solid-State Sens. Actuators," 1995, Vol. 2, pp. 368–371.

791. A. D. Johnson and E. J. Shahoian, Recent progress in thin film shape memory microactuators, in "Proceedings IEEE Micro Electro Mechanical Systems," 1995, pp. 216–220.

### Walk, Swim, and Fly Actuators

792. N. R. Tas, R. Legtenberg, J. W. Berenschot, M. C. Elwenspoek, and J. H. J. Fluitman, The electrostatic shuffle motor, in "Proceedings 6th Europ. Workshop on Micromachining, micromechanics and Microsystems," 1995, pp. 128–131.

793. T. Fukuda, A. Kawamoto, F. Arai, and H. Matsura, Mechanism and swimming experiment of micro mobile robot in water, in "Proceedings IEEE Micro Electro Mechanical Systems," 1994, pp. 273–278.

794. I. Shimoyama, Y. Kubo, T. Kaneda, and H. Miura, Simple microflight mechanism on silicon wafer, in "Proceedings IEEE Micro Electro Mechanical Systems," 1994, pp. 148–152.

795. I. Shimoyama, Y. Fulisawa, G. D. Getzan, H. Miura, M. Shimada, and Y. Matsumoto, Fluid dynamics of microwing, in "Proceedings IEEE Micro Electro Mechanical Systems," 1995, pp. 374–379.

**ENN**
*Encyclopedia of Nanoscience and Nanotechnology*
**www.aspbs.com/enn**

# Mesoscopic Organizations of Metal Nanocrystals

## G. U. Kulkarni, P. John Thomas, C. N. R. Rao

*Jawaharlal Nehru Center for Advanced Scientific Research,
Jakkur, Bangalore, India*

## CONTENTS

## 1. INTRODUCTION

A metal nanocrystal is a tiny chunk of the bulk measuring a few nanometers with a finite number of metal atoms in it. Nanocrystals in the size range of 1–50 nm are considered important and are obtainable as metal sols—a dispersion of a solid in a liquid, also called a colloidal sol. Metal sols possess fascinating colors and have long been used as dyes. The fact that such dyes indeed consist of tiny metal chunks was established as early as 1857 by Faraday [1]. Modern techniques of synthesis have enabled us to obtain sols that can be dried and redissolved like water colors. The colloidal particles display a remarkable tendency to remain single-crystalline and are hence named nanocrystals. However, the nanoparticles, depending on the method of synthesis, may exhibit multiply twinned domains sometimes even with a fivefold symmetry. Metal nanocrystals possess high surface area—a great fraction of the atoms in a nanocrystal is on its surface. A small nanocrystal of 1 nm diameter will have almost all of its atoms ($\sim$30) on the surface, while a larger nanocrystal of 10 nm ($\sim$1000 atoms) will have around 15% of its atoms on the surface [2].

An added dimension to research on nanocrystals is their size-dependent properties. The electronic, magnetic, and optical properties of a nanocrystal depend on its size [2]. In small nanocrystals, the electronic energy levels are not continuous as in the bulk metal but are discrete, due to the confinement of the electron wavefunction to the physical dimensions of the particles [3]. This phenomenon is called quantum confinement and therefore, nanocrystals are also known as quantum dots. The spacing between successive energy levels varies inversely as the diameter of the nanocrystal is changed; hence the observed changes in the properties. In fact, metal nanocrystals with volume less than 1 nm$^3$ have been shown to exhibit a definitive bandgap (few tens of meV) at room temperature. In other words, a small nanocrystal could be a very bad conductor although it is a tiny silhouette of the conducting bulk. Likewise, a tiny nanocrystal of a ferromagnetic metal can be paramagnetic in nature. In several respects, small nanocrystals behave like molecules. The nanocrystals can be discretely charged with electrons with characteristic charging energies. It means that a nanocrystal carrying an extra electron can exhibit properties different from a neutral species.

The electronic absorption spectrum of metal nanocrystals in the visible region is dominated by the plasmon band. This absorption is due to the collective excitation of the itinerant electron gas on the particle surface and is characteristic of a metal nanocrystal of a given size. In colloids, surface plasmon excitations impart characteristic colors to the metal sols, the beautiful wine-red color of gold sols being well known [4–10]. The theory of optical absorption in small metal particles was proposed at the turn of the last century by Mie [7, 10], who predicted the dependence of the plasmon peak on the dielectric constant of the surrounding medium and the diameter of the nanocrystal. Further, it was also predicted that the optical properties of metal nanocrystals would be highly anisotropic with a change in shape [8, 9]. The dependence of the absorption band of thiol-capped Au nanocrystals on solvent refractive index was recently verified by Templeton et al. [11]. Link and El-Sayed found that the absorption band splits into a longitudinal and a transverse band in Au nanorods [4, 5]. The positions of the two bands agree well with the theoretical prediction of Gans [8, 9].

The shrinking dimensions of the current microelectronic devices and the realization that current lithographic processes cannot extend to the nanoworld [12] have lent

tremendous thrust to research aimed at ordering nanocrystals into functional networks [13–18]. The nanocrystals akin to covalent systems self-assemble into ordered arrays in one, two, and three dimensions under the right conditions. Lattices of nanocrystals consist of interacting nanocrystals and may exhibit novel properties arising out of such interactions. The ability to engineer such assemblies, thus, extends the reach of current lithographic techniques and holds promise for a new generation of electronics of the nanoworld [13]. In this context, synthesis and programmed assembly of metal nanocrystals assume significance.

In this chapter, we discuss the structure and stability of mesoscopic organizations of nanocrystals in one, two, and three dimensions obtained by using a variety of surfactants. Some discussion is also devoted to unusual organizations such as clusters of nanocrystals and microcolloidal crystals. Though much of what is said holds good for semiconductor nanocrystals as well, we restrict ourselves only to metal nanocrystals for the sake of brevity.

## 2. SYNTHETIC STRATEGIES FOR METAL NANOCRYSTALS

### 2.1. General Methods

Bare metal nanocrystals of varying sizes are prepared by employing physical methods such as evaporation of metal in a vacuum by resistive heating or laser ablation. The nanocrystals are usually deposited on a solid substrate in a vacuum. Although the size of the nanocrystals cannot be exactly controlled during evaporation, it is possible to narrow the size distribution by controlling the rate of evaporation, varying the distance between the substrate and the evaporator, as well as by using nucleating inert gases. Complete control over size requires mass selection using a cluster beam apparatus. In the soft-landing method, nanoparticles generated in a stream of argon are made to land gently on a cold substrate covered with a bed of argon. The morphology of soft-landed clusters is quite different from that obtained from direct deposition, the former being more spherical and uniform.

Chemical reduction of metal salts dissolved in appropriate solvents yields small metal particles of varying size distributions [19–22]. The stabilizing agents employed include surfactants such as long-chain thiols or amines or polymeric ligands such as polyvinylpyrrolidone (PVP). A variety of reducing agents have been employed for reduction. These include electrides, alcohols, glycols, metal borohydrides, and certain specialized reagents such as tetrakis(hydroxymethyl) phosphonium chloride. The last reagent has enabled the preparation of gold hydrosols (down to ~2 nm) with a narrow size distribution. The polyol method has been quite popular in producing particles of Ag, Au, Pd, Ru, Co, Ni, and variety of other metals from nanometric to micron dimensions. Reverse micellar methods exploit the "water pools" in water-in-oil mixtures to synthesize nanocrystals and have been successful in the preparation of Ag, Au, Co, Pt, and Co nanocrystals [23, 24]. Microorganisms such as bacteria and fungi have also been harnessed to synthesize nanocrystals [25]. The synthesis of metal nanocrystals at the air-water interface as in Langmuir–Blodgett films or at a liquid-liquid

interface is currently attracting wide attention [14, 26, 27]. One such preparation involved a water-toluene interface, across which a film of Au nanocrystals was grown as shown in Figure 1 [28]. Other chemical techniques for the preparation of nanocrystals involve radiolytic, sonochemical, or electrochemical reactions [29, 30] or templates such as channels of zeolites [31]. Sonochemical reactions sometimes yield amorphous nanocrystals. Traditionally, clusters of controlled sizes have been generated by ablation of a metal target in vacuum followed by mass selection of the plume to yield cluster beams [32, 33]. Such cluster beams could be subject to *in-situ* studies or be directed on to solid substrates. In order to obtain nanocrystals in solution, Harfenist et al. [34] steered a mass-selected Ag cluster beam through a toluene solution of thiol and capped the vacuum-prepared particles. Alternatively, sols of Au and Ag have also been obtained by simply irradiating [35, 36] a strip of metal immersed in a solution containing the capping agent with laser light.

### 2.2. Size Control

The successful synthesis of metal nanocrystals involves three steps: nucleation, growth, and termination by the capping agent or ligand [19–21]. Though the reaction temperature and reagent concentrations provide a rudimentary control of the three steps, it is often impossible to independently control them and so the obtained nanocrystals usually exhibit a distribution in size. Typically, the distribution is log-normal with a standard deviation of 20% [21]. Given the fact that properties of the nanocrystals are size-dependent, it is significant to be able to synthesize nanocrystals of precise dimensions with minimal size distributions. This can be accomplished to a limited extent by size-selective precipitation either by centrifugation or by use of a miscible solvent-nonsolvent liquid mixture to precipitate nanocrystals. Lasers have also been used to alter the size distribution of nanocrystalline sols [37–41]. A breakthrough of sorts was achieved independently by two groups, led by Schmid [42] and Zamaraev [43], who succeeded in preparing truly monodisperse nanocrystals which they called "cluster compounds." They are like macromolecules with a core containing metal-metal bonds yet



**Figure 1.** Nanocrystalline film of Au formed at the toluene-water interface (middle). Gold is introduced as a toluene solution of Au(PPh$_3$)Cl while partially hydrolyzed THPC (tetrakishydromethylphosphonium-chloride) in water acts as a reducing agent. The film is obtained when the two layers are allowed to stand for several hours. When dodecanethiol is added to the toluene layer, the film breaks up forming an organosol (left) while mercaptoundecanoic acid added to water produces a hydrosol (right).

obtainable in definite stoichiometries, typical examples being $[Pt_{38}(CO)_{44}H_2]^{2-}$, $Au_{55}(PPh_3)_{12}Cl_6$. The enhanced stability of $Au_{55}$ was recently demonstrated clearly by Boyen et al. [44], who exposed a series of $Au_n$ nanocrystals to oxidation. These nanocrystals are bequeathed with special stability because they consist of a magic number of metal atoms which enables the complete closure of successive shells of atoms in a cubic close-packed arrangement. The magic numbers 13, 55, 147, 309, and 561 correspond to the closure of 1, 2, 3, 4, and 5 shells, respectively [45]. A schematic illustration of magic nuclearity nanocrystals is shown in Figure 2. Since the breakthrough, several magic nuclearity nanocrystals have been prepared including PVP-stabilized $Pd_{561}$ nanocrystals [46]. In Figure 3 are shown scanning tunneling and transmission electron micrographs of polymer-protected $Pd_{561}$ nanocrystals.

## 2.3. Shape Control

Since the properties of the nanocrystals follow from the confinement of the electrons to the physical dimensions of the nanocrystals, it would be interesting to vary the shape of the nanocrystals and study the effect of confinement of electrons in such artificial shapes [47]. This has led to the revival of interest in synthetic strategies yielding nonspherical nanocrystals. Conventional methods such as due to Turkevich [20] yield, in addition to spherical particles, a mixture of shapes—triangular, teardrop, etc.—which were once thought of as undesirable. Today, smarter synthetic schemes have been designed which yield selectively nanocrystals in the form of rods, elongated spheres, cubes, and hexagons. Au nanorods were first electrochemically synthesized by Yu et al. [48] and their optical properties were studied by Link et al. [47]. Murphy's group has pioneered a solution state method to obtain long nanorods of Au and Ag [49–51]. Their method involves a seed-mediated growth of nanocrystals into nanorods and is an easy method to produce large quantities of nanorods. Besides the above, channels of cationic micelles [52] and the polyol process [53] have been adapted to yield nanorods of Au or Ag. Puntes et al. [54] have obtained nanorods of Co by carefully decomposing cobalt carbonyl in high boiling organic solvent.
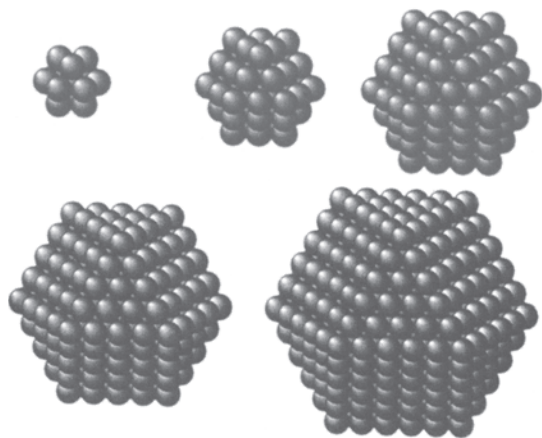


**Figure 2.** Metal nanocrystals in closed-shell configurations with magic number of atoms.
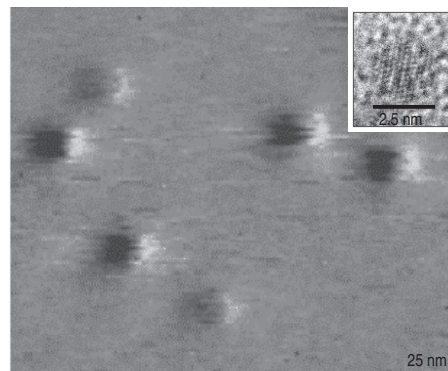


**Figure 3.** STM image of polymer-coated $Pd_{561}$ nanocrystals. The nanocrystals are seen as fluffy balls against plane background of the graphite substrate. The inset shows a high-resolution electron micrograph (HRTEM) of an individual nanocrystal. We see the characteristic 11 [111] fringes in the icosahedral shape measuring 2.5 nm. The diameter estimated from STM is ~3.4 nm, the difference being due to the ligand shell.

## 2.4. Tailoring the Ligand Shell

Nanocrystals in their native form are dominated by the surface species; the capping agents employed play a role in determining the properties of the nanocrystals [55]. Hence, in addition to controlling the size and the shape of the nanocrystal, it is also necessary to tailor its surface with the right capping agent. In addition to traditional capping agents that include ions, surfactants, and polymers, a new breed of ligands—dendrimers, hydrogen-bonding fragments of protein, DNA, and dyes—with pendent thiol groups as well as silica layers have been used as capping agents [56–58]. In some cases, a layer of a noble metal is used as a buffer between the core nanocrystal and the ligand shell [59]. Thus, a layer of gold lends special stability to Fe nanocrystals and helps in preventing oxidation and in preserving the magnetic properties of Fe (see Fig. 4).

Of special interest in this regard are reactions that enable the total replacement of one set of ligands with another [60–64]. These reactions also typically enable the transfer of nanocrystals from one phase to another. A novel method of thiol-derivatizing hydrosols of metals has been developed by Sarathy et al. [61, 62]. The procedure involves mixing vigorously a hydrosol containing metal particles of the desired size distribution with a toluene solution of an alkane thiol in the presence of a strong acid or reducing agent. The completion of the derivatization is marked by a vivid interchange of the colors from the aqueous layer to the hydrocarbon layer. The advantage of this method is that well-characterized metal particles can be easily thiol-derivatized in a nonaqueous medium. A variety of hydrosols of Au, Ag, and Pt has been thiolized by this procedure.

## 2.5. Alloy Nanocrystals

Bimetallic or alloy colloids have been made by the chemical reduction of the appropriate salt mixture in the solution phase. Thus, Ag-Pd and Cu-Pd colloids of varying composition have been prepared by alcohol reduction of mixtures of silver nitrate or copper oxide with palladium oxide [65].
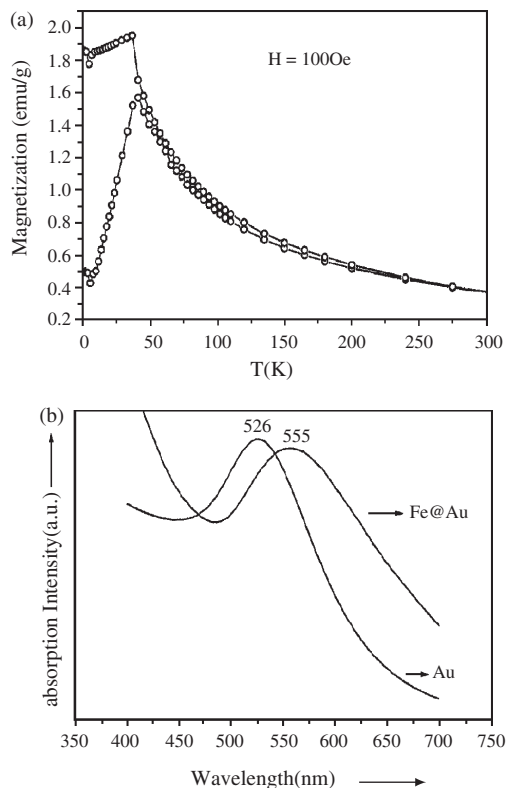
**Figure 4.** (a) Zero field cooled and field cooled magnetization curves for Fe-Au core-shell nanocrystals. The blocking temperature is 42 K. (b) Absorption spectrum showing the Au surface plasmon. For comparison, the spectrum of Au hydrosol is also shown. Reprinted with permission from [59], J. Lin et al., *J. Solid State Chem.* 159, 26 (2001). © 2001, Elsevier.

Fe-Pt alloy nanocrystals have been made by thermal decomposition of the Fe and Pt acetylacetonates in high boiling organic solvents [66]. Au-Ag alloy nanocrystals have been made by co-reduction of silver nitrate and chloroauric acid with sodium borohydride [67, 68]. Bare alloy nanocrystals have been made by thermal evaporation of alloy ingots in vacuum, typical examples being Ni-Cu, Ag-Au, Cu-Pd [69]. Lasers are being increasingly used to bring about alloying of nanocrystals. Au nanocrystals with their plasmon bands centered around 530 nm are ideal for laser irradiation studies. Au-Ag alloying and segregation have been brought about by the use of lasers on Au-Ag layered particles [70, 71].

## 3. METAL NANOCRYSTAL ASSEMBLIES

Like molecular systems, nanocrystals capped with suitable ligands spontaneously assemble into ordered aggregates. That such self-assembly can occur through a variety of weak forces is being recognized. Cooperative assemblies of ligated metal [13] as well as of colloidal polymer spheres seem to occur through the mediation of electrostatic and capillary forces [72–74]. The forces that govern the nanocrystal assembly, however, are different in many ways. Surface tension, for example, plays an important role [21] because in a nanocrystal, a large fraction of atoms is present at the surface. Surfactant molecules which self-assemble on

metal surfaces have proved to be the best means of obtaining ordered arrays of nanocrystals [74]. The way in which the nanocrystals organize themselves depends critically on the metal core diameter, the nature of the ligand, substrate, and even the dispersive medium used [75]. Thiolized nanocrystals readily arrange into two-dimensional arrays on removal of the solvent [13]. Using suitable methods, they can also be put into one-dimensional organization in the form of strings or assembled in a stepwise fashion in a three-dimensional superlattice (see Fig. 5).

### 3.1. One-Dimensional Arrangements

Hornayak and co-workers [76] used the ordered channels of porous alumina as templates to obtain linear arrangements of Au nanocrystals. By varying the pore size, the diameter of the nanowire could be controlled. A linear arrangement has also been obtained by coordinating Au particles (∼1.4 nm) stabilized with phosphine ligands to single-stranded DNA oligonucleotide of the desired length and specific sequence [77, 78]. Organization of particles in a 1D lattice has met with limited success. Heath and co-workers [79] have fabricated wires of Ag nanocrystals by compressing a dispersion of Ag (4.5 nm) nanocrystals in toluene (Fig. 6). The wires were one nanocrystal thick, a few nanocrystals wide, and extended in length from 20 to 300 nm. The interwire separation distance as well as the alignment of the wires could be controlled by compressing the film of nanocrystals.
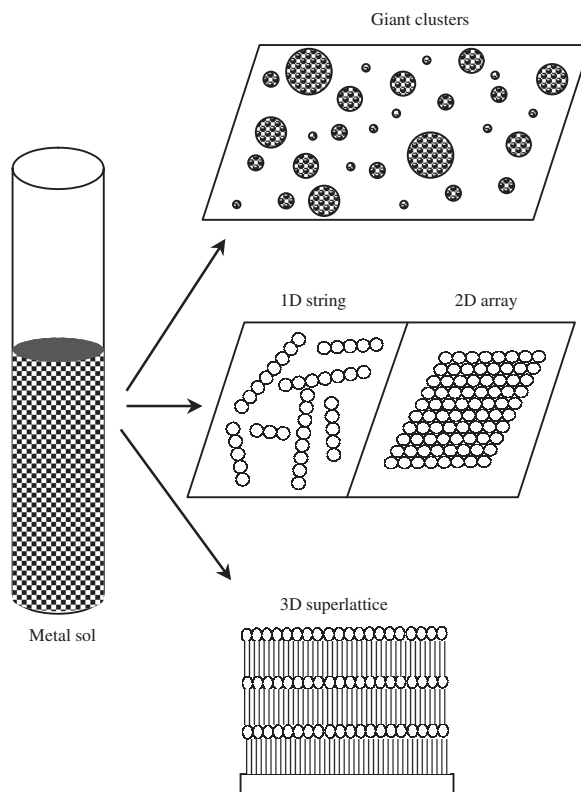


**Figure 5.** Schematic illustration of the various metal nanocrystal organizations.
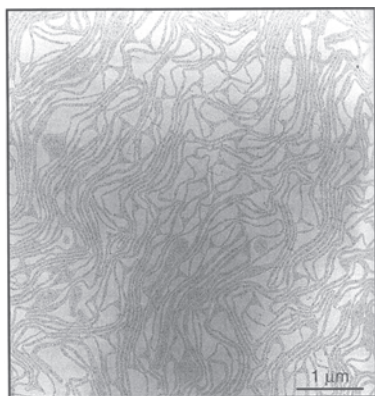
## 3.2. Two-Dimensional Arrays

Ligands based on long-chain thiols have served as good candidates for assembling nanocrystals on a flat substrate. Gold organosols using alkane thiols as surfactants were first prepared by Schiffrin and co-workers [80] by phase transferring gold ions and carrying out reduction in the presence of thiols. Several workers have adopted this procedure to obtain thiolized metal nanocrystals [81–84]. Whetten et al. [82] have centrifuged and separated out fractions containing particles of different mean sizes, to prepare 2D arrays of size-selected Au nanocrystals. A two-dimensional array of dodecanethiol-covered Ag nanocrystals obtained by Fitzmaurice and co-workers [83] is shown in Figure 7. Similarly, well-ordered arrays of magic nuclearity nanocrystals, $Pd_{561}$ and $Pd_{1415}$, have been successfully obtained after replacing their polymer coating by alkanethiols (Fig. 8) [85]. Harfenist et al. [34] found that Ag nanocrystals prepared by using a cluster beam were stable in air and formed extended 2D arrays. Ordered 2D lattices containing thiolized Au particles of two different sizes have been reported by Kiely et al. (see Fig. 9) [84]. They found that the
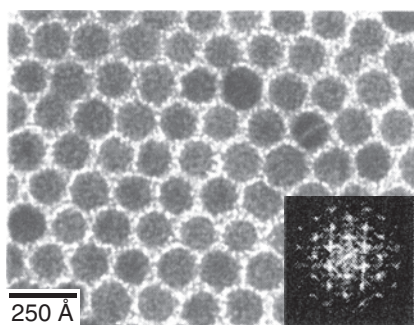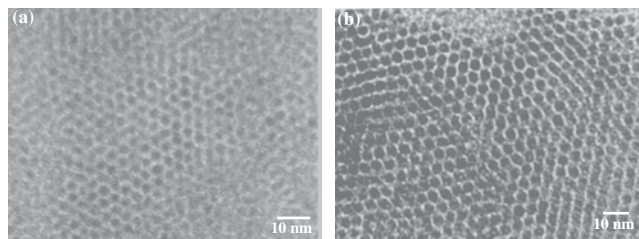


**Figure 8.** TEM micrographs showing hexagonal arrays of thiolized Pd nanocrystals: (a) $Pd_{561}$ octanethiol, (b) $Pd_{1415}$ octanethiol. Organized arrays of these nanocrystals extend to lengths over several microns.

nanocrystals of different radii follow the radius ratio rules formulated for alloying of different metals. Alloy arrays consisting of Au and Ag nanocrystals of different sizes have been made [86]. Similarly, arrays consisting of a mixture of $Fe_3O_4$ and Fe-Pt nanocrystals of several different sizes have been obtained [87]. Long-chain fatty acids have also been used for ligating metal nanocrystals. Colloidal dispersion of Co nanocrystals capped with fatty acids were found to self-assemble to yield hexagonally ordered arrays similar to those obtained with alkanethiols [88, 89]. Similarly, Ag nanocrystals capped with fatty acids of appropriate lengths yield cubic or hexagonal close-packed structures [90, 91]. It is possible to obtain micrometer-sized rings and hexagonal arrays of monodisperse nanocrystals instead of extended arrays by varying the solvent evaporation rate and exploiting the resulting fluid instabilities (the Marangoni effect) that occur during evaporation [92–96].

Schmid et al. [97] have reported an ordered two-dimensional array of small $Au_{55}$ nanocrystals (diameter ~1.4 nm) on a polymer film (see Fig. 10). At the other end of the size regime, big Au nanocrystals of 15–90 nm dimensions have also been organized into two-dimensional arrays [98]. Arrays of Au-Ag [67, 68] and Fe-Pt alloy nanocrystals [66] have been obtained. Magic nuclearity $Pd_{561}$ nanocrystals have been exploited to make Pd-Ni core-shell particles with variable Ni loadings [99]. The nanocrystals so obtained possess a core-shell structure, with the Pd seed in the middle and a Ni layer covering it. The magic nuclearity $Pd_{561}$ nanocrystals act as high-quality seeds and promote the formation of monodisperse Pd-Ni core-shell
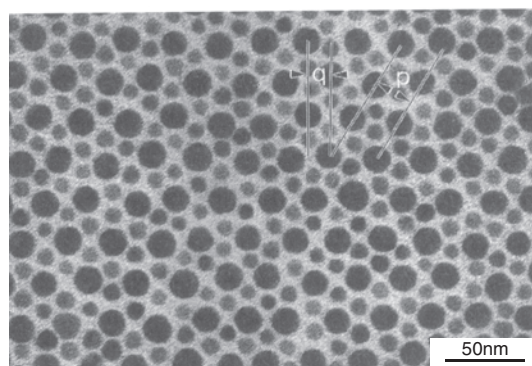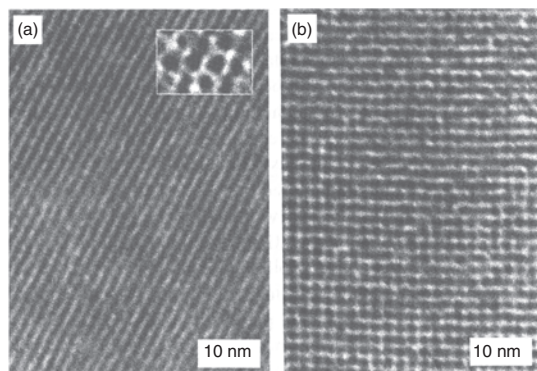
**Figure 10.** TEM images of Au$_{55}$ monolayers showing a hexagonal (a) and a cubic (b) structure. The monolayers were prepared on a polyethyleneimine functionalized carbon grid. The magnified inset in (a) shows single clusters in the hexagonal form. Reprinted with permission from [92], M. Maillard et al., *J. Phys. Chem.* B104, 11871 (2000). © 2000, American Chemical Society.

nanocrystals. Arrays of Pd$_{561}$Ni$_n$ ($n$ up to 10,000 atoms) have been prepared after thiolizing the core-shell nanocrystals (see Fig. 11) [100]. By a simple extension of this technique, arrays of triple-layer nanocrystals of the form Pd$_{561}$Ni$_{3000}$Pd$_{1500}$ were also obtained. Methods to organize nonspherical metal nanocrystals into two-dimensional arrays have met with limited success. A TEM image of an array of thiol-derivatized hexagonal Pt nanocrystals ($\sim$8 nm diameter) is shown in Figure 12. These were first prepared using an inverse micellar method, and thiol-derivatized without altering the shape or size. Elongated silver nanocrystals have been organized into ordered nanowire arrays [101].

The nanocrystal organizations mentioned are mainly entropy-driven. The two lengths involved—the nanocrystal diameter ($d$) and the ligand chain length ($\ell$)—play an important role in deciding the nature of the organization, that is, its orderliness. It has been observed experimentally that for a given diameter of the nanocrystal, the packing changes swiftly as the length of the thiol ligand is increased. The stability diagram in terms of $d$ and $\ell$ shown in Figure 13 illustrates that extended close-packed organizations of nanocrystals are found for $d/\ell$ values $\sim$2. Although entropy-driven, the above can not be treated as hard sphere organizations. Based on a study of the effect of the solvent polarity on the self-assembly of ligated nanocrystals, Korgel et al. [75, 83] proposed a soft sphere model taking the interparticle interaction into consideration.
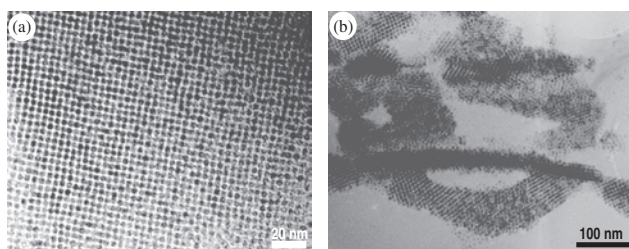


**Figure 11.** TEM image of an ordered array of octanethiol capped (a) Pd$_{561}$Ni$_{561}$ and (b) Pd$_{561}$Ni$_{3000}$ nanocrystals.
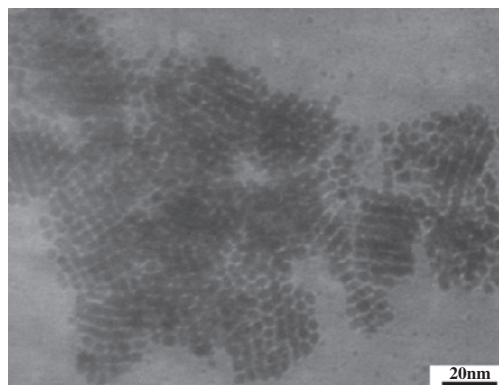


**Figure 12.** TEM image of thiol-derivatized Pt nanocrystals. The hexagonal nanocrystals form close-packed structures resembling a honeycomb pattern. The wiggly pattern in the TEM image is due to the second layer of the honeycomb structure sitting directly over the first layer in a AB-type packing.

Accordingly, a ligated nanocrystal allows for penetration of the ligand shell up to its hard sphere limit. In this model, the total potential energy, $E$, is considered to be a result of two types of forces between the nanocrystals,

$$E = E_{\text{steric}} + E_{v\,dW} \tag{1}$$

$$E_{v\,dW} = \frac{A}{12}\left\{ \frac{d^2}{\tau^2 - d^2} + \frac{d^2}{\tau^2} + 2\,\ln\left[\frac{\tau^2 - d^2}{t^2}\right] \right\} \tag{2}$$

$$E_{\text{steric}} = \frac{50 d \ell^2}{(\tau - d)\pi \sigma_a^3} kTe^{-\pi(\tau - d)} \tag{3}$$

The van der Waals interaction due to the polarization of the metal cores constitutes the attractive term and the steric interaction between the thiol molecules on the two surfaces forms the repulsive term, where $\tau$ is the interparticle distance. The Hamaker constant, $A$, for Pd nanocrystals in
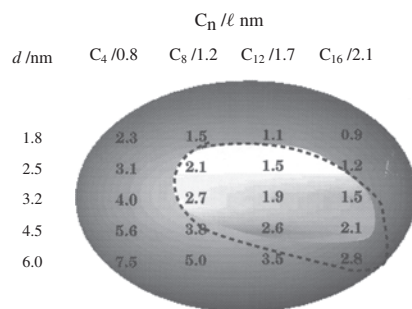


**Figure 13.** The $d - \ell$ phase diagram for Pd nanocrystals thiolized with different alkanethiols. The mean diameter, $d$, was obtained from the TEM measurements on as-prepared sols. The length of the thiol, $\ell$, is estimated by assuming an all-*trans* conformation of the alkane chain. The thiol is indicated by the number of carbon atoms, C$_n$. The bright area in the middle encompasses systems that form close-packed organizations of nanocrystals. The surrounding darker area includes disordered or low-order arrangements of nanocrystals. The area enclosed by the dashed line is derived from calculations from the soft sphere model. Reprinted with permission from [85], P. J. Thomas et al., *J. Phys. Chem.* B104, 8138 (2000). © 2000, American Chemical Society.

toluene has been estimated to be 1.95 eV [102]. The calculated diameter of the area occupied by the thiol molecule (sa) on the particle surface is 4.3 Å [83]. The total energy is attractive over a range of interparticle distances, the magnitude increasing with fall in distance. There could be a range of interparticle distances where the attractive energy from the van der Waals term exceeds the repulsive energy due to the steric factor, giving rise to net stabilization of the two-particle system. This is illustrated in Figure 14 in the case of 4.5-nm Pd particles. Stabilization energies of 17 and 2 meV are obtained from the calculation for particles coated with octanethiol and dodecanethiol, respectively. When the stabilization energies have moderate values, comparable to the thermal energy of the nanocrystals, ordered organizations can be expected (see the regime shown by dashed line in Fig. 13). If the $d/\ell$ and hence the stabilization energy is not favorable, collapsed monolayers of nanocrystals or loosely packed structures are seen. Clearly, the interdigitation of thiol molecules plays a major role in attributing hardness to the ligated nanocrystal, which in turn decides the nature of the two-dimensional organization.

## 3.3. Three-Dimensional Superlattices

Multilayer assemblies using monothiols are generally fragile. Multilayer deposition of nanocrystals is best achieved by exploiting bifunctional molecular spacers (see Fig. 15) [13, 14]. One end of the bifunctional molecule is tethered to the surface by chemisorption and the exposed amine or thiol moiety at the tail can now be used to anchor nanocrystals. Subsequent layers can be introduced by dipping the substrate sequentially into the respective spacer molecule solutions and the nanocrystal dispersion, with intermediate steps involving washing and drying. The formation of the multilayer assembly can be monitored using a variety of spectroscopy and microscopy tools. Thus, employing Au substrates and dithiols as spacers, multilayer assemblies of several metal nanocrystals have been accomplished [103]. One such example of layer-by-layer deposition of Pt (5 nm) nanocrystals is shown in Figure 14. Brust et al. [104] have reported the formation of multilayers of Au nanoparticles using dithiols. These workers have confirmed the layer-by-layer deposition of particle arrays by employing UV-vis spectroscopy and ellipsometry. Such assemblies
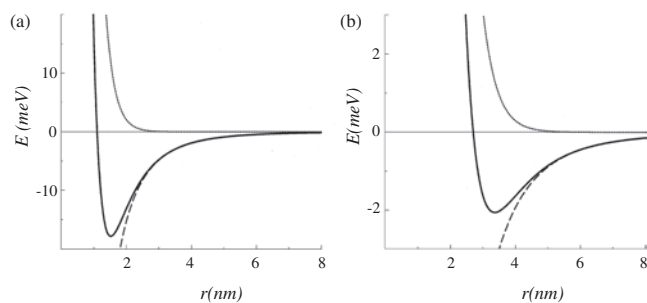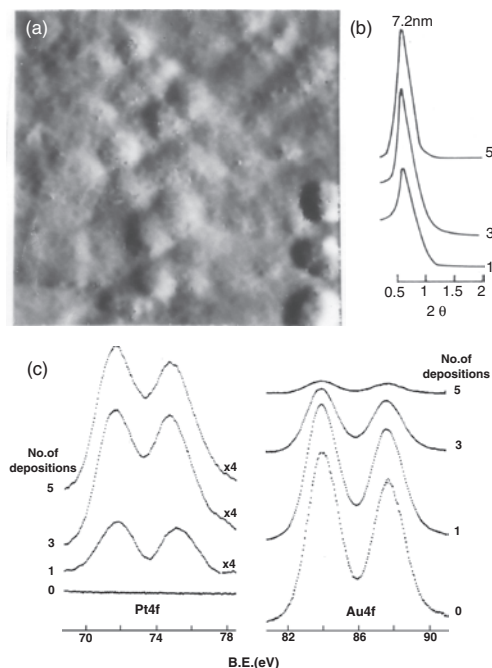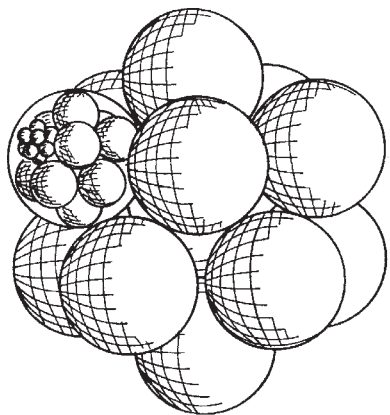


**Figure 15.** Multilayer deposition of Pt (5 nm) nanocrystals on a polycrystalline Au substrate. After each deposition, the structure was characterized by STM, X-ray diffraction, as well as by XPS. (a) STM image obtained after the second deposition showing the presence of regular arrays of nanoparticles with a interparticle spacing of 2 nm, extending over 300 nm, corresponding to the size of a typical flat terrace on the substrate. (b) X-ray diffraction pattern of the arrays after the first, third, and fifth depositions exhibiting low-angle reflections with the d-spacings reflecting the particle diameter and the interparticle distance. (c) X-ray photoelectron spectra in the Pt(4f) and Au(4f) regions for the 5 nm Pt/Au system. The intensity of the Pt(4f) feature increases with the number of depositions, accompanied by a decrease in the Au(4f) intensity as the substrate gets increasingly shadowed due to the limited escape depth of the photoelectrons.

can be made with ionic spacer molecules as well [105, 106]. Three-dimensional superlattices involving nanocrystals of different metals (e.g., Pt, Au) and of metals and semiconductors (e.g., Au, CdS) have also been prepared and characterized [103].
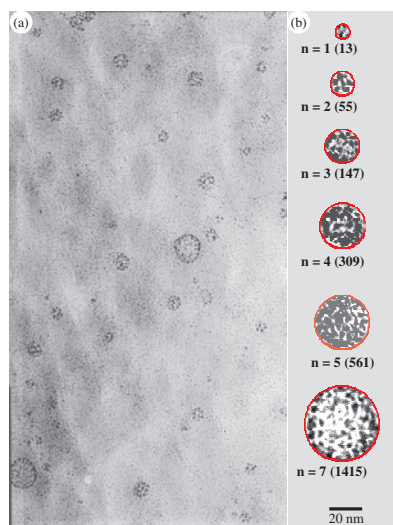
## 3.4. Superclusters

It has been proposed that self-similarity in metal nanocrystal organization would manifest in the form of a giant cluster whose shape and size are direct consequences of the nanocrystals themselves [107]. The invariance of the shell effects in metal nanocrystals with scaling is shown schematically in Figure 16. Thus, $Pd_{561}$ nanocrystals would be expected to self-aggregate into a giant cluster of the type $(Pd_{561})_{561}$ under suitable conditions. The monodisperse nature of the nanocrystals is thought to be important in assisting the self-aggregation process. Formation of such clusters was observed in the mass spectra of magic nuclearity $Au_{55}$ nanocrystals. Secondary ion mass spectrometry indicated the presence of species with large m/z values and these were attributed to $(Au_{13})_{55}$ giant clusters [108]. The giant clusters so obtained have, however, not been isolated



**Figure 14.** Variation of the two components and the total potential energy versus the separation distance between two Pd nanocrystals of 4.5 nm diameter coated with (a) octanethiol, (b) dodecanethiol. Reprinted with permission from [85], P. J. Thomas et al., *J. Phys. Chem. B* 104, 8138 (2000). © 2000, American Chemical Society.

**Figure 16.** Self-similarity: Schematic illustration of the formation of a cluster of metal nanocrystals (supercluster) and a cluster of superclusters. The size effects operating in nanocrystals could be invariant to scaling. Reprinted with permission from [107], H. G. Fritsche et al., *Z. Phys. Chem.* 199, 87 (1997). © 1997, Oldenburg Verlage.

or imaged. One such observation was made in the case of $Pd_{561}$ nanocrystals where the PVP covered nanocrystals aggregated to form giant clusters [109]. The TEM image in Figure 17 is revealing. There are regions where the nanocrystals are densely packed in the form of giant aggregates with estimated nanocrystal nuclearities corresponding to various magic numbers. It is possible that the formation of the giant clusters is facilitated by the polymer shell that encases them. Unlike in case of Pd nanocrystals coated with alkanethiols, which self-assemble to form ordered arrays, the polymer shell effectively magnifies the facets of the metallic core, thereby aiding a giant assembly of the nanocrystals.
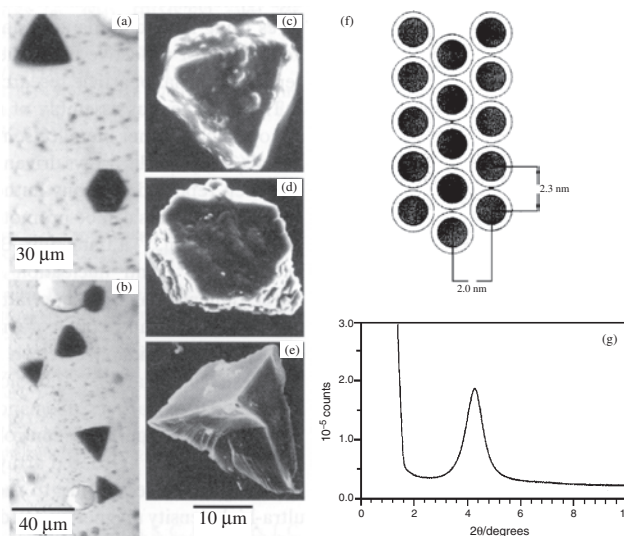
## 3.5. Colloidal Crystals

The tendency of monodisperse nanocrystals to arrange into ordered three-dimensional arrays extending to a few microns has been noticed [110]. Careful tuning of crystallization conditions has yielded crystallites of micrometer dimensions consisting of $Au_{55}$ nanocrystals and Fe-Pt alloy nanocrystals (4.5 nm) as shown in Figure 18 [111, 112]. However, it was observed that the nanocrystal arrangement in the crystallites was polymorphous. It is believed that such crystallites, consisting of ordered nanocrystals, could prove to be the best candidates to study the collective properties of an ensemble of nanocrystals.

# 4. APPLICATIONS OF METAL NANOCRYSTALS

Several applications have been envisaged for metal nanocrystals, ranging from simple dyes to magnetic-resonance-imaging contrast agents [113], as components of electronic circuitry [17, 114] and magnetic media [88], as ingredients in catalyst and sensors, and so on. The properties of a nanocrystal, however, depend critically on its size [2].
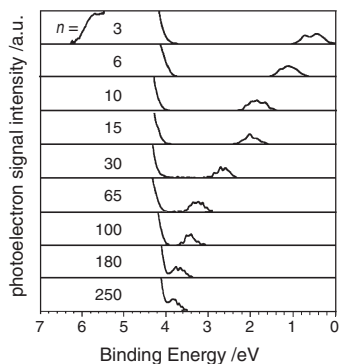
## 4.1. Isolated Nanocrystals

A nanocrystal undergoes a size-induced metal-insulator transition when the diameter of the particles is decreased to below a few nanometers [3, 115, 116]. Scanning tunneling spectroscopy measurements of nanocrystals of various metals have revealed that the nanocrystals of dimensions $\sim 1$ $nm^3$ exhibit a definitive bandgap (up to 70 meV) that decreases gradually as the volume of the nanocrystal increases [115]. Beyond 2 nm, the nanocrystal becomes essentially metallic. Photoelectron spectroscopic measurements on mass-selected $Hg_n$ nanoparticles ($n = 3$ to 250) in



**Figure 17.** TEM micrograph showing the giant clusters comprising $Pd_{561}$ nanocrystals. Sample for TEM was prepared by the slow evaporation of a $PVP - Pd_{561}$ hydrosol. Giant clusters are enclosed in circles whose diameters correspond to magic numbers. The $n$ and $L$ values indicate the number of nanocrystals and closed shells, respectively.



**Figure 18.** (a, b) Optical and (c, d, e) SEM images of Fe-Pt microcrystals. (f) Schematic illustration of a $Au_{55}$ nanocrystal arrangement in a microcrystal. (g) Small-angle X-ray diffraction pattern obtained from a $Au_{55}$ microcrystal. Reprinted with permission from [111], G. Schmid et al., *Chem. Commun.* 1303 (1999). © 1999, RSC Journals.

the gas phase reveal that the characteristic HOMO–LUMO ($s$–$p$) energy gap decreases gradually from ~3.5 eV for $n < 3$ to ~0.2 eV for $n < 250$, as shown in Figure 19. The bandgap closure is predicted at $n \sim 400$. The metal-to-nonmetal transition in gaseous Hg nanoparticles was examined by Rademann and co-workers [117] by measuring the ionization energies (IE). For $n < 13$, the dependence of IE on $n$ suggested a different type of bonding. A small Hg particle with atoms in the $6s^26p^0$ configuration held together by relatively weak van der Waals forces, is essentially nonmetallic. As the nanoparticle grows in size, the atomic $6s$ and $6p$ levels broaden into bands and an insulator-to-metal transition appears to occur driven by the physical dimensions of the individual particle. Note that this is the same element, Hg, behaving as either a metal or a nonmetal, depending upon its physical size! The change in the electronic structure of the nanocrystal manifests itself in many ways, one example being reactivity. Nanocrystals of the noble metal gold, in contact with an oxidic support such as silica, act as efficient catalysts for the oxidation of CO to $CO_2$, the activity depending on the size (see Fig. 20); maximum activity was observed for nanocrystals of ~3 nm diameter [118]. Sometimes, the reactivity is so specific to the nanocrystal size that literally "every atom counts" in determining the chemical reactivity [119]. A few studies have sought to exploit dependence of the plasmon absorption band on the dielectric constant of the surrounding medium in metal nanocrystals to detect binding events taking place at the ligand shell. Thus, Au nanocrystals could colorimetrically determine the successful hybridization of oligonucleotide strands bound to their surface [73, 77]. It has been proposed that colorimetric sensing of heavy metal ions could be obtained by the use of carboxylic acid terminated bifunctional thiols bound to metal nanocrystals [120, 121]. The changes in the electronic absorption spectra of ~5-nm Ag nanocrystals capped with lipoic acid, following the addition of the heavy ions, $Cu^{2+}$ and $Fe^{2+}$, is shown in Figure 21. Such a dampening also brings about a change in color. It is apparent that $Cu^{2+}$ ions dampen the plasmon band more effectively than $Fe^{2+}$. Nanocrystals are thought of as important in single-electron devices such as supersensitive electrometers and memory devices [114, 122]. Capped nanocrystals, by virtue of their
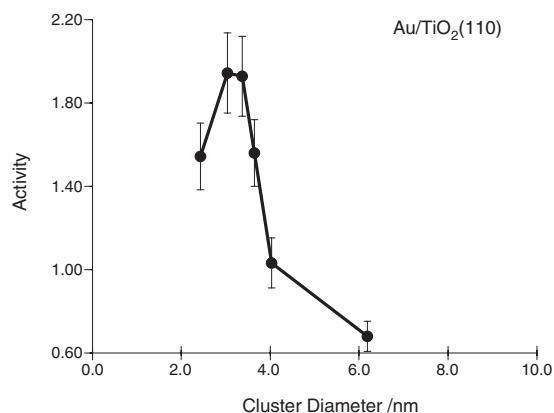


**Figure 20.** The activity (CO atoms/total Au atoms) for CO oxidation at 350 K as a function of the Au cluster diameter supported on a $TiO_2$ surface. The $CO/O_2$ mixture was 1:5 at a total pressure of 40 Torr. Reprinted with permission from [118], M. Valden et al., *Science* 281, 1647 (1998). © 1998, American Association for the Advancement of Science.

size, possess capacitance in the range of attofarad ($10^{-18}$ F). Charging a nanocrystal with an extra electron perturbs it to such an extent that the next electron requires an appreciable change in the charging potential. This is often seen as a "Coulomb staircase" in the current-voltage tunneling spectra. Indeed, the charging energy varies linearly with the inverse of the diameter of the nanocrystal [123, 124]. The sensitivity of a nanocrystal to single-electron charging makes it an ideal candidate for use in single-electron transistors and memory devices.

Size effects were perhaps first noticed in magnetic clusters [88]. Magnetic properties of nanoparticles of transition metals such as Co and Ni show marked variations with size. It is well known that in the nanometric domain, the coercivity of the particles tends to zero [125]. Thus, the nanocrystals behave as superparamagnets with no associated coercivity or retentivity. The blocking temperature which marks the onset of this superparamagnetism increases with the nanocrystal size. This scenario, however, changes in the case of interacting nanocrystals, where the interparticle interaction and hence their magnetic properties can be tuned by varying the interparticle distance. Thus, lattices of interacting magnetic nanocrystals are considered important in the future magnetic storage devices. Further, the magnetic
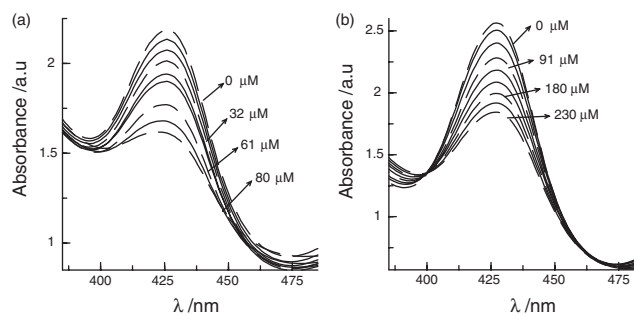


**Figure 19.** Photoelectron spectra of Hg clusters of varying nuclearity. The $6p$ feature moves gradually towards the Fermi level, emphasizing that the bandgap shrinks with increase in cluster size. Reprinted with permission from [117], K. Rademann et al., *Phys. Rev. Lett.* 69, 3208 (1992). © 1992, American Institute of Physics.



**Figure 21.** Electronic absorption spectra of ~5-nm Ag nanoparticles showing changes accompanying the addition of (a) $Cu^{2+}$ and (b) $Fe^{2+}$ ions. The concentrations of the ions are indicated.

moment per atom is seen to increase as the size of a particle decreases [126].

Creating patterns of nanocrystals on surfaces has attracted wide attention. Such patterned substrates can act as templates to grow nanowires, and etch masks to grow nanopillars and quantum dots [127–129]. Other than the layer-by-layer technique mentioned before, simple techniques such as spin-coating have been employed to create a nanocrystalline pattern on surfaces [130]. We have utilized dip-pen nanolithography, a direct write lithographic technique [131, 132], which relies on a cantilever used for atomic force microscopy (AFM) to write on a substrate to create patterns of Au nanocrystals on mica substrates. Figure 22 shows a contact AFM picture of nanocrystals patterned in rectangles of varying aspect ratios.

## 4.2. Collective Properties

The fact that the physical properties of metal nanocrystal organizations could be different from those of the isolated particles is being realized. Pellets of monodisperse nanocrystals, obtained by the use of bifunctional ligand that binds to more than one nanocrystal or by applying pressure on dried nanocrystalline matter, have been used for electrical transport measurements [133–136]. Pellets made of small Au and Pd nanocrystals exhibit nonmetallic behavior with specific conductivities in the range of $10^6 \ \Omega^{-1} \mathrm{cm}^{-1}$ [133–135]. The conductivity, however, increases dramatically with an increase in the diameter of the nanocrystals. An insulator-metal transition has indeed been reported from pellets made of ∼12.5 nm Au and Ag nanocrystals [136]. Electrical transport measurements on layer-by-layer assemblies of nanocrystals on conducting substrates have been carried out by adoption of a sandwich configuration [137–139]. Nanocrystalline films with bulk metallic conductivity have been realized with Au nanocrystals of 5 and 11 nm diameter spaced with ionic and covalent spacers [138, 139].
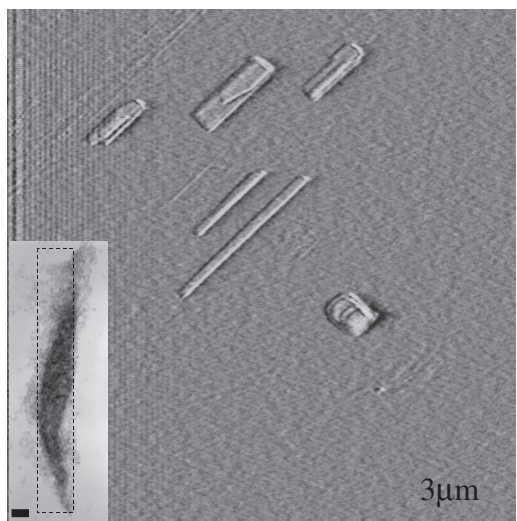


**Figure 22.** Contact AFM scan of a 9 $\mu$m$^2$ area on mica substrate showing rectangles of various aspect ratios filled with Au nanocrystals. The inset shows a TEM image of a similar pattern on a holey carbon copper grid. The scale bar in the inset corresponds to 50 nm.

The conductivity of monolayered two-dimensional arrays of metal nanocrystals have been studied with patterned electrodes [140–145]. Structural disorder and interparticle separation distance have been identified as key factors that determine the conductivity of such layers [140–143]. The conductivity of such layers has been enhanced by replacing alkane thiol with an aromatic thiol *in-situ* [144, 145]. That the interaction energy of nanocrystals in such organizations can be continually varied by changing the interparticle distance was exploited by Heath and co-workers [146, 147], who prepared a monolayer of Ag (∼3 nm) nanocrystals at air-water interface in a LB trough and varied the interparticle distance by applying pressure. A host of measurements including reflectivity and nonlinear optical spectroscopic techniques were carried out *in-situ*. This study led to the observation of a reversible Mott–Hubbard metal-insulator transition in the nanocrystal ensemble wherein the coulomb gap closes at a critical distance between the particles. Tunneling spectroscopic measurements on films of 2.6-nm Ag nanocrystals capped with dodecanethiol reveal a coulomb blockade behavior attributable to isolated nanocrystals [147]. On the other hand, nanocrystals capped with hexane and pentane thiol exhibit characteristics of strong interparticle quantum-mechanical exchange. Similar behavior was observed in the case of self-assembled two-dimensional arrays of Co nanocrystals and Au nanocrystals [148, 149].

Co nanocrystals when organized into two-dimensional arrays exhibit a higher superparamagnetic blocking temperature compared to isolated nanocrystals; that is, they display a higher resistance to thermal reversal of their spins than when they are isolated [150]. Sun et al. reported a lattice of nanocrystals each consisting of a Fe core and a Pt shell prepared by heating Fe-Pt alloy nanocrystals [66]. Following phase segregation, the interaction between the nanocrystals increased, leading to a ferromagnetic film. Exchange spring magnets—nanocomposites that consist of magnetically hard and soft phases interacting by magnetic exchange coupling—have been made by carefully annealing the mixed nanocrystal array consisting of Fe-Pt and Fe$_3$O$_4$ [87].

## 4.3. Nanocomputing

Ordered arrays of nanocrystals, in principle, could be thought of as arrays of SETs, where the electrostatic interaction between neighboring SETs acts as wireless communication means. It has been suggested by Korotkov [151] and Lent and co-workers [152] that simple logical operations can be performed on a circuitry consisting of arrays of SETs in the form of chains or cells with suitable insulating spacers. An electric field applied in one direction polarizes the strings into either the 1 or 0 state. Lent's scheme, named quantum cellular automata, instead uses a square cell consisting of five nanocrystals to denote the state of polarization. Preliminary experiments to evaluate the schemes are currently being pursued.

The realization that self-assembly driven fabrication process is not capable of producing defect-free structures has fuelled a search for algorithms that can compute even with defective circuitry. Heath and co-workers [153] have developed Teramac, a computer that works despite a high concentration of defects in its bank of microprocessors.

A more radical solution called amorphous computing aims to "engineer pre-specified, coherent behavior from cooperation of large numbers of unreliable parts interconnected in unknown, irregular and time varying ways" [154–156].

## 5. CONCLUSIONS

Nanocrystals of metals with diameters in the range 1 to 50 nm form a new class of materials with unusual properties which are size-dependent. Excellent electrical conductivity that primarily characterizes a metallic state becomes a rare entity in small nanocrystals (<2 nm) due to quantum confinement of the electronic states. Similarly, magnetic metals lose much of the coercivity with diminishing size. On the other hand, chemical properties such as reactivity may show up better at smaller sizes due to a greater number of surface bonding sites and other electronic effects. Considering the importance of nanocrystals in technological applications, a large number of synthesis methods have evolved in recent years which include reverse micelle and sonochemical methods besides laser ablation. Control over size and shape as well as encasing the nanocrystals with ligands of specialized functionalities have become subjects of urgent enquiry. While isolated metal nanocrystals are interesting by themselves, their organizations, especially those which are capable of self-assembling into well-ordered arrays, have attracted greater attention. Nanocrystals anchored to fragments of DNA or similar molecules essentially form one-dimensional organizations. When coated with long-chain alkane thiols, nanocrystals exhibit a tendency to assemble into hexagonal arrays on flat substrates. The stability of such a two-dimensional organization depends on the diameter of the nanocrystals and the length of the ligand. Multilayers of nanocrystal arrays can also be made in a programmed way by selecting suitable spacer molecules. Patterns of nanocrystals can be obtained using scanning probe techniques. Another mesoscalar aggregation known is the formation of giant clusters of nanocrystals with definite nuclearities. It would be ideal to grow crystals of nanocrystals, but such efforts have met with only a limited success to date, giving micron-sized crystals. Nanocrystal organizations may exhibit properties very different from those of the individual. They are amenable to unprecedented control over the lattice, the size of the nanocrystal and interparticle separation being continuously variable over a range. Exploratory experiments for measuring such collective properties are currently underway.

## GLOSSARY

**Atomic force microscopy**   A scanning probe microscopic technique which utilizes the weak forces between a sharp cantilever and the specimen to obtain a topographic image.

**Mesoscale**   A scale of higher order than the constituents.

**Metal-insulator transition**   A transition from a conducting to a nonconducting state induced by external stimuli or the size of the object.

**Nanocrystal**   A single crystal of a material with dimensions in the nanometer range.

**Scanning tunneling microscopy**   A scanning probe microscopic technique which uses the tunneling current between a metal tip and the conducting specimen to obtain a topographic image.

**Self-assembly**   Spontaneous assembly of objects under the influence of weak forces.

**Transmission electron microscopy**   An electron microscopic technique relying on electrons transmitted through the specimen to obtain atomic scale images.

## ACKNOWLEDGMENT

## REFERENCES

1. M. Faraday, *Philos. Trans. R. Soc. London* 147, 145 (1857).
2. C. N. R. Rao, G. U. Kulkarni, P. J. Thomas, and P. P. Edwards, *Eur. J. Chem.* 29, 27 (2002).
3. P. P. Edwards, R. L. Johnston, and C. N. R. Rao, in "Metal Clusters in Chemistry" (P. Braunstein, G. Oro, and P. R. Raithby, Eds.). Wiley-VCH, Weinham, 1999.
4. S. Link and M. A. El-Sayed, *J. Phys. Chem.* B105, 1 (2001).
5. S. Link and M. A. El-Sayed, *Int. Rev. Phys. Chem.* 19, 409 (2001).
6. P. Mulvaney, *Langmuir* 12, 788 (1996).
7. G. Mie, *Ann. Phys.* 25, 377 (1908).
8. R. Gans, *Ann. Phys.* 31, 881 (1911).
9. R. Gans, *Ann. Phys.* 47, 270 (1915).
10. G. C. Papavassilliou, *Prog. Solid State Chem.* 12, 185 (1980).
11. A. C. Templeton, J. J. Pietron, R. W. Murray, and P. Mulvaney, *J. Phys. Chem.* B104, 564 (2000).
12. R. F. Service, *Science* 274, 1834 (1996).
13. C. N. R. Rao, G. U. Kulkarni, P. J. Thomas, and P. P. Edwards, *Chem. Soc. Rev.* 29, 27 (2000).
14. A. N. Shipway, E. Katz, and I. Willner, *Chemphyschem* 1, 18 (2000).
15. M. P. Pileni, *J. Phys. Chem.* B105, 3358 (2001).
16. C. B. Murray, C. R. Kagan, and M. G. Bawendi, *Annu. Rev. Mater. Sci.* 30, 545 (2000).
17. U. Simon, *Adv. Mater.* 10, 1487 (1998).
18. G. Schmid and L. F. Chi, *Adv. Mater.* 10, 515 (1998).
19. G. Schmid, Ed., "Clusters and Colloids: From Theory to Applications." VCH, Weinham, 1994.
20. J. Turkevich, P. C. Stevenson, and J. Hillier, *J. Discuss. Faraday. Soc.* 11, 55 (1951).
21. A. I. Kirkland, D. E. Jefferson, D. G. Duff, P. P. Edwards, I. Gameson, B. F. U. Johnson, and D. J. Smith, *Proc. R. Soc. London. A* 440, 589 (1993).
22. L. J. de Jongh, Ed., "Physics and Chemistry of Metal Cluster Compounds." Kluwer, Dordrecht, 1994.
23. T. S. Ahmadi, L. Wang, A. Henglein, and M. A. El-Sayed, *Chem. Mater.* 8, 428 (1996).
24. M. P. Pileni, *J. Phys. Chem.* 97, 6961 (1993).
25. P. Mukherjee, A. Ahmad, D. Mandal, S. Senapati, S. R. Sainkar, M. I. Khan, R. Ramani, R. Parischa, P. V. Ajayakumar, M. Alam, M. Sastry, and R. Kumar, *Angew. Chem. Int. Ed.* 40, 3585 (2001).
26. I. Moriguchi, F. Shibata, Y. Teraoka, and S. Kagawa, *Chem. Lett.* 761 (1995).
27. M. Platt, R. A. W. Dryfe, and E. P. L. Roberts, *Chem. Commun.* 2324 (2002).
28. Unpublished results from our laboratory.

29. Y. Mizukoshi, K. Okitsu, Y. Maeda, T. A. Yamamoto, R. Oshima, and Y. Nagata, *J. Phys. Chem.* B101, 7033 (1997).

30. A. Henglein, *Ber. Bunsenges. Phys. Chem.* 99, 903 (1995).

31. J. H. Fendler, Ed., "Nanoparticles and Nanostructured Films." Wiley-VCH, Weinham, 1998.

32. K. Sattler, J. Mhlback, and E. Recknagel, *Phys. Rev. Lett.* 45, 821 (1980).

33. P. Milani and S. Iannotta, "Cluser Beam Synthesis of Nanostructured Materials." Springer, Berlin, 1999.

34. S. A. Harfenist, Z. L. Wang, R. L. Whetten, I. Vezmar, and M. M. Alvarez, *Adv. Mater.* 9, 817 (1997).

35. F. Mafuné, J.-Y. Kohno, Y. Takeda, and T. Kondow, *J. Phys. Chem.* B106, 7575 (2002).

36. F. Mafuné, J.-Y. Kohno, Y. Takeda, T. Kondow, and H. Sawabe, *J. Phys. Chem.* B104, 9111 (2000).

37. F. Mafuné, J.-Y. Kohno, Y. Takeda, and T. Kondow, *J. Phys. Chem.* B105, 9050 (2001).

38. H. Eckstein and U. Kreibig, *Z. Phys. D—Atoms, Molecules and Clusters* 36, 239 (1993).

39. P. V. Kamat, M. Flumiani, and G. V. Hartland, *J. Phys. Chem.* B102, 3123 (1998).

40. Y. Niidome, A. Hori, T. Sato, and S. Yamada, *Chem. Lett.* 310 (2000).

41. J. Neddersen, G. Chumanov, and T. M. Cotton, *Appl. Spectrosc.* 47, 1959 (1993).

42. G. Schmid, *Inorg. Synth.* 7, 214 (1990).

43. M. N. Vargaftik, V. P. Zagorodnikov, I. P. Stolyarov, I. I. Moiseev, V. A. Likholobov, D. I. Kochubey, A. L. Chuvili, V. I. Zaikovsky, K. I. Zamaraev, and G. I. Timofeeva, *Chem. Commun.* 937 (1985).

44. H.-G. Boyen, G. Kastle, F. Weigl, B. Koslowski, C. Dietrich, P. Ziemann, J. P. Spatz, S. Riethmuller, C. Hartmann, M. Moller, G. Schmid, M. G. Garnier, and P. Oelhafen, *Science* 297, 1533 (2002).

45. T. P. Martin, T. Bergmann, H. Göhlich, and T. Lange, *J. Phys. Chem.* 95, 6421 (1991).

46. T. Teranishi and M. Miyake, *Chem. Mater.* 10, 54 (1998); T. Teranishi, H. Hori, and M. Miyake, *J. Phys. Chem.* B101, 5774 (1997).

47. S. Link, M. B. Mohamed, and M. A. El-Sayed, *J. Phys. Chem.* B103, 3073 (1999).

48. Y. Yu, S. Chang, C. Lee, and C. R. C. Wang, *J. Phys. Chem.* B101, 6661 (1997).

49. C. J. Murphy and N. R. Jana, *Adv. Mater.* 14, 80 (2002).

50. C. J. Johnson, E. Dujardin, S. A. Davis, C. J. Murphy, and S. Mann, *J. Mater. Chem.* 12, 1765 (2002).

51. N. R. Jana, L. Gearheart, and C. J. Murphy, *Chem. Commun.* 617 (2001).

52. K. Esuni, M. Nawa, N. Aihara, and K. Usui, *New. J. Chem.* 719 (1998).

53. Y. Sun and Y. Xia, *Adv. Mater.* 14, 833 (2002).

54. V. F. Puntes, K. M. Krishnan, and A. P. Alivisatos, *Science* 291, 2115 (2001).

55. P. Zhang and T. K. Sham, *Appl. Phys. Lett.* 81, 736 (2002).

56. C. M. Niemeyer, *Angew. Chem. Int. Ed.* 40, 4128 (2001).

57. V. Chechik and R. M. Crooks, *J. Am. Chem. Soc.* 122, 1243 (2000).

58. P. Mulvaney, L. M. Liz-Marzan, M. Giersig, and T. Long, *J. Mater. Chem.* 10, 1259 (2002).

59. J. Lin, W. Zhow, A. Kumbhar, J. Wiemann, J. Fang, E. E. Carpenter, and C. J. O'Connor, *J. Solid State Chem.* 159, 26 (2001).

60. H. Harai, H. Aizawa, and H. Shiozaki, *Chem. Lett.* 8, 1527 (1992).

61. K. V. Sarathy, G. Raina, R. T. Yadav, G. U. Kulkarni, and C. N. R. Rao, *J. Phys. Chem.* B101, 9876 (1997).

62. K. V. Sarathy, G. U. Kulkarni, and C. N. R. Rao, *Chem. Commun.* 537 (1997).

63. D. I. Gittins and F. Caruso, *Angew. Chem. Int. Ed.* 40, 3001 (2001).

64. L. O. Brown and J. E. Hutchison, *J. Am. Chem. Soc.* 121, 882 (1999).

65. H. N. Vasan and C. N. R. Rao, *J. Mater. Chem.* 5, 1755 (1995).

66. S. Sun, C. B. Murray, D. Weller, L. Folks, and A. Maser, *Science* 287, 1989 (2000).

67. N. Sandhyarani, M. R. Reshmi, R. Unnikrishnan, K. Vidyasagar, S. Ma, M. P. Antony, G. P. Selvam, V. Visalakshi, N. Chandrakumar, K. Pandian, Y. T. Tao, and T. Pradeep, *Chem. Mater.* 12, 104 (2000).

68. S. T. He, S. S. Xie, J. N. Yao, H. J. Gao, and S. J. Pang, *Appl. Phys. Lett.* 81, 150 (2002).

69. K. R. Harikumar, S. Ghosh, and C. N. R. Rao, *J. Phys. Chem.* B101, 536 (1997).

70. Y.-H. Chen and C.-S. Yeh, *Chem. Commun.* 371 (2001).

71. J.-P. Abid, H. H. Girault, and P. F. Brevet, *Chem. Commun.* 829 (2001).

72. A. Terfort, N. Bowden, and G. M. Whitesides, *Nature* 386, 162 (1997).

73. C. A. Mirkin, R. L. Letsinger, R. C. Mucic, and J. F. Storhoff, *Nature* 382, 607 (1996).

74. C. P. Collier, T. Vossmeyer, and J. R. Heath, *Annu. Rev. Phys. Chem.* 49, 371 (1998).

75. B. A. Korgel and D. Fitzmaurice, *Phys. Rev. Lett.* 80, 3531 (1998).

76. G. L. Hornayak, M. Kröll, R. Pugin, T. Sawitowski, G. Schmid, J. O. Bovin, G. Karrson, H. Hofmeister, and S. Hopfe, *Eur. J. Chem.* 3, 195 (1997).

77. A. P. Alivisatos, K. P. Johnsson, X. Peng, T. E. Wilson, C. J. Loweth, M. P. Burchez, Jr., and P. G. Schultz, *Nature* 382, 609 (1996).

78. A. Kumar, M. Pattarkine, M. Bhadbhade, A. B. Mandale, K. N. Ganesh, S. S. Datar, C. V. Charmadhikari, and M. Sastry, *Adv. Mater.* 13, 341 (2001).

79. S. W. Chung, G. Markovich, and J. R. Heath, *J. Phys. Chem.* B102, 6685 (1998).

80. M. Brust, M. Walker, D. Bethell, J. D. Schiffrin, and R. Whyman, *Chem. Commun.* 801 (1994).

81. N. Sandhyarani and T. Pradeep, *Chem. Mater.* 12, 1755 (2000).

82. R. L. Whetten, J. T. Khoury, M. M. Alvarez, S. Murthy, I. Vezmar, Z. Wang, P. W. Stephens, Ch. L. Clevend, W. D. Luedtke, and U. Landman, *Adv. Mater.* 8, 428 (1996).

83. B. A. Korgel, S. Fullam, S. Connolly, and D. Fitzmaurice, *J. Phys. Chem.* B102, 8379 (1998).

84. C. J. Kiely, J. Fink, M. Brust, D. Bethell, and D. J. Schiffrin, *Nature* 396, 444 (1998).

85. P. J. Thomas, G. U. Kulkarni, and C. N. R. Rao, *J. Phys. Chem.* B104, 8138 (2000).

86. C. J. Kiely, J. Fink, J. G. Zheng, M. Brust, D. Bethell, and D. J. Schiffrin, *Adv. Mater.* 12, 639 (2000).

87. H. Zheng, J. Li, J. P. Llu, Z. L. Whang, and S. Sun, *Nature (London)* 420, 395 (2002).

88. S. Sun and C. B. Murray, *J. Appl. Phys.* 85, 4325 (1999).

89. C. Petit, A. Taleb, and M. P. Pileni, *J. Phys. Chem.* B103, 1805 (1999).

90. M. P. Pileni, *New. J. Chem.* 693 (1998).

91. K. Abe, T. Hanada, Y. Yoshida, N. Tanigaki, H. Takiguchi, H. Nagasawa, M. Nakamoto, T. Yamaguchi, and K. Yase, *Thin Solid Films* 327–329, 524 (1998).

92. M. Maillard, L. Motte, A. T. Ngo, and M. P. Pileni, *J. Phys. Chem.* B104, 11871 (2000).

93. M. Maillard, L. Motte, and M. P. Pileni, *Adv. Mater.* 16, 200 (2001).

94. P. C. Ohara and W. M. Gelbart, *Langmuir* 14, 3418 (1998).

95. T. Vossmeyer, S.-W. Chung, W. M. Gelbart, and J. R. Heath, *Adv. Mater.* 10, 351 (1998).

96. C. Stowell and B. A. Korgel, *Nano Lett.* 1, 595 (2001).

97. G. Schmid, M. Bäumle, and N. Beyer, *Angew. Chem. Int. Ed.* 1, 39 (2000).

98. B. Kim, S. L. Tripp, and A. Wei, *J. Am. Chem. Soc.* 123, 7955 (2001).

 *99.* T. Teranishi and M. Miyake, *Chem. Mater.* 11, 3414 (1999).

*100.* P. J. Thomas, G. U. Kulkarni, and C. N. R. Rao, *J. Nanosci. Nanotechnol.* 1, 267 (2001).

*101.* B. A. Korgel and D. Fitzmaurice, *Adv. Mater.* 10, 661 (1998).

*102.* D. Bargeman and F. V. V. Vader, *J. Electroanal. Chem.* 37, 45 (1972).

*103.* K. V. Sarathy, P. J. Thomas, G. U. Kulkarni, and C. N. R. Rao, *J. Phys. Chem.* B103, 399 (1999).

*104.* M. Brust, D. Bethell, C. J. Kiely, and D. J. Schiffrin, *Langmuir* 14, 5425 (1998).

*105.* R. Blonder, L. Sheeney, and I. Willner, *Chem. Commun.* 1393 (1998).

*106.* Y. Liu, Y. Wany, and R. O. Claus, *Chem. Phys. Lett.* 298, 315 (1998).

*107.* H. G. Fritsche, H. Muller, and B. Fehrensen, *Z. Phys. Chem.* 199, 87 (1997).

*108.* H. Feld, A. Leute, D. Rading, A. Benninghoven, and G. Schmid, *J. Am. Chem. Soc.* 112, 8166 (1990).

*109.* P. J. Thomas, G. U. Kulkarni, and C. N. R. Rao, *J. Phys. Chem.* B105, 2515 (2001).

*110.* M. Maillard, L. Motte, A. T. Ngo, and M. P. Pileni, *J. Phys. Chem.* B104, 11871 (2000).

*111.* G. Schmid, R. Pugin, T. Sawitowski, U. Simon, and B. Marler, *Chem. Commun.* 1303 (1999).

*112.* E. Shevchenko, D. Talapin, A. Kornowski, F. Wiekhorst, J. Kötzler, M. Haase, A. Rogach, and H. Weller, *Adv. Mater.* 14, 287 (2002).

*113.* C. R. Martin and D. T. Mitchell, *Anal. Chem.* 322A (1998).

*114.* D. L. Feldheim and C. D. Keating, *Chem. Soc. Rev.* 27, 1 (1998).

*115.* C. P. Vinod, G. U. Kulkarni, and C. N. R. Rao, *Chem. Phys. Lett.* 289, 329 (1998).

*116.* R. Busani, M. Folker, and O. Chesnovsky, *Phys. Rev. Lett.* 81, 3836 (1998).

*117.* K. Rademann, O. D. Rademann, M. Schlauf, V. Even, and F. Hensel, *Phys. Rev. Lett.* 69, 3208 (1992).

*118.* M. Valden, X. Lai, and D. W. Goodman, *Science* 281, 1647 (1998).

*119.* U. Heiz, A. Sanchez, S. Abbet, and W.-D. Schneider, *J. Am. Chem. Soc.* 121, 3214 (1999).

*120.* Y. Kim, R. C. Johnson, and J. T. Hupp, *Nano Lett.* 1, 165 (2001).

*121.* S. Berchmans, P. J. Thomas, and C. N. R. Rao, *J. Phys. Chem.* B106, 4651 (2002).

*122.* H. Graber and M. H. Devoret, Eds., "Single Charge Tunneling, Coulomb Blockade Phenomena in Nanostructures." NATO ASI Series B294. Plenum, New York, 1992.

*123.* P. J. Thomas, G. U. Kulkarni, and C. N. R. Rao, *Chem. Phys. Lett.* 321, 163 (2000).

*124.* J. Jortner, *Z. Phys. D—Atoms, Molecules and Clusters* 24, 247 (1992).

*125.* C. P. Bean and J. D. Livingston, *J. Appl. Phys.* 30, 1208 (1959).

*126.* Van de Heer, P. Milani, and A. Chatelain, *Z. Phys. D—Atoms, Molecules and Clusters* 19, 241 (1991).

*127.* H. Ago, T. Komatsu, S. Ohshima, Y. Kuriki, and M. Yumura, *Appl. Phys. Lett.* 77, 79 (2000).

*128.* Y. Cui, L. J. Lauhon, M. S. Gudisksen, J. Wang, and C. M. Lieber, *Appl. Phys. Lett.* 78, 2214 (2001).

*129.* P. A. Lewis, H. Ahamed, and T. Sato, *J. Vac. Sci. Technol.* B16, 2938 (1998).

*130.* Y.-K. Hong, H. Kim, G. Lee, W. Kim, J. Park, J. Cheon, and J.-Y. Koo, *Appl. Phys. Lett.* 80, 844 (2002).

*131.* R. D. Piner, J. Zhu, F. Xu, S. Hong, and C. A. Mirkin, *Science* 283, 661 (1999).

*132.* C. A. Mirkin, S. Hong, and L. Demers, *Chemphyschem* 2, 37 (2001).

*133.* M. Brust, D. Bethell, D. J. Schiffrin, and C. J. Kiely, *Adv. Mater.* 7, 795 (1995).

*134.* V. Torma, G. Schmid, and U. Simon, *Chemphyschem* 1, 321 (2001).

*135.* U. Simon, R. Flesch, H. Wiggers, G. Schn, and G. Schmid, *J. Mater. Chem.* 8, 517 (1998).

*136.* M. Aslam, I. S. Mulla, and K. Vijayamohanan, *Appl. Phys. Lett.* 79, 689 (2001).

*137.* R. H. Terrill, T. A. Postlewaite, C. Chen, C. D. Poon, A. Terzis, A. Chen, J. E. Hutchinson, M. R. Clark, G. Wignall, J. D. Londono, R. Superfine, M. Falvo, C. S. Johnson, Jr., E. T. Samulski, and R. W. Murray, *J. Am. Chem. Soc.* 117, 1237 (1995).

*138.* M. D. Musick, C. D. Keating, M. H. Keefe, and M. J. Natan, *Chem. Mater.* 9, 1499 (1997).

*139.* Y. Liu, Y. Wang, and R. O. Clauss, *Chem. Phys. Lett.* 298, 315 (1998).

*140.* R. Parthasarathy, X.-M. Lin, and H. A. Jaeger, *Phys. Rev. Lett.* 87, 186807 (2001).

*141.* J. Schmelzer, Jr., S. A. Brown, A. Wurl, H. Hyslop, and R. J. Blaikie, *Phys. Rev. Lett.* 88, 226802 (2002).

*142.* R. C. Doty, H. Yu, C. K. Shih, and B. A. Korgel, *J. Phys. Chem.* B105, 8291 (2001).

*143.* T. Ogawa, K. Kobayashi, G. Masuda, T. Takase, and S. Maeda, *Thin Solid Films* 393, 374 (2001).

*144.* R. G. Osifchin, W. J. Mahoney, J. D. Bielefeld, R. P. Andres, J. I. Henderson, and C. P. Kubiak, *Superlattices and Microstructures* 18, 283 (1995).

*145.* R. G. Osifchin, W. J. Mahoney, J. D. Bielefeld, R. P. Andres, J. I. Henderson, and C. P. Kubiak, *Superlattices and Microstructures* 18, 275 (1995).

*146.* G. Markovich, C. P. Collier, S. E. Hendricks, F. Ramacle, R. D. Levine, and J. R. Heath, *Acc. Chem. Res.* 32, 415 (1999).

*147.* G. Medeiros-Ribeiro, D. A. A. Ohlberg, R. S. Williams, and J. R. Heath, *Phys. Rev. B*59, 1633 (1999).

*148.* A. Taleb, F. Silly, A. O. Gusev, F. Charra, and M.-P. Pileni, *Adv. Mater.* 12, 633 (2000).

*149.* T. P. Bigioni, L. E. Harrell, W. G. Cullen, D. K. Guthrie, R. L. Whetten, and P. N. Fist, *Eur. Phys. J.* D6, 355 (1999).

*150.* V. Russier, C. Petit, J. Legrand, and M. P. Pileni, *Phys. Rev. B*62, 3910 (2000).

*151.* J. Jortner and M. Ratner, Eds., "Molecular Electronics." Blackwell Scientific, London, 1997.

*152.* A. O. Orlov, I. Amlani, G. H. Berstein, C. S. Lent, and G. L. Snider, *Science* 277, 928 (1997).

*153.* J. R. Heath, P. J. Kuekes, G. S. Snider, and R. S. Williams, *Science* 280, 1717 (1998).

*154.* H. Abelson, D. Allen, D. Coore, C. Hanson, G. Homsy, T. F. Knoght, Jr., R. Nagpal, E. Rauch, G. J. Sussman, and R. Weiss, Technical Report A. I. Memo 1665, Massachusetts Institute of Technology Artificial Intelligence Laboratory, 1999.

*155.* D. Coore, R. Nagpal, and R. Weiss, Technical Report A. I. Memo 1614, Massachusetts Institute of Technology Artificial Intelligence Laboratory, 1997.

*156.* H. Abelson, D. Allen, D. Coore, C. Hanson, G. Homsy, T. F. Knoght, Jr., R. Nagpal, E. Rauch, G. J. Sussman, and R. Weiss, *Commun. ACM*, May 2000.

**ENN**
*Encyclopedia of Nanoscience and Nanotechnology*
**www.aspbs.com/enn**

# Mesoscopic Phenomena in Nanotubes and Nanowires

## Junji Haruyama

*Aoyama Gakuin University, Setagaya, Tokyo, Japan*

## CONTENTS

## 1. INTRODUCTION

Evolution of recent nanotechnology is brilliant. It has made possible experimental observation of the nanoworld, leading to evolution of nanoscience. A variety of novel phenomena have been found in quantum and mesoscopic physics in the past decade. The mainstream of the nanotechnology is of course semiconductor nanotechnology, such as nanolithography using electron beams, dry etching with low damage, and two-dimensional electron gas formed in compound semiconductors. Besides, scanning probe microscopy also realized observation of nanoworld and manipulation of nanoscale materials. These methods are called top-down methods, because one artificially reproduces macroscopic-size materials down to nanosize. Using this way, one can reproduce materials mostly as one wants, while this method may accompany difficulties in its precise reproducibility and uniformity in nanostructure parameters because of the artificial method.

In contrast, self-organization is the other way relevant to produce nanostructures. Because this is not artificial but a natural method depending on automatic organization of molecules, this is called the bottom-up method. Since nanomaterials are naturally organized, this method brings high reproducibility and uniformity in nanoparameters.

Porous alumina membrane is one of the typical self-organized materials. This membrane consists of a honeycomb structure with nanosized diameter pores on the top view. Besides, these pores have straight shape vertical to the aluminum substrate without crossing each other. In this chapter, we report on a variety of quantum and mesoscopic phenomena observed in nanostructures realized by utilizing this alumina membrane as a template. We deposit nickel (Ni) and carbon nanotubes (CNT) into the pores of alumina template. These lead to successful study of nanoscience as follows.

In Section 3, we report on Coulomb blockade (CB), a typical phenomenon in single electron tunneling, observed in a single tunnel junction (STJ) attached to the bottom ends of Ni-nanowires and multiwalled carbon nanotubes (MWNTs). The first aim of this study was to confirm that CB could take place even in a STJ. The second aim was to investigate association of the CB with its external electromagnetic environment (EME). Many theoretical works reported that CB was very sensitive to its external EME in STJ systems (e.g., the so-called phase correlation theory), whereas only some researchers reported on this experimentally. In particular, we focused on identification of mesoscopic phenomena in Ni-nanowires and MWNTs. We reveal that Ni-nanowire has quasi-one-dimensional electron–electron interaction following Altshuler's theory and MWNT possesses weak localization (WL) resulting from phase interference of electron waves in the diffusive regime. We investigate how these electron interactions and WL contribute to the CB in STJ, as its external EME.

In Section 4, we focus on quantum phenomena observed in MWNTs, without the tunnel junction presented in Section 3, synthesized in the nanopores of alumina membranes (i.e., spintronics, superconductivity, and Y-junctions with nano-hetero-band junction). In Section 4.1.1, we found that phase interference in the MWNTs was sensitive to the materials slightly diffused into the top ends of MWNTs from the metal electrodes. We clarified that diffusion of heavy mass electrodes (e.g., gold and platinum) with the volume ratio of only about 5% yielded spin flipping due

to its spin–orbit interaction, changing the WL to antilocalization in bulk MWNTs. We propose a novel spintronics device, which operates like a CMOS transistor, using these MWNTs. In Section 4.1.2, we report how excess volume of cobalt, deposited into the bottom of the pores as catalyst for MWNT growth, changed structures of the MWNTs and spin interference in those. We found three anomalous behaviors. These phenomena imply strong spin coherence, which is maintained even with ferromagnetic impurities, of the MWNTs.

In Section 4.2, we report proximity-induced superconductivity (PIS) in niobium (Nb)/MWNT junctions. It is difficult to observe superconductivity in CNTs, because (1) the interface transparency of the metal electrode/CNT junction is poor due to misalignment of chemical potential and (2) strong one-dimensional repulsive electron interaction prevents Cooper pairs from those existences in the case of single walled CNTs. We realized a highly transparent interface by evaporating Nb electrodes on the top ends of our MWNTs with annealing. We found for the first time that conductance increases, on temperature decrease, due to PIS in the MWNTs. We also reveal that the increased conductance starts to decrease at lower temperature due to Thouless energy yielded by diffusion of Cooper pairs (i.e, reentrant effect).

In Section 4.3, we report electronic properties of Y-junction CNTs, consisting of a large diameter stem divided into two small diameter branches. This result implies automatic formation of a molecular heteroband junction controllable by a gate terminal utilizing one of the branches.

In Section 5, we report on quantum phenomena in ferromagnetic nanowire (Ni-nanowire). In Section 5.1, we report on abrupt magnetoresistance (MR) jump and reveal a possibility that this is due to macroscopic quantum tunneling of magnetic domain wall, which includes a large number of electron spins. In Section 5.2, we report on possible coexistence of phase coherence and ferromagnetism. We discuss whether ferromagnetism destroys phase coherence of electron waves based on our observation. Because these phenomena are quite strange, one may feel many open questions. We just present the observed results and one example for interpretation.
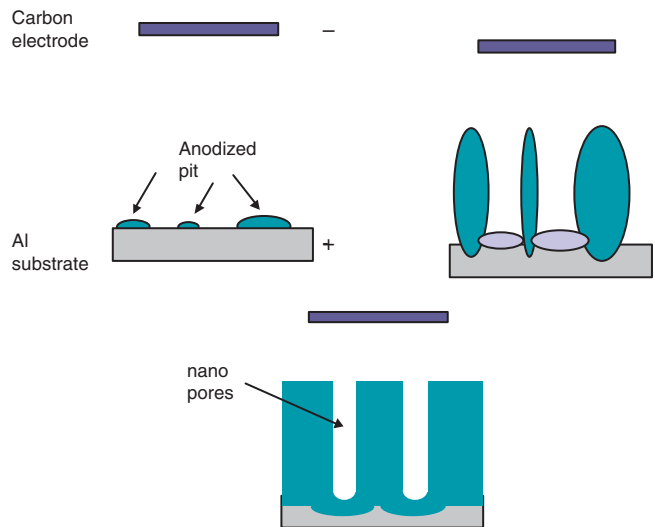
## 2. POROUS ALUMINA MEMBRANE

Porous alumina membrane was studied in early times. It shows extremely high uniformity of structure parameters in comparison with other many porous materials. For instance, it was studied as a magnetic recording media by depositing ferromagnetic materials into the pores. As mentioned in Section 1, porous alumina membrane has a honeycomb structure consisting of nanosized diameter pores on the top view (Fig. 1a). Besides, these pores have a straight shape vertical to the aluminum substrate without crossing each other (Fig. 1b). One can easily synthesize this membrane just only by anodizing pure aluminum substrate in some solutions (e.g., $H_2SO_4$, $H_3PO_4$) with applied voltage.

Figure 2 shows schematic cross-sectional view, which indicates how this alumina membrane with pores is formed. First, aluminum substrate starts to be anodized at random leading to pits (a). Because the distance between the top
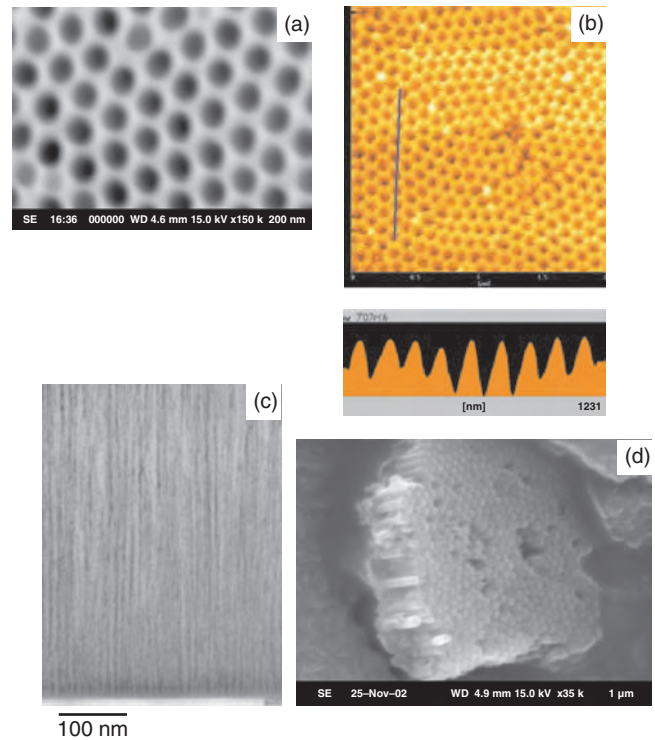


**Figure 1.** (a) SEM top view image of a porous alumina membrane. This looks like a honeycomb. (b) AFM top view image of a porous alumina membrane. This implies the presence of cell structures and defects. Lower part of the figure shows cross-sectional image, along the blue solid line in the top view, around the top portion of pores. This emphasizes a periodic location of nanopores with highly uniform diameter. (c) Cross-sectional SEM image of Ni-nanowire array deposited into (a) and (b). (d) SEM overview image of an exposed carbon nanotube array synthesized into (a) and (b). After the synthesis of nanotubes, alumina membrane was etched out. This implies that an alumina membrane with nanopores can be a template favorite to produce nanowire arrays consisting of a variety of materials.



**Figure 2.** Schematic views showing how to synthesize a porous alumina membrane.

part of the pit and the other electrode becomes smaller than the plane places without pits, electrical field concentrates on this part. This induces further anodization of the pits (b). Consequently, the parts where pits did not exist remain as pores, whereas the pits become alumina film (c). As this procedure goes ahead, alignment of the pores becomes highly regular to avoid energy loss (i.e., the distance between the pores becomes equal). This is the so-called self-organization. This leads to alumina membrane with high uniformity which looks like honeycomb on its top view (d). However, why alumina membrane has the highest uniformity is still an open question.

We developed successfully how to control the structure parameters of this alumina membrane down to nanoscale by optimizing anodization conditions, such as current density, applied voltage, and anodizing temperature, with relevant solutions. We can reduce pore diameter down to 5 nm now. We also realized deposition of a variety of materials into the nanopores (e.g., metals; gold, copper, cobalt, nickel, ferrite, semiconductors; CdS, CdTe, molecules; carbon nanotubes), leading to a variety of nanowires or nanotubes. In addition, those combinations are possible.

In this chapter, we evaporated electrodes on the top parts of arrays of nanowires or nanotubes and measured electric features by applying bias voltage between the top electrode and the Al substrate. Hence, the observed characteristics are the averaged features of the nanowires or nanotubes with numbers as large as $10^3$–$10^5$. Nevertheless, we find that even averaged results exhibit unique and interesting phenomena in quantum and mesoscopic regimes. From the next section, we show some such examples.

# 3. COULOMB BLOCKADE IN SINGLE TUNNEL JUNCTION ATTACHED TO NANOWIRE

## 3.1. Correlation with Electron–Electron Interaction in Metal Nanowire

### 3.1.1. Introduction

In this section, Coulomb blockade depending on mutual Coulomb interaction (MCI) in external electromagnetic environments is reported in an array system of single tunnel junctions connected directly to disordered Ni-nanowires (i.e., an array of disordered Ni-nanowire/$Al_2O_3$/Al located in parallel), fabricated using a nanoporous Al film template. Observed zero-bias conductance ($G_0$) anomaly and its linear $G_0$ vs temperature relation qualitatively agree with Zeller and Cleland's observations of CB. CB is also quantitatively confirmed from the extended Zeller's model in a tunnel-junction array. In the high voltage region, only one-dimensional (1D) MCI following Altshuler's formula in a disordered Ni-wire dominates the conductance mechanism with the absence of CB. In contrast, in the lower voltage region, the CB mentioned previously emerges at the temperatures below a phase transition temperature ($T_c$), accompanied by the 1D MCI in the Ni-wire. The MCI plays the key roles of high impedance EME and transmission line following phase correlation theory of CB. It is found that CB is very sensitive to the diffusion coefficient ($D$) of the MCI,

resulting in the linear $T_c$ vs $D^{1/2}$ relation. For this relation, we propose as one possible model that the charging energy of CB competes with the energy quantum of fluctuation of Nyquist phase breaking caused by multiple Coulomb scattering in the Ni-nanowire. This linear $T_c$ vs $D^{1/2}$ relation is reconfirmed by the Ni-wire diameter dependence of $T_c$. Magnetic field dependence of the $G_0$ vs temperature relation obviously supports the actual presence of $T_c$ with different conductance mechanisms between the temperatures above and below $T_c$.

Coulomb blockade has been experimentally reported in a variety of nanotunnel junction systems (e.g., metal nanoparticle array systems, quantum dots, and other nanojunction systems fabricated by semiconductor nanotechnologies and scanning probe microscopes). It is also successfully understood by many theoretical works (e.g., the orthodox theory proposed by Averin et al. [1]). Most of experiments have been basically performed in multi-tunnel-junction (MTJ) systems. For instance, Zeller et al. first reported a zero-bias conductance ($G_0$) anomaly and its linear $G_0$ vs temperature relation in the array of Sn nanoparticles located in parallel [1, 5]. They explained the $G_0$ anomaly by introducing the charging effect of the nanoparticle (i.e., capacitance model). The linear $G_0$ vs temperature relation was also interpreted by the contribution of many nanoparticles with distributed charging energy ($E_C$). In contrast, only a few reports have successfully reported on CB in a STJ system, because it is difficult to fabricate EME satisfying phase correlation (PC) theory of CB in a single junction system. In PC theory, unless the real part of the total impedance of EME ($\text{Re}[Z_t(\omega)]$) is larger than the resistance quantum $R_Q \sim h/e^2 = 25.8$ k$\Omega$, the tunneling electron cannot transfer its energy to the EME. In addition, unless the high impedance transmission line ($R_L > R_Q$) is more closely connected to a single junction, zero-point oscillations caused by the EME fluctuation fluctuate the surface charges on the junction. They easily smear out the CB [2, 3]. Furthermore, the geometry of the high $\text{Re}[Z_t(\omega)]$ including the high $R_L$ region also must have enough small parasitic capacitance to observe clear CB [1, 8]. Cleland et al. successfully reported on the $G_0$ anomaly and CB in one single junction system, turning out the PC theory [3]. The first goal of this work is to report on the $G_0$ anomaly and its linear $G_0$ vs temperature relation in an array of single junctions located in parallel, which was never fabricated in the past works, and to identify it as the CB. They are actually consistent with Zeller and Cleland's reports in some viewpoints, suggesting the presence of CB.

Here, since Coulomb blockade (CB) is very sensitive to the external environment (EME) as mentioned above, correlation of CB with the mesoscopic phenomena in EME has recently attracted much attention [4–9]. In multijunction systems, some works successfully revealed the correlation of CB with the phase interference of electron waves [4], the spin interaction of electrons [6], and the fluctuation (e.g., (1) electron phase coherence is never destroyed even in quantum dots inserted in an Aharonov–Borm ring except for the case of spin coherence [4]; (2) many body effects in artificial atoms [6]). On the other hand, in single junction systems, only our past work has experimentally reported on the CB associated with the repulsive MCI in the EME and

with the extended PC theory proposed by previously [10–12]. The second goal of this work is to clarify the detailed correlation of the CB with MCI in external environment, based on the confirmation of CB mentioned previously.

In our past works, we briefly discussed the CB and its correlation with MCI in the same system as that in this work [i.e., an array of Al/Al$_2$O$_3$/Ni-nanowire (STJs)] [10–12], from the following two viewpoints.

***From the Viewpoint of Nazarov's Theory* [11, 13]**
In PC theory, EME plays two key roles for CB in STJ. (1) Tunneling electron transfers its energy to the EME, leading to CB. (2) EME phase fluctuations ($\Delta\varphi$) cause a charge fluctuation ($\Delta Q$) on the junction surface by coupling with zero-point oscillation (or by commutation relation [$\Delta\varphi, \Delta Q$] = $ie$), smearing CB out. To cause the first process, Re[$Z_t(\omega)$] must be larger than $R_Q$, and to avoid the second process, high $R_L$ must be closely connected to a single junction. Since this connection of the high $R_L$ automatically results in the high Re[$Z_t(\omega)$], the first process can also occur in the $R_L$. Nazarov applied this PC theory to the CB depending on the MCI in the external environment [13]. We fit the second derivative of measured current ($d^2I/dV^2$) in our samples with different wire diameters by his theory at the fixed temperature ($T = 1.5$ K) and identified the tunnel structure parameters [11]. Since they were in good agreement and reasonable values, we concluded the results of CB related to the MCI following Nazarov's theory.

***From the Comparison with the Past Reports of CB and the Theory for MCI in Disordered Conductors* [10, 14]**
The linear $G_0$ vs temperature relation observed was very roughly compared with the past two experimental results [3, 15] and identified as the CB [10]. The presence of MCI in the Ni nanowire was also identified from the $G$ vs $V^{1/2}$ curve fitting by Altshuler's theory. We pointed out a possibility that the MCI plays the role of high $R_L$ for the CB. Altshuler's theory basically employs calculation of the density of states in which MCI was treated as its quantum correction [14]. Hence, it is very different from Nazarov's theory, because the charging effect $E_C$ of tunnel-junction capacitance was never considered. In this viewpoint, the CB and MCI were separately discussed. Also, other necessary conditions for CB were discussed (e.g., influence of many STJs located in parallel and the parasitic capacitance of the long resistive Ni-wire on the CB) [10].

Although they discussed the presence of CB related to the MCI, no detailed features of the CB, MCI, and their correlation were clarified. In particular, the correlation in the temperature dependence was never reported. In this work, we clarify them focusing on the temperature dependence of resistance (conductance), taking into account Altshuler's and CB theories. In Section 3.1.2, the experimental results are at first presented. $G_0$ anomaly and the linear $G_0$ vs temperature relation are discussed based on Zeller and Cleland's observations of CB. Based on the extended Zeller's capacitance model, it is quantitatively confirmed that the $G_0$ anomaly originated from CB in the array of junctions located in parallel with distributed $E_C$. The high resistance Ni-wire ($>R_Q$) plays the roles of the high Re[$Z_t(\omega)$] and $R_L$ for the CB. One-dimensional MCI following Altshuler's theory is discussed based on the temperature dependence of

the normalized resistance in the high voltage region. In contrast, that at the low voltages is discussed. The appearance of CB at the temperatures below a phase transition temperature ($T_c$) is identified with the 1D MCI at the high temperatures ($>T_c$). The MCI is the origin of the high resistance of the Ni-wire. Correlation of the CB with the 1D MCI is discussed. The CB is sensitive to a diffusion coefficient ($D$) of the MCI, resulting in the linear $T_c$ vs $D^{1/2}$ relation. The origin of the linear $T_c$ vs $D^{1/2}$ relation is interpreted from the comparison of $E_c$ with an energy quantum of phase fluctuation caused by the MCI. The linear $T_c$ vs $D^{1/2}$ relation is reconfirmed by the linear wire diameter dependence of $T_c$. The presence of $T_c$ and different conductance mechanisms classified at the $T_c$ are obviously reconfirmed by the magnetic field dependence of the $G_0$ vs temperature relation.

### 3.1.2. Experimental Results

***Sample Structure and Measurement Method*** Figure 3a shows a schematic overview of the sample structure fabricated by using novel nanomaterial (i.e., nanoporous alumina film template, NAT) [10–12]. The NAT with high packing density of nanosized diameter pores was simply fabricated by
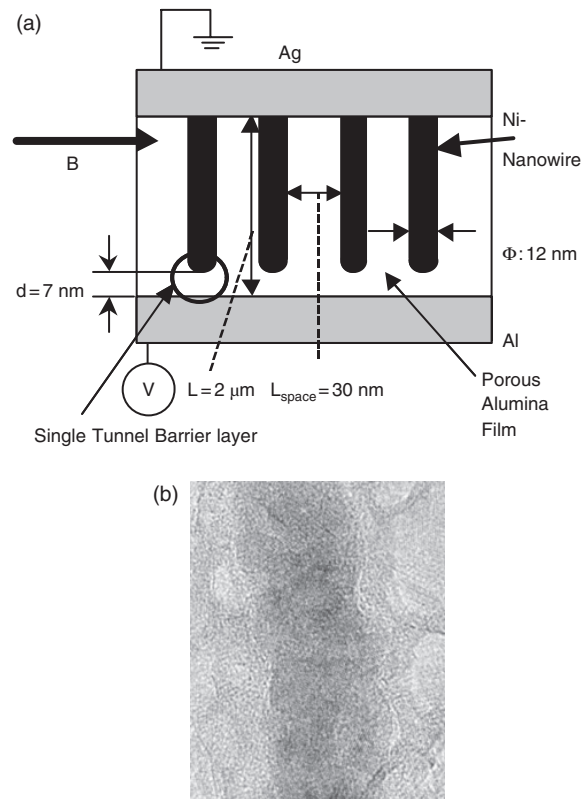


**Figure 3.** (a) Schematic overview of a sample structure, an array system of Ni-nanowire/Al$_2$O$_3$/Al (single tunnel junctions directly connected to Ni-nanowires) located in parallel. It was fabricated using a nanoporous alumina film template, which simply provides unique nanostructures by self-organized growth. (b) High resolution cross-sectional TEM image of one Ni-nanowire. We confirmed the presence of a thin tunnel barrier of 10 nm order thickness at the bottom end of this nanowire in [124]. Reprinted with permission from [124], J. Haruyama et al., *Phys. Rev. B* 62, 8420 (2000). © 2000, American Physical Society.

anodizing a pure Al film in $H_2SO_4$. Each pore automatically has a single tunnel barrier layer between its bottom and the Al substrate. Because of the self-organized growth, this NAT exhibits high uniformity, high repeatability, and high controllability of the nanostructure parameters (e.g., pore diameter and thickness of the tunnel barrier layer). In this work, Ni was electrochemically deposited into the nanopores. Thus, this system is an array structure of Ni-nanowire/$Al_2O_3$/Al (single junctions connected directly to Ni-nanowires) located in parallel. The structure parameters of the Ni-wire and the tunnel junction were confirmed by atomic force microscopy (AFM), scanning electron microscopy (SEM), and high resolution cross-sectional transmission electron microscopy (TEM) [10–12].

Figure 3b shows a typical high resolution cross-sectional TEM image of one Ni-wire including the bottom part. One can actually observe the tunnel barrier layer and Ni-nanowire with the order of 10 nm in the thickness and the diameter, respectively. In addition, very small interference patterns with the order of sub-nm diameter are visible in the Ni-wire. It suggests that the Ni-wire is in a disordered structure. This, however, never means the presence of electrical discontinuity grains, because the thickness of a grain boundary is as thin as sub-nm and any insulator layers cannot be introduced in our electrochemical deposition process. It also never indicates subnanoparticle arrays with charging effect like Zeller's system, because such thin boundary layers in the Ni cannot quantitatively have a tunnel resistance larger than $R_Q$. Furthermore, no Coulomb staircase (conductance oscillation) is observable in any current vs voltage (conductance vs voltage) curves unlike the many past reports of metal nanoparticle arrays [10], as mentioned in the next section. These strongly support that Ni-wire is electrically continuous in spite of a disordered structure, and our system is purely a single junction/Ni-nanowire array system. It is the key for our argument.

All electrical measurements were carried out by applying dc voltage between the Al substrate and the top of all Ni wires as shown in Figure 3a. The number of electrically active wire/junctions is estimated from the observed current order to be at most on the order of $10^4$. Magnetic field ($B$) was applied perpendicular to the axis of Ni-wire.

***Measurement Results and Analyses*** Figure 4 shows the temperature ($T$) dependence of conductance ($G$) vs $V^{1/2}$ curve in the plus voltage region. They obviously exhibit the $G_0$ anomalies. One corner voltage noted as $V_{1D}$ is observed around 0.3 V at each temperature, whereas the other corner voltage noted as $V_{CB}$ emerges around 0.12 V only at $T = 1.5$ K. No conductance oscillation is observable in any curves as mentioned. Although small conductance oscillations are observed at some voltage points, they originate from the simple measurement noise because they are independent of temperature. The inset of Figure 4 shows the temperature ($T$) dependence of $G_0$. The relation is mostly linear at temperatures below about 4 K. It is because this low temperature region could not be fit by any functions related to CB, electron transport in disordered conductors, and hopping conductance (e.g., $G$ vs $T^{1/2}$, $G$ vs $T^{1/4}$, $G$ vs $\log(T)$, $R$ vs $T^{-1/4}$) [1, 14, 16] and only the linear relation gave the best fit. The interpretation of this linear $G_0$ vs $T$ relation as the CB is discussed.
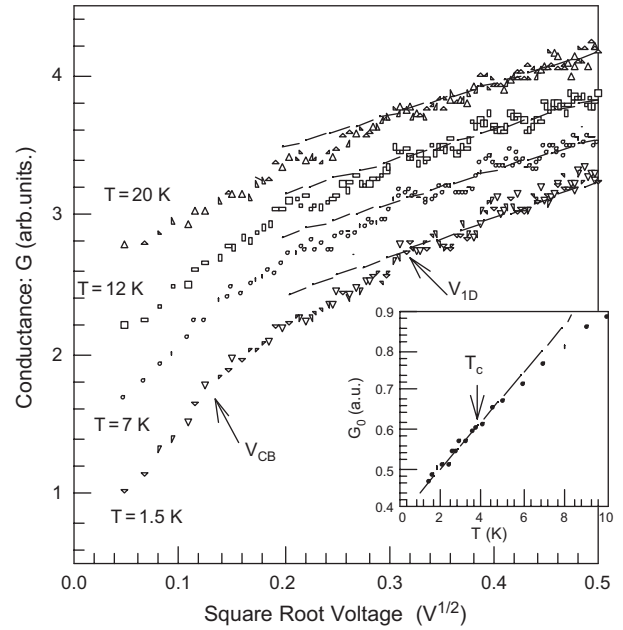


**Figure 4.** Temperature dependence of conductance ($G$) vs $V^{1/2}$ features in the positive voltage region, exhibiting the $G_0$ anomaly. The corner voltages ($V_{CB}$ and $V_{1D}$) were interpreted as the transition voltages from the one-dimensional mutual Coulomb interaction to the CB regimes and from the 3D to the 1D MCI regimes, respectively. Inset: Temperature dependence of $G_0$. The linear $G_0$ vs temperature relation as shown by the dotted line is interpreted as evidence for CB in the tunnel junction array. Reprinted with permission from [124], J. Haruyama et al., *Phys. Rev. B* 62, 8420 (2000). © 2000, American Physical Society.

Figure 5 shows the temperature dependence of the normalized resistance at each voltage point, which is below and slightly above $V_{CB}$, in Figure 3. Data fitting by the following Eq. (1), Altshuler's formula for 1D MCI in disordered conductors, basically gave the best fit to the linear $\delta R/R_n$ vs $T^{-1/2}$ parts,

$$\delta R(T)/R_n = (\rho e^2/8\hbar A)(4 + 3\lambda/2)(D\hbar/T)^{1/2} \qquad (1)$$

where $R_n, \rho, A, \lambda$, and $D$ are the resistance at the highest temperature, the resistivity (order of $10^{-7}$), the cross-sectional area (order of $10^{-16}$), the effective constant for MCI (order of 10), and the diffusion constant for MCI, respectively. In the data fitting, $D$ was used as only a free parameter, fixing the $R_n$ at the one end.

The temperature dependence can be classified into the following two voltage regions:

(1) **High voltage region:** lower four features (0.144–0.124 V of $V^{1/2}$). The temperature dependence can be fit by Eq. (1) at the entire temperatures measured. This high voltage region exists between $V_{1D}$ and $V_{CB}$.
(2) **Low voltage region:** upper eight features (0.114V–0.032 V). This low voltage region is smaller than $V_{CB}$.

The temperature dependence can be classified into the following two regimes by the $T_c$, defined as the temperature at which the deviation starts to emerge from the linear fitting
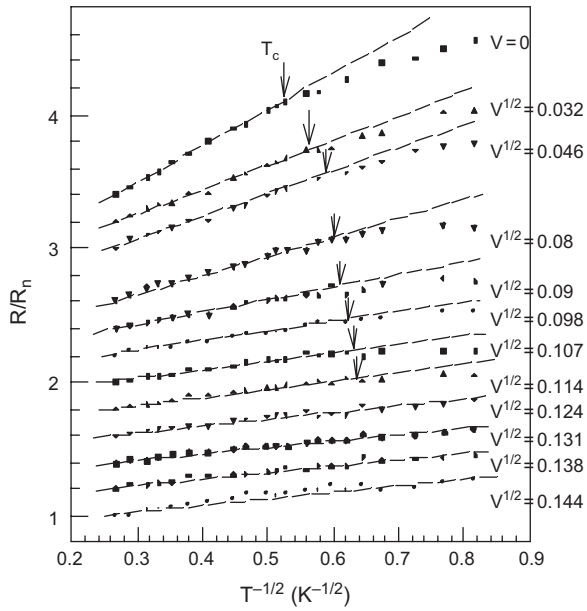
**Figure 5.** Temperature dependence of the normalized resistance at each voltage in Figure 4. The lower four and upper eight features were measured at the voltage points above and below $V_{CB}$, respectively. The dotted line shows the best fitting by Altshuler's formula for 1D MCI in disordered conductors. The arrows indicate phase transition temperatures ($T_c$) from the 1D MCI to the CB temperature regimes. Reprinted with permission from [124], J. Haruyama et al., *Phys. Rev. B* 62, 8420 (2000). © 2000, American Physical Society.

by Eq. (1):

(1) **a high temperature region** ($T_c > T$) that can be well fit by Eq. (1) and
(2) **a low temperature region** ($T_c < T$) in which the deviations appear from Eq. (1).

In the high temperature region, it should be noted that the slope value, $\alpha$, of the linear part increases in a decrease of voltage as shown in Figure 5. Figure 6a shows the inverse of the slope value ($\alpha^{-1}$) vs $V^{1/2}$ obtained from Figure 5. The interpretation assuming the linearity shown by the dotted line will be discussed. In addition, $T_c$ interestingly shifts to the lower temperature region in this increase of $\alpha$ in Figure 5. Figure 6b shows the $T_c$ vs $D^{1/2}$ relation. $D$ was determined from the parameter fitting to $\alpha$ by Eq. (1) at each voltage in Figure 5. The $T_c$ vs $D^{1/2}$ relation is mostly linear. Since it is the manifestation of the correlation of the CB with MCI in the Ni-wire, the interpretation is discussed.

Figure 7 shows the dependence of the $G_0$ vs temperature relation on the Ni-wire diameter ($\phi$). In each feature, the linear $G_0$ vs temperature relation and $T_c$ can be clearly observed. They are more obvious than those in the inset of Figure 4. The inset shows the dependence of $T_c$ on $\phi$ with the $T_c$ in the inset of Figure 4. It exhibits a mostly linear $T_c$ vs $\phi$ relation, although the sample number is only three. It is discussed that this linear relation is consistent with the linear $T_c$ vs $D^{1/2}$ relation.

Figure 8a shows the magnetic field ($B$) dependence of the $G_0$ vs temperature relation of the sample with
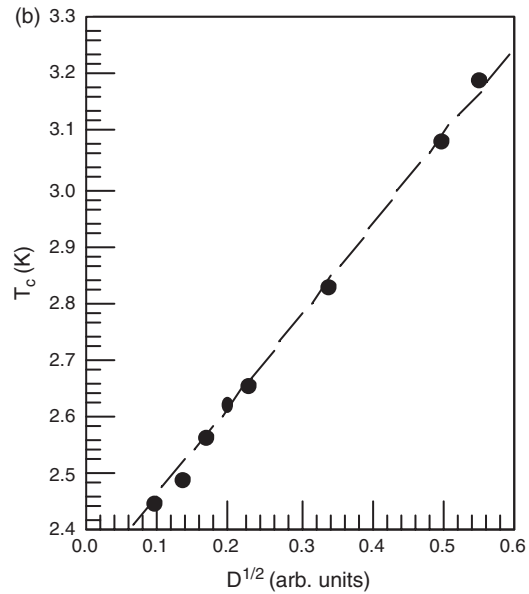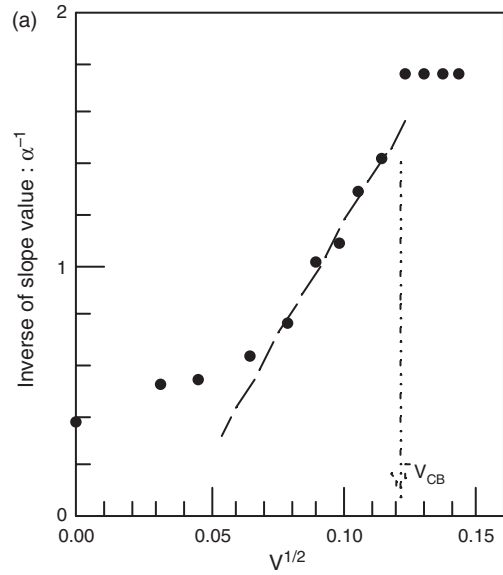




**Figure 6.** (a) $V^{1/2}$ dependence of the inverse of the slope value ($\alpha$) of the linear $\delta R(T)/R_n$ vs $T^{-1/2}$ parts obtained from Figure 3. $\alpha$ drastically increases within $V_{CB}$. The dotted line means a linear relation possibly assumed. (b) $T_c$ in Figure 3 vs the square root of the thermal diffusion coefficient ($D^{1/2}$) of MCI. $D$ was obtained from $\tilde{\alpha}$. It implies a mostly linear relation as shown by the dotted line. Reprinted with permission from [124], J. Haruyama et al., *Phys. Rev. B* 62, 8420 (2000). © 2000, American Physical Society.
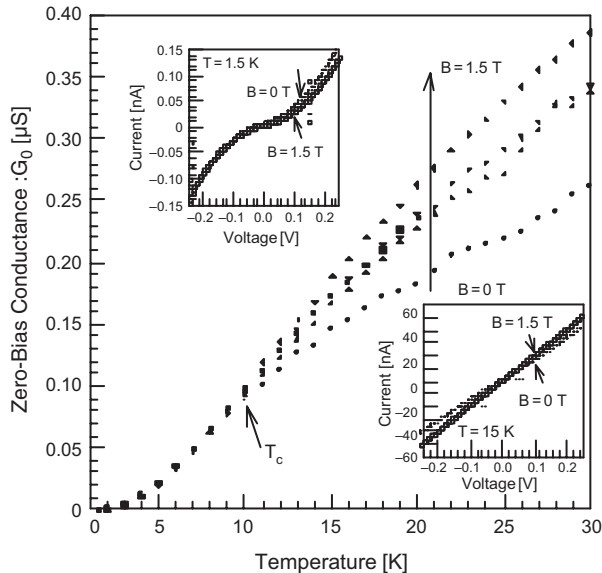
$\phi = 32$ nm in Figure 7. The magnetic field dependence remarkably changes around $T_c$. $G_0$ is mostly independent of the magnetic field at temperatures below $T_c$, whereas positive magnetoconductance emerges at temperatures above $T_c$. This result strongly supports the actual presence of $T_c$ with different mechanisms at the temperatures above and below $T_c$. Figure 8b shows the magnetic field dependence of the $I$–$V$ curves in each temperature region. The change of the $I$–$V$ curve is quite asymmetric at $T = 1.5$ K ($<T_c$). The current is reduced in the plus voltage region, whereas it mostly does not change in the minus voltage
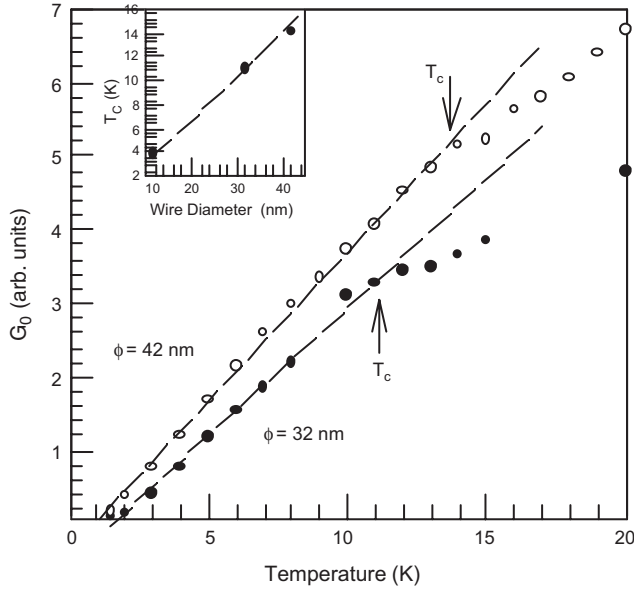
**Figure 7.** Dependence of $G_0$ vs temperature features on the Ni-wire diameters ($\phi$). Only $\phi$ was varied with keeping tunnel-junction parameters constant. Inset: Dependence of $T_C$ on $\phi$ with the $T_C$ of the inset in Figure 4 It supports the linear $T_C$ vs $D^{1/2}$ relation in Figure 6b. Reprinted with permission from [124], J. Haruyama et al., *Phys. Rev. B* 62, 8420 (2000). © 2000, American Physical Society.

region. They lead to mostly independent $G_0$ on the magnetic field. On the other hand, the change of $I$–$V$ is symmetric at $T = 15$ K ($> T_c$). Absolute values of the current are much increased in the entire voltage regions, leading to the



**Figure 8.** (a) Magnetic field ($B$) dependence of $G_0$ vs temperature in the sample with $\phi = 32$ nm shown in Figure 7. The $G_0$ vs temperature relation is mostly independent of $B$ at temperatures below $T_c$ (CB regime), whereas a positive magnetoconductance appears at temperatures above $T_c$ (1D MCI regime). (b) $B$ dependence of $I$–$V$ curves at the temperatures above and below $T_c$. Reprinted with permission from [124], J. Haruyama et al., *Phys. Rev. B* 62, 8420 (2000). © 2000, American Physical Society.

positive magnetoconductance. The possible mechanisms are speculated.

### 3.1.3. Interpretation and Discussion

**Coulomb Blockade in an Array of Single Junctions Located in Parallel** The $G_0$ anomaly with the linear $G_0$ vs temperature relation shown in Figure 4 can be interpreted as a result of CB from the following two viewpoints.

**From the Viewpoint of Zeller's Report of the CB [15]** Zeller et al. experimentally reported on the observation of the $G_0$ anomaly and its linear $G_0$ vs temperature relation. The system was an array of Sn nanoparticles with the surface oxide layers located in parallel (i.e., double nano-tunnel-junction array system). The linear $G_0$ vs temperature relation, which was observed at temperature below about 4 K in the Sn array with the mean radius of 15 nm, is qualitatively similar to our observation, although the quantitative discussion is difficult because the $G_0$ was presented in arbitrary units in their report. They theoretically explained the $G_0$ anomaly by the capacitance model (i.e., charging effect) of one Sn nanoparticle. It has basically the same meaning as the orthodox theory of CB. The linear $G_0$ vs temperature relation was also explained by the contribution of many particles, located in parallel, with distributed charging energy (i.e., $V_c$) as

$$G_0(T) = \int_0^\infty n(V_c) \exp(-eV_c/kT)\, dV_c \qquad (2)$$

where $n(V_c)$ is the area of all particles with activation energy $e^2/2C \pm eV_D = eV_c$. This equation can result in the linear $G_0$ vs temperature relation by assuming $n(V_c)$ as a constant and taking it out of the integral. It is, however, not relevant to directly employ Eq. (2) for explanation of our result, because Eq. (2) includes no consideration about the tunnel probability based on Fermi's golden rule and only Maxwell–Boltzmann statistics are introduced as the number of particles with $V_c$ in it.

Here, extending this model, we try to explain our linear $G_0$ vs temperature relation by using the orthodox theory of CB. Tunneling probability ($\Gamma$) for one STJ is simply given by the following equation including Fermi's golden rule, when the tunnel transition probability is assumed to be $(e^2 R_t)^{-1}$ and the influence of external environment is neglected:

$$\Gamma(V, T) = (1/e^2 R_t) \int_{-\infty}^\infty dE f(E)[1 - f(E + \delta E)]$$

$$= \frac{V - e/2C_j}{eR_t}\{1 - \exp[-(\delta E/kT)]\}^{-1} \qquad (3)$$

where $\delta E$ is the resultant energy change of system by a single electron tunneling (SET) event (i.e., $\delta E = eV - e^2/2C_j$). $C_j$ and $R_t$ are the junction capacitance and the tunnel resistance of single junction, respectively. Equation (3) can be rewritten by placing $V = 0$ and taking into account the $e^2/2C_j(= E_c) \gg kT$ as follows.

$$\Gamma(0, T) = \frac{1}{2C_j R_t} \exp[-(E_c/kT)] \qquad (4)$$

This equation gives the temperature dependence of zero-bias tunnel probability for one single junction. In this process, a thermal-exited electron occasionally causes the SET event. More detailed calculation for tunnel transition probability leads to the temperature dependence of $G_0$ in the orthodox theory. Here, the contribution of many single junctions located in parallel with the distributed $E_c$ can be introduced by integrating $E_c$ in Eq. (4) as

$$\Gamma_{\text{total}}(0, T) = \frac{1}{2C_j R_{t(\text{total})}} \int_0^\infty \exp[-(E_c/kT)] \, dE_c$$

$$= \frac{k}{2C_j R_{t(\text{total})}} T \qquad (5)$$

where $R_{t(\text{total})}$ is the total $R_t$. Equation (5) actually implies the linear $G_0$ vs temperature relation that is qualitatively consistent with our observation.

The coefficient of Eq. (5) also quantitatively agrees with the experimental result (slope value of the linear part of the inset of Fig. 4) as follows. Since we used a simple tunnel transition probability in Eq. (3), $R_t$ in Eq. (4) should be replaced by the total $R_t$ in Eq. (5). In contrast, $C_j$ should not be replaced by the total $C_j$, because the coupling among the neighboring junctions is weak in our system due to the sufficiently large junction spacing (~30 nm). Here, $R_{t(\text{total})}$ can be estimated to be on the order of $10^2\,\Omega$ from the $R_t$ of $10^6\,\Omega$ and the number of junctions of $10^4$. $C_j$ is also estimated to be on the order of $10^{-17}$ F from [10, 11]. Thus coefficient of temperature in Eq. (5) can be estimated to be on the order of $10^{-8}$. This value is in nice agreement with the slope value of the linear part(order of $10^{-8}$/1 K) in the inset of Figure 4. Therefore, one can conclude that the linear $G_0$ vs temperature relation can provide qualitatively and quantitatively strong evidence for the CB in the array of junctions located in parallel.

Although our system is a STJ array biased by voltage, this calculation is relevant, because of the presence of high $\text{Re}[Z_t(\omega)]$ with the high $R_L$ and the zero-bias tunneling probability. For more accurate discussion, both the phase correlation function ($P(E)$) and the actual distribution function of the junction parameters have to be introduced into Eq. (3).

### *From the Viewpoint of Cleland's Report* [3]    There is one large difference between our observation and Zeller's observation. The extrapolation of the linear $G_0$ vs temperature ($T$) relation to $T = 0$ K leads to no $G_0$ in Zeller's, whereas a nonvanishing $G_0$ exists even at $T = 0$ K in our case. From this viewpoint, Cleland's report is comparable with our observation. Cleland et al. reported on the $G_0$ anomaly, which strongly depends on the transmission line resistance $R_L$ and the normalized zero-bias resistance ($R_0/R_t$) vs $1/T$ relation. The relation exhibited a saturation (flattening) at the low temperatures near $T = 0$ K and a linear relation at the high temperatures. Since the $R_0/R_t$ vs $1/T$ relation can be basically replaced by the $G_0$ vs $T$ relation, both the saturation and the linear $R_0/R_t$ vs $1/T$ relation can qualitatively correspond to our observations (i.e., nonvanishing $G_0$ and linear $G_0$ vs T, respectively).

Their system was similar to ours, because the single junction was directly connected to the Ni transmission line with

2 $\mu$m wide. Since they explained the $G_0$ anomaly as CB following a theory like PC theory and successfully turned out environmental effect on CB, our results can be applied also qualitatively to CB. The saturation at the low temperatures was also explained by employing a fluctuation charge, $q$, caused by Nyquist voltage noise in the transmission line, into Eq. (4). It is consistent with our result, because there is a possibility of the presence of a Nyquist phase breaking process also in our Ni-nanowire as discussed later. The only main difference between our observation and Cleland's observation is that his result also indicates that even one single junction can exhibit the linear $G_0$ vs $T$ relation based on $q$.

When it is concluded that the $G_0$ anomaly in Figure 4a is CB from the previous discussion, our single junction system at least must satisfy the following four necessary conditions [10]: (1) $R_t \gg R_Q$, (2) $E_c \gg kT$, (3) $\text{Re}[Z_t(\omega)] \gg R_Q$, (4) half width of distributed tunnel junction parameters $<25\%$. The first and second conditions must be satisfied in any tunnel junction systems. The fourth condition, based on Mullen's calculation [10], is required only for the parallel located junction array system. The third condition is of core importance only for STJ systems. It was already confirmed in [10, 11] that our STJ system satisfied all of these conditions, except for the following one problem about parasitic capacitance ($C_{\text{par}}$). When we defined $L = \tau \times c$ (where $\tau \sim h/eV$, $c$ is the velocity of light in vacuum) as the geometry for an effective $C_{\text{par}}$ like the horizontal model, the $C_{\text{par}}$ in the $L$ was much larger than that estimated from the observed CB [10, 18]. To explain this difference, we may have to select a smaller velocity instead of $c$ in our very disordered Ni-nanowire. This problem is not yet clarified even in this work.

Here, the third condition is the key factor for this work. Measurement of the resistance ($R_{\text{Ni}}$) of one Ni-wire by scanning tunneling microscopy revealed that the $R_{\text{Ni}}$ was near 120 K$\Omega$ which was larger than $R_Q$. The Ni-wire is also directly connected to the single junction. Therefore, one can interpret that the Ni-wire automatically plays the roles of high $\text{Re}[Z_t(\omega)]$ and $R_L$ in our system. The $R_{\text{Ni}}$ of 120 K$\Omega$ is, however, three orders higher than that of bulk Ni. It is discussed in the next section that the origin for this anomalously high $R_{\text{Ni}}$ is in the mutual Coulomb interaction caused by disorder.

### *Mutual Coulomb Interaction in Disordered Ni-Nanowire at High Voltages*    The linear $G$ vs $V^{1/2}$ relation at the voltages above $V_{1D}$ in Figure 4 quantitatively indicated the presence of 3D MCI, in the disordered Ni-nanowire, following Altshuler's formula [10, 14]. In contrast, the temperature dependence in the first high voltage region ($V_{CB} < V < V_{1D}$) of Figure 5 was successfully fit by Eq. (1) in the entire temperature region. It qualitatively implies the presence of a 1D MCI following Altshuler's theory. One can confirm its relevance by comparing the thermal diffusion length $l_T$ with the localization length $\xi_{\text{loc}}$. They can be estimated as follows, by using $D$, which gives the best fit to the linear slope of the high voltages of Figure 5, and the $R_{\text{Ni}}$ of 120 K$\Omega$ for conductivity $\sigma$, respectively:

$$lT = [\hbar D/kT]^{1/2} \sim 10^{-8} \qquad (6)$$

$$\xi_{\text{loc}} = (2\hbar/e^2) A\sigma \sim 10^{-7} \qquad (7)$$

Since $\xi_{loc}$ is actually one order larger than $l_T$, it is reconfirmed that the Ni-wire is in the weak localization regime.

In addition, since this $l_T$ is larger than $\phi$ and smaller than wire length, it quantitatively supports the presence of one dimension of the MCI. Thus, it is concluded that the 1D MCI is the dominant conductance mechanism in the high voltage region and that $V_{1D}$ is the transition voltage from the 3D to the 1D MCI regimes in a decrease of voltage. Since $l_T$ becomes larger than $\phi$ at $V_{1D}$ with decreasing voltage in this transition, the MCI loses the two dimensions at $V_{1D}$ at the same time, because the cross section of Ni-wire has the two dimensions. It results in the direct transition from the 3D to 1D MCI regimes, which is consistent with our observation of the absence of the 2D MCI regime. Since this 1D MCI can lead to impedance higher than that of the 3D MCI because of the stronger scattering rate, it can play the roles of the high $\mathrm{Re}[Z_t(\omega)]$ and $R_L$ for the CB. However, note that any CB related characteristics are not observed in the voltage region higher than $V_{CB}$ in spite of this high impedance EME. The reason is discussed.

Why $l_T$ increases with decreasing voltage can be qualitatively interpreted as follows. In the formula of $l_T$, only diffusion constant $D$ has a voltage dependence because of the equation

$$D = vF^2\tau_{e-e}/d \qquad (8)$$

where $v_F$, $\tau_{e-e}$, and $d$ are the Fermi velocity, the relaxation (collision) time for electron–electron scattering, and the sample dimension, respectively [14]. Although $v_F^2$ decreases with decreasing voltage, $\tau_{e-e}$ can increase by decreasing the electron–electron scattering rate (i.e., $1/\tau_{e-e}$). If the increase of $\tau_{e-e}$ quantitatively exceeds the decrease of $v_F^2$, $D$ can increase with decreasing voltage.

***CB and 1D MCI Temperature Regimes Distinguished at $T_c$ at Low Voltages***    In the low voltage region, $T_c$ classified the temperature dependence into two regions. At low temperatures ($T<T_c$), conductance ($G$) vs temperature features show a mostly linear relation. In particular, it can be well represented by the linear $G_0$ vs temperature regime (below 4 K) shown in the inset of Figure 4. This is the straightforward indication that the temperature region below $T_c$ is the CB temperature regime. This CB temperature regime emerges only at voltages below $V_{CB}$ at $T = 1.5$ K. In this sense, $V_{CB}$ can be the transition voltage from the 1D MCI to the CB voltage regimes. In contrast, the linearity at the high temperatures ($T>T_c$) indicates the possible presence of Altshuler's 1D MCI as well as that of the high voltage region mentioned in the previous section.

There is, however, one large difference that the slope value, $\alpha$, of the linear part drastically increases with reducing voltage, as shown in Figure 6a. If one possibly assumes that this relation is mostly linear except for the saturation around 0 V as shown by the dotted line in Figure 6a, the increase of $\alpha$ can be also qualitatively interpreted by Altshuler's formula for the voltage dependence of $\tau_{e-e}$ (i.e., linear $\tau_{e-e}^{-1/2}$ vs $V^{1/2}$) in the 1D MCI as follows [14]. From Eq. (1) and the discussion in the previous section, $\alpha$ can have the following relation with $D^{1/2}$ and $\tau_{e-e}$:

$$\alpha \propto D^{1/2} \propto \tau_{e-e}^{1/2} \qquad (9)$$

Thus, if the linear $\alpha^{-1}$ vs $V^{1/2}$ relation is assumed, one can attain the following relation:

$$\alpha^{-1} \propto \tau_{e-e}^{-1/2} \propto V^{1/2} \qquad (10)$$

This qualitatively agrees with the linear $\tau_{e-e}^{-1/2}$ vs $V^{1/2}$ relation proposed by Altshuler as mentioned. This relation implies that the scattering rate of MCI (i.e., $\tau_{e-e}^{-1}$) decreases in a decrease of the applied voltage in 1D disorder systems. The reason for the saturation around 0 V, however, is not revealed here. It indicates that $\tau_{e-e}^{-1}$ does not become zero even at $V = 0$. There may exist other interesting mechanisms (e.g., influence of thermal diffusion at finite temperature). In the case, the linearity cannot be assumed and hence novel explanations for this increase of $\alpha$ will have to be introduced. We conclude that the high temperature regime ($T>T_c$) is also the 1D MCI regime as well as that in the first voltage region ($V>V_{CB}$), based on only the presence of the linear $\delta R/R_n$ vs $T^{-1/2}$ relation and the assumption of linearity in Figure 6a.

Consequently, one can conclude that $T_c$ is the phase transition temperature from the 1D MCI to the CB temperature regimes in a decrease of temperature. This means that the $G_0$ anomalies, which are observed at the temperatures above 7 K ($>T_c$) in Figure 4, are simply due to the MCI following Altshuler's theory. In contrast, that at $T = 1.5$ K ($<T_c$) originates from the CB. It is consistent that $V_{CB}$ is distinct only at $T = 1.5$ K in the $G$ vs $V^{1/2}$ curves in Figure 3, because even the largest $T_c$ is 3.2 K as shown in Figure 6b. However, note that the 1D MCI in the Ni-wire never disappears even in this CB temperature regime ($T<T_c$). It plays the key role to yield the CB as the high $\mathrm{Re}[Z_t(\omega)]$ and $R_L$ in the CB temperature regime. As mentioned in the next section, it is supported by the fact that this CB temperature regime is very sensitive to the diffusion constant ($D$) of the MCI. Here, MCI is basically an elastic process. Since, however, the origin of this MCI is the electron–phonon scattering by disordered potential, the tunneling electron may at least transfer the $E_c$ to there, although it is small energy transfer.

***Correlation of CB with 1D MCI in Ni-Wire***    For the correlation between CB and 1D MCI in the Ni-wire, we can find an interesting feature. $T_c$ shifts to the lower temperature region in an increase of $\alpha$ (i.e., $D$) by decreasing voltage as shown in Figure 5. The $T_c$ vs $D^{1/2}$ exhibits a mostly linear relation as shown in Figure 6b. Since $D$ is assumed to be proportional to $\tau_{e-e}$ as shown in Eq. (9), this linearity indicates that $T_c$ strongly depends on $\tau_{e-e}$ in the Ni-wire. Although there may be some interpretations for this linear $T_c$ vs $D^{1/2}$ relation, we propose one possible explanation as follows. All MCI processes yield some kinds of fluctuations. In particular, Altshuler et al. pointed out that multiple quasielastic MCI processes dominate the phase breaking process in 1D and 2D disordered conductors in the absence of other phase breaking mechanisms, the so-called Nyquist phase breaking [17]. According to [17], an energy quantum ($E_N$) of fluctuating field can be given by

$$E_N = h\omega_N \sim h[T/D^{1/2}N(E)]^{2/3} \qquad (11)$$

Where $h$, $\omega_N$, and $N(E)$ are the Planck constant, the frequency of the fluctuating field, and the density of states in a 1D conductor, respectively. Since $V_{CB}$ is in the 1D MCI voltage regime, Eq. (11) can be applied for this discussion. If the charging energy ($E_c$) of CB is smaller than the $E_N$, the CB will be smeared out by the fluctuation even if the temperature satisfies the thermal condition (i.e., $E_C \gg kT$). Hence, when $E_N$ is equal to $E_C$, Eq. (12) is given from Eq. (11):

$$T_c \sim [(E_c/h)^{3/2} N(E)^{-1}] D^{1/2} \qquad (12)$$

When it is assumed that both $E_c$ and $N(E)$ are basically constants, this equation immediately indicates the linear $T_c$ vs $D^{1/2}$ relation. Here, $E_c$ is actually a constant for the same one sample. In contrast, since $N(E)$ in a 1D conductor is generally proportional to the inverse of $E$ and applied voltage, it is not constant. $N(E)$ here, however, can be almost a constant, because this voltage region (i.e., $V < V_{CB}$) is around 0 V. In Figure 6b, the extrapolation to $D^{1/2} = 0$ leads to $T_c = 2.3$ K. This means that the CB temperature regime survives up to 2.3 K, even if the Ni-nanowire is in the strong localization regime.

This explanation implies that the $E_c$ and the $E_N$ compete at the $T_c$, which is characterized by diffusion constant $D$ depending on the $\tau_{e-e}^{-1}$ as shown in Eqs. (9) and (12). As applied voltage is decreased, $D$ becomes larger, because of the decrease of $\tau_{e-e}^{-1}$. It can reduce $E_N$ in Eq. (11). As a result, since $E_c$ exceeds $E_N$, $T_c$ increases in Eq. (12). In the other words, the CB temperature regime can be smeared out by the fluctuation energy quantum $E_N$ of the Nyquist phase breaking process in the EME. Of course, since CB requires essentially no phase coherence, the phase breaking process itself does not directly affect the CB except for the case of spin coherence. This result, however, indicates that the field fluctuation caused by phase breaking in the EME can affect the CB in single junction systems. Here, as discussed, our observation qualitatively agreed with Cleland's observation [3, 10, 18], which was explained by introducing the fluctuation charge, $q$, caused by a Nyquist voltage noise in the external transmission line [3]. This is consistent with the presence of a Nyquist phase breaking process in the Ni-nanowire in our system.

This discussion is also consistent with PC theory [2]. One can simply replace the excitation energy of an environmental mode ($h\omega_S$) in PC theory to the fluctuation energy quantum $h\omega_N$ and compare with $E_C$. In this sense, the tunneling electron can transfer its $E_c$ by exciting $h\omega_N$ in our system. Here, this MCI in the Ni-wire also plays the role of high $R_L$ to avoid the external environmental fluctuation in our system, leading to CB. However, when too large $E_N$ caused by the high $\tau_{e-e}^{-1}$ exists in our Ni-wire, it can excite too large $h\omega_N (h\omega_S)$. In such a case, the Ni-wire can no longer act as a high $R_L$, because the Ni-wire becomes only a large Nyquist noise source. This is also consistent with PC theory, because if $E_C$ is much smaller than the excited energy of environmental mode $h\omega_S$, phase correlation function ($J(t)$) and phase fluctuation $\Delta\varphi$ of the external environment become zero and the charge fluctuation $\Delta Q$ on junction surface diverges through the commutation relation $[\Delta\varphi, \Delta Q] = ie$ in PC theory. It easily smears out CB voltage. Here, since the high $\tau_{e-e}^{-1}$ (i.e., decrease of $\alpha$) is caused by the increasing of

voltage in Figure 4 and 5, it is suggested that the smearing out of the CB temperature regime in $V > V_{CB}$ is due to this too large $\tau_{e-e}^{-1}$ at 1.5 K in Figure 4. This explanation implies the necessity of the optimized $\tau_{e-e}^{-1}$, when the MCI is the origin of the high $R_L$ for the CB in single junction systems.

***Wire Diameter Dependence of $T_c$***   In order to reconfirm this discussion, quantitative comparison of the slope of the value of Figure 6b with the coefficient of Eq. (12) is required. However, since the coefficient has not been exactly fixed in any past works, it will be difficult at this stage. As one of the other works, dependence of $T_c$ on diameter ($\phi$) of Ni-nanowire was measured. In the previous section, decrease of the applied voltage made the diffusion constant $D$ varied. In contrast, since $D$ also strongly depends on $\phi$, it is expected that different $\phi$ also makes $T_c$ shifts. The result exhibited a mostly linear $T_c$ vs $\phi$ relation as shown in the inset of Figure 7. Here, $D$ has the following relation with the electron density, $n$, and the cross-sectional area of Ni-wire $A$:

$$D \propto 1/n \propto A = \pi(\phi/2)^2 \qquad (13)$$

Thus, $T_c$ can have the following relation with $D$, when the linear $T_c$ vs $\phi$ relation actually exists:

$$T_c \propto \phi = 2(A/\pi)^{1/2} \propto D^{1/2} \qquad (14)$$

Therefore, the linear $T_c$ vs $\phi$ relation in Figure 7 qualitatively supports the presence of the linear $T_c$ vs $D^{1/2}$ relation. In Figure 7, the extrapolation to $T_c = 2$ K results in $\phi$ of about 5 nm. It may mean that around the $\phi$, the Ni-nanowire may enter a strong localization regime as discussed.

The $G_0$ vs $T$ relations in Figure 7 have the following two slight differences from that in the inset of Figure 4a. (1) $G_0$ saturates around $T = 1.5$ K with a value of about $10^{-8}$ S. (2) The data fittings by Eq. (1) at temperature above $T_c$ become rougher, although they are still fit with the different slopes. Although these may originate from large wire diameters, the origins are not clear here.

***Magnetic Field Dependence of $G_0$ versus Temperature Relation and $I$–$V$ Curves***   The magnetic field ($B$) dependence of $G_0$ vs temperature ($T$) relation is drastically varied around $T_c$ as shown in Figure 8a. This result obviously supports the actual presence of a $T_c$ with a physical meaning, although $T_c$ was not distinct in the inset of Figures 4a and 5. It also implies the presence of quite different $G_0$ mechanisms between the temperature regions below and above $T_c$. In fact, the symmetry of the $I$–$V$ curves on the $B$ applied was quite different between the two temperature regions as shown in Figure 8b.

Here, applying a positive voltage corresponds to the injection of an electron from the Al substrate side, whereas a negative voltage corresponds to the injection from the Ni-wire side. The origin of Figure 8b may be speculated based on it as follows, although it is not the aim of this work.

The change of the $I$–$V$ curve by the applied $B$ is quite asymmetric in the CB temperature regime [$T = 1.5$ K($< T_c$)]. The most asymmetric part in our structure is the single tunnel barrier layer that exists between the one end of the Ni-nanowire and the Al substrate. When CB is the dominant

mechanism for electron transport in the system, the change in the $I$–$V$ curve with the $B$ will easily reflect this asymmetry from the following speculation. There may exist three effects related to the applied $B$ in the Al/Al$_2$O$_3$/Ni-wire (i.e., in Al and Ni) system: (1) differences in spin flip scattering, (2) different Zeeman energies (spin magnetic moments), (3) difference in spin–orbit interaction. In the first case, the electrons in the $d$ orbit of the Ni-nanowire are strongly spin-polarized by the applied $B$, whereas there is no spin polarization in the Al substrate. Thus, only when the electrons tunnel through from the Al to the Ni-wire is a large spin flip scattering caused at the entrance of the Ni-wire. Consequently, CB is enhanced in this process, because an electron has to get a larger energy to overcome the spin-flip scattering in addition to the $E_c$. In contrast, when the electrons tunnel into the Al, there is basically no influence of the spin polarization. Thus, the $I$–$V$ curve is mostly independent of $B$. These may lead to the asymmetric $I$–$V$ on the applied $B$.

Also, in the second case, when electrons tunnel into the Ni-wire, an additional energy for electrons is required in addition to $E_c$, because of Zeeman energy in the Ni. In contrast, this means that electrons can tunnel into the Al with smaller energies, because of the Zeeman energy of Ni. Therefore $I$–$V$ curves should strongly depend on the $B$ in all the voltage regions in this process. Hence, this case does not seem to explain the $B$ independent feature in the negative voltage region in Figure 8b. The third case may be less possible because Ni has a very small spin–orbit interaction.

On the other hand, the change of $I$–$V$ curve with applied $B$ is quite symmetric in the 1D MCI regime [$T = 15$ K($> T_c$)]. When CB has vanished at this high temperature region, the tunnel barrier becomes a simple tunneling resistance. Thus, the electron transport is dominated by the Ni-nanowire, which has the symmetric structure. It is consistent with the symmetric $I$–$V$ change on the applied $B$. As a typical example, positive magnetoconductances (MC) have been observed in weak localization as a result of phase interference effect of electron waves [e.g., $G = \log(B)$ in 2D weak localization]. Our case, however, may not correspond to it, because Altshuler's formula for MCI, which exists in our Ni-wire, took into account only charge of electrons for quantum correction. In addition, the $B$ dependence of the 1D MCI is not clearly reported, especially in ferromagnetic nanowires. Thus, it is difficult to identify the origin of positive MC and also its correlation with $T_c$ from this $B$ dependence.

Anyway, in order to reveal the mechanisms for magnetoconductance, detailed measurements are indispensable taking into account ferromagnetic nanowire.

### 3.1.4. Conclusion

Coulomb blockade depending on the one-dimensional mutual Coulomb interaction in the external electromagnetic environment was reported for the first time in an array of disordered Ni-nanowire/Al$_2$O$_3$/Al located in parallel, fabricated using nanoporous alumina film. Observed $G_0$ anomaly and its linear $G_0$ vs temperature relation qualitatively agreed with Zeller and Cleland's reports of CB. It was also quantitatively concluded from the extended Zeller's model in the tunnel junction array. At $V > V_{CB}$, only the 1D MCI following Altshuler's formula in the disordered Ni-wire governs the conductance mechanism. In contrast, at $V < V_{CB}$,

CB emerged accompanied with 1D MCI also following Altshuler's formula. The 1D MCI in the Ni-wire played the key roles of high Re[$Z_t(\omega)$] and $R_L$ in phase correlation theory for our CB in the single junction system. It was supported by the fact that CB was very sensitive to the diffusion constant $D$ of the MCI, yielding the linear $T_c$ vs $D^{1/2}$ relation. This relation was interpreted as a result of the correlation between the charging energy $E_c$ of CB and the energy quantum $E_N$ of the fluctuating field in the Ni-wire. Tunneling electrons could transfer $E_c$ to the EME by exciting this energy quantum $E_N$ ($= h\omega_N$), although it was a small energy transfer. It is consistent with PC theory. In contrast, MCI also acted as a high $R_L$. Too large a mutual Coulomb scattering rate, however, yielded large $E_N$, smearing the CB by the commutation relation [$\Delta\varphi, \Delta Q$] $= ie$. This linear $T_c$ vs $D^{1/2}$ relation was reconfirmed by the linear wire diameter dependence of $T_c$. The presence of $T_c$ and different conductance mechanisms classified at $T_c$ was also obviously reconfirmed by the magnetic field dependence of the $G_0$ vs temperature relation.

This work reported on the correlation of CB with the 1D MCI in the external environment in a single junction system. In contrast, when phase coherence of electron waves is conserved in disordered materials, a variety of mesoscopic phenomena emerges (e.g., AB effect, UCF, weak localization). They will bring us novel mesoscopic phenomena associated with single electron tunneling. We will report it in the very near future by utilizing our porous alumina film (e.g., by depositing multiwalled carbon nanotubes into the nanopores).

## 3.2. Correlation with Weak Localization in Carbon Nanotubes

### 3.2.1. Introduction

We report on correlation of Coulomb blockade in a single tunnel junction with phase interference effects of electron waves in its external electromagnetic environment, by utilizing multiwalled carbon nanotubes. Experimental results and analysis suggest that a high impedance external environment caused by weak localization in the MWNT can yield Coulomb blockade, in accordance with phase correlation theory. It is also revealed that the Coulomb blockade is very sensitive to phase modulation in the MWNT, which acts as a high impedance transmission line.

Coulomb blockade, a typical phenomenon associated with single electron tunneling, has been successfully observed in a variety of systems. Recently, the correlation with phase of electron waves and spins that exist in the EME has attracted much attention, because Coulomb blockade is very sensitive to EME. Most such studies have been performed in multijunction systems. For instance, Coulomb blockade was not observed to destroy the phase coherence of electron waves in quantum dots inserted to an Aharonov–Borm ring and did not require phase coherence with the EME [19], whereas it was drastically affected by the spin coherence of the electrons, according to many body effects in quantum dots (i.e., artificial atoms connected to lead) [20]. On the other hand, no work has reported it in single junction systems. It is because correlation between Coulomb blockade

and its external environment in single junction systems has characteristics quite different from those in multijunctions, although it is much more sensitive to the external environment. It has been well known as phase correlation theory [21, 22].

Phase correlation theory implies that the external electromagnetic environment plays the following two key roles. (1) The tunneling electron transfers a charging energy ($E_c$) to the external environment, yielding Coulomb blockade. (2) Fluctuation of the external environment fluctuate the junction surface charge by coupling with the zero-point oscillation, smearing out Coulomb blockade. To realize the first role and avoid the second role, the real part of the total impedance of the external environment ($\mathrm{Re}[Z_t(\omega)]$) must be much larger than resistance quantum ($R_Q = h/e^2 \sim 25.8$ k$\Omega$). This is the key factor in phase correlation theory. A part of $Z_t(\omega)$ also must be closely located to a single junction to avoid the second role as a high impedance transmission line $R_L$ ($\gg R_Q$). Since the connection of this high $R_L$ automatically results in a high $Z_t(\omega)$, the first role can occur also in the $R_L$ region.

Phase correlation theory has been experimentally confirmed [23]. Some works also reported good agreement with the current vs voltage [or conductance ($G$) vs voltage] feature observed in the weak tunneling case [24], and recently even in the strong tunneling case [25, 26].

Here, we focus on the correlation of Coulomb blockade in a single junction with the phase coherence of electron waves in its external environment, based on phase correlation theory. We ask the question, "Can weak localization play two such roles in a single junction system, yielding Coulomb blockade?" It corresponds to the question, "How different are the impedance mechanisms between phase correlation theory and weak localization theory?" The total external environment impedance $Z_t(\omega)$ employed by phase correlation theory is interpreted as a delay of surface electron charge decay in the external environment, because it is described by a set of harmonic oscillators (i.e., a set of $LC$ circuits in a circuit model) with energy quantum $\hbar\omega$ and originates from the commutation relation between phase $\varphi$ of tunneling electron and junction surface charge $Q$ (i.e., $[\varphi, Q] = ie$). Energy transfer is performed by exciting this $LC$ mode in a circuit model and hence it should correspond to electron-charge related phenomena in realistic systems (e.g., electron–phonon scattering). Here, electron–phonon scattering decreases as temperature lowers and phase interference effects of electron waves, which are represented by weak localization, can also yield high impedance ($>R_Q$) at such low temperature [27].

However, since the impedance caused by weak localization is quite different from $Z_t(\omega)$ for the following two points. (1) Since it is a result of phase interference of electron waves in the diffusive regime, electron charge is not basically related. (2) Since it is an elastic process, any energy transfer cannot occur. Therefore, if one follows phase correlation theory (at least from the viewpoint of the role of energy transfer), no Coulomb blockade may be observed under a high impedance external environment caused by weak localization. We try to examine this hypothesis by directly connecting multiwalled carbons (MWNTs) with weak localization to single tunnel junctions by utilizing a nanoporous alumina film

template. Although Coulomb oscillation has been already reported in single-walled carbon nanotube systems with multitunnel junctions [28], it should be noticed that this work has a quite different meaning from those.

### 3.2.2. Experiments and Discussion

We measured averaged static electric characteristics of the sample shown in Figure 9a. Figure 10a clearly exhibits a zero-bias $G$ ($G_0$) anomaly.

The shape of the $G_0$ anomaly is drastically varied near $T = 5$ K and the shape at 2 K is quite different from the inset shown as a reference [29]. It is evidence that the nanomaterials connected to single-tunnel junctions strongly
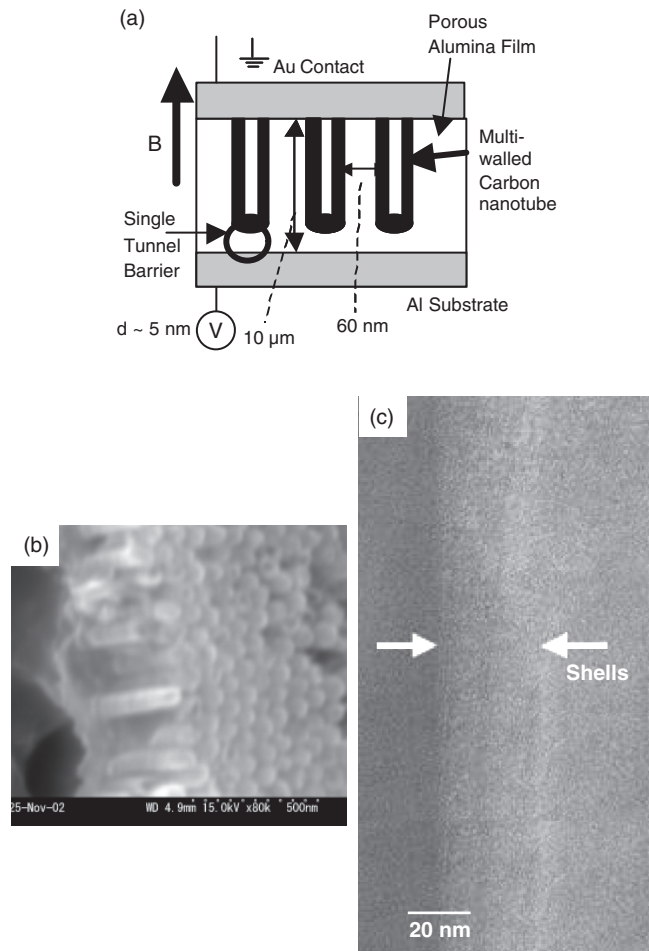


**Figure 9.** (a) Schematic cross-section of the sample, an array of single-tunnel junctions connected to multiwalled carbon nanotubes (i.e., array of Al/Al$_2$O$_3$/MWNTs). Nanoporous alumina film easily allows us to realize this structure, because single tunnel junctions are automatically formed at the bottom part of each nanopore filled by MWNTs. The absence of a tunnel barrier at the Au/MWNT interface was actually confirmed by high resolution cross-sectional TEM imaging and X-ray analysis. It is the key for this work. (b) SEM image of the exposed MWNT array, after the Al$_2$O$_3$ layer was etched out. (c) High resolution cross-sectional TEM image of one-side shells of MWNT with about 26 shells and the mean radius of 17.5 nm. Reprinted with permission from [40], J. Haruyama et al., *Phys. Rev. B* 63, 073406 (2001). © 2001, American Physical Society.
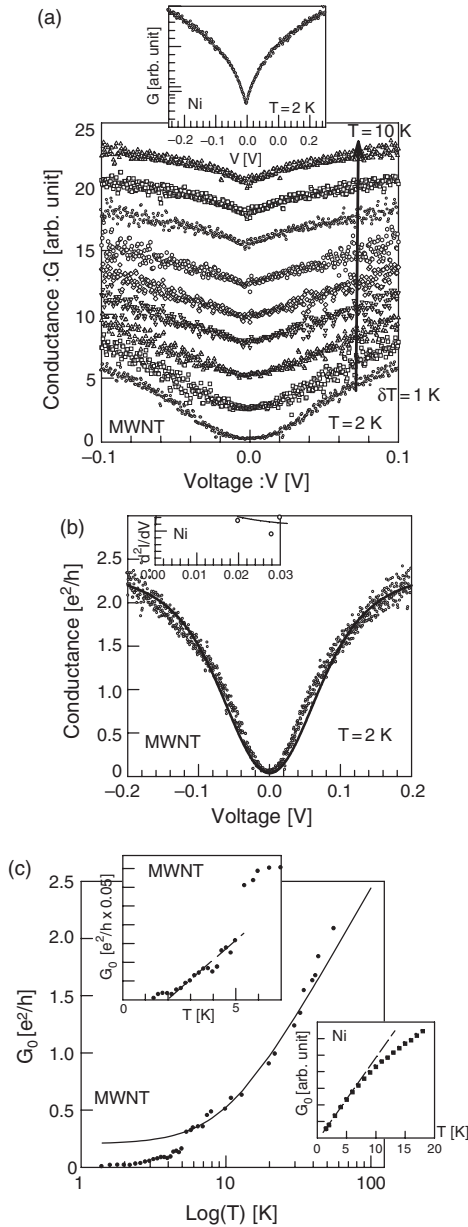
**Figure 10.** (a) Al/Al$_2$O$_3$/MWNT array. Temperature dependence of a typical conductance ($G = dI/dV$) vs voltage ($V$) curve, exhibiting a zero-bias $G$ ($G_0$) anomaly. The shape of the $G_0$ anomaly is drastically varied near $T = 5$ K. Inset: Al/Al$_2$O$_3$/Ni-nanowires array: $G$ vs $V$ curve, exhibiting a different shape of $G_0$ anomaly[29]. The sample was fabricated by depositing nickel into the nanopores of the alumina film with exactly the same nanostructure parameters as in Figure 1a. (b) MWNT system. Data fitting to $G$ vs. $V$ curve of Figure 2a by phase correlation theory. The solid line is the result calculated from Eqs. (1)–(3). The data and calculation results are in nice agreement, implying that the MWNT acts as the high external environment impedance for this Coulomb blockade. (c) MWNT system. Temperature ($T$) dependence of $G_0$ shown in Figure 2a. The solid line is the result calculated by the two-dimensional weak localization formula of MWNT. Upper inset: Linear $G_0$ vs temperature relation at temperatures below 5 K in (c), indicating evidence of Coulomb blockade in an array system[29]. Lower inset: Ni-nanowire system. Temperature dependence of $G_0$, indicating a linear $G_0$ vs temperature relation at low temperatures. Reprinted with permission from [40], J. Haruyama et al., *Phys. Rev. B* 63, 073406 (2001). © 2001, American Physical Society.

contribute to the $G_0$ anomaly. The $G_0$ anomaly in Figure 10a can be well fit by phase correlation theory as shown in Figure 10b and as explained in the next paragraph, whereas that in the inset of Figure 10a cannot be directly fit by phase correlation theory. Its first derivative (i.e., $dG/dV$ vs $V$ curve) is fit by Nazarov's theory introducing a mutual Coulomb interaction to the external environment of Coulomb blockade [30] as shown in the inset of Figure 10b. This large difference is also evidence that Coulomb blockade in the single junction system can be much influenced by mesoscopic phenomena in the nanowires directly connected.

Figure 10c is distinguished by the following three temperature regions; (1) above 10 K: $G_0$ vs $\log(T)$ relation is linear; (2) 5 k–10k: its saturation region; (3) below 5 K: $G_0$ vs temperature relation is linear (see the upper inset). This linear $G_0$ vs temperature relation is also observable in the lower inset. We have argued that it provides strong qualitative and quantitative evidence of Coulomb blockade in an array of single junctions located in parallel (i.e., as a temperature dependence of averaged $G_0$) [29]. The temperature of 5 K also agrees with that at which the shape of the $G_0$ anomaly starts to change in Figure 10a, suggesting that the $G_0$ anomaly below 5 K originates from Coulomb blockade.

In order to confirm Coulomb blockade in an Al/Al$_2$O$_3$/MWNTs array and clarify its connection with phase correlation theory, we first numerically calculate a $G$ vs $V$ curve, normalized by tunneling resistance ($R_t$) and the number of junctions, using Eqs. (1)–(3) from phase correlation theory [21, 22]. We then fit the $G$ vs $V$ curve measured at 2 K in the Coulomb blockade regime in Figure 10a by the calculation result. Since we know the $R_t$ of 300 k Ω (larger than $R_Q$) from the measurement, the fitting parameters are the resistance of the external transmission line ($R_L$) and junction capacitance ($C$) as $\omega_{RC} = 1/(R_L C)$.

$$I(V) = \frac{1 - e^{-\beta eV}}{eR_t} \int_{-\infty}^{+\infty} dE \frac{E}{1 - e^{-\beta E}} P(eV - E) \quad (15)$$

$$P(E) = \frac{1}{2\pi\hbar} \int_{-\infty}^{\infty} dt\, e^{J(t) + i\frac{E}{\hbar}t} \quad (16)$$

$$J(t) = 2 \int_{-\infty}^{\infty} \frac{d\omega}{\omega} \frac{\mathrm{Re}[Z_t(\omega)]}{R_Q} \frac{e^{-i\omega t}}{1 - e^{-\beta\hbar\omega}} \quad (17)$$

where $\beta$ is the $1/kT$ and $Z_t(\omega) = 1/[i\omega C + Z(\omega)^{-1}]$ is the total EME impedance consisting of junction capacitance $C$ in parallel with an external environment impedance $Z(\omega)$ in a circuit model. $J(t)$, $P(E)$, and $I(V)$ are phase correlation function, Fourier transform of $J(t)$, and the tunnel current, respectively.

These three equations well represent the argument of phase correlation theory mentioned in the Introduction. Phase fluctuation of the junction surface charges caused by the tunneling electrons and its time evolution result in Eq. (17) through the commutation relation between charge and phase. Tunneling current (probability) is obtained from Eq. (15) by purterbatively treating the tunneling Hamiltonian using Fermi's golden rule and $P(E)$, which is interpreted as a probability density for the tunneling electrons to transfer $E_c$ by exciting the external environment mode described by $J(t)$. If $\mathrm{Re}[Z_t(\omega)]/R_Q$ is much smaller than one in Eq. (17), $P(E)$ becomes delta function $\delta(E)$ and

thus Coulomb blockade disappears in Eq. (15). In addition, phase fluctuation $\varphi$ can be also neglected and thus charge fluctuation $Q$ on the junction surface diverges due to the commutation relation $[\varphi, Q] = ie$, smearing the Coulomb blockade voltage $e/2C$.

As shown by the solid line in Figure 10b, the measurement and calculation results are in excellent agreement in our weak tunneling case (i.e., $R_t$ of 300 k$\Omega > R_Q$). The best fitting gives the $R_L$ of 450 k$\Omega$ and the Re$[Z_t(\omega)]$ with mostly the same order value as $R_L$. This impedance of 450 k$\Omega$ mainly corresponds to the impedance of MWNT ($R_{NT}$) in our system, because the MWNT was directly connected to the single junction and the resistance of the gold contact layer including the gold/MWNT interface was at most on the order of 100 $\Omega$. We cannot find the impedance of 450 k$\Omega$ in any parts of the system other than the MWNT. The value of 450 k$\Omega$ as the resistance of MWNT is also in good agreement with that in a previous report [31]. In addition, note that this 450 k$\Omega$ is actually larger than $R_Q$. Therefore, we conclude that our Coulomb blockade is consistent with phase correlation theory, and that the MWNT acts as both a high $Z_t(\omega)$ for transferring charging energy and a high $R_L$ for avoiding external environment fluctuation, because the MWNT is closely connected to the single junction.

The origin of this high impedance of carbon nanotubes is the key point for this work. As we expected, it can be qualitatively understood as a result of weak localization from the curve fitting shown in Figure 10c. As shown by the solid line, the $G_0$ vs temperature characteristic is in nice agreement with the formula of 2D WL of MWNT [28], except for the Coulomb blockade temperature region,

$$G(T) = G(0) + \frac{e^2}{2\pi^2\hbar} \frac{n\pi d}{L} \ln\left[1 + \left(\frac{T}{T_c(B, \tau_s)}\right)^p\right] \quad (18)$$

where $n$, $d$, $L$, and $\tau_s$ are the number of shells, the diameter of the inner shell of the MWNT, the length of the MWNT, and the relaxation time of spin-flip scattering, respectively. The contribution of number of MWNTs and $R_t$ were taken into account by the term of $G(0)$. The best fitting gives $n = 18$, $p = 2.1$, and $T_c = 10$ K. Here, a main difference from the past reports [31] is the $T_c$ as high as 10 K. This high $T_c$ is understandable by the presence of magnetic impurities (cobalt), which was deposited into the nanopores as a reactant for carbon nanotube growth, in the MWNT with a very small volume [29]. In addition, the localization length $\xi_{loc}$ can be estimated to be on the order of 1 $\mu$m ($<$ the MWNT length of 10 $\mu$m) from the carbon nanotube impedance of 450 k $\Omega$. It also supports that our MWNT is in the weak localization regime.

Based on these confirmations [i.e., (1) Coulomb blockade following phase correlation theory with near 450 k$\Omega$ of the external impedance, (2) the impedance of 450 k$\Omega$ existing only in the MWNT in our system, (3) the origin of the highly resistive MWNT being weak localization], we finally conclude that the weak localization in the multiwalled carbon nanotube plays the roles of both high $Z_t(\omega)$ and high $R_L$ for the Coulomb blockade. This conclusion is controversial to our hypothesis mentioned in the Introduction. The reason may be interpreted as follows at this stage. Of course, even apart from this interpretation, observed facts and analyses strongly support our conclusion.

Unless the tunneling electrons cannot transfer their energy to the environment, a tunneling event is allowed and, hence, Coulomb blockade cannot be caused in any case, if one follows PC theory [i.e., Eqs. (4)–(6)]. This is of core importance also for MQC (MQT) following the spirit of Caldeira and Leggett. MQT is much smeared by energy dissipation in its external environment. There may exist, however, the following two exceptions [30]; (1) the Debye–Waller factor exp$(-\rho)$ in Mössbauer effect in $LC$ mode and (2) infrared divergence in $RC$ mode at finite temperature.

The latter comes from the analogy between the motion of free Brownian particle and the $RC$ environmental effect with the impedance $Z_t(\omega) = R$ and is relevant for the $RC$ environment with the impedance much larger than $R_Q$. With $Z_t(\omega) = R$, Re$[Z_t(\omega)]$ is given by $R/(1 + (\omega RC)^2)$ and then $(\pi/C)\delta(\omega)$ for very large $R$ at finite temperature. Hence, energy transfer is carried out only around $\omega = 0$ in accordance with $P(E) = \delta(E - E_c)$. This is the so-called infrared divergence. In this case, only thermal fluctuation yields a time evolution of phase $J(t)$ (i.e., diffuse the free Brownian particles), leading to $J(t) \propto t$ for long time, because the $RC$ mode at very low frequency has basically no time-fluctuated electromagnetic factor. Therefore, the tunneling electrons can have a chance to transfer the charging energy $E_c$ by exciting the $RC$ mode through thermal fluctuation even in the nondissipative electromagnetic environment, particularly in the environment sensitive to electron phase fluctuations like localization. This new interpretation means a possibility that thermal environment is taken into account as $P(E)$ in Eq. (4), if it is coupled with the electromagnetic environment. Our result may be qualitatively interpreted by this case at least from the following three points, (1) Re$[Z_t(\omega)]$ of about 450 k$\Omega$ is much larger than $R_Q$, (2) Resistance of MWNT is basically frequency independent. (3) The measurement temperature is 2 K.

Otherwise, $P(E)$ in Eqs. (4) and (5) may have to be reinterpreted as "*the other probability*," not associated with the energy transfer probability of the tunneling electrons to the EME. Here, $P(E)$ is the Fourier transform of $J(T) = \langle[\tilde{\varphi}(t) - \tilde{\varphi}(0)]\tilde{\varphi}(t)\rangle$, a time evolution of phase fluctuation $\tilde{\varphi}$ in the EME, and the origin of the phase was defined as $\varphi(t) = e/\hbar \int dt V(t)$, where $V(t) = Q(t)/C_j$ is the voltage across the tunnel junction. The phase interference effect in localization also originates from this definition. Hence, $J(t)$ is a time evolution of $\tilde{\varphi}$ but should be attached to the localization effect so as not to destroy phase coherence in the MWNT. In this sense, $P(E)$ may be reinterpreted as a transmission probability of electrons, associated with $J(t)$ in the localization regime, in the MWNT. This does not deny the energy dissipation in external environment. In this case, energy transfer may take place in the contact metal electrodes with lower impedances.

In addition, we may have to perform more careful data fitting from the following points.

(1) Junction capacitance $C$: We used $C$ obtained in our past report [28]. Since the $C$ was estimated from data fitting by Nazarov's theory, it is not yet experimentally confirmed.

(2) Parasitic capacitance $C_p$: We did not take into consideration the influence of the $C_p$ of MWNT. When we

define $L = \tau \times c$ (where $\tau \sim h/eV$, $c$ is the velocity of light in vacuum) as the geometry for an effective $C_p$ based on the horizontal model [33] and included the $C_p$ in the data fitting, it does not exhibit perfect agreement. $C_p$ for better agreement should be smaller than that calculated from $L = \tau \times c$. To explain this difference, a smaller velocity instead of $c$ may have to be employed, because our MWNT has very disordered surface.

(3) LCR model: We also have employed the *RC* mode as a lumped circuit model in PC theory here. Since, however, MWT has distributed *L*, *R*, and *C* including this $C_p$ in the actual system, the *LCR* transmission line model will have to be introduced.

However, even apart from these data fitting problems, the linear $G_0$ vs temperature dependence, the high impedance EME only in the MWNT directly connected to the junction, and its dependence on the localization effect will support our conclusion.

Here, why Coulomb blockade disappears near 5 K in Figure 10c is also not obvious with the $G_0$ discontinuity. In the Ni-nanowire system shown in Figure 10c, inset, Coulomb blockade also disappeared around 6 K due to the phase fluctuation caused by mutual Coulomb interaction in the Ni-wire [29]. Based on this result, we modulate the phase of electron waves in the MWNT by applying a magnetic field also in this case and observe its influence on the Coulomb blockade. As shown in Figure 11, the $G_0$ vs magnetic field ($B$) relation exhibits oscillation. Such oscillation
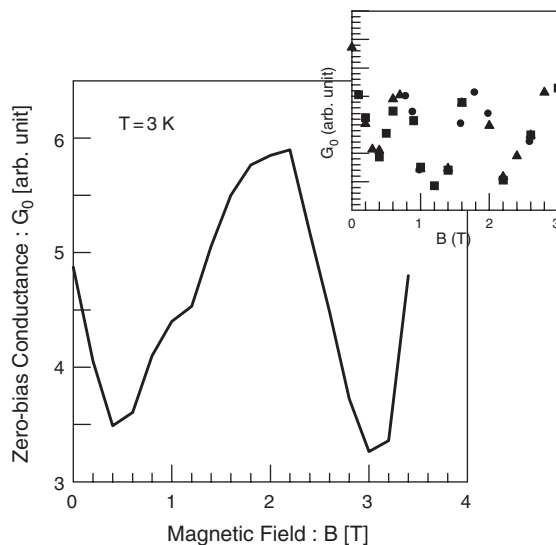


**Figure 11.** Magnetic field ($B$) dependence of $G_0$ in the CB temperature regime. Magnetic field was applied parallel to the tube axis within a few degrees as shown in Figure 1a. The radius of the AAS cylinder calculated from the first oscillation peak ($\Delta B = 2.2$ T) is in excellent agreement with the mean radius of the actual MWNT, although we did not take into account the contribution of the tube length, the misalignment angle of B to the tube axis, and the number of many MWNTs for the oscillation magnitude. It also indicates that the electron wave flows either in all of the shells or only in the midshells. Reprinted with permission from [40], J. Haruyama et al., *Phys. Rev. B* 63, 073406 (2001). © 2001, American Physical Society.

in MWNT has been understood as the Altshuler–Aronov–Spivak (AAS) effect in a graphite cylinder [32], which originates from phase interference of the electron waves encircling the cylinder in opposite directions and modulated by magnetic flux enclosed, with an oscillation period $\Delta B = (h/2e)/(\pi r^2)$ where $r$ is the radius of the cylinder. Here, the radius can be estimated to be 17.3 nm from the first oscillation peak. This radius is in excellent agreement with the mean radius of our actual MWNT of 17.5 nm. It is a straightforward indication that this conductance oscillation originates from AAS effect.

This result implies that the Coulomb blockade is very sensitive to the electron phase fluctuation of the MWNT even under a high $R_L$ ($>R_Q$) directly connected to a single junction. Since the high $R_L$ is caused by weak localization in the MWNT, this result may be relevant. It also suggests the possibility that the elimination of Coulomb blockade near $T = 5$ K in Figure 10c may be attributed to the dephasing process by strong spin-flip scattering in the MWNT, as well as that in the Ni-nanowire system.

# 4. MULTIWALLED CARBON NANOTUBES

## 4.1. Spintronics

### 4.1.1. Antilocalization Due to Spin–Orbit Interaction in Metal-Doped Nanotubes

***Introduction*** Electrode atoms are slightly diffused, with only about 5% volume-ratio, into the top end of MWNTs, standing in nanopores of porous alumina membranes. Diffusion of light-mass materials (carbon and aluminum) leads to weak localization in the AAS oscillations, which is qualitatively consistent with previous works on MWNTs. In contrast, we find that diffusion of heavy materials (gold and platinum) changes this weak localization into an antilocalization in the MWNT bulk. This effect is only observable when electrons are injected through the diffusion region and undergo a $\pi$-phase shift in their electron waves, caused by polarized injection of spin-flipped electrons due to spin–orbit interaction in the diffusion region of the MWNT bulk.

Single-walled carbon nanotubes are conducting molecular nanowires that exhibit a variety of mesoscopic phenomena. There is a renewed interest in these nanostructures because their characteristics are very sensitive to materials deposited onto the tube inner space [34]. In contrast, the physical properties of MWNTs have been interpreted only in terms of quantum phase interference effects of electron waves in the diffusive regime at the single-molecular level (e.g., WL [35–37], AAS oscillations [38–42], universal conductance fluctuation [35], possible metal–insulator transition [43], and strong spin coherence [44]). The investigation of correlation of such interference phenomena with dopant materials in the tube inner space or the MWNT itself has so far received no attention.

AAS oscillations and WL are the typical phase interference effects of electron waves observed in MWNTs. Constructive phase interference in current paths encircling MWNTs with time-reversal symmetry leads to WL, when the sample size is smaller than both the phase coherence length and the localization length [45–47]. The presence

of a resistance maximum and a negative magnetoresistance (MR) around zero-magnetic field reflect WL in the AAS oscillations [48]. Previous works on MWNTs reported only this type of AAS oscillation. On the other hand, the presence of a strong spin–orbit interaction (SOI) in thin metallic cylinders formed by heavy mass atoms leads to antilocalization (AL), reflected by a resistance minimum and a positive MR around zero-magnetic field, in the AAS oscillations [49]. This is because the SOI causes electron-spin flipping, thereby leading to change of the electron phase by $\pi$ [50–52]. No group, however, has yet successfully observed this electron-spin flipping and AL in the AAS oscillations in MWNTs.

In this chapter we find that diffusion of heavy-mass atoms, deposited onto the top end of MWNT electrodes *with only about 5% in volume-ratio* drastically changes this WL to AL in the bulk of the MWNTs. Based on a revised Altshuler's theory, we show that SOI, depending on the diffused atom mass and the diffusion volume-ratio, is the key for understanding the WL to AL change. We find that this phenomenon is observable only when electrons are injected through the diffusion region and is understood as spin flipping of electron waves (i.e., phase shift by $\pi$), caused by SOI in the diffusion region of the bulk of MWNTs.

***Experiments and Discussion*** In electrical measurements of MWNTs performed in previous works, an individual MWNT was deposited on a substrate [38, 39], and gold (Au) fingerlike electrodes were fabricated by lithography over the MWNT. Only the upper half-part of the MWNT that did not face the substrate, had an interface with the electrodes. Hence, it was difficult to diffuse by annealing the electrode-atoms into one entire end of the MWNT along the circumference of the NT (including the lower half-part facing the substrate). In contrast, we reported earlier on a different method to obtain the characteristics of MWNT arrays standing in nanosized diameter pores of porous Alumina membranes [40–42]. In this method, after the deposition of MWNTs into the nanopores (Fig. 12e), the top ends of the standing MWNTs were exposed from the surface of alumina membranes (Fig. 12a–d) and, then, a thick electrode was directly deposited on all of the top ends (Fig. 12f). Hence, diffusion of electrode-atoms takes places into the entire end of the standing MWNTs. For this reason, the diffusion region of the electrode-atoms forms the other nanotubelike structure on the top end of MWNTs (Fig. 12f). In fact, we confirmed that our sample clearly exhibited the diffusion of Au atoms, deposited as an electrode material, into the top end of MWNT, in [81].

Figure 13 shows typical MR oscillation characteristics observed in the samples with four different electrode materials. In this work, we measured a large number of MWNTs in one array sample at the same time. However, although this smears MR oscillation in some cases, we assumed that the observed characteristics were the simple superposition of the characteristic of each MWNT from the following three reasons: (1) The uniformity of the tube diameter was extremely high (e.g., half-width of distribution was less than 13). (2) The spacing between the MWNTs was relatively large. (3) According to [53], the characteristics of the individual MWNTs and the MWNT arrays fabricated by this method were basically consistent.
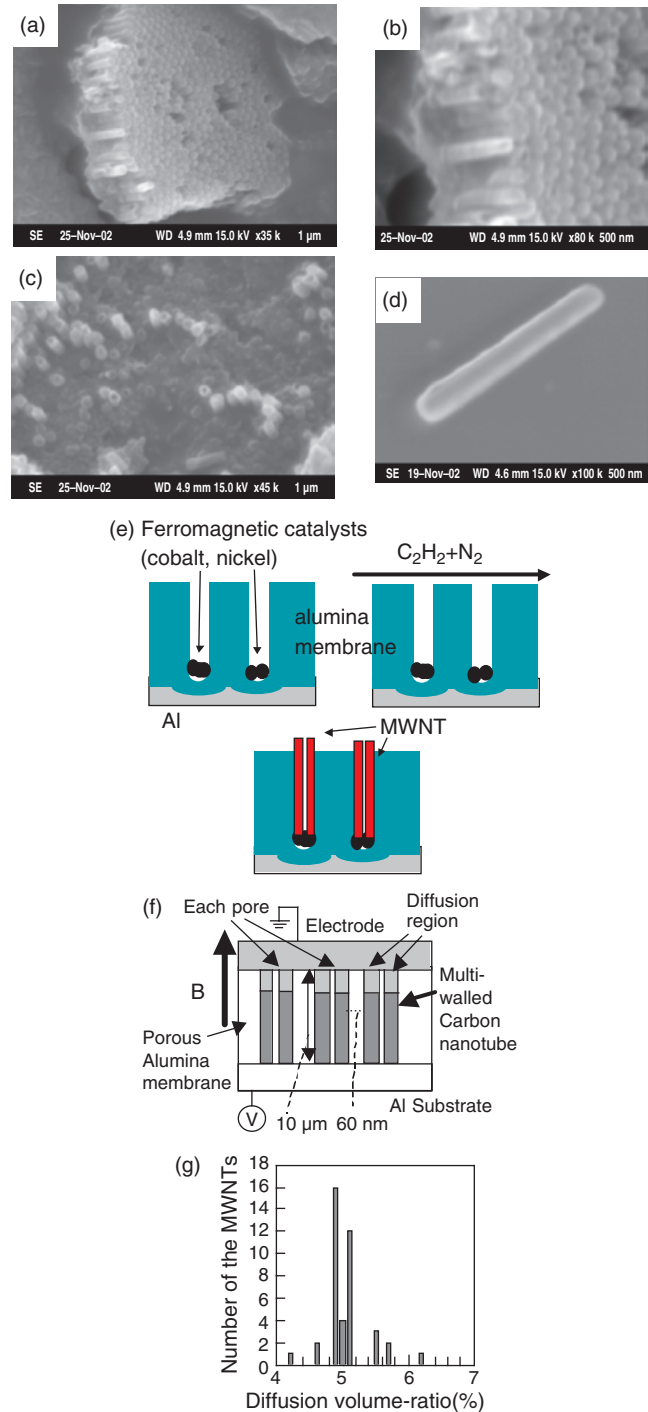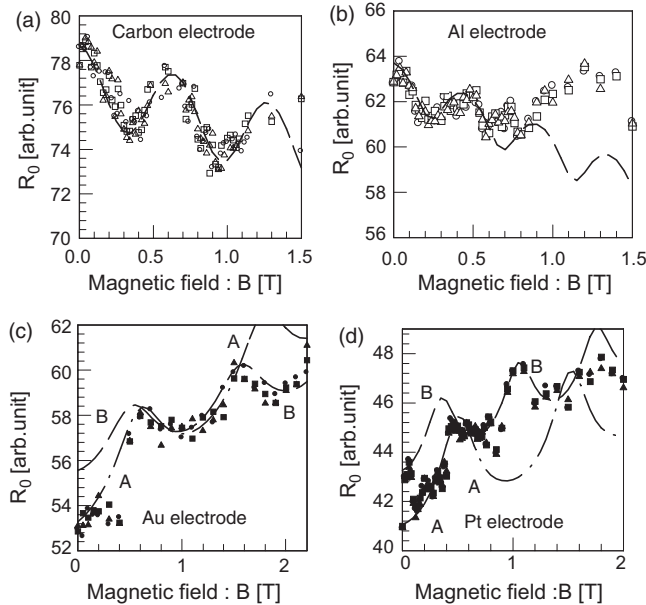


**Figure 12.** (a) SEM overview image of the exposed top part of a MWNT array, exhibiting a high regularity like a honeycomb. (b) High resolution image of (a). (c) SEM top view of (b), implying the opened top portion. (d) SEM image of one MWNT. (e) How to synthesize MWNTs in nanopores of alumina membrane by chemical vapor deposition. (f) Schematic cross-section of the MWNT array sample for this section. Thin tunnel barriers attached to the bottom end of MWNTs, used for Section 3, were basically deleted in the experiments of this section. Hence, MWNTs have direct contact to Al substrate. (g) Distribution of the diffusion volume ratio of Au electrode, obtained from CSTEM images of one array. The total number of MWNTs investigated is 41. Reprinted with permission from [81], J. Haruyama et al., *Phys. Rev. B* 65, 33402 (2002). © 2002, American Physical Society.
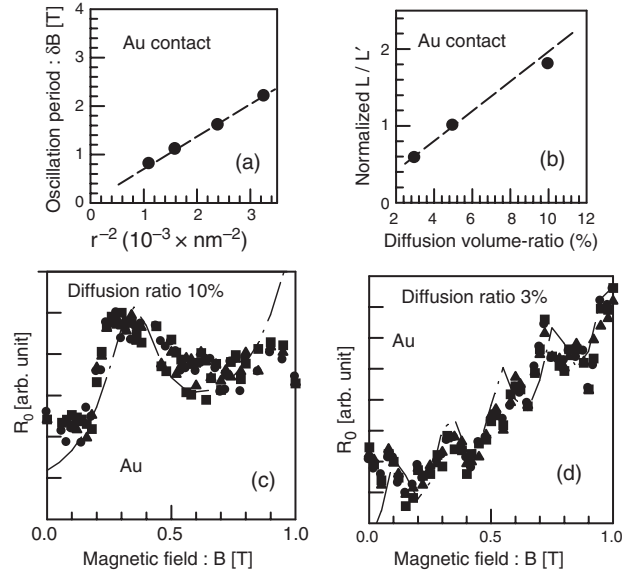
Since Figure 13a exhibits the MR maximum at $B = 0$ T and negative MR, the localization type is WL. This is qualitatively consistent with the previous works on AAS oscillations in MWNTs. Figure 13b also exhibits a MR oscillation with WL, although the decrease of MR saturates around $B = 0.5$ T. On the contrary, the MR oscillations shown in Figure 13c and d clearly reveal the MR minimums at $B = 0$ T and positive MRs which imply the presence of AL, although the oscillations themselves are not clear in comparison with (a) and (b). The positive MR is in contradiction with previous works [38–42].

In order to confirm the correlation between the observed MR oscillations and the AAS effect, we investigated the dependence of the oscillation period, $\Delta B$, on the MWNT radius, $r$. Figure 14a shows the result, which is a linear $\Delta B$ vs $r^{-2}$ relation with the slope value of $2.5 \times 10^{-16}$ (J•S/C). This is quantitatively in good agreement with the relation $\Delta B = (h/2e)/(\pi r^2)$ given by the AAS oscillation theory, with $(h/2e)/\pi \sim 6.5 \times 10^{-16}$.

Next, we discuss the influence of the electrode materials on the type of localization observed in the AAS oscillations as suggested by the results in Figure 13. The atomic numbers of Pt and Au are 78 and 79, respectively, whereas those of C and Al are 6 and 13. This indicates that the emergence of WL or AL strongly depends on the mass of the electrode-material atoms. Since AL is observable only in the samples with heavy-mass electrode materials (Pt and Au), this is qualitatively consistent with the previous works on thin Mg and Li cylinders [48, 49], which emphasizes the contribution of SOI. However, it should be noticed that the



**Figure 14.** (a) MR oscillation period vs square of mean tube radii. Mean tube radii of the array samples are confirmed by TEM and SEM images. (b) Normalized $L_\varphi/L'_\varphi$ vs diffusion volume ratio of Au atom to the MWNT. Each $L_\varphi/L'_\varphi$ was obtained from the best data fitting to Figure 3c and d by Eqs. (15)–(18) and then normalized by that for line A of the Figure 2c sample with 5% ratio. (c) MR oscillation in the sample with the diffusion volume ratio two times higher than the Figure 2c sample. Dotted line means the calculation result from Eqs. (15)–(18). (d) That with the diffusion volume ratio 0.6 times smaller than the Figure 2c sample. The smaller oscillation period is due to the larger tube radius caused by the fabrication process to get the longer tune length. Reprinted with permission from [81], J. Haruyama et al., *Phys. Rev. B* 65, 33402 (2002). © 2002, American Physical Society.

diffusion region of our electrode materials is only about 5% of the volume-ratio in our MWNTs. Hence, one deals with a qualitatively different phenomenon from any previous observations in thin metallic film systems, although nothing of this kind has been reported in MWNT systems.

In order to resolve this issue, we carry out a data fitting procedure based on Altshuler's equations for AAS oscillations [48]. In [48], the equations for AAS oscillations including the contribution of SOI can be rewritten as

$$\delta G = -(e^2/\pi h)(2\pi r/L_s)[(1/2 + \beta)Z_\phi(L_\varphi(H)) \\ - 3/2 Z_\phi(L'_\varphi(H))] + \alpha(H) \quad (19)$$

$$Z_\phi(L_\varphi(H)) = \ln(L_\varphi/\ell) + 2\sum_{n=1}^{\infty} k_0(n(2\pi r/L_\varphi)) \\ \times \cos[2\pi n(\Phi/(hc/2e))] \quad (20)$$

$$1/L_\varphi^2 = 1/D\tau_\varphi \quad (21)$$

$$1/L_\varphi'^2 = 1/L_\varphi^2 + 2/D\tau_{so} \quad (22)$$

where $L_s$, $\beta$, $L_\varphi$, and $L'_\varphi$ in Eq. (19) are the tube length, the constant depending on electron–electron interaction, and the phase coherent length without and with SOI, respectively. $\ell$, $k_0$, and $\Phi$ in Eq. (21) are the mean free path, the Macdonald function, and the magnetic flux ($\pi r^2 H$), respectively. $D$, $\tau_\varphi$, and $\tau_{so}$ in Eqs. (21) and (22) are the diffusion constant,



**Figure 13.** Dependence of magnetoresistance oscillations on the top electrode materials. Four samples with different electrode materials [i.e., (a) carbon, (b) aluminum, (c) gold, and (d) platinum] were measured. Magnetic field was applied parallel to the tube axis. We basically plot the three times measurement results at each magnetic field. Dashed and dotted lines are the calculation results by Eqs. (15)–(18). Reprinted with permission from [81], J. Haruyama et al., *Phys. Rev. B* 65, 33402 (2002). © 2002, American Physical Society.

the relaxation time for inelastic scattering, and the relaxation time for SOI, respectively. Here, $\alpha(H)$ in Eq. (19) represents the increase or decrease of the mean value of conductance, depending on magnetic field $H$. We also neglected the contribution of magnetic field on $L_\varphi$ in Eq. (21).

Equation (19) has very simple physical meaning: The first term related to $Z_\phi(L_\varphi(H))$ basically represents the AAS oscillations without SOI (i.e., WL), whereas the second term with $Z_\phi(L'_\varphi(H))$ reveals the influence of SOI (i.e., AL) on the AAS oscillations, using Eq. (22). Equation (22) includes the term $1/D\tau_{so}$ as the contribution of SOI. If SOI is very weak, $\tau_{so}$ diverges to an infinite value and, hence, $L_\varphi/L'_\varphi$ becomes "1" because of $(L_\varphi/L'_\varphi)^2 = 1 + 2(L_\varphi^2)/D\tau_{so}$, leading to WL. On the contrary, if $\tau_{so}$ has a finite value, $L_\varphi/L'_\varphi$ becomes larger than "1" because of $2(L_\varphi^2)D\tau_{so} > 0$, leading to the increase of the oscillation amplitude of the second term of Eq. (19) and thus AL. Therefore, the contribution of $\tau_{so}$ can be represented by $L_\varphi/L'_\varphi$. We selected this $L_\varphi/L'_\varphi$ as the fitting parameter.

As shown by the dashed line in Figure 13, the measurement and calculation results are in good agreement in all the samples. This is interpreted as strong evidence for AAS oscillations. The best fittings to Figure 13a and b give $L_\varphi/L'_\varphi = 1$, assuming $L_\varphi = 10^{-5}$ m and $\beta = 2$. This strongly supports the absence of SOI and the presence of WL for the reason mentioned previously. In particular, the measurement and calculation results are in excellent agreement in Figure 13a. On the other hand, both Figure 13c and d are fitted by two independent oscillation modes depending on magnetic field (i.e., bimodal behavior) as shown by lines A and B, assuming finite values for $\tau_{so}$. Compared with the value of $L_\varphi/L'_\varphi$ of the carbon electrode sample, the best fittings give $L_\varphi/L'_\varphi = 9.18$ and $L_\varphi/L'_\varphi = 9.3$ for lines A and B in Figure 13c and $L_\varphi/L'_\varphi = 9.28$ and $L_\varphi/L'_\varphi = 9.4$ for lines A and B in Figure 13d, respectively. These values of $L_\varphi/L'_\varphi \sim 9$ ($> 1$) are strong evidence for the contribution of SOI and, hence, the emergence of AL, also for the reason explained. The comment for the bimodal behavior is mentioned in the later part of this chapter.

The central issue of this chapter is the physical relevance of $L_\varphi/L'_\varphi$, as obtained from the best fit shown in Figure 13, because Eqs. (19)–(22) do not relate to actual material parameters. Two facts make it possible to physically identify this $L_\varphi/L'_\varphi$: There is a correlation (1) with the atomic numbers of the electrode materials (i.e., mass of the atoms) and (2) also with the volume-ratio of the diffusion region to the MWNT.

From the viewpoint of correlation (1), the atomic numbers ($Z$) of C and Pt are 6 and 78. Reference [48] indicates that $\tau_\varphi/\tau_{so}$ is given by $(3L_\varphi^2/\ell a)(aZ)^4$, where $a$ is the fine structure constant ($\approx 1/137$). In the case of carbon, $\tau_\varphi/\tau_{so}$ can be estimated to be on the order of $10^{-6}$ in our system from this equation. This is nearly consistent with $\tau_{so} = \infty$ (i.e., $L_\varphi/L'_\varphi = 1$) obtained from the best fits in Figure 13a and b. In contrast, in the case of Pt, $\tau_\varphi/\tau_{so}$ can be estimated to be on the order of $10^{-2}$. This does not quantitatively agree with $\tau_\varphi/\tau_{so} \approx 5$ estimated from $L_\varphi/L'_\varphi \approx 10$ obtained from the data fitting. In this case, only the increase of $\tau_\varphi/\tau_{so}$ with the atomic number is in qualitative agreement. Hence, based only on [48], the physical meanings of $L_\varphi/L'_\varphi$ cannot be quantitatively identified from the atomic numbers.

In order to clarify correlation (2), we varied the diffusion volume-ratio by changing the MWNT length with a constant diffusion length in the same electrode-material samples. $L_\varphi/L'_\varphi$ was obtained from the best fit of the experimental data in Figure 14c and d by Eqs. (19)–(22) by identifying each MWNT length with $L_S$ in Eq. (19). As shown in Figure 14b, the relation between the $L_\varphi/L'_\varphi$ values and the diffusion volume-ratio is mostly linear. This is the strong evidence that factor (2) is the key to determine $L_\varphi/L'_\varphi$ (i.e., the contribution of SOI) and $L_\varphi/L'_\varphi$ has a correlation with actual systems. It implies that the contribution of SOI to AL is linearly proportional to the volume-ratio of the diffused Au atom.

Consequently, the diffusion of heavy-mass atoms, deposited as the electrode materials on MWNTs, at only about 5% in volume-ratio can drastically change WL to AL in the bulk of NTs. This can be shown by a phase shift of the electron waves by $\pi$, caused by spin flipping due to SOI in the diffusion region of MWNT bulk. However, which conjugated conditions are formed between the atom of Au or Pt and the carbon nanotube by annealing and how it leads to SOI is still an open question. Further investigation is indispensable to clarify this issue.

Based on the linear relation mentioned, the bimodal behaviors and the two different $L_\varphi/L'_\varphi$ values obtained in Figure 13c and d suggest the presence of two different distribution peaks in the diffusion volume of Au and Pt atoms in one array sample. The equal ratio of $L_\varphi/L'_\varphi$ from line B to line A ($\sim 1.013$) in both (c) and (d) also supports this conclusion. As a confirmation, we exactly investigated the distribution of diffusion volume-ratio in an array. As shown in Figure 12d, we could actually find two peaks at 4.9% and 5.1% of the volume-ratio. Since the ratio of 5.1%/4.9% is 1.041, this is nearly consistent with the $L_\varphi/L'_\varphi$ ratio between lines A and B ($\sim 1.013$). However, the reason they independently emerge in the different magnetic-field regions is still unclear.

Finally, we show why such a small diffusion region only at the one end of MWNT drastically changes the phase interference in the bulk of MWNT. Figure 15a shows MR oscillations when electrons are injected into the MWNTs from either the Au electrode or Al substrate. It reveals a polarity of AL and WL; that is, only when electrons are injected through the Au diffusion region does a positive MR (i.e., AL) emerge. This strongly supports the contribution of SOI caused in the diffusion region. As shown in Figure 15b, when the electrons are injected through the Au diffusion region, the electron phases are spin-flipped by the strong SOI right after the injection, and then they cause phase interference. Since the spin coherence is strongly conserved in all the phase interference paths of electron waves encircling the MWNT [44], it leads to the AL in the bulk of the MWNTs. In contrast, when the electrons are injected from the Al substrate, they are spin-flipped in the diffusion region, after most of the interference procedure is completed (i.e., after the interference paths were already closed) as shown in (b). Such electrons no longer contribute to the phase interference. These phenomena are the direct evidence of the important role played by the small diffusion region in the phase interference in the bulk of the MWNTs.

For the application of this effect, we propose a phase switching device like a CMOS circuit, as shown in Figure 16.
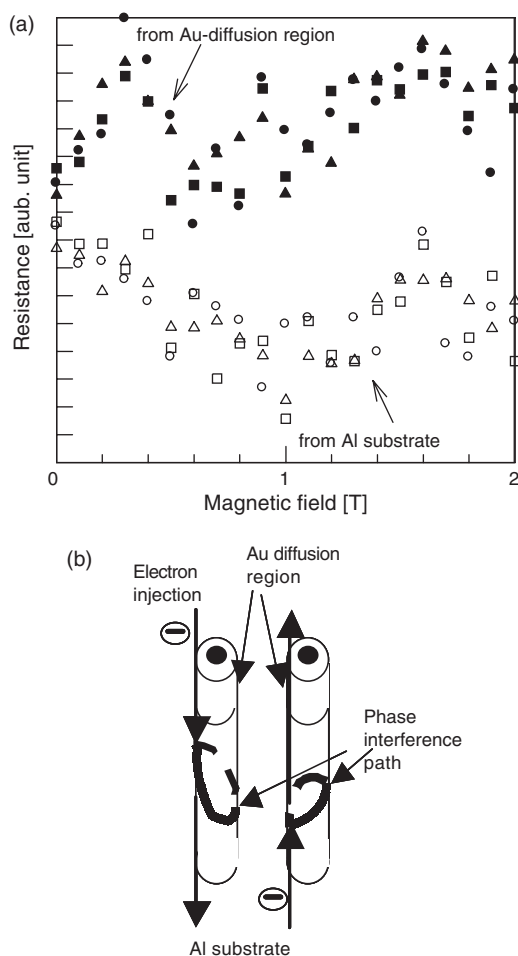
**Figure 15.** (a) MR features when electrons are injected from different electrode sides. Open and filled symbols are the MRs for the electron injection from the Al substrate and the Au electrode, respectively. (b) Schematic figures of MWNTs with the phase interference path, encircling the MWNT, for AAS oscillations and the direction of electron injection. Left and right figures mean the electron injections from the Au diffusion region and Al substrate sides, respectively.

When magnetic field is applied, WL is destroyed in the MWNT1 leading to high conductance, whereas AL is destroyed in the MWNT2 leading to low conductance. Hence, the current flows from $V_{DD}$ to $V_{out}$ and, hence, $V_{out}$ becomes "1" as shown in the left figure. In contrast, when magnetic field is not applied, MWNT1 and MWNT2 show WL and AL, respectively. Hence, no current flows between $V_{DD}$ and $V_{out}$. It makes the potential difference between earth and $V_{out}$ equal and, hence, $V_{out}$ becomes "0." This is a quite novel electron-phase switching device, although detailed adjustment of the resistances of MWNTs is of course required.

### 4.1.2. Anomalous Spin Interference Due to Excess Cobalt Catalyst and Strong Spin Coherence

**Introduction** We report on the sensitivity of localization effects, identified in conductance ($G$) versus logarithmic temperature (log [$T$]) relations ($G$ vs log [$T$] relations) and
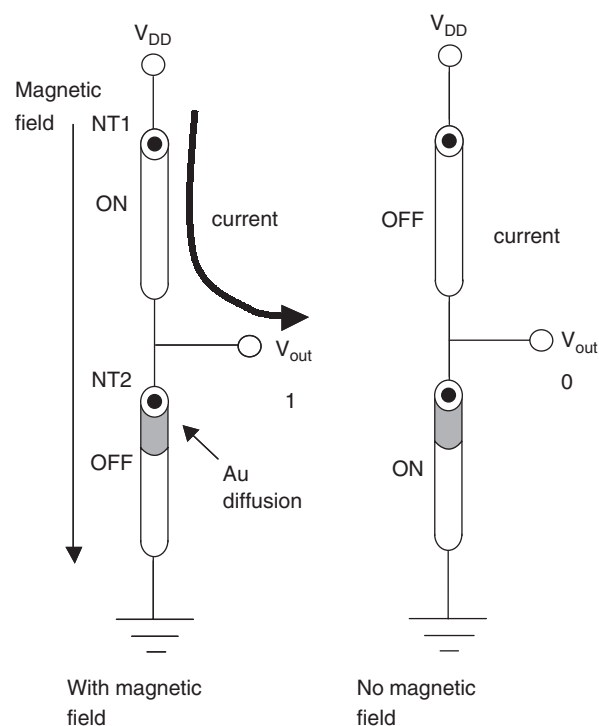


**Figure 16.** Novel electron-phase switching device utilizing the effect found here. MWNT1 is a general MWNT, exhibiting WL under no magnetic field. MWNT2 is our MWNT with an Au diffusion region, exhibiting AL under no magnetic field. Reprinted with permission from [81], J. Haruyama et al., *Phys. Rev. B* 65, 33402 (2002). © 2002, American Physical Society.

in MR oscillations, to excess volume of a cobalt catalyst in MWNTs synthesized in nanoporous alumina membranes. These localization effects bring about the following anomalies in bulk MWNTs. (1) A slight increase in the volume of excess cobalt changes AL to WL both in MR oscillations and in the $G$ vs log [$T$] relation. (2) A further increase in excess changes this WL back to the AL, but only in MR oscillation. (3) Even under this AL in MR, neither AL nor WL can be observed in the $G$ vs log [$T$] relation. We carry out data fitting to the MR oscillations by a revised formula for Altshuler–Aronov–Spivak oscillation and find a drastic change of phase coherence length depending on the excess cobalt deposition time. We also carefully observe each MWNT by high resolution cross-sectional transmission electron microscopy and find unique MWNT structures with cobalt particles and wire. Based on these, we propose interpretation for the anomalies. We interpret the first anomaly by the odd-time spin flip due to the cobalt particles remaining in MWNTs and spin polarization due to the short cobalt wires formed at the bottoms of MWNTs; these particles and wires are yielded by the slight increase in excess cobalt. The second and third anomalies are also interpreted by thick and highly disordered MWNT shells, which surround cobalt particle arrays. This is yielded by a further increase of the amount of cobalt. These phenomena can be basically universal in MWNTs that are synthesized by excess ferromagnetic catalysts, by virtue of the strong spin coherence.

Carbon nanotubes (CN), single-level molecular conductors, are attracting much attention, because they exhibit

unique quantum-mesoscopic phenomena and provide a variety of applications to novel molecular-quantum devices. It is well known that such quantum phenomena are very sensitive to the presence of impurities and defects in CNs. Here, one method of synthesizing CNs is a catalytic process of chemical vapor deposition using ferromagnetic catalysts (e.g., cobalt, nickel, and iron) [54]. Because these ferromagnetic catalysts remain in CNs even after synthesis under excess catalyst volume, it is of core importance to clarify how the excess volume of ferromagnetic catalysts contributes to changes in the physical characteristics of CNs.

Excess volume of the ferromagnetic catalysts affects CNs in at least two aspects: (1) During synthesis, excess volume changes CN structures, leading to changes in their physical characteristics, (2). After synthesis, excess volumes remaining in CNs are magnetic impurities, which change the physical characteristics of CNs. No work has been reported on the first of these aspects, whereas the second aspect, the influence of magnetic impurities, has been studied in both single-walled CNs and multiwalled CNs, as follows.

The influence of magnetic impurities in SWNTs has been studied mainly through electron spin resonance [55, 56]. Even a small concentration of magnetic impurities can relax the conducting electrons very efficiently [55], because SWNTs have a large carrier mean free path and a large spin diffusion length, like one-dimensional conductors. Spins and phases of electron waves in this ballistic regime are very sensitive to magnetic impurities. In addition, recently even a novel Kondo effect was reported, in which a SWNT serves as a one-dimensional host for conducting electrons, with magnetic clusters including a localized spin [56].

In contrast, the influence of magnetic impurities in MWNTs has been interpreted to be the origin of dephasing for quantum electron waves, as follows. The electrical properties of MWNTs are basically understood by the phase interference of quantum electron waves in the diffusive regime [54]. A typical example of such a phenomenon is a 2D WL, a constructive phase interference of electron waves. In thin metallic film and 2D electron gas systems, the conductance of 2D WL exhibits linearly logarithmic temperature ($\log[T]$) dependence with a saturation region forming at low temperatures. The Log $[T]$-dependent region is a manifestation of decoherence by electron–phonon scattering, whereas the saturation region implies decoherence by spin-flip scattering due to magnetic impurities.

Also in MWNTs, the conductance ($G$) vs log $[T]$ relation has exhibited such 2D WL behavior [57, 59–61], although the linear $G$ vs log $[T]$ relation survived at higher temperatures. The influence of magnetic impurities on the electrical properties of MWNTs has been reported in regards only to this decoherence for spin relaxation. For our MWNTs utilizing cobalt catalysts, we also reported previously that the transition temperature, $T_c$, between the linear $G$ vs log $[T]$ and its saturation regions was higher than the transition temperatures, $T_c'$, in thin metallic-film samples: about $T_c \sim 6$ K versus, for example, $T_c' \sim 1$ K [59–61].

However, no researchers have clarified how increases in the volume of excess cobalt change such phase interference phenomena in MWNTs. In this work, we reveal for the first time that phase interference, identified by $G$ vs log$[T]$ relations and magnetoresistance oscillations, is very sensitive to

increases in excess cobalt catalysts, based on our previous discovery of antilocalization in our MWNTs [64]. We find three anomalies in this sensitivity, and we interpret them in terms of correlation of AL and WL with complicated MWNT structures, observed by TEM (e.g., cobalt particles remaining in the MWNTs, short cobalt nanowires at the bottoms of the MWNTs, and thick and highly disordered MWNT shells), yielded by the excess cobalt catalyst.

### Experimental Results and Discussion

***Sample Structures and Measurement Methods*** Figure 17a shows the schematic cross section of our MWNT array synthesized into nanopores of an alumina membrane. After the membrane was formed by anodizing an aluminum substrate, a cobalt catalyst was electrochemically deposited
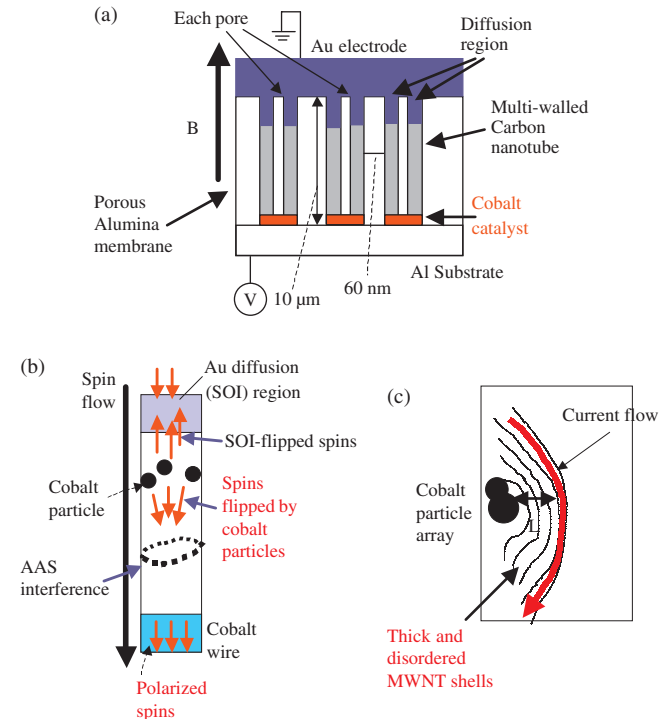


**Figure 17.** (a) Schematic cross-section of an MWNT array synthesized into nanopores of porous alumina membranes. We prepared three samples with three different times for cobalt deposition (i.e., 30, 120, and 360 seconds for samples 1, 2, and 3, respectively). The deposition time of 30 seconds corresponds to the optimal cobalt volume, whereas 120 and 360 seconds lead to the slightly and highly excess cobalt volumes, respectively. (b) Schematic cross-sectional model of the MWNT with the cobalt particles and the short cobalt nanowire accumulated at the bottom of the MWNT. This explains the first anomaly in this work. This model was obtained from the observation of high resolution cross-sectional TEM images (Fig. 20a–c), and the increase of spin scattering due to magnetic impurities obtained from the drastic decrease in $L_\varphi$ (change from Figure 19a to b in Table 1). Slight increase of excess cobalt catalyst yields this original structure. (c) Schematic cross-sectional model of the MWNT with thick and disordered shells surrounding a cobalt particle array. This explains the second and third anomalies. This model was obtained from a TEM image (Fig. 20c), the increase in $L_\varphi$ (change from Fig. 19b to c in Table 1), and the decrease in $T_c$ (change from Figs. 18b to c). High increase of excess cobalt catalyst leads to this original structure. Reprinted with permission from [81], J. Haruyama et al., *Phys. Rev. B* 65, 33402 (2002). © 2002, American Physical Society.

into the bottom of the nanopores at three different times. As we explain later, the deposition time of 30 seconds is around the optimal point for our parameters of alumina membranes. Hence, 120 and 360 seconds led to the excess deposition times. With this cobalt catalyst, MWNTs were synthesized by chemical vapor deposition of $C_2H_2$ and $N_2$ gases. Although we measured the physical properties of MWNTs as averaging about $10^3$ in the array, it was already confirmed in [65] that the averaged properties of such arrays were mostly the same as those of individual MWNTs because of the extremely high uniformity of the nanostructure parameters of this alumina membrane. It also turned out that even averaged measurement results could exhibit unique quantum-mesoscopic phenomena (see [59, 61–64]).

### Relationship between Conductance vs log [T] and Excess Cobalt Volume

Figure 18 shows the dependence of the zero-bias conductance ($G_0$ vs log [T] relation on the volume of cobalt catalyst in the samples with three different cobalt deposition times. The data reveal drastic changes in the $G_0$ vs log [T] relation, depending strongly on the deposition time. Figure 18a and its inset exhibit a slight decrease of $G_0$ as the temperature increases (i.e., negative $G_0$ behavior) up to $T = 2$ K. In contrast, Figure 18b, in which the cobalt deposition time was slightly increased, surprisingly implies that this decrease of $G_0$ disappears and only a saturation region (flatness) emerges at the lowest temperatures.

The further increase of the cobalt deposition time interestingly leads to the elimination of this saturation region (Fig. 18c). Even negative $G_0$ behavior, like that shown in
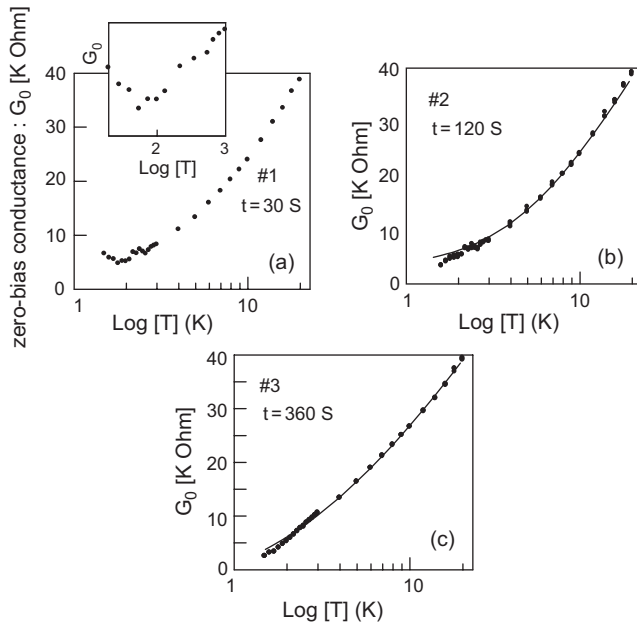


**Figure 18.** Dependence of zero-bias conductance ($G_0$) vs logarithmic temperature (log[$T$]) relation on the three different cobalt deposition times. (a), (b), and (c) correspond to the optimized cobalt volume, the slightly excess cobalt volume, and the highly excess cobalt volume, respectively. Solid lines are the calculation results by 2D weak-localization formula for MWNTs [Eq. (19)]. Reprinted with permission from [81], J. Haruyama et al., *Phys. Rev. B* 65, 33402 (2002). © 2002, American Physical Society.

Figure 18a, is unobservable. At almost all of the temperatures measured, only a linear and positive $G_0$ vs log [T] relation appears.

The characteristics in Figure 18 can be understood as follows. Figure 18a results from the presence of AL, a destructive phase interference phenomenon, which we reported previously [64]. In that study, we revealed that the gold-diffusion region at the top end of our MWNTs had SOI and the spins flipped by this SOI were injected into the bulk MWNT (Figs. 17a and b), leading to the phase shift by $\pi$ and, hence, the AL [64]. In this AL regime, decoherence due to the increased temperature leads to a negative $G_0$ vs log [T] relation because the destructive interference is eliminated.

In contrast, qualitatively Figure 18b means the emergence of 2D WL, consistent with previous reports on MWNTs [57], with magnetic-impurity (spin-flip) scattering at low temperatures as mentioned in the Introduction. Quantitatively, the relation was well fitted by the formula of 2D WL, as shown by the solid line in Figure 18b [59],

$$G(T) = G(0) + (e^2/\pi h)(n\pi d/L)\ln[1 + (T/T_c(B, \tau_s))^p] \tag{23}$$

where $n$, $p$, $d$, $L$, and $\tau_s$ are the number of shells, the parameter for dominant inelastic scattering, the diameter of the inner shell of the MWNT, the length of the MWNT, and the relaxation time of spin-flip scattering due to magnetic impurities, respectively. The contribution of the number of MWNTs is taken into account by the term $G(0)$. The good agreement between the data and calculation in Figure 18b supports presence of 2D WL. The best fitting to the experimental result gives $T_c = 5.4$ K, using $n = 18$, $p = 2.1$, $d = 50$ nm, and $L = 10$ mm. This $T_c$ as high as 5.4 K actually implies the presence of strong spin-flip scattering by magnetic impurities. In contrast, the best fitting to Figure 18c gives $T_c$ as low as 1.7 K, which actually emphasizes a mostly linear $G_0$ vs log[$T$] relation in the measured temperature range down to $T = 1.5$ K.

### Relationship between Magnetoresistance Oscillations and Volume of Excess Cobalt

In order to confirm these AL and 2D WL, we measured the MRs in the sample in each figure. Figure 19 shows the results. Figure 19a exhibits a positive MR around $B = 0$ T. This is actually consistent with decoherence in the AL regime shown in Figure 18a, with the bimodal oscillations (i.e., large- and small-magnitude oscillations, depending on the magnetic fields), as we already reported in [64]. In contrast, a negative MR surprisingly emerges around $B = 0$ T in Figure 19b. This is also consistent with the 2D WL regime shown in Figure 18b.
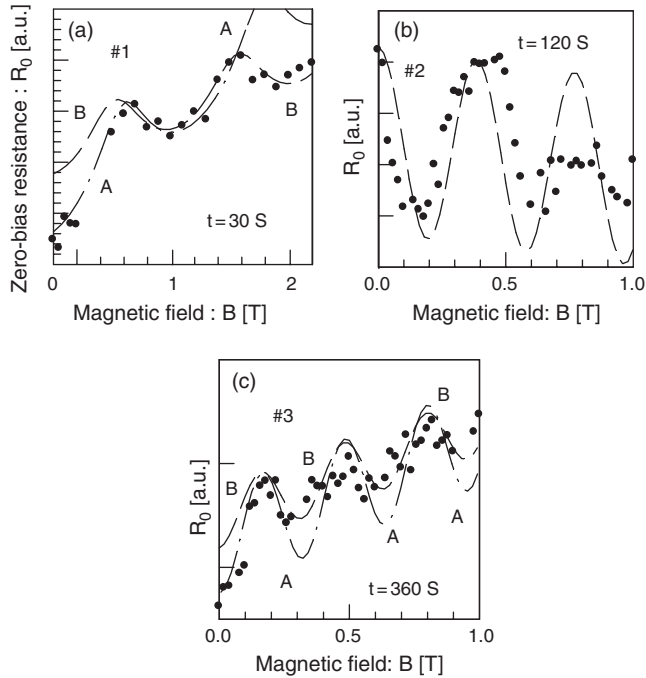
We performed data-fitting for Figure 19a and b by the revised Altshuler's formula for AAS oscillation [64],

$$\delta G = -(e^2/\pi h)(2\pi r/L_s)[(1/2 + \beta)Z_\phi(L_\varphi(H))$$
$$- 3/2Z_\phi(L'_\varphi(H))] + \alpha(H) \tag{24}$$

$$Z_\phi(L_\varphi(H)) = \ln(L_\varphi/\ell) + 2\sum_{n=1}^{\infty} k_0(n(2\pi r/L_\varphi))$$
$$\times \cos[2\pi n(\Phi/(hc/2e))] \tag{25}$$

$$1/L_\varphi^2 = 1/D\tau_\varphi \tag{26}$$

$$1/L_\varphi^2 = 1/L_\varphi^2 + 2/D\tau_{so} \tag{27}$$

**Figure 19.** Dependence of magnetoresistance features, corresponding to each figure in Figure 18. A magnetic field was applied in parallel with the tube axis. Lines A and B in (a) and (c) and the dotted line in (b) are the calculation results by the revised formula of Altshuler–Aronov–Spivak oscillation with and without spin–orbit interaction, respectively [Eqs. (20)–(23)]. Different oscillation periods in (a), (b), and (c) are due to the different tube diameters caused during the anodization procedure. They were also taken into account for the data fitting. Reprinted with permission from [81], J. Haruyama et al., *Phys. Rev. B* 65, 33402 (2002). © 2002, American Physical Society.

where $L_s$ $\beta$ $L_\varphi$, and $L'_\varphi$ in Eq. (24) are the tube length, the constant depending on electron–electron interaction, and the phase coherent length without and with SOI, respectively. $\ell$, $k_0$, and $\Phi$ in Eq. (25) are the mean free path, the Macdonald function, the magnetic flux ($\pi r^2 H$), respectively. $D$, $\tau_\varphi$, and $\tau_{so}$ in Eqs. (26) and (27) are the diffusion constant, the relaxation time for inelastic scattering, and the relaxation time for SOI, respectively. Here, $\alpha(H)$ in Eq. (24) represents the increase or decrease of the mean value of conductance, depending on magnetic field $H$. We also neglected the contribution of magnetic field on $L_\varphi$ in Eq. (26).

Equation (24) has a very simple physical meaning: The first term related to $Z_\phi(L_\varphi(H))$ basically represents the AAS oscillations without SOI (i.e., WL), whereas the second term with $Z_\phi(L'_\varphi(H))$ reveals the influence of SOI (i.e., AL) on the AAS oscillations, using eq. (27). Equation (27) includes the term $1/D\tau_{so}$ as the contribution of SOI. If SOI is very weak, $\tau_{so}$ diverges to an infinite value and, hence, $L_\varphi/L'_\varphi$ becomes "1" because of $(L_\varphi/L'_\varphi)^2 = 1 + 2(L_\varphi^2)/D\tau_{so}$, leading to WL. On the contrary, if $\tau_{so}$ has a finite value, $L_\varphi/L'_\varphi$ becomes larger than "1" because of $2(L_\varphi^2)/D\tau_{so} > 0$, leading to the increase of the oscillation amplitude of the second term of Eq. (24) and thus AL. Therefore, whether $\tau_{so}$ has infinite or finite values can decide emergence of either

AL or WL. Since this is represented by $L_\varphi/L'_\varphi$, we selected this $L_\varphi/L'_\varphi$ as the fitting parameter.

The results are shown in each figure by the solid and dotted lines. The agreement between data and theory is good in each figure also for the bimodal oscillation modes (i.e., large- and small-magnitude oscillations, depending on the magnetic fields, as we reported in [11]). This bimodal behavior means the presence of two different $L_\varphi/L'_\varphi$. Because $L_\varphi/L'_\varphi$ depended on the diffusion volume of gold atoms (Figure 20a), we clarified that this bimodal behavior was attributable to the presence of two distribution peak of this gold diffusion volume in one array. The best fitting to the
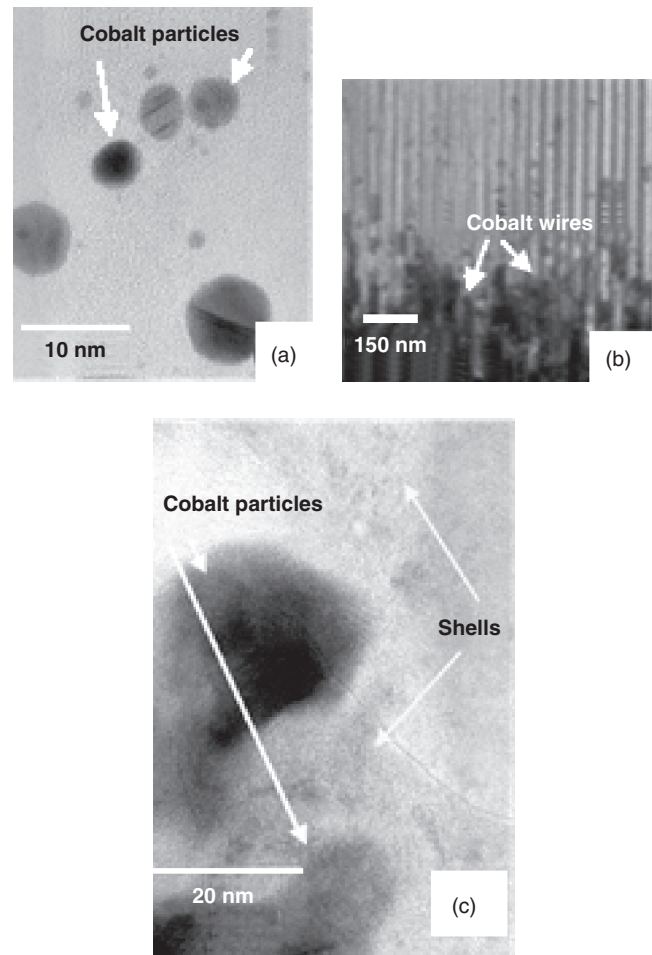


**Figure 20.** Typical high-resolution cross-sectional TEM images of each MWNT. (a) Example of a cobalt particle, without any shells, included in the MWNTs of the samples in Figures 18b and 19b. This sample includes high density of such particles. (b) Short cobalt wires formed at the bottom of MWNTs of the samples in Figures 18b and 19b. This is formed by accumulation of cobalt catalyst at the bottom of a nanopore of alumina membrane and has no diffusion during the synthesis. (c) Cobalt particle arrays surrounded by the disordered and thick shells in the samples in Figures 18c and 19c. Highly disordered shell structures (i.e., coffee-cup structures), which originated from the cobalt particle array, are also observable. Highly excess cobalt catalyst leads to this unique structure. (d) General shell structures of our MWNT, with about 36 shells, observable in the samples in Figures 18b and 19b. Reprinted with permission from [81], J. Haruyama et al., *Phys. Rev. B* 65, 33402 (2002). © 2002, American Physical Society.

line A in Figure 19a gives "$L_\varphi = 10.2$ $\mu$m" and $L'_\varphi = 1.1$ $\mu$m, respectively. Because $L_\varphi/L'_\varphi > 1$, this means the finite value of $\tau_{so}$ and hence quantitatively supports the presence of strong SOI and AL in Figure 18a. In contrast, the best fitting to Figure 19b actually gives "$L_\varphi = 0.13$ $\mu$m" and "$L'_\varphi = 1.02$ $\mu$m." In this case, $L_\varphi$ drastically decreases for reasons explained in the next section (d), whereas $L'_\varphi$ (i.e., the strength of the SOI) is nearly equal to that of Figure 19a. This decrease of $L_\varphi$ leads to $L_\varphi/L'_\varphi \sim 1$ under a constant $\tau_{so}$, because $(L_\varphi/L'_\varphi)^2 = 1 + 2(L^2_\varphi)/D\tau_{so}$. This $L_\varphi/L'_\varphi \sim 1$ is also consistent with the presence of 2D WL.

In Figure 19c, a positive MR emerges again with the bimodal oscillations. The best fitting to line A gives "$L_\varphi = 8.2$ $\mu$m" and $L'_\varphi = 0.75$ $\mu$m, implying the presence of AL, similar to Figure 19a. $L_\varphi$ increased again nearly up to the value found in Figure 19a under mostly the same $L'_\varphi$ as that in Figure 19b and we explain why in the next section. It should be noticed, however, that this is not consistent with the linear $G_0$ vs log$[T]$ relation shown in Figure 18c, because AL should exhibit a negative $G_0$ vs log $[T]$ relation like Figure 18a.

Consequently, Figure 18 and 19 imply that $G_0$ vs log $[T]$ relations and MRs (i.e., AL and WL) are very sensitive to the excess cobalt-deposition time (i.e., the volume of excess cobalt). We find the following three anomalies in these results. (1) A slight increase in the excess cobalt volume causes a transition from the AL to the 2D WL, in both the $G_0$ vs log $[T]$ relations and the MRs [i.e., from (a) to (b) in Figure 18 and 19]. (2) A further increase changes this WL back to the AL only in the MRs (Fig. 19c). (3) Despite that, AL is unobservable in the $G_0$ vs log $[T]$ dependence (Fig. 18c), exhibiting only the linear log $[T]$ relation.

***Proposal of the Models for the Three Anomalies*** What is the origin for these anomalies? In Table 1, we show the summary of the fitting parameters obtained from the best fit to each of Figure 19 and the density of cobalt particles, confirmed by high resolution cross sectional TEM (HRC-STEM) images, in each MWNT corresponding to Figure 19. As we explained, we note that only $L_\varphi$ changes drastically depending on the deposition time of cobalt catalyst, whereas $L'_\varphi$ is mostly constant. In general, $1/L^2_\varphi$ is given by $1/D\tau_{in} + 2/D\tau_s (= 1/L^2_{in} + 2/L^2_s)$, where $\tau_{in}$ is the relaxation times for inelastic scattering, when decoherence due to electron–electron interaction is neglected (e.g., at temperatures above $T = 1.5$ K). We can propose models as the origins for the anomalies, based on these.

In the first anomaly, $L_\varphi$ decreased drastically and we confirmed the increase of cobalt density in the MWNT by the HRCSTEM image (Fig. 20a). Because no change was found in the MWNT shell structure at least by the HRC-STEM image (Fig. 20d, i.e., no change in disorder of the MWNT), we have no reason for the change in $L_{in}$. Hence, the decrease of $L_\varphi$ can be due to the decrease of $L_s$. This $L_s$ decrease and the increased density of cobalt particles strongly suggest that the spin-flip scattering by the cobalt particles is the main reason for the first anomaly. Based on this, we propose a model representable by Figure 17b.

In the second anomaly, $L_\varphi$ increased drastically, whereas we found that the density of cobalt particles also increased further, leading to the arrays of cobalt particles (Fig. 20c), by HRCSTEM. These are not consistent. Besides, we also found the highly disordered shells of the MWNT by the HRTEM (Fig. 20c). This can bring strong electron–phonon interaction and hence decrease of $L_{in}$. This is also not consistent with the increase of $L_\varphi$. We found, however, that the cobalt particle arrays were surprisingly surrounded by the thick shells, by the HRCSTEM (Fig. 20c). If the current flows along the outer part of these thick MWNT shells, this large thickness reduces the influence of the spin scattering due to the cobalt particles, leading to the increase of $L_\varphi$. We propose a model explainable by Figure 17c, based on this.

The third anomaly is at least strongly associated with the strong disorder of the thick MWNT shells mentioned (Fig. 20c), because the linear $G_0$ vs log $[T]$ relation implies the presence of strong electron–phonon interaction caused by the disordered structure. We also propose an interpretation based on Figure 17c.

***Relationship among the First Anomaly, Cobalt Particles, and Short Cobalt Wires*** The AL observable in Figures 18a and 19a was attributed to the polarized injection of the spins, flipped by SOI in the gold-diffusion region at the top end of the MWNTs, into the bulk of MWNTs as we reported in [64]. Since the flipped spins led to the phase shift of electron waves by $\pi$ in the bulk MWNTs, the WL in the bulk MWNTs changed to the AL. This phase shift and AL are well represented by the negative $G_0$ vs log $[T]$ regime at low temperatures and the positive MR in Figures 18a and 19a, respectively. This AL was caused when the volume of the cobalt catalyst was optimal, because no cobalt particles could be detected in the bulk MWNTs.

However, when the volume of excess cobalt is increased slightly, the cobalt particles easily remain in the bulk MWNT even after the synthesis. We explain the first anomaly, based on Figure 17b, taking into consideration these cobalt particles, as we implied.

In general, this influence may lead to simply random flipping and the decoherence of these spins and hence to the elimination of both the negative $G_0$ vs log $[T]$ relation and

**Table 1.** Relation of deposition time of the cobalt catalyst vs magnetoresistance oscillation behavior, confirmed from Figure 19, around zero magnetic field. Phase coherence length without ($L_\varphi$) and with ($L'_\varphi$) spin–orbit interaction obtained from the best fit in Figure 19. Those ratios and density of cobalt particles confirmed by high resolution cross-sectional TEM image of each sample for Figure 3 (see Fig. 20), in MWNT after the synthesis.

| Cobalt deposition time | MR (at $B = 0$) | $L_\varphi$ | $L'_\varphi$ | $L_\varphi/L'_\varphi$) | Averaged density of cobalt particles in a MWNT |
|---|---|---|---|---|---|
| 30 S (Fig. 3a) | positive [AL] | 10.2 | 1.1 | 9.27 | ~0 |
| 120 S (Fig. 3b) | negative [WL] | 0.13 | 1.02 | 0.13 | 27 |
| 360 S (Fig. 3c) | positive [AL] | 8.2 | 0.75 | 10.9 | 55 [particle array] |

*Source:* Reprinted with permission from [81], J. Haruyama et al., *Phys. Rev. B* 65, 33402 (2002). © 2002, American Physical Society.

the positive MR (i.e., elimination of the AL). This scenario does not agree with Figures 18b and 19b. Here, if the spin, flipped by the SOI at the top of MWNT, is flipped by these cobalt particles in the $n$th time (here, $n$ should be the odd integer) during flowing through the MWNT before AAS interference occurs, the interference is caused by this flipped spin with opposite moment (Fig. 17b). Because this leads to phase shift by $\pi$ in the AAS interference, this changes the AL to the WL. These flipped spins, however, have fluctuation. Here, HRCSTEM detected the presence of cobalt wire as short as about 300 nm at the bottom end of the MWNTs in sample 2 (Fig. 20b). This wire was yielded by an accumulation of excess cobalt catalyst at the bottom part of the nanopores of the alumina membrane due to the excess deposition time, because such excess cobalt can no longer contribute to the growth of the MWNTs and no longer diffuse into the MWNTs as particles. After the AAS interference took place, such spins with fluctuation are injected into the short cobalt wire at the bottom end of the MWNT (Fig. 17b). If this cobalt nanowire plays a role of spin polarization for these spins, all such spins will be aligned reducing the fluctuation as they flow through the cobalt nanowire. This makes the magnitude of the WL increase. Consequently, the WL appears in Figures 18b and 19b, when the magnitude of this WL becomes dominant compared with that for the AL. In fact, it was reported that MWNTs connected to ferromagnetic electrodes exhibited strong spin polarization, characterized by strong spin coherence [63]. Besides, we confirmed that these phenomena could not be observed when electrons were injected from the Al substrate.

Quantitatively, in this case, SOI length ($L_{so}$) $\geq$ spin scattering length ($L_s$) must be satisfied, because the spin-flip scattering due to the cobalt particles has to beat the spin flipping by the SOI. Here, $L_{\varphi}$ in Figure 19b decreased remarkably from that in Figure 19a under the mostly constant $L'_{\varphi}$ (see Table 1). This led to $(L_{\varphi}/L'_{\varphi})^2 = 1 + 2(L_{\varphi}^2)/D\tau_{so} \sim 1$ and hence this WL. This change means $(L_{\varphi}^2)/(D\tau_{so}) = (L_{\varphi}/L_{so})^2 \sim 0$ and hence $L_{so} \geq L_{\varphi}$. As explained, this $L_{\varphi}$ decrease is due to the decrease of $L_s$. Therefore, $L_{so} \geq L_{\varphi}$ implies presence of $L_{so} \geq L_s$. This quantitatively supports our argument discussed. The high $T_c$ of 5.4 K in Figure 18b supports this explanation, because $T_c$ is the transition temperature for decoherence from the spin-flip scattering to the inelastic scattering regimes with increasing temperature.

These structures, that is, the presence of ferromagnetic particles remaining in the MWNTs and ferromagnetic electrodes formed at the bottom ends of MWNTs, can be yielded in any MWNTs, when excess volume of a ferromagnetic catalyst is used. Therefore, this phenomenon can be universal in such MWNTs. The strong spin coherence, which cannot surprisingly be dephased even after the $n$th time flipping, of the MWNTs makes this spin interference phenomenon possible.

***Relationship between the Second and Third Anomalies and Thick and Disordered Shells of MWNTs*** The second anomaly is more complicated, because a further increase in excess of the cobalt volume seems merely to induce further spin-flip scattering, leading to stronger decoherence of the 2D WL and hence the destruction of MR

oscillation in Figure 19b. We also explain this anomaly based on Figure 16c, as we mentioned.

In order to clarify the reason for this anomaly, we carefully observed, by HRCSTEM, the shell structures of the MWNTs around cobalt particles. In Figure 20c, we found the following. (1) There is a larger density of cobalt particles in the Figure 18c sample than in Figure 18b, and such cobalt particles were combined, in most cases, to cobalt-particle arrays. (2) Such cobalt-particle arrays were surrounded by the disordered and thick shells of the MWNTs. These structures can be yielded by a high increase in the excess volume of the cobalt catalyst, far from the optimal condition, because the growth of the MWNTs is very sensitive to the catalyst, especially in chemical vapor deposition. Here, quantum electron waves in our MWNTs flow along the outer portions of the shells [64]. Hence, these thick shells increase the distance ($L$) between the cobalt particles and the wave flow, reducing the influence of spin-flip scattering by the cobalt particle on phase coherence (Fig. 17c). This leads to the elimination of the 2D WL, because the origin for the 2D WL in Figure 19b was this spin-flip scattering. This in turn changes the WL back to the AL, similar to Figure 19a. This phenomenon can be also universal in MWNTs, when the excess volume of a catalyst is too high. Such unoptimized conditions easily lead to MWNTs with thick shells surrounding ferromagnetic catalysts. One should note that even such thick MWNTs can conserve strong spin coherence.

In this case, $L_{\varphi}$ increased up to about 8.2 $\mu$m with mostly constant $L'_{\varphi}$, leading to $L_{\varphi} > L'_{\varphi}$ again (Table 1). This quantitatively supports the explanation mentioned, because only $L_s$ can increase in this structure, along with decreased $L_{in}$ as will be mentioned.

In contrast, the third anomaly stresses decoherence by only strong electron–phonon scattering. The highly disordered shell structure observed in Figure 20c emphasizes the possible presence of strong electron–phonon scattering in this MWNT (i.e., a decrease in $L_{in}$), leading to the elimination of AL. Besides, dephasing by the cobalt particles leading to the low temperature saturation in the WL is also reduced by the thick shells as mentioned. Therefore, only the lineal and positive $G_0$ vs log $[T]$ relation can emerge (Fig. 18c). This behavior, however, can be consistent with the AL in MR (Fig. 19c) because of the following: (1) The positive MR in Figure 19c was yielded by decoherence of SOI due to the increase of magnetic field at the fixed temperature ($T = 1.5$ K), whereas the third anomaly is caused by decoherence of electron–phonon interaction due to the increase of temperature at the fixed magnetic field ($B = 0$). (2) Decoherence of SOI and electron–phonon scattering are very sensitive only to magnetic field and temperature, respectively. These second and third anomalies stress that the thick shell of MWNTs reduces the influence of spin-flip scattering due to the cobalt particles under the magnetic-field change, but its disorder enhances the electron–phonon interaction under the temperature change.

The coexistence of the second and third anomalies may be not universal, because it can be constructed only when there is a highly optimized balance among the thickness of MWNT shells, the strength of their disorder, and the location of

the cobalt particles in the MWNTs. Our system seems to occasionally have included such an optimized structure.

**Conclusion** In conclusion, we found for the first time that the $G_0$ vs log[$T$] relation and MRs were very sensitive to the excess increase of cobalt-catalyst volume in MWNT arrays, synthesized in nanoporous alumina membranes. We found the following three anomalies in these results. (1) A slight increase in the excess cobalt volume caused a transition from the AL to the 2D WL, in both the $G_0$ vs log[$T$] relations and the MRs. (2) A further increase changed this WL back to the AL only in the MRs. (3) Despite that, AL was unobservable in the $G_0$ vs log[$T$] dependence, exhibiting only the linear log[$T$] relation. We found drastic change of $L_\varphi$ in each anomaly, from the data fitting to the MR oscillations by revised AAS oscillation theory. We also performed careful observation of each MWNT by HRCSTEM and found the unique MWNT structures with the cobalt particles. We proposed interpretations for the anomalies, based on those.

Based on the drastic decrease of $L_\varphi$ and the increased density of cobalt particles, we qualitatively attributed the first anomaly to the odd-time flipping of electron spins by the cobalt particles remaining in the MWNTs, leading to the phase shift by $\pi$ and, hence, the change from AL to 2D WL. The polarization of those spins by the short cobalt wires, formed at the bottoms of the MWNTs, induced this. These structures resulted from the slightly excess cobalt volume. Quantitative comparison of change of $L_{so}$ and $L_s$ also supported this interpretation. We explained the second anomaly by the thick shell structures of the MWNTs, based on the increase of $L_\varphi$. The thick shells eliminated the 2D WL by surrounding the cobalt particle array and reducing the spin scattering due to the cobalt particles by detaching the current flow along the outer portion of MWNTs from the cobalt particles. This led to the re-emergence of AL. In contrast, the disordered shells strongly enhanced the decoherence by electron–phonon scattering, leading to the linear $G_0$ vs log[$T$] down to $T = 1.7$ K. We qualitatively attributed this third anomaly to the different sensitivity of decoherence between magnetic field increases and temperature increases. For further quantitative confirmation, estimation of $L_s$ from the $G_0$ vs log[$T$] relations will be at least indispensable.

It has been already reported that diffusive SWNT rings can, interestingly, exhibit WL and AL together with strong localization, depending on the temperature[66]. We also reported that 2D WL in the bulk MWNT was changed to AL by doping gold and platinum on the top end of the MWNT[64]. On the other hand, this chapter implies the possibility that bulk MWNTs themselves can provide AL, 2D WL, and the switching between them. In any case, it is important to note that we can control these by changing the volume of excess ferromagnetic catalyst. We believe that these phenomena are basically universal in MWNTs with excess volume of ferromagnetic catalysts, because these are reproducible. Only the strong spin coherence of MWNTs can make these anomalous spin interference phenomena possible. These phenomena will be also very useful to realize novel spintronics and phase interference devices that utilize MWNT networks synthesized by ferromagnetic catalysts networks.

## 4.2. Superconductivity

Proximity-Induced Superconductivity and Its Reentrance Effect in Niobium/Multiwalled Carbon Nanotube Junctions

### 4.2.1. Introduction

We report on an experimental study of the diffusive transport near interface of niobium(Nb)/multiwalled carbon nanotube junctions. Utilizing MWNTs synthesized in nanopores of alumina membranes makes a highly transparent interface possible. On the magnetic-field dependence of observed conductance increase and the transition temperatures versus nanotube length diagram, we observe proximity-induced superconductivity with an onset temperature of $T = 9$ K at the highest case. We reveal that this conductance decreases due to its reentrance effect at low temperature. These phenomena are the manifestation of the extremely large diffusion constant of Cooper pairs in the MWNTs. The drastic magnetic-field dependence of the reentrant conductance supports the presence of a reentrance effect associated with the Altshuler-Aronov-Spivak effect.

Superconductivity of carbon nanotube, a molecular conductor, is currently of great interest, because it was recently found that hole-doped $C_{60}$ and magnesium diboride that have structures similar to CNs, exhibit high-temperature superconductivity. Until recently, only two groups had reported superconductivity in single-walled carbon nanotubes [67–69]. The first group claimed to have observed superconductivity at $T = 15$ K only from the Meissner effect without actually showing vanishing resistance [67]. The other group reported a transition temperature as low as $T < 1$ K in both proximity-induced and intrinsic superconductivity [68, 69]. However, no other group has been able to reproduce successfully these results. In fact, Morpurgo et al. attribute the absence of proximity-induced superconductivity in niobium(Nb)/SWNT/Nb junctions [70] to the following two reasons: (1) Because charge carriers in SWNTs behave as a Luttinger liquid due to the strong one-dimensional repulsive electron interaction, unusual phonon modes would be capable of producing Cooper pairs with attractive electron interaction [69, 70, 78–80]. (2) High transparency of the metal electrode/CNs interface is hard to achieve because of the misalignment between Fermi levels. Only electrodes made of titanium(Ti), carbide(C), silicon(Si)C, or NbC by a special technique [68, 69] meet this criterion, but Ti and Si are not superconductors. Consequently, only NbC is a suitable candidate for highly transparent superconductor/CN interfaces.

In contrast, nobody has successfully reported superconductivity in multiwalled carbon nanotubes. Because MWNTs exclude the existence of Luttinger liquid (although this issue is debatable, we could not actually find any power law dependence in the conductance versus temperature and voltage characteristics of our samples), one can at least avoid the former handicap of SWNTs. In addition, it is well known that two-dimensional quantum electron waves generated from the molecular band in MWNTs have the longest phase coherence among many materials in the diffusive regime; therefore, it is crucial to show that Cooper pairs can exist with such strong phase coherence.

In this work, we for the first time, investigate "PIS" in Nb/MWNTs junctions. When the superconductor (S)/ normal conductor (N) interface is highly transparent, leakage of the Cooper pair wave function from the S into the N leads to PIS in the N. Recent experimental transport studies near a mesoscopic S/N interface (e.g., S/2D electron gas (2DEG)[71–73] and thin metal S/N junctions [74–77]), have revealed the presence of subtle physics implying the coexistence of Cooper pair wave functions with the 2D electron waves.

In particular, the "reentrance effect" has attracted much attention. This effect emerges when the conductance enhancement due to PIS suddenly decreases at energy below the "Thouless energy $(E_{Th})$" that arises from the uncertainty between the diffusion time of Cooper pair and its energy fluctuation [76]. Furthermore, when an Aharonov–Bohm (AB) ring is inserted on the N channel of such S/N junctions, the AB flux causes drastic changes in the reentrance effect, simultaneously with modifications of the effective channel length and the Andreev reflection at the S/N mirrors [73–77].

How can such phenomena take place in S-electrode/ MWNT junction systems? In this chapter, we report the existence of PIS at a temperature of $T = 9$ K at the highest case and its reentrant effect from the magnetic-field dependence of conductance behaviors and the dependence of the transition temperatures on the nanotube length in a high-transparency Nb/MWNT junctions. This junction is realized by utilizing MWNTs synthesized into the nanopores of alumina membranes. Next, we show that two magnetic-field dependences strongly support the "reentrance effect connected to the AB trajectory," with two anomalous behaviors.

### 4.2.2. Experiments and Discussion

Here, in any case, the low-transparency interface of S/N junctions prevents PIS from occurring. Figure 21a and b shows the schematic views of an array of Nb/MWNTs (S/N) junctions and a single Nb/MWNT junction, respectively. After the synthesis of MWNTs into the nanopores of alumina membranes [81–83], we performed the preannealing. Then, the surface of alumina membrane was etched out so that the top portion of the MWNTs was exposed. Right after we evaporated Nb/gold film (in high vacuum with each 1 $\mu$m thickness, superconducting transition temperature of about 8.1–9 K, and critical magnetic field of about 1500 Gauss) on these top ends of MWNTs, we carried out the annealing in vacuum, again. Hence, the annealing changes only the boundary conditions of the Nb/MWNT interface. We found that annealing at 650 °C for this structure led to high diffusion of Nb atoms into the top ends of all shells in MWNTs, due to the interface area being large enough for diffusion along the circumferential direction (Fig. 21b and d). Because this process leads to the generation of NbC (right panel of Fig. 21d), the interface became highly transparent. In contrast, we could not find any diffusion of Nb and the presence of NbC in the samples annealed at lower temperatures [150 (e) and 400 °C]. The end-bonded MWNT also contributes to the high transparency [85]. We also showed that even the normal metal electrodes, slightly diffusing into the top ends of MWNTs, actually led to a drastic change of phase interference in the bulk of our MWNTs [81].
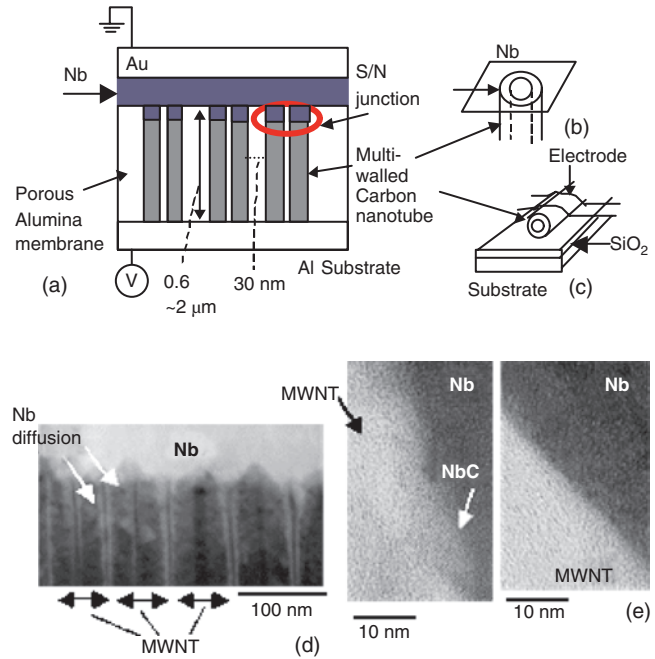


**Figure 21.** The schematic cross-sections of (a) an array of Nb/MWNT junctions and (b) one Nb/MWNT (S/N) junction, synthesized into the nanopores of alumina membranes by chemical vapor deposition. The mean outer and inner diameters of MWNT are 100 and 60 nm, respectively, with the shell thickness of 20 nm. The half width of the distribution of the outer diameter is as small as about 15%. The shell structure proving the MWNT was already reported in [82]. Because this system is not a S/N/S junction, there is no Josephson contribution in the measurement results. Although we measured the average characteristics of Nb/MWNTs junctions with about $10^4$ in one array, it was already confirmed that they could exhibit approximately the same quantum phenomena as those of an individual MWNT [81–83], due to the extremely high uniformity. (c) One of the general methods, much different from ours (b), used to provide electrical contact with the nanotube. It is difficult to provide high-transparency interface by this, because only half of the most outer shell along the circumferential direction has the interface with the electrode. (d) Left: High angle annular dark field image of cross-sectional TEM around the Nb/MWNT junction array [see (a)] annealed at 650 °C, implying the high diffusion of Nb atoms. Right: High resolution CSTEM image of an Nb/MWNT interface. The gray regions blended by the white (MWNTs) and black (Nb) regions are clearly visible at the boundary, implying the presence of NbC with the lattice constant of 0.35 nm. (e) High resolution CSTEM image of an Nb/MWNTs interface annealed at 150 °C, implying no gray region at the border between the MWNTs and Nb and hence the absence of NbC.

In the main panel of Figure 22a, we show the temperature dependences of zero-bias conductance $(G_0)$ in an Nb/MWNT array annealed at $T_{An} = 650$ °C. We successfully find the gradual but obvious conductance increases with the onset transition temperature ($T_{px}$ of $T_{px} = 5.4$ K under zero magnetic field $(H = 0)$. In contrast, we note that this conductance starts to drop from $T = 3.4$ K (i.e, transition temperature for the conductance decrease, $T_{re} = 3.4$ K). The $T_{px}$ was shifted to lower temperature when a magnetic field $(H)$ was applied in the Nb electrode (i.e., perpendicular to the tube axis). The critical magnetic field $(H_c)$ for the disappearance of the conductance increase was about 1400 Gauss, which is mostly the same as $H_c$ for the vanishing
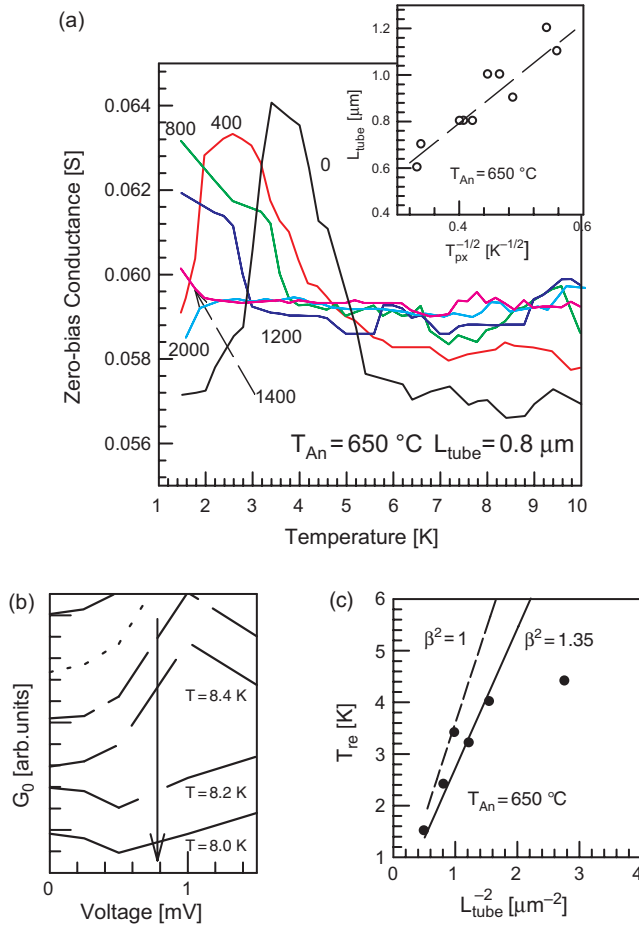
**Figure 22.** (a) Temperature dependences of zero-bias conductance ($G_0$), in an Nb/MWNT array annealed at $T_{An} = 650$ °C, measured for different values of the magnetic fields perpendicular to the MWNT axis. The labels on the curves correspond to the value of magnetic field in Gauss. The resistance of one MWNT with the interface resistance is around 100 KΩ to 1 MΩ at $H = 0$ Gauss, which is consistent with that of MWNTs with weak localization [81, 82]. Inset: The averaged tube length ($L_{tube}$) vs $T_{px}^{-1/2}$ relation obtained from the measurements of 10 samples, with different $L_{tube}$ annealed at $T_{An} = 650$ °C. The dotted linear line was obtained from the minimum square method. (b) Temperature dependences of conductance vs voltage relation, around the superconducting transition temperature of our Nb film, in an Nb/MWNTs array with $T_{px} = 3.5$ K. Conductance dip is observable above $T = 8.4$ K, whereas this abruptly changes to the conductance peak at $T = 8.2$ K in a decrease of temperature. We qualitatively confirm that this conductance peak originates from the emerging Andreev reflection, due to the superconducting transition of Nb film, at the Nb/MWNT junction, because (1) $T = 8.2$ K mentioned previously is approximately near $T_c$ of our Nb-film and (2) the voltage width of the conductance peak ($\sim$1.2 meV) is nearly equal to the $\Delta$ of Nb (i.e., $\Delta_{Nb} \sim$1.4 meV). (c) Transition temperature for reentrant conductance ($T_{re}$) vs $L_{tube}^{-2}$ relation obtained from the six samples in the inset of (a). We could not find reentrant conductance in other four samples in (a). The dot and solid lines are calculation results from $T_{Th} = \hbar D/kL^2 = (A/\beta)^2/L^2$ with $L = L_{tube}$, $A \sim 1.9 \times 10^{-6}$, and $\beta$ as a fitting parameter.

superconducting transition of our Nb electrode film, in contradiction to [3]. The $T_{re}$ also moved to lower temperature in $H = 400$ Gauss, and the conductance drop vanished above $H = 800$ Gauss. The conductance increase observable

mainly in the change from $H = 0$ to $H = 400$ Gauss at all the temperatures above $T = 5.4$ K is due to destruction of weak localization in the MWNTs [81], because this increase exhibited a linear and positive $G_0$ vs log($H$) relation. We do not discuss this phenomenon in this chapter.

These characteristics for the conductance increase and its $H$ dependence are similar to the behavior of superconducting transition. However, conductance does not increase up to infinite value like in general superconducting transition, due to the conductance drop. Besides, each curve in Figure 22a is inhomogeneous on temperature change unlike in general conductance vs temperature relations. Hence, in order to confirm the correlation of this conductance increase with superconducting transition, we investigated dependence of $T_{px}$ on the MWNT length. We found that $T_{px}$ decreased with increasing the averaged MWNT length ($L_{tube}$), following the linear $L_{tube}$ vs $T_{px}^{-1/2}$ relation (i.e., "$L_{tube} = A \cdot T_{px}^{-1/2}$," where $A$ is a coefficient constant) (inset of Fig. 22a). Besides, we found even $T_{px}$ as high as $T = 9$ K in the junction of Nb/MWNTs with $L_{tube} = 0.6$ $\mu$m. Importantly, this relation qualitatively agrees with the temperature dependence of $L_T$ [i.e., "$L_T = (\hbar D/kT)^{1/2}$," where $D$ is the diffusion constant]. This effect stresses that the "$L_T = (\hbar D/kT)^{1/2}$" relation becomes dominant in the MWNTs below $T_{px}$. This is the straightforward evidence that the conductance increase below $T_{px}$ is strongly associated with the PIS caused by the Nb electrode.

The conductance mechanism follows the smallest of the two parameters, $L_T$ or the phase coherence length ($L_\phi$). Because $L_\phi$ in our MWNTs is on the order of a few $\mu$m [81] around about $T = 10$ K, thereby implying $L_\phi > L_T$ below about $T = 10$ K, we believe that this discussion is relevant. We understand that such a conductance increase was never observed in any of our MWNTs without superconductor electrodes, despite the fact that we measured over 300 samples. They just exhibited monotonic conductance decreases due to weak localization. Besides, one should note that even the highest $T_{px} \sim 9$ K observed is below the superconducting transition temperature ($\sim$9.1 K) of our Nb film. This suggests a strong relation between the conductance increase with superconducting transition of Nb electrode and PIS. PIS can occur even at the N-channel length $\gg L_T$, leading only to the shrinkage of the normal conducting state length (e.g., by Maki–Thompson–Larkin fluctuations of the order parameters)[72]. However, this is not the case because the conductance increase does not exhibit strong dependence on the N-channel length.

We already mentioned that (high-temperature) PIS requires high-transparency interface of S/N junction (see Fig. 21). In fact, we confirmed that the conductance increase in the main panel of Figure 22a is also very sensitive to the interface transparency of Nb/MWNT junctions, as follows. An Nb/MWNT array annealed at $T_{An} = 150$ °C exhibited no conductance increase. This low-temperature annealing results in the low-transparency Nb/MWNTs interface due to absence of NbC by the poor diffusion of Nb into the MWNTs (see Fig. 21d and e). The interface resistance of the 150 °C-annealed Nb/MWNT junction can be estimated to be at least 10 times larger than that in the 650 °C-annealed sample. In addition, no current could be detected in the sample without annealing, indicating zero

transparency. Here, the abrupt onset of a conductance peak, which can be due to Andreev reflection (in which an incident electron coming from the N is converted into the Cooper pair in the S, leaving a reflected hole in the N, at the S/N junction [67, 84]), with decreasing temperature from $T = 8.2$ K (Fig. 22b) also supports the presence of this high-transparency interface in the 650 °C-annealed sample, because Andreev reflection can only take place at a highly transparent S/N interface.

We still need to establish evidence for the existence of PIS. Unlike in general superconductivity, the junction conductance does not reach infinite value but rather starts to drop at $T_{re} = 3.4$ K as temperature decreases. We argue that this is due to the "reentrance effect," which is critical for the manifestation of the PIS regime. The N-channel/N-reservoir (N/N′) junction attached to the other end of the N-channel plays an important role in this context. When the N/N′ interface is highly transparent, the proximity-induced Cooper pair amplitude is suppressed near the N/N′ junction because the Cooper pairs diffuse out of the N-channel, where they feel the $E_{Th}(= \hbar D/L^2)$ gap rather than $\Delta$. Here $\Delta$ and $L$ are the bulk superconducting gap and the N-channel length, respectively, there. This leads to "the spatially averaged normalized density of state $(N_N(E))$ in the N-channel $<$ its normal state value," at $E \leq E_{Th}$. Consequently, the conductance decreases at $E \leq E_{Th}$ (i.e., reentrance effect), whereas the PIS can survive only at $E \geq E_{Th}$.

In Figure 22c, we show the $T_{re}$ vs $L_{tube}^{-2}$ relation obtained from the measurement results for Figure 22b samples. Interestingly, this relation is mostly linear except at $L_{tube} = 0.6$ $\mu$m. This result agrees qualitatively with the Thouless temperature $(T_{Th})$ dependence on the N-channel length, $L$ (i.e., $T_{Th} = \hbar D/kL^2$), and is the first evidence that the conductance decrease from $T_{re}$ is due to the reentrance effect.

We show the second evidence for PIS as follows. As explained, because the "$L_{tube} = A \cdot T_{px}^{-1/2}$" relation in the inset of Figure 22a was qualitatively equivalent to "$L_T = (\hbar D/kT)^{1/2}$," we define $A = \beta(\hbar D/k)^{1/2}$, where $\beta$ is a constant coefficient. Hence, from the asymptotic value of $L_{tube}$ vs $T_{px}^{-1/2}$ ($A = 1.9 \times 10^{-6}$) and the value at which the dotted line crosses to the $Y$-axis ($0.04 \times 10^{-6}$), the data obtained in Figure 22b can be fitted by the expression $L_{tube} = (1.9 \times 10^{-6}) \cdot T_{px}^{-1/2} + 0.04 \times 10^{-6}$. With $T_{Th} = \hbar D/kL^2 = (A/\beta)^2/L^2$, we can derive the $T_{Th}$ vs $L_{tube}^{-2}$ relation, by using $A \sim 1.9 \times 10^{-6}$, $L = L_{tube}$, and $\beta$ as a fitting parameter. From the data shown in Figure 22c, the value $\beta^2 = 1.35$ gives the best fit to the measurements in the linear regime. This $\beta^2 = 1.35$ value establishes the relation $T_{re} = 0.74 \times T_{Th}$." In fact, similar relations were reported in the reentrance effect observed in the Nb/2DEG junction ("$T_{re} = 0.4 \times T_{Th}$")[72] and in the Al/Cu junction ("$T_{re} = 0.5 \times T_{Th}$")[70]. Our coefficient value of 0.74 approximately agrees with those. From this discussion, we conclude that the conductance drop at $T_{re} = 3.4$ K in the main panel of Figure 22a is attributed to the "reentrance effect." The particular "0.74" value is discussed.

The $L_{tube} = 0.6$ $\mu$m value for the departure from the linear regime shown in Figure 22c is associated with a weakening of the reentrance effect due to the decrease of Cooper pair diffusion in the MWNT. Indeed, the density of Cooper pairs is very high even around the MWNT/Al interface in

MWNTs with lengths as short as 0.6 $\mu$m. We speculate that the high-transparency MWNTs/Al (N/N') interface, the key for this reentrance effect, was also realized with the 650 °C annealing, because this temperature is near both the melting point of Al and the synthesis temperature of MWNT. The Al atoms and MWNT are actively connected in such conditions. Nevertheless, the instability and reproducibility of this junction lead to the reproducibility of the reentrant conductance with 60% probability.

The highest $T_{re} = 4.5$ K of the reentrance effect observed in this work is much higher than reported in the Nb/2DEG ($T_{re} = 0.5$ K) [72] and in the Al/Cu junctions ($T_{re} = 60$ mK)[74]. This is a manifestation of the extremely large diffusivity $D = 0.37$ m$^2$/s, estimated from the parameters $A \sim 1.9 \times 10^{-6}$ and $\beta^2 = 1.35$, in our MWNTs (e.g., $D = 0.08$ m$^2$/s at most, in the case of 2DEG and $D = 0.007$ m$^2$/s in the Cu film), resulting in the strong phase coherence. The discovery of the reentrance effect surprisingly implies that the diffusion of Cooper pair even into MWNTs, consisting of $\pi$ and $\sigma$ bands formed by $sp^2$- and $sp^3$-mixed orbitals, can lead to the reduction of $N_N(E)$, which is qualitatively similar to that in Nb/2DEG and metal S/N junctions. We put emphasis on this reentrant conductance as the other evidence for PIS. However, it is interesting to notice that the strong phase coherence did not enhance the critical magnetic field for the vanishing PIS in our MWNTs (main panel in Fig. 22a). This is in contradiction to that in SWNT, which reported the 10 times larger critical field [69].

The magnetic-field dependence [the inset of Fig. 23a and the relation at $\Phi/\Phi_0' = 1/2$ (where $\Phi_0' = \Phi_0/80$ and $\Phi_0$ is
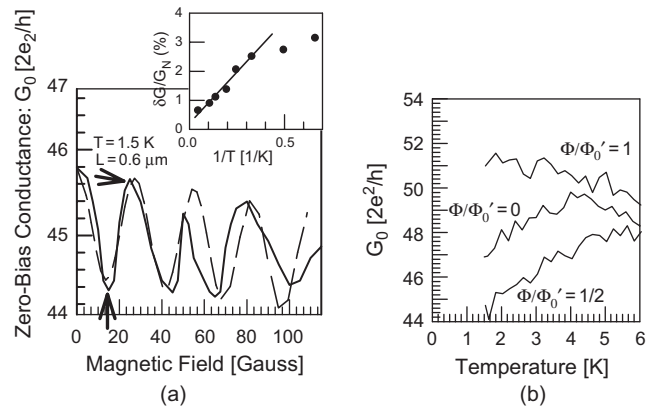


**Figure 23.** (a) Periodic magnetoconductance oscillation (solid line) observed in the reentrant regime. Magnetic flux was applied along the MWNT axis. This can be fitted by the formula of Altshuler-Aronov-Spivak oscillations (dotted line)[81], assuming the anomalous period of $\Delta\Phi = \Phi_0/80 = \Phi_0' = 25$ Gauss and the presence of spin-orbit interaction for the negative MC around zero magnetic field. This period of 25 Gauss corresponds to the magnetic flux $\Delta\Phi = \Phi_0/80 = \Phi_0'$, based on the best fit (dotted line) with the mean MWNT radius of 40 nm[81]. Inset: Power-law relation of the normalized magnitude of this MC oscillation ($\Delta G/G_N$) vs $1/T$ above $T_{re} = 4.5$ K and its saturation below $T_{re}$. $G_N$ is the normal state conductance. The solid line is a guide for the eyes. (b) Magnetic field dependence of the $G_0$ vs temperature relations around $T_{re}$ at the fields shown by the arrows in (a) (i.e., $\Phi/\Phi_0' = 1/2$ and $\Phi/\Phi_0' = 1$, respectively). At $\Phi/\Phi_0' = 1/2$, the $G_0$ maximum shifts up to about $T = 6$ K (enhancement of the reentrance regime). In contrast, at $\Phi/\Phi_0' = 1$, $G_0$ exhibited a monotonic increase (its shrinkage).

the superconducting quantum flux) in Fig. 23b] also supports the presence of reentrance effect, if we assume our Nb/MWNT structure is equivalent to an S/N junction connected to AAS trajectory, like a S/N junction connected to an AB ring [8] (Fig. 24a and b). The reentrance effect in this system has been successfully studied [73–76]. Reference [74] showed the power-law decay of $\Delta G/G_N$ on temperature increase with the ratio between 2.5% and 0.5% and its saturation below the $T_{re}$ ($= 50$ mK). These are quantitatively in precise agreement with the inset of Figure 23a. Besides, the enhancement of reentrance effect at the magnetic flux in the bottom of oscillation ($\Phi/\Phi_0' = 1/2$) in Figure 23b also qualitatively agrees, when we neglect that the magnetic flux was $\Phi/\Phi_0 = 1/2$ in [74]. These two results strongly support the presence of a reentrance effect associated with the AAS effect in our Nb/MWNT system.

The enhancement of the reentrance effect at $\Phi/\Phi_0 = 1/2$ is qualitatively explained by the decrease of the effective N-channel length ($L$), due to the destructive phase interference in the AB ring, for $E_{Th} = \hbar D/L^2$ in [74] (Fig. 24b). The $L$ for $E_{Th}$ consists of the $L'$ and $L''$ regions. Because the destructive phase interference at $\Phi/\Phi_0 = 1/2$ enhances the zero electron–hole pair amplitude at the $\gamma$ point and the $L''$ region, this effect leads to the reduction of $L$ down to $L'$. Consequently the conductance-maximum temperature shifts to higher temperatures. Our results are consistent with this interpretation (Fig. 24). In the following, we explain the "$T_{re} = 0.74 \times T_{Th}$" relation. We point out that in the data fitting for the $T_{Th}$ vs $L_{tube}^{-2}$ relation, we did not include the length of AAS trajectory. By using $\beta = 1$ and assuming a length of 500 nm for this AAS trajectory, we confirmed that it gave the best fit to the measured $T_{re}$ vs $L_{tube}^{-2}$ relation. Hence, the conductance-maximum temperature shifts to $T_{re} = 6$ K, indicating $L = 740$ nm, at $\Phi/\Phi_0' = 1/2$. For a AAS trajectory length of 500 nm, this means $L' = 240$ nm, based on the previous fitting. Interestingly, this implies that the main AAS trajectory is located at a distance of 240 nm from the Nb/MWNT interface (Fig. 24a).

However, (1) the AAS oscillations assuming $\Delta\Phi = \Phi_0/80 = \Phi_0'$ and influence of spin–orbit interaction (SOI) and (2) the "shrinkage" of the reentrance effect at $\Phi/\Phi_0' = 1$ are very anomalous. In (1), SOI is not required if one follows the aforementioned explanation. The negative MC around zero magnetic field in the MC oscillations can be qualitatively understood by the enhancement of the reentrant conductance (Fig. 23b) due to the destructive phase interference at $\Phi/\Phi_0' = 1/2$. When this conductance decrease due to the reentrance effect overcomes the conductance increase due to the destructive phase interference in the AAS effect, the negative MC can emerge However, the MC oscillation with "the period $\ll$ the quantum flux" has never been observed in our N electrode/MWNT junctions before [81]. Besides, only quantum flux should penetrate into the Nb electrode that exists on the inner space of MWNTs in Figure 24a, because the tops of the inner space of MWNTs are capped by the Nb film. In this sense, the small period may indicate that MC oscillations may be not associated with AAS oscillations. This is still in contradiction to the explanation supporting the reentrance effect.

For a possible interpretation, we may have to take into consideration (1) the contribution of the trajectory, which encircles a MWNT in the $n$th time, where $n$ is the integer, which leads to $\Delta\Phi = \Phi_0/n$, (2) the contribution of extra phases resulting from Andreev reflection, which takes place in AAS trajectories facing the Nb/MWNT interface, which leads to $\Delta\Phi = \Phi_0/2$ [75], and (3) multiple Andreev reflections due to the strong electron interaction [67, 77], which may lead to $\Delta\Phi = \Phi_0/2^n$.

Finally, we tried to eliminate the reentrance effect by reducing the interface transparency of the MWNT/Al substrate junction. In order to realize this, a thin tunnel barrier with a thickness of a few nanometers was formed at the bottom end of the pores (i.e., MWNTs) by optimizing the anodization condition of the alumina membrane. Annealing this sample after the synthesis of MWNTs leads to diffusion of this tunnel barrier and the bottom part of the MWNT (we confirmed this by TEM), yielding a lower transparency interface of the MWNT/Al-substrate junction. As explained, because this low transparency reduces diffusion out of Cooper pairs from the MWNT to the Al substrate, the reentrance effect must disappear. The result is shown in the inset of Figure 25. In fact, the $G_0$ increase is only observable from $T = 6$ K down to $T = 1.5$ K as temperature decreases. Because this $T = 6$ K approximately corresponds to $T_{px}$ of MWNTs with $L_{tube} = 0.8\ \mu$m, this conductance increase can be due to PIS. The main panel of Figure 25 also shows the temperature dependence of its $G_0$ vs voltage relationship. A conductance peak around zero voltage starts to grow in the region between $-0.65$ and $+0.65$ mV (i.e., $\Delta = 1.3$ meV) from $T = 6$ K corresponding to $T_{px} = 6$ K, whereas two conductance dips appear between the voltage regions of $\pm 0.6$ and $\pm 2$mV also at $T = 6$ K. This conductance peak monotonically reduces to $T = 1.5$ K with decreasing temperature, while the conductance dips also monotonically deepen. In addition, the very sharp conductance valley observable at a voltage of $+0.2$ mV disappears as the temperature decreases.

This disappearance of reentrant conductance strongly supports the claim that the highly transparent interface of the MWNT/Al substrate junction is the key factor in the reentrance effect. This growth in the conductance peak is also evidence of the high-transparency interface of the Nb/MWNT junction and the consequent PIS. It is already known that Andreev reflection (in which an incident electron coming from the N is converted into a Cooper pair in the S, leaving a reflected hole in the N, at the S/N junction)
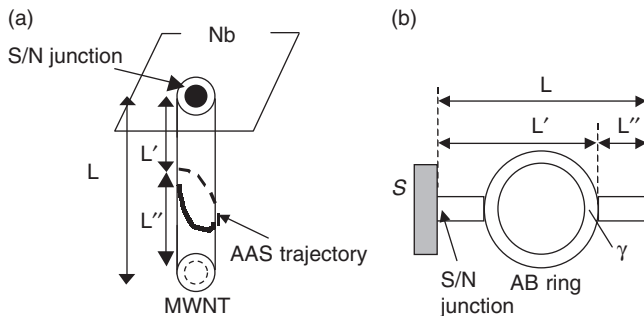


**Figure 24.** (a) An Nb/MWNT junction with a trajectory for AAS oscillation. (c) An S/N junction with the AB ring in its N-region [74]. This structure is assumed to be equivalent to (a) just by replacing the AB ring to the AAS trajectory.
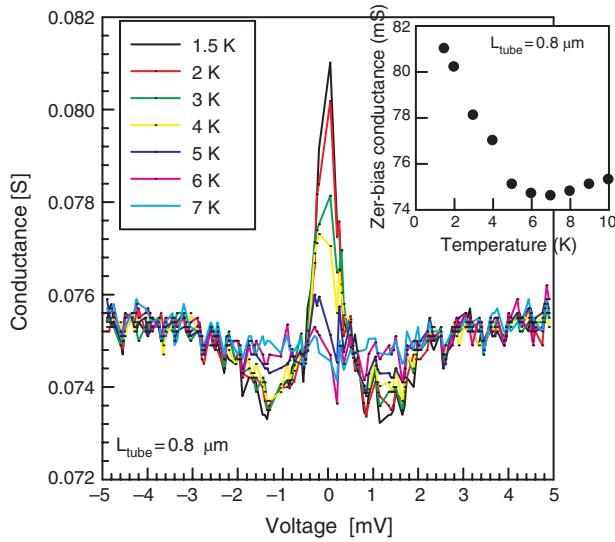
**Figure 25.** Temperature dependence of conductance vs voltage relationships in an Nb/MWNT/Al array with $L_{tube}$ of 0.8 $\mu$m and low-transparency interfaces of the MWNT/Al-substrate junctions. Inset: Temperature dependence of $G_0$ of the main panel.

with a highly transparent S/N interface leads to a conductance peak, particularly in one-dimensional N/S junctions [70, 84]. Our Nb/MWNT junction mostly corresponds to this case, because: (1) $T = 6$ K, at which the conductance peak emerges, agrees with $T_{px}$ as mentioned and is below $T_c$ of our Nb film. (2) The value of $\Delta = 1.3$ meV is approximately equal to the $\Delta$ of Nb (i.e., $\Delta_{Nb} \sim 1.4$ meV). (3) The phase coherence length, estimated from $D = 0.37$ m²/s as 523 nm, is larger than the circumferential length of the MWNT which is about 250 nm, so that our MWNT can be a one-dimensional conductor in the diffusive regime.

### 4.2.3. Conclusion

In conclusion, we reported a conductance increase with the onset temperature of $T_{px} = 9$ K as the highest case and its decreasing with decreasing temperature in Nb/MWNTs junctions with high-transparency interface. The junctions have been achieved by utilizing MWNTs synthesized in nanopores of alumina membranes. We argued that the former and the latter originated from the PIS and its reentrance effect, respectively. The estimated large diffusion constant of Cooper pairs in the MWNTs strongly contributed to these two effects, whereas it did not enhance the critical magnetic field for the vanishing PIS. The observed drastic magnetic-field dependences were also consistent with previous works but some questions remain open. Because of the high reproducibility, MWNTs must be a molecular material relevant for the investigation of superconductivity related phenomena.

### 4.3. Y-Junction Carbon Nanotubes

Self-gate Suppressed Rectification Property in Y-Junction Carbon Nanotube with a Large Diameter and Acute Angle of Two Branches.

### 4.3.1. Introduction

We successfully synthesize a variety of Y-junction multi-walled carbon nanotubes with different diameters and angles of two branches by utilizing porous alumina membranes realized by a two-step anodization method and investigate those electrical properties. We find here that even a Y-junction MWNT with a diameter as large as 50 nm in its stem can show a stable rectification property following the Anderson mode for macroscopic heteroband junction with 20 meV of built-in potential, when the two branches form acute angle. In contrast, we clarify the presence of a current-suppression mechanism deviating from the Anderson model, in the forward voltage region. We argue that this is due to a self-gating effect, caused by difference in an electrochemical potential between the two branches.

A carbon nanotube, a molecular conductor, is a strong candidate for nanoelectronics devices. It is theoretically known that the junction at which a larger diameter "stem" of a single-walled carbon nanotubes is divided into two smaller diameter "branches" (Y-junction or T-junction SWNTs) exhibits interesting electrical properties (such as nano-hetero-junctions of different bandgap semiconductors and nano-Schottky junctions) representing a rectifying nanodiode [86–88]. This is because SWNTs can be either metal or semiconductor with different bandgaps, depending on the diameter, chirality, and defects. Multiple connection of such SWNTs with differences in chiralities, diameters, and defects leads to the properties mentioned at the Y-junction [89].

In addition, the presence of the Y-junction implies the connection of one more SWNT to this two-terminal junction as the third terminal. This third terminal can act as a gate electrode which can control the electric features of two-terminal SWNT devices. A three-terminal operation of quantum conductivity, like a metal–oxide–semiconductor transistor, has also been predicted only theoretically [86].

Hence, Y- and T-junction SWNTs are expected to become a key component of carbon nanotube integration circuits, but synthesizing them with high reproducibility has proved to be very difficult. Only recently have some experiments [90–92] reported successful synthesis of Y-junction nanotubes and the presence of asymmetric current versus voltage features only at room temperature, possibly resulting from heteroband junctions. The details of the electrical properties are still ambiguous.

Even apart from carbon nanotube systems, the Y-branch nano-electron-wave guide is attracting large attention as a novel switching device in nanoelectronic junctions [93, 94]. It has been reported that capacitive coupled two branches led to switching of electron-wave flow between the branches up into THz range due to a self-gating effect in new class of gateless mesoscopic devices [93] and to switching gain increasing superlinearly with source–drain voltages due to side-gate voltages applied [94]. Both reports implied that even very small voltages applied on both sides of the branches (i.e., lateral electric field) efficiently switched flow of electron waves between the two branches. A Y-junction carbon nanotube can be a good candidate for such novel nano-electron-wave guides.

Here, in this work, we successfully synthesize a variety of Y-junction multiwalled carbon nanotubes with different

diameters and branch angles by utilizing Y-shaped nanopores of alumina membranes [95, 96] realized by a two-step anodization method. We clarify that even a Y-junction MWNT with a large diameter stem can lead to macroscopic heteroband junction representable by the Anderson model at the Y-junction, when the two branches form an "acute angle." We also find a deviation from the model, implying a self-gating effect due to capacitive coupling of the two branches.

### 4.3.2. Experimental Results and Discussion

We show the structural information of Y-shaped pores, in which Y-junction MWNTs were synthesized, in Figure 26. We have already confirmed that our carbon nanotubes synthesized in porous alumina membrane by chemical vapor deposition were MWNTs, which exhibited diffusive electron-wave transport at low temperature [95, 96]. Besides, nanotubes synthesized by similar methods showed semiconducting behavior at room temperature [91]. Hence, our MWNTs can have semiconducting characteristics in the diffusive regime. We prepared three different types of Y-junction MWNTs with one straight MWNT as a reference for this experiment, and their features are described in Table 2. SEM images of those pores are shown in Figure 26c. These imply that only type B1 has an acute angle between the two branches. In contrast, there is a spacing of 20–30 nm between two branches in types A and B2, due to the large diameter stems.

Figure 27 shows the current versus voltage ($J$ vs $V$) characteristics of each type of MWNT at room temperature. First, we find that only type B1 exhibits a strong asymmetry and rectification property similar to that noted in past reports (Fig. 27b). Because type C, which is not a Y-junction MWNT, exhibited a symmetric $J$ vs $V$ curve (Fig. 27d), we conclude that not the interface of electrode/MWNT junctions but the Y-junction is the origin for this asymmetric $J$ vs $V$ property of type B1. In contrast, second, we note that the $J$ vs $V$ feature of type A is mostly symmetric and shows poor reproducibility (Fig. 27a). Because the ratio of diameters between the stem and branches is the same as that of type B1, the very large diameter around 90 nm in the stem of type A can be the origin for the instability and elimination of the rectification property in Figure 27a. Third, we find that the $J$ vs $V$ feature of type B2 (Fig. 27c) even with a high diameter ratio (above 4) of the stem and branch is also symmetric. This also implies that a large diameter around 70 nm in the stem of type B2 eliminates the rectification property, even under such a high diameter ratio.

Why do the large diameter stems in types A and B2 eliminate the rectification property? Why can only type B1 have the rectification property? One main reason can be the angle between the two branches (i.e., whether the angle is obtuse or acute) as mentioned for Figure 27c, because only type B1 has the acute angle between the two branches. Reference [86] theoretically reported a rectification property in a (14,0) SWNT branching two (7,0) SWNTs with acute angle. The acute angle led to the presence of six heptagons clustered at the Y-junction, leading to the rectification property. In contrast, [86] also showed that a Y-junction SWNT, consisting of three (8,0) SWNTs, with an obtuse angle led
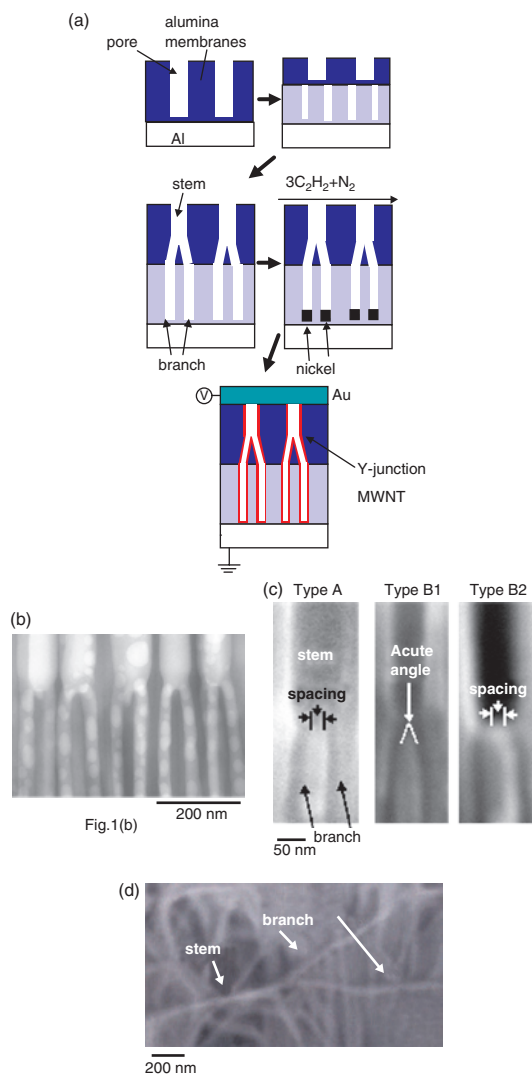


**Figure 26.** Schematic cross-section of alumina membrane with Y-shaped nanopores and its synthesis method. First, aluminum substrate, with applied positive bias voltage (50 V for type A and B1, 60 V for type B2), is anodized in $H_2C_2O_4$ under a current density and temperature of 10 °C (left upper). This leads to large-diameter pores for the stem in the alumina membrane. After this anodization is stopped, second, anodization with reduced bias voltage of 35 V was continuously performed under the same conditions, leading to smaller diameter pores for the branch (right upper). The total thickness of the alumina membrane is 5 $\mu$m in each sample. Y-shaped pores were synthesized by automatic alignment of the interface of the upper and lower membranes, due to self-organization (left lower). We also realized smaller diameter pores in type B by reducing current density for anodization, compared with type A. Consequently, we successfully prepared three types of Y-shaped pores for this experiment (Table 2). After the synthesis of the Y-shaped pores, nickel was electrochemically deposited into the bottom ends of the branch pores and then, Y-junction MWNTs were synthesized by chemical vapor deposition using the nickel as a catalyst (right lower and the lowest). Although we measured the averaged characteristics of Y-junction MWNTs with the number of about $10^4$, it was already confirmed that even this was mostly the same as those in an individual Y-junction nanotube [91]. (b) Cross-sectional TEM image of Y-shaped pore array for type B1 in an alumina membrane. (c) Cross-sectional SEM images of Y-shaped pores, for types A, B1, and B2 (see Table 2), in alumina membranes. (d) SEM overview image of a Y-junction nanotube (shown by an arrow) of type B1.

**Table 2.** Structure parameters for types A, B1, B2, and C of Y-shaped pores.

|            | Type A | Type B1 | Type B2 | Type C |
|------------|--------|---------|---------|--------|
| $\phi 1$ (nm) | 90  | 50  | 69  | 80 |
| $\phi 2$ (nm) | 26  | 15  | 17  | — |
| $\phi 3$ (nm) | 27  | 16  | 19  | — |
| $\phi 1/\phi 2$ | 3.5 | 3.3 | 4.1 | 1 |
| $\theta$   | obtuse | acute | obtuse | — |
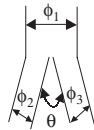
*Note:* The diameter corresponds to most outer diameters of MWNTs. We measured about 30 pores in each array to confirm these averaged structure parameters. Types A and B1 have mostly the same ratio of the stem and branch in diameter, but each pore diameter in type A is approximately two times larger than that in type B1. Types B1 and B2 have mostly the same diameter in the branch, but the ratios of the stem and branch in diameter in type B2 were increased from that of type B1 by increasing the stem diameter. These lead to acute angle of two branches only in type B1. Type C has just a straight shape like a general MWNT with a large diameter.

to only two heptagonal defects. These calculation results imply the presence of heptagon defects at the Y-junction parts with the acute angle in our nanotubes (i.e., in type B1), although we failed to observe actual chilarity of our
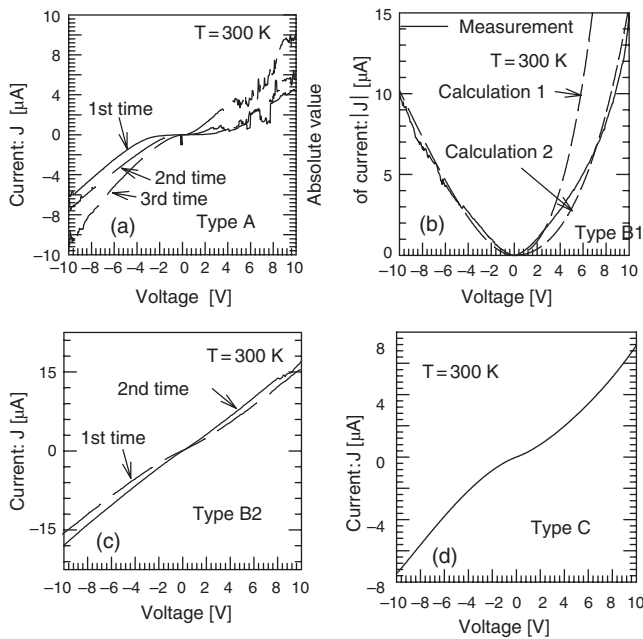


**Figure 27.** Current vs voltage ($J$ vs $V$) curves, measured three times, of type A. The first-time measurement exhibits weak asymmetry, whereas the asymmetry drastically degrades in the second- and third-time measurements, resulting in symmetric features. (b) "Absolute value of the $J$" vs $V$ curve of type B1. Solid line is the measurement result. Calculations 1 and 2 mean the calculation results using only the Anderson model [Eqs. (23) and (24)] and that with the self-gating effect [Eqs. (23)–(27)], respectively. (c) $J$ vs $V$ curves of type B2, implying a mostly symmetric property in the two-time measurements. (d) $J$ vs $V$ curves of type C, implying a perfect symmetric feature.

Y-junction MWNTs here. Besides, because one MWNT consists of many SWNTs, rolled up coaxially, with different chiralities and diameters, the acute angle between the branches in our Y-junction MWNT will introduce defects with the number larger than that of one Y-junction SWNT, at some of shells. Reference [86] implied that heptagonal defect had a positive charge and, hence, asymmetric locations of such defects in Y-junction tube easily led to the rectification property. Y-junction MWNTs can also easily introduce such asymmetric location of defects near the Y-junction parts at some of shells, due to the structural reasons mentioned with a larger number of defects. Therefore, we speculate that the presence of heptagon defects introduced by the acute angle of two branches and the asymmetric location yielded the rectification property in our Y-junction MWNTs. Anyway, these experimental results revealed that even a Y-junction MWNT with diameter as large as 50 nm in its stem could show a stable rectification property when the two branches formed the acute angle. In contrast, the Y-junction MWNTs including the diameters larger than 50 nm with obtuse angle between two branches could not show any rectification properties even if they had the high diameter ratio of the stem and branches.

Based on this result, we focus on detailed features of type B1. Figure 28 shows the logarithmic conductance ($\log[G]$) versus the inverse of temperature ($1/T$) relation, which are the so-called thermal-activation-type characteristics representing the semiconductor-like features, in type B1. We found that the $\log[G]$ vs $1/T$ relationships were very different between the positive (Fig. 28a and b) and negative (Fig. 28c) bias voltage regions. The $\log[G]$ vs $1/T$ relation in the negative bias voltages is linear and hence follows the thermal-activation type at high temperatures (Fig. 28c),
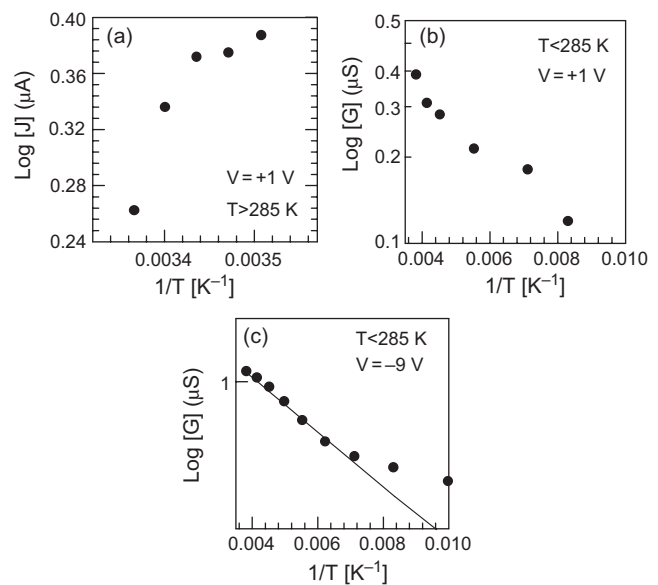


**Figure 28.** Logarithmic current ($\log[J]$) vs inverse of temperature ($1/T$) relation at $V = +1$ V above $T = 285$ K of type B1. (b) Logarithmic conductance ($\log[G]$) vs $1/T$ relation at $V = +1$ V below $T = 285$ K of the type B1. (c) Log [$G$] vs $1/T$ relation at $V = -9$ V of the type B1. The sold line shows the best fit by the thermal-activation relation.

whereas this relation saturates at low temperatures below a transition temperature. In contrast, the $\log[G]$ vs $1/T$ relation in the positive bias voltage regions does not follow the thermal-activation type. It increases as temperature increases above $T \sim 285$ K (Fig. 28a), whereas it decreases with decreasing temperatures below $T \sim 285$ K (Fig. 28b).

Because the asymmetric $J$ vs $V$ curve in Figure 27 (b) means the presence of either a heteroband junction or a Schottky junction, we carry out data fitting by the Anderson model for macroscopic semiconductor heterojunction as follows [97]. The $J$ vs $V$ characteristics are given by the following equation in the Anderson model:

$$J = (qA^*TV_{bi}/k)\exp(-qV_{bi}/kT)$$
$$\times (1 - V_{sd}/V_{bi}[\exp(qV_{sd}/kT) - 1] \quad (28)$$
$$A^* = 4\pi qm^*k^2/h^3 \quad (29)$$

$q$, $A^*$, $V_{bi}$, $V_{sd}$, and $m^*$ are the elementary charge of hole, the effective Richardson constant, the built-in potential at the heterojunction, the source–drain voltage applied between the electrodes for the stem and one branch, and the effective mass of hole, respectively. We used $V_{bi}$ as only a fitting parameter, normalizing the observed current by the number of measured Y-MWNTs in one array. The agreement between the experimental result and the calculation for the $J$ vs $V$ curve is good below $V = 2.4$ V (calculation 1 in Fig. 27b). In particular, the experimental result and the calculation exhibit excellent agreement in the negative bias voltage region. The current in this region does not reach saturation levels but decreases linearly proportional to the bias voltage. This implies the absence of a Schottky junction, because the current through a Schottky junction with reverse bias reaches saturation due to the Schottky barrier. This nonsaturated $J$ vs $V$ feature is a manifestation of a heteroband junction at the Y-junction. In addition, the $\log[G]$ vs $1/T$ relation in the negative voltage region is also in good agreement with the calculation result obtained from Eq. (28) (Fig. 28c). The best fitting in Figures 27b and 28c gives $V_{bi} = 20$ meV as the heterojunction barrier.

These results provide a configuration of a two-terminal macroscopic heteroband junction for the Anderson model at the junction of the stem and one branch (Fig. 29), when we neglect the influence of the other (third) branches. Because the bandgap is proportional to the inverse of the MWNT diameter in semiconducting carbon nanotubes, the branch with 15 (or 16) nm diameter should have a bandgap larger than that of the stem (50 nm diameter). We applied the positive and negative bias voltages to the braches and stems, respectively, in the measurement for Figure 27b. Because the positive and negative bias regions correspond to the forward and reverse bias regions, respectively, in Figure 29, the current carrier can be a hole. Hence, the band discontinuity at the valence band of heterojunction can be 20 meV as $V_{bi}$.

We have confirmed that a Y-junction MWNT even with the diameter as large as 50 nm in its stem, when the acute angle between the branches is formed, can exhibit the electrical properties of a macroscopic heteroband junction, mostly following the Anderson model. This emphasizes an advantage that one does not have to synthesize carbon nanotubes with diameters as small as a few nm,
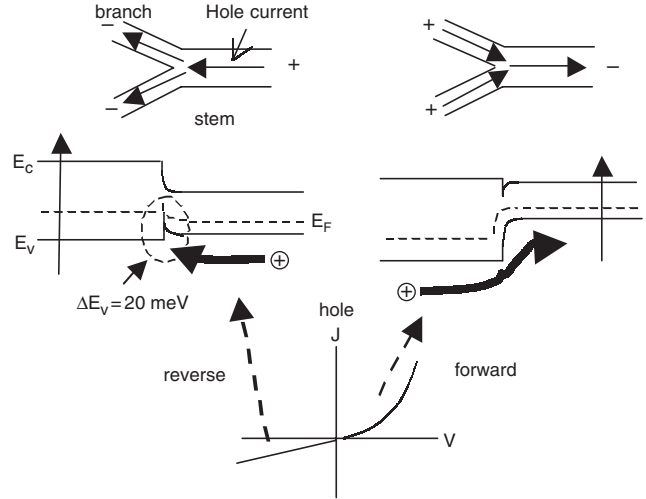


**Figure 29.** Configuration for a heteroband junction, corresponding to the reverse and forward bias voltage regions in the $J$ vs $V$ curve in Figure 27b, based on the measurement results and Anderson model.

to realize heteroband junction by connection of different carbon nanotubes. However, the following two problems remain in the interpretation of these experimental results: (1) disagreement between the measurement and calculation results above $V = +2.4$ V in Figure 27b and (2) conductance decrease accompanying a temperature decrease in Figure 28b. Because Eq. (28) indicates that there should be a larger current in the forward bias region in Figure 27b and conductance should increase with decreasing temperature in Figure 28b, the presence of a mechanism that prevents the current from increasing in accordance with the Anderson model, in the forward bias region, is implied.

Here, we can understand this current-suppression mechanism in accordance with a side-gating effect reported in [93, 94]. We have taken into consideration only the connection of the stem and one branch (i.e., two-terminal configuration) for the explanation of the rectification property. However, if resistances of the two branches are asymmetric (e.g., $R_{s1} + R_{b1} \ll R_{s2} + R_{b2}$ in Fig. 30), source–drain voltage ($V_{sd}$) applied between the stem and branches leads to difference in an electrochemical potential between the two branches ($\Delta\mu_{12}$). Because alumina film exists between the branches, this $\Delta\mu_{12}$ results in a capacitive coupled two-branch system (Fig. 30). Reference [93, 94] implied that even very small difference in voltages applied on both sides of the branches (i.e., lateral electric field) yielded a large difference in $\Delta\mu_{12}$, leading to efficient switching flow of electron waves between the two branches, in a nano-Y-branch waveguide. This is represented by the following equations taking into account only a self-gating effect.

$$\Delta V - sd = 2R_0J_1 = (1 + \gamma)/(1 - \gamma)$$
$$\times [(\Delta\mu_{12}/-e) - (\mu/-4e)] \quad (30)$$
$$\gamma = \tanh[\eta_{sg}(\Delta\mu_{12}/-e)/V_s] \quad (31)$$
$$\eta_{sg} = C_Q/(C_Q + 2C_{12}) \quad (32)$$

$R_0 = h/2e^2 \sim 13$ k$\Omega$, $J_1$ is the current represented by Anderson model in one branch channel (Fig. 30), $\mu$ is
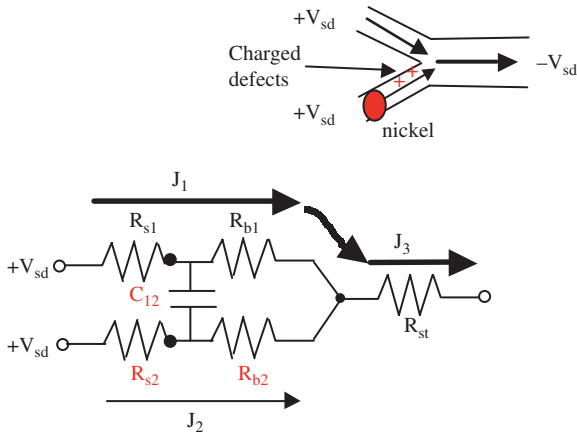
**Figure 30.** Equivalent circuit of a Y-junction nanotube. $R_s$, $R_b$, and $R_{st}$ are the resistances of the source contact (interface resistance at the Al/MWNT-branches), branches, and stem, respectively. $J_i$ is the hole current in each part of the Y-junction MWNT.

the electrochemical potential in electrode connecting to the stem, $V_s$ is the switching voltage which is a measure of how large a change in $\Delta\mu_{12}$ is required to affect $\gamma$, $C_Q = 2/R_0v_F \sim 2 \times 10^{-10}$ (F) is the quantum capacitance (i.e., $e^2 \times$ density of state), and $C_{12} \sim 10^{-14}$ (F) is the capacitive coupling between the two branches (Fig. 30). $\Delta V_{sd}$ in Eq. (30) means a voltage difference, yielded by $\Delta\mu_{12}$, between the electrodes for the stem and one branch. $\gamma$ in Eq. (31) is the switching parameter between the two branches. $\eta_{sg} \sim 0.95$ in Eq. (32) is the side-gating efficiency which is a measure of how well the $\Delta\mu_{12}$ follows the side-gating voltage which was yielded by $C_Q$ and $C_{12}$. Consequently, these equations imply that even very small $\Delta\mu_{12}$ leads to a large $\Delta V_{sd}$, induced by $C_Q$ and $C_{12}$ with asymmetrical located charges on the two branches, resulting in a large current only in one branch and, hence, efficient switching of current between the two branches. Because this current flow enhances $\Delta\mu_{12}$, this self-gating effect grows self-consistently. When this $\Delta V_{sd}$ plays the role of voltage relaxation for the heteroband junction in Figure 29, the rectified current can be reduced as we found.

We performed data fitting to Figure 27b introducing this $\Delta V_{sd}$ into Eq. (28) as the term of $(V_{sd} - \Delta V_{sd})$. The fitting parameters are $\Delta V_{sd}$, $(\Delta\mu_{12}/-e)$, and $V_s$. The result in a positive bias voltage region is shown in Figure 27b as calculation 2. The agreement between the data and the calculation result is good. The best fitting gives $\Delta V_{sd} = 0.3V_{sd}$, using $(\Delta\mu_{12}/-e) = 0.1V_{sd}$ and $V_s = 0.1$ (V). Therefore, this result implies that the origin for the current reduction deviating from the Anderson model is $\Delta\mu_{23}$. We confirmed that this $\Delta\mu_{12}$ is due to the following origin.

We investigated the structures of Y-junction MWNTs in detail and found that the amount of nickel, which was electrochemically deposited into the bottom of the pore branches as a catalyst, was asymmetric between the two pore branches of alumina membranes, by high-resolution cross-sectional TEM observation. This asymmetry is easily introduced, because the electrochemical deposition is very sensitive to electric field applied (i.e., positive and negative bias voltages applied between the Al substrate and the other electrode, respectively, in our case). Even very small struc-

tural asymmetry in the two branches of a Y-shaped pore leads to a large difference in the electric field and, hence, the asymmetric volume of nickel catalyst between the two pore branches. A larger volume of nickel in one branch still remains at the bottom of pore as particles even after the synthesis of Y-junction MWNTs. These nickel particles diffuse around the interface of the Al substrate/Y-MWNT branch junction by annealing [95], and then lead to high interface resistance (i.e., $R_{s1} \ll R_{s2}$ in Fig. 30) because it is well known that interface resistance of metal/carbon nanotube junction is basically high except for TiC, SiC, and NbC [98]. This asymmetric resistance can yield $\Delta\mu_{12}$.

Besides, [93] reported that the self-gating effect together with heptagon induced positive charge might lead to induction of the self-gating effect. Because it could be assumed that the heptagon induced positive charges located asymmetrically near the Y-junction in our Y-junction MWNT as mentioned, this is consistent with our model.

### 4.3.3. Conclusion

In conclusion, we found that even the Y-junction MWNT with diameter as large as 50 nm in its stem exhibited the rectification properties that were in good agreement with the Anderson model for macroscopic heteroband junctions with a hetero barrier of 20 meV, when the two branches formed the acute angle. The observed deviation from the Anderson model was also interpreted by the self-gating effect caused by $\Delta\mu_{12}$ due to the asymmetric resistance between the two branches. We also pointed out that the heptagonal defects introducible by the acute branch angle were the origin for the rectification property.

However, we failed to find actual chilarities and the presence of heptagons with asymmetric locations in the Y-junction MWNTs. Besides, it was not clarified how the heptagon leads to heteroband junctions. Hence, further investigation is expected to reveal them. In any cases, our results imply that porous alumina membrane is a favorite template for synthesis of a variety of Y-junction nanotubes that can be a strong candidate for a molecular rectification diode and transistor.

## 5. FERROMAGNETIC NANOWIRES

### 5.1. Macroscopic Quantum Tunneling of Magnetic Domain Walls

#### 5.1.1. Introduction

Detailed behavior of abrupt magnetoresistance jumps in Ni-nanowires, imbedded into nanoporous alumina membranes, is reported. Abrupt elimination of the MR hysteresis by the MR jump indicates abrupt motion and emission of magnetic domain walls (DWs) from the wires. We find that temperature dependence of the inverse of the normalized jump magnitude shows behaviors similar to those of thermal escape and macroscopic quantum tunneling (MQT) rates in Josephson junctions. We also find that the MR jump is also sensitive to wire diameters. These can be evidence for MQT of magnetic DWs. We also reveal the possible presence of weak localization in the Ni-wire and find that this MR jump is independent of it.

Macroscopic quantum tunneling is an interesting phenomenon, proving the presence of a single macroscopic degree of freedom governed by quantum mechanics. Since it also leads to macroscopic quantum coherence (MQC), useful for realization of quantum computation, it is currently of great interest. The possibility of MQT has been discussed in some material systems (e.g., Josephson junction systems [99], (anti)ferromagnetic nanomaterials [100–106], and organic nanomaterials with charge density wave [107]).

In particular, MQT has been successfully studied in Josephson junction systems. Clarke et al. observed phase difference across the Josephson junction and precisely measured an escape rate, $\Gamma$, of the particle associated with the phase difference from the washboard potential well as the function of current [99]. They found that the experimental results were in good agreement with the prediction by Caldeila and Leggett both in nondissipative and dissipative environmental cases. Hence, $\Gamma$ at low temperatures was interpretable as MQT. Recent observation of quantum oscillation between two charge states in a single Cooper-pair box, utilizing charging effect by single Cooper-pair tunneling, also exhibited a possible MQT and MQC.

In contrast, experimental identification of MQT in ferromagnetic materials still remains ambiguous, despite many theoretical and experimental papers on the subjects [2–8].

Abrupt MR jumps observed in ferromagnetic nanowires and -particles are such examples. They have been discussed from the viewpoint of MQT of magnetic domain walls, spin transition layers including a large number of electron spins. For instance, Hong et al. experimentally reported on a stochastic behavior of the critical magnetic fields for MR jumps and its dependence on microwave radiation in Ni-nanowires [2–4]. The results were interpreted by MQT of magnetic DWs through a tunnel barrier of a pinning potential well. In their interpretation, since the DW abruptly causes MQT through the tunnel barrier at the critical magnetic field, the total magnetization abruptly changes, leading to the abrupt MR jump. They, however, did not show detailed dependence (e.g., MR jump on hysteresis loop and wirediameter, jump magnitude on temperature), which can be more direct evidence for MQT.

In addition, another interpretation for the MR jump has been presented theoretically. It is a destruction of weak localization, the constructive phase interference effect of electron waves in the diffusive regime [105]. WL is strongly coupled with phase of electron spin in ferromagnetic materials. Hence, it argued that spin-flip scattering in the DW and the fluctuation caused by DW motion lead to the dephasing in WL and, hence, the negative MR. None, however, experimentally investigated this theory, including coexistence of phase-interference effects in ferromagnetic nanostructures.

In this work, we experimentally report on detailed behaviors of abrupt MR jumps observed in Ni-nanowires, imbedded into nanopores of alumina membranes. The observed features of hysteresis loops in MR, the temperature, and wire-diameter dependences of MR jumps can be evidence for MQT of magnetic DWs. We also find that possible WL, independent of the MR jump, exists in the Ni-nanowires.

## 5.1.2. Experiments and Discussion

The array sample of Ni-nanowires for MR measurements has been fabricated by electrochemically depositing Ni into nanopores of porous alumina membranes [106, 108–111]. This method leads to high confinement of only Ni-atoms into the pores and, hence, Ni-nanowires with less defects, impurities, and good morphology, compared with nanowires fabricated by the lithographic method and placed on substrates. In addition, since the aspect ratio between the wire length and the diameter is as high as 100, it provides high anisotropic MR as mentioned later. Wire-nanostructure parameters like diameters also can be easily controlled in this method. Therefore, this method is relevant for this study.

Figure 31a shows the typical MR jumps observed in our sample. It clearly exhibits abrupt MR jumps (MR increases) around $B = 0.7$–$0.9$ T [i.e., critical magnetic fields ($B_c$) for MR jumps]. The MR jumps have the following two characteristics. (1) The emergence of MR jump depends on the measured times at the same $B_c$. (2) $B_c$ are observable not
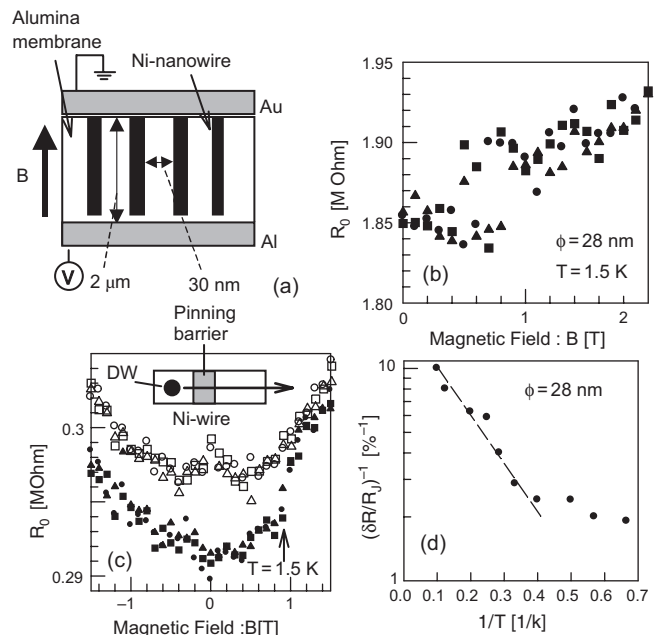


**Figure 31.** Typical magenetoresistance jumps observed in the Ni-nanowire array including the wire number of about $10^4$. Sample structures are mostly the same as those in Section 3, except for elimination of the thin tunnel barrier attached to the bottom ends of the Ni-nanowires. The mean wire diameter ($\phi$), length, and spacing between the wires are about 28 nm, 2 $\mu$m, and 18 nm, respectively. Since the interwire spacing is large enough, the MR value shown here means the superposition of individual wire's characteristics. The half width of the distributed diameter is about 15%, implying high uniformity. Magnetic fields were applied in parallel with the wire axis in all the measurements. (b) Hysteresis loop in the MR and its elimination by the MR jump. Sample-structure parameters are basically the same as those in (a). Arrows mean the MR jumps. Asymmetry of MR jump on the magnetic fields is due to a tunnel junction connected to the one end of the wire as explained elsewhere. (c) Temperature dependence of the inverse of normalized MR jump magnitude in the sample with the same parameters as (a). Dotted line is a guide for the eye. Reprinted with permission from [125], J. Haruyama et al., *Phys. Status Solidi A* 189, 609 (2002). © 2002, Wiley–VCH.

at one magnetic field point but at several field points (i.e., $B = 0.7$, 0.8, and 0.9 T). About the first point, three times we measured MR at each magnetic field and we plot them on Figure 31a. For instance, MR jump is unobservable at the first time measurement at $B = 0.7$ T, whereas it appears at the second and third time measurements at the same $B (= 0.7$ T). This implies that this MR jump is a stochastic phenomenon. In this sense, this is qualitatively consistent with Hong's observation [100–102]. About the second point, we measured a lot of wires ($\sim 10^4$) in one array sample at the same time. Since $B_c$ is sensitive to the wire diameter as revealed in the later part (Fig. 32), this will be due to the distributed wire diameter. When we measured an array sample with the wire number as large as $10^8$, the MR jump was actually smeared out by averaging. It supports this argument.

This MR exhibits a hysteresis loop as shown in Figure 31b. Presence of a hysteresis loop in ferromagnetic materials implies that spin flipping cannot follow the magnetic field in a reversed process in its some geometry parts, leading to geometry parts with different spin orientations (i.e., magnetic domains) and hence magnetic DWs. Therefore, this result suggests that two magnetic domains at least exist in our Ni-wires, although the presence of multidomains is suppressed as the wire diameter is reduced.

However, it should be noticed that this hysteresis loop is very different from that in the past reports in the following very important point; that is, this hysteresis loop is destroyed by MR jump (at magnetic fields higher than the $B_c \sim 1.0$ T) as shown in Figure 31b. This strongly implies that the magnetic DWs are abruptly emitted from the Ni-nanowires by this MR jump, based on the previous discussion.

Here, we investigate the correlation of MR jump with this abrupt motion of the DW by the following two measurements; (1) temperature dependence of the amplitude of MR jump and (2) wire diameter dependence of MR jump behavior.

Initially, Figure 31c shows the temperature dependence of the inverse of the normalized magnitude of MR jump, $(\Delta R/R_J)^{-1}$, where $R_J$ is the MR at the magnetic field right before the MR jump. Above $T \sim 3$ K, it exhibits the thermal-

activation-type characteristic

$$(\Delta R/R_J)^{-1} = A\exp(-\Delta E/kT) \tag{33}$$

where $A$ is the constant and $\Delta E$ is the activation energy. In contrast, it saturates below $T \sim 3$ K. This relation is very similar to the temperature dependence of thermal escape and MQT rates, $\Gamma$, of the particle associated with phase difference in Josephson junction, mentioned in the introduction and given by the equation [1]

$$\Gamma = (\omega_p/2\pi)\exp(-\Delta U/kT - \text{esc}) \tag{34}$$

where $\omega_p$ and $\Delta U$ are the plasma frequency of the particle in the potential well and the tunnel barrier height at the well, respectively. $T_{\text{esc}}$ was nearly equal to temperature at high temperatures (i.e., in classical regime), whereas $T_{\text{esc}}$ took temperature-independent values at temperatures lower than a critical temperature (i.e., in quantum regime) [99]. $\Gamma$ at high temperatures was interpreted as the thermal escape rate, whereas it was interpreted as MQT probability of the phase particle at low temperatures.

This qualitative agreement of $(\Delta R/R_J)^{-1}$ with $\Gamma$ on the temperature dependence implies a possibility that this MR jump, observed at the saturation region (temperatures below $T \sim 3$ K), is strongly associated with MQT in Ni-nanowires. Since the magnetic DWs move abruptly and are emitted from the wires at the MR jump as mentioned, this suggests a possibility that the MR jump is related to MQT of the magnetic DWs.

However, it should be noticed that $(\Delta R/R_J)^{-1}$ itself does not directly correspond to MQT probability in our case unlike the case of Josephson junctions. In Josephson junction systems, the thermal escape rate increased in an increase of temperatures, whereas it decreased at low temperatures, leading to MQT observed as a deviation from the relation. In contrast, although the thermal escape rate of the DW increases with an increase of temperatures like the Josephson junction case, it reduces $\Delta R/R_J$ by thermal smearing, because abrupt MR jumps can be caused only by the abrupt motion of DWs (i.e., MQT at a critical magnetic field). Thus, the $\log(\Delta R/R_J)^{-1}$ vs $1/T$ relation follows the thermal-activation type in this case. Therefore, only the $T_c$ can have a quantitative meaning as the transition temperature, at which the deviation from the thermal-activation relation emerges, indicating the emergence of MQT at lower temperatures. Hence, one cannot quantitatively compare Eq. (33) with Eq. (34).

In order to interpret $\Delta R/R_J$ from the viewpoint of MQT probability, the following relation must be required; $\Delta R/R_J \propto$ "emission rate of the magnetic DW from the entire parts of the nanowire: $\Gamma_{\text{em}}$" $\propto$ "MQT rates of the DW at the pinning potential barrier (i.e., $\Gamma$)." Hence, when $\Gamma_{\text{em}} = \Gamma$ is assumed, $\Delta R/R_J$ should be proportional to MQT probability (i.e., $\Delta R/R_J = A\Gamma$). This coefficient $A$ is the factor representing a sensitivity of DW emission to $\Delta R/R_J$ as follows.

There are the following two cases for the contribution of the presence of the magnetic DW to MR (i.e., representing coefficient $A$ of $\Delta R/R_J = A\Gamma$) in ferromagnetic systems.
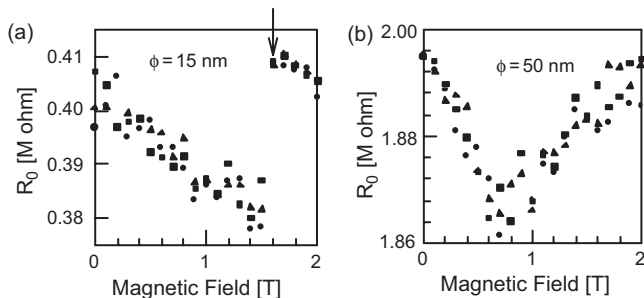


**Figure 32.** MR jumps in the samples with the diameters (a) smaller and (b) larger than that of the Figure 31a sample. The critical magnetic field $B_c$ for MR jump shifts to the higher field with the larger $\Delta R$ ($B_c = 1.5$ T, $\Delta R/R_J = 7.9\%$) in the smaller diameter sample, compared with the Figure 1a sample ($B_c = 0.8$ T, $\Delta R/R_J = 2.3\%$). In contrast, the MR jump disappears in the large diameter sample. Reprinted with permission from [125], J. Haruyama et al., *Phys. Status Solidi A* 189, 609 (2002). © 2002, Wiley–VCH.

(1) Negative contribution: Since this makes MR decreases by DWs, MR is increased by the emission of DWs and abrupt MR jump.

(2) Positive contribution: In this case, MR is reduced by the MR jump. Since MR increases by the abrupt MR jump in our case, the contribution of presence of the DW should be negative.

The following two models are possible for such negative contributions to the best of our knowledge; (1) destruction of weak localization and (2) anisotropic MR (AMR). Here, since the decoherence for weak localization does not explain our results as mentioned later, AMR can be the origin. Because our structure is a nanowire with the high aspect ratio as high as 100, it provides a strong anisotropy and, hence, AMR is more sensitive to magnetic DW with random spin orientations. Increase of the spin coherence by the emission of the DW can drastically make the MR increase in our system. Hence, it can easily reflect the emission rate of the DWs and hence the MQT rate through the pinning barrier. If this negative contribution of the DW is quantitatively revealed, one will be able to find the value of $A$ and, then, estimate $\Gamma$ from $\Delta R/R_J = A\Gamma$. Since, however, we could not find detailed information of the DWs (e.g., the number of DWs in one Ni-wire, DW thickness, the number of spins, and those exact orientations in one DW) in this work, it is difficult here.

The wire diameter dependence of the MR jump also supports this argument. Figure 32 shows the results. $B_c$ shits to the higher magnetic field in the smaller wire-diameter sample as shown in (a), whereas MR jump disappears in the larger diameter sample in (b). In the larger diameter sample, the pinning of the DWs and AMR becomes weak, leading to the elimination of the MR jump. In contrast, they are enhanced in the smaller diameter sample, leading to the increase of $B_c$ and $\Delta R/R_J$.

Consequently, we conclude that the elimination of the hysteresis loop by the MR jump, the temperature dependence of $(\Delta R/R_J)^{-1}$ similar to that in Josephson junction, and the wire diameter dependence of MR jumps are the direct evidence for MQT of the magnetic DWs. The critical temperature, $T_c \sim 3$ K, between the thermal escape and MQT regimes in Figure 31c is actually the same as that in report by Hong and Giordano [101]. This conclusion is also consistent with the stochastic behavior of the MR jumps and the dispersion of $B_c$ in Figure 31a.

Finally, we discuss correlation between this MQT of DW and weak localization in the Ni-wire. Figure 33a shows the temperature dependence of magnetoconductance at each magnetic field. At $B = 0$ T, it can be well fitted by the formula for two-dimensional WL with magnetic impurities, as shown in the upper inset of Figure 33a. The best fitting gives $T_c$, a transition temperature between electron–phonon scattering and spin scattering regimes for dephasing, of 6 K. This $T_c$, relatively higher than those of nonmagnetic wires, is consistent with strong AMR in ferromagnetic nanowires. In addition, positive logarithmic dependence of MC was also found over a wide magnetic-field range in many other samples as shown in Figure 33b, despite the presence of MR jumps in the region. Figure 31a and b samples also exhibit qualitatively the same positive $G_0$
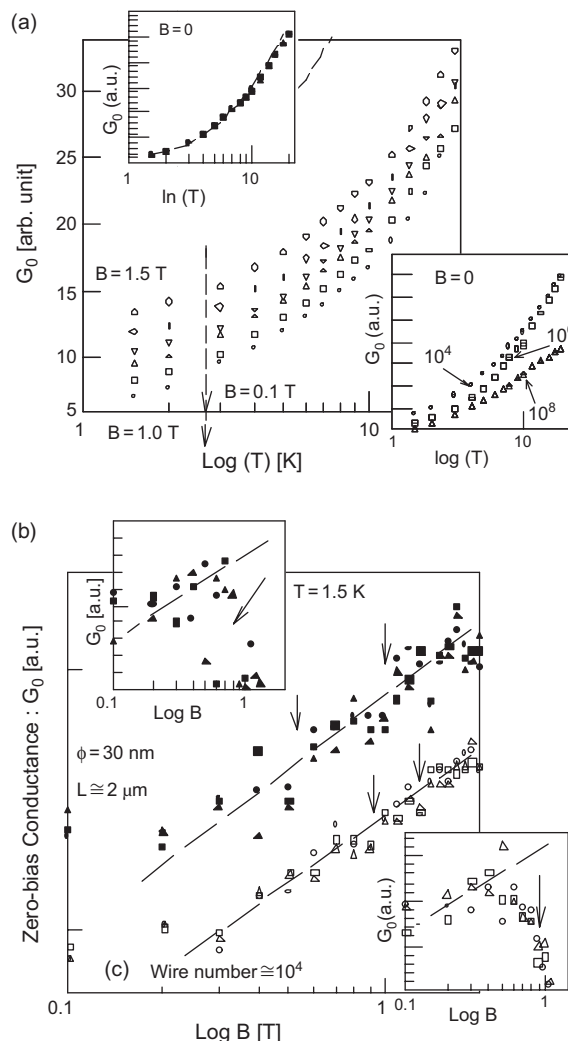


**Figure 33.** (a) Logarithmic temperature dependence of zero-bias magnetoconductance ($G_0$) around the critical magnetic field for MR jump ($B_c = 1.3$ T). Upper inset: Logarithmic temperature dependence of $G_0$ at zero magnetic field. Solid line is the calculation result by 2D weak localization formula. Lower inset: Dependence of the $G_0$ vs log($T$) relation on the number of the wires measured. $10^4$, $10^6$, and $10^8$ mean the number of the measured wires in each electrode area. All the electrodes were prepared on the same sample. (b) Typical logarithmic magnetic-field dependence of $G_0$ in two samples with mostly the same structure parameters. Arrows mean MR jumps. Dashed linear lines are only guides for the eye. Upper inset: That in the Figure 1a sample. Lower inset That of the upper curve in the Figure 1b sample. Reprinted with permission from [125], J. Haruyama et al., *Phys. Status Solidi A* 189, 609 (2002). © 2002, Wiley–VCH.

vs log[$B$] relations as shown in the insets of Figure 3b, although the range is smaller. These also qualitatively support 2D WL, although the relations saturate around $B = 0$ T. None successfully reported on such phase-interference effects in ferromagnetic nanostructures. One reason will be due to scattering by bad surface morphology due to surface anodization, because nanowires are directly placed on substrate surfaces in general measurement methods. In contrast, since our Ni-nanowires are imbedded into nanopores of alumina membrane, they can avoid such an influence leading to

this weak localization. However, electron phase coherence should easily destroyed by strong spin scattering in ferromagnetic structures, basically. Hence, more careful investigation will be indispensable to reconfirm our WL.

The problem is also "two-dimensional." The temperature dependence is mostly independent of the number of wires less than $10^6$, as shown in the lower inset of Figure 33a. It suggests that the dimension originates not from a large number of measured Ni-wires but from the individual Ni-nanowires, which should have only either 1D or 3D. Here, we have reported that the wire-array sample with smaller diameter (~10 nm) exhibited features following 1D electron–electron interaction reported by Davydov et al. [111]. Based on this, we propose a model in which current flows only along the wire surface in the wires with diameter larger than ~10 nm like that in carbon nanotubes (i.e., our nanowire consisted of a 2D Ni-sheet). Since our Ni-wire has an amorphous structure with strong disorder, current may flow only surface with low resistivity.

Here, it is of core importance to notice that the logarithmic temperature dependence in Figure 33a is independent of the abrupt MR jump caused around $B = 1.3$ T. The logarithmic magnetic-field dependence also still survives even with the MR jumps in Figure 33b. These imply that the MR jumps do not lead to dephasing in the WL regime. In this sense, our abrupt MR jump cannot be interpreted by the theory of Tatara and Fukuyama [105], if the WL is reconfirmed.

Caldeira and Leggett theoretically reported that MQT was easily suppressed by energy dissipation in its external environment [99, 104]. In contrast, in realistic magnetic systems, some candidates exist as the origin for such dissipation (e.g., magnons and phonons in ferromagnetic insulators, conducting electrons supporting magnetization moment in metallic weak ferromagnets with thin DW). Since our Ni-nanowire with WL does not correspond to any of such systems, further investigation will be required to clarify the energy dissipation mechanism.

This chapter still remains ambiguous at least as follows: (1) quantitative contribution of many wires to the MR jumps, (2) quantitative confirmation of MQT based on the temperature and wire-diameter dependence, (3) the reconfirmation of WL and, then, the reason for coexistence of 2D WL with ferromagnetism, (4) the reason for its "2D," and (5) the reason WL is independent of the MR jumps. To reveal these, more careful investigation will be expected theoretically and experimentally.

## 5.2. Coexistence of Phase Coherence and Ferromagnetism

Can Mesoscopic Phase Coherence of Electron Waves Coexist with Ferromagnetism in Ni-Nanowires Embedded into Alumina Membranes?

### 5.2.1. Introduction

We report possible coexistence of mesoscopic phase coherence of electron waves and ferromagnetism in Ni-nanowires, which are embedded into nano-pores of Alumina membranes. We successfully find the following phenomena: (1) positive and linear logarithmic dependence of zero-bias conductance on both temperature and magnetic field and (2)

periodic magnetoresistance oscillation, incredibly fittable by the revised formula of Altshuler–Aronov–Spivak oscillation, in the Ni-wires with larger diameters. These suggest the possible presence of two-dimensional weak localization in our Ni-nanowires. Our Ni-nanowires, which are electrochemically deposited and embedded into the pores of alumina membranes, provide high purity and good surface morphology. We argue that these reduce probabilities of parasitic spin scattering, leading to this coexistence.

Coexistence of mesoscopic and macroscopic phase coherence of quantum electron waves and ferromagnetism is recently of great interest. When sample sizes are reduced smaller than the phase coherent length of quantum electron waves, the phase of electron waves is conserved across the entire region of the sample. When the phase coherent length is on mesoscopic and macroscopic scales, this leads to mesoscopic and macroscopic phase coherence, respectively. A variety of phase interference effects emerge in such regimes, such as weak localization, Aharonov–Bohm effect, Altshuler–Aronov–Spivak oscillation, universal conductance fluctuation, metal–insulator transition, and superconductivity [113]. Mesoscopic coherence phenomena have been successfully studied in thin nonmagnetic metal films, semiconductor two-dimensional electron gas systems, and carbon nanotubes [114] in last the decade. Macroscopic coherence has been, of course, a manifestation of superconducting materials.

On the other hand, ferromagnetic materials have strong spin polarization, spin-flip scattering, and spin fluctuation. Hence, if the scattering lengths for such processes are smaller than phase coherent length, they will easily lead to decoherence and elimination of phase interference effects in ferromagnetic nanostructures. Tatara and Fukuyama also theoretically reported that abrupt motion of magnetic domain walls, including a large number of spins, yielded phase fluctuation and destroyed WL, a typical constructive phase interference phenomenon, in ferromagnetic nanowires [115]. In fact, none experimentally reported such coexistence. Therefore, coexistence of ferromagnetism and phase coherence seems to be theoretically and experimentally impossible in general respects.

In contrast, some recent works have surprisingly reported on the coexistence of macroscopic phase coherence and ferromagnetism in particular superconducting materials, (e.g., $d$-band metal $ZrZn_2$ [116] and $UGe_2$ [117]). With respect to mesoscopic phase coherence, our group also reported the possibility that abrupt motion of magnetic domain walls did not lead to dephasing for weak localization in nickel (Ni)-nanowires, which is a $d$-band metal embedded into porous alumina membranes [118–120]. Besides, very recently, Tatara and Barbara theoretically predicted that ferromagnetism did not affect the AB effect and AAS oscillation in 3$d$-band metals in an essential way. This is because AAS oscillation is suppressed for a minority spin channel in most 3$d$ metals due to strong $s$–$d$ scattering, whereas majority spin channel survives due to small density of sates in the $d$-band [121]. Therefore, coexistence of phase coherence and ferromagnetism is currently in the debating stage and none at least experimentally report on mesoscopic phase coherent phenomena in ferromagnetic nanostructures.

In this work, we for the first time report the possible coexistence of mesoscopic phase coherence and ferromagnetism

in Ni-nanowires, based on the following measurement results, e.g., (1) positive and linear logarithmic-temperature ($\log[T]$) dependence of zero-bias conductance ($G_0$) with the saturation region at low temperatures, which can be fitted by a formula of 2D WL, (2) positive and linear logarithmic magnetic-field ($\log[B]$) dependence of $G_0$ with the saturation region at low magnetic fields, and (3) periodic magnetoresistance oscillations, incredibly observed in the Ni-wires with larger diameters, like AAS oscillation. We point out that special structures of our Ni-nanowires, which are electrochemically deposited and embedded into the nanopores of alumina membranes, strongly contribute to coexistence of phase coherence and ferromagnetism.

### *5.2.2. Experiments and Discussion*

Figure 34 shows the schematic cross-section of our Ni nanowires, which were electrochemically deposited and embedded into nanopores of alumina membranes. We have



100 nm

**Figure 34.** Coss-sectional SEM image of a Ni-nanowire array, which was electrochemically deposited and embedded into nanopores of alumina membranes. We prepared arrays with three different mean pore diameters of about 30, 55, and 96 and with the same pore length of 2 mm for this work. This nanowire at least has the following three advantages. high purity, good surface morphology, and no surface oxidation. The first advantage arises from the electrochemical deposition and leads to reduction of scattering probabilities by impurities and defects. The second and third advantages arise from embedding the nanowires into the nanopores with good morphology of the inner walls and lead to reduction of probabilities of surface-spin scattering due to bad morphology and surface oxidation. Spin-flip scattering and spin fluctuation caused by such parasitic factors (i.e., impurities, defects, and poor surface morphology) lead to drastic reduction of phase coherence in ferromagnetic nanowires in an essential way. Hence, our special wire structure is relevant to realize coexistence of mesoscopic phase coherence and ferromagnetism. Magnetic field was applied along with the wire axis in all the measurements in this work.

actually reported a variety of quantum-mesoscopic phenomena using this membrane (e.g., [114, 118–120, 123, 124]). Since this membrane provides extremely high uniformity of structure parameters, observed characteristics in nanowire arrays, deposited into the nanopores, were the superposition of features of individual nanowires.

Figure 35a shows a typical $\log[T]$ dependence of $G_0$ at zero magnetic field. This implies the presence of a linear and positive $\log[T]$ dependence at high temperature and its saturation at low temperatures. There is a transition temperature, $T_c$, between these two regimes. The dotted line is the calculation result by the formula of 2D WL [122]

$$G(T) = G(0) + (e^2/2\pi^2\hbar)$$
$$\times (\pi d/L)\ln[1 + (T/T_c(B, \tau_s))^p] \qquad (35)$$

where $d$, $L$, $N_s$, and $p$ are the diameter and length of the wire, the relaxation time of spin-flip scattering, and the parameter for electron–electron interaction, respectively.

The measurement and calculation results are in excellent agreement. Based on the theory of 2D WL, the linear and positive $\log[T]$ regime at high temperatures means decoherence by electron–phonon scattering, whereas the saturation regime at low temperatures is the decoherence regime by
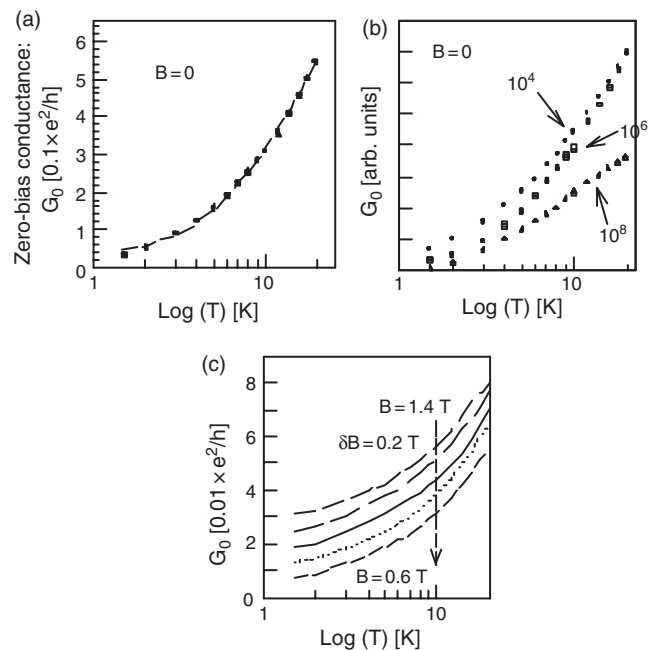


**Figure 35.** (a) Typical logarithmic temperature ($\log[T]$) dependence of zero-bias conductance $G_0$ in Ni-nanowires with mean radius of about 30 nm. Black symbols mean the measurement results and the dotted line is the calculation result by formula of two-dimensional weak localization [Eq. (35)]. They are in good agreement, implying strong spin-flip scattering. (b) Wire-number dependences of $10^4$, $10^5$, and $10^6$ are the number of the Ni-nanowires included in each array. This $G_0$ vs $\log[T]$ relation, however, did not mostly vary even in the array with the wire number up to $10^6$. This implies that this coexistence results not from collective phenomena of the wire array but from the individual Ni-nanowires. (c) Magnetic field dependence of the $G_0$ vs $\log[T]$ relation in Ni-nanowires similar to (a), exhibiting positive magnetoconductance, which is evidence for weak localization.

spin-flip scattering due to magnetic impurities. The best fitting gives $p = 1.9$ and $T_c = 6$ K in our case. This $T_c = 6$ K is much larger than that below 1 K in nonmagnetic nanomaterials with magnetic impurities in the WL regime and hence implies the presence of strong spin-flip scattering in our Ni-nanowires. This is qualitatively consistent with presence of strong spin-flip scattering in ferromagnetic materials. Therefore, this result suggests a possibility of coexistence of 2D WL and ferromagnetism in our Ni-nanowires.

Here, although we measured conductance of a Ni-nanowire array including the number of wires as large as about $10^4$, we conclude that this coexistence results not from collective phenomena of the wire array but from the individual Ni-nanowire, from the result of Figure 35b. Besides, we have already reconfirmed that electrical features of array samples are mostly consistent with those of individual wires, due to extremely high uniformity of the parameters of nanostructures in porous alumina membranes [114].

When a magnetic field is applied, this $G_0$ vs $\log[T]$ relation causes a parallel shift to higher conductance values, particularly in the saturation region at low temperatures (i.e., positive magnetoconductance behavior) (Fig. 35c). In contrast, the relation itself does not mostly change under applied magnetic field up to $B = 1.5$ T (Fig. 35c), although it is smeared by high magnetic field, particularly in the saturation region. This is also evidence of WL, because the electron phase is dephased by the magnetic field particularly in the spin-flip scattering regime, leading to an increase of conductance.

Associated with this respect, Figure 36 shows a typical $\log[B]$ dependence of $G_0$ in two samples with mostly the same structure parameters. First, we applied a high magnetic field of 7 T for initialization of magnetization and then we reduced magnetic field toward $B = 0$ T. Since magnetic length $[L_B = (h/eB)^{1/2}]$ is 88.9 nm which is shorter than phase coherence length $(L_\phi)$ of 490 nm (mentioned later) at $B = 0.1$ T, this field region above 0.1 T actually can contribute to decoherence by magnetic field. One can see a linear and positive $\log[B]$ dependence at high magnetic fields and its saturation at low magnetic fields in both the samples. These also qualitatively support the presence of 2D WL. The linear and positive $\log[B]$ dependence is attributed to decoherence by applied magnetic field, while its saturation is due to decoherence by spin fluctuation which becomes dominant around zero magnetic field with reversing magnetic field. This saturation regime without negative MC means the absence of spin–orbit interaction. This is also consistent with the fact that Ni has no spin–orbit interaction.

Consequently, positive $\log[T]$ and $\log[B]$ dependence of $G_0$ has revealed the possibility of coexistence of mesoscopic phase coherence and ferromagnetism in our Ni-nanowires. However, why two-dimensional WL exists is not answered. If the cross-section of nanowire has a circular shape, nanowire should not provide two dimensions in any cases, because smaller and larger diameter wires should have only one and three dimensions, respectively. In order to clarify this reason, we observed magnetoresistance of the Ni-wires with larger mean diameter, applying magnetic field along with the wire axis.

Figure 37a and b show the result. Surprisingly, one can find MR oscillations in both figures, although the behaviors are
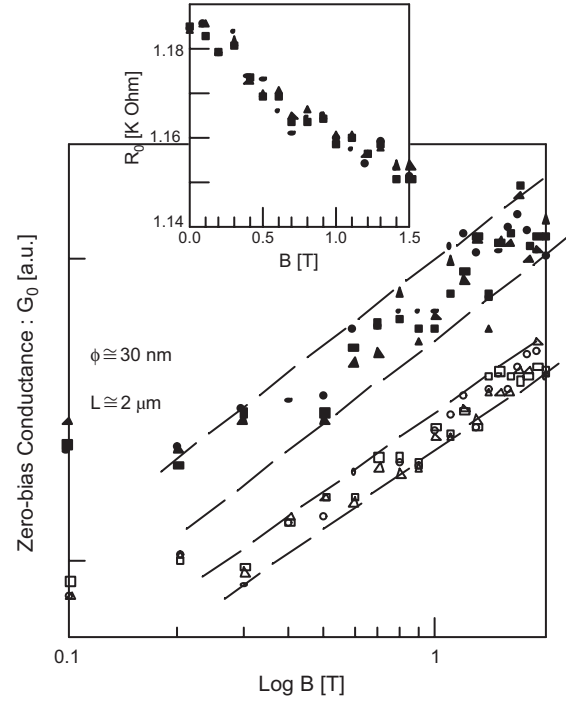


**Figure 36.** Typical logarithmic magnetic-field ($\log[B]$) dependence of $G_0$. We basically measured magnetoconductance three times at each field, except for some field points with high repeatability of $G_0$, and plotted them on the figure with circles, triangles, and square. Dotted lines are only guides to the eyes. Inset: Magnetoresistance obtained from the upper feature of the main panel, exhibiting smeared oscillation with very small magnitude.

complicated in (b). Since the wire diameter is large and this is metal nanowire, any quantized levels cannot exist. Hence, as one of possibilities for this MR oscillation, we performed data fitting by the formula of AAS oscillation [114]

$$\delta G = -(e^2/\pi h)(2\pi r/L_s)[(1/2 + \beta)Z_\phi(L_\varphi(H)) - 3/2 Z_\phi(L'_\varphi(H))] + \alpha(H) \tag{36}$$

$$Z_\phi(L_\varphi(H)) = \ln(L_\varphi/\ell) + 2\sum_{n=1}^{\infty} k_0(n(2\pi r/L_\varphi))$$

$$\times \cos[2\pi n(\Phi/(hc/2e))] \tag{37}$$

$$1/L_\varphi^2 = 1/D\tau_\varphi \tag{38}$$

$$1/L'^2_\varphi = 1/L_\varphi^2 + 2/D\tau_{so} \tag{39}$$

where $L_s$ $\beta$ $L_\varphi$, and $L'_\varphi$ in Eq. (36) are the tube length, the constant depending on electron–electron interaction, and the phase coherent length without and with SOI, respectively. $\ell$, $k_0$, and $\Phi$ in Eq. (37) are the mean free path, the Macdonald function, and the magnetic flux ($\pi r^2 H$), respectively. $D$, $\tau_\varphi$, and $\tau_{so}$ in Eqs. (38) and (39) are the diffusion constant, the relaxation time for inelastic scattering, and the relaxation time for SOI, respectively. Here, $\alpha(H)$ in Eq. (36) represents the increase or decrease of the mean value of conductance, depending on magnetic field $H$. We also neglected the contribution of magnetic field on $L_\varphi$ in Eq. (38). Hence, $L_\phi$ is basically only a fitting parameter.
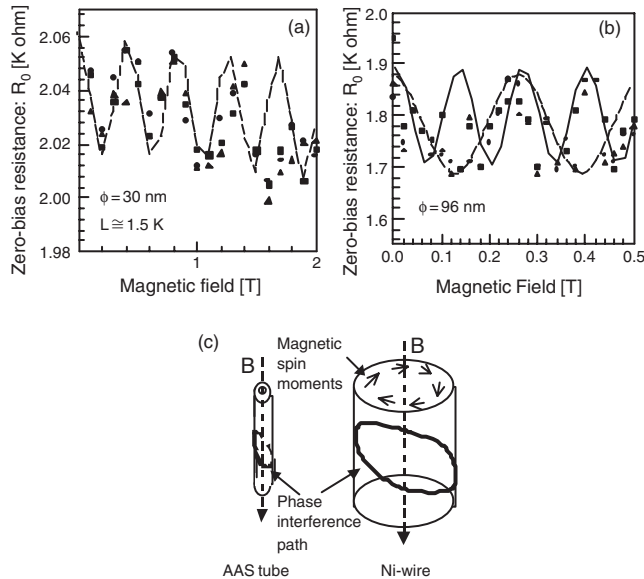
**Figure 37.** (a) Magnetoresistance oscillation in the Ni-wires with mean diameter of 55 nm. Black symbols mean the measurement results (also three times) and the dotted line is the calculation result by a revised formula of Altshuler-Aronov-Spivak oscillation [Eqs. (36)–(38)]. (b) Magnetoresistance oscillation in the Ni-wires with mean diameter of 96 nm, which is larger than (a). Solid and dotted lines are the calculation results by the AAS oscillation formula mentioned previously. These indicate the presence of bimodal behavior. Namely, MR oscillation with periods of 0.25 T exists at magnetic field lower than about 0.25 T (dotted line), while MR oscillation with period of 0.12 T exists above about 0.25 T (solid line). One of the reasons for this behavior is the presence of a two-distribution peak of the wire diameters in this one array. When pore diameter is increased, such distribution is yielded in our anodization method. (c) Left: Schematic view of an AAS tube. In general AAS oscillation, the phase interference path of electron waves encircles the circumferential direction of this AAS tube. Since magnetic fluxes penetrating into the tube inner space modulate the vector potential there, the phase of electron waves encircling the tube circumference is modulated, and hence periodic MR oscillation emerges. Right: Schematic view of a cylindrical-ferromagnetic structure (i.e., large-diameter wire). The magnetic spin moments encircling the circumference form a single domain structure. Magnetic flux also penetrates into the center part of the wire.

The data and calculation result by AAS oscillation theory is in good agreement in each figure. MR oscillation with period ($\Delta B$) of 0.4 T and negative MR around 0 T is confirmed by this fitting at $B < 1$ T in (a), while bimodal behavior is identified with $\Delta B = 0.12$ and 0.25 T in (b). This $\Delta B$ of 0.12 T in (b) is good agreement with the relation of $\Delta B \propto r^{-2}$ for AAS oscillation theory ($r$ is the radius of tube), in comparison with $\Delta B = 0.4$ T in (a). These results imply a possibility that these periodic MR oscillations are AAS oscillations.

This observation of AAS oscillation emphasizes that the phase interference path for 2D WL and AAS oscillation exists along with the circumferential direction of the Ni-wire (Fig. 35c). This is the reason for the presence of two dimensions. Phase coherence length, $L_\phi$, obtained from the best fitting in Figure 37a, is as large as 490 nm, which is actually larger than the length of the wire circumference of 170 nm. Of course, this is larger than $LB$ at 0.1 T as mentioned.

This seems to be very strange, because (1) such a phase interference path should not exist due to dephasing by strong spin-flip scattering caused by ferromagnetism, and (2) Ni-wire has no tubelike structure (i.e, vector potential cannot survive in the inner part of the ferromagnetic wire). From the viewpoint of (1), however, some recent works revealed that magnetic spin moments exist along with circumference in ferromagnetic structures with cylindrical and disk shapes, leading to single domain structure with a circlelike shape (Fig. 37c) [123]. If our Ni-wire also has such a spin structure and electron waves flow along with these spin moments (Fig. 37c), dephasing by spin-flip scattering will be not caused and hence such a phase interference path can survive. From the viewpoint of (2) this wire system is quite different from the AAS tube. This is a very serious problem and we have no idea how to explain this at the current stage. However, the measurement and calculation results strongly suggest the presence of AAS oscillation and phase interference path along with the wire circumference in our Ni-nanowire.

Such MR oscillation, which was imposed on the positive $G_0$ vs log[B] relation, can be found even in Figure 36a measured in the smaller diameter wires, although they are very smeared and oscillation magnitudes are much smaller. In contrast, Figure 37a also exhibits negative MR, which exists around $B = 0$ T and also as a background feature of MR oscillation, like that in Figure 36a, although the slope value is smaller than that in Figure 36a. These mean that magnitude of AAS oscillation (i.e., phase modulation by magnetic field) becomes less distinct and smaller as the wire diameter decreases, while only dephasing becomes dominant leading to negative MR.

As the wire diameter decreases down to a range of 20 or 30 nm, the phase interference path with a circlelike shape is smeared leading to smaller $L_\varphi$, because clear magnetic spin moments along with the wire circumference become difficult to exist due to limited geometry space.

Only an unclear but quasi-2D interference path along with the wire circumference still survives. This leads not to distinct modulation of phase but only to dephasing, caused by magnetic field applied along with the wire axis, if $L_\varphi$ is still larger than the length of the wire circumference. This discussion well explains the wire-diameter dependence mentioned. Hence, $L_\phi$ should be larger than about 93 nm in the samples for Figures 35 and 36.

Besides, we also actually reported emergence of one-dimensional electron–electron interaction in the Ni-nanowires with further smaller diameter (less 10 nm) [124]. This supports our discussion, because the Ni-nanowires with such small diameter no longer have an interference path along with the wire circumference. In this case, only transversal dimension of the nanowire should be compared with phase coherent length or thermal diffusion length. When either of them is larger than the wire diameter, 1D electron–electron interaction emerges.

### 5.2.3. Conclusion

In conclusion, we reported on the possible coexistence of ferromagnetism and mesoscopic phase coherence in the Ni-nanowires, which was electrochemically deposited and embedded into the nanopores of alumina membranes. All

the results reported here qualitatively and quantitatively suggested the coexistence. None, however, experimentally reported on such phenomena in ferromagnetic nanostructures fabricated by other methods before. Our results imply a possibility that this may be due to not essential spin scatterings and fluctuation of bulk nanowires but parasitic spin scattering by impurities, defects, and bad surface morphologies. For instance, nanowires placed on substrate are easily anodized on the surface and the morphology is also much affected by the roughness of substrate surface, leading to strong surface scattering of spins. In addition, even a small amount of defects and impurities introduced during the fabrication processes will have a serious influence as the scattering origins for spins because of the nanosize of the wires. Our fabrication method using the nanopores of alumina membranes and electrochemical deposition can easily avoid these problems. Only such highly pure ferromagnetic nanowires with good surface morphology will lead to coexistence of phase coherence and ferromagnetism in an essential way, as Tatara and Barbara predicted [121].

## 6. CONCLUSIONS

Novel quantum-mesoscopic phenomena observed in the nanostructures and nanomaterials, which were realized by utilizing porous alumina membranes, have been reviewed. Multiwalled carbon nanotubes, Ni-nanowires, and tunnel junctions attached to them exhibited a variety of interesting properties. The top down method, such as nanolithography in semiconductor transistors and two-dimensional electron gas, is of course an established powerful tool for creation of nanostructures and study of nanoscience. However, the bottom up method as presented here, using nanoporous alumina membranes, will be more promising for study of nanoscience and its applications, because of its high uniformity, reproducibility, controllability, and simplicity. One can realize a variety of nanostructures by utilizing a porous alumina membrane as a nanotemplate.

Some of the works presented here still remain open questions. In particular, Ni-nanowire related phenomena reported in Section 5 are very anomalous with our strange interpretation. Measurement of one Ni-nanowire, hence, is required. For this, one can resolve alumina membrane, pick up one Ni-nanowire, place this on Si-substrate, and measures its physical properties. However, this leads to an increase of parasitic spin scattering due to surface defects and roughness, like a general measurement method. Hence, probing only one Ni-nanowire embedded in an alumina membrane will be relevant way by scanning probe microscopy.

In contrast, carbon nanotube related phenomena are quite original and fascinating. These also imply how carbon nanotube is an attractive nanomaterial. In particular, one can speculate strong quantum entanglement of singlet spins forming Cooper pairs. Hence, the study based on Section 4 must open up a new door to realization of quantum computation utilizing quantum entanglement. Recently, this has been actually reported and discussed both theoretically and experimentally. My target is also in this quantum computation. I believe that no materials can realize quantum computation with enough dephasing time, except for carbon nanotubes.

Carbon nanotubes with special structures will induce this process.

No one doubt that nanotechnology and nanoscience can be the mainstream in the 21st century. These will reveal to us fantastic and exciting phenomena hiding in the quantum and mesoscopic world. Some of those will be far beyond our imagination. Besides, application of such phenomena will drastically change our future life. I believe that the future will be brilliant. Effective combination of top-down and bottom-up methods will be a key for certain and quick realization of the future.

## GLOSSARY

**Carbon nanotube (CN)** Molecular tube consisting of rolled up graphene sheet, with diameter as small as 0.4 to a few 10 nm. A single-walled CN is rolled up graphene sheet exhibiting electron transport in the ballistic regime, whereas a multiwalled CN is coaxially rolled up multiple graphene sheets with that in the diffusive regime.

**Macroscopic quantum tunneling (MQT)** Tunneling is a typical phenomenon caused by electron waves in either microscopic or mesoscopic worlds. Of course, a "macroscopic particle," like a baseball, basically should not cause tunneling because it cannot wave. However, MQT surprisingly implies the presence of a single macroscopic degree of freedom governed by quantum mechanics in special cases. MQT has been actually reported in Josephson junction systems, (anti)ferromagnetic nanomaterials, and organic nanomaterials.

**Phase interference of quantum electron waves** When sample size is smaller than phase coherence length of thermal diffusion length of electrons, phase of quantum electron waves is maintained across the entire region of the sample. This leads to a variety of phase interference phenomena, such as (weak, anti, and strong) localization, universal conductance fluctuation, Aharonov–Bohm (Altshuler–Aronov–Spivak) effect, etc.

**Porous alumina membrane** Membrane including dense nanopores (5 to a few 10 nm in diameters) looking like a honeycomb on its top view. This is obtained from simply anodizing pure aluminium in solutions, through self-organization process.

**Proximity-induced superconductivity** When a superconductor (S) is connected to a normal conductor (N) with a highly transparent S/N interface, the Cooper pair wave function diffuses from S to N. This leads to "proximity-induced superconductivity" in a part of N, and hence conductance of the part increases. When diffusion of the Cooper pair is dominant at the end of this part, Thouless energy, $E_{Th}$, is defined from the uncertainty principle of $\Delta E_{Th} \cdot \Delta \tau \approx h/2\pi$. Below this $E_{Th}$, conductance decreases due to "reentrance effects."

**Single electron tunneling (SET)** Tunneling effect of electron dominated by charging energy ($E_c = e^2/2C$, where $C$ is the junction capacitance) of the tunnel junction. This $E_c$ realizes manipulation of electrons one by one (single electron). Typical phenomena are Coulomb blockade, Coulomb staircase, Coulomb oscillation, etc. Tunneling is a phenomenon representative of electron "waves," whereas $e$ is elementary charge of an electron representative electron particle. One

can actually "feel" duality of waves and particles in quantum mechanics by macroscopic measurement of SET.

## REFERENCES

1. D. V. Averin and K. K. Likharev, in "Mesoscopic Phenomena in Solids" edited by B. L. Altshuler, P. A. Lee, and R. A. Webb, 173(North-Holland, 1991); Single Charge Tunneling edited by H. Grabert, and M. H. Devoret, (Plenum Press, New York and London, 1991).
2. G.-L. Ingold, Yu. V. Nazarov, in the second article of [1], p. 21.
3. A. N. Cleland, J. M. Schmidt, and J. Clarke, *Phys. Rev. Lett.* 64, 1565 (1990).
4. A. Yacoby, M. Heiblum, D. Mahalu, and H. Shtrikman, *Phys. Rev. Lett.* 74, 4047 (1995).
5. H. Akera, Abstract of Int. Nat. Sym. Nano-Physics and Electronics," NPE'97, (Tokyo), 1997, p. 83.
6. S. Tarucha, D. G. Austing, T. Honda, R. J. van der Hage, and L. P. Kouwenhoven, *Phys. Rev. Lett.* 77, 3613 (1996).
7. S. Drewes and S. R. Renn, *Phys. Rev. Lett.* 80, 1046 (1998).
8. Ya. M. Blanter, A. D. Mirlin, and B. A. Muzykantskii, *Phys. Rev. Lett.* 78, 2449 (1997).
9. J. A. Folk, S. R. Patel, S. F. Godijn, A. G. Huibers, S. M. Cronenwett, and C. M. Marcus, *Phys. Rev. Lett.* 76, 1699 (1996).
10. J. Haruyama, D. Davydov, D. Routkevitch, D. Ellis, B. W. Statt, M. Moskovits, and J. M. Xu, Solid-state electronics, in "Proc. NPE'97, 1998, Vol. 42, p. 1257.
11. D. Davydov, J. Haruyama, D. Routkevitch, D. Ellis, B. W. Statt, M. Moskovits, and J. M. Xu, *Phys. Rev. B* 57, 13550 (1998).
12. D. Routkevitch, A. A. Tager, J. Haruyama, D. Almawlawi, M. Moskovits, and J. M. Xu., *IEEE Electron Devices* 43, 1646 (1996); A. Tager, D. Routkevitch, J. Haruyama, D. Almawlawi, M. Moskovits, and J. M. Xu, *NATO ASI Ser. E* 323, 171 (1996).
13. Yu. V. Nazarov, *Sov. Phys. JETP* 68, 561 (1989); in [2], p. 99.
14. B. L. Altshuler and A. G. Aronov, in "Electron–Electron Interactions in Disordered Systems" (A. L. Efros and M. Pollak, Eds.), North-Holland, Amsterdam, 1985; B. L. Altshuler and A. G. Aronov, *Solid State Comm.* 30, 115 (1979).
15. H. R. Zeller and I. Giaever, *Phys. Rev.* 181, 789 (1969).
16. S. Kobayashi, *Surface Sci. Rep.* 16 (1992).
17. B. L. Altshuler, A. G. Aronov, and D. E. Khmelnitsky, *J. Phys. C* 15, 7367 (1982).
18. Yu. V. Nazarov, *Sov. Phys. JETP* 68, 561 (1989); J. P. Kauppinen and J. P. Pekola, *Phys. Rev. Lett.* 77, 3889 (1996); P. Delsing, K. K. Likharev, L. S. Kuzmin, and T. Claeson, *Phys. Rev. Lett.* 63, 1180 (1989).
19. Yacoby, M. Heiblum, D. Mahalu, and H. Shtrikman, *Phys. Rev. Lett.* 74, 4047 (1995).
20. S. Tarucha, D. G. Austing, and T. Honda, *Phys. Rev. Lett.* 77, 3613 (1996).
21. G.-L. Ingold and Y. V. Nazarov, in "Single Charge Tunneling" (H. Grabert and M. H. Devoret, Eds.), NATO ASI Series, p. 21. Plenum P, New York/London, 1991.
22. M. H. Devoret, D. Estive, H. Grabert, G.-L. Ingold, H. Pothier, and C. Urbina, *Phys. Rev. Lett.* 64, 1824 (1990).
23. A. N. Cleland, J. M. Schmidt, and J. Clarke, *Phys. Rev. Lett.* 64, 1565 (1990).
24. S. H. Farhangfar and J. P. Pekola, *Europhys. Lett.* 43, 59 (1998); T. Holst, D. Esteve, C. Urbina, and M. H. Devoret, *Phys. Rev. Lett.* 73, 3455 (1994).
25. X. H. Wang and K. A. Chao, *Phys. Rev. B* 56, 12404 (1997); 59, 13094 (1999).
26. P. Joyez, D. Esteve, and M. H. Devoret, *Phys. Rev. Lett.* 80, 1956 (1998).
27. Y. Imry, in "Introduction to Mesoscopic Physics." Oxford Univ. Press, London, 1997.
28. S. J. Tans, M. H. Devoret, and C. Dekker, *Nature* 386, 474 (1997); 394, 761 (1998).
29. J. Haruyama, I. Takesue, and Y. Sato, in "Quantum Mesoscopic Phenomena and Mesoscopic Devices in Microelectronics" (I. Kulik and R. Ellialtiogluet, Eds.), NATO Science Ser. C, Vol. 145, p. 559. Plenum, New York, 2000; J. Haruyama, I. Takesue, and Y. Sato, *Appl. Phys. Lett.* 77, 2891 (2000).
30. D. Davydov, J. Haruyama, D. Routkevitch, D. Ellis, B. W. Statt, M. Moskovits, and J. M. Xu, *Phys. Rev. B* 57, 13550 (1998).
31. L. Langer, V. Bayot, E. Grivei, J.-P. Issi, J. P. Heremans, C. H. Olk, L. Stockman, C. Van Haesendonck, and Y. Bruynseraede, *Phys. Rev. Lett.* 76, 479 (1996).
32. A. Bachtold and C. Strunk, *Nature* 397, 673 (1999).
33. Yu. V. Nazarov, *Sov. Phys. JETP* 68, 561 (1989); P. Delsing, K. K. Likharev, L. S. Kuzmin, and T. Claeson, *Phys. Rev. Lett.* 63, 1180 (1989).
34. S. Kazaoui, N. Minami, R. Jacquemin H. Kataura, and Y. Achiba, *Phys. Rev. B* 60, 13339 (1999); R. S. Lee, *Nature* 388, 255 (1997).
35. L. Langer, V. Bayot, E. Grivei, J.-P. Issi, J. P. Heremans, C. H. Olk, L. Stockman, C. Van Haesendonck, and Y. Bruynseraede, *Phys. Rev. Lett.* 76, 479 (1996).
36. S. N. Song, X. K. Wang, R. P. H. Chang, and J. B. Ketterson, *Phys. Rev. Lett.* 72, 697 (1994).
37. V. Bayot, L. Piraux, J.-P. Michenaud, and J.-P. Issi, *Phys. Rev. B* 40, 3514 (1989).
38. A. Bachtold, C. Strunk, et al., *Nature* 397, 673 (1999).
39. A. Fujiwara, K. Tomiyama, H. Suematsu, M. Yumura, and K. Uchida, *Phys. Rev. B* 60, 13492 (1999).
40. J. Haruyama, I. Takesue, T. Hasegawa, and Y. Sato, *Phys. Rev. B* 63, 073406 (2001).
41. J. Haruyama, I. Takesue, and Y. Sato, *Appl. Phys. Lett.* 77, 2891 (2000).
42. J. Haruyama, I. Takesue, and Y. Sato, in "Quantum Mesoscopic Phenomena and Mesoscopic Devices in Microelectronics"

(I. Kulik and R. Ellialtiogluet, Eds.), NATO Science Ser. C, Vol. 145, 559. Plenum, New York, 2000.

43. T. W. Ebbesen, H. J. Lezec, and H. Hiura, *Nature* 382, 54 (1996).
44. K. Tsukagoshi and B. W. Alphenaar, *Nature* 401, 572 (1999).
45. P. W. Anderson, *Phys. Rev.* 109, 1492 (1958).
46. E. Abrahams, P. W. Anderson, D. C. Licciardello, and T. V. Ramakrishnan, *Phys. Rev. Lett.* 42, 673 (1979).
47. C. van Haesendonck, L. Van den dries, and Y. Bruynseraede, and G. Deutscher, *Phys. Rev. B* 25, 5090 (1982).
48. B. L. Altshuler and A. G. Aronov, *JETP Lett.* 35, 588 (1982).
49. D. Y Sharvin and Y. V. Sharvin, *Sov. Phys. JETP Lett.* 34, 272 (1981).
50. S. Hikami, A. I. Larkin, and Y. Nagaoka, *Progr. Theor. Phys.* 63, 707 (1980).
51. F. Komori, S. Kobayashi, and W. Sasaki, *J. Phys. Soc. Jpn.* 51, 3136 (1982).
52. G. Bergman, *Phys. Rev. Lett.* 48, 1046 (1982).
53. C. Papadopoulos, A. Rakitin, J. Li, A. S. Vedeneev, and J. M. Xu, *Phys. Rev. Lett.* 85, 3476 (2000).
54. H. Dai, in "Carbon Nanotubes" (Mi. and G. Dresselhaus, Eds.), p. 29. Springer-Verlag, Berlin, 2001.
55. L. Forro and C. Schonenberger, in "Carbon Nanotubes" (Mi. and G. Dresselhaus, p. 329. Springer-Verlag, Berlin, 2001.
56. T. W. Odom, J.-L. Huang, C. L. Cheung, and C. M. Lieber, *Science* 290, 1549 (2000).
57. L. Langer, V. Bayot, E. Grivei, J.-P. Issi, J. P. Heremans, C. H. Olk, L. Stockman, C. Van Haesendonck, and Y. Bruynseraede, *Phys. Rev. Lett.* 76, 479 (1996).
58. Bachtold and C. Strunk, *Nature* 397, 673 (1999).
59. J. Haruyama, I. Takesue, T. Hasegawa, and Y. Sato, *Phys. Rev. B* 63, 073406 (2001).
60. J. Haruyama, I. Takesue, and Y. Sato, *Appl. Phys. Lett.* 77, 2891 (2000).
61. J. Haruyama, I. Takesue, and Y. Sato, in "Quantum Mesoscopic Phenomena and Mesoscopic Devices in Microelectronics" (I. Kulik and R. Ellialtiogluet, Eds.), NATO Science Ser. C, Vol. 145, p. 559. Plenum, New York, 2000.
62. T. W. Ebbesen, H. J. Lezec, and H. Hiura, *Nature* 382, 54 (1996).
63. K. Tsukagoshi and B. W. Alphenaar, *Nature* 401, 572 (1999).
64. J. Haruyama, I. Takesue, and T. Hasegawa, *Appl. Phys. Lett.* 79, 269 (2001); *Phys. Rev. B* 65, 33402 (2002).
65. C. Papadopoulos, A. Rakitin, J. Li, A. S. Vedeneev, and J. M. Xu, *Phys. Rev. Lett.* 85, 3476 (2000).
66. H. R. Shea, R. Martel, and Ph. Avouris, *Phys. Lev. Lett.* 84, 4441 (2000).
67. Z. K. Tang, *Science* 292, 2462 (2001).
68. M. Kociak, A. Yu. Kasumov, S. Guéron, B. Reulet, I. I. Khodos, Yu. B. Gorbatov, V. T. Volkov, L. Vaccarini, and H. Bouchiat, *Phys. Rev. Lett.* 86, 2416 (2001).
69. Yu. Kasumov, R. Deblok, M. Kociak, B. Reulet, H. Bouchiat, I. I. Khodos, Yu. B. Gorbatov, V. T. Volkov, C. Journet, and M. Burghard, *Science* 284, 1508 (1999).
70. F. Morpurgo, J. Kong, C. Marcus, and H. Dai, *Science* 286, 263 (1999).
71. H. Takayanagi, J. Bindslev Hansen, and J. Nitta, *Phys. Rev. Lett.* 74, 162; ibid. 166 (1995).
72. E. Toyoda, H. Takayanagi, and H. Nakano, *Phys. Rev. B* 59, R11653 (1999).
73. S. G. den Hartog, B. J. van Wees, Y. V. Nazarov, T. M. Klapwijk, and G. Borghs, *Phys. Rev. B* 56, 13738 (1997).
74. P. Charlat, H. Courtois, Ph. Gandit, D. Mailly, A. F. Volkov, and B. Pannetier, *Phys. Rev. Lett.* 77, 4950 (1996).
75. V. T. Petrashov, V. N. Antonov, P. Delsing, and R. Claeson, *Phys. Rev. Lett.* 70, 347 (1993).
76. A. Golubov, F. K. Wilhelm, and A. D. Zaikin, *Phys. Rev. B* 55, 1123 (1997-II).

77. O. Bourgeois, A. Frydman, and R. C. Dynes, *Phys. Rev. Lett.* 88, 186403 (2002).
78. Y. Wei, J. Wang, Hong Guo, H. Mehrez, and C. Roland, *Phys. Rev. B* 63, 195412 (2001).
79. D. L. Maslov, M. Stone, P. M. Goldbart, and D. Loss, *Phys. Rev. B* 53, 1548 (1996); R. Fazio, F. W. J. Hekking, and A. A. Odintsov, *Phys. Rev. B* 53, 6653 (1996).
80. D. Loss and T. Martin, *Phys. Rev. B* 50, 12160 (1994); ibid. 65, 165327 (2002).
81. J. Haruyama, I. Takesue, and T. Hasegawa, *Phys. Rev. B* 65, 33402 (2002); *Appl. Phys. Lett.* 79, 269 (2001); *Appl. Phys. Lett.* 81, 3031 (2002).
82. J. Haruyama, I. Takesue, and T. Hasegawa, *Phys. Rev. B* 63, 073406 (2001); *Appl. Phys. Lett.* 77, 2891 (2000).
83. C. Papadopoulos, A. Rakitin, J. Li, A. S. Vedeneev, and J. M. Xu, *Phys. Rev. Lett.* 85, 3476 (2000).
84. G. E. Blonder, M. Tinkham, and T. M. Klapwijk, *Phys. Rev. B* 25, 4515 (1982).
85. R. Martel, V. Derycke, C. Lavoie, J. Appenzeller, K. K. Chan, J. Tersoff, and Ph. Avouris, *Phys. Rev. Lett.* 87, 256805 (2001); Y. Zhang and S. Iijima, *Science* 285, 1719 (1999).
86. A. N. Andoriotis, M. Menon, D. Srivastava, and L. Chernozatonskii, *Phys. Rev. Lett.* 87, 066802 (2001).
87. M. Menon and D. Srivastava, *Phys. Rev. Lett.* 79, 4453 (1997).
88. Z. Yao and C. Dekker, *Nature* 402, 273 (1999).
89. R. Saito, M. Fujita, G. Dresselhaus, and M. S. Dresselhaus, *Phys. Rev. B* 46, 1804 (1992).
90. J. Li, C. Papadopoulos, and J. M. Xu, *Nature* 402, 253 (1999).
91. C. Papadopoulos, A. Rakitin, J. Li, A. S. Vedeneev, and J. M. Xu, *Phys. Rev. Lett.* 85, 3476 (2000).
92. C. Satishkumar and R. Rao, *Appl. Phys. Lett.* 77, 2530 (2000).
93. J.-O. J. Wesstrom, *Phys. Rev. Lett.* 82, 2564 (1999).
94. S. Reitzenstein, L. Worschech, P. Hartmann, M. Kamp, and A. Forchel, *Phys. Rev. Lett.* 89, 226804 (2002).
95. J. Haruyama, I. Takesue, and T. Hasegawa, *Phys. Rev. B* 65, 33402 (2002); *Appl. Phys. Lett.* 79, 269 (2001); *Appl. Phys. Lett.* 81, 3031 (2002).
96. J. Haruyama, I. Takesue, and T. Hasegawa, *Phys. Rev. B* 63, 073406 (2001); *Appl. Phys. Lett.* 77, 2891 (2000).
97. S. M. Sze, in "Physics of Semiconductor Devices." Wiley–Interscience, New York, 1981.
98. J. Haruyama, K. Takazawa, S. Miyadai, A. Takeda, N. Hori, Y. Kanda, and N. Sugiyama, submitted for publication.
99. J. Clarke, A. N. Cleland, M. H. Devoret, and D. Estive, *Science* 239, 992 (1988).
100. K. Hong and N. Giordano, *J. Magn. Magn. Mater.* 151, 396 (1995).
101. K. Hong and N. Giordano, *Eur. Phys. Lett.* 36, 147 (1996).
102. K. Hong and N. Giordano, *NATO ASI Ser. E* 301, 257 (1995).
103. See *NATO ASI Ser. E* 301 (1995).
104. G. Tatara and H. Fukuyama, *Phys. Rev. Lett.* 72, 772 (1994).
105. G. Tatara and H. Fukuyama, *Phys. Rev. Lett.* 78, 3773 (1997).
106. J. Haruyama, I. Takesue, S. Kato, K. Takazawa, and Y. Sato, in "Macroscopic Quantum Coherence and Quantum Computation" (D. Averin, B. Raggiero, and Silvestrini, Eds.), p. 427. Kluwer, Dordrecht, 2001.
107. A. Maiti and J. H. Miller, Jr., *Phys. Rev. B* 43, 12205 (1991).
108. J. Haruyama, I. Takesue, and Y. Sato, *Phys. Rev. B* 62, 8420 (2000); *Appl. Phys. Lett.* 76, 1698 (2000).
109. J. Haruyama, I. Takesue, T. Hasegawa, and Y. Sato, *Phys. Rev. B* 63, 073406 (2001); *Appl. Phys. Lett.* 77, 2891 (2000).
110. J. Haruyama, I. Takesue, and Y. Sato, in "Quantum Mesoscopic Phenomena and Mesoscopic Devices in Microelectronics" (I. Kulik and R. Ellialtiogluet, Eds.), NATO Science Ser. C, Vol. 145, p. 559. Plenum, New York, 2000.
111. D. Davydov, J. Haruyama, D. Routkevitch, D. Ellis, B. W. Statt, M. Moskovits, and J. M. Xu, *Phys. Rev. B* 57, 13550 (1998).
112. H. Gravert, *Phys. Rev. Lett.* 52, 2193 (1984).

*113.* Y. Imry, "Introduction to Mesoscopic Physics." Oxford Univ. Press, London, 1997.

*114.* J. Haruyama, I. Takesue, and T. Hasegawa, *Phys. Rev. B* 65, 33402 (2002); *Appl. Phys. Lett.* 79, 269 (2001).

*115.* G. Tatara and H. Fukuyama, *Phys. Rev. Lett.* 78, 3773 (1997).

*116.* C. Pfleiderer and M. Uhlarrz, *Nature* 412, 58 (2001).

*117.* S. S. Saxena and P. Agarwal, *Nature* 406, 587 (2000).

*118.* J. Haruyama, I. Takesue, S. Kato, K. Takazawa, and Y. Sato, in "Macroscopic Quantum Coherence and Quantum Computation" (D. Averin, B. Raggiero, and Silvestrini, Eds.), p. 427. Kluwer, Dordrecht, 2001.

*119.* J. Haruyama, I. Takesue, S. Kato, K. Takazawa, and Y. Sato, *Appl. Surf. Sci.* 175–176, 597 (2001).

*120.* J. Haruyama, S. Kato, and K. Takazawa, *Physica Status Solidi*, in press.

*121.* G. Tatara and B. Barbara, *Phys. Rev. B* 64, 172408 (2001).

*122.* J. Haruyama, I. Takesue, T. Hasegawa, and Y. Sato, *Phys. Rev. B* 63, 073406 (2001).

*123.* Yu. K. Guslienko and K. L. Metlov, *Phys. Rev. B* 63, 100403 (2001).

*124.* J. Haruyama, K. Hijioka, M. Tako, and Y. Sato, *Phys. Rev. B* 62, 8420 (2000).

*125.* J. Haruyama, S. Kato, and K. Takazawa, *Physica Status Solidi A* 189, 609 (2002).

# Metal Nanoclusters

## Yuan Wang, Yongge Wei

*Peking University, Beijing, China*

## CONTENTS

## 1. INTRODUCTION

Scientific interest in highly dispersed small metal particles could be traced back to the age of Faraday [1], who prepared Au colloids having beautiful color by chemical reduction in the presence of glutin. Currently small and highly dispersed nanoscopic metal or alloy particles with narrow size distributions are called metal or alloy nanoclusters in publications.

The difference between metal nanoclusters and metal colloids, dispersions of metal particles with average sizes ranging from 1 nm to submicrometer in a continuous media, is not rigorous in many cases. Herein we limit the discussions to metal or alloy particles having sizes in a range from 0.5 to 10 nm, which play an important role in so-called bottom-up architecture aiming to assemble functional structures or systems including catalyst, magnet, nanoelectronic, or optics devices, chemical or biochemical sensors, etc.

Subfields in this area have been well reviewed by Schmid and co-workers [2–9], the authors of three books [10–12], Toshima and co-workers [13–21], Templeton et al. [22], Rao et al. [23], Lewis [24], Schon and Simon [25, 26], Aiken and Finke [27], and Bonnemann [28]. A synopsis of the wet chemical preparation of mono- and bimetallic colloidal particles and survey of potential applications in catalysis and materials science have been contributed by Bonnemann and Richards [29] in 2001.

The properties of metal or alloy similar to other materials depend on the motion type of its electrons, which is confined by the space of the materials. Owing to the quantum mechanical rules, nanoscale particles, in which their electrons behave like "particles in a box," should have the so-called "quantum size effect" on their physical properties. Therefore there is a specific length scale, usually in the low edge region of nanodimension for metallic materials [30–32], below which the properties become sensitive to the physical size, which gives birth to a lot of novel and unique properties of the nanosized metal and alloy particles compared to their corresponding bulk materials.

It is well known that physical properties of a metal substance, such as optical, electrical, and magnetic properties, melting points, specific heats, and surface reactivity are size dependent. Metal nanoclusters exhibit size-dependent melting temperatures that are far below that of the bulk metal. Takagi in 1954 reported the earliest measurements on the reduced melting temperature of metal nanoclusters [33]. A brief summary of the research on the melting point of metal nanoclusters has been given recently by Martin and co-workers in their report for the research on the sintering temperatures of alkanethiol-capped Au and Pt nanoclusters with sizes of 6 and 4 nm, respectively. It is observed that the sintering temperature of the Au nanoclusters is close to 210 °C while that of the Pt nanoclusters is about 190 °C, much lower than the melting temperatures of 1064 and 1772 °C of bulk Au and Pt, respectively [34].

Some of new chemical, optical, and thermal properties of metallic nanocrystals and their dynamical processes have been investigated on the femto- to picosecond time scale [35].

One of the most important progresses in metal nanocluster catalysts during the last decade is that the impression of the inability of gold to catalyze has been scrapped due to the finding of excellent catalytic efficiency of supported gold nanocluster catalysts [36, 37]. The most attractive catalytic properties of supported gold nanoclusters are the high catalytic efficiency for the oxidation of CO in the presence of excess hydrogen and the notable selectivity in the oxidation of propylene to propylene oxide. This topic has been well reviewed by Choudhary and Goodman recently [38].

This chapter will deal with progress in some aspects of metal nanoclusters, including chemical preparation and

ISBN: 1-58883-061-6/$35.00
Copyright © 2004 by American Scientific Publishers
All rights of reproduction in any form reserved.

*Encyclopedia of Nanoscience and Nanotechnology*
Edited by H. S. Nalwa
Volume 5: Pages (337–367)

structure control, assembly or self-assembly of these attractive building blocks, and their current and potential applications in catalysts, biosensors, and magnetic materials. Applications of metal nanoclusters in micro- or nano-electronics have been well reviewed [2–7, 25, 26].

## 2. ART OF CHEMICAL PREPARATION

Interest in nanoscopic materials and their application to catalysts and nanodevices have greatly stimulated the research on developing new physical [23, 39] and chemical methods for the preparation and structure control of metal nanoclusters. The strategy usually adopted for chemically preparing metal nanoclusters is to lead metal atoms produced *in-situ* to aggregate and generate metal cores followed by depositing the further formed metal atoms on these cores. Because of the huge specific surface energy, colloidal nanoparticles are usually stabilized by protective agents including polymers, such as poly(*N*-vinyl-2-pyrrolidone) (PVP) and polyvinyl alcohol (PVA), coordination ligands such as PPh$_3$ and mercaptans, or surfactants to prevent them from aggregating during their preparation, application, and storage. On the other hand, the charge effect derived from adsorbed ions on the surface of small metal particles and the solvent effect, namely decreasing the surface energy of particles and activity of surface atoms by adsorbing various solvent molecules, have been known to be effective for stabilizing the tiny metals in colloidal solutions. Metal nanoclusters stabilized with only simple anions or infirmly adsorbed solvent molecules can be called "unprotected" or "naked" metal clusters. To study the influence of the protective agents on the properties of metal cores and to use small metal particles as building blocks effectively, a stable, "unprotected" metal colloid is desirable since the particles can be easily modified with various designed organic species or can be embedded in different materials with a wide range of loading.

Metal nanoclusters can be grouped under four heads according to the stabilizer in the products, namely polymer, surfactant or coordination ligands, solvent or anions, and solid support stabilized metal nanoclusters.

## 2.1. Polymer-Protected Metal Nanoclusters

### 2.1.1. Monometallic Nanoclusters

Polymer protected metal nanoclusters have a very long history of preparation. They are usually prepared by reducing metal ions with various reductants in the presence of suitable polymers usually having a nonpolar polymer chain and polar groups. Electrochemical or photochemical reductions are also effective for preparing polymer-protective metal nanoclusters; however, they are usually prepared by chemical reduction.

During the last two decades, lots of effort has been paid to prepare various polymer-protected metal nanoclusters and examine their catalytic properties. The most attractive polymer protective metal nanoclusters are PVP protected ones with metal particle sizes ranging from 1 to 3 nm, which were first prepared in the 1970s by refluxing a methanol or an ethanol (or alcohol/water) solution of noble metal chlorides containing PVP [40, 41]. Teranishi and Miyake examined in

detail the influence of preparation conditions such as the category and concentration of alcohols, ratio of PVP to Pd on the particle size, and distribution of PVP-protected Pd nanoclusters in 1998. It was observed in X-ray diffraction (XRD) measurements that the lattice constant of these Pd nanoclusters protected with PVP increased with a decrease in the metal particle size from 30 to 17 Å [42].

Recently, size-controllable synthesis of Ru nanoclusters has been done by Yan et al. [43]. In their work, series of PVP-stabilized ruthenium nanoparticles with various dimensions were prepared by heating or refluxing a polyol solution of ruthenium(III) salts; the average diameters of the resulting Ru nanoparticles can be controlled in the range of 1.4–7.4 nm with relative standard deviations of less than 0.3 by changing the polyols, the reduction temperature, and/or the amount of PVP. The factors affecting the size of PVP-stabilized Pd nanoparticles have also been investigated [44].

Besides PVP, functional polymers have also been chosen as protective agents to prevent metal nanoclusters from agglomeration. Narrowly dispersed gold nanoparticles of size less than 3 nm were synthesized by reducing metal ions with KBH$_4$ in the presence of linear polymers containing cyano or mercapto groups as protective agents [45].

An overview has been given by Mayer [46] on the generation of metal nanoparticles dispersed within amphiphilic polymeric systems, ranging from nonionic polymers and polyelectrolytes to amphiphilic diblock copolymers. Recently, $\pi$-conjugated polymer-protected gold nanoparticles of narrow size distribution, in a stable colloidal form, have been prepared, via reduction of HAuCl$_4$, in the presence of a $\pi$-conjugated poly(dithiafulvene) having electron donating properties [47].

Dendrimer-encapsulated Cu, Pd, Pt, Ag, and Au metal nanoclusters ranging in size from 1 to 3 nm have been prepared by reducing the corresponding metal ions in dendrites [48–62]. Hybrids of silver particles of 1 to 2 nm in size modified with highly branched amphiphilical polyethyleneimines could be adhered effectively to polar substrates providing environmentally friendly antimicrobial coatings [63] (see Fig. 1). Block copolymers of carbosilane dendrimers and polyisocyanopeptides may have the potential to be exploited as templates to direct the formation of nanowires of metal nanoclusters [64].

The self-assembly with ordered patterns of block copolymer micelles, which have dimensions of 10–100 nm and a good kinetic stability, is an interesting kind of template for generating two-dimensional (2D) arrays of inorganic nanoclusters [65–67]. Cohen and Boontongkong prepared a poly(styrene-*block*-acrylic acid) (PS-*b*-PAA) micellar thin film and loaded it with an aqueous AgAc solution treated with NaOH. Reduction of the sample in a hydrogen atmosphere (~2 atm at 85 °C for 30 h) resulted in a hexagonal array of silver clusters of ~4 nm in diameter within the thin film template. The uniform silver cluster size should be derived from the inherent size monodispersity of the individual micelles and their PAA cores [68] (see Fig. 2).

Stable Au, Pt, and Pd colloidal particles with average diameter of 4–6 nm have been prepared by reducing metal chlorides HAuCl$_4$, H$_2$PtCl$_6$, or Pd(NO$_3$)$_2$ with NaBH$_4$ during an acid catalytic hydrolysis process of *N*-[3-(trimethoxysilyl)propyl] ethylenediamine. These noble metal
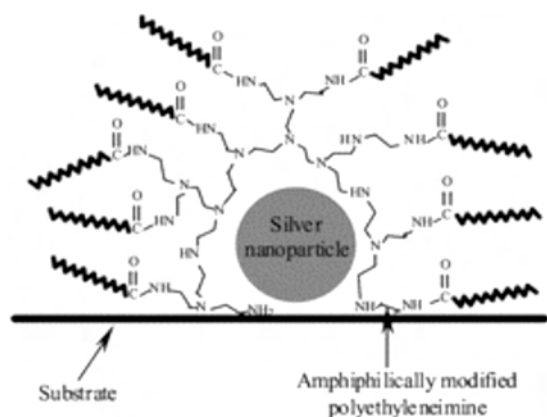
**Figure 1.** Ag nanoclusters encapsulated by highly branched amphiphilical polyethyleneimine dendrimers. Reprinted with permission from [63], J. C. Tiller et al., *Chem. Commun.* 3018 (2002). © 2002, Royal Society of Chemistry.

colloidal particles containing sol could be gelled to give monoliths of various shapes by allowing them to gel in a container with desired shape [69, 70].

Inorganic polymers with special nanoporous structures have been used as templates for the preparation of metal nanoclusters. For example, in mesopore silica or mercapto group functionalized mesopore silica, narrowly dispersed Ag [71–74], Au [75, 76], Pt [76, 77], and Co–Ru alloy [78] nanoclusters have been prepared by *in-situ* electrochemical and chemical reduction or thermal decomposition.

Carbon nanotubes are also attractive supports for the synthesis of metal nanoclusters. Fe–Ni alloy nanoparticles inside carbon nanotubes via wet chemistry have been prepared [79]. The growth of Pd, Pt, Ag, and Au nanoparticles on the outer surface of carbon nanotubes has also been reported [80].

An ultraviolet (UV) photolysis (253.7 nm wavelength) method [81, 82] was used to prepare PVP-protected Pd and Ag nanoclusters in a mixture of 2-propanol and acetone. The size of obtained Pd nanoparticles (2–3 nm) is independent of palladium acetate concentration, whereas those of
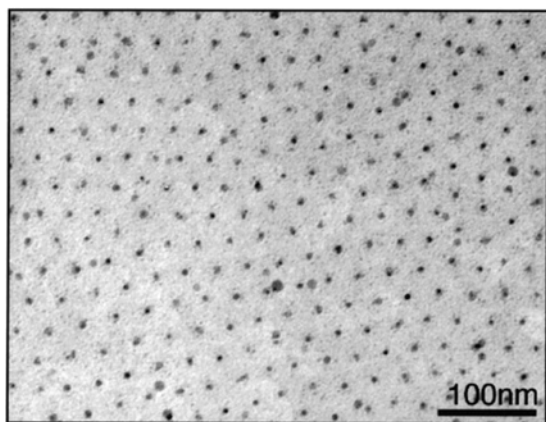


**Figure 2.** Plan-view TEM of PS-*b*-PAA micellar thin film containing Ag nanoclusters. Reprinted with permission from [68], Y. Boontongkong and R. E. Cohen, *Macromolecules* 35, 3647 (2002). © 2002, American Chemical Society.

Ag colloids increase from 3 to 9 nm with increasing concentration of silver perchlorate [83].

The photochemical reductions of $AuCl_4^-$ for preparing Au nanoclusters protected by PVP have been conducted in formamide in the presence of PVP. It was found that the diameters of prepared Au nanoparticles depended on the concentration of $AuCl_4^-$. Narrowly distributed Au colloids with average sizes from 6 to 18 nm have successfully prepared by this process. The effective photoreduction of $AuCl_4^-$ in the nonaqueous system is attributed to the higher degree of dissociation of $AuCl_4^-$ in formamide. Silver, palladium, and platinum colloidal particles could also be produced with this modified photochemical process [84].

A microwave dielectric heating method was first adopted to prepare polymer-stabilized metal nanoclusters with small particle size by Liu and co-workers, which opened up a way to synthesize polymer protected metal nanoclusters in a fast and continuous manner. Platinum colloidal particles having nearly spherical shape and size of 2 to 4 nm were prepared by this method [85].

Polymer-supported metal nanoclusters have been prepared in supercritical carbon dioxide by reducing metal ions in polymer matrixes [86]. The chemical and physical properties of carbon dioxide in the supercritical state differ from those of conventional organic solvents. The preparation of nanomaterials, including metal nanoclusters, in such a special condition has just been reviewed by Cooper [87].

Stable polymer-protected metal nanoclusters are usually prepared in a higher ratio of polymer to metal; otherwise, unstable turbid dispersion with large particle size or precipitates will appear. This fact has been thought of as one of the main drawbacks of polymer protected metal nanoclusters because it limits the application relating to electron transportation. This defect can be overcome by the reaction of polymer protective agents such as PVP with preformed "unprotected" small metal nanoclusters. A very stable colloidal solution of PVP-protected Pt nanoclusters, Pt particle size of 1.5 nm, with a PVP-monomeric-unit/Pt molar ratio of 0.35 was prepared by this strategy recently by Wang et al. [88]. This success in the preparation of small metal nanoclusters with an extraordinarily high ratio of Pt to PVP revealed that to stabilize some small noble metal nanoclusters, a high PVP/Pt ratio as usually used is not necessary. It suggests that in the usual preparation process (i.e., reducing noble metal ions in the presence of PVP) the largely excess amount of PVP is needed for kinetic control of the reduction process rather than preventing the small metal particles from aggregating. For the latter purpose, a much lower PVP/Pt ratio than that usually expected is enough at common conditions (see Fig. 3).

### 2.1.2. Bimetallic Nanoclusters

At the end of the 1980s, the alcohol-refluxing method was extended to prepare bimetallic nanoclusters composed of two kinds of noble metals. PVP-protected Pt–Pd [89], Pt–Rh [90], and Au–Rh bimetallic nanoclusters with average particle size less than 3 nm were prepared and their catalytic properties for the hydrogenation of olefins were examined. The stability against aggregation of a Pt–Rh bimetallic nanocluster is much higher than that of a Pt nanocluster prepared

**Figure 3.** TEM image of a stable PVP-protected Pt nanocluster with a high Pt/PVP ratio (monomeric unit of PVP/Pt mole ratio: 0.35) prepared by dissolving a precipitate of "unprotected" Pt nanoclusters. The average diameter of the Pt nanoparticles is 1.5 nm. Reprinted with permission from [88], Y. Wang et al., *Chem. Mater.* 12, 1622 (2000). © 2000, American Chemical Society.

by the same method. From an XRD study on the Pt/Rh bimetallic nanocluster, we suggested that the products have a structure of alloy or random solid solution of the metal atoms. On the other hand, an extended X-ray absorption fine structure (EXAFS) analysis on the Pd–Pt (4/1) bimetallic nanocluster made by Toshima et al. suggested that a model of a Pt core completely covered with a Pd shell could express its structure [91]. An infrared carbon monoxide (IR-CO) probe characterization study on this Pd–Pt (4/1) bimetallic colloid [92] implied that the surface of the bimetallic nanocluster is enriched in Pd.

In 1996 Esumi and co-workers [83] reported the preparation of a Pd/Ag alloy nanoclusters of 1 to 4 nm protected with PVP using an UV-irradiation method. The optical absorption bands of the prepared Pd/Ag alloy nanoclusters become sharp and shift to longer wavelengths with increasing molar ratio of Ag. The observed spectra are in good agreement with the calculated spectra of alloy colloids.

Preparation of Au–Ag bimetallic nanoclusters, which usually have only one plasmon absorption band that redshifts with increasing Au content, has been intensively studied [93–104].

From the view point of electron interaction and position assembly effects, bimetallic nanoclusters composed of a noble metal and a light transition metal such as Cu, Ni, or Co are more plausible because they provide a high potential for tailoring the structures of atomic self-assemblies and electron characteristics. Therefore, changing not only the size and shape but also the metal compositions could modulate properties of these materials in a wide range, such as catalytic and magnetic behavior. In the beginning of the 1990s, a strategy for the synthesis of polymer-protective bimetallic colloids composed of a noble metal and a light transition metal such as Co, Ni, and Fe was proposed. A stable polymer-protective bimetallic colloid can be obtained which is composed of some metal element strongly

protected by a polymer agent and another metal element or its compound which by itself cannot form a stable polymer-protective metal sol due to the low protective effect of the same polymer on it, as long as the first kind of metal atom can be present in the surface of the colloidal particles under the preparation conditions [105, 106].

Preparation of PVP-protected Cu/Pd bimetallic colloids by co-reducing a mixture of the corresponding metal acetates in 2-ethoxyethanol at 70–130 °C was reported by Bradley and co-workers [107, 108]. This method provided bimetallic $Cu_{30}Pd_{70}$ nanoclusters with particle sizes of $4 \pm 0.4$ nm as confirmed by transmission electron microscopy (TEM), IR-CO probe, and X-ray absorption spectroscopy measurements. For this co-reduction process, a mechanism was suggested in which Cu(0) was deposited on the surface of the preformed Pd particles and migrated into the Pd particles after deposition but only to within a few atomic layers of the surface [108]. When the Cu/Pd ratio is higher than 1:1, a part of the Cu ions cannot be reduced to a metallic state by this method according to our experience, suggesting that Pd may have an acceleration effect on the Cu ion reduction [109].

Small Cu/Pd and Cu/Pt alloy nanoclusters with average particle size of 1 to 2 nm and narrow size distributions were successfully prepared in the whole range of metal composition by Toshima and Wang using a so-called "cold alloying process" that involves two steps [110, 111]. First, hydroxide colloids (the real structure is more complex) containing both of the corresponding metal elements were prepared in glycol by adding NaOH to solutions of Cu and noble metal salts in the presence of PVP. The obtained bimetallic hydroxide colloidal solutions, in the second step, were refluxed at 198 °C for several hours with a nitrogen flow passing through the reaction systems to take away water and by-products. This is the first example of preparing metal and bimetallic nanoclusters using a polyol reduction process. TEM, XRD, UV-visible absorption spectroscopy (UV-vis), X-ray photoelectron spectroscopy (XPS), and Auger spectra of the products proved the bimetallic nanoclusters with structures of alloy or random solid solution of Cu and Pt or Pd could be prepared at the whole Cu/Pt or Cu/Pd ratios (see Fig. 4).

Unpublished data of energy dispersive X-ray (EDX) semi-quantitative analyses in high resolution TEM (HRTEM) revealed that each of the small particles prepared by this method contained both Cu and noble metal elements. Meanwhile it was also found that PVP-Pt nanoclusters prepared in glycol containing NaOH with a pH of 10 have a mean diameter of 1.1 nm with a narrow size distribution from 0.7 to 1.7 nm. Pt nanoparticles in this colloid are well separated from each other, which is quite different from those prepared with the alcohol refluxing method reported by Hirai and Toshima [40, 41]. The previous PVP-Pt colloid prepared by refluxing an alcohol solution of $H_2PtCl_6$ contains a lot of aggregators derived from gathering several or dozens of Pt particles with an average diameter of 1.6 nm and a size distribution from 1.2 to 2 nm. It is reasonable to believe that the unusual small particle size and perfect separation state of the PVP-protected Pt nanoparticles obtained in glycol containing NaOH are derived from the formation of Pt hydroxide precursors and the charging effect due to the adsorption of $OH^-$ groups on the Pt surface. The UV-vis
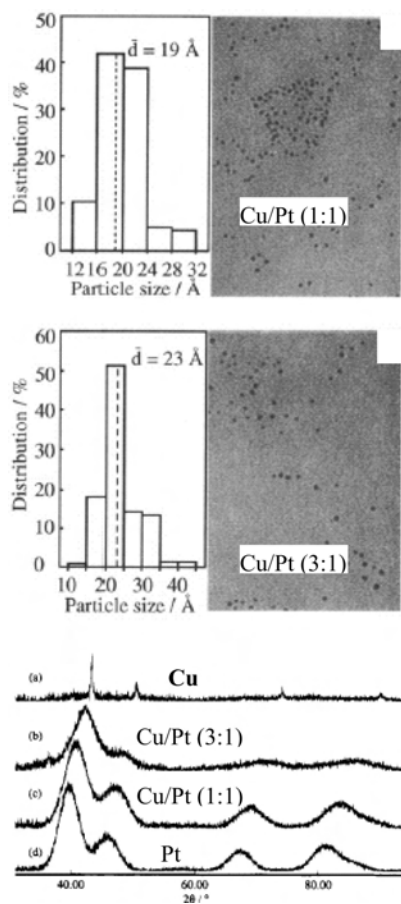
**Figure 4.** TEM micrographs and XRD diffraction patterns of PVP protected Cu/Pt bimetallic nanoclusters. Adapted with permission from [111], N. Toshima and Y. Wang, *Langmuir* 10, 4574 (1994). © 1994, American Chemical Society.

spectra of Pt/Cu alloy nanoclusters revealed that the plasmon band of Cu originally located at 562 nm shifts to the longer wavelength with increasing Pt content and decreases in intensity, depicting the changes in electronic structure in the alloy nanoclusters. A study on the EXAFS characterization of the structure of PVP-protected Cu/Pd alloy nanoclusters has been reported recently [112].

The cold alloying process was also adopted to prepare Cu/Rh, Co/Pt, and Ni/Pt bimetallic nanoclusters. PVP-protected Co/Pt and Ni/Pt alloy nanoclusters with diameters less than 3 nm and Co/Pt or Ni/Pt ratios up to 1:1 could be easily prepared by this method [109, 113].

Besides the formation of bimetallic alloy nanoclusters, small metal nanoclusters of a core–shell structure provide another practicable route to tailor the structure and property of bimetallic nanoclusters for the purpose of different potential applications. PVP-protected Pd–Pt bimetallic colloids in the size range from 1.5 to 5.5 nm with controllable core/shell structures have been successfully prepared by Wang and Toshima with a so-called "hydrogen-sacrificial protective strategy," in which hydrogen adsorbed on the preformed Pd cores is used to prevent the Pd cores from oxidizing by the added Pt (II) ions and to reduce Pt (II) ions under the catalytic function of the preformed small metal cores. A Pt or Pd shell of 1 or 2 atomic layers in thickness

covering the Pd or Pt cores having average diameters of 2.3 and 1.5 nm, respectively, was established as confirmed by TEM and IR-CO probe measurements [92] (see Fig. 5).

### 2.1.3. Shape Control

Shape control of colloidal metal nanoparticles protected by polymer has been conducted by several groups and is believed to be important for exploring the catalytic properties of nanoparticles with different shapes. During the process of reducing metal ions slowly, a shape selectivity may emerge if the catalytic reduction of the metal ions on a special crystal face of the preformed metal nanoparticles is much faster than those on the others. For example, if the reductive deposition rate of Pt atoms on the Pt{111} is much faster than those on Pt{100}, a high selectivity of cubic particles will form as the main product, whereas tetrahedral or octahedral Pt nanoparticles would be obtained when the ratio of the relative rates is reversed. Reaction conditions such as pH, temperature, adsorbent, reducing agent, and the metal precursors may have important influence on the final shape of the metal nanoparticles.

Ahmadi and co-workers reported the formation of tetrahedral, cubic, irregular-prismatic, icosahedral, and cubo-octahedral particles of Pt by reducing $K_2PtCl_4$ with $H_2$ in aqueous solutions of sodium polyacrylate. It was found that the ratio of polyacrylate to Pt ions is one of the key factors for controlling the shape of the products. Polyacrylate protected cubic and tetrahedral nanoparticles, 11 and 7 nm in size, respectively, were prepared with a shape selectivity of 80% and 60%, respectively [114, 115]. The shape distribution of platinum nanoparticles during the growth period and its dependence on the concentration of the capping polymer as well as the pH of the solution were studied with TEM [116]. The shape of platinum nanoparticles prepared by reduction of Pt(IV) ions in the presence of sodium polyacrylate (PAA) or PVP was also studied [117].

A poly(*N*-isopropylacrylamide) protected Pt colloid with a cubic shape selectivity of 68% was prepared using $H_2$ as a reductant by Miyazaki and Nakano at a temperature higher than the critical solution temperature [118].
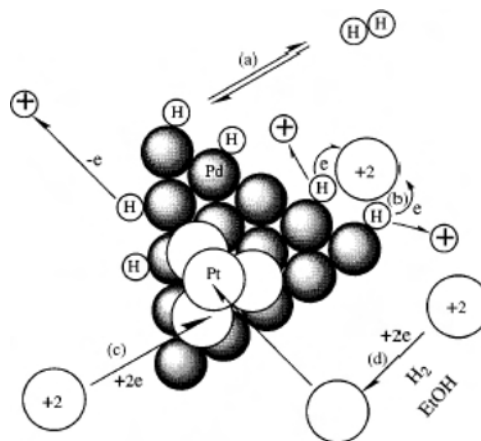


**Figure 5.** Hydrogen-sacrificial protective strategy for the preparation of bimetallic colloids with a core/shell structure. Reprinted with permission from [92], Y. Wang and N. Toshima, *J. Phys. Chem. B* 101, 5301 (1997). © 1997, American Chemical Society.

Five types of crystal morphologies, including triangular, hexagonal, pentagonal, square, and rhombohedral, have been observed in PVP-protected Pd nanoparticles prepared by Choo et al. [119]. Using different solvents as the reaction medium, different morphologies of PVP-protected silver colloids with charming colors could be obtained through microwave irradiation on a solution of silver nitrate [120].

### 2.1.4. Immobilization

Polymer-protective metal nanoclusters are usually prepared as stable colloidal solutions which need to be immobilized for the demands of some specific application purposes. Several strategies for the immobilization of polymer protected metal nanoclusters have been proposed. Solidification of Pt and Rh metal nanoclusters protected with a co-polymer of $N$-vinyl-2-pyrrolidone and methyl acrylate was realized by Hirai and co-workers through the reaction between the residue groups of methyl ester in the protective agent with amino groups in a poly(acrylamide) resin [121, 122]. It could be expected that using this method the structure feature of the polymer protected metal nanoclusters is almost the same as that prepared after the solidification process. Specially designed polymer protective agents and supports have to be used in this strategy.

In the end of the 1980s, we proposed a procedure, namely a "coordination capture method" [90, 123], to immobilize PVP-protected metal nanoclusters onto ligand anchored supports in order to prepare a high performance catalyst which could be easily separated from the catalytic system (Fig. 6a, b). The surface of a silica support was modified with -$(CH_2)_3SH$ and -$(CH_2)_3SR$ groups, respectively, and the obtained products were simply stirred in a colloidal solution of PVP-protected metal nanoclusters of Pd, Pt, Au, or Pt/Rh alloy, resulting in a complete immobilization of the metal nanoclusters on the supports. This method characterized by taking advantage of the coordination action of the anchored ligands to metal atoms at the nanocluster's surface or the specific reaction between mercaptan and surface metal atoms provided a route of universal significance to combine the techniques of metal nanocluster preparation and the surface modification. XPS measurements on the products revealed that only a very limited amount of PVP still hung on the immobilized metal nanoclusters. Two factors should be controlled to achieve an ideal experimental result. First, the interaction between the coordination ligands and the metal atoms at the surface should be stronger than that between the polymer protective agents and metal nanoclusters. Second, the support surface should be amicable to the colloid solutions, which usually could be easily fulfilled by adding a suitable organic solvent to the reaction system. Today, it is well known that the coordination capture method is not restricted to polymer-protected metal nanoclusters or powder supports; for supports of plate shape and other metal nanoclusters as well as other anchored ligands, it also works well [124, 125].

The concept of "coordination capture" was greatly expanded by using double-ended dithiols which can be bonded on the surface of a metal plate with one tail and confine small metal nanoclusters with another tail of mercaptan group (Fig. 6c), providing a universal route to develop a
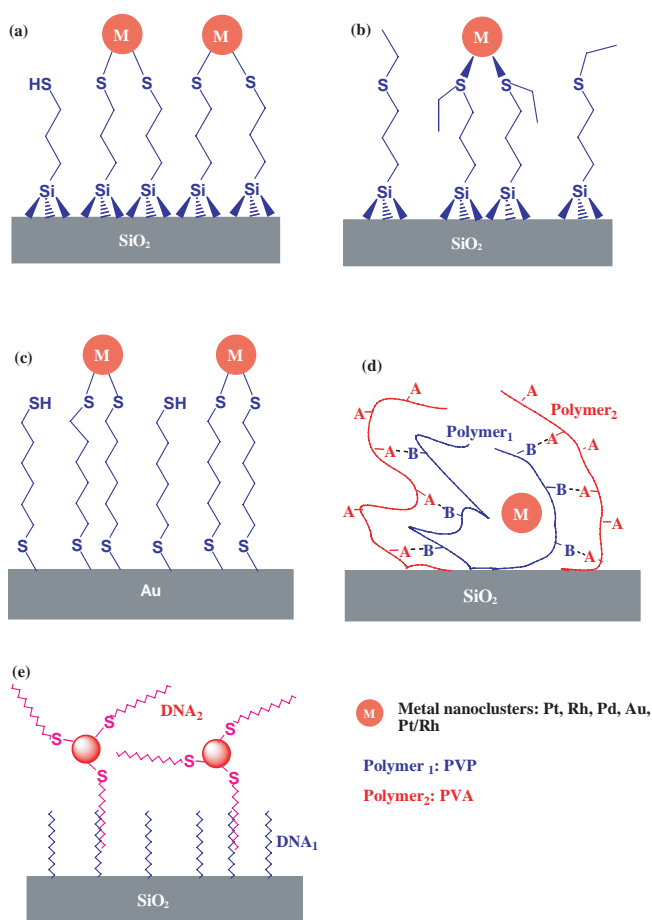


**Figure 6.** Schemes of several processes for immobilization of metal nanoclusters by anchored ligands or forming hydrogen-bonding complexes. (a) Immobilization of metal nanoclusters with anchored mercapto groups. Drawn according to [123], Y. Wang et al., *J. Chem. Soc., Chem. Commun.* 1878 (1989). (b) Immobilization of metal nanoclusters with anchored thioether groups. Adapted with permission from [90], Y. Wang and H. Liu, *Polymer Bull.* 25, 139 (1991). © 1991, Springer-Verlag. (c) Aryl or alkyl dithiol fixed metal nanoclusters on Au surface. Adapted with permission from [130], K. Vijaya Sarathy et al., *J. Phys. Chem. B* 103, 399 (1999). © 1999, American Chemical Society. (d) Immobilization of polymer-protected metal nanoclusters by forming polymeric hydrogen bond complexes. A and B are the residue groups located at different kinds of polymer chains. Drawn according to [139], Y. Wang et al., *Polym. Adv. Tech.* 7, 634 (1996). (e) Immobilization of metal nanoclusters by the specific hybridization of surface-bound and nanoparticle-anchored oligonucleotides. Adapted with permission from [300], T. A. Taton et al., *J. Am. Chem. Soc.* 122, 6305 (2000). © 2000, American Chemical Society.

film of metal nanoparticles [126–136]. This technique has been used in the study of the intrinsic electronic properties of individual metal nanoparticles using scanning tunneling microscopy (STM) [135, 136] and the development of new electronic switches based on a redox process of the bridging ligand [137].

It has been well known that ionic or hydrogen bond complexes of polymers can form as precipitates when two kinds of soluble polymer having groups for forming ionic or hydrogen bonds are mixed together in suitable conditions such as pH and solvent. Therefore, if the polymer-protective

agent for metal nanoclusters is a polyelectrolyte or a macro-molecule containing polar groups, immobilization of the corresponding metal nanoclusters could be easily conducted by forming polymer ionic complex [138] or polymer hydrogen bond complex (Fig. 6d) [139]. The latter, proposed by Wang and Liu, is more convenient for real applications because many of the usually adopted polymer protective agents such as PVP, PVA, PAA, and DNA belong to this group. When an aqueous colloidal solution of PVP-protected metal nanoclusters was mixed with an aqueous solution of PAA, for example, a network of hydrogen bond complex of PVP–PAA with the encapsulated metal nanoclusters formed as a black precipitate, leaving a clear, colorless solution containing metal nanoparticles of an ignorable amount. If the immobilization is conducted in the presence of an inorganic support with a large specific surface area such as a silica, a supported metal catalyst with well-dispersed metal nanoclusters can be obtained. Out of question, this immobilization method can also be used to prepare film of layered structure using a layer-by-layer cross-adsorption procedure.

Metal nanoclusters including those protected by polymers could be embedded in inorganic metal oxide matrixes by an *in-situ* hydrolysis of organometallic compounds such as $CH_3Si(OCH_3)_3$ or $Si(OCH_3)_4$. This sol–gel process provides a convenient way to encapsulate small metal particles originally stabilized with different protective agents in nano- or microporous inorganic supports [140–142].

Electrophoretic deposition of Pt nanoclusters protected with PVP on TEM grids was reported by Teranishi et al. A monolayer of closely stacked Pt nanoclusters could be obtained this way [143].

## 2.2. Ligand and Surfactant-Protected Metal Nanocluster

Different from the polymer-protected metal nanoclusters, these colloidal metal nanoparticles are covered with a layer of organic molecules with their heads or tails contacting the surface metal atoms depending on the solvent used. Therefore the thickness of the organic shell on the metal core can be roughly estimated from the dimension and configuration of the molecules. Some surfactants have been known to be effective for stabilizing colloidal metal particles for a long time. Current interest in the preparation of surfactant stabilized metal nanoclusters is to control the particle size, shapes, and metal compositions in order to achieve new catalyst precursors or specific superlattice patterns that may be of importance for potential applications in recording media or nanostructured electronic devices.

### 2.2.1. Ligand Stabilized Metal Nanoclusters

The ligand (such as mercaptan or triphenylphosphine) stabilized metal nanoclusters are considered to be a new kind of building block material for fabricating future new electronic devices or nanoelectric digital circuits based on the so-called quantum size effect or single electron transition effect, which have been investigated theoretically and experimentally [3, 25, 26, 136, 144, 145]. Besides operating the nanoswitch of a single metal nanoparticle, the possibility of future application of nanoclusters in this field and some

other functional system strongly depends on the availability of ordered organized nanomaterials. Therefore, intensive effort has been paid to fabricate superlattice of metal nanoclusters in one, two, or three dimensions during the last decade. Compared with possible future applications in nanoeletronics, more realistic are the use of these building blocks for chemical or biochemical sensors, magnetic recording media, and catalysts.

The ligand or surfactant metal nanoclusters are usually prepared by chemical reduction of corresponding metal ions in the presence of the protective agents; they can also be obtained by reactions of the preformed metal cores with the protective agents. The latter provides a convenient way to transfer metal nanoclusters between different phases [88, 146, 147].

The well known $Au_{55}(PPh_3)_{12}Cl_6$ nanocluster and some of its derivatives characterized by definite or near definite numbers of metal atoms of Au, Pd, Pt, or Rh, for example, and protective coordination ligands were created by Schmid and co-workers [148–152], and their structures, properties, and possible applications have been well reviewed [2, 3, 10]. Additionally, alkylphosphine or alkylphosphine oxide passivated Cr and Ni nanoclusters have also been prepared [153]. Important progress in alkylphosphine stabilized metal nanoclusters is that a $Pd_{145}$ nanocluster with pseudo-$I_h$ symmetry, $Pd_{145}(CO)_x(PEt_3)_{30}$, has recently been confirmed by single-crystal X-ray diffraction studies [154]. It has been found that this $Pd_{145}$ nanocluster contains a spherical-like three-shell $Pd_{115}$ kernel encapsulated by a metal carbonyl cluster shell consisting of 30 Pd atoms, 30 perpendicularly ligating triethylphosphine molecules, and about 60 edge-bridging carbon monoxide ligands. Especially, within the center of the $Pd_{115}$ kernel, there is a perfect two-shell icosahedral Mackay hard-sphere nucleus, $Pd_{55}$, which is the first experimental verification of Mackay theory [155] by X-ray crystallography, and it also makes the $Pd_{145}$ nanocluster an interesting model for testing size-dependent physical properties of metal nanoclusters.

Mercaptan is very important ligand for stabilizing metal nanoclusters and has been used to fix many small metal nanoclusters on the surface of a support [123]. In 1994, Brust et al. reported the preparation of thiol-stabilized gold nanoparticles in a two-phase liquid–liquid system [156]. In this preparation, $[AuCl_4]^-$ ions were extracted into an organic solution containing alkylthiol with a long chain; then the Au(III) ions were reduced with $NaBH_4$ to lead to the formation of mercaptan stabilized Au nanoclusters that can be separated by adding a precipitating agent of methanol or acetone and re-dissolved like a common compound after being completely dried. In fact, reducing Au(III) ions with $NaBH_4$ or $LiB(C_2H_5)_3H$ in the presence of mercaptans in organic media such as methanol or THF could simply prepare stable colloidal solutions of mercaptan-stabilized gold nanoclusters [157–159]. In addition to Au nanoclusters, mercaptan stabilized Ag [160, 161], Pt [159, 162], Ir [159], and gold-containing alloy [163] Au/Ag, Au/Cu, Au/Ag/Cu, Au/Pd, Au/Pd, Au/Ag/Cu/Pd nanoclusters have been reported. Either aromatic [164, 165] or alkyl mercaptan with different chain lengths [166, 167] which may contain other functional groups [168–174] has been adopted

as the protective agent, especially when a ligand containing photofunctional groups is used, and a way to develop novel photofunctional materials opens [169, 170, 174]. It has been revealed that using a higher Au/S ratio, lower reaction temperature, and addition of NaBH$_4$ with a high speed favor forming small and narrowly distributed metal nanoclusters [168, 175].

Recently, novel pyrrolylalkanethiolate-stabilized gold and palladium nanoparticles have been prepared, and electrochemical polymerization of them gave remarkably stable poly(pyrrole metal nanoparticle) films on metal electrodes [176].

Alkyl amine [177–181], carboxylic acid [182], or alkyl isocyanide [162] stabilized metal nanoclusters were also synthesized, although their stabilities are not as high as mercaptan stabilized metal nanoclusters. As shown in Figure 7 as an example, good quality, monodispersed long-chain alkylamine capped copper metal nanoparticles have been successfully synthesized in a nonhydrolytic approach by the thermal decomposition of a Cu(II) precursor, copper (II) 1-$N,N$-dimethylamino-2-propanolate, [Cu(OCH(Me)CH$_2$NMe$_2$)$_2$], in a hot coordinating solvent [181].

The special high stabilizing effect of mercaptan on the metal nanoclusters is derived from the oxidation addition reaction of mercaptan group and the surface Mattel atoms which remove two hydrogen atoms from mercapto groups and form metal–sulfur bonds on the surface. It has been observed that heating treatment of the mercaptan-stabilized Au nanocluster in organic solvent may change its particle size or shape [183]. Compared to those prepared using conventional mono-alkylthiols, a designed four-chained disulfide stabilizer enabled Yonezawa and co-workers to prepare small gold nanoclusters and control the particle size with atomic precision when NaBH$_4$ was used as a reducing agent [184].

Macrocyclic thiol compounds such as thiolated alpha- or beta-cyclodextrins have been used to cap metal nanoclusters of Au, Ag, and Pd. This development in the coordination chemistry of metal nanoclusters should be very promising in some specially designed assembly of nanostructured functional materials [185–193].

Because of the strong interaction between mercapto group and metal atoms, adding a mercaptan with a long chain into usually prepared colloidal solutions of various

metal nanoclusters could easily produce the corresponding mercaptan-stabilized metal nanoclusters or modify the nanoparticles with functional groups via ligand-exchanging reactions.

Gold nanoparticles functionalized with thiol dendrons containing three redox active amidoferrocenyl units via ligand exchange have been reported; these dendronized gold nanoparticles could recognize H$_2$PO$^{4-}$ [59].

Metal nanoparticles with size dispersion less than 10% are usually called monodispersed metal nanoclusters. Although adjusting the preparation conditions could narrow the size distribution, the separation of different sized metal nanoparticles should be given more attention. The methods of precipitation by stages (i.e., adding precipitating agents step by step [194, 195], liquid gravity column chromatography [196], or capillary electrophoresis [197]) have proven to be helpful in narrowing the size dispersion of metal nanoclusters and studying the size-dependent properties.

A fundamental question has been proposed for a long time; that is, what and how strong is the ligand effect on the electronic properties of small metal nanoclusters? To answer this question we need small metal nanoclusters having the same metal core and various modifying shells of organic ligands because the core-level binding energies of small metal nanoclusters are also dependent on the metal particle size [198, 199]. In general, higher binding energies of core levels in metal nanoparticles relative to the values of bulk metal can be observed when the metal particles are small enough, and values increase with decreasing particle size. This phenomenon has been interpreted in terms of final state relaxation [200]. Based on the successful synthesis of Pt nanoclusters having the same metal core, 1.3 nm in average size, stabilized by alkylamine, alkylthiol, PPh$_3$, PVP, and PVA, respectively, we have revealed that the size-dependent effect on the Pt 4$f$ binding energy of the Pt cores (average Pt core size 1.3 nm, size distribution 0.8–2.8 nm) is +0.5 eV. The thiol-bonded effect on the Pt core causes a further 0.3 eV increase in the Pt 4$f$ binding energy. PPh$_3$ has a weak influence on the Pt 4$f$ binding energy of the Pt core, whereas PVP, PVA, and alkylamine do not cause obvious changes in the Pt 4$f$ signals [147].

An ultrafast electron dynamic study revealed that chemically prepared Au nanoclusters with a Au$_{28}$ nanocore surrounded by 16 glutathione molecules show an induced transient absorption in the visible region from 2.58 to 1.65 eV (480–750 nm) with a maximum around 2.07 (600 nm) after excitation with femtosecond laser pulses. The excited state relaxation shows a biexponential decay with a subpicosecond and a longer nanosecond decay time which is different from those observed for larger gold nanoparticles, suggesting that the examined gold nanocluster exhibits molecular properties [201]. A broad luminescence extending over the entire spectral range from the visible to the infrared (2.0–0.8 eV) was observed by Link and co-workers [202].
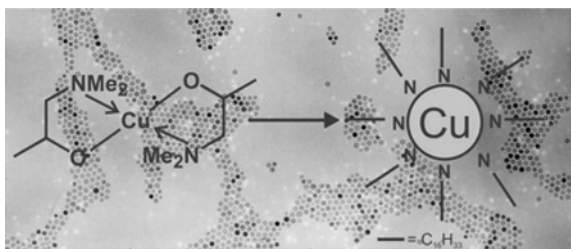


**Figure 7.** Good quality, monodispersed hexadecylamine stabilized Cu nanoclusters by the thermal decomposition of a precursor complex [Cu(OCH(Me)CH$_2$NMe$_2$)$_2$] in the hot hexadecylamine solvent. Reprinted with permission from [181], R. A. Fischer et al., *Chem. Commun.* 68, (2002). © 2002, Royal Society of Chemistry.

## 2.2.2. Surfactant Stabilized Metal Nanoclusters

Surfactant protected metal nanoclusters have been studied intensively and some new contributions will be mentioned here.

Goia and Matijevic studied the influence of difference in redox potentials of $M^{n+}/M$ and reductant/oxidation-product pairs on metal colloid formation in water and pointed out that the $\Delta E$ should be higher than 0.3–0.4 eV in usual cases. Suitable reductants and reaction conditions for the preparation of metal colloidal from various transition metal ions have been tabled [203].

Syntheses of cationic palladium nanoparticles stabilized by quaternary ammonium alkylisocyanides were reported. Reduction of $PdCl_4^{2-}$ by hydrazine in the presence of the surfactant gave rise to a stable aqueous dispersion of cationic palladium nanoparticles. The particle size depended on the alkyl chain lengths of the stabilizer molecules [204].

$NaBH_4$ is one of the widely used reducing agents in the preparation of metal colloids. However, when the reduction of light transition metal ions such as $Co^{2+}$ or $Ni^{2+}$ was conducted in water using $NaBH_4$, indefinite amounts of metal borides would be produced. A very smart strategy of universal significance for the preparation of various small metal nanoclusters (metal elements of 6–11 groups) in organic media stabilized with surfactant and ether or thioether was proposed by Bonnemann and co-workers [205]. The reaction is as follows: $MX_v + vNR_4(BEt_3H) + THF \rightarrow M_{colloid} + vBEt_3 + H_2$, where $NR_4^+$ works as the stabilizer.

A tetraoctylammonium-stabilized PtSn colloid, with nominal composition $Pt_3Sn$ as confirmed by point-resolved EDX analysis, was prepared by co-reduction of the metal salts and supported on silica. The supported bimetallic nanocluster, average size of 1.5 nm, has a highly disordered structure. By removing the stabilizer tetraoctylammonium by heating the samples in He to 200 °C, coalescence of neighboring particles produced a majority of cubic $Pt_{0.81}Sn_{0.19}$ particles, with average size of 3.1 nm and a minority phase of stoichiometric hexagonal PtSn of 4.4 nm in size [206].

A copper colloid stabilized by $N(octyl)_4^+$ with Cu particle size of 5 to 10 nm was prepared by the reduction of $[N(octyl)_4]_2[CuCl_2Br_2]$ in toluene using $Li[BEt_3H]$ as a reducing agent. An in-situ XANES (X-ray absorption near edge structure) investigation was performed for the first time during the colloid synthesis, which is helpful in giving direct insight into the mechanism of the colloid formation. An intermediate $Cu^+$ state prior to the nucleation of the particles was observed in this measurement [207].

Anionic surfactants such as alkylsulfate have also been used widely as the stabilizer of metal nanoclusters. Silver nanoparticles with well-defined size and shape distribution under sodium dodecylsulfate in solution were prepared by photochemical reduction of laser irradiation [208, 209]. Recently, a new method for the synthesis of surfactant-stabilized noble metal nanoparticles has been developed, whereby a sodium alkyl sulfate ($SC_nS$) surfactant bearing an alcohol-type functional group is used as the reductant, and there is no need for an external reducing agent. By changing the carbon chain length of the surfactant, the diameter of the nanoparticles could be controlled [210].

Polyfluorinated organic compounds are interesting in protecting metal nanoclusters due to their unique properties. Perfluorocarboxylate-stabilized silver nanoparticles have been prepared via the thermal decomposition of layered silver perfluorocarboxylates (Fig. 8) [211]. Palladium
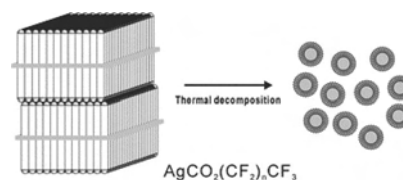


**Figure 8.** Perfluorocarboxylate-stabilized silver nanoparticles from the thermal decomposition of layered silver perfluorocarboxylates. Reprinted with permission from [211], K. Kim et al., *Chem. Commun.* 442 (2002). © 2002, Royal Society of Chemistry.

nanoparticles can also be prepared by reduction of palladium(II) chloride in the presence of different compounds featuring long perfluorinated carbon chains [212].

It is important to select a suitable reductant besides the control of other reaction conditions in order to obtain a stable colloidal solution of small metal nanoclusters by the method of reducing metal ions. The reduction ability on an electrode, however, could be easily adjusted by changing the potentials. Therefore the electrochemical process should be a very promising strategy for synthesizing metal nanoclusters especially for those metal elements having a relatively low redox potential.

Recently a detailed study on the size-selective electrochemical preparation of $R_4N^+Br^-$ stabilized Pd colloids was conducted by Reetz and co-workers, in which a sacrificial anode of Pd is used, and the surfactant serves as the electrolyte and stabilizer. The results showed that parameters such as solvent polarity, current density, charge flow, distance between electrodes, and temperature could be used to control the size of the Pd nanoparticles in a range of 1.2 to 5 nm. $(n\text{-}C_6H_{13})_4N^+Br^-$-stabilized nickel and $(n\text{-}C_8H_{17})_4N^+Br^-$-stabilized Pt/Pd colloids were successfully prepared [213].

Using standard Schlenck techniques Sobal et al. [214] prepared a well controllable core–shell structured Ag/Co bimetallic nanocluster. The method consists of a thermal decomposition of dicobalt octacarbonyl in combination with a transmetalation reaction with water-free $AgClO_4$ using oleic acid and tridodecylamine as protective surfactants the following reaction

$$Co_2(CO)_8 + 2AgClO_4 \rightarrow 2Ag + Co + 8CO + Co(ClO_4)_2$$
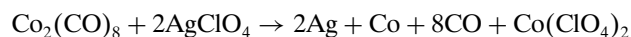
As a result, bimetallic Ag/Co particles were formed. The core–shell structures of these bimetallic nanoclusters of non-alloying elements were clearly characterized by TEM, electron energy-loss spectroscopy (EELS), and EDX as shown in Figures 9 and 10.

Formation of stable gold nanoparticles of different size and shape has been reported via UV photoactivation of $HAuCl_4$ in variable concentrations of TX-100. It is observed that small gold nanoparticles preferentially coalesce together at higher temperature in micelles. Temperature induced changes in the shape of the micelle provide the required template conditions for linear growth of gold nanoparticles. The smaller gold particles preferentially dissolved by cyanide at a faster rate in air in comparison to that for the larger particles because of higher mobility and possibly because of lower redox potentials of the smaller
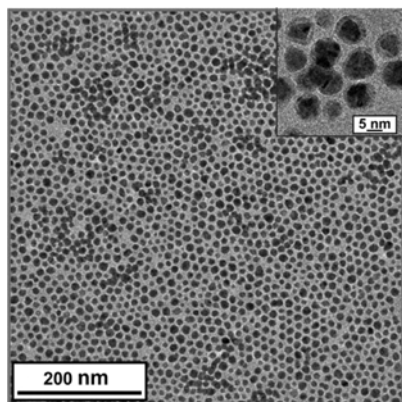
**Figure 9.** TEM image at low magnification of a monolayer of AgCo$_{0.81}$ particles deposited on a carbon coated copper grid. The core–shell structure is visible at higher magnification (inset). Reprinted with permission from [214], M. Hilgendorff et al., *Nano Lett.* 2, 621 (2002). © 2002, American Chemical Society.

particles. These interesting experiments provide a meaningful variant way to create metal nanoclusters with different shapes and particle sizes [215].

Chemicals inducing the formation of a specific shape of metal particles are called shape-directing agents. The function of a shape-directing agent, tetra-*n*-octylammonium glycolate, which bears a hydroxyl group at the $\alpha$-position, on the shape selectivity of trigonal cross-section particles of Ni was studied. An *in-situ* Fourier transform infrared (IR) study of the formation of colloidal nickel from bis(cyclooctadiene) nickel in the presence of tetra-*n*-octylammonium glycolate revealed that the interaction of the alpha-hydroxy carboxylate with the surface of the colloidal metal particle is likely to be the morphology-determining factor in the shape-selective preparation of these metal particles [216].

### 2.2.3. Assembly and Self-Assembly

The fabrication of superlattice structures of nanobuilding blocks is thought to be a key factor relating to future optical and electronic devices [124, 217–231].

When the colloidal solutions of metal nanoclusters are led to slowly evaporate their solvent on a flat surface,
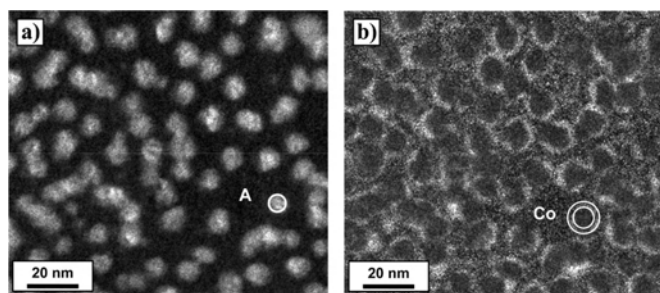


**Figure 10.** EELS element mapping of the Ag component (Ag $M_{4,5}$ edge) (a) and the Co component (Co $L_{2,3}$ edge) (b) in the bimetallic particles revealing an Ag$_{core}$Co$_{shell}$ structure. The element specific brightness of the same particle is marked by circles in both images. Reprinted with permission from [214], M. Hilgendorff et al., *Nano Lett.* 2, 621 (2002). © 2002, American Chemical Society.

nanoparticles with narrow size and shape distributions have a tendency to gather together and form two- or three-dimensional ordered superlattice patterns. This is one of the self-assembly processes. Perfect superlattice patterns of metal nanoclusters with the ordered scales up to submicrometer or even several micrometers have been constructed by simply evaporating solvent in a drop of colloidal solutions of metal nanoclusters stabilized by surfactant or coordinating ligands. For example, Au nanoclusters stabilized with alkylthiols [124, 232–236], 2,6-bis(1′-(8-thiooctyl)benzimidazol-2-yl)-pyridine [124], tetraalkylammonium salt [124, 237, 238], tetrapyridylporphine [239] or PPh$_3$ [240], Ag [241–247] and Pt nanoparticles [248] stabilized with alkylthiols, Pd nanoclusters stabilized with tetraalkylammonium salt [249], Co nanoparticles stabilized with carboxylic acid having a long chain [250], and Pt/Fe alloy stabilized with a mixture of oleic acid and oleic amine [251] have been successfully arranged into two- or three- dimensional superlattices, and the dynamic influence factors or driving forces in the self-assembly process have been discussed [244, 252–255]. Colloidal crystals of monodisperse Fe/Pt nanoparticles have also been grown by a three-layer technique of controlled oversaturation [256].

Highly ordered, hexagonally packed monolayer of gold nanoclusters protected with fluorinated alkane thiols has been reported by Yonezawa et al. These fluoro-alkylthiol-stabilized nanoparticles are soluble only in fluorocarbon media, and casting of these dispersions provided highly ordered, hexagonally packed monolayers on solid substrates [257]. Self-organized superstructures of fluorocarbon-stabilized Ag nanoparticles were also been studied [258].

Yonezawa and Kunitake synthesized a kind of gold nanoparticle stabilized with a water-soluble mercapto ligand (sodium 3-mercaptopropionate) by a modified citrate reduction of HAuCl$_4$. These gold nanoparticles were incorporated successfully into the interlayers of cast films of cationic bilayers by immersion of the film in gold nanoparticle dispersions [259]. Such amphiphilic gold nanoparticles were also obtained through ligand exchange reaction of alkanethiolate-protected gold nanoclusters with $\omega$-thiocarboxylic acids, and their assembly process was pH-controlled [260].

By use of the mercaptan stabilizer containing hydroxyl group, gold nanoparticles could be assembled with TiO$_2$ colloidal particle layer by layer resulting in a layered nanocomposite, which provided a convenient and universal process for assembling metal nanoclusters [261].

An organic/inorganic hybrid photoactive and electroactive functional film has also been made by this layer-by-layer deposition technique via alternate assemblies of aggregates of thionine dyes and Au nanoparticles on an amino functionalized support surface (Fig. 11) [262]. Hybrid nanocomposites of metal nanoclusters with silica such as highly ordered spherical mesoporous silica/gold [263] and silica/Ag [264] nanoparticles were also prepared through self-assembly recently. Pt nanoparticle-doped Nb$_2$O$_5$ composite films (~80 nm thickness) have been prepared by the liquid phase deposition method [265] (Fig. 12).

Gold nanoparticles and alkylthiols with various functional groups, including fullerene-C$_{60}$ [266], have also been used for fabricating novel photo- or electroactive nanostructures
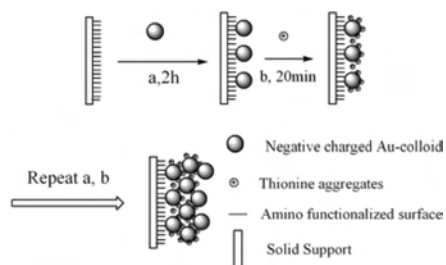
**Figure 11.** Alternate assemblies of thionine and Au nanoparticles on an amino functionalized surface. Reprinted with permission from [262], S. Dong et al., *Chem. Commun.* 1706 (2002). © 2002, Royal Society of Chemistry.
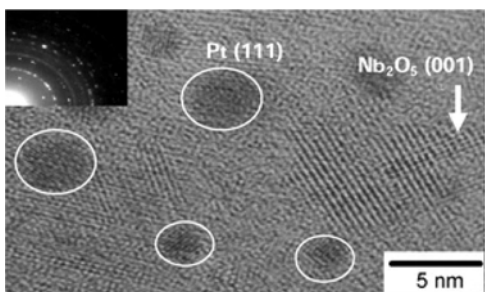


**Figure 13.** An alternative Pd/Au bimetal nanoparticle thin film with redox activity via electrooxidative deposition of palladium and gold nanoclusters attached with the same biferrocene-terminated thiolates. Reprinted with permission from [270], M. Yamada and H. Nishihara, *Chem. Commun.* 2578 (2002). © 2002, Royal Society of Chemistry.

[267–269] by self-assembly techniques. Recently, an alternative assembled nanoparticle thin film with redox activity has been formed by a combination of electrochemically oxidative deposition of palladium and gold nanoparticles attached with the same biferrocene-terminated thiolates (Fig. 13) [270].

It has been reported that IR light irradiation of a mixed toluene solution of ammonium salt-stabilized gold nanoparticles with a $3.8 \pm 0.8$ nm core and a porphyrin thioacetate derivative affords a thin photoactive film of the cluster–porphyrin network (Fig. 14) [271].

Three-dimensional Pt nanoparticle networks were prepared by cross-linking preformed aluminum-organic-stabilized Pt nanoparticles in solution with organic spacer molecules, through a protonolytic cross-linking reaction of reactive aluminum methyl groups at the particle surface. The hybrids were characterized by electron microscopy, IR spectroscopy, and anomalous small-angle X-ray scattering techniques [272].

One-dimensional organization of copper nanoparticles has been achieved by chemical reduction using lipid-copper hybrid nanofibers as a template; the reduction of copper ions resulted in the formation of copper nanoclusters at intervals of 2 to 5 nm along the nanofibers [273].

Spheric architectures of nanostructures containing Au or Ag could be obtained through the assembly of the corresponding smaller metal nanoclusters on spherelike templates [274, 275]. Direct self-assembly of thymine-functionalized Au nanoparticles with diaminopyridine-functionalized polyhedral oligomeric silsequioxanes (POSS) through tandem

hydrogen bonding and POSS recognition processes also forms well-defined spherical aggregates [276]. (Fig. 15).

Self-assembly of small metal nanoclusters, for example, of $Au_{55}$ into linear nanostructures, has been conducted with different strategies [277–280]. To arrange metal nanoclusters in a two-dimensional pattern of parallel rows of clusters with an adjustable periodicity down to a scale of several nm, however, is still a challenging task.

Dumpich and co-workers reported a method of fabricating metallic nanostructures by electron beam lithography on films of surfactant stabilized metal colloids. Destroying the organic stabilizers with high-energy electron beams may result in a patterned film of metal particles. This technique provides an interesting and powerful fabrication manner for metal nanostructures of various kinds of material and geometry [281].

The electron beam lithography technique has been demonstrated to be a very promising tool for making various designed patterns of assembled metal nanoclusters [282–285]. Figure 16 shows the nanowires of assembled Au nanoclusters derived from electron beam lithography on a Langmuir–Blodgett film of alkanethiol-capped 3 nm diameter gold nanoparticles reported by Werts and co-workers [286]. Nanowires with diameters less than 50 nm could be produced under controllability conditions; the patterns are formed by radiation-induced cross-linking of the alkyl chains and they can be contacted and studied electrically [286].

An electron beam can also be exploited in the growth of metal nanoparticles from small organometallic clusters or other metallic compounds on irradiation, and assemblies of Ru nanoparticle chains and wires [287] and 2D and 3D metal patterns [288] have been obtained directly.

Maoz and co-workers [289–292] developed a promising nanolithography technique in order to establish a



**Figure 12.** Pt nanoparticles dispersed in $Nb_2O_5$ composite films by liquid phase deposition. Reprinted with permission from [265], S. Deki et al., *J. Mater. Chem.* 1495 (2002). © 2002, Royal Society of Chemistry.
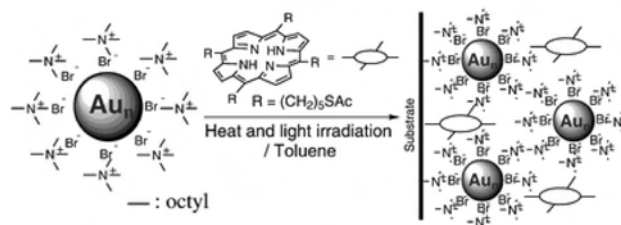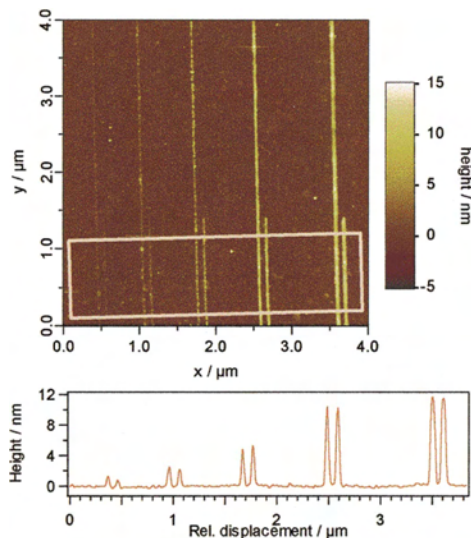


**Figure 14.** A thin photoactive film of the hybrid Au cluster–porphyrin network. Reprinted with permission from [271], H. Nishihara et al., *Chem. Commun.* 2476 (2001). © 2001, Royal Society of Chemistry.
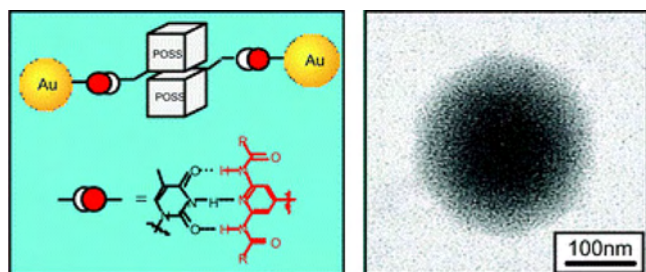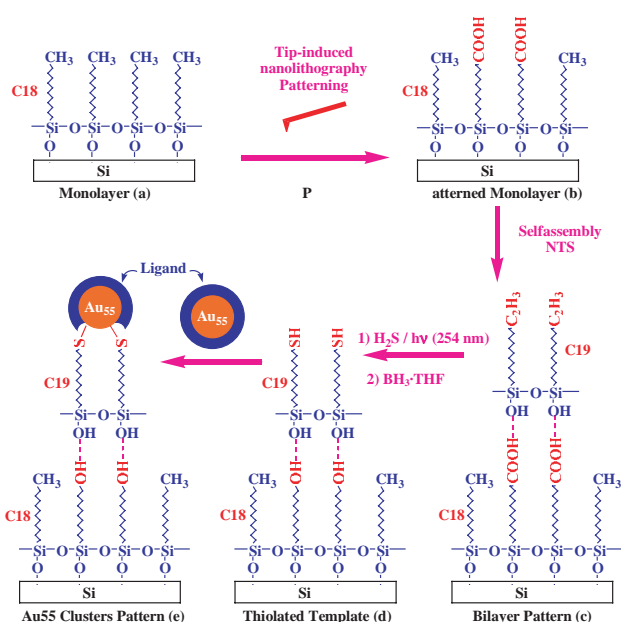
**Figure 15.** Spherical nanoaggregates induced by tandem hydrogen bonding and POSS recognition processes. Reprinted with permission from [276], V. M. Rotello et al., *Chem. Commun.* 1892 (2002). © 2002, Royal Society of Chemistry.

planed pattern of chemical information [i.e., using conductive atomic force microscopy (AFM) tip-induced nano-electrochemical oxidation of terminal $CH_3$ groups to carboxylic acid groups in a selected area of a methyl-terminated silane monolayer on silicon followed by a self-assembly process and chemical process to establish a chemical pattern of mercapto groups]. Nanostructured building blocks prepared *in-situ* could be fixed on the patterns of mercapto groups.

Using the "coordination capture" concept and manner, the organization of $[Au_{55}(Ph_2PC_6H_4SO_3Na)_{12}Cl_6]$ nanoclusters on various shaped patterns with top thiol groups created by the nanolithography technique has been well studied and perfectly assembled patterns with good stability of Au nanoclusters have been achieved by Liu and co-workers [293]. Figures 17 and 18 demonstrate the scheme of the nanolithography technique and the AFM image of the patterns of assembled organic template and parallel wires of gold nanoclusters.



**Figure 17.** Schematic representation of the fabrication of an organosilane template pattern with top thiol functional groups and the selective self-assembly of [Au55] clusters on the template. Adapted with permission from [293], J. Sagiv et al., *Nano Lett.* 2, 1055 (2002). © 2002, American Chemical Society.

These recent achievements in the template-guided assembly based on the nanolithography technique highlight a generic, controllable, and realizable assembly methodology to the nanoarchitectures.



**Figure 16.** AFM image of a pattern written at 25 keV on a three-layer thick Langmuir–Blodgett film of Au nanoparticles capped with *n*-hexanethiol. The e-beam dose is increased from 0.8 (left) to 6 mC/cm$^2$ (right). The lines are 40 nm wide, with a center-to-center distance of 100 nm. Reprinted with permission from [286], J. Bourgoin et al., *Nano Lett.* 2, 43 (2002). © 2002, American Chemical Society.
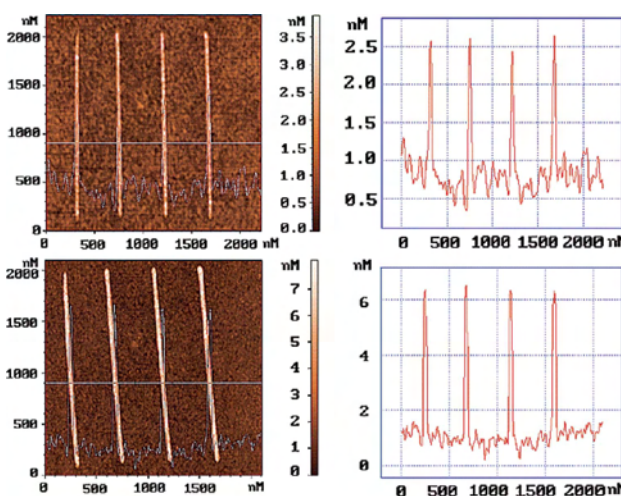


**Figure 18.** AFM semicontact mode topographic images of a pattern of parallel wires and distance–height profiles along the marked lines, taken (top image) after the assembly of the bilayer pattern (step c in Fig. 17), and (bottom image) after the final assembly of [Au55] on the thiolated template (step e in Fig. 17) and further annealing at 80 °C for 12 h. The size of the deposited gold particles is evaluated from the difference between the measured wire heights in the two images. Reprinted with permission from [293], J. Sagiv et al., *Nano Lett.* 2, 1055 (2002). © 2002, American Chemical Society.

Assembly of metal nanoclusters on proper templates could give rise to various promising structures. There is growing interest in attempts to combine biomaterials and nanoparticles in the fabrication of novel nanostructures as well as the investigation of their properties [294]. One of the research motivations for this combination is taking advantage of the well defined structures and special properties of biomolecules and their supermolecular structures to organize the nanoparticles into predefined, topologically intricate nanostructures or to synthesize miscellaneous materials for utilization in electronic, optical, and chemical devices. Several kinds of biomaterials have been used as templates for this purpose; for example, highly ordered protein assemblies, tobacco mosaic virus, and bacterial S-layers have been adopted for the generation of ordered arrays of metal and semiconductor nanoparticles [295–299].

DNA molecules have been used to mediate assembly of metal nanoparticles into linear, monolayer, and multilayer structures [300–306]. In addition, they have also been used to grow metal nanowires [307–310].

Very recently, we assembled Au or Pd nanoparticles respectively onto a self-assembled peptide nanofibril, used as a special 1D template, by mixing a preformed Au colloidal solution and the template directly or reducing Pd(II) ions with hydrogen in the presence of the template. It was found in surprise that double helical arrays of Au or Pd nanoparticles formed at a pH value near 6, whereas single-chain arrays of the metal nanoparticles formed at pH of 3.5. Pd nanowires in different shapes were also prepared. In addition, the assembled metal nanoparticles serving as labels were used to speculate the structure of the self-assembled peptide nanofibril [524].

Using the concepts of self-assembly of metal nanoclusters and the high specific selectivity of DNA segment combination, which were determined by the DNA configurations and the formation of hydrogen bonding, Elghanian and co-workers [311] reported a DNA sensing system in 1997, applicable to determine the sequence of a DNA or RNA molecules, which opened a new field to develop metal nanocluster-based biosensors having potential applications in medical and biological science. The development of biosensors is extremely significant in disease diagnosis and treatment, drug discovery, molecular biology and bioengineering, forensic identification, and environmental monitoring of biological agents and toxins [312, 313]. A biosensor, in principle, is based on the coupling of a ligand–receptor binding reaction [314] to a signal transducer, where the signal may have all sorts of physical characteristics including optical, radioactive, electrochemical, piezoelectric, magnetic, micromechanical, thermal, and mass spectrometric properties [315]. Since the metal nanocluster-based DNA sensor was published [311], there has been progressively increasing interest globally in studies on metal nanocluster-based biosensors. Due to their strong size-dependent natures and dimensional similarities to biomacromolecules, metal nanoclusters are most fascinating in making unique biosensors [316], for instance, DNA sensors [311, 316–340], glucose sensors [341–349], IgG protein sensors [350], and $H_2O_2$ sensors [351], when they are covalently hybridized with biological molecules such as peptides, proteins, enzymes, and nucleic acids. Recently, gold nanoparticles coated with haptenylated mercaptodextrans have been assembled, via binding specifically, to paramagnetic beads coated with a specific antibody, providing a way designed for biomolecule assay [352] (Fig. 19). Compared to traditional detecting techniques, metal nanocluster-based biosensors possess many desirable advantages; for example, it has low detection limits to picogram per ml, even to a single molecule, indestructive and highly selective detection, multiple modes of detection, and real-time detection, and it is label-free, environmentally friendly, cheap, and easy to miniaturize [353].

## 2.3. Anion and Solvent Stabilized Metal Nanoclusters

Stable colloidal solutions of "unprotected" small metal nanoclusters with a reasonable concentration of metal are of great importance in real applications such as fabrication of special electrode of fuel cells, catalysts, sensors and various composite materials. Successful examples for such preparations are still very limited. The unprotected metal nanoclusters are prepared in the absence of usual protective agents; however, they are not truly bare but stabilized by solvents or simple anions adsorbed on them, or by both. Cardenas-Trivino and co-workers prepared stable Pd colloids with average diameters of 6–8 nm in acetone or propanol using a solvated metal atom dispersion technique (SMAD). These Pd colloidal particles are "living" in the sense that they can be used to produce metal films [354]. Gold nanoparticles in acetone and films derived from their immobilization on functional group anchored surfaces have been studied [355]. A synthetic procedure for preparation of large quantities of monodisperse gold colloids based on the SMAD method was recently reported [356].

Recently, the authors succeeded in the effective preparation of small (1–3 nm) metal nanoclusters of Pt, Rh, Ru [88], and their alloys (unpublished data) in glycol containing NaOH without adding any other protective agent. These "unprotected" metal nanoclusters stabilized by organic solvent and $OH^-$ were prepared by reducing colloidal particles of the corresponding metal hydroxides or complexes. These metal nanoclusters are very tractable as building blocks for fabricating new function materials [357] in the sense that they can easily be separated from the solvent as precipitates by adding an aqueous solution of HCl and the precipitated metal nanoclusters are "resoluble" in many organic solvents.
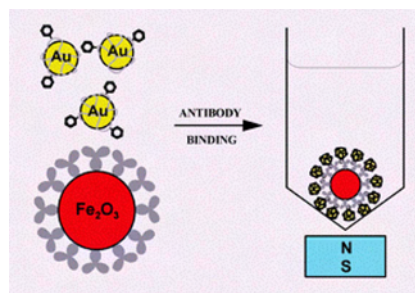


**Figure 19.** Haptenylated mercaptodextran-coated gold nanoparticles for biomolecular assays. Reprinted with permission from [352], R. Wilson, *Chem. Commun.* 108 (2003). © 2003, Royal Society of Chemistry.

Stable cyclohexanone or cyclopentanone colloidal solutions of Pt nanoclusters, average size 1–2 nm, with a Pt concentration higher than 200 g/L can be easily obtained by dissolving the precipitated Pt nanoclusters in the solvents. Colloidal solutions of thin Pt nanowires having diameters of 1–3 nm and lengths up to 70 nm have been succeefuly prepared by reducing $K_2PtCl_4$ with $H_2$ in the presence of our "unprotected" Pt nanoseeds [525].

Tano and co-workers reported the preparation of stable palladium colloids with average Pd particle size of 8–10 nm from the thermal decomposition of Pd complexes in methyl isobutyl ketone [358].

As ionic liquids have high polarity, robust physical stability, low volatility, and tunable properties, they are full of potentials in making metal nanoclusters under these green solvents [359], and narrowly dispersed germanium nanoclusters have been electrodeposited from a dilute solution of $GeCl_4$ in the ionic liquid 1-butyl-3-methylimidazolium hexafluorophosphate ([BMIm]$PF_6$) [360].

Colloidal early transition metals are of great interest in scientific research and applications. Organosols of zero valent Ti, Zr, V, Nb, and Mn with small particle size were prepared by Bonnemann and Brijoux by reducing the corresponding metal halides in tetra hydrofuran (THF) using K[$BEt_3H$] as a reductant [361]. Intensive studies on the Ti-THF nanocluster using HRTEM, EDX, XPS, XANES, and EXAFS analyses proved that this metal colloid consists of very small Ti particles in the zero valent state, stabilized by intact THF molecules [362].

Stable colloidal solutions of cubic Pt nanoparticles stabilized by oxalate with a particle size of 6.5 nm and shape selectivity larger than 90% were recently successfully prepared by the authors via the reduction of $K_2Pt(C_2O_4)_2$ in water with hydrogen at room temperature. It was observed that the shape selectivities of the Pt colloidal particles were strongly dependent on the precursors of metal salts used in the reactions, which should be related to the reaction speed and adsorption states on the formed metal nanoparticles. After the exposure to air and treatment with hydrogen, the oxalate stabilized Pt nanoparticles can self-assemble into Pt nanowires with diameters of those of the Pt nanoparticles and lengths of several hundreds of nm [363].

A stable colloidal solution of gold nanoparticles of 2 nm diameter was prepared in water containing $CS_2$ without adding any other stabilizers by reduction of $AuCl_4^-$ with $NaBH_4$. It was found that the surface plasmon band at around 520 nm was strongly damped due to small particle size and possibly chemisorption of a $CS_2$ derivative [364].

Polyoxometallates are important anionic stabilizers and supports for the preparation of metal nanoclusters due to their high surface charge plus significant steric bulk. Narrowly dispersed 2 or 3 nm Ir and Rh nanoclusters stabilized by $[P_2W_{15}Nb_3O_{62}]^{9-}$ were made by Finke et al. [365, 366] and their synthesis, characterization, and formation mechanisms were discussed in a recent review by Aiken and Finke [27]. Following Finke's precedent work using a Dawson polyoxmetallate as a nanocluster stabilizing agent, synthesis of Ag, Au, Pd, and Pt nanoparticles using Keggin polyoxometalates, such as $[SiW_{12}O_{40}]^{9-}$, as photocatalysts and stabilizers has also been conducted recently by Troupis et al. [367].

# 3. METAL NANOCLUSTER CATALYSTS

## 3.1. Quasi-Homogeneous Catalysts

PVP protected metal nanoclusters, which exhibit very high catalytic activities and stability in many organic reactions, and the well-known Nord colloid (PVA-protected Pd colloidal) [368] are representative examples of the quasi-homogeneous catalytic system.

In this catalytic system, the catalytic active species (i.e., metal nanoparticles) are similar to that of metal-supported catalysts but homogeneously dispersed as a colloid in the reaction media. Because of the very small particle size accompanied by a large specific surface area and high coordination unsaturating state of the surface metal atoms as well as the low resistance of mass transfer, the PVP-protected metal nanoclusters usually exhibit much higher catalytic activities than the corresponding traditional metal-supported catalysts. Recently, the hydrogen concentration–pressure isotherms of surfactant-stabilized palladium clusters and polymer-embedded palladium nanoclusters with diameters of 2, 3, and 5 nm were measured with the gas sorption method at room temperature. The results show that, compared to bulk palladium, the hydrogen solubility in the phase of the clusters is enhanced fivefold to tenfold [369].

Another important advantage of the metal nanocluster catalysts is that it provides many more possibilities than the traditional metal-supported catalyst to design and tailor the structures of the catalytic system such as the shape and size, metal element and composition in alloy nanoclusters, thickness and the core size in core–shell structured bimetallic colloidal particles, modifiers of small molecules adsorbed on the metal nanoparticles, structure and functional groups in the protective polymer. Stability of PVP-protective metal nanoclusters is quite good for many reactions in organic or water media; a reaction temperature higher than 150 °C is possible for some reactions if it is necessary. Polymer-protected metal nanocluster catalyst has an ascendency compared with nanoclusters stabilized with surfactants or coordination ligands in the stability and possibility of separation from the substrates and products. PVP-protected metal nanoclusters with a PVP molecular weight larger than 40,000 could be easily separated from solvent, without losing its catalytic activity, and washed with solvent in an ultrafilter equipped with a membrane having a cutoff molecular weight of 20,000 to 30,000, although this technique is not usually adopted in experiments. Addition of precipitate agents such as acetone to an alcohol colloidal solution of PVP-protective metal clusters could also separate the polymer-protective nanoclusters from the reaction system as a precipitate. For some special protective agents, changing pH or temperature will cause a separation of the catalyst as a precipitate.

Metal nanocluster catalysts have been successfully used in many reactions, such as the hydrogenation and selective hydrogenation of various unsaturated organic compounds, hydration of acrylonitrile to acrylamide, oxidation of organic compounds, Heck reaction, and visible light-induced hydrogen evolution, and various factors that may influence the catalytic properties have been investigated.

The Heck coupling reaction between aryl halides and olefins is usually conducted with a palladium complex

such as Pd acetate that decomposes during the reaction and forms Pd precipitate. Recently, series of well-defined homopolymer-stabilized Pd colloids with different metal particle sizes were used to catalyze the coupling reaction of *p*-bromobenzaldehyde with butyl acrylate. The PVP-protected Pd colloid catalyst exhibits very high stability and good activity. Extremely high total turnover numbers (TON, moles of substrate/moles of Pd; TON = 100,000) and turnover frequencies (TOF = TON/*h*; TOF > 80,000) were obtained [370].

Studies on the catalytic properties of colloidal bimetallic catalysts, a promising new kind of material, started about 10 years ago [90, 91, 371]. PVP-protected Pt/Rh and Pt/Pd bimetallic colloids with small metal particles exhibit much better activities than those of the corresponding monometallic colloids. The preparation, characterization, and application to catalysis of some polymer- or ligand-stabilized bimetallic nanoparticles have been reviewed by Toshima and Yonezawa [372].

The structure of the bimetallic nanoclusters has a significant influence on their catalytic properties. The catalytic properties of our Cu/Pd alloy nanocluster protected by PVP for the selective hydrogenation of 1,3-cyclooctadiene to corresponding monoene and selective hydration of acrylonitrile to acrylamide (see Scheme 1), an important industrial process, have been intensively studied. In the hydrogenation reaction, both the coexisting Cu in the alloy nanoclusters and PVP can improve the selectivity to the formation of monoene by several times; however, cooperation of both effects causes an extreme increase in the selectivity. An industrial process of producing acrylamide from acrylonitrile needs a very high selectivity, because a small amount of cyanohydrine in the product will cause a big problem in the following process of polymerization of acrylamide. Our Cu/Pd alloy nanoclusters not only exhibit a much higher activity than usual Cu-supported catalyst but also give rise to a selectivity near 100% to acrylamide and no cyanohydrine can be detected during the reaction. Both the catalytic selectivity and activity of the Cu/Pd alloy nanocluster catalysts for the aforementioned two reactions are sensitive to the Cu/Pd ratio in the alloy nanoclusters [111].

The selective hydrogenation of $\alpha,\beta$-unsaturated aldehydes to the corresponding unsaturated alcohols is an important step for the preparation of various fine chemicals (see Scheme 2). It is a challenging task to reduce the C=O group while leaving the C=C double bond since usual metal catalysts do in the reverse. The PVP-Pt/Co (3/1) alloy nanoclusters, narrowly distributed in a size range from 1 to 2.7 nm with an average diameter of 1.7 nm, prepared by the "cold alloying process" exhibit quite excellent catalytic properties for the selective hydrogenation of cinnamaldehyde to cinnamyl alcohol. The average activity of 114 mol CAL/mol



Selectivity: 99.8%
Conversion: 92.8%
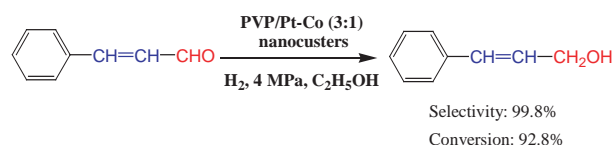
**Scheme 2**

metal per hr and a selectivity of 99.8% at a conversion of 96.2% could be easily achieved [113, 373].

PVP-protected Ni/Pd bimetallic colloids with narrow particle size distribution prepared by a similar method show high catalytic activity in the hydrogenation of nitrobenzene. The highest activity can be achieved for a bimetallic nanocluster with a molar ratio of Ni:Pd = 2:3, which exhibits 3.5 times greater activity than that of a typical colloidal palladium catalyst [374].

Monometallic, bimetallic, trimetallic, and tetrametallic nanoclusters, average size ranging 1.6–2.1 nm, containing Cu, Pd, Pt, and Ru have been prepared by reduction of corresponding metal chlorides with tetraoctylammonium formate in dimethylformamide. Catalytic properties of these colloidal catalysts for the coupling reaction of phenylboronic acid and iodobenzene to give biphenyl (see Scheme 3) have been investigated. Pd and Pd/Cu nanoclusters are more active than the others, and the Pd/Cu nanoclusters exhibit better activity at higher conversions. Ru and, surprisingly, Cu nanoclusters were found to be both active and stable for this reaction [375].

Catalyst modification is a widely applied strategy in heterogeneous hydrogenation. The chiral modification of metal nanoparticles in metal-supported catalysts has been a well-known strategy providing a high enantioselectivity in the hydrogenation of some organic compounds having potential to generate chiral center during the reactions. Heterogeneous Ni catalyst modified with tartaric acid and Pt catalyst modified with cinchona alkaloids are the most successful catalytic systems in enantioselective heterogeneous catalysts, which have been intensively studied in the field of heterogeneous catalyst. It has been concluded that supported Pt catalysts with relatively low dispersion (particle diameter larger than 2 nm) are preferred for the hydrogenation of $\alpha$-ketoester derivatives [376–382].

A platinum colloid prepared using the alkaloid dihydrocinchonidine was found to catalyze the hydrogenation of $\alpha$-ketoester pyruvates with a good enantioselectivity and high catalytic activity [383, 384]. A very interesting result was reported by Zuo et al. that an enantiomeric excess in favor of R-(+)-methyl lactate up to 97.6% could be obtained in the hydrogenation of pyruvate over a PVP-stabilized platinum colloidal catalyst with an average Pt particle size of only 1.4 nm (see Scheme 4) [385]. Molecular mechanics calculations of the modifier–reactant interaction on the



(Selectiveity > 99.6%)

**Scheme 1**



**Yield: near 100%**
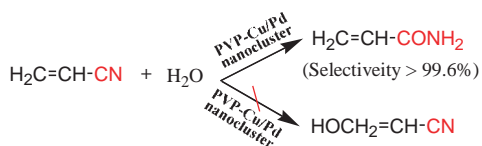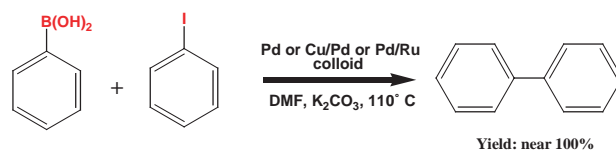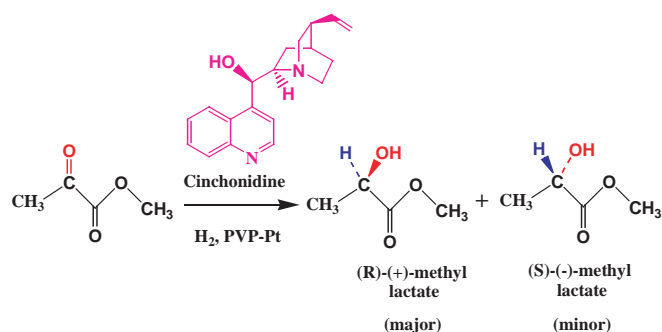
**Scheme 3**

**Scheme 4**

platform surface suggest that it is possible to obtain good enantioselectivity on the small clusters [386].

Metal cations can have significant modifying effects on the catalytic properties of metal nanoclusters. An acceleration effect of lanthanoid ions on the catalytic activity of Pd nanoparticles protected by lanthanoid polyacrylate (PAA-Pd-Ln) was observed in the hydrogenation of acrylic acid. However, $Ln^{3+}$ ions do not influence the catalytic activity of PVP-protected Pd colloid. On the other hand, the promotion effect of $Nd^{3+}$ ions on the PAA-Pd-catalyzed hydrogenation of methyl acrylate and allyl amine was observed, but not of 1-hexene. It was believed that the observed promotion effect stemmed from the following factors: $Ln^{3+}$ ions were concentrated around the Pd nanoparticles; the coordination of $Ln^{3+}$ ions to the substrates containing an oxygen or a nitrogen atom is an important factor for the promotion; and the dissociative hydrogen adsorption on the surface of Pd nanoparticles can be accelerated by the presence of $Ln^{3+}$ ions [387].

Selective hydrogenation of citronellal to citronellol was conducted over PVP-stabilized Pt and Ru colloids; metal cations were found to increase both the activity and the selectivity. The modification was assumed to be due to the adsorbed metal cations activating the C=O double bonds, resulting in accelerating the reaction rate and increasing the selectivity to unsaturated alcohols [388]. A similar positive influence of the metal cations was also observed in the hydrogenation of cinnamaldehyde to cinnamyl alcohol and of crotonaldehyde to crotyl alcohol over a polymer-protected Pt colloid catalyst [389].

The amazing promotion effect of metal cations appears again in the selective hydrogenation of *o*-chloronitrobenzene (*o*-CNB) to *o*-chloroaniline (*o*-CAN), in which eliminating chlorin is an obstacle to be overcome. The reaction was carried out in methanol at 303 K under 0.1 MPa of hydrogen over PVP-protected Ru–Pd and Ru–Pt bimetallic colloids [390] prepared by $NaBH_4$ reduction of the corresponding mixed-metal salts at room temperature. In the presence of cobalt ion, nearly 100% selectivity to (*o*-CAN) was achieved over PVP-Ru/Pt colloids at 100% conversion of *o*-CNB, with an activity two orders of magnitude higher than that of monometallic PVP-Ru colloid [391].

Besides simple metal cations, metal complexes were also found to enable an obvious improvement on the catalytic performance of metal nanoclusters dispersed in liquid [392], which revealed a new possibility to modify the surface of metal nanocluster catalysts with organometallic complexes of designed structures.

The size effect of Pd particles on the catalytic Suzuki reactions between phenylboronic acid and iodobenzene was investigated using catalysts of PVP-protected Pd colloids with varying particle size prepared by the stepwise growth reaction. The catalytic activity of the Pd nanoparticles was found to be in the order of Pd (3.9 nm) > Pd (3.0 nm) approximate to Pd (5.2 nm) > Pd (6.6 nm). The trend of increased catalytic activity with the decrease in particle size was believed to reflect the fact that the vertex and edge atoms of the particles are active sites for the Suzuki reaction. The lower catalytic activity for the smallest Pd nanoparticles might stem from a strong adsorption of the reaction intermediates on the particle surface [393]. The influence of protective agents, poly(amido-amine) dendrimers, block copolymer of polystyrene-*b*-poly(sodium acrylate), and PVP, on the catalytic properties of Pd nanoparticles in this reaction was also investigated [394].

Catalytic properties of colloidal Pt as electrocatalysts for the electrochemical oxidation of methanol were studied. Current efficiencies of $CO_2$ during methanol oxidation were determined by differential electrochemical mass spectrometry. It was observed that $CO_2$ formed via $CO_{ad}$ oxidation in a serial reaction, while formaldehyde and formic acid also formed in a parallel reaction. The further oxidation of these intermediates depends on the diffusion and convection conditions in connection with the surface structure of the Pt electrode. Ru promotes methanol oxidation to $CO_2$ via $CO_{ad}$, leading to a higher current efficiency of $CO_2$ [395].

Catalytic activities of palladium, platinum, rhodium, and Pd/Pt nanoclusters stabilized by various ligands with average sizes ranging from 1.3 to 3.2 nm and from 2.2 to 4.0 nm were evaluated by hydrogenation of 1,3-cyclooctadiene and methyl acrylate. The activities depend upon the particle size. The activities of heterogeneous catalysts prepared from supporting the metal nanoclusters on charcoal depend strongly on the covering strength of the stabilizer [396].

The catalytic properties of $Pd_{\sim561}phen_{\sim60}(OAC)_{\sim180}$ and $Pd_{\sim561}phen_{\sim60}O_{\sim60}(PF_6)_{\sim60}$ nanoclusters (where phen = phenanthroline) dispersed in water for several organic reactions have been studied by Vargaftik and co-workers [397–399].

Rh colloids stabilized with cationic surfactant have been demonstrated to be effective catalysts for the hydrogenation of arene derivatives such as anisole, toluene, and *p*-xylene in liquid–liquid biphasic systems in which the rhodium nanoparticles are suspended in an aqueous phase. A maximum TOF is obtained when the surfactant concentration is near the critical micellar concentration [400].

Microemulsion could be used as a microreactor for organic reaction catalyzed by metal nanoclusters. For example, in a water/AOT/*n*-heptane microemulsion, the reactions between $p$-$Me_2NC_6H_4NH_2$ and $Co(NH_3)_5Cl^{2+}$ forming *N,N*-dimethyl-*p*-semiquinonediimine, a process of relevance in color photography, over colloidal palladium catalysts with average diameter of 2.5 nm have been studied by Spiro and de Jesus. The palladium colloids were prepared by mixing microemulsions containing $K_2PdCl_4$ with ones containing 10 times this concentration of hydrazine, followed

by sonication. It was observed that the activation energies increased as the temperature fell [401].

The electrochemical mechanism in which electrons are transferred from reductant to oxidant through the nanoparticles of gold and other noble metals has been accepted to explain the catalytic functions of metal nanoclusters for many redox reactions occurring on the surface of metal nanoclusters, such as the reaction between $N,N$-dimethyl-$p$-phenylenediamine ($p$-Me$_2$NC$_6$H$_4$NH$_2$) and Co(NH$_3$)$_5$Cl$^{2+}$ forming $N,N$-dimethyl-$p$-semi-quinonediimine [401–404], the reduction of Fe(CN)$_6^{3-}$ to Fe(CN)$_6^{4-}$ by S$_2$O$_3^{2-}$ [405–407], or the reduction of water by reduced methyl viologen [408].

Usually when metal nanoclusters stabilized with surfactants or simple anions are used as catalysts, especially in the hydrogenation of organic compounds, a decrease in catalytic activity will soon be observed due to the easy aggregation of small metal nanoparticles under hydrogen, which should have relation to the adsorption of H$_2$ on the metal nanoparticles. Therefore, the lifetimes of these catalysts in a colloidal solution are usually not long enough for real applications, different from that of PVP-protected metal nanocluster catalysts. Aiken and Finke reported that the catalytic lifetime of a Rh nanocluster, particle size 2–4 nm, stabilized with polyoxoanion and tetrabutylammonium achieved a number $\geq 193{,}000$, which is near that of a heterogeneous catalyst, 5% Rh/Al$_2$O$_3$, and much higher than those of homogenous complex catalysts such as RhCl(PPh$_3$)$_3$ (Wilkinson's catalyst) or [(1,5-COD)Rh(CH$_3$CN)$_2$]BF$_4$. The Rh nanoclusters are prepared by the hydrogen reduction of [($n$-C$_4$H$_9$)$_4$N]$_5$Na$_3$[(1,5-COD)-Rh$_2$·W$_{15}$Nb$_3$O$_{62}$] [366, 409].

## 3.2. Immobilized Metal Nanocluster Catalysts

Research on adsorbing metal colloidal particles on a support could be traced back to before the 1970s. One example is the adsorption of Pd colloidal particles on Al$_2$O$_3$ contributed by Turkevich and Kim in 1970 [410]. Before 1990, the catalyst preparation procedure by immobilizing colloidal metal particles had not attracted reasonable attention, due to the lack of exciting results on the improvement of catalytic properties achieved in an unusual way, which seems a little complex compared with the traditional impregnation method in heterogeneous catalyst preparation. In 1989, Wang et al. prepared very active Rh and Pt nanocluster supported catalysts via coordination capturing Rh (3.5 nm) and Pt (1.6 nm) nanoclusters in PVP-protected metal colloids with mercapto group anchored on a silica support [123]. In the hydrogenation of hex-1-ene and cyclohexene, the catalytic activities of these mercaptan-fixed Rh and Pt nanoparticle catalysts are 100 to 300 times higher than those of commercial Rh/C and Pt/C catalysts at the same conditions. This is the first example of a mercapto-containing (which have been generally regarded as poisons for platinum metal catalysts) supported metallic catalyst with high activity for hydrogenation of alkenes. The as-prepared immobilized Pt and Rh nanoclusters are very stable during the reactions and can be reused many times. We have pointed out that the extremely high activities derived from the immobilization of metal nanoclusters via coordination capture can create favorable conditions for the substrates to easily access

the catalytic active sites in the catalyst and prevent the small colloidal particles from aggregating.

With thioether group anchored on silica such as -Si(CH$_2$)$_3$-S(CH$_2$)$_2$CH$_3$, Pd nanoclusters in PVP-protected Pd colloid can easily be immobilized. This catalyst shows a selectivity of 99% in the partial hydrogenation of cyclopentadiene (COD) to cyclopentene (COE) with an initial rate of 2.7 (mol H$_2$/s mol Pd) at room temperature and atmosphere pressure (unpublished data).

Immobilization of polymer (PVP)-stabilized metal colloids on different supports has also been realized by a modified coordination capture method in which the supports were pretreated with an ethanol solution of triphenylphosphine (TPP) and then were led to reaction with the PVP-protective metal colloidal solutions. TPP adsorbed on the surface of support captured the metal nanoparticles in colloidal solution. PVP and TPP in the solid products then were removed by washing with water and ethanol/toluene, resulting in a supported metal nanocluster catalyst having a similar size and size distribution of metal particles as their precursor. Platinum catalysts prepared in this way exhibited superior catalytic properties to their precursors in colloidal solution for the selective hydrogenations of $o$-chloronitrobenzene to $o$-chloroaniline and citronellal to citronellol. This revealed the great potential of nanoscale metal colloidal particles in catalysis [411].

Modification effects of metal cations on the catalytic properties of a Pt nanocluster supported catalyst, prepared by the modified coordination capture method, were investigated for the selective hydrogenation of $o$-chloronitrobenzene to $o$-chloroaniline, cinnamaldehyde to cinnamyl alcohol, and citronellal to citronellol. It was found that Ni$^{2+}$ and Co$^{2+}$ cations increased both the activity and the selectivity at the same time [412].

The immobilized polymer-protected metal colloid catalysts Wang et al. prepared in 1995 by the formation of polymer hydrogen bond complexes on inorganic support such as silica, like a skin of cross-linked polymer embedded with small metal nanoparticles, exhibit very high selectivity in the selective hydrogenation of COD to COE. The PVP-PAA-Pd catalyst supported on silica prepared by forming hydrogen bond complex between polyacrylic acid and PVP in a PVP-protected Pd colloid in the presence of a silica support can catalyze the reaction in a selectivity of 98% to COE at a COD conversion of 100% with a TOF of 2.25 mol H$_2$/mol Pd s. The catalytic selectivity of PVA-PAA-Pd catalysts prepared by the same is better than the PVP-PAA-Pd catalyst, although its catalytic activity is much lower than PVP-PAA-Pd catalyst, partly due to the large Pd particle size in the PAA-Pd colloid. PVP-Rh and PVP-Pt colloid catalysts can also be easily immobilized by this method and the obtained skin catalysts covered on silica support exhibit good activities in this hydrogenation reaction [139].

The selective partial hydrogenation of 3-hexyn-1-ol giving leaf alcohol, a valuable fragrance, and the selective oxidation of glucose giving sodium gluconate over supported nanosized metal colloidal particles originally stabilized with surfactant were examined by Bonnemann and co-workers. It has been described that independent of the support, the performance of these nanoparticle precursors may be optimized dependent on the size, composition, and structure of

the particles. Furthermore, the protective agents can shield the catalytic active surface of metal nanoclusters against poisons and addition of doping agents can enhance the catalytic properties [413, 414].

In 1999, Lange et al. reported a convenient method for preparing embedded polymer-protected metal nanocluster catalysts. The PVP-protected Pt nanoclusters with size of 1.4 nm embedded in amorphous microporous titania–silica mixed oxide by a sol–gel procedure exhibited a quite good selectivity to the formation of hexene in the hydrogenation of 2-hexyne. A 2-hexene selectivity of >94% was obtained at hexyne conversion up to 50%, and at complete conversion a selectivity to 2-hexenes of 88% (cis-2-hexene selectivity of 91%) was achieved. In colloidal dispersions of the PVP-stabilized catalyst in propanol, however, the initial hexene selectivity of 80% at a conversion less than 10% fell to ca. 45% at 100% conversion [140]. The obvious increases in the selectivity may be derived from the configuration confinement of PVP by the matrix of inorganic nanoparticles. This success showed an interesting variant procedure for developing new hybrid catalyst with some special catalytic properties.

SiO$_2$-embedded nanoscopic Pd/Au alloy colloids were prepared by embedding the alloy particles of 3 nm in size stabilized with tetraalkylammonium in a silica matrix using a sol–gel process with THF as the solvent. Removing the protecting agent could lead to a mesoporous texture with a comparatively narrow pore distribution and the SiO$_2$-embedded Pd/Au colloid preserves the size and the structural characteristics of the colloidal metal precursor. The new material exhibits good catalytic properties in selective hydrogenation of 3-hexyn-1-ol to the corresponding cis-hexanol derivatives [142].

Recently Niederer and co-workers reported the synthesis of metal nanoparticle containing [Me]($x$)-MCM-41 heterogeneous catalyst using surfactant stabilized palladium, iridium, and rhodium nanoparticles in the synthesis gel. Characterization results using XRD, inductively coupled plasma-atomic emission spectrometry (ICP-AES), thermogravimetric analysis (TA), TEM, and nitrogen sorption techniques on this catalyst revealed that the nanoparticles were present inside the pores of MCM-41. Catalytic properties for the hydrogenation of cyclohexene, cyclooctene, cyclododecene, and norbornene over these catalysts were examined [415].

Dendrimer-encapsulated Pd and Pt nanoparticles with narrow particle size distribution dispersed in supercritical CO$_2$ have been used as effective catalysts for the hydrogenation of styrene and Heck heterocoupling of iodobenzene and methacrylate [416].

Metal nanoclusters stabilized by surfactants can be easily adsorbed on supports to prepare metal supported heterogeneous catalysts. Mono- and bimetallic nanoparticles stabilized by lipophilic or hydrophilic surfactants of the cationic, anionic, or nonionic type have been used as precursors for preparing heterogeneous metal nanocluster catalysts, which are effective for the hydrogenation and oxidation of organic substrates. A comparison of catalytic results and CO chemisorption experiments revealed that the protecting surfactants still covered the nanoparticle surface after adsorption on supports, which markedly improved the lifetime of the catalysts [205].

A lanthanium oxide supported Ru colloid was used as the catalyst for the hydrogenation of benzene in an aqueous solution of sodium hydroxide. Selectivity to cyclohexene of higher than 50% at 50% conversion was achieved [417].

Frelink et al. reported in 1995 that the catalytic activities for oxidation of methanol of carbon-supported catalysts derived from colloidal techniques are 2–3 times higher than those prepared using either impregnation or ion-exchange methods [418].

Metal particle size would have an influence on the catalytic activity of a supported metal nanocluster electrocatalytic catalyst. Large particles are accompanied by a loss in specific area of the metal particles; however, if the small particles are entrapped in micropores of the support, an obvious decrease in the apparent catalytic activity may also be observed. It has been demonstrated that the optimal Pt particle size for reactions in a H$_2$/O$_2$ fuel cell is ~3 nm [419].

The microwave-assisted synthesis method has been used to prepare well-dispersed Pt nanoparticles, average size in 3.5–4 nm, supported on carbon for the application of fuel cells. This catalyst exhibits high electrocatalytic activity in the room-temperature oxidation of liquid methanol [420].

Highly active electrocatalytic electrodes of carbon–silica composites containing Pt nanoparticles of about 2 nm have been prepared by Anderson and co-workers [421] by embedding Vulcan carbon XC-72 carbon-supported Pt nanoparticles in a silica gel followed by a CO$_2$ supercritical drying process. The electrocatalytic activity for methanol oxidation over the colloidal-Pt-modified carbon–silica composite aerogels was reported to be 4 orders of magnitude higher than that over the native Pt-modified carbon powder. A further improvement in the activity was achieved by appropriately annealing the electrodes to increase the size of Pt nanoparticles to 3–4 nm.

Bimetallic colloidal nanoparticles containing Pt, especially the Pt/Ru nanoclusters with particle sizes of 1–2 nm stabilized by organoaluminum, were reported to be suitable for preparing fuel cell anode catalysts with an improved CO tolerance. The colloid precursors were supported and activated by thermal conditioning to remove the organic stabilizer [422–426]. It was also found that the size of organoaluminum-stabilized metal particles did not change during the thermal conditioning even at high metal loadings (20 wt% metal).

A Pt–Ru/graphitic carbon nanofibers nanocomposite containing Pt–Ru alloy nanoclusters having 6 nm average diameter and 1:1 bulk Pt/Ru ratio with a total metal content of 42 wt% has been prepared and used as an anode catalyst in a direct-methanol fuel cell. An average current density at 0.4 V of 0.21 A/cm$^2$ for the fuel cell was achieved [427].

Bimetallic Pt–Sn nanoclusters, PtSn (niggliite), and Pt$_3$Sn, with an average diameter of 5–8 nm, highly dispersed on a carbon powder support at a total metal loading of ca. 15 wt%, have been prepared and their electrocatalytic properties have also been investigated. It is observed that both the Pt–Sn/C nanocomposites as electrooxidation catalysts in a direct methanol fuel cell give fuel cell performances comparable to that expected for Pt–Sn catalysts prepared by more conventional methods [428].

Pt–Co bimetallic nanoclusters of 3–4 nm diameter prepared by Zhang and Chan using a water-in-oil reverse microemulsion of water-Triton X-100-propan-2-ol-cyclohexane were supported on a carbon electrode which has a high catalytic activity for methanol oxidation at room temperature [429].

Hydrogenation of butyronitrile and the adsorption of CO over Pt/Rh bimetallic nanoparticles supported on activated charcoal have been studied. The Pt/Rh ratio at the surface has an important influence on the catalytic activity and CO chemisorption ability. Maximum activity in this hydrogenation reaction and CO adsorption ability were observed at a Pt/Rh atomic ratio of 0.1. Detection of the different types of CO bonding at the surface by IR and the EXAFS characterization results revealed that Rh was enriched in the surface [430].

Catalytic properties for the selective hydrogenation of 3,4-dichloronitrobenzene to corresponding aniline under high pressure over a supported Pt catalyst prepared by immobilizing nanoparticles in surfactant-protected Pt hydrosols have been examined in batchwise and continuous manners [431].

$R_4N^+Br$-stabilized Pd colloids were embedded in inorganic matrix by an *in-situ* fluoride-catalyzed hydrolysis of $CH_3Si(OCH_3)_3$ and $Mg(OC_2H_5)_3$, resulting in micro/mesoporous hydrophobic sol–gel materials entrapped with individual Pd nanoclusters, which are active catalysts in the hydrogenation of 1,5-cyclooctadiene [141].

Multilayered polyelectrolyte films containing silver metal nanoparticles of 4–30 nm in average diameter were prepared by reducing silver ions in the films by heating or $NaBH_4$. These metal nanocluster embedded polyelectrolyte films exhibit obvious electrochemical catalytic properties and can be used as antimicrobial coatings [432].

Ag nanoparticles in a composite of organosulfur containing a conducting polymer (DMcT-PAn) component were found to have the capacity to improve the charge–discharge performance of the composite as a cathode material for lithium rechargeable batteries. Ag nanoparticles were bound to DMcT with a silver–sulfur bond in this composite system. The observed enhancement in the battery performance was attributed to the electrocatalytic activity of the metal nanoparticles and the increased conductivity of the composite films [433].

## 4. METAL NANOCLUSTER MAGNETIC MATERIALS AND DEVICES

Magnetism related to metal nanoclusters and cluster-assembled thin films has been reviewed recently [434]. In this section, we will give a brief description of metal nanoclusters and their assemblies as promising magnetic materials in order to make up for the lack of reviews in this aspect at present [435].

Nanoscale magnetic particles have attracted considerable growing interest [434–436], both theoretical and experimental, in recent years, because of their unique size-dependent magnetic properties and their potential in advanced magnetic functional materials. Both magnetic particles and their assemblies have attractive and extensive applications in various fields of materials science. Isolated magnetic particles can be used as magnetic fluid for magnetic separation

and magnetic sealing devices [437, 438]. Controlled assemblies of magnetic particles with other stuff will find their applications in smart AFM tips [439, 440], magnetic force-enhanced biomolecule recognition [441, 442], and magnetic field-assisted drug delivery [443–445]. Furthermore, self-assembly of magnetic nanoparticles as building blocks in chemically controllable manners can be used to build up novel magnetic nanostructures [446]. Due to collective physical phenomena of many elementary particulates magnetic properties of a nanostructured assembly are dominated by the interaction of its building blocks besides the nature of the blocks. This kind of nanoparticle-based self-assembly, which is governed by particle–particle and particle–substrate interactions, is extremely important in fabricating unique nanocomposite functional magnetic materials with potential in strong permanent magnets [447, 448], ultrahigh density data storage media [251, 449–451], and spintronic devices, including spin valves [452, 453] and spin-dependent tunneling junctions [454–456] based on the giant magnetoresistance (GMR) effect [457], for ultrasensitive magnetic heads [458, 459], and for nonvolatile magnetic random access memory (MRAM) [460–462].

In the design and preparation of nanostructured magnetic materials, controlled self-assembly of magnetic nanoparticles is an exciting and promising area and has stimulated great recent interest as it may offer a convenient tool for magnetic nanodevice fabrication [446]. Generally speaking, only the uniform nanoparticles as building blocks are, in principle, easy to self-assemble into well-defined 2D patterns and 3D architectures, which are considerably important in nanodevice fabrication. Recently developed solution-phase synthetic approaches (including the pyrolysis of organometallic compounds [463, 464], thermal [465, 466] or sonochemical decomposition of metal carbonyl compounds [467], and the reduction of metal salts by borohydride [468, 469], triethylborohydride [470, 471] or diols [251, 373], for preparing highly well-monodispersed elemental Fe [467, 472] and Co [465, 466, 468–471, 473–477], binary Fe–Pt [251, 478], Co–Pt [373, 464, 479–481], and Co–Ag [214], and ternary Fe–Co–Pt [482] and Fe–Pt–Ag [483] magnetic nanocrystals with narrow size distribution of standard deviation $\sigma$ within about 10%) have given scientists the chance to construct novel self-assembled magnetic nanostructures based on magnetic metal nanoclusters.

Chemical synthesis [484] and ordered assembly [485] of magnetic metal nanoparticles have just been reviewed. Electronic and magnetic properties of monodispersed FePt nanoparticles [486], arrays of ferromagnetic iron and cobalt nanoclusters wires along lines of magnetic flux of the applied field [487], control of the magnetic anisotropy of a Co/Pt nanomultilayer with embedded particles [488], and granular GMR sensors of Co/Cu and Co/Ag nanoparticles [489] have been reported recently. In the following examples of this section, we will focus on the potential applications of self-assembled nanostructures from magnetic metal nanoclusters.

### 4.1. Ultrahigh Density Data Storage Media

Magnetic data storage has been playing a key role in the development of audio, video facilities, and computers since its invention more than 100 years ago by Poulsen [490].

In 1956, the first hard disk drive was made by IBM and had a total storage capacity of 5 MB at a recording density of 2 kb/in$^2$. Since then the principle of magnetic data storage has been based on writing magnetic bits in plane on magnetic layers, which is the so-called longitudinal recording. In pursuit of lowering the cost and improving the performance, the areal density (i.e., the number of bits per unit area on a disk surface) has increased nearly 20 million-fold to more than 40 Gb/in$^2$ in modern disk drives and currently doubles every year. Recently, recording densities beyond 100 Gb/ in$^2$ have been reached in two laboratory demonstrations [491, 492]. This continued growth in areal density was achieved by scaling the critical physical dimensions of the constituted magnetic grains; however, there is a limit to this scaling that will be approached within the next few years [493]. One of these limits (i.e., thermal limits [494–496]) lies in the reduction in magnetic grain size, where due to enhanced thermal effects the onset of superparamagnetism at room temperature for small particles will define the size of the smallest possible particles to keep one from losing recording data. The size of a grain to block superparamagnetism is related to the thermal stability of the grain magnetization, which can be described by the stability ratio, $C = E/k_B T$, where $E$ stands for the magnetic anisotropy energy of the grain in question, $k_B$ is Boltzman's constant, and $T$ is the temperature. The magnetic anisotropy energy $E$ per grain is dependent on the grain volume $V_g$ and the anisotropy energy density $K_u$, and defined as $E = K_u V_g$. To store information reliably for 10 years, it requires $C = 60$ [494, 495]. If one assumes cylindrical particles with a height of the typical disk film thickness of 20 nm and $K_u$ of current media (about $3 \times 10^5$ J/m$^3$), this implies a minimum stable particle diameter of no less than about 7 nm for monodispersed particles.

To increase the storage density, however, the size of the grains needs to be reduced. This together with increasing magnetic isolation is the conventional way taken to scale media. Since ultimately the transition width is governed by the size of the grains, higher densities require smaller grains. Also, to maintain a satisfactory signal-to-noise ratio, it is imperative to keep the number of grains per bit constant, and thus the grain size is reduced as the density is increased. The anisotropy energy density $K_u$ can only be increased to some extent to uphold the thermal stability as the grain size is reduced, since the media switching field increases with $K_u$ and cannot go beyond the write field available from the head [493]. Various alternative routes to postpone perceived thermal limits [494–496] for acquiring higher recording densities have been proposed in recent years [493, 495–498]. One of the most promising ways is to use a nanoparticle medium, which is a magnetic film fabricated with metal nanoparticles. The present candidates for nanoparticle media are FePt [251] and CoPt [451] binary alloy with face-centered tetragonal structure, since they have high uniaxial magnetocrystalline anisotropy ($K_u \approx 7 \times 10^6$ and $5 \times 10^6$ J/m$^3$ for FePt and CoPt, respectively) and good chemical stability and show excellent hard magnetic properties [495, 499, 500]. Self-assembled FePt nanoparticulate film has been successfully used in preliminary longitudinal contact recording studies [251]. Earlier attempts to make FePt [501–503] and CoPt particle thin films [504, 505] have mainly relied upon sputter deposition or other vacuum techniques. But those methods

result in chemically disordered crystallites of face-centered cubic structure, which require high-temperature annealing to encourage the alloy films to adopt the magnetically advantageous face-centered tetragonal phase. A shortcoming of vacuum-deposition/annealing procedures is that they commonly lead to products characterized by a broad distribution of grain sizes, with a typical standard deviation of about $\sigma = 30$–35% [493], due to random nucleation in the initial stages of growth and subsequent agglomeration during annealing.

The broad distribution of grain sizes in a magnetic film is undesirable, because uniformity of grain size can help maintain a high signal-to-noise ratio in magnetic recording applications. In a recording medium with widely varying grain sizes, the smallest grains are most susceptible to demagnetization and losing their stored data, or they are superparamagnetic and not useful for magnetic storage, while the large grains contribute disproportionately to the noise. That is less of a problem when all grains are approximately the same size. In addition, today's magnetic reading heads detect signals from very small data bits most accurately when the bits are made up of grains with uniform size distribution. To produce high performance recording media with good thermal stability, large storage density, and low noise, one needs naturally to increase the number of grains of median size in a magnetic film with a simultaneous narrowing of their size distribution.

The keys to making nanoparticle media are controlling the size of magnetic grains and controlling their array from agglomeration in the films. In a recent report by Sun et al. [251], both problems have been solved primarily, using controllable solution-phase chemistry. The strategy adopted by Sun et al. is to make tiny bimetallic nanoparticles from iron and platinum compounds which as prepared are magnetically weak, allowing them to form self-assembled layers, followed by annealing at about 500 °C, and transforming them into stronger magnets at the end.

In this controllable procedure, monodisperse FePt nanoclusters, with a very narrow size distribution of standard deviation $\sigma < 5\%$, is first synthesized by reduction of platinum acetylacetonate with 1,2-hexadecanediol, and simultaneously thermal decomposition of iron pentacarbonyl in dioctylether, in the presence of oleic acid and oleyl amine stabilizers (see Fig. 20). The size and composition of these FePt nanoclusters can be readily controlled. Their composition is adjusted by controlling the molar ratio of iron carbonyl to the platinum salt. The size of FePt nanoclusters can be tuned from 3 to 10 nm by first growing 3-nm monodisperse seed nanoclusters *in-situ* and then adding more reagents to enlarge the existing seeds to the desired size. These nanoparticles are well isolated and purified easily by centrifugation after the addition of a precipitant such as ethanol and can be redispersed in a variety of nonpolar solvents.

To make a film, the resulting FePt nanoclusters are spread on a substrate. As the solvent is slowly evaporated, the weakly magnetic nanoparticles nestle down by self-assembly into a regular array. Within an array, the interparticle distance may be adjusted by replacing oleic acid and oleyl amine with shorter chain alkyl group via ligand exchange, and correspondingly the symmetry of the array can be controlled.
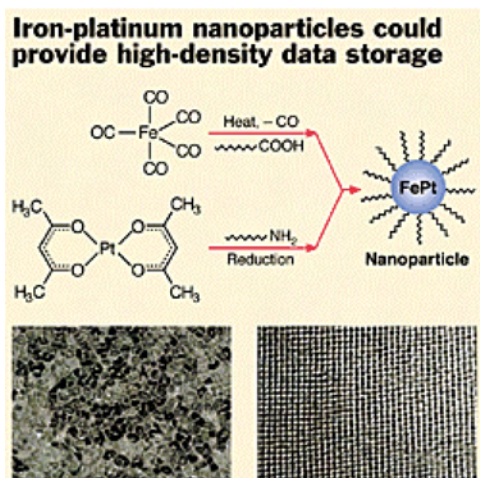
**Figure 20.** TEM micrograph of arrays of nanosized FePt particles (at right) that are smaller and more uniform in size than those obtained from a CoPtCrB material (left) that was used recently in a very high density data-storage demonstration. Reprinted with permission from [449], M. Jacoby, *C&E News* 78, 37 (2000). © 2000, Shouheng Sun.

Next, the films are annealed at 560 °C, for about half an hour, to convert the internal particle structure from a chemically disordered face-centered cubic phase to the chemically ordered, ferromagnetic face-centered tetragonal phase. During the annealing, no agglomeration occurs and the organic stabilizers are fused into a hard coat surrounding each magnetic nanoparticle. The resulting magnetic films are chemically and mechanically robust. Sun et al. have shown that these materials can store data faithfully at a density equivalent to that of CoCr-based alloy hard disks on the market today (see Fig. 20 for the film structure). On the basis of conventional grain size scaling arguments, these materials may even allow one to boost that density 10-fold using current read and write heads.

This strategy, developed by Sun et al. as well as by workers at IBM, to fabricate nanoparticle media is an important milestone for ultrahigh density magnetic data storage, which also bring forth the fascination of magnetic nanoclusters in the process of self-assembly chemistry. Now, more effort is still needed for future practical applications. For instance, the biggest problem is that it is necessary to find a way to orient the particle easy magnetization axes all perpendicularly to the film, since the tiny FePt nanoclusters can freeze in place facing any direction and conventional recording heads work only if all the magnetic particles on a disk have their crystalline axes aligned with the disk's surface. Ultimately, if one would like to record one bit per nanoparticle for patterned media using magnetic metal nanoclusters, which would correspond to higher recording densities of about 10–20 Tb/in$^2$, it requires one to make a long-range regular array of the nanoclusters—this will be a formidable challenge to future self-assembly chemistry.

## 4.2. Exchange-Spring Strong Magnets

Permanent magnets are one of the most technologically important magnetic functional materials in science and technology and in our everyday life. The performance of permanent-magnet materials is evaluated by their maximum magnetic energy product—this figure of merit is a measure of the maximum magnetostatic energy that would be stored in free space between the pole pieces of a magnet made from the material in question [506]. The larger its magnetic energy product, the greater the performance of a permanent magnet, and hence it is called a strong magnet.

The maximum magnetic energy product is proportional to the area closed in the saturated hysteresis loop of a magnet, which arises from plotting the magnetization of the material as the applied magnetic field is cycled under its saturation field. This hysteresis loop is characterized by the saturation magnetization, that is, maximum magnetization and the coercivity of the material, which is the reverse applied field strength to reduce the magnetization to zero. The larger the coercivity of a magnet, the harder it is, whereas the smaller the coercivity of a magnet, the softer it is. To gain a strong magnet with a large magnetic energy product, it requires that there are both lager magnetization and lager coercivity in the material.

Progress in making strong permanent magnets has been limited by the difficulty of finding new compounds with these two necessary properties. For instance, $Fe_{65}Co_{35}$ alloy, a material with the largest room-temperature saturation magnetization of 24 kG, should have a theoretical maximum magnetic energy product of 144 MG Oe—the upper bound on the magnetic energy product for strong magnets. But in practice this material does not have such a large magnetic energy product because it is a soft magnet (i.e., its coercivity is actually fairly low and a small reverse field is sufficient to reduce the magnetization to zero).

About a decade ago, the idea of exchange coupling between a hard material and a soft material with a large magnetization occurred to physicists [507–509], which brought a new hope of producing magnets with their maximum magnetic energy product approaching the upper bound of 144 MG Oe. These kinds of exchange-spring magnets are nanocomposites that are composed of magnetically hard and soft nanophases that interact by magnetic exchange coupling. In a two-nanophase mixture of such materials, exchange forces between the phases mean that the resulting magnetization and coercivity of the material will be some average of the properties of the two constituent phases [508]. In order to realize the effective exchange coupling, the relative sizes of the grains of the two nanophases must be chosen carefully [507]: In general, the characteristic dimensions of the soft magnetic phase cannot exceed about twice the wall thickness of magnetic domains in the hard one. Typically, this limits the soft magnetic phase to be about 10 nm in diameter. Correspondingly, the hard one must have dimensions of this order too, or the volume fraction of the soft magnetic phase will be rather low, thus reducing the magnetization of the composite.

Following the concept of magnetic exchange coupling, a lot of techniques, including melt-spinning [510–512], mechanical milling [513–515], and sputtering [516–518], have been exploited to prepare exchange-spring magnets. However, all of these techniques have had only limited success in fabricating two-phase nanostructures with a high magnetic energy product, as they could not afford

to effectively control the so-required nanostructures for exchange coupling.

Recently, Zen and co-workers [448] reported on how to use self-assembly of magnetic nanoparticles as building blocks to fabricate novel exchange-spring magnets. Their method of chemical synthesis under controlled self-assembly is attractive potentially in making three-dimensional bulk magnets with high magnetic energy product. When monodispersed 4 nm $Fe_{58}Pt_{42}$ and 4 nm $Fe_3O_4$ nanoclusters are mixed in hexane under ultrasonic agitation and allowed to self-assemble three-dimensionally by either evaporation of the hexane or addition of ethanol, they form nanoscale structures which, when heated and chemically reduced by $H_2$ under Ar gas at 650 °C for one hour, form homogeneous mixtures, at 5-nm scale, of a hard tetragonal FePt phase and a high-magnetization soft $Fe_3Pt$ phase. The admixture of Pt in the $Fe_3Pt$ nanograins results from sintering at a temperature of 650 °C, which is used to induce the phase transition from disordered FePt to ordered tetragonal FePt. The magnetic energy product of this two-nanophase material is 20.1 MG Oe, which considerably exceeds the theoretical limit of 13 MG Oe for non-exchange-coupled isotropic FePt magnet by over 50%.

This self-assembly protocol opens the door to make strong magnets for practical applications [447], since the size and composition of the individual building blocks can be independently tuned, and the self-assembly results in homogeneous mixtures, at the nanosacle, to effective exchange coupling of the hard and soft magnetic nanophases. However, there are still many practical challenges to be faced when producing magnets with their magnetic energy products approaching the magic number of 144 MG Oe. For example, ways of compressing the two-nanophase material into a high-density compact must be explored, as well as improved alignment of the axes of the hard particles to exploit the full magnetic potential of the nanocomposite system [447]. Nevertheless, it could be expected that highly monodispersed magnetic metal nanoclusters, especially the uniform nanoparticles with zero distribution, will play an important role in making superstrong magnets in the future.

## 4.3. Metal Spintronic Devices

Since the discovery of the GMR effect [457] in 1988, spintronics [519–521], an innovative emerging electronics based on electron spin as well as charge, has made great progress in information science and technology for outstripping the performance of traditional electronics devices. Spintronic devices use magnetic moment to carry information and can combine the performance of standard microelectronics with spin-dependent effects that arise from the interaction between spin of the carrier and the magnetic properties of the material. Introduction of the electron spin degree of freedom to such devices gives them various advantages, including low electric power consumption, nonvolatile data retention, excellent radiation protection, superfast data processing speed, and high integration densities. At present, spintronic hard disk drive read-heads are well established commercially [458], MRAMs appear to be set to follow suit [519], and an all-metallic magnetic logic NOT gate [522] has just been achieved in a laboratory demonstration. In the

future, spintronics will lead to very rapid quantum computers [523].

One of the promising applications of ferromagnetic metals or alloys materials is to make spintronic devices that stand for information by the magnetization direction of the ferromagnetic metal components. Spin valves and spin-dependent tunneling junctions are fundamentally metallic spintronic devices developed currently in the world for hard disk drive read-heads and MRAM [521]. Both devices are based on the giant magnetoresistive effect of thin-film materials composed of alternate ferromagnetic and nonmagnetic layers. A spin valve has two ferromagnetic layers (alloys of nickel, iron, and cobalt) sandwiching a thin nonmagnetic metal (usually copper), with one of the two magnetic layers being "pinned" (i.e., the magnetization in that layer is relatively insensitive to moderate magnetic fields, and the other being "free"; i.e., its magnetization can be changed by a relatively small applied magnetic field). A spin-dependent tunnel junction (SDTJ) is a device in which a pinned layer and a free layer are separated by a very thin insulating layer, commonly aluminum oxide. As the magnetizations in the two layers change from parallel to antiparallel alignment, the magnetoresistance of them rises typically from 5 to 10% for spin valves and 20 to 40% for SDTJ, respectively. Pinning is usually accomplished by using an antiferromagnetic layer that is in intimate contact with the pinned magnetic layer. The two films form an interface that acts to resist changes to the pinned magnetic layer's magnetization.

To date, all the metallic films for these devices, including the recent magnetic logic gates under development [522], are fabricated with vacuum techniques of metal vapor deposition such as sputter. The fundamental developing work exploiting the self-assembly technique of metal nanoparticles has just begun at IBM. In a recent report [226], using monodisperse Co nanoclusters with $\sigma = 5\%$, Black and co-workers have self-assembled nanoscale ordered arrays of 10-nm ferromagnetic Co nanoclusters between lithographically patterned metal contacts spaced about 100 nm apart, for the study of SDTJ devices. After annealing under Ar with 5% $H_2$ at 400 °C for about one hour, to strip off the organic ligands protecting the clusters, the arrays convert into films displaying spin-dependent electron transport. At low temperatures, the current–voltage characteristics of the junction reflect single-electron tunneling through the array, and the observed magnetoresistance is on the order of 10% ratio, approaching the maximum predicted theoretically for ensembles of cobalt islands with randomly oriented easy magnetic axes. This work demonstrates that self-assembled Co-nanocrystal superlattices are excellent model experimental systems for studying magnetotransport in nanostructured materials. The observed spin-dependent tunneling in such nanoscale devices of highly uniform magnetic-nanocrystal arrays implies that magnetic metal nanoclusters have vast potential in making advanced spintronic devices. It is reasonable to believe that novel spin valves, spin-dependent tunneling junctions, and magnetic logic elements made from metal nanoclusters might become realized in the future, if the spin-dependent electron transport within an array of metal nanoclusters takes place at room temperature.

From these examples, we can see that, in various potential applications of magnetic metal nanoclusters for fabricating

advanced magnetical materials and devices, self-assembly has played a key role. This technique is an attractive tool in future nanofabrication because it provides the way to precisely engineer structures on the nanometer scale over large sample areas. However, there is still a long and hard road to the well-developed self-assembly chemistry. It requires more convenient routines to largely prepare size-, shape-, and composition-controllable, even uniform nanoclusters, and easily controlled processes to assemble the nanoclusters into regular arrays or patterns with different symmetry at will.

## 5. SUMMARY

Nanoclusters with small particle sizes and narrow size distributions of noble metals such as Au, Pt, Pd, Rh, Ru, and Ir, light transition metals such as Cu, Co, and Ni, early transition metals such as Zr and Ti, and some alloys of these elements are available from chemical preparations. The structure and composition of them are usually characterized using techniques of TEM, HRTEM, EDX, XPS and Auger Spectroscopy, EELS, XRD, EXAFS, IR-CO probe, STM, AFM, etc. Current interests in metal nanocluster preparation are control of the size, shape, composition, and core–shell structures, especially tailoring the physical and chemical properties by alloying different metals.

The so-called "unprotected" metal nanoclusters stabilized with organic solvent and simple anions are tractable building blocks in nanochemistry and nanomaterial science because they can be easily prepared in large scale, modified with various preferred ligands and embedded in a functional or matrix materials with high loading.

Self-assembly of narrowly distributed metal nanoclusters into an ordered superlattice pattern of large area has been intensively studied and some promising progress has been achieved based on narrowly distributed metal nanoclusters stabilized by ligands or surfactants during last decade. However, obstacles still need to be overcome before this technique can be put into real applications. It requires more convenient routines to largely prepare size- and shape-controllable, even uniform, nanoclusters, and easily controlled processes to assemble the nanoclusters into regular arrays and patterns with different symmetry at will.

Electron beam lithography and especially the conductive-AFM-tip-induced nanolithography technique have highlighted the generic, controllable, and realizable assembly methodologies to the nanoarchitectures.

More realistic possibilities for wide applications of metal nanocluster building blocks are catalysts, nanostructured magnets, and chemical or biochemical sensors.

Polymer-protective metal nanoclusters are suitable candidates for quasi-homogeneous catalysts due to their high stability in the conditions of many organic reactions and the weak interaction between the metal surface atoms and residue groups in usual adopted polymer protective agents. PVP is still the most preferred polymer protective agent for such a purpose.

Immobilization of preformed structure-controllable metal and alloy nanoclusters originally stabilized with various protective agents provides a promising new concept and practice to generate heterogeneous catalyst for various applications. The "coordination capture method," which fixes individual nanoparticles on the outer surface of a support via anchored ligands, not only contributes the most active catalysts for hydrogenation of organic compounds because of the easy access of the substrates to the small metal and alloy nanoclusters but also has been adopted in the meaningful exploration of the specific properties of small metal nanoclusters and their self-assemblies.

Embedding metal nanoclusters in porous inorganic oxide matrixes by stacking metal oxide nanoparticles around the various preformed metal nanoclusters or the adsorbing metal nanoclusters on supports could produce a new type of catalyst that should find real applications in many catalytic reactions and in the fuel cells operated at a relatively low temperature.

Modifying the catalytically active metal nanocluster surfaces with chiral ligands, metal cations, or metal complexes can greatly improve their catalytic selectivities in many reactions.

The combination of metal nanoclusters with biomolecules is a very challenging approach to assemble nanoclusters in a designed pattern that would find applications in developing new biomaterials or biosensors, nanoelectronics, and evaluating the superstructures and functions of boimolecules or organisms.

Syntheses and assemblies of bimetallic magnetic nanoclusters with narrowly distributed sizes and shapes would produce promising magnetic media of the highest recording density. Self-assembly of different magnetic metal and alloy nanoclusters using a wet chemical process, followed by suitable chemical and physical treatment, is a very promising and realistic approach to create new magnetic materials and devices with superior properties that are difficult to be realize through other routes so far.

## GLOSSARY

**Alcohol refluxing method**  A method for reducing metal cations with refluxed alcohol.

**AOT**  bis(2-ethylhexyl)sulfosuccinate, a surfactant with two alkyl chains.

**Catalyst modification**  Optimizing the catalytic property of the active sites in a catalytic system by adding additives or changing its support structure.

**Coordination capture method**  A strategy for immobilizing metal nanoparticles characterized by the coordination action or specific reaction between ligands anchored on a support and surface atoms of the metal nanoparticles.

**Dendrimer**  A polymer with star-shaped or tree-like structure.

**Deoxyribonucleic acid (DNA)**  A naturally occurring polymer usually has a double-stranded structure and plays an important role in heredity of life.

**Electrocatalytic electrode**  An electrode having an ability to catalyze an electrochemical reaction occurring on it, which is useful in electrochemical devices such as a full cell sensor or detector.

**Electron beam lithography**  A process for fabricating a designed pattern on a material by destroying the structure at irradiated positions with high-energy electron beams.

**Electrophoretic deposition** Deposition of charged colloidal particles or molecules on electrodes immersed in a colloidal solution under the influence of an applied electric field.

**Exchange-spring magnet** A nanocomposite magnet composed of magnetically hard and soft nanophases that interact by magnetic exchange coupling.

**Fuel cell** An electrochemical cell in which the energy of a reaction between a fuel and an oxidant is converted directly and continuously into electrical energy.

**Giant magnetoresistance effect (GMR)** A physical phenomenon characterized by a dramatic increase in the electric resistance of a material under an applied magnetic field.

**Infrared carbon monoxide probe** An IR analysis method for species or structures based on the vibration of adsorbed carbon monoxide.

**Ionic liquids** Salts, typically possessing at least one organic ion, with low melting-points in a liquid state within a wide temperature range including room temperature. Ionic liquids are becoming widely recognized as solvents for "green" chemical synthesis because they have no measurable vapor pressure, are nonflammable, and show dramatic enhancements in reaction rate, yield, and selectivity.

**Magnetic random access memory (MRAM)** A novel non-volatile random access memory based on magnetic moment to carry information, it still keeps the recorded information in the memory when the power is off.

**Micelle** A submicroscopic or nanoscopic aggregation of molecules, as a droplet in a colloidal system.

**Polymer hydrogen bond complex** A complex derived from different polymers with hydrogen bonds between them.

**Polyoxometallates** A large family of metal-oxygen clusters of the early transition metals in high oxidation states, most commonly $V^V$, $Mo^{VI}$, and $W^{VI}$. Their diversity in composition and molecular structure allows a wide versatility in terms of shape, polarity, redox potentials, surface charge distribution, and acidity.

**Schlenck technique** A method for handling oxygen- or moisture-sensitive compounds under inert atmosphere.

**Sol–gel procedure** A wet chemical technique for fabricating nanostructured materials via hydrolysis and condensation processes in a suitable solvent with metal salts, silicon chloride and metal or non-metal alkoxides as the precursors.

**Solvated metal atom dispersion technique (SMAD)** A method for preparing metal nanoclusters or colloids involving vaporization of a metal under vacuum and codeposition of the atoms with the vapors of a solvent on cooled walls of a reactor. During a warming up process, metal nanoparticles formed, are stabilized both by solvation and negative charge.

**Spin-dependent tunnel junction (SDTJ)** A spintronic device in which a pinned and a free magnetic metallic layer is separated by a very thin insulating layer, commonly aluminum oxide. As the magnetization in the two layers changes from parallel to antiparallel alignment, the magnetoresistance of such a device rises typically from 20 to 40%.

**Spintronics** An innovative branch emerging in electronics based on not only the charge but also the spin of an electron.

**Spintronic device** A device based on spintronics, which carries information exploiting the charge and spin of an electron.

**Spin valve** A spintronic device composed of two ferromagnetic metal layers (alloys of nickel, iron, or cobalt) sandwiching a thin nonmagnetic metal (usually copper). Under a moderately applied magnetic field, the magnetization of one layer, called "pinned" layer, is relatively insensitive to the field, whereas the applied field can change that of the other layer, called "free" layer. As the magnetization in the two layers changes from parallel to antiparallel alignment, the magnetoresistance of such a device rises typically from 5 to 10%.

**Triton X-100** Polyethylene glycol mono [4-(1,1,3,3,-tetramethylbutyl)phenyl]ether.

**Ultraviolet photolysis** Inducing a chemical reaction by ultraviolet light irradiation.

# ACKNOWLEDGMENTS

# REFERENCES

1.  M. Faraday, *Philos. Trans. Roy. Soc. London* 147, 145 (1857).
2.  G. Schmid, *Chem. Rev.* 92, 1709 (1992).
3.  G. Schmid, M. Baumle, M. Geerkens, I. Heim, C. Osemann, and T. Sawitowski, *Chem. Soc. Rev.* 28, 179 (1999).
4.  G. Schmid and L. F. Chi, *Adv. Mater.* 10, 515 (1998).
5.  G. Schmid and G. L. Hornyak, *Curr. Opin. Solid State Mater. Sci.* 2, 204 (1997).
6.  G. Schmid, *J. Chem. Soc. Dalton Trans.* 7, 1077 (1998).
7.  G. Schmid, *Adv. Eng. Mater.* 3, 737 (2001).
8.  G. Schmid, *J. Mater. Chem.* 12, 1231 (2002).
9.  G. Schmid, V. Maihack, F. Lantermann, and S. Peschel, *J. Chem. Soc. Dalton Trans.* 5, 589 (1996)
10. "Cluster and Colloids" (G. Schmid, Ed.). VCH, Weinheim, 1994.
11. "Metal Nanoparticles: Synthesis, Characterization, and Applications" (D. L. Feldheim and C. A. Foss, Eds.). Dekker, New York/Basel, 2002.
12. "Nanosale Materials in Chemistry" (K. J. Klabunde, Ed.). Wiley, New York, 2001.
13. N. Toshima, in "Nanoscale Materials" (L. M. Liz-Marzán and P. Kamat, Eds.). Kluwer, New York, 2002.
14. T. Teranishi and N. Toshima, Preparation, characterization and properties of bimetallic nanoparticles, in "Catalysis and Electrocatalysis at Nanoparticle Surfaces" (A. Wieckowski, E. R. Savinova, and C. G. Vayenas, Eds.), Ch. 11, p. 379. Dekker, New York, 2002.
15. N. Toshima and Y. Shiraishi, in "Encyclopedia of Surface and Colloid Science" (A. T. Hubbard, Ed.), p. 879. Dekker, New York, 2002.
16. T. Yonezawa and N. Toshima, in "Advanced Functional Molecules and Polymers" (H. S. Nalwa, Ed.), Vol. 2, Ch. 3, p. 65. Gordon & Breach, New York, 2000.
17. N. Toshima, *Macromol. Symp.* 156, 45 (2000).
18. N. Toshima, in "Fine Particles: Synthesis, Characterization, and Mechanism of Growth" (T. Sugimoto, Ed.), Ch. 9, p. 430. Dekker, New York, 2000.
19. N. Toshima, *Pure Appl. Chem.* 72, 317 (2000).

20. N. Toshima, in "Nanostructured Materials in Biological and Artificial Systems" (A. Yamagishi and Y. Fukushima, Eds.), p. 395. Elsevier, Oxford, 1998.
21. N. Toshima and T. Yonezawa, *New J. Chem.* 22, 1179 (1998).
22. A. C. Templeton, W. P. Wuelfing, and R. W. Murray, *Acc. Chem. Res.* 33, 27 (2000).
23. C. N. R. Rao, G. U. Kulkarni, P. J. Thomas, and P. Edwards, *Chem. Soc. Rev.* 29, 27 (2000).
24. L. N. Lewis, *Chem. Rev.* 93, 2693 (1993).
25. G. Schon and U. Simon, *Colloid Polym. Sci.* 273, 101 (1995).
26. G. Schon and U. Simon, *Colloid Polym. Sci.* 273, 202 (1995).
27. J. D. Aiken III and R. G. Finke, *J. Mol. Catal. A* 145, 1 (1999).
28. H. Bonnemann, *Preparation Catalysts VI* 91, 185 (1995).
29. H. Bonnemann and R. M. Richards, *Eur. J. Inorg. Chem.* 10, 2455 (2001).
30. S. R. Liu, H. J. Zhai, and L. S. Wang, *Phys. Rev. B* 65, 113397 (2002).
31. S. R. Liu, H. J. Zhai, and L. S. Wang, *J. Chem. Phys.* 117, 9758 (2002).
32. S. R. Liu, H. J. Zhai, and L. S. Wang, *Phys. Rev. B* 64, 153398 (2001).
33. M. Takagi, *J. Phys. Soc. Jpn.* 9, 359 (1954).
34. J. E. Martin, J. Odinek, J. P. Wilcoxon, R. A. Anderson, and P. Provencio, *J. Phys. Chem. B* 107, 430 (2003).
35. M. A. El-Sayed, *Acc. Chem. Res.* 34, 257 (2001).
36. M. Valden, X. Lai, and D. W. Goodman, *Science* 281, 1647 (1998).
37. H. G. Boyen, G. Kastle, F. Weigl, B. Koslowski, C. Dietrich, P. Ziemann, J. P. Spatz, S. Riethmuller, C. Hartmann, M. Moller, G. Schmid, M. G. Garnier, and P. Oelhafen, *Science* 297, 1533 (2002).
38. T. V. Choudhary and D. W. Goodman, *Top. Catal.* 21, 25 (2002) and references therein.
39. For examples: K. Bromann, C. Félix, H. Brune, W. Harbich, R. Monot, J. Buttet, and K. Kern, *Science* 274, 956 (1996).
40. H. Hirai, Y. Nakao, and N. Toshima, *J. Macromol. Sci. Chem. A* 12, 1117 (1978).
41. H. Hirai, Y. Nakao, and N. Toshima, *J. Macromol. Sci. Chem. A* 13, 727 (1979).
42. T. Teranishi and M. Miyake, *Adv. Mater.* 10, 594 (1998).
43. X. Yan, H. Liu, and K. Y. Liew, *J. Mater. Chem.* 3387 (2001).
44. H. P. Choo, K. Y. Liew, and H. Liu, *J. Mater. Chem.* 934 (2002).
45. T. Teranishi, I. Kiyokawa, and M. Miyake, *Adv. Mater.* 10, 596 (1998).
46. A. B. R. Mayer, *Polym. Adv. Tech.* 12, 96 (2001).
47. Y. Zhou, H. Itoh, T. Uemura, K. Naka, and Y. Chujo, *Chem. Commun.* 613 (2001).
48. M. Zhao, L. Sun, and R. M. Crooks, *J. Am. Chem. Soc.* 120, 4877 (1998).
49. L. Balogh and D. A. Tomalia, *J. Am. Chem. Soc.* 120, 7355 (1998).
50. K. Esumi, A. Suzuki, N. Aihara, K. Usui, and K. Torigoe, *Langmuir* 14, 3157 (1998).
51. M. Zhao and R. M. Crooks, *Angew. Chem. Int. Ed.* 38, 364 (1999).
52. M. Zhao and R. M. Crooks, *Adv. Mater.* 11, 217 (1999).
53. V. Chechik, M. Zhao, and R. M. Crooks, *J. Am. Chem. Soc.* 121, 4910 (1999).
54. M. Zhao and R. M. Crooks, *Chem. Mater.* 11, 3379 (1999).
55. L. K. Yeung and R. M. Crooks, *Nano Lett.* 1, 14 (2001).
56. K. Esumi, A. Kameo, A. Suzuki, and K. Torigoe, *Colloid Surf. A* 189, 155 (2001).
57. E. H. Rahim, F. S. Kamounah, J. Frederiksen, and J. B. Christensen, *Nano Lett.* 1, 499 (2001).
58. F. Grohn, G. Kim, B. J. Bauer, and E. J. Amis, *Macromolecules* 34, 2179 (2001).
59. M.-C. Daniel, J. Ruiz, S. Nlate, J. Palumbo, J.-C. Blais, and D. Astruc, *Chem. Commun.* 2000 (2001).
60. M.-K. Kim, Y.-M. Jeon, W. S. Jeon, H.-J. Kim, S. G. Hong, C. G. Park, and K. Kim, *Chem. Commun.* 667 (2001).
61. T. Vossmeyer, B. Guse, I. Besnard, R. E. Bauer, K. Müllen, and A. Yasuda, *Adv. Mater.* 14, 238 (2002).
62. M. Ooe, M. Murata, T. M., K. Ebitani, and K. Kaneda, *Nano Lett.* 2, 999 (2002).
63. C. Aymonier, U. Schlotterbeck, L. Antonietti, P. Zacharias, R. Thomann, J. C. Tiller, and S. Mecking, *Chem. Commun.* 3018 (2002).
64. J. J. L. M. Cornelissen, R. van Heerbeek, P. C. J. Kamer, J. N. H. Reek, N. A. J. M. Sommerdijk, and R. J. M. Nolte, *Adv. Mater.* 14, 489 (2002).
65. J. P. Spatz, A. Roescher, and M. Moller, *Adv. Mater.* 8, 337 (1996).
66. J. P. Spatz, S. Mossmer, C. Hartmann, M. Moller, T. Herzog, M. Krieger, H. G. Boyen, P. Ziemann, and B. Kabius, *Langmuir* 16, 407 (2000).
67. M. Moffitt, L. McMahon, V. Pessel, and A. Eisenberg, *Chem. Mater.* 7, 1185 (1995).
68. Y. Boontongkong and R. E. Cohen, *Macromolecules* 35, 3647 (2002).
69. S. Bharathi, N. Fishelson, and O. Lev, *Langmuir* 15, 1929 (1999).
70. S. Bharathi and O. Lev, *J. Chem. Soc. Chem. Commun.* 2303 (1997).
71. Y. Zhang, F. Chen, J. Zhuang, Y. Tang, D. Wang, Y. Wang, A. Dong, and N. Ren, *Chem. Commun.* 2814 (2002).
72. K. S. Morley, P. C. Marr, P. B. Webb, A. R. Berry, F. J. Allison, G. Moldovan, P. D. Brown, and S. M. Howdle, *J. Mater. Chem.* 1898 (2002).
73. L. Armelao, R. Bertoncello, E. Cattaruzza, S. Gialanella, S. Gross, G. Mattei, P. Mazzoldi, and E. Tondello, *J. Mater. Chem.* 2401 (2002).
74. S. Besson, T. Gacoin, C. Ricolleau, and J.-P. Boilot, *Chem. Commun.* (2003).
75. Y. Guari, C. Thieuleux, A. Mehdi, C. Reye, R. J. P. Corriu, S. Gomez-Gallardo, K. Philippot, B. Chaudret, and R. Dutartre, *Chem. Commun.* 1374 (2001).
76. A. Fukuoka, H. Araki, Y. Sakamoto, N. Sugimoto, H. Tsukada, Y. Kumai, Y. Akimoto, and M. Ichikawa, *Nano Lett.* 2, 793 (2002).
77. L.-X. Zhang, J.-L. Shi, J. Yu, Z.-L. Hua, X.-G. Zhao, and M.-L. Ruan, *Adv. Mater.* 14, 1510 (2002).
78. F. Schweyer, P. Braunstein, C. Estournès, J. Guille, H. Kessler, J.-L. Paillaud, and J. Rosé, *Chem. Commun.* 1271 (2000).
79. H.-Q. Wu, X.-W. Wei, M.-W. Shao, J.-S. Gu, and M.-Z. Qu, *J. Mater. Chem.* 1919 (2002).
80. B. Xue, P. Chen, Q. Hong, J. Lin, and K. L. Tan, *J. Mater. Chem.* 2378 (2001).
81. N. Toshima, T. Takahashi, and H. Hirai, *Chem. Lett.* 1245 (1985).
82. M. Ohtaki, N. Toshima, M. Komiyama, and H. Hirai, *Bull. Chem. Soc. Jpn.* 63, 1433 (1990).
83. K. Esumi, M. Wakabayashi, and K. Torigoe, *Colloid Surf. A* 109, 55 (1996).
84. M. Y. Han and C. H. Quek, *Langmuir* 16, 362 (2000).
85. W. Yu, W. Tu, and H. Liu, *Langmuir* 15, 6 (1999).
86. K. S. Morley, P. C. Marr, P. B. Webb, A. R. Berry, F. J. Allison, G. Moldovan, P. D. Brown, and S. M. Howdle, *J. Mater. Chem.* 1898 (2002).
87. A. I. Cooper, *Adv. Mater.* 13, 1111 (2001).
88. Y. Wang, J. Ren, K. Deng, L. Gui, and Y. Tang, *Chem. Mater.* 12, 1622 (2000).
89. N. Toshima, K. Kushihashi, T. Yonezawa, and H. Hirai, *Chem. Lett.* 1769 (1989).
90. Y. Wang and H. Liu, *Polymer Bull.* 25, 139 (1991).
91. N. Toshima, M. Harada, T. Yonezawa, K. Kushibashi, and K. Asakura, *J. Phys. Chem.* 95, 7448 (1991).
92. Y. Wang and N. Toshima, *J. Phys. Chem. B* 101, 5301 (1997).
93. L. M. Liz-Marzan and A. Philipse, *J. Phys. Chem.* 99, 15120 (1995).
94. S. Link, Z. L. Wang, and M. A. El-Sayed, *J. Phys. Chem. B* 103, 3529 (1999).

95. L. Rivas, S. Sanchez-Cortea, J. V. Garcia-Ramos, and G. Morcillo, *Langmuir* 16, 9722 (2000).
96. I. Srnova-Sloufova, F. Lednicky, A. Gemperle, and J. Gemperlova, *Langmuir* 16, 9928 (2000).
97. I. Lee, S. Han, and K. Kim, *Chem. Commun.* 1782 (2001).
98. K. Mallik, M. Mandal, N. Pradhan, and T. Pal, *Nano Lett.* 1, 319 (2001).
99. N. Kometani, M. Tsubonishi, T. Fujita, K. Asami, and Y. Yonezawa, *Langmuir* 17, 578 (2001).
100. C. S. Ah, S. D. Hong, and D. Jang, *J. Phys. Chem. B* 105, 7871 (2001).
101. M. P. Mallin and C. J. Murphy, *Nano Lett.* 2, 1235 (2002).
102. D. Chen and C. Chen, *J. Mater. Chem.* 12, 1557 (2002).
103. L. Lu, H. Wang, Y. Zhou, S. Xi, H. Zhang, J. Hu, and B. Zhao, *Chem. Commun.* 144 (2002).
104. K. L. Kelly, T. R. Jensen, A. A. Lazarides, and G. C. Schatz, in "Metal Nanoparticles: Synthesis, Characterization and Applications" (D. L. Feldheim and C. A. Foss, Jr., Ed.). Dekker, New York, 2002.
105. Y. Wang, L. Gui, and Y. Tang, *Chin. J. Chem.* 12, 11 (1994).
106. Y. Wang, L. Gui, and Y. Tang, "Abstract of Materials Research Society 1992 Spring Meeting, Symposium O," O3.8, San Francisco, 1992.
107. J. S. Bradley, E. W. Hill, C. Klein, B. Chaudret, and A. Duteil, *Chem. Mater.* 5, 254 (1993).
108. J. S. Bradley, G. H. Via, L. Bonnevio, and E. W. Hill, *Chem. Mater.* 8, 1895 (1996).
109. N. Toshima and Y. Wang, *Adv. Mater.* 6, 245 (1994).
110. N. Toshima and Y. Wang, *Chem. Lett.* 1611 (1993).
111. N. Toshima and Y. Wang, *Langmuir* 10, 4574 (1994).
112. C.-R. Bian, S. Suzuki, K. Asakura, P. Lu, and N. Toshima, *J. Phys. Chem. B* 106, 8587 (2002).
113. W. Yu, Y. Wang, H. Liu, and W. Zheng, *Polym. Adv. Tech.* 7, 719 (1996).
114. T. S. Ahmadi, Z. L. Wang, T. C. Green, A. Henglein, and M. A. El-Sayed, *Science* 272, 1924 (1996).
115. T. S. Ahmadi, Z. L. Wang, A. Henglein, and M. A. El-Sayed, *Chem. Mater.* 8, 1161 (1996).
116. J. M. Petroski, Z. L. Wang, T. C. Green, and M. A. El-Sayed, *J. Phys. Chem. B* 102, 3316 (1998).
117. T. Teranishi, R. Kurita, and M. Miyake, *J. Inorg. Organomet. Polym.* 10, 145 (2000).
118. A. Miyazaki and Y. Nakano, *Langmuir* 16, 7109 (2000).
119. H. P. Choo, K. Y. Liew, W. A. K. Mahmood, and H. Liu, *J. Mater. Chem.* 2906 (2001).
120. R. He, X. Qian, J. Yin, and Z. Zhu, *J. Mater. Chem.* 3783 (2002).
121. H. Hirai, M. Ohtaki, and M. Komiyama, *Chem. Lett.* 149 (1987).
122. H. Hirai, M. Ohtaki, and M. Komiyama, *Chem. Lett.* 269 (1986).
123. Y. Wang, H. Liu, and Y. Jiang, *J. Chem. Soc. Chem. Commun.* 1878 (1989).
124. R. G. Freeman, K. C. Grabar, K. J. Allison, R. M Bright, J. A. Davis, A. P. Guthrie, M. B. Hommer, M. A. Jackson, P. C. Smith, D. G. Walter, and M. J. Natan, *Science* 267, 1629 (1995).
125. K. C. Grabar, K. J. Allison, B. E. Baker, R. M. Bright, K. R. Brown, R. G. Freeman, A. P. Fox, C. D. Keating, M. D. Musick, and M. J. Natan, *Langmuir* 12, 2353 (1996).
126. M. Brust, D. Bethell, D. Schiffrin, and C. Kiely, *Adv. Mater.* 7, 795 (1995).
127. R. Andres, S. Datta, M. Dorongi, J. Gomez, J. I. Henderson, D. B. Janes, V. R. Kolagunta, C. P. Kubiak, W. Mahoney, R. F. Osifchin, R. Reifenberger, M. P. Samanta, and W. Tian, *J. Vac. Sci. Technol. A* 14, 1178 (1996).
128. J. I. Henderson, S. Feng, G. Ferrence, T. Bein, and C. Kubiak, *Inorg. Chim. Acta* 242, 115 (1996).
129. D. Bethell, M. Brust, D. J. Schiffrin, and C. Kiely, *J. Electroanal. Chem.* 409, 137 (1996).
130. K. V. Sarathy, P. J. Thomas, G. U. Kulkarni, and C. N. R. Rao, *J. Phys. Chem. B* 103, 399 (1999).
131. S. W. Chen, *J. Phys. Chem. B* 104, 663 (2000).
132. N. Fishelson, I. Shkrob, O. Lev, J. Gun, and A. D. Modestov, *Langmuir* 17, 403 (2001).
133. M. Aslam, I. Mulla, and K. Vijayamohanan, *Langmuir* 17, 7487 (2001).
134. M. Brust and C. Kiely, *Coll. Surf. A* 202, 175 (2002).
135. M. Dorogi, J. Gomez, R. Osifchin, R. Andres, and R. Reifenberger, *Phys. Rev. B* 52, 9071 (1995).
136. R. P. Andres, T. Bein, M. Dorogi, S. Feng, J. I. Henderson, C. P. Kubiak, W. Mahoney, R. G. Osifchin, and R. Reifenberger, *Science* 272, 1323 (1996).
137. D. I. Gittins, D. Bethell, D. J. Schiffrin, and R. J. Nichols, *Nature* 408, 67 (2000).
138. Y. Nakamura and H. Hirai, *Chem. Lett.* 1197 (1976).
139. Y. Wang, H. Liu, and Y. Huang, *Polym. Adv. Tech.* 7, 634 (1996).
140. C. Lange, D. De Caro, A. Gamez, S. Storck, J. S. Bradley, and W. F. Maier, *Langmuir* 15, 5333 (1999).
141. M. T. Reetz and M. Dugal, *Catal. Lett.* 58, 207 (1999).
142. H. Bonnemann, U. Endruschat, B. Tesche, A. Rufinska, C. W. Lehmann, F. E. Wagner, G. Filoti, V. Parvulescu, and V. I. Parvulescu, *Eur. J. Inorg. Chem.* 5, 819 (2000).
143. T. Teranishi, M. Hosoe, and M. Miyake, *Adv. Mater.* 9, 65 (1997).
144. "Single-Charge Tunneling" (H. Grabert and M. H. Devoret, Eds.). Plenum, New York, 1992.
145. M. Kastner, *Nature* 389, 667 (1997).
146. H. Liu and N. Toshima, *J. Chem. Soc. Chem. Commun.* 1095 (1992).
147. X. Fu, Y. Wang, N. Wu, L. Gui, and Y. Tang, *J. Colloid Interf. Sci.* 243, 326 (2001).
148. G. Schmid, B. Morun, and J.-O. Malm, *Angew. Chem. Int. Ed. Engl.* 28, 778 (1989).
149. G. Schmid, *Inorg. Synth.* 7, 214 (1990).
150. G. Schmid, M. Hams, J.-O. Malm, J.-O. Bovin, J. v. Ruitenbeck, H. W. Zandbergen, and W. T. Fu, *J. Am. Chem. Soc.* 115, 2046 (1993).
151. G. Schmid, S. Emde, V. Maihack, W. Meyer-Zaika, and St. Peschel, *J. Mol. Catal. A* 107, 95 (1996).
152. G. Schmid, R. Pugin, J.-O. Malm, and J.-O. Bovin, *Eur. J. Inorg. Chem.* 813 (1998).
153. M. Green and P. O'Brien, *Chem. Commun.* 1912 (2001).
154. N. T. Tran, D. R. Powell, and L. F. Dahl, *Angew. Chem. Int. Ed.* 39, 4121 (2000).
155. A. L. Mackay, *Acta Crstallogr.* 15, 916 (1962).
156. M. Brust, M. Walker, D. Bethell, D. J. Schiffrin, and R. Whyman, *J. Chem. Soc., Chem. Commun.* 801 (1994).
157. M. Brust, J. Fink, D. Bethell, D. J. Schiffrin, and C. Kiely, *J. Chem. Soc., Chem. Commun.* 1655 (1995).
158. C. K. Yee, R. Jordan, A.Ulman, H. White, A. King, M. Rafailivich, and J. Sokolov, *Langmuir* 15, 3486 (1999).
159. C. K. Yee, M. Scotti, A. Ulman, H. White, A. King, M. Rafailivich, and J. Sokolov, *Langmuir* 15, 4314 (1999).
160. N. Sandhyarani, M. R. Resmi, R. Unnikrishnan, K. Vidyasagar, S. G. Ma, M. P. Antony, G. P. Selvam, V. Visalakshi, N. Chandrakumar, K. Pandian, Y. T. Tao, and T. Pradeep, *Chem. Mater.* 12, 104 (2000).
161. N. K. Chaki, S. G. Sudrik, H. R. Sonawane, and K. Vijayamohanan, *Chem. Commun.* 76 (2002).
162. S. L. Horswell, C. J. Kiely, I. A. O'Neil, and D. J. Schiffrin, *J. Am. Chem. Soc.* 121, 5573 (1999).
163. M. J. Hostetler, C.-J. Zhong, B. K. H. Yen, J. Anderegg, S. M. Gross, N. D. Evans, M. Porter, and R. W. Murray, *J. Am. Chem. Soc.* 120, 9396 (1998).
164. S. R. Johnson, S. D. Evans, S. W. Mahon, and A. Ulman, *Langmuir* 13, 51 (1997).
165. S. Chen and R. W. Murray, *Langmuir* 15, 682 (1999).

166. R. H. Terrill, T. A. Postlethwaite, C.-H. Chen, C.-D. Poon, A. Terzis, A. Chen, J. E. Hutchison, M. R. Clark, G. Wignall, J. D. Londono, R. Superfine, M. Falve, C. S. Johnson, E. T. Samulski, and R. W. Murray, *J. Am. Chem. Soc.* 117, 12537 (1995).

167. M. J. Hostetler, J. E. Wingate, C.-J. Zhong, J. E. Harris, R. W. Vachet, M. R. Clark, J. D. Londono, S. J. Green, J. J. Stokes, G. D. Wignall, G. L. Glish, M. D. Porter, N. D. Evans, and R. W. Murray, *Langmuir* 14, 17 (1998).

168. S. Chen and K. Kimura, *Langmuir* 15, 1075 (1999).

169. J. Hu, J. Zhang, F. Liu, K. Kittredge, J. K. Whitesell, and M. A. Fox, *J. Am. Chem. Soc.* 123, 1464 (2001).

170. J. Zhang, J. K. Whitesell, and M. A. Fox, *Chem. Mater.* 13, 2323 (2001).

171. M. Yamada, I. Quiros, J. Mizutani, K. Kubo, and H. Nishihara, *Phys. Chem. Chem. Phys.* 3377 (2001).

172. N. Kanayama, O. Tsutsumi, A. Kanazawa, and T. Ikeda, *Chem. Commun.* 2604 (2001).

173. S. Watanabe, M. Sonobe, M. Arai, Y. Tazume, T. Matsuo, T. Naka-mura, and K. Yoshida, *Chem. Commun.* 2866 (2002).

174. G. Wang, J. Zhang, and R. W. Murray, *Anal. Chem.* 74, 4320 (2002).

175. D. V. Leff, P. C. Ohara, J. R. Heath, and W. M. Gelbart, *J. Phys. Chem.* 99, 7036 (1995).

176. K. Hata and H. Fujihara, *Chem. Commun.* 2714 (2002).

177. D. V. Leff, L. Brandt, and J. R. Heath, *Langmuir* 12, 4723 (1996).

178. S. Gomez, K. Philippot, V. Collière, B. Chaudret, F. Senocq, and P. Lecante, *Chem. Commun.* 1945 (2000).

179. S. Mandal, P. R. Selvakannan, D. Roy, R. V. Chaudhari, and M. Sastry, *Chem. Commun.* 3002 (2002).

180. P. R. Selvakannan, S. Mandal, R. Pasricha, S. D. Adyanthaya, and M. Sastry, *Chem. Commun.* 1334 (2002).

181. J. Hambrock, R. Becker, A. Birkner, J. Weiss, and R. A. Fischer, *Chem. Commun.* 68 (2002).

182. C. Damle and M. Sastry, *J. Mater. Chem.* 1860 (2002).

183. C.-J. Zhong, W.-X. Zhang, F. L. Leibowitz, and H. H. Eichel-berger, *Chem. Commun.* 1211 (1999).

184. T. Yonezawa, K. Yasui, and N. Kimizuka, *Langmuir* 17, 271 (2001).

185. J. Liu, S. Mendoza, E. Roman, M. J. Lynn, R. L. Xu, and A. E. Kaifer, *J. Am. Chem. Soc.* 121, 4304 (1999).

186. J. Liu, J. Alvarez, and A. E. Kaifer, *Adv. Mater.* 12, 1381 (2000).

187. J. Alvarez, J. Liu, E. Roman, and A. E. Kaifer, *Chem. Commun.* 1151 (2000).

188. J. Liu, W. Ong, E. Roman, M. J. Lynn, and A. E. Kaifer, *Langmuir* 16, 3000 (2000).

189. J. Liu, J. Alvarez, W. Ong, E. Roman, and A. E. Kaifer, *J. Am. Chem. Soc.* 123, 11148 (2001).

190. J. Liu, J. Alvarez, W. Ong, E. Roman, and A. E. Kaifer, *Langmuir* 17, 6762 (2001).

191. J. Liu, J. Alvarez, W. Ong, and A. E. Kaifer, *Nano Lett.* 1, 27 (2001).

192. J. Alvarez, J. Liu, E. Román, and A. E. Kaifer, *Chem. Commun.* 2000, 1151 (2002).

193. J. Liu, W. Ong, A. E. Kaifer, and C. Peinador, *Langmuir* 18, 5981 (2002).

194. R. L. Whetten, J. T. Khoury, M. M. Alvarez, S. Murthy, I. Vezmar, Z. L. Wang, P. W. Stephens, C. L. Cleveland, W. D. Luedtke, and U. Landman, *Adv. Mater.* 8, 428 (1996).

195. X. M. Lin and C. M. Sorensen, *Chem. Mater.* 11, 198 (1999).

196. T. G. Schaaff, M. N. Shafigullin, J. T. Khoury, I. Vezmar, R. L. Wherren, W. G. Cullen, P. N. First, C. Gutiérrrez, J. Ascensio, and M. J. Jose-Yacamán, *J. Phys. Chem. B* 101, 7885 (1997).

197. T. G. Schaaff, G. Knight, M. N. Shafigulin, R. F. Borkman, and R. L. Whetten, *J. Phys. Chem. B* 102, 10643 (1998).

198. T. T. P Cheung, *Surf. Sci.* 140, 151 (1984).

199. W. Ederhardt, P. Fayet, D. M. Cox, Z. Fu, A. Kaldor, R. Sherwood, and D. Sondericker, *Phys. Rev. Lett.* 64, 780 (1990).

200. G. K. Wertheim, S. B. Dicenzo, and S. E. Young, *Phys. Rev. Lett.* 51, 2310 (1983).

201. S. Link, M. A. El-Sayed, T. G. Schaaff, and R. L. Whetten, *Chem. Phys. Lett.* 356, 240 (2002).

202. S. Link, A. Beeby, S. FitzGerald, M. A. El-Sayed, T. G. Schaaff, and R. L. Whetten, *J. Phys. Chem. B* 106, 3410 (2002).

203. D. V. Goia and E. Matijevic, *New J. Chem.* 1203 (1998).

204. T. Yonezawa, K. Imamura, and N. Kimizuka, *Langmuir* 17, 4701 (2001).

205. H. Bonnemann, G. Braun, W. Brijoux, R. Brinkmann, A. Tilling, K. Seevogel, and K. Siepen, *J. Organomet. Chem.* 520, 143 (1996).

206. H. Bonnemann, P. Britz, and W. Vogel, *Langmuir* 14, 6654 (1998).

207. J. Rothe, J. Hormes, H. Bönnemann, W. Brijoux, and K. Siepen, *J. Am. Chem. Soc.* 120, 6019 (1998).

208. J. P. Abid, A. W. Wark, P. F. Brevet, and H. H. Girault, *Chem. Commun.* 792 (2002).

209. N. Kometani, H. Doi, K. Asami, and Y. Yonezawa, *Phys. Chem. Chem. Phys.* 5142 (2002).

210. C.-L. Lee, C.-C. Wan, and Y.-Y. Wang, *Adv. Funct. Mater.* 11, 344 (2000).

211. S. J. Lee, S. W. Han, and K. Kim, *Chem. Commun.* 442 (2002).

212. M. Moreno-Manas, R. Pleixats, and S. Villarroya, *Chem. Commun.* 60 (2002).

213. M. T. Reetz, M. Winter, R. Breinbauer, T. Thurn-Albrecht, and W. Vogel, *Chem.-Eur. J.* 7, 1084 (2001).

214. N. S. Sobal, M. Hilgendorff, H. Möhwald, and M. Giersig, *Nano Lett.* 2, 621 (2002).

215. M. Mandal, S. K. Ghosh, S. Kundu, K. Esumi, and T. Pal, *Langmuir* 18, 7792 (2002).

216. J. S. Bradley, B. Tesche, W. Busser, M. Masse, and R. T. Reetz, *J. Am. Chem. Soc.* 122, 4631 (2000).

217. D. V. Averin and K. K. Likaharev, *J. Low Temp. Phys.* 62, 345 (1986).

218. A. Kumar and G. M. Whitesides, *Science* 263, 60 (1994).

219. R. H. Terrill, T. A. Postlethwaite, C. Chen, C.-D. Poon, A. Terzis, A. Chen, J. E. Hutchison, M. R. Clark, G. Wignall, J. D. Londono, R. Superfine, M. Falvo, C. S. Johnson, Jr., E. T. Samulski, and R. W. Murray, *J. Am. Chem. Soc.* 117, 12537 (1995).

220. A. P. Alivisatos, *Science* 271, 933 (1996).

221. R. P. Andres, J. D. Bielefeld, J. I. Henderson, D. B. Janes, V. R. Kolagunta, C. P. Kubiak, W. J. Mahoney, and R. G. Osifchin, *Science* 273, 1690 (1996).

222. D. L. Feldheim, K. C. Grabar, M. J. Natan, and T. E. Mallouk, *J. Am. Chem. Soc.* 118, 7640 (1996).

223. Y. Xia, E. Kim, M. Mrksich, and G. M.Whitesides, *Chem. Mater.* 8, 601 (1996).

224. G. Hornyak, M. Kroll, R. Pugin, T. Sawitowski, G. Schmid, J. O. Bovin, G. Karsson, H. Hofmeister, and S. Hopfe, *Chem.-Eur. J.* 3, 1951 (1997).

225. Z.-L. Wang, *Adv. Mater.* 10, 13 (1998).

226. C. T. Black, C. B. Murry, R. L. Sandstrom, and S. Sun, *Science* 290, 1131 (2000).

227. T. Teranishi, M. Haga, Y. Shiozawa, and M. Miyake, *J. Am. Chem. Soc.* 122, 4237 (2000).

228. J. Liu, T. Lee, D. B. Janes, B. L. Walsh, M. R. Melloch, J. M. Woodall, R. Reifenberger, and R. P. Andres, *Appl. Phys. Lett.* 77, 373 (2000).

229. D. B. Janes, T. Lee, J. Liu, M. Batistuta, N. P. Chen, B. L. Walsh, R. P. Andres, E. H. Chen, M. R. Melloch, J. M. Woodall, and R. Reifenberger, *J. Electron. Mater.* 29, 565 (2000).

230. V. Torma, T. Reuter, O. Vidoni, M. Schumann, C. Radehaus, and G. Schmid, *Chem. Phys. Chem.* 2, 546 (2001).

231. D. Wyrwa, N. Beyer, and G. Schmid, *Nano Lett.* 2, 419 (2002).

232. B. A. Korgel and D. Fitzmaurice, *Phys. Rev. Lett.* 80, 3531 (1998).

233. D. I. Gittins, A. S. Susha, B. Schoeler, and F. Caruso, *Adv. Mater.* 14, 508 (2002).

*234.* T. C. Rojas, J. M. de la Fuente, A. G. Barrientos, S. Penadés, L. Ponsonnet, and A. Fernández, *Adv. Mater.* 14, 585 (2002).

*235.* C. R. Mayer, S. Neveu, and V. Cabuil, *Adv. Mater.* 14, 595 (2002).

*236.* T. Hassenkam, K. Nŕrgaard, L. Iversen, C. J. Kiely, M. Brust, and T. Bjŕrnholm, *Adv. Mater.* 14, 1126 (2002).

*237.* J. Fink, C. J. Kiely, D. Bethell, and D. J. Schiffrin, *Chem. Mater.* 10, 922 (1998).

*238.* S. T. Liu, T. Zhu, R. S. Hu, and Z. F. Liu, *Phys. Chem. Chem. Phys.* 4, 6059 (2002).

*239.* I. Sloufova-Srnova and B. Vlckova, *Nano Lett.* 2, 121 (2002).

*240.* G. Schmid, M. Bäumle, and N. Beyer, *Angew. Chem. Int. Ed.* 39, 181 (2000).

*241.* S. A. Harfenist, Z.-L. Wang, M. M. Alvarez, I. Vezmar, and R. L. Whetten, *J. Phys. Chem.* 100, 13904 (1996).

*242.* B. A. Korgel and D. Fitzmaurice, *Adv. Mater.* 10, 661 (1998).

*243.* B. A. Korgel, S. Fullam, S. Connolly, and D. Fitzmaurice, *J. Phys. Chem. B* 102, 8379 (1998).

*244.* Z. L. Wang, S. A. Harfenist, R. L. Whetten, J. Bebtley, and N. D. Evans, *J. Phys. Chem. B* 102, 3068 (1998).

*245.* B. A. Korgel, N. Zaccheroni, and D. Fitzmaurice, *J. Am. Chem. Soc.* 121, 3533 (1999).

*246.* B. A. Korgel and D. Fitzmanurice, *Phys. Rev. B* 59, 14191 (1999).

*247.* H. I. S. Nogueira, P. C. R. Soares-Santos, S. M. G. Cruz, and T. Trindade, *J. Mater. Chem.* 2339 (2002).

*248.* K. V. Sarathy, G. Raina, R. T. Yadav, G. U. Kulkarni, and C. N. R. Rao, *J. Phys. Chem. B* 101, 9876 (1997).

*249.* M. T. Reetz, M. W. Winter, and B. Tesche, *Chem. Commun.* 147 (1997).

*250.* Z.- L. Wang, Z.-R. Dai, and S.-H. Sun, *Adv. Mater.* 12, 1944 (2000).

*251.* S. Sun, C. B. Murray, D. Weller, L. Folks, and A. Moser, *Science* 287, 1989 (2000).

*252.* S. A. Harfenist, Z.-L. Wang, M. M. Alvarez, I. Vezmar, and R. L. Whetten, *J. Phys. Chem.* 100, 13904 (1996).

*253.* W. D. Luedtke and U. Landman, *J. Phys. Chem.* 100, 13323 (1996).

*254.* Z. L. Wang, S. A. Harfenist, I. Vezmar, R. L. Whetten, J. Bentley, N. D. Evans, and K. B. Alexander, *Adv. Mater.* 10, 808 (1998).

*255.* J. R. Heath, C. M. Knobler, and D. V. Leff, *J. Phys. Chem. B* 101, 189 (1998).

*256.* E. Shevchenko, D. Talapin, A. Kornowski, F. Wiekhorst, J. Kötzler, M. Haase, A. Rogach, and H. Weller. *Adv. Mater.* 14, 287 (2002).

*257.* T. Yonezawa, S. Onoue, and N. Kimizuka, *Langmuir* 17, 2291 (2001).

*258.* T. Yonezawa, S. Onoue, and N. Kimizuka, *Adv. Mater.* 13, 140 (2001).

*259.* T. Yonezawa and T. Kunitake, *Colloid Surf. A* 149, 193 (1999).

*260.* J. Simard, C. Briggs, A. K. Boal, and V. M. Rotello, *Chem. Commun.* 1943 (2000).

*261.* T. Yonezawa, H. Matsune, and T. Kunitake, *Chem. Mater.* 11, 33 (1999).

*262.* W. Cheng, J. Jiang, S. Dong, and E. Wang, *Chem. Commun.* 1706 (2002).

*263.* R. I. Nooney, T. Dhanasekaran, Y. Chen, R. Josephs, and A. E. Ostafin, *Adv. Mater.* 14, 529 (2002).

*264.* H. Rensmo, A. Ongaro, D. Ryan, and D. Fitzmaurice, *J. Mater. Chem.* 2762 (2002).

*265.* H. Y. Y. Ko, M. Mizuhata, A. Kajinami, and S. Deki, *J. Mater. Chem.* 1495 (2002).

*266.* Y.-S. Shon and H. Choo, *Chem. Commun.* 2560 (2002).

*267.* K. i Uosaki, T. Kondo, M. Okamura, and W. Song, *Faraday Discuss.* 373 (2002).

*268.* A. W. Snow, M. G. Ancona, W. Kruppa, G. G. Jernigan, E. E. Foos, and D. Park, *J. Mater. Chem.* 1222 (2002).

*269.* S. D. Jhaveri, D. A. Lowy, E. E. Foos, A. W. Snow, M. G. Ancona, and L. M. Tender, *Chem. Commun.* 1544 (2002).

*270.* M. Yamada and H. Nishihara, *Chem. Commun.* 2578 (2002).

*271.* M. Yamada, A. Kuzume, M. Kurihara, K. Kubo, and H. Nishihara, *Chem. Commun.* 2476 (2001).

*272.* H. Bonnemann, N. Waldofner, H. G. Haubold, and T. Vad, *Chem. Mater.* 14, 1115 (2002).

*273.* M. Kogiso, K. Yoshida, K. Yase, and T. Shimizu, *Chem. Commun.* 2492 (2002).

*274.* T. Cassagneau and F. Caruso, *Adv. Mater.* 14, 732 (2002).

*275.* E. Hutter and J. H. Fendler, *Chem. Commun.* 378 (2002).

*276.* J. B. Carroll, B. L. Frankamp, and V. M. Rotello, *Chem. Commun.* 1892 (2002).

*277.* N. Lu, J. Zheng, M. Gleiche, H. Fuchs, L. Chi, O. Vidoni, T. Reuter, and G. Schmid, *Nano Lett.* 2, 1097 (2002).

*278.* S. Hoeppener, L. Chi, and H. Fuchs, *Nano Lett.* 2, 459 (2002).

*279.* D. Wyrwa, N. Beyer, and G. Schmid, *Nano Lett.* 2, 419 (2002).

*280.* T. Reuter, O. Vidoni, V. Torma, and G. Schmid, *Nano Lett.* 2, 709 (2002).

*281.* G. Dumpich, E. F. Wassermann, M. Winter, and M. T. Reetz, *Mater. Sci. Forum* 287, 413 (1998).

*282.* L. Clarke, M. N. Wybourne, M. D. Yan, S. X. Cai, and J. F. W. Keana, *Appl. Phys. Lett.* 71, 617 (1997).

*283.* X. M. Lin, R. Parthasarathy, and H. M. Jaeger, *Appl. Phys. Lett.* 78, 1915 (2001).

*284.* T. R. Bedson, R. E. Palmer, T. E. Jenkins, D. J. Hayton, and J. P. Wilcoxon, *Appl. Phys. Lett.* 78, 1921 (2001).

*285.* T. R. Bedson, R. E. Palmer, and J. P. Wilcoxon, *Appl. Phys. Lett.* 78, 2061 (2001).

*286.* M. H. V. Werts, L. Mathieu, J. Bourgoin, and M. Brust, *Nano Lett.* 2, 43 (2002).

*287.* B. F. G. Johnson, K. M. Sanderson, D. S. Shephard, D. Ozkaya, W. Zhou, H. Ahmed, M. D. R. Thomas, L. Gladden, and M. Mantle, *Chem. Commun.* 1317 (2000).

*288.* F. Stellacci, C. A. Bauer, T. Meyer-Friedrichsen, W. Wenseleers, V. Alain, S. M. Kuebler, S. J. K. Pond, Y. Zhang, S. R. Marder, and J. W. Perry, *Adv. Mater.* 14, 194 (2002).

*289.* R. Maoz, S. R. Cohen, and J. Sagiv, *Adv. Mater.* 11, 55 (1999).

*290.* R. Maoz, E. Frydman, S. R. Cohen, and J. Sagiv, *Adv. Mater.* 12, 424 (2000).

*291.* R. Maoz, E. Frydman, S. R. Cohen, and J. Sagiv, *Adv. Mater.* 12, 725 (2000).

*292.* S. Hoeppener, R. Maoz, S. R. Cohen, L. F. Chi, H. Fuchs, and J. Sagiv, *Adv. Mater.* 14, 1036 (2002).

*293.* S. Liu, R. Maoz, G. Schmid, and J. Sagiv, *Nano Lett.* 2, 1055 (2002).

*294.* C. M. Niemeyer, *Angew. Chem. Int. Ed.* 40, 4128 (2001).

*295.* S. Behrens, K. Rahn, W. Habicht, K.-J. Böhm, H. Rösner, E. Dinjus, and E. Unger, *Adv. Mater.* 14, 1621 (2002).

*296.* M. Mertig, R. Kirsch, W. Pompe, and H. Engelhardt, *Eur. Phys. J. D* 9, 45 (1999).

*297.* U. B. Slytr, P. Messner, D. Pum, and M. Sara, *Angew. Chem. Int. Ed.* 38, 1034 (1999).

*298.* W. Shenton, D. Pum, U. B. Sleytr, and S. Mann, *Nature* 389, 585 (1997).

*299.* W. Shenton, T. Douglas, M. Young, G. Stubbs, and S. Mann, *Adv. Mater.* 11, 253 (1999).

*300.* T. A. Taton, R. C. Mucic, C. A. Mirkin, and R. L. Letsinger, *J. Am. Chem. Soc.* 122, 6305 (2000).

*301.* L. M. Demers, S. J. Park, T. A. Taton, Z. Li, and C. A. Mirkin, *Angew. Chem. Int. Ed.* 40, 3071 (2001).

*302.* M. Sastry, A. Kumar, S. Datar, C. V. Dharmadhikari, and K. N. Ganesh, *Appl. Phys. Lett.* 78, 2943 (2001).

*303.* Y. Maeda, H. Tabata, and T. Kawai, *Appl. Phys. Lett.* 79, 1181 (2001).

*304.* S. J. Lin, M. Satjapipat, A. J. Baca, and F. Zhou, *Chem. Commun.* 609 (2001).

*305.* E. Dujardin, L. B. Hsin, C. R. C. Wang, and S. Mann, *Chem. Commun.* 1264 (2001).

*306.* A. N. Shipway and I. Willner, *Chem. Commun.* 2035 (2001).

*307.* E. Braun, Y. Eichen, U. Sivan, and G. Ben-Yoseph, *Nature* 391, 775 (1998).

308. J. Richter, R. Seidel, R. Kirsch, M. Mertig, W. Pomp, J. Plaschke, and H. K. Schackert, *Adv. Mater.* 12, 507 (2000).
309. J. Richter, M. Mertig, M. I. Pomp, and H. K. Schackert, *Appl. Phys. Lett.* 78, 536 (2001).
310. O. Harnack, W. E. Ford, A. Yasuda, and J. M. Wessels, *Nano Lett.* 2, 919 (2002).
311. R. Elghanian, J. J. Storhoff, R. C. Mucic, R. L. Letsinger, and C. A. Mirkin, *Science* 277, 1078 (1997).
312. A. P. F. Turner, *Science* 290, 1315 (2000).
313. B. H. Schneider, F. D. Quinn, and D. A. Shafer, *ACS Symp. Ser.* 815, 107 (2002).
314. I. M. Klotz, "Ligand–Receptor Energetics: A Guide for the Perplexed." Wiley, New York, 1997.
315. A. J. Haes and R. P. Van Duyne, *J. Am. Chem. Soc.* 124, 10596 (2002).
316. D. J. Maxwell, J. R. Taylor, and S. M. Nie, *J. Am. Chem. Soc.* 124, 9606 (2002).
317. J. J. Storhoff, R. Elghanian, R. C. Mucic, C. A. Mirkin, and R. L. Letsinger, *J. Am. Chem. Soc.* 120, 1959 (1998).
318. T. A. Taton, C. A. Mirkin, and R. L. Letsinger, *Science* 289, 1757 (2000).
319. R. A. Reynolds III, C. A. Mirkin, and R. L. Letsinger, *J. Am. Chem. Soc.* 122, 3795 (2000).
320. L. M. Demers, C. A. Mirkin, R. C. Mucic, R. A. Reynolds, R. L. Letsinger, R. Elghanian, and Viswanadham, *Anal. Chem.* 72, 5535 (2000).
321. R. A. Reynolds III, C. A. Mirkin, and R. L. Letsinger, *Pure Appl. Chem.* 72, 229 (2000).
322. T. A. Taton, G. Lu, and C. A. Mirkin, *J. Am. Chem. Soc.* 123, 5164 (2001).
323. S.-J. Park, T. A. Taton, and C. A. Mirkin, *Science* 295, 1503 (2002).
324. Y. W. C. Cao, R. C. Jin, and C. A. Mirkin, *Science* 297, 1536 (2002).
325. R. C. Jin, G. S. Wu, Z. Li, C. A. Mirkin, and G. C. Schatz, *J. Am. Chem. Soc.* 125, 1643 (2003).
326. K. T. Ranjit, A. Lichtenstein, F. Patolsky, and I. Willner, *Chem. Commun.* 1025 (2000).
327. O. Lioubashevski, F. Patolsky, and I. Willner, *Langmuir* 17, 5134 (2001).
328. Y. Weimann, F. Patolsky, and I. Willner, *Analyst* 126, 1502 (2001).
329. I. Willner, F. Patolsky, Y. Weimann, and B. Willner, *Talanta* 56, 847 (2002).
330. J. Wang, D. K. Xu, A. N. Kawde, and R. Polsky, *Anal. Chem.* 73, 5576 (2001).
331. J. Wang, R. Polsky, and D. K. Xu, *Langmuir* 17, 5739 (2001).
332. J. Wang, *Anal. Chim. Acta* 469, 63 (2002).
333. L. He, M. D. Musick, S. R. Nicewarner, F. G. Salinas, S. J. Benkovic, M. J. Natan, and C. D. Keating, *J. Am. Chem. Soc.* 122, 9071 (2000).
334. X. C. Zhou, S. J. O'Shea, and S. F. Y. Li, *Chem. Commun.* 953 (2000).
335. N. Stich, A. Gandhum, V. Matushin, C. Mayer, G. Bauer, and T. Schalkhammer, *J. Nanosci. Nanotech.* 1, 397 (2001).
336. J. H. Xu, J. J. Zhu, Y. L. Zhu, K. Gu, and H. Y. Chen, *Anal. Lett.* 34, 503 (2001).
337. H. Q. Zhao, L. Lin, J. R. Li, J. A. Tang, M. X. Duan, and L. Jiang, *J. Nanopart. Res.* 3, 321 (2001).
338. H. Q. Zhao, L. Lin, J. Tang, M. X. Duan, and L. Jiang, *Chin. Sci. Bull.* 46, 1074 (2001).
339. H. Cai, Y. Q. Wang, P. G. He, and Y. H. Fang, *Anal. Chim. Acta.* 469, 165 (2002).
340. H. Cai, Y. Xu, N. N. Zhu, P. G. He, and Y. Z. Fang, *Analyst* 127, 803 (2002).
341. S. Sampath and O. Lev, *Adv. Mater.* 9, 410 (1997).
342. S. Bharathi and O. Lev, *Anal. Commun.* 35, 29 (1998).
343. S. Bharathi, M. Nogami, and O. Lev, *Langmuir* 17, 2602 (2001).
344. S. Bharathi and M. Nogami, *Analyst* 126, 1919 (2001).
345. F. Q. Tang and L. Jiang, *Ann. NY Acad. Sci.* 864, 538 (1998).
346. F. Q. Tang, J. F. Shen, J. F. Zhang, and G. L. Zhang, *Chem. J. Chin. Univ.* 20, 634 (1999).
347. F. Q. Tang, Z. Wei, D. Chen, X. W. Meng, L. Gou, and J. G. Ran, *Chem. J. Chin. Univ.* 21, 91 (2000).
348. F. Q. Tang, X. W. Meng, D. Chen, J. G. Ran, and C. Q. Zheng, *Sci. Chin.: Chem. B* 43, 268 (2000).
349. F. Q. Tang and X. L. Ren, *Acta Chim. Sinica* 60, 393 (2002).
350. X. Su, S. F. Y. Li, and S. J. O'Shea, *Chem. Commun.* 755 (2001).
351. J. B. Jia, B. Q. Wang, A. G. Wu, G. J. Cheng, Z. Li, and S. J. Dong, *Anal. Chem.* 74, 2217 (2002).
352. R. Wilson, *Chem. Commun.* 108 (2003).
353. N. Stich, A. Gandhum, V. Matushin, J. Raats, C. Mayer, Y. Alguel, and T. Schalkhammer, *J. Nanosci. Nanotech.* 2, 375 (2002).
354. G. Cardenas-Trivino, K. Klabunde, and D. E. Brock, *Langmuir* 3, 986 (1987).
355. F. Tian and K. J. Klabunde, *New J. Chem.* 22, 1275 (1998).
356. S. Stoeva, K. J. Klabunde, C. M. Sorensen, and I. Dragieva, *J. Am. Chem. Soc.* 124, 2305 (2002).
357. X. Du, Y. Wang, Y. Mu, L. Gui, P. Wang, and Y. Tang, *Chem. Mater.* 14, 3953 (2002).
358. T. Tano, K. Esumi, and K. Meguro, *J. Colloid Interf. Sci.* 133, 530 (1999).
359. F. Endres, *Chem. Phys. Chem.* 3, 144 (2002).
360. F. Endres and S. Z. El Abedin, *Chem. Commun.* 892 (2002).
361. H. Bonnemann and W. Brijoux, *Nanostruct. Mater.* 5, 135 (1995).
362. R. Pranke, J. Rothe, J. Pollmann, J. Hormes, H. Bonnemann, W. Brijoux, and T. Hindenburg, *J. Am. Chem. Soc.* 118, 12090 (1996).
363. X. Fu, Y. Wang, N. Wu, L. Gui, and Y. Tang, *Langmuir* 18, 4619 (2002).
364. K. Torigoe and K. Esumi, *J. Phys. Chem. B* 103, 2862 (1999).
365. Y. Lin and R. G. Finke, *J. Am. Chem. Soc.* 116, 8335 (1994).
366. J. D. Aiken III and R. G. Finke, *J. Am. Chem. Soc.* 121, 8803 (1999).
367. A. Troupis, A. Hiskia, and E. Papaconstantinou, *Angew. Chem. Int. Ed.* 41, 1911 (2002).
368. L. D. Rampino and F. F. Nord, *J. Am. Chem. Soc.* 63, 2745 (1941).
369. C. Sachs, A. Pundt, R. Kirchheim, R, M. Winter, M. T. Reetz, and D. Fritsch, *Phys. Rev. B* 6407, 075408 (2001).
370. J. Le Bars, U. Specht, J. S. Bradley, and D. G. Blackmond, *Langmuir* 15, 7621 (1999).
371. Toshima, N., Yonezawa, T. Harada, M. Asakura, and K. Iwasawa, *Chem. Lett.* 815 (1990).
372. N. Toshima and T. Yonezawa, *New J. Chem.* 22, 1179 (1998).
373. W. Yu, Y. Wang, and H. Liu, *J. Mol. Catal. A* 112, 105 (1996).
374. P. Lu, T. Teranishi, K. Asakura, M. Miyake, and N. Toshima, *J. Phys. Chem. B* 103, 9673 (1999).
375. M. B. Thathagar, J. Beckers, and G. Rothenberg, *J. Am. Chem. Soc.* 124 11858 (2002).
376. Y. Izumi, *Adv. Catal.* 32, 2151 (1983).
377. A. Tai and T. Harada, in "Tailored Metal Catalysts" (Y. Iwasawa, Ed.), p. 265. Kluwer, Dordrecht, 1986.
378. A. F. Carley, M. K. Rajurnon, M. W. Roberts, and P. B. Wells, *J. Chem. Soc., Faraday Trans.* 91, 2176 (1995).
379. H. Blaser, H. Jalett, M. Muller, and M. Studer, *Catal. Today* 37, 441 (1997).
380. M. O. Lorenzo, C. J. Baddeley, and R. Muryn, *Nature* 404, 376 (2000).
381. L. A. M. M. Barbosa and P. Sautet, *J. Am. Chem. Soc.* 123, 6639 (2001).
382. V. Hurnhlot, S. Haq, C. Muryn, W. A. Hofer, and R. Raval, *J. Am. Chem. Soc.* 124, 503 (2002).
383. H. Bonnemann and G. A. Braun, *Chem.- Eur. J.* 3, 1200 (1997).
384. H. Bonnemann and G. A. Braun, *Angew. Chem. Int. Ed. Engl.* 35, 1992 (1996).

385. X. B. Zuo, H. F. Liu, and M. H. Liu, *Tetrahedron Lett.* 39, 1941 (1998).

386. X. B. Zuo, H. F. Liu, D. W. Guo, and X. Z. Yang, *Tetrahedron* 55, 7787 (1999).

387. T. Teranishi, K. Nakata, M. Iwamoto, M. Miyake, and N. Toshima, *React. Funct. Polym.* 37, 111 (1998).

388. W. Yu, H. Liu, M. Liu, and Z. Liu, *React. Funct. Polym.* 44, 21 (2000).

389. W. Yu, H. Liu, M. Liu, and Q. Tao, *J. Mol. Catal. A* 138, 273 (1999).

390. M. Liu, W. Yu, H. Liu, and J. Zheng, *J. Colloid Interf. Sci.* 214, 231 (1999).

391. M. Liu, W. Yu, and H. Liu, *J. Mol. Catal. A* 138, 295 (1999).

392. H. Feng and H. Liu, *J. Mol. Catal. A* 126, L5 (1997).

393. Y. Li, E. Boone, and M. A. El-Sayed, *Langmuir* 18, 4921 (2002).

394. Y. Li and M. A. El-Sayed, *J. Phys. Chem. B* 105, 8938 (2001).

395. H. S. Wang, C. Wingender, H. Baltruschat, M. Lopez, and M. T. Reetz, *J. Electroanal. Chem.* 509, 163 (2001).

396. N. Toshima, Y. Shiraishi, T. Teranishi, M. Miyake, T. Tominaga, H. Watanabe, W. Brijoux, H. Bonnemann, and G. Schmid, *Appl. Organomet. Chem.* 15, 178 (2001).

397. M. N. Vargaftik, V. P. Zargorodnikov, I. P. Stolarov, and I. I. Moiseev, *J. Chem. Soc. Chem. Commun.* 937 (1985).

398. I. I. Moiseev, M. N. Vargaftik, T. V. Chernysheva, T. A. Stromnova, A. E. Gekhman, G. A. Tsirkov, and A. M. Makhlina, *J. Mol. Catal. A* 108, 77 (1996).

399. M. N. Vargaftik, N. Y. Kozitsyna, N. V. Cherkashina, R. I. Rudyi, D. I. Kochubei, and B. N. Novgorodov, *Kinet. Catal.* 39, 740 (1998).

400. J. Schulz, S. Levigne, A. Roucoux, and H. Patin, *Adv. Syn. Catal.* 334, 266 (2002).

401. M. Spiro and D. M. de Jesus, *Langmuir* 16, 2464 (2000).

402. U. Nickel, C. Liu, P. Lachenmayr, and M. Schneider, *Bull. Soc. Chim. Fr.* 308 (1988).

403. U. Nickel and C.-Y. Liu, *J. Imaging Sci.* 34, 8 (1990).

404. Y.-H. Chen, U. Nickel, and M. Spiro, *J. Chem. Soc., Faraday Trans.* 90, 617 (1994).

405. P. L. Freund and M. Spiro, *J. Phys. Chem.* 89, 1074 (1985).

406. P. L. Freund and M. Spiro, *J. Chem. Soc., Faraday Trans.* 82, 2277 (1986).

407. M. Spiro, *Catal. Today* 17, 517 (1993).

408. A. Mills, P. Douglas, and T. Russell, *J. Chem. Soc., Faraday Trans.* 86, 1417 (1990).

409. J. D. Aiken III and R. G. Finke, *Chem. Mater.* 11, 1035 (1999).

410. J. Turkevich and G. Kim, *Science* 169, 873 (1970).

411. W. Yu, M. Liu, H. Liu, X. An, Z. Liu, and X. Ma, *J. Mol. Catal. A* 142, 201 (1999).

412. W. Yu, H. Liu, X. An, X. Ma, Z. Liu, and L. Qiang, *J. Mol. Catal. A* 147, 73 (1999).

413. H. Bonnemann, W. Brijoux, A. S. Tilling, and K. Siepen, *Top. Catal.* 4, 217 (1997).

414. H. Bonnemann, W. Brijoux, K. Siepen, J. Hormes, R. Franke, J. Pollmann, and J. Rothe, *Appl. Organomet. Chem.* 11, 783 (1997).

415. J. P. M. Niederer, A. B. J. Arnold, W. F. Holderich, B. Spliethof, B. Tesche, M. Reetz, and H. Bonnemann, *Top. Catal.* 18, 265 (2002).

416. Mi. Zhao and R. M. Crooks, *Angew. Chem. Inter. Ed.* 38, 364 (1999).

417. H. Bonnemann, P. Britz, and H. Ehwald, *Chem. Tech.* 49, 189 (1997).

418. T. Frelink, W. Visscher, and J. A. R. van Veen, *J. Electroanal. Chem.* 382, 65 (1995).

419. K. Kinoshita, *J. Electrochem. Soc.* 137, 845 (1990).

420. W. Chen, J. Lee, and Z. Liu, *Chem. Commun.* 2588 (2002).

421. M. L. Anderson, R. M. Stroud, and D. R. Rolison, *Nano Lett.* 2, 235 (2002).

422. T. J. Schmidt, M. Noeske, H. A. Gasteiger, R. J. Behm, P. Britz, W. Brijoux, and H. Bonnemann, *Langmuir* 13, 2591 (1997).

423. T. J. Schmidt, M. Noeske, H. A. Gasteiger, R. J. Behm, P. Britz, and H. Bonnemann, *J. Electrochem. Soc.* 145, 925 (1998).

424. T. J. Schmidt, M. Noeske, H. A. Gasteiger, R. J. Behm, P. Britz, and H. Bonnemann, *J. Electrochem. Soc.* 145, 3697 (1998).

425. U. A. Paulus, U. Endruschat, G. J. Feldmeyer, T. J. Schmidt, H. Bonnemann, and R. J. Behm, *J. Catal.* 195, 383 (2000).

426. H. Bonnemann, R. Brinkmann, P. Britz, U. Endruschat, R. Mortel, U. A. Paulus, G. J. Feldmeyer, T. J. Schmidt, H. A. Gasteiger, and R. J. Behm, *J. New Mat. Electrochem. Syst.* 3, 199 (2000).

427. E. S. Steigerwalt, G. A. Deluga, D. E. Cliffel, and C. M. Lukehart, *J. Phys. Chem. B* 105, 8097 (2001).

428. F. E. Jones, S. B. Milne, B. Gurau, E. S. Smotkin, S. R. Stock, and C. M. Lukehart, *J. Nanosci. Nanotech.* 2, 81 (2002).

429. X. Zhang and K. Chan, *J. Mater. Chem.* 1203 (2002).

430. K. Siepen, H. Bonnemann, W. Brijoux, J. Rothe, and J. Hormes, *Appl. Organomet. Chem.* 14, 549 (2000).

431. H. Bonnemann, W. Wittholt, J. D. Jentsch, and A. S. Tilling, *New J. Chem.* 22, 713 (1998).

432. J. Dai and M. L. Bruening, *Nano Lett.* 2, 497 (2002).

433. J. E. Park, S. Kim, O. Mihashi, O. Hatozaki, and N. Oyama, *Macromol. Symp.* 168, 35 (2001).

434. C. Binns, *J. Nanosci. Nanotech.* 1, 243 (2001).

435. D. L. Leslie-Pelecky and R. D. Rieke, *Chem. Mater.* 8, 1770 (1996).

436. J. L. Dormann, D. Fiorani, and E. Tronc, *Adv. Chem. Phys.* 98, 283 (1997).

437. K. Satoh, *J. Jpn. Soc. Tribol.* 41, 458 (1996).

438. G. D. Li, *Rare Metal Mat. Eng.* 31, 1 (2002).

439. S. H. Liou, *IEEE Trans. Mag.* 35, 3989 (1999).

440. O. Sqalli, M. P. Bernal, P. Hoffmann, and F. Marquis-Weible, *Appl. Phys. Lett.* 76, 2134 (2000).

441. D. R. Baselt, G. U. Lee, K. M. Hansen, L. A. Chrisey, and R. J. Colton, *Proc. IEEE* 85, 672 (1997).

442. D. K. Kim, Y. Zhang, J. Kehr, T. Klason, D. Bjelke, and M. Muhammed, *J. Magn. Magn. Mater.* 225, 256 (2001).

443. A. N. Rusetski and E. K. Ruuge, *J. Magn. Magn. Mater.* 85, 299 (1990).

444. A. Jordan, R. Scholz, P. Wust, H. Fahling, and R. Felix, *J. Magn. Magn. Mater.* 201, 413 (1999).

445. E. E. Carpenter, *J. Magn. Magn. Mater.* 225, 17 (2001).

446. S. Sun, S. Anders, H. F. Hamann, Jan-U. Thiele, J. E. E. Baglin, T. Thomson, E. E. Fullerton, C. B. Murray, and B. D. Terris, *J. Am. Chem. Soc.* 124, 2884 (2002).

447. D. J. Sellmyer, *Nature* 420, 374 (2002).

448. H. Zeng, J. Li, J. P. Liu, Z. L. Wang, and S. Sun, *Nature* 420, 395 (2002).

449. M. Jacoby, *C&E News* 78, 37 (2000).

450. R. F. Service, *Science* 287, 1902 (2000).

451. B. Warne, O. I. Kasyutich, E. L. Mayes, J. A. L. Wiggins, and K. K. W. Wong, *IEEE Trans. Mag.* 36, 3009 (2000).

452. B. Dieny, V. S. Speriosu, S. Metin, S. S. P. Parkin, B. A. Gurney, P. Baumgart, and D. R. Wilhoit, *J. Appl. Phys.* 69, 4774 (1991).

453. S. S. P. Parkin and D. Mauri, *Phys. Rev. B* 44, 7131 (1991).

454. J. S. Moodera, L. R. Kinder, T. M. Wong, and R. Meservey, *Phys. Rev. Lett.* 74, 3273 (1995).

455. T. Miyazaki and N. Tezuka, *J. Magn. Magn. Mater.* 139, L231 (1995).

456. T. Miyazaki and N. Tezuka, *J. Magn. Magn. Mater.* 151, 403 (1995).

457. M. N. Baibich, J. M. Broto, A. Fert, F. N. Van Dau, F. Petroff, P. Eitenne, G. Creuzet, A. Friederich, and J. Chazelas, *Phys. Rev. Lett.* 61, 2472 (1988).

458. C. Tsang, R. E. Fontana, B. A. Gurney, D. E. Heim, V. S. Speriosu, T. Lin, and M. L. Williams, *IEEE Trans. Magn.* 30, 3801 (1994).

459. J. C. Mallinson, "Magneto-Resitive Heads: Fundamentals and Applications," p. 103. Academic Press, New York, 1996.

460. S. S. P. Parkin, K. P. Roche, M. G. Samant, P. M. Rice, R.B. Beyers, R. E. Scheuerlein, E. J. Sullivan, S. L. Brown, J. Bucchigano, D. W. Abraham, Y. Lu, M. Rooks, P. L. Trouilloud, R. A. Wanner, and W. J. Gallagher, *J. Appl. Phys.* 85, 5828 (1999).

461. S. Tehrani, E. Chen, M. Durlam, M. DeHerrera, J. M. Slaughter, J. Shi, and G. Kerszykowski, *J. Appl. Phys.* 85, 5822 (1999).

462. S. Tehrani, B. Engel, J. M. Slaughter, E. Chen, M. DeHerrera, M. Durlam, P. Naji, R. Whig, J. Janesky, and J. Cader, *IEEE Trans. Mag.* 36, 2752 (2000).

463. J. Osuna, D. de Caro, C. Amiens, B. Chaudret, E. Snoeck, M. Respaud, J.-M. Broto, and A. Fert, *J. Phys. Chem.* 100, 14571 (1996).

464. T. O. Ely, C. Pan, C. Amiens, B. Chaudret, F. Dassenoy, P. Lecante, M.-J. Casanove, A. Mosset, M. Respaud, and J.-M. Broto, *J. Phys. Chem. B* 104, 695 (2000).

465. S.-J. Park, S. Kim, S. Lee, Z. G. Khim, K. Char, and T. Hyeon, *J. Am. Chem. Soc.* 122, 8581 (2000).

466. V. F. Puntes, K. M. Krishnan, and A. P. Alivisatos, *Science* 291, 2115 (2001).

467. K. S. Suslick, M. M. Fang, and T. Hyeon, *J. Am. Chem. Soc.* 118, 11960 (1996).

468. C. Petit, A. Taleb, and M. P. Pileni, *Adv. Mater.* 10, 259 (1998).

469. C. Petit, A. Taleb, and M. P. Pileni, *J. Phys. Chem. B* 103, 1805 (1999).

470. S. Sun and C. B. Murry, *J. Appl. Phys.* 85, 4325 (1999).

471. S. Sun, C. B. Murry, and H. Doyle, *Mater. Res. Soc. Symp. Proc.* 577, 395 (1999).

472. S.-J. Park, S. Kim, S. Lee, Z. G. Khim, K. Char, and T. Hyeon, *J. Am. Chem. Soc.* 122, 8581 (2000).

473. D. P. Dinega and M. G. Bawendi, *Angew. Chem., Int. Ed. Engl.* 38, 1788 (1999).

474. M. Giersig and M. Hilgendorff, *J. Phys. D* 32, L111 (1999).

475. U. Wiedwald, M. Spasova, and M. Farle, *J. Vac. Sci. Technol. A* 19, 1773 (2001).

476. S. I. Woods, J. R., Kirtley, S. Sun, and R. H. Koch, *Phys. Rev. Lett.* 87, 137205 (2001).

477. V. F. Puntes, K. M. Krishnan, and A. P. Alivisatos, *Appl. Phys. Lett.* 78, 2187 (2001).

478. S. Sun, E. E. Fullerton, D. Weller, and C. B. Murry, *IEEE Trans. Mag.* 37, 1239 (2001).

479. J.-I. Park and J. Cheon, *J. Am. Chem. Soc.* 123, 5743 (2001).

480. E. V. Shevchenko, D. V. Talapin, A. L. Rogach, A. Kornowski, M. Haase, and H. Weller, *J. Am. Chem. Soc.* 124, 11480 (2002).

481. C. Frommen, H. Rosner, and D. Fenske, *J. Nanosci. Nanotech.* 2, 509 (2002).

482. M. Chen and D. E. Nikles, *Nano Lett.* 2, 211 (2002).

483. S. Kang, J. W. Harrell, and D. E. Nikles, *Nano Lett.* 2, 1033 (2002).

484. T. Hyeon, *Chem. Commun.* in press.

485. A. L. Rogach, D. V. Talapin, E. V. Shevchenko, A. Kornowski, M. Haase, and H. Weller, *Adv. Funct. Mater.* 12, 653 (2002).

486. B. Stahl, N. S. Gajbhiye, G. Wilde, D. Kramer, J. Ellrich, M. Ghafari, H. Hahn, H. Gleiter, J. Weißmüller, R. Würschum, and P. Schlossmacher, *Adv. Mater.* 14, 24 (2002).

487. G. H. Lee, S. H. Huh, J. W. Park, H.-C. Ri, and J. W. Jeong, *Phys. Chem. B* 106, 2123 (2002).

488. I.-J. Jeon, D.-W. Kang, D.-E. Kim, D.-H. Kim, S.-B. Choe, and S.-C. Shin, *Adv. Mater.* 14, 1116 (2002).

489. S. Ram and P. S. Frankwicz, *Physica Status Solidi A* 188, 1129 (2001).

490. "Magnetic Recording: The First 100 Years" (E. D. Daniel, M. C. Denis, and M. H. Clark, Eds.). IEEE Press, New York, 1998.

491. J. Hong, J. Kane, J. Hashimoto, M. Yamagishi, K. Noma, and H. Kanai, presented at the 12th Magnetic Recording Conf., TMRC2001, Minneapolis, MN, 20–22 August 2001.

492. Z. Zhang, presented at Intermag Europe 2002, Amsterdam, The Netherlands, 28 April–May 2002.

493. S. Anders, S. Sun, C. B. Murray, C. T. Rettner, M. E. Best, T. Thomson, M. Albrecht, J.-U. Thiele, E. E. Fullerton, and B. D. Terris, *Microelectron. Eng.* 61-2, 569 (2002).

494. S. H. Charap, P.-L. Lu, and Y.-J. He, *IEEE Trans. Magn.* 33, 978 (1997).

495. D. Weller and A. Moser, *IEEE Trans. Magn.* 35, 4423 (1999).

496. R. L. White, *J. Magn. Mag. Mater.* 209, 1 (2000).

497. A. Moser, K. Takano, D. T. Margulies, M. Albrecht, Y. Sonobe, Y. Ikeda, S. Sun, and E. E. Fullerton, *J. Phys. D* 35, R157 (2002).

498. R. L. Comstock, *J. Mater. Sci.* 13, 509 (2002).

499. K. Inomata, T. Sawa, and S. Hashimoto, *J. Appl. Phys.* 64, 2537 (1988).

500. S. H. Liou, S. Huang, E. Klimek, R. D. Kirby, and Y. D. Yao, *J. Appl. Phys.* 85, 4334 (1999).

501. K. R. Coffey, M. A. Parker, and J. K. Howard, *IEEE Trans. Magn.* 31, 2737 (1995).

502. N. Li and B. M. Lairson, *IEEE Trans. Magn.* 35, 1077 (1999).

503. R. A. Ristau, K. Barmak, L. H. Lewis, K. R. Coffey, and J. K. Howard, *J. Appl. Phys.* 86, 4527 (1999).

504. C. Chen, O. Kitakami, S. Okamoto, Y. Shimada, K. Shibata, and M. Tanaka, *IEEE Trans. Magn.* 35, 3466 (1999).

505. M. Yu, Y. Liu, A. Moser, D.Weller, and D. J. Sellmyer, *Appl. Phys. Lett.* 75, 3992 (1999).

506. S. Chikazumi and C. D. Graham, Jr., "Physics of Ferromagnetism," 2nd ed. Oxford Univ. Press, New York, 1997.

507. E. F. Kneller and R. Hawig, *IEEE Trans. Magn.* 27, 3588 (1991).

508. R. Skomski and J. M. D. Coey, *Phys. Rev. B* 48, 15812 (1993).

509. T. Schrefl, H. Kronmüller, and J. Fidler, *J. Magn. Magn. Mater.* 127, L273 (1993).

510. D. H. Ping, K. Hono, and S. Hirosawa, *J. Appl. Phys.* 83, 7769 (1998).

511. R. Coehoorn, D. B. De Mooij, and C. De Waard, *J. Magn. Magn. Mater.* 80, 101 (1989).

512. T. Kobayashi, M. Yamasaki, and M. Hamano, *J. Appl. Phys.* 87, 6579 (2000).

513. W. Gong, G. C. Hadjipanayis, and R. F. Krause, *J. Appl. Phys.* 75, 6649 (1994).

514. P. G. McCormick, W. F. Miao, P. A. I. Smith, J. Ding, and R. Street, *J. Appl. Phys.* 83, 6256 (1998).

515. J. Zhang, S.-Y. Zhang, H.-W. Zhang, B.-G. Shen, and B.-H. Li, *J. Appl. Phys.* 89, 2857 (2001).

516. J. P. Liu, Y. Liu, R. Skomski, and D. J. Sellmyer, *J. Appl. Phys.* 85, 4812 (1995).

517. E. E. Fullerton, J. S. Jiang, C. H. Sowers, J. E. Pearson, and S. D. Bader, *Appl. Phys. Lett.* 72, 380 (1998).

518. J. P. Liu, C. P. Luo, Y. Liu, and D. J. Sellmyer, *Appl. Phys. Lett.* 72, 483 (1998).

519. G. Prinz, *Science* 282, 1660 (1998).

520. S. A. Wolf and D. M. Treger, *IEEE Trans. Magn.* 36, 2748 (2000).

521. S. A. Wolf, D. D. Awschalom, R. A. Buhrman, J. M. Daughton, S. von Molnár, M. L. Roukes, A. Y. Chtchelkanova, and D. M. Treger, *Science* 294, 1488 (2001).

522. D. A. Allwood, G. Xiong, M. D. Cooke, C. C. Faulkner, D. Atkinson, N. Vernier, and R. P. Cowburn, *Science* 296, 2003 (2002).

523. D. P. DiVincenzo, *Science* 270, 255 (1995).

524. X. Fu, Y. Wang, L. Huang, Y. Sha, L. Gui, L. Lai and Y. Tang, *Adv. Mater.* 15, 902 (2003).

525. X. Fu, Y. Wang, N. Wu, L. Gui and Y. Tang, *J. Mater. Chem.* 13, 1192 (2003).

# Metal Nanoclusters by Ion Implantation

Elti Cattaruzza, Francesco Gonella

*Università Ca' Foscari di Venezia, Venezia, Italy*

## CONTENTS

## 1. INTRODUCTION

One of the interesting suitable methods to modify the structure and properties of a near-surface region of a material along selected patterns is to implant accelerated ions at high velocity into the solid matrix. By ion implantation, the features of the host material may be dramatically changed, depending on the host matrix as well as on the ion-implanted species and the process parameters, namely, fluence, energy, temperature, and current density. The use of ion implantation to modify a solid matrix starts from the determination of the chemical, mechanical, optical, or magnetic properties required for achieving prescribed material properties. By ion implantation, very large dopant concentration values can be obtained in the ion-irradiated region, thus inducing important effects on the chemical and physical properties near the surface. A proper choice of implantation energies and fluences allows the implanted atoms to pre-determine the composition, the depth, and the spatial shape of the modified layers as desired. The implanted layer can then be considered as a new material, interconnected with the host one in a prescribed region under the surface of the original solid. This region has thickness values ranging from tens of nanometers to several microns, depending mainly on the implanted species and on the energy of implantation. Furthermore, the use of accelerators and mass separators of high resolution makes the ion implantation a synthesis technique with an intrinsic high level of cleanness, even permitting to implant a single isotope.

Taking a general look at the advantages of introducing fast atoms in a solid matrix, it is worth remarking that the new material is not formed under a thermodynamic equilibrium process. This is of crucial importance, because the usual solubility limits can be largely overcome, thus opening the possibility to achieve impurity local concentrations inaccessible by conventional synthesis routes. Moreover, the possibility to control the temperature of the solid during implantation allows in many cases the formation of chemical phases in the implanted layers which could not be synthesized by adding the dopant to the unmodified material in a conventional melting procedure. As far as the ion track inside the solid is concerned, the random nature of the energy loss and of the scattering processes during the slowing down of the implanted atoms results in a dispersed distribution of dopant, also for large concentrations of the implanted element. By selecting the temperature at which the implantation process is carried out, one can favor either the aggregation of the dopants or their diffusion into the solid. Actually, the diffusion coefficients of the different species can be enhanced by the production of defects due to ion irradiation, thus completely changing the diffusion rates inside the matrix. Moreover, enhanced diffusion in certain regions of a solid can be produced by implanting one ion species, and then exploited for enhancing the diffusion of a second ion species owing to enhanced mobility along the radiation damage pattern already formed. The radiation damage may be reduced or removed by an appropriate annealing of the solid during and/or after the ion implantation. In many situations, the radiation damage is not an undesired effect: the passage of fast atoms inside a solid can produce some desired property changes, such as the variation of the local density, or the creation of aggregation and precipitation centers for the implanted atoms.

The literature about ion implantation as a tool to modify the physical properties of semiconductors is enormous, with the first implantation experiments all devoted to the semiconductor physics. However, in the last ten years experiments of ion implantation in insulators have largely taken

place, mainly as a consequence of the rising technological interest in new optical materials. In this chapter, we describe the present grasp of the processes involved in ion implantation of metal atoms in a dielectric matrix, exploring the representative and largely investigated case of silica glass. Depending on the reactivity of the implanted metal atoms with the host matrix, formation of compounds or metal particles in the nanometer range of size takes place. The composite materials formed by metal nanoparticles embedded in glasses are shortly indicated with the acronym MNCGs, standing for metal nanocluster composite glasses. The main physical properties which make technologically interesting the MNCGs will be described, with particular emphasis to the linear and nonlinear optical properties. The relevant effects of the radiation damage in the case of ion implantation in silica glass will be also summarized. The processes governing the chemical and physical interaction between the implanted atoms and the atoms in the host matrix have not been fully understood nor phenomenologically described, so a comparison will be given among the different existing approaches to the comprehension of the chemical interaction in these systems. Two case studies of MNCGs will be presented, namely, copper nanoclusters obtained by copper ion implantation in fused silica, and copper-gold alloy nanoclusters obtained by sequential implantation of copper and gold in fused silica. The preparation protocols for the formation of single and binary alloy nanoparticles will be reported, together with the linear and nonlinear optical figures of merit interesting for technological applications of these MNCGs.

## 2. METAL NANOCLUSTERS IN SILICA GLASS

Composite materials formed by transition-metal clusters embedded in glass matrices (metal nanocluster composite glasses, MNCGs) have been used for artistic purposes since the fourth century A.D. by Roman glass-makers. Architects exploited their peculiar optical properties for the medieval cathedral windows through several European countries. These glasses exhibit a great variety of beautiful colors owing to the nanosized metal particles embedded in the matrix. Since Michael Faraday first gave a scientific description of the effects inducing the coloration in MNCGs [1], much attention has been continuously dedicated to study their physical and chemical properties, and to the development of fabrication methods. Physical properties of metal aggregates as well as of nanocomposites may change dramatically in the transition from atom to molecule to cluster to solid. In this chapter, some aspects will be presented and discussed, particularly related to situations in which cluster concentration is below percolation limit, and where cluster radius is much smaller than the wavelength $\lambda$ of the light used to probe its response (quasi-static regime, valid for clusters with size $R$ such that $R/\lambda \leq 0.01$, in which retardation effects of the electromagnetic field over the cluster diameter are negligible). Moreover, clusters larger than 1 nm diameter exhibit electronic behavior features of the metal, but are small enough (up to tens of nanometers diameter) to exhibit strong confinement effects.

As concerns the application aspects connected to MNCGs, the interest in these systems regards several different fields. Dielectric matrices containing dispersed nanoclusters may exhibit enhanced coercivity, shift of the hysteresis loop, superparamagnetic and large magnetotransport properties [2]. Nanostructured materials are studied also for catalysis, where high surface-to-volume ratios are required [3]. Glass-based composites are in general expected to play an important role as materials for various nanotechnology applications, due to the low cost, ease of processing, high durability and resistance, and high transparency, with the possibility of tailoring the behavior of the glass-based structures. Much attention has been dedicated to MNCGs in the last decade in the field of nonlinear integrated optics and photonics, where photons are used instead of electrons to acquire, store, process, and transmit information [4–8]. All-optical switching devices may be designed in which the intensity-dependent refractive index of the material, owing to the third-order electric susceptibility, $\chi^{(3)}$, is strongly enhanced. Nonlinear switching devices are based on optical waveguiding structures that provide strong beam confinement in prescribed patterns. In these devices, the intensity of an optical signal is used as the parameter that causes switching between two output channels that perform logic operations [9]. The main properties of MNCGs for applications in optoelectronics devices are short response times (ps or lower), low power switching threshold, wavelength tunability, thermal stability, low two-photon absorption, high threshold for laser-induced damage, and THz recycling frequency. In general, the optical properties of MNCGs are strongly dependent on several factors, among which are the nature and the chemical composition of the nanocrystals in the host matrix; the size and the shape of the clusters; the concentration of clusters and its gradient across the sample; the interaction of the cluster with the host matrix.

Besides the interest for their technological application, MNCGs are studied from several points of view, including the dynamics of cluster nucleation and growth, the stability of the clusters, as well as the conditions that determine the cluster structure in terms of composition, crystalline phase, size, and size distribution. MNCGs present also interesting peculiar properties related to the thermodynamics of cluster formation, as well as to the chemical and physical aspects of the composite structure in terms of reactivity, stability, transport phenomena, magnetic properties, and so on [10]. A great effort has been made to develop new preparation methods, among which are those based on ion implantation techniques, irradiation techniques of metal-doped glass matrices, deposition techniques, and chemical routes such as sol–gel.

In the literature, several updated reviews may be found on the technology of MNCGs. A very broad review on nanotechnology may be found in [11], in which a specific chapter is dedicated to MNCGs [12], while for example the Materials Research Society has dedicated one of the latest issues of its *Bulletin* to the topic of nanocrystals research [13]. Reference [14] specifically introduces quantum dot materials, including MNCGs. Glasses for optoelectronic devices, particularly MNCGs, are treated in [15] as well as in [16]. Concerning the theoretical aspects of MNCG properties, the literature offers a great variety of approaches. Reference

[17] extensively deals with the electronic properties of metal clusters, while [18] focuses on quantum size effect. Optical properties of small metal particles are treated in detail in [19] and [20], which present extended reviews on theoretical and experimental aspects of the optical response of metal clusters. Recent aspects concerning the interface properties of MNCGs are in [21], while [22] presents a review of all-optical switching via nonlinear optical materials.

In the following, we are going to treat in some detail the aspects concerning the optical response of MNCGs, since optical properties are the most appealing features of these materials. The first theoretical approach for describing the interaction of light with metal aggregates is due to Maxwell–Garnett, who in 1904 [23, 24] developed a model that is still used in some circumstances. Some years later, Gustav Mie [25] observed that the Maxwell-Garnett description was suitable only for some of the studied colloidal solutions with metal particles. Mie theory starts from a phenomenological approach, without a physical description involving the electron behavior inside the clusters. Collective plasmon oscillations of different multipole order, with the aim to interpret the Mie theory, was introduced only in the 1970s by Kreibig [26, 27]. In the quasi-static regime, an electromagnetic wave propagating in the composite does not resolve the individual scattering centers, and the medium appears homogeneous and characterized by an effective complex dielectric function. Its optical response may be approached following a discrete island model, in which each scattering center is considered, or an effective medium model, in which one scattering center is considered, the rest of the surrounding medium being averaged into a homogeneous medium. Bruggeman was the first [28] to develop an effective medium theory. A composite film is regarded as an array of two components, without constraints in the volume ratio of one component with respect to the other, arbitrarily considered as the host medium. This approach is particularly effective in the vicinity of the percolation threshold for the composite, when it abruptly increases its electrical conductivity. The composites of this kind are, however, typically formed by clusters larger than the nanometer range. On the other hand, Maxwell-Garnett [23, 24] considered metal clusters embedded in a surrounding medium of dielectric constant $\varepsilon_h$ (real), polarized by an optical field. The Lorentz local-field relationships derived in standard textbooks of electrodynamics give the effective frequency-dependent dielectric function $\tilde{\varepsilon}$ (complex) of the composite medium:

$$\frac{\tilde{\varepsilon} - \varepsilon_h}{\tilde{\varepsilon} + 2\varepsilon_h} = p\frac{\varepsilon_m - \varepsilon_h}{\varepsilon_m + 2\varepsilon_h} \tag{1}$$

where $p$ is the metal volume fraction (or filling factor), and $\varepsilon_m(\omega) = \varepsilon_1(\omega) + i\varepsilon_2(\omega)$ is the dielectric function of the metal particle. For small $p$ values, Eq. (1) may be expanded to the first order in the volume fraction, and recalling that the linear absorption coefficient $\alpha_0$ is related to the imaginary part of $\tilde{\varepsilon}$, one finds [20]

$$\alpha = 9p\frac{\omega\varepsilon_h^{3/2}}{c}\frac{\varepsilon_2}{(\varepsilon_1 + 2\varepsilon_h)^2 + \varepsilon_2^2} \tag{2}$$

This expression has a maximum at a frequency for which $\varepsilon_1 + 2\varepsilon_h \approx 0$. This is the absorption resonance condition

known as the surface plasmon resonance (SPR). The position, width, and shape of the SPR are determined by the metal dielectric function, as well as by the size and shape of the particles, the concentration of particles, and the surrounding dielectric. This absorption feature actually plays an important role in several optical properties interesting for application aspects, as discussed later. The resonant contribution to the absorption in MNCGs disappears when the nanoparticle diameter is lowered to about 1 nm. At that dimension, quantum corrections to the classical absorption become also significant [29]. When particle volume fraction is greater than a few percent, the interaction between the particles causes a redshift of the absorption band, an effect for which the Maxwell-Garnett picture can give account. On the other hand, increasing the concentration of the particles also leads to optical broadening due to statistical effects [30]. Mie was the first to derive an exact description of optical absorption and elastic scattering by a metal spherical cluster [25]. By adding the contribution of single clusters, the theory accounts correctly for many experimental cases, provided that interaction effects among the clusters as well as multiple scattering effects are missing. This concerns, however, a large class of inhomogeneous composite glasses, where the cluster density is anyhow sufficiently low to allow a description within this regime. Data for the optical extinction in the visible range of 52 metallic nanoparticles are given in [12, 31].

The optical absorption of the glass matrix containing metal clusters is usually expressed starting from either the Mie theory or from the Maxwell-Garnett effective dielectric function model [32]. In the first case, the contribution of each cluster to the absorption is calculated, so obtaining the absorption coefficient. In the second case, an effective dielectric function is calculated for the glass-clusters composite, and the absorption coefficient is obtained from the imaginary part of this function. Comprehensive reviews of the different models describing the absorption features are in [19, 27], with several tests of the reliability of the different models. In [19], an extended bibliography on optical spectroscopy experimental data for MNCG is also given. An estimation may be given of the size at which the cluster can be considered as a small metallic particle, with electronic behavior similar to that of solid metal. In alkali-metal clusters, the transition between covalent and metallic behavior may take place even with only a few atoms forming the cluster [33]. In the case of noble metals, the optical properties are due to $d$ and $s$-$p$ (conduction) electrons. In calculating the band structure, the outermost $d$ and $s$ electrons must be treated together, leading to six bands, five of which are flat, lying a few electon volts below the Fermi level ($d$-like bands); the other one is almost free-electron-like (it is the actual conduction band or $s$-$p$ band). As in the approach by [34], the metal-nonmetal transition occurs approximately at some critical size corresponding to the number of atoms

$$N_c \approx \sqrt{12f_c + 171} - 6 \tag{3}$$

where $f_c$ is a temperature-dependent function that can be determined from the bulk metal properties,

$$f_c(T) = \frac{W_b^2}{100k_B^2 T^2 Z_b} \tag{4}$$

where $W_b$ and $Z_b$ are the $d$-band width and effective coordination number, respectively. For example, the values of $N_c$ obtained for Fe, Co, and Ni are, respectively, of 50, 39, and 34 atoms. These values correspond to clusters of radius of about $\frac{1}{2}$ nm. Schematically, the original one-electron energy levels of an atom split into two components when a dimer is formed. The levels split further for larger clusters, finally giving rise to the quasi-continuous band structure of the bulk solid, with electrons filling the bands up to the Fermi energy $E_F$. The first ionization potential of the atoms correspondingly turns into the bulk work function.

As concerns the nonlinear optical properties of MNCGs, the second-order susceptibility vanishes because of the centrosymmetric structure of these composites. Moreover, the enhancement of the third-order susceptibility due to classical and quantum confinement effects [35] may be exploited in all-optical switching technology, since its real part is related to the nonlinear refractive index $n_2$, defined in terms of the linear index $n_0$ and of the light intensity, $I$, as $n = n_0 + n_2 I$ [5, 36–38]. In a similar way, the intensity-dependent absorption coefficient can be written as $\alpha = \alpha_0 + \beta I$, where $\beta$ is the nonlinear absorption coefficient. Let us take a composite consisting of small particles with a relative volume fraction $p \ll 1$ in a glass host, and denote the complex dielectric function of the metal cluster as $\varepsilon_m(\omega) = \varepsilon_1(\omega) + i\varepsilon_2(\omega)$. For low incident intensities, only the linear response of the composite is important; however, wherever light confinement is important, such as in waveguides, and for high-power pulsed laser irradiation, higher-order effects play an important role. The linear index of refraction $n_0$ and the linear absorption coefficient $\alpha_0$ are related to the real and the imaginary part of the first-order susceptibility, respectively. In an amorphous matrix such as in MNCGs composites, the third-order susceptibility of the material is related to the nonlinear index of refraction, $n_2$, and to the nonlinear absorption coefficient, $\beta$, as follows [39]

$$n_2\left(\frac{m^2}{W}\right) = \frac{120\pi^2}{cn_0^2}\,\mathrm{Re}\,\chi^{(3)} \text{ (electrostatic units)} \quad (5)$$

$$\beta\left(\frac{m}{W}\right) = \frac{240\pi^2\omega}{c^2 n_0^2}\,\mathrm{Im}\,\chi^{(3)} \text{ (electrostatic units)} \quad (6)$$

where $c$ is the light velocity in vacuum. The change in the refractive index of a material with the intensity of the optical field is called the optical Kerr effect. The effects of classical confinement on third-order susceptibility of the composite medium can be derived by considering the composite medium and applying Maxwell's equations for the case in which the susceptibility is nonlinear; the calculation is carried out to the first order in the electric field [40]. It can be shown that the effective nonlinear optical susceptibility of the composites at issue has the expression

$$\chi_{eff}^{(3)} = p \cdot \chi_{qd}^{(3)} \left|\frac{3\varepsilon_2}{\varepsilon_1 + 2\varepsilon_2}\right|^2 \left[\frac{3\varepsilon_2}{\varepsilon_1 + 2\varepsilon_2}\right]^2 \equiv p \cdot \chi_{qd}^{(3)} |f_c|^2 (f_c)^2 \quad (7)$$

where the quantity $f_c$ may be considered as a measure of the local-field enhancement of the polarization, and $\chi_{qd}^{(3)}$ is the intrinsic third-order nonlinear susceptibility of the

metal nanoparticle. More rigorous, self-consistent treatments using a jellium model for the metal particle yield the same result for this special case [41].

In the specific case of metal nanoclusters embedded in silicate glasses, three kinds of transitions in the cluster may actually occur, namely, (1) intraband transitions; (2) interband transitions; and (3) the hot-electron transitions. Intraband transitions originate in the filled conduction-band states near the Fermi level and terminate in other conduction-band states which satisfy the selection rules for electric-dipole transitions. Because both the initial and final states are free-electron-like, these transitions show the strongest quantum-confinement effects, since the initial and final states both "feel" the effects of the boundary surface of the quantum dot. For an absorptive nonlinearity, the resulting value of $\chi_{intra}^{(3)}$ has been calculated in a phenomenological theory [42] to be proportional to $1/a^3$ (where $a$ is the nanocluster radius) and to $T_1$ and $T_2$, that is, the relaxation times (energy lifetime and dephasing time, respectively) [14, 18]. Attempts to observe the intraband nonlinearity are complicated by the fact that this contribution to the third-order susceptibility is typically the smallest in magnitude, although it has the fastest response time. The interband transitions are from the $d$-like orbitals of the valence band to the empty conduction-band states, and these transitions are the ones which produce the characteristic colors of metals. These states are only weakly dependent on quantum-size effects because the initial state is already localized in space. Finally, the hot-electron transitions are those in which an electron in the conduction band absorbs a photon and is heated, losing its energy by electron-phonon scattering or collisions with the nanoparticle walls. Indeed, when light of frequency near that of plasmon resonance is incident upon a metal cluster-doped glass, part of the energy is transferred to the metal particles. This energy partly promotes $d$-electrons to the conduction band, and the rest is absorbed by the conduction electrons, which have relatively weak specific heat, and thus can be raised to high temperatures. The hot-electron effect is sometimes called "Fermi smearing," since it results in a broadening of the electron population distribution near the Fermi edge through electronic excitation. During the electron-lattice thermalization time, the Fermi–Dirac distribution is modified, part of the one-electron levels below the Fermi one being emptied and part of the levels above becoming occupied. This leads to a modification of the dielectric constant, originating a contribution to the third-order susceptibility. The hot-electron transitions can be particularly strong and can, under certain circumstances, be the dominant transitions for a metallic nanocluster in an optical field, giving positive imaginary (absorptive) contribution to the third-order susceptibility. While these transitions produce a third-order susceptibility with magnitudes 10 to $10^4$ times as large as the intraband transitions at a given wavelength, the excited states tend to have relaxation times on the order of hundreds of picoseconds. In fact, the hot-electron system thermalizes with the lattice by electron-phonon collisions and interaction with the nanoparticle surface on a time scale of a few picoseconds [43]. Then, on a typical time scale of tens of picoseconds, the excess thermal energy is removed by thermal diffusion toward the matrix [44], while on the scale of hundreds of picoseconds the

whole system reaches the initial temperature of the sample. However, besides the nonlinear $n_2$ coefficient, the suitability of MNCGs in the field of all-optical switching technology is also linked to other features, that is, high intensity threshold for laser-induced damage, low thermo-optic contribution to $n_2$, and very short response-recovery time (high recycling frequency). All these aspects concur to define some figures of merit of the material [7, 9, 38, 45], the determination of which is the basis for an effective reliable material design. The most quoted figures of merit are related to very important properties that a material must accomplish for application in ultrafast all-optical switching devices. For example, the possibility to process light signals without needing to convert them to electronic form should allow all-optical devices to operate in a frequency range inaccessible to electronics. However, high switching speeds must be coupled with low power switching threshold, to get high packing densities in optoelectronic or photonic devices. The nonlinear material must exhibit a large $n_2$ value to operate at watt peak power in centimeter-long devices. At the same time, it must have a low optical absorption (a nonlinear phase shift of at least $2\pi$ should be possible over one attenuation distance for reasonable device throughput), a high intensity threshold for laser-induced damage, a low thermo-optic contribution to $n_2$, and a very short response-recovery time (i.e., a high recycling frequency). Moreover, thermal stability and wavelength tunability are important peculiarities for promising nonlinear materials. Depending on the main absorption mechanism of a given material, that is, linear or nonlinear, two figures of merit have to be satisfied for $2\pi$ phase shift [38, 45]

$$W = \frac{|n_2| I_{\max}}{\alpha_0 \lambda} > 1, \qquad T = \frac{\beta \lambda}{|n_2|} < 1 \qquad (8)$$

where $n_2$ is the "fast" nonlinear refractive index, $\alpha_0$ and $\beta$ are the already defined linear and nonlinear absorption coefficients, $\lambda$ is the light wavelength, and $I_{\max}$ is the maximum permitted value of the light intensity. The figure of merit $T$ has an outstanding importance in semiconductor-based optical devices, for which the nonlinear absorption coefficient $\beta$ is positive in sign. MNCGs usually exhibit absorption saturation when large intensities of the incident radiation are used; that is, for these materials $\beta$ is negative in sign, thus fulfilling the condition $T < 1$ for any value of $\beta$ magnitude. Absorption can induce also refractive index changes due to thermo-optic effect: since they compete with the fast light-induced index change, for a useful device the thermal index change must be a small fraction of the fast one. A figure of merit has therefore been defined as [7, 9, 38]:

$$F = \left| \frac{\Delta n_{\text{fast}}}{\Delta n_{\text{th}}} \right| \qquad (9)$$

where $\Delta n_{\text{fast}}$ is the fast refractive index change required to give the switching, and $\Delta n_{\text{th}}$ is the resultant thermal refractive index change. F is a rough indication of the number of switching operations that can be achieved in a thermal recovery time, $\tau_{\text{th}}$, and must be therefore as large as possible. The maximum processing frequency of the device, $\mathscr{F}$, can be estimated by the ratio between $F$ and the thermal recovery time, $\tau_{\text{th}}$. For ultrafast applications, $\mathscr{F}$ must be larger

than 100 GHz. For MNCGs, the first estimation of these figures of merit appeared in literature in [38]. Negative values for the figure of merit $T$ are usually exhibited by these composites [38], and values around 0.1–0.2 for $W$ have been achieved recently [46]. Although it is reasonable to suppose an attainment of the needed conditions for $W$ in a near future, the values estimated for the processing frequency $\mathscr{F}$ are still unsatisfactory, being about two orders of magnitude lower than the requested value [38].

## 3. ION IMPLANTATION IN SILICA GLASS

Several ways to prepare metal-doped glasses are usually employed, namely, ion implantation, ion-exchange processes, quenching and heat treatments, processes that employ porous glasses, and chemical routes such as the sol–gel technique. The main advantages of ion implantation are the possibility to pattern the composite material, to control the concentration and the distribution of the dopant elements, to overcome the solubility limits, and of course to introduce virtually any element in any solid substrate. During implantation, the interaction between moving ions and solid substrate determines, via radiation damage, mechanical stresses as well as composition and density modifications; thus, the physical properties of the host glasses may change. Furthermore, it is possible to form chemical compounds which would not be realized by means of conventional techniques, leading for example to the formation of regions in which the linear refractive index is significantly different from that of the substrate. The glass modifications induced by the ion implantation depend on the glass composition, the ion species, the implantation energy, the fluence, and the current density. Several reviews of the research in the field of ion implantation in glasses have been published in the literature [47–50]. In addition to the cited literature in the following sections, many other experiments of metal ion implantation in glasses were reported in the last years. Among them, the most recent are for the case of Ag [51–63], Cu [52, 60, 61, 64–75], Au [52, 60, 61, 65, 76, 77], Ni [78], Si [79], Sn [80, 81], Ir [82], Ge [83], Cr and Zr [84], Ti and Zr [85], Er and Tb [86], Cu + Ni double ion implantations [87–91], Ag + S [88, 92–94], Ga + N and In + N [95–98], Zn + S, Cd + S, and Pb + S [99], Ga + As [100], Cd + Se and Cd + S [101], Cl + Cu [102], Si + Au [103], Au + Cu [90, 94, 104], Au + Ag [90, 94], Ag + Cu [90, 105, 106], Cu + Co [90, 91, 107], Pd + Cu and Pd + Ag [94, 108], Co + Ni [91, 94, 109–111].

### 3.1. Physical Effects

The physical interaction of an implanted ion with a glass matrix results in the deposition energy into electronic processes of ionization and excitation, and into atomic collisional events; these processes are now adequately understood [112]. The energy partition between the two different processes depends on the ion velocity relative to that of the matrix electrons, it is usually obtained through the TRansport of Ions in Matter (TRIM) code [113], that gives also the projected ion range, $R_p$, and the range straggling, $\Delta R_p$. The ion range $R_p$ is the mean value of the depth at which the implanted atoms stop inside the solid matrix, and

$\Delta R_p$ is related to the thickness of the implantation profile; both quantities depend mainly on the chosen implantation energy. Compared to other materials, only in insulators the electronic energy deposition significantly induces modifications of the physical properties. Most of the well-characterized defects which are formed by ion implantation in glasses [114] have been identified in the ion-implanted silica glass [115–118]. The silica glass consists of slightly distorted $SiO_4$ tetrahedra joined to each other at the corners: each silicon atom is tetrahedrally bonded to four oxygen atoms, and each oxygen atom is bonded to two silicon atoms, acting as a bridge between neighboring tetrahedra (hence called "bridging oxygen"). The nearest-neighbor distance is the Si–O bond at 1.62 Å. O–Si–O angles are nearly constant (109.5°), while Si–O–Si angles vary from 120° to 180°, with a maximum around 144° [119, 120]. The idealized structure of defect-free silica glass is then a "continuous random network" (CRN). After implantation, the main defect induced in silica is called E'-center: it can be described as an oxygen vacancy opposite an electron in a dangling Si $sp^3$ orbital [119]. The E'-center is a paramagnetic defect, and many variants of this center can be found in ion-implanted silica [114, 121]. The oxygen displacement can be originated by radiolytic processes. The electronic energy deposition component of the ion energy gives the driving energy needed for creating an electron–hole pair (about 9 eV in silica glass); if converted to atomic motion through nonradiative recombination, this energy is sufficient to overcome the Si–O chemical bond strength (about 4.5 eV). The displaced oxygen atom forms a new bond with a near-neighbor oxygen atom. The E'-center can also be formed by hole trapping at the Si–Si bond formed after the displacement of a bridging oxygen to a distant site due to collisional processes. As a consequence of E'-center formation, local atomic rearrangements occur. These rearrangements result in volume variations which in turn induce a variety of interesting physical property modifications [112]. The E'-center in silica gives rise to optical absorption around 215 nm of wavelength.

Another important implantation-induced defect in silica is the non-paramagnetic defect called the $B_2$-center, which is formed only by component of ion energy going into displacement processes [122]. This center is detected in silica as an optical absorption band centered around 245 nm of wavelength. The model proposed for this center is that of an oxygen vacancy which has trapped two electrons (Si–V–Si, where V stands for vacancy). The $B_2$-center concentration produced by a heavy ion can be greatly reduced by a subsequent $H^+$ implantation: hydrogen migrates to the defect to originate Si–H H–Si configurations.

Ion implantation in glasses results in defect-induced volumetric changes. These density changes in the implanted region lead to changes in refractive index, and in surface stress and hardness. For most simple silicate glasses, ion implantation usually results in compaction within the implanted region [123–126]; this is related to the large specific volume and more open structure of the glassy state compared to that of its crystalline counterpart. However, for high energy deposition values, a structural change from a compacted to an expanded state occurs [123]. The implanted layer being usually on the order of (or less than) 1 $\mu$m in depth, the constraint of the undamaged substrate is such

that the expansion (contraction) is normal to the surface. The changes in refractive index induced by density changes on ion-implanted silica were detected for the first time more than forty years ago [127]. In that case the positive change of the refractive index saturated at about 4%; later work has established that the change in index is usually of the order of 1–2% for most ions [128, 129]. Obviously, for implantation of atoms that react chemically with the host matrix forming compounds, larger variations of the refractive index are possible. As an example, in N-implanted silica anomalously large refractive index increases (about 6%) were observed for the first time in the 1970s [130]. These optical findings are explained considering that nitrogen implantation of silica gives rise to $SiO_xN_y$ oxynitride compounds in the implanted region [131–134]. In soda-lime glasses, ion implantation induces instead a decrease of the refractive index, due to the depletion of alkali atoms from the implanted layers during implantation [135–137].

## 3.2. Chemical Effects

Depending on the choice of the pair "implanted atom-dielectric host," ion implantation of metals in glass gives rise to the formation of new compounds and/or metallic nanoparticles. The processes governing the chemical and physical interaction between the implanted atoms and the atoms in the host matrix are not completely understood and still under debate. In this section, the metal nanocluster formation is studied after ion implantation in silica glass. Particular emphasis is given to the comparison among different existing approaches to the understanding of the chemical interactions taking place between the implanted atoms and the silica glass matrix. Since the physical properties of MNCGs depend on the cluster structure, composition, and size, it is of crucial importance to set procedures and preparation protocols for modifying these features.

Perez [138–140] made the first attempts to analyze the charge state of implanted atoms, using an interesting and very simple statistical model. In the case of Fe-implanted crystalline MgO, LiF, and $Al_2O_3$, he observed that the structure of the host matrix plays an important role in the determination of the final products (i.e., compounds) after ion irradiation. Consequently, he calculated the probability of finding different structural configurations of implanted atoms as a function of their atomic fraction, by using the binomial distribution. The possibility to find different chemical states of the implanted element, for an arbitrary local concentration $x$ of the dopant atoms, is determined by the binomial distribution:

$$P_N(n, x) = \binom{N}{n} x^n (1 - x)^{N-n} \qquad (10)$$

where $N$ stands for the number of neighboring atoms that originate the coordination shell(s) of the implanted probe atom. Other dopant atoms present inside the shell(s) can form complexes of $n$ implanted atoms. In other words, Eq. (10) represents the probability, for a given dopant concentration, to find exactly $n$ implanted atoms in a group of any $N$ neighboring atoms surrounding the implanted probe atom. As a consequence, the probabilities to find isolated dopant atoms ($n = 0$), dimers ($n = 1$), or trimers ($n = 2$)

inside the matrix can be easily calculated, depending on the number of the neighbor atoms $N$ of an implanted one. The agreement between calculations and data was excellent only for low to moderate fluences, because the increasing amount of damage at high fluence makes the concept of near-neighbors questionable. Thus, the statistical model of Perez gives results reliable only for ion implantation in crystalline substrates. However, even in Cr-implanted crystalline MgO and $Al_2O_3$ [141], calculations and experimental data actually disagree.

A few years later, Hosono [142] proposed a criterion to predict the formation of elementary colloids by ion implantation in $SiO_2$ glass, based on physical and chemical considerations. He observed that the major defects produced during ion implantation in silica are oxygen-deficient centers: Si–Si homobonds and neutral oxygen monovacancies. Concerning the Si–Si bonds, their concentration is highly ion-specific; that is, it depends on the chemical interactions among the implanted element and the atoms constituting the glass matrix (silicon and oxygen). For strong chemical interactions, implanted ions (M) form M–O bonds, leaving Si–Si bonds. On the other hand, when the chemical interactions are weak, a large fraction of implanted atoms does not react with oxygen atoms, so that the concentration of Si–Si bonds results very low. Implanted (M) and silicon ions compete for bonding oxygen: colloid formation will occur when the chemical affinity of M ions for the oxygen is smaller than that of $Si^{4+}$. Hosono proposed to take the free energy of oxide formation as the quantity which gives the measure of the chemical interaction; that is, colloid formation occurs when the Gibbs free energy of formation of oxides of an implanted element M, $\Delta G_T^0(M_xO_2)$, is greater than that for $SiO_2$, $\Delta G_T^0(SiO_2)$. The considered chemical reaction is the formation of the $M_xO_2$ oxide starting from the element M in the metallic form and oxygen in the molecular gaseous form, $O_2$:

$$M_x^{(met)} + O_2^{(gas)} \rightarrow M_xO_2 \tag{11}$$
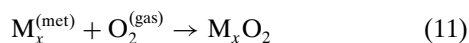
Since the Gibbs free energy depends on temperature, $T$, Hosono estimated the "fictive temperature" $T_f$ of the implanted layers to be around $T_f = 3000$ K, by considering the temperature of the thermal equilibrium between the detected concentration (in the implanted layers) of the Si–Si homobonds and that of the neutral oxygen monovacancies. Hosono proposed also a different estimation of $T$, based on the shift of the lattice vibrations of the silica network, originated by the decrease in the Si–O–Si bridging bond angle after irradiation. As the pure silica exhibits shifts of the lattice vibrations depending on the temperature, Hosono assumed that the silica implanted layers could be considered as unimplanted silica at a temperature, $T_f$, that results to be in agreement with the previous estimation, that is, $T_f \sim 3000$ K. Thus, for ion implantation in silica at room temperature, Hosono suggested that colloid formation of the implanted element (M) originates when $\Delta G_T^0(M_xO_2) > \Delta G_T^0(SiO_2)$ at $T \sim 3000$ K. The $\Delta G_{T=3000\,K}^0$ values are estimated by extrapolating the reported temperature dependence (see to this regard the so-called Ellingham diagrams [142], an example of which is reported in Fig. 1
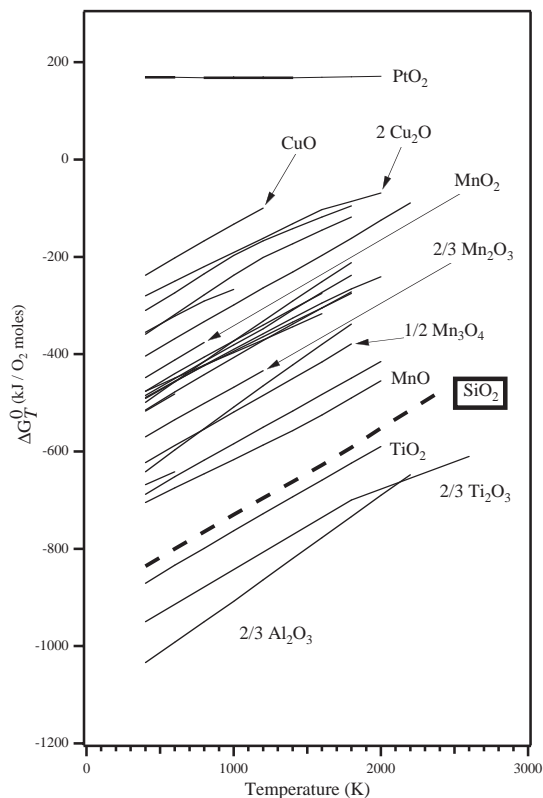


**Figure 1.** Ellingham diagram. Temperature dependence of the Gibbs free energy of formation $\Delta G_T^0$ for the reaction (11), as calculated from data in [143]. $\Delta G_T^0$ values are normalized to the $O_2$ moles involved in the reaction. For clarity, only few compound names are indicated.

starting from the Gibbs free energy tabulated data for inorganic substances [143]). The meaning of $T_f$ was related to the "thermal spike" model of particle irradiation damage [144].

A more general approach for understanding the different compounds originating in silica by ion implantation is due to Hosono and co-workers [145, 146]. Starting from the observation of the main implantation-induced defects in silica and their concentration, Hosono and co-workers pointed out the importance of the chemical interaction strength among implanted and host matrix atoms as a determining factor that influences the nature of the detected defects. They assumed that the primary factor controlling chemical interactions of implanted ions M with the substrate structure is the electronegativity [147] of the implanted element. Group I implants are those for which extraction of oxygen atoms from the silica network and formation of M–O bond take place; type II are implants that knock on oxygen atoms from the silica network, thereby forming Si–M bonds. Type III implants do not exhibit significant chemical reactions. The correlations found between the electronegativity (EN) of implanted elements and the three groups led Hosono and co-workers to classify into group I and II the implants for which the EN of the implanted element M is EN < 2.5 and EN > 3.5, respectively, while noble metal ion implants were considered to be of type III.

The model proposed by the Padua and Venice Universities research group originates from the investigation of Kelly

on the compositional modifications induced by ion implantation on alloys, oxides, and other substances [148, 149]. He observed that, in binary alloys, the mixing between atomic species induced by the ion beam is related to the heat of mixing, $\Delta H_m$ (usually few tenths of eV/atom). For metal pairs having a negative heat of mixing, the mixing induced by ion irradiation can be up to three times wider than in the case of metal pairs with $\Delta H_m = 0$, for which the mixing is induced by purely ballistic effects. These findings indicate a very important role for chemical guidance in ion-beam mixing, even though, during ion implantation, both the incoming ion energy (several keV) and the recoil energy of the atoms (tens of eV) are very large if compared to the chemical energies coming into play. Thus, the (high) energies involved in ion implantation suggest that thermal spike processes take place during irradiation. However, Kelly proposed an alternative and satisfactory description of the ion-mixing process [148, 149], by supposing the existence of a chemical driving force taking place at the end of the collisional cascades. He introduced a new term in the ion-beam mixing diffusion equations, which describes the effects of chemically guided steps along preferential trajectories. In this way, it is possible to understand how chemical guidance (in the broadest sense) could have considerable effects on the ion-mixing process in spite of the extreme energy disparity, that is, how the "reasonable" requirement (driving force $\geq kT$) could be satisfied. As a consequence, the thermal spike interpretation is not necessary. Molecular dynamics simulations of atomic motion in displacement cascades induced by ion implantation have helped to elucidate the role of thermal spikes [150]. After the first few tenths of a picosecond in the cascade (during which the temperature concept is meaningless), the effective local temperature is of the order of a few thousands K for a time interval of 10–20 ps: at this level the self-diffusion coefficient is typical of a liquid state, confirming the local-melt interpretation of the cascade thermal spike. However, after few tenths of a nanosecond the local temperature is the substrate temperature. Thus, these simulations suggest that the described chemical (thermodynamics) processes should take place at the substrate temperature.

The model proposed by the Padua and Venice group is called the *two-step* model [49, 151–156]. It distinguishes two different energy steps in the ion implantation process. The first is characterized by high-energy ballistic effects: they essentially cause the damage of the substrate (defects, knock-on events, etc.). The second is characterized by low-energy, chemically guided processes: they induce the formation of compounds predictable on the basis of thermodynamical considerations. The allowed compounds are determined by calculating $\Delta G_T^0$ for chemical reactions like the following (assuming ion implantation in silica of the element M)

$$M^{(gas)} + SiO_2 \rightarrow (compounds) \tag{12}$$
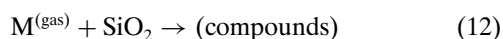
where $T$ is the temperature of the silica substrate during implantation. The more negative the $\Delta G_T^0$ values, the more likely is the formation of the particular compound.

To compare the prediction of the three described models, two different cases are briefly described. As a first example, the case of copper ion implantation in silica is outlined. It is

well known that copper implantation in silica glass originates the formation of metal copper particles in the nanometer range of size (see the following section for a list of literature references). For instance, copper nanoclusters are detected in 90 keV energy implanted silica, $5 \times 10^{16}$ ions/cm$^2$ of fluence, current density lower than 2 $\mu$A/cm$^2$ [137, 157]. The ion range $R_p$ and the range straggling $\Delta R_p$ are 70 nm and 23 nm, respectively, as calculated by TRIM code [113]. By using these implantation conditions, the sample temperature does not exceed 30 °C during irradiation. The chemical and compositional analyses performed by X-ray photoelectron and X-ray-excited Auger electron spectroscopies (XPS and XE-AES, respectively) reveal that at depths in which the copper atomic fraction is lower than about 2% (i.e., at the start and at the end of the in-depth copper concentration profile), the oxidation state of copper atoms is +1: at low metal concentrations, about all the copper atoms react with the host silica matrix, forming chemical bonds with oxygen atoms. At depths in which the copper concentration is higher, also metal copper is detected. Transmission electron microscopy confirms these findings, showing the presence of spherical copper nanoparticles, 6.5 nm of mean size. Starting from the Gibbs free energy tabulated data for inorganic substances [143], it is possible to calculate the Gibbs energy value for chemical reactions involving Cu and the silica substrate. Here are some chemical reactions originating metal copper or copper oxides:

$$Cu + SiO_2 \rightarrow Cu^{met} + SiO_2 \qquad \Delta G_{298\,K}^0 = -297 \text{ kJ mol}^{-1} \tag{13}$$

$$4Cu + SiO_2 \rightarrow 2Cu_2O + Si^{met} \qquad \Delta G_{298\,K}^0 = -631 \text{ kJ mol}^{-1} \tag{14}$$

$$2Cu + SiO_2 \rightarrow 2CuO + Si^{met} \qquad \Delta G_{298\,K}^0 = +3 \text{ kJ mol}^{-1} \tag{15}$$

There is a good agreement between the compounds predicted by the *two-step* model and the experimental findings. In particular, it indicates the formation of $Cu_2O$, not of $CuO$. Indeed, from the second reported reaction, it follows that the formation of $Cu_2O$ should be connected with the presence of silicon atoms in the metal form inside the matrix, anyway not observed. However, from a quantitative point of view, the total amount of metal silicon atoms (if present) should be well below the detection limit of the used spectroscopies. As far as the other two models are concerned, both the Hosono and the Hosono–Matsunami–Himagawa ones predict correctly the formation of metal copper nanoparticles, but the formation of copper oxides is not expected.

As a second example of comparison among the three models, the case of manganese ion implantation in silica [156] is summarized here. Manganese ions at 38 keV of energy are implanted in silica glass at three different fluences, namely 1, 5, and $10 \times 10^{16}$ ions/cm$^2$, with a current density lower than 2 $\mu$A/cm$^2$. During irradiation, the sample temperature does not exceed 30 °C. For manganese ions implanted in silica at 38 keV energy, the mean projected range $R_p$ and the range straggling $\Delta R_p$ are 36 nm and 12 nm, respectively [113]. In the sample implanted at the lowest fluence, for which the maximum atomic Mn concentration is around 5%, only the presence of Mn–O chemical bonds is detected. In the other two samples, for which the Mn

atomic concentration is larger than 10%, manganese silicide compounds are detected in addition to the manganese oxide and/or silicate. Here, the radiation damage induced a modification of the silica stoichiometry, causing an oxygen depletion at a depth slightly lower than $R_p$ and an increase at higher ones. No metal manganese is detected in the three different samples. From tabulated data in [143], it is possible to calculate the Gibbs energy value for chemical reactions involving Mn and the silica substrate. Here are some allowed chemical reactions:
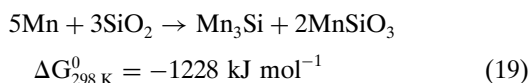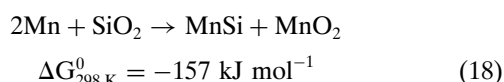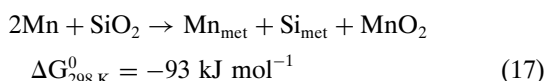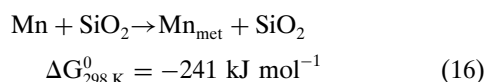
$$Mn + SiO_2 \rightarrow Mn_{met} + SiO_2$$
$$\Delta G^0_{298\,K} = -241 \text{ kJ mol}^{-1} \qquad (16)$$

$$2Mn + SiO_2 \rightarrow Mn_{met} + Si_{met} + MnO_2$$
$$\Delta G^0_{298\,K} = -93 \text{ kJ mol}^{-1} \qquad (17)$$

$$2Mn + SiO_2 \rightarrow MnSi + MnO_2$$
$$\Delta G^0_{298\,K} = -157 \text{ kJ mol}^{-1} \qquad (18)$$

$$5Mn + 3SiO_2 \rightarrow Mn_3Si + 2MnSiO_3$$
$$\Delta G^0_{298\,K} = -1228 \text{ kJ mol}^{-1} \qquad (19)$$

The agreement between the compounds predicted by the *two-step* model and the experimental evidence is good, even if the metal prediction is not experimentally confirmed. The Hosono model predicts incorrectly the formation of metal nanoparticles, while the Hosono–Matsunami–Himagawa rules predict the formation of only Mn–O bonds.

The investigations by the Padua and Venice group on the compounds formed in silica by single metal ion implantation are summarized in Figure 2. For each implanted (metal) element, the detected compounds are reported as a function of the atomic concentration of the implanted atom. The most important evidence is the formation of silicide compounds: among the described models, the *two-step* is the only one able to predict the formation of silicides when Cr, Mn, Pd, Pt, or Ti are implanted in silica. A direct comparison
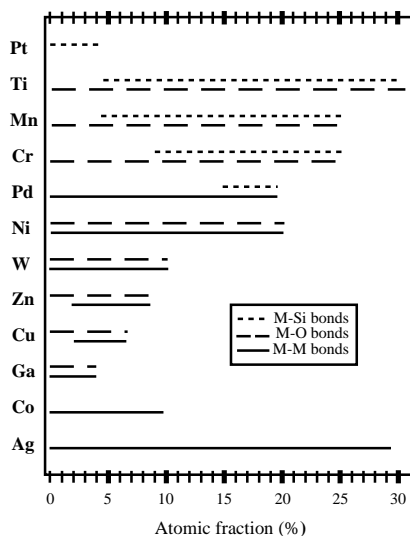
**Figure 2.** Chemical species involving the generic (metal) element M in M-implanted silica, as a function of the metal concentration.

among the Hosono, the Hosono–Matsunami–Imagawa, and the *two-step* model predictions is very interesting. The experimental findings regarding the compounds formed by metal ion implantation in silica, as they are found in the recent literature, are summarized in Table 1, where the prediction of the three different models is reported for each implanted element. The Hosono criterion predictions are correct for almost all the reported elements: it fails only for Cr and Pt. It is possible that, for higher Pt concentration, metallic cluster formation takes place. When chromium is considered, however, experimental findings seem to exclude the formation of a significant amount of metallic chromium clusters. The main limit of the Hosono model is its inability to predict the formation of any kind of compounds (oxides and silicides). This method is presumably more appropriate for dopant concentrations larger than few atomic %, as suggested; as a matter of fact, Hosono tested its criterion for ion irradiation performed at room temperature with doses of $5–10 \times 10^{16}$ atoms/cm$^2$, 50–200 nm of $R_p$ [142].

The Hosono–Matsunami–Imagawa model is able to predict the formation of both oxides and silicides of the implanted element, as well as the metallic cluster formation. It cannot predict the contemporary appearance of more than

**Table 1.** Compounds formed by single implantation of metal elements in silica glass (P and Se are included).

| Elements M (EN) | M–Si bonds | | M–O bonds | | | M–M bonds | | | |
|---|---|---|---|---|---|---|---|---|---|
| Ag (1.9) | | | | | | • [48] | ☆ | o | ◇ |
| Al (1.6) | | | • [158] | o | ◇ | | | | |
| As (2.2) | | | • [159] | o | | • [159] | ☆ | | ◇ |
| Au (2.5) | | | | | | • [48] | ☆ | o | ◇ |
| B (2.0) | | | • [160] | o | ◇ | | | | |
| Bi (2.0) | | | | o | | • [161] | ☆ | | ◇ |
| Cd (1.7) | | | | o | | • [162] | ☆ | | ◇ |
| Co (1.9) | | ◇ | | o | ◇ | • [163] | ☆ | | ◇ |
| Cr (1.7) | • [153] | ◇ | • [153] | o | ◇ | | ☆ | | |
| Cu (1.9) | | | • [48] | | ◇ | • [48] | ☆ | o | ◇ |
| Er (1.2) | | | • [164] | o | ◇ | | | | |
| Fe (1.8) | | ◇ | • [165] | o | ◇ | • [165] | ☆ | | ◇ |
| Ga (1.8) | | | • [166] | o | ◇ | • [166] | ☆ | | ◇ |
| Ge (2.0) | | | • [167] | o | | • [168] | ☆ | | ◇ |
| In (1.8) | | | | o | | • [169] | ☆ | | ◇ |
| Li (1.0) | | | • [145] | o | ◇ | | | | |
| Mn (1.5) | • [156] | ◇ | • [156] | o | ◇ | | ☆ | | ◇ |
| Ni (1.9) | | ◇ | • [170] | o | ◇ | • [170] | ☆ | | ◇ |
| P (2.2) | | | • [171] | o | ◇ | • [172] | ☆ | | ◇ |
| Pb (2.3) | | | • [47] | o | ◇ | • [47] | ☆ | | ◇ |
| Pd (2.2) | • [173] | ◇ | | o | ◇ | • [173] | ☆ | | ◇ |
| Pt (2.3) | • [174] | ◇ | | o | | | ☆ | | ◇ |
| Sb (2.0) | | | | o | | • [168] | ☆ | | ◇ |
| Se (2.5) | | | | | | • [175] | ☆ | | ◇ |
| Sn (2.0) | | | | o | ◇ | • [176] | ☆ | | ◇ |
| Ti (1.5) | • [177] | ◇ | • [177] | o | ◇ | | | | |
| W (2.4) | | | • [151] | o | ◇ | • [151] | ☆ | | ◇ |
| Zn (1.6) | | | • [178] | o | ◇ | • [178] | ☆ | | ◇ |

*Note:* EN stands for Pauling electronegativity [147]. Silicon implanted in silica originates substoichiometric silicon oxides and, for high local concentrations, also amorphous silicon precipitates [179].
• Experimental evidence.
☆ Hosono model prediction.
o H–M–H model prediction.
◇ *Two-step* model prediction.

one compound. It fails sometimes on the oxides formation and, very often, it does not predict the formation of metallic clusters. The silicide formation in the case of Cr, Mn, Pd, Pt, Ti is not expected. Figure 2 suggests that this method may be more suitable for predictions in the case of low dopant atomic concentrations, for example when low-fluence irradiations are performed.

The *two-step* model can predict the formation of more than one compound. In particular, it is the only one able to predict the formation of silicides for Cr, Mn, Pd, Pt, Ti implantation in silica. Moreover, its predictions are in good agreement with experimental evidences for the other considered implants. Starting from the reported chemical reaction, the formation of metallic clusters is always possible

$$M^{(gas)} + SiO_2 \rightarrow M_{met} + SiO_2 \quad \Delta G_T^0 < 0 \qquad (20)$$
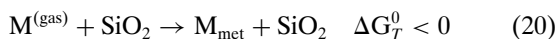
because at room temperature the $G_T^0$ value for $M^{(gas)}$ ($M_{met}$) is always positive (negative). However, in some cases (Al, B, Cr, Er, Li, and Ti) the formation of metallic clusters (even if possible) is not the most favored process, because of its very small $\Delta G_T^0$ absolute value compared to the formation of oxide and silicide species. The model fails mainly on the prediction of silicides formation in the case of Fe, Co and Ni, that is, for implantation with elements having particular magnetic properties. Concerning the importance of the first step, the ballistic–physical one, the experimental findings show that the formation of the predicted compounds actually takes place depending on the depth in the implanted region: for different dopant concentrations, as well as for different matrix damage, a certain compound can be present in different amounts. Unfortunately, for highly damaged regions in which the silica stoichiometry is modified, it is not possible to calculate correctly the Gibbs free energy variation for reactions like the one stated above, because the $G_T^0$ values for $SiO_x$ species are unknown. Exact calculations are possible only for stoichiometric silica, even if qualitative considerations can be put forward as well.

A conceptually critical assumption of the *two-step* model is the introduction of thermodynamical considerations. As an *a posteriori* justification, this approach provides reliable anticipations about chemical modifications of the implanted silica, even if a great care must be taken when equilibrium considerations are applied to an out-of-equilibrium process. Moreover, thermodynamical considerations are limited by uncertainties on the evaluation of the local temperature, as well as on the assumption that chemical interactions take place between the implanted atoms and the substrate chemical compounds (not the substrate separate atomic species).

# 4. SINGLE IMPLANTATION: THE CASE OF COPPER

Copper implantation in glasses has been explored in the last decade for both basic and application purposes. Indeed, copper-doped glasses have attracted a great interest for their blue-green luminescence properties, useful in laser technology, as well as for third-order nonlinear optical features of copper nanoclusters in glass. Several experimental studies on copper implantation were published by different research groups [137, 157, 180–189] exploring the different conditions

for the copper aggregation in nanometer-sized crystallites; typical implantation energies are up to 200 keV. In Section 3 we already described an experiment of copper ion implantation in silica from a chemical point of view.

The implantation of copper may easily give rise to a typical bimodal distribution, interpreted in terms of diffusivity of the implanted ions, deposited energy distribution, and defect migration upon implantation. Rutherford backscattering spectrometry (RBS) measurements of the copper depth profiles showed a near-Gaussian distribution for fluences lower than $2 \times 10^{16}$ ions/cm$^2$ and a bimodal distribution for fluences greater than $3 \times 10^{16}$ ions/cm$^2$ [12, 47, 48]. The larger peak in the bimodal distribution is approximately twice the size of the smaller, and nearer to the surface. Its position in depth lies inside the region of the maximum rate (eV/nm) of the collisional energy deposition, that is, in which the silica network is highly damaged. Indeed, another observed effect is that one related to the knock-on of oxygen atoms towards the deeper part of the implanted region. Figure 3 shows the in-depth concentration profiles of copper (absolute) and oxygen (subtracting the substrate oxygen level) after implantation in silica glass with 160 keV, $1 \times 10^{17}$ Cu$^+$/cm$^2$, as from secondary ion mass spectrometry (SIMS) analysis. A modification of the O distribution following the Cu profile is evident. An oxidation effect on copper particles linked to the matrix damage was also evidenced [190].

Optical absorption spectra of copper-implanted silica glasses exhibit an absorption band with a peak at about 2.2 eV (corresponding to about 560 nm of wavelength), depending on the implantation conditions [191]. This absorption feature is due to the surface plasmon resonance of metallic copper nanoparticles, even if a contribution from excitonic transition in cuprous oxide particles cannot in principle be ruled out. The temperature dependence of the two types of transition is, however, quite different: absorption due to plasma oscillations is not expected to depend on the temperature, while the widths of absorptions due to excitons decrease remarkably with decreasing temperature [192]. No changes were observed in the absorption spectra in most of the experimental findings, indicating that the observed absorption features should be attributed to metal copper particles. Direct evidence for the formation of copper colloids is anyhow obtained by transmission electron microscopy (TEM) analyses. The optical absorption at 2.2 eV may actually be modified by the fluence rate,
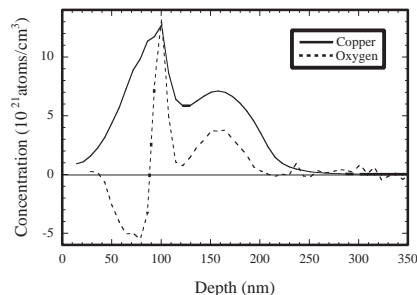


**Figure 3.** In-depth concentration profiles of copper (absolute) and oxygen (subtracting the substrate oxygen content) after implantation in silica glass with 160 keV, $1 \times 10^{17}$ Cu$^+$/cm$^2$, as from SIMS and RBS analyses.

for fluences greater than $3 \times 10^{16}$ ions/cm$^2$, without significant changing of the spatial distribution of copper ions. The observed nonlinear increase in absorption with increasing fluence rate has been connected to alteration of the shape of the clusters from spherical to prolate spheroids [183].

The effects of ion-beam current density on the physical and optical properties of Cu nanoclusters prepared by ion implantation were also studied [184]. The mean diameter and the standard deviation were shown to increase with the current density. The increase of the mean cluster size as well as the broader size distribution with increase of the dose rate can be ascribed to increased local heating in the implanted layer, with both enhanced diffusion of the implanted copper and growth kinetics. It is worth mentioning that subsequent irradiation of copper-implanted silica with nitrogen ions gives rise to the diffusion of copper towards the surface and possibly the clusters dissolution, due to the nitrogen reaction with both the silica substrate and the implanted copper, while no optical absorption structure is observed, connected to copper colloid formation, for other silicate glasses [137, 157, 193], indicating that the substrate structure and its reactivity with copper play a major role in the copper behavior. The colloid formation of Cu has been also studied [187] when other dopants (P, F, and Ge) are present in amorphous silica substrates.

Silica slides implanted at room temperature with 160 keV Cu$^+$ ions, at implant currents below 2 $\mu$A/cm$^2$, with fluences ranging from $5 \times 10^{16}$ to $1 \times 10^{17}$ Cu$^+$/cm$^2$, were studied in detail [190, 194] also after annealing in air at 700 °C for 30 min. Extended X-ray absorption fine structure (EXAFS) measurements at the Cu K-edge were performed at European Synchrotron Radiation Facility (ESRF) on the GILDA beamline. Copper metallic clusters were found to exhibit slightly different structural parameters with respect to the corresponding metal bulk. In particular, the particles with diameter <1 nm exhibit a contraction up to 1.5% of the first shell distance [195, 196], with a reduction of the first shell radius up to 0.04 Å. The pressure acting on the particles resulting from the embedding matrix and the surface tension of the particle was determined to be up to 5.8 GPa. The analysis also indicates a transition from fcc to a relaxed icosahedral structure for the copper clusters, as expected from molecular dynamics calculations for small diameters ($D < 50$ Å). Figure 4 shows the optical absorption spectra of a silica glass sample implanted with 160 keV, $5 \times 10^{16}$ Cu$^+$/cm$^2$, before and after annealing in air at 700 °C for 30 min; the inset of Figure 4 shows the histograms of the size distribution of metallic copper clusters before and after the annealing. The SPR band increases after heat treatment without modifying significantly its shape, indicating the increase of the cluster number. On the other hand, size distribution maximum shifts towards lower particle dimension. A TEM analysis before and after the annealing indicates that larger clusters remain almost unaltered, distributed in the implanted region nearest to the glass surface, while the number of smaller clusters increases, giving rise to the size distribution shift. Recently, negative copper ion implantation was also effectively performed for copper clusters formation in SiO$_2$ matrix [197]. Sixty kilo-electron-volt Cu ions were implanted into silica glasses at $3 \times 10^{16}$ ions/cm$^2$ fluence, up
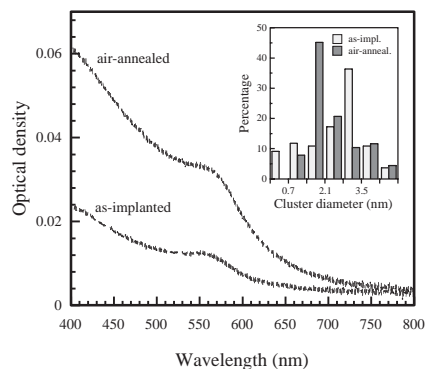


**Figure 4.** Optical absorption spectra of a silica glass sample implanted with 160 keV, $5 \times 10^{16}$ Cu$^+$/cm$^2$, before and after annealing in air at 700 °C for 30 min. The inset shows the histograms of the size distribution of metallic copper clusters before and after the annealing treatment.

to a current density of 260 $\mu$A/cm$^2$, giving rise to dose-rate-dependent metallic cluster formation. Finally, it is worth mentioning the study of copper implantation in silica glass performed either before or after a second implantation of fluorine [171, 188]. Nanosized particle structure has been observed to depend on the implants order; in fact, when the implantations are made following the Cu-F sequence, colloidal particles were identified by TEM presenting a dual structure composed of Cu metal (core) and Cu$_2$O (shell). Such result was explained in terms of oxidation of the outer part of Cu colloids, due to the recoil of energetic oxygens from the silica structure by F implantation.

## 5. DOUBLE IMPLANTATION: THE CASE OF GOLD + COPPER

In general, a double-implanted system is driven toward a stable structure (separated, alloy, or core-shell aggregates) by different factors: the miscibility of the implanted elements, their chemical interaction with the host matrix, and the radiation-induced defects, which can play a major role in the nucleation and clusters growth. In particular, it is shown that thermal annealings in different atmospheres may give rise to the formation of either alloy or separated systems. In general, nanoclusters do not undergo the strict requirements of miscibility as for the bulk alloying, due to the peculiar properties of nanometer-sized systems [198], that may exhibit novel alloy phases thermodynamically unfavored in the bulk.

In this section, a case study is presented on the formation of mixed Au-Cu nanoclusters upon sequential ion implantation of the two species into fused silica. Sequential ion implantations with different elements were performed on fused silica substrates at current densities lower than 2 $\mu$A/cm$^2$ and ion-beam energies to get the same projected range for the implanted species (typical energies were up to 200 keV, with ion doses from $1 \times 10^{16}$ ions/cm$^2$ to $4 \times 10^{17}$ ions/cm$^2$). Ion-implanted slides were then heat-treated at different temperatures and times in air, or in a H$_2$-Ar gas mixture. The obtained samples are named according to the following: XnYmZ means a first implantation of $n \times 10^{16}$ ions/cm$^2$ of the species X, followed by a second implantation

of $m \times 10^{16}$ ions/cm$^2$ of the species Y. The letter Z indicates the annealing atmosphere (if any): A stand for air, H for H$_2$-Ar mixture. Optical and structural techniques were used to detect the possible alloy formation. In the case of noble metal clusters, the SPR in the visible range is a clear fingerprint of nanoparticles formation [19], and when dealing with noble metals alloy the SPR resonance is located in between those of the pure elements, and is triggered by the complex interplay between the modified free electrons and interband absorptions [19, 25, 199].

Figure 5 shows the optical absorption spectra of the sample Au3Cu3 before (as-implanted) and after annealing either in oxidizing or reducing atmosphere, at 900 °C for 1 h. Gold and copper ions were implanted at 190 and 90 keV, respectively. The spectrum for the as-implanted sample exhibits a faint absorption band at about 560 nm, while the Au3Cu3A sample presents a well-defined absorption peak at 530 nm, consistent with the SPR of gold metal clusters in the nanometer range of size [19]. The optical absorption of the sample Au3Cu3H is similar to the as-implanted one, but with the absorption band sharper and more intense, suggesting that the average cluster size is increased. It is worth noting that the SPR peak position of Au3Cu3 and Au3Cu3H is located in between that of pure Au and Cu nanoclusters (located at about 530 and 570 nm [48], respectively), indicating that an intermetallic Au-Cu alloy possibly formed. Figure 6 shows the bright-field TEM planar views of Au3Cu3 (a), Au3Cu3H (b), and Au3Cu3A (c) samples. In the as-implanted sample, spherical crystalline clusters are visible with an average diameter $\langle D \rangle = (3.8 \pm 1.6)$ nm, with mutual random orientation as from selected area electron diffraction (SAED) analysis. Even if energy-dispersive X-ray spectroscopy (EDS) microanalysis shows the presence of both gold and copper in the examined area, the SAED pattern can be indexed according to a single fcc phase with lattice constant $a = (0.3958 \pm 0.0015)$ nm. This value is in between the experimental values for the pure bulk phases of either gold ($a_{Au} = 0.40786$ nm) or copper ($a_{Cu} = 0.36150$ nm), thus showing that an Au$_x$Cu$_{1-x}$ intermetallic alloy actually formed. Indeed, the lattice parameters of the continuous Au-Cu solid solution phase exhibits a positive deviation from
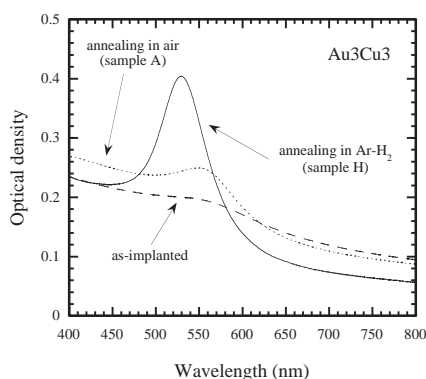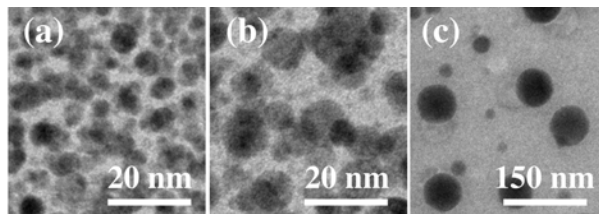


**Figure 6.** Bright-field TEM planar view of Au + Cu double-implanted silica samples before and after thermal treatments. (a) As-implanted sample (Au3Cu3); (b) sample annealed in reducing atmosphere (Au3Cu3H); (c) sample annealed in oxidizing atmosphere (Au3Cu3A).

an assumed Vegard's law [200], as in Eq. (21):

$$a_{alloy} = xa_{Au} + (1-x)a_{Cu} + 0.01198x(1-x) \qquad (21)$$

By inserting the measured lattice parameter in Eq. (21), a value of $x = 0.68$ is obtained, corresponding to a ratio $K = [Au]/[Cu] = 2.1$. Compositional analysis obtained from EDS data gives an average value $K_{EDS} = 1.5$, which is slightly lower than the SAED results. This suggests that part of the copper atoms do not participate in the alloying but remain in a different state, either atomic or oxidized. Figure 6b shows the bright-field TEM micrograph of the sample annealed in hydrogen atmosphere: the clusters are spherical and their average diameter ($\langle D \rangle = (8.7 \pm 2.5)$ nm) is higher than that for the as-implanted sample. In this case, SAED analysis indicates the formation of an ordered Au-Cu phase which is consistent with the tetra-auricupride phase (tetragonal, $a = 0.3960$ nm, $c = 0.3670$ nm) with equal Au-Cu atomic concentration. The sample Au3Cu3A presents near the surface large and irregularly shaped crystallites (not shown), with size up to the micron range, which give at EDS analysis a strong Cu signal with almost no presence of Au. SAED patterns show that these structures are composed of crystalline domains of CuO in the tenorite phase, with very small amount of crystalline Cu$_2$O. This indicates that during annealing in air Cu migrates toward the surface, where it is oxidized. This scenario is also confirmed by RBS measurements, which evidenced in the Au3Cu3A sample a significant rearrangement of copper ions, which pile up at the surface, whereas gold ions diffuse deeper in the samples. A loss of about 25% of copper was detected for this sample, while no loss occurs for the Au3Cu3H one. Au3Cu3 and Au3Cu3H samples exhibit almost coincident Gaussian in-depth distribution of the implanted species, while for Au3Cu3A sample a splitting of the two distributions occurs, with inward and outward migration of gold and copper, respectively. Furthermore, XPS measurements clearly indicate the presence of oxidized copper (CuO) at the surface. Below these copper oxide crystallites, the bright-field TEM micrograph in Figure 6c shows almost spherical clusters with mean diameter $\langle D \rangle = (33 \pm 15)$ nm. From the SAED results, an estimation of the lattice constant $a = (0.4067 \pm 0.0015)$ nm may be obtained for the fcc phase, consistent with that of the gold bulk lattice parameter.

The picture that emerges from TEM and optical results is summarized in Table 2, reporting some of the most relevant results of the Au-Cu experiments: sequential ion implantation may directly result in alloyed Au-Cu colloids, and subsequent annealing in reducing atmosphere can be used to



**Figure 5.** Optical absorption spectra of the sample Au3Cu3 before (as-implanted) and after annealing either in oxidizing or reducing atmosphere, at 900 °C for 1 h. Implantation fluence was $3 \times 10^{16}$ atoms/cm$^2$ for both gold and copper; energy was 190 and 90 keV, respectively.

**Table 2.** Summary of the TEM and optical absorption results for Au + Cu implanted samples.

| Sample | Annealing conditions | Size (nm) | Structure (SAED) | $x$ alloy | Lattice constant (nm) | SPR (nm) |
|---|---|---|---|---|---|---|
| Au3Cu3 | — | 3.8±1.6 | $Au_xCu_{1-x}$ fcc | 0.67(3) | $a = 0.3958(15)$ | 550 |
| Au3Cu3H | $H_2$-Ar (900 °C, 1 h) | 8.7±2.5 | $Au_xCu_{1-x}$ tetragonal | 0.50(3) | $a = 0.3960(12)$ $c = 0.3670(12)$ | 550 |
| Au3Cu3A | Air (900 °C, 1 h) | 33±15 | $Au_xCu_{1-x}$ fcc CuO (tenorite) | 0.97(3) | $a = 0.4060(12)$ | 532 — |
| Au3Cu3HA | $H_2$-Ar (900 °C, 1 h) + air (900 °C, 15 min) | 28±17 | $Au_xCu_{1-x}$ fcc $Cu_2O$ (cuprite, cubic) | 0.93(3) | $a = 0.4051(12)$ | 535 620 |

*Note:* Size is expressed as average diameter ± standard deviation as from TEM experimental size distribution.

increase the average size of the clusters, with a change in the structural ordering of the alloy. On the other hand, an oxidizing annealing induces a separation of the two species. The alloy formation process in the Au + Cu implanted sample should result from the enhanced diffusion of copper in small gold clusters [198, 201] during the implantation. The subsequent annealing in $H_2$-Ar at 900 °C drives copper atoms dispersed in the matrix toward the already formed clusters, increasing their size and shifting the Au/Cu concentration toward the nominal 1:1 ratio, and therefore inducing a structural disorder-order phase change. Moreover, from the phase diagrams of the Au-Cu system, 900 °C is actually the melting point temperature for the 1:1 Au:Cu alloy, that in turn could be lowered due to the thermodynamic size effect [202]. The annealing in air at the same temperature is able to separate the two species, and this may indicate that this transition is assisted by an intermediate solid-liquid one.

Starting from Au3Cu6H sample (i.e., from a composite system with AuCu alloy nanoparticles), after a subsequent thermal annealing in air at 900 °C for 15 min, copper atoms come out from the alloy forming $Cu_2O$ (cuprite, cubic, $a = 0.4267$ nm). The oxide and the alloy clusters form a double interconnected structure, in which the $Cu_2O$ structure is stabilized by the crystallographic cubic template of the $Au_xCu_{1-x}$ alloy [203]. If the annealing time reaches about 5 h, the system evolves toward a complete de-alloying: in the final configuration all the copper atoms are extracted from the alloy nanoparticles and oxidized in large polycrystalline clusters of CuO [203] (tenorite, monoclinic) located near the surface. The optical absorption spectra after different annealing intervals exhibit an evolution of both the position and the shape of the SPR bands [203], in agreement with the de-alloying process. Upon 5 h air-annealing, only a single SPR band of pure Au clusters is detected, while the band at 620 nm (due to $Cu_2O$) is gradually depressed, indicating a complete decoupling of the Au-Cu system.

## 6. CONCLUSIONS

Glass-based composites are drawing an enormous interest for several nanotechnology application fields, such as catalysis, integrated optics and photonics, magnetic materials, and so on. The low cost, the ease of processing, the durability, resistance, and transparency properties, as well as the compatibility with several different materials make silicate glasses privileged candidates for the preparation of nanocluster-containing dielectrics with prescribed properties.

Ion implantation is attracting increasing interest as a versatile technique to control the metal nanocluster formation in silicate glasses, so determining the functional properties of the composite. In this chapter, a review has been presented on the state of the art of the implantation technique to fabricate metal nanocluster doped glasses. An extended introduction was first given on the physics and chemistry of ion implantation-related phenomena in silica glass. The topic was then developed by examining two case studies, namely, implantation of copper and double sequential implantation of copper and gold in fused silica glass. In particular, it has been shown how the dynamics of cluster nucleation and growth, their stability, composition, crystalline phase, size, and size distribution could depend on the implantation parameters and the possible post-implantation treatments. Moreover, it has been pointed out how the nonequilibrium nature of the phenomena taking place during the cluster nucleation and growth upon ion implantation may give rise to structures that should be unfavored from the point of view of the thermodynamics of cluster formation.

All these factors contribute to define a scenario in which the number of degrees of freedom for controlling the final material structure and properties could be quite significant for ion implantation-based methodologies. This means that besides the experimental activity based on ion implantation, nanocluster materials research must develop a deeper insight into the basic physical processes that govern the cluster formation.

## GLOSSARY

**Confinement effects** Electronic and optical properties exhibited by metal nanoclusters due to the size of the particles, which in the nanometer range affects the electrons behavior in a peculiar way. Extrinsic cluster size effects are the collective electronic or lattice excitations, while quantum size effect refers to the electron-energy levels spacing.

**Fermi energy** Parameter representing the maximum electronic state energy at $T = 0$ K.

**Knock-on events** In ion implantation process, events for which the interaction between the implanted ion and the matrix gives rise to a displacement towards higher depths of the target atoms.

**Nonlinear optical properties** In the context of metal nanocluster glass composites, the nonlinear response of the material dependent on the intensity of the incoming light. In particular, intensity-dependent refractive index.

**Quantum dots** Nanoclusters, intended as the zero-dimension structure whose quantum behavior determines that of the composite material.

**Scattering** Process in which the incoming implanted ion undergoes a change of its wave vector $k$.

**Surface plasmon resonance** Resonant collective oscillation of electrons in the nanocluster due to an incoming electromagnetic wave, producing a surface polarization of the cluster.

## ACKNOWLEDGMENTS

## REFERENCES

1. M. Faraday, *Philos. Trans. R. Soc.* 147, 145 (1857).
2. M. Respaud, J. M. Broto, H. Rakoto, A. R. Fert, L. Thomas, B. Barbatra, M. Verelst, E. Snoek, P. Lecante, A. Mosset, J. Osuna, T. Ould Ely, C. Amiens, and B. Chaudret, *Phys. Rev. B* 57, 2925 (1998).
3. F. Tihay, J. M. Pourroy, A. C. Roger, and A. Kienneman, *Appl. Catal. A* 206, 24 (2000).
4. G. I. Stegeman and R. H. Stolen, *J. Opt. Soc. Am. B* 6, 652 (1989).
5. E. M. Vogel, *J. Am. Ceram. Soc.* 72, 719 (1989).
6. T. Kobayashi, *Nonlin. Opt.* 1, 91 (1991).
7. S. R. Friberg and P. W. Smith, *IEEE J. Quantum Electron.* QE-23, 2089 (1987).
8. K. W. DeLong, A. Gabel, C. T. Seaton, and G. I. Stegeman, *J. Opt. Soc. Am. B* 6, 1306 (1989).
9. R. F. Haglund Jr., *Mater. Sci. Eng. B* 54, 38 (1998).
10. G. Mattei, Ph.D. Thesis, University of Padova, Italy, 1998.
11. H. S. Nalwa, Ed., "Handbook of Nanostructured Materials and Nanotechnology." Academic Press, San Diego (2000)
12. F. Gonella and P. Mazzoldi, in "Handbook of Nanostructured Materials and Nanotechnology" (H. S. Nalwa, Ed.), Vol. 4, p. 81. Academic Press, San Diego, 2000.
13. L. M. Liz-Marzan and D. Norris, Eds., "New Aspects of Nanocrystals Research." Material Research Society, Pittsburgh, PA, 2001.
14. C. Flytzanis, F. Hache, M. C. Klein, D. Ricard, and Ph. Roussignol, *Progr. Opt.* 29, 321 (1991).
15. P. Mazzoldi and G. C. Righini, in "Insulating Materials for Optoelectronics" (F. Agulló-López, Ed.), p. 367. World Scientific, Singapore, 1995.
16. R. F. Haglund Jr., in "Handbook of Optical Properties II: Optics of Small Particles, Interfaces, and Surfaces" (R. E. Hummel and P. Wissmann, Eds.), Vol. 2, p. 191. CRC Press, New York, 1997.
17. J. A. A. J. Perenboom and P. Wyder, *Phys. Rep.* 78, 173 (1981).
18. W. P. Halperin, *Rev. Mod. Phys.* 58, 533 (1986).
19. U. Kreibig and M. Vollmer, "Optical Properties of Metal Clusters," Springer Series in Materials Science, Vol. 25. Springer, Berlin, 1995.
20. R. H. Doremus and P. Rao, *J. Mater. Res.* 11, 2834 (1996).
21. L. Yang, D. H. Osborne Jr., R. F. Haglund Jr., R. H. Magruder III, C. W. White, R. A. Zuhr, and H. Hosono, *Appl. Phys. A* 62, 403 (1996).
22. C. N. Ironside, *Contemp. Phys.* 34, 1 (1993).
23. J. C. Maxwell-Garnett, *Philos. Trans. R. Soc. A* 203, 385 (1904).
24. J. C. Maxwell-Garnett, *Philos. Trans. R. Soc. A* 205, 237 (1905).
25. G. Mie, *Ann. Phys. (Leipzig)* 25, 377 (1908).
26. U. Kreibig and P. Zacharias, *Z. Phys.* 231, 128 (1970).
27. U. Kreibig, in "Handbook of Optical Properties II: Optics of Small Particles, Interfaces, and Surfaces" (R. E. Hummel and P. Wissmann, Eds.), Vol. 2, p. 145. CRC Press, New York, 1997.
28. D. A. G. Bruggeman, *Ann. Phys. (Leipzig)* 24, 636 (1935).
29. W. C. Huang and J. T. Lue, *Phys. Rev. B* 49, 17279 (1994).
30. A. Dotsenko, S. Kuchinsky, and M. Prassas, *J. Non-Cryst. Solids* 218, 317 (1997).
31. J. A. Creighton and D. G. Eadon, *J. Chem. Soc. Faraday Trans.* 87, 3881 (1991).
32. D. E. Aspnes, *Am. J. Phys.* 50, 704 (1992).
33. F. Yonezawa, S. Sakamoto, and F. Wooten, *J. Non-Cryst. Solids* 117/118, 477 (1990).
34. J. Zhao, C. Xiaozhuang, and W. Guanghou, *Phys. Rev. B* 50, 15424 (1994).
35. C. Flytzanis and J. Hutter, in "Contemporary Nonlinear Optics" (G. P. Agrawal and R. W. Boyd, Eds.). Academic Press, San Diego, 1992.
36. F. Hache, D. Ricard, and C. Flytzanis, *J. Opt. Soc. Am. B* 3, 1647 (1986).
37. K. Koizumi, "Proceedings of XVI International Congress on Glass," Madrid 1992, Vol. 1, p. 45.
38. E. Cattaruzza, G. Battaglin, F. Gonella, R. Polloni, G. Mattei, C. Maurizio, P. Mazzoldi, C. Sada, M. Montagna, C. Tosello, and M. Ferrari, *Philos. Mag. B* 82, 735 (2002).
39. I. Tanahashi, H. Inouye, K. Tanaka, and A. Mito, *Jpn. J. Appl. Phys.* 38, 5079 (1999).
40. D. Stroud and V. E. Wood, *J. Opt. Soc. Am. B* 4, 778 (1989).
41. F. Hache, D. Ricard, and C. Girard, *Phys. Rev. B* 38, 7990 (1988).
42. F. Hache, D. Ricard, C. Flytzanis, and U. Kreibig, *Appl. Phys. A* 47, 347 (1988).
43. R. W. Schoenlein, W. Z. Lin, J. G. Fujimoto, and G. L. Eesley, *Phys. Rev. Lett.* 58, 1680 (1987).
44. A. Stella, M. Nisoli, S. De Silvestri, O. Svelto, G. Lanzani, P. Cheyssac, and R. Kofman, *Phys. Rev. B* 53, 15497 (1996).
45. G. I. Stegeman, E. M. Wright, N. Finlayson, R. Zanoni, and C. T. Seaton, *J. Lightwave Technol.* 6, 953 (1988).
46. E. Cattaruzza, G. Battaglin, P. Calvelli, F. Gonella, G. Mattei, C. Maurizio, P. Mazzoldi, S. Padovani, R. Polloni, C. Sada, B. F. Scremin, and F. D'Acapito, *Composites Sci. Technol.* 63, 1203 (2003).
47. A. Meldrum, R. F. Haglund, Jr., L. A. Boatner, and C. W. White, *Adv. Mater.* 13, 1431 (2001).
48. P. Mazzoldi, G. W. Arnold, G. Battaglin, F. Gonella, and R. F. Haglund Jr., *J. Nonlin. Opt. Phys. Mater.* 5, 285 (1996).
49. E. Cattaruzza, *Nucl. Instrum. Meth. B* 169, 141 (2000).
50. A. L. Stepanov and D. E. Hole, *Recent Res. Devel. Appl. Phys.* 5, 1 (2002).
51. D. E. Hole, A. L. Stepanov, and P. D. Townsend, *Nucl. Instrum. Meth. B* 148, 1054 (1999).
52. I. Okur, P. D. Townsend, and P. J. Chandler, *Nucl. Instrum. Meth. B* 148, 1069 (1999).
53. P. Magudapathy, P. Gangopadhyay, B. K. Panigrahi, K. G. M. Nair, and S. Dhara, *Phys. B* 299, 142 (2001).
54. A. L. Stepanov, D. E. Hole and A. A. Bukharaev, *Vacuum* 64, 169 (2002).
55. M. Dubiel, H. Hofmeister, E. Schurig, E. Wendler, and W. Wesch, *Nucl. Instrum. Meth. B* 166–167, 871 (2000).
56. A. L. Stepanov, D. E. Hole, and P. D. Townsend, *Nucl. Instrum. Meth. B* 161–163, 913 (2000).

57. A. L. Stepanov, D. E. Hole, and P. D. Townsend, *J. Non-Cryst. Solids* 260, 65 (1999).

58. A. L. Stepanov, D. E. Hole, and P. D. Townsend, *J. Non-Cryst. Solids* 244, 275 (1999).

59. A. L. Stepanov, D. E. Hole, and P. D. Townsend, *Nucl. Instrum. Meth. B* 149, 89 (1999).

60. A. L. Stepanov, V. A. Zhikharev, D. E. Hole, P. D. Townsend, and I. B. Khaibullin, *Nucl. Instrum. Meth. B* 166–167, 26 (2000).

61. A. Oliver, J. C. Cheang-Wong, J. Roiz, L. Rodriguez-Fernández, J. M. Hernández, A. Crespo-Sosa, and E. Muñoz, *Nucl. Instrum. Meth. B* 191, 333 (2002).

62. J. C. Pivin, M. A. Garcia, J. Llopis, and H. Hofmeister, *Nucl. Instrum. Meth. B* 191, 794 (2002).

63. J. C. Pivin, M. A. García, H. Hofmeister, A. Martucci, M. Sendova Vassileva, M. Nikolaeva, O. Kaitasov and J. Llopis, *Eur. Phys. J. D* 20, 251 (2002).

64. A. L. Stepanov, D. E. Hole, and P. D. Townsend, *Nucl. Instrum. Meth. B* 166–167, 882 (2000).

65. P. D. Townsend and D. E. Hole, *Vacuum* 63, 641 (2001).

66. M. Ikeyama, S. Nakao, M. Tazawa, K. Kadono, and K. Kamada, *Nucl. Instrum. Meth. B* 175–177, 652 (2001).

67. A. Oliver, J. C. Cheang-Wong, J. Roiz, J. M. Hernández, L. Rodríguez-Fernández, and A. Crespos, *Nucl. Instrum. Meth. B* 175–177, 495 (2001).

68. K. Fukumi, A. Chayahara, K. Ohora, N. Kitamura, Y. Horino, K. Fujii, M. Makihara, J. Hayakaya, and N. Ohno, *Nucl. Instrum. Meth. B* 149, 77 (1999).

69. Y. Takeda, V. T. Gritsyna, N. Umeda, C. G. Lee, and N. Kishimoto, *Nucl. Instrum. Meth. B* 148, 1029 (1999).

70. A. L. Stepanov, D. E. Hole, and P. D. Townsend, *Nucl. Instrum. Meth. B* 191, 468 (2002).

71. U. Pal, A. Bautista-Hernández, L. Rodríguez-Fernández, and J. C. Cheang-Wong, *J. Non-Cryst. Solids* 275, 65 (2000).

72. N. Umeda, N. Kishimoto, Y. Takeda, C. G. Lee, and V. T. Gritsyna, *Nucl. Instrum. Meth. B* 166–167, 864 (2000).

73. N. Kishimoto, N. Umeda, Y. Takeda, C. G. Lee, and V. T. Gritsyna, *Nucl. Instrum. Meth. B* 148, 1017 (1999).

74. Y. Takeda, V. T. Gritsyna, N. Umeda, C. G. Lee, and N. Kishimoto, *Nucl. Instrum. Meth. B* 148, 1029 (1999).

75. C. Maurizio, F. d'Acapito, M. Benfatto, S. Mobilio, E. Cattaruzza, and F. Gonella, *Eur. Phys. J. B* 14, 211 (2000).

76. Z. Dai, S. Yamamoto, K. Narumi, A. Miyashita, and H. Naramoto, *Nucl. Instrum. Meth. B* 149, 108 (1999).

77. D. Ila, R. L. Zimmerman, C. I. Muntele, P. Thevenard, F. Orucevic, C. L. Santamaria, P. S. Guichard, S. Schiestel, C. A. Carosella, G. K. Hubler, D. B. Poker, and D. K. Hensley, *Nucl. Instrum. Meth. B* 191, 416 (2002).

78. O. Cíntora-González, C. Estournès, D. Muller, J. Guille, and J. J. Grob, *Nucl. Instrum. Meth. B* 147, 422 (1999).

79. R. S. Brusa, W. Deng, G. P. Karwasz, A. Zecca, G. Mariotto, P. Folegati, R. Ferragut, and A. Dupasquier, *Appl. Surf. Sci.* 194, 106 (2002).

80. A. Markwitz, R. Grötzschel, K. H. Heinig, L. Rebohle, and W. Skorupa, *Nucl. Instrum. Meth. B* 152, 319 (1999).

81. T. Höche and T. Angermann, *J. Non-Cryst. Solids* 262, 114 (2000).

82. J. C. Cheang-Wong, A. Oliver, J. Roiz, J. M. Hernández, L. Rodríguez-Fernández, J. C. Morales, and A. Crespo-Sosa, *Nucl. Instrum. Meth. B* 175–177, 490 (2001).

83. K. Masuda, M. Yamamoto, M. Kanaya, and Y. Kanemitsu, *J. Non-Cryst. Solids* 299–302, 447 (2002).

84. E. M. Hunt and J. M. Hampikian, *Acta Mater.* 47, 1497 (1999).

85. A. Aboukaïs, L. D. Bogomolova, A. A. Deshkovskaya, V. A. Jachkin, N. A. Krasil'nikova, S. A. Prushinsky, O. A. Trul, S. V. Stefanovsky, and E. A. Zhilinskaya, *Opt. Mater.* 19, 295 (2002).

86. A. Deshkovskaya, Ch. Buchal, V. Komar, and I. Skornyakov, *Surf. Coat. Technol.* 158–159, 513 (2002).

87. F. D'Acapito, G. Battaglin, E. Cattaruzza, F. Gonella, C. Maurizio, P. Mazzoldi, S. Mobilio, and F. Zontone, *Eur. Phys. J. D* 10, 123 (2000).

88. E. Cattaruzza, G. Battaglin, R. Polloni, T. Cesca, F. Gonella, G. Mattei, C. Maurizio, P. Mazzoldi, F. D'Acapito, F. Zontone, and R. Bertoncello, *Nucl. Instrum. Meth. B* 148, 1007 (1999).

89. E. Cattaruzza, F. d'Acapito, F. Gonella, A. Longo, A. Martorana, G. Mattei, C. Maurizio, and D. Thiaudière, *J. Appl. Cryst.* 33, 740 (2000).

90. F. Gonella, E. Cattaruzza, G. Battaglin, F. D'Acapito, C. Sada, P. Mazzoldi, C. Maurizio, G. Mattei, A. Martorana, A. Longo, and F. Zontone, *J. Non-Cryst. Solids* 280, 241 (2001).

91. C. de Julián Fernández, C. Sangregorio, G. Mattei, C. Maurizio, G. Battaglin, F. Gonella, A. Lascialfari, S. Lo Russo, D. Gatteschi, P. Mazzoldi, J. M. Gonzalez, and F. D'Acapito, *Nucl. Instrum. Meth. B* 175–177, 479 (2001).

92. R. Bertoncello, S. Gross, F. Trivillin, F. Caccavale, E. Cattaruzza, P. Mazzoldi, G. Mattei, G. Battaglin, and S. Daolio, *J. Mat. Res.* 14, 2449 (1999).

93. L. Armelao, R. Bertoncello, E. Cattaruzza, S. Gialanella, S. Gross, G. Mattei, P. Mazzoldi, and E. Tondello, *J. Mater. Chem.* 12, 2401 (2002).

94. G. Mattei, *Nucl. Instrum. Meth. B* 191, 323 (2002).

95. E. Borsella, S. Dal Toè, G. Mattei, C. Maurizio, P. Mazzoldi, A. Saber, G. Battaglin, E. Cattaruzza, F. Gonella, A. Quaranta, and F. D'Acapito, *Mater. Sci. Eng. B* 82, 148 (2001).

96. E. Borsella, C. de Julián Fernández, M. A. García, G. Mattei, C. Maurizio, P. Mazzoldi, S. Padovani, C. Sada, G. Battaglin, E. Cattaruzza, F. Gonella, A. Quaranta, F. D'Acapito, M. A. Tagliente, and L. Tapfer, *Nucl. Instrum. Meth. B* 191, 447 (2002).

97. E. Borsella, M. A. Garcia, G. Mattei, C. Maurizio, P. Mazzoldi, E. Cattaruzza, F. Gonella, G. Battaglin, A. Quaranta, and F. D'Acapito, *J. Appl. Phys.* 90, 4467 (2001).

98. E. Borsella, C. de Julián Fernández, M. A. García, G. Mattei, C. Maurizio, P. Mazzoldi, S. Padovani, C. Sada, G. Battaglin, E. Cattaruzza, F. Gonella, A. Quaranta, F. D'Acapito, M. A. Tagliente, and L. Tapfer, *Nucl. Instrum. Meth. B* 191, 447 (2002).

99. A. Meldrum, C. W. White, L. A. Boatner, I. M. Anderson, R. A. Zuhr, E. Sonder, J. D. Budai, and D. O. Henderson, *Nucl. Instrum. Meth. B* 148, 957 (1999).

100. Y. Kanemitsu, H. Tanaka, T. Kushida, K. S. Min, and H. A. Atwater, *Phys. E: Low-Dimensional Syst. Nanostructures* 7, 322 (2000).

101. C. W. White, A. Meldrum, J. D. Budai, S. P. Withrow, E. Sonder, R. A. Zuhr, D. M. Hembree Jr., M. Wu, and D. O. Henderson, *Nucl. Instrum. Meth. B* 148, 991 (1999).

102. K. Fukumi, A. Chayahara, H. Kageyama, K. Kadono, T. Akai, N. Kitamura, H. Mizoguchi, Y. Horino, M. Makihara, K. Fujii, and J. Hayakawa, *J. Non-Cryst. Solids* 259, 93 (1999).

103. J. C. Cheang-Wong, A. Oliver, A. Crespo, J. M. Hernández, E. Muñoz, and R. Espejel-Morales, *Nucl. Instrum. Meth. B* 161–163, 1058 (2000).

104. F. Gonella, G. Mattei, P. Mazzoldi, C. Sada, G. Battaglin and E. Cattaruzza, *Appl. Phys. Lett.* 75, 55 (1999).

105. T. S. Anderson, R. H. Magruder III, J. E. Wittig, D. L. Kinser, and R. A. Zuhr, *Nucl. Instrum. Meth. B* 171, 401 (2000).

106. H. Tsuji, K. Kurita, Y. Gotoh, N. Kishimoto, and J. Ishikawa, *Nucl. Instrum. Meth. B* 195, 315 (2002).

107. E. Cattaruzza, F. D'Acapito, C. de Julian Fernandez, A. de Lorenzi, F. Gonella, G. Mattei, C. Maurizio, P. Mazzoldi, S. Padovani, B. F. Scremin, and F. Zontone, *Nucl. Instrum. Meth. B* 191, 406 (2002).

108. G. Battaglin, E. Cattaruzza, G. De Marchi, F. Gonella, G. Mattei, C. Maurizio, P. Mazzoldi, M. Parolin, C. Sada, and I. Calliari, *Nucl. Instrum. Meth. B* 191, 392 (2002).

109. C. de Julián, C. Sangregorio, G. Mattei, G. Battaglin, E. Cattaruzza, F. Gonella, S. Lo Russo, F. D'Orazio, F. Lucari,

G. De, D. Gatteschi, and P. Mazzoldi, *J. Magn. Magn. Mater.* 226–230, 1912 (2001).

110. C. de Julián Fernández, C. Sangregorio, G. Mattei, G. De, A. Saber, S. Lo Russo, G. Battaglin, M. Catalano, E. Cattaruzza, F. Gonella, D. Gatteschi, and P. Mazzoldi, *Mat. Sci. Eng. C* 15, 59 (2001).

111. F. D'Orazio, F. Lucari, C. de Julián, G. Mattei, S. Lo Russo, C. Maurizio, P. Mazzoldi, C. Sangregorio, D. Gatteschi, F. Gonella, E. Cattaruzza, C. Battaglin, and D. Fiorani, *J. Magn. Magn. Mater.* 242–245, 627 (2002).

112. G. W. Arnold and P. Mazzoldi, in "Ion Beam Modification of Insulator" (P. Mazzoldi and G. W. Arnold, Eds.), p. 195. Elsevier, Amsterdam, 1987.

113. J. P. Biersack and L. G. Haggmark, *Nucl. Instrum. Meth.* 174, 257 (1980).

114. W. J. Weber, R. C. Ewing, C. A. Angell, G. W. Arnold, A. N. Cormack, J. M. Delaye, D. L. Griscom, L. W. Hobbs, A. Navrotsky, D. L. Price, A. M. Stoneham, and M. C. Weinberg, *J. Mater. Res.* 12, 1946 (1997).

115. G. W. Arnold, *J. Non-Cryst. Solids* 179, 288 (1994).

116. H. Hosono, *J. Non-Cryst. Solids* 187, 457 (1995).

117. H. Hosono and H. Imagawa, *Nucl. Instrum. Meth. B* 141, 566 (1998).

118. M. Mizuguchi, H. Hosono, and H. Kawazoe, *Mater. Sci. Eng. A* 253, 275 (1998).

119. D. L. Griscom, *J. Non-Cryst. Solids* 73, 51 (1985).

120. A. K. Varshneya, in "Fundamentals of Inorganic Glasses." Academic Press, San Diego, 1994.

121. D. L. Griscom, *Nucl. Instrum. Meth. B* 1, 481 (1984).

122. G. W. Arnold, *IEEE Trans. Nucl. Sci.* NS-20, 220 (1973).

123. G. W. Arnold, G. Battaglin, G. Mattei, P. Mazzoldi, and S. Zandolin, *Nucl. Instrum. Meth. B* 166–167, 440 (2000).

124. F. Piao, W. G. Oldham, and E. E. Haller, *J. Non-Cryst. Solids* 276, 61 (2000).

125. A. Benyagoub, S. Klaumünzer, and M. Toulemonde, *Nucl. Instrum. Meth. B* 146, 449 (1998).

126. C. M. Johnson, T. D. Thompson, M. C. Ridgway and V. Gurarie, *Nucl. Instrum. Meth. B* 141, 629 (1998).

127. R. L. Hines and R. Arndt, *Phys Rev.* 119, 623 (1960).

128. E. P. EerNisse, *J. Appl. Phys.* 45, 167 (1974).

129. A. P. Webb, L. Allen, B. R. Edgar, A. J. Houghton, P. D. Townsend, and C. W. Pitt, *J. Phys. D* 8, 1567 (1975).

130. A. P. Webb and P. D. Townsend, *J. Phys. D: Appl. Phys.* 9, 1343 (1976).

131. C. Wang, Y. Tao, and S. Wang, *J. Non-Cryst. Solids* 52, 589 (1982).

132. I. K. Naik, *Appl. Phys. Lett.* 43, 519 (1983).

133. A. Carnera, P. Mazzoldi, A. Boscolo-Boscoletto, F. Caccavale, R. Bertoncello, G. Granozzi, I. Spagnol, and G. Battaglin, *J. Non-Cryst. Solids* 125, 293 (1990).

134. P. Mazzoldi, F. Caccavale, E. Cattaruzza, A. Boscolo-Boscoletto, R. Bertoncello, A. Glisenti, G. Battaglin, and C. Gerardi, *Nucl. Instrum. Meth. B* 65, 367 (1992).

135. P. Mazzoldi, *Nucl. Instrum. Meth.* 209/210, 1089 (1983).

136. F. Geotti-Bianchini, P. Polato, S. Lo Russo, and P. Mazzoldi, *J. Am. Ceram. Soc.* 67, 39 (1984).

137. R. Bertoncello, F. Trivillin, E. Cattaruzza, P. Mazzoldi, G. W. Arnold, G. Battaglin, and M. Catalano, *J. Appl. Phys.* 77, 1294 (1995).

138. A. Perez, G. Marest, B. D. Sawicka, J. A. Sawicki, and T. Tyliszczac, *Phys. Rev. B* 28, 1227 (1983).

139. A. Perez, *Nucl. Instrum. Meth. B* 1, 621 (1984).

140. C. J. McHargue, P. S. Sklad, C. W. White, G. C. Farlow, A. Perez, N. Kornilios, and G. Marest, in "Materials Modification by High-fluence Ion Beams" (R. Kelly and M. Fernanda da Silva, Eds.), p. 245. Kluwer Academic, Dordrecht, 1989.

141. T. Futagami, Y. Aoki, O. Yoda, and S. Nagai, *Nucl. Instrum. Meth. B* 88, 261 (1994).

142. H. Hosono, *Jpn. J. Appl. Phys.* 32, 3892 (1993).

143. O. Knacke, O. Kubaschewski, and K. Hesselmann, in "Thermo-chemical Properties of Inorganic Substances," 2nd ed. Springer-Verlag, Berlin, Heidelbergh, 1991.

144. W. Primak, E. Edwards, D. Keifer, and H. Szymanski, *Phys. Rev.* 133, 531 (1964).

145. H. Hosono and N. Matsunami, *Phys. Rev. B* 48, 13469 (1993).

146. H. Hosono and H. Imagawa, *Nucl. Instrum. Meth. B* 91, 510 (1994).

147. J. Emsley, "The Elements," 2nd ed. Oxford Univ. Press, New York, 1993.

148. R. Kelly, in "Structure–Property Relationships in Surface-Modified Ceramics" (C. J. McHargue, Ed.), Kluwer Academic, Dordrecht, 1989.

149. R. Kelly, *Mater. Sci. Eng. A* 115, 11 (1989).

150. H. Hsieh, T. Diaz de la Rubia, R. S. Averback, and R. Benedek, *Phys. Rev. B* 40, 9986 (1989).

151. R. Bertoncello, A. Glisenti, G. Granozzi, G. Battaglin, F. Caccavale, E. Cattaruzza, and P. Mazzoldi, *J. Non-Cryst. Solids* 162, 205 (1993).

152. G. Battaglin, *Nucl. Instrum. Meth. B* 116, 102 (1996).

153. E. Cattaruzza, R. Bertoncello, F. Trivillin, P. Mazzoldi, G. Battaglin, L. Mirenghi, and P. Rotolo, *J. Mat. Res.* 11, 229 (1996).

154. R. Bertoncello, S. Gross, F. Trivillin, F. Caccavale, E. Cattaruzza, P. Mazzoldi, G. Mattei, G. Battaglin, and S. Daolio, *J. Mat. Res.* 14, 2449 (1999).

155. G. Battaglin, R. Bertoncello, M. Casarin, E. Cattaruzza, G. Mattei, P. Mazzoldi, F. Trivillin, and M. Urbani, *J. Non-Cryst. Solids* 253, 251 (1999).

156. S. Barison, G. Battaglin, R. Bertoncello, E. Cattaruzza, A. Mascolo, P. Mazzoldi, M. Ruzzi, and F. Trivillin, *J. Mat. Chem.* 9, 2929 (1999).

157. P. Mazzoldi, F. Caccavale, E. Cattaruzza, P. Chakraborty, L. Tramontin, A. Boscolo-Boscoletto, R. Bertoncello, F. Trivillin, G. Battaglin, and G. W. Arnold, *Nucl. Instrum. Meth. B* 91, 505 (1994).

158. K. Fukumi, A. Chayahara, M. Makihara, K. Fujii, J. Hayakawa and M. Satou, *J. Am. Ceram. Soc.* 77 (1994) 3019.

159. H. Hosono, H. Tanoue, S. Hishita, and A. Nakamura, *Nucl. Instrum. Meth. B* 116, 178 (1996).

160. H. Hosono and N. Matsunami, *Nucl. Instrum. Meth. B* 141, 566 (1998).

161. S. Y. Park, T. Isobe, M. Senna, R. A. Weeks, and R. A. Zuhr, *Appl. Phys. Lett.* 73, 2687 (1998).

162. T. S. Anderson, R. H. Magruder III, D. L. Kinser, R. A. Zuhr, and D. K. Thomas, *Nucl. Instrum. Meth. B* 124, 40 (1997).

163. E. Cattaruzza, F. Gonella, G. Mattei, P. Mazzoldi, D. Gatteschi, C. Sangregorio, M. Falconieri, G. Salvetti, and G. Battaglin, *Appl. Phys. Lett.* 73, 1176 (1998).

164. A. Polman, D. C. Jacobson, D. J. Eaglesham, R. C. Kistler, and J. M. Poate, *J. Appl. Phys.* 70, 3778 (1991).

165. A. Perez, M. Treilleux, T. Capra, and D. L. Griscom, *J. Mat. Res.* 2, 910 (1987).

166. E. Cattaruzza et al., in preparation.

167. X. L. Wu, T. Gao, G. G. Siu, S. Tong, and X. M. Bao, *Appl. Phys. Lett.* 74, 2420 (1999).

168. G. K. Celler, L. E. Trimble, T. T. Sheng, S. G. Kosinski, and K. W. West, *Appl. Phys. Lett.* 53, 1178 (1988).

169. T. S. Anderson, R. H. Magruder III, R. A. Weeks, and R. A. Zuhr, *J. Non-Cryst. Solids* 203, 114 (1996).

170. E. Cattaruzza, F. Gonella, G. Mattei, P. Mazzoldi, G. Battaglin, D. Gatteschi, C. Sangregorio, R. Bertoncello, and F. Trivillin, in "Proceedings of the XVIII International Congress on Glass" (M. K. Choudhary, N. T. Huff, and C. H. Drummond III, Eds.), Chap. 11, p. 13. The American Ceramic Society, Westerville, OH, 1998.

171. H. Hosono, Y. Abe, Y. L. Lee, T. Tokizaki, and A. Nakamura, *Appl. Phys. Lett.* 61, 2747 (1992).

172. H. Hosono, Y. Y. Suzuki, Y. Abe, Y. L. Lee, K. Oyoshi, and S. Tanaka, *J. Non-Cryst. Solids* 142, 287 (1992).

173. G. Battaglin, R. Bertoncello, M. Casarin, E. Cattaruzza, G. Mattei, P. Mazzoldi, F. Trivillin, and M. Urbani, *J. Non-Cryst. Solids* 253, 251 (1999).

174. G. Battaglin, *Nucl. Instrum. Meth. B* 116 102 (1996).

175. D. O. Henderson, M. Wu, A. Ueda, Y. S. Tung, R. Mu, J. Chen, Z. Gu, W. E. Collins, C. W. White, J. Budai, A. Meldrum, R. A. Zuhr, and J. G. Zhu, *Nucl. Instrum. Meth. B* 141, 284 (1998).

176. Y. Takeda, T. Hioki, T. Motohiro, S. Noda, and T. Kurauchi, *Nucl. Instrum. Meth. B* 91, 515 (1994).

177. E. Cattaruzza, G. Mattei, P. Mazzoldi, R. Bertoncello, G. Battaglin, and L. Mirenghi, *Appl. Phys. Lett.* 67, 2884 (1995).

178. G. Battaglin, R. Bertoncello, E. Cattaruzza, P. Colombo, G. Mattei, P. Mazzoldi, and M. Ricci, "Proceedings of XIX International Congress on Glass," Vol. 2, p. 865, 2001.

179. U. Herrmann, H. H. Dunken, E. Wendler, and W. Wesch, *J. Non-Cryst. Solids* 204, 273 (1996).

180. K. Becker, L. Yang, R. F. Haglund Jr., R. H. Magruder, R. A. Weeks, and R. A. Zuhr, *Nucl. Instrum. Meth. B* 59–60, 1304 (1991).

181. R. F. Haglund Jr., R. H. Magruder III, S. H. Morgan, D. O. Henderson, R. A. Weller, L. Yang, and R. A. Zuhr, *Nucl. Instrum. Meth. B* 65, 405 (1992).

182. R. F. Haglund, L. Yang, R. H. Magruder III, J. E. Wittig, K. Becker, and R. A. Zuhr, *Opt. Lett.* 18, 373 (1993).

183. R. H. Magruder III, R. A. Zuhr, and R. A. Weeks, *Nucl. Instrum. Meth. B* 59–60, 1308 (1991).

184. R. H. Magruder III, R. F. Haglund Jr., L. Yang, J. E. Wittig, and R. A. Zuhr, *J. Appl. Phys.* 76, 708 (1994).

185. H. Hosono, Y. Abe, and N. Matsunami, *Appl. Phys. Lett.* 60, 2613 (1992).

186. H. Hosono, H. Fukushima, Y. Abe, R. A. Weeks, and R. A. Zuhr, *J. Non-Cryst. Solids* 143, 157 (1992).

187. H. Hosono and R. A. Zuhr, *J. Non-Cryst. Solids* 178, 160 (1994).

188. H. Hosono, *Phys. Rev. Lett.* 74, 110 (1995).

189. G. W. Arnold, P. Mazzoldi, L. Tramontin, A. Boscolo-Boscoletto, and G. Battaglin, *Mat. Res. Soc. Symp. Proc.* 279, 285 (1993).

190. F. D'Acapito, S. Mobilio, G. Battaglin, E. Cattaruzza, F. Gonella, F. Caccavale, P. Mazzoldi, and J. R. Regnard, *J. Appl. Phys.* 87, 1819 (2000).

191. F. Gonella, *Nucl. Instrum. Meth. B* 166–167, 831 (2000).

192. D. C. Reynolds and T. C. Collins, "Excitons." Academic Press, New York, 1981.

193. R. A. Weeks, H. Hosono, R. A. Zuhr, R. H. Magruder III, and H. Mogul, *Mat. Res. Soc. Symp. Proc.* 152, 115 (1989).

194. F. D'Acapito, S. Colonna, S. Mobilio, F. Gonella, E. Cattaruzza, and P. Mazzoldi, *Appl. Phys. Lett.* 71, 2611 (1997).

195. A. Balerna, E. Bernieri, P. Picozzi, A. Reale, S. Santucci, E. Burattini, and S. Mobilio, *Phys. Rev. B* 31, 5058 (1985).

196. M. Marcus, A. Andrews, M. P. Zegenhagen, J. A. S. Bommannavar, and P. Montano, *Phys. Rev. B* 42, 3312 (1990).

197. N. Kishimoto, V. T. Gritsyna, H. Kono, H. Amekura, and T. Saito, *Nucl. Instrum. Meth. B* 127–128, 579 (1997).

198. H. Yasuda, and H. Mori, *Z. Phys. D* 31, 131 (1994).

199. G. Battaglin, E. Cattaruzza, F. Gonella, G. Mattei, P. Mazzoldi, C. Sada, and X. Zhang, *Nucl. Instrum. Meth. B* 166–167, 857 (2000).

200. H. Okamoto, D. J. Chakrabarti, D. E. Laughlin, and T. B. Massalski, "Phase Diagrams of Binary Gold Alloys," Monograph Series on Alloy Phase Diagrams. American Society for Metals, Metals Park, OH, 1987.

201. H. Yasuda, K. Mitsuishi, and H. Mori, *Phys. Rev. B* 64, 094101 (2001).

202. P. Buffat and J.-P. Borel, *Phys. Rev. A* 13, 2287 (1976).

203. G. Battaglin, E. Cattaruzza, C. De Julian Fernandez, G. De Marchi, F. Gonella, G. Mattei, C. Maurizio, P. Mazzoldi, A. Miotello, C. Sada, and F. D'Acapito, *Nucl. Instrum. Meth. B* 175–177, 410 (2001).

# Metal Nanoclusters as Quantum Dots

## Günter Schmid

*University of Essen, Essen, Germany*

## CONTENTS

## 1. INTRODUCTION

Quantum dots can be defined as zero-dimensional particles of a matter, following quantum mechanical rules instead of the laws of classical physics. These have been developed for bulk materials where the number of building blocks, independent of their nature, is practically infinite. Keeping in mind that for instance 2 mg of gold still contains about $6 \times 10^{18}$ atoms, it becomes clear that even very small particles, say at the border of invisibility, still behave bulklike and so fit into our common idea of materials properties. However, if the dimensions fall below a distinct value, most of the known properties are going to be changed. A few examples will demonstrate this fascinating behavior which in principle has been known for a long time to mankind, of course without understanding the reasons.

Ruby red small gold particles have been used to color glasses since ancient times. Buildings in regions with cold winters would be damaged yearly if the water inside stones and concrete was not part of a nano- and microporous system, decreasing the melting point of water down until −60 °C. Nature uses the smallness of materials to change wettability of surfaces and so to keep them clean. A well-known example is the famous "Lotus effect." The huge leaves of the Lotus plant look always clean since, due to their nano- and microstructured surface, the wettability is so low that water droplets immediately fall down taking with them dust and other impurities. It is assumed that many other plants and even butterflies use those effects for cleaning themselves.

What happens if materials become small? In general one can say that it is the change of the surface:volume ratio when going from large to small. The smaller a particle or a droplet, the larger its surface compared with its volume. Surface atoms or surface molecules, however, differ characteristically from inner ones, since they have less neighbors and so behave differently in many respects. For instance it is known that ice, even at low temperatures, is always covered by a film of "liquid" water molecules. These are not fully incorporated into the crystal lattice and so become mobile. In the case of the "Lotus effect" it is the surface tension of the water droplets that cannot be overcome by the nanoparticles on the leaf surface.

Metals in general are characterized by their unique electronic bonding system, differing from nonmetals and semiconductors. It is based on *quasi* freely mobile electrons inside a piece of bulk metal. However, if the dimension of a metal decreases to a certain extent, this very special behavior is no longer possible: the electrons are trapped in a too small volume and then behave very differently and consequently also change the particles' physical and chemical properties. We will discuss the consequences in detail in the following sections.

This chapter on metal nanoparticles as quantum dots tries to elucidate these very special events that occur when quantum size effects dominate instead of classical bulk behavior. In a somewhat simplified manner metal quantum dots can be called "artificial atoms" since they exhibit more or less discrete electronic energy levels in contrast to bulk species owning electrons in energy bands. It becomes very clear that those species must have exciting properties promising completely novel applications.

## 2. ELECTRONS IN BULK METALS AND IN METAL NANOPARTICLES

Two-thirds of the chemical elements are metals. In most cases they form crystals of dense packed atoms, the valence electrons of which are part of a band of nondistinguishable states of energy. These can be fully or only partially occupied. If they are fully occupied, an energetically neighbored

empty band is necessary to make the electrons movable. Partially occupied bands fulfill this condition by themselves. The existence of conductivity bands is the most important characteristic of metals. If the energy gap between a fully occupied band and the next empty band is too large to overlap, semiconductors result. In principle, this consideration of a metallic state is derived from the molecular orbital (MO) description of molecules, where bonding and antibonding electronic states are formulated to describe the electronic situation. So the electronic bulk situation in a piece of lithium, for instance, is nothing but an extension of the MO description of a $Li_2$ molecule to the MO description of a $Li_\infty$ "molecule" with a practically infinite number of bonding and antibonding "MOs," now called bands. On the way from $Li_2$ to $Li_\infty$ the system must pass a situation when, for the first time, metallic properties become evident. The originally well defined energy levels become broader by the large number of narrow states, however. Finally, no longer is differentiation possible and the band formation is perfect. Moving from the opposite side, the question arises, when will typical bulk properties begin to disappear? Figure 1 illustrates these events by three typical situations: a molecular particle (a), consisting of only a few atoms, has very discrete electronic levels, the molecular orbitals. On the way to the bulk (c) with its typical band structure, here formed from $s$ and $d$ electrons, (b) illustrates the situation between molecule and bulk. We still see quite well pronounced electronic energy levels, however, of a less precise character than in (a).

The situation in (b) illustrates a piece of matter that still behaves electronically similar to an atom or a molecule and consequently has to be described by quantum mechanical rules and not by classical physics like its bulk relatives. Therefore, those particles are called "quantum dots" or the somewhat more spectacular "artificial atoms."

The transition from a bulk situation to molecular-like situation is also called a size-induced metal-insulator transition (SIMIT) [1–3]. The SIMIT is caused by the limited volume of extended states with a corresponding De Broglie wavelength. The effect, happening between ca. 1 $\mu$m and a few nm, was studied by microwave absorption measurements of solid or liquid indium particles dispersed in oil. Assuming that the conduction electrons form standing waves with multiples of $\lambda/2$ ($\lambda$ = De Broglie wavelength), it was concluded that boundaries of those metal particles act as potential
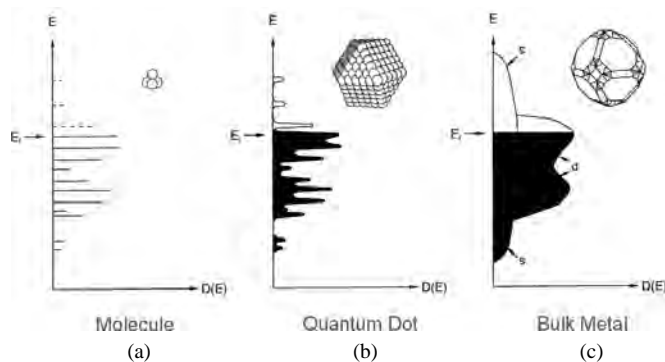
walls, trapping the electrons in between. The model of a "particle in a box," related to the textbook model of an "electron in the box," was created. Since the level spacing of those electrons in the size regime are still below the thermal energy $k_BT$, their temperature dependence is still metallic. However, the number of "metallic electrons" is limited due to the particles size. Nimtz et al. used this effect to generate the so-called cutoff wavelength transistor [3].

Of course, it is obvious that those artificial atoms should have exciting properties in many respects. The most spectacular one is to be expected in relation to the so-called single electron tunneling (SET). This means that electron transitions between particles can principally be performed by single electrons, as Likharev predicted [4]. The most important condition to realize SETs is the right size of the particle, the appropriate temperature to avoid thermally activated tunneling between particles, and finally the distance between the particles. These conditions are set into relation by the formula

$$\frac{e^2}{2C} \gg k_BT$$

where $C$ is the capacity of the tunnel contact, $C = \varepsilon\varepsilon_o\frac{A}{d}$, $\varepsilon$ is the dielectric constant, $\varepsilon_o$ is the electric field constant, $A$ is the surface of the electrode, and $d$ is the distance of the electrodes. If the electrostatic energy $E_e$ is very large compared with the thermal energy $E_t$, controlled tunneling of single electrons becomes possible. As the capacity $C$ depends on the surface and herewith on the size of the electrodes (i.e., the size of the participating particles), the formula tells us that the smaller a particle, the larger its electrostatic energy. Figure 2a elucidates the the experimental setup for measuring the current–voltage characteristic of an individual nanoparticle. Figure 2b informs on the theoretical relation between current ($I$) and voltage ($U$) in such



(a)



(b)
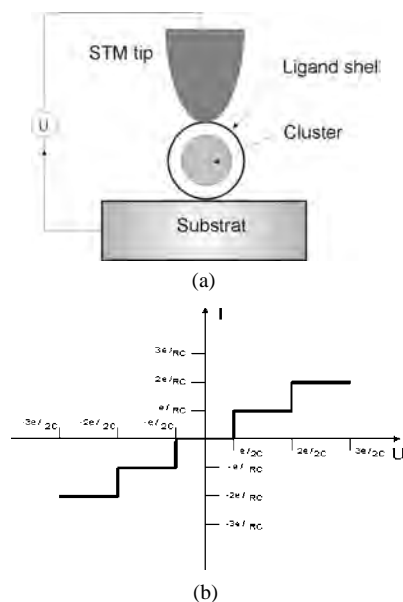
**Figure 2.** Experimental setup to register the current–voltage characteristics of a single metal nanocluster (a) and the corresponding theoretical staircase curve (b).



| Molecule | Quantum Dot | Bulk Metal |
| (a) | (b) | (c) |

**Figure 1.** Electronic situation in a molecule (a), a metal nanoparticle (b), and a bulk metal (c).

a system. The smallest possible increase of $U$ results in a smallest current $I$, forming so-called staircases.

Those stair cases, in other words, represent charge transport by single electrons. Figure 2a shows another detail that should be explained. As will be shown somewhat later, metal nanoparticles under investigation always bear a protecting shell of nonconducting molecules for several reasons. First, it would be impossible to prepare defined nanoparticles without those shells and, second, such isolating shells belong to a working system for building up a capacitance, necessary to observe SET.

Owning quantum dots as nanosized metal particles, if possible working at room temperature (if $E_e$ is large enough), give rise to thoughts reaching far into the future. For instance, if a system of organized quantum dots, working as transistors, could be created, a novel generation of computers would become available, surpassing the actual systems by magnitudes of orders.

In this connection it might be appropriate to briefly mention the two general strategies to develop nanosized structures for future electronics. There exists the so-called "top-down" strategy which is based on the miniaturization of bulk structures by various methods. It was and still is a unique story of success. Consider the development of the efficiency of computers! Their capacity is doubled every year and a half, as the famous Moore's law predicts. However, further miniaturization by conventional electron-beam lithography [5, 6] is known to be limited to, say, about 50 nm. This is probably far too large to really reach the quantum size regimes, especially if metals are considered as a matter of choice. The use of semiconductors in regions below 50 nm is problematic since the semiconductor properties are going to be lost when the structure units fall below a distinct dimension. So the opposite "bottom-up" strategy gains more and more importance. As we will see in the next section, the generation of metal nanoparticles is exclusively based on that technique. Bottom-up means that one starts with atoms, ions, or molecules which are then combined with nanoparticles of any, but well defined, size. Traditional chemical procedures can in general be applied. Particles in the size range of less than 1 nm, up to some dozens of nanometers, are available by relatively simple and cheap procedures. Section 3 will deal with some synthetic principles to prepare those metal nanoparticles.

# 3. SYNTHETIC STRATEGIES

There exist several wet-chemical procedures to generate metal nanoparticles. First of all it should be stated that all recipes are performed in solution and, very typical and important, the resulting particles are protected by different "skins." This has predominantly to do with the chemistry itself but is also a necessity to stabilize the particles kinetically. Without a protecting shell the particles would coalesce very quickly, and as a consequence only microcrystalline metal powders would be formed instead of individual particles.

The following methods include the most frequently used preparation techniques:

- salt reduction
- degradation of organometallic precursors
- electrochemical routes
- radiation induced synthesis
- ultrasound assisted methods

Among all, the salt reduction is by far the most important route to metal nanoparticles, since it is broadly applicable. The number of variations is huge and especially it is the opportunity to vary the conditions in an almost unlimited number. Furthermore, all metals under consideration are available as salts or complexes. Depending on the redox potentials, the choice of the reducing agents can also be varied in a wide range. No wonder that Faraday had already used salt reduction to prepare his famous purple–red colloidal gold solutions which partially still exist. The use of appropriate organometallic precursor molecules that can easily be degraded into metal atoms, followed by aggregation to nanoparticles, has developed as an interesting alternative to salt reduction, of course of less broad variability. The other methods mentioned are less important and shall not be considered further in this chapter which does not focus on synthetic aspects but rather on the properties of nanoparticles. However, some examples for salt reduction and the organometallic route will be discussed in the following section.

## 3.1. Salt Reduction

If a salt or a complex with positively charged metal atoms (not necessarily free ions) in solution is reduced by an appropriate reducing agent, metal atoms are generated in the very first step. Usually they are not long-lived and aggregate to continuously growing particles, sometimes even to small crystallites which, if big enough, precipitate. Mirrors on the glass walls of the reaction flasks are also very common and even practically used, for instance to make mirrors of silver, gold, or other noble metals. However, under distinct conditions it happens that the growth of the particles is restricted and nanoparticles of considerable stability are formed. The condition to yield size-limited particles is the presence of molecules, ions, charges, or even micelles to stop growth and to stabilize the particles. The number of species to protect naked particles is large.

Faraday originally used white phosphorus to reduce gold salts [7]. Turkevich for the first time reduced $AuCl_4^-$ with sodium citrate to prepare narrowly dispersed gold colloids [8]. Many modifications of that recipe became known in the course of the last few decades. Citrate was substituted by many other reducers such as $BH_4^-$ and $BEt_3H^-$ [9], $N_2H_4$ [10], $NH_2OH$ [11], $AlR_3$ [12, 13], $H_2$ [14–21], or alcohols [22–24], just to name a few. "Natural" systems like tannin [25, 26] and even living species like fungi [27] have been used to produce gold nanoparticles.

Besides gold, mainly silver, palladium, platinum, rhodium, but also less noble metals such as cobalt or nickel have been prepared in colloidal form. In any case, the particles were protected either directly by the oxidation products of the reducers, by ions, preventing coalescence due to electrical repulsion, or by solvent molecules, if polar enough. Polymers, stabilizing the particles due to their viscosity, have also been applied successfully, often in catalytic processes. Finally, special ligand molecules forming strong

bonds to surface atoms have turned out to protect metal nanoparticles best. Strong ligand shells even allow the isolation of the nanoparticles in solid state and their redispersion in appropriate solvents. This is not possible if ions, solvent molecules, or other less good binding species are used to cover the particle surface. Gold colloids, for instance, that have been prepared by the citrate method from $AuCl_4^-$ in water are weakly protected by a mixture of $Na^+$, $Cl^-$, citrate ions, and water. In water the stabilization is good enough to keep the red particles over long times in solution. However, if counterions are added or the concentration becomes too high, metallic precipitates are rapidly formed. The same particles can be isolated in solid state, if the ligand shell consists of the phosphine $P(C_6H_4SO_3Na)_3$ with strong Au–P bonds [28]. Nitrogen containing ligands, for instance phenanthroline and its derivatives [18, 19], amines and ammonium salts [9, 29], and, of special importance, thiols, have turned out to form very stable shells on the particle surfaces, depending on the kind of metal.

The synthesis of one special ligand stabilized gold nanoparticle shall be described in more detail, since it plays a decisive role in the following sections. It is $Au_{55}(PPh_3)_{12}Cl_6$ and some of its derivatives which become available by ligand exchange processes. As we will see later, $Au_{55}(PPh_3)_{12}Cl_6$ is of exceptional importance because, among the metal nanoparticles, it represents the prototype of a quantum dot. The $Au_{55}$ core is 1.4 nm in size; including the ligand shell of $PPh_3$ the diameter of the cluster is about 2.3 nm. It is prepared from $Ph_3PAuCl$ in benzene or toluene at 60 °C by reduction with $B_2H_6$ [30, 31]. Diborane is not only a very special agent that reduces Au(I) in the starting compound to Au(0) (with some restrictions due to the six Cl atoms), but it serves also as a Lewis acid to trap excessive $PPh_3$ with formation of $Ph_3P–BH_3$. This is an important aspect since the original $PPh_3$:Au ratio of 1:1 would not allow formation of nanoparticles. $Au_{55}(PPh_3)_{12}Cl_6$ can be isolated as a brown, microcrystalline powder in about 30% yield. Most of the gold is found as a metallic precipitate. The cluster compound is best soluble in dichloromethane; however, the stability in solution is rather low. It decomposes in the course of hours to gold and smaller cluster compounds. In contrast, the solid compound is stable over long periods of time as long as the temperature is kept at room temperature or below.

As already mentioned, $Au_{55}(PPh_3)_{12}Cl_6$ can be used for ligand exchange reactions. $PPh_3$ can be replaced by other phosphines or even better by thiols which are known as stronger ligands toward gold. Figure 3 summarizes some of the synthetic aspects concerning $Au_{55}$ particles.

## 3.2. Degradation of Organometallic Precursors

Controlled decomposition of appropriate organometallic complexes is another route to prepare metal nanoparticles. For instance, the decomposition of Ru(COD)(COT) (COD = 1,5-cyclooctadiene, COT = 1,3,5-cyclooctatriene) happens already at room temperature under an atmosphere of 1–3 bar $H_2$ in tetrahydrofurane in the presence of a stabilizer [32]. For instance, poly(vinyl pyrrolidone) (PVP) has been used to stabilize 1.1 nm Ru particles. Alkylamines and alkylthiols as protecting species gave 2–3 nm particles.



(a)

(b)
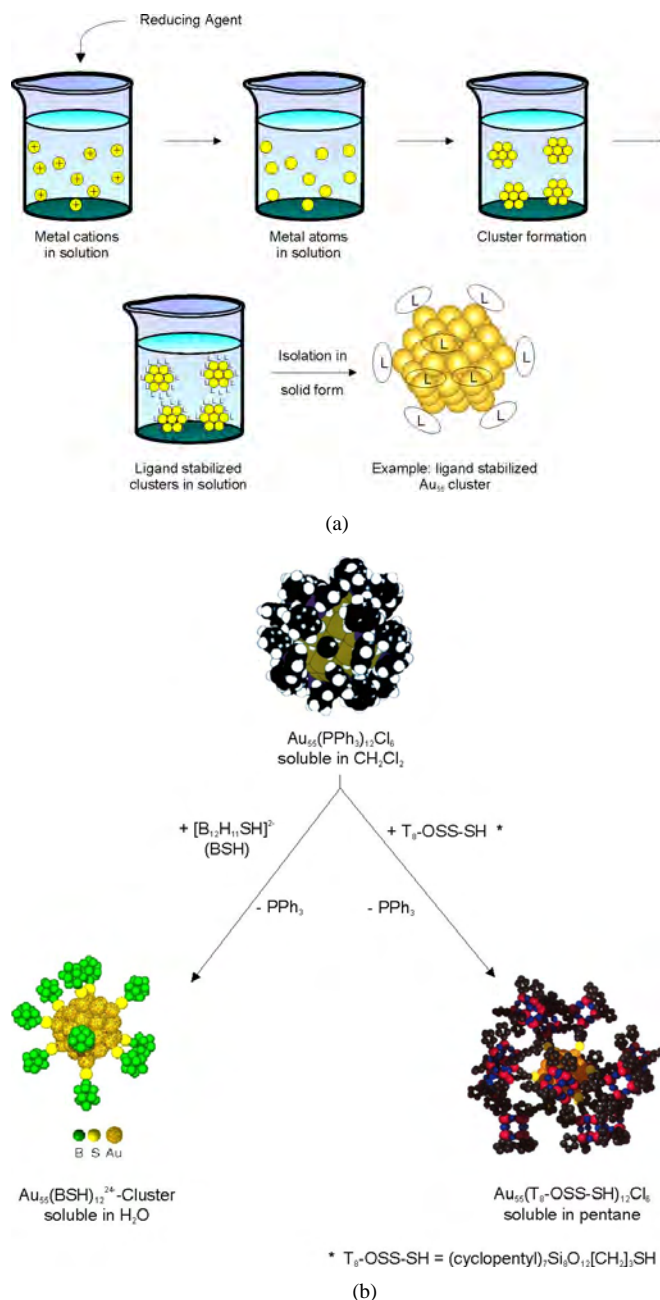
**Figure 3.** Formal sketch of the synthesis of ligand stabilized metal nanoparticles (a) and illustration of some ligand exchange reactions, combined with change of solubility properties (b).

High amine concentrations support formation of rod- and wormlike particles.

Bimetallic nanoparticles have also become available by this degradation method. $Co_xPt_{1-x}$ particles are formed if $Co(\eta^3-C_8H_{13})(\eta^4-C_8H_{12})$ and $Pt_2(dba)_3$ [dba = bis(dibenzylidene acetone)] are decomposed under hydrogen in the presence of PVP [33]. The composition of the alloylike particles depends on the initial ratio of the two precursors. $Co_3Pt_1$ and $Co_1Pt_1$ of 1 nm in size as well as $Co_1Pt_3$ of 1.5 nm have been characterized.

# 4. QUANTUM SIZE BEHAVIOR OF METAL NANOPARTICLES

Numerous investigations of metal nanoparticles in the size range of 1–15 nm of different metals using different methods have been performed in the course of the last 10–15 years. Size-dependent properties were frequently observed. However, it should be stated that each special method informs only on a distinct property. Therefore, it makes no sense to expect precise data for the transition between a typical bulk behavior and a quantum sized determined character. Rather it can be assumed that a less sharp continuation of properties will be observed, dependent on the applied method. In addition, an important factor is the temperature of observation. As discussed in Section 2, there is a direct relation between particle size and the electrostatic energy of electrons $E_e$, on the one hand, and, on the other hand, between $E_e$ and the temperature. *In summa* we will see that indeed all the different methods bring us to a quite reasonable understanding of what quantum size behavior of metal nanoparticles means and how large (or how small) those particles have approximately to be in order to justify the expression "quantum dot."

Strong deviations from bulk behavior have been predicted for the electronic susceptibility when the quantum size regime is reached, however, only at very low temperatures. So-called odd–even effects should become evident (i.e., half of the nanoparticles of a diamagnetic metal must statistically carry a spin). Each spin will interact with about six neighbored spins, assuming randomly packed particles that have to be small enough to make the effect strong enough to be observed. As subjects palladium nanoparticles of various size have been selected, namely those of 3.6, 3.0, and 2.5 nm in size, all protected by organic ligand shells, the diamagnetic contribution of which has been considered for the calculations [34]. Figure 4 shows the experimental as well as the calculated results.

The calculated solid curves fit quite well to the experimental data. These show a clear dependence of the susceptibility from the particle sizes. The susceptibility maxima indicate increasing interactions between spins on neighbored particles with decreasing size. For comparison: 15 nm Pd colloids as well as bulk palladium do not show any increase of susceptibility at lowest temperatures.

A quite different but also very impressive demonstration of the transition from the bulk to the quantum size regime succeeded by electronic relaxation processes in gold nanoparticles. Ligand protected 15 nm, 1.4 nm, and 0.7 nm Au nanoparticles in aqueous solution have been used for direct measurement of electronic energy relaxation using femtosecond laser spectroscopy [35]. The particles have been excited with a short 390 nm laser pulse to generate hot electrons, the relaxation of which was observed in the near infrared region. Figure 5 shows the decay profiles of the hot electrons probed at 790 nm for the three different particles. A fast rise is followed by a single or double exponential decay. The solid lines show the corresponding fits.

The relaxation time is in principle dependent on both electron–phonon coupling and surface collision. In larger particles the weakening of electron–phonon coupling dominates, expressed in slower electronic relaxation compared to bulk. Smaller particles are more strongly influenced by collision events, accelerating the relaxation. From Figure 5 it can be seen that the relaxation time for the 1.4 nm particles is much faster (1 ps) than for the 15 nm ones and is attributed to the increased surface collision processes. The 0.7 nm Au particles, on the contrary, exhibit a considerably longer relaxation time ($\approx$300 ps). The longer lived hot electrons demonstrate that the band description, still valid for the 1.4 nm particles, is no longer applicable. Those particles behave as molecules with localized electrons between the participating atoms. Finally, it can be stated that the transition from bulk to molecule with respect to the electronic relaxation of hot electrons happens between 1.4 and 0.7 nm.



**Figure 4.** Electronic magnetic susceptibility $\chi$ of Pd nanoparticles of different size, indicating increasing maxima with decreasing particle size. The maxima are caused by spin–spin interactions between neighboring particles. Solid curves represent the calculated behavior. Reprinted with permission from [34], Y. Volokitin et al., *Nature* 384 (1996). © 1996, Macmillan Magazines Ltd.



**Figure 5.** Time evolution profile of photogenerated hot electrons in gold nanoparticles of different size. Reprinted with permission from [35], B. A. Smith et al., *Chem. Phys. Lett.* 270, 139 (1997). © 1997, Elsevier Science.

Mössbauer spectroscopy is another valuable tool to get information on the electronic situation in metal nano-particles. [197]Au Mössbauer spectroscopic investigations on a series of Pt and Au nanoparticles of varying sizes have been performed [36, 37]. [197]Au Mössbauer spectroscopy of Pt nanoparticles became possible by irradiation with thermal neutrons, ending up in [197]Au isotopes. Size dependent Möss-bauer data can be expected since a large surface:volume ratio (increasing with decreasing size) leads to large con-tributions from surface atoms. The electron density near to a metal surface fluctuates due to screening of the sur-face (Friedel oscillations). In combination with quantum size effects those fluctuations can produce a net variation of the isomer shift (IS) inside the metal cores of the particles. For gold as well as for platinum nanoparticles up to 4 nm fluc-tuations could be observed. Gold particles >6 nm do not indicate fluctuations. Except for those larger gold colloids all the smaller nanoparticles show IS values which devi-ate slightly (<1 mm/sec) from the bulk values. This can be attributed to surface fluctuations in combination with quan-tum size effects. However, charge transfer via the different ligand molecules may additionally play a role by charging the surface atoms and herewith the core atoms. Detailed analyses of many IS and quadrupole splitting data suggest a description of the surface atoms, even ligated, to behave "metallic" in such a sense that they exchange free charge with the inner core atoms. Otherwise they would behave like atoms of different oxidation states as in complexes, which is not the case.

Among all investigated metal nanoparticles the 1.4 nm $Au_{55}$ clusters, equipped with various ligand shells, varying the total size, turned out to be of dominant importance. As the connecting link between bulk and molecule they earn special interest with respect to future applications. This is why we will consider from now mainly the properties and behavior of this unique type of nanoparticle.

Photoelectron spectroscopy of $Au_{55}(PPh_3)_{12}Cl_6$ indicates a more or less nonmetallic behavior as long as their ligand shell remains intact. Exposure to X-rays during the measure-ments leads to a degradation of the ligand shell with loss of the chlorine atoms. As a result a shift of the X-ray pho-toelectron spectroscopy (XPS) valence band toward that of bulk gold is observed, as can be seen from Figure 6 [38].

The removal of the chlorine atoms follows from the loss of the Cl-2$s$ signal over the course of 30 h. Figure 6 shows the XPS valence band spectra of bulk gold in comparison with $Au_{55}(PPh_3)_{12}Cl_6$, 1.6 nm bare gold particles on diamond and the $Au_{55}$ sample after two days of X-ray irradiation. It is clearly seen that there is a characteristic shift of the Au-5$d_{5/2}$ subband by about 1 eV toward the Fermi energy more or less coinciding with the spectrum of 1.6 nm Au particles on diamond. From this it can be concluded that the 55 Au atoms without bearing the electronegative Cl atoms behave metal-like.

Among the various physical methods to get informa-tion on the electronic "inner life" of metal nanoparticles the current–voltage (I–U) behavior of individual particles gives the most valuable results. Those measurements even allow observation of single electron transitions between elec-trodes and particle. First reports on SET behavior of metal nanoparticles came from van Kempen et al. [39, 40]. They
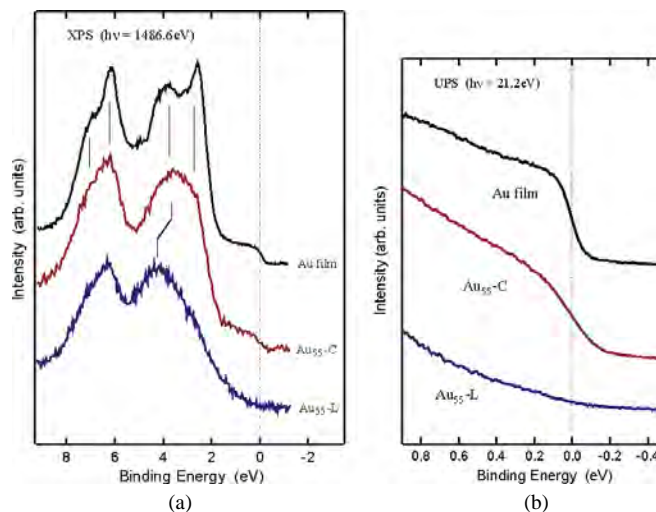


**Figure 6.** (a) XPS valence band spectra of a gold film, bare Au nano-particles of 1.6 nm on top of diamond, of $Au_{55}(PPh_3)_{12}Cl_6$ ($Au_{55}$-L) and of the cluster after two days of X-ray exposure ($Au_{55}$-C). (b) UPS valence band spectra in the vicinity of the Fermi energy of a Au Film, the intact $Au_{55}$ cluster ($Au_{55}$-L) and the cluster without Cl ($Au_{55}$-C). Reprinted with permission from [38], H.-G. Boyen et al., *Phys. Rev. Lett.* 87, 276401 (2001). © 2001, American Physical Society.

investigated ligand stabilized 1.8 nm Pt nanoclusters at 4.2 K by means of scanning tunneling microscopy on a Au(111) surface. The I–U characteristics showed well expressed charging effects. At about the same time Andres et al. inves-tigated 1.8 nm high Au nanoparticles, positioned on a self-assembled monolayer of xylene dithiol. They were able to indicate not only Coulomb blockade behavior [41] but also a distinct Coulomb staircase at room temperature [42, 43]. Dodecanethiol protected gold islands of various size (0.8 and 2.4 nm) on $MoS_2$ surfaces, generated by evaporating Au atoms onto the substrate, also showed well expressed SET effects [44].

Figure 7 shows the experimental setup and the result of the investigation of a relatively large particle as an exam-ple of how those measurements can be performed and how the temperature influences the result. This has to do with the relatively simple relation between the electrostatic
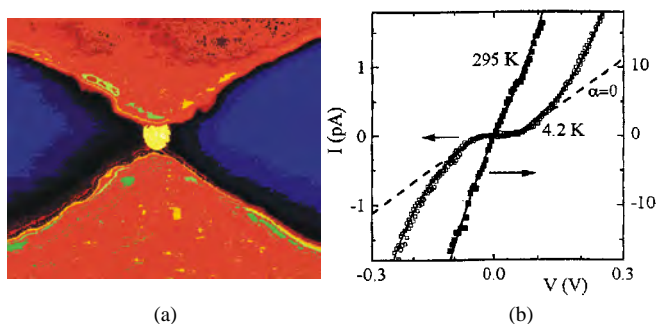


**Figure 7.** SEM image of a 15 nm gold particle between two Pt tips (a) and the I–U characteristics at 295 and 4.2 K with a well devel-oped Coulomb blockade (b). Reprinted with permission from [45], A. Bezryadin et al., *Appl. Phys. Lett.* 71, 1273 (1997). © 1997, American Institute of Physics.

and the thermal energy of an electron. SET can only be observed if the thermal energy $E_t$ is very small compared with the electrostatic energy $E_e$ (see Section 2).

Since the capacity $C$ of the system is directly linked to the size of the particle it can be seen that the smaller the particle, the larger $E_e$ becomes (i.e., the higher the temperature can be to observe SET processes).

The investigated particle, trapped between two platinum electrodes [45], consisted of a 15 nm gold colloid, protected by a ligand shell of $P(C_6H_4SO_3Na)_3$ molecules. The $I$–$U$ characteristic at 295 K shows a linear relation between current and voltage, indicating a simple metallic behavior (Ohm law) of this relatively large particle. However, at 4.2 K there is a characteristic so-called Coulomb blockade (CB) to be observed since $E_t$ is now small enough compared to $E_e$. CBs result if the particle is charged by a single electron which then blockades the transition of another one, until it is transported to the counterelectrode at a higher voltage: this is nothing but a single electron switch!

Due to the preceding formula, a drastic decrease of the particle size might enable SET at room temperature, essential for practical use. Indeed, $Au_{55}(PPh_3)_{12}Cl_6$ with its 1.4 nm core and a ca. 0.4 nm thick ligand shell fulfills these conditions ideally. Figure 8 presents the $I$–$U$ curve of that cluster at room temperature [46]. A well defined Coulomb blockade is to be seen perfectly supporting the predictions in relation to the $E_e/E_t$ relation.

The summit of those investigations succeeded by a scanning tunneling microscopic (STM) investigation of $Au_{55}(PPh_3)_{12}Cl_6$ at 7 K and ultrahigh vacuum conditions [48]. An individual cluster was imaged by STM with a resolution high enough that even phenyl rings of $PPh_3$ ligands could be localized. Figure 9 shows the STM image and the corresponding space filling model shows how the cluster seems to be positioned on a Au(111) surface.

Locally resolved scanning tunneling spectroscopy at two different positions on top of the cluster (marked by arrows) was performed. Figure 10 shows the two spectra. The dashed curve resulted when the tip was positioned aside the phenyl rings so that tunneling happened directly between tip and



(a)                    (b)
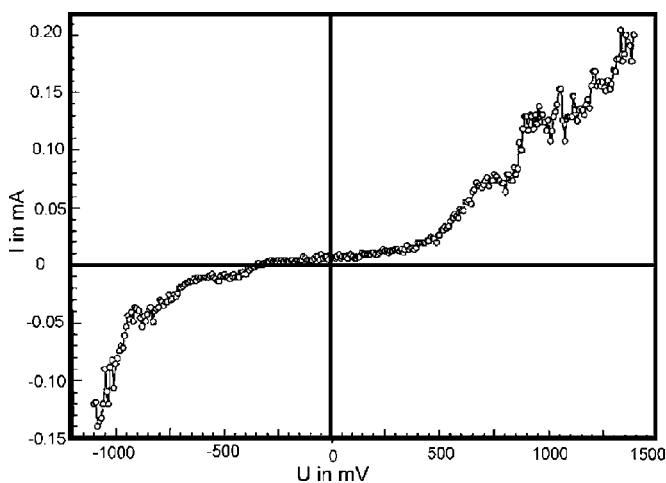
**Figure 9.** STM image of an individual $Au_{55}(PPh_3)_{12}Cl_6$ cluster and a space filling model. Light dots indicate $C_6H_5$ rings of the $PPh_3$ ligands. The arrows a and b indicate the positions of the STM tip for the two measurements, the results of which are shown in Figure 10 [48].

cluster, whereas the solid curve was gained by positioning the tip precisely on top of a phenyl ring. Both spectra exhibit a Coulomb blockade of 1.2 V; however, at 7 K tunneling processes within the CB can still be observed. Most of the signals of both spectra coincide showing that the $PPh_3$ ligands do not contribute to the electronic processes in this energy regime. Control experiments with $PPh_3$ molecules on Au(111) surfaces show that the significant unoccupied and occupied states are far above and below the Fermi level, respectively. This result indicates a finite density of electronic states in the cluster and so for the first time experimentally proves that the qualitative model, sketched in Figure 1 and describing nanoparticles of that size as intermediates between bulk and molecule, agrees quite well with the reality. The average level spacing in $Au_{55}(PPh_3)_{12}Cl_6$ can so be determined as 135 meV.

Summarizing this section it can be stated that metal nanoparticles in the size range of a few nanometers exhibit experimentally detectable quantum size behavior. Optimized quantum size character is shown by ligand stabilized $Au_{55}$ clusters with a core diameter of 1.4 nm. Among various physical investigations, current–voltage characteristics of individual particles contributed most considerably to our understanding of the electronic situation in those particles.



**Figure 8.** $I$–$U$ characteristic of $Au_{55}(PPh_3)_{12}Cl_6$ at room temperature [46, 47].
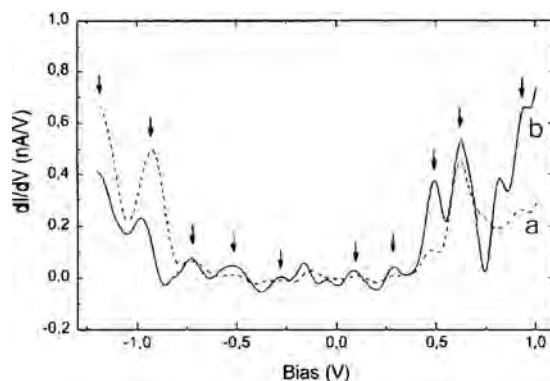


**Figure 10.** Current–voltage characteristics measured at two different positions above the $Au_{55}$ core: (a) tip positioned aside the ligand, (b) tip positioned on top of a phenyl ring of $PPh_3$ [48].
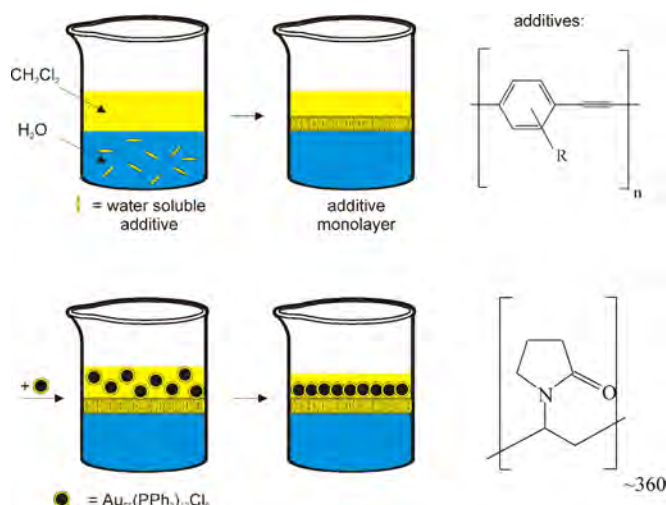
**Figure 11.** Illustration of the formation of ordered layers of $Au_{55}(PPh_3)_{12}Cl_6$ clusters on a polymer film at the phase transition between water and dichloromethane.

$Au_{55}(PPh_3)_{12}Cl_6$ shows well expressed quantum size properties even at room temperature (i.e., those particles could in principle be used as single electron switches and, under appropriate conditions, as single electron transistors in future nanoelectronic devices. For these reasons it is absolutely necessary to develop techniques on how to handle those quantum dots individually. In other words, it seems necessary to organize them two- or one-dimensionally or, as a final goal, even to write artificial structures. The next section therefore deals with efforts to organize quantum dots by various methods.

## 5. ORGANIZATION

Two-dimensional arrangements of metal nanoparticles usually are available by self-assembly processes on appropriate surfaces. Those processes sometimes happen just by themselves without applying special conditions. Numerous examples, especially of larger metal particles, have become known in the past [49–56]. Here we will focus on those nanoparticles that play a potential role in future applications (i.e., we will again consider the behavior of $Au_{55}$ clusters as outstanding particles due to their unique electronic properties).

Self-assembly processes of $Au_{55}(PPh_3)_{12}Cl_6$ clusters on various surfaces have occasionally been observed; however,
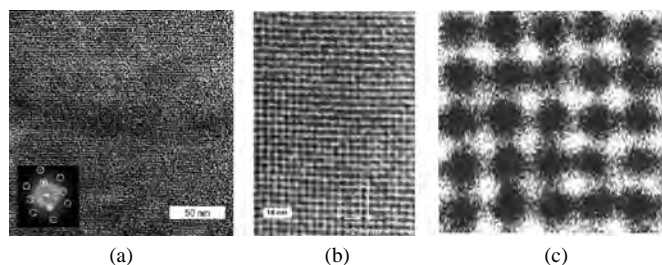


**Figure 12.** TEM images of square ordered monolayers of $Au_{55}(PPh_3)_{12}Cl_6$ clusters with increasing magnifications [47, 57, 58].
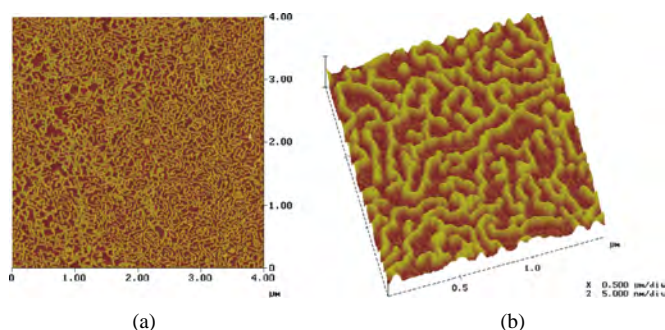


**Figure 13.** AFM image of PVP molecules, decorated with $Au_{55}(PPh_3)_{12}Cl_6$ clusters. Reprinted with permission from [62], T. Reuter et al., *Nano Lett.* 2, 709 (2002). © 2002, American Chemical Society.

those accidental processes are not very well suited for developing general routes with reproducible results. The best results to date have been gained using a liquid–liquid phase barrier to assemble clusters. The process is supported by a monomolecular film of a suited polymer, weakly interacting with the clusters [57]. Figure 11 illustrates the process.

In a first step a small amount of polymer molecules, preferably those with a weak attraction toward the phenyl rings of the $PPh_3$ ligands, is dissolved in the water phase. Poly(paraphenlyleneethynylene) (PPE) derivatives and PVP turned out to give best results by formation of a "molecular carpet" at the surface. "Innocent" alkyl chains like PMMA (plexiglass) do not give satisfying results. On the other hand, too strong interactions between support and the particles to be organized also may lead to poorer results, due to the hindered mobility of the deposited particles. Thereafter, a very thin film of a dichloromethane solution of the cluster is added onto the water surface. The clusters spontaneously organize at the phase boundary. After evaporation of the dichloromethane, the self-assembled cluster monolayer can be transferred to appropriate substrates for further investigation.

Surprisingly, two different structures of cluster monolayers were found: those of simple square arrangement of the
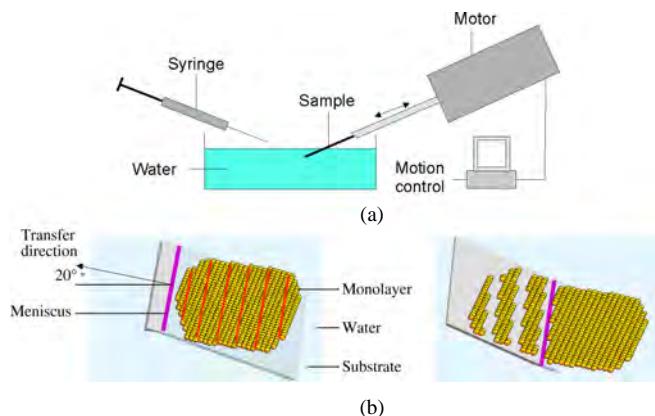


**Figure 14.** Langmuir–Blodgett device for generating cluster monolayers and the transfer to a support (a). (b) The mechanism of stripe formation from islands of ordered nanoparticles.
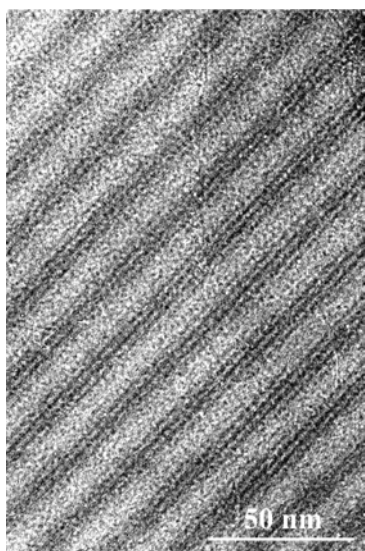
**Figure 15.** TEM image of an assembly of stripes of $Au_{55}(PPh_3)_{12}Cl_6$ clusters, consisting of three to four rows each. Reprinted with permission from [64], O. Vidoni et al., *J. Mater. Chem.* 11, 3188 (2001). © 2001, Royal Society of Chemistry.

particles, and another one of hexagonally ordered particles. The reason for this behavior is seen in the orientation of the ligand shells of a first few clusters at the very beginning of the process. Details shall not be discussed here. Figure 12 shows some transmission electron microscope (TEM) images of such regular arrangements of both types.

Areas of up to some hundred nm$^2$ could be generated by this method, of course still much too small for any kind of applications, but large and good enough for early investigations of the electronic characteristics.

First approaches to generate one-dimensional (1D) arrangements of $Au_{55}$ clusters have also become known in recent years. "One-dimensional" should, however, not be understood in its ideal sense. This would mean that rows of single clusters must be formed. We will also accept a few rows of clusters as being one-dimensional, to avoid the expression "*quasi*-one-dimensional" which would indeed be more correct.

One-dimensional arrangement of such small particles requires appropriate templates, since nature does not tend to organize matter one-dimensionally.

Templates for the 1D arrangements could be long-chained molecules, steps on surfaces, channels, and pores. Indeed, some promising results with nanoporous systems (alumina) have been achieved [59]. Nevertheless, this method is not yet satisfactory enough that reproducible results could be obtained. Experiments with corresponding channels do not really exist, except for a few preliminary approaches. The main problem is the generation of channels in a suited material of a diameter corresponding to the cluster's diameter. A promising approach has become known using the wetting instabilities of monolayers on solid substrates. L-$\alpha$-dipalmitoyl-phosphatidylcholine layers on water surface degrade when transferred to mica in a striped pattern [60]. Hydrophilic channels of 200–300 nm width are formed, of course much too large for assembling 2 nm particles in a row, but an opportunity to learn more about such hybrid systems. $Au_{55}(PPh_3)_{12}Cl_6$ clusters, deposited from solution, form aggregates in the channels of adjusted size.

As templates various polymers have been tested, among others PPEs [61], PVP [62], or DNA [63]. They all resulted in promising products. As an example some cluster–PVP hybrid systems shall be presented [62].

PVP molecules on the water surface of an LB trough were treated with $Au_{55}(PPh_3)_{12}Cl_6$ clusters in a dichloromethane solution. The clusters interact via their ligand shells with the polymers to form 1D chains that are linked together. The degree of linkage depends on the pressure applied. Figure 13 shows a pattern of those cluster covered PVP molecules. In contrast to bare PVP molecules, the cluster covered ones are intensively cross-linked. This is mostly due to clusters at the ends of the chains, where they act as multifunctional junctions. This finding might be of considerable interest with respect to the use of those quantum dots in imaginable two-dimensional electronic working systems.

A very unusual kind of two-dimensional arrangement has been found when ordered monolayers of $Au_{55}(PPh_3)_{12}Cl_6$
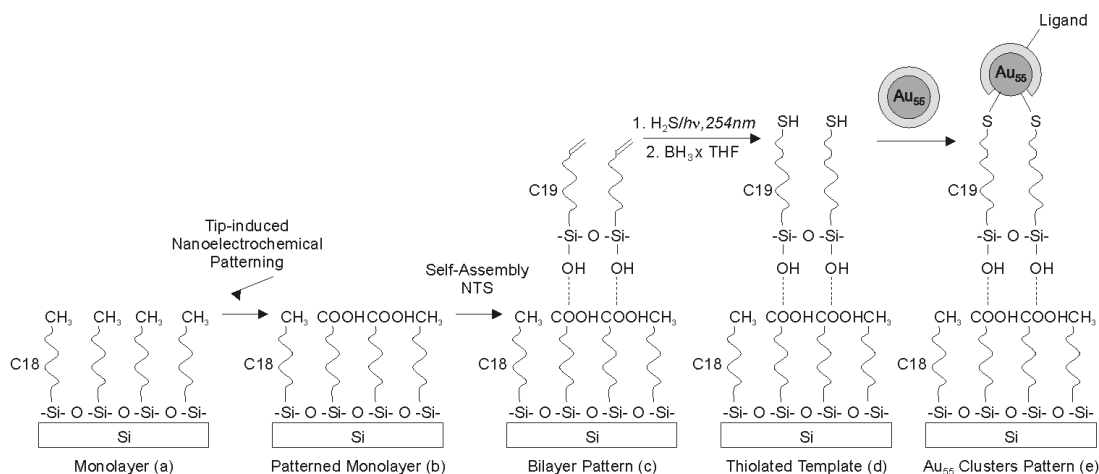


**Figure 16.** Sketch showing how chemically active tracks are written by an AFM tip, followed by additional chemical steps and addition of $Au_{55}(PPh_3)_{12}Cl_6$ clusters. Reprinted with permission from [65], S. Liu et al., *Nano Lett.* 2, 1055 (2002). © 2002, American Chemical Society.

(a)

(b)

(c)
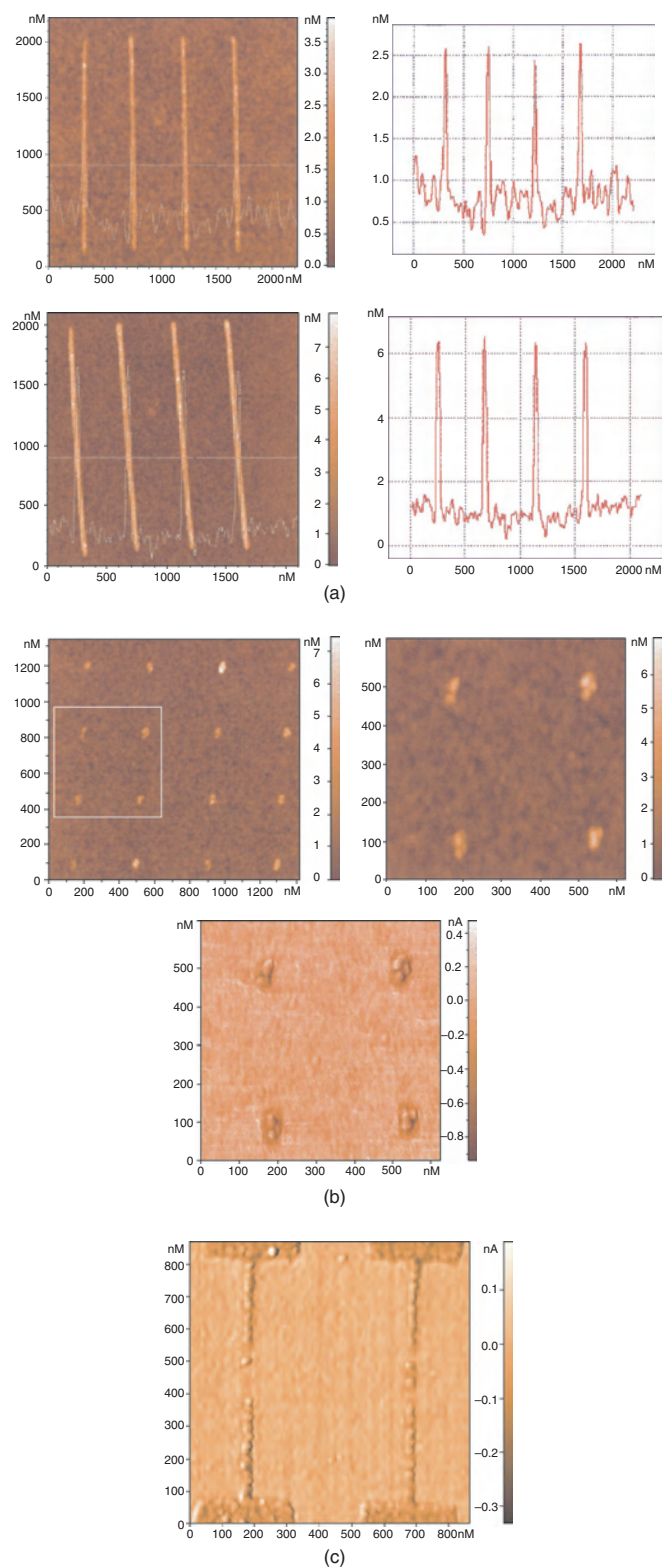
**Figure 17.** AFM images of artificial patterns of Au$_{55}$ clusters. (a) Stripes of modified tracks without (top) and with clusters (bottom). (b) Dots consisting of three to four particles. (c) Lines of single particles, interrupted to deposit one or two individual clusters in between. Reprinted with permission from [65], S. Liu et al., *Nano Lett.* 2, 1055 (2002). © 2002, American Chemical Society.

clusters on the water surface of a special Langmuir–Blodgett device are transferred to solid substrates under very distinct experimental conditions [64]. Self-assembled monolayers of these clusters without the support of a polymer (see above) are rather unstable with respect to mechanical stress. So, if a solid substrate is dipped underneath a self-assembled monolayer and is then drawn back under an angle of 20° and with a speed between 2 and 10 cm min$^{-1}$ the ordered structure is degraded in a very controlled way. Equidistant stripes of three to four cluster rows are formed under these conditions. This process can be achieved to the oscillating water meniscus at the water/air phase boundary on the substrate. The frequency of the oscillation depends decisively on speed and angle. Figure 14 elucidates the process. Figure 15 shows a TEM image of those stripes of cluster rows which have been generated on the surface of a carbon coated copper grid for electron microscopy.

In spite of all these promising approaches to organizing quantum dots in two or one dimensions we have to state that we are still very far from having systems that could be used as working devices. In any case we have to develop artificial structures with quantum dots positioned at distinct positions. Self-assembly processes therefore cannot be applied, and the hitherto obtained results should be considered as useful exercises.

A recently treaded path could be a guide, since it allows one for the first time to deposit individual Au$_{55}$ clusters to form any kind of pattern [65].

A self-assembled monolayer of CH$_3$ terminated alkyl chains on a flat substrate is treated by electrical pulses via a metal coated atomic force microscope (AFM) tip of the highest quality. Along the track of the tip the CH$_3$ groups are oxidized to COOH functions. These can then be derivatized to SH functionalized units on top of which Au$_{55}$ clusters can easily be deposited, due to their high affinity to thiol groups. Finally, Au$_{55}$ patterns are formed, the structure of which is simply a function of the software guiding the AFM tip. Figure 16 illustrates the chemistry necessary to bind the clusters. Figure 17a–c shows AFM images of various cluster patterns. Figure 17a shows stripes of appropriately modified tracks without (top) and with (bottom) clusters. The height difference agrees perfectly with the height of the clusters of 2.5 nm. Precisely placed dots of three to four clusters are shown in Figure 17b, whereas Figure 17c shows the real possibilities of this method. Using a perfect AFM tip, lines of individual clusters are generated, interrupted at distinct positions, followed by deposition of one or two individual clusters, and then continued as lines again.

Although no electronic characterizations of those architectures have yet been performed, it can be assumed that this or related techniques might finally open the door to novel applications of metal nanoclusters in nanoelectronics, future generations of computers, optoelectronics, and many other fields.

# 6. CONCLUSIONS

The miniaturization of metals to nanoscale provokes dramatic changes of properties. Decreasing melting points, optical properties and, most important, electronic properties make small metal particles into new materials. It is the

reduction of dimensionality to practically 0D forcing the electrons from a *quasi* delocalized state in the bulk into more or less discrete energy levels in particles of a few nanometers. This size-effect shifts the nature of a particle from bulk, described by the laws of classical physics, to quantum mechanics. Nanoparticles with electrons in discrete levels are therefore also called "quantum dots" or in a simplified version "artificial atoms." The specific property of those quantum dots is their special current–voltage behavior with a typical Coulomb blockade instead of a linear relation between $I$ and $U$, as is the case in bulk metals. This Coulomb blockade exhibits nothing but single electron transitions. Quantum dots with such properties therefore can in principle be used as single electron switches and also as single electron transistors. These properties make them highly promising candidates for applications in future nanoelectronic devices. As a perfect example, the cluster compound $Au_{55}(PPh_3)_{12}Cl_6$ and also its derivatives with other ligand molecules became important. They indeed exhibit perfect quantum size behavior even at room temperature. That is why numerous efforts have been made to organize them one- and two-dimensionally. Except well performed self-organized layers, the first steps to draw artificial structures with these $Au_{55}$ clusters have been successfully performed.

## GLOSSARY

**Atomic force microscopy** Measurement of atomic forces between a scanning tip and a sample surface reaching magnification up to 100,000,000 times.

**Coulomb blockade** Charging of a nanoparticle by a single electron, blocking the transfer of a second electron.

**Langmuir–Blodgett technique** Spreading and pushing together molecules on a liquid surface, followed by transfer onto a solid substrate.

**Quantum dot** Zero-dimensional particle to be described by quantum mechanical rules.

**Scanning tunneling microscopy** Technique for analyzing surfaces on an atomic level by measurement of a tunnel current between a conductive tip and a conductive surface.

**Self-assembly** Nonguided organization of molecules or nanoparticles on surfaces following the principles of close packing.

**Single-electron tunneling (SET)** Transition of individual electrons between nanoparticles by means of quantum mechanical tunneling.

**Size-induced metal–insulator transition (SIMIT)** Transition of a metallic to an insulating state by reduction of size generating localized energy levels from an energy band.

## REFERENCES

1. P. Marquardt, L. Börngen, G. Nimtz, H. Gleiter, R. Sonnberger, and Y. Zhu, *Phys. Lett. A.* 114, 39 (1986).
2. G. Nimtz, P. Marquardt, and H. Gleiter, *J. Cryst. Growth* 86, 66 (1988).
3. P. Marquardt and G. Nimtz, *Festkörperprobleme* 29, 317 (1989).
4. K. K. Licharev and T. Claeson, *Sci. Am.* 266, 50 (1992).
5. K. K. Licharev and A. Korotkov, in "Proceedings of the 190th Electrochemical Society," San Antonio, TX, 1996, Vol. 96, Ch. 2, p. 563.
6. T. Sato, H. Ahmed, D. Brown, and B. F. H. Johnson, *J. Appl. Phys.* 82, 696 (1997).
7. M. Faraday, *Philos. Trans.* 147, 145 (1857).
8. J. Turkevich, P. C. Stevenson, and J. Hillier, *Disc. Faraday Soc.* 11, 55 (1951).
9. H. Bönnemann and R. M. Richards, *Eur. J. Inorg. Chem.* 2455 (2001).
10. P. R. van Rheenen, M. J. McKelvey, and W. S. Glaunsinger, *J. Solid State Chem.* 67, 151 (1987).
11. D. G. Duff and A. Baiker, in "Preparation of Catalysts VI" (G. Poucelet, J. Martens, B. Deemon, P. A. Jacobs, and P. Grange, Eds.), p. 505. Elsevier Science, Amsterdam, 1995.
12. H. Bönnemann, W. Brijoux, R. Brinkmann, U. Endruschat, W. Hofstadt, and K. Angermund, *Rev. Roum. Chim.* 44, 1003 (1999).
13. J. Sinzig, L. J. de Jongh, H. Bönnemann, W. Brijoux, and R. Köppler, *Appl. Organomet. Chem.* 12, 387 (1998).
14. M. N. Vargavtik, V. P. Zargorodnikov, I. P. Stolarov, I. I. Moiseev, D. I. Kochubey, V. A. Likholobov, A. L. Chuvilin, and K. I. Zarnaraev, *J. Mol. Catal.* 53, 315 (1989).
15. M. N. Vargaftik, V. P. Zargorodnikov, I. P. Stolarov, I. I. Moiseev, V. A. Likholobov, D. I. Kochubey, A. L. Chuvilin, V. I. Zaikovsky, K. I. Zamaraev, and G. I. Timofeeva, *J. Chem. Soc. Chem. Commun.* 937 (1985).
16. V. V. Volkov, G. van Tendeloo, G. A. Tsirkov, N. V. Cherkashina, M. N. Vargaftik, I. I. Moiseev, V. M. Novotortsev, A. V. Kvit, and A. L. Chuvilin, *J. Cryst. Growth.* 163, 377 (1996).
17. I. I. Moiseev, M. N. Vargaftik, V. V. Vlokov, G. A. Tsirkov, N. V. Charkashina, V. M. Novotortsev, O. G. Ellett, I. A. Petrunenka, A. L. Chuvilin, and A. V. Kvit, *Mendeleev Commun.* 87 (1995).
18. G. Schmid, M. Harms, J.-O. Malm, J.-O. Bovin, J. van Ruitenbeck, H. W. Zandbergen, and W. T. Fu, *J. Am. Chem. Soc.* 115, 2046 (1993).
19. G. Schmid, V. Maihack, F. Lantermann, and S. Peschel, *J. Chem. Soc. Dalton Trans.* 589 (1996).
20. G. Schmid, in "Applied Homogeneous Catalysis with Organometallic Compounds" (B. Cornils and W. A. Herrmann, Eds.). VCH, Weinheim, 1996.
21. J. D. Aiken III and R. G. Finke, *J. Mol. Catal. A* 145, 1 (1999).
22. N. Toshima and T. Yonezawa, *New J. Chem.* 1179 (1998).
23. N. Toshima and K Hirakawa, *Polymer J.* 31, 1127 (1999).
24. P. Lu, T. Taramishi, K. Asakura, M. Miyake, and N. Toshima, *J. Phys. Chem. B* 103, 9673 (1999).
25. J. W. Slot and H. J. Geuze, *Eur. J. Cell Biol.* 38, 87 (1985).
26. H. Mühlpfort, *Experimenta* 38, 1127 (1982).
27. P. Mukherjee, A. Ahmad, D. Mandal, S. Senapati, S. R. Sainkar, M. I. Khan, R. Ramani, R. Parischa, P. V. Ajayakumar, M. Alam, M. Sastry, and R. Kumar, *Angew. Chem. Int. Ed.* 40, 3585 (2001).
28. G. Schmid and A. Lehnert, *Angew. Chem.* 101, 773 (1989); *Angew. Chem. Int. Ed. Engl.* 28, 780 (1989).
29. H. Bönnemann, W. Brijoux, R. Brinkmann, R. Fretzen, Th. Joussen, R. Köppler, P. Neiteler, and J. Richter, *J. Mol. Catal.* 86, 129 (1994).
30. G. Schmid, R. Boese, R. Pfeil, F. Bandermann, S. Meyer, G. H. M. Calis, and J. W. A. van der Velden, *Chem. Ber.* 114, 3634 (1981).
31. G. Schmid, *Inorg. Synth.* 7, 214 (1990).
32. C. Pan, K. Pelzer, K. Philippot, B. Chaudret, F. Dassenoy, P. Lecante, and M.-J. Casanove, *J. Am. Chem. Soc.* 123, 7584 (2001).
33. T. O. Ely, C. Pan, C. Amiens, B. Chaudret, F. Dassenoy, P. Lecante, M.-J. Casanove, A. Mosset, M. Respaud, and J.-M. Broto, *J. Phys. Chem. B* 104, 695 (2000).
34. Y. Volokitin, J. Sinzig, L. J. de Jongh, G. Schmid, M. N. Vargaftik, and I. I. Moiseev, *Nature* 384 (1996).
35. B. A. Smith, J. Z. Zhang, U. Giebel, and G. Schmid, *Chem. Phys. Lett.* 270, 139 (1997).

36. P. M. Paulus, A. Goossens, R. C. Thiel, G. Schmid, A. M. van der Kraan, and J. L. de Jongh, *Hyperfine Interactions* 126, 199 (2000).

37. P. M. Paulus, A. Goossens, R. C. Thiel, A. M. van der Kraan, G. Schmid, and L. J. de Jongh, *Phys. Rev. B* 64, 205418 (2001).

38. H.-G. Boyen, G. Kästle, F. Weigl, and P. Ziemann, *Phys. Rev. Lett.* 87, 276401 (2001).

39. H. van Kempen, J. G. A. Dubois, J. W. Gerritsen, and G. Schmid, *Physica B* 204. 51 (1995).

40. J. G. A. Dubois, J. W. Gerritsen, S. E. Shafranjuk, E. J. G. Boon, G. Schmid, and H. van Kempen, *Europhys. Lett.* 33, 279 (1996).

41. M. Dorogi, J. Gomez, R. Osifchin, R. Andres, and R. Reifenberger, *Phys. Rev. B* 52, 9071 (1995).

42. R. Andres, S. Datta, M. Dorogi, J. Gomez, J. Henderson, D. Janes, V. Kolagunta, C. Kubiak, W. Mahoney, R. Osifchin, R. Reifenberger, M. Samanta, and W. Tian, *J. Vac. Sci. Technol. A* 14, 1178 (1996).

43. R. Andres, T. Bein, M. Dorogi, S. Feng, J. Henderson, C. Kubiak, W. Mahoney, R. Osifchin, and R. Reifenberger, *Science* 272, 1323 (1996).

44. S. Hong, J. Bielefeld, R. Andres, and R. Reifenberger, in "Nanowires" (P. Serena and N. Garcia, Eds.), pp. 351–372. Kluwer Academic, Dodrecht, 1997.

45. A. Bezryadin, C. Dekker, and G. Schmid, *Appl. Phys. Lett.* 71, 1273 (1997).

46. L. F. Chi, M. Hartig, T. Drechsler, Th. Schwaack, C. Seidel, H. Fuchs, and G. Schmid, *Appl. Phys. A* 66, 187 (1998).

47. G. Schmid, *Adv. Eng. Mater.* 3, 737 (2001).

48. H. Zhang, G. Schmid, and U. Hartmann, to be published.

49. M. Brust, D. Bethell, D. J. Schiffrin, and C. J. Kiely, *Adv. Mater.* 7, 799 (1995).

50. M. Brust, M. Walker, D. Bethell, D. J. Schiffrin, and R. Whyman, *J. Chem. Soc. Chem. Commun.* 801 (1994).

51. J. Fink, C. J. Kiely, D. Bethell, and D. J. Schiffrin, *Chem. Mater.* 10, 922 (1998).

52. C. J. Kiely, J. Fink, M. Brust, D. Bethell, and D. J. Schiffrin, *Nature* 396, 444 (1998).

53. C. J. Kiely, J. G. Zheng, J. Fink, M. Brust, D. Bethell, and D. J. Schiffrin, *Adv. Mater.* 12, 640 (2000).

54. R. P. Andres, J. D. Bielefeld, J. I. Henderson, D. B. James, V. R. Kolagunta, C. P. Kubiak, W. J. Mahoney, and R. G. Osifchin, *Science* 273, 1690 (1996).

55. B. A. Korgel and D. Fitzmaurice, *Adv. Mater.* 10, 661 (1998).

56. J. P. Wilcoxon, J. E. Martin, and P. Provencio, *J. Chem. Phys.* 115, 998 (2001).

57. G. Schmid and N. Beyer, *Eur. J. Inorg. Chem.* 835 (2000).

58. G. Schmid, M. Bäumle, and N. Beyer, *Angew. Chem. Int. Ed. Engl.* 39, 181 (2000).

59. G. L. Hornyak, M. Kröll, R. Pugin, Th. Sawitowski, G. Schmid, J.-O. Bovin, G. Karsson, H. Hofmeister, and S. Hopfe, *Chem. Europ. J.* 3, 1951 (1997).

60. M. Gleiche, L. F. Chi, and H. Fuchs, *Nature* 403, 173 (2000).

61. D. Wyrwa, N. Beyer, and G. Schmid, *Nano Lett.* 2, 419 (2002).

62. T. Reuter, O. Vidoni, V. Torma, G. Schmid, L. Nan, M. Oleiche, L. Chi, and H. Fuchs, *Nano Lett.* 2, 709 (2002).

63. F. Patolsky, Y. Weizmann, O. Lionbashevski, and I. Willner, *Angew. Chem. Int. Ed.* 41, 2323 (2002).

64. O. Vidoni, T. Reuter, V. Torma, W. Meyer-Zaika, and G. Schmid, *J. Mater. Chem.* 11, 3188 (2001).

65. S. Liu, R. Maoz, G. Schmid, and J. Sagiv, *Nano Lett.* 2, 1055 (2002).

# Metal Nanoclusters on Oxide Surfaces

Gianfranco Pacchioni

*Università di Milano–Bicocca,*
*and Istituto Nazionale per la Fisica della Materia, Milano, Italy*

## CONTENTS

## 1. INTRODUCTION

Metal clusters do not represent an entirely new area in material science. In fact, their existence was proved and investigated both in the chemical and physical communities long before nanotechnology became a mature field [1]. Metal nanoclusters are well-defined objects, containing from a few to a few hundred atoms, whose dimensions are typically in the nanometer regime. They differ from molecules in the fact that molecules are stable units, while clusters are often in a metastable state, and do not exist in appreciable numbers in equilibrium conditions. In this respect, nanoclusters represent a new class of objects that, in order to be studied and used, must be stabilized in some way, either by encapsulation in shells of molecules (ligands) or by deposition on an inert substrate. When the size of a metal aggregate approaches 100 nm–1 $\mu$m, one is dealing with small metal particles whose properties are defined in terms of the statistical distribution of sizes. This is typical of the colloid state [2]. Metal colloids were already handled by Michael Faraday in the 19th century, and the term colloid was introduced in 1861 to describe the slow diffusion rates and nanocrystallizability in aqueous solutions of insoluble materials, such as silver chloride and gold [3]. These systems are of large practical importance (colloidal gold has been used for centuries to make ruby glass and for the coloring of ceramics), but it is questionable if colloids belong to the field of nanotechnology in a strict sense. The impact of metal clusters on nanoscience and nanotechnology is largely connected to a truly size-dependent understanding of the chemical and physical behavior of the individual units, and to the ability of tuning characteristics and properties by changing size. The generation, synthesis, and properties of nanoclusters are the object of this chapter.

The study of metal clusters goes back to the 1960s and even earlier, when the first examples of molecular metal clusters, that is, small metal aggregates of a few atoms surrounded by stabilizing ligands, were reported [4, 5]. In those years, the first cluster carbonyls, such as $Co_4(CO)_{12}$, $Fe_2(CO)_9$, and $Fe_3(CO)_{12}$, were discovered. This launched the field of organometallic cluster chemistry, and enormous advances were made in the 1970s in the synthesis of large cluster complexes. Compounds such as $Rh_{13}(CO)_{24}$, $Pt_{26}(CO)_{32}$, $Pt_{38}(CO)_{44}$, and so on, containing tens of metal atoms were reported, and their structure was determined by X-ray diffraction methods [4]. Some of these clusters, like the famous $Ni_{38}Pt_6(CO)_{44}$ cluster [6], contain a metal core which closely resembles a small fragment of bulk metal, with an atomic ordering typical of cubic close-packing crystals. The great success of metal clusters in ligand shells lies in the fact that they can be obtained by chemical synthesis, that they are sufficiently stable, and that they can be produced at relatively low cost in appreciable amounts. The use of vibrational, photoelectron, optical spectroscopies, and the possibility to characterize these systems structurally with X-ray diffraction methods opened new ways to study their structure–properties relationship [7]. The similarities between phenomena on surfaces and observations in organometallic cluster chemistry prompted, in the mid-1970s, the formulation of the so-called "cluster–surface analogy" [8]. This concept alerted both fields (surface scientists and cluster chemists) to the presence of each other. Many fundamental questions arise as a consequence. For example, why are small naked metal clusters such good catalysts, whereas clusters with ligands, often containing the same number of metal atoms, are usually rather inert? How many atoms must a cluster contain before its properties are indistinguishable from the bulk? And so on. Nowadays, these problems are better understood, although the questions are not yet completely answered. For instance, the

modest reactivity of ligated metal clusters is due to their high stability. A good catalyst must be able to reversibly bind an adsorbed species, activate the reactants, and transform them into the products with low activation barriers, a process which is highly dependent on the presence of active sites (often low-coordinated atoms). In organometallic clusters, the ligands are often too strongly bound to the metal cage, so that even if a given reaction takes place on its surface, the product does not leave the catalysts, thus preventing another reaction from occurring on the same cluster. Also, the question of the number of atoms needed to reach bulk properties has been, at least partly, clarified. In fact, this depends very much on the property one is interested in. Some properties converge quite rapidly (bond lengths, ionization potentials, etc.), some evolve quite slowly (cohesive energy, magnetic properties), and some require very large metal particles (conductivity).

Recently, the first principle calculations of large clusters containing more than 100 metal atoms have become accessible, shedding new light on the evolution of properties with size. Density functional calculations on Ni [9] and Au [10] clusters containing from 6 to 147 atoms have shown that the cluster cohesive energy varies linearly with the inverse of the cluster radius, indicating that the surface-to-volume ratio is the primary ingredient which determines the convergence of this quantity to the bulk. The force constants for the metal–metal stretching converge rather fast to the bulk modulus; both the ionization potential and the electron affinity of the clusters vary almost linearly with the reciprocal of the cluster radius; a cluster of 147 metal atoms shows a deviation from the metal work function of less than 10%. The electronic structure, as represented by the density of states, evolves rather quickly from a discrete behavior for the small clusters to the typical bands of the bulk metal. The gap decreases from about 2 eV in clusters with fewer than ten atoms to 0.2–0.3 eV for the larger aggregates [9, 10].

This does not mean that there are no open questions left about clusters and their properties—on the contrary. Several techniques were developed in the 1980s to better characterize these systems, and in particular to study naked clusters, that is, small aggregates of metal atoms without surrounding ligands [11–14]. One approach has been that of matrix isolation, where naked metal clusters were embedded in a rare gas matrix at low temperature to prevent coalescence to form larger particles [15]. In fact, small metal clusters represent a metastable state of condensed matter; in the absence of a separating agent, the clusters tend to aggregate to form large colloidal particles, a process also known as sintering. Matrix isolation has permitted, for the first time, the study of well-defined metal clusters with spectroscopic methods [15]. The assumption here (not always verified) was that the clusters interact with the matrix host sufficiently little to allow them to retain much of their gas-phase properties, such as geometry, electronic ground state, vibrational structure, and so on.

A completely different and very challenging approach has been to produce metal clusters in nozzle beams. Sources capable of producing free beams of nanoscale metal clusters with a wide range of sizes were reported 20 years ago [16, 17]. At the heart of most cluster sources is a region in which a supersaturated vapor of the material to be studied is generated with the aid of a pulsed laser beam. An inert gas flow is then added in the condensation region. The condensed vapor passes through a pair of apertures into a high-vacuum region where it forms a free supersonic beam. It is intuitive that ejecting a metal vapor into a cooled rare gas will produce condensation into small particles, but predicting the size distribution as a function of the source parameters from the first principles is difficult. Still, with this technique, it has been possible to generate mass-selected gas-phase clusters of various materials, and to study their properties (in particular, stability, but also spectroscopic and magnetic properties) as a function of cluster size. Thanks to this technique, the existence of the stable molecule $C_{60}$ was discovered [18]. The limitation with these techniques is that the amount of cluster material that can be produced in the beam is evidently quite small. Mass selection of ionized clusters in beams further reduces the yield so that, until very recently, experiments on mass-selected clusters were limited to *in-situ* spectroscopic studies.

The two fields, clusters from solution by chemical means and clusters from physical methods, developed further, and at the beginning of the 1990s, two independent and complementary ways to produce and study metal clusters were available: on one side, clusters in ligand shells at the solid state obtained via chemical synthesis, and on the other, gas-phase clusters obtained by vaporization–aggregation techniques. These systems, however, are of little practical interest until they are deposited and stabilized on some "inert" substrate so that their chemical, optical, and magnetic properties can be studied and used in practical applications. This leads us directly into the field of supported metal nanoclusters, an area which is opening new perspectives in nanotechnology.

## 2. SUPPORTED METAL CLUSTERS

There are several reasons why supported metal clusters can play a role in nanoscience and nanotechnology [19–23]. The most immediate application is related to catalysis [24]. Take a typical heterogeneous catalyst, such as those installed in automobiles to reduce car exhaust. Here, the catalyst consists of a monolithic backbone covered internally with a washcoat made of porous ceramic materials like alumina. On the surface of the ceramic are deposited small particles of noble metals like palladium, platinum, and rhodium. In order to be active, the metal particle must have the size of a few nanometers. The better is the control on the size distribution of the particles, the more efficient is the catalyst. However, despite several efforts to better characterize the relationships among the surface morphology, size, and shape of the metal particles, a deep understanding of the catalytic mechanisms is often lacking. Also, the nature of the bonding at the interface between the particle and the oxide support is known only very approximately. Ideally, one would like to be able to prepare monodispersed catalyst particles, all having the same number of atoms, and possibly of very small size. In fact, the active part of the catalyst is its surface, where the low-coordinated atoms are responsible for most of the chemistry. However, the surface atoms are only a small fraction of the total number of atoms in the

particle. Since heterogeneous catalysis often relies on precious metals, reducing the size of the particle immediately results in a better surface-to-volume ratio. In this way, it is possible, with a given quantity of material, to produce a much larger number of active sites, and to increase the efficiency of the catalyst. The second appealing aspect of good control of the size and shape of the particles is to achieve a better selectivity of the catalyst, as will be discussed below. The selectivity is the capability to produce a large fraction of just one product over the many products that can be obtained in a chemical reaction. A supported metal particle exhibits atoms with different coordinations, and hence, different reactivities (Fig. 1), thus giving rise to a mixture of products. A higher reactivity and a better selectivity are some of the final goals of nanocatalysis, an area aimed at preparing new catalysts in the nanometer scale with good perspectives in practical applications and bright potential for fundamental understanding. One should mention at this point that the preparation of small metal particles supported on an oxide substrate is at the heart of the research on supported metal catalysts. However, what makes the relatively mature field of supported metal catalysts different from nanocatalysis? Basically, it is the level of control on the dimensions, structure, and chemical mechanisms. Nanocatalysis is related to the possibility of producing new systems in the nanoscale under controlled conditions. Some new techniques have been developed in this direction in the last few years, as will be discussed in more detail below. In this respect, traditional catalysis by supported metal particles represents a well-established area with little connection to nanoscience.

Another field where supported metal clusters will play a role is in microelectronic technologies, and in particular, in the production of sensors. Sensors are often defined as "artificial noses." Their function is to detect the presence of molecules in the atmosphere by means of their chemical reaction with a metal particle which is part of a MOSFET (metal-oxide semiconductor field-effect transistor). In such a device, a thin metal film is separated from a semiconducting Si crystal by a very thin layer of an insulating oxide, $SiO_2$. The conductance of the semiconductor can be modulated by applying an electric field perpendicular to the surface of the semiconductor. A positive charge in the metal film results in a negative charge in the semiconductor; this in turn affects the lateral conductivity of the semiconductor. It is clear that the charging of the metal layer is critical, and may depend on several factors like film thickness, film morphology, and so on. One way to tune the charging of the metal layer is to adsorb molecules on its surface. This changes the charging of the film, and can lead to a direct measure of the amount of gas adsorbed. The performance, durability, and sensitivity of this kind of device depends very critically on the structure of the metal overlayer, and on our understanding of the mechanisms of nucleation and growth of metal particles to form the film. Cluster formation is a crucial step in the preparation of the device, and the possibility to better control the dependence of the gas adsorption on the shape and size of the metal islands would represent a considerable step for the improvement of these systems.
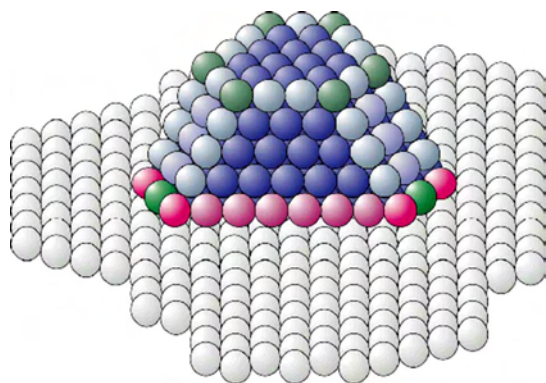
An area of potential use of supported clusters and nanoparticles is in magnetic recording. The magnetic properties of atoms are quite well understood, but the development of the magnetic order on a macroscopic scale in a solid is a rather complex problem. Long-range magnetic order is not simply the sum of the effects of the individual components (i.e., the isolated atoms). Rather, it is a collective effect of atoms which can result in the well-known ferromagnetic or antiferromagnetic orderings or in more complicated alignments. Magnetic clusters provide a link between the magnetism at the atomic level and in the condensed state [25]. Presently, our hard disks contain magnetic particles about 600 nm long and 50 nm wide, and can store up to 20 Gbits/in². A target of the present technology is to further reduce the size of these magnetic particles down to $150 \times 15$ nm², and possibly even smaller. It is essential in this context to be able to produce small particles of good quality in order to exploit the permanent magnetization of the material.

In general, the question of the magnetic behavior of small clusters is a fascinating problem which has been considered from the very early days of the study of clusters. Back in 1962, the seminal paper by Kubo [26] discussed the unusual thermodynamic properties of clusters, in particular, the specific heat and the magnetic susceptibility. It is well known that the magnetization of a small particle of a magnetic material is a function of the average coordination of the atoms in the particle. For instance, the surface atoms carry a higher magnetic moment than the bulk ones in Fe, Co, and Ni. Indeed, Stern–Gerlach measurements of gas-phase Fe, Co, and Ni clusters containing from a few to a few hundreds of atoms have shown enhanced total magnetic moments as the size of the cluster is reduced [27]. This has been explained theoretically by considering the evolution of the electronic structure of the cluster with size [28]. While small clusters of a magnetic metal, for example, Ni, have an average magnetic moment close to 1 Bohr magneton per atom, the increase of coordination progressively lowers the magnetization to the bulk value, 0.6 Bohr magnetons/atom, a value which is already observed for clusters containing 3–400 atoms [27, 29]. It is also interesting to note that the small dimensionality can lead nonferromagnetic materials to become ferromagnetic. This has been theoretically predicted



**Figure 1.** Schematic representation of a supported metal particle showing the existence on the particle surface of metal atoms with different coordinations. Each of these atoms has a potentially different reactivity toward adsorbed species.

for very small clusters containing about 10–20 atoms [30], and was later confirmed experimentally [31], thus opening new perspectives for the use of clusters in magnetic applications.

The problem of cluster magnetization was analyzed in detail in the early 1990s for the case of ligand-stabilized organometallic clusters. These systems, in fact, being produced in larger quantities, have permitted us to perform very accurate low-temperature magnetic measurements [7, 32]. As mentioned above, most of these clusters have a rather small metal core, like $Ni_5(CO)_{12}$ or $Ni_6(CO)_{12}$, where all metal atoms are on the cluster "surface," and hence, in direct contact with the ligands. However, examples of high-nuclearity clusters, like $Ni_{38}Pt_6(CO)_{44}$, have also been reported [6]. In this latter case, the six internal Pt atoms form an octahedron, which is included in the larger octahedron composed of the 38 Ni atoms. The CO ligands are thus bound to the Ni atoms, but not to the internal Pt ones [29, 32]. The great advantage of using these systems for magnetic measurements is that they are crystalline and monodispersed. In other words, a sample of a given cluster compound contains only one particular type of macromolecule (provided the compound is pure, of course), and thus presents a macroscopically large collection of identical metal clusters, mutually separated by the ligand shell, which provides a highly effective means of chemical stabilization of the small metal particles. In the absence of the ligands, this particle should exhibit a total magnetic moment of about 24 unpaired electrons (38 Ni atoms with 0.6 unpaired electrons per atom); the measurements have shown, on the contrary, that the cluster is diamagnetic [32]. This result has been completely rationalized theoretically [29, 32]. It has been shown that the ligands on the cluster surface induce a substantial change in the electronic structure of the metal atoms, and in particular, a local quenching of the magnetic moment. Thus, the magnetic behavior of ligated clusters or colloidal particles is strongly dependent on the surface-to-bulk atom ratio; when no internal or bulk atoms are present, as for very small clusters, the magnetic properties can be completely lost. This is an important observation since, when a bare metal cluster is deposited on an oxide surface, it is possible that the surface acts in the same way as the ligands in organometallic clusters, thus leading to a partial reduction of the magnetization due to the metal–oxide interface bonding (Fig. 2). This problem has only recently been addressed, and in fact, it seems that a small magnetic quenching occurs when the particle is deposited.

Cluster-assembled materials offer new opportunities in material science and technology. In fact, films can be made by depositing dense assemblies of preformed clusters. Tuning the impact energy of the clusters on the substrate, one can form continuous films by using energetic cluster impact, or granular films by using medium-energy impact. By depositing clusters in soft-landing conditions in conjunction with a beam of atoms from a conventional deposition source, one can produce cluster assemblies embedded in a matrix. This technology leads to the production of cluster-assembled materials, a field which appears to be relevant to the magnetic industries. In metals, magnetic clusters can produce an unusually large dependence of the resistance on the magnetic field, an effect known as giant magnetoresistance
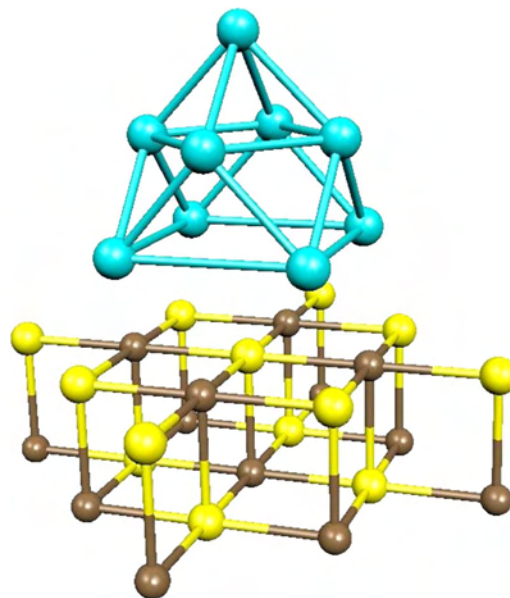


**Figure 2.** An $Ni_9$ nanocluster supported on the surface of magnesium oxide, MgO. Quantum–chemical calculations have shown that the magnetic moments of the cluster are partially quenched on the Ni atoms at the interface with the oxide surface.

(GMR), originally observed in magnetic multilayers [33]. The incorporation of magnetic clusters in semiconductors would allow for the integration of microelectronics with storage technologies and optoelectronic devices.

One last example of the potential application of clusters is in the field of optical properties. A spherical particle of a metal gives rise to a special collective excitation of its surface electrons which was discovered and described by Mie in 1908 [34]; it is also known as plasmon excitation, and it can fall in the visible region of the spectrum, thus giving rise to a colored cluster sample. This is indeed what happens in some old windows in ancient cathedrals where the red color is due to tiny Au particles in a glass matrix. However, as the size of the metal particle is decreased, the optical properties become size dependent, and do not obey the Mie theory anymore, but follow the laws of quantum mechanics, and in particular, of confined electrons in an external potential. Since, for small clusters, the energy levels are discrete with energy separations which depend on the size and shape of the cluster, this can lead to specific optical properties.

In the previous paragraphs, we have given some reasons why supported metal clusters can play a role in future nanotechnology applications. We have seen that, in order to be of practical use, the clusters must be deposited and stabilized on a substrate. This leads us to the second aspect of the problem, that of the supporting material. In particular, we will focus on oxide substrates as these are more widely used in the context of catalysis, sensors, and microelectronic applications.

# 3. OXIDE SUPPORTS

There are several strategies to prepare oxide surfaces for cluster deposition [35, 36]. A great deal of work has been done using high-surface-area polycrystalline oxides

prepared by chemical means (e.g., decomposition of the corresponding hydroxides or carbonates). Actually, these are the "natural" candidates for practical applications as they are normally used in catalysis as support for noble metal catalysts. Several attempts have also been made to deposit well-defined clusters onto the surface of polycrystalline oxides starting, for instance, from organometallic precursors [37]. The system is then treated thermally so that the ligands around the organometallic cluster are removed, and the metal cage is left on the surface. The characterization of the metal cluster formed in this manner is rather difficult, and is often based on indirect evidence. A key question in this context is if the original structure of the metal cage of the organometallic cluster is preserved once the ligands are removed. In fact, there is evidence that this often is not the case. The ligands not only provide a means to avoid coalescence of small metal aggregates into larger particles, but also have a stabilizing effect on the whole cluster. The thermal desorption of the ligands may lead to strong structural changes within the metal core, and even into the disaggregation of the original structure. Still, for some metals where strong metal–metal bonds are formed in the metal unit, it has been possible to prepare, by these techniques, very small, well-defined, metal nanoclusters deposited on an oxide. A recent example is that of an $Ir_4$ cluster which has been formed on two substrates, MgO and $Al_2O_3$, by deposition of $Ir_4(CO)_{12}$ organometallic cluster complexes followed by decarbonylation [38]. The existence of the metal unit after the removal of the ligands has been proved by extended X-ray absorption fine structure (EXAFS) measurements. These nanoclusters exhibit a specific catalytic activity, in particular, in propene hydrogenation. However, it has been found that replacement of the MgO with the $Al_2O_3$ support boosts the catalytic activity tenfold, showing the important role of the interface bonding on the electronic and chemical properties of the metal particle [38].

Another approach which has been widely followed in the past is to produce metal clusters in porous oxides by chemical impregnation with a solution of the metal cation, followed by a reduction in $H_2$ atmosphere [39]. If applied to a rough surface, this leads to metal particles with a broad distribution of sizes. If, however, the impregnation is done in a material with pores all having the same dimensions (e.g., nanoporous crystalline materials like zeolites), the aggregation is limited by the size of the pores, and an assembly of metal particles with similar sizes can be obtained.

One problem with these kinds of techniques is that, in general, there is little control of the size of the metal particles formed. The same applies to the synthesis of organometallic clusters. The formation of a cluster of a given nuclearity follows rules which are not yet understood, and it is not possible to direct the synthesis toward a cluster with a predetermined size (or shape) [4]. Things are even worse when the cluster is deposited on a rough surface: in most cases, even the exact nuclearity of the cluster is unknown, and sometimes the only information available is the existence of aggregates of metal atoms from measurements of the metal–metal distances in EXAFS. Another disadvantage is that oxide surfaces in normal conditions are generally covered by OH groups as they have the tendency to interact with water from the atmosphere, leading to water dissociation and surface hydroxilation. Polycrystalline oxides present a very complex surface morphology, a high number of defects, pores, impurities, and so on, and their use for detailed studies of metal–support interactions presents problems related to this surface complexity.

Therefore, other techniques have been developed in recent years to address this problem. It should be mentioned, however, that polycrystalline and amorphous oxides are the materials used in industrial and practical applications, and a direct comparison of the results obtained on these systems with better defined substrates or model systems has been of great help to better understand the surface structure and morphology.

The most direct way to prepare an oxide surface is by *in-situ* cleavage of a single crystal in an ultrahigh vacuum [40]. For some oxides, in particular, cubic oxides like MgO, NiO, and $SrTiO_3$, this works nicely; for other oxides, like $SiO_2$, $Al_2O_3$, and $TiO_2$, of great technological importance, this process is much more difficult as they tend to form rough surfaces by cleavage. Most of these oxides are good insulators or wide-gap semiconductors. This represents an additional problem for their study. In fact, the low conductivity of the material makes electron spectroscopies (photoemission in particular) quite difficult to use because of the charging of the sample under the irradiating light. Also, the low thermal conductivity of oxide single crystals represents a serious problem for the study of temperature desorption processes.

To overcome this problem, single-crystalline oxide surfaces are prepared by growing epitaxial thin films on single-crystal metal supports [35, 36]. Epitaxy (literally "placed" (epi) "arrangement" (taxy) from Greek) is essentially a recrystallization process in which gaseous atoms condense on a template created by a substrate to form a single-crystal film. At least three different major techniques have been developed in this context, and the growth of ultrathin oxide films a few layers thick has become a nanotechnology in itself [41]. One possibility is to oxidize the substrate by direct exposure of the metal surface to $O_2$ pressure. This is the method usually adopted to grow very thin films of $SiO_2$ on Si single crystals for microelectronic applications. In this case, however, the $SiO_2$ film is amorphous, a great advantage for the $Si/SiO_2$ interface properties when one is interested in the dielectric functions of the oxide, and a limitation if one is interested in obtaining very well-defined surfaces to deposit nanoclusters. Often, the direct oxidation of the metal single crystal presents problems connected to the different lattice constants of the metal and its oxide. When the lattice mismatch is larger than a few percent, no epitaxial growth is possible, and the film grows in microcrystalline form, with many additional interfaces and grain boundaries where the control at the microscopic level is low. In some cases, the direct oxidation of the metal substrate leads to good-quality films. This is the case, for instance, of NiAl alloys which are widely used to grow ultrathin, three-atomic-layers-thick films of $Al_2O_3$. In this case, the segregation of Al toward the surface of the alloy leads to a well-defined interface and a regular $Al_2O_3$ film. Probably, the most widely used method to grow oxide thin films in UHV conditions is by metal atom deposition in an oxygen atmosphere. Here, a metal is vaporized (e.g., in a Knudsen cell), and deposited onto a substrate

in a given background $O_2$ pressure. One grows, in this way, films of various thicknesses on the substrate whose quality is strongly dependent on a number of parameters (e.g., temperature of the substrate, flux of metal vapor, $O_2$ pressure, etc.). Films of MgO and NiO on Mo(100), Ag(100), or other metal substrates are usually produced in this way. It is important to mention that the surfaces of these films contain more defects than the surfaces of cleaved single crystals. On the other hand, it is, in principle, possible to grow films with different concentrations and kinds of defects, allowing us, in this way, to tune another important parameter of metal–oxide interfaces, that is, the defects concentration.

All of the oxide surfaces used to deposit clusters in controlled conditions need to be well characterized, both structurally and electronically. This is an essential prerequisite in order to study the properties of deposited metal clusters. As mentioned above, the use of thin oxide films instead of bulk crystals allows one to use a variety of spectroscopies, and to better characterize the material. It is important to mention a few of these characterization techniques. Low-energy electron diffraction (LEED) provides information on the long-range order of the film; this can be complemented by short-range order analysis like photoelectron diffraction (PD). Very important for the structural characterization are scanning tunneling microscopy (STM) and atomic force microscopy (AFM). STM is based on the measurement of the tunneling current from a tip to the sample; it provides an image of the empty or filled states of the atoms of the surface. When one is dealing with insulating materials, like MgO, $SiO_2$, or $Al_2O_3$, the use of STM is not possible unless one makes use of ultrathin thin films of a few layers' thickness. In fact, ultrathin films containing up to three oxide layers of MgO or $Al_2O_3$ grown on a conducting substrate permit us to obtain good STM images, even with atomic resolution. Very often, the structural characterization of the surface of the films is a complex problem. In fact, with few exceptions, most bulk oxides exhibit strong surface relaxation, and even reconstructions. In this respect, they do not resemble the ideal surface arising from a cleavage of the bulk along a given crystallographic direction. Examples are those of the surfaces of $Al_2O_3(0001)$, $Cr_2O_3(0001)$, $Fe_2O_3(0001)$, and even a relatively simple surface like $TiO_2(110)$ has been the subject of considerable debate. For some of these surfaces, however, a good level of structural characterization has been obtained.

Once the oxide substrate has been structurally characterized, one has to identify the characteristic features of its electronic properties, and in particular, the differences from the corresponding bulk oxides. In fact, the truncation of the bulk Madelung potential at the surface leads to considerable changes in the chemical bonding at the surface. One direct consequence of this is the reduction of the bandgap at the surface; this is even more pronounced at low coordinated sites like steps, edges, kinks, and corners, and can lead to a completely different reactivity from that expected for the regular surface. In this respect, several characterization techniques have been applied. Ultraviolet photoemission (UPS) provides a way to investigate the valence band structure of the films. The problem here is that one wants to analyze only the very top layers of the film which will directly affect the properties of the supported metal particle. UPS, on the

other hand, is sensitive to several internal layers, and the features of the surface can be difficult to identify in this way. For this reason, UPS measurements have recently been complemented by a new technique, metastable impact electron spectroscopy (MIES) [42], which makes use of energy transfer from He atoms in an excited state to the surface atoms of the films. The technique provides information about the valence band structure of the film, but has the advantage of being sensitive to the film top layer only. In this way, it has even been possible to identify states in the gap associated with surface defects which are not observable with UPS because of the low sensitivity to the surface. Other means to characterize the surface are based on the detection of surface species by vibrational spectroscopies (e.g., to identify the presence of OH groups) or optical transitions (this can be useful, in particular, in the presence of localized defects).

The properties of oxide surfaces are dominated to a large extent by the presence of extended or point defects. They become particularly important in the analysis of the chemical reactivity of supported metal atoms and clusters [43], and in the description of the nucleation and growth of supported clusters. Finally, the defects can also modify the catalytic activity of the deposited metal by affecting the bonding at the interface [44, 45].

Depending on the oxide electronic structure, more ionic or more covalent, on its crystalline structure and surface reconstruction, and on the preparation of the material (polycrystalline, thin film, etc.), a great variety of defect centers can form at the surface. Even on a simple stoichiometric oxide, like MgO, nine different point defects have been identified and described in the literature [46]. These defect centers can have rather different properties and characteristics, and exist in various concentrations. Low-coordinated O anions at steps and kinks are known to exhibit a pronounced basic character, and to be more reactive with incoming molecules than terrace sites via electron transfer from the surface to the adsorbate [47]. Oxygen vacancies, also called $F^+$ and F-centers, contain one or two electrons trapped in the cavity left by the missing O ion [48]. These centers can act as good electron sources for charge-transfer reactions [49]. Cation vacancies result in localized holes on surface O anions, which then exhibit enhanced reactivity because of their radical character. Hydroxyl groups, OH, can favor the nucleation of metal clusters [50], and introduce inhomogeneous electric fields at the surface. The complexity of the problem is increased by the fact that the point defects can be located at various sites, terraces, edges, steps, and kinks, and that they can be isolated, occur in pairs, or even in "clusters." Furthermore, the concentration of the defects is usually low, making their detection by integral surface-sensitive spectroscopies very difficult. A microscopic view of the metal/oxide interface and a detailed analysis of the sites where the deposited metal atoms or clusters are bound becomes essential in order to rationalize the observed phenomena, and to design new materials with known concentrations of a given type of defect.

In general, the good quality of the substrate is essential to analyze in detail the properties of the supported nanoclusters. In fact, as we will discuss below, the cluster–oxide interaction is such that it influences the shape and electronic structure of the deposited cluster. A deep understanding of

the cluster properties needs, therefore, a similarly profound knowledge of the interface bonding.

# 4. GENERATION OF METAL NANOCLUSTERS

Once a substrate oxide surface has been prepared, either in the form of a single crystal or a thin film, metal clusters can be generated and deposited by various techniques [51]. The most widely used is based on the simple deposition of the metal from a vapor [52]. After impinging on the surface, the metal atoms diffuse and aggregate to form clusters of various size, depending on the vaporization rate, substrate temperature, flux, and so on. Although, in principle, the level of control on the cluster dimensionality is not expected to be very high, leading to a broad distribution of sizes, it has been shown that, by this technique, rather well-defined clusters, almost monodisperse, and even single isolated atoms can be deposited on the surface [52]. The definition of the particle size is usually done by means of STM measurements, although other indirect methods can be used, as will be discussed in Section 5.

A second way to deposit clusters on surfaces follows a completely different and more sophisticated technique [51]. This is based on the production of metal clusters in a molecular beam in the gas phase, for instance, by laser vaporization sources or by high-energy ion sputtering. In the first case, light pulses from an Nd–YAG laser focused onto a suitable target, and can vaporize even refractory materials. Clustering occurs within the nozzle as the metal vapor encounters the rare gas, and continues in the strong expansion as the mixture is ejected. The mixture can contain a given fraction of ionized clusters, which can then be separated by mass by various methods; in most cases, this is done using a quadrupole mass spectrometer. It is also possible to increase the number of charged clusters by using a second laser of sufficient energy to ionize the neutral clusters. In this way, one obtains a beam of mass-separated metal clusters, all having the same size, and the problem becomes to deposit them on the surface in a soft way, in order to prevent damage to the oxide substrate, cluster fragmentation, and other undesired effects. Three impact energy regimes are usually distinguished: low energy ($\approx$.1 eV/atom), medium energy (1–10 eV/atom), and high energy ($>$10 eV/atom). In the low-energy regime, clusters suffer little distortion, there is no damage to the surface, and if a film is formed from the deposited clusters, this consists of a highly porous array of randomly stacked particles. At medium energies, the clusters remain intact, but their morphology is modified, and there may be some induced effect on the surface. It can happen that, for highly mobile clusters, medium-energy impact with the surface renders the particles immobile as a result of the surface damage. At high energies, clusters are completely disrupted, and there is damage to the surface that runs several layers deep. It should be mentioned that much insight into the mechanism of impact of the cluster with the surface has been gained thanks to molecular dynamics simulations.

If one is interested in depositing well-defined, separated clusters on the surface, one has to adopt a soft-landing technique. This can be done by applying a bias voltage to the substrate for deceleration of the ionized clusters as they approach the surface, so that the incident energy can be specified quite accurately. Another way to avoid fragmentation is to deposit the nanoclusters on a cold rare-gas film formed on a solid surface. The van der Waals matrix of rare-gas atoms at low temperature adsorbs the collision energy, resulting in a nondestructive landing of the nanoclusters.

# 5. STRUCTURE AND PROPERTIES OF SUPPORTED METAL NANOCLUSTERS

Supported metal clusters are difficult to characterize from a structural point of view. The small dimension, the low concentration on the surface, the existence of particles with slightly different sizes and shapes, and so on, are all effects that strongly limit the use of standard methods for structural characterization. In fact, the only way to directly identify the cluster size and shape is to use microscopies like transmission electron microscopy (TEM) for particles of hundreds of atoms and STM for very small clusters of a few atoms. This latter method, however, can only be used in connection with conductive substrates, thus limiting it to semiconducting oxides or ultrathin films on metals. An alternative to STM can be represented by AFM, although atomic resolution has not yet been achieved with this technique for supported clusters. A TEM micrograph is produced by transmitting electrons with an energy of 200–400 keV through a sample using the contrast produced by the electron density in the system for imaging. Excellent examples of TEM measurements have been reported for Pd nanocrystallites of typical size of $100 \times 100$ nm$^2$ grown on MgO [22]. STM images of Rh clusters deposited on $Al_2O_3$ films have shown that, upon vapor deposition of Rh at low temperature, small particles nucleate on point defects of the substrate, and a narrow distribution of the sizes of particles is generated [53]. If the deposition of Rh is performed at room temperature, the mobility of the Rh atoms is considerably higher, so that the nucleation at the line defects of the film becomes dominant. Consequently, all of the material nucleates on steps and domain boundaries. Also, in this case, the particles have a rather uniform size.

While STM provides the surface structure of the deposited clusters, their internal structure, in particular, as a function of the cluster size, and the structure of the interface are not accessible through STM. In this connection, TEM studies combined with STM measurements can provide a better picture. On the basis of several high-resolution TEM images (HRTEM), it has been possible to determine the lattice constants as a function of the size of the supported particles. The average metal–metal distance in a cluster is an important parameter. In fact, it is known mainly from theoretical calculations that gas-phase metal clusters of a few atoms have average distances considerably shorter than in the bulk. The HRTEM images have shown that Pt clusters of sizes from 10 to 30 Å deposited on $Al_2O_3$ have lattice constants up to 10% smaller than the bulk one [20]. On the other hand, for particles of 30 Å size, the interatomic Pt–Pt distances approach the corresponding bulk

value. The shorter distance for smaller cluster sizes is a typical manifestation of the lower average coordination of the atoms in the particle. In order to compensate for the smaller number of metal–metal bonds, there is a contraction of the distances which, for very small clusters of fewer than ten atoms, can be quite substantial. The HRTEM results show that, even when the cluster is deposited on a surface, this typical cluster property remains.

The electronic structure of a supported cluster reflects, to a large extent, its geometric structure and vice versa. A key question related to the electronic structure of small clusters is how the aggregation of metal atoms leads from a system with well-defined, discrete molecular levels to a system which is better described by means of band structure theory because of the delocalized nature of the valence electrons. As atoms are put together, the atomic levels split to form cluster orbitals, with splittings that are directly dependent on the strength of the interaction and the metal–metal distances. Already for clusters of tens of atoms, one can start to distinguish groups of levels in the positions corresponding to those of the bands in the bulk material. It is only for clusters containing a few hundred atoms, however, that the level spacing becomes small enough to approach the thermal energy $kT$ ($kT = 26$ meV at room temperature). This means that metal clusters of a few tens of atoms can have occupied and unoccupied levels that are separated by energy differences which are considerably larger than the thermal energy, in contrast to the bulk. Thus, small clusters can exhibit a semiconducting behavior, and in principle, the gap can be tuned by varying the cluster size. The size at which this gap vanishes varies with the metal, and is quite difficult to measure experimentally; on the other hand, this quantity is accessible from first-principle calculations [9, 10]. Spectroscopic measurements of transition metal clusters surrounded by CO ligands suggest that aggregates of 70–80 atoms are sufficient to close the gap. However, the presence of the ligands usually has the effect of changing the electronic structure of the metal aggregate, and in particular, results in a wider gap between occupied and unoccupied states than in the corresponding free cluster.

More interesting in the context of supported metal clusters are the measurements done with scanning tunneling spectroscopy (STS). These are obtained by recording current–voltage curves in a scanning tunneling microscope on a single, well-identified cluster. The technique is thus not giving an average measure over several objects, as in usual spectroscopies, but rather is providing information on the electronic structure of a specific cluster. Typical current–voltage curves have been reported for Au clusters on $TiO_2(110)$ [54]. Large Au particles of dimensions varying from $3 \times 1$ to $5 \times 3$ nm do not show a plateau near $I = V = 0$, indicating a metallic character for the particle as no gap is measured. On the other hand, small Au clusters of $2.5 \times 0.7$ nm size exhibit a gap of about 1 eV. This is a typical quantum size effect, where a nonmetal-to-metal transition is observed for the same element, Au, by only changing the particle dimension.

Another way to probe the electronic structure of supported metal clusters is via their optical response. Ag particles are known to give rise to collective excitations on a sphere, known as Mie plasmon [34], as discussed above.

However, when a spherical particle is deposited onto a substrate there is a change in its shape due to the adhesion to the surface, which results in a loss of spherical symmetry. As a consequence, more than one plasmon resonance can be measured for the supported particle. Indeed, this is what has been observed for Ag particles on mica [55]. The oscillation perpendicular to the surface appears at a higher energy than the corresponding oscillation parallel to the surface. The width of the bands and the relative shift depend on the size and shape distribution of the clusters. This technique, however, measures an average over several particles, and the results depend strongly on the level of dispersion of the cluster sizes. Experiments of this kind on individual clusters based on a scanning tunneling device have been recently reported [56] for Ag clusters on alumina.

A completely different approach to unravel the structure, shape, and to some extent, also the electron distribution of a metal cluster is by vibrational spectroscopy of adsorbed molecules. In this respect, carbon monoxide, CO, is widely used thanks to its low reactivity and high sensitivity of the C–O stretching to local modifications of the electron density of the underlying atoms. To this end, once clusters have been deposited on a given substrate, the sample is exposed to a CO gas atmosphere so that CO molecules adsorb on some specific sites of the particle. The ultrahigh vacuum conditions are then re-established, and Fourier transform infrared (FT–IR) spectra of adsorbed CO are recorded. There are several reasons why this technique is powerful for characterizing clusters on surfaces. For instance, in a recent set of experiments, mass-selected Pd, Pt, and Au clusters were generated in a beam, and deposited by soft-landing methods onto an MgO(100) film grown on an Mo(100) substrate [57, 58]. Even single metal atoms can be deposited at low temperature (90 K), and their existence is proved by FT–IR. In fact, on a single metal atom, only one or two CO molecules can bind on top of the atom, giving rise to a typical frequency, usually around 2050–2100 cm$^{-1}$. If no other IR bands exist at a lower frequency, for example, below 2000 cm$^{-1}$, this is a clear sign that no bridge-bonded CO molecules are present, and that no clusters are formed. If the sample is heated to 400 K, the metal atoms become mobile on the surface, and they aggregate to form small clusters. CO adsorption on the very small Pd clusters formed in this way, typically dimers or trimers, results in only one IR band around 1840 cm$^{-1}$, typical of bridge-bonded CO [59]. At even higher temperatures (800 K), small clusters coalesce to form large Pd particles of nanometer size. On these particles, one can identify various adsorption sites for CO, on-top, bridge, three-, or fourfold hollow sites. Each of these sites gives rise to a specific vibrational frequency for adsorbed CO, and the IR spectrum shows all of these bands together, indicating the formation of a larger aggregate. In a similar way, mass-selected Pt$_8$ clusters deposited on MgO only exhibit CO at bridge sites, while the larger Pt$_{20}$ cluster also shows a band typical of threefold hollow sites on Pt single crystals [57]. Therefore, the CO vibrational frequency provides a very efficient method to titrate the sites of the cluster, and to obtain some indirect information about the structure of the cluster.

# 6. ATOMIC LEVEL CHEMISTRY OF NANOCLUSTERS

As a last topic, we describe an example of how very small clusters can be used to direct the chemistry of adsorbed molecules [24]. This is a field which is known as nanocatalysis, and the reader is referred to this more specific topic for more detailed information [58]. Here, we simply stress that what has been long considered as a dream for catalytic chemistry, that is, the generation of an ensemble of identical, well-defined metal catalysts, all having the same size (and possibly the same shape), is nowadays possible, at least under some conditions.

The preparation of a collection of supported metallic particles that are truly monodisperse, that is, they all have exactly the same size, has long been considered to be virtually impossible [60]. As a consequence, it has been difficult to recognize size effects for small supported clusters, as size distributions have been broad. For clusters in the gas phase, however, strong size-dependent chemical properties have been discovered during the last two decades, and the obtained results lead to new concepts for understanding their chemical properties. Connections of these observations with real catalysis have often been stressed, and suggestions for the tuning efficiency and selectivity of a certain catalytic process by simply changing the cluster size were already made in early days. Efficient and selective conversion is indeed important in catalysis, as most catalytic surfaces assist a variety of reactions. It is, therefore, of interest to study the factors affecting the size-dependent selective and efficient behavior of catalytic systems. Recently, new experiments have been reported where model catalysts, consisting of a collection of metal particles of a single size deposited on oxide supports, have been generated. Strongly size-dependent efficiency and selectivity for the polymerization of acetylene on supported palladium clusters [61] have been reported. The clusters are prepared in a high-frequency laser evaporation source, and after mass selection, they are soft-landed on thin MgO(100) films under UHV conditions (Fig. 3).

Cyclotrimerization of acetylene has been intensively studied in the past, and therefore represents an ideal reaction to check the special reactivity of size-selected metal clusters. On Pd single crystals [62] and supported Pd particles [63], the reaction varies with size and shape, with Pd(111) found to be the most reactive facet. The formation of benzene on relatively large palladium particles a few nanometers in size is very similar to the analogous low-index single-crystal results, with desorption of benzene at 230 and 530 K [63]. The larger Pd particles in this series, regular polyhedra comprised exclusively of $\langle 111 \rangle$ and $\langle 100 \rangle$ facets, favor the low-temperature reaction pathway, whereas the smaller particles desorb benzene at 530 K. Whereas for Pd single crystals the polymerization reaction is highly selective and only benzene is formed, size-distributed Pd particles catalyze different reaction channels, and different types of hydrocarbons are observed [63].
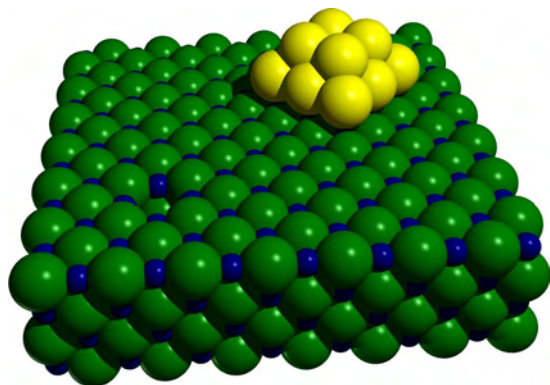
The same reaction has then been studied on very small, size-selected $Pd_n$ clusters deposited on MgO containing from 1 to 30 atoms [45]. Surprisingly, a single Pd atom already catalyzes the cyclotrimerization reaction, and for cluster sizes up to $Pd_3$, benzene desorbs at about 300 K. For $Pd_7$, an additional desorption peak of benzene is observed at about 430 K. Increasing the cluster size leads to a further intensity increase of this peak. For $Pd_8$, this feature becomes as important as the peak at 300 K, while for $Pd_{30}$, benzene desorbs around 430 K [45]. Thus, different reaction mechanisms occur, depending on the cluster size, with the very small clusters already producing benzene at room temperature. In addition, the polymerization reaction on small $Pd_n$ clusters reveals a strongly size-dependent selectivity [61]. Whereas up to $Pd_3$ one forms only benzene, with 100% selectivity, $Pd_{4-6}$ clusters lead to the formation of other hydrocarbons besides benzene, like $C_4H_6$. Even larger Pd clusters produce a third product, $C_4H_8$. This becomes the dominant product for the polymerization of acetylene on $Pd_{30}$. Thus, not only can one tune the reaction mechanism by varying the cluster size, but also the kind of product can be selected by depositing a specific Pd cluster with a well-defined number of atoms.

# 7. SUMMARY

The deposition and growth of well-defined metal clusters under controlled conditions onto a stabilizing substrate can open very important perspectives in various technological areas. Thus far, the generation of metal clusters has been possible either via chemical synthesis (and in this case, the clusters are surrounded by ligands shells) or in the gas phase from vaporization and aggregation techniques. In neither case is there complete control of the nuclearity of the cluster which one wants to produce, as this is governed by rules which are not yet completely understood. However, recent advances in the mass-selection and soft-landing deposition of gas-phase metal clusters seem to open the way to prepare ensembles of nanosized metal particles all having the same size. This can be extremely useful for exploiting the structure-dependent properties of the metal clusters, and for tuning these properties as required by a given application. So far, this approach has been restricted to cluster deposition on oxide thin films under ultrahigh vacuum conditions, in order to exploit the thermal and electrical conductive properties of the films. The approach is also limited by



**Figure 3.** Schematic representation of a Pd nanocluster deposited on the (100) surface of magnesium oxide, MgO. Pd clusters have been generated and used to study chemical reactivity as a function of the cluster dimensionality by varying the cluster size atom by atom.

the complexity and the cost of the experimental apparatus needed to generate the clusters. With other less sophisticated methods, it has been possible to deposit metal clusters that are almost monodisperse, showing that other technologies are available to reach the same objective. The hope is to be able to extend these technologies to more complex substrates without losing the characteristics which are typical of the small cluster dimensionality, often below the nanometer size. When this will be possible, spectacular advances are to be expected in various areas of material science, from heterogeneous catalysis to sensors, and from magnetic recording to sensors to optical problems.

## GLOSSARY

**Catalyst support**   Surface of an "inert" inorganic material, usually an oxide, where small metal particles or metal clusters are deposited and stabilized, forming the active part of the catalyst.

**Cluster**   Metastable state in condensed matter consisting of very small aggregates of atoms, usually metal atoms.

**Nanocatalyst**   Assembly of metal nanoparticles, ideally all having the same size, deposited on an inert support (catalyst support).

**Organometallic cluster**   System composed of a metal core of 2–50 atoms surrounded by a shell of ligand molecules.

## REFERENCES

1. See, for instance, G. Schmid (Ed.), "Clusters and Colloids: From Theory to Applications." VCH, Weinheim, 1994.
2. S. C. Davis and K. J. Klabunde, *Chem. Rev.* 82, 153 (1982).
3. T. Graham, *Phil. Trans. Royal Soc.* 151, 183 (1861).
4. M. Moskovits (Ed.), "Metal Clusters." Wiley-Interscience, New York, 1986.
5. D. M. P. Mingos and D. J. Wales, "Introduction to Cluster Chemistry." Prentice-Hall, Englewood Cliffs, NJ, 1990.
6. A. Ceriotti, F. Demartin, G. Longoni, M. Manassero, M. Marchionna, G. Piva, and M. Sansoni, *Angew. Chem. Int. Ed. Engl.* 24, 697 (1985).
7. L. J. De Jongh (Ed.), "Physics and Chemistry of Metal Cluster Compounds." Kluwer, Dordrecht, 1994.
8. M. R. Albert and J. T. Yates, "The Surface Scientist's Guide to Organometallic Chemistry." American Chemical Society, Washington, DC, 1987.
9. G. Pacchioni, S.-C. Chung, S. Krüger, and N. Rösch, *Chem. Phys.* 184, 125 (1994).
10. O. Häberlen, S.-C- Chung, M. Stener, and N. Rösch, *J. Chem. Phys.* 106, 5189 (1997).
11. G. Benedek, T. P. Martin, and G. Pacchioni, "Elemental and Molecular Clusters." Springer, Berlin, 1988.
12. S. Sugano and H. Koizumi, "Microcluster Physics." Springer, Berlin, 1998.
13. T. P. Martin, "Large Clusters of Atoms and Molecules," NATO ASI Series E, Vol. 313. Kluwer, Dordrecht, 1996.
14. M. M. Kappes, *Chem. Rev.* 88, 369 (1988).
15. M. Moskovits, (Ed.), "Metal Clusters." 185, Wiley Interscience, New York, 1986, 185 (1861).
16. K. Sattler, J. Muhlback, and E. Recknagel, *Phys. Rev. Lett.* 45, 821 (1980).
17. T. G. Diez, M. A. Duncan, D. E. Powers, and R. E. Smalley, *J. Chem. Phys.* 74, 6511 (1981).
18. H. W. Kroto, J. R. Heath, S. C. O'Brien, R. F. Curl, and R. E. Smalley, *Nature* 318, 162 (1985).
19. G. Schmid, M. Bäumle, M. Geerkens, I. Heim, C. Osemann, and T. Sawitowski, *Chem. Soc. Rev.* 28, 179 (1999).
20. H.-J. Freund, *Surf. Sci.* 500, 271 (2002).
21. C. T. Campbell, *Surf. Sci. Rep.* 27, 1 (1997).
22. C. Henry, *Surf. Sci. Rep.* 31, 231 (1998).
23. G. Renaud, *Surf. Sci. Rep.* 32, 1 (1998).
24. R. M. Lambert and G. Pacchioni (Eds.), "Chemisorption and Reactivity of Supported Clusters and Thin Films," NATO ASI Series E, Vol. 331. Kluwer, Dordrecht, 1997.
25. J. Shi, S. Gider, K. Babcock, and D. D. Awschalom, *Science* 271, 937 (1996).
26. R. Kubo, *J. Phys. Soc. Jpn.* 17, 975 (1962).
27. I. M. L. Billas, A. Chatelain, and W. A. de Heer, *Science* 265, 1682 (1994).
28. J. A. Alonso, *Chem. Rev.* 100, 637 (2000).
29. G. Pacchioni and N. Rösch, *Acc. Chem. Res.* 28, 390 (1995).
30. B. V. Reddy, S. N. Khanna, and B. I. Dunlap, *Phys. Rev. Lett.* 70, 3323 (1993).
31. A. J. Cox, J. G. Louderback, and L. A. Bloomfield, *Phys. Rev. Lett.* 71, 923 (1993).
32. D. A. van Leeuwen, J. M. van Ruitenbeek, L. J. de Jong, A. Ceriotti, G. Pacchioni, G. Longoni, O. Häberlen, and N. Rösch, *Phys. Rev. Lett.* 73, 1432 (1994).
33. A. Barthélémy, A. Fert, R. Morel, and L. Steren, *Phys. World* 7, 34 (1994).
34. A. Mie, *Ann. Phys.* 25, 377 (1908).
35. S. A. Chambers, *Surf. Sci. Rep.* 39, 105 (2000).
36. D. P. Woodruff (Ed.), "The Chemical Physics of Solid Surfaces—Oxide Surfaces," Vol. 9. Elsevier, Amsterdam, 2001.
37. H. H. Lamb, B. C. Gates, and H. Knözinger, *Angew. Chem. Int. Ed. Engl.* 27, 1127 (1988).
38. A. M. Argo, J. F. Odzak, F. S. Lai, and B. C. Gates, *Nature* 415, 623 (2002).
39. B. C. Gates, "Catalytic Chemistry." Wiley, New York, 1991.
40. V. E. Henrich and P. A. Cox, "The Surface Science of Metal Oxides." Cambridge University Press, Cambridge, 1994.
41. The surface science of metal oxides, *Faraday Discuss* 114 (1999).
42. L. N. Kantorovich, A. L. Shluger, P. V. Sushko, J. Günster, P. Stracke, D. W. Goodman, and V. Kempter, *Faraday Discuss* 114, 173 (1999).
43. H.-J. Freund, *Angew. Chem. Int. Ed. Engl.* 36, 452 (1997).
44. A. Sanchez, S. Abbet, U. Heiz, W.-D. Schneider, H. Häkkinen, R. N. Barnett, and U. Landmann, *J. Phys. Chem. A* 103, 9573 (1999).
45. S. Abbet, A. Sanchez, U. Heiz, W.-D. Schneider, A. Ferrari, G. Pacchioni, and N. Rösch, *J. Am. Chem. Soc.* 122, 3453 (2000).
46. G. Pacchioni, in "The Chemical Physics of Solid Surfaces" (P. Woodruff, Ed.), Vol. 9. Elsevier, Amsterdam, 2001.
47. G. Pacchioni, J. M. Ricart, and F. Illas, *J. Am. Chem. Soc.* 116, 10152 (1994).
48. A. M. Ferrari and G. Pacchioni, *J. Phys. Chem.* 99, 17010 (1995).
49. E. Giamello, M. C. Paganini, M. Chiesa, D. M. Murphy, G. Pacchioni, R. Soave, and A. Rockenbauer, *J. Phys. Chem. B* 104, 1887 (2000).
50. A. Bogicevic and D. R. Jennison, *Surf. Sci.* 437, L741 (1999).
51. C. Binnis, *Surf. Sci. Rep.* 44, 1 (2001).
52. M. Franck and M. Bäumer, *Phys. Chem. Chem. Phys.* 2, 3723 (2000).
53. J. Libuda, F. Winkelmann, M. Bäumer, H.-J. Freund, T. Bertrams, H. Neddermeyer, and K. Müller, *Surf. Sci.* 318, 61 (1994).
54. M. Valden, X. Lai, and D. W. Goodman, *Science* 281, 1647 (1998).
55. F. Stietz and F. Trager, *Phil. Mag. B* 79, 1281 (1999).
56. N. Nilius, N. Ernst, and H. J. Freund, *Phys. Rev. Lett.* 84, 3994 (2000).
57. U. Heiz, A. Sanchez, S. Abbet, and W. D. Schneider, *J. Am. Chem. Soc.* 121, 3214 (1999).

*58.* U. Heiz and W.-D. Schneider, *J. Phys. D: Appl. Phys.* 33, R85 (2000).

*59.* S. Abbet, E. Riedo, H. Brune, U. Heiz, A. M. Ferrari, L. Giordano, and G. Pacchioni, *J. Am. Chem. Soc.* 123, 6172 (2001).

*60.* G. C. Bond and D. T. Thompson, *Catal. Rev.—Sci. Eng.* 41, 319 (1999).

*61.* S. Abbet, A. Sanchez, U. Heiz, and W. D. Schneider, *J. Catal.* 198, 122 (2001).

*62.* W. T. Tysoe, G. L. Nyberg, and R. M. Lambert, *J. Chem. Soc., Chem. Commun.* 623 (1983).

*63.* P. M. Holmblad, D. R. Rainer, and D. W. Goodman, *J. Phys. Chem. B* 101, 8883 (1997).

# Metal Nano-Optics

## J. R. Krenn, A. Leitner, F. R. Aussenegg

*Karl-Franzens-University Graz, Graz, Austria*

## CONTENTS

## 1. INTRODUCTION

The optical properties of noble metal nanoparticles are strongly affected by the occurrence of plasmon modes, that is, resonant collective oscillations of the conduction electrons. These particle plasmons give rise to a variety of optical effects as spectrally selective absorption and scattering and a dramatic field enhancement localized to subwavelength volumes. Although plasmon-based sensor devices are readily available, their specific properties make particle plasmons also promising candidates for the tasks of guiding, routing, and manipulating light within a future subwavelength optical technology (nano-optics). However, the investigation of nanoparticle plasmon effects was often hindered by a lack of sample structures geometrically well defined on the nanoscale. This drawback was efficiently eliminated within the last decade due to improved lithographic fabrication methods. Here, we will review recent results on particle plasmons that originate from the improved control of sample morphology (individual particle size and geometry) as well as arrangement patterns of nanoparticle ensembles. In addition, the investigation of individual nanoparticles is discussed.

Just as in other fields such as electronics or material science, the size reduction of optical elements into the nanometer range gives rise to interesting novel or modified physical properties. It is somewhat surprising that noble metals, a material class not usually associated with optics, has been used in nanostructured form for centuries. As early as 2000 years ago, gold nanoparticles were used to color glasses, an effect that is based on the spectrally selective absorption of light: An exciting light wave drives the conduction electrons in the metal nanoparticle to a coherent oscillation. The finite size of the particle gives rise to repulsive forces, thus leading to a resonant character of the electron plasma oscillation. This resonance creates a spectrally narrow absorption band generating the aforementioned color effect. The resonance phenomenon is usually termed *surface plasmon* after its quantized energy values. For a clear discrimination from surface plasmon modes existing as propagating waves in flat interfaces, we use the term particle plasmon (PP) in the following.

PP effects have been investigated for a long time, and there are extensive reviews and excellent textbooks available [1, 2]. The nanoparticle sizes investigated cover a broad range from small clusters consisting of only a few atoms to particles with diameters of more than 100 nm. Within the last decade a variety of preparation techniques was developed, which enabled the production of monodisperse ensembles of particles with diameters up to a few nanometers. Optical experiments on highly diluted and therefore interaction-free samples of such nanoparticles allowed measurement to a good approximation of the optical properties of the individual particle [1]. On the other side, it turned out to be quite complicated to produce homogeneous ensembles of metal nanoparticles within the size range from 10 to 100 nm. In addition, usually no regular nanoparticle arrays on substrates could be formed to study the interaction of PP fields in a well-controlled way. Consequently, distributions in nanoparticle size and their mutual distance had to be introduced into theories modeling the optical properties of nanoparticle ensembles, which is a quite cumbersome task.

However, improvements in experimental techniques within the last few years offer nowadays unprecedented control over individual particle size and geometry and the lateral position of a particle when deposited on a substrate. Thereby well-defined nanoparticle samples (e.g., arrays of regularly arranged identically shaped particles) are available that can be probed with conventional optical methods. Besides improved production techniques, the capabilities

of optical microscopy were considerably expanded by the advent of scanning near-field optical microscopy. This method allows probing of PP fields of individual nanoparticles with subwavelength optical resolution. It is the aim of this chapter to discuss recent results for PP optics which rely on either (1) single nanoparticles or (2) samples produced with a high degree of control on particle geometry and position. Regarding materials, experimental and theoretical efforts focused mainly on the noble metals gold and silver owing to their low PP damping and consequently strong near-field effects.

The basics of PP excitation are summarized in Section 2. In Section 3 the relevant experimental techniques are introduced. Sections 4 and 5 are devoted to spectrally and spatially resolved measurements of the optical far- and near-field properties of isolated and electromagnetically coupled nanoparticles, respectively. Finally, Section 6 summarizes existing and envisaged applications of regular metal nanoparticles and nanoparticle ensembles.

## 2. PARTICLE PLASMONS

The basics of PP excitation are extensively discussed in [1, 2], so we give only a brief summary here. We restrict ourselves to a spheroidal particle much smaller than the wavelength of the exciting light $\lambda_0$, because for this special case the theoretical description of the PP effect is particularly simple and clear. For polarization of the exciting light along one of the spheroid principal axes $j = x$, $y$, or $z$ the polarizability $\alpha(\omega)_j$ of the spheroid takes the following form:

$$\alpha(\omega)_j = \epsilon_0 V \frac{\epsilon(\omega) - \epsilon_s}{\epsilon_s + [\epsilon(\omega) - \epsilon_s]L_j} \qquad (1)$$

$\epsilon(\omega)$ is the complex dielectric function of the metal, $\epsilon_0$ and $\epsilon_s$ are the dielectric functions of the vacuum and the surrounding medium, respectively, and $V$ is the spheroid volume. The shape factor $L_j$ describes the spheroid geometry [1]. For example, for a sphere $L_x = L_y = L_z = \frac{1}{3}$. We find $\alpha(\omega)_j$ to be maximal for the resonance conditions $\mathrm{Re}\{\epsilon(\omega)\} = \epsilon_s(1 - 1/L_j)$, its actual value only being restricted by the imaginary part of $\epsilon(\omega)$. These resonances correspond to PP excitation, leading in turn to enhanced absorption, scattering, and near-field intensity. As the crucial point we note that by controlling the nanoparticle geometry (described by $L_j$) we can tailor the spectral position of the PP resonances. Silver and gold are the most popular metals used for experimental PP investigations. Nanoparticles made from these noble metals sustain PP resonances in the visible and near-infrared spectral ranges, and owing to the particularly low values of their imaginary part of $\epsilon(\omega)$, PP damping is quite low and they are chemically stable. Clearly the simple model discussed cannot account for many aspects of real nanoparticles such as size effects for very small ($< \sim 5$ nm) or large ($> \sim 50$ nm) particles or the presence of a substrate or electromagnetic interaction between particles. Although Mie theory [3] and its various extensions can handle a few cases, generally numeric methods have to be applied [4–6].

## 3. EXPERIMENTAL

### 3.1. Preparation Methods

The production of samples with well-defined individual nanoparticle geometry and particle arrangement pattern has to rely on some lithographic techniques. Electron beam lithography (EBL) has proved to be the most universal tool for this purpose [7]. Producing a nanoparticle sample by EBL consists of the following steps. The desired sample pattern is transferred to an electron-sensitive resist, typically polymethyl methacrylate (PMMA) deposited on a substrate with a thickness of $\sim 100$ nm by exposure to an electron beam. Chemical development results in a resist mask for the deposition of the metal by evaporation in high vacuum. After lifting off the PMMA mask the metal structures remain on the substrate. Two examples of EBL-produced gold nanoparticle arrays (which will be further discussed in Section 6.A) are shown in Fig. 1a. The smallest lateral structure that can be produced by a typical EBL setup is $\sim 25$ nm; the write field is restricted to a few 100 $\mu$m. Alternatively, when the metal is deposited beneath the resist layer, the sample pattern can be transferred from the resist mask by reactive ion etching [8].

Self-assembled mono- or bilayers of latex spheres can also serve as a mask for an evaporation step [9, 10]. The particle distance can be controlled by the size of the latex spheres. However, the particle size is a function of particle distance and the ensemble pattern cannot be varied. Another technique allowing the production of particle ensembles with fairly narrow distributions in particle size and interparticle distance is based on micelle layers surrounding a metal precursor [11]. These two techniques allow the preparation of large sample areas; examples of gold nanoparticle arrays produced with the respective technique are shown in Figure 1b and c. Although in general providing no control over the lateral position of nanoparticles on a substrate, improved chemical synthesis methods allow preparation of an extended range of nanoparticle geometries that are of interest for single nanoparticle analysis (see [12, 13] and references therein). The production of monocrystalline metal nanowires was reported in [14].

### 3.2. Optical Methods

PP excitations can be conveniently probed by optical extinction spectroscopy. Thereby information about both resonance frequency and the PP damping (via the PP peak width) is gained. For EBL-produced samples the spectrometer usually has to be coupled to a microscope because of the small overall sample area. Provided the distance between the individual nanoparticles within a sample exceeds the optical resolution limit a conventional (far-field) optical microscope can be also used to investigate individual nanoparticles. A dark-field configuration is specifically suited for spectroscopic examination of single particles, because by suppressing the exciting light from reaching the detector the signal-to-noise ratio can be considerably enhanced.

For directly probing the PP near-field or spatially resolving closely packed nanoparticles, a scanning near-field optical

(a)



(b)



(c)
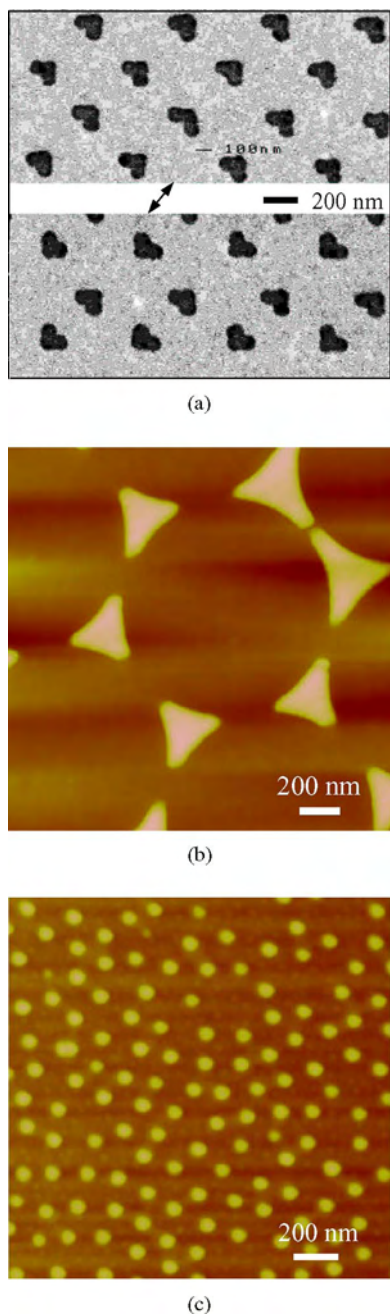
**Figure 1.** Lithographically produced gold nanoparticle ensembles: (a) Scanning electron micrographs of two EBL-produced samples consisting of identical non-centrosymmetric particles in two different arrangement patterns as shown in the upper and lower parts of the figure. The double arrow indicates the orientation of the particle symmetry axis (Courtesy of J. R. Krenn, University of Graz). (b) Scanning force microscope image of a sample produced with a latex sphere mask (Courtesy of M. Goncalves, University of Ulm). (c) Scanning force microscope image of a sample produced with a polymeric micelle-based technique (Courtesy of M. Ott, University of Ulm).

microscope (SNOM) [15, 16] rather than a conventional optical microscope has to be used. In a SNOM a nanoscale tip in the immediate vicinity of the sample surface allows inclusion of evanescent waves in the optical detection process.

Thereby the diffraction limit is overcome, because these evanescent waves carry the information about sample features smaller than the limit set by far-field diffraction. The measured light signal for a given lateral position of the tip is recorded and an image is acquired by raster scanning the tip over the sample. The distance between tip and sample is usually kept constant at a value $<10$ nm by measuring shear forces on the tip [17]. Alternatively, to exclude any mechanical interaction between the sample and the tip a series of successive scans at a constant height while the sample is approached can be performed [18, 19]. The spatial resolution of a SNOM is determined by the tip size and its distance to the sample surface rather than by the light wavelength.

SNOMs relying on a subwavelength light source (usually an aperture in an opaque metal film coating a sharpened glass fiber) yield information about the optical local density of states [20] of the sample, and thus the intrinsic optical mode structure of the sample. In contrast, a specific SNOM configuration dubbed the photon scanning tunneling microscope (PSTM) [21, 22] measures the local intensity of the electric field. Usually a dielectric fiber tip is used as a local probe of the optical near-field of the sample. The sample is optically coupled to a glass prism and illuminated by an evanescent wave generated by total internal reflection of a laser beam inside the prism. Light scattered locally by the tip is guided through the fiber to a detector and assigned to the lateral position of the tip. Besides suppressing the excitation light from the detecting fiber, the evanescent wave excitation creates a quasi two-dimensional optical wave at the prism/sample interface, which is convenient for the investigation of optical phenomena reduced to two dimensions as propagating surface plasmons. Alternatively the detection of light scattered by the tip might be accomplished by external optics, allowing the use of metal or semiconductor tips, a technique often called apertureless scanning near-field optical microscopy [23, 24]. With apertureless SNOMs, the optical excitation was also performed by shining light on the sample under an angle from the tip side.

## 4. INDIVIDUAL NANOPARTICLES

### 4.1. Far-Field Measurements

Measuring the spectral response of single nanoparticles by conventional optical techniques solves the problem of extremely low signal levels. The signal-to-noise ratio can be considerably enhanced by dark-field microscopy, in which the nanoparticle is excited either by an evanescent wave created by a totally reflected beam in a prism or by a dark-field condensor. The detection optics is designed to pick up exclusively light scattered by the nanoparticle [25]. As an example, two scattered light spectra are shown in Figure 2a [26]. The spectra are taken from a single 60 nm diameter gold sphere and a gold nanorod. The latter is a chemically produced elongated prolate particle with a cross-sectional diameter of $\sim 20$ nm and a long axis around 80 nm. The PP is driven along the long axis. As the spectra are acquired from single particles, the PP damping and thus the PP lifetime $\tau$ can be unambiguously deduced from the spectral peak width $\Gamma$. This parameter is usually not accessible with conventional spectroscopic measurements of nanoparticle
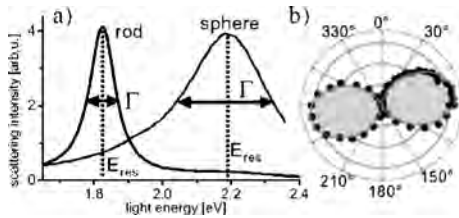
**Figure 2.** (a) Scattered light spectra of a 60 nm gold sphere and a gold nanorod excited along its long axis. (b) Polar plot of the scattered light intensity from the nanorod as a function of the polarization angle of the exciting light. Reprinted with permission from [26], C. Sönnichsen et al., *Phys. Rev. Lett.* 88, 077402 (2002). © 2002, American Physical Society.

ensembles because distributions in particle size and shape might inhomogeneously broaden the PP peak. However, it was shown that under certain conditions femtosecond time-resolved techniques give access to $\tau$ even for inhomogeneous broadening [27, 28]. From Figure 2a we find $\Gamma$ to be considerably smaller for the nanorod compared with the sphere, which is due to the smaller nanorod volume leading to lower radiation damping. Nanorods are thus expected to show a higher enhancement of the optical near-field, a key property for applications such as surface enhanced spectroscopy (see Section 4.2). Figure 2b displays a polar plot of the light intensity scattered from the long axis PP resonance of the nanorod as a function of the polarization angle of the exciting light. This plot (long rod axis oriented along the 170/350° direction) demonstrates the dipole characteristic of the PP resonance [26].

## 4.2. Near-Field Measurements

Although scattering spectroscopy gives access to the optical response of an individual particle, it cannot provide direct information about the spatial profile of PP near-fields. However, direct imaging of these fields is possible by near-field optical microscopy. A variety of PP investigations relying on the different SNOM types as outlined in Section 4.2 have been performed recently.

When optically excited, the PP field around a nanoparticle can be probed locally with a resolution given mainly by the tip dimension. It has been shown that for purely dielectric (uncoated) fiber tips the signal acquired with a PSTM is to an excellent approximation proportional to the local electric field intensity in absence of the tip. That means that perturbations of the PP near-field due to the presence of the tip can be neglected [29]. As an example, the PP field around an individual gold nanoparticle (diameter 100 nm, height 40 nm) excited resonantly at $\lambda_0 = 633$ nm and probed by a dielectric fiber tip is shown in the PSTM image in Figure 3a [18]. The projection of the incident wave vector on the substrate plane $k_\parallel$ points from bottom to top. We find two bright lobes around the particle position and a standing wave pattern due to interference of the exciting light wave and light scattered by the particle. The theoretical image in Figure 3b corresponds well to the experimental result and confirms the lateral particle position in between the two lobes (white square in Fig. 3b). To recover the measured field pattern the calculation had to be performed in a plane 100 nm above the
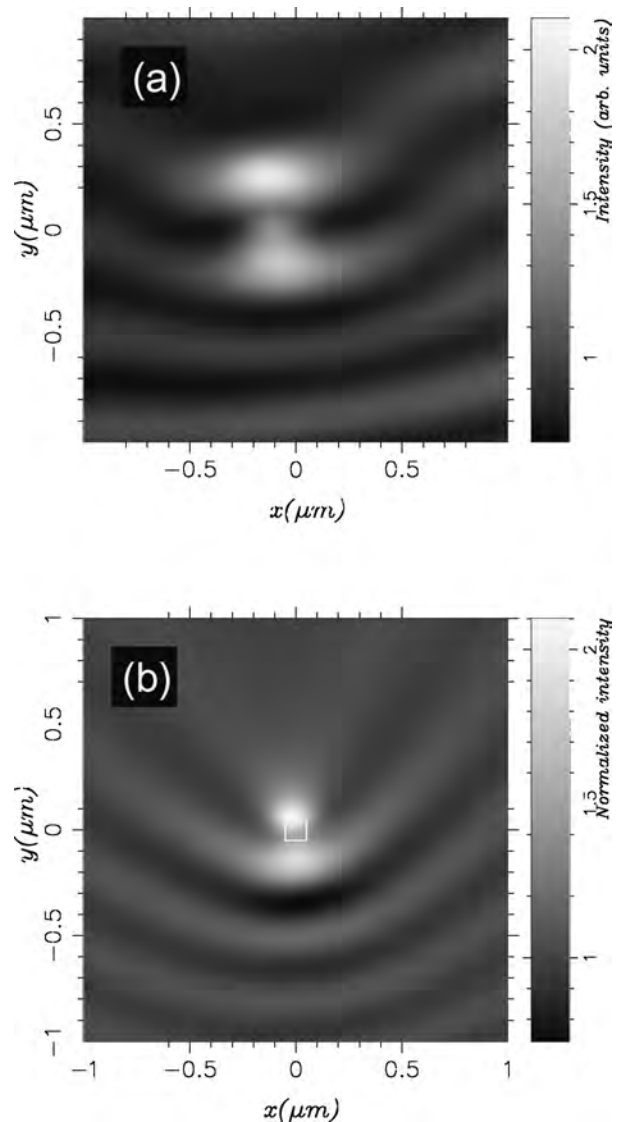


**Figure 3.** Optical PP near-field around a gold nanoparticle: (a) PSTM image; (b) numerical simulation. Reprinted with permission from [18], J. R. Krenn et al., *Phys. Rev. Lett.* 82, 2590 (1999). © 1999, American Physical Society.

particle, a distance that clearly exceeds the distance between the very tip of the probe and the sample, which is known from the experiment to be below 10 nm. This discrepancy is due to the finite detection volume of the dielectric tip. However, when metal coating of the tip is used to confine the detection volume, the measurement process cannot be considered noninvasive anymore because the presence of the metal is likely to change the optical response of the sample.

A spectroscopic study of the optical near-field of a single gold nanoparticle was performed with an apertureless SNOM equipped with a silicon tip [30, 31]. When different laser wavelengths were used for excitation, the relative intensity of the particle near-field with respect to the intensity level on the bare substrate changed. This information was processed to recover the near-field spectral response of the particle (Fig. 4). The authors showed that the observed
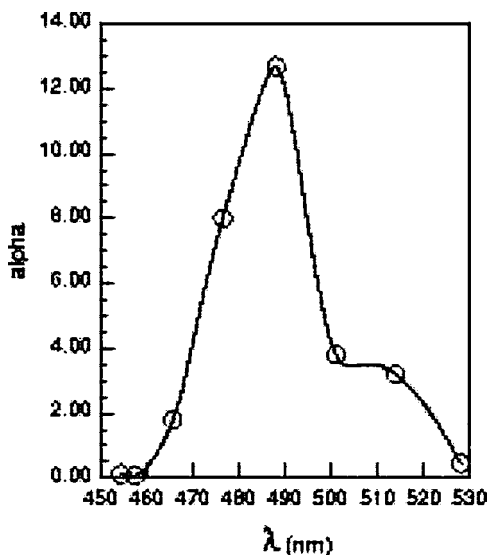
**Figure 4.** Near-field enhancement of a gold nanoparticle as a function of wavelength. The near-field enhancement is defined as the optical signal measured with a silicon tip above the particle normalized to the signal picked up above the bare substrate. Reprinted with permission from [30], P. M. Adam et al., *J. Appl. Phys.* 88, 6919 (2000). © 2000, American Institute of Physics.

intensity maximum around 488 nm corresponded to a PP mode oriented vertically to the substrate, thus demonstrating the capability of a apertureless SNOM to selectively probe individual PP modes. A similar technique has been used to reveal the PP field profile around gold nanoparticles [32].

Instead of probing PP fields locally, a SNOM can be used for local PP excitation by an apertured fiber tip. Again, varying the excitation wavelength allowed construction of the spectral dependence of the PP field of individual gold nanoparticles [33]. However, the presence of the aperture-forming metal exerts an influence on the optical PP properties, as outlined in [34].

## 5. COUPLED NANOPARTICLES

Nano-optical devices as well as conventional optical applications call for nanoparticle ensembles rather than isolated particles. Because in ensembles electromagnetic interactions between individual particles might occur, possible coupling mechanisms have to be analyzed. Because of the strong confinement of the PP field around the respective nanoparticles, electromagnetic coupling only takes place for nanoparticles in the immediate vicinity of each other (on the order of a few tens of nanometers; near-field coupling). Far-field radiation, however, can also exert a strong impact on the optical properties of the nanostructures. This is the case if grating effects occur; that is, if a periodic particle arrangement pattern gives rise to a coherent superposition of the individual (dipolar) scattered light fields.

### 5.1. Particle Pairs

Starting from an isolated nanoparticle as discussed in Section 4.2 the elementary system to test PP coupling is a pair of two nanoparticles with varying mutual distance.

The scanning electron micrographs in Figure 5a and b show two particle arrays built up from nanoparticles (diameter 140 nm, height 14 nm) arranged as pairs with respective center-to-center distances of $D = 250$ and 150 nm. The
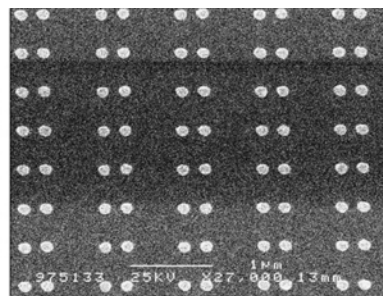


(a)
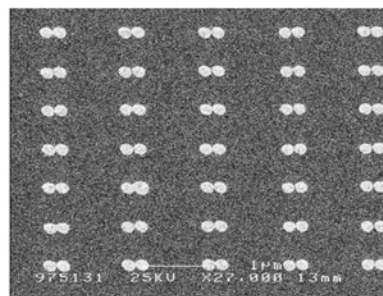


(b)
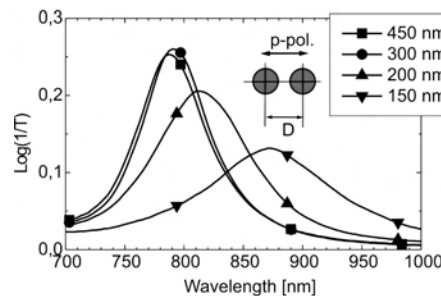


(c)
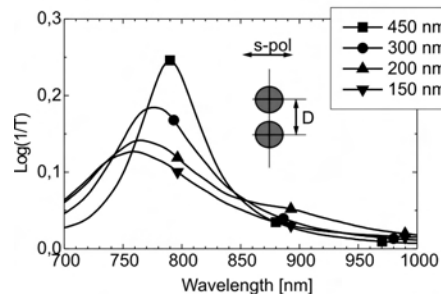


(d)

**Figure 5.** Scanning electron microscope images of exemplary gold nanoparticle pair arrays with particle pair distances $D$ (center-to-center) of (a) 250 nm and (b) 150 nm. Extinction (defined as log (1/transmission) spectra for samples with $D$ values of 150, 200, 300, and 450 nm are shown for polarization directions of the exciting light along (c) and parallel (d) to the particle pair axis (Courtesy of J. R. Krenn, University of Graz).

extinction spectra for a series of such particle pair samples is shown in Figure 5c for the polarization direction parallel to the long particle pair axis and in Figure 5d for the perpendicular polarization direction. In the first case a reduction of $D$ gives rise to a redshift of the PP peak whereas for the perpendicular polarization direction a weak blueshift is found. Both effects can be readily understood in terms of two coupled oscillators. Depending on their respective orientations, two spatially close dipolar oscillators strengthen or weaken each other's restoring forces acting on their oscillating electrons, leading to the observed spectral shifts of the PP resonances [35, 36]. Additionally, the near-field profile around the particle pair is drastically changed when $D$ decreases, giving rise to a strongly enhanced PP field confined between the two particles [5]. This effect is especially interesting for surface-enhanced optical spectroscopies relying on a high field enhancement (see Section 6.2). The electromagnetic coupling of two gold nanoparticles was also directly imaged by a PSTM [37]. In this experiment, PP excitation in a particle by the PP field of a nearby particle (which was excited directly by a laser beam) was demonstrated. This coupling effect was found to be extremely sensitive to the interparticle distance, indicating the localization of the interaction range to a nanoscale volume. Possible applications of such electromagnetically coupled nanoparticles include nanoscale switches or routers for light signals.

## 5.2. Regular Arrays

Increasing the number of interacting nanoparticles allows the realization of a variety of specific particle ensembles. Regular one-dimensional particle chains have triggered specific interest recently because they might be used as submicroscopic waveguides, relying on the near-field coupling of nanoparticles [38, 39]. Indeed, the coherent near-field interaction stemming from periodic particle arrangements has already been investigated experimentally. It was found that for an appropriately chosen particle distance the PP interaction leads to a squeezing of the respective PP fields. The lateral extension of the corresponding PP field maxima was found to measure only 80 nm, which for the excitation wavelengths of $\lambda_0 = 633$ nm corresponds to a value of about $\lambda_0/8$ [18]. The obvious difference of this squeezed mode from the PP field of a single nanoparticle (see Fig. 3a) indicates a strong localization of the chain PP mode, favorable when thinking of nanoscale waveguiding [38, 39].

For two-dimensional nanoparticle ensembles, again PSTM measurements revealed the PP field profile and the associated enhancement in near-field intensity [19]. These properties are crucially influenced by the periodicity of the two-dimensional particle arrangement, that is, the grating constant. This influence is particularly strong when the grating constant is on the order of the wavelength. Because such particle distances are beyond the near-field coupling regime, only grating effects can explain this behavior. Grating orders radiating at a grazing angle were identified to lead to enhanced local fields, shifting the PP band of the individual particles spectrally. On the other hand, a radiating grating order represents an open channel for radiation damping of the PP, lowering the PP lifetime [40]. These

effects are important when one deals with any kind of regular nanoparticle arrangement and their understanding allows the controlled design of the optical near-field profile and the PP lifetime. The latter was demonstrated in [40] by tuning the PP lifetime in a gold nanoparticle array from 2 to 8 fs.

Interesting optical properties emerge also from the combination of regular two-dimensional nanoparticle arrangements with a substrate exhibiting an optical functionality. If a dielectric waveguide is used as the substrate, interference effects can give rise to a spectrally selective suppression of extinction of the particle ensemble [41, 42]. This effect is due to the waveguide-mediated interaction of the exciting light and the nanoparticles. Another interesting system consists of nanoparticle arrays put on a flat metal film that supports a propagating surface plasmon. Bragg scattering of the surface plasmon from the particle array can give rise to a photonic bandgap [43, 44], inhibiting SP propagation in a certain frequency range [45]. Such systems have been used to realize mirror- and beamsplitter-like devices acting on propagating surface plasmons and allowing the realization of two-dimensional plasmon optics [46].

## 6. APPLICATIONS

Optical elements based on PP effects as discussed in Section 5 illustrate the application potential of geometrically well-controlled metal nanostructures. In the following we point out further applications ranging from spectroscopy to near-field detection and data storage.

## 6.1. Nonlinear Optics

When light field-driven metal electrons are hindered in or deviate from their collective linear motion by a surface or any other barrier, the polarization gets nonlinear contributions, which give rise to nonlinear optical (NLO) effects as, for example, harmonic generation. This intrinsic property of a metal surface is especially important for nanoparticles and nanostructures in which the polarizability of the electrons can be resonantly enhanced by PPs. Thus, strong enhancement of the nonlinear process compared with a flat metal surface is possible, leading to surface enhancement of NLO effects. In general, the lack of centrosymmetry in the system is the essential condition for second-order nonlinearity. A simple metal surface is obviously not centrosymmetric and thus shows second-order NLO effects in addition to the less symmetry-dependent third-order effects. Because of the high symmetry in spherical and spheroidal metal particles, the second-order NLO effects are forbidden. However, particles strongly deviating from highly symmetric shapes efficiently produce second-order NLO effects. Lamprecht et al. [47] showed that by EBL methods regular two-dimensional particle arrays with designed second-order NLO properties can be obtained. In addition they showed that in addition to symmetry considerations for the individual particle geometry, the symmetry properties of the particle arrangement pattern is of importance. Two two-dimensional regular arrays of non-centrosymmetrically shaped particles were fabricated, one with a parallel orientation of the particles (upper part of Fig. 1a) and a second array with pairwise antiparallel orientation (lower part of Fig. 1a). When the exciting

light is polarized parallel to the particle symmetry axis (indicated by the double arrow in Fig. 1a) the second-order nonlinear dipoles are also oriented parallelly and antiparallelly, respectively, in the two different cases. Although the linear optical properties were found to be identical in both cases, the second-order efficiency of the parallelly oriented case (Fig. 1a) was a factor of 40 larger than that of the higher symmetric antiparallel case. As expected from the particle shape, the linear spectra are highly dichroic; that is, the optical resonances are strongly different for the polarization direction parallel to the particle symmetry axis and normal to it. By appropriate choice of the aspect parameters one polarization resonance was tuned to a specific laser frequency. With such second harmonic generation-optimized two-dimensional particle arrays the PP decay time in metal nanoparticles was measured in the 10 fs timeframe by a second-order nonlinear autocorrelation method [47].

## 6.2. Surface Enhanced Spectroscopy

Since the first reports on surface-enhanced Raman scattering (SERS) the dominant problem has been a quantitatively correct explanation of the physical mechanism behind. Moreover, other related surface enhanced spectroscopic effects, such as surface-enhanced fluorescence and surface-modified photobleaching, have to fit in the model. Different models were proposed, based on both electrodynamic and chemical mechanisms [48–50].

As long as the phenomena were investigated at structurally poorly defined metal nanostructures such as roughened electrode surfaces or island films, chances to obtain a realistic estimate of the electromagnetic field enhancement factors were low. Again, much progress was made recently by investigating structurally highly defined systems. However, there are still enormous differences in the reported numbers of the Raman enhancement factor, depending on the kind of experiment, suggesting that there is a comparatively weak "standard" effect, well controllable by the electrodynamic parameters [51] and an effect at single "hot" particles. Nie and Emory [52] prepared a single molecule/single particle system using highly diluted single colloidal particles immobilized on a substrate and single molecules by applying a highly diluted incubation solution of rhodamine 6G (R6G) to the particles. An unexpected finding from their Raman and fluorescence investigations was that *a very small number of nanoparticles exhibited unusually high enhancement efficiencies*. These particles were termed "hot particles."

These experiments showed that the number of observed hot particles increases with the R6G concentration but finally saturates and that most of the R6G molecules are thus adsorbed on "inactive" particles. It was found by atomic force microscopy investigations that the optically active particles are typically three times larger than the inactive ones, but it could not be determined whether the hot particles contain specific absorption sites of unusually high affinities that could preferentially accumulate R6G molecules onto these particles. That question was solved by polarized Raman measurements, which gave evidence for single–molecule behavior. From these findings one had to conclude that SERS is a single molecule/single particle phenomenon,

which leads to the extremely high intrinsic enhancement factors of $10^{14}$–$10^{15}$ and that only one of, say, 100 to 1000 particles is optically hot. Similar findings corroborating the picture of hot particles were also obtained by Kneipp et al. [53]. However, the real nature of such hot particles is still unknown.

## 6.3. SNOM Tips

Spectrally selective scattering and near-field enhancement of PPs suggest the application of metal nanoparticles as near-field probes. Indeed, it was demonstrated that the light scattered by an individual metal nanoparticle can be used to probe optical near-fields with subwavelength resolution and enhanced signal levels compared with fiber tip probes [54–58]. On the other hand, metal nanoparticles can serve as nanoscale light emitters. In the so-called *tetrahedral tip* geometry a gold nanoparticle serves as such a subwavelength light source. The particle situated at the end of a three-sided pyramidal glass wedge is excited by surface plasmons propagating along a gold film evaporated on the flat sidewalls and edges of the wedge [59]. A similar tip geometry based on a silicon wedge was reported in [60]. A general review on the role of PPs for SNOM tips can be found in [61].

## 6.4. Data Storage

In optical storage media such as CDs and DVDs an increase in information density is possible when the conventional single laser wavelength technique is substituted by a multiple wavelength readout. Given $n$ as the number of different wavelengths, the number of possible information states per storage unit ("pit") is $2^n$. Consequently a single pit must contain spectral information that can be realized by a defined composition of spectrally differently scattering metal nanoparticles. The size of the pit can still be as small as the optical resolution limit. A realization of this principle was demonstrated experimentally for a two-wavelength system [62, 63]. On a transparent substrate different pits were fabricated by EBL, representing all (four) possible combinations of spectral states: 00, A0, 0B, and AB, where "A" and "B" designate the presence of a particle scattering at the wavelengths A and B, respectively, and "0" represents its absence. As spectrally differently scattering nanostructures, elongated particles of different orientations were used that show dichroic behaviour. This means that under polarized excitation two different plasmon resonances exist, which correspond to the orientation of the light field parallel or normal to the particle elongation direction. In a scattering experiment performed at the two different resonance wavelengths, the different pits of the sample showed different "on" and "off" states at the corresponding wavelengths. This is shown in Figure 6a, which is a scanning electron microscope image, showing the different compositions and orientations of the particles in each pit, and the corresponding scattering images at 488 and 633 nm, respectively. We note that the distance between the individual pits in Figure 6 was chosen larger than necessary for clarity of presentation.

(a)



(b)



(c)
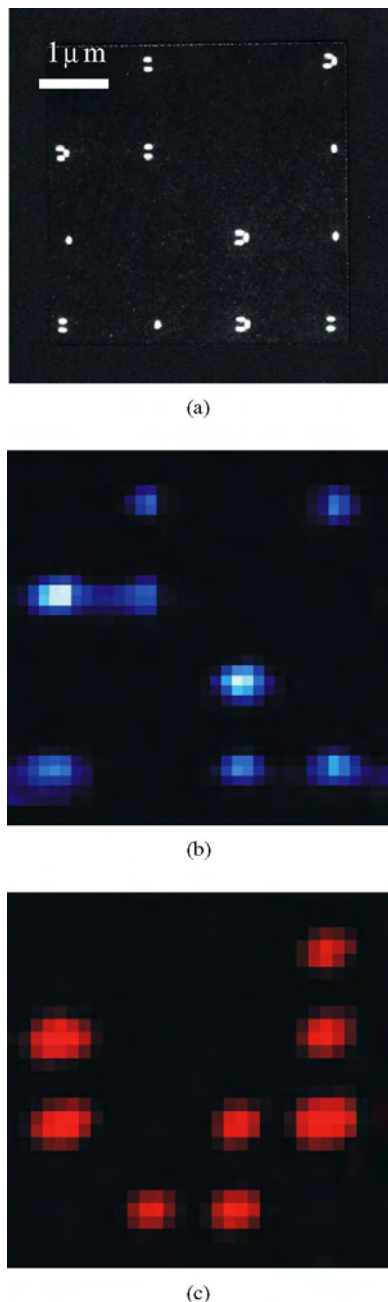
**Figure 6.** Data storage by metal nanoparticle pits. (a) Scanning electron micrograph of a representative sample section. The corresponding scattered light images with irradiating blue ($\lambda_0 = 488$ nm) and red ($\lambda_0 = 633$ nm) laser light are shown in (b) and (c), respectively. Reprinted with permission from [62], H. Ditlbacher et al., *Opt. Lett.* 25, 563 (2000). © 2000, Optical Society of America.

## 7. CONCLUSION

Lithography offers unprecedented control of geometry and position of individual metal nanoparticles and particle arrays. Such samples enable the detailed and specific investigation of PPs. From these investigations our understanding of PP properties such as the nanoscale localization of PP fields or their femtosecond lifetime improved considerably. These results also highlight the application potential

of metal nanostructures demonstrated by the first examples such as PP-based data storage or submicron waveguiding [38, 39, 64]. Further applications can easily be envisaged when thinking of the central role of optics in fields such as telecommunications or sensorics. Here metal nano-optics could contribute the optical part of nanotechnology. For any kind of mass production of metal nanostructure covered surfaces it would, however, be necessary to replace EBL by a faster technique. Recent demonstrations of nanoimprinting [65–67] and soft lithography [68] indicate that these techniques could fill that need.

## GLOSSARY

**Particle plasmon**   Resonant collective electron oscillation in a metal nanoparticle.

**Photon scanning tunneling microscope (PSTM)**   Scanning probe microscope relying on a subwavelength sized glass tip as a local probe.

**Scanning near-field optical microscope (SNOM)**   Scanning probe microscope relying on a subwavelength aperture as the light source.

**Surface enhanced Raman scattering (SERS)**   Enhancement of the Raman scattering cross-section by several orders of magnitude when molecules are positioned close to metal nanostructures.

**Surface plasmon**   Resonant collective electron oscillation at a metal/dielectric interface.

## ACKNOWLEDGMENTS

## REFERENCES

*1.* U. Kreibig and M. Vollmer, "Optical Properties of Metal Clusters." Springer-Verlag, Berlin, 1995.
*2.* C. F. Bohren and D. R. Huffman, "Absorption and Scattering of Light by Small Particles." J Wiley, New York, 1983.
*3.* G. Mie, *Ann. Phys.* 25, 377 (1908).
*4.* C. Girard and A. Dereux, *Rep. Prog. Phys.* 59, 657 (1996).
*5.* J. P. Kottmann and O. J. F. Martin, *Opt. Lett.* 26, 1096 (2001).
*6.* E. Moreno, D. Erni, C. Hafner, and R. Vahldieck, *J. Opt. Soc. Am. A* 19, 101 (2002).
*7.* M. A. McCord and M. J. Rooks, in "Handbook of Microlithography, Micromachining and Microfabrication" (P. Rai-Choudhury, Ed.), Vol. 1, Chap. 2, pp. 139–249. SPIE and The Institution of Electrical Engineers, Bellingham, WA, 1997.
*8.* J. R. Sheats and B. R. Smith, Eds. "Microlithography Science and Technology." Marcel Dekker, New York, 1998.
*9.* U. C. Fischer and H. P. Zingsheim, *J. Vac. Sci. Technol.* 19, 881 (1981).
*10.* T. R. Jensen, M. L. Duval, K. L. Kelly, A. A. Lazarides, G. C. Schatz, and R. P. Van Duyne, *J. Phys. Chem. B* 103, 9846 (1999).

11. J. P. Spatz, S. Mössmer, C. Hartmann, M. Möller, T. Herzog, M. Krieger, H.-G. Boyen, P. Ziemann, and B. Kabius, *Langmuir* 16, 407 (2000).

12. J. J. Mock, M. Barbic, D. R. Smith, D. A. Schultz, and S. Schultz, *Phys. Rev. B* 116, 6755 (2002).

13. R. Jin, Y. Cao, C. A. Mirkin, K. L. Kelly, G. C. Schatz, and J. G. Zheng, *Science* 294, 1901 (2001).

14. Y. Yu, S. Chang, C. Lee, and C. R. C. Wang, *J. Phys. Chem. B* 101, 6661 (1997).

15. D. W. Pohl, W. Denk, and M. Lanz, *Appl. Phys. Lett.* 44, 651 (1984).

16. B. Hecht, B. Sick, U. P. Wild, V. Deckert, R. Zenobi, O. J. F. Martin, and D. W. Pohl, *J. Chem. Phys.* 112, 7761 (2000).

17. K. Karrai and R. D. Grober, *Appl. Phys. Lett.* 66, 1842 (1995).

18. J. R. Krenn, A. Dereux, J. C. Weeber, E. Bourillot, Y. Lacroute, J. P. Goudonnet, B. Schider, W. Gotschy, A. Leitner, F. R. Aussenegg, and C. Girard, *Phys. Rev. Lett.* 82, 2590 (1999).

19. M. Salerno, N. Felidj, J. R. Krenn, A. Leitner, F. R. Aussenegg, and J. C. Weeber, *Phys. Rev. B* 63, 165422 (2001).

20. A. Dereux, C. Girard, and J. C. Weeber, *J. Chem. Phys.* 112, 7775 (2000).

21. D. Courjon, K. Sarayedine, and M. Spajer, *Opt. Commun.* 71, 23 (1989).

22. R. C. Reddick, R. J. Warmack, and T. L. Ferrell, *Phys. Rev. B* 39, 767 (1989).

23. V. Sandoghdar and J. Mlynek, *J. Opt. A: Pure Appl. Opt.* 1, 523 (1999).

24. In "Nano-Optics, Springer Series in Optical Sciences," Vol. 84, (S. Kawata, M. Ohtsu, and M. Irie, Eds.), Chap. 4, pp. 75–109. Springer-Verlag, Berlin, 2002.

25. C. Sönnichsen, S. Geier, N. Hecker, G. von Plessen, J. Feldmann, H. Ditlbacher, B. Lamprecht, J. R. Krenn, F. R. Aussenegg, V. Z.-H. Chan, J. P. Spatz, and M. Möller, *Appl. Phys. Lett.* 77, 2949 (2000).

26. C. Sönnichsen, T. Franzl, T. Wilk, G. von Plessen, and J. Feldmann, *Phys. Rev. Lett.* 88, 077402 (2002).

27. B. Lamprecht, J. R. Krenn, A. Leitner, and F. R. Aussenegg, *Appl. Phys. B* 69, 223 (1999).

28. T. Vartanyan, M. Simon, and F. Traeger, *Appl. Phys. B* 68, 425 (1999).

29. J. C. Weeber, E. Bourillot, A. Dereux, J. P. Goudonnet, Y. Chen, and C. Girard, *Phys. Rev. Lett.* 77, 5332 (1996).

30. P. M. Adam, S. Benrezzak, J. L. Bijeon, and P. Royer, *J. Appl. Phys.* 88, 6919 (2000).

31. S. Benrezzak, P. M. Adam, J. L. Bijeon, and P. Royer, *Surf. Sci.* 491, 195 (2001).

32. R. Hillenbrand and F. Keilmann, *Appl. Phys. B* 73, 239 (2001).

33. T. Klar, M. Perner, S. Grosse, G. von Plessen, W. Spirkl, and J. Feldmann, *Phys. Rev. Lett.* 80, 4249 (1998).

34. L. J. Richter, C. E. Jordan, R. R. Cavanagh, G. W. Bryant, A. Liu, S. J. Stranick, C. D. Keating, and M. J. Natan, *J. Opt. Soc. Am. A* 16, 1936 (1999).

35. H. Tamaru, H. Kuwata, H. T. Miyazaki, and K. Miyano, *Appl. Phys. Lett.* 80, 1826 (2002).

36. S. A. Maier, M. L. Brongersma, P. G. Kik, and H. A. Atwater, *Phys. Rev. B* 65, 193408 (2002).

37. J. R. Krenn, J. C. Weeber, A. Dereux, E. Bourillot, J. P. Goudonnet, B. Schider, A. Leitner, F. R. Aussenegg, and C. Girard, *Phys. Rev. B* 60, 5029 (1999).

38. M. Quinten, A. Leitner, J. R. Krenn, and F. R. Aussenegg, *Opt. Lett.* 23, 1331 (1998).

39. M. L. Brongersma, J. W. Hartman, and H. A. Atwater, *Phys. Rev. B* 62, 16356 (2000).

40. B. Lamprecht, G. Schider, R. T. Lechner, J. R. Krenn, A. Leitner, and F. R. Aussenegg, *Phys. Rev. Lett.* 84, 4721 (2000).

41. S. Linden, J. Kuhl, and H. Giessen, *Phys. Rev. Lett.* 86, 4688 (2001).

42. S. Linden, A. Christ, J. Kuhl, and H. Giessen, *Appl. Phys. B* 73, 311 (2001).

43. W. L. Barnes, T. W. Preist, S. C. Kitson, and J. R. Sambles, *Phys. Rev. B* 54, 6227 (1996).

44. S. C. Kitson, W. L. Barnes, and J. R. Sambles, *Phys. Rev. Lett.* 77, 2670 (1996).

45. S. I. Bozhevolnyi, J. E. Erland, K. Leosson, P. M. W. Skovgaard, and J. M. Hvam, *Phys. Rev. Lett.* 86, 3008 (2001).

46. H. Ditlbacher, J. R. Krenn, G. Schider, A. Leitner, and F. R. Aussenegg, *Appl. Phys. Lett.* 81, 1762 (2002).

47. B. Lamprecht, A. Leitner, and F. R. Ausseneg, *Appl. Phys. B* 68, 419 (1999).

48. R. K. Chang and T. E. Furtak, Eds. "Surface Enhanced Raman Scattering." Plenum, New York, 1982.

49. A. Otto, in "Light Scattering in Solids IV," Vol. 54, Topics in Applied Physics, Chap. 6, pp. 289–418. Springer-Verlag, Berlin, 1984.

50. M. Moskovits, *Rev. Mod. Phys.* 57, 783 (1985).

51. N. Felidj, J. Aubard, G. Levi, J. R. Krenn, M. Salerno, G. Schider, B. Lamprecht, A. Leitner, and F. R. Aussenegg, *Phys. Rev. B* 65, 075419 (2002).

52. S. Nie and S. R. Emory, *Science* 275, 1102 (1997).

53. K. Kneipp, Y. Wang, H. Kneipp, L. T. Perelman, I. Itzkan, R. R. Dasari, and M. S. Feld, *Phys. Rev. Lett.* 78, 1667 (1997).

54. U. Fischer and D. Pohl, *Phys. Rev. Lett.* 62, 458 (1989).

55. T. J. Silva and S. Schultz, *Appl. Phys. Lett.* 65, 658 (1994).

56. O. Sqalli, M.-P. Bernal, P. Hoffmann, and F. Marquis-Weible, *Appl. Phys. Lett.* 76, 2134 (2000).

57. J. M. T. Kalkbrenner, M. Ramstein and V. Sandoghdar, *J. Microsc.* 202, 72 (2001).

58. O. Sqalli, I. Utke, P. Hoffmann, and F. Marquis-Weible, *J. Appl. Phys.* 92, 1078 (2002).

59. J. Koglin, U. C. Fischer, and H. Fuchs, *Phys. Rev. B* 55, 7977 (1997).

60. T. Yatsui, M. Kourogi, and M. Ohtsu, *Appl. Phys. Lett.* 79, 4583 (2001).

61. S. Kawata, Ed. "Near-Field Optics and Surface Plasmon Polaritons," Vol. 81, Topics in Applied Physics. Springer-Verlag, Berlin, 2001.

62. H. Ditlbacher, J. R. Krenn, B. Lamprecht, A. Leitner, and F. R. Aussenegg, *Opt. Lett.* 25, 563 (2000).

63. H. Ditlbacher, J. R. Krenn, B. Lamprecht, A. Leitner, and F. R. Aussenegg, *Opt. Photonics News* 11, 43 (2000).

64. S. A. Maier, P. G. Kik, and H. A. Atwater, *Appl. Phys. Lett.* 81, 1714 (2002).

65. S. Y. Chou, P. R. Krauss, and P. J. Renstrom, *Science* 272, 85 (1996).

66. D.-Y. Khang and H. H. Lee, *Appl. Phys. Lett.* 75, 2599 (1999).

67. S. Y. Chou, C. Keimel, and J. Gu, *Nature* 417, 835 (2002).

68. Y. Xia and G. M. Whitesides, *Annu. Rev. Mater. Sci.* 28, 153 (1998).

# Metal Nanoparticle Superlattices

Toshiharu Teranishi, Mikio Miyake

*Japan Advanced Institute of Science and Technology,*
*and Japan Science and Technology Co., Tatsunokuchi, Nomi, Ishikawa, Japan*

## CONTENTS

## 1. INTRODUCTION

### 1.1. Definition

Metal nanoparticles are in the 1-nm to 1-$\mu$m size range. However, metal nanoparticles larger than a few tens of nanometers show similar physical and chemical properties to the bulk. The upper limit of the size of metal nanoparticles to show the interesting properties different from the bulk is at most 20 nm. Therefore, the size of metal nanoparticles that the current scientists are focusing on is restricted from 1 to 20 nm, consisting of 10 to $10^6$ atoms. Speaking strictly from the viewpoint of the electronic structure, the metal nanoparticles smaller than 5 nm (often called the *clusters*) are the target materials, because it was found from vigorous mass studies on metal nanoparticles that the binding energies of metal nanoparticles consisting of less than 1000 atoms varied periodically due to the quantum size effect [1], meaning that the metal nanoparticles are not just aggregates of metallic atoms. This size range will hold the secret of the genesis of a metal. Anyway, we deal with the metal nanoparticles (including bimetallic nanoparticles) from 1 to 20 nm in size.

### 1.2. Current Focus

The precise control of the primary structures of metal nanoparticles, such as size, shape, or composition, enables us to fabricate the secondary structures of nanoparticles, which means the regularly ordered metal nanoparticles with well-defined one- (1D), two- (2D), or three-dimensional (3D) spatial configuration. Since such ordered metal nanoparticles, so-called superlattices, are expected to show the novel properties that are not present in the isolated nanoparticles, the current interests in colloid chemistry have been focused on the fabrication of superlattices of size- and shape-controlled metal nanoparticles, as shown in Figure 1. The fabrication of ordered metal nanoparticles would enable us to produce optical devices, such as surface-enhanced Raman scattering (SERS) films [2, 3], optical grating [4], antireflective surface coating [5], selective solar absorbers [6], and data storage devices [7]. Moreover, the monodisperse metal nanoparticles have potentiality to be the building blocks for nanoelectronic devices using the single-electron tunneling effect [8, 9]. Especially, the metal nanoparticles smaller than 2 nm in size are required for such devices to make use of the phenomenon of Coulomb blockade at room temperature [9–15].

To order the metal nanoparticles on substrates by evaporating the solvent from the nanoparticle solutions, one has to use a rigid stabilizer such as ligand or surfactant for metal nanoparticles to form nanoparticle superlattices of well-defined configurations, because the volume change of stabilizer like linear polymer through the evaporation of the solvent may suppress the complete arrangement of nanoparticles. In fact, 2.6-nm polyacrylonitrile-protected Au nanoparticles formed only a partially hexagonal network in two dimensions [16]. Two approaches have been employed in order to form superlattice structures of metal nanoparticles. One is to self-assemble metal nanoparticles by placing a few drops of their solution on a substrate or by dipping it into the solution, followed by the solvent evaporation. The self-assembly technique is a widely used fabrication method of superlattices due to its ease and convenience. As indicated by Bowden and co-workers, the self-assembly technique has a great potential to produce the complex patterns of metal nanoparticles by endowing the nanoparticles with the direction of interaction [17]. Another approach is to use either external forces, such as an electrophoretic deposition [18, 19] and a LB technique [20, 21], or strong
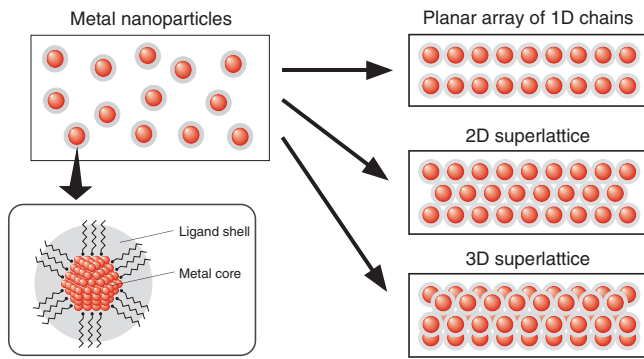
**Figure 1.** Schematic illustration of metal nanoparticle superlattices.

interactions, such as an electrostatic interaction [22–25] and a DNA hybridization [26–28].

Let us introduce the fabrication techniques, characterization techniques, novel physical properties, and applications of metal nanoparticle superlattices to nanodevices.

## 2. FABRICATION TECHNIQUES

Here we deal with the fabrication of low-dimensional (1D and 2D) superlattices of metal nanoparticles together with 3D ones [29]. Fabrication techniques of metal nanoparticle superlattices reported so far are listed in Table 1.

### 2.1. One-Dimensional Superlattices

The fabrication of 1D superlattices, or 1D chains, of metal nanoparticles is the most challenging subject when ordering metal nanoparticles, because it is quite difficult to self-assemble metal nanoparticles in low symmetry. If we are able to organize them in 1D configuration, the tunneling behavior between them can be investigated and the nanowiring between the nanodevices, such as single-electron transistor and single-electron memory, can be realized, which will open the door to generate the future ultralarge-scale integrated circuits (ULSI) beyond the ability of the current photolithography technique. In general, the template methods are very effective to order nanoparticles in 1D configuration. Here we introduce the fabrication methods of 1D chains of metal nanoparticles and then present our technique to fabricate planar array of 1D chains of Au nanoparticles.

Alumina membranes are excellent template materials because of their high degree of order, thermal and chemical stability, and optical clarity. The pores of the membranes are packed in a parallel hexagonal array formed by an electrochemical anodic process, and pore diameter is controlled by regulation of the applied anodic potential (ca. 1.4 nm V$^{-1}$) [30]. In 1997, Hornyak and co-workers succeeded in the fabrication of 1.4-nm Au$_{55}$ nanoparticles in 1D configuration by using porous alumina membranes as template materials [31]. They used an electrophoretic pore filling method under an electric field strength ranging from 5 to 20 V cm$^{-1}$. Along the distance of 70 nm, 20 or 21 T$_8$-OSS-protected Au$_{55}$ nanoparticles (T = RSiO$_{3/2}$, OSS = oligosilsesquioxane) of 4.2-nm diameter including the ligand shell were arranged in

**Table 1.** List of metal nanoparticle superlattices reported so far.

| Dimension of superlattices | Metal | Fabrication method | Size (nm) | Ref. |
|---|---|---|---|---|
| 1D | Au | Electrophoresis with porous alumina membrane | 1.4 | [31] |
| | Au | Step edge of carbon film | 5.0 | [32] |
| | Ag | DNA | — | [33] |
| | Au | Biopolymer | 1.4 | [34] |
| | Au | Ridge-and-valley carbon | 3.4 | [37] |
| 2D | Au | Self-assembly | 3.4–9.7 | [57, 58] |
| | Au | Self-assembly | 3–5 | [44] |
| | Au | Self-assembly | 6.7 | [65] |
| | Au | Self-assembly | 1.8–8.0 | [66] |
| | Au | Self-assembly | 4.7–5.9 | [67] |
| | Ag | Self-assembly | 5.0 | [41] |
| | Ag | Self-assembly | 2.3 | [40] |
| | Ag | Self-assembly | 4.2 | [42, 68] |
| | Pt | Self-assembly | 4.1 | [42, 68] |
| | Pd | Self-assembly | 5.9 | [43] |
| | Pt | Self-assembly | 2.7, 4.0, 4.6 | [50] |
| | Co | Self-assembly | 5.8 | [71] |
| | Co | Self-assembly | 10 | [73] |
| | Co | Self-assembly | 8.0 | [74, 75] |
| | Fe | Self-assembly | 2.0 | [77] |
| | Au | Ligand-substrate interaction | 1.4 | [79] |
| | Au | Interligand interaction | 1.9 | [80] |
| | Au | Electophoretic deposition | 3.5–18.5 | [18, 19] |
| | Au | LB | 2.9 | [81] |
| | Au | LB | 3.5 | [82] |
| | Au | LB | 17 | [83] |
| | Au | LB | 1.4 | [84] |
| | Ag | LB | 7.0 | [148] |
| 3D | Au | Self-assembly | 1.4 | [87] |
| | Au | Self-assembly | 3.5 | [88] |
| | CoPt$_3$ | Self-assembly | 1.5–7.2 | [89] |
| | Pt,Au | Mutilayer deposition | 1.5–6.0 | [91, 92] |
| | Ag | Self-assembly | 4.5, 5.2 | [45] |
| | Au | Alternative sputtering | 3.0–33.7 | [126] |
| | Au | Layer-by-layer | 2.5, 12 | [9] |
| | Au | Self-assembly | 2.0 | [146] |
| | Ag | Self-assembly | 3.5–7.7 | [147] |
| | FePt | Self-assembly | 4.0, 6.0 | [7, 158, 159] |
| | FePt | Polymer-mediated self-assembly | 6.0 | [162] |
| | Fept | Three-layer technique | 4.5 | [172] |
| | FePtAg | Self-assembly | 3.5 | [178] |

1D configuration, not exactly in a straight line but rather in a helical structure, in 7-nm pores.

Oku and Suganuma arranged Au nanoparticles in one dimension on amorphous carbon films using the adhesive force at the step edge of carbon films [32]. As shown in Figure 2, 1D self-assembled Au nanoparticles were fabricated by dispersing the toluene solution of 5-nm Au nanoparticles protected by $\alpha$-terpineol (C$_{10}$H$_{18}$O) on holey
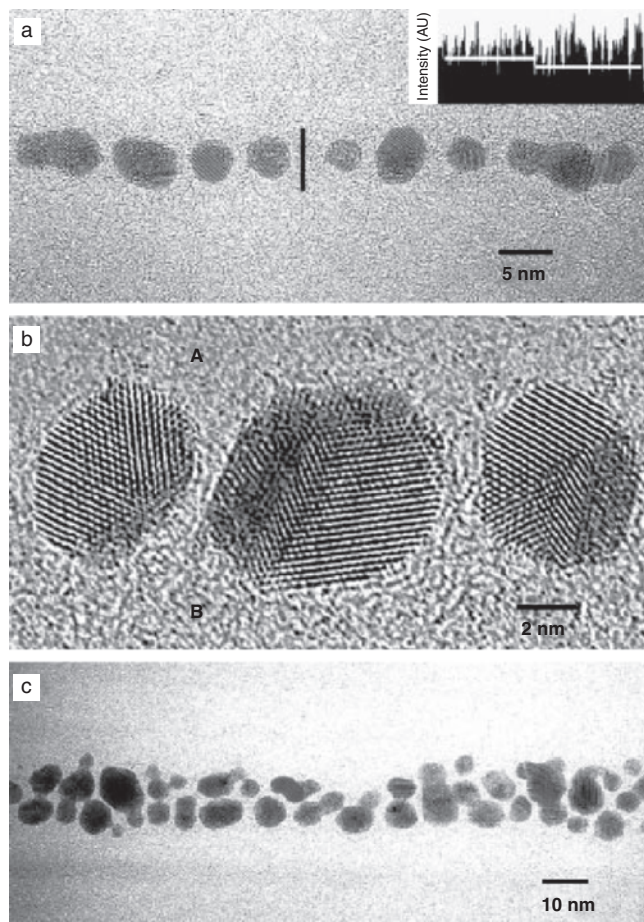
**Figure 2.** (a) Low magnification image of 1D self-assembled Au nanoparticles on amorphous carbon film with the intensity distribution across the interface indicated. (b) Enlarged HRTEM image of 1D self-assembled Au nanoparticles. (c) 1D self-assembly of Au nanoparticles with a width of ca. 15 nm. Reprinted with permission from [32], T. Oku and K. Suganuma, *Chem. Commun.* 2355 (1999). © 1999, Royal Society of Chemistry.

carbon grids with thickness ca. 15 nm. The longest size of the 1D ordering of 5-nm Au nanoparticles was ca. 1.5 $\mu$m, which is dependent on the length of step edge of the carbon thin films. The larger nanoparticles and nanowires encapsuled in carbon nanocapsules and nanotubes were obtained after annealing the specimens at 400 °C for 30 min under vacuum.

Also the fabrication techniques of 1D chains of Ag and Au nanoparticles between the electrodes using DNA [33] and biopolymers [34] were reported. DNA has the appropriate molecular-recognition and mechanical properties, but poor electrical characteristics prevent its direct use in electrical circuits. Braun and co-workers [33] first attached 12-base oligonucleotides, derivatized with a disulfide group at their 3′ end, to the electrodes through sulfur-gold interactions, the electrodes being each marked with specific but different oligonucleotide sequences. A connection was then made by hybridizing two distant surface-bound oligonucleotides with a 16-$\mu$m-long and fluorescently labeled $\lambda$-DNA that contained two 12-base sticky ends, where each of the ends was complementary to one of the two different sequences

attached to the gold electrodes and fluorescent groups were used to confirm the $\lambda$-DNA stretching. The silver ions were then selectively localized along the DNA through $Ag^+/Na^+$ ion-exchange to form the complexes between the silver and the DNA bases [35, 36]. The silver ion-exchanged DNA was reduced to produce nanometer-sized metallic Ag aggregates bound to the DNA skeleton. The Ag aggregates were subsequently further "developed" using an acidic solution of hydroquinone and silver ions under low light conditions, resulting in the formation of conductive Ag wires along the DNA skeleton, which unfortunately did not show the low-resistant and ohmic behavior.

In 2001, Berven and co-workers [34] succeeded in assembling 1.4-nm Au nanoparticles on a biopolymer template deposited between metal electrodes on an insulating substrate for an investigation on the room-temperature electrical behavior of Au nanoparticles. A thin film of the biopolymer poly-L-lysine (PLL) (MW = 54,000 amu) was initially deposited on the fingers of gold interdigitated array electrodes from aqueous methanol containing the $\alpha$-helical form of its hydrobromide salt. The exposed side chains of the dried film were subsequently deprotonated by soaking in dilute base. The 11-mercaptoundecanoic acid-stabilized Au nanoparticles were then assembled onto the biopolymer from an organic solvent through an electrostatic assembly to obtain the networks of Au nanoparticles composed of their 1D self-assembled array.

Recently we have developed a novel method to fabricate a planar array of 1D chains of Au nanoparticles size-controlled by the heat-treatment in the solid state in combination with a specially developed technique to produce nanoscale ridge-and-valley structured substrates using a vacuum process [37]. The 20-nm-thick NaCl overlayers were deposited by thermal evaporation onto the optical grade (110) polished NaCl single crystals (muscut angle <3°) at 250 °C. Since NaCl(110) is an unstable plane, the film surface becomes faceted with low-energy (100) and (010) planes during the homoepitaxial growth of NaCl. A 30-nm-thick carbon replica layer was deposited directly on the NaCl surface, as shown in Figure 3. The carbon layer was floated off from the NaCl substrate in water, and was then loaded on 400-mesh copper grids. As seen in Figure 3b presenting an AFM image of carbon replica layer, it preserved ridge-and-valley surface topography with long and straight in-plane macrosteps along [001] of the NaCl epilayer. It was found from the line profile in Figure 3c that the valley depth and its period are a few nanometers and ca. 20 nm, respectively. Placing a drop of 3.4-nm DT-Au nanoparticles onto this carbon substrate, followed by the solvent evaporation, led to the fabrication of a planar array of 1D chains of DT-Au nanoparticles, as shown in Figure 4a. However, almost all the 1D chains were bundles of a few chains. In order to avoid the production of such aggregated structures, the carbon substrate was dipped into DT-Au toluene solution, followed by withdrawal parallel to the valley direction. As seen in Figure 4b and c (magnified one), the number of bundles of chains was decreased, and the planar array of 1D chains of Au nanoparticles ordering in a line was formed throughout a few square millimeters of the carbon substrate. The 1D chains formed an array at a distance of ca. 10 nm or ca. 20 nm, which corresponds to a half or one valley period. From AFM measurement of
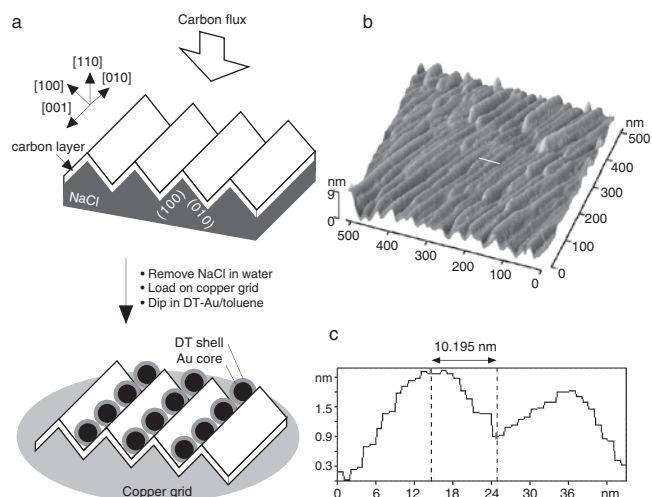
**Figure 3.** (a) Schematic illustration of a preparation of the carbon layer with ridge-and-valley structure and the formation of planar 1D chains of dodecanethiol-protected gold nanoparticles (DT-Au). (b) AFM image of a ridge-and-valley carbon layer on copper grid. (c) A line profile along the white line indicated in (b). Reprinted with permission from [37], T. Teranishi et al., *J. Am. Chem. Soc.* 124, 4210 (2002). © 2002, American Chemical Society.

this sample, there is likely to be one line of nanoparticles between two ridges, indicating that the Au nanoparticles were predominantly immobilized in valleys and partly on ridges. The formation mechanism is speculated as follows: When the substrate is withdrawn from the toluene, the Au nanoparticles are adsorbed and assembled mainly in valleys at the upper edge of the substrate by the adhesive [32] and attractive capillary forces [38], respectively. Then the growth of 1D chains of nanoparticles is caused through convective particle flux by solvent evaporation from the already ordered chains [39].

## 2.2. Two-Dimensional Superlattices

### 2.2.1. Self-Assembly During Solvent Evaporation

The fabrication of 2D superlattices of metal nanoparticles has been vigorously studied for a decade. The preparation technique mainly involves a self-assembly of organic ligand-protected metal nanoparticles larger than 2 nm. Since such nanoparticles are easily self-assembled in a hexagonal packing on various substrates due to the capillary force between the nanoparticles during the solvent evaporation, there are too many studies to mention [2, 3, 40–51].

Needless to say, precise control of particle size and shape is required to fabricate their perfect superlattices without mosaic structures. Since a number of investigations of Au nanoparticles and their self-assembly into 2D superlattices has been reported, following a synthesis by Brust et al. [52], understanding of their synthetic method of Au nanoparticles is very helpful. Their strategy consisted in growing the Au nanoparticles with the simultaneous attachment of self-assembled thiol monolayers on the growing nuclei. In order to allow the surface reaction to take place during Au nucleation and growth, the particles were grown
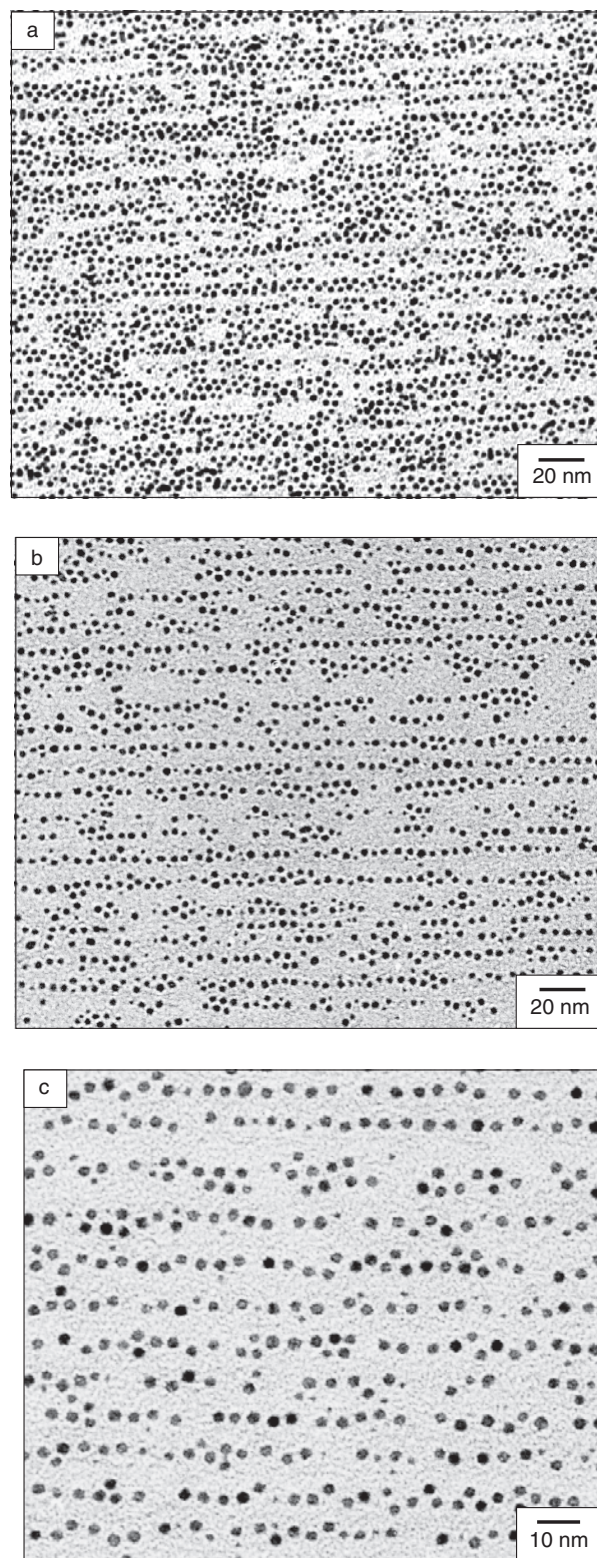


**Figure 4.** TEM images of 3.4-nm DT-Au nanoparticles on ridge-and-valley carbon layers. (a) Prepared by a drop method. (b) Prepared by a dip method. (c) A magnified image of (b). Reprinted with permission from [37], T. Teranishi et al., *J. Am. Chem. Soc.* 124, 4210 (2002). © 2002, American Chemical Society.

in a two-phase system. Two-phase redox reactions can be carried out by an appropriate choice of redox reagents present in the adjoining phases [53]. To be more specific, $[AuCl_4]^-$ was transferred from aqueous solution to toluene using tetraoctylammonium bromide (TOAB) as the phase-transfer reagent and reduced with aqueous sodium borohydride ($NaBH_4$) in the presence of the protective agent, dodecanethiol ($C_{12}H_{25}SH$). On addition of the reducing agent, the organic phase changes color from orange to deep brown within a few seconds. The overall reaction is summarized by Eqs. (1) and (2), where the source of electrons is $BH_4^-$.

$$[AuCl_4]^-(aq) + N(C_8H_{17})_4^+(toluene)$$
$$\rightarrow N(C_8H_{17})_4^+[AuCl_4]^-(toluene) \qquad (1)$$

$$m[AuCl_4]^-(toluene) + nC_{12}H_{25}SH(toluene) + 3me^-$$
$$\rightarrow 4mCl^-(aq) + (Au_m)(C_{12}H_{25}SH)_n(toluene) \qquad (2)$$
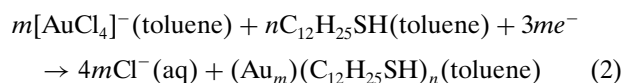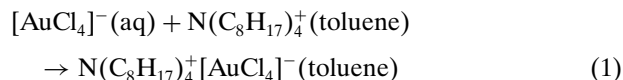
The conditions of the reaction determine the ratio of thiol to gold, that is, the ratio $n/m$, and make it possible to control the particle sizes [54]. The protective agent not only serves as a protective layer for the particles, which prevents direct contact between the particles and consequent collapse of the structure, but also provides interparticle bonding.

In 2001, we developed a simple and quite useful method to manipulate the size of Au nanoparticles by using the heat-treatment of small Au nanoparticles not in solution [55, 56] but in the solid state [57, 58], which is far from the conventional techniques [59–63]. A preparation of dodecanethiol-protected Au nanoparticles (DT-Au) as a source for the heat-treatment followed Brust's two-phase (toluene/water) reaction procedure [52]. The organic (toluene) phase was then separated, evaporated completely in a rotary evaporator at 40 °C, and dried *in vacuo* at 30 °C for a day. The crude solid obtained was heat-treated at 150–250 °C at the heating rate of 2 °C min$^{-1}$, and held for 30 min. The heat-treated product was dissolved in toluene and mixed with methanol to remove excess free dodecanethiol and TOAB. The dark brown precipitate was filtered off, washed with methanol, and redispersed in toluene. Octadecanethiol (ODT) was also used as a protective agent in place of dodecanethiol. This heat-treatment of as-prepared DT-Au nanoparticles at 150, 190, and 230 °C led to the thermodynamical particle growth, the particle sizes becoming $3.4 \pm 0.3$, $5.4 \pm 0.7$, and $6.8 \pm 0.5$ nm, respectively. Figure 5 presents the TEM images of DT-Au nanoparticles heat-treated at 150, 190, and 230 °C, respectively. The particle sizes are proportional to the heat-treatment temperatures in this region. These particles form 2D superlattices with almost completely hexagonal packing on flat carbon-coated copper grids for TEM. The formation area of 2D superlattices is extended with an increase in the concentration of Au nanoparticles in toluene. The thickness of ligand layer estimated from the mean diameters calculated from TEM and AFM images was 1.25 nm, which is smaller than the DT ligand length ($\sim$1.8 nm) [64]. This result suggests that the DT ligands are interpenetrating each other in 2D superlattices of DT-Au nanoparticles [18]. Using ODT in place of DT gives similar results except that the Au nanoparticles of $9.7 \pm 0.9$ nm are obtained by the heat-treatment at 250 °C [58]. Thus we can fabricate the
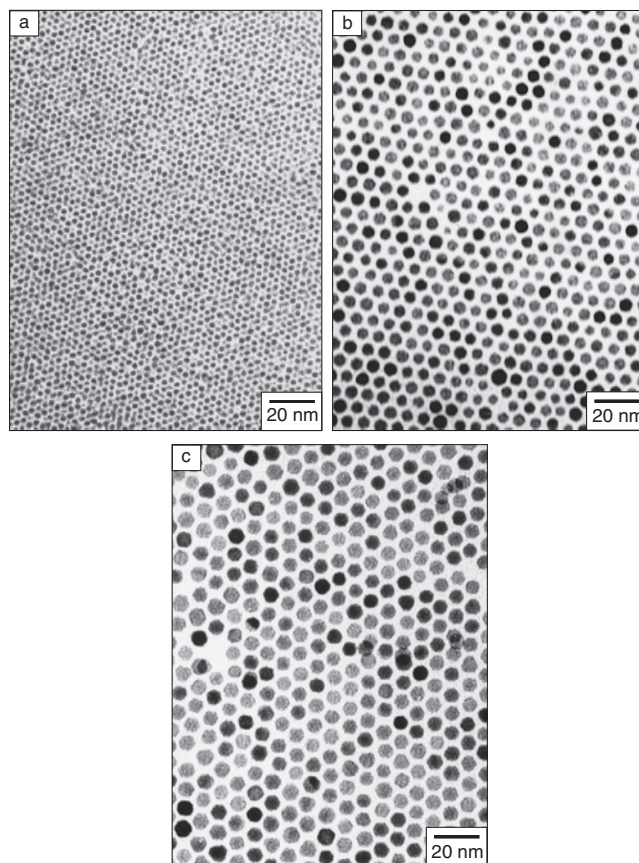


**Figure 5.** TEM images of DT-Au nanoparticles heat-treated at (a) 150 °C, (b) 190 °C, and (c) 230 °C. Reprinted with permission from [57], T. Teranishi et al., *Adv. Mater.* 13, 1699 (2001). © 2001, Wiley-VCH.

self-assembled 2D superlattices of Au nanoparticles ranging from 3.4 to 9.7 nm in size with hexagonal packing. The formation of self-assembled 2D superlattices of Au nanoparticles protected by quaternary ammonium bromide salts [44, 65] or amines [66] has been investigated as well.

An interparticle spacing in 2D superlattices is expected to be tuned by the ligand length. In 2000, Martin and co-workers investigated the interparticle spacings in 2D superlattices of Au nanoparticles synthesized in nonionic inverse micelles, and capped with alkanethiol ligands, with alkane chains ranging from $C_6$ to $C_{18}$ [67]. It was found that it was possible to control the interparticle spacing of superlattices by capping with organic thiols. Very small alkanethiols cause precipitation, but alkanethiols from $C_6SH$ to $C_{14}SH$ result in the formation of uniform superlattices with controlled interparticle spacings. Image analysis suggests that the particle gaps increase at the rate of 1.2 Å per carbon atom of the alkanethiols, as shown in Figure 6. The control of the particle spacings is important to some potential applications, such as single-electron tunneling devices.

Of course, there appeared many reports on 2D superlattices of metal nanoparticles besides Au nanoparticles. The formation of 2D superlattices of alkanethiol-protected Ag nanoparticles by Harfenist and co-workers is presented [41]. They prepared 5.0-nm dodecanethiol-protected Ag nanoparticles by an aerosol processing method. Depositing
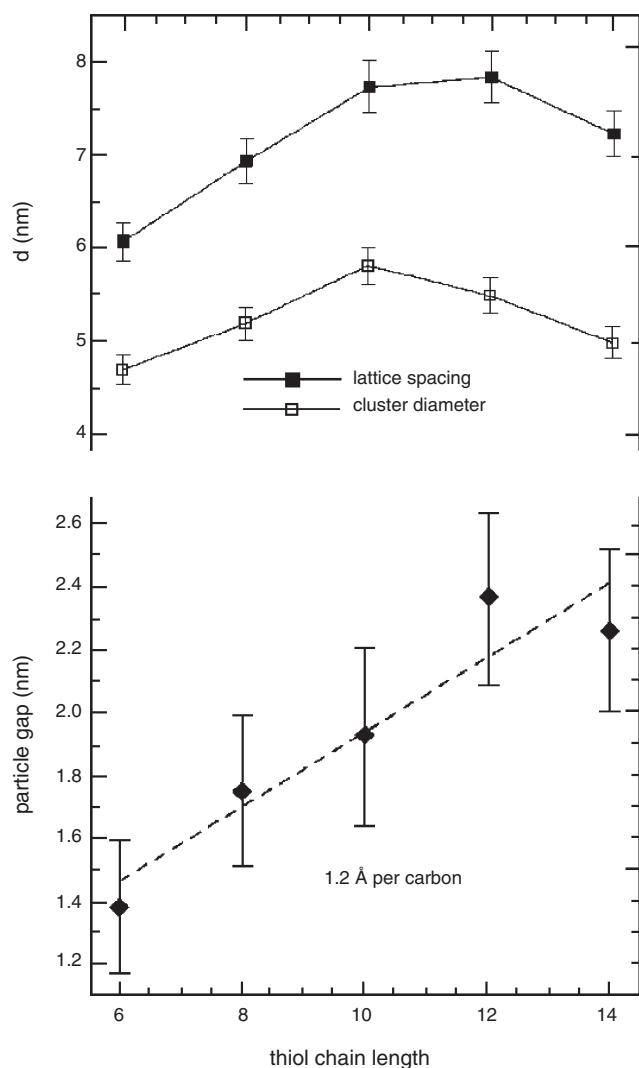
**Figure 6.** Dependence of the average particle size, lattice spacing, and nanoparticle gap on thiol chain length. Reprinted with permission from [67], J. E. Martin et al., *J. Phys. Chem. B* 104, 9475 (2000). © 2000, American Chemical Society.

a highly concentrated drop of their toluene solution on an ultrathin amorphous carbon film substrate and allowing it to dry slowly in air gave the self-assembled 2D superlattices of Ag nanoparticles with a hexagonal packing (sixfold symmetry) during the solvent evaporation. Also orientational ordering of faceted nanoparticles in superlattices was directly observed, which leads us to the determination of the nanoparticle's faceted morphology, as mediated by the interactions of ligands tethered to the facets on neighboring nanoparticles. Orientational ordering is crucial for the understanding of the fundamental properties of nanoparticles array, as well as for their optimal utilization in optical, electronic, and magnetic applications. Wang investigated the particle direction in 2D superlattices in detail using high-resolution TEM, as presented in Section 3 [48, 49].

Pileni's group has dedicated their efforts to the syntheses of metal nanoparticles in AOT reverse micelles and the formation of their superlattices. The preparation of Ag nanoparticles was achieved by mixing two AOT reverse micellar solutions

having the same water content, the first being made with 30% Ag(AOT), 70% Na(AOT) and the second with $N_2H_4$ with 100% of Na(AOT) [40]. Extraction of Ag nanoparticles from micelles by adding dodecanethiol to the aqueous solution and subsequent size-selected precipitation with pyridine induce flocculation of the Ag nanoparticles, resulting in the monodisperse 2.3-nm Ag nanoparticles. When the Ag nanoparticles dispersed in hexane were deposited on a support, a monolayer made of nanoparticles with spontaneous hexagonal assembly was observed.

Sarathy et al. prepared 4.2-nm Ag and 4.1-nm Pt nanoparticles protected by dodecanethiol as well as 4.2-nm Au nanoparticles [42, 68]. To the hydrosols containing metal nanoparticles prepared by the $NaBH_4$ reduction of the corresponding metal salts were added dodecanethiol, followed by an addition of concentrated HCl, resulting in the dodecanethiol-protected metal nanoparticles in toluene phase. The toluene solutions of these nanoparticles were deposited on the flat carbon substrates to produce self-assembled 2D superlattices.

In the same year, self-assembly of tetraalkylammonium salt ($NR_4X$)-protected Pd nanoparticles was reported by Reetz et al. [43]. Simple dip-coating using solutions of $N(C_4H_9)_4Br$-, $N(C_8H_{17})_4Br$-, or $N(C_{18}H_{37})_4Br$-protected Pd nanoparticles [69] having average core sizes of 2.5, 5.9, and 5.9 nm, respectively, was performed. In the case of 2.5-nm $N(C_4H_9)_4Br$-protected Pd nanoparticles, completely random distributions of nanoparticles on the surface were observed. Similar observations were made upon employing larger-sized Pd nanoparticles protected by $N(C_4H_9)_4Br$. In complete contrast, the Pd nanoparticles protected by $N(C_8H_{17})_4Br$ led to high degrees of ordering. The respective nanoparticles self-assemble in hexagonal close-packed 2D superlattices. Taking the thickness of the $N(C_8H_{17})_4Br$ protective coat surrounding Pd nanoparticles to be 1.2 nm into consideration [70], assumption of a bilayer between the ordered nanoparticles leads to the prediction that the distance between the centers of the Pd cores should amount to 8.3 nm. The observed value of 8.2 nm is in excellent agreement with this expectation, which means that the protective ligands on the surface touch each other without damage or interpenetration in this case. The 5.9-nm $N(C_{18}H_{37})_4Br$-protected Pd nanoparticles also self-assembled in a 2D superlattice with a hexagonal packing, the distance between the centers of the nanoparticles amounting to 10.2 nm, which is consistent with the predicted value. In addition, a usual square-packing (coordination number four in the 2D superlattice) was observed in the case of the $N(C_8H_{17})_4Br$-protected Pd nanoparticles, the distance between the centers of the nanoparticles amounting to 6.3 nm. The reason for the formation of such unusual ordered domains is unclear.

Martin et al. have succeeded in the formation of 2D superlattices of alkanethiol-protected Pt nanoparticles in 2002 [50]. The Pt nanoparticles were synthesized from $H_2PtCl_6 \cdot 6H_2O$ as a metal precursor in inverse micelles and stabilized by capping with an alkanethiol, followed by purification. The Pt nanoparticles of 2.7, 4.0, and 4.6 nm in size thus obtained formed self-assembled 2D superlattices on a TEM grid. One of the interesting differences between Pt and other nanoparticles is the frequent formation of square lattices. The interparticle spacing of 2D superlattices of Pt

nanoparticles can be controlled over a limited range by capping with alkanethiols. The lattice spacing increases by ~1.4 Å per carbon atom in the alkanethiol chains in the range of 8 to 18 carbons.

The 2D superlattices are fabricated not only from the monodisperse noble metal nanoparticles, such as Au, Ag, and Pt, but also from 3d-transition-metal nanoparticles. There are several reports on the fabrication of self-assembled 2D superlattices of magnetic Co [71–75] and Fe [76, 77]. As a representative, 2D self-assembly of Co nanoparticles by Puntes et al. is presented [75]. Their unique preparation technique of monodisperse Co nanoparticles is as follows: $Co_2(CO)_8$ dissolved in *o*-dichlorobenzene is injected in a refluxing *o*-dichlorobenzene in the presence of oleic acid and trioctylphosphine oxide (TOPO). As the reaction proceeds in time, the products evolve in a predictable pattern. Thus, quenching the reaction solution after 5 to 10 s yields samples with Co nanorods. As time evolves over minutes, the high-energy hexagonally close-packed rod-shaped particles disappear at the expense of monodisperse spherically shaped $\varepsilon$-Co nanoparticles. These $\varepsilon$-Co nanoparticles are self-assembled into 2D superlattices on a carbon-coated TEM grid as a *o*-dichlorobenzene solution of $\varepsilon$-Co nanoparticles is allowed to evaporate slowly in a controlled atmosphere.

Among these numerous researches on a self-assembly of metal nanoparticles, a noteworthy one is on the self-assembly of alkanethiol-protected Au nanoparticles of different and well-defined sizes reported by Kiely and co-workers [47, 78]. The crystallographic alloy structure adopted by a mixture of two different elements depends on the physical dimensions and properties of its constituent atoms. If two metallic species with atomic radii $R_A$ and $R_B$ (where $R_A < R_B$) are alloyed, the crystal structure adopted is determined by (i) the local number ratio of the two components ($n_A/n_B$), (ii) the ratio of the radii of the two components $R_A/R_B$, and (iii) polarizability effects. When the 2D superlattice is composed solely of alkanethiol-protected Au nanoparticles with a diameter of less than 10 nm and well-defined bimodal particle sizes, the superlattice structures formed depend primarily on the ratios $n_A/n_B$ and $R_A/R_B$, with polarization effects being negligible. For instance, when $n_A/n_B = 0.5$ and $0.482 < R_A/R_B < 0.624$, an $AB_2$ structure, analogous to $AlB_2$, can be generated (Fig. 7a). Alternatively, when $n_A/n_B = 1$ and $0.27 < R_A/R_B < 0.425$, an AB superlattice analogous to NaCl can crystallize as shown in Figure 7b. With other specific combinations of $n_A/n_B$ and $R_A/R_B$, effects such as phase segregation and random alloy formation have been demonstrated [47]. Two chemically different building blocks, namely alkanethiol-protected Au and Ag nanoparticles, can also spontaneously self-assemble to form true nanoscale colloidal alloy superlattices [78].

### 2.2.2. Weak Interactions

When one uses 2D superlattices of metal nanoparticles as nanoelectronic devices making use of Coulomb blockade phenomenon at room temperature, metal nanoparticles smaller than 2 nm in diameter are required. Since the formation of ordered structures of such small nanoparticles is difficult mainly due to the weak attractive capillary force
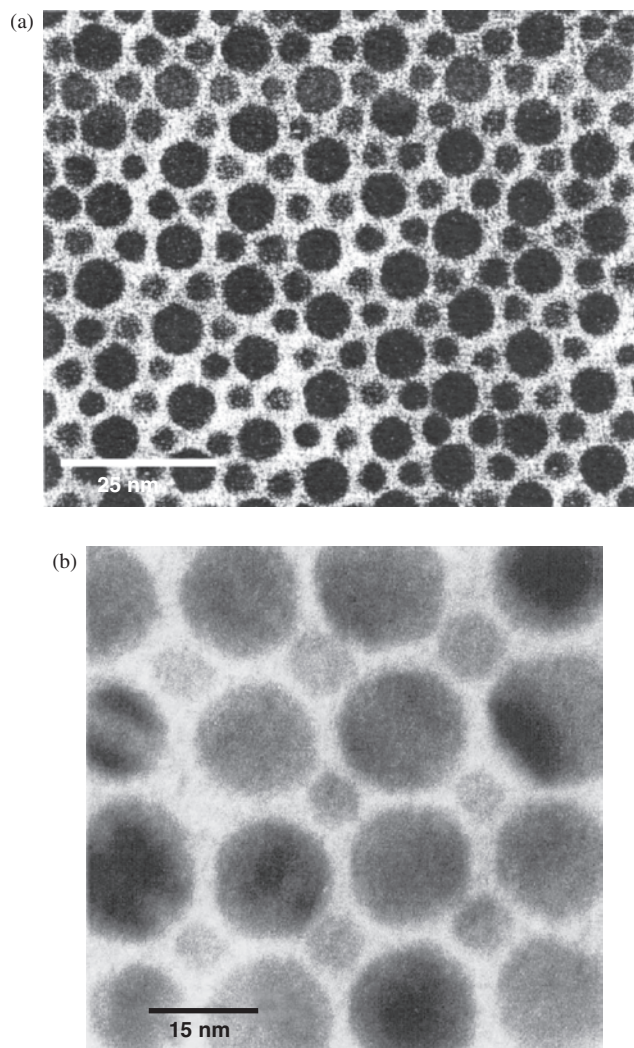
**Figure 7.** Rafts of bimodal nanoparticles forming (a) ordered $AB_2$ and (b) ordered AB superlattice arrays. Reprinted with permission from [78], C. J. Kiely et al., *Adv. Mater.* 12, 640 (2000). © 2000, Wiley-VCH.

between the nanoparticles, one should make use of weak interaction between the protective agents or between the protective agent and the substrate (Fig. 8). If these interactions are too strong to be reversible, precipitates of
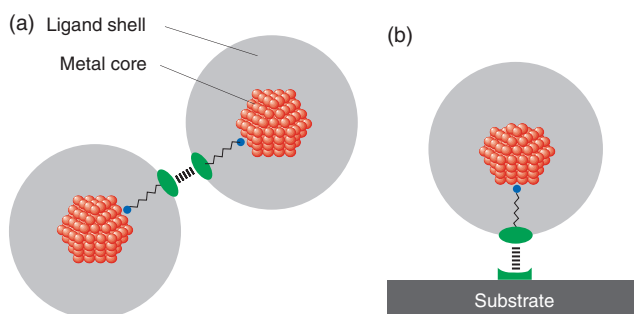
**Figure 8.** Strategy to fabricate 2D superlattices of metal nanoparticles smaller than 2 nm by using the interaction (a) between the protective ligands and (b) between the protective ligand and the substrate.

nanoparticles are formed in solution or no rearrangement of metal nanoparticles on substrates occurs, respectively. First research on 2D superlattice formation consisting of metal nanoparticles smaller than 2 nm was reported by Schmid and co-workers early in 2000 [79], where they used an interaction between the protective ligand and the modified substrate to generate 2D superlattices of 1.4-nm Au nanoparticles. The 2D hexagonal and square lattices of $Au_{55}$ nanoparticles on polymer films were successfully prepared by dipping a poly(ethyleneimine) (PEI)-covered carbon-coated copper grid (for TEM) into an aqueous solution of $[Au_{55}(Ph_2PC_6H_4SO_3H)_{12}Cl_6]$ nanoparticles, as shown in Figure 9. Classical acid-base reactions took place because of the NH functional groups on the PEI. Most of the nanoparticles were found in ordered arrangements of up to a few square micrometers. The reason for the formation of two different superlattices must be attributable to the influence of the polymer, since numerous nanoparticle samples on substrates without polymer have been investigated by TEM before, but such large ordered domains have never been observed. In this experiment a PEI with the lower molecular weight of 60,000 was used instead of the 600,000 used in former experiments, so as to avoid the coiling of the polymer on the surface. The details, however, have been unclear yet.

Recently, we succeeded in 2D self-assembly of 1.5- to 1.9-nm Au nanoparticles by using a newly synthesized protective ligand, 2,6-bis(1′-(n-thioalkyl)benzimidazol-2-yl)pyridine ($TC_nBIP$; see inset in Fig. 10a) [80]. This ligand was designed to have two functional groups, a disulfide group and 2,6-bis-(benzimidazol-2-yl)pyridine (BIP) group, the former serving to produce small Au nanoparticles and the latter inducing the interaction between the ligands. Figure 10a,b presents the TEM image of $TC_8BIP$-protected Au nanoparticles of 1.9 nm in size and the schematic illustration of the interdigitation of ligands. A $\pi$-$\pi$ interaction of BIP groups of protective ligands may contribute to the self-assembly of such small Au nanoparticles, which is also suggested by the formation of perfectly ordered 2D superlattice at air-water interface (Fig. 10c). Tuning the ligand length could control the interparticle spacing of 2D self-assembled super-
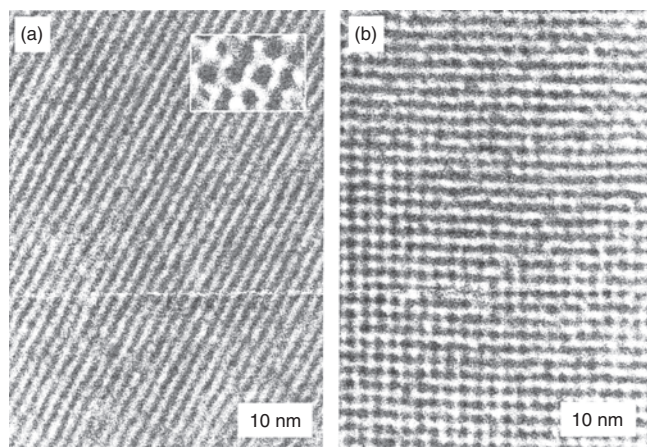


**Figure 9.** TEM images of $Au_{55}$ monolayers showing a hexagonal (a) and a cubic (b) structure. The magnified inset in (a) shows single particles in the hexagonal form. Reprinted with permission from [79], G. Schmid et al., *Angew. Chem. Int. Ed.* 39, 181 (2000). © 2000, Wiley-VCH.
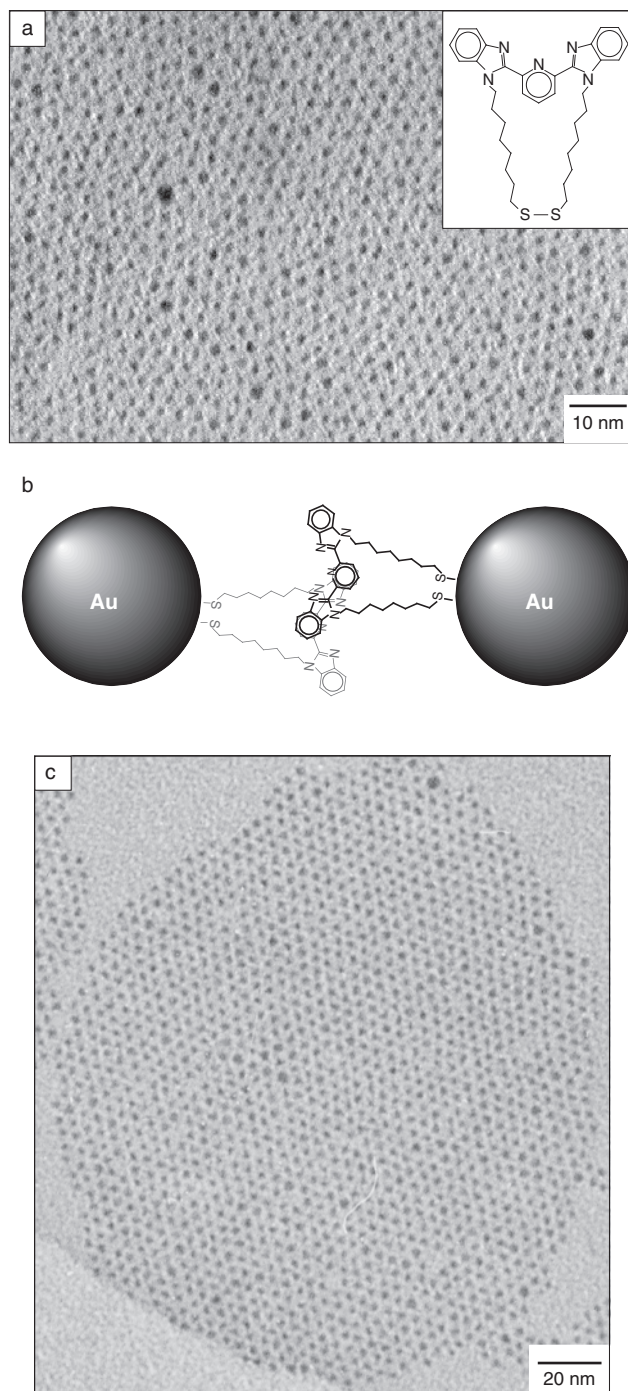


**Figure 10.** (a) TEM images of 1.9-nm $TC_8BIP$-protected Au nanoparticles ($TC_8BIP/Au = 1/1$ (mol/mol)). The inset stands for the chemical structure of $TC_8BIP$ ligand. (b) Schematic illustration of the interpenetration of $TC_8BIP$ ligands protecting Au nanoparticles. (c) Perfectly ordered 2D superlattices of $TC_8BIP$-protected Au nanoparticles at air-water interface. Parts (a) and (b) Reprinted with permission from [80], T. Teranishi et al., *J. Am. Chem. Soc.* 122, 4237 (2000). © 2000, American Chemical Society.

lattices from 1.9 to 2.6 nm. Furthermore, making use of an interligand complexation of $TC_nBIP$ with ferrous ions could expand the interparticle spacing of 2D superlattices to 3.6 nm.

### 2.2.3. External Forces

Although the self-assembly technique with or without using weak interaction between the protective ligand and substrate or the ligands themselves is very convenient to fabricate 2D superlattices of metal nanoparticles, it seems difficult to enlarge the assembly area. For an application of nanoparticle superlattices to nanodevices, an large-scale 2D assembly of nanoparticles using external forces to gather nanoparticles is required. An electrophoretic deposition [18, 19] and a Langmuir–Blodgett (LB) technique [81–84] are quite effective in this regard.

Giersig and Mulvaney demonstrated that the electrophoretic deposition is a useful technique for achieving the 2D assembly of Au nanoparticles of various sizes onto a carbon-coated TEM grid [18, 19]. They prepared Au nanoparticles larger than 10 nm using the citrate method described by Enüstün and Turkevich [85] and smaller particles using the protocol employed by Slot and Geuze [86] in which tannic acid is added together with citric acid to the auric salt solution. Octadecanethiol, dodecanethiol, octanethiol, mercaptopropionic acid, sodium 4-mercaptobenzoate, and sodium mercaptoethanoate were used as the protective agents. When the protecting citrate and chloride ions were to be replaced by water-soluble thiolates, the thiols were added as the sodium salts to the aqueous solution of Au nanoparticles. In the case of alkanethiols, the ligand-exchange reactions were carried out in THF-water mixed solution. The electrophoretic deposition was carried out by immersing TEM grid-pinned copper sheath (anode) and aluminum foil (cathode) into 5 mL solution with the electrode spacing of 0.2 cm. A conventional dc power supply was used to generate the applied voltage. Figure 11 shows the change in assembly of citrate-protected
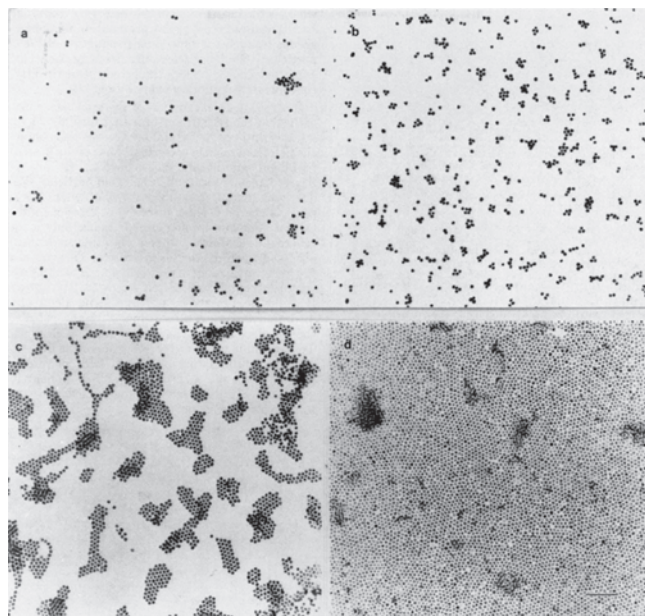


**Figure 11.** Electron micrographs of 2D Au nanoparticle lattices after different periods of electrophoretic deposition from a 0.5-mM Au nanoparticle solution. The polarization times are (a) 5 s, (b) 10 s, (c) 15 s, and (d) 35 s. Trisodium citrate ion was used as a stabilizer. Reprinted with permission from [18], M. Giersig and P. Mulvaney, *Langmuir* 9, 3408 (1993). © 1993, American Chemical Society.

Au nanoparticles by varying the time of polarization in the solution. After 5 s, the grids were sparsely covered, and the Au nanoparticles existed predominantly as randomly distributed isolated particles. After 10 s of polarization, 10–25% of the grid surface was coated, but there were clear signs of clustering. Au nanoparticle triplets were very common and could not be explained statistically. After 15 s, there was clear evidence for island formation. The triplets were no longer seen, and had apparently "grown." The island showed clear ordering, but the crystallographic axes of neighboring islands were not correlated. After 35 s, the grid was largely covered, and the individual domains had converged or coalesced. The Au nanoparticles of 3.5–18.5 nm in size protected by any ligands used here also formed 2D superlattices by the electrophoretic deposition technique. The interparticle spacing and the ligand monolayer geometry can be easily varied by changing the size of the protective ligand. The agreement at smaller chain lengths between observed and calculated chain lengths is good and suggests that the ligands are oriented almost vertically at the nanoparticle surface. At longer chain lengths, the observed particle-particle separation is clearly too small and suggests that the packing of the nanoparticles results in considerable interdigitation of the alkane chains.

For large-scale formation of metal nanoparticle superlattices, the Langmuir–Blodgett technique is quite attractive because any hydrophobic ligand-protected nanoparticles can be applied to LB methods and the assembly area can be expanded to a few hundred square centimeters [81–84]. Bourgoin and co-workers successfully prepared LB films of 2.9-nm dodecanethiol-protected Au nanoparticles on various substrates over macroscopic dimensions [81]. The 2.9-nm dodecanethiol-protected Au nanoparticles were prepared by using Brust's method [52] and suspended in trichloro-1,1,1-ethane ($10^{-4}$ M). This solution was spread on pure water surface in the LB trough and the Au nanoparticles were slowly compressed at constant speed. At the surface pressure of 6–8 mN m$^{-1}$, the area per particle lies around 1000–1300 Å$^2$, and roughly fits the expected area filled by one average dodecanethiol-protected Au nanoparticle. Above 6–8 mN m$^{-1}$, the area per particle is very small and multilayers are likely to form, at least in some parts of the film. The LB film obtained can be transferred onto various solid substrates by the classical dipping-withdrawing method. In this case, however, the LB films consist of a number of small rafts, in which the Au nanoparticles ordered spontaneously when the dilute nanoparticle solutions were developed onto water subphase.

In 2001, Huang and co-workers clarified the fabrication mechanism of LB monolayer of alkanethiol-protected Au nanoparticles [83]. The citrate-protected Au nanoparticles of 17 nm in size were prepared by the reduction of H[AuCl$_4$] with trisodium citrate and tannic acid, subjected to the ligand-exchange reaction with dodecanethiol in ethanol, redispersed in chloroform, and carefully cast on the water surface. After the Au nanoparticles spread over the water surface, the domain structures of the ordered particle arrays initially formed by the self-assembly process. As the barriers were moved, these domains were compressed, so that the distances between the domains decreased. As the barriers were moved further, the domains were getting closer

and closer, which resulted in a sharp increase in the surface pressure. By this stage, a densely packed monolayer of Au nanoparticles had formed on the water surface. It was concluded that once the domain structures had formed, it was very difficult to reconstruct them into a larger-area homogeneous structure by LB compression.

Brown and co-workers succeeded in expanding the average particle grain size by the subsequent compression followed by relaxation procedure [84]. The 1.4-nm Au nanoparticles they used were coated with triphenyl phosphine groups, some of which have *p-N*-methyl-carboxamidophenylphosphine groups in place of the triphenyl phosphine. On average, one of the *p-N*-methyl-carboxamidophenylphosphine groups on each particle has a reactive aminopropyl group in place of the methyl group attached to an amide. An amide linkage ties the amine part of the aminopropyl group to palmitic acid ($C_{14}H_{29}COOH$). Several nitrile groups may also be present in the coating. The overall effect is amphiphilic: a weakly polar particle with one nonpolar alkane tail and an otherwise stiff coating. These Au nanoparticles were dissolved in anhydrous ethanol or methanol and 2-propanol 50%/50 vol%, at concentrations of 1 nmol/10 $\mu$L and 1 nmol/25 $\mu$L. After the solution was deposited dropwise onto the water surface with a microsyringe, the films were concentrated through compression to a surface pressure of 35 mN m$^{-1}$, and barrier motion was stopped, allowing the surface pressure to decrease as the film relaxed. Cycles of compression and relaxation were repeated up to six times over times up to 36 h. Highly ordered 2D arrays were formed from the amphiphilic starting material by compression and relaxation of the Langmuir layers. Important factors in the formation of ordered arrays include the particle coating material and uniformity and the use of a compression/relaxation cycle to promote ordering. Array quality improved with multiple compression/relaxation cycles or with annealing time at a fixed surface pressure. Grains are approximately 30 nm in diameter immediately after the third compression at the surface pressure of 35 mN m$^{-1}$, but are ∼150 nm in diameter when held at constant area for 2.5 h after a fifth compression. When a film was transferred after 12 h of third compression, Au nanoparticle arrays with monolayer grains appeared to extend to more than 400 nm × 500 nm (Fig. 12).

Almost all the 2D superlattices of metal nanoparticles mentioned here have the sixfold symmetry. The fabrication of 2D superlattices with lower symmetry, such as twofold (wire), threefold (e.g., honeycomb), and fourfold (e.g., square), would be interesting and required for future nanodevices.

## 2.3. Three-Dimensional Superlattices

Three-dimensional superlattices of metal nanoparticles stand for nanometer- to micrometer-sized crystals of close-packed metal nanoparticles. Multilayer assemblies of metal nanoparticles are achieved by two approaches: one is to use the self-assembly technique and another is to adopt the multilayer deposition of 2D particle arrays.

In 1999, Schmid and co-workers found that micrometer-sized crystals (3D superlattices) of $Au_{55}(PPh_3)_{12}Cl_6$ nanoparticles were formed from dichloromethane solution
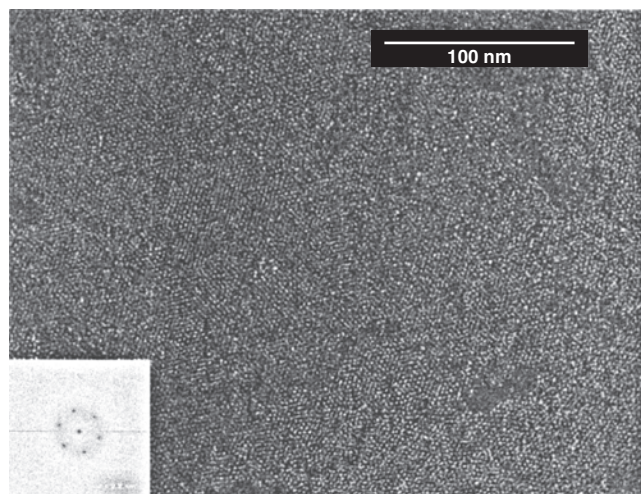


**Figure 12.** Monolayer grain with area 0.25 $\mu$m × 0.35 $\mu$m. This film was compressed three times; the maximum surface pressure reached was 35 mN/m. This image shows the film 12 h after it was last disturbed/compressed and 18 h from the time it was created. No grids were taken prior to this time to minimize disruption of the film. The inset shows the 2D Fourier transform of the image, indicating particle separation of 2.2 nm, and hexagonal close-packed order. Reprinted with permission from [84], J. J. Brown et al., *Langmuir* 17, 7966 (2001). © 2001, American Chemical Society.

[87]. Fast evaporation of the solvent from concentrated dichloromethane solutions of $Au_{55}(PPh_3)_{12}Cl_6$ resulted in the formation of well-shaped crystals in the size range of hundreds of nanometers up to a few micrometers, as shown in Figure 13. It was revealed from TEM (Fig. 14) that these superlattices corresponded to a hexagonal close-packing. Small-angle X-ray diffraction (SAXRD) showed only one strong reflection of $2\theta = 4.3°$, corresponding to a *d*-value of 2.05 nm in accord with the average distance from TEM of 2.05 nm. This might correspond to a hexagonal close-packing, if observed along the [111] direction. A crystal of the size of $1 \times 1 \times 1$ $\mu$m contains ca. $10^8$ nanoparticles. The fabrication of 3D superlattices will make it possible not only to investigate their solid-state researches in solutions but to apply them to 3D single-electron tunneling (SET) devices.

Kimura et al. have also successfully prepared micrometer-sized 3D superlattices of water-soluble mercaptosuccinic acid (MSA)-protected Au nanoparticles of 3.5 nm in size [88]. MSA-protected Au nanoparticles were prepared by adding aqueous NaBH$_4$ solution to the water/methanol mixed solution containing H[AuCl$_4$] and MSA. The crystallization of Au nanoparticles took place in 4–10 days with hydrochloric acid below pH 2 in a glass bottle giving numerous plate-like micrometer-sized 3D superlattices with clear crystal habit (majority triangle with minor rectangular fringe). The thickness was found by a laser microscope to be in the range of 0.1–1 $\mu$m.

Shevchenko and co-workers have succeeded in the synthesis and self-assembly of CoPt$_3$ magnetic nanoparticles [89]. Reduction of platinum acetylacetonate (Pt(acac)$_2$) and thermal decomposition of Co$_2$(CO)$_8$ in the presence of 1-adamantanecarboxylic acid (ACA) were employed in different coordinating mixtures (diphenyl ether and hexadecylamine (HDA), diphenyl ether and *n*-tetradecylphosphonic
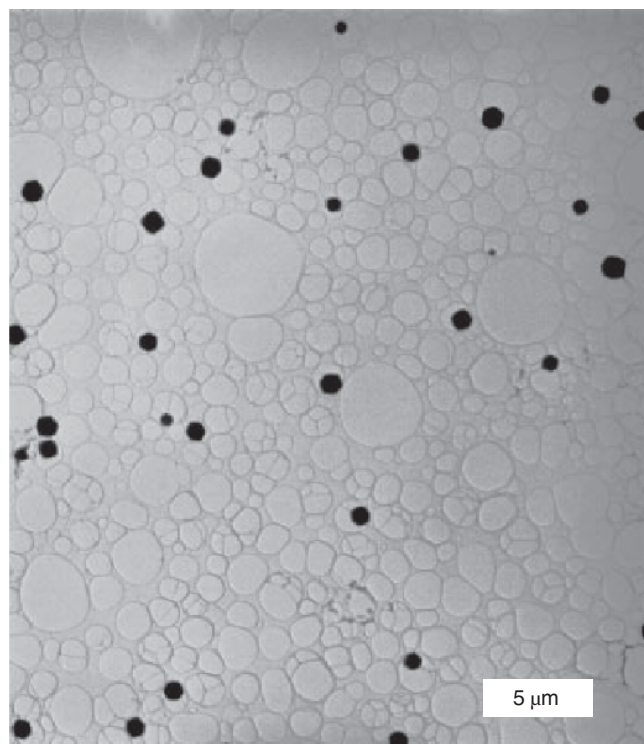
**Figure 13.** Transmission electron microscopic (TEM) image of well-shaped microcrystals of $Au_{55}(PPh_3)_{12}Cl_6$. Most of the crystals are ca. 1 $\mu$m in diameter. Reprinted with permission from [87], G. Schmid et al., *Chem. Commun.* 1303 (1999). © 1999, Royal Society of Chemistry.



**Figure 14.** High-resolution TEM image of a $Au_{55}(PPh_3)_{12}Cl_6$ microcrystal. The monocrystalline particle shows particle rows with a separation of 2.0–2.1 nm in accord with a hexagonal close-packed arrangement of the spherical particles. The particle distance can be determined as 2.3 nm. Reprinted with permission from [87], G. Schmid et al., *Chem. Commun.* 1303 (1999). © 1999, Royal Society of Chemistry.

acid (TDPA), and HDA and 1-hexadecanol) to produce monodisperse, highly crystalline $CoPt_3$ nanoparticles. The mean particle size can be varied from 1.5 to 7.2 nm by controlling the reaction conditions and the type of coordinating mixture. XRD patterns of 4.0-nm as-prepared $CoPt_3$ nanoparticles corresponded to the chemically disordered fcc $CoPt_3$ structure which was also observed for vapor-deposited $Co_xPt_{1-x}$ films [90]. The width of the diffraction peaks at wide angles was considerably broadened and increased with decreasing particle size. Due to their narrow size distributions and the uniform spherical shape, the $CoPt_3$ nanoparticles had a strong tendency to self-assemble into 2D and 3D superlattices. Spontaneous self-assembly was observed when the solutions of $CoPt_3$ nanoparticles were spread onto a substrate with subsequent slow evaporating of the carrier solvent. Depending on the particle size and conditions of solvent evaporation, several kinds of self-assembled superlattices were observed. Thus, Figure 15a shows a TEM overview image of a close-packed monolayer of 4.8-nm $CoPt_3$ nanoparticles. If the surface coverage with nanoparticles was higher than one monolayer, nanoparticles of the second layer occupied positions between the nanoparticles in the first layer (Fig. 15b,c). Due to the relatively large interparticle spacing of $\sim$2.5 nm presumably maintained by the bulky ACA capping ligands, two layers of $CoPt_3$ nanoparticles form the above-mentioned structure observable for different nanoparticle sizes (Fig. 15b,c). The third layer of nanoparticles occupied the positions typical for cubic close-packing (ccp) (Fig. 15d,e). Figure 15e

gives a magnified image of a three-layered assembly of 4.0-nm $CoPt_3$ nanoparticles. The difference in phase contrast between two underlying layers and a darker third layer allows us to attribute each nanoparticle to the layer it is placed in and permits us to conclude that $CoPt_3$ nanoparticles are packed into ccp-like superlattice, where the nanoparticles are separated from each other by thick (2.5 nm) organic shells. Figure 15f presents a TEM image of multilayer 3D superlattice where the 4.5-nm $CoPt_3$ nanoparticles are arranged in a nearly defect-free 3D structure exhibiting long-range order. Graphical illustration (Fig. 15g) clarifies the three-layer arrangement of $CoPt_3$ nanoparticles.

Sarathy and co-workers achieved the multilayer assemblies of metal nanoparticles by the sequential adsorption of dithiol molecules and metal nanoparticles of the desired size, as shown in Figure 16 [91, 92]. A clean polycrystalline metal substrate of gold or silver was immersed in a 50-mM toluene solution of 1,10-decanedithiol. After 2 h, it was washed with toluene and dried in air. The dithiol-covered substrate was then immersed in a dilute dispersion of metal nanoparticles of the desired size (obtained by the controlled reduction of metal ions complexed with tetra-*n*-octylammonium bromide in toluene using $NaBH_4$) in toluene for 12 h. After
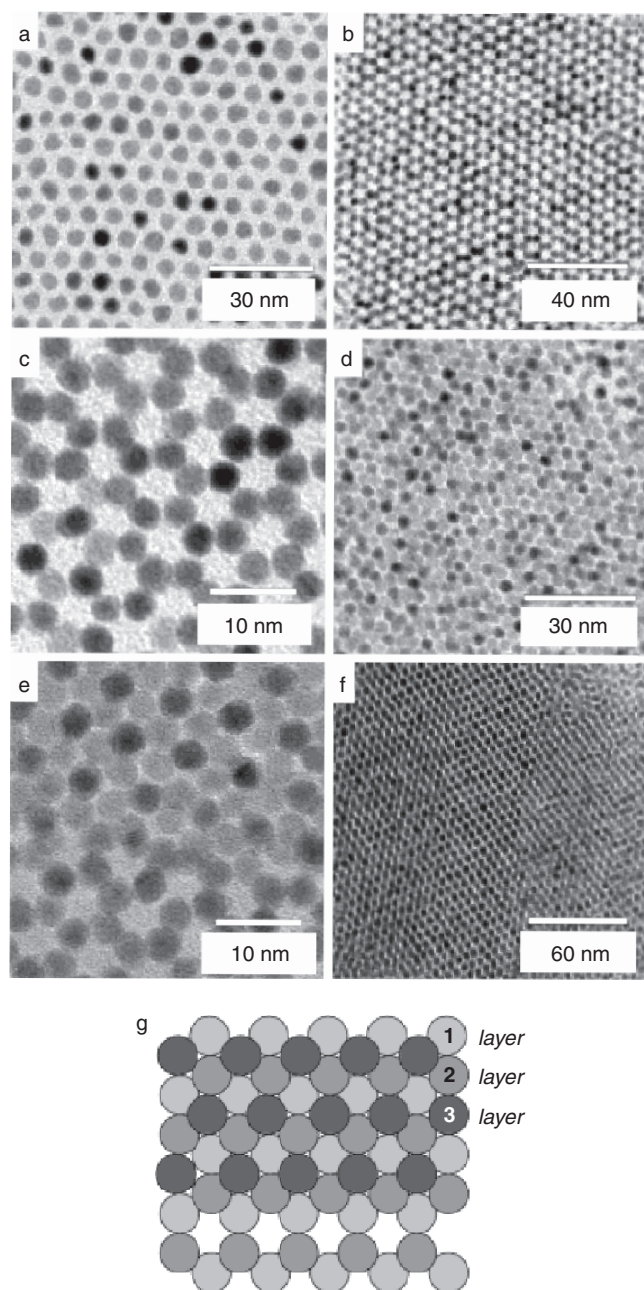
**Figure 15.** TEM images (a) of monolayer of 4.8-nm CoPt$_3$ nanoparticles, (b, c) of two layers of 3.6- and 4.0-nm CoPt$_3$ nanoparticles, (d) of three layers of 3.6-nm CoPt$_3$ nanoparticles, (e) of three layers of 4.0-nm CoPt$_3$ nanoparticles (HRTEM), (f) of more than five layers of 4.5-nm CoPt$_3$ nanoparticles, and a graphical illustration (g) of three-layer arrangement of CoPt$_3$ nanoparticles. Reprinted with permission from [89], E. V. Shevchenko et al., *J. Am. Chem. Soc.* 124, 11480 (2002). © 2002, American Chemical Society.



**Figure 16.** Schematic drawing depicting the layer-by-layer deposition of Pt particles onto a Au substrate, the layers being separated by dithiol molecules. Also shown is the formation of a heterostructure consisting of alternate layers of semiconductor and metal particles. Reprinted with permission from [91], K. V. Sarathy et al., *J. Phys. Chem. B* 103, 399 (1999). © 1999, American Chemical Society.

Other 3D superlattices of metal nanoparticles are presented in Section 4 together with their physical properties.

# 3. CHARACTERIZATION TECHNIQUES

## 3.1. Transmission Electron Microscopy

The unique physical and chemical properties of nanoparticles are determined not only by the large surface-to-volume ratio but also by the crystallographic structures of the particle surface. The former is determined by the particle size, and the latter depends on the particle shape. Crystal structures can be determined by X-ray and neutron diffraction, while transmission electron microscopy (TEM) is indispensable for characterization of nanoparticles and their superlattices. Although scanning probe microscopy (SPM), such as scanning tunneling microscopy (STM) and atomic force microscopy (AFM), can provide atomic-resolution images of large crystal surfaces, they are unlikely to clearly

the formation of a particulate layer by this means, it was washed with toluene and dried. The above steps employed for depositing the first layer of nanoparticles were repeated to obtain 3D superlattices. Using this procedure, several monometal, bimetal, and metal-semiconductor 3D superlattices have been prepared. Characterization of these 3D superlattices is presented in Section 3.

resolve the atomic lattices of nanoparticles because of the surface coating and the wobbling of the nanoparticles under the scanning tip. TEM is very powerful for revealing the atom distributions on nanoparticle surfaces even when they are protected with protective ligands. Today's TEM is a versatile tool that provides not only atomic-resolution lattice images but also chemical information at a spatial resolution of 1 nm or better, allowing direct identification of single nanoparticles [93–97].

If the nanoparticles can be taken as the building blocks, their 2D and 3D superlattices are unavoidably affected by the particle shape. TEM is unique in determining the relationship between particle orientations and the assembling crystallography of the ordered array. An example for an alkanethiol-protected Ag nanoparticle superlattice by Wang is described [49]. Figure 17a is a TEM image recorded from an Ag nanoparticle superlattice deposited on a carbon substrate, from which the orientation of the particles and the arrays can be identified. The Ag nanoparticles have a truncated octahedral shape (the inset in Fig. 17a), and they are oriented along the [110] of the Ag atomic lattice in the image, along which four {111} and two {100} facets are imaged edge-on. The unit cell of the nanoparticle superlattice is also oriented along $[110]_s$ of fcc, where the subscript refers to the superlattice. Therefore, the orientational relationship between the Ag nanoparticles and the nanoparticles lattice is [110] // $[110]_s$ and [001] // $[1\bar{1}0]_s$. This registered orientational order can be used to determine the orientations of the nanoparticles in the unit cell of the superlattice, as shown in Figure 17c. The nanoparticles are packed into a fcc lattice, and the nanoparticles are arranged following a principle of face-to-face. The image recorded from the same area at a slightly large defocus condition gives the channels (the white dots in Fig. 17b) enclosed by the bundling distributed thiolate molecules on the surface of the nanoparticles. This model has been proved by the energy-filtered chemical imaging technique in TEM [98]. The tetrahedral-shaped nanoparticles have sharp corners and their assembly may have long-range translational symmetry but the orientational order is limited only to a short range [99]. In the case of the 2D superlattice of tetrahedral Ag nanoparticles, the most dense packing is also the favorable configuration from the energy point of view in spite of the threefold symmetry of the packing due to the shape of the nanoparticles.

Particle shapes can be identified by HRTEM images, but in some cases the dark-field imaging is requisite for confirming the result. If the bright-field TEM images illustrate that the particles have triangular-like projected shapes, the projected triangles correspond to either tetrahedral or platelet-like structure. If the latter were the case, the dark-field image recorded using the diffracted electrons would show a uniform contrast across the particle because there is no variation in the projected thickness across the particle. In contrast, if the dark-field image showed bright spots at the center of particles, this indicates the tetrahedral shape because the dark-field image is sensitive to the projected density of the atoms under the first-order scattering approximation. On the other hand, the bright-field image cannot uniquely define the particle shape. Dark-field imaging can also be useful for identifying the number of stacking layers in 3D superlattices of nanoparticles [100]. Figure 18 is
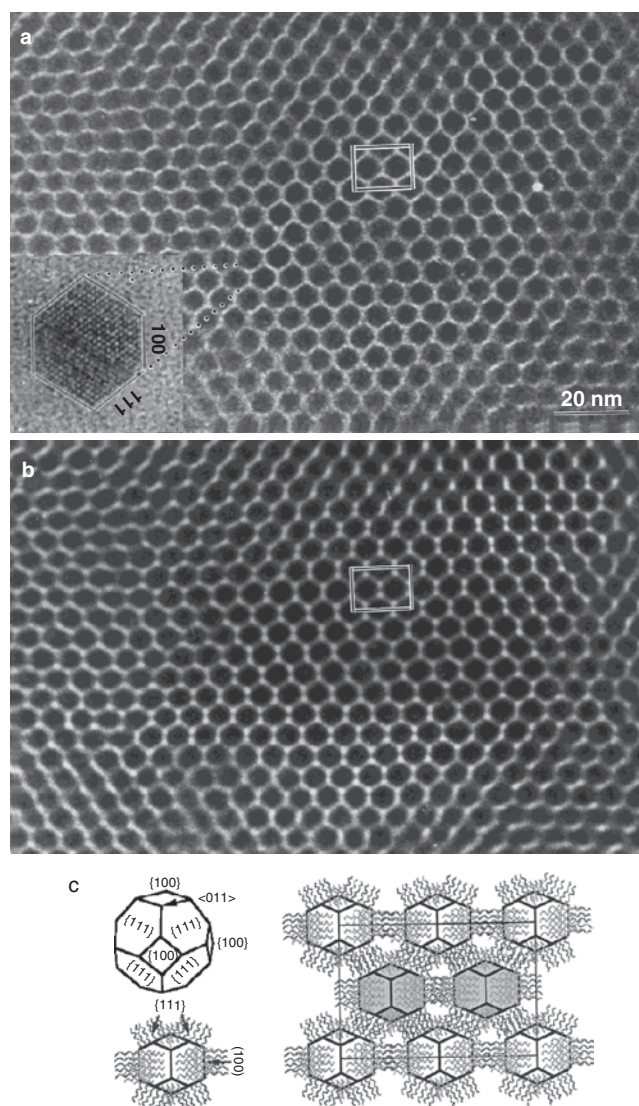


**Figure 17.** (a) TEM image of a face-centered cubic-packed Ag nanoparticle whose shape is dominated by truncated octahedral (TO) (see the inset HRTEM image of a single Ag nanoparticle). The image displays the orientational relationship between the nanoparticles and the assembled superlattice. (b) A TEM image recorded from the same specimen area under slightly defocused condition. The image in (a) is recorded at near focus condition, and it is sensitive to the particle shape, and the image in (b) is most sensitive to the phases caused by a variation in the projected mass thickness. (c) A structural model of the TO particle and the $[110]_s$ projection of the unit cell as indicated in (a), where the gray pasted particles are located at different $z$ heights. The channels enclosed by the bundled thiolates are presented. Reprinted with permission from [97], Z. L. Wang, *J. Phys. Chem. B* 104, 1153 (2000). © 2000, American Chemical Society.

such an example, which was recorded by positioning a small size objective aperture on the optic axis while the incident beam is scanned conically to average over the particle orientations. This type of image is called conical scan dark-field imaging and it is most sensitive to the local projected mass thickness, and the diffraction effect is minimized. The monolayer assembly preserves very well the translational symmetry. The second layer introduces a minor short-range
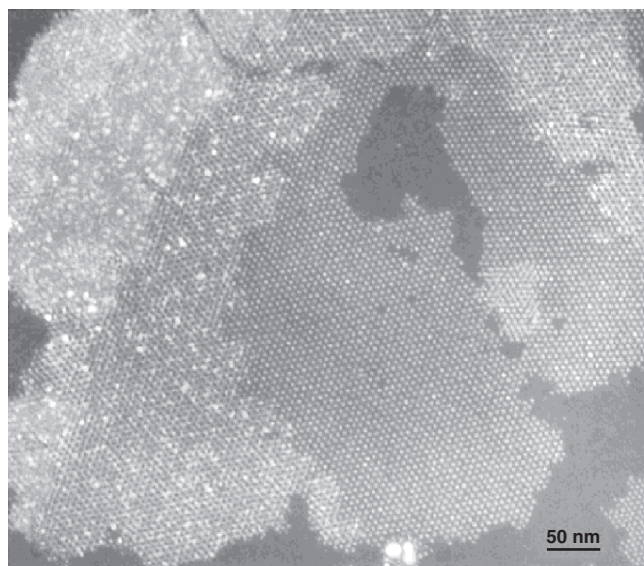
**Figure 18.** Dark-field TEM image recorded by scanning the incident beam conically, showing the monolayer, double-layer, and triple-layer self-assembly of Ag nanoparticles. Reprinted with permission from [97], Z. L. Wang, *J. Phys. Chem. B* 104, 1153 (2000). © 2000, American Chemical Society.

disorder, while the third layer is largely disordered. The reason for the increased disordered structure is likely due to the introduction of larger size particles, resulting in the creation of "interstitial" and vacancy point defects in the arrays. The contrast of this type of image is proportional to the specimen thickness for relatively thin specimens, allowing a direct identification of the number of stacking layers from the image.

## 3.2. Fast Fourier Transformation of Micrographs

In order to examine the ordering of the nanoparticles in 2D superlattices more statistically, SEM and TEM images are often subjected to the fast Fourier transformation (FFT). The general procedure is that the micrographs are scanned, the contrast in the images is enhanced, and 2D FFT is performed using a proper software such as NIH Image[1] [101]. In Figure 19a, a high-resolution micrograph of part of a single domain composed of 14.1-nm Au nanoparticles fabricated by an electrophoretic deposition is shown [18]. Figure 19b is the result obtained after FFT of the micrograph in Figure 19a. The 14.1-nm Au nanoparticles crystallize into a hexagonal close-packed lattice with an average core-to-core separation of 15.1 nm. Thus the thickness of the stabilizing layer between the particles is 1.0 nm. Furthermore, second- and third-order reflexes are evident which confirms the high degree of ordering in the 2D superlattice. Low-angle selected-area electron diffraction measurements of 2D superlattices are also useful for determining the ordering of nanoparticles as well as the FFT technique [66].

---

[1] NIH Image was developed at the U.S. National Institutes of Health and is available on the internet.
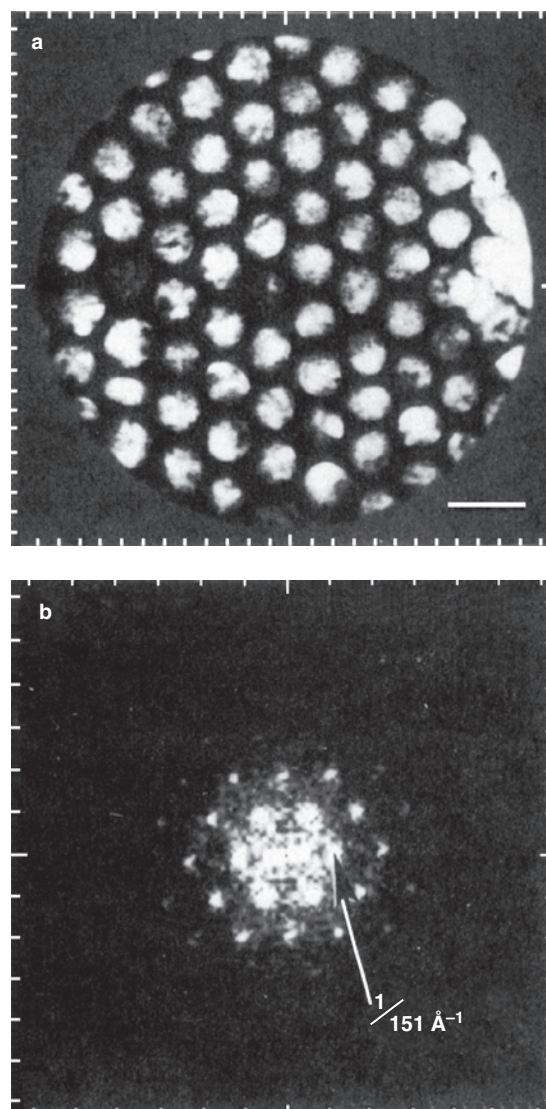


**Figure 19.** (a) Electron micrograph of part of a single 2D domain. Scale bar is 200 Å. (b) Power spectrum of (a) showing hexagonal close-packing with the first-, second-, and third-order reflexes. The first reflex, which also indicates the size of the lattice unit cell, amounts to $1/151$ Å$^{-1}$. Reprinted with permission from [18], M. Giersig and P. Mulvaney, *Langmuir* 9, 3408 (1993). © 1993, American Chemical Society.

## 3.3. Small-Angle X-ray Diffractometry

Small-angle X-ray difractometry (SAXRD) is also a powerful tool to investigate the ordering of metal nanoparticles in their 2D and 3D superlattices. Figure 20 shows SAXRD patterns obtained with the thiol-protected Au nanoparticles with the mean diameters of 4.2, 2.1, and 1.0 nm prepared by Sarathy et al. [42]. The Au nanoparticles with the mean diameter of 4.2 nm form a close-packed structure, while the smaller particles of mean diameters of 2.1 and 1.0 nm form superstructure islands, with voids in between. All of them, however, show characteristic SAXRD patterns, each particle giving small-angle peaks corresponding to *d*-spacings of 5.0, 4.5, and 3.8 nm, respectively. These diffraction peaks are likely to result from the nanoparticle arrays, in particular
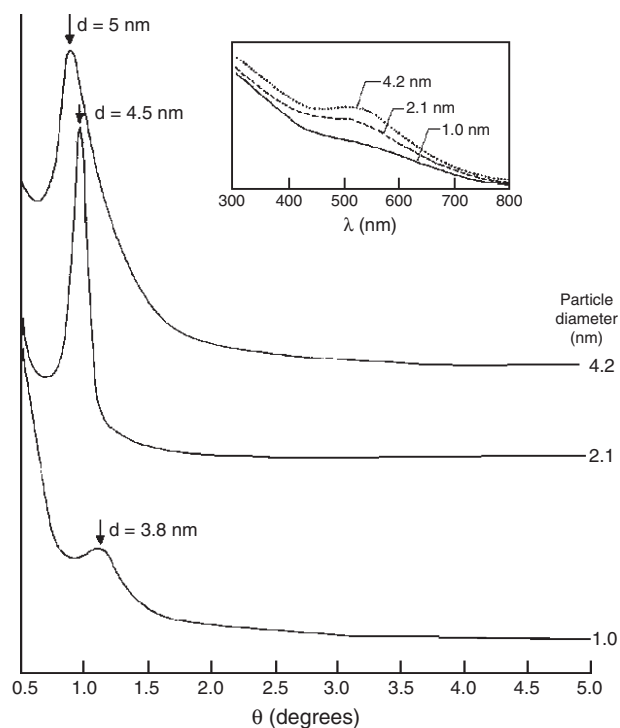
**Figure 20.** XRD patterns from the nanocrystalline arrays of Au nanoparticles of different mean diameters (4.2, 2.1, and 1.0 nm). Inset of the figure displays the UV-vis spectra of these particles. Reprinted with permission from [42], K. V. Sarathy et al., *J. Phys. Chem. B* 101, 9876 (1997). © 1997, American Chemical Society.

due to the (110) spacing of the bcc structure [102]. Higher-angle peaks could not be observed due to the limited thickness of the films and also possibly due to the presence of distribution of sizes. The distance between the nanoparticles deduced from the $d$-spacings is somewhat smaller than the expected value (twice the radius of the particle and the thiol layer thickness). Thus, in the case of the 4.2-nm nanoparticles, the $d$-spacing of 5.0 nm gives an interparticle distance of 0.8 nm, which is smaller than the estimated surfactant layer thickness of $\sim$1.5 nm. It appears that there is a significant overlap (or close-packing) of the passivating layers of the thiol molecules on the neighboring particles.

Schmid et al. also employed SAXRD for an investigation of the ordering of $Au_{55}(PPh_3)_{12}Cl_6$ nanoparticles in their 3D superlattices [87]. Samples for SAXRD experiments were prepared by fast evaporation of the solvent of concentrated dichloromethane solutions of $Au_{55}(PPh_3)_{12}Cl_6$. The black powder consisted almost exclusively of 3D superlattices. The result of the SAXRD experiments is shown in Figure 21. Only one strong reflection of $2\theta = 4.3°$ is registered, corresponding to a $d$-value of 2.05 nm in accord with the average distance from TEM of 2.05 nm. This might correspond to a hexagonal close-packing, if observed along the [111] direction.

## 3.4. X-ray Photoelectron Spectroscopy

X-ray photoelectron spectroscopy (XPS) can be employed for the characterization of 3D superlattices of metal nanoparticles. Figure 22 shows core-level XPS spectra of the
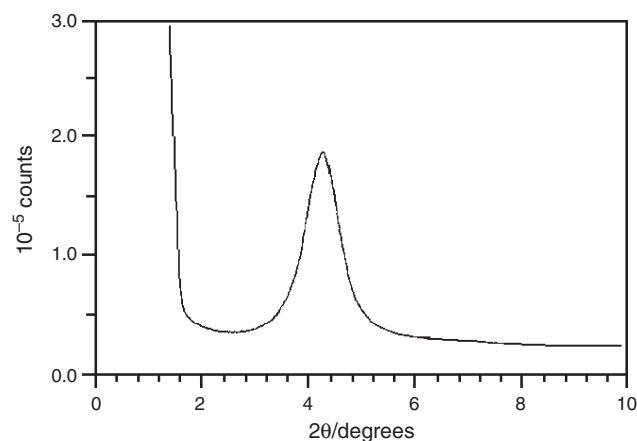


**Figure 21.** Result of small-angle X-ray diffraction (SAXRD) measurements on $Au_{55}(PPh_3)_{12}Cl_6$ microcrystals. The $2\theta$ angle of 4.3° corresponds to a $d$ value of 2.05 nm, in accord with the TEM results. Reprinted with permission from [87], G. Schmid et al., *Chem. Commun.* 1303 (1999). © 1999, Royal Society of Chemistry.

lattices formed by the multilayer deposition of 5-nm Pt nanoparticles with dithiols as cross-linkers on a gold substrate after the first, third, and fifth depositions [91, 92]. The intensity of the Pt(4f) feature increases with the number of depositions accompanied by a decrease in the Au(4f) intensity as the substrate gets increasingly shadowed due to the limited escape depth of the photoelectrons. The intensities
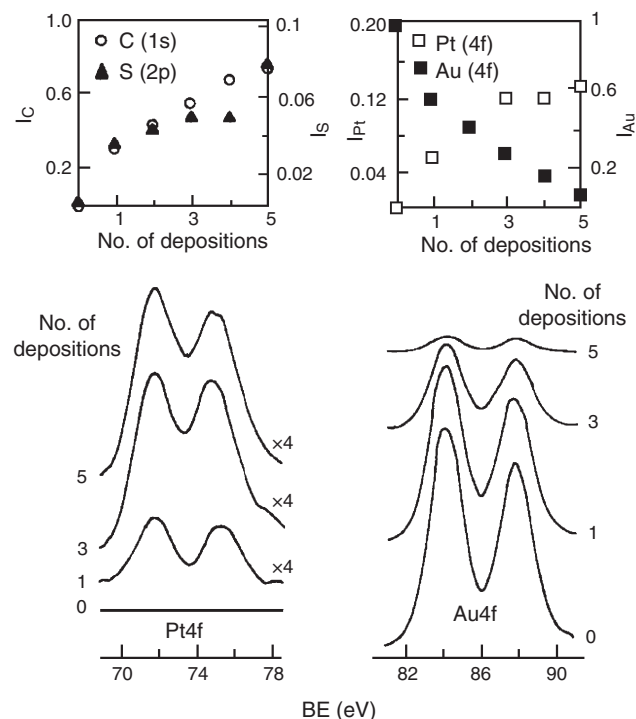


**Figure 22.** X-ray photoelectron spectra in the Pt(4f) and Au(4f) regions for the 5-nm Pt/Au system. Inset shows variations in the Pt(4f) and Au(4f) intensities as well as C(1s) and S(2p) intensities with the number of depositions. Reprinted with permission from [91], K. V. Sarathy et al., *J. Phys. Chem. B* 103, 399 (1999). © 1999, American Chemical Society.

of the C(1s) and S(2p) levels of the dithiol (at 285.0 and 163.6 eV, respectively) also increase with the increasing number of depositions. The observed variation of the relevant core-level intensities with successive depositions is clearly indicative of 3D superlattice formation as a result of layer-by-layer deposition.

XPS could also characterize a 3D bimetallic superlattice by alternative deposition of 6-nm Au nanoparticles and 5-nm Pt nanoparticles on a silver substrate, the particle layers being separated by decanedithiol molecules. In the core-level XPS spectra of Ag(3d), Au(4f), and Pt(4f), there is a decrease in the intensity of Ag(3d) with successive depositions, while the Au(4f) intensity appears after the first deposition and decreases after the deposition of Pt nanoparticles in the second layer. This technique provides further proof for the formation of 3D superlattices of metal nanoparticles.

# 4. PHYSICAL PROPERTIES AND APPLICATIONS

The engineering of nanoscale materials and devices is of greater current interest from the viewpoint of their novel optical, electronic, and magnetic properties than is the engineering of either isolated molecules or macroscopic solids. Confinement and quantization of conduction electrons within a small volume [103–105] enhance the optical and electronic conductance properties of materials composed of nanoparticles, and the reduction of magnetic recording unit drastically improves the magnetic recording density. In this section, the novel optical, electronic, and magnetic properties of nanoparticle superlattices are presented, which would be useful to the development of future nanooptical, nanoelectronic, and nanomagnetic devices.

## 4.1. Optical Property

Optical properties of isolated metal nanoparticles and, in particular, their dependence on size effect [106–109] have been intensively investigated. Absorption spectra of metal nanoparticle solutions exhibit broad bands in the UV-vis range due to the excitation of plasmon resonances or interband transitions. The UV-vis absorption spectra of a fairly dilute dispersion of metal nanoparticles can be calculated from the "Mie" theory [110]. The absorbance, $A$, for a dispersion of $N$ particles per unit volume is given by

$$A = \frac{CNl}{2.303} \quad (3)$$

where $C$ and $l$ are the absorption cross section and the optical path length, respectively. If the particle dimensions are smaller than the mean free path of the conduction electrons, collisions of these electrons with the particle surface take place. This lowers the effective mean free path. In the limit of $2\pi R < \lambda$ (where $R$ is the radius of the particles and $\lambda$ the wavelength of light in the media), only the electric dipole term, developed in Mie's theory, is significant. Then the cross section can be expressed as

$$C = \frac{(18\pi V \varepsilon_2(\omega)\varepsilon_m^{3/2})}{\lambda[(\varepsilon_1(\omega) + 2\varepsilon_m)^2 + \varepsilon_2(\omega)^2]} \quad (4)$$

where $V$ and $\lambda$ are, respectively, the volume of the spherical particle and the incident wavelength, corresponding to a frequency $\omega$. The complex relative permittivity of the metal, $\varepsilon(\omega)$, is expressed as

$$\varepsilon(\omega) = \varepsilon_1(\omega) + i\varepsilon_2(\omega) \quad (5)$$

When $\varepsilon_2$ is small or does not change so much around the band, the position of maximum absorption occurs for all $\varepsilon_1(\omega) = -2\varepsilon_m$. The wavelength of this plasma resonance is therefore given by the wavelength dependence of $\varepsilon_1(\omega)$. The width and height of the resonance are determined by the $\varepsilon_2(\omega)$ value at this wavelength. Furthermore, the plasmon peak width is related to the dielectric constant of the surrounding environment, $\varepsilon_m$ [111–113]. If the particle sizes are comparable to the mean free path of the conduction electrons, the collisions of conduction electrons with the particle surfaces become appreciable and thus the effective mean free path is less than that in bulk material. The electron energy bands are quantized and the number of discrete energy levels is related to the magnitude of the number of atoms; the intensities between the conduction band levels of metal particles are no longer smeared out thermally. This influences intraband transitions of the conduction electrons and leads to a damping of electron motion, which corresponds to the free path effect in the classical approach. This damping affects the dielectric constant.

Among the various metal nanoparticles, the optical properties of Cu, Ag, and Au nanoparticles should be focused on, because they have surface plasmon resonances (SPRs) in the UV-vis region, which are quite important for an application to the future nano-optical devices. For example, the UV-vis absorption spectra of toluene solutions of dodecanethiol-protected Au nanoparticles with different diameters are shown in Figure 23, in which the SPR at 520 nm increases with increasing particle sizes [58]. Well-defined, ordered superlattices prepared from these nanoparticle building blocks offer possibilities for observing interesting, new, and potentially useful collective optical phenomena.

Taleb and co-workers compared the optical properties of dodecanethiol-protected Ag nanoparticles dispersed in hexane solution and self-assembled in a 2D or 3D superlattice
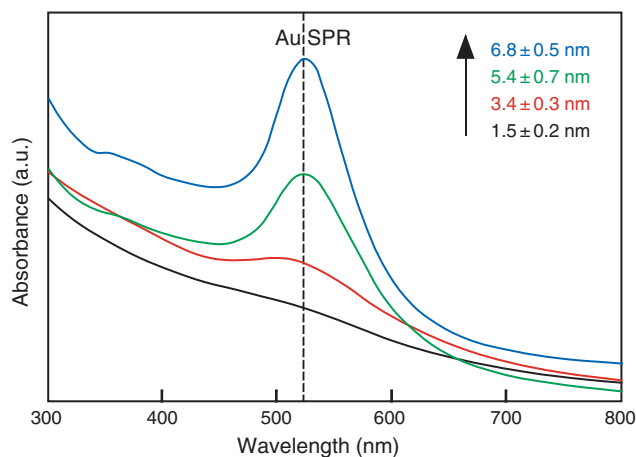


**Figure 23.** UV-vis absorption spectra of DT-Au nanoparticles with different diameters.

[40, 45]. When the Ag nanoparticles formed hexagonally packed 2D superlattices, the SPR peak of Ag nanoparticles was shifted toward an energy lower than that obtained in hexane solution. Such a shift is due to their self-assembly on the graphite support. The bandwidth of the SPR peak (1.3 eV) obtained after deposition is larger than that in solution (0.9 eV). This can be attributed to a change in the dielectric constant of the composite medium. It is concluded that the shift toward lower energy is due to an increase in the dielectric constant of the composite medium of the nanoparticles, which is the superposition of several factors [114] such as the spherical particles, the support, particle-particle interactions, and the air.

For isolated nanoparticles, the increase in the dielectric constant induces a shift to lower energy and an increase in the bandwidth of the SPR peak. For nanoparticles assembled in a fcc 3D structure, each nanoparticle is surrounded by 12 other particles. So in 3D superlattices, the dielectric constant must take into account the composite environment resulting from the external field, the dipole fields of all the other particles, and the contribution due to the support. There is no model actually which could evaluate quantitatively this effect, but all these effects must induce an increase in the total dielectric constant, which, as for isolated particles, induces a shift toward the low energy of the SPR peak. The 5.2-nm dodecanethiol-protected Ag nanoparticles dispersed in hexane ($[(Ag)_n] = 2.5 \times 10^{-3}$ M) was used to confirm such behavior. By addition of one drop of the solution on the graphite support, appearances of hole, mono-, and multilayers were observed, whose UV-vis absorption spectrum was shifted toward low energy (0.27 eV) compared to the absorption of nanoparticles dispersed in solution, as shown in Figure 24. The bandwidth of the plasmon peak (1.0 eV) is larger than that observed in solution (0.8 eV). By adding three drops instead of one to the support, it was totally covered, resulting in the formation of 3D superlattices. The absorption spectrum showed a large red shift of the SPR peak compared to the solution (0.47 eV). Furthermore, the bandwidth of the SPR peak decreased (0.70 eV) in comparison with that obtained with the monolayer (1.0 eV) and is smaller than that obtained with free
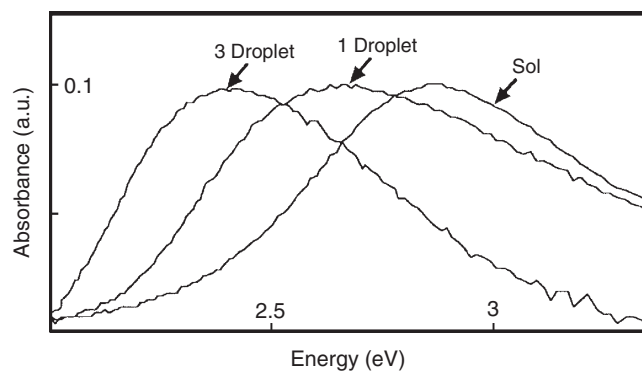


**Figure 24.** Absorption spectra of the 4.5-nm Ag nanoparticles dispersed in hexane before and after deposition and deduced from reflectivity when the particles are deposited on cleaved graphite ($[Ag]_n = 2.5 \times 10^{-3}$ M). Reprinted In part with permission from [45], A. Taleb et al., *J. Phys. Chem. B* 102, 2214 (1998). © 1998, American Chemical Society.

coated nanoparticles in hexane (0.80 eV). These results confirm the effect of the medium dielectric constant of the particle when assembled in 2D and 3D and show a decrease in the bandwidth and plasmon peak, which could be due to an increase in the mean free path conduction electrons of Ag nanoparticles through a barrier of 2 nm. Also the optical absorption properties of 3D superlattices of water-soluble Au nanoparticles have been investigated by Sato et al. [115].

Another important optical aspect of metal nanoparticles having SPR in the UV-vis region is to show the second- [116–118] and third-order [119–122] nonlinear optical properties. Especially, the third-order nonlinear optical materials are expected to be applied to future optical devices like an optical switch. Small metal nanoparticles embedded in glasses have been widely studied as resonant-type nonlinear optical materials for photonic devices [123, 124]. Recent studies have shown that the third-order optical nonlinearity in glasses doped with Au, Ag, and Cu nanoparticles is strongly enhanced near the SPR frequency because of the local-field enhancement [120, 125]. The time response of metal nanoparticles is theoretically very fast. There have been several attempts to measure the response time of Au [126, 127] and Cu [128] nanoparticles. In order to obtain large third-order nonlinear susceptibility $\chi^{(3)}$ ($\sim 10^{-6}$ esu), there is a wide variety of fabrication methods of glasses containing metal nanoparticles: melt quenching [129, 130], sol–gel [131, 132], ion implantation [133, 134], and sputtering [135, 136]. Although the large nonlinearity and the fast time response are expected for these glasses, the value of the third-order nonlinear susceptibility $\chi^{(3)}$ remains in the range of $10^{-13}$–$10^{-11}$ esu because of the low concentrations (typical volume fraction of $10^{-6}$) of metal nanoparticles in the glass prepared by the conventional melt-quenching technique. On the other hand, by the sputtering method, various kinds of metals can be embedded in the glass thin film and high concentrations of metal nanoparticles are easily achieved.

In 1996, Tanahashi and co-workers investigated third-order nonlinear optical properties of $Au/SiO_2$ composite thin films ($Au/SiO_2$ films) [126]. Au and $SiO_2$ were deposited alternatively onto a synthetic quartz glass or a GaAs substrate by a multitarget rf magnetron sputtering method. The concentration of Au in the films was controlled by both the deposition time and the input power. The third-order nonlinear susceptibility $\chi^{(3)}$ was measured by a degenerate four-wave mixing (DFWM) method at room temperature. The light source was an excimer-laser-pumped dye laser with a pulse duration of 20 ns, a spectral width of 0.2 cm$^{-1}$, and a maximum peak power of 1 MW cm$^{-2}$. The value of $\chi^{(3)}$ was estimated by the following equation:

$$\chi^{(3)} = \left( \frac{n^2 c \lambda}{32 \pi^3} \right) \left[ \frac{\alpha}{(1-T)T^{0.5}} \right] \left( \frac{\eta^{0.5}}{I_0} \right) \qquad (6)$$

where $\lambda$ is the wavelength of incident light (530 nm), $\alpha$ the absorption coefficient, $T$ the transmissivity, $\eta$ the diffraction efficiency, $n$ the refractive index, and $c$ the light velocity. $\eta$ is defined by the intensity ratio of the signal beam $I_s$ to the incident beam $I_0$. The value $\chi^{(3)}$ is obtained from the measurements of the intensities of incident, transmitted, and signal beams. Figure 25 shows the dependence of $\chi^{(3)}$ on the pumping wavelength, together with the absorption spectrum
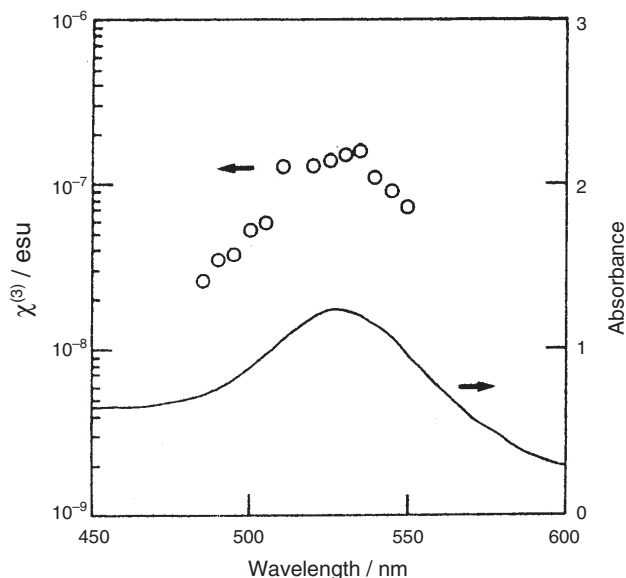
**Figure 25.** Dependence of $\chi^{(3)}$ on the pumping wavelength together with the absorption spectrum for the film with 8.0 at. % of Au. Reprinted with permission from [126], I. Tanahashi et al., *J. Appl. Phys.* 79, 1244 (1996). © 1996, American Institute of Physics.

for the film with 8.0 at. % (volume fraction of 0.031) of Au with a mean diameter of 33.7 nm. The absorption spectrum exhibits a SPR peak at around 530 nm and the values of $\chi^{(3)}$ exhibit also a peak at the absorption peak, indicating the resonant behavior of $\chi^{(3)}$ at the SPR frequency. The maximum value of $\chi^{(3)}$ is on the order of $10^{-7}$ esu, which is four orders of magnitude larger than those of Au nanoparticles in glasses prepared by the conventional melt-quenching method [120]. This is because the concentration of Au in the films is four orders of magnitude larger than that of the conventional glasses containing Au nanoparticles (volume fraction of $10^{-6}$).

In order to investigate the particle size dependence of $\chi^{(3)}$, a figure of merit $\chi^{(3)}/\alpha$ was introduced. The values of $\chi^{(3)}$ were normalized by the absorption coefficient $\alpha$ at the corresponding wavelength to the $\chi^{(3)}$, because the films contain different volume fractions of Au nanoparticles [137]. The value of $\chi^{(3)}/\alpha$ ($\alpha$: absorption coefficient) for the films was increased upon an increase of mean diameter of Au nanoparticles in the range of 3.0–33.7 nm, which was explained by the size dependences of the local-field factor and the imaginary part of dielectric constant of the nanoparticles.

To obtain the larger value of $\chi^{(3)}$, the 3D superlattices of ligand-protected Au and Ag nanoparticles with various sizes will be the most promising candidates, because the film containing high Au concentration can be easily fabricated.

## 4.2. Electronic Property

More recently, the electronic properties of metal nanoparticles have been investigated within the context of decreasing electronic device size features to the nanoscopic level [14]. Applications of individual nanoparticles as computer transistors, electrometers, chemical sensors, and in

wireless electronic logic and memory schemes have been described and in some cases demonstrated [138], albeit somewhat crudely at this point. Many of these studies have revealed that electronic devices based on nanoscopic objects will not function analogously to their macroscopic counterparts. Thus, a conventional MOSFET (metal oxide semiconductor field effect transistor), which uses $\sim 10^5$ electrons for switching function, will no longer be able to control the flow of electrons as its size reaches the sub–50-nm regime. At these dimensions, electron transport in n- and p-doped contacts is affected by the quantum mechanical probability that electrons simply tunnel through the interface. These tunneling processes will begin to dominate in the nanometer size regime, causing errors in electronic data storage and manipulation. The fabrication of ordered metal nanoparticles with well-defined 2D configurations would enable us to produce the novel nanoelectronic devices like a single-electron transistor (SET, see Fig. 26) which work with one electron at room temperature, allowing the drastic reduction of electric power [2, 3, 138, 139]. The monodisperse metal nanoparticles have potentiality to be the building blocks for nanoelectronic devices using the single-electron tunneling effect—the correlated transfer of electrons one-by-one through the object [140]. Single-electron tunneling was first hypothesized in the early 1950s [141], a time when many physicists pondered how the electronic properties of a material (e.g., a metal wire) would change as material dimensions were reduced to the micron or nanometer scale. Gorter and others argued that, provided the energy to charge a metal with a single-electron, $e/2C$ ($e$ is electron charge, $C$ is metal capacitance), was larger than $k_B T$, electrons would be forced to flow through the metal in discrete integer amounts rather than in fluid-like quantities normally associated with transport in macroscopic materials. Further reasoning led to the prediction that current-voltage ($I$-$V$) curves of a nanoscopic metal should be distinctly nonohmic; that is, current steps should appear corresponding to the transport of $1e^-$, $2e^-$, $3e^-$, etc., currents through the metal.

In fact, these predictions turned out to be true, although it was not until the late 1980s that well-defined single-electron tunneling steps were observed experimentally. Even then,
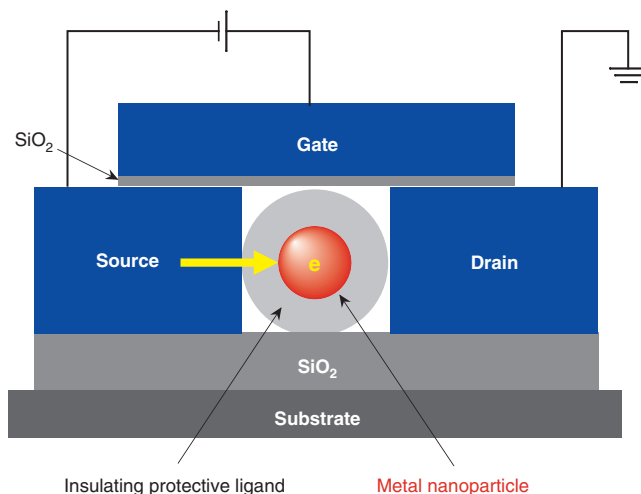


**Figure 26.** Schematic illustration of single-electron transistor (SET).

enthusiasm for single-electron devices was tempered by the fact that these initial experiments were performed on relatively large metal islands (micron sized) prepared with photolithography or metal evaporation [142–144]. Thus, in order to satisfy the requirement $e/2C > k_BT$, it was necessary to cool the microstructures to below 1 K. Herein lies perhaps the greatest obstacle to implementing single-electron devices: to avoid thermally induced tunneling processes at room temperature, the metal island of any single-electron device must be less than 10 nm, more restrictively 2 nm, in diameter. This dimension is difficult to reach with electron beam lithography or scanning probe microscopies, although it is now easily achieved by chemists using solution-phase nanoparticle synthesis methods.

Andres and co-workers investigated at first the electron transport ($I$-$V$) properties of $1.9 \pm 0.6$-nm Au nanoparticles bound to a bulk Au surface through a self-assembled monolayer (SAM) of the dithiol, $p$-xylene-$\alpha$, $\alpha'$-dithiol [14]. They produced the Au-dithiol-Au nanoparticles-air gap-STM tip double tunnel junction by placing an STM tip over a single Au nanoparticle. $I$-$V$ measurements provided us a lot of information that a Coulomb gap and one clear current step were observed at positive bias even at room temperature, and the resistance of a single dithiol molecule and the dithiol junction capacitance were $18 \pm 12$ M$\Omega$ and $1.7 \times 10^{-19}$ F, respectively. Then they fabricated 2D superlattices of decanethiol-protected Au nanoparticles between 450-nm gap Au electrodes. Coulomb blockade effects were again observed by the appearance of a high resistance gap around 0 V in the $I$-$V$ curves, which was backed by the fact that the $I$-$V$ response became ohmic when the nanoparticles were exposed to a conjugated aryl diisonitrile molecule.

Experiments similar to those described above were conducted by Green et al. [145]. The Au nanoparticles protected by alkanethiols of varying alkyl chain lengths ($C_8$, $C_{12}$, $C_{16}$) were assembled across the gaps of interdigitated array electrodes and investigated electronically. Nonlinear $I$-$V$ curves were reported for these systems which depended on the length of the alkane chain. Conductivities of the 2D arrays calculated from the $I$-$V$ curves revealed a two order of magnitude decrease for every four carbons in the alkane chain. It was pointed out that the $I$-$V$ properties observed in Au nanoparticle monolayers in the high potential limit fit well to models usually employed in interpreting electron transfer in redox polymer systems. These models provide additional insight into the Au nanoparticle-nanoparticle electron transfer mechanism, rate, coupling coefficient, and charging energy.

Feldheim and co-workers used a combination of layer-by-layer inorganic polyelectrolyte and Au nanoparticle self-assembly methods to fabricate bulk metal-insulator-nanoparticle-insulator-bulk metal (MINIM) devices [9]. First, a clean bulk substrate was immersed in a solution of mercaptoethylamine hydrochloride to immobilize cationic sites on the surface. The substrate was then alternately soaked in aqueous solutions containing single anionic sheets of lamellar inorganic solids [KTiNbO$_5$, $\alpha$-Zr(HPO$_4$)$_2$ · H$_2$O (ZrP)] and organic polyelectrolyte cations [polyallyamine hydrochloride (PAH)]. A "monolayer" of the desired polyelectrolyte ion exchanges onto the oppositely charged material deposited on the substrate during the previous immersion step (i.e., anionic ZrP to cationic PAH). Multilayers of the same material cannot form on the surface during a single immersion step because of electrostatic repulsion. The thickness of the resulting film was thus defined by the number of immersion cycles the substrate was subjected to. Once the desired junction thickness was assembled, Au nanoparticles were introduced into the film by soaking the substrate in a solution containing citrate-protected Au nanoparticles. The Au nanoparticles bind readily to the amine functionalities contained in PAH. Following Au nanoparticle deposition, a second insulating junction was formed by simply reversing the adsorption sequence used to form the first junction. Note that the two junctions may be designed to vary in thickness and/or composition (i.e., a different inorganic may be chosen for junction 2). A thin layer of the organic conducting polymer poly(pyrrole) was polymerized on top to complete the MINIM device. $I$-$V$ curves of MINIM devices fabricated with $2.5 \pm 1.5$-nm Au nanoparticles displayed Coulomb gap potentials at room temperature. The magnitude of the gap potential was somewhat tunable via the junction thickness; decreasing the junction thickness from 8 to 3 nm (by decreasing the number of polyelectrolyte pairs) decreased the Coulomb gap potential from 400 to 275 mV. In addition, changing the Au nanoparticle size also affected the $I$-$V$ properties of these devices. Figure 27 shows a series of $I$-$V$ curves recorded at various temperatures for a device fabricated with 12-nm Au nanoparticles. At temperature close to 25 °C, an ohmic response was observed because the capacitance of the particles was such that $k_BT > e/2C$. Upon cooling slightly, however, the $I$-$V$ curves became increasingly nonlinear as the single-electron charging energy began to dominate the tunneling process.

Recently, Ogawa et al. have investigated the electronic conductive characteristics of 3D superlattices made from 1,10-decanedithiol and 2-nm Au nanoparticles between 1-$\mu$m gap Au electrodes [146]. The 3D superlattices of 2-nm Au nanoparticles prepared by Brust's method [52] between 1-$\mu$m gap Au electrodes were fabricated as follows: A silicon chip of gold micro-gap electrodes with the gap size of approximately 1 $\mu$m was dipped in 10% toluene solution of 1,10-decanedithiol for approximately 48 h in nitrogen atmosphere. To this solution 2-nm Au nanoparticles suspension in toluene was added, and kept silent for a further 24 h. The chip was washed with toluene and acetone successively to remove excess dithiol and Au nanoparticles. The TEM image indicates that each Au nanoparticle is clearly distinguishable and no coagulation occurred, which means that organic dithiol molecules exist between the Au nanoparticles to prevent them "short circuiting." With these micro-gap electrodes, no current could be detected under 5 V, and a sigmoidal $I$-$V$ curve was observed over the voltage (Fig. 28). On the other hand, the $I$-$V$ response of the pressed pellet of Au nanoparticles was ohmic. Since approximately 300–500 Au nanoparticles are connected in series between the two electrodes of 1 $\mu$m, the 2-nm Au nanoparticles have a charging potential of the order of $10^{-2}$ V, which is roughly in agreement with the observed barrier potential. The activation energy for 3D superlattices was estimated to be $4 \times 10^{-3}$ eV, which is one order smaller than that of the pressed pellet. These
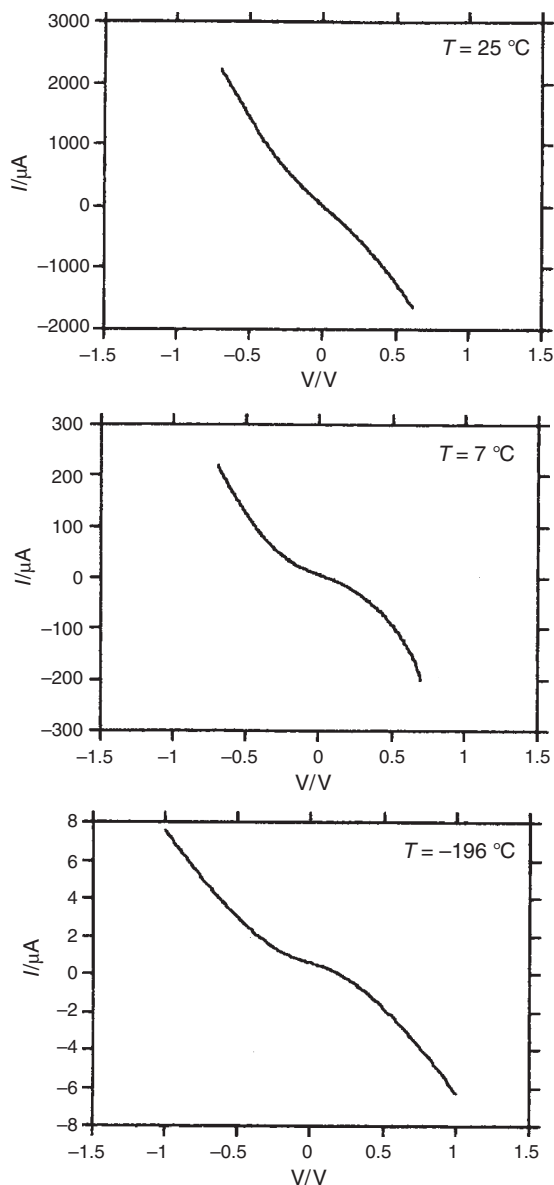
results clearly indicate that the electronic conduction mechanism of the bulk pellet is different from the microscopic network made on the micro-gap electrodes. In the former, interdomain hopping could be predominant with the activation energy of $6 \times 10^{-2}$ eV. In the smaller region measured by micro-gap electrodes, the activation energy was one order smaller ($4 \times 10^{-3}$ eV) than it, which is the consequence that the electrodes are connected only by covalent bonding and the interaction between the Au nanoparticles was more effective.

Doty and co-workers measured temperature-dependent electron transport through 3D superlattices of alkanethiol-protected Ag nanoparticles using interdigitated array
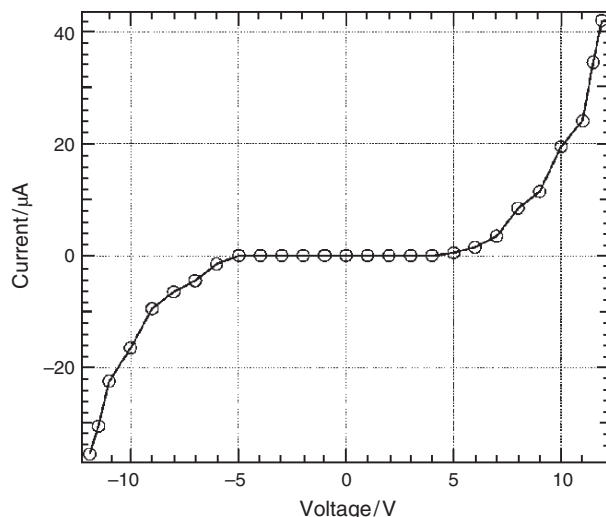
electrodes [147]. Nanoparticles ranging from 3.5 to 7.7 nm in diameter with Coulomb blockade energies well above $k_B T$ were studied. The nanoparticle superlattices exhibited linear *I-V* behavior for temperatures as low as 70 K. Ordered fcc superlattices exhibited a positive temperature coefficient of resistivity (TCR), characteristic of a metal, at temperatures above approximately 225 to 245 K, depending on the particle size. The values of the conductivity, on the order of $10^{-6}$ to $10^{-7}$ $\Omega^{-1}$ cm$^{-1}$, however, are characteristic of semiconductors. Below the transition temperature, the TCR for the monodisperse nanoparticle arrays became negative, characteristic of an insulator, and the conductance, $G$, of the ordered arrays scales exponentially with temperature as $G \propto \exp[-(T_0/T)^\nu]$. The exponent $\nu$ ranges from 0.67 to 1.34 for nanoparticles 7.7 to 3.5 nm in diameter, respectively, characteristic of a gap in the density of states in the overall electronic structure of the superlattice. It was concluded that electron transport occurs through a polaron hopping mechanism. In contrast to the organized superlattices, disordered close-packed nanoparticles exhibited insulating behavior at all temperatures studied due to (Anderson-type) disorder.

Beverly et al. reported a study of the effects of the systematic variation of particle size distribution, a significant source of disorder within the system, on the temperature-dependent electron transport characteristics of highly compressed 2D superlattices of dodecanethiol-protected Ag nanoparticles [148]. The 7-nm Ag nanoparticles protected by dodecanethiol were synthesized using the method developed by Brust et al. [52]. 2D superlattices of dodecanethiol-protected Ag nanoparticles were prepared by LB technique at an air-water interface and transferred to electrode patterned glass substrates. A transition temperature between the transport regimes of simple, activated transport to variable range hopping was observed to be in tune with increasing disorder of the monolayer. The overall transport behavior is described in terms of a mobility gap in the Anderson localized regime and an Efros–Shklovskii variable

range hopping between localized states in the gap below some temperature characterized by the degree of disorder. From these results, a true insulator-metal transition at narrow but still finite (<3%) size distributions is predicted.

We have also fabricated 2D superlattices of 5.4-nm dodecanethiol-protected Au nanoparticles between 500-nm gap Au electrodes on GaAs by the LB technique [149]. Figure 29 presents the preliminary $I$-$V$ curve of these 2D superlattices at 4.2 K. It was found that for large particles of $\sim$5 nm in diameter the electron behavior was dominated by the Coulomb blockade effect at low temperature, while the $I$-$V$ response was ohmic at room temperature.

For producing the nanoelectronic devices, ordering small nanoparticle building blocks in 2D and 3D configuration is important in order to make use of single-electron tunneling effect at room temperature. On the other hand, the construction of nanoscale circuits from such devices requires achieving interelement wiring and electrical interfacing to macroscopic electrodes. So many researches have been dedicated to the formation of metal nanowires through 1D chains of metal nanoparticles and the elucidation of their electronic properties [33, 34, 37]. In 1998, Braun and co-workers first used hybridization of the DNA molecule with surface-bound oligonucleotides to stretch it between two Au electrodes, the DNA molecule being then used as a template for the vectorial growth of a 12-$\mu$m long, 100-nm wide conductive Ag wire [34]. Unfortunately, the $I$-$V$ curves are highly nonlinear and asymmetric with respect to zero bias. The origin of the extremely high resistance at small bias, and of the dependence of the current on the voltage scan direction, are likely to be derived from the Coulomb blockade phenomenon or intergrain boundary resistance due to Ag corrosion. For future applications, the development of low-resistance, ohmic metal wires, for example, by making use of post-growth thermal treatment, is strongly required. Huang et al. have recently demonstrated one of the strategies to fabricate conductive networks of GaP, InP, and Si nanowires [150].

For the development of nanoelectronic devices using single-electron tunneling effect at room temperature, it is indispensable to arrange quite small nanoparticles in 2D or 3D configuration between the electrodes. Modification of organic ligands of metal nanoparticles is likely to be useful in this regard, and such nanoelectronic devices will be realized in the near future.
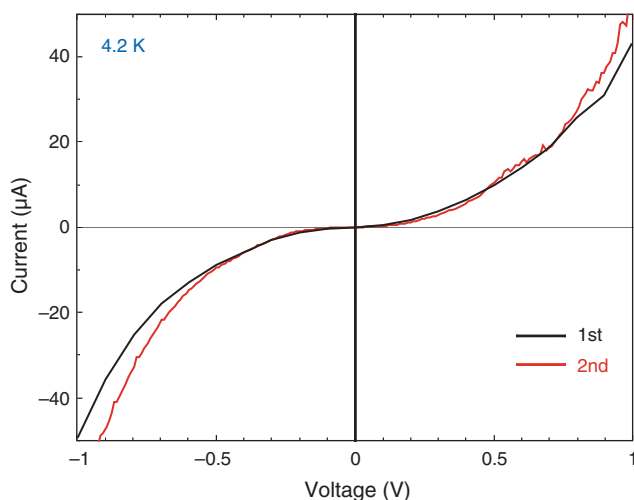
## 4.3. Magnetic Property

The magnetic properties of metal nanoparticles arise from the competition between strong, short-range exchange interactions and long-range, dipolar couplings of electron spins in the atoms that make up magnetic solids. These competing interactions favor parallel alignment of nearby spins and antiparallel alignment of distant spins, forming magnetic domains in "bulk" magnets. In a small particle, truncation of the long-range, dipolar forces results in a "single-domain" magnet with all of the spins aligned in a single direction. Further reducing the size of a single-domain particle decreases the number of spins exchange-coupled to resist spontaneous reorientation of its magnetization at a given temperature. A double-well potential (Fig. 30) is used to conceptualize the rotation of the magnetization direction for a uniaxial magnetic particle [151]. The energy barrier $\Delta E$ between the orientations is proportional to the particle volume and the material's anisotropy constant, which describes the preference for spins to align in a particular direction within the particle due to the influence of crystal symmetry, shape, and surface effects. As the particle size decreases, $\Delta E$ becomes comparable to thermal energy ($k_{\mathrm{B}}T$), and the energy barrier no longer pins the magnetization on the time scale of observation. The particle is said to be superparamagnetic. Mapping the scaling limits of magnetic storage technology [151, 152] and understanding spin-dependent transport phenomena in nanoscale devices [73] motivate studies of magnetic nanoparticles.

Progress in ultrahigh-density magnetic recording is due in part to the development of metal thin-film media with

**Figure 29.** Current-voltage curve of 2D superlattices of 5.4-nm DT-Au nanoparticles formed between 500-nm gapped gold electrodes.
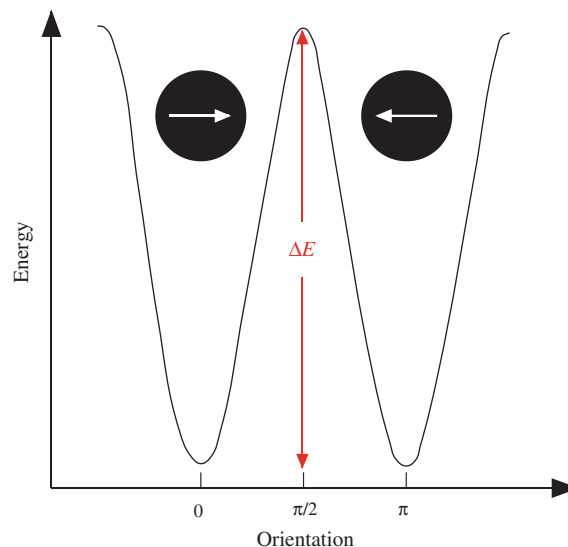
**Figure 30.** Graph of the energy dependence of nanoparticle magnetization. $\Delta E$ represents the energy barrier to the rotation of the magnetization. The left and right arrows represent spin states.

smaller particles, narrower size distributions, and optimized compositions [153]. In principle, the size-control of noble metal nanoparticles is relatively easy, while the formation of the uniform size of 3d-transition monometallic nanoparticles is quite difficult because it is hard to control the reduction rate of 3d-transition metal ions. Although the formation and 2D self-assemblies of Co [71–75], Fe [76, 77], and iron oxide [154, 155] have been achieved, recent interests have been focused on the bimetallic nanoparticles with large uniaxial magnetocrystalline anisotropy, $K_u$, because of their application to ultrahigh-density out-of-plane magnetic recording media. The bimetallic nanoparticles with good magnetic property usually contain 3d-transition metal, such as iron, cobalt, and nickel, as one of the elements. FePt and CoPt alloys are an important class of materials in permanent magnetic applications because of their large uniaxial magnetocrystalline anisotropy [$K_u \approx 7 \times 10^6$ and $5 \times 10^6$ J/m$^3$] (see Table 2) [156, 157] and good chemical stability. As the magnetic stability of individual particles scales with the anisotropy constant, $K_u$, and the particle volume, $V$, small FePt and CoPt nanoparticles may be suitable for future ultrahigh-density magnetic recording media applications [152]. Let us take a look at these two examples of magnetic nanoparticles.

In 2000, Sun and co-workers succeeded in synthesis of monodisperse FePt nanoparticles by the reduction of platinum acetylacetonate (Pt(acac)$_2$) with 1,2-hexadecanediol and thermal decomposition of iron pentacarbonyl (Fe(CO)$_5$) in the presence of oleic acid and oleylamine stabilizers [7, 158, 159]. The FePt nanoparticle composition is adjusted by controlling the molar ratio of iron carbonyl to the platinum salt. With dioctylether as solvent, a 3:2 molar ratio of Fe(CO)$_5$ to Pt(acac)$_2$ gave Fe$_{48}$Pt$_{52}$ particles, a 2:1 molar ratio yielded Fe$_{52}$Pt$_{48}$, and a 4:1 molar ratio produced Fe$_{70}$Pt$_{30}$. The FePt particle size can be tuned from 3 to 10 nm by first growing 3-nm monodisperse seed particles *in-situ* and then adding more reagents to enlarge the existing seeds to the desired size. When a drop of dilute FePt dispersion (~1 mg/ml) was deposited on a SiO-coated copper

grid, the particles readily self-assembled into 2D superlattices (Fig. 31) as well as 3D ones. In the 3D superlattice of 6-nm Fe$_{50}$Pt$_{50}$ nanoparticles, a nearest-neighbor spacing of ~4 nm is maintained by the oleic acid and oleylamine capping groups. Room-temperature ligand exchange of these long-chain capping groups for shorter RCOOH/RNH$_2$ (R = dodecyl down to hexyl chains) allows the interparticle distance to be adjusted. Ligand exchange with hexanoic acid/hexylamine yields a cubic-packed 3D superlattice of 6-nm Fe$_{50}$Pt$_{50}$ nanoparticles with ~1-nm spacings. Although, for a 180-nm thick, 4-nm Fe$_{52}$Pt$_{48}$ nanoparticle assembly annealed at 560 °C for 30 min, the HRSEM images show that the particles are well separated with no agglomeration occurring, interparticle spacings are reduced from ~4 to ~2 nm. Rutherford backscattering measurements on these annealed 4-nm Fe$_{52}$Pt$_{48}$ particle superlattices indicate 40 to 50 at. % carbon content, showing that annealing at high temperature does not result in the loss of stabilizing ligands; rather, they are converted to a carbonaceous coating around each particle. Thermal annealing converts the internal particle structure from a chemically disordered face-centered cubic (fcc) phase to the chemically ordered face-centered tetragonal (fct) phase, or L1$_0$ phase. Annealing induces the Fe and Pt atoms to rearrange into the long-range chemically ordered L1$_0$ structure. At annealing temperatures below 500 °C, only partial chemical ordering is observed. The chemical ordering can be increased by annealing at higher temperatures or by increasing the annealing time. Diffraction patterns of the samples annealed above 540 °C match those of L1$_0$ FePt. Annealing 4-nm FePt particles at higher temperature, for example, ≥600 °C, however, results in an increase of the average particle size and a broadening of the size distribution. Superconducting quantum interference device magnetometry measurements of 4-nm FePt nanoparticles show that the as-synthesized particle superlattices are superparamagnetic (coercivity $H_c = 0$ Oe) at room temperature. The temperature-dependent magnetization measurement in a 10-Oe field between 5 and 400 K with the standard zero-field-cooling (ZFC) and field-cooling procedures (FC) [160]

**Table 2.** Properties of hard magnetic materials.

| Alloy system | Material | $K_u$ (10$^7$ erg/cm$^3$) | $M_s$ (emu/cm$^3$) | $H_K$ (kOe) | $T_c$ (K) | $\delta_w$ (Å) | $\gamma$ (erg/cm$^3$) | $D_c$ ($\mu$m) | $D_p$ (nm) |
|---|---|---|---|---|---|---|---|---|---|
| Co-alloys | CoPtCr | 0.20 | 298 | 13.7 | — | 222 | 5.7 | 0.89 | 10.4 |
| | Co | 0.45 | 1400 | 6.4 | 1404 | 148 | 8.5 | 0.06 | 8.0 |
| | Co$_3$Pt | 2.0 | 1100 | 36 | — | 70 | 18 | 0.21 | 4.8 |
| L1$_0$ phase | FePd | 1.8 | 1100 | 33 | 760 | 75 | 17 | 0.20 | 5.0 |
| | FePt | 6.6–10 | 1140 | 116 | 750 | 39 | 32 | 0.34 | 3.3–2.8 |
| | CoPt | 4.9 | 800 | 123 | 840 | 45 | 28 | 0.61 | 3.6 |
| | MnAl | 1.7 | 560 | 69 | 650 | 77 | 16 | 0.71 | 5.1 |
| Rare-earth | Fe$_{14}$Nd$_2$B | 4.6 | 1270 | 73 | 585 | 46 | 27 | 0.23 | 3.7 |
| Trans. metals | SmCo$_5$ | 11–20 | 910 | 240–400 | 1000 | 22–30 | 42–57 | 0.71–0.96 | 2.7–2.2 |

*Source:* Reprinted with permission from ref. [157], D. Weller et al., *IEEE Trans. Magn.* 36, 10 (2000). © 2000, IEEE.
Anisotropy field $H_K = 2K_u M_s^{-1}$.
Domain wall width $\delta_w = \pi(A/K_u)^{1/2}$.
Domain wall energy $\gamma_w \approx 4(A \cdot K_u)^{1/2}$.
Single-particle domain size $D_c = 1.4\gamma_w M_s^{-2}$.
Exchange coupling constant $A = 10^{-6}$ erg cm$^{-1}$.
Minimal stable grain size $D_p = (60k_B T/K_u)^{1/3}$ ($\tau = 10$ years).
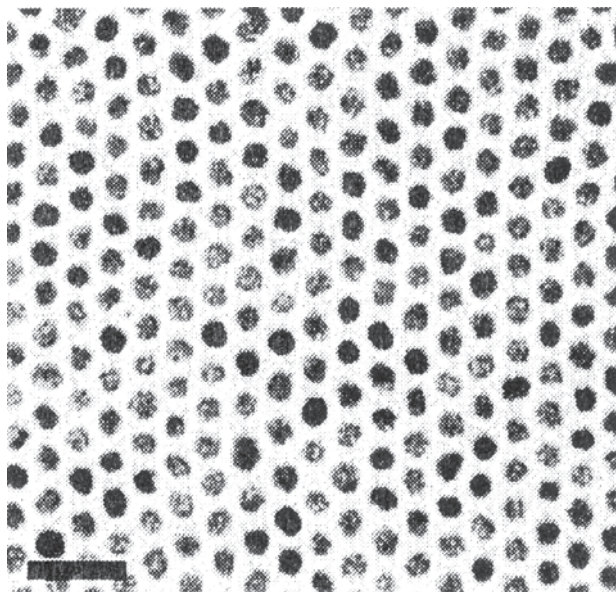
**Figure 31.** TEM image of a 2D assembly of 6-nm $Fe_{52}Pt_{48}$ particles (bar = 30 nm). Reprinted with permission from [159], S. Sun and D. Weller, *J. Mag. Soc. Jpn.* 25, 1434 (2001). © 2001, Magnetics Society of Japan.

indicate that superparamagnetic behavior is blocked at 20 to 30 K, consistent with low magnetocrystalline anisotropy of the fcc structure. Annealing converts the nanoparticles to the high-anisotropy $L1_0$ phase and transforms them into nanoscale ferromagnets. The coercivity of these ferromagnetic assemblies is tunable in the 0–10 kOe range by controlling annealing temperature and time, as well as the Fe:Pt ratio and particle size, as shown in Figure 32. Unfortunately,
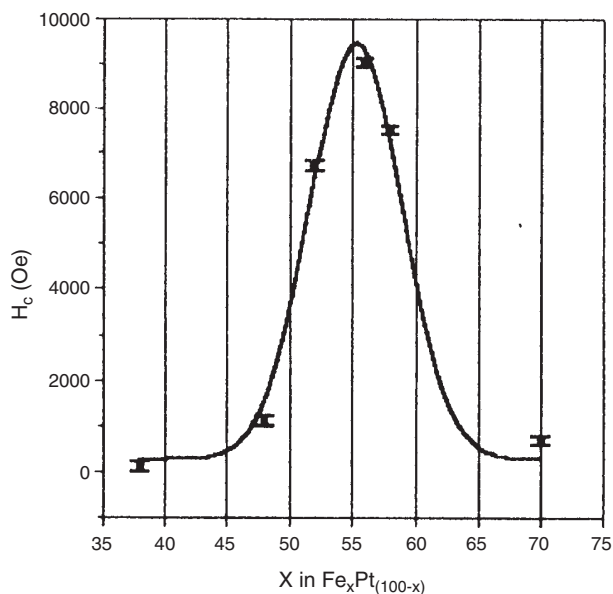


**Figure 32.** Composition-dependent coercivity $H_c$ of 580 °C annealed FePt nanoparticle-assemblies. Reprinted with permission from [159], S. Sun and D. Weller, *J. Mag. Soc. Jpn.* 25, 1434 (2001). © 2001, Magnetics Society of Japan.

there is little difference between in-plane and out-of-plane coercivities and hysteresis behavior, indicating random orientation of the easy axes of individual FePt nanoparticles. FePt stoichiometry-dependent coercivity data demonstrate that Fe-rich $Fe_xPt_{1-x}$ ($x \sim 0.52$ to 0.60) nanoparticle assemblies have the largest coercivity, consistent with earlier reports on vacuum-deposited FePt thin films [151, 161].

Although self-assembly of monodisperse magnetic nanoparticles via solvent evaporation yields magnetic nanoparticle arrays that exhibit high local ordering, at present time, such regular arrays are difficult to form over an extended area with controlled assembly structure and thickness, and generally, various gaps among groups of regular arrays exist. For the application in ultrahigh-density magnetic recording, the magnetic nanoparticles need to be assembled uniformly over a large area in only two to three nanoparticle layers. The polymer-mediated nanoparticle assembly technique reported by Sun et al. has the advantage of highly controlled assembly thickness and dimension and shows great potential for magnetic recording application [162]. The general principle of this process is based on polymer-assisted layer-by-layer assembly [163–168], and is applied first here to assemble FePt nanoparticles. The assembly process includes: (1) surface functionalization with a layer of polymer coating and (2) replacement of the particle stabilizers with a pendant functional group of the polymer. The pendant functional group extends out in the solution. By dipping the polymer-derivative substrate into the particle dispersion, ligand exchange occurs and a strong monolayer particle assembly is formed. A poly(ethyleneimine) (PEI)/FePt assembly is fabricated as follows: a HO-terminated substrate is immersed into chloroform solution of PEI for 30 s, then rinsed with ethanol and dried; subsequently, the dried substrate is immersed into hexane dispersion of the FePt nanoparticles for 30 s, followed by rinsing with hexane and drying. This gives one layer of FePt nanoparticle assembly. By repeating this simple two-step process in a cyclic fashion, a PEI/FePt multilayer assembly can be obtained. Near-edge X-ray absorption fine structure spectroscopy (NEXAFS) on the thin nanoparticle superlattices indicates that more metallic Fe exists in a multilayer film than in a one-layer film. Consequently, the coercivity of thin films is dependent on assembly thickness due to the iron/iron oxide ratio variation with the assembly thickness.

In 2002, Shevchenko and co-workers successfully prepared 3D superlattices of monodisperse 4.5-nm FePt nanoparticles using a three-layer technique based on slow diffusion of a nonsolvent into the bulk of the concentrated solution of nanoparticles through a buffer layer of a third component with low, but not negligible, solubility for nanoparticles [169]. According to this method, crystallization of 4.5-nm FePt nanoparticles in hexane prepared using Sun's method [7] was induced by slow diffusion of a nonsolvent (methanol) into a solution of FePt nanoparticles through a buffer layer of 2-propanol. Slow destabilization of a dispersion of FePt nanoparticles in toluene resulted in nucleation of 3D superlattices of FePt nanoparticles, preferentially on the walls of the glass tubes. Thicker black and thinner brownish colored superlattices that were visible to the naked eye were formed in approximately 4 months. Studies of the magnetic properties of the FePt 3D superlattices

were performed using standard ZFC and FC procedures and field-dependent magnetization measurements. The temperature-dependent magnetization between 5 K and 350 K was measured in a field of 200 Oe. FePt nanoparticles exhibited superparamagnetic behavior, which was blocked for temperatures below 14 K. The magnetic anisotropy constant was calculated to be $1.0 \times 10^6$ erg $cm^{-3}$ assuming spherical 4.5-nm FePt nanoparticles. The FC curve rose monotonically with decreasing temperature below the ZFC cusp, as observed in systems containing randomly oriented magnetic nanoparticles [170, 171]. In the field-dependent magnetization measurements, a hysteretic behavior and the increase of coercivity with decreasing temperature were observed below the blocking temperature, which is typical for the region of stable ferromagnetism. Other groups have been also investigating the assembly and physical properties of FePt nanoparticles and have given the similar results [172, 173].

Before an application of FePt nanoparticle superlattices to the high-density data storage magnetic hard disk drives can be realized, some basic materials science problems must be solved. One of the most challenging problems is the reduction in the phase transformation temperature from the fcc phase to the tetragonal ($L1_0$) phase. As prepared, the nanoparticles have an fcc structure and are superparamagnetic. The particles are coated with organic surfactants (oleic acid and oleylamine) and can be dispersed in hydrocarbon solvents. When the dispersions are cast onto solid substrates and the solvent evaporates, the nanoparticles self-assemble into close-packed arrays. After heat treatment at temperatures above 500 °C, the nanoparticles transform to the tetragonal phase, having high magnetocrystalline anisotropy and giving films with high coercivity. The coercivity depends on the heating temperature, and for complete phase transformation, the nanoparticles must be heated to nearly 580 °C; there is considerable particle coalescence and loss of particle positional order [174]. Particle coalescence leads to increased switching volumes, which defeats the point of making small particles. The loss of positional order comes from the decomposition of the surfactant layers allowing particle motion. It would be highly desirable if the temperature required for the fcc to tetragonal phase transformation were lower, at least below temperatures where the particles coalesce, preferably below the temperature where the organic surfactants decompose. There have been many recent reports of the effect of additives on the thermal ordering of sputtered films of either CoPt or FePt alloys. Kitakami et al. have found that the addition of Sn, Pb, Sb, Bi, or Ag into sputtered CoPt films promotes the disordered fcc to ordered tetragonal transformation, resulting in significant reductions in the temperature required for ordering [175, 176]. Maeda et al. observed a reduction of the ordering temperature for FePt sputtered films by adding Cu [177]. For films containing $[FePt]_{85}Cu_{15}$, the coercivity was 5000 Oe after annealing at 300 °C, while the $H_c$ for films containing FePt was only a few hundred Oe after annealing at 300 °C. These reports suggest a means of lowering the fcc to tetragonal phase transformation for FePt nanoparticles by adding either copper or silver.

Kang et al. reported the synthesis of $[Fe_{49}Pt_{51}]_{88}Ag_{12}$ nanoparticles and the beneficial effect of the added silver

on the phase transformation temperature [178]. An addition of Ag to FePt nanoparticles was achieved by the simultaneous polyol reduction of platinum acetylacetonate and silver acetate and the thermal decomposition of iron pentacarbonyl in the presence of oleic acid and oleylamine in phenyl ether. The 3.5-nm $[Fe_{49}Pt_{51}]_{88}Ag_{12}$ nanoparticles self-assembled into hexagonal closed-packed superlattices by the evaporation of the mixed solvent of hexane/octane. The (111) lattice spacing was expanded to 229 pm for the $[Fe_{49}Pt_{51}]_{88}Ag_{12}$ nanoparticle relative to 225 pm for $Fe_{53}Pt_{47}$, indicating that silver was substituting into the FePt lattice. The XRD measurements of $[Fe_{49}Pt_{51}]_{88}Ag_{12}$ annealed from 300 to 500 °C showed that very weak (001) and (011) peaks for the tetragonal FePt phase appeared after annealing at 350 °C. A shoulder appeared at the low $2\theta$ side of the FePt (111) peak indicating that Ag was phase separating from the particles. For $[Fe_{49}Pt_{51}]_{88}Ag_{12}$ the (111) lattice spacing approaches the bulk value for tetragonal FePt (d111 = 219.7 pm) at lower annealing temperatures than for $Fe_{53}Pt_{47}$. It appears that the Ag atoms leave the FePt lattice at temperatures less than 400 °C, leaving lattice vacancies, which increase the mobility of the Fe and Pt atoms, thus enhancing the kinetics for the phase transformation. The curves in Figure 33 compare the coercivity of the $[Fe_{49}Pt_{51}]_{88}Ag_{12}$ and $Fe_{53}Pt_{47}$ films as a function of annealing temperature. A coercivity $H_c$ increases more rapidly with increasing annealing temperature for the $[Fe_{49}Pt_{51}]_{88}Ag_{12}$ films. $H_c$ for the film annealed to 350 °C was more than 1000 Oe, indicating a significant amount of phase transformation at this temperature.

The CoPt alloy is also one of the candidates for ultrahigh-density magnetic recording media as well as the FePt alloy because of its high magnetic anisotropy and good chemical stability upon corrosion. Recently, Park and Cheon
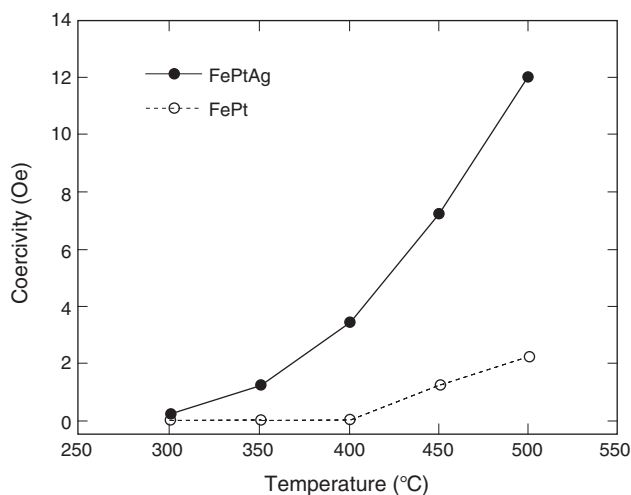


**Figure 33.** Plots of coercivity as a function of heat-treatment temperature for films containing self-assembled $[Fe_{49}Pt_{51}]_{88}Ag_{12}$ (solid circle) or $Fe_{53}Pt_{47}$ (open circle) nanoparticles. Substitution of Ag into FePt nanoparticles to give self-assembled $[Fe_{49}Pt_{51}]_{88}Ag_{12}$ nanoparticles (a) allowed transformation from the superparamagnetic fcc to the ferromagnetic $L1_0$ phase after heat treatment at 400 °C for 30 min (b) Reprinted with permission from [178], S. Kang et al., *Nano Lett.* 2, 1033 (2002). © 2002, American Chemical Society.

prepared the CoPt alloy nanoparticles smaller than 10 nm with different compositions and structures [179]. 1.8-nm $Co_1Pt_3$ and 1.9-nm $Co_1Pt_1$ alloy nanoparticles were synthesized by injecting $Co_2(CO)_8$ toluene solution into hot toluene solution containing platinum hexafluoroacetylacetonate ($Pt(hfac)_2$) with oleic acid as a stabilizing surfactant. The 6.3-nm $Co_{core}Pt_{shell}$ alloy nanoparticles were synthesized by refluxing both 6.3-nm Co nanoparticles prepared from the thermolysis of $Co_2(CO)_8$ in toluene and $Pt(hfac)_2$ in a nonane solution containing $C_{12}H_{25}NC$ as a stabilizer. The composition of the CoPt nanoparticles can be tuned by adjusting the ratio of reactants. SQUID measurements indicated that a blocking temperature ($T_B$) of 20 K and a $H_c$ of 6.9 kOe at 5 K were observed for $CoPt_3$ nanoparticles while a $T_B$ of 15 K and a $H_c$ of 5.3 kOe at 5 K were observed for $Co_1Pt_1$ nanoparticles. These values are higher relative to those observed for pure Co nanoparticles of similar size as a result of the increased anisotropy due to alloy formation. These solid solution type nanoparticles show superparamagnetic behavior at 300 K. On the other hand, the structures of the $Co_{core}Pt_{shell}$ alloy nanoparticles retain the properties of the pure Co core and are not significantly affected by the Pt shell. Self-assembled 2D and 3D superlattices of these CoPt nanoparticles would be easily fabricated. In addition, self-assembly and magnetic properties of FeCoPt nanoparticles have been studied by Chen and Nikles [180].

The thin films of FePt and CoPt nanoparticles are the most promising candidates for future ultrahigh-density magnetic recording media at areal densities in the terabits per square inch regime. Future requirements involve the expansion of an assembly area, the ordering of easy axes of nanoparticles, and the reduction of ordering temperature.

## 5. CONCLUSIONS

The 21st century is the age of nanotechnology. Since nanoscale metal nanoparticles are applicable to a number of areas of technological importance, the colloid chemistry will occupy much attention of scientists. It is certain that controlling the primary structures of metal nanoparticles, that is, size, shape, crystal structure, and composition, is still most important, because these structures determine the physical and chemical properties of metal nanoparticles. Now that techniques are readily available for detailed structural and spectroscopic analysis, the current interests of colloid chemists are focused on the fabrication of low-dimensional (1D and 2D) superlattices of metal nanoparticles as well as 3D ones. Now we have a variety of strategies for fabricating the 1D, 2D, and 3D superlattices, but it is still difficult to produce the desired patterns of nanoparticles at the desired places. The development of methodology to order size- and shape-controlled metal nanoparticles in desired patterns [181, 182] at arbitrary areas will be the key technology for developing the future nanodevices, such as nano-optical, nanoelectronic, and nanomagnetic devices.

## GLOSSARY

**Coulomb blockade** A phenomenon that the tunneling of electrons between a quantum dot and an electrode is prohibited due to an increase in the electrostatic energy when an electron is confined in a small quantum dot.

**Nonlinear optical property** A property to generate high frequency twice or third times as large as angular frequency of incident light resulting from the polarization proportional to the square or cube of intensity of incident light.

**Self-assembly** Spontaneous arrangement of molecules or materials in solvent or during the solvent evaporation.

**Superlattice** Long range ordered structure of crystallites with short-range ordered structure.

**Uniaxial magnetocrystalline anisotropy** A difference in energy between a hard axis and an easy axis.

## ACKNOWLEDGMENTS

## REFERENCES

1. A. Kawabata, *J. Phys. Soc. Jpn.* 29, 902 (1970).
2. R. G. Freeman, K. C. Grabar, K. J. Allison, R. M. Bright, J. A. Davis, A. P. Guthrie, M. B. Hommer, M. A. Jackson, P. C. Smith, D. G. Walter, and M. J. Natan, *Science* 267, 1629 (1995).
3. R. H. Terrill, T. A. Postlethwaite, C. Chen, C.-D. Poon, A. Terzis, A. Chen, J. E. Huthison, M. R. Clark, G. Wignall, J. D. Londono, R. Superfine, M. Falvo, C. S. Johnson, Jr., E. T. Samulski, and R. W. Murray, *J. Am. Chem. Soc.* 117, 12537 (1995).
4. A. Kumar and G. M. Whitesides, *Science* 263, 60 (1994).
5. P. Hinz and H. J. Dislich, *Non-Cryst. Solids* 82, 411 (1986).
6. R. E. Hahn and B. O. Seraphin, "Physics of Thin Film." Academic, New York, 1978.
7. S. Sun, C. B. Murray, D. Weller, L. Folks, and A. Moser, *Science* 287, 1989 (2000).
8. A. N. Korotkov, R. H. Chen, and K. K. Likharev, *J. Appl. Phys.* 78, 2520 (1995).
9. D. L. Feldheim, K. C. Grabar, M. J. Natan, and T. E. Mallouk, *J. Am. Chem. Soc.* 118, 7640 (1996).
10. T. P. Bigioni, L. E. Harrell, W. G. Cullen, D. E. Guthrie, R. L. Whetten, and P. N. First, *Eur. Phys. J. D* 6, 355 (1999).
11. L. O. Brown and J. E. Hutchison, *J. Am. Chem. Soc.* 119, 12384 (1997).
12. G. Schön and U. A. Simon, *Colloid Polym. Sci.* 273, 101 (1995).
13. G. Schön and U. A. Simon, *Colloid Polym. Sci.* 273, 202 (1995).
14. R. P. Andres, T. Bein, M. Dorogi, S. Feng, J. I. Henderson, C. P. Kubiak, W. Mahoney, R. G. Osifchin, and R. Reifenberger, *Science* 272, 1323 (1996).
15. D. B. Janes, V. R. Kolagunta, R. G. Osifchin, J. D. Bielefeld, R. P. Andres, J. I. Henderson, and C. P. Kubiak, *Superlattices Microstruct.* 18, 275 (1995).
16. T. Teranishi, I. Kiyokawa, and M. Miyake, *Adv. Mater.* 10, 596 (1998).
17. N. Bowden, A. Terfort, J. Carbeck, and G. M. Whitesides, *Science* 276, 233 (1997).
18. M. Giersig and P. Mulvaney, *Langmuir* 9, 3408 (1993).
19. M. Giersig and P. Mulvaney, *J. Phys. Chem.* 97, 6334 (1993).

20. J. R. Heath, C. M. Knobler, and D. V. Leff, *J. Phys. Chem. B* 101, 189 (1997).

21. K. S. Mayya, V. Patil, and M. Sastry, *Langmuir* 13, 2575 (1997).

22. S. Peschel and G. Schmid, *Angew. Chem. Int. Ed. Engl.* 34, 1442 (1995).

23. T. Zhu, X. Y. Fu, T. Mu, J. Wang, and Z. F. Liu, *Langmuir* 15, 5197 (1999).

24. J. Schmitt, P. Machtle, D. Eck, H. Mohwald, and C. A. Helm, *Langmuir* 15, 3256 (1999).

25. K. S. Mayya and M. Sastry, *Langmuir* 15, 1902 (1999).

26. C. A. Mirkin, R. L. Letsinger, R. C. Mucic, and J. J. Storhoff, *Nature* 382, 607 (1996).

27. C. J. Loweth, W. B. Caldwell, X. Peng, A. P. Alivisatos, and P. G. Schultz, *Angew. Chem. Int. Ed.* 38, 1808 (1999).

28. A. P. Alivisatos, K. P. Johnsson, X. Peng, T. E. Wilson, C. J. Loweth, M. P. Bruchez, Jr., and P. G. Schultz, *Nature* 382, 609 (1996).

29. T. Teranishi, Metallic Colloids in "Encyclopedia of Surface and Colloid Science" (Auther T. Hubbard, Ed.). Marcel Dekker, New York, 2002.

30. H. Masuda and F. Fukuda, *Science* 248, 1466 (1995).

31. G. Hornyak, M. Kröll, R. Pugin, T. Sawitowski, G. Schmid, J.-O. Bovin, G. Karsson, H. Hofmeister, and S. Hopfe, *Chem. Eur. J.* 3, 1951 (1997).

32. T. Oku and K. Suganuma, *Chem. Commun.* 2355 (1999).

33. E. Braun, Y. Eichen, U. Sivan, and G. Ben-Yoseph, *Nature* 391, 775 (1998).

34. C. A. Berven, L. Clarke, J. L. Mooster, M. N. Wyboune, and J. E. Hutchison, *Adv. Mater.* 13, 109 (2001).

35. T. G. Spiro, "Nucleic Acid-Metal Ion Interactions." Wiley Interscience, New York, 1980.

36. L. G. Marzilli, T. J. Kisternmacher, and M. J. Rossi, *J. Am. Chem. Soc.* 99, 2797 (1977).

37. T. Teranishi, A. Sugawara, T. Shimizu, and M. Miyake, *J. Am. Chem. Soc.* 124, 4210 (2002).

38. P. A. Kralchevsky, V. N. Paunov, I. B. Ivanov, and K. Nagayama, *J. Colloid Interface Sci.* 151, 79 (1992).

39. N. D. Denkov, O. D. Velev, P. A. Kralchevsky, I. B. Ivanov, H. Yoshimura, and K. Nagayama, *Nature* 361, 26 (1993).

40. A. Taleb, C. Petit, and M. P. Pileni, *Chem. Mater.* 9, 950 (1997).

41. S. A. Harfenist, Z. L. Wang, M. M. Alvarez, I. Vezmar, and R. L. Whetten, *J. Phys. Chem.* 100, 13904 (1996).

42. K. V. Sarathy, G. Raina, R. T. Yadav, G. U. Kulkarni, and C. N. R. Rao, *J. Phys. Chem. B* 101, 9876 (1997).

43. M. T. Reetz, M. Winter, and B. Tesche, *Chem. Commun.* 147 (1997).

44. J. Fink, C. J. Kiely, D. Bethell, and D. J. Schiffrin, *Chem. Mater.* 10, 922 (1998).

45. A. Taleb, C. Petit, and M. P. Pileni, *J. Phys. Chem. B* 102, 2214 (1998).

46. R. P. Andres, J. D. Bielefeld, J. I. Henderson, D. B. Janes, V. R. Kolagunta, C. P. Kubiak, W. J. Mahoney, and R. G. Osifchin, *Science* 273, 1690 (1996).

47. C. J. Kiely, J. Fink, M. Brust, D. Bethell, and D. J. Schiffrin, *Nature* 396, 444 (1998).

48. Z. L. Wang, *Adv. Mater.* 10, 13 (1998).

49. Z. L. Wang, *J. Phys. Chem. B* 104, 1153 (2000).

50. J. E. Martin, J. P. Wilcoxon, J. Odinek, and P. Provencio, *J. Phys. Chem. B* 106, 971 (2002).

51. S. Stoeva, K. J. Klabunde, C. M. Sorensen, and I. Dragieva, *J. Am. Chem. Soc.* 124, 2305 (2002).

52. M. Brust, M. Walker, D. Bethell, D. J. Schiffrin, and R. Whyman, *J. Chem. Soc. Chem. Commun.* 801 (1994).

53. V. J. Cunnane, D. J. Schiffrin, C. Beltran, G. Geblewicz, and T. Solomon, *J. Electroanal. Chem.* 247, 103 (1988).

54. D. V. Leff, P. C. Ohara, J. R. Heath, and W. M. Gelbart, *J. Phys. Chem.* 99, 7036 (1995).

55. M. M. Maye, W. X. Zheng, F. L. Leibowitz, N. K. Ly, and C. J. Zhong, *Langmuir* 16, 490 (2000).

56. M. M. Maye and C. J. Zhong, *J. Mater. Chem.* 10, 1895 (2000).

57. T. Teranishi, S. Hasegawa, T. Shimizu, and M. Miyake, *Adv. Mater.* 13, 1699 (2001).

58. T. Shimizu, T. Teranishi, S. Hasegawa, and M. Miyake, submitted to *J. Phys. Chem. B.* 107, 2719 (2003).

59. M. Green and P. O'Brien, *Chem. Commun.* 183 (2000).

60. T. Teranishi, I. Kiyokawa, and M. Miyake, *Adv. Mater.* 10, 596 (1998).

61. T. Teranishi, M. Hosoe, and M. Miyake, *Adv. Mater.* 9, 65 (1997).

62. T. Teranishi and M. Miyake, *Chem. Mater.* 10, 594 (1998).

63. T. Teranishi, M. Hosoe, T. Tanaka, and M. Miyake, *J. Phys. Chem. B* 103, 3818 (1999).

64. C. D. Bain, J. Evall, and G. M. Whitesides, *J. Am. Chem. Soc.* 111, 7155 (1989).

65. X. M. Lin and C. M. Sorensen, *Chem. Mater.* 11, 198 (1999).

66. L. O. Brown and J. E. Hutchison, *J. Phys. Chem. B* 105, 8911 (2001).

67. J. E. Martin, J. P. Wilcoxon, J. Odinek, and P. Provencio, *J. Phys. Chem. B* 104, 9475 (2000).

68. K. V. Sarathy, G. U. Kulkarni, and C. N. R. Rao, *Chem. Commun.* 537 (1997).

69. M. T. Reetz and W. Helbig, *J. Am. Chem. Soc.* 116, 7401 (1994).

70. M. T. Reetz, W. Helbig, S. A. Quaiser, U. Stimming, N. Breuer, and R. Vogel, *Science* 267, 367 (1995).

71. C. Petit, A. Taleb, and P. Pileni, *J. Phys. Chem. B* 103, 1805 (1999).

72. D. P. Dinega and M. G. Bawendi, *Angew. Chem. Int. Ed.* 38, 1788 (1999).

73. C. T. Black, C. B. Murray, R. L. Sandstrom, and S. Sun, *Science* 290, 1131 (2000).

74. V. F. Puntes, K. M. Krishnan, and A. P. Alivisatos, *Topics in Catalysis* 19, 145 (2002).

75. V. F. Puntes, K. M. Krishnan, and A. P. Alivisatos, *Science* 291, 2115 (2001).

76. D. de Caro, T. Ould Ely, A. Mari, B. Chaudret, E. Snoeck, M. Respaud, J.-M. Broto, and A. Fert, *Chem. Mater.* 8, 1987 (1996).

77. S. J. Park, S. Kim, S. Lee, Z. G. Khim, K. Char, and T. Hyeon, *J. Am. Chem. Soc.* 122, 8581 (2000).

78. C. J. Kiely, J. F. Fink, J. G. Zheng, M. Brust, D. Bethell, and D. J. Schiffrin, *Adv. Mater.* 12, 640 (2000).

79. G. Schmid, M. Bäumle, and N. Beyer, *Angew. Chem. Int. Ed.* 39, 181 (2000).

80. T. Teranishi, M. Haga, Y. Shiozawa, and M. Miyake, *J. Am. Chem. Soc.* 122, 4237 (2000).

81. J.-P. Bourgoin, C. Kergueris, E. Lefèvre, and S. Palacin, *Thin Solid Film* 327–329, 515 (1998).

82. M. Sastry, A. Gole, and V. Patil, *Thin Solid Film* 384, 125 (2001).

83. S. Huang, G. Tsutsui, H. Sakaue, S. Shingubara, and T. Takahagi, *J. Vac. Sci. Technol. B* 19, 115 (2001).

84. J. J. Brown, J. A. Porter, C. P. Daghlian, and U. J. Gibson, *Langmuir* 17, 7966 (2001).

85. B. V. Enüstün and J. Turkevich, *J. Am. Chem. Soc.* 85, 3317 (1963).

86. J. W. Slot and H. J. Geuze, *J. Cell Biol.* 38, 87 (1985).

87. G. Schmid, R. Pugin, T. Sawitowski, U. Simon, and B. Marler, *Chem. Commun.* 1303 (1999).

88. K. Kimura, S. Sato, and H. Yao, *Chem. Lett.* 372 (2001).

89. E. V. Shevchenko, D. V. Talapin, A. L. Rogach, A. Kornowski, M. Haase, and H. Weller, *J. Am. Chem. Soc.* 124, 11480 (2002).

90. A. L. Shapiro, P. W. Rooney, M. Q. Tran, F. Hellman, K. M. Ring, K. L. Kavanagh, B. Rellinghaus, and D. Weller, *Phys. Rev. B* 60, 12826 (1999).

91. K. V. Sarathy, P. J. Thomas, G. U. Kulkarni, and C. N. R. Rao, *J. Phys. Chem. B* 103, 399 (1999).

92. C. N. R. Rao, G. U. Kulkarni, P. J. Thomas, and P. P. Edwards, *Chem. Soc. Rev.* 29, 27 (2000).

93. Z. L. Wang, "Characterization of Nanophase Materials." Wiley-VCH, New York, 2000.

94. D. B. Williams and C. B. Carter, "Transmission Electron Microscope." Plenum, New York, 1996.

95. Z. L. Wang and Z. C. Kang, "Functional and Smart Materials—Structural Evolution and Structure Analysis." Plenum, New York, 1998.

96. R. F. Egerton, "Electron Energy-Loss Spectroscopy in the Electron Microscope." Plenum, New York, 1996.

97. Z. L. Wang, *J. Phys. Chem. B* 104, 1153 (2000).

98. Z. L. Wang, S. A. Harfenist, R. L. Whettern, J. Bentley, and N. D. Evans, *J. Phys. Chem. B* 102, 3068 (1998).

99. Z. L. Wang, S. A. Harfenist, I. Vezmar, R. L. Whettern, J. Bentley, and N. D. Evans, *Adv. Mater.* 10, 808 (1998).

100. S. A. Harfenist, Z. L. Wang, M. M. Alvarez, I. Vezmar, and R. L. Whetten, *Adv. Mater.* 9, 817 (1997).

101. http://rsb.info.nih.gov/nih-image/.

102. R. L. Whetten, J. T. Khoury, M. Alvarez, S. Murthy, I. Vezmar, Z. L. Wang, P. W. Stevens, C. L. Cleveland, W. D. Luedtke, and U. Landman, *Adv. Mater.* 8, 428 (1996).

103. Special issue: *Nanostructured Materials, Chem. Mater.* 8 (1996).

104. Special issue, *Science* 271, 920 (1996).

105. J. R. Heath, *Science* 270, 1315 (1995).

106. C. F. Bohren and D. R. Huffman, "Absorption and Scattering of Light by Small Particles." Wiley, New York, 1983.

107. S. Mochizuki and R. Ruppin, *J. Phys.: Condens. Matter* 5, 135 (1993).

108. K. P. Charlé and W. Schulze, *Ber. Bunsen-Ges. Phys. Chem.* 88, 350 (1984).

109. U. Kreibig and M. Vollmer, "Optical Properties of Metal Cluster." Springer-Verlag, Berlin, 1995.

110. G. Mie, *Ann. Phys.* 25, 377 (1908).

111. K. P. Charlé and W. Schulze, *Ber. Bunsen-Ges. Phys. Chem.* 88, 350 (1984).

112. H. Hövel, S. Fritz, A. Hilger, U. Kreibig, and M. Vollmer, *Phys. Rev. B* 48, 18178 (1993).

113. B. N. J. Persson, *Surf. Sci.* 281, 153 (1993).

114. B. W. Ninham and R. A. Sammut, *J. Theor. Biol.* 56, 125 (1976).

115. S. Sato, H. Yao, and K. Kimura, *Chem. Lett.* 526 (2002).

116. O. A. Aktsipetrov, P. V. Elyutin, A. A. Fedyanin, A. A. Nikulin, and A. N. Rubtsov, *Surf. Sci.* 325, 343 (1995).

117. B. Lamprecht, A. Leitner, and F. R. Aussenegg, *Appl. Phys. B* 68, 419 (1999).

118. P. Galletto, P. F. Brevet, H. H. Girault, R. Antoine, and M. Broyer, *J. Phys. Chem. B* 103, 8706 (1999).

119. T. Dutton, B. Vanwonterghem, S. Saltiel, N. V. Chestnoy, P. M. Renzepis, T. P. Shen, and D. Rogovin, *J. Phys. Chem.* 94, 1100 (1990).

120. F. Hache, D. Ricard, C. Flyzanis, and U. Kreibig, *Appl. Phys. A* 47, 347 (1988).

121. J. Matsuoka, R. Mizutani, S. Kaneko, H. Nasu, K. Kamiya, K. Kadono, T. Sakaguchi, and M. Miya, *J. Ceram. Soc. Jpn.* 101, 53 (1993).

122. C. Voisin, N. D. Fatti, D. Christofilos, and F. Vallée, *J. Phys. Chem. B* 105, 2264 (2001).

123. D. Ricard, P. Roussignol, and C. Flytzanis, *Opt. Lett.* 10, 511 (1985).

124. E. J. Heolweil and R. M. Hochestrasser, *J. Chem. Phys.* 82, 4762 (1985).

125. M. J. Blömer, J. W. Haus, and P. R. Ashley, *J. Opt. Soc. Am. B* 7, 790 (1990).

126. I. Tanahashi, Y. Manabe, T. Tohda, S. Sasaki, and A. Nakamura, *J. Appl. Phys.* 79, 1244 (1996).

127. M. Lee, T. S. Kim, and Y. S. Choi, *J. Non-Cryst. Solids* 211, 143 (1997).

128. H. H. Huang, F. A. Yan, Y. M. Kek, C. H. Chew, G. Q. Xu, W. Ji, P. S. Oh, and S. H. Tang, *Langmuir* 13, 172 (1997).

129. S. D. Stookey, *J. Am. Ceram. Soc.* 32, 246 (1949).

130. R. D. Maurer, *J. Appl. Phys.* 29, 1 (1958).

131. J. Matsuoka, R. Mizutani, S. Kaneko, H. Nasu, K. Kamiya, K. Kadono, T. Sakaguchi, and M. Miya, *J. Ceram. Soc. Jpn.* 101, 53 (1993).

132. I. Tanahashi and T. Mitsuyu, *J. Non-Cryst. Solids* 181, 77 (1995).

133. G. W. Arnold and J. A. Borders, *J. Appl. Phys.* 48, 1488 (1977).

134. K. Fukumi, A. Chayahara, K. Kadono, T. Sakaguchi, Y. Horino, M. Miya, J. Hayakawa, and M. Satou, *Jpn. J. Appl. Phys.* 30, 742 (1991).

135. T. Akai, K. Kadono, H. Yamanaka, T. Sakaguchi, M. Miya, and H. Wakabayashi, *J. Ceram. Soc. Jpn.* 101, 105 (1993).

136. I. Tanahashi, M. Yoshida, Y. Manabe, T. Tohda, S. Sasaki, T. Tokizaki, and A. Nakamura, *Jpn. J. Appl. Phys.* 33, 1410 (1994).

137. A. Nakamura, T. Tokizaki, H. Akiyama, and T. Kataoka, *J. Lumin.* 53, 105 (1992).

138. D. L. Feldheim and C. D. Keating, *Chem. Soc. Rev.* 27, 1 (1998).

139. H. Grabar and M. H. Devoret, "Single Charge Tunneling, Coulomb Blockade Phenomena in Nanostructures." Plenum, New York, 1992.

140. D. V. Averin and K. K. Likaharev, *J. Low Temp. Phys.* 62, 345 (1986).

141. C. J. Gorter, *Physica* 17, 777 (1951).

142. B. J. Barner and S. T. Ruggiero, *Phys. Rev. Lett.* 59, 807 (1987).

143. M. Amman, R. Wilkins, E. Ben-Jacob, P. D. Maker, and R. C. Jaklevic, *Phys. Rev. B* 43, 1146 (1991).

144. T. A. Fulton and G. Dolan, *Phys. Rev. Lett.* 59, 109 (1987).

145. S. J. Green, J. J. Stokes, M. J. Hostetler, J. Pietron, and R. W. Murray, *J. Phys. Chem. B* 101, 2663 (1997).

146. T. Ogawa, K. Kobayashi, G. Masuda, T. Takase, and S. Maeda, *Thin Solid Films* 393, 374 (2001).

147. R. C. Doty, H. Yu, C. K. Shih, and B. A. Korgel, *J. Phys. Chem. B* 105, 8291 (2001).

148. K. C. Beverly, J. F. Sampaio, and J. R. Heath, *J. Phys. Chem. B* 106, 2131 (2002).

149. T. Teranishi and Y. Yamamoto, unpublished results.

150. Y. Huang, X. Duan, Q. Wei, and C. M. Lieber, *Science* 291, 630 (2001).

151. P. L. Lu and D. H. Charap, *IEEE Trans. Magn.* 30, 4230 (1994).

152. D. Weller and A. Moser, *IEEE Trans. Magn.* 35, 4423 (1999).

153. J. S. Li, M. Mirzamaani, X. P. Bian, M. Doerner, S. L. Duan, K. Tang, M. Toney, T. Arnoldussen, and M. Madison, *J. Appl. Phys.* 85, 4286 (1999).

154. T. Fried, G. Shemer, and G. Markovich, *Adv. Mater.* 13, 1158 (2001).

155. T. Hyeon, S. S. Lee, J. Park, Y. Chung, and H. B. Na, *J. Am. Chem. Soc.* 123, 12798 (2001).

156. K. Inomata, T. Sawa, and S. Hashimoto, *J. Appl. Phys.* 64, 2537 (1998).

157. D. Weller, A. Moser, L. Folks, M. E. Best, W. Lee, M. F. Toney, M. Schwickert, J.-U. Thiele, and M. F. Doerner, *IEEE Trans. Magn.* 36, 10 (2000).

158. S. Sun, E. E. Fullerton, D. Weller, and C. B. Murray, *IEEE Trans. Magn.* 37, 1239 (2001).

159. S. Sun and D. Weller, *J. Mag. Soc. Jpn.* 25, 1434 (2001).

160. M. Hanson, C. Johansson, M. S. Pedersen, and S. Mørup, *J. Phys. Condens. Matter* 7, 9269 (1995).

161. M. H. Hong, K. Hono, and M. Watanabe, *J. Appl. Phys.* 84, 4403 (1998).

162. S. Sun, S. Anders, H. F. Hamann, J.-U. Thiele, J. E. E. Baglin, T. Thomson, E. E. Fullerton, C. B. Murray, and B. D. Terris, *J. Am. Chem. Soc.* 124, 2884 (2002).

163. J. H. Fendler, *Chem. Mater.* 8, 1616 (1996).

164. Y. Liu, A. Wang, and R. Claus, *J. Phys. Chem. B* 101, 1385 (1997).

165. T. Cassagneau, T. E. Mallouk, and J. H. Fendler, *J. Am. Chem. Soc.* 120, 7848 (1998).

*166.* J. Schmitt, P. Machtle, D. Eck, H. Mohwald, and C. A. Helm, *Langmuir* 15, 3256 (1999).

*167.* B. H. Sohn and B. H. Seo, *Chem. Mater.* 13, 1752 (2001).

*168.* J. W. Ostrander, A. A. Mamedov, and N. A. Kotov, *J. Am. Chem. Soc.* 123, 1101 (2001).

*169.* E. Shevchenko, D. Talapin, A. Kornowski, F. Wiekhorst, J. Kötzler, and M. Haase, *Adv. Mater.* 14, 287 (2002).

*170.* D. L. Leslie-Pelecky and R. D. Rieke, *Chem. Mater.* 8, 1770 (1996).

*171.* M. F. Hansen and S. Mørup, *J. Magn. Magn. Mater.* 203, 214 (1999).

*172.* B. Stahl, N. S. Gajbhiye, G. Wilde, D. Kramer, J. Ellrich, M. Ghafari, H. Hahn, H. Gleiter, J. Weimüller, R. Würschum, and P. Schlossmacher, *Adv. Mater.* 14, 24 (2002).

*173.* T. Teranishi, M. Miyake, Y. Tsuchiya, and K. Ito, unpublished results.

*174.* Z. R. Dai, S. Sun, and Z. L. Wang, *Nano Lett.* 1, 443 (2001).

*175.* C. Chen, O. Kitakami, S. Okamoto, and Y. Shimada, *Appl. Phys. Lett.* 76, 3218 (2000).

*176.* O. Kitakami, Y. Shimada, K. Oikawa, Hl. Daimon, and F. Fukamichi, *Appl. Phys. Lett.* 78, 1104 (2001).

*177.* T. Maeda, T. Kai, A. Kikitsu, T. Nagase, and J. Akiyama, *Appl. Phys. Lett.* 80, 2147 (2002).

*178.* S. Kang, J. W. Harrell, and D. E. Nikles, *Nano Lett.* 2, 1033 (2002).

*179.* J.-I. Park and J. Cheon, *J. Am. Chem. Soc.* 123, 5743 (2001).

*180.* M. Chen and D. E. Nikles, *Nano Lett.* 2, 211 (2002).

*181.* B. H. Sohn, J.-M. Choi, S. I. Yoo, S.-H. Yun, W.-C. Zin, J. C. Jung, M. Kanehara, T. Hirata, and T. Teranishi, *J. Am. Chem. Soc.* 125, 6368 (2003).

*182.* M. Kanehara, Y. Oumi, T. Sano, and T. Teranishi, *J. Am. Chem. Soc.* 125, 8708 (2003).

# Metal Nanoparticles

Colin C. Baker, Anshu Pradhan

*University of Delaware, Newark, Delaware, USA*

S. Ismat Shah

*University of Delaware, Newark, Delaware, USA; and Fraunhofer Center for Manufacturing and Advanced Materials, Newark, Delaware, USA*

## CONTENTS

## 1. INTRODUCTION

Nanotechnology has had an immense impact on nearly all existing scientific disciplines. The applications range from catalysis to biotechnology. Metal nanoparticles are at the top of the rapidly increasing list of materials being investigated in the nanostructured form. Although they are relatively easy to synthesize by wet chemical, electrochemical, and vacuum techniques, the barriers to the use of these particles are associated with the scale up limitations of most of these processes and the enhanced reactivity of the metal nanoparticles. The enhanced reactivity of metal nanoparticles emanates from the large surface area. Some metals that are essentially inert in bulk form may become pyrophoric at nanometer scale. Special safety precautions have to be used in the production of metal nanoparticles. There are also biological and environmental considerations that should be considered when experimenting with metal nanoparticles.

In this chapter we first describe some important applications of nanoparticles and relate these applications to the unique physical and chemical properties of metal nanoparticles. The application section is followed by detailed description of the synthesis techniques along with the

description of modes of metal nanoparticle growth in gaseous phase.

## 2. SYNTHESIS OF METAL NANOPARTICLES

A review of some of the methods for obtaining nanometer sized metal particles is given here. Chemical techniques are discussed first, but the emphasis in this chapter is on metal nanoparticles synthesized with gas phase techniques, such as physical vapor deposition (PVD) processes including Joule heating–inert gas condensation (IGC) and plasma sputtering–IGC as well as other aerosol processes. The nucleation and growth of particles for the PVD processes is then discussed.

### 2.1. Chemical Techniques

Unlike synthesis of nano-oxide particles that can be produced in fairly large amounts by chemical techniques, the chemical techniques for metal nanoparticle synthesis are generally limited in scale. Only small amounts are typically produced. However, producing nanoparticles with a nonvacuum technique is important and, therefore, is briefly summarized here.

#### 2.1.1. Template Synthesis of Nanoparticles

Metal nanoparticles produced without any constraints in the solid, liquid, or gaseous phase are often spherical in nature. However, for many existing and emerging applications it is desirable to produce such nanoparticles with high shape anisotropies.

The surface enhancement of Raman scattering and other optical processes depends strongly on the particle size and shape [1]. Metal nanowires having high aspect ratios have received extensive interest in recent years because of their

unique quantum properties and their potential for use as interconnects in nanoscale devices [2–5]. Anisotropic metal nanoparticles can also be used to fabricate sensitive biological and molecular sensors based on the principle of surface plasmon resonance spectroscopy [6]. Nonspherical particles can by synthesized by chemical reduction in solutions containing surfactants that influence the thermodynamics or the kinetics of crystal growth along a particular direction [7, 8]. Another approach commonly used involves electrodeposition of metal into the pores of suitable template [9–14]. Materials such as anodic aluminum oxide (AAO) and track etch membranes which have pores on the nanometer scale are commonly used as templates. Anodic aluminum oxide films consist of an array of nominally cylindrical pores and can be prepared by electrochemically etching aluminum metal in an acidic medium. By varying the process conditions, the anodic aluminum oxide film can be separated from the aluminum substrate, if desired [15]. Track etch membranes are prepared by exposing a thin polymer film, such as polycarbonates, to high-energy nuclear fission fragments, which create tracks in the polymer film. Track etch membranes are mechanically easier to handle because of their inherent flexibility, while the anodic aluminum oxide templates offer much higher pore densities and the pores are parallel to each other which can be useful for certain applications [15]. Both the anodic aluminum oxide as well as the track etch templates are commercially available.

Synthesis of metal nanoparticles using templates attached to a substrate simply involves deposition of the required metal within the pores by ac electrodeposition. The primary advantage of this method is the ease of material handling, as the AAO template is supported by the underlying aluminum substrate [15]. However, the pore filling is nonuniform resulting in granular disordered metal structures. Metal nanoparticle synthesis from freestanding templates such as those obtained after the AAO is separated from the aluminum substrate or track etch membranes is complicated by the fact that they are mechanically fragile, and that there is no suitable electrode to use for electrodeposition. The latter problem is solved by sputter depositing a thin film of a suitable metal (usually silver) onto one face of the template film to render it conductive [15]. This structure is then transferred to a electrochemical cell and a metal, which can be easily etched, is deposited onto the surface previously coated by sputtering to form a continuous metallic foundation on which the metal of interest can be deposited [15]. The second metal is then deposited and the first metal is etched in an acid bath to leave the nanoparticles of the desired metal embedded in the pores of the template. The length of the nanorods can be controlled by monitoring the total charge used for the electrodeposition and sequential electrodeposition of different metals can be carried out to create striped nanorods [16]. Under controlled conditions, electrodeposition can preferentially occur on the step edges of a single crystal surface which can also be used a template to grow nanowires. This technique is called step edge decoration [16–28] and yields very fine nanowires with a thickness of one or two atomic layers, but it is usually difficult to remove these ultrathin wires from the surfaces on which they have been deposited. Recently, Zach and co-workers [3] synthesized Mo nanowires by first selectively depositing

a "precursor wire" of molybdenum oxide from an alkaline solution of $MoO_4^{2-}$ on the step edges of a graphite crystal. These wires were reduced in $H_2$ and then lifted off the graphite surface by embedding the wires into a polystyrene film spun onto the graphite surface to yield hemicylindrical metallic nanowires. Another two step process that can be used to create nanowires has been described by Hong and co-workers [5]. They used the self-assembled nanotube arrays of calyx(4)hydroquinones (CHQs) as a template for silver nanowires. The hydroquinone subunits in the CHQ nantotube can capture metal ions in their pores with high affinity and reduce the silver ions to form silver aggregate in an acidic solution under photochemical conditions [29]. The procedure to fabricate the silver nanowires consists of soaking CHQ nantotube powder in an aqueous $AgNO_3$ solution, which sequesters the silver ions within the ordered nantotube array. This is followed by ultraviolet irradiation to reduce the silver ions [5]. The silver nanowires retain the morphology of the parent silver ions which are templated by the pores of the CHQ nanotubes yielding nanowires around 750 nm with well ordered one-dimensional (1D) structures [5].

### 2.1.2. Inverse Micelle Synthesis of Metal Nanoparticles

Inverse micelles or microemulsions are made by dissolving a suitable surfactant in a mixture of an apolar organic solvent and water. Surfactants are molecules consisting of both a hydrophilic and a hydrophobic end. When a surfactant is dissolved in the solvent, nanometer sized water droplets are formed within the volume and stabilized by the surfactant molecules. The hydrophilic ends of the surfactant lie along the outer surface of the water droplet and the hydrophobic end sticks into the nonpolar solvent, stabilizing the water droplet and providing mechanical separation from the solvent. Surfactants commonly used for nanoparticle synthesis include didodecyldimethylammonium bromide (DDAB), sodium di-Z-ethyl hexylsulfosuccinate, Marlipal O13/80 (alkyl polyethyleneglycol ether type $C_{13}E_8$), etc., dissolved in a suitable solvent. The radius of the droplets is proportional to the parameter $w_0$, which is the ratio of molar number of water to the molar number of surfactant. The droplet concentration (at constant $w_0$) is proportional to the water volume fraction in the microemulsions. In this way both the droplet size and concentration can be varied by adjusting the composition of the microemulsions [30, 31]. The droplets are in continuous Brownian motion, and the collisions of the droplets allows for rapid exchange of their contents. In order to produce nanoparticles, the appropriate reactants, which are soluble in water, are added to a microemulsion in a sequential manner. The droplet collisions lead to mixing of the reactants in the aqueous phase of the microemulsion and the reaction starts [31]. The reactants usually consist of a metal salt, which provides the metal ions, and a reducing agent such as sodium borohydride ($NaBH_4$). Nanoparticles are formed by the nucleation and growth mechanism within the water droplets. The growth of the nanoparticles is constrained by the reverse micelles, and a detailed model describing the process has been formulated by Lamer and Dinegar [32]. The

inversed micelle technique yields highly monodisperse particles whose size can be varied by controlling the microemulsion parameters. However, like many of the other chemical methods, it is not easy to scale up this method from a lab scale to a production scale [31]. However, within the scientific community this remains a popular method for synthesizing nanoparticles, and Co, Fe, Ni, Ag, Cu, Rh, Pt, and Pd nanoparticles have been successfully synthesized [30, 31, 33–56]. A typical case of the synthesis of Co nanoparticles is outlined here. The surfactant, DDAB, is first dissolved in deoxygenated toluene to a concentration of 10–12%. Cobalt chloride ($CoCl_2 \cdot 6H_2O$) is commonly used as the metal salt and is dissolved to a concentration of about 0.005–0.02 M. Under vigorous stirring, 5–10 M $NaBH_4$ aqueous solution is added to the concentration of $[BH_4^-]/[Co_2^+] = 3:1$. The solution changes color and a stable colloid of Co nanoparticles, with particle size as low as 2–3 nm, is obtained [35, 39, 40].

### 2.1.3. Dendrimer-Encapsulated Metal Nanoparticles

Dendrimers are highly branched organic molecules with a well defined repetitive structure that have been successfully used to create nanoparticles by sequestering metal ions at the dendrimer core and then reducing the same. The technique is similar to the use of porous templates for nanoparticle synthesis, with the dendrimer molecules acting as the template. Dendrimers have three basic anatomical features: a core, repetitive branch units, and terminal functional groups [46–49]. The physical and chemical properties of dendrimers depend on the chemical structure of the three components as well as the overall size and dimensionality of the dendrimer [60]. A dendrimer is characterized by the chemical repeat unit as well as the dimensionality or the generation number. The generation number for a dendrimer is the number of growth cycles undergone by the dendrimer. For example, generation 0 dendrimer (G0) is formed after the first cycle of reactions on the dendritic core, generation 1(G1) is formed after the second cycle, and so on. With each cycle, the diameter of the dendrimer increases linearly, while the number of surface functional groups increases exponentially, giving the symmetric, highly branched dendrimer structures. The steric crowding on the periphery of the dendrimer due to the exponential increase in the number of surface functional groups leads to geometric changes. For example in the case of PAMAM, G1 has an expanded or "open" configuration, while G4 has a porous globular structure and G8 is a spheroid [61]. Dendrimers of sufficiently high generation develop a three-dimensional shape with interior voids large enough to accommodate nanoscopic guest molecules [62, 63]. Dendrimers retain guest molecules selectively depending on the guest molecule, chemical composition of the dendrimer interior and periphery, and the cavity size [50–63].

Dendrimers are well suited to act as nanoparticle templates for the following reasons: (1) The dendrimer templates have uniform composition and structure and therefore yield well-defined nanoparticle replicas [61, 64–66]. (2) The nanoparticles are stabilized by encapsulation within the dendrimer, which prevents agglomeration [60, 61, 64–67]. (3) The terminal groups on the dendrimer can be tailored to control solubility and for linking of the encapsulated

to other molecules and surfaces [65, 68–71]. A solution containing the metal ion of interest and the dendrimer is mixed. The chemistry of the dendrimers can be used to trap metal ions exclusively within their interiors [60, 72]. This is followed by a chemical reduction with a reducing agent such as $NaBH_4$, which results in the formation of intradendrimer metal clusters [60, 72]. The ability to prepare well-defined intradendrimer nanoparticles depends on the chemical composition of the dendrimer. These metallic clusters are stable for a period of about one week in an oxygen-free atmosphere. However, on exposure to air, they revert back to the intradendrimer ions. Nanoparticles of Cu, Ag, Au, Pt, Pd, and Rh with particle size less than 2 nm $\pm 2$ Å can be synthesized with this technique [60, 61, 64, 69, 71–74]. Nanoparticles of some metals such as Ag, whose ions are not strongly complexed, can be prepared by a metal displacement reaction [170]. For example, the copper nanoparticles encapsulated in a dendrimer on exposure to $Ag^+$ will reduce silver and form dendrimer encapsulated silver nanoparticles [60, 61]:

$$Cu + 2Ag^+ \rightleftharpoons Cu^{2+} + 2Ag \qquad (1)$$
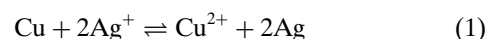
Bimetallic nanoparticles can also be formed in the same way by adding a smaller amount of the metal ions. Ag/Cu, Au/Cu, Pd/Cu, Pt/Cu bimetallic nanoparticles have been formed by adding less than a stoichiometric amount on the corresponding ion to the dendrimer encapsulated Cu nanoparticle [60, 61]. Bimetallic nanoparticles can also be obtained by co-complexation of the two metallic ions with the dendrimer followed by a single reduction step. Bimetallic nanoparticles such as Pt/Pd can also be prepared by sequential loading. In this method, a metal ion is complexed and reduced to form a dendrimer encapsulated nanoparticle. This is then complexed with the second metal ion which, on subsequent reduction, results in the formation of a bimetallic nanoparticle.

## 2.2. Gas Condensation Processes

The techniques of inert gas condensation, co-condensation, and plasma sputtering are gas phase PVD processes that are performed in a vacuum. Gas phase processes involve the generation of metal atoms through various means, and the homogeneous nucleation and subsequent condensation and coagulation of nanoparticles. To begin, it is necessary to define some terms. Definitions given by Flagan and Lunden are adopted [75]. Coagulation refers to particle combination due to processes such as Brownian motion. Coalescence refers to the sintering and diffusion of species within particles where contact is made. An agglomeration of particles occurs when the individual particles remain identifiable. Agglomerates can be either hard, sometimes referred to as an aggregate, where large amounts of energy are required to separate the individual particles, or soft, where small amounts of energy are needed.

The formation of particles involves supersaturation. This is generally achieved by rapid cooling of the particle nuclei by various means including loss of energy to a cooler inert gas, or chamber wall, or loss of energy by radiation.

### 2.2.1. Joule Heating–Inert Gas Condensation

Inert gas condensation is a desirable process for the synthesis of metal nanoparticles for several reasons. It is a relatively simple process capable of producing bulk quantities of particles, and since it utilizes vacuum deposition, it offers high purity particles and does not require hazardous chemicals. At present the commonly used form of the IGC process is generally attributed to the work of Gleiter [76] shown in Figure 1. In this process a source of metal nuclei is produced from a Joule (resistively) heated refractory metal evaporation source or "boat." The boat is heated to a temperature of evaporation that corresponds to the pressure in the chamber. The metal melts in the boat and subsequently evaporates in the presence of an inert carrier gas. The rapid cooling of the metal atoms through collisions with the inert gas initiates a large degree of supersaturation, resulting in nucleation. The nuclei are removed by either convective or forced flow from the heated region above the boat. The particles are often collected on a cold finger or other cold surface where the particles are scraped off at the end of the process [76].

Although the inert gas condensation process traditionally involved Joule heating of a source to form metal nuclei, many other processes for evaporation and nuclei generation are now used and will be discussed in subsequent sections. The development of the IGC process in fact began as far back as the 1930s when Pfund synthesized bismuth nanoparticles from a wire [77]. Other early studies were performed using argon and nitrogen as the inert gas species, and metals such as Au, Ag, Cu, Fe, Zn, and Mg were evaporated. In the early processes the particles were removed from the evaporation source by convective flow. It was found that the size of the particles could be varied by changes in gas pressure [78–85]. Later studies showed that helium gas provided the same effects but gave particle sizes that in general were much smaller than processes that use argon or nitrogen [81, 82]. It was speculated that the energy of the metal particles after evaporation allows them to escape from the area of the evaporation source thus stopping the growth process. However, the particles are supercooled by collisions with the inert gas atoms causing energy losses, and so the amount of supercooling determines the energy that the particles have for escape. Therefore, it was proposed that because of its lower mass, helium collisions with the metal particles do not provide as much supercooling as larger inert gas species. The metal particles therefore are able to escape from the evaporation source more easily, thus condensing in a region of fewer metal nuclei, giving smaller sizes [81, 82].
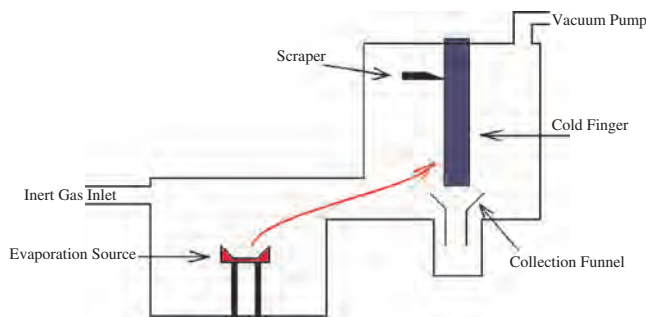
Granqvist and Burhman studied the IGC process extensively [86]. They studied the influence of pressure and inert gas species Ar, Xe, and He on metals such as Mg, Zn, Cr, Fe, Co, and Al and found a size and crystal habit dependence on inert gas pressure and species. In their study they defined a particle growth region above the surface of the evaporation source (Fig. 2). They concluded that it is the pressure in the growth region and time that the metal nuclei spend there that will determine their size and morphology. They found that if the pressure in the growth region is high, there are more metal nuclei available to coalesce and form larger particles. Thus if smaller amounts of metal nuclei are available, or the nuclei can be removed from the area quickly, the resultant particle size can be kept to a minimum. Furthermore, they found that a less massive inert gas species would not confine the particles in the growth region as effectively as a more massive species. Thus, helium would allow more metal to be removed from the growth region resulting in smaller particles [86]. They concluded that the pressure in the growth chamber is a more important parameter than the growth temperature. Other researchers have confirmed these results [87].

Flagan and Lunden elaborated on the Granqvist and Burhman studies by proposing that it is not the overall system pressure that determines the particle size, but the partial pressure of the vapor precursor [75]. The total pressure in the chamber serves to regulate the diffusion of vapor from the growth source. Lowering the total pressure increases diffusion, dispersing the particles and thus restricting the growth by coagulation.

In the early IGC processes metal particles were removed from the hot source by convective flow due to the large temperature gradient from the source to the surrounding vacuum. Convective flow of the particles is generally a low yield process, however. Therefore, in order to produce larger amounts of nanoparticles, forced flow gas condensation techniques were developed [88–91]. Haas et al. [92] developed a process where a nozzle was used to pass the inert gas in a jet stream over the evaporation source. This process increased production and, by removing the particles more quickly from the growth zone, reduced their size. Later, they pointed out that forced jet streams have inherent problems due to complex gas flows, where vortices are



**Figure 1.** A schematic of a simple inert gas condensation process.
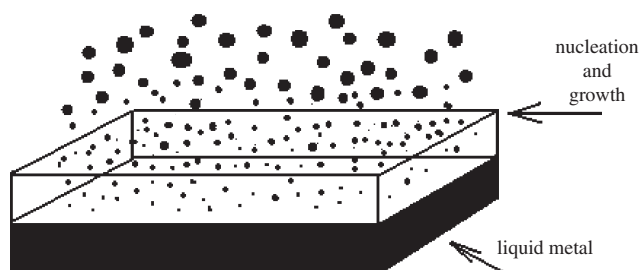


**Figure 2.** The nucleation and growth of metal nanoparticles from an evaporation source. Adapted with permission from [86], C. G. Granqvist and R. A. Buhrman, *J. Appl. Phys.* 47, 2200 (1976). © 1976, American Institute of Physics.

developed that may transport particles behind the evaporation source and onto the chamber walls [93]. These problems were overcome by developing a system of concentric nozzles. In this case four inner nozzles were used to deliver the inert gas directly over the evaporation source while a gas stream from an outer nozzle was used to envelop the flow from the inner nozzle [93]. The palladium nanoparticles produced in their apparatus had a median diameter 80% smaller and a geometric standard deviation 17% lower than those produced in a free convection process [93]. In contrast, Yamamuro et al. [94] observed a wider particle size distribution for increasing inert gas flow rates in a forced flow IGC system, and no decrease in the average particle size. They attribute this behavior to the gas flow disturbing the growth and thermalization process [94]. Brock et al. [95] found that if the inert gas jet was turbulent, the particle sizes were smaller and had a higher number concentration than for laminar jet flows. In the forced flow process developed by Haas et al., it was observed that agglomeration was more prevalent than in a simple condensation system where particles are removed by convective forces [93].

Currently, many researchers are using variations on the IGC process to obtain metals, oxides, and composites. Wegner et al. [96] developed a jet flow condenser where bismuth nanoparticles were evaporated from a crucible and passed through a system containing a center tube and three annular tubes forming a diluter and a heat exchanger. In the diluter, Ar gas is discharged in a stream opposite to the flow of the metal nanoparticles. This apparatus allowed them to study the complex flow patterns formed in the IGC process. Goldby et al. [97] constructed an IGC system where mass selected metal clusters with a controlled landing energy can be deposited onto substrates to form either clustered materials or thin films. In this apparatus the metal is evaporated at room temperature into a helium gas stream. The particles nucleate and form clusters that are passed through a nozzle and expand into an area where they are ionized by a cathode plasma ion source. The particles are then separated with a mass filter according to their mass to charge ratio. They were able to produce clusters of 2–300 Pd atoms and 20–300 Ag atoms, and the energy in which the particles landed was from ∼25 to 800 eV [97]. Oda et al. [98] constructed a system where after evaporation, nanoparticles were transported through a nozzle at 300 m/s to a spray chamber. In the spray chamber the nanoparticles were used to write micrometer-sized patterns onto a substrate. Shen et al. [99] and Busmann et al. [100] developed an IGC process where metal wire is fed continuously to the evaporation boat. The system was then operated in a continuous fashion without the need for recharging of the evaporation source.

Compounds are synthesized in the IGC process by methods that include evaporation of a compound precursor or by evaporation of separate precursors with a subsequent mixing of the gases. Shen et al. [99] used a Ag–63%Cu wire and were able to obtain a Ag–Cu nanocomposite. Weissmuller et al. [101] produced an Y–Fe alloy using the IGC process, where the precursor was a bulk Y–Fe alloy. This method, however, can pose difficulties because of the differences in vapor pressure of the constituents. In the Weissmuler research, the Fe vapor pressure is greater than that of Y so the particles were initially Fe rich [101]. Yamamoto et al.

[102] and Nakayama et al. [103] used a co-evaporation process to obtain iron oxide–silver nanocomposites. Other co-evaporated compounds have included Ge–Al [104], W–Ga [105], $Ni_3Al$ [106, 107], and TiAl [108]. Oxides of metals are often formed in a two step process where the metal is formed first and is subsequently oxidized by controlled addition of oxygen [109]. In our research we have synthesized Fe nanoparticles with an Fe-oxide passivation layer. The nanoparticles were produced in a continuous IGC process and oxidized by introducing a controlled amount of air into the chamber after synthesis [110]. The result was a Fe core/Fe-oxide shell geometry. The oxide shell is crystalline and is composed of $\gamma$-$Fe_2O_3$ or $Fe_3O_4$. In Figure 3 a transmission electron micrograph of an oxide passivated Fe nanoparticle is shown. Lattice fringes associated with the Fe core are evident, as well as fringes from the Fe-oxide shell. As can be seen, the oxide shell may be polycrystalline.

Techniques have been developed to coat the nanoparticles with other metals as they grow [111, 112]. Haubold et al. [112, 113] developed a co-evaporation process where inert gas is injected into the growth chamber through a nozzle carrying atoms of one element above an evaporation source of a second element. The atoms of the second source condense at the surface of the nanoparticles in the form of a thin coating. They report the successful coating of Cu nanocrystals with Bi by this process. Krauss and Gleiter [114] combined resistive evaporation with high pressure sputtering to form W nanocrystals surrounded by several layers of Ga.

Finally, structure changes in the evaporative heating process have been reported. Krauss and Birringer [115] demonstrated that metastable phases of Ta and W, and a modification of the structure of $Y_2O_3$, could be produced in the IGC system by varying process conditions such as level of under cooling and cooling rate of the metal nuclei. They synthesized metastable $\beta$-W and $\beta$-Ta nanoparticles, in which X-ray diffraction results were used to deduce that the metastable phases have different space groups and lattice parameters than their respective equilibrium structures. Similarly, they were able to synthesize either a cubic
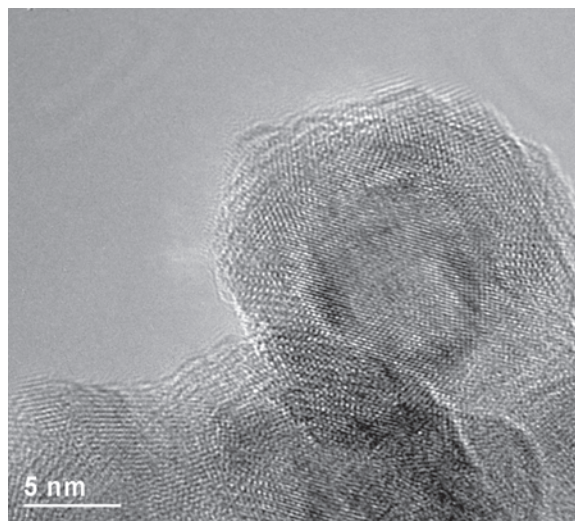


**Figure 3.** Transmission electron micrograph of an iron-oxide passivated iron nanoparticle.

form or a monoclinic phase of $Y_2O_3$ by changing the process conditions. In this synthesis, pure Y was evaporated and then oxidized in a separate step. Modifications of the structure of W, Cr, and Mo nanoparticles had also been previously demonstrated by other researchers [116].

### 2.2.2. Plasma Sputtering–Inert Gas Condensation

Plasma sputtering is a valuable technique for generating nanoparticles of refractory metals that have vapor pressures that are too low for the Joule heating process. Plasma sputtering is favorable due to other limitations in the Joule heating process. For example, some metal species such as Al will alloy with refractory metal evaporation boats such as W, leading to failure of the boat. Inhomogeneous temperature distributions may occur in the molten metal leading to irreproducibility in experiments, while in plasma sputtering the conditions are very stable and can be controlled easily by the current [117]. The production of alloys with controlled composition is much easier in plasma sputtering by using an alloy target of the same composition. Therefore the sputtered species are much more closely related to the target than are species evaporated in a Joule heating process. However, a disadvantage in sputtering processes is that product yields are much lower than for Joule heating.

In the plasma sputtering process a metal target material is bombarded with high-energy ions of an inert gas such as Ar or Kr. The source of high-energy ions is a plasma, which can be generated by direct current (dc) or radio frequency (rf) power sources. The high-energy ions created in the plasma are accelerated to the target and bombard it causing the ejection of predominantly neutral atoms and a small fraction of ions from the target surface. Often a static magnetic field is applied near the target of dc power sources to produce a high-density plasma, known as magnetron sputtering. The ejected materials are also of high energy and can be collected on a cooled substrate where their energy is not sufficient to form a thin film. The ejected particles can also be swept away by the inert gas atmosphere from the sputter source and condensed by the same process as described by the other gas condensation techniques (Fig. 4).

The plasma sputtering process for the deposition of thin films is a well established technique [118]. To favor nucleation and coagulation of the sputtered materials for the formation of metal nanoparticles, the apparatus is operated at higher pressures than for thin film deposition. Early research on diode sputtering to synthesize nanoparticles was done by Yatsuya et al. [119, 120] where they developed two different electrode arrangements. In one arrangement, they used a needlelike anode placed near a W filament. A discharge was induced between the two electrodes in an Ar atmosphere. The Ar gas was accelerated to the W wire where sputtering produced W nanoparticles. In the second arrangement two parallel plates composed of either Cu or Ag were placed in an Ar atmosphere and the application of several hundred volts induced a discharge producing either Cu or Ag nanoparticles [119, 120].

Hahn and Averback [117] applied dc and rf magnetron sputtering with Ar to produce nanoparticles of Al, Mo, $Cu_{91}Mn_9$, $Al_{52}Ti_{48}$, and $ZrO_2$ particles with diameters of
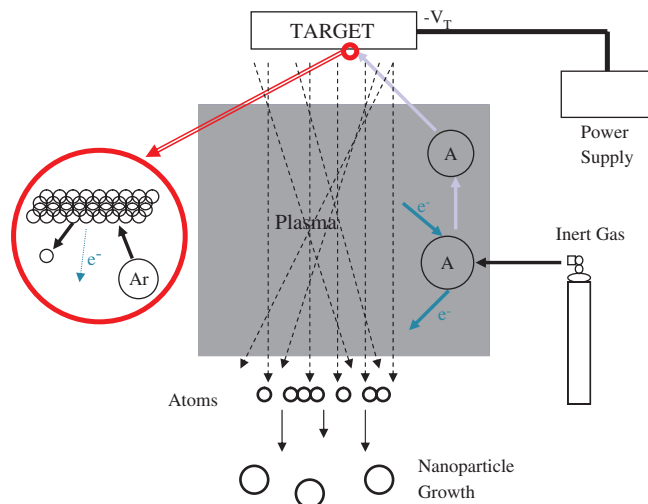


**Figure 4.** A schematic of a typical plasma sputtering process.

7–50 nm. They determined that the pressure needed for the formation of nanoparticles was ∼200 to 1500 mTorr. They also reported an increase in grain sizes for a $Cu_{91}Mn_9$ alloy from 7 to 14 nm by varying the current from 2 to 4.5 A [117]. Suh et al. [121] used dc magnetron sputtering to form 15–60 nm Cu and 5–25 nm $SnO_2$ particles. They also observed that pressures of 200–1100 mTorr were required for the deposition of nanoparticles, while noting that conventional sputter deposition processes for thin films involved operation at pressures in the range 0.1–10 mTorr. Similarly, they reported power level requirements of 1–3 kW were needed to form nanoparticles. Chow et al. [122–124] synthesized Mo nanocrystals and found that at pressures between 4 and 100 mTorr, Mo films were formed, while at pressures of 150 mTorr, Mo nanocrystals of two sizes, 20 and 5 nm, were obtained. Their experiments suggested that the size of these nanocrystals depended on the sputtering argon pressure in what seemed to be an anomalous manner. For pressures of 200–400 mTorr, the particle sizes decreased with increasing pressure and were found to be as small as 7 nm at 400 mTorr. This seemed to be in contrast to the pressure dependence for nanoparticles synthesized in a Joule heating system. This behavior, however, can be understood upon careful consideration of the sputter deposition process. The pressure increase near the cathode corresponds to a decrease in sputter rate, resulting in a decrease in the density of particles. Therefore fewer particles are available to coagulate and form larger particles. This is analogous to a decrease in the partial pressure of species in Joule heating systems. Above 400 mTorr, however, particle sizes increased, with particle agglomerates observed at 700 mTorr [122–124]. In this case pressures above 400 mTorr represented a threshold in which nanoparticles were confined in the vapor for longer periods of time thus increasing their size by growth through coagulation [122–124]. Terauchi et al. [125] used rf magnetron sputtering with Ar to synthesize Au nanoparticles and determined that Au nanoparticles formed when sputtered at pressures between 60 and 300 mTorr. In contrast to other studies, however, at pressures between 60 and 250 mTorr the particle size was increased from 3 to 12 nm. In this case, both pressure and

rf power were increased. They observed that an increase in pressure alone gave lower sputter rates. Thus power was increased. Therefore increasing power to increase sputter density offset the effect of increasing pressure, and so the pressure dependence of nanoparticles could not be solely determined. Further increases in power, however, resulted in film formation. In this case the energy of the ejected particles was not removed sufficiently upon deposition on the substrate [125].

An effective method to remove energy from ejected species is by forming a thermal gradient in the sputtering system. By depositing the nanoparticles onto a cooled substrate, they experience a thermal gradient between sputter target and substrate [123, 124]. The thermal gradient increases the convective velocity of the sputtered particles and reduces the frequency of collisions [126]. Similar to Joule heating processes, the thermal gradient is also effective in enhancing deposition rates. Chandra et al. [126] sputtered Ag with Ar and He. They observed that for sputtering under identical power and pressures, a substrate cooled to 80 K resulted in the formation of agglomerated Ag nanoparticles, while a substrate at 295 K resulted in an Ag film. They also observed that when sputtered with He, the nanoparticles formed were smaller than for sputtering with Ar [126]. This may be the result of less effective confinement of species through growth by coagulation due to the lower mass of He than Ar. Pressure and growth time are also varied to control particle size distributions as well. Kaatz et al. [127] found that narrow size distributions are attained if the particles are collected soon after sputtering, thus reducing time for agglomeration.

These observations seem to confirm that the growth of nanoparticles in sputtering processes is similar to that in Joule heating, where the growth occurs in the gas phase in flight to the substrate [127]. Furthermore, it is the partial pressure of species that determines the particle size with nucleation and growth being a function of supersaturation. In the case of sputtered species, supersaturation is a function of the distance from the substrate, sputtering rate, and the mean free path of species in the vapor [127].

Variations on sputtering geometry have been developed. Xenoulis et al. [128] used a hollow-cathode plasma sputtering source with a flowing inert gas to form an intense source of metal nanoparticles. The apparatus was shaped like a cone, with the inside surface acting as both a cathode of the desired metal species and a channel where the gas enters and discharges. The device was driven by a dc power supply with a potential of 340 V. The sputter gas was Ar, which served to both sputter the cathode and to carry the sputtered species away causing nucleation and growth. Clusters of Cu, Ag, Au, and Ta were produced, and species were found to increase in size with sputter current [128]. Urban et al. [129, 130] constructed a device where condensed nanoparticles were swept out of a 3 mm diameter converging–diverging exit nozzle, forming a low velocity beam. The beam was directed onto a substrate to write a patterned film. This process was used to produce Al, Cr, Fe, Ni, $Cu_{1-x}Co_x$, Cu, Zr, Mo, Ag, Ta, W, Pt, and Au films. Wagener et al. [131] used magnetron sputtering to deposit nanoparticles into low vapor pressure liquids such as silicone oil in a process known

as vacuum evaporation on running liquids. Surfactants were added to the oil to prevent agglomeration of the particles.

As previously discussed, the production of metal compound nanoparticles in the plasma sputtering process is often done by sputtering alloy targets. Some compound nanoparticles successfully produced have included TiAl [132, 133], AlAg [134], and CuMo [135]. The synthesis of metal oxides and nitrides can be accomplished by sputtering in the presence of a reactive gas. This, however, can lead to oxidative or nitride poisoning of the sputter target thus reducing yields. Alternatives to reactive sputtering with oxides include postsputter oxidation where the particles are oxidized in a controlled manner in the growth chamber after synthesis. This also can have difficulties, where grain growth and agglomeration have been observed [117].

## 2.2.3. Co-Condensation Synthesis of Metal Nanoparticles

Chemical methods of metal nanoparticle synthesis described previously involve clustering of metal atoms produced by a chemical reaction into nanoparticles. The key step in this process is the chemical reduction of the metal salts in an aqueous media which determines the particle size and size distribution. Although great success has been achieved in synthesizing nanoparticles of many metals with narrow size distribution, there are many challenges that prevent their scale up. The chemistry of the process is not well understood [136, 137]. As a result, researchers have reported numerous different conditions resulting in products of varying nature and composition [138–143]. However, it is known that maintaining exactly similar reaction conditions is important to achieve the narrow particle distribution. Without fundamental understanding of the processes involved, the scale up of chemical synthesis techniques has not been successful. In addition, purification of the nanoparticles is complicated and complete removal of the by-products of the metal salt reduction step is an important issue for these techniques.

To overcome these problems, many researchers have used the co-condensation (COCON) process of synthesizing metal nanoparticles. The COCON process involves co-deposition of metal vapors and a polar coordinating solvent on to the liquid nitrogen cooled walls of a reactor at low pressures (typically, a few mTorr). The solvent coordinates the growing nanoparticles and prevents the agglomeration of nanoparticles commonly observed in Joule heating IGC techniques (Section 2.2.1). The size of the nanoparticles synthesized by COCON is usually much lower than that obtained from IGC. Particles smaller than 5 nm with narrow size distribution can be obtained. In the COCON process the nanoparticle growth starts in vacuum and continues later in a polar solvent. The nanoparticle growth mechanisms in vacuum are well understood [144–146], and some of these results can also be applied to the particle growth in the COCON process. Other advantages of the process include the ease of scaling, good control over the particle size, and high purity of the nanoparticles obtained [147–149].

The COCON technique has its roots in an earlier technique called "vacuum evaporation onto a running oil substrate" demonstrated by Yatsuya and co-workers [150–154]. In this process, an oil of low vapor pressure is introduced

near the center of a vertically mounted rotating disk. The oil moves toward the edge due to the centrifugal force and thus, a thin layer of oil is present on the disk. An evaporation source placed facing the disk acts as a source of metal atoms. Any suitable source such as thermal evaporators, electron beam evaporators, or sputtering guns can be used. The metal is evaporated from the source and is deposited onto a running oil substrate on the rotating disk. The metallic particles formed move along with the oil and this suspension is collected at the edge of the disk. Yatsuya et al. [150, 153, 154] used an electron beam evaporator and typical deposition conditions were: metal evaporation rate ∼100 mg/min, source–substrate distance was around 15 cm, oil supply of ∼10 cm$^3$/min, and disk rotation speed ∼200 rpm. Nanoparticles between 20 and 80 Å were synthesized under these conditions, and the particle size could be controlled by rotation speed of the disk and its distance from the evaporation source [150]. Instead of a disk, any substrate such as a horizontal rotating drum on which an oil layer can be maintained by the centrifugal force can be used [131]. Metal deposition onto the mobile liquid surface prevents the formation a film which would result if a solid substrate is used. Thus, in this process, the oil prevents the coalescence of the nanoparticles by physically separating them.

An important modification to this process was made by Klabunde and co-workers, who used an organic solvent instead of the oil. This technique is referred to as the solvated metal atom dispersion technique [148–150, 155–172]. In this technique, the metal vapors and the solvent are introduced simultaneously into a reactor whose walls have been cooled with liquid nitrogen. For a small-scale setup this can be done by simply immersing the reactor vessel in a bath of liquid nitrogen. However, a double walled reactor is used for larger reactor dimensions. The solvent and the metal vapors co-condense onto the sides of the reactor. The temperature of the reactor is maintained below the freezing point of the solvent used. After the metal deposition step, the reactor walls are allowed to warm up and the colloidal suspension of the nanoparticles is obtained. The suspension can be collected directly in a flask connected to the reactor [156] or be allowed to flow over support material (such as alumina powder) placed inside the reactor, which on further heating transfers the nanoparticles onto the support [243]. This is extremely useful for the formation of highly dispersed active metallic catalysts.

The vaporized metal atoms start clustering in the vacuum phase as they travel toward the reactor walls, but the main growth occurs on the reactor walls as the solvent melts during the warming of the reactor [147, 173]. Thus, the COCON technique can be used to create nanoparticle suspensions without resorting to chemical reduction. A large number of metal nanoparticles have been synthesized including Au, Ag, Sn, Pt, Mo, In, Nd, Co, Re, Fe, and Ni [147–149, 155–172]. Depending on the metal, organic liquids such as alcohols, ketones, toluene, THF, etc. are chosen as the solvent. The choice of the solvent is important as the growing metal nanoparticle exhibits high reactivity with the host solvent. The solvent helps to solvate the metal atoms and the growing nanoclusters and prevents their agglomeration. The solvent causes the metal particles to develop a small negative charge. The agglomeration of the metal

particles is prevented due to the steric effects (solvation) which impede the motion of the clusters and because of the electrostatic repulsion (due to incorporation of the negative charge) [147]. It has been observed that polar solvents yield smaller crystallites. The solvent also prevents the interaction of nanoparticles with the atmosphere, thus reducing the oxidation of the metal. This is especially important as nanoparticles are characterized by high surface energy and are extremely prone to oxidation. Some of the chemical synthesis techniques have been able to avoid this problem by *in-situ* coating of the growing nanoparticles. However, since the synthesis and coating of the nanoparticles has to be carried out simultaneously, the chemistries of the two processes need to be matched, which reduces the freedom in selecting the coating material. In addition, for many applications, coating the nanoparticles changes the properties (e.g., magnetic properties) of the nanoparticle [174]. The suspensions synthesized by the COCON technique do not suffer from these limitations as the suspensions prevent oxidation of the nanoparticles for as long as a few months [156]. The coating of the particles can be done either *in-situ* during the metal deposition step [169, 170, 174] or in a two step process. Since the metal atoms are generated by evaporation and not by a chemical reaction, the restrictions on the coating chemistry can be relaxed. Bimetallic nanoclusters can also be synthesized by using two metal sources simultaneously. Under different process conditions either bimetallic nanoparticles of uniform composition or a nanoparticle with a core–shell morphology can be obtained [147–149, 165, 172]. In the case of some metals, digestive ripening can be carried out to further reduce the polydispersity, by adding suitable agents to the solvent. Stoeva et al. [156] have shown this in the case of gold, where they mixed dodecanethiol with the solvent before the metal evaporation step. The nanoparticle suspension subsequently obtained, which had particle sizes ranging from 1 to 40 nm, could be refluxed to obtain particle sizes of about 4 nm with a standard deviation below 4 Å [156].

Thus, it can be seen that the COCON technique is a powerful technique capable of synthesizing nanoparticle suspensions of various metals with high purity and good control over the particle size and size distribution. Since the underlying physics of the process is understood, it is possible to scale up the COCON reactor. We are currently using a scaled up COCON reactor to produce large quantities of silver and copper nanoparticle suspensions [175]. The reactor is a cylindrical vessel 2.3 m long and 0.4 m in diameter (Fig. 5). The reactor is designed to run in a continuous mode and approximately 300 mL of suspension can be produced per hour with a metal concentration of ∼1 mg/mL. The suspensions obtained from the reactor match those reported from smaller reactors in terms of particle size and distribution, which underlines the efficiency of scale up. To look at individual particles we have dispersed the metal nanoparticles in a film of PMMA by dissolving PMMA powder into the suspension and then spin casting the same (Fig. 6). It can be seen in Figure 6 that the COCON technique produces nanoparticles with narrow size distribution without agglomeration.
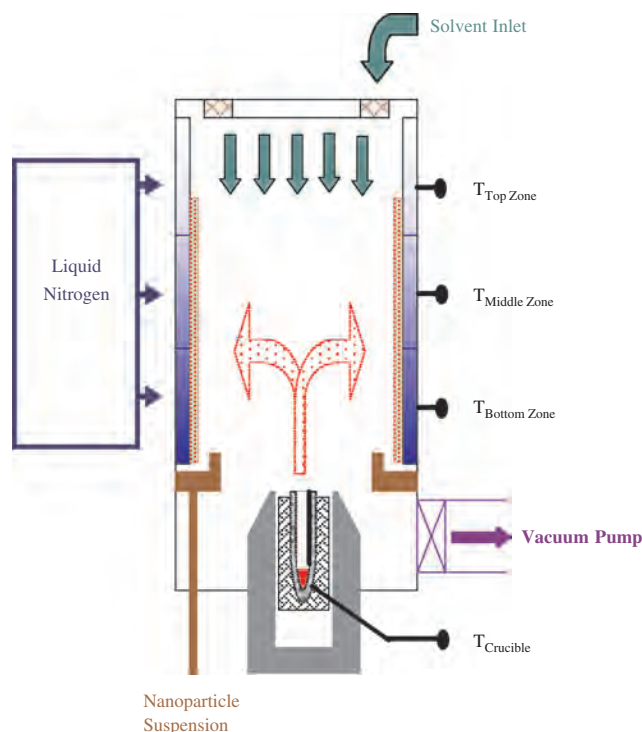
**Figure 5.** A schematic of the co-condensation process.

## 2.2.4. Other Gas Phase Processes

Other methods to produce metal nuclei in the gas phase include inductive heating, chemical vapor deposition (CVD) and chemical vapor condensation (CVC), and gas phase or liquid phase laser ablation. A brief treatment of each method is presented here.

The inductive heating process is a variation on the Joule heating process where an inductive heater is used to heat a crucible. Inductive heating is used when temperatures above
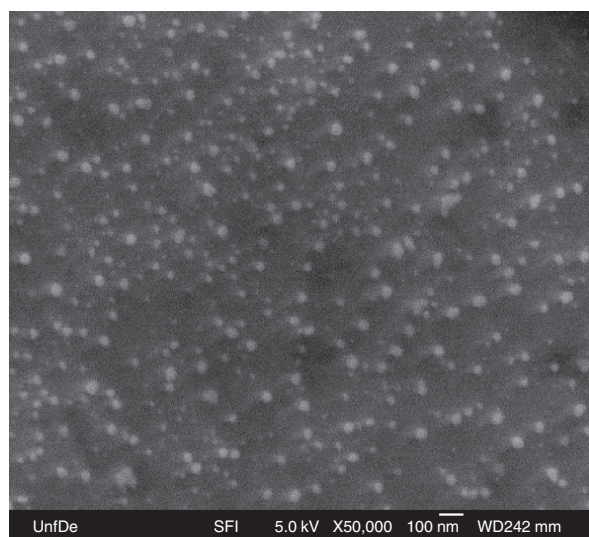


**Figure 6.** Silver nanoparticles dispersed in a film of PMMA. Reprinted with permission from [175], A. Pradhan et al., *Mater. Res. Soc. Symp. Proc.* 740, I6.10.1 (2003). © 2003, Materials Research Society.

2700 K are needed to evaporate the metal precursor [176]. In a typical system an induction coil is wrapped around the crucible to make thermal contact, and the crucible acts as a susceptor. A high frequency current of 500 kHz to 1 MHz is passed through the coil. The coil consists typically of copper with cooling water passed through it, while typical crucible materials are graphite or tungsten. Induction heating has been used successfully to evaporate some refractory metals [177] and other materials such as Pd [178]. A limitation to this process is the undesirable heating of other apparatus in the reactor that causes outgassing [176].

In the chemical vapor deposition and chemical vapor condensation processes, a chemical precursor is converted to the gas phase and subsequently dissociated by thermal energy or a plasma to generate nuclei [179]. The plasma in CVD processes is often generated using microwave radiation. The metal nuclei are carried away from the plasma reaction zone and coagulate as in other gas condensation processes. Powder precursors are sometimes used in this process as well. Oxide powders have been used where the oxides are reduced to their respective metals. Vissokov et al. [180] produced 5–50 nm particles of Mn, Fe, Co, Zn, and Mo by reducing their respective oxides in this technique. Metal alloy nanoparticles such as Fe–Ni and Fe–Cu have also been produced in a 50% $H_2$–50% Ar plasma [181]. In the CVC process, metallorganic precursors are often used. Choi et al. [182] used $Fe(CO)_5$ and $Co_2(CO)_8$ to produce nanoparticles of Fe and Co, respectively. The precursors were transported into a bubbler and then passed into a heated furnace by He gas, where they were subsequently decomposed. They found that the mean particle size was a function of the temperature of the decomposition process [182]. The CVC process is, however, used most widely in the production of metal oxides and ceramics [183, 184].

In the gas phase laser ablation process, high-powered laser pulses are directed onto a metal target to remove metal atoms and create nuclei. The synthesis is generally performed in an inert gas where a high degree of supersaturation results in the vapor phase above the target. The growth of nanoparticles continues by coalescence as in other vapor processes [185]. Unlike some other vapor phase techniques, however, the pressure regime is generally at or above ambient conditions [186]. The wavelength of the laser is chosen depending on the target material. Metals are often ablated with an excimer laser (ultravoilet radiation). This technique has been used to synthesize transition metals [187, 188]. Ozawa et al. [189] synthesized W nanoparticles under low He gas pressure using a $Q$-switched Nd:YAG laser. They found that at a power of 1.9 J/cm$^2$ particle size control was achieved from 10 to 80 nm depending on inert gas pressure in the system. Stepanov et al. [190] reported the synthesis of 25 nm yttrium nanoparticles by laser ablation in argon. Finally, intermetallics have also been synthesized by pulsed laser deposition. Pithawalla et al. [191] have reported the synthesis of nanopowders of Fe, Al, and ferromagnetic iron–aluminide particles of 6–10 nm. They used a $Q$-switched Nd:YAG laser at $\lambda = 532$ nm in an Ar or He environment and a Fe–40 at% Al target. They also reported the ability to produce "treelike" morphology in the samples by applying an electric field in the deposition chamber [191]. Laser ablation in a liquid medium is also a widely used method

for metal nanoparticle synthesis. In this case a metal target is immersed in a solution and laser pulses are directed onto the target as in the gas phase process. Ablation in a liquid medium is used as a cleaner alternative to chemical solution synthesis of metal nanoparticles. As the laser pulse hits the metal, clusters of metal particles are formed. These clusters are reduced in size to the nanometer scale by heating and vaporization of the laser. As reported by Bosbach et al. [192] the size of the nanoparticles can be tuned by changing the wavelength of light to the specific absorption frequency for the metal clusters.

Liquid solutions have most often been used to synthesize noble metal nanoparticles [193–195], but laser ablation in liquids has been used to generate other metals such as Ti [196], as well as compounds such as Ag$_2$Se nanoparticles [197]. The liquid medium has included such diverse species as water, ethanol, chloroform, and *n*-hexane [198], and a range of liquid solutions including NaCl [193] and sodium dodecyl sulfate [196] among others.

### 2.2.5. Nucleation and Growth in Gas Condensation Processes

In this section we discuss the nucleation and growth of metal nanoparticles in gas condensation processes. Synthesis of nanoparticles in inert gas condensation systems begins with the nucleation of clusters of metal atoms. The thermodynamics of nucleation are often modeled with the bulk free energy change per volume of the system [199]

$$\Delta G = 4\pi r^2 \sigma + \frac{4}{3}\pi r^3 \Delta G_v \qquad (2)$$

where $\Delta G$ is the Gibbs free energy of the system, $\Delta G_v$ is the energy change on going from vapor to solid, and $\sigma$ is the surface free energy of a nucleus. At equilibrium the change in free energy of the system is zero. This is used to find the critical radius $r_c$ for nucleation. Nucleation occurs at supersaturation, given by

$$\ln\left(\frac{C}{C^*}\right) = \ln S = \frac{2\sigma v}{kTr_c} \qquad (3)$$

A kinetic expression for the rate of nucleation $J$ is given by an Arrhenius type of equation,

$$J = C \exp\left(\frac{-\Delta G^*}{kT}\right) \qquad (4)$$

This is used to obtain a final expression for the rate of nucleation [75]:

$$J = \frac{p_v v}{\sqrt{2\pi m_v kT}}\sqrt{\frac{\sigma}{kT}}N_1 \exp\left(\frac{-16\pi\sigma^3 v^2}{3k^3 T^3 (\ln S)^2}\right) \qquad (5)$$

It can be seen from this expression that the nucleation of particles has a strong dependence on the degree of supersaturation and, as discussed earlier, the manner in which supersaturation is achieved is characteristic of the IGC process.

After nucleation, particle growth occurs by coagulation and subsequent coalescence of nuclei in a growth region near the evaporation source. Coagulation is a stepwise process where two nuclei meet and are joined causing

sintering. In the case of Joule heating, depending upon where in the hot growth region this process occurs, the sintering may be followed by complete coalescence, in which diffusion occurs between the two nuclei, forming a larger single particle. The driving force for diffusion is the excess surface area of the joined spheres. Conversely, the sintering may result in particle necking, where a strongly bonded neck joins smaller particles in a hard agglomeration of particles, sometimes referred to as an aggregate. Even further from the growth region, a "soft" agglomeration may result. The soft agglomeration can be dispersed with minimal energy input. These processes are depicted in Figure 7, where the schematic representation given by Granqvist and Burhman has been modified.

Granqvist and Burhman [86] proposed a growth model that was based on the statistical coalescence of nuclei. The model is generated assuming that the growth of nanoparticles is a stepwise process where the change in particle volume at a coalescence step is a random fraction of the particle volume from the previous step. Thus the primary particle size is a result of the number of coalescence steps [86]. The model leads to a log-normal particle size distribution [86, 200]

$$f_{LN}(x) = \frac{1}{(2\pi)^{1/2}\ln\sigma}\exp\left(-\frac{(\ln x - \ln\bar{x})^2}{2\ln^2\sigma}\right) \qquad (6)$$

where $x$ is the particle diameter, and $\sigma$ is the standard deviation.

The growth of nanoparticles in the IGC process is now thought to be through Brownian coagulation [201]. A model for this process often employs an integrodifferential equation [75, 201–203]

$$\frac{\partial N(t,V)}{\partial t} = \frac{1}{2}\int_0^V K(U, V-U)N(t,U)N(t,V-U)\,dU$$
$$- N(t,V)\int_0^\infty K(V,U)N(t,U)\,dU \qquad (7)$$

where $N(t,V)$ is a function characterizing the time dependant particle size distribution, $U$ and $V$ are the volumes of particles that coagulate, and $K(U,V)$ is the coagulation kernel, a collision rate function. The collision rate function is generally assumed to take the form of a free molecule coagulation that results from the kinetic theory of gases [204].
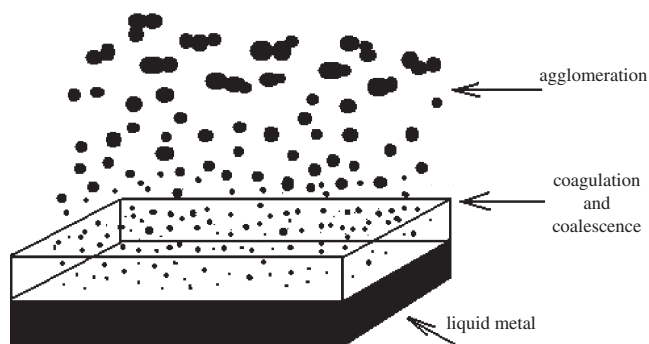


**Figure 7.** The coagulation and coalescence of metal nanoparticles with a subsequent agglomeration.

This, however, may only be valid early in the growth process for primary spherical particles where hard agglomerates are not considered.

In research by Flagan and Lunden [75], based on earlier work by Lai et al. [205], a self-preserving particle size distribution was incorporated into the integrodifferential equation to obtain a dynamic population balance for the IGC system [75]. The self-preserving distribution is similar in shape to a log-normal distribution, where the two are often confused [201]. The self-preserving size distribution is a function of a unitless volume, while the log-normal distribution is a function of the particle mean and standard deviation [201]. Flagan and Lunden applied the particle size distribution to the population balance in a simplified analysis where coagulation of nuclei leads to an initial growth of primary nanoparticles by coalescence. They obtained a time dependant relationship for the average nanoparticle volume [75]

$$\bar{v}(t) = \bar{v}_0 \left[ 1 + \frac{5}{12} \frac{\alpha \kappa_0 \rho_0 V t}{\bar{v}_0^{5/6}} \int_0^t \frac{dt}{\sqrt{T/T_0}} \right]^{6/5} \tag{8}$$

The second term in brackets is the characteristic time for coagulation of spherical particles with

$$\kappa_0 = \left( \frac{3}{4\pi} \right)^{1/6} \sqrt{\frac{6kT}{\rho_0}} \tag{9}$$

where $\alpha = 6.67$ for spherical particles [205], $\bar{v}_0$ is the average nucleus size, and $\rho_0$ is the density of a nucleus. This model is limited to an ideal gas, constant pressure, and a linear decrease in temperature from the evaporation source. Furthermore, the model only applies to coalescence of small particles leading to larger primary particles; it does not account for particle growth to form hard agglomerates. Their analysis was expanded to include growth of hard agglomerates where an accelerated growth occurs.

While agglomeration and sintering of nanoparticles are inherent to the growth process, this may represent problems for obtaining individual nanoparticles for subsequent processing and functionalization, or when compaction is necessary. Rapid removal of nanoparticles from the growth region, while stopping primary particle growth, may essentially freeze them during growth, causing sintered areas or necks between them. The result is a hard agglomerate or aggregate of nanoparticles that can be very difficult to disperse. The aggregation of particles depends on a competition between the time that it takes for particles to collide (coagulate) vs the time it takes for them to coalesce in the growth process [201, 206]. If particles coalesce much faster than they collide, they combine to form a larger single particle. If the collision time is much quicker, an aggregate of nanoparticle chains is observed. The collision and coalescence times are dependent on the rate at which particles are removed from the hot growth region of the evaporation source [201]. The viscous coalescence time $\tau_c$ for spheres of area $A$ has been given by [207]

$$\tau_c = \frac{\mu A}{\gamma} \tag{10}$$

where $\mu$ is the viscosity of the primary particle and $\gamma$ is the surface free energy. The characteristic time is considered to be time independent, even though this time is applied to aggregates that restructure during the growth process [208].

Models for agglomeration and subsequent aggregation of nanoparticles have been developed that incorporate characteristic agglomeration and aggregation times [75, 206, 208–213]. The first such model describing the simultaneous coalescence and aggregation of nanoparticles was formulated by Koch and Friedlander [214]. In the model, a particle sintering rate expression was used in the population balance for the system. The model was based on the principle that the driving force was the minimization of the surface area $A$ of an aggregate. In the sinter rate expression the particle surface area is reduced $dA/dt$ according to the ratio

$$\frac{dA}{dt} = -\frac{A - A_c}{\tau_c} \tag{11}$$

where $A_c$ is the surface area of a completely coalesced sphere, and $\tau_c$ is the characteristic sintering time. The Koch and Friedlander model was applied to the entire growth process from coagulation to agglomeration. The mechanism for sintering may change during the growth process, however, and may be a function of the aggregate size. This presents a difficulty for the model [214].

Xiong and Pratsinis [215] developed a two-dimensional model that describes the evolution of aggregate volume including a surface area distribution. The model incorporates particle coagulation, coalescence, and sintering rate terms. In their analysis they determined that irregularly shaped aggregates form as a result of the finite coalescence rate for particle nuclei, and that coalescence and collision have a specific dependence on the size and shape of the particles [215]. Park et al. [204] developed a model that did not consider just free molecular coagulation, a common assumption as discussed previously, but considered coagulation of particles in all size regimes including aggregates. They suggested that Brownian and turbulent coagulation occur simultaneously in the growth process, and the intensity of turbulence increases the particle size distribution [204].

Nanoparticle synthesis models have also included the concept of fractals to describe the aggregate growth [75, 216–218]. Aggregate size and shape can be characterized as mass fractals in which their dimensions determine the collision behavior of nanoparticles [217]. A relationship between the number of primary nanoparticles $N$ in a fractal and its radius of gyration $R_g$ is given by [219]

$$N = k_g \left( \frac{R_g}{a} \right)^{D_f} \tag{12}$$

where $a$ is the average primary particle radius, $D_f$ is the unitless fractal dimension, and $k_g$ is a unitless fractal prefactor. The fractal dimension is a measure of the openness of the aggregate structure. Thus primary particles that are aligned in a straight chain would have $D_f = 1$. The fractal prefactor is related to the voids between primary particles [220]. A simple method to determine the fractal dimension and prefactor is through a logarithmic plot of $N$ vs $(R_g/a)$, where the slope is the fractal dimension $D_f$ and the intercept is the fractal prefactor $k_g$ [220]. Brasil et al. [220] found

estimates of $k_g$ approximate to 1.27 and $D_f$ approximate to 1.82, which were approximately independent of aggregate size and composition. They also found that partial sintering in conjunction with the polydispersity of aggregates contributes to an increase in $k_g$, possibly justifying the differences between numerical and experimental results [220].

Monte Carlo simulations have also been used in which many growth processes are incorporated into one model [201, 203, 221, 222]. In Monte Carlo simulations the mass fractal dimension is often determined. However, these can be complicated processes.

During coalescence and sintering the particles minimize their energy by forming an area of adhesion between them where a grain boundary is present [223]. Large forces are required to separate particles sintered in this manner

$$F = \frac{3}{2}\pi\gamma_{\text{eff}}\frac{r_1 r_2}{(r_1 + r_2)} \tag{13}$$

where $\gamma_{\text{eff}}$ represents a contribution from the surface energy and the grain boundary energy of the sintered particles and $r_1$ and $r_2$ are the radii of two particles [223, 224]. These sintered nanoparticles can exhibit contrast fringes that are developed parallel to the area of contact. The fringes are often observed in transmission electron micrographs. Other types of adhesive force that are involved when metal nanoparticles come into contact with one another include van der Waals and electrostatic forces. Generally, the electrostatic force between particles is the smallest force [225]. Van der Waals forces have been postulated to cause the particles to coagulate and sinter forming aggregates even at room temperature [201].

Several approaches have been used to solve the problem of particle coalescence and sintering *in-situ*. Singhal et al. [226] reported the optimization of a vapor phase synthesis process by using a technique called combustion flame-chemical vapor condensation where particles pyrolyze downstream before being collected. The pyrolysis was done with a flat flame working at low pressure, which reduced residence time and minimized collisions. Andres et al. [227] used a process to spray a coating of alkyl thiol molecules onto Au nanoparticles as they are evaporated from the source. This reduced agglomeration of bare metal. Olynick et al. [201] coated Cu nanoparticles with a thin oxide layer to prevent sintering. And finally, Gotoh et al. [228] devised a system where Ag nanoparticles were evaporated onto a nylon filter media that was saturated with a cationic or dodecanethiol surfactant. The carrier gas was passed through the filter, and subsequent to an experiment, the filter medium was washed in toluene to remove the surfactant stabilized Ag nanoparticles.

# 3. CHARACTERIZATION OF METAL NANOPARTICLES

There are many techniques available for the characterization of metal nanoparticles. A brief introduction to some of the relevant techniques is given here, along with some of the important results that are applicable to the study of metal nanoparticles.

## 3.1. Electron Microscopy

Electron microscopy consists of the techniques of scanning electron microscopy (SEM) and transmission electron microscopy (TEM). SEM is valuable for allowing a more magnified view of a sample than is possible with optical microscopy. In the SEM experiment the sample is placed in a vacuum chamber and bombarded with a focused beam of electrons. The electrons are rastered across the surface of the sample. The electron bombardment causes several processes to occur in the sample, such as electron backscattering, secondary electron emission, and photon emission. In current electron microscopes the lateral resolution now achievable is approaching 1 nm.

TEM may be the single most important technique for characterizing metal nanoparticles. TEM allows the researcher the ability to probe the size, shape, internal structure, and, through electron diffraction and other accessories, the chemical species of the nanoparticles. The operation of a TEM is similar to that of SEM in that the sample is placed in vacuum and bombarded with a focused beam of electrons. Two types of imaging are obtained, bright field and dark field. In bright field imaging the electrons propagate through the sample and are focused and magnified. The image is formed from the electrons that transmit through the sample through contrast that depends on the scattering mechanisms. Electrons are also diffracted upon impinging on the sample. In dark field imaging, an image is formed from the electrons that are diffracted. This allows the imaging from specific crystalline planes. Current high-resolution TEM systems can achieve lateral resolutions of 0.1 nm or lower. Electron diffraction patterns allow the researcher the ability to determine the lattice constant of the particles, which can help in species identification. The technique of selected area diffraction allows the researcher to probe specific areas in nanostructured materials. There are now other analytical techniques available in a TEM package. Two such techniques include energy dispersive X-ray spectroscopy, in which characteristic X-rays emitted from the sample upon electron bombardment are analyzed, and electron energy loss spectroscopy where the electron energies are measured after they are elastically or inelastically scattered upon transmitting through the sample. Both of these techniques are available as an accessory to a TEM. A review of some of these analytical TEM methods has been given by Schneider [229].

Both SEM and TEM techniques can be destructive to the sample under study. TEM sample preparation may consist of dispersing the nanoparticles in a solvent and then drying them on a carbon coated copper grid. For thin film samples microtoming techniques are needed. SEM experiments generally require minimal preparation techniques.

## 3.2. X-Ray Diffraction

In X-ray diffraction (XRD) a collimated beam of X-rays is incident on the sample under study and is diffracted by the crystalline phases contained in the sample. XRD is a nondestructive technique that is important for identifying the crystalline phases, structural properties, defects and strain, crystal size, and epitaxy in a sample. The average nanocrystal size, both in powder and thin film samples, can be

estimated using the Scherrer equation based on diffraction peak broadening [230],

$$D = \frac{0.89\lambda}{(\Delta 2\theta)\cos\theta} \qquad (14)$$

where $\lambda$ is the X-ray wavelength, and $\Delta 2\theta$ is the full width at half maximum of the peak. Sample identification can be easy by comparing the experimental diffraction pattern to that in the JCPDS files [231]. Sample preparation is relatively simple; nanoparticles can be pressed into a disc, film, or smeared onto a substrate and the experiment does not require vacuum.

## 3.3. X-Ray Photoelectron Spectroscopy

X-ray photoelectron spectroscopy (XPS) uses soft X-rays to bombard the surface of a sample causing electrons to be ejected. The kinetic energy of the ejected electrons is measured and is converted to binding energy in the sample. XPS is a surface sensitive technique giving information from about 2–20 atomic layers into the sample. XPS is a valuable tool for characterizing the chemical state of atoms. Because metal nanoparticles have a high surface energy, surface passivation is a common method of particle treatment. XPS is often used to determine the effects of bonding of species to the surface [232], including the surface oxidation studies of metals [233]. XPS can be performed on thin films and powders, but the sample must be vacuum compatible. For a discussion on the quantitative analysis of nanostructures see Tougaard [234, 235].

## 3.4. Fourier Transform Infrared Spectroscopy

The vibrational motion of chemical bonds occurs in the infrared (IR) energy regime. Fourier transform infrared spectroscopy (FTIR) exploits this phenomenon by exposing the sample to IR energy, which couples to the IR energy in the sample at characteristic energies. If the impinging IR energy is in resonance with the energy of the chemical bond in the sample, the intensity of the beam will be reinforced. In the experiment the intensity of the beam is measured before and after it interacts with the sample. The incident radiation can be detected in transmission or reflection experiments. The intensity is then plotted as a function of the frequency in the IR spectrum. The principal use for FTIR in metal nanoparticle characterization is to detect chemical species bonded to the metal surface, and to monitor reactions at the surface [236, 237].

## 3.5. Raman Spectroscopy

In a Raman spectroscopy experiment, laser light impinges on the sample under study in a process where most of the light is scattered. This scattered light is known as Rayleigh scattering and appears as a large central band on a Raman spectrum. Some of the light, however, may excite molecular and crystalline vibrations. The photons in this case lose an amount of energy that is equal to the energy imparted to the sample. The photons are thus scattered with a longer wavelength, whose difference is known as the Stokes shift. The atoms that are excited by this process relax back to their ground state and release energy back to the incident beam in a process known as the anti-Stokes shift. The Stokes shift is generally measured in a Raman experiment, and the separation of the shifted light from the Rayleigh scattering is a measure of the vibrational frequency in the sample. Laser light is often used in the visible or ultraviolet region, and the technique is generally nondestructive. Nanoparticle powder samples can be pressed into pellets and the detector placed 90° to the sample. The laser light is detected as it is reflected from the surface.

An interesting combination of Raman spectroscopy and metal nanoparticles has been developed in a technique known as surface enhanced raman spectroscopy (SERS). SERS is used to enhance the surface selectivity of Raman spectroscopy by depositing metal nanoparticles onto the sample. The metal nanoparticles provide an electromagnetic enhancement by roughing up the surface and by localizing the metal's surface plasmons. SERS experiments are most often done with noble metal nanoparticles [238, 239], and results have shown that the Raman signal can be enhanced by a factor of $10^{14}$–$10^{15}$ [240, 241].

## 3.6. Solid State Nuclear Magnetic Resonance Spectroscopy

Solid state nuclear magnetic resonance (NMR) is a technique used to identify crystalline phases in materials. It is especially valuable for probing materials properties in disordered systems such as amorphous systems [242]. NMR is based on the interaction of nuclear magnetic moments with rf waves. The sample under study is placed in a magnetic field and irradiated with rf pulses over a varying range of frequencies. The nucleus of the atom is excited from its ground state to a higher magnetic spin state, and as it relaxes back to its ground state it re-emits energy at the excitation frequency. The atoms in a sample are thus identified based on the excitation energy. NMR can only be applied to nuclei with an odd mass or odd atomic number because these nuclei possess a permanent magnetic moment. In an experiment the excitation frequency is detected and plotted as intensity versus frequency. The area under a peak is directly proportional to the number of nuclei contributing to the effect. Sample structure and bonding information may also be obtained. NMR is an important tool for obtaining quantitative information and powders, single crystals, or thin films are all suitable for NMR analysis.

Researchers have used $^{13}C$ and $^{1}H$ NMR to investigate the interaction between alkanethiol coated Au nanoparticles [243, 244]. They have found that the alkanethiol Au bond is sensitive to the Au nanoparticle size, causing a size dependent shift in the NMR spectrum. Researchers have now also been able to correlate NMR chemical shifts to nanoparticle sizes encaged in zeolites [245]. Enderle et al. [246] used $^{129}Xe$ NMR to determine the size of platinum nanoparticles encaged in a zeolite. They found that the Xe chemical shift increases with particle size in the zeolite due to Xe–Pt interactions until finally the Xe atom was restricted from entering the cage as the Pt nanoparticle size increased to fill the cage.

## 3.7. Mössbauer Spectroscopy

Mössbauer spectroscopy is based on the Mössbauer effect, in which a transition occurs between the ground sate of an atom and a low-lying nuclear level involving the emission or absorption of a photon in the form of a $\gamma$-ray. This technique involves emitter atoms and absorber atoms, with the absorber being the sample under study. The emitter is a radioactive isotope that emits $\gamma$-rays toward the absorber. The emitter must be of the same element and isotope as the emitter, but with its atoms in the ground state. Upon absorption of the $\gamma$-ray the absorbing atom is raised to an excited level and subsequently emits the $\gamma$-ray. The $^{57}$Co isotope is ideally suited as an emitter, which produces 14.4 keV $\gamma$-rays. This makes $^{57}$Fe a common element under study as an absorber. Another common emitter is $^{197}$Pt with $^{197}$Au being the absorber. The emission and absorption of $\gamma$-rays by the emitter and the absorbing sample are recoilless for atoms bound in a solid below its Debye temperature; thus no energy loss is involved. This is a necessary condition for the Mössbauer effect to occur. A spectrum is obtained by using a synchrotron $\gamma$-ray beam of a radioactive material, while the Doppler effect is used to differentiate between the absorption and emission energy for absorbing samples in which the energy gap is different from that of the emitter. In utilizing the Doppler effect, the emitter (or sometimes the absorber) is oscillated in the direction of the absorber (emitter) thus changing the energy of the $\gamma$-rays. The change in velocity is converted to the energy, and so zero velocity is analogous to zero energy change between the emitter and absorber and any difference in energy therefore is due to interatomic or intraatomic interactions of the absorber. This shift is termed the isomer shift. If the sample has a nucleus with spin greater than 1/2, its nucleus will have an electric quadrupole moment. This momemt will interact with an electric field gradient arising from nonuniform distributions of electrons in the sample, or from nonuniform atoms bound to the Mössbauer active atom. The result is a split in the single absorption line. A magnetic field produced either internally from electron arrangements in the sample or externally results in further splits in the quadrupole doublets to give six lines in the spectrum [247].

Mössbauer spectroscopy results are most often obtained in transmission mode, where the $\gamma$-rays pass through the specimen to the detector. For thick specimens this is an inefficient process, and the technique of conversion electron Mössbauer spectroscopy can be used. In this case X-rays and Auger electrons are detected when the atom that is excited by the $\gamma$-rays decays to its ground state. The Mössbauer effect has been observed for over 40 elements [247] but it is most often used for Fe containing samples. Unlike many characterization techniques, in Mössbauer spectroscopy detailed information about individual atoms in a cluster can be obtained, rather than information averaged throughout the bulk [248].

As discussed, the absorption line from an atom will exhibit a single isomer shift due to electrostatic interactions in the sample. This shift is now being investigated for the study of metal nanoparticles. Paulus et al. [249] have characterized the isomer shift in 1–17 nm Au and Pt nanoparticles. They correlated the shift to size effects and concluded that

the large surface to volume ratio for nanoparticles makes surface effects such as screening important.

The size dependent magnetic properties of iron can be determined as it goes from a ferromagnetic to a superparamagnetic state as evidenced by a transition from an absorption sextext in the spectra to a doublet or singlet [250–254]. Researchers have also proposed that two components for the hyperfine magnetic field of nanostructured Fe powders compressed into discs are present, corresponding to nanoparticles and grain boundaries, with the grain boundary being an unusual gaslike phase [255–257] although the results have met with skepticism [258].

Finally, Mössbauer spectroscopy has been a valuable technique for examining nanoparticle Fe-core/Fe-oxide shell configurations [259]. It has been used to determine the nature of the oxide coatings such as differentiating between $\gamma$-$Fe_2O_3$ or $Fe_3O_4$ based on an absorption doublet or singlet, and to identify a superparamagnetic behavior in the oxide coatings [260].

An extensive review of the use of Mössbauer spectroscopy in nanostructured materials research has been given by Campbell and Gleiter [261].

## 3.8. Physical Adsorption

An important technique for determining the surface area of metal nanoparticles is the Brunauer, Emmett, and Teller (BET) method. The BET method is a standard method for determining surface area in catalysis research and has now been approved by the American Society for Testing in Materials. In the BET method, a gas phase adsorbate is exposed to the metal particle surface adsorbant, and the amount adsorbed is used to determine the surface area of the adsorbant. The adsorbate is attracted to the particle surface due to unbalanced forces [262]. The adsorption process is spontaneous and therefore results in a decrease in the free energy of the system. The adsorbate is bound to the adsorbant by van der Waals forces. In order to perform an experiment, the nanoparticles are placed in a glass container that is evacuated at 77 K. Sintering of nanoparticles may occur upon evacuation; thus maintaining the system at a suitable temperature is important [262]. The system volume is then determined by admitting a nonadsorbing gas such as helium into the system. The helium is then removed, and $N_2$ gas is admitted to the system. The decrease in pressure as the $N_2$ adsorbs in a monolayer on the particle surfaces is determined and then correlated with the volume of the gas admitted to the system. The volume and pressure are used in a simple expression and plotted to determine the monolayer volume of particles. The plot is known as a BET isotherm because the process is done at constant temperature.

## 4. PROPERTIES AND APPLICATIONS OF METAL NANOPARTICLES

There are several applications of interest for metal nanoparticles which exploit their unusual properties. In this section a brief survey of some of the interesting properties of metal nanoparticles is presented. We also highlight some of

the interesting current applications based on these properties. For a more detailed discussion the reader is referred to the appropriate literature.

## 4.1. Optical Properties and Applications

There is great interest in the optical properties of noble metal nanoparticles for optical energy transport [263–265], polarizers and color filters in liquid crystal displays [266], photonic crystals [267, 268], and chemical and biological sensors [269–271], among others. The optical properties of nanoparticles are being investigated because they undergo some remarkable changes as their size decreases. Fundamentally, electromagnetic waves incident upon a metal undergo scattering and absorption processes. At a particular energy, the electromagnetic field induces a collective oscillation of conduction electrons, creating surface polarization charges in the particle, which leads to a resonance frequency in the absorption spectrum. The band that results in the spectrum is known as the surface plasmon absorption band and is predicted by the extinction cross section for nanoparticles dispersed in a media [272]

$$C_{\text{ext}} = \frac{24\pi^2 R^3 \varepsilon_m^{3/2}}{\lambda} \frac{\varepsilon''}{\left(\varepsilon' + 2\varepsilon_m\right)^2 + \varepsilon''^2} \quad (15)$$

where $\lambda$ is the wavelength of the incident radiation, $R$ is the particle radius, $\varepsilon_m$ is the dielectric function for the media in which the nanoparticles are dispersed, and $\varepsilon'$ and $\varepsilon''$ are the real and imaginary parts of the complex dielectric function given by $\varepsilon = \varepsilon' + i\varepsilon''$. As is evident from Eq. (15), the extinction cross section and thus plasmon absorption band is characteristic of the complex dielectric function of the metal and the media in which it is dispersed [8, 272–273]. The real and imaginary parts of the complex dielectric function for free electron particles are given by

$$\varepsilon' = \varepsilon_\infty - \frac{\omega_p^2}{\omega^2 + \omega_d^2} \quad (16)$$

$$\varepsilon'' = \frac{\omega_d \omega_p^2}{\omega \left(\omega^2 + \omega_d^2\right)} \quad (17)$$

where $\varepsilon_\infty$ is the high frequency dielectric constant due to interband and core transitions, $\omega$ is the incident radiation frequency, $\omega_p$ is the bulk plasma frequency, and $\omega_d$ is the damping frequency which is dependent on the velocity of free electrons $v_F$ at the Fermi energy and the mean free path of the conduction electrons, $R_{\text{bulk}}$:

$$\omega_d = \frac{v_F}{R_{\text{bulk}}} \quad (18)$$

Changes in the peak given by Eq. (15) may evolve if the properties of the nanoparticle material and surrounding media are changed, which is reflected in the dielectric function of the nanoparticle and media. For example, the decrease in size of a nanoparticle to below 10 nm can change the mean free path for the conduction electrons [274]. This affects the dielectric function of the material, causing changes in the absorption band. If the radii of the

nanoparticles become smaller than the mean free path of electrons, the mean free path will become a function of the nanoparticle size. As given by Eq. (18), changes in the mean free path affect the damping frequency, and thus the real part of the dielectric constant, Eq. (16). When $\varepsilon' = -2\varepsilon$ in the denominator of Eq. (15), the absorption peak will broaden into a band, which will alter the color of the metal nanoparticle system [272].

The color of noble metals is a result of the reflection and transmittance of the incident light. These properties will change as the plasmon absorption band changes. This is apparent because reflection and transmittance of light by a metal are functions of the complex index of refraction of the material. The index of refraction is in turn related to the dielectric function through the relation [272, 273]

$$\varepsilon = (n + ik)^2 \quad (19)$$

where $n$ is the refractive index, and $k$ is the absorption coefficient. Therefore, changes in dielectric function affect the transmission and reflection of light in the species by shifting the reflection and absorption as the plasmon peak broadens.

Researchers have also observed plasmon band shifts to both higher and lower energies for decreasing particle size. The results are controversial, with no common trend being evident [274]. For silver nanoparticles, redshifts due to damping of electron motion with decreasing size are predicted with classical models and have been observed [274, 275]. However, blueshifts predicted by quantum size theories have also been observed [272, 274, 276]. Similarly, both blue-and redshifts have also been observed for Au nanoparticles [277–279].

The average metal nanoparticle shape, particle–particle separation, and molecular binding can also affect the position and width of the plasmon peak [272]. Dramatic color changes of metal nanoparticles due to particle separation were observed in experiments by Ung et al. [280] and Mulvaney [281]. In their experiments the color of films observed with transmitted light containing 15 nm Au particles coated with silica was changed from bluish gray to pink as the particle separation increased. This is shown in Figure 8. Increasing the thickness of the silica coating on the nanoparticles increased the particle separation, which served to decrease the concentration of gold nanoparticles in the gold silica matrix. Therefore they modeled the effect as concentration dependent. The dielectric function was given by an average dielectric function $\varepsilon_{\text{av}}$ of the silica matrix and Au nanoparticles that depended on the volume fraction of nanoparticles $\phi$ absorbed in the matrix [280]

$$\varepsilon_{\text{av}} = \varepsilon_m \left(1 + \frac{3\phi\beta}{1 - \phi\beta}\right) \quad (20)$$

where

$$\beta = \frac{\varepsilon - \varepsilon_m}{\varepsilon + 2\varepsilon_m} \quad (21)$$

The color change was proposed to be a result of the broadening of the plasmon absorption band, which shifted the reflected and absorbed light as discussed previously. In this
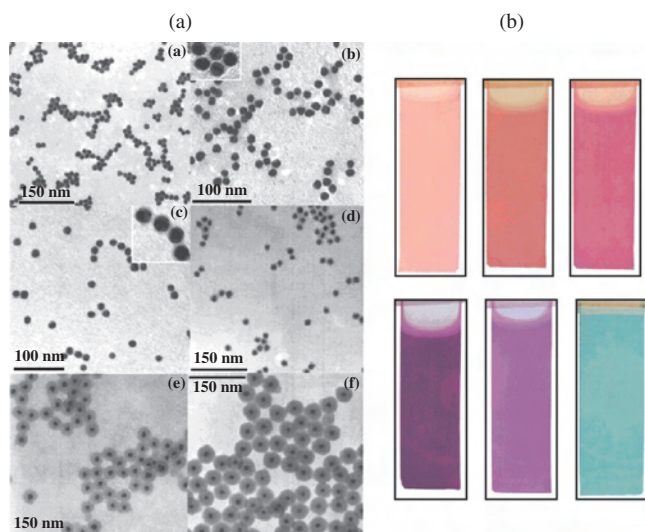
**Figure 8.** (a) Electron micrographs of silica coated 15 nm gold particles. The shell thickness is varied in each sample and increases from a to f. (b) Transmitted colors of the series of gold nanoparticles with different shell thicknesses. The colors correspond to an increase in thickness from top left to bottom right. Reprinted with permission from [280], T. Ung et al., *J. Phys. Chem. B* 105, 3441 (2001). © 2001, American Chemical Society.

case they proposed the shift to be the result of changes of dipole coupling between particles. When the particles are separated further, the coupling is reduced, and when the particles had a very small or no coating, their concentration increased to the point where they start acting as a regular Au thin film [280, 281].

Researchers are making use of the plasmon peak shift due to particle/molecule binding and particle–particle separation in biological applications. In work done by Malinsky et al. [282], alkanethiol self-assembled monolayers (SAMs) were incorporated onto Ag nanoparticles. A redshift in the surface plasmon peak was observed for every carbon atom increase of the alkanethiol chain length. A redshift was also observed in the surface plasmon peak when a cationic polypeptide was bound to the SAM modified Ag nanoparticle surface. Storhoff et al. [283] developed a bioassay technique in which DNA strands were linked to Au nanoparticles to form aggregates with redshifted plasmon peaks. The plasmon peak shift was found to depend on the DNA strand lengths and degree of particle agglomeration. Thus, these particle size and distance dependent applications are expected to change methods for biological tagging and probing, where molecular bonding of a target molecule to a solution of functionalized nanoparticles can change the nanoparticle optical properties [269].

## 4.2. Electronic Properties and Applications

The electronic properties of metal and semiconductor nanoparticles are being studied heavily. For a review of the electronic properties of semiconductor nanoparticles, sometimes referred to as quantum dots, see the review paper by Alivisatos [284].

As the size of a metal nanoparticle is decreased, the continuous density of electronic states in its band structure changes until, at small enough sizes, it is finally broken into discrete energy levels. In discrete energy levels the electrons are not freely mobile, and Ohm's law is no longer applicable. A resultant "Coulomb staircase" is observed experimentally in the current–voltage curves for nanoparticles. The shape corresponds to electronic tunneling via discrete energy levels where adding or removing one electron from the nanoparticle creates an excited state. This excited state has a voltage threshold that depends on an electrostatic charging energy [285, 286]

$$E = \frac{e^2}{2C} \tag{22}$$

where $e$ is the charge of an electron and $C$ is the capacitance of the particle. To observe this effect a single nanoparticle must be contacted between two electrodes, surrounded by a capacitance layer, and the thermal energy of the nanoparticle must also be smaller than the electrostatic charging energy [248]. Early investigations of this effect were performed on aluminum nanoparticles by Ralph et al. [287, 288] where it was observed that electrical measurements for <10 nm Al nanoparticles at temperatures of <1 K in a simple tunneling device showed quantization of the energy levels. Later, Klein et al. [289] found this staircase behavior with 5.8 nm Au nanoparticles at 4.2 K.

Electronic measurements for single metal nanoparticles are now often done by coating the particle with molecular ligands in what are known as monolayer protected clusters (MPCs). The MPCs are placed on metallic substrates and contacted with a scanning tunneling microscope (STM) tip [284, 285, 290]. The STM tip and metal substrate serve as the electrical contacts, while the ligand monolayer surrounding the nanoparticle provides the capacitance layer. This creates a double tunnel junction, where the staircase shaped $I$–$V$ curve is observed. This is shown schematically in Figure 9. MPCs can also be used to create a charged or ionizable surface to the nanoparticle. The electrostatic force is then useful for creating building blocks of the nanoparticles [291]. The requirement that the thermal energy be less than the
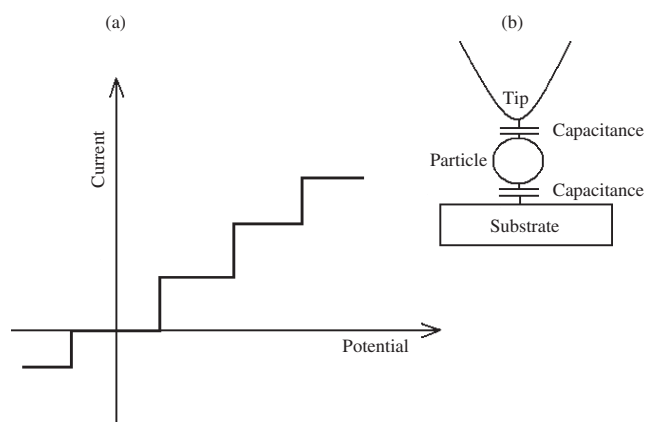


**Figure 9.** (a) Staircase shaped $I$–$V$ curve obtained from a nanoparticle double tunnel junction. (b) Schematic diagram of the tip–nanoparticle arrangement. An STM tip and metal substrate contact a ligand monolayer surrounding the nanoparticle.

electrostatic charging energy is realized at room temperature if the particle is less than 2 nm [292]. In a device developed by Andres et al. [286] Au nanoparticle clusters were bonded to aryl dithiols forming a SAM on a Au substrate. They observed staircase *I–V* curves at room temperature for varying tunnel currents (Fig. 10).

A device of interest for metal nanoparticles is the single electron transistor [293, 294]. The staircase behavior would represent a device that can be charged and discharged. This device would use one electron to switch a transistor, compared to a conventional silicon based device that uses $10^4$ electrons [286]. The single electron transistor would therefore require lower power consumption and result in smaller electronic devices. Fulton and Dolan [293] first developed a three terminal device with a 14 nm Al thin film. Their device exhibited Coulomb staircase behavior at 1.1–4.2 K. More recently, Ralph et al. [295] developed a nanoparticle transistor with a gate electrode, in which they were able to measure electronic spectra with different numbers of electrons in a single device. They formed Al nanoparticles on a substrate by depositing a 2.5 nm layer of Al, which beaded up due to surface tension to form particles less than 10 nm. The gate was formed by depositing a thin layer of Al insulated with $SiO_x$. The device exhibited Coulomb staircase behavior at temperatures below 4.2 K.

In order for a single electron transistor to be used in a practical application, it would need to be operated at room temperature. A recent paper by Gubin et al. [296] reported the development of devices made from metallorganic clusters of Pt, Pd, and Fe deposited onto highly oriented pyrolitic graphite substrates. The metallorganic clusters consisted of metal nuclei of 0.7–2.8 nm surrounded by a dielectric ligand shell. They reported the ability to synthesize single clusters, cluster chains, and two-dimensional
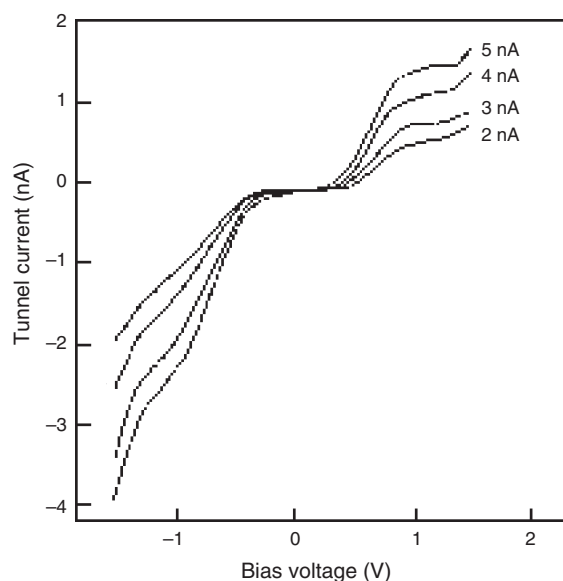
cluster structures. Contact was made to the clusters with an STM tip, and the Coulomb staircase effect was observed. This development may bring us a step closer to the realization of a single electron transistor.

## 4.3. Magnetic Properties and Applications

Ferromagnetic particles, some of which include Fe, Co, and Ni, exhibit a strong magnetic interaction due to unbalanced spins in their *d*-subshells. These materials are characterized by hysteresis on a magnetization vs applied field plot when the applied field is increased and then decreased in both a positive and negative direction. The hysteresis is characteristic of two processes that occur in the sample: the initial movement of magnetic domains in the sample at small applied magnetic fields and then, at sufficient energy, the rotation of the sample magnetization vector to align in the direction of the applied field until saturation, $M_s$, is reached. The energy required to bring the net magnetization in the sample back to zero in the reverse direction is given by the coercivity, $H_c$,

$$H_c = \frac{2K}{M_s} \qquad (23)$$

where $K$ is the anisotropy constant, which is characteristic of the energy required to align the magnetization of the sample along a particular direction. The anisotropy could arise from the particle structure (crystalline anisotropy), shape, stress, surface, or interaction with other particles. Equation (23) is applicable for systems without thermal activation.

If the size of a ferromagnetic particle is reduced to a few nanometers, it will have a single magnetic domain. Single domain particles exhibit greater coercivity values than larger multidomain particles because a greater applied field is needed to align only the magnetization vector. For spherical iron particles, the diameter where the transition to a single magnetic domain occurs has been proposed by Kittel to be approximately 15 nm [297]. Single domain particles with some form of anisotropy may exhibit an unusually large coercivity, sometimes indicating only two values of the magnetic moment, and thus are ideal for digital recording [298]. As the size of ferromagnetic particles is decreased even further, the particles may exhibit a change from ferromagnetic to superparamagnetic behavior. This is observed as a lack of hysteresis (zero coercivity) and occurs for particles where the thermal energy is sufficient to overcome anisotropy barriers.

One of the current issues in magnetic materials research is the understanding of the coercivity of particles and its variation with size and various forms of anisotropy. As the particle size decreases, the number of magnetic domains decreases, and the coercivity of the nanoparticles changes from domain dependent to thermal dependent, as previously discussed. In this case, the thermal energy in the sample must be great enough to overcome an anisotropy barrier for the magnetization vector to align with the applied field [299]. A particle size dependent plot of the coercivity vs size shows that as the particle size decreases, the coercivity increases above its bulk value until, at the size where a single domain is observed, the coercivity reaches a maximum. As the particle size decreases further, the coercivity decreases until it



**Figure 10.** Staircase shaped *I–V* curves at room temperature from a sample of gold nanoparticle clusters bonded to aryl dithiols forming a SAM onto a Au substrate. Reprinted with permission from [286], R. P. Andres et al., *Science* 272, 1323 (1996). © 1996, American Association for the Advancement of Science.

reaches zero where superparamagnetism is observed [299–302]. An illustration of this behavior is given in Figure 11. This particle size dependence was observed by Löffler et al. [303], where they recently observed that for room temperature Fe nanoparticles produced in an inert gas condensation process, the maximum in coercivity was ~100 Oe for 35 nm particles. Chen et al. [304] observed a maximum in coercivity at 18 nm for Fe particles embedded in an insulating matrix, while the coercivity was zero for particles less than 5 nm showing a superparamagnetic behavior.

The influence of the exchange anisotropy and surface anisotropy between a nanoparticle core and surrounding layers has been found to alter the magnetization behavior of nanoparticles. The exchange anisotropy arises from coating a magnetic particle with a antiferro or ferro magnetic shell, introducing an increased energy barrier. This is sometimes observed for Fe-oxide/Fe or Co-oxide/Co shell/core systems. Gangopadhyay et al. [305] found that at 10 K the coercivity of Fe-oxide/Fe particles increased drastically with decreasing core particle size, while the saturation magnetization decreased. These results were attributed to the larger oxide to metal ratio as the particles became smaller, which results in a larger exchange anisotropy. As the temperature was increased, the coercivity was reduced as a result of the reduced anisotropy barrier due to thermal superparamagnetism effects. At room temperature, the coercivity for Fe-oxide passivated Fe particles increased as particle size was increased, which may be expected due to the larger crystalline anisotropy. In this case as the core increases in size the influence of the anisotropy in the oxide shell is reduced [305]. Hsu et al. [306] found a large maximum in coercivity of 1300 Oe for room temperature 20 nm oxide coated Fe particles but also found that the coercivity for unoxidized particles was nearly as high. An increase in coercivity with decreasing particle size for Fe-oxide systems has been observed by others, but with no maximum in coercivity being observed [307].

Surface anisotropy also represents an increased energy barrier, in this case binding the magnetization to the particle due to the broken symmetry at the surface [299]. These effects are enhanced for nanoparticles where the fraction of
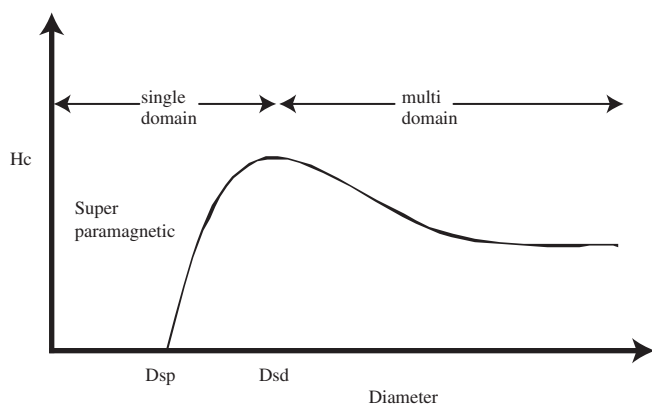
surface to bulk atoms increases as the particle size decreases. Labaye et al. [308] proposed that the competition between surface and bulk anisotropy imposes a "throttled" spin structure where the spins of outer shells tend to orient normal to the surface while the core spins remain parallel to each other. The result for large enough values of surface anisotropy is no net magnetization. Peng et al. [309] found that the anisotropy constant for oxide coated particles was an order of magnitude greater than that for nonpassivated iron nanoparticles.

Coatings can also influence the magnetic properties of nanoparticles by donating or grabbing electrons from the magnetic particle core. Coatings that donate electrons can reduce the magnetization, by filling empty $d$ shell levels, while those that grab electrons may increase magnetization [310]. The covalent bonding of polymers to the nanoparticle surface is also being investigated to enhance the magnetic properties of particles [311] and to help minimize magnetization losses due to oxidation [312].

There are a number of applications of interest for magnetic nanoparticles including data storage [313–315], ferrofluids [316–319] and ferrogels [320–322], and catalysts [323–325]. An exciting area for magnetic nanoparticle research is in biological applications. Researchers are using the magnetic properties to determine whether specific molecules bind in solution. In a recent study by Kötitz et al. [326], biotin molecules were bound to magnetic iron oxide nanoparticles, which were then reacted with a protein. The reaction was monitored by magnetic relaxation measurements. The magnetization of particles in solution is described by an expression that includes an exponential decay with time. This effective relaxation time has two components, the Neél relaxation and the Brownian relaxation. The dominant relaxation process, the Neél relaxation time, depends on the particle hydrodynamic radius. The hydrodynamic radius includes the particle radius along with the attached molecule. Thus by monitoring the relaxation time they were able to monitor the progress of the reaction [326]. This method can be used to determine whether various molecules will react.

Researchers are investigating the use of magnetic nanoparticles in cancer treatment [327–329]. Cancer therapy where cells are heated to 41 to 46 °C to cause cell inactivation is called hyperthermia. Researchers are using superparamagnetic nanoparticles to perform this procedure in what is known as magnetic fluid hyperthermia (MFH). MFH works by using an externally applied ac field to heat the nanoparticles. The nanoparticles can be delivered into cancer tumors in a ferrofluid without anesthesia. Nanoparticles are desirable for this process because they absorb much more power at magnetic fields that are tolerable than those of micrometer-sized particles [327, 328]. Jordan et al. [330] used dextran coated magnetite nanoparticles in MFH experiments and observed 44% tumor control in mice. This technique is now being used to treat humans with prostate tumors [330].

Another biological application of interest for magnetic nanoparticles is in separation processes. A common method for isolation of biologically active compounds is to separate them into biocompatible two-phase systems. Magnetic fluids have been added to the solutions where the application of



**Figure 11.** Particle coercivity vs size. The diameter for single magnetic domain is given by $D_{sd}$ and the diameter for superparamagnetism is given by $D_{sp}$. Adapted with permission from [299], C. M. Sorensen, in "Nanoscale Materials in Chemistry" (K. J. Klabunde, Ed.). Wiley, New York, 2001. © 2001, Wiley.

a magnetic field is used to speed up the phase separation [331]. Wikstrom et al. [332] demonstrated that the addition of a dextran stabilized ferrofluid to a mixture of dextran and polyethylene glycol and applying a magnetic field increased the separation time by a factor of 35.

## 4.4. Thermal Properties and Applications

As the size of particles is decreased to the nanometer scale, the ratio of surface area to volume increases dramatically. This effect has interesting results for the thermal properties of nanoparticles in comparison to bulk materials [333]. For example Buffat and Borel [334] showed that a decrease in size below ~5 nm results in a dramatic decrease in the melting point for Au nanoparticles. Their results indicated that the melting point was lowered by nearly 900 K. Because melting is a process in which the regular order of the lattice is rearranged and destroyed, surface atoms are more susceptible to this rearrangement. Therefore the greater percentage of surface atoms will lower the onset of this process [248]. A nearly linear relationship was observed by Allen et al. [335] for the melting point as a function of the reciprocal radius of nanoparticles. They performed size dependent melting experiments of Pb, Sn, In, and Bi nanocrystals. Other factors, such as shape and surface contamination, were also observed to affect the size dependent melting of nanoparticles [335]. A model for the lowering of the melting point for spherical nanoparticles was developed by Shi [336] and given by the equation

$$\frac{T_m(r)}{T_m(\infty)} = \exp\left(\frac{-(\alpha - 1)}{(r/3h - 1)}\right) \quad (24)$$

where $T_m(r)$ and $T_m(\infty)$ are the melting temperature of the nanocrystals of radius $r$ and the bulk material respectively, $h$ is the height of a monolayer of atoms on the crystal surface, and $\alpha$ is the ratio of the mean square displacement of atoms on the surface to that in the bulk [337].

The criterion for melting was proposed by Lindemann [338]. The crystal will melt if the root mean square displacement of its atoms exceeds a particular fraction of the interatomic distance. As the crystal heats up, the oscillations of its atoms increases until a particular limit where the bonds are broken and thus melting occurs. The atoms on the surface are not as strongly bound as are those in the bulk; therefore the process begins on the surface of the crystal. This is described by the mean square displacement of the surface atoms $\delta_s$ and the atoms in the bulk $\delta_v$ [339]:

$$\alpha = \frac{\delta_s}{\delta_v} \quad (25)$$

For values of $\alpha > 1$, the melting point decreases with decreasing particle size, while for $\alpha < 1$ the melting point increases with decreasing size. Values for which $\alpha < 1$ have been observed for nanoparticles embedded in a matrix, where the surface atoms vibrate at a lower frequency than in the bulk [340, 341].

Another enhanced thermal property of metal nanoparticles is their increased specific heat. Rupp and Birringer [341] observed that for 6 nm Pd and 8 nm Cu particles over the temperature range of 150–300 K the specific heat was increased by 40% and 10%, respectively, over their bulk values. The specific heat of a material is defined as the amount of heat required to increase its temperature by one degree and is a function of both phonons and electrons. At low temperatures, the specific heat at constant pressure $C_p$ is given by the Debye–Sommerfeld model

$$C_p = \gamma T + BT^3 \quad (26)$$

where $\gamma$ is the Sommerfeld parameter which represents the electronic contribution to the specific heat, while $B$ represents the phonon contribution. Experiments performed at low temperatures can be carried out to investigate both the electronic and phonon contributions to the specific heat. Bai et al. [342] studied the specific heat of Fe nanoparticles from 1.8 to 26 K. They found that the Sommerfeld parameter decreases by about 50%. This indicates that the electronic contribution to the specific heat for small particles at low temperatures is reduced. Conversely, at higher temperatures, increased lattice vibration of surface atoms increases the phonon contribution to give a larger specific heat. Therefore they concluded that a $T^2$ term should be incorporated into the specific heat equation [342].

Researchers have also observed other thermal property changes for metal nanoparticles. Li et al. [343] observed a crossover from a positive thermal expansion at low temperatures to a negative thermal expansion at high temperatures for 4 nm Au particles. The crossover was observed at about 125 K, and the particles retained their face-centered cubic cell parameter. They attributed this behavior to the effects of valence electronic excitations on the equilibrium lattice separation. Specifically, the allowed energy levels for valence electrons in a nanoparticle are inversely proportional to the particle volume, which can vary with temperature. The lattice shrinks as a result of the increased energy level spacing when the temperature is increased. This reduces the number of electrons occupying excited states but also raises the thermal energy of individual electrons in the excited states. These factors compete to lower the electronic potential energy and result in a crossover from expansion to contraction [343].

Applications for metal nanoparticles include their use in thermal management applications. For example, because they conduct heat by orders of magnitude greater than liquids, it is expected that the addition of metal particles can enhance the thermal conductivity of the liquid. Conduction enhancement is important for fluids such as pump oils, motor oils, and heat exchange fluids among others where heat dissipation can enhance performance. Metal nanoparticles have high thermal conductivity and large surface area and may not cause clogging associated with larger particles.

Early work on fluid thermal conduction enhancement was done with polystyrene particles, which have a low thermal conductivity but were easily dispersed in the fluid [344]. More recently, thermal conduction enhancement with metal and metal oxide nanoparticles has been studied by several researchers [345–351]. Choi [345] and Eastman et al. [349] added copper nanoparticles to ethylene glycol and found a 40% increase in thermal conductivity with the addition of only 0.3 vol% nanoparticles and thyoglicolic acid as a stabilizing agent. In our research we have used the techniques

of inert gas condensation and co-condensation to produce silver and copper nanoparticles which were added to hydrocarbon oil for thermal conductivity enhancement. We were able to increase the thermal conductivity of the oil by nearly 50% by adding $\sim 1.75 \times 10^{-4}$ wt% nanoparticles [352].

In the past, the theory of thermal conductivity enhancement of particles in solution has been modeled as a composite system in which stationary state diffusion equations were solved [353, 354]. These yielded solutions to the heat transport equations in which only particle loading and shape, not particle size, affected the thermal conductivity [355]. Conversely, particle size has been shown to affect the conductivity [355]. Recent researchers, however, have proposed that nanoparticles incur dispersion of heat by their random motions in the fluid, Brownian motion [356]. Keblinski et al. [355], however, have proposed that heat transfer may be from Brownian motion to a small degree, but a predominant effect may be from nanoparticle clusters being formed in the solution. In this case the heat transport is through ballistic transport, and not through diffusion [355]. However, clustering of particles may be detrimental to a real working system.

## 5. CONCLUSION

The numerous potential applications of metal nanoparticles are energizing the research in this area. The questions associated with the scale up of most of the metal nanoparticle synthesis processes need to be addressed before the application potential of the metal nanoparticles can be fully realized. Regardless of the current scale-up limitations, these materials are so unique and scientifically interesting that vigorous research in this area will surely continue for many years to come.

## GLOSSARY

**Agglomerate** Assembly of identifiable individual particles within a larger structure. The particles may be bonded weakly or strongly within the structure.

**Aggregate** An agglomerate of strongly bonded particles.

**Brownian motion** Random motion.

**Coagulation** Particle combination due to processes such as Brownian motion.

**Coalescence** Sintering and diffusion of species within particles where contact is made.

**Co-condensation** A nanoparticle synthesis technique involving the co-deposition of metal vapors and a polar coordinating solvent on to the liquid nitrogen cooled walls of a reactor at low pressures (typically, a few mTorr). The solvent coordinates the growing nanoparticles and prevents the agglomeration of nanoparticles commonly observed in Joule heating gas condensation techniques.

**Dendrimer** A highly branched organic molecule with a well defined repetitive structure. Dendrimers have been used to create nanoparticles by sequestering metal ions at the dendrimer core and then reducing them.

**Inert gas condensation** A nanoparticle synthesis technique involving the rapid cooling of atoms through collisions with an inert gas. The cooling initiates a large degree of supersaturation, resulting in nucleation of particles. The nuclei join to form larger nanoparticles.

**Inverse micelles** Microemulsion templates for nanoparticle synthesis. Microemulsions are made by dissolving suitable surfactants in a mixture of apolar organic solvents and water. When a surfactant is dissolved in the solvent, nanometer sized water droplets are formed within the volume and stabilized by the surfactant molecules. Reactants, which include a metal salt to provide the metal ions and a reducing agent, which are soluble in water, are added to the microemulsion in a sequential manner. The droplet collisions lead to mixing of the reactants in the aqueous phase of the microemulsion and the reaction starts. Nanoparticles can be formed by the nucleation and growth mechanism within the water droplets.

**Joule heating** A technique in which a metal charge is placed in or near a "boat" which is heated by electrical resistance. The metal charge is liquified and evaporated, releasing metal atoms for the inert gas condensation process.

**Physical vapor deposition** Any process in which atoms are released from a target due to physical processes such as heating, ion, or electron bombardment.

**Plasma sputtering** A physical vapor deposition technique used for the synthesis of nanoparticles or thin films. The process involves the ionization of an inert or reactive gas to form a plasma of charged species and electrons, etc. Positively charged ions from the plasma are accelerated to a target. The target is bombarded by the ions, releasing metal atoms, which are then available to form nanoparticles or thin films of the desired material.

## REFERENCES

1. K. L. Kelly, T. R. Jensen, A. A. Lazarides, and G. C. Schatz, in "Metal Nanoparticles" (D. L. Feldheim and C. A. J. Foss, Eds.), p. 89. Dekker, New York, 2002.
2. A. I. Yanson, G. R. Bollinger, H. E. van der Brom, N. Agrait, and J. M. v. Ruitenbeek, *Nature* 395, 783 (1998).
3. M. P. Zach, K. H. Ng, and R. M. Penner, *Science* 290, 2120 (2000).
4. Y. Kondo and K. Takayanagi, *Science* 289, 606 (2000).
5. B. H. Hong, S. C. Bae, C. W. Lee, S. Jeong, and K. S. Kim, *Science* 294, 348 (2001).
6. M. D. Malinsky, K. L. Kelly, G. C. Schatz, and R. P. V. Duyne, *J. Am. Chem. Soc.* 123, 1471 (2001).
7. V. F. Puntes, K. M. Krishnan, and A. P. Alivisatos, *Science* 291, 2115 (2001).
8. U. Kreibig and M. Vollmer, "Optical Properties of Metal Clusters," Vol. 25. Springer-Verlag, Heidleberg/Berlin, 1995.
9. S. A. Sapp, D. T. Mitchell, and C. R. Martin, *Chem. Mater.* 11 (1999).
10. C. A. Foss, M. J. Tierney, and C. R. Martin, *J. Phys. Chem.* 96, 9001 (1992).
11. D. Routkevitch, T. Bigioni, M. Moskovits, and J. M. Xu, *J. Phys. Chem.* 100, 14037 (1996).
12. C. K. Preston and M. Moskovits, *J. Phys. Chem.* 97 (1993).
13. L. Sun, P. C. Searson, and C. L. Chien, *Phys. Rev. B* 61, R6463 (2000).
14. T. M. Whitney, J. S. Jiang, P. C. Searson, and C. L. Chien, *Science* 261, 1316 (1993).
15. A. Fukuoka, H. Araki, Y. Sakamoto, N. Sugimoto, H. Tsukada, Y. Kumai, Y. Akimoto, and M. Ichikawa, *Nano Lett.* 2, 793 (2002).

16. C. A. J. Foss, in "Metal Nanoparticles" (D. L. Feldheim and C. A. J. Foss, Eds.), p. 119. Dekker, New York, 2002.

17. S. R. Nicewarner-Pena, R. G. Freeman, B. D. Reiss, L. He, D. J. Pena, I. D. Walton, R. Cromer, C. D. Keating, and M. J. Natan, *Science* 294, 137 (2001).

18. T. Jung, R. Schlittler, J. K. Gimzewski, and F. J. Himpsel, *Appl. Phys. A* 61, 467 (1995).

19. D. Y. Petrovykh, F. J. Himpsel, and T. Jung, *Surf. Sci.* 407, 189 (1998).

20. M. Blanc, K. Kuhnke, V. Marsico, and K. Kern, *Surf. Sci.* 414, L964 (1998).

21. P. Gambardella, M. Blanc, H. Brune, K. Kuhnke, and K. Kern, *Phys. Rev. B* 61, 2254 (2000).

22. R. J. Nichols, D. M. Kolb, and R. J. Behm, *J. Electroanal. Chem.* 313, 109 (1991).

23. S. Morin, A. Lachenwitzer, O. M. Magnussen, and R. J. Behm, *Phys. Rev. Lett.* 83, 5066 (1999).

24. E. A. Abd, El Meguid, P. Berenz, and H. Baltruschat, *J. Electroanal. Chem.* 467, 50 (1999).

25. J. Dekoster, B. Degroote, H. Pattyn, G. Langouche, A. Vantomme, S. Degroote, *Appl. Phys. Lett.* 75, 938 (1999).

26. D. W. G. Goad and M. Moskovits, *J. Appl. Phys.* 49, 2929 (1978).

27. A. Anderson, O. Hunderi, and C. G. Granqvist, *J. Appl. Phys.* 51, 754 (1980).

28. C. K. Presto and M. Moskovits, *J. Phys. Chem.* 92, 2957 (1988).

29. E. Braun, Y. Eichen, U. Sivan, and G. Ben-Yoseph, *Nature* 391, 775 (1998).

30. M. Lade, H. Mays, J. Schmidt, R. Willumeit, and R. Schomacker, *Colloids Surfaces A* 163, 3 (2000).

31. J. Schmidt, C. Guesdon, and R. Schomacker, *J. Nanoparticle Res.* 1, 267 (1999).

32. V. K. Lamer and R. H. Dinegar, *J. Am. Chem. Soc.* 72, 4847 (1950).

33. L. Yiping, G. C. Hadjipanayis, C. M. Sorensen, and K. J. Klabunde, *J. Appl. Phys.* 69, 5141 (1991).

34. H. Ago, T. Komatsu, S. Ohshima, Y. Kuriki, and M. Yumura, *Appl. Phys. Lett.* 77, 79 (2000).

35. H. Ago, S. Ohshima, K. Uchida, and M. Yumura, *J. Phys. Chem. B* 105, 10453 (2001).

36. M. Boutonnet, J. Kizling, P. Stenius, and G. Maire, *Colloids Surfaces* 5, 209 (1982).

37. D. H. Chen and S. H. Wu, *Chem. Mater.* 12, 1354 (2000).

38. J. P. Chen, K. M. Lee, C. M. Sorensen, K. J. Klabunde, and G. C. Hadjipanayis, *J. Appl. Phys.* 75, 5876 (1994).

39. J. P. Chen, C. M. Sorensen, K. J. Klabunde, and G. C. Hadjipanayis, *J. Appl. Phys.* 76, 6316 (1994).

40. J. P. Chen, C. M. Sorensen, K. J. Klabunde, and G. C. Hadjipanayis, *Phys. Rev. B* 51, 11527 (1995).

41. L. X. Chen, T. Liu, M. C. Thurnauer, R. Csencsits, and T. Rajh, *J. Phys. Chem. B* 106, 8539 (2002).

42. O. Cherniavskaya, A. Adzic, C. Knutson, B. J. Gross, L. Zang, R. Liu, and D. M. Adams, *Langmuir* 18, 7029 (2002).

43. An. I. Cooper, *Adv. Mater.* 13, 1111 (2001).

44. J. Y. Fang, K. L. Stokes, J. Wiemann, and W. L. Zhou, *Mater. Lett.* 42, 113 (2000).

45. J. Y. Fang, K. L. Stokes, J. A. Wiemann, W. L. Zhou, J. B. Dai, F. Chen, and C. J. O'Connor, *Mater Sci. Eng. B* 83, 254 (2001).

46. G. N. Glavee, K. J. Klabunde, C. M. Sorensen, and G. C. Hadjipanayis, *Inorg. Chem.* 32, 474 (1993).

47. G. N. Glavee, K. J. Klabunde, C. M. Sorensen, and G. C. Hadjipanayis, *Langmuir* 10, 4726 (1994).

48. G. N. Glavee, K. J. Klabunde, C. M. Sorensen, and G. C. Hadjipanayis, *Inorg. Chem.* 34, 28 (1995).

49. X. M. Lin, C. M. Sorensen, K. J. Klabunde, and G. C. Hadjipanayis, *J. Mater. Res.* 14, 1542 (1999).

50. An. Manna, B. D. Kulkarni, K. Bandyopadhyay, and K. Vijayamohanan, *Chem. Mater.* 9, 3032 (1997).

51. C. Petit and M. P. Pilen, *J. Magn. Magn. Mater.* 166, 82 (1997).

52. M. Sugiyama, H. Okazaki, and S. Koda, *Jpn. J. Appl. Phys. Part 1* 41, 4666 (2002).

53. T. Tago, Y. Shibata, T. Hatsuta, K. Miyajima, M. Kishida, S. Tashiro, and K. Wakabayashi, *J. Mater. Sci.* 37, 977 (2002).

54. C. M. Wai and H. Ohde, *J. Chinese Inst. Chem. Eng.* 32, 253 (2001).

55. J. P. Wilcoxon, U.S. Patent 5, 147, 841, 1992.

56. L. Yiping, G. C. Hadjipanayis, C. M. Sorensen, and K. J. Klabunde, *J. Appl. Phys.* 67, 4502 (1990).

57. F. W. Zeng and S. C. Zimmerman, *Chem. Rev.* 97, 1681 (1997).

58. W. Bosman, H. M. Janssen, and E. W. Meijer, *Chem. Rev.* 99, 1665 (1999).

59. M. Fischer and F. Vogtle, *Angew. Chem. Int. Ed.* 38, 885 (1999).

60. R. M. Crooks, V. Chechik, B. I. Lemon III, L. Sun, L. K. Yeung, and M. Q. Zhao, in "Metal Nanoparticles" (D. L. Feldheim and C. A. Foss, Jr., Eds.), pp. 261–296. Dekker, New York, 2002.

61. R. M. Crooks, M. Q. Zhao, L. Sun, V. Chechik, and L. K. Yeung, *Acc. Chem. Res.* 34, 181 (2001).

62. J. Jansen, E. M. M. Debrabandervandenberg, and E. W. Meijer, *Science* 266, 1226 (1994).

63. S. Stevelmans, J. C. M. vanHest, J. Jansen, J. vanBoxtel, E. vandenBerg, and E. W. Meijer, *J. Am. Chem. Soc.* 118, 7398 (1996).

64. M. Q. Zhao, L. Sun, and R. M. Crooks, *J. Am. Chem. Soc.* 120, 4877 (1998).

65. M. Q. Zhao and R. M. Crooks, *Adv. Mater.* 11, 217 (1999).

66. M. Q. Zhao and R. M. Crooks, *Angew. Chem. Int. Ed.* 38, 364 (1999).

67. V. Chechik and R. M. Crooks, *J. Am. Chem. Soc.* 122, 1243 (2000).

68. L. K. Yeung, C. T. Lee, K. P. Johnston, and R. M. Crooks, *Chem. Comm.* 2290 (2001).

69. H. Tokuhisa, M. Q. Zhao, L. A. Baker, V. T. Phan, D. L. Dermody, M. E. Garcia, R. F. Peez, R. M. Crooks, and T. M. Mayer, *J. Am. Chem. Soc.* 120, 4492 (1998).

70. V. Chechik, M. Q. Zhao, and R. M. Crooks, *J. Am. Chem. Soc.* 121, 4910 (1999).

71. L. Sun and R. M. Crooks, *Langmuir* 18, 8231 (2002).

72. Y. H. Niu, L. K. Yeung, and R. M. Crooks, *J. Am. Chem. Soc.* 123, 6840 (2001).

73. W. M. Lackowski, J. K. Campbell, G. Edwards, V. Chechik, and R. M. Crooks, *Langmuir* 15, 7632 (1999).

74. R. M. Crooks and M. Q. Zhao, *Chem. Mater.* 11, 3379 (1999).

75. M. M. Flagan and R. C. Lunden, *Mater. Sci. Eng. A* 204, 113 (1995).

76. H. Gleiter, *Progr. Mater. Sci.* 33, 223 (1989).

77. A. H. Pfund, *Phys. Rev.* 35, 1434 (1930).

78. L. Harris, D. Jeffries, and B. M. Siegel, *J. Appl. Phys.* 19, 741 (1947).

79. L. Harris, D. Jeffries, and B. M. Siegel, *J. Chem. Phys.* 18, 261 (1950).

80. K. Kimoto, Y. Kamiya, M. Nonoyama, and R. Uyeda, *Jpn. J. Appl. Phys.* 2, 702 (1963).

81. N. Wada, *Jpn. J. Appl. Phys.* 6, 553 (1967).

82. N. Wada, *Jpn. J. Appl. Phys.* 7, 1287 (1968).

83. S. Yatsuya, S. Kasukabe, and R. Uyeda, *Jpn. J. Appl. Phys.* 12, 1675 (1973).

84. S. Yatsuya, S. Kasukabe, and R. Uyeda, *J. Crystal Growth Appl. Phys.* 24/25, 319 (1974).

85. S. Kasukabe, S. Yatsuya, and R. Uyeda, *Jpn. J. Appl. Phys.* 13, 1714 (1973).

86. C. G. Granqvist and R. A. Buhrman, *J. Appl. Phys.* 47, 2200 (1976).

87. A. R. Thölen, *Acta Metal.* 27, 1765 (1979).

88. H. Abe, W. Schulze, and B. Tesche, *Chem. Phys.* 47, 95 (1980).

89. K. Sattler, J. Mühlbach, and E. Recknagel, *Phys. Rev. Lett.* 45, 821 (1980).

90. R. S. Bowles, J. J. Kolstad, J. M. Calo, and R. P. Andres, *Surf. Sci.* 106, 117 (1981).

91. R. W. Siegel and J. A. Eastman, *Mater. Res. Soc. Symp. Proc.* 132, 3 (1989).

*92.* V. Haas, H. Gleiter, and R. Birringer, *Scripta Metall. Mater.* 28, 721 (1993).

*93.* V. Haas, R. Birringer, H. Gleiter, and S. E. Pratsinis, *J. Aerosol Sci.* 28, 1443 (1997).

*94.* S. Yamamuro, K. Sumiyama, and K. Suzuki, *J. Appl. Phys.* 85, 483 (1999).

*95.* J. R. Brock, P. J. Kuhn, and D. Zehavi, *J. Aerosol Sci.* 6, 11 (1986).

*96.* K. Wegner, B. Walker, S. Tsantilis, and S. E. Pratsnis, *Chem. Eng. Sci.* 57, 1753 (2002).

*97.* I. M. Golby, L. Kuipers, B. von Issendorf, and R. E. Palmer, *Appl. Phys. Lett.* 69, 2819 (1996).

*98.* M. Oda, K. Setoguchi, E. Fuchita, and C. Hayashi, *J. Mater. Sci. Technol.* 13, 249 (1997).

*99.* H. Shen, B. Gunther, H. Schäfer, Z. Li, and Zh. Qi, *Scripta Metall. Mater.* 32, 1677 (1995).

*100.* H.-G. Busmann, B. Gunther, and U. Meyer, *Nanostruct. Mater.* 12, 531 (1999).

*101.* J. Weissmuller, R. D. Shull, G. Rixecker, R. D. McMichael, and L. H. Bennett, *Nanostruct. Mater.* 7, 161 (1996).

*102.* T. A. Yamamoto, R. D. Shull, and H. W. Hahn, *Nanostruct. Mater.* 9, 539 (1997).

*103.* T. Nakayama, T. A. Yamamoto, Y. H. Choa, and K. Niihara, *J. Mater. Sci.* 35, 3857 (2000).

*104.* B. Y. Miao, J. M. Hong, P. P. Chen, X. L. Yuan, M. Han, and G. H. Wang, *J. Phys.-Cond. Mater* 9, 10985 (1997).

*105.* H. Wolf, H. G. Zimmer, T. Filz, S. Lauer, T. Wichert, and W. Krauss, *Mater. Sci. Eng. A* 204, 43 (1995).

*106.* S. Van Petegem, D. Segers, C. Dauwe, F. dalla Torre, and H. Van Swygenhoven, *Monatsh. Chem.* 133, 829 (2002).

*107.* T. Haubold, R. Bohn, R. Birringer, and H. Gleiter, *Mater. Sci. Eng. A* 153, 679 (1992).

*108.* R. S. Averback, *Z. Phys. D* 26, 84 (1993).

*109.* R. W. Siegel and J. A. Eastman, *Mater. Res. Soc. Symp. Proc.* 123, 3 (1989).

*110.* C. Baker, S. Ismat Shah, S. K. Hasanain, B. Ali, L. Shah, G. Li, T. Ekiert, and K. M. Unruh, *Mater. Res. Soc. Symp. Proc.* 746, Q4.4.1 (2003).

*111.* U. Herr, *Solid State Comm.* 76, 197 (1990).

*112.* T. Haubold, F. Boscherini, S. Pascarelli, S. Mobilio, and H. Gleiter, *Philos. Mag. A* 66, 591 (1992).

*113.* H. Konrad, T. Haubold, R. Birringer, and H. Gleiter, *Nanostruct. Mater.* 7, 605 (1996).

*114.* W. Krauss and H. Gleiter, *Phys. Rev. B* 58, 11226 (1998).

*115.* W. Krauss and R. Birringer, *Nanostruct. Mater.* 9, 109 (1997).

*116.* Y. Saito, K. Mihama, and R. Uyeda, *Jpn. J. Appl. Phys.* 19, 1603 (1980).

*117.* H. Hahn and R. S. Averback, *J. Appl. Phys.* 67, 1113 (1990).

*118.* For a review see H. Haberland, M. Karrais, M. Mall, and Y. Thurner, *J. Vac. Sci. Technol. A* 10, 3266 (1992).

*119.* S. Yatsuya, K. Yamauchi, T. Kamakura, A. Yanagida, H. Wakayama, and K. Mihama, *Surface Sci.* 156, 1011 (1985).

*120.* S. Yatsuya, T. Kamakura, K. Yamauchi, and K. Mihama, *Jpn. J. Appl. Phys. Part 2 Lett.* 25, L42 (1986).

*121.* T. G. Suh, D. M. Umarjee, S. Prakash, H. J. Doerr, C. V. Deshpandey, and R. F. Bunshah, *Surface Coatings Technol.* 49, 304 (1991).

*122.* G. M. Chow, R. L. Holtz, A. Pattnaik, A. S. Edelstein, T. E. Schlesinger, and R. C. Cammarata, *Appl. Phys. Lett.* 56, 1853 (1990).

*123.* G. M. Chow, C. L. Chien, and A. S. Edelstein, *J. Mater. Res.* 6, 8 (1991).

*124.* G. M. Chow, A. Pattnaik, T. E. Schlesinger, R. C. Cammarata, M. E. Twigg, and A. S. Edelstein, *J. Mater. Res.* 6, 737 (1991).

*125.* S. Terauchi, N. Koshizaki, and H. Umehara, *Nanostruct. Mater.* 5, 71 (1995).

*126.* R. Chandra, P. Taneja, J. John, P. Ayyub, G. K. Dey, and S. K. Kulshreshtha, *Nanostruct. Mater.* 11, 1171 (1999).

*127.* F. H. Kaatz, G. M. Chow, and A. S. Edelstein, *J. Mater. Res.* 8, 995 (1993).

*128.* A. C. Xenoulis, P. Trouposkiadis, C. Potiriadis, C. Papastaikoudis, A. A. Katsanos, and Clouvas, *Nanostruct. Mater.* 7, 473 (1996).

*129.* F. K. Urban, A. Hosseini-Tehrani, P. Griffiths, A. Khabari, Y. W. Kim, and I. Petrov, *J. Vac. Sci. Technol. B* 20, 995 (2002).

*130.* F. K. Urban, A. Hosseini-Tehrani, A. Khabari, P. Griffiths, and G. Fernandez, *Thin Solid Films* 356, 513 (1999).

*131.* M. Wagener and B. J. Gunther, *J. Magn. Mag. Mater.* 201, 41 (1999).

*132.* H. Chang, C. J. Altstetter, and R. S. Averback, *J. Mater. Res.* 7, 2962 (1992).

*133.* S. Q. Xiao, A. H. Foitzik, G. Welsch, T. Haubold, and H. Gleiter, *Acta Metal. Mater.* 42, 2535 (1994).

*134.* P. G. Hockel and J. Weissmuller, *Scripta Mater.* 35, 647 (1996).

*135.* O. Alvarez-Fregoso, S. Lopez, J. A. Juarez-Islas, M. Garcia, E. Martinez, M. A. Alvarez-Perez, J. C. Ramirez, and S. Granados, *Phys. Status Solidi B* 220, 575 (2000).

*136.* G. N. Glavee, K. J. Klabunde, C. M. Sorensen, and G. C. Hadjipanayis, *Inorg. Chem.* 34, 28 (1995).

*137.* G. N. Glavee, K. J. Klabunde, C. M. Sorensen, and G. C. Hadjipanayis, *Langmuir* 10, 4726 (1994).

*138.* R. D. Rieke, *Science* 246, 1260 (1989).

*139.* A. Conias, G. Ennas, G. Licheri, G. Marongui, and G. Paschina, *Chem. Mater.* 2, 363 (1990).

*140.* H. I. Schlesinger, H. C. Brown, A. E. Finholt, J. K. Gilbreath, H. R. Hockstrue, and E. K. Hyde, *J. Am. Chem. Soc.* 75, 215 (1965).

*141.* S. Nafis, G. Hadjipanayis, C. M. Sorensen, and K. J. Klabunde, *IEEE Trans. Magn.* 25, 3641 (1989).

*142.* J. van Wontergham, S. Morup, C. J. W. Koch, S. W. Charlds, and S. Wells, *Nature* 322, 622 (1986).

*143.* A. L. Oppergard, F. J. Damell, and H. C. Miller, *J. Appl. Phys.* 32, 1845 (1961).

*144.* L. B. Kiss, J. Soderlund, G. A. Niklasson, and C. G. Granqvist, *Nanostruct. Mater.* 12, 327 (1999).

*145.* L. B. Kiss, J. Soderlund, G. A. Niklasson, and C. G. Granqvist, *Nanotechnology* 10, 25 (1999).

*146.* J. Soderlund, L. B. Kiss, G. A. Niklasson, and C. G. Granqvist, *Phys. Rev. Lett.* 80, 2386 (1998).

*147.* K. J. Klabunde, "Free Atoms, Clusters, and Nanoscale Particles." Academic Press, San Diego, 1994.

*148.* D. J. Zhang, G. Glavee, G. C. Hadjipanayis, K. J. Klabunde, and C. M. Sorensen, *High Temp. Mater. Sci.* 36, 93 (1996).

*149.* D. J. Zhang, K. J. Klabunde, C. M. Sorensen, and G. C. Hadjipanayis, *High Temp. Mater. Sci.* 36, 135 (1996).

*150.* S. Yatsuya, Y. Tsukasaki, K. Yamauchi, and K. Mihama, *J. Cryst. Growth* 70, 533 (1984).

*151.* S. Yatsuya, T. Hayashi, H. Akoh, E. Nakamura, and A. Tasaki, *Jpn. J. Appl. Phys.* 17, 355 (1978).

*152.* S. Yatsuya, K. Mihama, and R. Uyeda, *Jpn. J. Appl. Phys.* 13, 749 (1974).

*153.* S. Yatsuya, Y. Tsukasaki, K. Mihama, and R. Uyeda, *J. Cryst. Growth* 45, 490 (1978).

*154.* H. Akoh, Y. Tsukasaki, S. Yatsuya, and A. Tasaki, *J. Cryst. Growth* 45, 495 (1978).

*155.* K. Matsuo and K. J. Klabunde, *J. Org. Chem.* 47, 843 (1982).

*156.* S. Stoeva, K. J. Klabunde, C. M. Sorensen, and I. Dragieva, *J. Am. Chem. Soc.* 124, 2305 (2002).

*157.* A. Balerna, S. Coluccia, G. Deganello, A. Longo, A. Martorana, G. Martra, C. Meneghini, P. Pertici, G. Pipitone, E. Pitzalis, A. M. Venezia, A. Verrazzani, and G. Vitulli, *Eur. Phys. J. D* 7, 577 (1999).

*158.* T. Boronina, K. J. Klabunde, and G. Sergeev, *Environ. Sci. Technol.* 29, 1511 (1995).

*159.* B. J. Tan, K. J. Klabunde, and P. M. A. Sherwood, *J. Am. Chem. Soc.* 113, 855 (1991).

160. K. J. Klabunde, Y. X. Li, and B. J. Tan, *Chem. Mater.* 3, 30 (1991).
161. Y. X. Li and K. J. Klabunde, *New J. Chem.* 12, 691 (1988).
162. B. J. Tan, K. J. Klabunde, T. Tanaka, H. Kanai, and S. Yoshida, *J. Am. Chem. Soc.* 110, 5951 (1988).
163. V. Akhmedov and K. J. Klabunde, *J. Mol. Catal.* 45, 193 (1988).
164. Y. X. Li and K. J. Klabunde, *Hyperfine Interact.* 41, 665 (1988).
165. Y. X. Li, Y. F. Zhang, and K. J. Klabunde, *Langmuir* 4, 385 (1988).
166. Y. X. Li and K. J. Klabunde, *Langmuir* 3, 558 (1987).
167. Y. Tanaka, K. Matsuo, and K. J. Klabunde, *Abstr. Pap. Am. Chem. Soc.* 184, 26 (1982).
168. Y. Wang, Y. X. Li, and K. J. Klabunde, *ACS Symp. Ser.* 517, 136 (1993).
169. Y. X. Li and K. J. Klabunde, *Langmuir* 7, 1388 (1991).
170. Y. X. Li, K. J. Klabunde, and B. H. Davis, *J. Catal.* 128, 1 (1991).
171. Y. X. Li and K. J. Klabunde, *J. Catal.* 126, 173 (1990).
172. K. J. Klabunde, Y. X. Li, and K. F. Purcell, *Hyperfine Interact.* 41, 649 (1988).
173. K. J. Klabunde and R. S. Mulukutla, in "Nanoscale Materials in Chemistry" (K. J. Klabunde, Ed.), p. 229. Wiley-Interscience, New York, 2001.
174. D. J. Zhang, K. J. Klabunde, C. M. Sorensen, and G. C. Hadjipanayis, *Nanostruct. Mater.* 12, 1053 (1999).
175. A. Pradhan, S. Ismat Shah, and L. Pakstis, *Mater. Res. Soc. Symp. Proc.* 740, I6.10.1 (2003).
176. P. Milani and S. Ianotta, in "Cluster Beam Synthesis of Nanostructured Materials." Springer-Berlag, Berlin, 1999.
177. D. Bulgin, J. Dyke, J. Goodfellow, N. Jonathan, E. Lee, and A. J. Morris, *Electron Spectrosc.* 12, 67 (1977).
178. S. Tsantilis, S. E. Pratsinis, and V. Haas, *J. Aerosol Sci.* 30, 785 (1999).
179. K. E. Gonsalves, H. Li, R. Perez, P. Santiago, and M. Jose-Yacaman, *Coord. Chem. Rev.* 206, 607 (2000).
180. G. P. Vissokov, B. I. Stefanov, N. T. Gerasimov, D. H. Oliver, R. Z. Enikov, A. I. Vrantchev, E. G. Balabanova, and P. S. Pirgov, *J. Mater. Sci.* 23, 2415 (1988).
181. S. Ohno and M. Uda, *J. Jpn. Inst. Metals* 53, 946 (1989).
182. C. J. Choi, X. L. Dong, and B. K. Kim, *Scripta Mater.* 44, 2225 (2001).
183. Y. Chen, N. Glumac, B. H. Kear, and G. Skandan, *Nanostruct. Mater.* 9, 101 (1997).
184. W. Chang, G. Skandan, S. C. Danforth, M. Rose, A. G. Balogh, H. Hahn, and B. Kear, *Nanostruct. Mater.* 6, 321 (1995).
185. Z. Paszti, G. Peto, Z. E. Horvath, and A. Karacs, *Appl. Surface Sci.* 168, 114 (2000).
186. A. G. Gnedovets, A.V. Gusarov, and I. Smurov, *J. Phys. D* 32, 2162 (1999).
187. T. G. Dietz, M. A. Duncan, D. E. Powers, and R. E. Smalley, *J. Chem. Phys.* 74, 6511 (1981).
188. M. D. Morse, *Chem. Rev.* 86, 1049 (1986).
189. E. Ozawa, Y. Kawakami, and T. Seto, *Scripta Mater.* 44, 2279 (2001).
190. A. L. Stepanov, G. Bour, A. Reinholdt, and U. Kreibig, *Tech. Phys. Lett.* 28, 642 (2002).
191. Y. B. Pithawalla, S. C. Deevi, and M. S. El-Shall, *Mater. Sci. Eng. A* 329, 92 (2002).
192. J. Bosbach, D. Martin, F. Stietz, T. Wenzel, and F. Trager, *Appl. Phys. Lett.* 74, 2605 (1999).
193. C. H. Bae, S. H. Nam, and S. M. Park, *Appl. Surf. Sci.* 197, 628 (2002).
194. F. Mafune, J. Y. Kohno, Y. Takeda, and T. Kondow, *J. Phys. Chem. B* 106, 7575 (2002).
195. T. Tsuji, K. Iryo, N. Watanabe, and M. Tsuji, *Appl. Surf. Sci.* 202, 80 (2002).
196. S. I. Dolgaev, A. V. Simakin, V. V. Voronov, G. A. Shafeev, and F. Bozon-Verduraz, *Appl. Surf. Sci.* 186, 546 (2002).
197. Z. Y. Jiang, R. B. Huang, S. Y. Xie, Z. X. Xie, and L. S. J. Zheng, *Solid State Chem.* 160, 430 (2001).
198. G. Compagnini, A. A. Scalisi, and O. Puglisi, *Phys. Chem. Phys.* 4, 2787 (2002)
199. A. D. Randolph and M. A. Larson, "Theory of Particulate Processes," 2nd ed. Academic Press, New York, 1988.
200. C. Kaito, K. Fujita, H. Shibahara, and M. Shiojiri, *Jpn. J. Appl. Phys.* 16, 697 (1977).
201. D. L. Olynick, J. M. Gibson, and R. S. Averback, *Philos. Mag. A* 77, 1205 (1998).
202. H. Müller, *Kolloidbeihefte* 27, 223 (1928).
203. Y. Efendiev and M. R. Zachariah, *J. Colloid Interface Sci.* 249, 30 (2002).
204. S. H. Park, K. W. Lee, E. Otto, and H. Fissan, *J. Aerosol Sci.* 30, 3 (1999).
205. F. S. Lai, S. K. Friedlander, J. Pich, and G. M. Hidy, *J. Colloid Interface Sci.* 39, 395 (1972).
206. G. D. Ulrich and N. S. Subramanian, *Combust. Sci. Technol.* 17, 119 (1977).
207. J. Frenkel, *J. Phys.* 9, 385 (1945).
208. P. Tandon and D. E. Rosner, *J. Colloid Interface Sci.* 213, 273 (1999).
209. A. I. Medalia, *J. Colloid Interface Sci.* 24, 393 (1967).
210. H. M. Park and D. E. Rosner, *Chem. Eng. Sci.* 44, 2225 (1989).
211. H. M. Park and D. E. Rosner, *Chem. Eng. Sci.* 44, 2233 (1989).
212. M. Tassopoulos, J. A. O'Brien, and D. E. Rosner, *AIChE J.* 35, 967 (1989).
213. J. L. Castillo, P. L. Garcia-Ybarra, and D. E. Rosner, *J. Crystal Growth* 116, 105 (1992).
214. W. Koch and S. K. Friedlander, *J. Colloid Interface Sci.* 140, 419 (1990).
215. Y. Xiong and S. E. Pratsinis, *J. Aerosol Sci.* 24, 283 (1993).
216. P. Meakin, *Adv. Colloid Interface Sci.* 28, 249 (1988).
217. A. Gurav, T. Kodas, T. Pluym, and Y. Xiong, *Aerosol Sci. Technol.* 19, 411 (1993).
218. S. H. Park, R. Xiang, and K. W. Lee, *J. Colloid Interface Sci.* 231, 129 (2000).
219. U. O. Koylu, Y. C. Xing, and D. E. Rosner, *Langmuir* 11, 4848 (1995).
220. A. M. Brasil, T. L. Farias, and M. G. Carvalho, *Aerosol Sci. Technol.* 33, 440 (2000).
221. A. Kalani and P. D. Christofides, *Comput. Chem. Eng.* 26, 1153 (2002).
222. A. Maisels, F. E. Kruis, and H. Fissan, *J. Aerosol Sci.* 33, 35 (2002).
223. A. R. Thölen, in "Nanophase Materials Synthesis–Properties–Applications" (G. C. Hadjipanayis and R. W. Siegel, Eds.), p. 57. Kluwer Academic, Dordrecht, 1994.
224. K. L. Johnson, K. Kendall, and A. D. Roberts, *Proc. Roy. Soc. London Ser. A* 324, 301 (1971).
225. H. Masuda and K. Gotoh, in "Powder Technology Handbook" (K. Gotoh, H. Masuda, and K. Hiagashitani, Eds.), p. 133. Dekker, New York, 1997.
226. A. Singhal, G. Skandan, A. Wang, N. Glumac, B. H. Kear, and R. D. Hunt, *Nanostruct. Mater.* 11, 545 (1999).
227. R. P. Andres, J. D. Bielfeld, J. I. Henderson, D. B. Janes, V. R. Kolagunta, C. P. Kubiak, W. J. Mahoney, and R. G. Osifchin, *Science* 273, 1690 (1996).
228. A. Gotoh, K. Kamiya, and F. Ikazaki, *J. Mater. Sci. Lett.* 19, 217 (2000).
229. R. Schneider, *Anal. Biol. Chem.* 374, 639 (2002).
230. H. P. Klug and L. E. Alexander, "X-ray Diffraction Procedures for Polycrystalline and Amorphous Materials," 2nd ed., p. 689. Wiley Interscience, New York, 1974.
231. Powder Diffraction Data from the Joint Committee on Powder Diffraction Standards, Swarthmore, PA, 1976.
232. X. Y. Fu, Y. Wang, N. Z. Wu, L. L. Gui, and Y. Q. Tang, *J. Coll. Interface. Sci.* 243, 326 (2001).
233. J. C. Sanchez-Lopez, T. C. Rojas, J. P. Espinos, and A. Fernandez, *Scripta Mater.* 44, 2331 (2001).

*234.* S. Tougaard, *Surf. Inter. Anal.* 26, 249 (1998).

*235.* S. Tougaard *Appl. Surf. Sci.* 101, 1 (1996).

*236.* M.-I. Baraton, in "Handbook of Nanostructured Materials and Nanotechnology" (H. S. Nalwa, Ed.), Vol. 2, p. 89. Academic Press, San Diego, 1999.

*237.* F. Boccuzzi, A. Chiorino, and M. Manzoli, *Surf. Sci.* 454–456, 942 (2000).

*238.* M. Muniz-Miranda and G. Sbrana, *J. Mol. Struct.* 565, 159 (2001).

*239.* J. Wang, T. Zhu, M. Tang, S. M. Cai, and Z. F. Liu, *Jpn. J. Appl. Phys. Part 2 Lett.* 35, L1381 (1996).

*240.* A. M. Michaels, M. Nirmal, and L. E. Brus, *J. Am. Chem. Soc.* 121, 9932 (1999).

*241.* A. M. Michaels, J. Jiang, and L. Brus, *J. Phys. Chem. B* 104, 11965 (2000).

*242.* H. Eckert, Solid state nuclear magnetic resonance, in "Encyclopedia of Materials Characterization" (C. R. Brundle, C.A. Evans, Jr., and S. Wilson, Eds.), pp. 460–472. Butterworth-Heinemann, Boston, 1992.

*243.* B. S. Zelakiewicz, A. C. de Dios, and Y. Y. Tong, *J. Am. Chem. Soc.* 125, 18 (2003).

*244.* R. H. Terrill, T. A. Postlethwaite, C. H. Chen, C. D. Poon, A. Terzis, A. D. Chen, J. E. Hutchison, M. R. Clark, G. Wignall, J. D. Londono, R. Superfine, M. Falvo, C. S. Johnson, E. T. Samulski, and R. W. Murray, *J. Am. Chem. Soc.* 117, 12537 (1995).

*245.* A. Labouriau, G. Panjabi, B. Enderle, T. Pietrass, B. C. Gates, W. L. Earl, and K. C. Ott, *J. Amer. Chem. Soc.* 121, 7674 (1999).

*246.* B. A. Enderle, A. Labouriau, K. C. Ott, and B. C. Gates, *Nano Lett.* 2, 1269 (2002).

*247.* P. E. J. Flewitt and R. K. Wild, "Physical Methods for Materials Characterisation," pp. 231–243. Institute of Physics, Bristol, 1994.

*248.* G. Schmid, in "Nanoscale Materials in Chemistry" (K. J. Klabunde, Ed.). Wiley, New York, 2001.

*249.* P. M. Paulus, A. Goossens, R. C. Thiel, G. Schmid, A. M. van der Kraan, and L. J. de Jongh, *Hyperfine Interact.* 126, 199 (2000).

*250.* S. Morup, J. A. Dumesic, and H. Topsoe, in "Applications of Mössbauer Spectroscopy" (R. L. Cohen, Ed.), Vol. 2, p. 1. Academic Press, New York, 1982.

*251.* J. L. Dormann, D. Fiorani, R. Cherkaoui, E. Tronc, F. Lucari, F. D'Orazio, L. Spinu, M. Nogues, H. Kachkachi, and J. P. Jolivet, *J. Magn. Mag. Mater.* 203, 23 (1999).

*252.* S. Morup, *Europhys. Lett.* 28, 671 (1994).

*253.* S. Roy, D. Das, D. Chakravorty, and D. C. Agrawal, *J. Appl. Phys.* 74, 4746 (1993).

*254.* P. Brahma, S. Banerjee, D. Das, P. K. Mukhopadhyay, S. Chatterjee, A. K. Nigam, and D. Chakravorty, *J. Magn. Mag. Mater.* 246, 162 (2002).

*255.* U. Herr, J. Jing, R. Birringer, U. Gonser, and H. Gleiter, *Appl. Phys. Lett.* 50, 472 (1987).

*256.* S. Trapp, C. T. Limbach, U. Gonser, S. J. Campbell, and H. Gleiter, *Phys. Rev. Lett.* 75, 3760 (1995).

*257.* Y. Sasaki, M. Hyakkai, E. Kita, A. Tasaki, H. Tanimoto, and Y. Iwamoto, *J. Appl. Phys.* 81, 4736 (1997).

*258.* J. Balogh, L. Bujidoso, D. Kaptas, and T. Kemeny, *Phys. Rev. B* 61, 4109 (2000).

*259.* S. Giri, S. Ganguli, and M. Bhattacharya, *Appl. Surf. Sci* 182, 345 (2001).

*260.* Y. I. Petrov and E. A. Shafranovsky, *J. Nanoparticle Res.* 3, 419 (2001).

*261.* S. J. Campbell and H. Gleiter, in "Mössbauer Spectroscopy Applied to Materials and Magnetism" (G. J. Long and F. Grandjeab, Eds.), pp. 241–303. Plenum Press, New York, 1993.

*262.* D. J. C. Yates, Physical and chemical adsorption, in "Encyclopedia of Materials Characterization" (C. R. Brundle, C.A. Evans, Jr., and S. Wilson, Eds.), pp. 736–744. Butterworth–Heinemann, Boston, 1992.

*263.* T. W. Ebbesen, H. J. Lezec, H. F. Ghaemi, T. Thio, and P. A. Wolff, *Nature* 391, 667 (1998).

*264.* J. R. Krenn, A. Dereux, J. C. Weeber, E. Bourilott, Y. Lacroute, and J. P. Goudonnet, *Phys. Rev. Lett.* 82, 2590 (1999).

*265.* J. B. Pendry, *Science* 285, 1687 (1999).

*266.* Y. Dirix, C. Bastiaansen, W. Caseri, and P. Smith, *Adv. Mater.* 11, 223 (1999).

*267.* P. A. Rundquist, P. Photinos, S. Jagannathan, and S. A. Asher, *J. Chem. Phys.* 91, 4932 (1989).

*268.* X. Xu, G. Friedman, K. D. Humfeld, S. A. Majetich, and S. A. Asher, *Chem. Mater.* 14, 1249 (2002).

*269.* R. Elghanian, J. J. Storhoff, R. C. Mucic, R. L. Letsinger, and C. A. Mirkin, *Science* 277, 1078 (1997).

*270.* J. J. Storhoff, R. Elghanian, R. C. Mucic, C. A. Mirkin, and R. L. Letsinger, *J. Am. Chem. Soc.* 120, 1959 (1998).

*271.* T. A. Taton, C. A. Mirkin, and R. L. Letsinger, *Science* 289, 1757 (2000).

*272.* P. Mulvaney, in "Nanoscale Materials in Chemistry" (K. J. Klabunde, Ed.). Wiley, New York, 2001.

*273.* C. Kittel, "Introduction to Solid Sate Physics." Wiley, New York, 1996.

*274.* J. P. Wilcoxon, J. E. Martin, and P. Provencio, *J. Chem. Phys.* 115, 998 (2001).

*275.* R. Dupree and M. A. Smithard, *Phys. Status Solidi A* 11, 695 (1972).

*276.* S. K. Mandal, R. K. Roy, and A. K. Pal, *J. Phys. D* 35, 2198 (2002).

*277.* M. M. Alvarez, J. T. Khoury, T. G. Schaaff, M. N. Shafigullin, I. Vezmar, and R. L. Whetten, *J. Phys. Chem. B* 101, 3706 (1997).

*278.* K. Fauth, U. Kreibig, and G. Schmid, *Z. Phys. D* 12, 515 (1989).

*279.* J. P. Wilcoxon, R. L. Williamson, and R. J. Baughman, *J. Phys. Chem.* 98, 9933 (1993).

*280.* T. Ung, L. M. Liz-Marzán, and P. Mulvaney, *J. Phys. Chem. B* 105, 3441 (2001).

*281.* P. Mulvaney, *MRS Bull.* 26, 1009 (2001).

*282.* M. D. Malinsky, K. L. Kelly, G. C. Schatz, and R. P. Van Duyne, *J. Am. Chem. Soc.* 123, 1471 (2001).

*283.* J. J. Storhoff, A. A. Lazarides, R. C. Mucic, C. A. Mirkin, R. L. Letsinger, and G. C. Schatz, *J. Am. Chem. Soc.* 122, 4640 (2000).

*284.* J. P. Alivisatos, *Science* 271, 933 (1996).

*285.* C. B. Murray, C. R. Kagan, and M. G. Bawendi, *Annu. Rev. Mater. Sci.* 30, 545 (2000).

*286.* R. P. Andres, T. Bein, M. Dorogi, S. Feng, J. I. Henderson, C. P. Kubiak, W. Mahoney, R. G. Osifchin, and R. Reifenberger, *Science* 272, 1323 (1996).

*287.* D. C. Ralph, C. T. Black, and M. Tinkham, *Phys. Rev. Lett.* 74, 3241 (1995).

*288.* C. T. Black, D. C. Ralph, and M. Tinkham, *Phys. Rev. Lett.* 76, 688 (1996).

*289.* D. L. Klein, P. L. McEuen, J. E. Bowen, R. Roth, and A. P. Alivisatos, *Appl. Phys. Lett.* 68, 2574 (1996).

*290.* S. Ogawa, F.-R. F. Fan, and A. J. Bard, *J. Phys. Chem.* 99, 11182 (1995).

*291.* D. J. Schiffrin, *MRS Bull.* 26, 1015 (2001).

*292.* J. H. Fendler, *Chem. Mater.* 13, 3196 (2001).

*293.* T. A. Fulton and G. J. Dolan, *Phys. Rev. Lett.* 59, 109 (1987).

*294.* T. Sato, H. Ahmed, D. Brown, and B. F. D. Johnson, *J. Appl. Phys.* 82, 696 (1997).

*295.* D. C. Ralph, C. T. Black, and M. Tinkham, *Phys. Rev. Lett.* 78, 4087 (1997).

*296.* S. P. Gubin, Y. V. Gulayev, G. B. Khomutov, V. V. Kislov, V. V. Kolesov, E. S. Soldatov, K. S. Sulaimankulov, and A. S. Trifonov, *Nanotechnology* 13, 185 (2002).

*297.* C. Kittel, *Phys Rev.* 70, 965 (1946).

*298.* A. Morrish, "Physical Principles of Magnetism." IEEE Press, Piscataway, NJ, 2001.

*299.* C. M. Sorensen, in "Nanoscale Materials in Chemistry" (K. J. Klabunde, Ed.). Wiley, New York, 2001.

*300.* W. H. Meiklejohn, *Rev. Mod. Phys.* 25, 302 (1953).

*301.* F. E. Luborsky, *J. Appl. Phys.* 32, 171S (1961).

302. E. F. Kneller and F. E. Luborsky, *J. Appl. Phys.* 34, 656 (1963).

303. J. F. Löffler, H. B. Braun, W. Wagner, G. Kostorz, and A. Wiedenmann, *Mater. Sci. Eng. A* 304–306, 1050 (2001).

304. C. Chen, O. Kitakami, and Y. Shimada, *J. Appl. Phys.* 84, 2184 (1998).

305. S. Gangopadhyay, G. C. Hadjipanayis, C. M. Sorensen, and K. J. Klabunde, in "Nanophase Materials–Synthesis–Properties–Applications" (G. C. Hadjipanayis and R. W. Siegel, Eds.). Kluwer Academic, Dordrecht, 1994.

306. C.-M. Hsu, H.-M. Lin, K.-R. Tsai, and P.-Y. Lee, *J. Appl. Phys.* 76, 4793 (1994).

307. C. Prados, M. Multigner, A. Hernando, J. C. Sanchez, A. Fernandez, C. F. Conde, and Conde, *J. Appl. Phys.* 85, 6118 (1999).

308. Y. Labaye, O. Crisan, L. Berger, J. M. Greneche, and J. M. D. Coey, *J. Appl. Phys.* 91, 8715 (2002).

309. D. L. Peng, T. Hihara, K. Sumiyama, and H. Morikawa, *J. Appl. Phys.* 92, 3075 (2002).

310. U. Gradmann, *J. Magn. Magn. Mater.* 54-7, 733 (1986).

311. C. Gruttner, S. Rudershausen, and J. Teller, *J. Magn. Mag. Mater.* 225, 1 (2001).

312. J. Connolly and T. G. St. Pierre, *J. Magn. Magn. Mater.* 225, 156 (2001).

313. R. P. Cowburn, *J. Phys. D* 33, R1 (2000).

314. K. J. Kirk, *Contemp. Phys.* 41, 61 (2000).

315. B. Warne, O. I. Kasyutich, E. L. Mayes, J. A. L. Wiggins, and K. K. W. Wong, *IEEE Trans. Magn.* 36, 3009 (2000).

316. M. A. Sousa, F. A. Tourinho, J. Depeyrot, G. J. daSilva, and M. C. Lara, *J. Phys. Chem. B* 105, 1168 (2001).

317. F. Gazeau, C. Baravian, J. C. Bacri, R. Perzynski, and M. I. Shliomis, *Phys. Rev. E* 56, 614 Part B (1997).

318. K. T. Wu, Y. D. Yao, C. R. C. Wang, P. F. Chen, and E. T. Yeh, *J. Appl. Phys.* 85, 5959 Part 2B (1999).

319. K. Raj, B. Moskowitz, and R. Casciari, *J. Magn. Magn. Mater.* 149, 174 (1995).

320. M. Zrinyi, L. Barsi L, and A. Buki, *Polymer Gels Networks* 5, 415 (1997).

321. T. Mitsumata, K. Ikeda, J. P. Gong, Y. Osada, D. Szabo, and M. Zrinyi, *J. Appl. Phys.* 85, 8451 (1999).

322. G. Torok G, V. T. Lebedev, L. Cser, G. Kali, and M. Zrinyi, *Physica B* 297, 40 (2001).

323. J. Zhao, F. E. Huggins, Z. Feng, F. L. Lu, N. Shah, and G. P. Huffman, *J. Catal.* 143, 499 (1993).

324. L. Wang, L. X. Feng, T. Xie, and X. F. Qing, *J. Mater. Sci. Lett.* 18, 1489 (1999).

325. V. P. Zhdanov and B. Kasemo, *Phys. Rev. B* 55, 4105 (1997).

326. R. Kötitz, W. Weitschies, L. Trahms, W. Brewer, and W. Semmler, *J. Magn. Magn. Mater.* 194, 62 (1999).

327. A. Jordan, R. Scholz, P. Wust, H. Fahling, and R. Felix, *J. Magn. Magn. Mater.* 201, 413 (1999).

328. A. Jordan, R. Scholz, K. Maier-Hauff, M. Johannsen, P. Wust, J. Nadobny, H. Schirra, H. Schmidt, S. Deger, S. Loening, W. Lanksch, and R. Felix, *J. Magn. Magn. Mater.* 225, 118 (2001).

329. C. M. Niemeyer, *Angew. Chem. Int. Ed.* 40, 4128 (2001).

330. A. Jordan, R. Scholz, P. Wust, H. Fahling, J. Krause, W. Wlodarczyk, B. Sander, T. Vogl, and R. Felix, *Int. J. Hyperthermia* 13, 587 (1997).

331. I. Safarik and M. Safarikova, *Monatsh. Chem.* 133, 737 (2002).

332. P. Wikstrom, S. Flygare, A. Grondalen, and P. O. Larsson, *Anal. Biochem.* 167, 331 (1987).

333. M. Hu and G. V. Hartland, *J. Phys. Chem. B* 106, 7029 (2002).

334. P. Buffat and J. P. Borel, *Phys. Rev. A* 13, 2287 (1976).

335. G. L. Allen, R. A. Bayles, W. W. Gile, and W. A. Jesser, *Thin Solid Films* 144, 297 (1986).

336. F. G. Shi, *J. Mater. Res.* 9, 1307 (1994).

337. Q. Jiang, H. X. Shi, and M. Zhao, *J. Chem. Phys.* 111, 2176 (1999).

338. F. A. Lindemann, *Phys. Z.* 11, 609 (1910).

339. O. Koper and S. Winecki, in "Nanoscale Materials in Chemistry" (K. J. Klabunde, Ed.). Wiley, New York, 2001.

340. Z. Zhang, J. C. Li, and Q. Ziang, *J. Phys. D* 33, 2653 (2000).

341. J. Rupp and R. Birringer, *Phys. Rev. B* 36, 7888 (1987).

342. H. Y. Bai, J. L. Luo, D. Jin, and J. R. Sun, *J. Appl. Phys.* 79, 361 (1996).

343. W. H. Li, S. Y. Wu, C. C. Yang, S. K. Lai, K. C. Lee, H. L. Huang, and H. D. Yang, *Phys. Rev. Lett.* 89, 135504 (2002).

344. A. S. Ahuja, *J. Appl. Phys.* 46, 3408 (1975).

345. S. U. S. Choi, *ASME FED* 231, 99 (1995).

346. J. A. Eastman, S. U. S. Choi, S. Li, L. J. Thompson, and S. Lee, *Mater. Res. Soc. Symp. Proc.* 457, 3 (1997).

347. X. Wang, X. Xu, and S. U. S. Choi, *J. Thermophys. Heat Transfer* 13, 474 (1999).

348. S. Lee, S. U. S. Choi, S. Li, and J. A. Eastman, *J. Heat Transf.* 121, 280 (1999).

349. J. A. Eastman, S. U. S. Choi, S. Li, W. Yu, and L. J. Thompson, *Appl. Phys. Lett.* 78, 718 (2001).

350. H. Xie, J. Wang, T. Xi, Y. Liu, F. Ai, and Q. Wu, *J. Appl. Phys.* 91, 4568 (2002).

351. Y. Xuan and Q. Li, *Int. J. Heat Fluid Flow* 21, 58 (2000).

352. C. Baker, A. Pradhan, and S. Ismat Shah, unpublished.

353. D. J. Jeffrey, *Proc. Roy. Soc. London Ser. A* 335, 355 (1973).

354. R. H. Davis, *Int. J. Thermophys.* 7, 609 (1986).

355. P. Keblinski, S. R. Phillipot, S. U. S. Choi, and J. A. Eastman, *Int. J. Heat Mass Transf.* 45, 855 (2002).

356. Y. Xuan and W. Roetzel, *Int. J. Heat Mass Transf.* 43, 3701 (2000).

# Metal Nanoparticles in Catalysis

## Qiang Wang, Agnes E. Ostafin

*University of Notre Dame, Notre Dame, Indiana, USA*

## CONTENTS

## 1. INTRODUCTION

Metal nanoparticles used in catalysis range in size from crystallites containing only a few hundred atoms to much larger particles up to 100 nm in diameter. These particles may be supported on the surface of a secondary "inert" material, used as colloids in a liquid suspension or as powders. Their unifying feature is that the physical size of the metal particle is correlated with the efficiency and type of catalytic reactions that can take place in their presence [1]. The extremely high surface area-to-volume ratio of these particles means that surface-bound ligands, the surrounding solvent, or a solid support particle can be used to tune the chemical and physical properties of the particle surface to promote the catalytic behavior or make it more selective [2]. In this review, we describe methods used for the synthesis of metal nanoparticle catalysts, several examples of metal nanoparticle catalyst materials currently in use, and some of their observed size-dependent catalytic behavior.

Catalysts have been used for centuries to improve the yield and properties of chemicals and foodstuffs in everyday life and in industry, from alcoholic fermentation at the beginning of the Neolithic period [3] to the refining of petroleum, which had U.S. sales of over 8 billion barrels in the year 2000 [4]. The word "catalysis" originated with Berzelius, who in 1835 used it to describe a "catalytic force" that had the ability of "decomposition of substances." A catalyst can shift the activation energy for a reaction, or change the enthalpy or entropy of the reacting system, usually by forming a surface-bound product or reactant, or both [5]. The understanding of catalyst function as a molecular-scale phenomenon arose early in the twentieth century [6], with the development of

quantitative chemical reaction kinetics [7], transition state theory [8], and the adsorption phenomenon [9].

The use of metal nanoparticle catalysts really came of age in the latter half of the twentieth century, thanks to the stimulus provided by industrial demand for faster, more specific, and cheaper catalytic materials that could be easily recovered and reused [10, 11]. In the process of developing ever finer particulates with optimized surface bonding properties, it became clear that the types of catalytic reactions observed on the surfaces of larger-sized materials do not extrapolate predictably to nanosized particulates [12, 13]. In fact, materials that are chemically inert at macroscopic scales take on new chemical reactivity as smaller and smaller particles are produced.

The onset of catalytic behavior appearing in nanosized metal particles originates with the gradual transition from metallic to molecular properties and is not a simple function of the exposed surface area [14]. A critical minimum particle size exists for each element, beyond which the periodic arrangement of atoms of the bulk crystal lattice cannot be sustained. The shift in periodicity leads to changes in the optical, electronic, and chemical properties of the material [15]. A high concentration of surface defects and absorbed ions creates islands of reactivity on the nanoparticle surface [2]. Much ongoing computational and experimental research is aimed at understanding the number and nature of these surface sites, their interaction with the rest of the nanoparticle and the solvent, and the consequential chemical behavior [16, 17].

The chemical reactivity of metal nanoparticles is a complicated function of lattice structure [18], bond length [19], bandgap [20, 21], ionization potential [19, 22, 23], electron affinity [24], and oxidation potential [25] of the particles. Because each of these properties has a slightly different dependence on the particle size, it is possible to obtain a wide variety of chemical reactivities for the same element by simply adjusting the particulate size [26]. In addition to internal structural and electronic differences of nanosized versus bulk metal particles, steric and/or electronic effects may inhibit certain reactants from reaching the nanoparticle surface, altering the apparent activity and selectivity of the catalyst [27, 28].

Surface-bound stabilizers, ligands, and ions may form new chemically active sites on the nanoparticle surface and can change the chemical activity and selectivity of existing sites in several ways [29]: (1) They can create a specific solvent "environment" around the catalyst. This could influence the diffusion of the reactant to the surface and introduce hydrophobic, steric, or electrostatic effects that alter the strength of interaction between the reactant and the catalyst surface. (2) They can chemically modify the catalyst surface by forming organometallic complexes, or polarize the metal particle. (3) They may provide or absorb protons, which may influence the equilibrium of acid-base reactions. and (4) They can influence the morphology and solubility of the nanoparticles early in the preparation stage or during reactions. These features may be advantageously used in the separation of the nanosized catalysts from the resultant products.

The performance of catalytic metal nanoparticles can also be tuned by choice of support material composition and how it is synthesized. The catalytic rate and selectivity can be affected by whether the support matrix is coprecipitated with preexisting particles or metal salt precursors, or is impregnated subsequently with precursors, which are then reacted *in-situ* to form nanoparticles within their void spaces. Dopants may also be added that may interact with the reactant to activate or lower its transition state energy, interact with the nanoparticles via electron donor-acceptor interactions, depress the poisoning effect of reaction products and impurities, or modify the support structure in the vicinity of the nanoparticles. The bulk porosity of the support can further be used to increase the reaction selectivity by prohibiting certain reactants from reaching the active site.

## 2. SYNTHESIS OF NANOPARTICLES

Metal nanoparticle catalysts can be synthesized starting from the bulk metal with the use of mechanical milling, laser ablation, ion sputtering, combustion flame, or microwave plasma discharge (Table 1). They can also be synthesized from soluble metal salts via sol–gel methods, sometimes combined with sonolysis or radiolysis. As indicated below, these methods are not limited to the synthesis of metal nanoparticle catalysts, but have also been used for a wide variety of metal, metal oxide, and carbon-based nanomaterials.

### 2.1. Ball Milling

Ball milling, also called mechanical alloying, generates either amorphous or crystalline nanoparticles by grinding the bulk metal material with stainless steel balls about 1 mm in diameter in a rotating steel milling chamber for several hours. Although simple and convenient, this method suffers from the disadvantage of potential contamination by materials used in the steel ball [30] or the milling chamber, and low production rates averaging 1–5 g/h [31]. Nanoparticles prepared by the ball milling method include metallic nanoparticles such as Fe-Al [32, 33], Al-Ni [34], Fe-Cr [35, 36], Al-Ti-Fe [37], and Al-Ru [38]; ceramics such as $MoO_3$ [39], $Al_2O_3$ [40], $NiFe_2O_4$ [41], and $SrMnO_3$ [42]; and other materials such as carbon powders [43], SnS [44], $MoSi_2$ [45], $TiB_2$ [46], $V_2O_5$ oxidation catalyst [47], VPO oxidation catalyst [48], VHP ammoxidation catalyst [49], iron ore-based hydrogenation catalysts [50], and fuel cell catalysts [51].

The most commonly used mill is the planetary mill (Fig. 1). A support arm is mounted on a welded supporting framework via two bearing units. At one end of the arm a cylindrical milling chamber is mounted, and at the other end a counterbalance is mounted, the position of which along the arm can be adjusted for static structural balancing. The belt-driven, cylindrical milling chamber rotates along its own central shaft and centrifugally mixes the materials and balls in the chamber. The centrifugal force, which is much larger than gravity, is referred to as the milling force. During planetary milling, centrifugal forces alternately add and subtract. The grinding balls roll halfway around the chamber and then are thrown across it, colliding with the opposite wall at high speed. Grinding is further intensified by interaction of the balls with the sample particles. Planetary action gives up to $20g$ acceleration and reduces the grinding time to about two-thirds that of a simple centrifugal mill.

Because of the tremendous milling force experienced by the material during processing, the chemical and physical properties of the materials may be subject to change. In addition to the decrease in particle size [52], loss or alteration of crystallinity [53–58], changes in physical properties such as specific heat [59], and chemical reactions [60, 61] are observed. Some materials have higher catalytic activity after milling because of the lowered particle size [49] and better dispersion of the compounds [48], whereas others may decline in activity because of the change in the crystal structure [62].

The milling time, atmosphere in the vial, ball-to-powder ratio, and container temperature all must be controlled to get the desired products. For example, milling carbon nanotubes with stainless steel balls for 5 min yielded integrated nanotubes similar to the original structures. After 10 min, the proportion of broken nanotubes increased and some nanoparticles were found, and after 15 min many onion-like carbon particles were made [63]. When the mixture was milled for a full 60 min, the sample was mainly composed of amorphous carbon nanoparticles.

Depending on the material being milled, the environment may be an important parameter in the milling process. Natural graphite milled in nitrogen, argon, oxygen, and air can be considered as an example [64]. The first two atmospheres gave identical milling results and are referred to as inert atmospheres. However, when milled in an oxygen atmosphere, the carbon microstructure was found to evolve very differently. The specific surface area of samples milled in an inert atmosphere increases rapidly, from 6 $m^2/g$ to 150 $m^2/g$ within 3 h of milling. In contrast, the specific surface area of samples milled in air or oxygen was suppressed to below 25 $m^2/g$ even after milling for 10 h in oxygen, and a strong vacuum developed in the vial. This suggests that the oxygen may be adsorbed to the surface of the milled particles, suppressing particle growth.

Shelled structures may be formed if two different compounds are milled together. For example, iron powders with a particle size of 5–10 $\mu$m were mixed with 50–100-nm carbon black powder [65]. Milling for 5–10 min and then annealing at elevated temperatures resulted in the formation of encapsulated 10–20-nm iron crystallites covered with

**Table 1.** Summary of nanoparticle preparation methods and their features.

| Method | Description | Advantages | Disadvantages | Nanoparticles synthesized |
|---|---|---|---|---|
| 1. Ball milling | Bulk material ground to nanometer size with stainless steel balls | Simple, low-tech operation | Contamination from the instrument | Metal, bimetallic, metal oxide |
| 2. Laser ablation | Bulk material vaporized by laser pulse and collected on cooled substrate to form nanoparticles | Simple, clean process | Low productivity<br>High energy consumption<br>Hard to control the nanoparticle size/morphology | Mainly metal oxide and metal nitride |
| 3. Ion sputtering | Bulk material ablated by ion beam and collected on cooled substrate to form nanoparticles | Similar to laser ablation | Low productivity<br>Requires specialized ion source | Mainly metal nanoparticles |
| 4. Combustion flame | Metal precursor with or without fuel combusted and metal vapor collected on cooled substrate to form nanoparticles | High productivity<br>Uniform primary particles obtainable with special combustion chamber | Product aggregation | Mainly metal oxide and some metal nanoparticles |
| 5. Microwave plasma | Metal precursor decomposed in microwave-induced plasma and metal vapor collected on cooled substrate to form nanoparticles | High productivity synthesis at relatively low temperatures | Requires specialized microwave source | Metal, metal oxide, metal nitride |
| 6. Sol–gel | Dissolved metal precursor ions chemically reacted to form precipitate suspension | High productivity and repeatable synthesis at room temperature | Contamination from the solution | Metal, metal oxide |
| 7. Sonochemistry | Metal precursor decomposed and chemically reacted with reduction agents in cavitation bubbles with high local temperature and pressure generated by ultrasound | High productivity | Potential contamination by ultrasonic by-products and required high-powered ultrasound device | Metal, metal oxide, metal carbon |
| 8. Radiolysis | High-energy radiolysis generates hydrated electron and radicals which either directly reduce metal ions or produce reducing species *in-situ* | High productivity | Potential contamination by soluble radiation by-products and required specialized radiolysis sources | Metal (single or bimetallic composite) nanoparticles |

graphite layers about 5 nm thick. A controlled chemical reaction between the milled materials and the atmosphere in the vial may also be used to synthesize new composite materials. For example, maghemite nanoparticles were prepared by grinding iron in water, which reacts according to the reaction $2Fe + 3H_2O \rightarrow \gamma Fe_2O_3 + H_2$ [66].

## 2.2. Laser Ablation

In the laser ablation method, a pulsed laser beam is focused via an external lens onto a target located within a vacuum chamber (Fig. 2). The hot atoms ejected from the target surface undergo cooling collisions with the carrier gas present in the chamber and are collected in a condensation zone, typically a cold finger, located in front of the target. If a small concentration of reactant gas is also present it will react with the vaporized atoms to form new compounds. Laser ablation is a relatively simple process compared with other methods and can be applied to a variety of materials, both conducting and insulating. At commonly used laser wavelengths below 250 nm, almost all materials absorb the incident radiation. Laser ablation, however, presents some major disadvantages, such as low production rate, high energy consumption, and difficult control over particle homogeneity and reaction stoichiometry [67]. Laser ablation has been used to synthesize ceramic nanopowders [68] such as $Al_2O_3$ [69], $SnO_2$ [70, 71], iron oxides, strontium
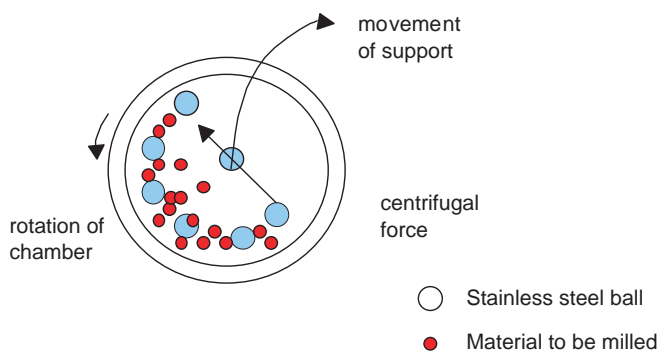
**Figure 1.** General motion of stainless steel balls in a planetary mill (top view). The centrifugal force impells them toward the chamber wall, where larger particles are broken into smaller ones.

ferrite [72], $ZrO_2$ [73], indium oxide [74], AlN [75], GaN [76, 77], carbon nitrides [78], tungsten [79], Si [80, 81, 82], $SiO_2$ [83], and $NbAl_3$ [84].

The nanoparticle size and phase are influenced by the laser power used, the substrate composition and structure, and the temperature, composition, and pressure of the background gas. Materials can only be ablated if the laser fluence (the laser pulse energy per unit area) on the target exceeds a critical value, called the threshold fluence. The threshold fluence depends on the material and the temporal profile of the laser pulse. When the material is highly absorbent and the pulse duration is short, the threshold fluence needed is small. Further manipulation of the fluence and lasing wavelength can be used to modify the size of the nanoparticles [85]. For example, the mean size of silver, gold, and permalloy nanoparticles formed as a result of the ablation obtained with radiation at 248 nm increases with increasing laser fluence. This trend for metallic nanoparticles is opposite that observed for glass, where the mean diameter decreases with increasing laser fluence [86].

Operating at lower target temperatures reduces the size of nanoparticles formed by decreasing the mobility of the deposited nanoparticles and preventing interparticle aggregates. Depending on the material, the structural form of the target material can also influence the size and phase of the final product. Anatase and rutile, two of the common crystallographic modifications of $TiO_2$, were compared [87]. With rutile as the ablation target, the product was always
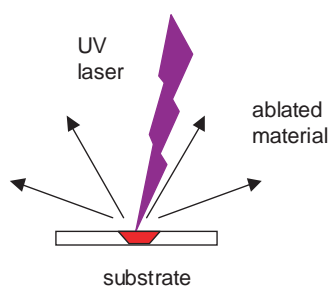
amorphous, nanoparticulate $TiO_2$. However, when anatase was used as a target, the collected sample consisted of a mixture of relatively larger particles (50–100 nm) of anatase, rutile, and amorphous $TiO_2$. It is possible that the difference arose partly from the rutile pellet being more fully sintered than the anatase pellet.

For the same pressure, the flow characteristics of the background gas, rather than its mass or reactivity, can be used to tailor nanoparticle size by modifying the ablation plume's spatial distribution and changing the frequency of collisions between metal atoms. For larger viscosity gases like Ne and Ar, the plume distributions are columnar, whereas in He, $O_2$, and $N_2$ mushroom-shaped distributions are formed [88]. The mean diameters of Si nanoparticles produced in an Ar background were significantly smaller than in those formed in air under the same experimental conditions. At low pressures, the mean free path of the gaseous species is comparable to the target-to-substrate separation, and a two-dimensionally continuous thin film tends to be formed on the substrate. With increasing gas pressure, the sputtered species are more likely to undergo collision-induced aggregation above the collection substrate and form discrete nanoparticles. Particle-particle collisions in lower viscosity gases allow the formation of larger particles at a faster rate. For example, the growth rate of the Si clusters in He was fastest, nearly eight times faster than that in $N_2$.

## 2.3. Ion Sputtering

The formation of nanoparticles by ion sputtering is similar to laser ablation. The difference is that an ion beam produced by either an arc discharge or an ion gun is used instead of a high-energy laser beam to vaporize the material (Fig. 3). To generate a beam of ions, a high potential difference is applied between two electrodes placed in a chamber that is filled with a gas like Ar. A few electrons emitted from the electrodes are accelerated by the large electric field toward the cathode. Inelastic collision of these electrons with the gaseous atoms in the chamber leads to excitation and ionization of the atoms, and collisions between these excited ions creates a second generation of electrons and ions, which also collide, forming the self-sustaining arc discharge [89]. If the material to be vaporized is the cathode, then the gaseous ions are allowed to sputter away the material of the electrode. Alternatively, they can be focused onto another target



**Figure 2.** High-energy laser light ablates atoms from the surface of a target material. The energized vapor atoms collide with each other and background carrier gas atoms, and nucleate small nanosized particulates, which are collected in a cold trap dowstream.
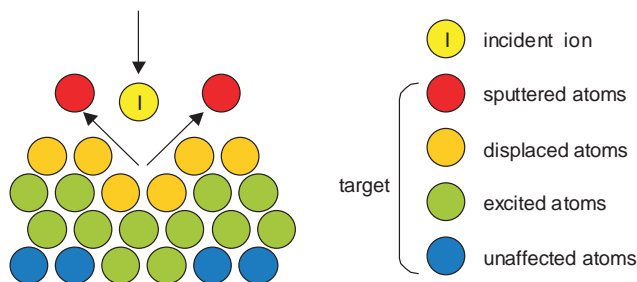


**Figure 3.** Incident high-energy ions ablate atoms from the surface of a target material that collide with each other and background gas atoms and nucleate nanoparticulates, which are collected downstream in a cold trap. The energy of the incident ions determines the energy transferred to subsurface layers.

material. Metal nanoparticles synthesized by the ion sputtering method include Al, Cr, Fe, Ni, $Cu_{1-x}Co_x$, Cu, Zr, Mo, Ta, W [90, 91], Ag [92, 93, 94], Au [95, 96], Pt [97, 98, 99], C [100, 101, 102], and $C_3N_4$ [103].

The chamber pressure and sputtering voltage both influence the morphology and growth rate of resulting nanoparticles and nanocrystalline films. At low chamber pressures and high sputtering voltages, the ionic species do not experience enough collisions in the vapor and are not cold enough to permit nucleation of sputtered materials. Instead of discrete particles, a polycrystalline film is formed on the surface of the collection substrate. At high chamber pressures, more frequent collisions of the sputtered species with the chamber gas atoms leads to a rapid decrease in the temperature of the sputtered atoms, and nucleation and growth of nanoparticles happen above the collection substrate. At even higher pressures the sputtering rate begins to be affected since ions from the arc discharge begin to lose energy by collisions before they even reach the target, resulting in a smaller fraction of ions with sufficient energy to sputter atoms off of the target. The sputtering voltage affects the chemical reactions between colliding molecules before they nucleate into particles or films. Nanocrystalline carbon films are formed from an adenine ($C_5H_5N_5$) target with an ion-sputtering energy of around 500 V at low gas pressures, whereas above 750 V, nanocrystalline carbon nitride films are deposited [103].

The chamber pressure affects the spatial development of particle growth and can be adjusted to obtain a specific particle size distribution [104]. At a sputtering threshold pressure of 150 mTorr, Mo nanoparticle formation occurs at relatively large distances from the source, and a bimodal size distribution is obtained. At 300 mTorr, the nanoparticle formation distance decreased to less than 4.5 cm from the target, and the particles had a wide size distribution.

A significant difference in the morphology of Ag nanoparticles and films was observed, depending on whether argon or nitrogen ions are used as sputtering ions [94]. Sputtering with argon ions leads to Ag nanoparticles, whereas sputtering with nitrogen ions leads to flatter structures.

Several materials can be sputtered simultaneously to form complex structured materials. With this approach, homogeneously distributed silver nanoparticles with an elongated shape along the direction of the thin film growth [105] and cobalt or copper nanocrystals encapsulated in graphite-like carbon have been synthesized by cosputtering of C-Co or C-Cu targets [105].

## 2.4. Combustion Flame

When an organic metal precursor is combusted in the presence of a gaseous hydrogen/oxygen mixture, the precursors experience rapid thermal decomposition in the hot zone of the flame and form metal vapor. When the vapor is cooled, a cloud consisting of fine metal particles is formed. Nanoparticles that have been synthesized with the combustion method are mainly ceramics such as $SiO_2$, $TiO_2$, $ZrO_2$, $Al_2O_3$, SiC [106, 107], $TiO_2$ [108], iron (III) oxide [109], $Y_2O_3$ [110], $BaTiO_3$ [111], Er-doped $CeO_2$ [112], and $V_2O_5$ [113]. Besides these, $C_{60}$, carbon onions, and higher fullerenes [114] have also been synthesized by the combustion flame method.

Different metals form different nanocrystalline structures when combusted. Some of the distinct morphologies found so far are as follows: (1) cubes for $\alpha$-Cr; (2) octahedra for fcc metals; (3) rhombic dodecahedra for $\alpha$-Fe, $\beta$-Mn, and Be; (4) tristetrahedra for $\alpha$-Mn; (5) icosatetrahedra for $\delta$-Cr; (6) hexagonal plates and polyhedra for Be, Mg, and Zn; (7) hexagonal rods with split ends for Te; (8) truncated triangular biprisms for fcc metals; and (9) pentagonal decahedra and/or icosahedra for fcc metals and $\gamma$-Fe. Morphologies (1) to (7) are single crystals. The nanoparticles formed in (8) are twinned and those in (9) are called multiply twinned particles [115].

The resulting nanoparticle size is strongly dependent on the combustion conditions, such as the shape of the flame, flame pressure, residence time of the particles in the flame, and flame temperature. Most of the experimental results can be explained with an empirical rule that particles become larger when nucleation occurs in a vapor of higher density. Therefore, simply increasing the precursor concentration will lead to smaller nanoparticles. For an analogous reason, the size and shape of nanoparticles will be quite different, depending on where they form in the metal cloud [116]. A typical metal cloud in an inactive gas looks like the flame of a candle. From the inside out, it consists of an inner zone nearest the evaporation source, an inner front, an outer zone, and an outer front. In the inner zone nanoparticles that form are relatively small and their size distribution is narrow, but the particles increase in size with increasing distance from the source. In the inner front, particles are several times larger in diameter than those in the inner zone and become larger as the distance from the source increases. In the outer zone, the nanoparticle size is nearly the same as that in the inner zone, although the density of the particles is much lower. Outside the outer zone, particles are usually aggregated as tangled chains and have various sizes. Here, aggregation may have taken place by collisions of particles during circulation by convection.

To decrease the size distribution, a stable flat flame process may be used [117]. Parallel to and below the flat burner is a water-cooled substrate maintained at slightly above room temperature. Nanoparticles condense on the cool substrate and are collected. Since the temperature profile, gas phase, residence time, and precursor concentration are uniform across the entire surface of the burner, the effect is to generate a beam of essentially monodispersed nanoparticles.

The residence time of the particles in the flame directly influences the size of the product. Longer residence times lead to larger particles. Samples taken from near the burner display a small mean diameter, and agglomerates consist of only two or three particles [118]. However, deposits collected near the chamber wall are much larger and more agglomerated. The spread in mean particle size suggests that the deposit consists of particles that follow two classes of trajectories: (1) those in which deposited particles collide with the substrate immediately after condensation, and (2) those in which the substrate is bypassed. In the former case, residence times are expected to be very short. Thus the particle size and degree of agglomeration are expected to be small. However, in case (2), the particles do not experience the

rapid quench induced by the substrate and thus would be expected to have time/temperature histories characterized by significantly longer periods of time in the hot region, leading to increased particle size and degree of agglomeration.

The flame temperature in the hot region also influences the resulting nanoparticle size by changing the collision frequency of atoms in the flame. By adjusting the ratio of glycine to nitrate, the combustion flame temperature can be lowered, and the size of rare-earth oxide nanoparticles like $Y_2O_3$:Eu and Er-doped $CeO_2$ phosphors is reduced [110, 112, 119]. However, if the pressure is too high, agglomeration of forming nanoparticles becomes troublesome. An improved method is combustion operating at low pressure in a stagnant flame [120]. Agglomeration is reduced because at lower temperatures results in less sintering of primary particles occurs. The flow rate of background gas should be adjusted appropriately; for example, for $TiO_2$ nanoparticles, increasing the oxygen content or flow rate of $O_2$/He gas releases a larger amount of water during the reaction and increases the probability of powder agglomeration in water vapor.

## 2.5. Microwave-Induced Plasma

Microwave-induced plasmas are ionized gases consisting of positive and negative ions and electrons, as well as neutral species, formed by microwaves in the frequency range from 300 MHz to 300 GHz (Fig. 4). The microwave plasma temperature can be adjusted in a range from 300 to 900 °C by properly selecting field strength, gas pressure, and gas species. In some cases, microwave heating of the containment vessel will release electrons from the vessel walls and allow autoignition of the plasma. The plasma is sustained by microwave energy continually transmitted from the source to the plasma gas. The nanoparticle precursors are allowed to flow into the plasma area along with an appropriate background gas. Although the overall temperatures of microwave plasmas are not as high as those in a DC or RF plasma, they are sufficient to enhance the kinetics of the chemical reactions through initiation of electron ionization and the dissociation or oxidation of the reactive molecules [121]. After the plasma has cooled, nanoparticles are formed. The nanoparticles synthesized by this method include ceramic powders [121, 122] such as $Cr_2O_3$ [123], $\gamma$-$Fe_2O_3$ [124, 125],
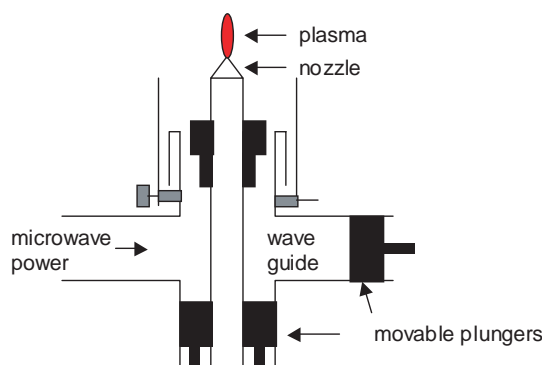


**Figure 4.** Schematic of a microwave waveguide design used to generate a plasma region for the synthesis of nanoparticles.

polymer-coated $\gamma$-$Fe_2O_3$ [126], $ZrO_2$ [127], $MoS_2$ [128, 129], $WS_2$ [128, 129], and AlN [130]; metal nanoparticles including Al [131], Mo [132], B [133], Fe [31], polymer-coated Fe [134], and carbon-supported Fe, Co, and Co-Mo nanoparticles [135]; and carbon nanotubes [136–142].

Choice of plasma gas may be used to terminate the growth of metal particles at a particular size or to keep the metal particles from agglomerating once on the substrate. With 10% $H_2$/Ar instead of pure Ar as a carrier gas, the mean particle diameters of carbon-supported monometallic (Fe, Co) and bimetallic (Co-Mo) materials could be decreased to less than 2 nm [135]. Carbon nanoparticle synthesized from the mixture of $H_2$ and $CH_4$ by microwave plasma chemical vapor deposition, and nanotubes were obtained from the mixture of $N_2$ and $CH_4$.

By manipulation of the plasma temperature, the morphology of the nanoparticles can be changed. In the case of $MoS_2$ nanoparticles formed by reaction of the metal hexacarbonyl with $H_2S$ in a microwave-induced plasma, irregularly shaped particles with a size from 5 to 8 nm are formed at 250 °C [128, 129]. At longer microwave plasma residence times and higher temperatures, bent planes of varying size and polyhedral crystals are formed. Because the microwave output power affects both the plasma temperature as well as the rate of particle nucleation and growth, the mean particle size can be tuned by both lowering of the microwave output power and manipulation of the feed rates of reactants and flow rates of the plasma-forming and carrier gases. A high flow rate of the plasma-forming gas shortens the residence time of the newly formed species in the reactor, which suppresses growth and coagulation. If the feeding rate of the precursor is increased or the flow rate of the carrier gas is decreased, a higher concentration of the reactive species will form in a localized region and will lead to accelerated nucleation and growth of larger nanoparticles.

## 2.6. Sol–Gel Method

Sol–gel methods are commonly used to prepare nanocomposite materials because these reactions occur readily with a wide variety of precursors and can be conducted at or near room temperature. In typical sol–gel syntheses, metal or main-group element compounds undergo hydrolysis and condensation reactions yielding gelled materials with extended three-dimensional structures. Water may be removed by calcination to get a porous nanopowder product. A second material may be coprecipitated with the metal, to yield a high-surface-area nanoparticle support loaded with a desired element. Sol–gel methods have been used to synthesize a wide variety of metal and metal oxide nanoparticles, including Zr [143], $CeO_2$-$ZrO_2$ [144], Ce-Mo oxide [145], bimetallic Au-Pd core shells [146], Ag-$SiO_2$ [147], Ag-Au [148], CuO [149], $TiO_2$ [150, 151], $Al_2O_3$-$TiO_2$ [152], $Al_2O_3$ [153], mesoporous aluminosilicate [154, 155], microporous hollandite-type hydrous manganese oxide [156], and Y zeolites [157]. $Fe_2O_3$-, ZnO-, PbO-, $VO_x$-, Cu-, $RhO_x$- Pt-, and Ru-loaded MCM-41 and MCM-48 [158–165], Ti-substituted silica-based mesoporous molecular sieves [166], Cu- and Co-loaded ZSM-5 [167], $TiO_2$ in activated carbon (AC), $\gamma$-$Al_2O_3$ and $SiO_2$ [168], Ni in amorphous silica and highly

porous alumina [169, 170]; and $Fe_2O_3$ nanoparticles in $SiO_2$ composites [171] have also been produced.

Water or alcohol is commonly used as the solvent in the sol–gel method. The size of $TiO_2$ catalysts prepared by hydrolysis of titanium alkoxides in an alcohol-water mixture can be controlled by the ratio of water to alcohol during the reaction [151]. At a constant $[H_2O]/[precursor]$ ratio, the particle size decreases rapidly with water addition and reaching a constant value at high water concentration. For higher water fractions a higher homogeneous nucleation rate is possible, therefore more and smaller gel spheres are produced.

Variation in the structure of the nanoparticle can be accomplished by varying the temperature and the surface of evaporation/volume ratio of the sol during gelation. When the sols gel with a lower $S/V$ ratio, a matrix forms with large pores, in which a great number of metal ions and solvent can be trapped. Calcination gives rise to large particles. For $Fe_2O_3/SiO_2$, low $S/V$ values and high temperatures in the gelation process favored the occurrence of $\gamma$-$Fe_2O_3$, whereas high $S/V$ ratios and low temperature give rise to $\alpha$-$Fe_2O_3$ formation [172]. At low $S/V$ values and high temperatures, both polycondensation and evaporation are faster, not all ethoxy groups from TEOS are hydrolyzed, and therefore part of the solvent remains trapped in the silica pores. At high $S/V$ ratios and low temperatures, the hydrolysis of the ethoxy group is almost total and no ethanol is trapped into the pore. Depending on the drying conditions, aerogel or xerogel materials can be formed [173]. When the gel is dried slowly, the capillary forces at the liquid/vapor interface result in shrinkage and cracking, so that the original porous structure is lost and dense xerogels are obtained. If the drying step is performed under supercritical conditions where no capillary forces are present, the original pore structure of the gel is retained and aerogels are formed.

## 2.7. Sonochemical Method

Sol–gel syntheses of metal nanoparticles may be assisted by the use of sonolysis to initiate reactions between precursors, avoiding contamination of the nanoparticle catalyst with unreacted reductants or oxidants [174]. High-intensity ultrasound causes the formation, growth, and collapse of bubbles in the irradiated liquids, a process called cavitation (Fig. 5) [175]. Bubble collapse results in an enormous concentration of energy from the conversion of the kinetic energy of the highly sheared and strained liquid motions at the bubble interface into heating of the contents of the bubble, which could generate localized hot spots with temperatures as high
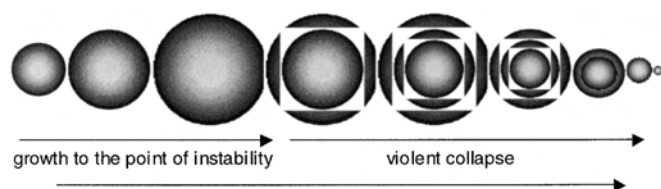


**Figure 5.** Progression of bubble formation and collapse during sonochemical excitation. As the bubble collapses the pressure and temperature within the bubble space increase dramatically, inducing chemical reactions at the gas/liquid interface until the bubble disappears.

as 5000 °K and pressures as high as 1000 atm, resulting in heating and cooling rates above 1010 °K/s [176, 177].

In the interfacial region around the bubbles high temperatures and pressures arise from the very large shear and strain gradients of liquid motion in the bubble vicinity. The high local temperatures and pressures, combined with extraordinarily rapid cooling, induce physical or chemical changes in the bubble or the interfacial region, depending on the volatility of the precursors. Volatile molecules penetrate the bubbles and react with one another in the inner vaporous phase [178], whereas involatile molecules react in the interfacial region [179]. Metal nanoparticle catalysts form via one of several mechanisms in these regions: (1) the nanoparticle precursors undergo decomposition and form nanoparticles [180]; (2) the reactions between reductant and precursor mixture solution could be promoted by the high temperatures and pressures [181]; (3) a high concentration of strong, highly reactive reductants could be generated in aqueous or alcohol solutions, and these could be used to reduce the precursors [182–185]; and (4) high-speed jets of liquid with velocities of hundreds of meters per second driven by rapidly breaking bubbles may break large brittle materials into nanoparticles [178] or accelerate the particles, causing interparticle collisions, melting, and nanoparticle growth [186]. If the reactions take place inside the collapsing bubble, the products obtained are usually amorphous as a result of the high cooling rates in the bubbles, which prevent crystallization from occurring [187]. On the other hand, if the reaction takes place at the bubble interface, crystalline products may be obtained [179].

Ultrasound sonolysis has been used to produce colloidal Pt [184, 188], nanosized Pd clusters on Y-zeolites [185, 189], Pd nanoparticles dispersed on $Al_2O_3$ for the hydrogenation of olefins [190], Cu nanoparticles for the condensation of aryl halides [191], Ni nanoparticles [192–194], Au nanoparticles [195, 196], Ru nanoparticles [197], Fe nanoparticles [193, 198–200], iron-molybdenum nanoparticles for the synthesis of single-walled carbon nanotubes [201], and various nanoparticle metal alloys such as Fe-Co, Pt-Pd, and M50 steel [193]. In addition to metal nanoparticle catalysts, this method has had broader applicability and has been used to synthesize metal oxide nanoparticles such as $Cu_4O_3$, $Cu_2O$, and $Fe_3O_4$ embedded in polyaniline [202, 203], CuO, ZnO, $Co_3O_4$, $MnO_2$ [204, 205], $Fe_2O_3$ [206], $Mo_2O_5$ [207], $TiO_2$ [208], $SnO_2$ [209], ceramic nanoparticles such as $PdC_x$ ($x$ less than or equal to 0.15) [181], PbS [210], CdS nanoparticles [211], nickel aluminate spinel particles [212], InP [213], $Ag_2S/PVA$, CuS/PVA [214], and $ThC_2$ [215].

The choice of nanoparticle surface-stabilizing protective reagents, the composition of the bulk solution, and ultrasound power can be used to influence the size and morphology of the product nanoparticles. Metal nanoparticles are often prepared in the presence of surfactants, polymers, or other coordinating reagents that bind to the surface of the nanoparticles. Such protective reagents favor nanoparticle nucleation by forming larger soluble complexes between the precursors and prevent nanoparticles from growing bigger [201, 216]. With this strategy, PbSe crystals were formed with polyethylene glycol (PEG) as a dispersant [217]. The stoichiometric ratio of tetramethylammonium hydroxide (TMAOH) surfactant stabilizer to reactive

species was used in the sonochemical preparation of $CeO_2$ nanoparticles to decrease the nanoparticle size from 5.9 nm to 3.3 nm, narrow the size distribution, and prevent aggregation [218]. Similarly, HgSe and $Fe_2O_3$ nanoparticles with different sizes could be obtained in the presence of complexing agents in the sonochemical method [219, 220].

Surfactants can be used to direct the morphological growth of product, influencing both its shape and size. CuSe nanocrystallites ranging from 25 to 30 nm spherical $Cu_{2-x}Se$, flakelike $\beta$-CuSe, and spherical $Cu_3Se_2$ were synthesized in different solutions at room temperature via sonochemical irradiation [221]. Lamellar structures of CuSe were obtained when the concentration of sodium dodecyl sulfate (SDS) was higher than 0.2 mol/liter [222]. With cetyltrimethylammonium bromide (CTAB) as a template instead, 25–30-nm spherical CuSe was obtained. Similarly elongated needles of Pb(OH)Br 900 nm in length and 150 nm in width were synthesized sonochemically in the presence of 1% CTAB surfactant [223].

The composition of bulk solution influences the physical properties or chemical activity of the reactants in the solution. Low viscosity, high surface tension, and low vapor pressure solutions favor maximum acoustic cavitation and sonochemical yields [224]. The temperature generated during the collapse of a gas-filled cavity is lower for higher vapor pressure solvents, because the energy is used to compress the solvent vapor in the bubble is not available for adiabatic heating, nor for chemical reactions inside the bubble and volatile solvents are used, the effective temperatures reached during bubble collapse are lower, and, the type of nanoparticle forming reactions that can take place may be affected [187]. For example, ZnO, CuO, $Co_3O_4$, and $Fe_3O_4$ nanoparticles were synthesized sonochemically from their metal acetates both in water and in 10% *N*,*N*-dimethylformamide (DMF) water solution [225]. Higher yields of nanoparticles were obtained in DMF solution than in water because the addition of DMF decreased the solvent viscosity and vapor pressure, yielding more cavitations during the sonication process. Similarly, in the preparation of nanocrystalline CuSe via sonochemistry, the addition of methanol decreased the $Cu^{2+}$ concentration and led to $Cu_3Se_2$ nanoparticles [221]. However, excess methanol could inhibit the generation of $H_2O_2$ and OH radicals [226], and prevented the oxidization of the $Cu^+$ into $Cu^{2+}$ ions, leading instead to the formation of $Cu_3Se_2$. The influence of solution pH on the production of MnO nanoparticles by sonochemistry showed that the size of the product was strongly dependent on the pH [204]. Increasing in pH produced particles of smaller size, from 100 nm at pH 7.5 to approximately 55 nm at pH 8.8 and 20 nm at pH 10, opposite the trends observed for sol–gel synthesis in the absence of ultrasound.

Ultrasound power can also influence nanoparticle formation in several ways [221]: (1) it can increase the solubility of certain reactants and enhance the speed of reactions; (2) it can create massive shock waves that drive high-speed microjets of liquid to impinge upon the surface of a metal nanoparticle catalyst or bulk precursor target, removing material in a localized erosion to produce a newly exposed and highly reactive surfaces; (3) it can improve mass transport in the solution through the turbulent mixing it creates; (4) it can

cause particle fragmentation; and (5) it can increase the temperature of the bulk solution. Tetrachloroaurate(III) hydrate was reduced in an aqueous 2-propanol solution to form colloidal gold nanoparticles with different powers of ultrasound [227]. An ultrasound intensity threshold must be achieved for the gold reduction to take place. No reduction was produced with a 100-W, 28-kHz ultrasonic cleaner; however, an ultrasound generator operated at 200 W and 200 kHz was intense enough to induce the generation of nanoparticles. The rates of Au nanoparticle production were increased with increased ultrasound power and resulted in a decrease in the average particle size from 71 to 35 nm as the power was increased from 0.5 to 1.43 $W/cm^2$.

## 2.8. Radiolysis Method

Radiolytic activation of metal nanoparticle precursors in solutions may be done with ultraviolet or X-ray radiation, MeV energy electrons, or gamma radiation. These methods have variously been used to prepare silver [228–231]; gold [232, 233], copper and mercury [234–236]; nickel [237]; cadmium [238]; Bi [239]; Pt, Pt-Au bimetallic, Au-Pt core-shell [240, 241]; and Hg-Ag bimetallic [242] nanoparticles. The radiation chemical method for colloid preparation has important advantages in comparison with the chemical reduction of metal ions: it is reproducible and can be applied at ambient temperature, no disturbing chemical impurities are introduced, and the reduction is initiated homogeneously (i.e., without local concentration gradients when reactants are mixed) [243]. The radiation sources used could be (a) continuous or steady-state and include X-ray machines, $Co^{60}$ $\gamma$-ray sources, and UV light, [229]; and (b) pulsed instrumentation such as electron accelerators, which generate pulses of high-energy electrons with a duration of $10^{-6}$ s or less [244–246].

When exposed to high-energy radiation, the water molecules of the solvent absorb the radiation and react with the following stoichiometry: $4.0H_2O = 2.6e^-_{aq} + 2.6OH\cdot + 0.6H\cdot + 2.6H^+ + 0.4H_2 + 0.7H_2O_2$, where the coefficients express the number of each species destroyed or formed per 100 eV of energy absorbed by the water (also called the $G$ value), and $e^-_{aq}$ refers to the hydrated electron [247]. The distinguishing feature of radiolysis is the formation of the products in isolated volume elements called spurs and tracks, which may contain one or more pairs of reactive $e^-_{aq}$, OH$\cdot$ radical, H$\cdot$ radical, and $H^+$. Within the spur or track, these species diffuse and react with each other, and a fraction of them combine to form the molecular products $H_2$, $H_2O_2$, and $H_2O$, while the remainder escape into the bulk solution and become homogeneously distributed [247]. During radiolysis roughly equal numbers of reducing and oxidizing radicals are produced. Scavengers such as aliphatic alcohols and formic acids are generally added to the solution and react with OH radicals to modify the system to be totally reducing [234, 248, 249].

Direct absorption of radiation by the metal precursors can be neglected when they constitute less than 1 mol/liter [247]. The main reactions involve hydrated electrons ($e^-_{aq}$), H$\cdot$ radicals, R$\cdot$ radicals, and OH$\cdot$ radicals reacting with metal precursors to form metal atoms, which subsequently coalesce to form nanoparticles. The hydrated electron is a strong
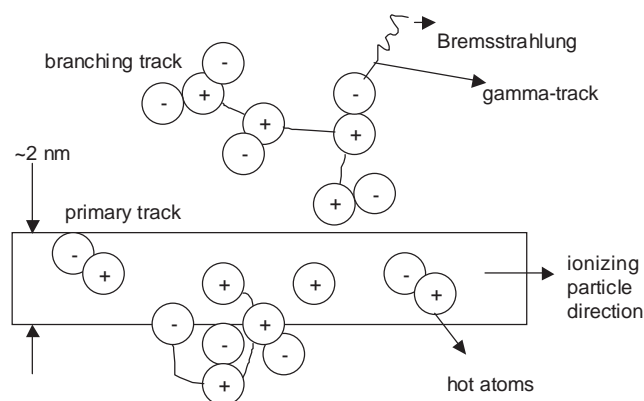
**Figure 6.** Ionized track formed by ionizing particles traveling through a liquid zone called the primary track. The cascade effect of ion formation and secondary radiation emission induces chemical reactions with radical species and metal precursors that lead to nanoparticle formation.

reducing agent, with a redox potential of about $-2.7$ V, and reacts with most metals, except the alkali and alkaline earth metals [250]. The hydroxyl radical, on the other hand, is a strong oxidizing agent ($E^0(OH/OH^-) = 1.9$ V) [247]. In many cases, the diffusion rate of the hydrated electron is the controlling step. Based on the fact that complexation of the metal ion with ligands other than $H_2O$ can produce a dramatic reduction in reaction rate [251]. H· radicals reduce metal ions via electron transfer, oxidizing metal ions, such as $Ti^{3+}$, $V^{2+}$, $Cr^{2+}$, $Fe^{2+}$, and $Pu^{3+}$ while being converted to molecular hydrogen [252, 253]. Secondary radicals formed from reaction of the primary radiolytically generated species with suitable additives are much less reactive than is the hydrated electron but can still lead to nanoparticle formation. The reactions of these radicals with metal ions could proceed via (a) an outer-sphere electron transfer mechanism, in which electron transfer takes place across metal-coordinating ligands without replacing them, and the reduced metal complex coagulates to form nanoparticles, or (b) a ligand-exchange chain mechanism, in which the radicals also combine with the metal complex and facilitate further complexation with another metal ion to form a larger intermediate complex and detached ligand. At some stage, the radical species must itself be detached from the growing metal cluster to initiate a new cycle of chain growth until all of the metal ions have been reduced to neutral metal or radical-radical interactions terminate the chain [249]. The formation of nanoparticles occurs via a nucleation step and growth step [234]. The ratio of nucleation rate to growth rate decides the size and number of nanoparticles. Normally, the redox potential of a free metal ion is much higher than that of a metal ion already absorbed on a surface [229, 232]. Thus, already formed nanoparticles could act as a catalyst for metal ion reduction by interaction with radicals and stored electrons [254]. For these two reasons, the nucleation rate is normally slower than the growth rate.

Chemical or physical factors that influence the formation and stability of the seed, the redox potential of the metal ions and radicals, and the stability of the nanoparticles also influence the size and shape of the final nanoparticles. Surface-stabilizing additives by quench agglomeration between forming nanoparticles. For example, polymers in small concentration, such as polyphosphate, polyacrylate, poly-(vinyl sulfate), poly(vinyl alcohol), and poly(ethyleneimine), are used to synthesize silver nanoparticles from silver salt such as $AgClO_4$ [243]. Surfactants [235] and salts [230] have also been used as stabilizers. Small clusters, mainly $Ag_4^{2+}$, are first formed and stabilized on the polymer chains by interacting with the functional groups of the polymers [231]. The Coulomb repulsion between the chains prevents the clusters from coagulating, and these are the seeds for further growth. The stabilizer can influence the size of the nanoparticles. Six-nanometer particles with a rather narrow size distribution could be prepared by $\gamma$-irradiating a $Cu^{2+}$ solution and polyethyleneimine [255]. In the first step $Cu^{2+}$ is converted into $Cu^+$, which is strongly bound to the polymer, and, in a second step, reduction of $Cu^+$ takes place. A rather strict separation between the formation and growth of nuclei as a result of the metal bonding to the polymer ensures a narrow size distribution of the colloidal particles. For instance, Colloidal silver sols were formed by $\gamma$-irradiation of $AgClO_4$ solutions with sodium citrate as stabilizer [230]. At low citrate concentrations, partly agglomerated large particles were formed, whereas well-dispersed particles with smaller size and narrower size distribution were formed with increasing citrate concentration. At still higher concentrations, more citrate was absorbed to the nuclei seeds, decreasing the rate at which other Ag ions absorb to the seed and reducing the metal, resulting in more seeds of smaller size [256, 257]. For example, the reduction rate constant of $Ag^+$ by $e_{aq}$ ($Ag^+ + e_{aq} = Ag^0$) was decreased from $4.8 \times 10^{10}$ $M^{-1}$ $s^{-1}$ to $1.0 \times 10^{10}$ $M^{-1}$ $s^{-1}$ in the presence of polyacrylate [258]. Similar effects were found in the preparation of copper nanoparticles, with poly($N$-vinyl pyrrolidone) (PVP) and poly(vinyl alcohol) (PVC) as stabilizers [235].

In many cases, the stabilizer can also be converted to radicals by the incident radiation and participate in the reaction. Radicals generated from different stabilizers could have different reactivities, which may influence the reaction mechanism. For example, methanol used as a stabilizer led to 1-hydroxyalkyl radical, ·$CH_2OH$, and *tert*-butyl alcohol led to 2-hydroxyalkyl radical, ·$CH_2(CH_3)_2COH$. In the reactions of $K_2PtCl_4$ with these radicals, 1-hydroxyalkyl followed a radical-exchange mechanism, in which $PtCl_4^{2-}$ ions formed larger intermediate complexes in a chain reaction upon attack by 1-alkoxyalkyl radicals; however, 2-hydroxyalkyl directly reduced $PtCl_4^{2-}$ to Pt nanoparticles [248]. The radical localized at the 1-position in the 1-alkoxyalkyl species makes the addition of a lone electron pair on the O atom possible and thus allows the radical-exchange mechanism. However, 2-hydroxyalkyl radicals could add to $PtCl_4^{2-}$ only via the C atom, which had a stronger reduction ability and a weaker complex ability compared with O. In the preparation of Cu nanoparticles from $CuSO_4$ solution, the isopropyl alcohol radical reduced sample is less polydisperse than the $CO_2^-$ radical [259].

The dose of the radiation influences the reduction rate and final particle size. Increasing the radiolysis dose decreased the formation time of colloids [260]. The kinetics of reduction $KAuCl_4$ with $\gamma$-irradiation had a similar effect [232]. At high dosage, Au(III) was quickly reduced to Au(I)

and then to Au(0), leading to nanoparticles as small as 7 nm. At low dosage, the reduction of Au(I) to Au(0) was relatively slow because of the negative value of $E^0(Au^1/Au^0)$. The longer lifetime of Au(I) in the solution allowed it to absorb more ions and form larger nanoparticles (25 nm). Smaller (20–100 nm) colloidal Cu particles were formed with increasing $\gamma$-irradiation dosage of $KCu(CN)_2$ aqueous solution [234]. In the preparation of silver colloids by $\gamma$-irradiation, the particle number increases with increasing dose, which may be explained by an increase in nuclei formation at a higher dosage [261]. Radiolysis of mixed Au(III) and Ag(I) solutions at different dose rates led to different nanoparticle structures [262]. At low dosage, a Au core and Ag shell structure was formed, whereas high dosages led to Au-Ag alloys. Because of the lower $E^0(Au(III)/Au)$ compared with $E^0(Ag(I)/Ag)$, at low dosage reduced silver atoms transfer electrons to gold ions. Thus Au(III) ions are first reduced to form gold nanoparticles, and then reduction of the silver ions occurred at the surface of gold clusters. At high dose rate, reduction rates of both type of metal ions are much faster than the electron transfer rate, and Ag and Au metal deposit together to form alloy nanoparticles.

The addition of ions to the irradiated solution may interfere with the metal precursor or radicals and change the metal reduction rate or further modify the shape or size of the product nanoparticles. For example, $H^+$ reacts with hydrated electrons ($e_{aq}$) to form a hydrogen atom ($e_{aq} + H_3O^+ = H + H_2O$), which is a weaker reducing agent than is $e_{aq}$ [235]. Thus at lower pH, the metal ion reduction rate is lower. Excess $CN^-$ could decrease the rate of Cu reduction in the $\gamma$-irradiation of aqueous solutions of $KCu(CN)_2$ and increase the size of the final nanoparticles because it complexes strongly with $Cu^{2+}$, making it harder to reduce [234].

# 3. METAL NANOPARTICLES AS CATALYSTS

In this section, several examples of metal nanoparticle catalysts such as gold, silver, platinum, palladium, rhodium, and ruthenium as well as bimetallic nanomaterials are discussed. The samples listed here show that not only does decreasing the size of the particle effectively increase the metal nanoparticle catalyst activity for the same amount of metal because of increased surface area [263], but that it also alters the nanoparticle's electronic structure, surface property, and metal-environment interaction [12]. By thoughtful control of the preparation methods to adjust these features, improved catalysts may be developed.

## 3.1. Gold

Nanosized colloidal gold is one of the most well known of all metal nanoparticles, but only recently has been identified as a catalyst [264]. The activity is strongly size dependent, since particles larger than 50 nm have no observed catalytic activity, whereas activity rises sharply for particles 2 to 3 nm in diameter. Gold nanoparticle catalysts retain their catalytic properties while left unsupported in an aqueous suspension, making them ideal for the study of the size dependence of

catalytic behavior without the influence of the support [265]. In contrast to other materials, gold nanoparticles have distinctive surface plasmon absorption in the visible region of the electromagnetic spectrum that can conveniently be used to follow size and surface property changes [266].

Gold nanoparticles less than 20 nm in diameter can catalyze a variety of reactions [264], including the oxidation of carbon monoxide [267], the selective oxidation of hydrocarbons [268], dehydrogenation of alcohols [269], the water-gas shift reaction [270], the hydrochlorination of ethyne [271], and the oxidative decomposition of $CCl_2F_2$ and $CH_3Cl$ [272].

Catalytic activity evaluated against different units has different size-dependence trends, showing convincingly that besides total surface area, some other size-dependent factor is involved. For example, the activity per gold particle decreases with increasing size except for 14.5 nm particles, which are unexpectedly highly active, while activity per unit area decreases from 10 to 12.6 nm, and increases from 14.4 to 46.4 nm [265]. In contrast, the activity per unit area per unit mass decreases continuously with particle size over this range.

Gold nanoparticles can catalyze other reactions if they are supported on a suitable material that can interact with the metal. Among the variety of reactions that have been reported are the epoxidation of propene with the use of Au-Ti-MCM-41 and Au-Ti-MCM-48 [273] and the ring-opening reactions of propylene oxide on Au-MgO [274], the NO-CO reaction on $Au-TiO_2$ and $Au-Al_2O_3$ [275], the hydrogenation of 1,3-butadiene and crotonaldehyde [276, 277], the selective reduction of $NO_x$ compounds [278], the oxidation of ethylene glycol to glycolate [279], the hydrogenation of but-2-ethanol by Au/ZnO [280], cleavage of 2,4-dinitrophenyl acetate with the use of $N$-methylimidazole-functionalized gold [281], and $N_2O$ decomposition with the use of Au nanoparticles supported over $Co_3O_4$ [282].

The preparation method, chemistry of the supporting matrix, and gold nanoparticle concentration each can have an effect on the final catalyst activity and stability [264]. Supported gold catalysts prepared by impregnation of gold salt into an inert support by ion exchange, followed by reduction to form gold nanoparticles, form poorer catalysts than those prepared by coprecipitation of gold and support materials [283]. Calcination of the composite material leads to a less active catalyst because the high temperatures tend to reduce the permeability of the support or fuse adjacent nanoparticles together [283]. The electron-donating ability of the matrix can be chosen to improve the gold catalyst activity. For example, in the carbon monoxide reaction, alumina and magnesia-supported gold were found to be significantly more active than unsupported gold [284]. EXAFS studies have shown that the low-temperature oxidation of CO on $Au-\gamma-Al_2O_3$ catalysts was actually dependent on the presence of a specific Au-O bond [285, 286]. The structure of this bond varies with the solution pH used during the deposition of Au in the $\gamma-Al_2O_3$ support, and the active form is a polymeric $Au(OH)_3$ that forms under basic conditions. The interaction of the metal atoms with $O^-$ and $OH^-$ from the oxide support can affect the size of the gold particle or cluster and therefore its effectiveness as a catalyst. Both TEM and EXAFS studies of supported Au catalysts coprecipitated with $Fe(OH)_3$ and $Ti(OH)_4$ showed

**Table 2.** A summary of the reactions catalyzed by the metal nanoparticles discussed in this review.

| Nanoparticle | Catalytic reactions |
| --- | --- |
| Au | Oxidation reactions of carbon monoxide [267], hydrocarbons [268], $CCl_2F_2$ [272], dehydrogenation of alcohols [269], water-gas shift reaction [270], hydrochlorination [271] |
| Au supported | Epoxidation [273], ring-opening [274], NO-CO rxn [275], hydrogenation [276, 277, 279], $NO_x$ reduction [278], oxidation [279], cleavage [281], $N_2O$ decomposition [282] |
| Ag | Redox catalysis of aromatic and nitro compounds [302, 303], selective oxidation of alkenes [304] |
| Ag supported | $NO_x$ reduction to $N_2$ [318] |
| Pt | NO reduction [333], $H_2$ and $O_2$ reaction [334] |
| Pt supported | CO hydrogenation to methane [339, 340]. Ring opening of methylcyclopentane [349, 335, 336] |
| Pd | Hydrogenation of unsaturated alcohols [27, 351], hydrolysis [354, 355], hydrogenation of cyclohexene, alkenes, and styrene [353, 355, 361], reduction of dyes [362] |
| Pd supported | Oxidation [367] hydrogenation [368, 373], methanol decomposition [374], photoreduction [375] |
| Cu | Water-gas shift reaction [377, 378], oxidation [379–382, 387], dehydrogenation [384–386], condensation [190] |
| Cu supported | Methanol synthesis [391], hydrogenation [385, 396, 398–401], CO removal [397] |
| Rh | Dissociation of CO [402–406], hydrolytic cleavage of alkanes [407, 408] |
| Rh supported | Formation of ethanol [409], formation of acetic acid and acetaldehyde [411], $H_2$ reduction [412, 416], NO dissociation [413] |
| Ru | — |
| Ru supported | Ammonia synthesis [416, 417], hydrogenation [421–425, 427, 430, 432–437], $N_2O$ decomposition [164], $N_2$ dissociation [437] |
| Ni | Nanotube synthesis [439–442] |
| Ni supported | Reforming of syngas [443], hydrodehalogenation [444], hydrogenation [445–447], CO dissociation [457], nanotube synthesis [458–462] |
| Co | Nanotube synthesis [467, 470, 478], Fischer-Tropsch synthesis [479, 480] |
| Co supported | Fischer-Tropsch synthesis [481–487], hydroformylation [488, 494, 499], CO conversion [495], cyclodehydration [496], olefin production [497] |
| Fe | Nanotube synthesis [501–507], olefin production [514], hydrogenation [516] |
| Fe supported | Nanotube synthesis [508–510], coal liquefaction [519], Fisher-Tropsch synthesis [512], hydrogenation [522], reduction [523] |
| Mo | — |
| Mo supported | Reduction [529, 530], nitration [532], disproportionation [533], hydrodesulfurization [534–538, 556, 557], crude oil upgrading [543], polymerization [544], hydrotreatment [545] |
| Bimetallic | Hydrogenation [531, 559–562, 564, 566, 567, 569], hydrodechlorination [563], removal of organic pollutants [565, 569, 580, 581], $H_2$ dissociation [568, 583], electrooxidation [570–573], fuel cell [574–578], carbon nanotubes [579], hydrocracking [582], dehydrogenation [584], hydrotreating [585–588], oxidation [589, 591, 592], hydrodesulfurization and hydrodenitrogenation [590], isomerization [593] |

*Note:* These metal nanoparticles may catalyze more reactions, depending on how they are synthesized and used.

that the precipitation agents $NaCO_3$ and $NH_4OH$ influenced both the support structure and catalyst activity [287, 288]. Au-Fe(OH)$_3$ precipitated by $NaCO_3$ had higher activity than that precipitated by $NH_4OH$, because the ammonia-precipitated material had larger pores and larger Au particles and thus had smaller activity. In contrast, no pore size or catalytic performance difference could be observed for Au-Ti(OH)$_4$ catalysts obtained with either precipitation agent. A comparative study of the CO oxidaton by Au-TiO$_2$ catalysts showed that gold nanoparticle-impregnated, sol–gel-derived, anatase-structured TiO$_2$ with smaller pores has higher activity than commercial TiO$_2$ that has both an anatase and a rutile phase [289].

## 3.2. Silver

Silver nanoparticles can be synthesized in reverse micelles [290], by radiolysis [291], and by citrate reduction [292]. The lattice structures of bulk silver and gold are very similar [293]; however, their nanoparticle catalytic properties are quite different. For example, unlike gold, whose catalytic activity increases with decreasing particle size, the rate of ethylene oxidation on silver is faster for larger silver particles than for smaller particles [294].

Reaction sites differing in the surface lattice structure, type of adsorbed oxygen species, and reaction selectivity [295] have been identified for catalytically active silver nanoparticles smaller than about 50 nm [296–298]. After the

absorption of $O_2$ on the Ag nanoparticle surface, the surface of silver nanoparticles smaller than 8 to 10 nm is dominated by molecular oxygen, whereas for particles larger than 30 nm, an ionic oxygen species is also present. This kind of "ionic" oxygen was shown to be preferred for the nucleophilic attack of ethylene in complete combustion reactions [174]. The catalytic activity of PAA-Ag could be promoted by adding Cs(I) and Re(VII) ions to the system, which was shown to increase the surface oxygen concentration of Ag powders up to fivefold [305].

The distribution of active oxygen species on the silver nanoparticle surface is not random and varies with particle size [299]. The catalytically active surface center occurs on Ag{111} surfaces and consists of two adjacent adsorbed oxygen states with different ionicities of the Ag-O bond [300]. The "ionic" oxygen was responsible for ethylene adsorption and the "covalent" oxygen for the ethylene oxide formation [301]. As the particle size decreases, the concentration of edge and corner atoms per unit mass increases, favoring the two-electron reaction pathway for oxygen oxidation in KOH solution, either $O_2 + H_2O + 2e^- \rightarrow HO_2^- + OH^-$ or $HO_2^- + H_2O + 2e^- \rightarrow 3OH^-$. On crystal faces of large silver nanoparticles supported on carbon, a four-electron pathway $O_2 + 2H_2O + 4e^- \rightarrow 4OH^-$ is observed.

Suspensions of coated silver nanoparticles are commonly used for redox catalysis of aromatic nitro compounds and organic dyes [302, 303]. Silver nanoparticles between 4.0 and 4.3 nm in diameter protected by poly(sodium acrylate) (PAA) were used as a catalyst for the oxidation of ethylene to ethylene oxide [304].

Silver nanoparticles have been supported on $ZrO_2$ [306], $SiO_2$ [307, 308], $TiO_2$-$SiO_2$ [309, 310], $Ce_{0.16}Zr_{0.84}O$ [53], $Al_2O_3$ [311], and ZSM-5 [312]. Ag supported on a nonporous $\gamma$-alumina is the preferred catalyst for $NO_x$ conversion of automotive exhaust and organic compounds like ethylene oxide, ethanol, formic acid, and acetic acid [313–317], and has been prepared by precipitation from inverse microemulsion [311], sol–gel methods [314], and impregnation of $Al_2O_3$ powders with an aqueous solution of silver nitrate and then drying at 393 K [315].

The effectiveness of supported silver nanoparticle catalysts depends on metal loading, dispersion, and size of particles in the support. For example, lean $NO_x$ reduction with $C_3H_6$ is higher at 2% metal loading than at 6% metal loading [318]. At 6 wt% Ag-$Al_2O_3$ there are significant amounts of metallic Ag after reaction at 523 K, whereas none is found for 2 wt% Ag-$Al_2O_3$. Between 0.5 wt% and 3 wt% Ag the dispersion of small nanoparticles in the support increases and the maximum catalytic efficiency is found at 2 wt% Ag [316]. Multiple impregnation in 0.5 wt% steps up to total 2% loading, followed by 1 h of calcination at 500 °C, improved the effectiveness further. Oxidative post-treatment of the catalyst changes the surface structure as well as the morphology of silver particles and improves both the activity and selectivity relative to reduced catalyst for removing $NO_x$ in lean exhaust gas with ethanol and propene [319]. The maximum activity and selectivity for supported silver particles on highly crystalline zirconium phosphate is about 48 nm in average diameter, whereas 4.6 nm particles had negligible activity [320].

Improvement in $NO_x$ conversion performance or selectivity of Ag-$\gamma$-$Al_2O_3$ and Ag-ZSM-5 was observed with the addition of cations like Cs [311, 321–323] or Ce [324] to help convert NO to $NO_2$. Once $NO_2$ is available, it is then reduced to $N_2$ by $Ag^+$ sites. In ZSM-5, the effectiveness of cation addition decreases with increasing cation loading. For larger (100 nm) Ag particles, 0.2% of Cs increased ethylene oxide formation slightly, whereas 0.5% Cs sharply decreased the activity. Other cations used include $Na^+$, which gives the highest total conversion and $K^+$, which gives the best selectivity for ethylene oxide formation, and excessive Cs was found to suppress the reaction completely.

Reaction selectivity is influenced by the presence of water, which must be competitively desorbed by the reactants in order for reaction to occur. In the case of $n$-alkanes their adsorption enthalpy increases with increasing carbon number, meaning that smaller alkanes like propane and $n$-butane are inhibited from reaction more than are longer alkanes like $n$-octane and $n$-hexane. In addition, since the mean energy of one C-H bond decreases as the carbon number in $n$-alkanes is increased, the turnover of these is favored. The effect is significant even without NO, because the efficiency of oxidation of hydrocarbons by $O_2$ also increases with carbon number.

Atmospheric $SO_2$ suppresses the conversion of ethanol and $NO_x$ on supported silver catalysts below 700 K [315]. The support composition also assists in recovery and the resistance of the support to deactivation by atmospheric conditions. For example, a $Ce_{0.16}Zr_{0.84}O$ support acts as a sink for $SO_2$ and improves the sulfur resistance of the catalyst [306]. In contrast, only limited regeneration of Ag/$Al_2O_3$ catalysts could be achieved under the same gas-phase composition and time of reduction for temperatures as high as 600 °C.

## 3.3. Platinum

The method used to prepare Pt nanoparticles was shown to significantly affect their catalytic property, sometimes in unexpected ways. Pt nanoparticles prepared by radiolysis, hydrogen, and citrate reduction showed different abilities for the conversion of methylviologen ($MV^{2+}$) to $MV^{+\cdot}$ radical [325, 326]. Particles prepared by the reduction of $H_2PtCl_6$ with alcohol had an average diameter of 2.7 nm, whereas those prepared with $KBH_4$ had a smaller average diameter of 1.6 nm. In this case the alcohol-reduced nanoparticles had higher activity because the by-product from the $KBH_4$ reduction remained absorbed to the nanoparticle surface and blocked part of the active sites [327].

Stabilizers used in the formation of Pt nanoparticles influence their resultant morphology and reactivity. For example, in the preparation of polyacrylate-stabilized Pt nanoparticles from the reduction of $K_2PtCl_4$, a range of morphologies, tetrahedral, cubic, irregular-prismatic, icosahedral, and cubo-octahedral, were formed simply by changing the ratio of polymer to platinum cation [328]. Stabilizers absorbed on the surface may also change the activity by controlling the size of the nanoparticle in the preparation stage [329]. Longer alkyl chain surfactants led to smaller nanoparticles because the stronger hydrophobic property of the longer chains prevented the coagulation of nanoparticles [330].

Which crystal facet is exposed to the surface determines the Pt nanoparticle shape and reactivity [331]. Cubic nanoparticles prepared by hydrogen reduction of $K_2PtCl_4$ had mainly {100} facets and only small amounts of {111} and {110} facets, whereas truncated tetrahedral particles exhibited {111} and {100} facets [332]. Octahedron-like Pt particles also had both {111} and {100} facets. The correlation between facet exposure and catalytic activity extends to supported Pt nanoparticle catalysts and may lead to unexpected complications. For example, Pt nanocrystallites with mainly {100} facets were loaded on $\gamma$-$Al_2O_3$ and used as a catalyst for NO reduction by $CH_4$. Compared with traditional polycrystalline Pt/$\gamma$-$Al_2O_3$, the product of this reaction was mainly $N_2$, $H_2O$, and $CO_2$ instead of $NH_3$ and CO [333]. The reason for this is that adsorbed oxygen was more active on the {100} facet, which converted the $CH_x$ and absorbed hydrogen to $H_2O$ and $CO_2$, preventing the formation of $NH_3$ and CO.

Pt nanoparticles between 2 nm and 6 nm in size mounted on carbon electrodes are used as a catalyst for reactions of $H_2$ with $O_2$ [334]. Because the density of states of the catalyst is smaller as the size decreases, the adsorption of hydrogen on smaller particles is weaker and the particles are more prone to oxidation. Pt nanoparticles in the range from about 5 nm to 20 nm in diameter loaded on an $Al_2O_3$ support used as catalysts for NO and CO reaction had increasing activity with decreasing particle size [330].

Other phenomena observed include the size-dependent catalytic ring opening of methylcyclopentane to *n*-hexane (*n*-H), 2-methylpentane (2-MP), and 3-methylpentane (3-MP) [335, 336, 349], and formation of butyraldehyde from the hydrogenation of C=C crotonaldehyde and the hydrogenation of C=O to crotylalcohol [338, 350]. The particle size is correlated with the face of the Pt crystal exposed and the extent of its interaction with the support. For example, in the ring opening reactions the ionic site of alumina attacks the easily ionized tertiary carbon of MCP, but, since the adjacent carbon atom could be bound to the Pt nanoparticle surface, the intermediate preferred the formation of *n*-H. For larger nanoparticles, the C=O group of crotonaldehyde adsorbs better on the Pt (111) surface than on smaller particles. On smaller particles, although both bonds absorb equally strongly, the C=C reaction of crotonaldehyde is kinetically favored.

As with gold and silver, Pt nanocatalysts are often supported on oxide matrices such as $Al_2O_3$ [335], $SiO_2$ [336], MCM-41 [337], and $TiO_2$ [338]. For CO hydrogenation to methane, the turnover frequency of Pt-$TiO_2$ after reduction at high temperature was several orders of magnitude higher than unsupported Pt or Pt-$SiO_2$ [339, 340]. This enhancement originates from a strong metal-support interaction that changes the electronic state of Pt or creates active sites on the metal-support phase boundary [341]. Of all the supports, $TiO_2$ has the strongest enhancement because parts of the $Ti^{4+}$ sites are easily reduced to $Ti^{3+}$ and $Ti^{2+}$, and other $TiO_x$ sites can migrate over the Pt surface. Enhancements are also found for other supports such as $Al_2O_3$ [342–345], MgO [346], $ZrO_2$ [347], and $CeO_2$ [348].

## 3.4. Palladium

Pd nanoparticles are used as catalysts for hydrogenation reactions of many compounds, including allyl alcohol and *N*-isopropyl acrylamide in water [351], unsaturated alcohols [27], olefin and styrene [352], cyclohexene, triethylallylammonium bromide [353], and transfer hydrolysis of bromotoluene and 1-butenyltrimethylammonium bromide [354, 355]. Heterogeneous palladium metal catalysts employed for the Heck reaction are mainly soluble palladium (II) complexes [356, 357].

Stabilization of Pd nanoparticles against aggregation with organic or polymeric coatings can be used to control particle size, morphology, and solubility, all of which affect catalyst performance. Some examples of stabilizing coatings that have been employed include poly(amidoamine) dedrimers [351], tetraoctylammonium surfactants [352], polyacids [358], PVA [359], and poly(*N*-isopropylacrylamide) [360].

Reverse microemulsions of water-trioctylmethylammonium(aliquat)-dichloroethane can be used to form Pd nanoparticles for use in the transfer hydrolysis of bromotoluene [354]. The reversed micelles had three functions: to direct the formation of the metal nanoparticle by restricting the reduction of the metal precursor $K_2PdCl_4$ by alcohol to the inside of the micelles, to stabilize nanoparticles against further aggregation, and to restrict the catalytic reaction of the hydrogenation of bromotoluene to within the micelles. Water concentration and reduction temperature had an important influence on the curvature of the reversed micelles and nucleation of Pd, thus influencing the morphology of the Pd nanoparticles and their activity. At high water concentration, the curvature of the micelles decreased, resulting in larger Pd nanoparticles and lower activity, while at high Pd reduction temperatures, the nucleation rate was faster and the nanoparticles were smaller and more active.

Dendrimer-stabilized particles are prepared by absorption of Pd (II) ions to hydroxyl-terminated poly(amidoamine) (PAMAM) dendrimers, where they complexed with interior amine groups. Chemical reduction of the metal ions with $BH_4^-$ yielded dendrimer-encapsulated Pd nanoparticles with a number of atoms equal to that initially preloaded onto the dendrimer, and nearly monodispersed palladium nanoparticles $1.7 \pm 0.2$ nm in size were prepared [27]. These nanoparticles catalyze the hydrogenation of unsaturated alcohols such as allyl alcohol and *N*-isopropyl acrylamide in water [351]. The reaction rate can be controlled with the use of dendrimers of different generations. The turnover frequencies for Pd encapsulated in the sixth generation and the eighth generation of dendrimers were 10% and 5% of that of the fourth generation because higher generation materials are less porous. The generation also affects the reaction selectivity. The hydrogenation rate of allyl alcohol, the simplest unsaturated alcohol, was five times faster than that of 3-methyl-1-penten-3-ol, for fourth-generation dendrimers containing less than 1 nm Pd nanoparticles (about 40 atoms). For the same dendrimer generation and substrate, the activity of the Pd catalysts increases with particle size from 40 to 164 to 659 atoms.

Tetraoctylammonium-stabilized Pd nanoparticles synthesized by laser ablation are generally much smaller in size, with narrower size distributions ($2.4 \pm 0.5$ nm), than bare

Pd $12.7 \pm 5.7$ nm [352]. The smaller size and more uniform distributions improve the efficiency of hydrogenation of olefin and styrene, as well as the work life of the catalyst. Polyacid stabilization produces slightly larger nanoparticles about 10 nm in size because the strong interaction between polyacid and palladium precursor slows the reduction process [29]. However, Pd nanoparticles protected by polyacids had unexpectedly low catalytic activity for the hydrogenation of cyclohexene than those protected by nonionic polymers, possibly because the strong interaction of polyacid with Pd decreased the availability of the surface for catalysis. The effect was more severe with even larger particles. Modification of the surfaces of Pd and Pt nanoparticles by the adsorption of cinchona alkaloids cinchonidine (CD) or cinchonine (CN) resulted in different enantioselective hydrogenation of pyruvate esters [361]. For Pt nanoparticles, CD coating favored the (R)-enantiomer and CN coating favoring the (S)-enantiomer.

Pd nanoparticles stabilized by a cationic surfactant (CTAB), anionic surfactant (SDS), and nonionic surfactant (TX-100) exhibited selective reactivity toward the reduction of several dyes, including methylene blue (MB), phenosafranin (PS), fluorescein (F), 2,7-dicholrofluorescein (DCF), eosin (E), and rose bengal (RB), when several reductants were used, such as $NaBH_4$, $N_2H_4$, and ascorbic acid [362]. The activity was found to be a function of the concentration of the surfactants (below or above CMC concentration) and the charge of the surfactants and the reactants.

Mixed coatings allow better control of the catalytic behavior of Pd catalysts. Cyclodextrin-stabilized Pd nanoparticles used in the hydrogenation of alkenes such as 1-butenyltrimethylammonium bromide could be selectivity tuned by the addition of molecules such as cationic ferrocene derivatives [355]. Some derivatives inhibited reaction by occupying the active sites and repelling the positively charged reactant from the Pd surface by their own positive charges. Pd nanoparticles multiply coated with hydroxylated polyisoprene (PHI), cross-linked poly(2-cinnamoyloxyethyl methacrylate) (PCEMA), and poly(acrylic acid) (PAA) have been used for the hydrogenation of triethylallylammonium bromide (TEAA) [353]. Compared with Pd black, the activity of encapsulated Pd was lower because of the barrier effect of the encapsulation, which also changed the reaction order from zero order to first order. However, one of the advantages of the encapsulated Pd was the ability to modify the pH-dependent activity of the catalyst via the encapsulating environment. The hydrogenation activity of TEAA-coated Pd was slower at pH 3 than at pH 10. The amine groups of the PAA center had a pKa of 5.7; therefore at pH values higher than 5.7, reactant diffused more easily into the nanosphere because of the negative pressure, resulting in better performance. Pd nanoparticles stabilized with lanthanide-doped PPA showed 10 times improved performance [359]. The lanthanide ions transfer electrons to Pd nanoparticles, making them electron rich and promoting the donation of electrons from the Pd $d$ band to the $H_2$ $\sigma u^*$ band. As a result $H_2$ is better able to dissociatively adsorb to the Pd surface. In contrast, PVA-coated Pd nanoparticles were unaffected by the addition of lanthanides because of

weak binding interaction between the lanthanide and the polymer.

One of the major drawbacks of homogeneous metal catalysis lies in the separation of the reaction product from the catalyst. With an appropriate stabilizer, the hydrophilic properties of nanoparticles can be changed, and this may be used in the separation of the nanocatalysts from the products. Stabilizers may be chosen such that they do not influence the resulting catalytic behavior of the particles, only their physical stability. For instance, 1–4-nm palladium nanoparticles prepared by citrate or ethanol reduction and stabilized by citrate, polypyrrolidone, or poly(vinylalcohol) were used to catalyze the Heck, Suzuki, and Stille coupling reactions independently of the stabilizer [363]. In another example, phosphine-coated Pd can be converted into water-soluble derivatives by adsorption of polar groups on the surface, including carboxylate, sulfonate, and ammonium [364]. Complexation of Pd-dendrimer composites with perfluorinated carboxylic acids renders the resulting nancomposites preferentially soluble in fluorinated hydrocarbons [365]. When the hydrogenation reaction was carried out, the catalyst was in the fluorous phase, and the reactants were in the organic phase. Stirring, sonicating, and/or heating of the mixture led to formation of a fine emulsion, and the catalytic reaction proceeded at the interface of the microemulsions. When the reaction was over, the product was isolated form the organic phase, and the catalyst-containing fluorous layer was recycled. One catalyst preparation was recycled 12 times without appreciable loss of catalytic activity.

Core-shell structured nanoparticles containing 2-nm Pd particles as the core and a 2-nm amorphous carbon layer as the shell can be formed by sonication, starting with an organic precursor like tris-$\mu$-[dibenzylideneaceton]-dipalladium $[(\phi\text{-CH}=\text{CH-CO-CH}=\text{CH-}\phi)_3Pd_2]$ [366]. Sonication generates collapsing bubbles in the solvent, and two regions suitable for chemical reaction are formed: region 1 is the bubble phase, where elevated temperatures and high pressures are produced and nanoparticle formation reactions take place, and region 2 is the thin liquid layer immediately surrounding the bubbles, where the temperature is lower than in the bubble but still high enough for decomposition reactions. The product of the decomposition reactions was dibenzylidene acetone (DBA) ligands, which bound to the freshly formed Pd nanoparticles and underwent palladium-mediated cracking to atomic carbon.

Highly dispersed Pd(II) bound to the surface of pretreated glassy carbon electrode by covalent interaction of oxygen atoms on the electrode surface and Pd(II) electrocatalytically oxidizes hydrazine [367]. Montmorillonite-supported Pd nanoparticles prepared by mixng MTABr surfactant-stabilized Pd nanoparticles ranging from 1.5 to 6.2 nm in size with sodium montmorillonite are used for the hydrogenation of styrene to ethylbenzene, and hydrogenation of 1-phenyl-1-butyne to *cis*- and *trans*-alkenes in tetrahydrofuran (THF) [368, 369]. These catalysts exhibit an increase in activity with decreasing particle size that could be attributed to more edge and corner atoms found in small particles. Pd nanoparticles in the range between 2.8 and 5 nm generated *in-situ* on EXM-534 montmorillonite pillared by aluminum oxide (Al-PILC) is used for

the hydrogenation of cyclohexene to cyclohexane [370, 371]. Laboratory-prepared Pd-loaded sol–gel porous $\gamma$-alumina spheres with a higher surface area (300 m$^2$/g) relative to commercial product (80 m$^2$/g) contained more Pd evenly distributed, leading to a higher hydrogen-oxygen reaction rate [372]. Pd colloids prepared in polystyrene-poly-4-vinylpyridine micelles (PS-b-P4VP-Pd) and deposited on Al$_2$O$_3$ exhibited high activity and selectivity in hydrogenation of the triple bond of acetylene alcohols to the double bond of olefin alcohols [373]. Pd nanoparticles with an average size of 6 nm and predominantly exposed {111} facets grown on a well-ordered Al$_2$O$_3$ film in ultra-high-vacuum conditions were used as a model catalyst for the methanol decomposition reaction [374]. A titania-modified MCM-41 (MCM-41-TiO$_2$) support was used to synthesize Pd nanoparticles *in-situ* by impregnating with H$_2$PdCl$_4$ and irradiating by UV light with a wavelength less than 400 nm [375]. The modified catalyst showed higher activity than MCM-14-TiO$_2$ for the photoreduction of Cr(VI) to Cr(III).

The synthesis method used to form supported Pd catalysts may alter the effectiveness of the material. Pd nanoparticles of the same size and concentration precipitated onto a ZrO$_2$ support *in-situ* performed better than impregnated material [376]. XPS showed that there was a stronger interaction in precipitated material between the ZrO$_2$ support and surface oxygen, suggesting that in the precipitation stage the ZrO$_2$ surface alters the particle morphology.

## 3.5. Copper

Copper nanoparticles have been used as catalysts for a number of reactions, including the water-gas shift reaction [377, 378]; oxidation of CO [379], ammonia [380], benzene, phenol, and pyridine [381, 382], and graphite [383]; dehydrogenation of *n*-butanol [384, 385] and isopropyl alcohol [386]; and the condensation of iodobenzene to biphenyline [190].

Unlike Au, Ag, Pd, and Pt, copper nanoparticles are generally less active on an active center basis. Activity decreases as the copper crystallite size increases for particle size in the range from less than 1 nm to 3 nm in the CH$_4$ oxidation reaction [387]. As with Au and Pd, the Cu crystallite size can be correlated with specific crystal surfaces, which have different catalytic activities [388]. The rate of reverse water-gas shift reaction from CO$_2$/H$_2$ to CO/H$_2$O and methanol synthesis was higher on the Cu {110} surface than on Cu {100} and polycrystalline copper. On Cu {110} surfaces, there are more coordinately unsaturated copper atoms, which resemble ultrathin islands with high chemisorption ability.

Because Cu nanoparticles sinter more easily during reaction and lose their activity, they are mostly used loaded on supports. Supports such as SiO$_2$, ZnO, and Cr$_2$O$_3$ have been shown to stabilize the Cu nanoparticle against sintering [389, 390] and increase the dispersion of small Cu particles in the support, with a positive effect on catalytic activity. Preparation conditions have a significant influence on the size, structure, and surface properties of the supported Cu catalysts [391]. Cu/ZnO catalysts prepared in four solvents (H$_2$O, dimethylformamide, ethanol, and diethylene glycol) used for methanol synthesis via hydrogenation from CO$_2$ were compared. Smaller particles were obtained when more viscous solvents were used, suggesting that higher viscosity solvents prevent the nucleation growth of nanoparticle catalysts [391]. Electroless deposition of Cu/SiO$_2$ produces smaller copper crystals with higher activity than impregnation methods [392].

Support-copper interactions in some systems may increase the activity of the Cu nanoparticle catalyst. CO oxidation on samaria-doped ceria (SDC) supports was more efficient than on SDC/gamma-alumina supports [393]. The oxygen vacancy in the SDC support can reduce the CuO on the nanoparticle surface to form metallic Cu, thought to be the active center [394]. In the SDC-gamma-alumina support, the support-metal interaction was weaker and the activity was lowered. Other supports improved the Cu catalytic activity by either activating the reactant or changing the selectivity of the supported copper [395, 396]. Cu/TiO$_2$ showed the highest turnover frequency for methanol synthesis via CO$_2$ hydrogenation compared with Al$_2$O$_3$, and SiO$_2$ supported because the interface of TiO$_2$ and Cu helps activate the H$_2$. A basic alumina-mixed oxide (Cu/Al$_2$O$_3$-MO$_x$; M = Al, Cr, Mg, Mn, and Zn) support favors dehydrogenation, yet acidic support favored dehydration [385, 396]. Cu/Al$_2$O$_3$-MgO is used to remove CO residues arising from methanol synthesis and to produce methyl ethyl ketone from 2-butanol dehydrogenation mainly over Cu/MgO, and butane over Cu/SiO$_2$, because CO removal was carried out by reaction with H$_2$O. The order of the activity for Cu/Al$_2$O$_3$-MO$_x$ with different M was Zn > Al > Cr > Mn > Mg. On an Al$_2$O$_3$-ZnO support, a spinel compound, CuZn$_2$O$_4$, is formed, which leads to better Cu dispersion in the support upon reduction. Chromium addition presents higher catalyst activity for the dehydrogenation of *n*-butanol via increased copper dispersion and decreased copper crystallite size, and lower deactivation rates [397]. This phenomenon was also found in Cu/Ti/$\gamma$-Al$_2$O$_3$ catalyst for the hydrogenation of CO$_2$ [398], B$_2$O$_3$-doped Cu/ZnO/Al$_2$O$_3$ catalyst [399], Cu/CeOx/Al$_2$O$_3$ [400], and metal hydroxide-doped supported Cu catalysts [401].

## 3.6. Rhodium

The catalytic reactions of Rh nanoparticles including the dissociation of CO and hydrolytic cleavage of the C-C bond in alkanes are size dependent [402–404]. For Rh particles ranging from 0.6 to 64 Å in size, the dissociation ratio of CO on the nanoparticles increases when the nanoparticle size increases from about 100 atoms per particle to 1000 atoms per particle, and then decreases as the particle becomes even larger [405]. This observation is related to changes in the concentration of steps and edges in the nanoparticle surface and the presence of coordination sites as the size of the particle is increased. The reaction rate of CO with O$_2$ by Rh nanoparticles supported on the Al$_2$O$_3$ polycrystalline surface was about two orders of magnitude higher for 2.5-nm nanoparticles than for 5-nm nanoparticles, and an order of magnitude higher than plain Rh foil [406]. From studies of the hydrolytic cleavage of a variety of alkanes, it appears that the active site on the Rh surface consists of large specific assembles of Rh atoms, which have a greater chance to form on larger particles. The cleavage of bonds involving quaternary carbons appears to be more size-dependent

than bonds involving primary, secondary, and tertiary carbons [407]. For example, as the size of Rh increased from less than 1 nm to 15 nm, the cleavage rate of *n*-hexane (*n*-H) increased 6 times, however, 2,2,3,3-tetramethylbutane (2233TMB) increased 10,000 times [407]. An explanation for the relative ease of breaking between the two adjacent quaternary carbon bonds may be explained by the ability of the two quaternary carbons to participate in a four-carbon ring intermediate with the two adjacent carbons after the molecule is adsorbed on the Rh surface [408]. In comparison, a secondary-quaternary bond is more difficult to cleave [407].

The addition of other metals can influence the activity and selectivity of Rh catalysts via different mechanisms [409]. For V-promoted Rh-SiO$_2$, the product was exclusively ethanol [410], whereas Mn-promoted Rh-SiO$_2$ catalyst formed acetic acid and acetaldehyde [411]. A detailed study showed that after H$_2$ reduction, part of the Rh in Rh-Mn-SiO$_2$ was in the +1 state; however, the Rh in Rh-V-SiO$_2$ was mainly in the 0 state [412]. The CO formed a bridging intermediate on the Rh-V-SiO$_2$ surface and a twin intermediate on the Rh-Mn-SiO$_2$. Although there was no direct evidence to show that the bridging CO led to ethanol production, and the twin CO led to acetic acid and acetaldehyde production, this configuration difference could be responsible for the different behaviors of the two kinds of catalysts. The effects of V, Nb, and Ta on the CO hydrogenation to oxygenated products of Rh/SiO$_2$ catalysts were compared [409]. These metals could form metal oxides and spread over the Rh surface during the calcination process, following the order Ta < Nb < V. This led to an activity order of V < Nb < Ta and different adsorption intermediates of CO on the Rh surface. When more of the nanoparticle surface was covered by metal oxide, the ratio of linear CO adsorption on the Rh surface to bridging CO adsorption increased. A different mechanism is thought to be at work for sodium, which causes an increase in the catalytic activity of Rh for NO and CO reaction by giving electrons to Rh during the electron transfer from Rh to the antibonding orbital of NO, thus promoting the NO dissociation [413].

As with the other materials discussed, the morphology of the support may change the catalytic property of the nanoparticles by influencing the loading of the Rh precursor into the support and changing the structure of the final nanoparticles [414 ]. This was shown with three kinds of activated carbon supports: peat-based Norit Rox (N), coconut-based carbon (C), and wood-based Takeda Shirasaki (T), each loaded with Rh(NO$_3$)$_3$ and then reduced to form nanoparticles. The difference in pore structure and surface-active groups of these materials decided the final structure of the Rh nanoparticles. Rh nanoparticles were distributed more uniformly on T and N supports, which had more mesopores (pore diameter range from 2 to 50 nm) and macropores (pore diameter larger than 50 nm) than the C support, which had mainly micropores (pore diameter smaller than 2 nm). Because the T support had more acidic groups, which have strong interaction with Rh$^{3+}$ precursor, fewer Rh nanoparticles aggregated in T support than in N support.

Modification of the surface of the nanoparticle support can be used to adjust both the particle size and distribution of the Rh nanoparticle catalyst [415]. In silica supports, the Ru precursor can diffuse into the silica-forming nanoparticles in the pore, which block them, preventing access and reducing performance. After modification of the silica membrane by a silylation agent H$_2$N(CH$_2$)$_2$NH(CH$_2$)$_3$Si(OCH$_3$)$_3$, which decreased the pore of the membrane, the Rh precursor could only be loaded onto the outer surface of the particle. This preserved the pore structure and formed partly covered Rh nanoparticles only on the outer surface.

## 3.7. Ruthenium

The activity of Ru catalyst used for ammonia synthesis is also strongly dependent on particle size [416]. The control step of ammonia synthesis is the dissociation of N$_2$ on the catalyst surface [417]. Studies showed that the rate of N$_2$ dissociation on step atoms of the Ru surface was at least 9 orders of magnitude higher than that on the flat Ru surface [418]. An active site containing five Ru atoms, with two atoms from the higher coordination of the step and an adjacent three compact atoms from the lower coordination of the step, may be involved [419]. One nitrogen atom in the N$_2$ molecule bridges the two atoms, while the other sits in the center of the three atoms. The relationship between the number of active sites and crystal size on nickel surfaces was studied by van Hardeveld and van Montfoort [420]. They found that the presence of this kind of site was strongly size dependent, and no such site was present if the particles were smaller than 1.5 nm in diameter. The Ru particles that have the maximum number of active sites have a diameter from 1.8 to 7 nm. Above this, the number of sites decreases dramatically because of the decrease in step atoms on the nanoparticle surface.

Supported Ru nanoparticles have been used as catalysts for the selective hydrogenation of carbonyl groups (C=O) in the vicinity of conjugated or isolated double bonds to produce α- and β-unsaturated alcohols [421], the hydrogenation of benzene and toluene to their corresponding cycloakenes and aldehydes to their corresponding alcohols [422], and as a replacement for iron in ammonia synthesis [423–425], N$_2$O decomposition [164].

Ru nanoparticles with an average diameter between about 3.7 nm and 16.8 nm on an active carbon support catalyzes the reaction of cinnamaldehyde to cinnamyl alcohol, with a side reaction of hydrogenation of C=C to hydrocinnamaldehyde. The specific activity (expressed per atom of Ru on the surface) was constant as the nanoparticle size was increased, while the selectivity increased as the particle size increased [422]. On larger particles, the aromatic ring of cinnamaldehyde may prevent the C=C group from bonding close to the surface, meaning that only the C=O group located at one terminal of the molecule could reach the catalyst. As with other metal nanoparticles, the loading percentage can be correlated with the average nanoparticle size within the support. The activity of nanoparticle Ru increases from 0.5 wt% to 5 wt%, but further increase in the loading leads to aggregation of the nanoparticles and a decrease in activity [421].

Choice of nanoparticle precursor may be used to tailor the interaction of the metal with the forming support

and affect the ultimate catalytic behavior. The dispersion of Ru in MCM-41 prepared from Ru(OH)₃ was better than that prepared from RuCl₃ or Ru₃(CO)₁₂ and had the highest activity for N₂O decomposition [164]. This may be due to the stronger interaction between the support and Ru(OH)₃. Other precursors, RuCl₃, Ru(acac)₃, K₂RuO₄, Ru(NO)(NO₃)₃, and Ru₃(CO)₁₂, resulted in a varied nanoparticle dispersion [426]. Some precursors, such as Cl from RuCl₃, were potential contamination sources for the reaction, and the catalyst performance could be improved by working at higher temperatures to allow the chlorine to dissipate [427].

Ru supported on zeolites had higher selectivity for α, β-unsaturated aldehydes because the pore structure made it harder for the C═C bond to adsorb on the Ru particles [428]. Sn, Fe, and Ge promoters increased the selectivity of Rh-alumina catalyst in the hydrogenation of acetophenone by helping to activate the C═O bond [429]. The selectivity of Ru-SiO₂ for hydrogenation of 3-methyl-2-butenal to its corresponding unsaturated alcohol was increased in the presence of alkali metals (Na, K, Cs) [427, 430–437]. One possible explanation for this was that part of the alkali promoters were reduced to the metallic state in the reaction conditions. The alkali metals immediately transferred their electron to Ru because Ru had a higher ionization potential than alkali metal. N₂ molecules were easier to dissociate on the electron-rich Ru [436]. Another explanation was the direct interaction of the alkali metal and the reactant. A self-consistent density functional calculation showed that instead of interacting with the Ru particle, the Na and Cs lower the dissociation activation energy of N₂ on the Ru(0001) surface [437]. Without the promoter, the dipole moment induced when N₂ absorbed to the Ru surface in the transition state had a high energy level. The electric field formed by the alkali promoters stabilized the dipole moment and lowered the transition state energy. For the Ru-γ-Al₂O₃ catalysts used for ammonia synthesis, La, Ce, Sm, and Cs could all be used as promoters. To get the same activity, more Cs than the other three elements was needed. This was due to the fact that Cs(OH) had the lowest melting point and easily spread over the whole Al₂O₃ support in the catalyst preparation process, whereas other promoters located on the surface of the Ru nanoparticles or the interface of the Ru and the support [426]. Use of K and Cs promoters increased the activity of Ru catalysts for the hydrogenation of unsaturated aldehydes by neutralizing poisonous impurities such as Cl.

The interaction of support and nanoparticles sometimes should be avoided. The acidity of Al₂O₃ support withdraws electrons from Ru nanoparticles and decreases the activity of ammonia synthesis. To minimize this effect, Ru-Al₂O₃ was prepared by loading stabilized Ru nanoparticles with an average diameter of 5 nm on the Al₂O₃ support [438]. The stabilizer of the nanoparticles minimized the interaction with the support. The activity was more than 10 times higher than that of the catalyst prepared by the impregnation method. In contrast, in a study using Ru-MaAl₂O₄ as an ammonia synthesis catalyst, the activity progressively increased during the initial running of the catalyst. This was attributed to the aggregation of the smallest Ru crystals, which were too small to have active sites, into larger crystals with more active sites [416].

## 3.8. Nickel

Ni nanoparticles have been used to catalyze the synthesis of nanotubes and nanofibers of carbon [430], dititanium sulfide (Ti₂S) [440], GaN [441], and TiC [442]. Apart from the above, supported Ni/MgO catalysts were used for the dry reforming of methane to produce syngas [443], Ni/SiO₂ catalysts for the hydrodehalogenation of halogenated aromatic compounds [444], and Ni/Al₂O₃ for benzene hydrogenation [445, 446] and hydrogenation of beta-keto esters [447].

The relationship of reaction mechanism, growth rate, and morphology of carbon nanotube formation with the morphology, size, and support choice for Ni nanoparticle catalysts provides a good example with which to demonstrate the character of Ni nanoparticle catalysts and is discussed below. The basic mechanism of carbon nanotube growth with Ni metal nanoparticle catalysts is the decomposition of carbon sources on the catalyst particle forming carbon atoms that accumulate on the catalyst surface and form tubes. This process is accomplished by either a yarmulke mechanism in which carbon diffuses on the nanoparticle surface and incorporates at the root of the growing nanotube [448], or by another mechanism in which the carbon decomposes, dissolves, and diffuses into the nanoparticle, where it is incorporated at the root of the nanotubes [449]. A hollow structure is obtained because certain faces favor the precipitation of carbon, whereas other faces are incapable of such a process and result in the formation of hollow structures [450]. It was shown that Ni{100} and Ni{110} nanocrystal planes facilitated the formation of filamentary carbon [451].

The morphology and size of the nanoparticles are key factors in determining the shape and dimension of the carbon tubes [452]. Different shapes of carbon nanotubes, such as bidirectional, twisted, helical, or branched, may form, depending on the shape and movement of the nanoparticles during growth of the nanotubes [452]. For example, if carbon tubes could growth on both ends of the nanoparticle, a bidirectional carbon nanotube would form, with the nanoparticle remaining in the middle of the tube. During the tube growth process, if the nanoparticle suddenly burst into several smaller particles, branched nanotubes could be formed. If the nanoparticle was rotating during the growth process, twisted or helical tubes could be formed.

When the catalytic metal particles are several nanometers in size, approximately the same size as the nanotube diameter, the catalyst particle is found trapped in the tip of the single-walled tube, and the diameter of the tube can be directly related to the particle size [453, 454]. When the metal particle diameter is several tens of nanometers in size, the precipitation of a large number of single-walled tubes onto a single nanoparticle was observed [455]. This was explained by a large number of active sites for nanotube growth present on the larger nanoparticles. During the synthesis of carbon nantubes in the polyethylene-water-Ni system at 100 MPa and 730–800 °C, flake-like graphite or carbon tubules from 70 to 1300 nm in diameter could be formed, depending on the size of the Ni catalyst particles used [456]. Finally, the growth rate of nanotubes also varies with different Ni nanoparticle diameters. Ni clusters containing 11, 20, or 30 atoms were deposited onto thin MgO{100} films. Monodispersed Ni-30 clusters showed a higher reactivity for CO dissociation than Ni-11 and Ni-20 [457]. The high

surface-to-volume ratio and the distinctive electronic properties of clusters of this size may account for the differences in reactivity.

As with the other metal nanoparticle catalyst materials already discussed, the selection of support material could also change the Ni nanoparticle electronic properties or keep the nanoparticle stable against coagulation, thereby influencing the growth of nanotubes. In fact, catalyst-support interactions can be critical for nanotube synthesis. Obtaining electrons from the support increases the electron density of nickel nanoparticles and its ability to donate electrons to the antibonding orbitals of the carbon source, making it easier to dissociate [458]. Ni/TiO$_2$ had a strong SMSI effect [459], whereas Ni/SiO$_2$ [460] and Ni/Al$_2$O$_3$ [461] were much weaker. Ni on TiO$_2$, Al$_2$O$_3$, SiO$_2$, and CaO supports as catalysts for carbon nanotube synthesis from hydrocarbon were compared. Ni/TiO$_2$ was the most active one, Ni/Al$_2$O$_3$ and Ni/SiO$_2$ were much less active, and Ni/CaO had no activity at all [462]. The TiO$_2$ support was partially reduced to Ti$^{2+}$ and Ti$^{3+}$, which can donate electrons to the nickel nanoparticles and increase its electron density and catalytic activity.

Nickel nanoparticles easily aggregate under preparation and reaction conditions. For example, a highly loaded Ni/SiO$_2$ catalyst (90%) used for the direct cracking of methane to nanotubes was aggregated to a size of 30–40 nm from 7 nm by the end of the first reaction hour [463]. Some supports could prevent the aggregation. Ni diffused in and reacted with $\gamma$-Al$_2$O$_3$ nanoparticles to form finely dispersed crystalline Ni-aluminates, which were stable up to 1000–1100 °C. This material shows remarkable catalytic activity in CH$_4$ oxidation [464]. Nickel nanoparticles with an average size of 28 nm were prepared from the reduction of perovskite-like mixed oxides, La$_2$NiO$_4$. La$_2$O$_3$ prevents Ni particles from agglomerating and promotes the dispersion of nanoscale Ni particles [465]. Compared with unsupported nanoparticles, supported Ni nanoparticles had a better-controlled size distribution and thus generated nanotubes with more uniform diameters [466].

Besides Ni, Co and Fe nanoparticles can also be used as catalysts for carbon nanotube synthesis. Nickel nanoparticle catalyst yields the highest growth rate, whereas Co results in the lowest growth rate [467]. This might be due to the fact that carbon diffuses and segregates faster on Ni particles than on Co and Fe. A flame synthesis method was used to produce single-walled carbon nanotubes and nanofibers with the use of Fe and Ni catalysts [468]. Fe reacts preferentially with CO/H$_2$/He mixtures to produce single-walled nanotubes. In contrast, Ni reacts preferentially with C$_2$H$_2$/H$_2$/He mixtures to yield nanofibers [469].

## 3.9. Cobalt

Besides being used as a catalyst for carbon nanotube synthesis [470–478], Co nanoparticles could also used as Fischer-Tropsch (FT) synthesis catalysts to produce chemicals, gasoline, diesel fuel, and other high-value long-chain hydrocarbons from relatively cheap natural and associated gases formed by vapor reforming and partial oxidation of carbon monoxide and hydrogen. The FT products are predominantly linear; hence the quality of the diesel fuel is very high, with octane numbers of up to 75 [479]. Rather than

burning off unused gas or leaving it untapped, FT synthesis yields products that are useful, cleaner (lower in sulfur and heavier metals than crude oil), and easier and cheaper to transport [480].

The product distribution of FT synthesis on Co/Al$_2$O$_3$ catalysts is affected by the crystalline size of Co and its degree of reduction from cobalt precursors [481]. The average carbon number in the final product is decided by the ratio of chain propagation rate to chain termination rate. The propagation rate is higher if the reactants, CO and H$_2$, are easier to activate on the catalyst surface, whereas the termination rate is higher if the adsorption of intermediates is fast. A common observation is that the selectivity for producing lighter hydrocarbon products is decreased by a decrease in particle size [481, 482]. However, the increase in product carbon number with decreasing Co nanoparticle size was observed so far only with a Co/Al$_2$O$_3$ catalyst [483]. Different conditions in the catalyst preparation process, such as the pH [483] or contaminants [482], may influence the CO adsorption or intermediate desorption. The presence of residual Co oxide species in the Co metal nanoparticles strongly influences the activity for FT synthesis [484–487]. The selectivity of CO hydrogenation to hydrocarbon was decreased at lower CoO reduction degree, and most of the product was CO$_2$ and H$_2$O. The activity was also decreased with higher CoO content.

The synthesis of small size Co nanoparticle catalysts on supports requires the initial formation of very small CoO or Co$_3$O$_4$ crystallites as precursors [488]. Strong interactions between the support and Co precursor could promote the formation of such small oxide clusters, but, in turn, such strong interactions generally lower the degree of reduction of the precursors to Co metal [489]. The effects of MgO, CaO, SrO, BaO, $\gamma$-Al$_2$O$_3$, and SiO$_2$ supports on Co catalyst reduction and stability were investigated [490]. Among these supports, only MgO exhibited a high interaction with Co precursors. A solid solution of CoO and MgO was formed in the calcined MgO supported catalyst, but not in the other supports. Because the oxygen atoms in the solid solution were shared by both Mg and Co, and their interactions with Mg were strong, only part of the solid solution was reducible, and small clusters of metallic Co were generated. Being at least partially embedded in the substrate, these clusters were more stable against sintering than the others. This effect that the addition of MgO both decreased the extent of Co reduction and increased the dispersion of cobalt was also found in the addition of MgO to the Co/SiO$_2$ [491]. ZrO$_2$, on the other hand, favored the reduction of cobalt oxides and increased the activity for FT synthesis [492]. Nanosized zirconia-silica bimodal catalyst supports prepared by direct introduction of zirconia sol into silica gel, which improved supported cobalt catalyst activity significantly via a spatial effect and the chemical promotional effect of zirconia in liquid-phase FT synthesis [493].

The addition of small amounts of metals to supported Co catalysts was used to increase the reduction degree of the catalyst and increased the efficiency of the cobalt while at the same time avoiding an increase in the particle size. Small amounts of Pt, Pd, and Ru promoters affected the characteristics and performance of Co/SiO$_2$ catalyst used for the hydroformylation of 1-hexene [494]. The addition of a

small amount of Ru greatly increased the reduction degree of CoO to Co in 50% to 98% yield; however, the reduced Co nanoparticle size was a little bit large at 13.7 nm. Pt and Pd increased the reducibility of CoO to Co and at the same time kept the Co nanoparticles small, at 4.2 and 5.7 nm, respectively, which led to a great improvement in the activity for hydroformylation of 1-hexene. When Ru, Pt, and Pd were added to a Co/SiO$_2$ catalyst for FT synthesis, Ru increased the reduction degree and Pd, Pt-promoted cobalt dispersion was observed [488]. The addition of Cr on Co/silicalite-1 for CO conversion to hydrocarbons was found to be an effective way to enhance the catalytic activity as a result of a decrease in the particle size of Co [495]. The addition of Au made the cobalt reducible at significantly lower temperatures, in comparison with those of the nonpromoted catalysts on the cyclodehydration of 1,4-butanediol [496].

The support could interact with Co or directly with the reactant via acid-base or electron transfer interactions, thus changing the reaction kinetics. For the FT synthesis of long-chain hydrocarbons over supported cobalt catalysts [492], the interaction between Co species and an acidic support led to a decrease in the number of available Co metal sites and a decrease in the activity and selectivity of chains longer than five carbon atoms. Negatively charged silicate crystallite mesoporous materials (SCMMs) were applied as Co particle supports for FT synthesis [497]. Olefins and branched hydrocarbons were efficiently produced, compared with linear hydrocarbons as the main product for ordinary Co/silica catalyst. This may be due to the charge of the SCMM, which affects the chemical state of the Co catalyst, making it cationic and harder to absorb H$_2$ and become activated.

The nature of pores of the metal nanoparticle support could have a great effect on the reduction degree and the size of the supported Ni nanoparticles and thus influence the final catalytic properties. With larger pores, the size of supported cobalt species can be bigger, as can its extent of overall reduction [498]. FT reaction rates and selectivities over different sizes of cobalt/silica (SBA-15 and MCM-41) catalysts were studied [498]. The reaction rates were found to be much higher with the pore diameter exceeding 30 Å than on narrower pore catalysts because of the fully reduced Co present. Optimally sized pores led to significantly higher reaction selectivities for hydroformylation of 1-hexene with Co/SiO$_2$ catalyst [499]. It was found that cobalt catalysts supported on silica with an appropriate pore size, about 6–10 nm, were active for reaction with very high selectivity to oxygenates. Cobalt nanoparticle catalysts supported on zirconia-coated silica aerogel lead to heavy products such as syngas [500], whereas cobalt catalysts supported on ZrO$_2$-SiO$_2$ in mixed aerogel produced middle-sized distillates, mainly C$_5$ products.

## 3.10. Iron

Fe nanoparticles have also been used to synthesize single-walled carbon nanotubes [501–503], multiwalled carbon nanotubes [504], and aligned nanotubes (20–35 nm thick) on flat substrates [505–507] or within the pores of alumina membranes [508]. They are used to form other types of nanowires such as gallium nitride [509] and SiC [510]. The use of nanoparticles to synthesize carbon nanotubes has

been discussed, and in detail for Ni catalysts. This section focuses on the use of Fe nanoparticles for other uses, such as FT synthesis and coal liquefaction.

Decreasing Fe catalyst particle size generally results in higher catalytic activity for many Fe-catalyzed reactions [511], whereas sintering of Fe into larger particles is often cited as the reason for catalyst degradation [512]. Very small Fe particles have exhibited higher selectivities for olefins than do bulk iron catalysts under comparable conditions [513]. Small Fe crystallites provide higher olefin/paraffin ratios, shorter chain lengths, and better catalytic activity maintenance [514]. In direct coal liquefaction, decreasing the particle size was shown to be an important way of increasing the activity of Fe catalysts [515]. However, in some systems, the activity decreases with decreasing particle size. The turnover number of the Fe/C catalyst was lower for the CO hydrogenation reaction [516] and might be due to the fact that in this system, planar surfaces, instead of corners and edges of the nanoparticles, were involved [517].

Choice of the proper porous support matrix could help maintain the small Fe particle size by preventing small iron nanoparticles from sintering [518]. With active carbon with different size distribution as a support, the Fe particle size decreased if the volume of the meso- and macropore pores of the activated carbon decreased [519]. The relatively small pore size of active carbon limits the amount of relatively large Fe$_3$(CO)$_{12}$ molecules in the pore, and, thus, nanoparticles as small as 1 nm could be synthesized [519]. A wetness impregnation method was used to prepare coal-supported Fe nanoparticles [520]. The interaction between Fe and the coal support was increased by this method, and the particle size could be decreased from 50 to 27 nm. This catalyst exhibited high activity in the coal liquefaction reaction.

Fe metal and Fe oxide catalyze different reactions, thus the degree of reduction directly influences the catalyst activity and/or selectivity [521]. The activity of Fe/C catalyst for CO hydrogenation (FT synthesis) is gradually lost if metal Fe oxidizes to FeO during use [512]. The reduction degree varies with time, and complete reduction can take up to 16 h [514]. The presence of other metal ions may also influence the reduction process. For example, the addition of manganese to Fe/silicalite-1 catalysts causes an increase in the amount of the oxide phase and an increase in alkene product during CO hydrogenation [522]. The presence of potassium increased the threshold reduction temperature by about 100 °C for Fe/ZrO$_2$ catalyst [523], possibly because of the coverage of the Fe compound by potassium carbonate or filling of the catalyst pores, limiting its accessibility for hydrogen and impeding the removal of water vapor produced in the reduction.

The nanoparticle-support interaction may influence the Fe oxide reduction degree. Fe oxide was easier to reduce with MgO supports prepared from magnesium nitrate than with MgO from magnesium acetate, because MgFe$_2$O$_4$ was formed with acetate as the precursor. The nitrate-formed sample showed activity one order of magnitude higher than that of the acetate-formed sample [524]. Complete reduction was similarly prevented by strong interactions between the Fe nanoparticle and many oxide supports, such as Y and ZSM-5 zeolites [525], alumina [526], ZrO$_2$ [527], and

La$_2$O$_3$-γ-Al$_2$O$_3$ [528]. For this reason, carbon as a support was widely used for Fe nanoparticle catalysts [514].

## 3.11. Molybdenum

Molybdenum nanoparticle catalysts have mainly been used as supported catalysts. Among their many uses, they have been used for the reduction of SO$_2$ and NO [529, 530], CO and H$_2$ reaction [531], nitration of toluene [532], disproportionation of CO [533], hydrodesulfurization [534–538], epoxidation [539, 540], olefin functionalization [541], crude oil upgrading [542], catalytic polymerization [543], and hydrotreatment of anilines, quinolines, pyridines, thiols, sulfides, and thiophenes [544].

A primary effect of the support is to tailor the oxidation state and complexation of Mo [545, 546]. Molybdenum-based catalysts supported on graphite form oxide clusters that appear to be elliptical, with sizes ranging from 10 to 20 nm in length and 6 nm in width. When produced in the presence of Co, ringed CoMoO$_x$ structures are formed. When sulfur is added large slabs of CoMoSO$_x$ are formed that are about 10 to 15 nm in size, and small MoS$_2$ crystallites and large needle-shaped CoS nearly 30 nm to 60 nm in length are seen. The clusters are stable, indicating a strong interaction between the cluster and the graphite support that affects the catalyst performance [547].

The Co-Mo-S structure is better than other metal-sulfur structures for the formation of a carbonyl sulfide (COS) intermediate because of the optimum strength of the metal-sulfur bond and support interaction [548]. The reactivities of ethanethiol and 1,2-ethanedithiol were studied on the clean Mo{110}, defective p(4 × 4)-C/Mo{110}, and p(4 × 4)-C/Mo{110} surfaces, demonstrating that the presence of multiple sulfhydryl (SH) groups influences the surface chemistry and product distribution. Ethanethiol experiments performed on clean Mo{110} surfaces yielded ethane and ethylene as reaction products, whereas 1,2-ethanedithiol experiments produced acetylene, ethylene, vinyl thiol, and ethanethiol. Ethanethiol experiments showed that no significant differences in reactivity, selectivity, or reaction pathways exist between clean Mo{110} and the defective p(4 × 4) surfaces. 1,2-Ethanedithiol experiments performed on the clean Mo{110} and p(4 × 4)-C/Mo{110} surfaces produced similar reaction products, although significant changes were observed in selectivity. On the clean surface, the major desorption products were acetylene, ethylene, vinyl thiol, and ethanethiol. However, the reaction of 1,2-ethanedithiol on the p(4 × 4)-C/Mo(110) surface produced only acetylene and ethylene. Thus, complete desulfurization of 1,2-ethanedithiol occurs on the p(4 × 4) surface upon decomposition, yielding only hydrocarbon products [549]. Comparing with γ-Al$_2$O$_3$-supported sulfide catalysts of transition metals Co, Mo, Fe, and FeMo, the sulfided CoMo/Al$_2$O$_3$ exhibited the most outstanding activity for the complete conversion of SO$_2$ at 300 °C at a molar feed ratio of CO/SO$_2$ = 2 [550]. The presence of Co strongly affects the sensitivity of the catalyst activity to the sulfide pretreatment but does not affect the fine structure of the Mo site [551]. The catalytic activity of MoS$_2$ supported on activated carbons for the reduction of SO$_2$ is strongly related to the reaction temperature and the CH$_4$:SO$_2$ feed ratio, with a secondary dependency on the loading of the MoS$_2$ [552].

Promoters like potassium and samarium, added to MgO/γ-Al$_2$O$_3$ catalyst, change the relative acidities of the catalysts, with K-promoted catalyst having lower acidity, followed by Sm, whereas the unpromoted sample showed the highest acidity. The higher the acid character of the catalyst, the lower the selectivity to propene. A parallel between Mo$^{6+}$ reducibility and resultant catalytic activity was reported [553]. For TiO$_2$-Al$_2$O$_3$ mixed-support catalysts, the hydrodesulfurization of 4-methyl-DBT (4-MDBT) and 4,6-dimethyl-DBT (4,6-DMDBT) is much higher than the conversion obtained over Al$_2$O$_3$-supported materials [554]. Chelating reagents like NTA, EDTA, and CyDTA added to Co-Mo/Al$_2$O$_3$ catalyst promote the catalyst activity by formation of highly active sites [555]. Addition of sodium or magnesium ions to Ni-Mo catalyst supported on alumina affected the size and distribution of pores. It was found that sodium ions prevented the formation of aluminum molybdate, whereas magnesium ions increased the thermal stability of the catalyst [556].

Matrix stability and ion migration can alter the structure, composition, and distribution of supported Mo catalyst materials. In the Al-Ni-Mo catalyst, crystalline α-NiMoO$_4$ arranged in the near-surface layer. An increase in the annealing temperature results in the migration of the molybdenum component to the edges of catalyst granules. Fast heating and short annealing times result in some shift of the molybdenum distribution inside the granule, and surface molybdate structures and a disordered beta-phase of nickel molybdate, stabilized by aluminum atoms, become the main compounds [557]. Mechanical activation of Mg-Mo-ZnO$_x$ and Mg-Mo-Ko$_x$ can be used to "activate" the catalyst, to change or intensify its selectivity [558].

## 3.12. Bimetallic Nanoparticles

Many of the metal elements mentioned above can be combined to form catalytic bimetallic nanoparticles. Among those reported include Pd-Cu bimetallic nanoparticles used for CO and NO reaction [559]; Pd-Ln used for NO reduction by CH$_4$ [560]; Pd-Zn, Pd-Au, and Pd-Pt nanoparticles in polystyrene-block-poly-4-vinylpyridine micelles for the hydrogenation of dehydrolinalol [561]; Au-Pd core-shell nanoparticles for hydrogenation of 4-pentenoic acid [562]; Pd-Pt for formic acid oxidation [563]; Pd-Ru catalyst for the reaction between cinnamylacetate and benzylamine [564]; Pd-Ru cluster for the hydrogenation of alkenes [565]; Pd-Ag/SiO$_2$ for the hydrodechlorination of 1,2-dichloroethane into ethylene [566]; poly(N-vinyl-2-pyrrolidone)-protected Pd-Ni for the hydrogenation of nitrobenzene [567]; reduction removal of organic pollutant by Pd-Fe and Pd-Zn nanoparticle catalysts [568], Ru-Sn nanoparticle used as a catalyst for the hydrogenation of polyenes [569]; Rh-Ti/alumina as a catalyst for cinnamaldehyde hydrogenation [570]; Cu-Rh for H$_2$ dissociation [571] and hydrogenation of hexane [572]; Pt-Ru [573–575] and Pt-Ni [576] used for the electroxidation of methanol; Pt-Ru on graphitic carbon as the anode of a direct methanol fuel cell [577–581]; Fe-Au nanoparticle used to synthesize carbon nanotubes [582]; Fe-Pt and Fe-Ni nanoparticle for the reduction removal of organic pollutants [568]; Ag/Fe for the dechlorination of pentachlorophenol in supercritical carbon dioxide [583]; Co-Ag used for

decomposition of ethylene to grow filamentous carbon [584]; Ni-Mo for the hydrocracking of vacuum oil [585]; Mo-S, Co-Mo-S, and Ni-Mo-S for hydrogen dissociation and dehydrogenation of indole [586, 587]; Co-Mo for hydrotreating hydrocarbons at atmospheric pressure, hydrodesulfurization, and carbon monoxide hydrogenation [588–591]; Fe-Mo for methanol oxidation [592]; B-Ni-Mo for hydrodesulfurization and hydrodenitrogenation [593]; Na-Cr-Mo and Sn-Mo-O for the oxidation of methanol [594, 595]; and $MoO_3/SiC$ catalyst for hydrocarbon isomerization [596].

## 4. SUMMARY

The activity and selectivity of metal nanoparticle catalysts are determined primarily by their size. The size can be controlled by the preparation method, choice of particle support, choice of stabilizer molecules, presence of ions that absorb on the nanoparticle surface, and material composition. Apart from the change in specific surface area, the change of nanoparticle size influences the electron structure of the particle, the density and energies of edge and step atoms on the particle surface, and the nature of active binding sites on the nanoparticle surface. The specific combination determines the catalytic properties of nanoparticles. Besides the above effects, using a composition of two or metals to prepare nanoparticles could further change the catalytic properties.

Depending on the preparation method, nanoparticles of similar size but with different crystal structures (if the nanoparticle is a nanocrystal), surface morphology, or nanoparticle shape and size may be obtained. For many materials, which crystal plane is exposed determines the particle's ability to catalyze a given reaction. Among the many ways of preparing metal nanoparticle catalysts, the sol–gel method is the most frequently preferred because of its simplicity, but other methods may be more amenable to scaling up.

Many nanoparticles are loaded on supports as catalysts. The supports may affect the activity and selectivity of nanoparticles by its pore structure, the metal-support interaction, helping to absorbing reactants, or by forming new active sites on the support-particle interface. Either in solution or on a support, the surface of many metal nanoparticles must be covered by stabilizers to keep them from coagulation or sintering at the high reaction temperatures used for reaction. Stabilizers could be ligands, surfactant, or polymers, which may also have donor-acceptor interactions with the nanoparticle or control the accessibility of reactants with the nanoparticle surface by steric or electric effects.

In general, the size of metal nanoparticles can be used to tune the activity and selectivity of the catalysts, offering more opportunities to find better catalysts, while at the same time providing greater challenges for the catalysis engineer to understand the molecular and atomic phenomena that give rise to catalysis.

## GLOSSARY

**Activity**  Used to evaluate the ability of the catalyst to accelerate the reaction. Could be evaluated by the rate of the reaction at the presence of the catalyst.

**Ball milling**  Also called mechanical alloying. A method for nanoparticle synthesis in which bulk material ground to nanometer size with stainless steel balls.

**Catalyst**  A substance that increases the rate at which a chemical reaction reaches equilibrium.

**Combustion flame**  A method for nanoparticle synthesis in which a metal precursor with or without fuel combusted and metal vapor collected on cooled substrate to form nanoparticles.

**Critical micelle concentration (CMC)**  The concentration at which a surfactant would form a micelle structure.

**CTAB (Hexadecyltrimethylammonium bromide)**  A surfactant with a 16-carbon chain as a tail and trimethylammonium as a head group.

**Dehydrogenation**  An oxidation reaction in which the reactant loses hydrogen atoms.

**Dendrimer**  A polymer with a tree-like structure built up from branched monomer.

**Extended X-ray absorption fine structure (EXAFS)**  Refers to the sinusoidal variation of the X-ray absorption coefficient as a function of X-ray photon energy, which occurs after each absorption edge of an element and extends for up to a further 1500 eV. This technique can be used to obtain structural information about molecules without the need for obtaining single crystals.

**Fischer-Tropsch synthesis**  Synthesis of hydrocarbon from CO and $H_2$.

**Hydrogenation**  A reduction reaction in which the reactant gets hydrogen atoms.

**Ion sputtering**  Bulk material ablated by an ion beam and collected on a cooled substrate to form nanoparticles.

**Laser ablation**  Bulk material vaporized by a laser pulse and collected on a cooled substrate to form nanoparticles.

**MCM-41**  A mesoporous molecular sieve that possesses hexagonally arranged uniform pore structures.

**Metal nanoparticle**  Metal particle ranging in size from a few hundred atoms to up to 100 nm in diameter.

**Microwave plasma**  A region of hot ions and free radicals created by microwaves that decomposes that is metal precursors cooled substrate to form nanoparticles.

**Poly(acrylic acid) (PAA)**  A polymer stabilizer.

**PAMAM**  Hydroxyl-terminated poly(amidoamine). A dendrimer molecule.

**PCEMA**  Poly(2-cinnamoyloxyethyl methacrylate). A polymer used as a stabilizer.

**Radiolysis method**  High-energy radiolysis generating hydrated electrons and radicals which either directly reduce metal ions or produce reducing species *in-situ*.

**Selectivity**  The ratio of reactant converted to desired product to the total reacted amount.

**Size dependence**  The properties of a nanoparticle change as its size changes.

**Sol–gel method**  A method to synthesize nanoparticles in which dissolved metal precursor ions chemically reacted to form a precipitate suspension.

**Sonochemistry method**  A method to synthesize nanoparticles in which metal precursor decomposed and

chemically reacted with reduction agents in cavitation bubbles with high local temperature and pressure generated by ultrasound.

**Stabilizer** A molecule bound to the surface of nanoparticles, making them stable by static and/or electronic effects. The molecule could be a ligand, surfactant, or polymer.

## REFERENCES

1. C. N. R. Rao, G. U. Kulkarni, P. J. Thomas, and P. P. Edwards, *Chem. Eur. J.* 8, 29 (2002).
2. G. Schmidt, "Clusters and Colloids: From Theory to Application." Weinheim, New York, 1994.
3. M. Prettre, "Catalysis and Catalysts." Dover, New York, 1963.
4. Bureau of Economic Analysis, GDP and Related Data: Current-Dollar and 'Real' GDP. Bureau of Economic Analysis, 2002.
5. W. P. Jencks, *Catal. Chem. Enzymol.* Wiley, New York, 1969.
6. H. S. Taylor, *J. Am. Chem. Soc.* 53 (1931).
7. K. J. Laidler, "Reaction Kinetics," Vol. 1. Macmillan, New York, 1963.
8. H. Eyring, *J. Chem. Phys.* 3, 107 (1935).
9. I. Langmuir, *J. Am. Chem. Soc.* 40, 1361 (1918).
10. C. N. Satterfield, "Heterogeneous Catalysis in Industrial Practice," 2nd Ed. McGraw-Hill, New York, 1991.
11. J. Anderson and M. Boudart, "Catalysis: Science and Technology." Springer-Verlag, New York, 1981.
12. A. Henglein, *Top. Curr. Chem.* 143, 113 (1988).
13. J. D. Aiken III and R. G. Finke, *J. Mol. Catal. A* 145, 1 (1999).
14. R. S. Naidu and B. K. Banerjee, Challenges in Catalysis Science and Technology (1987). Vol. 1, p. 16.
15. A. Henglein, *Chem. Rev.* 89, 1861 (1989).
16. T. Wang, C. Lee, and L. D. Schmidt, *Surf. Sci.* 163, 181 (1985).
17. V. I. Bukthiyarov and M. G. Slin'ko, *Russ. Chem. Rev.* 70, 147 (2001).
18. J. Flad, H. Stoll, and H. Preuss, *J. Chem. Phys.* 71, 3042 (1979).
19. M. D. Morse, *Chem. Rev.* 86, 1049 (1986).
20. V. Kumar and R. Car, *Phys. Rev. B* 44, 8243 (1991).
21. G. Grosso, "Solid State Physics." Academic, San Diego, London, 2000.
22. I. Boustani, W. Pewestorf, P. Fantucci, V. Bonacic-Koutecky, and J. Koutecky, *Phys. Rev. B* 35, 9437 (1987).
23. T. H. Upton, *Phys. Rev. Lett.* 56, 2168 (1986).
24. Y. D. Glinka, S. H. Lin, L. P. Hwang, Y. T. Chen, and N. H. Tolk, *Phys. Rev. B* 64, article NO. 085421 (2001).
25. J. Belloni, *Curr. Opin. Colloid Interface Sci.* 1, 184 (1996).
26. G. Schmidt, *Chem. Rev.* 92, 1709 (1992).
27. Y. Niu, L. K. Yeung, and R. M. Crooks, *J. Am. Chem. Soc.* 123, 6840 (2001).
28. Y. Li and M. A. EI-Sayed, *J. Phys. Chem. B* 105, 8938 (2001).
29. A. B. R. Mayer, J. E. Mark, and S. H. Hausner, *J. Appl. Polym. Sci.* 70, 1209 (1998).
30. F. H. Sanchez, C. E. Rodriguez-Torres, A. F. Cabrera, M. Meyer, L. M. Zelis, and M. B. F. van Raap, *Mater. Sci. Forum* 269-2, 443 (1998).
31. R. Kalyanaraman, S. Yoo, M. S. Krupashshankare, T. S. Sudarshan, and R. J. Dowding, *Nanostruct. Mater.* 10, 1379 (1998).
32. F. Charlot, F. Bernard, E. Gaffet, D. Klein, and J. C. Niepce, *Acta Mater.* 47, 619 (1999).
33. F. Bernard, F. Charlot, E. Gaffet, and Z. A. Munir, *J. Am. Ceram. Soc.* 84, 910 (2001).
34. S. K. Pabi and B. S. Murty, *Bull. Mater. Sci.* 19, 939 (1996).
35. P. Delcroix, T. Ziller, C. Bellouard, and L. E. G. Caer, *Mater. Sci Forum* 360-3, 329 (2001).
36. C. Lemoine, A. Fnidiki, D. Lemarchand, and J. Teillet, *J. Magn. Magn. Mater.* 203, 184 (1999).
37. A. V. Leonov, V. I. Fadeeva, O. E. Gladilina, and H. Matyja, *J. Alloys Compd.* 281, 275 (1998).
38. E. Hellstern, H. J. Fecht, Z. Fu, and W. L. Johnson, *J. Appl. Phys.* 65, 305 (1989).
39. G. Mestl, B. Herzog, R. Schlogl, and H. Knozinger, *Langmuir* 11, 3027 (1995).
40. J. Naser, W. Riehemann, and H. Ferkel, *Mater. Sci Eng., A* 234, 467 (1997).
41. M. Gotic, I. Czako-Nagy, S. Popovic, and S. Music, *Philos. Mag. Lett.* 78, 193 (1998).
42. Q. W. Zhang, T. Nakagawa, and F. Saito, *J. Alloys Compd.* 308, 121 (2000).
43. H. Hermann, T. Schubert, W. Gruner, and N. Mattern, *Nanostruct. Mater.* 8, 215 (1997).
44. P. Balaz, T. Ohtani, Z. Bastl, and E. Boldizarova, *J. Solid State Chem.* 144, 1 (1999).
45. C. Gras, F. Bernard, F. Charlot, E. Gaffet, and Z. A. Munir, *J. Mater. Res.* 17, 542 (2002).
46. D. D. Radev and D. Klisurski, *J. Alloys Compd.* 206, 39 (1994).
47. V. O. Kharlamov, O. I. Bacherykova, I. V. Komashko, G. A. Khalameida, S. V. Bogutska, L. V. Byl, O. G. Stoch, J. Koval, and A. Zazhygalov, *Teor. Eksp. Khim.* 34, 180 (1998).
48. J. Haber, V. A. Zazhigalov, J. Stich, L. V. Bogutskaya, and I. V. Batcherikova, *Catal. Today* 33, 39 (1997).
49. L. Wilde, U. Steinike, A. Martin, M. Fait, and B. Muller, *Mater. Sci Forum* 343–346, 859 (2000).
50. P. Kuznetsov, L. I. Kuznetsova, V. G. Chumakov, and G. A. Moiseeva, *Mater. Res. Innovation* 3, 340 (2000).
51. R. Wilkenhoener, R. Vassen, H. P. Buchkremer, and D. Stover, *J. Mater. Sci.* 34, 257 (1999).
52. A. Calka and D. Wexler, *Mater. Sci Forum* 360-3, 301 (2001).
53. E. O. Krist, A. Z. Juhasz, and I. Vassanyi, *Clays Clay Miner.* 41, 608 (1993).
54. S. Gialanella and Feal, *Intermetallics* 3, 73 (1995).
55. E. Kristof-Mako and A. Z. Juhasz, *Thermochim. Acta* 342, 105 (1999).
56. E. Kristof-Mako and A. Z. Juhasz, *Powder Technol.* 75, 145 (1993).
57. J. M. Filio, K. Sugiyama, F. Saito, and Y. Waseda, *Powder Technol.* 78, 121 (1994).
58. B. Kollath and A. Z. Juhasz, *Hungar. J. Ind. Chem.* 24, 263 (1996).
59. E. Hellstern, H. J. Fecht, Z. Fu, and W. L. Johnson, *J. Appl. Phys.* 65, 305 (1988).
60. P. N. Kutnetsov, L. I. Kuznetsova, A. M. Zhizhaev, S. M. Kolesnikova, G. L. Pashkov, and V. V. Boldyrev, *Russ. J. Inorg. Chem.* 47, 393 (2002).
61. P. Balaz, L. Takacs, J. Z. Jiang, V. Soika, and M. Luxova, *Mater. Sci. Forum* 386-3, 257 (2002).
62. A. S. Kharitonov, V. B. Fenelonov, T. P. Voskresenskaya, N. A. Rudina, V. V. Molchanov, L. M. Plyasova, and G. I. Panov, *Zeolites* 15, 253 (1995).
63. Y. B. Li, B. Q. Wei, J. Liang, Q. Yu, and D. H. Wu, *Carbon* 37, 493 (1999).
64. T. S. Ong and H. Yang, *Carbon* 38, 2077 (2000).
65. B. Bokhonov and M. Korchagin, *J. Alloys Compd.* 333, 308 (2002).
66. R. Janot and D. Guerard, *J. Alloys Compd.* 333, 302 (2002).
67. J. F. Hamet and B. Mercey, *Curr. Opin. Solid State Mater. Sci.* 3, 144 (1998).
68. K. Yatsui, C. Grigoriu, K. Masugata, W. H. Jiang, and T. Sonegawa, *Jpn. J. Appl. Phys. Part* 36, 4928 (1997).
69. G. P. Johnston, R. E. Muenchausen, D. M. Smith, W. Fahrenholtz, and S. Foltyn, *J. Am. Ceram. Soc.* 75, 3293 (1992).
70. J. Naser, H. Ferkel, W. Riehemann, and B. L. Mordike, *Lasers Eng.* 9, 195 (1999).
71. T. K. H. Starke, G. S. V. Coles, and H. Ferkel, *Sens. Actuators, B* 85, 239 (2002).
72. S. R. Shinde, S. D. Kulkarni, A. G. Banpurkar, R. Nawathey-Dixit, S. K. Date, and S. B. Ogale, *J. Appl. Phys.* 88, 1566 (2000).

73. G. Williams and G. S. V. Coles, *J. Mater. Chem.* 8, 1657 (1998).

74. A. Murali, A. Barve, V. J. Leppert, S. H. Risbud, I. M. Kennedy, and H. W. H. Lee, *Nano Letters* 1, 287 (2001).

75. G. P. Johnston, R. E. Muenchausen, D. M. Smith, and S. R. Foltyn, *J. Am. Ceram. Soc.* 75, 3465 (1992).

76. T. J. Goodwin, V. J. Leppert, S. H. Risbud, I. M. Kennedy, and H. W. H. Lee, *Appl. Phys. Lett.* 70, 3122 (1997).

77. V. J. Leppert, C. J. Zhang, H. W. H. Lee, I. M. Kennedy, and S. H. Risbud, *Appl. Phys. Lett.* 72, 3035 (1998).

78. S. Matsumoto, E. Q. Xie, and F. Izumi, *Diamond Relat. Mater.* 8, 1175 (1999).

79. P. Heszler, *Appl. Surf. Sci.* 186, 538 (2002).

80. T. Okada, *Mater. Sci. Forum* 301, 95 (1999).

81. L. A. Chiu, A. A. Seraphin, and K. D. Kolenbrander, *J. Electron. Mater.* 23, 347 (1994).

82. L. Patrone, D. Nelson, V. Safarov, M. Sentis, and W. Marine, *J. Lumin.* 80, 217 (1998).

83. C. B. Juang, H. Cai, M. F. Becker, J. W. Keto, and J. R. Brock, *Appl. Phys. Lett.* 65, 40 (1994).

84. J. Mazumder, H. Chung, T. Yamamoto, T. P. Duffey, H. Sehitoglu, M. H. Jilavi, and W. M. Kriven, *Nanostruct. Mater.* 9, 75 (1997).

85. M. F. Brcker, J. R. Brock, H. Cai, D. E. Henneke, J. W. Keto, J. Lee, W. T. Nichols, and H. D. Glicksman, *Nanostruct. Mater.* 10, 853 (1998).

86. C. Juang, H. Cai, M. Becher, J. Keto, and J. Grock, *Appl. Phys. Lett.* 65, 40 (1994).

87. A. Harano, K. Shimada, T. Okubo, and M. Sadakata, *J. Nanoparticle Res.* 4, 215 (2002).

88. Y. Nakata, J. Muramoto, T. Okada, and M. Maeda, *J. Appl. Phys.* 9, 1640 (2002).

89. J. C. Pivin, *J. Mater. Sci.* 18, 1267 (1983).

90. R. T. Yadav, V. S. Ramamurthy, D. P. Mahapatra, and G. V. Raviprasad, *Phys. Rev. A* 49, 1908 (1994).

91. F. K. Urban, P. Hosseini-Tehrani, P. Griffiths, A. Khabari, Y. W. Kim, and I. Petrov, *J. Vac. Sci. Technol. B* 20, 995 (2002).

92. M. X. Yang, D. H. Gracias, P. W. Jacobs, and G. A. Somorjai, *Langmuir* 14, 1458 (1998).

93. Z. Paszti, G. Peto, Z. E. Horvath, A. Karacs, and L. Guczi, *Solid State Commun.* 107, 329 (1998).

94. Y. Xiong, H. Wu, Y. Guo, Y. Sun, D. Yang, and D. Da, *Thin Solid Films* 375, 300 (2000).

95. A. Maekawa and F. Okuyama, *Surf. Sci.* 481, L427 (2001).

96. G. Peto, G. L. Molnar, Z. Paszti, O. Geszti, A. Beck, and L. Guczi, *Mater. Sci. Eng., C* 19, 95 (2002).

97. P. W. Jacobs, F. H. Ribeiro, G. A. Somorjai, and S. J. Wind, *Catal. Lett.* 37, 131 (1996).

98. P. W. Jacobs, S. J. Wind, F. H. Ribeiro, and G. A. Somorjai, *Surf. Sci.* 372, L249 (1997).

99. A. S. Eppler, J. Zhu, E. A. Anderson, and G. A. Somorjai, *Top. Catal.* 13, 33 (2000).

100. V. I. Ivanovomskii, V. I. Siklitsky, A. A. Sitnikova, A. A. Suvorova, A. V. Tolmatchev, T. K. Zvonariova, and S. G. Yastrebov, *Philos. Mag. B* 76, 973 (1997).

101. S. G. Yastrebov, V. I. Ivanov-Omskii, V. I. Siklitsky, and A. A. Sitnikova, *J. Non-Cryst. Solids* 230, 622 (1998).

102. Z. Wang, F. Zhu, W. Wang, and M. Ruan, *Phys. Lett. A* 242, 261 (1998).

103. J. Wu, T. Lu, T. Wang, L. Chen, K. Chen, C. Kuo, T. Chen, Y. Yu, C. Wang, and E. Lin, *Diamond Relat. Mater.* 8, 605 (1999).

104. F. H. Kaatz, G. M. Chow, and A. S. Edelstein, *J. Mater. Res.* 8, 995 (1993).

105. D. Babonneau, T. Cabioc'h, A. Naudon, J. C. Girard, and M. F. Denanot, *Surf. Sci.* 409, 358 (1998).

106. G. Skandan and B. H. Kear, *Mater. Sci. Forum* 243, 217 (1997).

107. Y. J. Chen, N. G. Glumac, G. Skandan, and B. H. Kear, *Synth. Characterization Adv. Mater. ACS Symp. Ser.* 681, 158 (1998).

108. B. K. Kim, G. G. Lee, H. M. Park, and N. J. Kim, *Nanostruct. Mater.* 12, 637 (1999).

109. J. H. Yi, S. Son, and M. Choi, *Key Eng. Mater.* 206, 135 (2002).

110. T. Ye, G. W. Zhao, W. P. Zhang, and S. D. Xia, *Mater. Res. Bull.* 32, 501 (1997).

111. F. R. Hu, L. Li, D. N. Zheng, and C. C. Ge, *J. Univ. Sci. Technol. Beijing* 9, 188 (2002).

112. X. J. Yu, P. B. Xie, and Q. D. Su, *Phys. Chem. Chem. Phys.* 3, 5266 (2001).

113. G. G. Amatucci, F. Badway, A. Singhal, B. Beaudoin, G. Skandan, T. Bowmer, I. Plitza, N. Pereira, T. Chapman, and R. Jaworski, *J. Electrochem. Soc.* 148, A940 (2001).

114. M. P. Johnson, J. B. Donnet, T. K. Wang, C. C. Wang, R. W. Locke, B. E. Brinson, and T. Marriott, *Carbon* 40, 189 (2002).

115. R. Uyeda, *J. Cryst. Growth* 24–25, 69 (1974).

116. S. Yatsuya, S. Kasukabe, and R. Uyeda, *J. Cryst. Growth* 24–25, 319 (1974).

117. Y. Chen, N. Glumac, B. H. Kear, and G. Skandan, *Nanostruct. Mater.* 9, 101 (1997).

118. N. G. Glumac, G. Skandan, Y. J. Chen, and B. H. Kear, *Nanostruct. Mater.* 12, 253 (1999).

119. L. A. Chick, L. R. Pederson, G. D. Maupin, J. L. Bates, L. E. Thomas, and G. J. Exarhos, *Mater. Lett.* 10, 6 (1990).

120. A. Singhal, G. Skandan, N. Glumac, and B. H. Kear, *Scr. Mater.* 44, 2203 (2001).

121. D. Vollath, D. V. Szabo, and J. Haußelt, *J. Eur. Ceram. Soc.* 17, 1317 (1997).

122. D. Vollath and K. E. Sickafus, *J. Mater. Sci.* 28, 5943 (1993).

123. D. Vollath, D. V. Szabo, and J. O. Willis, *Mater. Lett.* 29, 271 (1996).

124. D. Vollath, D. V. Szabo, R. D. Taylor, J. O. Willis, and K. E. Sickafus, *Nanostruct. Mater.* 6, 941 (1995).

125. D. Vollath, D. V. Szabo, R. D. Taylor, and J. O. Willis, *J. Mater. Res.* 12, 2175 (1997).

126. D. Vollath, D. V. Szabo, and J. Fuchs, *Nanostruct. Mater.* 12, 433 (1999).

127. M. Orker, J. Schmidberger, D. V. Szabo, and D. Vollath, *Phys. Rev. B* 1, 1014 (2000).

128. D. Vollath and D. V. Szabo, *Mater. Lett.* 35, 236 (1998).

129. D. V. Szabo and D. Vollath, *Nanostruct. Mater.* 12, 597 (1999).

130. R. K. Kalyanaraman, S. H. Yoo, M. S. Krupashankara, and T. S. Sudarshan, *Powder Metall.* 43, 380 (2000).

131. J. H. Eng, P. J. Hong, S. S. Dai, D. Vollath, and D. V. Szabo, *J. Mater. Sci. Technol.* 14, 173 (1998).

132. B. H. Liu, H. C. Gu, and Q. L. Chen, *Mater. Chem. Phys.* 59, 204 (1999).

133. J. L. Boulanger and D. Autissier, *J. Phys. IV* 3, 1305 (1993).

134. H. Srikanth, R. Hajndi, C. Chirinos, and J. Sanders, *Appl. Phys. Lett.* 79, 3503 (2001).

135. J. R. Brenner, J. B. L. Harkness, M. B. Knickelbein, G. K. Krumdick, and C. L. Marshall, *Nanostruct. Mater.* 8, 1 (1997).

136. S. H. Tsai, C. W. Chao, C. L. Lee, and H. C. Shih, *Appl. Phys. Lett.* 74, 3462 (1999).

137. M. Tammler, J. Ristein, T. Habermann, A. Gohl, K. Janischowsky, D. Nau, G. Muller, and L. Ley, *Diamond Relat. Mater.* 8, 792 (1999).

138. X. Wang, Z. Hu, X. Chen, and Y. Chen, *Scr. Mater.* 44, 1567 (2001).

139. B. D. Yao and N. Wang, *J. Phys. Chem. B* 105, 11395 (2001).

140. J. Yu, J. Ahn, Q. Zhang, S. F. Yoon, Y. J. Li Rusli, B. Gan, K. Chew, and K. H. Tan, *J. Appl. Phys.* 91, 433 (2002).

141. S. G. Wang, J. H. Wang, and Y. Qin, *Acta Chim. Sinica* 60, 957 (2002).

142. J. Yu, Q. Zhang, J. Ahn, S. F. Yoon, Y. J. Li Rusli, B. Gan, K. Chew, and K. H. Tan, *Mater. Sci. Eng. B* 90, 16 (2002).

143. J. A. Wang, M. A. Valenzuela, J. Salmones, A. Vázquez, A. García-Ruiz, and X. Bokhimi, *Catal. Today* 68, 21 (2001).

*144.* M. Thammachart, V. Meeyoo, T. Risksomboon, and S. Osuwan, *Catal. Today* 68, 53 (2001).

*145.* W. Kuang, Y. Fan, and Y. Chen, *Catal. Today* 68, 75 (2001).

*146.* K. Itsu, M. Murakami, S. Tanabe, and H. Matsumoto, *Chem. Lett.* 11, 1336 (2000).

*147.* T. Li, J. Moon, A. A. Morrone, J. J. Mecholsky, D. R. Talham, and J. H. Adair, *Langmuir* 15, 4328 (1999).

*148.* X. L. Ren and F. Q. Tang, *Acta Chim. Sinica* 60, 393 (2002).

*149.* A. A. Eliseev, A. V. Lukashin, A. A. Vertegel, L. I. Heifets, A. I. Zhirov, and Y. D. Tretyakov, *Mater. Res. Innovations* 3, 308 (2000).

*150.* A. J. Maira, K. L. Yeung, J. Soria, J. M. Coronado, C. Belver, and C. Y. Lee, *Appl. Catal., B* 29, 327 (2001).

*151.* A. J. Maira, K. L. Yeung, Y. Lee, P. L. Yue, and C. K. Chan, *J. Catal.* 192, 185 (2000).

*152.* G. Xiong, X. Wang, L. D. Lu, X. J. Yang, and Y. F. Xu, *J. Solid State Chem.* 141, 70 (1998).

*153.* N. Yao, G. Xiong, Y. Zhang, M. He, and W. Yang, *Catal. Today* 68, 97 (2001).

*154.* D. Zhao, C. Nie, Y. Zhou, S. Xia, L. Huang, and Q. Li, *Catal. Today* 68, 11 (2001).

*155.* L. Zhu, F. Xiao, Z. Zhang, Y. Sun, Y. Han, and S. Qiu, *Catal. Today* 68, 2091 (2001).

*156.* Z. Wang, S. Tezuka, and H. Kanoh, *Catal. Today* 68, 111 (2001).

*157.* X. Liu and Z. Yan, *Catal. Today* 68, 145 (2001).

*158.* S. E. Dapurkar, S. K. Badamali, and P. Selvam, *Catal. Today* 68, 63 (2001).

*159.* P. Selvam, S. E. Dapurkar, S. K. Badamali, M. Murugasan, and H. Kuwano, *Catal. Today* 68, 69 (2001).

*160.* P. Van Der Voort, M. Baltes, and E. F. Vansant, *Catal. Today* 68, 119 (2001).

*161.* X. Hu, F. L. Y. Lam, L. M. Cheung, K. F. Chan, X. S. Zhao, and G. Q. Lu, *Catal. Today* 68, 129 (2001).

*162.* R. S. Mulukutla, T. Shido, K. Asakura, and Y. Iwasawa, *Scr. Mater.* 44, 1695 (2001).

*163.* S. C. Shen and S. Kawi, *Catal. Today* 68, 245 (2001).

*164.* S. Kawi, S. Y. Liu, and S. C. Shen, *Catal. Today* 68, 237 (2001).

*165.* R. Köhn and M. Fröba, *Catal. Today* 68, 227 (2001).

*166.* W. Ahn, N. Kim, and S. Jeong, *Catal. Today* 68, 83 (2001).

*167.* F. Seyedeyn-Azad and D. Zhang, *Catal. Today* 68, 161 (2001).

*168.* Z. Ding, X. Hu, P. L. Yue, G. Q. Lu, and P. F. Greenfield, *Catal. Today* 68, 173 (2001).

*169.* R. Naci, A. Musinu, G. Piccaluga, and G. Pinna, *Mater. Sci. Forum* 195, 1 (1995).

*170.* K. Hwang, H. Y. Zhu, and G. Q. Lu, *Catal. Today* 68, 183 (2001).

*171.* G. Ennas, A. Musinu, G. Piccaluga, D. Zedda, D. Gatteschi, C. Sangregorio, J. L. Stanger, G. Concas, and G. Spano, *Chem. Mater.* 10, 495 (1999).

*172.* S. Solinas, G. Piccaluga, M. P. Morales, and C. J. Serna, *Acta Mater.* 49, 2805 (2001).

*173.* M. Casula, A. Corrias, and G. Paschina, *J. Non-Cryst. Solids* 293–295, 25 (2001).

*174.* A. Henglein, *Chem. Mater.* 10, 444 (1998).

*175.* K. S. Suslick, "Ultrasound: Its Chemical, Physical and Biological Effects." VCH, Weinheim, 1988.

*176.* K. S. Suslick, D. A. Hammerton, and R. E. Cline, *J. Am. Chem. Soc.* 108, 5641 (1986).

*177.* W. B. McNamara III, Y. T. Didenko, and K. S. Suslick, *Nature* 401, 772 (1999).

*178.* K. S. Suslick and G. J. Price, *Annu. Rev. Mater. Sci.* 29, 295 (1999).

*179.* J. P. Ge, Y. D. Li, and G. Q. Yang, *Chem. Commun.* 17, 1826 (2002).

*180.* K. S. Suslick, M. Fang, and T. Hyeon, *J. Am. Chem. Soc.* 118, 11960 (1996).

*181.* K. Okitsu, Y. Mizukoshi, H. Bandow, T. A. Yamamoto, Y. Nagata, and Y. Maeda, *J. Phys. Chem. B* 101, 5470 (1997).

*182.* Y. Nagata, Y. Mizukoshi, K. Okitsu, and Y. Maeda, *Radia. Res.* 146, 333 (1996).

*183.* F. Grieser, R. Hobson, J. Sostaric, and P. Mulvaney, *Ultrasonics* 34, 547 (1996).

*184.* Y. Mizukoshi, E. Takagi, H. Okuno, R. Oshima, Y. Maeda, and Y. Nagata, *Ultrasonics Sonochem.* 8, 1 (2001).

*185.* Y. Mizukoshi, R. Oshima, Y. Maeda, and Y. Nagata, *Langmuir* 15, 2733 (1999).

*186.* S. J. Doktycz and K. S. Suslick, *Science* 247, 1067 (1990).

*187.* M. W. Grinstaff, A. A. Cichowlas, S. B. Choe, and K. S. Suslick, *Ultrasonics* 30, 168 (1992).

*188.* R. A. Caruso, M. Ashokkumar, and F. Grieser, *Colloids Surf., A* 169, 219 (2000).

*189.* K. Okitsu, A. Yue, S. Tanabe, and H. Matsumoto, *Bull. Chem. Soc. Jpn.* 75, 449 (2002).

*190.* K. Okitsu, A. Yue, S. Tanabe, and H. Matsumoto, *Chem. Mater.* 12, 3006 (2000).

*191.* N. A. Dhas, C. P. Raj, and A. Gedanken, *Chem. Mater.* 10, 1446 (1998).

*192.* Y. Koltypin, G. Katabi, X. Cao, R. Prozorov, and A. Gedanken, *J. Non-Cryst. Solids* 201, 159 (1996).

*193.* K. E. Gonsalves, H. Li, R. Perez, P. Santiago, and M. Jose-Yacaman, *Coord. Chem. Rev.* 206, 607 (2000).

*194.* D. H. Chen and C. H. Hsieh, *J. Mater. Chem.* 12, 2412 (2002).

*195.* W. Chen, W. P. Cai, C. H. Liang, and L. D. Zhang, *Mater. Res. Bull.* 36, 335 (2001).

*196.* W. Chen, W. P. Cai, Z. P. Zhang, and L. Zhang, *Chem. Lett.* 2, 152 (2001).

*197.* S. Gao, J. Zhang, Y. F. Zhu, and C. M. Che, *New J. Chem.* 24, 739 (2000).

*198.* T. Prozorov, R. Prozorov, K. V. P. M. Shafi, and A. Gedanken, *Nanostruct. Mater.* 12, 669 (1999).

*199.* X. Cao, Y. Koltypin, G. Kataby, R. Prozorov, and A. Gedanken, *J. Mater. Res.* 10, 2952 (1995).

*200.* R. Vijayakumar, Y. Koltypin, I. Felner, and A. Gedanken, *Mater. Sci. Eng. A* 286, 101 (2000).

*201.* Y. Li, J. Liu, Y. Q. Wang, and Z. L. Wang, *Chem. Mater.* 13, 1008 (2001).

*202.* R. V. Kumar, Y. Mastai, and A. Gedanken, *Chem. Mater.* 12, 3892 (2000).

*203.* R. V. Kumar, Y. Mastai, Y. Diamant, and A. Gedanken, *J. Mater. Chem.* 11, 1209 (2001).

*204.* V. Ganesh Kumar, D. Aurbach, and A. Gedanken, *J. Mater. Res.* 17, 1706 (2002).

*205.* V. G. Pol, D. N. Srivastava, O. Palchik, V. Palchik, M. A. Slifkin, A. M. Weiss, and A. Gedanken, *Langmuir* 18, 3352 (2002).

*206.* K. V. P. M. Shafi, A. Ulman, X. Z. Yan, N. L. Yang, C. Estournes, H. White, and M. Rafailovich, *Langmuir* 17, 5093 (2001).

*207.* N. A. Dhas and A. Gedanken, *Chem. Mater.* 9, 3144 (1997).

*208.* J. C. Yu, L. Z. Zhang, and J. G. Yu, *New J. Chem.* 26, 416 (2002).

*209.* J. J. Zhu, Z. H. Lu, S. T. Aruna, D. Aurbach, and A. Gedanken, *Chem. Mater.* 12, 2557 (2000).

*210.* Y. P. Sun, R. Guduru, F. Lin, and T. Whiteside, *Ind. Eng. Chem. Res.* 39, 4663 (2000).

*211.* G. Z. Wang, W. Chen, C. H. Liang, Y. W. Wang, G. W. Meng, and L. D. Zhang, *Inorg. Chem. Commun.* 4, 208 (2001).

*212.* P. Jeevanandam, Y. Koltypin, and A. Gedanken, *Mater. Sci. Eng. B* 90, 125 (2002).

*213.* B. Li, Y. Xie, J. X. Huang, Y. Liu, and Y. T. Qian, *Ultrasonics Sonochem.* 8, 331 (2001).

*214.* R. V. Kumar, O. Palchik, Y. Koltypin, Y. Diamant, and A. Gedanken, *Ultrasonics Sonochem.* 9, 65 (2002).

*215.* S. I. Nikitenko, P. Moisy, I. A. Tcharushnikova, P. Blanc, and C. Madic, *Ultrasonics Sonochem.* 7, 177 (2000).

*216.* S. Xu, H. Wang, J. J. Zhu, and H. Y. Chen, *J. Cryst. Growth* 234, 263 (2002).

*217.* T. Ding, H. Wang, S. Xu, and J. J. Zhu, *J. Cryst. Growth* 235, 517 (2002).

218. L. X. Yin, Y. Q. Wang, G. S. Pang, Y. Koltypin, and A. Gedanken, *J. Colloid Interface Sci.* 246, 78 (2002).

219. H. Wang, S. Xu, X. Zhao, J. Zhu, and X. Xin, *Mater. Sci. Eng. B* 96, 60 (2002).

220. T. Prozorov, G. Kataby, R. Prozorov, and A. Gedanken, *Thin Solid Films* 340, 189 (1999).

221. Y. Xie, X. W. Zheng, X. C. Jiang, J. Lu, and L. Y. Zhu, *Inorg. Chem.* 41, 387 (2002).

222. L. M. Qi and J. M. Ma, *Chem. J. Chin. Univ.* 20, 507 (1999).

223. P. Jeevanandam, Y. Koltypin, Y. Mastai, and A. Gedanken, *J. Mater. Chem.* 10, 2143 (2000).

224. H. G. Flynn, "Physical Acoustics: Principles and Methods" (W. P. Mason, Ed.), p. 165. Academic Press, New York, 1964.

225. R. Vijaya Kumar, Y. Diamant, and A. Gedanken, *Chem. Mater.* 12, 2301 (2000).

226. A. Henglein and C. Korman, *Int. J. Radiat. Biol.* 48, 251 (1985).

227. K. Okitsu, A. Yue, S. Tanabe, H. Matsumoto, and Y. Yobiko, *Langmuir* 17, 7717 (2001).

228. N. Yanagihara, Y. Tanaka, and H. Okamoto, *Chem. Lett.* 8, 796 (2001).

229. A. Henglein, *Chem. Mater.* 10, 444 (1998).

230. A. Henglein and M. Giersig, *J. Phys. Chem. B* 103, 9533 (1999).

231. B. G. Ershov and A. Henglein, *J. Phys. Chem. B* 102, 10663 (1998).

232. E. Gachard, H. Remita, J. Khatouri, B. Keita, L. Nadjo, and J. Belloni, *New J. Chem.* 22, 1257 (1998).

233. L. Francois, M. Mostafavi, J. Belloni, J. F. Delouis, J. Delaire, and P. Feneyrou, *J. Phys. Chem. B* 104, 6133 (2000).

234. A. Henglein, *J. Phys. Chem. B* 104, 1206 (2000).

235. S. S. Joshi, S. F. Patil, V. Iyer, and S. Mahumuni, *Nanostruct. Mater.* 10, 1135 (1998).

236. S. Kapoor, H. G. Salunke, B. M. Pande, S. K. Kulshreshtha, and J. P. Mittal, *Mater. Res. Bull.* 33, 1555 (1998).

237. S. Kapoor, H. G. Salunke, A. K. Tripathi, S. K. Kulshreshtha, and J. P. Mittal, *Mater. Res. Bull.* 35, 143 (2000).

238. S. Kapoor, S. Adhikari, C. Gopinathan, and J. P. Mittal, *Mater. Res. Bull.* 34, 1333 (1999).

239. M. Gutierrez and A. Henglein, *J. Phys. Chem.* 100, 7656 (1996).

240. R. Vijayalakshmi, S. Kapoor, and S. K. Kulshreshtha, *Solid State Sci.* 4, 489 (2002).

241. A. Henglein, *J. Phys. Chem. B* 104, 2201 (2000).

242. S. Kapoor and T. Mukherjee, *Mater. Res. Bull.* 36, 2543 (2001).

243. A. Henglein, *J. Phys. Chem.* 97, 5457 (1993).

244. A. J. Swallow, "Radiation Chemistry." Longman, London, 1973.

245. M. S. Matheson and L. M. Dorfman, "Pulse Radiolysis." MIT Press, Cambridge, MA, 1969.

246. E. Janata, A. Henglein, and B. G. Ershov, *J. Phys. Chem.* 98, 10888 (1994).

247. G. V. Buxton, *Coord. Chem. Rev.* 22, 195 (1977).

248. B. G. Ershov, E. Janata, M. Michaelis, and A. Henglein, *J. Phys. Chem.* 95, 8996 (1991).

249. E. Janata, A. Henglein, and B. Ershov, *J. Phys. Chem.* 100, 1989 (1996).

250. J. H. Raxendale, *Radia. Res. Suppl.* 4, 139 (1964).

251. M. Anbar, *Q. Rev.* 22, 573 (1968).

252. G. G. Jayson, J. P. Keene, D. Stirling, and A. J. Swallow, *Trans. Faraday Soc.* 65, 2453 (1969).

253. H. Cohen and D. Meyerstein, *J. Chem. Soc. Dalton Trans.* 2559 (1974).

254. A. Henglein and M. Giersig, *J. Phys. Chem.* 98, 6931 (1994).

255. T. Sosebee, M. Giersig, A. Holzwarth, and P. Mulvaney, *Ber. Bunsen-Ges. Phys. Chem.* 99, 40 (1995).

256. S. Kapoor, *Langmuir* 15, 4365 (1999).

257. S. Kapoor, D. Lawless, P. Kennepohl, D. Meisel, and N. Serpone, *Langmuir* 10, 3018 (1994).

258. B. G. Ershov and A. Henglein, *J. Phys. Chem. B* 102, 10667 (1998).

259. S. Kapoor and C. Gopinathan, *Radiat. Phys. Chem.* 53, 165 (1998).

260. B. G. Ershov, E. Janata, and A. Henglein, *Radiat. Phys. Chem.* 39, 123 (1992).

261. H. K. Wu, X. L. Xu, X. W. Ge, and Z. C. Zhang, *Radiat. Phys. Chem.* 50, 585 (1997).

262. M. Treguer, C. de Cointet, H. Remita, J. Khatouri, M. Mostafavi, J. Amblard, J. Belloni, and R. de Keyzer, *J. Phys. Chem. B* 102, 4310 (1998).

263. J. M. Thomas and W. J. Thomas, "Introduction to the Principles of Heterogeneous Catalysis," p. 241. Academic Press, London, New York, 1967.

264. G. Bond and D. Thompson, *Catal. Rev. Sci. Eng.* 41, 319 (1999).

265. T. K. Sau, A. Pal, and T. Pal, *J. Phys. Chem. B* 105, 9266 (2001).

266. S. Link and M. A. El-Sayed, *J. Phys. Chem. B* 103, 4212 (1999).

267. S. Galvagno and G. Parravano, *J. Catal.* 55, 178 (1978).

268. N. W. Cant and W. K. Hall, *J. Phys. Chem.* 75, 2914 (1971).

269. M. W. Robert and T. I. Stewart, "Chemisorption and Catalysis," p. 16. Institute of Petroleum, London, 1972.

270. D. Andreeva, V. Idakiev, T. Tabakova, and A. Andreev, *J. Catal.* 158, 354 (1996).

271. G. J. Hutchings, *Gold Bull.* 29, 123 (1996).

272. T. Aida, R. Higuchi, and H. Niiyama, *Chem. Lett.* 1990, 2247 (1990).

273. B. S. Uphade, T. Akita, T. Nakamura, and M. Haruta, *J. Catal.* 209, 331 (2002).

274. A. Fasi, I. Palinko, K. Hernadi, and I. Kiricsi, *Catal. Lett.* 81, 237 (2002).

275. T. Uematsu, L. Fan, T. Maruyama, N. Ichikuni, and S. Shimazu, *J. Mol. Catal. A* 182, 209 (2002).

276. M. Okumura, T. Akita, and M. Haruta, *Catal. Today* 74, 265 (2002).

277. P. Bera and M. S. Hegde, *Catal. Lett.* 79, 75 (2002).

278. E. Seker and E. Gulari, *Appl. Catal., A* 232, 203 (2002).

279. F. Porta, L. Prati, M. Rossi, S. Coluccia, and G. Martra, *Catal. Today* 61, 165 (2000).

280. J. E. Bailie, H. A. Abdullah, J. A. Anderson, C. H. Rochester, N. V. Richardson, N. Hodge, J. G. Zhang, A. Burrows, C. J. Kiely, and G. J. Hutchings, *Phys. Chem. Chem. Phys.* 3, 4113 (2001).

281. L. Pasquato, F. Rancan, P. Scrimin, F. Mancin, and C. Frigeri, *Chem. Commun.* 2000, 2253 (2000).

282. L. Yan, X. M. Zhang, T. Ren, H. P. Zhang, X. L. Wang, and J. S. Suo, *Chem. Commun.* 2002, 860 (2002).

283. F. Pinna, *Catal. Today* 41, 129 (1998).

284. M. Haruta, *Catal. Today* 36, 153 (1997).

285. C. H. Lin, S. H. Hsu, M. Y. Lee, and S. D. Lin, *J. Catal.* 209, 62 (2002).

286. H. Liu, A. I. Kozlov, A. P. Kozlova, T. Shido, K. Asakura, and Y. Iwasawa, *J. Catal.* 185, 252 (1999).

287. A. I. Kozlov, A. P. Kozlova, K. Asakura, Y. Matsui, T. Kogure, T. Shido, and Y. Iwasawa, *J. Catal.* 196, 56 (2000).

288. A. P. Kozlova, S. Sugiyama, A. I. Kozlov, K. Asakura, and Y. Iwasawa, *J. Catal.* 176, 426 (1998).

289. M. Moran-Pineda, S. Castillo, and R. Gomez, *React. Kinet. Catal. Lett.* 76, 375 (2002).

290. A. Taleb, C. Petit, and M. P. Pileni, *Chem. Mater.* 9, 950 (1997).

291. B. G. Ershov, E. Janata, and A. Henglein, *J. Phys. Chem.* 97, 339 (1993).

292. P. C. Lee and D. Meisel, *J. Phys. Chem.* 86, 3391 (1982).

293. T. Shibata, H. Tostmann, B. Bunker, A. Henglein, D. Meisel, S. Cheong, and M. Boyanov, *J. Synchrotron Radiat.* 8, 545 (2001).

294. V. I. Bukhtiyarov, A. I. Boronin, and V. I. Savchenko, *J. Catal.* 150, 262 (1994).

295. V. I. Bukhtiyarov, A. F. Carley, L. A. Dollard, and M. W. Roberts, *Surf. Sci.* 381, L605 (1997).

296. X. E. Verykios, F. P. Stein, and R. W. Coughlin, *J. Catal.* 66, 368 (1980).

297. J. Wu and P. Harriott, *J. Catal.* 39, 359 (1975).

298. R. Santen and C. Groot, *J. Catal.* 530 (1986).

*299.* Y. Yang and Y. Zhou, *J. Electroanal. Chem.* 397, 271 (1995).

*300.* R. B. Grant and R. M. Lambert, *J. Catal.* 92, 364 (1985).

*301.* V. I. Bukhtiyarov, A. I. Boronin, I. P. Prosvirin, and V. I. Savchenko, *J. Catal.* 150, 268 (1994).

*302.* N. Pradhan, A. Pal, and T. Pal, *Colloids Surf., A* 196, 247 (2002).

*303.* N. Jana, T. Sau, and T. Pal, *J. Phys. Chem. B* 103, 115 (1999).

*304.* Y. Shiraishi and N. Toshima, *Colloids Surf., A* 169, 59 (2000).

*305.* H. Suzuki and A. Ayame, *Nippon Kagaku Kaishi* 9, 930 (1992).

*306.* N. Hickey, P. Fornasiero, J. Kaspar, M. Graziani, G. Martra, S. Coluccia, S. Biella, L. Prati, and M. Rossi, *J. Catal.* 209, 271 (2002).

*307.* C. Mao and A. Vannice, *J. Catal.* 154, 230 (1995).

*308.* J. Li, W. Dai, Y. Dong, and J. Deng, *Mater. Lett.* 44, 233 (2000).

*309.* Q. Liu, Y. Cal, W. Dao, and J. Deng, *Catal. Lett.* 55, 87 (1998).

*310.* S. R. Seyedmonir, J. K. Plischke, M. A. Vannice, and H. W. Young, *J. Catal.* 123, 534 (1990).

*311.* A. Martinez-Arias, M. Fernandez-Garcia, A. Iglesias-Juez, J. A. Anderson, J. C. Conesa, and J. Soria, *Appl. Catal., B* 28, 29 (2000).

*312.* Z. J. Li and M. Flytzani-Stephanopoulos, *J. Catal.* 182, 313 (1999).

*313.* T. Miyadera, *Appl. Catal., B* 2 (2-3): 199-205 Jun 15, 1993

*314.* K. Shimizu, A. Satsuma, and T. Hattori, *Appl. Catal., B* 25, 239 (2000).

*315.* A. Abe, N. Aoyama, S. Sumiya, N. Kakuta, and K. Yoshida, *Catal. Lett.* 51, 5 (1998).

*316.* T. E. Hoost, R. J. Kudla, K. M. Collins, and M. S. Chattha, *Appl. Catal., B* 13, 59 (1997).

*317.* E. M. Cordi and J. L. Falconer, *Appl. Catal., B* 151, 179 (1997).

*318.* K. A. Bethke and H. H. Kung, *J. Catal.* 172, 93 (1997).

*319.* N. Aoyama, K. Yoshida, A. Abe, and T. Miyadera, *Catal. Lett.* 43, 249 (1997).

*320.* S. Cheng and A. Clearfield, *J. Catal.* 94, 455 (1985).

*321.* B. S. Bal'zhinimaev, S. N. Goncharova, and E. A. Paukshtis, *Appl. Catal., B* 126, 67 (1995).

*322.* I. H. Son, M. C. Kim, H. L. Koh, and K. L. Kim, *Catal. Lett.* 75, 191 (2001).

*323.* W. D. Moross, *Catal. Rev. Sci. Eng.* 591 (1983).

*324.* C. Yokoyama and M. Misono, *Catal. Lett.* 29, 1 (1994).

*325.* A. Henglein, B. G. Ershov, and M. Malow, *J. Phys. Chem.* 99, 14129 (1995).

*326.* B. G. Ershov, *Russ. Chem. Bull. Int. Ed.* 50, 626 (2001).

*327.* A. B. R. Mayer, J. E. Mark, and S. H. Hausner, *Angew. Makromol. Chem.* 259, 45 (1998).

*328.* T. S. Ahmadi, Z. L. Wang, T. C. Green, A. Henglein, and M. A. El-Sayed, *Science* 272, 1924 (1996).

*329.* Y. Shiraishi, M. Nakayama, E. Takagi, T. Tominaga, and N. Toshima, *Inorg. Chim. Acta* 300, 964.

*330.* M. Ikeda, S. Takeshima, T. Tago, M. Kishida, and K. Wakabayashi, *Catal. Lett.* 58, 195 (1999).

*331.* F. Garin, S. Aeiyach, P. Legare, and G. Maire, *J. Catal.* 77, 323 (1982).

*332.* Z. L. Wang, T. S. Ahmad, and M. A. El-Sayed, *Surf. Sci.* 380, 302 (1997).

*333.* I. Balint, A. Miyazaki, and K. Aika, *Appl. Catal., B* 37, 217 (2002).

*334.* Y. Takasy, Y. Fujii, K. Yasuda, Y. Iwanaga, and Y. Matsuda, *Electrochim. Acta* 34, 453 (1989).

*335.* R. Kramer and H. Zuegg, *J. Catal.* 80, 446 (1983).

*336.* R. Kramer and H. Zuegg, *J. Catal.* 85, 530 (1984).

*337.* Q. H. Xia, K. Hidajat, and S. Kawi, *Catal. Today* 68, 255 (2001).

*338.* F. Delbecq and P. Sautet, *J. Catal.* 152, 217 (1995).

*339.* S. J. Tauster, S. C. Fung, and R. L. Garten, *J. Am. Chem. Soc.* 100, 170 (1978).

*340.* M. A. Vannice and C. Sudhakar, *J. Phys. Chem.* 88, 2429 (1984).

*341.* M. A. Vannice, *J. Mol. Catal.* 59, 165 (1990).

*342.* B. Sen and M. A. Vannice, *J. Catal.* 113, 52 (1988).

*343.* K. Otto, L. P. Haack, and J. E. Devries, *Appl. Catal., B* 1, 1 (1992).

*344.* K. Kunimori, T. Okouchi, and T. Uchijima, *Chem. Lett.* 12, 1513 (1980).

*345.* R. Y. Tang, R. A. Wu, and L. W. Lin, *Appl. Catal.* 10, 163 (1984).

*346.* P. Claus, H. Berndt, C. Mohr, J. Radnik, E. J. Shin, and M. A. Keane, *J. Catal.* 192, 88 (2000).

*347.* K. Ebitani, J. Konishi, and H. Hattori, *J. Catal.* 130, 257 (1991).

*348.* S. E. Golunski, H. A. Hatcher, R. R. Rajaram, and T. J. Truex, *Appl. Catal., B* 5, 367 (1995).

*349.* F. G. Gault, "Advances in Catalysis and Related Subjects," Vol. 30, p. 1. Academic Press, New York, London, 1981.

*350.* M. Englisch, A. Jentys, and J. A. Lercher, *J. Catal.* 166, 25 (1997).

*351.* M. Zhao and R. M. Crooks, *Angew. Chem. Int. Ed.* 38, 364 (1999).

*352.* C. B. Hwang, Y. S. Fu, Y. L. Lu, S. W. Jang, P. T. Chou, C. R.C. Wang, and S. J. Yu, *J. Catal.* 195, 336 (2000).

*353.* R. S. Underhill and G. Liu, *Chem. Mater.* 12, 3633 (2000).

*354.* Y. Berkovich and N. Garti, *Colloids Surf., A* 128, 91 (1997).

*355.* J. Liu, J. Alvarez, W. Ong, E. Roman, and A. Kaifer, *Langmuir* 17, 6762 (2001).

*356.* A. Biffis, M. Zecca, and M. Basato, *Eur. J. Inorg. Chem.* 2001, 1131 (2001).

*357.* C. Rocaboy and J. A. Gladysz, *Org. Lett.* 4, 1993 (2002).

*358.* A. B. R. Mayer, J. E. Mark, and S. H. Hausner, *J. Appl. Polym. Sci.* 10, 1209 (1998).

*359.* T. Teranishi, K. Nakata, M. Iwamoto, M. Miyaka, and N. Toshima, *React. Funct. Polym.* 37, 111 (1998).

*360.* C. Chen and M. Akashi, *Langmuir* 13, 6465 (1997).

*361.* P. J. Collier, J. A. Iggo, and R. Whyman, *J. Mol. Catal., A* 146, 149 (1999).

*362.* N. Jana, Z. L. Wang, and T. Pal, *Langmuir* 16, 2457 (2000).

*363.* S. Pathak, M. T. Greci, R. C. Kwong, K. Mercado, G. K. S. Prakash, G. A. Olah, and M. E. Thompson, *Chem. Mater.* 12, 1985 (2000).

*364.* J. P. Genet and M. Savignac, *J. Organomet. Chem.* 576, 305 (1999).

*365.* V. Checkik and R. M. Crooks, *J. Am. Chem. Soc.* 122, 1243 (2000).

*366.* N. A. Dhas, H. Clhen, and A. Gedanken, *J. Phys. Chem. B* 101, 6834 (1997).

*367.* F. Li, B. Zhang, S. Dong, and E. Wang, *Electrochem. Acta* 42, 2563 (1997).

*368.* B. Veisz, Z. Kiraly, L. Toth, and B. Pecz, *Chem. Mater.* 14, 2882 (2002).

*369.* A. Mastalir, Z. Kiraly, G. Szollosi, and M. Bartok, *J. Catal.* 194, 146 (2000).

*370.* A. Szucs, Z. Kiraly, F. Berger, and I. Dekany, *Colloids Surf., A* 139, 109 (1998).

*371.* Z. Kiraly, I. Dekany, A. Mastalir, and M. Bartok, *J. Catal.* 161, 401 (1996).

*372.* V. R. Palker, *Eur. Phys. J. D* 16, 253 (2001).

*373.* E. Sulman, V. Matveeva, A. Usanov, Y. Kosivtsov, G. Demidenko, L. Bronstein, D. Chernyshov, and P. Valetsky, *J. Mol. Catal., A* 146, 265 (1999).

*374.* S. Schauermann, J. Hoffmann, V. Johanek, J. Hartmann, J. Libuda, and H. Freund, *Angew. Chem. Int. Ed.* 41, 2532 (2002).

*375.* S. Zheng, L. Gao, Q. Zhang, and J. Sun, *J. Solid State Chem.* 162, 138 (2001).

*376.* Y. Matsumura, M. Okumura, Y. Usami, K. Kagawa, H. Yamashita, M. Anpo, and M. Haruta, *Catal. Lett.* 44, 189 (1997).

*377.* J. R. Mellor, N. J. Coville, S. H. Durbach, and R. G. Copperthwaite, *Appl. Catal., A* 171, 273 (1998).

*378.* J. R. Mellor, N. J. Coville, A. C. Sofianos, and R. G. Copperthwaite, *Appl. Catal., A* 164, 185 (1997).

*379.* J. T. Kummer, *Prog. Energy Combust. Sci.* 6, 177 (1980).

*380.* L. Gang, B. G. Anderson, J. van Grondelle, and R. A. van Santen, *Catal. Today* 61, 179 (2000).

*381.* S. C. Kim, *J. Hazard. Mater.* 91, 285 (2002).

*382.* G. Vitulli, M. bernini, S. Bertozzi, E. Pitzalis, P. Salvadori, S. Coluccia, and G. Martra, *Chem. Mater.* 14, 1183 (2002).

*383.* E. A. Heintz and W. E. Parker, *Carbon* 4, 473 (1996).

*384.* C. Y. Shiau and Y. R. Lee, *J. Chin. Inst. Chem. Eng.* 30, 475 (1999).

385. J. N. Keuler, L. Lorenzen, and S. Miachon, *Appl. Catal., A* 218, 171 (2001).
386. A. J. Marchi, J. L. G. Fierro, J. Santamaria, and A. Monzon, *Appl. Catal., A* 142, 375 (1996).
387. P. W. Park and L. S. Ledford, *Appl. Catal., B* 15, 221 (1998).
388. J. Yoshihara and C. T. Campbell, *J. Catal.* 161, 776 (1996).
389. M. Schildenberger, Y. C. Bonetti, J. Gobrecht, and R. Prins, *Top. Catal.* 13, 109 (2000).
390. M. V. Twigg and M. S. Spencer, *Appl. Catal., A* 212, 161 (2001).
391. Y. Ma, Q. Sun, D. Wu, W. H. Fan, Y. L. Zhang, and J. F. Deng, *Appl. Catal., A* 171, 45 (1998).
392. C. Y. Shiau and J. C. Tsai, *J. Chem. Technol. Biotechnol.* 73, 414 (1998).
393. J. B. Wang, W. H. Shih, and T. J. Huang, *Appl. Catal., A* 203, 191 (2000).
394. T. S. Askgaard, J. K. Norskov, C. V. Ovesen, and P. Stoltze, *J. Catal.* 156, 229 (1995).
395. K. K. Bando, K. Sayama, H. Kusama, K. Okabe, and H. Arakawa, *Appl. Catal., A* 165, 391 (1997).
396. K. Sekizawa, S. Yano, K. Eguchi, and H. Arai, *Appl. Catal., A* 169, 291 (1998).
397. C. Y. Shiau and Y. R. Lee, *Appl. Catal., A* 220, 173 (2001).
398. G. X. Qi, X. M. Zheng, J. H. Fei, and Z. Y. Hou, *Indian J. Chem. Sect. A* 40, 588 (2001).
399. J. G. Wu, M. Saito, and H. Mabuse, *Catal. Lett.* 68, 55 (2000).
400. M. Fernandez-Garcia, E. G. Rebollo, A. G. Ruiz, J. C. Conesa, and J. Soria, *J. Catal.* 172, 146 (1997).
401. X. B. Ma, Z. H. Li, B. W. Wang, and G. H. Xu, *React. Kinet. Catal. Lett.* 76, 179 (2002).
402. P. A. Vuissoz, T. Yonezawa, D. Yang, J. Kiwi, and J. J. van der Klink, *Chem. Phys. Lett.* 264, 366 (1997).
403. A. Eichler, J. Hafner, J. Furthmuller, and G. Kresse, *Surf. Sci.* 346, 300 (1996).
404. G. A. Del Angel, B. Coq, G. Ferrat, F. Figueras, and S. Fuentes, *Surf. Sci.* 156, 351 (1985).
405. M. Frank, S. Andersson, J. Libuda, S. Stempel, A. Sandell, B. Brena, A. Giertz, P. A. Bruhwiler, M. Baumer, N. Martensson, and H. J. Freund, *Chem. Phys. Lett.* 279, 92 (1997).
406. V. Nehasil, I. Stara, and V. Matolin, *Surf. Struct.* 352–354, 305 (1996).
407. B. Coq and F. Figueras, *J. Mol. Catal.* 40, 93 (1987).
408. F. Garin, P. Girard, F. Weisang, and G. Maire, *J. Catal.* 70, 215 (1981).
409. T. Beutel, O. S. Alekseev, Y. A. Ryndin, V. A. Likholobov, and H. Knozinger, *J. Catal.* 169, 132 (1997).
410. H. Y. Luo, H. W. Zhou, L. W. Lin, D. B. Liang, C. Li, D. Fu, and Q. Xin, *J. Catal.* 145, 232 (1994).
411. T. P. Wilson, P. H. Kasai, and P. C. Ellgen, *J. Catal.* 69, 193 (1981).
412. P. Z. Lin, H. Y. Luo, S. B. Xie, H. W. Zhou, C. H. Xu, S. Y. Huang, L. W. Lin, D. B. Liang, P. L. Yin, and Q. Xin, *J. Mol. Catal., A* 122, 115 (1997).
413. F. W. Williams, A. Palermo, M. S. Tikhov, and R. M. Lambert, *J. Phys. Chem. B* 104, 11883 (2000).
414. M. E. Halttuen, M. K. Niemela, A. O. I. Krause, T. Vaara, and A. I. Vuori, *Appl. Catal., A* 205, 37 (2001).
415. N. K. Raman, T. L. Ward, C. J. Brinker, R. Sehgal, D. M. Smith, Z. Duan, M. Hampden-Smith, J. K. Bailey, and T. J. Headley, *Appl. Catal., A* 96, 65 (1993).
416. C. J. H. Jacoben, S. Dahl, P. L. Hansen, E. Tornqvist, L. Jensen, H. Topsoe, D. V. Prip, P. B. Moenshaug, and I. Chorkendorff, *J. Mol. Catal., A* 163, 19 (2000).
417. G. Rambeau and H. Amariglio, *J. Catal.* 72, 1 (1981).
418. S. Dahl, A. Logadottir, R. C. Egeberg, J. H. Larsen, and I. Chorkendorff, *Phys. Rev. Lett.* 83, 1814 (1999).
419. S. Dahl, E. Tornqvist, and I. Chorkendorff, *J. Catal.* 192, 381 (2000).
420. R. van Hardeveld and A. van Montfoort, *Surf. Sci.* 4, 396 (1966).

421. P. Kulson and L. Cerveny, *Appl. Catal., A* 128, 13 (1995).
422. S. Galvagno, G. Capannelli, G. Neri, A. Donato, and R. Pietropaolo, *J. Mol. Catal.* 64, 237 (1991).
423. S. I. Niwa, F. Mizukami, M. Kuno, K. Takeshita, H. Nakamura, T. Tsuchiya, K. Shimizu, and J. Imamura, *J. Mol. Catal.* 34, 247 (1986).
424. M. C. Schoenmaker-Stolk, J. W. Verwijs, J. A. Don, and J. J. F. Scholten, *Appl. Catal.* 29, 73 (1987).
425. J. R. Jennings, "Catalytic Ammonia Synthesis." Plenum, New York, 1991.
426. S. Murata and K. Aika, *J. Catal.* 136, 110 (1992).
427. A. Waghray, R. Oukaci, and D. G. Blacjmond, *Stud. Surf. Sci.* 75, 2480 (1993).
428. D. G. Blackmond, R. Oukaci, B. Blanc, and P. Gallezot, *J. Catal.* 131, 131 (1991).
429. P. Kulson, L. Cerveny, and J. Had, *Catal. Lett.* 23, 299 (1994).
430. S. Murata and K. Aika, *Appl. Catal., A* 82, 1 (1992).
431. K. I. Aika, T. Takano, and S. Murata, *J. Catal.* 136, 126 (1992).
432. Z. Kowalczyk, S. Jodzis, W. Rarog, J. Zielinski, and J. Pielaszek, *Appl. Catal., A* 173, 153 (1998).
433. K. Aika, M. Kumasaka, T. Oma, O. Kato, H. Matsuda, N. Watanabe, K. Yamazaki, A. Ozaki, and T. Onishi, *Appl. Catal.*, 28, 57 (1986).
434. P. Moggi, G. Albanesi, G. Predieri, and G. Spoto, *Appl. Catal., A* 123, 145 (1995).
435. H. Baris, M. Glinski, J. Kijenski, A. Wokaun, and A. Baiker, *Appl. Catal.* 28, 295 (1986).
436. I. Rossetti, N. Pernicone, and L. Forni, *Appl. Catal., A* 208, 271 (2001).
437. J. J. Mortensen, B. Hammer, and J. K. Norskov, *Phys. Rev. Lett.* 80, 4333 (1998).
438. A. Miyazaki, I. Balint, K. Aika, and Y. Nakano, *J. Catal.* 204, 364 (2001).
439. Y. S. Cho, G. S. Choi, S. Y. Hong, and D. Kim, *J. Cryst. Growth* 243, 224 (2002).
440. C. H. Liang, G. W. Meng, G. Z. Wang, L. D. Zhang, and S. Y. Zhang, *Chem. Mater.* 13, 2150 (2001).
441. K. S. Nahm, Y. H. Mo, M. Shajahan, and S. H. Lee, *Korean J. Chem. Eng.* 19, 510 (2002).
442. C. H. Liang, G. W. Meng, W. Chen, Y. W. Wang, and L. D. Zhang, *J. Cryst. Growth* 220, 296 (2000).
443. B. Q. Xu, J. M. Wei, H. Y. Wang, K. Q. Sun, and Q. M. Zhu, *Catal. Today* 68, 217 (2001).
444. C. Menini, C. Park, R. Brydson, and M. A. Keane, "Electron Microscopy and Analysis 1999," Institute of Physics Conference Series, 1999, Vol. 161, p. 553.
445. S. Lefondeur, S. Monteverdi, S. Molina, M. M. Bettahar, Y. Fort, E. A. Zhilinskaya, A. Aboukais, and M. Lelaurain, *J. Mater. Sci.* 36, 2633 (2001).
446. R. Monaci, A. Musinu, G. Piccaluga, and G. Pinna, *Nanophase Mater. Mater. Sci. Forum* 195, 1 (1995).
447. T. E. Jones and C. J. Baddeley, *Surf. Sci.* 513, 453 (2002).
448. H. Dai, A. G. Rinzler, P. Nikolavev, A. Thesi, D. T. Colbert, and R. E. Smalley, *Chem. Phys. Lett.* 260, 471 (1996).
449. A. Oberlin, M. Endo, and T. Koyama, *J. Cryst. Growth* 32, 335 (1976).
450. J. Nakamura, H. Hirano, M. Xie, I. Mastsuo, T. Yamada, and K. Tanaka, *Surf. Sci.* 222, L809 (1989).
451. V. V. Kriventsov, D. I. Kochubey, V. V. Goidin, V. V. Molchanov, and V. V. Chesnokov, *Top. Catal.* 18, 91 (2002).
452. N. M. Rodriguez, *J. Mater. Res.* 8, 3233 (1993).
453. J. F. Colomer, C. Stephan, S. Lefrant, G. Van Tendeloo, I. Willems, Z. Konya, A. Fonseca, C. Laurent, and J. B. Nagy, *Chem. Phys. Lett.* 317, 83 (2000).
454. G. G. Tibbetts, *J. Cryst. Growth* 66, 632 (1984).
455. Y. Saito, K. Kawabata, and M. Okuda, *J. Phys. Chem.* 99, 16076 (1995).

*456.* J. Libera and Y. Gogotsi, *Carbon* 39, 1307 (2001).

*457.* U. Heiz, F. Vanolli, A. Sanchez, and W. D. Schneider, *J. Am. Chem. Soc.* 120, 9668 (1998).

*458.* S. C. Davis and K. J. Klabunde, *Chem. Rev.* 82, 153 (1982).

*459.* S. J. Tauster, S. C. Fung, and R. L. Garten, *J. Am. Chem. Soc.* 100, 170 (1978).

*460.* M. Arai, T. Ishikawa, T. Nakayaman, and Y. Nishiyama, *J. Colloid Interface Sci.* 97, 255 (1984).

*461.* K. Kunimori, Y. Ikenda, M. Soma, and T. Uchijima, *J. Catal.* 79, 185 (1983).

*462.* R. L. Vander Wal, T. M. Ticich, and V. E. Curtis, *Carbon* 39, 2277 (2001).

*463.* M. A. Ermakova, D. Y. Ermakov, L. M. Plyasova, and G. G. Kuvshinov, *Catal. Lett.* 62, 93 (1999).

*464.* D. Mazza, A. Delmastro, and S. Ronchetti, *J. Eur. Ceramic Soc.* 20, 699 (2000).

*465.* Q. Liang, L. Z. Gao, Q. Li, S. H. Tang, B. C. Liu, and Z. L. Yu, *Carbon* 39, 897 (2001).

*466.* R. T. K. Baker, M. A. Barber, P. S. Harris, F. S. Feates, and R. J. Waite, 26, 51 (1972).

*467.* Z. P. Huang, D. Z. Wang, J. G. Wen, M. Sennett, H. Gibson, and Z. F. Ren, *Appl. Phys. A* 74, 387 (2002).

*468.* R. L. Vander Wal and L. J. Hall, *Chem. Phys. Lett.* 349, 178 (2001).

*469.* J. Gavillet, A. Loiseau, F. Ducastelle, S. Thair, P. Bernier, O. Stephan, J. Thibault, and J. C. Charlier, *Carbon* 40, 1649 (2002).

*470.* A. Fonseca, K. Hernadi, J. B. Nagy, D. Bernaerts, and A. A. Lucas, *J. Mol. Catal., A* 107, 159 (1996).

*471.* J. M. Mao, L. F. Sun, L. X. Qian, Z. W. Pan, B. H. Chang, W. Y. Zhou, G. Wang, and S. S. Xie, *Appl. Phys. Lett.* 72, 3297 (1998).

*472.* B. C. Liu, L. Z. Gao, Q. Liang, S. H. Tang, M. Z. Qu, and Z. L. Yu, *Catal. Lett.* 71, 225 (2001).

*473.* M. Nath, B. C. Satishkumar, A. Govindaraj, C. P. Vinod, and C. N. R. Rao, *Chem. Phys. Lett.* 322, 333 (2000).

*474.* C. H. Kiang, W. A. Goddard, R. Beyers, and D. S. Bethune, *Carbon* 33, 903 (1995).

*475.* J. P. Pinheiro, M. C. Schouler, and E. Dooryhee, *Solid State Commun.* 123, 161 (2002).

*476.* N. Nagaraju, A. Fonseca, Z. Konya, and J. B. Nagy, *J. Mol. Catal., A* 181, 57 (2002).

*477.* Z. J. Liu, Z. Y. Yuan, W. Z. Zhou, L. M. Peng, and Z. D. Xu, *Phys. Chem. Chem. Phys.* 3, 2518 (2001).

*478.* N. S. Kim, Y. T. Lee, J. H. Park, H. Ryu, H. J. Lee, S. Y. Choi, and J. B. Choo, *J. Phys. Chem. B* 106, 9286 (2002).

*479.* S. W. Kim, S. U. Son, S. S. Lee, T. Hyeon, and Y. K. Chung, *Chem. Commun.* 2001, 2212 (2001).

*480.* A. M. Thayer, *Chem. Eng. News* March 13, 20 (2000).

*481.* J. H. Lee, D. K. Lee, and S. K. Ihm, *J. Catal.* 113, 544 (1988).

*482.* E. Kikuchi, R. Sorita, H. Takahashi, and T. Matsuda, *Appl. Catal. A* 186, 121 (1999).

*483.* L. Fu and C. H. Bartholomew, *J. Catal.* 92, 376 (1985).

*484.* A. R. Belambe, R. Oukaci, and J. G. Goodwin, Jr., *J. Catal.* 166, 8 (1997).

*485.* B. G. Johnson, C. H. Bartholomew, and D. W. Goodman, *J. Catal.* 128, 231 (1991).

*486.* S. W. Ho, M. Hovalla, and D. M. Hercules, *J. Phys. Chem.* 94, 6396 (1990).

*487.* R. C. Reuel and C. H. Bartholomew, *J. Catal.* 85, 78 (1984).

*488.* N. Tsubaki, S. L. Sun, and K. Fujimoto, *J. Catal.* 199, 236 (2001).

*489.* R. C. Reuel and C. H. Bartholomew, *J. Catal.* 85, 63 (1984).

*490.* E. Ruckenstein and H. Y. Wang, *Appl. Catal., A* 204, 257 (2000).

*491.* M. K. Niemela and A. O. I. Krause, *Catal. Lett.* 34, 75 (1995).

*492.* D. H. Yin, W. H. Li, W. S. Yang, H. W. Xiang, Y. H. Sun, B. Zhong, and S. Y. Peng, *Microporous Mesoporous Mater.* 47, 15 (2001).

*493.* Y. Zhang, Y. Yoneyama, and N. Tsubaki, *Chem. Commun.* 2002, 1216 (2002).

*494.* X. Q. Qiu, N. Tsubaki, S. L. Sun, and K. Fujimoto, *Fuel* 81, 1625 (2002).

*495.* D. Das, G. Ravichandran, and D. K. Chakrabarty, *Catal. Today* 36, 285 (1997).

*496.* L. Leite, V. Stonkus, L. Ilieva, L. Plyasova, T. Tabakova, D. Andreeva, and E. Lukevics, *Catal. Commun.* 3, 341 (2002).

*497.* T. Iwasaki, M. Reinikainen, Y. Onodera, H. Hayashi, T. Ebina, T. Nagase, K. Torii, K. Kataja, and A. Chatterjee, *Appl. Surf. Sci.* 132, 845 (1998).

*498.* A. Y. Khodakov, A. Griboval-Constant, R. Bechara, and V. L. Zholobenko, *J. Catal.* 206, 230 (2002).

*499.* X. Q. Qiu, N. Tsubaki, and K. Fujimoto, *J. Chem. Eng. Jpn.* 34, 1366 (2001).

*500.* Y. Q. Zhang, H. W. Xiang, B. Zhong, and Q. Wang, *Petroleum Sci. Technol.* 17, 981 (1999).

*501.* R. L. Vander Wal, *Combust. Flame* 130, 37 (2002).

*502.* B. C. Liu, S. H. Tang, Z. L. Yu, B. L. Zhang, T. Chen, and S. Y. Zhang, *Chem. Phys. Lett.* 357, 297 (2002).

*503.* R. L. V. Wal, G. M. Berger, and L. J. Hall, *J. Phys. Chem. B* 106, 3564 (2002).

*504.* A. Kukovecz, Z. Konya, N. Nagaraju, I. Willems, A. Tamasi, A. Fonseca, J. B. Nagy, and I. Kiricsi, *Phys. Chem. Chem. Phys.* 2, 3071 (2000).

*505.* Z. F. Ren, Z. P. Huang, J. W. Xu, J. H. Wang, P. Bush, M. P. Siegal, and P. N. Provencio, *Science* 282, 1105 (1998).

*506.* P. Mauron, C. Emmenegger, A. Zuttel, C. Nutzenadel, P. Sudan, and L. Schlapbach, *Carbon* 40, 1339 (2002).

*507.* J. B. Park, G. S. Choi, Y. S. Cho, S. Y. Hong, D. Kim, S. Y. Choi, J. H. Lee, and K. I. Cho, *J. Cryst. Growth* 244, 211 (2002).

*508.* G. L. Che, B. B. Lakshmi, C. R. Martin, and E. R. Fisher, *Langmuir* 15, 750 (1999).

*509.* H. W. Seo, S. Y. Bae, J. Park, H. N. Yang, K. S. Park, and S. Kim, *J. Chem. Phys.* 116, 9492 (2002).

*510.* G. W. Meng, L. D. Zhang, Y. Qin, F. Phillipp, S. R. Qiao, H. M. Guo, and S. Y. Zhang, *Chin. Phys. Lett.* 15, 689 (1998).

*511.* A. V. Cugini, D. Krastman, D. V. Martello, E. F. Frommell, A. W. Wells, and G. D. Holder, *Energy Fuels* 8, 83 (1994).

*512.* J. Schwar, P. W. Jahn, L. Wiedmann, and A. Benninghoven, *J. Vac. Sci. Technol., A* 9, 238 (1991).

*513.* H. J. Jung, P. L. Walker, and M. A. Vannice, Jr., *J. Catal.* 75, 416 (1982).

*514.* J. M. Martin-Martinez and M. A. Vannice, *Ind. Eng. Chem. Res.* 30, 2263 (1991).

*515.* F. Derbyshire and T. Hager, *Fuel* 73, 1087 (1994).

*516.* V. K. Jones, L. R. Neubauer, and C. H. Bartholomew, *J. Phys. Chem.* 90, 4832 (1986).

*517.* C. S. Kellner and A. T. Bell, *J. Catal.* 75, 416 (1982).

*518.* A. Brenner and D. A. Hucul, *Inorg. Chem.* 18, 2836 (1979).

*519.* C. Moreno-Castilla, M. A. Salasperegrin, and F. J. Lopezgarzon, *Fuel* 74, 830 (1995).

*520.* A. V. Cugini, D. Krastman, R. G. Lett, and V. D. Balsone, *Catal. Today* 19, 395 (1994).

*521.* D. P. Hoffmann, M. Houalla, A. Proctor, and D. M. Hercules, *Appl. Spectrosc.* 46, 489 (1992).

*522.* G. Ravichandran, D. Das, and D. K. Chakrabarty, *J. Chem. Soc., Faraday Trans.* 90, 1993 (1994).

*523.* L. A. Boot, A. J. Vandillen, J. W. Geus, and F. R. Vanburen, *J. Catal.* 163, 186 (1996).

*524.* P. Putanov, E. Kis, G. Boskovic, and K. Lazar, *Appl. Catal.* 73, 17 (1991).

*525.* Z. Gao, B. Zhang, and J. Cui, *Appl. Catal.* 2, 331 (1991).

*526.* M. L. Cubeiro, F. Gonzalez-Jimenez, M. R. Goldwasser, M. J. Perez-Zurita, E. Pietri, and L. Garcia, *Hyperfine Interact.* 134, 13 (2001).

*527.* E. Guglielminotti, *J. Phys. Chem.* 98, 4884 (1994).

*528.* Y. H. Ge, Y. M. Zhou, J. S. Qian, and Y. R. Ding, *J. Rare Earths* 15, 11 (1997).

*529.* W. H. Zhang, J. J. Peng, Y. S. Ma, L. Q. Hao, and S. X. Zhuang, *Acta Phys. Chim. Sinica* 18, 901 (2002).

530. S. X. Zhuang, M. Yamazaki, K. Omata, Y. Takahashi, and M. Yamada, *Appl. Catal., B* 31, 133 (2001).
531. H. Kim, K. H. Lee, and J. S. Lee, *Res. Chem. Intermed.* 26, 427 (2000).
532. W. Skupinski and M. Malesa, *Appl. Catal., A* 236, 223 (2002).
533. D. E. Resasco, W. E. Alvarez, F. Pompeo, L. Balzano, J. E. Herrera, B. Kitiyanan, and A. Borgna, *J. Nanoparticle Res.* 4, 131 (2002).
534. S. Yamada, W. H. Qian, A. Ishihara, G. D. Wang, L. Li, and T. Kabe, *Sekiyu Gakkaishi J. Jpn. Petroleum Inst.* 44, 217 (2001).
535. K. Tawara, J. Imai, H. Iwanami, *Sekiyu Gakkaishi J. Jpn. Petroleum Inst.* 43, 105 (2000).
536. M. Nagai, J. Takada, and S. Omi, *J. Phys. Chem.* 103, 10180 (1999).
537. S. Yoshinaka and K. Segawa, *Catal. Today* 45, 293 (1998).
538. J. Sarlis and D. Berk, *Chem. Eng. Commun.* 140, 73 (1996).
539. K. Vassilev, S. Ivanov, and S. Tanielyan, *Oxidation Commun.* 22I, 387 (1999).
540. J. O. Oludipe, S. E. Iyuke, and B. O. Aderemi, *J. Chem. Technol. Biotechnol.* 63, 147 (1995).
541. O. Brummer, A. Ruckert, and S. Blechert, *Chem.—Eur. J.* 3, 441 (1997).
542. C. Ovalles, E. Filgueiras, A. Morales, I. Rojas, J. C. de Jesus, and I. Berrios, *Energy Fuels* 12, 379 (1998).
543. S. W. Xia, Q. Zhao, and P. Zhang, *Chem. J. Chin. Univ.* 17, 1297 (1996).
544. S. J. Liaw, A. Raje, K. V. R. Chary, and B. H. Davis, *Appl. Catal., A* 123, 251 (1995).
545. R. A. Akhmedyanova, I. Y. Litvintsev, A. Y. Monayenkov, and V. N. Sapunov, *Petroleum Chem.* 34, 413 (1994).
546. N. F. D. Erbruggen, L. M. J. Vonhippel, G. Mestl, B. Lengeler, and H. Knozinger, *Langmuir* 10, 3073 (1994).
547. H. Permana, S. Lee, and K. Y. S. Ng, *Catal. Lett.* 24, 363 (1994).
548. S. X. Zhang, H. Magara, M. Yamazaki, Y. Takahashi, and M. Yamada, *Appl. Catal., B* 24, 89 (2000).
549. C. L. Roe and K. H. Schulz, *Stud. Surf. Sci. Catal.* 127, 121 (1999).
550. N. Koizumi, M. Yamazaki, M. Iijima, and M. Yamada, *Appl. Surf. Sci.* 121, 429 (1997).
551. S. Kasahara, Y. Udagawa, and M. Yamada, *Appl. Catal., B* 12, 225 (1997).
552. T. S. Wiltowski, K. Sangster, and W. O'Brien, *J. Chem. Technol. Biotechnol.* 67, 204 (1996).
553. M. C. Abello, M. F. Gomez, and L. E. Cadus, *Catal. Lett.* 53, 185 (1998).
554. C. Pophal, F. Kameda, K. Hoshino, S. Yoshinaka, and K. Segawa, *Catal. Today* 39, 21 (1997).
555. K. Hiroshima, T. Mochizuki, T. Honma, T. Shimizu, and M. Yamada, *Appl. Surf. Sci.* 121, 433 (1997).
556. M. Lewandowski and Z. Sarbak, *Cryst. Res. Technol.* 33, 315 (1998).
557. V. I. Mikhailov, T. V. Dovganyuk, and L. I. Zadko, *Kinet. Catal.* 34, 990 (1993).
558. N. I. Rybakova, O. D. Sterligov, and S. Vadelson, *Petroleum Chem.* 34, 201 (1994).
559. A. B. Hungria, A. Iglesias-Juez, A. Martinez-Arias, M. Fernandez-Garcia, J. A. Anderson, J. C. Conesa, and J. Soria, *J. Catal.* 206, 281 (2002).
560. A. Rath, E. Aceves, J. Mitome, J. Liu, U. S. Ozkan, and S. G. Shore, *J. Mol. Catal., A* 165, 103 (2001).
561. L. M. Bronstein, D. M. Chernyshov, I. O. Volkov, M. G. Ezernitskaya, P. M. Valetsky, V. G. Matveeva, and E. M. Sulman, *J. Catal.* 196, 302 (2000).
562. Y. Mizukoshi, T. Fujimoto, Y. Nagata, R. Oshima, and Y. Maeda, *J. Phys. Chem. B* 104, 6028 (2000).
563. P. Waszcauk, T. M. Barnard, C. Rice, R. I. Masel, and A. Wieckowski, *Electrochem. Commun.* 4, 599 (2002).
564. B. F. J. Johnson, S. A. Raynor, D. B. Brown, D. S. Shephard, T. Mashmeyer, J. M. Thomas, S. Hermans, R. Raja, and G. Sankar, *J. Mol. Catal., A* 182–183, 89 (2002).
565. R. Raja, G. Sankar, S. Hermans, D. S. Shephard, S. Bromley, J. M. Thomas, and B. F. G. Johnson, *Chem. Commun.* 1999, 1571 (1999).
566. B. Heinrichs, F. Noville, J. Schoebrechts, and J. Pirard, *J. Catal.* 192, 108 (2000).
567. P. Liu, T. Teranishi, K. Asakura, M. Miyake, and N. Toshima, *J. Phys. Chem. B* 103, 9673 (1999).
568. W. Zhang, C. Wang, and H. Lien, *Catal. Today* 40, 387 (1998).
569. S. Hermans, R. Raja, J. N. Thomas, B. F. G. Johnson, G. Sankar, and D. Gleeson, *Angew. Chem. Int. Ed.* 40, 1211 (2001).
570. M. Kuzma and L. Cerveny, *Res. Chem. Intermed.* 26, 347 (2000).
571. S. Gonzalez, C. Sousa, M. Fernandez-Garcia, V. Bertin, and F. Illas, *J. Phys. Chem. B* 106, 7839 (2002).
572. D. S. Shephard, T. Maschmeyer, G. Sankar, J. M. Thomas, D. Ozkaya, B. F. G. Johnson, R. Raia, R. D. Oldroyd, and R. G. Bell, *Chem.—Eur. J.* 4, 1214 (1998).
573. Y. Takasu, H. Itaya, T. Iwazaki, R. Miyoshi, T. Ohnuma, W. Sugimoto, and Y. Murakami, *Chem. Commun.* 2001, 341 (2001).
574. P. Waszczuk, J. Solla-Gullon, H. S. Kim, Y. Y. Tong, V. Montiel, A. Aldaz, and A. Wieckowski, *J. Catal.* 203, 1 (2001).
575. T. Kessler and A. M. Castro Luna, *J. Appl. Electrochem.* 32, 825 (2002).
576. K. Park, J. Choi, B. Kwon, S. Lee, Y. Sung, H. Ha, S. Hong, H. Kim, and A. Wieckowski, *J. Phys. Chem. B* 106, 1869 (2002).
577. E. S. Steigerwalt, G. A. Deluga, D. E. Cliffel, and C. M. Lukehart, *J. Phys. Chem. B* 105, 8097 (2001).
578. E. S. Steigerwalt, G. A. Deluga, and C. M. Lukehart, *J. Phys. Chem. B* 106, 760 (2002).
579. D. R. Rolison, P. L. Hagans, K. E. Swider, and J. W. Long, *Langmuir* 15, 774 (1999).
580. Y. Takasu, T. Fujiwara, Y. Murakami, K. Sasaki, M. Oguri, T. Asaki, and W. Sugimoto, *J. Electrochem. Soc.* 147, 4421 (2000).
581. D. L. Boxall, G. A. Deluga, E. A. Kenik, W. D. King, and C. M. Lukehart, *Chem. Mater.* 13, 891 (2001).
582. X. Wang, J. Lu, Y. XIe, G. Du, Q. Guo, and S. Zhang, *J. Phys. Chem. B* 106, 933 (2002).
583. A. Kabir and W. D. Marshall, *Green Chem.* 3, 47 (2001).
584. A. Chambers, N. M. Rodriguez, and R. T. K. Baker, *J. Phys. Chem.* 100, 4229 (1996).
585. Y. Miki, K. Honna, Y. Araki, Y. Iwata, K. Sato, and Shimada, *J. Jpn. Petroleum Inst.* 45, 279 (2002).
586. A. Travert, H. Nakamura, R. A. van Santen, S. Cristol, J. F. Paul, and E. Payen, *J. Am. Chem. Soc.* 124, 7084 (2002).
587. S. C. Kim and F. E. Massoth, *J. Catal.* 189, 70 (2000).
588. V. D. Ryabov, O. B. Chernova, and I. M. Kolesnikov, *Chem. Technol. Fuels Oils* 36, 266 (2000).
589. C. E. Burgess and H. H. Schobert, *Fuel Process Technol.* 64, 57 (2000).
590. M. Kamil, S. S. Alam, and S. K. Saraf, *Indian J. Chem. Technol.* 1, 319 (1994).
591. H. Chen and A. A. Adesina, *Appl. Catal., A* 112, 87 (1994).
592. K. Ivanov, *Appl. Catal., A* 116, L1 (1994).
593. M. Ewandowski and Z. Sarbak, *Fuel* 79, 487 (2000).
594. K. Ivanov, S. Krustev, and P. Litcheva, *J. Alloys Compd.* 279, 132 (1998).
595. N. G. Valente, L. E. Cadus, O. F. Gorriz, L. A. Arrua, and J. B. Rivarola, *Appl. Catal., A* 153, 132 (1997).
596. A. P. E. York, C. PhamHuu, P. DelGallo, and M. J. Ledoux, *Catal. Today* 35, 51 (1997).

# Metal Oxide Nanostructures as Gas Sensors

Oomman K. Varghese, Craig A. Grimes

*The Pennsylvania State University, University Park, Pennsylvania, USA*

## CONTENTS

## 1. INTRODUCTION

Gas sensors are used extensively to detect and monitor a wide variety of gases including toxic and explosive gases, organic and inorganic vapors, humidity, and odors. In many applications gas sensors capable of monitoring ppb (parts per billion) concentrations are required. For example, they are widely used for the detection of carbon monoxide in the home. In automobiles, oxygen sensors (also called lambda sensors) are highly essential for controlling engine combustion and hence fuel efficiency. For greenhouse cultivation humidity, oxygen and carbon dioxide are all monitored using metal oxide sensors. In the food industry, alcohol sensors are widely used for control of fermentation processes. As the range of applications continues to increase, highly reliable and precise sensors that can monitor processes in real time become increasingly important. In this article we begin with a discussion of metal oxide based gas sensors, and then review the use of nanotechnology in the gas sensor field.

Conventionally, gases are measured using techniques such as gas chromatography, nondispersive infrared spectroscopy, UV-Vis spectroscopy, mass spectrometry, and ion mobility spectrometry. These methods are precise for measuring components within a mixture of gases; however application is limited by cost, instrumentation complexity, and the relatively large physical size of the instrumentation, which inhibits use outside the laboratory. In contrast solid-state gas sensors are not as precise but are relatively inexpensive, simple to operate, and are able to detect the presence of a gas species within a fraction of a second.

Solid-state gas sensors transform chemical information originating from a chemical reaction into an analytically useful signal [1, 2]. A chemical sensor has two basic functional units: a receptor and a transducer. The receptor part transforms a chemical information into a form of energy, and the transducer part converts this energy into a useful, typically electrical signal. Metal oxide gas sensors, which include both semiconducting and insulating materials, are based on changes in their electrical properties with gaseous ambient [1, 3–7]. In this article, we primarily discuss metal oxide semiconductor gas sensors operating at elevated temperatures and insulating metal oxide humidity sensors that operate at room temperature.

## 2. METAL OXIDE GAS SENSORS

It has long been known that the electrical resistance of semiconductors is affected by the composition of the gaseous ambient, with systematic studies on this phenomena initiated by Brattain and Bardeen [8] in the early 1950s. However the initial changes seen in electrical properties with gas ambient were too small to achieve a useful sensor, and the changes induced by the gases were often found to be irreversible [1, 9]. A major advancement in sensor technology came in 1962, when Seiyama [10] reported on the gas sensing properties of zinc oxide. Simultaneously Taguchi [11] made a commercial sensor using tin oxide. The metal oxides, especially tin oxide, were found to be stable and the gas sensing properties highly reproducible. Since this pioneering work, a large number of oxide materials, including *n*- and *p*-type materials, have been studied for their gas sensing properties. However only a handful of materials, mostly *n*-type, have proven suitable for practical application as gas sensing materials [1, 12, 13]; some of these materials are listed in Table 1.

**Table 1.** Metal oxides used as gas sensors.

| Material | Response to gas | Ref. |
|---|---|---|
| $SnO_2$ | $H_2$, CO, $CH_4$, $H_2S$, $C_3H_8/C_4H_{10}$, $Cl_2$ $CH_3OH$, humidity, $C_2H_5OH$, $NO_x$, $O_2$, $AsH_3/PH_3$, $C_3H_6$, Trimethyl amine (TMA), $CCl_4$, $CHCl_3$, $CO_2$ | [16, 251–264] |
| $Fe_2O_3$ | CO, $C_2Cl_4$, $C_4H_{14}$, Acetone, $C_2H_4$, humidity | [54, 265–268] |
| ZnO | $H_2$, $O_2$, $C_2H_5OH$, CO, $NH_3$, TMA, $CH_4$, $AsH_3$, $PH_3$ | [269–275] |
| YBCO | $C_2H_5OH$, acetone, diethylether, $O_2$, $NO_x$ | [276–278] |
| $Ba_{0.5}Sr_{0.5}TiO_3$ | Humidity | [279] |
| $MgAl_2O_4$ | Humidity | [280] |
| $SnO_2$-$TiO_2$ | $C_4H_{10}$ | [281] |
| $Sn_{1-x}Fe_xO_y$ | CO | [282] |
| $TiO_2$ | LPG, TMA, $NO_x$, CO, $H_2$, humidity, $O_2$, | [283–290] |
| $Ga_2O_3$ | $O_2$, $H_2$, CO, $CH_4$ | [291–294] |
| $WO_3$ | $H_2S$, $NO_x$, $H_2$, formaldehyde | [295–298] |
| Indium Tin Oxide (ITO) | $NO_x$, $Cl_2$, $CCl_4$, $CO_2$ | [299–302] |
| $Al_2O_3$ | LPG, humidity | [283, 303] |
| $SrTiO_3$ | $O_2$ | [304] |
| $ZrO_2$ | LPG | [283] |
| $CeO_2$ | $O_2$ | [304] |
| $Cr_2O_3$ | Ethanol | [305] |
| $ZnSnO_3$ | Ethanol | [306] |
| $SrSnO_3$ | Humidity | [307] |
| $Nb_2O_5$ | $O_2$ | [308] |
| $BaTiO_3$ | $O_2$ | [304] |
| $BaCeO_3$ | $CO_2$ | [309] |
| $CuO$-$BaSnO_3$ | $CO_2$ | [310] |
| $Pr_6O_{11}$ | Ethanol | [311] |

The most thoroughly studied, as well as the most promising materials for gas sensing, are titania and tin oxide, while alumina appears most useful for humidity sensing.

## 2.1. Sensor Parameters

Sensitivity is the ability of the sensor to detect a given concentration of gas, a primary concern in selecting a material for a given sensing application [13]. In the case of metal oxide sensors, sensitivity is generally defined in terms of resistance, conductance, or conductivity. For an *n*-type metal oxide in the presence of a reducing gas, or *p*-type metal oxide in the presence of an oxidizing gas, sensitivity $S$ is usually defined as

$$S = \frac{R_0 - R_{gs}}{R_{gs}} \approx \frac{R_0}{R_{gs}} \quad \text{if} \quad R_{gs} \ll R_0$$

where $R_0$ and $R_{gs}$ are the stable values of the resistance of the material before and after exposure to gas. For an *n*-type material in presence of a reducing gas, or a *p*-type material

in the presence of an oxidizing gas,

$$S = \frac{R_{gs} - R_0}{R_0} \approx \frac{R_{gs}}{R_0} \quad \text{if} \quad R_{gs} \gg R_0$$

A sensor parameter related to sensitivity is the dynamic range; ideally sensors should have appreciable sensitivity over a wide range of gas concentrations. Reversibility is another critical aspect of sensor performance. Unless specifically used as a dosimeter, the changes in resistance/impedance with gas exposure should be reversible; a reliable sensor should not show hysteresis on cycling between different ambients. When the sensor is exposed to a mixture of gases, the sensor should discriminate between them; this property is called selectivity. semiconductor gas sensors are mostly sensitive to many gases simultaneously and hence have poor selectivity; however several methods can be adopted for improving the selectivity as discussed by Morrison [9] as well as Egashira and Shimizu [14]. The most commonly employed method is to load metal catalysts, such as Pt or Pd, onto the surface of the sensing material, or to dope the sensing material with acidic/basic oxides. These catalysts or additives increase the rate of a particular gas–solid reaction compared to others, or enable only one reaction route to occur, which enables the constituent gases to be identified.

Another important sensor parameter is the response time as well as recovery time of the sensor. The response time is the time required for a sensor to respond to a step increase in analyte gas concentration. Since most sensors approach the final signal asymptotically, the response time is commonly defined as the time needed to reach 90 percent of the final signal for a given concentration of gas. The recovery time is usually expressed as the time for the signal to fall below 10 percent of the maximum response. A good sensor should respond quickly when the analyte is introduced, and it should recover immediately after its removal. Response and recovery times are in part determined by material topology relative to the molecular size of the sensed parameter, temperature, and binding energy between the material and analyte.

The sensor element should be stable with time and repeated operational cycles. The drift in sensor resistance with time is often a problem in metal oxide gas and humidity sensors. In metal oxide gas sensors, the drift is mainly due to factors such as grain growth at the operating temperature, loss of porosity (or structural changes), change in the bulk stocihiomtery, surface poisoning, etc. [1, 15]. In humidity sensors, the drift is mainly due to the gradual formation of a stable chemisorbed OH- layer [16] on the surface. The magnitude of performance change, or drift, for a given material depends on duration of operation, operating temperature, ambient in which the sensor works, the frequency in which the sensor is exposed to the gaseous ambient of interest, and also the concentration of the reactive species.

## 3. GAS SENSING MECHANISMS

Several reactions have been identified as responsible for the gas sensing properties of oxide semiconductor materials [1]. The mechanisms vary with the material and the gas being sensed. Important reactions responsible for gas sensing are discussed next.

## 3.1. Adsorption

Gas adsorption [17], which includes physisorption and chemisorption, is one of the most commonly reported mechanisms associated with the gas-sensing behavior of metal oxide gas and humidity sensors. Physisorption is associated with dipole–dipole interaction (van der Waals) between the adsorbate (gas species) and adsorbent (metal oxide), with a comparatively weak binding energy on the order of 0.1 eV. Physisorption is characterized by high surface coverage at relatively low temperatures, and low surface coverage at higher temperatures. Since there is no charge transfer due to physisorption, the conductivity of the material will be unaffected due to physisorption; however, the electrical impedance of the sensor can be affected by charge transfer through the multiple physisorbed layers. As discussed in the following section, metal oxide based humidity sensors operate on the principle of physisorption.

Chemisorption refers to strong adsorbate to adsorbent bonding, which can lead to compound formation. The binding energy of chemisorption is normally greater than 0.4 eV. Chemisorption with charge transfer is also called ionosorption. In some cases, chemisorption with and without charge transfer is called strong and weak chemisorption, respectively. In the process of strong chemisorption, the adsorbate acts as a surface state effecting partial charge transfer between the adsorbate and adsorbent and is held to the surface by electrostatic attraction. Chemisorption is limited to one monolayer and occurs at elevated temperatures due to the requirement of an activation energy, commonly associated with breaking the bonds of the incoming gas species. However chemisorption will occur at room temperature if the material has highly active surface sites.

Chemisorption of an oxidizing gas, such as oxygen, traps surface electrons from the donor levels inside the material [1, 4, 18–23]. Electron extraction creates an electron-depleted region (in other words a positive space charge region of donor ions) near the surface. This reduces the conductance of a $n$-type metal oxide while increasing that of a $p$-type oxide. The most commonly observed chemisorbed species on metal oxide surface operating in air is $O_2^-$ and/or $O^-$ where $O^-$ is more active compared to $O_2^-$. Although oxygen chemisorption in the form of highly active $O^{2-}$ is possible, it cannot be retained on the surface due to its high charge unless the adsorption site has a high Madelung potential [1]. Mostly at temperatures, near room temperature, $O_2^-$ dominates the coverage, whereas at higher temperatures and/or lower partial pressures, $O^-$ dominates. Oxygen chemisorption reduces the conductance of the metal oxide due to the removal of electrons from the conduction band.

Reducing gases interact with metal oxides either through direct chemisorption or through a surface state associated with adsorbed oxygen. Interaction of the reducing gas with preadsorbed oxygen ions results in desorption of the product, leaving the electron in the conduction band. Removal of adsorbed oxygen decreases the resistance of the $n$-type semiconductor while that of the $p$-type semiconductor is increased. The sensitivity of the material electrical resistance to adsorbed oxygen coverage leads to a direct relation between the resistance and the partial pressure of the reducing agent. In the case of direct chemisorption, the reducing gases inject electrons into an $n$-type material, thereby creating a negatively charged space charge layer near the surface of the material; this layer is called the accumulation region, and it increases the conductance of the $n$-type material. In the case of $p$-type material, the reducing gases extract holes from the material, and hence the conductance is reduced.

Chemisorption results in bending of energy bands in the solid [24–26]. Band bending due to chemisorbed oxidizing (acceptor) or reducing (donor) species is schematically represented in Figure 1 [25]. Charge transfer to or from the adsorbate continues until the Fermi level of the solid equilibrates with the energy level of the adsorbate. The surface energy barrier $qV_s$ shown in Figure 1 takes a maximum value of 0.5 to 1 eV, and hence the concentration of surface charge is limited to $10^{12}$ to $10^{13}$ ions cm$^{-2}$; this is called the Weisz limitation [27]. Sensors operating on the basis of chemisorption have nominal operating temperatures 300 °C to 500 °C.

## 3.2. Reduction, Oxidation, and Dissociation

At the surface of a metal oxide, reducing gases can attack lattice oxygen [1, 28]. The adsorbing reducing gas species extracts oxygen from the lattice, creating a singly ionized oxygen vacancy along with an electron. This electron goes to the conduction band and hence the resistance of the material is reduced (for $n$-type). In the case of sensors operating in air, upon removing the reducing gas, the ambient oxygen reoxidizes the material surface. The reoxidation involves
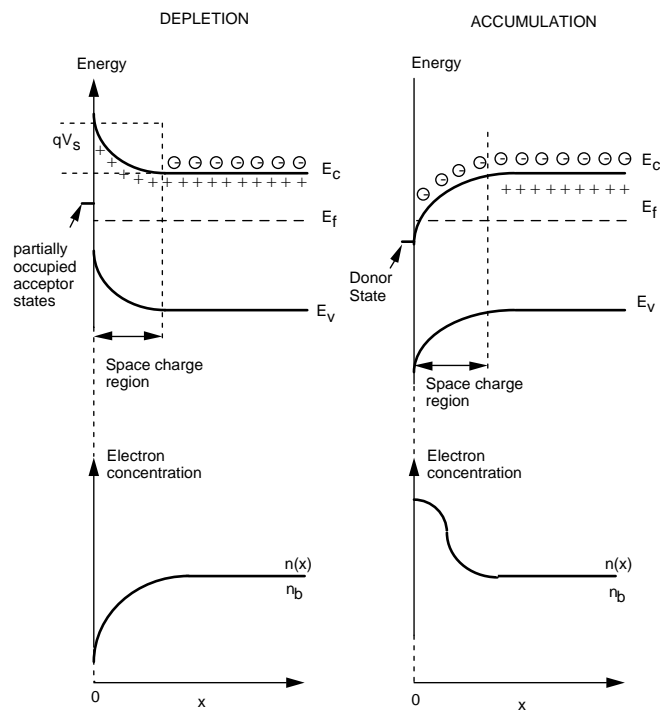


**Figure 1.** Energy band bending at the surface of an $n$-type metal oxide semiconductor as a result of chemisorption. Electron concentration at the conduction band is also shown. $E_C$ represents conduction band edge, $E_v$ the valence band edge, $E_F$ the Fermi level, $qV_s$ the energy barrier at the surface, $n(x)$ the electron concentration in the conduction band, and $n_b$ the electron concentration within the bulk [25].

adding electrons to $O_2$ gas, forming adsorbed $O_2^-$ then $O^-$ and finally combining with an oxygen vacancy to form $O_{Lattice}^-$ whereupon the material regains its original resistance. These processes typically occur between 400 °C to 600 °C [1].

A process of importance for high-temperature oxygen sensors is lattice dissociation. At low oxygen, partial pressure and/or high temperature oxygen vacancies are created in the bulk of the oxide material [1, 12, 29]. The reoxidation process is the same as that mentioned previously. A change in oxygen partial pressure changes the concentration of oxygen vacancies that act as electron donors. Conductance of an $n$-type oxide decreases on increasing the oxygen partial pressure. Oxygen sensors based on $TiO_2$, $Ga_2O_3$, and $SrTiO_3$ belong to this category. These sensors operate between 700 °C to 1000 °C. The effectiveness of both these mechanisms depends on the rate of reaction, mobility of the vacancies, and stability of the lattice structure.

### 3.3. Humidity Sensors

Metal oxide humidity sensors operate both at room temperature and at elevated temperatures, and are respectively classified as ionic or electronic type sensors [16]. In electronic type humidity sensors, electronic transfer between the water and oxide material takes place. Depending upon the material, water interacts with the oxide through the processes discussed in the previous section: removal of chemisorbed oxygen, direct chemisorption, or reduction of the oxide lattice at the surface.

Ionic type metal oxide humidity sensors operating at room temperature rely on the mechanism of physisorption. The fundamental process is the physisorption of water molecules on an initially chemisorbed layer of hydroxyl ions [16, 30–32]. At very low humidity levels, chemisorption of water molecules on the oxide surface takes place. This chemisorbed layer remains unaffected by further changes in humidity; however an increase in humidity causes water molecules to physisorb onto this hydroxyl layer. During formation of the first physisorbed layer, a water molecule gets attached to two neighboring hydroxyl groups through hydrogen double bonds, and a proton may be transferred from a hydroxyl group to the water molecule to form an $H_3O^+$ ion. When the physisorption occurs within less than a monolayer, that is, when clusters of physisorbed molecules are present at the surface, $H_3O^+$ diffusion within hydroxyl groups and proton transfer between adjacent water molecules in a cluster takes place [30]. Another conduction process based on the phonon-assisted electron tunneling mechanism was also suggested [33–35] to explain the sensing behavior at low humidity levels. At higher humidity levels, the number of physisorbed layers increases, allowing each water molecule to be singly bonded to a hydroxyl group, and proton hopping between adjacent water molecules in the continuous water layer takes place. The conduction process is same as that of pure water and is called Grotthuss chain reaction [30]. The dominant charge carrier in high humidity environment is therefore the $H^+$ ions (protons). The concentration of $H^+$ increases with increasing humidity and $H^+$ move freely through the water-like layer. Therefore, the presence of an adsorbed layer of water at the surface reduces the total sensor impedance due to the increase in the ionic conductivity, as well as capacitance due to the high dielectric constant of water.

## 4. NANOSTRUCTURES

Nanotechnology refers to the ability to manipulate atoms to form nanodimensional objects commonly referred to as nanostructures. These structures include atom clusters such as quantum dots, nanotubes, nanorods, nanowires, nanoporous architectures, nanoscale multilayers, nanocrystalline thin films, and nanophase materials [36]. Commonly, the prefix "nano" is used before crystallite, pore, tube, rod, or wire when their diameter falls to 250 nm or less. Many years before nanotechnology was of interest, researchers in the gas sensor field used metal oxide nanostructures for sensing applications and realized the importance of such structures in controlling gas-sensing properties. For example, in 1981 Ogawa et al. [37] reported the use of tin oxide thin films consisting of ultrafine crystallites of dimension 5 to 20 nm for gas-sensing applications. These films showed excellent humidity, ethanol, and isobutane sensitivities, depending upon the preparation condition and the operating temperature of the sensor. In the 1990s, with the development and ready access of devices for atomic scale resolution, such as the field emission scanning electron microscope (FESEM), the correlation between sensitivity and nanostructure became readily evident [38].

### 4.1. Porous Structure

Enhancing the surface area of a material without a corresponding increase in the geometric area has long been realized as a matter of utmost technological importance for metal oxide gas sensors, since the increase in porosity provides more area for the gas to interact with the material. Porous structures possess large surface areas relative to smooth planar structures. Both pore diameter distribution and pore length affects the gas-sensing and humidity-sensing characteristics of metal oxide sensors [39].

In porous humidity sensors, in addition to the process of physisorption, capillary condensation may also take place. At a particular temperature and relative humidity (RH), water condensation occurs in pores up to $r_K$ in radius given by Kelvin's relation [40]

$$r_K = \frac{2\gamma M}{\rho RT \ln(Ps/P)} \tag{1}$$

$P$ is the water-vapor pressure, $Ps$ the water vapor pressure at saturation, $\gamma$ the surface tension, $R$ the universal gas constant, $T$ the temperature in Kelvin, and $\rho$ and $M$ are respectively the density and molecular weight of water. Condensed water inside the pores reduces the impedance of the material drastically. Since capillary condensation enhances the sensing capabilities of a material, pore size distribution has been widely considered to be an important parameter in determining the sensitivity in a particular humidity range [41, 42]. A pore size distribution over a wide range, from 0.1 nm to 100 nm, has been considered as necessary in a sensing element to detect humidity from a few percents to about 90% [41]; however achieving this wide pore size distribution consistently in sintered bodies is a challenging task.

Advances in nanotechnology have enabled the preparation of highly ordered nanoporous architectures and

nanotubes with well-defined pore dimensions and tremendous surface area [43, 44]. Most of the fabrication techniques are simple, and there is a high level of consistency in the production of these structures. In many cases, the pore dimensions and distribution are tunable over a wide range, enabling user-defined pore and tubular structures. Having realized the advantages of such nanostructures, the sensor community has started using these for gas and humidity sensing applications.

## 4.2. Crystallite Dimension

Early studies on the gas-sensing properties of metal oxide single crystals revealed that they cannot be sufficiently sensitive to gases to make a useful device unless the number of electrons exchanged with the surface is comparable with the number of electrons inside the crystal [1], a consequence of Weisz limitation [27]. Although bulk and thin film single crystals show selectivity, reproducibility, and stability, the role of these structures is limited to the study of gas sensing mechanisms, as the observed sensitivity is low [14, 45–49].

In the case of polycrystalline materials (in the form of sintered bodies, pellets, of thick or thin films), the contact resistance between the grains dominates the electrical resistance of the sensor. Figure 2 shows a schematic diagram of the electron depletion region around the surface of each grain, and at the intergranular contact region of $n$-type grains operating in the presence of oxygen, along with corresponding band model [1]. As shown in the figure, the charge carriers must overcome an energy barrier $qV_s$ in order to move from one grain to another. $V_s$, and hence resistance, may be controlled by adsorbed oxygen or surface states other than oxygen at the grain boundaries or an oxygen in-diffusion along the grain boundary [24]. The conductance of the sensing material in this case can be written as [1]

$$G = G_0 \exp\left(\frac{-qV_s}{kT}\right) \tag{2}$$
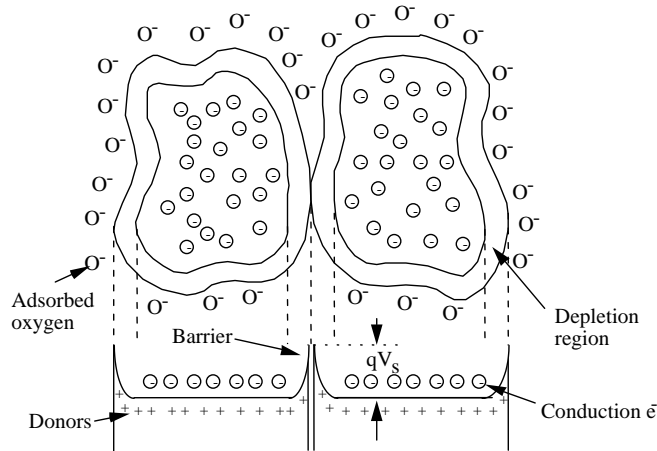
where $q$ is electron charge, $k$ is the Boltzmann's constant, $T$ is the operating temperature in Kelvin, and $G_0$ is a proportionality constant. Since the space charge region is more resistive than the bulk, the intergranular contact provides most of the sample resistance. However, the intergranular contact resistance strongly depends on surface processes, and hence sufficient sensitivity for a useful sensing device can be obtained in these samples, even in bulk form.

In polycrystalline materials, especially those prepared by sintering, grains may be joined by so-called necks [38, 50–52]. If the neck size is small, the space charge layer spreads throughout the region and the sensor resistance and hence sensitivity are effectively determined by the necks [38, 50–52]. If the size is large, the neck does not have much control over sensor resistance and sensitivity. Ogawa et al. [53] explained the high sensitivity of ultrafine particle thin films on the basis of the neck model. They arrived at this conclusion by examining the variation in electron mobility observed through Hall effect studies. They calculated the Debye length $L_D$ given by

$$L_D = \left(\frac{\varepsilon \varepsilon_0 kT}{q^2 n_b}\right)^{1/2} \tag{3}$$

in their films as 3 nm. Here $\varepsilon$ is the dielectric constant of the material, $\varepsilon_0$ the permittivity of free space, and $n_b$ the carrier concentration. According to Ogawa's model [53], when the particle size and channel joining them are comparable to twice the Debye length, the mobility of the charge carriers are highly modulated by the gas species, and thus the material shows high sensitivity.

Yamazoe's group [38, 51] studied the effect of crystallite size on the sensitivity of tin oxide and found that the sensitivity increases dramatically upon reducing the crystallite to less than 6 nm. On the basis of other reports and their own observations Yamazoe [51] suggested a model for grain size effects. This model is schematically represented in Figure 3.



**Figure 2.** Physical model showing the role of intergranular contact regions in determining the resistance of a polycrstalline $n$-type metal oxide semiconductor; the corresponding band model is given at the bottom [1].
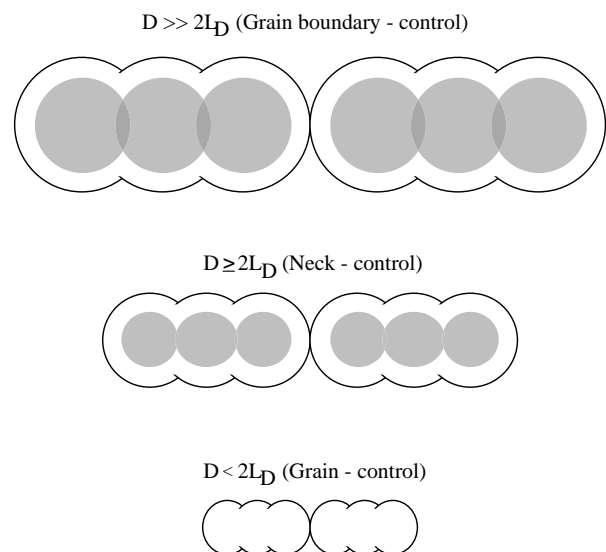


**Figure 3.** Grain size effect in metal oxide sensors. The shaded portion represents the electron-rich region and the blank portion represents the space charge (electron-depleted) region [51].

The thickness of the surface charge layer $L$ as well as the surface potential barrier height are determined by the surface charge, which is in turn dependent upon the amount of adsorbed oxygen (for example) and the Debye length ($L_D$), which is a characteristic of the semiconductor material for a particular donor concentration. For crystallite diameter $D \gg 2L_D$, the grain boundary contacts dominate the sensor resistance, and hence largely determine the gas sensitivity of the material. In this regime, electron-conducting channels through necks are wide and hence not affected by formation of a space charge region; in this region, the sensitivity is almost independent of the diameter of the crystallite. When $D$ becomes comparable to $2L_D$, the neck region will be highly resistive and control the sensor resistance and hence sensitivity (referred to as the neck control regime); sensors in the grain control regime show high sensitivities [54]. When $D < 2L_D$, the grains are completely depleted of charge carriers, and hence the grains control the resistance and sensitivity of the sensor material.

On the basis of work function measurements on polycrystalline $SnO_2$ samples, Schierbaum et al. [55] and Gopel and Schierbaum [56] proposed a model for the energy-level diagrams and electron concentrations of the three cases mentioned in the previous paragraph with reference to Figure 3, before and after exposure to a reducing gas such as CO. These diagrams are shown in Figure 4. The dotted and dashed lines in the energy diagram show the situation before and after exposure to CO, respectively. It can be seen from Figure 4a and Figure 4b that the band bending at the grain boundaries or necks occurs without variation in the bulk value of ($E_C - E_F$); that is to say $\Delta(E_C - E_F)_b \approx 0$ and $\Delta n_b \approx 0$, where $E_C$ is the conduction band edge, $E_F$ the Fermi level, $n$ the electron concentration, and $b$ the bulk properties. In the case of Figure 4c, no difference exists between the surface and bulk value of $E_C$, that is

$\Delta(E_C - E_F)_b \approx \Delta(E_C - E_F)_s$, where the subscript $s$ denotes surface properties. Therefore, for nanosized grains where $D < 2L_D$, the interaction with gas shifts the band homogeneously across the grains upon charge transfer reactions at their surfaces, and hence the flat band conditions are approximately satisfied. The temperature dependence of the conductance $G$ of nanoscale grains is proportional to

$$\exp\left[-\left(\frac{E_C - E_F}{kT}\right)\right] \qquad (4)$$

This equation is in contrast with Eq. (2), the behavior of which depends on band bending. Hence the Schottky barrier mechanism of electron transport across the grain boundaries cannot be applied once the grain size is smaller than the Debye length of the electrons.

Nanocrystallites/nanoparticles possess a specific surface area of several hundred $m^2/g$ [57]. The smaller the feature size, the higher the number of surface atoms will be compared to the bulk; hence the properties of a nanoarchitectured material are largely governed by the surface. These features have resulted in a considerable interest in using nanocrystalline materials for gas-sensing applications. Among all metal oxide nanostructures, the majority of the gas sensor studies have been conducted on nanocrystalline structures.

## 4.3. Nanocrystalline Structures

Nanocrystalline structures in the form of sintered disks and thick and thin films are used in the gas sensor field. In the case of disks and thick films, nanoparticle powders are first made using an appropriate technique. These powders are then converted into pressed disks, or in the case of thick films, a slurry of the nanoparticle powder is applied onto a substrate such as alumina, which is then sintered at elevated temperatures to remove binders and to increase strength. The resulting pellets and thick films are porous, allowing access of the gas species to a maximum number of grains.

Sol–gel is one of the most successful methods in creating nanocrystalline oxides. It is an economical and relatively easy method to prepare powders and thin films of desired nano- to microstructure. In general, it is a process based on the hydrolysis and condensation reactions of organic or inorganic precursors. Various methods in sol–gel have been employed for preparing nanoparticle powders and nanocrystalline thin films of metal oxide nanocrystals for sensing applications. The nanocrystalline structures of oxides such as $SnO_2$ [58–66], $TiO_2$ [67–70], $WO_3$ [71], and various composite oxides like $MoO_3$-$SnO_2$ [58, 72], $MoO_3$-$TiO_2$ [73], $V_2O_5$-$TiO_2$ [74], and $TiO_2$-$SnO_2$ [75] were prepared by several groups using sol–gel and successfully employed for gas-sensing applications. A transmission electron microscope (TEM) image and diffraction pattern of a nanocrystalline titania thin film prepared by our group using sol–gel is shown in Figure 5; the film has an average crystallite size of 6 nm. The sol was prepared by dissolving titanium isopropoxide in ethanol and hydrochloric acid in the molar ratio 0.007:2.56:0.059 by stirring and refluxing the mixture at 80 °C for 6 hours. The resulting solution was kept open for aging in an ambient of relative humidity (RH) less than 10%
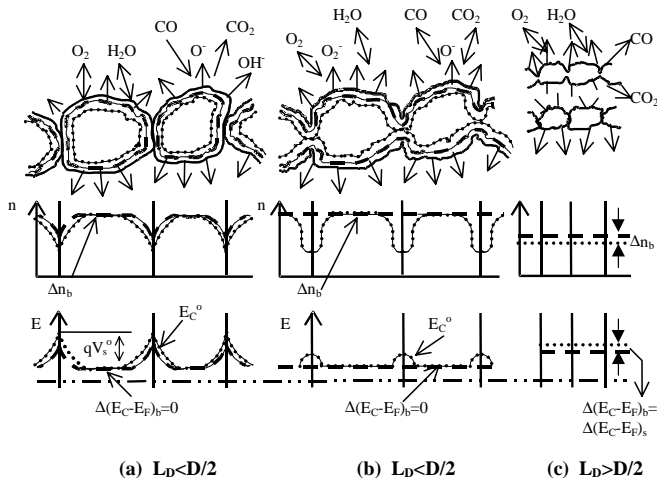


**Figure 4.** The effect of oxidizing and reducing gases on the depletion region inside the grains (shown at the top), electron concentration (middle), and energy bands (bottom) with respect to the change in the grain diameter $D$ of an $n$-type metal oxide semiconductor. The dashed line represents the situation before and the dotted line that after exposure to the reducing gas. $b$ and $s$ represent the bulk and surface properties, respectively [55].
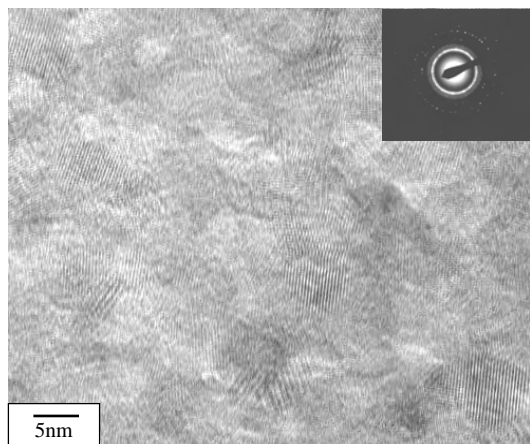
**Figure 5.** Transmission electron microscope image of a nanocrystalline thin film prepared by sol–gel technique. The selected area diffraction pattern showing the presence of anatase phase is given in the inset.

and temperature 21 °C for 72 hours. Films were deposited from the sol onto substrates using dip coating at low humidity levels, followed by immediate placement in a constant high-humidity ambient for drying. The resulting film was sintered at 500 °C in an argon environment for 3 hours to achieve nanocrystalline films in anatase phase.

Varghese et al. [76] prepared nanocrystalline tin oxide thin films of grain size 4.5 nm using $SnCl_2$-$2H_2O$ as a precursor for ethanol sensing. Chiorino et al. [58, 72] used sol-route to make $SnO_2$ and $MoO_x$-$SnO_2$ nanosized powders with particle size 30 to 50 nm; sensors were fabricated out of a paste made of these particles. Through hydrothermal treatment of a sol made by suspending stannic acid gel in an ammonia solution, uniform tin oxide thin films with a crystallite size of 6 nm were made by Baik et al. [62].

Another commonly employed fabrication method is precipitation [71, 77–80], with coprecipitation used for making composite materials. Nanoparticles are obtained by washing and then annealing a precipitate obtained by reaction of metal-containing chemicals. Lee et al. [71] used precipitation to prepare nanocrystalline $TiO_2$ and $WO_3$ films, and coprecipitation for $WO_3$-$TiO_2$ films, obtaining a crystallite size of less than 10 nm. Chu et al. [78, 79] used coprecipitation to prepare nanosized powders of $CoTiO_3$ and $CdO$-$In_2O_3$; the particle size obtained ranged from 14.5 to 26 nm, depending on the sintering temperature [79].

Several other fabrication techniques such as laser-assisted pyrolysis [80, 81], laser ablation [26, 82–84], radio-frequency sputtering [85–90], gas condensation [91], solid-state reaction [92, 93], aerosolization [94], mechanical alloying [95], spray pyrolysis [96, 97], rheotaxial growth and thermal oxidation (RGTO) [98–101], arc plasma [102], reactive-gas evaporation [103, 104], and supercritical fluid drying method [105, 106] have been used for the preparation of various types of nanocrystalline metal oxides. Panchapakesan et al. [107] used metal seed layers of iron, cobalt, nickel, copper, or silver deposited by vacuum evaporation to prepare nanocrystalline tin oxide. The particle size of the tin oxide deposited upon these seed layers was determined by the topology of the seed layers. A method combining decomposition of an organometallic precursor and controlled sur-

face hydrolysis, as well as their oxidation, was used by Nayral et al. [108] and Fau et al. [109] to form stable noncoalescing nanoparticles of tin oxide.

## 4.4. Nanoporous Architectures

Nanoporous architectures are generally formed by using templates as well as through self-organization processes. Sol–gel [110–114], cationic or anionic surfactant template method [115–125], nanoparticle route [126], sonochemical synthesis [127], radio-frequency sputtering, anodic oxidation [128–129], plasma spraying [130], chemical precipitation [131, 132], two-step replication process with anodic porous alumina as template [133], and various other innovative and conventional techniques [134] have been used for the fabrication of nanoporous architectures of metal oxides such as $TiO_2$, $SnO_2$, $ZnO$, and $WO_3$. In the case of nanocrystalline metal oxide sensors, many of the researchers who use nanoporous structures for sensing prepare powders of nanoporous particles and later compact them into disks or apply them onto a substrate in paste form using techniques such as screen printing. Wang et al. [115, 120] used a cationic surfactant method for the fabrication of nanoporous tin oxide particles of 368 $m^2$/g surface area that were applied to an alumina tube for sensor fabrication. Hyodo et al. [117] also used a cationic surfactant method for the fabrication of nanoporous tin oxide particles of 4.1 nm pore size; they subsequently made thick films out of these nanoparticles for sensing studies. Devi et al. [111] used sol–gel with polyethylene glycol as a pore-creating template to fabricate nanoporous titania powders that were later pressed in the form of a disk for sensing studies. A problem with this templating approach to sensor fabrication is that in many cases the original porosity, pore size distribution, and surface area are lost during the fabrication process.

Self-organization of nanoporous architectures can provide superior control over pore distribution and dimensions compared to the structures formed using physical templates. Anodization is a highly useful and simple technique for the fabrication of self-organized nanoporous structures of metal oxides. Images of nanoporous alumina and titanium oxide films fabricated by our research group for the use in humidity and gas sensing studies using anodization are shown in Figures 6a to 6c. The alumina film shown in Figure 6a and 6b is made using a two-step anodization technique [135–137], while the titanium oxide film was prepared using single-step anodization. The aluminum substrate was first anodized in an oxalic or sulfuric acid solution. The anodization was stopped after consuming a few microns of aluminum, and the porous alumina film was removed through etching. The etchant, a mixture of chromic acid and phosphoric acid, is highly selective, attacking alumina much faster than aluminum. The remaining aluminum is dimpled, with the dimples serving as a uniform seed layer upon which a highly uniform porous layer could then be achieved through a second anodization step at the same voltage. For the fabrication of titanium oxide nanotubes, a solution of hydrofluoric acid in water was used as the electrolyte. An anodization voltage of 3 V was used for preparing the film shown in Figure 6c. Recently Shimizu et al. [128] also prepared nanoporous titania through anodization but used sulfuric acid as the electrolyte.
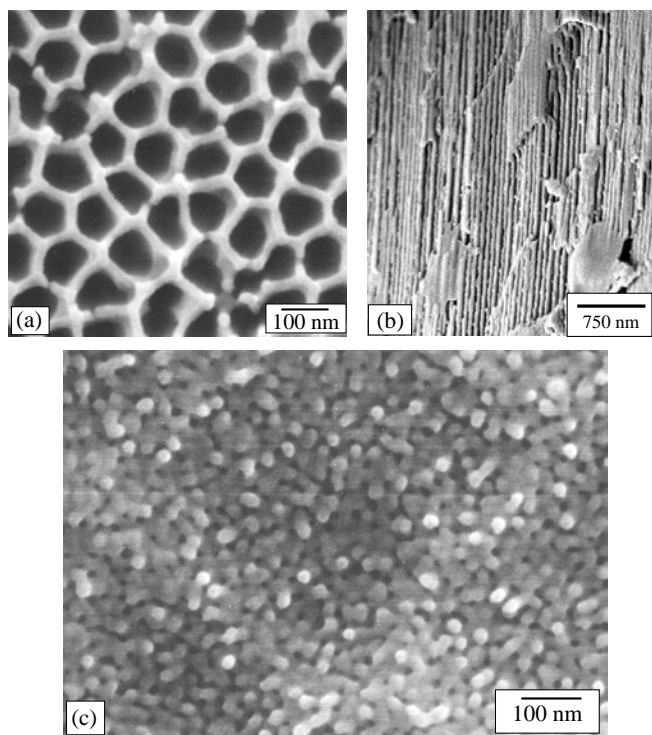
**Figure 6.** The field emission scanning electron microscope (FESEM) image of (a) nanoporous alumina prepared by a two-step anodization process, (b) a cleaved alumina sample showing the pore channels, and (c) nanoporous titania prepared by single-step anodization.

## 4.5. Nanotubes, Nanorods, Nanowires, and Nanoribbons

Like nanoporous films, nanotubes also provide tremendous surface area for the gas to interact with. The introduction of carbon nanotubes by Ijima [138] in 1991 led to the fabrication of nanotubes composed of a variety of materials including metal oxides such as $Al_2O_3$ [139–142], $SnO_2$ [143], $TiO_2$ [144–162], $VO_x$ [154, 163–170], $V_2O_5$ [141], $ZrO_2$ [171], ZnO [172, 173], and $MoO_3$ [141]. Most efforts were concentrated on developing titania nanotubes because of their potential as advanced sensor, photocatalytic, and photovoltaic materials.

Titania nanotubes have been fabricated by various techniques based on both templated growth and self-assembly. Techniques such as sol–gel, anodization, electrodeposition, and sonochemical, as well as some chemical routes have so far been employed for making titania nanotubes. For example Hoyer [148] made a polymer mold first from porous alumina, then used an electrochemical method to deposit titania onto the polymer rod-like template structure. After deposition, the polymer mold was removed to obtain a titania nanotube array. Imai et al. [150] prepared titania nanotubes having inner diameters of 50 to 150 nm by dipping porous alumina in a titanium tetrafluoride, water, and ammonia solution; the diameter of the tube was found to be dependent on the dipping time. Lakshmi et al. [156], M. Zhang et al. [161], X. Zhang et al. [174], and Liu et al. [158] also used alumina as a template. Liu et al. [158] obtained polycrystalline, nanocrystalline, and

single crystalline tubes of inner diameter 2.5 to 5 nm with outer diameter 20 to 40 nm. Adachi et al. [149] used an alkyl amine as a structure-directing agent for the fabrication of titania nanotubes. Nontemplate methods have also been used for titania nanotube fabrication. Kasuga et al. [147, 152] treated sol–gel derived powders with NaOH to obtain titania nanotubes of 400 $m^2$/g surface area; Zhang et al. [153] and Lin et al. [160] used similar fabrication routes. Zhu et al. [151] sonicated titania nanoparticles in a NaOH solution to obtain titania nanotubes. Gong et al. [162] describe an anodization technique to fabricate titanium oxide nanotubes. The process [162] consists of anodizing titanium foil in an electrolyte of 0.5% hydrofluoric acid in water. Nanotubes of inner diameter from 22 nm to 90 nm can be achieved by varying the anodization voltage from 10 V to 25 V. FESEM images of a nanotube array prepared using an anodization voltage of 20 V is shown in Figure 7.

Like titania, alumina nanotubes can be fabricated using anodic oxidation. Pu et al. [139] prepared branched alumina nanotubes using anodization. Carbon nanotube templates have been used for preparing metal oxide nanotubes [140, 171, 175]. $VO_x$ nanotubes are generally prepared using amines as structure-directing agents [164, 165, 167–170]. Zhang et al. [173] used precipitation, while Wu et al. [172] used pyrolysis of zinc acetylacetonate to prepare zinc nanotubes.

Nanorod, nanowire and nanoribbon metal oxides such as $TiO_2$ [156, 161, 174, 176], $SnO_2$ [143, 177], ZnO [156, 178–185], $Ga_2O_3$ [141, 186, 187], $MoO_3$ [154], $WO_3$ [156], and $Fe_2O_3$ [188] have been fabricated by methods including gas phase synthesis and high temperature processing, as well as templated synthesis. Figure 8 shows a $TiO_2$ nanowire mat, fabricated by the authors, made by filling the pores of an alumina membrane via sol gel, letting the film dry, and then subsequently removing the alumina template by a sodium hydroxide etch.

## 4.6. Structural Stability

As most metal oxide gas sensors operate at elevated temperatures, their structural stability is a critical factor in determining the suitability of a material for a given application. At high temperatures, grain growth, phase transition of the crystalline phase, pore widening or shrinking, and even complete collapse of the structure can take place [189–191], leading to undesired changes in sensor performance. The high surface areas of nanocrystalline structures makes them
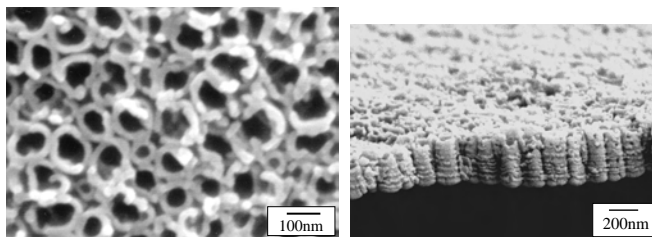


**Figure 7.** (a) The surface morphology of a titania nanotube array prepared by single step anodization process employing an anodization voltage of 20 V. (b) A lateral view of the nanotubes.
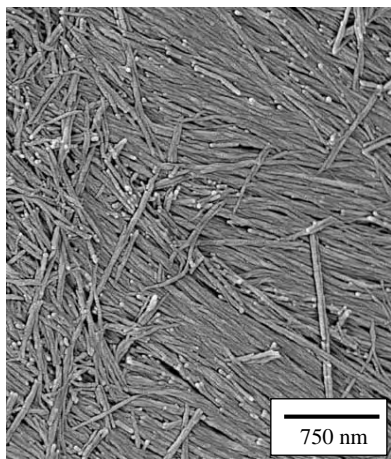
**Figure 8.** The FESEM image of TiO$_2$ nanowire mat prepared by filling an alumina template with sol and then removing the template after drying the sample.

prone to solid-state sintering at elevated temperatures, leading to grain growth with a corresponding reduction in grain surface area. Li et al. [92] studied the stability of tin oxide nanoparticles, prepared using a solid-state reaction route, while performing high temperature annealing. They observed an increase in grain size from 8.5 to 13.4 nm on sintering at 400 °C and 600 °C with a corresponding reduction in surface area from 83 to 57 m$^2$/g. On the other hand, nanocrystalline tin oxide thin films of 6 nm grain size deposited by Baik et al. [62] using a hydrothermal method were found stable to 600 °C with no appreciable change in grain size observed below this temperature. Willett et al. [83] observed a reduction in surface area of the disk samples made of nanocrystalline tin oxide powders on annealing at elevated temperatures.

In the case of nanoporous architectures and nanotubes, if the as-prepared samples are amorphous prior to use, they need to be converted into a desired crystalline phase by heat treatment. Metal oxides used in high temperature sensing applications do not show appreciable gas sensitivity in the amorphous state. In the case of thin-walled nanoporous and nanotube structures, particular attention should be given to crystallization of the walls; if the wall thickness is comparable to the critical size of the nuclei, then it is difficult to crystallize the walls [192, 193]. The critical size of the nucleus may be reduced by adding impurities [189, 194–198]; however the crystallization or phase transformation to a stable phase is accompanied by densification and hence a reduction in volume [199] that may lead to the pore shrinkage or pore widening and, ultimately, collapse of the porous or tubular structures. Wang et al. [115] observed an increase in pore diameter from 2.2 to 3.9 nm, a reduction in surface area from 368 to 136 m$^2$/g, and an increase in particle size from 1.8 to 7.8 nm when crystalline nanostructured tin oxide samples were annealed at 300 °C and 400 °C. The authors have observed that titania nanotubes prepared by anodization (see Fig. 7) are stable to about 580 °C on annealing in an oxygen or argon environment, even though crystallization in anatase phase occurred at 280 °C and phase transformation to rutile started at about 430 °C [200]. No discernible vari-

ation in the tube dimensions were observed below 580 °C; however above this temperature the grain growth from the underlying titanium support (see Figs. 9a–9b) disturbed the nanotubes and led to the collapse of the structure. Figure 9c is an FESEM image of the titania nanotubes subjected to rapid heating and cooling (10 °C/min) cycles, as in when subjected to nonisothermal conditions. It can be seen that the solid-state sintering led to the coalescence of the tube walls, resulting in a worm like pattern.

The structural stability of the structures can be improved with the help of impurity addition or chemical treatment. Ferroni et al. [80] doped titania films with Nb and Ta, which inhibited the grain growth and phase transformation from anatase to rutile phase. Hyodo et al. [117] stabilized the nanoporous SnO$_2$ particles prepared by the surfactant method using a phosphoric acid treatment before calcination. The treated particles conserved the large surface area of 305 m$^2$/g after calcination at 600 °C. The ordered nanoporous structure of untreated particles was completely destroyed on annealing at this temperature; however they observed a reduction in pore size and surface area on annealing above 600 °C. It was believed that the phosphoric acid treatment made the wall thickness comparable to the crystallite size, which avoided the crystallite growth and pore destruction.

## 5. GAS SENSING PROPERTIES

### 5.1. Nanocrystalline Structures

The gas-sensing properties of a material significantly increase when the crystallite size is comparable to or less than the twice the Debye length. A considerable amount of literature is available that demonstrates that the reduction
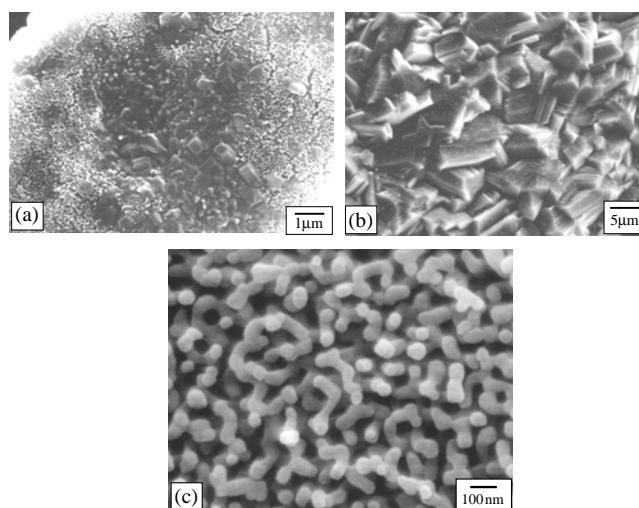


**Figure 9.** Thermal stability of titania nanotubes prepared by anodization technique. (a) A low magnification image of the nanotubes (shown in Figure 7) after annealing in oxygen ambient for three hours at 680 °C showing the grain growth from the titanium support destroying the nanotubes, (b) the image after annealing the sample at 880 °C showing the complete collapse of the nanotubes, and (c) the image of the nanotubes showing the coalescence of the walls after subjecting them to fast heating and cooling rates and taken to 820 °C.

in crystallite size to nanoscale dimensions improves the sensitivity [59–109, 201–212]. The ethanol sensitivity enhancement in a sol–gel deposited nanocrystalline tin oxide thin film on reducing the grain size from 9.0 nm to 4.5 nm is shown in Figure 10. Lu et al. [105] observed a drastic increase in CO sensitivity in $SnO_2$ when the crystallite size was reduced below 10 nm. Ansari et al. [60] obtained a hydrogen sensitivity of three orders of magnitude in tin oxide thick films at 200 °C with 20 nm crystallite size. It was reported [82] that $BaTiO_3$ in nanocrystalline (grain size 25 nm) thick film form showed appreciable sensitivity to $CO_2$. $WO_3$ based nanocrystalline thick films were shown able to detect sub-ppm levels of $NO_x$ [71]. Tan et al. [95] prepared nanocrystalline $xSnO_2$-$(1 - x)\alpha$ $Fe_2O_3$ using mechanical alloying and found that ethanol sensitivity was very high ~845 for 1000 ppm ethanol when the particle size was ~10 nm. Panchapakesan et al. [107], using metal seed layers, made tin oxide thin films of grain size from 20 to 121 nm, with the smaller grain sizes showing significantly higher sensitivities. Solis et al. [103] showed that nanocrystalline $WO_3$ films with 15 nm grain size can yield a sensitivity of $10^4$ to 10 ppm hydrogen-sulfide at room temperature. Nayral et al. [212] made tin oxide nanoparticles highly sensitive to carbon monoxide, with tin at the core surrounded by a sheath of tin oxide using thermolysis; the inner core had a diameter of 11 nm with a 4 nm thick sheath.

As indicated in Figure 10, Vlachos and Xenoulis [213] demonstrated that an optimum value of atomic cluster size exists where the nanostructures exhibit optimal sensitivity. The size at which maximum sensitivity occurs depends on the carrier concentration and the energy gap of the semiconductor. The carrier concentration depends on factors such as degree of oxidation, the existence of additives, and poisoning of the surface parameters. The critical size of the cluster can be approximately calculated using the relation $a_{max} = 10^{15}/n_0$, where $n_0$ is the electron concentration in the flat band condition. For larger grain size, the sensitivity decreases with increasing cluster size, since the depletion width becomes smaller compared to the cluster radius and also because of the lower fraction of charge carriers moved to surface states. In smaller clusters, complete carrier depletion takes place; the sensitivity increases with an increase in cluster size because the variation of Fermi level with respect to valence band increases as cluster size increases.
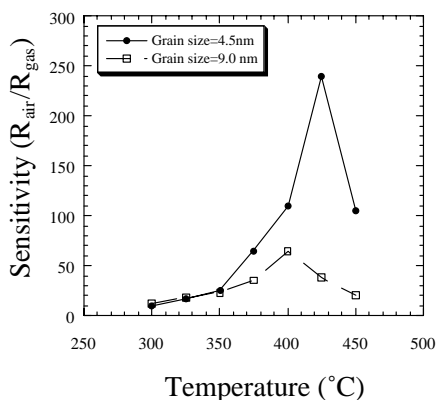
Varghese and Malhotra [214, 215] observed an electrode sample capacitance effect in nanocrystalline tin oxide thin films. They attributed this to the migration of adsorbed oxygen on the application of a dc bias at temperatures above 300 °C. The samples were highly selective to ethanol compared to hydrogen and liquefied petroleum gas (LPG). Tan et al. [95] reported $xSnO_2$-$(1 - x)\alpha$ $Fe_2O_3$ based ethanol sensors with high selectivity to CO and $H_2$; they suggest that mechanical milling of the nanoparticles created high concentrations of dangling bonds, which in turn resulted in high sensitivity and selectivity.

Reduction in thin film thickness can also increase the sensitivity [216]. Sakai et al. [207] observed an enhancement in sensitivity upon reducing the thickness of a nanocrystalline tin oxide thin film while keeping the particle size constant. Ultra thin films of $SnO_2$ and ZnO deposited by Yamasaki et al. [217] showed a thickness dependent sensitivity; the sensitivity of tin oxide was optimum for 3 to 20 nm films, whereas ZnO was highly sensitive for films 5 nm or less.

## 5.2. High Temperature Gas Sensing

Recently developed high surface area nanoporous materials have not yet effectively been employed as high temperature gas sensors. However there are reports in the literature indicating the utility of employing nanopororous architectures for gas sensing [111, 115–117, 119, 125, 128, 131, 134, 218–220]. For example, Wang et al. [125] obtained a high ethanol sensitivity of ~280 for nanostructured tin oxide with a surface area 136 $m^2$/g. Li and Kawi [116] used nanoporous tin oxide having a surface area of 156.8 $m^2$/g for sensing hydrogen and observed that the sensitivity increased considerably with surface area. Li and Kawi also [119] found a surface area dependent hydrogen sensitivity in tin oxide. Shimizu et al. [128] made a heterojunction out of anodically oxidized nanoporous $TiO_2$ and Pd observing excellent hydrogen sensitivity at 250 °C in air. Devi et al. [111] obtained appreciable sensitivity to hydrogen and CO for pellets made of nanocrystalline/nanoporous titiania particles of surface area 299 $m^2$/g, and observed a reduction in surface area and sensitivity when annealing the sample.

## 5.3. Room Temperature Humidity Sensing

The humidity sensing properties of alumina, discovered almost fifty years ago [33, 221–230], are based on ionic conduction. As discussed earlier, while porous metal oxides are in demand for use as humidity sensors [16, 40, 231–239], nanoporous structures have not been effectively applied to the task since earlier reports indicated that a pore size distribution of 0.1 to 100 nm was needed to sense humidity in a wide range [41]. However recent work on the humidity sensing abilities of uniformly nanoporous alumina films made through anodization showed that an easily built and highly reproducible wide range humidity sensor could be achieved using nanodimensional pores of a narrow size distribution [240].

Starting from adhesive-backed aluminum tape (99% pure), purchased from Tesa Tape Inc., subsequently anodized sensors SO50, SO30, DO15, and DS15 were prepared under the conditions given in Table 2. Per sample



**Figure 10.** Grain size dependent variation of sensitivity as a function of temperature for a tin oxide thin film prepared by sol–gel.

**Table 2.** Anodization conditions used for making nanoporous alumina films.

| Sample | Anodizing voltage | Duration of anodization (min.) | No. of anodization stages |
|--------|-------------------|-------------------------------|---------------------------|
| SO50 | 50 V | 120 | one |
| SO30 | 30 V | 120 | one |
| DO15 | 15 V | 120 | two |
| DS15 | 15 V | 120 | two |

*Note:* Oxalic acid (2 wt% in water) was used as the electrolyte in all the cases except for DS15 where anodization was performed in 4 wt% sulfuric acid.

notation, the first letter denotes a single-S or double-D step anodization process; the second letter denotes the use of oxalic O acid in the anodization bath; the two-digit number denotes the anodization voltage. It was observed that single-step anodization results in disordered pore structures at low voltages. Hence a double-step process was used for making samples DO15 and DS15. Samples SO50, SO30, DO15, and DS15 have, respectively, average pore diameters of 45.2 nm, 38.4 nm, 22.7 nm, and 13.6 nm with a corresponding standard deviation of 3.4 nm, 7.8 nm, 4.9 nm, and 2.6 nm. All samples have a predominantly ordered pore structure. An evaporated gold interdigital capacitor pattern of dimension 1.2 cm × 1.2 cm formed on the surface of the alumina films was used electrodes. Sensor impedance was measured over the frequency range 5 Hz to 13 MHz using a computer-controlled Hewlett-Packard impedance analyzer (4192A) fitted with an impedance test fixture.

Figure 11 shows the measured 5 kHz sensor impedance of the different sensors as a function of humidity. The humidity-sensitive region of DS15 is 20% to 90% RH (relative humidity) and that of DO15 is ∼45% to 95% RH. Sensors SO30 and SO50 become sensitive to humidity at approximately 65% and 75% RH, respectively. Smaller pore size increases the range of humidity values over which the sensor is responsive, and increases the sensitivity at lower humidity levels. Therefore optimal pore size can be selected for the operating region of interest. It was observed that as frequency decreases, the width of the sensitive region increases, and the point at which the sensor becomes responsive shifts to lower relative humidity values. As a typical case the response of the sensor DO15 to humidity at different measurement frequencies is shown in Figure 12; for a given pore size, the humidity-sensitive region of operation can be
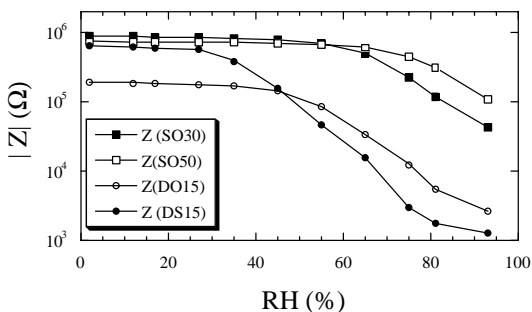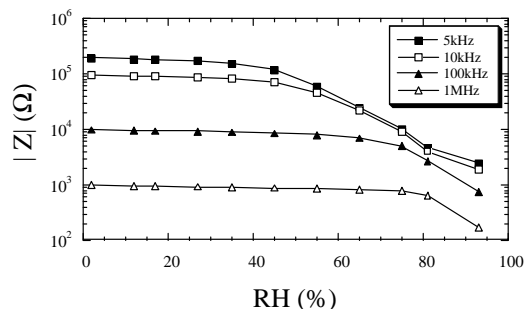


**Figure 12.** Humidity dependent variation of impedance of the sensor DO15 at different measurement frequencies.

selected by frequency tuning. A typical response/recovery graph of the sensor SO50 when the humidity was cycled between 2% and 45% of sensor SO50 is shown in Figure 13. All sensors were completely reversible, regaining their original impedance values even after repeated exposure to high humidity levels. The minimum response/recovery times were observed for SO50, the sample with the largest pore size. From impedance spectroscopy studies, it was inferred that anions become incorporated into the alumina film during the anodization process [34, 35, 241] where they act as proton donors and facilitate the adsorption of water molecules. Hence liquid-like networks are formed at relatively lower humidity levels for the smaller pore sized sensors DS15 and DO15. This process, along with capillary condensation, is responsible for the observed humidity-sensing behavior of the uniformly nanoporous alumina sensors.

## 5.4. Nanotubes

Immediately after the introduction of carbon nanotubes a considerable amount of interest focused on studying their gas-sensing properties [138, 242–248]; however it is to be expected that metal oxide nanotubes will have much superior gas-sensing properties. Hydrogen gas-sensing experiments have recently been conducted using titanium nanotube arrays prepared by anodization (see Fig. 7); the nanotubes demonstrate superior hydrogen-sensing characteristics than any of the metal oxide structures previously studied [249]. The results of titania nanotubes fabricated using anodization voltages of 20 V, 12 V, and 10 V are discussed here. These tubes have, respectively, inner diameters



**Figure 11.** Variation of electrical impedance of nanoporous alumina of different pore size with respect to relative humidity.
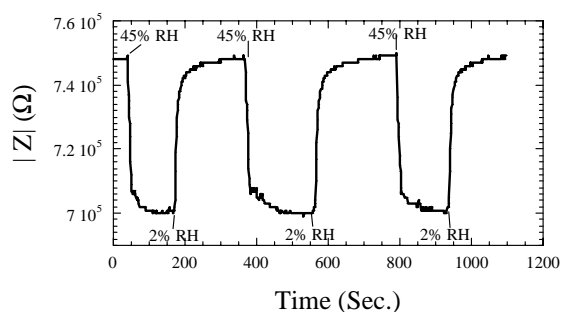


**Figure 13.** Response of the sensor SO50 when the relative humidity was cycled between 2% and 45%.
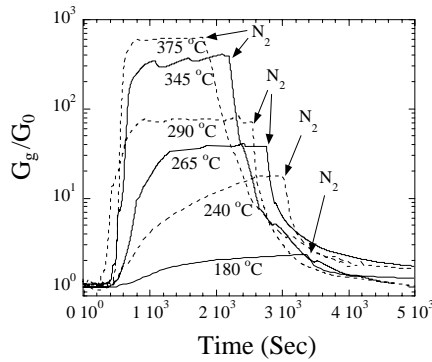
**Figure 14.** Variation of normalized conductance of nanotubes of pore size 76 nm with respect to time on exposure to 1000 ppm hydrogen at different temperatures.

of 76 nm with standard deviation SD = 15 nm, 46 nm (SD = 8 nm), and 22 nm (SD = 5 nm); wall thickness 27 nm (SD = 6 nm), 17 nm (SD = 2 nm), and 13 nm (SD = 2 nm); and lengths 400 nm, 240 nm, and 200 nm. Prior to sensing studies, samples were annealed at 500 °C in a pure oxygen ambient for 6 hours with a heating and cooling rate of 1 °C. The sensor consists of a base titanium metal foil with a nanotube array grown on top. An insulating barrier layer separates the nanotubes from the conducting titanium foil. Electrical connections were made by two parallel 10 mm × 2 mm platinum pads of 100 $\mu$m thickness.

Figure 14 shows the response of the 20 V (76 nm diameter) nanotube sample as a function of ambient temperature as it is switched from a nitrogen environment to one containing 1000 ppm hydrogen, and then back to nitrogen. The plot is made using normalized conductance $G_g/G_0$ versus time where $G_0$ is the base conductance of the sensor, that is, the sensor resistance before introducing the test gas, and $G_g$ the conductance in the presence of the test gas. The magnitude of the conductance variation increases with temperature, starting from a marginal variation at 180 °C to a variation of three orders of magnitude at approximately 400 °C.

The variation in electrical conductance of 76 nm, 46 nm, and 22 nm diameter TiO$_2$ nanotube arrays with exposure to 1000 ppm hydrogen at 290 °C is shown in Figure 15. It is clear that the conductance variation is more prominent with smaller diameter nanotubes. The 22 nm diameter nanotube
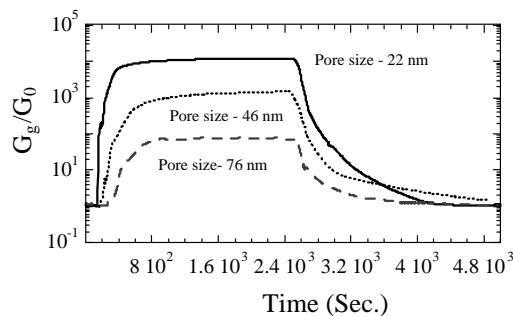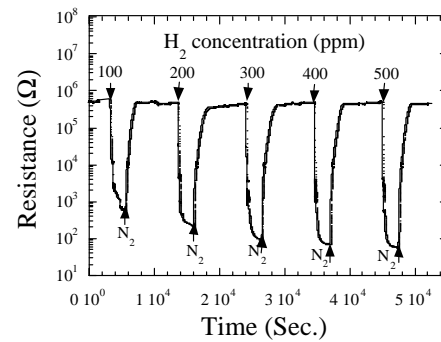


**Figure 16.** Response of the nanotube sensor with pore size 22 nm at 290 °C on cycling hydrogen concentration from 0 to 500 ppm in discrete steps of 100 ppm.

sample shows a four orders of magnitude change in conductance. Figure 16 shows the variation in resistance of a 22 nm diameter nanotube sample at 290 °C when the hydrogen concentration is cycled from 0 to 500 ppm in discrete steps of 100 ppm. A three orders of magnitude variation in the resistance is seen with exposure of 100 ppm hydrogen. It is clear from this that the nanotubes respond without hysteresis. The nanotubes respond to hydrogen over a wide range of concentrations; a typical conductance isotherm of the 22 nm diameter nanotubes is shown in Figure 17. Furthermore, the sensors showed high selectivity to hydrogen compared to carbon monoxide, ammonia and carbon dioxide. Although, the resistance of the nanotubes increased in the presence of oxygen, the change was not completely reversible.

Studies indicated that chemisorption of hydrogen spilled over onto the nanotube surface by platinum electrodes is the process behind the sensing action of the nanotubes [250]. Hydrogen acts as an electron donor on chemisorption. However the high sensitivity shown by the 22 nm diameter nanotubes cannot be explained merely by simple chemisorption. A factor that may be influencing the sensitivity is the wall thickness of the nanotubes. Once the wall thickness is comparable to the size of the negative space charge region created by the chemisorbed hydrogen, the sensitivity may increase drastically. The nanotube contact points may also play a key role in determining the high hydrogen sensitivity. For a given electrode, separation number of contact points increases as the diameter of the nanotubes decreases. However, detailed investigations are needed to study the unusual



**Figure 15.** Influence of the dimensions of the tube on the conductance variation of the sensor when exposed to 1000 ppm hydrogen at 290 °C.
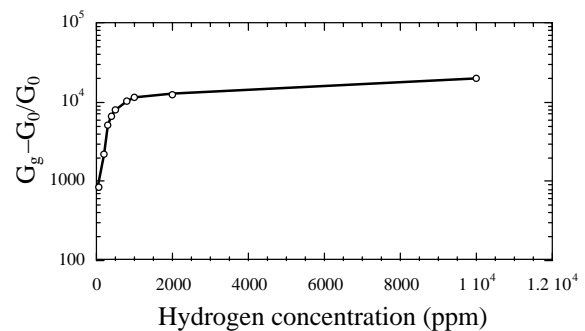


**Figure 17.** Conductance isotherm of 22 nm inner-diameter nanotubes at 290 °C.

sensing behavior shown by the nanotubes. The example illustrates the exciting opportunities offered for incorporating novel nanoarchitectured materials into gas sensors having advanced properties.

# 6. CONCLUSIONS

Due to their size and geometry, metal oxide nanostructures exhibit gas sensing capabilities of extraordinary sensitivity. Most gas sensor studies have focused on the application of titania and tin oxide, although many different materials have been investigated. For all materials, excellent sensing characteristics have been demonstrated with scaling of material feature size to the nanoscale. An extensive literature survey shows that while the nanoarchitectured materials achieve excellent gas sensitivities, the issue of structural stability at elevated temperatures limits their immediate application. However once the issue of feature stability is successfully addressed, the outstanding gas sensing properties of the materials indicate that nanotechnology will dominate the metal oxide gas sensor field in the near future.

# GLOSSARY

**Adsorbate** The species that get adsorbed on the surface of a material.

**Adsorbent** The material on which the adsorption occurs.

**Debye length** The distance beyond which a given charge is effectively shielded by the other charges in the material.

**Madelung potential** The potential at a site in or on the crystal, arising due to all the point charges in the crystal.

**Sensor** A device that responds to a physical or chemical stimulus and expresses this response in the form of a recordable signal.

# ACKNOWLEDGMENTS

# REFERENCES

1. M. J. Madou and S. R. Morrison, "Chemical Sensing with Solid State Devices," Academic Press, New York, 1989.
2. A. Hulanicki, S. Glab, and F. Ingman, *Pure Appl. Chem.* 63, 1247 (1991).
3. T. Seiyama, "Chemical Sensor Technology," Elsevier, Amsterdam, 1988, Vol. 1 & 2, p. 1.
4. U. Lampe, M. Fleischer, N. Reitmeier, H. Meixner, J. B. Mcmonagle, and A. Marsh, in "Sensors Update" H. Baltz, W. Gopel, and J. Hesse, Eds., 1996, Vol. 2, p. 1.
5. W. Gopel and G. Reinhardt, in "Sensors Update," H. Baltz, W. Gopel, and J. Hesse, Eds., 1996, Vol. 1, p. 49.
6. G. Sberveglieri, "Gas Sensors," Kluwer, Boston, 1992.
7. S. R. Morrison, in "Semiconductor Sensors," S. M. Sze, Ed., Wiley, New York, 1994.
8. W. H. Brattain and J. Bardeen, *Bell Systems Technical Journal* 32, 1 (1953).
9. S. R. Morrison, *Sens. Actuators* 12, 425, 1987.
10. T. Seiyama, A. Kato, K. Fujiishi, and M. Nagatani, *Anal. Chem.* 34, 1502 (1962).
11. N. Taguchi, U.S. Patent No. 3644795 (1972).
12. P. T. Moseley, *Sens. Actuators, B* 6, 149 (1992).
13. C. N. R. Rao, A. R. Raju, and K. Vijayamohanan, in "New Materials" S. K. Joshi, C. N. R. Rao, T. Tsurma, and S. Nagakma, Eds., Narosa Publishing, New Delhi, 1992, p. 1.
14. M. Egashira and Y. Shimizu, "SPIE Proceedings of the International Conference on Thin Film Physics and Applications," Vol. 1519, p. 467, 1991.
15. K. H. Kim and C. G. Park, *J. Electrochem. Soc.* 138, 2408 (1991).
16. E. Traversa, *Sens. Actuators, B* 23, 135 (1995).
17. A. Dabrowski, *Adv. Colloid Interface Sci.* 93, 135 (2001).
18. J. Ding, T. J. McAvoy, R. E. Cavicchi, and S. Semancik, *Sens. Actuators, B* 17, 597 (2001).
19. W. Gopel and R. Feierabend, *Phys. Rev. B* 28, 3427 (1983).
20. S. R. Morrison, *Surf. Sci.* 13, 85 (1969).
21. L. Ottaviano, E. Maccallini, and S. Santucci, *Surf. Sci.* 492, L700 (2001).
22. K.-D. Schierbaum, *Sens. Actuators, B* 24–25, 239 (1995).
23. K. D. Schierbaum, H. D. Wiemhofer, and W. Gopel, *Solid State Ionics* 28–30, 1631 (1988).
24. A. M. Gaskov and M. N. Rumyantseva, *Russ. J. Appl. Chem.* 74, 440 (2001).
25. D. Kohl, *Sens. Actuators* 18, 71 (1989).
26. T. G. G. Maffeïs, G. T. Owen, M. W. Penny, T. K. H. Starke, S. A. Clark, H. Ferkel, and S. P. Wilks, *Surf. Sci.* 520, 29 (2002).
27. P. B. Weisz, *J. Chem. Phys.* 21, 1531 (1953).
28. J. N. Zemel, *Thin Solid Films* 163, 189 (1988).
29. P. T. Moseley and D. E. Williams, *Polyhedron* 8, 1615 (1989).
30. W. J. Fleming, *Soc. Automot. Eng. Trans.* Section 2, 90, 1656 (1981).
31. T. Moromoto, M. Nagao, and F. Tokuda, *J. Phys. Chem.* 73, 243 (1969).
32. L. Marcussen, *Chem. Eng. Sci.* 25, 1487 (1970).
33. T. Seiyama, K. Fueki, J. Shiokawa, and S. Suzuki (Eds.), "Chemical Sensors," Elsevier, New York, 1983.
34. V. K. Khanna and R. K. Nahar, *Appl. Surf. Sci.* 28, 247 (1987).
35. V. K. Khanna and R. K. Nahar, *J. Phys. D: Appl. Phys.* 19, L141 (1986).
36. R. W. Siegel, in "Fundamental Properties of Nanostructured Materials," D. Fiorani and G. Sberveglieri, Eds., 1993, p. 3.
37. H. Ogawa, A. Abe, M. Nishikawa, and S. Hayakawa, *J. Electrochem. Soc.* 128, 2020 (1981).
38. C. Xu, J. Tamaki, N. Miura, and N. Yamazoe, *Sens. Actuators, B* 3, 147 (1991).
39. J. W. Gardner, *Sens. Actuators* 18, 373 (1989).
40. H. Arai and T. Seiyama, in "Sensors: A Comprehensive Survey," W. Gopel, J. Hesse, and J. N. Zemel (Eds.), VCH, Weinheim, 1992, Vol. 3, p. 155.
41. Y. Shimizu, H. Arai, and T. Seiyama, *Sens. Actuators* 7, 11 (1985).
42. S. H. Tao, W. M. Tang, L. Ping, and Y. Xi, *Sens. Actuators* 19, 61 (1989).
43. A. Sayari, M. Jaroniec, and T. J. Pinnavaia, "Nanoporous Materials II," Elsevier, Amsterdam, 2000.
44. A. Sayari and M. Jaroniec, "Nanoporous Materials III," Elsevier, Amsterdam, 2002.
45. S. Semancik and T. B. Fryberger, *Sens. Actuators, B* 1, 97 (1990).
46. R. M. Geatches, A. V. Chadwick, and J. D. Wright, *Sens. Actuators, B* 4, 467 (1991).
47. B. Bott, T. A. Jones, and B. Mann, *Sens. Actuators* 5, 65 (1984).
48. G. E. Poirier, R. E. Cavicchi, and S. Semancik, *J. Vac. Sci. Technol. A* 11, 1392 (1993).
49. W. Gopel, U. Kirner, and H. D. Wiemhofer, *Solid State Ionics* 28–30, 1423 (1988).
50. B. Chwieroth, B. R. Patton, and Y. Wang, *J. Electroceramics* 6, 27 (2001).
51. N. Yamazoe, *Sens. Actuators, B* 5, 7 (1991).

52. X. Wang, S. S. Yee, and W. P. Carey, *Sens. Actuators, B* 24–25, 454 (1995).
53. H. Ogawa, M. Nishikawa, and A. Abe, *J. Appl. Phys.* 53, 4448 (1982).
54. G. Sberveglieri, C. Perego, F. Parmigiani, G. Dinelli, and G. Quattroni, *Sens. Actuators, B* 20, 163 (1994).
55. K. D. Schierbaum, U. Weimar, W. Gopel, and R. Kowalkowski, *Sens. Actuators, B* 3, 205 (1991).
56. W. Gopel and K. D. Schierbaum, *Sens. Actuators, B* 26–27, 1 (1995).
57. J. Scoonman, *Solid State Ionics* 135, 5 (2000).
58. A, Chiorino, G. Ghiotti, F. Prinetto, M. C. Carotta, M. Gallana, and G. Martinelli, *Sens. Actuators, B* 59, 203 (1999).
59. Q. Pan, J. Xu, X. Dong, and J. Zhang, *Sens. Actuators, B* 66, 237 (2000).
60. S. G. Ansari, P. Boroojerdian, S. R. Sainkar, R. N. Karekar, R. C. Aiyer, and S. K. Kulkarni, *Thin Solid Films* 295, 271 (1997).
61. G. Zhang and M. Liu, *Sens. Actuators, B* 69, 144 (2000).
62. N. S. Baik, G. Sakai, N. Miura, and N. Yamazoe, *Sens. Actuators, B* 63, 74 (2000).
63. S. V. Manorama, C. V. G. Reddy, and V. J. Rao, *Nanostruct. Mater.* 11, 643 (1999).
64. X. Liu, J. Yang, L. Wang, X. Yang, L. Lu, and X. Wang, *Mater. Sci. Eng. A* 289, 241 (2000).
65. M. Z. Atashbar, H. T. Sun, B. Gong, W. Wlodarski, and R. Lamb, *Thin Solid Films* 326, 238 (1998).
66. Z. A. Ansari, S. G. Ansari, T. Ko, and J.-H. Oh, *Sens. Actuators, B* 87, 105 (1991).
67. C. Garzella, E. Comini, E. Bontempi, L. E. Depero, C. Frigeri, and G. Sberveglieri, *Sens. Actuators, B* 83, 230 (2002).
68. E. Comini, G. Faglia, G. Sberveglieri, Y. X. Li, W. Wlodarski, and M. K. Ghantasala, *Sens. Actuators, B* 64, 169 (2000).
69. G. Sberveglieri, E. Comini, G. Faglia, M. Z. Atashbar, and W. Wlodarski, *Sens. Actuators, B* 66, 139 (2000).
70. X. Liu, J. Yang, L. Wang, X. Yang, L. Lu, and X. Wang, *Mater. Sci. Eng. A* 289, 241 (2000).
71. D.-S. Lee, S.-D. Han, J.-S. Huh, and D.-D. Lee, *Sens. Actuators, B* 60, 57 (1999).
72. A. Chiorino, G. Ghiotti, F. Prinetto, M. C. Carotta, D. Gnani, and Martinelli, *Sens. Actuators, B* 58, 338 (1999).
73. Y. X. Li, K. Galatsis, W. Wlodarski, M. Passacantando, S. Santucci, P. Siciliano, and M. Catalano, *Sens. Actuators, B* 77, 27 (2001).
74. S. Zhuiykov, W. Wlodarski, and Y. Li, *Sens. Actuators, B* 77, 484 (2001).
75. W.-P. Tai and J.-H. Oh, *Sens. Actuators, B* 85, 154 (2002).
76. O. K. Varghese, L. K. Malhotra, and G. L. Sharma, *Sens. Actuators, B* 55, 161 (1999).
77. X. Ge, Y. Liu, and X. Liu, *Sens. Actuators, B* 79, 171 (2001).
78. X. Chu, X. Liu, G. Wang, and G. Meng, *Mater. Res. Bull.* 34, 1789 (1999).
79. X. Chu, X. Liu, and G. Meng, *Mater. Res. Bull.* 34, 693 (1999).
80. J. Xu, Q. Pan, Y. Shun, and Z. Tian, *Sens. Actuators, B* 66, 277 (2000).
80. M. Ferroni, M. C. Carotta, V. Guidi, G. Martinelli, F. Ronconi, M. Sacerdoti, and E. Traversa, *Sens. Actuators, B* 77, 163 (2001).
81. M. C. Carotta, M. Ferroni, D. Gnani, V. Guidi, M. Merli, G. Martinelli, M. C. Casale, and M. Notaro, *Sens. Actuators, B* 58, 310 (1999).
82. P. Keller, H. Ferkel, K. Zweiacker, J. Naser, J.-U. Meyer, and W. Riehemann, *Sens. Actuators, B* 57, 39 (1999).
83. M. J. Willett, V. N. Burganos, C. D. Tsakiroglou, and A. C. Payatakes, *Sens. Actuators, B* 53, 76 (1998).
84. T. K. H. Starke, G. S. V. Coles, and H. Ferkel, *Sens. Actuators, B* 85, 239 (2002).
85. M. Ferroni, V. Guidi, G. Martinelli, G. Gaglia, P. Nelli, and G. Sberveglieri, *Nanostruct. Mater.* 7, 709 (1996).
86. E. Comini, G. Sberveglieri, M. Ferroni, V. Guidi, and G. Martinelli, *Sens. Actuators, B* 68, 175 (2000).
87. A. Karthigeyan, R. P. Gupta, K. Scharnagl, M. Burgmair, M. Zimmer, S. K. Sharma, and I. Eisele, *Sens. Actuators, B* 78, 69 (2001).
88. M. Ferroni, V. Guidi, G. Martinelli, P. Nelli, and G. Sberveglieri, *Sens. Actuators, B* 44, 499 (1997).
89. M. C. Carotta, M. Ferroni, V. Guidi, and G. Martinelli, *Adv. Mater.* 11, 943 (1999).
90. G. Sberveglieri, L. E. Deero, M. Ferroni, V. Guidi, G. Martinelli, P. Nelli, C. Perego, and L. Sangaletti, *Adv. Mater.* 8, 334 (1996).
91. H.-M. Lin, C.-H. Keng, and C.-Y. Tung, *Nanostruct. Mater.* 9, 747 (1997).
92. F. Li, J. Xu, X. Yu, L. Chen, J. Zhu, Z. Yang, and X. Xin, *Sens. Actuators, B* 81, 165 (2002).
93. F. Li, L. Chen, Z. Chen, J. Xu, J. Zhu, and X. Xin, *Mater. Chem. Phys.* 73, 335 (2002).
94. G. Korotcenkov, V. Brinzari, J. Schwank, and A. Cerneavschi, *Mater. Sci. Eng. C* 19, 73 (2002).
95. O. K. Tan, W. Zhu, Q. Yan, and L. B. Kong, *Sens. Actuators, B* 65, 361 (2000).
96. M. Ferroni, M. C. Carotta, V. Guidi, G. Martinelli, F. Ronconi, O. Richard, D. V. Dyck, and J. V. Landuyt, *Sens. Actuators, B* 68, 140 (2000).
97. M. N. Rumyantseva, M. N. Bulova, T. A. Kuznetsova, L. I. Ryabova, A. M. Gaskov, G. Loucaseau, and M. Labeau, *Russ. J. Appl. Chem.* 74, 434 (2001).
98. G. Sberveglieri, G. Faglia, S. Groppelli, P. Nelli, and A. Camanzi, *Semicond. Sci. Technol.* 5, 1231 (1990).
99. G. Sberveglieri, *Sens. Actuators, B* 6, 239 (1992).
100. G. Sberveglieri, S. Groppelli, P. Nelli, and C. Perego, *Sens. Actuators, B* 15–16, 86 (1993).
101. G. Sberveglieri and P. Nelli, in "Fundamental Properties of Nanostructured Materials," D. Fiorani and G. Sberveglieri, Eds., 1993, p. 288.
102. L. F. Dong, Z. L. Cui, and Z. K. Zhang, *Nanostruct. Mater.* 8, 815 (1997).
103. J. L. Solis, S. Saukko, L. Kish, C. G. Granqvist, and V. Lantto, *Thin Solid Films* 391, 255 (2001).
104. H.-M. Lin, C.-M. Hsu, H.-Y. Yang, P.-Y Lee, and C.-C. Yang, *Sens. Actuators, B* 22, 63 (1994).
105. F. Lu, Y. Liu, M. Dong, and X. Wang, *Sens. Actuators, B* 66, 225 (2000).
106. F. Lu, S. Chen, and S. Peng, *Catal. Today* 30, 183 (1996).
107. B. Panchapakesan, D. L. DeVoe, M. R. Widmaier, R. Cavicchi, and S. Semancik, *Nanotechnology* 12, 336 (2001).
108. C. Nayral, T. O. Ely, A. Maisonnat, B. Chaudret, P. Fau, L. Lescouzerez, and A. P. Lavigne, *Adv. Mater.* 11, 61 (1999).
109. P. Fau, M. Sauvan, S. Trautweiler, C. Nayral, L. Erades, A. Maisonnat, and B. Chaudret, *Sens. Actuators, B* 78, 83 (2001).
110. Z. Jin, H.-J. Zhou, Z.-L. Jin, R. F. Savinell, and C.-C. Liu, *Sens. Actuators, B* 52, 188 (1998).
111. G. S. Devi, T. Hyodo, Y. Shimizu, and M. Egashira, *Sens. Actuators, B* 87, 122 (2002).
112. W. Qu, W. Wlodarski, and J.-U. Meyer, *Sens. Actuators, B* 64, 76 (2000).
113. H. Hirashima, H. Imai, and V. Balek, *J. Non-Cryst. Solids* 285, 96 (2001).
114. R. Konenkamp and I. Rieck, *Mater. Sci. Eng. B* 69–70, 519 (2000).
115. Y.-D. Wang, C.-L. Ma, X.-H. Wu, X.-D. Sun, and H.-D. Li, *Sens. Actuators, B* 85, 270 (2002).
116. G.-J. Li and S. Kawi, *Talanta* 45, 759 (1998).
117. T. Hyodo, N. Nishida, Y. Shimizu, and M. Egashira, *Sens. Actuators, B* 83, 209 (2002).
118. L. Qi, J. Ma, H. Cheng, and Z. Zhao, *Langmuir* 14, 2579 (1998).
119. G.-J. Li, and S. Kawi, *Mater. Lett.* 34, 99 (1998).
120. Y. Wang, C. Ma, X. Sun, and H. Li, *Microporous Mater.* 49, 171 (2001).

121. S. Cabrera, J. E. Haskouri, C. Guillem, J. Latorre, A. B. Porter, and D. B. Porter, *Solid State Sciences* 2, 405 (2000).
122. M. M. Yusuf, H. Imai, and H. Hirashima, *J. Non-Cryst. Solids* 285, 90 (2001).
123. K. M. S. Khalil and M. I. Zaki, *Powder Technol.* 120, 256 (2001).
124. Y. Zhang, A. Weidenkaff, and A. Reller, *Mater. Lett.* 54, 375 (2002).
125. Y.-D. Wang, C.-L. Ma, X.-H. Wu, X.-D. Sun, and H.-D. Li, *Talanta* 57, 875 (2002).
126. Y. K. Hwang, K.-C. Lee, and Y.-U. Kwon, *Chem. Commun.* 1738 (2001).
127. Y. Wang, X. Tang, L. Yin, W. Huang, Y. R. Hacohen, and A. Gedanken, *Adv. Mater.* 12, 1183 (2000).
128. Y. Shimizu, N. Kuwano, T. Hyodo, and M. Egashira, *Sens. Actuators, B* 83, 195 (2002).
129. H. Masuda, H. Yamada, M. Satoh, H. Asoh, M. Nakao, and T. Tamamura, *Appl. Phys. Lett.* 71, 2770 (1997).
130. Y. C. Zhu and C. X. Ding, *Nanostruct. Mater.* 11, 319 (1999).
131. L. Gao, Q. Li, Z. Song, and J. Wang, *Sens. Actuators, B* 71, 179 (2000).
132. J. Zhao, Z. Wang, L. Wang, H. Yang, and M. Zhao, *Mater. Chem. Phys.* 63, 9 (2000).
133. P. Hoyer and H. Masuda, *J. Mater. Sci. Lett.* 15, 1228 (1996).
134. I. Hayakawa, Y. Iwamoto, K. Kikuta, and S. Hirano, *Sens. Actuators, B* 62, 55 (2000).
135. H. Masuda and K. Fukuda, *Science* 268, 1466 (1995).
136. H. Masuda, F. Hasegwa, and S. Ono, *J. Electrochem. Soc.* 144, L127 (1997).
137. O. Jessensky, F. Muller, and U. Gosele, *Appl. Phys. Lett.* 72, 1173 (1998).
138. S. Ijima, *Nature* 354, 56 (1991).
139. L. Pu, X. Bao, J. Zou, and D. Feng, *Angew. Chem.* 113, 1538 (2001).
140. Y. Zhang, J. Liu, R. He, Q. Zhang, X. Zhang, and J. Zhu, *Chem. Phys. Lett.* 360, 579 (2002).
141. J.-S. Lee, K. Park, S. Nahm, S.-W. Kim, and S. Kim, *J. Cryst. Growth* 244, 287 (2002).
142. J. Zou, L. Pu, X. Bao, and D. Feng, *Appl. Phys. Lett.* 80, 1079 (2002).
143. Z. R. Dai, J. L. Gole, J. D. Stout, and Z. L. Wang, *J. Phys. Chem. B* 106, 1274 (2002).
144. M. Zhang, Y. Bando, and K. Wada, *J. Mater. Res.* 16, 1408 (2001).
145. C. Hippe, M. Wark, E. Lork, and G. S. Ekloff, *Microporous Mater.* 31, 235 (1999).
146. Z. Shunli, Z. Jingfang, Z. Zhijun, D. Zuliang, A. V. Vorontsov, and J. Zhensheng, *Chin. Sci. Bull.* 45, 1533 (2000).
147. T. Kasuga, M. Hiramatsu, A. Hoson, T. Sekino, and K. Niihara, *Langmuir* 14, 3160 (1998).
148. P. Hoyer, *Langmuir* 12, 1411 (1996).
149. M. Adachi, Y. Murata, M. Harada, and S. Yoshikawa, *Chem. Lett.* 942 (2000).
150. H. Imai, Y. Takei, K. Shimizu, M. Matsuda, and H. Hirashima, *J. Mater. Chem.* 9, 2971 (1999).
151. Y. Zhu, H. Li, Y. Koltypin, Y. R. Hacohen, and A. Gedanken, *Chem. Commun.* 2616 (2000).
152. T. Kasuga, M. Hiramatsu, A. Hoson, T. Sekino, and K. Niihara, *Adv. Mater.* 11, 1307 (1999).
153. Q. Zhang, L. Gao, J. Sun, and S. Zheng, *Chem. Lett.* 226 (2000).
154. G. R. Patzke, F. Krumeich, and R. Nesper, *Angew. Chem.* 41, 2446 (2002).
155. A. Michailowski, D. Almawlawi, G. Cheng, and M. Moskovits, *Chem. Phys. Lett.* 349, 1 (2001).
156. B. B. Lakshmi, P. K. Dorhout, and C. R. Martin, *Chem. Mater.* 9, 857 (1997).
157. R. A. Caruso, J. H. Scaattka, and A. Greiner, *Adv. Mater.* 13, 1577 (2001).
158. S. M. Liu, L. M. Gan, L. H. Liu, W. D. Zhang, and H. C. Zeng, *Chem. Mater.* 14, 1391 (2002).
159. Y. Zhang and A. Reller, *Chem. Commun.* 606, (2002).
160. C.-H. Lin, S.-H. Chien, J.-H. Chao, C.-Y. Sheu, Y.-C. Cheng, Y.-J. Huang, and C.-H. Tsai, *Catal. Lett.* 80, 153 (2002).
161. M. Zhang, Y. Bando, and K. Wada, *J. Mater. Sci. Lett.* 20, 167 (2001).
162. D. Gong, C. A. Grimes, O. K. Varghese, W. Hu, R. S. Singh, Z. Chen, and E. C. Dickey, *J. Mater. Res.* 16, 3331 (2001).
163. K. S. Pillai, F. Krumeich, H.-J. Muhr, M. Niederberger, and R. Nesper, *Solid State Ionics* 141–142, 185 (2001).
164. X. Chen, X. Sun, and Y. Li, *Inorg. Chem.* 41, 4524 (2002).
165. F. Bieri, F. Krumeich, H.-J. Muhr, and R. Nesper, *Helv. Chi. Acta* 84, 3015 (2001).
166. A. Dobley, K. Ngala, S. Yang, P. Y. Zavalij, and M. S. Whittingham, *Chem. Mater.* 13, 4382 (2001).
167. M. Niederberger, H.-J. Muhr, F. Krumeich, F. Bieri, D. Gunther, and R. Nesper, *Chem. Mater.* 12, 1995 (2000).
168. H.-J. Muhr, F. Krumeich, U. P. Schonholzer, F. Bieri, M. Niederberger, L. J. Gauckler, and R. Nesper, *Adv. Mater.* 12, 231 (2000).
169. M. E. Spahr, P. S. Bitterli, R. Nesper, O. Haas, and P. Novak, *J. Electrochem. Soc.* 146, 2780 (1999).
170. M. E. Spahr, P. Bitterli, R. Nesper, M. Muller, F. Krumeich, and H. U. Nissen, *Angew. Chem.* 37, 1263 (1998).
171. C. N. R. Rao, B. C. Satishkumar, and A. Govindaraj, *Chem. Commun.* 1582 (1997).
172. J.-J. Wu, S.-C. Liu, C.-T. Wu, K.-H. Chen, and L.-C. Chen, *Appl. Phys. Lett.* 81, 1312 (2002).
173. J. Zhang, L. Sun, C. Liao, and C. Yan, *Chem. Commun.* 262 (2002).
174. X. Zhang, B. Yao, L. Zhao, C. Liang, L. Zhang, and Y. Mao, *J. Electrochem. Soc.* 148, G398 (2001).
175. B. C. Satishkumar, A. Givindraj, E. M. Vogl, L. Basumallick, and C. N. R. Rao, *J. Mater. Res.* 12, 604 (1997).
176. Y. X. Zhang, G. H. Li, Y. X. Jin, Y. Zhang, J. Zhang, and L. D. Zhang, *Chem. Phys. Lett.* 365, 300 (2002).
177. Z. R. Dai, Z. W. Pan, and Z. L. Wang, *Solid State Commun.* 118, 351 (2001).
178. H. Kind, H. Yan, B. Messer, M. Law, and P. Yang, *Adv. Mater.* 14, 158 (2002).
179. J.-J. Wu and S.-C. Liu, *Adv. Mater.* 14, 215 (2002).
180. M. H. Huang, Y. Wu, H. Feick, N. Tran, E. Weber, and P. Yang, *Adv. Mater.* 13, 113 (2001).
181. P. Yang, H. Yan, S. Mao, R. Russo, J. Johnson, R. Saykally, N. Morris, J. Pham, R. He, and H.-J. Choi, *Advanced Functional Materials* 12, 323 (2002).
182. X. M. Sun, X. Chen, Z. X. Deng, and Y. D. Li, *Mater. Chem. Phys.* 78, 99 (2002).
183. Y. Dai, Y. Zhang, Q. K. Li, and C. W. Nan, *Chem. Phys. Lett.* 358, 83 (2002).
184. L. Guo, J. X. Cheng, X.-Y. Li, Y. J. Yan, S.H. Yang, C. L. Yang, J. N. Wang, and W. K. Ge, *Mater. Sci. Eng. C* 16, 123 (2001).
185. J. Y. Li, X. L. Chen, H. Li, M. He, and Z. Y. Qiao, *J. Cryst. Growth* 233, 5 (2001).
186. W. Q. Han, P. K. Redlich, F. Ernst, and M. Ruhle, *Solid State Commun.* 115, 527 (2000).
187. Y. H. Gao, Y. Bando, T. Sato, Y. F. Zhang, and X. Q. Gao, *Appl. Phys. Lett.* 81, 2267 (2002).
188. K. E. Gonsalves, H. Li, and P. Santiago, *J. Mater. Sci.* 36, 2461 (2001).
189. K.-N. P. Kumar, J. Engell, J. Kumar, K. Keizer, T. Okubo, and M. Sadakata, *J. Mater. Sci. Lett.* 14, 1784 (1995).
190. J. A. Varela, O. J. Whittemore, and E. Longo, *Ceramics International* 16, 177 (1990).
191. O. J. Whittemore and J. J. Sipe, *Powder Technol.* 9, 159 (1974).
192. K.-N. P. Kumar, K. Keizer, A. J. Burggraaf, T. Okubo, and H. Nagamoto, *J. Mater. Chem.* 3, 1151 (1993).

*193.* Y. Ohya, H. Saiki, T. Tanaka, and Y. Takahashi, *J. Am. Ceram. Soc.* 79, 825 (1996).

*194.* X.-Z. Ding and X.-H. Liu, *J. Mater. Sci. Lett.* 15, 1392 (1996).

*195.* K. J. D. MacKenzie, *Transactions and Journal of the British Ceramic Society* 74, 29 (1975).

*196.* F. C. Gennari and D. M. Pasquevich, *J. Mater. Sci.* 33, 1571 (1998).

*197.* Y. Iida and S. Ozaki, *J. Am. Ceram. Soc.* 44, 120 (1961).

*198.* K.-N. P. Kumar, K. Keizer, A. J. Burggraaf, T. Okuba, and H. Nagamoto, *J. Mater. Chem.* 3, 923 (1993).

*199.* K.-N. P. Kumar, K. Keizer, A. J. Burggraaf, T. Okubo, H. Nagamoto, and S. Morooka, *Nature* 358, 48 (1992).

*200.* O. K. Varghese, D. Gong, M. Paulose, C. A. Grimes, and E. C. Dickey, *J. Mater. Res.*, in press, (2003).

*201.* I. Kosacki and H. U. Anderson, *Sens. Actuators, B* 48, 263 (1998).

*202.* T. K. H. Starke, G. S. V. Coles, and H. Ferkel, *Sens. Actuators, B* 85, 239 (2002).

*203.* D.-S. Lee, H.-Y. Jung, J.-W. Lim, M. Lee, S.-W. Ban, J.-S. Huh, and D.-D. Lee, *Sens. Actuators, B* 71, 90 (2000).

*204.* M. A. E. Khakani, R. Dolbec, A. M. Serventi, M. C. Horrillo, M. Trudeau, R. G. S. Jacques, D. G. Rickerby, and I. Sayago, *Sens. Actuators, B* 77, 383 (2001).

*205.* D.-S. Lee, D.-D. Lee, S.-W. Ban, M. Lee, and Y. T. Kim, *IEEE Sensors Journal* 2, 140 (2002).

*206.* V. Guidi, M. C. Carotta, M. Ferroni, G. Martinelli, L. Paglialonga, E. Comini, and G. Sberveglieri, *Sens. Actuators, B* 57, 197 (1999).

*207.* G. Sakai, N. S. Baik, N. Miura, and N. Yamazoe, *Sens. Actuators, B* 77, 116 (2001).

*208.* Y. Li, M. Z. Atashbar, M. K. Ghantasala, W. Wlodarski, and M. W. Austin, "1998 Conference on Optoelectronic and Microelectronic Materials and Devices Proceedings," IEEE, p. 310, 1999.

*209.* A. V. Chadwick, N. V. Russell, A. R. Whitham, and A. Wilson, *Sens. Actuators, B* 18–19, 99 (1994).

*210.* M.-I. Baraton, L. Merhari, P. Keller, K. Zweiacker, and J.-U. Meyer, *Mater. Res. Soc. Symp. Proc.* 536, 341 (1999).

*211.* E. Comini, V. Guidi, C. Frigeri, I. Ricco, and G. Sberveglieri, *Sens. Actuators, B* 77, 16 (2001).

*212.* C. Nayral, E. Viala, P. Fau, F. Senocq, J.-C. Jumas, A. Maisonnat, and B. Chaudret, *Chem.—Eur. J.* 6, 4082 (2000).

*213.* D. S. Vlachos and A. C. Xenoulis, *Nanostruct. Mater.* 10, 1355 (1998).

*214.* O. K. Varghese and L. K. Malhotra, *Sens. Actuators, B* 53, 19 (1998).

*215.* O. K. Varghese and L. K. Malhotra, *J. Appl. Phys.* 87, 7457 (2000).

*216.* G. Bläser, Th. Rühl, C. Diehl, M. Ulrich, and D. Kohl, *Physica A* 266, 218 (1999).

*217.* T. Yamazaki, S. Wada, T. Noma, and T. Suzuki, *Sens. Actuators, B* 13–14, 594 (1993).

*218.* T. Dittrich, J. Weidmann, F. Koch, I. Uhlendorf, and I. Lauermann, *Appl. Phys. Lett.* 75, 3980 (1999).

*219.* G. Neri, A. Bonavita, S. Galvagno, P. Siciliano, and S. Capone, *Sens. Actuators, B* 82, 40 (2002).

*220.* G. Li and S. Kawi, *Sens. Actuators, B* 59, 1 (1999).

*221.* F. Ansbacher and A. C. Jason, *Nature* 171, 177 (1953).

*222.* V. K. Khanna and R. K. Nahar, *Sens. Actuators* 5, 187 (1984).

*223.* S. Basu, S, Chatterjee, M. Saha, S. Bhandyopadhay, K. K. Mistry, and K. Sengupta, *Sens. Actuators, B* 79, 182 (2001).

*224.* G. Sberveglieri, R. Anchisini, R. Murri, C. Ercoli, and N. Pinto, *Sens. Actuators, B* 32, 1 (1996).

*225.* L. H. Mai, P. T. M. Hoa, N. T. Binh, N. T. T. Ha, and D. K. An, *Sens. Actuators, B* 66, 63 (2000).

*226.* S. Chatterjee, S. Basu, S. Bandyopadhay, K. K. Mistry, and K. Sengupta, *Rev. Sci. Instrum.* 72, 2792 (2001).

*227.* R. K. Nahar, *Sens. Actuators, B* 63, 49 (2000).

*228.* Z. Chen, M.-C. Jin, and C. Zhen, *Sens. Actuators* 2, 167 (1990).

*229.* S. Basu, M. Saha, S. Chatterjee, K. K. Mistry, S. Bandyopadhay, and K. Sengupta, *Mater. Lett.* 49, 29 (2001).

*230.* Y. Sadaoka, Y. Sakai, and S. Matsumoto, *J. Mater. Sci.* 21, 1269 (1986).

*231.* B. M. Kulwicki, *J. Am. Ceram. Soc.* 74, 697 (1991).

*232.* N. Yamazoe and Y. Shimizu, *Sens. Actuators* 10, 379 (1986).

*233.* T. Seiyama, N. Yamazoe, and H. Arai, *Sens. Actuators* 4, 85 (1983).

*234.* L. Ketron, *Ceramic Bulletin* 68, 860 (1989).

*235.* M. K. Jain, M. C. Bhatnagar, and G. L. Sharma, *Sens. Actuators, B* 55, 180 (1999).

*236.* G. Sberveglieri, R. Murri, and N. Pinto, *Sens. Actuators, B* 23, 177 (1995).

*237.* K.-S. Chou, T.-K. Lee, and F.-J. Liu, *Sens. Actuators, B* 56, 106 (1999).

*238.* Y.-C. Yeh, T.-Y. Tseng, and D.-A. Chang, *J. Am. Ceram. Soc.* 72, 1472 (1989).

*239.* C. Cantalini, M. Faccio, G. Ferri, and M. Pelino, *Sens. Actuators, B* 15–16, 293 (1993).

*240.* O. K. Varghese, D. Gong, M. Paulose, K. G. Ong, C. A. Grimes, and E. C. Dickey, *J. Mater. Res.* 17, 1162 (2002).

*241.* R. K. Nahar, V. K. Khanna, and W. S. Khokle, *J. Phys. D: Appl. Phys.* 17, 2087 (1984).

*242.* J. Kong, N. R. Franklin, C. Zhou, M. G. Chapline, S. Peng, K. Cho, and H. Dai, *Science* 287, 622 (2000).

*243.* P. G. Collins, K. Bradley, M. Ishigami, and A. Zettl, *Science* 287, 1801 (2000).

*244.* S. Frank, P. Poncharal, Z. L. Wang, and W. A. de Heer, *Science* 280, 1744 (1998).

*245.* O. K. Varghese, P. D. Kichambre, D. Gong, K. G. Ong, E. C. Dickey, and C. A. Grimes, *Sens. Actuators, B* 81, 32 (2001).

*246.* C. Dillon, K. M. Jones, T. A. Bekkedahl, C. H. Kiang, D. S. Bethune, M. J. Heben, *Nature* 386, 377 (1997).

*247.* U. Sumanasekera, C. K. W. Adu, F. Fang, and P. C. Eklund, *Phys. Rev. Lett.* 85, 1096 (2000).

*248.* A. Zahab, L. Spina, and P. Poncharal, *Phys. Rev. B* 62, 10000 (2000).

*249.* C. Christofides and A. Mandelis, *Jpn. J. Appl. Phys.* 68, R1 (1990).

*250.* U. Roland, T. Braunschweig, and F. Roessner, *J. Mol. Catal. A* 127, 61 (1997).

*251.* J. Vetrone, Y.-W. Chung, R. Cavicchi, and S. Semancik, *J. Appl. Phys.* 73, 8371 (1993).

*252.* T. Oyabu, T. Osawa, and T. Kurobe, *J. Appl. Phys.* 53, 7125 (1982).

*253.* M. Ippommatsu, H. Ohnishi, H. Sasaki, and T. Matsumoto, *J. Appl. Phys.* 69, 8368 (1991).

*254.* J. R. Brown, P. W. Haycock, L. M. Smith, A. C. Jones, and E. W. Williams, *Sens. Actuators, B* 63, 109 (2000)

*255.* R. Rella, A. Serra, P. Siciliano, L. Vasanelli, G. De, A. Licciulli, and A. Quirini, *Sens. Actuators, B* 44, 462 (1997).

*256.* J.-J. Choi, H. P. Kim, H.-W. Cheong, Jong.-M. Kim, and Jae.-M. Kim, *Sens. Actuators, B* 13–14, 515 (1993).

*257.* G. Huyberechts, M. Honore, and J. Roggen, *Sens. Actuators, B* 15–16, 281 (1993).

*258.* P. V. Geloven, M. Honore, J. Roggen, S. Leppavuori, and T. Rantala, *Sens. Actuators, B* 4, 185 (1991).

*259.* G. Ghiotti, A. Chiorino, W. X. Pan, and L. Marchese, *Sens. Actuators, B* 7, 691 (1992).

*260.* A. E. Varfolomeev, A. I. Volkov, A. V. Eryshkin, V. V. Malyshev, A. S. Rasumov, and S. S. Yakimov, *Sens. Actuators, B* 7, 727 (1992).

*261.* S.-C. Chang, *J. Vac. Sci. Technol., A* 1, 296 (1983).

*262.* S. Zhao, P. Wei, and S. Chen, *Sens. Actuators, B* 62, 117 (2000).

*263.* J.-J. Choi, H. P. Kim, H.-W. Cheong, Jong.-M. Kim, and Jae.-M. Kim, *Sens. Actuators, B* 13–14, 515 (1993).

*264.* D. H. Kim, J. Y. Yoon, H. C. Park, and K. H. Kim, *Sens. Actuators, B* 62, 61 (2000).

*265.* J. Peng and C. C. Chai, *Sens. Actuators, B* 13–14, 591 (1993).

*266.* M. Fukazawa, H. Matuzaki, and K. Hara, *Sens. Actuators, B* 13–14, 521 (1993).

*267.* T. Morimoto, M. Nagao, and F. Tokuda, *J. Phys. Chem.* 73, 243 (1969).

268. A. A. Vasiliev and M. A. Polykarpov, *Sens. Actuators, B* 7, 626 (1992).
269. A. R. Raju and C. N. R. Rao, *Sens. Actuators, B* 3, 305 (1991).
270. S. P. S. Arya and O. N. Srivastava, *Cryst. Res. Technol.* 23, 669 (1988).
271. I. Stambolova, K. Konstantinov, S. Vassilev, P. Peshev, and T. S. Tsacheva, *Mater. Chem. Phys.* 63, 104 (2000).
272. A. Jones, T. A. Jones, B. Mann, and J. G. Firth, *Sens. Actuators* 5, 75 (1984).
273. H. Nanto, T. Minami, and S. Takata, *J. Appl. Phys.* 60, 482 (1986).
274. H. Nanto, H. Sokooshi, and T. Kawai, *Sens. Actuators, B* 13–14, 715 (1993).
275. A. E. Varfolomeev, A. I. Volkov, A. V. Eryshkin, V. V. Malyshev, A. S. Rasumov, and S. S. Yakimov, *Sens. Actuators, B* 7, 727 (1992).
276. E. Grantscharova, A. R. Raju, and C. N. R. Rao, *Chem. Lett.* 1759 (1991).
277. N. Li and T.-C. Tan, *Sens. Actuators, B* 9, 91 (1992).
278. N. Koshizaki, K. Yasumoto, and K. Suga, *Sens. Actuators, B* 9, 17 (1992).
279. Y. C. Yeh and T. Y. Tseng, *J. Mater. Sci.* 24, 2739 (1989).
280. G. Gusmano, G. Montesperelli, E. Traversa, and A. Bearzotti, *Sens. Actuators, B* 13–14, 525 (1993).
281. W.-Y. Chung, D.-D. Lee, and B.-K. Sohn, *Thin Solid Films* 221, 304 (1992).
282. G. Sberveglieri, C. Perego, F. Parmigiani, G. Dinelli, and G. Quattroni, *Sens. Actuators, B* 20, 163 (1994).
283. A. R. Raju, K. Seshadri, and C. N. R. Rao, *Talanta* 39, 1543 (1992).
284. Y. Takao, K. Fukuda, Y. Shimizu, and M. Egashira, *Sens. Actuators, B* 10, 235 (1993).
285. Y. Takao, Y. Iwanaga, Y. Shimizu, and M. Egashira, *Sens. Actuators, B* 10, 229 (1993).
286. J. Huusko, V. Lantto, and H. Torvela, *Sens. Actuators, B* 15–16, 245 (1993).
287. K. D. Schierbaum, U. K. Kirner, J. F. Geiger, and W. Gopel, *Sens. Actuators, B* 4, 87 (1991).
288. L. A. Harris, *J. Electrochem. Soc.* 127, 2657 (1980).
289. A. Bearzotti, A. Bianco, G. Montesperelli, and E. Traversa, *Sens. Actuators, B* 18–19, 525 (1994).
290. T. Y. Tien, H. L. Stadler, E. F. Gibbons, and P. J. Zacmanidis, *Ceramic Bulletin* 54, 280 (1975).
291. M. Fleischer and H. Meixner, *Sens. Actuators, B* 5, 115 (1992).
292. M. Fleischer and H. Meixner, *Sens. Actuators, B* 6, 257 (1992).
293. M. Fleischer and H. Meixner, *Sens. Actuators, B* 13–14, 259 (1993).
294. G. K. Flingelli, M. M. Fleischer, and H. Meixner, *Sens. Actuators* 48, 258 (1998).
295. H. Ming, H. C. Ming, Y. H. Yih, L. P. Yew, and Y. C. Cheng, *Sens. Actuators, B* 22, 63 (1994).
296. P. Shaver, *Appl. Phys. Lett.* 11, 255 (1967).
297. L. Daza, S. Dassy, and B. Delmon, *Sens. Actuators, B* 10, 99 (1993).
298. D. J. Smith, J. F. Vetelino, R. S. F. Elmer, and L. Wittman, *Sens. Actuators, B* 13–14, 264 (1993).
299. G. Sberveglieri, G. Faglia, S. Groppelli, and P. Nelli, *Sens. Actuators, B* 8, 79 (1992).
300. A. Galdikas, Z. Martnas, and A. Setkus, *Sens. Actuators, B* 7, 633 (1992).
301. N. G. Patel, K. K. Makhija, C. J. Panchal, D. B. Dave, and V. S. Vaishnav, *Sens. Actuators, B* 23, 49 (1995).
302. N. G. Patel, K. K. Makhija, C. J. Panchal, D. B. Dave, and V. S. Vaishnav, *Sens. Actuators, B* 21, 193 (1994).
303. B. M. Lacquet and P. L. Swart, *Sens. Actuators, B* 17, 41 (1993).
304. U. Lampe, J. Gerblinger, and H. Meixner, *Sens. Actuators, B* 7, 787 (1992).
305. Z. Chen and K. Colbow, *Sens. Actuators, B* 9, 49 (1992).
306. S. Y. Sheng and Z. T. Shu, *Sens. Actuators, B* 12, 5 (1993).
307. Y. Shimizu, M. Shimabukuro, H. Arai, and T. Seiyama, *J. Electrochem. Soc.* 136, 1206 (1989).
308. M. Ohtaki, J. Peng, K. Eguchi, and H. Arai, *Sens. Actuators, B* 13–14, 495 (1993).
309. T. Hibino and H. Iwahara, *Sens. Actuators, B* 13–14, 483 (1993).
310. T. Ishihara, K. Kometani, Y. Mizuhara, and Y. Takita, *Sens. Actuators, B* 13–14, 470 (1993).
311. S. C. Tsang and C. Bulpitt, *Sens. Actuators, B* 52, 226 (1998).

# Metal Polyhedral Nanorods

## Jeong Won Kang, Ho Jung Hwang

*Chung-Ang University, DongJak-Ku, Seoul, Korea*

**CONTENTS**

## 1. INTRODUCTION

In nanoscience, one of the fundamental answers sought by both experimental and theoretical studies is the clarification of the stable geometrical structures of nanorods and nanowires, since the properties of nanometer-sized structures, rods, and wires are often different from those of the corresponding bulk material. The development of new experimental techniques, such as mechanically controllable break junctions and the use of the scanning tunneling microscope (STM), have made it possible to fabricate and study atomic-size junctions or contacts between macroscopic metals. The mechanical and electrical properties of nanocontacts between metallic bodies have been the subject of intensive research [1–13]. Quantum point contacts are structures in which a "neck" comprising just a few atomic diameters forms a bridge between two electrical contacts. The results observed when a metal surface is contacted using a STM [1–8] or by other some method [9–13] have typically displayed a conductance that is quantized in steps of $2e^2/h$, where $e$ is the electron charge and $h$ is Planck's constant. The mechanical properties of nanocontacts have shown that, before the first yield point, nanowires exhibit an elastic stage and, thereafter, elongation deformation proceeds in alternating quasi-elastic and yielding stages [6, 7, 14, 15]. The density of states (DOS) of ultrathin Au nanowires shows molecular-like features, having many sharp and discrete energy peaks [16]. As the diameter of the Au nanowire increases, the discrete energy levels gradually overlap and form continuous electronic bands. The shape of the DOS of nanowires with diameters of several

nanometers is not very sensitive to the diameter of the wire, while the width of the electronic band gradually narrows as the wire becomes thicker. This band narrowing can be understood from the two-dimensional quantum confinement effect in nanowires. High-resolution transmission electron microscopy (HRTEM) allows us to collect valuable information on the structure of ultrathin nanowires prepared by different methods [17–25]. *Multishelled polyhedral nanostructures* have been found in several inorganic layered materials, such as $WS_2$, $MoS_2$, and $NiCl_2$ [17–19]. HRTEM images have revealed that long metallic nanowires fabricated using different methods [5, 20–24] have well-defined structures and, in particular, novel helical multishelled (HMS) structures are observed in ultrathin Au [5, 20–22] and Pt [23] nanowires.

Multiply twinned particles (MTPs) (including icosahedra, decahedra, and Mark decahedra) with fivefold symmetry axes are a type of structure unique to nanometer-sized particles [26–28]. The structure and the stability of these MTPs have been well documented [29] and a comprehensive review [30] has been given on experimental studies of small particles with fivefold symmetry accompanied by an in-depth theoretical description of their characteristics and computer modeling. Multiply twinned rodlike or needle-shaped particles, sometimes also called whiskers or dendrites, of more or less established growth anisotropy, reflected by the corresponding aspect ratio of the elongated particles, have been known for decades. The materials and processes involved may be summed up in brief. Melmed and Hayward [31] observed Ni, Fe, and Pt whiskers of pentagonal shape grown from the vapor phase on tungsten substrates. Although this was only the second paper on multiply twinned structures, it gave a model consisting of five face-centered cubic (fcc) twin-related subunits with only slight lattice distortions. Ogburn et al. [32] reported the observation of pentagonal dendrites of Cu grown from the vapor phase. DeBlois [33, 34] found pentagonal Ni whiskers by hydrogen reduction of $NiBr_2$. Digard et al. [35] clearly showed the presence of particles of pentagonal prism shape capped by pentagonal pyramids, besides various multiply twinned structures formed by electrodeposition of Ag. Hayashi et al. [36] reported on particles

of rodlike shape obtained by a gas evaporation technique of Pd which exhibit characteristic features of fivefold twinning. Brieu and Gillet [37–39] studied by means of TEM tilt series the internal structure of rodlike decahedra grown by reduction of $NiBr_2$ in organic solution. Elongated *copper* particles of several hundred nanometers length having fivefold axes and aspect ratios up to around 10 were observed by Smith and Gai [40] using selected area electron diffraction to identify the multiply twinned structure. Dahmen and Westmacott [41] found pentagonal, needle-shaped precipitates of Ge in aluminum matrix. Millers and Kuzjukjevics [42] observed fivefold twinned rodlike particles of chemical vapor deposition-grown TiN having additional re-entrant {111} faces at their prism edges. Arita et al. [43] found Yb fivefold twinned pentagonal rods from inert gas aggregation synthesis. Romanov et al. [44] observed multiply twinned whiskers of CdTe. Yu et al. [45] and Wang et al. [46] reported Au nanorods prepared by an electrochemical method. Lisiecki et al. [24] studied recently the internal structure of rodlike particles of Cu of truncated decahedron shape formed by hydrazine reduction of an organometallic copper compound. A short report on pentagonal *nanorods of silver* prepared by inert gas aggregation was given by Nepijko et al. [47]. Canizal et al. [48] presented a method to produce *Au nanorods* based on the bioreduction process. Hofmeister et al. [25] very recently found that *silver nanorods* prepared by aggregation have the characteristic shape of a pentagonal prism capped by pentagonal pyramids on both ends. The optical properties [49] and thermal stability of the *Au nanorods in* solution have been reported by Mohamed [50]. Thiolate ligands, which produce colloidal solutions, have been used to fabricate Au nanostructures [51–54]. These passivated clusters are relatively stable and can be easily observed experimentally. Techniques using ligands can also be used to create passivated nanorods, and these may have great technological importance in the fabrication of nanoscale devices. However, long nanorods would not be expected to be oriented along a fivefold axis [24], and since there is the possibility of other structures of pentagonal nanorods, more precise and comprehensive research is still required to obtain unambiguous conclusions regarding ultrathin nanorod structures under the above conditions.

In recent theoretical research, the structures of ultrathin metal nanowires, such as Au [16, 25, 55–58], Cu [58–64], Pb and Al [62–64], Pt and Ag [65], and Ti [66], have been investigated using molecular dynamics (MD) simulations. These results have shown that HMS structures exist for ultrathin nanowires of several fcc metals. Previous work using atomic scale simulations under various conditions has shown many different polygonal Cu nanowire structures, such as rectangular, pentagonal, and hexagonal forms [61]. A freestanding pentagonal Cu nanowire has also been studied in the tensile testing of a HMS Cu nanowire investigated using the steepest descent (SD) and MD methods [67]. Many studies on the structure of nanoclusters or nanowires have shown that some nanostructures are related to a *decahedron model* in, for example, Ag [68, 69], Ni [68], Au [68, 70–72], Cu [73, 74], Na [75], and La [76]. The minimization of surface energy on approaching a sphere is most effectively realized by an icosahedron consisting of 20 twin-related tetrahedra arranged around a common corner [30].

Polyhedral metal nanorods with multiply twinned boundaries have attracted much interest for several reasons. One is the shape anisotropy enabling severe changes in surface-sensitive properties. Another is the issue of their composition and lattice structure, which should be sensitive somehow to shape changes. This chapter provides information on these questions for polyhedral metal nanorods.

## 2. COMPOSITION OF POLYHEDRAL NANORODS

### 2.1. Composition Methods

The physical and chemical states of metal nanorod growth depend on their respective formation process. The methods applied are the plasma-arc method, the vapor condensation method (in vacuum or in inert gas), the electrosap method, the colloidal assembly method, various chemical methods, etc.

### 2.1.1. Colloidal Self-Assembly: Copper Nanorods

Lisiecki et al. [24] prepared copper metal nanorods by reduction of $Cu(AOT)_2$, in $Cu(AOT)_2$–isooctane–NaCl–water colloidal self-assemblies. Hydrazine is used as the reducing agent, with an overall concentration of 0.15 M, and the reaction takes place under a $N_2$ atmosphere starting immediately after hydrazine has been added to the colloidal solution. In a Pyrex tube, 3 ml of $5 \times 10^{-2}$ M $Cu(AOT)_2$–isooctane is mixed with 36.1 $\mu$l of 10-1 M sodium chloride previously dissolved in water. The $Cu(AOT)_2$, water, and chloride concentrations are $5 \times 10^{-2}$, 0.55, and $10^{-3}$ mol dm$^{-3}$, respectively. The system is kept for 20 h at room temperature (20–22 °C). Then, 21.9 $\mu$l of 20.6 mol dm$^{-3}$ hydrazine is added to the colloidal solution, which is vigorously stirred. Under these conditions, the ratio of $Cu(AOT)_2$ to hydrazine is equal to 1/3. The colloidal assembly immediately turns dark, which is due to the reduction of $Cu(AOT)_2$ to Cu(O), and the solution becomes darker with time. After 2 h, a drop of the solution is placed on a carbon film supported by a copper grid. Investigations which were performed a few minutes after the hydrazine was added to the colloidal system shared the presence of water in oil interconnected cylinders [77]. In terms of the local $Cu(AOT)_2$ number of molecules at the interface, this turns out to be much higher than the overall concentration given above. Thus, when the chemical reduction starts, the space is limited by the water in oil cylinders in a very high supersaturation regime. The copper nuclei formed are close to the interface, which favors crystallization in a preferential direction. With time, the production of copper nuclei is reduced and the viscosity at the interface remains high. Finally, slow crystallization, which allows control of the physical parameters, also allows the formation of long rods of copper.

### 2.1.2. Electrochemical Method: Gold Nanorods

Wang et al. [46] prepared gold nanorods of different aspect ratios using the electrochemical method. The electrolyte consisted of a hydrophilic cationic surfactant,

hexadecyltrimethylammonium bromide, and a hydropho-
bic cationic co-surfactant, tetradecylammonium bromide
or tetraoctylammonium bromide. The length of the gold
nanorods could be controlled by changing the ratio between
the surfactant and the co-surfactant. The electrolysis was
carried out under ultrasonication with an applied current of
5 mA and at a temperature of 42 °C for about 45 min.

### 2.1.3. Inert Gas Aggregation:
### Silver Nanorods

Hofmeister et al. [25] prepared the silver particles by the
inert gas aggregation technique in ultrahigh vacuum equip-
ment and deposited them on NaCl (001) cleavage planes.
Silver was evaporated from a Knudsen cell in an argon
atmosphere and the mixture of gas and metal atoms was
transferred to a nucleation zone. In this region of lami-
nar flow particles were formed at high enough supersat-
uration and grew according to the applied conditions as
reported in more detail by Frank et al. [78]. After removal
of the argon gas, particles of the cluster beam were col-
lected on a sampling probe where the substrate crystal was
mounted. Subsequently, this substrate crystal was coated by
a thin amorphous carbon film of about 10 nm thickness and
removed from the chamber.

## 2.2. HRTEM Images

The carbon films containing the as-deposited metal
nanorods were detached from the substrate by floating in
distilled water and were mounted on metal microgrids. Elec-
tron microscopy characterization, including HRTEM and
selected area electron diffraction, was done. A rotation/tilt
sample holder was employed to adjust a well-defined particle
orientation with respect to the electron beam. The spacings
of lattice plane fringes and their angular and spatial rela-
tions were determined from digitized electron micrographs
by digital image processing. Mostly, the Fourier transform
procedure was employed to obtain a reciprocal-space repre-
sentation, that is, a diffractogram, of an image.

The structure of metal nanorods as prepared according
to the presentations above was explained clearly as trun-
cated large decahedra [24, 25, 46]. Obviously, due to the
additional surfactant in the present preparation at the deca-
hedral nuclei, the growth can be hindered and can only take
place in the [110] direction (i.e., the fivefold axis), resulting
in well-defined long nanorods.

In order to obtain more information on structural details,
electron diffraction, HRTEM images, and power spectra
(PS) have been used for the tilt series of the nanorods. The
long axis of the rods was always taken as the tilt axis. The tilt
angle with respect to the substrate of the nanorods started
from 0°, and surprisingly, after tilting the particles, a peri-
odic sequence could be observed (i.e., every 36° a complete
repetition of the image, clearly displayed in the PS, was
achieved).

Figure 1 shows a HRTEM image of an Au nanorod ori-
ented along [110] obtained from Wang et al. [46]. The Au
nanorod is a single crystallite without dislocations, stacking
faults, or twins. The facets enclosing the nanorods are identi-
fied from the electron diffraction pattern, and the dominant
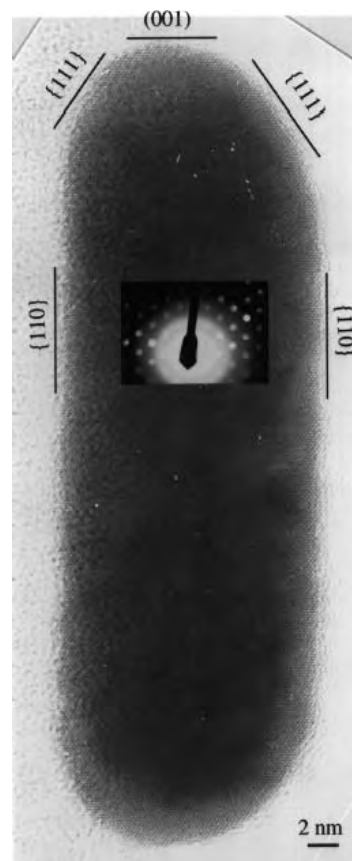


**Figure 1.** HRTEM image recorded from an Au nanorod oriented along
the [110] direction, displaying the {100}, {111}, and {110} faceted crys-
tal structure of the rod. The inset is the electron diffraction pattern
recorded from the rod, which proves the single crystalline structure of
the rod. Reprinted with permission from [46], Z. L. Wang et al., *Surf.
Sci.* 440, L809 (1999). © 1999, Elsevier Science.

side facets are {110} and the growth direction is [001]. The
(001) and {111} facets of small areas terminate the ends of
the nanorods.

To find out the possibility of forming {100}-type facets at
the sidewall of the nanorods, dark-field imaging is used. The
dark-field TEM image is recorded using a {111} reflected
beam under the two-beam condition when the nanorod is
oriented nearly parallel to the [110] direction (Fig. 2a).
From the two-beam dynamic diffraction theory, the inten-
sity of the dark-field image under the Bragg condition fol-
lows $\sin^2(\pi d/\xi_g)$ [79], where $d$ is the sample thickness and
$\xi_g$ is the so-called extinction distance depending on the
crystal structure factor and the electron wavelength. Thus,
the thickness fringes should be equally spaced if the spec-
imen thickness increases linearly across the specimen. The
two possible configurations are schematically presented in
Figure 2b. For a nanorod oriented along [011], the thickness
fringes observed across the nanorod in the dark-field image
would be symmetric around its axis. Considering the thick-
ness variation across the Au nanorod, the thickness fringes
would be equally separated at each side of the axis (indi-
cated by the dashed line in Fig. 2a) if only four {100} facets
enclosed the nanorods. The thickness fringes are not equally
spaced and there is a broad center band if {110}- and
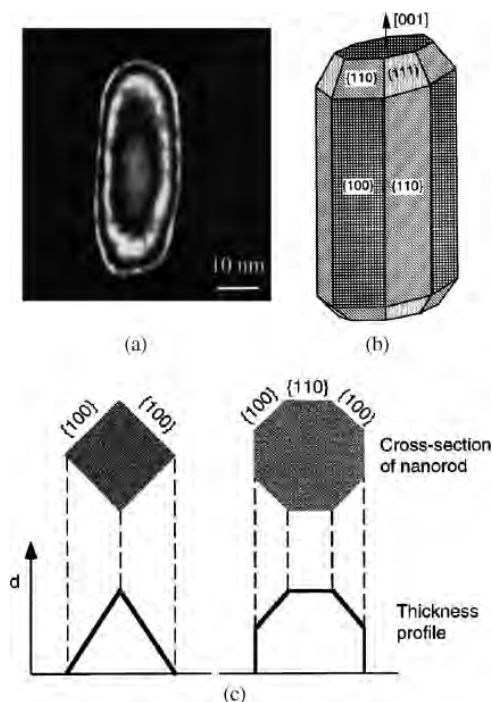
**Figure 2.** (a) Dark-field TEM image recorded using a {111} reflected beam when a rod is oriented nearly parallel to the [110] direction. (b, c) Two possible cross-sections of the nanorod and the corresponding profiles of crystal thickness variation across the rod. (d) A structural model of the Au nanorod. Reprinted with permission from [46], Z. L. Wang et al., *Surf. Sci.* 440, L809 (1999). © 1999, Elsevier Science.



**Figure 3.** Characteristic image contrast patterns obtained upon rotation around the long axis of a rodlike particle supplemented by corresponding diffractograms, where (a) shows the symmetric contrast pattern corresponding to orientation {111} and (b) shows the nonsymmetric one corresponding to orientation {220}. Reprinted with permission from [25], H. Hofmeister et al., *J. Cryst. Growth* 234, 773 (2002). © 1999, Elsevier Science.

{100}-type facets (Fig. 2c) enclose the nanorod. In comparison with the experimental image shown in Figure 2a, the finite width of the band at the center and its uniformity in intensity indicate that the thickness at the center region is nearly constant with a lateral width of ∼5 nm, whereas the thickness fringes around the center band are unequally spaced, apparently suggesting that the cross-section of the nanorod is consistent with the model shown in Figure 2c. As a summary of the experimental results presented in Figures 1 and 2, Figure 3d gives a schematic model of the geometrical structure of the Au nanorod.

The rodlike particles by inert gas aggregation synthesis are deposited with their long axes parallel to the substrate plane as shown in Figure 3. Rotation around this axis by means of the microscope tilting stage reveals two characteristic image contrast patterns which both have a rotational periodicity of 36° (i.e., backward and forward rotations lead to the same result). One of them, corresponding to the {111} orientation lattice plane, exhibits a symmetric contrast pattern with respect to the long axis, as shown in Figure 3a, and the other one, corresponding to two orientations, is separated from {111} by 18° rotation and exhibits a nonsymmetric contrast pattern {220}, as shown in Figure 3b. The characteristic image contrast patterns result from different lattice planes contributing to the image which is reflected by the corresponding diffractogram. From HRTEM images of both orientations information on the spatial extension of the involved lattice planes may be extracted. At first sight, in orientation {111} lattice plane fringes and certain Moiré

fringes may clearly be recognized and their spacing $d_{111}$ and $d_M$ can be measured. The {200} lattice plane fringes, clearly visible by their reflections in the diffractogram, are somewhat hidden in the image. This superposition pattern will be discussed below in more detail. For orientation B the situation is rather clear: the upper half exhibits two sets of {111} fringes as being characteristic of a fcc lattice in ⟨110⟩ zone axis orientation, and the lower half exhibits one set of {220} fringes perpendicular to the long axis. This contrast pattern is mirrored upon 36° rotation around the nanorod axis.

## 3. COMPUTER SIMULATIONS

To describe the multi-shelled-type nanorods and nanowires when the nanowire consisted of coaxial tubes with $n, n', n'', n'''$ helical atom rows ($n > n' > n'' > n'''$), one used the $n–n'–n''–n'''$ notation introduced by Kondo and Takayanagi [22]. The initial structure of the copper nanorods was obtained from the results of previous studies on ultrathin metal nanowires. Gülseren et al. [64] showed that 5–1 and 6–1 Al and Pb nanowires exist using a simulated annealing method, Hwang and Kang [60] showed that 5–1 and 6–1 Cu nanowires exist in a cylinder using the SD method, and Wang et al. [66] showed that 5–1 and 6–1 Ti nanowires exist using a genetic algorithm. Wilson and Johnston [80] modeled Au clusters that could be extended to nanorods by using a simulated annealing method and also showed the existence of some clusters that were similar to those of ultrathin nanorods [81]. These nanorods were multiple twinned structures composed of tetrahedral subunits and were stabilized

with needlelike edges. The subunits of the nanorods had slightly deviated from the shape of a regular tetrahedron to avoid spatial discontinuities. Several studies [82–84] on the atomistic simulations of ultrathin metal nanorods have been investigated by an empirical potential based on the second-moment-approximation of the tight binding scheme [85].

## 3.1. Ultrathin Needlelike Polyhedral Nanorods

Hexahedrons, octahedrons, decahedrons, and dodecahedrons consist of three, four, five, and six twin-related tetrahedrons arranged around one common edge that is a three-, four-, five-, and sixfold axis of a cluster, respectively. Figure 4 shows the smallest hexahedral, octahedral, decahedral, and dodecahedral nanocluster structures, and these are denoted by 3–1, 4–1, 5–1, and 6–1, respectively, and are composed of five, six, seven, and eight atoms, respectively. The initial atomic arrangements shown in Figure 4 were selected using the atomic coordinates given in [56, 76] for metal clusters and nanowires. Then, the optimized structures for Cu were fully relaxed using the SD method. Except for the dodecahedron, all the structures have been described in previous papers [30, 69–76, 86] on cluster motifs. Since ultrathin helical 6–1 configuration nanowires have been investigated in previous work [55, 60, 62, 66], the dodecahedron structure was included in this investigation, even though the dodecahedral structure shown in Figure 4d is not the most stable $Cu_8$ cluster.

Figure 5 shows the structures of nanorods optimized using the SD method. Before the SD simulation, MD simulations were performed using structures created by a fourfold
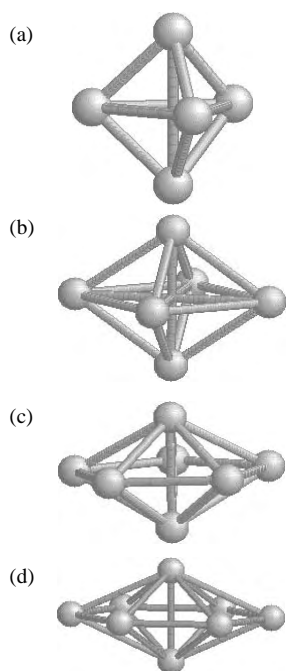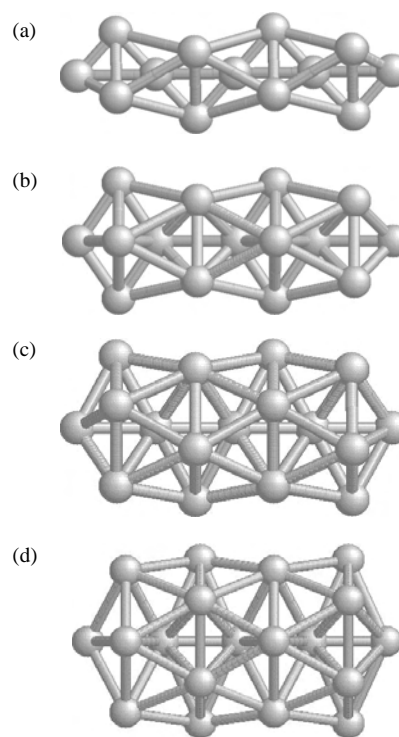


**Figure 5.** Structures assumed after MD simulation of structures composed of a fourfold expansion of the polyhedrons shown in Figure 4: (a) hexahedron, (b) octahedron, (c) decahedron, and (d) dodecahedron. Reprinted with permission from [84], J. W. Kang and H. J. Hwang, *Nanotechnology* 13, 524 (2002). © 2002, Institute of Physics Publishing.

expansion of the polyhedrons shown in Figure 4 along the core axis. Although the most stable nanostructures were generally spherical structures, to focus on metal nanorods, clusters that were optimized as rodlike structures were selected. These structures are in good agreement with the structures found in HMS-type nanowires. The central atomic strand is a straight line, and the outer shells are composed of helical atomic rows. Since the polygonal outer rings have different side angles appearing sequentially, the atomic rows in the outer shells form helices. In nanorods composed of one shell in addition to the central atomic strand, the outer polygon occurs in the sequence *A–B–A–B*, in which *A* and *B* are the same polygon but rotated around the axis of the polygon center. When outer rings are composed of triangles, rectangles, pentagons, and hexagons, the rotation angles are 60°, 45°, 36°, and 30°, respectively. From these patterns, the structure of semi-infinite nanowires has a hexagonal-like surface, such as that seen in HMS-type nanowires [56, 60, 62, 66]. In the simulation results presented in this chapter, the stable, ultrathin nanorods always had a needlelike structure with multiple twinned boundaries.

The nanorods shown in Figure 5 can also be explained by tetrahedral connections. For example, when a decahedron nanostructure is composed of two outer rings and three core atoms, then after relaxation this converts into an icosahedron nanostructure with 20 twin-related tetrahedrons arranged around common corners. Table 1 shows the number of tetrahedra arranged in an ultrathin polyhedral nanorod as a function of the polygon and the number of



**Figure 4.** The smallest polyhedra of: (a) hexahedron, (b) octahedron, (c) decahedron, and (d) dodecahedron. Reprinted with permission from [84], J. W. Kang and H. J. Hwang, *Nanotechnology* 13, 524 (2002). © 2002, Institute of Physics Publishing.

**Table 1.** The number of tetrahedra in nanorods comprised of one shell.

| Number of rings | Number of tetrahedra (vertex number of ring = $p$) | | Total number of tetrahedra |
|---|---|---|---|
| | 1 ring and 2 cores | 2 rings and 1 core | |
| 1 | $p$ | | $p$ |
| | | $2p$ | |
| 2 | $p$ | | $4p$ |
| | | $2p$ | |
| 3 | $p$ | | $7p$ |
| | | $2p$ | |
| 4 | $p$ | | $10p$ |
| | | $2p$ | |
| • | • | • | • |
| • | • | • | • |
| • | • | • | • |
| $n-1$ | $p$ | | $(3n-5)p$ |
| | | $2p$ | |
| $n$ | $p$ | | $(3n-2)p$ |

outer rings. For the smallest structure shown in Figure 1, the number of tetrahedra, $p$, is the vertex number of one outer ring. Hence, the number of tetrahedra consisting of a single outer ring and two core atoms is $p$, and the number of tetrahedra consisting of two outer rings and one core atom is $2p$. Therefore, if a polyhedral nanorod is composed of $n$ outer rings and $n+1$ core atoms, then the number of tetrahedra in the nanorod is $(3n-2)p$.

Since ultrathin metal nanowires have multishelled structures [59, 62, 65], the structure of a nanorod, when the larger outer shell surrounds the nanorods, is investigated as shown in Figure 5. Nanorods consisting of two shells were constructed using the procedure shown in Figure 1. A 10–5–1 nanorod also has structures with an outer ring sequence of $A$–$B$–$C$–$B$. (A) and (C) in Figure 6 denote pentagonal rings, and (B) denotes a decagonal ring, which is nearly circular. Each ring in Figure 4 is also represented along with its cell. The 10–5–1 nanowire formed by a circular folding of the {111} sheets has a HMS-type structure, composed of $A$, $B$, and $C$ cells, with a cell sequence of $A$–$B$–$C$–$B$ along the wire axis. Both edges of the 12–6–1 and 10–5–1 nanorods always have a needle-like structure. From this characteristic structural property of nanorods
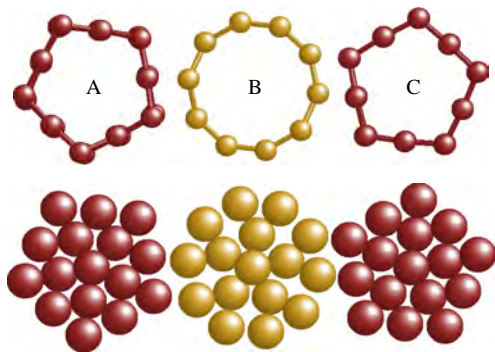


**Figure 6.** The outer ring sequence of a decahedron cluster. (A) and (C) denote pentagonal rings and (B) denotes a decagonal ring that is nearly circular. Each ring also is represented with its cell. Reprinted with permission from [84], J. W. Kang and H. J. Hwang, *Nanotechnology* 13, 524 (2002). © 2002, Institute of Physics Publishing.

having two shells, one can predict the properties of nanorods with larger diameters. In the case of a nanorod having three shells, the outer ring sequence would be $A$–$B$–$C$–$D$–$C$–$B$, and in case of a nanorod with four shells, the outer ring sequence would be $A$–$B$–$C$–$D$–$E$–$D$–$C$–$B$, and so on. The surfaces of these nanorods will always have a {111}-like structure, and their edges will always have a needlelike structure.

From the above results, the geometric information on polyhedral nanorods can be obtained, and this provides much help in furthering our understanding of polyhedral nanorods. Table 2 shows the relationship between the number of tetrahedrons and the number of shells. The atomic ring of the largest shell consists of $N_r$ atoms, and the number of shells is given by $N_s$; therefore, the number of tetrahedrons for the base polyhedron with multiple twinned boundaries, $p$, is $N_r/N_s$. Whenever the outer rings of a nanorod are increased by $N_s$ times, the number of identical tetrahedra increases. When $N_r - 1 = n \times N_s$, then the total number of tetrahedra forming the polyhedral nanorods is equal to $(3n-2)p$.

One can also calculate the number of atoms in a tetrahedron as a function of the number of shells, as shown in Table 3. The vertex number of a tetrahedron is always four, and since there are six edges on a tetrahedron, the number of atoms on the edges is a multiple of six, with the general formula $6(N_s - 1)$ for $N_s \geq 2$. As the area of the face of a tetrahedron increases, then the number of atoms on the face is given by $(N_s - 2)(N_s - 1)/2$ for $N_s \geq 3$. Since the number of faces on a tetrahedron is four, then the number of atoms on all faces is four times the number of atoms on a face. The number of atoms in tetrahedron is given by $(N_s - 3)(N_s - 2)(2N_s - 5)/6$ for $N_s \geq 4$.

## 3.2. Pentagonal Needlelike Polyhedral Nanorods

The results and discussion given above cannot explain the structures observed in previous work in self-assembled pentagonal Cu [25], Ag [26], and Au [46] nanorods having a

**Table 2.** The number of tetrahedra in nanorods comprising of $N_s$ shells, in which the outer ring consists of $N_r$ atoms.

| Number of rings | Number of tetrahedra ($p = N_r/N_s$) | | Total number of tetrahedra |
|---|---|---|---|
| | 1 ring $N_s + 1$ cores | $N_s + 1$ rings and 1 core | |
| 1 | $p$ | | $p$ |
| | | $2p$ | |
| $N_s + 1$ | $p$ | | $4p$ |
| | | $2p$ | |
| $2N_s + 1$ | $p$ | | $7p$ |
| | | $2p$ | |
| $3N_s + 1$ | $p$ | | $10p$ |
| | | $2p$ | |
| • | • | • | • |
| • | • | • | • |
| • | • | • | • |
| $(n-1)N_s + 1$ | $p$ | | $(3n-5)p$ |
| | | $2p$ | |
| $nN_s + 1$ | $p$ | | $(3n-2)p$ |

**Table 3.** The number of atoms composing the basic tetrahedron as a function of the number of shells.

| Number of shells | 1 | 2 | 3 | 4 | 5 | 6 | ...... | $N_s$ |
|---|---|---|---|---|---|---|---|---|
| Number of atoms on vertices | 4 | 4 | 4 | 4 | 4 | 4 | ...... | 4 |
| Number of atoms on edges | — | 6 | 12 | 18 | 24 | 30 | ...... | $6(N_s - 1)$ |
| Number of atoms on faces | — | — | 4 | 12 | 24 | 40 | ...... | $2(N_s - 2)(N_s - 1)$ |
| Number of inner atoms | — | — | — | 1 | 5 | 15 | ...... | $(N_s - 3)(N_s - 2)(2N_s - 5)/6$ |
| Total number of atoms in unit tetrahedron | 4 | 10 | 20 | 35 | 57 | 89 | ...... | |

{100} surface. Figure 7 shows the simulated nanorods with larger diameters having the decahedron and dodecahedron structures shown in Figure 4. Figure 7a, c, and e shows square {100} surface lattices of needlelike nanorods optimized using the SD method with diameters of 15, 33, and 40 Å, consisting of 1175, 3505, and 3550 atoms, respectively. The axial direction of the nanorods having multiple twinned boundaries was always in the ⟨110⟩ direction [24, 25, 46, 87]. Figure 7a and c shows pentagonal multishelled nanorods having four and eight shells, respectively, and Figure 7e shows a hexagonal multishelled nanorod having eight shells. Figure 7b, d, and f shows structures obtained from MD simulations over 100 ps at 300 K. The temperature of the MD simulations was increased from 0 to 300 K in 1 ps by rescaling the atomic velocities.

At 300 K, the pentagonal multishelled nanorod with diameter = 15 Å was transformed into a nanorod with an outer ring sequence similar to that in the above discussion. All the facets on this nanorod were triangles, and most of its surface



(a)  (b)

(c)  (d)

(e)  (f)
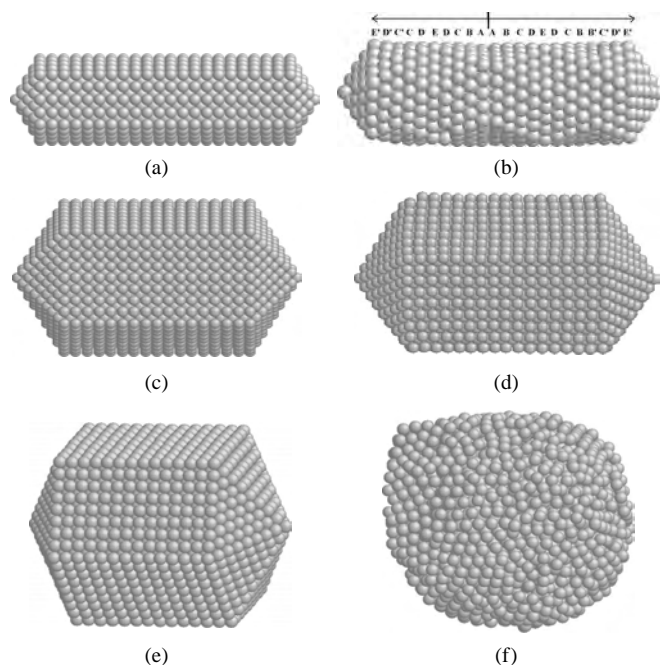
**Figure 7.** Pentagonal multishelled nanorods with (a) four shells and (c) eight shells, respectively, and hexagonal multishelled nanorods with eight shells. The structures obtained using MD simulations of (a), (c), and (e) over 100 ps at 300 K are shown in (b), (d), and (f), with (b) showing the outer ring sequence denoted by label. The SD method was used for (a), (c), and (e). Reprinted with permission from [84], J. W. Kang and H. J. Hwang, *Nanotechnology* 13, 524 (2002). © 2002, Institute of Physics Publishing.

was composed of a hexagonal lattice, as shown in Figure 7b. All facets on the polyhedral nanorod shown in Figure 7b are triangles. If each facet of the nanorod is very close in form to a regular triangle, then the facets were arranged in a close-packed {111} surface. In particular, the facets of the icosahedron model nanorod are satisfied best using the above conditions, in which all the facets of the nanorod are close to those of a regular triangle. Therefore, pentagonal nanostructures, nanorods, and nanowires have a particular importance in nanoscience, as emphasized in the Introduction. The final rings of both sides in Figure 7b are always pentagonal rings. The labels in Figure 7b denote the outer ring sequence. Since the number of outer rings and shells in the nanorod of Figure 7a does not satisfy the conditions shown in Table 2, the nanorod is not composed of the same tetrahedrons as those shown in Figure 7b. Nevertheless, in general, the nanorod of Figure 7b is composed of several tetrahedrons and its structure is in good agreement with icosahedron model discussed above.

A pentagonal multishelled nanorod with a diameter = 33 Å maintains its original decahedral model structure at 300 K. However, although a hexagonal multishelled needlelike nanorod with a square surface lattice was obtained from the SD simulation in the case of the initially defined structure, the hexagonal multishelled nanorod did not maintain its original structure in the MD simulations at 300 K but was transformed into a spherical-like cluster.

In view of the above results, one infer that ultrathin needlelike polyhedral nanorods are composed of different outer ring connections, with all facets on the polyhedral nanorods becoming triangles, and form the surface of a tetrahedron. The conditions of the ultrathin nanorods of icosahedral models are satisfied using the above, and all their facets are close to those of a regular triangle. However, pentagonal multishelled nanorods having diameters of several nanometers are stable using the decahedral model. Therefore, needlelike polyhedral nanorods can also be composed solely of pentagonal tubes, which have a square surface lattice and triangular facets on both edges. Hexagonal multishelled nanorods having diameters of several nanometers are unstable.

It is also investigated whether semi-infinite hexagonal multishelled nanowires having diameters of several nanometers maintain their original structure. A periodic boundary condition along the wire axis was used in the simulation of nanowires related to polyhedral nanorods. The lengths of the supercells optimized by the SD method were 63.128 Å. The nanowires shown in Figure 8a and b were composed of 4525 and 4774 atoms, respectively, and were obtained from MD simulations of nanowires at 300 K corresponding to those shown in Figure 7c and e, respectively. While the pentagonal multishelled nanowire with a square surface
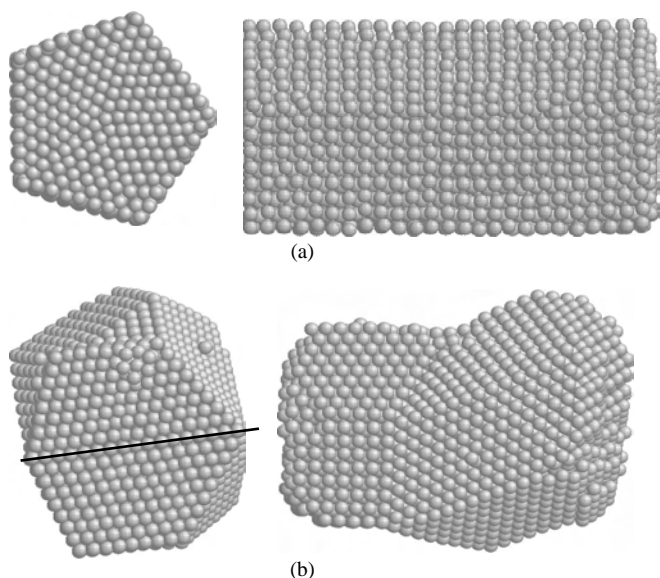
**Figure 8.** Structures obtained from MD simulations over 100 ps at 300 K. (a) The pentagonal multishelled nanowire corresponds to the structure in Figure 7c. (b) The structure obtained from a hexagonal multishelled nanowire corresponds to the structure in Figure 7e. The line on the left-hand side of (b) denotes a twin boundary. Reprinted with permission from [84], J. W. Kang and H. J. Hwang, *Nanotechnology* 13, 524 (2002). © 2002, Institute of Physics Publishing.



**Figure 9.** (a) The subunit of a pentagonal multishelled nanorod. (b) The triangular– and quadrangular–pyramid shapes. The base plane of the quadrangular pyramid and the surface of pentagonal multishelled nanorod are in the form of a regular tetragon. Reprinted with permission from [84], J. W. Kang and H. J. Hwang, *Nanotechnology* 13, 524 (2002). © 2002, Institute of Physics Publishing.

lattice maintains its original structure, the hexagonal multishelled nanowire with a square surface lattice was transformed into a nanowire with multifacets that were composed of close-packed surfaces. Pure {111} nanowires have non-close-packed surfaces. However, the nanowire of Figure 8b has a spiral structure and was composed of completely close-packed surfaces with both {100} and {111} surfaces. Applying a variable periodic boundary condition along the wire axis in the case of the hexagonal multishelled nanowire may cause formation of other structures. Figure 8b shows TEM images revealing this aspect relating to nonlinear nanowires [88–90] and a nanospring [89]. The cross-section on the left-hand side of Figure 8b is a twin boundary, and the atomic rows in the all facets are composed of nine atoms. MD simulations show that hexagonal multishelled nanowires with multiple twinned boundaries are unstable. The reason for this can be understood by the fact that pentagonal multishelled nanorods forming a square surface lattice are stable, as is discussed in the following paragraph.

The pentagonal multishelled nanorod can be divided into five subunits, with one subunit being a triangular nanorod composed of a connection of regular triangles skewed by about 30°, as shown in Figure 9a. However, the opposite edge of the pentagonal multishelled nanorods could not be constructed using this triangle series. The structure of the subunit can be explained by the structural properties using two polyhedrons. One was a triangular pyramid (a regular tetrahedron), and the other was a quadrangular pyramid, as shown in Figure 9b. The base plane of the quadrangular pyramid is the surface of the pentagonal multishelled nanorods, and this forms a regular tetragon. The inclined
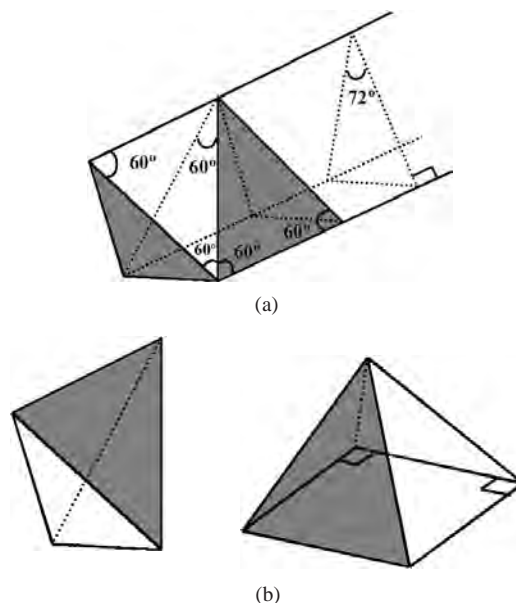
plane of the quadrangular pyramid forms the base plane of the triangular pyramid. Two pyramids are connected alternately along the axis of the pentagonal multishelled nanorods. The polyhedrons of both edges along the wire axis are always triangular pyramids, and all the triangles within the two pyramids are the same regular triangles. Therefore, since the atoms on all the regular triangles are on close-packed {111} surfaces and the base plane of the quadrangular pyramid is a {100} surface, the subunits of the pentagonal multishelled nanorods can be composed of a perfect fcc structure. However, the subunit of the hexagonal multishelled nanorods cannot satisfy the condition that the subunit of the multishelled nanorods has to form a perfect fcc structure. Therefore, while no hexagonal multishelled nanorod having a diameter of several nanometers has been found in previous works, hexagonal polyhedral nanorods with a diameter below 1 nm can be formed. Since pentagonal multishelled nanorods are composed of fcc subunits, they maintain their stable structure at 300 K. However, nanorods connected by different outer rings, such as those shown in Figures 5 and 6, are more stable than those of a pure pentagonal multishelled structure. Moreover, long nanorods are not expected to be oriented along only the fivefold axis [24, 25]. There is the possibility of other structures related to the pentagonal multishell.

The pentagonal multishelled nanorod shown in Figure 7b is compared with a multishelled nanorod having a different structure, but possessing the same number of atoms as the pentagonal multishelled nanorod shown in Figure 7b. Since each shell of an HMS-type nanowire is composed of a circular folding {111} sheet [21, 55, 56, 60], an HMS-type

needlelike nanorod having a sequence of 40–35–30–25–20–15–10–5–1 was composed of the circular folding of {111} sheets and was then relaxed using the SD method. The relaxed structure was related to a decagonal discus structure, and Figure 10 shows the relaxed decagonal multishelled 40–35–30–25–20–15–10–5–1 nanorod with a hexagonal-like surface lattice that was obtained using an MD simulation at 300 K. Table 4 highlights the differences between the pentagonal multishelled nanorod shown in Figure 7b having a square surface lattice and the decagonal multishelled nanorod shown in Figure 10 having a hexagonal surface lattice. While the number of atoms in the pentagonal multishelled nanorod in Figure 7b is the same as that of the decagonal multishelled nanorod in Figure 10, the properties of the pentagonal multishelled nanorod in Figure 7b, such as the average energy per atom, the aspect ratio, and the lattice constant of nanorod along the axis, are different than those of the decagonal multishelled nanorod in Figure 10. Since pentagonal tubes are composed of 5-times-folded $\{100\}\langle110\rangle$ sheets, and decagonal tubes are composed of 10-times-folded $\{111\}\langle111\rangle$ sheets, the lattice constants of pentagonal and decagonal nanorods are close to the lattice constants of $\langle110\rangle$ and $\langle111\rangle$ fcc structures, respectively. The outer rings of Figures 7a and 10 have sequences of A–A–A–A and A–B–A–B, respectively. The average diameter of the nanorod in Figure 10 is larger than that in Figure 7b, and the length of the nanorod in Figure 10 is shorter than that in Figure 7b. Since the volume of the nanorod in Figure 7b is greater than that in Figure 10, the decagonal multishelled nanorod is more close-packed than the pentagonal multishelled nanorod.

Pentagonal nanorods can assume three forms based on the diameter. When the diameter is below 2 nm, pentagonal nanorods can be modeled using an icosahedral structure. As the diameter increases above 3 nm, pentagonal nanorods can be modeled using two types of structure: (1) decahedral and (2) decagonal discus. When the core region of a needlelike nanorod is described using the decahedron model, the whole shape of the nanorod becomes that of a pentagonal multishelled nanorod with a {100} surface. When the icosahedral model describes the core region of the needlelike nanorod, the whole shape of the nanorod becomes that of a decagonal multishelled nanorod with a {111} surface. This has not been detected in any previous theoretical work or HRTEM image. Therefore, briefly, the core regions of nanorods determine the structures of larger diameter needlelike nanorods.

**Table 4.** Comparison of a pentagonal multishelled nanorod with a decagonal multishelled nanorod.

| Property | Figure 5b 40–35–30–25–20–15–10–5–1 | Figure 8 40–35–30–25–20–15–10–5–1 |
|---|---|---|
| Total number of atoms | 3,505 | 3,505 |
| Total cohesive energy (eV) | −11,797.326 | −11,765.889 |
| Average energy per atom (eV) | −3.366 | −3.357 |
| Average diameter of center (Å) | 33 | 35 |
| Length (Å) | 60.746 | 53.913 |
| Aspect ratio | 1.840 | 1.540 |
| Lattice constant (Å) | 2.462 | 2.185 |
| Surface lattice | square | hexagon |
| Cross-sectional shape | pentagon | decagon |
| Outer ring sequence | A–A–A–A | A–B–A–B |



**Figure 10.** A decagonal multishelled 40–35–30–25–20–15–10–5–1 nanorod with a hexagonal surface lattice. Reprinted with permission from [84], J. W. Kang and H. J. Hwang, *Nanotechnology* 13, 524 (2002). © 2002, Institute of Physics Publishing.
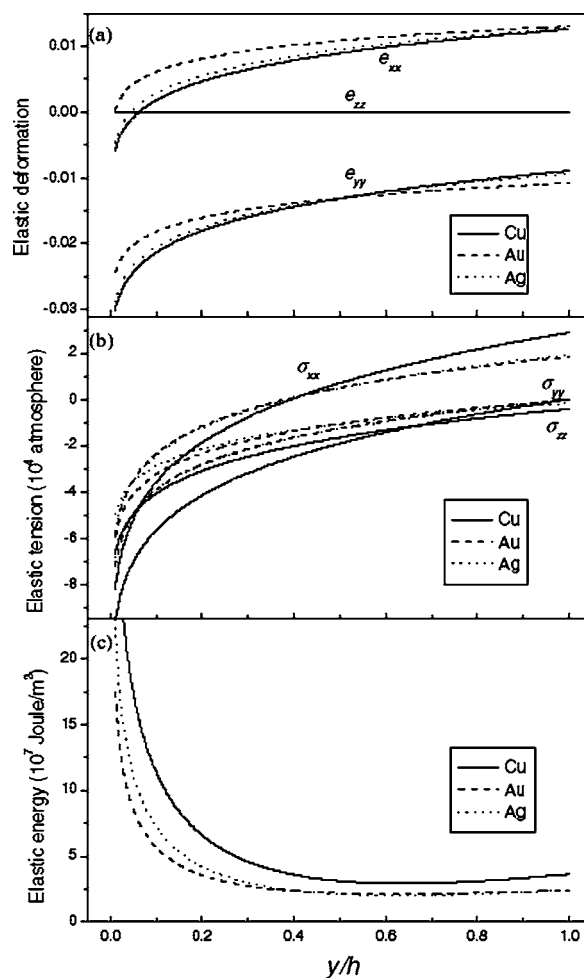


**Figure 11.** The elastic deformation (a), tension (b), and energy distribution (c) in the multiply twinned rods (MTRs) of Cu (full curves), Au (broken curves), and Ag (dotted curves) at zero external pressure and zero deformation in the axial direction. Reprinted with permission from [82], F. Ding et al., *J. Phys.: Condens. Matter* 14, 113 (2002). © 2002, Institute of Physics Publishing.

## 3.3. Stability and Elastic Deformation of Pentagonal Nanorods

Ding et al. [82] discussed the stability and elastic deformation in the polyhedral nanorods, a pentagonal nanorod with multiple twin boundaries, on the basis of elastic theory, and indicated that the polyhedral nanorods are metastable and will disappear at a certain critical size around several tens of nanometers.

### 3.3.1. Distribution of Elastic Deformation in Decahedral Metal Nanorods

Figure 11a–c shows the distribution of elastic deformation, elastic stress, and elastic energy in the decahedral metal nanorods of Ag, Au, and Cu at zero surface pressure and
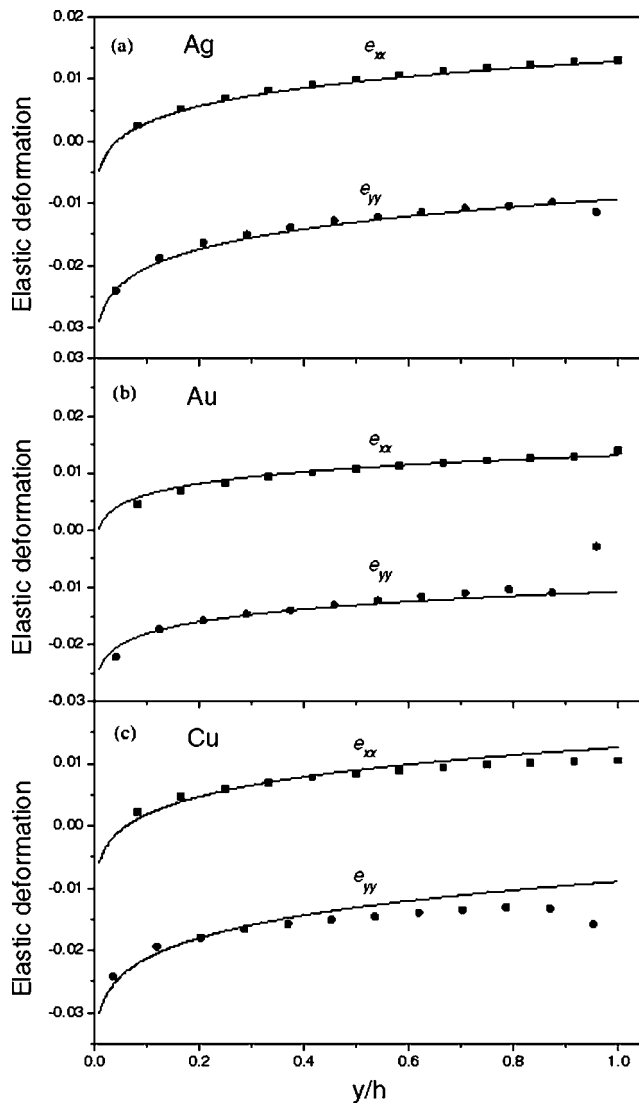
zero deformation in the axial direction. It is clear that the central part of the decahedral metal nanorod is more compressed than the outer part, and the elastic energy in the central part is many times higher than that in outer part. The elastic stress $\sigma_{xx}$ in the central part (about $y < 0.4h$) is negative whereas $\sigma_{xx}$ in the outer part (about $y > 0.4h$) is positive. This indicates that the central part of the icosahedron is compressed whereas the outer part is tensioned in the $x$ direction. Such a distribution of the elastic stress is favorable for keeping the force balanced.

In Figure 11b, the elastic pressure ranges from 50,000 to 80,000 atm in the center whereas the tension in outer part is about 20,000 atm. It is well known that many physical and chemical properties of materials (such as the Raman spectrum, DOS, and melting point) depend on the pressure. So a high nonuniform distribution of elastic stress in the decahedral metal nanorods may make these properties different from those of the corresponding bulk material. Further study on how the nonuniform elastic deformation in decahedral metal nanorods influences their properties is needed. See Figure 12.

### 3.3.2. Stability of Decahedral Metal Nanorods

In order to discuss the stability of the decahedral metal nanorod structure, Ding et al. [82] considered other rods with bulk structure (fcc structure). There are many possible shapes for nanorods with a fcc structure. They considered hexagonal rods because of their lower surface energy. As shown in Figure 13, four of the six surfaces of such a nanorod are (111) facets and the other two are (100) facets.



**Figure 12.** Comparison of the results of the numerical simulation (scatter symbols) with those of the present theory (curves) for elastic deformation for Au (a), Ag (b), and Cu (c) at zero external pressure and zero deformation in the axial direction. Reprinted with permission from [82], F. Ding et al., *J. Phys.: Condens. Matter* 14, 113 (2002). © 2002, Institute of Physics Publishing.
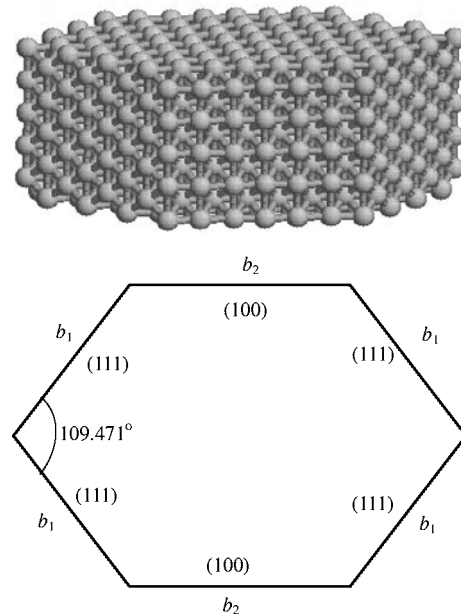


**Figure 13.** The structure of hexagonal rods with an fcc structure. (a) A three-dimensional photo of a section of a hexagonal rod. (b) The structure of a projection of the hexagonal rod with edge lengths $b_1$ and $b_2$, (111) and (100) denoting the two kinds of crystal plane in the fcc structure. Reprinted with permission from [82], F. Ding et al., *J. Phys.: Condens. Matter* 14, 113 (2002). © 2002, Institute of Physics Publishing.

The surface energies of the (111) facet and the (100) facet of the fcc structure are often lower than those of other kinds of facets.

The difference in energy between a decahedral metal nanorod and bulk material with the same volume is

$$\Delta E_{MTR} = 5\gamma_{100}al + \frac{5}{2\cos\left(\frac{3}{10}\pi\right)}\gamma_t al + \frac{5}{2}la^2\sin\left(\frac{3}{10}\pi\right)\bar{\varepsilon} \quad (1)$$

where $l$ is the height of the nanorod and $\gamma_{100}$ and $\gamma_t$ are the surface energy density of (100) facets and the twin boundaries. The first term of Eq. (1) is the surface energy of the five external surfaces, the second term is the surface energy of the five twin boundaries, and the third term is the elastic energy in the decahedral metal nanorod. The first two terms are proportional to the edge length $a$ whereas the third term is proportional to $a^2$. The surface energy dominates for thin rods whereas the elastic energy dominates for large ones. The energy difference between a hexagonal nanorod and the bulk material with same volume is

$$\Delta E_{hex} = 4\gamma_{111}b_1 l + 2\gamma_{100}b_2 l \quad (2)$$

where $\gamma_{111}$ is the surface energy density of (111) facets and $b_1$, $b_2$ are the edge lengths of the hexagonal nanorod (in Fig. 12b). The volume of such a hexagonal nanorod with unit height is $V = 1.633b_1b_2 + 0.942\,81b_1^2$. For hexagonal rods with constant volume and height, the energy varies with the ratio of $b_2$ to $b_1$. Simple calculation can provide the ratio of $b_2$ to $b_1$ of the hexagonal nanorod with the lowest energy when its volume and height are kept constant: $b_2/b_1 = 2((\gamma_{111}/\gamma_{100}) - 0.5773)$. Figure 14 shows the volume dependence of the energy difference between Cu decahedral metal nanorods and hexagonal rods with the lowest energy. It is clear that the energy of such a hexagonal nanorod is lower than that of a decahedral metal nanorod with same volume. This indicates that the decahedral metal nanorod structure is a kind of metastable structure but the global minimum structure of the nanorods. Similar results
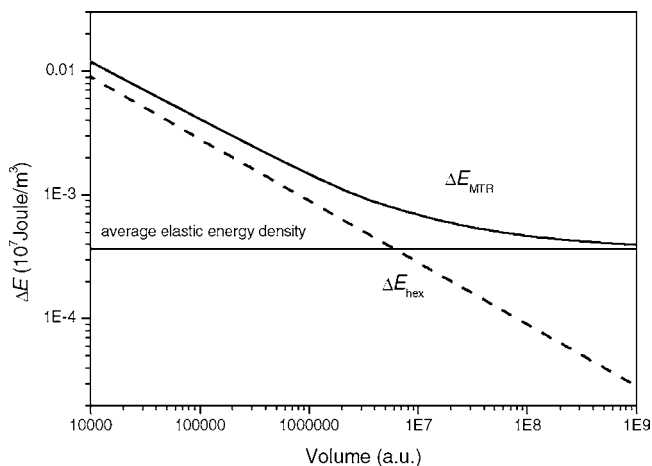


**Figure 15.** A gap of 9.75° will appear at one of the twin boundaries if a MTR becomes unstable with increasing size. Reprinted with permission from [82], F. Ding et al., *J. Phys.: Condens. Matter* 14, 113 (2002). © 2002, Institute of Physics Publishing.

are obtained for other fcc metals such Au, Ag, and Ni. Maybe this is the reason nanorods with multiple twin structures are rarely observed. Whereas the decahedral metal nanorod structure can exist at nanometer size, it will disappear with an increase in size because of its nonperiodic structure. At a certain critical size the decahedral metal nanorod structure is impossible to stabilize: in fact it is the elastic energy in a decahedral metal nanorod that makes it unstable. If a decahedral metal nanorod is unstable, a gap of 9.75° will appear at one of its five twin boundaries (as shown in Fig. 15) and the elastic energy will disappear. So Ding et al. [82] gave a criterion for instability of the decahedral metal nanorod structure: a decahedral metal nanorod will be unstable if the energy of the decahedral metal nanorod with a gap of 9.75° is lower than that of a perfect decahedral metal nanorod. The critical size $a_c$ of the decahedral metal nanorod from this criterion is defined as

$$a_c = \frac{4\gamma_{111} - 2\gamma_t}{5\sin\left(\frac{3}{5}\pi\right)\bar{\varepsilon}} \quad (3)$$

Table 5 lists the average elastic energy density and the critical size for some metals with a fcc structure. The critical size for these metals varies from 20 to 100 nm. For Cu the critical size is 53.1 nm, which is in good agreement with the size of the rods obtained in experiments (25 nm).



**Figure 14.** The solid curve (broken line) is the volume dependence of the energy difference between the MTRs (hexagonal rods) and the corresponding bulk materials. Reprinted with permission from [82], F. Ding et al., *J. Phys.: Condens. Matter* 14, 113 (2002). © 2002, Institute of Physics Publishing.

**Table 5.** The average elastic energy density in MTRs of some metals with bulk fcc structure and their critical size.

|  | Cu | Au | Ag | Pb | Ni | Al | Pd |
|---|---|---|---|---|---|---|---|
| Elastic energy ($10^8$ erg cm$^{-3}$) | 3.646 | 2.414 | 2.457 | 0.7198 | 12.77 | 1.648 | 3.777 |
| Critical size $a$ (nm) | 53.1 | 68.2 | 51.4 | 78.8 | 20.4 | 86.2 | 49.6 |

*Source:* Reprinted with permission from [82], F. Ding et al., *J. Phys.: Condens. Matter* 14, 113 (2002). © 2002, Institute of Physics Publishing.

## 4. CONCLUSIONS

This chapter has given experimental and theoretical studies of ultrathin needlelike metal nanorods with fivefold symmetry and briefly discussed the shape anisotropy of their compositions and the shape changes. Metal nanorods prepared have the characteristic shape of a pentagonal prism capped by pentagonal pyramids on both ends. The atomistic simulations of polyhedral metal nanorods have shown that the shape changes with diameter and the elastic deformation calculation has also shown their stability and instability. The polyhedral metal nanorods were found to be a quasi-stable structure and such a structure will disappear at a size of around several tens of nanometers. However, although not discussed in this chapter, the passivated nanorods prepared by the colloidal solutions are relatively stable, and these may have great technological importance in the fabrication of nanoscale devices.

We have attempted to provide an overview concerning recent developments involving experimental and theoretical results. It is almost certain we have not done justice to the many scientists and engineers who have contributed to this field. We think this is mainly a representative list of examples determined by the usual constraints of space, time, and energy.

## GLOSSARY

**Colloid** In 1861 Thomas Graham coined the term colloid (which means "glue" in Greek) to describe Selmi's "pseudo-solutions." The term emphasizes their low rate of diffusion and lack of crystallinity. Graham deduced that the low rate of diffusion implied that the particles were fairly large—at least 1 nm in diameter in modern terms. On the other hand, the failure of particle sedimentation implied an upper size limit of 1 micrometer. Graham's definition of the range of particle sizes that characterize the colloidal domain is still widely used today.

**High-resolution transmission electron microscopy (HRTEM)** HRTEM can provide structural information at better than 0.2 nm spatial resolutionl. In most crystalline inorganic materials, including ceramics, semiconductors and metals, the positions of individual atomic columns can be resolved, at least in low-index zones. When recorded under optimum conditions, electron micrographs can be directly interpreted in terms of the projected crystal potential. In other cases, image simulations are necessary to match proposed structures to image features.

**Molecular dynamics** Solution of equation of motion of individual particles. Kinetic energy is related to the temperature and interaction between particles is related to the interatomic potential functions.

**Molecular modeling** A computer-aided design process in which computational chemistry software programs are used to create models of macromolecules based on electronic structure, and molecular mechanics calculations coupled with 3D experimental data.

**Multiple twined particle (MTP)** Particle with the multiple twined boundaries such as decahedron and icosahedron.

**Nanorod** Rod in the range of nanometers.

**Scanning tunneling microscopy (STM)** The STM provides a picture of the atomic arrangement of a surface by sensing corrugations in the electron density of the surface that arise from the positions of surface atoms.

## ACKNOWLEDGMENTS

## REFERENCES

1. N. Agrait, J. G. Rodrigo, and S. Vieira, *Phys. Rev. B* 47, 12345 (1993).
2. L. Olesen, E. Lagegaard, I. Stensgaard, F. Besenbacher, J. Schiotz, P. Stoltze, K. W. Jacobsen, and J. K. Norskov, *Phys. Rev. Lett*. 72, 2251 (1994).
3. J. I. Pascual, J. Mendex, J. Gomez-Herrero, A. M. Baro, N. Garcia, U. Landman, W. D. Luedtke, E. N. Bogachek, and H. P. Cheng, *Science* 267, 1793 (1995).
4. M. Diaz, J. L. Costa-Krammer, A. L. Escobar, N. Leon, and A. Correia, *Nanotechnology* 13, 43 (2002).
5. H. Ohnishi, Y. Kondo, and K. Takayanagi, *Nature* 395, 780, (1998).
6. G. Rubio, N. Agrait, and S. Vieira, *Phys. Rev. Lett.* 76, 2302 (1996).
7. C. Untiedt, G. Rubio, S. Vieira, and N. Agrait, *Phys. Rev. B* 56, 2154 (1997).
8. J. L. Costa-Krammer, *Phys. Rev. B* 55, 5416 (1997).
9. C. J. Muller, J. M. Krans, T. N. Todorov, and M. A. Reed, *Phys. Rev. B* 53, 1022 (1996).
10. U. Landman, W. D. Luedtke, B. E. Salisbury, and R. L. Whetten, *Phys. Rev. Lett.* 77, 1362 (1996).
11. J. L. Costa-Kramer, N. Garcia, R. Garcia-Mochales, and P. A. Serena, *Surf. Sci.* 342, L1144 (1995).
12. K. Hansen, E. Lagsgaard, I. Stensgaard, and F. Besebacher, *Phys. Rev. B* 56, 2208 (1997).
13. C. A. Stafford, *Phys. Status Solidi B* 230, 481 (2002).
14. J. W. Kang and H. J. Hwang, *J. Korean Phys. Soc.* 38, 695 (2001).
15. J. W. Kang and H. J. Hwang, *Nanotechnology* 12, 295 (2001).
16. B. Wang, S. Yin, G. Wang, A. Buldum, and J. Zhao, *Phys. Rev. Lett.* 86, 2046 (2001).
17. R. Tenne, L. Margulis, M. Genut, and G. Hodes, *Nature* 360, 444 (1992).
18. L. Margulis, G. Salitra, R. Tenne, and M. Tallenker, *Nature* 365, 113 (1993).
19. Y. R. Hacohen, E. Grunbaum, R. Tenne, and M. Tallenker, *Nature* 395, 336 (1998).
20. Y. Kondo and K. Takayanagi, *Phys. Rev. Lett*. 79 3455 (1997).
21. Y. Kondo and K. Takayanagi, *Science* 289, 606 (2000).
22. V. Rodrigues, T. Fuhrer, and D. Ugarte, *Phys. Rev. Lett.* 85, 4124 (2000).
23. Y. Oshima, H. Koizumi, K. Mouri, H. Kirayama, and K. Takayanagi, *Phys. Rev. B* 65, 12401 (2002).
24. I. Lisiecki, A. Filankembo, H. Sack-Kongehl, K. Weiss, M.-P. Pileni, and J. Urban, *Phys. Rev. B* 61, 4968 (2000).
25. H. Hofmeister, S. A. Nepijiko, D. N. Ievlev, W. Schulze, and G. Ertl, *J. Cryst. Growth* 234, 773 (2002).
26. T. P. Martin, *Phys. Rep.* 273, 199 (1996).
27. C. L. Cleveland and U. Landman, *J. Chem. Phys.* 94, 7376 (1991).
28. W. Miehle, O. Kandler, and I. Leisner, *J. Chem. Phys.* 91, 5940 (1989).

29. S. Ino, *J. Phys. Soc. Japan* 27, 941 (1969).
30. V. G. Gryaznov, J. Heydenreich, A. M. Kaprelov, S. A. Nepijko, A. E. Romanov, and J. Urban, *Cryst. Res. Technol.* 34, 1091 (1999).
31. A. J. Melmed and D. O. Hayward, *J. Chem. Phys.* 31, 545 (1959).
32. F. Ogburn, B. Paretzkin, and H. S. Peiser, *Acta Cryst.* 17, 774 (1964).
33. R. W. DeBlois, *J. Appl. Phys.* 36, 1647 (1965).
34. R. W. DeBlois, *J. Vac. Sci. Technol.* 3, 146 (1966).
35. C. Digard, M. Maurin, and J. Robert, *Met. Corros. Ind.* 51, 255 (1976).
36. T. Hayashi, T. Ohno, S. Yatsuya, and R. Uyeda, *Jpn. J. Appl. Phys.* 16, 705 (1977).
37. M. Brieu and M. Gillet, *Thin Solid Films* 100, 53 (1983).
38. M. Brieu and M. Gillet, *Thin Solid Films* 167, 149 (1988).
39. M. Gillet and M. Brieu, *Z. Phys. D* 12, 107 (1989).
40. B. C. Smith and P. L. Gai, in "Proceedings of the Eighth European Congress Electron Microsc.," Programme Comm. 8. European Congress EM, Budapest, 1984, Vol. 2, p. 1151.
41. U. Dahmen and K. H. Westmacott, *Science* 233, 875 (1986).
42. T. N. Millers and A. A. Kuzjukevics, *Progr. Cryst. Growth Charact.* 16, 367 (1988).
43. M. Arita, N. Suzuki, and I. Nishida, *J. Cryst. Growth* 132, 71 (1993).
44. A. E. Romanov, I. A. Polonsky, V. G. Gryaznov, S. A. Nepijko, T. Junghanns, and N. I. Vitrykhovski, *J. Cryst. Growth* 129, 691 (1993).
45. Y. Y. Yu, S. S. Chang, S. L. Lee, and C. R. Wang, *J. Phys. Chem. B* 101, 6661 (1997).
46. Z. L. Wang, M. B. Mohamed, S. Link, and M. A. El-Sayed, *Surf. Sci.* 440, L809 (1999).
47. S. A. Nepijko, D. N. Ievlev, W. Schulze, J. Urban, and G. Ertl, *Chem. Phys. Chem.* 3, 140 (2000).
48. G. Canizal, J. A. Ascencio, J. Gardea-Torresday, and M. Jose Yacaman, *J. Nanoparticle Res.* 3, 475 (2001).
49. S. Link, C. Burda, M. B. Mohamed, and M. A. El-Sayed, *J. Phys. Chem. B* 103, 1165 (1998).
50. M. B. Mohamed, K. Z. Ismail, S. Link, and M. A. El-Sayed, *J. Phys. Chem. B* 102, 9370 (1998).
51. C. L. Cleveland, U. Landman, M. N. Shafigullin, P. W. Stephens, and R. L. Whetten, *Z. Phys. D* 40, 503 (1997).
52. C. L. Cleveland, U. Landman, T. G. Schaaff, M. N. Shafigullin, P. W. Stephens, and R. L. Whetten, *Phys. Rev. Lett.* 79, 1873 (1997).
53. T. G. Schaaff, M. N. Shafigullin, J. T. Khoury, I. Vezmar, R. L. Whetten, W. G. Cullen, P. N. First, C. Gutierrez-Wing, M. J. Ascensio, and M. J. Jose-Yacaman, *J. Phys. Chem. B* 101, 7885 (1997).
54. M. M. Alvarez, J. T. Khoury, T. G. Schaaff, W. Shafigullin, I. Vezmar, and R. L. Whetten, *Chem. Phys. Lett.* 266, 91 (1997).
55. E. Tosatti, S. Prestipino, S. Kostlmeier, A. Dal Corso, and F. D. Di Tolla, *Science* 291, 288 (2001).
56. G. Bilalbegović, *Phys. Rev. B* 58, 15412 (2000); G. Bilalbegović, *Solid State Commun.* 115, 73 (1998).
57. J. A. Torres, E. Tosatti, A. Dal Corso, F. Ercolessi, J. J. Kohanoff, F. D. Di Tolla, and J. M. Soler, *Surf. Sci.* 426, L441 (1999).
58. G. Bilalbegović, *Comp. Mater. Sci.* 18, 333 (2000).
59. H. J. Hwang and J. W. Kang, *J. Korean Phys. Soc.* 40, 283 (2002).
60. J. W. Kang and H. J. Hwang, *Mol. Sim.* 28, 1021 (2002).
61. J. W. Kang and H. J. Hwang, *Comp. Mater. Sci.*, in press (preprint:/cond-mat/0202032).
62. O. Gülseren, F. Erolessi, and E. Tosatti, *Phys. Rev. Lett.* 80, 3775 (1998).
63. F. Di Tolla, A. Dal Corse, J. A. Torres, and E. Tosatti, *Surf. Sci.* 456, 947 (2000).
64. O. Gülseren, F. Erolessi, and E. Tosatti, *Phys. Rev. B* 51, 7377 (1995).
65. G. M. Finbow, R. M. Lynden-Bell, and I. R. McDonald, *Mol. Phys.* 92, 705 (1997).
66. B. Wang, S. Yin, G. Wang, and J. Zhao, *J. Phys.: Condens. Matter* 13, L403 (2001).
67. W. W. Kim, J. W. Kang, T. W. Kim, H. J. Hwang, and G. Y. Lee, *J. Korean Phys. Soc.* 40, 889 (2002).
68. K. Michaelian, N. Rendon, and I. L. Garzon, *Phys. Rev. B* 60, 2000 (1999).
69. S. Erkoc and T. Yilmaz, *Physica E* 5, 1 (1999).
70. S. Erkoc, *Physica E* 8, 210 (2000).
71. T. X. Li, S. Y. Yin, Y. L. Ji, B. L. Wang, G. H. Wang, and J. J. Zhao, *Phys. Lett. A* 267, 403 (2000).
72. C. R. A. Catlow, V. L. Bulatov, and R. W. Grimes, *Nucl. Instrum. Methods B* 122, 301 (1997).
73. L. Rongwu, P. Zhengying, and H. Yukun, *Phys. Rev. B* 53, 4156 (1996).
74. U. Lammers and G. Borstel, *Phys. Rev. B* 49, 17360 (1994).
75. U. Landman, *Solid State Commun.* 107, 693 (1998).
76. S. Erkoc, T. Bastug, M. Hirata, and S. Tachimori, *Chem. Phys. Lett.* 314, 203 (1999).
77. M. P. Pileni, T. Gulik, J. Tanori, A. Filankembo, and J. C. Dedieu, *Langmuir* 22, 7359 (1998).
78. F. Frank, W. Schulze, B. Tesche, J. Urban, and B. Winter, *Surf. Sci.* 156, 90 (1985).
79. R. L. Whetten, J. T. Khoury, M. M. Alvarez, S. Murthy, I. Vezmar, Z. L. Wang, P. W. Stephens, C. L. Cleveland, W. D. Luedtke, and U. Landman, *Adv. Mater.* 8, 428 (1996).
80. N. T. Wilson and R. L. Johnston, *Eur. Phys. J. D* 12, 161 (2000).
81. N. T. Wilson and R. L. Johnston, http://www.tc.bham.ac.uk/bcweb/ACABU/.
82. F. Ding, H. Li, J. Wang, W. Shen, and G. Wang, *J. Phys.: Condens. Matter* 14, 113 (2002).
83. J. W. Kang and H. J. Hwang, *J. Phys.: Condens. Matter* 14, 2629 (2002).
84. J. W. Kang and H. J. Hwang, *Nanotechnology* 13, 524 (2002).
85. F. Cleri and V. Rosato, *Phys. Rev. B* 48, 22 (1993).
86. L. Rongwu, P. Zhengying, and H. Yukun, *Phys. Rev. B* 53, 4156 (1996).
87. Y. F. Zhang, Y. H. Tang, N. Wang, D. P. Yu, C. S. Lee, I. Bello, and S. T. Lee, *Appl. Phys. Lett.* 72, 1835 (1998).
88. Z. L. Wang, Z. R. Dai, R. P. Gao, and Z. G. Bai, and J. L. Gole, *Appl. Phys. Lett.* 77, 3349 (2000).
89. Y. F. Zhang, Y. H. Tang, H. Y. Peng, N. Wang, C. S. Lee, I. Bello, and S. T. Lee, *Appl. Phys. Lett.* 75, 1842 (1999).
90. D. N. Mcllroy, D. Zhang, Y. Kranov, and M. G. Norton, *Appl. Phys. Lett.* 79, 1540 (2001).

# Metallic State in Conducting Polymers

## Kwanghee Lee

*Pusan National University, Pusan, Korea*

## CONTENTS

## 1. INTRODUCTION

In 1976, Alan MacDiarmid, Hideki Shirakawa, and Alan Heeger discovered conducting polymers (i.e., doped conjugated polymers) and the ability to dope these polymers over the full range from insulator to metal [1]. This created a new field of research on the boundary between chemistry and condensed-matter physics [2] and also offered a new class of materials which exhibit the electrical and optical properties of metals or semiconductors and which retain the attractive mechanical properties and processing advantages of polymers [3]. As a consequence, the significance of their works has been recognized by the award of the Nobel Prize in chemistry for 2000 [4].

Conjugated polymers in a nondoped state have an anisotropic, quasi-one-dimensional electronic structure with a gap of typically 1–3 eV, corresponding to the conventional semiconductor gap size. As a result, the chemistry and physics of these polymers in their nondoped semiconducting state are of great interest because they provide a route to "plastic electronic" devices. In particular, the discovery of light-emitting diodes (LEDs) in these materials in 1990 [5] provided the stimulus for a major push in this direction, and now prototype devices meet realistic specifications for applications [6]. The polymer LED is, however, only one of a larger class of devices in the emerging class of polymer optoelectronic devices, including lasers, high-sensitivity polymer photodiodes and photovoltaic cells, thin-film transistors, and all-polymer integrated circuits [7]. All of these sophisticated electronic components are fabricated by casting the semiconducting and/or metallic polymer layers from solution.

In addition to the polymer electronics, conducting polymers also emerge as promising candidate materials for nanotechnology materials. Conducting polymers are inherently "molecular wires" with a dimension of ~10 nm and therefore principally satisfy the role of interconnecting wire for future nanosized integrated circuits [8]. "Molecular electronics" is also a field that conducting polymers would play an important role in as promising nanotechnology materials. Recently molecular-scale electronics have received much attention because of their promise of future electronic devices, which operate at nanometer size and also at THz speeds. Such a molecular-scale electronic concept also requires use of single or few molecules as major electronic components such as diodes, transistors, and laser diodes [9].

For the realization of such nanometer scale devices using conducting polymers, it is crucial to understand the mechanism of charge conduction and to evaluate physical properties of those materials in a nanometer scale. However, although the electrical and optical properties of conducting polymers have been investigated for over a decade, the nature of the metallic states and the corresponding metal–insulator transition are not fully understood. This mainly originates from their complex morphologies inherent to typical polymer systems and also from their novel reduced dimensionality. In this chapter, therefore, current understanding of the metallic conducting polymers is briefly given, with an emphasis on the influence of disorder and dimensionality on their transport and optical properties.

## 2. CHEMICAL AND ELECTRONIC STRUCTURES

Since conventional polymers are considered to be insulators, they were viewed as uninteresting from the point of view of electronic materials. Although this is true for

typical saturated polymers, the electronic configuration of conjugated polymers is fundamentally different. In conjugated polymers, the chemical bonding leads to one unpaired $\pi$-electron per carbon atom, in which the carbon orbitals are in the $sp^2p_z$ configuration. Since these orbitals of successive carbon atoms overlap each other, it leads to electron delocalization along the backbone of the polymer. This electronic delocalization provides the origin of peculiar charge mobility along the backbone of the conjugated polymers.

The classical example is polyacetylene, $(-CH)_n$, in which each carbon is $\sigma$-bonded to two neighboring carbons and one hydrogen atom. Then there is one $\pi$-electron left on each carbon. In such a case, if the $\sigma$-bond lengths of carbon–carbon were equal, the fundamental band structure consideration would imply that the electronic structure of the polyacetylene is that of a typical metal with one unpaired electron per formular unit. In real situations, however, the structure of polyacetylene is dimerized as a result of the Peierls instability with two carbon atoms in the repeat unit, $(-CH=CH)_n$, leading to the bond-alternated structure characteristic of conjugated polymers [2, 10]. Thus the $\pi$ band is divided into $\pi$ and $\pi^*$ bands. Since each band can hold two electrons per atom (spin up and spin down), the $\pi$ band is filled and the $\pi^*$ band is empty. The energy difference between the highest occupied state in the $\pi$ band and the lowest unoccupied state in the $\pi^*$ band is the $\pi-\pi^*$ energy gap ($E_g$). Since there are no partially filled bands, conjugated polymers are typically semiconductors with a gap of $E_g \approx 1$–3 eV. Because $E_g$ depends upon the molecular structure of the repeat unit, synthetic chemists are provided with the opportunity and the challenge to control the energy gap by design at the molecular level. As a consequence, the opportunity to synthesize new conducting polymers with improved/desired properties began to attract the attention of synthetic chemists, and now the family of $\pi$-conjugated polymers has been greatly enlarged as shown in Figure 1.

Although the electronic structures of nondoped conjugated polymers correspond to those of semiconductors, they exhibit peculiar electronic and optical properties associated with their strong electron–phonon interaction inherent in these quasi-one-dimensional systems. In contrast with conventional inorganic semiconductors with rigid bands, upon doping or photoexcitation the carriers are self-localized and form the nonlinear excitations on the polymer chains: solitons, polarons, or bipolarons, depending on the ground state degeneracy [2, 10, 11]. Much of the new physics associated with conjugated polymers is related to the formation and properties of such nonlinear excitations. New subgap optical transitions occur with a corresponding shift of oscillator strength from $\pi-\pi^*$ transition to the localized gap states associated with these novel quasi-particles. In the case of "photodoping," the redistribution of oscillator strength associated with subgap infrared absorption and the corresponding bleaching of the interband ($\pi-\pi^*$) transition provide a route to nonlinear optical response. Moreover, these nonlinear quasi-particle excitations are believed to be responsible for the electronic transport in the dilute and intermediate doping level, illustrating a moderate electrical conductivity without significant Pauli susceptibility.
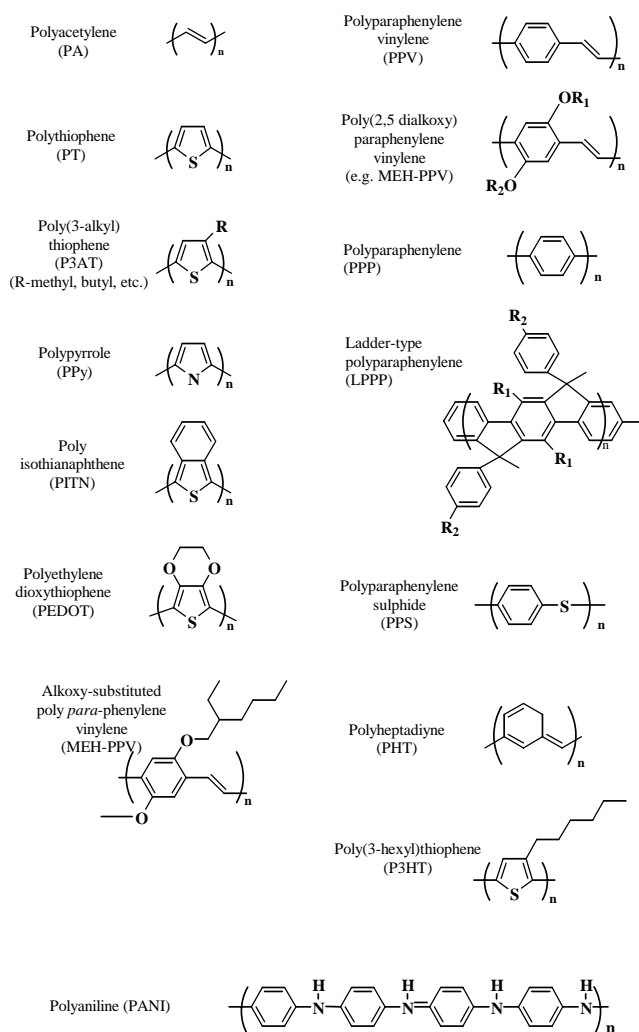


**Figure 1.** Molecular structures of conjugated polymers.

Upon chemical or electrochemical doping above some critical dopant level, many conjugated polymers undergo a transition from such a nonlinear excitation state to a metallic state at high doping level [12]. The metallic state is verified by measurements of the Pauli spin susceptibility, linear dependence of the thermopower with temperature, and the linear term in heat capacity, that is, properties which all originate in the appearance of a finite density of states at the Fermi level ($E_F$) [12].

In principle, it has been frequently pointed out that the metallic state with finite density of states at $E_F$ does not reconcile with the general concept of a quasi-one-dimensional conjugated polymer, for such a system should be subject to the Peierls instability. Therefore, the existence of the metallic state in conjugated polymers requires the involvement of additional interactions, notably electron–electron interaction, interchain coupling, and dopant-mediated interaction. Such additional interactions would result in high dimensionality in the electronic structure of the metallic state, thereby avoiding and stabilizing the Peierls instability.

Another peculiarity of the metallic state is a persistence of the infrared-active vibrational (IRAV) modes into the

metallic state with enhanced oscillator strength [13]. In principle, the IRAV modes arise from the localized vibrational modes caused by local deviations from the symmetry of the perfectly dimerized pattern in the vicinity of the nonlinear excitations and constitute the characteristics of these quasi-one-dimensional systems [14, 15]. However, it has also been argued that the linear dependence of IRAV intensity with doping concentration does not reconcile with the metallic state in which one would expect the Peierls energy gap to close. Therefore, the metallic state is believed to be a dimerized structure with a high density of localized structural distortions rather than uniform bond-length structure as suggested earlier.

The electronic structure of the metallic state is expected to be fundamentally different from the low doping regime where nonlinear excitations (solitons or bipolarons) are important excitations. Although such nonlinear excitations are self-localized in the dilute doping regime, they start to interact at high concentration. As a result, the wave functions of the adjacent nonlinear excitations overlap sufficiently to form a continuum of energy levels, leading to the suggested soliton lattice band [16] for degenerate ground state systems (Fig. 2a) and bipolaron lattice band [17] for nondegenerate ground state systems (Fig. 2b). However, since such lattice bands are empty, they are not appropriate for the description of the metallic state requiring the finite density of state at the Fermi level. Indeed, in order to make such band models compatible with the metallic state, there was a suggestion that the metallic state could be understood as a merging of a soliton (bipolaron) lattice band with a valence band (or a conduction band for n-type doping) to form a partially filled conduction band [16, 17].

The polaron lattice model (Fig. 2c) is an alternative, retaining a doping induced half-filled polaron band in the $\pi-\pi^*$ energy band gap, consistent with expectation of a traditional metallic state [18]. In this model, the sharp increase in the Pauli susceptibility of $trans$-$(CH)_x$ could be understood in terms of a first order phase transition from a soliton lattice to a polaron lattice [18]. Because the polaron lattice model has a half-filled subband within the $\pi-\pi^*$ gap, there is a finite density of states at the Fermi level, and transport occurs by coherent electron motion through this subband. This polaron lattice metal concept can be generalized in case of most nondegenerate ground state systems as well as polyacetylene. In this case, the bipolaron state is driven toward polaron lattice conformation with increasing
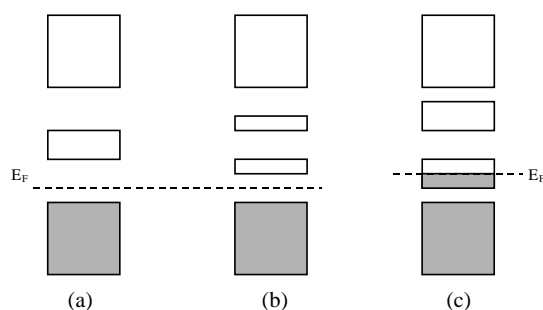
dopant concentration. However, there was a theoretical calculation which predicted weak IRAV modes in the polaron lattice [19], in contrast with the experimental observations. This result has been used as the main argument against the polaron lattice model together with the fact the polaron lattice is expected to be unstable toward a Peierls distortion in such a one-dimensional system. In contrast, it is notable that there is recent theoretical consideration [20], indicating that the polaron lattice provides for significant charge polarization along the polymer chains and can also lead to intensive IRAV modes. In any case, despite a decade of research on the metallic state of conjugated polymers, many of the fundamental issues remain unsolved. In particular, the existence of IRAV modes demonstrates that the heavily doped conjugated polymers are not simple metals.

## 3. DOPING AND PROCESSIBILITY

The electrical conductivity of conducting polymers can be controlled over the full range from insulator to metal either by chemical doping or by electrochemical doping. In fact, the initial discovery of the ability to dope conjugated polymers involved charge-transfer redox chemistry by chemical doping: oxidation ($p$-type doping) or reduction ($n$-type doping) [21, 22]. When the doping level is sufficiently high, the electronic structure evolves to that of a metal [23]. In such a case, the electrochemical potential is shifted either by a redox reaction or an acid–base reaction into a region of energy with a high density of electronic states. On the other hand, however, charge neutrality of the entire system is maintained by the introduction of counterions. In this sense doped conjugated polymers are kinds of salts.

Doped polyacetylene has been the prototype system since the initial report of the achievement of a conductivity of $\sigma_{dc} \sim 100$ S/cm upon doping with iodine [1]. Subsequently, polyacetylene was synthesized by alternate routes that yields higher conductivities of $\sigma_{dc} \sim 10^5$ S/cm, approaching that of a traditional metal [24–26]. Recent advances in the processing of other conducting polymer systems, for example polyaniline [27], polypyrrole [28], and poly($p$-phenylenevinylene) [29], have led to improvements in their $\sigma_{dc}$ to the range of $\sim 10^3$–$10^4$ S/cm.

The electrical conductivity results from the existence of charge carriers and from the ability of those charge carriers to move along the $\pi$-bonded backbone. In principle, broad $\pi$-electron bandwidths can lead to relatively high carrier mobility, which is extended into three dimensions through interchain electron transfer. Disorder, however, limits the carrier mobility and therefore the electrical conductivity. Indeed, research directed toward conjugated polymers with improved structural order and hence higher mobility is a focus of current activity in the field.

Although polyacetylene exhibits high conductivity in its doped state, this system is unstable in the ambient air. In fact, even as late as last decade there were no known examples of stable metallic polymers which could be processed in the metallic form. This is a prerequisite requirement for broad use of these systems in industrial products. This major outstanding problem was first solved with polyaniline.



**Figure 2.** Schematic representations of the band structures of (a) soliton lattice, (b) bipolaron lattice, and (c) polaron lattice forms.

Polyaniline provides the prototypical example of a chemically distinct doping mechanism [30]. Protonation by acid–base chemistry leads to an internal redox reaction and the conversion from the emeraldine base (semiconducting) to the emeraldine salt (metallic), as shown schematically in Figure 3. Upon protonation of the emeraldine base to the emeraldine salt, the proton-induced spin unpairing mechanism leads to a structural change with one unpaired spin per repeat unit, but without change in the number of electrons [31]. The result is a half-filled band and, potentially, a metallic state in which there is a positive charge in each repeat unit and an associated counterion.

Polyaniline has been investigated extensively for over 100 years and attracted interest as a conducting material for several important reasons: the monomer is inexpensive, the polymerization reaction is straightforward and proceeds with high yield, and polyaniline has excellent stability. Processing high-molecular-weight polyaniline into useful objects and devices has been a difficult problem. Cao et al. made important progress in 1991 by using functionalized protonic acids to both convert polyaniline to the metallic form and, simultaneously, render the resulting polyaniline complex soluble in common organic solvents [27]. The functionalized counterion acts like a "surfactant" in that the charged head group is ionically bound to the oppositely charged protonated polyaniline chain, and the tail is chosen to be compatible with nonpolar or weakly polar organic liquids. Moreover, the processibility of polyaniline induced by the sulfactant counterions has made possible the fabrication of conducting polymer blends with a variety of host polymers [32]. Since the

blends are melt-processible as well, the counterion-induced processibility of polyaniline provides a route to conducting polymer blends for use in industrial products.

Although chemical doping is an efficient and straightforward process, it is typically difficult to control the doping level. Complete doping to the highest concentrations yields reasonably high quality materials. However, attempts to obtain intermediate doping levels often result in inhomogeneous doping. Electrochemical doping was invented to solve this problem [33]. In electrochemical doping, the electrode supplies the redox charge to the conducting polymer, while ions diffuse into (or out of) the polymer structure from the nearby electrolyte to compensate the electronic charge. The doping level is determined precisely by the voltage between the conducting polymer and the counterelectrode. Typical examples are electrochemically synthesized polypyrrole doped with $PF_6$ (PPy-$PF_6$) [28] and poly(3,4-ethylenedioxythiophene) doped with $PF_6$ (PEDOT-$PF_6$) [34].

Because the interchain electron transfer interactions of conjugated polymers are relatively strong compared to the van der Waals and hydrogen bonding interchain interactions typical of saturated polymers, conducting polymers tend to be insoluble and infusible. Thus this was a serious problem in the early years just after the discovery of $\pi$-conjugated polymers.

Since then, significant progress in the processing of $\pi$-conjugated polymers has been made with four basic approaches as follows: the first is the "side-chain functionalization" method, which is typically used for processing undoped conjugated polymers from solution in organic solvents or from water. Derivatives of polythiophene, the poly(3-alkylthiphene), and the soluble derivative-poly(phenylene vinylene) (PPV) are typical examples of this approach. Since the side chains decrease the interchain coupling and increase the entropy, these derivatives can be processed from solution.

The second is the "precursor route" chemistry, principally used for processing polyacetylene and pure PPV into thin films. The versatile precursor route involves the preparation of a processible precursor (saturated) polymer and the subsequent conversion of that precursor to the conjugated polymer [35–37]. After conversion to the conjugated form, the resulting polymer is insoluble and intractable, but thermally stable; for example PPV is stable at temperatures in excess of 300 °C.

The third approach is the counterion-induced processing, principally used for processing polyaniline in the metallic form from organic solvents, as explained previously. The counterion-induced processibility of metallic polyaniline utilizes bifunctional counterions such as dodecylbenzenesulfonate to render the polymer soluble [27]. The charge on the $SO_3^-$ head group forms an ionic bond with the positive charge (proton) on the polyaniline chain. The hydrocarbon tail likes organic solvents. Processing polyaniline in the conducting form resulted in materials with improved homogeneity and crystallinity, and with correspondingly improved electrical conductivities [38].

Finally, the forth approach is the aqueous colloidal dispersions created by template synthesis, principally used for processing polyaniline [39] and PEDOT [40]. Template-guided
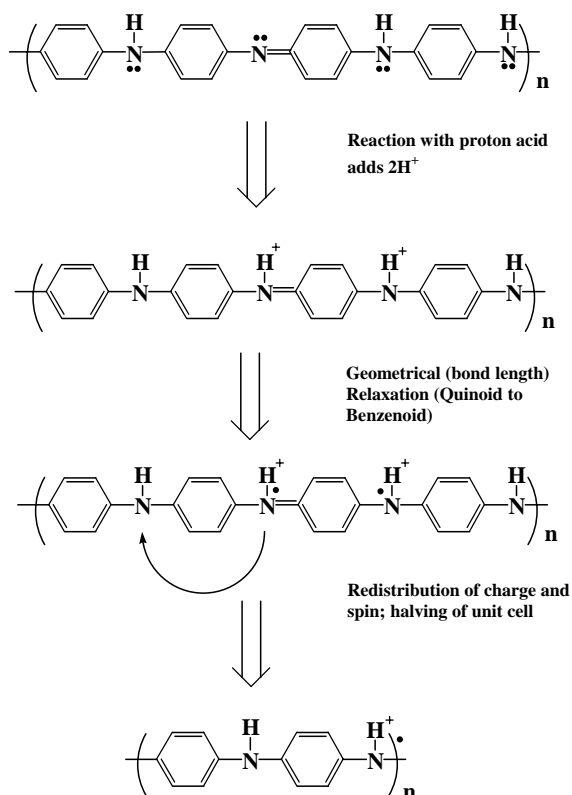


**Figure 3.** Proton-induced spin unpairing in polyaniline.

synthesis of conducting polymers was first reported by Sun and Yang [39]. The molecular template, in most cases polyacids such as polystyrene sulfonic acid, binds the monomer, for example aniline, to form molecular complexes that are dispersed in water as colloidal particles. Upon polymerization, the aniline monomers form the template-polyaniline complex. By judicious choice of the template molecule and the polymerization conditions, stable submicrometer-size colloidal particles of polyaniline–template aggregate can be formed during polymerization. The stabilization against coagulation arises from the Coulomb repulsion between particles, which is a result of the surface charge provided by the extra sulfonic acid groups in polystyrene sulfonic acid. Very stable dispersions of polyaniline–polystyrene sulfonic acid complexes can be made with particle size less than 1 $\mu$m.

Poly(ethylenedioxythiophene)-polystyrene sulfonate (PEDOT-PSS) can be prepared as a stable dispersion in water [40, 41]. Films of PEDOT-PSS are semitransparent and can be spin cast with a surface resistance of approximately 500 $\Omega$/square and with 75% transmission. This material, therefore, is successfully utilized as a promising transparent electrode or buffer layer in the recent polymer optoelectronic devices.

# 4. MORPHOLOGY AND STRUCTURE DISORDER

Conducting polymers are known as complex systems with typical polymeric morphology. X-ray diffraction studies confirm that they consist of relatively well-ordered crystalline regions with structural coherence length ($\xi_c$) of $\sim$30–100 Å, interconnected through less-ordered amorphous regions [24, 42–46]. A schematic view of such structural inhomogeneity in the conducting polymers is shown in Figure 4, in which individual polymer chains pass through both ordered regions and less-ordered regions. The percent crystallinity may vary from near zero to 50% or 60% for polypyrrole [42, 43] and polyaniline [44–46], respectively, to greater than 80% for polyacetylene [24].

In recognition that disorder generally plays a crucial role in the physics of conducting polymers, the question of
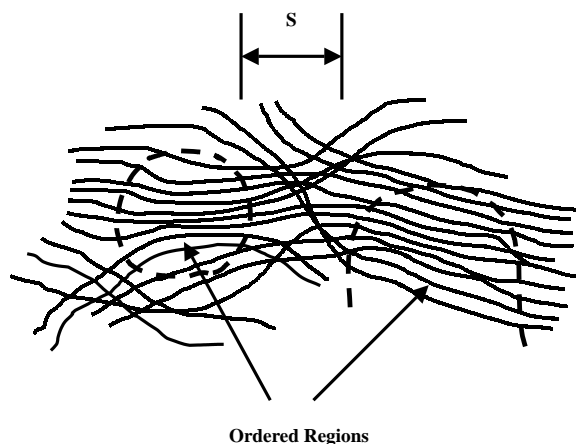


**Figure 4.** Schematic view of the inhomogenous disorder in conducting polymers.

whether such structural inhomogeneities of mesoscopic scale totally complicate their physical properties (so-called "inhomogeneous limit") [47–50], or whether disorder is present over a wide range of length scales and can be treated by an averaged manner (so-called "homogeneous limit") [51–53], has been a subject of considerable discussion. In the former case, the metal–insulator (M–I) transition would be better described in terms of percolation between metallic islands with an emphasis on the one-dimensional localization in the less-ordered regions, while in latter case, the M–I transition would be described by conventional localization theory (e.g., Anderson transition).

In the inhomogeneous limit [47–50], the localization effects in the conducting polymers are proposed to originate from one-dimensional localization in the less-ordered regions. The inhomogeneous disorder model represents the doped polymer chains as relatively ordered (or crystalline) islands interconnected through polymer chains traversing disordered regions. The individual chains are often assumed to be longer than the island and interisland length scales. Within this model, conducting electrons are three-dimensionally delocalized in the crystalline ordered regions. In order to transit between ordered regions, the conducting electrons must diffuse along electronically isolated chains through the disordered regions where the electrons readily become localized. In this model, the localization length of the electrons depends upon the details of the disorder. Three-dimensional crystalline order facilitates delocalization. If the localization length for some conduction electrons exceeds the separation between the ordered regions then the total delocalization will be substantially enhanced.

Although it is true that the structural mesoscopic inhomogeneities have strongly dominated the physical properties of earlier conducting polymer materials, recent progress in the processing of conducting polymers has significantly improved the quality of the materials with corresponding improvements in the physical properties [51–53]. The examples are polyaniline doped with functionalized sulfactant acid CSA [27, 38, 54], electrochemically fabricated polypyrrole doped with $PF_6$ (PPy-$PF_6$) [28, 55, 56], and $PF_6$-doped poly(3,4-ethylenedioxythiophene) [34, 57, 58]. Transport studies [38, 51, 55, 57] demonstrated that those improved materials are more highly conducting and more homogeneous than those studied earlier; the relevant length scales which are used to characterize the electronic properties near the M–I transition [i.e., the inelastic scattering length ($L_{in} \approx 300$ Å) in the metallic regime and the localization length ($L_c \approx 200$–300 Å) in the insulating regime] are larger than the characteristic size of inhomogeneities (i.e., $\xi_c$). In such a case the scale of disorder can be treated by an average manner, hence the homogeneous limit. In fact, recent comprehensive transport studies on the improved systems [38, 51, 55, 57] are quite successful in describing the transport properties within the framework of conventional localization–interaction theory [59–61], which was originally developed for homogeneously disordered materials.

Infrared reflectance studies have also played an important role in clarifying the metal physics of conducting polymers [52–54, 56, 58]. For the optical measurements of charge transport, the involved processes might have a different implication with the dc transport measurements. Whereas

dc transport experiments measure the bulk properties of the samples with a limitation to the slowest transport process in the system, optical measurements probe the charge dynamics with a characteristic length scale of $L_\omega = (D/\omega)^{1/2}$ (here $D$ is the electron diffusion coefficient and $\omega$ is the probing frequency), probably less than structural inhomogeneity size $\xi_c$. Therefore, considering the percent crystallinity of typical metallic polymers is almost 50–60%, the inhomogeneous limit would place the optical spectroscopic data to be understood in the framework of effective medium theory or percolation model. However, recent optical spectroscopic studies [52–54, 56, 58] clearly demonstrated that the conventional Drude model modified with weak localization effect is a good description for the optical response of these systems, again supporting the homogeneous limit as in the transport studies.

# 5. METAL–INSULATOR TRANSITION IN CONDUCTING POLYMERS

## 5.1. Role of Disorder

Although the nature of the M–I transition in conducting polymers is still a subject of considerable discussion, it is generally recognized that disorder plays an important role in the physics of metallic polymers [51, 52]. Therefore, it is worth considering conventional disorder-induced M–I transition [59–62] as a starting point of this section. Ioffe and Regel argue that as the extent of disorder increases in a metallic system, the mean free path ($\ell$) approaches the interatomic spacing, limiting metallic behaviors of the system [63]. In such a case the Ioffe–Regel criterion is defined as $k_F\ell \approx 1$, where $k_F$ is the Fermi wave number. The metallic regime corresponds to $k_F\ell \gg 1$.

Based on the Ioffe–Regel criterion, Mott [59, 62] proposed that a M–I transition must occur when the disorder is sufficiently large that $k_F\ell < 1$. In such a case coherent metallic transport would not be possible. In recognition of Anderson's early work on disorder-induced localization, Mott called this M–I transition the Anderson transition [64]. In the limit where $k_F\ell \ll 1$ (i.e., where the strength of the random disorder potential is large compared to the bandwidth), all states become localized and the system is called a Fermi glass [65]. A Fermi glass is an insulator with a continuous density of localized states occupied according to Fermi statistics. Although there is no energy gap, the behavior is that of an insulator because the states at the Fermi energy are spatially localized.

The scaling theory of localization demonstrated that the disorder-induced M–I transition was a true phase transition with a well-defined critical point [66]. McMillan [67] and Larkin and Khmelnitskii [68] showed that near the critical regime of Anderson localization a power-law temperature dependence is to be expected for the conductivity.

## 5.2. Transport Properties

Recently critical behavior of Anderson localization has been observed over a relatively wide temperature range in a number of structurally improved conducting polymer systems, including polyacetylene [69], polypyrrole [55],

poly(p-phenylenevinylene) [70, 71], polyaniline [38], and poly(3,4-ethylenedioxythiophene) [57]. In each case, the metallic, critical, and insulating regimes near the M–I transition have been identified from Zabrodskii plots [72] of the logarithmic derivative of the conductivity $W = (\Delta \ln \sigma / \Delta \ln T)$ vs $T$. In the metallic and insulating regime $W(T)$ exhibits positive and negative temperature coefficients, respectively, while in the critical regime, $W(T)$ is temperature independent.

The resistivity, $\rho(T)$, and the resistivity ratio, $\rho_r = \rho(1.4\ K)/\rho(300\ K)$, have been successfully used to quantify the relative disorder in different samples and for sorting out the various regimes [51]. In general, as the disorder increases, the materials become more insulating, and the conductivity decreases more rapidly upon lowering the temperature (i.e., $\rho_r$ increases). In fact, the resistivity ratio $\rho_r$ has proven to be useful as an "effective order parameter" for the M–I transition in conducting polymers [38, 51, 55].

The critical regime is easily tunable in conducting polymers by varying the extent of disorder, or by applying external pressure and/or magnetic field. The transitions from metallic to critical behavior and from critical to insulating behavior have been induced with a magnetic field, and from insulating to critical and then to metallic behavior with increasing external pressure [38, 51, 55, 69–71].

In the metallic regime, the zero-temperature conductivity remains finite with magnitude that depends on the extent of the disorder. Metallic behavior has been demonstrated for conducting polymers with $\sigma(T)$ remaining constant as $T$ approaches zero. Well into the metallic regime where the mean free path extends over many repeat units, the residual resistivity will become small, as in a typical metal. However, this truly metallic regime, with $k_F\ell \gg 1$, has not yet been achieved.

In the critical region, theory predicts that the resistivity $\rho(T)$ should follow the power law [67, 68]. Extension of the power law dependence to $T = 0$ requires that the system be precisely at the critical point. The power law is universal and requires only that the disordered system be in the critical regime. The power law dependence for $\rho(T)$ has been observed over a wide temperature range in a number of metallic polymers near the M–I transition. Log–log plots of $W(T)$ vs $T$ are quite sensitive and enable the precise identification of the critical regime. Moreover, the detailed evolution of $\rho(T)$ in the critical regime at low temperatures can be observed in $W(T)$ plots as the system is changed from metal to insulator. In the insulating regime, transport occurs through variable range hopping among localized states, where $\ln \rho$ is proportional to $T^{-1/x}$ where $x$ is determined by details of the hopping mechanism [59, 62, 73].

## 5.3. Infrared Reflectance Studies

Reflectance measurements provide information on the electronic structure over a wide spectral range. Measurements in the infrared (IR) probe the intraband (free carrier) excitations, while measurements at higher photon energies probe the interband transitions [74]. The corresponding optical conductivity provides information on the metal physics and the disorder-induced M–I transition, and the joint density of

states associated with interband transitions at higher energies. IR reflectance measurements, therefore, have played an important role in clarifying the metal physics of conducting polymers [52–54, 56].

High-precision reflectance measurements were carried out over a wide spectral range on a series of PPy-PF$_6$ samples (A–F) in the insulating, critical, and metallic regimes near the M–I transition [53]. Based on the transport characterization, sample A is in the metallic regime, and sample F is in the insulating regime. For samples B through E, the electronic properties gradually evolve from the metallic side of the M–I transition to the insulating side via the critical regime. Since the reflectance in the IR is sensitive to the charge dynamics of carriers near the Fermi energy ($E_F$), such a systematic reflectance study can provide information on the electronic states near $E_F$ and how those states evolve as the system passes through the M–I transition. The data demonstrate that metallic PPy-PF$_6$ is a disordered metal and the M–I transition is driven by disorder; similar results were obtained for conducting polyaniline [54, 75].

Figure 5 shows $R(\omega)$ for samples A–F as measured at room temperature. For the most metallic sample (A), $R(\omega)$ exhibits distinct metallike signatures, a free carrier plasma resonance as indicated by the minimum in $R(\omega)$ around $1.5 \times 10^4$ cm$^{-1}$ and high $R(\omega)$ in the far-IR ($R \geq 90\%$ for $\omega < 20$ cm$^{-1}$). As PPy-PF$_6$ goes from the metallic to the insulating regime via the critical regime, $R(\omega)$ is gradually suppressed in the IR. In the insulating regime (F), $R(\omega)$ remains well below that of the metallic sample (A) throughout the IR. The $R(\omega)$ spectra are in excellent correspon-

dence with the transport results; the better the quality of the sample, as defined by the higher $\sigma_{dc}(300$ K), the higher $R(\omega)$ in the IR.

In the far-IR (below 100 cm$^{-1}$), the Hagen–Rubens approximation [76] provides an excellent fit to $R(\omega)$

$$R_{\text{H-R}}(\omega) = 1 - (2\omega/\pi\sigma_{\text{H-R}})^{1/2} \qquad (1)$$

where $\sigma_{\text{H-R}}$ is the $\omega$-independent conductivity. The $\sigma_{\text{H-R}}$ values obtained from the Hagen–Rubens fits are in remarkably good agreement with the measured values of $\sigma_{dc}(300$ K) [53].

The optical conductivity, $\sigma(\omega)$, can be obtained by the Kramers–Kronig analysis of $R(\omega)$ as shown in Figure 6. The corresponding $\sigma(\omega)$ are not typical of a Drude metal for which $\sigma_{\text{Drude}} = (\omega_p^2\tau/4\pi)/[1+\omega^2\tau^2]$, where $\omega_p$ is the $\pi$-electron plasma frequency, and $\tau$ is the mean scattering time. Even for the most metallic sample (A), $\sigma(\omega)$ decreases with decreasing $\omega$ below 2500 cm$^{-1}$ and thus deviates from Drude behavior. On moving toward the insulating regime (from A to F), $\sigma(\omega)$ is suppressed, and the maximum in $\sigma(\omega)$ gradually shifts to higher frequencies.

The $\sigma(\omega)$ data are fully consistent with the "localization-modified Drude model" (LMD) [52]. This LMD model, originally proposed by Mott and Kaveh [77], has been modified by Lee and Heeger [54] and successfully introduced into the analysis of optical spectra of metallic conducting polymers [52–54, 56]. This model is a first order correction of the Drude model in the regime of weak localization, as given by [52, 54]

$$\sigma_{\text{LMD}} = \sigma_{\text{Drude}}\{1 - C[1 - (3\tau\omega)^{1/2}]/(k_F\ell)^2\} \qquad (2)$$

where $k_F$ is the Fermi wave number and $\ell$ is the mean free path. In this model, the zero-frequency limit determines the constant $C$, while a fit to $\sigma(\omega)$ determines $k_F\ell$. The suppressed $\sigma(\omega)$ data from the various regimes were fit with the functional dependence predicted by the LMD model; Figure 6 illustrates the excellent agreement of the fits to the data with the parameters summarized in the inset. The phonon



Figure 5. Reflectance spectra of sample A–F of PPy-PF$_6$, demonstrating plasma resonance in the near-IR. Bottom plot shows the far-IR reflectance with the Hagen–Rubens extrapolation to zero frequency. Reprinted with permission from [53], K. Lee et al., *Adv. Mater.* 10, 456 (1998). © 1998, Wiley–VCH.
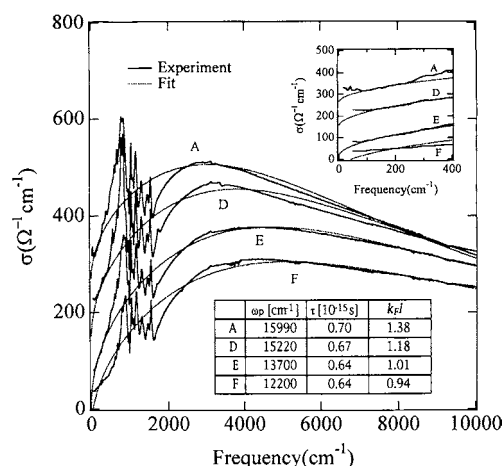


Figure 6. Optical conductivity $\sigma(\omega)$ of sample A–F of PPy-PF$_6$. Dashed lines are fitted to the localization-modified Drude model. Fit parameters are given in the table. Reprinted with permission from [53], K. Lee et al., *Adv. Mater.* 10, 456 (1998). © 1998, Wiley–VCH.

| | $\omega_p$ [cm$^{-1}$] | $\tau$ [10$^{-15}$s] | $k_F\ell$ |
|---|---|---|---|
| A | 15990 | 0.70 | 1.38 |
| D | 15220 | 0.67 | 1.18 |
| E | 13700 | 0.64 | 1.01 |
| F | 12200 | 0.64 | 0.94 |

features around 400–2000 cm$^{-1}$ are, of course, not included in the LMD model. There are small deviations for $\omega < 100$ cm$^{-1}$, below which phonon-assisted hopping makes a measurable contribution to $\sigma(\omega)$ and to the dc conductivity.

The parameters obtained from the fits are reasonable. The screened plasma frequency, $\Omega_p = \omega_p/(\varepsilon_\infty)^{1/2} = 1.5 \times 10^4$ cm$^{-1}$, is in good agreement with the frequency of the minimum in $R(\omega)$, and $\tau$ is typical of disordered metals ($\tau \sim 10^{-14}$–$10^{-15}$ s). The quantity $k_F\ell$ is of particular interest, for it characterizes the extent of disorder and is often considered as an order parameter in localization theory [59–62]. For all four samples represented in Figure 6, $k_F\ell \approx 1$, implying that all are close to the M–I transition. As the disorder increases and the system moves from the metallic regime (sample A with $k_F\ell = 1.38$) to the critical regime (sample E with $k_F\ell = 1.01$), $k_F\ell$ approaches the Ioffe–Regel limit [63], precisely as would be expected. In the insulating regime (sample F), $k_F\ell = 0.94 < 1$, consistent with localization of the electronic states at $E_F$.

Thus the IR reflectance data obtained for metallic polymers indicate that they are disordered metals near the disorder-induced M–I transition. There is remarkable consistency between the conclusion obtained from transport studies [51, 55] and from IR reflectance measurements [52, 53].

# 6. DIMENSIONALITY CONSIDERATION

## 6.1. Quasi-One-Dimensional Electronic Structure

Conducting polymers are principally one-dimensional (1D) systems with a typical conjugated backbone structure [2]. As a consequence, the electrical properties improve, as the degree of chain extension and chain alignment is improved. Polyacetylene is the prototype example; the conductivity increases approximately linearly with the mechanical tensile-draw ratio in the iodine-doped polyacetylene films [78]. X-ray diffraction studies of these drawn films exhibited a high degree of structural order that improves with the draw ratio. Furthermore, consistent with the chain orientation and the improved structural order, the anisotropy ($\sigma_{//}/\sigma_\perp$) in the electrical conductivity increased with the draw ratio. These data demonstrate that heavily doped polyacetylene is a highly anisotropic metal with relatively weak interchain coupling [78].

Although the electrical conductivity is enhanced by the relatively high mobility associated with intrachain transport, one must have the possibility of interchain charge transfer to avoid the localization inherent to systems with a 1D electronic structure [59, 62]. The electrical conductivity becomes three dimensional (and thereby truly metallic) only if there is high probability that an electron will have diffused to a neighboring chain prior to traveling between defects on a single chain.

In fact, the establishment of a delocalized 3D metallic state from an array of quasi-1D chains is governed by the interplay between interchain transfer integral $t_\perp$ and intra-chain mean free time $\tau$ [79]. If the interchain coupling is

sufficiently strong that $t_\perp \gg \hbar/\tau$, the electron wave functions become delocalized in three dimensions (or perhaps 2D). In such a case, the conductor is on the metallic side of the M–I transition and the interchain transport is coherent. On the other hand, if $t_\perp \ll \hbar/\tau$, the electronic wave functions will be localized onto individual chains and localized within these chains by intrachain backscattering. Therefore, since a large $t_\perp$ value is usually expected for well-ordered crystalline materials in which the chains have precise phase order, the achievement of metallic polymers with improved chain extension and chain alignment is a major opportunity and also a challenge in the conducting polymer research.

## 6.2. Optical Investigation of Intra- and Interchain Charge Dynamics

Although finite interchain coupling is essential for the metallic state of conducting polymers, there are relatively few measurements of the strength of $t_\perp$ and the anisotropy in the metallic properties [80]. In particular, since tensile drawing induces anisotropy in the physical properties of the films by chain extension and chain alignment, high-precision reflectance studies on such materials enable a separation of the parallel and perpendicular contributions to the optical constants.

Polarized reflectance measurements [81] were carried out on high-quality, stretch-oriented (tensile-drawn with a draw ratio $\ell/\ell_0 \approx 1.5$) films of metallic PPy-PF$_6$. Although separation of the intrachain and interchain contributions to the charge transport has been attempted in dc [82, 83] and frequency-dependent measurements [84], the complex morphology of conducting polymers complicates the analysis of the data. Moreover, since the dc transport properties are limited by the slowest process (i.e., the weakest link), it is difficult to obtain information on the intrinsic properties from such measurements. In contrast, infrared optical measurements [85] on anisotropic samples are capable of probing the anisotropic charge dynamics parallel to and perpendicular to the orientation axis.

Figure 7 shows $R(\omega)$ of partially oriented PPy-PF$_6$ measured in both polarization directions, parallel to and perpendicular to the draw axis [81]. Data from an as-grown sample
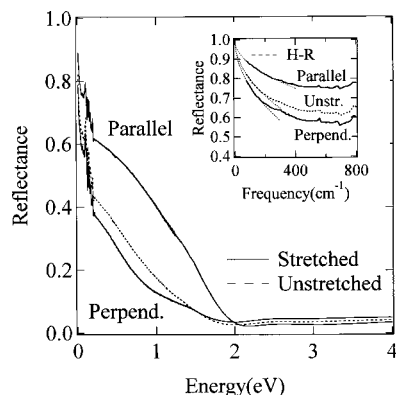


**Figure 7.** Reflectance spectra of stretch-oriented PPy-PF$_6$. Reprinted with permission from [81], K. Lee and A. J. Heeger, *Synth. Met.* 128, 279 (2002). © 2002, Elsevier Science.

(not oriented) are shown for comparison. $R(\omega)$ of the as-grown sample is typical of the highest quality PPy-PF$_6$ with a well-defined plasma frequency as indicated by the minimum in $R(\omega)$ around 2.0 eV [53, 56]. The oriented sample exhibits significant anisotropy in $R(\omega)$. For parallel polarization, $R(\omega)$ is well above that of the unoriented sample throughout the IR ($\hbar\omega < 2$ eV), while for the perpendicular direction $R(\omega)$ remains just below that of the unoriented sample with a pronounced feature around 1.4 eV.

Figure 8 displays the optical conductivity, $\sigma(\omega)$, and dielectric function, $\varepsilon_1(\omega)$, as obtained from Kramers–Kronig analysis of $R(\omega)$ with appropriate extrapolation beyond the measured range [53, 56]. For $\omega < 50$ cm$^{-1}$, the Hagen–Rubens (H-R) relation was used to extrapolate to $\omega \to 0$, as shown in the inset of Figure 7. The IR spectra of the oriented sample exhibit significant differences in the intraband region ($\hbar\omega \leq 2$ eV) in comparison with the nonoriented sample. For the parallel direction, $\sigma(\omega)$ increases and sharpens below 1 eV with a weak feature around 1.4 eV. The feature at 1.4 eV is more pronounced in the perpendicular direction.

The $\sigma(\omega)$ data obtained from the stretched sample are consistent with the dc transport results. The uniaxial orientation of the as-grown PPy-PF$_6$ (dc conductivity $\sigma_{dc} \approx 350$ S/cm at 300 K) with $\ell/\ell_0 \approx 1.5$ results in substantial increase in $\sigma_{dc}$ along the draw axis ($\sigma_{dc//} \approx 800$ S/cm at 300 K) together with a strong anisotropy ($\sigma_{dc//}/\sigma_{dc\perp} \approx 4.6$ with $\sigma_{dc\perp} \approx 175$ S/cm). Both are in agreement with optically measured $\sigma(\omega \to 0)$ as shown in the inset to Figure 8a. This remarkable agreement provides confidence in the accuracy and precision of our $R(\omega)$ measurements.

Chain orientation has a strong influence on the spectral dependence of $\varepsilon_1(\omega)$. PPy-PF$_6$ is a disordered metal close to the metal–insulator transition with $\omega_p\tau \sim 1$ [53, 56]. Thus, $\varepsilon_1(\omega)$ of the unstretched sample does not cross zero even
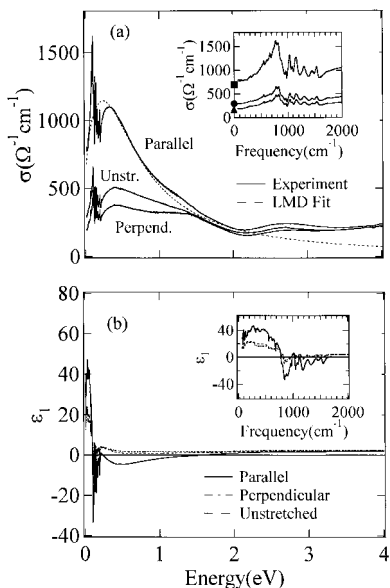
at the plasma frequency because the plasma oscillation is overdamped. In contrast, however, for a good metal with $\omega_p\tau > 1$, $\varepsilon_1(\omega)$ is expected to cross zero at the screened plasma frequency, $\Omega_p = \omega_p/(\varepsilon_\infty)^{1/2}$, where $\varepsilon_\infty$ is the high-energy contribution to $\varepsilon_1$ [74]. This is the case for the parallel direction in the stretched sample; $\varepsilon_1(\omega)$ crosses zero at 1.6 eV and goes to negative values deeper in the IR. This is supported by theoretical analysis using the LMD model [52] as shown in Figure 8. The fits to the data yield $\omega_p \approx 2.3$ eV and $\tau \approx 1.2 \times 10^{-15}$ sec for the parallel polarization. Using these values, we obtain $\Omega_p \approx 1.6$ eV with $\varepsilon_\infty \approx 2$ and $\omega_p\tau \approx 4.2 > 1$. However, in contrast to simple Drude behavior, weak localization [53] causes $\varepsilon_1(\omega)$ cross zero again at 0.24 eV and remain positive down to $\approx 50$ cm$^{-1}$ (our low frequency measurement limit).

Although one hopes to obtain information on the parallel and perpendicular charge dynamics from the data, the samples are only partially oriented. In such partially aligned 1D systems, both $\sigma(\omega)$ for polarization parallel [$\sigma_{//}(\omega)$] and perpendicular [$\sigma_\perp(\omega)$] to the draw axis are given by a combination of intrinsic intrachain part, $\sigma_{0//}(\omega)$, and interchain component, $\sigma_{0\perp}(\omega)$, in the context of effective mediumlike approach. Using the degree of chain orientation for those samples as obtained from independent experiment, $\sigma_{0//}(\omega)$ and $\sigma_{0\perp}(\omega)$ are obtained from the analysis of $\sigma_{//}(\omega)$ and $\sigma_\perp(\omega)$ as displayed in Figure 9.

The $\sigma_{0//}(\omega)$ spectrum is typical of a disordered Drude metal [52] with a dominant response in the low energy for $\hbar\omega \leq 0.5$ eV. On the other hand, $\sigma_{0\perp}(\omega)$ exhibits spectral features of strongly localized conductors with $\sigma_{0\perp}(\omega) \approx 0$ for $\hbar\omega \leq 0.3$ eV and a peak around 1.4 eV. These imply the interchain charge dynamics is incoherent and severely limits the charge transport process in conducting polymers. This is attributed to the weak interchain coupling as compared with the intrachain scattering rate; when estimated to be $\hbar/\tau \approx 0.5$ eV from the spectral shape of $\sigma_{0//}(\omega)$, it is larger than the usual value of $t_\perp$ ($\approx 0.01$–0.2 eV) for conducting polymers; hence $t_\perp < \hbar/\tau$. In such a case, theories [79] predict that the interchain charge motion is incoherent with a strong localization, as consistent with the experimental observation. Finally, the value $\sigma_{0//}(\omega \to 0) \approx 2 \times 10^3$ S/cm is considerably larger than the experimentally measured conductivity ($\sigma_{//dc} \approx 800$ S/cm). This suggests that significant



**Figure 8.** (a) Optical conductivity spectra $\sigma(\omega)$ and (b) real part of the dielectric function $\varepsilon_1(\omega)$ of stretch-oriented PPy-PF$_6$. Reprinted with permission from [81], K. Lee and A. J. Heeger, *Synth. Met.* 128, 279 (2002). © 2002, Elsevier Science.
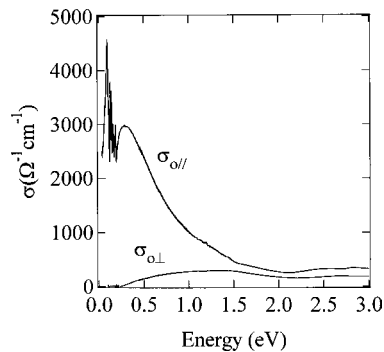


**Figure 9.** Intrachain [$\sigma_{0//}(\omega)$] and interchain optical conductivity [$\sigma_{0\perp}(\omega)$] for PPy-PF$_6$. Reprinted with permission from [81], K. Lee and A. J. Heeger, *Synth. Met.* 128, 279 (2002). © 2002, Elsevier Science.

improvement in the performance of conducting polymers can be achieved by better control of morphology and by improving chain alignment.

# 7. CONDUCTING POLYMERS AS NANOTECHNOLOGY MATERIALS

According to Moore's law, it is expected that the dimensions of integrated circuit components will be reduced to approximately 10 nm by the year 2020. In such a case the interconnecting wires within such circuits would approach the ultimate limit: so-called "molecular wires" in which a linear array of single atoms just provides building blocks of the components. One of the potential candidates for such semiconductive and/or metallic "molecular wires" is the $\pi$-conjugated polymer system [8, 86].

Another promising aspect for conducting polymers as nanotechnology materials is the "molecular electronics" [9, 87, 88]. Recently molecular-scale electronics have received much attention because of their promise of future electronic devices, which operate at nanometer size and also at THz speeds. Such a molecular-scale electronic concept also requires use of single or few molecules as major electronic components such as diodes, transistors, and laser diodes. For the realization of such nanometer scale devices, therefore, it is crucial to control the synthesis of a conducting polymer in a nanometer scale and to evaluate the performance and mechanism of molecular conduction. In recent years there have been several pioneering works focusing on those subjects, and some examples are introduced here.

Grozema and co-workers [89] measured hole mobility along isolated chains of $\pi$-conjugated polymers after irradiating polymer solutions with Van de Graaff accelerator. Pulsed irradiation produces radical cations and excess electrons in the solutions. Then, the change in the conductivity of a solution was monitored using the time-resolved microwave conductivity technique at a frequency of 30 GHz. They showed that mobilities well in excess of 0.1 cm$^2$/Vs are possible for hole transport along isolated chains. They conclude that conformational disorder and/or structural defects in the backbone plays a decisive role in determining the magnitude of the mobility and that values in excess of 1 cm$^2$/Vs would be realizable, if the disorder can be reduced by either chemical or physical means.

Nonresonant tunnel conduction through a self-assembled monolayer of conjugated molecules fabricated on gold (111) was reported by Sakaguchi and co-workers [90]. In their experiment, conjugated molecules with different numbers of oligothiophene rings were fabricated on gold to form the self-assembled monolayer (SAM), which was covalently bonded to the metal surface. Nanometer-scale electrical measurements were performed in a manner of contacting the Pt-coated cantilever having a 20 nm sphere radius with the SAM surface using a conductive atomic force microscope. The sample current image was obtained by monitoring the current with a two-dimensional scan of metal-coated cantilever on the sample surface. This work proved that the electrical measurements with nanometer spatial resolution enable mapping of tunnel current as well as efficiency of tunnel conduction through molecular wire by analyzing length

dependence on current; a series of conjugated molecules with different numbers of oligothiophene rings possess a high tunnel-conduction efficiency.

Boggild et al. [91] also reported the direct measurements of the microscale conductivity on thin polymer films by mapping the conductivity of single uniaxially ordered domains and surrounding disordered areas. This was possible due to a novel scanning micro four-point probe that allows the source, drain, and voltage electrodes to be positioned within the same domain. Exceptionally high conductivities were observed on the single domain level, while the disordered regions exhibited much poorer conduction. This indicates that the in-plane alignment of polymer molecules in a monolayer is a crucial parameter for the electrical properties.

Devices based on conjugated polymers usually make use of the polymers as solution cast thin films. Since the electronic and optical properties of the films are inherently related to their local structure, it is important to achieve a greater control of the self-assembly process that takes the polymers from a disordered state in solution into a semi ordered solid state. The desire to make nanometer scale devices for future electronic applications further emphasizes the need for such nanoscale control.

In an effort to achieve such a purpose, Bjornholm and co-workers [92] reported on the formation of conjugated polymer nanowires by collapsing a monolayer of amphiphilic polythiophene on a Langmuir–Blodgett trough. Isothermic compression leads to dense packed monolayers in which the polythiophene backbones are $\pi$-stacked parallel to the water surface as shown in Figure 10. The stacking of the polymers is highly ordered. From X-ray diffraction data, the domain size of the highly ordered $\pi$-stacked polymer has been estimated to be 6 nm in the stacking direction. The average length of the polymers is $\leq 40$ nm (i.e., $\leq 50$ repeat units). The room temperature conductivity of the undoped wires is less than $10^{-5}$ S/cm, while the iodine-doped sample reaches a value of $\sigma \approx 40$ S/cm.

Since application of conducting polymers in molecular sensors or electronic devices requires nanosized polymer dots or wires, nanosized conducting polymer fibers have been prepared electrochemically using hollowed templates made from polycarbonates with neutron beams [93] or chemically using zeolites with linear pores [94]. However, for practical applications in electronic circuits of nanometer size, preparation of nanosized conducting polymer
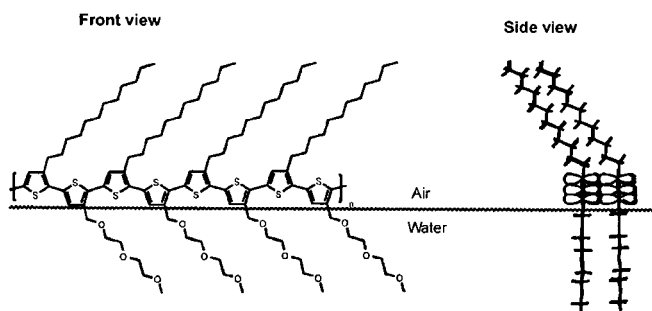


**Figure 10.** Molecular structure of the amphiphilic polythiophene derivative. Reprinted with permission from Ref. [92], T. Bjornholm et al., *Adv. Mater* 11, 1218 (1999). © 1999, Wiley-VCH.

dots and/or wires needs to be simplified. Nanowires prepared inside zeolite pores or polycarbonate templates could eventually be used for electronic circuits; however, it would not be trivial to separate them from the template materials although the nanowires thus prepared may be manipulated with nanotweezers [95].

Recently Choi and Park [96] have developed a new concept to grow nanosized conducting polymer wires and rings by *in situ* electrochemical techniques. Conducting polymer nanowires and nanorings were synthesized using electrochemical growth on gold electrodes modified with SAMs of well-separated thioated cyclodextrins in an alkanethiol "forest." Thiolated aniline monomer is anchored to the surface within the cyclodextrin cavity and forms an initiation point for polymer wire growth. The polymer wires appear to be made of numerous single strands several tens of nanometers thick and a few micrometers long. They claimed that a single nanowire thread of a conducting polymer has been isolated for the first time [96].

In addition to the fields of electronics and optics, conducting polymers are also promising candidate materials for biomedical applications [97–101]. As a next generation of implantable biomaterials, the capability of communication with surrounding tissues would be essential; those materials should incorporate stimulatory cues (such as electrical signals) directly into tissues for regulating cell attachment, proliferation, and differentiation. Moreover, the use of electroactive materials would allow one to locally deliver an electrical stimulus at the site of damage, while also providing a physical template for cell growth and tissue repair. Therefore conducting polymers, such as polypyrrole and polythiophene, are expected to play a crucial role in such biomedical applications [97–101]. In fact, *in vitro* enhancement of nerve cell axonal extension has been reported using polypyrrole with application of either constant current or constant voltage [97–99]. Polypyrrole has also been used as a substrate to increase electronic interfacing between neurons and micromachined microelectrodes for potential applications in neural probes and prosthetic devices [100].

Recently Rivers and co-workers [101] reported the synthesis and characterization of a novel biodegradable, electrically conducting polymer that demonstrates good tissue compatibility. The polymer was synthesized from conducting oligomers of pyrrole and thiophene that are connected together via degradable ester linkages. They addressed that the material has broad potential for tissue engineering applications as a temporary scaffold for cell attachment and as a source of electrical signals to stimulate tissue regeneration. They also expect that the material will be useful to some bioelectronic application in which a transient electronic–tissue interface is desired.

## 8. CONCLUDING REMARKS

As a new class of materials which exhibit the electrical and optical properties of semiconductors or metals together with the processing advantages of typical polymers, conjugated polymers provide a route to "plastic electronic" devices, including polymer LEDs, polymer lasers, high-sensitivity polymer photodiodes and photovoltaic cells, thin-film transistors, and all-polymer integrated circuits. In addition to such polymer electronics and optoelectronics, conjugated polymers also emerge as promising candidate materials for nanotechnology materials in the form of "molecular wires" for molecular electronics.

For the realization of such novel devices using conjugated polymers, it is crucial to understand the mechanism of charge conduction and to evaluate the physical properties of those materials on a nanometer scale. However, although the electrical and optical properties of conducting polymers have been investigated for over a decade, the nature of the metallic states and the corresponding metal–insulator transition are not still fully understood. This mainly originates from their complex morphologies inherent to typical polymer systems and also from their novel reduced dimensionality.

Although the structural mesoscopic inhomogeneities have strongly dominated the physical properties of earlier conducting polymers, recent progress in the processing has significantly improved the quality of the materials with corresponding improvements in the physical properties. The transport and optical measurements on the improved materials have proved that the relevant electronic length scales are larger than the characteristic size of structural inhomogeneities, and the conventional localization theory is a good description for the physical properties of the improved systems. In such a case the intrachain charge dynamics is typical of a disordered Drude metal with a weak interchain coupling, while the interchain responses are dominated by spectral features of strongly localized conductors. This suggests that significant improvement in the performance of conducting polymers can be achieved by better control of morphology and by improving chain alignment. The desire to make nanometer scale devices using these materials further emphasizes the need for such nanoscale control and improvement.

## GLOSSARY

**$\pi$–$\pi^*$ Transition** An electronic transition described approximately as a promotion of an electron from a "bonding" orbital to an "antibonding" orbital (designated as *) generally in the conjugated polymer systems.

**Hagen–Rubens approximation** The approximate relation for infrared reflectivity of typical metals at low frequencies.

**Ioffe–Regel limit** A limit to conventional metallic behaviors as the extent of disorder increases in a metallic system.

**Infrared active vibrational modes (IRAV)** Molecular vibration modes originating from a local symmetry breaking by introducing doping charges to the backbone of conjugated polymers. These modes are optically observed in the infrared region.

**Kramers–Kronig relation** Dispersion relation between the real part and imaginary part of the response function of a linear passive system, such as complex dielectric constant, complex refractive index, and reflectivity.

**Langmuir–Blodgett (LB) films** A set of monolayers, or layers of organic material one molecule thick, deposited on a solid substrate. An LB film can consist of a single layer or many, up to a depth of several visible-light wavelengths.

**Molecular electronics**   Research and development of electronic devices at a molecular level of miniaturization with electrons as signal carriers.

**Peierls instability**   The phenomenon of opening bandgap by lattice distortion due to the modulation of the charge density wave with wave vector $2k_F$ in one-dimensional materials.

## ACKNOWLEDGMENTS

## REFERENCES

1. C. K. Chiang, C. R. Fincher, Y. W. Park, A. J. Heeger, H. Shirakawa, and E. J. Louis, *Phys. Rev. Lett.* 39, 1098 (1977).
2. A. J. Heeger, S. Kivelson, J. R. Schrieffer, and W. P. Su, *Rev. Mod. Phys.* 60, 781 (1988).
3. See, for example, "Handbook of Conducting Polymers," 2nd ed. (T. A. Skotheim, R. L. Elsenbaumer, and J. R. Reynolds, Eds.), Dekker, New York, 1998.
4. A. J. Heeger, *Rev. Mod. Phys.* 73, 681 (2001).
5. J. H. Burroughes, D. D. C. Bradley, A. R. Brown, R. N. Marks, R. H. Friend, P. L. Burns, and A. B. Holmes, *Nature* 335, 539 (1990).
6. R. H. Friend, R. W. Gymer, A. B. Holmes, J. H. Burroughes, R. N. Marks, C. Taliani, D. D. C. Bradley, D. A. Dos Santos, J. L. Bredas, M. Logdlund, and W. R. Salaneck, *Nature* 397, 121 (1999).
7. See, for example, "Semiconducting Polymers" (G. Hadziioannou and P. F. van Hutten, Eds.), Wiley–VCH, Weinheim, 2000.
8. B. Wessling, in "Handbook of Nanostructured Materials and Nanotechnology"(H. S. Nalwa, Ed.), Vol. 5, p. 501. Academic Press, San Diego, 2000.
9. C. Joachim, J. K. Gimzewski, and A. Aviram, *Nature* 408, 541 (2000).
10. W. P. Su, J. R. Schrieffer, and A. J. Heeger, *Phys. Rev. Lett.* 42, 1698 (1979).
11. Y. Lu, "Solitons and Polarons in Conducting Polymers." World Scientific, Singapore, 1988.
12. J. Chen, T.-C. Chung, F. Moraes, and A. J. Heeger, *Solid State Commun.* 53, 757 (1985).
13. Y. H. Kim and A. J. Heeger, *Phys. Rev. B* 40, 8393 (1989).
14. B. Horovitz, *Solid State Commun.* 41, 729 (1982).
15. E. Ehrenfrund, E. Vardeny, O. Brafman, and B. Horovitz, *Phys. Rev. B* 36, 1535 (1987).
16. E. M. Conwell, H. A. Mizes, and S. Jeyadev, *Phys. Rev. B* 40, 1630 (1989).
17. E. M. Conwell and H. A. Mizes, *Phys. Rev. B* 44, 937 (1985).
18. S. Kivelson and A J. Heeger, *Phys. Rev. Lett.* 55, 308 (1985).
19. H. Y. Choi and E. J. Mele, *Phys. Rev. B* 34, 8750 (1986).
20. S. Stafstrom and J. L. Bredas, *Phys. Rev. B* 38, 4180 (1988).
21. C. K. Chiang, S. C. Gau, C. R. Fincher, Y. W. Park, and A. G. MacDiarmid, *Appl. Phys. Lett.* 33, 18 (1978).
22. H. Shirakawa, E. J. Louis, A. G. MacDiarmid, C. K. Chiang, and A. J. Heeger, *Chem. Commun.* 578 (1977).
23. C. K. Chiang, C. R. Fincher, Y. W. Park, A. J. Heeger, H. Shirakawa, and E. J. Louis, *Phys. Rev. Lett.* 39, 1098 (1977).
24. J. Tsukamoto, *Adv. Phys.* 41, 509 (1992).
25. N. Basescu, Z.-N.X. Liu, D. Moses, A. J. Heeger, H. Naarmann, and N. Theophilou, *Nature* 327, 403 (1987).
26. H. Shirakawa, Y.-X. Zhang, T. Okuda, K. Sakamaki, and K. Akagi, *Synth. Met.* 65, 14 (1994).
27. Y. Cao, P. Smith, and A. J. Heeger, *Synth. Met.* 48, 91 (1992).
28. K. Sato, M. Yamaura, T. Hagiwara, K. Murata, and M. Tokumoto, *Synth. Met.* 40, 35 (1991).
29. T. Ohnishi, T. Noguchi, T. Nakano, M. Hirooka, and I. Murase, *Synth. Met.* 41–43, 309 (1991).
30. W. R. Salaneck, I. Lundstrom, W. S. Haung, and A. G. MacDiarmid, *Synth. Met.* 13, 291 (1986).
31. F. Wudl, R. O. Angus, F. L. Lu, P. M. Allemand, D. J. Vachon, M. Nowak, Z. X. Liu, and A. J. Heeger, *J. Am. Chem. Soc.* 109, 3677 (1987).
32. Y. Cao, P. Smith, and A. J. Heeger, U.S. Patent 5, 232, 631.
33. P. J. Nigrey, A. G. MacDiarmid, and A. J. Heeger, *Chem. Commun.* 96, 594 (1979).
34. R. Kiebooms, A. Aleshin, K. Hutchison, and F. Wudl, *J. Phys. Chem.* 101, 11037 (1997).
35. J. H. Edwards and E. J. Feast, *Polym. Commun.* 21, 595 (1980).
36. D. R. Gagnon, J. D. Capistran, F. E. Karasz, and R. W. Lenz, *Polym. Bull.* 12, 93 (1984).
37. I. Murasi, T. Ohnishi, and M. Hirooka, *Polym. Commun.* 25, 327 (1984).
38. R. Menon, Y. Cao, D. Moses, and A. J. Heeger, *Phys. Rev. B* 497, 1758 (1993).
39. L. Sun and S. C. Yang, *Polym. Prepr.* 33, 379 (1992).
40. G. Heywang and F. Jonas, *Adv. Mater.* 4, 116 (1992).
41. J. Friedrich and K. Werner, U.S. Patent 5, 300, 575.
42. M. Yamaura, K. Sato, T. Hagiwara, and K. Ieata, *Synth. Met.* 48, 337 (1992).
43. Y. Nogami, J.-P. Pouget, and T. Ishiguro, *Synth. Met.* 62, 257 (1994).
44. J. Joo, Z. Oblakowski, G. Du, J. P. Pouget, E. J. Oh, J. M. Weisinger, Y. G. Min, A. G. MacDiarmid, and A. J. Epstein, *Phys. Rev. B* 49, 2977 (1994).
45. J. P. Pouget, Z. Oblakowski, Y. Nogami, P. A. Albouy, M. Laridjani, E. J. Oh, Y. Min, A. G. MacDiarmid, J. Tsukamoto, T. Ishiguro, and A. J. Epstein, *Synth. Met.* 65, 131 (1994).
46. Z. H. Wang, E. M. Scherr, A. G. MacDiarmid, and A. J. Epstein, *Phys. Rev. B* 45, 4190 (1992).
47. R. S. Kohlman, J. Joo, and A. J. Epstein, in "Physical Properties of Polymers Handbook" (J. E. Mark, Ed.), Am. Inst. of Phys., New York, 1996.
48. R. S. Kohlman, J. Joo, Y. Z. Wang, J. P. Pouget, H. Kaneko, T. Ishiguro, and A. J. Epstein, *Phys. Rev. Lett.* 74, 773 (1995).
49. R. S. Kohlman, J. Joo, Y. G. Min, A. G. MacDiarmid, and A. J. Epstein, *Phys. Rev. Lett.* 77, 2766 (1996).
50. R. S. Kohlman, A. Zibold, D. B. Tanner, G. G. Ihas, T. Ishiguro, Y. G. Min, A. G. MacDiarmid, and A. J. Epstein, *Phys. Rev. Lett.* 78, 3915 (1997).
51. R. Menon, C. O. Yoon, D. Moses, and A. J. Heeger, in "Handbook of Conducting Polymers," 2nd ed. (T. A. Skotheim, R. L. Elsenbaumer, and J. R. Reynolds, Eds.), Dekker, New York, 1998.
52. R. Kiebooms, R. Menon, and K. Lee, in "Handbook of Advanced Electronic and Photonic Materials and Devices" (H. S. Nalwa, Ed.), Vol. 8. Academic Press, San Diego, 2001.
53. K. Lee, E. K. Miller, A. N. Aleshin, R. Menon, A. J. Heeger, J. H. Kim, C. O. Yoon, and H. Lee, *Adv. Mater.* 10, 456 (1998).
54. K. Lee, A. J. Heeger, and Y. Cao, *Phys. Rev. B* 48, 14884 (1993).
55. C. O. Yoon, R. Menon, D. Moses, and A. J. Heeger, *Phys. Rev. B* 49, 10851 (1994).
56. K. Lee, R. Menon, C. O. Yoon, and A. J. Heeger, *Phys. Rev. B* 52, 4779 (1995).
57. A. Aleshin, R. Kiebooms, R. Menon, and A. J. Heeger, *Phys. Rev. B* 56, 3659 (1997).
58. Y. Chang, K. Lee, R. Kiebooms, A. Aleshin, and A. J. Heeger, *Synth. Met.* 105, 203 (1999).

59. N. F. Mott, "Metal–Insulator Transitions." Taylor and Francis, New York, 1990.
60. T. G. Castner, in "Hopping Transport in Solids" (M. Pollak and B. I. Shklovskii, Ed.). North-Holland, Amsterdam, 1990.
61. P. A. Lee and T. V. Ramakrishnan, *Rev. Mod. Phys.* 57, 287 (1985).
62. N. F. Mott and E. A. Davis, "Electronic Processes in Noncrystalline Materials." Oxford Univ. Press, Oxford, 1979.
63. A. F. Ioffe and A. R. Regel, *Progr. Semicond.* 4, 237 (1960).
64. P. W. Anderson, *Phys. Rev.* 109, 1492 (1958).
65. P. W. Anderson, *Comments Solid State Phys.* 2, 193 (1970).
66. E. Abrahams, P. W. Anderson, D. C. Licciardello, and T. V. Ramakrishnan, *Phys. Rev. Lett.* 42, 695 (1979).
67. W. L. McMillan, *Phys. Rev. B* 24, 2739 (1981).
68. A. I. Larkin and D. E. Khmelnitskii, *Sov. Phys. JETP* 56, 647 (1982).
69. M. Reghu, K. Vakiparta, Y. Cao, and D. Moses, *Phys. Rev. B* 49, 16162 (1994).
70. M. Ahlskog, M. Reghu, A. J. Heeger, T. Noguchi, and T. Ohnishi, *Phys. Rev. B* 53, 15529 (1996).
71. M. Ahlskog, M. Reghu, A. J. Heeger, T. Noguchi, and T. Ohnishi, *Phys. Rev. B* 55, 6777 (1997).
72. A. G. Zabrodskii and K. N. Zinovjeva, *Zh. Eksp. Teor. Fiz.* 86, 727 (1984).
73. B. I. Shklovskii and A. L. Efros, "Electronic Processes in Doped Semiconductors." Springer, Heidelberg, 1984.
74. F. Wooten, "Optical Properties of Solids." Academic Press, New York, 1972.
75. K. Lee, A. J. Heeger, and Y. Cao, *Synth. Met.* 72, 25 (1995).
76. E. Hagen and H. Rubens, *Ann. Phys.* 11, 873 (1903).
77. N. F. Mott and M. Kaveh, *Adv. Phys.* 34, 329 (1985).
78. Y. Cao, P. Smith, and A. J. Heeger, *Polymer* 32, 1210 (1991).
79. Y. A. Firsov, in "Localization and Metal–Insulator Transition" (H. Fritzsche and D. Adler, Ed.), Plenum Press, New York, 1985.
80. A. J. Heeger, *Faraday Discuss. Chem. Soc.* 88, 1 (1989).
81. K. Lee and A. J. Heeger, *Synth. Met.* 128, 279 (2002).
82. J. Joo, S. M. Long, J. P. Pouget, E. J. Oh, A. G. MacDiarmid, and A. J. Epstein, *Phys. Rev. B* 57, 9567 (1998).
83. C. O. Yoon, H. K. Sung, J. H. Kim, E. Barsoukov, J. H. Kim, and Hosull Lee, *Synth. Met.* 99, 201 (1999).
84. J. A. Reedijk, H. C. F. Martens, H. B. Brom, and M. A. J. Michels, *Phys. Rev. Lett.* 83, 3904 (1999).
85. G. Leising, *Phys. Rev. B* 38, 10313 (1988).
86. See, for example, "Nanostructure Physics and Fabrication" (M. A. Reed and W. P. Kirk, Eds.), Academic Press, New York, 1989; "Nanostructures and Mesoscopic Systems" (M. A. Reed and W. P. Kirk, Eds.), Academic Press, New York, 1992.
87. M. Pope and C. Swenberg, "Electronic Processes in Organic Crystals and Polymers," 2nd ed., p. 1172. Oxford Univ. Press, Oxford, 1999.
88. See, for example, "Molecular Electronics: Science and Technology Conference Proceedings No. 262." Am. Inst. of Physics, New York, 1992.
89. F. C. Grozema, L. D. A. Siebbeles, J. M. Warman, S. Seki, S. Tagawa, and U. Scherf, *Adv. Mater.* 14, 228 (2002).
90. H. Sakaguchi, A. Hirai, F. Iwata, A. Sasaki, and T. Nagamura, *Appl. Phys. Lett.* 79, 3708 (2001).
91. P. Boggild, F. Grey, T. Hassenkam, D. R. Greve, and T. Bjornholm, *Adv. Mater.* 12, 947 (2000).
92. T. Bjornholm, T. Hassenkam, D. R. Greve, R. D. McCullough, M. Jayaraman, S. M. Savoy, C. E. Jones, and J. T. McDevitt, *Adv. Mater.* 11, 1218 (1999).
93. C. R. Martin, *Acc. Chem. Res.* 28, 61 (1995).
94. C. G. Wu and T. Bein, *Science* 264, 1757 (1994).
95. P. Kim and C. M. Lieber, *Science* 286, 2148 (1999).
96. S.-J. Choi and S.-M. Park, *Adv. Mater.* 12, 1547 (2000).
97. C. E. Schmidt, V. R. Shastri, J. P. Vacanti, and R. Langer, *Proc. Nat. Acad. Sci. USA* 94, 8948 (1997).
98. A. Kotwal and C. E. Schmidt, *Biomaterials* 22, 1055 (2001).
99. J. H. Collier, J. P. Camp, T. W. Hudson, and C. E. Schmidt, *J. Biomed. Mater. Res.* 50, 574 (2000).
100. X. Cui, V. A. Lee, Y. Raphael, J. A. Wiler, J. F. Hetke, D. J. Anderson, and D. C. Martin, *J. Biomed. Mater. Res.* 56, 261 (2001).
101. T. J. Rivers, T. W. Hudson, and C. E. Schmidt, *Adv. Funct. Mater.* 12, 33 (2002).

ENN
*Encyclopedia of Nanoscience and Nanotechnology*
www.aspbs.com/enn

# Micro and Nanocantilever Sensors

P. G. Datskos, T. Thundat, Nickolay V. Lavrik

*Oak Ridge National Laboratory, Oak Ridge, Tennesee, USA*

## CONTENTS

## 1. INTRODUCTION

Cantilever structures are the simplest micro-electro-mechanical systems (MEMS) that can be easily micromachined and mass produced. The ability to detect extremely small displacements make the cantilever beams ideal for detection of extremely small forces and stresses. Here we assume that the displacement is directly proportional to the force acting on the cantilever beam. In general, small cantilever beams execute thermal motion (Brownian motion) with amplitudes proportional to the square root of the thermal energy. Measuring the thermal motion amplitude as a function of frequency enables the determination of resonance frequency of the cantilever beam.

Adsorption of molecules on the surface of a cantilever changes the total mass and, consequently, the resonance frequency of the cantilever. The resonance frequency of a microcantilever varies sensitively as a function of mass loading due to molecular adsorption [1–7]. The resonance frequency of a cantilever beam depends on its dimensions, elastic modulus, and density. By changing the dimensions, the resonance frequency can be varied from hundreds of Hz to hundreds of MHz. In fact, depending on the material when the cantilever is of nanoscale dimensions, GHz frequencies can be expected. For a given thickness, shorter cantilevers have higher resonance frequency than longer cantilevers. For a cantilever of given mass, higher resonance frequency implies a larger spring constant. The effect of damping due to medium density is higher for higher resonance frequencies. Although many cantilever sensors take advantage of adsorption-induced bending as the transduction method, an approach based on resonance frequency shifts can potentially provide ultimate sensitivity for detection of a single molecule.

If molecular adsorption is confined to one side of the cantilever, the cantilever undergoes bending due to adsorption-induced variation in surface stress [1–4, 8]. Molecular adsorption onto cantilevers that have two chemically different surfaces results in a differential stress between the top and bottom surfaces of the cantilever. The differential stress produces microcantilever bending. Generally, adsorption decreases the surface energy. For small bending of a cantilever, the surface stress variation can be equated to the variation of surface-free energy. The extent of cantilever bending is often directly proportional to the surface-free energy variation due to molecular adsorption. Therefore, the cantilever bending due to molecular adsorption depends on the change in free energy per adsorbate and the total number of molecules taking part in the adsorption process. The extent of bending depends on the spring constant of the cantilever. In fact, for smaller spring constant cantilevers, the deflection of the cantilever will be larger.

## 2. CANTILEVER SENSORS

The typical thickness of commonly used microcantilevers is approximately $1\mu$m. The length of the cantilever can vary from tens of $\mu$m to a few hundred $\mu$m. The spring constants of the cantilevers are typically in the range of 0.01–1 N/m. Microcantilevers are usually fabricated from silicon or silicon nitride using standard photolithographic and etching techniques. A silicon nitride or a silicon dioxide film is deposited on a single-crystal silicon wafer by a low-pressure chemical vapor deposition (LPCVD) process. By varying the conditions of LPCVD, efforts are made to reduce the stress and stress gradient in the film so that the cantilevers are flat and undeformed when fabricated. The nitride or oxide films are then patterned by photolithography, and the cantilever shapes are defined on the top surface and the etch masks on the bottom surface. The silicon substrate is then etched away to produce free-standing cantilevers. A metal layer such as gold can be coated onto either side of the cantilever, either to provide a surface for chemical modification

through alkanethiol linkers or to make the surface nonreactive for silane-amino linkages of molecules that bind to the oxide surface.

Adsorption-induced cantilever deflection and resonance frequency variation can form the basis of a universal platform for real-time, *in-situ* measurement of physical, chemical, and biochemical properties. A plethora of physical, chemical, and biological sensors, based on the micromachined cantilever platform, have already been demonstrated [1–4, 8–18]. Because cantilever bending and resonance frequency can be measured simultaneously, sensors can be based on adsorption-induced resonance frequency shifts and/or cantilever bending. The resonance frequency shifts and bending of a cantilever can be measured with very high precision using different readout techniques [19], such as optical beam deflection, variations in piezoresistivity, capacitance, and piezoelectric properties.

## 2.1. Thermal Motions of a Cantilever

The resonance frequency of a cantilever, $f$, is given by

$$f = \frac{1}{2\pi}\sqrt{\frac{K}{m^*}} \qquad (1)$$

where $K$ is the spring constant and $m$ is the effective mass of the cantilever. The effective mass can be related to the mass of the beam, $m$, through the relation $m^* = nm$, where $n$ is a unitless geometric parameter. For a rectangular cantilever, $n$ has a typical value of 0.24 [20]. For a rectangular cantilever sensor, the spring constant for vertical deflection is given by [19]:

$$K = \frac{Ewt^3}{4L^3} \qquad (2)$$

where $E$ is the modulus of elasticity for the composing material and $w$, $t$, $L$ are the width, thickness, and length of the beam, respectively. From eq. (1), it is clear that longer cantilevers have smaller spring constants. Therefore, longer cantilevers are more sensitive for measuring surface stresses. However, increasing the length also increases the thermal vibrational noise of the cantilever [19], which from statistical physics, is

$$\delta_n = \sqrt{\frac{2K_B TB}{\pi k f_0 Q}} \qquad (3)$$

Here, $k_B$ is the Boltzmann constant ($1.38 \times 10^{-23}$ J/K), $T$ is the absolute temperature (300 K at room temperature), $B$ is the bandwidth of measurement (typically about 1000 Hz for dc measurement), $f_0$ is the resonant frequency of the cantilever, and $Q$ is the quality factor of the resonance which is related to damping.

It is clear from eq. (3) that lower spring stiffness produces higher thermal noise. It is important to note that the resonance frequency $f_0$ may undergo noticeable fluctuations, $\Delta f_0$, due to exchange between the mechanical and thermal energy of the cantilever [21]:

$$f_0 = \frac{1}{A}\sqrt{\frac{2\pi k_B TB}{KQ f_0}} \qquad (4)$$

where $T$ is the absolute temperature, $Q$ is the quality factor of the cantilever oscillator, $A$ is the oscillation amplitude, and $B$ is the measurements bandwidth. Although eq. (4) predicts increased absolute fluctuations of the resonance frequency, $f_0$, as the resonance frequency $f_0$ increases, relative frequency instability, $\Delta f_0/f_0$, decreases in the case of higher frequency oscillators

$$\frac{\Delta f_0}{f_0} = \frac{1}{A}\sqrt{\frac{2\pi k_B TB}{KQ f_0}} \qquad (5)$$

## 2.2. Q-Factor

The quality factor, or $Q$-factor, of a resonator is a measure of the spread of the resonance peak, $\Delta f_0$, and is thus related to energy loss due to damping ($Q = \Delta f_0/f_0$). The lower the $Q$-factor, the more damped the oscillator. The $Q$-factor depends on parameters such as cantilever material, geometrical shape, and the viscosity of the medium. Typically, the $Q$-factor of a rectangular silicon cantilever in air is approximately 30. However, in liquids, the $Q$-factor decreases by a factor of 10. Therefore, measurements of adsorbed mass based on resonance frequency variation suffer from low resolution in liquid environment. Recently, it has been shown that the effective $Q$-factor can be increased by two to three orders of magnitude by a feedback mechanism [22]. In the feedback technique, the position sensitive detector (PSD) signal is fed back to a piezoelectric element that drives the cantilever into resonance. This technique also works with thermal motion of the cantilever.

## 2.3. Signal Transduction

For a cantilever with a dimension in tens of microns, the bending and resonance frequency shifts are measured with high precision using optical reflection, piezoresistive, capacitance, and piezoelectric methods. One great advantage of the cantilever technique is that both bending and resonance frequency can be measured simultaneously. Moreover, other resonance parameters such as phase, amplitude, and $Q$-factor can be determined if a frequency spectrum is obtained. All the signal transduction methods are compatible with an array format.

### 2.3.1. Optical Beam Deflection

The simplest way of measuring cantilever deflection is by using optical beam deflection [19, 23]. In optical beam deflection technique, a laser diode is focused at the free end of the cantilever. The reflected beam is monitored using a position-sensitive detector. Displacement of the order of 0.1 nm can be measured using optical beam deflection. Optical beam deflection has many advantages such as being compatible with use under liquid and lack of electrical contact to the cantilever beam.

### 2.3.2. Piezoresistance Method

Piezoresistivity is the variation of bulk resistivity with applied stress. Doped silicon exhibits a strong piezoresistive effect [24–27]. The resistance of a doped region on a cantilever

can change reliably when the cantilever is stressed with deflection. This deflection can be caused by changes in adsorption-induced stress or by externally applied stress, such as thermal stress. The variation in cantilever resistance can be measured using an external, dc-biased, Wheatstone bridge. Typical resistance of a silicon microcantilever with a doped boron channel is a few k$\Omega$. If the resistances in the Wheatstone bridge is assumed to have identical values, $R$, and an applied voltage $V$, the differential voltage across the bridge can be expressed as $\Delta V = V \Delta R / (4R)$. If the cantilever is designed to have two identical legs, the current can flow in and out of the cantilever through boron channels. Metallic interconnects can be made to the boron channels at the base of the cantilever for application of external power. The disadvantage of the piezoresistive technique is that it requires passing a current through the cantilever for displacement measurements. This results in electronic noises and thermal drift in cantilever deflection. In addition, the cantilever beam is at a higher temperature due to resistive losses in the cantilever. Since the cantilever temperature is above ambient temperature, any changes in flow rate or thermal conductivity of the ambient can cause parasitic cantilever deflection.

### 2.3.3. Piezoelectric Method

Piezoelectric technique utilizes cantilevers with overlayers that are piezoelectric. Thin layers of piezoelectric materials such as ZnO induces transient charge due to cantilever movement [28–30]. One disadvantage of the piezoelectric technique is that it requires electrodes to the piezoelectric film. In addition, for measurable piezoelectric signals, the film needs to be thicker. Piezoelectric technique is difficult to use when static cantilever deflection measurements are needed. Piezoelectric cantilevers are ideal for resonance, frequency-based approaches.

### 2.3.4. Capacitance Method

The capacitance variation technique of measuring cantilever deflection makes use of the variation in capacitance between cantilever and a fixed substrate [17, 31]. The capacitance varies sensitively as a function of cantilever bending. Capacitance technique, however, is not suitable for liquid environments. Also, variation in the dielectric constant of ambient can contribute to cantilever bending signal.

## 2.4. Advantages of Cantilever Sensors

One great advantage of the cantilever-based sensors is that four resonance response parameters (resonance frequency, phase, amplitude, and $Q$-factor) can be measured simultaneously. Another compelling feature of microcantilever sensors is that they can be operated in air, vacuum, or liquid. The damping effect in a liquid medium, however, reduces the resonance response of a microcantilever. In most liquids, the observed resonance response is approximately an order of magnitude smaller than that in air. The bending response, however, remains unaffected by the presence of a liquid medium. Therefore, the feasibility of operating a microcantilever in a solution with high sensitivity makes the microcantilever an ideal choice for biochemical sensors. Therefore, microfabricated cantilevers can provide the basis for a universal platform for real-time, *in-situ* measurement, and determination of physical, chemical, and biochemical properties. Cantilever sensors offer improved dynamic response, greatly reduced size and high precision, and increased reliability compared to conventional sensors. They are the simplest micromechanical systems that can be mass-produced with conventional micromachining techniques. They can be fabricated into multielement sensor arrays and fully integrated with on-chip electronic circuitry. Because the thermal mass of microcantilevers is extremely small, they can be heated and cooled with a thermal time-constant of less than a millisecond. This is advantageous for rapid reversal of molecular absorption processes and regeneration purposes. Therefore, the micromechanical platform offers an unparalleled opportunity for the development and mass production of extremely sensitive, low-cost sensors for real-time *in-situ* sensing of many chemical and biological species. Therefore, cantilever sensors with extremely high sensitivity can be fabricated by simply reducing the cantilever dimensions. These cantilevers with reduced sizes belong to a class known as nano-electro-mechanical systems (NEMS). Reducing the dimension increases energy efficiency, time response, and sensitivity. However, decreasing the cantilever size results in increased difficulties in fabrication as well as monitoring cantilever response.

## 3. CANTILEVER SENSOR CHARACTERISTICS

The most important aspects of any sensor are its sensitivity, selectivity, and the ability for regeneration. Cantilever-based sensors are extremely sensitive displacement sensors, but they do not offer any intrinsic chemical selectivity. For cantilever-based sensors, the chemical selectivity is obtained by utilizing chemically selective layers such as polymeric films, self-assembled monolayers, or antibody-antigen layers. Regeneration of the sensor originates from thermodynamics. If the analyte-substrate interaction energy is large, the sensor may not regenerate at room temperature.

As pointed out earlier, the cantilever sensor can be operated in two modes: resonance frequency variation and adsorption-induced cantilever bending. The sensitivity of the cantilever bending increases as the spring constant of the cantilever is reduced. Therefore, longer cantilevers with very small spring constants are attractive for use with the adsorption-bending method. However, thermal motion of the cantilever severely limits the extent by which the spring constant of the cantilever can be reduced. On the other hand, the sensitivity of resonance frequency shifts based-approach increases as a function of frequency of operation. Therefore, shorter, higher frequency cantilevers are more suitable for increasing the detection limit when utilizing an approach that takes advantage of frequency shifts.

## 3.1. Sensitivity of Resonance Frequency-Based Approach

Assuming the contribution from variation in spring constant is small, a mass dependence of the fundamental frequency can be written by combining eqs. (1) and (2) as

$$f = \frac{1}{2\pi}\sqrt{\frac{K}{m^*}} = \frac{t}{2\pi(0.98)L^2}\sqrt{\frac{E}{\rho}} \qquad (6)$$

where $\rho$ is the density of the cantilever material. The mass of the adsorbed material can be determined from the initial and final resonance frequency and the initial mass of the cantilever as

$$\frac{(f_1^2 - f_2^2)}{f_1^2} = \frac{\Delta m}{m} \qquad (7)$$

where $f_1$ and $f_2$ are the initial and final frequency, respectively, and $\Delta m$ and $m$ are adsorbed mass and initial mass of the cantilever, respectively. If the adsorption is uniform on the cantilever surface, eq. (7) needs to be modified appropriately in order to take into account the effective mass of the cantilever.

The mass sensitivity of a cantilever sensor can be written as

$$S_m = \lim_{\Delta m \to 0} \frac{1}{f}\frac{\Delta f}{\Delta m} = \frac{1}{f_0}\frac{df}{dm} \qquad (8)$$

where $\Delta m$ and $dm$ are normalized to the active sensor area of the device ($\Delta m = \delta m / A$, where $A$ is the area of the cantilever). As can be seen from the expression in eq. (8), the sensitivity is the fractional change of the resonant frequency of the structure with addition of mass to the sensor. When applying this definition to the case of the cantilever sensor, the sensitivity can be expressed as

$$S_m = \frac{1}{\rho f}\frac{df}{dt} \qquad (9)$$

where $\rho$ and $t$ are the density and the thickness of the adsorbate, respectively. If mass is added uniformly on a cantilever, its resonance frequency decreases as a function of adsorbed mass. Note that the sensitivity of a cantilever sensor depends only on its thickness and material density.

Another characterization parameter of a cantilever sensor is its minimum detection mass density. The minimum detectable mass density can be obtained by rearranging eqs. (6) and (7) as

$$\Delta m_{\min} = \frac{1}{S_m}\frac{\Delta f_{\min}}{f} \qquad (10)$$

where $\Delta m_{\min}$ is the minimum detectable mass density and $\Delta f_{\min}$ is the minimum detectable frequency shift. Typically, minimum detectable mass density values are experimentally quoted results due to specifics of the sensor as well as the frequency detection limitations determining $\Delta f_{\min}$. Therefore, by changing the physical dimension of a cantilever, one can increase its detection limits by many orders of magnitude.

The absolute limit of minimum detection can be derived by combining eqs. 4 and 5. The smallest (noise limited) detectable change in the resonator mass per unit area can be expressed as

$$\Delta m_{\min} = 8\sqrt{\frac{2\pi^5 K k_B T B}{f_0^5 Q}} \qquad (11)$$

## 3.2. Sensitivity of Adsorption-Induced Cantilever Deflection Approach

As mentioned earlier, thin microcantilevers also undergo bending due to mechanical forces generated by molecular adsorption, one of the most overlooked yet fascinating aspects of adsorption. These adsorption-induced forces can be easily detected on so-called "real surfaces" such as the surface of a microcantilever operated in air or under liquid. Adsorption-induced forces are applicable only for monolayer films and should not be confused with bending due to dimensional changes such as the swelling of thicker polymer films on cantilevers. Adsorption-induced stress sensors have sensitivities three orders of magnitude higher than frequency variation (for resonance frequencies in the range of tens of kHz) based on adsorbed mass. In addition, adsorption-induced cantilever bending is ideal for liquid-based applications.

Using Stoney's formula [32], we can express the radius of curvature of cantilever bending due to adsorption as to adsorption as

$$\frac{1}{R} = 6\frac{(1-v)}{Et^2}\Delta\sigma \qquad (12)$$

where $R$ is the cantilever's radius of curvature; $v$ and $E$ are Poisson's ratio and Young's modulus for the substrate, respectively; $t$ is the thickness of the cantilever; and $\Delta\sigma$ is the differential surface stress. The differential surface stress is the difference between the surface stress of the top and bottom surfaces of the cantilever beam in units of N/m or J/m$^2$. Typically, the microcantilevers have spring constants in the range of 0.1 N/m. Using geometry, a relationship between the cantilever displacement and the differential surface stress can be expressed as

$$z = \frac{3L^2(1-v)}{Et^2}\Delta\sigma \qquad (13)$$

where $L$ is the length and $h$ is the deflection. Equation 13 shows a linear relation between cantilever bending and differential surface stress. Therefore, any variation in the differential surface stress can result in cantilever bending. When confined to one surface, molecular adsorption on a thin cantilever can cause large changes in surface stress. Surface stress, $\sigma$, and surface free energy, $\gamma$, can be related using the Shuttleworth eqn. [33]

$$\sigma = \gamma + \left(\frac{\partial\gamma}{\partial\varepsilon}\right) \qquad (14)$$

where $\sigma$ is the surface stress. The surface strain $\partial\varepsilon$ is defined as a ratio of change in surface area, $\partial\varepsilon = \delta A / A$. Since the bending of the cantilever is very small compared to the

length of the cantilever, the strain contribution is only in the ppm ($10^{-6}$) range while the surface free-energy changes are in the $10^{-3}$ range. Therefore, one can easily neglect the contribution from surface strain effects and equate the free-energy change to surface stress variation.

# 4. NANOCANTILEVERS

Microcantilevers designed for scanning probe microscopy (SPM) applications have a resonance frequency in the 10–300 kHz range depending on the spring constant. The cantilevers used in SPM typically have dimensions in the 100 microns range and are fabricated by micromachining. These cantilevers demonstrated to be excellent sensors based on resonance frequency variation or cantilever bending. For a microcantilever, the sensitivity of mass detection increases with higher spring constant while bending signal sensitivity increases with lower spring constant. It has been demonstrated that a mass resolution of approximately 1 pg can be achieved for a 200-micron-long cantilever with a resonance frequency of 25 kHz. The mass sensitivity of a microcantilever sensor can be greatly increased by decreasing its dimensions [34–36]. It is conceivable that reducing the dimensions of a cantilever sensor can lead to detection of individual binding events of molecular adsorption on a cantilever.

The cantilevers with reduced dimensions are called nanocantilevers. Nanocantilevers typically have a length of approximately 1 $\mu$m. The thickness and width of a nanocantilever are adjusted such that the cantilever is free from size-induced deformations. One advantage of decreasing the length of the cantilever is that its resonance frequency can be increased into GHz. Higher resonance frequency implies higher spring constant. Since these cantilevers have high spring constants, they are not suitable for detecting adsorption-induced cantilever bending. Therefore, the nanocantilevers are more suited for a resonance frequency variation-based sensing approach than a bending-based method. However, it is possible to design a nanocantilever with a spring constant around 1 N/m by adjusting the length, width, and thickness. Davis et al. calculated a resonance frequency of 179.9 MHz for a cantilever of 2.82 microns long with a spring constant of 1 N/m [37].

In the case of resonating cantilevers scaled down to the nanosize, further dramatic increases in their sensitivity to chemical or biological stimuli are expected providing an opportunity to achieve ultra-high mass sensitivity, ultimately, approaching detection to the single molecule level [38]. The minimum detectable mass strongly depends on $K$ and $Q$ and is given by [38]:

$$\Delta m_{\min} = \frac{8G}{\langle z^2 \rangle^{1/2}} \frac{m_0^{5/4}}{K^{3/4}} \sqrt{\frac{k_B T B}{Q}} \qquad (15)$$

where $G$ is a geometrical factor of the cantilever, $k_B$ is the Boltzmann constant, $T$ is the temperature of the cantilever, $B$ is the bandwidth of the measurement, $m_0$ is the initial cantilever mass, and $\langle z^2 \rangle^{1/2}$ is the root mean-square amplitude of the cantilever motion. Therefore, both increased stiffness and the mass of the externally actuated resonator can influence the mass sensitivity. From eq. (15), however, it is clear

that there is a connection between effects of the resonator stiffness mass and the $Q$-factor. Obviously, accurate predictions of the mechanical quality factors are needed in order for eq. (15) to accurately predict the mass detection limit for nanocantilevers.

In addition to analytical implications, single-molecule detection is also very important for many fundamental areas of physics, chemistry, and biology. Nanomechanical structures capable of detecting single-molecule interactions have the potential for providing real-time information that cannot be obtained using the currently available methods.

In addition to sensing applications, nanocantilevers may also find applications in imaging such as scanning probe microscopy where fast imaging is needed. In this case, the cantilever beam is used for detecting force gradients that exists on the sample surface. The detectable force resolution of the cantilever is given by $(Kk_B/f_0Q)^{1/2}$. By varying the dimension, the cantilevers can be made sensitive to detect force gradients or to increase the resonance frequency and thus the scanning speed. It is possible to increase the resonance frequency without significantly changing the spring constant by optimizing the dimensions. In other applications, smaller dimensions of the nanocantilever will tend to increase the spatial resolution in techniques for *in-situ* mapping of molecular beams [39].

It should be pointed out that many of the signal transduction techniques for cantilever deflection measurements discussed in Section 2, such as optical beam deflection, are not suitable when cantilever length is reduced below a few micrometers. Davis et al. demonstrated a cantilever signal detection based on capacitive readout [37]. In this sensor, the nanocantilever was excited into resonance electrostatically by means of a lateral electrode. The detection of oscillation amplitude of the cantilever was achieved by measuring displacement current in the capacitor formed by the cantilever and the driver electrode. The length of the cantilever was 50 microns. Kawakatsu et al. [40] fabricated nanocantilevers (nanometric oscillators) using silicon-etching processes. The cantilever was a nanometric tip with an elastic neck where the tip was fabricated by anisotropic etching of silicon by KOH. Burger et al. demonstrated nanocantilever fabrication based on focused ion beam (FIB) patterning/milling and KOH etching [41]. These nanocantilevers were 30 nm thin and 100 nm wide with lengths ranging from 0.5–2 microns.

As mentioned earlier, signal transduction is a formidable challenge for nanocantilevers. This challenge, however, can be overcome by utilizing a signal transduction method based on electron transfer that is ideally suited for detection of nanocantilever motion. As an electrically driven cantilever vibrates between two biased electrodes, a current flows through the system due to charge transfer between the electrodes through the floating cantilever. The basic concept of charge transport is similar to a electrostatic charge shuttle demonstrated by Tuominen et al. [42].

## 4.1. Nanocantilever Fabrication

Single crystal and polycrystalline cantilever structures routinely fabricated by a number of conventional processes of wet or dry etching. The dry etching process involves

etching in inductively coupled plasma systems. Cantilevers can also be fabricated using photo-electrochemical etching using etch stops. These conventional techniques of fabricating cantilevers using micromachining techniques are ideal for cantilevers that are tens of $\mu$m in size. However, fabrication of cantilevers with dimensions of only a few $\mu$m or smaller is still a formidable task. There exist a number of ways by which nanocantilevers can be fabricated, such as FIB or a combination of FIB and etching. Abadal et al. [7] have demonstrated two different types of fabrication techniques—one based on a combination of laser and atomic force microscopy (AFM) lithography and a second one based on electron beam lithography (EBL) [43]. In AFM lithography, a cantilever is fabricated on an Al-coated SiO$_2$ surface by oxidation. Electron beam lithography utilized a lift-off defined chrome layer as a mask for SF$_6$-based reactive ion etching. Cantilevers with a width of 100 nm and with varied lengths between 10 $\mu$m to 40 $\mu$m have been fabricated. However, none of these techniques are compatible with mass production.

Nanofabrication using a FIB is more compatible with mass production [38, 44]. In the FIB technique, a focused Ga ion beam with energy in tens of KeV is used to physically cut out cantilevers from thin silicon membranes. We used this technique where the starting surfaces for fabricating cantilevers were single-crystal Si membranes having an initial thickness of 10 $\mu$m. Prior to cantilever fabrication, the FIB was used to reduce the thickness of the Si membrane down to a few micrometers.

Cantilevers with dimensions 0.8 to 2 $\mu$m in length, 50 nm to 500 nm in width, and 25 to 100 nm in thickness, have been fabricated using FIB. The calculated resonance frequency of a rectangular Si cantilever with these dimensions is 265 MHz. The FIB technique can be used to nanofabricate devices from different materials and not limited to only Si.

A different approach that involves a combination of a focused ion beam and anisotropic wet etching can also be used for single-crystal substrates [41, 43, 45]. In this case, the focused Ga ion beam is used to dope specific parts of the target, single-crystal surface. Selective Ga ion implantation and subsequent milling by FIB exposure followed by wet chemical etching can be used to fabricate nanomechanical structures in single-crystal Si. Nanobridges and nanocantilevers with around 30 nm thickness can be made by controlled selective underetching between unexposed and exposed areas. In Figure 1, we show an example of nanomechanical bridges fabricated using the FIB doping technique. The patterned Ga ion implantation was performed on a (100) Si wafer and the effective doping depth was estimated to be around 70 nm. Anisotropic etching was performed on the implanted samples at 83 °C using KOH.

## 4.2. Nanocantilever Measurements

As indicated earlier, optical detection of cantilever motion of nanocantilevers and nanocantilever arrays at their resonance frequency is extremely difficult due to the reduced reflection (scattered) signal from the cantilever surface. Other techniques, such as piezoelectric and
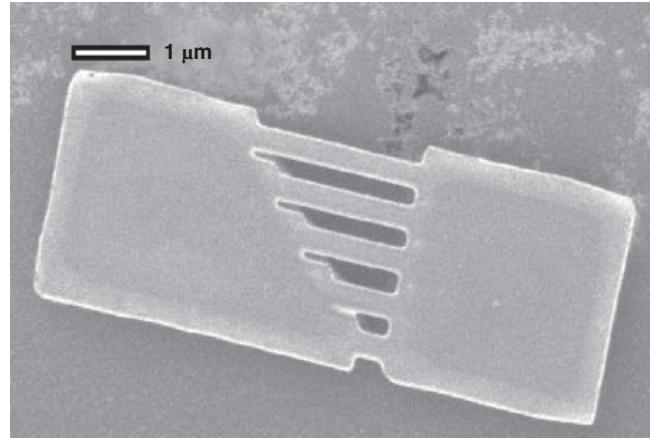


**Figure 1.** An ion micrograph of an array of nanobridges fabricated from a single-crystal silicon using a focused ion beam doping technique.

piezoresistive techniques, are harder to implement at nanoscale. Davis et al. [37] demonstrated capacitive-based signal transduction for 30–50 $\mu$m long cantilevers. However, as the cantilever dimensions are reduced, the capacitance signal will become comparable to parasitic capacitance from lead wires and bonding pads. Direct integration of CMOS circuitry on the cantilever chip can reduce the parasitic capacitance. Other techniques, such as electron tunneling and electron shuttling, can be used as signal transduction techniques for nanocantilevers since the amplitude of vibration is within nanometer range. In an electron tunneling device, the electrons tunnel between two surfaces maintained at a potential difference and separated by a few nanometers. In electron shuttling, the cantilever is vibrated between two surfaces maintained at a potential difference. Both electron tunneling and shuttling mechanisms can be used with ease when nanocantilevers are involved.

In electron shuttling signal transduction, a nanocantilever is nanofabricated between two fixed electrodes using FIB. The cantilever and the associated electrode system were fabricated monolithically using an FIB from a silicon membrane. A scanning ion micrograph of the monolithic
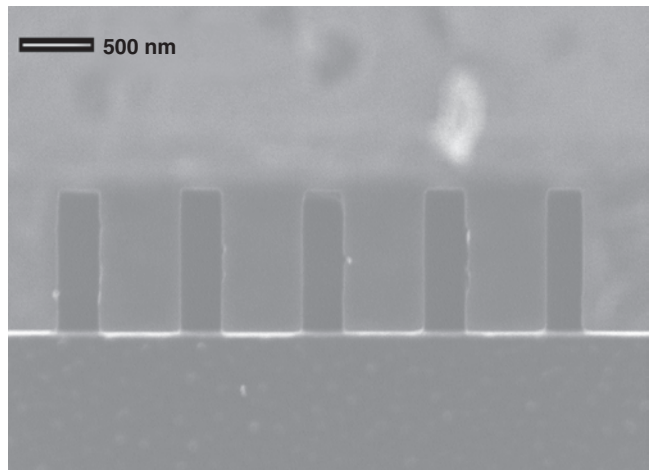


**Figure 2.** An ion micrograph of an array of nanocantilevers fabricated from commercially available microcantilevers using a focused ion beam.

cantilever and detection system is shown in Figure 3. The length of the cantilever was 4.5 $\mu$m and the thickness of the cantilever was 0.5 $\mu$m. This type of geometry allowed in-plane motion of the cantilever. The motion of the cantilever was in the plane of the image. The micrograph shows the thickness of the cantilever. Two electrodes (labeled as source and drain) were micromachined in such a way that the cantilever can oscillate between these two structures. The source and drain electrodes were equidistant from the cantilever beam. The separation distance between the cantilever and the source and drain was approximately 50 nm. All three components—cantilever (gate), source, and drain—were electrically isolated from each other. The nanocantilever was excited into resonance using an acoustic excitation source. The source and drain electrodes were electrically biased and the current flowing through the system was measured using a pico-ammeter.

## 4.3. Nanocantilever Resonance Response Characterization

The motion of the nanofabricated cantilevers was studied using the experimental set-up described above [44]. When a bias voltage is applied between the source and drain electrodes, no electron current flowed through the system under d.c. voltage condition because of the air gap between the cantilever and the two electrodes. It is possible that when the system is biased with a d.c., the cantilever can bend due to applied electrostatic force. However, such cantilever bending due to electrostatic force was too small to cause the cantilever to bend enough and make contact with the electrodes. Also, since d.c. bias voltage is used, no displacement current flowed through the system. When the cantilever was excited into resonance (using an acoustic source), the oscillatory motion caused the cantilever to make electrical contact with the source and the drain electrode. Electronic charge was transferred to the electrically floating cantilever "gate" when the cantilever made contact with the source electrode. The electron charge on the cantilever was subsequently transferred to the drain electrode as the cantilever oscillated in the opposite direction and made contact with
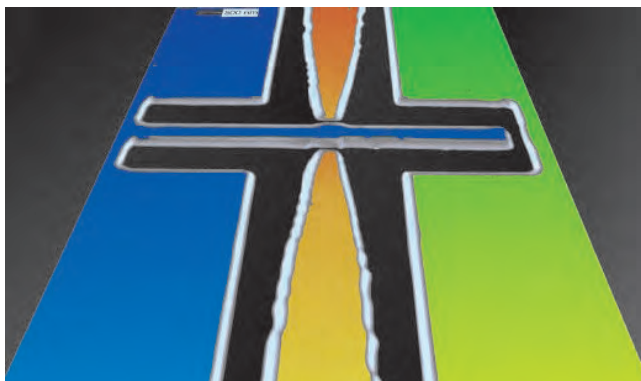
the drain electrode. As the cantilever made alternating contact with the source and drain electrodes, electrical charge was transferred from the source to the drain electrode causing a net electron current to flow through the system.

The applied bias voltage between the source and the drain electrode was 500 mV. When the cantilever was acoustically excited, the current through the circuit exhibited a peak at 5.2 MHz (see Fig. 4). At resonance, the acoustic frequency used for cantilever excitation matches with natural frequency of the cantilever. In Figure 4, we show the electron current through the system measured with a pico-ammeter as a function of the acoustic frequency that excited the cantilever into motion. From the data in Figure 4, it appears that at resonance the electron current increases to 7 pA against the noise floor of 1.7 pA. The mechanical $Q$-factor of the cantilever was calculated to be around 10 when the device was operated in air. The $Q$-factor can be increased by an order of magnitude by operating in a He gas environment; when the cantilever oscillates in a low viscosity medium such as He oscillation damping is reduced. At the resonance frequency, the measured electron current was approximately 7 pA.

The flow of electron current between the source and drain electrodes, facilitated by the cantilever motion, can be understood as follows. As the cantilever comes in contact with the energized source electrode, the cantilever will pick up charge $q$, either by electron tunneling or by physical contact. This charge will then be transferred to the drain electrode as the cantilever oscillates and makes contact with the drain electrode. The total current due to electron transfer can be expressed as

$$i = 2nef \tag{16}$$

where $n$ is the number of charge quanta (electrons) transferred to the cantilever, $e$ is the electronic charge, and



**Figure 3.** An ion micrograph of a nanocantilever with a readout system fabricated from a single-crystal silicon using an FIB. The cantilever "gate" was actuated acoustically and had a resonance frequency of 5.2 MHz.
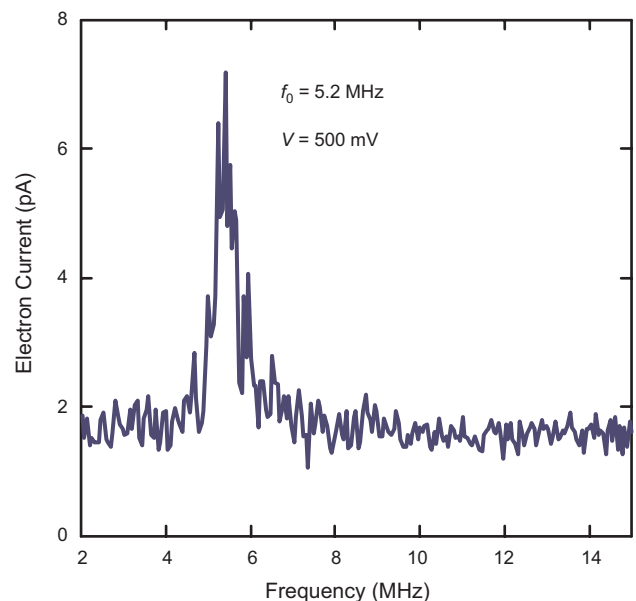


**Figure 4.** Electron current measured as a function of frequency. The nanocantilever gate was actuated acoustically around its first harmonic resonance and the effective electron transport was monitored for an applied bias of 500 mV.

$f$ is the excitation frequency. From the data presented in Figure 4, we obtain a value of $n = 5$ at resonance and $n = 1$ at frequencies far away from resonance. These values correspond to 1.7 pA noise current and 7 pA current at resonance, respectively.

From the physical dimensions of the Si nanocantilever, a cantilever mass of $10^{-15}$ g can be calculated. If the resonance frequency can be measured with a resolution of 100 Hz, the minimum detection limit for adsorbed mass can be calculated as $10^{-19}$ g at a resonance frequency of 5.2 MHz. This detection limit is ample to detect changes in adsorbed mass due to a single biomolecule of a large protein or a DNA strand of 50 nm in length. The detection limit can be further improved by increasing the $Q$-factor of the cantilever. The $Q$-factor can be possibly amplified by a feedback system, which was demonstrated for optical signal transduction.

## 4.4. Femtogram Mass Sensitivity

Mass sensitivity of a few femtograms was demonstrated using small-size cantilevers in the air. The smaller cantilevers were fabricated from commercially available cantilevers (200 $\mu$m long, 50 $\mu$m wide, and 1.5 $\mu$m thick) and were coated with a 35-nm gold layer on one side to increase optical reflectivity and response to photothermal actuation [38]. An FIB milling instrument (FEI 200) was used to fabricate cantilevers that measured 2 to 6 $\mu$m long, 50 to 100 nm thick, and had resonance frequencies in the range of 1–6 MHz [38]. It was reported that all these fabricated resonators exhibited very similar normalized widths of the resonances in air, which was almost independent of the cantilever thicknesses and shapes. The explanation offered [38] was that for cantilevers in air, viscous damping by the medium is the predominant energy dissipation mechanism. Based on the width of the measured resonance curves, a $Q$-factor of 25 was estimated. At a lower air pressure, the $Q$-factor increased by at least five-fold. A very important conclusion that can be drawn from these observations is that minimization of intrinsic mechanical losses may not be practical in the case of nanomechanical mass-sensitive transducers operating in the air at room temperature and atmospheric pressure [38].

A rectangular, gold-coated silicon cantilever with a resonance frequency of 2.25 MHz with an approximate 2 $\mu$m width and 6 $\mu$m length was exposed to 11-mercaptoundecanoic acid vapor. Upon exposure of the cantilever to 11-mercaptoundecanoic acid vapors, the resonance frequency was found to decrease, which was attributed to chemisorption of the analyte molecules onto the gold-coated surface of the cantilever. The measured frequency shift of 2 KHz was found to correspond to an added mass of $5.5 \times 10^{-15}$ g, a value that is close to a 50% coverage of a monolayer of 11-mercaptoundecanoic with a total mass of $6 \times 10^{-15}$ g over the area of the cantilever which is 12 $\mu$m$^2$.

## 4.5. Controlling *Q*-Factor of a Cantilever

The $Q$-factor of a cantilever, defined as the ratio of resonance frequency to FWHM of a resonance curve, determines the efficiency of oscillations. The $Q$ of a microcantilever vibrating in air is typically in the range of 30–100. In liquids $Q$ drops to a small value close to 1. The resolution of the resonance frequency measurement increases with $Q$. Therefore, techniques to improve the $Q$-factor of vibrating cantilevers will have important implications in imaging and sensor applications. Recently, it has been demonstrated that the $Q$ of a cantilever vibration can be manipulated using a feedback technique [22, 46]. It is shown that the $Q$ can be increased by a factor 10–1000 using feedback. Even Brownian motion (thermal motion) of a cantilever can be amplified.

As pointed out earlier, a low $Q$-factor leads to a lower resolution in resonance frequency detection and thus a low sensitivity in mass detection. When the cantilever sensor is operated in a medium, the damping decreases the $Q$-factor leading to lower sensitivity. Therefore, despite its suitability for liquid operations resonance, frequency-based, cantilever sensors have not attracted much attention as sensitive biological and chemical sensors. The $Q$-factor of a cantilever can be increased by utilizing a feedback technique. For an optical beam deflection technique, the feedback can be accomplished by feeding back the output of the PSD to a piezoelectric cantilever holder. A phase shifter and a gain controller placed between the PSD and piezoelectric holder determines the feedback condition. By adjusting the phase shift and gain, the $Q$-factor can be manipulated in a controlled fashion.

The governing equation of motion for a feedback-driven cantilever, modeled as a damped harmonic oscillator, is

$$m_{eff} \frac{d^2 z}{dt^2} + \gamma \frac{dz}{dt} + kz = G e^{i\phi} z(t) \tag{17}$$

where, $m_{eff}$ is the effective mass of the cantilever, $\gamma$ is the resistance or damping force on the cantilever, $k$ is the spring constant, $G$ is the gain of the feedback amplifier, $\phi$ is the phase shift added by the phase shifter, and $z$ is the vertical displacement of the cantilever. Thus the system can be thought of as a harmonic oscillator with an effective spring constant $k_{eff} = (k - G e^{i\phi})$. The general form of the solution for $z(t)$ can be written as

$$z(t) = (C_1 \cos \omega^* t + C_2 \sin \omega^* t) e^{-\frac{\gamma t}{2 m_{eff}}};$$
$$\text{where } \omega^* = \sqrt{\frac{k_{eff}}{m_{eff}} - \frac{\gamma^2}{4 m_{eff}^2}} \tag{18}$$

The gain of the feedback amplifier ($G$) and phase shift ($\phi$) is critical in tuning the feedback signal to achieve resonance and amplification. The magnitude of the gain and phase shift was a function of the physical dimensions and material properties of the cantilever. We have shown that the $Q$-factor of a silicon-nitride cantilever oscillating under a solution can be varied. In air, we were able to increase the $Q$ from 20 to 3000 for silicon-nitride cantilevers resonating by Brownian motion. The smaller FWHM achieved with the feedback allows frequency measurements at a smaller linewidth, improving the minimum detectable frequency shift. Similar $Q$-factor enhancement can be achieved for other signal transduction methods [7, 22, 46].

## 5. CONCLUSIONS

As the technology to fabricate nanosize mechanical structures further develops, we envision a plethora of new application where these systems can play an important role. As the frequency of these devices approaches or even exceeds GHz nanomechanical devices will be in the same time and frequency domain reserved now only for electronic devices.

One very important issue that need to be addressed is the efficient readout of nanocantilevers not only because of the small size but also because of the readout of large arrays. Compared to presently used signal transduction methods, electron transfer using a cantilever system is ideally suited for NEMS nanocantilevers. Conventional techniques of measuring the resonance frequency, such as optical beam deflection, fall short when applied to micromachined nanocantilevers. For example, in optical beam deflection, the cantilever motion is measured by reflecting a laser diode off the free end of a cantilever into a position-sensitive detector. The shortcomings of optical techniques are simply due to the lack of a sufficient reflected (or scattered) optical signal from the cantilever beam. Optical beam deflection is extremely sensitive when used for cantilevers that are 5 $\mu$m to a few hundreds of micrometers long while the electron transfer signal transduction is extremely sensitive for cantilevers that are a few hundred nanometers to a few microns in length.

The applicability of electron transfer signal transduction for aqueous environments remains extremely challenging. Presence of electro active ions in the water can cause a large Faraday leakage current that can overwhelm electron transfer signal. The leakage current, however, can be significantly reduced using proper insulation, reduced bias voltage, and a reduced number of charge carriers in the solution. However, this technique may be applicable for biosensors that can be operated in humid atmosphere.

## GLOSSARY

**B** Bandwidth of measurements, a frequency range, within which measured signals are analyzed, a very narrow bandwidth of measurements can be achieved by collecting and averaging the data for prolonged periods of time.

**Cantilever** Suspended beam structure with a single clamping point; suspended structures with shapes more complex than a rectangular beam and more than one (typically two) clamping points are also refereed to as cantilevers. An example of the latter is a V-shaped cantilever, often used in scanning probe microscopy.

**K** Spring constant, can be used to quantify the elasticity of suspended beams and analogous structures; assumes linear relationship between the force exerted on the beam and its deformation (Hook's law) and is defined as a force that would displace the reference point (usually an end of the cantilever) by 1 meter; spring constants of typical microcantilevers are in the range of $10^{-2}$ to 10 N/m.

**Microcantilever** Cantilever with characteristic sizes on the order of microns; microcantilever devices that are widely used as force probes in scanning probe microscopy have lengths, widths and thicknesses in the range of, respectively, 50–300 $\mu$m, 20–100 $\mu$m, and 0.5–5 $\mu$m.

**Micro-electro-mechanical systems (MEMS)** Term coined to denote microfabricated devices that rely on mechanical phenomena and mechanical energy, may integrate micromechanical and traditional microelectronic components.

**Nano-electro-mechanical-systems (NEMS)** Devices that rely on mechanical phenomena and mechanical energy and has characteristic dimensions less than 1 micron.

**Q-factor** Quality factor, parameter that quantifies energy dissipation in the resonating device, can be defined as the ratio of the average energy stored in the resonator to the energy dissipated per oscillation cycle.

**Thermal energy** Kinetic energy of atoms, molecules and any microscopic particles at nonzero temperatures.

**Thermal motion** Motion of microscopic objects in equilibrium with their thermal environment ("thermal bath") due to continuous dynamic exchange of thermal energy.

## REFERENCES

1. T. Thundat, R. J. Warmack, Chen, and D. P. Allison, *Appl. Phys. Lett.* 64, 2894 (1994).
2. T. Thundat, G. Y. Chen, R. J. Warmack, D. P. Allison, and E. A. Wachter, *Anal. Chem.* 67, 519 (1995).
3. T. Thundat, E. A. Wachter, S. L. Sharp, and R. J. Warmack, *Appl. Phys. Lett.* 66 (1995).
4. P. G. Datskos, C. M. Egert, and I. Sauers, *Sensors and Actuators B* 61, 75 (2000).
5. J. K. Gimzewski, C. Gerber, E. Meyer, and R. R. Schlittler, *Chem. Phys. Lett.* 217, 589 (1994).
6. R. Berger, C. Gerber, H. P. Lang, and J. K. Gimzewski, *Microelectronic Engineering* 35, 373 (1997).
7. G. Abadal, Z. J. Davis, B. Helbo, X. Borris, R. Ruiz, A. Boisen, F. Campabadal, J. Esteve, E. Figueras, F. Perez-Murano, and N. Barniol, *Nanotechnology* 12, 100 (2001).
8. T. Thundat, P. I. Oden, P. G. Datskos, G. Y. Chen, and R. J. Warmack, in "The 16th Warner Brandt Workshop on Charged Particle Penetration Phenomena." Oak Ridge, TN, 1996.
9. N. V. Lavrik, C. A. Tipple, M. J. Sepaniak, and P. G. Datskos, *Biomedical Microdevices* 3, 33 (2001).
10. N. V. Lavrik, C. A. Tipple, M. J. Sepaniak, and P. G. Datskos, *Proc. SPIE* 4560, 152 (2001).
11. N. V. Lavrik, C. A. Tipple, M. J. Sepaniak, and P. G. Datskos, *Chem. Phys. Lett.* 336, 371 (2001).
12. H. P. Lang, R. Berger, F. Battistion, J. P. Ramseyer, E. Meyer, C. Andreoli, J. Brugger, P. Vettiger, M. Despont, T. Mezzacasa, L. Scandella, H.-J. Guntherodt, C. Gerber, and J. K. Gimzewski, *Appl. Phys. A* 66, S61 (1998).
13. H. P. Lang, M. K. Baller, R. Berger, C. Gerber, J. K. Gimzewski, F. M. Battison, P. Fornaro, J. P. Ramseyer, E. Meyer, and H. J. Gÿntherodt, *Anal. Chim. Acta* 393, 59 (1999).
14. H. P. Lang, R. Berger, C. Andreoli, J. Brugger, M. Despont, P. Vettiger, C. Gerber, J. K. Gimzewski, J. P. Ramseyer, E. Meyer, and H.-J. Güntherodt, *Appl. Phys. Lett.* 72, 383 (1998).
15. P. G. Datskos, M. J. Sepaniak, C. A. Tipple, and N. Lavrik, *Sensors and Actuators B-Chemical* 76, 393 (2001).
16. P. G. Datskos, S. Rajic, M. J. Sepaniak, N. Lavrik, C. A. Tipple, L. R. Senesac, and I. Datskou, *J. Vac. Sci. Tech. B* 19, 1173 (2001).
17. J. C. L. Britton, R. L. Jones, P. I. Oden, Z. Hu, R. J. Warmack, S. F. Smith, W. L. Bryan, and J. M. Rochelle, *Ultramicroscopy* 82, 17 (2000).

*18.* R. Berger, E. Delamarche, H. P. Lang, C. Gerber, J. K. Gimzewski, E. Meyer, and H.-J. Güntherodt, *Science* 276, 2021 (1997).

*19.* D. Sarid, "Scanning Force Microscopy with Applications to Electric, Magnetic, and Atomic Forces." Oxford University Press, New York, 1991.

*20.* G. Y. Chen, T. Thundat, E. A. Wachter, and R. J. Warmack, *J. Appl. Phys.* 77, 3618 (1995).

*21.* T. R. Albrecht, P. Grutter, D. Horne, and D. Rugar, *J. Appl. Phys.* 69, 668 (1991).

*22.* A. Mehta, S. Cherian, D. Hedden, and T. Thundat, *Appl. Phys. Lett.* 78, 1637 (2001).

*23.* E. A. Wachter, T. Thundat, P. G. Datskos, P. I. Oden, R. J. Warmack, and S. L. Sharp, *Rev. Sci. Instrum.* 67 (1996).

*24.* M. Tortonese, H. Yamada, R. C. Barrett, and C. F. Quate, in "The Proceedings of Transducers '91." *IEEE,* Pennington, NJ, 1991.

*25.* M. Tortonese, R. C. Barrett, and C. F. Quate, *Appl. Phys. Lett.* 62, 834 (1996).

*26.* J. A. Harley and T. W. Kenny, *J. Microelectromechanical Systems* 9, 226 (2000).

*27.* P. I. Oden, E. A. Wachter, P. G. Datskos, T. Thundat, and R. J. Warmack, *Infrared Technology and Applications XXII,* SPIE 2744, 345 (1996).

*28.* D. L. DeVoe and A. P. Pisano, *J. Microelectromechanical Systems* 6, 266 (1997).

*29.* S. Zurn, M. Hseih, G. Smith, D. Markus, M. Zang, G. Hughes, Y. Nam, M. Arik, and D. Polla, *Smart Materials and Structures* 10, 252 (2001).

*30.* Q. M. Wang and L. E. Cross, *Ferroelectrics* 215, 187 (1998).

*31.* R. Amantea, C. M. Knoedler, F. P. Pantuso, V. K. Patel, D. J. Sauer, and J. R. Tower, in "SPIE," Vol. 3061, p. 210. Orlando, FL, 1997.

*32.* G. G. Stoney, *Proc. Royal Soc. London* 82, 172 (1909).

*33.* R. Shuttleworth, *Proc. Phys. Soc. London* 63A, 444 (1950).

*34.* Y. T. Yang, K. L. Ekinci, X. M. H. Huang, L. M. Schiavone, and M. L. Roukes, *Appl. Phys. Lett.* 78, 162 (2001).

*35.* D. W. Carr, L. Sekaric, and H. G. Craighead, *J. Vac. Sci. Tech. B* 16, 3821 (1998).

*36.* A. Olkhovets, S. Evoy, D. W. Carr, J. M. Parpia, and H. G. Craighead, *J. Vac. Sci. Tech.* B18, 3549 (2000).

*37.* Z. J. Davis, G. Abadal, O. Kuhn, O. Hansen, F. Grey, and A. Boisen, *J. Vac. Sci. Tech. B* 18 (2000).

*38.* N. V. Lavrik and P. G. Datskos, *Appl. Phys. Lett.* 82, 2697 (2003).

*39.* U. Drodofsky, M. Drewsen, T. Pfau, S. Nowack, and J. Mlynek, *Microelectronic Engineering* 30, 383 (1996).

*40.* H. Kawakatsu, H. Toshiyoshi, D. Saya, K. Fukushima, and H. Fujita, *Appl. Surf. Sci.* 57, 320 (2000).

*41.* J. Brugger, G. Beljakovic, M. Despont, N. F. deRooij, and P. Vettiger, *Microelectronic Engineering* 35, 401 (1997).

*42.* M. T. Tuominen, R. V. Krotkov, and M. L. Breuer, *Phys. Rev. Lett.* 83, 3025 (1999).

*43.* J. Xu and A. J. Steckl, *Appl. Phys. Lett.* 65, 2081 (1994).

*44.* P. G. Datskos and T. Thundat, *J. Nanosci. Nanotech.* 2, 369 (2001).

*45.* A. J. Steckl, H. C. Mogul, and S. Mogren, *Appl. Phys. Lett.* 60, 1833 (1992).

*46.* J. Tamayo, A. D. L. Humphris, and M. J. Miles, *Appl. Phys. Lett.* 77, 582 (2000).

# Micro- and Nanomechanics

Barton C. Prorok

*Auburn University, Auburn, Alabama, USA*

Yong Zhu, Horacio D. Espinosa,* Zdeněk P. Bažant, Zaoyang Guo

*Northwestern University, Evanston, Illinois, USA*

Yufeng Zhao, Boris I. Yakobson

*Rice University, Houston, Texas, USA*

## CONTENTS

## 1. MECHANICS OF SCALE

It has been known for quite some time that materials and structures with small-scale dimensions do not behave in the same manner as their bulk counterparts. This aspect was first observed in thin films where certain defect structures were found to have deleterious effects on the film's structural integrity and reliability. This became a significant concern because thin films are routinely employed as components in microelectronics and microelectromechanical systems (MEMS). Their properties frequently allow essential device functions and therefore accurate identification of these properties is key to the development of new technologies. Unfortunately, most of our knowledge is based on bulk material behavior, which many times fails to describe material response in small-scale dimensions because of the dominance of surface and interface effects, finite number

of grains in a given structure (e.g., through the thickness), and the role played by the manufacturing process (e.g., texture, residual stress, and dislocation structure). This last feature is particularly important since material surfaces and microstructures are the result of the process employed to deposit or remove material [1].

### 1.1. Thin Films

As thin film dimensions begin to approach that of the films microstructural features, the material mechanical properties begin to exhibit a dependence on the specimen size. In metallic thin films this translates to plastic yielding occurring at increased stresses over their bulk counterparts. Although this phenomenon was observed as early as 1959 [2], no consensus or common basic understanding of it yet exists. In addition to plastic behavior, other mechanical properties can exhibit size effects, such as fracture toughness and fatigue resistance. Each of these properties operates on a characteristic length scale that can be compared to the physical dimensions of microelectronics, microdevices, or nanodevices. This is shown schematically in Figure 1, which utilizes a logarithmic length scale map beginning at the atomic scale and ending at the macro scale. On the left are four categories of structures and the regime where their dimensional size fits on the length scale. On the right are regimes indicating where dimensional size effects begin to affect the material mechanical properties and theories used to predict behavior. Elastic properties are dependent on the bonding nature of the material and only exhibit size effects at the atomic scale. In contrast, plastic, fatigue, and fracture toughness properties all exhibit size effects in the micrometer and submicrometer regime. These properties all depend on defect generation and evolution, which are mechanisms

---

* Corresponding author.
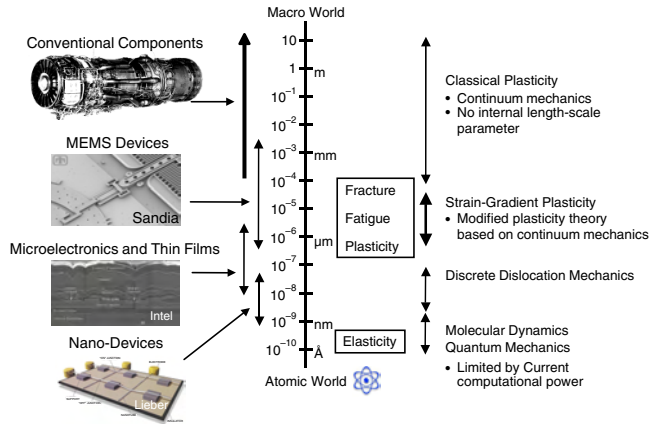
**Figure 1.** Illustration of length-scale effects on the mechanical properties of materials.

that operate on characteristic length scales [3]. These fundamental changes in mechanical behavior occur in the size scale of MEMS and microelectronics devices, and thus, a better understanding of inelastic mechanisms is required to better predict their limits of strength and reliability.

The right side of Figure 1 also lists the theories used to predict material behavior and the length scale where they are applicable. These include classical plasticity, strain gradient plasticity, discrete dislocation mechanics, molecular dynamics, and quantum mechanics. Classical plasticity is described in terms of traditional continuum mechanics, which describes the relationships between stress and strain and is applicable for predicting behavior from a size of approximately 100 micrometers and greater. Molecular dynamics (MD) is at the other end of the scale and involves the generation, mobility, and interaction between individual dislocations, twinning, stacking faults, and other defects. It is only applicable at the lower end of the scale since it is based on large scale numerical simulation. Therefore, it is subsequently limited by current computational power (i.e., systems approximately one million atoms in size). In the regime between classical plasticity and discrete dislocation mechanics, a theory called strain gradient plasticity has been developed in the last decade to describe material behavior [4]. It considers the effect of gradients in strain in the description of flow behavior. A large number of theories have been proposed. However, as will be discussed in Section 4, most of these theories exhibit unreasonable predictions as the size of the structure approaches one nanometer. For this reason, its applicability is limited to structures with minimum dimension of a few hundred nanometers. Between this theory and molecular dynamic, a model based on discrete dislocation dynamics has been postulated [5–7]. These models are currently in an early stage of development so they are not discussed here in detail.

The mechanical response of thin films depends on many factors. Of particular importance is the existence of film thickness effects that arise because of geometrical constraints on dislocation motion. Size effects on mechanical properties begin to play a dominant role when one or more of the structure's dimensions begins to approach the scale of the material microstructural features. The onset of plastic

deformation depends strongly on the ability of dislocations to move under an induced stress [8, 9]. The ease of their movement can be hindered by any number of obstacles such as grain boundaries, precipitates, interfaces, etc. Specimen size then begins to govern plastic behavior by creating geometrical constraints, surface effects, and the competition of deformation mechanisms (i.e., dislocation motion versus twinning or phase transitions). Other effects that specimen size can have on plastic deformation involve microstructural changes. This includes grain size, morphology, and crystallographic texture. Preferential grain orientations can result from a minimization of surface energies [10, 11]. The average grain size is also typically on the order of the film thickness, due to an effect called the "specimen thickness effect" which depends upon grain boundaries being pinned by their surface grooves, occurring when the mean equivalent grain diameter is on the order of the film thickness [12, 13].

Several theoretical models, based on single dislocation motion, have been proposed to explain the size effect phenomenon [14–16]. However, each predicts strength increases far below experimentally obtained values. The higher yield point of metallic thin films is likely the result of a combined interaction between strain hardening and deformation mode transition from dislocation motion to twinning.

Several pioneering studies have experimentally identified the existence of size effects on the plasticity of metals. These studies were able to obtain experimental nanoindentation data showing a strong size effect as evidenced by material hardness decrease as indentation depth increases [17–19]. Figure 2 is a reproduction of the data from Ma and
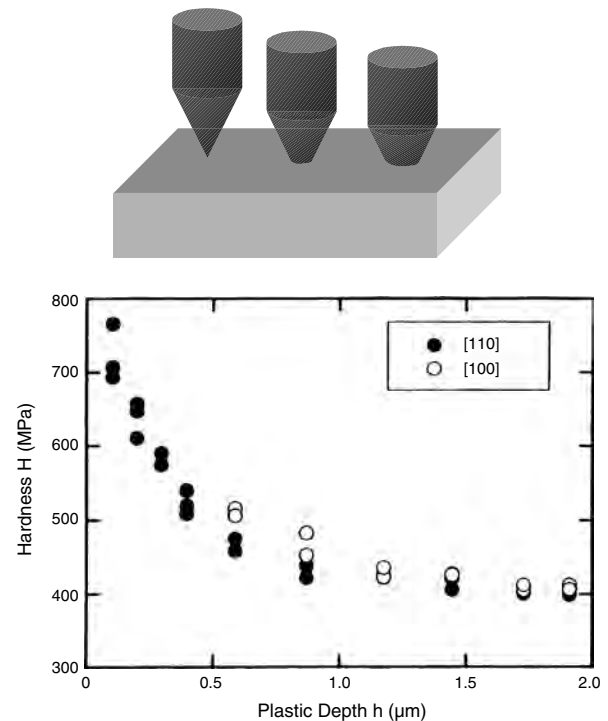


**Figure 2.** Plot of hardness vs plastic depth illustrating how hardness increases with smaller plastic depth. Reprinted with permission from [18], Q. Ma and D. R. Clarke, *J. Mater. Res.* 10, 853 (1995). © 1995, Materials Research Society.

Clarke [18] of nanoindentation performed on epitiaxially grown silver on sodium chloride and shows that the hardness increases by a factor of two to three as penetration depth decreases. Their results have been verified and expanded upon in subsequent studies [20–27].

Other pioneering work involved bending strips of metal of varying thickness around a rigid rod [28] and applying a torque load to copper rods of varying diameter [29]. The strips varied in thickness from 12, 25, and 50 $\mu$m and each was bent around a rigid rod whose diameter was scaled to the film thickness to ensure identical states of strain in each strip. Figure 3 shows the results in the form of normalized bending moment versus surface strain. It is clear from this plot that as each strip was strained to the same degree, the thinner strips required a larger bending moment. The copper rod experiment used rods of varying diameter, 12–170 $\mu$m. A torque was applied to each rod in order to twist them all to the same degree (i.e. to identical states of strain). A plot of torque versus twist per unit length is shown in Figure 4 and indicates an increase in strength by a factor of three for the smallest rod over the largest. Direct tensile tests were also performed on identically sized copper rods (Fig. 4). The authors concluded that for the most part, no size effects existed when subjected to direct tension. The results of these tests show a strength increase for smaller structures over larger ones when subject to bending and torsional loads.

In these pioneering studies, the size dependence of the mechanical properties was considered to be a result of nonuniform straining [23, 29, 30]. It was shown that classical continuum plasticity could not predict the size dependence
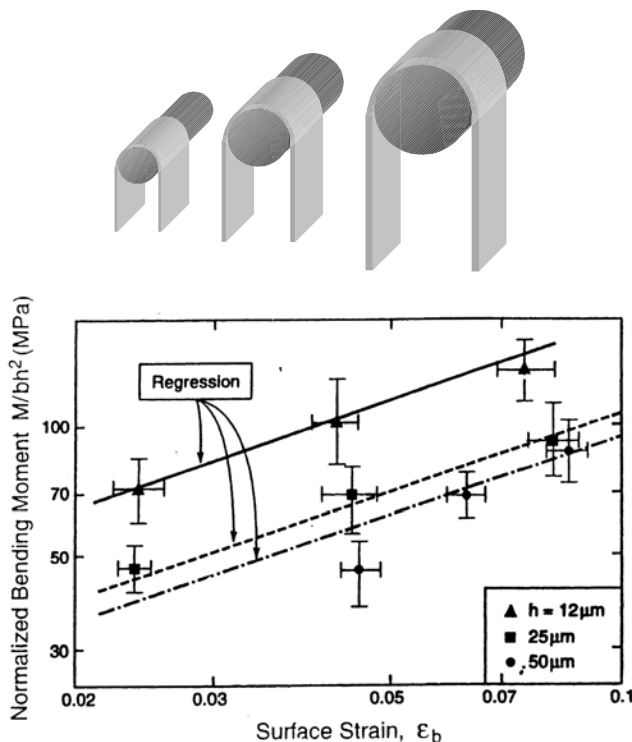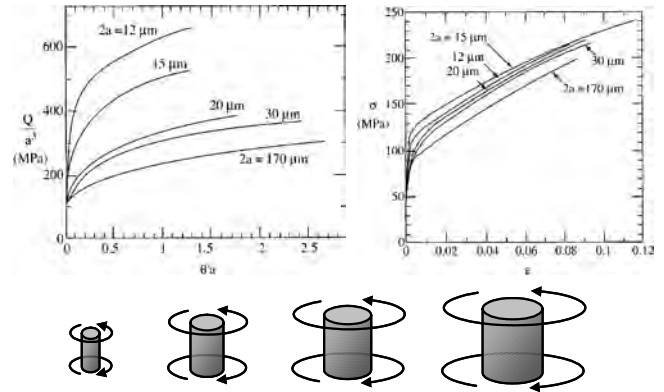


**Figure 4.** Plot of applied torque vs twist for copper rods of varying diameter and stress–strain of identical rods subject to direct tension. Reprinted with permission from [29], N. A. Fleck et al., *Acta Metal. Mater.* 42, 475 (1994). © 1994, Elsevier Science.

in this regime. The generally accepted size limit for accurate description of plasticity by the classical theory is systems with dimensions greater than approximately 100 $\mu$m. As previously mentioned, molecular mechanics can accurately describe material behavior at the atomic level. However, due to the computational cost and limitations on performing atomistic simulations for more than one million atoms, the maximum size regime computationally approachable is systems with dimensions <0.1 $\mu$m [30]. This leaves an intermediate region where a continuum strain gradient plasticity theory, to describe material behavior, is highly desirable [4, 29–35].

In the aforementioned work of Fleck et al. [29], the authors concluded that for the most part, no size effects existed for direct tension. It should be noted that the smallest rod diameter investigated by this group was only 12 $\mu$m. The homogeneous manner in which the uniaxial tests were conducted appears to have hindered gradients in plasticity from occurring. Can size effects then exist in the absence of strain gradients? Recent work on tensile testing of thin gold films of submicrometer thickness has shown that strong size effects do indeed exist in the absence of strain gradients [36–39]. In these studies, grain size was held constant at approximately 250 nm while specimen thickness and width were varied systematically. Figure 5a is a composite scanning electron microscopy (SEM) image showing the side view of the three studied membranes with different thicknesses. For each thickness, there is a characteristic number of grains composing the film ranging from one to five. Stress–strain plots for these films are presented in Figure 5b. They show that the yield stress more than tripled when film thickness was decreased from 1 to 0.3 $\mu$m, with the thinner specimens exhibiting brittle-like failure and the thicker a strain softening behavior. It is believed that these size effects stem from the limited number of grains in the film thickness, which limits the number of dislocation sources and active slip systems. In such case, other deformation modes such as twining and grain boundary shearing accompanied by diffusion become dominant [36]. The same features were observed in other face center cubic (fcc) metals [36].

Clearly there are many things to learn about materials at this scale. Future investigations should be pursued and focus



**Figure 3.** Plot of normalized bending moment vs surface strain illustrating how the thinner films require more bending moment for the same state of strain. Reprinted with permission from [28], J. S. Stolken and A. G. Evans, *Acta Mater.* 46, 5109 (1998). © 1998, Elsevier Science.
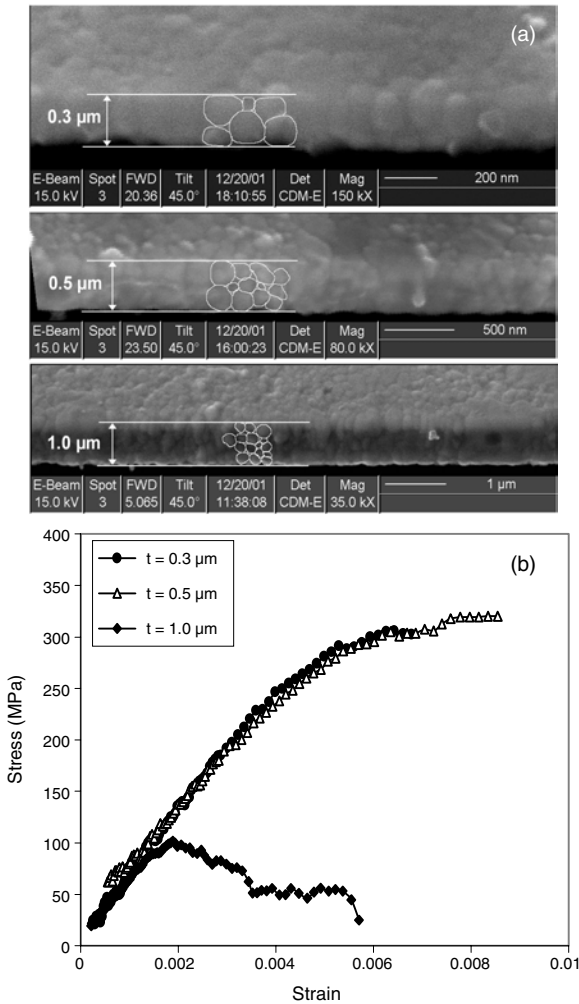
**Figure 5.** SEM image highlighting the number of grains existing through the film thickness (a). Note the various magnifications and 45° tilt employed during imaging. Stress–strain plot for a gold membranes 0.3, 0.5, and 1.0 $\mu$m thick (b). Reprinted with permission from [36], H. D. Espinosa et al., *J. Mech. Phys. Solids*, in press, 2004. © 2004, Elsevier Science.

on varying the material microstructure systematically to gain further insight into its effects on the size dependent plasticity phenomenon. Further progress can also be made by combining experimental results with analytical and computational studies to better understand the fundamental deformation mechanisms, particularly the mechanics of dislocation generation, motion, interaction, and the competition between inter- and intragranular deformation processes.

## 1.2. Nanostructures

As structures move beyond the submicrometer to the nanometer scale, description of mechanical behavior focuses on issues other than the traditional ensemble of defects. For instance, the length scale of a typical dislocation and the volume of material required for it to have significant influence on deformation are large compared to the typical volume of a nanosized object. Therefore, it can be argued that beyond

a certain point, other types of defects, surface forces, and intermolecular processes control mechanical behavior.

Nanostructures can be described as either a bulk material with a grain structure of a nominal size in the range of 1 to 100 nanometers, or structures with one or more dimensions below 100 nm. A more rigorous definition is based on the functionality of the structure (i.e., when dimensions are such that new and unique properties can be achieved). An example of a nanostructure is a carbon nanotube, which is a molecular scale fibrous structure made of carbon atoms. They were discovered by Sumio Iijima in 1991 and are a subset of the family of fullerene structures [40]. The simplest way to describe the structure of a carbon nanotube is to imagine a flat plane of carbon graphite rolled into a tube, much the same as a sheet of paper; see Figure 6. Like
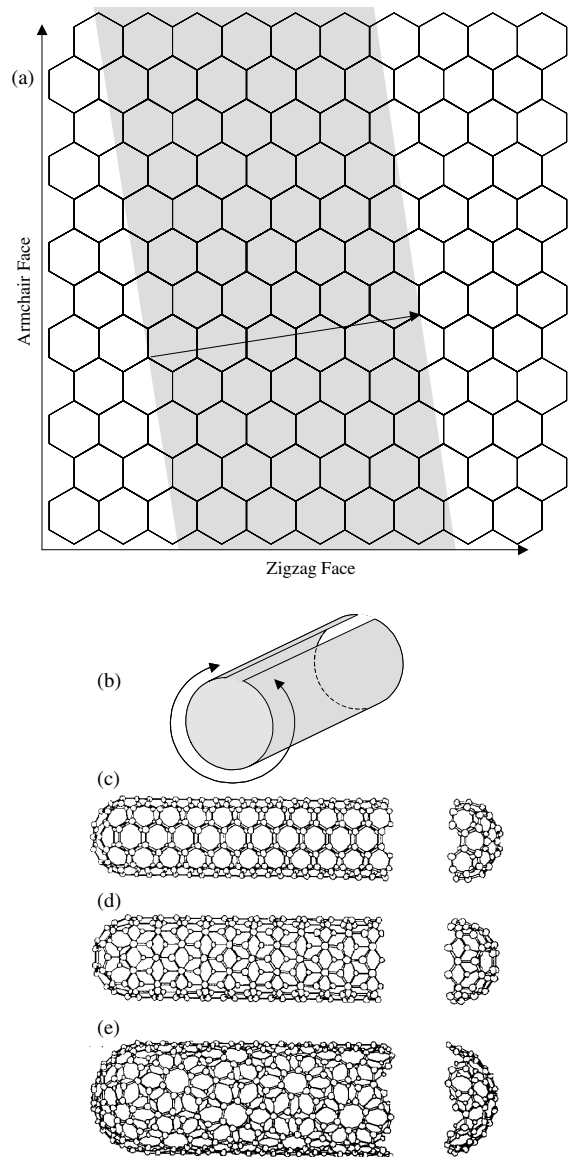


**Figure 6.** Schematic drawings of a two-dimensional graphene sheet (a), rolled-up sheet (b), and armchair (c), zigzag (d), and chiral (e) nanotubes. (c)–(e) Reprinted with permission from [41], M. S. Dresselhaus et al., *Carbon* 33, 883 (1995). © 1995, Elsevier Science.

paper, a graphene plane can be rolled in several directions to achieve varying structures [41]. Figure 7 shows transmission electron microscopy (TEM) images of carbon nanotubes as a gathered bunch and in a rope-like form [42]. Since their discovery, many scientists have been fascinated by their unique and outstanding properties. Extensive articles and books have been dedicated to carbon nanotubes. Among those, Qian et al. [43] contributed a comprehensive review article, "Mechanics of Carbon Nanotube," from the perspective of both experimentation and modeling.

Dislocation theory has been used to describe relaxation and intramolecular plasticity in carbon nanotubes (CNTs) [44]. By analyzing the dynamic topology of the graphene wall of a CNT, Yakobson argued that dislocations dipoles resulting from Stone–Wales (SW) diatomic interchanges play a key role in CNT relaxation under tension. The dislocation core is identified as a 5/7 pentagon–heptagon and the dipole as a 5/7 attached to an inverted 7/5 core; see Figure 8. When the dislocations unlock, one of two possible mechanisms occurs as a function of temperature. At low temperatures, a mechanism of transformations 7/8/7 and then 7/8/8/7, etc., leads to the brittle failure upon formation of larger molecular openings such as 7/14/7. At high temperatures, the two dislocations glide away from each other in a spiral path. When enough glide has taken place, they leave behind a nanotube of smaller diameter and changed electrical properties; see Figure 8.

A dominant characteristic of nanostructures is that they possess a rather large surface area to volume ratio. As this ratio increases, interfaces and interfacial energy as well as surface topography are expected to play a commanding role in deformation and failure processes. The picture of nanoscale behavior can be viewed as the following: At the larger end of the length scale, 50 to 100 nanometers, dislocation generation and motion will continue to dictate material behavior. As the grain size or structural dimensions fall below this range, behavioral control is transitioned to surface and intermolecular mechanisms. Understanding the mechanics of these materials and structures, and the competition and relationship between their deformation mechanisms, will be essential to predicting their behavior in applications of nanoscale electronics and devices. These
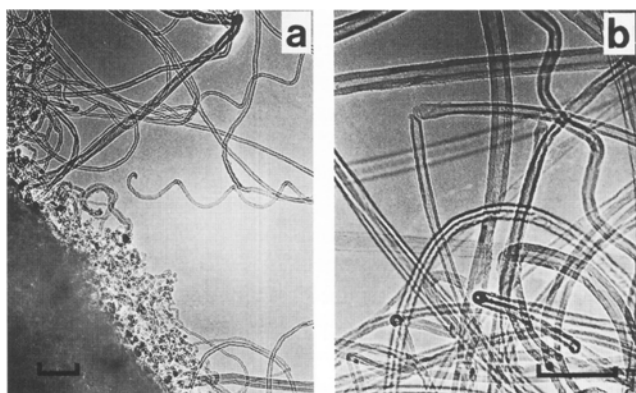


**Figure 8.** (a) In an armchair CNT, the first Stone–Wales rotation of an equatorially oriented bond into a vertical position creates a nucleus of relaxation. SW rotations marked by arrows show further evolution as (b) a brittle crack or (c) a couple of dislocations gliding away from each other. (d) The change of the CNT chirality and a stepwise change of diameter cause the corresponding variations of electrical properties. Formation of the next SW defect continues the necking process, unless the dislocations pile up at insufficient temperature. Reprinted with permission from [44], B. I. Yakobsons, *Appl. Phys. Lett.* 72, 918 (1998). © 1998, American Institute of Physics.

types of concerns compose the field of nanomechanics, the foundation of which is currently being laid out.

## 2. MICRO- AND NANOSCALE MEASUREMENT TECHNIQUES

Mechanical testing at the micro- and nanoscales is quite challenging. Since the physical dimensions of specimens range from a few hundred micrometers down to as small as 1.0 nanometer, novel mechanical testing methods have been developed to successfully measure their properties. Specimens of such size are easily damaged through handling and it is difficult to position them to ensure uniform loading along specimen axes. They are also difficult to attach to the instrument grips. Testing has been shown to suffer from inadequate load resolution as well as having data reduction formulae that are hypersensitive to precise dimensional measurements. To minimize these effects, a variety of micro- and nanoscale testing techniques have been employed to investigate size effects on mechanical properties. Reviews detailing the particulars are given in [15, 45–47].



**Figure 7.** TEM image of a gathered collection of carbon nanotubes (a) and bunched in a ropelike form. Reprinted with permission from [42], V. Ivankov et al., *Carbon* 33, 1727 (1995). © 1995, Elsevier Science.

## 2.1. Thin Film Measurement Techniques

The mechanical testing of thin films has been pursued for a few decades. The developed methods are quite unique and diverse. They can be grouped into four categories: depth sensing indentation, bending or curvature, tensile tests, and microelectromechanical system approaches.

### 2.1.1. Depth Sensing Indentation

Depth sensing indentation is a widely used method for estimating the mechanical properties of materials whereby a material's resistance to a sharp penetrating tip is continuously measured as a function of depth into the material. The result is a load-displacement signature with loading and unloading segments that describe material response. In recent years, instruments have been developed possessing subnanometer accuracy in displacement and submicro-Newton accuracy in load [48–52]. Another major improvement in the indentation methodology is the ability to continuously measure contact stiffness at any point during the test. These new tools have fueled interest in studying the mechanical properties of thin films and nanostructured materials by nanoindentation.

In indentation testing, the indenter tip geometry is generally pyramidal or spherical in shape and fashioned from single crystal diamond. In micro- and nanoscale testing the most frequently used indenter is the three-sided Berkovich tip. This geometry allows the tip to be ground to a very fine point, as opposed to the chisel-like point in four-sided Vickers indenters, resulting in self-similar geometry over a wide range of indentation depths. Other indenter geometries include spherical (good for defining the elastic-plastic transition of a material; however, there is great difficulty in obtaining high-quality spheres of sufficient hardness), cube-corner (sharper than the Berkovich, but produces much higher stresses and strains in the indenter vicinity that results in cracking), and conical (has self-similarity like the Berkovich with an additional advantage of no stress concentrations from sharp edges; however, like the spherical indenter there is difficulty in manufacturing high quality tips). Table 1 summarizes the various indenter geometries.

The process of driving the indenter into the material can be described as follows. After making contact, load is applied to either maintain a constant tip displacement rate or a constant strain rate. Initially, deformation constitutes only elastic displacement of the material, which quickly evolves into permanent or plastic deformation as the load is increased. Thus, zones of elastic and plastic deformation

surround the penetrating tip with plasticity mostly occurring in the vicinity of the tip and elasticity occurring ahead of the plastic front. The situation is best described as a complex interplay of elastic and plastic deformation processes. After the prescribed maximum depth is achieved the unloading process begins. As the load on the indenter is reduced, elastic recovery of the material forces the indenter upward. The measured load-deflection signature of this unloading process is then governed only by the elastic properties of the material. Typical loading and unloading curves are shown in Figure 9. These curves show the behavior for a hard ($\bigcirc$) and a ductile ($\bullet$) material. In comparison, the harder material requires a larger load to drive the indenter to the same
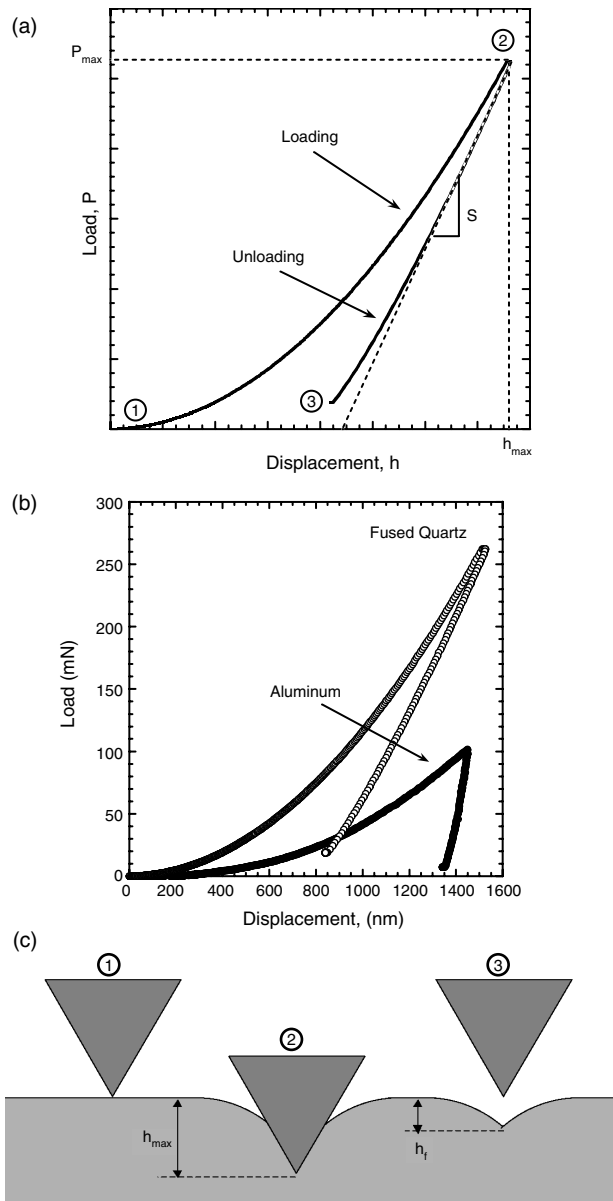


**Figure 9.** Schematic of the typical load-displacement signature obtained by nano-indentation (a). Comparison between hard (fused quartz) and soft (aluminum) materials (b), and side-view schematic of the nano-indentation process where the circled numbers correspond to the points in the load-displacement curve above (c).

**Table 1.** Geometries of various indenters.

| Parameter | Berkovich | Cube-corner | Cone | Spherical | Vickers |
|---|---|---|---|---|---|
| Shape | | | | | |
| C-f angle Projected | 65.35° | 35.264° | — | — | 68° |
| Contact area | $24.5600d^2$ | $2.5981d^2$ | $\pi a^2$ | $\pi a^2$ | $24.5044d^2$ |

C-f stands for centerline to face angle, $d$ stands for indentation depth, and $a$ stands for tip radius for cone and spherical indenters.

penetration depth, reflective of its higher atomic cohesion. The harder material also stores more elastic energy than the softer material and undergoes less permanent deformation. This is seen during unloading where the harder material traces a path closer to its loading curve than the softer material. The softer material has a nearly vertical unloading signature. This is indicative of very little elastic recovery. When comparing the residual indentation marks the softer material exhibits a larger and deeper mark.

Indentation testing uses the maximum point of the load-deflection signature to determine the hardness ($H$) of the material, defined as the ratio of applied load ($P$) to the indenter/material contact area ($A$):

$$H = \frac{P}{A} \tag{1}$$

The contact area is determined using the relationship describing the surface area of the indenter with indentation depth, given in Table 1 for the various tip geometries. This value is referred to as the "universal hardness" and includes contributions from both elastic and plastic deformation. With today's instrumentation testing systems, this can be calculated on a continuous basis as a function of indentation depth.

Young's modulus ($E$) is another important material property that can be determined with nanoindentation testing. There are two methods for determining these properties based on the load displacement signature of the indent. The first involves a technique developed by Doerner and Nix [53] who took the approach that during the early stages of unloading, the contact area between the indenter and material is constant. Thus the unloading stiffness, $S$, is related to the materials modulus via

$$S = \frac{dP}{dh} = \frac{2}{\sqrt{\pi}} E_r \sqrt{A} \tag{2}$$

where $S$ is measured stiffness of the upper portion of the unloading curve, $dP$ is the change in load, $dh$ is the change in displacement, $A$ is the projected contact area, and $E_r$ is the effective modulus determined by

$$\frac{1}{E_r} = \frac{(1 - \nu^2)}{E} + \frac{(1 - \nu_i^2)}{E_i} \tag{3}$$

where $E$ and $\nu$ are the elastic modulus and Poisson's ratio for the specimen and $E_i$ and $\nu_i$ are the same parameters for the indenter. An important aspect of this method is the accurate determination of contact area. By extrapolating the linear portion of the unloading curve to zero load (see Fig. 9), an extrapolated depth can be used to determine contact area. A perfect pyramid can be assumed at indentation depths above 1 $\mu$m. However, below 1 $\mu$m a correction factor must be used in order to account for blunting of the tip point [53]. This was accomplished by employing the TEM replica technique to determine the Berkovich indenter shape. Deviations from a perfect Berkovich tip below 1 $\mu$m were identified.

Oliver and Pharr [54] built on these solutions by realizing that unloading data is usually not linear but better described with a power law,

$$P = A(h - h_f)^m \tag{4}$$

where $P$ is the load, $h$ is the displacement, and $A$, $m$, and $h_f$ are constants determined by a least squares fitting procedure. Elastic modulus is then obtained from a variation of Eq. (2),

$$S = \frac{dP}{dh} = \frac{2}{\sqrt{\pi}} E_r \sqrt{A} \beta \tag{5}$$

where $\beta$ describes the correction of the area function due to tip blunting, approximately 1.034 for a Berkovich indenter [54]. The advantage of the Oliver and Pharr method is that the indent shape does not need to be directly measured. The method is based on the assumption that elastic modulus is independent of indentation depth. By modeling the load frame and specimen as two springs in series the total compliance, $C$, can be expressed as

$$C = C_f + C_s = C_f + \frac{\sqrt{\pi}}{2E_r} \frac{1}{\sqrt{A}} \tag{6}$$

where $C_f$ is the load frame compliance and the compliance of the specimen, $C_s$, is $\frac{1}{S}$; see Eq. (2). If the elastic modulus is constant with indentation depth, then a plot of $C$ vs $A^{-1/2}$ is a linear function whose intercept is $C_f$. For large indentation depths, the area function for a perfect Berkovich indenter can be used, namely,

$$A(h_c) = 24.5 H_c^2 \tag{7}$$

Equation (7) is also a good starting place to estimate the area function of the Berkovich tip. The area function for the tip is ascertained from a series of indents at periodic depths, 100, 200, 400, 600, 1200, 1800 nm. For large indent depths it also gives initial estimates of $C_f$ and $E_r$. These values can then be plugged back into Eq. (6) to further estimate the contact area for the successively smaller indents. This data can be fit to the function

$$A(h_c) = 24.5 H_c^2 + C_1 h_c^1 + C_2 h_c^{1/2} + C_3 h_c^{1/4} + \cdots + C_8 h_c^{1/128} \tag{8}$$

where $C_1$ through $C_8$ are constants. The first term is the perfect Berkovich tip and the others describe the blunting of the tip. In order to obtain the most accurate area function, this new value must be plugged into Eq. (6) again, the process being iterated until convergence is attained.

Oliver and Pharr confirmed their method by obtaining data for nine materials of varying properties and plotting the computed contact area versus indentation depth with all materials falling on an identical linear line defining the tip area function. See Figures 24 and 25 in Oliver and Pharr [54]. Once the area function is known, it can be used to calculate $E$ and $H$ of other materials.

One inherent feature of these studies is that $E$ and $H$ are not directly measured and that some of the assumptions used in the data reduction procedure may be violated. One of the key assumptions is the power law given in (3), which is obtained from a contact elasticity solution of a half space. These assumptions become quite relevant in thin films for which substrate effects are part of the experimental signatures [55–57]. Bückle [58] has recommended that indentation depth in microindentation should not exceed 10% of

the film thickness in order to obtain reliable results. This is currently used as a guideline in nanoindentation, which limits the minimum film thickness that can be reliably tested, using the standard data reduction procedure given by Oliver and Pharr to approximately 1–2 $\mu$m and larger. In general, this limit is a function of substrate properties and film roughness. Nix and co-workers developed a methodology to account for the substrate effect, which enables the property measurement of much thinner films.

The load-depth signature is a complex quantity that is affected by events such as cracking, delamination, plastic deformation, strain hardening, phase transitions, etc. In particular, gradients in elastic and plastic strains exist and are a function of indentation depth [22, 23, 33, 35, 59]. Thus, many interpretative methodologies have been devised in an attempt to deconvolute these effects [60, 61].

A major complication of the nanoindentation technique, observed in some materials, is the so-called "pile-up" and "sink-in" of the material around the indenter tip [24, 62, 63]. Both effects are primarily a result of the plastic behavior of the material and have a significant effect on the contact area between the tip and specimen. Furthermore, the solutions given are based on elastic contact mechanics and do not consider the effects of plasticity in the indentation process. The inclusion of plasticity into the solution is a complex process since the constitutive equations are nonlinear. Also, material properties such as yield stress and work hardening must be included, which are heavily dependent on microstructural aspects that can vary from specimen to specimen.

Figure 10 illustrates the problems of "pile-up" and "sink-in." Pile-up occurs in soft materials, such as metals, whereby the ease of deformation results in localized deformation in the region near the indenter tip. The result is material piling up around the indenter and effectively increasing the contact area between sample and indenter. By contrast, stiffer materials are more difficult to deform and the strain fields emanating from the penetrating indenter spread further into the material and effectively distribute the deformation to more volume, further away from the indenter. The sink-in effect arises from this feature and results in less contact area between the indenter and sample. The result is that pile-up



**Figure 10.** Schematic representation illustrating how the contact area changes during pile-up and sink-in effects. Reprinted with permission from [24], K. W. McElhaney et al., *J. Mater. Res.* 13, 1300 (1998). © 1998, Materials Research Society.

tends to overestimate hardness and modulus due to higher contact areas and sink-in tends to underestimate hardness and modulus due to lower contact area.

Attempts to deconvolute the substrate effects were investigated by Saha and Nix [56]. In this work, soft films that were deposited on a variety of relatively harder substrates were probed by nanoindentation; see Table 2. These systems included cases where elastic homogeneity existed between the film and substrate, that is, when the expected elastic modulus of the film was equivalent to the substrate (e.g., aluminum on glass), and cases where elastic modulus differed significantly (aluminum on sapphire). By employing the parameter $P/S^2$, where $P$ is the indenter load and $S$ is the contact stiffness, and plotting it versus indentation depth, a description of material behavior is obtained. This parameter was first proposed by Joslin and Oliver [64], who realized that both components, $P$ and $S$, are directly measured in the test. They examined and combined their analytical relations, Eq. (1) for $P$ and Eq. (5) for $S$, to obtain

$$\frac{P}{S^2} = \frac{1}{\beta^2}\frac{\pi}{4}\frac{H}{E_r^2} \qquad (9)$$

which shows that the parameter is independent of the contact area (i.e., tip calibration) and thereby is also not corrupted by pile-up or sink-in effects. Since $H$ and $E$ remain constant with indentation depth for homogeneous materials, the parameter $P/S^2$ should be independent of depth as well. By this method, Saha and Nix have shown that when elastic homogeneity between film and substrate is met, the Oliver and Pharr data reduction method [54] allows the decoupling of indentation size effects, at small depths, and substrate induced strain gradient effects, at large depths whereby a plateau representing true intrinsic material behavior is obtained.

In the same work, Saha and Nix [56] also developed a method to account for substrate effects in cases that do not possess elastic homogeneity. Using the elastically homogeneous aluminum (Al) film on glass substrate as a starting point, they first assumed that since the glass substrate is much harder than the aluminum, all plastic deformation is accommodated by the Al film with no deformation occurring in the substrate until the indenter makes contact with it. This allowed them to make a second assumption, basically that the film hardness measured for the Al/glass system was its intrinsic value and therefore also representative of the film hardness for the Al/sapphire system. With this knowledge they calculated the reduced modulus via Eq. (9) and corresponding true contact area from Eq. (5). These values
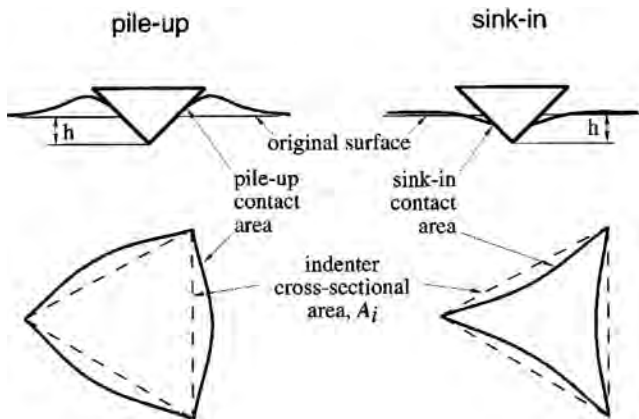
**Table 2.** Film/substrate systems tested by Saha and Nix. Al/Al, Al/glass, W/sapphire are elastically homogenous systems.

| Films | Substrates | $E$ (GPa) | $H$ (GPa) |
|---|---|---|---|
| Aluminum (Al) $E = 75$ GPa $H = 1$ GPa | aluminum | 75 | 1 |
| | glass | 73 | 6 |
| Tungsten (W) $E = 410$ GPa $H = 15$ GPa | silicon | 172 | 13 |
| | sapphire | 440 | 30 |

provided a means to compare experimental work with an existing model developed by King [65]. The King model was actually a modification of a treatment developed by Doerner and Nix [53] who, in the specific case they studied, were able to include a term in the reduced modulus, $E_r$, to account for the substrate effect. The King treatment built on this by modeling the system with a flat triangular indenter geometry resulting in a reduced modulus given by

$$\frac{1}{E_r} = \frac{1-\nu_i^2}{E_i} + \frac{1-\nu_f^2}{E_f}(1-e^{-\alpha t/a}) + \frac{1-\nu_s^2}{E_s}(e^{-\alpha t/a}) \quad (10)$$

where $E_s$ and $\nu_s$ are the elastic modulus and Poisson's ratio of the substrate respectively, $a$ is the square root of the projected contact area, $t$ is the thickness of the film below the indenter, and $\alpha$ is a scaling parameter that depends on $a/t$, which varies with indenter geometry. Saha and Nix have modified this analysis through incorporating a Berkovich indenter geometry by replacing $t$ in Eq. (10) with $(t-h)$, where $h$ is the indenter displacement into the film. Thus,

$$\frac{1}{E_r} = \frac{1-\nu_i^2}{E_i} + \frac{1-\nu_f^2}{E_f}(1-e^{-\alpha(t-h)/a}) + \frac{1-\nu_s^2}{E_s}(e^{-\alpha(t-h)/a}) \quad (11)$$

Substituting constants for $E$ and $\nu$ of each component, with $E_f$ taken from the elastically homogeneous case, yields the reduced modulus as a function of indentation depth that can be compared with the experimental $E_r$ calculated through Eq. (9). Saha and Nix found that these two methods are in good agreement for up to 50% of the film thickness, after which the experimentally obtained $E_r$ begins to decrease. Finally, by incorporating the experimentally obtained $E_r$ values into the modified King model, a plot of the film modulus versus indentation depth is obtained; see Figure 11. Here $E_f$ is seen to agree well up to 50% of the film thickness before beginning to decrease indicating that the King model is overpredicting the effect of the substrate. These data show that the modified analysis based on Eq. (11) is an effective method for estimating thin film modulus wherever substrate effects become relevant.

Hardness and elastic modulus are the properties most routinely measured by nanoindentation. However, it has also been shown to be an effective method for measuring other material properties such as fracture toughness in small volumes [66, 67], strain rate sensitivity and internal friction [68], and thermally activated plastic flow [69]. The frontier of nanoindentation revolves around combining current measurement and analysis with finite-element techniques [61, 70–73]. This combination will further aid the study of material mechanical behavior, especially those with nonlinear features. Finally, the so-called "Holy Grail" of nanoindentation will be the generation of material stress-strain behavior from indentation data in order that mechanical properties, such as yield and postyield properties, can be estimated. Further information on recent progress in nanoindentation can be found in the literature [74–76].
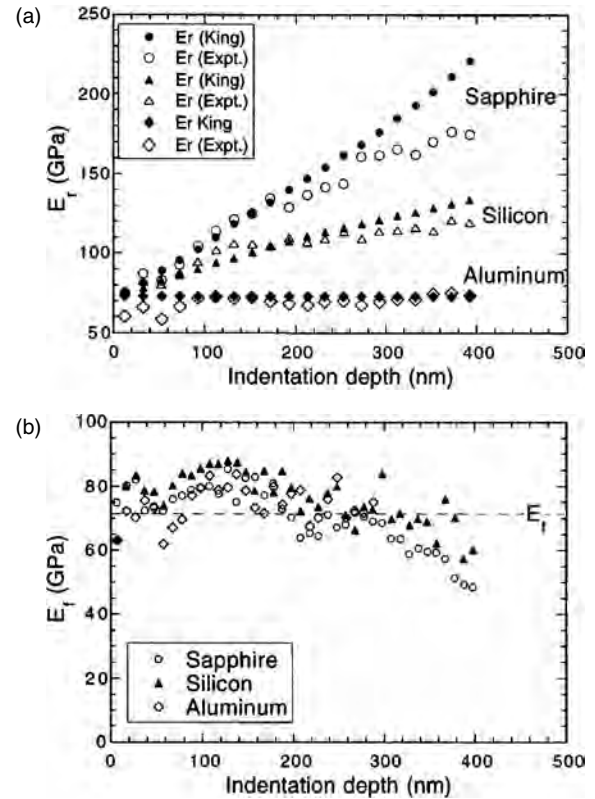


**Figure 11.** Comparison between modified King model and Saha and Nix experimental data for reduced modulus (a) and film modulus (b) of aluminum film on the substrates indicated. Reprinted with permission from [56], R. Saha and W. D. Nix, *Acta. Mater.* 50, 23 (2002). © 2002, Materials Research Society.

### 2.1.2. Bending and Curvature

Bending and curvature testing consists of microbeam bending, wafer curvature, and the bulge test. Bending tests on micromachined beams were first performed by Weihs et al. [77] and repeated by others [78–85]. The method involves deflecting a freestanding cantilever-like beam fixed at one end to the substrate. Building such structures on the micrometer scale is achieved with standard microfabrication procedures borrowed from the microelectronics field. Dimensions are on the order of a few micrometers to submicrometer thickness, tens of micrometers wide and hundreds of micrometers in length. Structures of this size have an extremely low stiffness and therefore high-resolution load cells are required to perceive the response of the beam. Nanoindenters have been shown to provide such load resolution and are routinely used to deflect such structures. A schematic of a typical microcantilever structure being deflected by a nanoindenter is shown in Figure 12. By this method, simple elastic beam theory can be applied. Namely,

$$k = \frac{Eb}{4(1-\nu^2)}\left(\frac{t}{l}\right)^3 \quad (12)$$

where $k$ is the stiffness, $E$ is the elastic modulus, $b$ is the cantilever width, $\nu$ is Poisson's ratio, $t$ is the thickness, and $l$ is the length of the cantilever at the point of contact.
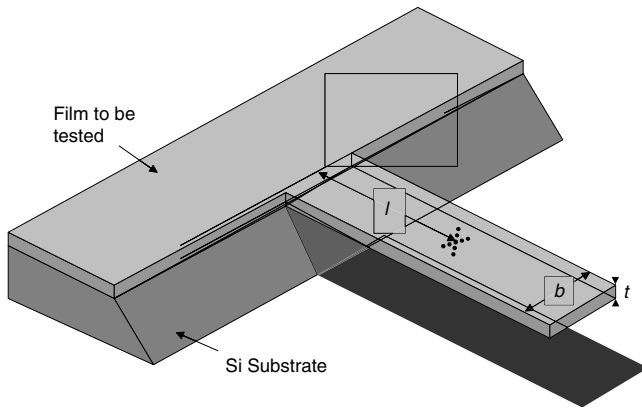
**Figure 12.** Schematic three-dimensional (3D) view of a freestanding cantilever structure. Parameters are defined in the text.



**Figure 14.** Load-deflection curves comparing load-displacement signatures for cantilevers lengths of 60, 80, 100, and 120 $\mu$m. Reprinted with permission from [84], H. D. Espinosa et al., *Exp. Mech.* (2003). © 2003, Society for Experimental Mechanics.

An example of results obtained from this method are shown in Figures 13 and 14. Figure 13 is an optical image of a common single crystal Si atomic force microscopy (AFM) tapping-mode tip and the corresponding load-deflection signature obtained after deflecting it with a nanoindenter [84]. In this structure the Si is oriented such that the length of the cantilever is parallel to the [110] direction. The stiffness, $k$, was found to vary between $2.58 \times 10^{-4}$ to $2.61 \times 10^{-4}$ mN/nm which corresponds to a modulus of 166 to 168 GPa when using Eq. (12), close to that of the [110] direction for Si, 170 GPa [86]. Another example of microcantilever bending results is shown in Figure 14 for thin film ultra-nanocrystalline diamond (UNCD). The figure shows load-deflection results on UNCD freestanding cantilevers at various cantilever lengths [84, 85]. As expected, the stiffness decreased as cantilever length increased. Using Eq. (12), the modulus was found to be between 945 and 963 GPa. The microcantilever bending test has shown to be a viable method to measure elastic properties; however, the technique exhibits some unique features. For example, the analytical solution is very sensitive to the measured thickness, as seen in Eq. (12) where its influence is to the third power warranting that extra care must be taken to accurately measure the specimen thickness. Undercutting during the release step introduces uncertainties in the measurement

of the cantilever length. Defining an equivalent cantilever length circumvented this problem [84]. The technique also suffers from boundary bending effects and inhomogeneous distribution of the strain since the bending moment is not constant along the length of the beam. Florando et al. [83] have put forth a solution to this issue by using a beam with a triangular width. Stress-strain behavior for the material can then be more accurately obtained.

Another bending based test is the wafer curvature method. Typically when a thin film is deposited on a substrate at elevated temperatures and then cooled to room temperature, the difference in the thermal expansion coefficient between the two materials will cause curvature in the structure to accommodate the strain. Whether this curvature is convex or concave is determined by which material has the greater coefficient of thermal expansion and if the film has tensile or compressive residual stress. This technique determines film properties by taking advantage of the fact that stress in the film is proportional to the radius of curvature of the substrate [87],

$$\sigma = \frac{E_s}{(1-\nu_s)}\frac{t_s^2}{6t_f}K_f \qquad (13)$$

where $t_f$ is the film thickness, $t_s$ if the substrate thickness, $E_s/(1-\nu_s)$ is the biaxial modulus of the substrate, and $K_f$ is the change in curvature. This equation relies on the assumption that the film completely accommodates lattice mismatch with the much thicker substrate [88]. A further constraint limits its application when the maximum bending deflection exceeds more than half the thickness of the substrate, $t_s/2$. Elastic and plastic properties can also be examined by varying the temperature. The technique has been used to examine a variety of thin films [15, 88–99]. There are some complexities of the wafer curvature method that hinder accurate property measurement such as nonuniformity of substrate-material adhesion and temperature. All in all, the method yields information on the material properties when confined by the substrate.

The third major bending based test is the bulge test, developed by Beams in 1959 [100], where a freestanding film is deflected by applying pressure with a compressed gas or liquid. These specimens also take advantage of standard microfabrication procedures to define their structures.



**Figure 13.** Optical images of (a) a silicon AFM tapping-mode tip and (b) corresponding load-displacement curve. Reprinted with permission from [84], H. D. Espinosa et al., *Exp. Mech.* (2003). © 2003, Society for Experimental Mechanics.

The geometry of the typical specimen consists of a thin film membrane that spans a cylindrical or rectangular chamber beneath. The film is fixed at the edges of the chamber such that the remainder of its structure is freestanding. The chamber is pressurized in a controlled manner that results in the freestanding film bulging upward. The resulting "bulge" height can then be measured by interferometry and other techniques. The test is designed to determine the in-plane mechanical properties of the film by eliminating specimen edge effects. Moreover, it also avoids the complexities of substrate material adhesion problems.

The technique has evolved over the years to settle on high aspect ratio rectangular chambers due to the "wrinkling effect" caused by biaxial states of stress that develop near the corners. This geometry confines the effect to the vicinity of the rectangle's short ends and allows uniform deformation to occur in the middle of the structure. Figure 15 is a cross-section of this region. Here, $H$ is the bulge height, $a$ is the membrane half-width, and $P$ is the applied gas pressure. Pressure is related to bulge height through the relation

$$P = \frac{2\sigma_0 t}{a^2} H + \frac{4Et}{3a^4(1-\nu^2)} H^3 \qquad (14)$$

where $\sigma_0$ is the residual stress, $t$ is the film thickness, $E$ is the material elastic modulus, and $\nu$ is the Poisson's ratio. The result of a test is a pressure-deflection plot describing the membrane behavior. A typical membrane response with several loading and unloading cycles is shown in Figure 16a for a freestanding Au film 1.8 $\mu$m thick. A comparison between the bulge and tensile tests was made for $Si_3N_4$ by Edwards et al. [101], whereby the elastic modulus of each technique was found to vary by as little a 1 GPa, $257 \pm 5$ GPa for tensile and $258 \pm 1$ GPa for bulge, and validating the bulge test as a viable wafer-level technique.

The method is able to examine both elastic and plastic properties. As in the case of nanoindentation, the stress-strain state in the film is not measured directly and requires a data reduction procedure that accounts for boundary effects. However, in the case the high aspect ratio membrane, stress and strain are nearly uniform in the short direction and can be approximated by

$$\varepsilon = \frac{2}{3a^2} H^2 \qquad (15)$$

$$\sigma = \sigma_0 + \frac{E}{(1-\nu^2)} \varepsilon = \frac{a^2}{2t} \frac{P}{H} \qquad (16)$$
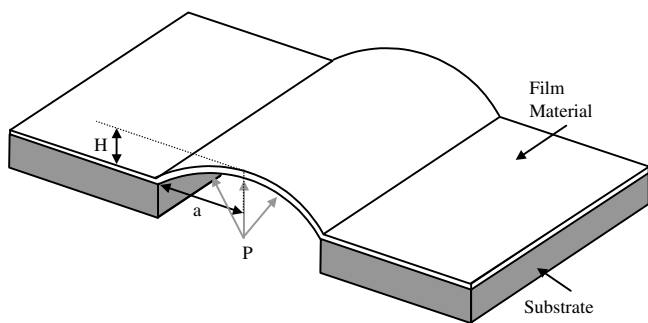


**Figure 15.** Cross-section of the middle of a high aspect ratio rectangular membrane; parameters are defined in the text.
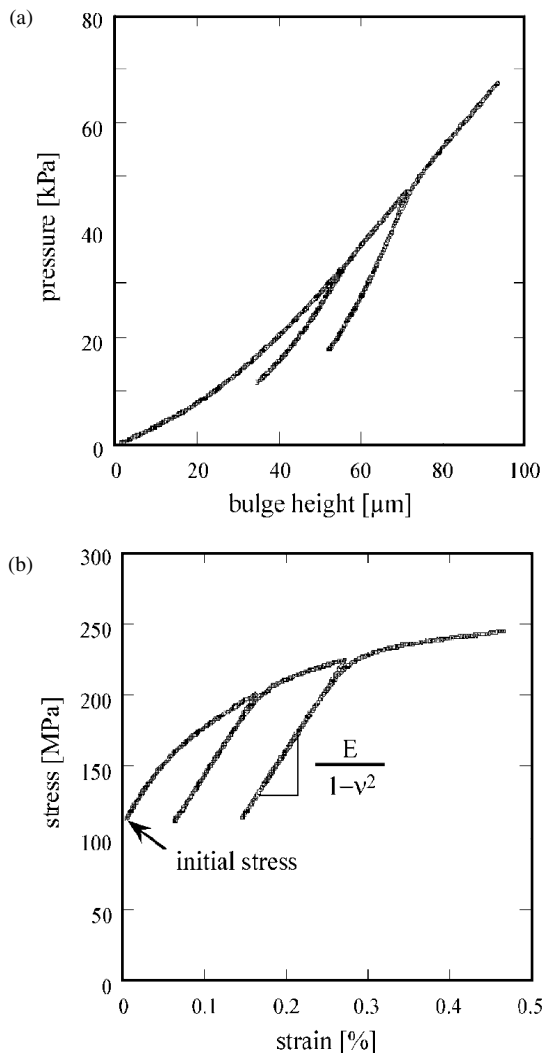


**Figure 16.** Pressure–height plot (a) and stress–strain plot (b) for bulge testing of an evaporated Au membrane 1.8 $\mu$m thick. Reprinted with permission from [46], O. Kraft and C. A. Volkert, *Adv. Eng. Mater.* 3, 99 (2001). © 2001, Wiley-VCH.

Using these equations, stress and strain can be extracted from the data. A plot of the stress-strain response of the data in Figure 16a is shown in Figure 16b. Several studies have utilized this technique to test thin films [102–107]. The apparatus required to perform a bulge test is simple and the method is an easy way of evaluating the in-plane mechanical properties. However, sample preparation is involved and is restricted to thin films with tensile residual stresses. Films with compressive stresses can buckle; in such a case the initial dome height must be determined as accurately as possible to avoid large errors in the experimental results. The experimental values are more accurate when the membrane is flatter.

### 2.1.3. Tensile Testing

The previously mentioned techniques can all be characterized as methods that subject the specimen to gradients of strain, which at the micro- and nanoscales can complicate

extraction of material property data. Also, their flexibility for testing specimens of varying geometry is limited. Thus, the equivalent of a tensile test, customarily to that performed on bulk samples, is desirable in this regard. *Tensile testing* is the most direct method for obtaining a material's mechanical properties. Loads and strains are measured directly and independently, and no mathematical assumptions are needed to identify quantities describing the material response. Many researchers have been involved in an effort to establish a scale-equivalent test [36–39, 83–85, 108–125]. However, tensile testing at the micro- and nanoscales has been difficult to achieve. Difficulties arise from load resolution, specimen fabrication, handling and mounting, uniformity of geometry from specimen to specimen, and independent measurement of stress and strain. The most attractive features of direct tensile testing are that data reduction is straightforward and the tests are much less susceptible to geometrically induced errors. Nonetheless, results reported in the many referenced studies vary somewhat, reinforcing the need for an easy to use tensile test that minimizes sample preparation, handling, and mounting that can produce numerous specimens of identical features.

Several noteworthy tensile testing schemes are worth detailing here. Sharpe et al. [114–118] have developed a micromachined frame containing the specimen. The fabrication process involves patterning the dog-bone specimen on a silicon wafer and then etching a window underneath. The final structure is shown in Figure 17. The finished tensile specimen is then mounted in the testing rig and grips are attached at either end. The two narrow sides are then cut with a rotary tool to free the specimen from the frame support. A piezoelectric actuator is employed to displace the specimen and subject it to uniaxial tension. Load is measured with a load cell possessing a resolution of 0.01 g and a load range of $\pm 100$ g, and strain with an interferometric strain displacement gauge. The typical width of specimens is 600 $\mu$m and the gauge length is 400 mm. Two sets of orthogonal strips are patterned on the surface of the specimen to reflect the laser beam used in the interferometric strain displacement gauge setup. When illuminated with the laser, the strips produce interference fringe patterns that are used to measure strain with a resolution of $\pm 5$ microstrain.

Another tensile testing technique, developed by Tsuchiya et al. [122, 124, 125], employs an electrostatic force gripping system to load the film. The specimen is fabricated as a freestanding thin-film cantilever fixed at one end and with a large pad at the other end. Schematics of the architecture and gripping process are shown in Figure 18. After fabrication and release of the cantilever specimen, a probe is aligned and brought into contact with the specimen free end to be gripped. An electrostatic attractive force is generated between the two surfaces with an applied voltage. Up to certain specimen dimensions, this force is rather large compared to the force required to deform the specimen in tension; therefore, the two remain rigidly fixed together as long as the voltage is applied. Tensile testing is then achieved through piezoelectric actuation of the probe along the axis of the specimen with displacements measured by a strain gauge at the probe. Specimen dimensions in the gauged region are on the order of: length 30–300 $\mu$m; width 2–5 $\mu$m; and thickness 0.1–2.0 $\mu$m.

Chasiotis and Knauss [112, 113] developed a testing procedure similar to that of Tsuchiya et al. Their test employs electrostatic forces to pull the specimen pad to the substrate while an ultraviolet curing adhesive then fixes a probe to it. This process ensures that the specimen experiences minimum handling during attachment and improves alignment between the specimen and probe since the specimen is temporarily fixed to the substrate. The electrostatic force is then reversed through identical poling of each side to release the



**Figure 17.** A tensile specimen fabricated at MIT (a) and at CWRU (b). Reprinted with permission from [118], K. M. Jackson et al., *Mater. Res. Soc. Symp. Proc.* 687 (2001). © 2001, Materials Research Society.
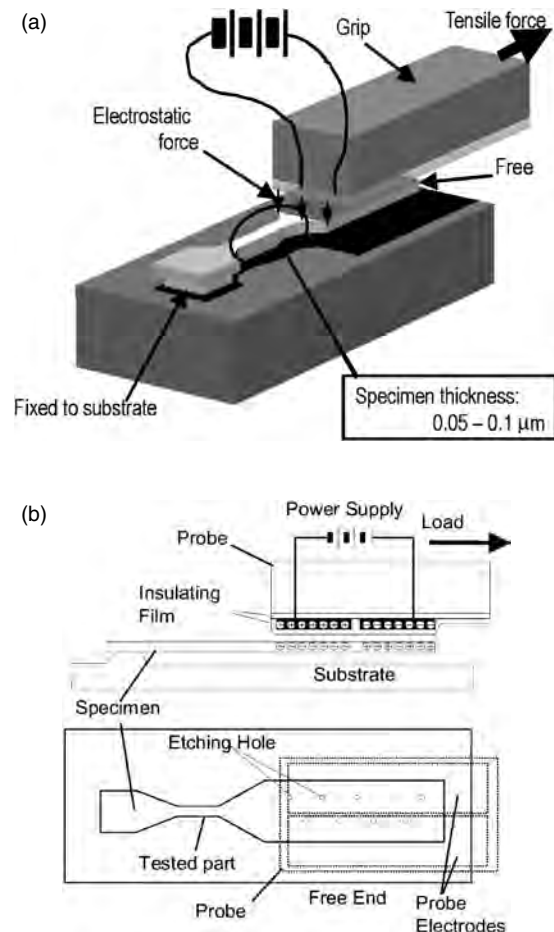


**Figure 18.** Schematics showing the architecture of the electrostatic grip system. Reprinted with permission from [125], T. Tsuchiya et al., *Mater. Res. Soc. Symp. Proc.* 687 (2002). © 2002, Materials Research Society.

combined pair from the substrate. Tensile testing proceeds in a similar manner to that of Tsuchiya et al. with the main difference being that measurement of strain fields is performed through AFM and digital image correlation (DIC).

Another variation of the microscale tensile test employs the cantilever architecture, but it possess a ring at the free end rather than a gripping pad [120, 126]; see Figure 19. A probe with a diameter just smaller than the inner diameter of the ring is inserted and then pulled in the direction of the specimen axis to apply direct tension. An optical encoder is used to independently measure displacement. Results were compared for two groups of specimens of significantly varying lengths to eliminate the error in stiffness due to deformation of the ring. By assuming that the effective stiffness was the same for each measurement the effect of the ring was canceled out. A problem with this test is the difficulty of eliminating friction between probe and substrate. This feature complicates the data reduction procedure and interpretation of the data.
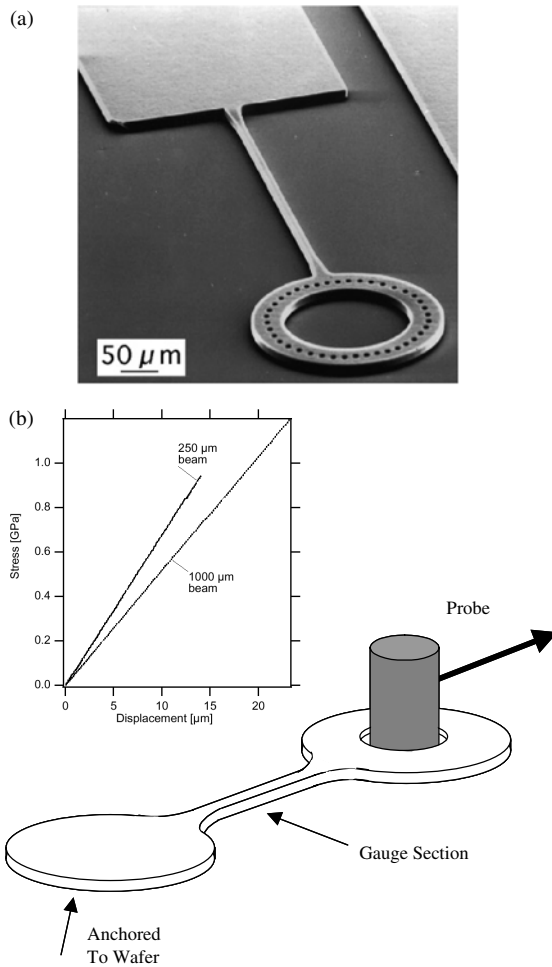


**Figure 19.** SEM image of the cantilever-ring architecture (a) and schematic of the loading process with experimental results for two specimens of different lengths (b). Reprinted with permission from [126], S. Greek et al., *J. Micromech. Microeng.* 9, 245 (1999). © 1999, Institute of Physics.
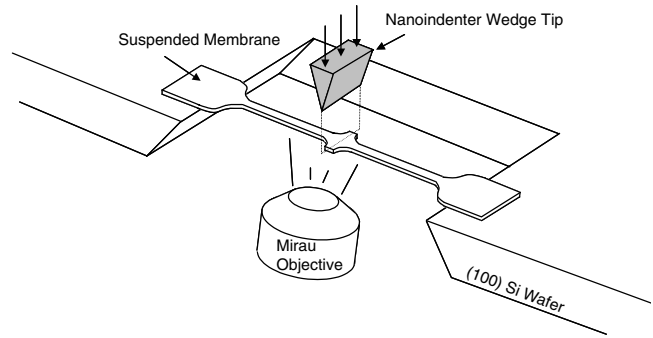


**Figure 20.** 3D schematic view of the membrane deflection experiment.

Another noteworthy microscale tensile test, called the membrane deflection experiment (MDE), was developed by Espinosa and co-workers [36–39, 119]. It involves the stretching of freestanding, thin-film membranes in a fixed–fixed configuration with submicrometer thickness. In this technique, the membrane is attached at both ends and spans a micromachined window beneath (see Fig. 20). A nanoindenter applies a line-load at the center of the span to achieve deflection. Simultaneously, an interferometer focused on the bottom side of the membrane records the deflection. The result is direct tension in the gauged regions of the membrane with load and deflection being measured independently. The geometry of the membranes is such that they contain tapered regions to eliminate boundary-bending effects and ensure failure in the gauge region (see Fig. 21). The result is direct tension, in the absence of bending and strain gradients of the specimen.

The MDE test has certain advantages; for instance, the simplicity of sample microfabrication and ease of handling results in a robust *on-chip* testing technique. The loading procedure is straightforward and accomplished in a highly sensitive manner while preserving the independent measurement of stress and strain. It can also test specimens of widely varying geometry, thickness from submicrometer to several micrometers, and width from one micrometer to tens of micrometers.
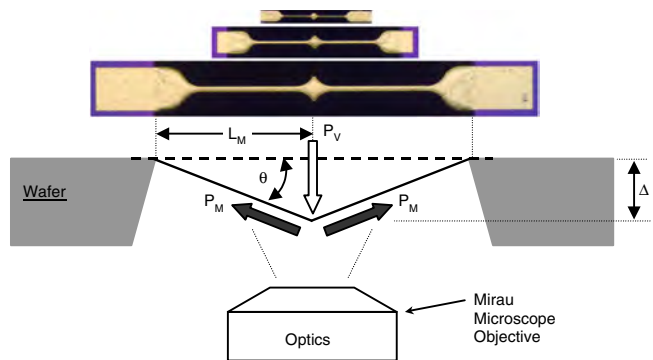


**Figure 21.** Side view of the MDE test showing vertical load being applied by the nanoindenter, $P_V$, the membrane in-plane load, $P_M$, and the position of the Mirau microscope objective. Reprinted with permission from [36], H. Espinosa et al., *J. Mech. Phys. Solids* (2003). © 2003, Elsevier Science.

The data directly obtained from the MDE test must then be reduced to arrive at a stress-strain signature for the membrane. The load in the plane of the membrane is found as a component of the vertical nanoindenter load by the equations

$$\tan\theta = \frac{\Delta}{L_M} \quad \text{and} \quad P_M = \frac{P_V}{2\sin\theta} \quad (17)$$

where (from Fig. 21) $\theta$ is the angle of deflection, $\Delta$ is the displacement, $L_M$ is the membrane half-length, $P_M$ is the load in the plane of the membrane, and $P_V$ is the load measured by the nanoindenter. Once $P_M$ is obtained the nominal stress, $\sigma(t)$, can be computed from

$$\sigma(t) = \frac{P_M}{A} \quad (18)$$

where $A$ is the cross-sectional area of the membrane in the gauge region. The cross-sectional area dimensions are typically measured using AFM [37].

The interferometer yields vertical displacement information in the form of monochromatic images taken at periodic intervals. The relationship between the spacing between fringes, $\delta$, is related through the wavelength of the monochromatic light used. Assuming that the membrane is deforming uniformly along its gauge length, the relative deflection between two points can be calculated, independently of the nanoindenter measurements, by counting the total number of fringes and multiplying by $\lambda/2$. Normally, part of the membrane is out of the focal plane and thus all fringes cannot be counted. By finding the average distance between the number of fringes that are in the focal plane of the interferometer, an overall strain, $\varepsilon(t)$, for the membrane can be computed from the following relation:

$$\varepsilon(t) = \frac{\sqrt{\delta^2 + (\lambda/2)^2}}{\delta} - 1 \quad (19)$$

This relationship is valid when deflections and angles are small. Large angles require a more comprehensive relation to account for the additional path length due to reflection off of the deflected membrane. This task and further details are given by Espinosa et al. [37].

The interferometer allows for *in-situ* monitoring of the test optically. Figure 22 shows combined interferometric images and stress-strain plots obtained from a typical membrane deflection experiment. The figure shows three instances of stress in stretching a thin gold strip obtained from the test. The first is at zero stretch and the second is at an intermediate stretch where the elastic–plastic behavior transition is exceeded and the strip is being permanently deformed. The third is at a large stretch and shows large local deformation indicating the strip is near failure. Data from MDE tests of thin gold, copper, and aluminum membranes have indeed shown that strong size effects exist in the absence of strain gradients [36].

Recently, the membrane deflection experiment was extended to measure fracture toughness of freestanding films [127]. In this method, two symmetric edge cracks are machined using a focused ion beam. A tip radius of 100 nm
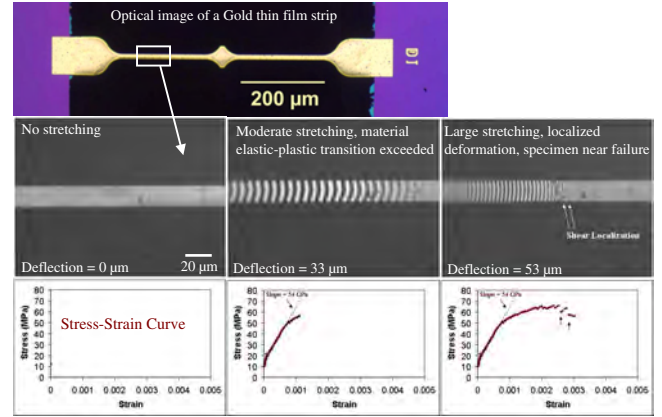


**Figure 22.** Magnified area of a thin gold membrane as it is stretched until it breaks. Three time points of stretching are shown that include the interferometric displacement image and the resulting stress–strain curve. Reprinted with permission from [36], H. Espinosa et al., *J. Mech. Phys. Solids* (2003). © 2003, Elsevier Science.

is achieved; see Figure 23. The toughness is computed from the equations

$$K_{IC} = \sigma_f \sqrt{\pi a} f\left(\frac{a}{W}\right) \quad (20)$$

$$f\left(\frac{a}{W}\right) = 1.12 + 0.429\left(\frac{a}{W}\right) - 4.78\left(\frac{a}{W}\right)^2$$
$$+ 15.44\left(\frac{a}{W}\right)^3 \quad (21)$$

where $\sigma_f$ is the fracture stress, $a$ is the length of the crack, and $W$ is the width of the gauge region as shown in Figure 23c.
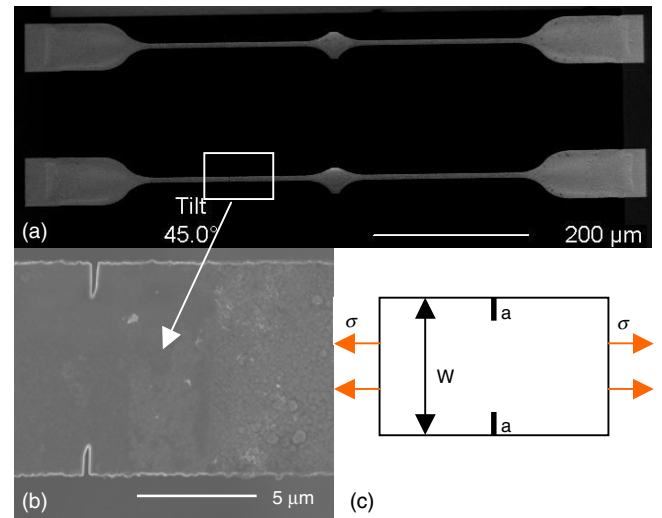


**Figure 23.** (a) A scanning electron micrograph of the geometry of the UNCD membranes, (b) a magnified area of the edge cracks, and (c) the schematic drawing of the two-symmetric-edge-cracks model.

### 2.1.4. Testing Methods Based on Microelectromechanical System Technology

Microelectromechanical systems can be advantageously employed in the testing of micro- and nanoscale specimens. These devices consist of micromachined elements such as comb-drive actuators and strain sensors that are integrated components on the wafer. They have the potential to impact the small-scale testing field through high resolution force and displacement measurements. Several possibilities for actuation and deformation measurement exist. The methology is based on the fabrication of numerous specimens of identical geometry and microstructure through standard micromachining techniques.

A promising MEMS-based testing approach has been developed by Saif et al. [128–132]. A single crystal micro-machined structure is used for stressing submicrometer thin films. *In-situ* SEM or TEM can be performed using this structure; see Figure 24. One end of the structure is attached to a bulk piezoelectric actuator while the other end is fixed. Folded and supporting beams are employed to uniformly transfer the load to the specimen, which is attached to a supporting fixed–fixed beam. This beam, of known spring constant, is then used as the load sensor. Two displacement elements are placed at either end of the specimen where the magnitude of displacement is imaged directly from the separation of beam elements. An innovative feature of the design is that the supporting beam structure is configured such that it can compensate and translate nonuniaxial loads into direct tensile loads on the specimen. In other words, the piezoelectric actuator is not required to pull on the structure exactly in a direction aligned with the specimen, thus solving the difficult issue of loading device–specimen alignment.

Another MEMS-based testing approach employs a comb-drive actuator to achieve time dependent stressing of the specimen through voltage modulation [133–139]. The device architecture consists of the microscale specimen with one
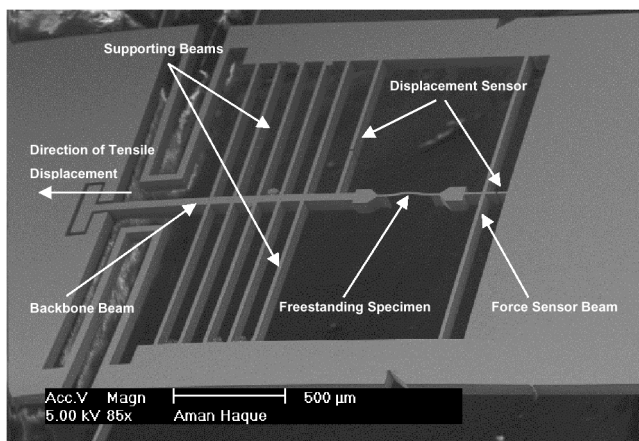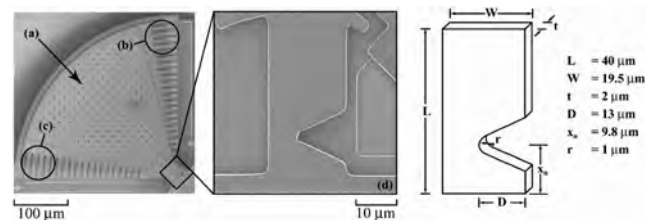


**Figure 25.** SEM micrographs of the fatigue test structure; (a) mass, (b) comb-drive actuator, (c) capacitive displacement sensor, and (d) notched cantilever beam specimen are shown. The nominal dimensions of the specimen are as indicated in the schematic. Reprinted with permission from [137], C. L. Mohlstein et al., *Mater. Res. Soc. Symp. Proc.* 687 (2002). © 2002, Materials Research Society.

end attached to a rigid mount and the other to a large perforated plate, which sweeps in an arc-like fashion when driven electrostatically by a comb-drive actuator (see Fig. 25). The resulting motion of the structure is recorded capacitively by the comb-drive sensor on the opposite side. The result is mode I stress concentration at the specimen notch. The specimen is tested until failure occurs and yields fracture and fatigue information about the material. Further details can be found in the cited literature.

Other MEMS techniques have also employed electrostatically driven comb-drives to perform other types of loadings. One such approach studied the effect of microstructure on fracture toughness through controlled crack propagation [140, 141]. The testing rig consists of a specimen anchored to a rigid support at one end and linked perpendicularly to a comb-drive actuator. The other end is attached to a beam that connects to a comb-drive actuator (see Fig. 26). A notch is either micromachined into the specimen (blunt notch) or a crack is propagated into the specimen through a Vickers microindent made in close proximity to the specimen. This step is performed as an intermediate step during the micro-fabrication of the specimen. The cracks, which radiate from the indent corners, travel into the specimen. Upon actuation of the comb-drive, the connecting beam applies mode I



**Figure 24.** A SEM micrograph of the tensile test chip can be performed *in-situ* inside a SEM or TEM. The freestanding specimen is cofabricated with force and displacement sensors by microelectronic fabrication. Reprinted with permission from [132], M. A. Hague and M. T. A. Saif, in "Proc. of the SEM Ann. Conf. on Exp. and Appl. Mech.," Milwaukee, WI, (2002). © 2002, Society for Experimental Mechanics, Inc.



**Figure 26.** SEM images a MEMS fracture device. (a) is the overall device architecture, (b) is a close-up of the specimen, (c) gives the relative dimensions, and (d) shows a buckled support beam, a problem stemming from residual stress during fabrication that plagues many MEMS devices. Image courtesy of R. Ballerini.

loading at the specimen notch or sharp crack. At a critical value of displacement, controlled fracture is attained.

Another MEMS-based technique utilizes electrothermal actuation to load specimens in direct tension [142, 143]. The device is designed such that slanted or axial beams impose a deformation on the sample (see Fig. 27). The produced Joule effect causes local heating and expansion of the beams. The thermal actuator pulls directly on the specimen, stressing it in uniform tension. Strain is determined from an integrated capacitive sensor and verified through digital image correlation. The rig can also be employed for fatigue testing by using a modulated voltage. However, thermal actuation is hindered by a relatively slow response time.

These MEMS techniques show great promise to test ever-smaller specimens and are expected to have a great impact on the development of nanoscale devices. When coupled with finite element multiphysics modeling they should be able to provide an accurate description of nanoscale structural response and associated features needed to predict their behavior. These data are important for exploiting micro- and nanoscale properties in the design of novel and reliable devices with increased functionality.

## 2.2. Nanoscale Measurement Techniques

The property measurement of one-dimensional nano-objects, such as nanowires (NWs) and CNTs, is extremely challenging because of the miniscule size. As such, early studies of their mechanical properties focused on theoretical analyses and numerical simulations. They allowed the prediction of Young's modulus, buckling and local deformation, and tensile strength [144–147]. Owing to advances in microscopy, especially scanning probe microscopy (SPM) and electron microscopy, nanoscale experiments employing these tools have been developed. The main challenges in the experimental study of one-dimensional nanosize specimens are: (1) constructing appropriate tools to manipulate and position specimens; (2) applying and precisely measuring forces in the nano-Newton range, and (3) measuring local mechanical deformation precisely. In the next sections,
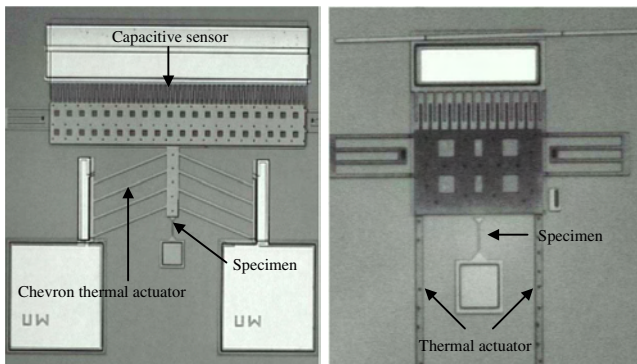
we review techniques and methodologies addressing these challenges.

### 2.2.1. Manipulation and Positioning of Nanotubes

There are several methods used today to synthesize CNTs including electric arc-discharge [148, 149], laser ablation [150], and catalytic chemical vapor deposition [151]. CNTs made by these methods are commercially available, although still very expensive. During synthesis, nanotubes are usually mixed with residues including various types of carbon particles. For applications or tests, a purification process is required in most cases. In the most common approach, nanotubes are ultrasonically dispersed in a liquid (e.g., iso-propanol) and the suspension is centrifuged to remove large particles. Other methods including dielectriphoretic separation are being developed to provide improved yield.

***Random Dispersion***   Random dispersion is the easiest method for most of the mechanical testing experiments to date, but it is only modestly effective. After purification, a small aliquot of the nanotube suspension is dropped onto a substrate. The result is CNTs randomly dispersed on the substrate. A metal layer is then uniformly deposited on top of the substrate and patterned by a photolithography process, after which some of the nanotubes become pinned by a grid of pads [152]. To improve the probability of nanotube coverage, CNTs on the substrate are imaged inside a scanning electron microscope and then this image is digitized and imported to the mask drawing software, where the mask for the subsequent electron beam lithography (EBL) is designed. In the mask layout, the pads are designed to superimpose over the CNTs [153]. This process requires an alignment capability of lithography with a resolution of 0.1 $\mu$m or better.

***Nanomanipulation***   SPM can be used both to image and to manipulate carbon nanotubes [154]. Using AFM, an individual multiwalled carbon nanotube (MWCNT) was successfully isolated from a group of overlapped MWCNTs. A "NanoManipulator" AFM system, comprising an advanced visual interface, teleoperation capabilities for manual control of the AFM tip, and tactile presentation of the AFM data, was developed at the University of North Carolina [155–157]. The NanoManipulator can take control of the AFM's probe, move it to the desired location, and manipulate atomic-scale structures. A software program integrates force feedback and AFM. A haptic interface, which is a penlike device, enables the users to remotely operate the NanoManipulator. More recently, they combined AFM, SEM, and the NanoManipulator interface to produce a manipulation system with simultaneous microscopy imaging [294].

Electron microscopy provides the imaging capability for manipulation of CNTs and NWs with nanometer resolution. Various sophisticated nanomanipulators under either SEM [294, 158, 159] or TEM [160–163] have been developed. These manipulators are usually composed of both a coarse micrometer-resolution translation stage and a fine nanometer-resolution translation stage; the latter is based on piezo-driven mechanisms. The manipulators have the



**Figure 27.** Micromechanical fatigue testers with: (a) an eight-beam chevron actuator and (b) a two-beam actuator. Reprinted with permission from [142], E. E. Fischer and P. E. Labossiere, in "Proc. of the SEM Ann. Conf. on Exp. and Appl. Mech.," Milwaukee, WI, 2002. © 2002, Society for Experimental Mechanics, Inc.

capability of motion in three linear degrees of freedom, and some even have rotational capabilities. Several probes are attached to the manipulator and can be operated independently. In general, the manipulation and positioning of nanotubes is accomplished in the following manner: (1) a source of nanotubes is positioned close to the manipulator inside the microscope; (2) the manipulator probe is moved close to the nanotubes under visual surveillance of the microscope monitor until a protruding nanotube is attracted to the manipulator due to either van der Waals forces or electrostatic forces; (3) the free end of the attracted nanotube is positioned in contact with the probe and is "spot welded" by the electron beam [164]; (4) the other end of the nanotube is placed at the desired location and "spot welded." Nanodevices can be made using this approach. The technique is being implemented with force feedback for haptic control. Limitations in perception depth are so alleviated [155, 159].

***External Field Alignment***  Dc and ac/dc electric fields have been used for the alignment of CNTs and nanoparticles [165, 166, 301]. Microfabricated electrodes are typically used to create an electric field in the gap between them. A droplet containing CNTs in suspension is dispensed into the gap with a micropipette. The applied electric field aligns the nanotubes, due to the dielectrophoresis effect, which results in the bridging of the electrodes by a single nanotube. The voltage drop that arises when the circuit is closed (dc component) ensures the manipulation of a single nanotube. Dc/ac fields have been successfully used in the manipulation of nanowires [167], nanotubes [165, 295], and bioparticles [168–170].

Huang [171] demonstrated another method of aligning nanotubes. A laminar flow was employed to achieve preferential orientation of nanotubes on chemically patterned surfaces. This method was successfully used in the alignment of silicon nanowires. Magnetic fields have also been used to align carbon nanotubes [172].

***Direct Growth***  Instead of manipulating and aligning CNTs after their manufacturing, researchers have also examined methods for controlled direct growth. Huang et al. [173] used the microcontact printing technique to directly grow aligned nanotubes vertically. Dai et al. [174, 298–300] reported several patterned growth approaches developed in their group. The idea is to pattern the catalyst in an arrayed fashion and control the growth of CNTs from specific catalytic sites. The author successfully carried out patterned growth of both MWCNTs and single-walled carbon nanotubes (SWCNTs) and exploited methods including self-assembly and external electric field control.

***Nanomachining***  It is of scientific interest to open the cap of MWCNTs to investigate the nanotube inner structure and intershell frictional behavior. Cumings and Zettl [253] have implemented an electric sharpening method to open the ends of MWCNTs using TEM. The process involves the electrically driven vaporization of successive outer layers from the end of the MWCNT, leaving the nanotube core intact and protruding from the bulk of the nanotube. This peeling and sharpening process can be applied repeatedly to the same multiwalled nanotube until the innermost tube

protrudes, with a tip having a radius of curvature comparable to that of a single-walled nanotube.

### 2.2.2. High Resolution Force and Displacement Measurements

SEM, TEM, and SPM have been widely used in characterizing nanotubes. These provide effective ways of measuring dimension and deformation of nanotubes with nanometer resolution. Electron microscopy uses high-energy electron beams for scattering (SEM) and diffraction (TEM). Field emission gun SEM has a resolution of about 1 nm and TEM is capable of achieving a point-to-point resolution of 0.1–0.2 nm. The resolution of SEM is limited by the interaction volume between the electron beam and the sample surface. The resolution of TEM is limited by the spread in energy of the electron beam and the quality of the microscope optics.

AFM has become a powerful tool in the characterization of CNTs due to its capability not only to map the surface topography with nanometer resolution but also to manipulate CNTs. AFM can be operated in several modes: contact mode, tapping mode (or force modulation mode), noncontact mode, and lateral force mode [176–180]. The tapping mode has been used to induce radial deformation of nanotubes in addition to the contact mode and the lateral force mode [154, 181]. Scanning tunneling microscopy (STM) has not been widely used in the mechanical testing of CNTs at this stage, but it shows enormous potential since it can reveal the atomic structure and the electronic properties of CNTs [154]. The STM can be operated in two modes: constant current mode and constant height mode. Figure 28 provides several typical images taken by SEM, TEM, AFM, and STM.

Commercial force sensors usually cannot reach nano-Newton resolution. Therefore, AFM cantilevers have been effectively employed as force sensors [164, 187, 188], provided that their spring constant has been accurately calibrated. Alternatively, MEMS technology offers the capability to measure force with nano-Newton resolution. This point will be further discussed in Section 2.3.

To date, the experimental techniques employed in the mechanical testing of nanotubes can be grouped into five categories: resonance, bending, radial, tensile, and torsion loading.

### 2.2.3. Measurement Techniques for Nanotubes and Nanowires

***Resonance***  Treacy et al. [184] estimated the Young's modulus of MWCNTs by measuring the amplitude of their thermal vibrations during *in-situ* TEM imaging (Fig. 29). The nanotubes were attached to the edge of a hole in 3-mm-diameter nickel rings for TEM observation, with one end clamped and the other free. The TEM images were blurred at the free ends, and increasing specimen temperature significantly increased the blurring. This indicated that the vibration was of thermal origin. Blurring occurs because the vibration cycle is much shorter than the integration time needed for capturing the TEM image.

A nanotube can be considered as a homogeneous cylindrical cantilever of length $L$ with outer and inner radii $a$
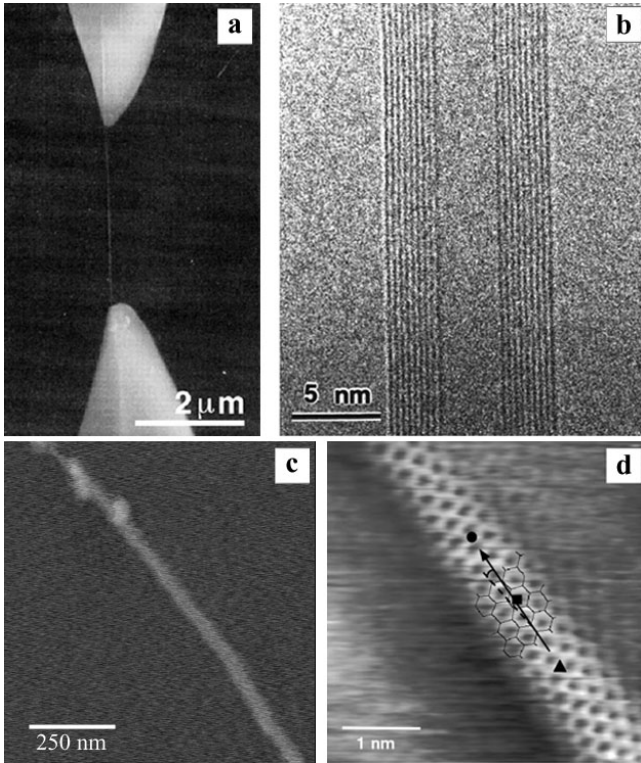
**Figure 28.** Typical images of CNTs taken by (a) SEM (reprinted with permission from [164], M. F. Yu et al., *Science* 287, 637 (2000). © 2000, American Association for the Advancement of Science.); (b) TEM (reprinted with permission from [293], R. H. Baughman et al., *Science* 297, 787 (2002). © 2002, American Association for the Advancement of Science); (c) AFM (image courtesy of C. Ke); and (d) STM (reprinted with permission from [183], T. W. Odom et al., *Nature* 391, 62 (1998). © 1998, Macmillan Publishers Ltd.). The imaging resolution of various instruments is illustrated.

and *b*, respectively. For such a structure, the square of the thermal vibration amplitude is given by

$$A^2 = \frac{16L^3kT}{E(a^4 - b^4)} \sum_j \beta_j^{-4} \approx 0.4243 \frac{L^3kT}{E(a^4 - b^4)} \qquad (22)$$

where $A$ is the amplitude at the free end, $k$ is the Boltzmann constant, $T$ is the temperature, $E$ is Young's modulus, and $\beta_j$ is a constant for free vibration mode $n$. By comparing the blurred images, one can estimate the vibration amplitude and deduce the value of Young's modulus.

This method is fairly simple to implement and exploits available instrumentation, including TEM holders with heating capability. As a matter of fact, this was one of the first experiments to measure Young's modulus of carbon nanotubes. There are some drawbacks associated with this method. Its accuracy to determine the vibration amplitude by comparing the blurred images is limited, the shape of the nanotubes is not exactly identical to a cylindrical cantilever, and the boundary conditions present some uncertainty. Krishnan et al. [185] later applied this method to SWCNTs.

Poncharal et al. [160] measured Young's modulus by using a method based on the mechanical resonance of cantilevered
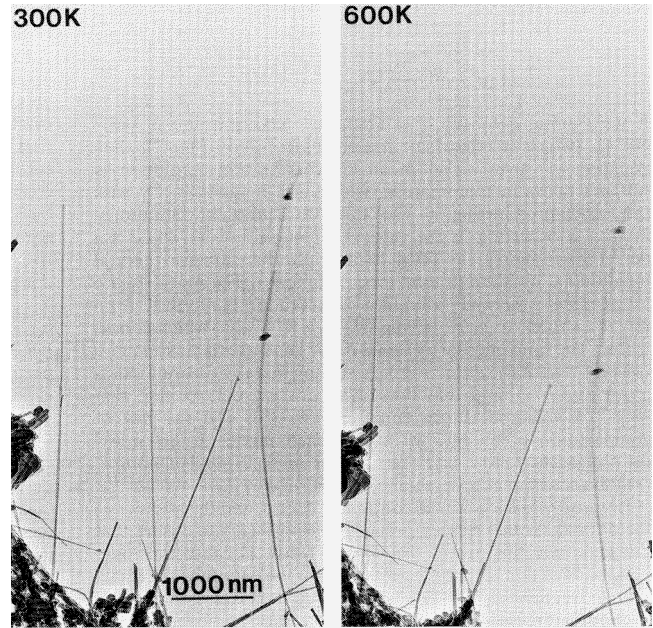


**Figure 29.** TEM micrographs showing the blurring at the tips due to thermal vibration at 300 and 600 K, respectively. Reprinted with permission from [184], M. M. J. Treacy et al., *Nature* 381, 678 (1996). © 1996, Macmillan Publishers Ltd.

MWCNTs. The actuation was achieved utilizing an ac electrostatic field within a TEM (Fig. 30). In the experiment, the nanotubes were attached to a fine gold wire, on which a potential was applied. In order to precisely position the wire
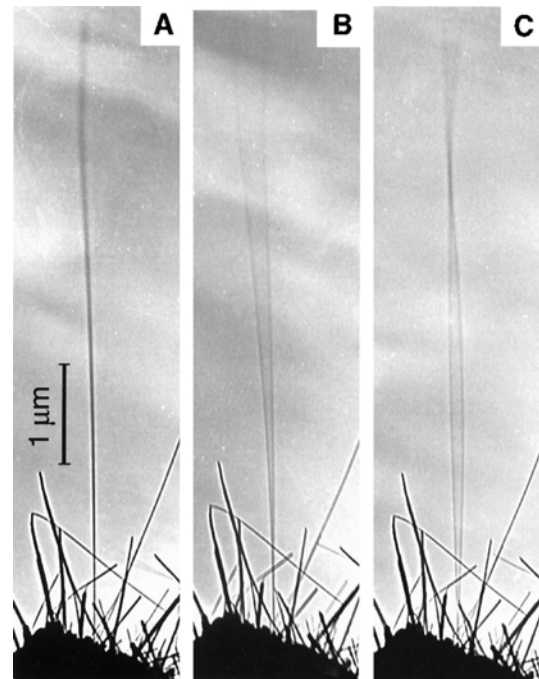


**Figure 30.** Dynamic responses to alternate applied potentials, (A) absence of a potential, (B) at fundamental mode, and (C) at second harmonic mode. Reprinted with permission from [160], P. Poncharal et al., *Science* 283, 1513 (1999). © 1999, American Association for the Advancement of Science.

near the grounded electrode, a special TEM holder with a piezo-driven translation stage and a micrometer-resolution translation stage was used. Application of an ac voltage to the nanotubes caused a time-dependent deflection. The resonant frequencies were then related to Young's modulus, viz.,

$$\nu_j = \frac{\beta_j^2}{8\pi} \frac{1}{L^2} \sqrt{(a^2 + b^2)} \sqrt{\frac{E}{\rho}} \tag{23}$$

where $a$ is the outer diameter, $b$ is the inner diameter, $E$ is the elastic modulus, $\rho$ is the density, and $\beta_j$ is a constant for the $j$ harmonic. The elastic modulus can then be estimated from the observed resonance frequencies. This method requires the precise positioning of the nanotubes against the counterelectrode, which can only be achieved by a high-precision manipulator. The advantage is that the resonance frequency can be much more precisely measured than the vibration amplitude.

***Bending and Curvature***   Falvo et al. [156] used AFM in contact mode to manipulate and bend a MWCNT resting on a substrate with the assistance of a nanomanipulator. The AFM tip was used to apply lateral force at locations along the tube to produce translation and bending. One end of the nanotube was pinned to the substrate by e-beam carbon deposition. After the bending, some of the deformed nanotubes were fixed by the friction between the nanotubes and the substrate and some returned to the undeformed configuration. Falvo et al. [157] applied this method to investigate the rolling and sliding behaviors of nanotubes.

Wong et al. [152] measured Young's modulus, strength, and toughness of MWCNTs by using AFM in lateral force mode (Fig. 31). In their method, nanotubes were dispersed randomly on a flat surface and pinned to this substrate by means of microfabricated patches. Then AFM was used to bend the cantilevered nanotubes transversely. At a certain location ($x$) along the length of each nanotube, the force versus deflection ($F$–$d$) curve was recorded to obtain the spring constant of the system. Multiple $F$–$d$ curves were
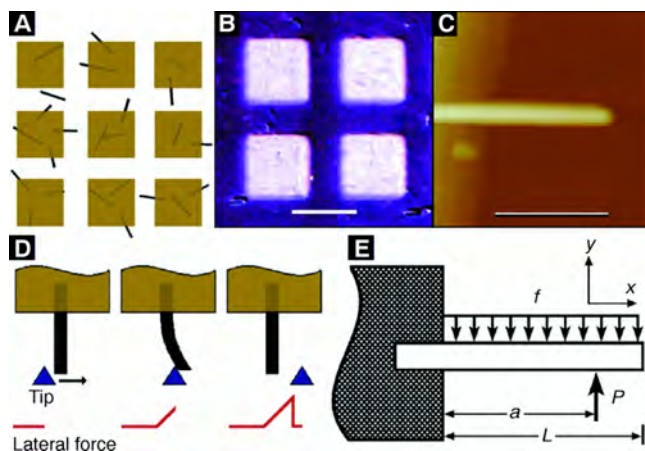
recorded at various locations along the nanotube. Single crystal $MoS_2$ was used as the substrate due to its low friction coefficient. By modeling the nanotube as a beam, the $F$–$d$ data acquired by this method were used to estimate Young's modulus. In Figure 31e, the response of a beam to a force $P$ applied at a distance $a$ (along the $x$ axis) from the fixed point ($x = 0$) is schematically illustrated. The governing equation for the elastic curve is

$$EI\frac{d^4y}{dx^4} = -f + P\delta(x - a) \tag{24}$$

where $y$ is the deflection, $I$ is the moment of inertia of the nanotube, and $f$ is the friction force between nanotube and substrate. This term was considered small and omitted in the analysis. By integrating this equation and defining the spring constant at position $x$ as $k(x) = dP/dy$, one can express it in terms of Young's modulus and tube geometry, viz.,

$$k(x) = \frac{3\pi r^4}{4x^3}E \tag{25}$$

where $\pi r^4/4$ is the moment of inertia for a solid cylinder of radius $r$.

Bending of nanotubes resting on a substrate is straightforward to implement. Nevertheless, it cannot eliminate the effect of adhesion and friction from the substrate. To solve the friction issue, Walters et al. [186] suspended the nanotube over a microfabricated trench and bent the nanotube repeatedly in lateral force mode. Salvetat et al. [187, 188] introduced a similar method to measure Young's modulus of SWCNTs and MWCNTs. The nanotubes were dispersed in ethanol and a droplet was deposited on a commercially available alumina ultrafiltration membrane with 200 nm pores (Whatman Anodics). Some nanotubes were suspended over the pores. The adhesion between the nanotubes and the membrane was found sufficiently strong, so that the nanotubes were effectively clamped. Using AFM in contact mode, the authors applied vertical load to the suspended nanotubes and recorded the force and deflection simultaneously. In this case, the nanotubes behaved like clamped beams subjected to a concentrated load.

***Radial Compression***   Shen et al. [154] performed an indentation test on MWCNTs using AFM. After separating the overlapped nanotubes using AFM in indentation/scratch mode, the authors used AFM in tapping mode to scan the tubes and selected a well-shaped tube to perform further testing. The sample stage was lifted against the AFM tip. After the tube made contact with the tip, the AFM cantilever was bent and the tube was compressed. The cantilever bending changed the position of the laser spot on the four-quadrant photodectector and thereby produced a voltage signal proportional to it. When the signal reached a trigger value, the sample was retracted. The radial compression was obtained from the stage motion and cantilever deflection, and the force was calculated using the known spring constant of the AFM cantilever and its deflection. In summary, Shen et al. actually squeezed the nanotubes by moving them against the AFM cantilever, similar to nanoindentation. However, to study the same problem with the same tool, Yu et al. [181] took a different strategy. They compressed the nanotubes by AFM while imaging the nanotubes



**Figure 31.** Overview of the approach used to probe mechanical properties of NRs and nanotubes. Reprinted with permission from [152], E. W. Wong et al., *Science* 277, 1971 (1997). © 1997, American Association for the Advancement of Science.

in tapping mode. In tapping-mode AFM, the cantilever was oscillated with amplitude $A_0$ above the surface. When scanning the sample, the tip struck the sample at the bottom of each oscillation cycle. Such intermittent contacts lead to a decrease of cantilever amplitude of value $A$. The set point $S$ was defined as the ratio of $A/A_0$. From the value of the set point, the authors deduced the contact force.

***Tensile Testing***  Tensile testing is the most widely used technique in macro- and microscale material characterization. In the testing of nano-objects, gripping and measuring force–displacement signatures is a major challenge. Direct stretch testing of nanotubes is hard to perform; however, ingenious experiments have been carried out.

Pan et al. [189] used a stress–strain rig to pull a very long ($\sim$2 mm) MWCNT rope containing tens of thousands of parallel tubes. They reported Young's modulus and tensile strength for this very long MWCNT. Yu et al. [164] conducted an *in-situ* SEM tensile testing of MWCNTs with the aid of a SEM nanomanipulator (Fig. 32). A single nanotube was clamped to the AFM tips by localized electron beam induced deposition of carbonaceous material inside the SEM chamber. The experiment setup consisted of three parts: a soft AFM probe (force constant less than 0.1 N/m) as a load sensor, a rigid AFM probe as an actuator, which was driven by a linear picomotor, and the nanotubes mounted between two AFM tips. Following the motion of the rigid cantilever, the soft cantilever was bent by the tensile load, equal to the force applied on the nanotube. The nanotube deformation was recorded by SEM imaging, and the force was measured by recording the deflection of the soft cantilever. The force–displacement signature was then converted to stress versus strain data, allowing modulus and strength of the MWCNTs to be measured. Yu et al. [296, 297] applied the same method to investigate the mechanical properties of ropes of SWCNTs, and the intershell friction of MWCNTs.

Cumings and Zettl [175] accomplished an *in-situ* TEM tensile testing of MWCNTs with the configuration shown
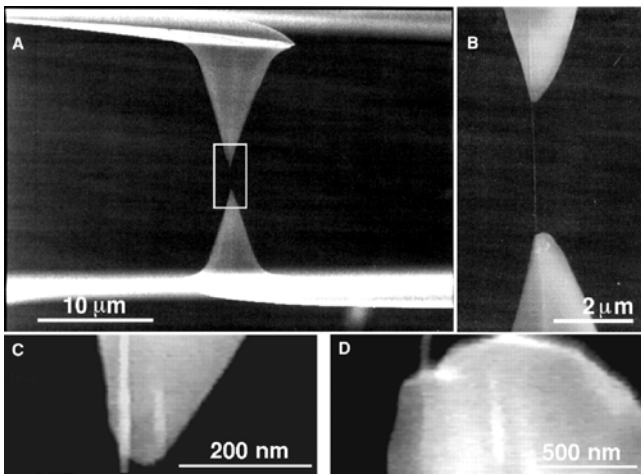


**Figure 32.** An individual MWNT mounted between two opposing AFM tips and stretched uniaxially by moving one tip. Reprinted with permission from [164], R. H. Baughman et al., *Science* 297, 787 (2002). © 2000, American Association for the Advancement of Science.
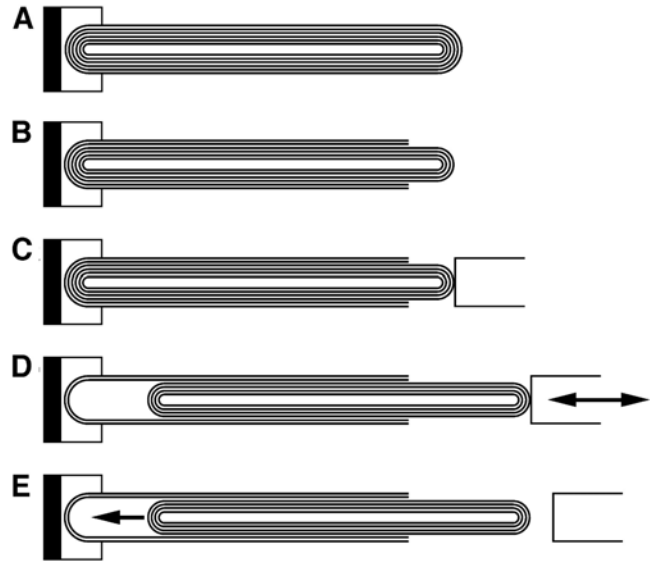


**Figure 33.** Schematic representation of the intershell experiments performed inside a TEM. Reprinted with permission from [175], J. Comings and A. Zettl, *Science* 289, 602 (2000). © 2000, American Association for the Advancement of Science.

schematically in Figure 33. A MWCNT was fixed at one end (Fig. 33a) and nanomachined at the other end to expose the inner tubes (Fig. 33b). A nanomanipulator was brought into contact with the core tubes and was spot-welded to the core by means of a short, controlled electrical current pulse (Fig. 33c). In Figure 33d and e two deformation modes are illustrated. In Figure 33d, the manipulator was moved right and left, thus telescoping the core out from or reinserting it into the outer housing of nanotube shells. The extraction and reinsertion process was repeated many times while being viewed at high TEM resolution to examine for atomic-scale nanotube surface wear and fatigue. In Figure 33e, the manipulator first telescoped the inner core out, then fully disengaged, which allowed the core to be drawn back into the outer shells by the intertube van der Waals force, consequently lowering the total system energy. A real-time video recording of the core bundle dynamics gave information pertaining to van der Waals and frictional forces between the tube shells.

***Torsional Testing***  Williams et al. [153] recently introduced a microfabricated device which offers the capability to conduct torsion tests (Fig. 34). They used an advanced fabrication technique to make this task possible. They started with depositing metal pads by photolithography. Then, alignment marks were deposited on a substrate by EBL and lift-off. The dispersion of MWCNTs onto the surface followed. SEM images were taken to help determine accurate locations of the paddles. Then the underlying silicon oxide was etched to suspend the paddles. The suspended paddles were deflected with an AFM installed inside the SEM. The AFM/SEM setup allowed direct measurements of the applied force and the paddle deflection. Assuming there is no bending, one could calculate the torque and the corresponding rotation of the nanotube. This is an original method to perform torsion test of nanotubes. However, an apparent drawback is that the applied force by the
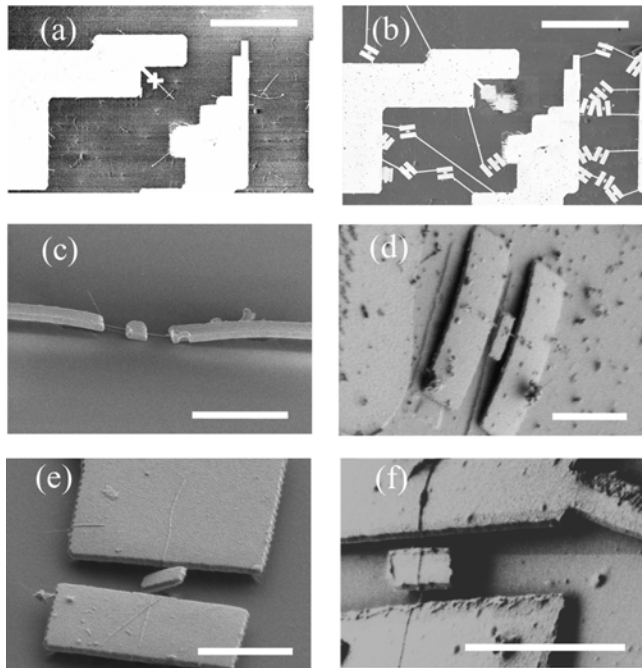
**Figure 34.** (a) Photolithographically patterned leads and EBL-patterned alignment marks (two crosshairs). (b) The same area with patterned paddles; the scale bars in (a) and (b) correspond to 40 $\mu$m. (c) The paddle touched the substrate due to the large curvature of the undercut metal leads. (d) Residual stress in the metal film and imperfect adhesion caused the leads to lift off the substrate. (e) One end of the paddle stuck to the substrate. (f) A Successfully suspended paddle. The scale bars in (c)–(f) correspond to 2 $\mu$m. Reprinted with permission from [153], P. A. Williams et al., *Appl. Phys. Lett.* 82, 805 (2003). © 2003, American Institute of Physics.

AFM introduces not only torsion but also bending of the nanotube.

## 2.3. Frontiers in Nanoscale Experimental Techniques

### 2.3.1. Limitations of Existing Techniques

Thin films have been studied with a variety of techniques including nanoindentation [15], tensile testing on millimeter and micrometer sized specimens [190–194], membrane deflection experiments [36–39, 84, 119], and *in-situ* high-resolution transmission electron microscopy (HRTEM) [195]. These techniques provided insight on various size scales including grain size effects and demonstrated that, in the case of metals, below a characteristic grain size, a transition occurs in the plastic deformation mechanism from intragranular dislocation motion to grain boundary sliding accompanied by substantial grain rotation and/or diffusion of clusters of vacancies. For the case of gold films, a grain size of 25 nm was identified as the characteristic size at which the transition is observed [195]. It should be noted that *in-situ* HRTEM findings are preliminary and that much work lays ahead. Despite these important advances, one can highlight the following limitations:

- In the case of nanoindentation and most microtensile testing of small samples, the defects responsible for the material deformation mechanisms are not imaged at the nanoscale at various loading states. Postmortem studies are conducted after unloading and further specimen micromachining.
- In the case of *in-situ* HRTEM, the current loading stages can only apply a prescribed displacement and thus do not possess the capabilities for independently measuring loads with adequate resolution. Hence the observed deformations are not accurately correlated with loading history. One exception is the MEMS-based stage being developed by Haque and Saif [131, 132].
- In the case of functional or intelligent materials, the current experimental setups do not have the electrodes and architecture needed for investigating electrical properties under stress (i.e., electromechanical coupling).

Single walled and multiwalled carbon nanotubes have been studied experimentally by means of AFM, SEM, and TEM. *A major issue in all of these studies is the scatter of the data*. For instance Young's modulus may present a scatter of more than 100%; failure strains are much smaller than the strain predicted by means of MD calculations [44]. The mechanics community has a special interest in assessing possible sources of errors and limitations of developed techniques. Among the most obvious, one can mention:

- They do not *directly and independently* measure load and deformation, as is the case in larger scale experiments. In fact, beam or string mechanics is used to infer local deformations.
- They assume homogeneous deformations because they cannot identify CNT atomic defects and monitor their evolution.
- Some use the same AFM tip to image and load the CNTs. As a result, imaging under loading is not possible.
- They cannot sense local deformations at attachment or loading points and therefore premature failure due to local deformations is not identified nor quantified.
- Most experimental configurations cannot measure specimen electronic properties under well-defined loading conditions.

New measurement tools, which can be integrated into high-resolution imaging instruments, are necessary in order to make further advances in the mechanics of CNTs, NWs, single crystal films, and polycrystalline films. MEMS technology offers unique features such as generation of micro-Newton load and nanometer displacement measurements with high resolution. It also provides the means to bridge size scales across several orders of magnitude as needed to investigate nano-objects.

### 2.3.2. A Novel MEMS Approach for In-situ Electron and Probe Microscopy

In order to overcome the aforementioned limitations, Espinosa and co-workers [196, 197] developed a new experimental setup for the testing of thin films, nanowires, and

nanotubes. The setup is an integrated MEMS device consisting of three well-defined components: an actuator, a specimen, and load sensor; see Figures 35. For the testing of thin films, the setup consists of a thermal actuator, a specimen, and a load sensor based on differential capacitance measurement. Thermal actuators have been used in the past to produce up to several milli-Newton forces. In the device shown in Figure 35a, a set of slanted beams connected to a trunk provides the actuation when a current is circulated between the fixed pads. Thermal expansion of the doped polysilicon beams results in a displacement of the trunk and, consequently, the loading of the sample [142]. The device works in displacement control, which is very advantageous in the study of thin films.

Sensors based on differential capacitance measurements are well established (e.g., Analog Devices' and Motorola's MEMS accelerometers). In this approach, the differential capacitor serves as a load sensor upon proper calibration. A readout chip, manufactured by Microsensors Co. [198], is being employed to measure differential capacitance with femtofarad resolution. The chip suppresses parasitic capacitance and provides adjustable internal capacitors to select range and resolution. Here the concept of a two-chip system, a MEMS chip for sample loading and another complementary metal oxide semiconductor chip for capacitance measurement, is employed; see Figure 35c. The movement



of the movable electrode is equal to the deformation of the folded beams in the axial direction. Capacitance change is proportional to the displacement of the movable electrode when such displacement is sufficiently small [198]. If a voltage bias $V_0$ is applied on each fixed electrode there will be a voltage change in the moving electrode, $V_{\text{sense}}$, given as

$$\frac{V_{\text{sense}}}{V_0} = \frac{\Delta d}{d} + o\left(\frac{\Delta d}{d}\right)^3 \qquad (26)$$

where $d$ is the gap between movable and fixed electrodes, $\Delta d$ is the movable electrode displacement in the axial direction, and $V_0$ is the bias voltage. If $\Delta d$ is much smaller than the gap $d$, $V_{\text{sense}}$ is proportional to $\Delta d$. When the spring constant of the folded beams is characterized, the force applied on the load cell is proportional to $V_{\text{sense}}$. Measurements of specimen deformation are achieved by *in-situ* microscopy. Direct measurement of local displacements and strains is very important. It is known that peculiarities observed in the elastic, plastic, fracture, and transport properties of thin films are directly related to atomic structure and associated defects. This point is addressed further later.

The lumped model of this device is shown in Figure 35b. Compatibility and equilibrium equations are also given in the figure. To illustrate the approach, tensile testing of polysilicon film can be examined as an example for design purposes. Considering the failure strain of polysilicon is about 1% [117], the required force from the thermal actuator to break the polysilicon specimen was calculated. The structure of the thermal actuator (e.g., number of slanted beams and geometry of each beam) was then designed after thermal analysis [199, 302]. These estimates were also verified using ANSYS multiphysics (from ANSYS Inc.). They show that the polysilicon specimen can be deformed to failure and that the resolution of a differential plate capacitor can be used to measure the load sensor motion.

For the case of CNT testing, the experimental setup is similar to that of thin film testing. One difference is that a comb-drive actuator is used (force control) instead of a thermal actuator (Fig. 36). The force to break a CNT is only several micro-Newtons, which can be achieved by a comb-drive actuator. A comb-drive actuator can accommodate a several micrometers motion range, which is required to study the nanotribological behavior of MWCNTs after the outside shell failure. Due to the limitation in space we do not provide all the details of the lumped model analysis for this device; however, we just mention that the analysis is very similar to one previously discussed for the thermal actuator.

The 3D nanomanipulator shown in Figure 37 is used to mount the nanosize specimen between the comb-drive actuator and the capacitive load sensor (Fig. 36). Several imaging tools are employed to measure specimen deformation and to identify defect initiation and evolution. In the next section, we report displacement measurement performed by DIC of AFM images obtained at various deformation levels.

### 2.3.3. In-situ AFM Results

Using the MEMS device shown in Figure 35, testing of polysilicon thin films with *in-situ* AFM displacement and strain measurements of the specimens was performed. AFM was employed to scan the specimen surface before and after
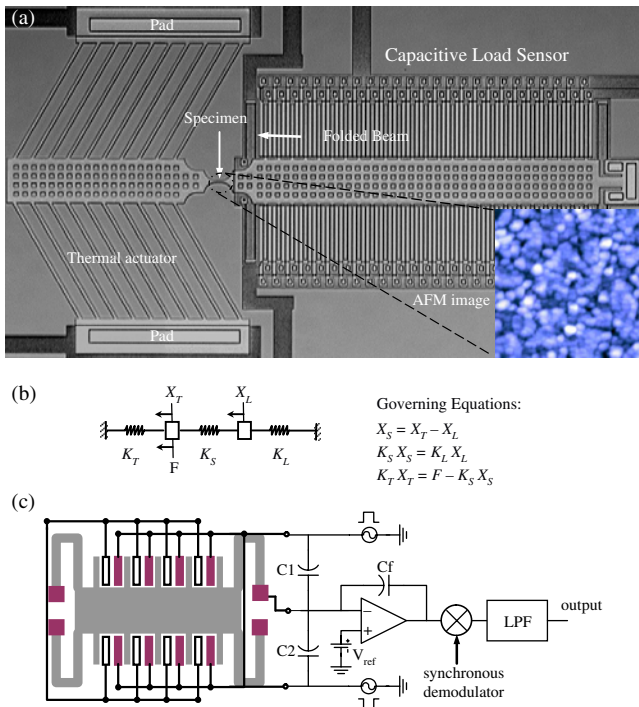
**Figure 35.** (a) MEMS device for *in-situ* AFM/SEM/TEM electromechanical characterization of polycrystalline nanoaggregates films. The whole system can fit in a 3 mm × 3 mm area. (b) Lumped model of the device shown in (a), where $X_S$ is the deformation of the specimen, $X_L$ is the displacement of the load sensor, $X_T$ is the displacement of the thermal actuator, $K_S$ is the stiffness of the specimen, $K_L$ is the stiffness of the load sensor, $K_T$ the stiffness of the thermal actuator, and $F$ is the total force generated by the thermal actuator. (c) Two-chip architecture used for measuring the load.
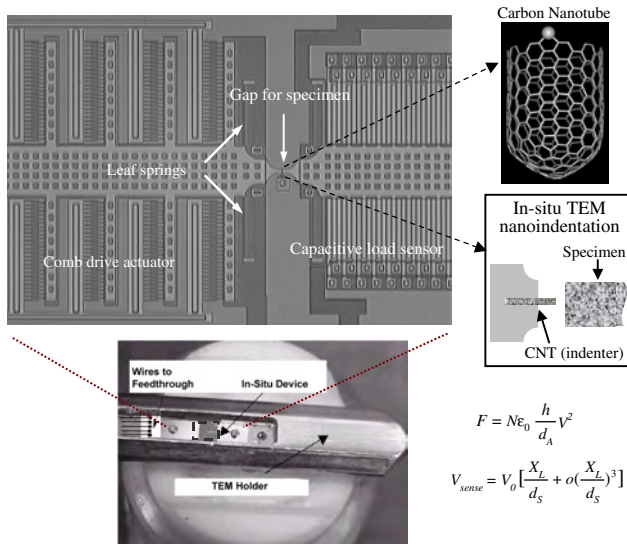
**Figure 36.** MEMS actuator for *in-situ* SEM/TEM/STM electromechanical characterization of carbon nanotubes. Various configurations will be investigated. The dimensions of the device will be such that the chip will fit in a TEM holder. Actuation and sensing pads will be wire bonded to a small breadboard and from there will be wired through the TEM holder feedthrough (see bottom image).

the loading. DIC was then used to process the AFM data to quantify the displacement/strain field. Figure 38a and b shows two AFM images of the specimen before and after loading [196, 197]. The first image was obtained before the application of a voltage to the thermal actuator, while the second image was obtained when a 5 V was applied. Figure 38c shows the displacement field obtained using DIC for a scanned area of 8 $\mu$m $\times$ 2 $\mu$m. The displacement contours show that the thermal actuator symmetrically stretched the specimen, in the *x*-direction, as expected. Moreover, the planarity of the device was investigated with an optical surface profiler and it turned out that the device was flat and parallel to the substrate within 40 nm.
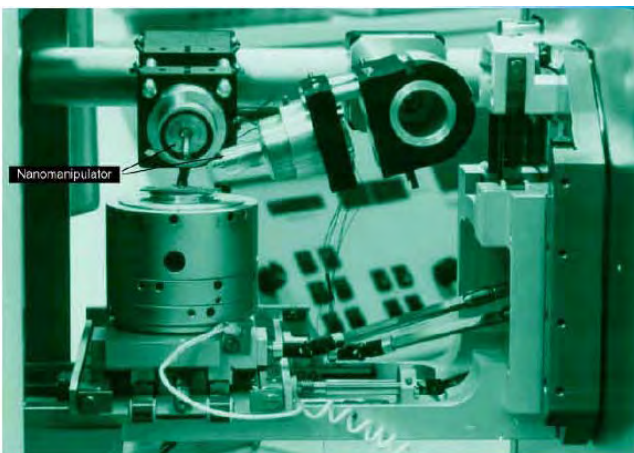


**Figure 37.** Klocke Nanotechnik nanomanipulator within a LEO field-emission SEM [159].
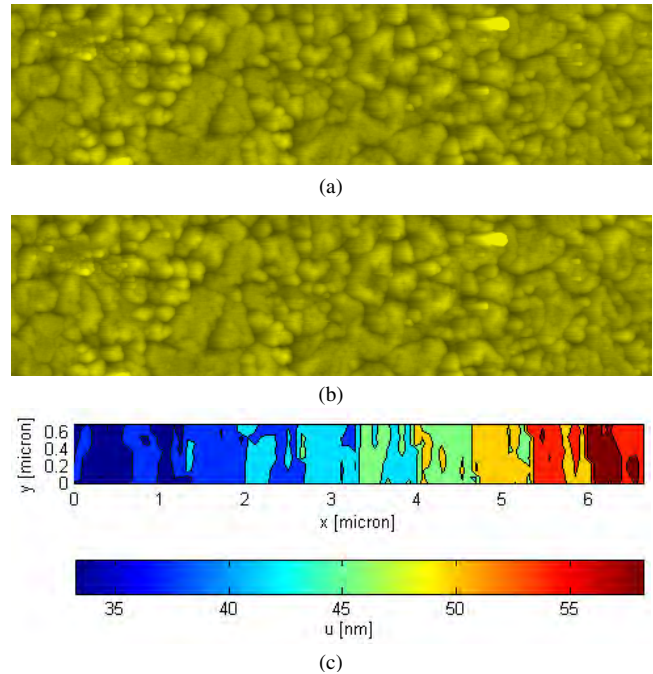


**Figure 38.** (a) AFM image of the topography of the specimen surface before loading. (b) AFM image during the loading. (c) Displacement contour computed by DIC within the area shown in (a) and (b). The load was applied in the *x*-direction. Reprinted with permission from [197], Y. Zhu et al., in "Proc. of the SEM Ann. Conf. on Exp. and Appl. Mech.," 2003. © 2003, Society for Experimental Mechanics, Inc.

## 2.3.4. Opportunities in Nanomechanical Imaging of Deformation

In this section we summarize efforts underway to elucidate deformation and failure mechanisms in thin films, nanowires, and nanotubes. Special emphasis is placed on techniques that are being used in conjunction with the MEMS setup discussed in the previous section.

In the investigation of thin films, extensive *in-situ* TEM work is essential to reveal the material behavior under stress at the grain level. Diffraction contrast and convergent beam electron diffraction at and around defects, with a beam diameter of a few angstroms, can be used to obtain lattice parameters and strain under load on ultrathin specimens. Higher order Laue zone line patterns can be compared to computer simulations of the deformed grains for this purpose. A critical aspect is the identification of dislocation sources and their densities, which are commonly assumed in atomistic, discrete dislocation, and other models.

Other TEM techniques such as weak-beam dark-field microscopy and Moire patterns for defect characterization are also possible. These techniques enhance the observation of defects such as dislocations, twins, and stacking faults on real space in real time. This effort is particularly relevant to assess the effectiveness of atomistic models in capturing defect distribution, annihilation, interaction with grain boundaries, and free surfaces. Defects sources, density, speed, and its relationship to material nanostructure and composition can also be quantified through this approach. Moreover, the onset of inelasticity and fracture characterization at the atomic level is also possible.

Stack and collaborators [161, 200, 201] have performed *in-situ* nanoindentation TEM studies by employing a TEM holder containing a piezo-actuator and a specially microfabricated wedge-shaped specimen. Observations of film deformation and nucleation of dislocations were observed in real time. Unfortunately, due to the hysterisis of the piezo-actuator and other experimental limitations, quantitative measurements of force–displacement were not possible. The MEMS device shown in Figure 36 may be one approach to overcome this limitation. Here the specimen is integrated to the load sensor during the microfabrication steps and a sharp indenter (e.g., a CNT) is mounted to the trunk of the MEMS thermal actuator using a 3D nanomanipulator (Klocke Nanotechnik Co.); see Figure 37. This 3D nanomanipulator has already been implemented for *in-situ* SEM site-specific nanowelding of carbon and other nanostructures [159].

Currently, the best TEM in the world has a point-to-point resolution of about 1 angstrom. It is anticipated that transmission electron microscopes will reach a resolution of subangstrom in the next few years by means of spherical and achromatic aberration corrections. This will make feasible the identification of *interatomic potentials* through atomic imaging of crystal planes. Using the device shown before, experiments performed on single crystal and bicrystal specimens could be employed to identify the interatomic potentials used in atomistic and molecular dynamic simulations. For particular crystal orientations, selected *a priori*, the atomic displacement field around a dislocation core or an interface could be mapped. HRTEM images of the crystal structure can be interpreted using software based on fast Fourier transform formalism and other approaches [202–204]. A cross-correlation technique can be used to assess the accuracy of the simulated images. This work would certainly constitute a milestone in materials research.

For the study of nanotubes and nanowires, TEM can provide information on chirality and other structural feature [205] but is unlikely to provide atomic images from which deformations can be computed. By contrast, ultravacuum STM has been successfully employed to obtain atomic images of CNTs [182, 183]. It remains to be determined if this imaging capability could be performed in combination with the MEMS device presented here. Capturing atomic structure under various loading degrees would be the ultimate goal in these studies.

Electromechanical properties of CNTs are of particular interest due to their potential in NEMS. Previous work by Tombler et al. [206] has shown that the conductivity of CNTs can change by several orders of magnitude when deformed by an AFM tip. The MEMS setup shown in Figure 36 has embedded interconnects and pads for electromechanical characterization of nanotubes under loading. By connecting the sensing pads to a signal analyzer, the electrical conductance can be measured under stress. Likewise, for the case of MWCNTs, sliding forces between outer and inner shells can be measured upon outer shell fracture. Therefore, on-chip nanoscale tribological properties can be identified with subnano-Newton force resolution and subnanometer displacement resolution. The main difference between previous work and the experimental approach here discussed is

that forces and atomic displacement are measured independently and directly.

# 3. MICRO- AND NANOSCALE MEASURED MATERIAL PROPERTIES

Thin films have long been harvested by the microelectronics industry for their unique properties. Conventional thinking has usually categorized their electrical properties as the property of primary importance. In the past decade and a half though, other nonelectronic, chemical and mechanical properties have also been found to have great significance [15, 93]. Mechanical properties, in particular, are critical when one is concerned with the fact that devices must have structural integrity and also be reliable throughout their life expectancy.

Thin film materials that are widely used in microdevices include metallic, silicon-based, and carbon-based substances. As diverse as these materials are in the atoms that compose them so are their properties. Processing techniques and parameters for films are numerous and directly affect the film microstructure. It is not surprising then that films of the same material that are processed by different methods can have widely varying properties. The methods employed to measure the properties listed in this section also vary significantly and therefore so do data values as well.

This section is designed to introduce the reader to thin film properties that have been measured thus far. No contrasts or categorizations are made to separate how processing or test methods affect the measured data in most cases. The scientific community has not yet come to a consensus on a uniform testing and characterization methodology by which measurements can be made and classified in a uniform and reproducible manner. Much work lies ahead before thin film behaviors, such as size effects, are fully understood and before theories capable of predicting behavior are developed. It should be noted that a number of the references garnered for this section have been previously collected in a review by Sharpe [207] and readers are directed there for additional citations.

## 3.1. Metallic Materials

Metallic materials serve many engineering functions in microdevices including both electrical and mechanical components. Metals display a wide range of mechanical behavior including elasticity, plasticity, creep, fatigue, and fracture. Only in recent years has the mechanical behavior of thin film metals become of concern in the design of microdevices. Metal films have been found to be susceptible to electromigration and other diffusion driven processes, stress and defect formation due to thermal effects, and changes in electrical behavior due to straining. These processes have deleterious effects that often lead to device failure.

The more popular metals used in microdevices include gold, aluminum, copper, and nickel. These materials are mainly deposited by sputtering or electron-beam evaporation, processes that contain numerous parameters directly

affecting microstructure. They are normally in polycrystalline form with grain size on the order of film thickness. They typically possess significant textures. Table 3 lists properties for the metals listed. With the exception of Au, Young's modulus of thin films mostly agrees with bulk polycrystalline values. Several materials showed increases in yield stress as specimen size decreased, as was previously shown for Au in Figure 5. In general, the yielding behavior of thin films tends to require larger stresses than their bulk counterparts. This is a topic of high interest to researchers and is currently a major research thrust toward the development of theories and models that can accurately predict their behavior.

## 3.2. Silicon-Based Materials

Most materials used in microdevices are silicon-based, which typically exhibit linear elastic behavior followed by brittle fracture. Silicon and silicon-based materials have been the dominant materials in the microelectronics revolution of the 20th century and the precursor to the microelectromechanical/nanoelectromechanical systems revolution currently underway. It has been the material of choice for current MEMS devices, mainly because devices can be fashioned using standard microfabrication techniques [215, 216]. The materials discussed in this section include single crystal silicon, polycrystalline silicon, silicon dioxide, silicon carbide, and silicon nitride.

Single crystal silicon has been a vehicle for the fabrication of microelectronics for several decades. It also serves as the most common structural material used in MEMS. Its electrical properties have been well characterized over the years; however, the mechanical properties, such as fatigue and fracture toughness, have only recently begun to be tackled. The mechanical properties measured thus far have been shown to be dependent on the micromachining process utilized to prepare specimens and their resulting surface conditions. The techniques employed to test single crystal specimens have been diverse and include many of the methods listed in the previous section. Table 4 provides a compilation of some results achieved over the past several years. Most of these results, in terms of Young's modulus, agree well with established benchmark values. Fracture strength varies considerably and is governed by the orientation of the crystal as well as the surface features particular to each micromachining process [217].

Polycrystalline silicon has become a commonly employed material in microdevices. It is normally employed as the structural part of the device due to its high melting point, ease of growth and micromachineability, and somewhat favorable mechanical behavior [219]. It also has the distinction of having appreciable piezoresistive behavior for the transduction of deflection or other electromechanical coupled variables. Polysilicon has been the focus of more thin film micromechanical properties measurements than any other material thus far. Table 5 lists the results from recent studies. A more complete list of experimental reports can be found in [207].

For the most part, it can be said that Young's modulus varies moderately between techniques. The same can be said for fracture strength when considering that it is a function of the surface flaws present. The effect of specimen size on fracture strength was extensively studied by Sharpe et al. [229] and Tsuchiya et al. [122]. These pioneering studies were able to show that as specimen size decreased, translating to a reduction in surface area, the fracture strength increased due to a lower population of surface flaws.

Silicon Oxide ($SiO_2$), nitride ($Si_3N_4$), and carbide (SiC), and combinations thereof, are silicon-based materials of growing importance in microdevices. They are less common than single or polycrystalline silicon as structural components due to residual stresses that develop during processing. Silicon dioxide and silicon nitride are commonly used as sacrificial layers, etch stops, or electrical/environmental passivation layers. Silicon nitride and silicon carbide are extensively used to make membranes for micropumps, pressure sensors, support for X-ray masks, etc. Table 6 lists a summary

**Table 3.** Summary of data on thin film metals.

| Material | Young's modulus (GPa) | Yield strength (GPa) | Tensile strength (GPa) | Method | Ref. |
|---|---|---|---|---|---|
| Au-size effect | 53–55 | 0.055–0.220 | 0.78–0.35 | MDE | [36, 38] |
| Au | 40–80 | — | 0.2–0.4 | tension | [2] |
| Au | 74 | 0.26 | — | indentation | [77, 208] |
| Au | 57 | — | — | bending | [77, 208] |
| Al-size effect | 65–70 | 0.150–0.180 | 0.240–0.375 | MDE | [36] |
| Al | 24.2–30.0 | 0.087–0.105 | 0.124–0.176 | tension | [209] |
| Al | 69 | — | — | tension | [128] |
| Al | 69–85 | — | — | bending | [210] |
| Cu-size effect | 125–129 | 0.200–0.345 | 0.45–0.80 | MDE | [36] |
| Cu-size effect | 120–132 | 0.120–0.480 | | tension | [211] |
| Cu | 86–173 | 0.12–0.24 | 0.33–0.38 | tension | [212] |
| Cu | 108–145 | — | — | indentation | [212] |
| Ni-thick | $176 \pm 30$ | $0.32 \pm 0.03$ | 0.55 | tension | [114] |
| Ni-thin | $231 \pm 12$ | $1.55 \pm 05$ | $2.47 \pm 0.07$ | tension | [213] |
| Ni-LIGA | $181 \pm 36$ | $0.33 \pm 0.03$ | $0.44 \pm 0.04$ | tension | [214] |
| Ni | $156 \pm 9$ | $0.44 \pm 0.03$ | — | tension | [212] |

MDE = membrane deflection experiment.

**Table 4.** Summary of data on single crystal silicon.

| Direction | Young's modulus (GPa) | Fracture strength (GPa) | Method | Ref. |
|---|---|---|---|---|
| $\langle 100 \rangle$, $\langle 110 \rangle$, $\langle 111 \rangle$ | 130, 170, 185 | — | benchmark | [86] |
| $\langle 100 \rangle$ | 168 | — | indentation | [218] |
| $\langle 100 \rangle$ (doped Si) | 60–200 | — | indentation | [151, 219] |
| $\langle 110 \rangle$ | 163–188 | 3.4 | indentation, MCD | [208] |
| $\langle 110 \rangle$ | 166–168 | — | MCD | [84, 85] |
| $\langle 110 \rangle$ | $177 \pm 18$ | 2.0–4.3 | bending | [220] |
| $\langle 110 \rangle$ (different fab.) | — | 1.0–6.8 | tension | [125] |
| $\langle 111 \rangle$, $\langle 110 \rangle$ | — | 1.3, 2.3 | tension | [221] |
| $\langle 110 \rangle$ | — | 1.2 | tension | [222] |
| $\langle 110 \rangle$ | 150 | 0.3 | tension | [223] |
| $\langle 110 \rangle$ | 147 | 0.26–0.82 | tension | [224] |
| $\langle 100 \rangle$, $\langle 110 \rangle$, $\langle 111 \rangle$ | 125–180 | 1.3–2.1 | tension | [225] |
| $\langle 100 \rangle$ | $142 \pm 9$ | 1.73 | tension | [213] |
| $\langle 110 \rangle$ | $169.2 \pm 3.5$ | 0.6–1.2 | tension | [226] |
| $\langle 100 \rangle$, $\langle 110 \rangle$, $\langle 111 \rangle$ | 115–191 | — | tension | [121] |
| $\langle 110 \rangle$ | — | 8.5–20 | torsion | [227] |
| | 75 (shear) | — | torsion | [228] |

MCD = microcantilever deflection.

of properties measured thus far. Silicon nitride and carbide both show future potential as mechanical components for microdevices due to their high Young's modulus. However, more extensive studies are required to understand how their thin film structure affects fracture strength, etc.

## 3.3. Carbon-Based Materials

Carbon in its various forms may become a key material for the manufacturing of MEMS/NEMS devices in the 21st century and will most probably displace silicon-based materials in devices. Carbon materials have exceptional and tailorable properties with the potential to meet the stringent demands that MEMS/NEMS devices and other thin film applications require. These include UNCD, diamond-like carbon, amorphous diamond, and carbon nanotubes. To date, the aggregate of testing performed on these materials is preliminary and much work is needed to confirm property measurements and comprehend their meaning.

Table 7 summarizes the current data on thin film diamond materials. The data are separated into four groups

that include ultrananocrystalline diamond, nanograined diamond, micrograined diamond, and diamond-like carbon. Each of these materials is fabricated using varying processing schemes to achieve their microstructures with the resulting mechanical behavior being a function of these processes, microstructures, and bonding characteristics. Diamond materials typically have large elastic moduli reflective of their strong cohesive binding and, being brittle in nature, fail by means of crack propagation initiated at flaw sites. The UNCD and micro- and nanograined materials all yield large elastic moduli since they are composed of crystalline grains. Diamond-like carbon is described as having an amorphous structure consisting of a mixture of $sp^2$ and $sp^3$ bonding from both graphite and diamond bonding and therefore possessing a lower elastic modulus.

Fracture strength has only recently been measured; results are listed in Table 7. It varies from 0.55 to 5.03 GPa depending on the type of material and testing technique. A typical stress–strain result for a UNCD specimen is given in Figure 39. In the gauge region, the specimen was 10 $\mu$m wide and 0.5 $\mu$m thick. The membrane deflection experiment described in Section 4 was employed. The stress–strain response of the specimen increases in a linear fashion until

**Table 5.** Summary of data on polysilicon.

| | Young's modulus (GPa) | Fracture strength (GPa) | Method | Ref. |
|---|---|---|---|---|
| MUMPs21 | 136–174 | 1.3–2.8 | tensile | [112] |
| MUMPs19 | 132 | — | tensile | [112] |
| Stress concentrations | — | 1.3–1.5 | tensile | [230] |
| Size effect | 154.1–159.6 | 1.51–1.67 | tensile | [229] |
| Size effect—doped | — | 2.0–2.8 | tensile | [122] |
| Microcantilever | $174 \pm 20$ | $2.8 \pm 0.5$ | bending | [231] |
| AFM deflection | $173 \pm 10$ | $2.6 \pm 0.4$ | bending | [232] |
| Bulk | 181–203 | — | indentation | [219] |
| Doped–undoped | 95–175 | — | indentation | [233] |

**Table 6.** Summary of data on silicon-based materials.

| Material | Young's modulus (GPa) | Fracture strength (GPa) | Method | Ref. |
|---|---|---|---|---|
| $SiO_2$ | — | 0.6–1.9 | tension | [234] |
| $SiO_2$ | 83 | — | bending | [77] |
| $SiO_2$ | 64 | 0.6 | indentation | [77] |
| $Si_3N_4$ | $222 \pm 3$ | — | bulge | [105] |
| $Si_3N_4$ | $216 \pm 10$ | — | indentation | [105] |
| SiC | $470 \pm 10$ | — | bending | [235] |
| SiC | 395 | — | indentation | [236] |

**Table 7.** Summary of data on thin film carbon-based materials.

| Material | Young's modulus (GPa) | Fracture strength (GPa) | Method | Ref. |
|---|---|---|---|---|
| UNCD (nanoseeded) | 945–963 | 3.95–5.03 | MDE | [84] |
| UNCD (microseeded) | 930–970 | 0.89–2.42 | MDE | [84] |
| UNCD | 916–959 | — | MCD | [84] |
| UNCD | 960 | — | nanoindentation | [237] |
| Nanograined diamond | 910–1150 | — | nanoindentation | [238] |
| Nanograined diamond | 675–765 | — | indentation | [239] |
| Nanograined diamond | 510 | — | laser-acoustic | [240] |
| Micrograined diamond | 1250 | — | nanoindentation | [241] |
| Micrograined diamond | 1155–1207 | — | nanoindentation | [242] |
| Micrograined diamond | 1000 | — | indentation | [243] |
| Micrograined diamond | 884–940 | — | indentation | [239] |
| Micrograined diamond | 830 | 2.72 | MCD | [244] |
| Micrograined diamond | — | 0.55–0.82 | mode I | [245, 246] |
| Diamond-like carbon | 800 | 0.7 | nanoindentation | [247, 248] |
| Diamond-like carbon | 700 | — | laser-acoustic | [249] |
| Diamond-like carbon | — | 0.8–1.0 | three-point bend | [250] |
| Diamond-like carbon | 260 | — | indentation | [251] |
| Diamond-like carbon | 60–145 | — | nanoindentation | [252] |

failure at 5.03 GPa. The slope of the plot represents the elastic modulus and was found to be 949 GPa.

It should also be mentioned that Table 7 contains data for a limited number of specimens of varying size and processing schemes and therefore effects of flaw size in relation to specimen size and processing are not defined. Fracture strengths of 0.7 to 5.03 GPa have been measured for UNCD films with the nanoseeded UNCD yielding by far the highest tensile strength [84, 85, 127].

Espinosa and co-workers have also interpreted the strength of UNCD based on Weibull statistics [127]. They showed that the Weibull parameters are highly dependent on the seeding process used in the growth of the films. When seeding was performed with micrometer size diamond particles, using mechanical polishing, the stress resulting in a probability of failure of 63% was found to be 1.74 GPa, and



**Figure 39.** Stress–strain curve representative of a typical UNCD MDE sample. An elastic modulus of 949 GPa, fracture stress of 5.03 GPa, and an estimated initial stress of 100 MPa were identified. Reprinted with permission from [84], H. D. Espinosa et al., *Exp. Mech.* (2003). © 2003, Society for Experimental Mechanics.

the Weibull modulus was 5.74. By contrast, when seeding was performed with nanosize diamond particles, using ultrasonic agitation, the stress resulting in a probability of failure of 63% increased to 4.13 GPa and the Weibull modulus was 10.76. The investigation highlights the role of microfabrication defects on material properties and reliability, as a function of seeding technique, when identical MPCVD chemistry is employed. This group is currently examining how strength is affected when specimen size is reduced to a degree where it becomes comparable to the flaw size. By employing the new membrane deflection toughness experiment developed by Espinosa and co-workers [127], the toughness of UNCD was measured to be approximately 7 MPam$^{1/2}$.

The results collected thus far demonstrate the significant mechanical advantages that carbon-based films can provide to MEMS/NEMS and their applications over other materials, particularly when extrinsic flaws such as pores and surface flaws can be further minimized and/or eliminated.

Clearly, much remains to be learned about the mechanical behavior of thin film materials. Researchers in the field must come to a consensus on a standard technique by which properties can be measured in an accurate and repeatable manner. Finally, the understanding of mechanisms involved in microstructural and specimen size effects as well as fracture and fatigue will allow the development of models capable of predicting film behavior.

### 3.3.1. Carbon Nanotubes

Most of the experimental techniques to date have been reviewed in this chapter. All have been performed to characterize the mechanical or related properties of carbon nanotubes. This section lists in tabular form the results of measurements of mechanical properties of MWCNTs and SWCNTs with focus on Young's modulus and strength. This section is intended to provide the reader not only values of mechanical properties but also the corresponding references and test methods employed in their identification.
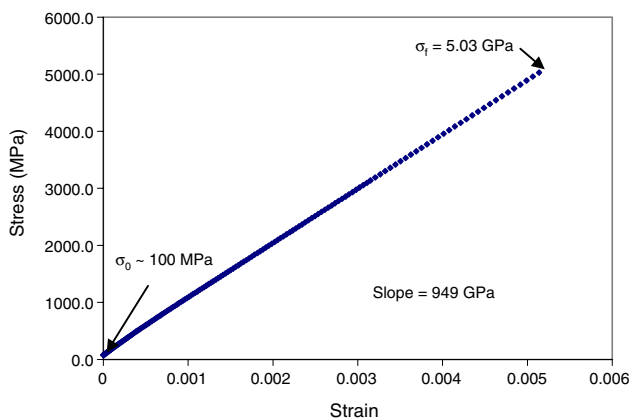
Most of the experimental measurements were conducted on MWCNTs and ropes of SWCNTs, with only one exception, that of Krishnan et al. [185] who measured Young's modulus of SWCNTs using the thermal resonance method. There exists a wide range in the reported properties primarily owing not only to different synthesis methods but also to the various assumptions used in the calculations of stress and strain.

Presently, there are several debatable issues related to the interpretation of the data. One such issue is whether CNTs behave more like a beam or a string. Most experiments have modeled the nanotube as a beam and obtained the Young's modulus based on this assumption. A typical example is the measurement done by Wong et al. [152], which correlated the distance along the nanotube and corresponding force constant. However, Walters et al. [186] argued that nanotubes behave as a string rather than a beam (Fig. 40).

Another contentious issue is whether there exists a relationship between nanotube diameter and Young's modulus. Poncharal et al. [160] and Salvetat et al. [187, 188] observed that Young's modulus decreases with increase in tube diameter. In the experiment of Poncharal et al., increasing diameter resulted in a sharp decrease of modulus. This decrease was explained due to a wavelike distortion or ripple on the inner arc of the bent nanotube for relatively thick nanotubes (Fig. 41). However, other measurements did not reveal a direct relation between the Young's modulus and tube diameter.

The existence and migration of buckles during the bending of nanotubes was observed by Falvo et al. [156]. The raised points along the tube were interpreted as buckles (Fig. 42), consistent with the increase in height as shown on the right in Figure 42a. The location of the buckles shifted dramatically, which can be seen from Figure 42b–c. The buckles in (c) appeared in regions which had been featureless, and the buckles of (b) mainly disappeared. Table 8 summarizes measured data on multiwalled carbon nanotubes.

In NEMS applications, it is essential to understand how friction, wear, and lubrication effect the relative motion of objects in contact. The tribology of carbon nanotubes includes two parts: intershell friction and nanotube/substrate
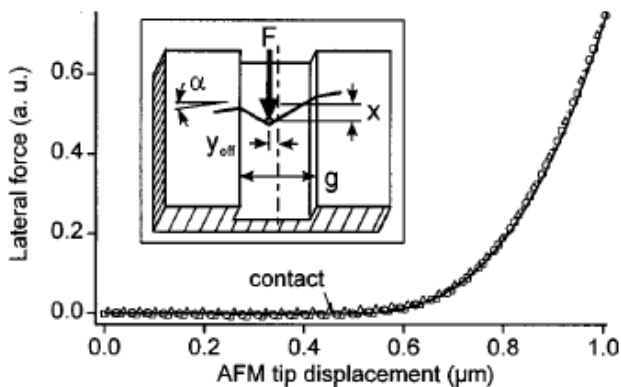


**Figure 40.** Lateral force on SWCNT rope as a function of AFM tip position. The four symbols represent data from four consecutive lateral force curves on the same rope, showing that this rope is straining elastically with no plastic deformation. Inset: the AFM tip moves along the trench, in the plane of the surface, and displaces the rope as shown. Reprinted with permission from [186], D. A. Walters et al., *Appl. Phys. Lett.* 74, 3803 (1999). © 1999, American Institute of Physics.
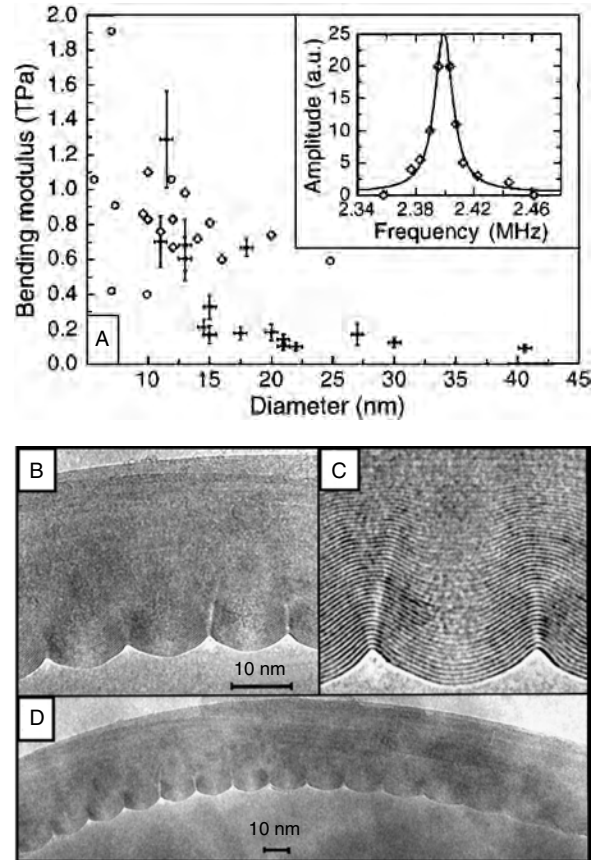


**Figure 41.** Elastic properties of nanotubes. (A) $E_b$ as a function of diameter: the dramatic drop in $E_b$ for $D \approx 12$ nm is attributed to the onset of a wavelike distortion, which appears to be the energetically favorable bending mode for thicker nanotubes. There is no remarkable change in the Lorentzian line shape of the resonance (inset) for tubes that have large or small moduli, although the low-modulus nanotubes appear to be more damped than the high-modulus tube. (D) TEM image of a bent nanotube showing the characteristic wavelike distortion. (B) and (C) Magnified views of a portion of (D). Reprinted with permission from [160], P. Poncharal et al., *Science* 283, 1513 (1999). © 1999, American Association for the Advancement of Science.

friction. Yu et al. [164] pulled the outermost shell and measured the force due to outer shell/inner shell interaction until the outermost shell broke. Cumings et al. [253] opened the end of a MWCNT and exposed the core tubes. The repeated extension and retraction of the core tubes against the outer shell did not reveal any wear or fatigue. The static friction force was estimated to be less than $6.6 \times 10^{-15}$ N/Å² and the dynamic friction force was less than $4.3 \times 10^{-15}$ N/Å².

Falvo et al. [157] studied the frictional behavior of a nanotube on two substrates: mica and graphite. On different substrates, the nanotubes preferred either rolling or sliding, depending on the pulling location. Figure 43 shows the rolling process of a CNT on a graphene substrate and the measured lateral force as a function of tip position.

The effect of mechanical deformation on the electrical properties of CNTs is of particular interest owing to the potential of CNTs in the development of nanoelectromechanical systems. Paulson et al. [254] found that changes
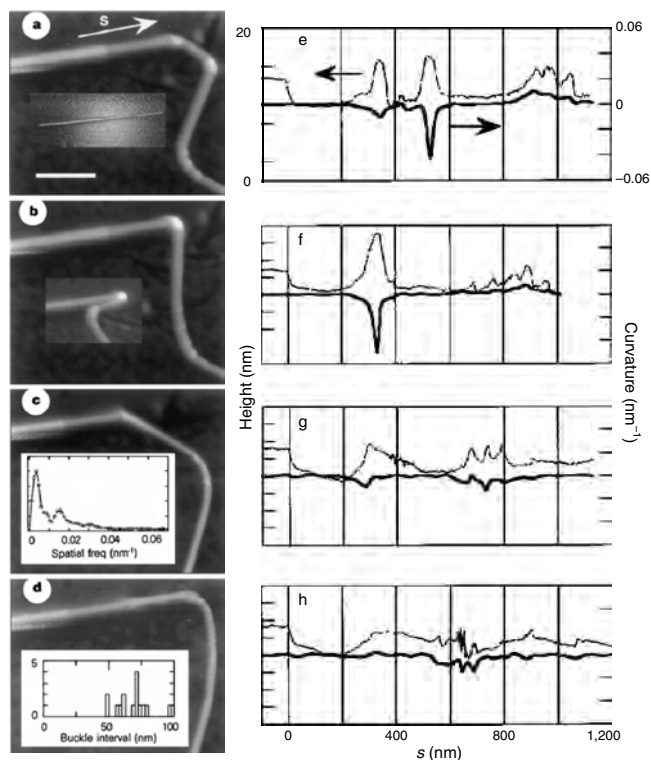
**Figure 42.** Curvature and height of buckles along a bent carbon nanotube. The white scale bar (in (a) represents 300 nm and all figures are to the same scale. A 20-nm-diameter tube was manipulated from its straight shape [(a), inset] into several bent configurations (a)–(d). The height and curvature of the bent tubes along its centerline [indicated by the arrow in (a)] are shown in (e)–(h). The upper trace in each graph depicts the height relative to the substrate; the lower trace depicts the curvature data. Height values are relative to substrate height. The "ripple"-like buckles migrate as the tube is manipulated into different configurations. The appearance and disappearance of the ripple buckles, as well as the severe buckle at $s \approx 500$ nm (e)–(f), suggest elastic reversibility. The large buckle at $s \approx 325$ nm (e), (f) retains its raised topographical features even after straightening (g), (h), suggesting that damage has occurred at this point; but the tube does not fracture. The average of the buckle interval histogram [(d), inset] and the average of the Fourier transforms [(c), inset] for a wide range of bent configurations establish the dominant interval as 68 nm. Reprinted with permission from [156], M. R. Falvo et al., *Nature* 389, 582 (1997). © 1997, American Association for the Advancement of Science.

in nanotube resistance were small unless the nanotubes fractured or the metal–nanotube contacts were perturbed. However, Tombler et al. [206] succeeded in bending individual SWNTs with an AFM tip and measuring conductance as a function of deflection. The study revealed that the conductance of SWCNT changed dramatically under the applied deformation. Figure 44 represents the schematic of their experiment and measured values. Quantum mechanical modeling was employed to verify and explain the experimental findings. The conclusion reached by the authors was that interaction between the AFM tip and the SWCNT deformed the nanotube to a point where the bonding in the nanotube was converted from $sp^2$ to $sp^3$. However, in previous studies, the nanotubes were more or less uniformly bent or strained; hence, the chemical bonding evidently remained $sp^2$.

**Table 8.** Multiwalled carbon nanotube.

| Method | Young's modulus (TPa) | Strength (GPa) | Comments | Ref. |
|---|---|---|---|---|
| Thermal vibration | 1.8 | — | | [184] |
| Electrostatic vibration | 0.1–1 | — | varies with diameter | [160] |
| Lateral force bending | $1.28 \pm 0.59$ | $14.2 \pm 8.0$ | | [152] |
| Contact force bending | $0.81 + 0.41$ $0.81–0.16$ | | arc-discharge MWCNT | [188] |
| Radial indentation | 0.0097–0.08 | >5.3 | compressive modulus and strength | [154] |
| Tensile test | $0.45 \pm 0.23$ | $1.72 \pm 0.64$ | very long MWCNT | [189] |
| Tensile test | 0.27–0.95 | 11–63 | outermost layer | [164] |
| Torsion test | $0.6^a$ | | | [153] |

$^a$ Shear modulus $G$.
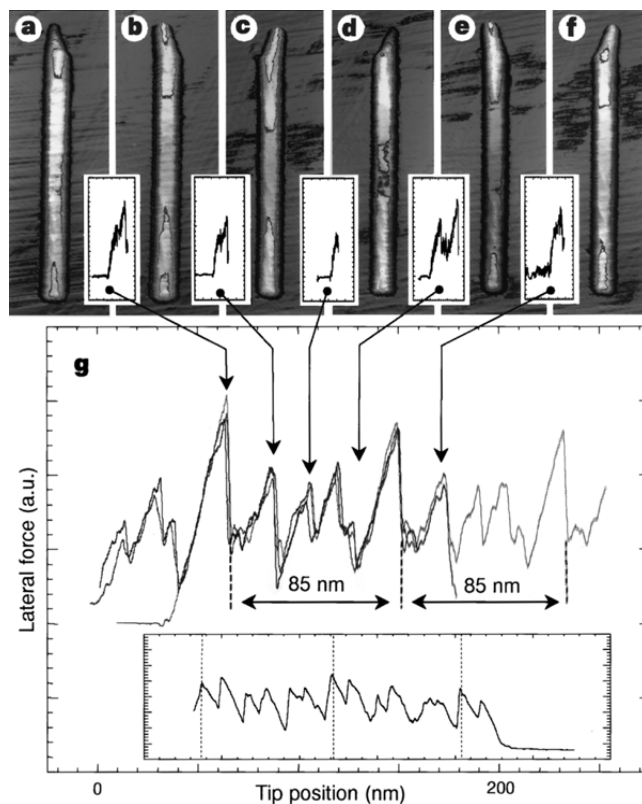


**Figure 43.** Rolling behavior of CNTs on the graphene substrate (a)–(f) as it is manipulated from left to right. The tube is imaged before and after each of the five manipulations. The insets between each topographical image show the lateral force during each manipulation. The tube is moving from left to right, not gradually but in sudden slips in a stick–slip type rolling motion. In (g), three overlapped signals from separate rolling trials are shown for the lateral force as the tube is pushed through several revolutions of stick–slip rolling motion. The features of the force traces are reproducible. The 85 nm periodicity in the signal, indicated by the dashed lines, is equal to the circumference of the tube at its ends. Reprinted with permission from [157], M. R. Falvo et al., *Nature* 397, 236 (1999). © 1999, Macmillan Publishers Ltd.
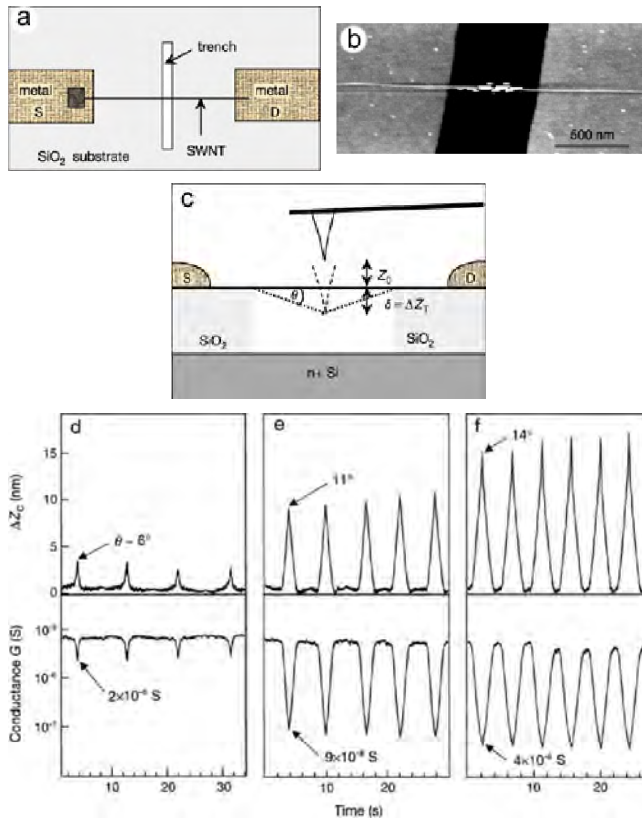
**Figure 44.** Bending of SWCNT by an AFM tip and the corresponding electrical conductance evolution. (a) Top view of an SWCNT partly suspended over a trench for electromechanical measurements; (b) AFM image of an SWCNT with suspended length $l \approx 605$ nm; (c) Side view of the AFM pushing suspended SWCNT. (d)–(f) cantilever deflection and nanotube electrical conductance evolution during repeated cycles of pushing the suspended SWCNT. $\theta$ is the tube bent angle. Initial tip–tube distance is 65 (d), 30 (e), and 8 nm (f), and the speed of the tip motion was about 22 (d), 34 (e), and 44 nm/s (f). It is seen that the conductance of an SWCNT is reduced by two orders of magnitude when deformed by an AFM. Reprinted with permission from [206], T. W. Tombler et al., *Nature* 405, 769 (2000). © 2000, Macmillan Publishers Ltd.

# 4. THEORETICAL MODELING AND SCALING

During the 1980s and 1990s, a host of experiments on the micrometer and submicrometer scale, including microindentation [15], microtorsion [29, 30], and microbending [28], revealed a strong size effect on the yield strength and hardening of metals. Similar size effects were observed also in metal matrix composites with particle diameters in the micrometer and submicrometer scale [255, 256]. The classical plasticity theories cannot predict these size effects because they involve no material characteristic length. To explain them, several strain gradient theories were developed. The first one was a phenomenological theory by Fleck and Hutchinson [30] based on the existence of a potential. This theory was later extended and improved, in several versions [31, 257, 258] while retaining the same basic structure. Another strain gradient theory which received considerable attention was the mechanism-based strain-gradient

(MSG) theory [33, 35] derived under certain simplifying assumptions from the concept of geometrically necessary dislocations. Based on numerical experience, this theory was recently improved as the Taylor-based nonlocal (TNT) theory [259], and the improvement consisting in the form of strain gradient dependence of the hardening function, made the theory conform to a revision proposed by Bažant [260, 261] on the basis of scaling analysis. Another noteworthy theory was Acharya and Bassani's strain gradient plasticity theory based on the idea of lattice incompatibility [262, 263], which represented a generalization of the incremental theory of plasticity. The asymptotic characters of these strain gradient theories were analyzed recently and it was found that the small-size asymptotic size effect predicted by some of the theories is excessive and unreasonable [259–261].

It might seem that the small-size asymptotic behavior of gradient plasticity is irrelevant because it is approached only at sizes below the range of validity of theory, for which the spacing of the geometrically necessary dislocations (about 10 to 100 nm) and the crystal size are not negligible, and other physical phenomena, such as surface tension, gradation of crystal size, and texture, intervene. However, knowledge of both the small-size and large-size asymptotics is very useful for developing asymptotic matching approximations for the intermediate range, for which the solutions are much harder to obtain. For the purpose of asymptotic matching, the asymptotic behavior must be physically reasonable even if attained outside the range of validity of the theory (this has been demonstrated in the modeling of cohesive fracture when the small-size plastic asymptote is often approached only for specimen sizes much smaller than the inhomogeneity size, e.g., the aggregate size in concrete [260]).

The present chapter reviews and summarizes several recent papers in which it was shown that the main theories proposed in the past, including couple stress theory, stress and rotation gradient theory, MSG, TNT, and the Acharya and Bassani's theory, suffer from excessive asymptotic size effect and some exhibit an unrealistic shape of the load-deflection curve. Simple adjustments of all these theories suffice to achieve reasonable asymptotic behavior and thus to make asymptotic matching approximations feasible.

The main strain gradient theories will be briefly introduced and their asymptotic analysis presented by Bažant and Guo [264] will be outlined. After that, a simple asymptotic-matching approximation, suitable for predictions of yield limit and plastic hardening on the micrometer scale, will be presented.

## 4.1. Strain Gradient Theories

First we will consider Fleck and Hutchinson's phenomenological strain gradient theory [29, 30] and its successive versions. In these theories, the effect of strain gradient tensor is incorporated into the potential energy density function, in a manner similar to the classical theories of Toupin [265] and Mindlin [266] in which only linear elasticity was considered. A higher order stress tensor needs to be introduced in these theories to provide a work conjugate to the strain gradient tensor, and the boundary condition of classical solid mechanics also needs to be modified as well. The classical $J_2$ deformation theory of plasticity (i.e., Hencky-type solid

strain theory) is chosen as the basis of strain gradient generalization.

Gao and Huang's MSG theory [33, 35] does not use the potential energy approach (and actually, potential energy even does not exist in that theory). Rather, this theory is based on the Taylor relation between the shear strength and dislocation density. A multiscale framework is used to introduce the higher order stress tensor and to establish the virtual work balance. Numerical simulations showed that while the higher order stress tensor is affected by the material length characterizing the size of the framework cell (called the mesoscale cell), the stress and strain tensors are almost unaffected. This observation triggered a reformulation in the form of the TNT theory [259], in which the strain gradient is numerically simulated as a nonlocal variable and the higher order stress disappears. This reformulation coincided with a revision proposed by Bažant [260, 261] for entirely different reasons—namely, the observation that the presence of couple stresses, dictated by the use of a strain gradient tensor as an independent kinematic variable, causes an excessive small-size asymptotic size effect, indicating that couple stresses should be removed from the formulation.

Acharya and Bassani's strain gradient theory [262, 263] differs significantly from the previous theories. It represents a generalization of incremental plasticity rather than total strain theory. The effect of a strain gradient is considered by changing the tangential modulus in the constitutive relation, while the framework of classical plasticity theory remains.

### 4.1.1. Fleck and Hutchinson's Theories

The first phenomenological strain-gradient theory developed by Fleck and Hutchinson [29, 30] is called the couple stress theory (denoted by CS). The subsequent modification [31] is called the stretch and rotation gradients theory (denoted by SG). Since the main idea of these two theories is the same, we will consider them jointly. To simplify the problem, only incompressible materials will be considered and the elastic part will be ignored because it is negligible compared to large plastic deformation of metals.

In the classical work of Toupin [265] and Mindlin [266], and dealing only with the linear elasticity case, the strain gradient is introduced into the strain energy density $W$ as

$$W = 1/2\lambda\varepsilon_{ii}\varepsilon_{jj} + \mu\varepsilon_{ij}\varepsilon_{ij} + a_1\eta_{ijj}\eta_{ikk} + a_2\eta_{iik}\eta_{kjj}$$
$$+ a_3\eta_{iik}\eta_{jjk} + a_4\eta_{ijk}\eta_{ijk} + a_5\eta_{ijk}\eta_{kij} \qquad (27)$$

where $\lambda$ and $\mu$ are the usual Lamé constants, $\varepsilon_{ij} = (u_{i,j} + u_{j,i})/2$ is the strain, $\eta_{ijk} = u_{k,ij}$ is the component of strain gradient tensor $\boldsymbol{\eta}$, and $a_n$ is the additional elastic stiffness constant of the material. The sum of the first two terms on the right-hand side is the classical strain energy density function, while the other five terms are the contributions of the strain gradient tensor. Based on the strain energy density defined as (27), the Cauchy stress $\sigma_{ij}$ can be defined as a work conjugate to $\varepsilon_{ij}$ (i.e. $\sigma_{ij} = \partial W/\partial\varepsilon_{ij}$). A higher order stress tensor $\boldsymbol{\tau}$, work conjugate to the strain gradient tensor $\boldsymbol{\eta}$, needs to be defined as $\tau_{ijk} = \partial W/\partial\eta_{ijk}$. The strain energy $W$ defined by (22) represents a linear elastic constitutive relation. There are many ways to extend it to a general nonlinear plastic material. Fleck and Hutchinson [31] chose to

do it by defining a new variable, a scalar called the combined strain quantity, $E$, which involves both the strain tensor and the strain gradient tensor, to replace the effective strain in the $J_2$ theory. $W$ is then assumed, for a general nonlinear plastic material, to be a nonlinear function of $E$. To define $E$, the strain gradient tensor $\boldsymbol{\eta}$ needs to be decomposed into a hydrostatic part $\boldsymbol{\eta}^H$ and deviatoric part $\boldsymbol{\eta}'$:

$$\eta_{ijk}^H = (\delta_{ik}\eta_{jpp} + \delta_{jk}\eta_{ipp})/4 \qquad \boldsymbol{\eta}' = \boldsymbol{\eta} - \boldsymbol{\eta}^H \qquad (28)$$

Due to incompressibility, we have $\varepsilon_{ij}' = \varepsilon_{ij}$, $\eta_{ijk}' = \eta_{ijk}$. Furthermore, $\boldsymbol{\eta}'$ is decomposed into three orthogonal parts $\boldsymbol{\eta}' = \boldsymbol{\eta}'^{(1)} + \boldsymbol{\eta}'^{(2)} + \boldsymbol{\eta}'^{(3)}$ such that $\eta_{ijk}'^{(m)}\eta_{ijk}'^{(n)} = 0$ when $m \neq n$ [31]; the three invariants $\eta_{ijk}'^{(n)}\eta_{ijk}'^{(n)}$ are used to define $E$,

$$E = \sqrt{2\varepsilon_{ij}'\varepsilon_{ij}'/3 + \ell_1^2\eta_{ijk}'^{(1)}\eta_{ijk}'^{(1)} + \ell_2^2\eta_{ijk}'^{(2)}\eta_{ijk}'^{(2)} + \ell_3^2\eta_{ijk}'^{(3)}\eta_{ijk}'^{(3)}}$$
$$(29)$$

where $\ell_i$ are three length constants which are given different values in different version of the theory.

$$\text{For CS:} \quad \ell_1 = 0 \quad \ell_2 = \ell_{CS}/2 \quad \ell_3 = \sqrt{5/24}\ell_{CS} \qquad (30)$$

$$\text{For SG:} \quad \ell_1 = \ell_{CS} \quad \ell_2 = \ell_{CS}/2 \quad \ell_3 = \sqrt{5/24}\ell_{CS} \qquad (31)$$

Here $\ell_{CS}$ is called the material characteristic length. If the strain gradient part is ignored, scalar $E$ becomes identical to the effective strain $\varepsilon$ used in the classical plasticity theories.

Now the strain energy density $W$ can be expressed as a function of $E$ instead of $\varepsilon$ as $W = W(E)$; thus the Cauchy stress tensor $\boldsymbol{\sigma}$ and the higher order stress tensor $\boldsymbol{\tau}$ can be expressed as

$$\sigma_{ij} = \frac{\partial W}{\partial\varepsilon_{ij}} = \frac{dW}{dE}\frac{\partial E}{\partial\varepsilon_{ij}} = \frac{2\varepsilon_{ij}}{3E}\frac{dW}{dE} \qquad (32)$$

$$\tau_{ijk} = \frac{\partial W}{\partial\eta_{ijk}} = \frac{dW}{dE}\frac{\partial E}{\partial\eta_{ijk}}$$

$$= \frac{dW}{E\,dE}\left(\ell_1^2\eta_{lmn}'^{(1)}\frac{\partial\eta_{lmn}'^{(1)}}{\partial\eta_{ijk}} + \ell_2^2\eta_{lmn}'^{(2)}\frac{\partial\eta_{lmn}'^{(2)}}{\partial\eta_{ijk}} + \ell_3^2\eta_{lmn}'^{(3)}\frac{\partial\eta_{lmn}'^{(3)}}{\partial\eta_{ijk}}\right)$$

$$= \frac{\ell_{CS}^2 C_{ijklmn}\eta_{lmn}dW}{E\,dE} \qquad (33)$$

Here $C_{ijklmn}$ is a six-dimensional constant dimensionless tensor [264]. Since the values of $\ell_i$ are different in CS and SG theories, the tensor $\mathbf{C}$ will also be different in these two theories, although for each of them $\mathbf{C}$ is a constant tensor, that is, independent of $\varepsilon$, $\boldsymbol{\eta}$, and $\ell_{CS}$. Because of the existence of higher order stress, the field equations of equilibrium must be generalized as

$$\sigma_{ik,i} - \tau_{ijk,ij} + f_k = 0 \qquad (34)$$

where $f_k$ is the body force.

### 4.1.2. Gao and Huang's MSG Theory and TNT Theory

As the first strain gradient theory based on geometrically necessary dislocations, the MSG theory is a generalization of the incremental theory of plasticity [267]. In the MSG theory, the definition of strain gradient tensor $\eta_{ijk} = u_{k,ij}$ is the same as it is in Fleck and Hutchinson's theories, but the definition of higher order stress is different. It is defined by virtual work balance in a multiscale framework. The final constitutive relation reads [33, 260, 261, 264]

$$\sigma_{ik} = K\delta_{ik}\varepsilon_{nn} + \frac{2\sigma}{3\varepsilon}\varepsilon'_{ik} \qquad \tau_{ijk} = l^2_\varepsilon \left( \frac{K}{6}\eta^H_{ijk} + \sigma\Phi_{ijk} + \frac{\sigma^2_Y}{\sigma}\Psi_{ijk} \right) \tag{35}$$

where

$$\Phi_{ijk} = \frac{1}{\varepsilon}(\Lambda_{ijk} - \Pi_{ijk}) \qquad \Psi_{ijk} = f(\varepsilon)f'(\varepsilon)\Pi_{ijk} \tag{36}$$

$$\varepsilon = \sqrt{2\varepsilon'_{ij}\varepsilon'_{ij}/3} \qquad \eta = \sqrt{\eta'_{ijk}\eta'_{ijk}/2} \tag{37}$$

$$\sigma = \sigma_Y\sqrt{f^2(\varepsilon) + l\eta}$$

and

$$\Lambda_{ijk} = [2\eta_{ijk} + \eta_{kji} + \eta_{kij} - (\delta_{ik}\eta_{ppj} + \delta_{jk}\eta_{ppi})/4]/72$$

$$\Pi_{ijk} = [\varepsilon_{ik}\eta_{jmn} + \varepsilon_{jk}\eta_{imn} - (\delta_{ik}\varepsilon_{jp} + \delta_{jk}\varepsilon_{ip})\eta_{pmn}/4] \\ \times \varepsilon_{mn}/54\varepsilon^2 \tag{38}$$

$$\eta^H_{ijk} = (\delta_{ik}\eta_{jpp} + \delta_{jk}\eta_{ipp})/4 \qquad \eta'_{ijk} = \eta_{ijk} - \eta^H_{ijk}$$

where $K$ is the elastic bulk modulus. Equation (37) defines the new hardening rule of the material in which $\sigma_Y$ is the yield stress; $\varepsilon$ and $\sigma$ are the effective strain and stress; $\eta$ is the effective strain gradient, which is proportional to the density of geometrically stored dislocations; $\sigma_Y f(\varepsilon)$ represents the classical plastic hardening function; $l$ is the material intrinsic length (similar to parameter $\ell_{CS}$ used in Fleck and Hutchinson's theories [29–31]); $\varepsilon'_{ij} = \varepsilon_{ij} - \varepsilon_{nn}/3$ is the deviatoric strain; $\eta^H_{ijk}$ is the volumetric part of strain gradient tensor; and $l_\varepsilon$ is the size of the so-called "mesoscale" cell which is expressed by Gao et al. [33] as

$$l_\varepsilon = \beta(G/\sigma_Y)b \tag{39}$$

Here $G$ is the shear modulus, $b$ is the Burgers vector, and $\beta$ is an empirical factor whose value is suggested to be between 1 to 10 [33]. The equilibrium equations are the same as (29). It is also interesting to consider a more general hardening relation,

$$\sigma = \sigma_Y[f^q(\varepsilon) + (l\eta)^p]^{1/q} \tag{40}$$

where $p$ and $q$ are positive exponents; and MSG theory corresponds to the case $p = 1$, $q = 2$.

When the MSG theory is used in numerical simulations, the results show that when the value of $l_\varepsilon$ is changed, the stress and strain do not change much, although the higher order stress does. This means that the existence of the higher order stress offers no advantage [35] (aside from the fact that they make the asymptotic scaling problematic

[261, 264]). Upon noticing this fact, the MSG theory has been replaced by the TNT theory, in which the higher order stress tensor is removed.

In the TNT theory, the strain gradient is not an independent variable but a nonlocal variable defined by numerical integration. The gradient term $\varepsilon_{ij,k}$ can be numerically approximated in a nonlocal form as follows [259]

$$\varepsilon_{ij,k} = \int_{V_{cell}} [\varepsilon_{ij}(\mathbf{x} + \xi) - \varepsilon_{ij}(\mathbf{x})]\xi_m \, dV \left( \int_{V_{cell}} \xi_k \xi_m \, dV \right)^{-1} \tag{41}$$

in which $V_{cell}$ is a sufficiently small representative cell surrounding point described by $\mathbf{x}$. To simplify the integration, $V_{cell}$ can be chosen as a cube centered at $\mathbf{x}$, and then the strain gradient $\eta_{ijk}$ can be expressed as

$$\eta_{ijk} = \frac{1}{I_\varepsilon} \int_{V_{cell}} [\varepsilon_{ik}\xi_j + \varepsilon_{jk}\xi_i - \varepsilon_{ij}\xi_k] \, dV \quad \text{with}$$

$$I_\varepsilon = \int_{V_{cell}} \xi^2_1 \, dV = \frac{1}{12}l^5_\varepsilon \tag{42}$$

where $l_\varepsilon$ is the size of the cube. Furthermore, one may introduce the volumetric part $\boldsymbol{\eta}^H$ and the deviatoric part $\boldsymbol{\eta}'$ of tensor $\boldsymbol{\eta}$, and the effective strain gradient invariant $\eta = \sqrt{\eta'_{ijk}\eta'_{ijk}/2}$, which is identical to that defined in the MSG theory. Because the strain gradient tensor does not function in (40) as an independent kinematic variable, we need not define the corresponding work-conjugate higher order stress tensor. For $p = 1$, $q = 2$, the constitutive relation is [259]

$$\sigma_{ik} = K\delta_{ik}\varepsilon_{nn} + \frac{2\sigma}{3\varepsilon}\varepsilon'_{ik}$$

where

$$\sigma = \sigma_Y\sqrt{f^2(\varepsilon) + l\eta} \tag{43}$$

Since the new higher order stress is absent, the equilibrium equation of the TNT theory is the same as in the classical theory (i.e., $\sigma_{ij,i} + f_j = 0$).

### 4.1.3. Acharya and Bassani's Theory

Acharya and Bassani's strain gradient theory is a generalization of the classical incremental plasticity theory, in which the strain gradient is assumed to affect only the instantaneous modulus. The strain gradient is considered to be a measure of lattice incompatibility and is introduced only through the second-order tensor as [262, 263]

$$\alpha_{ij} = e_{jkl}\varepsilon^p_{il,k} \tag{44}$$

where $e_{jkl}$ is the alternating symbol and $\varepsilon^p$ is the plastic strain. Introducing the invariant:

$$\alpha = \sqrt{2\alpha_{ij}\alpha_{ji}} \tag{45}$$

Acharya and Bassani modified the classical $J_2$ flow theory as follows [262, 263]:

$$\tau = \sqrt{\sigma'_{ij}\sigma'_{ij}/2} \qquad \dot{\tau} = \dot{\tau}_{cr} = h(\gamma^p, \alpha)\dot{\gamma}^p \tag{46}$$

$$\dot{\varepsilon}^p_{ij} = (\dot{\gamma}^p/2\tau)\sigma'_{ij} \qquad \dot{\sigma}_{ij} = C_{ijkl}(\dot{\varepsilon}_{kl} - \dot{\varepsilon}^p_{kl}) \qquad \gamma^p = \sqrt{2\varepsilon^p_{ij}\varepsilon^p_{ij}/3} \tag{47}$$

Here the instantaneous hardening modulus $h$ depends not only on plastic strain invariant $\gamma^p$ but also on plastic strain gradient invariant $\alpha$. An example of this function is as follows [262, 263]

$$h(\gamma^p, \alpha) = h_0\left(1 + \frac{\gamma^p}{\gamma_0}\right)^{N-1}\left[1 + \frac{l^2(\alpha/\gamma_0)^2}{1 + c(\gamma^p/\gamma_0)^2}\right]^{1/2} \quad (48)$$

where $l$ is the material intrinsic length, and $h_0$, $\gamma_0$, $c$, and $N$ are positive material constants.

There exist other strain gradient theories, but generally they are similar to one of the theories introduced here. For example, Chen and Wang's [268, 269] strain gradient theory is similar to Fleck and Hutchinson's theories.

## 4.2. Asymptotic Analysis of Strain Gradient Theories

For the purpose of scaling analysis, we need to consider geometrically similar structures of different sizes. This means that the structures are also similarly loaded. It is obvious that the strain gradient theories must reduce to the classical plasticity theory when the structure size is very large. To discuss the asymptotic cases, it is necessary to introduce dimensionless variables. Diverse sets of such variables could be chosen but only the following one is easy to interpret,

$$\bar{x}_i = x_i/D \qquad \bar{u}_i = u_i/D \qquad \bar{\varepsilon}_{ij} = \varepsilon_{ij}$$
$$\bar{\eta}_{ijk} = \eta_{ijk}D \qquad \bar{f}_k = f_k D/\sigma_N \quad (49)$$

where $D$ is the characteristic length of the structure, and $\sigma_N$ is the nominal strength. For geometrically similar structures the strain distribution may often be assumed to be the same, and then $\bar{x}_i$, $\bar{u}_i$, $\bar{\varepsilon}_{ij}$, and $\bar{\eta}_{ijk}$ will be size independent; that is, they will be the same for structures of different sizes. Consequently, the asymptotic behavior of the strain gradient tensor must be $\eta_{ijk} \propto 1/D$.

### 4.2.1. Asymptotic Analysis of Fleck and Hutchinson's Theories

***Scaling and Size Effect*** Fleck and Hutchinson's strain gradient theory can be used to generalize various particular forms of classical constitutive relations for plasticity. A stress–strain relation in the form of a general power law relation may be chosen as an example, in which the strain energy density is [29–31]

$$W = \frac{n}{n+1}\sigma_0 E_0\left(\frac{E}{E_0}\right)^{(n+1)/n} \quad (50)$$

where $\sigma_0$, $E_0$, and $n$ are positive material constants. For hardening materials, $n \geq 1$; typically $n \approx 2$–$5$ for normal metals. According to (32) and (33), the constitutive relation then reads

$$\sigma_{ik} = \frac{2}{3}\sigma_0\left(\frac{1}{E_0}\right)^{1/n}E^{(1-n)/n}\varepsilon_{ik} \quad (51)$$

$$\tau_{ijk} = \sigma_0\left(\frac{1}{E_0}\right)^{1/n}\ell_{CS}^2 E^{(1-n)/n}C_{ijklmn}\eta_{lmn} \quad (52)$$

It is now useful to define dimensionless variables:

$$\bar{\tau}_{ijk} = \tau_{ijk}/(E_0\ell_{CS}) \qquad \bar{\sigma}_{ij} = \sigma_{ij}/\sigma_0 \qquad \overline{E} = E$$
$$\bar{\eta}_{ijk}^{(l)} = \eta_{ijk}^{\prime(l)}D \qquad (l = 1, 2, 3) \quad (53)$$

Then the constitutive relation can be expressed as

$$\bar{\sigma}_{ik} = \frac{2}{3}\left(\frac{1}{E_0}\right)^{1/n}\overline{E}^{(1-n)/n}\bar{\varepsilon}_{ik} \quad (54)$$

$$\bar{\tau}_{ijk} = \left(\frac{1}{E_0}\right)^{1/n}\frac{\ell_{CS}}{D}\overline{E}^{(1-n)/n}C_{ijklmn}\bar{\eta}_{lmn} \quad (55)$$

The equilibrium equation (29) can be rewritten as

$$\partial_i\bar{\sigma}_{ik} - \frac{\ell_{CS}}{D}\partial_i\partial_j\bar{\tau}_{ijk} + \frac{\sigma_N}{\sigma_0}\bar{f}_k = 0 \quad (56)$$

where $\partial_i = \partial/\partial\bar{x}_i = $ derivatives with respect to the dimensionless coordinates. Substituting (49) and (55) into (56), one obtains the dimensionless field equation of equilibrium in the form

$$\frac{2}{3}\left(\frac{1}{E_0}\right)^{1/n}\partial_i\left(\overline{E}^{(1-n)/n}\bar{\varepsilon}_{ik}\right) - \left(\frac{\ell_{CS}}{D}\right)^2\left(\frac{1}{E_0}\right)^{1/n}$$
$$\times \partial_i\partial_j\left(C_{ijklmp}\overline{E}^{(1-n)/n}\bar{\eta}_{lmp}\right) = -\frac{\sigma_N}{\sigma_0}\bar{f}_k \quad (57)$$

Following Bažant [260, 261] and Bažant and Guo [264], we may simplify the analysis by replacing the surface fractions with body forces applied in a very thin boundary layer, the thickness of which tends to zero. This ensures that all the boundary conditions are homogeneous. When the structure is sufficiently large, $\ell_{CS}/D \to 0$, $\bar{\tau}_{ijl}$ vanish, according to (55), and the equilibrium equations reduce to the classical equilibrium equations, as required. The combined strain quantity, $E$, reduces to the classical effective strain because the strain gradient part can be ignored compared to the strain part. Then the strain energy density function takes the normal form as a function of the strain only.

As proposed by Bažant and Guo [264], it is interesting to look at the opposite asymptotic character of the theory when the structure size tends to zero, $\ell_{CS}/D \to \infty$. At first, the dimensionless combined strain quantity can be rewritten as

$$\overline{E} = \sqrt{2\varepsilon_{ij}'\varepsilon_{ij}'/3 + \left(\ell_1^2\bar{\eta}_{ijk}^{\prime(1)}\bar{\eta}_{ijk}^{\prime(1)} + \ell_2^2\bar{\eta}_{ijk}^{\prime(2)}\bar{\eta}_{ijk}^{\prime(2)} + \ell_3^2\bar{\eta}_{ijk}^{\prime(3)}\bar{\eta}_{ijk}^{\prime(3)}\right)/D^2}$$
$$\propto D^{-1} \qquad \text{for } \ell_{CS}/D \to \infty \quad (58)$$

If one defines a size-independent dimensionless variable

$$\overline{H} = \sqrt{\ell_1^2\bar{\eta}_{ijk}^{\prime(1)}\bar{\eta}_{ijk}^{\prime(1)} + \ell_2^2\bar{\eta}_{ijk}^{\prime(2)}\bar{\eta}_{ijk}^{\prime(2)} + \ell_3^2\bar{\eta}_{ijk}^{\prime(3)}\bar{\eta}_{ijk}^{\prime(3)}}/\ell_{CS} \quad (59)$$

the asymptotic behavior is seen to be

$$\overline{E} \approx \frac{\ell_{CS}}{D}\overline{H} \qquad \text{for } \ell_{CS}/D \to \infty \quad (60)$$

Substituting (60) into (57), the asymptotic form of the equilibrium equation reads

$$\frac{2}{3}\left(\frac{\ell_{CS}}{D}\right)^{(1-n)/n}\left(\frac{1}{E_0}\right)^{1/n}\partial_i\left(\overline{H}^{(1-n)/n}\bar{\varepsilon}_{ik}\right)-\left(\frac{\ell_{CS}}{D}\right)^{(1+n)/n}$$

$$\times\left(\frac{1}{E_0}\right)^{1/n}\partial_i\partial_j\left(C_{ijklmp}\overline{H}^{(1-n)/n}\bar{\eta}_{lmp}\right)=-\frac{\sigma_N}{\sigma_0}\bar{f}_k \quad (61)$$

After multiplying this equation by $(D/\ell_{CS})^{(n+1)/n}$ and taking the limit of the left-hand side for $\ell_{CS}/D \to \infty$, one gets the following asymptotic form of the equilibrium equations:

$$\partial_i\partial_j\left(C_{ijklmp}\overline{H}^{(1-n)/n}\bar{\eta}_{lmp}\right)=\chi\bar{f}_k$$

$$\text{with } \chi=\overline{E}_0^{1/n}\frac{\sigma_N}{E_0}\left(\frac{D}{\ell_{CS}}\right)^{(n+1)/n} \quad (62)$$

Because the left-hand side of the foregoing equation, as well as the dimensionless body force $\bar{f}_k$, is independent of size $D$ and because the boundary conditions are homogeneous and thus size independent, the parameter $\chi$ must be size independent. Thus, upon solving $\sigma_N$ from (62), one finds that the small-size asymptotic scaling law is

$$\sigma_N=\sigma_0\chi\overline{E}_0^{-1/n}\left(\frac{\ell_{CS}}{D}\right)^{(n+1)/n} \quad (63)$$

or

$$\sigma_N\propto D^{-(n+1)/n} \quad (64)$$

For plastic hardening materials, we have $1 < (n+1)/n \le 2$. Although the result (64) applies only to the special case of strain energy density function given by (50), the analytical technique used here is general. It is even suitable to the strain energy density function defined directly in terms of strain and strain gradients, rather than as the combined strain quantity. For example, if the strain energy density function is defined as (27) for the case of linear elasticity, a similar analysis can be made and it is found that the size effect law for very small sizes reads [264]

$$\sigma_N\propto D^{-2} \quad (65)$$

This also shows that (64) is quite general because (65) can be regarded as a special case of (64) in which the strain hardening exponent $n = 1$.

### Small-Size Asymptotic Load–Deflection Response

For some special cases (e.g., the pure torsion of a long thin wire or the bending of a slender beam), the symmetry conditions require displacement distribution to remain similar during the loading process. For such cases, the dimensionless displacement $\bar{u}_k$ can be related to a single parameter, $w$, and characterized by displacement profile $\hat{u}_k$ as $\bar{u}_k = w\hat{u}_k$ [260, 261, 264]. Since $\hat{u}_k$ is dimensionless, it must be independent of the size $D$. Displacements $\bar{u}_k$ evolve during the proportional loading process while the distribution profile remains constant. Thus the parameter $w$ can be considered as the displacement norm, $\|\bar{u}_k\|$. It follows that the strain, strain gradient, and combined strain quantity are all proportional to $w$. Therefore, $\overline{E}$ can be similarly represented as $\overline{E} = w\widehat{E}$, where $\widehat{E}$ is a size independent profile function, and

$w$ can be regarded as the deflection magnitude. Substituting this relation into the dimensionless constitutive relation (54) and (55), one can easily get

$$\bar{\sigma}_{ik}=w^{1/n}\hat{\sigma}_{ik} \qquad \bar{\tau}_{ijk}=w^{l/n}\hat{\tau}_{ijk} \quad (66)$$

where $\hat{\sigma}_{ik}$ and $\hat{\tau}_{ijk}$ are both size independent profile functions. Substituting these relations into dimensionless equilibrium equation (56), one finds that the load-deflection curve must have the form

$$\bar{f}_k\propto w^{1/n} \quad (67)$$

This relation is similar to the traditional strain–stress relation derived from the strain energy density function (50). The reason the load deflection curve begins with a vertical tangent is that the initial elastic response is assumed to be negligible.

***Example*** One important example is the microtorsion of a thin wire, for which a strong size effect was demonstrated [29–31] and described by strain gradient theories. The strain energy density function $W$ is defined as $W = \sigma E^{N+1}/(N+1)$. Compared with (50), one finds that $N = 1/n$. The radius of the wire, $D$, is chosen as the characteristic size of the structure. The deformation is characterized by the twist angle per unit length, $\kappa$. The nominal stress can be defined as $\sigma_N = T/D^3$, where $T$ is the torque. For different radii of the wire, we compare the $\sigma_N$ values corresponding to the same dimensionless twist $\bar{\kappa} = \kappa D$. The nominal stress can be expressed according to the CS theory as follows:

$$\sigma_N=\frac{T}{D^3}=\frac{6}{N+3}\sigma_0\bar{\kappa}^N\left\{\left[\frac{1}{3}+\left(\frac{\ell_{CS}}{D}\right)^2\right]^{(N+3)/2}-\left(\frac{\ell_{CS}}{D}\right)^{N+3}\right\}$$

$$(68)$$

When $\ell_{CS}/D \to \infty$, one has

$$\left[\frac{1}{3}+\left(\frac{\ell_{CS}}{D}\right)^2\right]^{(N+3)/2}-\left(\frac{\ell_{CS}}{D}\right)^{N+3}$$

$$\approx\frac{N+3}{2}\left(\frac{D}{3\ell_{CS}}\right)^2\left(\frac{\ell_{CS}}{D}\right)^{N+3} \quad (69)$$

from which

$$\sigma_N\propto D^{-N-1}=D^{-(n+1)/n} \quad (70)$$

For the load-deflection response, we now obtain the following relation between the load $T$ and the deformation $\bar{\kappa}$:

$$T\propto \kappa^N=\kappa^{1/n} \quad (71)$$

### 4.2.2. Asymptotic Analysis of Gao and Huang's MSG Theory and TNT Theory

**Scaling and Size Effect**  The dimensionless variables defined in (49) also need to be used here, and further dimensionless variables need to be defined as follows:

$$\bar{\varepsilon} = \varepsilon \qquad \bar{\eta} = \eta D \qquad \bar{\sigma}_{ij} = \sigma_{ij}/\sigma_Y$$
$$\bar{\tau}_{ijk} = \tau_{ijk}/(\sigma_Y l) \qquad \bar{\sigma} = \sigma/\sigma_Y \tag{72}$$

$$\bar{\eta}^H_{ijk} = \eta^H_{ijk} D \qquad \bar{\Lambda}_{ijk} = \Lambda_{ijk} D \qquad \bar{\Pi}_{ijk} = \Pi_{ijk} D$$
$$\bar{\Phi}_{ijk} = \Phi_{ijk} D \qquad \bar{\Psi}_{ijk} = \Psi_{ijk} D \tag{73}$$

These definitions are meaningful because $\eta^H_{ijk}$, $\Lambda_{ijk}$, and $\Pi_{ijk}$ are all homogeneous functions of degree 1 of tensors $\eta_{ijk}$ and $\varepsilon_{ij}$. It is not difficult to obtain a dimensionless version of the constitutive law of the MSG theory

$$\bar{\sigma}_{ik} = \frac{K}{\sigma_Y}\delta_{ik}\bar{\varepsilon}_{nn} + \frac{2\bar{\sigma}}{3\bar{\varepsilon}}\bar{\varepsilon}'_{ik}$$
$$\bar{\tau}_{ijk} = \frac{l^2_\varepsilon}{lD}\left(\frac{K}{6\sigma_Y}\bar{\eta}^H_{ijk} + \bar{\sigma}\bar{\Phi}_{ijk} + \frac{1}{\bar{\sigma}}\bar{\Psi}_{ijk}\right) \tag{74}$$

where $l$ and $l_\varepsilon$ are two characteristic material lengths. The corresponding dimensionless equilibrium equation reads

$$\partial_i\bar{\sigma}_{ik} - \frac{l}{D}\partial_i\partial_j\bar{\tau}_{ijk} + \frac{\sigma_N}{\sigma_Y}\bar{f}_k = 0 \tag{75}$$

Same as before, the boundary conditions can again be considered as homogeneous and the applied loads replaced by body forces $\bar{f}_k$ applied within a thin surface layer. The asymptotic behavior for a very large structure is simple. When $l/D \to 0$, we also have $l_\varepsilon/D \to 0$. Thus $\bar{\tau}_{ijk}$ tends to zero, according to Eq. (69), and all the equations reduce to the standard equations of classical plasticity theory, which means that there is no size effect, as required by classical plasticity.

The opposite asymptotic character for sufficiently small structures ($l/D \to \infty$ and $l_\varepsilon/D \to \infty$) is more interesting. The general hardening rule (40) can be rewritten with dimensionless variables as

$$\bar{\sigma} = [f^q(\varepsilon) + (l\bar{\eta}/D)^p]^{1/q} \tag{76}$$

Thus, we have $\bar{\sigma} \approx (l\bar{\eta}/D)^{p/q}$ when $l/D \to \infty$. Substituting (74) into (75), we can express the equilibrium equation as follows:

$$\partial_i\left[\frac{K}{\sigma_Y}\delta_{ik}\bar{\varepsilon}_{nn} + \frac{2}{3\bar{\varepsilon}}\left(\frac{l\bar{\eta}}{D}\right)^{p/q}\bar{\varepsilon}'_{ik}\right] - \left(\frac{l_\varepsilon}{D}\right)^2$$
$$\times \partial_i\partial_j\left[\frac{K}{6\sigma_Y}\bar{\eta}^H_{ijk} + \left(\frac{l\bar{\eta}}{D}\right)^{p/q}\bar{\Phi}_{ijk} + \left(\frac{D}{l\bar{\eta}}\right)^{p/q}\bar{\Psi}_{ijk}\right]$$
$$= -\frac{\sigma_N}{\sigma_Y}\bar{f}_k \tag{77}$$

When $l/D \to \infty$, the five terms on the left-hand side of the foregoing equation are, in sequence, of the order of

$$O(1) \quad O(D^{-p/q}) \quad O(D^{-2}) \quad O(D^{-2-p/q}) \quad O(D^{2+p/q}) \tag{78}$$

When $D \to 0$, the fourth term is generally the dominant one, and so we get the asymptotic form of the equilibrium equation,

$$\partial_i\partial_j(\bar{\eta}^{p/q}\bar{\Phi}_{ijk}) = \chi_1\bar{f}_k \tag{79}$$

with

$$\chi_1 = \left(\frac{l}{l_\varepsilon}\right)^2\frac{\sigma_N}{\sigma_Y}\left(\frac{D}{l}\right)^{2+p/q} \tag{80}$$

Since $D$ is not present in the left-hand side of (80) and the boundary conditions are also homogeneous, the parameter $\chi$ must be independent of $D$. Thus, the general small-size asymptotic scaling law of MSG theory reads [260, 261, 264]

$$\sigma_N = \sigma_Y\chi_1\left(\frac{l_\varepsilon}{l}\right)^2\left(\frac{l}{D}\right)^{2+p/q}$$

and for $\frac{p}{q} = \frac{1}{2}$

$$\sigma_N \propto D^{-5/2} \tag{81}$$

This asymptotic size effect is very strong [260, 261, 264]. It is much stronger than the normal linear elastic fracture mechanics size effect, which is $\sigma_N \propto D^{-1/2}$, or the typical Weibull size effect, which is around $\sigma_N \propto D^{-0.1}$.

There are also some special cases. For example, in the case of microbending, $\bar{\Phi}_{ijk} = 0$ for all $i, j, k$, which makes the fourth term on the left-hand side of (77) vanish; in the case of incompressible material, $\eta^H_{ijk} = 0$, which makes the third term on the left-hand side of (77) zero. So the general size effect law will change to $\sigma_N \propto D^{-2}$ for microbending of a compressible material, and to $\sigma_N \propto D^{-2+p/q}$ for microbending of an incompressible material (in detail, see [264]).

The size effect $D^{-5/2}$, as well as $D^{-2}$, is enormous and unrealistic. This is a consequence of the last three terms on the left-hand side of (77), which represent contributions from the couple stresses. A detailed analysis showed that the couple stresses are not necessary to fit the test results and to ensure the virtual work balance [264]. Based on this analysis, Bažant [260, 261] and Bažant and Guo [264] proposed a modified version of the MSG theory in which the couple stresses are made to vanish. This led to a theory identical to the TNT theory [260, 261, 264], which was proposed on the basis of numerical experience with varying the "mesoscale cell size" $l_\varepsilon$. Let us now analyze the asymptotic size effect of this theory. The dimensionless variables defined for the MSG theory may again be used for TNT theory. The dimensionless constitutive relation of the TNT theory reads

$$\bar{\sigma}_{ik} = \frac{K}{\sigma_Y}\delta_{ik}\bar{\varepsilon}_{nn} + \frac{2\bar{\sigma}}{3\bar{\varepsilon}}\bar{\varepsilon}'_{ik} \tag{82}$$

and the differential equation of equilibrium in terms of the dimensionless variables takes the form

$$\partial_i\bar{\sigma}_{ik} + \frac{\sigma_N}{\sigma_Y}\bar{f}_k = 0 \tag{83}$$

For large enough sizes, $D/l \to \infty$, the asymptotic behavior will be identical to the classical theory of plasticity, which implies no size effect. For very small sizes, $D/l \to 0$, we have

$$\bar{\sigma} = [f^q(\varepsilon) + (l\bar{\eta}/D)^p]^{1/q} \approx (l\bar{\eta}/D)^{p/q} \tag{84}$$

and the equilibrium equation can be rewritten as follows:

$$\partial_i \left[ \frac{K}{\sigma_Y} \delta_{ik} \bar{\varepsilon}_{nn} + \frac{2}{3\bar{\varepsilon}} \left( \frac{l\bar{\eta}}{D} \right)^{p/q} \bar{\varepsilon}'_{ik} \right] = -\frac{\sigma_N}{\sigma_Y} \bar{f}_k \qquad (85)$$

Obviously, the second term on the lefthand side dominates when $D/l \to 0$, and so the asymptotic form of the equilibrium equation is

$$\partial_i \left( \bar{\eta}^{p/q} \frac{\bar{\varepsilon}'_{ijk}}{\bar{\varepsilon}} \right) = \chi \bar{f}_k \qquad \text{with } \chi = -\frac{3}{2} \frac{\sigma_N}{\sigma_Y} \left( \frac{D}{l} \right)^{p/q} \qquad (86)$$

Same as before, $\chi$ is sizeindependent, and consequently the small-size asymptotic scaling law for the TNT theory is

$$\sigma_N = -\frac{2\sigma_Y}{3} \chi \left( \frac{l}{D} \right)^{p/q}$$

and for $\frac{p}{q} = \frac{1}{2}$

$$\sigma_N \propto D^{-1/2} \qquad (87)$$

Four possible cases of small-size asymptotic scaling for the MSG theory and the TNT theory are shown in Figure 45.

### Small-Size Asymptotic Load-Deflection Response

The characteristic features of the small-size asymptotic load-deflection curves will now be determined. The MSG theory will be analyzed first, and the TNT theory can be treated as a special limiting case of the MSG theory. Again we consider only the special cases where the relative displacement profile does not change during the loading process. Same as before, the displacement can be characterized by parameter $w$ as $\bar{u}_k = w\hat{u}_k$, where $\hat{u}_k$ is the displacement profile, which is not only independent of $D$ but also invariable during the proportional loading process. Similarly, the strain and strain gradient can be expressed as $\bar{\varepsilon}_{ij} = \varepsilon_{ij} = w\hat{\varepsilon}_{ij}$, $\bar{\varepsilon} = \varepsilon = w\hat{\varepsilon}$, $\bar{\eta}_{ijk} = w\hat{\eta}_{ijk}$, $\bar{\eta} = w\hat{\eta}$. Since variables $\Lambda_{ijk}$ and $\Pi_{ijk}$ are homogeneous functions of degree 1 of both $\boldsymbol{\eta}$ and $\boldsymbol{\varepsilon}$, their corresponding dimensionless variables can also be expressed as products of $w$ and a dimensionless profile function (i.e., $\overline{\Lambda}_{ijk} = w\widehat{\Lambda}_{ijk}$ and $\overline{\Pi}_{ijk} = w\widehat{\Pi}_{ijk}$). Because of the factor $1/\varepsilon$ in the definition of $\Phi_{ijk}$ [see Eq. (36)], we have $\overline{\Phi}_{ijk} = \widehat{\Phi}_{ijk}$,
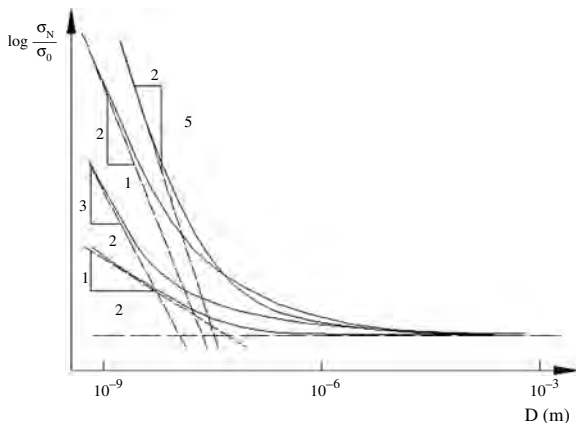


**Figure 45.** Four possible small-size asymptotic scaling curves for the MSG theory and the TNT theory.

which means that $\overline{\Phi}_{ijk}$ is independent of $w$. When we consider the beginning of the load-deflection diagram at $D \to 0$, we also have $w \to 0$, which is a limit not discussed during previous sizeeffect analysis. When the effect of $w$ is considered, the five terms on the left-hand side of (77) are proportional, in sequence, to the functions as follows:

$$w \qquad (w/D)^{p/q} \qquad w/D^2 \qquad w^{p/q}/D^{2+p/q}$$
$$w^{1-p/q} \qquad w^{1-p/q}/D^{2-p/q} \qquad (88)$$

In the case of MSG theory with $p = 1$, $q = 2$, these functions are

$$w \qquad \sqrt{w/D} \qquad w/D^2 \qquad w^{1/2}/D^{5/2} \qquad w^{1/2}/D^{3/2} \qquad (89)$$

and (77) can then be expressed as

$$-\frac{\sigma_N}{\sigma_Y} \bar{f}_k = a_1 w + a_2 w^{p/q} D^{-p/q} + a_3 w D^{-2} + a_4 w^{p/q} D^{-2-p/q}$$
$$+ a_5 w^{1-p/q} D^{-2+p/q} \qquad (90)$$

where parameters $a_i$ are constants independent of $D$ and $w$. Since the force $\bar{f}_k$ should decrease when $w$ decreases, one knows that $1 - p/q > 0$, which implies $p < q$. As we discussed before, if only $D \to 0$ is considered (or, in other words, $D \ll w$), the dominant term is $a_4 w^{p/q} D^{-2-p/q}$, which means that

$$\bar{f}_k \propto w^{p/q} \qquad \text{(for } w \gg D\text{)} \qquad (91)$$

For the MSG theory, this gives

$$\bar{f}_k \propto w^{1/2} \qquad \text{(for } w \gg D\text{)} \qquad (92)$$

We need to consider another asymptotic case in which $w \ll D$ (e.g., at the beginning of the load-deflection diagram). The dominant term in this case is either $a_4 w^{p/q} D^{-2-p/q}$ or $a_5 w^{1-p/q} D^{-2+p/q}$, depending on the value of $p/q$. The asymptotic load-deflection behavior is

$$\bar{f}_k \propto w^r \qquad r = \min\{p/q, 1 - p/q\} \qquad \text{(for } w \ll D\text{)} \qquad (93)$$

For MSG theory, the dominant term is $a_4 w^{1/2} D^{-5/2}$, and so the load $\bar{f}_k$ initially increases in proportion to $w^{1/2}$. Thus one has the asymptotic load-deflection relation for MSG theory as

$$\bar{f}_k \propto w^{1/2} \qquad \text{for all } w \qquad (94)$$

As discussed in the preceding section, some terms in (77) may vanish in some special cases, and a similar analysis can be applied to these special cases. For example, for microbending of an incompressible material, the third and fourth terms in (77) vanish, and as a result (92) changes as follows:

$$-\frac{\sigma_N}{\sigma_Y} \bar{f}_k = a_1 w + a_2 \sqrt{w/D} + a_5 w^{1/2}/D^{3/2} \qquad (95)$$

The asymptotic load-deflection curve is simple because the last term on the right-hand side of (95) dominates when

$D$ is small, regardless of the ratio of $w/D$, and so the asymptotic load-deflection relation for this special case is again

$$\bar{f}_k \propto w^{1/2} \qquad \text{for all } w \qquad (96)$$

This means the vanishing of some terms in flexure problems will not change the asymptotic load-deflection behavior. The TNT theory can be treated as a special case of the MSG theory. If the last three terms on the right-hand of the MSG equilibrium equation (77) vanish, the equation becomes identical to equilibrium equation (85) of the TNT theory. So (85) can be expressed as

$$-\frac{\sigma_N}{\sigma_Y}\bar{f}_k = a_1 w + a_2\sqrt{w/D} \qquad (97)$$

For small enough $D$ and $w$, the dominant term will be the second term on the right-hand side of (97), and so we have

$$\bar{f}_k \propto w^{1/2} \qquad \text{for all } w \qquad \text{(TNT theory)} \qquad (98)$$

It should be noted that the elastic part of the response has been neglected, which is why the load-deflection curves in (94), (96), and (98) begin with a vertical tangent.

**Example** The experiment of microtorsion of a thin wire can also be analyzed by the MSG theory [35] or TNT theory. Equation (35) in [35] can be transformed to the dimensionless formula

$$\sigma_N = \frac{T}{D^3} = \sigma_Y \frac{2\pi\bar{\kappa}}{3}\int_0^1\left\{\frac{\bar{\sigma}}{\bar{\varepsilon}}\left(\rho^2 + \frac{l_\varepsilon^2}{12D^2}\right) + \frac{l_\varepsilon^2 f(\bar{\varepsilon})f'(\bar{\varepsilon})}{12D^2\bar{\sigma}}\right\}\rho\,d\rho \qquad (99)$$

where $\sigma_N$ is the nominal stress, $T$ is the torque, $D$ is the radius of wire (which is also chosen as the characteristic length of the structure), $\sigma_Y$ is the yield stress of macroscale metal, and $\bar{\kappa} = \bar{\eta} = \kappa D$ is the dimensionless specific angle of twist, where $\kappa = $ actual specific angle of twist (i.e., the rotation angle per unit length of wire). Substituting $\bar{\sigma} = \sqrt{f^2(\bar{\varepsilon}) + l\bar{\eta}/D} \approx \sqrt{l\bar{\kappa}/D}$ into this formula, we find that, for $D \to 0$, the dominant part is obtained by integration of the second term, which leads to the following small-size asymptotic form:

$$\sigma_N = \sigma_Y\left(\frac{\pi}{18}l_\varepsilon^2 l^{1/2}\int_0^1\frac{\rho}{\hat{\varepsilon}}d\rho\right)\bar{\kappa}^{1/2}D^{-5/2} \qquad (100)$$

This result verifies the conclusions (81) and (89), where $\bar{\kappa}$ is considered as a measure of deflection, analogous to $w$ in (89). The asymptotic load-deflection behavior of the TNT theory can be obtained similarly.

Another special case is the application of the MSG theory to the microbending of incompressible metals [35]. Equation (29) in [35] can be transformed to the dimensionless version

$$\sigma_N = \frac{M}{D^2} = 2\sigma_Y\int_0^{1/2}\left[\frac{2}{\sqrt{3}}\bar{\sigma}\rho + \frac{\bar{\kappa}l_\varepsilon^2 f(\bar{\varepsilon})f'(\bar{\varepsilon})}{9D^2\bar{\sigma}}\right]d\rho \qquad (101)$$

where $D$ is the beam depth (the characteristic dimension of the structure), $M$ is the bending moment, $\bar{\kappa} = \bar{\eta} = \kappa D$ is the dimensionless bending curvature, and $\kappa$ is the actual bending curvature. When $D \to 0$, the small-size asymptotic form is

$$\sigma_N = \sigma_Y\left(\frac{2}{9}l_\varepsilon^2 l^{-1/2}\int_0^{1/2}f(\bar{\varepsilon})f'(\bar{\varepsilon})d\rho\right)\bar{\kappa}^{1/2}D^{-3/2} \qquad (102)$$

This verifies for this special case the asymptotic behavior $\sigma_N \propto D^{-2+p/q}$, as well as (96). Letting $l_\varepsilon = 0$, one finds that this asymptotic character also applies to the TNT theory.

### 4.2.3. Asymptotic Analysis of Acharya and Bassani's Theory

Let us now give a simple analysis of the asymptotic behavior of Acharya and Bassani's strain gradient theory [263]. We define dimensionless variables $\bar{u}_i = u_i/D$, $\bar{\varepsilon}_{ij,k} = \varepsilon_{ij,k}D$, and that $\bar{\alpha}_{ij} = \alpha_{ij}D$. When $D \to 0$, the asymptotic behavior of the plastic hardening modulus ($\bar{\gamma}^p = \gamma^p$) defined by (48) is found to be

$$h(\gamma^p, \alpha) = h_0\left(1 + \frac{\gamma^p}{\gamma_0}\right)^{N-1}\left[1 + c(\gamma^p/\gamma_0)^2\right]^{-1/2}\frac{\bar{\alpha}}{\gamma_0}\frac{l}{D}$$
$$\propto D^{-1} \qquad (103)$$

This shows that, at the same strain level, the plastic hardening modulus (slope of load deflection curve) increases as $D^{-1}$ when $D \to 0$. If the elastic part is neglected for very large plastic strain, the nominal stress must also scale asymptotically as $D^{-1}$. This asymptotic size effect is again quite strong (but not as strong as in the MSG theory). This size effect can be reduced by modifying the hardening function $h(\gamma^p, \alpha)$. For example, if the hardening modulus is redefined as

$$h(\gamma^p, \alpha) = h_0\left(1 + \frac{\gamma^p}{\gamma_0}\right)^{N-1}\left[1 + \frac{l\alpha/\gamma_0}{1 + c(\gamma^p/\gamma_0)}\right]^{1/2} \qquad (104)$$

then the asymptotic scaling becomes more reasonable:

$$h(\gamma^p, \alpha) \propto D^{-1/2} \quad \text{when } D \to 0 \qquad (105)$$

### 4.3. Asymptotic-Matching Approximation Formula

After determining the asymptotic behaviors of strain gradient plasticity theories, one can obtain an asymptotic matching approximation for a smooth transition of the nominal strength in the intermediate size range. In [260, 261, 264], a smooth transition between the case of no size effect for $D \to \infty$ and the case of power law size effect $\sigma_N \propto D^{-s}$ for $D \to 0$ ($s > 0$) has been described by the simple asymptotic-matching approximation

$$\sigma_N = \sigma_0\left[1 + \left(\frac{D_0}{D}\right)^{2s/r}\right]^{r/2} \qquad (106)$$

where $r$ is a constant to be determined by data fitting, while parameters $\sigma_0$ and $D_0$ can be determined by either the asymptotic size effect formula or data fitting. This formula
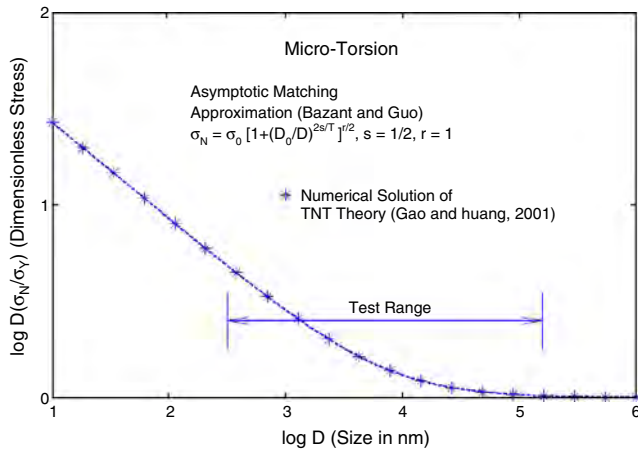
**Figure 46.** Asymptotic-matching approximation for micro-torsion.

was shown to fit the results for microtorsion and microbending (Figs. 46 and 47).

## 4.4. Concluding Remarks on Strain Gradient Theories

In many applications of interest (e.g., microelectronics and MEMS), characteristic dimensions are in excess of 100 nm–1 $\mu$m. Modeling the mechanics of such systems at the atomistic level is beyond present computational capabilities. Therefore, extension of continuum theories to account for size scales is of high relevance. Here we have discussed many of the existing theories. At the same time, their range of applicability was examined through small-size asymptotics.

Even though the small-size asymptotic behavior is obtained only below the size range of applicability of the theory ($>100$ nm), it is useful to pay attention to it. Several main theories show unreasonable small-size asymptotic behavior, which impairs the representation of experimentally observed behavior in the practical size range and spoils asymptotic matching approximations. Simple adjustments of the theories suffer to obtain reasonable asymptotics and make asymptotic matching approximation meaningful.
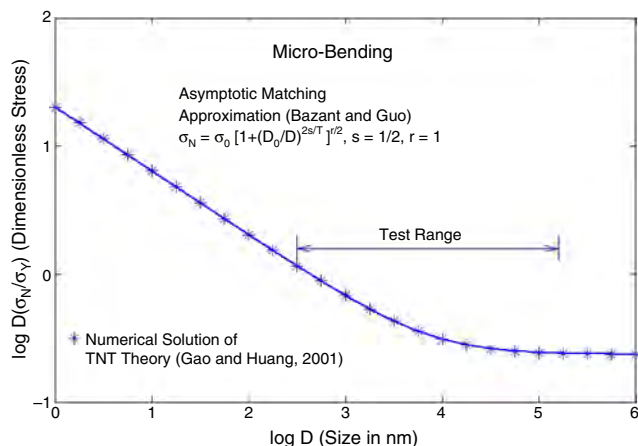


**Figure 47.** Asymptotic-matching approximation for micro-bending.

Finally, an analogy with quasibrittle materials such as concrete, rocks, sea ice, and fiber composite may be mentioned [270]. For them, too, the small size as well as large size asymptotic behaviors are attained only outside the range of validity of the theoretical models (cohesive crack model, crack band model, nonlocal damage models), that is, for specimen sizes much smaller than the inhomogeneity size or much larger than the largest constructable structures. Yet the knowledge of two-sided asymptotics has been shown to be very helpful to achieving good asymptotic matching approximations for the intermediate practical range.

It is also important to emphasize that strain gradient theories cannot explain the size scale effects observed in fcc metals in the absence of strain gradients [36, 37]. Clearly, new continuum theories are needed to be able to predict these size effects.

## 5. MODELING ONE-DIMENSIONAL MATERIALS: NANOTUBES AND NANOWIRES

One-dimensional nanoscale materials, that is, nanotubes (carbon CNT, boron nitride BNNT, etc.) and nanowires (e.g., silicon SiNW), are drawing ever more attention due to their promising properties for a variety of future applications. Mechanical strength of CNTs and BNNTs along with their electrical (for carbon) and thermal conductivity (for both), are appealing for composite applications. Although SiNWs have little advantage in strength, their chemical properties enable ease of doping, and they could be outstanding light-emitters due to a quantum confinement effect. These nanowires have the additional advantage that can be straightforwardly integrated in Si circuits. Here, we review some of the recent results concerning the mechanical yield and failure as well as the possible coalescence or welding mechanisms of C and BN nanotubes. Fundamental structures and energetics of SiNWs are also discussed.

Interest in composite application of CNTs is due to their mechanical strength combined with the electrical and thermal conductivity that together could lead to development a multifunctional material basis for a variety of novel purposes ranging from textile to aerospace applications. Besides the economical aspects, like low cost volume production of CNT, the limiting factors for their utilization in composites include their proper dispersion in matrix media, matrix-CNT adhesion and load transfer, intertubular connectivity and shear resistance, and internal strength of individual tubes. While manufacturing and cost issues remain mostly a subject of experimental empirical study, the mechanics of nanotubes has been a topic of detailed theoretical investigations and multiscale computational modeling.

Theoretical studies of CNT mechanics have been motivated by experimental evidence of great resilience and by expectations of extraordinary strength. These are based upon the strength of the individual carbon bonds and the elegance of two-dimensional carbon network structures. CNT mechanics, including buckling, yielding, and failure mechanisms, have been extensively investigated and are

summarized in recent reviews [145, 271], while the studies of elastic behavior, both linear and nonlinear, and buckling have made the transition from science to engineering (via the demonstrated correspondence of atomistic modeling methods and continuum elasticity and finite elements [145, 271]). Many issues of inelastic behavior still require analysis at the atomic scale utilizing the solid state physics and quantum chemistry formulations.

As an important example, we have recently undertaken a systematic series of quantum *ab initio* calculations of structures and moduli [272, 273] for C, BN (boron nitride or "white graphite," shown in Fig. 48) and $CF_x$ (fluorinated carbon) shells. They utilize density functional based computations (within Gaussian package) with periodic boundary conditions that yielded a set of accurate elastic parameters [272] that can be further employed in engineering shell models for CNT elasticity, vibrations, or postbuckling deformations. This careful discussion is also timely since somewhat controversial data have recently emerged in the literature, caused mainly by different interpretations of the effective cross-section of nanostructures, referred to recently as *Yakobson's paradox* [274].

SiNW is another type of 1D structure of high interest due mostly to the strategy of building nanoscale technology via the developed infrastructure of the silicon microelectronics industry. Recent efforts have demonstrated that ultrathin SiNWs indeed have properties that make them very competitive in many aspects of nanoscale electronics. First, Si is fairly reactive, enabling it to be easily doped. Second, faster and lower energy-consuming electronic devices have been suggested that are constructed of arrays of SiNWs, preliminary forms of which have already been built [275]. Finally, the quantum confinement effect opens a direct bandgap as wide as 2.0–3.0 eV, laying a potential foundation for effective visible-light emitters and making the so-called *all-photonic* technology possible using silicon materials alone [276]. Additionally, this direct bandgap has the potential to enable photovoltaics of ultrahigh efficiency, that is, if bulk quantities of SiNWs could be produced reasonably cheaply.

Recently, we found the ground-state structure of ultrathin, pristine SiNWs by utilizing theoretical analysis and large-scale computations [277]. Surprisingly, these SiNWs are polycrystalline and favor a whisker growth mode (i.e., they grow much faster along their axis than circumferentially). Their structures and energetics will be shown in comparison to other single crystalline nanowires. Moreover, faceting and matching of the facets at the wire's edges were found to play a critical role in stabilizing the SiNWs.
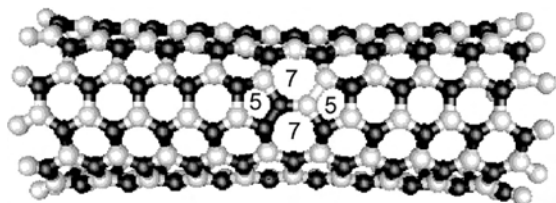


**Figure 48.** Stone–Wales 5/7/7/5 defect in (5, 5) BN nanotube. Reprinted with permission from [273], H. F. Bettinger et al., *Phys. Rev. B* 65, 041406 (2002). © 2002, American Physical Society.

## 5.1. Strength, Failure, and Healing Mechanisms in Nanotubes

### 5.1.1. Energies and Thermodynamics of the Yield Defects

The transition from yield to tensile strength for CNTs and its underlying atomic mechanism has been a subject of particular interest. It has been proposed that two alternative yield-failure paths in CNT are generally possible [44, 278]: (i) a brittle fracture through a nucleation and growth of a crack as in Figure 49, or (ii) a dislocation relaxation (i.e. *intramolecular plasticity*) in case of a miniscule fiber-nanotube. Indeed, it has been observed in detailed computer simulations that the primary yield defect, an event at the atomic scale, is represented by individual bond rotation, which leads to the formation of two pentagon–heptagon pairs in the hexagonal lattice, 5/7/7/5 in Figure 48. In the chemistry of fullerenes and nanotubes, this corresponds to "pyracylene" or Stone–Wales transformation. A computational study of this defect energy at different levels of applied tension allows one to determine the strain $\varepsilon$ at which the defect formation becomes thermodynamically favorable, whereby the nanotube can then possibly yield to the external tensile load.

Classical empirical potentials, tight binding approximations (TBA), and *ab initio* density functional theory calculations all identify the range of thermodynamic instability with respect to yield as $\varepsilon$ exceeds 6–7%. More recently we applied the same approach to isomorphic BN nanotubes, where the Stone–Wales defect (Fig. 48) again has been shown to have the lowest energy, below that of the competing structure of 4/8/8/4 polygons. The determined defect formation energy under strain approximately follows a linear relationship, namely,

$$E_{SW} = 5.5\text{–}46\varepsilon \text{ eV} \tag{107}$$

(cf. $E_{SW} = 3.1\text{–}45\varepsilon$ eV in case of armchair carbon). Thus, density functional analysis of yield thermodynamics for carbon (C, purely covalent) and boron nitride (BN, covalent-ionic) permits a comparison of their yield strength with the conclusion that partially ionic BN can be more resistant to yield than the homoelemental C.
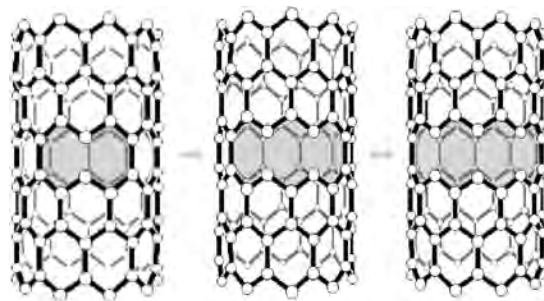


**Figure 49.** Quantum-mechanical relaxation of a nanocrack in H-terminated CNT. Reprinted with permission from [281], T. Dumitrica et al., *J. Chem. Phys.* 119, 1281 (2003). © 2003, American Institute of Physics.

### 5.1.2. Kinetic Theory of Strength

In any practical situation, a system is expected to sustain tension only within a finite time limit, while thermodynamic equilibrium implies time-unlimited conditions. A more consistent approach to failure [279, 280] comes from one based on rate equations and leads to more realistic estimates of strength. A kinetic theory approach to strength evaluation is an important step in this regard where the key point is to determine the probability, $P$, of defect formation (yield) as a function of time. It therefore can be calculated, provided that the computed activation barriers $E^*$ are available, by

$$P = 10^{15} L d \Delta t \, \text{sec}^{-1} \, \text{nm}^{-2} \exp[-E^*(\varepsilon, \chi)/k_b T] \sim 1 \quad (108)$$

where $L$ is the CNT length and $d$ is its diameter. Following extensive computational examination of the saddle-point activation barriers $E^*$ (Fig. 50a), this equation enabled calculation of the breaking strains $\varepsilon$ for a variety of temperatures $T$, duration times $\Delta t$, and chiral symmetries $\chi$ of SWNT, as shown in Figure 50b. With more accurate *ab initio* calculations of the transition state barriers $E^*$, the process can be enhanced.

Kinetic analysis shows that although thermodynamic requirements for yield can be relatively low (strains of 6–7%), overcoming activation barriers the strain level must exceed 15–20% (depending on chiral symmetry of the tube and the test duration). At this high strain level, nanotubes can in principle undergo brittle failure through "direct" bond breaking via a series of metastable radical states that include dangling bonds or unpaired electrons. We have recently [281] performed quantum mechanical structure relaxations which determined the energies of several of the first metastable defect states corresponding to one, two, or three broken bonds in the lattice. As an example, Figure 49 shows a singular broken-bond structure that emerges as metastable at approximately 16% tensile strain. From a chemistry viewpoint, such structures represent a biradical, $R^{\cdot} + {}^{\cdot}R$, that would immediately recombine under normal conditions. Unlike the Stone–Wales defect, these *virtual* defects do not exist in free lattice structures but can only emerge beyond the bifurcation point at high tension.
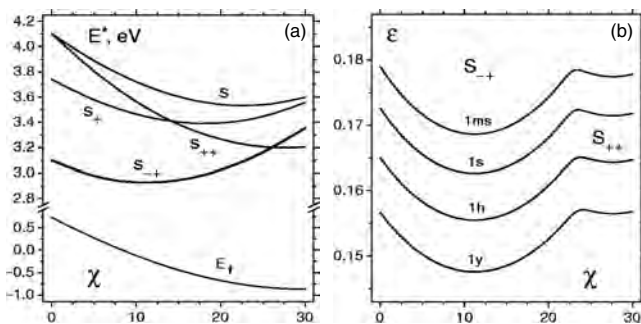


**Figure 50.** Activation barriers at $\varepsilon = 5\%$ (a), and breaking strain values (b) of CNT. Reprinted with permission from [280], G. G. Samsonidze and B. I. Yakobson, *Phys. Rev. Lett.* 88, 065501 (2002). © 2002, American Physical Society.

### 5.1.3. Welding and Reversible Failure

The possibility of nanotube coalescence, which is either a lateral or a butt-welding process of merging separate entities into one, has been investigated in detail due to its importance in formation of CNT networks, and its effect on overall electrical conductance, thermal transport, and mechanical strength [282]. We have discovered a mechanism of welding that consists exclusively of Stone–Wales bond rotations. It therefore appears as a feasible physical process at elevated temperatures or under irradiation. An example is shown in Figure 51 that illustrates the intermediate steps (as numbered) of (10,10)-CNT pair butt-welding, at high temperature or under irradiation (e-beam or laser):

$$(10, 10) + (10, 10) \rightarrow (10, 10) \qquad \text{or}$$
$$(15, 0) + (15, 0) \rightarrow (15, 0) \qquad (109)$$
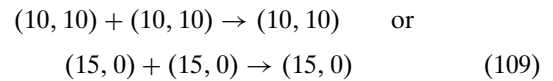
Emerging intermediate structures must possess unique and possibly useful electronic properties as they represent quantum dots with already attached nanotube-wires. Detailed calculations of the intermediate energies, $E$, shown in Figure 52 allow us to compare the energy barriers. The main data are obtained with TBA; open squares correspond to density functional results, and open circles are obtained from high-temperature molecular dynamics simulations. The data also show a possible reduction of the barriers by application of external mechanical forces, $F$, compression or tension, in transition from energy to enthalpy criteria, $H = E + FL$. This is important for engineering new nanostructures through stretching [283] or welding [281], as well as for improvement of bulk materials due to increased connectivity of the tubules in CNT bundles or possibly in composites.

### 5.2. Silicon Nanowires: Structure and Energetics

Although SiNWs possess much weaker bonds, they have higher rigidity (originating from the higher coordination [284, 285]) making the tiny wires extremely fragile compared to carbon nanotubes. Any practical construction of Si nanowires should not be too small in order to allow them to be sustainable in natural ambient conditions. Obviously, extremely thin ($d < 1$ nm) 1D Si structures could not emulate bulk structuring because all the atoms are actually located on a surface. Therefore, reconstruction will conform them into clusters or a chain of clusters even at zero temperature. The modeling of cluster chains considered as a SiNW currently accounts for a big portion of theoretical studies [286, 287]. Recently, a chain of fullerene-like clustered $Si_{20}$
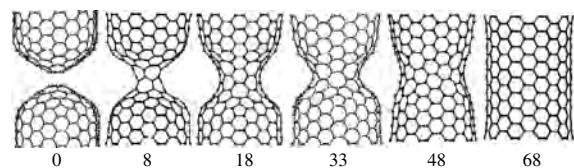


**Figure 51.** Steps of (10,10) + (10,10) coalescence via Stone–Wales bond rotations.
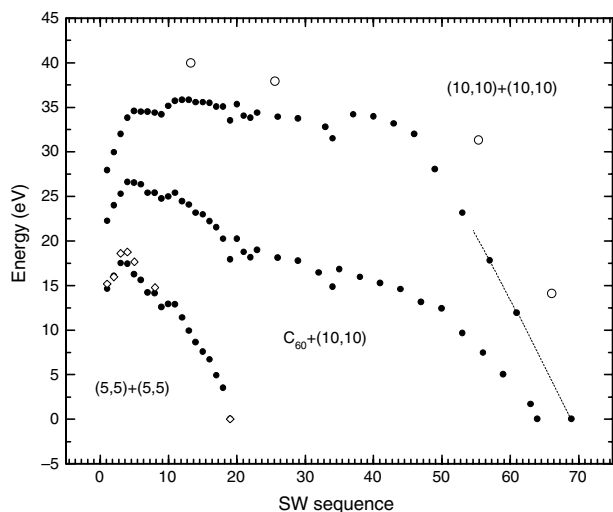
**Figure 52.** Computed energies of intermediate structures in coalescence. Reprinted with permission from [282], Y. F. Zhao et al., *Phys. Rev. Lett.* 88 185501 (2002). © 2002, American Physical Society.



**Figure 53.** Energy and structure (only cross-section on the right three) of three types of SiNWs. On the energy curve, diamonds and squares denote two surface reconstructions of the square SiNW; solid and open pentagons denote two types of pentagonal SiNWs. The five radial lines in the pentagonal model (right bottom) are {111} interfaces of stacking faults. Reprinted with permission from [277], Y. F. Zhao and B. I. Yakobson, *Phys. Rev. Lett.* 91, 035501 (2003).

was found to have a reasonably low energy [288]. If one adds more atomic layers to the cluster, chains will systematically accumulate strain, become distorted, and rapidly increase the energy of the system. Above a particular thickness ($d \sim 1.5$ nm for pristine SiNW), crystalline whiskers are more favorable and the process of faceting is the decisive factor to reduce energy.

Conventionally, the equilibrium shape of a faceted crystal is determined by minimization of Wulff's free energy, which neglects the interaction of facets (edge effect) and assumes a fixed bulk. This is a good approximation for relatively large crystals but poorly applicable to ultrathin SiNWs with $d < 10$ nm.

In [277, 289] we generalize Wulff's free energy as

$$F = s\gamma_s + E_e + E_b \tag{110}$$

to include the energy of matching the adjacent facets, $E_e$, and certain changes in the bulk, $E_b$, including possible internal granularity or elastic strain toward lowering the overall energy. Because the shape of a crystalline SiNWs is scalable with its diameter, the energy of an isomorphic family (with the same shape but various thickness) can be evaluated without full-scale computation. Several families of pristine whiskers with four-, five-, and six-fold symmetry in cross-section have been investigated and the relative energy is shown in Figure 53.

Surprisingly, a polycrystalline family has the lowest overall energy at $d < 6$ nm due to the perfect matching of the facets along the edges with very little cost to the bulk energy. This type of SiNW also has an important growth kinetics property: the dimer rows along the axis make the adatoms diffuse much faster in the axis direction than along the circumference.

Because the structures of the SiNW will influence their properties [290], the creation of new structures with controlled thickness and crystallographic orientation [291] is very important in practical applications. The new crystallographic structure with cross-sectional fivefold symmetry potentially provides opportunity for novel properties. It is known that the unique growth kinetics make it possible to produce SiNWs with identical crystallographic orientation (i.e., [110] direction).

In recent experiments, bundles of pristine SiNWs with diameters of 3–7 nm and lengths of >100 nm were formed in high vacuum [288] (see Fig. 54), which might be of the pentagonal type according to its growth kinetics. The hexagonal single crystalline SiNW with hydrogen-terminated facets has also been recently identified in [292].
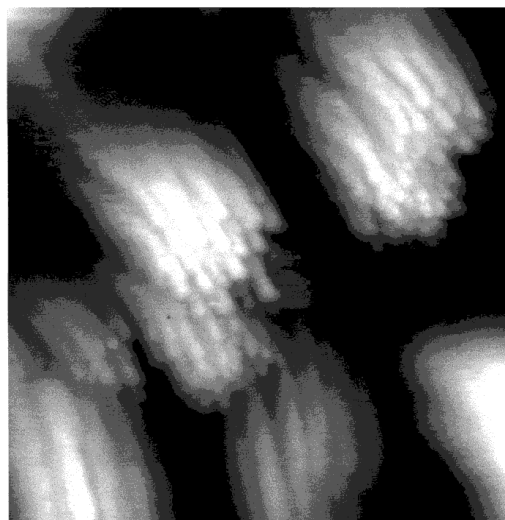


**Figure 54.** Bundles of the pristine SiNW, produced in high vaccum. Reprinted with permission from [288], B. Marsen and K. Sattler, *Phys. Rev. B* 60, 11593. (1999). © 1999, American Physical Society.

# GLOSSARY

**Micromechanics**   The field of mechanics dealing with properties and characteristics affecting deformation processes of microscale specimens.

**Multi-Scale Modeling**   Numerical modeling that takes into account mechanisms and properties of matter at multiple size scales.

**Nanomaterial**   A material possessing a nominal grain size in the range of 1 to 100 nm.

**Nanomechanics**   The field of mechanics dealing with properties and characteristics affecting deformation processes of nanoscale specimens.

**Nanotube**   A cylindrically shaped tube of nanoscale dimensions comprised of single- or multi-layered sheets of atoms.

**Nanowire**   A solid, cylindrically shaped rod of nanoscale dimensions.

**Size Effect**   The behavioral change in a material's property that manifests from reduced specimen size or reduced boundary conditions.

# ACKNOWLEDGMENTS

# REFERENCES

1. C. V. Thompson, *Annu. Rev. Mater. Sci.* 30, 159 (2000).
2. C. A. Neugebauer, J. B. Newkirk, and D. A. Vermilyea, "Structure and Properties of Thin Films." Wiley, New York, 1959.
3. E. Arzt, *Acta Mater.* 46, 5611 (1998).
4. J. W. Hutchinson, *Int. J. Solids Struct.* 37, 225 (2000).
5. A. Needleman and E. Van der Giessen, *Mater. Sci. Eng. A* 309, 1 (2001).
6. D. Weygand, L. H. Friedman, E. van der Giessen, and A. Needleman, *Mater. Sci. Eng. A* 309, 420 (2001).
7. J. Y. Shu, N. A. Fleck, E. Van der Giessen, and A. Needleman, *J. Mech. Phys. Solids* 49, 1361 (2001).
8. J. Weertman and J. R. Weertman, "Elementary Dislocation Theory." Oxford Univ. Press, Oxford, 1992.
9. D. Hull and D. J. Bacon, "Introduction to Dislocations." Pergamon, Oxford, 1984.
10. P. Lejcek and V. Sima, *Mater. Sci. Eng.* 60, 121 (1983).
11. M. M. Borodkina and T. S. Orekhova, *Fiz. Metallov Metalloved.* 54, 1204 (1982).
12. P. A. Beck, J. C. Kremer, L. J. Demer, and M. L. Holzworth, *Trans. Am. Inst. Mining Metall. Eng.* 175, 372 (1948).
13. W. W. Mullins, *Acta Metall.* 6, 414 (1958).
14. C. V. Thompson, *J. Mater. Res.* 8, 237 (1993).
15. W. D. Nix, *Metall. Trans. A* 20, 2217 (1989).
16. P. Chaudhari, *Philos. Mag. A* 39, 507 (1979).
17. M. S. De Guzman, G. Neubauer, P. Flinn, and W. D. Nix, *Mater. Res. Soc. Symp. Proc.* 308 (1993).
18. Q. Ma and D. R. Clarke, *J. Mater. Res.* 10, 853 (1995).
19. N. A. Stelmashenko, M. G. Walls, L. M. Brown, and Y. V. Milman, *Acta Metall. Mater.* 41, 2855 (1993).
20. M. Atkinson, *J. Mater. Res.* 10, 2908 (1995).
21. W. J. Poole, M. F. Ashby, and N. A. Fleck, *Scr. Mater.* 34, 559 (1996).
22. W. D. Nix, *Mater. Sci. Eng. A* 234, 37 (1997).
23. W. D. Nix and H. J. Gao, *J. Mech. Phys. Solids* 46, 411 (1998).
24. K. W. McElhaney, J. J. Vlassak, and W. D. Nix, *J. Mater. Res.* 13, 1300 (1998).
25. M. Goken and M. Kempf, *Acta Mater.* 47, 1043 (1999).
26. S. Suresh, T. G. Nieh, and B. W. Choi, *Scr. Mater.* 41, 951 (1999).
27. M. R. Begley and J. W. Hutchinson, *J. Mech. Phys. Solids* 46, 2049 (1998).
28. J. S. Stolken and A. G. Evans, *Acta Mater.* 46, 5109 (1998).
29. N. A. Fleck, G. M. Muller, M. F. Ashby, and J. W. Hutchinson, *Acta Metall. Mater.* 42, 475 (1994).
30. N. A. Fleck and J. W. Hutchinson, *J. Mech. Phys. Solids* 41, 1825 (1993).
31. N. A. Fleck and J. W. Hutchinson, in "Advances in Applied Mechanics" (J. W. Hutchinson and T. Y. Wu, Eds.), Vol. 33, p. 295. San Diego, Academic, 1997.
32. E. C. Aifantis, *Int. J. Eng. Sci.* 30, 1279 (1992).
33. H. Gao, Y. Huang, W. D. Nix, and J. W. Hutchinson, *J. Mech. Phys. Solids* 47, 1239 (1999).
34. H. Gao, Y. Huang, and W. D. Nix, *Naturwissenschaften* 86, 507 (1999).
35. Y. Huang, H. Gao, W. D. Nix, and J. W. Hutchinson, *J. Mech. Phys. Solids* 48, 99 (2000).
36. H. D. Espinosa, B. C. Prorok, and B. Peng, *J. Mech. Phys. Solids*, in press.
37. H. D. Espinosa, B. C. Prorok, and M. Fischer, *J. Mech. Phys. Solids* 51, 47 (2003).
38. H. D. Espinosa and B. C. Prorok, *Mater. Res. Soc. Symp. Proc.* 688 (2001).
39. B. C. Prorok and H. D. Espinosa, *J. Nanosci. Nanotechnol.* 2, 427 (2002).
40. S. Iijima, *Nature* 354, 56 (1991).
41. M. S. Dresselhaus, G. Dresselhaus, and R. Saito, *Carbon* 33, 883 (1995).
42. V. Ivanov, A. Fonseca, J. B. Nagy, A. Lucas, P. Lambin, D. Bernaerts, and X. B. Zhang, *Carbon* 33, 1727 (1995).
43. D. Qian, G. J. Wagner, W. K. Liu, M. F. Yu, and R. S. Ruoff, *Appl. Mech. Rev.* 55, 495 (2002).
44. B. I. Yakobson, *Appl. Phys. Lett.* 72, 918 (1998).
45. F. R. Brotzen, *Int. Mater. Rev.* 39, 24 (1994).
46. O. Kraft and C. A. Volkert, *Adv. Eng. Mater.* 3, 99 (2001).
47. R. P. Vinci and J. J. Vlassak, *Annu. Rev. Mater. Sci.* 26, 431 (1996).
48. Nano Indenter XP, MTS Systems Corp., http://www.mts.com/.
49. Triboscope, Hysitron Inc., http://www.hysitron.com/.
50. UMIS-2000, CSIRO, http://www.csiro.au/.
51. Nano Hardness Tester, CSM Instruments, http://www.csm-instruments.com/.
52. Fischerscope, Helmut Fischer Gmbh, http://www.fischer-technology. com/home.html.
53. M. F. Doerner and W. D. Nix, *J. Mater. Res.* 1, 601 (1986).
54. W. C. Oliver and G. M. Pharr, *J. Mater. Res.* 7, 1564 (1992).
55. R. Saha, Z. Xue, Y. Huang, and W. D. Nix, *J. Mech. Phys. Solids* 49, 1997 (2001).
56. R. Saha and W. D. Nix, *Acta Mater.* 50, 23 (2002).
57. R. Saha and W. D. Nix, *Mater. Sci. Eng. A* 319–321, 898 (2001).
58. H. Buckle, "The Science of Hardness Testing and Its Research Applications." ASM, Metals Park, OH, 1973.
59. H. Yuan and J. Chen, *Int. J. Solids Struct.* 38, 8171 (2001).
60. A. B. Mann, R. C. Cammarata, and M. A. Nastasi, *J. Mater. Res.* 14, 2195 (1999).
61. A. E. Giannakopoulos and S. Suresh, *Scr. Mater.* 40, 1191 (1999).
62. T. Y. Tsui and G. M. Pharr, *J. Mater. Res.* 14, 292 (1999).
63. Y. Y. Lim, M. M. Chaudhri, and Y. Enomoto, *J. Mater. Res.* 14, 2314 (1999).
64. D. L. Joslin and W. C. Oliver, *J. Mater. Res.* 5, 123 (1990).
65. R. B. King, *Int. J. Solids Struct.* 23, 1657 (1987).

66. C. B. Ponton and R. D. Rawlings, *Mater. Sci. Technol.* 5, 865 (1989).
67. C. B. Ponton and R. D. Rawlings, *Mater. Sci. Technol.* 5, 961 (1989).
68. J.-L. Loubet, B. N. Lucas, and W. C. Oliver, *Mater. Res. Soc. Symp. Proc.* 436, 233 (1996).
69. M. J. Mayo and W. D. Nix, *Acta Metall.* 36, 2183 (1988).
70. A. Bolshakov, W. C. Oliver, and G. M. Pharr, *Mater. Res. Soc. Symp. Proc.* 436, 141 (1996).
71. A. Bolshakov and G. M. Pharr, *J. Mater. Res.* 13, 1049 (1998).
72. J. C. Hay, A. Bolshakov, and G. M. Pharr, *J. Mater. Res.* 14, 2296 (1999).
73. M. Dao, N. Chollacoop, K. J. Van Vliet, T. A. Venkatesh, and S. Suresh, *Acta Mater.* 49, 3899 (2001).
74. A. C. Fischer, "Nanoindentation." Springer, New York, 2002.
75. S. P. Baker, R. F. Cook, S. G. Corcoran, and N. R. Moody, "Fundamentals of Nanoindentation and Nanotribology II." Material Research Society, 2001.
76. N. R. Moody, W. W. Gerberich, and S. P. Baker, *Mater. Res. Soc. Symp. Proc.* 522 (1998).
77. T. P. Weihs, S. Hong, J. C. Bravman, and W. D. Nix, *J. Mater. Res.* 3, 931 (1988).
78. J. A. Schweitz, *MRS Bull.* 17, 34 (1992).
79. S. P. Baker and W. D. Nix, *J. Mater. Res.* 9, 3131 (1994).
80. M. Knauss, Thesis, University of Stuttgart, 1996.
81. O. Kraft, R. Schwaiger, and W. D. Nix, *Mater. Res. Soc. Symp. Proc.* 518, 39 (1998).
82. R. Schwaiger and O. Kraft, *Scr. Mater.* 41, 823 (1999).
83. J. Florando, H. Fujimoto, Q. Ma, O. Kraft, R. Schwaiger, and W. D. Nix, *Mater. Res. Soc. Symp. Proc.* 563, 231 (1999).
84. H. D. Espinosa, B. C. Prorok, B. Peng, K.-H. Kim, N. Moldovan, O. Auciello, J. A. Carlisle, D. M. Gruen, and D. C. Mancini, *Exp. Mech.*, 43, 256 (2003).
85. H. D. Espinosa, B. Peng, K.-H. Kim, B. C. Prorok, N. Moldovan, X. C. Xiao, J. E. Gerbi, J. Birrell, O. Auciello, J. A. Carlisle, D. M. Gruen, and D. C. Mancini, *Mater. Res. Soc. Symp. Proc.* 741 (2002).
86. Y. A. Burenkov and S. P. Nikanorov, *Soviet Phys.-Solid State* 16, 963 (1974).
87. G. G. Stoney, *Proc. Roy. Soc. London* 82, 172 (1909).
88. F. J. von Preissig, *J. Appl. Phys.* 66, 4262 (1989).
89. J. T. Pan and I. Blech, *J. Appl. Phys.* 55, 2874 (1984).
90. P. A. Flinn, *Mater. Res. Soc. Symp. Proc.* 130, 41 (1989).
91. D. S. Gardner and P. A. Flinn, *IEEE Trans. Electron Devices* 35, 2160 (1987).
92. D. S. Gardner and P. A. Flinn, *Mater. Res. Soc. Symp. Proc.* 130, 69 (1989).
93. P. H. Townsend and T. A. Brunner, *J. Appl. Phys.* 62, 4438 (1987).
94. J. D. Romero, M. Khan, H. Fatemi, and J. Turlo, *J. Mater. Res.* 6, 1996 (1991).
95. V. T. Gillard and W. D. Nix, *Z. Metall.* 84, 874 (1993).
96. E. M. Zellinski, R. P. Vinci, and J. C. Bravman, *Mater. Res. Soc. Symp. Proc.* 391, 103 (1995).
97. O. Kraft and W. D. Nix, *Mater. Res. Soc. Symp. Proc.* 516, 201 (1998).
98. R. M. Keller, S. P. Baker, and E. Arzt, *J. Mater. Res.* 13, 1307 (1998).
99. T. S. Park and S. Suresh, *Acta Mater.* 48, 3169 (2000).
100. J. W. Beams, "Structure and Properties of Thin Films." Wiley, New York, 1959.
101. R. L. Edwards, G. Coles, and W. N. Sharpe, Jr., *Exp. Mech.*, in press.
102. E. I. Bromley, J. N. Randall, D. C. Flanders, and R. W. Mountain, *J. Vac. Sci. Technol. B* 1, 1364 (1983).
103. M. G. Allen, M. Mehregany, R. T. Howe, and S. D. Senturia, *Appl. Phys. Lett.* 51, 241 (1987).
104. O. Tabata, S. Sugiyama, and M. Takigawa, *Appl. Phys. Lett.* 56, 1314 (1990).
105. J. J. Vlassak and W. D. Nix, *J. Mater. Res.* 7, 3242 (1992).
106. V. M. Paviot, J. J. Vlassak, and W. D. Nix, *Mater. Res. Soc. Symp. Proc.* 356, 579 (1994).
107. V. Ziebart, O. Paul, U. Munch, J. Schwizer, and H. Baltes, *J. Microelectromech. Syst.* 7, 320 (1998).
108. D. T. Read, *Int. J. Fatigue* 20, 203 (1998).
109. D. T. Read and J. W. Dally, *J. Mater. Res.* 8, 1542 (1993).
110. J. A. Ruud, D. Josell, F. Spaepen, and A. L. Greer, *J. Mater. Res.* 8, 112 (1993).
111. D. Josell, D. van Heerden, D. Read, J. Bonevich, and D. Shechtman, *J. Mater. Res.* 13, 2902 (1998).
112. I. Chasiotis and W. G. Knauss, *Proc. SPIE* 3512, 66 (1998).
113. I. Chasiotis and W. G. Knauss, *Proc. SPIE* 4175, 96 (2000).
114. W. N. Sharpe, B. Yuan, and R. L. Edwards, *J. Microelectromech. Syst.* 6, 193 (1997).
115. W. N. Sharpe, Jr., S. Brown, G. C. Johnson, and W. C. Knauss, *Mater. Res. Soc. Symp. Proc.* 518, 57 (1998).
116. D. A. LaVan and W. N. Sharpe, *Exp. Mech.* 39, 210 (1999).
117. W. N. Sharpe, K. T. Turner, and R. L. Edwards, *Exp. Mech.* 39, 162 (1999).
118. K. M. Jackson, R. L. Edwards, G. F. Dirras, and W. N. J. Sharpe, *Mater. Res. Soc. Symp. Proc.* 687 (2001).
119. H. D. Espinosa, B. C. Prorok, and M. Fischer, in "Proc. of the SEM Ann. Conf. on Exp. and Appl. Mech.," Portland, OR, 2001, p. 446.
120. S. Greek and S. Johansson, *Proc. SPIE* 3224, 344 (1997).
121. T. Yi and C. J. Kim, in "Proc. MEMS (MEMS-Vol. 1), ASME Int. Mechanical Engineering Congress and Exposition," Nashville, TN, 1999, pp. 81–86.
122. T. Tsuchiya, O. Tabata, J. Sakata, and Y. Taga, *J. Microelectromech. Syst.* 7, 106 (1998).
123. G. Cornella, R. P. Vinci, R. S. Iyer, and R. H. Dauskardt, *Mater. Res. Soc. Symp. Proc.* 518, 81 (1998).
124. J. Amano, T. Ando, M. Shikida, K. Sato, and T. Tsuchiya, *Mater. Res. Soc. Symp. Proc.* 687 (2002).
125. T. Tsuchiya, J. Sakata, M. Shikida, and K. Sato, *Mater. Res. Soc. Symp. Proc.* 687 (2002).
126. S. Greek, F. Ericson, S. Johansson, M. Furtsch, and A. Rump, *J. Micromech. Microeng.* 9, 245 (1999).
127. H. D. Espinosa, B. Peng, B. C. Prorok, N. Moldovan, O. Auciello, J. A. Carlisle, D. M. Gruen, and D. C. Mancini, *J. Appl. Phys.* 94, 6076 (2003).
128. M. T. A. Saif, S. Zhang, M. A. Haque, and K. J. Hsia, *Acta Mater.* 50, 2779 (2002).
129. M. A. Haque and M. T. A. Saif, *Scr. Mater.* 47, 863 (2002).
130. M. A. Haque and M. T. A. Saif, *Sens. Actuator A* 97-8, 239 (2002).
131. M. A. Haque and M. T. A. Saif, *Exp. Mech.* 42, 123 (2002).
132. M. A. Haque and M. T. A. Saif, in "Proc. of the SEM Ann. Conf. on Exp. and Appl. Mech.," Milwaukee, WI, 2002.
133. J. A. Connally and S. B. Brown, *Science* 256, 1537 (1992).
134. S. B. Brown, W. Van Arsdell, and C. L. Muhlstein, in "Transducers 97, International Conference on Solid-State Sensors and Actuators," 1997, p. 591.
135. W. W. Van Arsdell and S. B. Brown, *J. Microelectromech. Syst.* 8, 319 (1999).
136. C. L. Muhlstein, S. B. Brown, and R. O. Ritchie, *Mater. Res. Soc. Symp. Proc.* 657 (2000).
137. C. L. Muhlstein, S. E. A. Stach, and R. O. Ritchie, *Mater. Res. Soc. Symp. Proc.* 687 (2002).
138. C. L. Muhlstein, S. B. Brown, and R. O. Ritchie, *J. Microelectromech. Syst.* 10, 593 (2001).
139. C. L. Muhlstein, S. B. Brown, and R. O. Ritchie, *Sens. Actuator A* 94, 177 (2001).
140. H. Kahn, R. Ballarini, and A. H. Heuer, *Mater. Res. Soc. Symp. Proc.* 657, 543 (2001).
141. H. Kahn, R. Ballarini, R. L. Mullen, and A. H. Heuer, *Proc. Roy. Soc. London Ser. A* 455, 3807 (1999).

*142.* E. E. Fischer and P. E. Labossiere, in "Proc. of the SEM Ann. Conf. on Exp. and Appl. Mech.," Milwaukee, WI, 2002.

*143.* L. Que, J. S. Park, and Y. B. Gianchandani, *J. Microelectromech. Syst.* 10, 247 (2001).

*144.* B. I. Yakobson, C. J. Brabec, and J. Bernholc, *Phys. Rev. Lett.* 76, 2511 (1996).

*145.* B. I. Yakobson and R. E. Smalley, *Am. Scientist* 85, 324 (1997).

*146.* X. Zhou, J. J. Zhou, and Z. C. Ou-Yang, *Phys. Rev. B* 62, 13692 (2000).

*147.* J. P. Lu, *Phys. Rev. Lett.* 79, 1297 (1997).

*148.* C. Journet, W. K. Maser, P. Bernier, A. Loiseau, M. L. delaChapelle, S. Lefrant, P. Deniard, R. Lee, and J. E. Fischer, *Nature* 388, 756 (1997).

*149.* T. W. Ebbesen and P. M. Ajayan, *Nature* 358, 220 (1992).

*150.* A. Thess, R. Lee, P. Nikolaev, H. J. Dai, P. Petit, J. Robert, C. H. Xu, Y. H. Lee, S. G. Kim, A. G. Rinzler, D. T. Colbert, G. E. Scuseria, D. Tomanek, J. E. Fischer, and R. E. Smalley, *Science* 273, 483 (1996).

*151.* W. Z. Li, S. S. Xie, L. X. Qian, B. H. Chang, B. S. Zou, W. Y. Zhou, R. A. Zhao, and G. Wang, *Science* 274, 1701 (1996).

*152.* E. W. Wong, P. E. Sheehan, and C. M. Lieber, *Science* 277, 1971 (1997).

*153.* P. A. Williams, S. J. Papadakis, A. M. Patel, M. R. Falvo, S. Washburn, and R. Superfine, *Appl. Phys. Lett.* 82, 805 (2003).

*154.* W. D. Shen, B. Jiang, B. S. Han, and S. S. Xie, *Phys. Rev. Lett.* 84, 3634 (2000).

*155.* R. M. I. Taylor and S. R., in "Advanced Interfaces to Scanning Probe Microscopes" (H. S. Nalwa, Ed.), Vol. 2. Academic Press, New York, 1999.

*156.* M. R. Falvo, G. J. Clary, R. M. Taylor, V. Chi, F. P. Brooks, S. Washburn, and R. Superfine, *Nature* 389, 582 (1997).

*157.* M. R. Falvo, R. M. Taylor, A. Helser, V. Chi, F. P. Brooks, S. Washburn, and R. Superfine, *Nature* 397, 236 (1999).

*158.* M. F. Yu, M. J. Dyer, G. D. Skidmore, H. W. Rohrs, X. K. Lu, K. D. Ausman, J. R. von Ehr, and R. S. Ruoff, *Nanotechnology* 10, 244 (1999).

*159.* Klocke Nanotechnik Co., http://www.nanomotor.de.

*160.* P. Poncharal, Z. L. Wang, D. Ugarte, and W. A. de Heer, *Science* 283, 1513 (1999).

*161.* E. A. Stach, T. Freeman, A. M. Minor, D. K. Owen, J. Cumings, M. A. Wall, T. Chraska, R. Hull, J. W. Morris, A. Zettl, and U. Dahmen, *Microsc. Microanal.* 7, 507 (2001).

*162.* Z. Lin, Ph.D. Thesis, Northwestern University, 2000.

*163.* Nanofactory Instruments, http://www.nanofactory.com/.

*164.* M. F. Yu, O. Lourie, M. J. Dyer, K. Moloni, T. F. Kelly, and R. S. Ruoff, *Science* 287, 637 (2000).

*165.* X. Q. Chen, T. Saito, H. Yamada, and K. Matsushige, *Appl. Phys. Lett.* 78, 3714 (2001).

*166.* A. Bezryadin, C. Dekker, and G. Schmid, *Appl. Phys. Lett.* 71, 1273 (1997).

*167.* P. A. Smith, C. D. Nordquist, T. N. Jackson, T. S. Mayer, B. R. Martin, J. Mbindyo, and T. E. Mallouk, *Appl. Phys. Lett.* 77, 1399 (2000).

*168.* M. P. Hughes, in "Handbook of Nanoscience, Engineering and Technology" (B. D. S. Lyshevski, G. Iafrate, and W. A. Goddard III, Eds.). Boca Raton, CRC Press, 2002.

*169.* M. P. Hughes and H. Morgan, *J. Phys. D* 31, 2205 (1998).

*170.* A. Ramos, H. Morgan, N. G. Green, and A. Castellanos, *J. Phys. D* 31, 2338 (1998).

*171.* Y. Huang, X. F. Duan, Q. Q. Wei, and C. M. Lieber, *Science* 291, 630 (2001).

*172.* M. Fujiwara, E. Oki, M. Hamada, Y. Tanimoto, I. Mukouda, and Y. Shimomura, *J. Phys. Chem. A* 105, 4383 (2001).

*173.* S. M. Huang, L. M. Dai, and A. W. H. Mau, *J. Phys. Chem. B* 103, 4223 (1999).

*174.* H. J. Dai, *Acc. Chem. Res.* 35, 1035 (2002).

*175.* J. Cumings and A. Zettl, *Science* 289, 602 (2000).

*176.* B. Bhushan, "Handbook of Micro/Nano Tribology." CRC Press, Boca Raton, 1999.

*177.* S. Morita, R. Wiesendanger, and E. Meyer, "Nanocontact Atomic Force Microscopy." Springer-Verlag, Berlin, 2002.

*178.* V. J. Morris, A. P. Gunning, and A. R. Kirby, "Atomic Force Microscopy for Biologists." Imperial College Press, London, 1999.

*179.* R. Wiesendanger, "Scanning Probe Microscopy and Spectroscopy: Methods and Applications." Cambridge Univ. Press, Cambridge, UK, 1995.

*180.* D. Bonnell, "Scanning Probe Microscopy and Spectroscopy: Theory, Techniques, and Applications." Wiley, New York, 2000.

*181.* M. F. Yu, T. Kowalewski, and R. S. Ruoff, *Phys. Rev. Lett.* 85, 1456 (2000).

*182.* J. W. G. Wildoer, L. C. Venema, A. G. Rinzler, R. E. Smalley, and C. Dekker, *Nature* 391, 59 (1998).

*183.* T. W. Odom, J. L. Huang, P. Kim, and C. M. Lieber, *Nature* 391, 62 (1998).

*184.* M. M. J. Treacy, T. W. Ebbesen, and J. M. Gibson, *Nature* 381, 678 (1996).

*185.* A. Krishnan, E. Dujardin, T. W. Ebbesen, P. N. Yianilos, and M. M. J. Treacy, *Phys. Rev. B* 58, 14013 (1998).

*186.* D. A. Walters, L. M. Ericson, M. J. Casavant, J. Liu, D. T. Colbert, K. A. Smith, and R. E. Smalley, *Appl. Phys. Lett.* 74, 3803 (1999).

*187.* J. P. Salvetat, G. A. D. Briggs, J. M. Bonard, R. R. Bacsa, A. J. Kulik, T. Stockli, N. A. Burnham, and L. Forro, *Phys. Rev. Lett.* 82, 944 (1999).

*188.* J. P. Salvetat, A. J. Kulik, J. M. Bonard, G. A. D. Briggs, T. Stockli, K. Metenier, S. Bonnamy, F. Beguin, N. A. Burnham, and L. Forro, *Adv. Mater.* 11, 161 (1999).

*189.* Z. W. Pan, S. S. Xie, L. Lu, B. H. Chang, L. F. Sun, W. Y. Zhou, G. Wang, and D. L. Zhang, *Appl. Phys. Lett.* 74, 3152 (1999).

*190.* J. R. Weertman and P. G. Sanders, *Solid State Phenom.* 35–36, 249 (1993).

*191.* T. Volpp, E. Goring, W. M. Kuschke, and E. Arzt, *Nanostruct. Mater.* 8, 855 (1997).

*192.* R. Z. Valiev, "Mechanical Properties and Deformation Behavior of Materials Having Ultra-Fine Microstructures." Kluwer Academic, Dordecht, 1993.

*193.* J. E. Carsley, W. W. Milligan, X. H. Zhu, and E. C. Aifantis, *Scr. Mater.* 36, 727 (1997).

*194.* J. E. Carsley, A. Fisher, W. W. Milligan, and E. C. Aifantis, *Metall. Mater. Trans. A* 29, 2261 (1998).

*195.* W. W. Milligan, S. A. Kachney, M. Ke, and E. C. Aifantis, *Nanostruct. Mater.* 2, 267 (1993).

*196.* H. D. Espinosa, Y. Zhu, and B. Peng, in "Proc. of the SEM Ann. Conf. on Exp. and Appl. Mech.," Milwaukee, WI, 2002.

*197.* Y. Zhu, F. Barthelat, P. E. Labossiere, N. Moldovan, and H. D. Espinosa, in "Proc. of the SEM Ann. Conf. on Exp. and Appl. Mech.," Charlotte, NC, 2003.

*198.* MicroSensors, Inc., http://www.microsensors.com.

*199.* C. D. Lott, T. W. McLain, J. N. Harb, and L. L. Howell, *Sens. Actuator A* 101, 239 (2002).

*200.* A. M. Minor, E. T. Lilleodden, E. A. Stach, and J. W. Morris, *J. Electron. Mater.* 31, 958 (2002).

*201.* A. M. Minor, J. W. Morris, and E. A. Stach, *Appl. Phys. Lett.* 79, 1625 (2001).

*202.* J. C. Spence, "Experimental High-Resolution Electron Microscopy," 2nd ed. Oxford Univ. Press, Oxford, 1988.

*203.* D. B. Williams and B. C. Carter, "Transmission Electron Microscopy, A Textbook for Materials Science." Plenum, New York, 1996.

*204.* P. Buseck, J. M. Cowley, and L. Eyring, "High Resolution Transmission Electron Microscopy—Theory and Applications." Oxford Univ. Press, Oxford, 1990.

*205.* M. Gao, J. M. Zuo, R. D. Twesten, I. Petrov, L. A. Nagahara, and R. Zhang, *Appl. Phys. Lett.* 82, 2703 (2003).

206. T. W. Tombler, C. W. Zhou, L. Alexseyev, J. Kong, H. J. Dai, L. Lei, C. S. Jayanthi, M. J. Tang, and S. Y. Wu, *Nature* 405, 769 (2000).
207. W. N. Sharpe, Jr., in "The MEMS Handbook" (M. Gad-el-Hak, Ed.). CRC Press, Boca Raton, 2002.
208. T. P. Weihs, S. Hong, J. C. Bravman, and W. D. Nix, *Mater. Res. Soc. Symp. Proc.* 402, 87 (1989).
209. D. Read, Y. Cheng, R. Keller, and J. McColskey, *Scr. Mater.* 45, 583 (2001).
210. B. T. Comella and M. R. Scanlon, *J. Mater. Sci.* 35, 567 (2000).
211. M. Hommel and O. Kraft, *Acta Mater.* 49, 3835 (2001).
212. T. E. Buchheit, T. R. Schmale, and D. A. LaVan, *Mater. Res. Soc. Symp. Proc.* 546, 121 (1999).
213. S. Greek and F. Ericson, *Mater. Res. Soc. Symp. Proc.* 518, 51 (1998).
214. W. N. Sharpe, Jr. and A. McAleavey, *Proc. SPIE* 3512, 130 (1998).
215. J. J. Sniegowski and M. P. de Boer, *Ann. Rev. Mater. Res.* 30, 299 (2000).
216. J. M. Bustillo, R. T. Howe, and R. S. Muller, *Proc. IEEE* 86, 1552 (1998).
217. T. Yi and C. J. Kim, *Meas. Sci. Technol.* 10, 706 (1999).
218. X. D. Li and B. Bhushan, *Thin Solid Films* 340, 210 (1999).
219. B. Bhushan and X. D. Li, *J. Mater. Res.* 12, 54 (1997).
220. S. Johansson, J. A. Schweitz, L. Tenerz, and J. Tiren, *J. Appl. Phys.* 63, 4799 (1988).
221. C. J. Wilson and P. A. Beck, *J. Microelectromech. Syst.* 5, 142 (1996).
222. W. Suwito, M. L. Dunn, and S. J. Cunningham, in "Int. Solid-State Sensors and Actuators Conf.—Transducers' 97," Chicago, 1997, p. 611.
223. K. E. Peterson, *Proc. IEEE* 70, 5 (1982).
224. S. J. Cunningham, S. Wan, and D. T. Read, in "Int. Solid-State Sensors and Actuators Conf.—Transducers' 95," Stockholm, Sweden, 1995, p. 25.
225. K. Sato, M. Shikida, T. Yoshioka, T. Ando, and T. Kawbata, in "Int. Solid-State Sensors and Actuators Conf.—Transducers' 97," Chicago, 1997, p. 595.
226. T. Yi and C. J. Kim, in "Int. Solid-State Sensors and Actuators Conf.—Transducers' 99," Sendai, Japan, 1999, p. 518.
227. M. T. A. Saif and N. C. MacDonald, in "9th Int. Workshop on Micro Electro Mechanical Systems," San Diego, 1996.
228. J. Dual, E. Mazza, G. Schiltges, and D. Schlums, *Proc. SPIE* 3225, 12 (1997).
229. W. N. Sharpe, Jr., K. M. Jackson, K. J. Hemker, and Z. Xie, *J. Microelectromech. Syst.* 10, 317 (2001).
230. J. Bagdahn and W. N. Sharpe, Jr., *Mater. Res. Soc. Symp. Proc.* 687 (2002).
231. W. N. Sharpe, Jr., B. Yuan, and R. Vaidyanathan, in "10th Int. Workshop on Micro Electro Mechanical Systems," Nagoya, Japan, 1997, p. 424.
232. P. T. Jones, G. C. Johnson, and R. T. Howe, *Mater. Res. Soc. Symp. Proc.* 518, 197 (1998).
233. B. Bhushan and L. Xiaodong, *Thin Solid Films* 340, 210 (1999).
234. T. Tsuchiya, A. Inoue, and J. Sakata, in "Int. Solid-State Sensors and Actuators Conf.—Transducers' 99," Sendai, Japan, 1999, p. 488.
235. C. Seere, A. Perez-Rodriguez, A. Romano-Rodriguez, J. R. Morante, J. Esteve, and M. C. Acero, *J. Micromech. Microeng.* 9, 190 (1999).
236. S. Sundararajan and B. Bhushan, *Wear* 217, 251 (1998).
237. A. V. Sumant, O. Auciello, A. R. Krauss, D. M. Gruen, D. Ersoy, J. Tucek, A. Jayatissa, E. Stach, N. Moldovan, D. Mancini, H. G. Busmann, and E. M. Meyer, *Mater. Res. Soc. Symp. Proc.* 657 (2000).
238. S. A. Catledge, J. Borham, and Y. K. Vohraa, *J. Appl. Phys.* 91, 5347 (2002).
239. M. I. De Barros and L. Vandenbulcke, L. Chinsky, D. Rats, and J. von Stebut, *Diamond Related Mater.* 10, 337 (2001).
240. E. A. Ekimov, E. L. Gromnitskaya, S. Gierlotka, W. Lojkowski, B. Palosz, A. Swiderska-Sroda, J. A. Kozubowski, and A. M. Naletov, *J. Mater. Sci. Lett.* 21, 1699 (2002).
241. S. A. Catledge and Y. K. Vohra, *J. Appl. Phys.* 83, 198 (1998).
242. R. L. Newton and J. L. Davidson, in "Mechanical Properties of Structural Films" (C. L. Muhlstein and S. B. Brown, Eds.), p. 318. ASTM, West Conshohocken, PA, 2001.
243. A. Kant, M. D. Drory, N. R. Moody, W. J. MoberlyChan, J. W. Ager, and R. O. Ritchie, *Mater. Res. Soc. Symp. Proc.* 505, 611 (1998).
244. P. Gluche, M. Adamschik, A. Vescan, W. Ebert, E. Kohn, A. Floter, R. Zachai, H. J. Fecht, and F. Szucs, *Diamond Related Mater.* 7, 779 (1998).
245. M. D. Drory, R. H. Dauskardt, A. Kant, and R. O. Ritchie, *J. Appl. Phys.* 78, 3083 (1995).
246. A. Kant, M. D. Drory, and R. O. Ritchie, *Mater. Res. Soc. Symp. Proc.* 383 (1995).
247. S. Christiansen, M. Albrecht, and H. P. Strunk, *J. Mater. Res.* 11, 1934 (1996).
248. K. H. Lai, C. Y. Chan, M. K. Fung, I. Bello, C. S. Lee, and S. T. Lee, *Diamond Related Mater.* 10, 1862 (2001).
249. D. Schneider, C. F. Meyer, H. Mai, B. Schoneich, H. Ziegele, H. J. Scheibe, and Y. Lifshitz, *Diamond Related Mater.* 7, 973 (1998).
250. S. E. Coe and R. S. Sussmann, *Diamond Related Mater.* 9, 1726 (2000).
251. T. Michler, M. Grischke, I. Traus, K. Bewilogua, and H. Dimigen, *Diamond Related Mater.* 7, 1333 (1998).
252. J. C. Sanchez-Lopez, C. Donnet, J. L. Loubet, M. Belin, A. Grill, V. Patel, and C. Jahnes, *Diamond Related Mater.* 10, 1063 (2001).
253. J. Cumings, P. G. Collins, and A. Zettl, *Nature* 406, 586 (2000).
254. S. Paulson, M. R. Falvo, N. Snider, A. Helser, T. Hudson, A. Seeger, R. M. Taylor, R. Superfine, and S. Washburn, *Appl. Phys. Lett.* 75, 2936 (1999).
255. D. J. Lloyd, *Int. Mater. Rev.* 39, 1 (1994).
256. M. T. Kiser, F. W. Zok, and D. S. Wilkinson, *Acta Mater.* 44, 3465 (1996).
257. N. A. Fleck and J. W. Hutchinson, *J. Mech. Phys. Solids* 49, 2245 (2001).
258. N. A. Fleck, M. F. Ashby, and J. W. Hutchinson, *Scr. Mater.* 48, 179 (2003).
259. Y. Guo, Y. Huang, H. Gao, Z. Zhuang, and K. C. Hwang, *Int. J. Solids Struct.* 38, 7447 (2001).
260. Z. P. Bazant, Theoretical and Applied Mechanics Report 00-12/C99s, Northwestern University (2000).
261. Z. P. Bažant, *J. Mech. Phys. Solids* 50, 435 (2002).
262. J. L. Bassani, *J. Mech. Phys. Solids* 49, 1983 (2001).
263. A. Acharya and J. L. Bassani, *J. Mech. Phys. Solids* 48, 1565 (2000).
264. Z. P. Bazant and Z. Y. Guo, *Int. J. Solids Struct.* 39, 5633 (2002).
265. R. A. Toupin, *Arch. Ration. Mech. Anal.* 11, 385 (1963).
266. R. D. Mindlin, *Int. J. Solids Struct.* 1, 417 (1965).
267. M. Jirasek and Z. P. Bazant, "Inelastic Analysis of Structures." Wiley, New York, 2002.
268. S. H. Chen and T. C. Wang, *Acta Mater.* 48, 3997 (2000).
269. S. H. Chen and T. C. Wang, *Int. J. Plast.* 18, 971 (2002).
270. Z. P. Bazant, "Scaling of Structural Strength," Hermes-Penton Science (Kogan Publishing), London, 2002.
271. B. I. Yakobson and P. Avouris, *Topics Appl. Phys.* 80, 287 (2001).
272. K. N. Kudin, G. E. Scuseria, and B. I. Yakobson, *Phys. Rev. B* 64, 235406 (2001).
273. H. F. Bettinger, T. Dumitrica G. E. Scuseria, and B. I. Yakobson, *Phys. Rev. B* 65, 041406 (2002).
274. O. A. Shenderova, V. V. Zhirnov, and D. W. Brenner, *Crit. Rev. Solid State Mater. Sci.* 27, 227 (2002).

*275.* D. Appell, *Nature* 419, 553 (2002).
*276.* P. Ball, "Made to Measure." Princeton Univ. Press, Princeton, NJ, 1997.
*277.* Y. F. Zhao and B. I. Yakobson, *Phys. Rev. Lett.* 91, 035501 (2003).
*278.* M. B. Nardelli, B. I. Yakobson, and J. Bernholc, *Phys. Rev. Lett.* 81, 4656 (1998).
*279.* G. G. Samsonidze and B. I. Yakobson, *Comput. Mater. Sci.* 23, 62 (2002).
*280.* G. G. Samsonidze and B. I. Yakobson, *Phys. Rev. Lett.* 88, 065501 (2002).
*281.* T. Dumitrica, T. Belytschko, and B. I. Yakobson, *J. Chem. Phys.* 119, 1281 (2003).
*282.* Y. F. Zhao, B. I. Yakobson, and R. E. Smalley, *Phys. Rev. Lett.* 88 185501 (2002).
*283.* B. I. Yakobson, U.S. Patent, 2001.
*284.* D. J. Jacobs and M. F. Thorpe, *Phys. Rev. Lett.* 75, 4051 (1995).
*285.* D. J. Jacobs and M. F. Thorpe, *Phys. Rev. E* 53, 3682 (1996).
*286.* B. X. Li, P. L. Cao, R. Q. Zhang, and S. T. Lee, *Phys. Rev. B* 65, 125305 (2002).
*287.* P. Sen, O. Gulseren, T. Yildirim, I. P. Batra, and S. Ciraci, *Phys. Rev. B* 65, 235433 (2002).
*288.* B. Marsen and K. Sattler, *Phys. Rev. B* 60, 11593 (1999).
*289.* S. Ismail-Beigi and T. Arias, *Phys. Rev. B* 57, 11923 (1998).
*290.* H. Yorikawa, H. Uchida, and S. Muramatsu, *J. Appl. Phys.* 79, 3619 (1996).
*291.* J. D. Holmes, K. P. Johnston, R. C. Doty, and B. A. Korgel, *Science* 287, 1471 (2000).
*292.* D. D. D. Ma, C. S. Lee, F. C. K. Au, S. Y. Tong, and S. T. Lee, *Science* 299, 1874 (2003).
*293.* R. H. Baughman, A. A. Zakhidov, and W. A. de Heer, *Science* 297, 787 (2002).
*294.* P. A. Williams, S. J. Papadakis, M. R. Falvo, A. M. Patel, M. Sinclair, A. Seeger, A. Helser, R. M. Taylor II, S. Washburn, and R. Superfine, *Appl. Phys. Lett.* 80, 2574 (2002).
*295.* J. Chung and J. Lee, *Sensors Actuators A* 104, 229 (2003).
*296.* M. F. Yu, B. S. Files, S. Arepalli, and R. S. Ruoff, *Phys. Rev. Lett.* 84, 5552 (2000).
*297.* M. F. Yu, B. I. Yakobson, and R. S. Ruoff, *J. Phys. Chem. B* 104, 8764 (2000).
*298.* Y. Zhang, A. Chang, J. Cao, Q. Wang, W. Kim, Y. Li, N. Morris, E. Yenilmez, J. Kong, and H. Dai, *Appl. Phys. Lett.* 79, 3155 (2001).
*299.* H. Dai, *Phys. World* 13, 43 (2000).
*300.* J. Kong, H. T. Soh, A. M. Cassell, C. F. Quate, and H. Dai, *Nature* 395, 878 (1998).
*301.* K. Yamamoto, S. Akita, and Y. Nakayama, *J. Phys. D* 31, L34 (1998).
*302.* L. Lin and M. Chiao, *Sensors Actuators A* 55, 35 (1996).

ENN
*Encyclopedia of Nanoscience and Nanotechnology*
www.aspbs.com/enn

# Low-Dimensional Nanocrystals

## Shu-Hong Yu, Jian Yang, Yi-Tai Qian

*University of Science and Technology of China, Hefei, Anhui, China*

## CONTENTS

## 1. INTRODUCTION

Nanostructured semiconductors with a size range of 1–100 nm have been the focus of recent scientific research because of their important nonlinear optical properties [1], luminescent properties [2, 3], quantum size effects [4, 5], and other important physical and chemical properties [6]. In past decades, low-dimensional materials such as nanometer-size inorganic dots, tubes, and wires have exhibited a wide range of electronic and optical properties that depend sensitively on both size and shape, and are of both fundamental and technological interest [7, 8]. They are potentially ideal building blocks for nanoscale electronics and optoelectronics [9]. The ability to control the shapes of semiconductor nanocrystals affords an opportunity to further test theories of quantum confinement and yields samples with desirable optical characteristics from the point of view of application [10, 11].

The exciting emerging important applications of low-dimensional semiconductor nanocrystals include using QDs in biological assays [12–15], building blocks for assembly semiconductor nanodevices [16], hybrid nanorod-polymer solar cells that combine semiconducting polymers and nano-particles in useful photovoltaic devices with relatively high conversion efficiencies [17], room-temperature ultraviolet lasing using ZnO nanowire (NW) arrays [18], light-emitting diodes (LEDs) [9], and nanosensors for biological and chemical species [19–21].

One of the current hottest issues in nanotechnology and nanoscience is how to control the size, shape, and dimensionality of nanocrystals because of their important applications in the design of new materials and devices in various fields such as catalysis, electronics, medicine, ceramics, pigments, cosmetics, and biotechnology [11–22]. For example, shape control is of significant importance in the fabrication of semiconductor nanocrystals [11], metal nano-crystals [24], and other inorganic materials [25], which may add alternative variables in the tailoring of properties of nanomaterials and provide more possibilities in the fabrication of nanodevices. The key issue in the study and application of 1D materials is how to assemble individual atoms into 1D nanostrucutres in an effective and controllable way [23]. Scheme 1 shows a schematic illustration of ideal semiconductor nanocrystals with well-defined shapes and sizes, and the relationship of the band gap to nano-particle size [26].

Considerable progress and a lot of effort have been made in the synthesis of technologically important semiconductors from the group II–VI, III–VI, and IV families of crystallites or nanocrystallines, which have been reviewed recently [27, 28]. However, all of these methods can only produce nanocrystallites with shapes never very far from spherical [23, 27–33]. Although several examples have been demonstrated, shape control has been more difficult to achieve. An intensive recent review by Yang et al. summarized the general strategies for the synthesis of various kinds of one-dimensional NWs or nanorods (NRs) [23]. In addition, a review by Nesper et al. [34] of the synthesis of oxide NR and nanotube (NT) materials appeared very recently.

This chapter will give a general overview of the state of the art for the variety of different synthesis routes of low-dimensional nanocrystals, with a focus on 1D NRs/NWs by solution pathways and emerging new approaches. Since the synthesis of NTs and oxide NWs/NRs has been reviewed very recently [23, 34], we will focus more on the synthesis of nonoxide low-dimensional nanocrystals by mild solution processes and introduce some promising new strategies for self-assembly of 1D, 2D nanocrystals and more complex structures.

The chapter is organized into the following parts: in the first part, a grand survey of research activities and progress
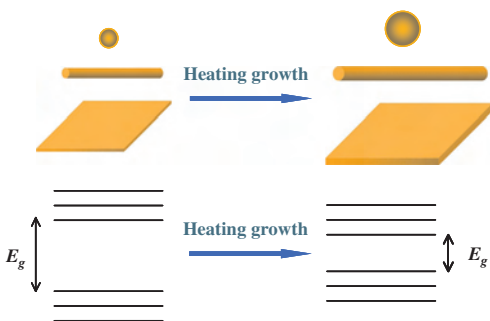
**Scheme 1.** Schematic illustration of the preparation of semiconductor nanocrystals with ideal shapes and sizes, and the relationship of the band gap to nanoparticle size. Reprinted with permission from [26], S. H. Yu, *J. Ceram. Soc. Jpn.* 109, S65 (2001). © 2001, Ceramic Society of Japan.

on the various low-dimensional nanocrystals was summarized in the form of tabulation.

The second part will discuss the main methodologies and emerging promising approaches for the synthesis of various important inorganic NWs/NRs, hierarchical nanostructures, and more complex superstructures with strong application potential. Generally, the synthetic strategies can be classified into two types, the "hard" and "soft" approaches, according to the preparation characteristics and reaction conditions. Among the "hard" approaches, usually foreign hard templates or drastic reaction conditions are needed; for example, the reaction medium is usually gas phase, and a high vacuum system and high temperature are applied. The main existing "hard" approaches for synthesis of 1D nanomaterials include four types: (i) The template-directed growth method, in which hard templates such as carbon nanotubes [7, 8, 35, 36] and porous aluminum template [37–40] are used. (ii) The vapor-liquid-solid (VLS) mechanism, which was previously proposed by Wagner in the 1960s [41]. This mechanism has been applied for the synthesis of various semiconductor NWs [42–47]. A laser ablation-based VLS catalytic growth process (LCG) makes it possible to synthesize semiconductor NWs with many different compositions [48]. (iii) The vapor-solid (VS) mechanism [49], in which NWs are generated directly from vapor condensation onto a substrate. Various metal oxides such as MgO, $Al_2O_3$, ZnO, and $SnO_2$ NWs or nanobelts (NBs) have been grown by either a carbon-thermal reduction process [50, 51] or direct thermal evaporation [52, 53]. (iv) The oxide-assisted NW growth route [54–59] was reported by Lee's group for growing GaAs, GaN NWs and Si NWs with the advantages of not having to use a metal catalyst or a template.

In contrast, the "soft" approaches are based on solution reactions and do not need a foreign hard template. They do not involve the use of drastic conditions, and the reaction is usually initiated under mild conditions or under natural conditions. The emerging main approaches also include four types: (i) A solvothermal process, which has been emerging as a versatile solution route for the synthesis of various semiconductor nanocrystals with different sizes and shapes [26, 34, 60–65]. (ii) A solution-liquid-solid (SLS) mechanism, which is used for growing III–V group nanofibers in hydrocarbon solvents at relatively low temperatures [60, 66–69] (group IV Ge, Si NWs can also be generated by a supercritical fluid solution-phase approach [70, 71]). (iii) Capping agent/surfactant-assisted synthesis [11, 25, 72–79]. Well-defined nanostructures can be obtained under hot conditions or natural/mild conditions. (iv) A bio-inspired approach for complex superstructures [73, 80–95]. In this approach, soft templates such as polymers, organic additives, or supramolecular templates are employed as crystal growth modifiers [88–90] and templates [94]. (v) An oriented attachment growth mechanism [96–103]. The spontaneous aggregation of smaller nanoparticles into well-structured nanocrystals has been reported in the case of $TiO_2$ [97–99], ZnO [100, 102], and CdTe [103]. These main strategies will be discussed in more detail with specific examples in the following parts after the general grand survey on the synthesis methodologies. Finally, we will give our own perspectives.

# 2. SYNTHETIC ROUTES FOR LOW-DIMENSIONAL NANOCRYSTALS

The intensive research and ongoing advances in the synthesis of various nanomaterials make it more and more difficult to keep up to date with all of the new achievements. However, in this section, we will try our best to briefly summarize various low-dimensional nanocrystals with strong application potentials synthesized by different routes in the past decade. We will focus more on the synthesis of 1D, 2D nanocrystals and more complex structures built up based on simple synthesis strategies, which we call "emerging and promising approaches" here.

Since intensive reviews on the synthesis of semiconductor nanodots (0D) have been published very recently [27, 28], we only focus on 1D and 2D nanomaterials such as NWs, NRs, NBs, nanoribbons, NTs, nanosheets (2D), and more complex structures. Table 1 is a general survey of various oxide NRs, NWs, NTs, and NBs or other novel/new nanostructures prepared by different strategies. Table 2 gives an intensive survey of nonoxide inorganic nanomaterials such as metal, semiconductor, and carbide- or nitride-based nanomaterials (NRs, NWs, NTs, nanoribbons, NBs, etc.).

## 2.1. Templated-Directed Growth Method

Template-based synthesis of low-dimensional nanomaterials has been widely employed in past decades. The characteristic of this method is the use of various templates to limited reactions to a confined nanoscale space such as channels or on a surface. Conventional templates include porous solid-state materials such as carbon NTs, anode aluminum oxide, zeolites, MCM-41 mesoporous silica, and porous polymers. Representative examples are given below to illustrate the application of these templates in the formation of various kinds of one-dimensional nanocrystals.

**Table 1.** Synthetic routes for oxide low-dimensional nanocrystals (published since 1995).

| Nanomaterials | Synthetic method | Ref. |
|---|---|---|
| $BaTiO_3$ NRs | Solution-phase decomposition of bimetallic alkoxide precursors in the presence | [104] |
| $SrTiO_3$ NRs | of coordinating ligands | [104] |
| $BaSO_4$ NWs and superstructures | Mineralization from aqueous solution in the presence of polymers | [88, 89] |
| $BaCrO_4$ NWs and chain structures | Reversed micelle templating method | [25, 75] |
| $BaCrO_4$ NWs and superstructures | Mineralization from aqueous solution in the presence of polymers | [89–91] |
| $BaCO_3$ NWs | A reverse micelle-based approach | [77] |
| $BaWO_4$ NRs | Reversed micelle templating method | [78] |
| $BaWO_4$ NWs | Cationic reverse micelles | [79] |
| $BaWO_4$ NWs arrays | Langmuir-Blodgett assembly of 1D nanostructures | [105, 106] |
| $CaSO_4$ NWs | A water-in-oil microemulsions route | [107] |
| CdO NBs | Evaporation of metal oxide powders at high temperatures, VS | [52] |
| $CdWO_4$ Nanosheets | Hydrothermal treatment in the presence of block copolymers | [92] |
| $CdWO_4$ NBs | Double jet reaction at room temperature | [92] |
| $CdWO_4$ NRs | Hydrothermal treatment of $CdCl_2$ and $Na_2WO_4$ | [108] |
| $Co_3O_4$ NRs | Template method with alumina membranes | [109] |
| $Co_3O_4$ NRs | Calcination of precursor powders prepared in a novel inverse microemulsion | [110] |
| CuO NRs | Room-temperature reaction of $CuCl_2 \cdot 2H_2O$ and NaOH with PEG 400 | [111] |
| CuO NRs | Heating copper substrates in air | [112] |
| $Eu_2O_3$ NRs | Sonication of an aqueous solution | [113] |
| $Fe_2O_3$ NRs | Thin-film processing method | [114] |
| $Fe_2O_3$ NRs | Grown onto a polycrystalline (or single-crystalline) substrate from an aqueous solution of ferric salts | [115] |
| $Fe_3O_4$ NRs | Sonication of aqueous iron(II) acetate in the presence of $\beta$-cyclodextrin | [116] |
| $Fe_4[Fe(CN)_6]_3 \cdot xH_2O$ NWs | Electrodeposition with two-step anodizing anodic aluminum oxide films | [117] |
| $Ga_2O_3$ NRs | Catalytic growth by arc discharge of GaN powders in $Ar/O_2$ mixture | [118] |
| $Ga_2O_3$ | Gas reaction method starting from Ga and $O_2$ | [119] |
| $Ga_2O_3$ | Physical evaporation at 300 °C from a bulk gallium target | [120] |
| $Ga_2O_3$ | DC arc discharge (GaN, graphite, nickel powder) | [121] |
| $Ga_2O_3$ | Electric arc discharge of GaN powders mixed with Ni and Co | [122] |
| $Ga_2O_3$ | Heat treatment of Ga with $SiO_2$ powder and a $Fe_2O_3$ catalyst | [123] |
| $Ga_2O_3$ NTs, NWs Nano-paintbrushes | Molten gallium and microwave plasma containing a mixture of monatomic oxygen and hydrogen | [124] |
| $Ga_2O_3$ NWs | Heating raw materials in $N_2$ or Ar without metal catalysts | [125] |
| $GeO_2$ NRs | Carbon-NT confined reaction of metallic Ge | [126] |
| $GeO_2$ NWs | Carbothermal reduction reaction between germanium dioxide and active carbons | [127] |
| $GeO_2$ NWs | Thermal oxidation of suboxide at high temperature | [128] |
| $In_2O_3$ NBs | Evaporation of metal oxide powders at high temperatures, VS | [52] |
| $In_2O_3$ NWs | A rapid heating process on Au-coated InP substrates in oxygen | [129] |
| $IrO_2$ | Templating against carbon NTs | [130] |
| $K_2Ti_6O_{13}$ | Calcination of KF and $TiO_2$ | [131] |
| $LaPO_4$:Eu NWs | Hydrothermal synthesis | [132] |
| $LaPO_4$:Ce NWs | Hydrothermal synthesis | [132] |
| MgO NRs | Vapor-solid growth process with *in-situ* generated Mg vapor | [51] |
| MgO NWs | Oxide-assisted catalytic growth method | [133] |
| MgO NWs | Vapor-phase method using $MgB_2$ as precursor | [134] |
| MgO NRs | Heating of $MgCl_2$ at 750 °C in mixture gas $(Ar/H_2)$ | [135] |
| $Mg(OH)_2$ NRs | Hydrothermal reaction of Mg, $H_2O$, and ethylenediamine | [136] |
| $MnO_2$ NRs | Template method with alumina membranes by a sol–gel approach | [137] |
| $MnO_2$ NRs | Hydrothermal synthesis | [138] |
| $Mn_3O_4$ NWs | Thermolysis of carbonates in NaCl flux and a surfactant NP9 at 850 °C | [139] |
| $Mg_{2.11}Mn_{5.46}O_{12} \cdot xH_2O$ nano-ribbons | A combination of techniques consisting of a sol–gel process for tetraethylammonium manganese oxide layered material, an ion-exchange method to a thin-film Mg-buserite precursor, and a hydrothermal reaction to transform the Mg-buserite to nanoribbonlike Mg-todorokite material | [140] |
| $MoO_3$ NRs | Template-directed reaction of molybdic acid and subsequent leaching process | [141] |
| $MoO_3$ NRs | Templating against carbon nanotubes | [130] |
| $MoO_2$ NRs | Templating against carbon NTs | [130] |
| $Ni(OH)_2$ NRs | Hydrothermal synthesis and deposition in a carbon-coated anodic alumina film | [142] |

**Table 1.** Continued

| Nanomaterials | Synthetic method | Ref. |
|---|---|---|
| NiO NRs | Thermal decomposition of a precursor in NaCl flux | [143] |
| PbTiO$_3$ NWs | Sol–gel electrophoresis, deposition in polycarbonate membrane | [144] |
| RuO$_2$ NRs | Templating against carbon NTs | [130] |
| Sb$_2$O$_3$ NRs | Microemulsion method for the system AOT-water-toluene | [145] |
| Sb$_2$O$_3$ NRs | A vapor-solid route using Sb$_2$S$_3$ nanopowders as raw material, VS | [146] |
| Sb$_2$O$_3$ NRs | Templated against carbon NTs | [147] |
| Sb$_2$O$_5$ NRs | Microemulsion method for the system AOT-water-toluene | [145] |
| SnO$_2$ NRs | Calcining precursors that are produced in inverse microemulsions | [148, 149] |
| SnO$_2$ NBs | Evaporation of metal oxide powders at high temperatures, VS | [52] |
| SnO$_2$ NWs, nanoribbons, NTs | Elevated temperature synthesis techniques using layered mixtures of Sn foil and SnO powder or simply SnO powder, VS | [150] |
| SnO$_2$ diskettes | Evaporating techniques using SnO or SnO$_2$ powders, VS | [151] |
| SnO nanoribbons | Evaporating SnO powders, VS | [152] |
| SiO$_2$ NWs | Helical mesostructured tubules from the Taylor vortex-assisted surfactant templates | [153] |
| SiO$_2$ NWs | Oxidation of Si wafer induced by molten gallium | [154] |
| SiO$_2$ NWs and bunches | Vapor-liquid-solid (VLS) process using molten gallium as a catalyst | [155] |
| SiO$_2$ NTs, NWs | Pyrolysis of mixed Si and SiO$_2$ powders | [156] |
| SiO$_2$ NWs | Using Au nanoparticle catalysts on a silicon substrate | [157] |
| SiC/SiO$_2$ helical core-shell NWs | Chemical vapor deposition technique | [158] |
| TiO$_2$ NWs | Electrochemically preparation using nanochannel alumina | [159] |
| TiO$_2$ NWs | Sol–gel template method employing alumina membranes | [160] |
| TiO$_2$ NWs | Electrochemically induced sol–gel preparation | [161] |
| TiO$_2$ NTs | Sol–gel-derived fine TiO$_2$-based powders were treated with NaOH aqueous solution | [162] |
| TiO$_2$ NTs | Solution growth method by hydrolyzing TiF$_4$ under acidic condition | [163] |
| TiO$_2$ NTs | Sol–gel method and removing the polymer thermally | [164] |
| TiO$_2$ NTs | Calcination of an organic gelator prepared from supramolecular assemblies | [165] |
| VO$_x$ NTs | Hydrothermal using long-chain amine as templates | [166–168] |
| V$_2$O$_5$ NRs | Vanadium pentoxide gels | [169] |
| V$_2$O$_5$ NRs | Templating against carbon NTs | [130] |
| WO$_3$ NRs | Templating against carbon NTs | [130] |
| WO$_3$ NRs | Direct oxidation of tungsten metal | [170] |
| YBCO NRs | Laser ablation of a high $T_c$ superconductor YBa$_2$Cu$_3$O$_7$ | [171] |
| ZnO NRs | Gas reaction employing Zn and H$_2$O | [172] |
| ZnO NWs | Heating Zn in N$_2$ or Ar without metal catalysts | [125] |
| ZnO NWs | Catalytic growth by vapor transport, VLS | [45, 173] |
| ZnO NBs | Evaporation of metal oxide powders at high temperatures, VS | [52] |
| ZnO NWs | Thermal evaporation, VS | [174] |
| ZnO NWs | Catalyzed epitaxial growth, VLS | [46] |
| ZnO NRs | Catalyst-free CVD method | [175] |
| ZnO NRs | Thermal decomposition of the precursor of ZnC$_2$O$_4$ in the presence of surfactant nonyl phenyl ether and NaCl flux | [176] |
| ZnO NWs | Site-specific growth by catalysis-driven molecular beam epitaxy | [177] |
| ZnO NWs arrays | Electrodeposited in the pores of anodic alumina membranes | [178] |
| ZnO NWs on CNTs | Multiwall carbon NTs were treated with Zn | [179] |
| ZnO NRs | Oriented attachment growth from ZnO nanoparticles from solution | [102] |
| ZnO hierarchical nano-structures | Vapor transport and condensation process on In$_2$O$_3$ core NWs | [53] |
| ZnO helical NRs | Biomimetic controlled nucleation and growth on ZnO NR arrays | [95] |

Carbon NTs, which were discovered in 1991 [352], are a good candidate for template-induced growth. The first example using carbon NTs as templates came from the synthesis of metal carbide NRs [35]. In this approach, carbon NTs as a reactant were directly converted into MC$_x$ NRs by the reactions of volatile metal oxide species. Herein, MO should be a metal oxide or nonmetal oxide with a relatively high vapor pressure at the desired reaction temperature.

$$MO + C(\text{nanotubes}) \Longrightarrow MC(\text{nanorods}) + CO \quad (1)$$
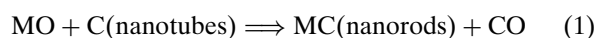
Similarly, GaN NRs were fabricated through the reaction of carbon NTs with MO (metal oxide) under an ammonia atmosphere [36]. Figure 1 shows typical TEM images of the original C NTs and GaN NRs templated from C NTs. Herein, MO should be a metal oxide or nonmetal oxide with a relatively high vapor pressure at the desired reaction temperature. The total reaction formula could be expressed as the following:

$$2Ga_2O(g) + C(\text{nanotubes}) + 4NH_3$$
$$\Longrightarrow 4GaN(\text{nanorods}) + H_2O + CO + 5H_2 \quad (2)$$
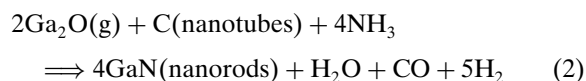
**Table 2.** Synthetic routes for nonoxide low-dimensional nanocrystals (published since 1995).

| Nanomaterials | Synthetic method | Ref. |
|---|---|---|
| Ag ultrathin NWs | Grow inside the pores of self-assembled calyx [4] hydroquinone NTs by electro/photochemical redox reaction in an ambient aqueous phase | [180] |
| Ag NWs | Templated from the mesoporous silica | [181, 182] |
| Ag NWs | Metal NW formation using $Mo_3Se_3^-$ as reducing and sacrificing templates | [183] |
| Ag NRs and dendrites | Ultraviolet photoreduction technique at room temperature using poly(vinyl-alcohol) (PVA) as protection agent | [184] |
| Ag NRs, NWs | Seed-mediated growth in a rodlike micellar medium | [185] |
| Ag nanoprisms | A photoinduced method for converting large quantities of silver nanospheres into triangular nanoprisms | [186] |
| Ag NWs | Electron-beam-induced growth from zeolite crystallites | [187] |
| Ag NWs | Templated from AgBr nanocrystals | [188] |
| Ag nanoarrays | Formed inside micellar arrays of a template consisting of a (dendritic polysilane)/polyisocyanide block copolymer reduced under the TEM electron beam | [189] |
| Ag NWs | Solid-liquid phase arc discharge method | [190] |
| Ag truncated triangular nanoplates | A solution phase method in the presence of cetyltrimethylammonium bromide micelles | [191] |
| Ag nanodisc | Mixing two reverse micellar solutions | [192] |
| Ag nanoprisms | Boiling $AgNO_3$ in $N,N$-dimethyl formamide, in the presence of poly(vinylpyrrolidone) | [193] |
| Ag NWs | Solvothermal reaction using Pt nanoparticles as seeds in ethylene glycol at 160 °C | [194] |
| 2D Ag NWs arrays | Evaporating a drop of chloroform-dispersed dodecanethiol-capped prolate Ag nanocrystals on a carbon substrate, which were synthesized in the presence of tetraoctylammonium bromide | [195] |
| Au NRs | Electrochemical oxidation/reduction within a simple two-electrode-type cell in the presence of cationic surfactant $C_{16}TAB$ | [196] |
| Au NWs | Templated from the mesoporous silica | [182] |
| Au NWs | Metal NW formation using $Mo_3Se_3^-$ as reducing and sacrificing templates | [183] |
| Au NRs | A solution seeding growth approach in the presence of an aqueous micellar template CTAB | [197, 198] |
| Au NRs | UV irradiation of $HAuCl_4$ solutions with 253.7-nm light in the presence of rodlike micelles of hexadecyltrimethylammonium chloride | [199] |
| Au NWs | DNA-directed assembly of gold NWs on complementary surfaces | [200] |
| 2D Au NWs | Self-assembly of gold nanoparticles on water surfaces in the presence of surfactants | [201] |
| Au NWs | Ultrahigh vacuum TEM with the electron beam thinning technique | [202] |
| 3D aggregates of Au NRs | DNA-driven self-assembly of gold NRs | [203] |
| $Au_{core}Ag_{shell}$ NRs | Reducing $AgCl_4^{3-}$(aq) with $NH_2OH$ selectively on the surface of gold NRs | [204] |
| Co NRs | The early stage of the thermal decomposition of $Co_2(CO)_8$ in a mixture of oleic acid and trioctylphosphine oxide (TOPO) | [205] |
| Co NW array | Vertical arrays of Co NWs with high densities through direct current electrodeposition created by using ultra-high-density arrays of nanopore of diblock copolymer templates | [206] |
| Co NWs | The potentiostatic electrochemical template synthesis of NWs in polycarbonate track-etched membranes with nominal pore diameters | [207] |
| Cu NWs | The potentiostatic electrochemical template synthesis of NWs in polycarbonate track-etched membranes with nominal pore diameters | [207] |
| Fe NRs | Thermal decomposition of organometallic precursor $(Fe(CO)_5)$ in the presence of a stabilizing surfactant TOPO at 340 °C under an argon atmosphere | [208] |
| In NWs | Room-temperature organometallic route using long-chain amines (hexadecylamine) as templates | [209] |
| $In_3Sb$ NWs | Room-temperature organometallic route using long-chain amines (hexadecylamine) as templates | [209] |
| Ni NRs | Surfactants hexadecylamine (HDA) or TOPO as capping agents in THF | [210] |
| Pb NWs | The NWs were embedded in tracked-etched polycarbonate membranes by electrodeposition | [211] |
| Pb NWs | Electrodeposition into anodic alumina membranes | [212] |
| Pd tetrahedras and octahedras | Reduction of metal ions in sodium dodecyl sulfate (SDS)/poly(acrylamide) gel by UV irradiation | [213] |
| Pd NWs | Using a mesoporous silica template via chemical vapor infiltration | [214] |
| Pd dendrites | Ultrasonically assisted synthesis using skeleton nickel as templates | [215] |
| Pt tetrahedra | Tetrahedral, cubic, irregular-prismatic, icosahedral, and cube-octahedral particle shapes were prepared with sodium polyacrylate as a capping agent | [216] |
| Mo NWs | A two-step process involving the electrodeposition of $MoO_2$ NWs on a highly oriented pyrolytic graphite (HOPG) surface followed by reduction | [217] |

**Table 2.** Continued

| Nanomaterials | Synthetic method | Ref. |
|---|---|---|
| W NRs | Thermal decomposition of surfactant-inorganic mesostructures | [218] |
| B NWs | VLS growth of amorphous boron NWs | [219] |
| B NWs | Amorphous boron NWs by magnetron sputtering | [220] |
| B NWs | Chemical vapor deposition using a diborane-$(B_2H_6)$-in-Ar gas mixture | [221] |
| Bi NTs | Hydrothermal reaction | [222] |
| Ge NWs | Liquid solution synthesis, reduction of $GeCl_4$ and phenyl-$GeCl_3$ by sodium metal in an alkane solvent at elevated temperature and pressure | [70] |
| Ge NWs | Nucleation and growth seeded by organic monolayer-coated Au nanocrystals | [223] |
| Si NWs | Laser-assisted growth, VLS | [44] |
| Si NWs | Chemical vapor deposition of $SiCl_4$, VLS | [43] |
| Si NWs | Vapor-liquid-solid (VLS) reaction using $SiCl_4$ as the Si source gas and Au as the mediating solvent | [224] |
| Si nanoribbons | Thermal evaporation of silicon monoxide (SiO) without templates or catalysts | [59] |
| Si NWs | Thermal evaporation | [225–227] |
| Si NWs | Laser ablation SiO | [228] |
| Si NWs | Supercritical fluid solution-phase growth, SLS | [71] |
| Si NW arrays | Electrochemistry approach by etching Si wafer in HF solution containing $AgNO_3$ | [229] |
| Si/SiGe Superlattice NWs | Block-by-block growth by hybrid pulsed laser ablation/chemical vapor deposition (PLA-CVD) process | [230] |
| Carbon-sheathed Sn-Pb NWs | Electrolytic formation of carbon-sheathed mixed Sn-Pb nanowires | [231] |
| Se NWs | Using cytochrome $c_3$ to make selenium NWs | [232] |
| Se NWs | Solution phase process | [233–234] |
| Te NTs | Reflexing a solution of orthotelluric acid in ethylene glycol at ~197 °C | [235] |
| Te nanobelts, NTs, nano-helices | Controlled hydrothermal route by reaction of sodium tellurite $(Na_2TeO_3)$ in aqueous ammonia solution at 180 °C | [236] |
| GaN NRs | Templating against carbon nanotubes | [32] |
| GaN NWs | Catalytic growth using Ga and $NH_3$, VLS | [237–239] |
| GaN NWs | Catalytic synthesis using gallium acetylacetonate and $NH_3$ gas, VLS | [240] |
| GaN NBs | Thermal reaction of gallium, gallium nitride, and ammonia using iron and boron oxide as catalysts | [241] |
| GaN NWs | Laser-assisted catalytic growth, VLS | [48, 242] |
| GaN NWs | Oxide-assisted growth by laser ablating GaN mixed with gallium oxide | [56] |
| GaN NWs | Silica-assisted catalytic growth | [57] |
| GaN NWs | Hot-filament chemical vapor deposition | [243, 244] |
| GaN arrays of nanopillars | MOCVD using a single molecule precursor | [245] |
| GaN NRs | Pyrolysis of gallium dimethylamide and ferrocene under an $NH_3$ atmosphere | [246] |
| GaAs NWs | Laser-assisted catalytic growth, VLS | [48] |
| GaAs NWs | Oxide-assisted method | [55] |
| GaAs NWs | Solution-liquid-solid growth, SLS | [66, 69] |
| GaAs NWs | Molecular beam epitaxy, CVD | [247–249] |
| GaP NWs | Laser-assisted catalytic growth, VLS | [48, 250] |
| GaP NWs | Laser ablation of a powder mixture of GaP and $Ga_2O_3$ | [251] |
| GaP NWs | Carbon NTs template against carbon NTs | [252] |
| GaP NWs | Hydride vapor phase epitaxy method | [253] |
| GaP NRs | Solution-liquid-solid growth, SLS | [66, 68] |
| GaP NRs | Thermal decomposition of $Ga(P^tBu_2)_3$ in trioctylamine (TOA), which was injected into a mixture of TOA and hexadecylamine (HDA) at 330 °C | [254] |
| $Al_xGa_{1-x}As$ NRs | Solution-liquid-solid growth, SLS | [69] |
| $GaAs_{0.6}P_{0.4}$ NWs | Laser-assisted catalytic growth, VLS | [48] |
| InAs NRs | Solution-liquid-solid growth, SLS | [66] |
| InAs NRs | Molecular beam epitaxy and metal-organic vapor phase epitaxy | [249, 255] |
| InP NWs | Laser-assisted catalytic growth, VLS | [48] |
| InP NRs | Solution-liquid-solid growth, SLS | [66] |
| $InAs_{0.6}P_{0.5}$ NWs | Laser-assisted catalytic growth, VLS | [48] |
| AlN NWs | Aluminum chloride-assisted nanowhisker growth | [256, 257] |
| AlN NRs | Templated against carbon nanotubes | [258] |
| AlN NWs | Silica assisted catalytic growth (same as GaN) | [57] |
| InN NWs | Catalyzed growth from azido-indium precursors, SLS | [259] |
| InN NWs | Thermal selective-area growth on gold-patterned Si substrates | [260] |
| BN NWs | Reaction of a mixture gas of $N_2$ and $NH_3$ over $\alpha$-FeB particles | [261] |
| BN NTs | Catalytic growth of boron nitride NTs | [262] |

**Table 2.** Continued

| Nanomaterials | Synthetic method | Ref. |
|---|---|---|
| BN NTs, nanobamboos, nanocables | Chemical vapor deposition method using B-N-O precursor | [263] |
| BN NWs | Magnetron sputtering for producing featherlike NWs | [264] |
| $Si_3N_4$ NWs | Heating Si or $(Si/SiO_2)$ in $N_2$ without catalyst | [125] |
| $Si_3N_4$ NRs | From borosilicate glass | [265] |
| $Si_3N_4$ NRs | Carbothermal reduction of SiO with amorphous activated C as a reductant | [266] |
| $Si_3N_4$ NRs | Solvothermal reaction of $SiCl_4$ with $NaN_3$ at 670 °C | [267] |
| $Ge_3N_4$ NBs | Thermal reduction $Ge/SiO_2$ in $NH_3$ | [268] |
| SiC NWs | Thermal evaporation | [269] |
| SiC NWs | Thermal evaporation of SiC powders using iron as a catalyst | [270] |
| SiC NWs | Laser ablation synthesis | [271] |
| SiC NRs | Template against carbon NTs | [35] |
| SiC nanocables | Reaction of $SiO_2$ with nanoscale C particles in Ar | [125] |
| SiC NWs | Reaction of arrays CTNs with SiO | [272] |
| SiC NWs | From the mixture of activated carbon and sol–gel-derived silica embedded with Fe nanoparticles | [273] |
| SiC NWs | Grown from $SiO_x$ thin films deposited on Si(100) substrate | [274] |
| SiC NWs | Reduction-carburization route | [275] |
| SiC NWs | Solvothermal reaction | [276] |
| $B_xC$ NRs | Template against carbon NTs | [35] |
| $B_xC$ nanosprings | Fe-catalyzed helical growth, VLS | [277] |
| AlC NWs | Lithium-assisted self-assembly | [278] |
| TiC NRs | Template against carbon NTs | [35] |
| TiC NWs | Reaction of TiO gas with methane in the presence of catalyst Fe, VLS | [279] |
| TiC NRs | Solvothermal reaction using $C_2Cl_4$, Ti, and N-containing nucleophilic solvents | [280] |
| $MgB_2$ NWs | Transport reaction using B NWs as template | [219] |
| $MMo_3Se_3$ NWs | Cation exchange in organic solution (M = $Li^+$, $Na^+$, $Rb^+$, $Cs^+$, $NMe^{4+}$) | [281] |
| $ErSi_2$ NWs | Epitaxial growth on silicon substrate | [282] |
| $NiSi_2/Si$ | Metal vapor vacuum arc implantation | [283] |
| $CoSi_2/Si$ | Metal vapor vacuum arc implantation | [283] |
| $TiSi_2$ NWs | Ti-catalyzed Si NWs by chemical vapor deposition | [284] |
| CdS NWs | Laser-assisted catalytic growth | [48] |
| CdS NWs | Electrodeposit in porous anodic aluminum oxide templates | [40, 285] |
| CdS NWs arrays | Sol–gel template synthesis with porous alumina template | [286] |
| CdS NRs | A single-source molecular procursor route to CdS nanorods | [287] |
| CdS NRs | Solvothermal reactions in ethylenediamine media | [61, 288] |
| CdS NRs | Solvothermal reaction in $n$-butylamine | [65] |
| CdS NRs, twinrod-, tetrapod-shaped | Solvothermal reaction in ethylenediamine media | [289] |
| CdS NWs | Polymer-controlled growth | [290] |
| Flat CdS triangle | Using $Cd(AOT)_2$/isooctane/$H_2O$ | [291] |
| CdS, CdSe NRs | Arrested precipitation from inorganic ions in a CTAB micellar solution | [292] |
| CdS, CdSe NRs | Controlled synthesis of multi-armed architectures using monosurfactant hexadecy-lamine (HAD) | [293] |
| CdSe NWs | Laser-assisted catalytic growth, VLS | [48] |
| CdSe NWs arrays | Electrodeposit in porous anodic aluminum oxide templates | [294] |
| CdSe NRs and other shapes | Growth of nanoparticles in a mixture of hexylphosphonic acid and TOPO | [11, 72] [295] |
| CdSe NRs | Capping agent-driven solution reaction using CdO as precursor | [296] |
| CdSe NRs | Solvothermal reaction in ethylenediamine | [61, 297] |
| CdSe NRs | Solvothermal reaction in $n$-butylamine | [65] |
| CdSe NWs | PVA-assisted solvothermal synthesis | [298] |
| CdSe nanorods and dendrites | Hydrothermal method | [299] |
| CdS/ZnS shells on CdSe NRs | Epitaxial growth of graded CdS/ZnS shells on colloidal CdSe NRs | [300] |
| CdTe NWs | Electrodeposition in alumina membrane | [37] |
| CdTe NRs | Capping agent-driven solution reaction using CdO as precursor | [296] |
| CdTe NWs | Spontaneous oriented attachment from nanoparticles | [103] |
| CdTe NRs | Solvothermal reaction | [61] |
| CdTe NWs | PVA-assisted solvothermal synthesis | [298] |
| $CdS_xSe_{1-x}$ | Solvothermal reaction | [301] |
| PbS NRs | Confined growth within the channels of mesoporous silica SBA-15 | [302] |

**Table 2.** Continued

| Nanomaterials | Synthetic method | Ref. |
|---|---|---|
| PbS NRs | Oriented growth in the presence of surfactant | [303] |
| Closed PbS NWs | Solvothermal reaction in the presence of poly[$N$-(2-aminoethyl)acrylamide] in ethylenediamine/$H_2O$ (3:1, v/v) solvent | [304] |
| PbS NRs | Solvothermal interface reaction route | [305] |
| PbSe NWs | Solution reaction at room temperature | [306] |
| PbSe NWs arrays | Direct current electrodeposition within anodic alumina membrane | [307] |
| ZnS NWs | Laser-assisted catalytic growth, VLS | [48] |
| ZnS NWs | Synthesis in liquid crystal systems | [308] |
| ZnS NWs | Simultaneous formation in a liquid crystal template by gamma-irradiation | [309] |
| ZnS NWs | Micelle-template inducing synthesis | [310] |
| ZnS nanosheets | Templating from a sheet-like molecular precursor $ZnS \cdot (NH_2CH_2CH_2NH_2)_{0.5}$ | [64] |
| ZnSe NWs | Laser-assisted catalytic growth, VLS | [48] |
| ZnSe NRs | Solvothermal reaction in $n$-butylamine | [65] |
| ZnSe NWs | Solvothermal reaction in ethylenediamine | [297] |
| ZnSe NWs | Electrodeposition in a porous alumina film | [311] |
| ZnTe NRs | Thermal decomposition of a monomeric molecular precursor, [Zn(TePh)$_2$][TMEDA] | [312] |
| ZnTe NRs | Thermal decomposition of the precursor derived from a solvothermal reaction using Zn, Te, and $N_2H_4 \cdot H_2O$ as reactants | [313] |
| Bi$_2$S$_3$ NWs | Solvothermal decomposition process | [314, 315] |
| Bi$_2$S$_3$ NRs | Hydrothermal ripening and crystallization | [316] |
| Bi$_2$S$_3$ NWs arrays | Electrochemical deposition | [317] |
| Bi$_2$Se$_3$ flakes | Solvothermal reaction | [318] |
| Bi(S, Se) NWs | Solvothermal reaction | [319] |
| Bi$_2$Te$_3$ NWs | Electrodeposition into porous alumina membrane | [320, 321] |
| Arrays | Pulsed electrodeposition in anodic alumina membranes | [322] |
| Sb$_2$S$_3$ NRs | Solvothermal decomposition process | [323] |
| | Electrodeposition within a porous polycarbonate membrane | [324] |
| Sb$_2$Se$_3$ NWs | Solvothermal reaction of SbCl$_3$ and Se with Na$_2$SO$_3$ in ethylene glycol | [325] |
| Ag$_2$S NRs | Room-temperature solution-growth method with AgNO$_3$, thiourea, and NaOH as the reagents | [326] |
| Ag$_2$Se NWs | Template-directed synthesis using porous alumina | [327] |
| Ag$_2$Se NWs | Solution reaction using Se NWs as templates | [328, 329] |
| Cu$_2$S NWs | Oxide-assisted nucleation and growth | [330] |
| Cu$_2$S NWs | Growth on copper surface at room temperature | [331] |
| Cu$_2$S/Au core/sheath NWs | Redox deposition method | [332] |
| CuS NTs | Organic amine-assisted hydrothermal process | [333] |
| MnS NRs Cd$_{1-x}$Mn$_x$S NRs | Thermal decompostion of Mn(S$_2$CNEt$_2$)$_2$ or Cd(S$_2$CNEt$_2$)$_2$ in the presence of hexadecylamine | [334] |
| MoS$_2$ NWs | Solvothermal reaction | [335] |
| MoS$_2$ NTs | Heating trisulfide molybdenum complexes in a stream of H$_2$ | [336] |
| MoS$_2$ NTs | Catalyzed transport method using C$_{60}$ as a growth promoter, VS | [337] |
| MoS$_2$ NTs | Gas-solid reaction, VS | [338] |
| WS$_2$ NTs | After the heating of thin tungsten films in an atmosphere of H$_2$S | [339] |
| WS$_2$ NTs | A two-step reaction using a tungsten oxide precursor | [340, 341] |
| WS$_2$ NTs bundles, foils | After the heating of WO$_3$ in mixed gas of H$_2$S and H$_2$/N$_2$ | [342] |
| NbS$_2$-sheathed CNTs | Using carbon NT template-promoted growth | [343] |
| NbS$_2$ NTs | Employing carbon NT template-promoted growth | [344] |
| HfS$_2$, ZrS$_2$, TiS$_2$ NTs | Using carbon NT template-promoted growth | [343] |
| SnS$_2$ nanoflakes | Thermal decomposition of (CH$_2$CH$_2$CH$_2$CH$_3$)$_4$Sn | [345] |
| CdIn$_2$S$_4$ NRs | Converting CdS NRs via the hydrothermal reaction | [346] |
| CuInS$_2$ NRs | Solvothermal reaction of In(S$_2$CNEt$_3$)$_3$ and Cu(S$_2$CNEt$_2$)$_2$ in ethylenediamine | [347] |
| AgInS$_2$ NRs | Solvothermal reaction of In(S$_2$CNEt$_3$)$_3$ and Ag(S$_2$CNEt$_2$) in ethylenediamine | [347] |
| AgBiS$_2$ NRs | Solvothermal process with AgCl, BiCl$_3$, and K$_2$S in ethylenediamine | [348] |
| Ag$_3$CuS$_2$ | Hydrothermal reaction using AgCl and CuCl and thiourea as reactants | [349] |
| Cu$_3$SnS$_4$ NRs | Solvothermal reaction using CuCl$_2 \cdot$ 2H$_2$O, SnCl$_4 \cdot$ 5H$_2$O, CH$_3$CSNH$_2$ as reactants in absolute ethanol | [350] |
| PbSnS$_3$ NRs | An iodine transport hydrothermal route | [351] |

The templating effect can be confirmed by a series of experiments. The mixture of Ga$_2$O$_3$ and Ga was used to produce gaseous Ga$_2$O, which is about 1 torr at 880 °C [353]. The powder mixture was separated from carbon NTs by porous alumina membrane, which can ensure that only gaseous Ga$_2$O flows up toward the side of carbon NTs to participate in the reaction. In such a reaction, carbon NTs act as templates to confine the reaction on NTs, which led
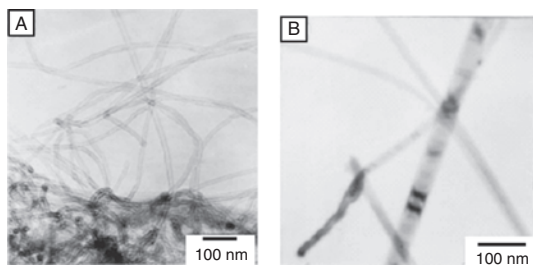
**Figure 1.** (A) TEM image of carbon nanotubes. (B) TEM image of GaN nanorods. Reprinted with permission from [36], W. Q. Han et al., *Science* 277, 1287 (1997). © 1997, American Association for the Advancement of Science.



**Figure 2.** (Left) SEM image of a top view of $Bi_2Te_3$ nanowires electrodeposited in AAO. Reprinted with permission from [321], A. L. Prieto et al., *J. Am. Chem. Soc.* 123, 7161 (2001). © 2001, American Chemical Society. (Right) SEM image of a side view of $Bi_2Te_3$ nanowires in AAO. Reprinted with permission from [320], M. S. Sander et al., *Adv. Mater.* 14, 665 (2002). © 2002, Wiley-VCH.

to the formation of NRs. If carbon NTs are not present in this reaction, GaN powders still can be obtained by another reaction:

$$Ga_2O + 2NH_3 \Longrightarrow 2GaN + H_2O + 2H_2 \qquad (3)$$

However, no GaN NRs were observed in this product [354]. On the other hand, carbon NTs did not change without Ga-$Ga_2O_3$ mixtures, in spite of the presence of ammonia. The results confirmed the evidence that the formation of GaN NRs took place on the surface of carbon NTs according to Eq. (2).

Other examples include GaP NWs [252], AlN NRs [258], SiC NRs, and $B_xC$ NRs [35]. The carbon NT-templated oxide NRs include $GeO_2$ [126], $IrO_2$ [130], $V_2O_5$, $WO_3$ [130], $MoO_3$, $MoO_2$ [130], $Sb_2O_3$ [147], and ZnO [179].

Recently, the range of the compounds, which can be prepared by the use of carbon NTs as templates, has been extended widely [258, 355]. Now, not only ternary NRs/NWs such as $CoFe_2O_4$ [355], but also disulfide NTs $ReS_2$ [356], $NbS_2$ [357], $HfS_2$, $ZrS_2$, and $TiS_2$ [343] can be fabricated with the use of carbon NTs as templates. However, in the case of the synthesis of disulfide NTs, carbon NTs do not participate in the reactions and just act as deposition substrates of disulfides.

In contrast to the above vapor-phase synthesis by hard template, another versatile methodology was solution-phase electrodeposition for the formation of various NWs with anode aluminum oxide (AAO) as a template. This methodology was first pioneered by Martin and Moskovits [37–40]. Since the electrodeposition is caused by electron transfer from the surface of the conducting material, the wires nucleate at the bottom of the channels of the AAO and grow continuously along the channels. Achieving continuous wires is a key advantage of electrodeposition, particularly for applications in which conductivity is important (e.g., thermoelectric devices, opto-electronic devices). On the other hand, porous alumina is a good choice for a template, because the pore diameters are easily adjusted (down to 9 nm) to sizes enabling quantum confinement. Moreover, the pore densities ($10^{10}$ pores/cm$^2$) and aspect ratio ($>100$) are high, which is appropriate for the growth of NWs. Figure 2 shows that $Bi_2Te_3$ NW arrays were electrodeposited in anode alumina oxide channels [320, 321]. A lot of inorganic NWs have been fabricated through this approach, such as Ag, Au, Pt,

$TiO_2$, $MnO_2$, ZnO, $SnO_2$, CdS, and CdSe [358]. It should be pointed out that most of the wires are polycrystalline by the electrodeposition process, which could limit its applications in electronic transport study [23].

A report by Zhu et al. [229] shows that large-area silicon NW arrays can be fabricated on silicon wafers without the use of a template, but based on a so-called microelectrochemical process that occurs at the surface of the silicon wafer in ionic metal (such as $Ag^+$) HF solution. However, the applicability of this method must be further extended.

The above templates have to be removed by heating carbon NTs in air or by dissolving the anode aluminum oxide in a strong basic solution to get pure NWs. It is worth noting that such post-treatments will more or less affect the as-prepared NWs.

## 2.2. Vapor-Liquid-Solid Mechanism

Another extensive method is one-dimensional growth based on the VLS mechanism. Initially, the VLS mechanism was proposed by Wagner [41] to explain the growth of crystal whiskers. In 1992, Yazawa et al. demonstrated that high densities of InAs nanowhiskers with diameters of 20–30 nm can be epitaxially grown on InAs (111) substrates onto which one monolayer of Au atoms have been deposited [42]. They argued that the wirelike growth appears to be induced by ultrafine alloy droplets generated by the reactions between Au clusters and InAs substrates. Again, silicon NWs were grown on Si(111) via the VLS reaction, with silane as the Si source gas and Au as the mediating solvent [43].

Lieber's group [7, 8] proposed a general mechanism to illustrate the growth process of the nanowires. The main points of the mechanism are the orientation growth directed by the metal droplet on the tip of crystals. The metal droplet acts as an energetically favored site for absorption of gas-phase reactants. When the clusters dissolve in the metal droplet supersaturates, they will crystallize and grow one-dimensional nanowires. The process is illustrated in Scheme 2.

This group made a great contribution to the improvement of the application of this mechanism to the synthesis of various semiconductor NWs by employing the laser ablation technique to produce nanosized metal catalysts, which
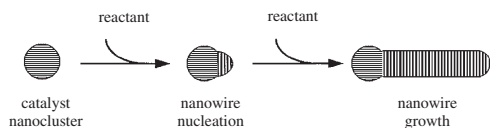
**Scheme 2.** Schematic illustration on the catalytic growth based on the VLS mechanism, including three stages: alloying, nucleation, and axial growth. Reprinted with permission from [7], J. T. Hu et al., *Acc. Chem. Res.* 32, 435 (1999). © 1999, American Chemical Society.

defines the diameter of NWs grown by the VLS mechanism. A pulsed Nd-yttrium-aluminum-garnet laser (wavelength 532 nm) was used to bombard targets, which were composed of NWs and catalysts. The laser ablation on $Si_{0.9}Fe_{0.1}$ generated NWs with a uniform diameter on the order of 10 nm and a length on the order of micrometers (Fig. 3A) [44]. Element analysis revealed that these NWs were Si cores coated by an amorphous $SiO_2$ shell as shown in Figure 3B. All of the nanowires terminated at one end in metal nanoparticles, which have a slightly larger diameter than that of NWs. The appearance of these metal nanoparticles on the tips of NWs confirmed that the growth of NWs relies on the VLS mechanism. The authors proposed that the main composition of the catalyst solid should be $FeSi_2$, because $FeSi_2$ is stable at the Si-rich region of the phase diagram. In addition, the NWs will stop growing when the temperature is below 1207 °C, since there will be no liquid catalyst at such a low temperature. The agreement between experimental data and theoretical predictions indicates that it is possible to rationally design new catalysts and appropriate growth conditions for other NWs.

$$FeSi_2(l) + nSi(g) \Longrightarrow FeSi_x(l) + mSi(s) \qquad (4)$$

It should be noted that the metal selected as a catalyst has a certain solubility with reactants. Meanwhile, since the catalyst should become liquid at the desired reaction temperature, the melting point of the catalyst should be taken into account. The known phase diagrams of binary compounds will be helpful for the design of reactions and selection of catalysts; however, we still know little about the ternary phase diagrams.

This idea has been successfully implemented by the preparation of a broad range of binary NWs and ternary NWs such as III–V materials (GaAs, GaP, GaAsP, InAs, InP, InAsP), II–VI compounds (ZnS, ZnSe, CdS, CdSe), and SiGe alloys, with LCG, based on the VLS mechanism [48]. However, the mechanism also has its inherent weaknesses. First, to ensure that the catalyst remains liquid, the reaction temperature has to be relatively high (700–1200 °C). This impedes the application of this approach with compounds that are unstable at high temperatures. Second, the products based this approach are not pure materials, because of the metal catalyst attached to the tip of the NWs. It is difficult to remove these catalysts from the as-prepared NWs. Third, the size distribution of these NWs is not ideal. Because the metal catalyst clusters tend to aggregate at high temperatures, this will lead to the decentralization of the size distribution of the NWs.

Yang et al. combined the conventional epitaxial crystal growth technique with the VLS mechanism to achieve precise orientation control during NW growth [46]. The result shows that this vapor-liquid-solid epitaxy (VLSE) is particularly powerful in controlling the synthesis of NW arrays. This group successfully epitaxially grew the highly oriented and well-aligned NW arrays on a patterned substrate by using a Au thin film as the catalyst for NW growth. Typical scanning electron microscopy (SEM) images of NW arrays grown on sapphire (110) substrates with patterned Au thin film fabricated by photolithography (Fig. 4) confirm that the ZnO NWs grow only in the Au-coated areas. The diameters of these wires range from 20 to 150 nm, whereas more than
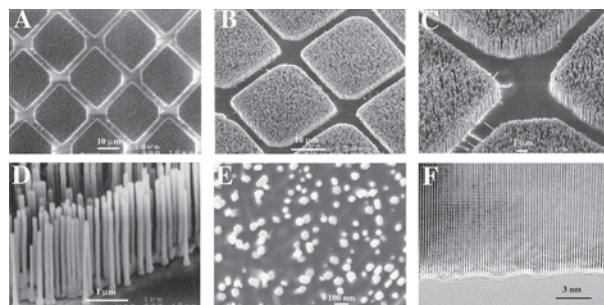


**Figure 4.** (A through E) SEM images of ZnO nanowire arrays grown on sapphire substrates. A top view of the well-faceted hexagonal nanowire tips is shown in (E). (F) High-resolution TEM image of an individual ZnO nanowire showing its ⟨0001⟩ growth direction. For the nanowire growth, clean (110) sapphire substrates were coated with a 10- to 35-Å-thick layer of Au, with or without TEM grids as shadow masks (micro-contact printing of thiols on Au followed by selective etching has also been used to create the Au pattern). Equal amounts of ZnO powder and graphite powder were ground and transferred to an alumina boat. The Au-coated sapphire substrates were typically placed 0.5 to 2.5 cm from the center of the boat. The starting materials and the substrates were then heated to 880 ° to 905 °C in an Ar flow. Zn vapor is generated by carbothermal reduction of ZnO and transported to the substrates where the ZnO nanowires grew. The growth generally took place within 2 to 10 min. Reprinted with permission from [46], M. Huang et al., *Science* 292, 1897 (2001). © 2001, American Association for the Advancement of Science.



**Figure 3.** (A) TEM image of the nanowires produced following ablation of a $Si_{0.9}Fe_{0.1}$ target. The white scale bar corresponds to 100 nm. (B) TEM image of a typical nanowire with crystalline Si core and an amorphous $SiO_x$ sheath. The scale bar corresponds to 10 nm. Inset: Electron diffraction recorded along the [211] zone axis. Reprinted with permission from [44], A. M. Morales and C. M. Lieber, *Science* 279, 208 (1998). © 1998, American Association for the Advancement of Science.

95% of them have diameters of 70 to 100 nm. The room temperature ultraviolet lasing was successfully demonstrated within ZnO NW arrays [46]. More recently, Yang et al. [21] discovered that certain superstructures of ZnO NWs can readily be formed with Zn as vapor source. A large yield of comb-like structures made of ZnO NWs can be synthesized, in which the NWs are uniformly distributed on the side of the comb stem. Other interesting structures such as tetrapods and tapered NWs can also be synthesized by varying the vapor conditions [21].

This approach can also be extended to the synthesis of carbide materials such as TiC NWs [279] and $B_xC$ nanosprings [277].

## 2.3. Vapor-Solid Mechanism

In fact, NWs can also be achieved in the absence of catalysts, with the classical VS mechanism [49]. Compared with the VLS mechanism, this route can avoid problems with the purity of products, because of the absence of catalysts. However, it is hard to find a strong and obvious driving force for the formation of NWs by this approach. So far, the researchers are inclined to assign the formation of NWs to the anisotropic growth rates of nanocrystals in different directions. However, these growth rates are related to many specific experimental conditions. The specific requirements for 1D crystal growth, such as the presence of a dislocation at the vapor-solid interface, are still controversial. One of the key factors is the control of supersaturation, the degree of which determines the prevailing growth morphology. The size of NWs can be controlled by supersaturation, nucleation sizes, and the growth process.

MgO, $Al_2O_3$, ZnO, and $SnO_2$ NWs have been synthesized by a carbon-thermal reduction process by Yang's group [50, 51]. Recently, Wang's group has shown an elegant example of the application of the VS mechanism to the synthesis of semiconductor NWs and NBs [52]. In a typical experimental procedure, oxide powders were placed in an alumina tube. The products were collected by an alumina substrate at the downstream end of the tube. The pressure in the alumina tube, the reaction time, and the flow rate of Ar were kept at 300 torr, 2 h, and 50 sccm, respectively, for all of the experiments. The evaporation temperatures were determined by the melting points of individual oxides. The as-obtained hexagonal ZnO exhibits a unique belt-like shape as shown in Figure 5. The detailed structure characterization shows uniform structure, single crystals, and two different growth directions ([0001] and [01$\bar{1}$0]). The subsequent success with $SnO_2$, $In_2O_3$, and CdO NBs indicates that this method is not a minor approach to NBs. The crystal growth was governed by a vapor-solid process. Oxide vapor was generated by the oxide powders, was deposited on a substrate at a lower temperature zone, and grew into NBs.

More recently, Ren's group has shown that a variety of novel hierarchical ZnO nanostructures with 6-, 4-, and 2-fold symmetries can be grown by a vapor transport and condensation technique from a mixture of ZnO, $In_2O_3$, and graphite powders as raw materials, as shown in Figure 6 [53]. Since
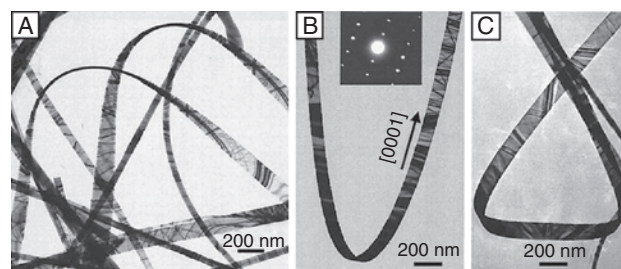


**Figure 5.** TEM and HRTEM images of ZnO nanobelts, showing their geometrical shape. (A to C) TEM images of several straight and twisted ZnO nanobelts, displaying the shape characteristics of the belts. Reprinted with permission from [52], Z. W. Pan et al., *Science* 291, 1947 (2001). © 2001, American Association for the Advancement of Science.

no catalyst is used in such a system, the $In_2O_3$ NW growth should be based on the VL mechanism. It was found that the major core NWs are single-crystal $In_2O_3$ with six, four, and two facets, and the secondary NRs are single-crystal hexagonal ZnO and grow either perpendicularly on or slanted to all of the facets of the core $In_2O_3$ NWs (Fig. 4). The growth of ZnO NRs could also grow based on the VS mechanism because the $In_2O_3$ core is covered by a ZnO layer that can be the basis for further ZnO NR growth. The high vapor pressure is necessary for the growth of the hierarchical structures compared with the aligned ZnO grown by the VLS mechanism [46]. The growth conditions, such as temperature, pressure, and source component ratios, are correlated to affect the supersaturation rate and the structure formed. This intriguing method could be extended for growing other oxide, carbide, and nitride materials with novel hierarchical nanostructures.

Based on the VS mechanism, various novel metal oxide nanostructures can also be synthesized, such as $Sb_2O_3$ NRs [146], $SnO_2$ NWs/nanoribbons/NTs [150], $SnO_2$ nanodiskettes [151], SnO nanoribbons [152], and $MoS_2$ NT bundles [337].
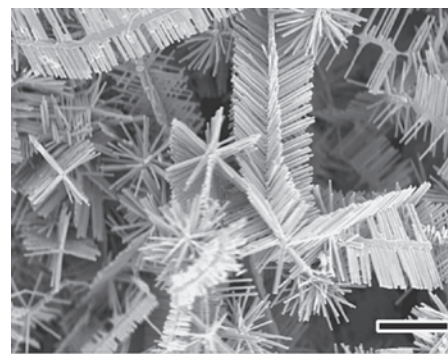


**Figure 6.** SEM image of ZnO nanostructures, showing the various structural symmetries. Three major basic symmetries of 6-, 4-, and 2-fold are clearly seen. Scale bar, 3 $\mu$m. Reprinted with permission from [53], J. Y. Lao et al., *NanoLetters* 2, 1287 (2002). © 2002, American Chemical Society.

## 2.4. Oxide-Assisted Growth Route

The oxide-assisted growth mechanism of NWs was recently developed by Lee's group [54]. It is somewhat like the VLS mechanism, but with the metal droplets in VLS replaced by an oxide in this mechanism. Therefore, this process has an advantage of being free of a metal catalyst or a template compared with the VLS mechanism.

GaE (E = N, P, As) NWs were fabricated by laser ablation of the corresponding powders mixed with gallium oxide ($Ga_2O_3$) under the flow of a carrier gas consisting of Ar and $H_2$ [55–57]. The diameter of GaAs core wires and the thickness of the $GaO_x$ sheath was in the range of 10–120 nm and 2–10 nm, respectively. The interface between the crystal core and amorphous sheath has an undulant contour. The following reactions were suggested during the growth process:

$$GaAs(s) \Longrightarrow Ga(g) + As(g) \tag{5}$$

$$4Ga(g) + Ga_2O_3(s) \Longrightarrow 3Ga_2O(g) \tag{6}$$

$$3Ga_2O(g) + 4As(g) \Longrightarrow 4GaAs(s) + Ga_2O_3(s) \tag{7}$$
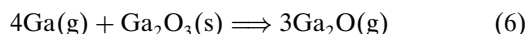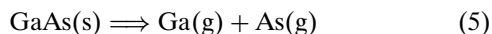
The results show that if a target made of pure GaAs powder without $Ga_2O_3$ was used for laser ablation, no NWs were found in the products. This indicates that the presence of the oxide $Ga_2O_3$ in the target is critical for the reaction in Eq. (6). Similar results were also observed in GaP, GaN NWs prepared by the same method, indicating that these NWs were grown by an oxide-assisted mechanism.

This mechanism can be further extended for the synthesis of Si NWs [58, 59]. Freestanding quasi-two-dimensional silicon nanoribbons have been realized in the present work with an oxide-assisted growth method (Fig. 7). Two kinds of morphology of the nanoribbons have been observed (Fig. 1A). Most of the ribbons have rippling edges (Fig. 1B), and a small portion of the ribbons has smooth edges (Fig. 1C). The thickness of the ribbons was estimated to be 10–20 nm. The rippling and curling features at the edge of most ribbons also further confirm that the nanoribbons are a quasi-two-dimensional structure and are distinctly different in shape from the one-dimensional silicon NWs with a smooth surface.

The oxide-assisted growth model is illustrated in Figure 8 with Si NWs as an example. Silicon oxide ($Si_xO$) was deposited from the vapor phase and generated silicon nanoparticles on the surface (Fig. 8a). Because the surface melting temperatures of nanoparticles can be much lower than that of their bulk materials, this enhances atomic absorption, diffusion, and deposition in a growth process. At the same time, the $SiO_2$ shell around silicon can effectively retard the radial growth of nanoparticles and impede the aggregation of nanoparticles. The structure defects at the tip of NWs provide favorable conditions for the faster axial growth of NWs (Fig. 8b). A detailed description of this mechanism and its application to Si NWs have been reported recently [58]. The characteristic of the product generated
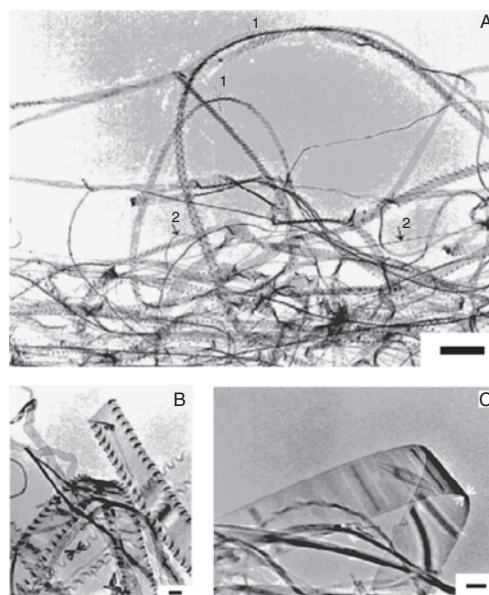


**Figure 7.** TEM images of (A) silicon nanoribbons collected from the substrate. Arrows 1 indicate the edge-on position, and arrows 2 indicate silicon nanowires grown together with nanoribbons. (B) Some rippling-edge ribbons. (C) A smooth-edge ribbon. The thicknesses of the ribbons estimated from the arrows indicating parts in B and C are 13 and 14 nm, respectively. Scale bars: 1 $\mu$m in A and 100 nm in B and C. Reprinted with permission from [59], W. S. Shi et al., *J. Am. Chem. Soc.* 123, 11095 (2001). © 2001, American Chemical Society.

by this mechanism is that the desired NW materials were surrounded by an amorphous oxide sheath.

## 2.5. Solvothermal Process

A challenging trend in synthetic chemistry and materials science is determining how the traditional solid-state reaction can be conducted in round-bottom flasks (i.e., turning down the heat for the fabrication of crystals) [60, 67]. Recent developments in soft solution processing may provide an alternative, convenient, lower-temperature, and environmentally friendly pathway for the fabrication of advanced ceramic materials with desirable shapes and sizes [359]. As
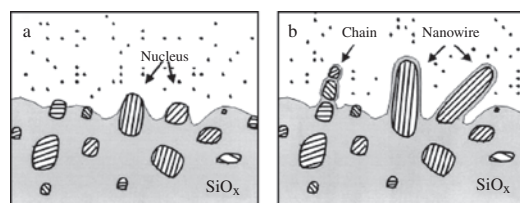


**Figure 8.** Schematic illustration of the oxide-assisted mechanism of nanowires. The parallel lines indicate the $\langle 112 \rangle$ orientation. (a) Si oxide vapor is deposited and forms the matrix within which the Si nanoparticles are precipitated. (b) Nanoparticles in a preferred orientation grow fast and form nanowires. Reprinted with permission from [58], S. T. Lee et al., *Mater. Sci. Eng., A* 286, 16 (2000). © 2000, Elsevier Science.

one kind of solution-based chemical process, the hydrothermal process has been widely used for the synthesis of a vast range of solid-state compounds such as oxides, sulfides, and halides [26, 34, 360–363] and molecular, zeolite, and other microporous phases [363], since the pioneering work from the 1960s to the 1980s.

Hydrothermal synthesis can be defined as the use of water as a solvent in a sealed reaction container when the temperature is raised above 100 °C. Under these conditions, the autogenous pressure (i.e., self-developing and not externally applied) is developed. The pressure within the sealed reaction container is found to increase dramatically with temperature, but it will also depend on other experimental factors, such as the percentage fill of the vessel and any dissolved salts. Figure 9 shows these data and demonstrates first the dramatic rise in pressure when a high percentage fill of the reaction vessel is used, and second how the pressure inside the reaction container can be controlled by choice of temperature and/or the volume of solvent used. Below the critical point of water, and even below 200 °C, a high percentage fill allows access to pressures of hundreds of atmospheres [365].

The use of hydrothermal conditions can exert significant effects on the reactivity of inorganic solids and the solubility of the compounds under conditions of elevated pressure and temperatures. The chemical reactivity of usually insoluble reagents can be much enhanced, and many sluggish solid-state reactions can be initiated under hydrothermal conditions. Usually hydrothermal synthesis occurs at higher temperatures (above 300 °C) and often takes place in the supercritical regime. However, even milder reaction conditions (temperature < 250 °C) can be applied not only to provide a convenient low-temperature route to materials with practical application, but also in the exploratory synthesis of new solids [364, 365].

The concepts embodied in the hydrothermal process have been extrapolated to nonaqueous system; therefore, its counterpart, the so-called solvothermal process, has emerged, in which an organic solvent is used as the reaction medium instead of water, at an elevated temperature near its boiling point. As the counterpart of the hydrothermal process, the solvothermal process has emerged in recent years and has received great attention in synthetic chemistry and materials science.
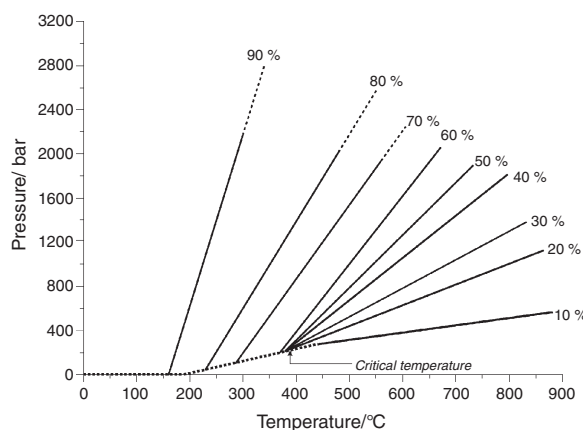
Solvothermal reactions are usually performed in a Teflon-lined, stainless steel autoclave, as shown in Figure 10. The use of an autoclave is necessitated by the pressures developed in the solvothermal reactions, and the inert liner is used to protect the stainless steel outer shell from the corrosive reagents and solvents typically used in the synthesis. Such autoclaves can be used at up to 270 °C, and, depending on the engineering specifications of the steel walls, pressures of ~150 bar can be maintained [365]. The synthetic procedure is simple; however, the rational design of the reaction requires multidisciplinary and interdisciplinary knowledge.

There are several advantages of the solvothermal technique that distinguish it from the traditional solid-state reactions and hydrothermal process. First, many inorganic precursors can be solubilized in a suitable solvent similar to that in which reactants were solubilized in the molten flux of the solid-state reaction at high temperatures [366]. Second, the solvothermal technique removes diffusion control by the use of a suitable solvent under mild conditions [366]. Third, the conventional hydrothermal method is confined to the conditions that some reactants will decompose in the presence of water or the precursors are very sensitive to water, or some reactions will not happen in the presence of water, resulting in the failure of the synthesis of the desired compounds. By the substitution of nonaqueous solvents (both polar and apolar solvents) such as alcohols, $C_6H_6$, polyamines, $NH_2NH_2$, or liquid $NH_3$ for water, solvothermal process allows many possibilities for the preparation of various nanocrystalline compounds and the initiation of some conventional solid-state reactions in organic media under mild conditions [26]. It can even be used to prepare carbonides, nitrides, phosphides, silicides, chalcogenides, and so on.

In the solvothermal process, one or several kinds of precursors are dissolved in nonaqueous solvents. The reactants are dispersed in solution and become more active. The reactions happen in the liquid phase or under supercritical status. The solvothermal process is relatively simple and easy

**Figure 9.** Pressure as a function of temperature and percentage fill of water in a sealed vessel. Reprinted with permission from [365], R. I. Walton, *Chem. Soc. Rev.* 31, 230 (2002). © 2002, Royal Society of Chemistry. Adapted from [361], A. Rabenau, *Angew. Chem., Int. Ed. Engl.* 24, 1026 (1985). © 1985, Wiley-VCH.
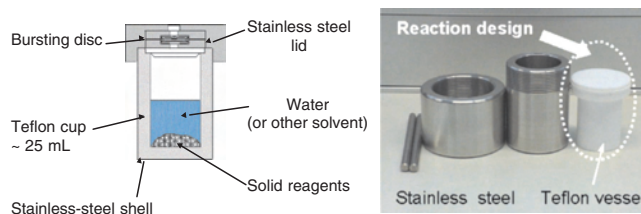
**Figure 10.** Left: A schematic of a Teflon-lined, stainless steel autoclave typically used in the laboratory to perform subcritical solvothermal synthesis. Reprinted with permission from [365], R. I. Walton, *Chem. Soc. Rev.* 31, 230 (2002). © 2002, Royal Society of Chemistry. Right: A set of autoclaves.

to control with several changeable parameters such as solvents, temperature, and reaction time. The sealed system can effectively prevent the contamination of the toxic and air-sensitive precursors. With the substitution of nonaqueous solvents such as polar and nonpolar solvents for water, the so-called solvothermal process can be widely extended to prepare various kinds of nonoxide nanocrystalline materials whose precursors are very sensitive to water.

In the past two decades, a trend toward very mild conditions (100–200 °C) has become increasingly apparent for inorganic synthesis chemistry and materials synthesis. The potential of this technique for preparative solid-state chemistry has been intensively reviewed [365–368]. Various oxide ceramic ultrafine powders were prepared by the solvothermal process [367]. Morris and Weigel [368] summarized some of the results of the recent works in the synthesis of molecular sieves from nonaqueous solvents.

In recent years, rational solution routes to nanocrystals have been extensively explored [26, 34]. Various nonoxide compound nanocrystals such as metal chalcogenides [61–65, 310, 323, 369, 370, 372–379], phosphides [380], and metal nitrides can be synthesized [381–383]. The results showed that the physicochemical properties of the solvents have strong effects on the reactivity, shapes, sizes, and phases of the particles, since solvent properties such as polarity, viscosity, and softness will strongly influence the solubility and transport behavior of precursors under solvothermal conditions. Various kinds of inorganic NRs/NWs/NTs can be synthesized by solvothermal/hydrothermal processes as listed in Tables 1 and 2.

In the following sections, the latest development of the fabrication of nonoxide low-dimensional semiconductor nanocrystals with different shapes, sizes, and phases by mild solution routes will be reviewed with a focus on the emerging solvothermal processing of 1D NRs/NWs. Specific examples will be given to illustrate the reaction activity, the principle, and key parameters that dominated the synthesis process.

### 2.5.1. Fabrication of II–VI Group Low-Dimensional Nanocrystals

**Shape, Size, and Phase Control of CdE Nanocrystals**
Several solvothermal routes were designed for the synthesis of CdS nanoparticles with different shapes, sizes, and phases [61, 62, 369]:

$$CdC_2O_4 + E \xrightarrow{\text{solvent}} CdE + 2CO_2 \uparrow \quad (E = S, Se, Te) \quad (8)$$

$$Cd^{2+} + NH_2CSNH_2 \xrightarrow{\text{solvent}} CdS \quad (9)$$

$$Na_2S_3 + CdSO_4 \xrightarrow{\text{solvent}} CdS + Na_2SO_4 + 2S \quad (10)$$
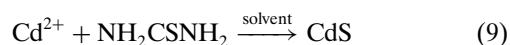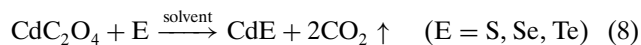
The reaction was conducted in a Teflon-lined autoclave with a 40-ml capacity (as shown in Fig. 10), which was filled with a solvent up to 80% of the total volume. The autoclave was maintained at 80–180 °C for 3–12 h and air-cooled to room temperature. Different solvents were chosen to investigate the influence on the reactivity, crystal shape, size, and phase.

The shape, particle size, and phase of II–VI group semiconductor nanparticles can be synthesized conveniently with high yield by the solvothermal process [61]. A CdS sample synthesized in ethylenediamine (en) via the reaction shown in Eq. (8) at 160 °C for 12 h can be indexed as the hexagonal phase of CdS (wurtzite structure) with cell constants $a = 4.140$ Å, $c = 6.72$ Å, which are close to the reported data for CdS (JCPDS card file no. 41-1049). The TEM image in Figure 11A shows that the CdS crystallites synthesized in ethylenediamine are uniform NRs with diameters of 20–50 nm and lengths of 200–1300 nm. In addition, CdS crystallites synthesized in other polyamines such as diethylene triamine (dien) and triethylene tetraamine (trien) under the same experimental conditions display the same morphology. The CdS powders obtained in dien consist of uniform NRs with diameters of 30–60 nm and lengths of 200–4800 nm. Wurtzite CdSe NRs with diameters of 6–20 nm and lengths up to 100–500 nm can also be synthesized in en, dien, and trien. Similarly, CdTe NRs with a zinc-blende structure were obtained in en.

Solvent effects on the morphology of the products were investigated. Disc-like particles with a size of 40 nm were produced in pyridine (py) as shown in Figure 11B. A lower temperature is unfavorable for the growth of CdE NRs. The CdS particles formed in en at 120 °C for 12 h consist of both uniform spherical particles and shorter NRs. If the temperature is lower than 120 °C, the reaction is incomplete and may not even occur. These results suggest that relatively higher temperature and pressure in the system are necessary for the oriented growth of the NRs. The results indicate that the morphology of CdS, CdSe, and CdTe crystallites can be controlled by choosing different solvents.

Remarkable control over the shape, size, and phase of CdS can be readily realized with the choice of different solvents and reaction conditions and other modified solvothermal reactions as expressed in Eqs. (9) and (10) [62, 369]. The widths and sizes of CdS NRs can be varied by controlling the temperature and reaction time. The TEM image
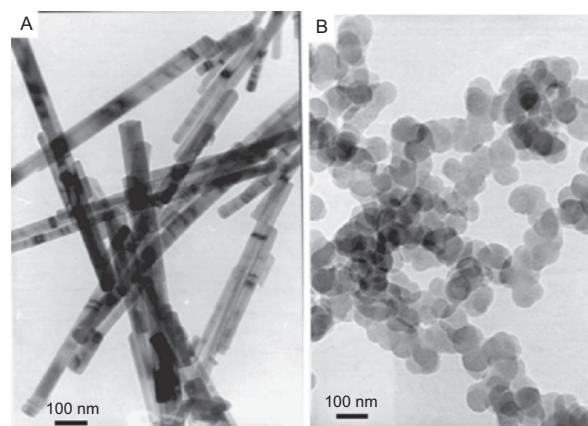


**Figure 11.** TEM images and ED patterns for the obtained CdS samples. (A) CdS synthesized in en at 160 °C for 12 h. (B) CdS nanoparticles synthesized in pyridine at 160 °C for 12 h. Reprinted with permission from [61], S. H. Yu et al., *Chem. Mater.* 10, 2309 (1998). © 1998, American Chemical Society.

in Figure 12a shows that the CdS powders obtained at 100 °C for 12 h consist of uniform NRs with diameters of 6–13 nm and lengths up to 140–480 nm. As the temperature approached 180 °C, the product was found to be uniform NRs with widths of 30–40 nm and lengths up to 280–900 nm (Fig. 12b). The CdS NRs show [001] preferential orientation as shown in a typical high-resolution transmission electron microscopy (HRTEM) image in Figure 12c, corresponding to a stronger and sharper (002) diffraction peak in the X-ray diffraction (XRD) pattern. The SEAD inserted in Figure 12c indicated the CdS NRs are polycrystalline with a wurtzite structure. Further results show that single-crystal CdS NRs can also be obtained at higher temperatures [63].

In addition to the shape control, both sizes and the phase of CdS nanocrystals can be controlled. A modified solvent thermal process as expressed in Eq. (10) was applied to prepare spherical CdS nanocrystals with different sizes via the reaction of $CdSO_4$ with $Na_2S_3$ in benzene at 80–120 °C. It was found that solvent, temperature, and reactant have significant effects on the crystal structure and particle size of CdS nanocrystals. Increased temperature and use of a solvent with a low dielectric constant benefit the preparation of CdS nanocrystals with hexagonal structure. The water content in the system not only induces the presence of cubic phase CdS nanocrystals, but also leads to increasing particle size. Compared with the result from the solvothermal process, pure cubic CdS nanocrystals with an average size of 7 nm were obtained via the hydrothermal process at 100 °C for 12 h, with $CdSO_4 \cdot 8/3H_2O$ and $Na_2S$ as reactants [369].

It is well known that the free energy difference between cubic and hexagonal structures for CdS is small [384, 385]. It is believed that solvents with a lower dielectric constant may minimize the free energy difference between the hexagonal and cubic phases and thus favor the formation of hexagonal phase CdS. In addition, the solvent has a significant effect on the shifting of the following equilibrium:

$$(CdS)_{crystalline} \longleftrightarrow Cd^{2+}_{Sol} + S^{2-}_{Sol} \qquad (11)$$

In this route, the presence of benzene, with a lower dielectric constant than water, will shift the equilibrium (11) to the left and slows the dissolution rate of CdS crystallites. Thus, it will lead to a difference in particle size of the final products. The effects of the solvent on crystal structures and particle size are also consistent with those reported by Ramsden et al. [386].

A modified solvothermal process produced CdTe crystals with different sizes, phase, and morphologies, with $CdCO_3$ reacting with Te in the presence of $N_2H_4 \cdot H_2O$ in the different solvents [370]. More interestingly, the meta-stable wurtzite CdTe phase and its conversion to the stable cubic CdTe phase under mild conditions were observed.

***Shape and Phase Control Synthesis of ZnS Nanocrystals***  A rational design of the solvothermal reaction makes it possible to control both the dimensionality (dots, rods, and sheets) of ZnS nanocrystals and the phase. The solvothermal reaction of zinc salts such as $Zn(CH_3COO)_2 \cdot 2H_2O$ or $ZnCl_2$, and with thiourea in en at 120–180 °C for 6–12 h, results in a white precipitate with the composition $ZnS \cdot (en)_{0.5}$ [64].

The XRD pattern in Figure 13a shows that a new molecular precursor was obtained at 180 °C. It has been confirmed that either a solvothermal reaction of $Zn^{2+}$ with thiourea or a similar reaction between Zn (or $Zn^{2+}$) and sulfur in en medium at 120–180 °C resulted in the same product. The SEM image in Figure 14a shows that all of the particles are sheet-like. EDX analysis of this lamellar precursor gave a Zn:S ratio of 1.00:0.98, indicating that this sulfide had the expected composition. In addition, both N and C signals were detected in the EDX spectrum. After removal of the en template, no N signal was detected in the EDX



**Figure 12.** TEM and HRTEM images of CdS nanowires synthesized by a solvothermal reaction of $Cd^{2+}$ with thiourea in ethylenediamine (a) at 100 °C for 12 h. (b) 180 °C for 12 h. (c) HRTEM image indicating a typical CdS nanorod with a diameter of ~12 nm and well-resolved (002) lattice planes, which was obtained under condition (a). An inserted electron diffraction pattern (ED) shows that the CdS nanorods are of polycrystalline nature and can be indexed as the wurtzite structure. Reprinted with permission from [26], S. H. Yu, *J. Ceram. Soc. Jpn.* 109, S65 (2001). © 2001, Ceramic Society of Japan.



**Figure 13.** XRD patterns of the products. (a) A lamellar precursor $ZnS \cdot (en)_{0.5}$ obtained by solvothermal reaction of $Zn(CH_3COO)_2 \cdot 2H_2O$ with thiourea in ethylenediamine (en) at 180 °C for 12 h. (b) and (c) Wurtzite ZnS nanoparticles obtained by thermal decomposition of lamellar $ZnS \cdot (en)_{0.5}$ precursor at 250 °C, 500 °C for 0.5 h under vacuum, respectively. (d) Sphalerite ZnS (S) nanoparticles obtained by a similar solvothermal reaction in ethanol at 120 °C for 12 h. Reprinted with permission from [64], S. H. Yu and M. Yoshimura, *Adv. Mater.* 14, 296 (2002). © 2002, Wiley-VCH.
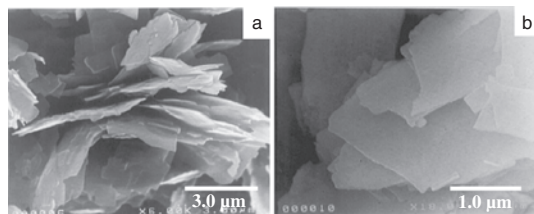
**Figure 14.** SEM images of (a) the lamellar precursor $ZnS \cdot (en)_{0.5}$ obtained by solvothermal reaction at 180 °C for 12 h and (b) ZnS nanosheets obtained by thermal decomposition of the precursor in vacuum at 250 °C for 0.5 h. Reprinted with permission from [64], S. H. Yu et al., *Adv. Mater.* 14, 296 (2002). © 2002, Wiley-VCH.

spectrum. TG-DTA analysis shows that the decomposition events of the precursor obtained at 120–180 °C happened at 362 °C, accompanying the weight loss of en. The net weight loss for the precursor obtained at 120 °C and 180 °C in this stage is 23.5%, which suggests a molecular precursor with a composition of $ZnS \cdot (en)_{0.5}$ (theory: 23.62%).

Pure wurtzite ZnS (W) was produced by removing the en by thermal decomposition at 250–500 °C under vacuum as confirmed by the XRD patterns in Figure 13c and d. The SEM image in Figure 14b and TEM images in Figure 15a show that ZnS nanoparticles are sheet-like with rectangle lateral dimensions in a range of 0.3–2 $\mu$m. The oxidization of the lamellar molecule in air produced wurtzite ZnO flake-like dendrites [64]. The nanosheets are well-crystallized single crystals with a growth direction along the *a* and *c* axes, as indicated by the SAED pattern in Figure 15a. The sharp nature of the (002) peak in Figure 13b and c suggests that the nanosheets grow along the *c* axis. The HRTEM image shows well-resolved (100) lattice planes with a lattice spacing of 3.3 Å, indicating that the preferred orientation is along the *a* axis (Fig. 15b). EDX analysis shows that the weight composition of Zn and S in the product is 67.24% and 32.76%, which is in good agreement with the stoichiometric composition of ZnS.

The synthetic method is both flexible and reproducible for controlling the phase, shape, and sizes of ZnS nanocrystals. By a similar solvothermal reaction at 120 °C, with
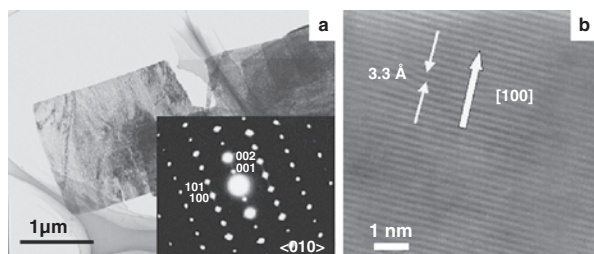


**Figure 15.** (a) TEM images and SAED patterns for wurtzite ZnS single-crystal nanosheets obtained by thermal decomposition of lamellar $ZnS \cdot (en)_{0.5}$ precursor at 500 °C for 0.5 h in vacuum. The inserted SEAD pattern was recorded along the $\langle 010 \rangle$ zone. (b) Well-resolved HRTEM image of the wurtzite ZnS single-crystal nanosheet. Reprinted with permission from [64], S. H. Yu and M. Yoshimura, *Adv. Mater.* 14, 296 (2002). © 2002, Wiley-VCH.

ethanol instead of en as a solvent, sphalerite ZnS (S) nanoparticles with a size of ∼3 nm can easily be synthesized. Furthermore, wurtzite ZnS NRs can also be synthesized by using *n*-butylamine, a monodentate amine, as a solvent [65]. A typical TEM image is shown in Figure 16. In addition, the NRs could be aligned together to form bundle structures or arrays under limited experimental conditions. The further oxidation of ZnS NRs can generate ZnO wurtzite NRs. The general synthetic strategies for ZnS nanocrystals with different phases and shapes and ZnO dendrites are shown in Scheme 3. The results show that both shape and phase of the ZnS nanocrystals can be well controlled by choosing solvents.

These facile mild solution-based methods shed light on the possibility of controlling shape, dimensionality (0D, 1D, 2D), size, and phase. The unusual 1D, 2D wurtzite ZnS single-crystal NRs and nanosheets, flake-like ZnO dendrites, and ZnO NRs can easily be generated based on the solvothermal reactions. This synthetic strategy implies that other semiconductor nanocrystals could also be synthesized along the same line by using a suitable "shape controller" under solvothermal conditions that we will discuss in next section.

***Formation Mechanism and General Synthesis of II–VI Nanorods*** As stated above, only CdS nanocrystals prepared by the solvothermal reactions in en display a rod-like shape. If en were replaced by other organic molecules as solvents, CdS nanocrystals would be irregular or spherical. What dominates this process and results in the formation of NRs? If this mechanism is revealed, one can expect to make use of it to control the shape and size of nanocrystals. Moreover, this mechanism can be expanded to design a general and rational pathway to other 1D semiconductors. In this section, the detailed formation process of CdS NRs under solvothermal conditions was discussed at first. Then a general solvothermal synthesis of II–VI NRs was presented.

CdS nanocrystals were prepared with a previous synthetic method [62]. In a typical procedure, an appropriate amount of $Cd(NO_3)_2 \cdot 4H_2O$ and $NH_2CSNH_2$ (molar ratio 1:3) was added to a Teflon-lined stainless steel autoclave that had been filled with en to 80% of its capacity. Samples (a), (b), (c), and (d) were taken out of the autoclave after the reaction had been carried out at 120 °C for 1 h, 1.5 h, 2.5 h, and 3.5 h, respectively. Then the mixtures were cooled to room temperature immediately. The precipitates were filtered and
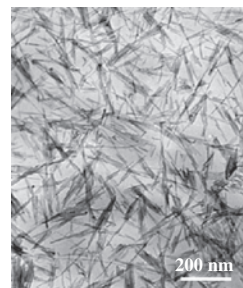


**Figure 16.** Wurtzite ZnS nanorods synthesized in *n*-butylamine at 250 °C for 12 h.
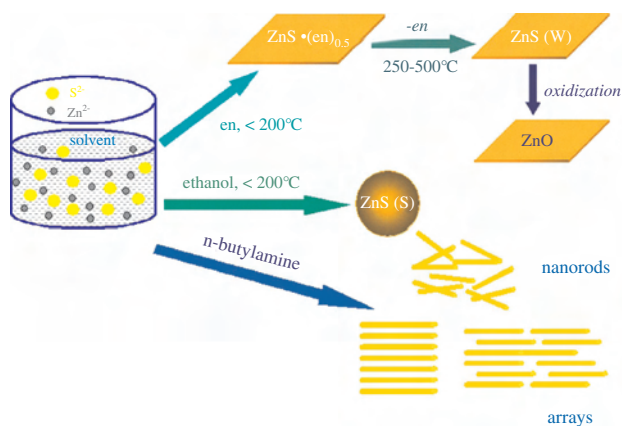
**Scheme 3.** Illustration of the controlled synthesis of ZnS nanocrystals with different dimensionalities and phases: ZnS dots, nanosheets, nanorods, and bundles. Partially adapted with permission from [64], S. H. Yu and M. Yoshimura, *Adv. Mater.* 14, 296 (2002). © 2002, Wiley-VCH.

washed repeatedly with distilled $H_2O$ and absolute ethanol to remove the excessive thiourea and other impurities. Finally the samples were dried in vacuum at 70 °C for 0.5 h.

The crystallinity of the samples is improved with the reaction time prolonged during the whole process, as shown in Figure 17. Furthermore, a preferential orientation and a rod-like shape were observed in the samples after a longer reaction time. TEM photographs show that there is an accordion-like folding process in the morphology evolution of the samples. The poorly crystallized sample (a) displayed a lamellar shape, as shown in Figure 18a, whereas the SAED pattern (inset of Fig. 18a) indicates that it was poorly crystallized, as confirmed by the XRD pattern in Figure 17a. A TEM photograph (Fig. 18b) of sample (b) reveals that the number of folds increased and these folds spontaneously agglomerated together. It seems that the shrinkage of the lamellae leads to both the increase and the agglomeration
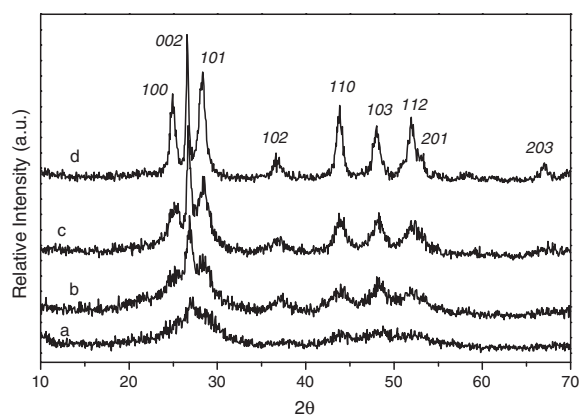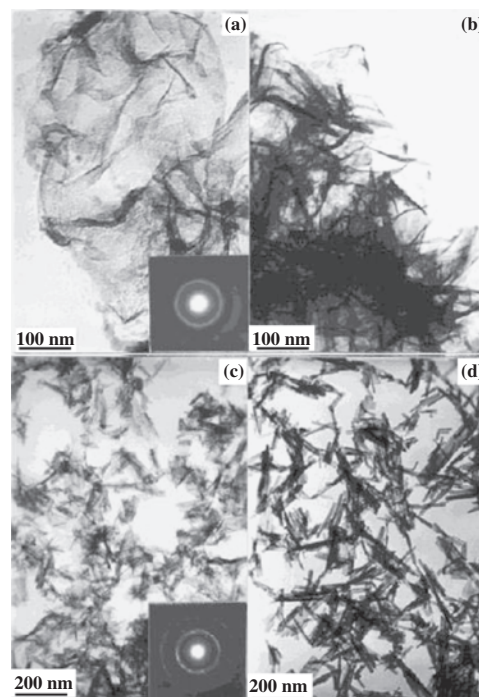


**Figure 18.** TEM images of the morphology evolution of CdS samples obtained at 120 °C in ethylenediamine. (a)–(d) With time prolonged by 1, 1.5, 2.5, and 3.5 h, respectively. Reprinted with permission from [63], J. Yang et al., *Chem. Mater.* 12, 3259 (2000). © 2000, American Chemical Society.

of the folds. Subsequently, there was an interesting shape change in the sample (c). The previously agglomerated folds broke into needle-like fragments as shown in Figure 18c, which is very critical in the formation process of CdS NRs. The SAED pattern shows a preferential orientation along (002), which coincides with the result from the XRD pattern. The sample (d) is composed of short NRs with widths of 12–17 nm and lengths of 40–160 nm.

According to these results, the formation of the obtained NRs can be divided into several steps. First cadmium nitrate and thiourea reacted to produce the lamellar CdS with many folds. After that, the folds on the lamellae agglomerated together. Then these folds broke into needle-like fragments. Finally these needles further grew into well-crystallized NRs. This transition process is interesting and is obviously different from the known 1D growth mechanisms. It is believed that en molecules adsorbed to the samples determined this morphology transition, and en molecules in the solution were not relevant to this transition process. If the sample (a) after filtering but without washing was put in a solvent such as absolute ethanol and solvothermally treated at 120 °C for 10 h, the products obtained were composed of CdS needles exclusively. However, if en molecules absorbed to sample (a) were removed by washing several times with distilled $H_2O$, most of the products prepared under the same conditions were uniform spherical particles. The results suggested that the transition process depends on en molecules absorbed to the initial sample.



**Figure 17.** XRD patterns for the CdS samples obtained at 120 °C, en. (a)–(d) With time prolonged by 1, 1.5, 2.5, and 3.5 h, respectively. Reprinted with permission from [63], J. Yang et al., *Chem. Mater.* 12, 3259 (2000). © 2000, American Chemical Society.

Although the close relationship between en molecules adsorbed to the surface and the formation of one-dimensional nanocrystals has been proved according to the above results, it is still not clear how en molecules control the formation of NRs. The IR spectrum of the starting solution was similar to that of $[Cd(en)_3]^{2+}$, which is similar to the data reported in the literature [387]. This implies that the en molecule in the starting solution uses a *gauche* conformation to chelate with $Cd^{2+}$ just like that in $[Cd(en)_3]^{2+}$ [388]. Although there is thiourea in the solution, the coordination capacity of thiourea is much smaller than that of the en molecule [389]. Therefore, a complex between thiourea and the $Cd^{2+}$ ion was not observed in the IR spectra. The IR spectra of the CdS samples were close to that of $Cd(en)Cl_2$, in which an en molecule uses a *trans* conformation to bridge an adjacent cadmium ion [391, 392]. This result indicates that the en molecule probably uses a *trans* conformation to coordinate with $Cd^{2+}$ on the surface of CdS, which we assume to be due to the fact that sulfur bonded with $Cd^{2+}$ impeded the formation of the chelate structure between the en molecule and $Cd^{2+}$ on the surface of the CdS.

The *trans* conformation of the en molecule adsorbed to the surface of CdS is important for the formation of CdS NRs through this process. To certify this conclusion, *o*-phenanthroline was chosen as the solvent to prepare CdS powders by the same reaction at 210 °C for 36 h, since it merely forms the chelate structure with $Cd^{2+}$ and its chelate ability is close to that of en [389]. Only irregularly shaped particles were observed in the product. This result demonstrates the importance of the conformation of the en molecule from the back. Reetz and co-workers also reported a nonchelating mode of coordination for $\alpha$-hydroxy carboxylates on the metal surface, which is likely to be the morphology-determining factor in the shape-selective preparation [393].

Although the IR spectra of the samples obtained at the different times were similar to each other, it was noted that the intensity of absorption peaks of the en molecules adsorbed to the surface of the CdS gradually decreased with regard to the adsorption peak of $NO_3^-$ at 1384.6 cm$^{-1}$. This indicates that the en molecule dissociates from the surface of CdS nanocrystallites during the morphology transition. The high temperature weakens the interaction between the en molecule and $Cd^{2+}$ on the surface of CdS, which leads to the dissociation of en molecules from the CdS surface. When the obtained samples without post-treatment were heated in a vacuum at 70 °C for 1 h, the absorption peaks that belonged to the en molecule adsorbed to the surface of CdS greatly decreased in intensity. However, there was no shift in the position of the IR peaks, indicating that the interaction between the en molecule and $Cd^{2+}$ on the surface of the CdS was destroyed.

If the dissociation of the en molecule absorbed to the surface of CdS is restrained, the morphology transition will slow down and even stop. For example, when sample (a) without post-treatment was put into benzene at 120 °C for 10 h, the products kept almost their original morphology. This can be attributed to the fact that the low solubility of the en molecule in benzene limits the dissociation of the en molecule. The result confirmed that the dissociation of the en molecule absorbed to the surface of CdS leads to the

morphology transition of CdS. This result also indicates that the dissociation of the en molecule in an apolar solvent is much slower than that in a polar solvent. In other words, the physicochemical properties of solvents have a great influence on the dissociation of the en molecule from CdS.

Based on all of these results, the whole forming process of CdS NRs can be expressed as follows:

$$Cd(en)_3^{2+} + S^{2-} \Longrightarrow CdS(en)_m \Longleftrightarrow CdS(en)_{m-n} + n(en) \tag{12}$$
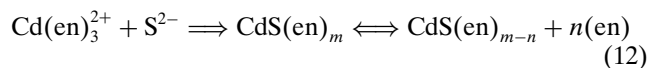
First, the $Cd^{2+}$ ion coordinated with the en molecule to form $Cd(en)_3^{2+}$ [387]. Thiourea decomposed to produce $S^{2-}$ at low temperatures in the base environment. Then the reaction between $Cd(en)_3^{2+}$ and $S^{2-}$ produced CdS powder with its surface-adsorbed en molecule. Meanwhile, the conformation of the en molecule coordinated with $Cd^{2+}$ changed from the *gauche* conformation to the *trans* conformation. However, the interaction between the en molecule and $Cd^{2+}$ on the surface of CdS was weak when the en molecule was used in the *trans* conformation. Therefore, this structure was destroyed at higher temperatures. This dissociation of the en molecule from the surface of CdS resulted in the evolution process of the morphology. In fact, the en molecule with the *trans* conformation acted as an intermediate.

There are still two questions to be resolved. One is to further ascertain the coordination mode between $Cd^{2+}$ on the surface and the en molecules. Because it is difficult to judge whether the coordination mode between $Cd^{2+}$ on the surface and the en molecules is monodentate (Scheme 4a) or bridging (Scheme 4b) based only on IR data, the en molecules in both cases are in the *trans* configuration. The other is to expand the controlling mechanism to the syntheses for other important one-dimensional semiconductors.

In as much as *n*-butylamine can act only as a monodentate ligand, the coordination between it and metal ions must be in a monodentate mode, as shown in Scheme 4c. Thus, it is employed as the solvent to answer the first question. CdS nanocrystals were chosen as the target to examine whether the same reaction in a monodentate ligand can produce NRs. In the IR spectrum of the as-prepared CdS nanocrystals, the characteristic absorption peak at 1573.0 cm$^{-1}$ can be undoubtedly assigned to the -NH$_2$ bending vibration, which shifts to lower frequencies as compared with pure *n*-butylamine [394]. At the same time, the red shift of C-N bending vibration caused by this coordination is also observed in the IR spectrum [394]. These results indicate
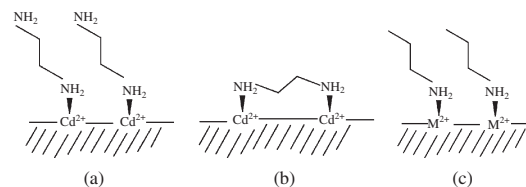


**Scheme 4.** Illustration of the possible coordination mode on the surface (a) monodentate mode of en molecules, (b) polydentate mode of en molecules, (c) monodentate mode of *n*-butylamine. Reprinted with permission from [65], J. Yang et al., *Angew. Chem. Ed. Int.* 41, 4697 (2002). © 2002, Wiley-VCH.

that *n*-butylamine also uses the nitrogen atom to coordinate with metal ions on the surface of CdS nanocrystals in a monodentate mode.

As shown in Figure 19a, the XRD pattern of CdS obtained at 220 °C for 12 h can be identified as a hexagonal phase CdS (JCPDS card no. 41-1049). The crystal size, which can be roughly estimated by using the Scherrer equation, are 50 nm and 9 nm, based on the (002) and (110) diffraction peaks, respectively. The great difference between the coherence length in the [002] direction and that in the [110] direction implies the unusual shape of the products [394]. Short NRs 7–10 nm in width and 30–55 nm in length can be readily observed in Figure 19b. It is believed that plenty of (002) planes in NRs and the anisotropic shape of NRs result in a remarkable increase in the intensity and narrowing of the FWHM of the (002) diffraction.

That a number of rod-like CdS nanoparticles can be obtained in *n*-butylamine indicates that one anchor atom in a ligand is necessary and adequate to the formation of NRs, even though more anchor atoms may be present in a ligand. The close interaction between anchor atoms in ligands (Lewis base) and metal ions on the surface (Lewis acid) is another prerequisite for the formation of NRs, because the result of this weak interaction will be that ligand molecules will not impose effective influence on the nucleation and growth of nanoparticles [62]. Altering this kind of interaction strength between ligands and metal ions could control the shape and size of various chalcogenide nanocrystals, as demonstrated previously in the synthesis of CdS nanocrystals [62].

To verify whether a monodentate ligand can be used as a "shape controller" for the synthesis of other semiconductor NRs, a series of similar solvothermal reactions were performed in *n*-butylamine. A mixture of hexagonal phase CdSe and cubic phase CdSe was obtained at 160 °C for 12 h. The TEM image in Figure 20a shows that the CdSe nanocrystals are composed of NRs 12–16 nm in width and 200–400 nm in length. Similarly, wurtzite ZnSe nanoparticles can also be obtained at 220 °C for 12 h. The ZnSe nanocrystals are composed of NRs with diameters in the range of 25–50 nm and lengths up to 1000 nm. A well-crystallized single ZnSe NR with a growth direction along the *c* axis is presented in Figure 20b. Wurtzite ZnSe NRs were achieved for the first
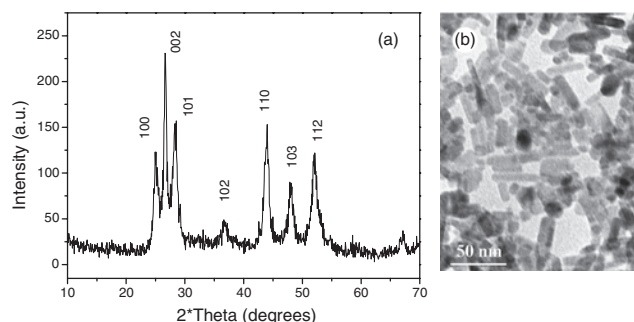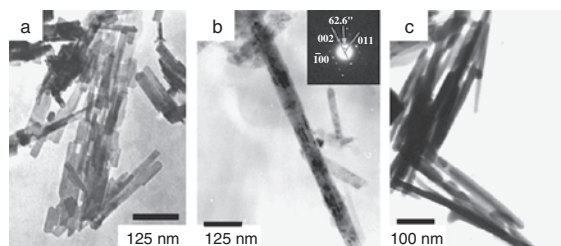


**Figure 20.** TEM images of (a) CdSe nanocrystals (160 °C, 12 h), (b) ZnSe nanocrystals (220 °C, 12 h), and (c) PbSe nanocrystals (80 °C, 12 h). Reprinted with permission from [65], J. Yang et al., *Angew. Chem. Ed. Int.* 41, 4697 (2002). © 2002, Wiley-VCH.

time in a solution system under mild conditions. Again, cubic PbSe NRs 12–20 nm in width and 200–450 nm in length as shown in Figure 20c can be obtained at 80 °C for 12 h. The growth direction of the NRs was along ⟨200⟩. These results indicate that selecting the proper experimental conditions is important for the formation of NRs, although NRs can be synthesized in *n*-butylamine.

This solvent-mediated controlling mechanism has been demonstrated to be successful in the synthesis of a variety of semiconductor NRs/NWs. In this mechanism, ligands control the shape of nanocrystals through the interaction between ligands and metal ions on the surface of nuclei. One anchor atom in a ligand such as *n*-butylamine is necessary and sufficient for the formation of 1D nanocrystals, even though more anchor atoms may be present in a ligand. The close interaction between anchor atoms in ligands and metal ions on the surface is another important prerequisite for NR formation. Furthermore, this route provides not only a possible general route to other chalcogenide NRs on a large scale but also a guide for further rational design of 1D chalcogenides.

## 2.5.2. Fabrication of Group V–VI Low-Dimensional Nanocrystals

$A_2^V B_3^{VI}$ (A = Sb, Bi, As and B = S, Se, Te) semiconductor compounds find applications in television cameras with photoconducting targets, thermoelectric devices, electronic and optoelectronic devices, and IR spectroscopy [395]. Bismuthinite ($Bi_2S_3$) and stibnite ($Sb_2S_3$) are direct band-gap materials that are useful for photodiode arrays or photovoltaics [396, 397]. $Bi_2S_3$ and $Sb_2S_3$ also belong to a family of solid-state materials with applications in thermoelectric cooling technologies based on the Peltier effect [398]. These materials may be a starting material for the synthesis of semiconductors based on sulfo salts of bismuth and related compounds and sulfoantimonates of antimony and related compounds such as $M(NH_3)_6Cu_8Sb_3S_{13}$ (M = Mn, Fe, Ni) [399].

Conventionally, $Bi_2S_3$ and $Sb_2S_3$ can be prepared by direct reaction of elements and sulfur vapor in a quartz vessel at high temperature [395, 400]. The liquid solution syntheses of $Bi_2S_3$ and $Sb_2S_3$ generally yield products that are mostly amorphous, poorly crystallized, or colloidal particles [401]. Thermal degradation of metal complexes with sulfur-containing ligands seems to be an attractive method for the synthesis of metal sulfides [398, 402]; however,



**Figure 19.** (a) XRD pattern and (b) TEM image of CdS nanocrystals obtained at 220 °C for 12 h. Reprinted with permission from [65], J. Yang et al., *Angew. Chem. Ed. Int.* 41, 4697 (2002). © 2002, Wiley-VCH.

high temperature is required to decompose the complex. In contrast, chemical solution reaction methods that do not involve sophisticated vacuum systems and heating apparatus have some advantages for the preparation of $Bi_2S_3$ and $Sb_2S_3$.

To avoid the hydrolysis of the bismuth and antimony salts in the presence of water, a so-called solvothermal decomposition process (SPD) was developed for the fabrication of $Bi_2S_3$ and $Sb_2S_3$ NWs (or NRs) [314–316], with $BiCl_3$ or $SbCl_3$ and thiourea (Tu) or thioacetamide (TAA) as starting reactants in polar solvents:

$$M^{3+} + Tu \xrightarrow{solvent} M_2S_3 \text{ NWs (or NRs)} \quad (M = Bi, Sb) \quad (13)$$
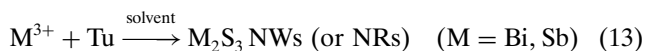
$Bi_2S_3$ nanoparticles can also be prepared by a hydrothermal crystallization method, by using ethylene diamine tetraacetic acid (EDTA) as a chelating agent to prevent the hydrolysis of $Bi^{3+}$ in water:

$$2Bi^{3+}(EDTA) + 3Na_2S \longrightarrow Bi_2S_3(sol)$$
$$+ EDTA + 6Na^+ \quad (14)$$
$$Bi_2S_3(sol) \xrightarrow{hydrothermal} Bi_2S_3(crystalline) \quad (15)$$
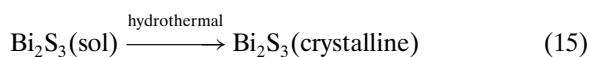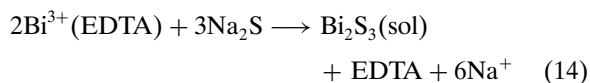
The methods make it possible to produce $Bi_2S_3$ and $Sb_2S_3$ NRs/NWs conveniently with yields as high as 95%. The particle sizes can be well controlled through the choice of different solvents or different processes. The influence of solvents, reaction temperature, and reaction time on the formation of $Bi_2S_3$ NWs was investigated. Since many metal ions can complex with thiourea or selenurea, the present technique is expected to synthesize other nanostructured metal chalcogenides.

The controllable synthesis of $Bi_2S_3$ nanocrystals is illustrated in Scheme 5. $Bi_2S_3$ NWs/NRs with controllable sizes can be selectively synthesized conveniently by the solvothermal decomposition process (SDP) and the hydrothermal process under suitable conditions, as shown in Figure 21.

Pure $Bi_2S_3$ can be easily obtained in high yield in several polar solvents. The products can be indexed orthorhombic structure with cell constants $a = 11.127$, $b = 11.265$, $c = 3.976$ Å, which are in agreement with the reported data (JCPDS card file 17-320). Different solvents were chosen for the investigation of the solvent effects on the
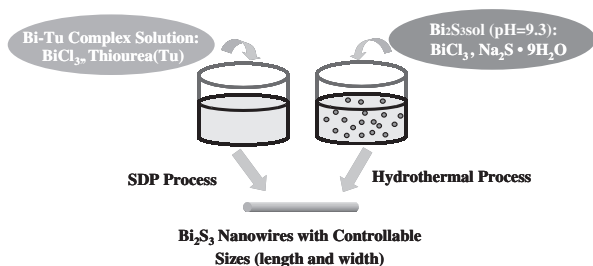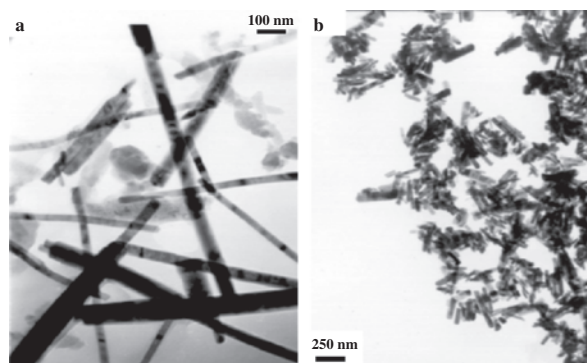


**Figure 21.** TEM images of (a) $Bi_2S_3$ nanowires fabricated by the solvothermal decomposition process at 140 °C, 12 h, ethanol (eth) and (b) rod-like $Bi_2S_3$ particles prepared by hydrothermal treatment of the sol (pH = 9.3) at 150 °C for 6 h. Reprinted with permission from [26], S. H. Yu, *J. Ceram. Soc. Jpn.* 109, S65 (2001). © 2001, Ceramic Society of Japan.

formation of $Bi_2S_3$. The solvents used included ethanol (eth), pyridine (py), ethylene glycol (EG), water, tetrahydrofuran (THF), en, 1,2-dimethoxyethane (DME), *N,N*-dimethylformamide (DMF), diethyl ether (DEE), benzene, and toluene. The effects of solvents on the synthesis of $Bi_2S_3$ and their physicochemical properties are listed in Table 3. The results confirmed that the $Bi_2S_3$ phase can be obtained in many polar solvents such as eth, py, EG, $H_2O$, DME, THF, en, and DMF. However, pure $Bi_2S_3$ nanowires can only be obtained in eth, py, EG, $H_2O$, and DME. Some unidentified phases besides the $Bi_2S_3$ phase in the products prepared in THF, en, and DMF were detected by XRD. In contrast, the Bi-Tu complex is difficult to form because of its poor solubility in apolar solvents such as DEE, benzene, and toluene due to the poor solubility of $BiCl_3$ and thiourea in apolar solvents. Both $BiCl_3$ and thiourea easily dissolve in polar solvents to form a yellow solution, which indicates the formation of Bi-Tu complexes.

The results confirmed that the polar solvents are more favorable for the formation of $Bi_2S_3$ NWs. The difference in the width and length of the $Bi_2S_3$ NWs may be related to the different physicochemical properties of the solvents. Solvent physicochemical properties such as polarity, viscosity, and softness will strongly influence the solubility and transport behavior of the precursors [366]. It has been reported that dielectric constants and dipole moments have been used in the quantitative characterization of solvent polarity [366]. These parameters are generally used to describe the overall solvation ability of a solvent. From Table 3, one can see that the dielectric constants are in the order $H_2O$ > EG > DMF > eth > en > py > THF, whereas the dielectric constants for DEE, benzene, and toluene are much smaller than those polar solvents. The Bi-Tu complexes are more easily formed in polar solvents than in apolar solvents. It is believed that the difference in particle sizes (width and length) could be attributed to the influence of the solvents on the solubility of Bi-Tu complexes and the decomposition reaction rate of the Bi-Tu complexes.



**Scheme 5.** Schematic illustration of the preparation of $Bi_2S_3$ nanowires with controllable sizes. Reprinted with permission from [26], S. H. Yu, *J. Ceram. Soc. Jpn.* 109, S65 (2001). © 2001, Ceramic Society of Japan.

**Table 3.** Effect of solvents on the synthesis of $Bi_2S_3$ and physical properties of solvents [403].

| Solvent | Dielectric[403] constant | Boiling point[403] (°C) | Temperature (°C) | Time (h) | Product | Particle sizes |
|---|---|---|---|---|---|---|
| eth | 24.55 | 78.3 | 140 | 12 | $Bi_2S_3$ | 30 nm × 500 nm |
| py | 12.3 | 115.2 | 140 | 12 | $Bi_2S_3$ | 20–30 nm × 1–3 $\mu$m |
| EG | 38.66 | 197.6 | 140 | 12 | $Bi_2S_3$ | 130–200 nm × 3.5 $\mu$m |
| $H_2O$ | 80.1 | 100 | 140 | 12 | $Bi_2S_3$ | 300 nm × 2.25 $\mu$m + short rods |
| $H_2O$[a] | 80.1 | 100 | 150 | 6 | $Bi_2S_3$ | 40 nm × 150 nm |
| $H_2O$[a] | 80.1 | 100 | 100 | 6 | $Bi_2S_3$ | 40 nm × 80 nm |
| DME | 7.20 | 85.2 | 140 | 12 | Bi-Tu | |
| THF | 7.58 | 66 | 140 | 12 | $Bi_2S_3$ + others | |
| en | 14.2 | 117.3 | 140 | 12 | $Bi_2S_3$ + others | |
| DMF | 36.71 | 153 | 140 | 12 | $Bi_2S_3$ + others | |
| DEE | 4.335 | 34.6 | 140 | 12 | No reaction | |
| Benzene | 2.275 | 80.1 | 140 | 12 | No reaction | |
| Toluene | 2.568 | 110.8 | 140 | 12 | No reaction | |

[a] The $Bi_2S_3$ powders were obtained by the hydrothermal treatment in [316].

The structural analysis shows that the infinite linear chains within the $M_2S_3$ (M = Sb, Bi) crystal structure will play a crucial role in the anisotropic growth characteristics as shown in Scheme 6. In fact, the one-dimensional growth of nanocrystals is actually the outside embodiment of inside crystal structures. However, the autogenous pressure in the solvothermal/hydrothermal process was found to play a key role in the orientation growth of the nanocrystals.

The reaction was conducted in a closed solution system, which may be similar to the sealed-tube pyrolysis reaction of $Bi(SBn)_3$ (Bn = $CH_2C_6H_5$) [398]. The solid-liquid interactions between the formed Bi-Tu complexes and the solvent and the decomposition of the complexes under sealed conditions could be responsible for the formation of the $Bi_2S_3$ NWs. In addition, the solvent acts as both reaction medium and dispersion medium so that it will prevent the aggregation of the particles and favor the production of uniform $Bi_2S_3$ powder with good dispersivity in the SDP.
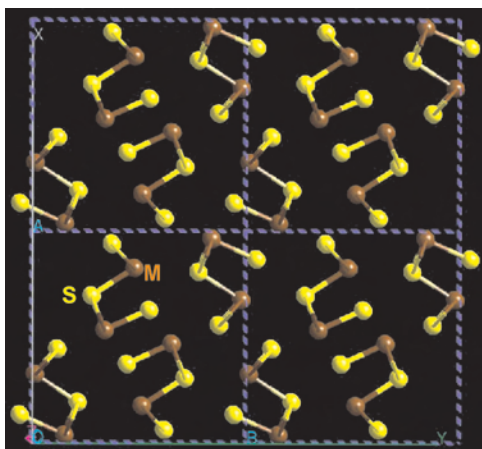


**Scheme 6.** The $XY$ projection of the structural view of $M_2S_3$ (M = Bi, Sb), showing the infinite chain structure. The modeling was done with the Cerius[2] software (Accelrys).

The $Bi_2S_3$ NWs prepared by SDP are much longer than those obtained by the hydrothermal treatment of an alkaline sol (pH = 8.0–10.0) from $BiCl_3$ and $Na_2S \cdot 9H_2O$, with EDTA as a complexing agent, as shown in Figure 21. The direct mixing of $Bi^{3+}$ with free $S^{2-}$ with EDTA as complex in aqueous solution will result in spontaneous nucleation and produce a large number of nuclei. Then the nucleation is more accelerated than the growth. Therefore, only smaller particles can be produced. In contrast, the decomposition of the Bi-Tu complexes in the SDP will proceed slowly and produce a smaller number of nuclei in the solution than the direct ion-exchange reaction due to the position-resistance effect of the formed Bi-Tu complexes and its relatively stable property, which would be favorable for the oriented growth of the NWs. Therefore, the growth stage is more accelerated than the nucleation stage, since the system can finish the nucleation stage with a smaller number of nuclei.

$Sb_2S_3$ NRs can also be easily produced with high yield by the same procedure [315]. When anhydrous $SbCl_3$ was added to the methanol solution of thiourea, the solution immediately turned yellow, which implies that the $Sb^{3+}$-thiourea complex is formed in the solution. The formation of such a complex was confirmed by the IR spectrum, UV-vis spectrum, and $^1H$ NMR spectrum.

In the IR spectrum of the $Sb^{3+}$-thiourea complex (Fig. 22a), three characteristic absorption peaks at 3370 cm$^{-1}$, 3290 cm$^{-1}$, and 3184 cm$^{-1}$ can undoubtedly be assigned to the -$NH_2$ stretching vibration. The -$NH_2$ bands did not shift to lower frequencies with regard to pure thiourea (Fig. 22b), which indicates that a bond from the nitrogen to the metal is not present [404]. Meanwhile, the frequency of the C-N stretching vibration of the complex blue shifted from 1474 cm$^{-1}$ in pure thiourea to 1511 cm$^{-1}$, which approaches the value for a double bond. The blue shift of the C-N stretching vibration implies that thiourea uses the sulfur atom to coordinate with the metal ion in the complex [405]. The C=S stretching vibration of the complex at 1413 cm$^{-1}$ was split into two peaks because of the
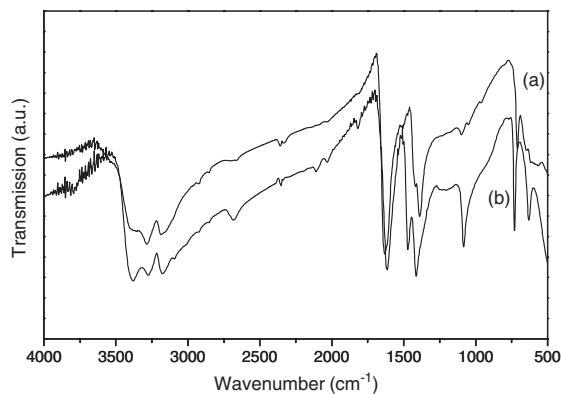
**Figure 22.** IR spectra of the as-prepared complex (a) and pure thiourea (b). Reprinted with permission from [323], J. Yang et al., *Chem. Mater.* 12, 2924 (2000). © 2000, American Chemical Society.

formation of a metal-sulfur bond [405]. Another very apparent difference in the IR spectrum between pure thiourea and the Sb³⁺-thiourea complex appeared at approximately 1100 cm⁻¹. The strong absorption peak of pure thiourea at 1084 cm⁻¹ was extremely weakened in the complex. In addition, another band associated with a C=S vibration of the complex was red shifted from 729 cm⁻¹ in pure thiourea to 709 cm⁻¹. The red shift can be attributed to the reduced double-bond character of the C=S bond due to the sulfur bonding with the metal. ¹H NMR spectrum presents one broad unresolved peak at 6.96 ppm that is shifted to the high field with regard to pure thiourea. It seems that the increase in electron density around the hydrogen atom is caused by the coordination of the ligand with the metal ion.

The crystallization process of the $Sb_2S_3$ NRs from the complex was followed by the XRD technique. The results show that the crystallinity of stibnite has been improved greatly with the prolonged reaction time. Figure 23a shows that no diffraction peaks corresponding to the starting
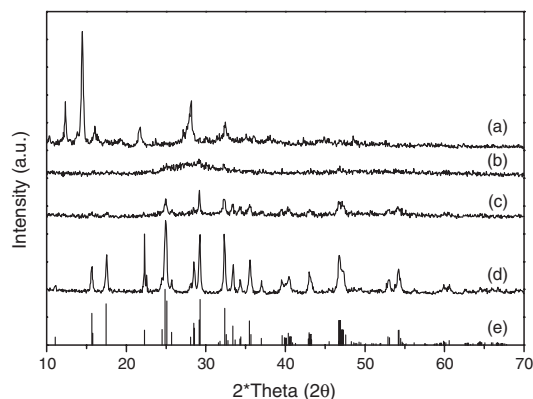
materials were observed. When the precursor was treated in an autoclave for 2 h at 120 °C, amorphous stibnite was obtained, as shown in Figure 23b. When the treatment time was prolonged to 3 h, the violet-red stibnite obtained was poorly crystallized, as shown in Figure 23c. Until the treatment time reached 6 h, the black-gray stibnite obtained was not well crystallized. The crystalline products (Fig. 23d) were identified as orthorhombic stibnite with cell constants $a = 11.228$ Å, $b = 11.329$ Å, $c = 3.844$ Å, which are close to the values in the literature (JCPDS file no. 6-0474).

The time-dependent shape evolution of the nanocrystals during the crystallization was followed. When the reaction lasted for 2 h at 120 °C, the $Sb_2S_3$ powders obtained were composed of amorphous nanoparticles with irregular shape and an average size of about 65 nm. When the reaction time was prolonged to 3 h, some NRs appeared in the poorly crystallized $Sb_2S_3$ powders. After 6 h all of the initial irregular particles transformed into well-crystallized NRs with an average diameter of 60 nm that is close to the size of the initial amorphous nanoparticles. In this transformation process, many neck-like connections were observed among the adjacent nanoparticles. Meanwhile, in the head or edge of the NRs just formed, there were many obvious bulges formed by different nanoparticles. The results suggest that probably the initial adjacent nanoparticles self-assemble together to form the final $Sb_2S_3$ NRs with the crystallinity improved.

The transformation from amorphous nanoparticles to crystallized NRs is much faster in a closed system than that in an open system. When the same solution was refluxed for 6 h in an oil bath, the products obtained were still irregular nanoparticles, as shown in Figure 24a. When the reflux time was prolonged to 10 h, some NRs did appear in the products, although the majority of the latter remained as irregular particles (Fig. 24b). When the initial amorphous nanoparticles were taken out and were washed to remove the adsorbed reactants and by-products, they were still transformed into NRs from the initial irregular nanoparticles as shown in Figure 24c, when they were treated in a closed autoclave for 10 h at 120 °C. With increasing reaction temperature, large $Sb_2S_3$ single crystalline NRs with lengths of 5 $\mu$m and 100 nm in diameter can be synthesized in



**Figure 23.** XRD patterns of the products obtained by solvothermal decomposition at different times at 120 °C. (a) The precursor. (b) 2 h. (c) 3 h. (d) 6 h. (e) The standard. Reprinted with permission from [323], J. Yang et al., *Chem. Mater.* 12, 2924 (2000). © 2000, American Chemical Society.
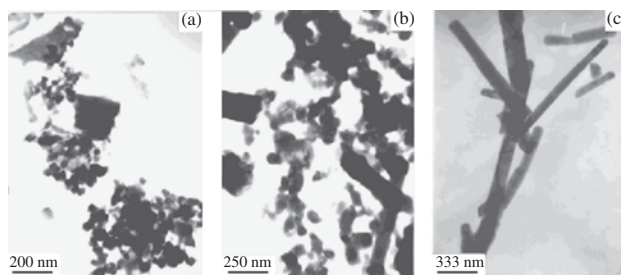


**Figure 24.** TEM photographs of the products obtained by (a) refluxing the methanol solution of the precursor for 6 h at 120 °C in a flask; (b) refluxing the methanol solution of the initial nanoparticles for 10 h in a flask at 120 °C; (c) maintaining the methanol solution of the initial nanoparticles at 120 °C for 10 h in an autoclave. Reprinted with permission from [323], J. Yang et al., *Chem. Mater.* 12, 2924 (2000). © 2000, American Chemical Society.

methanol at 180 °C for 12 h. The $Bi_2S_3$ and $Sb_2S_3$ NWs/NRs with high aspect ratios may be useful for important applications. The time dependence of the shape evolution of the nanocrystals during the crystallization controlled by pressure can be illustrated as in Scheme 7.

The above solvothermal process can be rapidly extended for the synthesis of other chalcogenide nanomaterials through the choice of suitable reaction conditions and precursors. A recent report shows that $Sb_2Se_3$ NWs with a diameter of 30 nm and lengths as long as 8 $\mu$m can be synthesized in diethylene (DEG) media at 120–140 °C by the solvothermal reaction, with $SbCl_3$, ammonia, $NaSO_3$, and Se as reactants [325]. The further optimization of the solvothermal reaction will make it possible to readily synthesize well-defined 1D III–IV nano-building blocks, which could be very useful for the synthesis of other 1D semiconductors based on sulfo salts of bismuth and related compounds and sulfoantimonates of antimony and related compounds.

### 2.5.3. Growth of Other Metal Chalcogenide Crystals

Both solvents and temperatures play important roles in the formation of different phases, their phase transformation, and morphologies of the products. It is possible to selectively synthesize metal chalcogenide nanostructured materials and grow large single crystals with perfect shapes and preferred sizes by choosing the suitable conditions. These materials with different phases and unusual shapes may have interesting catalytic, semiconducting, and magnetic properties. In this section, the influence of solvents on phase, shapes, and reactivity will be discussed with specific examples.

Various metal chalcogenide materials can be synthesized under mild conditions by the following solvothermal reaction [318, 372, 373]:

$$MC_2O_4 + E \xrightarrow{\text{solvent}} ME + 2CO_2 \uparrow$$
$$(M = \text{Metal}; E = S, Se, Te) \qquad (16)$$
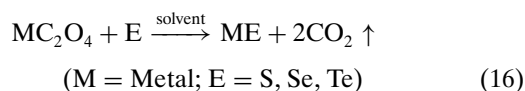
Table 4 lists experimental conditions for the synthesis of various metal chalcogenide materials and the characterization of the powders. As shown in Table 4, the solvothermal reactions in en proceed more completely than in other solvents such as py and THF, suggesting that the higher reactivity in en can be achieved compared with other solvents. Both solvent and temperature play key roles in the reaction, shapes, sizes, and phases. Solvent in particular has a significant effect on the morphology of the particles as shown in Table 4. The reaction of bismuth oxalate with selenium and tellurium proceeded in a manner similar to that of lead
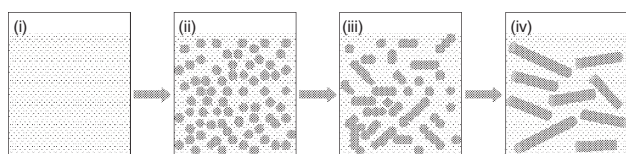
oxalate. $Bi_2Se_3$ particles with flake-like morphology are single crystal [318].

The influence of solvents on the phase transformation during the solvothermal reaction was well demonstrated by a Ni-S system [377]. A detailed study of the synthesis of various phases of nickel sulfide materials such as NiS, $Ni_3S_2$, $NiS_{1.03}$, $NiS_2$, metastable $Ni_3S_4$, and their phase transformation and the phase transformation under solvothermal conditions was recently reported to be studied with a liquid-solid interfacial reaction between nickel substrate and sulfur, and the reaction $Ni^{2+}$ ion with sulfur in different solvents such as en, water, ethanol, toluene, and py at lower temperatures ($\leq$200 °C) [377]. When the nickel salt was used instead of metal Ni, the reaction proceeded more easily. The main results of the reaction between $Ni^{2+}$ and S in en at different temperatures are summarized in Scheme 8.

Through control of the reaction time, the phase transformation process from NiS (M) to $NiS_2$ (cubic) can be nicely captured. The SEM image in Figure 25a shows that NiS (M) whiskers, with diameters ranging from 1 $\mu$m and lengths up to several micrometers, and spherical $NiS_2$ particles with a size of 1.2 $\mu$m were found to coexist in the product obtained at 200 °C for 12 h. EDX analysis confirmed that the spherical particles and whiskers in Figure 25 are composed of exact compositions of $NiS_2$ and NiS (M) phases, respectively. The tips of the NiS whiskers tend to bend, "melt," or dissolve further as shown in Figure 25b, indicating that the formation of the $NiS_2$ phase was at the expense of NiS (M) whiskers, and the transformation process from the NiS (M) phase to $NiS_2$ indeed exists during the reaction with the prolonging of the reaction time, which corresponds to the XRD results. Pure $NiS_2$ single crystals with well-defined dodecahedron crystals and uniform sizes of about 1.5–2.7 $\mu$m can be obtained by further prolonging the reaction time to 18 h at 200 °C as shown in Figure 25c. Figure 25d shows a typical $NiS_2$ single crystal with a well-developed dodecahedron {101} unit polytype shape and a size of 1.8 $\mu$m. Cubic $NiSe_2$ single crystals with a perfect octahedral shape and a size of 15 $\mu$m were obtained by a reaction of $NiC_2O_4 \cdot 2H_2O$ with Se in en [373]. $FeSe_2$, $CoSe_2$ crystals can be synthesized by a modified solvothermal process [374].

Various ternary metal chalcogenide NRs such as $CdIn_2S_4$ [346], $CuInS_2$, $AgInS_2$ [347], $AgBiS_2$ [348], $Ag_3CuS_2$ [349], $Cu_3SnS_4$ [350], and $PbSnS_3$ [351] have been synthesized by solvothermal/hydrothermal approaches under mild conditions. Even though the mechanism of the reaction and the formation of 1D NRs are still not clear, solvothermal/hydrothermal processes have already shown powerful versatilities and capabilities in the controlled solution synthesis of nonoxide 1D nanocrystals, in contrast to previous high-temperature approaches.

### 2.5.4. Controlled Growth of 1D Chalcogen Nanocrystals with More Complexity

Chalcogens are a group of important elements with unique combinations of many interesting and useful properties [406], which are also important reactant sources for the generation of metal chalcogenides, such as for the synthesis of semiconductor materials.



**Scheme 7.** Pressure-controlled formation process of the $Bi_2S_3$ and $Sb_2S_3$ NRs.

**Table 4.** Summary of various metal chalcogenides synthesized by a solvothermal process, including experimental conditions such as reactants and mole ratio (M/E) (M = metal source, E = S, Se, Te), solvent, temperature, and time; the phases were detected by X-ray powder diffraction, symmetry, and the particle shape.

| Reactants (M/E ratio) | Solvent | Reaction conditions | Phase | Symmetry | Shape |
|---|---|---|---|---|---|
| $CdC_2O_4 + S(2:1)$ | en | 120–180 °C, 12 h | CdS | Hexagonal | Rod-like |
| $CdC_2O_4 + S(2:1)$ | py | 160–180 °C, 12 h | CdS | Hexagonal | Spherical |
| $CdC_2O_4 + S(2:1)$ | EG | 160–180 °C, 12 h | CdS | Hexagonal | Spherical |
| $CdC_2O_4 + Se(2:1)$ | en | 140 °C, 12 h | CdSe | Hexagonal | Rod-like |
| $CdC_2O_4 + Se(2:1)$ | py | 160 °C, 12 h | CdSe | Hexagonal | Spherical |
| $CdC_2O_4 + Se(2:1)$ | py | 140 °C, 12 h | Se + CdSe[a] | | |
| $CdC_2O_4 + Te(2:1)$ | en | 180 °C, 12 h | CdTe | Cubic | Rod-like |
| $PbC_2O_4 + S(1:1)$ | en | 120 °C, 12 h | PbS | Cubic | Square |
| $PbC_2O_4 + S(1:1)$ | py | 120 °C, 12 h | PbS | Cubic | Square |
| $PbC_2O_4 + Se(1:1)$ | en | 160 °C, 12 h | PbSe | Cubic | Square |
| $PbC_2O_4 + Se(1:1)$ | py | 160 °C, 12 h | PbSe + Se[a] | | |
| $PbC_2O_4 + Te(1:1)$ | en | 160 °C, 12 h | PbTe | Cubic | Square |
| $PbC_2O_4 + Se(1:1)$ | py | 160 °C, 12 h | PbTe + Te[a] | | |
| $SnC_2O_4 + S(1:1.2)$ | en | 240 °C, 8 h | SnS | Orthorhombic | Plate-like |
| $SnC_2O_4 + Se(1:1.2)$ | en | 180 °C, 8 h | SnSe | Orthorhombic | Rod-like |
| $SnC_2O_4 + Te(1:1.2)$ | en | 170 °C, 8 h | SnTe | Cubic | Spherical |
| $Ag_2C_2O_4 + S(1:1)$ | en | 140 °C, 12 h | $Ag_2S$ | Monoclinic | Spherical |
| $Ag_2C_2O_4 + S(1:1)$ | py | 140 °C, 12 h | $Ag_2S$ | Monoclinic | Spherical |
| $Ag_2C_2O_4 + S(1:1)$ | THF | 140 °C, 12 h | $Ag_2S$ | Monoclinic | Spherical |
| $Ag_2C_2O_4 + Se(1:1)$ | en | 140 °C, 12 h | $Ag_2Se$ | Orthorhomic | Plate-like |
| $Ag_2C_2O_4 + Se(1:1)$ | py | 140 °C, 12 h | $Ag_2Se + Se$[a] | | |
| $Ag_2C_2O_4 + Se(1:1)$ | py | 160 °C, 12 h | $Ag_2Se + Ag$[a] | | |
| $Ag_2C_2O_4 + Se(1:1)$ | THF | 140 °C, 12 h | $Ag_2Se + Se$[a] | | |
| $Ag_2C_2O_4 + Te(1:1)$ | en | 180 °C, 12 h | $Ag_2Te + Se$[a] | Monoclinic | |
| $Ag_2C_2O_4 + Te(1:1)$ | en | 160 °C, 12 h | $Ag + Ag_2Te$[a] | | |
| $Ag_2C_2O_4 + Te(1:1)$ | py | 180 °C, 12 h | $Ag + Ag_2Te$[a] | | |
| $Ag_2C_2O_4 + Te(1:1)$ | THF | 180 °C, 12 h | $Ag + Ag_2Te$[a] | | |
| $Bi_2(C_2O_4)_3 + Se(1:1)$ | en | 140 °C, 12 h | $Bi_2Se_3$ | Hexagonal | Plate-like |
| $Bi_2(C_2O_4)_3 + Se(1:1)$ | py | 140 °C, 12 h | $Bi_2Se_3 + Se$[a] | | |
| $NiC_2O_4 \cdot 2H_2O + Se(1:2.4)$ | en | 170 °C, 8 h | $NiSe_2$ | Cubic | Octahedral |
| $NiC_2O_4 \cdot 2H_2O + Se(1:1)$ | en | 200 °C, 8 h | $Ni_{0.85}Se$ | Hexagonal | Starfish-like |
| $NiC_2O_4 \cdot 2H_2O + Se(3:2)$ | en | 220 °C, 8 h | $Ni_3Se_2$ | Triclinic | Dendritic |
| $NiC_2O_4 \cdot 2H_2O + Se(1:1)$ | en | 180 °C, 8 h | $NiSe_2$ | Cubic | Spherical |
| $NiC_2O_4 \cdot 2H_2O + Se(1:2.2)$ | py | 180 °C, 8 h | $NiSe_2$ | Cubic | Octahedral |
| $NiC_2O_4 \cdot 2H_2O + Se(1:2.2)$ | THF | 170 °C, 8 h | $NiSe_2$ | Cubic | Octahedral |

From [61, 318, 372, 373, 375].
[a] Dominant phase in the sample.
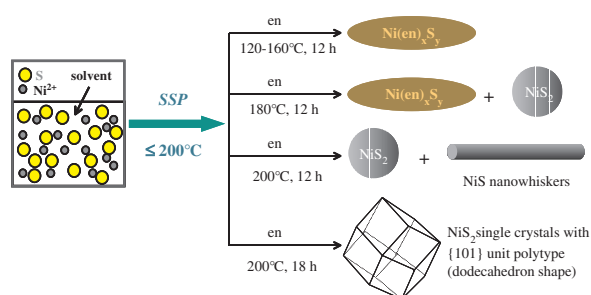


**Scheme 8.** Summary of the results of the reaction of $Ni^{2+}$ with S in ethylenediamine under different conditions. Reprinted with permission from [377], S. H. Yu and M. Yoshimura, *Adv. Funct. Mater.* 12, 277 (2002). © 2002, Wiley-VCH.

Trigonal selenium NWs with well-defined sizes and aspect ratios have been synthesized by a solution-phase approach [233, 234]. The first step of this approach involved the formation of amorphous $\alpha$-Se in an aqueous solution through the reduction of selenious acid with excess hydrazine by refluxing this reaction mixture at 100 °C:

$$H_2SeO_3 + N_2H_4 \rightarrow Se \downarrow + N_2 \uparrow + 3H_2O \qquad (17)$$
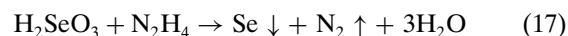
When this solution was cooled to room temperature, the small amount of selenium dissolved in the solution precipitated out as nanocrystallites of trigonal $t$-Se. Cooling the solution to room temperature will produce a small amount of trigonal Se in the solution, which will act as seeds for the formation of a large amount of trigonal Se NWs during further aging of the solution in a dark place [233]. The 1D
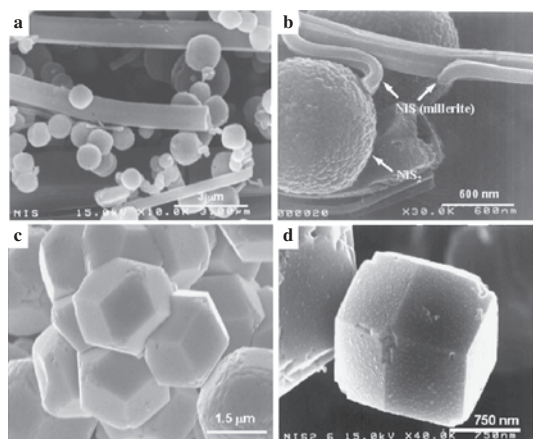
**Figure 25.** SEM images for products of the reaction of $Ni(NO_3)_2 \cdot 6H_2O$ with S in ethylenediamine. (a) and (b) Coexistence of NiS nanowhiskers with uniform spherical $NiS_2$ nanoparticles obtained at 200 °C, 12 h, $[Ni^{2+}] = [S] = 0.005$ mol. (c) Uniform and well-developed $NiS_2$ single crystals obtained at 200 °C for 18 h, $[Ni^{2+}]:[S] = 1:3$, $[S] = 0.005$ mol. (d) A typical $NiS_2$ single crystal displayed well-developed {101} poly-type with dodecahedron shape and a size of 1.2 $\mu$m. Reprinted with permission from [377], S. H. Yu and M. Yoshimura, *Adv. Funct. Mater.* 12, 277 (2002). © 2002, Wiley-VCH.

morphology of the final product was determined by the linearity of infinite, helical chains of Se atoms contained in the trigonal phase.

A recent report by Xia et al. shows that single crystalline NWs of $Ag_2Se$ can be synthesized by templating against the trigonal Se NWs [328, 329] at room temperature as shown in Figure 26.

In addition, trigonal tellurium NBs, NTs, and nanohelices can be synthesized [235, 236]. The tellurium NTs were synthesized by reflexing a solution of orthotelluric acid in ethylene glycol at ~197 °C [235] as shown in Figure 27. The early stage shows that tubular structures grew from the cylindrical seeds as shown in Figure 27a.

A very simple controlled hydrothermal route has been developed for the synthesis of tellurium NBs, NTs, and nanohelices by reaction of sodium tellurite ($Na_2TeO_3$) in aqueous ammonia solution at 180 °C [236]. The NBs have thicknesses of about 8 nm with widths of 30–500 nm and lengths up to several hundred micrometers, as shown in Figure 28a. The NBs tend to twist and form helices as shown in Figure 28b. When the NBs were further
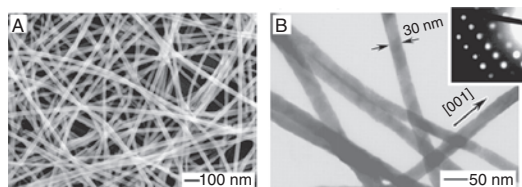


**Figure 26.** SEM (A) and TEM (B) images of uniform nanowires of $Ag_2Se$ that were synthesized through a reaction between the 32-nm nanowires of *t*-Se and an aqueous solution of $AgNO_3$ at room temperature. Reprinted with permission from [328], B. Gates et al., *J. Am. Chem. Soc.* 123, 11500 (2001). © 2001, American Chemical Society.
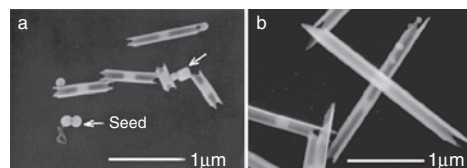


**Figure 27.** SEM images of the Te nanotubes synthesized by refluxing a solution of orthotelluric acid in ethylene glycol for (a) 4 min and (b) 6 min. The white arrow indicates the presence of seeds. Reprinted with permission from [235], B. Mayers and Y. N. Xia, *Adv. Mater.* 14, 279 (2002). © 2002, Wiley-VCH.

twisted and rolled, NTs formed. In addition, an interesting nanostructure, a "coaxed nanobelt within a nanotube," was observed, as shown in Figure 28c. The template-roll-growth mechanism and template-twist-joint-growth mechanism were proposed to explain the formation of such special nanostructures [236]. However, the detailed mechanism still needs to be investigated further.

The above novel chalcogen nanostructures can be rapidly used as templates for the synthesis of other, more specialized and more complex 1D and 2D metal chalcogenide nanostructures, which could find interesting applications.

## 2.6. Solution-Liquid-Solid Mechanism

The solution-liquid-solid (SLS) growth mechanism, which is analogous to the well-known VLS mechanism, was first discovered by Buhro et al. [66]. This route is mainly for growing group III–V nanofibers (InP, InAs, GaAs, $Al_xGa_{1-x}As$, InN) in hydrocarbon solvents at relatively low temperatures (less than or equal to 203 °C) [66–69]. More features about this route have been summarized in [67], as shown in Figure 29. The synthesis involved the methanolysis of $\{t\text{-}Bu_2In[\mu\text{-}P(SiMe_3)_2]\}_2$ in aromatic solvents to produce polycrystalline InP fibers (dimensions 10–100 nm × 50–1000 nm) at 111–203 °C [68]. The chemical pathway consists of a molecular component, in which precursor substituents are eliminated, and a nonmolecular component, in which the InP crystal lattices are assembled. The two components working in concert comprise the SLS mechanism. The molecular component proceeds through a sequence of isolated and
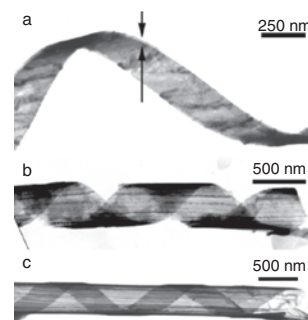


**Figure 28.** TEM images of (a) a typical tellurium nanobelt, (b) a helical nanobelt, (c) a typical helical nanobelt within a nanobelt-roll nanotube. Reprinted with permission from [236], M. S. Mo et al., *Adv. Mater.* 14, 1658 (2002). © 2002, Wiley-VCH.
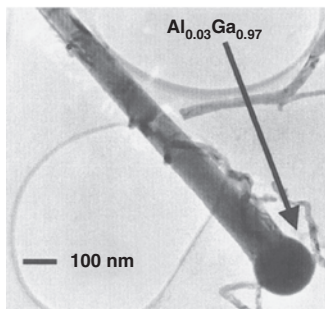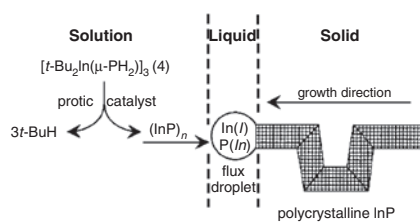
**Figure 29.** Solution-liquid-solid (SLS) mechanism and a representative $Al_{0.1}Ga_{0.9}As$ nanowhisker grown by the SLS mechanism. Reprinted with permission from [68], T. J. Trentler et al., *J. Am. Chem. Soc.* 119, 2172 (1997), and [69], P. D. Markowitz et al., *J. Am. Chem. Soc.* 123, 4502 (2001). © 1997, 2001, American Chemical Society.

fully characterized intermediates to form the $[t\text{-}Bu_2In(\mu\text{-}PH_2)]_3$ complex. The complex, which is alternatively prepared from $t\text{-}Bu_3In$ and $PH_3$, undergoes alkane elimination catalyzed by the protic reagent MeOH, PhSH, $Et_2NH$, or $PhCO_2H$. In the subsequent nonmolecular component of the pathway, the resulting $(InP)_n$ fragments dissolve into a dispersion of molten In droplets and recrystallize as InP fibers [68].

This approach has been extended for the synthesis of InN NWs by solution-state thermolysis of the dialkyl(azido)-indane precursor [259].

Group IV Si and Ge crystals can be generated by a supercritical fluid solution-phase approach [70]. Recently, Korgel et al. reported a supercritical fluid solution-phase self-assembly approach with a similar SLS mechanism for growing bulk quantities of defect-free Si NWs with diameters of about 4–5 nm and aspect ratios greater than 1000 by using alkanethiol-coated gold nanocrystals as uniform seeds to direct one-dimensional Si crystallization in supercritical hexane [71]. In this process, the sterically stabilized Au nanoparticles were dispersed in supercritical hexane together with diphenylsilane, which underwent decomposition at 500 °C and 270 bar. The phase diagram for Si and Au indicated that at temperatures above 363 °C, Si and Au will form an alloy in equilibrium with pure solid Si when the Si concentration with respect to Au is greater than 18.6%. Under this condition, the Si atoms dissolve into the sterically stabilized Au nanocrystals until the supersaturation is reached, at which point they are expelled from the particles as a thin nanometer-scale wire. The supercritical fluid medium with high temperature promotes Si crystallization. The Au nanocrystals will be maintained to seed NW growth under supercritical conditions.

## 2.7. Capping Agent/Surfactant-Assisted Synthesis

### 2.7.1. Self-Assembly under Hot Conditions

Capping agent/surfactant-assisted synthesis has been widely explored for the fabrication of NRs, NTs, and more complex structures. Recently, Alivisato's group synthesized the elongated CdSe nanocrystallites by injecting a solution of dimethylcadmium and selenium in tributylphosphine into a mixture of hexylphosphonic acid (HPA) and trioctylphosphine oxide (TOPO) at 340–360 °C [11, 72].

The surfactant molecules adsorb and desorb rapidly from the nanocrystal surface at the growth temperature, permitting the addition and removal of atoms from the crystallites, while aggregation is suppressed by the presence of (on average) one monolayer of surfactant at the crystallite surface. It is well known that the solubility of crystals increases as the size of the crystals decreases, according to the Gibbs-Thompson law. This law plays an important role in determining the growth kinetics of the nanocrystals. Peng et al. observed that if the monomer concentration in the solution is higher than the solubility of all existing nanocrystals, all nanocrystals in the solution grow and the size distribution narrows. The so-called focusing of size distribution can be exploited for the spontaneous formation of close to monodisperse colloidal nanocrystals and can form a three-dimensional orientation. The CdSe NRs with variable aspect ratios can be well achieved by kinetic control growth of the nanoparticles (Fig. 30).

The diverse range of observed shapes can be understood as arising from three basic effects: the nanocrystals will eventually tend toward nearly spherical shapes at slow growth rates; rods form at high growth rates by unidirectional growth of one face; and HPA accentuates the differences in the growth rates among various faces. A large injection
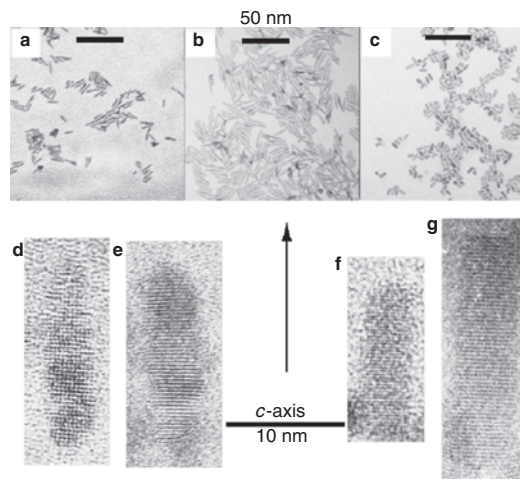


**Figure 30.** TEM images of different samples of quantum rods. (a–c) Low-resolution TEM images of three quantum-rod samples with different sizes and aspect ratios. (d–g) High-resolution TEM images of four representative quantum rods. (d) and (e) are from the sample shown in (a); (f) and (g) are from the sample shown in (c). Reprinted with permission from [11], X. G. Peng et al., *Nature* 402, 393 (1999). © 1999, Macmillan Magazines Ltd.

volume or a very high monomer concentration favors rod growth.

Recently, Peng et al. proposed a diffusion-controlled crystal growth model based on their careful observation of the shape evolution of CdSe NRs as shown in Scheme 9 [407]. They believed that a typical temporal shape evolution of CdSe quantum rods occurs in three distinguishable stages. When the Cd monomer concentration in the solution was between 1.4% and 2% of cadmium element by mass, all of the nanocrystals grew almost exclusively along their long axis, and both the aspect ratio and the volume of the crystals increased rapidly. This stage is called the "1D-growth stage." The second stage, the "3D-growth stage," occurred when the Cd monomer concentration dropped to between 0.5% and 1.4%. In this stage, crystals grew simultaneously in three dimensions [Fig. 31]. The aspect ratio remained constant, but the crystal volume increased. It should be mentioned that this stage was not observed before [11], probably because of the higher growth rates. The final stage, called "1D-to-2D ripening," was identified when the Cd concentration was constant at 0.5%. The aspect ratio of the rods dropped noticeably, because the dimension of the crystals increased along the short axis and decreased along the long axis. Nanocrystal volumes and number remained constant, and there was no noticeable net growth or net dissolution of nanocrystals. This indicates that the monomers very likely moved on the surface of a crystal from one dimension ($c$ axis) to the other two dimensions in an intraparticle manner.

The 1D-growth stage was confirmed by a reaction whose monomer concentration was maintained in the corresponding 1D-growth range for a longer time through the addition of more monomers to the reaction system at certain time intervals. The long axis of the quantum rods can be further extended from about 35 nm to over 100 nm by the secondary injections, but the short axis remained almost constant, at about 3–4 nm.

In this model, each crystal is surrounded by a diffusion sphere as shown in Scheme 9 [407]. The monomer concentration gradient between the bulk solution and the stagnant solution, as well as the diffusion coefficient of the monomers, determines the direction (out of or into the diffusion sphere) and the diffusion flux. The monomer concentration in the stagnant solution maintains the solubility of a given facet by the rapid growth onto or dissolution from the facet.



**Figure 31.** HRTEM image (a) of a typical tetrapod-shaped CdSe nanocrystal, looking down the [001] direction of one arm. Lattice spacings confirm that all four arms are of the wurtzite structure. In image (b), we see a tetrapod that has branches growing out of each arm. There are zinc blende layers near the ends of the original arms, and the branches are wurtzite with some stacking faults. Reprinted with permission from [72], L. Manna et al., *J. Am. Chem. Soc.* 122, 12700 (2000). © 2000, American Chemical Society.

The wurtzite structural characteristics are shown in Scheme 10, showing that all of the atoms on both facets perpendicular to the $c$ axis (unique facets) have only one dangling bond without surface reconstruction [407]. The facets terminated by negatively charged Se atoms and positively charged Cd atoms are the (00$\underline{1}$) facet and (001) facet, respectively. The negatively charged (00$\underline{1}$) facet is more or less uncoated, because the ligands in the solution are all electron-donating ligands and should bind exclusively to cationic species. Additionally, without surface reconstructions, any surface Cd atom grown on the (00$\underline{1}$) facet has to possess three dangling bonds, even if the surface Cd atoms reach a full monolayer. These unique structural features of the (00$\underline{1}$) facet and the dipole moment along the $c$ axis significantly increase the chemical potential of the unique facets, especially the (00$\underline{1}$) facet, compared with the others [407].

The above surfactant-driven shape-controlled synthesis strategy was further extended for the synthesis of group III–VI semiconductor NRs for the first time by Cheon's group



**Scheme 9.** A schematic diagram for the proposed mechanisms of the three stages of the shape evolution. The circle in each stage is the interface between the bulk solution and the diffusion sphere. Arrows indicate the diffusion directions of the monomers. The double-headed arrows represent the diffusion equilibrium in the 1D-to-2D ripening stage. Reprinted with permission from [407], Z. A. Peng and X. G. Peng, *J. Am. Chem. Soc.* 123, 1389 (2001). © 2001, American Chemical Society.



**Scheme 10.** Schematic structure of CdSe quantum rods in growth. The most stable form of a rod is shown on the left; its (00$\underline{1}$) facet terminated by Se atoms does not have any ligands. After growing a monolayer of Cd atoms on the (00$\underline{1}$) (right), this facet is still relatively active compared with the other facets, because the surface Cd atoms on this facet have three dangling bonds. See text for more details. Reprinted with permission from [407], Z. A. Peng and X. G. Peng, *J. Am. Chem. Soc.* 123, 1389 (2001). © 2001, American Chemical Society.

[254]. Gallium phosphide semiconductor nanocrystals can be synthesized by using thermal decomposition of a single molecular precursor, tris(di-*tert*-butylphosphino)gallane $(Ga(PtBu_2)_3)$, in a hot mixture of amine stabilizers. As in the case of CdSe, the shape of GaP nanocrystals can also be varied from nanospheres to rods with highly monodispersed size distributions by controlling the type and amount of stabilizing surfactants.

When only trioctylamine (TOA) was used as a stabilizer, spherical GaP nanoparticles with zinc blende structure were formed. Increasing the stabilizer ratio of HAD to TOA leads to the formation of NRs [254]. The addition of HDA to TOA leads to changes in the shape and crystalline phase of the GaP nanocrystals. Figure 32 shows that wurtzite GaP NRs with a diameter of 8 nm and a length of 45 nm were grown by thermal decomposition of the precursor in TOA solution, which was injected into a mixture of TOA and hexadecylamine (HDA) at 330 °C. A low HDA-to-TOA ratio seems to favor the formation of zinc blende nanospheres, but a high concentration of HDA leads to the formation of the wurtzite phase and induces anisotropic growth of the nanocrystals [254].

The steric effects of the stabilizers during crystal growth are illustrated in Scheme 11 [254]. The thermodynamically stable GaP zinc blende structure is a staggered conformation with $\langle 111 \rangle$ directions, and the kinetically stable wurtzite structure is an eclipsed conformation with $\langle 002 \rangle$ directions (Scheme 11). Kinetic stability of the wurtzite structure is induced by strong dipole interaction of incoming GaP monomers with surface GaP lattice atoms. The conformation of crystal structures is highly affected by changes in the stabilizer, since stabilizers can dynamically bind to the crystal surfaces during the GaP crystal growth. When the highly bulky tertiary amines (e.g., TOA) are used as stabilizers, a staggered conformation is favored, minimizing steric hindrance between these ligands and GaP lattices (Scheme 11, path A), and zinc blende GaP is preferred over wurtzite. In contrast, when an excess amount of less sterically hindered HDA is added to TOA, the rotational barrier between GaP-HDA complexes and GaP lattices is reduced. Therefore, the formation of the kinetically stable wurtzite GaP is now facilitated (Scheme 11, path B) under the kinetic growth regime induced by a high monomer concentration [254].
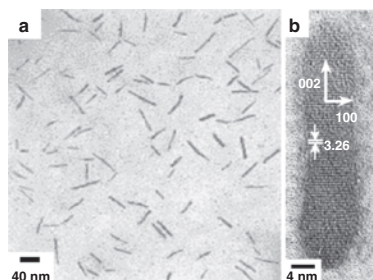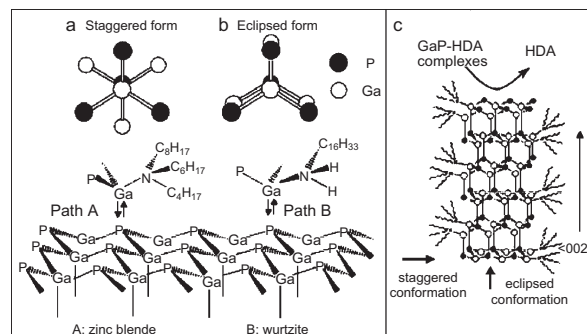


**Scheme 11.** Proposed mechanism for surfactant-driven steric effects on the crystalline phases (a, b) and rod growth (c) of GaP nanocrystals. Reprinted with permission from [254], Y.-H. Kim et al., *J. Am. Chem. Soc.* 124, 13656 (2002). © 2002, American Chemical Society.

The steric difference between these two stabilizers seems to induce the anisotropic growth of the wurtzite GaP. It is likely that, when wurtzite seeds are formed, sterically bulky TOA selectively binds to the other faces (e.g., 100 and 110 faces) with staggered conformation rather than to 002 faces and blocks growth on these faces. On the other hand, GaP-HDA complexes continuously supply monomers on the 002 faces with high surface energy and therefore promote growth along the *c* axis (Scheme 11c). In addition, the thermolysis of a monomeric precursor $[Zn(TePh)_2][TMEDA]$ prepared from $Zn(TePh)_2$ and donor ligand TMEDA in a mixed surfactant trioctylamine-dimethylhexylamine produced ZnTe NRs [312], which could be templated from the rod-like micelles formed in the mixed-solvent system.

Currently, this approach has been successfully applied to the synthesis of transition metal NRs such as Co [205], Fe [208], and Ni [210], as well as perovskite $BaTiO_3$, $SrTiO_3$ NRs [104].

### 2.7.2. Self-Assembly under Natural/Mild Conditions

In contrast to the above capping agent/surfactant-driven synthesis of semiconductor NRs in hot solvent, self-assembly of nanofiber bundles, NTs, NWs, and their structure modulation under natural/mild conditions have emerged recently [25, 72–79]. The reverse micelle reaction medium usually consists of either the anionic surfactant AOT (sodium bis(2-ethylhexyl)sulfosuccinate) or nonionic surfactants. Various kinds of 1D inorganic NRs/NWs such as $BaCrO_4$, [25, 75], $BaSO_4$ [74, 75], $BaCO_3$ [77], and $BaWO_4$ [78], $CaSO_4$ [107], $CaCO_3$ [408], CdS [292, 409], and Cu [410] have been synthesized in reverse micelle media or microemulsions. Other novel nanostructures, such as Ag nanodisc [192], flat CdS triangles [291], and CdS, CdSe NTs/NWs [76], can also be synthesized by this approach.

The strong binding interactions between surfactants and inorganic nuclei effectively inhibit the crystal growth and put the spontaneous structure reconstruction and self-organization of the primary nanoparticles under control. Micrometer-long twisted bundles of $BaSO_4$ and $BaCrO_4$ nanofilaments in water-in-oil microemulsions were prepared from the anionic surfactant AOT [25]. The reaction occurs at



**Figure 32.** Large-area TEM image (a) and a HRTEM image (b) of GaP nanorods. Reprinted with permission from [254], Y.-H. Kim et al., *J. Am. Chem. Soc.* 124, 13656 (2002). © 2002, American Chemical Society.

room temperature in unstirred isooctane containing a mixture of Ba(AOT)$_2$ reverse micelles and NaAOT microemulsions with encapsulated sulfate (or chromate) anions. The reverse micelles are about 2 nm in diameter and consist of a spherical cluster of about 10 Ba$^{2+}$ ions strongly associated with the sulfonic acid headgroups of the surfactant, along with the water of hydration [25]. In contrast, the microemulsions are larger (4.5 nm across) because they contain bulk water (aqueous Na$_2$SO$_4$ or Na$_2$CrO$_4$) at a water-to-surfactant molar ratio of $w = 10$. When mixed together, the two reaction fields interact so that the constituents are slowly exchanged and BaSO$_4$ or BaCrO$_4$ nanoparticles nucleate and grow within the delineated space. With time, other filaments are formed parallel to the original thread to produce a small bundle of coaligned inorganic nanofilaments held together by surfactant bilayers. The locking in of new filaments by surfactant interdigitation generates a bending force in the nonattached segment of the longer primary thread. This results in the coiling of the bundle into a characteristic spiral-shaped structure several hundred nanometers in size that becomes self-terminating at one end because further addition of the primary nanoparticles is prevented by spatial closure.

The construction of higher-order structures from inorganic nanoparticle building blocks was successfully demonstrated by achieving sufficient informational content in the preformed inorganic surfaces to control long-range ordering through interactive self-assembly [25]. The NRs have flat surfaces with low curvature so that the hydrophobic driving force for assembly can be strengthened through intermolecular interaction, resulting in the formation of a bilayer between adjacent particles by the interdigitation of surfactant chains attached to nanoparticle surfaces. When the [Ba$^{2+}$]:[SO$_4^{2-}$] (or [Ba$^{2+}$]:[CrO$_4^{2-}$]) molar ratio is equal to 1.0, remarkable linear chains of individual BaSO$_4$ or BaCrO$_4$ NRs are formed as shown in Figure 33.



**Figure 33.** TEM image showing ordered chains of prismatic BaSO$_4$ nanoparticles prepared in AOT microemulsions at [Ba$^{2+}$]:[SO$_4^{2-}$] molar ratio = 1 and $w = 10$. Scale bar = 50 nm. Reprinted with permission from [25], M. Li et al., *Nature* 402, 393 (1999). © 1999, Macmillan Magazines Ltd.

Semiconductor NTs and NWs have recently been obtained with the use of nonionic surfactants such as $t$-octyl-(OCH$_2$CH$_2$)$_x$OH, $x = 9, 10$ (Triton-X) and anionic surfactant AOT [76]. NWs of sulfides and selenides of Cu, Zn, and Cd with high aspect ratios can be prepared with Triton 100-X. The results show that it is possible to obtain both NTs and NWs of CdSe and CdS by this surfactant-assisted synthesis. For the synthesis of CdSe NTs, a suspension of cadmium oxide (10 mmol) was prepared in 20 ml of Triton 100-X (~24 mmol). A solution of NaHSe (NaBH$_4$/Se in 40 ml of water) was added dropwise under constant stirring to the suspension at 40 °C in an argon atmosphere. The resulting mixture was refluxed for 12 h and left overnight. The NTs are generally long, with lengths up to 5 $\mu$m, as shown in Figure 34. The outer diameter of the NTs is in the 15–20-nm range, and the diameter of the central tubule is in the 10–15-nm range. The wall thickness is therefore around 5 nm. The formation mechanism of the NTs in the presence of surfactant is still not clear.

It should be pointed out that the poor crystallinity of the nanostructures obtained by this approach as well as the use of large excess surfactants could restrict the applicability of this approach.

## 2.8. Bio-Inspired Approach for Complex Superstructures

### 2.8.1. Polymer-Controlled Crystallization

Bio-inspired approaches to the synthesis of inorganic minerals have been a hot research subject [73, 80, 81]. Recently it was shown that so-called double-hydrophilic block copolymers (DHBCs) [81–94] can exert a strong influence on the external morphology and/or crystalline structure of inorganic particles such as calcium carbonate [82–85], calcium phosphate [86], barium sulfate [87, 88], barium chromate [89–91], cadmium tungstate [92], and zinc oxide [93].

Elegant nested calcium phosphate nanofibers were mineralized in the presence of DHBC poly(ethylene oxide)-*b*-alkylated poly(methacrylic acid) (PEO-*b*-PMAA-C$_{12}$), which was synthesized from PEO-*b*-PMAA by partial alkylation with dodecylamine [411]. Through the control of the pH of the Ca$^{2+}$-loaded polymer solution, delicate mesoskeletons of interconnected calcium phosphate nanofibers with star-like, neuron-like, and more complex nested forms can be obtained, as shown in Figure 35 [86].



120 nm
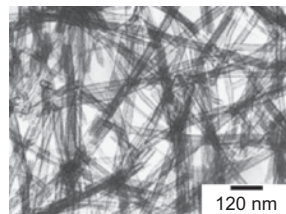
**Figure 34.** TEM image of CdSe nanotubes obtained with Triton 100-X as the surfactant. Reprinted with permission from [76], C. N. N. Rao et al., *Appl. Phys. Lett.* 78, 1853 (2001). © 2001, American Institute of Physics.
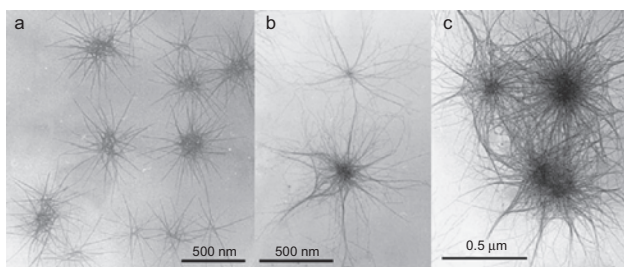
**Figure 35.** TEM images of calcium phosphate block copolymer nested colloids. (a) Star-like form at early stage at pH 3.5. (b) Later stage showing complex central core. (c) Neuron-like tangles produced at pH 5. Reprinted with permission from [86], M. Antonietti et al., *Chem. Eur. J.* 4, 2491 (1998). © 1998, Wiley-VCH.

Very long $BaSO_4$ and $BaCrO_4$ nanofibers and fiber bundles with remarkable similarity have been successfully fabricated by a polymer-controlled crystallization process at room temperature [88–90]. More complex morphologies of hashemite can be formed in the presence of partially phosphonated block copolymer poly(ethylene glycol)-*block*-poly(methacrylic acid) (PEG-*b*-PMAA-$PO_3H_2$, PEG = 3000 g mol$^{-1}$, 68 monomer units; PMAA = 700 g mol$^{-1}$, 6 monomer units) [84]. Figure 36a and b shows SEM images of fibrous superstructures with sharp edges composed of densely packed, highly ordered, parallel nanofibers of $BaCrO_4$. The TEM micrograph with higher resolution in Figure 35c shows the self-organized nature of the superstructure. Whereas the majority of the fibers appear to be aligned in a parallel fashion, gaps between the single fibers can form but are also closed again. An electronic diffraction pattern taken from such an oriented planar bundle as shown in Figure 36d (right) confirmed that the whole structure

scatters as a well-crystallized single crystal where scattering is along the [001] direction and the fibers are elongated along [210].

The initially formed nanoparticles stabilized by polymers are amorphous with sizes of up to 20 nm, which can aggregate to larger clusters. Evidently, this state of matter is the typical starting point for all types of highly inhibited reactions. The very low solubility product of barium chromate ($K_{sp} = 1.17 \times 10^{-10}$) shows that the superstructures do not really grow from a supersaturated ion solution but by aggregation/transformation of the primary clusters formed [89].

All structures always grow from a single starting point, implying that the fibers grow against the glass wall or other substrates such as TEM grids, which obviously provide the necessary heterogeneous nucleation sites. The growth front of the fiber bundles is always very smooth, suggesting the homogeneous joint growth of all single nanofilaments with the ability to cure occurring defects, in line with the earlier findings for $BaSO_4$ [88]. The opening angle of the cones is always rather similar, which seems to depend on temperature, degree of phosphonation of the polymer, and polymer concentration [89]. The control experiments show that the higher the temperature, the more linear the structures become. The superstructure developed more clearly, and to a much larger size, when the mineralization temperature was lowered to 4 °C, as shown in Figure 37a. A rather lower phosphonation degree (∼1%) of a PEG-*b*-PMAA is already powerful enough to induce the formation of the fiber bundles and the superstructures, as shown in Figure 37b.

Interestingly, secondary cones can nucleate from either the rim or defects onto the cone, thus resulting in a tree-like structures (Fig. 37a). The fact that a cone stops growing once a second cone has nucleated at one spot on the rim shows that the growth presumably is slowing down with time, favoring the growth of the secondary cone. The cone-like superstructures tend to grow farther into a self-similar, multi-cone "tree" structure, which was observed before for barite mineralized in the presence of polyacrylates, but only under very limited experimental conditions [88]. From a structural viewpoint, the hashemite/barite crystals have a mirror plane perpendicular to the *c* axis, implying that a homogeneous nucleation will always result in crystals with identical charges of the opposite faces, and no dipole crystals can be formed. However, a dipole crystal may be favored



**Figure 36.** SEM and TEM images of highly ordered $BaCrO_4$ nanofiber bundles obtained in the presence of PEG-*b*-PMAA-$PO_3H_2$ (21%, phosphonation degree) (1 g liter$^{-1}$) ([$BaCrO_4$] = 2 mM), pH 5. (a) Two fiber bundles with cone-like shape and length about 150 $\mu$m. (b) Very thin fiber bundles. (c) TEM image of the thin part of the fiber bundles, inserted electronic diffraction pattern taken along the $\langle 001 \rangle$ zone, showing the fiber bundles are well-crystallized single crystals and elongated along [210]. Reprinted with permission from [89], S. H. Yu et al., *Chem. Eur. J.* 8, 2937 (2002). © 2002, Wiley-VCH.



**Figure 37.** (a) A typical cone-like superstructure contains densely packed $BaCrO_4$ nanofiber bundles in the presence of PEG-*b*-PMAA-$PO_3H_2$ (21%, phosphonation degree) (1 g liter$^{-1}$) ([$BaCrO_4$] = 2 mM, pH 5), 2 days, 4 °C; (b) multi-funnel-like superstructures with remarkable self-similarity in the presence of PEG-*b*-PMAA-$PO_3H_2$ (1%, phosphonation degree) (1 g liter$^{-1}$) ([$BaCrO_4$] = 2 mM, pH 5). Reprinted with permission from [89], S. H. Yu et al., *Chem. Eur. J.* 8, 2937 (2002). © 2002, Wiley-VCH.

for a heterogeneous nucleation as one end of the crystal is determined by the heterogeneous surface, the other by the solution/dispersion. The crystal has a dipole moment $\mu = Q \cdot l$ ($Q$ = charge and $l$ = length of the crystal), which increases while the crystal is growing. This implies self-limiting growth so that a new heterogeneous nucleation event on the rim should become favorable after the dipole moment has reached a critical value due to energy minimization [89].

Based on the foregoing experimental observation and understanding, a self-limiting growth mechanism was proposed to explain the remarkable similarity of the superstructures [89] as shown in Scheme 12: (i) At the beginning, amorphous nanoparticles are formed, which are stabilized by the DHBCs (stage 1). (ii) Heterogeneous nucleation of fibers occurs on glass substrates, and the fibers grow under the control of a functional polymer, presumably by multipole field-directed aggregation of amorphous nanoparticles as proposed in [88]. (iii) The growth is continuously slowed down until secondary nucleation or overgrowth becomes more probable than the continuation of the primary growth. The secondary cone will grow as the first ones have done. (iv) The secondary heterogeneous nucleation event taking place on the rim can occur repeatedly, depending on the mass capacity of amorphous nanoparticles in the system.

A very recent observation shows that low-molecular-weight polyacrylic acid sodium salt serves as a very simple structure-directing agent for the room-temperature, large-scale synthesis of highly ordered cone-like crystals or very long, extended nanofibers made of $BaCrO_4$ or $BaSO_4$ with hierarchical and repetitive growth patterns as shown in Figure 38, where temperature and concentration variation permit control of the finer details of the architecture, namely length, axial ratio, opening angle, and mutual packing [90]. The formation of interesting hierarchical and repetitive superstructures is worth exploring further for other mineral systems.

Interestingly, single uniform $BaCrO_4$ nanofibers can also be synthesized by a combination of polymer-controlled crystallization process and controlled nucleation by colloidal species producing locally a high supersaturation of both DHBCs and $Ba^{2+}$. The addition of a minor amount of a cationic colloidal structure such as PSS/PAH polyelectrolyte capsule (PSS/PAH: poly(styrene sulfonate, sodium salt)/polyallylamine hydrochloride) in the same reaction system can promote the independent growth of a number of
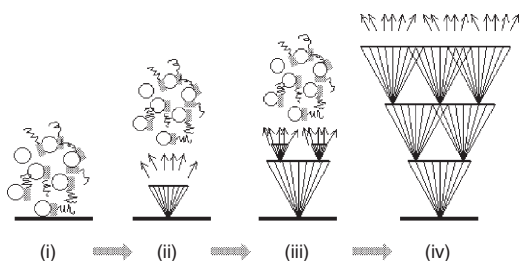


**Figure 38.** Complex forms of $BaSO_4$ bundles and superstructures produced in the presence of 0.11 mM sodium polyacrylate (Mn = 5100), at room temperature, $[BaSO_4]$ = 2 mM, pH = 5.3, 4 days. (a) Detailed superstructures with repetitive patterns. (b) Well-aligned bundles. Reprinted with permission from [90], S. H. Yu et al., *NanoLetters*, in press. © American Chemical Society.

fibers, thus leading to the dynamic discrimination of side nucleation and the resulting altered superstructures.

In addition to the formation of the mentioned superstructures under the control of block copolymers, DHBCs can also be used to fine-tune the nanostructural details of other inorganic crystals. Very thin 1D and 2D $CdWO_4$ nanocrystals with controlled aspect ratios were conveniently fabricated at ambient temperature or by hydrothermal ripening under the control of DHBC [92]. The TEM image in Figure 40a shows very thin, uniform $CdWO_4$ NRs/NBs with lengths in the range of 1 to 2 $\mu$m and a uniform width of 70 nm along their entire length (aspect ratio of about 30). The thickness of the NBs is ~6–7 nm. The slow and controlled reactant addition by the double-jet technique under stirring maintains the formation of intermediate amorphous nanoparticles at the jets [84] so that nanoparticles are the precursors for further particle growth rather than ionic species. Successive hydrothermal ripening after the double-jet reaction leads to a rearrangement of the rods into 2D lens-shaped, raft-like superstructures with a resulting lower aspect ratio, as shown in Figure 40b. In contrast, very thin and uniform nanofibers with a diameter of 2.5 nm, a length of 100–210 nm, and an aspect ratio of 40–85 as shown in Figure 40c



**Scheme 12.** Proposed mechanism for the formation of $BaCrO_4$ complexity superstructure with self-similarity by polymer-controlled crystallization. Reprinted with permission from [89], S. H. Yu et al., *Chem. Eur. J.* 8, 2937 (2002). © 2002, Wiley-VCH.
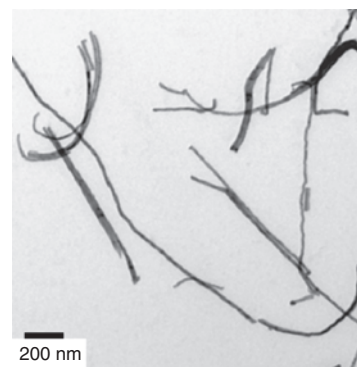


**Figure 39.** TEM images and electron diffraction pattern of the separated and very long $BaCrO_4$ nanofibers with high aspect ratio obtained in the presence of a small amount of PSS/PAH capsules (20 $\mu$l), PEG-*b*-PMAA-PO$_3$H$_2$, 1 g liter$^{-1}$, $[BaCrO_4]$ = 2 mM, pH 5, 25 °C. (a) A full view of the nanofibers. Reprinted with permission from [91], S. H. Yu et al., *Adv. Mater.*, in press. © Wiley-VCH.
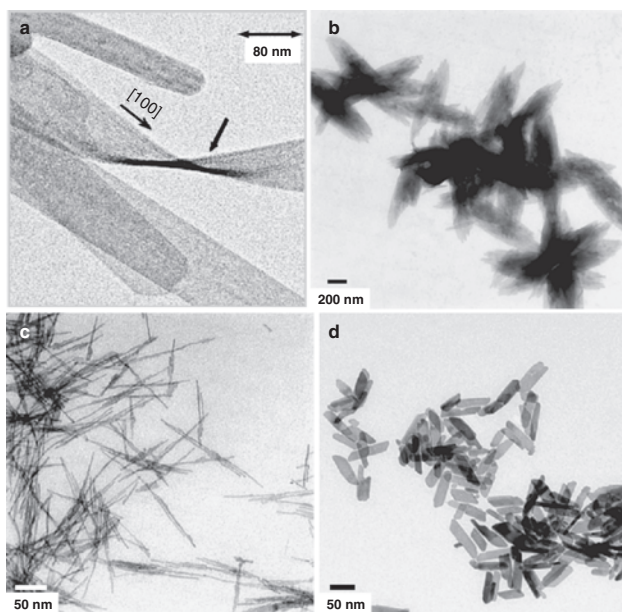
**Figure 40.** TEM images of the samples obtained under different conditions. (a) and (b) No additives: (a) pH = 5.3, double jet, $[Cd^{2+}]:[WO_4^{2-}] = 8.3 \times 10^{-3}$ M (final solution), at room temperature; (b) pH = 5.3, double jet, $[Cd^{2+}]:[WO_4^{2-}] = 8.3 \times 10^{-3}$ M (final solution), then hydrothermal crystallization: 80 °C, 6 h. (c) pH = 5.3, in the presence of PEG-*b*-PMAA (1 g liter$^{-1}$), 20 ml, double jet, $[Cd^{2+}]:[WO_4^{2-}] = 8.3 \times 10^{-3}$ M (final solution), then hydrothermal crystallization: 80 °C, 6 h. (d) Direct hydrothermal treatment of 20-ml solution containing equal molar $[Cd^{2+}]:[WO_4^{2-}] = 8.3 \times 10^{-2}$ M, pH = 5.3, at 130 °C, 6 h, in the presence of 1 g liter$^{-1}$ PEG-*b*-PMAA-PO$_3$H$_2$ (21%). Reprinted with permission from [92], S. H. Yu et al., *Angew. Chem. Int. Ed.* 41, 2356 (2002). © 2002, Wiley-VCH.

can readily be obtained when the DHBC PEG-*b*-PMAA is added to the solvent reservoir before the double-jet crystallization process, and the mixture is then hydrothermally ripened at 80 °C. When the partly phosphonated hydrophilic block copolymer PEG-*b*-PMAA-PO$_3$H$_2$ (21%) (1 g liter$^{-1}$) is added at an elevated temperature of 130 °C, even without the use of the double jets but at higher concentrations and coupled supersaturation, very thin platelet-like particles with a width of 17–28 nm, a length of 55–110 nm, and an aspect ratio of 2–4 are obtained by a direct hydrothermal process, as shown in Figure 40d. The nanoparticles display an interesting shape-dependent evolution of the luminescent properties, which may be of interest for applications.

Polymer-controlled crystallization in water at ambient temperature provides an alternative and promising tool for the morphogenesis of inorganic nanocrystals and superstructures that could be extended to various systems.

### 2.8.2. Supramolecular Self-Assembly

Supramolecular directed self-assembly of inorganic and inorganic/organic hybrid nanostructures has been emerging as an active area of recent research. The recent advance shows the remarkable feasibility of mimicking a natural mineralization system by a designed artificial organic template.

The supramolecular functional polymer can be directly employed for mineralization template of novel inorganic nanoarchitectures. CdS helices were successfully templated from supramolecular nanoribbons [94]. This novel inorganic nanostructure has a coiled morphology with a pitch of 40–60 nm, which can be rationalized in terms of the period of the twisted organic ribbons. A triblock architecture termed "dendron rodcoils" (DRC) can hydrogen bond in head-to-head fashion through dendron segments and self-assemble into nanoribbons [94]. The mineralization of the helical structures was done in both 2-ethylhexyl methacrylate (EHMA) and ethyl methacrylate (EMA). Figure 41 shows a typical CdS helix with a zigzag pattern and a pitch of 40–50 nm, which was isolated from a 1 wt% gel of the DRC in EHMA, to which a solution of cadmium nitrate in THF had been added prior to exposure to hydrogen sulfide gas [94]. HRTEM studies revealed that the polycrystalline zinc blende CdS is made up of small domains with grain sizes of about 4–8 nm. The results suggest that it is possible to achieve good control over the morphology of the templated product by using extremely uniform, stable, nonaggregated supramolecular objects as templates.

A peptide-amphiphile (PA) molecule was designed for the mineralization of PA nanofibers and hydroxyapatite (HAp) nanofibers [412]. This amphiphile molecule can assemble in water into cylindrical micelles because of the amphiphile's overall conical shape, resulting in alkyl tails packed in the center of the micelle while the peptide segments are exposed to the aqueous environment [412]. The PA molecules were found to self-assemble at acidic pH but disassemble at neutral and basic pH. After self-assembly into nanofibers, the nanofibers were cross-linked by the oxidation of the cysteine thiol groups through treatment with 0.01 M I$_2$. The cross-linked PA fibers contained intermolecular disulfide bonds, and intact fiber structures were still kept. These cross-linked fibers with negative charged surfaces are able to direct mineralization of HAp to form a composite material in which the crystallographic *c* axes of HAp are coaligned with the long axes of the fibers. The alignment of HAp nanofibers resembles the lowest level of hierarchical organization of bone [413].

In addition, supramolecular self-assembly using organogelators as template to transcribe inorganic nanostructures has been intensively studied. Organogelators are low-molecular-weight compounds that can gelate organic fluids at low
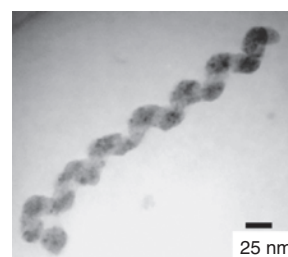


**Figure 41.** TEM micrograph of a typical CdS helix with a pitch of 40–50 nm precipitated in gels of the DRC in EHMA. Reprinted with permission from [94], E. D. Sone et al., *Angew. Chem. Int. Ed.* 41, 1705 (2002). © 2002, Wiley-VCH.

concentrations [414–419]. The gelators can gelate in organic solvents to form unique superstructures, which can transcribe inorganic nanostructures [420–429].

A helically structured silica has been successfully templated by a sol–gel transcription in chiral organogel systems [420–426]. The results show that certain cholesterol derivatives can gelate even tetraethoxysilane (TEOS), which can be used to produce silica by sol–gel polymerization [420]. Sol–gel polymerization of gelated TEOS solutions produces silica with a novel hollow fiber structure due to the template effect of the organogel fibers [420–426]. The formation of a three-dimensional network based on fibrous aggregates in organic fluids could be responsible for the formation of the gelling phenomenon.

This approach can be extended to the production of other metal oxide nanofibers or NTs with chiral structures. TiO$_2$ fibers were fabricated with the use of an amphiphilic compound, *trans*-(1$R$,2$R$)-1,2-cyclohexanedi(11-aminocarbonylundecylpyridinium) hexafluorophosphate as template [427]. The amphiphilic compound containing cationic charge moieties is expected to electrostatically interact with anionic titania species under basic conditions in the sol–gel polymerization process of Ti[OCH(CH$_3$)$_2$]$_4$. Transition-metal (Ti, Ta, V) oxide fibers with chiral, helical, and nanotubular structures can be prepared by the sol–gel polymerization of metal alkoxides, with *trans*-(1$R$,2$R$)- or *trans*-(1$S$,2$S$)-1,2-di(undecylcarbonylamino)cyclohexane as structure-directing agents [428]. A recent report describes well-defined TiO$_2$ helical ribbons and NTs obtained through sol–gel polymerization of titanium tetraisopropoxide [Ti(O$_i$Pr)$_4$] in gels of a neutral dibenzo-30-crown-10-appended cholesterol gelator [429]. These chiral helical tubes could have various applications in electronics, optics, and photocatalysts.

### 2.8.3. Small Molecular Organic Species-Mediated Crystallization

In contrast to the previously mentioned polymer-controlled crystallization and supramolecular template synthesis, some small molecular organic species can also exert significant influence on crystal orientation growth.

A very recent report by Liu et al. describes unusually oriented and extended helical ZnO nanostructures grown from a synthetic ceramic method, which is surprisingly very similar to the growth morphology of nacreous calcium carbonate [95]. The helical ZnO nanostructures were grown on a glass substrate containing oriented ZnO NR arrays [430], which was placed in a solution containing Zn(NO$_3$)$_2$, hexomethylenetetramine, and sodium citrate and was reacted at 95 °C for 1 day. Figure 42 shows the similarity of SEM images of the helical ZnO nanocolumns (Fig. 42a and b) and the growth tip of a young abalone shell containing oriented columns of aragonite nanoplates (Fig. 42c). In the secondary growth on the helical NRs, aligned and well-defined nanoplates are formed, as in nacre. The side-width growth of the ZnO nanoplates leads to hexagonal ZnO plates that begin to overlap with one another.
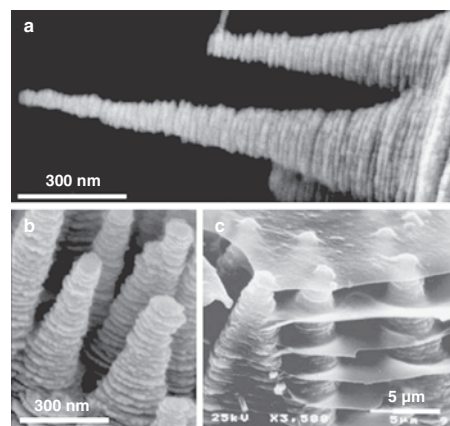


**Figure 42.** Comparison of ZnO helical structures with nacre. (a) and (b) High-magnification image of oriented ZnO helical columns. (c) Nacreous calcium carbonate columns and layers near the growth tip of a young abalone. Reprinted with permission from [95], Z. R. Tian et al., *J. Am. Chem. Soc.* 124, 12954 (2002). © 2002, American Chemical Society.

The organic species were reported to act as simple physical compartments or to control nucleation or to terminate crystal growth by surface poisoning in the biomineralization of nacre [431, 432]. The similarity of the biomimetic structures of helical ZnO rods to nacreous CaCO$_3$ indicated that helical growth might play some role in the formation of organized nacreous calcium carbonate. However, the organic species citrate ion still plays critical roles in the formation of such structures since the citrate ion has a large tendency to inhibit the growth of the (002) surfaces, possibly through selective surface adsorption.

The discussed polymer controlled mineralization and small molecular organic species-mediated mineralization could shed new light on the morphology and orientation control of inorganic crystals.

### 2.9. Oriented Attachment Growth Mechanism

Traditionally, crystal growth can be described as an Ostwald ripening process. The formation of tiny crystalline nuclei in a supersaturated medium occurred first and then was followed by crystal growth. The larger particles will grow at the cost of the small ones because of the difference between large particles and the smaller particles of a higher solubility. Penn and Banfield [96–98] confirmed that both anatase and iron oxide nanoparticles with sizes of a few nanometers can coalesce under hydrothermal conditions in a way called "oriented attachment" (Fig. 43). The crystal lattice planes may be almost perfectly aligned, or dislocations at the contact areas between the adjacent particles lead to defects in the finally formed bulk crystals. The so-called oriented attachment was also proposed by other authors for the crystal growth of TiO$_2$ [99] and for micrometer-sized ZnO particles during the formation of rod-like ZnO microcrystals [100]. However, until now, no direct evidence has been reported.
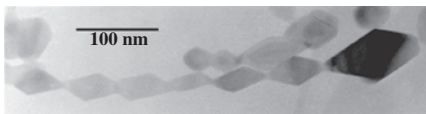
**Figure 43.** TEM micrograph of a single crystal of anatase that was hydrothermally coarsened in 0.001 M HCl, showing that the primary particles align, dock, and fuse to form oriented chain structures. Reprinted with permission from [98], R. L. Penn and J. F. Banfield, *Geochim. Cosmochim. Acta* 63, 1549 (1999). © 1999, Elsevier Science.

A very recent report by Weller et al. provided some strong evidence that ZnO NRs can be conveniently self-assembled from small ZnO quasi-spherical nanoparticles based on the oriented attachment mechanism by the evaporation and reflux of a solution containing 3–5-nm smaller nanoparticles [102]. Previously, self-assembly of nanoparticles capped by ligands was mainly driven by the interactions of the organic ligands rather than by the interaction of the particle cores.

ZnO sol with an average particle size of approximately 3 nm as shown in Figure 44a was easily prepared by adding dropwise a 0.03 M solution of KOH (65 ml) in methanol to a solution of zinc acetate dihydrate (0.01 M) in methanol (125 ml) under vigorous stirring at about 60 °C. Refluxing of the concentrated solution leads to the formation of rod-like nanoparticles. Prolonging the heating time mainly leads to an increase in the elongation of the particle along the *c* axis. After refluxing for 1 day, single crystalline NRs with average lengths of 100 nm and widths of approximately 15 nm were formed, as shown in Figure 44b. The authors argued that oxide nanoparticles are very favorable for oriented attachment for two reasons: first, organic ligands, which prevent intimate contact of crystal planes, are usually not needed for stabilization; and second, crystalline fusion of correctly attached particles leads to a gain not only in lattice-free energy but also in the free energy of polycondensation [102].

The spontaneous aggregation and self-assembly of the small nanoparticles into very elongated NRs/NWs was again observed in the case of CdTe when the protective shell of organic stabilizer on the surface of the initial CdTe nanoparticles was removed [103]. The presence of "pearl-necklace" agglomerates as intermediates of the
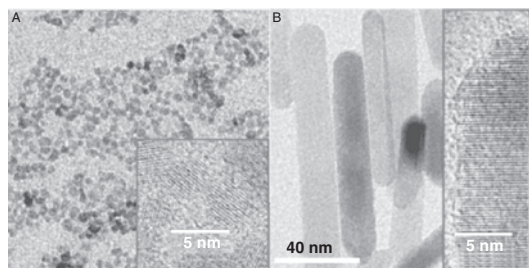
nanoparticle-NW transition suggested that the growth mechanism could be related to a special interaction/attraction between the nanoparticles. A dipole-dipole interaction was believed to be the driving force for such self-organization of the nanoparticles [103]. This approach provides a new pathway to high-quality luminescent CdTe NWs, even though the yield is still low.

Although there have been only few reports on the self-organization of nanoparticles, this new growth mechanism could offer an additional tool for the design of advanced materials with anisotropic material properties and could be used for the synthesis of more complex crystalline three-dimensional structures in which the branching sites could be added as individual nanoparticles, and could even lead to nearly perfect crystals [101, 102].

## 3. SUMMARY

In this chapter, the state of art of the synthesis of low-dimensional nanocrystals and more complex superstructures through the different approaches has been overviewed. The current advances in synthetic methodologies demonstrated that it is possible to rationally design 1D, 2D, and even more complex superstructures.

The "hard" approaches, such as template-directed growth method, the VLS mechanism, the VS mechanism, and oxide-assisted NW growth routes, have shown their powerful and straightforward pathways to the target 1D nanomaterials and their superstructures with high crystallinity, although they usually require either a carefully and costly predesigned template or rather strict reaction conditions.

The "soft" approaches show very promising alternative pathways for the synthesis of 1D nanocrystals. In addition to the strategies of solvent-mediated shape and structure modulation, the soft-hard interface between polymers/surfactants (or organic species) and inorganic crystals is also an area of great interest at present. The current progress indubitably emphasizes that all crystals will probably be amenable to morphosynthetic control by use of the appropriate templating molecules. The emerging new solution routes to 1D NRs/NWs and more complex superstructures, such as the solvothermal process, the SLS mechanism, capping agent/surfactant-assisted synthesis, bio-inspired approaches, and the oriented attachment growth mechanism, open alternative doorways to low-dimensional nanocrystals and more complex superstructures. Among these solution strategies, the solvothermal process shows possibilities and versatility for selective synthesis of various semiconductor nanocrystals with controllable shape, size, phase, and dimensionalities under mild conditions. The successful synthesis of various semiconductor NRs/NWs with the use of a suitable ligand solvent as a "shape controller" indicates that the solvothermal process is indicative of a fruitful and promising route to 1D and 2D semiconductor nanocrystals in the future.

The further understanding on the nucleation, crystallization, self-assembly, and growth mechanism of the nanocrystals in these solution strategies should open new rational pathways to prepare various kinds of highly crystalline nanowires/nanorods, nanotubes with well-defined monodispersed, sizes, and aspect ratios, and highly ordered/oriented



**Figure 44.** TEM images of ZnO. (A) Starting sol. (B) After 1 day of reflux of the concentrated sol. The insets show high-resolution TEM images of individual nanoparticles. Reprinted with permission from [102], C. Pacholski et al., *Angew. Chem. Int. Ed.* 41, 1188 (2002). © 2002, Wiley-VCH.

complex superstructures. Furthermore, it is no doubt needed to investigate the relationship between the structural specialties (shape, sizes, phases, dimensionality, and complexity etc.) of the low dimensional nanocrystals and their properties, which could shed light on their novel applications and fundamental properties as building blocks in nanoscience and nanotechnology.

## ACKNOWLEDGMENTS

## REFERENCES

1. M. G. Bawendi, M. L. Steigerwald, and L. E. Brus, *Annu. Rev. Phys. Chem.* 41, 477 (1990).
2. M. G. Bawendi, W. L. Wilson, L. Rothberg, P. J. Carrol, T. M. Jedju, M. L. Steigerwald, and L. E. Brus, *Phys. Rev. Lett.* 65, 1623 (1990).
3. W. Hoheisel, V. L. Colvin, C. S. Johnson, and A. P. Alivisatos, *J. Chem. Phys.* 101, 8455 (1994).
4. A. P. Alivisatos, *Science* 271, 933 (1996).
5. H. Weller, *Angew. Chem. Int. Ed. Engl.* 32, 41 (1993).
6. S. Mann, *Nature* 322, 119 (1988).
7. J. T. Hu, T. W. Odom, and C. M. Lieber, *Acc. Chem. Res.* 32, 435 (1999).
8. C. M. Lieber, *Solid State Commun.* 107, 607 (1998).
9. X. Duan, Y. Huang, Y. Cui, J. Wang, and C. M. Lieber, *Nature* 409, 66 (2001).
10. K. Leung, S. Pokrant, and K. B. Whaley, *Phys. Rev. B* 57, 12291 (1998).
11. X. G. Peng, L. Manna, W. D. Yang, J. Wickham, E. Scher, A. Kadavanich, and A. P. Alivisatos, *Nature* 404, 59 (2000).
12. G. P. Mitchell, C. A. Mirkin, and R. L. Letsinger, *J. Am. Chem. Soc.* 121, 8122 (1999).
13. M. J. Bruchez, M. Maronne, P. Gin, S. Weiss, and A. P. Alivisatos, *Science* 281, 2016 (1998).
14. W. C. W. Chan and S. M. Nie, *Science* 281, 2016 (1998).
15. M. Y. Han, X. H. Gao, J. Z. Su, and S. M. Nie, *Nat. Biol.* 19, 631 (2001).
16. Y. Cui and C. M. Lieber, *Science* 291, 851 (2001).
17. W. U. Huynh, J. J. Dittmer, and A. P. Alivisatos, *Science* 295, 2425 (2002).
18. P. Yang, in "Global Photonics Applications and Technology," World Markets Series, Business Briefing, p. 42. 2002.
19. Y. Cui, Q. Q. Wei, H. K. Park, and C. M. Lieber, *Science* 293, 1289 (2001).
20. M. Law, H. Kind, B. Messer, F. Kim, and P. D. Yang, *Angew. Chem. Int. Ed.* 41, 2405 (2002).
21. P. D. Yang, H. Q. Yan, S. Mao, R. Russo, J. Hohnson, R. Saykally, N. Morris, J. Pham, R. R. He, and H. J. Choi, *Adv. Funct. Mater.* 12, 323 (2002).
22. E. Matijević, *Curr. Opin. Colloid Interface Sci.* 1, 176 (1996).
23. P. D. Yang, Y. Y. Wu, and R. Fan, *Int. J. Nanotechnol.* 1, 1 (2002).
24. T. S. Ahmadi, Z. L. Wang, T. C. Green, A. Henglein, and M. A. El-Sayed, *Science* 272, 1924 (1996).
25. M. Li, H. Schnablegger, and S. Mann, *Nature* 402, 393 (1999).
26. S. H. Yu, *J. Ceram. Soc. Jpn.* 109, S65 (2001).
27. T. Trindade, P. O'Brien, and N. L. Pickett, *Chem. Mater.* 13, 3843 (2001).
28. M. Green, *Curr. Opin. Solid State Mater. Sci.* 6, 355 (2002).
29. C. B. Murray, D. J. Norris, and M. G. Bawendi, *J. Am. Chem. Soc.* 115, 8706 (1993).
30. X. G. Peng, J. Wickham, and A. P. Alivisato, *J. Am. Chem. Soc.* 120, 5343 (1998).
31. L. Spanhel, M. Haase, H. Weller, and A. Henglein, *J. Am. Chem. Soc.* 109, 5649 (1987).
32. J. E. B. Katari, V. L. Colvin, and A. P. Alivisatos, *J. Phys. Chem.* 98, 4109 (1994).
33. A. C. Jones, *Chem. Soc. Rev.* 101 (1997).
34. G. R. Patzke, F. Krumeich, and R. Nesper, *Angew. Chem. Int. Ed.* 41, 2447 (2002).
35. H. Dai, E. W. Wong, Y. Z. Lu, S. Fan, and C. Lieber, *Nature* 375, 769 (1995).
36. W. Q. Han, S. S. Fan, Q. Q. Li, and Y. D. Hu, *Science* 277, 1287 (1997).
37. J. D. Klein, R. D. Herrick, D. Palmer, M. J. Sailor, C. J. Brumlik, and C. R. Martin, *Chem. Mater.* 5, 902 (1993).
38. C. R. Martin, *Science* 266, 1961 (1994).
39. D. Almawlawi, C. Z. Liu, and M. Motskovits, *J. Mater. Res.* 9, 1014 (1994).
40. D. Routkevitch, T. Bigioni, M. Moskovits, and J. M. Xu, *J. Phys. Chem.* 100, 14037 (1996).
41. R. S. Wagner and W. C. Elhs, *Appl. Phys. Lett.* 4, 89 (1964).
42. M. Yazawa, M. Koguchi, A. Muto, M. Ozawa, and K. Hiruma, *Appl. Phys. Lett.* 61, 2051 (1992).
43. J. Westwater, D. P. Gosain, S. Tomiya, S. Usui, and H. Ruda, *J. Vac. Sci. Technol., B* 15, 554 (1997).
44. A. M. Morales and C. M. Lieber, *Science* 279, 208 (1998).
45. M. H. Huang, Y. Wu, H. Feick, E. Webber, and P. Yang, *Adv. Mater.* 13, 113 (2000).
46. M. Huang, S. Mao, H. Feick, H. Yan, Y. Wu, H. Kind, E. Weber, R. Russo, and P. Yang, *Science* 292, 1897 (2001).
47. Y. Y. Wu, H. Q. Yan, M. Huang, B. Messer, J.-H. Song, and P. D. Yang, *Chem. Eur. J.* 8, 1260 (2002).
48. X. F. Duan and C. M. Lieber, *Adv. Mater.* 12, 298 (2000).
49. R. S. Wagner, in "Whisker Technology" (A. P. Levitt, Ed.), p. 47. Wiley, New York, 1970.
50. P. Yang and C. M. Lieber, *J. Mater. Res.* 12, 2981 (1997).
51. P. Yang and C. M. Lieber, *Science* 273, 1836 (1996).
52. Z. W. Pan, Z. R. Dai, and Z. L. Wang, *Science* 291, 1947 (2001).
53. J. Y. Lao, J. G. Wen, and Z. F. Ren, *NanoLetters* 2, 1287 (2002).
54. S. T. Lee, N. Wang, Y. F. Zhang, and Y. H. Tang, *MRS Bull.* 24, 1116 (2000).
55. W. S. Shi, Y. F. Zheng, N. Wang, C.-S. Lee, and S.-T. Lee, *Adv. Mater.* 13, 591 (2001).
56. W. S. Shi, Y. F. Zheng, N. Wang, C. S. Lee, and S. T. Lee, *Chem. Phys. Lett.* 345, 377 (2001).
57. C. C. Tang, S. S. Fan, H. Y. Dang, P. Li, and Y. M. Liu, *Appl. Phys. Lett.* 77, 1961 (2000).
58. S. T. Lee, N. Wang, and C. S. Lee, *Mater. Sci. Eng., A* 286, 16 (2000).
59. W. S. Shi, H. Y. Peng, N. Wang, C. P. Li, L. Xu, C. S. Lee, R. Kalish, and S. T. Lee, *J. Am. Chem. Soc.* 123, 11095 (2001).
60. A. Stein, S. W. Keller, and T. E. Mallouk, *Science* 259, 1558 (1993).
61. S. H. Yu, Y. S. Wu, J. Yang, Z. H. Han, Y. Xie, Y. T. Qian, and X. M. Liu, *Chem. Mater.* 10, 2309 (1998).
62. S. H. Yu, J. Yang, Z. H. Han, Yong Zhou, Ru-Yi Yang, Yi Xie, Yi-Tai Qian, and Yu-Heng Zhang, *J. Mater. Chem.* 9, 1283 (1999).
63. J. Yang, J. H. Zeng, S. H. Yu, L. Yang, G. E. Zhou, and Y. T. Qian, *Chem. Mater.* 12, 3259 (2000).
64. S. H. Yu and M. Yoshimura, *Adv. Mater.* 14, 296 (2002).

65. J. Yang, C. Xue, S. H. Yu, J. H. Zeng, and Y. T. Qian, *Angew. Chem. Ed. Int.* 41, 4697 (2002).
66. T. J. Trentler, K. M. Hickman, S. C. Goel, A. M. Viano, P. C. Gibbons, and W. E. Buhro, *Science* 270, 1791 (1995).
67. W. E. Buhro, K. M. Hickman, and T. J. Trentler, *Adv. Mater.* 8, 685 (1996).
68. T. J. Trentler, S. C. Goel, K. M. Hickman, A. M. Viano, M. Y. Chiang, A. M. Beatty, P. C. Gibbons, and W. E. Buhro, *J. Am. Chem. Soc.* 119, 2172 (1997).
69. P. D. Markowitz, M. P. Zach, P. C. Gibbons, R. M. Penner, and W. E. Buhro, *J. Am. Chem. Soc.* 123, 4502 (2001).
70. J. R. Heath and F. K. LeGoues, *Chem. Phys. Lett.* 208, 263 (1993).
71. J. D. Holmes, K. P. Johnston, R. C. Doty, and B. A. Korgel, *Science* 287, 1471 (2000).
72. L. Manna, E. C. Scher, and A. P. Alivisatos, *J. Am. Chem. Soc.* 122, 12700 (2000).
73. S. Mann, *Angew. Chem. Int. Ed.* 39, 3392 (2000).
74. J. D. Hopwood and S. Mann, *Chem. Mater.* 9, 1819 (1997).
75. M. Li and S. Mann, *Langmuir* 16, 7088 (2000).
76. C. N. N. Rao, A. Govindaraj, F. L. Deepak, and N. A. Gunari, *Appl. Phys. Lett.* 78, 1853 (2001).
77. L. Qi, J. Ma, H. Cheng, and Z. Zhao, *J. Phys. Chem. B* 101, 3460 (1997).
78. S. Kwan, F. Kim, J. Akana, and P. Yang, *Chem. Commun.* 447 (2001).
79. H. T. Shi, L. M. Qi, J. M. Ma, and H. M. Cheng, *Chem. Commun.* 1704 (2002).
80. E. Dujardin and S. Mann, *Adv. Mater.* 14, 775 (2002).
81. H. Cölfen, *Macromol. Rapid Commun.* 22, 219 (2001).
82. M. Sedlak, M. Antonietti, and H. Cölfen, *Macromol. Chem. Phys.* 199, 247 (1998).
83. M. Sedlak and H. Cölfen, *Macromol. Chem. Phys.* 202, 587 (2001).
84. H. Cölfen and M. Antonietti, *Langmuir* 14, 582 (1998).
85. S. H. Yu, H. Cölfen, J. Hartmann, and M. Antonietti, *Adv. Funct. Mater.* 12, 541 (2002).
86. M. Antonietti, M. Breulmann, C. G. Goltner, H. Cölfen, K. K. W. Wong, D. Walsh, and S. Mann, *Chem. Eur. J.* 4, 2491 (1998).
87. L. M. Qi, H. Cölfen, and M. Antonietti, *Angew. Chem. Int. Ed.* 39, 604 (2000).
88. L. M. Qi, H. Cölfen, M. Antonietti, M. Li, J. D. Hopwood, A. J. Ashley, and S. Mann, *Chem. Eur. J.* 7, 3526 (2001).
89. S. H. Yu, H. Cölfen, and M. Antonietti, *Chem. Eur. J.* 8, 2937 (2002).
90. S. H. Yu, M. Antonietti, and H. Cölfen, *NanoLetters* 3, 379 (2003).
91. S. H. Yu, H. Cölfen, and M. Antonietti, *Adv. Mater.* 15, 133 (2003).
92. S. H. Yu, M. Antonietti, H. Cölfen, and M. Giersig, *Angew. Chem. Int. Ed.* 41, 2356 (2002).
93. M. Öner, J. Norwig, W. H. Meyer, and G. Wegner, *Chem. Mater.* 10, 460 (1998).
94. E. D. Sone, E. R. Zubarev, and S. I. Stupp, *Angew. Chem. Int. Ed.* 41, 1705 (2002).
95. Z. R. Tian, J. A. Voigt, J. Liu, B. Mckenzie, and M. J. Mcdermott, *J. Am. Chem. Soc.* 124, 12954 (2002).
96. F. Banfield, S. A. Welch, H. Zhang, T. T. Ebert, and R. L. Penn, *Science* 289, 751 (2000).
97. R. L. Penn and J. F. Banfield, *Science* 281, 969 (1998).
98. R. L. Penn and J. F. Banfield, *Geochim. Cosmochim. Acta* 63, 1549 (1999).
99. A. Chemseddine and T. Moritz, *Eur. J. Inorg. Chem.* 235 (1999).
100. M. A. Verges, A. Mifsud, and C. J. Serna, *J. Chem. Soc., Faraday Trans.* 86, 959 (1990).
101. A. P. Alivisatos, *Science* 289, 736 (2000).
102. C. Pacholski, A. Kornowski, and H. Weller, *Angew. Chem. Int. Ed.* 41, 1188 (2002).
103. Z. Y. Tang, N. A. Kotov, and M. Giersig, *Science* 297, 237 (2002).
104. J. J. Urban, W. S. Yun, Q. Gu, and H. Park, *J. Am. Chem. Soc.* 124, 1186 (2002).
105. P. Yang and F. Kim, *Chem. Phys. Chem.* 3, 503 (2002).
106. F. Kim, S. Kwan, J. Akana, and P. Yang, *J. Am. Chem. Soc.* 123, 4360 (2001).
107. G. D. Rees, R. Evans-Gowing, S. J. Hammond, and B. H. Robinson, *Langmuir* 15, 1993 (1999).
108. H.-W. Liao, Y.-F. Wang, X.-M. Liu, Y.-D. Li, and Y.-T. Qian, *Chem. Mater.* 12, 2819 (2000).
109. B. B. Lakshmi, C. J. Patrissi, and C. R. Martin, *Chem. Mater.* 9, 2544 (1997).
110. Y. K. Liu, G. H. Wang, C. K. Xu, and W. Z. Wang, *Chem. Commun.* 1486 (2002).
111. W. Wang, Y. Zhan, and G. Wang, *Chem. Commun.* 727 (2001).
112. X. Jiang, T. Herricks, and Y. Xia, *NanoLetters* 2, 1333 (2002).
113. V. G. Pol, O. Palchik, A. Gedanken, and I. Felner, *J. Phys. Chem. B* 106, 9737 (2002).
114. N. Beermann, L. Vayssieres, S.-E. Lindquist, and A. Hagfeldt, *J. Electrochem. Soc.* 147, 2456 (2000).
115. L. Vayssieres, N. Beermann, S.-E. Lindquist, and A. Hagfeldt, *Chem. Mater.* 13, 233 (2001).
116. R. Kumar, Y. Koltypin, X. N. Xu, Y. Yeshurun, A. Gedanken, and I. Felner, *J. Appl. Phys.* 89, 6324 (2001).
117. P. Zhou, D. Xue, H. Luo, and X. Chen, *NanoLetters* 2, 845 (2002).
118. Y. C. Choi, W. S. Kim, Y. S. Park, S. M. Lee, D. J. Bae, Y. H. Lee, G.-S. Park, W. B. Choi, N. S. Lee, and J. M. Kim, *Adv. Mater.* 12, 746 (2000).
119. J. Y. Li, Z. Y. Qiao, X. L. Chen, L. Chen, Y. G. Cao, M. He, H. Li, Z. M. Cao, and Z. Zhang, *J. Alloys Compd.* 306, 300 (2000).
120. H. Z. Zhang, Y. C. Kong, Y. Z. Wang, X. Du, Z. G. Bai, J. J. Wang, D. P. Yu, Y. Ding, Q. L. Hang, and S. Q. Feng, *Solid State Commun.* 109, 677 (1999).
121. W. Q. Han, P. Kohler-Redlich, F. Ernst, and M. Rühle, *Solid State Commun.* 115, 527 (2000).
122. G.-S. Park, W.-B. Choi, J.-M. Kim, Y. C. Choi, Y. H. Lee, and C.-B. Lim, *J. Cryst. Growth* 220, 494 (2000).
123. C. C. Tang, S. S. Fan, de la Chapelle, and P. Li, *Chem. Phys. Lett.* 333, 12 (2000).
124. S. Sharma and M. K. Sunkara, *J. Am. Chem. Soc.* 124, 12288 (2002).
125. Y. Zhang, N. Wang, S. Gao, R. He, S. Miao, J. Liu, J. Zhu, and X. Zhang, *Chem. Mater.* 14, 3564 (2002).
126. Y. Zhang, J. Zhu, Q. Zhang, Y. Yan, N. Wang, and X. Zhang, *Chem. Phys. Lett.* 317, 504 (2000).
127. X. C. Wu, W. H. Song, B. Zhao, Y. P. Sun, and J. J. Du, *Chem. Phys. Lett.* 349, 210 (2001).
128. J. Q. Hu, Q. Li, X. M. Meng, C. S. Lee, and S. T. Lee, *Adv. Mater.* 14, 1396 (2002).
129. C. H. Liang, G. W. Meng, Y. Lei, F. Phillipp, and L. D. Zhang, *Adv. Mater.* 13, 1330 (2001).
130. B. C. Satishkumar, A. Govindaraj, M. Nath, and C. N. R. Rao, *J. Mater. Chem.* 10, 2115 (2000).
131. G. L. Li, M. Liu, and G. H. Wang, *J. Mater. Res.* 16, 3614 (2001).
132. H. Meyssamy, K. Riwotzki, A. Kornowski, S. Naused, and M. Haase, *Adv. Mater.* 11, 840 (1999).
133. C. Tang, Y. Bando, and T. Sato, *J. Phys. Chem. B* 106, 7449 (2002).
134. Y. Yin, G. Zhang, and Y. Xia, *Adv. Funct. Mater.* 12, 293 (2002).
135. Z. Cui, G. W. Meng, W. D. Huang, G. Z. Wang, and L. D. Zhang, *Mater. Res. Bull.* 35, 1653 (2000).
136. Y. Li, M. Sui, Y. Ding, G. Zhang, J. Zhuang, and C. Wang, *Adv. Mater.* 12, 818 (2000).
137. B. B. Lakshmi, C. J. Patrissi, and C. R. Martin, *Chem. Mater.* 9, 2544 (1997).
138. X. Wang and Y. Li, *J. Am. Chem. Soc.* 124, 2880 (2002).
139. W. Z. Wang, C. K. Xu, G. H. Wang, Y. K. Liu, and C. L. Zheng, *Adv. Mater.* 14, 837 (2002).
140. J. Liu, J. Cai, Y. C. Son, Q. M. Gao, S. L. Suib, and M. Aindow, *J. Phys. Chem. B* 106, 9761 (2002).

141. M. Niederberger, F. Krumeich, H.-J. Muhr, M. Müller, and R. Nesper, *J. Mater. Chem.* 11, 1941 (2001).
142. K. Matsui, T. Kyotani, and A. Tomita, *Adv. Mater.* 14, 1216 (2002).
143. W. Z. Wang, Y. K. Liu, C. K. Xu, C. L. Zheng, and G. H. Wang, *Chem. Phys. Lett.* 362, 119 (2002).
144. S. J. Limmer, S. Seraji, M. J. Forbess, Y. Wu, T. P. Chou, C. Nguyen, and G. Cao, *Adv. Mater.* 13, 1269 (2001).
145. L. Guo, Z. Wu, T. Liu, W. Wang, and H. Zhu, *Chem. Phys. Lett.* 318, 49 (2000).
146. C. H. Ye, G. W. Meng, L. D. Zhang, G. Z. Wang, and Y. H. Wang, *Chem. Phys. Lett.* 363, 34 (2002).
147. S. Friedrichs, R. R. Meyer, J. Sloan, A. I. Kirkland, J. L. Hutchison, and M. L. H. Green, *Chem. Commun.* 929 (2001).
148. Y. Liu, C. Zheng, W. Wang, C. Yin, and G. Wang, *Adv. Mater.* 13, 1883 (2001).
149. Y. Liu, C. Zheng, W. Wang, Y. Zhan, and G. Wang, *J. Cryst. Growth* 233, 8 (2001).
150. Z. R. Dai, J. L. Gole, J. D. Stout, and Z. L. Wang, *J. Phys. Chem. B* 106, 1274 (2002).
151. Z. R. Dai, Z. W. Pan, and Z. L. Wang, *J. Am. Chem. Soc.* 124, 8673 (2002).
152. Z. L. Wang and Z. W. Pan, *Adv. Mater.* 14, 1029 (2002).
153. S.-M. Yang and W.-J. Kim, *Adv. Mater.* 13, 1191 (2001).
154. B. Zheng, Y. Wu, P. Yang, and J. Liu, *Adv. Mater.* 14, 122 (2002).
155. Z. W. Pan, Z. R. Dai, C. Ma, and Z. L. Wang, *J. Am. Chem. Soc.* 124, 1817 (2002).
156. Z. L. Wang, R. P. Gao, J. L. Gole, and J. D. Stout, *Adv. Mater.* 12, 1938 (2000).
157. Z. Q. Liu, S. S. Xie, L. F. Sun, D. S. Tang, W. Y. Zhou, C. Y. Wang, W. Liu, Y. B. Li, X. P. Zou, and G. Wang, *J. Mater. Res.* 16, 683 (2001).
158. H.-F. Zhang, C.-M. Wang, and L.-S. Wang, *NanoLetters* 2, 941 (2002).
159. X. Y. Zhang, L. D. Zhang, W. Chen, G. W. Meng, M. J. Zheng, and L. X. Zhao, *Chem. Mater.* 13, 2511 (2001).
160. M. Zhang, Y. Bando, and K. Wada, *J. Mater. Sci. Lett.* 20, 167 (2001).
161. Z. Miao, D. Xu, J. Ouyang, G. Guo, X. Zhao, and Y. Tang, *NanoLetters* 2, 717 (2002).
162. T. Kasuga, M. Hiramatsu, A. Hoson, T. Sekino, and K. Niihara, *Langmuir* 14, 3160 (1998).
163. S. M. Liu, L. M. Gan, L. H. Liu, W. D. Zhang, and H. C. Zeng, *Chem. Mater.* 14, 1391 (2002).
164. R. A. Caruso, J. H. Schattka, and A. Greiner, *Adv. Mater.* 13, 1577 (2001).
165. S. Kobayashi, K. Hanabusa, N. Hamasaki, M. Kimura, and H. Shirai, *Chem. Mater.* 12, 1523 (2000).
166. M. E. Spahr, P. Bitterli, R. Nesper, M. Müller, F. Krumeich, and H.-U. Nissen, *Angew. Chem. Int. Ed.* 37, 1263 (1998).
167. F. Krumeich, H.-J. Muhr, M. Niederberger, F. Bieri, B. Schnyder, and R. Nesper, *J. Am. Chem. Soc.* 121, 8324 (1999).
168. H.-J. Muhr, F. Krumeich, U. P. Schönholzer, F. Bieri, M. Niederberger, L. J. Gauckler, and R. Nesper, *Adv. Mater.* 12, 231 (2000).
169. J. Livage, *Chem. Mater.* 3, 578 (1991).
170. G. Gu, B. Zheng, W. Q. Han, S. Roth, and J. Liu, *NanoLetters* 2, 849 (2002).
171. Y. F. Zhang, Y. H. Tang, X. F. Duan, Y. Zhang, C. S. Lee, N. Wang, I. Bello, and S. T. Lee, *Chem. Phys. Lett.* 323, 180 (2000).
172. J. Y. Li, X. L. Chen, H. Li, M. He, and Z. Y. Qiao, *J. Cryst. Growth* 233, 5 (2001).
173. P. D. Yang, H. Q. Yan, S. Mao, R. Russo, J. Johnson, R. Saykally, N. Morris, J. Pham, R. R. He, and H. J. Choi, *Adv. Funct. Mater.* 12, 323 (2002).
174. B. D. Yao, Y. F. Chan, and N. Wang, *Appl. Phys. Lett.* 81, 757 (2002).
175. J.-J. Wu and S.-C. Liu, *J. Phys. Chem. B* 106, 9546 (2002).
176. C. K. Xu, G. D. Xu, Y. K. Liu, and G. H. Wang, *Solid State Commun.* 122, 175 (2002).
177. Y. W. Heo, V. Varadarajan, M. Kaufman, K. Kim, D. P. Norton, F. Ren, and P. H. Fleming, *Appl. Phys. Lett.* 81, 3046 (2002).
178. Y. Li, G. S. Cheng, and L. D. Zhang, *J. Mater. Res.* 15, 2305 (2000).
179. H. Kim and W. Sigmund, *Appl. Phys. Lett.* 81, 2085 (2002).
180. B. H. Hong, S. C. Bae, C. W. Lee, S. Jeong, and K. S. Kim, *Science* 294, 348 (2001).
181. M. H. Huang, A. Choudrey, and P. D. Yang, *Chem. Commun.* 1063 (2000).
182. Y.-J. Han, J. M. Kim, and G. D. Stucky, *Chem. Mater.* 12, 2068 (2000).
183. J. H. Song, Y. Wu, B. Messer, H. Kind, and P. Yang, *J. Am. Chem. Soc.* 123, 10397 (2001).
184. Y. Zhou, S. H. Yu, C. Y. Wang, X. G. Li, Y. R. Zhu, and Z. Y. Chen, *Adv. Mater.* 11, 850 (1999).
185. N. R. Jana, L. Gearheart, and C. J. Murphy, *Chem. Commun.* 617 (2001).
186. R. C. Jin, Y. W. Cao, C. A. Mirkin, K. L. Kelly, G. C. Schatz, and J. G. Zheng, *Science* 294, 1901 (2001).
187. M. J. Edmondson, W. Zhou, S. A. Sieber, I. P. Jones, I. Gameson, P. A. Anderson, and P. P. Edwards, *Adv. Mater.* 13, 1608 (2002).
188. S. Liu, J. Yue, and A. Gedanken, *Adv. Mater.* 13, 656 (2001).
189. J. J. L. M. Cornelissen, R. van Heerbeek, P. C. J. Kamer, J. N. H. Reek, N. A. J. M. Sommerdijk, and R. J. M. Nolte, *Adv. Mater.* 14, 489 (2002).
190. Y. Zhou, S. H. Yu, X. P. Cui, C. Y. Wang, and Z. Y. Chen, *Chem. Mater.* 11, 545 (1999).
191. S. H. Chen and D. L. Carroll, *NanoLetters* 2, 1003 (2002).
192. M. Maillard, S. Giorgio, and M. P. Pileni, *Adv. Mater.* 14, 1084 (2002).
193. I. Pastoriza-Santos and L. M. Liz-Marzan, *NanoLetters* 2, 903 (2002).
194. Y. G. Sun, B. Gates, B. Mayers, and Y. Xia, *NanoLetters* 2, 165 (2002).
195. B. A. Korgel and D. Fitzmaurice, *Adv. Mater.* 10, 661 (1998).
196. Y. Yu, S. Chang, C. Lee, and C. R. C. Wang, *J. Phys. Chem. B* 101, 6661 (1997).
197. N. R. Jana, L. Gearheart, and C. J. Murphy, *J. Phys. Chem. B* 105, 4065 (2001).
198. C. J. Murphy and N. R. Jana, *Adv. Mater.* 14, 80 (2002).
199. K. Esumi, K. Matsuhisa, and K. Torigoe, *Langmuir* 11, 3285 (1995).
200. J. K. N. Mbindyo, B. D. Reiss, B. R. Martin, C. D. Keating, M. J. Natan, and T. E. Mallouk, *Adv. Mater.* 13, 249 (2001).
201. T. Hassenkam, K. Nørgaard, L. Iversen, C. J. Kiely, M. Brust, and T. Bjørnholm, *Adv. Mater.* 14, 1126 (2002).
202. Y. Kondo and K. Takayanagi, *Science* 289, 606 (2000).
203. E. Dujardin, L. B. Hsin, C. R. C. Wang, and S. Mann, *Chem. Commun.* 1264 (2001).
204. C. S. Ah, S. D. Hong, and D.-J. Jang, *J. Phys. Chem. B* 105, 7871 (2001).
205. V. F. Puntes, K. M. Krishnan, and A. P. Alivisatos, *Science* 291, 2115 (2001).
206. T. Thurn-Albrecht, J. Schotter, C. A. Kastle, N. Emley, T. Shibauchi, L. Krusin-Elbaum, K. Guarini, C. T. Black, M. T. Tuominen, and T. P. Russell, *Science* 290, 2126 (2000).
207. C. Schonenberger, B. M. I. van der Zande, L. G. J. Fokkink, M. Henny, C. Schmid, M. Kruger, A. Bachtold, R. Huber, H. Birk, and U. Staufer, *J. Phys. Chem. B* 101, 5497 (1997).
208. S.-J. Park, S. Kim, S. Lee, Z. G. Khim, K. Char, and T. Hyeon, *J. Am. Chem. Soc.* 122, 8581 (2000).
209. K. Soulantica, A. Maisonnat, F. Senocq, M.-C. Fromen, M.-J. Casanove, and B. Chaudret, *Angew. Chem., Int. Ed. Engl.* 40, 2983 (2001).
210. N. Cordente, M. Respaud, F. Senocq, M.-J. Casanove, C. Amiens, and B. Chaudret, *NanoLetters* 1, 565 (2001).

211. G. Yi and W. Schwarzacher, *Appl. Phys. Lett.* 74, 1746 (1999).
212. Y.-T. Pang, G.-W. Meng, L.-D. Zhang, Y. Qin, X.-Y. Gao, A.-W. Zhao, and Q. Fang, *Adv. Funct. Mater.* 12, 719 (2002).
213. K. Torigoe and K. Esumi, *Langmuir* 11, 4199 (1995).
214. K.-B. Lee, S.-M. Lee, and J. Cheon, *Adv. Mater.* 13, 517 (2001).
215. J. Xiao, Y. Xie, R. Tang, M. Chen, and X. Tian, *Adv. Mater.* 13, 1887 (2001).
216. T. S. Ahmadi, Z. L. Wang, T. C. Green, A. Henglein, and M. A. El-Sayed, *Science* 272, 1924 (1996).
217. M. P. Zach, K. Inazu, K. H. Ng, J. C. Hemminger, and R. M. Penner, *Chem. Mater.* 14, 3206 (2002).
218. Y. Li, X. Li, Z.-X. Deng, B. Zhou, S. Fan, J. Wang, and X. Sun, *Angew. Chem., Int. Ed. Engl.* 41, 335 (2002).
219. Y. Wu, B. Messer, and P. Yang, *Adv. Mater.* 13, 1487 (2001).
220. L. M. Cao, Z. Zhang, L. L. Sun, C. X. Gao, M. He, Y. Q. Wang, Y. C. Li, X. Y. Zhang, G. Li, J. Zhang, and W. K. Wang, *Adv. Mater.* 13, 1701 (2001).
221. C. J. Otten, O. R. Lourie, M. F. Yu, J. M. Cowley, M. J. Dyer, R. S. Ruoff, and W. E. Buhro, *J. Am. Chem. Soc.* 124, 4564 (2002).
222. Y. D. Li, J. W. Wang, Z. X. Deng, Y. Y. Wu, X. M. Sun, D. P. Yu, and P. D. Yang, *J. Am. Chem. Soc.* 123, 9904 (2001).
223. T. Hanrath and B. A. Korgel, *J. Am. Chem. Soc.* 124, 1424 (2002).
224. Y. J. Zhang, Q. Zhang, N. L. Wang, Y. J. Yan, H. H. Zhou, and J. Zhu, *J. Cryst. Growth* 226, 185 (2001).
225. J. L. Gole, J. D. Stout, W. L. Rauch, and Z. L. Wang, *Appl. Phys. Lett.* 76, 2346 (2000).
226. Q. Gu, H. Y. Dang, J. Cao, J. H. Zhao, and S. S. Fan, *Appl. Phys. Lett.* 76, 3020 (2000).
227. W. S. Shi, H. Y. Peng, Y. F. Zheng, N. Wang, N. G. Shang, Z. W. Pan, C. S. Lee, and S. T. Lee, *Adv. Mater.* 12, 1343 (2000).
228. Y. H. Tang, Y. F. Zhang, N. Wang, W. S. Shi, C. S. Lee, I. Bello, and S. T. Lee, *J. Vac. Sci. Technol., B* 19, 317 (2001).
229. K.-Q. Peng, Y.-J. Yan, S.-P. Gao, and J. Zhu, *Adv. Mater.* 14, 1164 (2002).
230. Y. Wu, R. Fan, and P. Yang, *NanoLetters* 2, 83 (2002).
231. W. K. Hsu, S. Trasobares, H. Terrones, M. Terrones, N. Grobert, Y. Q. Zhu, W. Z. Li, R. Escudero, J. P. Hare, H. W. Kroto, and D. R. M. Walton, *Chem. Mater.* 11, 1747 (1999).
232. A. Abdelouas, W. L. Gong, W. Lutze, J. A. Shelnutt, R. Franco, and I. Moura, *Chem. Mater.* 12, 1510 (2000).
233. B. Gates, Y. D. Yin, and Y. N. Xia, *J. Am. Chem. Soc.* 122, 12582 (2000).
234. B. Gates, B. Mayers, B. Cattle, and Y. N. Xia, *Adv. Funct. Mater.* 12, 219 (2002).
235. B. Mayers and Y. N. Xia, *Adv. Mater.* 14, 279 (2002).
236. M. S. Mo, J. H. Zeng, X. M. Liu, W. C. Yu, S. Y. Zhang, and Y. T. Qian, *Adv. Mater.* 14, 1658 (2002).
237. C. C. Chen, C. C. Yeh, C. H. Chen, M. Y. Yu, H. L. Liu, J. J. Wu, K. H. Chen, L. C. Chen, J. Y. Peng, and Y. F. Chen, *J. Am. Chem. Soc.* 123, 2791 (2001).
238. C. C. Chen and C. C. Yeh, *Adv. Mater.* 12, 738 (2000).
239. J. Zhang, X. S. Peng, X. F. Wang, Y. W. Wang, and L. D. Zhang, *Chem. Phys. Lett.* 345, 372 (2001).
240. K. W. Chang and J. J. Wu, *J. Phys. Chem. B* 106, 7796 (2002).
241. S. Y. Bae, H. W. Seo, J. Park, H. Yang, J. C. Park, and S. Y. Lee, *Appl. Phys. Lett.* 81, 126 (2002).
242. X. Duan and C. M. Lieber, *J. Am. Chem. Soc.* 122, 188 (2000).
243. H. Y. Peng, X. T. Zhou, N. Wang, Y. F. Zheng, L. S. Liao, W. S. Shi, C. S. Lee, and S. T. Lee, *Chem. Phys. Lett.* 327, 263 (2000).
244. H. Y. Peng, N. Wang, X. T. Zhou, Y. F. Zheng, C. S. Lee, and S. T. Lee, *Chem. Phys. Lett.* 359, 241 (2002).
245. A. Wohlfart, A. Devi, E. Maile, and R. A. Fischer, *Chem. Commun.* 998 (2002).
246. W. Q. Han and A. Zettl, *Appl. Phys. Lett.* 80, 303 (2002).
247. K. Hiruma, M. Yazawa, T. Katsuyama, K. Ogawa, K. Haraguchi, M. Koguchi, and H. Kakibayashi, *J. Appl. Phys.* 77, 447 (1995).
248. K. Haraguchi, K. Hiruma, K. Hosomi, M. Shirai, and T. Katsuyama, *J. Vac. Sci. Technol., B* 15, 1685 (1997).
249. T. Shimada, K. Hiruma, M. Shirai, M. Yazawa, K. Haraguchi, T. Sato, M. Matsui, and T. Katsuyama, *Superlattices Microstruct.* 24, 453 (1998).
250. M. S. Gudiksen and C. M. Lieber, *J. Am. Chem. Soc.* 122, 8801 (2000).
251. W. S. Shi, Y. F. Zheng, N. Wang, C. S. Lee, and S. T. Lee, *J. Vac. Sci. Technol., B* 19, 1115 (2001).
252. C. Tang, S. Fan, M. Lamy de la Chapelle, H. Dang, and P. Li, *Adv. Mater.* 12, 1346 (2000).
253. H.-M. Kim, D. S. Kim, Y. S. Park, D. Y. Kim, T. W. Kang, and K. S. Chung, *Adv. Mater.* 14, 991 (2002).
254. Y.-H. Kim, Y.-W. Jun, B.-H. Jun, S.-M. Lee, and J. Cheon, *J. Am. Chem. Soc.* 124, 13656 (2002).
255. M. Yazawa, M. Koguchi, A. Muto, and K. Hiruma, *Adv. Mater.* 5, 577 (1993).
256. J. A. Haber, P. C. Gibbons, and W. E. Buhro, *J. Am. Chem. Soc.* 119, 5455 (1997).
257. J. A. Haber, P. C. Gibbons, and W. E. Buhro, *Chem. Mater.* 10, 4062 (1998).
258. Y. Zhang, J. Liu, R. He, Q. Zhang, X. Zhang, and J. Zhu, *Chem. Mater.* 13, 3899 (2001).
259. S. D. Dingman, N. P. Rath, P. D. Markowitz, P. C. Gibbons, and W. E. Buhro, *Angew. Chem., Int. Ed. Engl.* 39, 1470 (2000).
260. C. H. Liang, L. C. Chen, J. S. Hwang, K. H. Chen, Y. T. Hung, and Y. F. Chen, *Appl. Phys. Lett.* 81, 22 (2002).
261. K. F. Huo, Z. Hu, F. Chen, J. J. Fu, Y. Chen, B. H. Liu, J. Ding, Z. L. Dong, and T. White, *Appl. Phys. Lett.* 80, 3611 (2002).
262. C. C. Tang, Y. Bando, and T. Sato, *Chem. Phys. Lett.* 362, 185 (2002).
263. R. Ma, Y. Bando, and T. Sato, *Adv. Mater.* 14, 366 (2002).
264. L. M. Cao, K. Hahn, Y. Q. Wang, C. Scheu, Z. Zhang, C. X. Gao, Y. C. Li, X. Y. Zhang, L. L. Sun, W. K. Wang, and M. Rühle, *Adv. Mater.* 14, 1294 (2002).
265. C. C. Tang, X. X. Ding, X. T. Huang, Z. W. Gan, W. Liu, S. R. Qi, Y. X. Li, J. P. Qu, and L. Hu, *Jpn. J. Appl. Phys., Part 2* 41, L589 (2002).
266. Y. H. Gao, Y. Bando, K. Kurashima, and T. Sato, *Microsc. Microanal.* 8, 5 (2002).
267. K. Tang, J. Hu, Q. Lu, Y. Xie, J. Zhu, and Y. Qian, *Adv. Mater.* 11, 653 (1999).
268. Y. H. Gao, Y. Bando, and T. Sato, *Appl. Phys. Lett.* 79, 4565 (2001).
269. Z. L Wang, Z. R. Dai, R. P. Gao, Z. G. Bai, and J. L. Gole, *Appl. Phys. Lett.* 77, 3349 (2000).
270. Z. S. Wu, S. Z. Deng, N. S. Xu, J. Chen, J. Zhou, and J. Chen, *Appl. Phys. Lett.* 80, 3829 (2002).
271. W. S. Shi, Y. F. Zheng, H. Y. Peng, N. Wang, C. S. Lee, and S. T. Lee, *J. Am. Ceram. Soc.* 83, 3228 (2000).
272. Z. W. Pan, H. L. Lai, F. C. K. Au, X. F. Duan, W. Y. Zhou, W. S. Shi, N. Wang, C. S. Lee, N. B. Wong, S. T. Lee, and S. S. Xie, *Adv. Mater.* 12, 1186 (2000).
273. C. H. Liang, G. W. Meng, L. D. Zhang, Y. C. Wu, and Z. Cui, *Chem. Phys. Lett.* 329, 323 (2000).
274. J. C. Li, C. S. Lee, and S. T. Lee, *Chem. Phys. Lett.* 355, 147 (2002).
275. J. Q. Hu, Q. Y. Lu, K. B. Tang, B. Deng, R. R. Jiang, Y. T. Qian, W. C. Yu, G. E. Zhou, X. M. Liu, and J. X. Wu, *J. Phys. Chem. B* 104, 5251 (2000).
276. Q. Y. Lu, J. Q. Hu, K. B. Tang, Y. T. Qian, G. Zhou, X. M. Liu, and J. S. Zhu, *Appl. Phys. Lett.* 75, 507 (1999).
277. D. N. McIlroy, D. Zhang, Y. Kranov, and M. G. Norton, *Appl. Phys. Lett.* 79, 1540 (2001).
278. H.-F. Zhang, A. C. Dohnalkova, C.-M. Wang, J. S. Young, E. C. Buck, and L.-S. Wang, *NanoLetters* 2, 105 (2002).
279. S. R. Qi, X. T. Huang, Z. W. Gan, X. X. Ding, and Y. Cheng, *J. Cryst. Growth* 219, 485 (2000).
280. X. Wang, J. Lu, P. Gou, and Y. Xie, *Chem. Lett.* 820 (2002).

*281.* J. H. Song, B. Messer, Y. Wu, H. Kind, and P. Yang, *J. Am. Chem. Soc.* 123, 9714 (2001).

*282.* Y. Chen, D. A. A. Ohlberg, G. Medeiros-Ribeiro, Y. A. Chang, and R. S. Williams, *Appl. Phys. Lett.* 76, 4004 (2000).

*283.* C. P. Li, N. Wang, S. P. Wong, C. S. Lee, and S. T. Lee, *Adv. Mater.* 14, 218 (2002).

*284.* T. I. Kamins, R. S. Williams, D. P. Basile, T. Hesjedal, and J. S. Harris, *J. Appl. Phys.* 89, 1008 (2001).

*285.* D. S. Xu, Y. J. Xu, D. P. Chen, G. L. Guo, L. L. Gui, and Y. Q. Tang, *Chem. Phys. Lett.* 325, 340 (2000).

*286.* H. Q. Cao, Y. Xu, J. M. Hong, H. B. Liu, G. Yin, B. L. Li, C. Y. Tie, and Z. Xu, *Adv. Mater.* 13, 1393 (2001).

*287.* P. S. Nair, T. Radhakrishnan, N. Revaprasadu, G. A. Kolawole, and P. O'Brien, *Chem. Commun.* 564 (2002).

*288.* Y. D. Li, H. W. Liao, Y. Ding, Y. T. Qian, L. Yang, and G. E. Zhou, *Chem. Mater.* 10, 2301 (1998).

*289.* M. Chen, M. Y. Xie, J. Lu, Y. J. Xiong, S. Y. Zhang, Y. T. Qian, and X. M. Liu, *J. Mater. Chem.* 12, 748 (2002).

*290.* J. H. Zhan, X. G. Yang, D. W. Wang, S. D. Li, Y. Xie, Y. Xia, and Y. T. Qian, *Adv. Mater.* 12, 1348 (2000).

*291.* N. Pinna, K. Weiss, J. Urban, and M. P. Pileni, *Adv. Mater.* 13, 261 (2001).

*292.* C.-C. Chen, C.-Y. Chao, and Z. H. Lang, *Chem. Mater.* 12, 1516 (2000).

*293.* Y.-W. Jun, S.-M. Lee, N.-J. Kang, and J. Cheon, *J. Am. Chem. Soc.* 123, 5150 (2001).

*294.* D. Xu, X. Shi, G. Guo, L. Gui, and Y. Tang, *J. Phys. Chem. B* 104, 5061 (2000).

*295.* Z. A. Peng and X. G. Peng, *J. Am. Chem. Soc.* 124, 3343 (2002).

*296.* Z. A. Peng and X. G. Peng, *J. Am. Chem. Soc.* 123, 183 (2001).

*297.* W. Z. Wang, Y. Geng, P. Yan, F. Y. Liu, Y. Xie, and Y. T. Qian, *Inorg. Chem. Commun.* 2, 83 (1999).

*298.* Q. Yang, K. Tang, C. Wang, Y. Qian, and S. Zhang, *J. Phys. Chem. B* 106, 9227 (2002).

*299.* Q. Peng, Y. J. Dong, Z. X. Deng, and Y. D. Li, *Inorg. Chem.* 41, 5249 (2002).

*300.* L. Manna, E. C. Scher, L.-S. Li, and A. P. Alivisatos, *J. Am. Chem. Soc.* 124, 7136 (2002).

*301.* S. H. Yu, J. Yang, Z. H. Han, R. Y. Yang, Y. T. Qian, and Y. H. Zhang, *J. Solid State Chem.* 147, 637 (1999).

*302.* F. Gao, Q. Y. Lu, X. Y. Liu, Y. S. Yan, and D. Y. Zhao, *NanoLetters* 1, 743 (2001).

*303.* S. H. Wang and S. H. Yang, *Langmuir* 16, 389 (2000).

*304.* D. B. Yu, D. B. Wang, Z. Y. Meng, J. Lu, and Y. T. Qian, *J. Mater. Chem.* 12, 403 (2002).

*305.* M. S. Mo, M. W. Shao, H. M. Hu, L. Yang, W. C. Yu, and Y. T. Qian, *J. Cryst. Growth* 244, 364 (2002).

*306.* W. Z. Wang, Y. Geng, Y. Qian, M. R. Ji, and X. M. Liu, *Adv. Mater.* 10, 1479 (1998).

*307.* X. S. Peng, G. W. Meng, J. Zhang, X. F. Wang, C. Z. Wang, X. Liu, and L. D. Zhang, *J. Mater. Res.* 17, 1283 (2002).

*308.* Y. Li, J. H. Wan, and Z. N. Gu, *Mol. Cryst. Liquid Cryst.* 337, 193 (1999).

*309.* X. Jiang, Y. Xie, J. Lu, L. Y. Zhu, W. He, and Y. T. Qian, *Chem. Mater.* 13, 1213 (2001).

*310.* Q. S. Wu, N. W. Zheng, Y. P. Ding, and Y. D. Li, *Inorg. Chem. Commun.* 5, 671 (2002).

*311.* N. Kouklin, L. Menon, A. Z. Wong, D. W. Thompson, J. A. Woollam, P. F. Williams, and S. Bandyopadhyay, *Appl. Phys. Lett.* 79, 4423 (2001).

*312.* Y. W. Jun, C. S. Choi, and J. Cheon, *Chem. Commun.* 101 (2001).

*313.* Y. D. Li, Y. Ding, and Z. Y. Wang, *Adv. Mater.* 11, 847 (2002).

*314.* S. H. Yu, Y. T. Qian, L. Shu, Y. Xie, L. Yang, and C. S. Wang, *Mater. Lett.* 35, 116 (1998).

*315.* S. H. Yu, L. Shu, J. Yang, Z. H. Han, Y. T. Qian, and Y. H. Zhang, *J. Mater. Res.* 14, 4157 (1999).

*316.* S. H. Yu, J. Yang, Y. S. Wu, Z. H. Han, Y. Xie, and Y. T. Qian, *Mater. Res. Bull.* 33, 1661 (1998).

*317.* X. S. Peng, G. W. Meng, J. Zhang, L. X. Zhao, X. F. Wang, Y. W. Wang, and L. D. Zhang, *J. Phys. D: Appl. Phys.* 34, 3224 (2001).

*318.* S. H. Yu, J. Yang, Y. S. Wu, Z. H. Han, J. Lu, Y. Xie, and Y. T. Qian, *J. Mater. Chem.* 8, 1949 (1998).

*319.* H. L. Su, Y. Xie, P. Gao, H. Lu, Y. J. Xiong, and Y. T. Qian, *Chem. Lett.* 790 (2000).

*320.* M. S. Sander, A. L. Prieto, R. Gronsky, T. Sands, and A. M. Stacy, *Adv. Mater.* 14, 665 (2002).

*321.* A. L. Prieto, M. S. Sander, M. S. Martin-Gonzalez, R. Gronsky, T. Sands, and A. M. Stacy, *J. Am. Chem. Soc.* 123, 7161 (2001).

*322.* Y. Zhang, G. H. Li, Y. C. Wu, B. Zhang, W. H. Song, and L. Zhang, *Adv. Mater.* 14, 1227 (2002).

*323.* J. Yang, J. H. Zeng, S. H. Yu, L. Yang, Y. H. Zhang, and Y. T. Qian, *Chem. Mater.* 12, 2924 (2000).

*324.* E. Roy, P. Fricoteaux, and K. Yu-Zhang, *J. Nanosci. Nanotechnol.* 1, 323 (2001).

*325.* D. Wang, D. Yu, M. Shao, W. Yu, and Y. Qian, *Chem. Lett.* 1056 (2002).

*326.* Q. Lu, F. Gao, and D. Zhao, *Angew. Chem., Int. Ed. Engl.* 41, 1932 (2002).

*327.* Y. J. Glanville, D. G. Narehood, P. E. Sokol, A. Amma, and T. Mallouk, *J. Mater. Chem.* 12, 2433 (2002).

*328.* B. Gates, Y. Y. Wu, Y. D. Yin, P. D. Yang, and Y. N. Xia, *J. Am. Chem. Soc.* 123, 11500 (2001).

*329.* B. Gates, B. Mayers, Y. Y. Wu, Y. G. Sun, B. Cattle, P. D. Yang, and Y. N. Xia, *Adv. Funct. Mater.* 12, 679 (2002).

*330.* N. Wang, K. K. Fung, S. Wang, and S. Yang, *J. Cryst. Growth* 233, 226 (2001).

*331.* S. H. Wang, S. H. Yang, Z. R. Dai, and Z. L. Wang, *Phys. Chem. Chem. Phys.* 3, 3750 (2001).

*332.* X. G. Wen and S. H. Yang, *NanoLetters* 2, 451 (2002).

*333.* Q. Y. Lu, F. Gao, and D. Y. Zhao, *NanoLetters* 2, 725 (2002).

*334.* Y.-W. Jun, Y.-Y. Jung, and J. Cheon, *J. Am. Chem. Soc.* 124, 615 (2002).

*335.* H. Liao, Y. Wang, S. Zhang, and Y. Qian, *Chem. Mater.* 13, 6 (2001).

*336.* M. Nath, A. Govindaraj, and C. N. R. Rao, *Adv. Mater.* 13, 283 (2001).

*337.* M. Remskar, A. Mrzel, Z. Skraba, A. Jesih, M. Ceh, J. Demsar, P. Stadelmann, F. Levy, and D. Mihailovic, *Science* 292, 479 (2001).

*338.* J. Chen, S. L. Li, Q. Xu, and K. Tanaka, *Chem. Commun.* 1722 (2002).

*339.* R. Tenne, L. Margulis, M. Genut, and G. Hodes, *Nature* 360, 444 (1992).

*340.* A. Rothschild, J. Sloan, and R. Tenne, *J. Am. Chem. Soc.* 122, 5169 (2000).

*341.* Y. Q. Zhu, W. K. Hsu, N. Grobert, B. H. Chang, M. Terrones, H. Terrones, H. W. Kroto, and D. R. M. Walton, *Chem. Mater.* 12, 1190 (2000).

*342.* R. Rosentsveig, A. Margolin, Y. Feldman, R. Popovitz-Biro, and R. Tenne, *Chem. Mater.* 14, 471 (2002).

*343.* M. Nath and C. N. R. Rao, *Angew. Chem., Int. Ed. Engl.* 41, 3451 (2002).

*344.* Y. Q. Zhu, W. K. Hsu, H. W. Kroto, and D. R. M. Walton, *J. Phys. Chem. B* 106, 7623 (2002).

*345.* Q. Yang, K. B. Tang, C. R. Wang, D. Y. Zhang, and Y. T. Qian, *J. Solid State Chem.* 164, 106 (2002).

*346.* J. Q. Hu, B. Deng, W. X. Zhang, K. B. Tang, and Y. T. Qian, *Inorg. Chem.* 40, 3130 (2001).

*347.* Y. Cui, J. Ren, G. Chen, Y. Qian, and Y. Xie, *Chem. Lett.* 236 (2001).

*348.* B. Xie, S. W. Yuan, Y. Jiang, J. Lu, Q. Li, Y. Wu, W. C. Yu, H. B. Zhang, and Y. T. Qian, *Chem. Lett.* 612 (2002).

*349.* J. Q. Hu, B. Deng, W. X. Zhang, K. B. Tang, and Y. T. Qian, *Int. J. Inorg. Mater.* 3, 639 (2001).

*350.* Y. Xiong, Y. Xie, G. Du, and H. Su, *Inorg. Chem.* 41, 2953 (2002).

*351.* C. R Wang, K. B. Tang, Q. Yang, G. Z. Shen, B. Hai, C. H. An, J. Zuo, and Y. T. Qian, *J. Solid State Chem.* 160, 50 (2001).

*352.* S. Iijima, *Nature* 354, 56 (1999).

*353.* C. J. Frosch and C. D. Thurmond, *J. Phys. Chem.* 66, 877 (1962).

*354.* C. M. Balkas and R. E. Davis, *J. Am. Ceram. Soc.* 79, 2309 (1996).

*355.* C. Pham-Huu, N. Keller, C. Estournes, G. Ehret, and M. J. Ledoux, *Chem. Commun.* 1882 (2002).

*356.* M. Brorson, T. W. Hansen, and C. J. H. Jacobsen, *J. Am. Chem. Soc.* 124, 11582 (2002).

*357.* Y. Q. Zhu, W. K. Hsu, H. W. Kroto, and D. R. M. Walton, *Chem. Commun.* 2184 (2001).

*358.* A. Huczko, *Appl. Phys. A* 70, 365 (2000).

*359.* M. Yoshimura, W. Suchanek, and K. Byrappa, *MRS Bull.* 9, 17 (2000).

*360.* K. Byrappa and M. Yoshimura, Eds., "Handbook of Hydrothermal Technology." LLC/Noyes Publications, Park Ridge, NJ, 2000.

*361.* A. Rabenau, *Angew. Chem., Int. Ed. Engl.* 24, 1026 (1985).

*362.* J. P. Corbett, *Chem. Rev.* 85, 383 (1985).

*363.* H. Schafer, *Annu. Rev. Mater. Sci.* 15, 1 (1985).

*364.* S. Feng and R. Xu, *Acc. Chem. Res.* 34, 239 (2001).

*365.* R. I. Walton, *Chem. Soc. Rev.* 31, 230 (2002).

*366.* W. S. Sheldrick and M. Wachhold, *Angew. Chem., Int. Ed. Engl.* 36, 206 (1997).

*367.* G. Demazeau, *J. Mater. Chem.* 9, 15 (1999).

*368.* R. F. Morris and S. J. Weigel, *Chem. Soc. Rev.* 26, 309 (1997).

*369.* S. H. Yu, L. Shu, Y. S. Wu, K. B. Tang, Y. Xie, Y. T. Qian, and Y. H. Zhang, *Nanostruct. Mater.* 10, 1307 (1998).

*370.* J. Yang, X. L. Yang, S. H. Yu, X. M. Liu, and Y. T. Qian, *Mater. Res. Bull.* 35, 1509 (2000).

*371.* S. H. Yu, J. Yang, Y. T. Qian, and M. Yoshimura, *Chem. Phys. Lett.* 361, 362 (2002).

*372.* S. H. Yu, Z. H. Han, J. Yang, R. Y. Yang, Y. Xie, and Y. T. Qian, *Chem. Lett.* 1111 (1998).

*373.* Z. H. Han, S. H. Yu, Y. P. Li, H. Q. Zhao, F. Q. Li, Y. Xie, and Y. T. Qian, *Chem. Mater.* 11, 2302 (1999).

*374.* J. Yang, G. H. Cheng, J. H. Zeng, S. H. Yu, X. M. Liu, and Y. T. Qian, *Chem. Mater.* 13, 848 (2001).

*375.* Z. H. Han, Y. P. Li, S. H. Yu, C. Zhong, X. Y. Chen, H. Q. Zhao, and Y. T. Qian, *J. Cryst. Growth* 223, 1 (2001).

*376.* S. H. Yu, L. Shu, Y. S. Wu, Y. Xie, Y. T. Qian, and L. Yang, *J. Am. Ceram. Soc.* 82, 457 (1999).

*377.* S. H. Yu and M. Yoshimura, *Adv. Funct. Mater.* 12, 277 (2002).

*378.* J. Yang, S. H. Yu, X. L. Yang, and Y. T. Qian, *Chem. Lett.* 839 (1999).

*379.* J. Yang, S. H. Yu, Z. H. Han, Y. T Qian, and Y. H. Zhang, *J. Solid State Chem.* 146, 387 (1999).

*380.* S. H. Yu, J. Yang, Y. S. Wu, Z. H. Han, L. Shu, Y. Xie, and Y. T. Qian, *J. Mater. Res.* 13, 3365 (1998).

*381.* Y. Xie, Y. T. Qian, W. Z. Wang, S. Y. Zhang, and Y. H. Zhang, *Science* 272, 1926 (1996).

*382.* J. Q. Hu, Q. Y. Lu, K. B. Tang, S. H. Yu, Y. T. Qian, G. E. Zhou, X. M. Liu, and J. X. Wu, *J. Am. Ceram. Soc.* 83, 430 (2000).

*383.* J. Q. Hu, Q. Y. Lu, K. B. Tang, S. H. Yu, Y. T. Qian, G. E. Zhou, X. M. Liu, and J. X. Wu, *J. Solid State Chem.* 148, 325 (1999).

*384.* R. Rossetti, R. Hull, J. M. Gibson, and L. E. Brus, *J. Chem. Phys.* 82, 552 (1995).

*385.* R. J. Bandaranayake, G. W. Wen, J. Y. Lin, H. X. Jiang, and C. M. Sorensen, *Appl. Phys. Lett.* 67, 831 (1995).

*386.* J. J. Ramsden, S. E. Webber, and M. Gratzel, *J. Phys. Chem.* 89, 2740 (1985).

*387.* K. Krishnan and R. A. Plane, *Inorg. Chem.* 5, 852 (1966).

*388.* K. Nakamoto, in "Infrared and Raman Spectra of Inorganic and Coordination Compounds," Chap. 3, 3rd ed. Wiley, New York, 1978.

*389.* J. A. Dean, in "Lange's Handbook," 12th ed. McGraw-Hill Book Company, New York, 1987.

*390.* A. Sabatini and S. Callfano, *Spectrochim. Acta* 16, 677 (1960).

*391.* G. Newman and D. B. Powell, *J. Chem. Soc.* 477 (1961).

*392.* T. Iwamoto and D. F. Shriver, *Inorg. Chem.* 10, 2428 (1971).

*393.* J. S. Bradley, B. Tesche, W. Busser, M. Maase, and M. T. Reetz, *J. Am. Chem. Soc.* 122, 4631 (2000).

*394.* X. Y. Jing, S. L. Chen, and S. Y. Yao, in "Practical Guide to Infrared Spectrum," Chap. 6. Tianjin Science and Technology Press, 1992.

*395.* D. Arivuoli, F. D. Gnanam, and P. Ramasamy, *J. Mater. Sci. Lett.* 7, 711 (1988).

*396.* L. J. Farrugia, F. J. Lawlor, and N. C. Norman, *Polyhedron* 14, 311 (1995).

*397.* B. B. Nayak, H. N. Acharya, G. B. Mitra, and B. K. Mathur, *Thin Solid Films* 105, 17 (1983).

*398.* P. Boudjouk, M. P. Remington, Jr., D. G. Grier, B. R. Jarabek, and G. J. McCarthy, *Inorg. Chem.* 37, 3538 (1998).

*399.* H. O. Stephan and M. G. Kanatzidis, *Inorg. Chem.* 36, 6050 (1997).

*400.* C. Kaito, Y. Saito, and K. Fujita, *J. Cryst. Growth* 94, 967 (1989).

*401.* B. F. Variano, D. M. Hwang, C. S. Sandroff, P. Wiltzius, T. W. Jing, and N. P. Ong, *J. Phys. Chem.* 91, 6455 (1987).

*402.* W. S. Rees and G. Kräuter, *J. Mater. Res.* 11, 3005 (1996).

*403.* J. A. Dean, in "Lange's Handbook of Chemistry," 13th ed. McGraw-Hill Book Company, New York.

*404.* G. F. Svatos, C. Curran, and J. V. Quagliano, *J. Am. Chem. Soc.* 77, 6159 (1955).

*405.* A. Yamaguchi, R. B. Penland, S. Mizushima, T. J. Lane, C. Curran, and J. V. Quagliano, *J. Am. Chem. Soc.* 80, 527 (1958).

*406.* L. I. Berger, Ed., "Semiconductor Materials," pp. 86–88. CRC Press, Boca Raton, FL, 1997.

*407.* Z. A. Peng and X. G. Peng, *J. Am. Chem. Soc.* 123, 1389 (2001).

*408.* D. Kuang, A. Xu, Y. Fang, H. Ou, and H. Liu, *J. Cryst. Growth* 244, 379 (2002).

*409.* B. A. Simmons, S. Li, V. T. John, G. L. McPherson, A. Bose, W. Zhou, and J. He, *NanoLetters* 2, 263 (2002).

*410.* M. P. Pileni, *Langmuir* 17, 7476 (2001).

*411.* M. Antonietti and M. Weissenberger, *Macromol. Chem. Rapid Commun.* 18, 295 (1997).

*412.* J. D. Hartgerink, E. Beniash, and S. I. Stupp, *Science* 294, 1684 (2001).

*413.* W. Traub and S. Weiner, *Proc. Natl. Acad. Sci. U.S.A.* 86, 9822 (1989).

*414.* P. Terech and R. G. Weiss, *Chem. Rev.* 97, 3133 (1997).

*415.* S. Shinkai and K. Murata, *J. Mater. Chem.* 8, 485 (1997).

*416.* O. Gronwald and S. Shinkai, *Chem. Eur. J.* 7, 4329 (2001).

*417.* K. Hanabusa, K. Hiratsuka, M. Kimura, and H. Shirai, *Chem. Mater.* 11, 649 (1999).

*418.* K. Hanabusa, M. Yamada, M. Kimura, and H. Shirai, *Angew. Chem., Int. Ed. Engl.* 35, 1949 (1996).

*419.* K. Murata, M. Aoki, T. Suzuki, T. Harada, H. Kawabata, T. Komori, F. Ohseto, K. Ueda, and S. Shinkai, *J. Am. Chem. Soc.* 116, 6664 (1994).

*420.* Y. Ono, K. Nakashima, M. Sano, Y. Kanekiyo, K. Inoue, J. Hojo, and S. Shinkai, *Chem. Commun.* 1477 (1998).

*421.* J. H. Jung, Y. Ono, and S. Shinkai, *J. Chem. Soc., Perkin Trans 2* 1289 (1999).

422. Y. Ono, K. Nakashima, M. Sano, J. Hojo, and S. Shinkai, *Chem. Lett.* 1119 (1999).
423. J. H. Jung, Y. Ono, and S. Shinkai, *Angew. Chem., Int. Ed. Engl.* 39, 1862 (2000).
424. J. H. Jung, Y. Ono, and S. Shinkai, *Chem. Eur. J.* 6, 4552 (2000).
425. J. H. Jung, Y. Ono, K. Hanabusa, and S. Shinkai, *J. Am. Chem. Soc.* 122, 5008 (2000).
426. Y. Ono, K. Nakashima, M. Sano, J. Hojo, and S. Shinkai, *J. Mater. Chem.* 11, 2412 (2001).
427. S. Kobayashi, K. Hanabusa, N. Hamasaki, M. Kimura, H. Shirai, and S. Shinkai, *Chem. Mater.* 12, 1523 (2000).
428. S. Kobayashi, N. Hamasaki, M. Suzuki, M. Kimura, H. Shirai, and K. Hanabusa, *J. Am. Chem. Soc.* 124, 6550 (2002).
429. J. H. Jung, H. Kobayashi, K. J. C. Bommel, S. Shinkai, and T. Shimizu, *Chem. Mater.* 14, 1445 (2002).
430. B. C. Bunker, P. C. Rieke, B. J. Tarasevich, A. A. Campbell, G. E. Fryxell, G. L. Graff, L. Song, J. Liu, and J. W. Virden, *Science* 264, 48 (1994).
431. G. Falini, S. Albeck, S. Weiner, and L. Addadi, *Science* 271, 67 (1996).
432. A. M. Belcher, X. H. Wu, P. K. Christensen, P. K. Hansma, G. D. Stucky, and D. E. Morse, *Nature* 381, 56 (1996).

ENN
*Encyclopedia of Nanoscience and Nanotechnology*
**www.aspbs.com/enn**

# Modification of Carbon Nanotubes

Hansoo Kim, Wolfgang M. Sigmund

*University of Florida, Gainesville, Florida, USA*

## CONTENTS

## 1. INTRODUCTION

Carbon nanotubes (CNTs) were first introduced in 1991 as a new allotrope of carbon [1]. While Iijima was carrying out an experiment on fullerenes (another allotrope of carbon discovered in 1985 [2]) using an arc process, he found carbon clusters including various shapes of carbon particles. Some of them were graphitic sheets rolled up into cylinders. When CNTs are composed of one graphitic sheet they are called single wall nanotubes (SWNTs), and when they consist of more than one graphitic sheet they are called multiwalled nanotubes (MWNTs). They have an appearance similar to carbon fibers which are a lot less graphitic but have a hollow core. Figure 1a and b shows a drawing and a transmission electron microscopy (TEM) image of an armchair SWNT synthesized by the arc discharge technique. Armchair SWNTs are one of three kinds of SWNTs classified according to their helicity. The helicity has an impact on the properties of the pure as well as modified SWNTs. The strongest impact is on the electronic and optical properties. These will be described more in the following sections. In Figure 1c a clear high resolution TEM image of a MWNT with a diameter of about 200 Å which is filled with samarium oxide by wet chemistry is presented where the fringes representing the graphitic walls are separated by ~3.4 Å corresponding to that between walls of a large MWNT and carbonaceous particles reside on the outer surface of the nanotube. After intensive research it was found that CNTs have very attractive thermal, mechanical, electrical, and even optical properties. However, for utilizing CNTs in the industrial fields formidable technical hurdles should be overcome. To fabricate efficient CNT–polymer composites, CNTs must be homogenously dispersed in the matrix to avoid sliding on

the shells of other CNTs. Besides, the strong adhesion of CNTs to the matrix is necessary for effective stress transfer from the matrix to CNTs. For the assembly of nanometer-sized electronic devices using CNTs the charge densities should be adjustable as in the silicon-based circuits. The agglomeration of CNTs needs to be avoided, which induces the perturbation of the electronic structure of nanotubes. The homogeneous dispersion of CNTs is also required when they are mixed with a solvent for the optical applications. To satisfy these requisite conditions, many efforts have been made to date coating, doping, and functionalization of the surface of CNTs. In the following sections each modification method will be explained in detail, and how the properties of CNTs can be improved with these surface and structural modifications will be described.

## 2. MODIFICATION OF CARBON NANOTUBES

### 2.1. Graphitization

CNTs fabricated by various methods [especially nanotubes synthesized by chemical vapor deposition (CVD) have a number of structural defects which produce negative effects on their original properties. Andrews et al. heat-treated CNTs (synthesized by a low temperature CVD method) between 1600 and 3000 °C in an inert gas atmosphere and thereafter characterized them for chemical purity, interlayer spacing, and defect healing [3]. This graphitization procedure led the CNTs (the nanotubes annealed over 1800 °C) to remove essentially all residual metal catalyst inside and at the tips of the nanotubes along with structural reordering, which was confirmed by higher order diffraction spots from these heat-treated nanotubes. Furthermore, it was found by X-ray diffraction that the interlayer gap between the graphene shells as well as the numbers of the wall defects was reduced by the graphitization procedure. A similar result was also reported by Hamwi et al. in the process of fluorination of CNTs [4]. Hereby obtained ordered periodicity in the crystal structure of CNTs will help to attain the stability in thermal and electrical conductivity.
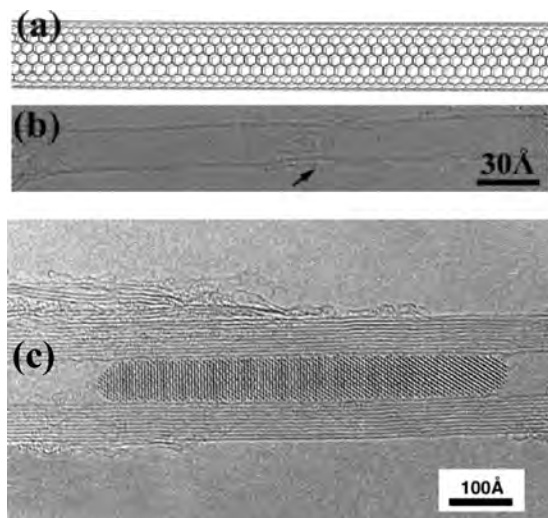
**Figure 1.** (a) Drawing of an armchair SWNT. (b) TEM image of a SWNT. The arrow indicates the shell of the SWNT. Reprinted with permission from [111], J. Sloan et al., *Chem. Commun.* 8, 699 (1999). © 1999, Royal Society of Chemistry. (c) TEM image of a MWNT filled with samarium oxide from http://www.chem.ox.ac.uk/icl/catcentre/nanogrp.htm.

## 2.2. Opening and Oxidation

Synthesized CNTs normally have closed caps at the tips. These closed caps can be removed by oxidation with heat treatment or oxidizing acids. Ajayan et al. reported that CNTs were oxidized after annealing for a short time above around 700 °C causing the etching away of the tube caps and the thinning of nanotube walls through layer-by-layer peeling of the outer layers (beginning with the cap region) [5]. Tsang et al. put CNTs into concentrated nitric acid and refluxed before washing and drying [6]. The product showed about 80–90% of the nanotubes became open-ended. Figure 2 shows an inverted bright field TEM image



**Figure 2.** Inverted bright field TEM image of a MWNT opened by annealing at 700 °C. Courtesy of H. Kim and W. Sigmund, unpublished data.

of a MWNT opened after heat treatment at 700 °C. Mazzoni et al. calculated the energetics of the oxidation and opening of CNTs [7]. In their study it was found that the cap oxidation is much more favorable than the wall oxidation because the extra elastic strain energy accumulated at the cap region of CNTs can be dramatically released from the very start of the oxidation and the that carbon–oxygen–carbon structure generated at the cap is energetically stable.

Graphitization and oxidation procedures are also considered to be methods for purification since these two treatments can help to get rid of residual catalyst metals and carbonaceous particles. In addition, various purification procedures have been reported, most of them using acids such as HCl, $H_2SO_4$, $HNO_3/H_2SO_4$, and other oxidizing reactants like $H_2O_2$.

## 2.3. Coating

CNTs have been coated with various metals and nonmetals to enhance the properties of CNTs or to acquire nanowires and composites. Zhang et al. coated CNTs (suspended across a TEM grid) with diverse metals such as titanium, iron, and nickel by electron beam deposition and directly observed these coated CNTs with TEM [8]. They found some metals such as titanium, nickel, and palladium can make a continuous coating on the surface of CNTs whereas some metals such as gold, aluminum, and iron form isolated particles. They explained this by mentioning that in general the ability of transition metals to bond with carbon atoms increases with the number of unfilled $d$-orbitals. Therefore, metals like titanium can make a strong bonding (having covalent bonding characteristics) to the outer shell of CNTs and this accounts for the very high condensation and sticking coefficient of them since many vacancies in the $d$-shell of metals like titanium may form by rehybridization with curvature-induced $sp^2$ orbitals of CNTs. This compares well with the experiment by Guerret-Plecourt et al., which is about filling of CNTs with metals (filling will be discussed more in detail later) [9]. In their study they put a mixture of graphite and metal powders into a hole in the anode and applied high current and voltage (100–110 amp dc and 20–30 V). The condensation of formed plasma yields CNTs filled with the metals used. The result shows that metals with an incomplete electronic shell in the most stable ionic state of the metals can fill the cavities of CNTs while metals with no incomplete shell such as tungsten and zinc only exist in the form of carbide at the tips of CNTs and no true filling was found. Accordingly, since the most stable ionic state of titanium ($Ti^{4+}$) does not have an incomplete shell, titanium cannot fill CNTs. This apparent discrepancy (that is, titanium can coat the outer surface of CNTs but cannot fill the inner cavity) may be explained by the fact that the filling materials are in fact crystalline metallic carbide. Titanium carbide (TiC) has no vacancies in the $d$-orbital, which makes it difficult to form a stable bonding to the inner wall of CNTs. Accordingly, it can be said that vacancies in the $d$-orbitals of transition metals play an important role in coating or filling CNTs.

Kim and Sigmund showed various shapes of zinc oxide (ZnO) nanostructures grown on the outermost shell of MWNTs. In their report heat treatment with a mixture of

zinc and nanotubes at various temperatures forms quantum dots, thin films, nanowires, and nanorods of ZnO on the surface of CNTs. These ZnO nanowires and nanorods were synthesized without the presence of any catalyst contrary to the generally accepted vapor–liquid–solid (VLS) theory for the growth of nanowires [10]. In the VLS theory constituent atoms such as gallium and arsenide are supposed to be supplied in the "vapor" state, dissolved into a molten catalyst (liquid) like gold, and reprecipitated as nanowires (solid) [11, 12]. This theory has sometimes been used to explain the formation of CNTs [13–16]. In Figure 3 ZnO nanorods on CNTs are shown where the hexagonal cross section of one of the nanorods indicates it was grown along the ⟨0001⟩ direction of ZnO crystal.

Seeger et al. reported silicon oxide ($SiO_x$) coating of MWNTs using a sol–gel technique [17]. In their experiment MWNTs fabricated by the standard arc discharge technique were dispersed in polyelectrolyte polyethylemine aqueous solution followed by sonication and centrifugation. After repeating this process the CNT dispersion was mixed with sol which was produced with a mixture of tetraethoxysilane, water, and ethanol. After sonication and centrifugation $SiO_x$-coated MWNTs were synthesized. Figure 4 shows a $SiO_x$-coated MWNT on which some parts are covered with amorphous phase while some other parts are demarcated by the distinct fringes with a gap $0.30 \pm 0.02$ nm corresponding to that of {111} planes of silicon.

Coating on CNTs is also used for the fabrication of nanowires. Bezryadin et al. deposited CNTs and suspended them over a slit etched in the substrate and sputtered a superconducting alloy of amorphous molybdenum–germanium ($Mo_{79}Ge_{21}$) film for the synthesis of nanowires to find out whether quantum phase slips can destroy superconductivity in very narrow wires [18]. Quantum phase slips are a controversial source of electric resistance for ultra-thin nanowires to cease being superconducting. Here CNTs were utilized as a template for metal deposition. Besides the aforementioned various methods for coating CNTs thermal evaporation deposition has also been used. In a report on



**Figure 4.** High resolution TEM micrograph of a coated CNT. The inset is a magnified image of the part indicated by the arrow. Reprinted with permission from [17], T. Seeger et al., *Chem. Phys. Lett.* 339, 41 (2001). © 2001, Elsevier Science.

coating CNTs with tungsten, tungsten filament was heated to evaporate tungsten atoms to deposit on CNTs [19].

## 2.4. Doping

Two types of doping for CNTs have been attempted. The first method was inspired by the previous silicon-based technique, that is, the incorporation of dopants into CNT networks. Yi and Bernholc investigated the atomic and electronic structures of doped CNTs by *ab initio* molecular dynamics [20]. They calculated the alteration in the electronic properties of semiconducting SWNTs by the substitution of nitrogen or boron for carbon in the nanotube. When nitrogen was doped into the carbon sites the SWNT becomes an *n*-type semiconductor while with boron it becomes a *p*-type semiconductor.

Miyamoto et al. studied the atomic and electronic structures of nanotubes forming from a hexagonal boron–carbon nitride ($BC_2N$) sheet [21]. Figure 5 shows $BC_2N$ (4, 4)



**Figure 3.** Zinc oxide nanorods grown on a MWNT. Reprinted with permission from [10], H. Kim and W. Sigmund, *Appl. Phys. Lett.* 81, 2085 (2002). © 2002, American Institute of Physics.
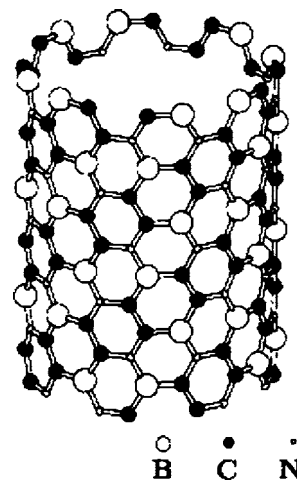


**Figure 5.** $BC_2N$ (4,4) nanotube. Reprinted with permission from [21], Y. Miyamoto et al., *Phys. Rev. B* 50, 4976 (1994). © 1994, American Physical Society.

nanotubes. According to their calculation $BC_2N$ nanotubes are energetically stable with the stability being intermediate between those of carbon and boron nitride (BN) nanotubes (BN nanotubes are the most stable among these three kinds of nanotubes). Due to the anisotropic geometry of the $BC_2N$ sheet these nanotubes were found to consist dominantly of chiral structures, which can be *n*-type or *p*-type semiconductors by tailoring the atomic stoichiometry; the substitution of carbon for boron and nitrogen sites results in *n*-doped and *p*-doped semiconductors, respectively. The anisotropy of the $BC_2N$ sheet al.so results in anisotropy in the electronic conductivity and thus helical currents along the shell of the nanotubes. Based on these theoretical studies an empirical attempt was made to dope CNTs with boron and nitrogen by the substitutional method.

Stephan et al. synthesized composite carbon–boron nitride nanotubes by the arc discharge technique [22]. They put a mixture of boron and graphite powder into a hole in the graphite anode and the electric arc was discharged in an inert atmosphere. Fabricated nanotubes contain up to 50% of boron and nitrogen concentration (generally 0 to 10%), of which measurements were taken by electron energy loss spectroscopy. It was found by TEM diffraction patterns that the basal planes of these nanotubes are separated from each other with the same spacing of those of MWNTs ($\sim$0.34 nm) and in rare cases two sets of diffraction spots indicate the possible simultaneous presence of separated graphite and boron nitride domains.

However, this type of doping has some problems; first, it is hard to adjust the amount of dopants to specific cases and, second, the inhomogeniety in the arrangement of the constituent atoms in the nanotubes causes the increment in electric resistivity. These could be serious impediments to the development of various electronic and photonic devices and the circuit integration.

The second type of doping is carried out by depositing dopants on the surface on CNTs through thermal or electrical evaporation of the dopants. This is similar to "coating" in terms of covering CNTs with some materials but its main purpose is to control the charge density in nanotubes. Lee et al. reported the enhancement in the electronic conductivity of SWNT bundles doped with potassium and bromine [23]. They used unoriented nanotube bundles synthesized by the laser ablation method as the matrix, bromine as an acceptor which was frozen with liquid nitrogen and then molten to dope CNTs, and potassium as a donor which was heated with a small temperature gradient for doping. Doped with bromine the nanotube bundle reduced its resistivity by an order and this new resistivity was not changed by its exposure to air. Annealing the sample led to recovering only half the original resistivity value and redoping with bromine decreased the resistivity to the initially reduced value. They attributed this behavior to the existence of at least two different bromine populations, weakly and strongly bound, in the doped material, or to the existence of a stable phase with intermediate bromine concentration. Additional measurements with the samples such as X-ray diffraction could detect the presence of the stable phase with intermediate bromine concentration. Doping with potassium also shows similar phenomena except

that exposing this potassium-doped sample to air immediately led to a large increase in resistivity to several times greater than the pristine values. We expect that this might be ascribed to the immediate oxidation of the potassium since the small size of potassium can react with oxygen at a violent rate. Figure 6 shows the effect of doping with potassium where curve (a) is for the pristine SWNT bundle, curve (b) is for the doped bundle, and curves (c) and (d) are for the doped and annealed bundle. In the figure the slopes of curves (a) (above $\sim$250 K) and (b) are similar while those of curves (c) and (d) appear to have the same value even though the authors mentioned in the report that these curves have almost the same slope. An explanation for this phenomenon might be the appearance of a new phase by the heat treatment at 580 K. This would hold true if the speculation that the resistivity is limited by electron–electron interaction (suggested by Lee et al.) is excluded.

This second type of doping is accomplished by the charge transfer between the contacting materials which is induced by the difference in the work functions. For example, in the previous report the work function of potassium is 2.29 eV [24] while that of a SWNT is known to be 4.8–5.1 eV [25, 26], so that electrons can be transferred from potassium to a SWNT to make the semiconducting SWNT an *n*-type semiconductor. In this way the electron density in CNTs can be controlled by the amount of the dopant. Also, since there is no substitutional or interstitial incorporation of the dopant into the matrix (CNTs) needed, the scattering and the increase in the resistivity by doping do not result. Therefore, currently the second type of doping is preferred.

Zhou et al. reported doping of CNTs by heating a dopant source and the resultant current–voltage characteristics in the selectively doped SWNT [27]. In their experiment after part of a SWNT was covered with polymethylmethacrylate the remaining uncovered part was exposed to the potassium vapor (electronic donor). Since the original SWNT behaves like a *p*-doped semiconductor the exposure of the uncovered part to potassium makes a *p–n* junction in one SWNT. Jhi et al. reported that the *p*-type behavior is induced by the adsorbed $O_2$ from the ambient and each $O_2$ molecule
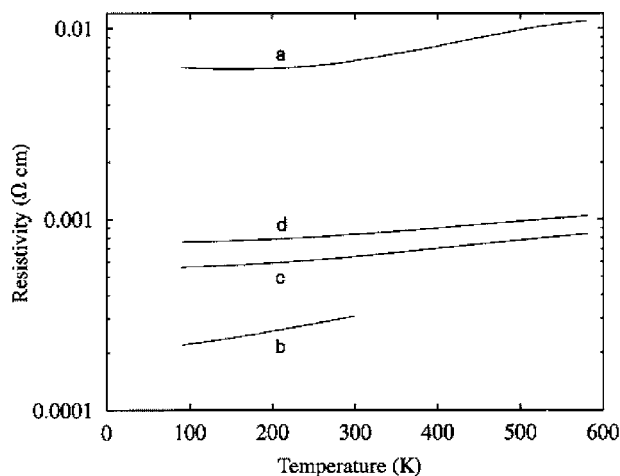


**Figure 6.** Resistivity versus temperature for a bulk SWNT sample. Reprinted with permission from [23], R. S. Lee et al., *Nature* 388, 255 (1997). © 1997, Macmillan Magazines, Ltd.

attracts about 10% of an electron from a SWNT [28]. However, it is controversial whether the pristine SWNT acts as a *p*-doped semiconductor or not. Derycke et al. prepared CNT transistors and measured the effects of heating (in vacuum or in air) or doping (with potassium) CNTs on the current–voltage characteristics [29]. Even though with a large amount of oxygen introduced the CNT functioned like a *p*-type semiconductor, it could act ambiploar (conducting either electrons or holes) with intermediate oxygen doses and an *n*-type semiconductor when it was annealed in vacuum, which are not the anticipated behaviors of a doped semiconductor. Doped semiconductors are expected to recover their intrinsic electronic property instead of taking the opposite charge carriers when the dopant from the semiconductors is eliminated. The authors suggested that the main effect of the oxygen adsorption is to modify the barrier property at the electrode–CNT contacts rather than to dope the bulk of the nanotube.

## 2.5. Functionalization

Functionalization of CNTs is to break carbon–carbon bonds and attach chemical functional groups such as phenol and carboxyl to the open tips, the outer shells, or less possibly the inner cavities of CNTs. Chen et al. reported the dissolution of shortened SWNTs functionalized with long alkyl chain in various organic solvents [30]. Shortened SWNTs were stirred in a mixture of $SOCl_2$ and dimethylformamide. After centrifugation and washing the resultant SWNTs were mixed with octadecylamine (ODA) and heated, which made soluble SWNTs having the long-chain molecule ODA to the open ends of shortened SWNTs. These SWNTs are soluble in common organic solvents such as chloroform and dichloromethane even though they are insoluble in water, ethanol, and acetone. It was also confirmed by proton nuclear magnetic resonance that there were magnetically different types of SWNTs in the sample.

Mickelson et al. succeeded in fluorination of the side wall of SWMTs [31]. After purification of SWNTs through refluxing, centrifugation, and filtering, the purified SWNT suspensions were filtered again and washed to form a free-standing film of SWNTs called bucky paper. This bucky paper was fluorinated by fluorine ($F_2$) after mixing with the helium inert gas through appropriate annealing below 500 °C (above 500 °C SWNTs were destroyed forming a nested tubelike graphitic structure similar to MWNTs). The fluorine was covalently bonded to the side wall of the SWNTs. These fluorinated nanotubes were defluorinated by anhydrous hydrazine below 400 °C (this time above 400 °C the nanotubes were annihilated during the defluorination procedure). These fluorinated nanotubes can be functionalized further; they can be reacted with sodium methoxide to produce methoxylated SWNTs [32].

Bahr et al. reported the functionalization of small diameter SWNTs via electrochemical reduction of aryl diazonium salts using a bucky paper electrode [33]. This type of reduction process allowed an aryl radical to covalently attach to the outer surface of CNTs, which also has been successfully applied to the functionalization of other allotropes of carbon such as highly ordered pyrolitic graphite and glassy carbon.

Ni and Sinnott studied the functionalization process of CNTs by energetic bombardment of $CH_3$ radicals through classical molecular dynamics simulations [34]. They used a system consisting of a bundle of six $(10, 10)$ SWNTs arranged in two layers, each of which is 50 Å long and comprised with 800 carbon atoms. Three different incident energies (10, 45, and 80 eV) of the radicals were considered. The simulation results were the scattering of $CH_3$ radicals, the adsorption of the fragments (C, CH, etc.) of the radicals on the outer walls of the SWNTs, and the knocking out the carbon atoms from the walls. In addition, defects and defect complexes such as pentagons, heptagons, and octagons could be generated, defects could be healed when the impacts occurred directly on the defects, or cross-linking between the SWNTs in the bundle through bombardment at 80 eV was predicted to happen.

Wong et al. used covalently functionalized nanotubes attached to atomic force microscope (AFM) tips as probes [35]. Previously Dai et al. showed that a CNT attached to the AFM tip could serve as an advanced probe with an improved resolution compared to the conventional silicon tips because of the high aspect ratio and the flexibility of CNTs [36]. The well-defined drop in the adhesion force characteristic of the deprotonation of a carboxyl acid was employed for validation of the existence of carboxyl groups at the tips of CNTs. With this carboxylic acid-terminated CNT (Fig. 7) it was demonstrated that two methyl-terminated and carboxylic acid-terminated sample areas, respectively, but without any height difference could be discerned through chemically sensitive detection. Also, it was proved that these functional
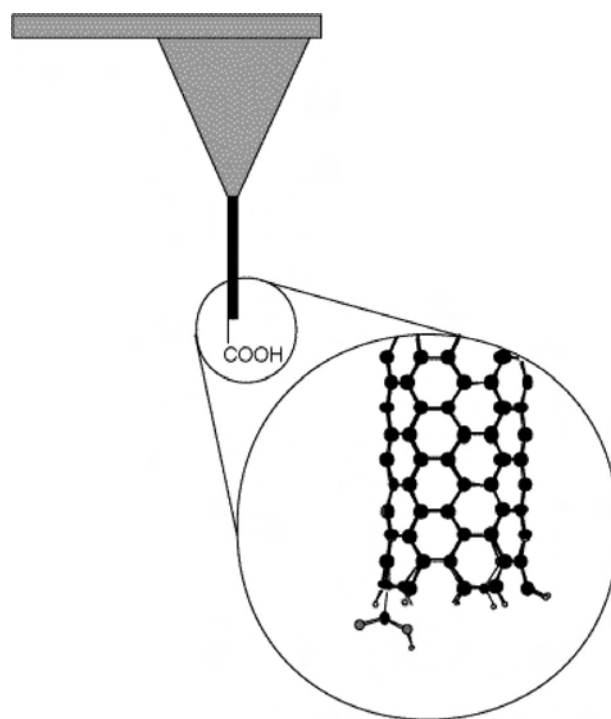


**Figure 7.** Schematic of carboxyl acid-terminated CNT attached to the AFM tip. Reprinted with permission from [35], S. S. Wong et al., *Nature* 394, 52 (1998). © 1998, Macmillan Magazines, Ltd.

group-terminated CNTs were useful for probing biological systems at the nanometer scale.

## 2.6. Filling

Filling is the process to put materials into the empty cavities of CNTs, which is accomplished mainly by one of three well-known procedures. However, the common mechanism applied for the first two procedures introduced is the capillary force. To find out if the capillary force can work for the encapsulation of a material by CNTs, it is important to know whether the material is capable of wetting the surface of the nanotubes; the contact angle between the surface and the material in a liquid state should be less than 90° to fill the nanotubes according to the Laplace equation.

First, Ajayan and Iijima succeeded in filling CNTs with lead [37]. In their experiment lead particles were deposited onto the nanotubes, which were supported on a holey carbon grid, and then pure lead was evaporated by electron beam in vacuum. The grid containing the sample was annealed in air for about 30 min at a temperature higher than the melting point of lead. This caused the nanotubes to be filled with lead or lead compound, which were not identified in the paper. Anyway, melting lead in air in the presence of CNTs breaks open the caps of the nanotubes and sucks up the molten lead into the empty cavities by the capillary force until the inner hydrostatic pressure equilibrates the outer pressure. When these two processes were done separately, that is, when CNTs opened before filling were heated with lead, the yield of filling was so low that CNTs encapsulated by lead or lead compound could not be observed [5]. The authors suggested that it might be caused by the fact that the inner cavity of the closed CNTs forms a vacuum, or a near-vacuum, so that the opened nanotubes come to lack the ability of capillary force to compete with the factors such as surface tension and metal viscosity and to suck up the molten lead. The reason that the closed nanotubes can keep lower atmospheric pressure inside the cavities than outside is expected to be that at the high synthetic temperature CNTs produce cavities with low density. Since the caps are also formed at the high temperature (or slightly lower than the synthetic temperature assuming they are formed during cooling) the lower pressure inside the cavities of nanotubes can be maintained even after cooling.

Dujardin et al. examined various materials to investigate the criteria for wetting the surface of CNTs, which are also applicable for filling [38]. The experiment came to the conclusion that to wet the surface (and therefore to fill the empty cavities by the capillary force) the surface tension of a material should be lower than 200 mN/m. This conclusion helps to indirectly vindicate that an element with surface tension higher than 200 mN/m can only fill CNTs when it forms a compound with sufficiently low surface tension to be drawn in by the capillarity or when it is under high pressure to push itself into the cavities.

Ajayan et al. filled CNTs with vanadium oxide ($V_2O_5$) by melting pure $V_2O_5$ powders in the presence of arc-fabricated nanotubes [39]. They obtained crystalline $V_2O_5$ (aligned along the *b*-axis of $V_2O_5$) embedded in the cavities of nanotubes. Intercalation by $V_2O_5$ into the gap where nanotube layers were missing was also found.

The second popular method to confine materials inside CNTs is wet chemistry. Tsang et al. demonstrated a way to fill nanotubes according to which CNTs were suspended in nitric acid solution containing metal nitrate, such as hydrated nickel nitrate, uranyl nitrate, iron nitrate, and cobalt nitrate, and refluxed [40]. The resultant materials found inside the cavities are oxides of the metals used and these were confirmed with the fringe separation of the material observed by high resolution TEM. They reported that many (60–70%) of the nanotubes opened by nitric acid were filled with the metal oxide but in case of separate opening filling the yield of encapsulation was low. Figure 1c shows one example of a filled CNT where samarium oxide with ordered atomic periodicity is encaged in the nanotube. They also succeeded in confining silver, gold, and gold chloride inside the cavities of nanotubes using a similar method [41]. In this report it was found that the confined materials do not always fill to clog the whole cavities but they might also fill a part of the of CNTs.

Third, CNTs can be filled with a residual catalyst or materials added on purpose to the carbon source at the time that they are produced. It has been reported that catalysts such as nickel, cobalt, and iron used typically for the synthesis of CNTs can fill inside the nanotubes in the forms of nanoparticles and nanorods. The synthetic method employed normally for encapsulating materials other than catalysts is the arc discharge technique. Materials to be encased by CNTs are put into the electrode, and the condensation of plasma yielded with applied high current and voltage forms CNTs filled with the materials used. We mentioned the representative experiment by Guerret-Plecourt et al. when discussing coating in Section 2.3. Moreover, many reports have been introduced about filling CNTs with diverse materials by this method [42, 43].

The advantages that can be acquired from filling CNTs with many materials are as follows: first, nanosized wires with high aspect ratios can be synthesized after filling CNTs with desired materials and getting rid of the nanotubes by heat treatment. Even though a great number of methods to directly synthesize nanowires such as gallium nitride and zinc oxide were reported [44, 45], this method has its own merit since it keeps the metal nanowires from being oxidized at the laboratory atmosphere for a long time protected by the graphene sheath of the CNTs like ~4 Å of silver nanowires covered with self-assembled calix hydroquinone nanotubes [46]. Hereby grown nanowires can be used as advanced catalysts for the chemical reactions where an oxidizing condition is maintained at least at the early stage of the reaction, so that the graphene sheath is eliminated before the catalytic reaction starts. The greatly increased surface to volume ratio of these nanowires helps them act as promising catalysts.

Second, the confinement of a material other than carbon inside the cavities of CNTs can modify the original electrical and optical properties of the nanotubes because of the interaction between the confined material and the nanotubes. This will be discussed more in detail in the following section.

Third, the encapsulated materials inside CNTs may generate a rich subtlety in the phase diagram; that is, there may be shifts in the freezing or melting transition points in

the narrow pore different from the cases of bulk materials. A recent report on the result of computational modeling with water confined inside nanotubes can be explained in the same way [47]. It is about a simulation by which it was vindicated that ice can form new phases inside CNTs different from the 13 polymorphic phases of bulk ice identified experimentally so far. It was also calculated that water confined in CNTs may have a solid–liquid critical point not shown in bulk materials and can exhibit a continuous transformation. Experimental reports about the unusual behavior inside the cavities were also introduced. Kim et al. carried out research on iron once used as a catalyst for the synthesis of CNTs and encased inside and at the tips of the nanotubes [48]. They reported that iron residues inside the nanotubes may have face-centered cubic crystal structure (high temperature phase; $\gamma$-Fe) instead of base-centered cubic structure ($\alpha$-Fe) stable at the laboratory atmosphere in spite of the fact that the synthetic temperature was lower than the phase transition temperature. Meyer et al. also reported the crystallography of a one-dimensional crystal of potassium iodide encapsulated within a small SWNT after investigation by high resolution TEM [49]. According to their result the lattice parameters of the potassium iodine are quite different from those in bulk potassium iodine. They suggested that this large shift in the lattice parameters is caused by the adjustment of the potassium iodine crystal to the arrangement of carbon atoms in the inner wall of the SWNT and the reduction in the number of neighboring atoms in the case of surface atoms of potassium iodine.

# 3. PROPERTIES OF MODIFIED CARBON NANOTUBES

In the previous section diverse methods for the modification of CNTs were discussed. These modified CNTs are reasonably expected to show mechanical, thermal, electrical, and optical properties different from those of pristine CNTs, some of which have been reported. In this section these novel properties of CNTs will be introduced with those of pristine CNTs.

## 3.1. Mechanical Properties

The reason that CNTs have been very attractive is that they have outstanding mechanical, electronic, and optical properties. Because of the very stable covalent bonding between carbon atoms and the network structure in the basal plane, CNTs have a high modulus of elasticity. The bonding between shells in MWNTs is formed by van der Waals force which causes the spacing between nanotube shells to range from 0.34 to 0.39 nm according to the diameter of synthesized MWNTs [50].

The value of the Young's modulus for SWNTs has some range because of the different interpretation of the wall thickness of the SWNT. When the wall thickness is considered to have a van der Waals radius of 3.4 Å the calculated Young's modulus is 1 TPa [51] which is similar to that of highly oriented pyrolytic graphite ($\sim$1.06 TPa) [52]. When the value is normalized by density it is higher than that of steel wire and even that of silicon carbide

nanorods [52]. However, with the radius of a carbon atom (0.7 Å) assumed to be the wall thickness, the Young's modulus is greatly increased to about 5 TPa [53]. The Young's modulus for MWNTs is estimated to be about 1.28 TPa [51]. The high modulus of CNTs leads several groups to synthesizing nanotube-reinforced composite materials.

CNTs are the ideal fiber as a reinforcing additive for composite materials since CNTs have not only a high aspect ratio and Young's modulus but also the lengths are short enough to flow through conventional polymer processing equipment so that parts can be molded into complex shapes (standard continuous fiber composites are expensive to process and limited to only simple shapes) [54]. Quian et al. [55] suggested a way of fabricating MWNT-dispersed polystyrene composite using an ultrasonic assisted solution-evaporation method. According to their result only a small amount (1 wt%) of nanotube can be incorporated into the polystyrene matrix to increase the Young's modulus by $\sim$40%. Figure 8 shows a TEM image of the propagation of a crack induced by thermal stress, which tends to nucleate at low nanotube density areas. The addition of CNTs to polymer composites also can increase their conductivities in order to dissipate charge buildup which can cause explosions while preventing degradation of other important factors such as mechanical properties and the low melt flow viscosity needed for thin-wall molding applications [56].

However, as mentioned, to fabricate good composite materials a strong bonding between individual CNTs and the matrix is necessary to transfer the applied load to the CNTs. For this purpose functionalization of CNTs is very useful. Activation of the surface of CNTs by the functionalization opens a way of linking to the polymer matrix. However, calculations of the chemical functionalization of SWNTs predict that functionalization decreases the Young's modulus of the nanotubes by about 15% [57]. When making nanotube composites, SWNTs are preferred since the slippage between the inner layers of MWNTs may contribute little to the carrying load, so that the stiffness for a given volume fraction of the nanotubes would be reduced [54]. Graphitization is applied to get rid of defects in the wall of CNTs
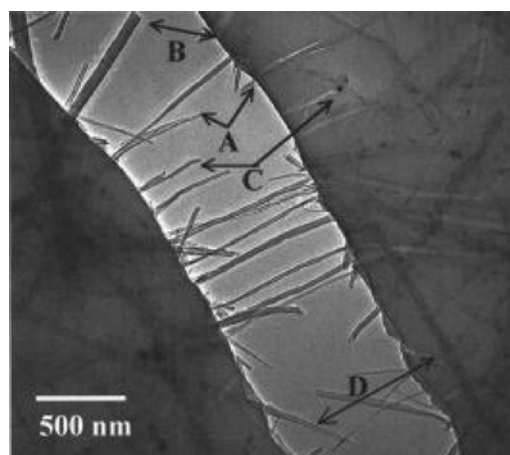


**Figure 8.** Propagation of a crack by thermal stress in MWNT-reinforced polystyrene. Reprinted with permission from [55], D. Qian et al., *Appl. Phys. Lett.* 76, 2511 (2000). © 2000, American Institute of Physics.

and to obtain structural order, which will help the homogeneous distribution of the applied force in the nanotubes leading to the increased mechanical strength.

## 3.2. Thermal Properties

Just like the electronic spectra of CNTs or other nanosized systems which are quantized because of their reduced dimension, phonon spectra in SWNTs were observed to have one-dimensional quantized phonon subbands via measuring the temperature-dependent specific heat of purified SWNTs [58]. According to their result the specific heat of SWNTs differs substantially from that of two-dimensional graphene or three-dimensional graphite.

Thermal conductivities of CNTs have been calculated through computer simulation and measured experimentally by many groups but still there is a wide range in their results. For reference, in case of high quality graphite the thermal conductivity in the basal plane is controlled by acoustic phonons and the value is as high as about 6000 W/mK at the maximum and 2000 W/mK at room temperature. Ruoff and Lorents suggested that the thermal conductivity of CNTs would be higher than any other material [59]. Hone et al. took a measurement for it with SWNT mats which were entangled therein and the value for the intrinsic longitudinal thermal conductivity was induced to be 1750–5800 W/mK from the acquired value (35 W/mK for the SWNT mat) with the assumption that the ratio of the intrinsic longitudinal thermal conductivity to the bulk thermal conductivity is similar to that of the intrinsic longitudinal electrical conductivity to the bulk electrical conductivity [60]. They speculated that the thermal conductivity of SWNTs is dominated at all temperatures by phonons rather than electrons since the empirically derived Lorentz number of the SWNT samples is about two orders of magnitude higher than that for the materials ruled by an electron system. However, when the thermal conductivity was measured with magnetically aligned SWNT films the resultant value was around 200 W/mK, one order lower than above value even though it was still effective that the electronic contribution to the thermal conductivity is insignificant compared to the thermal contribution [61].

Kim et al. also measured the thermal conductivity of individual MWNTs bridging two suspended islands which act as heating elements [62]. They reported that the value for the thermal conductivity is more than 3000 W/mK at room temperature and maintained that this value is a lower bound of the intrinsic axial thermal conductivity of a MWNT since they neglected the junction thermal conductance and assumed a solid isotropic material to correct geometric factors. Even though this value is comparable to that acquired through molecular dynamics simulations by Berber et al. [63], it is still different from that measured and induced with MWNT films by Yang et al., which is $2 \times 10^2$ W/mK [64]. Although the thermal conductivity of MWNTs in the radial direction is believed to be lower than that in the axial direction, the coefficient of thermal expansion is isotropic in both directions for MWNTs and SWNTs, which is caused by the network structure of the nanotubes [59].

Thermoelectric power reveals directly the sign of the charge carriers in a metallic conductor while for semiconductors it pinpoints the sign of the dominant carriers and the magnitude of the energy bandgap. Therefore, many groups measured the thermoelectric power of CNTs exploiting various mechanisms such as electron–hole symmetry breaking and Kondo effects to explain their experimental results [65–67]. However, these values came to be considered to have been affected by the surrounding atmosphere after finding the sensitive change in the thermoelectric power through doping CNTs with oxygen, which was completed by exposing the nanotubes to oxygen [68]. According to the report the thermoelectric power of SWNTs could be altered from positive to negative when oxygen doping of the surface of SWNTs was removed, which makes the p-type oxygen-doped SWNTs transform into the n-type oxygen-free nanotubes. Also, the sensitivity of SWNTs to oxygen was so high that the change in the thermoelectric power of the nanotubes could be detected even with the changing oxygen partial pressure from $10^{-8}$ to $10^{-10}$ Torr. Grigorian et al. measured how much the thermoelectric power of SWNT mats changes by Cesium (Cs) and iodine (I) doping with temperature [69]. They reported that pristine SWNTs exhibited a large and positive value ($\sim$40–50 $\mu$V/K) for the thermoelectric power at 300 K while that of the basal planes of graphite is much smaller and negative ($\sim$−4 mV/K). Upon Cs doping, the value changed to negative and the magnitude dropped significantly having a distinct minimum at 160 K. When SWNTs were doped with iodine the value remained positive but its magnitude at 300 K was decreased by a factor of 3–4 from that in pristine SWNTs mats, indicating that iodine doping created a large number of free hole carriers.

Even though the effect of graphitization of CNTs on the thermal (and electronic) properties has not reported until now it is easily anticipated that the periodic repetition of carbon atoms in the shells of CNTs obtained by graphitization will give well-ordered paths for phonon (and electron) propagation greatly reducing scattering by structural defects to the increment of thermal (and electrical) conductivity.

## 3.3. Electrical Properties

Graphite is known to be a semimetal material in which the valence and conduction bands overlap and thus no bandgap exists. When this graphite sheet is rolled up into the seamless cylinder shape of CNTs the situation is dramatically changed; the electrons are confined in a very short peripheral distance of CNTs, so that the quantum mechanical effect plays a major role in defining the electrical properties of CNTs. Depending upon a pair of integers $(n, m)$ that specify the diameter and the chirality of a SWNT, the nanotube can be metallic or semiconducting (Fig. 9) [70]. When $n$ is equal to $m$ a SWNT is called an armchair nanotube and has a band structure corresponding to that of metal. When $m$ is zero it is a zigzag nanotube and all the other combinations of $n$ and $m$ are called the chiral type. In case of the latter two types, SWNTs with $n - m = 3q$ ($q$: an integer) are expected to be metallic and those with $n - m \neq 3q$ are predicted to be semiconducting.

Using a scanning tunneling microscope (STM) the diameter and the chiral angle of individual SWNTs can be defined and the electrical property can be identified [70]. Semiconducting SWNTs have an energy gap of the order of $\sim$0.5 eV which is in fact inversely proportional to the diameter.
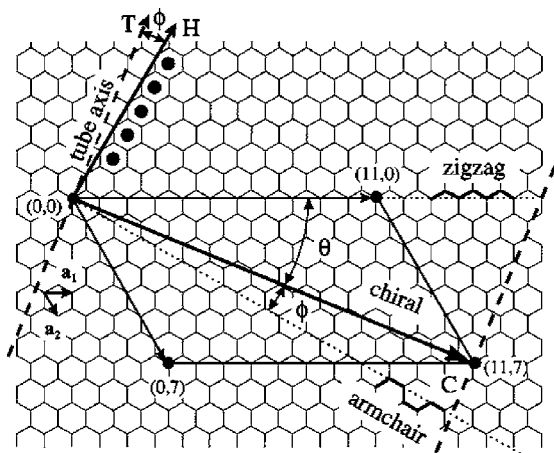
**Figure 9.** Relation between the hexagonal carbon lattice and the chirality of carbon nanotubes. Reprinted with permission from [70], J. W. G. Wilder et al., *Nature* 391, 59 (1998). © 1998, Macmillan Magazines, Ltd.

Since the diameter of CNTs is controllable depending on the size of the catalyst the energy gap of CNTs can be tunable indirectly during the synthesis [71].

Conductivity of nanotubes has been measured up to now but the values obtained are in the wide range of several orders of magnitude because of, first, the quality of the contact between a CNT and the electrode, second, the existence of defects and their complexes on the surface of the nanotubes, and, third, the presence of added functional groups such as OH and CO or adsorbed molecules such as $O_2$ and $NH_3$, and so forth. While it is generally accepted that the conductance of SWNTs is based on a ballistic mechanism of charge transfer [72], the mechanism for the electronic conductance of MWNTs is not clear up to now. Bachtold et al. measured the resistance of an individual nanotube and the contact resistance at a boundary with current feeders [73]. Using the tip of the AFM as a local voltmeter the electrostatic force acting between the tip and the nanotube was measured. The resistivity of a MWNT (9 nm in diameter) was gauged to be 10 k$\Omega$/$\mu$m and the contact resistance was calculated to be about as much as 5 kW. Previously, they reported pronounced resistance oscillations, called Aharonov–Bohm oscillations, as a function of magnetic flux from magnetoresistance measurements on individual MWNTs [74]. Along with a weak localization of carriers the resistance oscillations at low temperatures imply that the electronic conductance in a MWNT is dominated by the diffusive charge transfer. Langer et al. also supported the diffusive electronic transport mechanism for the conductance in MWNTs by measuring resistance of individual MWNTs down to a temperature of 20 mK under a magnetic field [75]. However, according to Frank et al. the conductance of MWNTs is quantized and depends on the ballistic charge transport mechanism [76]. Yoon et al. maintain that the interwall conductance of a MWNT is vanishingly small, so actually only the outermost wall is responsible for the electron transport (ballistic) in capped MWNTs by a theoretical analysis [77].

Great industrial and academic research into applications using these electronic properties has been done, one of which is the very flat panel display field where SWNTs and MWNTs have been successfully employed as field emission electron sources [78, 79]. When a voltage is applied across CNTs and anode [indium tin oxide (ITO) glass on which a phosphor material is deposited], electrons tunnel from the nanotube tip into the vacuum and excite the phosphor, so that visible light is produced from the phosphor and comes out of the transparent ITO glass for the flat panel display. Compared to thermal emission electron guns from hot tungsten wires and heated materials with low work functions, field emission from the tips of CNTs does not need extreme conditions such as ultrahigh vacuum and high voltages (It is for this reason that the former two field electron emitters have not been widely adopted in industry.) In addition, nanotube electron guns have very large amplification factors and greatly stable electron beams with a long lifetime (over 10,000 hours) [80, 81]. This field emission based on CNTs can be utilized in other fields; an X-ray source capable of practical medical imaging using a room-temperature array of nanotubes and gas discharge tube based on nanotubes for protection from lightning and alternating current power cross faults on the telecom network were reported [82, 83].

Another promising way to utilize the outstanding electronic properties of CNTs is to assemble electronic devices and integrate circuits with SWNTs or MWNTs. As current silicon-based technology gets incapable of shrinking the size of electronic devices due to Moore's law, so-called "bottom-up" technology developed from molecular electronics has stood in the spotlight of many research institutes as a replacement for the "top-down" process and CNTs are at the center as one of the leading materials. Dekker's group succeeded in fabricating CNT-based field effect transistor and logic circuits [84, 85]. Also, SWNTs have been used as building blocks to fabricate diodes and, recently, an inverter [86, 87]. However, to supersede the long-dominating silicon technology this new CNT-based technology should attain various technical prerequisites such as easy manipulation of CNTs to locate them at designated positions, prevention of CNTs from aggregation which perturbs the electronic structure of the nanotubes, and facilitated selection of semiconducting and metallic SWNTs.

Since the fields of electronics and optoelectronics using CNTs as the main constituent material are the most promising, active research on the electrical properties of modified CNTs has been extensively carried out. Opened CNTs can be used as electron guns for field emission microscopy. Saito et al. compared MWNTs having closed caps with open-ended MWNTs by observing emission patterns when they were used as electron guns in a microscope [88]. Figure 10 shows the result from which it can be deduced that electrons are emitted from the circular edges of the graphite layers of a nanotube.

Dimitrijevic et al. showed that CNTs coated with tetrahedrally bonded amorphous carbon (preferably called diamondlike carbon) using a cathodic arc deposition process can produce a more efficient field emission property than uncoated CNTs [89]. According to the result carbon-coated nanotubes can start to emit electrons into vacuum at lower threshold voltage. Another merit of the carbon-coated CNTs as field emission gun is the lower turn-on field ($E_{TO}$) than the uncoated CNTs; $E_{TO}$ was found to be 2.4 and 1.5 V/$\mu$m for the uncoated CNTs and for the CNTs coated with 20 nm
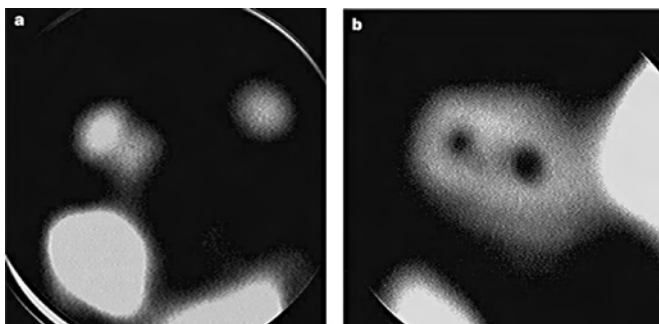
**Figure 10.** Field emission patterns from multiwalled carbon nanotubes. Reprinted with permission from [88], Y. Saito et al., *Nature* 389, 554 (1997). © 1997, Macmillan Magazines, Ltd.

thickness of amorphous carbon, respectively. $E_{\text{TO}}$ is defined to be the macroscopic electric field needed to produce a current density of 10 $\mu$A/cm$^2$. The authors attribute the advanced properties to the increase in the amount of $sp^3$ bonding induced by the introduction of amorphous carbon into the surface of CNTs and the inhomogeneity of the carbon coating.

Doping CNTs is mainly about modifying the electrical property, so that semiconducting nanotubes can be changed into *n*- or *p*-type semiconductors (refer to Section 2.4). Collins et al. measured the changes in various properties of CNTs after the nanotubes were doped with oxygen [68], one of which was introduced in Section 3.2. It was mentioned that the oxygen-doped semiconducting SWNTs behave like *p*-type semiconductors. With alternating atmospheres from vacuum to air or vise versa the electrical resistance switched by 10 to 15% in a relatively short time with dilute SWNT films. They also found with a STM that after oxygen treatment the electronic density of state of some nanotubes was increased and acted like metals or semimetals. Kong et al. also studied the effect of NO$_2$ and NH$_3$ doping on the electrical resistance of a semiconducting SWNT [90]. In their study they observed that the electronic conductance of semiconducting SWNTs was heightened by about three orders of magnitude by exposure to NO$_2$ while it was lowered after NH$_3$ treatment. Because of the high sensitivity of CNTs to various kinds of gases such as oxygen, NO$_2$, and NH$_3$ one of the most promising applications using CNTs is expected to be a sensitive chemical sensors.

The electronic conductance of CNTs will be greatly dominated by doping since the charge density in the nanotubes is dependent on the amount of the dopant and the charge mobility is not affected by the usual second type doping (Section 2.4).

As is mentioned in Section 2.6, by encapsulation of a material inside CNTs the original properties of the nanotubes can be affected. After Smith et al. reported encapsulation of fullerenes (C$_{60}$) in CNTs [91] various methods to insert fullerenes or metallofullerenes (fullerene-encapsulated metal) into the cavities of nanotubes have been introduced [43, 92]. The effect of this encapsulation of metallofullerenes on the electronic energy band structure of semiconducting CNTs was reported [93]. Authors put gadolinium-including fullerene (Gd@C$_{82}$) into semiconducting SWNTs forming a peapodlike structure by heating

the mixture of the two materials in a sealed glass ampoule. It was observed by a low temperature STM that the energy band structure could be modified by the periodically arranged metallofullerenes inside the nanotube. Kim et al. also suggested systematically that by encapsulation of two phases of iron inside a semiconducting nanotube using the electronic beam of TEM the nanotube can be transformed into *n*- or *p*-type semiconductors as a result of asymmetric modification of the energy band by the strain induced from the encapsulation of the two phases of iron and the charge transfer between iron and the nanotube [94].

Functionalization can also alter the electronic properties of CNTs. Shim et al. functionalized SWNTs by submerging them in polyethylene imine (PEI) solution and rinsing, and they measured the drain-source current with a few different gate voltage biases [95]. It was observed that the SWNTs were changed from *p*-type to *n*-type semiconductors after the functionalization, electron mobility in a field effect transistor based on the functionalized nanotube was high (600 cm$^2$/V s under a drain-source voltage of 10 mV), and photodesorption of O$_2$ from PEI-coated SWNTs raised the electron density to a higher level. Mickelson et al. reported that fluorinated SWNTs increase their resistance (higher than 20 M$\Omega$), making themselves insulators, compared to that of pristine untreated nanotubes (10–15 $\Omega$ two-probe resistance across the length of the $\sim 10 \times 3$ mm $\times 30$ $\mu$m bucky paper samples) [31]. These fluorinated nanotubes could recover most of their original electrical conductivity after defluorination.

## 3.4. Optical Properties

While the optical properties of SWNTs were calculated to be dominated by the chiral structures [96] those of a well-aligned MWNT bundle were found to be similar to graphite and insensitive to the chiral structures and small variation in the radius of MWNTs [97].

De Heer et al. measured the optical properties with aligned CNT films by ellipsometry [98]. They found the CNT films with their surface parallel to that of the substrate are optically isotropic, whereas the CNT films with their surface perpendicular to that of the substrate are highly anisotropic. Recently, O'Connell observed that SWNTs with direct bandgap fluoresce brightly in the 800 to 1600 nm wavelength region of the near infrared and the intensity of photoluminescence is drastically suppressed by aggregation of the isolated nanotubes or by acidification of the SWNT suspension [99]. According their report SWNTs were dispersed in aqueous sodium dodecyl sulfate surfactant, and this suspension was strongly agitated by sonication followed by centrifugation to detach individual SWNTs from bundles. This well-dispersed SWNT suspension shows the more distinct electronic absorption spectrum than the mixture which was prepared without centrifugation and thus preponderant with nanotube bundles.

Carbon black and fullerene suspensions have a peculiar property; that is, when the suspensions are exposed to laser pulses the energy transmittance is constant below a critical incident fluence. However, in excess of the critical value the transmittance decreases as the incident fluence increases, which is called the optical limiting property [100, 101].

This unique property can be used for the eye protection of aviators when exposed to intense laser applied by enemies. CNTs, whether they are SWNTs or MWNTs, also have the optical limiting property when they are dispersed in various solvents [102, 103]. While optical limiting behavior observed with fullerene ($C_{60}$) suspension occurs due to reversible saturable absorption and subsequent nonlinear refraction and scattering, optical limiting behavior in MWNT suspension may be ascribed to the nonlinear scattering stemming from expanding microplasmas as in carbon black suspension [103, 104]. Figure 11 shows the change in the transmittance of carbon black, fullerene, and SWNT suspensions with increase in the input energy using a 532 nm laser line [105].

Ago et al. measured work functions of MWNTs using ultraviolet photoelectron spectroscopy [106]. They found that pristine MWNTs have a slightly lower work function (4.3 eV) than that of highly oriented pyrolytic graphite (4.4 eV). MWNTs oxidized by various methods (heat treatment at 900 °C, oxygen plasma treatment, or acid oxidation) have different work functions (4.4–5.1 eV).

Doping was found to have a tremendous effect on the optical properties of CNTs [107]. For this research SWNTs of 1.2 to 1.6 nm in diameter with various helical structures were doped with iodine ($I_2$), potassium (K), bromine ($Br_2$), and cesium (Cs). When the SWNTs were doped with I2 and K an absorption peak assigned to the interband optical transition in semiconducting SWNTs was removed and the peak was recovered after undoping, suggesting that no chemical degradation during doping was involved. With SWNTs doped by $Br_2$ and Cs an additional disappearance of other absorption peaks and the emergence of new absorption peaks related to the involvement of energy states in the valence or conduction bands were observed.

The first type of doping (substitution of dopant atoms for carbon atoms in CNTs) can also exert a strong influence on the optical properties of SWNTs [108]. This type of doping was found to increase greatly the second-order hyperpolarizabilities, which is crucial for photonic applications including all optical switching, data processing, and detector protection. The second-order hyperpolarizabilities are used to characterize third-order optical nonlinearity of molecules.
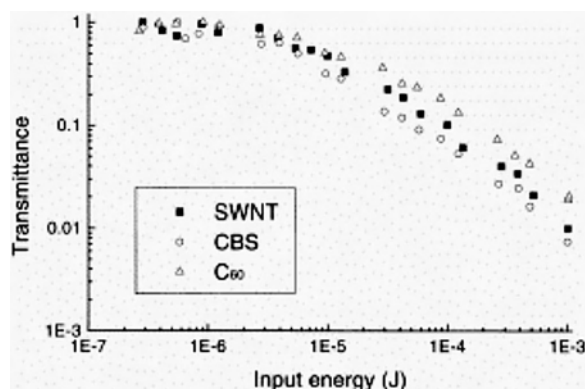


**Figure 11.** Optical limiting properties of SWNTs, carbon black, and fullerens in ethanol. Reprinted with permission from [105], L. Vivien et al., *Chem. Phys. Lett.* 307, 317 (1999). © 1999, Elsevier Science.
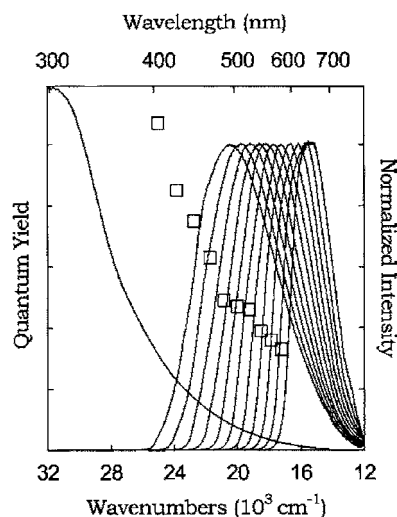


**Figure 12.** Progressive changes of the luminescence spectra and quantum yields of S-MWNT-PPEI-EI in homogeneous chloroform solution with excitation wavelengths (from left to right: 400–600 nm for the spectra and 400–580 nm for the quantum yields in 20 nm increments). Reprinted with permission from [109], J. E. Riggs et al., *J. Am. Chem. Soc.* 122, 5879 (2000). © 2000, American Chemical Society.

Riggs et al. measured the luminescence property with CNTs solubilized by covalently attaching them to highly soluble linear polymers [109]. They used the method suggested by Chen et al. [30] except that poly-(propionylethylenimine-co-ethylenimine) (PPEI-EI) was employed instead of ODA. Thus-synthesized polymer-bound nanotubes were found to be soluble in both organic solvents and water, forming highly colored homogeneous solution. In addition, the polymer-bound nanotubes were luminescent in the region of visible light with the luminescent center dependent on excitation energy (Figure 12). Luminescence yields of the polymer-bound shortened SWNTs and MWNTs, which were of the same order of magnitude, were higher than those of unshortened SWNTs bound to the same polymer. However, all these shortened or unshortened nanotubes show higher yield than fullerene by at least an order of magnitude.

## 4. SUMMARY

We have introduced diverse methods to modify the properties of SWNTs and MWNTs. They enable us to tailor the properties of CNTs to the requirements for various applications; CNTs are able to possess a higher order cyrstallinity after graphitization to show their original attractive properties, the work function of CNTs can be altered after oxidation, field emission properties of CNTs can be enhanced through coating, control of the charge density in CNTs can be obtained for CNT-based electronics as in silicon-based technology by doping, a localized modulation of the electronic energy bands of CNTs is possible through filling, and CNTs can be homogeneously dispersed in a solvent by functionalization. Even though many fascinating properties of pristine and modified CNTs have been reported some of them are controversial even now and ought to be clarified. Furthermore, there are still many difficulties to conquer; one, for example, is to sort SWNTs according to

their helicities to select semiconducting or metallic nanotubes. Although there was a report by Kusunoki et al. on a method to selectively synthesize zigzag-type CNTs [110] the synthesis method should progress to be acceptably efficient. Accordingly, much more pains should be taken in many fields including modification of CNTs. However, the hereby introduced modification methods are really indispensable for utilizing CNTs and the development of new modification processes is still ongoing by many scientists around the world, so that they will be fundamental in realizing nanotechnologies in the near future.

## GLOSSARY

**Multiwalled nanotube (MWNT)**  A nanosized structure composed of more than one graphite sheets which are rolled up coaxially into a seamless tubular shape.

**Optical limiting property**  A property of a material to reduce the transmittance radically from a critical intensity of an optical beam. It results from intensity dependent optical nonlinear processes. This property may be used to protect fine components of devices or eyes of the aviators from intensity optical radiation.

**Single wall nanotube (SWNT)**  A nanosized structure composed of a single graphite sheet which is rolled up into a seamless tubular shape.

**Vapor-liquid-solid (VLS) theory**  A theory suggested for the growth of semiconductor wires. In the theory a metal catalyst is used to dissolve feeding source atoms (vapor) in the molten state of the catalyst (liquid) and reprecipitate them as wires (solid). This theory is often employed to explain the formation of various nanowires and nanotubes.

**Work function**  A minimum energy required to remove an electron of a material, occupying the Fermi level, to the vacuum. The values for work function (typically 1–6 eV for elements) are characteristic of each material. The Fermi level is the energy level in which the probability to find an electron is 0.5, which is also the uppermost energy level occupied by electrons at absolute zero temperature.

**Young's modulus**  A magnitude of the stress necessary to induce a until strain in the elastic region of a material where the stress and the strain are proportional ($= \sigma/\varepsilon\sigma$: stress, $\varepsilon$: strain). Stress is force divided by area ($\sigma = F/A$) and strain is deformation in length of a material divided by the original length of the material.

## REFERENCES

1. S. Iijima, *Nature* 354, 56 (1991).
2. H. W. Kroto, J. R. Heath, S. C. Obrien, R. F. Curl, and R. E. Smalley, *Nature* 318, 162 (1985).
3. R. Andrews, D. Jacques, D. Qian, and E. C. Dickey, *Carbon* 39, 1681 (2001).
4. A. Hamwi, H. Alvergnat, S. Bonnamy, and F. Beguin, *Carbon* 35, 723 (1997).
5. P. M. Ajayan, T. W. Ebbesen, T. Ichihashi, S. Iijima, K. Tanigaki, and H. Hiura, *Nature* 362, 522 (1993).
6. S. C. Tsang, Y. K. Chen, P. J. F. Harris, and M. L. H. Green, *Nature* 72, 159 (1994).
7. M. S. C. Mazzoni, H. Chacham, P. Ordejon, D. Sanchez-Portal, J. M. Soler, and E. Artacho, *Phys. Rev. B* 60, R2208 (1999).
8. Y. Zhang, N. W. Franklin, R. J. Chen, and H. J. Dai, *Chem. Phys. Lett.* 331, 35 (2000).
9. C. Guerret-plecourt, Y. Lebouar, A. Loiseau, and H. Pascard, *Nature* 372, 761 (1994).
10. H. Kim and W. Sigmund, *Appl. Phys. Lett.* 81, 2085 (2002).
11. R. S. Wagner and W. C. Ellis, *Appl. Phys. Lett.* 4, 89 (1964).
12. D. H. Cobden, *Nature* 409, 32 (2001).
13. J. Gavillet, A. Loiseau, F. Ducastelle, S. Thair, P. Bernier, O. Stephan, J. Thibault, and J. C. Charlier, *Carbon* 40, 1649 (2002).
14. J. Gavillet, A. Loiseau, C. Journet, F. Willaime, F. Ducastelle, and J. C. Charlier, *Phys. Rev. Lett.* 8727 (2001).
15. E. F. Kukovitsky, S. G. L'Vov, and N. A. Sainov, *Chem. Phys. Lett.* 317, 65 (2000).
16. H. Kanzow and A. Ding, *Phys. Rev. B* 60, 11180 (1999).
17. T. Seeger, P. Redlich, N. Grobert, M. Terrones, D. R. M. Walton, H. W. Kroto, and M. Ruhle, *Chem. Phys. Lett.* 339, 41 (2001).
18. A. Bezryadin, C. N. Lau, and M. Tinkham, *Nature* 404, 971 (2000).
19. Y. J. Zhang, Q. Zhang, Y. B. Li, N. L. Wang, and J. Zhu, *Solid State Commun.* 115, 51 (2000).
20. J. Y. Yi and J. Bernholc, *Phys. Rev. B* 47, 1708 (1993).
21. Y. Miyamoto, A. Rubio, M. L. Cohen, and S. G. Louie, *Phys. Rev. B* 50, 4976 (1994).
22. O. Stephan, P. M. Ajayan, C. Colliex, P. Redlich, J. M. Lambert, P. Bernier, and P. Lefin, *Science* 266, 1683 (1994).
23. R. S. Lee, H. J. Kim, J. E. Fischer, A. Thess, and R. E. Smalley, *Nature* 388, 255 (1997).
24. D. R. Lide, "CRC Handbook of Chemistry and Physics," 81st ed. CRC Press, New York, 2000.
25. S. Suzuki, C. Bower, Y. Watanabe, and O. Zhou, *Appl. Phys. Lett.* 76, 4007 (2000).
26. D. Lovall, M. Buss, E. Graugnard, R. P. Andres, and R. Reifenberger, *Phys. Rev. B* 61, 5683 (2000).
27. C. W. Zhou, J. Kong, E. Yenilmez, and H. J. Dai, *Science* 290, 1552 (2000).
28. S. H. Jhi, S. G. Louie, and M. L. Cohen, *Phys. Rev. Lett.* 85, 1710 (2000).
29. V. Derycke, R. Martel, J. Appenzeller, and P. Avouris, *Appl. Phys. Lett.* 80, 2773 (2002).
30. J. Chen, M. A. Hamon, H. Hu, Y. S. Chen, A. M. Rao, P. C. Eklund, and R. C. Haddon, *Science* 282, 95 (1998).
31. E. T. Mickelson, C. B. Huffman, A. G. Rinzler, R. E. Smalley, R. H. Hauge, and J. L. Margrave, *Chem. Phys. Lett.* 296, 188 (1998).
32. E. T. Mickelson, I. W. Chiang, J. L. Zimmerman, P. J. Boul, J. Lozano, J. Liu, R. E. Smalley, R. H. Hauge, and J. L. Margrave, *J. Phys. Chem. B* 103, 4318 (1999).
33. J. L. Bahr, J. P. Yang, D. V. Kosynkin, M. J. Bronikowski, R. E. Smalley, and J. M. Tour, *J. Am. Chem. Soc.* 123, 6536 (2001).
34. B. Ni and S. B. Sinnott, *Phys. Rev. B* 61, R16343 (2000).
35. S. S. Wong, E. Joselevich, A. T. Woolley, C. L. Cheung, and C. M. Lieber, *Nature* 394, 52 (1998).
36. H. J. Dai, J. H. Hafner, A. G. Rinzler, D. T. Colbert, and R. E. Smalley, *Nature* 384, 147 (1996).
37. P. M. Ajayan and S. Iijima, *Nature* 361, 333 (1993).
38. E. Dujardin, T. W. Ebbesen, H. Hiura, and K. Tanigaki, *Science* 265, 1850 (1994).
39. P. M. Ajayan, O. Stephan, P. Redlich, and C. Colliex, *Nature* 375, 564 (1995).
40. S. C. Tsang, Y. K. Chen, P. J. F. Harris, and M. L. H. Green, *Nature* 372, 159 (1994).
41. A. Chu, J. Cook, R. J. R. Heesom, J. L. Hutchison, M. L. H. Green, and J. Sloan, *Chem. Mater.* 8, 2751 (1996).
42. J. Sloan, J. Cook, J. R. Heesom, M. L. H. Green, and J. L. Hutchison, *J. Cryst. Growth* 173, 81 (1997).
43. H. Kataura, Y. Maniwa, T. Kodama, K. Kikuchi, K. Hirahara, K. Suenaga, S. Iijima, S. Suzuki, Y. Achiba, and W. Kratschmer, *Synth. Metals* 121, 1195 (2001).

44. Y. Huang, X. F. Duan, Y. Cui, and C. M. Lieber, *Nano Letters* 2, 101 (2002).
45. M. H. Huang, S. Mao, H. Feick, H. Q. Yan, Y. Y. Wu, H. Kind, E. Weber, R. Russo, and P. D. Yang, *Science* 292, 1897 (2001).
46. B. H. Hong, S. C. Bae, C. W. Lee, S. Jeong, and K. S. Kim, *Science* 294, 348 (2001).
47. K. Koga, G. T. Gao, H. Tanaka, and X. C. Zeng, *Nature* 412, 802 (2001).
48. H. Kim, M. J. Kaufman, W. M. Sigmund, D. Jaques, and R. Andrews, *J. Mater. Res.* 18, 1104, (2003).
49. R. R. Meyer, J. Sloan, R. E. Dunin-Borkowski, A. I. Kirkland, M. C. Novotny, S. R. Bailey, J. L. Hutchison, and M. L. H. Green, *Science* 289, 1324 (2000).
50. C. H. Kiang, M. Endo, P. M. Ajayan, G. Dresselhaus, and M. S. Dresselhaus, *Phys. Rev. Lett.* 81, 1869 (1998).
51. E. W. Wong, P. E. Sheehan, and C. M. Lieber, *Science* 277, 1971 (1997).
52. D. H. Robertson, D. W. Brenner, and J. W. Mintmire, *Phys. Rev. B* 45, 12592 (1992).
53. B. I. Yakobson, C. J. Brabec, and J. Bernholc, *Phys. Rev. Lett.* 76, 2511 (1996).
54. P. Calvert, *Nature* 399, 210 (1999).
55. D. Qian, E. C. Dickey, R. Andrews, and T. Rantell, *Appl. Phys. Lett.* 76, 2868 (2000).
56. See www.fibrils.com.
57. A. Garg and S. B. Sinnott, *Chem. Phys. Lett.* 295, 273 (1998).
58. J. Hone, B. Batlogg, Z. Benes, A. T. Johnson, and J. E. Fischer, *Science* 289, 1730 (2000).
59. R. S. Ruoff and D. C. Lorents, *Carbon* 33, 925 (1995).
60. J. Hone, M. Whitney, C. Piskoti, and A. Zettl, *Phys. Rev. B* 59, R2514 (1999).
61. J. Hone, M. C. Llaguno, N. M. Nemes, A. T. Johnson, J. E. Fischer, D. A. Walters, M. J. Casavant, J. Schmidt, and R. E. Smalley, *Appl. Phys. Lett.* 77, 666 (2000).
62. P. Kim, L. Shi, A. Majumdar, and P. L. McEuen, *Phys. Rev. Lett.* 87, 215502 (2001).
63. S. Berber, Y. K. Kwon, and D. Tomanek, *Phys. Rev. Lett.* 84, 4613 (2000).
64. D. J. Yang, *Phys. Rev. B* 66, 165440 (2002).
65. J. Hone, I. Ellwood, M. Muno, A. Mizel, M. L. Cohen, A. Zettl, A. G. Rinzler, and R. E. Smalley, *Phys. Rev. Lett.* 80, 1042 (1998).
66. M. L. Tian, F. Q. Li, L. Chen, Z. Q. Mao, and Y. H. Zhang, *Phys. Rev. B* 58, 1166 (1998).
67. L. Grigorian, G. U. Sumanasekera, A. L. Loper, S. L. Fang, J. L. Allen, and P. C. Eklund, *Phys. Rev. B* 60, R11309 (1999).
68. P. G. Collins, K. Bradley, M. Ishigami, and A. Zettl, *Science* 287, 1801 (2000).
69. L. Grigorian, G. U. Sumanasekera, A. L. Loper, S. Fang, J. L. Allen, and P. C. Eklund, *Phys. Rev. B* 58, R4195 (1998).
70. J. W. G. Wilder, L. C. Venema, A. G. Rinzler, R. E. Smalley, and C. Dekker, *Nature* 391, 59 (1998).
71. C. L. Cheung, A. Kurtz, H. Park, and C. M. Lieber, *J. Phys. Chem. B* 106, 2429 (2002).
72. W. J. Liang, M. Bockrath, D. Bozovic, J. H. Hafner, M. Tinkham, and H. Park, *Nature* 411, 665 (2001).
73. A. Bachtold, M. S. Fuhrer, S. Plyasunov, M. Forero, E. H. Anderson, A. Zettl, and P. L. McEuen, *Phys. Rev. Lett.* 84, 6082 (2000).
74. A. Bachtold, C. Strunk, J. P. Salvetat, J. M. Bonard, L. Forro, T. Nussbaumer, and C. Schonenberger, *Nature* 397, 673 (1999).
75. L. Langer, V. Bayot, E. Grivei, J. P. Issi, J. P. Heremans, C. H. Olk, L. Stockman, C. VanHaesendonck, and Y. Bruynseraede, *Phys. Rev. Lett.* 76, 479 (1996).
76. S. Frank, P. Poncharal, Z. L. Wang, and W. A. de Heer, *Science* 280, 1744 (1998).
77. Y. G. Yoon, P. Delaney, and S. G. Louie, *Phys. Rev. B* 66, (2002).
78. A. G. Rinzler, J. H. Hafner, P. Nikolaev, L. Lou, S. G. Kim, D. Tomanek, P. Nordlander, D. T. Colbert, and R. E. Smalley, *Science* 269, 1550 (1995).
79. W. B. Choi, Y. W. Jin, H. Y. Kim, S. J. Lee, M. J. Yun, J. H. Kang, Y. S. Choi, N. S. Park, N. S. Lee, and J. M. Kim, *Appl. Phys. Lett.* 78, 1547 (2001).
80. Y. Saito and S. Uemura, *Carbon* 38, 169 (2000).
81. Y. Saito, K. Hamaguchi, R. Mizushima, S. Uemura, T. Nagasako, J. Yotani, and T. Shimojo, *Appl. Surf. Sci.* 146, 305 (1999).
82. G. Z. Yue, Q. Qiu, B. Gao, Y. Cheng, J. Zhang, H. Shimoda, S. Chang, J. P. Lu, and O. Zhou, *Appl. Phys. Lett.* 81, 355 (2002).
83. R. Rosen, W. Simendinger, C. Debbault, H. Shimoda, L. Fleming, B. Stoner, and O. Zhou, *Appl. Phys. Lett.* 76, 1668 (2000).
84. S. J. Tans, A. R. M. Verschueren, and C. Dekker, *Nature* 393, 49 (1998).
85. A. Bachtold, P. Hadley, T. Nakanishi, and C. Dekker, *Science* 294, 1317 (2001).
86. Z. Yao, H. W. C. Postma, L. Balents, and C. Dekker, *Nature* 402, 273 (1999).
87. J. L. Yang, H. J. Liu, and C. T. Chan, *Phys. Rev. B* 6408 (2001).
88. Y. Saito, K. Hamaguchi, K. Hata, K. Uchida, Y. Tasaka, F. Ikazaki, M. Yumura, A. Kasuya, and Y. Nishina, *Nature* 389, 554 (1997).
89. S. Dimitrijevic, J. C. Withers, V. P. Mammana, O. R. Monteiro, J. W. Ager, and I. G. Brown, *Appl. Phys. Lett.* 75, 2680 (1999).
90. J. Kong, N. R. Franklin, C. W. Zhou, M. G. Chapline, S. Peng, K. J. Cho, and H. J. Dai, *Science* 287, 622 (2000).
91. B. W. Smith, M. Monthioux, and D. E. Luzzi, *Nature* 396, 323 (1998).
92. G. H. Jeong, T. Hirata, R. Hatakeyama, K. Tohji, and K. Motomiya, *Carbon* 40, 2247 (2002).
93. J. Lee, H. Kim, S. J. Kahng, G. Kim, Y. W. Son, J. Ihm, H. Kato, Z. W. Wang, T. Okazaki, H. Shinohara, and Y. Kuk, *Nature* 415, 1005 (2002).
94. H. Kim, M. J. Kaufman, and W. M. Sigmund, submitted for publication.
95. M. Shim, A. Javey, N. W. S. Kam, and H. J. Dai, *J. Am. Chem. Soc.* 123, 11512 (2001).
96. R. H. Xie and Q. Rao, *Chem. Phys. Lett.* 313, 211 (1999).
97. M. F. Lin, F. L. Shyu, and R. B. Chen, *Phys. Rev. B* 61, 14114 (2000).
98. W. A. de Heer, W. S. Bacsa, A. Chatelain, T. Gerfin, R. Humphrey-baker, L. Forro, and D. Ugarte, *Science* 268, 845 (1995).
99. M. J. O'Connell, S. M. Bachilo, C. B. Huffman, V. C. Moore, M. S. Strano, E. H. Haroz, K. L. Rialon, P. J. Boul, W. H. Noon, C. Kittrell, J. P. Ma, R. H. Hauge, R. B. Weisman, and R. E. Smalley, *Science* 297, 593 (2002).
100. L. W. Tutt and A. Kost, *Nature* 356, 225 (1992).
101. K. Mansour, M. J. Soileau, and E. W. Van Stryland, *J. Opt. Soc. Am. B* 9, 1100 (1992).
102. X. Sun, R. Q. Yu, G. Q. Xu, T. S. A. Hor, and W. Ji, *Appl. Phys. Lett.* 73, 3632 (1998).
103. P. Chen, X. Wu, X. Sun, J. Lin, W. Ji, and K. L. Tan, *Phys. Rev. Lett.* 82, 2548 (1999).
104. S. R. Misha, H. S. Rawat, M. P. Joshi, and S. C. Mehendale, *J. Phys. B* 27, L157 (1994).
105. L. Vivien, E. Anglaret, D. Riehl, F. Bacou, C. Journet, C. Goze, M. Andrieux, M. Brunet, F. Lafonta, P. Bernier, and F. Hache, *Chem. Phys. Lett.* 307, 317 (1999).
106. H. Ago, T. Kugler, F. Cacialli, W. R. Salaneck, M. S. P. Shaffer, A. H. Windle, and R. H. Friend, *J. Phys. Chem. B* 103, 8116 (1999).
107. N. Minami, S. Kazaoui, R. Jacquemin, H. Yamawaki, K. Aoki, H. Kataura, and Y. Achiba, *Synth. Metals* 116, 405 (2001).
108. R. H. Xie, *Chem. Phys. Lett.* 310, 379 (1999).
109. J. E. Riggs, Z. X. Guo, D. L. Carroll, and Y. P. Sun, *J. Am. Chem. Soc.* 122, 5879 (2000).
110. M. Kusunoki, T. Suzuki, C. Honjo, T. Hirayama, and N. Shibata, *Chem. Phys. Lett.* 366, 458 (2002).
111. J. Sloan et al., *Chem. Commun.* 8, 699 (1999).

# Molecular Electronic Devices

## J. Chen, T. Lee, J. Su, W. Wang, M. A. Reed

*Yale University, New Haven, Connecticut, USA*

## CONTENTS

## 1. INTRODUCTION

The ability to utilize single molecules that function as self-contained electronic devices has motivated researchers around the world for years, concurrent with the continuous drive to minimize electronic circuit elements in the semiconductor industry. The microelectronics industry is presently close to the limit of this minimization trend dictated by both laws of physics and the cost of production. It is possible that electronically functional molecular components can not only address the ultimate limits of possible miniaturization but also provide promising new methodologies for novel architectures, as well as nonlinear devices and memories.

Molecular electronics [1–3] is conceptually different from conventional solid-state semiconductor electronics. It allows chemical engineering of organic molecules with their physical and electronic properties tailored by synthetic methods, bringing a new dimension in design flexibility that does not exist in typical inorganic electronic materials. It is well known that semiconductor devices are fabricated from the "top-down" approach that employs a variety of sophisticated lithographic and etch techniques to pattern a substrate. This approach has become increasingly challenging as feature size decreases. In particular, at nanometer scale, the electronic properties of semiconductor structures fabricated via conventional lithographic processes are increasingly difficult to control. In contrast, molecules are synthesized from the "bottom-up" approach that builds small structures from the atomic, molecular, or single device level. It in principle allows a very precise positioning of collections of atoms or molecules with specific functionalities. For example, one can selectively add an oxygen atom to a molecule with a precision far greater than an oxidation step in microfabrication using state of the art lithography and etching. Chemical synthesis makes it possible to make large quantities of nanometer-size molecules with the same uniformity but at significantly less cost, compared to other batch-fabrication processes such as microlithography. One can envision that in assembling molecular circuits, instead of building individual components on a chip one will synthesize molecules with structures possessing desired electronic configurations and attach/interconnect them into an electronic circuit using surface attachment techniques like self-assembly. Self-assembly is a phenomenon in which atoms, molecules, or groups of molecules arrange themselves spontaneously into regular patterns and even relatively complex systems without outside intervention [2].

## 2. BASIC CONCEPTS OF MOLECULAR ELECTRONICS

### 2.1. Self-Assembled Monolayers

Self-assembled monolayers (SAMs) are ordered molecular structures formed by the adsorption of an active surfactant on a solid surface (Fig. 1). A SAM film can be deposited on a substrate surface simply by exposing the surface to an environment containing surface active molecular species for a certain period of time (solution or vapor phase deposition). The molecules will be spontaneously oriented toward the substrate surface and form an energetically favorable ordered layer. During this process, the surface active head group of the molecule chemically reacts with and chemisorbs onto the substrate. Because a self-assembling system attempts to reach a thermodynamically stable state driven by the global minimization of free energy, it tends to eliminate growing foreign or faulty structures of molecules during the assembly process. This simple process with its intrinsic error-correction advantage makes SAMs inherently manufacturable and thus technically attractive and cost effective.
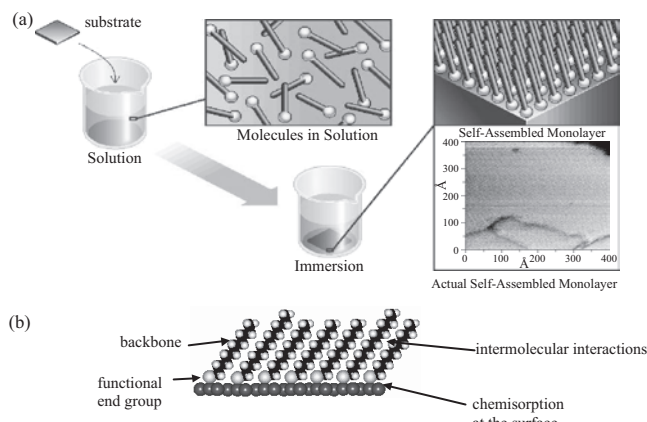
**Figure 1.** (a) Schematics illustrating self-assembly. Self-assembled monolayers are formed by immersing a substrate (e.g., a piece of metal) into a solution of the surface-active material. The functional end groups of molecules chemically react with the substrate material spontaneously, forming a two-dimensional assembly. Its driving force includes chemical bond formation of functional end groups of molecules with the substrate surface and intermolecular interactions between the backbones. (b) Cross-sectional schematic of self-assembled monolayers formed on a substrate.

In addition, SAMs can be designed and engineered to provide extremely high functional density. For example, one can realize a switch or a memory out of a single monolayer. On the other hand, in order to perform highly complex functions as those of current integrated circuits, a self-assembly strategy that enables easy formation of complex patterns to "program" the structures and (electrical) properties of materials at nanometer levels needs to be developed.

Aimed at understanding charge transport properties of SAMs and applying them to electronic applications, we focus our attention on conjugated SAMs in this study.

## 2.2. Conjugated Oligomeric Systems

The two basic requirements for electronic conduction in a material are (1) a continuous system of a large number of strongly interacting atomic orbitals leading to the formation of electronic band structures, and (2) the presence of an insufficient number of electrons to fill these bands. In inorganic semiconductors and metals, the atomic orbitals of each atom overlap with each other in the solid state creating a number of continuous energy bands, with the electrons provided by each orbital delocalized throughout the entire array of atoms. The strength of interaction between the overlapping orbitals determines the extent of delocalization, giving rise to the band width. Likewise, in a molecule, a set of overlapping delocalized electronic states across the entire molecule is necessary for efficient electronic conduction.

### 2.2.1. Delocalized $\pi$ Bonds and Benzene

More than two adjacent $p$ orbitals can combine to form a set of molecular orbitals where the electron pairs are shared by more than two atoms. These form "delocalized" $\pi$ bonds. In the case of benzene ($C_6H_6$), the $p$ orbital of each carbon
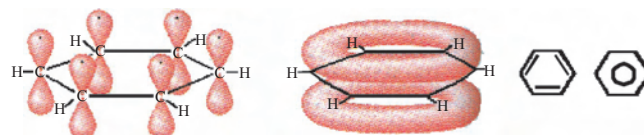


**Figure 2.** Delocalized $\pi$ Bonds of benzene and its symbols.

atom overlaps equally well with both neighboring $p$ orbitals, leading to a picture of benzene in which the six $\pi$ electrons are completely delocalized around the ring. Benzene therefore has doughnut-shaped clouds of electrons, one above and one below the ring (Fig. 2) [4].

### 2.2.2. Aliphatic versus Aromatic

Molecules with saturated C—C and C—H single ($\sigma$) bonds are referred to as aliphatic molecules. There are no conjugated $\pi$ orbitals in them, and they act as insulators. Molecules containing benzene rings are generally referred to as aromatic molecules.

### 2.2.3. Conjugated Oligomers

The term conjugated means an alternation of multiple and single bonds linking a sequence of bonded atoms, such that there is an extended series of overlapping $p$ orbitals, and the electrons involved are $\pi$ electrons. Oligomers are synthesized by joining one molecular unit to itself a few times. This repeated unit is the analog of the unit cell in the solid state; it is referred to as a monomer. Different from the more commonly encountered polymers that generally consist of strands of large molecules with varying length, structure, and morphology, oligomers are synthesized by precisely controlled processes producing well-defined chains [5, 6]. It is often the case that in oligomers, the MOs are $\sigma$ orbitals which are spatially not suited for extensive overlapping and impede significant electron delocalization. However, in conjugated oligomers, in addition to the $\sigma$ framework that establishes the structure of molecules, $\pi$ electrons are delocalized throughout the molecules. Good examples of conjugated oligomers are polyphenylene and polyphenylene-based molecules [7].

### 2.2.4. Polyphenylene and Polyphenylene-Based Molecules

The delocalization in benzene can be extended to other adjacent atoms. For example, one can bind benzene rings to each other (Fig. 3a), forming a chainlike structure called polyphenylene. Borrowing the idea of diblock copolymers[1] from bulk organic materials, one can also insert other types of molecular groups into a polyphenylene chain [e.g., singly bonded aliphatic groups (—$CH_2$—$CH_2$—), doubly bonded ethenyl groups (—HC=CH—), and triply bonded

---

[1] Copolymer refers to the combination of two different monomers, A and B; diblock indicates that they are combined in the ratio of one monomer each to make the new unit cell (A + B). Diblock copolymer opens up the possibility of creating polymer heterostructures with unique band structures.
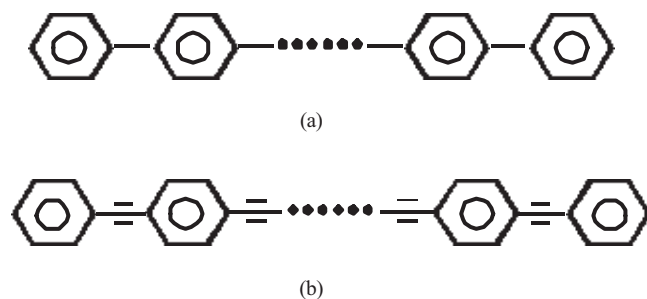
**Figure 3.** (a) Polyphenylenes and (b) polyphenylene-based conjugated oligomers.

ethynyl groups (—C≡C—)] to obtain polyphenylene-based molecules (Fig. 3b). In polyphenylenes or polyphenylene-based molecules with multiply bonded groups, delocalized $\pi$ orbitals extend across and merge with the neighboring aromatic ring and multiple bonded groups, maintaining delocalization throughout the length of the molecule.

For electronic transport studies, one needs to know the following important terminology: the highest occupied molecular orbital (HOMO) and the lowest unoccupied molecular orbital (LUMO), similar to the valence band and the conduction band in solid-state materials, respectively, but with discrete energy levels caused by quantization effects in constricted dimension of a molecule. The difference in HOMO and LUMO is referred to as the energy bandgap ($E_g$).

## 2.3. Basic Charge Transport Mechanisms

### 2.3.1. Bulk Organic Materials

Electron transport in bulk organic materials can be characterized by the macroscopic conductivity [8]. Most conjugated polymer systems are electrically nonconducting unless they are doped.[2] This may appear to be similar to semiconductors, but the physics of conjugated polymer semiconductors differs markedly from that of inorganic semiconductors such as Si or GaAs. In three-dimensionally bonded materials, the fourfold (or sixfold, etc.) coordination of each atom to its neighbors through covalent bonds leads to a rigid structure, and the rigidity of the lattice ensures that charge carriers added to the system are accommodated in the conduction and valence bands with negligible rearrangement of the bonding. In such systems, therefore, the electronic excitations can usually be considered in the context of this rigid structure, leading to the conventional concept of electrons and holes as the dominant excitations. In organic conductors, the bonding has reduced dimensionality (in that the interactions within the molecular chain are much stronger than those between adjacent chains). The twofold coordination makes these systems generally more susceptible to structural distortion. As a result, the dominant electronic excitations are inherently coupled to chain distortions, and

the equilibrium geometry is determined by the occupancy of the electronic levels via electron-phonon coupling. When a polymer chain is doped, it can usually better accommodate an added charge if the charge becomes localized over a smaller section of the chain. This is because, on one hand, charge localization along the chain requires a local rearrangement of the bonding configuration in the vicinity of the charge (the polymer lattice relaxes to a new bonding geometry) and hence costs the system a gain in elastic energy; on the other hand, the generation of this local lattice distortion also lowers the ionization energy of the distorted chain. If the gain in elastic energy is offset by the reduction of the ionization energy of the chain, charge localization will take place at the expense of complete charge delocalization [9]. The specific types of charged defects formed on the polymer backbone during doping depend on the structure of the polymer chain: those with degenerate ground-state structures such as polyacetylene and those with nondegenerate ground-state structures such as poly($p$-phenylene) [10].

For example, in the case of poly($p$-phenylene) (Fig. 4), when an electron is removed from the $\pi$-system of its backbone (chemical oxidation), an unpaired electron with spin 1/2 (a free radical) and a spinless positive charge (cation) are created. The radical and cation are coupled to each other via a local bond rearrangement, creating a polaron which appears in the band structure as localized electronic states symmetrically located within the gap with the lower energy states being occupied by a single unpaired electron. Further oxidation creates dications in the polymer. An electron can be removed from either the polaron or the remaining neutral portion of the chain. In the former case, the free radical of the polaron is removed and a dication is created composed of two positive charges coupled through the lattice distortion, creating a new spinless defect bipolaron. Removal of an additional electron from a neutral portion of the chain would create two polarons. Because the formation of a bipolaron produces a larger decrease in ionization energy compared to the formation of two polarons, the
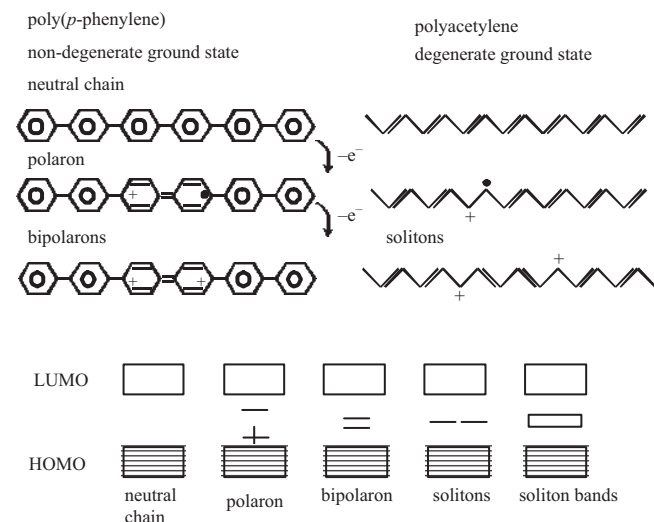


**Figure 4.** Neutral chain and oxidation of poly($p$-phenylene) (left) and polyacetylene (right) and the creation of polaron, bipolaron, and solitons states.

---

[2] That is, exposed to suitable electron acceptors (oxidizing agents) or electron donors (reducing agents). Doping through chemical oxidation (or reduction) involves the creation of a charged polymeric backbone and the introduction of a counterion that ensures charge neutrality.

former process is thermodynamically favorable. These new empty bipolaron states are also located symmetrically within the bandgap. Further doping creates additional localized bipolaron states, which eventually overlap to form continuous bipolaron bands at high enough doping levels.

In the case of conjugated polymers with degenerate ground-state structures, the situation is different. The initial oxidation of *trans*-polyacetylene also creates polarons as discussed earlier. When it is further oxidized, since its ground state is twofold degenerate, the bonding configurations on either side of the charged defects only differ by a reversed orientation of the conjugated system and are energetically equivalent resonance forms. It in turn creates isolated, noninteracting charged defects that form domain walls separating two phases of opposite orientation but identical energy. Such defects are called solitons, which result in the creation of new localized electronic states that appear in the middle of the energy gap. As the doping level increases, these states can overlap to form soliton bands.

It is now well accepted that in conducting polymers, transport occurs by the movement of charge carriers between localized states or between soliton, polaron, or bipolaron states [10]. The result is that transport in conducting polymers is dominated by thermally activated hopping (or tunneling processes) in which carriers hop across (or tunnel through) barriers created by the presence of isolated states or domains. These include, for example, intersoliton hopping [11], hopping between localized states assisted by lattice vibrations [12], interchain hopping of bipolarons [13], variable range hopping in three dimensions, and charging energy limited tunneling between conducting domains [11]. These latter two mechanisms are characterized by conductivities that vary as $T^{-1/4}$ in the case of variable range hopping [14] and $T^{-1/2}$ in the case of charging energy limited tunneling [15]. This is in contrast to processes related to the thermal activation of carriers across a bandgap into extended states in which the conductivity varies as $T^{-1}$. In summary, conjugated polymers have a bulk conductivity limited not by carrier mobility in a molecule but by interchain hopping, and macroscopic conductivity measurements do not directly probe single molecule properties. The mechanism of bulk conductivity involves incoherent diffusive intra- and intermolecular electron transport where the electrons thermalize with the matrix and are dissipative.

### 2.3.2. Nanoscale Molecular Wires

When these organic materials are reduced to their molecular components, what does conductivity mean? How will the chemical structure of a molecule affect the transport properties? Can one construct nanoscale molecular "wires"[3] that are capable of transporting charge easily from one end to the other, when the rigidity of the system frustrates polaron formation? Based on computation, modeling, measurement, and analogy, one can suggest several different mechanisms that take place when electrons transport through nanoscale molecules [16].

***Coherent Electron Motion: Nonresonant*** Nonresonant coherent electron motion occurs in the absence of strong dissipation or trapping effects, and the molecular orbitals associated with the molecular wire provide a pathway for the electron to transport down the wire without loss of energy or phase information. An important factor in determining the conductance of molecular wires is the location of the Fermi energy of the metallic contact relative to the energy levels of the wires. The molecules we will be considering have a HOMO-LUMO gap of several eV. Similar to the situation in metal-semiconductor contacts, the Fermi level will lie in the gap regardless of the nature of the molecule or the metal. It is similar to metal-semiconductor contacts, where the Fermi energy lies close to the charge neutrality level near the center of the gap; otherwise there would be too much excess charge in the semiconductor. The conduction is considered nonresonant because the electronic states in the wires are far above the energy of the tunneling electrons.

In nonresonant coherent electron motion, the rate of electron transport is exponentially dependent on the length of the molecular bridge [17–20]. The conductance $g$ can be expressed as

$$g = Ae^{-\beta N}$$

where $N$ indicates the number of sites in the wire and is proportional to wire length, $\beta$ is the characteristic decay parameter and depends on the internal wire electronic structure, and the prefactor $A$ is related to the contact conductance, depends on the electrode-wire end interactions, and can have a polynomial electric field term dependent on details of the system under study. This exponential decay should hold for short wires with large HOMO-LUMO gaps, such as oligoalkanes.

***Coherent Electron Motion: On-Resonance*** On-resonance coherent electron motion occurs when the energy of the tunneling electrons is resonant with the conduction band of the wires and in the absence of dissipative effects. The rate of electron transport will obey the Landauer formula [21, 22], independent of the length of the molecular bridge (distinctively different from nonresonant coherent electron motion). The conductance should scale linearly with the transmission coefficient and therefore with the number of eigenmodes in the wire.

The linear increase in conductance with the number of modes has been observed in atomic point contacts [23, 24], where the transmission probability $T$ is essentially unity for each available channel. However, given the nature of the molecular eigenstates, $T$ is much smaller in the wires. This is because the electronic orbitals in a molecule are often spatially localized on constituent atoms of the molecule (Fig. 5). An incoming electron with a specific energy can only be in resonance with part of the molecule, causing average transmission through the entire molecule much less than unity. Recent low-temperature conductance measurement in metallic carbon nanotubes apparently belongs to this regime of behavior [25].

---

[3] A molecular wire generally refers to a linear chain of $\pi$-type molecular structure intended to connect two electronic components [3].
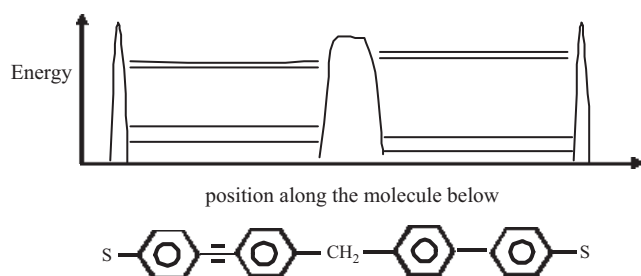
**Figure 5.** Molecular structure and schematics of electron orbital energy levels for a proposed molecule.

***Incoherent Transfer—Ohmic Behavior*** Incoherent transfer occurs when the electronic levels in the molecular wire couple either to nuclear motions (vibration, rotation) in the wire or to modes of the environment. The electronic states in the wire will develop an effective intramolecular lifetime, and inelastic scattering can become important. Under these conditions, the wire should behave very much like a regular electrical resistive wire, with its conductivity inversely proportional to length. In long, nonrigid molecular wires with smaller gaps, electron/vibration coupling, electron/electron scattering, or electron/defect scattering can be strong enough that electron localization on the wire occurs and can inhibit coherent electron transport. Under these circumstances, exponential decay dependence characterizing coherent electron motion should no longer be expected as in short wires with large gaps. This is similar to the situation of electron transfer through tunneling barriers in semiconductor devices, where incoherent processes arising from inelastic scatterings can result in the transformation from exponential decay to ohmic behavior, with the current dominated by inelastic processes and decreasing only slowly as the inverse of the length of the wire [26].

***Quasiparticle Formation and Diffusion*** In long molecular wires, quasiparticle motions could provide effective conduction. Quasiparticles like solitons and bipolarons are considered to be the primary charge carriers at ambient temperature in conducting polymer systems as discussed earlier (transport mechanisms in bulk organic materials). Ratner et al. [16] proposed that defects like solitons and bipolarons can be important transport mechanisms in longer molecular wire.

***Gated Electron Transfer Mechanisms*** One important characteristic of molecules is that they are capable of undergoing dynamic stereochemical change. Molecules can change their shapes from one local minimum to another. These different geometries have different electronic structures and therefore different conductances. An example from Closs et al. [27] shows that as a substituent on a cyclohexane ring changes its position from equatorial to axial, the rate of electron transfer changes by roughly a factor of 10. It is different from other nanoscale structures such as atomic wires, quantum dots, or mesoscopic junctions. This type of electron-transfer process is considered gated. Different molecular conformations can be caused by chemical reaction or thermal activation, etc.

These five mechanisms appear to be the important, limiting behaviors that can characterize conduction in molecular wires. By changing such parameters as the molecular and electronic structures of the molecular bridge, the metal-molecule attachment (energy level alignment), and coupling with nuclear or environmental modes (e.g., through solvent or coating), one can modify the nature of the conductance of these molecular wires.

## 2.4. Initial Studies in Molecular Electronics

In 1974, Aviram and Ratner suggested the field of molecular electronics by first proposing a D-$\sigma$-A unimolecular rectifier[4] [28] (i.e., a molecular $p$-$n$ junction). However, the proposal was premature in that both the chemical synthesis of such a rectifying molecule and the fabrication of such a device, involving vertically stacking nanometer-scale thick organic monolayers in between two metal electrodes, were not technically feasible. With recent developments in chemical synthesis and microfabrication, many of these challenging experiments have now been done. For example, Metzger et al. realized the D-$\sigma$-A rectification through Langmuir–Blodgett (L–B) multilayers[5] and monolayers of hexadecylquinolinium tricyanoquinodimethanide [29] in 1997.

Instead of using L–B films, Reed [30, 31] proposed conjugated oligomers with precisely controlled lengths as molecular devices using self-assembly techniques. Nevertheless, to electrically contact these functionalized rigid rod conjugated oligomers with lengths on the order of nanometer is technically challenging.

Mechanically controllable break junctions were originally used to study conductance quantization [32]. In 1997, Reed et al. first applied this technique to measure electronic transport through a single molecule [33]. Using a similar technique, Kergueris et al. employed a microfabricated break junction [34] to study transport through oligothiophene molecules. Zhou et al. [35] applied a vertical electrode method, first developed by Ralls et al. [36], to characterize molecular junctions. This technique realizes direct and robust metal-molecule contacts and allows for variable-temperature measurements, leading to further understanding of metal-SAM contacts [37, 38] and nonlinear molecular devices [38, 39].

In the meantime, the discovery of the scanning tunneling microscope (STM) opened a new horizon for the study of molecular-scale electronics. It allows for imaging, probing, and manipulation of single molecules [40–43]. For instance, the first demonstration of conduction through a single

---

[4] The D end is a good organic one-electron donor (but poor acceptor), $\sigma$ is a covalent saturated bridge, and A is a good organic one-electron acceptor (but poor donor). It is predicted to exhibit rectifying electron transfer from A to D because the barrier to form zwitterionic state $D^+$-$\sigma$-$A^-$ is several eV lower than that of $D^-$-$\sigma$-$A^+$.

[5] The L–B technique involves the vertical movement of a solid substrate through the monolayer/air interface. A classic L–B material has two distinct regions in the molecule: a hydrophilic headgroup and a long alkyl chain which provides a hydrophobic or oleophilic tail. L–B monolayer formation is governed by its hydrophilic/hydrophobic interaction with substrate, which is of a physical nature, unlike SAM which chemically reacts with its substrate.

molecule was made by Bumm et al. [42] who measured electron transport through individual molecules isolated in an insulating alkanethiol[6] matrix using STM. Combining self-assembled nanoclusters with conjugated molecules, Dorogi et al. [43] succeeded in extracting the conductance of xylene-dithiol by measuring current-voltage (I(V)) characteristics with an STM tip placed above gold cluster on a xylene-dithiol SAM covered gold surface.

Other than electrical characterization of conducting molecules, the search for individual molecules with the ability to behave as switches has been ongoing for a long time. It began with the Aviram and Ratner theory on molecular rectification in 1974 [28] and was furthered by Aviram's proposal on a molecular spiro switch in 1988 [44]. In addition, a molecular shift register was proposed by Hopfield et al. to be used for molecular electronic memories [45]. Only recently experimental results on switching and memory behavior have been reported in molecular devices. Collier et al. reported an irreversible switch with a low current density utilizing a L–B film [46]. Several months later, Chen et al. [38] realized a reversible switching device exhibiting a large peak to valley ratio negative difference resistance behavior using a redox SAM, which is the first of its kind. Moreover, we recently first demonstrated a molecular memory device with long bit retention time [39] working at ambient temperature.

Combining individual molecular elements such as wires, switches, and memories mentioned above to create devices with more complex functionality is the logical next step in further development of molecular electronics. However, the problem of interconnection on molecular scale is not a trivial one. Unlike bulk solid-state electronics, when small sections of molecular components are combined into larger molecular devices, strong Coulomb interaction and quantum interference among electrons can change the transport properties of individual elements.

## 3. FABRICATION OF MOLECULAR TRANSPORT DEVICES

Investigations of the electronic conduction through conjugated molecules that are end-bound onto a surface have been demonstrated using a STM [42, 43], using micromachined silicon nanopores [35, 37, 38], and between proximal probes [33, 34]. Although a good deal of information about the structural properties of various functional terminal moieties on both aliphatic and aromatic molecules has been obtained, very little is known about the electronic properties of through-bond transport.

STM techniques allow for the investigation of surface properties at high spatial resolution. Since a STM tip can be positioned with atomic accuracy, local experiments (electronic transport) can be performed (e.g., the conductances of single molecules can be measured) [42, 43]. However, the close proximity between the probe tip and the sample surface can also modify what is measured, by tip-induced modification of the local surface electronic structure, especially at small tip-surface distances. The perturbation of

the electronic structure can be very significant so that tip-induced localized states may be formed [47, 48]. In addition, other tip-surface interactions may become important (e.g., the electrostatic and van der Waals force interaction). The presence of a vacuum gap between tip and molecule often complicates analysis,[7] and the mechanical stability that the STM has to meet during spectroscopy measurements (under disengaged feedback loop) is quite demanding.

Another category of proximal probes aimed at defining nanometer-sized tunnel gaps is called a "break junction." Mechanically controllable break junctions [33] have been used to measure electronic conduction through benzene-1,4-dithiol. An alternative approach is a current-controlled break junction, fabricated using electromigration of metal atoms by passing current through metallic nanowires [49–51]. Recently Kushmerick et al. [52] have developed a cross-wire tunnel junction where the molecular layer sandwiched between wires (whose spacing is controlled by their mutual Lorentz force) is measured.

Fabrication of planar metallic electrodes with separation down to the length of conjugated oligomers is another approach to realize charge transport measurements through molecules. Lombardi [53] deposited 12-nm conjugated oligomers in between 10-nm metallic gaps, fabricated with a combination of standard electron-beam lithography on a bilayer resist and angle evaporation, but observed no appreciable conduction through the gaps. They concluded that either the molecules are sterically inhibited to bridge across the gap or they are not conductive at such length scales. More recently, Bezryadin et al. [54] demonstrated a 4-nm metallic gap by sputtering Pt across a slit in a freestanding silicon nitride membrane and then electrostatically trapped Pd colloids in between the nanoelectrodes. The electrostatic trapping method works well for colloids and DNA [55]. However, if one would electrostatically trap molecules, the strong trapping field may change the polarization, conformation, or structure of molecules undesirably.

To reliably measure transport through metal-molecule-metal system, we employ a fabrication technique to directly measure the conduction through a small number of self-assembled molecules sandwiched between top and bottom metallic contacts [35]. Figure 6 is a schematic flow diagram of the fabrication process. A scanning electron microscope (SEM) image of a fabricated device is shown in Figure 7. This technique guarantees good control over the device area and intrinsic contact stability, and produces a large number of devices with acceptable yield so that statistically significant results can be produced. Two features are essential to the process, the first of which is the employment of nano-scale device area. The area is made to be smaller than the domain size of the SAM and thus the adsorbed organic layer is highly ordered and (mostly) defect-free. The second feature is that during the deposition (evaporation) of the contact onto the SAM, several measures are taken to ensure that the deposited metal atoms accumulate at the SAM surface and do not penetrate into the organic layer. Particularly, liquid nitrogen is kept flowing through the cooling stage

---

[6] Alkanethiol molecules are the type of molecules with $(CH_2)_n SH$ structure.

[7] For example, narrow features in the local density of states of STM tip apex atom can give rise to negative differential resistance. See Y. Xue et al., *Phys. Rev. B* 59, R7852 (1999).
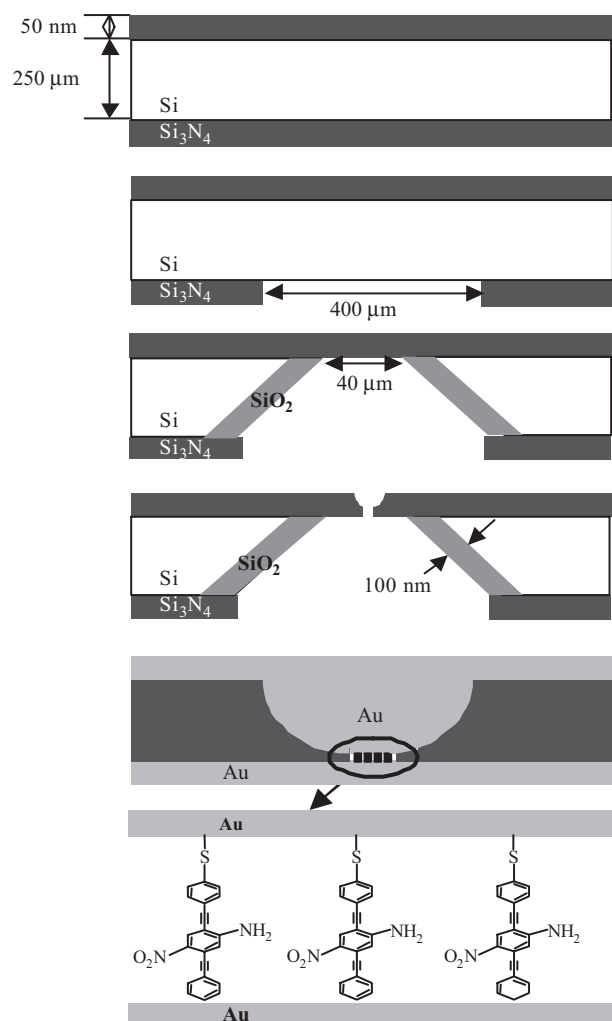
**Figure 6.** Schematics of the fabrication process.



**Figure 7.** (a) SEM graph from the bottom side of a fabricated device (Fig. 6), showing a pyramid structure of silicon and freestanding silicon nitride membrane. (b) SEM graph of nanopore (indicated as circle) after the first evaporation of metal from the top side.

during the thermal evaporation, in order to avoid thermal damage to the molecular layer. This technique reduces the kinetic energy of evaporated Au atoms at the surface of the monolayer, thus preventing Au atoms from diffusing through the monolayer. For the same reason the evaporation rate is kept very low.

## 4. BASIC TRANSPORT MEASUREMENT IN MOLECULAR LAYERS

In charge transport across a metal-SAM-metal system, both the electronic structure of the SAM and the metal-SAM coupling play important roles. Given the simplest conjugated SAM, one can study the effects of metal-SAM contact. The most well-known and studied SAM-metal system is thiolate on gold surfaces [56–60]. Reed et al. [33] have measured transport properties through a gold-thiolate SAM-gold junction. They proposed that the current is largely limited by Au-S contacts, which was later confirmed by theoretical calculations of Di Ventra et al. [61]. Recently, Vondrak et al. [62] reported that the interfacial electronic structure of thiolate SAM on metal surfaces is dominated by $\sigma^*$ orbitals localized to the C-S-metal anchor, is strongly coupled to the metal substrate, and is independent of the nature of the backbone, further emphasizing the importance of the interface metal-SAM contact. In this section we will discuss a second type of SAM-metal junction, specifically 1,4-phenylene diisocyanide with metal (Au or Pd) contacts [37]. This system has significant electronic advantages over the thiol and other group-VI systems (e.g., Se, Te) [63].

To understand the electrical conduction of a metal-molecule system, the energy level matching (or mismatching) of the available electrons in the metal (the Fermi level) and the available molecular orbital in the terminal molecule must be considered. In general, the Fermi level of the metallic contact does not energetically line up with either the HOMO or LUMO levels in the molecule [64]. This mismatch gives rise to a contact barrier, analogous to a Schottky contact. Electron (or hole) transport through such a contact will exhibit a range of phenomena, depending on the height of the barrier, the effective barrier thickness, and the presence of defects; the most prevalent are thermionic emission, direct tunneling, and defect-mediated transport such as hopping [65–67].

## 4.1. Conduction Mechanisms

Table 1 lists the possible conduction mechanisms with their characteristic behavior, temperature dependence, voltage dependence, and schematic band diagrams. Schottky emission is a process in which carriers overcome the metal-dielectric barrier by thermionic emission, whose current is a strong function of temperature. The extra voltage term on the exponential lowers the barrier at the metal-insulator interface due to image-force correction. Frenkel-Poole (FP) conduction is due to field-enhanced thermal excitation of trapped electrons into the conduction band, a process similar to Schottky emission. Instead of the metal-dielectric barrier height found in Schottky emission, the barrier height in FP conduction represents the depth of the trap potential with respect to the edge of the conduction band. Its current has the same temperature dependence as that of Schottky emission, but with different voltage dependence. As seen from its characteristics, the barrier lowering is twice that observed in Schottky emission, because of the immobility of the positive charge associated with the trap. Hopping conduction refers to the process in which thermally excited electrons hop from one isolated state to the next, whose conductance also depends strongly on temperature. Different from Schottky emission, there is no barrier lowering effect. The tunneling processes (both Fowler–Nordheim tunneling and direct tunneling) do not depend on temperature (to first order), but strongly depend on film thickness and voltage.

For a given metal-dielectric film-metal system, certain conduction mechanisms may dominate in certain voltage and temperature regimes. For example, Schottky emission usually plays an important role at high temperatures and low barrier heights; Frenkel–Poole conduction will dominate if there is a high density of traps in the dielectrics; tunneling current will be a major contribution if the dielectrics are thin and under high voltage biases; and for a dielectric film that has a very low density of thermally generated free carriers in the conduction band, hopping conduction is more likely to be observed, especially at low applied voltages and high temperatures.

To elucidate the dominant specific mechanism and effective barriers, we schematically plot the current density $\ln J$ versus $V^{1/2}$ for thermal emission, hopping, and tunneling transport as shown in Figure 8. The effect of thermionic emission for two different barrier heights ($\Phi_{th}$) is shown for $\Phi_{th2}(1.0 \text{ eV}) > \Phi_{th1}(0.5 \text{ eV})$. The effect of defect (e.g., hopping) conduction is shown for different defect densities $N(1.25N_0 > N_0 > 0.85N_0)$ even though the hopping barrier may be the same ($\Delta E_h = 0.5$ eV). The tunneling component (with $\Phi_{tunnel} = 0.5$ eV) is shown for the same barrier; it has a significantly smaller contribution than the other mechanisms. Depending on the value of $\Phi_{th}$, $\Delta E_h$, $N$, and $\Phi_{tunnel}$, one may observe different mechanisms; for example, both thermionic emission and hopping are observable for a barrier of 0.5 eV and defect concentration of $N_0$, if $\Delta E_h = \Phi_{th1} = 0.5$ eV. With the same barrier heights, if the defect density is too high, (e.g., $1.25N_0$), only hopping conduction can be observed; on the other hand, if the defect density is low enough, in this case, $0.85N_0$, one will only observe thermionic conduction.

Previous work on self-assembled thiol-terminated (but asymmetric) oligomers illustrated that one can deduce the basic transport mechanisms (illustrated in Fig. 8) by measuring the temperature-dependent current-voltage ($I(V,T)$) characteristics. In previous work, it has been found that the physisorbed aryl-Ti interface gave a thermionic emission barrier of approximately 0.25 eV [35], whereas the Au-thiol (and other group-VI termini such as Se and Te) bond exhibited a hopping barrier of roughly 0.2 eV [63]. This is consistent with other transport measurements on a single molecule [33] that measured an apparent gap of 0.7 eV, and the interpretation of the observed gap as the mismatch between the contact Fermi level and the LUMO of the molecule was supported by theoretical calculations [61]. That is because the contribution from the 0.2-eV defect-mediated hopping barrier (not present in the single molecule experiment) is significantly larger than that from the 0.7-eV barrier symmetric structures. The measured $I(V)$ should not (and does not, Fig. 9) show the resultant rectification of such a barrier asymmetry.

In the following, we investigate two self-assembled molecular systems: (1) the simple tunneling dominated conduction in Au-alkanethiol-Au junctions, and (2) the transport through the self-assembled functional termini of isocyanides, each with its effective electron transport barrier in the nanopore configurations (Fig. 6).

**Table 1.** Possible conduction mechanisms.

| Conduction mechanism | Characteristic behavior | Temperature dependence | Voltage dependence | Schematic band diagram |
|---|---|---|---|---|
| Schotty emission | $I \sim T^2 \exp\left(-q\frac{[\phi - \sqrt{qV/4\pi\epsilon d}]}{kT}\right)$ | $\ln\left(\frac{I}{T^2}\right) \sim \frac{1}{T}$ | $\ln(I) \sim V^{1/2}$ | |
| Frankel–Pool conduction | $I \sim VT^2 \exp\left(-q\frac{[\phi - 2\sqrt{qV/\pi\epsilon d}]}{2kT}\right)$ | $\ln\left(\frac{I}{T^2}\right) \sim \frac{1}{T}$ | $\ln\left(\frac{I}{V}\right) \sim V^{1/2}$ | |
| Hopping conduction | $I \sim V \exp\left(-\frac{\Delta E}{kT}\right)$ | $\ln\left(\frac{I}{V}\right) \sim \frac{1}{T}$ | $I \sim V$ | |
| Fowler–Nordheim tunneling | $I \sim V^2 \exp\left(-\frac{4d\sqrt{2m}}{3q\hbar V}(q\Phi)^{1.5}\right)$ | — | $\ln\left(\frac{I}{V^2}\right) \sim 1/V$ | |
| Direct tunneling | $I \sim V \exp\left(-\frac{4\pi d}{h}\sqrt{2m\Phi}\right)$ | — | $I \sim V$ | |
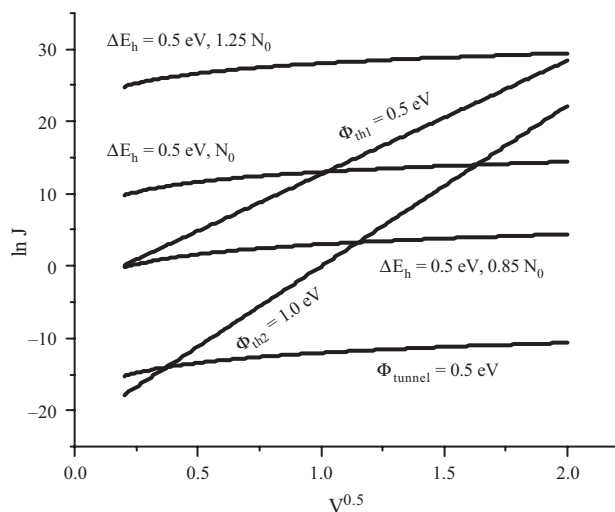
**Figure 8.** Dependencies of $\ln J$ versus $V^{1/2}$ for thermal emission, hopping, and tunneling transport. The effect on thermionic emission for two different barrier heights is shown; for $\Phi_{th2}$ (1.0 eV) > $\Phi_{th1}$ (0.5 eV), the thermionic emission component drops (exponentially). The effect of defect (e.g., hopping) conduction is shown for different defect densities ($1.25N_0 > N_0 > 0.85N_0$) even though the hopping barrier may be the same ($\Delta E_h = 0.5$ eV). The tunneling component (with $\Phi_{tunnel} = 0.5$ eV) is much smaller than the others. Depending on the value of $\Phi_{th}\Delta E_h$, N, and $\Phi_{tunnel}$, one may observe different mechanisms; for example, both are observable for $\Phi_{th1}$ and $N_0$, if $\Delta E_h = \Phi_{th1}$.

## 4.2. Alkanethiol SAM Metal-Insulator-Metal Tunneling

When the molecular layer is a large bandgap insulator, well-defined metal-insulator-metal (MIM) tunneling should occur. Temperature-independent electron transport due to direct tunneling should be the dominant conduction mechanism. Other mechanisms will be discussed in further sections; however, a MIM signature is important to determine if the transport is determined by the bandstructure of the molecular layer, or due to other less intrinsic
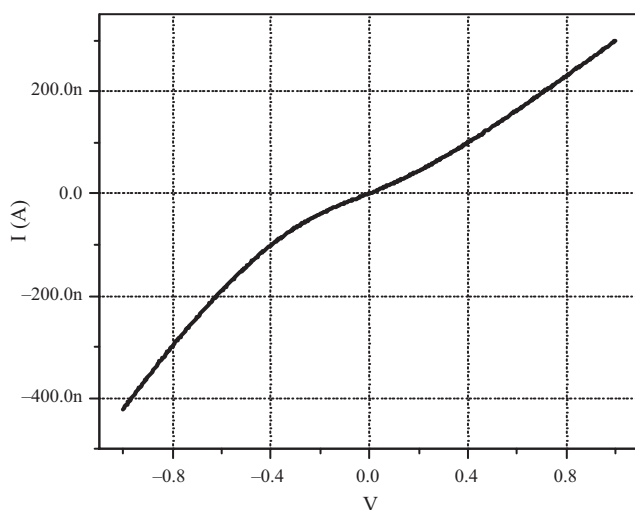


**Figure 9.** $I(V)$ of Pd-SAM-Pd junction at 290 K.

effects. An investigation of these systems has been done [29, 35, 38, 68, 69], specifically alkanethiol [$CH_3(CH_2)_{n-1}SH$] because it forms a robust SAM on Au surfaces [56–60, 70]. A few groups have utilized the scanning tunneling microscope [71], the conducting atomic force microscope [72, 73], or mercury-drop junctions [74], to investigate electron transport through alkanethiols at room temperature, and they claimed that the transport mechanism is tunneling. Although the electron conduction is expected to be tunneling when the Fermi levels of contacts lie within the HOMO-LUMO gap of a short length molecule as for the case of these alkanethiols [16], in the absence of $I(V, T)$ characteristics such a claim is unsubstantiated since other conduction mechanisms (such as thermionic or hopping conduction) can contribute and complicate the analysis.

In this section, electron transport through alkanethiol self-assembled monolayers is investigated with $I(V, T)$ measurements [75] using the device structure similar to one reported in the previous section (see Section 3) [35, 36]. For our experiments, a ~5 mM alkanethiol solution is prepared by adding ~10 $\mu$L alkanethiols into 10 mL ethanol. The deposition is done in solution for 24 hr inside a nitrogen filled glove box with an oxygen level of less than 100 ppm. Three molecules of different molecular lengths: octanethiol [$CH_3(CH_2)_7SH$; denoted as C8, for the number of alkyl units], dodecanethiol [$CH_3(CH_2)_{11}SH$; denoted as C12], and hexadecanethiol [$CH_3(CH_2)_{15}SH$; denoted as C16] were used to form the active molecular components.

As listed in Table 1[8] [67], based on whether thermal activation is involved, the conduction mechanisms fall into two distinct categories: (i) thermionic or hopping conduction which has temperature-dependent $I(V)$ behavior, and (ii) direct tunneling or Fowler-Nordheim tunneling which does not have temperature-dependent $I(V)$ behavior. For example, thermionic and hopping conductions have been observed for 4-thioacetylbiphenyl SAMs [35] and 1,4-phenelyene diisocyanide SAMs [37]. On the other hand, the conduction mechanism through alkanethiols is expected to be direct tunneling because the Fermi levels of contacts lie within the large HOMO-LUMO gap (~8 eV) of the alkanethiols with short molecular lengths (~1–2.5 nm) [16, 74].

Previous work on Langmuir–Blodgett alkane monolayers [76,77] exhibited a large impurity-dominated transport component, complicating the analysis. $I(V)$ measurements on self-assembled alkanethiol monolayers have also been reported [71–74, 78–80]. However, all of these measurements were performed at a fixed temperature (300 K) which is insufficient to prove tunneling as the dominant mechanism. Without $I(V, T)$ characterization, other conduction mechanisms (such as thermionic or hopping conduction) cannot be simply ruled out.

Figure 10 shows a representative $I(V, T)$ characteristic of dodecanethiol (C12) measured with similar device structure as that shown in Figure 6. Positive bias corresponds to electrons injected from the physisorbed Au contact (bottom contact in Fig. 6) into the molecules. By using the contact area of 45 $\pm$ 2 nm in diameter (estimated from SEM image [75]), a current density of 1500 $\pm$ 200 A/cm$^2$ at 1.0 V is

---

[8] The models listed in Table 1 apply to solid-state insulations with one band.
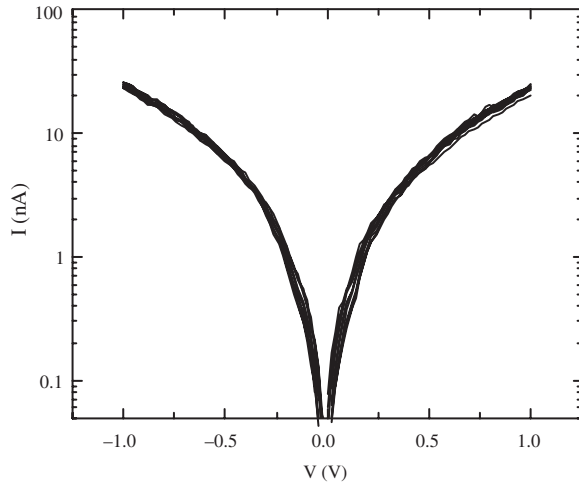
**Figure 10.** Temperature-dependent $I(V)$ characteristics of dode-canethiol (C12). $I(V)$ data at temperatures from 300 to 80 K with 20 K steps are plotted on a log scale.



**Figure 11.** (a) Arrhenius plot generated from the $I(V)$ data in Figure 10, at voltages from 0.1 to 1.0 V with 0.1 V steps. (b) Plot of $\ln(I^2/V)$ versus $1/V$ at selected temperatures.

determined. No significant temperature dependence of the characteristics (from $V = 0$ to 1.0 V) is observed over the range from 300 to 80 K. An Arrhenius plot [$\ln(I)$ versus $1/T$] of this is shown in Figure 11a, exhibiting little temperature dependence in the slopes of $\ln(I)$ versus $1/T$ at different bias and thus indicating the absence of thermal activation. Therefore, we conclude that the conduction mechanism through alkanethiol is tunneling, either direct or Flower–Nordheim. Direct tunneling happens when the applied bias is less than the barrier height ($V < \Phi_B/e$), while Fowler–Nordheim tunneling is dominant when the applied bias becomes larger than the barrier height ($V > \Phi_B/e$). These two tunneling mechanisms can be distinguished due to their distinct voltage dependencies. Analysis of $\ln(I^2/V)$ versus $1/V$ [in Fig. 11b] shows no significant voltage dependence, indicating no obvious Fowler–Nordheim transport behavior in this bias range (0 to 1.0 V) and thus determining that the barrier height is larger than the applied bias, that is, $\Phi_B > 1.0$ eV. This study is restricted to applied biases $\leq 1.0$ V. The transition from direct tunneling to Fowler-Nordheim tunneling requires higher applied bias.

To describe the tunneling transport through a molecular system having HOMO and LUMO energy levels, one of the applicable models is the Franz two-band with a gap model [81–84]. This model provides a nonparabolic energy-momentum ($E$-$k$) dispersion relationship by considering the contributions of both conduction band (corresponding to LUMO) and valence band (corresponding to HOMO) [81],

$$k^2 = \frac{2m^*}{\hbar^2} E \left(1 + \frac{E}{E_g}\right) \qquad (1)$$

where $k$ is the imaginary part of the wave vector of electrons, $m^*$ is the electron effective mass, $h$ $(= 2\pi\hbar)$ is Planck's constant, $E$ is the electron energy, and $E_g$ is the bandgap.

From this nonparabolic $E$-$k$ relationship, the effective mass of the electron tunneling through the molecular wires can be deduced by knowing the barrier height of the metal-SAM-metal junction [82]. When the Fermi level of the metal
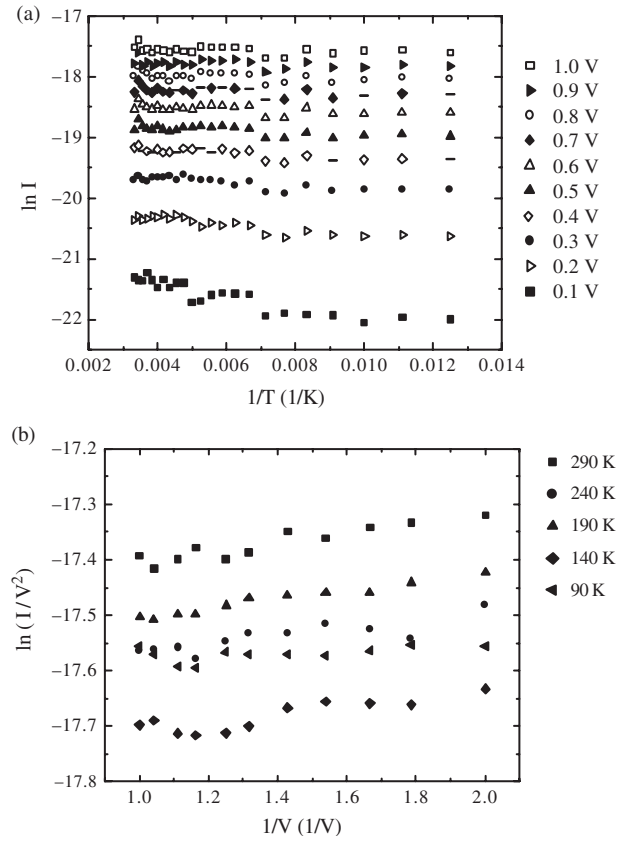
is aligned close enough to one band, the effect of the other distant band on the tunneling transport is negligible, and the widely used Simmons model [85] is an excellent approximation [86]. In the following we use the Simmons model to characterize our experimental $I(V)$ data, and later compare it to the Franz model to examine the validity of the approximation.

From the Simmons model, the tunneling current density through a barrier in the direct tunneling regime ($V < \Phi_B/e$) is given by [74, 85]

$$
\begin{aligned}
J = &\left(\frac{e}{4\pi^2\hbar d^2}\right)\left\{\left(\Phi_B - \frac{eV}{2}\right)\exp\left[-\frac{2(2m)^{1/2}}{\hbar}\right.\right. \\
&\times \alpha\left(\Phi_B - \frac{eV}{2}\right)^{1/2} d\bigg] - \left(\Phi_B + \frac{eV}{2}\right) \\
&\times \exp\left[-\frac{2(2m)^{1/2}}{\hbar}\alpha\left(\Phi_B + \frac{eV}{2}\right)^{1/2} d\right]\bigg\} \quad (2)
\end{aligned}
$$

where $m$ is electron mass, $d$ is barrier width, $\Phi_B$ is barrier height, $V$ is applied bias, and $\alpha$ is a unitless adjustable parameter that is introduced to modify the simple rectangular barrier model or to account for an effective mass [73, 74, 85]. $\alpha = 1$ corresponds to the case for a rectangular barrier and bare electron mass and previously has been shown not

to fit $I(V)$ data well for some alkanethiol measurements at fixed temperature (300 K) [74].

From Eq. (2), by adjusting two parameters $\Phi_B$ and $\alpha$, a nonlinear least-squares fitting can be performed to fit the measured C12 $I(V)$ data.[9] By using a device size of 45 nm in diameter, the best fitting parameters (minimized $\chi^2$) for the room temperature C12 $I(V)$ data were found to be $\Phi_B = 1.42 \pm 0.06$ eV and $\alpha = 0.65 \pm 0.02$ (C12, 300 K), where the error ranges of $\Phi_B$ and $\alpha$ are dominated by potential device size fluctuations of 7 nm (estimated from SEM image [75]). A second independently fabricated device with C12 gave values of $\Phi_B = 1.37 \pm 0.06$ eV and $\alpha = 0.66 \pm 0.02$. Likewise, a data set was obtained and fitting was done for hexadecanethiol (C16), which yielded values of $\Phi_B = 1.40 \pm 0.04$ eV and $\alpha = 0.68 \pm 0.02$ (C16, 300 K).

Using $\Phi_B = 1.42$ eV and $\alpha = 0.65$, a calculated $I(V)$ for C12 is plotted as a solid curve in Figure 12. A calculated $I(V)$ for $\alpha = 1$ and $\Phi_B = 0.65$ eV (which gives the best fit at low bias range) is shown as the dashed curve in the same figure, illustrating that with $\alpha = 1$ only limited regions of the $I(V)$ can be fit (specifically here, for $V < 0.3$ V). Although the physical meaning of $\alpha$ is not unambiguously defined, it provides a way of applying the tunneling model of a rectangular barrier to tunneling either through a nonrectangular barrier [74], a proposed effective mass ($m^*$) of the tunneling electrons through the molecules [73, 82], (i.e., for $\alpha = 0.65$, $m^*$ would be 0.42 m here), or a combination of both. Note that the $I(V)$ data can be fit to arbitrary accuracy over the entire bias range by allowing a slight bias dependence of $\alpha$ (or $\Phi_B$).

Nonlinear least-squares fittings on C12 $I(V)$ data at all temperatures allow us to determine $\{\Phi_B, \alpha\}$ over the entire temperature range and show that $\Phi_B$ and $\alpha$ values are temperature-independent in our temperature range (300 to 80 K). For the first C12 sample reported, values of $\Phi_B = 1.45 \pm 0.02$ eV and $\alpha = 0.64 \pm 0.01$ were obtained [$1\sigma_M$ (standard error)].

Equation (2) can be approximated in two limits: low bias and high bias as compared with the barrier height $\Phi_B$. For the low bias range, Eq. (2) can be approximated as [85]

$$J \approx \left(\frac{(2m\Phi_B)^{1/2}e^2\alpha}{h^2 d}\right)V \exp\left[-\frac{2(2m)^{1/2}}{\hbar}\alpha(\Phi_B)^{1/2}d\right] \quad (3a)$$

To determine the high bias limit, we compare the relative magnitudes of the first and second exponential terms in Eq. (2). At high bias, the first term is dominant and thus the current density can be approximated as

$$J \approx \left(\frac{e}{4\pi^2\hbar d^2}\right)\left\{\left(\Phi_B - \frac{eV}{2}\right)\exp\left[-\frac{2(2m)^{1/2}}{\hbar}\right.\right.$$
$$\left.\left. \times \alpha\left(\Phi_B - \frac{eV}{2}\right)^{1/2}d\right]\right\} \quad (3b)$$

According to the Simmons model, at low bias, the tunneling current is dependent on the barrier width $d$ as $J \propto$
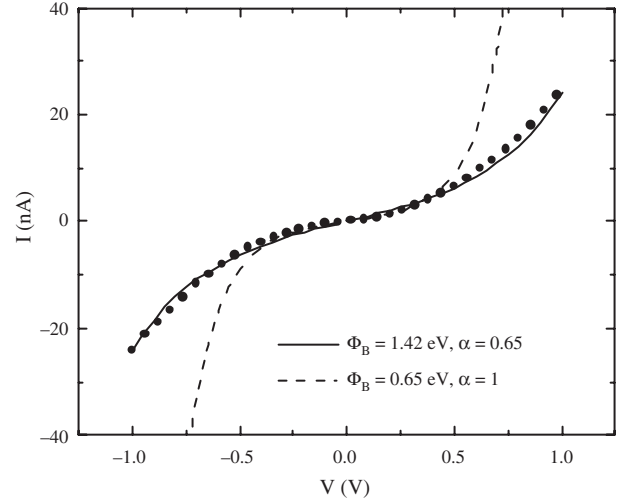


**Figure 12.** Measured C12 $I(V)$ data (circular symbols) are compared with the calculated ones (solid curve) using the optimum fitting parameters of $\Phi_B = 1.42$ eV and $\alpha = 0.65$. Calculated $I(V)$ from the simple rectangular model ($\alpha = 1$) with $\Phi_B = 0.65$ eV is also shown as a dashed curve.

$(1/d)\exp(-\beta_0 d)$, where $\beta_0$ is the bias-independent decay coefficient:

$$\beta_0 = \frac{2(2m)^{1/2}}{\hbar}\alpha(\Phi_B)^{1/2} \quad (4a)$$

while at high bias, $J \propto (1/d^2)\exp(-\beta_V d)$, where $\beta_V$ is the bias-dependent decay coefficient:

$$\beta_V = \frac{2(2m)^{1/2}}{\hbar}\alpha\left(\Phi_B - \frac{eV}{2}\right)^{1/2} = \beta_0\left(1 - \frac{eV}{2\Phi_B}\right)^{1/2} \quad (4b)$$

At high bias $\beta_V$ decreases as bias increases [Eq. (4b)], which results from the barrier lowering effect due to the applied bias.

We define the high bias range somewhat arbitrarily by comparing the relative magnitudes of the first and second exponential terms in Eq. (2). Using $\Phi_B = 1.42$ eV and $\alpha = 0.65$ obtained from nonlinear least-squares fitting of the C12 $I(V)$ data, the second term becomes less than $\sim 10\%$ of the first term at $\sim 0.5$ V that is chosen as the boundary of low and high bias ranges.

To determine the decay coefficient values for alkanethiols used in this study, three alkanethiols of different molecular length, octanethiol (C8), dodecanethiol (C12), and hexadecanethiol (C16), were investigated to generate length-dependent $I(V)$ data. Figure 13 is a log plot of tunneling current densities multiplied by molecular length ($Jd$ at low bias and $Jd^2$ at high bias) as a function of the molecular length for these alkanethiols. The molecular lengths used in this plot are 13.3, 18.2, and 23.2 Å for C8, C12, and C16, respectively (each molecular length was determined by adding an Au-thiol bonding length to the length of the molecule [72]). Note that these lengths implicitly assume "through-bond" tunneling, that is, along the tilted molecular chains between the metal contacts [72].

---

[9] Nonlinear least-squares of fittings were performed using Microcal Origin 6.0.
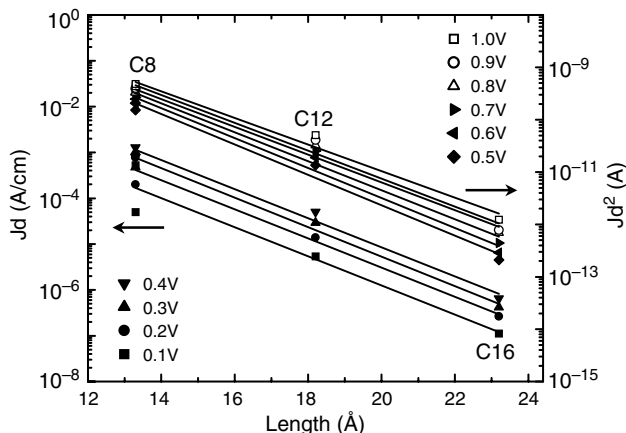
**Figure 13.** Log plot of tunneling current densities multiplied by molecular length $d$ at low bias and by $d^2$ at high bias (symbols) versus molecular lengths. The lines are plotted from linear fittings.



**Figure 15.** Summary of $\Phi_B$ (square symbols) and $\alpha$ (circular symbols) values obtained from alkanethiol $I(V)$ fittings and $\beta_V^2$-$V$ fitting.

As seen in Figure 13, the tunneling current shows exponential dependence on molecular length. The $\beta$ values can be determined from the slope at each bias and are plotted in Figure 14. The error bar of an individual $\beta$ value in this plot was obtained by considering both the device size uncertainties and the linear fitting errors.

According to Eq. (4b), $\beta_V^2$ depends on bias $V$ linearly in the high bias range. The inset in Figure 14 is a plot of $\beta_V^2$ versus V in this range (0.5 to 1.0 V) along with linear fitting of the data. From this fitting, $\Phi_B = 1.32 \pm 0.18$ eV and $\alpha = 0.63 \pm 0.03$ were obtained from the intercept and the slope, respectively, consistent with the more precise values obtained from the nonlinear least-squares fitting previously. The $\Phi_B$ (square symbols) and $\alpha$ (circular symbols) values obtained by the C12 and C16 $I(V)$ data fittings and $\beta_V^2$-$V$ linear fitting are summarized in Figure 15. The combined values are $\Phi_B = 1.39 \pm 0.01$ eV ($1\sigma_M$) and $\alpha = 0.65 \pm 0.01$

$(1\sigma_M)$. Using Eq. (4a), we can derive a zero field decay coefficient $\beta_0$ of $0.79 \pm 0.01$ Å$^{-1}$.

Decay coefficients for alkanethiol tunneling obtained by various experimental techniques have previously been reported [71–74, 78–80]. These reported decay coefficients were mainly deduced from the equation [16, 20]

$$G = G_0 \exp(-\beta d) \tag{5}$$

which has no explicit length factor $d$ in $G_0$. The $\beta$ values determined from Eq. (5) are generally different from those determined from $J \propto 1/d \exp(-\beta_0 d)$ or $J \propto 1/d^2 \exp(-\beta_V d)$ that were deduced from the Simmons model.

In order to compare with the previously reported $\beta$ values, we also performed length-dependent analysis on our experimental data according to Eq. (5). This gives a $\beta$ value from 0.83 to 0.72 Å$^{-1}$ in the bias range from 0.1 to 1.0 V, which is within the range of the results reported previously. For example, Holmlin et al. reported a $\beta$ value of 0.87 Å$^{-1}$ by mercury-drop experiments [74]. Wold et al. [72] have reported $\beta$ of 0.94 Å$^{-1}$ and Cui et al. [73] reported $\beta$ of 0.64 Å$^{-1}$ for various alkanethiols by using the conducting atomic force microscope technique. These reported $\beta$ values were treated as bias-independent quantities, contrary to the results reported here and that observed in a slightly different alkane system (ligand-encapsulated nanoparticle/alkane-dithiol molecules) [87].

We have also analyzed our experimental data using the Franz two-band model [81, 83, 84]. Since there is no reliable experimental data on the Fermi level alignment in these metal-SAM-metal systems, $\Phi_B$ and $m^*$ are treated as adjustable parameters. We performed least-squares fitting on our data with the Franz nonparabolic $E$-$k$ relationship [Eq. (1)] using the alkanethiol HOMO-LUMO gap of 8 eV [88].[10] Figure 16 shows the resultant $E$-$k$ relationship



**Figure 14.** Plot of $\beta$ versus bias in low bias range (square symbols) and high bias range (circular symbols). The inset shows a plot of $\beta_V^2$ versus bias with a linear fitting.

[10] Although the HOMO-LUMO gap of alkyl chain type molecules has been reported (See [88]), three are no experimental data on HOMO-LUMO gap for Au/alkanethiol SAM/Au system. Eight eV is commonly used as HOMO-LUMO gap of alkanethiol.
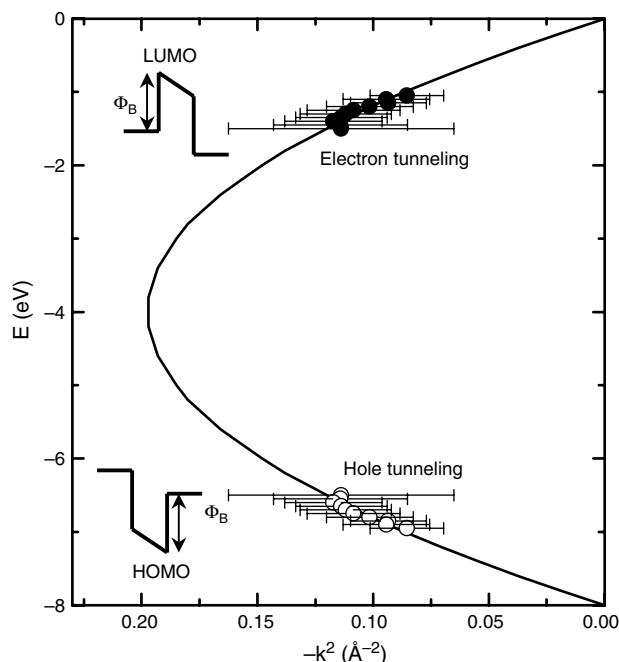
Figure 16. *E-k* relationship (symbols) generated from the length-dependent measurement data for alkanethiols. Solid and open symbols correspond to electron and hole tunnelings, respectively. The insets show the corresponding energy band diagrams. The solid curve is the Franz two-band expression for $m^* = 0.38$ m.

(following [83, 84]) and the corresponding energy band diagrams. The best fitting parameters by minimized $\chi^2$ were obtained as $\Phi_B = 1.55 \pm 0.59$ eV and $m^* = (0.38 \pm 0.20)$ m. Both electron tunneling around LUMO and hole tunneling around HOMO in the forbidden gap can be described by these parameters. $\Phi_B = 1.55$ eV indicates that the Fermi levels are aligned close to one band in either case; therefore the Simmons model is a valid approximation. The previous best fits obtained from the Simmons model of $\Phi_B = 1.39$ eV and $\alpha = 0.65$ (corresponding to $m^* = 0.42$ m for the rectangular barrier case) are in reasonable agreement.

## 4.3. Isocyanide SAM

Unlike alkanethiol, conjugated molecules (e.g., phenylene-type molecules) have delocalized $\pi$ orbitals throughout the length of the molecules, thus exhibiting different electronic properties (see Section 2.2). In the following, we investigate the through-bond electronic conduction for metal/phenylene diisocyanide SAM-metal junctions to study the transport mechanism as well as the effect of isocyanide-metal contacts.

Unlike the extensive research on thiol SAMs, very little has been reported on isocyanide SAMs. Angelici and co-workers reported the binding of aryl isocyanides to gold powder [89, 90]; their infrared spectroscopy measurements on 1,4-phenylene diisocyanide-gold show there exist two CN bands: an unbound CN and a CN bound perpendicular to gold. Henderson et al. [58] studied surface structure properties of aryl diisocyanides on gold film deposited on silicon substrate and reached the same conclusion.

Isocyanides have a high affinity for transition metals (e.g., W, Pd, Pt, etc.). When they bind to metal surfaces, it forms
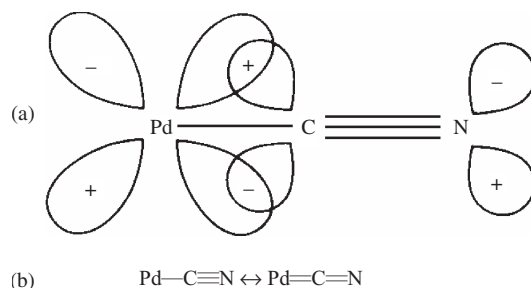


Figure 17. (a) $\pi$ bond between *d* orbital on Pd and antibonding orbital ($\pi^*$) on the isocyanide group. (b) Partial double bond resonance between Pd and CN.

so-called "backbonding" [91]. In the language of molecular orbital theory, that means that the metal (e.g., Pd) *d* orbital overlaps with the $\pi^*$ orbital of the ligand, for example, isocyanide (Fig. 17a). In this way, the delocalization of the electron density occurs via the overlap of *d* orbitals on the metal with orbitals of the ligand. The electron density is shifted via the $\pi$ bond from the metal atom to the ligand. The greater the amount of metal-C $\pi$ bonding, the less $\pi$ bonding can occur between C and N, giving rise to the partial double bond resonance structure as illustrated in Figure 17b. The metal-1,4 phenylene-diisocyanide-metal thus forms a delocalized $d\pi$-$p\pi$-$d\pi$ system (Fig. 18a), whereas Au-1,4 dithiol benzene-Au forms a $\sigma$-$p\pi$-$\sigma$ system (Fig. 18b). For symmetry reasons, the delocalized $\pi$ states within the conjugated molecule cannot couple strongly to the localized $\sigma$ states at the interface. These $\sigma$ states do not serve as efficient "bridging states" between the molecule and the metal. Therefore we expect a smaller contact barrier in the CN-metal (e.g., CN-Pd) system with $d\pi$-$p\pi$-$d\pi$ orbital overlap than that in S-Au system with $\sigma$-$p\pi$-$\sigma$ orbital overlap.
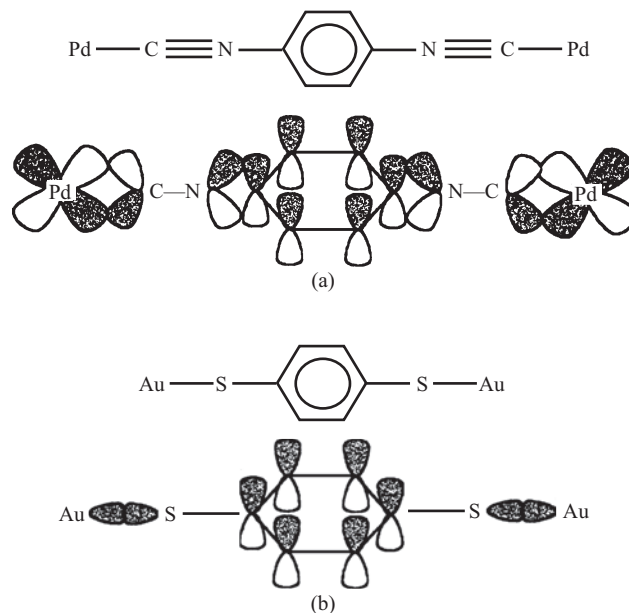


Figure 18. Bonding molecular orbital for metal bridged with (a) aromatic isocyanide and (b) aromatic thiols.

### 4.3.1. Au-Isocyanide-Au Junctions

Electronic measurements were performed in a nano-structure that has a metal top contact, a SAM active region, and a metal bottom contact. This nanostructure is similar to that reported previously (Section 3) [36], and is illustrated in Figure 19. To deposit the SAM layer onto the first metallic contact, the sample is transferred immediately into 1 mM 1,4-phenylene diisocyanide in toluene (Aldrich) under an inert atmosphere of Ar. After 48 hr, the sample is taken out, rinsed with fresh toluene, and gently blown dry with $N_2$ gas. It is then loaded into a high vacuum chamber right away for the top layer metallization.

Although the Au-isocyanide SAM-Au system appears to be symmetric, there is a subtle difference in the two SAM-metal interfaces formed during the fabrication process (Fig. 19). The first interface is formed when isocyanide chemisorbs onto gold surface; the second interface is formed when gold is evaporated onto isocyanide as pointed out in Figure 19. We refer to them as the chemisorbed contact and the evaporated contact, respectively.

To determine the effective transport characteristics, $I(V, T)$ measurements are performed from 300 to 20 K with the voltage swept between $-1$ to $+1$ V.[11] Figure 20 shows the $I(V)$ characteristics of a gold-isocyanide SAM-gold junction from 20 K to 300 K in 20-K increments. Positive bias corresponds to electron injection from the evaporated metal-SAM contact. Current changes five orders of magnitude over 300 K and freezes out at low temperature. This dramatic change of current with temperature suggests an activated type of behavior. Figure 21 illustrates reduced $I(T)$ characteristics at various voltages; one sees that the dependence of $\ln(I/T^2)$ versus $1/T$ (0.1 to 1 V) has a clear linear dependence at biases less than 0.7 V. This dependence is characteristic of thermionic emission [65–67], where

$$I = A^* T^2 \exp\left(-\frac{q\Phi - a\sqrt{V}}{kT}\right), \qquad a = q\sqrt{\frac{q\Phi}{4\pi\varepsilon_0\varepsilon d}}$$

where $A^*$ is the effective Richardson constant multiplied by the current injection area, $\Phi$ is the thermal emission barrier height, $k$ is Boltzmann's constant, $q$ is the electron charge, $\varepsilon_0$ is the vacuum dielectric constant, $\varepsilon$ is the relative dielectric constant of the isocyanide SAM, and $d$ is the thickness of the film.[12] For $V > 0.7$ ($E \sim 7$ MV/cm), deviation from a linear dependence is observed; the origin is not known, but it is probably due to high field breakdown effects. One possible scenario is that at high field, impact ionization generates electron-hole pairs, and the resulting hole current cancels the electron injection.

Below 0.1 V, the dependence does not have the voltage dependence characteristic of thermionic emission, and instead one finds a linear dependence of $\ln(I/V)$ versus $1/T$. This dependence is characteristic of hopping conduction, where

$$\ln(I/V) = f(N) - \Delta E/(kT)$$

[11] At low temperatures ($\sim$40 K), biases higher than 1 V are applied.

[12] The length of 1,4 phenylene-diisocyanide is calculated to be 10 Å with the molecule oriented normal to the gold surface. It agrees with the ellipsometry measurement by Henderson et al. [58].
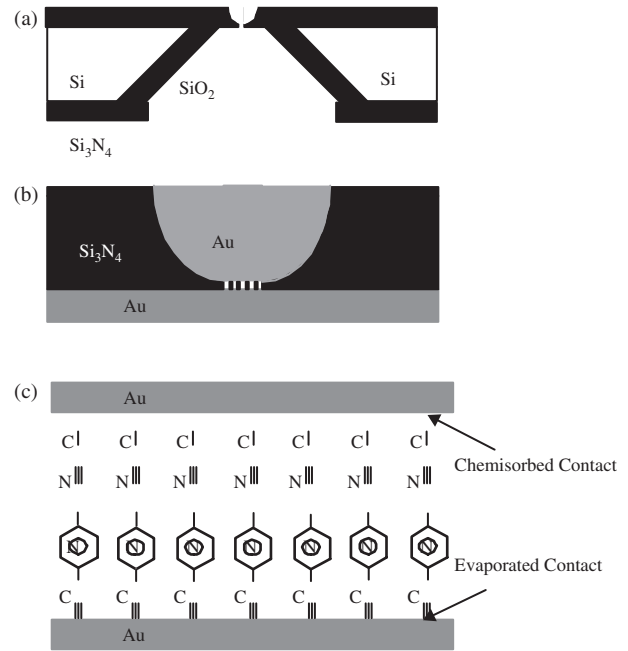


**Figure 19.** Schematics of device fabrication: (a) cross section of a silicon wafer with a nanopore etched through a suspended silicon nitride membrane. (b) Au-SAM-Au junction in the pore area. (c) Blowup of (b) showing 1,4-phenylene diisocyanide sandwiched in the junction, with the chemisorbed and evaporated contacts pointed out by the arrows.

where $\Delta E$ is the activation energy to hop from one site to another and $f(N)$ is a function of the trap concentration [66]. Figure 22 shows this dependence in the regime of bias less than 0.1 V. Whereas the physical interpretation of the thermionic transport barrier is clearly the molecule-metal contact potential, the physical site giving rise to hopping transport is less well defined. Structural defects in the nanopore or edge defects are potential candidates for the low-bias defect-mediated transport.
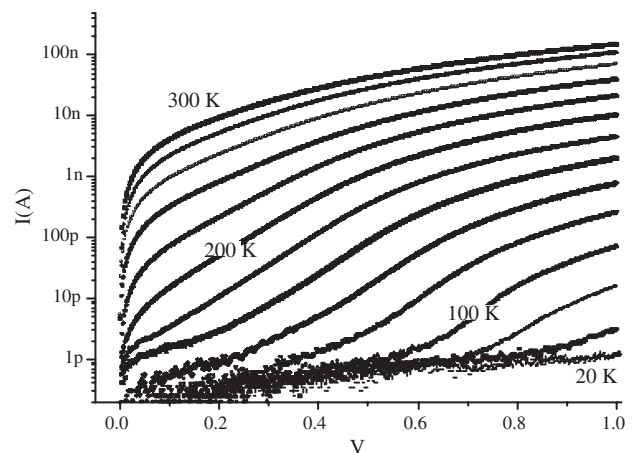


**Figure 20.** $I(V)$ characteristics of a Au-isocyanide SAM-Au junction from 20 to 300 K, with 20 K increments. Positive bias corresponds to electron injection from evaporated SAM-Au contact. The curves at 20 and 40 K overlap with each other.
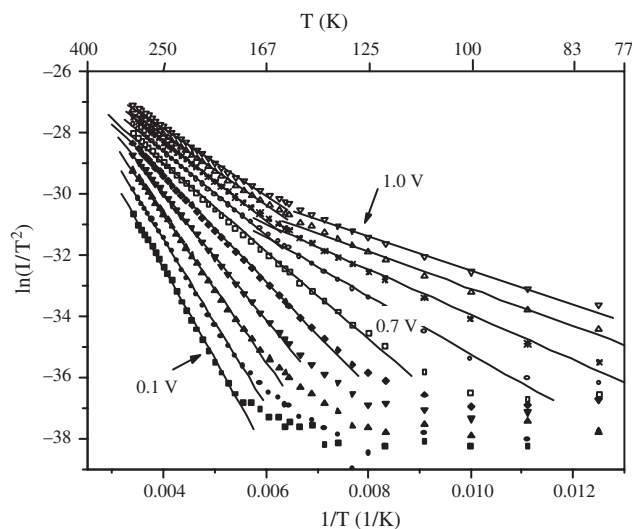
**Figure 21.** Series of plots of $\ln(I/T^2)$ versus $1/T$ at biases from 0.1 to 1.0 V with 0.1 V increments, for the Au-SAM-Au junctions. All the straight lines are $\chi^2$ fits for respective data sets.

To determine the energetic barriers, we plot the slope of $(\ln(I/T^2)$ versus $1/T)$ versus $V^{0.5}$ in Figure 23. For the isocyanide-Au contact, we obtain for 0.1 V $< V <$ 1 V that the intercept of the line fit gives $-q\Phi/k$, with a thermionic barrier of $\Phi = 0.38$ ($\pm 0.01$) eV; the slope of the line fit gives $a/k$, where $a = q(q\Phi/(4\pi\varepsilon_0\varepsilon d))^{0.5}$, with the dielectric constant of the isocyanide film $\varepsilon$ of 3.5. The effective Richardson constant can be obtained from Figure 21. With a device area of $300 \times 300$ Å$^2$, the effective Richardson constant was found to be around 120 A/cm$^2$ at low electrical field and 40 A/cm$^2$ at high fields ($E > 7$ MV/cm). This could be caused by reduced effective area at high current density/high electrical fields around nonuniform metal-SAM interfacial regions. For 0 V $< V <$ 0.1 V, the slope does not depend on bias voltage. A hopping barrier of $\Delta E = 0.3$ ($\pm 0.01$) eV is obtained from the slope $[\ln(I/V)$ versus $1/T]$ of Figure 22.
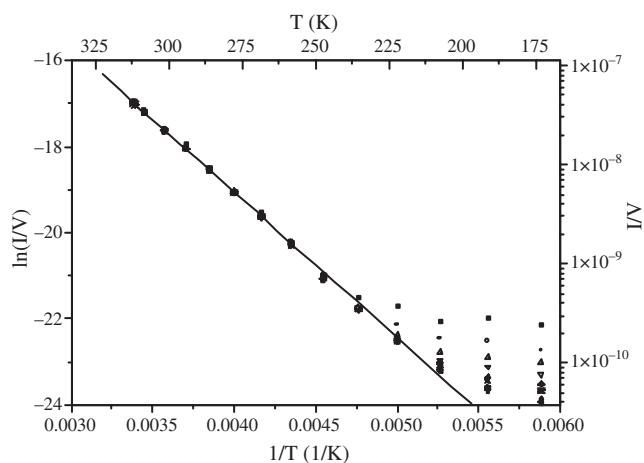


**Figure 22.** $\ln(I/V)$ versus $1/T$ at biases less than 0.1 V, for the Au-SAM-Au junctions. The straight line is the $\chi^2$ fit for the data set.
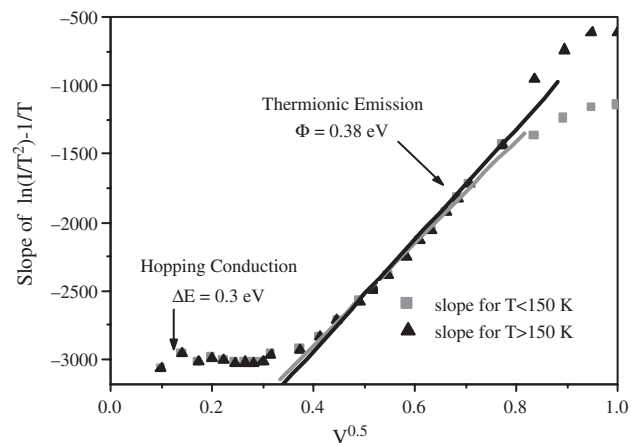


**Figure 23.** Plot of the slope of $[\ln(I/T^2)$ versus $1/T]$ versus $V^{0.5}$: at $0 < V < 0.1$ V, no bias dependence; at $V > 0.1$ V, linear dependence. Thermal barrier height of the Au-SAM-Au junction can be deduced from the intercept of the straight line.

When the junction is biased in the reverse direction such that electrons are injected from the chemisorbed Au-isocyanide contact, similar activation behavior is observed from $-0.01$ to $-1$ V (Fig. 24). The current changes more than five orders of magnitude over 200 K at both low and high bias regime. The barrier height is determined in Figure 25, where the slope of $[\ln(I/T^2)$ versus $1/T]$ was plotted against $V^{0.5}$. The intercept of the line fit gives a thermionic barrier of $\Phi = 0.35$ ($\pm 0.01$) eV and an effective Richardson constant of 120 A/cm$^2$. As schematically denoted in Figure 8, the observation of the various mechanisms in a given junction will depend on both the magnitude of the various barriers and the defect density. If the thermionic emission barrier is too large, such as in the case of thiol-like termini onto Au, only the hopping barrier would be observable. As defect-mediated conduction is a complicated function of trap concentration and details, a significantly more extensive study would be necessary to elucidate
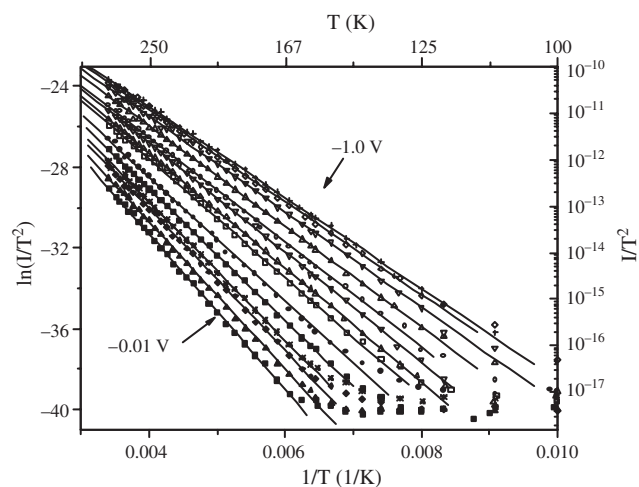


**Figure 24.** A series of plots of $\ln(I/T^2)$ versus $1/T$ at biases from $-0.01$ V to $-1.0$ V for the Au-SAM-Au junctions. All the straight lines are $\chi^2$ fits for respective data sets.
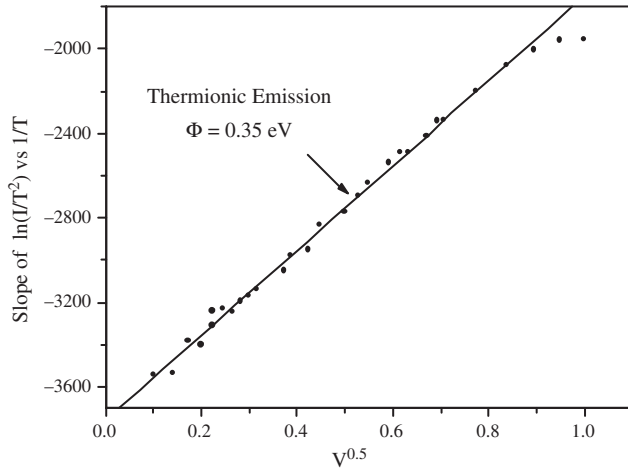
**Figure 25.** Plot of the slope of $[\ln(I/T^2)$ versus $1/T]$ versus $V^{0.5}$ of a Au-SAM-Au junction shows a linear dependence. Thermal barrier height of the junction can be deduced from the interception of the straight line. The straight line is the $\chi^2$ fit for the data set.

the nature and effects of process on the defects. The present study serves to identify the characteristic energy, although the origin and density (and thus the current magnitude) are not well controlled. From our experiment, under negative bias (chemisorbed metal-SAM contact), we only observe thermionic emission, with an unobservable defect component. Under positive bias (evaporated metal-SAM contact), the defect component is larger, and we observe both simultaneously. The above result suggests that defects are likely located at the evaporated metal-SAM interface, possibly introduced during metal evaporation onto the organic film surface.

### 4.3.2. Pd-Isocyanide-Pd Junctions

Because the fabrication technique is generalizable to different termini and metals, it is easy to compare the effects of different contacts. Utilizing the same fabrication technique but instead substituting the metal Au with Pd, Pd-1,4-phenylene diisocyanide-Pd junctions were fabricated and measured as before. Figure 26 shows the $I(V)$ characteristics from 50 to 290 K at 20-K increments when electrons were injected from the chemisorbed Pd-isocyanide contact. Notice that currents are larger than those of a Au-SAM-Au junction as shown in Figure 20, suggesting a smaller contact barrier. Figure 27 shows plots of: (a) $\ln(I/V)$ versus $1/T$ (low bias), illustrating hopping conduction; and (b) $\ln(I/T^2)$ versus $1/T$ (high bias), illustrating thermionic emission. The barrier heights are obtained in Figure 28, which illustrates the slope of $[\ln(I/T^2)$ versus $1/T]$ versus $V^{0.5}$ at negative bias, and we have (a) for $-0.1 < V < 0$ V, a hopping barrier of $\Delta E = 0.19$ ($\pm 0.02$) eV; (b) for $V < -0.1$ V, a thermionic emission barrier of $\Phi = 0.22$ ($\pm 0.02$) eV, with a fitted Richardson constant of 130 A/cm$^2$ at low field and 30 A/cm$^2$ at high electrical field ($E > 5$ MV/cm). The larger fitted Richardson constant could be caused by deviation in device area, while the smaller fitted Richardson constant could be due to reduced effective area at high current density/high electrical fields around nonuniform metal-SAM interfacial regions. In this case, the unidentified defect component was
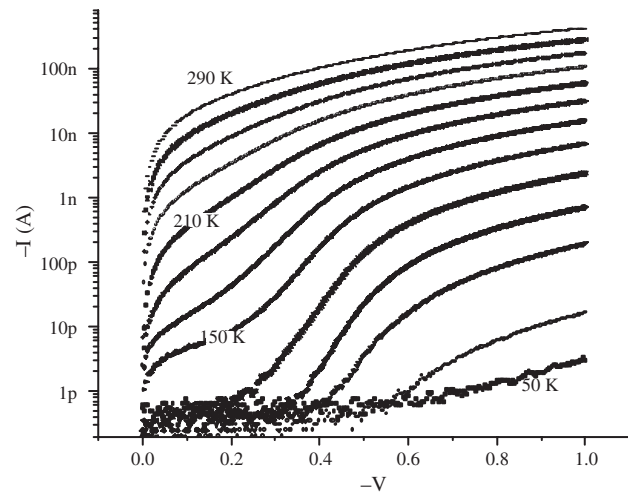


**Figure 26.** $I$-$V$ characteristics of a Pd-isocyanide SAM-Pd junction from 50 to 290 K, with 20-K increments. Negative voltage bias corresponds to electron injection from the chemisorbed SAM-Pd contact. The axes are converted into positive values such that $I$ can be expressed in ln scale.
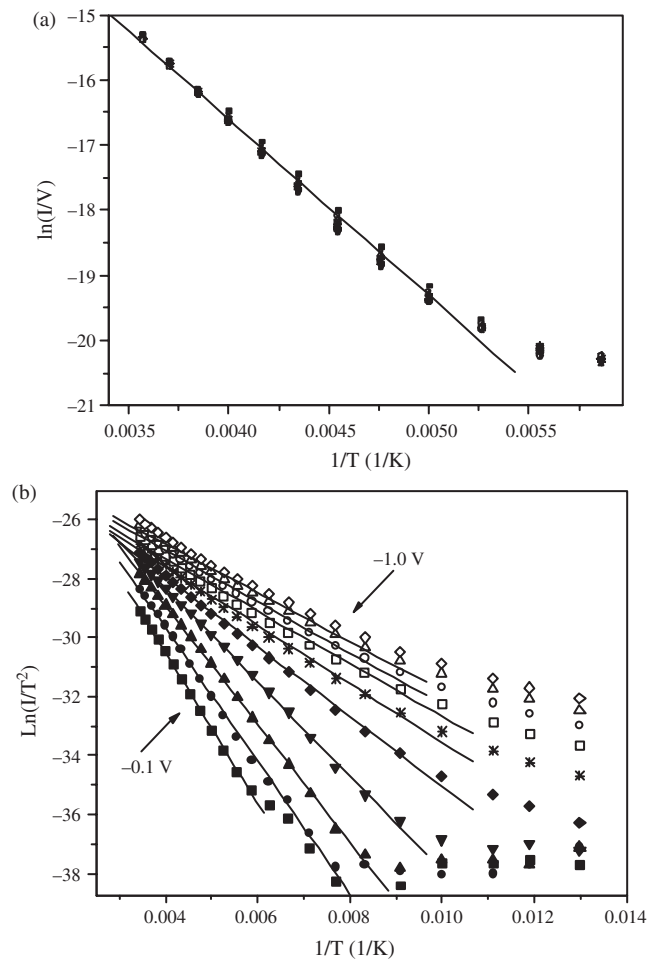


**Figure 27.** Pd-SAM-Pd junction: (a) $\ln(I/V)$ versus $1/T$ at biases larger than $-0.1$ V; (b) series of plots of $\ln(I/T^2)$ versus $1/T$ at biases from $-0.1$ to $-1.0$ V at $-0.1$-V increments. All the straight lines are $\chi^2$ its for respective data sets.
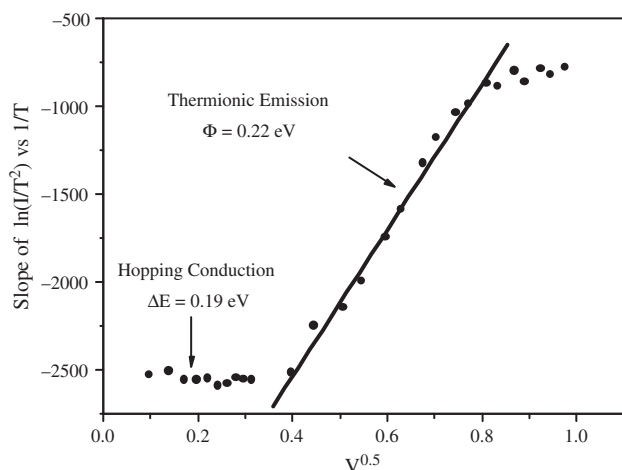
**Figure 28.** Plot of the slope of $[\ln(I/T^2)$ versus $1/T]$ versus $V^{0.5}$: at $-0.1V < V < 0$, no bias dependence; at $V < -0.1$ V, linear dependence. Thermal barrier height of the Pd-SAM-Pd junction can be deduced from the interception of the straight line.

large enough such that both thermionic emission and hopping are observed. When electrons are injected from the evaporated Pd-CN contact, the defect component is so large that only hopping is observed, with a barrier height of 0.21 ($\pm 0.02$) eV.

As seen from above results, the contact barrier between Au-isocyanide SAM is larger than that of Pd-isocyanide SAM. The difference is most likely caused by different electronic configurations between the two metals. In the noble metal Au, the $d$ shell is completely occupied and there is a single valence $s$ electron on the outer shell. The Fermi level of Au lies far enough above the $d$ band for the $s$ band to intersect $\varepsilon_F$ (Fermi surface) at points where it is still quite similar to the free electron band [92]. Consequently, the Fermi surface of Au is a slightly distorted free electron sphere. In the transition metal Pd, electrons are regarded as occupying overlapping $s$ and $d$ bands [93]. Unlike noble metals, the $d$ band in transition metals extends through the Fermi energy. When levels on the Fermi surface are $d$-derived levels, the Fermi surface no longer resembles a slightly distorted free electron sphere. According to Mott [94], the valence electrons (of Pd) are shared between a wide, low density of states $s$ band and a narrow, high density of states $d$ band. This high density of states arises because the spatial extension of the $d$-electron wave functions is much less than that for the $s$ electrons, with consequently less overlap from atom to atom. Hence the $d$ band is narrower, yet it has to accommodate ten electrons compared to the $s$-band's two electrons. Shown in Figure 29 are some qualitative features of the $d$-band and $s$-band contributions to the density of states of a transition metal [92]. In a word, the $d$ band plays a dominant part in the electronic properties of a transition metal such as Pd. When Pd is brought into contact with isocyanide ligand, its $d$ orbital overlaps with the $\pi^*$ orbital of a ligand and forms a $d\pi$-$p\pi$ bond. However, when Au comes into contact with isocyanide, since its $d$ bands lie far below the Fermi surface, it cannot "backbond" to isocyanide effectively. The delocalization between Au and isocyanide is therefore not as efficient as that between Pd
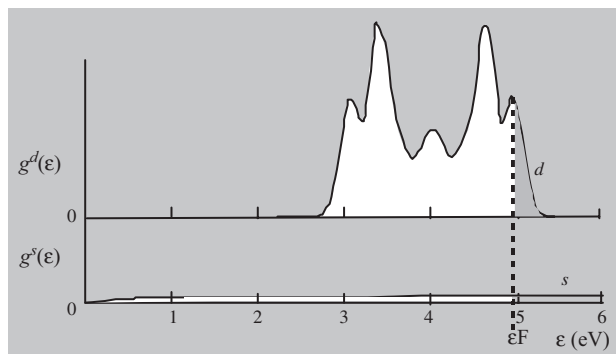


**Figure 29.** Some qualitative features of the $d$-band and $s$-band contributions to the density of states of a transition metal. The $d$ band is narrower and contains more levels than the $s$ band. Consequently, when the Fermi level (separating the shaded and unshaded regions) lies within the $d$ band, the density of states $g(\varepsilon_F)$ is very much larger than the free-electron-like contribution of the $s$ band alone. Reprinted with permission from J. M. Ziman, "Electrons and Phonons: The Theory of Transport Phenomena in Solids." Oxford Univ. Press, New York, 1960. © 1960, Oxford University Press. Adapted with permission from G. F. Foster, *Phys. Rev.* 98, 901 (1955). © 1955, American Physical Society.

and isocyanide. This could be responsible for the larger barrier height measured in Au-isocyanide SAM junctions.

Table 2 summarizes the results of the transport barriers of through-bond transport of isocyanide on the metals measured in this study. It is observed that thermal emission is the dominant conduction mechanism in chemisorbed metal-isocyanide junctions, while in the evaporated metal-isocyanide contact, both hopping and thermal emission can play an important role depending on the defect level introduced during the fabrication process. The barriers of both the chemisorbed and the evaporated contact are approximately the same, which is expected given the symmetry of the structure. It appears that the hopping component in the chemisorbed metal-molecule junction is less significant than that in the evaporated metal-molecule junction, which suggests that there are less defects in the chemisorbed metal-molecular interface. Overall, the Pd-CN contact barrier is smaller than that of a Au-CN junction. The technique reported here elucidates the relevant electronic transport barriers and conduction mechanisms of through-bond metal-molecule contacts, which have been possible through the implementation of microfabricated electronic devices utilizing SAMs. The technique should be applicable to a large range of inorganic and biomolecular transport measurements, to quantitatively measure the dominant electron transport mechanisms.

**Table 2.** Summary of the contact barriers and conduction mechanisms for various metal-isocyanide SAM interfaces.

| Metal | AU | Pd |
|---|---|---|
| Chemical contact | $0.35 \pm 0.01$ eV, thermionic | $0.22 \pm 0.02$ eV, thermionic ($0.19 \pm 0.02$ eV hopping at low bias) |
| Evaporated contact | $0.38 \pm 0.01$ eV, thermionic ($0.3 \pm 0.01$ eV hopping at low bias) | $0.21 \pm 0.02$ eV hopping |

# 5. DEVICE APPLICATIONS OF MOLECULAR LAYERS

Electronic switching and memory effects are known to exist in a wide variety of inorganic and organic materials. In 1979, Potember et al. [95] reported bistable, reproducible, and nanosecond electronic switching and memory phenomena in an organometallic charge-transfer complex salt CuTCNQ formed by TCNQ (7,7,8,8-tetracyano-$p$-quinodimethane), which acts as an electron acceptor with metallic copper as the electron-rich donor. In these materials the switching and memory phenomena are given rise to by the field-assisted structural changes such as phase transitions, crystallization, and metal filament formation assisted by highly localized Joule heating. However, the electronic behavior of these materials is mostly not stable or reproducible and usually requires high switching voltage [96].

In this section we discuss stable and reproducible switching and memory effects in SAM. We first present results on conformation-induced transition behavior and then demonstrate the realization of stable and reproducible large negative differential resistance (NDR) and charge storage in electronic devices that utilize a single redox-center-contained SAM as the active component. The devices exhibit electronically programmable and erasable memory bits with bit retention times greater than 15 min at room temperature.

## 5.1. Conductor-Insulator Transition Caused by Molecular Conformation

Molecular conformation[13] is one of the most important aspects of chemistry. When molecular systems have sufficient degrees of freedom to adopt a variety of shapes or forms, some of these forms can be associated with stretching or bending of bonds. For example, studies on mechanical distortions of bent nanotubes and crossing nanotubes show that they can exhibit substantial tubular deformations as well as bending and buckling, a factor in turn influencing their electronic transport characteristics [97].

On the other hand, molecular conformation is often associated with rotations of substituents around specific bonds. Zhou [63] observed that there exists a transition temperature below which the benzene rings of a tolane-like molecule assume a perpendicular configuration, but above which they assume a coplanar one. These devices are nanoscale Au/Ti/ethyl-substituted 4,4′-di(phenylene-ethynylene)-benzothiolate/Au junctions, fabricated using an inverted nanopore structure [63]. The experiments show that current first decreases gradually as temperature varies from room temperature to 30 K due to thermal activation; then a sharp decrease of two orders of magnitude in conductance resembling a transitional behavior is observed around 25 K (Fig. 30). Calculations by Seminario et al. show that the relative angle between two benzene rings in each tolane molecule determines its conductivity, being maximum at 0° and minimum at 90° [98]. At 10 K, phenyl rings in the tolane molecules show very little tendency to rotate and perpendicular tolanes are more stable than parallel tolane

---
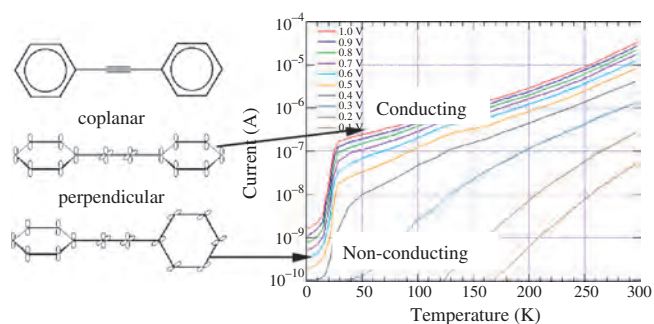


**Figure 30.** $I$-$T$ characteristics at different biases (0.1–1 V) of a Au/Ti/ethyl-substituted 4,4′-di(phenylene-ethynylene)-benzothiolate/Au junction. A sharp decrease in conductivity is observed around 25 K.

molecules—giving rise to smaller conductivity. At 30 K, the tolane rings are able to freely rotate with respect to each other, allowing the tolane molecules to be planar at some instant in time, consequently reaching higher conductivity.

## 5.2. Negative Differential Resistance in Molecular Junctions

The discovery of NDR in semiconductor diodes has opened a new chapter in semiconductor device physics and device development [98–104]. Through the use of NDR devices, circuits with complicated functions can be implemented with significantly fewer components [105–110]. There are various NDR devices such as Esaki tunnel diodes [98], Gunn effect diodes [99], resonant tunneling diodes [100], etc. caused by various physical mechanisms. For example, a Gunn effect diode, also known as a transferred electron diode, is given rise to by a field-induced transfer of conduction band electrons from a low-energy, high-mobility valley to higher-energy, low-mobility satellite valleys [101].

NDR was first discovered by Esaki [98] in 1958 in a tunnel diode (a highly degenerate $p$-$n$ junction). The physical basis of the tunnel diode, which is also called the Esaki diode, is interband tunneling between the valence band and the conduction band.

Another type of well-known NDR device is the resonant tunneling diode (RTD). Tsu and Esaki and co-worker proposed resonant tunneling shortly after molecular beam epitaxy (MBE) appeared in the field of compound semiconductor crystal growth in 1973 [100]. A RTD typically consists of an undoped quantum well layer (GaAs) sandwiched between undoped barrier layers (AlGaAs) and heavily doped emitter and collector contact regions [108]. Resonant tunneling through the double barrier structure occurs when the energy of the electrons flowing from the emitter coincides with the energy of the quantum well state (resonant state) in the quantum well. The effect of the external bias, $V$, is to sweep the alignment of the emitter and resonant states ($E_0$). Thus a resonant tunneling current starts to flow when the Fermi level $E_F$ in the emitter reaches the resonant state.

There are also some organic switching devices that exhibit NDR behavior, whereas their NDR behavior has been attributed to the formation of highly conducting filaments [111–113]. These filaments are formed by local joule heating which produces material rearrangement or even melting.

---

[13] Structures that differ only by rotation about one or more bonds are defined as conformations of a compound.

This type of organic switching device is insensitive to the polarity of the applied field but suffers from some material rearrangement or damage. Besides, the devices also need high switching power consumption, and the type of metal that was used for contacts also plays an important role. For instance, Gundlach and Kadlec have observed NDR in Al-(Al oxide)-arachidic acid-Al (or Au) junctions using the L–B technique [111], but short circuits were observed when they used Au for both junction electrodes. The presence of Al oxide is vital for their experiment to block leakage current around domain boundaries or defects in the L–B film (with a sample area of approximately 1 mm$^2$). The NDR they observed is not repeatable.

Here we discuss the realization of large NDR behavior and room temperature operation in an electronic device that utilizes special molecules as the active component. Unlike in Esaki diodes or in RTDs, the monolayer thickness is determined by the SAM thickness, which inherently/ultimately solves the monolayer fluctuation problem at the interfaces. Being different from bulk organic switching devices, our nanoscale NDR devices are both reproducible and reversible [38].

A molecule containing a nitroamine redox center [2′-amino-4,4′-di(ethynylphenyl)-5′-nitro-1-benzenethiolate] is used in the active SAM in the nanopore configuration discussed previously (Section 3). Its structure is illustrated in Figure 31. Apart from the ethynylphenyl-based backbone, there is a redox center introduced in the middle benzene ring: the electron-withdrawing nitro (-NO$_2$) group and the electron-rich amino (-NH$_2$) group.

To deposit the SAM layer onto gold electrode, we transfer the prefabricated nanopores into a 0.5-mM 2′-amino-4,4′-di(ethynylphenyl)-5′-nitro-1-(thioacetyl)benzene (**1a**)[14] in THF solution. The thioacetyl groups are then selectively hydrolyzed with ammonium hydroxide (concentrated aqueous 14.8M NH$_4$OH, 5 $\mu$L per mg of **1a**) in THF to yield the free thiol, 2′-amino-4,4′-di(ethynylphenyl)-5′-nitro-1-benzenethiol (**1b**), which forms the thiolate, 2′-amino-4,4′-(diethynylphenyl)-5′-nitro-1-benzenethiolate (**1**) upon exposure to Au after 48 hr [60] under an inert atmosphere of Ar. The sample was then prepared and characterized as discussed previously.

A device containing a SAM of conjugated molecules similar to **1** but not bearing the nitroamine functionalities was fabricated and measured in nearly identical conditions [63] and did not exhibit any NDR behavior. Therefore, the nitroamine redox center is responsible for the NDR behavior.

Typical $I(V)$ characteristics of a Au-(**1**)-Au device at 60 K are shown in Figure 32. Positive bias corresponds to hole injection from the chemisorbed thiol-Au contact and electron injection from the evaporated contact. The peak current density for this device was greater than 53 A/cm$^2$, the NDR is less than $-380$ $\mu\Omega$ cm$^2$, and the peak-to-valley (PVR) is 1030:1. Unlike previous devices that also used molecules to form the active region[15] [114], this device

---

[14] The starting compound (**1a**) was prepared by sequential Pd/Cu-catalyzed coupling of 2,5-dibromo-4-nitroacetanilide with phenylacetylene and 4-ethynyl (thioacetyl) benzene.

[15] Weak room-temperature NDR has been previously reported; See [114].
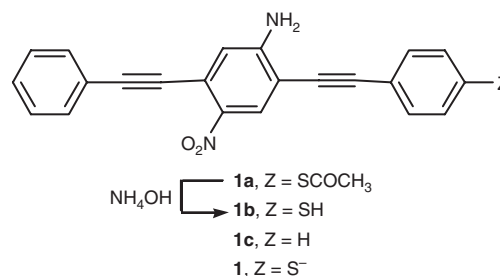


**Figure 31.** The structures of active molecular compound **1**, and its precursors, the free thiol **1b** and the thiol-protected system **1a**.

exhibits a robust and large NDR. Some device-to-device variations of peak voltage position ($\sim \times 2$) and peak current ($\sim \times 4$) were observed as shown in Figure 33.

Curve clusters 1–3 are from three different devices (numbered 1 through 3, respectively) on two different batches of wafers fabricated. Curves within each cluster are from the same device but from different runs at different time. Device-to-device current fluctuations can be attributed to fluctuations in the pore diameter size. As total voltage applied to the molecular junction can be divided into the voltage drop on the molecules and the voltage drop on the metal-molecule contacts, device-to-device peak voltage fluctuations can be caused by different voltage drops on the metal-molecule contacts. As shown by Di Ventra et al. [61], the detailed metal-molecule contact configuration plays an important part in the conductance of metal-molecular junctions. Different contact geometries caused by differences in fabrication processes, such as in etching and metallization, could result in different contact potentials.

The $I(V)$ curve is fully reversible upon change in bias sweep direction (from negative bias to positive bias) as shown in Figure 34; for a given device, small fluctuations ($\sim$1% in voltage peak position and $\sim$6% in peak current) are observed with consecutive positive and negative sweeps but could be attributed to temperature fluctuations of $\sim$2 K (within the experimental thermal stability). The
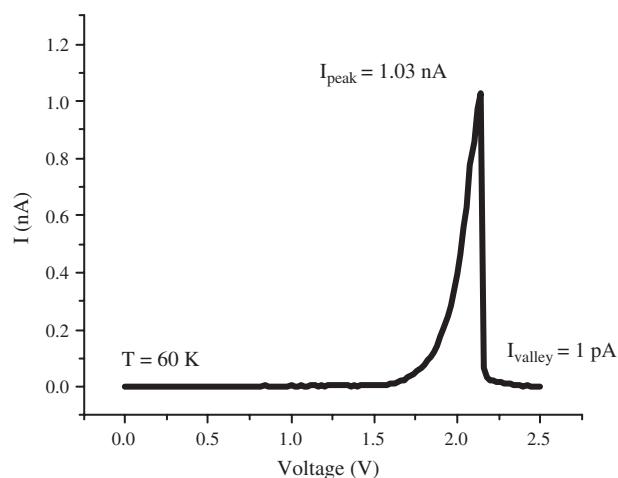


**Figure 32.** $I(V)$ characteristics of a Au-**1**-Au device at 60 K. The peak current density is $\sim$50 A/cm$^2$, the NDR is $\sim-400$ $\mu\Omega$ cm$^2$, and the PVR is 1030:1.
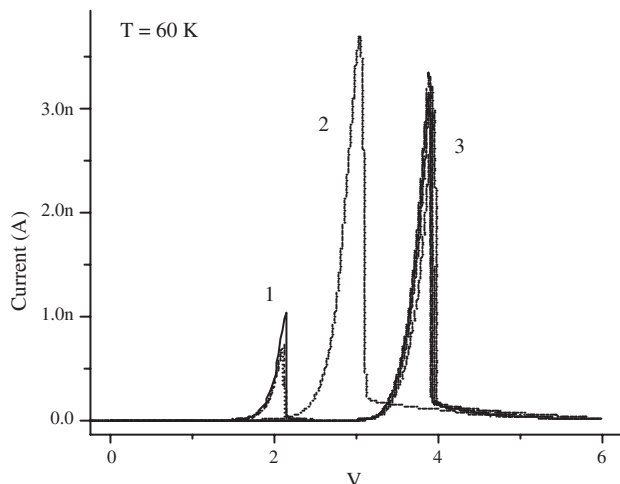
**Figure 33.** $I(V)$ characteristics of Au-**1c**-Au devices at 60 K. Curve clusters 1–3 are measured from different samples, while curves within one cluster are from the same sample but from different runs.

performance exceeds that observed in typical solid-state quantum well resonant tunneling heterostructures [115–118]. In addition to the obvious size advantages for scaling, the intrinsic device characteristics (that is, the valley current shutoff) may be superior to that of solid-state devices. The intrinsic PVR of the molecule may be considerably greater than that reported here because the valley currents observed (on the order of picoamperes) are comparable to typical leakage currents in the silicon nitride film.

## 5.3. Temperature Dependence

All of the Au-**1c**-Au devices examined exhibit peak voltage position and current magnitude shifts with temperature such as shown in Figure 35. We observe a decrease in peak intensity with increasing temperature. This could be caused by scattering in the junction. However, the fact that the peak intensity has a maximum at 60 K is not understood yet. It
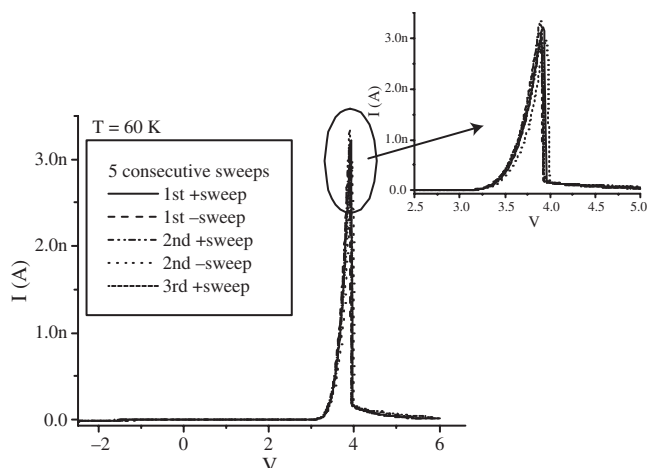


**Figure 34.** Forward $(-2 \rightarrow 6)$ V and reverse $(6 \rightarrow -2)$ V sweeps on a Au-**1c**-Au junction at 60 K. The inset shows the blowup of the sweeps around peak.
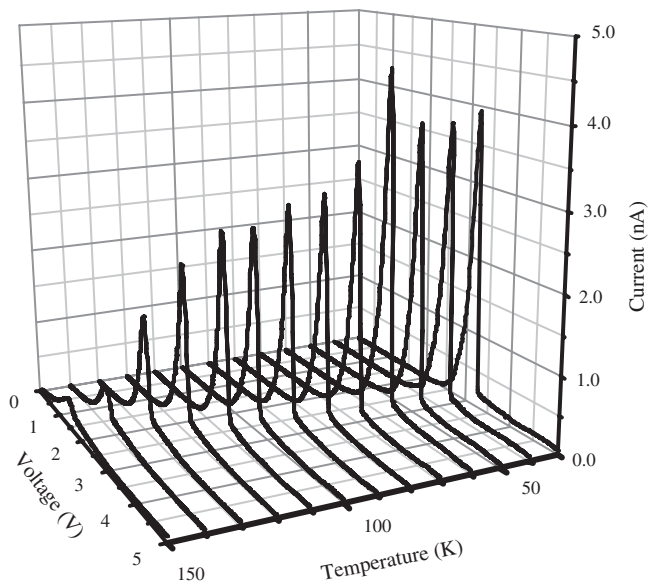


**Figure 35.** $I(V, T)$ characteristics of a Au-**1c**-Au device.

could be caused by thermally activated conformation change in the SAM layer. We also observe that the peak position shifts to smaller voltage with increasing temperature (Fig. 36a). The shift can be fit by the following expression:

$$\Delta V_{\text{peak}} = \frac{c_1}{1 + e^{-(34(10.7)meV/kT)}}$$

This expression can be explained by a two energy level model using a Boltzmann distribution, where the 34 $(\pm 0.7)$ meV corresponds to the activation barrier from the
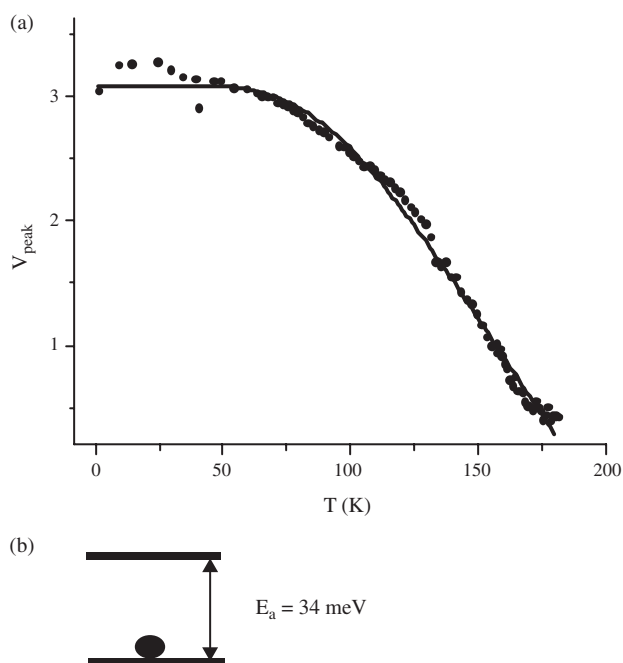


**Figure 36.** (a) Peak voltage versus temperature relationship of the same device. (b) Possible physical picture of the trap state.

bound state as proposed in Figure 36b, and $c_1$ is a proportionality constant. More supporting evidence for the above model comes from the temperature dependence of peak width (Fig. 35). It remains constant at low temperature and widens at higher temperature. Further discussions on temperature dependencies and comparison with other compounds will be carried on next.

Similar NDR behavior is also observed in devices with nitro only moiety (**2**). The PVR is smaller than that of **1**, but NDR behavior persisted from low temperature to room temperature. $I(V)$ characteristic of a Au-(**2**)-Au device at 300 K is shown in Figure 37a. The device has 300 K characteristics of a peak current density greater than 16 A/cm², NDR smaller than −144 mΩ cm², and a PVR of 1.5:1. At 190 K (Fig. 37b), the NDR peak is much sharper than that of **1**, although its PVR is not as big as that of **1**. The degradation in PVR (decreasing in peak current) can probably be caused by increased inelastic scattering with increasing temperature. Figure 38 shows the cyclic voltammagram curve for compound **2c** where the reduction potentials peaked at −1.39 V and −2.09 V, respectively. The potentials are shifted about 0.3 V less than that of the nitro-amino device.

The next experiment that naturally follows is the electronic transport and electrochemistry experiments of



**Figure 38.** Cyclic voltammagram of compound **2c** shows two distinct reduction peaks at −1.39 V and −2.09 V.

an amino only molecule [2′-amino-4,4′-di(ethynylphenyl)-1-benzenethiolate, compound **3**]. We observe no NDR behavior in **3** at both low temperature (60 K) and room temperature, as shown in Figure 39. To avoid breakdown of the molecular junction, bias at room temperature was restricted to 1 V to limit current through the junction. Its CV curve did not exhibit any reduction peak in the range of interest. Concluding from above experimental results, we suggest that the nitro group is responsible for the NDR behavior. Further understanding of the underlying mechanism and experimentation with various redox centers should allow us to engineer molecular compounds in the future to improve PVR at room temperature and above.

Shown in Figure 40 is the temperature dependence of peak positions of a Au-**2**-Au device. The peak voltage is observed to drop linearly with increasing temperature: $\Delta V_{\text{peak}} = -0.025 \, \Delta T$. It appears to be very different from
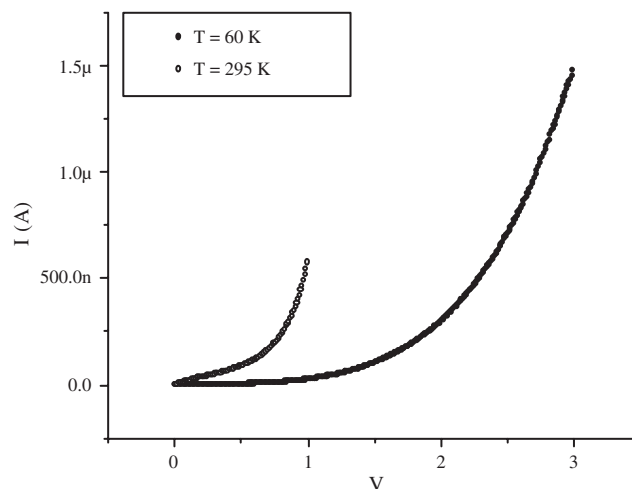




**Figure 39.** $I(V)$ characteristic of 2′-amino-4,4′-di(ethynylphenyl)-1-benzenethiolate (**3**) at 60 and 295 K. No NDR behavior was observed. Bias across **3** was restricted to 1 V at room temperature to avoid junction breakdown.

**Figure 37.** $I(V)$ characteristics of a Au-**2**-Au device at (a) 300 K and (b) 190 K.
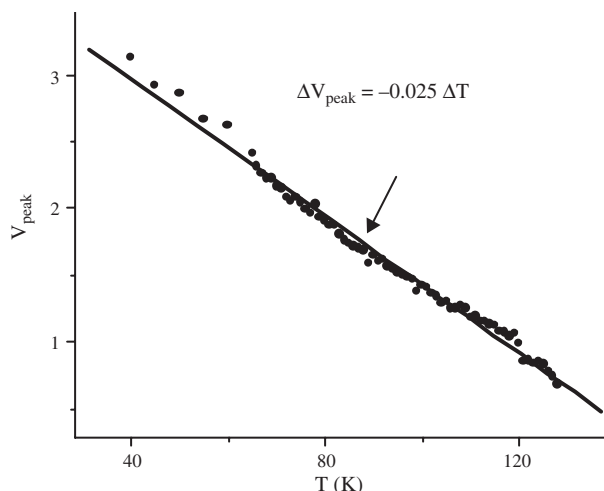
**Figure 40.** Peak voltage versus temperature of a Au-**2**-Au device.

that of a Au-**1c**-Au device. To compare possible effects of different redox centers on temperature dependence, we show in Figure 41 a plot of temperature versus voltage values at a constant current of 10 nA of a Au-**3**-Au device. Interestingly, it can also be fit to a two-level model,

$$\Delta V_{@10\,nA} = \frac{c_3}{1 + e^{(-30(meV)/kT)}}$$

where $c_3$ is a proportionality constant and the binding energy for the trap state on **3** is around 30 ($\pm$0.2) meV. On the other hand, the transition region of $V_{peak}$ versus $T$ of a nitro-amine redox molecule can be fit in piecewise to linear relationship as shown in Figure 42a, with $\Delta V = -0.014\,\Delta T$ and $\Delta V = -0.034\,\Delta T$, respectively, and the transition region of $V_{@10\,nA}$ versus $T$ of an amine-only moiety can also be fit to a linear relationship as shown in Figure 42b, with $\Delta V = -0.005\,\Delta T$. The fitting results and comparison between compounds **1c**, **2**, and **3** of positive voltage sweeps (referred to S1$^+$s) are summarized in Table 3. As shown in Table 4, the temperature dependence of subsequent positive voltage
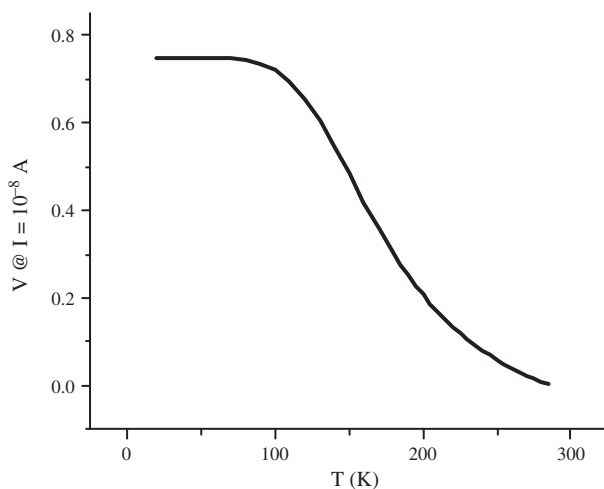


**Figure 41.** Voltage values at a constant current of 10 nA versus temperature of a Au-**3**-Au device.
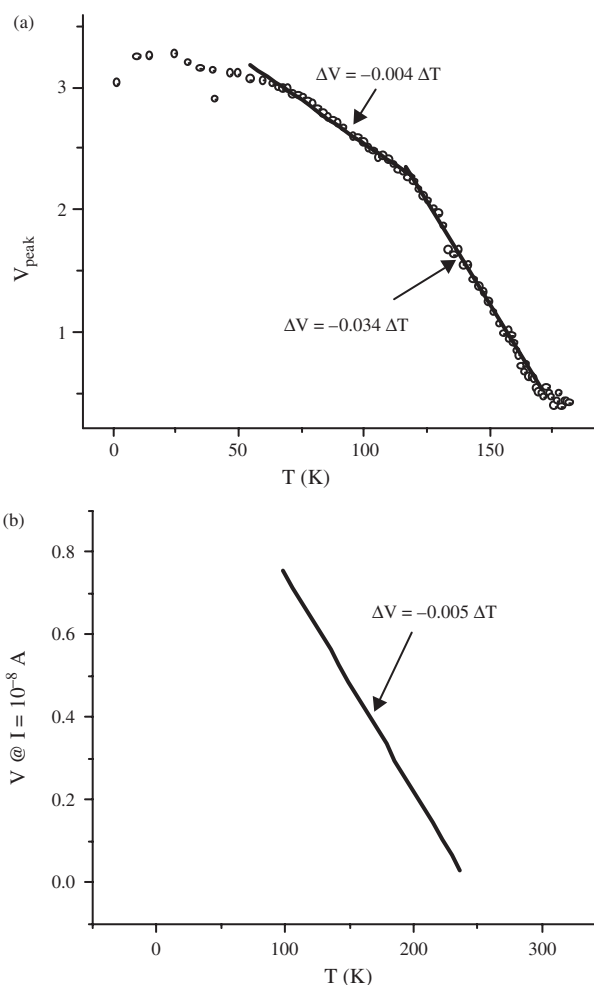


**Figure 42.** Piecewise linear fitting in the transition region of (a) peak voltage versus temperature of a Au-**1c**-Au device; (b) Voltage values at a constant current of 10 nA versus temperature of a Au-**3**-Au device.

sweeps (referred to S2$^+$s) is very similar to that of sweeps S1$^+$s. The difference has to do with the memory effects that will be discussed next.

The above result suggests that the presence of the amine group gives rise to a bound state around 30 meV in the molecule, whereas the nitro group is responsible for NDR behavior. The exact mechanism of linear shift of peak position with temperature is not understood at this stage. Possible explanations can be complex; for example, interactions with vibrational modes can cause instantaneous dipole changes in the molecule (Fig. 43) which in turn interact with electrons passing through the molecule, changing the transmission coefficient.

Based on our experiments, the electron-withdrawing nitro group is responsible for NDR behavior, whereas the electron-donating amine group gives rise to a bound state in the molecule of approximately 30 meV. We have learned that conformational change (rotation) and/or charging can change the conjugation of molecular orbitals. Further exploration on design and engineering of molecules with various redox substituents should help to realize nonlinear electronic devices with multiple functionalities.

**Table 3.** Comparison between compounds **1c**, **2**, and **3** on temperature dependence of S1$^+$ sweeps.

| Redox center | NDR | V versus T | | $E_{binding}$ |
|---|---|---|---|---|
| | | Best fit | Piecewise linear fit | |
| Nitro-only (**2**) | ✓ | $\Delta V_{peak} = -0.025\ \Delta T$ | | |
| Nitro-amine (**1c**) | ✓ | $\Delta V_{peak} = \frac{c_1}{1 + e^{[-(34(\text{meV})/kT)]}}$ | $\Delta V = -0.014\ \Delta T$ | 34 meV |
| | | | $\Delta V = -0.034\ \Delta T$ | |
| Amine-only (**3**) | ✕ | $\Delta V_{@10\ nA} = \frac{c_3}{1 + e^{[-30(\text{meV})/kT]}}$ | $\Delta V = -0.005\ \Delta T$ | 30 meV |

## 5.4. Molecular Memory Effects

The programmable storage of digital information as packets of charge is beginning to reach not only technological but fundamental limits. Electronic memories that operate at the charge limit (e.g., by single electron effects) have been demonstrated[16] [120, 121] but have not yet addressed the dimensional limit (i.e., a single molecule). Although memory phenomena have been studied in bulk organic materials (such as organometallic charge-transfer complex salts [95]), we will demonstrate nanoscale electronically programmable and erasable memory devices utilizing molecular SAM and a memory cell applicable to a random access memory (RAM).

Figure 44 lists the molecules used in this study. (They were introduced previously; we list them again for convenience.) The four systems studied are: Au-(**1**)-Au [**1**: 2′-amino-4,4′-di(ethynylphenyl)-5′-nitro-1-benzenethiolate]; Au-(**2**)-Au [**2**: 4,4′-di(ethynylphenyl)-2′-nitro-1- benzenethiolate]; Au-(**3**)-Au [**3**: 2′-amino-4,4′-di(ethynylphenyl)-1-benzenethiolate]; as well as Au-(**4**)-Au [**4**: 4, 4′-di(ethynylphenyl)-1-benzenethiolate] that had neither the nitro nor amine functionalities.

The memory device operates by the storage of a high or low conductivity state. Figure 45 shows the write, read, and erase sequences for (**1**). An initially low conductivity state (low $\sigma$) is changed (written) into a high conductivity state (high $\sigma$) upon application of a voltage pulse. The direction of current that flows during this "write" pulse is diagrammed. The high $\sigma$ state persists as a stored "bit," which is unaffected by successive read pulses. Molecules with the nitro moieties (**1** and **2**) are observed to change conductivity state, whereas the amine only (**3**) and the unfunctionalized molecule (**4**) do not exhibit storage. In the following, we first describe the characteristics obtained by linear voltage sweeps (so as to generate $I(V)$ characteristics). Second, we demonstrate the same effects and a circuit using voltage pulses.

Figure 46 shows the $I(V)$ characteristics of a Au-(**1**)-Au device at 200 K initially (defined as "0") and after (defined as "1") a write pulse, as well as the difference between the two (defined as "1"−"0"). Positive bias corresponds to hole injection from the chemisorbed thiol-Au contact. The device initially probed with a positive voltage sweep from 0 to 2 V exhibits a low conductivity state. Subsequent positive sweeps show a high conductivity state with $I(V)$ characteristics identical to the previous values ("1"). Device bias swept in the reverse bias direction from 0 to −2 V causes the $I(V)$ to

be identically reset to the initial, "0" $I(V)$ characteristic. The characteristics are repeatable to high accuracy and device degradation is not observed. This ability to program, read, and refresh the state of the molecular device accomplishes the functionality of a RAM. Figure 47 shows the difference characteristic ("1"−"0") of (**1**) as a function of temperature. The peak current difference decreases approximately linearly with increasing temperature.

A characteristic bit retention time was obtained by measuring the stored high conductivity state at various time intervals after programming the Au-(**1**)-Au device. After an initial positive write sweep from 0 to 2 V, a second sweep was measured at different time intervals, and the difference between the first and the second sweeps at peak current position was taken and plotted against time in Figure 48a. It is found that the difference "1"−"0" exhibits an exponential decay with a time constant ($\tau$) of approximately 800 seconds at 260 K. Similar measurements were performed from 260 to 190 K.[17] The stored state was found to decay exponentially with increasing time constants at lower temperatures. Shown in Figure 48b is a plot of the decay time constant (retention time) at different temperatures, exhibiting an exponential dependence with 1/T. It indicates an activation behavior: $\tau = \tau_0 \exp(E_a/kT)$, suggesting activation over a single trap state. The activation energy $E_a$ for this molecule over this bias regime was found to be approximately 80 meV.

A similar memory effect was also observed under negative bias [122]. Contrary to the positive bias, the molecular junction initially is in a higher conductivity state, whereas it is changed to a lower conductivity. After applying a positive sweep, we observe that the junction is set back to the initial negative trace.

Memory effects are also observed in devices with the molecules having only the nitro moiety (**2**), although in this case the storage was of a *low* conductivity state[18] after an initial positive sweep, opposite to that of molecule (**1**) [122]. A characteristic bit retention time of approximately 900 seconds at 300 K was observed.

Memory effects are not observed in molecule (**3**) with the amine-only group. Shown in Figure 49 are typical $I(V)$ characteristics of an Au-(**3**)-Au device at 60 and 295 K, respectively. The first and second traces at a constant temperature overlap with each other. The current level is higher than that of both Au-(**1**)-Au and Au-(**2**)-Au devices, suggesting that

---

[16] A single electron memory operating at 4 K was demonstrated in [121].

[17] Below 190 K, the $I(V)$ characteristic changes considerably, with the NDR peak shifting much toward higher voltage. No appreciable decay of current was observed.

[18] Not including the NDR region, where current level is higher than the initial state.

**Table 4.** Comparison between compounds **1c**, **2**, and **3** on temperature dependence of S2$^+$ sweeps.

| Redox center | NDR | V versus T | | $E_{binding}$ |
| | | Best fit | Piecewise linear fit | |
|---|---|---|---|---|
| Nitro-only (**2**) | √ | $\Delta V_{peak} = -0.005\Delta T$ | | |
| | | $\Delta V_{peak} = -0.010\Delta T$ | | |
| Nitro-amine (**1c**) | √ | $\Delta V_{peak} = \dfrac{c_1}{1 + e^{-[(32(meV)/kT)]}}$ | $\Delta V = -0.02\Delta T$ | 32 meV |
| Amine-only (**3**) | × | $\Delta V_{@10\ nA} = \dfrac{c_3}{1 + e^{[(-30(meV)/kT)]}}$ | $\Delta V = -0.005\Delta T$ | 30 meV |
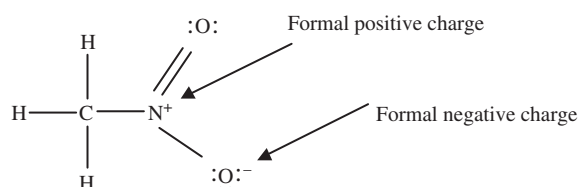


**Figure 43.** Nitromethane and its dipole.

the presence of nitro group impedes charge transport, causing a high conductivity state in (**1**) (with nitro-amine group) and a low conductivity state in (**2**) (with nitro-only group). Consequently, the 80 meV energy level observed in (**1**) is most likely associated with the nitro group.

The above observation leads us to the following preliminary model for the memory effect (Fig. 50). We have identified from above experimental results that the nitro group is responsible for the memory effect, while the presence of the amine group changes the initial conductivity states of the molecule (most likely caused by the different dipole distribution it introduces to the molecule). Here we use molecule **1** as an example. Depending on its history, **1** can be in one of the two states, L (low conductivity state) or H (high conductivity state). We propose that the different conductivity states are caused by different trap levels occupied by electrons as shown in Figure 50a. Different trap levels occupied by electrons in a molecule could mean either different electronic states with different charge distributions (such as different dipole distribution), or different conformation states in a molecule (such as rotational conformations, about various axes), or both. The microscopic origin of the trap states is at this point unknown; we stress that regardless of the microscopic origin, we have determined here that the origin



**Figure 45.** The operation principle of the storage and memory. The memory device operates by the storage of a high or low conductivity state. An initially low conductivity state (low $\sigma$) is changed into a high conductivity state (high $\sigma$) upon application of a voltage. The directions of current that flows during the "write" and "erase" pulses are diagrammed by the arrows. The high $\sigma$ state persists as a stored "bit."

is a trap state, and the energetic characteristics of that trap state.

These trap levels can cause different electronic distributions, leading to various conductivity states of the molecule. From Figure 46, **1** is initially in a low conductivity state (L). As the junction is biased positively, the barrier is tipped over, and the electron falls into state H (Fig. 50b). When the bias is removed, the electron remains undisturbed in the same localized state H it occupied under bias for a period of time equal to $(\nu P)^{-1}$ where $\nu$ is the attempting frequency



**Figure 44.** The molecular junctions (**1**–**3**) used in this study. Junction 4 was studied by Zhou [63], drawn here for comparison purpose. There are approximately 1000 molecules sandwiched between the two Au contacts. Only one molecule is drawn for simplicity.
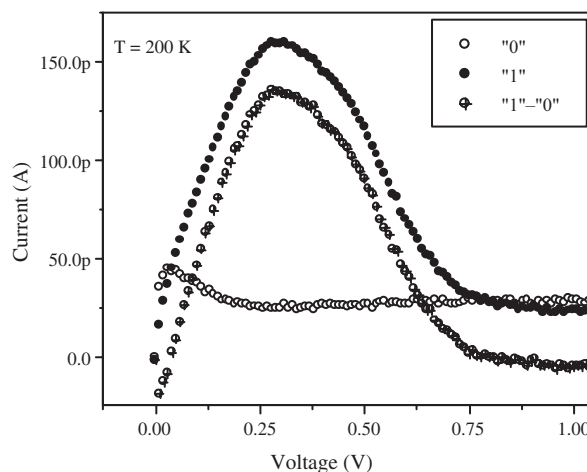


**Figure 46.** $I(V)$ characteristics of a Au-(**1**)-Au device at 200 K. "0" denotes the initial state, "1" the stored written state, and "1"−"0" the difference of the two states.
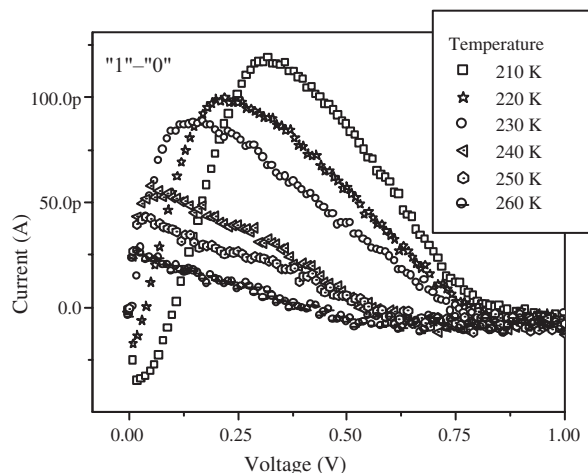
**Figure 47.** Difference $I(V)$ characteristics ("1"−"0") of a Au-(1)-Au device as a function of temperature.



**Figure 49.** $I(V)$ characteristic of 2'-amino-4,4'-di(ethynylphenyl)-1-benzenethiolate (**3**) at 60 and 295 K. First and second traces overlap with each other.



**Figure 48.** Bit retention as a function of time and temperature. (a) Bit retention for (1) exhibits an exponential decay with a time constant ($\tau$) of 790 seconds at 260 K. (b) Temperature dependence of $\tau$ gives an activation energy $E_a = 76 \pm 7$ meV.

to escape and $P$ is the probability of escaping the localized state H. In general $P$ is proportional to the Boltzmann factor $\exp(-E/kT)$, where $E$ denotes the energy barrier of the localized state H. It corresponds to the measured 80 meV as shown in Figure 48. For subsequent positive biases at times $t < (\nu P)^{-1}$, the electron is trapped in state H (Fig. 50c). Only with negative bias can the electron be "liberated" and go back to state L (Fig. 50d). At times $t > (\nu P)^{-1}$, the electron leaks through the barrier and finally returns to state L. The electron will be trapped in state L with following negative sweeps, and it can only be refreshed to the H state by positive bias. This explains well that the first negative sweep on the junction shows a high conductivity state (i.e., the initial H state after positive sweeps). The following negative
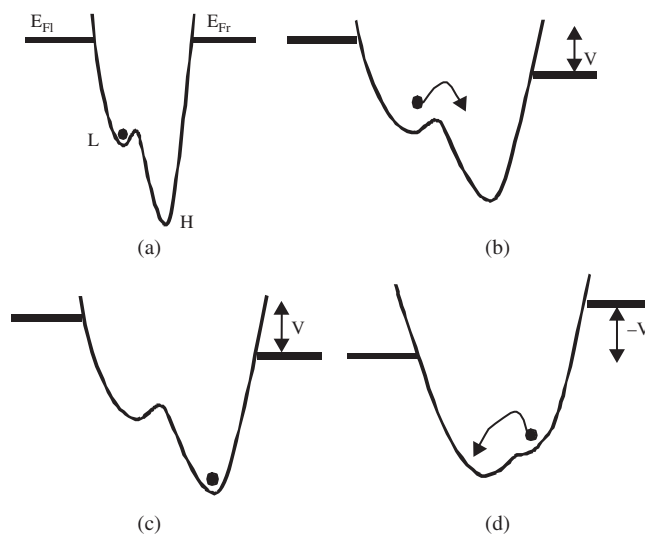


**Figure 50.** Proposed model for the memory effect. Lowering of $E_{Fr}$ corresponds to positive bias. (a) Initial low conductivity state, zero bias; (b) first positive sweep, "write," changed into a high conductivity state—H; (c) consecutive positive sweeps, "read," remained in the high conductivity state; (d) first negative sweep, "erase," back to low conductivity state.

traces show low conductivity state, and a positive trace resets the state.

In Figure 51, we see a final example of a molecule (biphenyl dinitro) that exhibits this large resettable conductivity at room temperature. Here the high conductivity state on probe is set into the low conductivity state, which is persistent until the application of a negative bias pulse, after which the high conductivity state is recovered. This type of behavior is illustrated with the above model of a bistable state; although the microscopic origin of these states is complex, the same generic behavior is generically seen in this class of oligomer systems.

## 5.5. Demonstration of a Molecular Memory Storage Cell

Figure 52 shows a constructed sense circuit diagram for a molecular memory cell operation. Transistor transistor logic (TTL) level signal (5 V) from a function generator is first converted to the operating point of the memory cell (set at the points diagrammed in Fig. 53, 1.5 V) and applied to the molecular junction (DUT). The current through DUT is measured via a feedback resistor $R_{sense}$ and amplified 10 times using low noise operational amplifiers. Then the signal is fed into a comparator (LM339) and compared with the "1" set-point (*low* conductivity state) as measured in Figure 52. To demonstrate the storage of a low conductivity state, the signal is inverted and gated with the input pulse from the function generator. A measured logic diagram utilizing the above sensing circuit and a Au-**2**-Au device is shown in Figure 54, demonstrating a molecular RAM cell at ambient temperature.
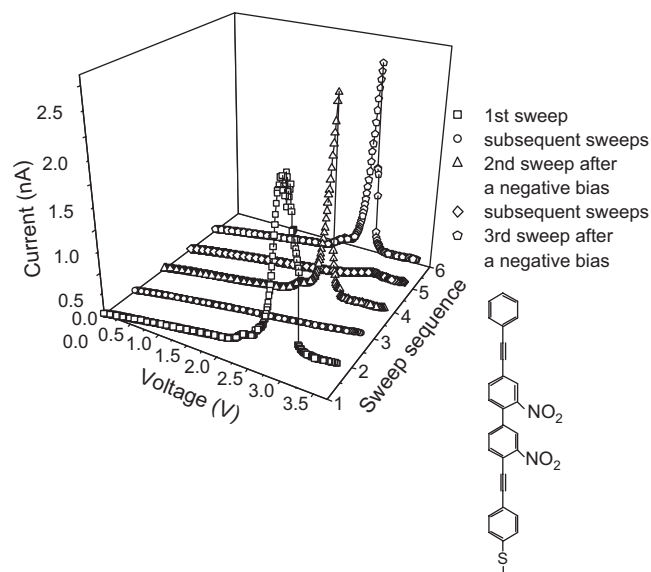


**Figure 51.** *I-V* characteristics of a Au-biphenyl-dinitro-Au device. (a) First sweep shows a high-conductivity ON state and two NDR peaks; the prominent peak current is 2.5 nA, the PVR is 7:1. The subsequent sweeps show a low-conductivity OFF state. After a negative sweep, the high conductivity ON state recovered and repeated with the first sweep. The subsequent sweeps show same low conductivity. After a negative sweep, the high-conductivity ON state recovers.
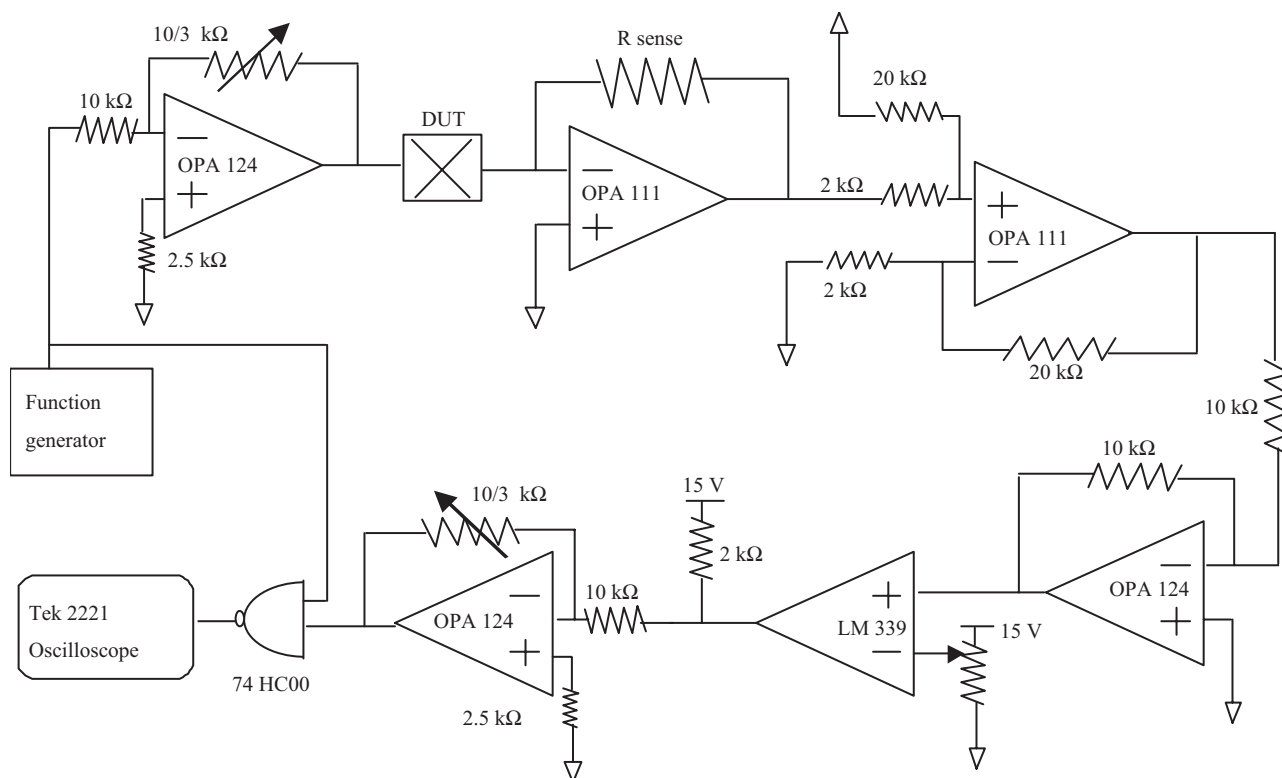


**Figure 52.** Diagram of the sense circuit for a molecular memory cell.
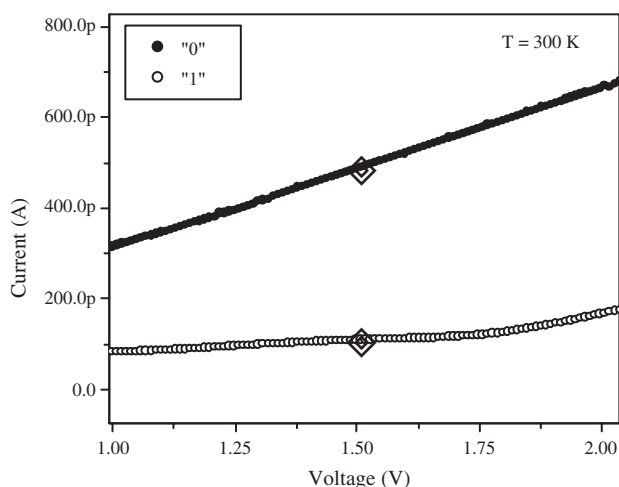
**Figure 53.** $I(V)$ characteristics of stored and initial/erased states in Au-(**2**)-Au at 300 K. The set-point indicated is the operating point for the circuit of Figure 52.

The upper trace shown in Figure 54 is an input waveform applied to the device, and the lower is the RAM cell output. The first positive pulse configures the state of the cell by writing a bit, and the second and third positive pulses read the cell. The third pulse (and subsequent read pulses, not shown here for simplicity) demonstrates that the cell is robust and continues to hold the state up to the limit of the bit retention time. This demonstration highlights the dramatically long bit retention time. The negative pulse erases the bit, resetting the cell. The second set of four pulses repeats this pattern, and many hours of continuous operation have been observed with no degradation in performance. Currently the speed of the memory device is limited by the RC time constant of the circuit. There is a 1 pF capacitance between the two Au electrodes in the nanopore configuration. The current level of the devices is less than 10 nA, which can be attributed to the 0.7-eV S-Au barrier [33, 61] in the molecular junction. Engineering of molecules with smaller contact barriers (e.g., use CN terminated molecules and Pd contacts) to obtain a higher current level while minimizing contact area to decrease parasitic capacitance should improve the RC limit.
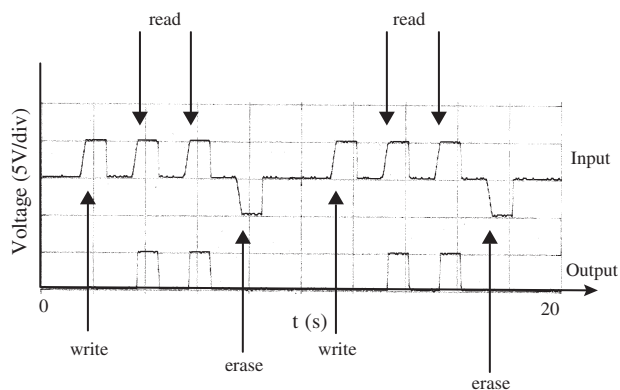


**Figure 54.** Measured logic diagram of the molecular random access memory.

The present devices utilize nanoscale structures that limit the number of molecules in the active region to ~1000, which is determined by lithographic limitations in defining the contacts. We have seen no evidence in the device characteristics indicating that limitations exist for scaling the number of molecules in the active region to one, assuming that an appropriate fabrication scheme can be identified.

## 6. CONCLUSIONS

Molecular electronics uses molecular structures whose function involves discrete molecules, which are distinguished from organic thin-film transistors that use bulk materials and bulk-effect electron transport. It provides a bottom-up way to produce subnanometer-sized functional devices.

We have developed a nanolithography technique to demonstrate directed self-assembly, generating intermixed SAMs—conjugated SAM in an insulating background. In particular, we have demonstrated that programmable patterning of a SAM of dodecanethiol can be performed by applying voltage pulses from a STM tip. After patterning, conjugated oligomers are introduced and they are observed to be subsequently chemisorbed onto the patterned sites. This technique combines a scanning probe microscope-based lithography technique and the design of molecular units with specific structural, chemical, and electronic properties. It can be used to generate SAMs with arbitrary compositions and geometries at ambient temperature, opening up many new possibilities for molecular-scale bottom-up fabrication.

Up to now, molecular electronics has been mostly about conductance measurements of molecules. For nanoscale molecules, most conductance measurements are restricted to two terminals because of fabrication issues and screening effects. Molecule-metal contact plays a vital part in these measurements. The quest for a small SAM-metal contact barrier has thus been long going, and has become a bottleneck in through-bond transport in molecular systems. We have investigated the contact barrier between isocyanide SAM and metal systems. Nonohmic behaviors—thermionic and hopping conduction—are observed to be the dominant conduction mechanisms. We have shown that thermal emission is the dominant conduction mechanism in chemisorbed metal-isocyanide junctions, while in the evaporated metal-isocyanide contact, both hopping and thermal emission can play an important role depending on the defect level introduced during the fabrication process, suggesting that there are less defects in the chemisorbed metal-molecular interface. Overall, the Pd-CN contact barrier is smaller than that of a Au-CN junction, in agreement with the more efficient $\pi$ bond formed between Pd-CN. Our results also show that the contact barrier between $\pi$-bonded isocyanide SAM-metal is less than that of the more extensively studied $\sigma$-bonded thiol SAM-metal systems. The technique reported here elucidates the relevant electronic transport barriers and conduction mechanisms of through-bond metal-molecule contacts, which have been possible through the implementation of microfabricated electronic devices utilizing SAMs. The technique should be applicable to a large range of inorganic and biomolecular transport measurements, to quantitatively measure the dominant electron transport mechanisms.

We demonstrated novel non-FET switching devices and a prototype of memory cell using single SAMs as the active component. We learned that conformational change like rotation of molecular bonds can change the conjugation of molecular orbitals, leading to the observed conductor-insulator type of transition that can be thermally controlled. We have realized two-terminal NDR devices with large PVR at low temperature and NDR devices at room temperature. The NDR behavior is caused by the reduction nature of substituents on ethynylphenyl molecules. Based on our experiments, the electron-withdrawing nitro group is responsible for NDR behavior, whereas the electron-donating amine group gives rise to a bound state in the molecule of approximately 30 meV. Through the design of the molecular switches we learned that incorporation of different redox centers can change charge distribution and/or conformation in a molecule, leading to different conjugation of molecular orbitals. Further exploration on design and engineering of molecules with various redox substituents should help to realize nonlinear electronic devices with multiple functionalities. We also discovered erasable storage effects in redox-center-containing ethynylphenyl molecules. The storage behavior can be discretely added on a molecule by engineering electron-withdrawing or/and electron-donating sidegroups onto its backbone. We have concluded from our experiments that the electron-withdrawing nitro group is responsible for the observed memory effects, while the presence of the electron-donating amine group changes the storage of different conductivity states. Our results show that the storage behavior is controlled by a single thermal activation process, associated with the nitro group. Further experiments with various redox centers should make molecular memories with different retention times possible. Finally, we successfully demonstrated an erasable molecular memory cell that can store a high conductivity state with a bit retention time orders of magnitude longer than that of a DRAM. Further engineering of different molecules shall permit potential applications such as nonvolatile memories on flexible substrates.

We have mainly focused on polyphenylene-based molecular wires in this study. What we have sampled and studied consists of only a tiny portion of a copious family of prospective molecules that possess unique characteristics for electronic applications. Even with the subject of our work, there still remains a lot to be explored. For instance, to further investigate through-bond transport of metal-molecule-metal systems, engineering and measurements of molecules with different backbones should help to elucidate its role versus the role of metal-molecule contacts. As to a molecule with specific end groups, one can vary its length (e.g., single ring vs multiple ring), conjugation (e.g., aliphatic ring vs aromatic ring), and charge distribution (electron-withdrawing group vs electron-donating group), and map out the functional table of each component. To minimize metal-molecule contact barriers, different kinds of end groups need to be explored (e.g., what will happen if there is no end group, what if one introduces electron-withdrawing group on one end but electron-donating group on the other end?). To improve the film robustness (e.g., against post-process heating or top metallization), novel organic-inorganic complex SAMs may be designed and engineered, which could preserve band engineering flexibility through the organic component and in the mean time improve film robustness through the inorganic component. To reduce the number of interconnects between different molecules, one can integrate the demonstrated prototype molecular switches and memories by synthesizing one specific molecule with different functional parts capable of performing the desired tasks. Will the various functional components behave as expected when they are "assembled" into one new unit (molecule)?

Molecular electronics is still in its infancy but holds great promise in that it potentially provides a conceptually new path without the inherent tolerance problems of a lithographic approach. We believe that the most exciting discovery in molecular electronics is its ability to explore new architectures and devices unique to molecular-based systems themselves, which are yet to be made.

## GLOSSARY

**Alkanethiol** A molecule with a structure of $CH_3(CH_2)_{n-1}SH$.

**Conjugated oligomer** A molecular type consisting of an alternation of multiple and single bonds linking a sequence of bonded-atoms, such that there is an extended series of overlapping $p$ orbitals.

**Highest occupied molecular Orbital (HOMO)** The highest orbital among the molecular orbitals that contain electrons.

**Langmuir–Blodgett monolayer** A molecular monolayer formed on a substrate by the physical attachment due to molecular hydrophilic/hydrophobic interaction with the substrate surface.

**Lowest unoccupied molecular orbital (LUMO)** The lowest orbital among the molecular orbitals that do not contain electrons.

**Molecular electronics** A new concept in electronics of utilizing molecules as self-contained electronic device components.

**Negative differential resistance** An electronic property that resistance (conductance) increases (decreases) over a certain voltage range.

**Self-assembled monolayer** A molecular monolayer formed on a substrate surface by the chemical interaction process of functional end groups of molecules with the substrate surface materials.

**Tunneling** An electronic transport process such that charge carriers tunnel through a thin barrier.

## ACKNOWLEDGMENT

## REFERENCES

*1.* M. A. Reed and T. Lee, Eds., "Molecular Nanoelectronics," American Scientific Publishers, Stevenson Ranch, California, 2003.

*2.* R. R. Birge, Ed., "Molecular and Biomolecular Electronics." American Chemical Society, Washington, DC, 1991.

3. A. Aviram and M. A. Ratner, Ed., "Molecular Electronics: Science and Technology," Annals of the New York Academy of Sciences, Vol. 852. New York Academy of Sciences, 1998.

4. J. McMurry, "Organic Chemistry." Brooks/Cole, Belmont, MA, 1996.

5. J. S. Schumm, D. L. Pearson, and J. M. Tour, *Angew. Chem. Int. Ed. Engl.* 33, 1360 (1994).

6. J. M. Tour, R. Wu, and J. S. Schumm, *J. Am. Chem. Soc.* 113, 7064 (1991).

7. J. C. Ellenbogen and J. C. Love, *Proc. IEEE* 88, 386 (2000).

8. T. A. Skotheim, Ed., "Handbook of Conducting Polymers." Dekker, New York, 1986.

9. D. D. C. Bradley, *Chem. in Britain* 719, August (1991).

10. M. F. Rubner, in "Molecular Electronics" (G. J. Ashwell, Ed.). Wiley, New York, 1992.

11. S. Kivelson, *Phys. Rev. B* 25, 3798 (1982).

12. D. Emin, in "Handbook of Conducting Polymers" (T. A. Skotheim, Ed.), Vol. 2, p. 915. Dekker, New York, 1986, and references therein.

13. R. R. Chance, J. L. Bredas, and R. Silbey, *Phys. Rev. B* 29, 4491 (1984).

14. N. F. Mott and E. A. Davis, "Electronic Processes in Non-Crystalline Materials." Clarendon, Oxford, 1979.

15. P. Sheng, B. Abeles, and Y. Arie, *Phys. Rev. Lett.* 31, 44 (1973).

16. M. A. Ratner, B. Davis, M. Kemp, V. Mujica, A. Roitberg, and S. Yaliraki, *Ann. N. Y. Acad. Sci.* 852, 22 (1998).

17. M. Magoga and C. Joachim, *Phys. Rev. B* 56, 4722 (1997).

18. M. A. Ratner, *J. Phys. Chem.* 94, 4877 (1990).

19. J. W. Evenson and M. Karplus, *Science* 262, 1247 (1993).

20. M. P. Samanta, W. Tian, S. Datta, J. I. Henderson, and C. P. Kubiak, *Phys. Rev. B* 53, R7636 (1996).

21. R. Landauer, *IBM J. Res. Dev.* 1, 223 (1957).

22. S. Datta, "Electronic Transport in Mesoscopic Systems." Cambridge Univ. Press, 1995.

23. C. Zhou et al., in "Molecular Electronics" (J. Jortner and M. Ratner, Eds.). Blackwell Science, Oxford, UK, 1997.

24. J. I. Pascual et al., *Science* 267, 1793 (1995).

25. S. J. Tans et al., *Nature* 386, 474 (1997).

26. G. Neofotistos, R. Lake, and S. Datta, *Phys. Rev. B* 43, 2442 (1991).

27. G. L. Closs et al., *J. Am. Chem. Soc.* 110, 2652 (1988).

28. A. Aviram and M. A. Ratner, *Chem. Phys. Lett.* 29, 277 (1974).

29. R. M. Metzger, B. Chen, U. Holpfner, M. V. Lakshmikantham, D. Vuillaume, T. Kawai, X. Wu, H. Tachibana, T. V. Hughes, H. Sakurai, J. W. Baldwin, C. Hosch, M. P. Cava, L. Brehmer, and G. J. Ashwell, *J. Am. Chem. Soc.* 119, 10455 (1997).

30. M. A. Reed, U.S. Patent 5, 475, 341, 1995.

31. M. A. Reed, U.S. Patent No. 5, 589, 629, 1996.

32. C. J. Muller, Ph.D. Thesis, Leiden, Netherlands, 1991.

33. M. A. Reed, C. Zhou, C. J. Muller, T. P. Burgin, and J. M. Tour, *Science* 278, 252 (1997).

34. C. Kergueris, J.-P. Bourgoin, S. Palacin, D. Esteve, C. Urbina, M. Magoga, and C. Joachim, *Phys. Rev. B* 59, 12505 (1999).

35. C. Zhou, M. R. Deshpande, M. A. Reed, L. Jones II, and J. M. Tour, *Appl. Phys. Lett.* 71, 611 (1997).

36. K. S. Ralls, R. A. Buhrman, and T. C. Tiberio, *Appl. Phys. Lett.* 55, 2459 (1989).

37. J. Chen, L. C. Calvet, M. A. Reed, D. W. Carr, D. S. Grubisha, and D. W. Bennett, *Chem. Phys. Lett.* 313, 741 (1999).

38. J. Chen, M. A. Reed, A. M. Rawlett, and J. M. Tour, *Science* 286, 1550 (1999).

39. M. A. Reed, J. Chen, et al., "1999 International Electron Device Meeting," 1999.

40. G. Binnig, H. Rohrer, C. Gerber, and H. Weibel, *Phys. Rev. Lett.* 49, 57 (1982).

41. D. M. Eigler and E. K. Schweizer, *Nature* 344, 524 (1990).

42. L. A. Bumm, J. J. Arnold, M. T. Cygan, T. D. Dunbar, T. P. Burgin, L. Jones II, D. L. Allara, J. M. Tour, and P. S. Weiss, *Science* 271, 1705 (1996).

43. M. Dorogi, J. Gomez, R. Osifchin, R. P. Andres, and R. Reifenberger, *Phys. Rev. B* 52, 9071 (1995).

44. A. Aviram, *J. Am. Chem. Soc.* 110, 5687 (1988).

45. J. J. Hopfield, J. Nelson, and D. Beratan, *Science* 241, 817 (1988).

46. C. P. Collier, E. W. Wong, M. Belohradský, F. M. Raymo, J. F. Stoddart, P. J. Kuekes, R. S. Williams, and J. R. Heath, *Science* 285, 391 (1999).

47. E. Tekman and S. Ciraci, *Phys. Rev. B* 40, 10286 (1989).

48. S. Ciraci, A. Baratoff, and I. P. Batra, *Phys. Rev. B* 41, 2763 (1990).

49. H. Park, A. K. L. Lim, J. Park, A. P. Alivisatos, and P. L. McEuen, *Appl. Phys. Lett.* 75, 301 (1999).

50. J. Park, A. N. Pasupathy, J. I. Goldsmith, C. Chang, Y. Yaish, J. R. Petta, M. Rinkoski, J. P. Sethna, H. D. Abruna, P. L. McEuen, and D. C. Ralph, *Nature* 417, 722 (2002).

51. W. Liang, M. P. Shores, M. Bockrath, J. R. Long, and H. Park, *Nature* 417, 725 (2002).

52. J. G. Kushmerick, D. B. Holt, S. K. Pollack, M. A. Ratner, J. C. Yang, T. L. Schull, J. Naciri, M. H. Moore, and R. Shashidhar, *J. Am. Chem. Soc.* 124, 10654 (2002).

53. D. R. Lombardi, Ph.D. Dissertation, Yale University, 1997.

54. A. Bezryadin, C. Dekker, and G. Schmid, *Appl. Phys. Lett.* 71, 1273 (1997).

55. D. Porath, A. Bezryadin, S. de Vries, and C. Dekker, *Nature* 403, 635 (2000).

56. P. E. Laibinis, G. M. Whitesides, D. L. Allara, A. Parikh, Y. T. Tao, and R. G. Nuzzo, *J. Am. Chem. Soc.* 113, 7152 (1991).

57. C. D. Bain, J. Evall, and G. M. Whitesides, *J. Am. Chem. Soc.* 111, 7155 (1989).

58. J. I. Henderson, S. Feng, G. M. Ferrence, T. Bein, and C. P. Kubiak, *Inorg. Chim. Acta* 242, 115 (1996).

59. J. J. Hickman, C. Zou, D. Offer, P. D. Harvey, M. S. Wrighton, P. E. Laibinis, C. D. Bain, and G. M. Whitesides, *J. Am. Chem. Soc.* 111, 7271 (1989).

60. J. M. Tour, L. Jones II, D. L. Pearson, J. S. Lamba, T. P. Burgin, G. M. Whitesides, D. L. Allara, A. N. Parikh, and S. Atre, *J. Am. Chem. Soc.* 117, 9529 (1995).

61. M. Di Ventra, S. T. Pantelides, and N. D. Lang, *Phys. Rev. Lett.* 84, 979 (2000).

62. T. Vondrak, H. Wang, P. Winget. C. J. Cramer, and X.-Y. Zhu, *J. Am. Chem. Soc.* 122, 4700 (2000).

63. C. Zhou, Ph.D. Dissertation, Yale University, 1999.

64. S. Datta, W. Tian, S. Hong, R. Reifenberger, J. Henderson, and C. P. Kubiak, *Phys. Rev. Lett.* 79, 2530 (1997).

65. E. Burstein and S. Lundqvist, "Tunneling Phenomena in Solids." Plenum, New York, 1969.

66. D. R. Lamb, "Electrical Conduction Mechanisms in Thin Insulating Films." Methuen, London, 1967.

67. S. M. Sze, "Physics of Semiconductor Devices," 2nd ed. Wiley, New York, 1981.

68. C. P. Collier, G. Mattersteig, E. W. Wong, Y. Luo, K. Beverly, J. Sampaio, F. M. Raymo, J. F. Stoddart, and J. R. Heth, *Science* 289, 1171 (2000).

69. M. A. Reed, J. Chen, A. M. Rawlett, D. W. Price, and J. M. Tour, *Appl. Phys. Lett.* 78, 3735 (2001).

70. A. Ulman, "An Introduction to Ultrathin Organic Films from Langmuir-Blodgett to Self-Assembly." Academic Press, Boston, 1991.

71. L. A. Bumm, J. J. Arnold, T. D. Dunbar, D. L. Allara, and P. S. Weiss, *J. Phys. Chem. B* 103, 8122 (1999).

72. D. J. Wold, R. Haag, M. A. Rampi, and C. D. Frisbie, *J. Phys. Chem. B* 106, 2813 (2002).

73. X. D. Cui, X. Zarate, J. Tomfohr, O. F. Sankey, A. Primak, A. L. Moore, T. A. Moore, D. Gust, G. Harris, and S. M. Lindsay, *Nanotechnology* 13, 5 (2002).

*74.* R. Holmlin, R. Haag, M. L. Chabinyc, R. F. Ismagilov, A. E. Cohen, A. Terfort, M. A. Rampi, and G. M. Whitesides, *J. Am. Chem. Soc.* 123, 5075 (2001); M. A. Rampi and G. M. Whitesides, *Chem. Phys.* 281, 373 (2002).

*75.* W. Wang, T. Lee, and M. A. Reed, *Phys. Rev. B* 68, 035416 (2003).

*76.* B. Mann and H. Kuhn, *J. Appl. Phys.* 42, 4398 (1971).

*77.* E. E. Polymeropoulos and J. Sagiv, *J. Chem. Phys.* 69, 1836 (1978).

*78.* F. F. Fan, J. Yang, L. Cai, D. W. Price, S. M. Dirk, D. V. Kosynkin, Y. Yao, A. M. Rawlett, J. M. Tour, and A. J. Bard, *J. Am. Chem. Soc.* 124, 5550 (2002).

*79.* K. Slowinski, H. K. Y. Fong, and M. Majda, *J. Am. Chem. Soc.* 121, 7257 (1999).

*80.* J. F. Smalley, S. W. Feldberg, C. E. D. Chidsey, M. R. Linford, M. D. Newton, and Y. Liu, *J. Phys. Chem.* 99, 13141 (1995).

*81.* W. Franz, in "Handbuch der Physik" (S. Flugge, Ed.), Vol. 17, p. 155. Springer-Verlag, Berlin, 1956.

*82.* C. Joachim and M. Magoga, *Chem. Phys.* 281, 347 (2002).

*83.* G. Lewicki and C. A. Mead, *Phys. Rev. Lett.* 16, 939 (1966); R. Stratton, G. Lewicki, and C. A. Mead, *J. Phys. Chem. Solids* 27, 1599 (1966); G. H. Parker and C. A. Mead, *Phys. Rev. Lett.* 21, 605 (1968).

*84.* B. Brar, G. D. Wilk, and A. C. Seabaugh, *Appl. Phys. Lett.* 69, 2728 (1996).

*85.* J. G. Simmons, *J. Appl. Phys.* 34, 1793 (1963).

*86.* J. G. Simmons, *J. Phys. D* 4, 613 (1971); J. Maserjian and G. P. Petersson, *Appl. Phys. Lett.* 25, 50 (1974).

*87.* X. D. Cui, A. Primak, X. Zarate, J. Tomfohr, O. F. Sankey, A. L. Moore, T. A. Moore, D. Gust, L. A. Nagahara, and S. M. Lindsay, *J. Phys. Chem. B* 106, 8609 (2002).

*88.* C. Boulas, J. V. Davidovits, F. Rondelez, and D. Vuillaume, *Phys. Rev. Lett.* 76, 4797 (1996); M. Fujihira and H. Inokuchi, *Chem. Phys. Lett.* 17, 554 (1972); S. G. Lias, J. E. Bartmess, J. F. Liebman, J. L. Holmes, R. D. Levin, and W. G. Mallard, *J. Phys. Chem. Ref. Data* 17, Suppl. 1 (1988).

*89.* M. J. Robertson and R. J. Angelici, *Langmuir* 10, 1488 (1994).

*90.* K. Shih and R. J. Angelici, *Langmuir* 11, 2539 (1995).

*91.* J. E. Huheey, "Inorganic Chemistry." Harper & Row, New York, 1983.

*92.* N. W. Ashcroft and N. D. Mermin, "Solid State Physics." p. 290. Harcourt Brace, Orlando, FL, 1976.

*93.* H. Jones, in "Handbuch der Physik" (S. Flugge, Ed.), Vol. 19, p. 227. Springer-Verlag, Berlin, 1956.

*94.* N. F. Mott, *Proc. Roy. Soc. London Ser. A* 153, 699 (1936).

*95.* R. S. Potember, T. O. Pochler, and D. O. Cowan, *Appl. Phys. Lett.* 34, 405 (1979).

*96.* R. S. Potember, T. O. Poehler, D. O. Cowan, and A. N. Bloch, in "The Physics and Chemistry of Low-Dimensional Solids", (L. Alcbcer, Ed.). Reidel, Dordrecht, 1980.

*97.* T. Hertel, R. E. Walkup, and Ph. Avouris, *Phys. Rev. B* 58, 13870 (1993).

*98.* L. Esaki, *Phys. Rev.* 109, 603 (1958).

*99.* L. B. Gunn, *Solid State Commun.* 1, 88 (1963).

*100.* L. L. Chang, L. Esaki, and R. Tsu, *Appl. Phys. Lett.* 24, 593 (1974).

*101.* H. Kroemer, *Proc. IEEE* 52, 1736 (1964).

*102.* L. G. Sollner et al., *Appl. Phys. Lett.* 43, 588 (1983).

*103.* M. Tsuchiya, H. Sakaki, and J. Yoshino, *Jpn. J. Appl. Phys.* 24, L466 (1985).

*104.* S. M. Sze, Ed., "High-Speed Semiconductor Devices." Wiley, New York, 1990.

*105.* F. Capasso and R. A. Kiehl, *J. Appl. Phys.* 58, 1366 (1985).

*106.* N. Yokoyama, K. Imamura, S. Muto, S. Hiyamizu, and N. Nishi, *Jpn. J. Appl. Phys. Part 2* 24, L583 (1985).

*107.* F. Capasso, in "Picosecond Electronics and Optoelectronics" (G. A. Mourou, D. M. Bloom, and C. H. Lee, Eds.). Springer, Berlin, 1985.

*108.* L. Esaki, *IEEE Trans. Electron Dev.* 12, 374 (1965).

*109.* Seabaugh and R. Lake, *Encycl. Appl. Phys.* 22, 335 (1998).

*110.* H. Mizuta and T. Tanoue, "The Physics and Applications of Resonant Tunneling Diodes." Cambridge Univ. Press, 1995.

*111.* K. H. Gundlach and J. Kadlec, *Phys. Status Solidi A* 10, 371 (1972).

*112.* C. Hamann et al., *Phys. Status Solidi A* 50, K189 (1978).

*113.* A. R. Elsharkawi and K. C. Kao, *J. Phys. Chem. Solids* 38, 95 (1977).

*114.* M. A. Reed, *Proc. IEEE* 87, 652 (1999).

*115.* J. H. Smet, T. P. E. Broekaert, and C. G. Fonstad, *J. Appl. Phys.* 71, 2475 (1992)

*116.* J. R. Söderström, D. H. Chow, and T. C. McGill, *J. Appl. Phys.* 66, 5106 (1989)

*117.* J. Day et al., *J. Appl. Phys.* 73, 1542 (1993).

*118.* H. H. Tsai et al., *IEEE Trans Electron. Devices. Lett.* 15, 357 (1993).

*119.* H. J. Gao et al., *Phys. Rev. Lett.* 84, 1780 (2000).

*120.* S. Tiwari, F. Rana, H. Hanafi, A. Hartstein, E. F. Crabbe, and K. Chan, *Appl. Phys. Lett.* 68, 1377 (1996).

*121.* N. J. Stome and H. Ahmed, *IEEE Trans, Electron. Devices Lett.* 20, 583 (1999).

*122.* J. Chen, Ph.D. Dissertation, Yale University, 2000.

# Molecular Gradient Nanoassemblies

Jan Genzer, Rajendra R. Bhat, Tao Wu, Kirill Efimenko

*North Carolina State University, Raleigh, North Carolina, USA*

## CONTENTS

## 1. INTRODUCTION

It is generally agreed that the concept of nanotechnology was conceived by Richard Feynman's visionary lecture at Caltech in 1959 [1]. However, it was only the last decade that saw key advances made in the manipulation and control of materials on a "small" scale [2]. This sudden outburst has been fueled, in part, by the potential for exploiting unique properties of nanostructures in commercially important applications, including sensors [3], high-efficiency solar cells [4], single-molecule detectors [5], and electroluminescent devices [6]. One of the milestones on the pathway toward materializing the grand vision of nanotechnology is to assemble the "small" building blocks at a desired location on a tangible substrate. To this end, recent advances in the field of self-assembly combined with new deposition technologies, such as soft-lithography techniques [7], have enabled alternative means of fabricating two- and three-dimensional surface structures.

Most soft-lithography techniques are based on selective and controlled deposition of self-assembled monolayers (SAMs) on material surfaces [8]. Various structural patterns with lateral dimensions ranging from hundreds of nanometers to several micrometers are created on the material surface using an elastomeric "pattern-transfer element" (or stamp) that has a three-dimensional structure molded onto its surface. Because of the molecular nature of the SAMs, the surface patterns generated via "soft lithography" are rather thin (thicknesses range from several angstroms to several nanometers). Some applications, particularly those involving subsequent microfabrication steps, such as etching, require that thicker layers of the surface coating be formed. Hence, techniques involving the patterning of thicker polymer layers grafted to the substrate have been developed [9–15]. The latter group of technologies is based on selectively decorating the material surfaces with polymerization initiators and then growing the macromolecules directly from the surface (so-called "grafting from"). Using this method, the thickness of the overcoat film can be adjusted by simply varying the polymerization conditions (time, monomer concentration, temperature).

The soft-lithography technologies always produce sharp boundaries between the distinct chemical regions on the substrate. This feature makes soft lithography useful for decorating substrates with well-defined chemical patterns of various shapes and dimensions. However, for some applications, it is desirable that the physicochemical characteristics, such as wetting of the substrate, change gradually. This can be accomplished by producing surfaces with a position-dependent and gradually varying chemistry. In these so-called "gradient surfaces," the gradient in surface energy is responsible for a position-bound variation in physical properties, most notably the wettability [16]. Recent studies have reported on the preparation of molecular gradients on length scales ranging from nanometers to centimeters [17, 18], thus offering the prospect of meeting the demands of a variety of novel applications. For example, such gradient substrates can be useful in high-throughput studies of the interfacial behavior of molecules and macromolecules [19] (the entire behavioral spectrum can be accessed in a single experiment), they can serve as templates for further processing, or they can be used as active elements in controlled surface transport of materials.

The aim of this review is to demonstrate the usefulness of the gradient substrates in nanotechnology. Several examples will be referenced documenting the utility of the

wettability gradients in combinatorial studies of adsorption, phase behavior in thin liquid and polymer films, templating, and material transport on surfaces. The dual nature of the molecular gradients (discrete on molecular scales, continuous on meso scales) endows them with unique properties that can be exploited to generate combinatorial libraries, which, in turn, will find use in the discovery of new materials and phenomena. Moreover, utilizing molecular gradients will provide simple means of mimicking molecular and biomolecular transport.

## 2. METHODS OF PREPARING GRADIENTS

Over the past 40 years, several strategies for making molecular gradients have been conceived and developed. Each has its advantages and disadvantages and each is best applied on one length scale (Table 1). These methods are briefly described below and discussed in a recent review [20].

The first report describing the formation of wettability gradients dates back to the mid-1960s. Carter described a technique based on evaporating palladium metal on cellulose acetate–covered glass [21]. A short length of stainless-steel rod was first placed in contact with the cellulose acetate film and a small amount ($\approx$2 mg) of fine palladium wire, positioned at a distance of approximately 10 cm from the rod, was evaporated under vacuum. This setup produced a relatively heavy deposition of palladium, which clearly outlined the intervening rod. However, owing to the scattering of metal particles, a much finer deposit of palladium extended beyond the visibly shadowed area and tapered in the narrowing angle under the curved surface of the rod. The technique is very simple, but does not offer much control over the gradient properties.

In the mid-1980s, Elwing et al. proposed a new method for preparing molecular gradients [22]. In this technique (Fig. 1a), the wettability gradient on the solid silicon oxide–covered substrate was produced by diffusion of dichlorodimethyl silane (DDS) between two organic solvents that have different densities but are mutually soluble. In a typical experiment, a silica-covered substrate was placed vertically into a container that was filled with xylene (XYL). Trichloroethylene (TCE) was mixed with a small amount of DDS and was delivered under the XYL phase in the container. During incubation, the two solvents interdiffused; the DDS diffused to the XYL region and was simultaneously attached to the silica surface. The technique is relatively simple, but it offers limited control over the gradient properties—except the length, which can be controlled by varying the diffusion time. The main limitation of the liquid diffusion technique—namely, that the shape of the diffusion profile was always Fickian—was removed in the density gradient solution method developed by Gölander and co-workers [23]. In this technique (Fig. 1b), a solution of TCE was mixed continuously and pumped from a mixing chamber into the bottom of a container containing vertically positioned silica-covered substrates. Simultaneously, the TCE solution was replenished in the mixing chamber with a solution from a second flask that contained DDS dissolved in diiodomethane (DIM). The concentration of DDS in the mixing chamber increased with time, and, as a result, a vertical density gradient containing a DDS concentration gradient built up in the container containing the substrates (with increasing concentration from the bottom). The wettability gradient was formed upon chemisorption of DDS to the silica substrate. While it allows for multiple gradient profiles, this technique is rather laborious.

Ueda-Yukoshi and Matsuda showed that poly(vinylene carbonate) (PVCa) can be hydrolyzed to produce poly(hydroxyl methylene) (PHM) in an alkaline solution (Fig. 1c). These researchers utilized this chemical conversion method to produce a wettability gradient on a PVCa surface [24]. A glass slide was first covered with a thin layer of PVCa, dried, and gradually immersed into an alkaline solution of NaOH. This process produced a surface, whose position-dependent wettability changed from hydrophobic (PVCa) to hydrophilic (PHM). By controlling the immersion speed, the gradient steepness was allowed to vary from several millimeters to several centimeters.

**Table 1.** Comparison of various methods used to produce chemical gradients.

| Gradient preparation method | Spatial range | | | |
| --- | --- | --- | --- | --- |
| | nm | $\mu$m | mm | cm |
| Shadowing evaporation [21] | | | ←·············→ | |
| Liquid diffusion [22] | | | ←·············→ | |
| Density gradient solution [23] | | | ←·············→ | |
| Hydrolysis of poly(vinylene carbonate) [24] | | | ←·············→ | |
| Radio frequency plasma discharge [25] | | | ←··········→ | |
| Corona discharge [26] | | | ←··············→ | |
| Gradient UVO treatment of hydrophobic SAMs [27] | | | ←··········→ | |
| Vapor evaporation [16] | | | ←·············→ | |
| Vapor evaporation on flexible substrates [17] | | | ←··············→ | |
| Diffusion of alkanethiols in polysaccharide [28, 29] | | | ←··········→ | |
| Electrochemical desorption of alkanethiols [30] | | | ←··········→ | |
| Replacement lithography [18] | | ←··············→ | | |
| Polyatomic deposition [31] | | ←··············→ | | |
| Heterobifunctional photolinkers [32, 33] | | | ←··········→ | |
| Microfluidic networks [34–37] | | ←··············→ | | |
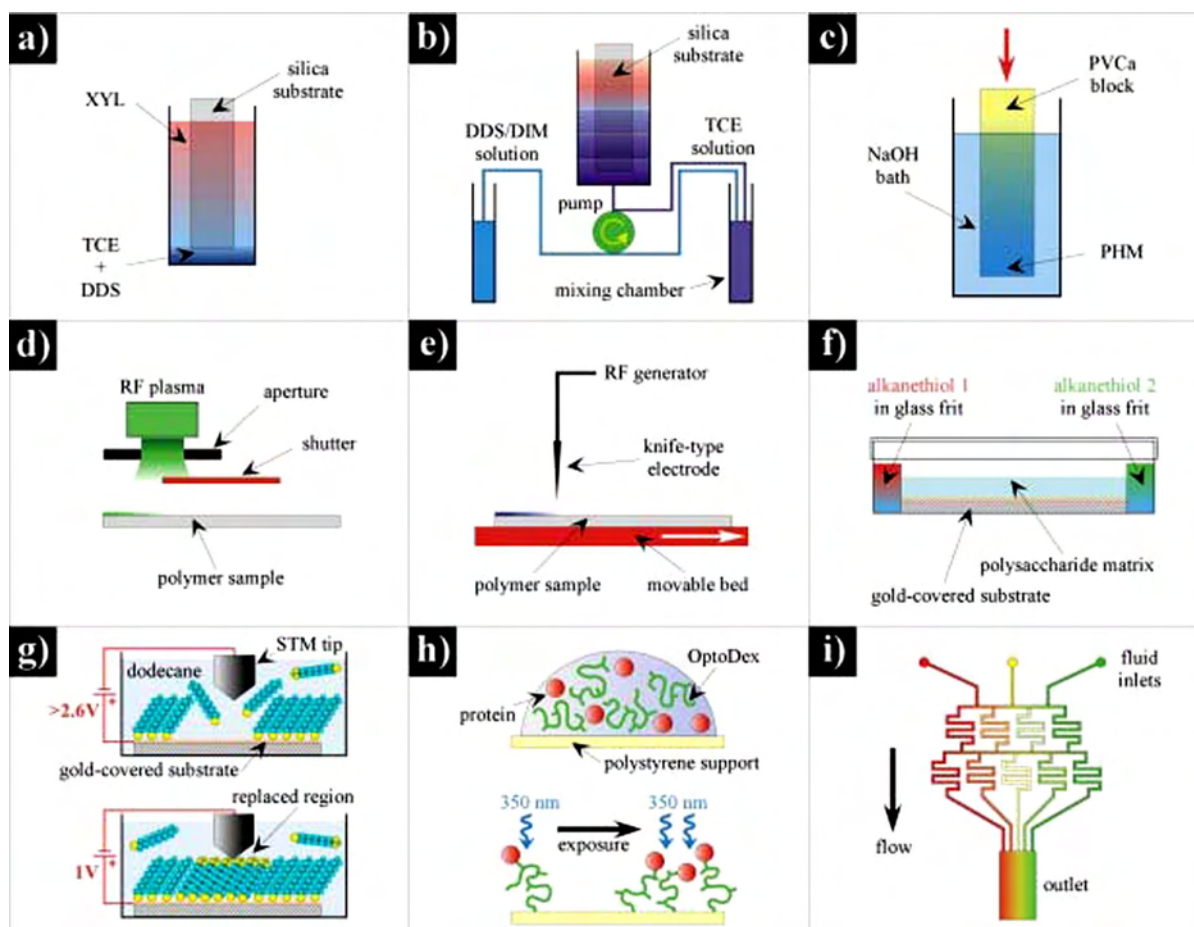
**Figure 1.** Schematic illustrating the formation of wettability gradient using (a) liquid diffusion technique, (b) density gradient solution method, (c) hydrolysis of poly(vinylene carbonate), (d) radio frequency plasma discharge, (e) plasma discharge, (f) diffusion of alkanethiols in polysaccharide matrix, (g) molecular gradients via replacement lithography, (h) gradients of proteins by means of heterobifunctional photolinkers, and (i) solution and surface gradient using microfluidics.

A versatile method for decorating polymer surfaces with chemical gradients is based on moving a shutter over the polymer surface during exposure of the surface to a radio frequency plasma discharge [25] (Fig. 1d). This technique is capable of producing various gradient shapes on a variety of polymers under various gas conditions. However, the chemical nature of the plasma-modified surfaces is not well defined—the surface consists of a mixture of various hydrophilic groups and radicals. Moreover, some materials have a tendency to roughen when exposed to a radio frequency plasma discharge. Lee and co-workers produced a wettability gradient on a low-density polyethylene surface by treating the polymer sheets in air with the corona from a knife-type electrode whose power gradually increased along the sample length [26] (Fig. 1e). While this method has the same characteristics as that based on a radio frequency plasma discharge, it is easier to accomplish and the treatment can be done under ambient conditions.

Roberson and co-workers developed a simple method for preparing surfaces with gradually varying wetting properties on a millimeter scale [27]. They first deposited SAMs made of *n*-octyl trichlorosilane (OTS) on flat silica surfaces

and exposed such surfaces to a gradient UV/ozone (UVO) radiation. To produce the gradient of UVO, Roberson and co-workers used a variable-density filter made of fused silica that was modified with inconel (a Ni, Cr, Fe alloy). The optical density varied from 0.04 to 1.0 (measured at $\lambda = 330$ nm) across the fused silica optical filter in 11 equidistant steps (4 mm each), giving a linear transmission gradient in the intensity of the UV radiation. The filter was placed close to the SAM-covered surface. Atomic oxygen, generated from molecular oxygen in the proximity of the surface by the UV radiation, converted a fraction of the —$CH_2$— and —$CH_3$ groups in the hydrophobic OTS moieties into hydrophilic functional groups (e.g., —COOH). The molar concentration of the atomic oxygen (and thus the density of the hydrophilic groups on the surface) was directly proportional to the incident UV intensity. Measurements using contact angle and time-of-flight secondary ion mass spectrometry confirmed the existence of linear wettability gradients; the surface energy was shown to increase from 26 mJ/m$^2$, on the untreated side, to 72 mJ/m$^2$, close to the UVO-modified side of the substrate.

Liedberg and Tengvall prepared molecular gradients by cross-diffusion of two different ω-substituted alkanethiols from opposite ends of a polysaccharide matrix deposited on top of a gold-covered planar substrate [28] (Fig. 1f). As the two alkanethiols interdiffused, they bonded to the underlying gold substrate and formed a self-assembled monolayer, whose composition changed along the diffusion path. Liedberg and co-workers demonstrated that this methodology can be used to prepare one-dimensional molecular gradients with hydrophilic/hydrophobic variation [28] as well as ordered/disordered structures [29].

The ability to control electrochemically the adsorption/desorption of alkanethiol molecular assemblies on/from a noble metal surface and its utilization in preparing structures with spatiotemporal characteristics has been exploited by Bohn and co-workers [30]. They first formed a self-assembled monolayer of *n*-octanethiol (OT) on a gold-coated substrate. OT gradients were formed by applying a 15-nV/mm in-plane potential gradient, which selectively removed the OT molecules from the regions exposed to a higher potential. After washing with pure solvent, the sample was reimmersed into another solution containing a hydrophilic mercapto propionic acid (MPA), whose molecules filled the bare areas on the gold substrate. A two-component linear gradient in composition (and hence wettability) was thus generated.

Gorman and co-workers recently developed a novel technique for preparing molecular gradients, whose dimensions can be controlled on the nanometer scale [18] (Fig. 1g). In their methodology, an organized SAM of an ω-substituted alkanethiol was formed on an atomically flat gold substrate. Such a substrate was then immersed into a dodecane solution containing another ω-substituted alkanethiol. The substrate-bound SAM was repeatedly imaged with scanning tunneling microscopy without apparent change in its appearance under conditions of set-point bias of +1 V (positive substrate bias) and set-point current between 6 and 8 pA. Upon changing the bias to +3.0 V or slightly higher (up to +4.0 V), replacement of the thiolate on the surface by the different thiol in solution occurred. This replacement was observed by scanning the tip in one area at the higher voltage, reducing the set-point voltage back to 1 V, and scanning the tip across a larger area. By rastering the tip in a defined pattern above the substrate, features with a resolution of approximately 10–15 nm and a variety of pattern shapes were generated.

Wijesundara and co-workers showed that surfaces with gradient wettabilities can be obtained by hyperthermal polyatomic ion deposition [31]. A poly(methyl methacrylate) (PMMA)/fluorocarbon gradient was produced by exposure of the PMMA surface to $C_3F_5^+$ ions. A linear variation in wettability was achieved by linearly increasing the fluence of the $C_3F_5^+$ ions while allowing the ion source to scan across the PMMA substrate. The researchers also established that a polyatomic deposition method can be used to form wettability gradients on other materials, including polymers (polystyrene, PS), semiconductors (H-terminated silicon), and oxides ($Al_2O_3$). In each case, the parameters of the gradients can be tuned by varying the ion type, the fluence, and the scanning speed.

Hypolite and co-workers proposed a method for creating microscale gradients using photoreactive cross-linking agents [32] (Fig. 1h). In their methodology, a conjugation reagent containing a photoactive benzophenone (BP), a water-soluble tetraethylene glycol (TEG) spacer, and an amine-reactive *N*-hydroxysuccinimide (NHS) ester was prepared and used to derivatize a protein, R-phycoerythrin (PE). A surface with a PE concentration gradient was created by scanning a Cd/He laser beam across the surface in a raster pattern but with increasing scanning speed in consecutive lines. Exposure to the laser beam activated the BP, which set up a reaction scheme that resulted in protein immobilization on the substrate. Increasing the exposure time of the surface to the laser beam increased the amount of BP–TEG–PE immobilized on the surface. Higher scanning velocities (shorter exposure times) resulted in lower concentrations of immobilized protein relative to the slower velocities. Caelen and co-workers utilized similar technology to form discrete gradients of immobilized proteins on surfaces [33]. They mixed protein probes with the photolinker polymer OptoDex (a polysaccharide-based polymer substituted with aryldiazirines). The solution was deposited on the surface in a gradient fashion via ink-jet printing. After drying, the surface was irradiated with light of 350 nm wavelength. Photoactivation of the aryldiazirine molecules led to the formation of reactive carbenes. Some carbenes underwent insertion reactions with covalent bonds of probe proteins; others bound to the underlying polystyrene surface. A discrete protein gradient on the surface was formed by removing the non-covalently attached protein by washing.

Caelen and co-workers proposed that gradients of immobilized proteins on surfaces can be prepared by utilizing microfluidic networks [34]. In this methodology, a poly(dimethyl siloxane) (PDMS) substrate was placed across the channels of a microfluidic network made on micromachined silicon to pattern lines of proteins onto the PDMS substrate. Capillary forces between a solution containing proteins and the hydrophilized walls of the microfluidic network induced filling of the channels and the protein was gradually depleted by fast adsorption of the proteins to the hydrophobic regions of the PDMS substrate exposed to the filled channels. After separating the PDMS from the microfluidic network, the underivatized areas of PDMS were blocked with bovine serum albumin. In the final step, fluorescently labeled immobilized antigens with antibodies were attached to the protein gradient areas to visualize the gradient. Whitesides and co-workers utilized a network of multi-inlet microfluidic channels to fabricate gradients in composition in solution and gradients in topography on the surface [35–37] (Fig. 1h). A microfluidic gradient generator comprising multiple generation branches in a poly(dimethyl siloxane) network was fabricated by rapid prototyping [37] and soft lithography. Multiple solutions were simultaneously infused into the network through the inlets. As the fluid streams traveled down the network, they were repeatedly split, mixed, and recombined. After several generations of branched systems, each branch contained different proportions of the infused solutions. A gradient was established—perpendicular to the flow—in a single large channel that combined all branches. Various gradient shapes and profiles were generated, including periodic gradients,

asymmetric gradients, superposed gradients, and dynamic gradients. By flowing hydrofluoric acid through the microfluidic network, a gradient in the surface topography was also generated on the silica.

In this review, we will outline several strategies for producing gradient-based surfaces. All the methodologies are based on generating the wettability gradient using the vapor deposition technique suggested more than 10 years ago by Chaudhury and Whitesides [16]. In this method, shown schematically in Figure 2, an organosilane (either chloro- or alkoxy-based) is mixed with paraffin oil (PO) and the mixture is placed in an open container that is positioned close to an edge of a silicon wafer. As the silane evaporates, it diffuses in the vapor phase and generates a concentration gradient along the hydrophilic substrate. Upon impinging on the substrate, the silane molecules react with the substrate —OH functionalities and form an organized SAM. The breadth and position of the silane molecular gradient can be tuned by varying the silane diffusion time and the flux of the silane molecules. The latter can be conveniently adjusted by varying the silane : PO ratio and/or the temperature of the silane : PO mixture. After the gradient SAM deposition, any physisorbed silane molecules are removed by thoroughly washing the substrates with warm deionized water (75°C; resistivity, >16 M$\Omega \cdot$m) for several minutes. In some instances, the molecular gradients serve as precursors for further processing. Specifically, we document later that molecular gradients can be used as templates for the adsorption of nanosized objects and the formation of three-dimensional (3D) structures by allowing polymer chains to grow from the molecules within the gradient (the so-called "grafting from" technology).

# 3. METHODS OF MEASURING GRADIENT PROPERTIES

Many different surface analytical techniques can be applied to study the properties of the gradient substrates. Perhaps the easiest and most widely available technique is based on measuring the wettability using either static or dynamic contact angles. In static contact angle experiments, one measures the wetting angle of a small volume of probing liquid on the surface. While in some instances contact angles are reported for cases where the droplet is separated from the needle, most measurements are performed under conditions where the needle and the probing liquid are not separated. The latter set of measurements allows for determining so-called advancing and receding contact angles. Contact angle measurements on wettability gradients are usually performed such that the needle is in contact with the probing liquid. Separating the needle from the liquid

would allow the liquid to move on the surface (see [16]), particularly in gradients with steep boundaries between the hydrophobic/hydrophilic regions. The dynamic contact angle (DCA) measurements are usually performed using the Wilhelmy plate techniques. Examples of the DCA measurements on gradient substrates can be found elsewhere [38].

While useful in providing macroscopic-level information about the chemistry of the gradient surfaces, contact angle methods are not capable of delivering information about the structural properties of the gradients on a molecular level (such as concentration of a particular chemical group, orientation of molecules, etc.). For information regarding the above, one has to turn to more sophisticated methods. Ruardy and co-workers discuss several examples describing the utilization of X-ray photoelectron spectroscopy (XPS) and infrared spectroscopy (IR) [38]. Recently, near-edge X-ray absorption fine structure (NEXAFS) spectroscopy has been applied to study the physicochemical characteristics of the gradient surfaces. NEXAFS turned out to be very beneficial because it allowed for simultaneous investigation of both the surface chemistry and the molecular orientation.

## 3.1. NEXAFS Spectroscopy

NEXAFS involves the resonant soft X-ray excitation of a K or L shell electron to an unoccupied low-lying antibonding molecular orbital of $\sigma$ or $\pi$ symmetry, $\sigma^*$ and $\pi^*$, respectively [39]. The initial-state K or L shell excitation gives NEXAFS its element specificity, while the final-state unoccupied molecular orbitals provide NEXAFS with its bonding or chemical selectivity. A measurement of the intensity of NEXAFS spectral features enables identification of chemical bonds and determination of their relative population density within the sample. Because of the fixed geometry between the sample and the X-ray beam and the fact that the $1s \rightarrow \sigma^*$ and $1s \rightarrow \pi^*$ excitations are governed by dipole selection rules, the resonance intensities vary as a function of the direction of the electric vector $\mathbf{E}$ of the incident polarized X-ray relative to the axis of the $\sigma^*$ and $\pi^*$ orbitals. This, coupled with the fact that sharp core-level excitations for elements C, N, O, and F occur in the soft X-ray spectral region, makes NEXAFS an ideal technique for probing the molecular orientations of organic molecules. Since its first introduction as a routine analytical technique, NEXAFS has proven advantageous in determining the orientation of both small molecules, as well as large macromolecular systems. Recently, we have demonstrated that NEXAFS can be used to sense the chemistry and determine the molecular orientation of gradient materials surfaces [40, 41]. To measure the spatial distribution of a given molecule, the sample is mounted onto a goniometer, which controls the orientation of the sample with respect to the polarization vector of the X-rays and enables horizontal and vertical sample motion. After tuning the monochromator energy to that corresponding to a given characteristic $1s \rightarrow \sigma^*$ (or $1s \rightarrow \pi^*$) transition, the sample is moved with small increments (usually between 0.5 and 1 mm), and after each step a new NEXAFS data set is recorded. To determine the concentration of a given chemical moiety, the angle between the sample normal and the electric vector $\mathbf{E}$ of the polarized X-ray beam, $\theta$, is set at $\theta \approx 50$–55°. At this angle—the so-called "magic angle"—the



**Figure 2.** Schematic showing the method of preparing molecular gradient by vapor deposition of organosilanes onto hydrophilic substrates.

NEXAFS intensity is independent of the molecular orientation on the substrate. If orientation information is required, the above procedure is repeated for at least three different angles $\theta$ (usually 20°, 50°, and 90°), and the molecular orientation is evaluated using standard techniques (for details, see [39, 40]).

# 4. PROPERTIES OF MOLECULAR GRADIENTS

One of the most important properties of a molecular gradient is its wettability, which is determined primarily by the terminal group of the SAM and the concentration of molecules attached to the substrate at a given position along the gradient. In Figure 3, we show the contact angles of water measured on "double" molecular gradients made by vapor deposition of OTS (OTS : PO = 1 : 5) from two opposite ends of the silica-covered silicon substrate. The data in Figure 3 show that at short diffusion times the two diffusion profiles stay isolated, forming a "wettability well." However, upon increasing the diffusion time of the molecules in the vapor, the two profiles start to interfere and the wettability well starts to fill up. The notion of double gradients can be further extended to form gradients of two chemically different species. Such heterogeneous double gradients on planar silica-covered substrates were recently prepared by forming mixed molecular gradients prepared by vapor interdiffuson of aminopropyl triethoxysilane (APTES) and $1H,1H,2H,2H$-perfluorodecyltrichlorosilane ($t$-F8H2) [42].

The gradual variation of the grafting density of the surface-bound molecules is expected to have a profound influence on the organization of the molecules in the gradients. By studying how the gradient-forming molecules are arranged across the gradient interfacial region, one can learn more about the mechanisms and nature of
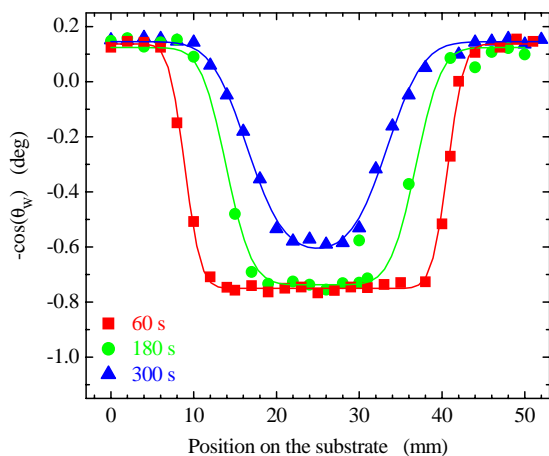
self-assembly in organosilane SAMs. The gradient geometry offers the advantage of constraining the self-assembly growth in a given direction. This is in contrast to the classical case of "uniform" self-assembly on a substrate, where the incorporation of the molecules in the final SAM takes place at random in all directions. The ability of NEXAFS to determine the molecular orientation of the surface-bound molecules can be utilized to study the orientation of the SAMs across the gradient. In Figure 4, we plot the dependence of the fraction of the F8H2 molecules on the surface (normalized by the maximum SAM coverage) (solid lines) and the variation of the average tilt of the semifluorinated part of the F8H2 molecule with respect to the surface normal, $\langle \tau_{F8} \rangle$, (dashed lines) as a function of the position on the silica surface for mono-, di-, and trifunctional $1H,1H,2H,2H$-perfluorodecyl organosilanes, $m$-F8H2, $d$-F8H2, $t$-F8H2, respectively (for chemical formulas, see the Appendix). By comparing the information about the concentration and orientation of F8H2 in the molecular gradient, the following picture emerges. Close to the diffusing sources, the density of the F8H2 molecules is high and, as a result, complete SAMs form, similar to homogeneous F8H2 SAMs [40, 43]. At larger distances from the diffusing sources, the concentration of F8H2 molecules decreases. Interestingly, the functional dependence of the concentration profiles varies, depending on the type of bonding on the substrate. This can be due to several factors. First, with the exception of the monofunctional $m$-F8H2



**Figure 3.** Cosine of contact angles of deionized water measured on "double" molecular gradients prepared by vapor deposition of $n$-octyl trichlorosilane (OTS) from two opposite ends of a silica-covered silicon wafer for 60 s (squares), 180 s (circles), and 300 s (triangles). The solid lines are the best fits to the data using the Fickian diffusion profile.
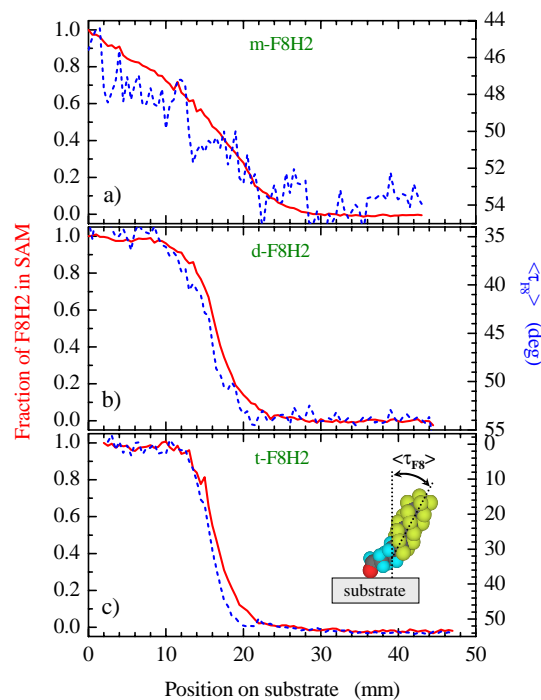


**Figure 4.** Fraction (solid lines) and molecular orientation (dashed lines) of F8H2 in the molecular gradients made of (a) $m$-F8H2, (b) $d$-F8H2, and (c) $t$-F8H2 organosilanes as a function of the position on the substrate. The inset to the figure shows a schematic of the molecular orientation of a single F8H2 molecule and denotes the definition of $\langle \tau_{F8} \rangle$.

molecules, both $d$-F8H2 and $t$-F8H2 species have a tendency to form larger multimolecular clusters. This behavior has been known for some time and is relatively well documented [44]. These clusters can form either in the vapor phase or after the molecules hit the silica surface. Recall that only minute concentrations of water are needed to hydrolyze the Si–Cl bond, thus converting it into Si–OH [8]. Hydrogen bonds between the hydroxyls from several molecules can be responsible for the formation of a relatively stable cluster. Moreover, the long life of such clusters is further facilitated by rather strong intermolecular van der Waals forces acting between two or more $-(CF_2)_8-$ helices [8]. Thus, unlike the $m$-F8H2 SAMs, which are formed primarily by deposition of single molecules, the $d$-F8H2 and $t$-F8H2 SAMs may be built by inserting clusters containing multiple molecules. The second factor, which is closely associated with the first one, has to do with the way the F8H2 organosilanes are packed. Genzer and co-workers have recently reported that the orientation of the F8H2 molecules in homogeneous SAMs depends on the bonding environment of the F8H2 molecule. The average tilt angles of the semifluorinated part of $t$-F8H2, $d$-H8H2, and $m$-F8H2 moieties from the surface normal, $\langle \tau_{F8} \rangle$, were $10 \pm 2°$, $35 \pm 2°$, and $45 \pm 3°$, respectively [45]. The increase in the tilt angle with increasing number of methyl groups attached to the silicon terminus was associated with the steric hindrance of those methyl groups close to the bonding substrate. From Figure 4, $\langle \tau_{F8} \rangle$ increases as one moves away from the diffusing source along each gradient. This behavior suggests that the chains start deviating from the tilt angles in their respective homogeneous SAMs. This molecular reorganization of the F8H2 molecules is in part due to the decreasing grafting density on the surface. Considering that the spot size of the X-ray beam on the sample during the NEXAFS experiments, about 1 mm$^2$, is much larger than the area occupied by a single $t$-F8H2 molecule, the tilt angle $\langle \tau_{F8} \rangle$ determined from NEXAFS represents only an *average* value. Hence, there is no straightforward way to discriminate between the case of all $t$-F8H2 molecules homogeneously tilting by the same angle and the case of a disordered system with a broad distribution of tilt angles. Therefore, the increase in $\langle \tau_{F8} \rangle$ observed in the region of the gradient in which the concentration decreases cannot be unambiguously interpreted by using the NEXAFS data alone. Complementary measurement of another physical property along the gradient—such as the density and/or the thickness—is required [40].

One of the limitations of the vapor deposition technique is that the current setup produces rather broad wettability gradients with very little tunability. Hence, our goal was to develop technologies leading to greater control over the characteristic size of the gradients. On a flexible substrate, this can be achieved by fine-tuning the grafting density of the molecules by fabricating mechanically assembled monolayers (MAMs), structures that are based on the synergism between self-assembly and mechanical manipulation of the grafted molecules on the surfaces [46]. The technique (Fig. 5) is based on the combination of (i) the well-known grafting reaction between $\omega$-(CH$_2$)$_n$SiCl$_3$ molecules (typically, $\omega = -CH_3$, $-CF_3$, $-NH_2$, $-CH=CH_2$, $-CN$) and $-OH$ functionalities present on silicon-based surfaces, [Si]≡substrate (Scheme 1), and (ii) mechanical manipulation
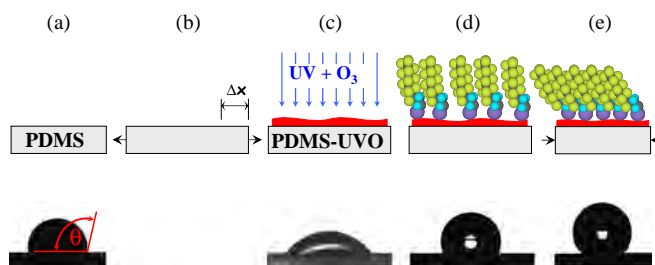


**Figure 5.** Top panels are schematics illustrating the technological steps leading to the production of MAMs. (a) A pristine PDMS network film is prepared by casting a mixture of PDMS and a cross-linker into a thin ($\approx$0.5 mm) film and curing it at 55 °C for about 1 h. (b) After soxhlet extraction in chloroform for 24 h, which removes any non-cross-linked PDMS oligomers, the film is cut into small strips ($\approx$1 × 5 cm$^2$) and mechanically stretched by a certain length, $\Delta x$. (c) Subsequent exposure to a UVO treatment produces hydrophilic PDMS surfaces (PDMS–UVO) composed mainly of hydroxyl groups as revealed from Fourier transform infrared and NEXAFS experiments. By increasing the length of the UVO treatment, the number of surface hydrophilic groups increases, causing the water contact angle to decrease. The HO–[Si]$_{surface}$ groups are particularly important because they serve as attachment points for the chlorosilane molecules. (d) The FyHx molecules are deposited from vapor onto this stretched substrate and form an organized SAM. (e) Finally, the strain is released from the PDMS–UVO film, which returns to its original size, causing the grafted FyHx molecules to form a densely organized MAM. To remove weakly physisorbed FyHx molecules, we wash the samples thoroughly in warm ($\approx$60 °C) distilled water for 1 min and dry them with nitrogen. The bottom panels show photographs of a water droplet spreading on each of the substrates. Reprinted with permission from [46], J. Genzer and K. Efimenko, *Science* 290, 2130 (2000). © 2000, American Association for the Advancement of Science.

of the grafted $\omega$-(CH$_2$)$_n$SiCl$_3$ molecules on the substrate. The method consists of five operational steps. First, a pristine poly(dimethyl siloxane) (PDMS) network film is prepared by casting a mixture of PDMS and a cross-linker into a thin film (thickness $\approx$ 0.5 mm) and curing at 55° C for about 1 h. In the second step, the cross-linked PDMS substrate is cut into small strips ($\approx$1.5 × 5 cm$^2$) and uniaxially stretched to various strains, $\Delta x$. The stretched substrate is then exposed to an ultraviolet/ozone (UVO) treatment to produce the $-OH$ surface functionalities (PDMS–UVO) [47]. The molecular gradient of $\omega$-(CH$_2$)$_n$SiCl$_3$ SAM is then formed following the vapor diffusion technique [16] described earlier. Finally, the strain is released from the PDMS–UVO film, which returns to its original size, causing the grafted $\omega$-(CH$_2$)$_n$Si molecules to form a gradient with a steeper concentration profile as compared to a nonstretched PDMS–UVO substrate. Figure 6 shows static contact angles of deionized water along gradient
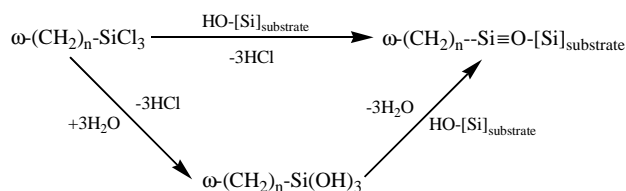


**Scheme 1.**
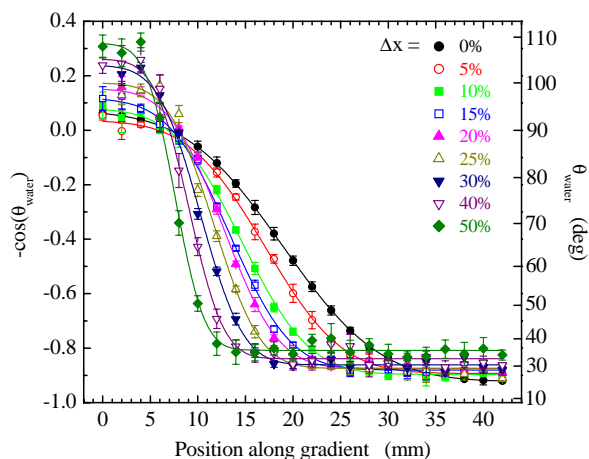
**Figure 6.** Contact angles of deionized water along gradient substrates prepared on PDMS network films that were previously extended by $\Delta x$ ranging from 0 to 50% [$\Delta x$ equal to 0% ($\bullet$), 5% ($\bigcirc$), 10% ($\blacksquare$), 15% ($\square$), 20% ($\blacktriangle$), 25% ($\triangle$), 30% ($\blacktriangledown$), 40% ($\triangledown$), and 50% ($\blacklozenge$)] and treated with UVO for 30 min. The gradients were deposited from vapor (as described in the text) for 5 min. The vapor source consisted of OTS:PO = 1:10 mixtures. Reprinted with permission from [17], K. Efimenko and J. Genzer, *Adv. Mater.* 13, 1560 (2001). © 2001, Wiley-VCH.

substrates prepared with $\Delta x$ ranging from 0 to 50%. In all cases, the exposure time of the PDMS to the UVO was 30 min, and the vapor diffusion time for a 1:10 OTS:PO mixture was 5 min. The data show that, as expected, the gradient steepness changes with changing $\Delta x$. Specifically, the span of gradient decreases from about 40 mm down to 15 mm as $\Delta x$ increases from 0 to 50%. In all cases, the profiles exhibit excellent Fickian-type diffusion profiles [17].

# 5. APPLICATIONS OF GRADIENTS ON SUBSTRATES

Continuous or discrete molecular gradients represent a chief tool for combinatorial chemistry and materials science [48, 49]. The combinatorial approach leads to rapid technological development with improved efficiency and lower research cost [50]. In addition, as documented below, the unique properties of the gradient substrates can also be utilized to study transport phenomena on surfaces.

## 5.1. Combinatorial Studies of Cell/Substrate Interactions

Successful application of a biomaterial inside the body necessitates that it mimic the function of the body part where it will be implanted. This requires that the implants respond to protein adsorption, cellular adhesion, and inflammatory reactions in the same way as the body part does. Most of the above-mentioned functions are influenced by wettability of the biomaterial surface. Traditional experiments designed to study the effect of wettability suffered from the different surface chemistries of the various biomaterials used to achieve a wide behavioral spectrum. For example, it was often difficult to segregate the effect of wettability on the studied phenomenon from that of the surface

chemistry of the surface. This incertitude is minimized to a great extent by studying protein and cell adsorption on a molecular gradient surface, where the observed response can be attributed primarily to variation in wettability along the surface. In addition, it has been recognized that immobilization of proteins and peptides on the surface of a material offers a powerful method for probing cell response and migration, biodetection, and activity control. The need for such well-defined surfaces as well as the requirement of reducing the number of specimens necessary for these studies has stimulated the development of methodologies providing gradients of biological macromolecules. Several techniques listed previously have been utilized in these studies. A recent review summarizes the progress in the application of gradient substrates in studies of cellular interaction phenomena up until 1997 [38].

## 5.2. Thin-Film Behavior on Gradient Substrates

There is a considerable need for understanding the structure, stability, and phase behavior of thin liquid and polymer films. Several studies have appeared that reported on utilizing combinatorial approaches to study the coalescence of droplets on chemically heterogeneous gradient substrates [51], order–disorder transition in grafted oligoalkanes on surfaces [29], phase separation in immiscible polymer blends [52], and interfacial behavior of block copolymer melts [53]. For example, Genzer and Kramer studied the phase separation in thin films of poly(ethylene propylene) (PEP) and its deuterated analog (dPEP) deposited on wettability gradient substrates prepared using the diffusion of alkanethiols in polysaccharide matrix [28]. By adjusting the composition of the alkanethiol solutions used to produce the wettability gradient, the surface energy ($\gamma_{SAM}$) was allowed to vary over a narrow window (from 30 to 21 mJ/m$^2$). Elastic recoil detection was used to measure the volume fraction profiles of dPEP and PEP in the samples. In Figure 7, we plot a series of such volume fraction versus depth profiles of dPEP for various positions along the gradient substrate (open circles). It is evident that the air/mixture interface is always wet by the dPEP-rich phase. The situation at the mixture/SAM interface is more complex. For $\gamma_{SAM} < 25$ mJ/m$^2$, the mixture/substrate interface is wet by a dPEP-rich phase. However, the thickness of this layer depends strongly on $\gamma_{SAM}$ and decreases with increasing $\gamma_{SAM}$. At $\gamma_{SAM} = 25.6$ mJ/m$^2$, the mixture/SAM interface is wet by the PEP-rich phase. The results in Figure 7 also show that, as the thickness of the dPEP phase at the mixture/substrate interface decreases, the thickness of the dPEP-rich phase at the air/mixture interface increases. This observation indicates that as $\gamma_{SAM}$ increases there is a redistribution of dPEP material from the mixture/SAM interface to the air/mixture interface. This pre-transitional behavior was shown to originate from the long-range nature of the van der Waals interaction between layers and was predicted by a simple model that considered the dependence of the free energies of the two dPEP-rich layers at the surface and substrate interfaces on their thicknesses.
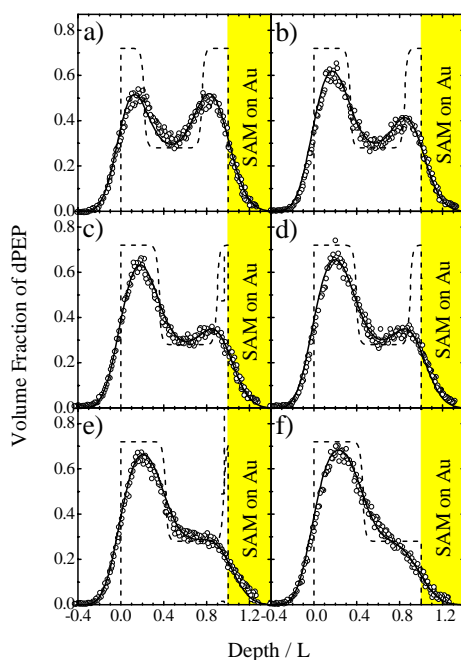
**Figure 7.** Volume fraction profiles of deuterated poly(ethylene propylene) (dPEP) in PEP/dPEP mixtures measured by elastic recoil detection (ERD) (open circles) for samples cast on substrates with $\gamma_{SAM}$ equal to (a) 20.5, (b) 21.2, (c) 21.7, (d) 22.3, (e) 23.3, and (f) 25.6 mJ/m$^2$ and annealed at 41 °C for 2 weeks. The dashed and solid lines denote the actual dPEP volume fraction profiles and the volume fractions corrected for the finite ERD resolution (ca. 90 nm), respectively. The depth coordinate has been normalized by the total film thickness, *L*. Reprinted with permission from [52], J. Genzer and E. J. Kramer, *Europhys. Lett.* 44, 180 (1998). © 1998, EDP Sciences.

## 5.3. Motion of Liquids on Gradient Substrates

Chemical gradients are capable of transporting materials in a directional manner and are responsible for driving many important biological and physical processes [38]. Initial empirical observations have evolved into deliberate efforts to direct liquid motion along chemical gradients [54]. It has long been known that a continuous liquid film can spontaneously break into droplets that move freely over surfaces without application of an obvious external force. For example, the formation of wine drops from a continuous liquid film spreading over the wineglass surface is driven by the change in surface tension caused by the evaporation of alcohol. Variations in surface tension and the resulting changes in wetting behavior of the liquid by composition or temperature gradient were studied and explained over 100 years ago and are associated with the name of the Italian physicist Carlo Marangoni [55]. Motion due to chemical gradients on the substrate was demonstrated by Chaudhury and Whitesides [16] with droplets of water moving on a surface of varying hydrophobicity created by coating a silicon wafer partially with *n*-decyl trichlorosilane (DTS). A drop of water moved from the hydrophobic end to the hydrophilic end of the wafer, but only very slowly and only over a distance on the order of 1 mm. Very recently, much higher drop speeds

have been observed for small water droplets formed by condensation of steam onto a gradient surface [56] and droplets on vibrating gradient surfaces [57].

## 5.4. Molecular Gradients as Two-Dimensional Templates

Gradient substrates have also been utilized as molecular templates for controlling the spatial distribution of nonpolymeric objects. Plummer and Bohn reported on electrochemically generating a gradient of amino-terminated thiol-based self-assembled monolayer on a gold-covered substrate [58]. To produce particle gradients, Plummer and Bohn attached carboxylic acid–modified, fluorescently doped polystyrene nanospheres (diameter of 200 nm) to the amino termini of the gradient SAM. Bhat and co-workers prepared assemblies of 17-nm gold nanoparticles with continuous gradients in number density on flat silica-covered substrates [59] (Fig. 8). Their methodology consisted of first forming a one-dimensional molecular gradient of amino groups ($-NH_2$) on the substrate by vapor diffusion of amine-terminated silane molecules, followed by attachment of gold nanoparticles to the $-NH_2$ functional groups by immersing the substrate in a colloidal gold solution. Experiments
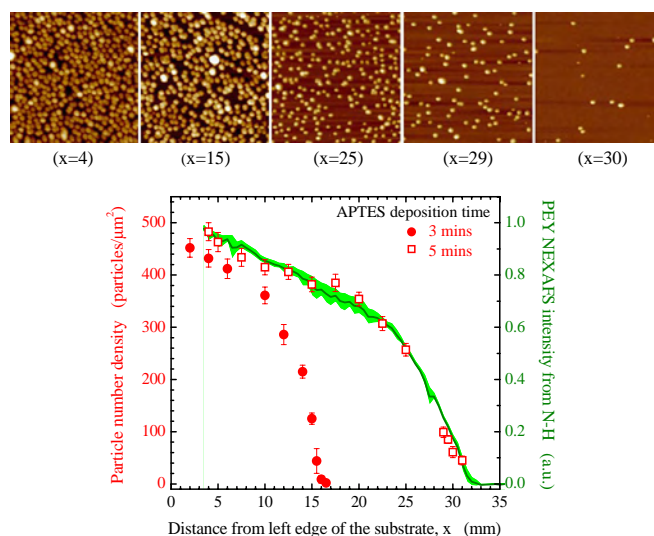


**Figure 8.** (Upper panel) Scanning force microscopy images of gold nanoparticles (diameter ≈ 7 nm) adsorbed along a substrate prepared by evaporating a (3-aminopropyl) triethoxysilane (APTES)/paraffin oil (PO) mixture (50/50 w/w) for 5 min followed by immersion in colloidal gold solution (pH ≈ 6.5) for 24 h (edge of each image = 1 $\mu$m). (Lower panel) Particle number density profile (left) for two gradients prepared by evaporating APTES/PO mixtures for 3 (●) and 5 (■) min. The data points represent an average from three transverse scans along the gradient taken at the center of the sample ($y = 0$ mm) and $y = -3$ mm, and $y = +3$ mm. The line represents the partial electron yield (PEY) near-edge X-ray absorption fine structure (NEXAFS) profile (right) of N–H bonds from an ATEPS gradient prepared by evaporating an APTES/PO mixture for 5 min. The area around the PEY NEXAFS line denotes the measurement uncertainty (based on nine line scans along the gradient taken between −3 mm and +3 mm from the center of the sample). Reprinted with permission from [59], R. R. Bhat et al., *Langmuir* 18, 5640 (2002). © 2002, American Chemical Society.

using scanning force microscopy revealed that the number density of nanoparticles on the substrate varied continuously as a function of the position on the substrate. NEXAFS studies confirmed that the nanoparticle number density gradient was closely correlated with the concentration gradient of —NH$_2$ groups anchored to the substrate. Bhat and co-workers demonstrated that the number density of nanoparticles within the gradient and the length of the gradient can be tuned by controlling the vapor diffusion of the silane molecules. In addition, this simple methodology can be further extended to create double gradients, thus producing "a valley in nanoparticle concentration." The adhesive molecular template can be modified to attract different kinds of particles for different applications, all of them arranged in a gradient pattern. The ability to vary and control the concentration of captured particles allows one to devise sensors, filters, and so on. Some components of fluids, for example, could pass through the gaps in the less-concentrated part of the particle gradient, but be blocked by the thicker concentration. Such filters could also be tailored to detect or capture harmful viruses or toxins. The controlled variation in distribution of particles also allows rapid testing of potential catalysts—always in demand by industry.



**Figure 9.** Dry ($h$, open symbols) and wet ($H$, closed symbols) thickness of the PAAm brush and the CMPE concentration (solid line) as a function of the position on the substrate. Reprinted with permission from [63], T. Wu et al., *J. Am. Chem. Soc.* 124, 9394 (2002). © 2002, American Chemical Society.

## 6. EXTENSION OF TWO-DIMENSIONAL GRADIENTS TO THREE DIMENSIONS

Recently, it has been recognized that molecular gradients can serve as useful templates for creating three-dimensional structures. For example, Lee and co-workers utilized the corona discharge method to produce a molecular gradient of radicals on the surface of poly(ethylene). This gradient surface was then used as a template for "grafting from" radical polymerization of poly(acrylic acid) [60] and poly(ethylene oxide) [61] with gradual variation of grafting densities. Wu and co-workers recently prepared substrates with a gradient variation of grafting densities on silica substrates [62, 63]. A gradient of 1-trichlorosilyl-2-(*m/p*-chloromethylphenyl) ethane (CMPE), the polymerization initiator, was formed on the surface using the vapor deposition technique, and the unexposed regions on the substrate containing unreacted —OH functionalities were treated with OTS in order to minimize any physisorption of the monomer and/or the polymer formed in solution on the parts of the substrate that do not contain the CMPE–SAM. NEXAFS was utilized to measure the concentration of the CMPE along the SAM gradient. The concentration of CMPE in the sample decreased as one moved from the CMPE side of the sample toward the OTS–SAM; the functional form closely resembled that of a diffusion-like profile (Fig. 9). Experiments using variable-angle spectroscopic ellipsometry (VASE) confirmed that only a single monolayer was formed on the substrate. Monodisperse poly(acryl amide) (PAAm) chains with gradual variation in grafting densities were synthesized by the "grafting from" reaction of acryl amide using atom transfer radical polymerization (ATRP), as described earlier [64–66]. VASE was used to measure the thickness of the dry polymer film, $h$, as a function of the position on the substrate. Because the polymers grafted on the substrate have all roughly the same degree of
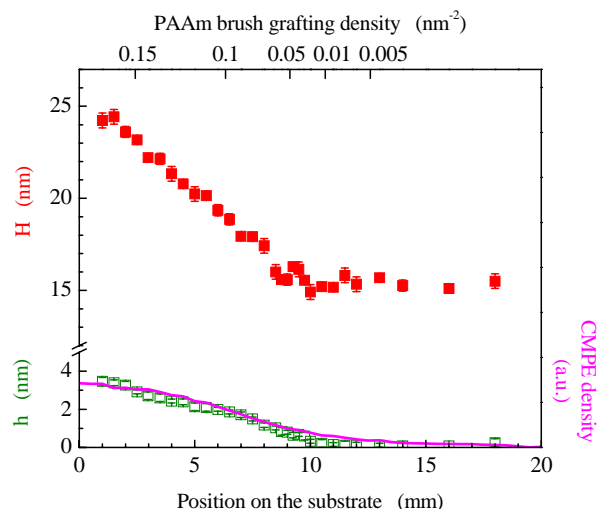
polymerization, the variation of the polymer film thickness can be attributed to the difference in the density, $\sigma$, of the CMPE grafting points on the substrate. The data in Figure 9 (for CMPE : PO = 1 : 1) reveal that $h$ decreases gradually as one moves across the substrate starting at the CMPE edge. Note that the concentration profile of the polymer follows that of the initiator (solid line in Fig. 9). The substrates with the grafted PAAm were placed into a solution cell that was filled with deionized (DI) water (pH $\approx$ 7), a good solvent for PAAm, and incubated for at least 5 h. The wet thickness of PAAm-grafted polymer in DI water, $H$, was measured using VASE. The values of $H$ for samples prepared on CMPE : PO = 1 : 1 gradients are shown in the top part of Figure 9. The data show that $H$ decreases as one traverses across the substrate starting at the CMPE side. In Figure 10, we plot the wet polymer thickness as a function of the PAAm grafting density on the substrate. The data in Figure 10 reveal that, at low $\sigma$, $H$ is independent of the grafting density. Hence, the chains are in the mushroom regime. At high polymer grafting densities, $H$ increases with increasing $\sigma$, indicating the brush behavior. The crossover between the two regimes occurred at $\sigma \approx 0.065$ nm$^{-2}$. By fitting the data in the brush regime to $H \sim N\sigma^n$, we get $n$ equal to $0.37 \pm 0.04$ (CMPE : PO = 1 : 1), $0.39 \pm 0.05$ (CMPE : PO = 1 : 2), and $0.40 \pm 0.06$ (CMPE : PO = 1 : 5). These results are in close agreement with the predicted value of $n = 1/3$ [67, 68].

We previously demonstrated that wettability measurements provide quick and reliable means of probing the physicochemical properties of gradient substrates. In Figure 11, we plot the negative cosine of $\theta_{DIW}$ as a function of the grafting density of PAAm on substrates comprising CMPE : PO = 1 : 1 (squares) and CMPE : PO = 1 : 5 (triangles) gradients. As anticipated, the data collapse on a single master curve. A close inspection of the results in Figure 11 reveals that the data can be divided into three distinct regions. For $\sigma > 0.1$ nm$^{-2}$, the chains are
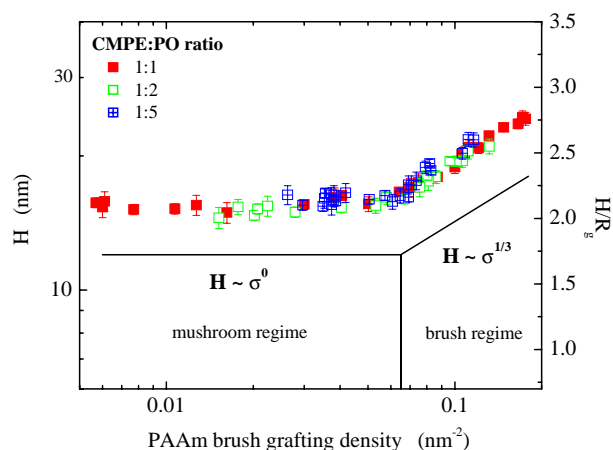
**Figure 10.** Wet thickness of the PAAm brush ($H$) as a function of the PAAm brush grafting density. Results for three different ratios of CMPE : PO are shown: 1 : 1 (■), 1 : 2 (□), and 1 : 5 (⊞). Reprinted with permission from [63], T. Wu et al., *J. Am. Chem. Soc.* 124, 9394 (2002). © 2002, American Chemical Society.

expected to be in a brush regime—the wettabilities are close to that of pure PAAm $[-\cos(\theta_{DIW}) \approx -0.79]$. For $\sigma < 0.02$ nm$^{-2}$, the PAAm chains form mushroom conformations on the substrate. In this regime, the wettabilities change slightly because the distance between the chains also changes, although they are already loosely separated on the substrate. At grafting densities $0.02$ nm$^{-2} < \sigma < 0.1$ nm$^{-2}$, the slope of $-\cos(\theta_{DIW})$ changes rather rapidly. The data in Figure 11 show that the position of the mushroom-to-brush crossover determined using the wettability approach is in accord with the ellipsometric measurements (the transition location was established to be at $\sigma \approx 0.065$ nm$^{-2}$). However, in the former case, the transition region extends over almost one order of magnitude in $\sigma$, which is broader than the transition region predicted by the $H$ versus $\sigma$ data.
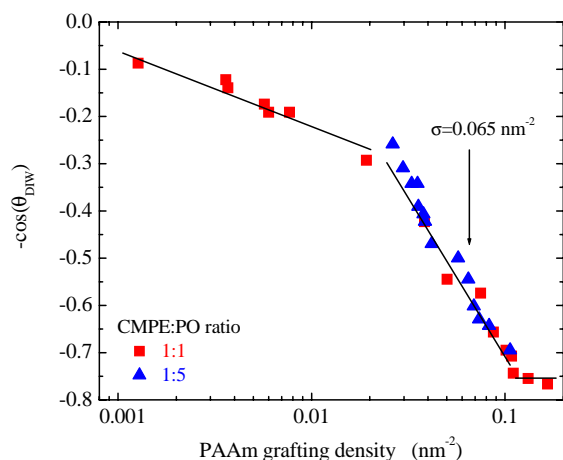


**Figure 11.** Negative of cosine of the contact angle of DI water as a function of the PAAm grafting density on the substrate for samples prepared on substrates containing the initiator gradients made of CMPE : OTS mixtures (w/w) 1 : 1 (squares) and 1 : 5 (triangles). The lines are meant to guide the eyes.

We speculate that the small difference between the widths of the mushroom-to-brush region inferred from both types of experiments is likely associated with the inaccuracy in $H$, which was obtained indirectly by the model fitting of the VASE data.

## 7. SUMMARY

We have reviewed various methodologies leading to the fabrication of molecular and macromolecular gradients on material substrates. Several examples were referenced documenting that wettability gradients can be utilized in combinatorial studies of bioadsorption, phase behavior in thin liquid and polymer films, templating, and material transport on surfaces. The dual nature of molecular gradients (discrete on molecular scales, continuous on meso scales) endows them with unique properties that can and will be further exploited in the synthesis of novel materials, generating combinatorial libraries, which, in turn, will find use in the discovery of new material phenomena. Utilizing molecular gradients will provide simple means of mimicking molecular and biomolecular transport. These structures are thus expected to provide a new paradigm for advancing the fundamental understanding of the structure–property relationship of material behavior.

## GLOSSARY

**Macromolecular gradient** Assembly of surface-anchored polymers with a position-dependent gradual variation of length, and/or grafting density, and/or composition on the substrate.

**Molecular gradient** Array of surface-bound self-assembled oligomers with a position-dependent gradual variation of grafting density on the substrate.

**Near-edge X-ray absorption fine structure spectroscopy (NEXAFS)** Provides information about bond population density in and orientation of surface-adsorbed molecules.
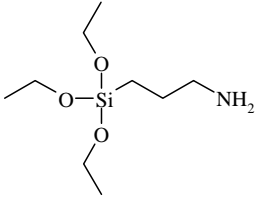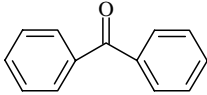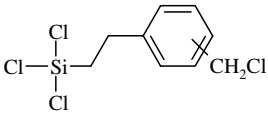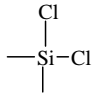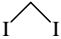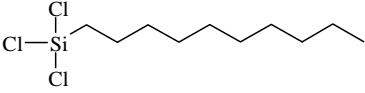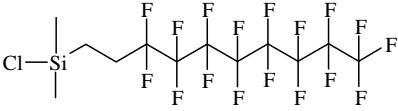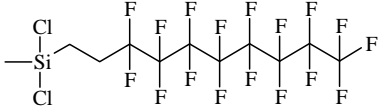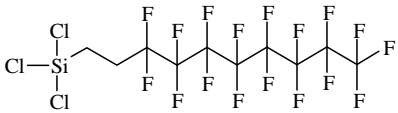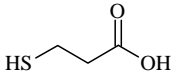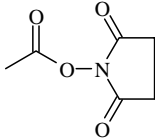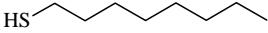
**Organosilane** Chloro- or alkoxy-terminated molecule, typically alkane or alkane-based, capable of self-assembly on oxide-covered surfaces.

**Self-assembled monolayer** Organized array of amphiphiles chemically bound to a substrate.

## ACKNOWLEDGMENTS

## APPENDIX: CHEMICAL FORMULAS

| Abbreviation | Compound | Chemical formula |
|---|---|---|
| APTES | Aminopropyl triethoxysilane | |
| BP | Benzophenone | |
| CMPE | 1-Trichlorosilyl-2-(*m*/*p*-chloromethylphenyl) ethane | |
| DDS | Dichlorodimethyl silane | |
| DIM | Diiodomethane | |
| DTS | *n*-Decyl trichlorosilane | |
| *m*-F8H2 | 1*H*,1*H*,2*H*,2*H*-Perfluorodecyl dimethylchlorosilane | |
| *d*-F8H2 | 1*H*,1*H*,2*H*,2*H*-Perfluorodecyl methyldichlorosilane | |
| *t*-F8H2 | 1*H*,1*H*,2*H*,2*H*-Perfluorodecyl trichlorosilane | |
| MPA | Mercapto propionic acid | |
| NHS | *N*-Hydroxysuccinimide ester | |
| OT | *n*-Octanethiol | |

continued

| Abbreviation | Compound | Chemical formula |
|---|---|---|
| OTS | n-Octyl trichlorosilane | |
| PAAm | Poly(acryl amide) | |
| PDMS | Poly(dimethyl siloxane) | |
| PEP | Poly(ethylene propylene) | |
| PHM | Poly(hydroxyl methylene) | |
| PMMA | Poly(methyl methacrylate) | |
| PS | Polystyrene | |
| PVCa | Poly(vinylene carbonate) | |
| TCE | Trichloroethylene | |
| TEG | Tetraethylene glycol | |
| XYL | Xylene | |

# REFERENCES

1. R. P. Feynman, *Eng. Sci.* 23, 22 (1960). A copy of Feynman's famous talk is also available on the Internet at http://www.zyvex.com/nanotech/feynman.html.
2. "Engineering a Smaller World: From Atomic Manipulation to Microfabrication," Special issue of *Science* 254, 1277 (1991); C. N. R. Rao and A. K. Cheetham, *J. Mater. Chem.* 11, 2887 (2001).
3. H. Wohltjen and A. W. Snow, *Anal. Chem.* 70, 2856 (1998).
4. B. Oregan and M. Gratzel, *Nature* 353, 737 (1991).
5. S. Nie and R. S. Emory, *Science* 275, 1102 (1997).
6. V. L. Colvin, M. C. Schlamp, and A. P. Alivisatos, *Nature* 370, 354 (1994).
7. Y. Xia and G. M. Whitesides, *Angew. Chem., Int. Ed. Engl.* 37, 550 (1998); Y. Xia, J. A. Rogers, K. E. Paul, and G. M. Whitesides, *Chem. Rev.* 99, 1823 (1999).
8. A. Ulman, "An Introduction to Ultrathin Organic Films from Langmuir–Blodgett to Self Assembly." Academic Press, New York, 1991.
9. M. Husseman, D. Mecerreyes, C. J. Hawker, J. L. Hedrick, R. Shah, and N. L. Abbott, *Angew. Chem., Int. Ed. Engl.* 38, 647 (1999).
10. R. Shah, D. Mecerreyes, M. Husemann, I. Rees, N. L. Abbott, C. J. Hawker, and J. L. Hedrick, *Macromolecules* 33, 597 (2000).
11. N. L. Jeon, I. S. Choi, G. M. Whitesides, N. Y. Kim, P. E. Laibinis, Y. Harada, K. R. Finnie, G. S. Girolami, and R. G. Nuzzo,

*Appl. Phys. Lett.* 75, 4201 (1999); N. Kim, N. L. Jeon, I. S. Choi, S. Takami, Y. Harada, K. R. Finnie, G. S. Girolami, R. G. Nuzzo, G. M. Whitesides, and P. E. Laibinis, *Macromolecules* 33, 2793 (2000).

12. B. de Boer, H. K. Simon, M. P. L. Werts, E. W. van der Vegte, and G. Hadziioannou, *Macromolecules* 33, 349 (2000).

13. P. Ghosh, W. M. Lackowski, and R. M. Crooks, *Macromolecules* 34, 1230 (2001).

14. D. M. Jones and W. T. S. Huck, *Adv. Mater.* 13, 1256 (2001).

15. J. Hyun and A. Chilkoti, *Macromolecules* 34, 5644 (2001).

16. M. K. Chaudhury and G. M. Whitesides, *Science* 256, 1539 (1992).

17. K. Efimenko and J. Genzer, *Adv. Mater.* 13, 1560 (2001).

18. R. R. Fuierer, R. L. Carroll, D. L. Feldheim, and C. B. Gorman, *Adv. Mater.* 14, 154 (2002).

19. J. C. Meredith, A. Karim, and E. J. Amis, *MRS Bull.* 27, 330 (2002).

20. J. Genzer, in "Encyclopedia of Materials Science" (K. H. J. Buschow, R. W. Cahn, M. C. Flemings, B. Ilschner, E. J. Kramer, and S. Mahajan, Eds.). Elsevier, Oxford, 2002.

21. S. B. Carter, *Nature* 208, 1183 (1965).

22. H. Elwing, S. Welin, A. Askendal, U. Nilsson, and I. Lundström, *J. Colloid Interface Sci.* 119, 203 (1987).

23. C. G. Gölander, K. Caldwell, and Y.-S. Lin, *Colloids Surf.* 42, 165 (1989).

24. T. Ueda-Yukoshi and T. Matsuda, *Langmuir* 11, 4135 (1995).

25. W. G. Pitt, *J. Colloid Interface Sci.* 133, 223 (1989).

26. J. H. Lee, H. G. Kim, G. S. Khang, H. B. Lee, and M. S. Jhon, *J. Colloid Interface Sci.* 151, 563 (1992).

27. S. V. Roberson, A. J. Fahey, A. Sehgal, and A. Karim, *Appl. Surf. Sci.* 9427, 1 (2002).

28. B. Liedberg and P. Tengvall, *Langmuir* 11, 3921 (1995).

29. M. Lestelius, I. Enquist, P. Tengvall, M. K. Chaudhury, and B. Liedberg, *Colloids Surf., B* 15, 57 (1999).

30. R. H. Terrill, K. M. Balss, Y. Zhang, and P. W. Bohn, *J. Am. Chem. Soc.* 122, 988 (2000).

31. M. B. Wijesundara, E. Fuoco, and L. Hanley, *Langmuir* 17, 5721 (2001).

32. C. L. Hypolite, T. L. McLernon, D. N. Adams, K. E. Chapman, C. B. Herbert, C. C. Huang, M. D. Distefano, and W.-S. Hu, *Bioconjug. Chem.* 8, 658 (1997).

33. I. Caelen, H. Gao, and H. Sigrist, *Langmuir* 18, 2463 (2002).

34. I. Caelen, A. Bernard, D. Juncker, B. Michel, H. Heinzelmann, and E. Delamarche, *Langmuir* 16, 9125 (2000).

35. N. L. Jeon, S. K. W. Dertinger, D. T. Chiu, I. S. Choi, A. Stroock, and G. M. Whitesides, *Langmuir* 16, 8311 (2000).

36. S. K. W. Dertinger, D. T. Chiu, N. L. Jeon, and G. M. Whitesides, *Anal. Chem.* 73, 1240 (2001).

37. D. C. Duffy, J. C. McDonald, O. J. A. Schueller, and G. M. Whitesides, *Anal. Chem.* 70, 4974 (1998).

38. T. G. Ruardy, J. M. Schakenraad, H. C. van der Mei, and H. J. Busscher, *Surf. Sci. Rep.* 29, 1 (1997).

39. J. Stöhr, "NEXAFS Spectroscopy." Springer-Verlag, Berlin, 1992.

40. J. Genzer, D. A. Fischer, and K. Efimenko, *Appl. Phys. Lett.*, 82, 266 (2003).

41. The NEXAFS experiments were carried out at the NIST/Dow Soft X-Ray Materials Characterization Facility at the National Synchrotron Light Source at Brookhaven National Laboratory. For detailed information about the NIST/Dow Soft X-ray Materials Characterization Facility at NSLS BNL, see http://nslsweb.nsls.bnl.gov/nsls/pubs/newsletters/96-nov.pdf.

42. K. Efimenko and J. Genzer, unpublished data.

43. J. Genzer, E. Sivaniah, E. J. Kramer, J. Wang, H. Körner, M. Xiang, K. Char, C. K. Ober, B. M. DeKoven, R. A. Bubeck, M. K. Chaudhury, S. Sambasivan, and D. A. Fischer, *Macromolecules* 33, 1882 (2000).

44. R. Banga, J. Yarwood, A. M. Morgan, B. Evans, and J. Kells, *Langmuir* 11, 4393 (1995); B. C. Bunker, R. W. Carpick, R. A. Assink, M. L. Thomas, M. G. Hankins, J. A. Voight, D. Sipola, M. P. de Boer, and G. L. Gulley, *Langmuir* 16, 7742 (2000).

45. J. Genzer, D. A. Fischer, and K. Efimenko, *Langmuir*, 18, 9307 (2002).

46. J. Genzer and K. Efimenko, *Science* 290, 2130 (2000).

47. K. Efimenko, W. E. Wallace, and J. Genzer, *J. Colloid Interface Sci.* 254, 306 (2002).

48. R. B. van Dover, L. F. Scheemeyer, and R. M. Fleming, *Nature* 392, 162 (1998).

49. B. Jandeleit, D. J. Schaefer, T. S. Powers, H. W. Turner, and W. H. Weinberg, *Angew. Chem., Int. Ed. Engl.* 38, 2494 (1999).

50. E. J. Amis, X.-D. Xiang, and J.-C. Zhao, *MRS Bull.* 27, 295 (2002).

51. H. Zhao and D. Beysens, *Langmuir* 11, 627 (1995).

52. J. Genzer and E. J. Kramer, *Europhys. Lett.* 44, 180 (1998).

53. A. Karim, personal communication.

54. C. D. Bain, *Chemphyschem* 2, 580 (2001).

55. L. E. Scriven and C. V. Sternling, *Nature* 187, 186 (1960).

56. S. Daniel, M. K. Chaudhury, and J. C. Chen, *Science* 291, 633 (2001).

57. S. Daniel and M. K. Chaudhury, *Langmuir* 18, 3404 (2002).

58. S. T. Plummer and P. W. Bohn, *Langmuir* 18, 4142 (2002).

59. R. R. Bhat, D. A. Fischer, and J. Genzer, *Langmuir* 18, 5640 (2002).

60. H. G. Kim, J. L. Lee, H. B. Lee, and M. S. Jhon, *J. Colloid Interface Sci.* 157, 82 (1993).

61. B. J. Jeong, J. H. Lee, and H. B. Lee, *J. Colloid Interface Sci.* 178, 757 (1996).

62. J. Genzer, T. Wu, and K. Efimenko, *Mat. Res. Soc. Symp. Proc.* 705, Y8.8.1 (2002).

63. T. Wu, K. Efimenko, and J. Genzer, *J. Am. Chem. Soc.* 124, 9394 (2002).

64. X. Huang, L. J. Doneski, and M. J. Wirth, *CHEMTECH* 19 (1998); *Anal. Chem.* 70, 4023 (1998).

65. X. Huang and M. J. Wirth, *Macromolecules* 32, 1694 (1999).

66. T. Wu, K. Efimenko, and J. Genzer, *Macromolecules* 34, 684 (2001).

67. M. S. Kent, *Macromol. Rapid Commun*. 21, 243 (2000) and references therein.

68. J. F. Douglas, M. S. Kent, S. K. Satija, and A. Karim, in "Encyclopedia of Materials: Science and Technology," pp. 7218–7223. Elsevier, Amsterdam, 2001.

# Molecular Logic Gates

## Françisco M. Raymo, Silvia Giordani

*University of Miami, Coral Gables, Florida, USA*

## CONTENTS

## 1. MINIATURIZATION OF ELECTRONIC DEVICES

The advent of integrated circuits has improved dramatically our ability to communicate, process, and store information [1]. These arrays of tiny electronic devices can manipulate large volumes of data at amazing speeds. Their impact on practical applications has been and continues to be revolutionary. Not only do they rule our computers; they also control our cars, watches, telephones, faxes, CD players, washing machines, and the many other electronic gadgets that have become part of our everyday lives. The secret of their success has been the continuous miniaturization of their functional components, which allows manufacturers to cram increasing numbers of them into single chips [2]. For example, the number of transistors in microprocessors has increased exponentially over the past three decades [3]. The Intel 4004 processor, built in 1971, had only 2,300 transistors [4]. The Intel Pentium 4 processor, fabricated in 2000, had 42,000,000 transistors. The dramatic raise in the number of components has translated into a huge enhancement in speed from $10^5$ to $10^9$ Hz. This amazing improvement in performance is mainly a result of effective miniaturization.

Miniaturization has progressed at a tremendous pace since the early days of integrated circuits [5]. Transistors continue to be scaled down at an exponential rate and their number on a chip doubles approximately every 18 months [3, 5]. Unfortunately, the fabrication of remarkably small features is inherently difficult, and present electronic devices have reached dimensions that are not too far from the nanoscale [3]. Shrinking their sizes below 100 nm is expected to be a major technological challenge. Cost-effective miniaturization might not persist below this limit. Furthermore, the bulk properties of semiconductors, which are the constituent materials of most electronic components, vanish at the nanoscale [6–9]. It follows that the operating principles of present microscale devices cannot survive in potential nanoscale counterparts. Alternative design criteria, materials, and fabrication procedures must be devised.

## 2. LOGIC GATES

Logic gates are the fundamental components of digital circuits [10]. These electronic devices process binary data encoded in electrical signals. More precisely, they transduce electrical inputs into electrical outputs according to predefined logic functions. The three basic logic gates and their truth tables are illustrated in Figure 1. The NOT gate converts one input ($I$) into one output ($O$). The output is *1* when the input is *0*. The output is *0* when the input is *1*. The AND and OR gates convert two inputs ($I1$ and $I2$) into a single output ($O$). In the AND gate, the output is *1* only when both inputs are *1*. It is *0* in the other three cases. In the OR gate, the output is *0* only when both inputs are *0*. It is *1* in the other three cases.

Networks of interconnected logic gates can be assembled by contacting their input and output terminals [10]. The logic functions of the resulting arrays are a combination of the operations executed by the individual gates. It follows that digital circuits able to perform specific functions can be designed by choosing the right number, type, and configuration of their constituent gates. This modular approach offers access to an unlimited number of combinational and sequential logic circuits and provides the opportunity to implement all conceivable logic functions.
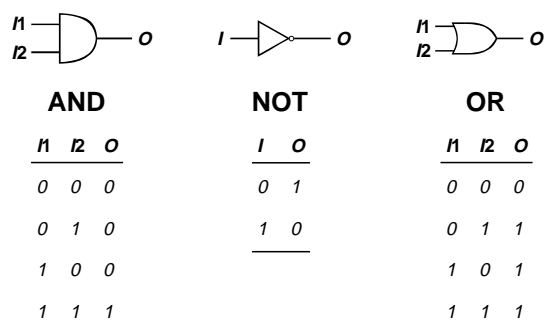
**Figure 1.** The three basic logic gates and their truth tables [10].

The signals that enter the input terminals of logic circuits, propagate across the network of gates, and leave the output terminals are electrical [10]. Binary digits are encoded in them by the application of simple logic conventions. Arbitrary logic thresholds are established first. Then, in a positive logic convention, binary *0* and *1* are assigned to the signals that are below and above, respectively, the fixed threshold. Alternatively, the assignment can be reversed in a negative logic convention. Relying on these simple considerations, complex strings of binary digits can be encoded in the electrical signals elaborated by interconnected logic gates.

## 3. MOLECULAR SWITCHES

Organic molecules are emerging as possible building blocks for innovative information storage, processing, and communication devices [11–14]. The tremendous power of modern chemical synthesis offers easy access to billions of potential molecular building blocks with designed properties and nanometer-sized dimensions [15]. Furthermore, organic molecules can be engineered to produce detectable outputs in response to input stimulations [16]. Indeed, simple binary switching operations can be reproduced at the molecular level with these chemical systems, which are commonly referred to as molecular switches [17].

The obvious analogy between logic gates and molecular switches continues to stimulate the design of chemical systems able to execute AND, NOT, and OR operations as well as more complex logic functions [18–22]. One of the major challenges in the implementation of molecular logic gates is the identification of viable procedures to address them and to detect their response. In the case of conventional logic gates, electrical wires carry the information that reaches their input terminals and departs from their output terminals. However, the direct connection of individual molecules or even collections of them to electrical wires is not an easy task [23–29]. Fortunately, molecules can be stimulated effectively in solution phase with chemical, optical, or redox stimulations [16–18]. Their response can be probed with conventional spectroscopic and electrochemical techniques. As result, most of the work on molecular logic gates has focused so far on the analysis of the logic behavior of molecular switches dissolved in organic or aqueous phases [18]. In this chapter we illustrate the operating principles and properties of the numerous molecular logic gates that have been developed in less than a decade.

## 4. MOLECULAR NOT GATES

A NOT operator (Fig. 1) converts an input signal into an output signal [10]. In particular, the output is high when the input is low and vice versa. Numerous organic molecules satisfy this relatively simple signal transduction protocol and, therefore, can execute NOT operations. For example, a fluorescent molecule that loses its ability to emit light upon protonation is, indeed, a molecular NOT gate. The fluorescence is high when the concentration of $H^+$ is low. The fluorescence is low when the concentration of $H^+$ is high. If a positive logic convention (low = *0*, high = *1*) is applied to the optical output and the chemical input, this signal transduction translates into the truth table of the NOT operator (Fig. 1).

In 1993, de Silva recognized the analogy between NOT gates and pH-sensitive fluorophores [30]. In a seminal article, he demonstrated that the pyrazole derivative **1** (Fig. 2) emits only when the concentration of $H^+$ is low. Photoinduced electron transfer from the central pyrazoline unit to the pendant benzoic acid quenches the fluorescence of the protonated form. Thus, a change in the concentration of $H^+$ from a low to a high value switches the emission intensity from a high to a low value. The inverse relation between the chemical input (concentration of $H^+$) and the optical output (fluorescence intensity) corresponds to a NOT operation.

A related example of a molecular NOT gate is the anthracene derivative **2** (Fig. 2) [31]. This molecular switch
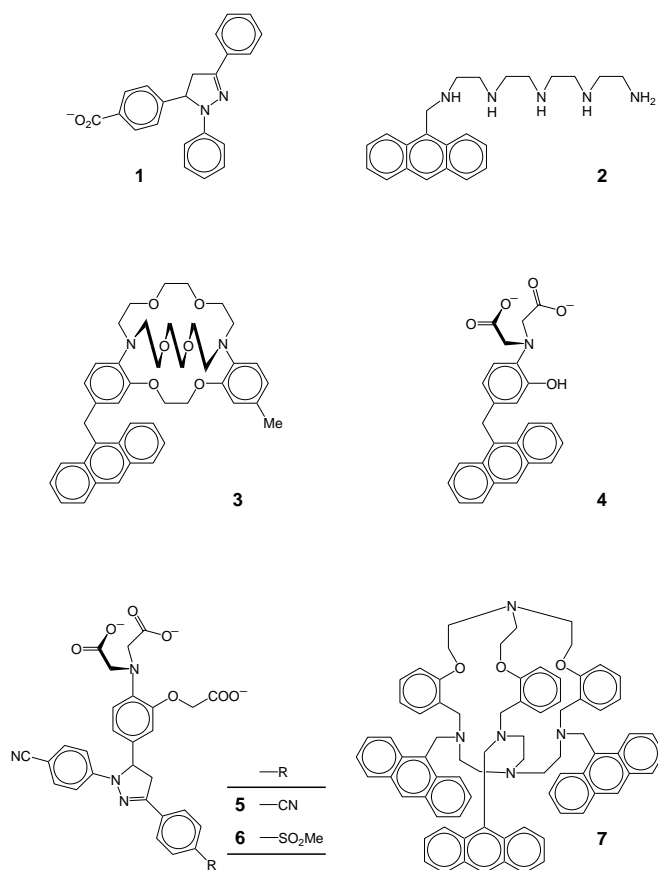


**Figure 2.** Molecular NOT and OR gates based on chemical inputs and optical outputs [30–34].

is extremely versatile. Depending upon the choice of pH and metal ions, different logic functions can be implemented. In particular, NOT operations can be executed at a pH of 4.5. Under these conditions, the anthracene fluorophore emits. The oligoamino arm appended to the fluorophore, however, can chelate metal ions, forming stable complexes. The bound metal center affects the emissive response of the anthracene fragment. In fact, the addition of $Cu^{2+}$ ions produces a drastic decrease in the fluorescence intensity. Once again, the optical output (fluorescence intensity) of the molecular switch is high only when its chemical input (concentration of $Cu^{2+}$) is NOT high.
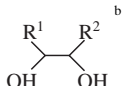
It is important to note that the inverse relation between the input and output of a NOT gate is not limited to pH-induced fluorescence quenching. Similar correlations can be found between chemical inputs and redox outputs, for example. It follows that a careful search in the chemical literature would almost certainly reveal hundreds of molecules capable of similar signal transductions. Most of them, however, have not been recognized or described as molecular NOT gates.

## 5. MOLECULAR OR GATES

An OR operator (Fig. 1) combines two inputs into a single output [10]. To reproduce this logic function at the molecular level, compounds able to respond to two input signals must be identified. In particular, they have to produce a detectable output when one or both inputs are applied. The compounds **3–7** (Table 1, Fig. 2) satisfy these conditions

**Table 1.** Molecular and supramolecular logic gates with one or two input terminals and a single output terminal.[a]

| Logic | Compound | Input 1 ($I1$) | Input 2 ($I2$) | Output ($O$) | Ref. |
|---|---|---|---|---|---|
| NOT | **1** | $H^+$ | — | Fluorescence | [30] |
|  | **2** | $Cu^{2+}$ | — | Fluorescence | [31] |
| OR | **2** | $Cd^{2+}$ | $Zn^{2+}$ | Fluorescence | [31] |
|  | **3** | $K^+$ | $Rb^+$ | Fluorescence | [30] |
|  | **4** | $Ca^{2+}$ | $Mg^{2+}$ | Fluorescence | [32] |
|  | **5** | $Ca^{2+}$ | $Mg^{2+}$ | Fluorescence | [32] |
|  | **6** | $Ca^{2+}$ | $Mg^{2+}$ | Fluorescence | [32] |
|  | **7** | $Cu^{2+}$ | $Ni^{2+}$ | Fluorescence | [33, 34] |
| AND | **8** | $H^+$ | $Na^+$ | Fluorescence | [30] |
|  | **9** | $H^+$ | $K^+$ or $Na^+$ | Fluorescence | [35] |
|  | **10** | $H^+$ | $Na^+$ | Fluorescence | [35] |
|  | **11** | $H^+$ | $Na^+$ | Fluorescence | [36] |
|  | **12** | $H^+$ | $Ca^{2+}$ | Fluorescence | [37] |
|  | **13** | $R\text{-}NH_3^{+b}$ | $R^1 \quad R^2$ [b] $\underset{OH \quad\quad OH}{\diagup\!\!\!\diagdown}$ | Fluorescence | [38] |
|  | **14** | $Ba^{2+}$ or $Ca^{2+}$ | $SCN^-$ | Fluorescence | [39] |
|  | **15** | $Ba^{2+}$ or $Ca^{2+}$ | $SCN^-$ | Fluorescence | [39] |
|  | **16** | $Cs^+$, $K^+$, $Li^+$, $Na^+$, or $Rb^+$ | Light | Absorbance | [40] |
|  | **18** | $H^+$ | Light | Fluorescence | [41, 42] |
|  | **20** | $H^+$ | Light | Absorbance | [43, 44] |
|  | **22** | $H^+$ | Voltage | Current | [45] |
|  | **23** | Magnetic field | Light | Absorbance | [46] |
|  | **24** | Light | Light | Absorbance | [47] |
|  | **25** | Light | Light | Fluorescence | [48] |
| NAND | **26** | $H^+$ | $ATP^c$ | Fluorescence | [49] |
|  | **27** | $dAMP^d$ | $dTMP^d$ | Fluorescence | [50] |
| NOR | **2** | $Cu^{2+}$ | $Ni^{2+}$ | Fluorescence | [31] |
|  | **28** | $H^+$ | $O_2$ | Luminescence | [51] |
|  | **29** | $H^+$ | $Zn^{2+}$ | Fluorescence | [52] |
|  | **30** | $H^+$ | $Hg^{2+}$ | Fluorescence | [52] |
| XOR | **31** | $Ca^{2+}$ | $H^+$ | Transmittance | [37] |
|  | **39 • 40** | Butylamine | $H^+$ | Fluorescence | [59] |
|  | **43 + 45** | Light | Light | Absorbance | [61] |
| XNOR | **31** | $Ca^{2+}$ | $H^+$ | Absorbance | [37] |
|  | **41 • 42** | Voltage | Voltage | Absorbance | [60] |
| INH | **32** | $H^+$ | $O_2$ | Luminescence | [53, 54] |

[a] The inputs and outputs are chemical, electrical, magnetic, or optical signals. The chemical inputs are the concentrations of the species listed. The electrical and magnetic inputs/outputs are the magnitudes of the parameters indicated. The optical inputs/outputs are the light intensities, the fluorescence intensities, or the magnitude of the parameters listed.
[b] The behavior of **13** was studied in the presence of D-glucosamine. However, distinct alkylammonium and diol components could be employed to reproduce the same signal transduction.
[c] ATP stands for adenosine triphosphate.
[d] dAMP and dTMP stand for deoxyadenosine monophosphate and deoxythymidine monophosphate, respectively.

[30, 32–34]. They generate an optical output (fluorescence) in response to one or two chemical inputs (metal cations). In the absence of metal cations, photoinduced electron transfer from the tertiary amino groups to the anthracene appendages in **3**, **4**, and **7** and to the pyrazoline fragment in **5** and **6** quenches their fluorescence. After the complexation of a metal cation in the cryptands of **3** and **7** and in the carboxylate clefts of **4–6**, the quenching process is suppressed and high fluorescence intensity is detected. It is important to note that each of these compounds responds to either one of two different metal cations. Thus, the fluorescence intensity is high when one OR the other metal cation is added. If a positive logic convention (low = 0, high = 1) is applied to the fluorescence intensity (optical output) and to the concentrations of the two metal cations (chemical inputs), the signal transduction of **3–7** translates into the truth table of the OR operator (Fig. 1).

The anthracene derivative **2** (Table 1, Fig. 2) reproduces a NOT operation at a pH of 4.5 and an OR function at a pH of 10 [31]. Under basic conditions, photoinduced electron transfer from the oligoamino arm to the anthracene fluorophore quenches the emission. In the presence of $Cd^{2+}$ and/or $Zn^{2+}$, the quenching efficiency of the amino groups is suppressed as a result of metal coordination. Thus, the behavior of this compound at a pH of 10 is equivalent to that of the molecular OR gates **3–7**. In all cases, an optical output (fluorescence intensity) is controlled by two chemical inputs (concentrations of two metal cations) according to an OR function.

## 6. MOLECULAR AND GATES

An AND operator (Fig. 1) combines two inputs into a single output [10]. Thus, molecules able to respond to two input signals must be designed to execute this particular logic function. In addition, the molecule has to produce a detectable output only when the two input stimulations are applied simultaneously. The compounds **8–12** (Table 1, Fig. 3) satisfy these conditions [30, 35–37]. They generate an optical output (fluorescence) only when two chemical inputs ($H^+$ and metal cation) are applied simultaneously. In the absence of $H^+$, photoinduced electron transfer from their tertiary amino group to the anthracene fluorophore quenches the emission. In the absence of metal cations, photoinduced electron transfer from the benzocrown ether or tetracarboxylate cleft to the anthracene fluorophore quenches the emission. Thus, a high emission intensity (optical output) is observed only when the concentrations of $H^+$ AND a metal cation (chemical inputs) are high. The fluorescence intensity is low in the other three cases. If a positive logic convention (low = 0, high = 1) is applied to the optical output and the two chemical inputs, this signal transduction translates into the truth table of the AND operator (Fig. 1).

The compounds **13–15** (Table 1, Fig. 3) share similar operating principles with **8–12**. They all convert two chemical inputs into an optical output according to an AND operation. In the case of **13**, the two chemical inputs are the concentrations of an ammonium cation and a diol, and the optical output is the anthracene fluorescence [38]. Indeed, a high emission intensity is observed only after
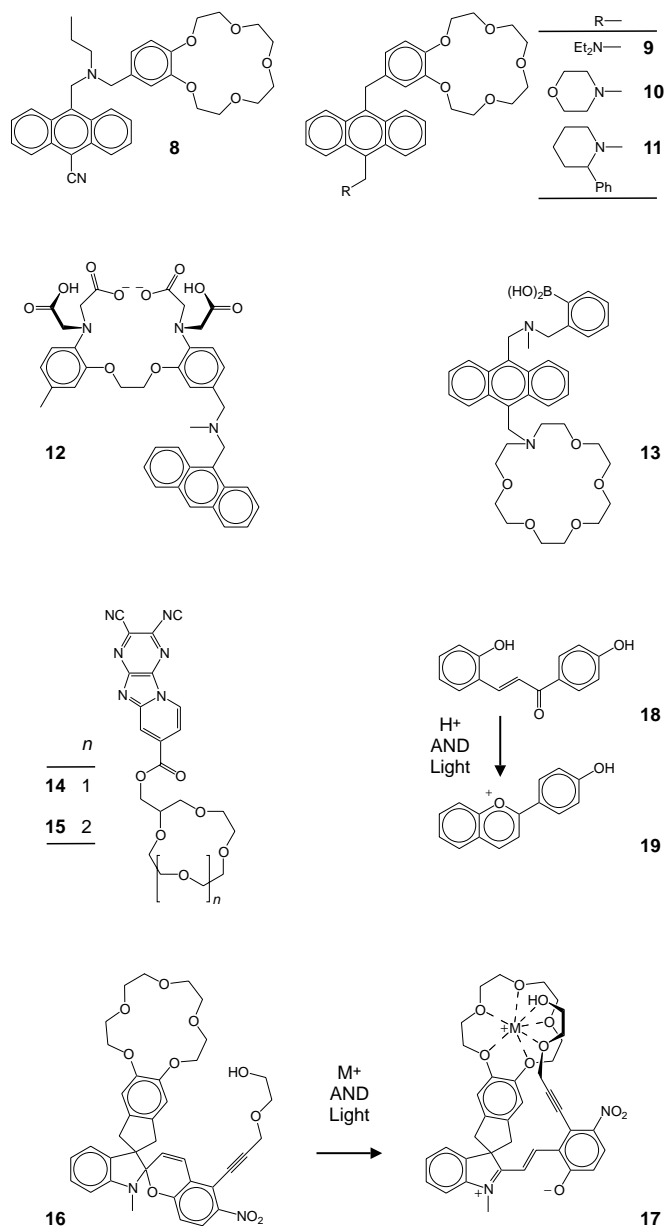


**Figure 3.** Molecular AND gates based on chemical and optical inputs and optical outputs [30, 35–42].

the complexation of an ammonium cation in the azacrown ether receptor AND the chelation of a diol by the boronic acid fragment. Under these conditions, the photoinduced electron transfer processes from the two tertiary amino groups to the anthracene fluorophores are suppressed. In the case of **14** and **15**, the two chemical inputs are the concentrations of a metal cation ($Ba^{2+}$ or $Ca^{2+}$) and $SCN^-$, and the optical output is the pyridoimidazopyrazine fluorescence [39]. Indeed, a low emission intensity is detected when the concentrations of $Ba^{2+}$ or $Ca^{2+}$ AND $SCN^-$ are high. Under these conditions, photoinduced electron transfer from the $SCN^-$ anion to the heteroaromatic fragment efficiently quenches the emission. If a positive logic convention (low = 0, high = 1) is applied to the chemical inputs and the optical output of **13** while a negative logic convention

(low = *1*, high = *0*) is applied to the fluorescence outputs of **14** and **15**, the signal transductions operated by **13–15** translate into the truth table of the AND operator (Fig. 1).

The molecular AND gates **16**, **18**, and **20** combine chemical and optical inputs into an optical output (Table 1, Figs. 3 and 4). The chemical input of **16** is the concentration of a metal cation (Cs$^+$, K$^+$, Li$^+$, Na$^+$, or Rb$^+$), and its optical input is the intensity of an ultraviolet pulse [40]. No significant changes in the absorption spectrum of **16** can be observed when one of the metal cations is added. Ultraviolet irradiation produces a colored merocyanine, which reisomerizes thermally to **16** in the absence of a metal cation. Instead, the irradiation of **16** in the presence of Cs$^+$, K$^+$, Li$^+$, Na$^+$, or Rb$^+$ generates the complex **17**, which is stabilized by the metal cation bound in the crown ether appendage. Under these conditions the photogenerated species does not reisomerize thermally, and a strong band is observed in the visible region of the absorption spectrum. Thus, the absorbance of this band (optical output) is high only when the concentration of a metal cation (chemical input) AND the intensity of the ultraviolet stimulation (optical input) are high. Similarly, the compound **18** can be operated with ultraviolet light (optical input) and H$^+$ (chemical input) [41, 42]. The irradiation promotes a *trans* to *cis* isomerization. The resulting *cis* isomer reisomerizes thermally to the original form **18** under neutral conditions. However, it switches to the 4′-hydroxyflavylium cation **19** in acidic media. This particular compound is fluorescent and emits (optical output) in the visible region. Thus, H$^+$ AND ultraviolet light promote the interconversion of **18** into **19**, producing an increase in the emission intensity. In a similar fashion, the compound **20** responds to H$^+$ (chemical input) and visible light (optical input) [43, 44]. The irradiation promotes the ring opening of the dihydroazulene fragment at one end of the *trans*-tetraethynylethene core. The addition of H$^+$ protonates the dimethylaniline fragment at the other end. Thus, the simultaneous application of the two inputs produces the compound **21**, which has a strong absorption band at 500 nm (optical output). It follows that the absorbance at this particular wavelength is high only when the optical AND the chemical inputs are applied. In summary, the signal transductions operated by **16**, **18**, and **20** translate into the truth table of the AND operator (Fig. 1), if a positive logic convention (low = *0*, high = *1*) is applied to their inputs and outputs.

The [2]catenane **22** is a unique example of a molecular AND gate able to transduce chemical and electrical inputs into an electrical output (Table 1, Fig. 4) [45]. Its macrocyclic polyether component encircles one of the two bipyridinium dications, as a result of cooperative electrostatic and charge-transfer terms. This co-conformation imposes distinct redox responses on the encircled and free bipyridinium dications. Indeed, the cyclic voltammogram shows four consecutive monoelectronic reduction processes. The first and second redox waves correspond to the reduction of the free and encircled, respectively, bipyridinium dications to the corresponding radical cations. The third and fourth redox waves are associated with the reduction of the free and encircled, respectively, radical cations to the corresponding neutral forms. These observations indicate that the macrocyclic polyether remains around the same
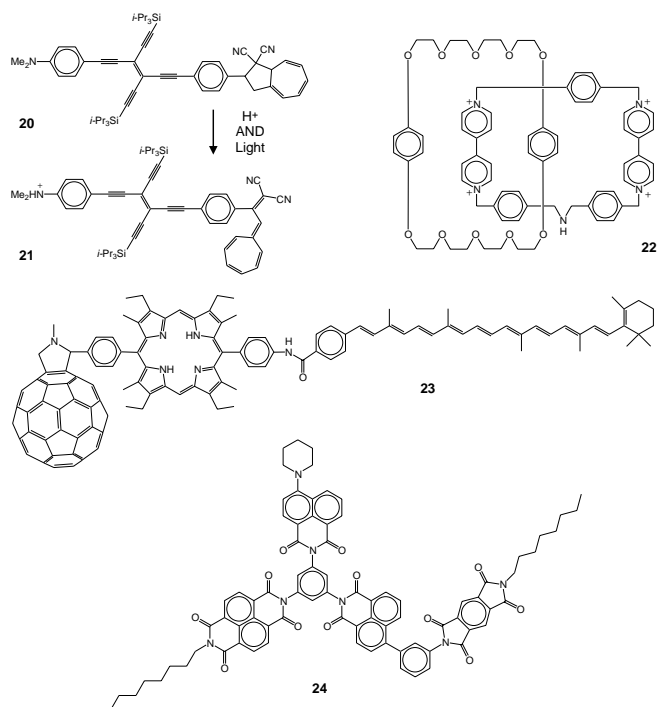


**Figure 4.** Molecular AND gates based on chemical, electrical, magnetic, and optical inputs and electrical or optical outputs [43–48].

bipyridinium unit after the first reduction process. In the presence of H$^+$, however, the secondary amino group is protonated and the cyclic voltammogram shows only three reduction waves. The first and second waves correspond, once again, to the reduction of the free and encircled bipyridinium dications, respectively, to the corresponding radical cations. After these two reduction processes, the macrocyclic polyether shuttles from the encircled radical cation to the secondary alkylammonium cation. In the resulting co-conformation, the two radical cations are identical and only one redox wave is observed for their simultaneous reduction to the corresponding neutral forms. Thus, the reduction of the encircled bipyridinium unit (electrical input) and the addition of H$^+$ (chemical input) result in the disappearance of the fourth redox wave (electrical output) in the cyclic voltammogram. The current for this particular redox wave is low when the voltage is lowered below the second reduction potential AND the concentration of H$^+$ is high. If a negative logic convention (low = *1*, high = *0*) is applied to the electrical input and output and a positive logic convention (low = *0*, high = *1*) is applied to the chemical input, the signal transduction operated by the [2]catenane **22** translates into the truth table of the AND operator (Fig. 1).

The carotenoid-porphyrin-fullerene triad **23** combines magnetic and optical inputs into an optical output (Table 1, Fig. 4) [46]. Excitation of the porphyrin core at 590 nm is followed by electron transfer to the fullerene end. The photogenerated hole in the porphyrin is filled after a second electron transfer from the carotenoid fragment. The final result is a charge-separated state, which absorbs light at 980 nm and undergoes charge recombination on a microsecond time scale at 77 K. Under the influence of a magnetic field, the lifetime of the charge separated state increases by

50%. Thus, the absorbance at 980 nm (optical output) measured after an appropriate interval of time from excitation (optical input) is high only when a high magnetic field (magnetic input) is applied. This signal transduction corresponds to the truth table of the AND operator (Fig. 1), if a positive logic convention (low $= 0$, high $= 1$) is applied to inputs and outputs.

The compound **24** and $HNO_3$ (**25**) are all-optical AND gates (Table 1, Fig. 4). Both convert two optical inputs into a single optical output. The irradiation of **24** at 420 nm (optical input) excites selectively the piperidinylnaphthalene imide donor, and it is followed by the transfer of an electron to the naphthalene diimide acceptor [47]. After 2 ns, a second laser pulse at 480 nm (optical input) promotes the electron transfer from the reduced form of the naphthalene diimide to the naphthalene imide spacer and finally to the benzene diimide tail. The reduction of the benzene diimide acceptor is accompanied by the appearance of an absorption band at 720 nm (optical output). Thus, only when both optical inputs are applied one after the other is an optical output detected. Similarly, an infrared stimulation (optical input) followed by an ultraviolet stimulation (optical input) induces the dissociation of $HNO_3$ (**25**) into OH and the fluorescent $NO_2^*$ [48]. Thus, the fluorescence of the photogenerated $NO_2^*$ is only observed when both inputs are applied. The signal transduction behavior of **24** and **25** corresponds to an AND operation, if a positive logic convention (low $= 0$, high $= 1$) is applied to their inputs and outputs.

# 7. COMBINATIONAL LOGIC WITH MOLECULAR SYSTEMS

Combinational logic circuits can be assembled by connecting the input and output terminals of the three basic logic gates AND, NOT, and OR [10]. The resulting arrays execute logic functions that are a combination of the three basic logic operations. Figure 5 illustrates simple examples of combinational logic circuits able to convert two binary inputs (*I1* and *I2*) into a single output (*O*) according to the functions summarized in the corresponding truth tables. To reproduce their logic behavior at the molecular level, molecular switches that respond to two input signals producing a detectable output must be designed. For example, the two compounds **26** and **27** (Table 1, Fig. 6) convert two chemical inputs into an optical output according to a NAND function (Fig. 5). At neutral pH, the anthracene fluorophore of **26** emits [49]. After the addition of either $H^+$ or adenosine triphosphate (ATP), the fluorescence (optical output) remains high. However, the optical output drops in intensity when both chemical inputs ($H^+$ and ATP) are applied. The protonation of the oligoamino arm encourages the supramolecular association of **26** with ATP and, as a result, the quenching of the anthracene fluorescence. Similarly, the fluorescence of the diamidinoindole derivative **27** changes in response to deoxyadenosine monophosphate (dAMP) and deoxythymidine monophosphate (dTMP) [50]. In mixtures of dimethylsulfoxide and water, this compound has an emission band at 475 nm. After the addition of either dTMP or dAMP, the emission intensity probed at 455 nm
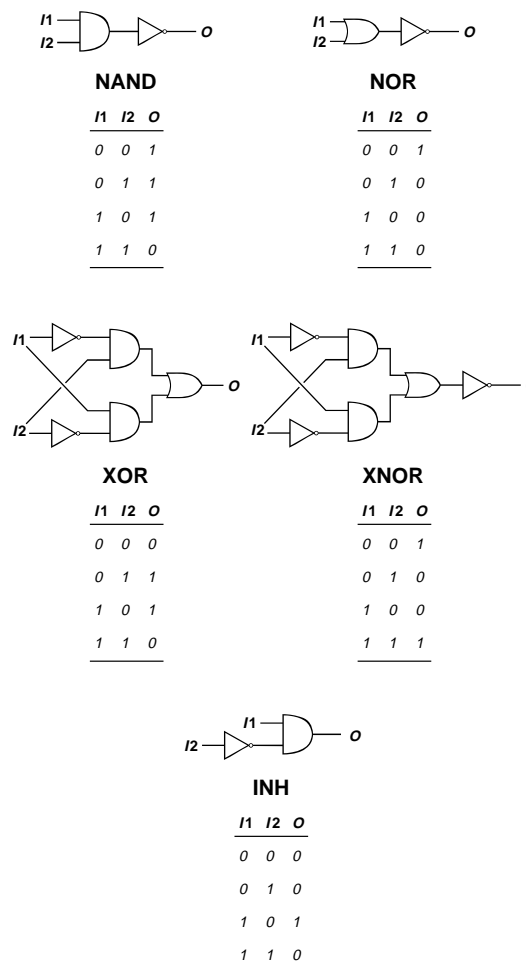


**Figure 5.** Combinational logic circuits with two inputs and one output [10].

does not change significantly. However, a shift of the emission maximum to shorter wavelengths and a concomitant decrease in emission intensity at 455 nm occur when the two deoxynucleotides are added simultaneously. The formation of a ternary complex between the base pair and the indole derivative is responsible for these changes. Thus, the fluorescence intensity (optical output) is low when the concentrations of dAMP and dTMP are high (chemical inputs). The signal transduction operated by **26** and **27** corresponds to a NAND function (Fig. 5), if a positive logic convention (low $= 0$, high $= 1$) is applied to their inputs and outputs.

The compounds **28–30** (Table 3, Fig. 6) convert two chemical inputs into an optical output according to a NOR operation (Fig. 5). The chemical inputs of the terbium complex **28** are the concentrations of $H^+$ and $O_2$, and the optical output is the luminescence intensity of the lanthanide [51]. In the presence of $H^+$, excitation at 304 nm is followed by the fluorescence of the phenanthridine appendage. In the absence of $H^+$, the excitation of the phenanthridine fragment is followed by intersystem crossing, electron transfer to the terbium center, and delayed emission from the lanthanide. In the presence of $O_2$, the tripled state of the phenanthridine appendage is quenched and the terbium emission is not observed. Thus, the optical output (terbium
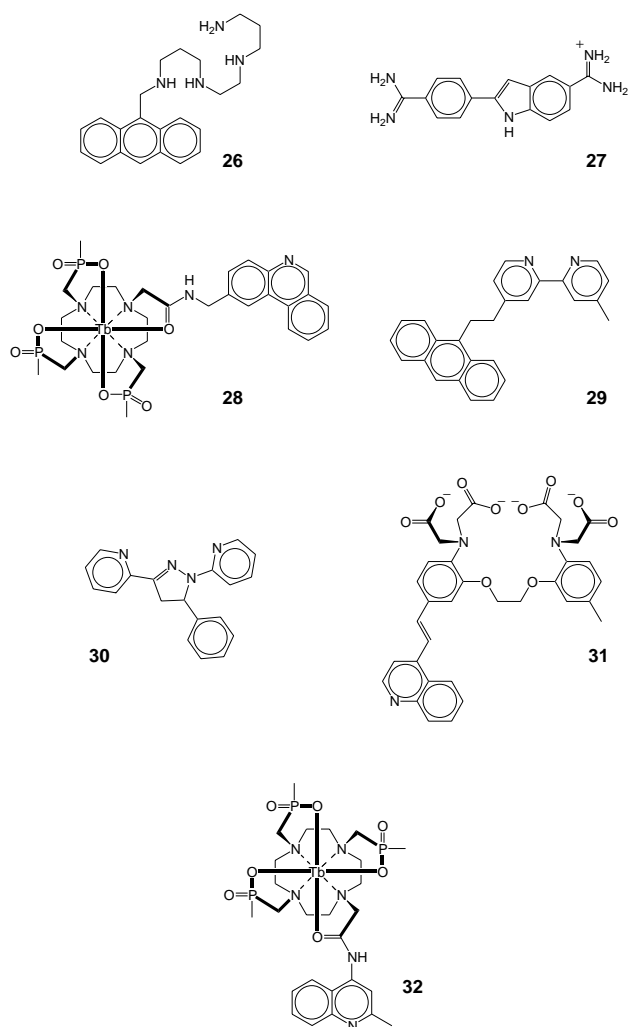
**Figure 6.** Molecular NAND, NOR, XOR, XNOR, and INH gates based on chemical and optical inputs and optical outputs [37, 49–54].

emission) is detected only when the two chemical inputs (H$^+$ and O$_2$) are not applied. Similarly, the anthracene fluorescence (optical output) of **29** is observed only when its two chemical inputs (H$^+$ and Zn$^{2+}$) are not applied [52]. In the presence of H$^+$ and/or Zn$^{2+}$, photoinduced electron transfer from the anthracene to the appended 2,2′-bipyridine ligand quenches the fluorescence. In the case of **30**, the fluorescence of the pyrazoline unit (optical output) is detected only in the absence of H$^+$ and Hg$^{2+}$ (chemical inputs). Efficient fluorescence quenching occurs in the presence of one or both cationic species. Thus, the optical output of **28–30** is high only when the chemical inputs are not applied. This signal transduction translates into the truth table of the NOR operator (Fig. 5), if a positive logic convention (low = 0, high = 1) is applied to the inputs and outputs.

The anthracene derivative **2** (Table 1, Fig. 2) reproduces a NOT operation at a pH of 4.5, an OR operation at a pH of 10, and a NOR function at a pH of 7 [31]. Under neutral conditions, the anthracene fluorescence (optical output) can be observed only in the absence of Cu$^{2+}$ and Ni$^{2+}$ (chemical inputs). Indeed, the binding of one of the two metal

cations to the oligoamino arm is accompanied by the efficient quenching of the anthracene fluorescence. Thus, the behavior of this versatile compound at a pH of 7 is equivalent to that of the molecular NOR gates **28–30**. In all cases, an optical output (fluorescence) is controlled by two chemical inputs (metal cations) according to a NOR function.

Comparison of the truth tables for the XOR and XNOR gates (Fig. 5) reveals an inverse relation between their output values. The input combinations leading to an output of *0* in the XOR produce an output of *1* in the XNOR and vice versa. Interestingly, both logic functions can be implemented with compound **31** (Table 1, Fig. 6) simply by careful selection of the output parameter [37]. The absorption spectrum of this compound shows a band at 390 nm. The complexation of Ca$^{2+}$ in the tetracarboxylate cleft shifts this band to shorter wavelengths. Instead, the protonation of the quinoline fragment pushes the same band to longer wavelengths. The opposing effects of the two chemical inputs, however, cancel each other when Ca$^{2+}$ and H$^+$ are added simultaneously. Under these conditions, the absorption band remains at the same wavelength. It follows that the absorbance probed at 390 nm decreases when only one of the two chemical inputs is applied. In contrast, the transmittance at the very same wavelength increases when only one of the two chemical inputs is applied. Thus, if a positive logic convention (low = *0*, high = *1*) is applied to inputs and output, this compound reproduces a XNOR function, when the absorbance is taken as the output, and a XOR function, when the transmittance is considered as the output.

The INH function (Fig. 5) can be implemented at the molecular level with the terbium complex **32** (Table 1, Fig. 6) [53, 54]. This compound transduces two chemical inputs (H$^+$ and O$_2$) into an optical output (terbium luminescence) according to this particular logic function. Under basic conditions, the complex **32** has a weak emission band at 548 nm in either aerated or degassed solutions. After the addition of H$^+$, the emission intensity increases dramatically only if O$_2$ is absent. The protonation of the quinoline fragment facilitates the energy transfer from the quinoline excited state to the lanthanide excited state, enhancing the emission intensity. In the presence of O$_2$, however, the partial quenching of the quinoline triplet state suppresses the energy transfer process. Thus, the emission intensity is high only when the concentration of H$^+$ is high and that of O$_2$ is low. If a positive logic convention (low = *0*, high = *1*) is applied to the two chemical inputs ($I1$ = H$^+$, $I2$ = O$_2$) and the optical output, the signal transduction of **32** translates into the truth table of the INH circuit (Fig. 5).

The three combinational logic circuits *a–c* in Figure 7 have three inputs and one output. The circuit *d* has an additional output terminal and converts three inputs into two outputs. The logic functions of these four circuits have been reproduced at the molecular level with the compounds **18** and **33–38** (Table 4, Figs. 3 and 8). The *trans*-chalcone **18** switches to the 4′-hydroxyflavylium cation **19** upon irradiation at 365 nm and the addition of either H$^+$ or sodium dodecyl sulfate (SDS) [55]. The transformation of **18** into **19** is accompanied by an increase in absorbance at 450 nm. Thus, this system responds to an optical ($I1$) and two chemical ($I2$ and $I3$) inputs producing an optical output ($O$).
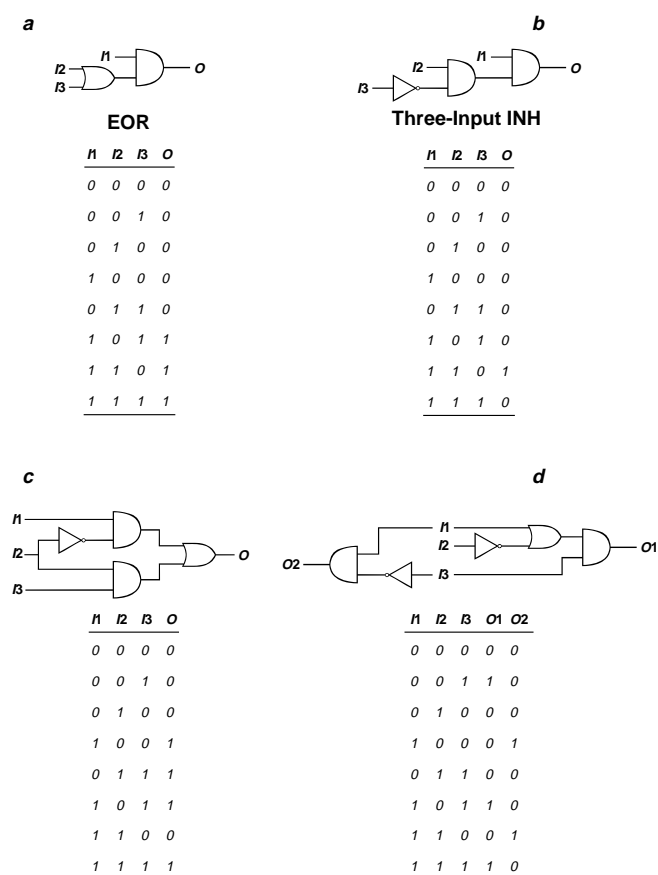
**Figure 7.** Combinational logic circuits with three inputs and one or two outputs [10].



**Figure 8.** Compounds able to reproduce complex combinational logic functions relying on chemical and optical inputs and optical outputs [55–58].

The output is high when the optical input is high and one or both chemical inputs are high. If a positive logic convention (low = 0, high = 1) is applied to the three inputs and the two outputs, this signal transduction translates into the truth table of the EOR gate (*a* in Fig. 7).

The compound **33** (Table 2, Fig. 8) responds to three chemical inputs (*I1* = $Ca^{2+}$, *I2* = β-cyclodextrin, *I3* = $O_2$) producing an optical output (naphthalene phosphorescence) [52]. The naphthalene phosphorescence is high only when the concentrations of $Ca^{2+}$ and β-cyclodextrin are high and that of $O_2$ is low. Under these conditions, the metal cation enters the tetracarboxylate cleft, suppressing photoinduced electron transfer from the tertiary amino groups to the naphthalene phosphor. The β-cyclodextrin encircles the naphthalene fragment, preventing bimolecular triplet–triplet annihilation. Finally, the absence of $O_2$ ensures that the naphthalene triplet is not quenched. Thus, the signal transduction operated by this compound translates into the truth table of the three-input INH (*b* in Fig. 7), if a positive logic convention (low = 0, high = 1) is applied to the three inputs and the single output.

The compounds **34** and **35** (Fig. 8) incorporate an anthracene core bridging two recognition sites [56, 57]. In both instances, photoinduced electron transfer from the azacrown ether appendage to the anthracene fluorophore quenches its emission. After the complexation of $K^+$ in the azacrown ether, the quenching mechanism is suppressed and

a fluorescence enhancement is observed. In contrast, the complexation of either $Na^+$ in the benzocrown ether receptor of **34** or $Cs^+$ in the calixarene receptor of **35** has no influence on the emission intensity. In the presence of $H^+$, the amino group of the azacrown of **34** and **35** is protonated and the complexation of $K^+$ prevented. However, protonation activates the photoinduced electron transfer from the catechol fragment to the anthracene fluorophore. The complexation of either $Na^+$ in the benzocrown ether of **34** or $Cs^+$ in the calixarene of **35** suppresses this quenching mechanism, enhancing the fluorescence intensity. In summary, these molecules respond to $K^+$ in the absence of $H^+$ and to either $Cs^+$ or $Na^+$ in the presence of $H^+$. Three chemical inputs (*I1* = $K^+$, *I2* = $H^+$, and *I3* = $Cs^+$ or $Na^+$) are transduced into a single optical output (fluorescence). This signal transduction translates into the truth table of the circuit *c* in Figure 7, if a positive logic convention (low = 0, high = 1) is applied to the three inputs and the single output.

The three-state molecular switch **36–38** (Table 2, Fig. 8) responds to two optical and one chemical input producing two optical outputs [58]. The inputs are ultraviolet stimulations (*I1*), visible light (*I2*), and $H^+$ (*I3*). The outputs are the absorbance at 401 nm (*O1*) of **38** and the absorbance at 563 nm (*O2*) of **37**. Ultraviolet irradiation of **36** induces the formation of **37** and the concomitant appearance of a band at 563 nm in the absorption spectrum. Either in the dark or under the influence of visible light, **37** reisomerizes to **36**, and the absorbance at 563 nm fades. The addition of $H^+$ to **36** produces **38** and the concomitant appearance of a band at 401 nm in the absorption spectrum. Under the influence of visible light, **38** reverts to **36** and the absorbance at 401 nm fades. Furthermore, the direct interconversion of **37** and **38** and the associated changes in absorbance at 563 and 401 nm

can be achieved by controlling the concentration of H$^+$. In summary, three inputs are converted into two outputs by this three-state molecular switch. If a positive logic convention (low = 0, high = 1) is applied to all inputs and outputs, this signal transduction translates into the truth table of the circuit *d* in Figure 7.

## 8. COMBINATIONAL LOGIC WITH SUPRAMOLECULAR SYSTEMS

Combinational logic functions can also be implemented with supramolecular systems. In particular, certain host-guest complexes can execute XOR and XNOR functions (Fig. 5) combining chemical, electrical, and optical inputs and outputs. The macrocyclic polyether **39** (Fig. 9) binds the 2,7-diazapyrenium dication **40** as a result of electrostatic and charge-transfer terms [59]. The supramolecular association encourages the quenching of the naphthalene fluorescence (optical output). After the addition of H$^+$ (chemical input), the crown ether slips off the guest and a high fluorescence intensity is detected. Similarly, the addition of butylamine (chemical input) produces an amine/diazapyrenium adduct, which promotes the dissociation of **39** from **40**. As a result, a high naphthalene fluorescence can be detected once again. When the two chemical inputs are added simultaneously, the protonation of butylamine occurs and the nonfluorescent supramolecular assembly remains unaffected. Thus, the optical output (fluorescence) is high when only one of the two chemical inputs (H$^+$ and butylamine) is applied. The signal transduction operated by the supramolecular system **39 • 40** translates into the truth table of the XOR gate (Fig. 5), if a positive logic convention is applied to the two inputs and the single output.

The supramolecular association of the tetracationic cyclophane **41** and the tetrathiafulvalene polyether **42** produces a rotaxane-like complex [60]. The attractive interactions between the complementary electron-deficient and electron-rich aromatic units are accompanied by the appearance of
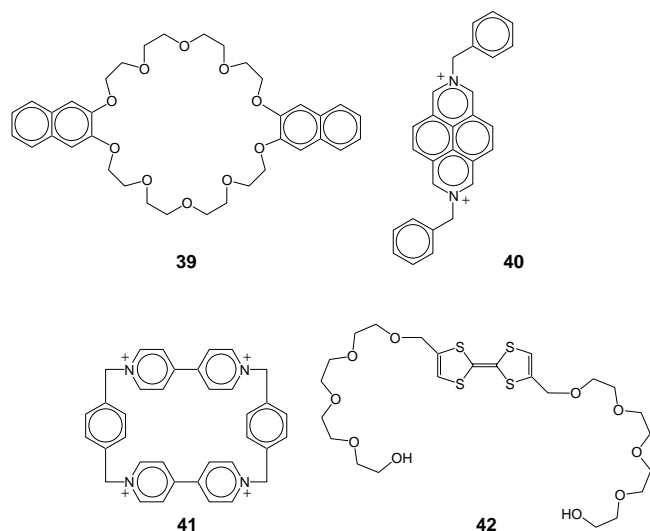
a charge-transfer band (optical output) at 830 nm in the absorption spectrum. The oxidation of the neutral tetrathiafulvalene to its radical cation encourages the dissociation of the complex and the disappearance of the charge-transfer band. Similarly, the reduction of the dicationic bipyridinium units to their radical cations results in a dramatic decrease in the magnitude of the supramolecular forces maintaining host and guest together. Under these conditions, the complex dissociates, and, once again, the charge-transfer band disappears. The oxidation of the tetrathiafulvalene unit and the reduction of the bipyridinium dications can be induced electrochemically by the application of appropriate voltages to a working electrode. If the voltage is raised above +0.5 V (*I1*), the oxidation of the guest occurs and the optical output fades. If the voltage is lowered below −0.3 V (*I2*), the reduction of the bipyridinium dications occurs and the optical output fades. In principle, a solution of the supramolecular assembly **41 • 42** can be stimulated with both inputs with the use of two independent working electrodes. Under these conditions, the charge-transfer absorbance (*O*) is high only when the voltage input *I1* is low and the voltage input *I2* is high or vice versa. This behavior corresponds to a XNOR function (Fig. 5), if a positive logic convention (low = 0, high = 1) is applied to *I1* and *O* and a negative logic convention (low = 1, high = 0) is applied to *I2*.

## 9. COMBINATIONAL AND SEQUENTIAL LOGIC WITH MULTIPLE MOLECULAR COMPONENTS

The relatively complex logic circuits in Figures 5 and 7 can be reproduced at the molecular level with individual compounds rather than networks of communicating molecular gates. There is no need for the output of one molecular logic gate to become the input of another. The overall combinational logic function can be integrated within a single molecular switch. This fascinating approach to digital processing with chemical systems is extremely elegant but has a major limitation. A new molecular switch has to be designed and synthesized every time a different logic function has to be implemented. In contrast, conventional digital circuits are assembled, relying always on the same three basic building blocks. Appropriate combinations of AND, NOT, and OR gates are assembled, interconnecting their input and output terminals. The contact established between them ensures the propagation of binary data across the network of gates and the implementation of specific sequences of the three basic logic operations. To reproduce this modular approach with chemical systems, efficient methods to operate multiple molecular components and, eventually, to communicate signals between them are starting to be developed. The XOR and NOR operations (Fig. 5) and the functions of the combinational and sequential logic circuits illustrated in Figure 10 have all been reproduced with ensembles of cooperating molecular components.

The *trans*-chalcone **43** (Fig. 11) isomerizes to a *cis* form upon irradiation at 365 nm [61]. At a pH of 4.5, the photogenerated *cis* isomer switches to the 4′-methoxyflavilyium cation **44**. This compound reverts to the original form **43**,



**Figure 9.** The molecular components of supramolecular XOR and XNOR gates based on chemical and electrical inputs and optical outputs [59, 60].

**Half-Adder**

| I1 | I2 | O1 | O2 |
|----|----|----|----|
| 0  | 0  | 0  | 0  |
| 0  | 1  | 1  | 0  |
| 1  | 0  | 1  | 0  |
| 1  | 1  | 0  | 1  |

| I1 | I2 | O      |
|----|----|--------|
| 0  | 0  | 0 or 1 |
| 0  | 1  | 1      |
| 1  | 0  | 0      |
| 1  | 1  | 0      |

| I1 | I2 | I3 | O |
|----|----|----|---|
| 0  | 0  | 0  | 1 |
| 0  | 0  | 1  | 0 |
| 0  | 1  | 0  | 1 |
| 1  | 0  | 0  | 0 |
| 0  | 1  | 1  | 1 |
| 1  | 0  | 1  | 0 |
| 1  | 1  | 0  | 0 |
| 1  | 1  | 1  | 0 |

**Three-Input NOR**

| I1 | I2 | I3 | O1 | O2 |
|----|----|----|----|----|
| 0  | 0  | 0  | 1  | 1  |
| 0  | 0  | 1  | 0  | 1  |
| 0  | 1  | 0  | 1  | 1  |
| 1  | 0  | 0  | 0  | 0  |
| 0  | 1  | 1  | 1  | 1  |
| 1  | 0  | 1  | 0  | 1  |
| 1  | 1  | 0  | 0  | 0  |
| 1  | 1  | 1  | 0  | 1  |

| I1 | I2 | I3 | O |
|----|----|----|---|
| 0  | 0  | 0  | 1 |
| 0  | 0  | 1  | 0 |
| 0  | 1  | 0  | 0 |
| 1  | 0  | 0  | 0 |
| 0  | 1  | 1  | 0 |
| 1  | 0  | 1  | 0 |
| 1  | 1  | 0  | 0 |
| 1  | 1  | 1  | 0 |

**Figure 10.** Combinational and sequential logic circuits with two or three inputs and one or two outputs [10].



**Figure 11.** Molecular components of combinational and sequential circuits based on the interplay of optical inputs and outputs [61, 62].

if the pH is increased. These transformations can be followed by monitoring the change in intensity of the absorption bands of **44**. In water, the irradiation of $K_3Co(CN)_6$ (**45**) at 365 nm results in the release of a $CN^-$ anion, which combines with $H^+$, increasing the pH. When **43** and **45** are codissolved in water, the continuous irradiations at 365 nm produce initially **44** and then $CN^-$. The released anion alters the pH, promoting the transformation of **44** back into **43**. A similar result is obtained under pulsed irradiation. A single pulse promotes the formation of **44**, and a second pulse induces the $CN^-$ release and the reformation of **43**. The two

pulses can be considered as two independent optical inputs and the absorbance of **44** as an optical output. It follows that the output is high when only one input is applied. This behavior corresponds to a XOR function (Fig. 5) if a positive logic convention (low = 0, high = 1) is applied to the two inputs and the single output.

The logic function of the half-adder (**a** in Fig. 10) can be implemented by operating in parallel an AND and a XOR gate sharing the same two inputs. The compounds **12** and **31** (Table 1, Figs. 3 and 6) execute AND and XOR functions, respectively, in response to $H^+$ and $Ca^{2+}$ inputs [37]. Their outputs are the fluorescence (**O2**) of **12** and the transmittance (**O1**) of **31**. When these two compounds are dissolved in the same solution, they can be operated simultaneously by application of the two chemical inputs. It follows that the signal transduction operated by a solution of **12** and **31** is equivalent to that executed by the circuit **a** in Figure 10, since the truth table of the half-adder is a combination of the truth tables of an AND and XOR gates.

Ultraviolet irradiation of the spiropyran **36** (Fig. 8) produces the merocyanine **37** [58]. The *p*-nitrophenolate fragment of the photogenerated isomer can abstract a proton from a compatible acid, generating the protonated merocyanine **38**. Indeed, ultraviolet irradiation (optical input) of an equimolar solution of **36** and the azopyridinium **46** (Fig. 11) encourages the formation of **38** and the azopyridine **47**, as

a result of photoinduced proton transfer [62]. Upon visible irradiation (optical input), the protonated merocyanine **38** reverts to the spiropyran **36**, releasing H⁺, which promotes the transformation of **47** into its conjugate acid **46**. The photoinduced transformation of **46** into **47** and vice versa can be followed by monitoring the change in absorbance (optical output) for the characteristic visible absorption band of **46**. Thus, ultraviolet (*I1*) and visible (*I2*) inputs modulate the intensity of an optical output (*O*) as a result of the intermolecular communication of a chemical signal (proton transfer) between compatible molecular components. In particular, the intensity of *O* changes from a high to a low value when *I1* is turned on and remains low after *I1* is turned off. The intensity of *O* returns to a high value if *I2* is turned on and remains high after *I2* is turned off. It follows that this multimolecular system has the ability to memorize the influence of the optical inputs and maintain the value imposed on the output even when the inputs are not applied. This intriguing behavior is equivalent to the *sequential* logic circuit *b* in Figure 10, if a positive logic convention (low = *0*, high = *1*) is applied to the two inputs and the single output. It is important to note that the output for the input combination *00* of this particular circuit can be either *0* or *1*. Its value is dictated by the *sequence* of events leading to that particular combination of inputs.

The different absorption properties of **36–38** (Fig. 8) can be exploited to control the emission intensity of pyrene (**48**) as a result of intermolecular fluorescence modulation [63]. This particular fluorophore emits in a wavelength range where only the two merocyanine forms **37** and **38** absorb significantly. Thus, high fluorescence intensity (*O*) is detected for an equimolar solution of **36** and **48**. However, ultraviolet

irradiation (*I1*) or addition of H⁺ (*I3*) promotes the interconversion of **36** into **37** or **38**, respectively. Under these conditions, the fluorescence of **48** is absorbed by either **37** or **38**, and a low emission intensity is detected. Upon irradiation with visible light (*I2*), the merocyanine forms revert to **36** and a high fluorescence intensity is restored. It follows that the optical output can be modulated by addressing the solution of the emitting and absorbing components with two optical and one chemical inputs. If a positive logic convention (low = *0*, high = *1*) is applied to all signals, this signal transduction translates into the truth table of the combinational logic circuit *c* in Figure 10. The logic behavior of this multimolecular system is based on the transmission of an optical signal from the emitting to the absorbing component. Since light can travel through space, the two communicating molecular components do not necessarily need to be in the same solution. The design of the optical network in Figure 12 relies on this simple consideration [64]. It incorporates a quartz cell containing an equimolar solution of naphthalene (**49**), anthracene (**50**), and tetracene (**51**) and a second quartz cell with a solution of the spiropyran **36**. The excitation source stimulates the emission of the three fluorophores contained in the first cell. These compounds emit light at three different wavelengths. The emitted light passes through the second cell before reaching the detector. Ultraviolet (*I1*), visible (*I2*), and H⁺ (*I3*) inputs control the interconversion of the three states **36–38**. The emission of **49** is absorbed equally by **36–38**. The emission of **50** (*O1*) is not absorbed by **36**, but it is "blocked" by **37** and **38**. The emission of **51** (*O2*) is absorbed and blocked only by **37**. Thus, three input stimulations modulate in parallel the fluorescence of three different compounds with three
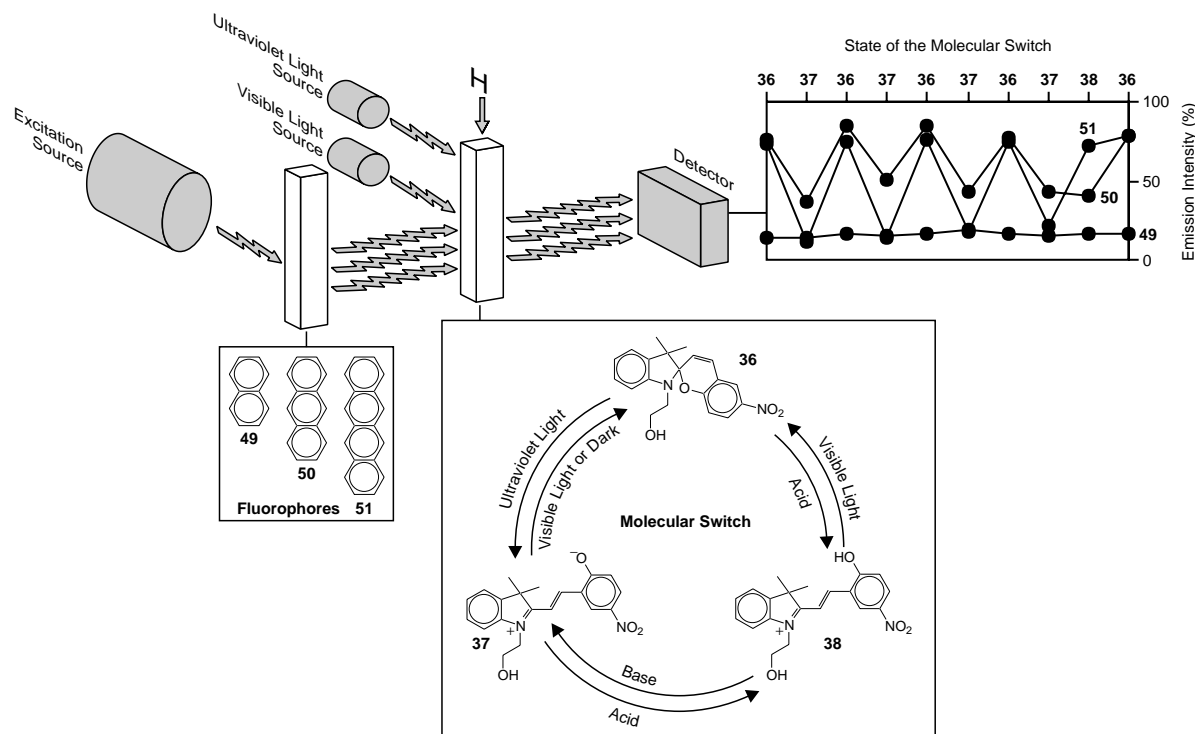


**Figure 12.** An optical network for the modulation of multiple optical signals in parallel [64].

distinct protocols that are dictated by the overlap of the emission and absorption bands of six molecular components. The plots in Figure 12 illustrate the correlation between the emission intensities of **49–51** and the state of the molecular switch. If a positive logic convention (low = 0, high = 1) is applied to the three inputs *I1–I3* and the two outputs *O1* and *O2*, the truth table for the circuit *d* of Figure 10 can be assembled. The outputs *O1* and *O2* switch between low and high values as the molecular switch is operated. In contrast, the fluorescence of **49** is always low, since its emission is always blocked by the switching element. As a result, this particular output is not included in the truth table and logic circuit.

An alternative optical network based exclusively on optical inputs and optical outputs is illustrated in Figure 13 [65]. In this case, a monochromatic beam travels from the visible light source to the detector, passing through three quartz cells containing a solution of the spiropyran **36**. Each cell can be addressed independently with ultraviolet inputs. When an ultraviolet source is turned on, the spiropyran **36** in the corresponding cell isomerizes to the merocyanine **37**. When the ultraviolet input is turned off, **37** reisomerizes thermally to **36**. If the wavelength of the monochromatic signal traveling from the source to the detector is chosen to match the visible absorption band of **37**, a high optical output reaches the detector only when all three ultraviolet inputs are not applied. Indeed, if only one of the inputs is turned on, the intensity of the output drops to 3–4%. If two or all three inputs are switched on, the output fades to 0%. Thus, a high output reaches the detector only when all three inputs are off. This particular signal transduction corresponds to the three-input NOR circuit (*e* in Fig. 10). Interestingly, if one of the three switching elements is removed, the logic operation executed becomes equivalent to the two-input NOR (Fig. 5). If only one switching element is left along the path of the traveling light, the logic function reduces to a simple NOT operation (Fig. 1). In all cases, a high output intensity is detected only when all inputs are NOT on.
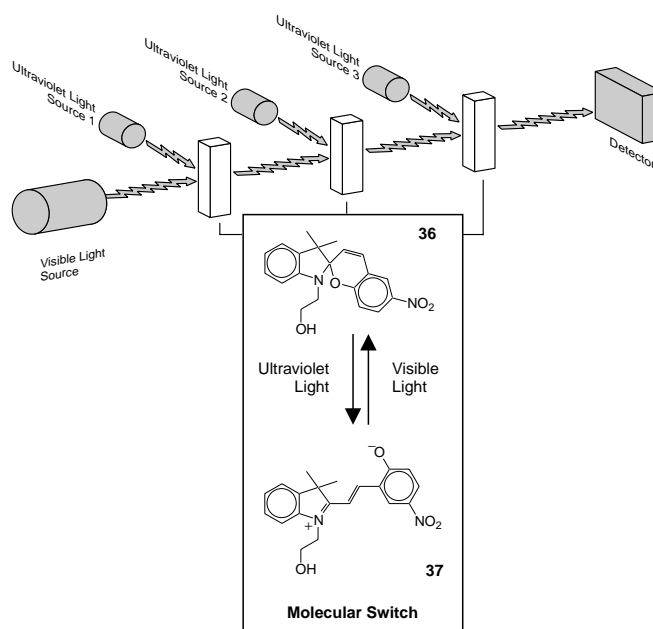


**Figure 13.** An all-optical three-input NOR gate based on three independent switching elements [65].

# 10. SOLID-STATE MOLECULAR LOGIC GATES

The molecular logic gates listed in Tables 1 and 2 have been investigated in solution. Experimental procedures reproducing their operating principles in solid-state configurations are only starting to be explored. For example, the [2]rotaxanes **52** and **53** (Fig. 14) have been incorporated successfully into two-terminal electronic devices [66, 67]. The [2]rotaxane **52** has a bipyridinium backbone encircled by a macrocyclic polyether. The two bulky tetraarylmethane groups prevent the electron-rich macrocycle from slipping off of the electron-deficient backbone. The [2]rotaxane **53** has an electron-deficient macrocycle threaded on the linear

**Table 2.** Molecular logic gates with two or three input terminals and one or two output terminals.[a, b]

| Compound | Input 1 (*I1*) | Input 2 (*I2*) | Input 3 (*I3*) | Output 1 (*O1*) | Output 2 (*O2*) | Ref. |
|---|---|---|---|---|---|---|
| **12 + 31** | $Ca^{2+}$ | $H^+$ | — | Fluorescence | Transmittance | [37] |
| **18** | Light | $H^+$ | SDS[c] | Absorbance | — | [55] |
| **33** | $Ca^{2+}$ | β-Cyclodextrin | $O_2$ | Phosphorescence | — | [52] |
| **34** | $Cs^+$ or $Na^+$ | $H^+$ | $K^+$ | Fluorescence | — | [56, 57] |
| **35** | $Cs^+$ or $Na^+$ | $H^+$ | $K^+$ | Fluorescence | — | [56] |
| **36** | $H^+$ | Light | Light | Absorbance | Absorbance | [58] |
| **36 × 3** | Light | Light | Light | Light | — | [65] |
| **36 + 46** | Light | Light | — | Absorbance | — | [62] |
| **36 + 48** | $H^+$ | Light | Light | Fluorescence | — | [63] |
| **36 + 49–51** | $H^+$ | Light | Light | Fluorescence | Fluorescence | [64] |

[a] The inputs and outputs are chemical or optical signals. The chemical inputs are the concentrations of the species listed. The optical inputs/outputs are the light, fluorescence, and phosphorescence intensities or the magnitude of the parameter listed.
[b] The circuits and truth tables corresponding to these molecular logic gates are illustrated in Figures 7 and 10. The half-adder (*a* in Fig. 10) is equivalent to the combination of **12** and **31**. The EOR (*a* in Fig. 7) corresponds to **18**. The three-input INH (*b* in Fig. 7) is equivalent to **33**. The circuit *c* in Figure 7 corresponds to **34** or **35**. The circuit *d* in Figure 7 is equivalent to **36**. The three-input NOR (*e* in Fig. 10) is equivalent to the all-optical network based on three switching elements each containing **36**. The circuit *b* in Figure 10 corresponds to the combination of **36** and **46**. The circuit *c* in Figure 10 is equivalent to the combination of **36** an **48**. The circuit *d* in Figure 10 is equivalent to the optical network based on **36** and **49–51**.
[c] SDS stands for sodium dodecyl sulfate.
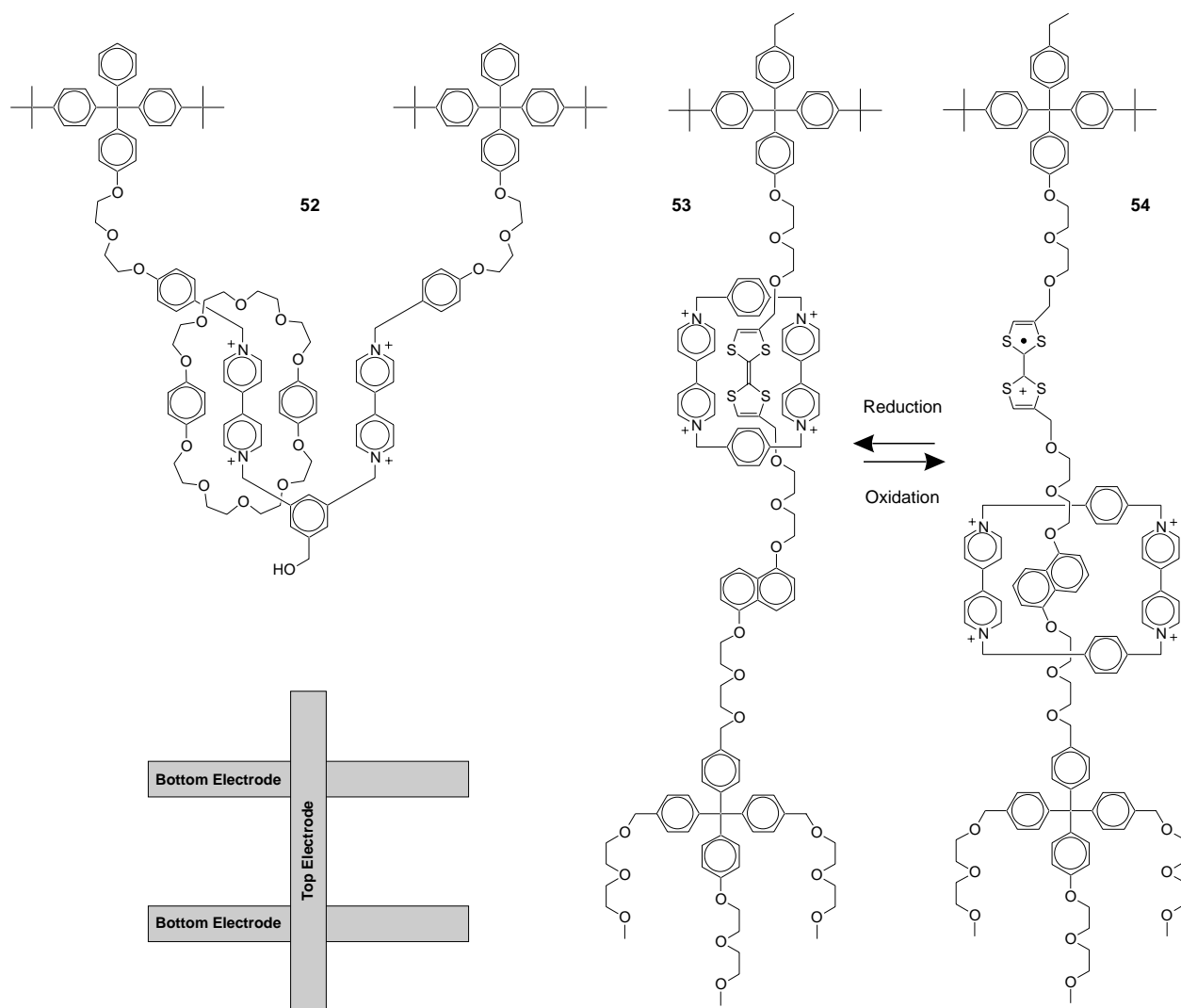
**Figure 14.** The molecular components of solid-state logic gates consisting of interconnected electrode/molecular layer/electrode cross-junctions [66, 67].

portion of an electron-rich dumbbell-shaped component. Once again, terminal tetraarylmethane groups mechanically trap the macrocyclic component. Attractive electrostatic and charge-transfer interactions maintain the bipyridinium cyclophane around the tetrathiafulvalene fragment of the dumbbell-shaped component. After the tetrathiafulvalene oxidation, electrostatic repulsion forces the tetracationic cyclophane to move away from the newly formed cationic unit, producing the [2]rotaxane **54**. After reduction, the neutral form of the tetrathiafulvalene fragment is restored and the original [2]rotaxane **53** is regenerated. Thus, the reversible interconversion between **53** and **54** can be controlled by oxidizing and reducing the electroactive tetrathiafulvalene unit.

The fabrication of solid-state devices incorporating the [2]rotaxanes **52** and **53** relies on the amphiphilic character of these compounds. Indeed, these molecules can be compressed into organized monolayers at the air/water interface of a Langmuir trough. The resulting films can be transferred on the surface of parallel electrodes patterned lithographically on silicon chips. Then the deposition of a top elec-

trode perpendicular to the bottom electrodes can produce pairs of interconnected cross-junctions (Fig. 14). In the case of the [2]rotaxane **52**, aluminum fingers covered by an aluminum oxide layer are used for the bottom electrodes. In the case of the [2]rotaxane **53**, the bottom electrodes are silicon wires with a silicon dioxide overlayer. In both instances, the top electrode is a titanium wire covered by an aluminum overlayer.

For a cross-junction containing a monolayer of the [2]rotaxane **52**, high current is measured at the top electrode only when the voltage of the bottom electrode is lowered below −0.7 V [66]. Under these conditions, the bipyridinium centered LUMOs mediate the tunneling of electrons from the bottom to the top electrode. An AND gate can be constructed by operating two cross-junctions with a common top electrode in parallel. Indeed, voltage inputs can be applied to the two independent bottom electrodes, and a single current output can be measured at the common top electrodes. Only when both voltage inputs are lowered below −0.7 V is a current output greater than 3 pA measured. When a negative voltage convention is applied to the inputs (low = *1*,

high = *0*) and a positive logic convention (low = *0*, high = *1*) is applied to the output, the signal transduction translates into an AND operation. If the logarithm of the current is taken as the output and the same logic conventions are applied, an OR function can be implemented. The logarithm of the current is greater than −9, when at least one voltage input is below −0.7 V. Furthermore, a three-input OR gate can also be realized by the operation of three cross-junctions with a common top electrode, following the same logic conventions. The voltages of the three bottom electrodes can be varied independently while the current at the top electrode is monitored. Once again, the logarithm of the current is greater than −9, when at least one voltage input is below −0.7 V.

In the case of the [2]rotaxane **53**, the junction conduction probed at +0.2 V can be switched between high and low values with the application of voltage pulses of −2 and +2 V to the bottom electrode [67]. A positive voltage pulse promotes the oxidation of the tetrathiafulvalene unit and the shuttling of the tetracationic cyclophane to produce the [2]rotaxane **54**. The redox-induced change in the stereoelectronic properties of the molecules sandwiched between the two crossing electrodes significantly affects their ability to mediate the tunneling of electrons through the junction. As a result, the conduction probed at +0.2 V grows significantly after a +2 V pulse. However, the original value can be restored by applying a −2 V pulse. The negative voltage pulse promotes the reduction of the cationic form of the tetrathiafulvalene fragment back to its neutral state. This process is accompanied by the shuttling of the bipyridinium cyclophane to the original position, regenerating the [2]rotaxane **53**. Following this strategy, it is possible to configure two-dimensional logic circuits consisting of interconnected cross-junctions. Indeed, appropriate voltage pulses can be exploited to predefine the conduction of each junction and impose desired current/voltage characteristics on the overall circuit. The potential of this approach for the implementation of logic functions was demonstrated by configuring nine interconnected cross-junctions to execute a XOR function [67].

In addition to rotaxanes, single-wall carbon nanotubes have also been exploited to reproduce logic functions with solid-state devices [68]. Individual nanotubes have been incorporated into ultraminiaturized transistors. One of them is illustrated schematically in Figure 15. The carbon nanotube lies on an insulating aluminum oxide layer deposited on an aluminum electrode. The two ends of the carbon nanotubes are in contact with gold electrodes. The voltage applied to the aluminum gate affects the electronic properties of the carbon nanotube, altering its ability to mediate the flow of electrons from the gold source to the gold drain. More precisely, the drain current at a source to drain bias of *ca.* −1.3 V jumps from *ca.* 0 to *ca.* 50 nA when the gate voltage is lowered from −1.0 to −1.3 V. This behavior is equivalent to that of a conventional enhancement-mode *p*-type field effect transistor [1]. A moderate change in the gate voltage produces a dramatic change in the drain current.

Multiple nanotube transistors can be fabricated on the same silicon chip, and the interconnection of their terminals with appropriate configurations results in the assembly of nanoscale digital circuits. For example, NOT and NOR gates have been implemented with this approach [68]. The NOT
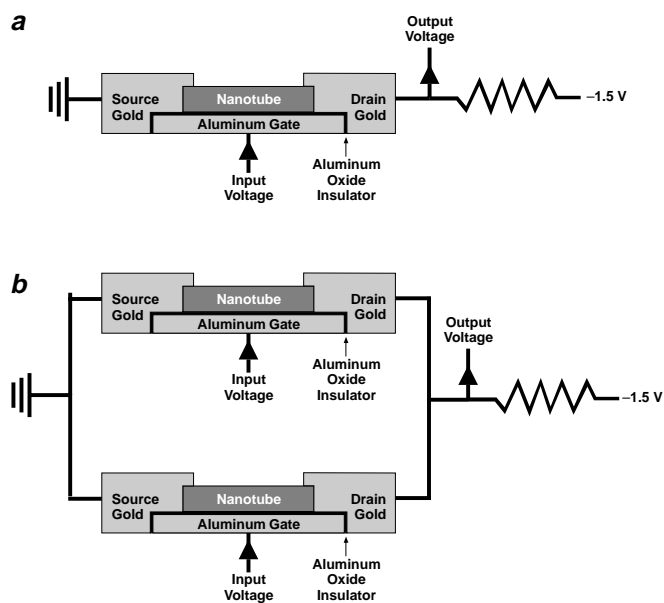


**Figure 15.** Solid-state logic gates based on single-wall carbon nanotube transistors [68].

gate (*a* in Fig. 15) consists of an off-chip bias resistor connected to the drain terminal of a nanotube transistor with the source grounded. The voltage output probed at the drain terminal varies with a voltage input applied to the gate, since the nanotube conductance is determined by the gate voltage. In particular, the nanotube resistance decreases below that of the bias resistor when a voltage input of −1.5 V is applied. Under these conditions, the voltage output drops to 0 V. The nanotube resistance increases above that of the bias resistor when the voltage input is raised to 0 V. As a result, the voltage output becomes −1.5 V. In summary, the output switches from a high (0 V) to a low (−1.5 V) level when the input changes from a low (−1.5 V) to a high (0 V) value. The inverse relation between input and output corresponds to a NOT operation, if a negative logic convention (low = *1*, high = *0*) is applied to both signals.

The NOR gate (*b* in Fig. 15) incorporates two nanotube transistors. Their source terminals are grounded. Their drain terminals are connected to an off-chip bias resistor. The two transistors are operated by independent input voltages but share the same output voltage. The common output is 0 V when the resistance of at least one of the two nanotubes is below that of the bias resistor. The output is −1.5 V when the resistance of both nanotubes is higher than that of the bias resistor. Thus, the output is high (0 V) if a low voltage input (−1.5 V) is applied to one or both transistors. The output is low (−1.5 V) when both voltage inputs are high (0 V). If a negative logic convention (low = *1*, high = *0*) is applied to all signals, the signal transduction behavior translates into the truth table of a NOR gate (Fig. 5).

## 11. CONCLUSIONS

The three basic logic operations AND, NOT, and OR can be implemented with chemical systems relying on fascinating molecular switches. These compounds respond to

chemical, electrical, magnetic, and/or optical inputs producing detectable electrical or optical outputs. Relatively complex combinational logic functions able to transduce two or three inputs into one or two outputs can be also reproduced at the molecular level. Indeed, the combined functions of multiple basic operators can be designed into single molecular switches thanks to the high level of sophistication reached by chemical synthesis. In addition, combinational and sequential logic functions can be reproduced with ensembles of cooperating molecular components. In these systems, distinct molecular switches share the same input stimulations and can be operated in parallel. Alternatively, the output of one molecular component can be communicated intermolecularly to a second component, offering the opportunity of operating molecular switches sequentially. The intermolecular communication of signals can rely on the transfer of protons from one molecule to another, or it can exploit the transmission of optical signals from emitting to absorbing species.

This exploratory research in the realm of molecular switches and digital processing has demonstrated already that information can be manipulated at the molecular level. However, the chemical systems developed so far are rudimentary examples of digital processors. At this stage, they remain far from potential applications in information technology. In addition, most of these studies rely on the bulk addressing of molecular switches in solution, rather than on the stimulation of single molecules in solid-state configurations. The major challenge in this research area lies in the identification of practical methods to scale these operating principles down to the unimolecular level and to reproduce the functions already demonstrated in solution with molecule-based solid-state devices. Fundamental studies in these directions will reveal if similar chemical processors for the elaboration and storage of binary data can, indeed, evolve into practical devices for information technology.

## GLOSSARY

**Digital circuits**   Networks of interconnected logic gates.

**Fluorescence**   Emission of light from a singlet excited state of a molecule.

**Logic gates**   Devices able to convert binary inputs into binary outputs according to defined logic functions.

**Molecular switches**   Molecules undergoing reversible transformations under the influence of external stimulations.

**Supramolecular chemistry**   Area of the chemical sciences studying the noncovalent association of independent molecular building blocks into multicomponent assemblies.

## REFERENCES

1. R. S. Muller and T. I. Kamins, "Device Electronics for Integrated Circuits." Wiley, New York, 2002.
2. M. J. Madou, "Fundamentals of Microfabrication: The Science of Miniaturization." CRC Press, Boca Raton, FL, 2002.
3. "International Technology Roadmap for Semiconductors." International SEMATECH, Austin, TX, 2000.
4. Processor Hall of Fame, Intel Corporation, Santa Clara, CA, 2002.
5. G. E. Moore, *Electronics* 114 (1965).
6. D. Goldhaber-Gordon, M. S. Montemerlo, J. C. Love, G. J. Opiteck, and J. C. Ellenbogen, *Proc. IEEE* 85, 521 (1997).
7. M. Schultz, *Nature* 399, 729 (1999).
8. D. A. Muller, T. Sorsch, S. Moccio, F. H. Baumann, K. Evans-Lutterodt, and G. Timp, *Nature* 399, 758 (1999).
9. J. D. Meindl, Q. Chen, and J. D. Davies, *Science* 293, 2044 (2001).
10. R. J. Mitchell, "Microprocessor Systems: An Introduction." Macmillan, London, 1995.
11. A. J. Bard, "Integrated Chemical Systems: A Chemical Approach to Nanotechnology." Wiley, New York, 1994.
12. A. P. Alivisatos, P. F. Barbara, A. W. Castleman, J. Chang, D. A. Dixon, M. L. Klein, G. L. McLendon, J. S. Miller, M. A. Ratner, P. J. Rossky, S. I. Stupp, and M. E. Thompson, *Adv. Mater.* 10, 1297 (1998).
13. Special issue on Photochromism: Memories and Switches, *Chem. Rev.* 100, 1683 (2000).
14. Special issue on Molecular Machines, *Acc. Chem. Res.* 34, 409 (2001).
15. K. C. Nicolau and E. C. Sorensen, "Classics in Total Synthesis." VCH, Weinheim, 1996.
16. V. Balzani, A. Credi, F. M. Raymo, and J. F. Stoddart, *Angew. Chem. Int. Ed.* 39, 3348 (2000).
17. B. L. Feringa, Ed., "Molecular Switches." Wiley-VCH, Weinheim, 2001.
18. M. D. Ward, *J. Chem. Ed.* 78, 321 (2001).
19. A. P. de Silva, N. D. McClenaghan, and C. P. McCoy, "Electron Transfer in Chemistry" (V. Balzani, Ed.), p. 156. Wiley-VCH, Weinheim, 2001.
20. A. P. de Silva, G. D. McClean, N. D. McClenaghan, T. S. Moody, and S. M. Weir, *Nachr. Chem.* 49, 602 (2001).
21. A. P. de Silva, D. B. Fox, T. S. Moody, and S. Weir, *Pure Appl. Chem.* 73, 503 (2001).
22. F. M. Raymo, *Adv. Mater.* 14, 401 (2002).
23. C. Y. Liu and A. J. Bard, *Acc. Chem. Res.* 32, 235 (1999).
24. R. M. Metzger, *Acc. Chem. Res.* 32, 950 (1999).
25. J. K. Gimzewski and C. Joachim, *Science* 283, 1683 (1999).
26. C. Joachim, J. K. Gimzewski, and A. Aviram, *Nature* 408, 541 (2000).
27. M. A. Reed and J. M. Tour, *Sci. Am.* 282, 86 (2000).
28. J. R. Heath, *Pure Appl. Chem.* 72, 11 (2000).
29. A. R. Pease, J. O. Jeppesen, J. F. Stoddart, Y. Luo, C. P. Collier, and J. R. Heath, *Acc. Chem. Res.* 34, 433 (2001).
30. A. P. de Silva, H. Q. N. Gunaratne, and C. P. McCoy, *Nature* 364, 42 (1993).
31. S. Alves, F. Pina, M. T. Albeda, E. García-España, C. Soriano, and S. V. Luis, *Eur. J. Inorg. Chem.* 405 (2001).
32. A. P. de Silva, H. Q. N. Gunaratne, and G. E. M. Maguire, *J. Chem. Soc., Chem. Commun.* 1213 (1994).
33. P. Ghosh, P. K. Bharadwaj, S. Mandal, and S. Ghosh, *J. Am. Chem. Soc.* 118, 1553 (1996).
34. P. Ghosh, P. K. Bharadwaj, J. Roy, and S. Ghosh, *J. Am. Chem. Soc.* 119, 11903 (1997).
35. A. P. de Silva, H. Q. N. Gunaratne, and C. P. McCoy, *J. Am. Chem. Soc.* 119, 7891 (1997).
36. S. A. de Silva, B. Amorelli, D. C. Isidor, K. C. Loo, K. E. Crooker, and Y. E. Pena, *Chem. Commun.* 1360 (2002).
37. A. P. de Silva and N. D. McClenaghan, *J. Am. Chem. Soc.* 122, 3965 (2000).
38. C. R. Cooper and T. D. James, *Chem. Commun.* 1419 (1997).
39. S. Iwata and K. Tanaka, *J. Chem. Soc., Chem. Commun.* 1491 (1995).
40. M. Inouye, K. Akamatsu, and H. Nakazumi, *J. Am. Chem. Soc.* 119, 9160 (1997).
41. F. Pina, A. Roque, M. J. Melo, M. Maestri, L. Belladelli, and V. Balzani, *Chem. Eur. J.* 4, 1184 (1998).
42. F. Pina, M. Maestri, and V. Balzani, *Chem. Commun.* 107 (1999).

43. L. Gobbi, P. Seiler, and F. Diederich, *Angew. Chem. Int. Ed.* 38, 674 (1999).

44. L. Gobbi, P. Seiler, F. Diederich, V. Gramlich, C. Boudon, J. P. Gisselbrecht, and M. Gross, *Helv. Chim. Acta* 84, 743 (2001).

45. P. R. Ashton, V. Baldoni, V. Balzani, A. Credi, H. D. A. Hoffmann, M.-V. Martínez-Díaz, F. M. Raymo, J. F. Stoddart, and M. Venturi, *Chem. Eur. J.* 7, 3482 (2001).

46. D. Kuciauskas, P. A. Liddell, A. L. Moore, and D. Gust, *J. Am. Chem. Soc.* 120, 10880 (1998).

47. A. S. Lukas, P. J. Bushard, and M. R. Wasielewski, *J. Am. Chem. Soc.* 123, 2440 (2001).

48. T. Witte, C. Bucher, F. Remacle, D. Proch, K. L. Kompa, and R. D. Levine, *Angew. Chem. Int. Ed.* 40, 2512 (2001).

49. M. T. Albelda, M. A. Bernardo, E. Garcia-España, L. Godino-Salido, S. V. Luis, M. J. Melo, F. Pina, and C. Soriano, *J. Chem. Soc., Perkin Trans. 2* 11, 2545 (1999).

50. H. T. Baytekin and E. U. Akkaya, *Org. Lett.* 2, 1725 (2000).

51. D. Parker and J. A. G. Williams, *Chem. Commun.* 245 (1998).

52. A. P. de Silva, I. M. Dixon, H. Q. N. Gunaratne, T. Gunnlaugsson, P. R. S. Maxwell, and T. E. Rice, *J. Am. Chem. Soc.* 121, 1393 (1999).

53. T. Gunnlaugsson, D. A. Mac Dónail, and D. Parker, *Chem. Commun.* 93 (2000).

54. T. Gunnlaugsson, D. A. Mac Dónail, and D. Parker, *J. Am. Chem. Soc.* 123, 12866 (2001).

55. A. Roque, F. Pina, S. Alves, R. Ballardini, M. Maestri, and V. Balzani, *J. Mater. Chem.* 9, 2265 (1999).

56. H.-F. Ji, R. Dabestani, and G. M. Brown, *J. Am. Chem. Soc.* 122, 9306 (2000).

57. H. Xu, X. Xu, R. Dabestani, G. M. Brown, L. Fan, and S. Patton, *J. Chem. Soc., Perkin Trans. 2* 636 (2002).

58. F. M. Raymo and S. Giordani, *J. Am. Chem. Soc.* 123, 4651 (2001).

59. A. Credi, V. Balzani, S. J. Langford, and J. F. Stoddart, *J. Am. Chem. Soc.* 119, 2679 (1997).

60. M. Asakawa, P. R. Ashton, V. Balzani, A. Credi, G. Mattersteig, O. A. Matthews, M. Montalti, N. Spencer, J. F. Stoddart, and M. Venturi, *Chem. Eur. J.* 3, 1992 (1997).

61. F. Pina, M. J. Melo, M. Maestri, P. Passaniti, and V. Balzani, *J. Am. Chem. Soc.* 122, 4496 (2000).

62. F. M. Raymo and S. Giordani, *Org. Lett.* 3, 3475 (2001).

63. F. M. Raymo and S. Giordani, *Org. Lett.* 3, 1833 (2001).

64. F. M. Raymo and S. Giordani, *J. Am. Chem. Soc.* 124, 2004 (2002).

65. F. M. Raymo and S. Giordani, *Proc. Natl. Acad. Sci. USA* 99, 4941 (2002).

66. C. P. Collier, E. W. Wong, M. Belohradsky, F. M. Raymo, J. F. Stoddart, P. J. Kuekes, R. S. Williams, and J. R. Heath, *Science* 285, 391 (1999).

67. Y. Luo, C. P. Collier, J. O. Jeppesen, K. A. Nielsen, E. Delonno, G. Ho, J. Perkins, H.-R. Tseng, T. Yamamoto, J. F. Stoddart, and J. R. Heath, *Chemphyschem* 3, 519 (2002).

68. A. Batchtold, P. Hadley, T. Nakanishi, and C. Dekker, *Science* 294, 1317 (2001).

# Molecular Nanotechnology with 2D Protein Crystals

Uwe B. Sleytr, Dietmar Pum, Margit Sára, Bernhard Schuster

*Universität für Bodenkultur Wien, Vienna, Austria*

## CONTENTS

## 1. INTRODUCTION

The cross-fertilization of biology, chemistry, and material sciences is opening up a great variety of new opportunities for innovation in nanosciences and biomimetics. Moreover, one of the most relevant areas of research in the nanosciences will be at the interface between biology and solid state physics. One of the key challenges is the technological utilization of self-assembly systems, wherein molecules spontaneously associate under equilibrium conditions into reproducible supramolecular aggregates ("bottom-up" strategy). The attractiveness of such "bottom up" processes lies in their capability to build uniform, ultra small functional units and the possibility to exploit such structures at meso- and macroscopic scale for life and nonlife science applications. The immobilization of biomolecules in an ordered fashion on solid substrates and their controlled confinement in definite areas of nanometer dimensions are key requirements for many applications, including the development of bioanalytical sensors, biochips, molecular electronics, biocompatible surfaces, and signal processing between functional membranes, cells, and integrated circuits.

The use of crystalline bacterial cell surface proteins (S-layer proteins) provided innovative approaches for the assembly of supramolecular structures and devices with dimensions of a few to tens of nanometers (for review see [1–5]). S-layers have proven to be particularly suited as building blocks in a biomolecular construction kit involving all major classes of biological molecules (protein, lipids, glycans, nucleic acids, and combinations of them) and nanoparticles. This chapter will provide a survey on the application potential of S-layers in life and nonlife sciences.

## 2. S-LAYER PROTEINS

S-layer proteins form the outermost cell envelope component of a broad spectrum of bacteria and archaea (for review see [1–9]) (Fig. 1). S-layers are composed of a single protein or glycoprotein species with an apparent relative molecular mass of 40,000–230,000 and exhibit either oblique (p1, p2), square (p4), or hexagonal (p3, p6) lattice symmetry with unit cell dimensions in the range of 3–30 nm (Fig. 2). One morphological unit consists of one, two, three, four or six identical subunits, respectively. S-layers are generally 5–10 nm thick and show pores of identical size (diameter, 1.5–8 nm) and morphology. In general, the topography of the outer face (with respect to the orientation of the S-layer on the bacterial cell) is smooth and the surface exhibits a charge neutral characteristic, while the inner face is often corrugated and net negatively or positively charged. Due to the crystalline character of S-layers functional groups, such as carboxyl or amino groups, are repeated with the periodicity of the protein lattice. This property of S-layer enables
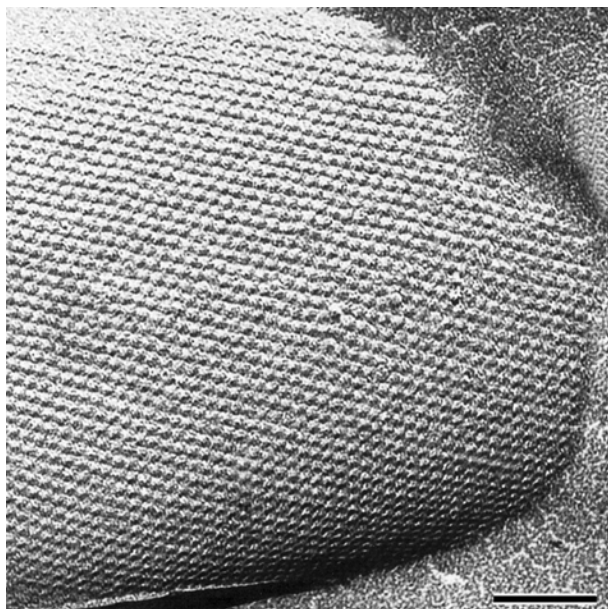
**Figure 1.** Transmission electron micrograph of a freeze-etching preparation of a bacterial cell showing an S-layer with hexagonal lattice symmetry. Bar, 100 nm.

a geometrically controlled immobilization of molecules and nanoparticles. Up to now, most nanotechnological applications have focused on S-layers present in gram-positive bacteria. In these organisms S-layers are linked to a rigid supporting layer [6].

## 3. SECONDARY CELL WALL POLYMERS

The rigid cell wall of Gram-positive bacteria contains, beside peptidoglycan, large amounts of accessory (secondary) cell wall polymers (SCWPs) composed of either teichoic acids, teichuronic acids, lipoteichoic acids, or lipoglycans [10]. Depending on the type, the polymer chains are either
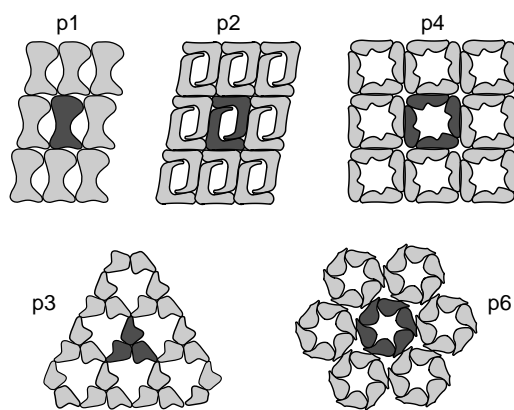


**Figure 2.** Schematic drawing of different S-layer lattice types. The regular arrays exhibit either oblique (p1, p2), square (p4), or hexagonal (p3, p6) lattice symmetry. One morphological unit (darker shades) consists of one, two, three, four, or six identical subunits, respectively [1]. Reprinted with permission from [1], U. B. Sleytr et al., *Angew. Chem. Int. Ed.* 38, 1999. © 1999, Wiley-VCH.

tethered to a lipid anchor or covalently linked to the peptidoglycan backbone. Although SCWPs are essential for cell viability, their exact physiological role is not really understood. Thus, very general functions such as binding of bivalent cations, keeping the peptidoglycan sacculus in an expanded state by charge repulsion, binding proteins to create an acidic cell wall during bacterial growth and division, or providing a biophysical barrier to prevent diffusion of nutrients and metabolites have been assigned to these polymers. Recently, evidence was provided that in Gram-positive bacteria, SCWPs function as anchoring structures for S-layer proteins [11, 12]. Accordingly, S-layer proteins can be considered as cell-surface-carbohydrate-binding proteins and the binding mechanism could correspond with that occurring between polysaccharides and lectins [12].

By sequence comparison, S-layer-homologous (SLH) motifs [13] have been identified at the N-terminal part of many S-layer proteins [14–19]. Typically, S-layer proteins possess three repeating SLH motifs each consisting of 50–60 amino acids. Secondary cell wall polymers have now been recognized to serve as binding sites for the SLH motifs of S-layer proteins [13]. In addition, SCWPs are highly specific for binding only S-layer proteins from those organisms from which they had been originally isolated [11]. As SCWP can be functionalized (e.g., by the introduction of thiol groups) gold substrates, but also other relevant inorganic surfaces can be covered by the SCWP to provide a specific binding matrix for a certain S-layer protein in a well-defined orientation. In addition, the concept of generating oriented functional protein lattices may also imply that appropriate glycolipids comprising the smallest functional units of SCWPs are synthesized and incorporated into liposomes or Langmuir lipid films [20].

## 4. S-LAYER FUSION PROTEINS

For production of S-layer–based biosensors [21], affinity microparticles [22], and solid-phase immunoassays [23–25], functional groups in the S-layer lattice were exploited as covalent binding sites for biologically active macromolecules, such as enzymes, antibodies, or ligands. As alternatives to the existing technology, namely, immobilization by chemical methods, genetic approaches are particularly attractive for incorporation of functional peptide sequences into S-layer proteins, which have to be done at positions that do not interfere with their self-assembly properties and interaction with SCWP. To guarantee that the integrated or fused functional sequence remains located on the outer surface of the S-layer lattice and available for further binding reactions, the specific interactions with the SCWP is used to achieve an oriented binding of S-layer fusion proteins on artificial supports.

By the fusion of streptavidin to the S-layer protein SbsB of *Geobacillus stearothermophilus* PV72/p2, new templates for nanopatterned molecular arrays and building blocks for nanobiotechnology have been generated [26]. The fusion proteins and streptavidin were produced independently in *E. coli*, isolated and mixed to refold heterotetramers of 1:3 stoichiometry (Fig. 3). Self-assembled chimeric S-layers could be performed in suspension, on liposomes, silicon wafers, and SCWPs containing cell wall fragments. The
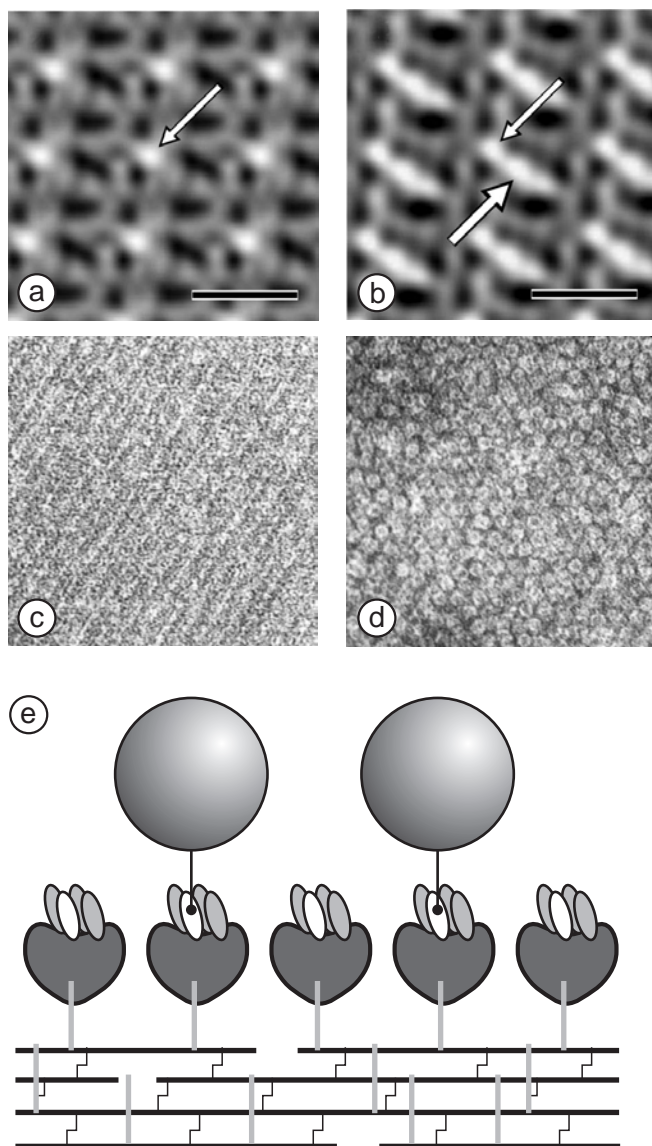
**Figure 3.** Digital image reconstructions from transmission electron micrographs of negatively stained preparations of *Geobacillus stearothermophilus* PV72/p2 (SbsB) (a) and streptavidin S-layer fusion protein (S1)3S1B1 (b). The region of highest protein mass in the SbsB lattice is the SLH-domain (a, thin arrow). In the lattice of the fusion protein, streptavidin showed up as additional protein mass (b, thick arrow) attached to the SLH-domain. Bars, 10 nm. Cell wall fragments carrying a chimeric S-layer formed by the fusion protein BS1(S1)3 (c) were capable of binding biotinylated ferritin (d), Bars, 100 nm. The lattice of bound ferritin molecules resembles the underlying S-layer lattice. The cartoon in (e) shows the orientation of BS1(S1)3 after SLH-enabled self-assembly with the streptavidin carrying outer face of the S-layer exposed. Self-assembly was enabled by the specific interaction between an accessory cell wall polymer that is part of the cell wall of *G. stearothermophilus* PV72/p2 and the SLH-domain of the fusion protein. Reprinted with permission from [26], D. Moll et al., *Proc. Natl. Acad. Sci. USA* 99, (2002). © 2002, National Academy of Sciences.

two-dimensional protein crystals displayed streptavidin in defined, repetitive spacing and were capable of binding D-biotin and biotinylated proteins in a regular fashion (Fig. 3). Therefore, the chimeric S-layer can be used as a

self-assembling, nanopatterned molecular affinity matrix to arrange biotinylated compounds on a surface.

In a further example, the *sbpA* gene encoding the S-layer protein SbpA of *B. sphaericus* CCM2177 was sequenced, cloned, and expressed in *E. coli* [27]. As a C-terminally truncated form revealed an improved accessibility compared to the recombinant SbpA, the chimeric gene encoding an S-layer fusion protein comprising the sequence of Bet v1, the major birch pollen allergen, was cloned and expressed in *E. coli*. The SbpA/Bet v1 fusion proteins self-assembled to regularly structured protein lattices. The functional sequences are aligned at a predefined distance in the nanometer range on the outermost surface of the S-layer lattice and therefore remain available for further binding reactions (e.g., with antibodies directed to Bet v1). These specific features of S-layer fusion proteins imply a considerable application potential as patterning elements and as nanostructures as required for biochip developments, proteomics, or genomics.

## 5. S-LAYER MONOLAYER FORMATION ON SOLID SURFACES

One of the most remarkable properties of isolated S-layer proteins is their capability to reassemble into monomolecular arrays in suspension, at the liquid-air interface, solid surfaces, floating lipid monolayers, and on liposomes (for review see [1–5]).

An important key to the fabrication of highly ordered functional arrays of nanoparticles and functional molecules lies in the development of suitable templates for spatially controlled particle deposition. S-layer proteins seem to be perfectly suited for this purpose since they have the intrinsic property to reassemble into two-dimensional arrays at various surfaces, including silicon, metals, and polymers. Functional groups are repeated (with the periodicity of the S-layer lattice) at a distance of approximately 10 nm, leading to regular arrays (superlattices) of bound functional molecules and particles [2, 3].

Crystal growth at interfaces, such as the liquid-solid interface, starts at several nucleation sites and proceeds in plane until the front edges of the growing crystalline areas meet [28, 29]. In this way, a closed mosaic of crystalline domains is formed. Nucleation points may be either protomers, oligomers, or small self-assembly products adsorbed from the solution. Size and orientation of the crystalline domains are mainly determined at a very early stage in the process of crystal formation by the lateral density and orientation of the nucleation points. It is assumed that a higher mobility of the proteins will lead to larger crystalline domains since the chance of an S-layer protein to contribute to an already existing domain is higher. Depending on the bacterial strain from which the S-layer was derived and the surface properties of the substrate used, an average patch size of individual crystalline domains of up to 20 $\mu$m in diameter may be obtained. The reciprocal influence of the surface properties of the solid support and the S-layer proteins determines which S-layer face (inner or outer face) will be attached to the support. This is a consequence of the asymmetry in the physicochemical surface properties of S-layer proteins. For

example, the S-layer protein SbsB of *Geobacillus stearother-mophilus* PV72/p2 forms monolayers with individual areas larger than 10 $\mu$m in diameter on silicon surfaces within 4 hours, whereas on gold the recrystallization takes much longer and the size of the monocrystalline patches is much smaller. Despite the different recrystallization behavior on solid surfaces ($SiO_2$ or Au), in both cases, the S-layer lattice of SbsB was attached with its outer surface to the substrate. In a similar way, S-layer protein SbpA from *Bacillus sphaericus* CCM2177 forms extended crystalline domains on hydrophilic silicon surfaces (patch size up to 5 $\mu$m in diameter), while only small patches are found on hydrophobic ones (patch size ca. 500 nm in diameter) (Györvary, unpublished results). Furthermore, accurate control of chemical composition of the subphase (e.g., pH, ion content, and ion concentration), temperature, and recrystallization time are important for obtaining large scale coherent S-layer domains. For example, the S-layer protein SbsB requires a pH of 4.1, while SbpA needs a pH of 9.0 and calcium in the subphase [29, 30].

Recently, different types of genetically engineered S-layer proteins were investigated with respect to their recrystallization behavior on solid surfaces (Györvary et al., unpublished results). These studies are particularly important since genetically modified S-layer proteins incorporating functional domains will play a key role in the specific and regular binding of appropriately functionalized nanoparticles [26]. Based on the results from the recrystallization experiments with wild-type S-layer proteins, it has to be decided where functional domains (e.g., binding regions of streptavidin) have to be inserted in the polypeptide chain. For example, from six streptavidin-SbsB heterotetrameric fusion protein constructs only one retained the capability of forming monocrystalline domains (patch size of ca. 400 nm in diameter) on silicon wafers. An alternative approach for inducing crystallization of S-layer proteins in an appropriate orientation with respect to solid supports or lipid films induces binding or adsorption of SCWP on surfaces and interfaces (see Section 3 on SCWP).

## 6. S-LAYER TEMPLATING OF NANOPARTICLE ARRAYS

Current state-of-the-art methods for self-assembly of nanoparticle arrays that generally involve bifunctional linkers, molecular recognition, or Langmuir–Blodgett techniques, do not offer the control and flexibility of the S-layer systems. The S-layer approach features adjustable lattice constants and control over template surface properties by chemical or genetic modifications [1–5] (Fig. 4).

The first approach in using S-layers as lithographic templates in the formation of ordered nanoparticle arrays was developed by Douglas and Clark [31]. In a three-step process, S-layer fragments of *Sulfolobus acidocaldarius* were deposited on a smooth carbon surface, metal coated by evaporation (1 nm thick Ta/W), and finally thinned by ion milling. Under ion bombardment, 15 nm diameter holes appeared in the protein-metal structure resembling the hexagonal lattice symmetry with a spacing of 22 nm. Subsequently, in a similar approach, a nanostructured titanium
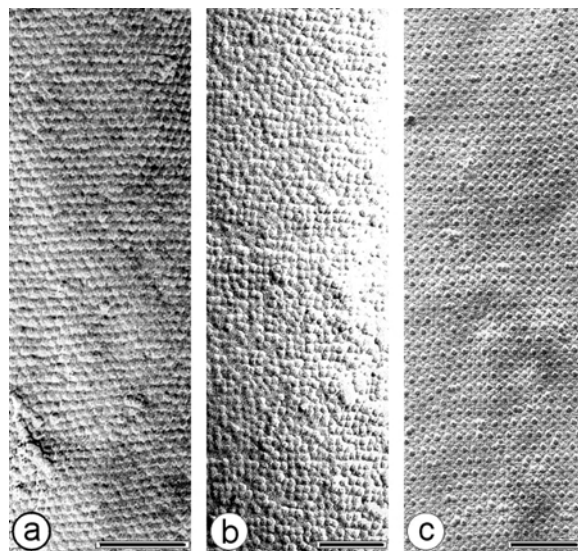


**Figure 4.** Freeze-etched preparations showing ferritin molecules bound by (a, b) covalent or (c) electrostatic interactions to S-layer lattices with different lattice symmetries and spacing. The regularly arranged ferritin molecules (12 nm diameter) resemble the underlying S-layer lattice. Bar in (a) and (b), 100 nm; bar in (c) 200 nm. Reprinted with permission from [2], U. B. Sleytr et al., "Supramolecular Polymerization" (A. Ciferri, Ed.), p. 177. Marcel Dekker, New York, 2000. © 2000, Marcel Dekker.

oxide layer with 10 nm pores was derived after coating S-layer fragments deposited on a smooth graphite surface [32]. Recently, the same group used low-energy "electron enhanced etching" to pattern the surface properties of silicon through the regularly arranged pores of the S-layer [33]. After etching and removal of the S-layer, the resulting structure was oxidized in an oxygen plasma yielding a regular array of etched holes with an 18 nm diameter. In the final step, evaporation of titanium onto the surface led to the formation of an ordered array of metal clusters. In a similar approach using argon-ion etching the S-layer of *Deinococcus radiodurans* was used for patterning ferromagnetic films [34]. A uniform hexagonal pattern of 10 nm wide dots and lattice constants of 18 nm was fabricated from 2.5 nm-thick sputter-coated Co, FeCo, Fe, FeNi, and NiFe films.

More recently, wet chemical processes were developed for the fabrication of metallic and semiconducting nanoparticle arrays using S-layers as templates [35–38]. In a first approach, self-assembly products from the S-layer protein of *Geobacillus stearothermophilus* NRS2004/3a variant 1 and *Bacillus sphaericus* CCM2177 were used for biocrystal templating of CdS superlattices [35]. Addition of a Cd(II) solution followed by slow reaction with hydrogen sulfide ($H_2S$) resulted in site-specific nucleation in the pore regions producing organized arrays of CdS nanoparticles. These experiments were repeated with the S-layer protein from *Bacillus sphaericus* CCM2177 recrystallized as monolayers on silicon wafers. After introduction of thiol groups on the S-layer surface, the protein structure was used as template for the precipitation of a tetrachloroauric (III) acid solution [36] (Fig. 5). Reduction of the gold (Au(III)) was either
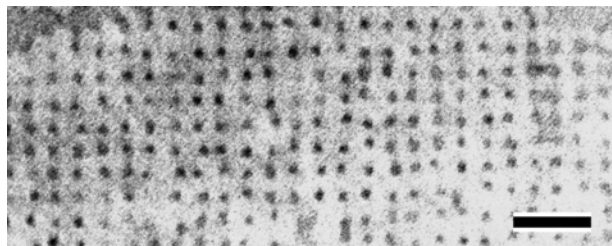
**Figure 5.** Transmisson electron micrographs of gold nanoparticles (5 nm diameter) formed in the pores of the square lattice of the S-layer of *Bacillus sphaericus* CCM2177 by wet chemistry. The S-layer has square lattice symmetry and a lattice constant of 13.1 nm. Bar, 50 nm.

performed by exposing the metalized S-layer to an electron beam in a transmission electron microscope or by slow reaction with $H_2S$. Gold nanoparticles with diameters of 4–5 nm were formed. Transmission electron microscopical studies in combination with digital image processing demonstrated that the metal nanoparticles had been formed in the pore region of the S-layer. As determined by electron diffraction, the gold nanoparticles were crystalline (cubic lattice symmetry) but in the long-range order not crystallographically aligned. The wet chemical approach was also used in our group in the precipitation of palladium, nickel, platinum, lead, and iron nanoparticle arrays (unpublished results). Wet chemistry was also applied for producing platinum nanoparticles on the S-layer of *Sporosarcina ureae* [37–38]. One morphological unit of the S-layer lattice of *Sp. ureae* revealed seven Pt cluster sites with diameters of ca. 1.9 nm.

An alternative method for generating regularly arranged nanoparticles arrays on S-layers is based on the binding of preformed standardized nanoparticles. Based on the work on binding biomolecules, such as enzymes or antibodies, onto S-layers (Fig. 4) it has already been demonstrated that gold or CdSe nanoparticles can be electrostatically bound in regular arrangements on S-layers [39, 40] (Fig. 6). The formation of superlattices was possible due to the repetitive arrangement of functional groups such as carboxylic acid, hydroxyl, and amino groups. The nanoparticles were either negatively charged due to surface citrate ions or positively charged due to surface capping with poly-L-lysine.
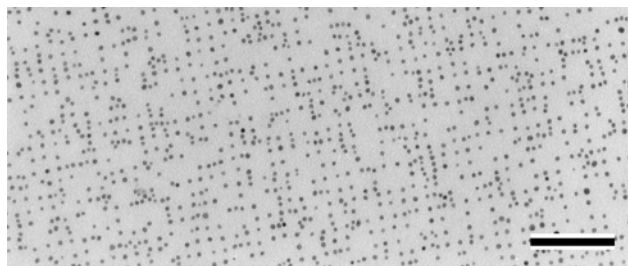


**Figure 6.** Transmission electron micrograph of preformed gold nanoparticles (5 nm diameter) regularly bound on the square lattice of the S-layer of *Bacillus sphaericus* CCM2177. Bar, 100 nm.

# 7. SPATIAL CONTROL OF THE S-LAYER REASSEMBLY

While S-layer protein templates allow a precise deposition of nanoparticles with spatial resolution on the molecular scale, it is also necessary to spatially control the assembly of S-layers within (sub)micrometer resolution on the substrate. This will allow the deposition of nanoparticle arrays as functional units on target areas with micrometer scale spacing. This may be especially useful when hybrid micro-nanoelectronic structures are developed. To approach this task, inexpensive conventional optical lithography [41] and soft lithography (micromoulding) has already been utilized.

Deep ultraviolet radiation (ArF; wavelength = 193 nm) was used to pattern monolayers of the S-layer protein of *Bacillus sphaericus* CCM2177 recrystallized on silicon wafers (Fig. 7). The S-layer was ablated from the silicon surface at the exposed regions but retained its crystalline and functional integrity in the unexposed areas. Subsequently, the remaining unexposed S-layer areas could be used to bind functional molecules or nanoparticles. For using patterned S-layers as nanonatural resists, the S-layer was reinforced for subsequent reactive ion-etching by silylation.

Micromoulding in capillaries was also used for spatially controlling the recrystallization of S-layer proteins on silicon
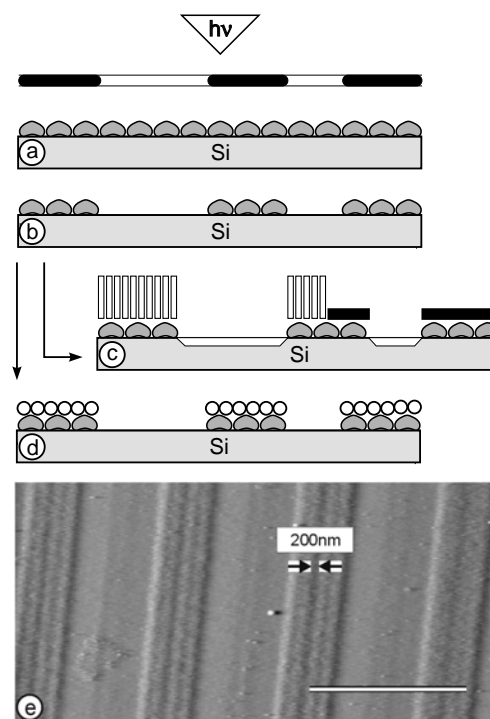


**Figure 7.** Schematic drawing of patterning S-layer protein monolayers on silicon substrates by optical lithography. A microlithographic mask is brought in direct contact with the S-layer (a). Upon exposure to ArF excimer laser irradiation the S-layer is removed in the exposed regions but remains unaffected in the unexposed areas (b). The remaining S-layer may either be used as an ultra high resolution resist after enhancement by a metallization procedure (c) or for binding molecules and nanoparticles (d). Scanning force microscopical image of a patterned S-layer (e), Bar, 3 $\mu$m. Reprinted with permission from [1], U. B. Sleytr et al., *Angew. Chem. Int. Ed.* 38, 1034 (1999). © 1999, Wiley-VCH.

wafers. For this approach, a poly(dimethylsiloxane) (PDMS) mould was placed on a silicon wafer and the empty channels were filled with S-layer protein solution. Subsequently, the PDMS mould was removed after a defined recrystallization time and a network of S-layer protein monolayers was obtained [42].

## 8. LIPID MEMBRANES

A fascinating intrinsic feature of S-layer proteins is the possibility to self-assemble the isolated constituent protein subunits and oligomeric precursors on liquid/lipid interfaces like Langmuir films, and on planar and spherical bilayer lipid membranes to form closed crystalline S-layer lattices [43]. This section focuses on the formation and application potential of these composite structures mimicking the supramolecular assembly of archaeal cell envelope structures (Fig. 8a) composed of a cytoplasmic membrane and a closely associated S-layer [44, 45]. In this biomimetic architecture (Fig. 8b) either a tetraether lipid monolayer or a phospholipid mono- or bilayer replaces the cytoplasmic membrane and bacterial S-layer proteins are recrystallized on one or both sides of the lipid film [3, 4, 43]. The aim of this biomimetic approach is to reinforce the fragile lipid membranes [46–49], but retaining its fluidity and also isolating structural and dynamic properties [50–56]. Since a great variety of biological processes are membrane-mediated, there has always been lively interest in the meso- and macroscopic reconstitution of biological membranes.

Particularly functional integral and peripheral membrane proteins have a broad potential for biomimetic, biotechnological, and bioanalytical applications.

Langmuir lipid films [57–58], the most simple model lipid membranes, are very suitable to study the recrystallization process of S-layer subunits since the charge and size of the lipid head groups and the phase state of the lipid layer at the air/water interface can be reproducibly controlled (Fig. 9a). Moreover, the mutual influence of the S-layer lattice and the lipid monolayer can be investigated in great detail. Generally, the recrystallization of S-layer proteins forming a closed monolayer on phospholipid films depends on (1) the phase state of the lipid film; (2) the nature of the lipid head group (size, polarity, and charge); and (3) the ionic content and pH of the subphase [59–60].

The binding force between exposed domains on the S-layer protein and certain lipid head groups is primarily electrostatic interaction. Large, closed S-layer monolayers could be obtained on lipid films with positively charged and zwitterionic head groups [60]. In contrast, S-layer proteins crystallized poorly under most lipids with negatively charged



**Figure 8.** Schematic illustration of (a) an archaeal cell envelope structure composed of the cytoplasma membrane with integral membrane proteins and an S-layer lattice integrated into the cytoplasma membrane. (b) Copying this supramolecular architecture, biomimetic membranes have been generated. The cytoplasma membrane is replaced by a phospholipid bilayer or a membrane-spanning (tetraether) lipid monolayer and bacterial S-layer proteins are crystallized from the subphase to form a closed lattice on the lipid film. Subsequently, integral membrane proteins can be reconstituted in the composite S-layer-supported lipid membrane. Reprinted with permission from [4], U. B. Sleytr et al., *Progr. Surf. Sci.* 68, 231 (2001). © 2001, Elsevier Science.



**Figure 9.** Schematic illustrations of lipid films generated by different procedures and the crystallization of S-layer protein, which has been injected into the subphase. A coherent S-layer lattice can be generated on (a) phospholipid or tetraetherlipid monolayers floating on the air/subphase interface; (b) spontaneously self-assembled spherical phospholipid bilayer membranes (liposomes); and (c) a phospholipid bilayer spanning a Teflon aperture that separates two compartments filled with subphase. On the right-hand-side, a TEM image of each composite S-layer/lipid membrane is given. The bar in the TEM-images represents 100 nm. Modified with permission from [4], U. B. Sleytr et al., *Progr. Surf. Sci.* 68, 231 (2001). © 2001, Elsevier Science.

head groups. The crystallization process could be facilitated by adding a small amount of positively charged lipid analogue [61] and surfactants like hexadecylamine [50, 62] to the zwitterionic lipids.

The influence of an attached S-layer lattice on the hydrophobic part of the lipid film was investigated [59]. At a low surface pressure of the lipid monolayer (∼5 mN/m), the protein crystallization affected the order of the alkane chains and drove the fluid lipid into a state of higher order. Injection of S-layer protein underneath a condensed monolayer (∼28 mN/m) resulted only in a slight increase in the segmental alkyl chain order [52–54, 59]. However, the results provided definite evidence that the S-layer protein did not interpenetrate the hydrophobic section of the lipid monolayer.

By contrast to the hydrophobic part, a partial insertion of domains on the S-layer protein into the head group region of the lipid monolayer has been observed [52–54]. Presumably, one amino acid side chain per three to four lipids dips into the lipid head group region at least to the phosphate moieties and probably further beyond. To accommodate the interpenetrating amino side chains, the orientation of the lipid head groups was tilted toward the surface normal. It is not known whether the amino acid side chains interpenetrated the lipid monolayer rather homogeneously, or, more likely, peptides might cluster within the polar part of the lipid membrane. In the latter case, some lipid head groups directly associated with amino acid side chain groups were strongly affected while others, for example, located at the membrane region spanning the pore of the S-layer, were not [52].

## 9. LIPOSOMES

Lipid molecules spontaneously self-assemble in an aqueous environment forming closed, spherical structures called liposomes [63–65]. In order to enhance the stability of liposomes and provide a biocompatible outermost surface structure for controlled immobilization, isolated S-layer proteins were crystallized on the outer shell of vesicles (Fig. 9b) [55, 62, 66–68]. These S-layer–coated liposomes are biomimetic structures resembling the supramolecular construction principle of virus envelopes and cell wall envelope structures of archaea. The crystallization of S-layer proteins resulted in a completely covered surface and did not affect the morphology of the liposomes [62, 68]. In order to enhance the stability of liposomes composed of a single lipid bilayer and provide a biocompatible outermost surface structure, S-layer lattices are recrystallized on their surface. Specific physicochemical surface properties and functions of S-layer–coated liposomes are introduced by crosslinking and/or chemical modifications of S-layer lattices, by immobilization of functional molecules or by using genetically engineered S-layer fusion proteins. The potential of S-layer–coated liposomes is currently exploited for new drug delivery and cell targeting vehicles in medicine, adjuvants in vaccination, signal enhancers carriers in medical diagnostics as well as in analytical biochemistry, and solubilizers for various ingredients [2–5].

## 10. PLANAR LIPID MEMBRANES

Lipid bilayers as relevant models for biological membranes have improved the knowledge on structure and function of cell envelopes. It became evident that a stabilization of lipid bilayers is imperatively necessary to utilize the function of cell membrane components for practical applications, as typically free-standing bilayer lipid membranes (BLMs) only survive for minutes to hours and are very sensitive toward vibration and mechanical shocks [48–49, 69]. S-layer proteins can be exploited as supporting structures for BLMs (Fig. 9c), since they stabilize the lipid film and largely retain their physical features (e.g., thickness, fluidity).

An uniform hydrostatic pressure has been applied to unsupported and S-layer–supported lipid membranes [70]. Unsupported lipid membranes, independent from which side pressurized and S-layer–supported lipid membranes pressurized from the lipid-faced side revealed a pronounced increase in capacitance. A maximal hydrostatic pressure gradient of 11 N/m$^2$ resulted in an almost doubling of the capacitance of the bilayers. By contrast, the S-layer–supported lipid membrane pressurized from the protein-faced side revealed only a minute increase in capacitance reflecting only minor pressure induced area expansion. In this context, it is interesting to note that mechano-sensitive ion channels like the family of epithelial Na$^+$-channels (ENaCs) can be activated by a hydrostatic pressure difference [71, 72]. Thus, S-layer–supported lipid membranes may be used to investigate the water flow-induced activation of ENaCs by excluding at the same time a curvature-induced mechanical activation if the composite structure is pressurized from the protein-faced side.

Up to now, the membrane-active peptides alamethicin, gramicidin, and valinomycin and the pore-forming protein α-hemolysin have been reconstituted in planar S-layer–supported lipid membranes [73–75]. All membrane-active molecules exhibited the same ion-selectivity and channel conductance, respectively, compared with the reconstitution in corresponding freestanding lipid membranes. But most important, functionalized S-layer/lipid structures showed the advantage of an enhanced long-term stability [73–74]. In addition, the gating of single α-hemolysin pores reconstituted in composite S-layer/lipid membranes could be performed [75].

## 11. S-LAYER ULTRAFILTRATION MEMBRANE (SUM)-SUPPORTED LIPID MEMBRANES

The following two subsections describe the most promising methods to attach lipid membranes on porous or solid supports (Fig. 10) in order to generate attractive membrane protein-based devices for technical applications. In general, lipid membranes generated on a porous support combine the advantage of possessing an essentially unlimited ionic reservoir on each side of the bilayer lipid membrane and easy manual handling. However, the surface properties of porous supports, like roughness or great differences in pore size, significantly impaired the stability of attached BLMs. In this section, the strategy to use an S-layer ultrafiltration
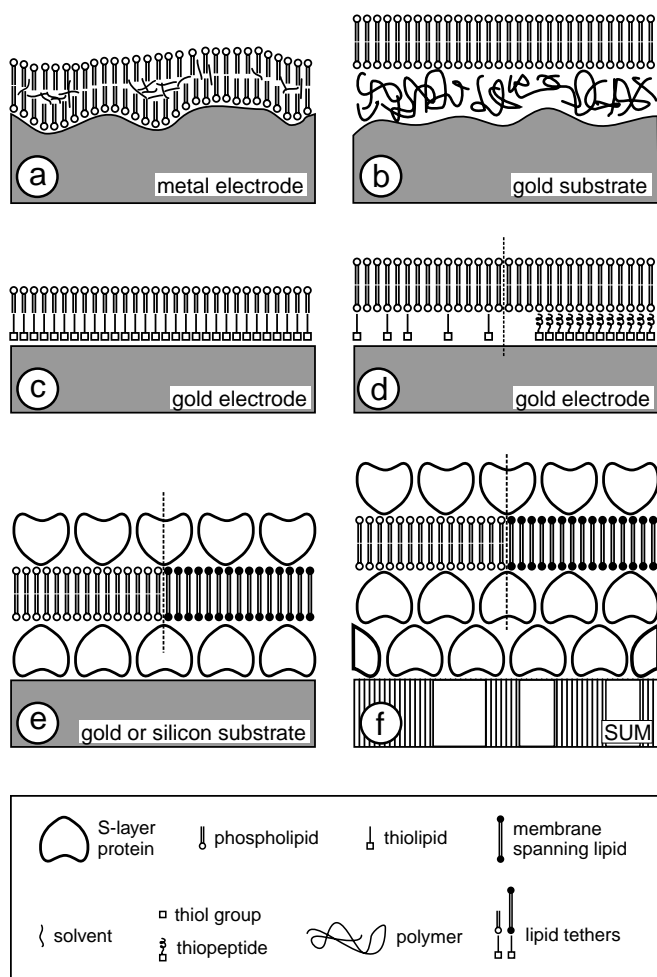
**Figure 10.** Schematic drawings illustrating the concept of solid-supported lipid membranes. In (a), a painted lipid membrane was generated on a metal electrode. The roughness of the metal surface causes a considerable amount of solvent in-between the two phospholipid leaflets. In (b), a soft polymer cushion (actual thickness is much larger than that of the lipid bilayer) is present as separating, biocompatible layer. In (c), the generation of the lipid bilayer makes use of the strong chemisorption of thiolipids to gold. The second leaflet of phospholipids was transferred from a Langmuir trough or by vesicle fusion onto the thiolipid monolayer. (d) The increase of the ionic reservoir between the membrane and the gold electrode can be accomplished by the addition of tether lipid molecules or thiopeptides. (e) As an alternative, an S-layer is located between the solid support and the lipid layer. Optionally, the external leaflet of the lipid bilayer can be stabilized by the attachment of an S-layer cover. In (f), the lipid bilayer has been generated on the S-layer on the surface of an S-layer ultrafiltration membrane. Again, the external leaflet of the lipid bilayer can be stabilized by an attached S-layer cover. Reprinted with permission from [4], U. B. Sleytr et al., *Progr. Surf. Sci.* 68, 231 (2001). © 2001, Elsevier Science.

membrane (SUM) with the S-layer as a stabilizing and biochemical layer between the BLM and the porous support is described (Fig. 10f). S-layer ultrafiltration membranes are isoporous structures with very sharp molecular exclusion limits and were manufactured by depositing S-layer–carrying cell wall fragments under high pressure on commercial microfiltration membranes (MFMs) with an average pore

size of approximately 0.4 $\mu$m [76–78]. After deposition, the S-layer lattices are crosslinked leading to a coherent smooth surface ideally suited for depositing lipid membranes. Due to the additional S-layer cover, SUMs revealed a smoother surface than MFMs.

Composite SUM-supported bilayers are tight structures with breakdown voltages well above 500 mV during their whole life-time of about 8 hours [79]. For a comparison, lipid membranes on a plain nylon MFM revealed a lifetime of about 3 hr. When voltage ramps were applied, the BLM on the MFM ruptured at a magnitude of about 210 mV. Specific capacitance measurements and reconstitution experiments revealed that the lipid membrane on the SUM consisted of two layers as the pore-forming protein $\alpha$-hemolysin could be reconstituted into lytic channels. For the first time, opening and closing behavior of even single $\alpha$HL pores could be measured with membranes generated on a porous support. In contrast, no pore formation was observed with BLMs generated on the MFM [79]. The present results indicated that the S-layer lattices of the SUM represent a water-containing layer for the closely attached lipid bilayer and provide also a natural environment for protein domains protruding from the membrane.

The main phospholipid (MPL) of *Thermoplasma acidophilum*, a membrane-spanning tetraether lipid, has also been transferred on a SUM by a modified Langmuir–Blodgett technique [80]. This is a very easy and reproducible method to generate supported lipid membranes. Again, SUM-supported MPL membranes allowed reconstitution of functional molecules, as proven by gramicidin, and measurements on single pores could be performed. S-layer ultrafiltration membrane-supported MPL membranes showed a lifetime of $8.3 \pm 2.9$ hr. An additional monomolecular S-layer protein lattice, recrystallized on the lipid-faced side, increased the lifetime significantly to $21.2 \pm 3.1$ hr [80]. In addition, the thermal, chemical, and long-term stability of tetraether lipids [81–83] and mechanical stability of SUM-supported membranes [79] have attracted interest in their potential with respect to biotechnological applications such as membrane protein-based biosensors for DNA-sequencing and high throughput screening and may finally end up in the lab-on-a-chip technology [84–87].

## 12. SOLID-SUPPORTED LIPID MEMBRANES

Solid-supported membranes were developed in order to overcome the fragility of freestanding BLMs, but also to enable biofunctionalization of inorganic solids (e.g., semiconductors, gold-covered surfaces) for the use at sensing devices [88–90]. Various types of solid-supported lipid membranes are reported in the literature (Fig. 10a–d) [43, 91–96]. However, they often show considerable drawbacks as there is a limited ionic reservoir at the side facing the solid support, membranes often appear to be leaky (noninsulating), and large domains protruding from the membrane may become denatured by the inorganic support. Again, S-layer proteins have been studied to elucidate their potential as stabilizing and separating ultrathin layers, which also maintains the structural and dynamic properties of the lipid membranes (Fig. 10e).

Silicon substrates have been covered by a closed S-layer lattice and bilayers were deposited by the Langmuir–Blodgett technique [57, 58, 97]. Lateral diffusion of fluorescently labeled lipid molecules in both layers have been investigated by fluorescence recovery after photobleaching studies [51]. In comparison with hybrid lipid bilayers (lipid monolayer on alkylsilanes) and lipid bilayers on dextran, the mobility of lipids was highest in S-layer–supported bilayers. Most important, the S-layer cover could prevent the formation of cracks and other inhomogenities in the bilayer [51]. These results have demonstrated that the biomimetic approach of copying the supramolecular architecture of archaeal cell envelopes opens new possibilities for exploiting functional lipid membranes at meso- and macroscopic scale. Moreover, this technology has the potential to initiate a broad spectrum of developments in many areas like sensor technology, diagnostics, (nano)biotechnology, electronic or optical devices, and high throughput screening for drug discovery.

## 13. CONCLUSIONS

Basic and applied S-layer research has demonstrated that nature provides most elegant examples for nanometer size, molecular self-assembly systems. The remarkable intrinsic features of S-layer proteins and the possibility for combining S-layer lattices with other functional molecules (e.g., proteins, lipids, glycans, and nucleic acids) in a spatial predictable way make them unique structural and patterning elements in molecular nanotechnology and biomimetics. The infrastructure needs for nanobiotechnology and, in particular, for S-layer technology are similar to those for other fields: multiuser facilities providing access to specialized technologies, funding mechanisms, and organization structures encouraging multidisciplinary teams for breaking new grounds.

## GLOSSARY

**Secondary cell wall polymer (SCWP)** The rigid cell wall of Gram-positive bacteria contains, beside peptidoglycan, large amounts of accessory (secondary) cell wall polymers (SCWPs) composed of either teichoic acids, teichuronic acids, lipoteichoic acids, or lipoglycans.

**S-layer** Bacterial surface layer. Crystalline bacterial cell surface layers (S-layers) are one of the most common outermost cell envelope components of prokaryotic organisms (archaea and bacteria).

**S-layer fusion protein** Genetically engineered functionalized protein consisting of a (truncated) S-layer protein and a (biochemical) functionality fused to it either at the N- or C-terminal end.

**S-layer ultrafiltration membrane (SUM)** Ultrafilter membranes consisting of a porous microfiltration membrane and a complete S-layer coating attached to it. The effective pore size is defined by the pores in the S-layer. Cut-off in the ultrafiltration range.

**Solid-supported lipid membrane** A lipid membrane often functionalized by incorporated or attached biochemically active molecules attached to a solid support.

## REFERENCES

1. U. B. Sleytr, P. Messner, D. Pum, and M. Sára, *Angew. Chem. Int. Ed.* 38, 1034 (1999).
2. U. B. Sleytr, M. Sára, and D. Pum, in "Supramolecular Polymerization" (A. Ciferri, Ed.), p. 177. Marcel Dekker, New York, 2000.
3. U. B. Sleytr, M. Sára, D. Pum, and B. Schuster, in "Nano-Surface Chemistry" (M. Rosoff, Ed.), p. 333. Marcel Dekker, New York, 2001.
4. U. B. Sleytr, M. Sára, D. Pum, and B. Schuster, *Progr. Surf. Sci.* 68, 231 (2001).
5. U. B. Sleytr, M. Sára, D. Pum, B. Schuster, P. Messner, and C. Schäffer, in "Biopolymers" (A. Steinbüchel and S. Fahnestock, Eds.), Vol. 7, p. 285, Wiley-VCH, Weinheim, 2002.
6. U. B. Sleytr and T. J. Beveridge, *Trends Microbiol.* 7, 253 (1999).
7. M. Sára and U. B. Sleytr, *J. Bacteriol.* 182, 859 (2000).
8. U. B. Sleytr, P. Messner, D. Pum, and M. Sára, in "Crystalline Bacterial Cell Surface Layer Proteins (S-Layers)" (U. B. Sleytr, P. Messner, D. Pum, and M. Sára, Eds.), p. 5. R. G. Landes Company, Austin, 1996.
9. T. J. Beveridge, *Curr. Opin. Struct. Biol.* 4, 204 (1994).
10. A. R. Archibald, in "Bacillus Subtilis and Other Gram-Positive Bacteria" (A. L. Sonnenshein, Ed.), p. 381. ASM Press, New York, 1993.
11. M. Sára, *Trends Microbiol.* 9, 47 (2001).
12. M. Sára and U. B. Sleytr, *J. Bacteriol.* 182, 859 (2000).
13. A. Lupas, H. Engelhardt, J. Peters, U. Santarius, S. Volker, and W. Baumeister, *J. Bacteriol.* 176, 1224 (1994).
14. R. D. Bowditch, P. Baumann, and A. A. Yousten, *J. Bacteriol.* 171, 4178 (1989).
15. S. Ebisu, A. Tsuboi, H. Takagi, Y. Naruse, H. Yamagata, N. Tsukagoshi, and S. Udaka, *J. Bacteriol.* 172, 1312 (1990).
16. H. Engelhardt and J. Peters, *J. Struct. Biol.* 124, 276 (1998).
17. N. Ilk, P. Kosma, M. Puchberger, E. M. Egelseer, H. F. Mayer, U. B. Sleytr, and M. Sára, *J. Bacteriol.* 181, 7643 (1999).
18. B. Kuen, A. Koch, E. Asenbauer, M. Sára, and W. Lubitz, *J. Bacteriol.* 179, 1664 (1997).
19. M. Lemaire, I. Miras, P. Gounon, and P. Beguin, *Microbiol.* 144, 211 (1998).
20. U. B. Sleytr, M. Sára, C. Mader, B. Schuster, and F. M. Unger, *Austrian Patent No. A* 409, 423 (2002).
21. D. Pum, M. Sára, and U. B. Sleytr, in "Immobilised Macromolecules: Application Potential" (U. B. Sleytr, P. Messner, D. Pum, and M. Sára, Eds.), p. 141. Springer-Verlag, London, 1993.
22. C. Weiner, M. Sára, and U. B. Sleytr, *Biotechnol. Bioeng.* 43, 321 (1994).
23. A. Breitwieser, S. Küpcü, S. Howorka, S. Weigert, C. Langer, K. Hoffmann-Sommergruber, O. Scheiner, U. B. Sleytr, and M. Sára, *BioTechniques* 21, 918 (1996).
24. A. Breitwieser, C. Mader, I. Sochor, K. Hoffmann-Sommergruber, W. Aberer, O. Scheiner, U. B. Sleytr, and M. Sára, *Allergy* 53, 786 (1998).

25. U. B. Sleytr and M. Sára, *Trends Biotechnol.* 15, 20 (1997).
26. D. Moll, C. Huber, B. Schlegel, D. Pum, U. B. Sleytr, and M. Sára, *Proc. Natl. Acad. Sci. USA* 99, 14646 (2002).
27. N. Ilk, C. Völlenkle, E. M. Egelseer, A. Breitwieser, U. B. Sleytr, and M. Sára, *Appl. Environ. Microbiol.* 68, 3251 (2002).
28. D. Pum, M. Weinhandl, C. Hödl, and U. B. Sleytr, *J. Bacteriol.* 175, 2762 (1993).
29. D. Pum and U. B. Sleytr, *Supramol. Sci.* 2, 193 (1995).
30. D. Pum and U. B. Sleytr, *Colloids and Surfaces A: Physicochem. Eng. Aspects* 102, 99 (1995).
31. K. Douglas and N. A. Clark, *Appl. Phys. Lett.* 48, 676 (1986).
32. K. Douglas, G. Devaud, and N. A. Clark, *Science* 257, 642 (1992).
33. T. A. Winningham, H. P. Gillis, D. A. Choutov, K. P. Martin, J. T. Moore, and K. Douglas, *Surf. Sci.* 406, 221 (1998).
34. M. Panhorst, H. Brückl, B. Kiefer, G. Reiss, U. Santarius, and R. Guckenberger, *J. Vac. Sci. Technol. B* 19, 722 (2001).
35. W. Shenton, D. Pum, U. B. Sleytr, and S. Mann, *Nature* 389, 585 (1997).
36. S. Dieluweit, D. Pum, and U. B. Sleytr, *Supramol. Sci.* 5, 15 (1998).
37. M. Mertig, R. Kirsch, W. Pompe, and H. Engelhardt, *Europ. Phys. J.* 9, 45 (1999).
38. W. Pompe, M. Mertig, R. Kirsch, R. Wahl, L. C. Ciachi, J. Richter, R. Seidel, and H. Vinzelberg, *Z. Metallkd.* 90, 1085 (1999).
39. S. R. Hall, W. Shenton, H. Engelhardt, and S. Mann, *Chem. Phys. Chem.* 3, 184 (2001).
40. E. Györvary, A. Schroedter, D. V. Talapin, H. Weller, D. Pum, and U. B. Sleytr, *J. Nanosci. Nanotechnol.* (submitted) (2003).
41. D. Pum, G. Stangl, C. Sponer, W. Fallmann, and U. B. Sleytr, *Colloids and Surfaces B: Biointerfaces* 8, 157 (1997).
42. E. S. Györvary, A. O'Riordan, A. Quinn, G. Redmond, D. Pum, and U. B. Sleytr, *Nanoletters*, in press.
43. B. Schuster and U. B. Sleytr, *Rev. Mol. Biotechnol.* 74, 233 (2000).
44. O. Kandler, in "Archaebacteria" (O. Kandler, Ed.), p. 149. Gustav Fischer Verlag, Stuttgart, 1982.
45. H. König, *Can. J. Microbiol.* 34, 395 (1988).
46. H. F. Knapp, W. Wiegräbe, M. Heim, R. Eschrich, and R. Guckenberger, *Biophys. J.* 69, 708 (1995).
47. X. Lu, A. Ottova-Leitmannova, and T. H. Tien, *Bioelectrochem. Bioenerg.* 39, 285 (1996).
48. T. H. Tien and A. L. Ottova, *J. Membr. Sci.* 189, 83 (2001).
49. M. Zviman and H. T. Tien, *Biosens. Bioelectron.* 6, 37 (1991).
50. B. Schuster, U. B. Sleytr, A. Diederich, G. Bähr, and M. Winterhalter, *Eur. Biophys. J.* 28, 583 (1999).
51. E. Györvary, B. Wetzer, U. B. Sleytr, A. Sinner, A. Offenhäusser, and W. Knoll, *Langmuir* 15, 1337 (1999).
52. M. Weygand, B. Wetzer, D. Pum, U. B. Sleytr, K. Kjaer, P. B. Howes, and M. Lösche, *Biophys. J.* 76, 458 (1999).
53. M. Weygand, M. Schalke, P. B. Howes, K. Kjaer, J. Friedman, B. Wetzer, D. Pum, U. B. Sleytr, and M. Lösche, *J. Mater. Chem.* 10, 141 (2000).
54. M. Weygand, K. Kjaer, P. B. Howes, B. Wetzer, D. Pum, U. B. Sleytr, and M. Lösche, *J. Phys. Chem. B* 106, 5793 (2002).
55. C. Mader, S. Küpcü, M. Sára, and U. B. Sleytr, *Biochim. Biophys. Acta* 1418, 106 (1999).
56. B. Wetzer, D. Pum, and U. B. Sleytr, *J. Struct. Biol.* 119, 123 (1997).
57. A. Zasadzinski, R. Viswanathan, L. Madson, J. Garnaes, and K. D. Schwartz, *Science* 263, 1726 (1994).
58. I. Langmuir and V. J. Schaefer, *J. Am. Chem. Soc.* 59, 1406 (1937).
59. A. Diederich, C. Hödl, D. Pum, U. B. Sleytr, and M. Lösche, *Colloids and Surfaces B: Biointerfaces* 6, 335 (1996).
60. B. Wetzer, A. Pfandler, E. Györvary, D. Pum, M. Lösche, and U. B. Sleytr, *Langmuir* 14, 6899 (1998).
61. R. Hirn, B. Schuster, U. B. Sleytr, and T. M. Bayerl, *Biophys. J.* 77, 2066 (1999).
62. S. Küpcü, M. Sára, and U. B. Sleytr, *Biochim. Biophys. Acta* 1235, 263 (1995).
63. D. Papahadjopoulos, *Ann. N. Y. Acad. Sci.* 308, 1 (1978).
64. D. D. Lasic, in "Structure and Dynamics of Membranes" (R. Lipowsky and E. Sackmann, Eds.), p. 491. Elsevier, Amsterdam, 1995.
65. D. D. Lasic. *Am. Sci.* 80, 20 (1992).
66. C. Mader, S. Küpcü, U. B. Sleytr, and M. Sára, *Biochim. Biophys. Acta* 1463, 142 (2000).
67. T. Hianik, S. Küpcü, U. B. Sleytr, P. Rybár, R. Krivánek, and U. Kaatze, *Coll. Surf. A* 147, 331 (1999).
68. S. Küpcü, K. Lohner, C. Mader, and U. B. Sleytr, *Molec. Membrane Biol.* 15, 69 (1998).
69. B. Raguse, V. Braach-Maksvytis, B. A. Cornell, L. G. King, P. D. J. Osman, R. J. Pace, and L. Wieczorek, *Langmuir* 14, 648 (1998).
70. B. Schuster and U. B. Sleytr, *Biochim. Biophys. Acta* 1563, 29 (2002).
71. I. I. Ismailov, V. G. Shlyonsky, and D. J. Benos, *Proc. Natl. Acad. Sci. USA* 94, 7651 (1997).
72. M. S. Awayda, I. I. Ismailov, B. K. Berdiev, and D. J. Benos, *APStracts* 2, 49 (1995).
73. B. Schuster, D. Pum, and U. B. Sleytr, *Biochim. Biophys. Acta* 1369, 51 (1998).
74. B. Schuster, D. Pum, O. Braha, H. Bayley, and U. B. Sleytr, *Biochim. Biophys. Acta* 1370, 280 (1998).
75. B. Schuster and U. B. Sleytr, *Bioelectrochem.* 55, 5 (2002).
76. M. Sára and U. B. Sleytr. *J. Bacteriol.* 169, 2804 (1987).
77. S. Weigert and M. Sára, *J. Membrane Sci.* 106, 147 (1995).
78. S. Weigert and M. Sára, *J. Membrane Sci.* 121, 185 (1996).
79. B. Schuster, D. Pum, M. Sára, O. Braha, H. Bayley, and U. B. Sleytr, *Langmuir* 17, 499 (2001).
80. B. Schuster, S. Weigert, D. Pum, M. Sára, and U. B. Sleytr, *Langmuir*, in press.
81. M. G. L. Elfterink, J. G. de Wit, A. J. M. Driessen, and W. N. Konings, *Biochim. Biophys. Acta* 1193, 247 (1994).
82. C. Nicolini, *Biosens. Bioelectron.* 10, 105 (1995).
83. B. A. Cornell, G. Krishna, P. D. Osman, R. D. Pace, and L. Wieczorek, *Biochem. Soc. Trans.* 29, 613 (2001).
84. J. J. Kasianowicz, E. Brandin, D. Branton, and D. W. Deamer, *Proc. Natl. Acad. Sci. USA* 93, 13770 (1996).
85. T. Stora, J. H. Lakey, and H. Vogel, *Angew. Chem. Int. Ed.* 38, 389 (1999).
86. D. W. Deamer and M. Akeson, *Trends Biotechnol.* 18, 147 (2000).
87. H. Bayley and P. S. Cremer, *Nature* 413, 226 (2001).
88. E. Sackmann, *Science* 271, 43 (1996).
89. E. Sackmann and M. Tanaka, *Trends Biotechnol.* 18, 58 (2000).
90. B. A. Cornell, V. L. Braach-Maksvytis, L. G. King, P. D. Osman, B. Raguse, L. Wieczorek, and R. J. Pace, *Nature* 387, 580 (1997).
91. H. M. McConnell, T. H. Watts, R. M. Weis, and A. A. Brian, *Biochim. Biophys. Acta* 864, 95 (1986).
92. E. Kalb, S. Frey, and L. K. Tamm, *Biochim. Biophys. Acta* 1103, 307 (1992).
93. A. L. Plant, *Langmuir* 9, 2764 (1993).
94. S. Heyse, T. Stora, E. Schmid, J. H. Lakely, and H. Vogel, *Biochim. Biophys. Acta* 1376, 319 (1998).
95. D. P. Nikolelis, T. Hianik, and U. J. Krull, *Electroanalysis* 11, 7 (1999).
96. W. Knoll, C. W. Frank, C. Heibel, R. Naumann, A. Offenhäusser, J. Rühe, E. K. Schmidt, W. W. Shen, and A. Sinner, *Rev. Mol. Biotechnol.* 74, 137 (2000).
97. K. J. Blodgett, *J. Am. Chem. Soc.* 57, 1007 (1935).

# Molecular Planar Technology

## J. M. Köhler

*Institute for Physical High Technology, Jena, Germany*

## W. Fritzsche

*Technical University Ilmenau, Ilmenau, Germany*

## CONTENTS

## 1. INTRODUCTION

### 1.1. Development of Planar Technology

Planar technology represents a class of fabrication methods used in the development and production of electronic and other miniaturized devices. The whole computer industry, consumer electronics, and communication technology are currently based on chip devices made by planar technology. Planar technology also plays an important role in recent research developments in nanofabrication.

The main issue in planar technology is the use of planar surfaces as a working plane or at least as a reference plane for all operations (Fig. 1). The limitation to planar surfaces is the key prerequisite for precise positioning of single micro- or nanofabricated, structural, and/or functional elements in relation to each other and in relation to an outside coordinate system. In addition, the convention of an operation plane supports a series of important fabrication technologies, in which the control of the third dimension is critical for achieving high quality in processes (including lithographic operations like photolithography and electron beam lithography) and in detection procedures using microscopic imaging by light, particle beams, or scanning probes. The possibility to control not only the size and shape but also the coordinates of all produced microdevices as well as nanofeatures in relation to outside coordinate systems is the precondition of the construction of physical interfaces between functional elements of different micro- and nanodevices and conventional devices including interfaces between machines and people. Thus, well-defined coordinates enable us to integrate huge numbers of single micropatterned functional elements inside microdevices and to integrate sets of integrated microdevices like integrated circuits (ICs), sensors, and interfaces, for example, in hierarchically organized complex device systems.

Planar technology has its roots in traditional mechanical procedures, in which plane surfaces are produced or reproduced, such as mechanical planning. In addition to mechanical techniques, optical methods call for geometrical restriction to a planar reference surface. So the restrictions in the third dimension connected with the depth of optical focus have required the use of plane layers for light-sensitive films since the beginning of photography about 170 years ago. In photolithography, the use of a plane of optical focus in the exposure system has relied up to now on plane surfaces for the exposure of a photosensitive layer (e.g., in resist technologies in IC fabrication). The beginning of lithographic planar technology is connected with the development of art lithographs, of printed lithographs, and of printing technology in general.

The use of planar surfaces is strongly connected with film technology. The deposition and the patterning of films, particularly thin-film technology, allow the construction of devices composed of different materials by planar technology. In many cases of thin-film technology application, the vertical dimension of thin-film structures can be neglected in comparison with the lateral extension of a surface. In other cases, the plane surface is reconstructed after patterning of films by planarization techniques.

The preparation of plane surfaces for lithographic purposes started with the preparation of lithographic plates
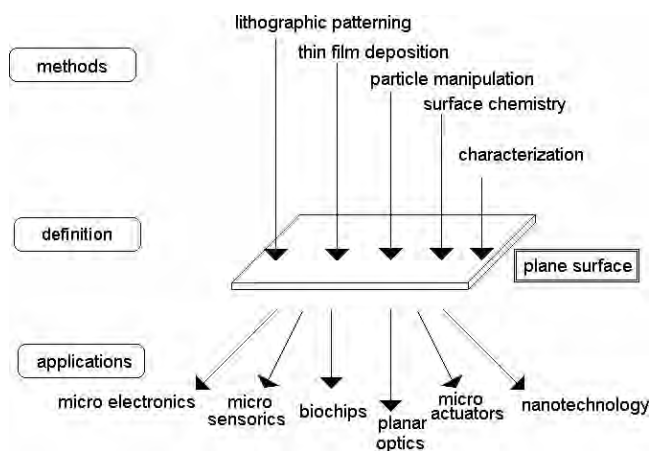
**Figure 1.** Planar technology as a fundamental principle for technological operations in lithographic micro- and nanofabrication.

by mechanical splitting of natural layered limestone. Alternatively, the mechanical preparation of plane and smooth surfaces was developed by different cutting, sawing, and polishing technologies. The plane surface of clean molten liquids is used in the fabrication of high-quality glass surfaces. Ultimate high-quality surfaces were obtained by splitting or sawing of single crystalline material along crystallographic planes with low Miller indices. This technique is used, for example, in the case of semiconductor single crystalline material like silicon or compound semiconductors. It is also practiced in the preparation of very smooth substrates for scanning probe techniques, in which mica is used because of its very good ability to separate along a crystal plane.

With increasing aspect ratios (ratio of height to width of lithographic pattern), an urgent need for technical methods of high-quality planarization evolved. In addition to planarization by spinning processes for resists and other polymeric materials, chemo-mechanical polishing (CMP) was developed as a procedure for the planarization of topographic microfeatures consisting of inorganic materials or covered by inorganic top layers.

Thin-film techniques are very essential for the buildup of micro- and nanodevices. Planar technology offers a powerful toolbox for the deposition of very different materials of homogeneous thickness on plane substrates. By techniques like chemical surface modification, spin-on deposition, evaporation, sputtering, reactive sputtering, chemical vapor deposition, galvanic film deposition, and molecular beam epitaxy, a material spectrum ranging from metals and alloys, semiconductors, and semiconductor compounds over different inorganic dielectric materials, piezoelectric materials to organic compounds, very different types of particular polymers are available. The typical thickness of thin films is in the range of about a few hundred nanometers up to a few micrometers. The homogeneity of thickness is better than 3% in most cases. The same techniques can also be used for the deposition of films with thicknesses in the range below 100 nm. Films of 10 to about 50 nm are particularly important for recent nanofabrication. Several techniques allow the preparation of homogenous films with a thickness of a few nanometers and in some cases down to one or a few atomic monolayers.

For the patterning of thin films, additive, subtractive, and lift-off-techniques are used. The basic methods of micropatterning were mainly developed in the context of microelectronic fabrication between about 1965 and 1980. Subtractive patterning by etching represents the most important group of patterning methods. Some wet etching techniques have been used for the characterization of semiconductor materials since the middle of the twentieth century. Dry etching methods like plasma etching (PE), sputter etching, reactive ion etching (RIE), ion beam etching (IBE), and reactive ion beam etching (RIBE) are preferentially used for the preparation of submicrometer and nanometer features (Fig. 2). Its application in the submicrometer and in the nanometer range dates mainly from the end of the 1970s. Under well-controlled conditions and in case of low aspect ratios, wet chemical etching techniques are also applied for the preparation of submicrofeatures and nanofeatures in thin films.

## 1.2. Molecular Methods in Traditional Micropatterning and Nanofabrication

Molecular materials and chemical processes involving inorganic as well as organic molecules already play an important role in conventional lithographic technologies. In film formation, chemical vapor deposition (CVD) techniques and plasma polymerization are typical examples of molecular methods. In CVD processes, molecular species are transported in the gaseous phase onto the substrate surface and chemically decomposed by physical activation processes releasing solid material at the surface. The by-products are gaseous and are removed through the gas phase. In addition to simple decomposition processes, interaction of different gas molecules takes place in many CVD processes, for example, for the formation of dielectrical layers containing silicon, like silicon oxide or silicon nitride made by reaction for halogen silanes or low-molecular-weight siloxanes with oxygen or ammonia. Organic films are made by surface polymerization processes. For this purpose, organic monomers are deposited through the gas phase onto a substrate surface and polymerize under plasma activation. Thin films of polymers are formed as a result.
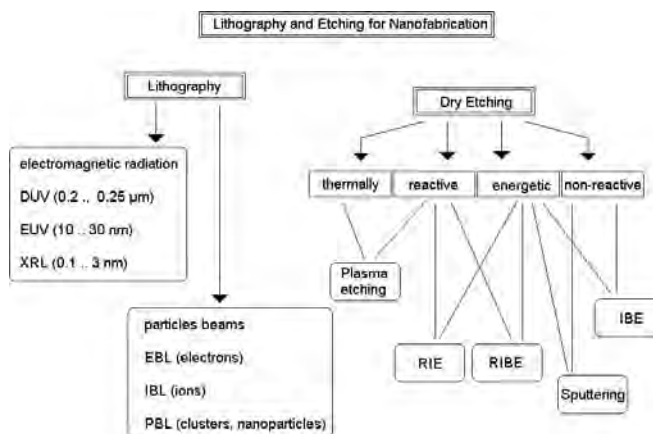


**Figure 2.** Scheme of important lithographic and etching methods for nanofabrication in planar technology.

Lithographic resist technologies represent the most important class of molecular-based techniques in IC fabrication. The formation of adhesive micromasks on top of functional layers to be patterned is a fundamental step in the major part of lithographic procedures. Therefore organic materials are needed that are stable against the attack in etching processes and can be processed by spinning, exposition, development, and rinsing. Different types of polymers and specific additives are used, depending on the lithographic procedures. Photosensitive additives based on naphthochinonbisazides are mainly used in positive photoresist processes to get high differences in the solubility of novolak polymer films in weak alkaline solutions used as developers. Acrylate-based polymers or similar materials are applied as resists in lithographical procedures using higher energy radiation, such as deep ultraviolet (DUV) lithography, in electron beam lithography (EBL), in ion beam lithography (IBL) and in X-ray lithography (XRL).

Molecular processes are also used in conventional planar technology for the improvement of adhesion of films. The local adhesive forces of surfaces regarding further material deposition can be enhanced by the reaction of small molecules with reactive sites at the surface of substrates and deposited films. A hydrophobization of surfaces is of particular importance because of the strong chemisorption of water molecules in the presence of surface OH groups, which can bind water by dipole-dipole interaction and hydrogen bridge bonds and enhance the probability of adhesion of ions by ion-dipole interactions. Such surface layers containing water and ions considerably reduce the interface interactions between the substrate and a deposited film, could disturb film growth, and often leads to the destruction of films during micro- or nanopatterning. In addition, such films can cause local dielectric or semiconducting islands, which influence the electrical properties of the interface. These effects can be reduced, if the hydrogen of surface OH groups is replaced by small hydrophobic groups like trimethylsilyl. A typical example is hexamethyldisalazane (HMDS), which is often used for surface hydrophobization. It reacts by the formation of trimethylsiloxane groups at the surface and release of ammonia, which is easily be solved in aqueous solutions or quickly desorbed in the case of a gas-phase treatment. The capture of surface oxygen atoms suppresses the adsorption of water and ions at the substrate surface.

Many etching procedures are also connected with molecular processes. Molecular interactions take place in a variety of wet etching processes as well as in reactive dry etching procedures. Molecular components in etching baths are used for the formation of soluble material from the film elements, which have to be removed. In addition to oxidizing agents, ligands for the formation of soluble complex compounds of ions formed by the chemical or electrochemical oxidation of film or substrate material are of particular importance in wet etching processes. For this purpose, small chemical species like halogenids or other ions and small molecules like ammonia are used, as are organic compounds. Multifunctional organic molecules like dicarbonic acids, dialcohols, hydroxycarbonic acids, diamines, amino acids, or related compounds are frequently introduced as chelated ligands in baths for wet etching.

Gaseous species or chemical species with high vapor pressure must be formed in dry etching procedures. Therefore, the atmospheres in reactive dry etching procedures contain gases supplying components for the formation of fast-desorbing molecules formed from the film materials, which have to be removed. Typically halogen gases and halogen-substituted low-weight alkanes as well as halogen sulfur compounds are constituents of various dry etch gases that provide halogen atoms for the formation of halogen compounds of metals and semiconductors with much lower evaporation temperatures than the metals, semiconductors, or their oxides. Organic polymers can easily be etched in oxygen plasmas because of the formation of $CO$, $CO_2$, and water, which are all gaseous at the reduced pressure in the vacuum etching devices and are always quickly desorbed from the surface.

## 1.3. Methodical and Geometrical Gaps

Molecules themselves are nanoobjects. With the reduction of lithographic patterns down to the deep submicrometer range and into the nanometer range, the number of molecules included in single features of micro- or nano-devices or involved in their preparation has been reduced more and more. Conventional planar technology is changing from the use of a lot of anonymous molecules to the use of small ensembles of molecules or even single molecules.

Both living nature and synthetic chemistry offer today a huge number of very different molecules. Only a small number of them are really applied in planar technology. The molecular materials used play an assisting role. The use of special molecular properties is restricted to their advantages in technological procedures. But up to now, specific functions of single molecules have not yet been used for the realization of new functions in devices. There is a broad discussion and extended research on the use of properties of single molecules in new electronic or sensing devices as well as in nanoactuators. However, most developments are far from real applications today.

In the first view, the dimension of single molecules seems to be the important threshold in the merging of single molecular operations and planar technology. Small molecules are no larger than about half a nanometer on one side, and the standard nanofabrication by EBL and IBE produces in general patterns down to about 50 nm, which means there is a gap in the linear dimension of about two orders of magnitude. But there are much larger molecules. Folded macromolecules have diameters in the range of about 2 and 10 nm (Fig. 3). Stretched linear macromolecules are often much longer than the critical dimension of microfabrication in the mass production of ICs. The DNA of the lambda phage has a length of 16 $\mu$m. This length is about two orders of magnitude higher then the smallest features made in IC mass production. In addition to linear structures, rings are also available from the biomolecular toolbox: plasmid DNA forms molecular rings with a diameter of several hundred nanometers. Therefore, the geometry cannot be the only and deciding gap between molecular and planar technology. More than geometry, the differences in technical methods are hindering the fast functional merging of molecular construction and lithographic operations.
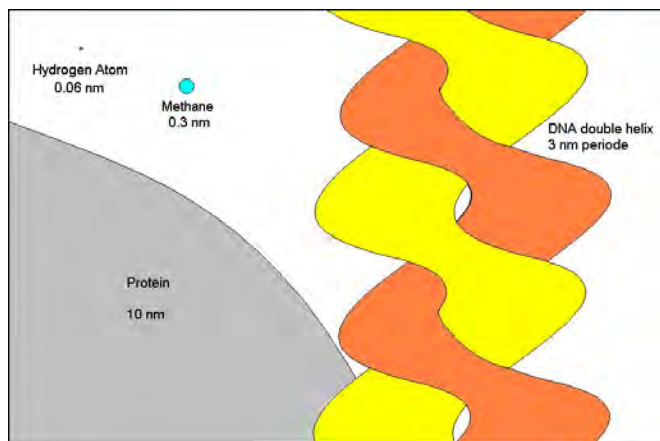
**Figure 3.** Comparison of the sizes of a small atom (hydrogen), a small molecule (methane), and biomacromolecules (proteins) and DNA (schematically).

The development of planar technology was mainly driven by physical thinking and mechanical, electrical, and electronic engineering. Plasma and particle physics, optics and sophisticated mechanical arrangements have mainly governed the development of the methods. Inorganic materials, metals, semiconductors as well as inorganic dielectrics play a much more important role than organic materials in the construction of micro and nanodevices up to now. Planar technology is traditionally connected with solid-state technology. Well-defined solids, single crystals, and stiff features determine the character of devices and the related preparation processes.

The largest methodical gap lies in the differences concerning the relation of chemical or planar technological elements in space. Chemists are working with gases and fluids, which means ensembles of molecules consisting of huge numbers of single particles, which are oriented and positioned in a random manner. The number of molecules in a given system can be determined more or less precisely by measuring the concentration, but in normal cases the exact number of molecules in a given system is not known and often is not of importance. Chemistry and biochemistry offer many very small and well-differentiated new functional elements, but they do not supply them in the right spatial order, and so the production of suitable interfaces between molecules and solid-state planar devices is a strong challenge.

## 1.4. Geometries, Topologies, and the Problem of Related Coordinate Systems

Chemistry and biochemistry deal with molecules, that means with very tiny objects of well-defined structure in the nanometer and in the subnanometer range. The atoms inside molecules have a very strong order because of their interconnection by chemical bonds. The bond network is described by the chemical structure. But this chemical structure is in general not a description of a certain geometry. It describes only a network of binding, a topology in the arrangement of atoms. Whereas in the case of small molecules the bond architecture allows one to describe the

geometry of a molecule on the basis of chemical structures in general, the overwhelming number of larger synthetical molecules possess only a defined binding topology, but this topology of chemical bonds allows the formation of a variety of different geometries due to rotable bonds. The number of possible geometries increases very quickly with the number of rotable bonds (Fig. 4). It can be restricted by stiff structural motifs in molecules (Fig. 5).

In larger biomolecules like nucleic acids and particularly in proteins, a well-defined three-dimensional geometry is achieved by the self-organized formation of a secondary and a tertiary structure. The self-organizing folding procedure leads to highly organized structures in space, which can work like single nanomachines. Biology has learned during evolution to integrate these molecular nanomachines in supermolecular arrangements, which form the basic working units on the subcellular level. Therefore, molecular bilayers of membranes or rodlike supramolecular aggregates of proteins are used as skeleton structures. The combination of self-organizing molecules and the reduction of spatial dimension is one of the fundamental principles in the spatial organization in living beings at the molecular and subcellular level. It includes primarily the formation of linear molecules by condensation processes of standardized building units and the subsequent folding of these linear arrangements into three-dimensional nano-objects, as well as the subdivision of the three dimensions of a cell with membranes as two-dimensional objects. So living nature connects the inside coordinate systems of different molecular elements. The principle of merging of coordinate systems is successfully achieved by nature from the level of small molecules through macromolecules, organelles, and cells up to tissues, organs, and organisms.

In synthetic chemistry, the internal coordinates of atoms are influenced not only by the motion of molecule parts due to movable bonds. In addition, the mobility of molecules in gases and liquids decouples the internal coordinate systems of all molecules (Fig. 6). Whereas the internal geometries at least in stiff molecules can be very precise, there is no defined relation between arbitrarily considered molecules inside a molecular ensemble. Supramolecular chemistry was
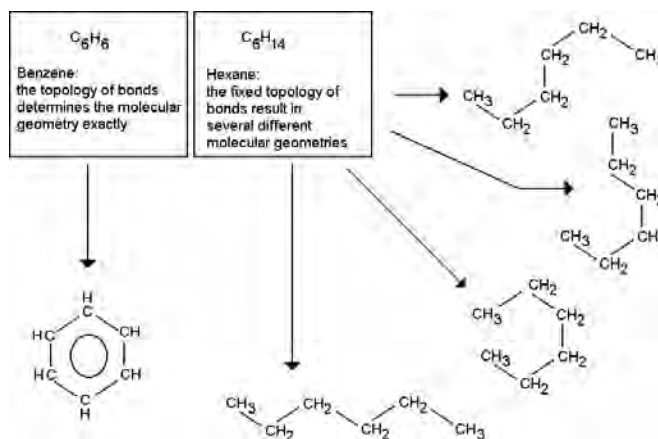


**Figure 4.** The role of formation of chains and rings for the molecular geometry for a given binding topology. Example: organic molecules with six carbon atoms.
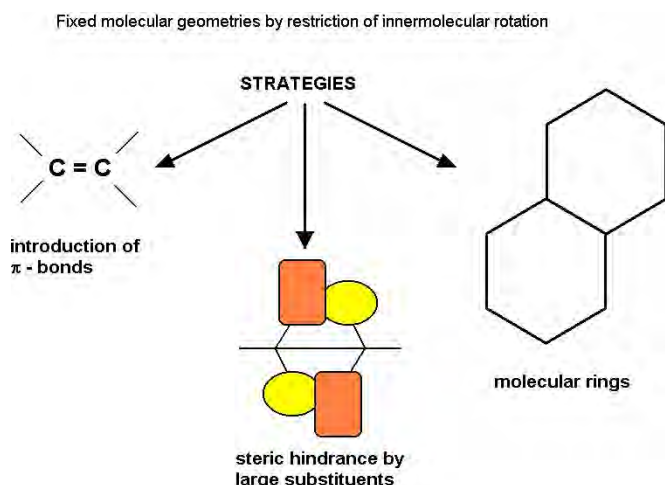
**Figure 5.** Stiffness in molecular construction modules: strategies for the reduction of rotational freedom.

started during the last two decades to overcome this problem. The synthesis of stiff molecules is one important step in the improvement of spatial organization of artificial molecules.

The physical thinking in micro- and nanodevice development is determined by the construction of single elementary devices like a transistor, for example, and combining them into complex functional systems. If physicists and electronic engineers are planning and preparing new devices, they are working with well-defined numbers and well-defined positions and orientations of each elementary device in an integrated system. Each small feature has its own position and orientation.

Planar technology provides organized micro- and nano-objects with a certain precision in space. It is particularly suited for the arrangement of numerous elements in the frame of a unique internal coordinate system. It can also connect this internal coordinate system with external technical coordinates.
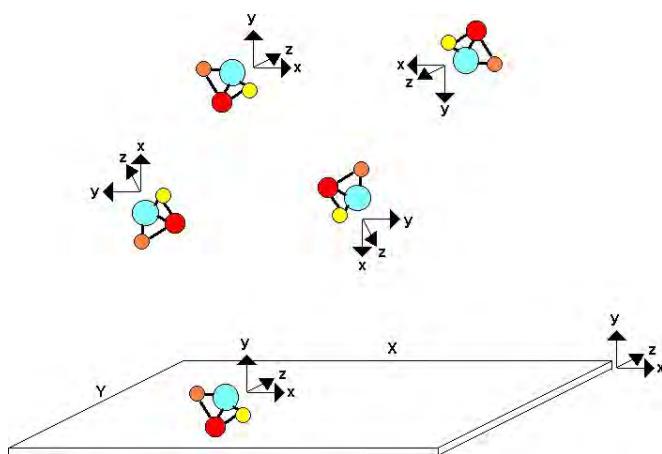


**Figure 6.** Problem of five coordinates in the oriented immobilization of molecules at chip surfaces for molecular nanoconstruction: positions $x$ and $y$, orientation (3 axis).

Therefore, there is an urgent need for the positioning and orientation of molecules and for their spatially well-defined integration in solid-state devices. The challenge of molecular planar technology is the development of methods and interfaces for the connection of molecules and synthetic procedures with planar micro- and nanodevices made by lithographic procedures. The integration of planar technology and chemical as well as biomolecular technologies gives us the hope of developing techniques in both fields within a common method pool that enable us to construct future single-molecule-based integrated devices.

## 2. LIMITS OF NANOPATTERNING BY CONVENTIONAL PLANAR TECHNOLOGY

### 2.1. Resolution Limits Caused by Lithographic Proximity Effects

Standard lithographic methods are based on the interaction of resist materials with radiation. For the realization of a highly resolved pattern, radiation is focused. There are two factors that influence the localization of the action of radiation. At first, the miniaturization of the diameters of foci is principally restricted by the wavelength of the radiation used. Second, radiation penetrating and absorbed by the resist acts not only directly but also by secondary processes, which are connected with a certain length (which is characteristic for the specific processes), wavelengths, particle energies, temperatures, and materials. The spatial effects of the influence of focused radiation in the proximity of areas that have to be exposed are called proximity effects.

In optical lithography, the diffraction of light is the main factor in proximity effects. In general, the probability of deposition of light energy decays with the characteristic length of the half-wavelength. This means that in case of the use of visible light, optical proximity effects influence thin-film elements in the area around lithographic edges with an extension between of about 0.2 and 0.4 $\mu$m. This value can be reduced in the case of application of deep UV light (200 nm wavelength) to about 0.1 $\mu$m. To reduce it below 100 nm, it is necessary to apply vacuum UV light. The increasing absorbance with decreasing wavelength of the most technical materials is a serious problem for the extension of UV lithography far into the vacuum UV region.

The proximity effect of optical lithography can be enhanced by diffusion processes. In positive resist processes, the photoproduct—the chemical species formed by exposition—has a low molecular weight and is comparatively mobile in the polymer matrix. In the case of increasing temperature, and influenced by the pH value of the matrix, the photoproduct can diffuse out of the exposed region and enhance the solubility of resist in regions near the edges outside the exposed areas. In consequence, enlarged microfeatures are observed after the resist development.

A strong reduction of exposure wavelength can reduce the diffraction-caused proximity effect significantly. Decreased diffraction effects are observed in the case of the use of weak X-rays (wavelengths typically in the range between 0.2 and 2 nm) or extreme UV light (EUV lithography, wavelengths typically in the range between 10 and 20 nm) for

the exposition. If a negative resist is used, the mobility of radiation products by diffusion is low, and, therefore, product diffusion does not enhance the small proximity effects. Unfortunately, XRL and EUV lithography suffer from difficulties in the construction of optical devices and the fabrication of lithographic masks. In addition, high-intensity and high-quality X-rays are only available from synchrotron rings and therefore are not available for local manufacturing.

The generation of patterns by low-wavelength radiation is more easily realized with the use of particle beams, particularly accelerated electrons in EBL. Electron beams can be focused down to about 1 nm and are therefore particularly suited for nanolithographic purposes. However, the impact of high-energy electrons with target materials is accompanied by a cascade of electron molecule interactions, leading to the generation of an excitation volume around the axis of the incident beam inside the resist. This area has a diameter of up to some hundreds of nanometers, depending on beam energy and on the average atomic weight of the resist material. So this EBL proximity effect is also serious for the limitation of lithographic resolution. Fortunately, this effect can be reduced by several measures, for example, by the application of special local intensities near the edges of lithographic features, the application of multilayer resist technologies, and contrast-enhancing etching procedures.

## 2.2. Energy and Radiation Damages

Radiation with particles or photons of higher energy is necessary to get lithographic probes that can be highly focused and thus supply high resolution. The problem is that molecular processes and the cleavage of chemical bonds inside solids are always activated by the interaction of one bond with one photon, electron, or ion. At lower energy of single particles, chemical processes are not activated or their activation can be controlled specifically by the choice of resonance energies. This effect is mainly used in photolithography in the visible range or the near-UV range. Incident photons activate only electrons of the dye molecules that should be brought to reaction, but the polymer matrix of resist and—still more important—the underlying material remain unaffected by the radiation. Preferably, electronic transitions between nonbinding orbitals and antibinding orbitals are used, to address specific photoprocesses by the absorption of photons of a certain wavelength.

Photochemistry becomes more nonspecific if the energy in photolithography is shifted to the DUV photon range. Below a wavelength of 300 nm and particularly in the border range to the vacuum UV range, transitions between binding and antibinding orbitals can be caused. In addition to $\pi$-$\pi^*$ transitions, which only reduce double-bond interactions, $\sigma$-$\sigma^*$ transitions are addressed in the low-wavelength range, causing immediate photoinduced bond cleavage. Typically radicals are formed in this process. They can undergo further less or more nonspecific chemical reactions.

The problem of nonspecific photochemical activation becomes more serious if EUV or X-ray photons are used for lithography. The absorption of this radiation does not primarily promote valence electrons, but leads to ionization from lower electronic shells. Cascades of relaxation processes are the consequence. In most materials, different processes of cleavage and new formation of chemical bonds are

induced. The specifity of the process is low. Single photons cause many chemical reactions, because the photon energy is a multiple of single activation energies. So, a single photon of a weak X-ray with a wavelength of about 1 nM contains enough energy for the activation of 200 molecules.

The ratio of energy transported by single particles to the activation energy of chemical processes is still higher in the case of electron and ion beam lithography. In EBL, acceleration voltages of about 20,000 to 40,000 V are usual. An electron energy of 20 kV exceeds the energy of a single chemical bond by 4 orders of magnitude. In the case of the application of high-energy ions, neutrons, or other heavy particles, this factor increases by up to 6 orders of magnitude when radiation in the MeV range is used.

High-energy radiation penetrating resist layers can deposit their energy to a significant extent into underlying functional layers. So radiation damage is observed in single crystalline as well as in glassy materials. Molecular films are particularly sensitive to radiation damage. The danger of radiation damage is especially high in the case of EBL because electrons possess much higher penetration potency than ion beams. In addition, X-radiation which is secondarily formed by the impact of high-energy particles in the target, can contribute to the radiation damage.

So the advantage of low diffraction of low-wavelength radiation is only one side of the coin. The effect of this radiation on certain target volumes instead of single molecules or bonds is the other side. Therefore, the application of high-energy lithographic probes is a compromise for nanotechnology. EBL and IBL are of high importance for the generation of nanofeatures in the range below 100 nm and down to a few nanometers. EUV lithography and XRL are candidates for the mass production of ICs and other devices with critical dimensions in the range down to a few tens of nanometers. All of these techniques can be handled and advantageously used if thin film-technology of solid material is scaled down into the micrometer and submicrometer range. But the application of this technology could become critical if the lower nanometer range is addressed. The applicability of processes with single molecules and for the activation of single bonds is very problematic because of the high-energy input, which has to be dissipated.

In addition to these difficulties, it is expected that EBL, XRL, and related techniques will play a deciding role in nanofabrication. At the least, these techniques are needed for the preparation of medium nanometer-sized structural environments and interfaces for ultimate nanostructures. But they have to be accomplished by other techniques, which are able to address specifically molecules, supramolecular objects, and other nano-objects.

## 3. PATTERNED MOLECULAR MONOFILMS

### 3.1. Preparation of Patterned Molecular Surface Films

The strategy of miniaturization in planar technology as well as in nanotechnology is frequently connected with the reduction of dimension. The ultimate extension of the principle

of thin-film technology is the reduction of film thickness to one molecular or one atomic layer. Monolayer technologies are, therefore, very important for nanotechnology.

The well-defined construction of monocrystalline inorganic thin films is usually achieved by so-called epitactic deposition processes. They are frequently applied for the production of highly pure compound semiconductor films [1]. These films consist of stacks of several dozen to several thousand atomic layers. A more sophisticated procedure is applied in the case of magnetic multilayer stacks for giant magnetoresistance devices. An alternating stack of ferroelectric and nonferroelectric films, each consisting of only a very few atoms, is built up by vacuum deposition processes and results in the specific magnetic coupling behavior of ferroelectric films [2]. In these films the atoms are more or less randomly distributed, so that the films are not defined by an exact number of atomic layers. Strongly alternating films of only atomic monolayers can be produced by the so-called ALE processes. ALE process is an atomic layer epitaxy realized by alternating CVD processes (chemical vapor deposition [3]) producing single atomic layers with a specific reactive surface for the chemical coupling of the molecules generating the following layer [4]. These inorganic monofilms can be patterned lithographically by standard resist procedures like photolithography, EBL, or IBL.

In addition to ultrathin inorganic layers, molecular monofilms are of particular interest in nanotechnology. They provide the possibility of introducing organic materials in a well-defined way [5]. Molecular monofilms are the basic procedure for molecular construction at plane surfaces (Fig. 7). Ordered molecular monofilms can be produced by the technique of self-assembled monolayers (SAM) [6] or by the Langmuir–Blodgett Technique (LB technique) [7]. In SAMs, the ability of self-arrangement of molecules is used, which are adsorbed at a solid surface but possesses a high surface mobility. This effect is well characterized for thiol-containing molecules at metal and semiconductor surfaces (particularly in the case of alkyl thiols at gold); another example is silane layers on silicon surfaces. A broader spectrum of film-forming organic materials can be processed by LB
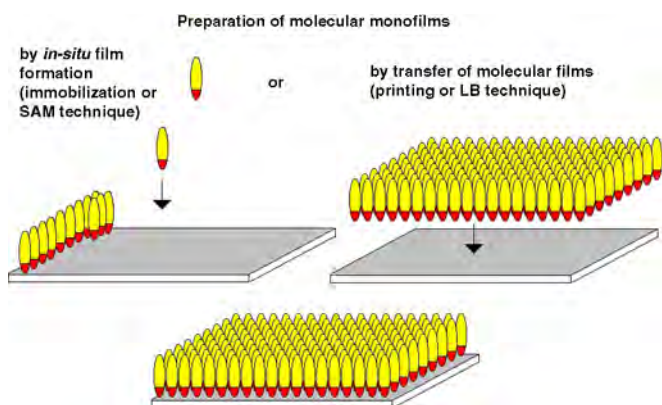
techniques. Thereby, a liquid is used as an assisting phase to achieve a high mobility of amphiphilic molecules, which occupy a liquid surface. A molecular monofilm is produced by mechanical compression of amphiphilic molecules in the film at the liquid surface. This film can be transferred in a second step to a plane solid surface. The disadvantage of the LB technique is the comparatively high tendency of formation of holes in the films. These defects are transferred to the solid surface together with the films. Micro- and nanopatterning of molecular films can be easily realized by nanoimprinting or soft printing procedures [8]. Free-standing LB films work as nanoporous membranes and are suited for separation processes [9].

SAMs of functionalized alkanethiols on gold surfaces are a well-studied system. They rely on a simple principle: an alkane chain, typically with 10–20 methylene units, is given a head group with a strong preferential adsorption for the substrate used. Thiol (S-H) head groups and Au (111) substrates yield excellent results. A preferred adsorption of the thiol molecules from solution to the gold can be observed, creating a dense monolayer with the tail group pointing away from the surface. By variation of the tail groups, the resulting chemical surface functionality can be widely varied. Furthermore, it is also possible to chemically functionalize the tail groups by performing reactions after assembly of the SAM.

The (111) direction is the preferred crystal face for alkanethiolate SAM preparation on gold substrates. It can be obtained either by using single crystal substrates or by evaporation of thin Au films on flat supports, typically glass or silicon. Several different solvents are usable at the low thiol concentrations in the lower millimolar range that are used in preparation of SAMs. Ethanol is the most commonly used solvent. Although the monolayer formation takes place very rapidly on the substrate, it is necessary to use incubation times of 12 h or more to obtain well-ordered, defect-free SAMs. Multilayers do not form, and adsorption times of several days are optimal for the formation of the highest quality monolayers.

Molecular monofilms for planar nanotechnology can also be produced by the attachment of molecules at plane surfaces. The interaction of single molecules with surfaces can be based on nonspecific adsorption, more or less specific chemisorption, and highly specific chemical bonding. In general, the strength of a certain chemical bond alone does not decide the character of binding between molecules and surfaces. The kind of interaction, the mobility of the attached molecule, and the number and the local arrangement of bonds determine the character of immobilization. Therefore, the strategies of binding of molecules at surfaces are rather diverse. They range from simple van der Waals interactions through dipole-dipole interactions, interactions between antagonistic charged surfaces and molecules, charged molecules and permanent or induced dipole groups to more specific covalent and coordinative bonds as well as polyvalent interactions, for example, by groups of ionic and dipole-dipole interactions and including groups of directed H-bridge bonds.

Molecular monofilms are sensitive against lithographic radiation. So some types of LB films and SAMs were patterned by EBL because of their intrinsic sensitivity for



**Figure 7.** Variants of the use of self-organized molecular films in planar technology. Left: *In-situ* formation by amphiphilic species (SAM technique). Right: Film formation at an assistant interface (liquid surface) and transfer of the completely formed monofilm or molecular multilayer film to the solid surface.

electron beams [10–13]. Minimal lateral feature sizes of 50 nm and less can be achieved. Molecular monofilms can also be patterned with scanning force microscopes or scanning tunneling microscopes. Here feature sizes down to about 10 nm were realized [14].

Nanopatterned molecular monofilms support the construction of more complex molecular compositions at surfaces, if they contain additional functional groups for secondary coupling processes. So such film elements can be used in different film synthesis strategies like the introduction of special film geometries, the control of surface density of functional groups, the control of chemical surface compatibility, the embedding of special guest molecules like dyes or enzymes in patterned ultrathin films, or combinatorial surface-directed chemical synthesis.

A special case of nanofunctional molecular monofilms is represented by biomembranes or biomimetic membranes including functional nanomachineries like membrane proteins. Such films can be transferred from solutions to chip surfaces to put them in a planar technological surrounding [15]. Biomembranes or bioanalogous membranes can be modified by the incorporation of different organic molecules, but also by the inclusion of metal and semiconductor nanoparticles [16].

### 3.2. Pattern Transfer from Molecular Films into Inorganic Layers

In some cases, lateral nanopatterned molecular monofilms are interesting for the realization of nanotechnical functions. More frequently, they are applied as masks for the patterning of underlying inorganic functional films.

Monomolecular films are suited as masks for wet chemical etching processes as well as for dry etching processes if the resistance of the monofilm against the etching medium is high enough. SAMs of octylthiole were tested as masks for the nanofabrication of GaAs films. Radiation by 50-keV EBL results in a positive resist behavior of the octadecylthiol film. The remaining film elements are resistive against an ammonia/hydrogen peroxide mixture, which was applied as an etchant for GaAs [17]. The exposure of a SAM film of an aromatic thiole by low-energy electron beams led to a negative contrast.

In addition to monofilms, ultrathin organic films are used for pattern transfer. Arrays of SiO$_2$ and metal pillars with diameters down to about 10 nm were fabricated by imprinting of ultrathin PMMA films and pattern transfer by a lift-off process [18].

### 3.3. Application of Micro- and Nanopatterned Monofilms

Lateral micro- or nanopatterned monofilms can be used for the introduction of molecular components in chemical and biochemical sensors and in electronic and optoelectronic micro- and nanodevices. So molecular monofilms are under investigation in the development of immobilization layers for biomolecules and synthetic recognition molecules for chemical and biochemical sensing. Protein-containing membranes are studied extensively because of their high potential for specific interaction or specific catalytic activity [19]. During the last decade, such films found particular interest for the construction and modification of molecule libraries in the form of biochips, which have been used meanwhile in medical diagnostics and drug development.

The typical length of amphiphilic molecules applied in SAMs and LB films is in the range of about 2 to 3 nm. This length is very well defined by the structure of the molecules. It determines the thickness of the molecular films. Therefore, it can be used for the construction of dielectric films with a determined thickness in the range of the typical tunneling distances for electrons. This property is of great interest for the development of tunneling devices, for example, single-electron tunneling (SET) devices, or for electron pair tunneling devices (Josephson electronics). Arrangements of nano- or micropatterned film stacks consisting of molecular monofilm and thin metal films are of particular interest for molecular electronics in connection with single-electron handling. Molecular films can be used for tunneling barriers as well as for molecular diodes or more complex functions in the connection of localization and transport control of single elementary charges [20]. The length of molecules in monofilms between electrodes determines the thickness of the tunneling barrier and hence the tunneling probability (Fig. 8). Theoretical investigations point to the possibility of integration of Josephson devices with single-photon devices with the use of tunneling barriers [21].

## 4. MOLECULES AND NANOPARTICLES AS LITHOGRAPHIC MASKS

### 4.1. Particle Templating

Nanoparticles are not only important as a special kind of material. They are very promising in different fields of nanotechnology because of the specific properties of individual particles. This concerns electronic, optical, and chemical functions as well as possibilities for immobilization, designing arrangements of nanoparticles, and nanopatterning of plane surfaces with the use of single nanoparticles and nanoparticle arrays [22].
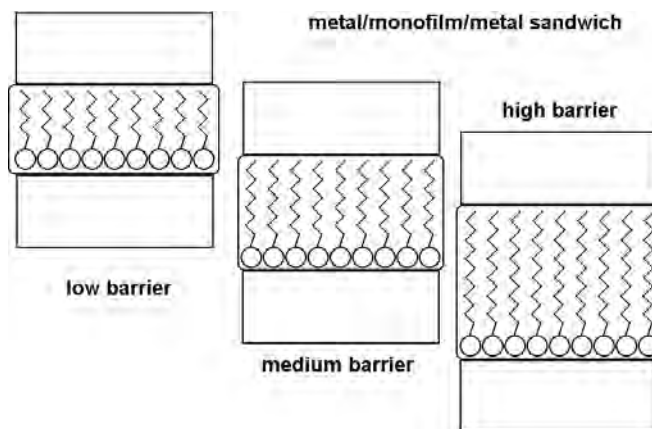


**Figure 8.** Control of barrier height for electron tunneling in metal/molecular film/metal contacts by variation of the length of alkyl chains in dielectric monofilms.

Nanoparticles tend to arrange in regular patterns at surfaces [23]. So it is possible to use them to transfer regular structures with space frequencies of the nanoparticle superlattice from the particle arrangement into substrate layers (Fig. 9) [24].

Colloidal gold particles were used as etch masks for the fabrication of silicon nanopillars. Nanopillars with minimal tip radii below 5 nm were obtained with the use of Au particles with diameters between 10 and 15 nm and silicon etching by RIE in a $CCl_4$ atmosphere [25]. Self-forming clusters of Au, Ag, and Fe also acted as etch masks in the production of silicon nanopatterns with high aspect ratios. The positioning of clusters was achieved by EBL, metal deposition, and a subsequent cluster-forming process at the lithographically patterned surface [26].

## 4.2. Molecular Templating

Molecular geometries, in addition to electron density distribution, quantum states, and charge, determine the strength and specifity of chemical bonds. The key/lock model for interactions between enzymes and substrates gives an important example of this fact. A particular artificial solution of molecular recognition consists of the imprinting of molecular shape in technical surfaces. Therefore, larger or smaller molecules are embedded in a polymer film or a monomolecular film at a surface. After stabilization of the film, these molecules are removed by a dissolution process without destruction of the shape of the rigid matrix [27]. Holes the shape of molecules remain in the matrix because of the dissolution process, which matches exactly with the shape of the formerly embedded molecules. Molecules of this shape interact preferably with these holes. Therefore, films or surfaces prepared according to this scheme can be used for chemical sensing.
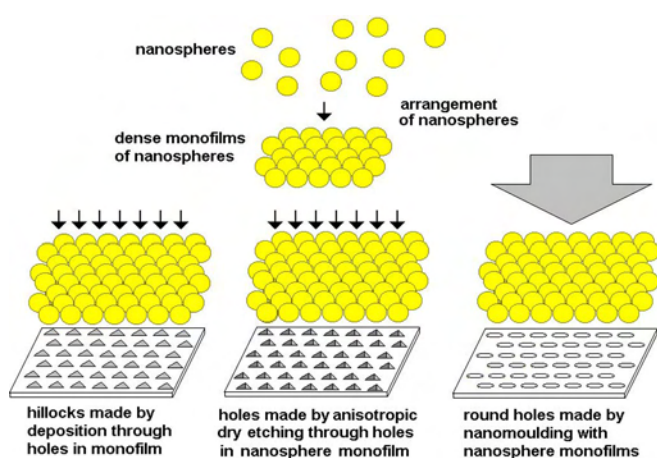
## 4.3. Molecular Networks for Lithographic Masking

Techniques have to be developed to transfer the molecular dimensions of, for example, biomolecules into applicable technical structures. This development is needed for technical access to the potential of molecular structures. A first step in this process is the use of the dimensions of molecular structures by transfer into traditional materials and processes of thin-film technology. The principle schemes are described in Figure 10. One approach is based on the application of molecular structures as masks in an etching process (left). Therefore, a thin film with the material of interest is deposited on a substrate, and molecules are immobilized on top of this layer. A subsequent etching step removes the film, except in the regions protected by the molecule. This technique provides an elegant way to utilize the potential of complex structures accessible by (bio)chemical synthesis also for technical purposes by transforming these geometries into, for example, a conductive pattern.

Proof-of-principle experiments were conducted with microtubules. Microtubules are tube-like protein assemblies that serve in cells primarily as a cytoskeleton. They can be assembled in vitro and result in rigid structures in the micrometer range, thereby providing ideal parameters for experiments. A demonstration used a gold layer as functional layer [28]. Microtubules were adsorbed on this layer and served as a mask in a subsequent dry etching step for the creation of a thin wire beneath the immobilized microtubules. To characterize the yielded nanowires, substrates with prestructured microelectrodes were used, which were connected to the nanowires by electron beam-induced deposition. So electrical measurements were possible, which clearly indicated the fabrication of a continuous metal nanowire by this technique (Fig. 11).

Although the demonstration was successful, it did not open the way for a standard technology, for at least two



**Figure 9.** Formation of regular nanopatterns in planar arrangements by the application of self-organized arrays of nanospheres: deposition through the regular holes between spheres (left), formation of holes in the planar surface of chip by anisotropic etching through the regular holes between spheres (center), and molding of the material at the planar surface by the spheres (right).



**Figure 10.** Pattern transfer using molecules for patterning of conducting film material: subtractive patterning. Left: 1. Deposition of a chain-like molecule immobilized with both ends at adjacent thin-film electrodes. 2. Etching of the underlying thin film of conductive material by use of the molecule as mask (lift-off). Right: 1. Immobilization of molecule. 2. Deposition of film. 3. Lifting of film elements by removal of the molecule due to a selective etching or dissolution process.
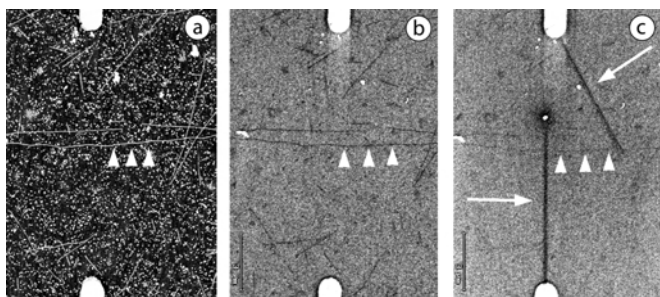
**Figure 11.** Nanowire preparation by molecular masking. Microtubules (protein assemblies) protect an underlying gold layer in a dry etching step. Scanning force micrograph (a) and scanning electron micrographs (b, c) were made of microtubules (arrowheads) positioned between microelectrodes and wired by electron-beam-induced line structures (arrows in c). Reprinted with permission from [28], W. Fritzsche et al., *Appl. Phys. Lett.* 75, 2654 (1999). © 1999, American Institute of Physics.

reasons. First, the resulting structure size depends on several factors during the processes and does not yet show a subnanometer precision. A second and more fundamental point regards the control over the position of the structure. The microtubules were randomly distributed over the surface, and only some electrodes positioned nearby were selected for experiments. Moreover, the final wiring to the prestructured electrodes was realized by nanocontacts based on an electron-beam-induced deposition [29]. The potential of the method is hampered by the missing positional control and the resulting requirement for an additional sophisticated wiring step.

Another example of the application of molecular masks used regular 2D arrangements of proteins. Typical examples are the S-layers, a sheet-like compound of bacteria that can be extracted and recrystallized on a variety of technical surfaces [30]. It consists predominantly of proteins with highly specific intermolecular interactions and results in a defined regular pattern with exact dimensions (depending on the species) in the lower nanometer range. The topographic aspect of this pattern can be used for metal coating prior to ion milling, which results in a regularly structured metal film due to differential metal removal and rearrangement due to the protein-metal heterostructure [31]. Another approach utilizes the regular pattern of the charge distribution in the protein, by applying metal deposition techniques catalyzed by charged surface regions [32]. So it is possible to achieve metal clusters in a highly ordered array with defined distances in the lower nanometer range, which is a unique possibility for the study of phenomena related to electron tunneling.

# 5. SUPERMOLECULAR CONSTRUCTIONS AT SURFACES

## 5.1. Macromolecules and Supermolecules at Surfaces

Planar nanotechnology with supermolecules is based on the physical and chemical handling of supermolecules at surfaces [33]. In general, molecules tend to adsorb at solid surfaces. van der Waals forces cause a positive interaction between molecules and solids. The number of atoms contributing to an attachment by van der Waals forces increases with increasing size of a molecule. That is why macromolecules like synthetic polymers, polysaccharides, or proteins like to adsorb at nearly every surface. In addition, charges, dipoles, and interactions between charges, dipoles, and induced dipoles may enforce attractive interactions between molecules and surfaces. So there is not the requirement of attaching them at a planar surface, but it is necessary to look for possibilities of specific and localized application of large molecules at plane technical surfaces. This can only be achieved by the choice of suitable solvents, thermal activation, and rinsing procedures, in which the solvent competes with the surface in the interaction with the molecules. Differentiation of adsorption is mainly controlled by the choice of rinsing protocols.

More specific interactions can be caused by coordinative binding. The formation of complex compounds requires the existence of coordinating groups in the molecules and at the surface and the presence of metal ions in the solution. The strength of attachment by coordinative bonds can be controlled over large ranges by adjusting the pH value and the concentration of suitable ions. Specific binding can also be achieved by means of ensembles of weak bonds. The strength of such polyvalent bonds can become comparable to that of strong chemical bonds, if a sufficiently high number of single bonds contribute to the cooperative effect. In particular, groups of H-bridges offer a good possibility of specific interactions because of their directionality.

The highest specificity of attachment and high binding strength are achieved by covalent coupling of molecules. Covalent coupling can be performed either by the binding of presynthesized molecules at the chip surface or by stepwise synthesis of molecules at the surface itself. Both techniques are under development now. The stepwise synthesis of linear macromolecules corresponds to the well-known strategy of solid-phase synthesis with the chemistry of protective groups. Variants of this strategy are used, for example, for the *in-situ* synthesis of oligo-DNA for biochip production by light-directed cleavage of protective groups.

The construction or immobilization of supermolecules at a surface demands more sophisticated strategies. Supermolecules are marked by a well-defined three-dimensional geometry. In contrast to most polymers, the real geometry of bonds in space is fixed in addition to the topology of chemical bonds. In standard polymers, the major part of bonds is free for rotation, which means one chemical structure (topology of bonds) can result in a huge number of possible conformations. In supermolecules, the rotability of bonds is restricted by the application of stiff parts, in which the atoms are connected by nonrotatable $\pi$-bonds, conjugated $\pi$-bonds, or aromatic systems. Supermolecules contain mostly ring structures, which contribute significantly to the stiffness of a molecule. Synthetic supermolecules are built up, in most cases, by the use of a hierarchy of chemical binding strength. First, molecular modules are synthesized by covalent coupling of atoms and small groups of them. Then these modules are connected by the application of weaker interactions. Therefore, in general, polyvalent bonds are used, like groups of H-bridges and coordinative

bonds, often supported by electrostatic and van der Waals interactions.

## 5.2. Molecular Architectures at Plane Surfaces by Immobilization of Supermolecules

The tools of conventional chemical synthesis can be largely used if molecules are presynthesized completely in solution and attached to the surface after the molecular construction is finished. This concept is already applied for the immobilization of peptides, proteins, and synthetic recognition structures for biosensors. Meanwhile, sophisticated strategies are developed for highly specific recognition of molecules at the surface and for transduction of molecular interactions into electronic signals [34, 35]. The immobilization of presynthesized molecules was extended to nucleic acids in connection with the production of DNA chips.

The fixation of larger molecules with certain functions is the main issue in all of these cases. The molecules must be stable against rinsing processes. The place of supermolecules or recognition structures has to be accessible for the diffusion of molecules of interest. And the chemical or biomolecular function of the immobilized molecules should be not affected by the immobilization. But the precise localization and orientation of the molecule are not of interest or are only of secondary importance.

In molecular nanotechnology there is a need for precise localization and orientation of very small ensembles of molecules or even single molecules. Therefore, strategies are needed that combine the localization of attachment at the plane surface and the precise choice of the reacting site for immobilization at the molecule itself. A rather sophisticated way of managing large molecular complexes consists of the connection between the spontaneous self-assembly of biogenic supermolecules and the introduction of functional groups realizing a position-specific attachment at chip surfaces (Fig. 12) [36].

## 5.3. *In-situ* Synthesis of Supramolecular Constructions at Plane Surfaces

Instead of immobilization of complex molecules, it is often necessary to form the supermolecules by modular construction at a certain reaction site at the planar surface.

Supermolecular chemistry offers different methods of construction of larger molecules, which are distinguished from classical polymer molecules by an exact atomic composition, a high rigidity, and, consequently, a much more precisely defined geometry. Comparatively simple examples are given by crown ethers and other host/guest compounds. More complex structures were realized in artificial helical structures like the so-called helicates [37], in catenanes, and in rotaxanes [38].

A simple strategy of constructing larger molecules and particularly spherical molecules is the buildup of dendrimers by initiating dendrimer growth with an immobilized starter molecule.

A convincing way to create functional supermolecular architectures at plane surfaces consists of the reassembly or *de novo* assembly of biomacromolecules or of artificially
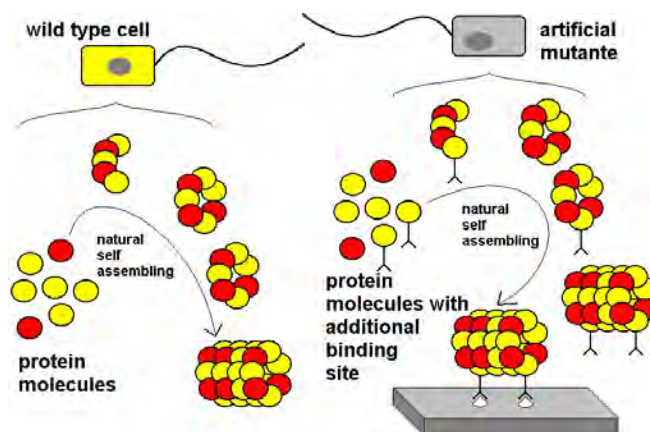


**Figure 12.** Use of recombinant building units of protein complexes to achieve oriented immobilization of large molecules by addressing specifically introduced linking elements.

modified biomacromolecules at chips. The reassembly of bacterial surface proteins forming regular patterns can extend to chip areas of several square centimeters. So two-dimensional crystals of regular nanoporous protein layers—so-called S-layers—can be obtained [39]. The formation of a rotating nanomachine made by genetically engineered ATP synthetase coupled with a fluorescence-labeled actin filament succeeded by such an assembly procedure [40–43].

Translational nanomachines can be taken from living nature and transferred into technical surroundings in addition to rotating nanomachines. The tubulin/kinesin system is particularly suited for such experiments [44]. Immobilized kinesin molecules at chip surfaces cause a linear transport of large tubulin supermolecule in the presence of ATP in a suitable buffer [45, 46].

## 5.4. Application of Chip-Integrated Supermolecules and Molecular Nanodevices

New types of electronic devices can be realized by the substitution of inorganic dielectric films with molecular films. Particular interest is attracted by molecular monofilms with a thickness in the range of typical electronic tunneling, meaning thicknesses up to about 3 nm. In addition to the tunneling effect, specific molecular electronic properties of molecular films can contribute to the function of devices with sandwich arrangements of metal or semiconductor nanoelectrodes with intermediate molecular films, namely films with asymmetries in the donor and acceptor properties of chemical end groups of the film-forming species. Such molecules show, in general, diode effects for charge transport [47]. Triode arrangements are realized in transistors with the use of molecular films. Single-electron transistors are realized, if the Coulomb blockade effect of an electronic nanoconfinement can be controlled by a gate electrode [48].

The inclusion of very small molecule ensembles can be detected in planar arrangements electronically if nanogaps in ultrathin metallic films are so small that the electrical conductivity inside the gaps is considerably influenced by adsorption of molecules in the gap region. In principle, the

electrical conductivity can reflect the number of molecules attached in the critical area [49].

Chip-integrated molecular architectures and supermolecules have been discussed as a basic idea in molecular electronics for a long time. Electron transport control in larger extended $\pi$-electron systems will probably become a key element in molecular logic architectures [50].

# 6. NANOPARTICLE ARRANGEMENTS AT PLANAR SURFACES

## 6.1. Preparation and Modification of Nanoparticles for Surface Technology

Nanoparticles are of particular interest for the bottom-up concept in nanotechnology because of their stiffness and their interesting optical and electronic properties. In contrast to many molecules, the atoms of a nanoparticle are interconnected by a high density of strong bonds, resulting in a nano-object with a fixed and rather stable geometry. This object is, compared with most macromolecules, chemically and mechanically stable. In addition to their stability, nanoparticles provide an interesting feature to molecular constructs: they can act as active components by optical or electronic effects.

Nanoparticles are commercially available today in a large spectrum of materials, like metals, dielectric inorganic materials, organic polymers, and elementary and compound semiconductors. Of particular importance for the properties and the processing of nanoparticles is the composition of their surface, in addition to their material composition.

Nanoparticles are mostly generated under the formation of charged surfaces to get a stabilization of nanoheterogenous systems. Surface charges cause repulsion between two particles. The aggregation of small particles is avoided by this repulsion.

A chemical modification of nanoparticle surface is achieved by exchange reaction of ligands in the molecular shell of particles. In this way DNA-carrying Au nanoparticles are prepared by the substitution of small organic molecules in the molecular shell of the nanoparticles with thiolated oligonucleotides, which attach to the Au surface by their thiol groups. The restoration of surface charge is important for the stabilization of the colloidal state. In the case of exchange of citrate by DNA, the negatively charged small molecule is replaced with a nucleid acid molecule of the same charge.

## 6.2. Interaction and Immobilization of Functionalized Nanoparticles

Functionalized particles can react with each other. They can also react with complementary functionalized surfaces. Spontaneous aggregation of particles can often be observed if the surface charge is removed. Otherwise, antagonistic charged particles will aggregate.

A more specific interaction of nanoparticles can be achieved by complementary binding groups. So the principle of hybridization between two single strands of nucleic acids can be transferred to a hybridization of beads. It was shown that beads possessing surfaces covered with complementary oligonucleotides aggregate spontaneously [51, 52].

The idea of specific interaction between beads can also be applied to the localized immobilization of nanoparticles in planar technology. Thus the hybridization of oligonucleotide-covered gold beads is possible at microspots of complementary DNA [53, 54]. Lithographically defined binding sites at a chip surface can be used for the localized immobilization of small ensembles of nanoparticles or for the positioning of single beads.

The oriented immobilization of GaP, InP, and Si nanowires succeeded by production and subsequent lifting of the semiconductor nanoparticles and reimmobilization under the influence of shear forces by liquid flow. Thus networks of nanowires could be constructed [55].

The position of immobilization of nanoparticles can be controlled by means of manipulating probes or by chemical micropatterning of the chip surface. Therefore, either resist technologies or light-directed chemical processes on chip surfaces can be used. Thus the localized immobilization of gold nanoparticles was done by the UV-initiated cleavage of light-sensitive protecting groups at a reactive monomolecular surface film [56].

The site-selective immobilization of single-stranded DNA-covered Au nanoparticles can be performed by hybridization with complementary DNA at micropatterned molecular spots at chip surfaces [57].

The combination of lithographically patterned surfaces with particular growth processes can be applied to different materials. Regular nanopatterns with high aspect ratios were realized by the production of immobilized single-wall carbon nanotubes at micropatterned catalyst areas at chip surfaces [58].

## 6.3. Nanoparticles in Labeling Technologies

Labeling techniques are an essential tool in microscopic methods for increasing sensitivity and improving the signal-to-background ratio. Today's standard label is based on fluorescence dyes with applications to microscopy and even to DNA array techniques.

Metal nanoparticles have been used in labeling techniques for microscopy for decades. In recent years, they have become more and more important for fast optical readout of biochips and in sensor device arrangements. Thus metal nanocluster labels can be used for an efficient readout of binding events of biomolecules at chip surfaces by optical enhancement effects [59].

A simpler readout is based on optical reflection from areas covered with nanoparticles. This effect can be used for DNA chip detection, as demonstrated with the use of microstructured DNA arrays on glass substrates [54]. To increase the dynamic range, a metal enhancement procedure known from electron and optical microscopy can be applied to nanoparticle-labeled surfaces. This development process results in the specific deposition of metal on the nanoparticles, leading to larger particles and therefore stronger signals. This increased signal enables the use of a simple flatbed scanner for the detection of DNA hybridization events [60] or the extremely fast (millisecond time scale) data collection of microstructured arrays [53]. In addition to

reflective or transmissive measurement, optical readout of nanobead-labeled surfaces can also be done by fluorescence [61] or SPR detection [62].

A combination of protein-modified polymer microspheres with gold nanoparticle labeling was successfully tested for an immunoassay at chip surfaces by means of an electrical readout. The selectively immobilized metallic nanoparticles were thereby used as catalysts for the production of conductive thin films by metal-catalyzed open-circuit metal deposition [63]. This approach was adapted to nanoparticle-labeled DNA on chip substrates containing microelectrode structures [64, 65]. Capture DNA was immobilized at the chip surface in the electrode gap. In the presence of complementary DNA that is nanoparticle labeled, a specific binding occurs and the labeled DNA is situated in the gap. With the metal enhancement, a metal layer is created by the enlargement of the particles on the surface. This metal layer is sensed by a significantly increased conductance over the gap.

## 6.4. Realization of Nanodevices by Nanoparticle Arrangements at Planar Surfaces

The specific immobilization of nanoparticles at well-defined places on chip surfaces attracts much attention in the contemporary research. Therefore, these techniques enable us to construct a new class of chip devices. These devices are in an intermediate situation between integrated circuits for solid-state electronics and (the more or less realized ideas of) molecular electronics. This new class of devices could be called "nanoparticle chip devices" because of the crucial role of nanoparticles, which are functionally integrated.

Metal nanowires can be manipulated on chip surfaces like charged molecules by the application of an electrical field. Thus they can brought into bridging functions between lithographically defined electrical thin-film elements for nanocontacts [66].

Carbon nanotubes are a very promising class discussed for molecular electronic devices. Planar arrangements of nanotube contact arrays were proposed for the realization of nonvolatile RAMs for molecular computing [67].

Nanoparticles exhibit interesting electronic properties due to size-related quantum effects. One example of the potential is the proposed SET transistor based on DNA positioning of a colloidal nanoparticle [68]. SET devices are a promising development toward lower energy consumption, which would minimize problems connected with the higher integration densities in today's microelectronic circuits. However, SET devices need an electron confinement in the lower nanometer size range. Today's structures are still larger, so they require low temperatures (below 1 K or even 0.1 K) for successful operation. The application of colloidal metal particles, as in electron confinement, was demonstrated, but the seamless integration of these particles into a technological environment is still missing. DNA-based positioning could be the solution, as described in the scheme in Figure 13a–d. A long DNA molecule is positioned between prestructured electrodes as already demonstrated [69]. In a subsequent step, the immobilized molecule is used to position a colloidal particle based on sequence-specific interactions between DNA on the particle and the long
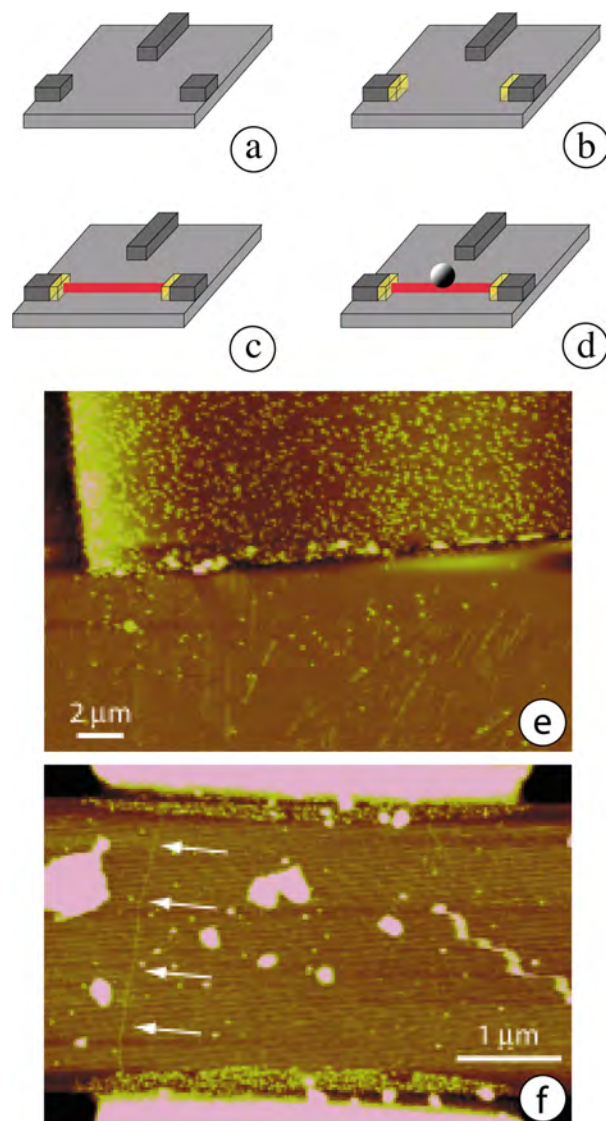


**Figure 13.** Nanoparticle arrangement using biomolecules. Microelectrode structures (a) are modified (b) to bind an individual DNA molecule (c). (d) This molecule serves as a positioning tool for the specific binding of a DNA-modified nanoparticle. (e) Demonstration of successful passivation of the substrate (bottom part) compared to the electrode (top) against binding of DNA, tested with nanoparticle-labeled DNA. (f) Scanning force micrograph of an individual DNA molecule positioned between microelectrodes. Reprinted with permission from [68], W. Fritzsche et al., in "DNA-Based Molecular Construction" (W. Fritzsche, Ed.), AIP Conference Proceedings, 2002, Vol. 640, p. 83. © 2002, American Institute of Physics.

DNA. Key steps of this procedure could be demonstrated in experiments. The specific binding of nanoparticles modified with DNA to surfaces with immobilized complementary DNA is shown in the upper part of Figure 13e. The lower part shows a background region, which was passivated by chemical modification to suppress nonspecific binding. The low number of particles (especially compared with the strong binding in the upper part) confirms the successful passivation. Figure 13f shows a combination of these principles of specific binding to defined surface regions on an otherwise passivated surface and its application to long (lambda)

DNA. Electrode structures (visible as bright regions at the top and bottom) were positively charged to induce binding of the negatively charged ends of the DNA. After passivation of the remaining areas and incubation with lambda DNA in a liquid flow, the imaged structure with an individual DNA molecule connecting the two electrodes was achieved. Further steps, such as the positioning of the colloidal particle along the immobilized DNA and the preparation of nanoparticles with a defined tunneling barrier based on self-assembly monolayers, were already demonstrated in the literature and have to be integrated in this setup.

## 6.5. Arrangement of Single Atoms and Small Atom Ensembles at Plane Surfaces

The ultimate nanofabrication technology uses single atoms instead of molecules for the construction of nanopatterns at plane surfaces. Such arrangements can be performed, if atoms are adsorbed at a surface but can be moved by a slight activation. The activation energy can be applied with probes like STM or AFM sensors. The conditions of manipulation are depending on the interaction energy between atoms and solid surface. The manipulation of noble gas atoms can only be performed at very low temperatures, but metal atoms at semiconductor or salt crystal surfaces can also be handled at room temperature. Arrangements of small numbers of atoms can be produced by manipulation of single atoms at plane surfaces by means of scanning probe devices. Dimers and trimers of gold atoms were prepared with an AFM moving single adsorbed atoms on a NaCl single crystal surface [70]. A particular illustrative example of artificially arranged atoms at a plane surface was given by M. F. Crommie et al. They built up a ring of 48 Fe atoms at a Cu single crystal surface. Concentric wavelike signal structures inside this atomic construct were interpreted as the quantum structure of a single electron inside the planar nanoconfinement [71].

## 7. OUTLOOK

### 7.1. Merging of Single-Molecule Techniques and Physical Nanofabrication

Obviously, the whole potential of nanopatterning can only be used if the self-assembly potential of molecules is technically controlled. On the other hand, molecule-based devices should be integrated into the planar technological concept. The need for technological bridging between supramolecular chemistry and planar nanotechnology for nanofabrication is particularly required for concepts of electronic devices using monomolecular functional elements [72]. The use of molecules for nanoelectronics must always address a highly specific coupling chemistry to get a localized immobilization and orientation of molecules (Fig. 14). Subsequent reinforcement of molecular wires by metal deposition leads to a technology for the preparation of molecular supported nanowires with low electrical resistances of nanowire networks (Fig. 15).

In addition to nanowires, electronic switches, or logic elements, the development of transducers for the construction of higher parallelized interfaces between the molecular and the electronic world can come to nanodimensions only if
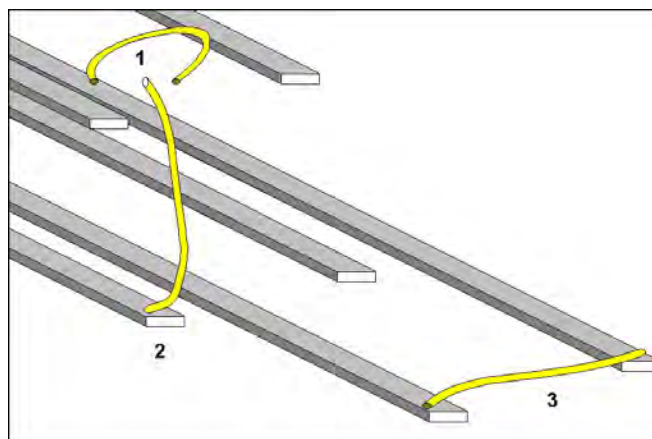


**Figure 14.** Steps of immobilized chain molecules for supporting nano-contacts between micro- or nanolithographically prepared planar electrodes. (1) Immobilization of one end of the molecule at the line electrode and of the other one in the dielectric space between lines resulting in no electrical contact. (2) One-sided immobilization results in no electrical contact. (3) Two-sided immobilization at different thin film electrodes (contact).

the merging between planar technology and single-molecule techniques is successful. The basic functions necessary for molecular transduction are solved in the framework of microchemical and microbiochemical sensing, as demonstrated in a variety of examples [73, 74].

Physical nanofabrication is mainly based on beam lithographic technologies like EBL or IBL and related techniques. Gas-phase processes like thin-film deposition and dry etching are essential for the nanopatterning of thin inorganic films. Both groups of techniques are developed in the frame work of planar technology concepts. But they are not well adapted to single-molecule handling procedures.

### 7.2. Single-Molecule Techniques

Single-molecule manipulation nearby or on planar surfaces requires techniques that address the molecular scale. For manipulations in the liquid phase, methods based on optical
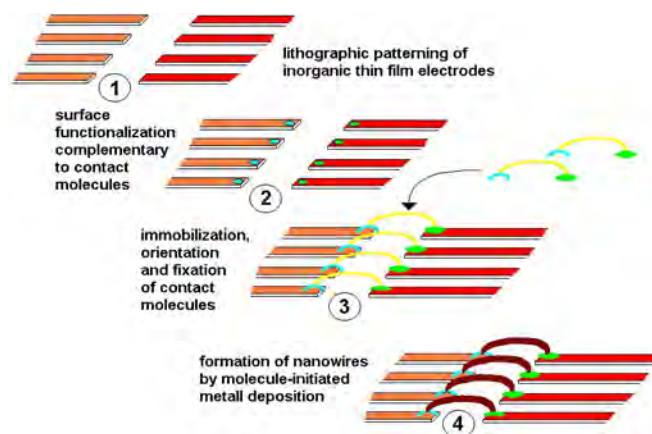


**Figure 15.** Steps for the preparation of molecule-supported nanocontacts in planar arrangement.

interactions are widely distributed [75]. Typical examples are optical tweezers, which can be used for the manipulation of particles in the medium nanometer range [76]. However, molecular manipulations (e.g., the study of DNA restriction on single molecules [77]) usually rely on optical "handles," particles (e.g., polymeric beads) large enough to be visible in the optical contrast. Therefore, the molecular scale cannot be addressed directly. Another example of optical methods aimed at the lower limits of optical resolution is the focused laser beam (microbeam), which is used, for example, for manipulations of chromosomes inside cells. It was shown that this method achieves cut widths below 200 nm [78]. This experiment was realized using chromosomes spread on a planar surface, thereby demonstrating the general applicability of optical methods to the manipulation of molecules on surfaces. However, the example also points to the limits of the approach: the method requires molecular structures visible in the optical contrast. This problem can be minimized with fluorescence markers, but the resolution is still limited. Thus the advantage of optical manipulation techniques, the combination of imaging and manipulation tools, is also a restriction.

To reach molecular dimensions by keeping a combination of imaging and manipulation capabilities, one could aim toward higher resolution imaging techniques. Electron microscopy is the method of choice for imaging molecular structures, such as DNA or proteins. There is also the possibility of manipulating surfaces with the electron beam in scanning electron microscopes by electron beam-induced deposition, as mentioned before. However, this approach is not widely used because of severe restrictions regarding molecular manipulations. The requirements of vacuum conditions and surface metallization are hardly compatible with (bio)molecular modifications, and the needed equipment is expensive and is not standard.

A fully new field of imaging methods was opened over 20 years ago with the introduction of the scanning tunneling microscope (STM) [79]. This was the start for the development of scanning probe microscopes (SPMs, also SXM because of the large variety of contrast mechanisms developed in the following years). In principle, SPM methods are based on the interaction of a probe scanned very close (lower nanometer range) over the sample surface (Fig. 16). The initial contrast was based on a tunneling current between a probe tip and a sample surface; both had to be electrically conductive. Tip and sample are engaged, until a predefined tunneling current is reached as the setpoint for a feedback mechanism. The sample height in this point is determined based on the movement of usually piezoceramic actuators, and an adjacent position is addressed. A raster-like scanning over the surface finally results in a 2D array of height values, which represent the final image of the measured surface area. Because of the strong distance dependency of the tunneling current, the very end of the tip interacts with the surface. Because STM, like all SPM methods, is limited regarding the resolution by the probe dimension (comparable to profilometry), the confinement of this interaction to an atomic tip results in atomic resolution. By utilization of the contrast used for imaging also for manipulations, individual atoms can be moved in special cases in an ultrahigh vacuum [80]. Although this resolution
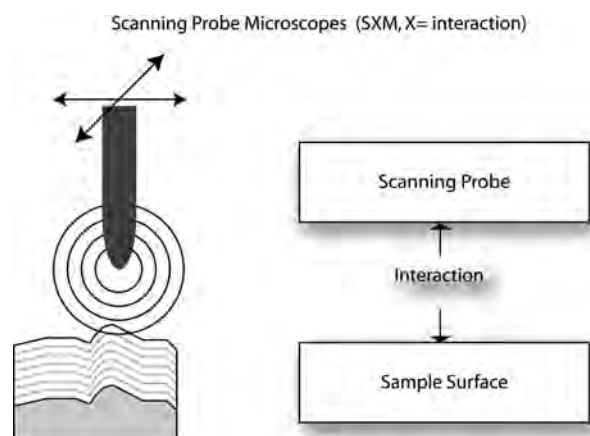


**Figure 16.** Scheme of scanning probe microscopy. A probe is raster-scanned over a surface controlled by a feedback mechanism based on highly localized probe-surface interactions.

for both imaging and manipulation is ultimate, STM is not the method of choice for the characterization of molecular structures on surfaces. It requires usually a conductive surface, thereby limiting the range of applicable substrates and molecules. Although there are now methods available for the imaging of isolator surfaces, they are not yet applicable as standard tools [81]. The need for a microscopic method with comparable resolution for isolating substrates led to the development of the scanning force microscope (SFM; also atomic force microscope, AFM) [82].

This SPM method probes the surface topography by raster-scanning a sharp tip (mounted at the end of a flexible cantilever) over the sample. As in the case of a STM, a piezoelectric scanner moves the sample relative to the tip and allows movements with Angstrom precision in the $x$, $y$, and $z$ directions. The deflection of the cantilever due to changing surface topography is usually monitored with a light pointer: a laser beam is reflected from the back side of the cantilever top toward a divided photodiode. The signal of the photodiode can be used through a feedback mechanism for keeping the deflection of the cantilever constant by adjusting the $z$ height of the scanner. This mode is called "constant force" (also "isoforce" or "constant deflection"); thereby the height movement of the cantilever represents the sample topography and is used for visualization. Turning the feedback off and monitoring the changing deflection by the diode signal results in an image in the "constant height" mode, which can improve the detection of edge features. The SFM can operate in gases or liquids, thereby opening a huge potential for imaging biological processes in their native environment with nanometer resolution.

Two modes differing in the duration of tip-sample contact are in general use. The first is based on steady contact (therefore denoted as "contact mode") that results in significant shear forces applied to the specimen. Soft molecules or samples with low substrate adsorption (as in the case of molecules adsorbed in buffer) are often unstable in this mode of operation. The "tapping mode" minimizes the shear forces by decreasing the tip-sample interaction, which is achieved by oscillation of the tip normal to the surface. In this case the amplitude of the oscillation is monitored and

the feedback mechanism is based on the damping due to surface contact (as detected by the photodiode).

A variety of complementary SPM methods were developed based on these basic principles. They exhibit a contrast mechanism based on the determination of tip-sample interactions and result in a mapping of the chosen interaction. Thus sample properties like viscosity, hardness, electrical conductivity, electrostatic interactions, optical absorbance or reflection, temperature or thermal conductivity, magnetic characteristics, etc., can be determined with a resolution in the lower nanometer range. These methods are aimed at minimal tip-sample interactions to avoid sample damages.

On the other side, the unique positioning capabilities of the SPM methods lead to another development aimed at surface manipulation. Almost all of the mentioned contrast mechanisms for imaging can also be used to modify the sample surface in a very localized manner (Fig. 17). Thus the SPM family also provides nanofabrication tools that approach the resolution of electron beam fabrication but show fewer restrictions regarding sample preparation, fabrication environment, or applied interaction mechanism.

One subset of SPM-based manipulations utilizes a voltage applied between a conductive tip (in STM or SFM mode) and the surface. In the case of thin metal films, an oxidation occurs, which can be used to create nonconductive regions that define (surround) a nanowire. This approach was applied to create a SET transistor, a device that requires nanometer-sized electron confinements contacted by defined tunneling barriers [83]. In addition to this process aimed at reducing the conductivity of surface areas, another voltage-based approach leads to the creation of metal wires by transferring metal (gold) from the tip to the surface with voltage pulses [84]. Thus metal structures smaller than 30 nm could be realized, demonstrating the potential for nanowiring.

Other methods for surface manipulation are based on the voltage-induced oxidation of silicon surfaces [85], the electrochemical deposition of silver on graphite surfaces [86], the manipulation of nanoparticles with a SFM tip [87, 88], or nanolithography based on tip-based mechanical manipulation on the substrate surface [89, 90].

The described SPM-based methods have the potential to modify surface regions in the lower nanometer scale. They can be utilized to define binding sites for small ensembles or even individual molecules as a prerequisite for defined molecular structures in a planar technology. Their advantage

compared with other nanofabrication tools is their compatibility with molecular manipulations. The SPM is a standard characterization method in laboratories involved in molecular surface modifications, and this wide availability leads to fast development and further enhancement of manipulation techniques in this field.

## 7.3. Development of a Technical Culture of Localized Chemistry

Nanotechnology is not only strongly related to the size of single molecules. It is a class of technologies addressing the overlap between physical engineering and chemistry. Engineers are following a top-down strategy to realize smaller and smaller dimensions. They have to learn that the individual molecules and even single atoms can no longer be neglected in the materials used, if the dimensions are reduced. But the problem of reduced numbers of particles is still more serious for chemistry than for physical engineering. Chemists think in molecular structures, which means thinking about the shape and size of single molecules. But classical chemistry deals with huge numbers of equal molecules in technology and in scientific experiments. The exact position and orientation of an individual molecule are of no interest in classical processes. In nanotechnology, chemists have to learn to transport, activate, and characterize single molecules. This is currently possible only under particular circumstances. New diagnostic tools are needed for the manipulation of molecules, the initiation of spontaneous arrangement, coupling and decoupling of molecules, and the destructionless characterization of products. And all of these processes have to be performed with respect to an outside coordination system. In a nanotechnology-orientated chemistry, a technical culture of localized chemical processing with single particles is strongly demanded.

This challenge includes the development of a complete set of procedures for single molecular handling and control of spontaneous processes. Chemistry must no longer be a stochastic method regarding the acting molecules, but each chemical step has to become a strongly determined operation with exactly predictable results related to individual particles. Process parameter windows, the frame of operational conditions, must be strongly defined for such a control.

The effort spent on the exact definition of individual molecular processes is of particular importance, if many nanotechnical functional elements based on molecular nanotechnology are to be integrated into complex devices.



**Figure 17.** SPM-based fabrication applies various interactions to achieve highly localized modifications of the surface.

## 7.4. Biomolecular Nanoengineering Using Lithographic Tools

DNA provides a huge potential for molecular construction. It is mainly based on the highly specific but variable binding of complementary sequences and on the sophisticated toolbox extracted from nature and used in the laboratory (e.g., enzymatic manipulations), but also on the highly developed technology of manipulating and characterizing DNA (e.g., PCR and gel electrophoreses). Well-known examples of the possibilities of DNA superstructures were demonstrated by the group of Seeman [91]. Moreover, because of

the large demand, an industry has been developed that provides DNA molecules in a chosen sequence, quantity, and quality.

On the other hand, the characterization tools for molecular structures on surfaces reached a level that allowed the high-resolution imaging of molecular structures on surfaces even under physiological conditions [92] and in their dynamic [93]. Moreover, techniques developed for the characterization of individual molecules now provide access to the properties of single molecules by integration of molecules into macroscopic measurement setups [94]. This integration is a key point for the technological use of the promising molecular materials and devices, but so far there have been only isolated solutions to this problem. The embedding of molecular structures in a solid substrate is the favored method, based on the above-mentioned microscopic and technological developments.

This process uses but is not limited to an adsorption of molecules such as DNA on surfaces, realized, for example, by surface modifications with silanes [95, 96]. It requires a defined orientation and a control over the position of the molecule. The application of prestructured electrodes and alternating voltages to guide DNA molecules in a defined position was demonstrated [97, 98]. Thus different molecules can be positioned by switching the voltage between different electrodes and exchanging the molecules in solution. However, this rather serial approach is limited to a low number of different constructs. A much higher variety could be realized based on self-assembly using a variety of specific binding pairs, as provided by the variability of DNA sequences. Moreover, this process is applicable in a parallel manner, as an important prerequisite for technological applications. The scheme in Figure 16 illustrates this approach. An extended molecule (1) binds with one end to a modified area on a substrate through specific interactions, (2), and in another step the free end of the molecule binds to another specified area, resulting in a molecule positioned in a defined orientation in a planar environment (3). This general approach was realized using about 16-$\mu$m-long double-stranded DNA molecules (originating from the lambda phage, therefore called lambda DNA), which exhibit single-stranded overhangs on both ends. Short DNA molecules with a sequence complementary to the ends were immobilized on planar electrode structures, so that the lambda DNA could be immobilized in a stretched state between the electrodes [69]. Such a structure with a DNA molecule of known sequence in a defined position could be used as a positioning tool for higher-order structures. One example is the proposed SET transistor based on immobilized DNA as a positioning tool for a metal nanoparticle [68].

In addition to this rather device-oriented application, DNA-based positioning also provides an interesting access to single-molecule studies in biology and biophysics. It should be possible to position, for example, individual enzymes along the stretched DNA in a defined way with nanometer precision based on specific DNA–DNA interactions. Thus one could arrange different interacting enzymes in a defined geometry and in the focus of additional characterization methods based on electrical or optical principles, or a predefined number of enzymes could be arranged in one reaction chamber.

All mentioned examples rely on the positioning by long DNA and therefore on the defined immobilization of this DNA molecule on a surface. This immobilization requires a prestructured surface, realized either by lithographic tools in a conventional way (photo- or e-beam lithography) or based on novel developments like soft lithography [99], scanning probe-base surface modification [100], or nanoimprint lithography [101]. The combination of prestructured surfaces with (bio)chemical surface modifications, which results in binding sites for small numbers or even individual molecules, is the technological basis for an integration of molecular constructions in today's technology.

## 7.5. Construction of Cell Organelle-like Functional Supermolecules

Living nature teaches us how complex organized microsystems have evolved. The theory of endocytosymbiosis shows that compartmented cells with specialized subsystems started with the integration of multifunctional individual cells into one supercell, which was followed by a reduction of functional complexity and specialization inside the integrated compartments. The formation and conservation of membranes separating the compartments is the most important morphological precondition for the specialization process. Nanopores and membrane-integrated transfer molecules are responsible for interaction and cooperation between compartments. Separation in space and coupling by transmitters and other signal paths are complementary aspects of working in complex biological micro- and nanosystems.

The biomimeting construction of molecular-based nanosystems must copy the biogenic philosophy of the definition of subsystems and morphological separation. Therefore, the compartmentation and the integration of nanopores and functional molecules or nanoparticles in artificial membranes are important strategies for the construction of biomimetic technical nanosystems by bottom-up processes. Cell-organell mimetic systems could be photochemically active like chloroplasts, redox-active like mitochondria, or responsible for storage and transport like liposomes. Many other functions could be addressed. In addition to poor chemical coupling, interactions by exchange of charges or excitation states will probably be the most important communication paths between subsystems. In contrast to biological systems, solid-state nanodevices and functional inorganic nanoparticles can be integrated in such complex technical nanodevices. This vision will come true if molecular self-organization can be connected with positioning and patterning at plane surfaces of technical substrates.

## 7.6. Vacuum Processes for Supramolecular Construction

The spontaneous organization of natural complexity with biomolecular building units is exclusively based on movable particles in a condensed state. The liquid phase dominates biomolecular processes. In addition to some processes in liquids at or near the surface of solids, phases with movable states like gels or liquid crystalline phases are typical for biomolecular self-organizing systems.

In semiconductor fabrication as well as in microsystem development, the solid phase is the most important state. The movable phases are used only for the modifications of the surfaces or near-surface films of solids. The role of the movable phase in physical micro- and nano-engineering shows an interesting contrast to biological systems. In planar technology, the route from microfabrication to nanotechnology was guided from more liquid phase operations to gas-phase operations at solid surfaces. Thus earlier deposition and etching procedures frequently used process liquids. The downscaling of technical nanopatterns was accompanied by a shift from wet procedures to dry procedures, from liquids to gases. The substitution of wet etching processes in solid-state electronics with dry etching is a typical example.

The question arises, how complex molecular-based nanosystems can be produced by gas-phase processes. Recent analytical operations have shown us that it is possible to transport heavy synthetic molecules as well as proteins through the gas phase, if they can be activated without destruction. This effect is used by laser-stimulated evaporation for time-of-flight mass spectroscopy (MALDI-TOF), for example. In the future nanotechnologists should learn how film deposition techniques can be qualified for the transport and strongly localized deposition of oriented single macro-molecules and individual nanoparticles.

## 7.7. Problems of Molecular Self-Organization in Integrated Planar Devices

Molecular self-organization is essential for the construction of complex functional systems in living beings. It is assumed that molecular self-organization can also be used for the construction of technical nanosystems. However, there are some important differences between technical and living systems: living beings are realizing a complete spectrum of functions in all phases of their individual development. The functional set of a technical system is necessary only after completion of, not during, the construction. This fact represents a fundamental advantage of technical systems in comparison with biological ones. In contrast to biological systems, technical construction and preparation strategies can be decoupled from the finally addressed functions.

Technology must be efficient and reliable. Yields have to be high, and the set of preparation steps must be reproducible. In living systems, we find two principal strategies of ecological survival. The so-called r-strategy is oriented on high output in the number of offspring with low investment in the single offspring. The r-strategy includes normally high variability, but low yield and low reproducibility. It is the typical case for lower-developed organisms and quickly changing surrounding conditions. The k-strategy is marked by competence. The number of offspring is low, but the investment is high. This strategy corresponds to high reliability and high yield. Technical development is frequently marked by variability and trials and errors. Technical production knows nearly no variation, no modification, and no mutation. Thus it seems that research and development is more comparable to the r-strategy, but the production to the k-strategy. Living systems are a model for technical solutions only to some extent. But there is a necessity to make much more

reproducible and reliable systems during production and to generate more variability and degrees of freedom during development. Thus we cannot assume that occasionally self-organization of molecules will solve all future technical problems. However, we can use the spontaneous effects of molecular self-organization for the search for new degrees of freedom in nanotechnical development and in new technology procedures. In a further developed phase, efficient and reproducible self-organization procedures can be included in the production of new devices and technical systems.

Miniaturization in the nanometer range with the inclusion of many different materials and more or less sensitive molecular species is accompanied by the problem of a large number of single functional units (nanodevices or molecular complexes) in a highly integrated system. Redundancy concepts are needed, in addition to a maximum of reliability of the single components. The typical lifetime of biological nanosystems and even of synthetic nanomolecular systems is, in general, not sufficient for most technical applications. The stability problem, particularly in connection with excited molecular states (which are frequently necessary for interfaces like nanotransducers), demands biomolecular functions that are technology-adapted and robust for inclusion in technical systems.

It is assumed that no molecular systems adapted to the aqueous environment of biological cells will solve this problem. It seems more probable that the combination of small solids with molecular units will enable us to construct nanomachines with new molecular-based functions. Clusters and nanoparticles possess many interesting properties and introduce robustness into the system. The included molecules are responsible for variability, mobility, molecular recognition, and specificity in the interaction of components as well as conversion by chemical processes.

The self-organization of nano-objects has to be controlled by the choice of components and the control of interaction conditions. This control includes both chemical and geometrical parameters. Therefore, an integration of planar technology with single-molecule handling and single-particle and single-cluster techniques is required.

## GLOSSARY

**Electron beam lithography (EBL)**   Preparation of micro or nano patterns by exposition and development of a plane thin film of a beam sensitive polymer by a focussed ray of highly accelerated electrons.

**Langmuir–Blodgett (LB) film**   Molecular monolayer transferred from a liquid-air interface onto a solid substrate.

**Optical lithography**   Preparation of micro patterns by use of a photochemical active resist layer and exposure through a partially transparent mask by an optical device.

**Self-assembled monolayers (SAM)**   Molecular assemblies spontaneously formed by the immersion of an appropriate substrate into a solution of an active surfactant in an organic solvent.

**Supermolecules**   Large molecules with well defined composition, binding topology and geometry, preferably formed by reversible interactions between smaller molecular subunits.

# REFERENCES

1. H. F. Hadamovsky (Ed.), "Halbleiterwerkstoffe." Deutscher Verlag für Grundstoffindustrie, Leipzig, 1972.
2. R. L. Edelstein, P. E. Tamanaha, P. E. Sheehan, M. M. Miller, D. R. Baselt, L. J. Whitman, and R. J. Colton, *Biosens. Bioelectron.* 14, 805 (2000).
3. A. Sherman, "Chemical Vapour Deposition for Microelectronics." Noyes, Park Ridge, NJ, 1987.
4. T. Suntola, *Mater. Sci. Rep.* 4, 261 (1989).
5. T. Salditt and U. S. Schubert, *Rev. Mol. Biotechnol.* 90, 55 (2002).
6. Y. Xia and G. M. Whitesides, *Angew. Chem.* 110, 568 (1998).
7. A. Ulman, "Ultrathin Organic Films." Academic Press, London, 1991.
8. A. Kumar and G. M. Whitesides, *Appl. Phys. Lett.* 63, 2002 (1993).
9. G. Lieser, S. Mittler-Neher, J. Spinke, and W. Knoll, *Biochim. Biophys. Acta* 192, 14 (1994).
10. W. Geyer, V. Stadler, W. Eck, M. Zharnikov, A. Gölzhäuser, and M. Grunze, *Appl. Phys. Lett.* 75, 2401 (1999).
11. J. Hartwich, M. Sundermann, U. Kleineberg, and U. Heinzmann, *Appl. Surf. Sci.* 144–145, 538 (1999).
12. R. C. Tiberio, H. B. Craighead, M. Lercel, T. Lau, C. W. Sheen, and D. L. Allara, *Appl. Phys. Lett.* 62, 476 (1993).
13. P. M. St. John and H. G. Craighead, *J. Vac. Sci. Technol., B* 14, 69 (1996).
14. M. A. McCord and R. F. W. Pease, *J. Vac. Sci. Technol., B* 4, 86 (1986).
15. E. Sackmann and M. Tanaka, *Trends Biotechnol.* 18, 58 (2000).
16. J. H. Fendler, *Chem. Rev.* 87, 877 (1987).
17. R. C. Tibero, H. G. Craighead, M. Lercel, T. Lau, W. Sheen, and D. L. Allara, *Appl. Phys. Lett.* 62, 476 (1993).
18. S. Y. Chou, P. R. Krauss, W. Zhang, L. Guo, and L. Zhuang, *J. Vac. Sci. Technol., B* 15, 2897 (1997).
19. P. Bianco, *Rev. Mol. Biotechnol.* 82, 393 (2002).
20. C. Zhou, M. R. Despande, M. A. Reed, L. Jones II, and J. M. Tour, *Appl. Phys. Lett.* 71, 611 (1997).
21. M. L. Roukes, *Physica B* 263–264, 1 (1999).
22. A. N. Shipway, E. Katz, and I. Willner, *Chem. Phys. Chem.* 1, 18 (2000).
23. P. Pileni, *Pure Appl. Chem.* 72, 53 (2000).
24. M. Pileni, *Cryst. Res. Technol.* 33, 1155 (1998).
25. P. A. Lewis, H. Ahmed, and P. Sato, *J. Vac. Sci. Technol.* 16, 2938 (1998).
26. T. Tada and T. Kanayama, *J. Vac. Sci. Technol., B* 16, 3934 (1998).
27. V. M. Mirsky, T. Hirsch, S. A. Piletsky, and O. S. Wolfbeis, *Angew. Chem.* 111, 1179 (1999).
28. W. Fritzsche, K. J. Böhm, E. Unger, and J. M. Köhler, *Appl. Phys. Lett.* 75, 2654 (1999).
29. W. Fritzsche, K. J. Böhm, E. Unger, and J. M. Köhler, *Nanotechnology* 9, 177 (1998).
30. U. B. Sleytr, M. Sara, D. Pum, and B. Schuster, *Prog. Surf. Sci.* 68, 231 (2001).
31. K. Douglas, N. Clark, and K. J. Rothschild, *Appl. Phys. Lett.* 48, 676 (1986).
32. M. Mertig, R. Kirsch, W. Pompe, and H. Engelhardt, *Eur. Phys. J. D* 9, 45 (1999).
33. R. C. Merkle, *Nanotechnology* 11, 89 (2000).
34. I. Willner, B. Willner, and E. Katz, *Rev. Mol. Biotechnol.* 82, 325 (2002).
35. F. W. Scheller, U. Wollenberger, C. Lei, W. Jin, B. Ge, C. Lehmann, F. Lidsat, and V. Fridman, *Rev. Mol. Biotechnol.* 82, 425 (2002).
36. K. Busch and R. Tampé, *Rev. Mol. Biotechnol.* 82, 3 (2001).
37. J. M. Lehn, A. Rigault, J. Siegel, J. Harrowfield, B. Chevrier, and D. Moras, *Proc. Natl. Acad. Sci. USA* 84, 2565 (1987).
38. J. Y. Ortholand, A. M. Z. Slavin, N. Spencer, J. F. Stoddart, and D. J. Williams, *Angew. Chem.* 101, 1402 (1989).
39. D. Pum, M. Weinhandl, C. Hödl, and U. B. Sleytr, *J. Bacteriol.* 175, 2762 (1993).
40. H. Noji, R. Yasuda, M. Yoshida, and K. J. Kinosita, *Nature* 386, 299 (1997).
41. O. Pänke, K. Gumbiowski, W. Junge, and S. Engelbrecht, *FEBS Lett.* 472, 34 (2000).
42. T. M. Duncan, V. V. Bulygin, Y. Zhou, M. L. Hutcheon, and R. L. Cross, *Proc. Natl. Acad. Sci. USA* 92, 10964 (1995).
43. D. Sabbert, S. Engelbrecht, and W. Junge, *Proc. Natl. Acad. Sci. USA* 94, 4401 (1997).
44. J. Howard, A. J. Hunt, and S. Baek, *Methods Cell Biol.* 39, 137 (1993).
45. L. Limberis and R. J. Stewart, *Nanotechnology* 11, 47 (2000).
46. R. Stracke, K. Böhm, J. Burgold, H.-J. Schacht, and E. Unger, *Nanotechnology* 11, 52 (2000).
47. A. Vilan, A. Shanzer, and D. Cahen, *Nature* 404, 166 (2000).
48. W. A. Schooveld, J. Wildeman, D. Fichou, P. A. Bobbert, B. J. v. Wees, and T. M. Klapvijk, *Nature* 404, 977 (2000).
49. C. Z. Li, H. X. He, A. Bogozi, J. S. Bunch, and N. J. Tao, *Appl. Phys. Lett.* 76, 1333 (2000).
50. J. C. Ellenbogen and J. C. Love, *IEEE Proc.* 88, 386 (2000).
51. A. P. Alivisatos, K. P. Johnsson, X. Peng, T. E. Wilson, C. J. Loweth, M. P. Bruchez Jr., and P. G. Schultz, *Nature* 382, 609 (1996).
52. C. A. Mirkin, R. L. Letsinger, R. C. Mucic, and J. J. Storhoff, *Nature* 382, 607 (1996).
53. J. M. Köhler, A. Csáki, J. Reichert, R. Möller, W. Straube, and W. Fritzsche, *Sens. Actuators, B* 76, 166 (2001).
54. J. Reichert, A. Csáki, J. M. Köhler, and W. Fritzsche, *Anal. Chem.* 72, 6025 (2000).
55. Y. Huang, X. Duan, Q. Wei, and C. M. Lieber, *Science* 291, 630 (2001).
56. T. Vossmeyer, E. DeIonno, and J. R. Heath, *Angew. Chem.* 109, 1123 (1997).
57. C. M. Niemeyer, B. Ceyhan, S. Gao, L. Chi, S. Peschel, and U. Simon, *Colloid Polym. Sci.* 279, 68 (2001).
58. A. M. Cassell, C. L. Asplund, and J. M. Tour, *Angew. Chem.* 111, 2565 (1999).
59. G. Bauer, F. Pittner, and T. Schalkhammer, *Mikrochim. Acta* 131, 107 (1999).
60. T. A. Taton, C. A. Mirkin, and R. L. Letsinger, *Science* 289, 1757 (2000).
61. J. R. Taylor, M. M. Fang, and S. Nie, *Anal. Chem.* 72, 1979 (2000).
62. L. He, M. D. Musick, S. R. Nicewarner, F. G. Salinas, S. J. Benkovic, M. J. Natan, and C. D. Keating, *J. Am. Chem. Soc.* 122, 9071 (2000).
63. O. D. Velev and E. W. Kaler, *Langmuir* 15, 3693 (1999).
64. R. Möller, A. Csáki, J. M. Köhler, and W. Fritzsche, *Langmuir* 17, 5426 (2001).
65. S. J. Park, T. A. Taton, and C. A. Mirkin, *Science* 295, 1503 (2002).
66. P. A. Smith, C. D. Nordquist, T. N. Jackson, T. S. Mayer, B. R. Martin, J. Mbindyo, and T. E. Mallouk, *Appl. Phys. Lett.* 77, 1399 (2000).
67. T. Rueckes, K. Kim, E. Joselevich, G. Y. Tseng, C.-L. Cheung, and C. M. Lieber, *Science* 289, 94 (2000).
68. W. Fritzsche, G. Maubach, D. Born, J. M. Köhler, and A. Csaki, in "DNA-Based Molecular Construction" (W. Fritzsche, Ed.), AIP Conference Proceedings, 2002, Vol. 640, p. 83.
69. E. Braun, Y. Eichen, U. Sivan, and G. Ben-Yoseph, *Nature* 391, 775 (1998).
70. X. Bouju, C. Joachim, and C. Girard, *Phys. Rev. B* 50, 11 (1994).
71. M. F. Crommie, C. P. Lutz, and D. M. Eigler, *Science* 262, 218 (1993).
72. C. Joachim, J. K. Gimzewski, and A. Aviram, *Nature* 408, 541 (2001).
73. A. B. Kharitonov, M. Zayatis, A. Lichtenstein, E. Katz, and I. Willner, *Sens. Actuators, B* 70, 222 (2000).
74. F. Scheller and F. Schubert, "Biosensoren." Akademieverlag, Berlin, 1989.

75. K. O. Greulich, "Micromanipulation by Light in Biology and Biomedicine: Laser Microbeam and Optical Tweezers." Birkhäuser, Basel, 1998.

76. N. Endlich, C. Hoyer, A. Harim, S. Monajembashi, and K. O. Greulich, *Exp. Tech. Phys.* 41, 303 (1995).

77. B. Schäfer, H. Gemeinhardt, V. Uhl, and K. O. Greulich, *Single Molecule* 1, 33 (2000).

78. K. König, I. Riemann, and W. Fritzsche, *Opt. Lett.* 26, 819 (2001).

79. G. Binnig, H. Rohrer, C. Gerber, and E. Weibel, *Phys. Rev. Lett.* 50, 120 (1983).

80. D. M. Eigler and E. K. Schweizer, *Nature* 344, 524 (1990).

81. M. Heim, R. Eschrich, A. Hillebrand, H. F. Knapp, R. Guckenberger, and G. Cevc, *J. Vac. Sci. Technol., B* 14, 1498 (1996).

82. G. Binnig, C. F. Quate, and C. Gerber, *Phys. Rev. Lett.* 56, 930 (1986).

83. K. Matsumoto, M. Ishii, and K. Segawa, *J. Vac. Sci. Technol., B* 14, 1331 (1996).

84. S. Hosaka, H. Koyanagi, A. Kikukawa, M. Miyamoto, R. Imura, and J. Ushiyama, *J. Vac. Sci. Technol., B* 13, 1307 (1995).

85. P. Avoris, T. Hertel, and R. Martel, *Appl. Phys. Lett.* 71, 285 (1997).

86. W. Li, J. A. Virtanen, and R. M. Penner, *Appl. Phys. Lett.* 60, 1181 (1992).

87. R. Resch, A. Bugacov, C. Baur, A. Madhukar, A. A. G. Requicha, and P. Will, *Appl. Phys. A* 67, 265 (1998).

88. T. Junno, K. Deppert, L. Montelius, and L. Samuelson, *Appl. Phys. Lett.* 66, 3627 (1995).

89. B. Klehn and U. Kunze, *J. Appl. Phys.* 85, 3897 (1999).

90. S. Miyake, *Appl. Phys. Lett.* 67, 2925 (1995).

91. N. C. Seemann, H. Wang, X. Yang, F. Liu, C. Mao, W. Sun, L. Wenzler, Z. Shen, R. Sha, H. Yan, M. H. Wong, P. Sa-Ardyen, B. Liu, H. Qiu, X. Li, J. Qi, S. M. Du, Y. Zhang, J. E. Mueller, T.-J. Fu, Y. Wang, and J. Chen, *Nanotechnology* 9, 257 (1997).

92. D. J. Müller, D. Fotiadis, and A. Engel, *FEBS Lett.* 430, 105 (1998).

93. S. Kasas, N. H. Thomson, B. L. Smith, H. G. Hansma, X. Zhu, M. Guthold, C. Bustamante, E. T. Kool, M. Kashlev, and P. K. Hansma, *Biochemistry* 36, 461 (1997).

94. D. Porath, A. Bezryadin, S. de Vries, and C. Dekker, *Nature* 403, 635 (2000).

95. A. Bensimon, A. Simon, A. Chiffaudel, V. Croquette, F. Heslot, and D. Bensimon, *Science* 265, 2096 (1994).

96. D. C. Schwartz and A. Samad, *Curr. Opin. Biotechnol.* 8, 70 (1997).

97. F. F. Bier, N. Gajovic-Eicherlmann, and R. Hölzel, in "DNA-Based Molecular Construction" (W. Fritzsche, Ed.), AIP Conference Proceedings, 2002, Vol. 640, p. 61.

98. M. Washizu, in "DNA-Based Molecular Construction" (W. Fritzsche, Ed.), AIP Conference Proceedings, 2002, Vol. 640, p. 51.

99. Y. Xia and G. M. Whitesides, *Angew. Chem. Int. Ed. Engl.* 37, 550 (1998).

100. R. Wiesendanger, *Proc. Natl. Acad. Sci. USA* 94, 12749 (1997).

101. S. Y. Chou, P. R. Krauss, and P. J. Renstrom, *Science* 272, 85 (1996).

# Molecular Sieve Silica Membranes

João C. Diniz da Costa, Victor Rudolph, G. Q. Lu

*The University of Queensland, Brisbane, Australia*

## CONTENTS

## 1. INTRODUCTION

This chapter presents an overview on the development of molecular sieve silica (MSS) membranes. It starts with a brief review of a membrane's background and general features. The review is then focused on MSS membrane synthesis and characterization processes with an introduction to the theory and principles applicable to sol–gel processing, templates, and film coating. The importance of micropore formation is discussed, in particular related to fractal branched systems, which are responsible for micropore size tailoring. As high-quality MSS membranes generally result in 3 Å average pore sizes, an activated diffusion model is developed to elucidate the transport mechanism. Finally, MSS membranes are reviewed in terms of their performance, transport characteristics, and application.

### 1.1. Background

The development of membranes for gas separation remained a dormant field for almost one century as greater research efforts were directed towards liquid filtration. As early as 1831, rates of escape of gases from natural rubber balloons were known [1]. The first serious efforts to develop inorganic membranes as a technology for gas separation started in the 1940s for the separation of uranium isotopes by the process of gaseous diffusion applied to $UF_6$ [2–4]. In the 1960s, the first attempts to commercially develop membrane gas separation systems were carried out. Initial membranes consisted of a thick dense polymer layer. A major problem experienced in this pioneering work was the serious limitation encountered with productivity (high flux) [5] because the permeation rate is inversely proportional to the thickness of a membrane's selective layer [6]. Conversely, by reducing the thickness of membranes, productivity increased at the expense of selectivity.

A breakthrough in membrane application was achieved in the 1960s by the development of asymmetric organic membranes by Loeb and Sourirajan [7]. These membranes consisted of a very thin top layer (thickness $< 5$ $\mu$m) supported by a porous sublayer (thickness 50–200 $\mu$m) [6]. By having a very thin dense top layer or a dense selective layer, productivity could be enhanced while adequate mechanical support was provided by a porous support which offers very low resistance to mass flux.

In the late 1970s, commercial polymeric membranes including polyether sulfone, polycarbonate, polydimethylsiloxane (PDMS), and polytrimethylsilylpropyne became available for gas applications [5], while dense metal membranes have also been used to purify hydrogen since 1965 [8]. In the second half of the 1980s, industrial laboratories and a large number of universities started focusing on developments of inorganic membranes, most significantly those made of ceramics [2]. The thrust behind inorganic membranes development originated from the inherent limitations of organic membranes for industrial and environmental applications. Incompatible conditions for organic membrane systems included high pressures, temperature, and chemical instability [9, 10]. Inorganic materials such as high-temperature thermally stable alumina composite membranes developed by Lin and Burggraaf [11] overcame these limitations as they have relatively high thermal and chemical stability and good capabilities to operate under high pressure [12]. This allowed applications to be extended into processes involving chemicals, temperature, or pressure conditions far beyond the limitations of the organic polymeric membranes.

Koresh and Sofer [13] pioneered the work on the development of carbon molecular sieve (CMS) membranes, initiating extensive research activity in micropore tailoring. CMS membranes were synthesized from different polymeric materials, including cellulose acetate, polyamides, and polyimides [14] with pore sizes typically in the region

of 3–6 Å [15]. However, Jones and Koros [9] found that organic compounds ($C_6$ and higher hydrocarbons) with concentration as low as 0.1 ppm caused severe deterioration in the performance of CMS membranes.

The evolution towards MSS membranes started with zeolite and pillared clays in the early 1990s. Zeolite based materials offer the potential to organize matter and manipulate molecules with high spatial precision at the nanometer scale [16]. Various researchers have worked on ceramic zeolite composite membranes for gas separation using templated method [17] or embedding zeolites in the polymer matrix [18–20]. However, most zeolite membranes were prepared using hydrothermal methods which are relatively simple, but have difficulties in controlling the thickness of the membrane layers and the orientation of particles [21]. Pillared clay membranes were tailored using lamellas of nanometer thickness in layered clay as natural blocks suitable to build a framework of nanometer dimension [22]. Dispersed into an aqueous solution, Na-montmorillonite clay lamellas exfoliate and even delaminate due to hydration of the interlayer cations, resulting in crystalline, quasi-two-dimensional sheets that are 0.96 nm thick and a few micrometers in diameter [23, 24]. Vercauteren et al. [25] synthesized pillared clay membranes and reported low permeation. They found that clay platelets are oriented mainly parallel to the surface of the support, thus resulting in a high degree of tortuosity and resistance to permeation.

Shelekhin and Dixon [26] provided the initial attempts towards MSS membranes by producing microporous glass hollow fibers resistant to organic solvents with extremely high selectivities but low flows. For some glass membranes, the silica microstructure is not chemically stable due to the existence of active silanols. This has been overcome partially by using chemical agents to make the surfaces of glass membranes hydrophobic [4, 27].

By the mid-1990s, major research efforts were directed towards what is now known as molecular sieving silica (MSS) membranes, which are novel amorphous microporous membranes [28]. Microporous apertures of molecular dimension are formed from polycondensation of silicon co-polymers. MSS membranes are generally synthesized from deposition on a substrate of a liquid film containing a hydrolyzed tetraethylorthosilicate in ethanol solution. MSS membranes can be tailored to have excellent thermal and chemical stability and high mechanical strength. Apart from gas separation, other potential applications of microporous inorganic membranes include catalytic reactors, gasification of coal, molten-carbonate and solid-electrolyte fuel cells, and water decomposition by thermochemical reactions [28].

## 1.2. General Features

A membrane can be described as a semipermeable barrier separating two phases [6]. As depicted in Figure 1, a membrane unit is constituted of a feed stream which generally faces the membrane's selective layer. For a component of a feed mixture to diffuse through the membrane, there must be a driving force. Depending on the application, the driving forces can be temperature, pressure, concentration, or electrical fields. The flux of gases through the membrane is
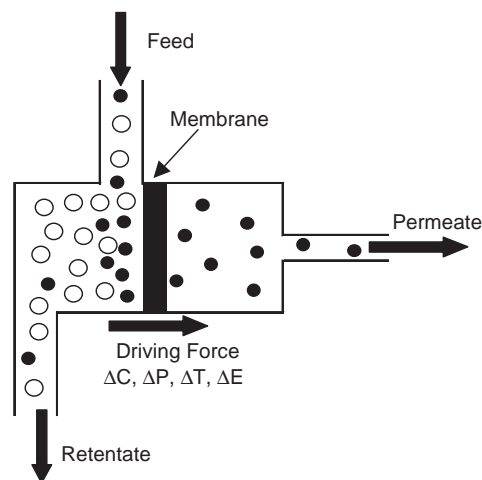


**Figure 1.** Schematic representation of a membrane system.

in most cases driven by a pressure gradient [29]. The filtrate and concentrated streams are generally referred to as permeate and retentate, respectively.

Two of the most important parameters that describe the performance of a membrane are productivity (i.e., permeability) and quality (i.e., selectivity). Permeability is typically used to provide an indication of the capacity of a membrane for processing the permeate: a high permeability means a high throughput [4]. Permeability denotes the flux of mass through a membrane per unit of area and time, and per unit pressure gradient. Gas permeability is often expressed:

- in Barrer units ($10^{-10} \cdot cm^3(STP) \cdot cm \cdot cm^{-2} \cdot s^{-1} \cdot cm\,Hg^{-1}$)
- or in gas permeation units ($10^{-6} \cdot cm^3(STP) \cdot cm^{-2} \cdot s^{-1} \cdot cm\,Hg^{-1}$) as pressure normalized flux
- or as a mole flux ($mol \cdot s^{-1} \cdot m^{-2} \cdot Pa^{-1}$).

Selectivity generally expresses the membrane's capacity to separate a desired component from the feed mixture. Selectivity is often calculated as permselectivity (ratio of permeation of single gases) or as a separation ratio $\alpha$ for a binary mixture. For good-quality inorganic membranes, a gas with large kinetic diameter is likely to be blocked while a gas with small kinetic diameter will diffuse through the membrane's selective microporous layer. For poor-quality membranes, selectivities are closer to unity. This gives an indication that the selective layer has large pores or a wide pore size distribution or pinhole defects rendering the membrane ineffective for separation purposes.

## 2. SYNTHESIS AND FABRICATION OF MSS MEMBRANES

### 2.1. Sol–Gel Process

The sol–gel process is a very useful route for producing molecular sieve films which are essentially of microporous dimensions ($p_{size} < 20$ Å). Polymeric silicate gels are often synthesized by hydrolyzing monomeric tetrafunctional alkoxide precursors employing a mineral acid (e.g., HCl) or a base (e.g., $NH_3$) as a catalyst. The sol–gel process is controlled

by the hydrolysis and condensation reactions as described by Eqs. (1) to (3). In the hydrolysis reaction (Eq. (1)), the alkoxide groups (OR) are replaced with hydroxyl groups (OH) where R is an alkyl group $C_xH_{2x+1}$. The silanol groups are subsequently involved in the condensation reaction producing siloxane bonds (Si-O-Si) plus by-products alcohol (ROH) (Eq. (2)) and water (Eq. (3)) [30]:

$$\equiv \text{Si-OR} + H_2O \leftrightarrow \equiv \text{Si-OH} + \text{ROH}$$

$$\text{(hydrolysis)} \quad (1)$$

$$\equiv \text{Si-OR} + \text{HO-Si} \equiv \leftrightarrow \equiv \text{Si-O-Si} \equiv +\text{ROH}$$

$$\text{(alcohol condensation)} \quad (2)$$

$$\equiv \text{Si-OH} + \text{HO-Si} \equiv \leftrightarrow \equiv \text{Si-O-Si} \equiv +H_2O$$

$$\text{(water condensation)} \quad (3)$$
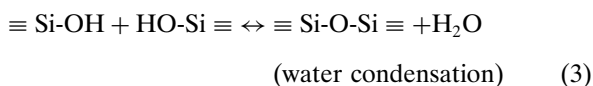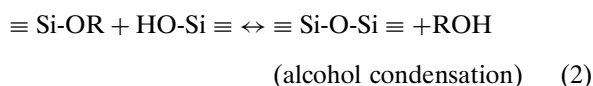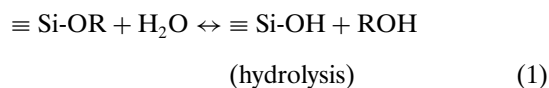
Various research groups [10, 31–33] have reported the production of high-quality molecular sieving films using a variety of sol–gel formulations as presented in Table 1. The molar ratio $r$ ($H_2O$:Si) of these gels was generally limited to values of 5.1 to 6.4 though in the literature $r$ values range from nonhydrolyzed to 50 [30]. Reasonably low $r$ values in acid catalyzed hydrolysis leads to the formation of weakly branched polymeric sols consistent with the formation of microporous materials. A two-step catalyzed hydrolysis with an initial step ($r = 1$) followed after 90 minutes by an additional step ($r \sim 3$) also produced weakly branched structures [34]. For lower $r$ values, the condensation rate is inhibited, forming rather weakly branched systems, which is addressed in Section 2.4.

The hydrolysis and condensation reactions lead to the growth and aggregation of clusters resulting in gel formation. Upon gelation, the gel commences to shrink and densify. This process is defined as syneresis and is caused by the spontaneous expulsion of solvents from its pores [30]. Gelation also serves the purpose to freeze in a particular sol configuration [35]. The gelation phenomenon plays a fundamental role in gel microstructure formation. Therefore, the film microstructure of membranes depends upon the preceding formulation and preparation procedures of sols to the gel point as well as the proceeding aging, drying, and heat treatment processes of gels.

The aging process of gels observed by nuclear magnetic resonance (NMR) has been investigated by Vega and Scherer [36], and Raman spectroscopy by Orcel et al. [37].

It was found that condensation of silica gels is an ongoing process after gelation due to the substantial amount of hydroxyl groups. Aging causes increased connectivity (crosslink) of the network produced by condensation reactions [30]. In other words, the gel structure stiffens due to the condensation reaction. According to Iler [38], surface tension forces created in a gel during solvent removal will cause the network to collapse. However, the stiffening of the gel network will resist the compressive forces of surface tension and the shrinkage rate is greatly reduced, resulting in greater pore volumes. Conversely, if the condensation reaction rate is inhibited, the gel network collapses, resulting in lower pore volumes.

The structural changes of xerogels (dried gels) have been investigated by infrared and Raman spectroscopy and NMR. Bertolluzza et al. [39] showed that both infrared and Raman spectroscopy complemented each other for gels prepared with TEOS. For instance, it was reported that the characteristics of xerogel spectra showed characteristic bands of fused quartz for IR ($\sim$1220, $\sim$1080, $\sim$800, $\sim$460 cm$^{-1}$) and Raman ($\sim$1180, $\sim$1070, $\sim$800, $\sim$430 cm$^{-1}$). These bands are associated with siloxane bonds (Si-O-Si). Duran et al. [40] investigated the structural evolution of xerogels calcined at various temperatures. It was found that the band associated with silanol groups (Si-OH) at $\sim$3740 and $\sim$960 cm$^{-1}$ reduced in intensity while the siloxane bands at $\sim$800 and $\sim$1070 cm$^{-1}$ enhanced their intensity with increasing temperature. These results suggest continuing condensation reactions during heat treatment leading to the strengthening of the network due to cross-linking.

For NMR studies, the $Q^n$ nomenclature is conventionally used to describe the silicon centers in silicates, where $Q^n$ represents the $n$(0,1,2,3,4) number of Si-O-Si linkages attached to silicon [41]. $Q^4$ are fully condensed species having a silicon nucleus with four bridging oxygen atoms while the other species are ascribed to silanol environments (i.e., $Q^2$ has a Si nucleus with two bridging oxygen atoms). Abidi et al. [41] investigated the chemical shifts for xerogels heat treated at various temperatures with NMR chemical shifts for the uncondensed species $Q^3$ and $Q^2$ at $-101$ and $-92$ ppm for xerogels treated from 60 to 350 °C. It was found that heat treatment enhanced the contribution of condensed species at the expense of uncondensed species. Similar results have been reported by Klemperer et al. [42] for loss of hydroxyl groups and the reduction in intensity of peaks associated with uncondensed species. This phenomenon can be explained by the condensation reactions (Eqs. (2) and (3)) and are in agreement with IR and Raman spectroscopy results.

Buckley and Greenblatt [43] investigated the pore characteristics of xerogels prepared with TEOS, ethanol, and water and calcined at 300 °C. It was reported that at low $r$ values (e.g., $H_2O$/Si = 4), the xerogel was characterized by $N_2$ adsorption isotherms of type I, characteristic of microporous materials. By increasing $r$ to a value of 20, the surface area increased and the adsorption isotherm changed to type IV. The latter indicated that the xerogel had less microporosity and a broader pore size distribution. It was also found that no significant effect in the xerogel structure was observed by increasing the ethanol content. Hence, excess

**Table 1.** Sol formulations of MSS membranes.

| Chemical composition | Process | Ref. |
|---|---|---|
| 1.0TEOS:3.8EtOH:6.4H$_2$O:0.085HNO$_3$ | single-step | [31] |
| 1.0TEOS:5.0EtOH:6.8H$_2$O:0.125HNO$_3$ | single-step | [32] |
| xMTES:(1−x)TEOS:3.8EtOH:5.1H$_2$O:0.056HCl | template two-step | [10] |
| 1TEOS:3.8EtOH:5.1H$_2$O:0.05HCl plus surfactant templates | template two-step | [48] |
| 1.0TEOS:3.8EtOH:6.0H$_2$O:0.10HNO$_3$ | two-step | [33] |

TEOS—tetraethylorthosilicate; MTES—methyltriethoxysilane.

water has a detrimental impact in the formation of micropore xerogels. These results can be explained as phase separation of solvents in the micropore during gel formation as ethanol preferentially evaporates, leaving excess water in the pore fluid. Condensation reactions and diminishing solvent quality (e.g., too much water) during drying probably helps to stiffen the xerogel structure and broadens the pore size distribution [35].

## 2.2. Molecular Imprinting

An important technique to tailor the pore size of xerogels is to add organic template agents during the sol–gel process [35]. During gel formation, organic templates are trapped in the gel structure. By heat treating the xerogel above 400 °C, organic templates are burnt off leaving within the xerogel matrix a cavity with similar dimensions to those of the template molecules [44]. This process seemingly produces microporous materials based on the imprint of molecular dimension of the template. In other words, the template provides a freeze in xerogel structure of micropore dimension ($r_{pore} < 20$ Å). There are two methods of sol–gel composites derived from template agents. The first one is a covalently bonded organic template, such as methyl groups ($CH_3$) in methyltriethoxysilane (MTES), which has a co-monomer nonhydrolyzable functionality. The second method employs an organic oligomer or surfactant, which interacts with the sol by weak van der Waals forces, hydrogen or ionic bonds, or hydrophilic-hydrophobic interactions.

Raman et al. [35] extensively reviewed the template based approach to the preparation of amorphous nanoporous silica. It was stated that the potential advantages of the template approach are that the organic ligand volume fraction may be used to control the volume fraction of the gel network while the pore size is independently controlled by the template size and shape. For gas separation applications, these features will fundamentally determine the overall performance of membrane films as the volume fraction controls permeance (defined as the thickness normalized flux of diffusing molecules transported across the film per pressure difference across the film) while selectivity (separation factor) is determined by pore size and pore size distribution.

Raman and Brinker [10] successfully prepared high-quality molecular sieve membranes derived from templated xerogel films using TEOS and MTES, a precursor which contains methyl as a covalently bonded organic template. It was reported that templated xerogels treated at 150 and 400 °C had $N_2$ sorption isotherms of type I (microporous). Increasing the calcination temperature of the templated xerogel to 550 °C yielded type-II isotherms, characteristic of nonporous materials. However, the partial $CO_2$ isotherm showed that the 550 °C sample was also microporous. These templated xerogels showed a good pore size control capability because $CO_2$ ($d_k = 3.3$ Å) has a lower molecular kinetic diameter than $N_2$ ($d_k = 3.64$ Å).

Kusakabe et al. [45] employed three different templates (octyl-, dodecyl- and octadecyltriethoxy-silanes) in order to test the role that template plays in tailoring pore sizes. They found that the alkyl chain of the template controls the pore size distribution. Hence, the shorter alkyl length produced the narrower pore size distribution. Kim et al. [46]

prepared microporous silica membranes by reacting TEOS and MOTMS (methacryloxypropyltrimethoxysilane), where the latter one controlled the pore structure formation in the region of pore size of 6 Å. Lu et al. [47] embedded methacryloxypropyl groups into the silica film matrix. They reported that as long as the template ligand volume has been below a critical percolation threshold, the secondary microporosity was inaccessible to $N_2$. The amount of primary pores only accessible to $CO_2$ decreased with the amount of added organic ligands (covalently bonded templates).

The employment of non-covalently bonded organic templates has also been investigated for silica derived membranes, including C6- and C16-surfactants [48] and alkyltriethoxysilanes [49]. Tsai et al. [48] claimed that by applying surfactants the flow resistance through the layers can be minimized and the inherent support defects can be overcome as well as that a narrow PSD can be attained. They used a C6-surfactant (triethyl-hexylammonium bromide) resulting in microporous ($d_p = 10$–12 Å) membranes with a high surface area (575 m$^2 \cdot$g$^{-1}$). Yuan et al. [49] used dodecyldimethylbenzylammonium chloride surfactants to achieve surface areas larger than 1000 m$^2 \cdot$g$^{-1}$ and uniform pore sizes around 10 Å. Ayral et al. [50] prepared silica membranes using TEOS and amphiphilic surfactants (Triton with varying polyoxyethylenic chains). Increasing the chain length of the surfactants resulted in a wider PSD in the same manner as observed by Kusakabe's co-workers [45] for covalently bonded ligand templates. The broadening of pore size is of particular concern as it leads to poor performance as separation capabilities of membranes are rendered ineffective. On the other hand, surface area and porous volume increased, which facilitates the transport of diffusing molecules through the membrane.

Various research groups [51–53] investigated the effect of methyl ligand template by NMR spectroscopy. The chemical shift of species containing methyl ligands was observed in the region of 50~70 ppm. To differentiate from the silicon nomenclature, the peaks associated with methyl ligands are referred to as $T^n \cdot T^3$ species are bound by three Si-O-Si links and one carbon ($CH_3$) while $T^2$ is formed by two Si-O-Si links, one Si-OH, and one carbon. Fahrenholtz et al. [51] reported that the peaks allocated to $T^n$ species increased in intensity with increase in the organic template molar ratio at the expense of $Q^n$-species.

Fahrenholtz et al. [51] also investigated the pore structure of templated xerogels calcined at 100 °C by varying the MTES/TEOS molecular ratio in a base catalyzed process. In mixtures ranging from 0/100 to 50/50, it was reported that the highest surface area (900 m$^2 \cdot$g$^{-1}$) and lowest pore volume (0.4 cm$^3 \cdot$g$^{-1}$) was obtained at 20/80 mixtures. However, these results cannot be compared against the work of Raman and Brinker [10] because the sample calcination was limited to 100 °C only. Farenholtz et al. [51] also reported that for mixtures in excess of 50/50 molar ratio, both surface area and total pore volume drastically reduced to zero at ~70/30 mixtures. Raman and Brinker [10] limited their mixtures to a maximum molar ratio of 50/50. As the molar ratio of MTES increased, the contribution of uncondensed species ($Q^2$, $Q^3$, and $T^n$) also increased, leading to very highly packed structures of no pore volume. Diniz da Costa et al. [54] reported that a higher template MTES:TEOS molar ratio induced the

collapse of the xerogel matrix due to capillary stress, promoting dense xerogels with a broader pore size distribution.

## 2.3. Fractal Branched Systems

Brinker et al. [55] investigated the bulk gel formation in weakly branched systems prepared by a two-step catalyzed hydrolysis of TEOS with $r = 5$. It was reported that there was a strong relation between weakly branched systems with $^{29}$Si NMR uncondensed species ($Q^2$ and $Q^3$) consistent with fractal dimension $d_f < 2$. In $^{29}$Si NMR spectroscopy, siloxane bridges are called $Q^4$ sites, single silanols $Q^3$ sites, and geminal silanols $Q^2$ sites [56]. The mass fractal theory which dictates steric constraints in silicate systems was developed by Mandelbrot [34] and is expressed as

$$M_{1,2} \propto R_f^{d_{f,1}+d_{f,2}-d} \tag{4}$$

where $R_f$ is a radius, $M_{1,2}$ is the number of intersections, $d_{f,1}$ and $d_{f,2}$ are the fractal dimensions of two structures, and $d$ is the dimension of space ($d = 3$). Mandelbrot [34] showed that for two structures of radius $R_f$ placed independently in the same region of space, the probability of intersections will decrease indefinitely as $R_f$ increases if $d_f < 1.5$. Hence, the structures are mutually transparent and they freely interpenetrate one another as they are forced into close proximity by the increasing concentration [57]. For weakly branched systems, there is a higher tendency for structures to interpenetrate, forming large structures of micropore size, resulting in densification.

According to de Lange et al. [58], the density of the final individual fractal structure is also dependent on the fractal dimension and $R_f$, according to

$$\text{density} \propto \frac{\text{mass}}{\text{volume}} = \frac{R_f^{d_f}}{R_f^3} = R_f^{d_{f,1}+d_{f,2}-d} \tag{5}$$

where the density decreases as $R_f$ increases. Dense films are undesirable in view of high resistance to permeation of diffusing molecules. Membrane film structures should have high porosity with small pore size. Hence, a balance must be attained between the two competing parameters to optimize film microstructure. Provided that sol fractals do not completely interpenetrate during film formation, the porosity may be controlled by the size of the fractal species prior to film formation.

The bulk gels prepared by Brinker et al. [55] showed extremely low BET surface areas ($\sim 1$ cm$^2$.g$^{-1}$) consistent with the exterior surface of nonporous materials. It was explained that weak branching combined with limited condensation during film formation promotes dense packing and low pore volume. However, de Lange et al. [58] found that dense films also formed for binary sols containing TEOS and metal oxides with $d_f > 1.5$. It was argued that the prediction of the porosity based on fractal dimension and interpenetration alone was difficult. In their view, the condensation rate, penetration rate, and drying rate are also important as far as the film final morphology is concerned. The work of de Lange and co-workers [58] is of considerable importance as it attempts to investigate the potential interaction between a silica film and the metal oxide supports. This is a feature of key technological importance for the production of membranes.

Recently, Diniz da Costa et al. [33] investigated the fractal formation of single-step and two-step sol–gel processes. The deconvoluted $^{29}$Si NMR spectra showed that the two-step process had a high concentration of silanol groups ($Q^3$ and $Q^2$) while the single-step process had a high contribution of siloxane bonds ($Q^4$). By using molecular probing, Diniz da Costa and co-workers reported that membranes prepared by the two-step process had a higher activation energy for helium than the single-step membranes. As the activation energy increases as the pore size decreases [59], these results strongly suggest that in fact pore size control and reduction can be achieved by enhancing the concentration of silanol groups as initially proposed by Mandelbrot [34].

## 2.4. MSS Film Technology

### 2.4.1. Membrane Film Coating

Preparation of MSS membranes is generally conducted by a sol–gel film formation process, namely dip-coating of ceramic oxide supports with colloidal sols containing silica precursors. According to Brinker and Scherer [30], sol–gel film formation requires considerably less equipment and is potentially less expensive than conventional thin-film forming processes such as chemical vapor deposition (CVD), evaporation, or sputtering. It was also indicated that a major advantage of sol–gel process over conventional coating methods is the ability to control precisely the microstructure of the deposited film (i.e., pore volume, pore size, and surface area). Coupled with mechanical, chemical, and thermal stability, MSS composite membranes derived from the sol–gel process potentially offer greater tailorability with respect to the pore size distribution.

### 2.4.2. Support Effect

Most silica thin films are cast on ceramic supports made from oxide powders such as ZrO$_2$, Al$_2$O$_3$, TiO$_2$, and CeO$_2$. Alumina supports are most suitable for gas separation [60]. Particle stacking is a major principle behind the preparation of ceramic membranes in order to obtain very narrow pore size distributions [61]. The stacking of particles with different grain sizes allows a reduction in pore volume and pore size as small particles are layered on top of large particles. These materials have been widely used as substrates for the preparation of molecular sieving membranes. According to Bonekamp [62], only a multilayered system can provide a substrate which is sufficiently smooth and flawless to serve as a support on which an almost defect-free microporous membrane can be made.

The literature indicates that substrates used for the preparation of MSS membranes are mainly $\alpha$-AlO$_3$ and $\gamma$-AlO$_3$ [10, 29, 31, 58, 63]. The principle of asymmetric membrane is also extensively used for tailoring MSS membranes. By stacking smaller colloids ($\gamma$-alumina) on top of larger colloids ($\alpha$-alumina), a membrane support can be produced in layers in a way that its pore size is reduced from the bottom to the top layer. The membrane's selective layer is therefore cast on the top layer. The primary function of the support

is to reduce flux resistance of diffusing molecules due to its large pores while providing mechanical stability and integrity to the microporous thin films.

Various research groups have prepared high-quality $\gamma$-alumina support with 40–60% porosities [11, 58, 61]. Using boehmite ($\gamma$-AlOOH), Lenaars et al. [61] produced nonsupport $\gamma$-alumina films with pore diameter ranging from 3.7 to 8.9 nm calcined at 200–900 °C. However, at 1000 °C calcination temperature, $\gamma$-alumina turns into $\alpha$-alumina resulting in pore diameter enlargement by one order of magnitude to 78 nm. Lin and Burggraaf [11] reported large pore radius in the region of 31 nm for support membranes treated at 450 °C, while the pore size increased up to 132 nm as the calcination temperature increased to 1200 °C. De Lange et al. [58] reported pore diameter in the region of 38 nm, while the inclusion of PVA (polyvinyl alcohol) in the sol–gel process caused the pore diameter to increase slightly to 42 nm.

Support characteristics play a vital role in the morphology of the sol–gel films. Bonekamp [62] reviewed the morphological requirements of supports for dip-coat film processing. In his view, layer homogeneity is fundamental in preparing thin films without defects and the support should have (i) small pore size, (ii) low surface roughness, and (iii) low void defect concentration. When large pores and voids are emptied by evaporation, the wall between adjoining pores is subjected to uneven stress that can cause cracking. Similarly, rough surfaces (e.g., edgelike shapes) induce film stress, resulting in microcracks. Support roughness can be reduced by polishing the supports [11, 32].

Although pore size of supports can be reduced by lowering the calcination temperature, this process is clearly dependent upon the calcination temperature of silica thin films. As crystal growth occurs with increasing calcination temperature and pore diameter likewise, there must be a trade-off between the heat treatment that provides the best microporous film while having the least detrimental impact to the support's integrity. In the literature, supports are generally precalcined prior to film deposition at temperatures ranging from 400 to 600 °C and heating rates of 0.5–1.0 °C · min$^{-1}$ [10, 31–33]. Precalcination emulates the conditions of film heat treatment in order to minimize the effect of interparticle heat stress on silica films.

### 2.4.3. Film Formation

Scriven [64] extensively reviewed the dip-coating process and proposed five stages: immersion, start-up, deposition, drainage, and evaporation. In the immersion stage, a substrate or membrane support is immersed in a liquid sol (coating bath) followed by the start-up stage which results in liquid adhering to the substrate surface. As the substrate is withdrawn from the coating bath, deposition (film formation) occurs. The moving substrate entrains the liquid in a fluid mechanical layer that splits in two above the liquid bath surface, returning the outer layer to the bath [64]. Drainage and evaporation of the coating sol occurs during and after withdrawal of the substrate from the coating bath.

Brinker et al. [65] also reviewed the sol–gel thin-film formation and suggested a more complete model based on the steady-state dip-coating process. In their model, there is a sequential order of structural development that results from draining accompanied by solvent evaporation, continued condensation reactions, and capillary collapse. During withdrawal of the substrate from the coating bath, the concentration of the polymeric materials increases close to the surface of the substrate due to gravitational drainage in tandem with severe evaporation and further condensation reactions. Gelation occurs concomitantly and is related to the moment when the condensing network is sufficiently stiff to withstand flow due to gravity, yet is filled with solvent [30]. For sol–gel film formation, aggregation, gelation, and drying occur in seconds [65].

Scriven [64] reported that film thickness is determined by the competition among viscous forces, capillary (surface tension) force, and gravity. According to Brinker and Scherer [30], when the substrate withdrawing speed ($U$) and viscosity are low (often the case for sol–gel film deposition), the balance of forces is modulated by the ratio of viscous drag to liquid-vapor surface tension ($\gamma_{LV}$). Hence, the thickness of a film ($h$) is proportional to $U^{2/3}$ in accordance with the Landau and Levich equation. In other words, increasing the speed of withdrawal in the dip-coating process will yield thicker films.

Many of the MSS membrane preparation methods cited in the literature do not state withdrawal speed. Researchers at the University of Twente in the Netherlands generally have a slight variation using the dip-coating pendulum system with very high tangential withdrawal speed. On the other hand, withdrawal speeds of 20 cm · min$^{-1}$ have been reported by Raman and Brinker [10]. The major advantage of the pendulum method is that just one side of the substrate is film-coated because the substrate is immersed tangentially to the coating bath. The normal right-angle dip-coating method requires that one coated side of the membrane is removed by sanding or scraping.

Deviations in predicted behavior in film formation were discussed by Brinker et al. [55] and Brinker and Scherer [30]. It was indicated that deviations may be caused by several other factors such as pH, viscosity regimes, and evaporation which increases concentration and viscosity resulting in non-Newtonian behavior. According to Brinker et al. [55], the concentration of the deposited film increases 18- to 36-fold due to evaporation. In turn, this causes the precursors to come into close proximity with each other resulting in closer aggregation, then gelation and drying with significant reorganization of the film matrix. During this process, chemical reaction rates increase quite considerably until gelation occurs and the film matrix continues to evolve during drying, aging, and thermal treatment.

### 2.4.4. Film Structure

The best technique to characterize deposited membrane films is molecular probing, which uses gas molecules of different kinetic diameters to determine the average pore size. However, the characterization of film structures always poses significant technical problems if further information such as surface area and pore volume is required. A qualitative and easy approach is to characterize the bulk xerogels. The disadvantage is that, although the underlying physics and chemistry that govern polymer growth and gelation are

essentially the same for films as bulk gels, other factors influence structural evolution in films [30]. For instance, the properties of a deposited thin film may be quite different due to nonequivalent gelation and drying conditions [55, 63].

Nonsupported thin films have been prepared by de Lange et al. [58] and de Vos and Verweij [31] for sorption characterization. These films were characterized by $N_2$ sorption isotherms of type I (microporous materials). The preparation procedure of nonsupported films included the evaporation of a sol in a Petri dish leading to gelation. Subsequently, the thin film was dried and then calcined at the desired temperature. De Vos and Verweij [31] reported that the pore sizes of nonsupported and supported membranes were very similar. However, de Lange et al. [58] used $\gamma$-alumina and reported that the pore sizes of supported membranes were slightly higher than those of nonsupported membranes. One point of consideration here relates to the fact that nonsupported films are cast on nonporous glass rather than porous metal oxide supports. As the membrane films are very thin, the morphology of the support or substrate may influence the final structure of the film morphology.

A further important parameter to control the microstructure of films relates to the aging of sols. Brinker et al. [65] investigated the effect of aging on silica films. It was reported that the porosity, surface area, and pore size increased monotonically with aging time employed to grow the fractal species prior to film deposition. Their films were microporous for sols aged within 3 days. However, the films became mesoporous with sols aged in excess of 3 days. This trend is also observed in membrane preparation. Various research groups [31–33, 58, 63] used nonaged sols to prepare microporous films. A variation from this approach is used by Raman and Brinker [10] who aged their templated sols for several days. However, their sols contained a methyl ligand template which induces capillary stress resulting in films with low pore volume. Hence, by aging the templated sols a form of pore control is achieved due to cross-linking.

### 2.4.5. Defects

A major problem arising from ceramic membranes relates to defect formation. According to de Vos and Verweij [31], the size and surface density of the defects depend on drying rate, amount and size of particles in the preparation atmosphere, and the thermal processing schedule. The stress in the film formation is large and nearly equal to the tension in the liquid ($\sigma = P$) [30]. According to Brinker et al. [65], it is commonly observed for films that adhere well to the support that cracking does not occur if the film thickness is below a critical thickness $h_c \sim 0.5$–$1$ $\mu$m. It was argued that cracking did not occur for films thinner than $h_c$ because the energy required to extend the crack was greater than the energy gained from relief of stresses near the crack. However, Leenaars et al. [61] observed that gel films dried at room temperature and relative humidities of 40 to 80% had no cracks if film thickness was less than 20 $\mu$m. Although reducing film thickness is one of the strategies to avoid stress fractures, some process conditions as reported by Leenaars may allow crack-free thicker films.

Many defects in silica films may reflect the morphology of the support or substrate which hampers the functional performance of membranes. Burggraaf [66] indicated that voids cause bubbles in the coating, resulting in pinholes. He also mentioned that cracks can be caused by pinholes and stress buildup due to the difference in expansion coefficient between the top film and substrate. Further defects can be caused by the membrane preparation process. Dust deposition during the film coating and calcining process can cause defects resulting in membranes of poor quality. De Vos and Verweij [31] and Tsai et al. [48] prepared silica films with thickness in the region of 30–90 nm (well below $h_c \sim 0.5$–$1$ $\mu$m) in clean rooms (class 1000) to avoid dust. Saracco et al. [67] reported that permselectivities are greatly enhanced due to the reduction of the statistical interference of particle dust in sol–gel deposition films in clean rooms versus normal laboratories. A method to repair a small concentration of defects in very thin silica films is to repeat the dipping and calcining process of the first silica layer.

## 3. SPECTROSCOPY AND CHARACTERIZATION

The characterization of film structures always poses significant technical problems in view of several factors affecting very thin film formation (i.e., micron scale). A qualitative and easy approach is to characterize xerogels based on the findings of Brinker and Scherer [30] that the underlying physics and chemistry that govern polymer growth and gelation are essentially the same for films as bulk gels. By studying xerogels, the microstructural evolution of the silica matrix can be fully analyzed at different steps of heat treatment process. Hence, fundamental information can be evaluated to tailor pore size of MSS membranes.

Several surface characterization techniques such as FTIR (Fourier transform infrared), $^{29}$Si NMR (nuclear magnetic resonance) spectroscopy, and TGA (thermogravimetic analysis) are employed to obtain information on the reaction mechanisms involved in the sol–gel processing. *In-situ* film characterization techniques such as XPS (X-ray photoelectron spectroscopy) and SEM (scanning electron microscopy) spectroscopy are also used to determine main features of membrane films.

Nitrogen adsorption is also used to determine important microstructural characteristics of xerogels such as micropore surface area, pore volume, pore size, and pore size distribution. Adsorption isotherms for gases of interest are obtained using gravimetric methods to determine the isosteric heat of adsorption, an important thermodynamic parameter used in the transport characteristic of MSS membranes.

### 3.1. Characterization of Xerogels

#### 3.1.1. Thermogravimetry

TGA is used to determine weight loss of xerogels during calcination and the temperature at which the compounds are oxidized and burnt off from the xerogel matrix. A typical weight loss curve of the templated and nontemplated xerogels as a function of temperature is depicted in Figure 2. Initial weight losses from room temperature to ~150 °C are mainly attributed to water molecules trapped in the xerogel matrix. From ~150 to ~450 °C, the rate of weight loss is
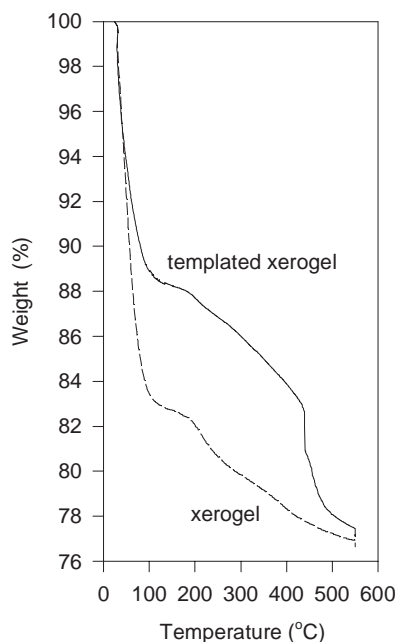
**Figure 2.** TGA weight loss curves. Reprinted with permission from [95], J. C. Diniz da Costa, Synthesis and Characterisation of Molecular Sieve Silica (MSS) Membranes, Ph.D. Thesis, University of Queensland, Brisbane, Australia, 2000.
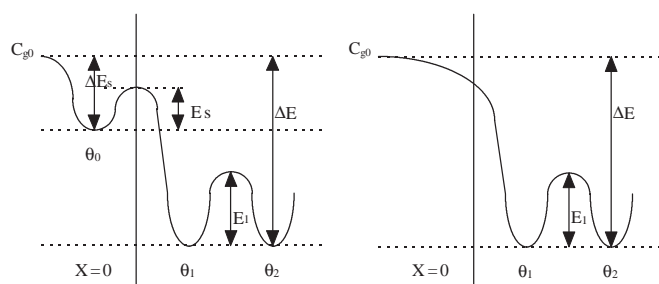


**Figure 3.** FTIR spectra of typical xerogel. Reprinted with permission from [95], J. C. Diniz da Costa, Synthesis and Characterisation of Molecular Sieve Silica (MSS) Membranes, Ph.D. Thesis, University of Queensland, Brisbane, Australia, 2000.

basically constant for both xerogel and templated xerogel, suggesting that water and alcohol are continuously expelled from the xerogel matrix due to condensation reactions. The sharp weight loss at about ∼450 °C for templated xerogels is attributed primarily to the oxidative pyrolysis of organic templates [10].

### 3.1.2. Infrared Spectroscopy

Infrared transmission spectroscopy is a volume rather than a surface specific technique because the interactions of sample volume with radiation do not define a surface at the atomic scale [68]. Therefore, FTIR spectroscopy is intentionally carried out to determine the molecular functional groups embedded in the bulk xerogel matrix only. As xerogels are optically too dense to measure the transmission spectra directly [69], bulk xerogels are crushed into very small particles and are pressed into KBr pellets.

Representative IR spectra of xerogels are depicted in Figure 3. The IR bands corresponding to silanol and silicon alkoxide groups generally appear in the range from ∼1400 to ∼600 $cm^{-1}$. The bands assigned to siloxane bonds at ∼800, 1080, and 1220 $cm^{-1}$ are listed in Table 2. The silanol band at ∼940 $cm^{-1}$ which appears very strongly at 50 °C decreases in intensity with increase in the calcination temperature [39, 40, 68]. This supports the view that polycondensation is the underlying process responsible for the transformation of silanols to silicons, as is also evidenced by the fact that the siloxane bands at ∼1092 $cm^{-1}$ increase in intensity at high calcination temperatures. It is also observed that siloxane bands at ∼1058 $cm^{-1}$ at 50 °C shift towards ∼1087 $cm^{-1}$ at 400 °C and ∼1092 $cm^{-1}$ at 550 °C. According to Duran et al. [40], this shift involves the strengthening of
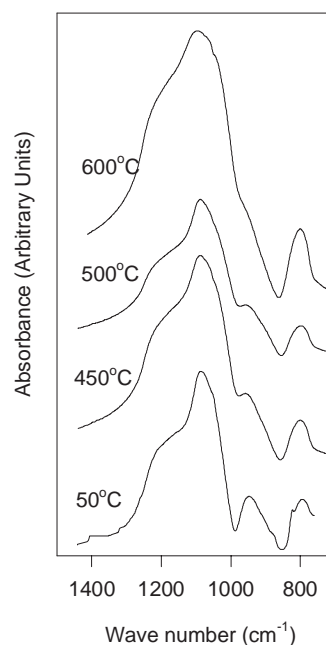
the xerogel network and can be interpreted as a shrinkage produced by polymeric bonding.

### 3.1.3. Nuclear Magnetic Resonance

Solid-state NMR spectroscopy complements IR spectroscopy because IR classifies the surface hydroxyls according to their bond strength (free and bridged silanols) while $^{29}$Si NMR distinguishes single (either isolated or vicinal) from double (geminal) silanols [56]. Xerogel samples are crushed in small particles and spun at a frequency of 2.5 KHz with cross polarization contact time of 8 ms, which is sufficient to allow cross polarization of the silicon functional groups. A typical $^{29}$Si NMR spectrum of a templated xerogel sample is depicted in Figure 4. The spectrum can be deconvoluted using Gauss–Lorentz curve fitting software in order to determine the proportion of the functional groups embedded in the xerogel matrix.

In Figure 4, three peaks are observed with chemical shifts ($\delta$) in the region of −90 to −120 ppm, denoting the presence of $Q^2$, $Q^3$, and $Q^4$ species, and the peaks with chemical shifts relative to kaolin at −60 to −70 ppm are associated with $Me(OH)_2$Si-O-Si bonds [41, 42, 51–53, 56]. To differentiate from the silicon nomenclature, these peaks are referred to as $T^n \cdot T^3$ species are bound by three Si-O-Si links and one

**Table 2.** Assignment of IR absorption spectra for templated xerogels.

|  |  | Ref. |
|---|---|---|
| 800 $cm^{-1}$ | Stretching mode Si-O-Si symmetric | [39, 40] |
| 960 $cm^{-1}$ | Stretching mode Si-OH | [39, 40, 68] |
| 1080 $cm^{-1}$ | TO mode Si-O-Si asymmetric | [40] |
| 1220 $cm^{-1}$ | LO mode Si-O-Si asymmetric | [39, 40] |
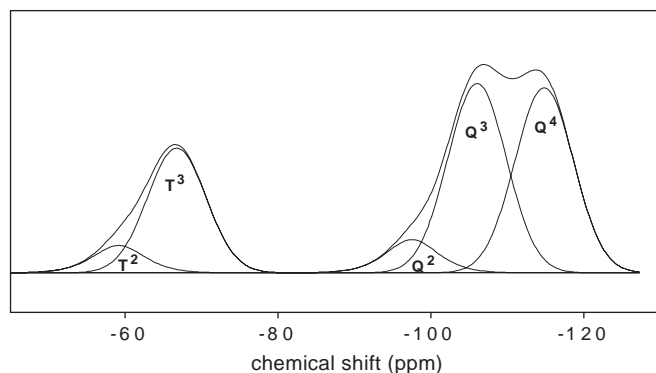
**Figure 4.** Deconvoluted NMR spectrum of sample 10/90 (400 °C). Reprinted with permission from [95], J. C. Diniz da Costa, Synthesis and Characterisation of Molecular Sieve Silica (MSS) Membranes, Ph.D. Thesis, University of Queensland, Brisbane, Australia, 2000.

carbon while $T^2$ is formed by two Si-O-Si links, one Si-OH, and one carbon. In practical terms, NMR spectroscopy is a powerful tool to assist researchers in developing xerogels with the microstructure required for MSS membranes, in particular directed to inference to fractal theory.

### 3.2. Adsorption

#### 3.2.1. Volumetric Adsorption

Gas adsorption/desorption is one of the most important and extensively used methods in the characterization (porous volume, specific surface area, and pore size distribution) of porous inorganic materials [3, 70]. Physical characterization of bulk xerogels is carried out by nitrogen adsorption at 77 K to determine the micropore volume, surface area, and pore size. In this technique, the samples must be degassed for a period of 3 hours or even longer at 250 °C prior to sorption experiments.

Typical $N_2$ sorption isotherms for a xerogel sample as a function of calcination temperature are shown in Figure 5. These isotherms are of type I, characteristic of microporous materials. Table 3 shows the results of micropore surface, volume, and average pore size for several xerogel samples. These results are obtained based on the t-plot method. The trend is quite clear that an increase in the calcination temperature reduces micropore surface and volume. There is a strong indication that the xerogel matrix continues to condense as calcination temperature increases. Despite this, no significant changes are observed in Table 3 with respect to pore size, suggesting that pore size remains quite constant in the calcination temperature range of 400–550 °C. These trends are generally observed for various sol–gel formulations and are attributed to the densification of the base-catalyzed xerogel matrix [51] and the HCl catalyzed xerogels [10].

Pore size distributions as plots of $dV/dr_h$ as function of the corresponding $r_h$ are shown in Figure 6. $V$ is the micropore volume ($cm^3 \cdot g^{-1}$) and $r_h$ is the hydraulic radius (Å). The pore size distribution was calculated according to the improved MP method developed by Zhu et al. [71] and based on nonporous silica adsorption data from Gregg and Sing [70]. For microporous materials, other methods
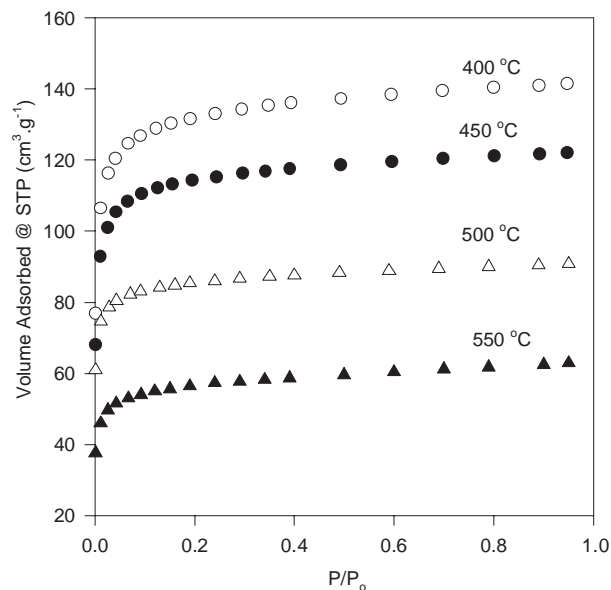


**Figure 5.** $N_2$ sorption isotherms of sample 50/50. Reprinted with permission from [95], J. C. Diniz da Costa, Synthesis and Characterisation of Molecular Sieve Silica (MSS) Membranes, Ph.D. Thesis, University of Queensland, Brisbane, Australia, 2000.

(HK and SF) for the determination of the pore size distribution can also be used. The pore size distribution ranges in the microporous region, suggesting that these xerogels can be used ideally for molecular sieving applications. It is observed that prominent peaks appear in the pore size range of $\sim$7.4 $\sim$8.9 $\sim$8.4 Å corresponding to pore filling at lower partial pressures as observed from the $N_2$ sorption experiments. As the calcination temperature increases, it promotes densification of the xerogel matrix and reduction in peak height (pore volume), but not much in pore size reduction.

#### 3.2.2. Gravimetric Adsorption

Gravimetric adsorption measurements are performed to determine thermodynamic conditions of xerogel materials. This is generally carried out by measuring the displacement of a quartz spring due to the sorption of gas molecules (sorbate) on the xerogel samples (sorbant). The sorption isotherms can be determined for various sorbates in order to calculate the isosteric heat of adsorption. Xerogel samples are degassed overnight at $P < 10^{-3}$ Torr at 300 °C prior to gas adsorption experiments. In this experiment, the bulk xerogel samples are subjected to a step change in sorbate pressure from an initial zero to a final atmospheric pressure.

**Table 3.** Pore structure data of various xerogel samples.

| Calcination temperature (°C) | Micropore volume ($cm^3 \cdot g^{-1}$) | Micropore surface ($m^2 \cdot g^{-1}$) | Average pore radius (Å) | Total pore volume ($cm^3 \cdot g^{-1}$) |
|---|---|---|---|---|
| 400 | 0.193 | 451.7 | 8.6 | 0.199 |
| 500 | 0.153 | 350.2 | 8.8 | 0.161 |
| 600 | 0.078 | 176.6 | 8.9 | 0.084 |
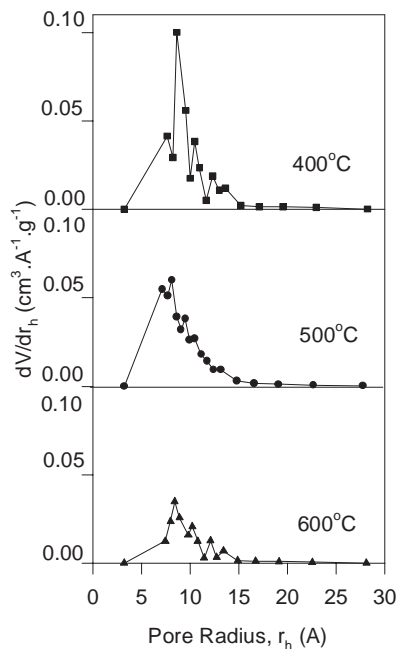
**Figure 6.** Pore size distribution of xerogel calcined at 400, 500, and 600 °C. Reprinted with permission from [95], J. C. Diniz da Costa, Synthesis and Characterisation of Molecular Sieve Silica (MSS) Membranes, Ph.D. Thesis, University of Queensland, Brisbane, Australia, 2000.

The weight adsorbed is measured as a function of partial pressure.

In Figure 7, representative $CO_2$ sorption isotherms are shown at temperatures 273–373 K for xerogels. The isotherms are given by plotting the amount adsorbed
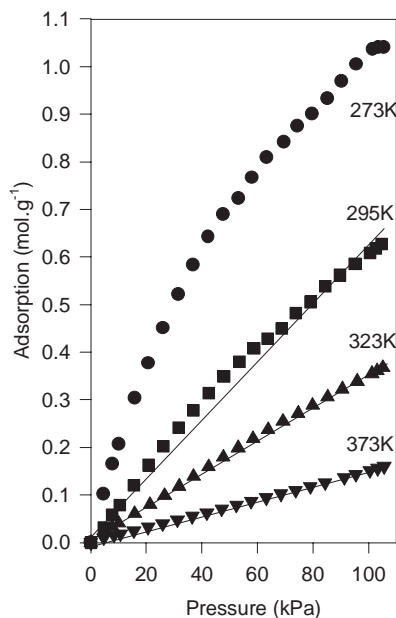


**Figure 7.** $CO_2$ adsorption isotherms for two-step xerogels. Reprinted with permission from [95], J. C. Diniz da Costa, Synthesis and Characterisation of Molecular Sieve Silica (MSS) Membranes, Ph.D. Thesis, University of Queensland, Brisbane, Australia, 2000.

$(mol \cdot g^{-1})$ versus pressure (kPa). The isotherms at 273–295 K are nonlinear and of Langmuir type. The Langmuir theory is based on the kinetic principle of equilibria; that is, the rate of adsorption is equal to the rate of desorption from the surface [72]. The Langmuir theory assumes that surfaces are homogeneous (all sites are energetically equivalent) and each site can hold one adsorbate molecule only with no interaction between molecules adsorbed on neighboring sites. The Langmuir adsorption isotherm which gives the relation of the amount of gas adsorbed as a function of the pressure at a given temperature is expressed as follows:

$$\theta = \frac{c\rho}{c_s\rho} = \frac{q}{q_s} = \frac{bp}{1+bp} \qquad (6)$$

where $c$ is the concentration $(mol \cdot m^{-3})$, $c_s$ is the concentration at saturation $(mol \cdot m^{-3})$, $q$ is the amount adsorbed $(mol \cdot gram^{-1})$, $b$ is the adsorption equilibrium constant $(Pa^{-1})$, $p$ is the pressure (Pa), and $\theta$ is the surface coverage. For adsorption on a uniform surface at sufficiently low concentrations, the equilibrium relationship between the gas phase and adsorbed phase concentration will be linear and generally referred to Henry's law [73]. Hence, Eq. (6) can be simplified to

$$q = q_s \, bp = Kp \qquad (7)$$

where $K$ is the Henry constant $(mol \cdot Pa^{-1} \cdot gram^{-1})$. At temperatures in excess of 323 K for $CO_2$ adsorption, the isotherms are practically linear implying that they comply with Henry's law [74] as it is observed in Figure 7.

One of the basic quantities in adsorption studies is the isosteric heat, which is the ratio of the infinitesimal change in the adsorbate enthalpy to the infinitesimal change in the amount adsorbed [72]. If $Q_{st}$ is taken to be independent of temperature, the temperature dependence of the Henry constant obeys the Van't Hoff equation [73]:

$$K = K_0 \exp\left(\frac{Q_{st}}{RT}\right) \qquad (8)$$

where $K_0$ is a temperature-independent proportionality constant, $Q_{st}$ is the isosteric heat of adsorption $(J \cdot mol^{-1})$, $R$ is the gas constant $(J \cdot mol^{-1} \cdot K^{-1})$, and $T$ is the absolute temperature (K). In accordance with Eq. (8), the slope of the natural logarithm of the $K$ versus $1/T$ yields $Q_{st}$.

The Arrhenius plots of the Henry constant $(\ln(K)$ versus $T^{-1})$ for single-step and double-step xerogels for several gases are depicted in Figure 8. The isosteric heats of adsorption $(Q_{st})$ reported in the literature for silica xerogel and silicalite zeolites are presented in Table 4 for comparison.

## 3.3. Characterization of Membrane Films

### 3.3.1. X-ray Photoelectron Spectroscopy

X-ray photoelectron spectroscopy is widely used as a surface analysis technique capable of providing an element analysis of surface within a 10% accuracy [75]. XPS sputter profiles and scanning Auger microscopy are also used in order to complement the silica film thickness SEM characterization, in particular to determine the interface between the silica film and aluminum substrate. In this experimental
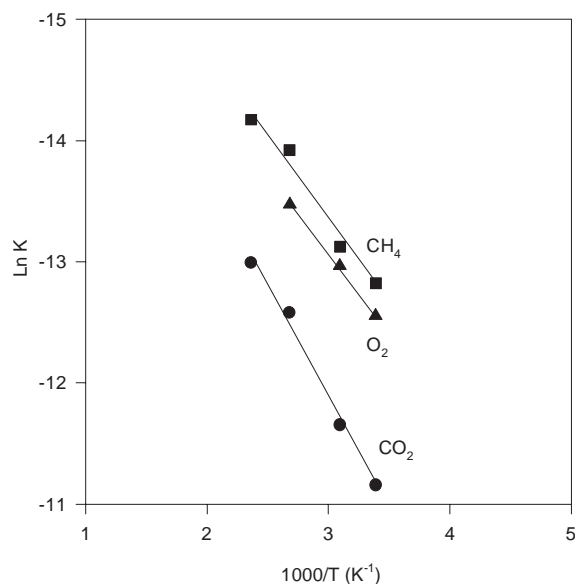
**Figure 8.** Arrhenius plot of the Henry constant. Reprinted with permission from [95], J. C. Diniz da Costa, Synthesis and Characterisation of Molecular Sieve Silica (MSS) Membranes, Ph.D. Thesis, University of Queensland, Brisbane, Australia, 2000.

technique, sputter rates by $Ar^+$ ion bombardment are used and are calculated from the calibrated sputter rate for dense $Ta_2O_5$. [58, 76]. The order of sputter rates for $Si_2$ is in the region of 60 nm $\cdot$ h$^{-1}$ using $Ar^+$ at 4 keV and 4.5 $\mu$A. The sputtered area formed a rhombus of $9 \times 9$ mm. The analyzed surface is centered in the rhombus with a diameter of 4 mm.

A typical XPS spectrum for intermediate silica templated film layer cast on $\alpha$-$Al_2O_3$ substrate and dried at 50 °C is shown in Figure 9a with an indication of the peaks for oxygen, carbon groups, aluminum, and silica. XPS is an *in-situ* technique useful to characterize the surface morphology of membrane films. Figure 9b depicts the stratum profiles of a representative MSS membrane which contains four intermediate layers of templated xerogel and four layers of silica xerogel. It shows the XPS sputter profiles for the relative concentration of aluminum, carbon, oxygen, and silica as a function of the sputter depth.

The resulting profiles show a decrease of silica concentration with an associated increase of aluminum concentration from a sputter depth of 60 nm. The interface between the silica film and the $\alpha$-$Al_2O_3$ substrate occurs approximately at a crossover sputter depth of 240 nm. From there on, the concentration of silica reduces at a rate of $2.5 \times 10^{-2}$ atoms
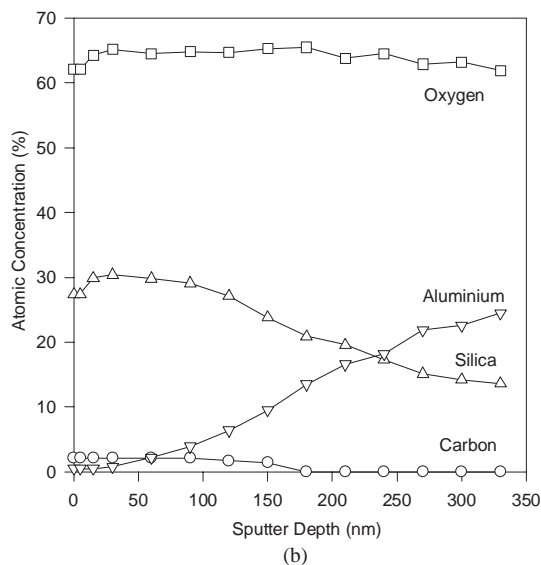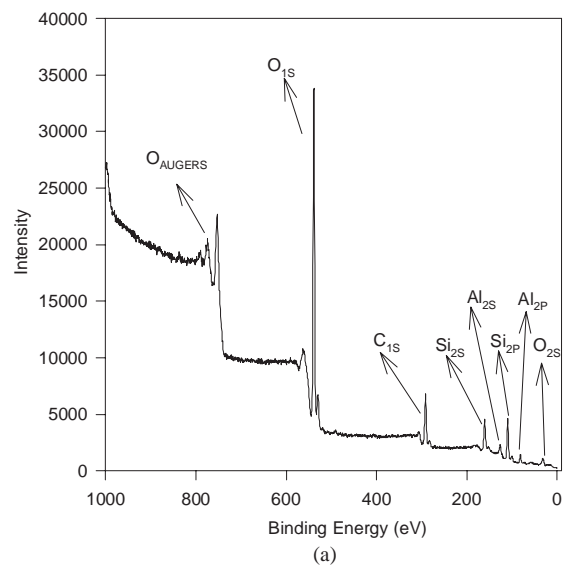




**Figure 9.** (a) XPS of a templated xerogel film dried at 50 °C and (b) XPS sputter profile. Reprinted with permission from [95], J. C. Diniz da Costa, Synthesis and Characterisation of Molecular Sieve Silica (MSS) Membranes, Ph.D. Thesis, University of Queensland, Brisbane, Australia, 2000.

% per nanometer. The carbon concentration profiles are mainly attributed to templates trapped in the silica matrix, indicating that concentrations of carbon groups are between 1 and 2% up to sputter depth of 180 nm with residual levels of less than 1% from there on.

### 3.3.2. Scanning Electron Microscopy

Several researchers [58, 62] have reported that scanning electron microscopy is a relevant *in-situ* technique to verify the individual layers (microporous) and substrates (mesoporous/macroporous) of membranes. SEM is carried out on a typical membrane to show its profile (cross section) and to determine the silica film thickness. Membrane cross sections are generally platinum or gold coated in high-purity Ar. Transmission electron microscopy (TEM) has also

**Table 4.** Typical isosteric heat of adsorption $Q_n$(kJ $\cdot$ mol$^{-1}$).

| Material | $CO_2$ | $CH_4$ | $H_2$ | $N_2$ | $O_2$ | Ref. |
|---|---|---|---|---|---|---|
| xerogel | 15.9 | 11.7 | 7.9 | 11 | 11 | [95] |
| silica | 22.3 | 10.3 | 6.1 | | | [77] |
| silicalite | 24.6 | 20 | | 17.3 | | [96] |
| silicalite | 24 | 18.6 | 6 | 15 | | [97] |
| silicalite | 20 | 28 | | | | [98] |
| silicalite | 24 | 20 | 6 | 17.6 | 16.3 | [99] |

been employed by researchers [31, 48] to analyze the profile layers of MSS membranes.

Typical cross sections of a MSS membrane are shown in Figure 10. The $\alpha$-Al$_2$O$_3$ substrate is very coarse while its coarseness decreases considerably very close to the silica top film. The silica film thickness varies throughout the membrane mainly due to the roughness of the substrate. The SEM does not show a good resolution at 100 nm dimensions.

# 4. MSS MEMBRANES AND APPLICATIONS

## 4.1. Modeling Gas Transport

### 4.1.1. Transport Mechanisms

The mechanisms that govern gas transport in mesoporous membranes (2 nm $< d_p <$ 50 nm) are (i) Knudsen diffusion, (ii) Poiseuille flow, and (iii) surface diffusion. Uhlhorn and Burggraaf [8] have shown that transport rate of gas molecules through mesoporous membranes decreases with increasing temperature according to the following:

(i) Knudsen diffusion

$$F_{Kn} = \frac{2\varepsilon_p \mu_{Kn} \overline{vr}}{3RT\ell} \quad \text{with} \quad \bar{v} = \sqrt{\frac{8RT}{\pi M}} \quad (9)$$

where $F_{Kn}$ is the Knudsen permeation (mol·m$^{-2}$·s$^{-1}$·Pa$^{-1}$), $\varepsilon_p$ is the porosity, $\mu_{Kn}$ is a shape factor (equal to $1/\tau$), $\tau$ is the tortuosity, $R$ is the gas constant (J·mol$^{-1}$·K$^{-1}$), $T$ is the absolute temperature (K), $\bar{v}$ is the average molecular velocity (m.s$^{-1}$), $\bar{r}$ is the modal pore radius (m), $\ell$ is the layer thickness (m), and $M$ is the gas molecular mass (kg·mol$^{-1}$).

(ii) Poiseuille permeation

$$F_P = \frac{\varepsilon_p \mu_P \overline{r^2}}{8RT\eta\ell} P_m \quad (10)$$

where $F_P$ is the Poiseuille permeation (mol·m$^{-2}$·s$^{-1}$·Pa$^{-1}$), $\mu_P$ is the reciprocal tortuosity, $\eta$ is the gas viscosity (N·s·m$^{-2}$), and $P_m$ is the mean pressure across the membrane (Pa).

(iii) Surface diffusion

$$J_S = \rho_{app} D_S \mu_S \frac{dq}{d\ell} \quad (11)$$

where $J_s$ is the surface diffusion flux (mol·m$^{-2}$·s$^{-1}$), $\rho_{app}$ is the apparent density (kg·m$^{-3}$), $D_s$ is the surface diffusion coefficient (m$^2$·s$^{-1}$), $\mu_s$ is the reciprocal tortuosity, and $dq/d\ell$ is the surface concentration gradient (mol·kg$^{-1}$·m$^{-1}$).

On the other hand, de Lange et al. [77] have shown that the transport of diffusing molecules through microporous membranes is activated in which the flux $J$ (mol·m$^{-2}$·s$^{-1}$) increases as a function of temperature according to

$$J \propto J_0 \exp\left(\frac{-E_{act}}{RT}\right) \quad (12)$$

where $J$ is the flux (mol·m$^{-2}$·s$^{-1}$) through the membrane, $E_{act}$ (kJ·mol$^{-1}$) is an apparent activation energy, $R$ is the gas constant, and $T$ is the absolute temperature (K).

### 4.1.2. Single-Gas Transport Mechanism Through Microporous Materials

Barrer [78] proposed a model of transport through microporous (single crystal zeolite) membranes as shown in Figure 11. The model can be best described in three sequential steps, namely ($j$) transport from the gas phase to the micropore, ($jj$) migration through the micropore, and ($jjj$) transport from the micropore to the gas phase. Gas-phase transport to the micropore ($j$) can take place by two parallel fluxes: ($j_1$) directly from the gas phase to the pore entrance and ($j_2$) via the external surface involving surface diffusion.

**Figure 10.** SEM of a middle cross section of a MSS membrane. Reprinted with permission from [95], J. C. Diniz da Costa, Synthesis and Characterisation of Molecular Sieve Silica (MSS) Membranes, Ph.D. Thesis, University of Queensland, Brisbane, Australia, 2000.
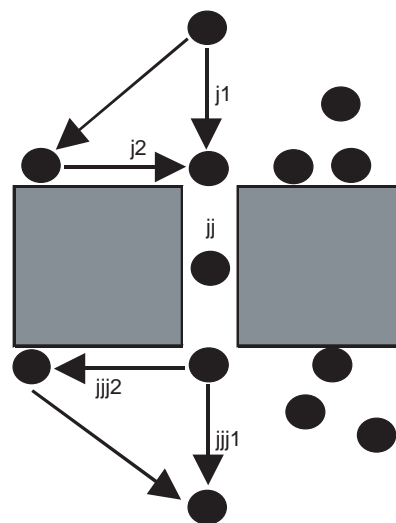
**Figure 11.** Model of gas transport through microporous membranes. Reprinted with permission from [95], J. C. Diniz da Costa, Synthesis and Characterisation of Molecular Sieve Silica (MSS) Membranes, Ph.D. Thesis, University of Queensland, Brisbane, Australia, 2000.

At the pore entrance at the retentate side to the pore exit at the permeate side, micropore diffusion ($jj$) takes place. Transport from the micropore to the gas phase ($jjj$) at the permeate side can also take place by two parallel fluxes: ($jjj_1$) desorption from the pore exit directly to the gas phase and ($jjj_2$) desorption via an external surface to the gas phase.

The potential energy profiles for both parallel fluxes ($j_1$ and $j_2$) are shown in Figure 12. $E_1$ is the apparent activation energy for micropore diffusion, $\Delta E$ is the energy difference between the gas phase and the molecules present in the micropore which is a heat of adsorption and is equal to $-Q_{st}$, $E_s$ is the activation energy for pore entrance from the external surface, and $\Delta E_s$ is the energy difference between the molecules adsorbed on the external surface and the gas phase [77]. For a molecule to permeate from the retentate side to the permeate side of a membrane, energy barriers ($E_s + \Delta E - \Delta E_s - E_1$) in 12a or ($\Delta E - E_1$) in Figure 12b must be overcome in the case where both internal and external adsorption obey Henry's law. Using Barrer's model, de Lange et al. [77] conducted an extensive assessment of the role of the surface diffusion of $CO_2$ and $H_2$ in microporous silica membranes. They found that the surface diffusion contributes only 2% to the total $H_2$ flux while $CO_2$ surface diffusion is not rate determining in the situations studied (291 $K < T < 573$ $K$ and $0 < p < 4$ bar).

In the case where interface process does not play a significant role, the surface barriers ($E_s$ and $\Delta E_s$) are extremely low and the gas-phase diffusion limitations can be neglected. Hence, microporous diffusion is the rate-limiting step as thermodynamic equilibrium is assumed at the interface [31]. As microporous diffusion is an activated transport, external surface diffusion can not be rate determining. According to de Lange et al. [77], the transport from the gas phase to the membrane is not likely to be rate determining either. Using the kinetic gas theory, they determined that even in a pessimistic scenario with a porosity of 1% and sticking probability of 1%, the collisional flux would exceed permeation by more than one order of magnitude.

If microporous flux ($jj$) is rate determining, the energy barriers are $\Delta E$ and $E_1$ where $E_1$ can be described as the mobility energy ($E_m$). According to the atomic jump theory, $E_m$ represents the energy barrier between two adsorption sites [79]. Hence, $E_m$ can be determined from apparent activation energy for permeation ($E_a$):

$$E_m = E_a - \Delta E \qquad (13)$$



**Figure 12.** Potential energy profiles of gas transport in membranes. Reprinted with permission from [95], J. C. T. Diniz da Costa, Synthesis and Characterisation of Molecular Sieve Silica (MSS) membranes, Ph. D. Thesis, University of Queensland, Brisbane, Australia, 2000.

where $\Delta E$ can be determined from the isosteric heat of adsorption ($Q_{st}$) by assuming that the contribution of the external surface can be neglected:

$$\Delta E = -Q_{st} \qquad (14)$$

The discussion so far is clearly limited to gases operating in the Henry regime. This type of approach may not be applicable to large and branched molecules (i.e., hydrocarbons) because direct entrance is unlikely and an adsorption step at the external surface is necessary [80]. However, hydrocarbons are large molecules and are likely to be discriminated from permeation in micropore membranes by size exclusion.

### 4.1.3. Activated Transport in Single Gas Permeation

Microporous diffusion is assumed to be the rate-limiting step. Hence, the diffusion of molecules in microporous materials is modelled as an activated process according to an Arrhenius relation:

$$D = D_0 \exp\left(\frac{-E_m}{RT}\right) \qquad (15)$$

where $D_0$ is a temperature-independent proportionality constant, $E_m$ is the mobility energy ($J \cdot mol^{-1}$), $R$ is the gas constant ($J \cdot mol^{-1} \cdot K^{-1}$), and $T$ is the absolute temperature (K). De Lange et al. [77] and da Costa et al. [74] showed that the sorption of several gases ($H_2$, $CO_2$, $O_2$, Ar, $N_2$, and $CH_4$) complied with Henry's law except $CO_2$ which showed a slight nonlinearity for temperatures below 50 °C. Hence, gas adsorption is in the low coverage of Henry's regime:

$$c = Kp \qquad (16)$$

where $p$ is pressure (Pa) and $K$ is Henry's constant as a function of temperature according to a van't Hoff relation (Eq. (8)). Substituting Eqs. (15), (16), and (8) into Fick's law gives a temperature dependency flux Eq. (17) in the Henry regime:

$$J_x = -D_0 K_0 \exp\left(\frac{Q_{st} - E_m}{RT}\right)\frac{dp}{dx} \qquad (17)$$

The permeance ($P/\ell$) may be defined as an activated transport normalized pressure flux ($mol \cdot m^{-2} \cdot s^{-1} \cdot Pa^{-1}$) as follows:

$$\frac{P}{\ell} = \frac{D_0 K_0}{\ell} \exp\left(\frac{E_m - Q_{st}}{RT}\right) \qquad (18)$$

Having determined permeance values at different temperatures, the slope of the natural logarithm of permeance versus $1/T$ will yield $E_a$, the activation energy of diffusing molecules in amorphous silica membranes given by Eq. (19) (see Eqs. (13) and (14)):

$$E_a = E_m - Q_{st} \qquad (19)$$

Permselectivity ($F_\alpha$) is a parameter that describes the separation efficiency of membranes based on single-gas permeation results for gases "A" ($J_A$) and "B" ($J_B$):

$$F_\alpha = \frac{J_A}{J_B} \qquad (20)$$

Permselectivity of molecular sieve membranes must be superior as measured against a benchmark separation factor known as the Knudsen ideal separation parameter ($\alpha^*$) as given by Eq. (21). In other words, membranes with permselectivity close to Knudsen's ideal separation parameters are likely to have pore sizes larger than those of molecular sieve materials. Membranes which comply with Knudsen diffusion result in low permselectivity while molecular sieve membranes show high permselectivity:

$$\alpha^* = \sqrt{\frac{M_A}{M_B}} \qquad (21)$$

## 4.2. MSS Membranes

MSS membranes reported in the literature generally do not have the same architectural structures, as their configuration and synthesis processes from substrate to top layer may differ. The establishment of appropriate criteria for performance comparison presents some difficulty. Having said that, high-quality membranes are generally characterized by high fluxes, selectivities, and activation energies. A summary of typical permeation results is shown in Table 5 for the production of defect-free MSS membranes using the sol–gel processes such as:

- a single-step catalyzed hydrolysis using $HNO_3$ as a catalyst [31, 32, 58]
- a templated single-step [45]
- or templated two-step catalyzed hydrolysis using HCl followed by pore tuning using nonhydrolyzed tetraethoxysilane diluted in ethanol [10]
- a templated two-step catalyzed hydrolysis [48]
- a two-step catalyzed hydrolysis [33]

Nair et al. [32] reported improved permeation results for MSS membranes and high $He/N_2$ permselectivities of 514 using a single-step sol–gel process. Raman and Brinker [10] prepared membranes using an organic ligand template (MTES) and an unhydrolyzed sol for micropore tuning. Although no separation between He and $CO_2$ was observed,

**Table 5.** Permeation of membranes ($10^{-9}$ mol · m$^{-2}$ · s$^{-1}$ · Pa$^{-1}$).

| Type | $P_{He}$ | $P_{H_2}$ | $P_{CO_2}$ | $P_{N_2}$ | $P_{CH_4}$ | Ref. |
|------|------|------|------|------|------|------|
| S |  36 |  |  | 0.07 |  | [32] |
| S |  | 740 | 80 |  |  | [58] |
| S |  | 591 | 228 | 10 | 0.7 | [31] |
| Tmp -T | 53 | 44 | 8 | 0.14 | 0.03 | [48] |
| T | 51 | 12 | 0.20 | 0.08 | 0.06 | [33] |
| Tmp -T | 44 |  | 68 |  | 0.95 | [10, 45] |
| Tmp |  | 100 | 9 | 1.2 | 2.5 | [45] |

Tmp (template), T (two-step), S (single-step).

the templated MSS membranes resulted in $CO_2/CH_4$ permselectivity of 71, indicating a high pore tailorability between the molecular kinetic diameters of $CO_2$ ($d_k = 3.3$ Å) and $CH_4$ ($d_k = 3.8$ Å). Kusakabe et al. [45] also prepared templated membranes using TEOS and alkyltriethoxysilanes (e.g., octyl and dodecylgrietoxysilanes) as template agents. They reported high permeation results for $H_2$, but permselectivities were relatively low in the order of 10 ($H_2/CO_2$) and less than 1 for $N_2/CH_4$. The latter permselectivity result indicates that a large diffusing molecule ($CH_4$) was diffusing preferentially in favor of smaller molecule ($N_2$).

De Vos and Verweij [31] reported high permeances and selectivities of $H_2$ and $CO_2$. The $H_2/CO_2$ permselectivity ranged between 2.5 and 7.5, while for the membranes calcined at 600 °C permselectivity increased to values between 18 and 130 with a half reduction in $H_2$ permeance. De Vos and co-workers were able to produce 30-nm-thick silica films by using clean rooms of class 1000 [67]. MSS films prepared in typical non-clean room laboratory facilities have thickness ranging between 500 and 2000 nm, which are 17 to 67 times thicker than the films prepared in clean-room facilities. As the flux of gases is inversely proportional to film thickness, membranes synthesized in clean rooms are likely to achieve $H_2$ permeances in excess of $1.0 \times 10^{-6}$ mol · m$^{-2}$ · s$^{-1}$ · Pa$^{-1}$ and $H_2/CO_2$ selectivities of as high as 150 due to extremely low dust concentration.

Brinker et al. [55] have reported that the two-step catalyzed hydrolysis process of bulk gels resulted in pore size reduction as compared to the single-step process. However, the two-step sol–gel process has only been employed recently by Tsai et al. [48] and Diniz da Costa et al. [33] in the preparation of MSS membrane films. Tsai et al. [48] used a two-step process and added C6 or C16 surfactants (triethylhexylammonium or cetyltrimethylammonium). They reported very high selectivities for $H_2/N_2$ (316) and $CO_2/CH_4$ (150–190), indicating that a high degree of pore size control was achieved for the separation of molecules with kinetic diameters higher than $CO_2$. Diniz da Costa et al. [33] reported that two-step MSS membranes had average pore sizes of 3.0 Å according to the separation of He ($d_k = 2.6$ Å), $H_2$ ($d_k = 2.89$ Å), and $CO_2$ ($d_k = 3.3$ Å). High selectivities were observed for $He/CO_2$ (255) and $H_2/CO_2$ (60) while permeation of He and $H_2$ was relatively high as listed in Table 5.

The literature also presents results for MSS membranes derived from other synthesis processes. Using microporous glass fibers, Shelekhin et al. [26] reported permselectivities as high as 11674 for He and $CH_4$. Although their He permeation results were very low, in the order of $3.5 \times 10^{-11}$ mol · m$^{-2}$ · s$^{-1}$, they clearly indicated high control of pore size as permeation decreased by several orders of magnitude with increase in the kinetic diameter of gases. Lin et al. [81] and Wu et al. [82] reported the production of silica membranes with similar qualities made by the CVD method. The He and $H_2$ permeance of their high-quality membranes were in the region of $1.0 \times 10^{-10}$ to $1.0 \times 10^{-11}$ mol · m$^{-2}$ · s$^{-1}$ with $He/H_2$ and $H_2/N_2$ permselectivities ranging between 1.0 and 7.0 and 2.4 and 513, respectively. Ha et al. [83] and Tsapatsis et al. [84] also made silica membranes by CVD deposition using Vycor glass tubes as substrate. The $H_2$ permeances are similar to those reported by Lin, Wu, and co-workers, but with

good $H_2/N_2$ selectivities of 880–2040 [83] and 125–1200 [84]. MSS membranes derived by CVD have permeances four to five orders of magnitude below the dip-coating results presented earlier.

Discussion of permeance and permselectivity should also include the apparent energy of activation as an extra assessment parameter of membrane quality. The apparent energy of activation for $H_2$ permeation gives a good correlation with the separation factor and may be used as a measure of quality [80]. According to de Lange and co-workers [85], high-quality membranes should have an apparent energy of activation for $H_2$ permeance of at least 10 kJ·mol$^{-1}$. Typical results of the apparent activation energy of two-step sol–gel membranes for $H_2$ permeance values range between 10.5 and 17.6 kJ·mol$^{-1}$ with the majority of the values in excess of 14.0 kJ·mol$^{-1}$ [33]. These results are higher than the apparent energy of activation for $H_2$ permeance of single-step MSS membranes of 10 kJ·mol$^{-1}$ or lower [31, 58].

There are two major contentious points in the literature regarding the thermodynamic properties of diffusing molecules. De Vos and Verweij [31] reported that the activation energy for the permeation of $CO_2$ is negative ($-2$ to $-4$ kJ·mol$^{-1}$) for membranes prepared by the single-step silica process. In some cases, the $CO_2$ permeation increased up to 50–100 °C, then decreased. However, Diniz da Costa and co-workers [33] found the opposite behavior for two-step membranes. They reported that the $CO_2$ permeation decreased up to 50–100 °C, then increased thereafter. Hence, the activation energy for $CO_2$ permeation was positive (4 to 7 kJ·mol$^{-1}$). The permeation model discussed above assumes linearity and $CO_2$ permeation shows nonlinearity at low temperatures [74]. It is not clear how this anomalous transport occurs in molecular sieving materials. Hence, the $CO_2$ transport in these materials merits further research.

The second contentious point is related to the sorption characteristics of silica films. The major dilemma in this situation is to determine the $Q_{st}$ representative of the microstructure of supported silica films (i.e., excluding membrane support and intermediate layers). The comparison of the isosteric heat of adsorption results with values given in the literature is very important because in principle there is an endeavor to determine $Q_{st}$ values that reflect the molecular sieving characteristics of amorphous silica microporous film. This comparison is made against silicalite which is a pure silica zeolite with elliptical straight channels (5.7 Å × 5.1 Å) and sinusoidal channels of $4.5 - 5.5$ Å pore diameter [31, 86]. The pore radius of the produced bulk xerogel is in the order of 8–9 Å [54] which is clearly greater than the silicalite pore radius.

In principle, the calculated $Q_{st}$ values for bulk xerogels may not reflect the true $Q_{st}$ of the final membrane molecular sieving silica films in view of different morphology (i.e., pore size). The $Q_{st}$ results of de Lange et al. [58] for unsupported silica films are in the same range of silicalite for $CO_2$ (20–28 kJ·mol$^{-1}$) and $H_2$ (6 kJ·mol$^{-1}$) and approximately half for $CH_4$ (19–28 kJ·mol$^{-1}$). However, the structural morphology of unsupported silica films and supported membrane films may also differ. The former is prepared on Petri dishes (i.e., nonporous surface) while the latter is cast on porous metal oxides. The substrate morphology affects the

overall film microstructure. In view of the considerable technical difficulties to simulate unsupported silica films with the same characteristics as supported silica films, de Vos and Verweij [31] argued that the $Q_{st}$ of silicalite can be regarded as a model system for the microporous membrane silica. In this context, it is important to observe that $CH_4$ has a very strong adsorption capacity in silicalite but a low capacity in unsupported silica films or xerogels.

## 4.3. Applications

In view of molecular separation and pore size tailorability, MSS membranes are ideal for applications requiring gas separation and/or gas stream enrichment. The main advantages of membranes are their high recoveries and versatility in handling different feed compositions under varying feed conditions. Also membranes can be built as compact operational modules which require low capital investment. Some examples of application include:

- *Petrochemical*—separation and/or enrichment of hydrogen gas streams
- *Petrochemical*—hydrogenation and dehydrogenation reactions
- *Fuel Cells*—portable energy generators and vehicles
- *Energy Generation*—integrated gasification combined-cycle systems (IGCC)
- *Flue Gas*—$CO_2$ separation

### 4.3.1. Transportation and Industrial Applications

MSS membrane employment is directly concerned with polymeric electrolyte membrane (PEM) fuel cells, which is a technology being developed for motor vehicles (50–100 kW), residential (2–10 kW), and commercial (250–500 kW) power generation, as well as small/portable generators and battery replacement. PEM fuel cells require a pure hydrogen source for operation. Hydrogen is typically obtained by reforming a hydrocarbon fuel (methanol or gasoline). In this reaction, the product is $H_2$, CO, $CO_2$, and water. CO levels of 50 parts per million (ppm) or greater are detrimental for the fuel cell operation due to catalyst poisoning and severe fuel cell degradation [87, 88]. As a modular system, MSS membranes can be easily installed in a fuel cell system to clean partially or totally CO. The use of MSS membrane reactors for the water gas shift reaction in fuel cells is now under investigation as an attractive commercial application.

Membrane technology in applications such is fuel cells is part of a system that will reduce airborne emissions compared with traditional internal combustion engines. Fuel cells emit less carbon dioxide and nitrogen oxides per kilowatt of power generated [89]. This technology is likely to be extremely beneficial for cities around the world where health problems are closely related to urban car emissions. As processes become more efficient by employing membranes, they greatly reduce energy consumption, leading to lower usage of fossil fuels and lower emission of greenhouse gases.

California and New York in the United States are leading a regulatory clampdown on $CO_2$ emissions, not only from industry, but also from motor vehicles. Legislation requires

that by 2005, 10% of the vehicles sold by vehicle manufacturers in the states be either zero emission vehicles, or a compliance program be offered for assessment which includes a progression to this target through partial zero emission vehicles, starting in 2004. Emphasis on zero emission in future transportation and/or energy generation is paramount and hydrogen fuel cell technology is foreseen as the preferred technology in view of zero tail-pipe emissions. These sorts of regulations are "encouraging" industry to invest in the alternative technologies of the future, with definite timelines being imposed for results.

In terms of energy efficiency, membrane reactors can improve conversions up to sixfold depending on the reaction. According to the U.S. Department of Energy, an energy saving of 10 trillion BTU per year (equivalent to 10 billion joules per year) could result from the use of catalytic membrane reactors as replacements for conventional reactors for dehydrogenation reactions [90]. Low-temperature fuel cells with membranes for hydrogen and carbon monoxide have electrical efficiency of 42% [91], which is much higher than the conventional combustion engines' efficiency of up to 33%. Regarding electrical power generation for buildings, fuel cells are likely to achieve higher energy efficiencies as losses in traditional power distribution lines are as high as 15% and thermoelectric power generation systems have efficiencies on the order of 38–40%.

The development in recent years of silica based membranes having consistent quality has paved the way for the application of membranes in high-temperature reactors. MSS membranes can operate up to temperatures of 500–600 °C, which is in the range of the majority of the reactions set up in Table 6. In many of these dehydrogenation processes, hydrogen is the reaction product which limits the overall conversion to a maximum dictated by the reaction equilibrium. By removing the hydrogen from the reactor, for example through a membrane process, the reaction is "pushed" to completion rather than equilibrium limited, providing an enhancement of conversion (5–8 times in some reactions) into product materials. According to Julbe et al. [92], membrane reactors are being explored in various configurations, but can be classified as follows:

- *Extractor*—removal of product(s) to enhance conversion by shifting the reaction equilibrium
- *Distributor*—to limit side reaction by controlled addition of reactant(s)
- *Active Contactor*—an engineered catalytic reaction zone by controlled diffusion of reactant(s)

**Table 6.** Application of porous inorganic membrane reactors [100].

| Reaction | Operating conditions |
|---|---|
| Dehydrogenation of ethane | 450–600 °C |
| Dehydrogenation of propane | 480–625 °C |
| Dehydrogenation of n-butane | 400–500 °C |
| Dehydrogenation of cyclohexane | 187–297 °C |
| Dehydrogenation of ethylbenzene | 550–640 °C |
| Dehydrogenation of methanol | 300–500 °C |
| Reduction of nitrogen oxide with ammonia | 300–350 °C |
| Steam reforming of methane | 445–590 °C |

There are also several new applications and innovative membrane reactor configurations. Generally, these systems are still in the research or development stages, addressing identified industrial and commercial concerns, for which current technological solutions are inadequate. These include [67]:

- Membrane reactors with separate feed-stock, where the reactants are mixed at different sides of the membrane
- Membrane reactors with condensing products
- Three-phase membrane reactors for sustained interface between liquids and gases
- Gas-phase filter reactors for simultaneous reduction of fly-ash and noxious gases
- Diesel exhaust soot converters to destroy incomplete combustion by-product aggregates (soot), which are carcinogenic agents
- Fluid bed membrane reactors for filtering slurry

Gas separation and enrichment are well-established industrial practices [5]. These include $H_2$ separation and recovery in petrochemical purge stream from hydro-processor, and $CH_4/CO_2$ separation in landfill gas for energy recovery applications. Air separation cannot be achieved with MSS membranes. The kinetic molecular diameters of $O_2$ and $N_2$ are very similar and pore size exclusion cannot be attained. However, $CO_2$ flue gas separation technologies are now attracting major research and industrial attention. Coal power generation plants are responsible for 36% $CO_2$ [93] emissions worldwide. As $CO_2$ sequestration techniques are now becoming socially and technically acceptable, the practicalities of energy supply are leading not to the abandonment of fossil fuels, but to the development of technologies directed towards flue gas separation and $CO_2$ sequestration.

### 4.3.2. Competitive Advantages

In application, membrane systems have to produce clear economic benefits in the form of reduced capital and operating costs, to be used in place of competing traditional separation technology methods for achieving the same outcome such as cryogenics, distillation, and pressure swing adsorption (PSA). The tendency appears for the noncryogenic technologies (membranes and PSA) to dominate the technology at medium to higher capacities, while cryogenics continues to dominate the highest capacities and ultrahigh purities [5]. It is expected that the situation for hydrogen separation will be very similar.

Metal (palladium and its alloys—Pd), zeolite, and polymeric membranes are major competitors for MSS membrane technology. Commercial polymeric membranes now have very high selectivity for hydrogen separation though temperature is limited to a maximum of 120 °C. Zeolite membranes are very stable up to 500 °C, but the pore size of zeolite is generally around 0.5 nm, resulting in very poor separation for hydrogen and other gases. On the other hand, Pd membranes show almost perfect hydrogen separation (close to 100% purity) while hydrogen permeation is similar to MSS membranes. Indeed, Pd membranes are the significant competitor to MSS membranes. However, Pd membranes are very unstable in environments containing steam. Furthermore, carbon monoxide blocks hydrogen, leading to lower permeation. Pd membranes are also very expensive,

on the order of US\$1250 to US\$2000 per square meter of membrane area [94].

The current barriers to broader introduction of inorganic MSS membrane technologies relate to the demonstration of long-term reliability and durability, robustness in processing with attention to processing potentially dirty streams, or developing *in-situ* regeneration and self-cleaning technologies. Further economic issues play a fundamental role regarding lowering the maintenance costs, scaled up methods to manufacture very large surface areas at commercially competitive prices, and the risk factor compared with established processes.

## 5. CONCLUSION

The key issues associated with the fabrication of membranes generally include support, sol–gel, and film technologies. Support substrates must have a narrow pore size distribution, low surface roughness, and extreme low defect density. Nonhomogeneous surfaces propagate stresses resulting in microporous films with a high defect density of large undesirable pores, pinholes, and microcracks. Membrane supports fundamentally provide the mechanical stability and integrity to the microporous thin films at the expense of increased flux resistance of diffusing molecules.

The preparation of microporous films depends upon the preceding formulation and preparation procedures of sols as well as the proceeding aging, drying, and heat treatment processes of gels. Based on the fractal theory, weakly branching polymer system promotes dense packing and low pore volume, resulting in microporous films. A primary condition to achieve weakly branching systems is to inhibit the condensation reactions during film formation. This is achievable by preparing sols with low $H_2O/Si$ molar ratio in a single-step or two-step catalyzed hydrolysis process. In film technology, sol–gel film dip-coating is extensively used as compared with chemical vapor deposition. In the dip-coating process, the thickness of the film increases as a function of the withdrawal speed of the substrate from a sol. MSS films are generally calcined between 400 and 600 °C at ramping rates of 0.5–1.0 °C·min$^{-1}$. Film defect concentration can be largely reduced by depositing films in dust-free environments (i.e., clean rooms). The transport of diffusing molecules through microporous silica films is activated diffusion as a function of the isosteric heat of adsorption $Q_{st}$ and the mobility energy $E_m$.

There are two major contentious issues within the literature review related to the characterization of the microstructure of the final deposited film. Based on the principle that the underlying physics and chemistry that govern polymer growth and gelation are the same for films and bulk gels, the characterization of bulk gels poses no technical problems as experienced by thin films. However, the gelation and drying conditions of thin films are quite different from bulk gels, which may lead to nonequivalent microstructure. The contentious issue of film morphology is also extended to the adsorption characteristics of films. Although it is relatively easy to conduct adsorption experiments in bulk gels or unsupported films, their structures may not be equivalent to the film microstructure. $CO_2$ permeation also shows anomalous results and further research is required to understand $CO_2$ diffusion in micropores.

The outlook for MSS membrane application is excellent, particularly with the forthcoming commercialization of fuel cell vehicles. It is particularly important to clean up the reformate gas as CO poisons fuel cell catalysts, with a potential second spin-off application for the water gas shift reaction. Although membrane reactor industrial applications have yet to materialize to a large extent, MSS membranes have the capability to operate at temperatures up to 500–600 °C, ideal for hydrogenation and dehydrogenation reactions in the petrochemical industry. MSS membranes still have to compete against traditional separation technologies. The market outlook for MSS membranes is likely to be small in medium module systems delivering medium- to high-purity separation and recovery.

## GLOSSARY

**Activated transport** A transport process in which the permeation (flux) increases with temperature.

**Activation energy** The total energy barrier for the micropore diffusion of a molecule.

**Adsorption** A process in which molecules attach themselves to the surface of a solid material.

**Asymmetric membranes** Membranes having layers with different structural characteristics such as pore size, surface area and pore volume.

**Fractal structures** In silica derived materials, fractal structures refer to a random formation of polyfunctional monomers.

**Gel** It is a substance that contains a continuous solid skeleton enclosing a continuous liquid phase [30].

**Membrane** A physical barrier device capable of separating gas and liquid molecules.

**Microporous** Pores diameter lower than 20 Å.

**Mobility energy** The energy barrier between two adsorption sites in micropore diffusion.

**Molecular imprint** A cavity left in a material matrix by burning off an organic template.

**MSS membranes** Membranes derived from a sol–gel process results in pore sizes of molecular dimension.

**Permeance** A parameter indicating the flow of molar mass per area of membrane per unit time per pressure difference across the membrane.

**Permselectivity** A ratio of permeance of two different gases in a single gas permeation test.

**Selectivity** A ratio of permeance of two different gases in a gas mixture permeation test.

**Silanol** A silica (Si) atom bonded to a hydroxyl (OH) group.

**Siloxane** An oxygen atom bonded to silica (SI—O—SI).

**Sol** It is a colloidal suspension of solid particles in a liquid [30].

**Template** A central structure allows network formation. Subsequently, the template can be removed creates a morphological cavity directly related to the features of the template.

**Xerogel** Dry gel.

## REFERENCES

1. P. Meares, in "Membranes in Gas Separation and Enrichment," (P. Meares, Ed.), p. 1. The Royal Society of Chemistry, London, 1986.
2. J. Gillot, in "Inorganic Membranes Synthesis, Characteristics and Application," (R. R. Bhave, Ed.), p. 1. Chapman and Hall, New York, 1991.
3. K. Keizer and H. Verweij, *Am. Chem. Soc.* 26, 37 (1996).
4. H. P. Hsieh, "Inorganic Membranes for Separation and Reaction." Elsevier, Amsterdam, 1996.
5. W. J. Koros and G. K. Flemming, *J. Membr. Sci.* 83, 1 (1993).
6. M. Mulder, "Basic Principles of Membrane Technology." Kluwer, Dordrecht, 1991.
7. S. Loeb and S. Sourirajan, *Adv. Chem. Ser.* 38, 117 (1962).
8. R. J. R. Uhlhorn and A. J. Burggraaf, in "Inorganic Membranes Synthesis, Characteristics and Application," (R. R. Bhave, Ed.), p. 155. Chapman and Hall, New York, 1991.
9. C. W. Jones and W. J. Koros, *Carbon* 32, 1427 (1994).
10. N. K. Raman and C. J. Brinker, *J. Membr. Sci.* 105, 273 (1995).
11. Y. S. Lin and A. J. Burggraaf, *J. Am. Ceram. Soc.* 74, 219 (1991).
12. A. J. Burggraaf and L. Cot, in "Fundamentals of Inorganic Membrane Science and Technology," (A. J. Burggraaf and L. Cot, Eds.), p. 1. Elsevier, Amsterdam, 1996.
13. J. Koresh and A. Sofer, *Sep. Purif. Tech.* 18, 723 (1983).
14. C. W. Jones and W. J. Koros, *Carbon* 32, 1419 (1994).
15. V. C. Geiszler and W. J. Koros, *Ind. Eng. Chem. Res.* 35, 2999 (1996).
16. T. Bein, *Chem. Mater.* 8, 1636 (1996).
17. M. D. Jia, K. V. Peinemann, and R. D. Behling, *J. Membr. Sci.* 82, 15 (1993).
18. J. M. Duval, B. Folkers, M. Mulder, G. Desgrandchamps, and C. A. Smolders, *J. Membr. Sci.* 80, 189 (1993).
19. I. F. J. Vankelecom, C. Dotremont, M. Morobe, J. B. Uytterhoeven, and C. I. Vadescasteele, *J. Phys. Chem. B* 101, 2160 (1997).
20. C. Dotremont, I. F. J. Vankelecom, M. Morobe, J. B. Uytterhoeven, and C. I. Vadescasteele, *J. Phys. Chem. B* 101, 2160 (1997).
21. Z. A. E. P. Vroon, Synthesis and Transport Studies of Thin Ceramic Supported Zeolite (MFI) membranes, Ph.D. Thesis, University of Twente, Enschede, the Netherlands, 1995.
22. E. R. Kleinfeld and G. S. Ferguson, *Science* 265, 370 (1994).
23. R. M. Barrer, "Zeolites and Clay Minerals as Sorbents and Molecular Sieves." Academic Press, London, 1975.
24. A. C. D. Newman, "Chemistry of Clays and Clay Minerals." Longmans, London, 1987.
25. S. Vercauteren, J. Luyten, R. Leysen, and E. F. Vansant, *J. Membr. Sci.* 119, 161 (1996).
26. A. B. Shelekhin and A. G. M. Dixon, *J. Membr. Sci.* 75, 233 (1992).
27. R. Schnabel and W. Vaulant, *Desalination* 24, 249 (1978).
28. S. Morooka and K. Kusakabe, *MRS Bull.* 25 (1999).
29. A. J. Burggraaf and K. Keizer, in "Inorganic Membranes Synthesis, Characteristics and Application" (R. R. Bhave, Ed.), p. 10. Chapman and Hall, New York, 1991.
30. C. J. Brinker and G. W. Scherer, "Sol Gel Science: The Physics and Chemistry of the Sol Gel Processing." Academic Press, San Diego, 1990.
31. R. M. de Vos and H. Verweij, *J. Membr. Sci.* 143, 37 (1998).
32. B. N. Nair, T. Yamaguchi, T. Okubo, H. Suematsu, K. Kaizer, and S. I. Nakao, *J. Membr. Sci.* 135, 237 (1997).
33. J. C. Diniz da Costa, G. Q. Lu, V. Rudolph, and Y. S. Lin, *J. Membr. Sci.* 198, 9 (2002).
34. B. B. Mandelbrot, "Fractals, Form and Chance." Freeman, San Francisco, 1977.
35. N. K. Raman, M. T. Anderson, and C. J. Brinker, *Chem. Mater.* 8, 1682 (1996).
36. A. J. Vega and G. W. Scherer, *J. Non-Cryst. Sol.* 111, 153 (1989).
37. G. Orcel, L. L. Hench, I. Artaki, J. J. Jonas, and T. W. Zerda, *J. Non-Cryst. Sol.* 105, 223 (1988).
38. R. K. Iler, "The Chemistry of Silica." Wiley, New York, 1979.
39. A. Bertolluzza, C. Gagnano, M. A. Morelli, V. Gottardi, and M. Guglielmi, *J. Non-Cryst. Sol.* 48, 117 (1982).
40. A. Duran, C. Serna, V. Fornes, and J. M. Fernadez Navarro, *J. Non-Cryst. Sol.* 82, 69 (1986).
41. N. Abidi, B. Deroide, J. V. Zanchetta, L. C. de Menorval, and J. B. d'Espinose, *J. Non-Cryst. Sol.* 231, 49 (1998).
42. W. G. Klemperer, V. V. Mainz, and D. M. Millar, in "Better Ceramics Through Chemistry II" (C. J. Brinker, D. E. Clark, and D. R. Ulrich, Eds.), p. 15. Materials Research Society, Pittsburgh, PA, 1986.
43. A. M. Buckley and M. Greenblatt, *J. Non-Cryst. Sol.* 143, 1 (1992).
44. J. S. Beck, J. C. Vartuli, G. J. Kennedy, C. T. Kresge, W. J. Roth, and S. E. Schramm, *Chem. Mater.* 6, 1816 (1994).
45. K. Kusakabe, S. Sakamoto, T. Saie, and S. Morooka, *Sep. Purif. Tech.* 16, 139 (1999).
46. Y. S. Kim, K. Kusakabe, S. Morooka, and S. M. Yang, *Korean J. Chem. Eng.* 18, 106 (2001).
47. Y. Lu, G. Cao, R. P. Kale, S. Prabakar, G. P. Lopez, and C. J. Brinker, *Chem. Mater.* 11, 1223 (1999).
48. C. Tsai, S. Tam, Y. Lu, and C. J. Brinker, *J. Membr. Sci.* 169, 255 (2000).
49. Z. Y. Yuan, W. Z. Zhou, and L. M. Peng, *Chem. Lett.* 10, 1150 (2000).
50. A. Ayral, C. Balzer, T. Dabadie, C. Guizard, and A. Julbe, *Catal. Today* 25, 219 (1995).
51. W. G. Fahrenholtz, D. M. Smith, and D. W. Hua, *J. Non-Cryst. Sol.* 144, 45 (1992).
52. J. J. Yang, I. M. El-Nahhal, I. S. Chuang, and G. E. Maciel, *J. Non-Cryst. Sol.* 209, 19 (1997).
53. F. Brunet, *J. Non-Cryst. Sol.* 231, 58 (1998).
54. J. C. Diniz da Costa, G. Q. Lu, and V. Rudolph, *Coll. Surf. A* 179, 261 (2001).
55. C. J. Brinker, A. J. Hurd, and K. J. Ward, in "Ultrastructure Processing of Advanced Ceramics" (J. D. Mackenzie and D. R. Ulrich, Eds.), p. 223. Wiley, New York, 1988.
56. E. F. Vansant, P. Van Der Voort, and K. C. Vrancken, "Characterisation and Chemical Modification of the Silica Surface." Elsevier, Amsterdam, 1995.
57. T. A. Witten and M. E. Gates, *Science* 232, 1607 (1986).
58. R. S. A. de Lange, J. H. A. Hekkink, K. Keizer, and A. J. Burggraaf, *J. Membr. Sci.* 99, 57 (1995).
59. M. F. M. Post, in "Introduction to Zeolite Science and Practice" (H. van Bekkun, E. M. Flanigen, and J. C. Jansen, Eds.), p. 1123. Elsevier, Amsterdam, 1991.
60. A. F. M. Lenaars and A. J. Burggraaf, *J. Coll. Int. Sci.* 105, 27 (1985).
61. A. F. M. Lenaars, K. Keizer, and A. J. Burggraaf, *J. Mater. Sci.* 19, 1077 (1984).
62. B. C. Bonekamp, in "Fundamentals of Inorganic Membrane Science and Technology" (A. J. Burggraaf and L. Cot, Eds.), p. 141. Elsevier, Amsterdam, 1996.
63. D. L. Meixner and P. N. Dyer, *J. Membr. Sci.* 140, 81 (1998).
64. L. E. Scriven, in "Better Ceramics Through Chemistry III" (C. J. Brinker, D. E. Clark, and D. R. Ulrich, Eds.). Materials Research Society, Pittsburgh, PA, 1988.
65. C. J. Brinker, A. J. Hurd, P. R. Schunk, G. C. Frye, and C. S. Ashley, *J. Non-Cryst. Sol.* 147, 424 (1992).

66. A. J. Burggraaf, in "Fundamentals of Inorganic Membrane Science and Technology" (A. J. Burggraaf and L. Cot, Eds.), p. 259. Elsevier, Amsterdam, 1996.

67. G. Saracco, H. W. J. P. Neomagus, G. F. Versteeg, and V. S. W. P. M., *Chem. Eng. Sci.* 54, 1997 (1999).

68. A. Burneau and J. P. Gallas, in "The Surface Properties of Silicas" (A. P. Legrand, Ed.), p. 147. John Wiley & Sons, Chichester, UK, 1998.

69. C. J. Brinker and D. M. Haaland, *J. Am. Ceram. Soc.* 66, 758 (1983).

70. S. J. Gregg and K. S. W. Sing, "Adsorption, Surface Area and Porosity." Academic Press, New York, 1982.

71. H. Y. Zhu, G. Q. Lu, N. Maes, and E. F. Vansant, *J. Chem. Soc. Faraday Trans.* 93, 1417 (1997).

72. D. D. Do, "Adsorption Analysis: Equilibria and Kinetics." Imperial College Press, London, 1998.

73. D. M. Ruthven, "Principles of Adsorption and Adsorption Processes." John Wiley & Sons, New York, 1984.

74. J. C. D. da Costa, G. Q. Lu, and V. Rudolph, in "Adsorption Science and Technology" (D. D. Do, Ed.), p. 381. World Scientific, Singapore, 2000.

75. R. J. Ward and B. J. Wood, *Surf. Interf. Anal.* 16, 679 (1992).

76. C. G. Morris and B. J. Wood, *Mater. Forum* 15, 44 (1991).

77. R. S. A. de Lange, K. Keizer, and A. J. Burggraaf, *J. Membr. Sci.* 104, 81 (1995).

78. R. M. Barrer, *J. Chem. Soc. Faraday Trans.* 86, 1123 (1990).

79. P. G. Shewmon, "Diffusion in Solids." McGraw-Hill, New York, 1963.

80. A. J. Burggraaf, in "Fundamentals of Inorganic Membrane Science and Technology" (A. J. Burggraaf and L. Cot, Eds.), p. 331. Elsevier, Amsterdam, 1996.

81. C. L. Lin, D. L. Flowers, and P. K. T. Liu, *J. Membr. Sci.* 92, 45 (1994).

82. J. C. S. Wu, H. Sabol, G. W. Smith, D. L. Flowers, and P. K. T. Liu, *J. Membr. Sci.* 96, 275 (1994).

83. H. Y. Ha, S. Woo-Nam, S. A. Hong, and W. K. Lee, *J. Membr. Sci.* 85, 279 (1993).

84. M. Tsapatsis and G. Gavalas, *J. Membr. Sci.* 87, 281 (1994).

85. R. S. A. de Lange, J. H. A. Hekkink, K. Keizer, and A. J. Burggraaf, *Microporous Mater.* 4, 169 (1995).

86. W. J. Bakker, L. J. P. van den Broeke, F. Kapteijn, and J. A. Moulijn *A I Ch E J.* 43, 2203 (1997).

87. O. Korotkikh and R. Ferrauto, *Catal. Today* 62, 249 (2000).

88. K. I. Sotawa, Y. Hasegawa, K. Kusakabe, and S. Morooka, *Int. J. Hydrogen Energy* 27, 339 (2002).

89. ECW, "Fuel Cells for Distributed Generation: A Technology and Marketing Summary." Energy Centre of Wisconsin, Madison, WI, 2000.

90. H. S. Fogler, in, "Elements of Chemical Engineering Reaction." Prentice-Hall, Englewood Cliffs, NJ, 1999.

91. D. Rastler, D. Herman, R. Goldstein, and J. O'Sullivan, "State of the Art Fuel Cell Technologies for Distributed Power." Electric Power Research Institute, Palo Alto, CA, 1996.

92. A. Julbe, D. Farrusseng, and C. Guizard, *J. Membr. Sci.* 181, 3 (2001).

93. IEA, "$CO_2$ Emissions from Fuel Combustion." International Energy Agency, Paris, France, 1997.

94. U. Illgen, R. Schäfer, M. Noack, P. Kölsch, A. Kühnle, and J. Caro, *Catal. Com.* 2, 395 (2001).

95. J. C. Diniz da Costa, Synthesis and Characterisation of Molecular Sieve Silica (MSS) Membranes Ph.D. Thesis, The University of Queensland, Brisbane, Australia, 2000.

96. L. V. C. Rees, P. Bruckner, and J. Hampson, *Gas Sep. Purif.* 5, 67 (1991).

97. T. C. Golden and S. Sircar, *J. Coll. Int. Sci.* 162, 183 (1994).

98. V. R. Choudary and S. Mayadevi, *Zeolites* 17, 501 (1996).

99. J. Dunne, R. Mariwala, M. Rao, S. Sircar, R. J. Gorte, and A. L. Myers, in "Fundamentals of Adsorption" (M. D. LeVan, Ed.), p. 277. Kluwer Academic Boston, 1996.

100. J. Zaman and A. Chakma, *J. Membr. Sci.* 92, 1 (1994).

# Molecular Tectonics in Sol–Gel Chemistry

## Marc Henry

*Université Louis Pasteur, Strasbourg, France*

## CONTENTS

## 1. INTRODUCTION

Molecular tectonics [1] is the art of iterating programmed recognition patterns at the molecular level in order to obtain hybrid organic–inorganic infinite networks displaying a wide range of physical or chemical properties (Fig. 1). It is an interdisciplinary area where geometrical and topological concepts are more important than the nature of the chemical bonds formed between atoms. On one hand, some people prefer to play with the whole palette of noncovalent interactions (van der Waals, dipolar, or hydrogen bonding) in order to build fascinating new supramolecular compounds. On the other hand, solid-state chemists use much stronger chemical bonds (covalent, ionic, coordination) leading to amazing microporous architectures. At the present level of knowledge, it is not yet possible to predict the final structure, knowing the nature of the individual tectons (building blocks carrying chemical information imprinted in their molecular structure). This comes in part from our inability to set out a quantitative energy scale for the molecular interactions in which an individual tecton may be engaged, even if all these interactions derive from the single and unique fundamental electromagnetic interaction. At the very beginning, sol–gel chemistry was designed to

obtain glasses [2] or ceramic materials [3] after hydrolysis, condensation, and gelation of metal alkoxides $M(OR)_n$ or of metal complexes in aqueous solutions [4, 5] (Fig. 2). Soon after, it was realized that a much broader range of molecular precursors could be used, leading to new hybrid organic–inorganic materials [6]. It then became obvious that sol–gel chemistry and molecular tectonics were indeed two very complementary approaches to the synthesis of materials.

In this chapter, we have chosen to focus on materials based on titanium dioxide elaborated through hydrolysis and condensation of hybrid organic–inorganic titanium(IV)-based molecular complexes. This choice was motivated by the technological and strategic importance of titanium dioxide and by the lack of a comprehensive review dealing with all the crystalline aspects of Ti—O chemical bonds. In fact, most past studies and reviews in sol–gel chemistry focused on materials based on $SiO_4$, $AlO_4$, and $PO_4$ tetrahedral building units. Interest in transition metal–based chemistry came from the need to bring electrical, optical, or magnetic properties to an otherwise amorphous gel [7, 8]. With the growing development of the synthesis of tailored porous materials [9–11], it became obvious that hybrid organic–inorganic crystalline assemblies were no longer limited to tetrahedral building block units. Unveiling the assembly route of materials based on octahedral units is thus a real scientific challenge. For that purpose, molecular complexes or solid-state compounds based on titanium(IV) species are probably the best candidates for setting out basic rules that may be further used for a rational design and synthesis of new hybrid materials. Accordingly, with their $d^0$ electronic configuration, $Ti^{IV}$ cations may be found under four-, five-, six-, seven- and eightfold coordination, in stark contrast with other p-element ($Si^{IV}$, $Al^{III}$) or late transition metals. Moreover, in contrast with silicon- or aluminum-based compounds, the $Ti^{III}$ oxidation state may appear upon irradiation or application of an adequate potential, establishing the most simple link toward other transition metals characterized by a partial filling of atomic d orbitals. This unique
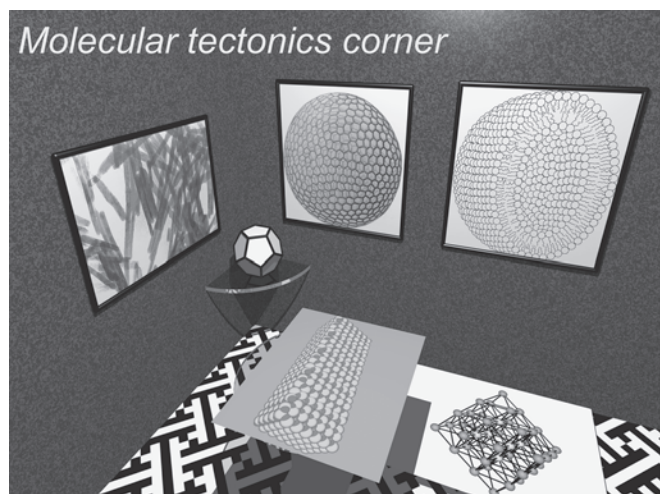
**Figure 1.** Pictorial survey of molecular tectonics aims and goals. On the floor, one may recognize nanoscale synthesis (electron sink cluster $Ni_{38}Pt_6$). The unmounted painting on the table represents interfacial recognition around colloidal units ($Al_2O_3$ nuclei). On the corner glass shelf is represented microstructural fabrication (Al—Mn quasicrystal). Crystal engineering (acircular $Al_2O_3$ nanocrystals) is pictured on the left wall. Finally, on the right wall, supramolecular preorganization (micellar vesicles and liposomes at the right) and cellular processing in biomineralization (radiolar skeleton at the left) may be identified.

position in the periodic table, at the frontier between elements using s, p, and d orbitals (Al, Ga, Si, Sn) and elements using d, s, and p orbitals (transition metals), makes titanium a very attractive element. However, to keep this
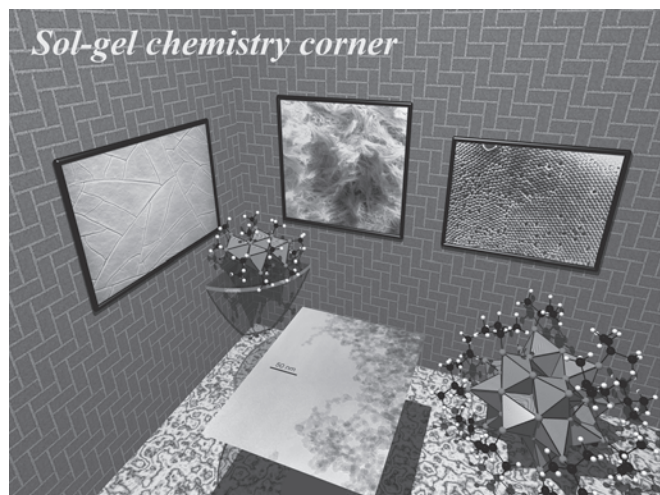


**Figure 2.** Pictorial survey of sol–gel chemistry aims and goals. The first steps involve synthesis of functional building units ($[Ti_{18}O_{28}H(OBu^t)_{17}]$ oxo-alkoxide on the floor) from metal alkoxides (corner glass shelf). The unmounted micrograph on the table illustrates the hydrothermal synthesis of monodisperse anatase nanocrystals after base hydrolysis of titanium alkoxides. On the right wall is represented fabrication of opal-like materials after base hydrolysis at room temperature (right) and design of titanium oxo-acetate fibers via acetic acid modification (left). Finally, the left wall shows elaboration of titania thin films via acetylacetone modification.

review to a reasonable length, we have chosen to focus on chemical compounds displaying only Ti—O or Ti—N bonds, which are the most stable ones for applications in materials chemistry. As most hybrid organic–inorganic compounds based on the Ti—O bond display an inorganic titanium–oxygen core surrounded by an otherwise organic shell, this review has been organized as follows. Section 2 is devoted to recent theoretical advances in the understanding of the electronic structure and chemical reactivity of chemical compounds displaying large molecular weights (solids and molecular species displaying hundreds or thousands of constituent atoms). It focuses on aqueous sol–gel chemistry as well as on the structure and properties of solid crystalline phases displaying the $TiO_2$ stoichiometry. To the best of our knowledge, such a comprehensive review is still lacking, and it is of the utmost importance to have an accurate knowledge of the final limiting term common to all these Ti—O-based hybrid compounds. In the same spirit, Section 3 is devoted to the other limiting term: coordination chemistry of molecular metallo-organic titanium(IV) complexes. Finally, Section 4 will deal with hybrid organic–inorganic $TiO_2$-based materials, either as molecular species or as reticulated networks. In conclusion, we will outline some interesting perspectives concerning this important class of compounds.

# 2. SOL–GEL CHEMISTRY AND MOLECULAR TECTONICS OF INORGANIC COMPOUNDS

This section is devoted to a comprehensive review of the structural chemistry and practical applications of purely inorganic phases based on Ti—O bonds. It covers the aqueous chemistry of $Ti^{IV}$ species, the structural chemistry of crystalline phases displaying the $TiO_2$ stoichiometry, and the various applications of titanium dioxide in materials chemistry. Accordingly, it was our feeling that a good understanding of the structural aspects of hybrid organic–inorganic systems could not be reached without a deep knowledge of purely inorganic phases. In this field, two important theoretical tools developed in our group are also introduced, providing the first systematic rational approach for the understanding of the experimental behavior of such complex systems. It was thus hoped that the philosophy and methodology exemplified here in the case of systems based on Ti—O bonds could serve as a general template for compounds based on other metallic centers.

## 2.1. Aqueous Chemistry of $Ti^{IV}$ Species

The partial charge model (PCM) was introduced more than 13 years ago in its most rudimentary form in an attempt to understand the chemical reactivity of silicon and transition metal alkoxides using Allred–Rochow electronegativity data [7, 12]. Soon after, it was extensively used for the modeling of aqueous sol–gel chemistry [4, 5].

### 2.1.1. Hydrolysis/Condensation Behavior

With the help of this model, it is rather easy to justify the experimental trends observed for metal ion hydrolysis as a function of oxidation state $z$ and pH (Fig. 3). Moreover,
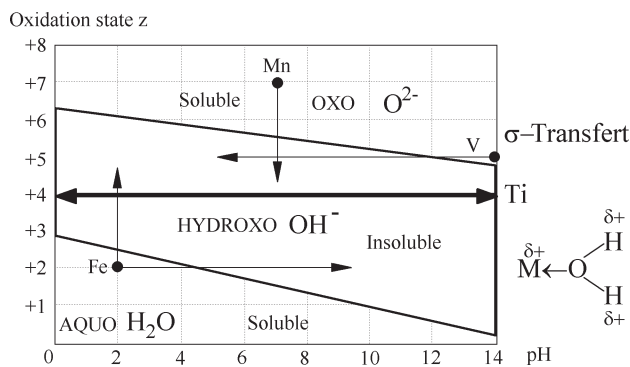
**Figure 3.** Theoretical charge–pH diagram according to the partial charge model. This diagram helps to explain why tetravalent species such as $Ti^{IV}$ display a very limited aqueous solution chemistry. It also emphasizes the spontaneous hydrolysis of trivalent species and the four basic processes commonly used in aqueous sol–gel syntheses: acid addition ($V_2O_5$ gels) or reduction ($MnO_2$ gels) for high-valence species (oxy-anions) and base addition and/or oxidation ($Fe_3O_4$ and $Fe_2O_3$ gels) for low-valence species (aquo-cations).

it was also possible to predict from the sole knowledge of the oxidation state $z$, electronegativity $\chi$, and preferred coordination number $N$ the hydrolytic behavior of metal cations in aqueous solutions. From the basic PCM equations, it is possible to predict the equilibrium hydrolysis ratio $h$ for the following hydrolysis reaction: $[M(OH_2)_N]^{z+} \rightarrow [MO_N H_{2N-h}]^{(z-h)+} + h[H^+]_{aq}$. It mainly depends on the relative electronegativities of the free proton $H = EN(H^+)$, the water molecule $W = EN(H_2O)$, the solvated proton $R_p = EN[H(H_2O)_p^+]$, the aquo-cation $M_N^z = EN[M(H_2O)_N^{z+}]$, and the solution pH according to [4, 5]:

$$h = \frac{\sigma_N \times (S - M_N^z)}{\sigma_H \times (S - H)} \Leftrightarrow S = R_p + (W - R_p) \times (pH/7)$$

$$= \frac{\sigma_N \times M_N^z - h\sigma_H \times H}{\sigma_N - h\sigma_H} \quad (1)$$

Here

$$\sigma_N = \sigma[M(H_2O)_N] = \sigma_M + N\sigma_W$$

$$= \sigma_M + N(\sigma_O + 2\sigma_H) \quad (2)$$

is the global softness of the hydrated cation computed by adding individual atomic softnesses $\sigma_i$ according to the complex stoichiometry. For the Allred–Rochow electronegativity scale, atomic electronegativities $\chi$ and softnesses $\sigma$ are linked according to $\sigma = (1.36\chi^{1/2})^{-1}$ [4, 5]. With $\chi_O = 3.50$, $\chi_H = 2.10$, we get $\sigma_H = 0.5074$, $H = \chi_H + 1/\sigma_H = 4.071$, $\sigma_W = 1.408$, $W = 2.491$, and $R = 2.732$ (assuming p = 2, i.e., a proton bridging two water molecules). Now, for $Ti^{IV}$ species ($z = 4$, $\chi = 1.32$, i.e., $\sigma_N = 0.640 + N \times 1.408$), the characteristic coordination number is pH dependent with $N_a = 6$ under acid conditions as evidenced in the crystal structure of $TiO(SO_4) \cdot H_2O$ [13] (Fig. 4a). Under basic conditions, the coordination number is reduced to $N_b = 4$, as evidenced in the crystal structure of $\beta$-$Ba_2TiO_4$ [14] (Fig. 4b). Consequently, with $\sigma_6 = 9.087$, $M_6^4 = 2.849$, one may write $h(N_a) = (2.095 + 0.627 \times pH)/(1.339 + 0.035 \times pH)$, while with $\sigma_4 = 6.271$, $M_4^4 = 3.009$ it becomes $h(N_b) =$
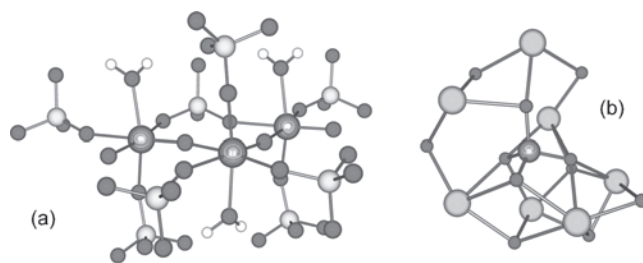


**Figure 4.** Sixfold coordination and fourfold coordination numbers for $Ti^{IV}$ as found in the crystal structures of titanyl sulfate monohydrate (a) and dibarium titanate (b).

$(3.424 + 0.433 \times pH)/(1.339 + 0.035 \times pH)$. Figure 5 shows how the hydrolysis ratio $h = \min[h(N_a), h(N_b)]$ is predicted to change as the pH is increased from 0 to 14.

Within this model, the existence domain (vertical lines in Fig. 5) of a given hydrolyzed complex, $[MO_N\text{-}H_{2N-h}]^{(z-h)+}$, is defined by the following inequality: $pH(h - 0.5) < pH < pH(h + 0.5)$. On the acid side, the prediction is in full agreement with experimental data showing that the titanyl cation $[TiO(H_2O)_5]^{2+}$ ($h = 2$) should be the most acidic species in aqueous solutions [15, 16]. On the basic side, however, the most basic species ($[TiO(OH)_3]^-$ anion) remains hypothetical as it has never been experimentally detected. A first possibility is that it does not exist at all. This would, however, be a rather puzzling situation with respect to the existence of anionic aqueous complexes for the closely related $Zr^{IV}$ species [17]. Another possibility is that the equilibrium between the solid phase and the solution is too slow to establish. This last explanation is probably the right one as up to 45 days were needed to reach equilibrium in the case of $Zr^{IV}$ [17]. Another clue is provided by the fact that, as shown in Figure 6a, Zr—OH—Zr bridges are well known in the molecular state (see, e.g., the crystal structure of the basic salt $ZrOCl_2 \cdot 8H_2O$ [18]). This is in stark contrast with $Ti^{IV}$ (Fig. 6b) where only oxo bridges (Ti—O—Ti) have been characterized (see, e.g., the crystal structure of the basic salt $Ti_8O_{12}(H_2O)_{24}Cl_8 \cdot HCl \cdot 7H_2O$ [19]).

The same conclusion is also reached after consideration of the general electronegativity charge plot for solid-phase
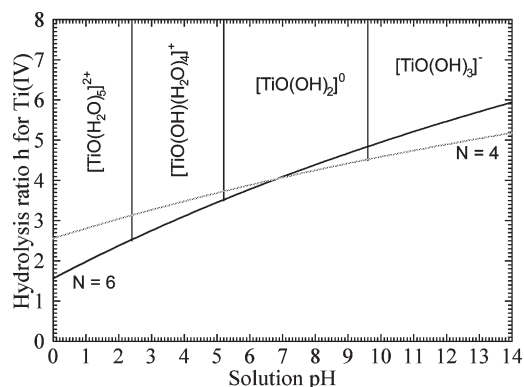


**Figure 5.** Theoretical $Ti^{IV}$ hydrolysis diagram according to the partial charge model. The solid curves were computed using $z = +4$ (oxidation state), $\chi^0 = 1.32$ (Allred–Rochow electronegativity), $N_a = 6$, and $N_b = 4$ (see text for details). The vertical lines correspond to the existence domains of each $[MO_N H_{2N-h}]^{(z-h)+}$ complex.
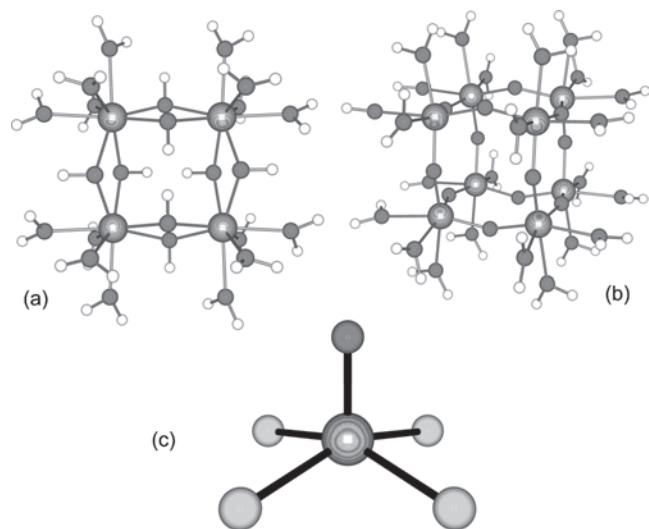
**Figure 6.** Molecular complexes isolated from hydrochloric solutions containing $Zr^{IV}$ and $Ti^{IV}$ cations. (a) Hydroxy-based cyclic polymer $[Zr_4(OH)_8(H_2O)_{16}]^{8+}$. (b) Oxo-based cage polymer $[Ti_8O_{12}(H_2O)_{24}]^{8+}$. In both cases, chloride ions behave as simple counterions hydrogen-bonded with coordinated water molecules. (c) Square pyramidal $[TiOCl_4]^{2-}$ ion with its very short terminal Ti—O bond.

nucleation (Fig. 7) [4, 5]. Owing to their charge ($z = +4$) and electronegativity ($\chi^0 = 1.32$), $Ti^{IV}$ cations falls inside the "insoluble oxides" domain. This illustrates the instability of any Ti—OH—Ti bridges ($2Ti—OH \rightarrow Ti—O—Ti + H_2O$ favored over $Ti—OH + Ti—OH_2 \rightarrow Ti—OH—Ti + H_2O$). On the other hand, $Zr^{IV}$ cations are found borderline and, consequently, both behaviors may be observed, depending on experimental conditions. Now, for hydroxy-bridged species, the limiting step for dissolution should be
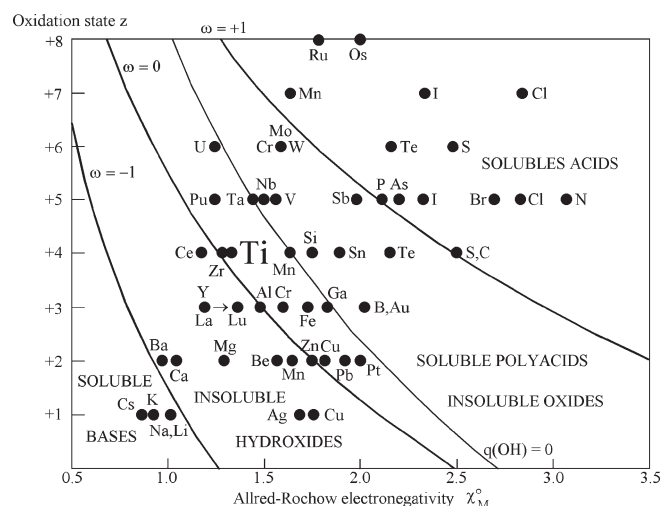


**Figure 7.** General charge–electronegativity plot for hydrolysis/condensation reactions. Solid lines are derived after application of the partial charge model using the following critical conditions: $EN[MO_{N-1}H_{2N-z-1}^+] = EN(H_2O)$ ($\omega = -1$ curve for M—OH $\rightarrow$ M$^+$+ $OH^-$ ionization), $EN[MO_NH_{2N-z}] = EN(H_2O)$ ($\omega = 0$ curve for olation versus oxolation behavior), $EN[MO_NH_{2N-z-1}^-] = EN(H_2O)$ ($\omega = +1$ curve for M—OH $\rightarrow$ M—O$^-$ + H$^+$ ionization), and $EN[MO_{z/2}] = EN(OH)$ ($q_{OH} = 0$ curve for infinite versus limited oxolation).

the breaking of a coordinate bond (M—OH—M + OH$^-$ $\rightarrow$ M—OH + M—OH$^-$). In contrast, oxide phase dissolution requires the breaking of a much stronger covalent bond (M—O—M + OH$^-$ $\rightarrow$ M—O$^-$ + M—OH). Consequently, owing to the very slow kinetics observed for the formation of $[Zr(OH)_5]^-$ anions from solid $ZrO_x(OH)_{4-2x}$ phases, one may anticipate an extremely slow kinetics for the formation of soluble $[TiO(OH)_3]^-$ anions from $TiO_2$ solid phases.

## 2.1.2. Complexation by Anionic Species

In its most simple form, the PCM is also able to explain the complexation behavior of anionic species toward aqueous $Ti^{IV}$ precursors. Here, the PCM equations [4, 5] furnish a fundamental link between the electronegativity of the $q$-protonated form of an $n$-valent anion $X^{n-}$ ($Q = EN[H_qX^{(n-q)-}]$) and the other electronegativities $H$, $M_N^z$, $S$, $W$ governing the hydrolysis behavior of the cation $[M(H_2O)_N]^{z+}$:

$$\sigma_M\left(\frac{H - M_N^z}{H - S}\right) = \frac{\sigma_M(H - M_N^z) - \alpha\sigma_W(H - W)}{H - Q} + q\sigma_H + \alpha\sigma_W \tag{3}$$

In this equation, $\alpha$ corresponds to the number of water molecules removed from the coordination sphere of the hydrated cation after its association with the anion (coordination mode). For $Ti^{IV}$ species ($z = 4$, $N = 6$, $\chi = 1.32$), (3) leads to

$$\frac{11.108}{4.071 - S} = \frac{11.108 - 2.225 \times \alpha}{4.071 - Q} + 0.507 \times q + 1.408 \times \alpha \tag{4}$$

Consequently, for a given $n$-valent anion $X^{n-}$ characterized by its coordination mode $\alpha$, the critical pH for complexation with aqueous $Ti^{IV}$-based species may be derived for each protonated form $H_qX^{(n-q)-}$ of the ligand, using the $S$ value computed from (4): $pH^* = 7 \times (S - R)/(W - R)$.

***Complexation by Chloride Ions*** Let us consider, for example, the case of the chloride ion characterized by $EN[Cl(H_2O)_6^-] = 2.395$ ($q = 0$ form) and $EN(HCl) = 2.438$ ($q = 1$ form). Assuming a monodentate coordination mode ($\alpha = 1$), the domain of stability of $Ti^{IV}$ complexes is found to be pH = 7.1 ± 2.1. Above pH $\sim$ 9, complexes should be dissociated into hydroxo complexes and chloride ions, while, below pH $\sim$ 5, they should be hydrolyzed, leading to aquo complexes and again chloride counterions. These results could help to explain why no chloride ions are found within the coordination sphere of $Ti^{IV}$ centers in the molecular cube $[Ti_8O_{12}(H_2O)_{24}]^{8+}$ (right complex in Fig. 6). Accordingly, such a complex derives formally from the oxolation of eight $[TiO(OH)(H_2O)_4]^+$ ions ($h = 3$ term) that are formed according to the PCM when pH = 3.8 ± 1.4 (Fig. 5). Owing to the very small overlap between both domains, only outer-sphere complexes are possible, in good agreement with experiments. Let us recall that these conclusions only apply when water molecules are in large excess relative to all present solute species (dilute solutions). Owing to the mass action law, increasing the chloride ion concentration (typically above 1 M) will always favor complexation.

Accordingly, tetragonal pyramidal $[TiOCl_4]^{2-}$ ions displaying a very short terminal Ti—O bond (Fig. 6c) have been evidenced in the crystal structure of $[NEt_4]_2[TiOCl_4]$ [20].

***Complexation by Fluoride Ions*** Interestingly enough, a quite different behavior may be anticipated for complexation by fluoride anions that are characterized by $EN[F(H_2O)_4^-] = 2.586$ ($q = 0$ form) and $EN(HF) = 2.934$ ($q = 1$ form). Assuming again a monodentate coordination mode ($\alpha = 1$), the domain of stability of $Ti^{IV}$ complexes is now found to be pH $= -0.5 \pm 5.3$ (Fig. 8). The stability of Ti—F bonds in aqueous solution is demonstrated by the isolation in the crystalline state of four different phases. Thus, linear chains of corner-sharing octahedra have been evidenced in the crystal structure of $(NH_4)_2TiOF_4$ ($\mu_2$-oxo bridges) [21] and $(H_3O)TiF_5$ ($\mu_2$-fluoro bridges) [22]. In contrast, monomeric $[TiF_6]^{2-}$ ions have been characterized in the crystal structures of $(H_3O)(H_5O_2)TiF_6$ and $(H_5O_2)_2TiF_6 \cdot 2H_2O$ [23].

***Complexation by Acetate Ions*** Acetate ions characterized by $EN[CH_3COO^-] = 2.246$ ($q = 0$ form) and $EN(CH_3COOH) = 2.493$ ($q = 1$ form) are expected to behave in a very similar way to chloride ions in aqueous solutions. Accordingly, considering a monodentate coordination mode ($\alpha = 1$), as evidenced in the crystal structure of acetato-titanatrane $[Ti_2\{N(CH_2CH_2O)_3\}_2-(CH_3COO)_2]$ [24], leads to pH $= 8.2 \pm 4.3$ (Fig. 9). As such a pH range overlaps with the pH range for $TiO_2$ precipitation, it is not surprising to find no evidence in the literature of crystalline phases involving the coexistence of aquo, hydroxo, oxo, or acetato ligands within the $Ti^{IV}$ coordination sphere. To stabilize such acetato complexes, one thus has to turn toward titanium alkoxides in nonaqueous solvents (*vide infra*).

***Complexation by Perchlorate and Nitrate Ions*** Other common inorganic monovalent anions such as perchlorate ($EN[ClO_4^-] = 2.857$, $EN[HClO_4] = 3.101$) and nitrate $[NO_3]^-$ ($EN[NO_3^-] = 2.762$, $EN[HNO_3] = 3.077$) provide examples of a bidentate behavior ($\alpha = 2$) toward $Ti^{IV}$ as evidenced by the crystal structures of $Ti(ClO_4)_4$ [25] and $Ti(NO_3)_4$ [26]. As shown in Figure 10, perchlorate complexes should be largely dissociated in aqueous solutions (pH $= -3.6 \pm 3.6$), explaining why anhydrous conditions are necessary for their isolation and characterization. Figure 11 shows that nitrate ions are expected to behave in a rather similar way, even if one cannot completely rule out some complexation at very low pH (pH $= -2.4 \pm 4.3$).

***Complexation by Oxalate and Sulfate Ions*** As expected, complexes involving multivalent anions are much more stable than those involving monovalent anions. For example, Figure 12 shows the expected complexation range for oxalate species that are characterized by $EN(C_2O_4^{2-}) = 2.329$, $EN(HC_2O_4^-) = 2.623$, $EN(H_2C_2O_4) = 2.832$, and $\alpha = 2$. With critical pH $= -3.8$ for $Ti—O_2C—CO_2H + H_3O^+ \rightarrow Ti—OH_2^+ + H_2C_2O_4$, pH $= 1.8$ for $Ti—O_2C—CO_2H + H_2O \rightarrow Ti—OH_2 + [HC_2O_4]^-$, and pH $= 9.7$ for $Ti—O_2C—CO_2 + 2OH^- \rightarrow Ti(OH)_2 + [C_2O_4]^{2-}$, oxalate complexes can thus be destroyed only under strongly basic conditions. Consequently, under acidic or neutral conditions, crystalline complexes may be easily isolated from the aqueous solutions. The most common species encountered in the presence of such oxalate is thus the
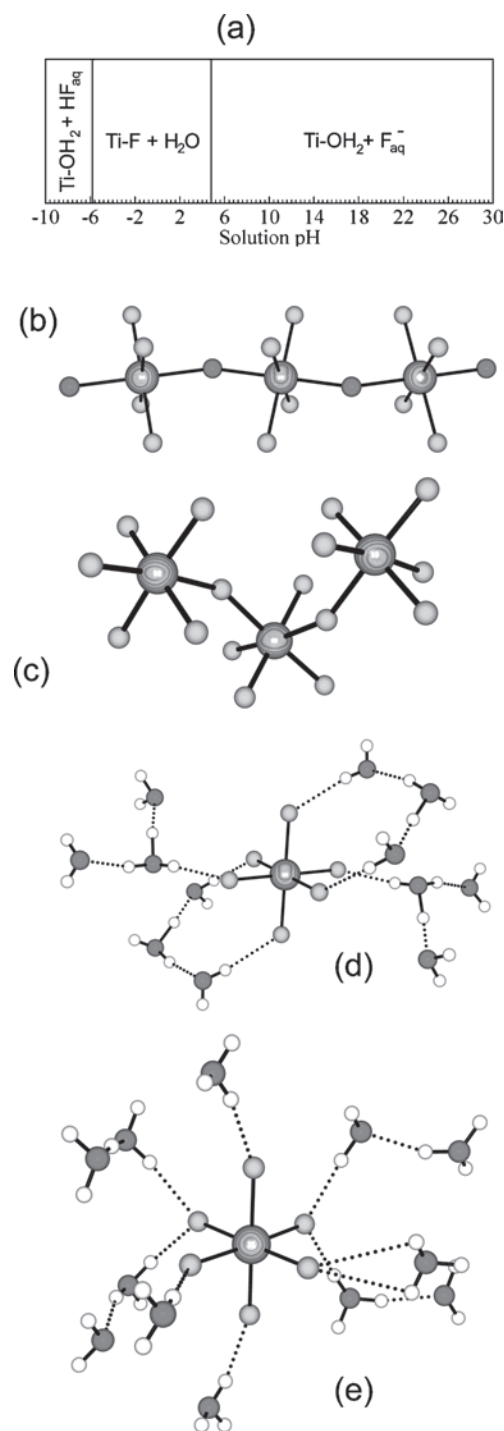


**Figure 8.** Complexation of aqueous $Ti^{IV}$ species by fluoride anions. (a) Theoretical complexation range according to the PCM. (b) Molecular chain found in the crystal structure of $(NH_4)_2TiOF_4$. (c) Molecular chain found in the crystal structure of $[H_3O^+][TiF_5]^-$. (d) H-bond pattern around the $[TiF_6]^{2-}$ anion found in the crystal structure of $[H_3O^+][H_5O_2^+][TiF_6]^{2-}$. (e) H-bond pattern around the $[TiF_6]^{2-}$ anion found in the crystal structure of $[H_5O_2^+]_2[TiF_6]^{2-}$.

tetrameric hybrid oxo-anion $[Ti_4O_4(C_2O_4)_8]^{8-}$, which may be crystallized in the presence of ammonium [27], potassium [28, 29], or cesium ions [30]. A still wider range of complexation is predicted for sulfate ions characterized by $\alpha = 1$
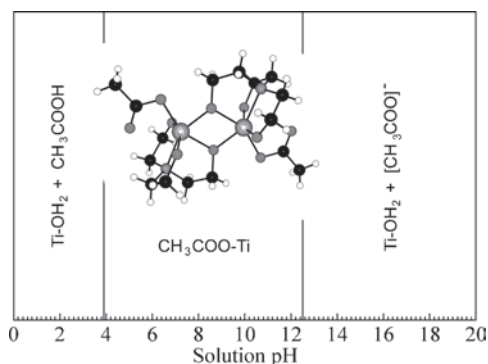
**Figure 9.** Theoretical complexation range predicted by the PCM for Ti$^{IV}$ aqueous species in the presence of acetate ions. A monodentate coordination mode has been assumed in view of the crystal structure of acetato-titanatrane [Ti$_2$\{N(CH$_2$CH$_2$O)$_3$\}$_2$(CH$_3$COO)$_2$]. Owing to the overlap with the TiO$_2$ precipitation range, such complexes can be isolated only in nonaqueous solvents.
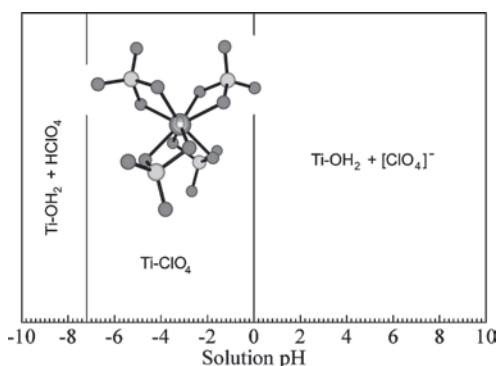


**Figure 10.** Theoretical complexation range predicted by the PCM for Ti$^{IV}$ aqueous species in the presence of perchlorate ions. A bidentate coordination mode has been assumed in view of the crystal structure of Ti(ClO$_4$)$_4$. Owing to the negative pH range, complexes can be isolated only under anhydrous conditions.
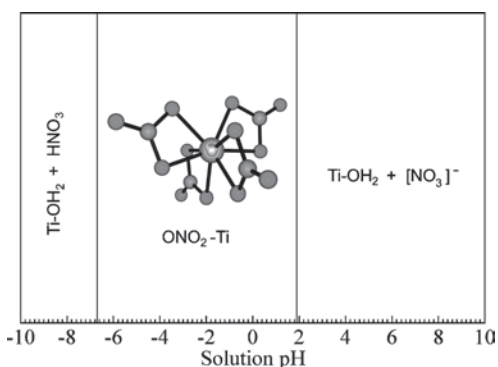


**Figure 11.** Theoretical complexation range predicted by the PCM for Ti$^{IV}$ aqueous species in the presence of nitrate ions. A bidentate coordination mode has been assumed in view of the crystal structure of Ti(NO$_3$)$_4$. As most of the complexation domain lies below pH 0, stable complexes are expected only at very low pH.
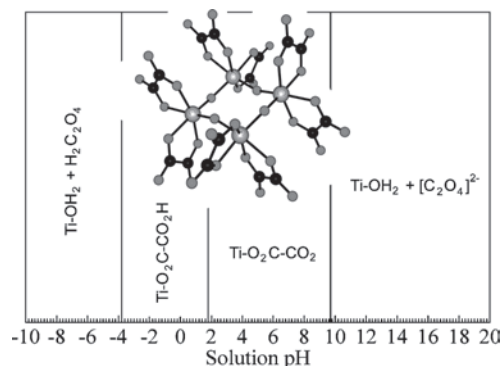


**Figure 12.** Theoretical complexation range predicted by the PCM for Ti$^{IV}$ aqueous species in the presence of oxalate anions. A bidentate coordination mode has been assumed in view of the crystal structures of M$_2$TiO(C$_2$O$_4$)$_2$(M = Li, Na, K, Rb, Cs, NH$_4$).

(Fig. 13), EN(SO$_4^{2-}$) = 2.277 (pH* = 11.8), EN(HSO$_4^-$) = 2.634 (pH* = 1.0), and EN(H$_2$SO$_4$) = 2.872 (pH* = −6.1). This large domain of stability could explain why at least three different crystalline phases have been isolated and characterized in the TiO$_2$—SO$_3$—H$_2$O phase diagram. All phases are basic salts ($h = 2$) that may be formulated as TiOSO$_4 \cdot$ H$_2$O [13, 31, 32] and that can be further dehydrated to form $\alpha$-TiOSO$_4$ [33] or $\beta$-TiOSO$_4$ [13, 32]. The crystal structures of TiOSO$_4 \cdot$ H$_2$O and $\beta$-TiOSO$_4$ are closely related, as they both contain zigzag [TiO]$_n$ chains (*cis* disposition of the two $\mu_2$-oxo groups within the Ti$^{IV}$ coordination sphere). In TiOSO$_4 \cdot$ H$_2$O (Fig. 13b), two $\mu_3$-sulfato groups are found in the *trans* position relative to the two $\mu_2$-oxo groups, while a third $\mu_3$-sulfato group in the axial position is used to bridge two zigzag chains together. The last octahedral axial position is occupied by an aquo ligand forming two
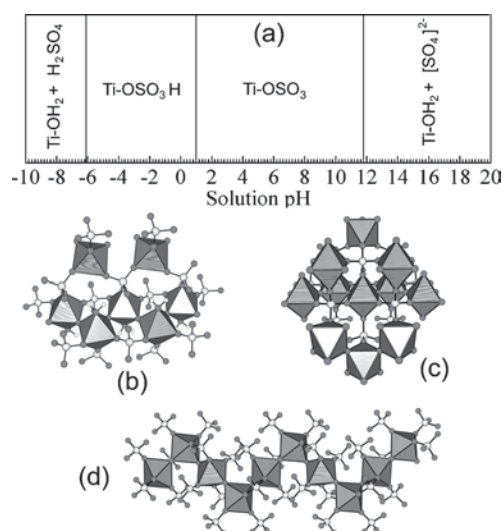


**Figure 13.** (a) Theoretical complexation range of Ti$^{IV}$ aqueous species by monodentate sulfate ions according to the PCM. (b) Crystal structure of TiOSO$_4 \cdot$ H$_2$O displaying zigzag [TiO]$_n^{2n+}$ chains linked together through $\mu_3$-sulfato bridges. (c) Crystal structure of $\beta$-TiOSO$_4$ displaying the same chains as in TiOSO$_4 \cdot$ H$_2$O but now linked together through $\mu_4$-sulfato bridges. (d) Crystal structure of $\alpha$-TiOSO$_4$ with [(*cis,trans*)Ti$_2$O$_2$]$_n^{4n+}$ zigzag chains linked together through $\mu_4$-sulfato bridges.

H bonds with the free vertices of two neighboring $\mu_3$-sulfato groups. Similar zigzag chains have also been evidenced in the crystal structure of $\beta$-TiOSO$_4$, but here we have a full bridging $\mu_4$-sulfato coordination mode between the chains (Fig. 13c). Another kind of zigzag chain has been found in the crystal structure of $\alpha$-TiOSO$_4$, a phase obtained after digestion of ilmenite FeTiO$_3$ in sulfuric acid above 180 °C (Fig. 13d) [33]. Such chains display two kinds of TiO$_6$ octahedra, one sharing *cis* vertices and the other one sharing *trans* vertices with two adjacent octahedra. The remaining four vertices of both octahedra are shared with SO$_4$ tetrahedra, which then behave again as $\mu_4$-sulfato bridging ligands.

***Complexation by Phosphate Ions***  Phosphate ions are also known to bind to Ti$^{IV}$ in a bridging monodentate way ($\alpha = 1$), as evidenced in the crystal structures of Na$_5$Ti(PO$_4$)$_3$ [34] ($\mu_2$-phosphato bridges; Fig. 14c) or MTi$_2$(PO$_4$)$_3$, with M = Na [35, 36], K [37], Rb [38, 39] ($\mu_4$-phosphato bridges; Fig. 14b). However, owing to the additional anionic charge, EN(PO$_4^{3-}$) = 1.707 (pH* = 23.5), EN(HPO$_4^{2-}$) = 2.170 (pH* = 10.1), EN(H$_2$PO$_4^-$) = 2.481 (pH* = 1.4), and EN(H$_3$PO$_4$) = 2.705 (pH* = −4.7), a twofold increase in the complexation domain is observed (Fig. 14a). One may notice the very high pH predicted for the occurrence of the ionic cleavage Ti—OPO$_3$ + 3OH$^-$ → Ti(OH)$_3$ + [PO$_4$]$^{3-}$. Taking into account the fact that a [PO$_4$]$^{3-}$ ion cannot exist in aqueous solutions without extensive H bonding with the solvent and assuming one H bond per negative charge would lead to EN(PO$_4^{3-}$ · 3H$_2$O) = 2.232 (i.e., pH* = 12.8), a much more reasonable value. It remains, nevertheless, that the stability range of Ti$^{IV}$—PO$_4$ complexes covers almost all the accessible pH range, which could help to explain why numerous crystalline phases have been isolated from such solutions. For example, we were able to get 173 hits by searching for phases containing Ti, P, and O atoms in the October 2001 release of the ICSD Database in Karlsruhe. By comparison, the same search for Ti, S, and O atoms yielded only 29 hits. This high coordinating power of phosphate ions is immediately evidenced by the existence of three normal hydrogenophosphate salts ($h = 0$).

The most common one, $\alpha$-Ti(HPO$_4$) · H$_2$O, is based on a hexagonal layer of TiO$_6$ octahedra linked together through $\mu_3$-O$_3$POH bridges and holding a water layer with each water molecule engaged in two H bonds with P—OH moieties (Fig. 15a) [40–43]. It is readily formed after heating a mixture of amorphous titanium dioxide [41–43] or titanium [40] and phosphoric acid. If one starts from titanium fluoro complexes, another hydrated-phase $\gamma$-Ti(PO$_4$)(H$_2$PO$_4$) · 2H$_2$O may be formed [40]. This new layered structure (Fig. 15b) involves an equal amount of $\mu_4$-PO$_4$ and $\mu_2$-O$_2$P(OH)$_2$ bridges, with free moieties of dihydrogenophosphate bridges engaged into H bonds with water molecules. The same layer-like arrangement of TiO$_6$ and PO$_4$ tetrahedra is found in the dehydrated form $\beta$-Ti(PO$_4$)(H$_2$PO$_4$), but H bonds are now made directly between [PO$_2$(OH)$_2$]$^-$ tetrahedra [44].

A hydrated normal orthophosphate salt ($h = 0$) [Ti$_3$(PO$_4$)$_4$(H$_2$O)$_2$] · NH$_3$ has also been obtained after prolonged heating at 190 °C of a mixture of TiCl$_3$, HCl, H$_3$PO$_4$, and urea CO(NH$_2$)$_2$ [45]. Interestingly enough, the preparation from TiCl$_4$ was not successful. Two kinds of Ti atoms in a 1 : 2 ratio are found within this three-dimensional (3D)
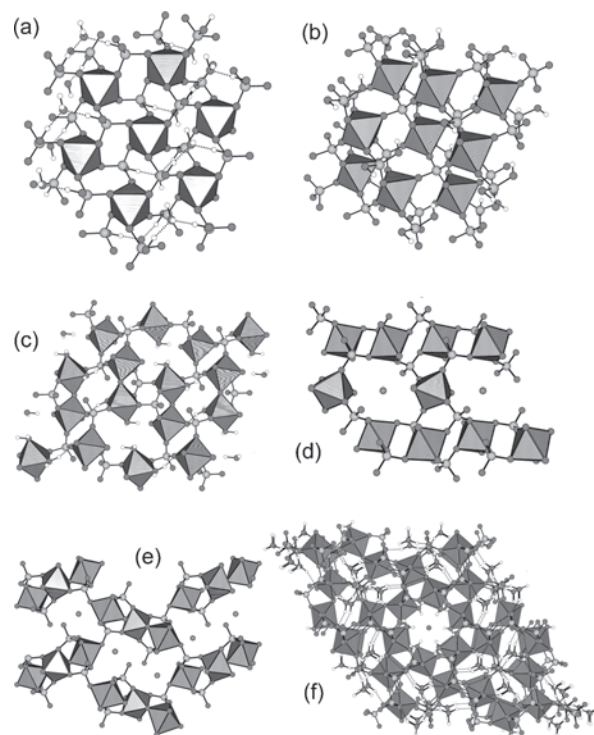


**Figure 15.** (a) Hybrid hydrated layer based on TiO$_6$ octahedra and $\mu_3$-hydrogenophosphato tetrahedra found in the crystal structure of $\alpha$-Ti(HPO$_4$)$_2$ · H$_2$O. (b) Hybrid layer based on TiO$_6$ octahedra and mixed ($\mu_4$-phosphato, $\mu_2$-dihydrogenophosphato) tetrahedra found in the crystal structure of $\beta$-Ti(PO$_4$)(H$_2$PO$_4$) and $\gamma$-Ti(PO$_4$)(H$_2$PO$_4$) · 2H$_2$O. (c) 3D network based on [Ti$_2$O]$^{6+}$ dimers and $\mu_4$-phosphato bridges in the crystal structure of [Ti$_2$O(PO$_4$)$_2$(H$_2$O)$_2$]. (d) Microporous 3D network based on $\mu_4$-phosphato bridges in the crystal structure of [Ti$_3$(PO$_4$)$_4$(H$_2$O)$_2$] · NH$_3$. (e) 3D network based on [Ti$_3$O$_2$]$^{8+}$ dimers and mixed ($\mu_4$-phosphato, $\mu_3$-hydrogenophosphato) bridges in the crystal structure of M$_2$[(Ti$_3$O$_2$)(HPO$_4$)$_2$(PO$_4$)$_2$](M = Rb, NH$_4$). (f) Microporous 3D network based on mixed ($\mu_4$-phosphato, $\mu_3$-phosphato) bridges in the crystal structure of (H$_3$O)$_3$[Ti$_6$O$_3$(PO$_4$)$_7$(H$_2$O)$_3$] · H$_2$O.





**Figure 14.** Molecular tectonics of titanium phosphates. (a) Theoretical complexation range predicted by the PCM for Ti$^{IV}$ aqueous species in the presence of monodentate phosphate ions. (b) Crystal structure of MTi$_2$(PO$_4$)$_3$(M = Na, K, Rb) showing the $\mu_4$-bridging monodentate coordination mode of phosphate ions. (c) Crystal structure of Na$_5$Ti(PO$_4$)$_3$ showing that phosphate ions may also adopt a $\mu_2$-bridging monodentate coordination mode.

structure (Fig. 15d). The first one displays two aquo ligands in the *trans* position and four $\mu_4$-phosphato bridges in the equatorial plane, while the second one is surrounded by six $\mu_4$-phosphato bridges, leading to the overall stoichiometry $Ti(H_2O)_2(PO_4)_{4/4}Ti_2(PO_4)_{12/4} \equiv Ti_3(PO_4)_4(H_2O)_2$ for the 3D network. This linking of Ti octahedra by phosphate oxygen via Ti—O—P bonds defines channels running along the *c* axis of the crystal, with ammonia molecules located at the center of eight-membered rings involving an equal amount of $TiO_6$ octahedra and $PO_4$ tetrahedra.

Besides these crystal structures involving nonhydrolyzed $Ti^{IV}$ species ($h = 0$) and protonated $[H_qPO_4]^{(3-q)-}$ species ($q = 0, 1, 2$), basic salts involving hydrolyzed precursors ($0 < h \leq 2$) have also been found. The crystal structure of $[Ti_2O(PO_4)_2(H_2O)_2]$ provides the first evidence of a 3D network based on a corner-sharing octahedral dimer ($h = 1$) and $PO_4$ tetrahedra (Fig. 15c) [45, 46]. This compound may be obtained under hydrothermal conditions ($T = 190\ °C$ during 1 week) from a concentrated mixture of $TiCl_4$ and $H_3PO_4$. Here, $\mu_2$-oxo $[Ti_2O]^{6+}$ octahedral dimers appear to be complexed on one side by two *cis*-disposed aquo ligands and three $\mu_4$-phosphato bridges, and on the other side by five $\mu_4$-phosphato bridges, leading to a 3D network displaying a $TiO_{1/2}(H_2O)_2$ $(PO_4)_{3/4}TiO_{1/2}(PO_4)_{5/4} \equiv Ti_2O(PO_4)_2(H_2O)_2$ stoichiometry. Another example based on the $h = 1$ $Ti^{IV}$ precursor is provided by the crystal structure of MIL-18 (Fig. 15f) prepared under hydrothermal conditions ($T = 210\ °C$) from an aqueous mixture of hydrous titanium oxide, $H_3PO_4$, HF, and 1,3-diaminopropane [47]. In this structure, $\mu_2$-oxo $[Ti_2O]^{6+}$ octahedral dimers are found complexed on one side by one water molecule and four $\mu_4$-phosphato bridges, and on the other side by four $\mu_4$- and one $\mu_3$-phosphato bridges, leading to a charged 3D network displaying a $[TiO_{1/2}(H_2O)$ $(PO_4)_{4/4}TiO_{1/2}(PO_4)_{4/4}(PO_4)^-_{1/3}]_3 \equiv [Ti_6O_3(PO_4)_7(H_2O)_3]^{3-}$ stoichiometry. Charge compensation appears to be ensured by three $[H_3O]^+$ countercations in strong interaction with one water molecule [47]. A linear corner-sharing $[Ti_3O_2]^{8+}$ trimer ($h = 4/3$) could be identified in the crystal structures of $(NH_4)_2[(Ti_3O_2)(HPO_4)_2(PO_4)_2]$ obtained under heating at 190 °C of a mixture containing $TiCl_4$, $H_3PO_4$, and urea (Fig. 15e) [45]. An isostructural rubidium salt of this phase has also been isolated [48]. In both phases, the terminal Ti atoms of $[Ti_3O_2]^{8+}$ trimers appear to be complexed by two $\mu_3$-$HPO_4$ and three $\mu_4$-$PO_4$ bridges, while the central Ti atom appears to be bonded to two $\mu_3$-$HPO_4$ and two $\mu_4$-$PO_4$ bridges. The overall stoichiometry may then be written as $[TiO_{1/2}(\mu_3$-$HPO_4)_{2/3}(\mu_4$-$PO_4)_{3/4}]_2[TiO_{2/2}(\mu_3$-$HPO_4)_{2/3}$ $(\mu_4$-$PO_4)_{2/4}]^{2-} \equiv [Ti_3O_2(\mu_3$-$HPO_4)_2(\mu_4$-$PO_4)_2]^{2-}$, with charge compensation ensured by two ammonium or rubidium countercations.

This corner-sharing condensation process via $\mu_2$-oxo groups can be continued until the formation of infinite linear chains that are characteristic building units of crystalline structures involving $TiO^{2+}$ ($h = 2$) precursors. The most simple and symmetric chain is found in the crystal structure of $Na_4TiO(PO_4)_2$ (Fig. 16a) [49]. In this chain, each Ti octahedron displays two *trans* $\mu_2$-oxo groups with four symmetrically disposed $\mu_2$-phosphato bridges, explaining the overall $[TiO_{2/2}(PO_4)_{4/2}]^{4-}$ stoichiometry and the occurrence of four sodium countercations between the chains. More
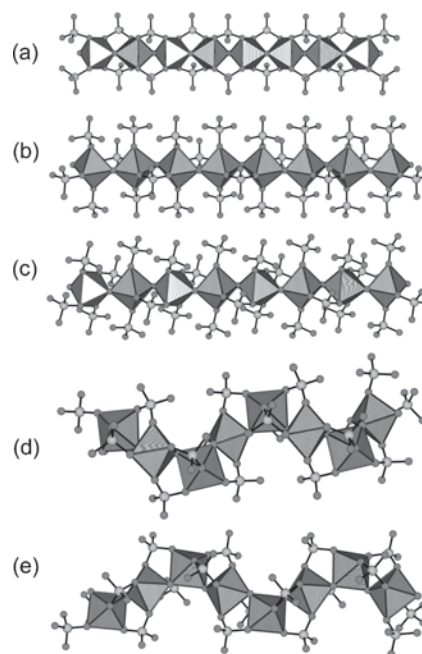


**Figure 16.** Observed chain conformations in the crystal structures of titanyl phosphates. (a) Complexation of linear *trans*-$TiO^{2+}$ chains by $\mu_2$-phosphato bridges in the crystal structure of $Na_4TiO(PO_4)$. (b) Linear *trans*-$TiO^{2+}$ chain in the crystal structure of $\beta$-$LiTiOPO_4$. (c) Alternated *trans*-$TiO^{2+}$ chain in the crystal structure of $\alpha$-$LiTiOPO_4$ and $\alpha$-$NaTiOPO_4$. (d) Skewed *cis*-$TiO^{2+}$ chain in the crystal structure of $\beta$-$NaTiOPO_4$. (e) Mixed (*cis*-$TiO^{2+}$, *trans*-$TiO^{2+}$) chain in the crystal structure of $KTiPO_4$ and $RbTiOPO_4$.

complex chains occur in the crystal structures of phases displaying the $MOPO_4$ (M = Li, Na, K) stoichiometry (Fig. 16). The chain occurring in the crystal structure of $\beta$-$LiTiOPO_4$ (Fig. 16b) is very similar to that found in the crystal structure of $Na_4TiO(PO_4)_2$ (Fig. 16a), except that it now involves $\mu_4$-phosphato bridges leading to the new $[TiO_{2/2}(PO_4)_{4/4}]^-$ stoichiometry [50, 51]. An alternate version of this *trans*-$TiO^{2+}$ chain occurs in the crystal structures of $\alpha$-$LiTiOPO_4$ [52] and $\alpha$-$NaTiOPO_4$ [53, 54] (Fig. 16c), while the full *cis*-$TiO^{2+}$ chain (Fig. 16d) has been characterized in the crystal structure of $\beta$-$NaTiOPO_4$ [55]. Finally, a mixed alternate (*cis*-$TiO^{2+}$, *trans*-$TiO^{2+}$) chain forms the building unit of the crystal structure of $KTiOPO_4$ [56–61] and $RbTiOPO_4$ [62–64] (Fig. 16e). Owing to the high polarizability of the Ti—O bonds and their mutual disposition inside strongly distorted octahedra (172.3 pm < $d_{Ti—O}$ < 215.0 pm), such crystals are characterized by large nonlinear optical properties. Compared to similar organic materials, they also display a high radiation damage threshold arising from their rigid framework of $PO_4$ tetrahedra.

**Complexation by Silicate Ions**   Our last concern will be the case of silicate ions, which, like phosphate ions, bind to $Ti^{IV}$ through monodentate ($\alpha = 1$) $\mu_4$-silicato bridges, as evidenced in the crystal structures of natisite $Na_2TiO(SiO_4)$ [65, 66] and $Li_2TiO(SiO_4)$ [67] (Fig. 17b). The interesting feature of these 3D networks is the fivefold square pyramidal coordination observed for titanium atoms. The same coordination polyhedron occurs in the two low-temperature (Fig. 17c) and high-temperature (Fig. 17d) polymorphic
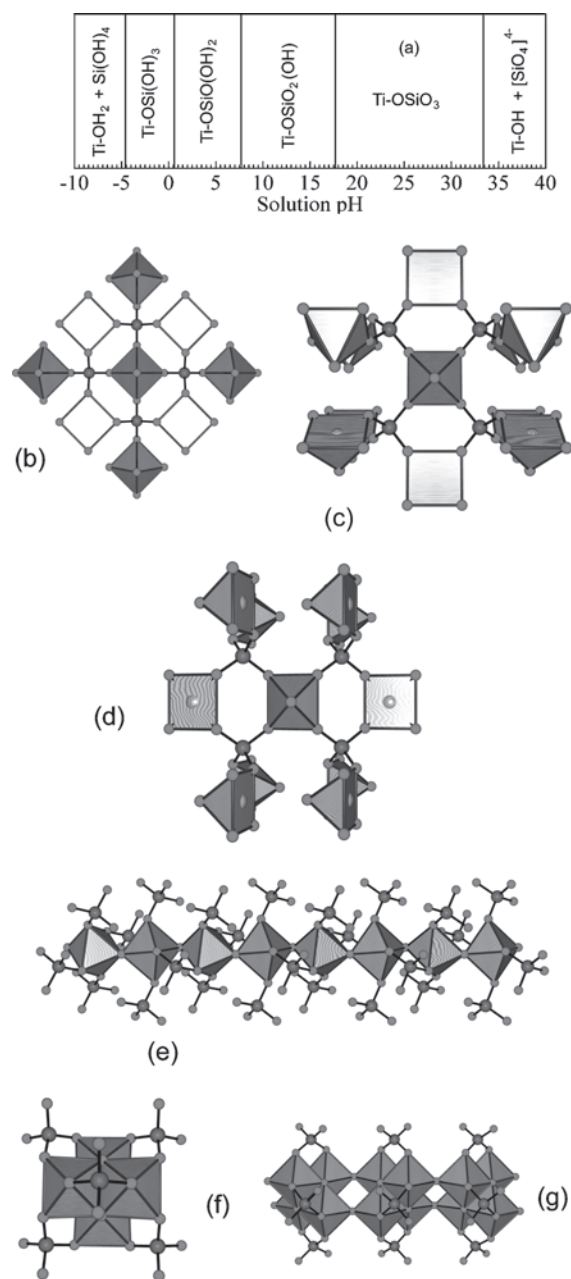
**Figure 17.** Molecular tectonics of silicotitanates. (a) Theoretical complexation range predicted by the PCM for Ti$^{IV}$ aqueous species in the presence of nonsolvated monodentate silicate ions. (b) Crystal structure of natisite Na$_2$TiO(SiO$_4$) and Li$_2$TiO(SiO$_4$) showing the $\mu_4$-bridging monodentate coordination mode of silicate ions and the square pyramidal fivefold coordination of Ti atoms. (c) Low-temperature modification of a polymorph of Na$_2$TiO(SiO$_4$) network. (d) High-temperature modification of the polymorph shown in (c). (e) *trans*-TiO$^{2+}$ octahedral chain occurring in the crystal structure of titanite or sphene CaTiO(SiO$_4$). (f) Cubane-like arrangement of Ti and O atoms in the crystal structures of M$_4$Ti$_4$O$_4$(SiO$_4$)$_3$ · 4H$_2$O phases (M = H, Na, K, Cs) that are structural analogs of the mineral pharmacosiderite. (g) Chains of cubane-like Ti$_4$O$_4$ cages linked through linear oxo-bridges in the crystal structures of M$_2$Ti$_2$O$_3$SiO$_4$ · $n$H$_2$O (M = H, Na).

modifications of Na$_2$TiO(SiO$_4$) [68], whereas an alternate *trans*-TiO$^{2+}$ octahedral chain, similar to that observed in $\alpha$-LiTiOPO$_4$ or $\alpha$-NaTiOPO$_4$, occurs in the crystal structure of titanite or sphene CaTiO(SiO$_4$) (Fig. 17e) [69–75]. The PCM complexation diagram for this tetravalent ion, characterized by EN(SiO$_4^{4-}$) = 1.161 (pH* = 33.4), EN(HSiO$_4^{3-}$) = 1.721 (pH* = 17.7), EN(H$_2$SiO$_4^{2-}$) = 2.100 (pH* = 7.7), EN(H$_3$SiO$_4^-$) = 2.374 (pH* = 0.6), and EN(H$_4$SiO$_4$) = 2.581 (pH* = −4.6), is shown in Figure 17a. As with the case of phosphate ions, we notice the very large values obtained for ionic dissociation of [HSiO$_4$]$^{3-}$ and [SiO$_4$]$^{4-}$. Allowing for some H bonding with the surrounding water molecules would lead to EN(SiO$_4^{4-}$ · 4H$_2$O) = 2.126 (pH* = 15.1), EN(HSiO$_3^{3-}$ · 3H$_2$O) = 2.195 (pH* = 9.6), and EN(H$_2$SiO$_4^{2-}$ · 2H$_2$O) = 2.285 (pH* = 4.7). Even with these reasonable corrections, we see that titanosilicate complexes are stable throughout the whole range of pH. This may help to explain the occurrence of more than 500 known crystalline phases (exactly 561 phases containing Si, Ti, and O atoms in the October 2001 release of the ICSD Database in Karlsruhe). There is also another reason to explain the complexity of titanosilicate chemistry. As shown in Figure 7, all previously studied C$^{IV}$-, N$^V$-, P$^V$-, S$^{VI}$-, and Cl$^{VII}$-based oxyanions cannot undergo spontaneous oxolation in aqueous solutions owing to their location at the upper right of the diagram in the domain of soluble acids. With Si$^{IV}$, we have moved to the polyacid domain, meaning that spontaneous oxolation 2Si—OH → Si—O—Si + H$_2$O may now readily occur in aqueous solutions, leading to polysilicate species. With two systems both able to undergo oxolation after pH changes, we may thus span the whole palette from silicotitanates (titanium oxo-compounds complexed by orthosilicate anions) to titanosilicates (polysilicates complexed by titanyl TiO$^{2+}$ cations). To keep this review within reasonable limits and in view of our interest in titanium oxo chemistry, we have limited ourselves to the study of silicotitanates gathered in Figure 17.

The striking feature is, then, that besides the previously discussed phases (titanite and natisite) only two phases remain to be considered, as most crystalline phases are found to involve Si—O—Si bonds. The overwhelming abundance of titanosilicates over silicotitanates may be the consequence of the very high affinity of Si—O bonds for Ti$^{IV}$, allowing for some depolymerization of the Ti—O—Ti bonds. Consequently, only the most symmetrical molecular arrangements of the Ti—O—Ti bonds should be able to resist silicate species. In fact, this is just what has been found experimentally in the crystal structures of M$_4$Ti$_4$O$_4$(SiO$_4$)$_3$ · 4H$_2$O phases with M = H, K, Cs [76, 77], or Na [78], which are structural analogs of the mineral pharmacosiderite KFe$_4$(OH)$_4$(AsO$_4$)$_3$ · 6H$_2$O. These phases can be prepared under hydrothermal conditions ($T$ = 160–200 °C, $t$ = 48–100 h) from amorphous TiO$_2$–SiO$_2$ gels having Si : Ti = 2. In this 3D network, cubane-like Ti$_4$O$_4$ oxo-cages are complexed by six $\mu_4$-silicato bridges (Fig. 17f) with each SiO$_4$ tetrahedra bridging two Ti$_4$O$_4$ cubes. It is interesting to compare this very compact cube to the much larger Ti$_8$O$_{12}$ (see Fig. 6) isolated from solutions containing noncoordinating Cl$^-$ counteranions [19]. Other related phases Na$_2$Ti$_2$O$_3$SiO$_4$ · 2H$_2$O [79] and Ti$_2$(OH)$_2$OSiO$_4$ · 1.5H$_2$O [80] could be obtained upon prolonged heating ($t$ = 10 days at $T$ = 200 °C) of

solutions obtained by mixing $TiCl_4$, $H_2O_2$, silicic acid, and NaOH. As shown in Figure 17g, these 3D networks involve exactly the same $Ti_4O_4$ building units associated again to $\mu_4$-silicato bridges, but the cubes are now linked to linear chains through four $\mu_2$-oxo bridges. Each cube is complexed by four $SiO_4$ tetrahedra common to two cubes leading to a negatively charged ($[Ti_4O_4O_{4/2}(SiO_4)_{4/2}]^{4-} \equiv [Ti_2O_3SiO_4]^{2-}$) hybrid network needing two countercations ($H^+$ or $Na^+$) to ensure charge neutrality.

## 2.2. Crystalline Titanium(IV) Oxides

After this review of the aqueous chemistry of $Ti^{IV}$ species, it should be obvious that our PCM approach provides considerable help in rationalizing and understanding the experimental facts. In its most simple form, it suffers, however, from its blindness to the detailed molecular or crystalline structure. For example, if the model readily explains why, under acidic conditions (pH $\sim$ 0), a titanyl cation ($h = 2$) should be formed (the fully aquo $Ti^{IV}$ complex is just much more electronegative than the most acidic species $[H_5O_2]^+$ compatible with a water medium), it makes absolutely no distinction between $[Ti(OH)_2(OH_2)_4]^{2+}$ or $[TiO(OH_2)_5]^{2+}$ species. Referring to the above experimental results showing the occurrence of monomeric $[TiO]^{2+}$ cation (natisite), dimeric $[Ti_2O]^{6+}$ (phosphate counteranion), trimeric linear $[Ti_3O_2]^{8+}$ (phosphate counteranion), tetrameric square planar $[Ti_4O_4]^{8+}$ (oxalate counteranion), cubane-like $[Ti_4O_4]^{8+}$ (silicate counteranion), cubic-like $[Ti_8O_{12}]^{8+}$ (chloride counteranions), and chainlike (cis, trans, or mixed) $[TiO]_n^{2n+}$ (fluoride, sulfate, phosphate, and silicate counteranions), it should be clear the real $h = 2$ aqueous species should be written as $[TiO(OH_2)_5]^{2+}$ and not $[Ti(OH)_2(OH_2)_4]^{2+}$. Similarly, if the PCM rightly predicts that the final term of condensation should be a hydrated oxide $TiO_2 \cdot nH_2O$ and not a hydroxide $Ti(OH)_4$, absolutely no distinction is possible among the three common polymorphs of titanium dioxide (rutile, anatase, and brookite). Consequently, during the decade following the achievement of the above formalism [4], considerable work was performed along the following lines:

1. Elaboration of a structure-dependent version based on the Sanderson electronegativity scale in order to compute NMR chemical shifts [81] and treat nonmolecular 3D networks [82].
2. Use of the Mulliken scale for individual electronegativities and of covalent radii for approximating chemical hardnesses [83, 84].
3. Improved evaluation of chemical shifts and electric field gradient tensors from crystalline [85] or molecular structures [86].
4. Use of the Allen spectroscopic electronegativity scale and *ab initio* atomic radii, allowing probing molecular interactions [87–90] and performing crystal structure optimization [90–92].

### 2.2.1. PACHA Formalism

In the following, we examine this new powerful approach known as PACHA (partial atomic charge and hardness analysis). This model is then applied to the study of $TiO_2$ crystalline phases and some $Ti^{IV}$-based hybrid organic–inorganic

molecular networks. Briefly stated, the PACHA model states that for any chemical compound four global mean values, symbolized hereafter as $\langle EN \rangle$, $\langle GH \rangle$, $\langle EB \rangle$, and $\langle GI \rangle$, may be defined. At a local scale (atomic sites), it is further characterized by $2 \times n$ local indexes in the form of $n$ partial charges ($q_i$) and $n$ frontier indexes ($f_i$). The parameter $\langle EN \rangle$ corresponds to the mean electronegativity (in volts) of the system that may be identified with the energy situated halfway between the HOMO and the LUMO (Fig. 18). It can then be used to determine if a given compound will act as an electron donor (low or negative value) or as an electron acceptor (high $\langle EN \rangle$ value). The parameter $\langle GH \rangle$ measures the global hardness that should scale like a HOMO–LUMO gap (molecule) or band gap (solids). It can be used to compute the paramagnetic contribution to the chemical shielding of an NMR active atomic nucleus. The $\langle EB \rangle$ parameter reflects the energetic balance between all atomic pairs, either attractive ($\delta^+ \cdots \delta^-$) or repulsive ($\delta^+ \cdots \delta^+$ or $\delta^- \cdots \delta^-$). A negative value is an indication of a stable compound, whereas a positive value points to a species that must heavily rely on covalent interactions to become stabilized. This parameter can also be used to probe energetic interactions between molecular fragments [87–92].

Briefly stated, within the density functional theory (DFT) framework [93, 94], the total molecular energy $E$ can always be partitioned between the purely electrostatic contribution EB and a purely electronic functional $F[\rho]$, which takes care of all the exchange and electronic correlation: $E_{tot} = EB + F[\rho]$. Now, for the same molecular fragment placed into two different chemical environments (in a vacuum, on one hand, and inside a crystalline lattice, on the other hand, for example), our basic assumption is that $F_1[\rho] \sim F_2[\rho]$. If this approximation holds, then the interaction energy can be readily evaluated as $E_{int} \sim EB(1) - EB(2)$. This EB value can also be used, through a simplex minimization technique,
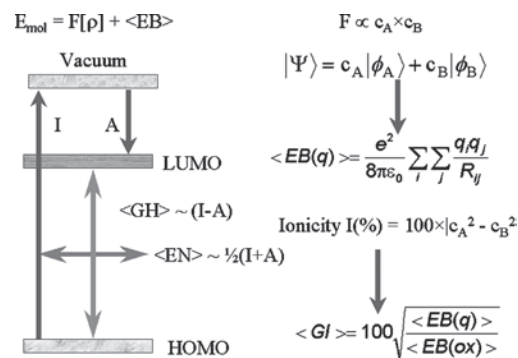


**Figure 18.** Relationships between the PACHA model (mean electronegativity, EN; global hardness, $\langle GH \rangle$; partial charge, $q$; global ionicity, $\langle GI \rangle$; electrostatic balance, $\langle EB \rangle$), LCAO–MO theory (wave function, $|\Psi\rangle$; HOMO, LUMO, LCAO–MO coefficients $c_A$ and $c_B$), and density functional theory DFT (electronic density, $\rho$; exchange-correlation functional, $F[\rho]$; electrostatic functional, $\int v_{ne}\rho \, d\tau$). From DFT requirements, $\langle EN \rangle$ should correspond to an electronic chemical potential governing electronic density flows between atoms, that is, to a Fermi level, while $\langle GH \rangle$ should correspond to the HOMO–LUMO or band gap. A key feature of the model is the spherical charge approximation ($\int v_{ne}\rho \, d\tau \sim \langle EB \rangle$), providing a very efficient algorithm for the quantification of molecular and crystalline interactions.

to find the most favorable position for an atom or an atomic group within a molecule or a crystalline network [90–92]. For metal alkoxides, this is particularly useful as it allows us to get a reliable estimate of the atomic coordinates of H atoms. Accordingly, these coordinates are often not included in the refinement process of X-ray data but are nevertheless absolutely needed to get realistic partial charge distributions. Such a minimization technique can also be used to get reliable charge distributions from strongly disordered crystals. Finally, the $\langle GI \rangle$ parameter is a global ionicity index, ranging from 0 to 100%, that helps to decide whether a given compound should be considered as ionic or covalent. A purely covalent structure ($q_i \sim 0$) will then be characterized by GI $\sim$ 0%, while a purely ionic one ($q_i$ values close to the oxidation states) will have GI $\sim$ 100%.

***Electronic Signatures*** The PACHA equations provide a fundamental mathematical link between atomic properties (electronegativities $e\chi_i^0$, atomic sizes $r_i$) and molecular or crystalline structure via partial charge ($q_i$) and frontier index ($f_i$) distributions. Chemical objects are introduced via the knowledge of stoichiometric coefficients $n_i$, oxidation numbers $z_i$, Madelung matrix $M_{ij}$ (in Å$^{-1}$), total charge $Q$, and number of formula units $Z$ per unit cell:

$$n_i e \langle EN \rangle = n_i e \chi_i^0 + n_i \eta_i q_i + 14.4 \sum_j M_{ij} q_j$$

$$\text{with } \sum_i n_i q_i = Q \qquad (5)$$

$$n_i e^2 \langle GH \rangle = n_i \eta_i f_i + 14.4 \sum_j M_{ij} f_j \quad \text{with } \sum_i n_i f_i = Z \quad (6)$$

$$\langle EB(q)/eV \rangle = \sum_i \sum_j M_{ij} q_i q_j \qquad (7)$$

$$\langle GI/\% \rangle = 100 (EB(q)/EB(z))^{1/2} \qquad (8)$$

In its *ab initio* final form, the PACHA model uses the configuration energy of the elements [95, 96] and atomic orbital radii $r_i$ [97] to approximate electronegativity values $\chi_1^0$ and chemical hardnesses $\eta_i (\text{eV}) = 1440/r_i$ (pm), respectively. This particular choice confers an absolute character on the reported charge distributions, as these values are fixed by quantum-mechanical laws and not by empirical data commonly used to define other electronegativity or radius scales. This allows us to treat on the same quantitative basis organic or inorganic objects, a very important point if we want to cope with complex mixed organic–inorganic compounds. Another nice aspect linked with this absolute character is the possibility to establish a quantitative correlation between partial charges borne by oxygen atoms $q_O$ and protonation constants ($-pK_a = 17.3 + 39.5 \times q_O$) [87–90]. With this relationship in hand, stating that the higher the charge on the oxygen atom, the higher its acidity, we have a very convenient way to infer acidobasic properties directly from the molecular or crystalline structure. Finally, electrostatic interactions cannot be the whole story for understanding the chemical reactivity of mixed organic–inorganic complexes. Consequently, the model gives us, besides the partial charge $q_i$, a set of frontier indexes $f_i$ that can be used as a local probe for hard–soft interactions. To sum up, with four global parameters ($\langle EN \rangle$, $\langle GH \rangle$, $\langle EB \rangle$, and $\langle GI \rangle$) and $2n$ local

ones ($q_i$ and $f_i$), we may define what we call an "electronic signature" (ES) within the PACHA formalism.

***Case Study: Carbon Monoxide*** A good illustration of our strategy is provided by the very simple example of carbon monoxide (CO). First, quantum mechanics or atomic spectroscopy tells us that an isolated carbon atom has an electronegativity $\chi_C^0 = 15.05$ V [95] and that the radii of the valence orbitals of this element are $r_{2s} = 62$ pm and $r_{2p} = 59.6$ pm [97]. Similarly, for the oxygen atom, we have $\chi_O^0 = 21.36$ V [95], $r_{2s} = 45$ pm, and $r_{2p} = 41.4$ pm [97]. In the following, we will always assume that the atomic chemical hardness is governed by the most diffuse atomic orbital (here 2s orbitals for both carbon and oxygen atoms). Now we have to introduce the crystalline structure of carbon monoxide (space group $P2_13$) [98]. Using an Ewald summation procedure [99], we find that the $2 \times 2$ Madelung matrix characterizing this structure is $M_{CC} = -0.47897$ Å$^{-1}$, $M_{CO} = M_{OC} = 3.41636$ Å$^{-1}$, and $M_{OO} = -0.44559$ Å$^{-1}$ (optimum convergence parameter $G = 0.32$ Å$^{-1}$). Inserting these data into the PACHA equations given above leads to the following electronic signature: $\langle EN \rangle = 17.18$ V, $\langle GH \rangle = 18.4$ eV, $\langle EB \rangle = -2.98$ eV, $\langle GI \rangle = 11.6\%$, $q_C = -q_O = +0.231$, $f_C = 0.663$, and $f_O = 0.334$. From this absolute signature, it is possible to deduce that CO should be a very stable and strongly covalent (low ionicity index $\langle GI \rangle$) molecule with a low-lying HOMO (high electronegativity $\langle EN \rangle$) and a wide HOMO–LUMO gap (large global hardness $\langle GH \rangle$). Even if the oxygen atom is found to be negatively charged, it should have no affinity for protons (p$K_a \sim -8.5$). For covalent-based interactions (coordination chemistry), the largest $f$ index is found on the C atom and not the O atom, explaining the preferred coordination mode M—C≡O and not M—O≡C. Fortunately, all these predictions are confirmed by experiments.

The interesting point is that these properties were derived without any reference to any MO scheme. In particular, the occurrence of a triple carbon–oxygen bond in this molecule has been completely ignored. This example shows the power of our approach, as chemical stability and properties can be predicted without solving the Schrödinger equation. Nevertheless, it also pinpoints its weakness concerning the ignorance of the nature of frontier orbitals and our total inability to predict any spectroscopic properties. A further step is achieved by considering that all these physicochemical properties are not driven by the crystalline structure, but are already engraved in the molecular structure of a single molecule. To check this point, let us forget the whole crystalline network and keep just the single essential information: CO is a molecule displaying a very short C—O bond (106.3 pm). Physically speaking, this means that the CO network has been vaporized and that we now face a free isolated CO molecule. For this much simpler situation, the Madelung matrix is just $M_{AA} = M_{BB} = 0$ (no C$\cdots$C or O$\cdots$O interactions) and $M_{AB} = 1/1.063 = 0.941$ Å$^{-1}$ (no intermolecular C$\cdots$O interactions). Inserting this new matrix into the same equations leads to $\langle EN \rangle = 17.22$ V, $\langle GH \rangle = 19.9$ eV, $q(C) = -q(O) = 2 \times \langle GI \rangle = +0.224$, and $f(C) = 1 - f(O) = 0.656$. A simple comparison with previous values derived after a full Madelung summation process will immediately convince the reader that CO forms

a truly molecular crystal. This comes from the fact that its electronic signature changes by a very tiny 0.1% on going from the crystalline lattice to the free molecule. This clearly demonstrates that, at least in the case of the CO molecule, the pertinent chemical information is completely included in the knowledge of the molecular geometry and not in the way the molecules are packed inside a crystalline structure. Moreover, we also are now in a position to get a quantitative evaluation of the lattice packing energy for this highly covalent network. Accordingly, for the crystalline network, we know that $\langle EB_{net} \rangle = -2.98/4 \text{ eV} = -71.9 \text{ kJ mol}^{-1}$, as we have four CO molecules per unit cell ($Z = 4$). For a positively charged carbon atom ($q = +0.224$) situated at 1.063 Å of a negatively charged oxygen atom ($q = -0.224$) in a free molecule, we should have $\langle EB_{mol} \rangle = -694.68 \times 2(0.224)^2/1.063 = -65.6 \text{ kJ mol}^{-1}$. As expected, $\langle EB_{net} \rangle$ is lower than $\langle EB_{mol} \rangle$ owing to the intermolecular interactions occurring in the solid state and which are absent in the free molecule. The difference $\langle EB_{net} \rangle - \langle EB_{mol} \rangle \sim -6 \text{ kJ mol}^{-1}$ is thus a direct measure of all the attractive intermolecular forces acting in the crystalline state. In this particular case, it is found to be rather weak (typical of van der Waals interactions) in agreement with the low molecular weight and low polarity of the CO molecule. The good news is now that this procedure is quite general and not limited to molecular networks. It can be easily applied in a systematic way to any crystalline network or isolated molecule.

***Errors in Evaluation of Electronic Signatures***   Another important aspect of the PACHA model concerns the systematic inclusion of errors in the electronic signature. First, one has to notice that, given structural $M_{ij}$ input, (4)–(8) lead to a unique electronic signature. If some errors are made concerning the determination of unit-cell parameters and/or atomic positions, the corresponding signature will be more or less affected depending on the accuracy of the structure determination. For experimental data coming from X-ray or neutron diffraction, the evaluation of errors is straightforward as these techniques give not only the structural parameters but also the estimated standard deviations (esd or $\sigma$) on each optimized parameter. From a single input, it is then possible to generate $N$ slightly different crystal structures by allowing random variations of the structural parameters within $3\sigma$ (99.9% confidence level). By computing a Madelung matrix for each of these $N$ crystal structures (typically $N = 100$), it is possible to perform a statistical analysis on the derived $\langle EN \rangle$, $\langle GH \rangle$, $\langle EB \rangle$, $\langle GI \rangle$, $q_i$, and $f_i$ quantities. Corresponding errors on the PACHA parameters may then be reported as $3\sigma$. This systematic evaluation of errors allows us to know how many significant digits should be reported in the electronic signature. However, the same crystal structure may have been determined several times by different authors. In these cases, errors may not be computed from the individual esd, but rather from a statistical analysis performed over all available structural refinements. Such errors will be reported in boldface characters to distinguish them from the errors associated with a single refinement. Finally, if errors are reported in italics, they have been computed from an average over structural data of good quality obtained by rejecting from the statistics all structures with unknown $R$ values or having $R$ values typically higher than 10%.

A direct and useful consequence of this systematic evaluation of errors in the electronic signature concerns the accuracy of the determination of the Madelung matrix. If structural data of the highest quality ($R < 5\%$) is available, convergence would be reached as soon as the relative variation between two successive evaluations of the same matrix element is typically less than $10^{-4}$. Increasing the accuracy beyond this point will increase severely the computation time for a statistically nonsignificant improvement of the electronic signature. Reciprocally, if the crystal structure has a huge unit cell, it will surely not be well refined ($R > 10\%$). In such cases, it may be perfectly correct to use nonconverged Madelung matrices having a relative accuracy as low as $10^{-2}$ or higher in order to minimize the computation time.

***Situation Relative to ab initio Models***   Another interesting point concerns the accuracy of structural data derived from first-principles calculations with absolutely no experimental input. The use of the term "accurate" is here important, as it refers to the difference between a *calculation* and the *true value of an observable*. Because the true value of an observable is, in principle, unknowable, it is virtually impossible to judge the accuracy of a calculation. Such is not the case if we have some idea of the *uncertainty* (expressed as a standard deviation $\sigma$ through a statistical analysis) attached to the measure of the observable. If this uncertainty is very low, we may safely identify the mean value measured with the true value of the observable. Now it is easy to check how many standard deviations separates the result of a calculation from a measured value. If theory lies within $3\sigma$ of experience, the model can claim to reproduce accurately the experimental values; otherwise, it should be considered as not good enough to reproduce experimental trends. Consequently, the reported combined standard uncertainty on each electronic parameter (which depends on the crystalline short-range and long-range order) allows us to judge, in a quantitative and objective way, how far a theoretical structure is from the experimental one. A good agreement between theory and experiment should be claimed only when all electronic parameters of the theoretical structure lie within $3\sigma$ of the experimental data.

Figure 19 presents the PACHA model in relation to other quantum-mechanical tools. As can be seen, owing to the total absence of empirical parameters, it can be considered as an *ab initio* approach based on a spherical charge approximation of DFT equations. Its very high efficiency lies in the encapsulation of all the problematic electron–electron correlations into just two parameters per chemical element: the configuration energy identified with the electronegativity and an atomic radius identified with the chemical hardness. The interesting point is that the previously used PCM approach may be viewed as a particular case of the PACHA equations. The PCM is obtained by putting $M_{ij} = 0$ and by using the Allred–Rochow scale to get electronegativities and hardnesses. In this case, the chemical hardness is approximated as the square root of the electronegativity through an empirical constant $k$ in order to mimic the atomic radius dependence. This allows keeping just one parameter per chemical element instead of two in the PACHA approach. In the following, this PACHA model will be extensively used to
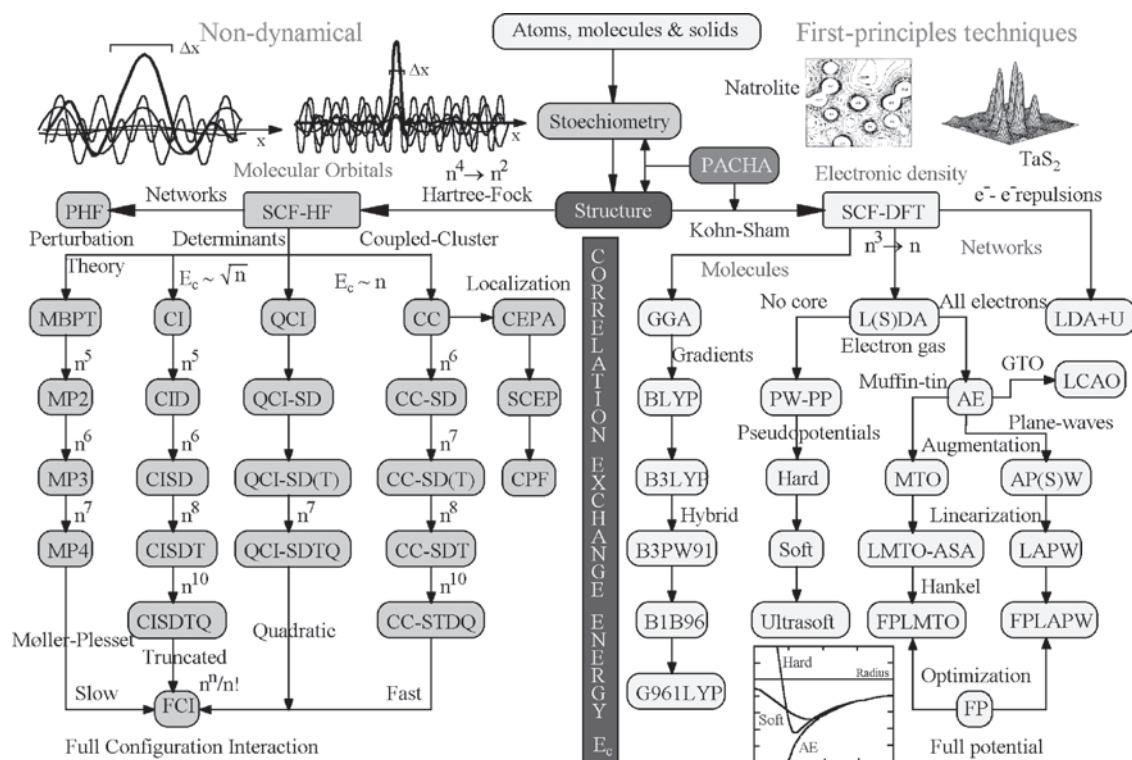
**Figure 19.** PACHA model relative to other quantum-mechanical tools. The Hartree–Fock (HF) approaches based on the determination of the total wave function after resolution of the Schrödinger equation are represented on the left of the figure. Here $n$ scales like the total number of electrons and gives an idea of the computational cost of each method. SCF, self-consistent field; MBPT, many-body perturbation theory; MP, Moller–Plesset development; CI, configuration interaction with S, single; D, double; T, triple; Q, quadruple excited configurations; FCI, full CI; QCI, quadratic CI; CC, coupled cluster; CEPA, coupled-electron-pair approximation; SCEP, self-consistent electron pair; CPF, coupled-pair functional approach. The approaches based on density functional theory (DFT) using the Kohn–Sham equations are represented on the right of the figure. GGA, generalized gradient-corrected approximation; B, Bethe exchange functional; LYP, Lee–Yang–Parr correlation functional; PW, Perdew–Wang; L(S)DA, local (spin) density approximation; PW, plane wave; PP, pseudo-potential; AE, all electrons; MTO, muffin-tin orbital; L, linearized; ASA, atomic sphere approximation; FP, full potential; APW, augmented PW; GTO, Gaussian-type orbital; LCAO, linear combination of atomic orbitals; U, correction for electron–electron repulsions.

discriminate between known $TiO_2$ polymorphs or to understand the chemical properties of various complexes or building blocks that can be used in a rational design of hybrid organic–inorganic networks.

### 2.2.2. Application to $TiO_2$ Polymorphs

With at least six different known polymorphs, $TiO_2$ provides a challenge for theoretical models devoted to chemical bonding in the solid state. Surprisingly enough, these crystalline $TiO_2$ phases have never been systematically reviewed and compared using the same theoretical framework.

**Rutile** This is the thermodynamically stable high-temperature polymorph. It is very well known that tetragonal crystal structure is based on linear chains of $TiO_6$ octahedra sharing a pair of opposite edges and which are further linked by shared vertices to form a 3D structure of 6:3 coordination (Fig. 20). In this structure, oxygen atoms are in an approximate hexagonal closest packing configuration with titanium atoms filling half of the available octahedral holes. Each $TiO_6$ octahedron is in contact with 10 other ones (2 through edge sharing and 8 through corner sharing). The room-temperature rutile structure has been

refined several times [100–117], allowing us to compute the following low-accuracy electronic signature:

| Global | Local | |
|---|---|---|
| $\langle EN \rangle = 5.83 \pm 0.23$ V | $q(Ti) = 1.631 \pm 0.035$ | |
| $e^2\langle GH \rangle = 3.04 \pm 0.05$ eV | $q(O) = -0.815 \pm 0.018$ | (9) |
| $\langle EB \rangle = -23.5 \pm 1.3$ eV | $f(Ti) = 1.178 \pm 0.017$ | |
| $\langle GI \rangle = 40.77 \pm 0.88\%$ | $f(O) = -0.089 \pm 0.009$ | |

In comparison with $\alpha$-quartz ($\langle EN \rangle = 12.78 \pm 0.07$ V, $e^2\langle GH \rangle = 8.86 \pm 0.06$ eV, $\langle EB \rangle = -10.5 \pm 0.4$ eV, $\langle GI \rangle = 25.8 \pm 0.4\%$, $q_{Si} = +1.03 \pm 0.02$, and $q_O = -0.516 \pm 0.008$) [118], rutile appears to be a much more ionic and less electronegative oxide material in agreement with common chemical knowledge. To match the experimental room-temperature band gap, $E_g(\text{direct}) = 3.062$ eV and $E_g(\text{indirect}) = 3.101$ eV [119], with the global hardness, we have to set $G = 0.47$ Å$^{-1}$. This value is very close to the optimum $G$ value minimizing the computation time ($G = 0.49$ Å$^{-1}$). The large frontier index found for titanium reflects the rather large orbital radius of the titanium 4s orbital (147.7 pm) used to approximate the chemical hardness of this atom. Limiting statistical analysis to the 20 structures
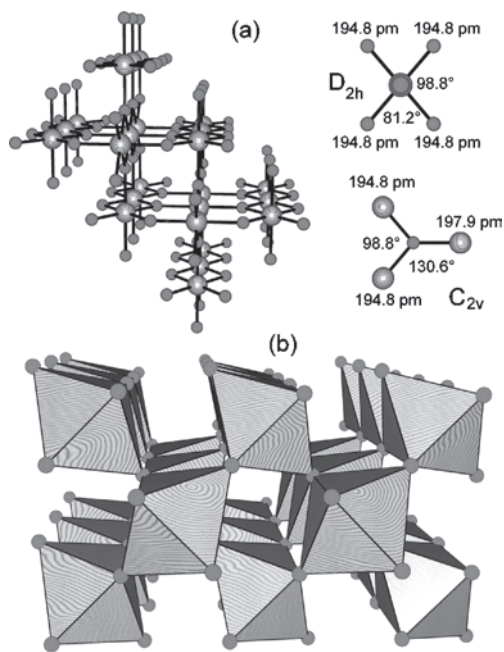
**Figure 20.** Rutile crystal structure (space group $P4_2/mnm$). (a) Local geometry at Ti and O sites and ball-and-stick view of the chemical bond patterns. (b) Topology of the 3D framework is evidenced as corner sharing between chains of *trans* edge-sharing octahedra.

having $R < 5\%$ leads to the following much more accurate electronic signature:

| Global | Local |
|---|---|
| $\langle EN \rangle = 5.838 \pm 0.014$ V | $q(Ti) = 1.6286 \pm 0.0022$ |
| $e^2 \langle GH \rangle = 3.046 \pm 0.002$ eV | $q(O) = -0.8143 \pm 0.0011$ |
| $\langle EB \rangle = -23.41 \pm 0.08$ eV | $f(Ti) = 1.1768 \pm 0.0011$ |
| $\langle GI \rangle = 40.72 \pm 0.06\%$ | $f(O) = -0.0884 \pm 0.0005$ |

$$(10)$$

Finally, selecting one of the most recent and best crystal structure determinations ($R = 1.1\%$ [112]) leads to this very high accuracy signature:

| Global | Local |
|---|---|
| $\langle EN \rangle = 5.8354 \pm 0.0023$ V | $q(Ti) = 1.6290 \pm 0.0004$ |
| $e^2 \langle GH \rangle = 3.0464 \pm 0.0010$ eV | $q(O) = -0.81449 \pm 0.00019$ |
| $\langle EB \rangle = -23.420 \pm 0.013$ eV | $f(Ti) = 1.17700 \pm 0.00018$ |
| $\langle GI \rangle = 40.725 \pm 0.009\%$ | $f(O) = -0.08850 \pm 0.00009$ |

$$(11)$$

The 41% global ionicity found for this network may be compared to other ionicity indexes given in the literature. With $\chi(Ti) = 1.4$ and $\chi(O) = 3.5$, it is found that GI = 55% from the Pauling equation $I(Ti-O) = 100\{1 - \exp[-0.18(\chi_{Ti} - \chi_O)^2]\}$ [120] against GI $= -50 \times q(O) = 37.4\%$ from optical basicity–derived charges $q(O) = -0.86/(\chi_{Ti} - 0.25)$ [121]. Accurate X-ray charge density studies of the rutile structure [109] have revealed a rather high degree of covalence but with $q(Ti) = -2 \times q(O) \sim +3$, leading to GI $\sim 75\%$. This value is similar to that derived from LO–TO splitting [122] (GI = 66%) or from band structure calculations that show that the valence DOS has 2/3 O-2p character and 1/3 Ti-3d character [123, 124]. Semiempirical INDO

[125] and *ab initio* [126] calculations lead to very similar values $q(Ti) = -2 \times q(O) = 2.516$ and 2.610, respectively. Consequently, it is clear that the rutile structure should have at least 40% covalent character, ruling out definitively the picture $Ti^{4+}-O^{2-}$ for the Ti—O bond.

Knowing the room-temperature electronic signature of rutile, we may take a look at the effect of changing the temperature as crystal data are available from $T = 15$ K up to $T = 1883$ K [107, 112–114, 127]. Figure 21 shows that, with the exception of the $T = 15$ K point [113], smooth variations are obtained. Moreover, data points coming from different studies are found to be in rather close agreement. It is clear from these graphs that, above room temperature, higher temperatures mean higher $\langle EN \rangle$, $\langle EB \rangle$, $q(O)$, $f(O)$ and lower $\langle GH \rangle$, $\langle GI \rangle$, $q(Ti)$, $f(Ti)$. The absorption spectra of rutile crystals have shown that both band gaps, $E_g(\text{direct})$ and $E_g(\text{indirect})$, decrease on lowering the temperature [119]. At 1.6 K, $E_g(\text{direct}) = 3.033$ eV ($\Delta E_g = -0.029$ eV) and $E_g(\text{indirect}) = 3.049$ eV ($\Delta E_g = -0.052$ eV). A decrease in $\langle GH \rangle$ is also noted in Figure 21. However, it is so small ($\Delta E_g \sim -0.001$ eV) that we cannot rule out an artifact coming from the experimental data used. Accordingly, for $T = 16$ K, the refinement of the structure was made using powder neutron diffraction data, while single-crystal X-ray diffraction has been used for other temperatures. On the other hand, between 298 and 100 K, we find that $\Delta \langle EN \rangle = -0.050$ eV, a value of the same order of magnitude as the experimental $\Delta E_g$. Concerning the high-temperature domain, a slight increase in the electric field gradient at titanium sites $|V_{zz}|$ with temperature $|V_{zz}|$ (V Å$^{-2}$) $= 2.1 + 6 \times 10^{-4}T$ and a strong temperature dependence of the asymmetry parameter $\eta_Q = 0.26 - 3 \times 10^{-4}T$ were reported [128]. Using our charge distributions to compute these two parameters leads to a small decrease in $|V_{zz}|$ with temperature (0.5 V Å$^{-2}$ between 300 and 1900 K). It also leads to a parabolic variation from $\eta_Q = 0.35$ at room temperature up to $\eta_Q = 0.94$ at 943 K and then down to $\eta_Q = 0.49$ at 1900 K. These
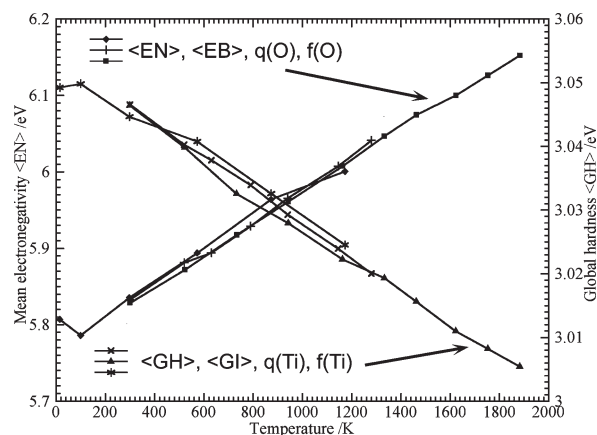


**Figure 21.** Evolution of the electronic signature of the rutile structure with temperature. Upon increasing temperature, $\langle EN \rangle$, $\langle EB \rangle$, $q(O)$, and $f(O)$ are found to increase in a parallel way with the following increments: $\Delta(\langle EB \rangle) = +2$ eV, $\Delta[q(O)] = +0.03$, and $\Delta[f(O)] = +0.015$. Conversely, $\langle GH \rangle$, $\langle GI \rangle$, $q(Ti)$, and $f(Ti)$ are decreasing functions of temperature with the following decrements: $\Delta(\langle GI \rangle) = -1.3\%$, $\Delta[q(Ti)] = -0.06$, and $\Delta[f(Ti)] = -0.03$.

variations are of the right order of magnitude for both $|V_{zz}|$ and $\eta_Q$ but are at the opposite of the experimental findings ($|V_{zz}|$ increases and $\eta_Q$ decreases with temperature). Interestingly enough, the temperature at which $\eta_Q^{th}$ reaches its maximum value ($T = 943$ K) is very close to the temperature ($T = 980$ K) at which $\eta_Q^{exp} \sim 0$. Consequently, if our electronic signatures are able to explain the amplitudes of the observed variations, they fail to reproduce the signs. More work is thus needed to get both amplitudes and signs.

Figure 22 shows that increasing the pressure has the opposite effect of increasing the temperature, as higher pressure leads to higher $\langle GH \rangle$, $\langle GI \rangle$, $q(Ti)$, $f(Ti)$ and to lower $\langle EN \rangle$, $\langle EB \rangle$, $q(O)$, $f(O)$. The $\langle GH \rangle$ curve (not shown), however, displays an anomaly at $P = 7.6$ GPa, which parallels the nonlinear variation of the $c$ parameter of the unit cell. The reported data were as follows: 2.959 Å (ambient pressure), 2.948 Å (3100 MPa), 2.946 Å (5000 MPa), 2.921 Å (7600 MPa), and 2.940 Å (8600 MPa) [129]. To conclude this section, we may note that at least four theoretical models have tried to reproduce the rutile crystal structure starting from first principles. Table 1 shows the results, taking the very accurate electronic signature (11) as the experimental reference for the esd. As can be seen, only the Car–Parinello method appears to be successful. All other methods are completely out of range by at least an order of magnitude.

***Anatase*** This is the other common tetragonal low-temperature polymorph of titanium oxide displaying spiral chains of edge-sharing octahedra that are further linked by sharing edges and corners to form another 3D structure of $6:3$ coordination (Fig. 23). In contrast with rutile, oxygen atoms are found in an approximate cubic closest packing configuration. In this structure, each $TiO_6$ octahedron is in contact with eight other ones (four through edge sharing and four through corner sharing). Among the six crystal structure determinations available [113, 115, 134–137], only
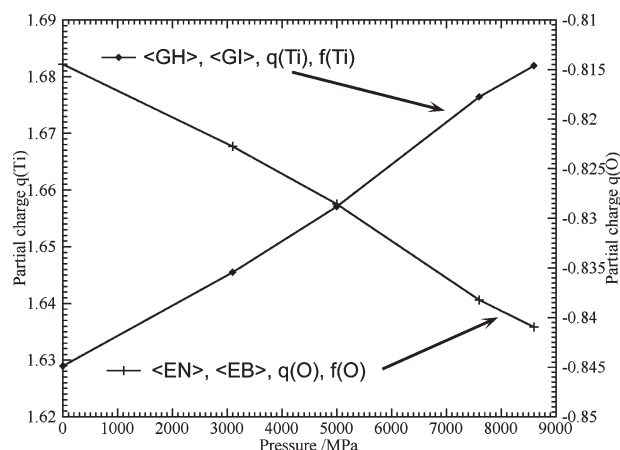


**Figure 22.** Evolution of the electronic signature of the rutile structure with pressure. Upon increasing pressure, $\langle EN \rangle$, $\langle EB \rangle$, $q(O)$, and $f(O)$ are found to decrease in a parallel way with the following decrements: $\Delta(\langle EB \rangle) = -2$ eV, $\Delta(\langle EN \rangle) = -0.4$ eV, and $\Delta[f(O)] = -0.015$. Conversely, $\langle GH \rangle$, $\langle GI \rangle$, $q(Ti)$, and $f(Ti)$ are increasing functions of pressure with the following increments: $\Delta(\langle GH \rangle) = +0.03$ eV, $\Delta(\langle GI \rangle) = +1.4\%$, and $\Delta[f(Ti)] = +0.03$. Note the mirror effect of pressure and temperature (cf. Fig. 21).

three are accurate enough ($R < 5\%$) to compute a reasonable electronic signature:

$$
\begin{array}{ll}
\textit{Global} & \textit{Local} \\
\langle EN \rangle = 5.998 \pm 0.008 \ V & q(Ti) = 1.6363 \pm 0.0011 \\
e^2 \langle GH \rangle = 3.1203 \pm 0.0015 \ eV & q(O) = -0.8182 \pm 0.0005 \\
\langle EB \rangle = -23.68 \pm 0.04 \ eV & f(Ti) = 1.1647 \pm 0.0006 \\
\langle GI \rangle = 40.91 \pm 0.03\% & f(O) = -0.0824 \pm 0.0003
\end{array}
$$
(12)

The best structural refinement ($R = 2.3\%$) available for this anatase structure [136] leads to a very similar signature:

$$
\begin{array}{ll}
\text{Global} & \text{Local} \\
\langle EN \rangle = 5.997 \pm 0.024 \ V & q(Ti) = 1.6363 \pm 0.0035 \\
e^2 \langle GH \rangle = 3.120 \pm 0.025 \ eV & q(O) = -0.8182 \pm 0.0018 \\
\langle EB \rangle = -23.68 \pm 0.04 \ eV & f(Ti) = 1.1647 \pm 0.0018 \\
\langle GI \rangle = 40.91 \pm 0.09\% & f(O) = -0.0824 \pm 0.0009
\end{array}
$$
(13)

Anatase is, then, slightly more ionic than rutile. The quite modest $\Delta q(Ti) = 0.008$ increase in ionicity from rutile to anatase is just slightly larger than that found by *ab initio* calculations $q(Ti) = -2 \times q(O) = +2.610 \Rightarrow \Delta q(Ti) = 0.003$ [126]. As with the rutile structure, electron density studies have revealed strong covalent bonds between titanium and oxygen [138], while band structure calculations show considerable mixing between O(2p) and Ti(3d) orbitals in both the valence and the conduction bands [139]. Optical investigations have shown that the band gap is slightly wider in anatase ($E_g = 3.2$ eV at RT and $E_g = 3.3$ eV below 100 K) than in rutile [140, 141]. The 0.1-eV experimental increase in $E_g$ is thus well in line with the 0.1-eV increase obtained for $\langle GH \rangle$ or $\langle GI \rangle$. This result is also in line with the thermochemical value $\Delta E = 12$ kJ mol$^{-1}$ $\sim 0.12$ eV measured for the anatase $\rightarrow$ rutile transition [142]. This increase in $E_g$ also explains the $-195$-ppm shielding observed in $^{47, 49}$Ti-NMR [143] and the 31-ppm shielding observed in $^{17}$O-NMR [144]. To check this point, we may refer to the general theory of magnetic screening [145], allowing us to write on an absolute scale the isotropic part of the chemical shielding tensor of the $^{17}$O nucleus in the following form [85]:

$$
\sigma_{iso}(ppm) = \sigma_{dia}(ppm) - 966 \times [(R° + \kappa q) \times P_u]/\Delta E \ (eV)
$$
(14)

where $\sigma_{dia}$ is a diamagnetic contribution, $\Delta E$ an average excitation energy, $R°$ the average value of the function $\langle (a_0/r)^3 \rangle$ over the O-2p atomic orbital, $q$ the electronic density around the nucleus, $\kappa$ a parameter close to unity, and $P_u$ an orbital contribution varying in a parabolic way with the atomic charge $q$. Referencing $^{17}$O chemical shifts against water leads to the following relationship between screening constants $\sigma$ and chemical shifts $\delta$ [146]: $\delta(^{17}O) = 324.0 - \sigma$. The diamagnetic contribution may be evaluated directly from the crystal structure as [147]:

$$
\sigma_{dia}(ppm) = \sigma_{at}^{dia}(q) + 9.393 \times \sum_\alpha Z_\alpha/r_\alpha \ (\text{Å})
$$
(15)

Using Hartree–Fock–Slater wave functions, we can assume that for the $^{17}$O nucleus $\sigma_{at}^{dia} = 418$ ppm, $R° = 5.03$, and $\kappa \sim 1$ [148, 149]. On the other hand, assuming isotropic p-orbital

**Table 1.** Accuracy checking of theoretical rutile structures computed from first-principles methods against signature (11).

| Method | Reference | $\langle EN \rangle$ | $\langle GH \rangle$ | $\langle GI \rangle$ | $\langle EB \rangle$ | $q(Ti)$ | $f(Ti)$ | $q(O)$ | $f(O)$ |
|--------|-----------|------|------|------|------|--------|--------|-------|-------|
| esd | Signature (2) | 0.0047 | 0.0010 | 0.0185 | 0.0262 | 0.0007 | 0.0004 | 0.0004 | 0.0002 |
| NLPPMD | [130] | $4\sigma$ | $0\sigma$ | $3\sigma$ | $3\sigma$ | $4\sigma$ | $4\sigma$ | $3\sigma$ | $4\sigma$ |
| PEG | [131] | $32\sigma$ | $44\sigma$ | $21\sigma$ | $20\sigma$ | $22\sigma$ | $28\sigma$ | $19\sigma$ | $28\sigma$ |
| SCSPP | [132] | $47\sigma$ | $13\sigma$ | $43\sigma$ | $43\sigma$ | $46\sigma$ | $42\sigma$ | $40\sigma$ | $42\sigma$ |
| SCSPP | [133] | $62\sigma$ | $19\sigma$ | $57\sigma$ | $56\sigma$ | $60\sigma$ | $55\sigma$ | $53\sigma$ | $55\sigma$ |

*Note:* SCSPP, self-consistent soft pseudo-potentials with LDA approximation; NLPPMD, nonlocal pseudo-potentials in molecular-dynamical density functional theory with LDA approximation; PEG, polarization-induced electron-gas model.

populations ($P_{xx} = P_{yy} = P_{zz}$) and an s-orbital population close to 2 leads to $P_u = 1.5[1 - (q_O - 1)^2/9]$ [85]. Now with $q(O) = -0.81445$ and $\Delta E \sim \langle GH \rangle = 3.046$ eV for rutile [from signature (11)], $P_u = 0.95127$, $(R^\circ + \kappa q) = 4.2155$, leading to

$$\delta(\text{rutile}) = 324 - [734.5 - (966 \times 4.2155 \times 0.95127)/3.046]$$

$$= 861 \text{ ppm} \qquad (16)$$

Similarly, for anatase, $q(O) = -0.8182$ and $\Delta E \sim \langle GH \rangle = 3.120$ eV [signature (13)], $P_u = 0.94903$, $(R^\circ + \kappa q) = 4.2118$, leading to

$$\delta(\text{anatase}) = 324 - [736.1 - (966 \times 4.2118 \times 0.94903)/3.12]$$

$$= 826 \text{ ppm} \qquad (17)$$

The ca. + 270-ppm difference found between (16) or (17) and experimental chemical shifts reflects all the errors made by using atomic values for $(R^\circ, \kappa)$ and approximate $P_u$



**Figure 23.** TiO$_2$ anatase crystal structure (space group $I4_1/amd$). (a) Local geometry at Ti and O sites and ball-and-stick view of the chemical bond patterns. (b) Topology of the *cis* edge sharing between TiO$_6$ octahedra. (c) Topology of the 3D framework is evidenced as edge sharing between spiral octahedral chains.

values. It also reflects the errors coming from the approximation $\Delta E \sim \langle GH \rangle$ and from the deviation of signature (16) or (17) from experimental reality. With so many approximations in hand, finding values at 50% from experimental reality is by itself a very encouraging result. Moreover, assuming the same systematic errors between rutile and anatase leads to $\delta(\text{anatase}) - \delta(\text{rutile}) = -35$ ppm, which compares favorably with the $-32$-ppm experimental value. It may then be said that an increase in the global hardness difference of 0.074 eV between rutile and anatase is enough to explain to the 30-ppm shielding observed for the $^{17}$O nucleus. Concerning the $^{47}$Ti nucleus, the isotropic part of the shielding tensor may be written as

$$\sigma_{\text{iso}}(\text{ppm}) = \sigma_{\text{dia}}(\text{ppm}) - 966 \times [(R^\circ + \kappa q) \times D_u]/\Delta E \text{ (eV)} \qquad (18)$$

$R^\circ$ is now the average value of the function $\langle (a_0/r)^3 \rangle$ over the Ti-3d atomic orbitals ($R^\circ = 2.016343$ a.u. and from Roothaan–Hartree–Fock atomic wave functions $\kappa \sim 0.63$ [149]) with the population unbalance $D_u$ in titanium d orbitals approximated as [145]:

$$D_u \sim 3(P_0 + P_{\pm 1} + P_{\pm 2}) - \tfrac{3}{2}[4P_{-2}P_{+2} + P_0(P_{-1} + P_{+1})]$$

$$- \tfrac{1}{2}[(P_{-2} + P_{+2})(P_{-1} + P_{+1}) + P_{-1}P_{+1}] \qquad (19)$$

Here $P_0$, $P_{-1}$, $P_{+1}$, $P_{-1}$, and $P_{-2}$ stand for populations of orbitals $d(z^2)$, $d(yz)$, $d(xz)$, $d(xy)$, and $d(x^2 - y^2)$, respectively. Assuming an empty 4s orbital, a $t_{2g}$–$e_g$ splitting under an octahedral field ($P_{-2} = P_0 = 0$), and an isotropic repartition of the $(4 - q_{Ti})$ remaining electrons in the $t_{2g}$ set [$P_{+1} = P_{-1} = P_{+2} = P = (4 - q)/3$] leads to $D_u \sim P(9 - 3P/2) = [56 - q_{Ti}(10 + q_{Ti})]/6$. With $\sigma_{\text{at}}^{\text{dia}}(Ti) = 1643$ ppm [148], the absolute shielding of the titanium atom in the rutile phase ($q_{Ti} = +1.6290 \Rightarrow D_u = 6.176$, $\langle r^{-3} \rangle = 3.0426$, and $\Delta E \sim \langle GH \rangle = 3.046$ eV) may then be approximated as

$$\sigma(\text{rutile}) = 1873.2 - (966 \times 3.0426 \times 6.176)/3.046$$

$$= -4086 \text{ ppm} \qquad (20)$$

On the other hand, for the absolute shielding of the titanium atom in the anatase polymorph ($q_{Ti} = +1.6363 \Rightarrow D_u = 6.160$, $\langle r^{-3} \rangle = 3.0472$, and $\Delta E \sim \langle GH \rangle = 3.120$ eV), it becomes

$$\sigma(\text{anatase}) = 1874.2 - (966 \times 3.0472 \times 6.16)/3.120$$

$$= -3938 \text{ ppm} \qquad (21)$$

According to these values, we predict that $\delta(\text{anatase}) - \delta(\text{rutile}) = \sigma(\text{rutile}) - \sigma(\text{anatase}) \sim -148$ ppm, in reasonable agreement with the $-195$-ppm experimental value.

As both $^{47,49}$Ti and $^{17}$O isotopes have nuclear quadrupole moments, it may be of interest to compare the electric field gradients in both structures. For the $^{17}$O nucleus, experimental values are $V_{xx} = +1.6$ V Å$^{-2}$, $V_{yy} = -23.8$ V Å$^{-2}$, $V_{zz} = +22.2$ V Å$^{-2}$, $\eta_Q = 0.89$ in the rutile phase [151], and $K_Q = |e^2 V_{zz} Q/h|(1 + \eta_Q^2/3)^{1/2} = 1.5$ and 1.1 MHz in the rutile and anatase polymorphs respectively [144]. Let us now use signatures (11) and (13) with a Sternheimer antishielding factor $|1 - \gamma_\infty| = 3.1$ (adjusted value to reproduce the $V_{yy}$ component of the rutile phase). We then predict $V_{xx} = +19.0$ V Å$^{-2}$, $V_{yy} = -23.8$ V Å$^{-2}$, $V_{zz} = +4.8$ V Å$^{-2}$, $\eta_Q = 0.60$ in the rutile phase ($K_Q = 1.66$ MHz), and $V_{xx} = -24.0$ V Å$^{-2}$, $V_{yy} = +22.9$ V Å$^{-2}$, $V_{zz} = +2.8$ V Å$^{-2}$, $\eta_Q = 0.90$ in the anatase phase ($K_Q = 1.67$ MHz). We are thus not able to explain the experimental 0.4-MHz decreases in the $K_Q$ of anatase relative to rutile. With reference to the general theory of the origin of electric field gradients [152], we may write:

$$V_{zz} = (1 - \gamma_\infty)V_{zz}^{\text{ext}} + (1 - R)V_{zz}^{\text{loc}} \qquad (22)$$

Our failure to reproduce electric field gradient (efg) values may then be linked to the assumption that $V_{zz}^{\text{loc}} = 0$. This just means that the local contribution that arises from the nonspherical filling of O-2p orbitals cannot be neglected in these phases. Similarly, concerning the efg at the $^{49}$Ti nuclei, experiments [128] lead to $V_{xx} = +8.6$ V Å$^{-2}$, $V_{yy} = +13.4$ V Å$^{-2}$, $V_{zz} = -22.0$ V Å$^{-2}$, $\eta_Q = 0.22$ for the rutile phase ($^{49}C_Q = 13.9 \pm 0.1$ MHz, $\eta_Q = 0.19 \pm 0.1$ [143]). For the anatase phase, $^{49}C_Q = 4.79 \pm 0.01$ MHz, $\eta_Q = 0$ [143]. Using signatures (11), (13) and a Sternheimer antishielding factor $|1 - \gamma_\infty| = 9.9$ (adjusted value to reproduce the $^{49}C_Q$ value of the anatase phase) leads to $^{49}C_Q = 1.9$ MHz, $\eta_Q = 0.25$ for the rutile polymorph. If the agreement on the $\eta_Q$ value is good, the 9.1-MHz decrease observed on going from rutile to anatase is not reproduced. According to LAPW calculations, the very high $C_Q$ value of the rutile phase comes from the polarization of "semi-core" 3p orbitals [151], and it is thus not surprising that a model based on valence contributions failed in such a case.

Consequently, our electronic signatures are able to explain on a semiquantitative basis chemical shift variations on all NMR-active nuclei, but fail to reproduce electric field gradients owing to the neglect of valence contributions and core polarization. It is then evident that, as in the case of silica polymorphs and in agreement with *ab initio* calculations, stoichiometry and local order (TiO$_6$ octahedron and edge and/or corner sharing between octahedra) mainly govern charge distributions. Taking into account the long-range crystalline order (unit-cell repetition) leads only to rather small variations. As shown in Figure 24, the effect of temperature on the electronic signature of anatase is very similar to what has been found for the rutile structure. No pressure data appear to be available for this structure.

**Brookite**   This is the third natural form of titanium dioxide. Its orthorhombic structure is based on zigzag chains of edge-sharing octahedra that are further linked by sharing
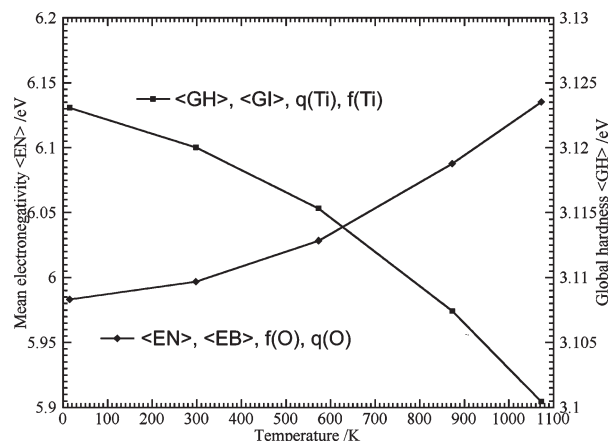


**Figure 24.** Evolution of the electronic signature of the anatase structure with temperature. Upon increasing temperature, $\langle\text{EN}\rangle$, $\langle\text{EB}\rangle$, $q(\text{O})$, and $f(\text{O})$ are found to increase in a parallel way with the following increments: $\Delta(\langle\text{EB}\rangle) = +1$ eV, $\Delta[q(\text{O})] = +0.015$, and $\Delta[f(\text{O})] = +0.006$. Conversely, $\langle\text{GH}\rangle$, $\langle\text{GI}\rangle$, $q(\text{Ti})$, and $f(\text{Ti})$ are decreasing functions of temperature with the following decrements: $\Delta(\langle\text{GI}\rangle) = -0.8\%$, $\Delta[q(\text{Ti})] = -0.03$, and $\Delta[f(\text{Ti})] = -0.012$.

corners to form a third type of 3D structure with 6:3 coordination (Fig. 25). As with the rutile structure, the idealized structure of brookite may be derived from hexagonal close-packed layers of oxygen atoms. However, in contrast with rutile, each TiO$_6$ octahedron is in contact with nine other ones (three through edge sharing and six through corner sharing). Three refinements are available for this crystal structure [107, 153, 154], leading to the following electronic
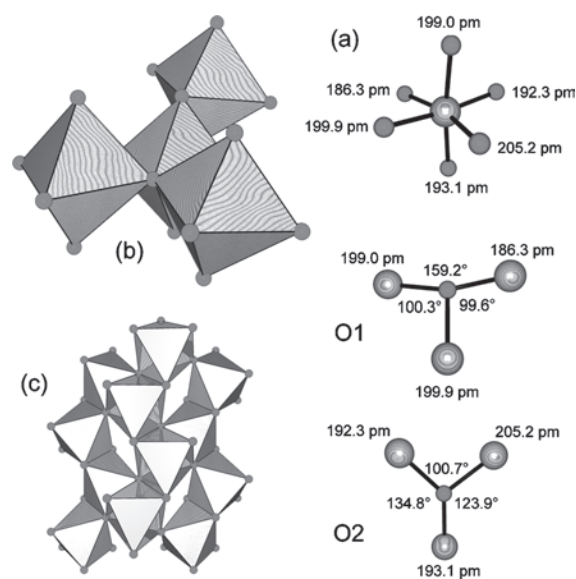


**Figure 25.** TiO$_2$ brookite crystal structure (space group *Pbca*). (a) Local $C_1$ geometry at Ti and O sites. Atoms O1 and O2 are situated 8.8 pm and 8.3 pm, respectively, above the plane formed by the three Ti atoms. (b) Topology of the *cis* edge sharing between four TiO$_6$ octahedra. (c) Topology of the 3D framework is evidenced as corner sharing between zigzag octahedral chains.

signature:

<div style="text-align:center">

**Global**          **Local**

$\langle EN \rangle = 5.919 \pm 0.010$ V    $q(Ti) = 1.6285 \pm 0.0004$
$e^2 \langle GH \rangle = 3.084 \pm 0.008$ eV    $\langle q(O) \rangle = -0.814 \pm 0.006$
$\langle EB \rangle = -23.404 \pm 0.013$ eV    $f(Ti) = 1.1707 \pm 0.0008$
$\langle GI \rangle = 40.713 \pm 0.009\%$    $\langle f(O) \rangle = -0.085 \pm 0.005$

</div>

$$\tag{23}$$

The charge difference between the two crystallographically nonequivalent oxygen atoms being statistically insignificant, $q(O1) = -0.813 \pm 0.004$ and $q(O2) = -0.816 \pm 0.004$, only mean values have been reported in signature (23). The following electronic signature was computed from the best structural refinement available for this structure ($R = 3.9\%$ [107]):

<div style="text-align:center">

Global          Local

$\langle EN \rangle = 5.914 \pm 0.022$ V    $q(Ti) = 1.629 \pm 0.003$
$e^2 \langle GH \rangle = 3.085 \pm 0.005$ eV    $\langle q(O) \rangle = -0.815 \pm 0.007$
$\langle EB \rangle = -23.43 \pm 0.12$ eV    $f(Ti) = 1.1711 \pm 0.0017$
$\langle GI \rangle = 40.73 \pm 0.08\%$    $\langle f(O) \rangle = -0.086 \pm 0.002$

</div>

$$\tag{24}$$

This shows that the rather low errors obtained in signature (23) come from the very limited set of data used (only 3) and thus cannot be considered as significant. This is not the case for signature (24) where averaging has been performed over 100 randomly generated structures. Brookite is, then, more electronegative and harder than rutile but less than anatase. It has, however, almost the same ionicity or electrostatic balance as rutile. To the best of our knowledge, a single band structure calculation has been performed for this crystal structure, using the orthogonalized LCAO method with the LDA approximation [139]. The results have shown very similar band structures and DOS and PDOS features among rutile, anatase, and brookite. This is in line with the close similarities of signatures (11), (13), and (24). According to these calculations, brookite should, however, have a direct band gap 0.42 eV higher than that of rutile and 0.16 eV higher than that of anatase [139]. Its static dielectric constant $\varepsilon_s = 7.89$ should also be much higher than that of rutile ($\varepsilon_s^{th} = 6.62$ and $\varepsilon_s^{exp} = 6.33$) or anatase ($\varepsilon_s^{th} = 6.04$ and $\varepsilon_s^{exp} = 5.62$). This is not in agreement with the $\langle EN \rangle$ and $\langle GH \rangle$ parameters found for this polymorph, which suggests that brookite should have an electronic structure intermediate between rutile and anatase. Our result probably reflects the number of common edges found in these three phases that are rutile (two edges), brookite (three edges), and, finally, anatase (four edges).

No $^{17}$O-NMR data are available for brookite, but according to $^{47,49}$Ti-NMR, this polymorph displays approximately the same chemical shift as rutile [143]. This experimental result would be very difficult to explain assuming a 0.4-eV band gap increase relative to the rutile polymorph. Assuming the same charge distribution in both phases would lead, according to (18), to $\sigma$(brookite) $\sim 1873.3 - (966 \times 3.0426 \times 6.176)/3.5 = -3313$ ppm, that is, to a ca. 800-ppm shielding relative to rutile. Using signature (24) to compute the absolute shielding of brookite would predict $\sigma$(brookite) $\sim 1873.3 - (966 \times 3.0426 \times 6.176)/3.085 = -4011$ ppm, a much

more reasonable 75-ppm shielding relative to rutile and 63-ppm deshielding relative to anatase. Recent measurements have been made [155, 156], but the authors do not seem to agree on the reported values (brookite intermediate between anatase and rutile [155] and brookite more shielded than anatase [156]). Nevertheless, in both cases, chemical shift differences among the three polymorphs are found to be about 100 ppm, in good agreement with the above analysis. Concerning the electric field gradient at the titanium site, signature (24) would lead to $^{49}C_Q = 2.9$ MHz, $\eta_Q = 0.54$. This is a much lower value than in anatase and should be compared with the experimental values $^{47}C_Q = 7.3$ MHz [155], $^{49}C_Q = 10.0$ MHz [156], $\eta_Q = 0.55$ [155, 156]. Consequently, if the asymmetry parameter is well reproduced, problems remain with the absolute value of $C_Q$ as already noted for rutile and anatase. For $^{17}$O nuclei, we would predict for the two crystallographically nonequivalent sites: $\delta(O1) = 846$ ppm (15-ppm shielding from rutile), $\delta(O2) = 844$ ppm (17-ppm shielding from rutile), $C_Q(O1) = 1.54$ MHz, $C_Q(O2) = 1.44$ MHz, $\eta_Q(O1) = 0.93$, $\eta_Q(O2) = 0.78$. Experiments [156] have revealed a shielding of 12.5 and 44.5 ppm relative to rutile. Owing to the very similar partial charge on the O atom, one may conclude that the $P_u$ contribution cannot be isotropic as assumed above (see Fig. 25 for a comparison of distortions around both sites). Brookite behaves exactly the same way as rutile or anatase concerning the variation of its electronic signature with temperature (Fig. 26). Again, as with anatase, no pressure data are available for this structure.

**TiO$_2$(B)** This is a synthetic phase that may be obtained by proton exchange and subsequent dehydration of layered titanates having the formula $A_2Ti_nO_{2n+1}$ (A = Na, K, Cs; $3 \leq n \leq 6$) at temperatures below $T = 350$ °C [157]. Above 550 °C or by applying pressure (60 MPa at room temperature), this phase transforms into anatase [158]. Its monoclinic structure is very similar to that found for the covalent
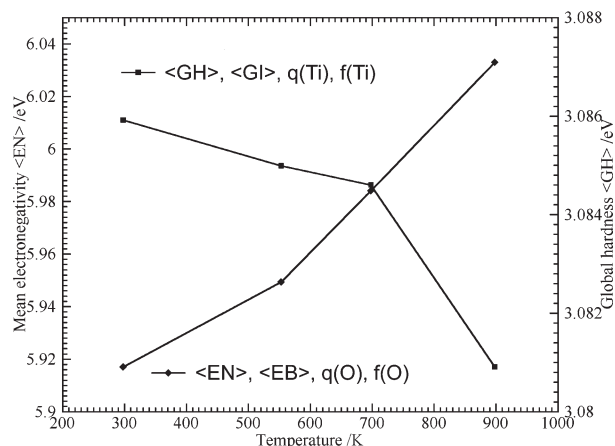
**Figure 26.** Evolution of the electronic signature of the brookite structure with temperature. Upon increasing temperature, $\langle EN \rangle$, $\langle EB \rangle$, $q(O)$, and $f(O)$ are found to increase in a parallel way with the following increments: $\Delta(\langle EB \rangle) = +0.6$ eV, $\Delta[q(O)] = +0.010$, and $\Delta[f(O)] = +0.005$. Conversely, $\langle GH \rangle$, $\langle GI \rangle$, $q(Ti)$, and $f(Ti)$ are decreasing functions of temperature with the following decrements: $\Delta(\langle GI \rangle) = -0.5\%$, $\Delta[q(Ti)] = -0.02$, and $\Delta[f(Ti)] = -0.010$.

framework of the $Na_xTi_4O_8$ bronze. It is based on double chains of edge-sharing octahedra, which are further linked by sharing corners to form a fourth type of 3D structure with oxygen atoms in fourfold, threefold, and twofold coordination (Fig. 27). In this structure, $TiO_6$ octahedra are in contact either with nine other ones (four through corner sharing and five through edge-sharing for the Ti1 site) or with eight other ones (four through corner sharing and four through edge sharing for the Ti2 site). As with the anatase structure, the ideal structure of $TiO_2$(B) may be derived from a cubic close packing of oxygen atoms. In terms of ordered vacancies (□) within a NaCl-type network, anatase may be written as $[Ti□][O_2]$, whereas $TiO_2$-B may be written as $[Ti_4□_5][O_8□]$. Only one crystal structure determination is available [156] leading to the following signature:

$$
\begin{array}{ll}
\text{Global} & \text{Local} \\
\langle EN \rangle = 6.15 \pm 0.33 \text{ V} & \langle q(\text{Ti}) \rangle = 1.63 \pm 0.16 \\
e^2 \langle GH \rangle = 3.32 \pm 0.28 \text{ eV} & \langle q(\text{O}) \rangle = -0.82 \pm 0.11 \\
\langle EB \rangle = -23.5 \pm 1.0 \text{ eV} & \langle f(\text{Ti}) \rangle = 1.15 \pm 0.13 \\
\langle GI \rangle = 40.9 \pm 0.6\% & \langle f(\text{O}) \rangle = -0.08 \pm 0.13
\end{array}
\tag{25}
$$

The rather high errors reported for atomic coordinates explain the low accuracy of the reported signature. $TiO_2$(B) appears to be much more electronegative than anatase. If it also displays a high global hardness, its ionicity is found very close to that of other polymorphs. If the two symmetrically nonequivalent titanium atoms in the asymmetric cell are found to be not significantly different, this is not the case for oxygen atoms in twofold $q(\text{O1})[\mu_2 - \text{Ti}] = -0.76 \pm 0.07$, and fourfold coordination, $q(\text{O2})[\mu_4 - \text{Ti}] = -0.85 \pm 0.03$. Threefold coordinated oxygen atoms are very similar, $q(\text{O3})[\mu_3 - \text{Ti}] = -0.83 \pm 0.05$ and $q(\text{O4})[\mu_3 - \text{Ti}] =$
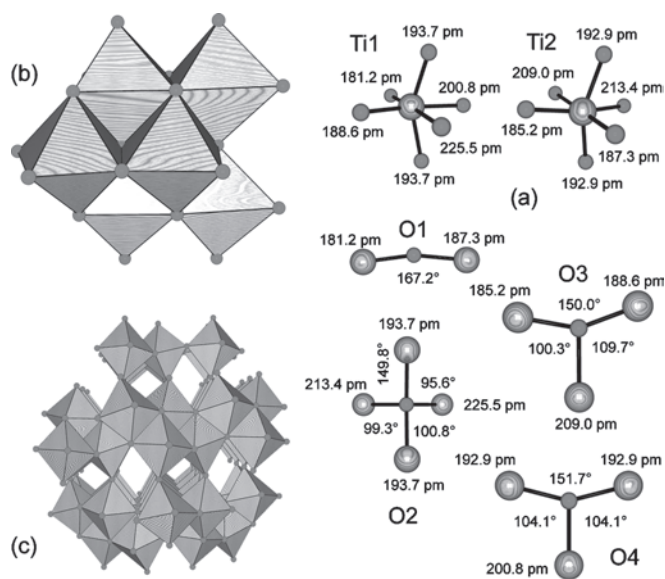
$-0.82 \pm 0.02$, and are not significantly different from O2. To the best of our knowledge, very few experimental and theoretical studies have been devoted to this phase. Table 2 shows the predicted NMR parameters for this phase if signature (25) is correct.

***$TiO_2$(R)*** This synthetic phase may be obtained after topotactic oxidation of the lithium titanate bronze $Li_{0.5}TiO_2$ by acidic solutions of hydrogen chloride [159]. Its orthorhombic structure is based on double chains of edge-sharing octahedra that are further linked by sharing corners to form a 3D structure similar to that of ramsdellite ($\gamma$-$MnO_2$) or of diaspore ($\alpha$-AlOOH) (Fig. 28). All oxygen atoms are found in threefold coordination with each $TiO_6$ octahedron sharing four edges and four corners with eight other octahedra as in anatase. However, when heated above 640 K, $TiO_2$(R) transforms into brookite. As with the $TiO_2$(B) structure, only one crystal structure determination is available [159], leading to the following electronic signature:

$$
\begin{array}{ll}
\text{Global} & \text{Local} \\
\langle EN \rangle = 6.71 \pm 0.04 \text{ V} & q(\text{Ti}) = 1.559 \pm 0.007 \\
e^2 \langle GH \rangle = 3.590 \pm 0.012 \text{ eV} & \langle q(\text{O}) \rangle = -0.780 \pm 0.024 \\
\langle EB \rangle = -21.0 \pm 0.2 \text{ eV} & f(\text{Ti}) = 1.111 \pm 0.003 \\
\langle GI \rangle = 38.99 \pm 0.18\% & \langle f(\text{O}) \rangle = -0.055 \pm 0.013
\end{array}
\tag{26}
$$

$TiO_2$(R) appears, then, to be one of the most electronegative, hardest, and least ionic polymorphs of all the titanium oxides studied until now. Contrary to other titania polymorphs, there is a clear relationship between the network topology and the charge distribution. Concerning the two crystallographically nonequivalent oxygen atoms, they bear a very similar partial charge, $q(\text{O1}) = -0.788 \pm 0.003$ and $q(\text{O2}) = -0.772 \pm 0.005$, but they should be easily distinguished by $^{17}$O-NMR. Taking rutile as the reference signature (26) would lead to $\delta(\text{O1}) = -165$ ppm and $\delta(\text{O2}) = -150$ ppm, with a very clear differentiation through the efg: $C_Q(\text{O1}) = 1.48$ MHz ($\eta_Q = 0.87$) and $C_Q(\text{O2}) = 0.58$ MHz ($\eta_Q = 0.30$). For $^{47, 49}$Ti-NMR, we predict a strong shielding of the titanium nucleus, $\delta(\text{Ti}) = -851$ ppm (rutile as the reference), with a rather large quadrupolar coupling constant, $^{49}C_Q = 4.5$ MHz and $\eta_Q = 0.43$.

***$TiO_2$(H)*** This synthetic phase may be obtained by topotactic oxidation of the potassium bronze $K_{0.25}TiO_2$ [160]. Its tetragonal structure is based on the same double chains of edge-sharing octahedra found in $TiO_2$(R) but which are now further linked by sharing corners to form a 3D structure typical of the hollandite family (Fig. 29). The local environment of oxygen and titanium atoms in this structure is very similar to that found in $TiO_2$(R). All oxygen atoms are found



**Figure 27.** $TiO_2$(B) crystal structure (space group $C2/m$). (a) Local $C_s$ geometry at all atomic sites. Atoms O3 and O4 are situated 0.0 pm and 0.9 pm, respectively, above the plane formed by the three Ti atoms. (b) Polyhedral view of the topology of the edge-sharing pattern between five $TiO_6$ octahedra. (c) Topology of the 3D framework is evidenced as corner sharing between fused double octahedral chains.

**Table 2.** Theoretical predicted NMR parameters for the $TiO_2$(B) polymorph.

| Atomic site | O1 | O2 | O3 | O4 | Ti1 | Ti2 |
|---|---|---|---|---|---|---|
| Charge $q$ | −0.7607 | −0.8486 | −0.8305 | −0.8210 | 1.6071 | 1.6537 |
| $\delta$/ppm (rutile) | +46 | −222 | −122 | −109 | −459 | −497 |
| $C_Q$ (MHz) | 2.4 | 1.2 | 1.8 | 1.5 | 1.6 | 3.2 |
| $\eta_Q$ | 0.04 | 0.17 | 0.71 | 0.96 | 0.51 | 0.66 |
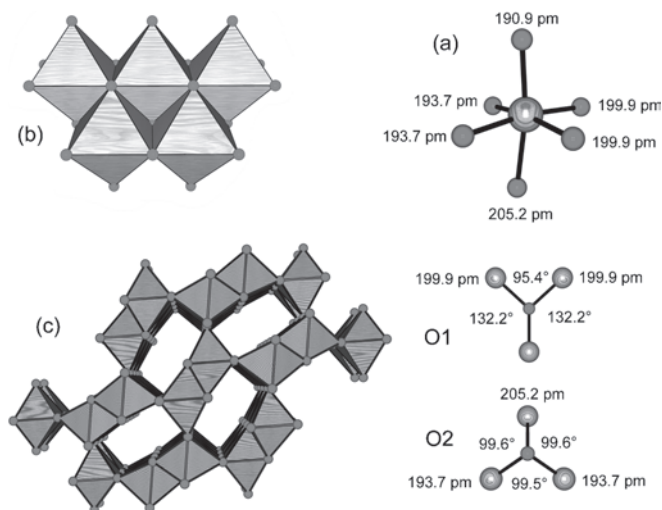
**Figure 28.** TiO$_2$(R) crystal structure (space group *Pbnm*). (a) Local $C_s$ geometry at all atomic sites. Atoms O1 and O2 are situated 4.1 pm and 93 pm, respectively, above the plane formed by the three Ti atoms. (b) Polyhedral view of the topology of the edge-sharing pattern between five TiO$_6$ octahedra. (c) Topology of the 3D framework is evidenced as corner sharing between fused double octahedral chains.

in threefold coordination, with each TiO$_6$ octahedron sharing four edges and four corners with eight other octahedra. However, contrary to TiO$_2$(R), heating TiO$_2$(H) above 410 °C leads to the anatase polymorph and not to the brookite one. As with the TiO$_2$(B) and TiO$_2$(R) structures, only one crystal structure determination is available, involving some disordered potassium atoms [160]. Based on the assumption that the TiO$_2$ framework would not be very much changed
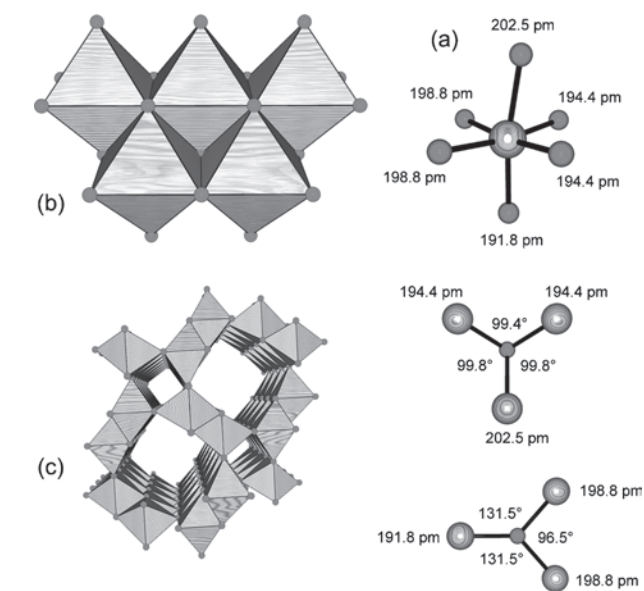


**Figure 29.** TiO$_2$(H) crystal structure (space group *I*4/*m*). (a) Local $C_s$ geometry at all atomic sites. Atoms O1 and O2 are situated 92.7 pm and 7.8 pm, respectively, above the plane formed by the three Ti atoms. (b) Polyhedral view of the topology of the edge-sharing pattern between five TiO$_6$ octahedra. (c) Topology of the 3D framework is evidenced as corner sharing between fused double octahedral chains.

upon potassium removal, we have been able to compute the following electronic signature for this interesting phase:

| Global | Local |
|---|---|
| $\langle EN \rangle = 7.14 \pm 0.05$ V | $q(\text{Ti}) = 1.563 \pm 0.006$ |
| $\langle GH \rangle = 4.517 \pm 0.012$ eV | $\langle q(\text{O}) \rangle = -0.78 \pm 0.05$ |
| $\langle EB \rangle = -21.1 \pm 0.2$ eV | $f(\text{Ti}) = 1.078 \pm 0.003$ |
| $\langle GI \rangle = 39.08 \pm 0.16\%$ | $\langle f(\text{O}) \rangle = -0.04 \pm 0.08$ |

$$(27)$$

Concerning the global ionicity, TiO$_2$(R) and TiO$_2$(H) are virtually indistinguishable. This result was foreseeable as both structures are built from the same double octahedral chains. The two structures are, however, completely different concerning the mean electronegativity and the global hardness, which display much higher values in TiO$_2$(H) than in TiO$_2$(R). This should mean that the NMR parameters of these phases should be completely different. Concerning the two crystallographically nonequivalent oxygen atoms, we get $q(\text{O1}) = -0.766 \pm 0.005$ and $q(\text{O2}) = -0.796 \pm 0.002$, leading to $\delta(\text{O1}) = -376$ ppm and $\delta(\text{O2}) = -400$ ppm (rutile as the reference). Nuclear quadrupolar coupling constants are expected to be very similar to those of TiO$_2$(R) with $C_Q(\text{O1}) = 0.59$ MHz ($\eta_Q = 0.21$) and $C_Q(\text{O2}) = 1.46$ MHz ($\eta_Q = 0.81$). For $^{47,\,49}$Ti-NMR, the very high value found for $\langle GH \rangle$ means a very strong shielding of the titanium nucleus relative to the rutile phase, $\delta(\text{Ti}) = -101$ ppm. The nuclear quadrupolar coupling constant is expected to be much larger than in TiO$_2$(R), $^{49}C_Q = 5.68$ MHz, with a very low asymmetry parameter, $\eta_Q = 0.02$.

***TiO$_2$-II*** This metastable phase was first prepared from anatase, brookite, or rutile by heating at 450 °C under 400 MPa [161]. It can also be prepared at room pressure by dissolving Ti$_3$O$_5$ in sulfuric acid at elevated temperature (150–200 °C) [162]. Upon heating at 600 °C at atmospheric pressure, it transforms into rutile in a few hours. The phase boundary between rutile and TiO$_2$-II in a pressure–temperature diagram is not linear but changes from having a negative to having a positive slope with increasing temperature at about 6 GPa and 850 °C [163]. TiO$_2$-II is isostructural with $\alpha$-PbO$_2$ and displays zigzag chains of edge-sharing octahedra joined by common vertices to form a 3D structure with 6 : 3 coordination (Fig. 30). In this structure, each TiO$_6$ octahedron is in contact with 10 other ones (2 through edge sharing and 8 through corner sharing). Two crystal structure refinements are available for this compound. Using the most recent one from X-ray powder diffraction ($R = 2.5\%$ [162]) leads to the following electronic signature:

| Global | Local |
|---|---|
| $\langle EN \rangle = 5.72 \pm 0.02$ V | $q(\text{Ti}) = 1.634 \pm 0.004$ |
| $e^2 \langle GH \rangle = 2.992 \pm 0.007$ eV | $q(\text{O}) = -0.8172 \pm 0.0018$ |
| $\langle EB \rangle = -23.61 \pm 0.13$ eV | $f(\text{Ti}) = 1.1858 \pm 0.0015$ |
| $\langle GI \rangle = 40.86 \pm 0.09\%$ | $f(\text{O}) = -0.0929 \pm 0.0008$ |

$$(28)$$

This phase appears to be slightly less electronegative and slightly more ionic than rutile. Owing to its lower global hardness, this polymorph should appear deshielded relative to rutile, $\delta(^{17}\text{O}) = +21$ ppm and $\delta(^{47,\,49}\text{Ti}) = +108$ ppm. Asymmetric electric field gradients are expected at both sites, $C_Q(^{17}\text{O}) = 1.41$ MHz ($\eta_Q = 0.89$) and $C_Q(^{49}\text{Ti}) = 3.2$ MHz ($\eta_Q = 0.35$).
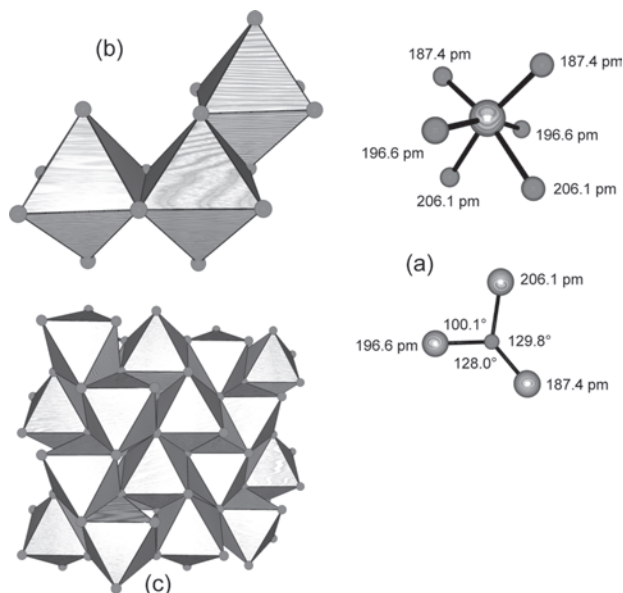
**Figure 30.** TiO$_2$-II crystal structure (space group *Pbcn*). (a) Local geometry for Ti and O atoms. The O atom is situated 16.1 pm above the plane formed by the three Ti atoms. (b) Polyhedral view of the topology of the edge-sharing pattern between three TiO$_6$ octahedra. (c) Topology of the 3D framework is evidenced as corner sharing between zigzag octahedral chains.

**TiO$_2$-III** At room temperature, rutile is stable up to 12 GPa, undergoing a direct transition to a structure displaying the same crystalline environment as ZrO$_2$ (baddeleyite) [164], with titanium atoms in sevenfold coordination (Fig. 31). Upon the release of pressure, this baddeleyite-type phase converts to the $\alpha$-PbO$_2$-type polymorph. In this structure, the titanium atom is sandwiched between a square and a triangle of oxygen atoms defining a nonahedron. These nonahedra are linked into double sheets by sharing triangular edges. A dense stacking, through the remaining square edges, of these double sheets along the $a$ axis leads to the 3D structure. Only unit-cell parameters are available for this phase [164]. However, it was possible to give an approximate electronic signature for this phase using the well-known atomic positions for the zirconium compound [165]:

| Global | Local |
|---|---|
| $\langle EN \rangle = 4.805 \pm 0.013$ V | $q(Ti) = 1.747 \pm 0.002$ |
| $e^2 \langle GH \rangle = 3.230 \pm 0.006$ eV | $\langle q(O) \rangle = -0.874 \pm 0.040$ |
| $\langle EB \rangle = -27.79 \pm 0.07$ eV | $f(Ti) = 1.2551 \pm 0.0010$ |
| $\langle GI \rangle = 43.69 \pm 0.04\%$ | $\langle f(O) \rangle = -0.128 \pm 0.033$ |

$$(29)$$

This baddeleyite phase would thus be the most ionic and least electronegative of all the TiO$_2$ polymorphs. Its global hardness should be close to that found for the TiO$_2$(B) polymorph. A shielding of the $^{17}$O and $^{47, 49}$Ti nuclei relative to rutile is also anticipated. According to signature (29), a clear distinction between sites O1 ($q = -0.8604 \pm 0.0027$, $\delta = -132$ ppm, $C_Q = 1.62$ MHz, $\eta_Q = 0.96$) and O2 ($q = -0.8869 \pm 0.0016$, $\delta = -245$ ppm, $C_Q = 0.69$ MHz, $\eta_Q = 0.69$) is expected. The 113-ppm difference between both sites is well in line with the 77-ppm value found in
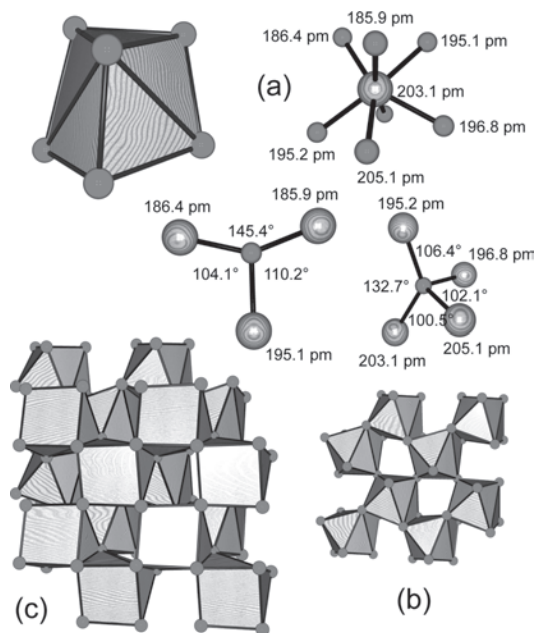


**Figure 31.** TiO$_2$-III crystal structure isostructural with baddeleyite (space group $P2_1/c$). (a) Seven-, three-, and fourfold coordination polyhedra for titanium and oxygen atoms. The O1 atom is situated 5.5 pm above the plane formed by the three Ti atoms. (b) Polyhedral view of the topology of the corner-sharing pattern within a single layer. (c) Topology of the 3D framework is evidenced as stacking of the layers displayed in (b).

ZrO$_2$–baddeleyite [144]. In $^{47, 49}$Ti-NMR a strong deshielding (+485 ppm) relative to rutile is expected with a moderately large efg, $^{49}C_Q = 4.0$ MHz ($\eta_Q = 0.29$).

Raman spectroscopy has shown that this baddeleyite phase may also be formed starting from the anatase polymorph between 13 and 17 GPa [166]. Between 4.5 and 7 GPa, anatase transforms into the $\alpha$-PbO$_2$ network, while above 60 GPa, the baddeleyite polymorph seems to transform into a higher symmetry and coordination structure. As only one X-ray reflection is available for this new phase, its crystal structure remains unknown.

**General Discussion** Using the previous results, we are ready to draw the electronegativity–hardness map [167] for all titania polymorphs (Fig. 32). Reading from left to right (increasing electronegativity), we find the following sequence of apparition: baddeleyite $\rightarrow$ rutile(P) $\rightarrow$ TiO$_2$(II) $\rightarrow$ rutile(T) $\rightarrow$ anatase $\rightarrow$ brookite $\rightarrow$ TiO$_2$(B) $\rightarrow$ TiO$_2$(R) $\rightarrow$ TiO$_2$(H). As can be seen in Table 3, this is virtually the order found by dividing the unit-cell volume $V$ by the number of TiO$_2$ formula units $Z$. The only exception concerns the phases TiO$_2$(B) and TiO$_2$(R). This correlation between $\langle EN \rangle$ and $V/Z$ is easily explained by elementary quantum-mechanical considerations. Assuming that $\langle EN \rangle$ is a measure of the Fermi level of electrons $-\varepsilon_F$ in the structure and treating a crystal as a three-dimensional box of volume $V \sim L^3$ filled with $N$ electrons, we may write

$$k_F^2 = (2\pi/L)^2 n_F^2 = (2\pi/L)^2 (n_x^2 + n_y^2 + n_z^2)$$
$$= (3\pi^2 N/V)^{2/3} \Rightarrow \varepsilon_F = (\hbar^2/2m_e)k_F^2 \sim V^{-2/3} \quad (30)$$
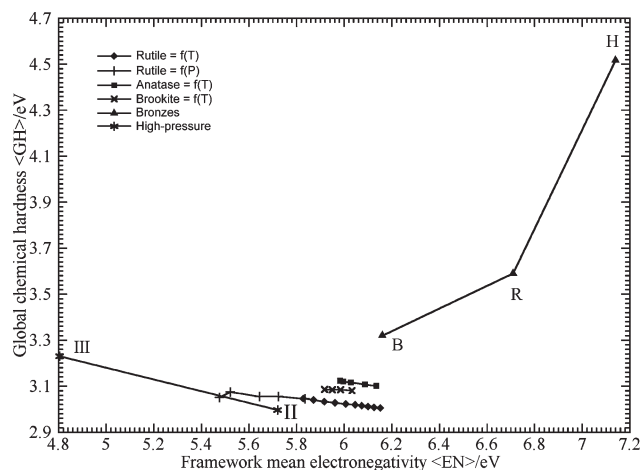
**Figure 32.** Electronegativity–hardness map for titania polymorphs. Lines connecting points refer to the effect of changing pressure (rutile, $TiO_2$-II, and $TiO_2$-III) or temperature (rutile, anatase, and brookite). Labels B, R, and H refer to $TiO_2$(B), $TiO_2$(R), and $TiO_2$(H) networks, respectively.

Relation (30) tells us that $-\varepsilon_F \propto \langle EN \rangle$ should decrease as $V$ decreases in agreement with Figure 32 and Table 3. The inversion observed between $TiO_2$(B) and $TiO_2$(R) suggests that a crystal cannot always be assimilated to a box filled with electrons. The mode of linking of $TiO_6$ polyhedra may thus have a nonnegligible effect ($\sim 0.5$ eV $\sim 50$ kJ mol$^{-1}$) on electronic parameters.

Another sequence is found by reading the map from bottom to top (increasing chemical hardness): $TiO_2$(II) $\rightarrow$ rutile(T) $\rightarrow$ rutile(P) $\rightarrow$ anatase $\rightarrow$ brookite $\rightarrow$ $TiO_2$(B) $\sim$ baddeleyite $\rightarrow$ $TiO_2$(R) $\rightarrow$ $TiO_2$(H). Theoretically, this order should be related to the energy difference existing between the centers of gravity of valence and conduction band (average band gap). As chemical bonding studies in titania polymorphs have been mainly limited to rutile, anatase, and brookite, it is very difficult to check this point. Band structure calculations on rutile, anatase, and brookite structures lead to very similar DOS curves [139]. This is well in line with the very close charge distributions given above. Our review has, however, shown that the electronic structure of rutile, anatase, brookite, and $TiO_2$-II polymorphs should be quite different from that of $TiO_2$(B), $TiO_2$(R), $TiO_2$(H), or $TiO_2$-III. For rutile, anatase, and $TiO_2$-II, this

**Table 3.** Classification of $TiO_2$ polymorphs according to the volume occupied by one $TiO_2$ formula unit (RTP means room temperature and pressure conditions).

| Phase | $V(\text{Å})^3$ | $Z(TiO_2)$ | $V/Z(\text{Å}^3)$ |
| --- | --- | --- | --- |
| $TiO_2$ (baddeleyite) | 104.43 | 4 | 26.11 |
| $TiO_2$(II) | 122.33 | 4 | 30.58 |
| Rutile (RTP) | 62.43 | 2 | 31.22 |
| Brookite (RT) | 256.84 | 8 | 32.11 |
| Anatase (RT) | 136.30 | 4 | 34.08 |
| $TiO_2$(R) | 137.16 | 4 | 34.29 |
| $TiO_2$(B) | 284.15 | 8 | 35.52 |
| $TiO_2$(H) | 307.49 | 8 | 38.44 |

result has been fully confirmed through Ti-2p and O-1s X-ray absorption studies [168]. For other polymorphs, experimental or theoretical data are still lacking. This review should then be considered as a very first step toward the characterization of chemical bonding in $TiO_2$ polymorphs. In particular, it would have been interesting to extend this study to other rutile-based structures (M = Ti, Zn, V, Cr, or Ru with X = O or F) that have been fully investigated using FPLAPW calculations [169].

In view of Figure 32 and Table 3, there does not emerge a clear reason for the well-known thermodynamic stability of the rutile phase. Taking the full unit-cell volume $V$ as an index of thermodynamic stability would lead to the correct identification of the most stable phase, that is, rutile, as it displays the smallest volume. However, one may also think that the volume occupied by one $TiO_2$ formula unit $V/Z$ would be a more logical choice, in which case the winner is the baddeleyite phase. Alternatively, most stable compounds are characterized by a large band gap (i.e., a high global hardness) and a low Fermi level (i.e., a high electronegativity), in which case the wheel turns in favor of $TiO_2$(H). This is in clear contrast with experimental data that show without any ambiguity that upon heating all polymorphs are transformed into the rutile phase. Similarly, upon release of pressure, $TiO_2$-II and $TiO_2$-III are again transformed into rutile. Experiments also show that at low temperature the rutile phase is seldom obtained and that most syntheses end up with the anatase network. Other polymorphs are usually obtained only under carefully controlled conditions or by increasing the pressure.

Unfortunately, after a comprehensive review of the literature devoted to this stability problem, we have not been able to find a reasonable explanation for the dominant position of the anatase and rutile structures over other polymorphs. Worse, we have been faced with the puzzling glass paradox when we have tried to introduce entropy considerations. Accordingly, most thermodynamic textbooks state that, for a perfect crystal at $T = 0$ K, the absolute entropy $S$ should be equal to 0 (Nernst theorem or third law of thermodynamics). From this principle and from the second principle stating that the entropy should be a positive quantity, it directly follows that, for any structural motif, a disordered arrangement (glass) should always have a higher entropy than a well-ordered one (crystal). For example, let us call $S_c$ the entropy of a 3D network like that of $\alpha$-quartz (crystal displaying a Dirac distribution of Si—O—Si bond angles). Similarly, let us call $S_g$ the entropy of a *static* disordered array having an equivalent number of corner-sharing $SiO_4$ tetrahedra (glass displaying a Gaussian distribution of Si—O—Si bond angles). According to the third law of thermodynamics, $S_g > S_c$, meaning that, for the transformation crystal $\rightarrow$ glass, we should have $\Delta S = S_g - S_c > 0$. Now, for any spontaneous process to occur, we must have a decrease in the Gibbs free energy, that is, $\Delta G = \Delta H - T \times \Delta S < 0$. Consequently, if we want to avoid this "spontaneous" transformation, we must have $\Delta G > 0$, that is, $\Delta H > T \times \Delta S$. Here lies the glass paradox. At the left of this inequality, we have a finite quantity, $\Delta H$, which can be either positive (endothermic process) or negative (exothermic process), as it depends on the way chemical bonds are rearranged during the transition. At the right, the situation is completely different as we have a

strictly positive quantity, $T \times \Delta S$ ($T > 0$, $\Delta S > 0$ according to established thermodynamic principles), which has absolutely no limits owing to its temperature dependence. Consequently, if at low temperature the crystal is in the stable thermodynamic state ($\Delta G > 0$ because $\Delta H > T \times \Delta S$), there will nevertheless always exist a finite temperature allowing the spontaneous disappearance of the crystalline order. In other words, if you start from a crystal and increase the temperature very slowly (to maintain equilibrium conditions at any time), you should always get a glass before fusing the sample! The amazing thing is that in the real world, to make a glass, you never proceed like that. First, you have to go to the liquid state and then quench your system very rapidly in order to avoid spontaneous crystallization. Moreover, even if you have succeeded to get a glass from a given material, it will be very hard to avoid crystallization between $T_g$ and fusion. Obviously, Nature tells us that a crystal is more stable than a glass and that our starting theorem $S = 0$ for a perfect crystal should be urgently revised.

Fortunately, if we switch to information theory [170–172] (Fig. 33), such a paradox is easily avoided. As a crystal is always more symmetric than a glass, one must have $S_c > S_g$, leading to a complete reversal of the above inequalities. With this more correct definition, an entropy increase is always correlated with an information loss or an increase in symmetry. Glasses, being less symmetric than crystals, are then systematically devitrified as soon as the temperature is raised, and if you want to obtain them, you have to be very clever in order to avoid crystallization.

With the help of Figure 33, all we have to do is to compare the space-group orders of the eight $TiO_2$ polymorphs. Moreover, as it is always possible to choose a primitive cell for describing a crystal structure, we can drop the Bravais symbol (A, B, C, I, F, R) and focus on the remaining symmetry elements. The result is rutile = anatase (16) > brookite = ramsdellite = hollandite = $TiO_2$-II (8) > bronze = $TiO_2$-III (4). One may also use the number of refined parameters needed to obtain the atomic coordinates from the X-ray diffraction pattern to get a better discrimination, which becomes rutile = anatase (3) < $TiO_2$-II (7) < hollandite (8) < ramsdellite (9) < brookite (12) < $TiO_2$-III (13) < bronze (16). The situation is now perfectly clear. Rutile and anatase are the phases that display the lowest information content and thus the highest entropy. Consequently, at sufficiently high temperature, all other polymorphs are expected to end up in one of these two phases. To differentiate between these two polymorphs, one must go a step further by looking at the local symmetry elements. For rutile displaying $D_{2h}$ local symmetry for Ti atoms, eight and three bond angles are fixed by symmetry to be equal to 90° and 180°, respectively. Consequently, the full description of the $TiO_6$ octahedron is achieved by the specification of just one arbitrary bond angle $\theta$, the three remaining ones being $\theta$ and $2(180° - \theta)$ by symmetry. The situation is quite different in anatase with $D_4$ symmetry for Ti atoms. Here, the full description of the $TiO_6$ octahedron requires the specification of at least three bond angles $\theta$, $\psi$, and $\varphi$, the 12 other bond angles being 180°, $\theta$, $3\psi$, $3\varphi$, and $4(180° - \varphi)$ by symmetry. As less information is required to describe the $TiO_6$ octahedron in rutile, this last phase should have higher entropy than anatase. The anatase phase should then also
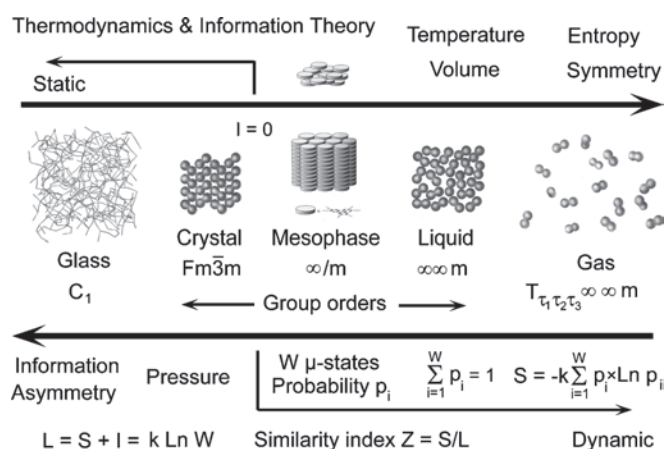


**Figure 33.** Relationships between entropy, symmetry, information, and thermodynamic stability. From the differential of the Gibbs free energy, $dG = V\,dP - S\,dT < 0$, it follows that any kind of matter will try to reduce its volume $V$ and increase its entropy $S$ after an increase in pressure and temperature, respectively. According to the fundamental equation of information theory, $S = -k \sum_i p_i \ln p_i$. In this relationship, $k$ is the Boltzmann constant and $p_i$ is the probability of the occurrence of a microstate compatible with a set of macrovariables ($E, N, V, T, P$) and such that $\sum_i p_i = 1$. From this definition, it follows that if the permutation symmetry is maximum (i.e., all the $W$ possible microstates are degenerate in energy), then $p_i = 1/W$ and $S = L = k \ln W$. Now, for a system to hold some information, an energetic difference between the various microstates is required. It then follows that the amount of information $I$ contained in any material system displaying $W$ microstates should be given by $I = k \ln W - S$, where $S$ denotes the entropy. A good rule of thumb to judge the entropy level of a material system is then to look at the group order $G$ of all its symmetry elements. For a glass $G = 1$ (just identity as the symmetry element), entropy should be at a minimum and information at its maximum (about $10^{23}$ $x, y, z$ triplets to describe the structure). On the other hand, a dilute gas $G$ displays a fivefold infinity (most symmetric continuous group for translations, rotations, and reflections). As $S = L$, the information content here is $I = 0$ (full ignorance of the $10^{23}$ $x, y, z$ triplets). With this diagram, it becomes obvious that, upon increasing the temperature, a glass should crystallize, a crystal should melt (with or without mesophase formation), and a liquid should vaporize. The amazing point is that most thermodynamic textbooks make no distinction between static disorder (glass) and dynamic disorder (gas), with the consequence that $S$ is assumed to be 0 for a perfect crystal (Nernst theorem). This misconception leads to the "glass paradox" described in the text.

be transformed into rutile upon heating in agreement with experiments. After rutile and anatase, the phase that should display the highest entropy is $TiO_2$-II. The fact that this phase could be chemically synthesized without pressure is nice evidence of its good thermodynamic stability at moderate temperature [162]. The case of brookite deserves special attention. It is well known that this phase can be obtained only under hydrothermal conditions starting from aqueous solutions [173–175] or from organic solutions [176–179]. The rather low symmetry of brookite could help to explain the difficulty in obtaining it not mixed with rutile or anatase. Exactly the same conclusion may be drawn from the fact that at high pressure and temperature one obtains the $TiO_2$-II polymorph rather than brookite. Similarly, at room temperature and above 12 GPa, rutile transforms directly into $TiO_2$-III (baddeleyite) and not into brookite. This clearly

shows that under a physical constraint low-symmetry phases may be obtained if they minimize their unit-cell volume. Consequently, the occurrence of the brookite phase cannot be related to the pressure increase coming from the use of hydrothermal conditions. It should rather be explained by the presence of a chemical constraint providing the necessary negative enthalpic contribution to overcome the loss of entropy relative to rutile or anatase. For example, structural defaults in the form of uncondensed Ti—OH groups may be responsible for the stabilization of brookite. Similar considerations obviously apply to the $TiO_2$ polymorphs (B, R, and H) synthesized after proton exchange and moderate heating of alkali-containing titanates. It may well be that in all these phases the true stoichiometry is not $TiO_2$ but rather $X_\varepsilon TiO_2$. The foreign species X should then be responsible, through the introduction of structural defaults, for the stabilization of a particular network over that of rutile or anatase. The fact that $TiO_2(R)$ transforms upon heating into brookite, a phase of lower symmetry, is also strong evidence that negative enthalpic contributions not linked to the $TiO_2$ stoichiometry are lurking around.

## 2.3. Titanium Dioxide in Materials Chemistry

In this section, we present a brief overview of the practical and potential applications of purely inorganic materials based on titanium oxides. The case of hybrid organic–inorganic materials will be treated after the section devoted to titanium(IV) coordination chemistry.

### 2.3.1. White Pigments

One of the most important aspects of $TiO_2$ compositions lies in their chemical inertness, associated with their nontoxicity to living matter. This nontoxicity has led, for example, to the replacement after 1920 of all previously used white pigments [ZnO, $2PbCO_3 \cdot Pb(OH)_2$, $ZnS \cdot BaS$] by $TiO_2$ owing to its large refraction index under the rutile (2.7 at 590 nm) or anatase (2.55 at 590 nm) form. These values are among the highest for a transparent inorganic material (e.g., diamond, ZnS, ZnO, and NaCl are characterized by 2.45, 2.38, 2.2, and 1.54). Moreover, as they are associated with a high reflectivity (a prerequisite for efficient light scattering), one may anticipate that $TiO_2$ is a very attractive optical material. All these properties come, in fact, from a rather wide band gap (3.2 eV) [119], high enough to lead to transparent materials but low enough to provide a highly refractive solid medium. Since 1920, all white commercial materials (paints, plastics, paper, fabrics, rubber, pharmaceuticals, etc.) have been mainly of the rutile form (85%) and sometimes of the anatase form (15%). To fix the ideas, about 60% of the total production is devoted to paints, the remaining being equally distributed among plastics, papers, and fabrics. At an industrial scale, two processes are used. The older one involves leaching of poor ilmenite minerals (less than 60% $TiO_2$) by sulfuric acid at moderate temperature (around 200 °C). After thermolysis of the resulting solution at 110 °C for several hours, the resulting precipitate is fired at 1000 °C [180]. If no rutile seeds are added prior to heating, one ends up with the anatase polymorph [181, 182]. The growth mechanism of the anatase particles under such conditions has been well studied [183–186]. Alternatively, one may use

hydrochloric acid as a leaching agent and add sulfate or fluoride anions to control the structure, size, and shape of the resulting particles [187, 188]. Around 1960, a new process was proposed involving carbochloration between 800 and 1000 °C of ilmenites containing more than 60% $TiO_2$, giving rise to the formation of titanium chloride: $TiO_2 + 2C + 2Cl_2 \rightarrow TiCl_4\uparrow + 2CO\uparrow$. $TiCl_4$ may then be reacted with dioxygen above 1400 °C to yield only the rutile polymorph: $TiCl_4 + O_2 \rightarrow TiO_2\downarrow + 2Cl_2\uparrow$. As a matter of fact, a direct interesting consequence of this is the easy detection of paint forgeries. If anatase is detected, the picture was probably painted between 1920 and 1953; if rutile is present, the picture cannot be older than 50 years. If $TiO_2$ is not detected, the picture was surely painted before 1920. As a dense nonporous material, synthesis of bulk titania is also interesting for making high-refractive-index coatings on silica glasses [189]. The most striking feature of these coatings deposited from organic solutions is that their optical properties are dependent on the type of glass substrate. Thus, on alkali-free substrate, the anatase polymorph is always obtained, while, on a soda glass, a mixed $Na_2O \cdot xTiO_2$ phase is formed [189]. The organic precursor is also important as $Ti(OEt)_4$ leads to anatase at a temperature as low as 150 °C [190], while a $TiCl_2(OEt)_2$ solution leads to brookite [189]. The addition of a mineral acid such as $HNO_3$ or HCl [190] or of diethanolamine [191] has been described to obtain clear solutions from $Ti(OEt)_4$ or $Ti(OPr^i)_4$ precursors.

### 2.3.2. Photocatalysts and Gas Sensors

It has long been recognized that an inherent drawback in the application of $TiO_2$ in coatings is the "chalking" effect resulting from photoredox processes at the pigment surface [192]. Interestingly enough, these parasite reactions can be used to design efficient photoelectrochemical [193] cells or new photocatalysts [194] for the destruction of both organic and inorganic pollutants. For example, photocatalytic activity may be linked to the creation of active radical centers following generation of photocarriers that are able to perform interfacial redox processes. A good example of such a photocatalytic activity is provided by $TiO_2$ thin films prepared by dip coating from $Ti(OPr^i)_4$ dissolved in $\alpha$-terpineol in the presence of acetylacetone and acetic acid [195]. After calcination at 450 °C for 1 h, 1-$\mu$m-thick films of anatase were obtained that were able to perform the photooxidation of nitric oxide (1 ppm concentration) into nitrate ions $NO_3^-$ under dry air conditions. Another example concerns the photocatalytic oxidation of organic pollutants during water treatment using $TiO_2$-based nanostructured sol–gel coatings [196]. It is noteworthy that anatase displays a far higher photocatalytic activity than rutile [197] and that the photoluminescence of anatase is quite different from that of rutile [192]. Consequently, the complete photoelectrolysis of water to $H_2$ and $O_2$ is thermodynamically possible on anatase only [198]. This stresses again the importance of controlling the anatase-to-rutile transformation, as rutile is desired for paints whereas anatase is preferred for photocatalysts. The presence of brookite, known to catalyze the anatase → rutile transformation, and the crystallite size (the bigger, the more stable) seem to be the key factors ruling the transition in the absence of doping ions [197].

Closely related applications concern the elaboration of gas sensors for environmental purposes. It has been reported that nanosized $TiO_2$ thin films were able to detect 20 ppm of $NO_2$ at a temperature suitable for monitoring of exhaust gases from engines [199]. Undoped anatase thin films were also reported to display rapid responses to $O_2$, $H_2$, and ethanol [200]. Similarly, nanostructured thick films elaborated via screen-printing technology from sol–gel-derived anatase powders may be used for atmospheric pollutant monitoring such as carbon monoxide [201]. In all these applications, the thickness uniformity of these films should be very precisely controlled. Consequently, special coating techniques have been developed for that purpose such as atomic layer epitaxy using $Ti(OR)_4$ (R = Et, $Pr^i$) [202, 203] or $TiCl_4$ [204] in the presence of water. Notice that a 2D sol–gel process has also been developed for the synthesis of oxide semiconductor nanofilms [205]. Accordingly, using the Langmuir–Blodgett technique and titanium butoxide, it was possible to form ultrathin $TiO_2$ nanofilms exhibiting the quantum size effect [205]. However, care must be taken in the use of variations of optical properties of many forms of $TiO_2$-derived compounds as a straightforward probe of the particle size [206]. Finally, a very promising property of $TiO_2$ surfaces is their amphiphilic character (both hydrophilic and oleophilic) upon ultraviolet irradiation, leading to antifogging and self-cleaning coatings [207]. The proposed explanation for such a remarkable fact lies in the creation of surface oxygen vacancies at bridging sites upon ultraviolet irradiation. This results in a conversion of relevant $Ti^{4+}$ sites to $Ti^{3+}$ sites that are more favorable for dissociative water adsorption. Consequently, without irradiation, the surface is completely hydrophobic, displaying contact angles with water of $72° \pm 1°$. After irradiation, hydrophilic domains surrounding the photogenerated defects appear, allowing the complete spreading of water droplets (contact angles of $0° \pm 1°$) onto the surface. Self-cleaning properties are intimately linked to this amphiphilic character.

### 2.3.3. Photovoltaics

Titanium oxide is also found at the very heart of dye-sensitized solar cells, which provide a technically and economically credible alternative to present-day p–n junction photovoltaic devices [208–210]. Hydrothermal syntheses are here ideally suited to obtain the active nanocrystalline $TiO_2$ colloids. A widely used method starts from $TiCl_4$ or $Ti(OR)_4$ precursors that are hydrolyzed under acidic ($HNO_3$, HCl, or $MePhSO_3H$) and moderate heating (60–230 °C) conditions [156, 211–213]. It was also reported [214, 215] that switching to base hydrolysis with tetramethylammonium hydroxide ($Me_4NOH$) allowed good control over the crystal structure, size, shape, and organization of $TiO_2$ nanocrystals. Self-assembling processes of these nanocrystals into superlattices may then be exploited, leading to highly structured titania films [215]. In this process, it was also shown that the use of carboxylate-modified titanium alkoxides displaying a higher information content than unmodified alkoxides significantly influenced the final size and size distribution of the nanocrystals [216]. The transition from amorphous gels to the crystalline state in these systems was

followed by $^{47, 49}$Ti-NMR [156, 217] and $^{17}$O-NMR [218] techniques. Quantification of the rutile-to-anatase ratio was thus possible [156], whereas detection of ($\mu_3$-O, $\mu_4$-O) as core species and of ($\mu_3$-O, $\mu_2$-O, Ti—OH, Ti—$OH_2$, Ti—OR) as surface species was reported [217, 218]. Concerning the Ti atoms, XANES spectra are consistent with fivefold coordinated surface species in these nanocrystals. They have also confirmed that apparent band gaps do not vary in a simple way with particle size [219]. One may also notice that nonhydrolytic solution-based reactions involving [$TiCl_4$, $Ti(OR)_4$] or ($TiCl_4$, $R_2O$) mixtures may also lead to the formation of $TiO_2$ nanocrystals [220]. The underlying chemistry of these nonhydrolytic sol–gel routes has been reviewed [221]. Self-organized nanocrystalline anatase films are also prospective electrode materials for 2-V lithium ion batteries due to their convenient formal potential around 1.8 V (Li/$Li^+$) [222]. Owing to the following insertion–extraction process $TiO_2(s) + xLi^+ + xe^- = Li_xTiO_2(s)$ with $x < 0.5$, the specific capacity of $TiO_2$-based electrodes is 170 mA h $g^{-1}$, allowing the realization of electrochromic devices [223] and of new types of intercalation batteries [224].

### 2.3.4. Ceramics

Titania nanoparticles are also widely used for the preparation of ceramic-based microporous membranes [225] and are able to decrease significantly the sintering temperature of titania ceramics [226–228]. The mechanism of nucleation and growth of these nanoparticles has been studied for both $Ti(OEt)_4$ [229] and $Ti(OPr^i)_4$ [230] hydrolysis. With titanium tetraethoxide, it was shown that $v_{nucl} = k[H_2O]^3 [Ti(OEt)_4]^{-1}$, the last ethoxy group being lost during growth [229]. With titanium isopropoxide, hydrolysis seems to be complete at low water concentration, resulting in the creation of nanosized nuclei [230]. Moreover, as the total mass of the nuclei seems to be conserved during the precipitation process, particle growth should involve nucleus aggregation. This difference in growth mechanism may explain why monodispersed powders are easily obtained with $Ti(OEt)_4$, while polydispersed powders are formed with $Ti(OPr^i)_4$. The PCM has been applied to this system and helps to explain these differences at the molecular level [231]. Interestingly enough, supercritical drying of titania gels [232] leads to highly porous aerogels based on a framework of connected fractal aggregates [233, 234]. These materials provide good supports for catalysis purposes. They may also be used as adsorbents or as thermal and phonic insulators [232] and are particularly useful for commercial applications in the elaboration of soft abrasives or of solar screens for cosmetics.

With a melting point above 1800 °C, $TiO_2$ is also an attractive material to make protective coatings. Accordingly, in deep contrast with other transition metal alkoxides, the output of titanium alkoxides by the chemical industry can be reckoned in tons per annum. The origin of this remarkable difference may be traced back about 50 years ago when it was demonstrated that titanium butoxide could be used in making coatings stable for prolonged periods at 600 °C (heat-resistant paints) [235]. Another application linked to this good thermal stability is refractory fiber drawing from solutions containing $Ti(OPr^i)_4$–$H_2O$–EtOH–HCl [236].

### 2.3.5. Mixed SiO₂–TiO₂ Oxides

We now focus our attention on some mixed systems based on $TiO_2$ materials. In this field, titanium alkoxides are frequently used in conjunction with other metal alkoxides to get very useful multicomponent oxide materials. For example, interesting compositions are found in the $SiO_2$–$TiO_2$ binary system. Below 10 wt% $TiO_2$, one may get ultralow thermal expansion $SiO_2$–$TiO_2$ glasses. Such compositions may be readily prepared from $Ti(OPr^i)_4$–$Si(OEt)_4$–EtOH–HCl–$H_2O$ mixtures [237]. Above 10 wt%, alkali-resistant $SiO_2$–$TiO_2$ fibers may be directly drawn from these solutions [238]. Finally, using similar compositions, 30- to 95-mol% $TiO_2$ amorphous oxide films can be obtained that display a refractive index ranging from 1.63 to 2.17, allowing the elaboration of antireflective coatings for silicon solar cells [239].

In catalysis, $TiO_2$–$SiO_2$ systems are active compositions for acid-catalyzed reactions such as phenol amination, ethene hydration, butene isomerization, cumene dealkylation, 2-propanol dehydration, and 1,2-dichloroethane decomposition [240]. The essential problem in the elaboration of these mixed $SiO_2$–$TiO_2$ materials is the homogeneity of component mixing at the molecular level. Since Ti and Si alkoxide precursors do not hydrolyze at the same rate, small titania-rich domains may be formed in the mixed oxides [240]. Consequently, some fundamental studies have been devoted to the real chemical species that may be found in solutions after mixing Si(OR)₄ with Ti(OR)₄ with or without the addition of water. Concerning the possible transesterification reaction between both alkoxides in the absence of water $Si(OEt)_4 + Ti(OPr^i)_4 \rightarrow Si(OEt)_{4-x}(OPr^i)_x + Ti(OPr^i)_{4-x}(OEt)_x$, it was shown using multinuclear NMR and X-ray absorption techniques that possible $x$ values were mainly dependent on the relative ratio of the reactant [241]. For Si/Ti = 1, all possible species were detected and it was shown that the substitution of isopropoxy groups by ethoxy groups in the monomeric $Ti(OPr^i)_4$ leads to the formation of oligomeric species $Ti(OPr^i)_{4-x}(OEt)_x$ displaying pentacoordinated Ti atoms. The direct formation of Si—O—Ti bonds upon hydrolysis may be clearly evidenced using $^{17}O$-NMR and seems to be favored when the alkoxide is added to a prehydrolyzed solution of tetraethoxysilane [242, 243]. Moreover, a careful study of molecular compounds has established the main spectroscopic features of such Si—O—Ti bridges [244]. By reference with well-known Si—O—Si bridges characterized by NMR parameters $\delta$(Si—O—Si) < 100 ppm, $C_Q$(Si—O—Si) > 4.0 MHz, it was found that $C_Q$(Si—O—Ti) < 4.0 MHz, $\delta$(Si—O—$TiO_5$) > 300 ppm, and $\delta$(Si—O—$TiO_3$) > 200 ppm [244, 245]. The lowering of the quadrupolar constant is thus consistent with a more ionic Si—O—Ti bond, while the deshielding observed would be coherent either with a more anisotropic charge distribution in the p orbitals of O atoms or with a reduced HOMO–LUMO gap. Owing to the large deshielding observed and to the fact that Ti atoms have low-lying empty d levels, this last contribution seems more plausible. Concerning titanium atoms, an EXAFS study has shown that, for Ti contents below 10 mol%, Ti atoms were found in fourfold coordination, whereas, above 40 mol%, a majority of them were found in sixfold coordination [246]. At intermediate compositions, the $TiO_6$/$TiO_4$ was found to increase with the $TiO_2$ content and decrease upon increasing the temperature.

### 2.3.6. Barium Titanate

When $TiO_2$ is mixed with an alkaline earth oxide (MgO, CaO, SrO, BaO) or with lead oxide (PbO), a wide array of ferroelectric, piezoelectric, and pyroelectric materials are obtained which may be structurally characterized by solid-state multinuclear NMR techniques [247]. The most studied one is obviously barium titanate ($BaTiO_3$) owing to its high permittivity ($K \sim 6000$ at 25 °C for 0.7- to 1-$\mu$m grain size), explaining its widespread use in ceramic multilayer capacitors [248]. At an industrial scale, $BaTiO_3$ is prepared either by firing $BaCO_3$ and $TiO_2$ around 1000–1200 °C or through the thermal decomposition above 800 °C of barium titanyl oxalate salts ($BaTiO[C_2O_4]_2 \cdot 4H_2O$) [248]. However, finely divided (5–15 nm) stoichiometric $BaTiO_3$ agglomerated powders can be readily prepared at a temperature as low as 50 °C after hydrolysis in isopropanol or benzene of an equimolar mixture of $Ba(OPr^i)_2$ and $Ti(OAm^t)_4$ [249].

Consequently, there has been intensive research into the synthesis of mixed (Ba, Ti) alkoxides, which has led to the characterization of several complexes. One of the first isolated species, $BaTiO(OPr^i)_4 \cdot 7/8Pr^i$-OH, was obtained after refluxing Ba metal in a solution containing $Ti(OPr^i)_4$ and isopropanol [250]. Two crystallographically different tetrameric bimetallic oxoalkoxides have been identified in the crystal structure of this compound [250, 251]. The first tetramer may be formulated as $Ba_4Ti_4(\mu_4$-O)$_4(\mu_3$-OPr$^i)_2(\mu$-OPr$^i)_8$(OPr$^i)_6$(Pr$^i$OH)$_4$ (Fig. 34a) and is characterized by a distorted cube with alternating barium atoms and oxo groups. It may also be viewed as a [(Pr$^i$OH)Ba]$_4$ tetrahedron capped on all its faces by fivefold coordinated TiO(OPr$^i)_4$ groups. The second tetramer has a very similar structure (Fig. 34b) but should be formulated as $Ba_4Ti_4(\mu_4$-O)$_4(\mu_3$-OPr$^i)_2(\mu$-OPr$^i)_{10}$(OPr$^i)_4$(Pr$^i$OH)$_3$]. Such a complex may also be obtained alone by reaction between barium and titanium isopropoxide (1:1 ratio) in the presence of toluene and acetone [252]. Similarly, for $Ba(OEt)_2$:$Ti(OEt)_4 = 1:2$ in ethanol, the compound [Ba(OEt){$Ti_2$(OEt)$_9$}] $\cdot$ 5EtOH was isolated displaying the characteristic [$Ti_2$(OR)$_9]^-$ building block made of two $TiO_6$ octahedra sharing one face (Fig. 34c) [251, 253]. The same [$Ti_2$(OR)$_9]^-$ building block was also evidenced in the complex Ba[$Ti_3(\mu_3$-OPr$^i)_2(\mu_2$-OPr$^i)_5$(OPr$^i)_7$] obtained with $Ba(OPr^i)_2$:$Ti(OPr^i)_4 = 1:3$ in isopropanol/toluene solutions (Fig. 34d) [254] and in the complex Ba[$Ti_2${$(\mu_3$-OEt)$(\mu_2$-OEt)$_3$(OEt)$_4$}$_2]_2$ obtained with $Ba(OEt)_2$:$Ti(OEt)_4 = 1:4$ in ethanol (Fig. 34e) [253]. In all cases, the [$Ti_2(\mu_3$-OR)$_2(\mu_2$-OR)$_3$(OR)$_4]^-$ unit was found to behave as a tetradentate ligand toward $Ba^{2+}$ ions. On the other hand, two kinds of octahedral dimers, [$Ti_2(\mu$-OMe)$_2$(OMe)$_8]^{2-}$ (edge sharing) and [$Ti_2$O$(\mu$-OMe)$_3$(OMe)$_5]^{2-}$ (face sharing), have been characterized in the reaction product [Ba(MeOH)$_2$][Ba(MeOH)$_5$] [$Ti_2$O(OMe)$_8$] [$Ti_2$(OMe)$_{10}$]2 $\cdot$MeOH of $Ba(OMe)_2$ with $Ti(OMe)_4$ in a 1:2 ratio in methanol solutions (Fig. 34f) [255]. Interestingly, for the very similar $Ca(OR)_2$–$Ti(OR)_4$–ROH system, only one complex, [Ca{$Ti_2$(OR)$_9$}$_2$], could be identified [253]. The transferability of the [$Ti_2$(OR)$_9]^-$ building block to more complex ternary systems is also possible, as evidenced in the molecular structure of [{Cd(OPr$^i)_3$} Ba{$Ti_2$(OPr$^i)_9$}]$_2$ (Fig. 34g) obtained by reaction between ICdTi$_2$(OPr$^i)_9$ and KBa(OPr$^i)_3$ in toluene [256].
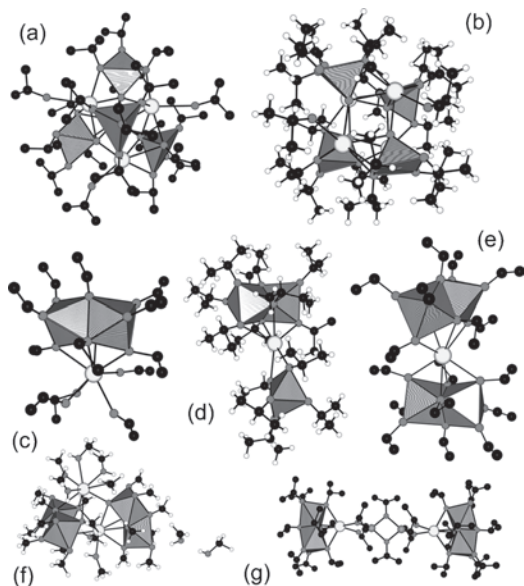
**Figure 34.** Crystal structures of some mixed barium–titanium(IV) alkoxides. (a) Fivefold coordination for Ti atoms in the molecular structure of tetrakis($\mu_4$-oxo)-bis($\mu_3$-isopropoxo)-octakis($\mu_2$-isopropoxo)-hexakis(isopropoxy)-tetrakis(isopropanol)-tetra-barium-tetra-titanium. (b) Fivefold coordination for Ti atoms in the molecular structure of tetrakis($\mu_4$-oxo)-bis($\mu_3$-isopropoxo)-decakis($\mu_2$-isopropoxo)-tetrakis(isopropoxy)-tris(isopropanol)-tetra-barium-tetra-titanium. (c) Face-sharing octahedral coordination for Ti atoms in the crystal structure of bis($\mu_3$-ethoxo)-tris($\mu_2$-ethoxo)-tetraethoxy-tetrakis(ethanol)-barium-di-titanium(IV) ethoxide ethanol solvate. (d) Mixed (octehedral, trigonal bipyramidal) coordination for Ti atoms in the crystal structure of bis($\mu_3$-isopropoxo)-pentakis($\mu_2$-isopropoxo)-heptaisopropoxy-barium-tri-titanium. (e) Face-sharing octahedral coordination for Ti atoms in the crystal structure of bis[bis{($\mu_3$-ethoxo)-tris($\mu_2$-ethoxo)-tetraethoxy}-di-titanium(IV)]-barium. (f) Mixed octahedral coordination for Ti atoms in the crystal structure of hexakis($\mu_3$-methoxo)-($\mu_3$-oxo)-bis($\mu_2$-methoxo)-decakis(methoxy)-hepta(methanol)-di-barium-tetra-titanium di-methanol solvate. (g) Face-sharing octahedral coordination for Ti atoms in the crystal structure of bis[bis($\mu_3$-isopropoxo)-hexakis($\mu_2$-isopropoxo)-tetrakis(isopropoxy)-barium-cadmium-di-titanium] toluene solvate.

The formation of $BaTiO_3$ precursors is obviously not limited to bimetallic oxoalkoxides. Preparation of barium titanyl oxalate, $BaTiO(C_2O_4)_2 \cdot 5H_2O$, has thus been described from aqueous solutions containing barium nitrate and ammonium titanyl oxalate [257]. As already observed for other oxalates, the molecular structure of this complex is based on eight-membered Ti—O rings composed of two pairs of nonequivalent $[TiO(C_2O_4)_2]^{2-}$ moieties, which are related by an inversion center (Fig. 35a). Similarly, preparation of barium titanium citrate, $BaTi(C_6H_6O_7)_3 \cdot 6H_2O$, has been described in the literature [258], but the detailed molecular structures of this complex remain largely unknown. This is not the case for barium titanium glycolate, $BaTi(C_2H_4O_2)_3 \cdot 4C_2H_6O_2 \cdot H_2O$, that has been prepared by reaction between ethylene glycol, BaO, $Ti(OPr^i)_4$, and isopropanol [258]. As shown in Figure 35b, the structure may be described using two building-block units: a monomeric octahedral tris(glycolate) complex, $[Ti(OCH_2CH_2O)_3]^{2-}$, H-bonded to a nine-coordinate Ba atom $[Ba(HOCH_2CH_2OH)_4(OH_2)]^{2+}$.
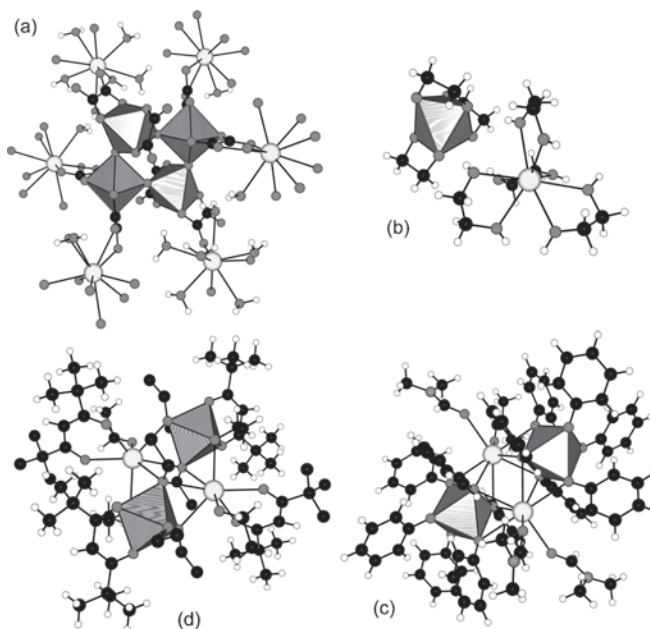


**Figure 35.** Molecular structures of organometallic precursors of barium titanate ($BaTiO_3$). (a) Tetrameric octahedral coordination in the crystal structure of barium titanyl oxalate pentahydrate. (b) Monomeric octahedral coordination in the crystal structure of aqua-tetrakis (ethylene glycol)-barium tris(ethylene glycolato)-titanium(IV). (c) Monomeric octahedral coordination in the crystal structure of tetrakis[($\mu_3$-phenoxo)-($\mu_2$-phenoxo)-(phenoxy)-(dimethylformamide)]- di-barium-di-titanium dichloroethane solvate. (d) Monomeric octahedral coordination in the crystal structure of bis[($\mu_3$-ethoxo)-bis($\mu_2$-ethoxo)-bis(2,2,6,6-tetramethylheptandionato-$O,O'$)-(ethoxy)-(ethanol)-barium-titanium].

Another kind of $BaTiO_3$ precursor could be obtained by reacting barium metal with phenol and $Ti(OPr^i)_4$ [259]. Recrystallization from $DMF/Et_2O$ mixtures leads to a complex displaying the $[BaTi(OC_6H_5)_6(DMF)_2]_2$ stoichiometry with Ti atoms in octahedral coordination and $Ba^{2+}$ ions adopting a bicapped trigonal prismatic coordination (Fig. 35c). A last precursor, $Ba_2Ti_2(thd)_4(\mu_3\text{-}OEt)_2(\mu\text{-}OEt)_4(OEt)_2(EtOH)_2$, may be obtained by reacting $Ti(OEt)_4$ with $Ba(thd)_2$ (thd = 2,2,6,6-tetramethylheptane-3,5-dione) in hexane [260]. This structure is built from neutral, centrosymmetrical, and tetranuclear units with a rhombus-shaped $Ba_2Ti_2O_6$ core that are preserved in solution (Fig. 35d). The geometry is octahedral for titanium and monocapped trigonal prismatic for the $Ba^{2+}$ ions. Obviously, if all these complexes lead to $BaTiO_3$ powders upon hydrolysis and/or calcination, they should nevertheless promote different microstructures in the final powders.

## 2.3.7. Strontium and Lead Titanate

Closely related to $BaTiO_3$ is strontium titanate ($SrTiO_3$), which may be used as a substrate for the deposition of high-temperature oxide superconductors, as symmetrical, voltage-dependent varistors, and in many electronic devices, relays, and switching transistors. $SrTiO_3$ nanocrystals with grain sizes ranging from 26 to 86 nm have been prepared by the stearic acid gel method [261]. Concerning mixed alkoxides, a $SrTi_4(OEt)_{18}$ complex, isostructural with $BaTi_4(OEt)_{18}$

(Fig. 34e), was characterized after reaction with Sr metal, EtOH, and $Ti(OEt)_4$ under reflux [262]. Similarly, using the same procedure with $Ti(OPr^i)_4$ and isopropanol leads to the complex $[Sr_2Ti(OPr^i)_8(Pr^iOH)_3] \cdot 2Pr^i\text{-}OH$ with sixfold coordinated strontium and titanium atoms associated into a triangular unit (Fig. 36a) [262].

Another interesting compound for its piezoelectric properties is lead titanate ($PbTiO_3$), which is widely used in microelectronics (actuators, sensors, and nonvolatile memories) [263]. It can be prepared under hydrothermal conditions [264] as most other perovskite-based titanates [265]. Here also, several mixed alkoxides have been described in the literature. The first isolated compound was $Pb_2Ti_4O_2$ $(CH_3COO)_2(OEt)_{14}$ obtained by reacting $Pb(CH_3COO)_2 \cdot 3H_2O$ and $Ti(OEt)_4$ in a 1:2 ratio in ethanol [266]. Its molecular structure is made of two $[Ti_2(\mu\text{-}O)(\mu\text{-}OAc) \cdot$

$(\mu\text{-}OEt)(OEt)_6]^{2-}$ dimers bridged by two lead atoms in fourfold coordination (Fig. 36b). Attempts to get a complex with 1:1 stoichiometry were successful, and the compound $Pb_2Ti_2O(OPr^i)_{10}$ was isolated after refluxing $Pb(OPr^i)_2$ and $Ti(OPr^i)_4$ in toluene [267]. This compound may be formulated as $Pb_2Ti_2(\mu_4\text{-}O)(\mu_3\text{-}OPr^i)_2(\mu\text{-}OPr^i)_4(OPr^i)_4$ and could be described as a corner-sharing $[Ti_2(\mu\text{-}O)(OPr^i)_{10}]^{4-}$ dimer in close association with two lead atoms in fourfold and fivefold coordination, respectively (Fig. 36c). Another possibility is to add $Ti(OPr^i)_4$ to a suspension of lead acetate (3:1 ratio) in hexane, leading to the compound $Pb_2Ti_2(\mu_4\text{-}O)(\mu\text{-}O_2CCH_3)_2(OPr^i)_8$ [268]. As shown in Figure 36d, the molecular structure of this complex may be described as $[Ti_2(\mu\text{-}O)(\mu\text{-}OAc)(\mu\text{-}OPr^i)(OPr^i)_6]^{2-}$ edge-sharing dimers in strong association with $[Pb_2(\mu\text{-}OAc)(\mu\text{-}OPr^i)]^{2+}$ units. To increase the volatility of these mixed complexes, reactions between $Ti(OPr^i)_4$ and lead amides such as $Pb(NBu^t)_2SiMe_2$ have been investigated, leading to the isolation of $Pb_4TiO(OPr^i)_4(NBu^t)_3$ [269]. Figure 36e shows the monomeric trigonal bipyramidal structure of this complex, which appears to be an addition product between $Ti(OPr^i)_4$ and the lead-containing cage ligand $Pb_4O(NBu^t)_3$. Figure 36f shows another kind of addition product obtained by reacting $SmI_2$ with $NaTi(OPr^i)_5$ or $Sm_5O(OPr^i)_{13}$ with $Ti(OPr^i)_4$ [270]. The interesting feature of this complex $[Sm_4Ti(\mu_5\text{-}O)(\mu_3\text{-}OPr^i)_2(\mu\text{-}OPr^i)_6(OPr^i)_6]$ is the occurrence of a rather rare $\mu_5$-oxo bridge, which has also been characterized in the hydrolysis product of $[LiTi(OPr^i)_5]$ [271] (Fig. 36g). Other compositions based on ternary systems $Pb(Zr, Ti)O_3$, $(Sr, Ba)TiO_3$, and so on, or on other multicomponent systems [272, 273] will not be discussed here.



**Figure 36.** Molecular structures of organometallic precursors of some miscellaneous titanates. (a) Monomeric octahedral coordination in the crystal structure of bis($\mu_3$-isopropoxy)-tris($\mu_2$-isopropoxy)-tris(isopropanolato)-tris(isopropoxy)-di-strontium-titanium isopropanol solvate. (b) Dimeric edge-sharing octahedral coordination for Ti atoms in the crystal structure of bis[($\mu_4$-oxo)-($\mu_2$-acetato-$O,O'$)-tetrakis($\mu_2$-ethoxy)-triethoxy-lead(II)-di-titanium]. (c) Dimeric corner-sharing octahedral coordination for Ti atoms in the crystal structure of ($\mu_4$-oxo)-bis($\mu_3$-isopropoxo)-tetrakis($\mu_2$-isopropoxo)-tetrakis(isopropoxy)-di-lead-di-titanium. (d) Dimeric edge-sharing octahedral coordination for Ti atoms in the crystal structure of tetrakis($\mu_4$-oxo)-bis($\mu_2$-acetato)-pentakis($\mu_2$-isopropoxo)-pentakis(isopropoxy)-di-lead-di-titanium. (e) Monomeric trigonal bipyramidal coordination for Ti atoms in the crystal structure of ($\mu_4$-oxo)-tris($\mu_3$-tert-butylamine)-tetrakis(isopropoxy)-tetra-lead-titanium. (f) Monomeric trigonal bipyramidal coordination for Ti atoms in the crystal structure of ($\mu_5$-oxo)-bis($\mu_3$-isopropoxo)-hexakis($\mu_2$-isopropoxo)-hexakis(isopropoxy)-tetra-samarium(III)-titanium. (g) Mixed (octahedral, trigonal bipyramidal) coordination of Ti atoms in the crystal structure of bis($\mu_5$-oxo)-tetrakis[($\mu_3$-isopropoxo)-($\mu_2$-isopropoxo)]-bis($\mu_2$-oxo)-tetrakis(isopropoxy)-tetra-lithium-tetra-titanium.

# 3. TITANIUM(IV) METALLO-ORGANIC COMPLEXES

The previous section has emphasized the widespread use of titanium(IV) alkoxides in materials chemistry. With so many potential applications in view for titanium alkoxides, a good understanding of their chemical reactivity is absolutely needed. A quick survey of the literature shows that, despite a very large number of publications referring to the use of these alkoxides, most published studies deliberately ignore that these compounds are oligomeric in solution and in the solid state. Worse, it seems rather amazing that the crystalline molecular structure of very basic compounds such as $Ti(OPr^i)_4$ and $Ti(OBu^n)_4$ remain completely unknown. Similarly, if numerous crystalline structures of the first hydrolysis products of $Ti(OR)_4$ compounds are available, very few studies have been devoted to their mechanism of formation. The same situation holds for chemically modified (oxo)alkoxides. Several compounds have been synthesized and characterized by X-ray diffraction techniques. Their molecular structure or chemical reactivity has, however, never been really understood despite their extensive use in supramolecular or sol–gel chemistry for the design of hybrid organic–inorganic materials displaying new original physical properties. Consequently, it was thought that we could fill a real scientific gap by making this critical study of the coordination chemistry of titanium(IV) centers. It

was hoped that by investigating in detail some well-selected hybrid organic–inorganic Ti(IV) complexes, very fundamental trends of the chemical reactivity of the Ti—O—C bond could be identified. This would provide very useful guidelines for anybody interested in the rational chemical design of hybrid TiO$_2$-based materials. Consequently, this section will begin by showing how our PACHA model could explain the chemical reactivity of titanium alkoxides toward protic species. This work is part of a systematic research program based on the molecular programming of titanium(IV) alkoxides that has been engaged in Strasbourg since 1993. Then, titanium(IV)-based complexes isolated in the crystalline state will be reviewed with a particular emphasis on their potential applications in homogeneous catalysis for example. Notice that for this review we have deliberately chosen to discard all organotitanium compounds (molecules with direct Ti—C bonds). If we are fully aware of the importance of these complexes in homogeneous catalysis, their usefulness for the elaboration of stable hybrid organic–inorganic TiO$_2$-based materials has not yet been demonstrated. Consequently, it was thought that a better coherence could be reached by limiting this study to complexes displaying only Ti—O—C, Ti—N—C, or Ti—O—X (X = Si, P) bonds within their molecular structure.

## 3.1. Titanium(IV) Alkoxides

It has long been known that titanium(IV) alkoxides are oligomeric compounds displaying various kind of Ti—OR—Ti bridges. When R is a primary aliphatic group, the basic structural unit is a compact edge-sharing tetramer [274–277] (Fig. 37). From a mechanistic point of view, the formation of a [Ti(OR)$_4$]$_4$ oligomer from tetrahedral Ti(OR)$_4$ monomers may be rationalized by noticing that direct addition of two Ti(OR)$_4$ tetrahedra leads to a dimer [(RO)$_4$Ti(OR)$_2$Ti(OR)$_4$] displaying edge sharing between a Ti(OR)$_6$ octahedron and a Ti(OR)$_4$ tetrahedron (Fig. 37a). Repetition of this process may lead either to a tetramer Ti$_4$(OR)$_{16}$ (smallest cyclic species containing only sixfold coordinated titanium atoms) or to an infinite edge-sharing octahedral chain [(RO)$_2$Ti(OR)$_{4\times1/2}$] ≡ Ti(OR)$_4$. Although for R = CH$_3$ both structures have been characterized in the solid state [277], only in the case of the tetrameric unit was its structure elucidated by a single-crystal X-ray diffraction study [276]. Three kinds of OR groups (10 terminal OR positions, 4 $\mu_2$-OR bridges, and 2 $\mu_3$-OR bridges) may be identified in this tetrameric structure. This raises the question of their relative reactivity toward hydrolysis or substitution upon reaction with X—OH molecules. To answer this question, this tetrameric structure was studied using the PACHA formalism and its electronic signature is given in Table 4. Several interesting features may be derived from these data. First, Ti atoms are found to be strongly electrophilic and thus highly prone to nucleophilic attack. This positive charge is counterbalanced by large negative charges on the methoxy groups. Interestingly enough, the negative charge distribution is quite anisotropic with $Q(\mu_3$-OMe) = −0.86, $Q(\mu_2$-OMe) = −0.71 (O7) and −0.70 (O6), and $Q$(OMe) = −0.54 (O1, O2), −0.50 (O3), −0.45 (O4), and −0.42 (O5). Bridging methoxy groups should, then, be better proton acceptors than terminal groups. Consequently,
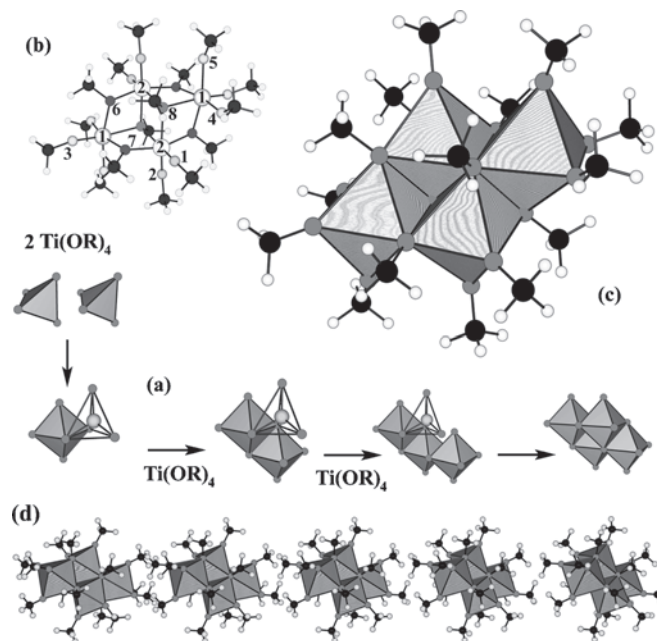


**Figure 37.** Molecular structures of primary titanium(IV) alkoxides. (a) Formation of the planar tetramer [Ti$_4$(OR)$_{16}$] through successive addition of monomeric Ti(OR)$_4$ tetrahedra. (b) Labeling scheme for terminal and bridging OR groups. (c) Polyhedral view of the molecular structure of bis[($\mu_3$-methoxo)-bis($\mu_2$-methoxo)-heptamethoxy-dititanium]. (d) van der Waals 1D network for titanium tetramethoxide in the solid state.

**Table 4.** Electronic PACHA signature for the molecular crystal containing [Ti$_4$(OMe)$_{16}$] tetramers.

| Atom | Charge $q$ | Index $f$ | Atom | Charge $q$ | Index $f$ |
|---|---|---|---|---|---|
| O8 ($\mu_3$-Ti) | −0.740 | −0.013 | H60 (C6) | +0.007 | 0.049 |
| O6 ($\mu_2$-Ti) | −0.665 | −0.004 | H71 (C7) | +0.008 | 0.052 |
| O7 ($\mu_2$-Ti) | −0.663 | −0.003 | H30 (C3) | +0.008 | 0.052 |
| O1 (Ti2) | −0.583 | 0.011 | H50 (C5) | +0.008 | 0.041 |
| O2 (Ti2) | −0.580 | 0.012 | H70 (C7) | +0.011 | 0.051 |
| O3 (Ti1) | −0.527 | 0.013 | H20 (C2) | +0.013 | 0.055 |
| O4 (Ti1) | −0.495 | 0.018 | H10 (C1) | +0.020 | 0.053 |
| O5 (Ti1) | −0.484 | 0.020 | H52 (C5) | +0.021 | 0.056 |
| C8 (O8) | −0.128 | 0.014 | H51 (C5) | +0.024 | 0.049 |
| C6 (O6) | −0.088 | 0.018 | H72 (C7) | +0.025 | 0.050 |
| C7 (O7) | −0.082 | 0.018 | H31 (C3) | +0.026 | 0.055 |
| C3 (O3) | −0.048 | 0.022 | H41 (C4) | +0.027 | 0.055 |
| C2 (O2) | −0.042 | 0.023 | H42 (C4) | +0.028 | 0.051 |
| C1 (O1) | −0.041 | 0.024 | H22 (C2) | +0.031 | 0.054 |
| C4 (O4) | −0.021 | 0.021 | H11 (C1) | +0.031 | 0.054 |
| H81 (C8) | −0.003 | 0.043 | H12 (C1) | +0.032 | 0.052 |
| H82 (C8) | +0.003 | 0.045 | H21 (C2) | +0.034 | 0.056 |
| H61 (C6) | +0.005 | 0.045 | H62 (C6) | +0.034 | 0.049 |
| C5 (O5) | +0.006 | 0.020 | H32 (C3) | +0.038 | 0.052 |
| H40 (C4) | +0.006 | 0.043 | Ti1 (3$\mu$-O) | +2.250 | 0.299 |
| H80 (C8) | +0.007 | 0.047 | Ti2 (4$\mu$-O) | +2.485 | 0.277 |

*Note:* Global parameters were ⟨EN⟩ = 12.37 V, ⟨GH⟩ = 5.7 eV, ⟨EB⟩ = −139.2 eV = −13,435 kJ mol$^{-1}$, and ⟨GI⟩ = 31.3%. See Figure 3 for O- and Ti-atom numbering scheme. The symbol in parentheses refers to the immediate neighborhood.

one may understand that, faced with a molecule bearing a reactive hydroxy group X—OH, Ti atoms should be easily attacked by nucleophilic oxygen centers. Following this attack, the bridging O atoms should also be preferentially protonated by the H atom residing on the hydroxo moiety of the attacking group. Titanium(IV) alkoxides thus display a rather high susceptibility toward hydrolysis with preferential attacks at the heart of their tetrameric core. To get a better visualization of this reactivity toward water, one may transform the partial charges found on O atoms into $pK_a$ values. The result clearly demonstrates a significantly higher basic character for bridging groups ($pK_a$: O8 = 11.9, O6 = 9.0, and O7 = 8.9) relative to terminal groups ($pK_a$: O1 = 5.7, O2 = 5.6, O3 = 3.5, O4 = 2.3, and O5 = 1.8).

These considerations help to explain why Ti(OEt)$_4$ hydrolysis products, heptameric $[Ti_7(\mu_4\text{-O})_2(\mu_3\text{-O})_2(\mu_2\text{-}$ OEt)$_8$(OEt)$_{12}$] [278–280], decameric $[Ti_{10}(\mu_4\text{-O})_4(\mu_3\text{-O})_2$ $(\mu_2\text{-O})_2(\mu_2\text{-OEt})_{10}$(OEt)$_{14}$] [279], and hexadecameric $[Ti_4(\mu_4\text{-O})(\mu_3\text{-O})_2(\mu_2\text{-O})(\mu_2\text{-OEt})_4$(OEt)$_4]_4$ [281] (Fig. 38), cannot be considered as condensation oligomers of tetrameric units. This would have happened only if terminal positions were more susceptible to hydrolysis than bridging positions. For the reverse situation (bridging positions more reactive than terminal positions), one may expect to find new compact structural units with oxo groups at the core (preferential hydrolysis) and unaffected terminal ligands. This is precisely what is observed experimentally. Another interesting aspect of this structure is the formation of a van der Waals chain of tetramers in the solid state (Fig. 37d). The very weak interactions responsible for the formation of this chain may be probed after isolation of a tetramer from its crystalline network, leading to $\langle EB \rangle =$ $-13{,}430.9$ kJ mol$^{-1}$. Knowing that the full network was characterized by $\langle EB \rangle = -13{,}435.0$ kJ mol$^{-1}$, we got an interaction energy of $\Delta E = (-13{,}435.0 + 13{,}430.9) =$

$-4.1$ kJ mol$^{-1}$, a value typical of weak van der Waals attractions. Also notice that in the liquid state an alkoxide such as Ti(OEt)$_4$ is no longer tetrameric but rather trimeric with a cyclic structure based on fivefold coordinated Ti atoms [282]. The reason for the occurrence of such a reduction in coordination number is still unclear and needs further theoretical investigations well beyond the scope of this review.

Detailed structural crystalline data for nonhydrolyzed secondary or tertiary titanium(IV) alkoxides are still lacking. The only structural information available was obtained in solutions using XANES and EXAFS spectroscopy [282] or $^{47,\,49}$Ti-NMR spectroscopy [283]. These techniques point to tetrahedral monomeric structures for Ti(OPr$^i$)$_4$, Ti(OBu$^t$)$_4$, and Ti(OAm$^t$)$_4$. This is not, however, the case for hydrolyzed species (Fig. 39) where crystalline data have been reported for trimeric $[Ti_3(\mu_3\text{-O})(\mu_3\text{-OMe})(\mu_2\text{-OPr}^i)_4$ (OPr$^i$)$_6$] [284], undecameric $[Ti_{11}(\mu_3\text{-O})_{10}(\mu_2\text{-O})_3(\mu_2\text{-O}$ Pr$^i$)$_4$(OEt)$_5$(OPr$^i$)$_6$] [285], dodecameric $[Ti_{12}(\mu_3\text{-O})_{14}$ $(\mu_2\text{-O})_2(\mu_2\text{-OPr}^i)_4$(OEt)$_6$(OPr$^i$)$_6$] [286, 287], heptadecameric $[Ti_{17}(\mu_4\text{-O})_4(\mu_3\text{-O})_{16}(\mu_2\text{-O})_4(\mu_2\text{-OPr}^i)_4$(OPr$^i$)$_{16}$] [288], and octadecameric $[Ti_{18}(\mu_4\text{-O})_4(\mu_3\text{-O})_{20}(\mu_2\text{-O})_3(\mu_2\text{-}$ OH)(OBu$^t$)$_{17}$] [289].
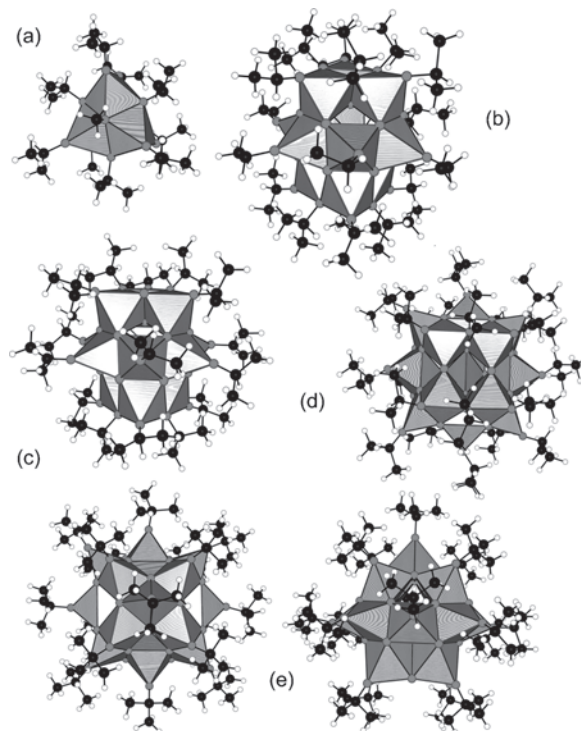


**Figure 39.** Molecular structures of titanium(IV) tetraisopropoxide hydrolysis products. (a) Octahedral coordination in the crystal structure of ($\mu_3$-methoxy)-($\mu_3$-oxo)-tris($\mu_2$-isopropoxy)-hexakis(isopropoxy)-tri-titanium(IV). (b) Decakis($\mu_3$-oxo)-tris($\mu_2$-oxo)-heptakis($\mu_2$-isopropoxo)-hexakis(isopropoxy)-pentakis(ethoxy)-undeca-titanium ethanol solvate. (c) Tetradecakis($\mu_3$-oxo)-bis($\mu_2$-oxo)-tetrakis($\mu_2$-isopropoxo)-hexakis(ethoxy)-hexakis(isopropoxy)-dodeca-titanium. (d) Tetrakis[($\mu_4$-oxo)-tris($\mu_3$-oxo)-($\mu_2$-oxo)-($\mu_2$-isopropoxo)-tetrakis(isopropoxy)]-heptadeca-titanium unknown solvate. (e) Tetrakis($\mu_4$-oxo)-icosakis($\mu_3$-oxo)-tris($\mu_2$-oxo)($\mu_2$-hydroxo)-heptadecakis(*tert*-butoxy)-octadeca-titanium *tert*-butanol solvate.



**Figure 38.** Molecular structures of titanium(IV) tetraethoxide hydrolysis products. (a) Bis($\mu_4$-oxo)-bis($\mu_3$-oxo)-octakis($\mu_2$-ethoxo)-dodecakis(ethoxy)-hepta-titanium. (b) Tetrakis($\mu_4$-oxo)-bis($\mu_3$-oxo)-bis($\mu_2$-oxo)-decakis($\mu_2$-ethoxo)-tetradecakis(ethoxy)-deca-titanium toluene solvate. (c) Tetrakis[($\mu_4$-oxo)-bis($\mu_3$-oxo)-($\mu_2$-oxo)-tetrakis($\mu_2$-ethoxo)-tetrakis(ethoxy)-tetra-titanium].

## 3.2. Reaction with Tripodal Ligands

Based on the above results, we have investigated the possibility of substituting all reactive bridging OR groups by suitable multidentate ligands. The planar geometry of the tetramer and the triangular disposition of the bridging OR groups suggested the use of tripodal ligands of the type $XC(CH_2OH)_3$. A survey of the Cambridge Structural Database showed that tris(hydroxymethyl)ethane or tris(hydroxymethyl)propane react with titanium isopropoxide to yield a tetrameric complex in the expected way [290], despite the fact that titanium isopropoxide is known to be monomeric in the liquid state [282, 283]. This result points to the high flexibility and lability of Ti—OR bonds and the existence, in solution, of a chemical equilibrium between $Ti(OR)_4$ monomers and $Ti_4(OR)_{16}$ tetrameric forms, not only for R = Me, Et, but also for R = $Pr^i$. Upon addition of a suitable well-shaped molecule able to chemically recognize the spatial disposition of bridging OR groups, equilibrium is probably displaced toward the tetramer owing to its consumption by the complexation process.

To clearly elucidate the influence of the OR group, we have undertaken a structural investigation of the products formed by reacting $Ti(OR)_4$ (R = $CH_2CH_3$, $CH(CH_3)_2$, and $CH_2CH_2CH_2CH_3$) with tris(hydroxymethyl)nitromethane (THMNM) [88]. This particular ligand was selected as it allows for the performance of $^{17}O$- and $^{14}N$-NMR studies and also displays a chemically reactive function allowing side-chain addition for forthcoming studies. The results of the study were as expected: conservation of the substituted tetrameric core in each case (Fig. 40). The fact that it was possible to change the OR group while maintaining the molecular structure clearly demonstrates the strong structuring role of the THMNM ligand. Similarly, the possibility of performing an oxolation reaction with minor changes to the tetrameric core is a good illustration of the protective role of multidentate ligands. Such reactions are obviously reminiscent of advanced organic synthesis, playing with the protective groups to obtain a better selectivity of the chemical reaction. Consequently, there is a clear benefit in this case for substituting bridging OR groups by multidentate ligands. However, the most interesting aspect is that we may have a deeper insight into the basic molecular mechanisms by looking at the electronic signatures of these substituted tetramers.

### 3.2.1. Reaction with Titanium(IV) Ethoxide

Table 5 gives the electronic signature for the ethoxy-based THMNM derivative (Fig. 40a). A comparison between ⟨EN⟩ and ⟨GH⟩ values shows that, from a MO point of view, the substituted tetramer is indeed more stable (higher ⟨EN⟩ and ⟨GH⟩, i.e., lower HOMO and wider HOMO–LUMO gap) than the methoxy-based one. This increased stability is also confirmed by the lower ⟨EB⟩ term. Notice that, owing to the occurrence of strongly covalent N—O bonds, the substituted tetramer has a more covalent character relative to the nonsubstituted one (lower ⟨GI⟩). At an atomic scale, we may immediately notice the inversion of charge between atoms Ti1 and Ti2 and the significant higher electrophilic character of Ti atoms in the THMNM derivative. Moreover, the predicted $pK_a$ values for oxygen
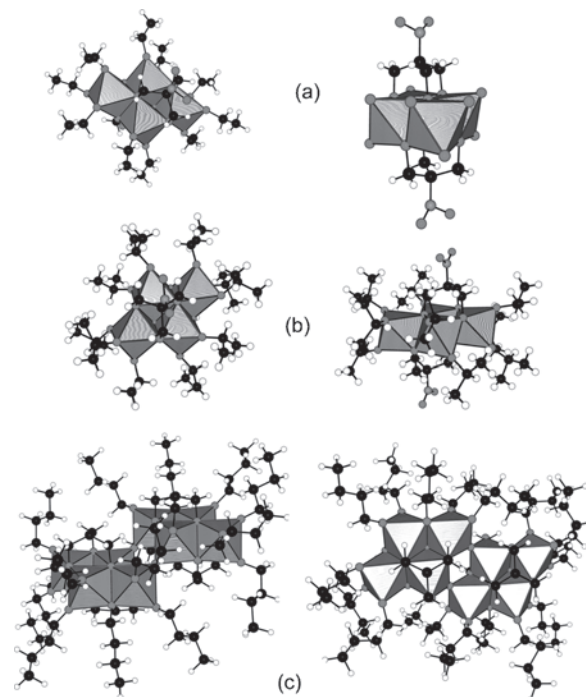


**Figure 40.** Molecular structures of the reaction products of $Ti(OEt)_4$ (a), $Ti(OPr^i)_4$ (b), and $Ti(OBu^n)_4$ (c) with the tripodal ligand tris(hydroxymethyl)nitromethane (THMNM). Owing to its particular geometry, a perfect geometric match exists between the ligand and the six $\mu_n$-OR bridges ($n = 2, 3$) found on a $[Ti_4(OR)_{16}]$ tetramer.

atoms of the ligand range from −8 for the nitro group to +11.0 for the $\mu_3$-$OCH_2$ moiety of the THMNM ligand. Terminal OEt groups are more basic than OMe groups ($4.7 \leq pK_a \leq 5.6$), while for the remaining $\mu_2$-$OCH_2$ moieties a value around 8.6 is obtained. Consequently, and in agreement with experiment [290], these substituted titanium alkoxides should be as reactive toward hydrolysis as unmodified ones. A more contrasted view of the overall charge distribution in this molecule is provided by summing individual charges according to the ligand stoichiometry, leading to $Q(OEt1) = −0.51$, $Q(OEt2) = −0.54$, $Q(OEt3) = Q(OEt10) = −0.49$, $Q(OEt9) = −0.47$, and $Q(THMNM) = −2.42$. The strong accumulation of electronic density on the tripod ligand relative to the terminal ethoxy renders them highly prone to protonation, in agreement with the above $pK_a$ values.

### 3.2.2. Reaction with Titanium(IV) Isopropoxide

Table 6 shows the electronic effects associated with the replacement of OEt groups by $OPr^i$ groups (Fig. 40b), while keeping intact the topology of the molecular object. As expected, these effects are rather weak and in coherence with the well-known better electron-donating properties of isopropoxy groups relative to ethoxy ones. Accordingly, lower positive charges are found on Ti atoms and a large decrease in the global ionicity index is observed. Surprisingly, if the HOMO is stabilized, the HOMO–LUMO gap is strongly reduced. This means that the isopropoxy-based tetramer should be slightly less reactive toward hydrolysis than the ethoxy-based derivative. Concerning $pK_a$ values for

**Table 5.** Electronic PACHA signature for the molecular crystal containing $[Ti_4(OEt)_{10}\{(\mu_2\text{-OCH}_2)_2\ (\mu_3\text{-OCH}_2)C(NO_2)\}_2]$ tetramers.

| Atom | Charge $q$ | Index $f$ | Atom | Charge $q$ | Index $f$ |
|---|---|---|---|---|---|
| O5 (2Ti2, C9) | −0.7176 | −0.0046 | H3 (C2) | +0.0374 | 0.0215 |
| O8 (C10, Ti1,Ti2) | −0.6574 | −0.0005 | H11 (C5) | +0.0383 | 0.0199 |
| O4 (Ti1, Ti2,C7) | −0.6541 | −0.0003 | H5 (C2) | +0.0412 | 0.0223 |
| O3 (Ti1, C5) | −0.5801 | 0.0043 | H19 (C9) | +0.0424 | 0.0180 |
| O9 (Ti2, C11) | −0.5789 | 0.0045 | H18 (C9) | +0.0436 | 0.0180 |
| O10 (Ti2, C13) | −0.5777 | 0.0049 | H23 (C11) | +0.0439 | 0.0180 |
| O2 (Ti1, C3) | −0.5680 | 0.0053 | H14 (C6) | +0.0473 | 0.0245 |
| O1 (Ti1, C1) | −0.5564 | 0.0053 | H22 (C11) | +0.0479 | 0.0179 |
| O6 (N1) | −0.2382 | 0.0197 | H21 (C10) | +0.0516 | 0.0193 |
| O7 (N1) | −0.2287 | 0.0216 | H4 (C2) | +0.0523 | 0.0249 |
| C12 (C11) | −0.1918 | −0.0097 | H30 (C14) | +0.0547 | 0.0259 |
| C6 (C5) | −0.1734 | −0.0076 | H8 (C4) | +0.0553 | 0.0240 |
| C14 (C13) | −0.1729 | −0.0061 | H28 (C13) | +0.0558 | 0.0183 |
| C2 (C1) | −0.1587 | −0.0021 | H10 (C4) | +0.0560 | 0.0252 |
| C4 (C3) | −0.1575 | −0.0025 | H15 (C6) | +0.0570 | 0.0242 |
| C9 (O5, C8) | −0.1012 | 0.0021 | H26 (C12) | +0.0572 | 0.0260 |
| C10 (O8, C8) | −0.0885 | 0.0027 | H17 (C7) | +0.0595 | 0.0203 |
| C7 (O4, C8) | −0.0880 | 0.0023 | H13 (C6) | +0.0614 | 0.0246 |
| C3 (O2, C4) | −0.0335 | 0.0075 | H20 (C10) | +0.0620 | 0.0211 |
| C1 (O1, C2) | −0.0287 | 0.0073 | H25 (C12) | +0.0658 | 0.0259 |
| N1 | −0.0117 | 0.0161 | H12 (C5) | +0.0671 | 0.0194 |
| C5 (O3, C6) | −0.0090 | 0.0059 | H31 (C14) | +0.0695 | 0.0253 |
| C8 (N1) | −0.0044 | 0.0153 | H29 (C14) | +0.0729 | 0.0238 |
| C13 (O10, C14) | −0.0003 | 0.0077 | H9 (C4) | +0.0749 | 0.0258 |
| H7 (C3) | +0.0083 | 0.0191 | H16 (C7) | +0.0791 | 0.0221 |
| C11 (O9, C12) | +0.0196 | 0.0083 | H1 (C1) | +0.0800 | 0.0227 |
| H6 (C3) | +0.0253 | 0.0185 | H24 (C12) | +0.0826 | 0.0246 |
| H2 (C1) | +0.0259 | 0.0185 | Ti2 (2OEt) | +2.3984 | 0.1019 |
| H27 (C13) | +0.0312 | 0.0193 | Ti1 (3OEt) | +2.5115 | 0.1118 |

*Note:* Global parameters were $\langle EN\rangle$ = 13.03 V, $\langle GH\rangle$ = 6.1 eV, $\langle EB\rangle$ = −14,874.6 kJ mol$^{-1}$, and $\langle GI\rangle$ = 25.7%. The symbol in parentheses refers to the immediate neighborhood.

**Table 6.** Electronic PACHA signature for the molecular crystal containing $[Ti_4(OPr^i)_{10}\{(\mu_2\text{-OCH}_2)_2(\mu_3\text{-OCH}_2)C(NO_2)\}_2]$ tetramers.

| Atom | Charge $q$ | Index $f$ | Atom | Charge $q$ | Index $f$ |
|---|---|---|---|---|---|
| O4 ($\mu$-Ti$_3$) | −0.712 | −0.003 | H37 (C18) | +0.046 | 0.016 |
| O5 ($\mu$-Ti$_2$) | −0.655 | 0.000 | H18 (C8) | +0.047 | 0.017 |
| O8 ($\mu$-Ti$_2$) | −0.653 | −0.000 | H23 (C10) | +0.047 | 0.015 |
| O1 (Ti1) | −0.575 | 0.003 | H31 (C15) | +0.048 | 0.017 |
| O9 (Ti2) | −0.574 | 0.003 | H14 (C6) | +0.051 | 0.019 |
| O2 (Ti1) | −0.559 | 0.003 | H7 (C3) | +0.053 | 0.017 |
| O10 (Ti2) | −0.558 | 0.004 | H24 (C12) | +0.053 | 0.015 |
| O3 (Ti1) | −0.548 | 0.004 | H19 (C9) | +0.054 | 0.022 |
| O7 (N) | −0.242 | 0.018 | H30 (C15) | +0.054 | 0.018 |
| O6 (N) | −0.236 | 0.017 | H32 (C16) | +0.054 | 0.019 |
| C8 (C7) | −0.173 | −0.002 | H29 (C15) | +0.056 | 0.020 |
| C3 (C1) | −0.168 | −0.002 | H2 (C2) | +0.056 | 0.019 |
| C19 (C17) | −0.166 | −0.002 | H36 (C18) | +0.057 | 0.017 |
| C18 (C17) | −0.166 | −0.001 | H12 (C6) | +0.057 | 0.019 |
| C5 (C4) | −0.165 | −0.002 | H20 (C9) | +0.058 | 0.019 |
| C6 (C4) | −0.163 | −0.002 | H34 (C16) | +0.058 | 0.018 |
| C15 (C14) | −0.162 | −0.003 | H3 (C2) | +0.059 | 0.018 |
| C16 (C14) | −0.162 | −0.002 | H10 (C5) | +0.061 | 0.018 |
| C9 (C7) | −0.159 | −0.003 | H4 (C2) | +0.062 | 0.021 |
| C2 (C1) | −0.158 | −0.002 | H16 (C8) | +0.062 | 0.019 |
| C10 (O4) | −0.104 | 0.002 | H39 (C19) | +0.063 | 0.019 |
| C13 (O8) | −0.092 | 0.003 | H13 (C6) | +0.064 | 0.018 |
| C12 (O5) | −0.088 | 0.002 | H25 (C12) | +0.065 | 0.016 |
| N1 | −0.020 | 0.013 | H33 (C16) | +0.065 | 0.019 |
| C11 ($\mu_3$-C) | −0.005 | 0.012 | H5 (C3) | +0.066 | 0.020 |
| C4 (O2) | +0.003 | 0.011 | H38 (C18) | +0.067 | 0.018 |
| H8 (C4) | +0.007 | 0.012 | H40 (C19) | +0.070 | 0.019 |
| C17 (O10) | +0.009 | 0.011 | H11 (C5) | +0.074 | 0.019 |
| C1 (O1) | +0.012 | 0.011 | H21 (C9) | +0.074 | 0.021 |
| C14 (O9) | +0.013 | 0.011 | H9 (C5) | +0.078 | 0.021 |
| C7 (O3) | +0.013 | 0.011 | H27 (C13) | +0.078 | 0.015 |
| H15 (C7) | +0.014 | 0.013 | H26 (C13) | +0.083 | 0.015 |
| H35 (C17) | +0.024 | 0.015 | H17 (C8) | +0.094 | 0.020 |
| H1 (C1) | +0.029 | 0.013 | H41 (C19) | +0.098 | 0.020 |
| H22 (C10) | +0.036 | 0.015 | Ti2 (4$\mu$-O) | +2.396 | 0.079 |
| H28 (C14) | +0.037 | 0.013 | Ti1 (3$\mu$-O) | +2.497 | 0.086 |
| H6 (C3) | +0.042 | 0.017 | | | |

*Note:* Global parameters were $\langle EN\rangle$ = 13.22 V, $\langle GH\rangle$ = 3.6 eV, $\langle EB\rangle$ = −155.0 eV = −14,950.2 kJ mol$^{-1}$, and $\langle GI\rangle$ = 21.8%. The symbol in parentheses refers to the immediate neighborhood.

the O atom, a slightly reduced range is spanned (from −7.8 for the nitro group up to 10.8 for the $\mu_3$-OCH$_2$ moiety of the THMNM ligand). Terminal OPr$^i$ groups are slightly less basic than OEt groups (4.3 ≤ p$K_a$ ≤ 5.4), while for the remaining $\mu_2$-OCH$_2$ moieties a p$K_a$ value around 8.6 is obtained. This value is almost the same as that obtained for the ethoxy-based THMNM tetramer. The very similar character of both tetramers is further evidenced through the global charge repartition: $Q$(OPr$^i$1) = −0.52, $Q$(OPr$^i$2) = −0.49, $Q$(OPr$^i$3) = −0.46, $Q$(OPr$^i$9) = −0.51, $Q$(OPr$^i$10) = −0.46, and $Q$(THMNM) = −2.44.

### 3.2.3. Reaction with Titanium(IV) Butoxide

Finally, Table 7 shows the electronic signature of the octameric species obtained after oxolation between two tetramers in the case of the *n*-butoxy ligand (Fig. 40c). As with the (Et → Pr$^i$) substitution, the HOMO continues to be stabilized, though to a much lesser extent [$\Delta$(EN) = 0.07 V versus 0.19 V previously], and the HOMO–LUMO gap is further reduced. Due to the existence of two $\mu_2$-oxo groups in the structure, a higher global ionicity is found relative to the isopropoxy-based tetramer. This ionicity remains, however, lower than that of the ethoxy-based tetramer. The remarkable feature of this structure is the occurrence of a strongly basic oxo ligand (p$K_a$ = 15.2). This obviously

means that such a $\mu_2$-oxo bridge should be stable only in aprotic solvents and would be immediately destroyed upon addition of water. As observed before, we found the logical sequence: p$K_a$($\mu_3$-O—C) = 11.2 > p$K_a$($\mu_2$-O—C) = 8.7 > p$K_a$(Ti—O—C) = 4.8 > p$K_a$(NO$_2$) = −8.1. Consequently, it appears obvious that the chemical nature of the OR chain plays a very minor role in fixing the acid–base properties of the tetramer. Concerning the global charge repartitions, we get the following distributions: $Q$($\mu$-OBu1) = −0.71, $Q$(OBu2) = −0.53, $Q$(OBu3) = −0.46, $Q$(OBu14) = −0.51, $Q$(OBu15) = −0.48, $Q$(OBu16) = −0.50, $Q$(OBu18) = −0.49, $Q$(OBu19) = −0.43, $Q$(THMNM14) = −2.53, and $Q$(THMNM18) = −2.20. If we exclude the OBu1 and THMNM14 ligands, we recover very similar values to those obtained with R = Et or Pr$^i$. This is completely in line with the fact that all these groups display exactly the same coordination mode in the three structures [terminal position for butoxy groups and fully bridging position ($\mu_3$-O, $\mu_2$-O′, $\mu_2$-O″) for the THMNM ligand]. For the butoxy chain

**Table 7.** Electronic PACHA signature for the molecular crystal containing $[Ti_4(OBu^n)_7(\mu_2\text{-}OBu^n)\{(\mu_2\text{-}OCH_2)_2(\mu_3\text{-}OCH_2)C(NO_2)\}\{(OCH_2)(\mu_2\text{-}OCH_2)(\mu_3\text{-}OCH_2)C(NO_2)\}O]_2$ octamers.

| Atom | Charge $q$ | Atom | Charge $q$ | Atom | Charge $q$ |
|---|---|---|---|---|---|
| O17 ($\mu_2$-O) | −0.823 | C33 (O18) | −0.031 | H134 (C32) | +0.039 |
| O8 ($\mu$-Ti$_3$, C16) | −0.728 | C25 (O15) | −0.030 | H81 (C10) | +0.039 |
| O9 ($\mu$-Ti$_3$, C17) | −0.715 | C37 (O19) | −0.026 | H102 (C25) | +0.040 |
| O1 ($\mu$-Ti$_2$, C1) | −0.662 | C29 (O16) | −0.024 | H130 (C36) | +0.040 |
| O4 ($\mu$-Ti$_2$, C13) | −0.661 | C21 (O14) | −0.016 | H101 (C23) | +0.040 |
| O10 ($\mu$-Ti$_2$, C19) | −0.656 | C5 (O2) | −0.013 | H110 (C30) | +0.040 |
| O5 ($\mu$-Ti$_2$, C15) | −0.654 | C9 (O3) | −0.012 | H106 (C27) | +0.040 |
| O19 (Ti4, C37) | −0.576 | N1 (O6, O7) | −0.010 | H124 (C39) | +0.041 |
| O2 (Ti1, C5) | −0.575 | N2 (O11, O12) | −0.010 | H142 (C3) | +0.041 |
| O15 (Ti3, C25) | −0.564 | C14 (N1) | −0.009 | H107 (C27) | +0.041 |
| O16 (Ti3, C29) | −0.563 | H89 (C16) | −0.006 | H112 (C31) | +0.041 |
| O3 (Ti1, C9) | −0.562 | C18 (N2) | −0.003 | H133 (C32) | +0.041 |
| O14 (Ti3, C21) | −0.552 | H66 (C1) | +0.001 | H138 (C24) | +0.041 |
| O13 (Ti2, C20) | −0.545 | H67 (C1) | +0.006 | H74 (C6) | +0.041 |
| O18 (Ti4, C33) | −0.544 | H103 (C25) | +0.007 | H123 (C38) | +0.041 |
| O7 (N1) | −0.236 | H109 (C29) | +0.011 | H131 (C36) | +0.042 |
| O12 (N2) | −0.234 | H114 (C33) | +0.014 | H141 (C3) | +0.042 |
| O11 (N2) | −0.229 | H115 (C33) | +0.014 | H127 (C40) | +0.043 |
| O6 (N1) | −0.229 | H79 (C9) | +0.015 | H147 (C12) | +0.043 |
| C40 (C39) | −0.116 | H86 (C15) | +0.016 | H69 (C2) | +0.044 |
| C32 (C31) | −0.116 | H96 (C21) | +0.017 | H75 (C6) | +0.045 |
| C28 (C27) | −0.115 | H108 (C29) | +0.021 | H135 (C28) | +0.046 |
| C24 (C23) | −0.114 | H92 (C17) | +0.023 | H116 (C34) | +0.047 |
| C36 (C35) | −0.113 | H122 (C38) | +0.024 | H87 (C15) | +0.048 |
| C12 (C11) | −0.111 | H97 (C21) | +0.025 | H68 (C2) | +0.048 |
| C8 (C7) | −0.111 | H144 (C8) | +0.029 | H84 (C13) | +0.049 |
| C4 (C3) | −0.110 | H77 (C7) | +0.030 | H132 (C32) | +0.049 |
| C16 (O8) | −0.090 | H146 (C8) | +0.031 | H118 (C35) | +0.050 |
| C10 (C9, C11) | −0.087 | H94 (C19) | +0.033 | H82 (C11) | +0.050 |
| C26 (C25, C27) | −0.086 | H72 (C5) | +0.035 | H99 (C22) | +0.053 |
| C6 (C5, C7) | −0.084 | H143 (C4) | +0.035 | H85 (C13) | +0.055 |
| C2 (C1, C3) | −0.084 | H98 (C22) | +0.036 | H104 (C26) | +0.055 |
| C35 (C36, C34) | −0.081 | H125 (C39) | +0.036 | H88 (C16) | +0.056 |
| C27 (C26, C28) | −0.080 | H140 (C24) | +0.036 | H148 (C12) | +0.056 |
| C3 (C2, C4) | −0.080 | H83 (C11) | +0.036 | H105 (C26) | +0.057 |
| C22 (C21, C23) | −0.079 | H149 (C12) | +0.037 | H120 (C37) | +0.063 |
| C23 (C22, C24) | −0.079 | H113 (C31) | +0.037 | H136 (C28) | +0.066 |
| C7 (C6, C8) | −0.078 | H117 (C34) | +0.037 | H119 (C35) | +0.072 |
| C31 (C30, C32) | −0.078 | H93 (C17) | +0.038 | H80 (C10) | +0.072 |
| C38 (C37, C39) | −0.077 | H78 (C9) | +0.038 | H128 (C40) | +0.073 |
| C11 (C10, C12) | −0.077 | H100 (C23) | +0.038 | H111 (C30) | +0.074 |
| C30 (C29, C31) | −0.077 | H139 (C24) | +0.038 | H126 (C40) | +0.079 |
| C17 (O9) | −0.075 | H70 (C3) | +0.038 | H90 (C20) | +0.084 |
| C34 (C33, C35) | −0.074 | H137 (C28) | +0.038 | H95 (C19) | +0.087 |
| C39 (C38, C40) | −0.069 | H145 (C8) | +0.039 | H91 (C20) | +0.105 |
| C15 (O5) | −0.067 | H129 (C36) | +0.039 | Ti2 (HMNM) | +2.302 |
| C1 (O1) | −0.066 | H121 (C37) | +0.039 | Ti1 (2 × OBu) | +2.406 |
| C13 (O4) | −0.061 | H71 (C3) | +0.039 | Ti4 (O3 × OBu) | +2.442 |
| C19 (O10) | −0.060 | H73 (C5) | +0.039 | Ti3 (3 × OBu) | +2.516 |
| C20 (O13) | −0.037 | H76 (C7) | +0.039 | | |

*Note:* Global parameters were $\langle EN \rangle = 13.29$ V, $\langle GH \rangle = 1.8$ eV, $\langle EB \rangle = -28{,}873.6$ kJ mol$^{-1}$, and $\langle GI \rangle = 24.4\%$. The symbol in parentheses refers to the immediate neighborhood.

bonded to atom O1, we find a more negative charge owing to its bridging position. Reciprocally, the THMNM moiety based on atom C18 does not display a full bridging mode as before, but rather a ($\mu_3$-O, $\mu_2$-O′, $\mu$-2O″) coordination mode. Consequently, it bears less negative charge than the other one based on atom C14.

### 3.2.4. General Discussion

We are now in a position to draw some conclusions from this series of three related crystal structures. Full substitution of bridging positions in $Ti_4(OR)_{16}$ tetramers does not alter very much the acid–base properties of these complexes. With electronic density mainly localized on THMNM moieties,

protic reagents such as water are expected to react preferentially with these ligands and less favorably with the remaining terminal OR chains. However, the removal of such a ligand would require the simultaneous attack of three water molecules upon a single tetramer, a rather unlikely process for entropy reasons. Consequently, the tripod should remain bonded to the tetramer even after hydrolysis, preventing the destruction of the initial tetrameric core. The fact that water molecules effectively attack the THMNM ligand is demonstrated by the butoxy-based structure. The observed octamer may be obviously derived from two tetrameric species, after partial hydrolysis and further oxolation of four terminal butoxy groups. If the THMNM ligand were significantly inert in this process, the octamer would have displayed only terminal butoxy groups. As shown in Figure 40c, this is not the case as two butoxy ligands are found in bridging positions. The occurrence of these $\mu_2$-OBu$^n$ groups may be explained if the $\mu_3$-OCH$_2$ moiety has been first hydrolyzed as suggested by our charge distributions and predicted p$K_a$ values. Since the THMNM ligand is still linked to the tetramer by the two other arms, it cannot be eliminated. Consequently, the free arm is able to react with a neighboring terminal butoxy group, leading to the formation of a new link between the OCH$_2$ moiety and the titanium atom. Now recall that, at room temperature, bridging and terminal positions are generally not distinguishable on the NMR time scale. Owing to the intrinsic lability of Ti—O bonds in such compounds, a fast cyclic permutation between the three groups ($\mu_2$-OCH$_2$ $\rightarrow$ $\mu_3$-OH $\rightarrow$ $\mu_1$-OBu$^n$) bonded to the same Ti atom may occur. This would then lead to a hydroxy group in the terminal position ($\mu_1$-OH) ideally placed to undergo the final oxolation reaction and to the final observed structure: $\mu_2$-OBu$^n$ and $\mu_3$-OCH$_2$.

## 3.3. Crystal Engineering of Hybrid Organic–Inorganic Networks

Crystal engineering has been defined as the understanding of intermolecular interactions in the context of crystal packing and the use of such understanding in the design of new solids with desired physical and chemical properties [291]. Consequently, this field shares many concepts with molecular tectonics or sol–gel chemistry, and we thought it interesting to see to what extent titanium-based molecular precursors commonly used in sol–gel chemistry can be tailored to meet crystal engineering requirements. In fact, it soon appears that titanium alkoxides were much too flexible to be used in a reliable way for the rational design of hybrid organic–inorganic networks. Moreover, as our PACHA model is able to provide us with a direct measure of molecular interactions in the solid state, it is a rather easy job to classify the observed crystalline networks along a universal energy scale.

### 3.3.1. Titanium Methoxide Ti(OMe)₄

For example, let us go back to the crystal structure of titanium(IV) tetramethoxide. We have seen that the whole packing energy of Ti$_4$(OMe)$_{16}$ tetramers into a 1D van der Waals chain (Fig. 37d) through methyl groups was indeed not very impressive ($-4.1$ kJ mol$^{-1}$). But we can do more

than that by looking at which kinds of methyl groups are involved in the stacking. Table 8 shows the retrosynthetic indexes [84] computed for the free tetramer after extraction from the network. Recall that these indexes are electronic probes defining which parts of a molecular fragment are deeply involved in the building of the lattice. They are simply defined as RI $= 100 \times (|q_{mol} - q_{cryst}|/q_{cryst})0$, where $q_{mol}$ is the charge of a given atom in the isolated fragment and $q_{cryst}$ its charge in the crystal. A low RI index means that the computed atomic charge is not under the control of the network, while a high value points to an atom strongly affected by the removal of the crystalline environment. For the methoxy-based tetramer, one may immediately see from Table 8 that stacking in the solid state involves interactions between bridging OMe groups. Assuming a reasonable threshold of at least 10% to define significant molecular interactions in the solid state, one gets an average H···H van der Waals interaction of $-4.1/7 = -0.6$ kJ mol$^{-1}$. This rather low value is in line with the fact that interactions between methyl groups are mainly responsible for the building of the network.

### 3.3.2. Tris(hydroxymethyl)nitromethane Derivatives

If the above conclusions were correct, one would expect that after replacement of bridging OR groups by THMNM ligands (Fig. 40) a much stronger interaction should be found. This was indeed shown to be the case after comparison of the $\langle EB \rangle$ value for the full network ($-14{,}950.2$ kJ mol$^{-1}$) to the $\langle EB \rangle$ value of an isolated isopropoxy-based tetramer ($-14{,}922.7$ kJ mol$^{-1}$), leading to a difference $\Delta E = -25.7$ kJ mol$^{-1}$. As shown in Table 9, the networking interactions are found to involve now the nitro group with, by decreasing order of importance:

**Table 8.** WinPacha retrosynthetic indexes after extraction of a [Ti$_4$(OMe)$_{16}$] tetramer from its crystalline network.

| | |
|---|---|
| O10, O4 ⇔ O7 = $-0.663$ ⇒ 0% | H36, H24 ⇔ H42 = $+0.028$ ⇒ 2% |
| O5, O6 ⇔ O8 = $-0.740$ ⇒ 0% | H4, H46 ⇔ H20 = $+0.014$ ⇒ 3% |
| O3, O14 ⇔ O6 = $-0.665$ ⇒ 0% | H21, H33 ⇔ H32 = $+0.039$ ⇒ 3% |
| O1, O15 ⇔ O1 = $-0.584$ ⇒ 0% | H32, H20 ⇔ H31 = $+0.027$ ⇒ 5% |
| Ti3, Ti2 ⇔ Ti1 = $+2.251$ ⇒ 0% | H28, H10 ⇔ H70 = $+0.011$ ⇒ 5% |
| Ti4, Ti1 ⇔ Ti2 = $+2.484$ ⇒ 0% | H47, H5 ⇔ H21 = $+0.032$ ⇒ 6% |
| O2, O16 ⇔ O2 = $-0.580$ ⇒ 0% | C13, C9 ⇔ C5 = $+0.006$ ⇒ 7% |
| O9, O13 ⇔ O5 = $-0.483$ ⇒ 0% | H37, H25 ⇔ H50 = $+0.009$ ⇒ 7% |
| O8, O12 ⇔ O4 = $-0.495$ ⇒ 0% | H27, H39 ⇔ H52 = $+0.022$ ⇒ 8% |
| O7, O11 ⇔ O3 = $-0.526$ ⇒ 0% | H38, H26 ⇔ H51 = $+0.026$ ⇒ 8% |
| C4, C10 ⇔ C7 = $-0.082$ ⇒ 0% | H29, H11 ⇔ H71 = $+0.009$ ⇒ 8% |
| C2, C16 ⇔ C2 = $-0.042$ ⇒ 0% | H23, H35 ⇔ H41 = $+0.030$ ⇒ 8% |
| C5, C6 ⇔ C8 = $-0.127$ ⇒ 0% | H43, H1 ⇔ H10 = $+0.018$ ⇒ 10% |
| C11, C7 ⇔ C3 = $-0.048$ ⇒ 0% | H13, H16 ⇔ H80 = $+0.006$ ⇒ 10% |
| C12, C8 ⇔ C4 = $-0.021$ ⇒ 1% | H18, H15 ⇔ H82 = $+0.004$ ⇒ 15% |
| H6, H48 ⇔ H22 = $+0.031$ ⇒ 1% | H34, H22 ⇔ H40 = $+0.005$ ⇒ 20% |
| H12, H30 ⇔ H72 = $+0.025$ ⇒ 1% | H42, H9 ⇔ H62 = $+0.027$ ⇒ 20% |
| C15, C1 ⇔ C1 = $-0.041$ ⇒ 1% | H19, H31 ⇔ H30 = $+0.010$ ⇒ 30% |
| C14, C3 ⇔ C6 = $-0.086$ ⇒ 2% | H40, H7 ⇔ H60 = $+0.004$ ⇒ 39% |
| H2, H44 ⇔ H11 = $+0.030$ ⇒ 2% | H8, H41 ⇔ H61 = $+0.007$ ⇒ 43% |
| H3, H45 ⇔ H12 = $+0.033$ ⇒ 2% | H17, H14 ⇔ H81 = $-0.005$ ⇒ 47% |

*Note:* The syntax is molecular labels ⇔ crystalline label = molecular charge ⇒ retrosynthetic index RI.

**Table 9.** WinPacha retrosynthetic indexes after extraction of a $[Ti_4(OPr^i)_{10}(THMNM)_2]$ tetramer from its crystalline network.

| | |
|---|---|
| O15, O2 ⇔ O2 = −0.559 ⇒ 0% | H44, H50 ⇔ H29 = +0.059 ⇒ 5% |
| O16, O3 ⇔ O3 = −0.548 ⇒ 0% | H5, H36 ⇔ H23 = +0.050 ⇒ 5% |
| Ti4, Ti1 ⇔ Ti1 = +2.497 ⇒ 0% | O20, O18 ⇔ O7 = −0.228 ⇒ 5% |
| O4, O10 ⇔ O4 = −0.712 ⇒ 0% | H28, H82 ⇔ H21 = +0.079 ⇒ 6% |
| Ti2, Ti3 ⇔ Ti2 = +2.395 ⇒ 0% | H70, H15 ⇔ H7 = +0.056 ⇒ 6% |
| O12, O8 ⇔ O9 = −0.574 ⇒ 0% | C15, C22 ⇔ C17 = +0.010 ⇒ 6% |
| O13, O9 ⇔ O10 = −0.558 ⇒ 0% | H72, H18 ⇔ H10 = +0.057 ⇒ 7% |
| O5, O11 ⇔ O5 = −0.654 ⇒ 0% | H38, H7 ⇔ H25 = +0.070 ⇒ 7% |
| O1, O14 ⇔ O1 = −0.574 ⇒ 0% | H1, H62 ⇔ H1 = +0.027 ⇒ 7% |
| C34, C8 ⇔ C3 = −0.168 ⇒ 0% | H49, H55 ⇔ H34 = +0.062 ⇒ 7% |
| C29, C23 ⇔ C19 = −0.167 ⇒ 0% | H42, H60 ⇔ H40 = +0.075 ⇒ 8% |
| C26, C24 ⇔ C15 = −0.163 ⇒ 0% | C3, C32 ⇔ C7 = +0.012 ⇒ 8% |
| O7, O6 ⇔ O8 = −0.654 ⇒ 0% | H39, H33 ⇔ H28 = +0.040 ⇒ 9% |
| C16, C28 ⇔ C18 = −0.165 ⇒ 0% | H73, H19 ⇔ H11 = +0.067 ⇒ 9% |
| C4, C19 ⇔ C10 = −0.104 ⇒ 1% | H37, H6 ⇔ H24 = +0.058 ⇒ 9% |
| C31, C2 ⇔ C4 = +0.003 ⇒ 1% | H67, H12 ⇔ H4 = +0.068 ⇒ 10% |
| H59, H41 ⇔ H39 = +0.064 ⇒ 1% | H25, H79 ⇔ H18 = +0.042 ⇒ 10% |
| C20, C5 ⇔ C12 = −0.089 ⇒ 1% | H11, H66 ⇔ H3 = +0.065 ⇒ 10% |
| H57, H30 ⇔ H37 = +0.045 ⇒ 2% | H68, H13 ⇔ H5 = +0.059 ⇒ 11% |
| C30, C1 ⇔ C1 = +0.012 ⇒ 2% | H16, H58 ⇔ H38 = +0.060 ⇒ 11% |
| C7, C33 ⇔ C2 = −0.161 ⇒ 2% | H27, H81, H74, H20 ⇔ H12 = +0.064 ⇒ 11% |
| C12, C38 ⇔ C9 = −0.162 ⇒ 2% | H4, H35 ⇔ H22 = +0.040 ⇒ 11% |
| C25, C27 ⇔ C16 = −0.165 ⇒ 2% | H43, H61 ⇔ H41 = +0.086 ⇒ 12% |
| C36, C10 ⇔ C6 = −0.167 ⇒ 2% | H75, H21 ⇔ H13 = +0.072 ⇒ 12% |
| O17, O19 ⇔ O6 = −0.231 ⇒ 2% | C13, C14 ⇔ C11 = −0.006 ⇒ 12% |
| H46, H52 ⇔ H31 = +0.047 ⇒ 2% | H76, H22 ⇔ H14 = +0.057 ⇒ 12% |
| H23, H77 ⇔ H16 = +0.061 ⇒ 3% | H26, H80 ⇔ H19 = +0.060 ⇒ 13% |
| C35, C9 ⇔ C5 = −0.159 ⇒ 3% | H48, H54 ⇔ H33 = +0.075 ⇒ 15% |
| H14, H69 ⇔ H6 = +0.043 ⇒ 3% | H53, H47 ⇔ H32 = +0.063 ⇒ 17% |
| H45, H51 ⇔ H30 = +0.056 ⇒ 4% | H2, H63 ⇔ H8 = +0.008 ⇒ 17% |
| C11, C37 ⇔ C8 = −0.166 ⇒ 4% | H3, H64 ⇔ H15 = +0.016 ⇒ 19% |
| C18, C21 ⇔ C14 = +0.013 ⇒ 4% | H9, H32 ⇔ H27 = +0.061 ⇒ 23% |
| N1, N2 ⇔ N1 = −0.019 ⇒ 5% | H71, H17 ⇔ H9 = +0.059 ⇒ 25% |
| H56, H29 ⇔ H36 = +0.059 ⇒ 5% | H8, H31 ⇔ H26 = +0.062 ⇒ 26% |
| H10, H65 ⇔ H2 = +0.059 ⇒ 5% | H24, H78 ⇔ H17 = +0.069 ⇒ 27% |
| C6, C17 ⇔ C13 = −0.087 ⇒ 5% | H40, H34 ⇔ H35 = +0.017 ⇒ 32% |

*Note:* The syntax is molecular labels ⇔ crystalline label = molecular charge ⇒ retrosynthetic index RI.

1. The methine group (C17) of a terminal OPr$^i$ group borne by the Ti2 atom (32%). Methyl groups of this moiety interact more weakly (11% and 12%).
2. The methyl group (C8) of a terminal OPr$^i$ group borne by the Ti1 atom (27%). After come the methine group (19%) and the other methyl group (13%).
3. One methylene arm (C13, $\mu$-Ti$_2$) of the tripod ligand (26% and 23% for both H atoms). The other $\mu$-Ti$_2$ arm (C12) displays negligible interaction (<10%), while the $\mu$-Ti$_3$ arm (C10) and central carbon (C11) interact weakly (11% and 12%, respectively).
4. The methyl group (C5) of another terminal OPr$^i$ group borne by the Ti1 atom (25%). After come the methine group (17%) and the other methyl group (11–12% for the three H atoms).
5. One methyl group (C16) of the other terminal OPr$^i$ group borne by the Ti2 atom (15–17%). The methine group and the other methyl group display negligible interactions (<10%).

Having identified 18 Pr$^i \cdots$O$_2$N interactions with RI < 10%, the average interaction energy should be −25.7/18 =

−1.4 kJ mol$^{-1}$. This is 2.5 times stronger than the previously mentioned Me $\cdots$ Me interaction and is in full agreement with the well-known increase in strength of the van der Waals interaction with the atomic number. Figure 41 shows the hexagonal 2D packing resulting from these interactions between nitro and isopropoxy groups.

One may also take a look at van der Waals interactions found in the very similar ethoxy-based tetramer. Comparison of the ⟨EB⟩ value for the full network (−14,874.6 kJ mol$^{-1}$) to the ⟨EB⟩ value of an isolated ethoxy-based tetramer (−14,855.7 kJ mol$^{-1}$), leads to a difference $\Delta E = -18.9$ kJ mol$^{-1}$. As shown in Table 10, the networking interactions are found to be completely different from the previous case. Again, by decreasing order of importance:

1. Interaction between four terminal OEt groups, one borne by the Ti2 atom and the three others by the Ti1 atom. The Ti2-OEt group is characterized by 952% for the C13 methine carbon, (27%, 20%) for the methine H atoms, and (19%, 12%) for the methyl H atoms. The large value (952%) found for the C13 atom comes from an almost null charge in the network associated with a change in sign of the charge on going from the crystal to the free state. The most involved Ti1-OEt moiety is based on atom C5: 71% for the methine carbon, (29%, 28%) for the methine H atoms, and (23%, 16%) for the methyl H atoms. The least involved is based on the C3 atom with 47% for just one H atom of the methylene group. The last Ti1-OEt group interacts mainly through its H atoms: (60%, 15%, 12%) for the H atoms of the methyl group, (29%, 14%) for the H atoms of the methylene group, and only 16% for the methine carbon.
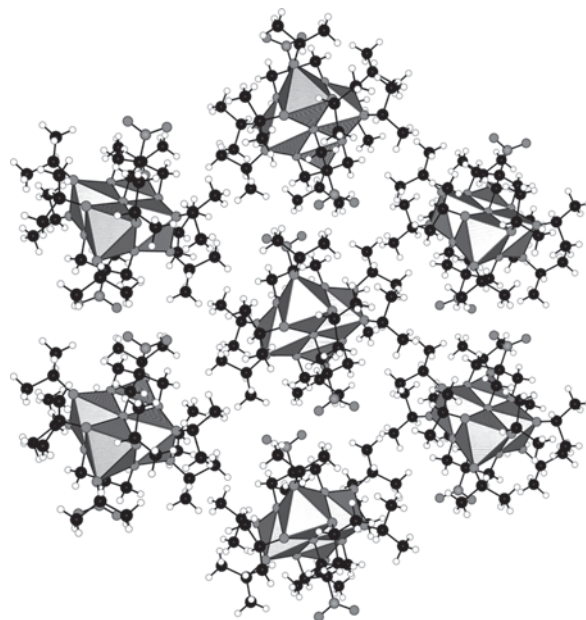


**Figure 41.** Hexagonal compact 2D network formed by $[Ti_4(OPr^i)_{10}(THMNM)_2]$ derivatives involving van der Waals contact between nitro and isopropoxy groups. The interaction energy was found to be very weak (ca. −1.4 kJ mol$^{-1}$ on average).

**Table 10.** WinPacha retrosynthetic indexes after extraction of a $[Ti_4(OEt)_{10}(THMNM)_2]$ tetramer from its crystalline network.

| | |
|---|---|
| O7, O6 ⇔ O5 = −0.718 ⇒ 0% | O20, O18 ⇔ O6 = −0.221 ⇒ 7% |
| C21, C15 ⇔ C14 = −0.173 ⇒ 0% | H9, H34 ⇔ H20 = +0.057 ⇒ 8% |
| O4, O11 ⇔ O4 = −0.654 ⇒ 0% | H44, H29 ⇔ H31 = +0.076 ⇒ 10% |
| Ti4, Ti1 ⇔ Ti1 = +2.510 ⇒ 0% | H61, H18 ⇔ H10 = +0.061 ⇒ 10% |
| O5, O10 ⇔ O8 = −0.658 ⇒ 0% | H10, H35 ⇔ H21 = +0.057 ⇒ 11% |
| O13, O9 ⇔ O10 = −0.577 ⇒ 0% | H26, H47 ⇔ H25 = +0.058 ⇒ 11% |
| Ti2, Ti3 ⇔ Ti2 = +2.400 ⇒ 0% | H43, H41 ⇔ H30 = +0.061 ⇒ 12% |
| O8, O12 ⇔ O9 = −0.578 ⇒ 0% | H15, H60 ⇔ H5 = +0.046 ⇒ 12% |
| C5, C18 ⇔ C10 = −0.089 ⇒ 0% | C11, C10 ⇔ C8 = −0.005 ⇒ 13% |
| O16, O3 ⇔ O3 = −0.581 ⇒ 0% | H24, H39 ⇔ H23 = +0.050 ⇒ 14% |
| C8, C27 ⇔ C4 = −0.158 ⇒ 0% | H31, H12 ⇔ H19 = +0.048 ⇒ 14% |
| O15, O2 ⇔ O2 = −0.566 ⇒ 0% | H51, H2 ⇔ H2 = +0.030 ⇒ 14% |
| H49, H3 ⇔ H6 = +0.025 ⇒ 0% | H14, H59 ⇔ H4 = +0.060 ⇒ 15% |
| O1, O14 ⇔ O1 = −0.559 ⇒ 1% | H21, H62 ⇔ H14 = +0.055 ⇒ 16% |
| N2, N1 ⇔ N1 = −0.012 ⇒ 2% | C23, C1 ⇔ C1 = −0.024 ⇒ 16% |
| C16, C6 ⇔ C9 = −0.103 ⇒ 2% | H30, H11 ⇔ H18 = +0.051 ⇒ 17% |
| C2, C24 ⇔ C3 = −0.033 ⇒ 2% | H28, H42 ⇔ H29 = +0.059 ⇒ 19% |
| H54, H20 ⇔ H13 = +0.060 ⇒ 2% | H33, H23 ⇔ H28 = +0.045 ⇒ 20% |
| H8, H37 ⇔ H17 = +0.061 ⇒ 2% | H36, H7 ⇔ H16 = +0.063 ⇒ 20% |
| C9, C26 ⇔ C6 = −0.178 ⇒ 3% | H55, H22 ⇔ H15 = +0.070 ⇒ 23% |
| C13, C22 ⇔ C12 = −0.186 ⇒ 3% | H25, H46 ⇔ H24 = +0.062 ⇒ 25% |
| C19, C4 ⇔ C7 = −0.085 ⇒ 3% | H32, H27 ⇔ H27 = +0.023 ⇒ 27% |
| O17, O19 ⇔ O7 = −0.221 ⇒ 3% | H53, H5 ⇔ H11 = +0.027 ⇒ 28% |
| H16, H56 ⇔ H8 = +0.057 ⇒ 4% | H45, H6 ⇔ H12 = +0.048 ⇒ 29% |
| C7, C28 ⇔ C2 = −0.165 ⇒ 4% | H50, H1 ⇔ H1 = +0.057 ⇒ 29% |
| H48, H40 ⇔ H26 = +0.060 ⇒ 5% | H52, H4 ⇔ H7 = +0.012 ⇒ 47% |
| C12, C20 ⇔ C11 = +0.019 ⇒ 5% | H13, H58 ⇔ H3 = +0.060 ⇒ 60% |
| H57, H17 ⇔ H9 = +0.070 ⇒ 6% | C25, C3 ⇔ C5 = −0.003 ⇒ 71% |
| H38, H19 ⇔ H22 = +0.045 ⇒ 7% | C17, C14 ⇔ C13 = +0.003 ⇒ 952% |

*Note:* The syntax is molecular labels ⇔ crystalline label = molecular charge ⇒ retrosynthetic index RI.

2. The second Ti2-OEt moiety is more weakly involved in the stacking: (25%, 11%) for the methyl group and 14% for the methylene group.
3. Last comes the THMNM ligand with 20% for one methylene group ($\mu$-Ti$_2$) and (17%, 14%) for the other $\mu$-Ti$_3$ methylene.

With quite different van der Waals interactions, it is not surprising to find a different mode of stacking. Whereas the isopropoxy-based tetramer leads to 2D planes, the ethoxy-based one forms rather linear chains (Fig. 42a). With about 25 Et···Et interactions, we get an average van der Waals energy of −0.8 kJ mol$^{-1}$, slightly stronger than Me···Me interactions (as expected) and significantly weaker than Pr$^i$···O$_2$N interactions.

We will not give the full crystal engineering analysis in the case of the butoxy-based octamer, owing to the fact that H-atom coordinates have not been experimentally determined. Instead, they have been added by our software in order to compute a meaningful electronic signature. Nevertheless, according to our crystal structure optimization algorithm, we may say that the octamers should form in the solid a van der Waals 1D chain (Fig. 42b). With $\langle EB \rangle_{net} = -28,873.6$ kJ mol$^{-1}$ and $\langle EB \rangle_{free} = -28,822.9$ kJ mol$^{-1}$, the packing energy should be at least −50.7 kJ mol$^{-1}$ for 48 kinds of van der Waals interactions involving mainly Bu$^n$···Bu$^n$ but also Bu$^n$···THMNM contacts. The average interaction energy is thus estimated at about −1.1 kJ mol$^{-1}$,
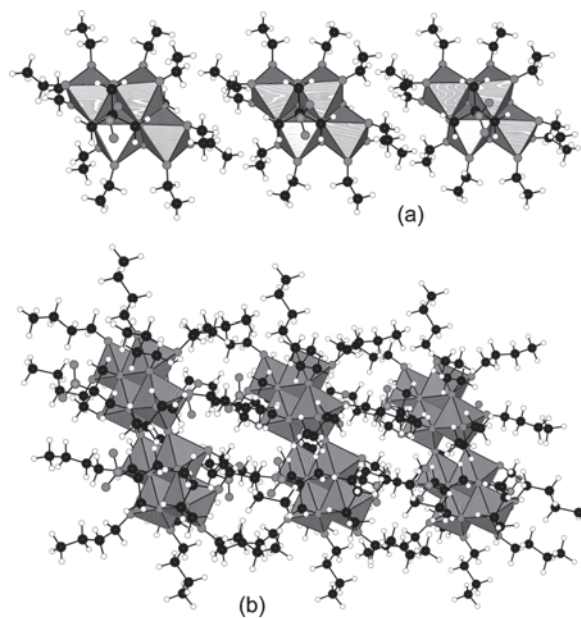


**Figure 42.** 1D van der Waals chains formed by $[Ti_4(OEt)_{10}(THMNM)_2]$ tetramers (a) and $[Ti_8O_2(OBu^n)_{16}(THMNM)_4]$ octamers (b). The stacking energy was found to be typical of van der Waals interactions (−0.8 kJ mol$^{-1}$ for R = Et and about −1.1 kJ mol$^{-1}$ for R = Bu$^n$).

that is, intermediate between that found for Et···Et and Pr$^i$···O$_2$N contacts.

We have detailed the crystal engineering analysis of the THMNM-based derivatives to convince the reader that it is possible, in a quantitative and routine way, to study very weak van der Waals interactions for such hybrid organic–inorganic networks. In fact, the method is completely general and can be applied to any crystalline network with weak but also stronger interactions. For example, one could cut the two $\mu_2$-oxo bridges in the previous octameric species, leaving two fragments characterized by $\langle EB \rangle = -13,019.3$ kJ mol$^{-1}$. Referring to the $\langle EB \rangle$ value of the free octamer, the energetic cost of this breaking is readily evaluated as $2 \times E_{Ti-O} = -2 \times 13,019.3 - 28,822.9 = -2784.3$ kJ mol$^{-1}$. This is, as expected from basic chemical knowledge, a considerable value ($E_{Ti-O} \sim -1400$ kJ mol$^{-1}$), typical of ionocovalent bonding between titanium and oxygen. Consequently, if we were ideally allowed to cut anywhere in the crystal or in the molecules, not all cuts would have the same energetic costs. This means that we are perfectly able to discriminate with no prior chemical knowledge, between strong and weak bonds.

### 3.3.3. Hybrid Organic–Inorganic Calixarenes

We now turn our attention toward more sophisticated hybrid organic–inorganic building blocks specially designed for their ability to be used in sol–gel chemistry, molecular tectonics, or crystal engineering. Let us go back once more to our basic tetrameric species $[Ti_4(OR)_{16}]$ and try to modify its reactivity by keeping intact its molecular structure. This was readily done [87] by noticing that the ligand 2,6-bis(hydroxymethyl)-$p$-cresol (BHMPC) has the right geometry to perform a chemical recognition of one or two consecutive edges of a compact tetramer (Fig. 43a).
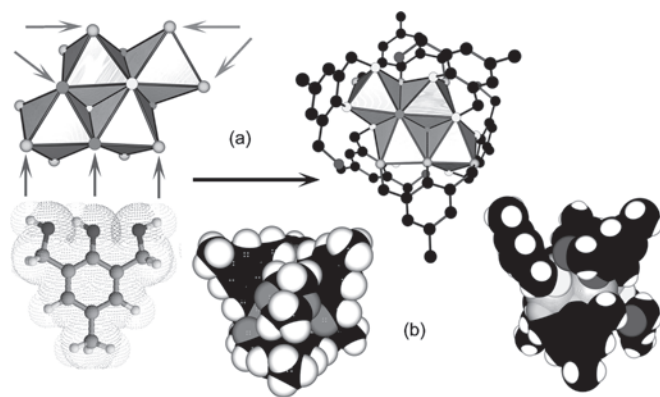
**Figure 43.** Molecular structures of the reaction products of $Ti(OR)_4$ with the tridentate ligand 2,6-bis(hydroxymethyl)-*p*-cresol ($H_3BHMPC$). (a) Molecular recognition between the trident and octahedral edges of $[Ti_4(OR)_{16}]$ tetramers. (b) Space-filling views of the divergent association of six phenyl rings around an inorganic $Ti_4O_2$ core (doubly fused calix[3] shape) displaying dioxane molecules trapped inside the two cavities.

Consequently, after reacting titanium(IV) alkoxides with BHMPC in a dioxane/ethanol mixture, an esthetic divergent association of six phenyl rings around an inorganic $Ti_4O_2$ core (doubly fused calix[3] shape) was obtained [87]. This very particular structure presents several interesting aspects. First, two dioxane molecules are found trapped inside the two divergent cavities (Fig. 43b). Second, an intramolecular system of four hydrogen bonds involving free arms of BHMPC molecules is found in this structure (Fig. 44). Third, dioxane and ethanol molecules are linked to the double calix by four intermolecular additional hydrogen bonds. Fourth, the tetramers are stacked in the solid state through van der Waals interactions, leading to a 1D network (Fig. 45). Last, the tetramer is stable toward hydrolysis, allowing its use as a building block in more complex hybrid networks.

Table 11 gives the electronic signature of this molecular crystal. As with previous tetramers, Ti atoms are found to bear a strong positive charge with negatively charged O atoms. Associated $pK_a$ values range from 17.1 for the $\mu_3$-oxo bridge to $-3.8$ for the free $CH_2OH$ arms of the BHMPC ligands. As expected, O atoms bridging two Ti atoms are found to be more basic ($pK_a = 9.0$ and 7.6) than O atoms bonded to one Ti atom ($pK_a = 2.6$–4.1). The least basic O atoms belong to dioxane ($pK_a \sim -6$) and ethanol ($pK_a \sim -4$) molecules. The stability of this hybrid tetramer toward
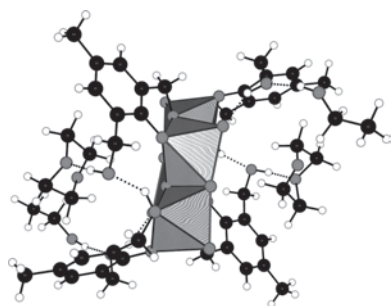


**Figure 44.** Intramolecular system of four hydrogen bonds involving free arms of BHMPC molecules.
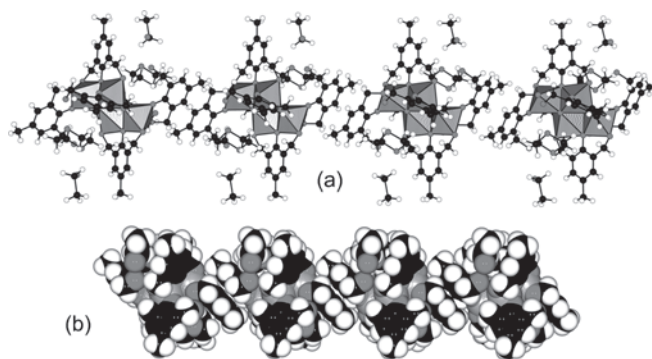


**Figure 45.** 1D van der Waals chain solvated by ethanol molecules based on $[Ti_4O_2(BHPMC)_2(HBHMPC)_2(H_2BHMPC)_2]$ tetramers. (a) Polyhedral view of the chain, including dioxane and ethanol molecules. (b) Space-filling view, showing the $\pi$-stacking between the aromatic groups.

hydrolysis may then be explained by the rather acid character of terminal Ti—O—C bonds that prevents the elimination of the BHMPC ligand after protonation of more basic $\mu_2$-O sites. The observed stability is also well in line with the rather high $\langle EN \rangle$ value (13.7 V) of the aromatic hybrid tetramer relative to the aliphatic ones (12.4–13.3 V). As a water molecule is characterized by $\langle EN \rangle = 14.7$ V, the electronegativity difference, and hence the reactivity, is strongly decreased in the case of the aromatic hybrid tetramer. Note that another increase in electronegativity ($\langle EN \rangle = 14.0$ V) is observed upon extraction of the aromatic hybrid tetramer from its network, meaning that the free tetramer should be still less reactive toward water.

It is also interesting to look at the global charge distributions. For the BHMPC ligands, we get $Q[Ph(Me)(O)(CH_2OH)_2] = -0.85$, $Q[Ph(Me)(O)(CH_2O)(CH_2OH)] = -1.17$, and $Q[Ph(Me)(O)(CH_2O)_2] = -1.58$, while for the two additional solvent molecules we get $Q(dioxane) = -0.20$ and $Q(EtOH) = +0.01$. Consequently, the dioxane molecules, which are more deeply encrusted inside the two divergent cavities, are logically more polarized than the ethanol molecules found in the outer positions. A comparison between the global charges found for the three deprotonated forms of the BHMPC ligands and the corresponding formal charges ($-1$, $-2$, and $-3$, respectively) shows the almost ionic character ($-0.85$ versus $-1$) of the bond between Ti atoms and the $Ph(Me)(O)(CH_2OH)_2$ ligand. The other ligands are more deeply involved with a transfer of almost one electron in the case of $Ph(Me)(O)(CH_2O)(CH_2OH)$ and one and a half electrons for the fully deprotonated form $Ph(Me)(O)(CH_2O)_2$.

For the quantification of molecular interactions in such a compound, one may identify several useful fragments: the free and empty double-calix shape $[Ti_4O_2(BHMPC)_6]$, which is characterized by $\langle EB_{cal} \rangle = -14{,}191.1$ kJ mol$^{-1}$; the free dioxane molecule, which has $\langle EB_{diox} \rangle = -70.9$ kJ mol$^{-1}$; and the free ethanol molecule with $\langle EB_{EtOH} \rangle = -110.9$ kJ mol$^{-1}$. Now, if we insert two dioxane molecules inside the two divergent cavities, we get a new chemical object $\{C_4H_8O_2 \subset [Ti_4O_2(BHMPC)_6]\}$ with $\langle EB_1 \rangle = -14{,}439.7$ kJ mol$^{-1}$. The total interaction energy is then estimated as $E_{tot}(C_4H_8O_2) = \langle EB_{cal} \rangle + 2 \times \langle EB_{diox} \rangle - \langle EB_1 \rangle = -106.8$ kJ mol$^{-1}$. Each

**Table 11.** Electronic PACHA signature for the molecular crystal containing $[Ti_4(\mu_3\text{-}O)_2\{Ph(\mu_2\text{-}O)(OCH_2)_2\}_2\{Ph(O)(\mu_2\text{-}OCH_2)(CH_2OH)\}_2\{Ph(O)(CH_2OH)_2\}_2]$ tetramers.

| Atom | Charge $q$ | Index $f$ | Atom | Charge $q$ | Index $f$ |
|---|---|---|---|---|---|
| O1 (Ti1, 2Ti2) | −0.871 | −0.004 | H3 (C7) | +0.040 | 0.011 |
| O5 (Ti1, Ti2, C10) | −0.666 | −0.000 | C1 (O2, C2, C6) | +0.040 | 0.011 |
| O10 (Ti2, C25, Ti1) | −0.630 | 0.000 | H88 (C32) | +0.040 | 0.014 |
| O2 (Ti1, C1) | −0.541 | 0.003 | H27 (C27) | +0.040 | 0.011 |
| O8 (Ti1, C19) | −0.541 | 0.004 | H76 (C28) | +0.040 | 0.013 |
| O3 (Ti1, C7, H89) | −0.518 | 0.002 | H10 (C10) | +0.041 | 0.011 |
| O9 (Ti2, C27) | −0.509 | 0.004 | C16 (C11, C15, O7) | +0.045 | 0.011 |
| O7 (Ti2, C16) | −0.504 | 0.004 | H82 (C30) | +0.045 | 0.014 |
| O6 (C18, H92) | −0.354 | 0.007 | H11 (C10) | +0.048 | 0.013 |
| O4 (C9, H91) | −0.343 | 0.008 | H85 (C33) | +0.052 | 0.013 |
| O13 (C33, H90) | −0.341 | 0.009 | H87 (C32) | +0.053 | 0.017 |
| O12 (C29, C30) | −0.285 | 0.008 | H86 (C32) | +0.054 | 0.016 |
| O11 (C28, C31) | −0.281 | 0.010 | H79 (C29) | +0.055 | 0.014 |
| C8 (C4) | −0.170 | −0.002 | H83 (C30) | +0.055 | 0.013 |
| C26 (C22) | −0.166 | −0.001 | H21 (C21) | +0.058 | 0.013 |
| C17 (C13) | −0.166 | −0.001 | H78 (C29) | +0.059 | 0.014 |
| C32 (C33) | −0.108 | 0.006 | H80 (C31) | +0.060 | 0.013 |
| C10 (O5, C11) | −0.074 | 0.003 | H13 (C14) | +0.061 | 0.013 |
| C7 (C2, O3) | −0.069 | 0.003 | H1 (C3) | +0.061 | 0.013 |
| C12 (C11, C13) | −0.066 | 0.008 | H20 (C19) | +0.062 | 0.014 |
| C14 (C13, C15) | −0.065 | 0.008 | H81 (C31) | +0.062 | 0.010 |
| C5 (C4, C6) | −0.065 | 0.008 | H22 (C23) | +0.064 | 0.013 |
| C21 (C20, C22) | −0.062 | 0.008 | H2 (C5) | +0.064 | 0.012 |
| C27 (C24, O9) | −0.060 | 0.003 | H16 (C17) | +0.065 | 0.015 |
| C3 (C2, C4) | −0.059 | 0.008 | H18 (C18) | +0.066 | 0.012 |
| C23 (C24, C22) | −0.057 | 0.008 | H15 (C17) | +0.066 | 0.015 |
| C19 (O8, C20) | −0.053 | 0.003 | H9 (C9) | +0.066 | 0.012 |
| C9 (C6, O4) | −0.040 | 0.004 | H6 (C8) | +0.066 | 0.016 |
| C18 (C15, O6) | −0.039 | 0.004 | H8 (C9) | +0.067 | 0.012 |
| C20 (C19, C21, C25) | −0.036 | 0.011 | H17 (C18) | +0.068 | 0.011 |
| C29 (C28, O12) | −0.032 | 0.007 | H25 (C26) | +0.068 | 0.014 |
| C11 (C10, C12, C16) | −0.031 | 0.011 | H23 (C26) | +0.069 | 0.016 |
| C2 (C1, C3, C7) | −0.027 | 0.011 | H12 (C12) | +0.070 | 0.013 |
| C24 (C23, C25, C27) | −0.023 | 0.012 | H14 (C17) | +0.070 | 0.014 |
| C33 (C32, O13) | −0.019 | 0.008 | H7 (C8) | +0.074 | 0.014 |
| C31 (O11, C30) | −0.013 | 0.006 | H5 (C8) | +0.074 | 0.016 |
| C6 (C1, C5, C9) | −0.012 | 0.012 | H26 (C27) | +0.074 | 0.013 |
| C15 (C14, C16, C18) | −0.011 | 0.012 | H4 (C7) | +0.075 | 0.012 |
| C13 (C12, C14, C17) | −0.011 | 0.013 | H84 (C33) | +0.078 | 0.014 |
| C4 (C3, C5, C8) | −0.010 | 0.012 | H24 (C26) | +0.078 | 0.015 |
| C30 (O12, C31) | −0.009 | 0.006 | H91 (O4) | +0.187 | 0.011 |
| C22 (C21, C26, C23) | −0.005 | 0.014 | H89 (O3) | +0.192 | 0.010 |
| C25 (C24, O10, C20) | +0.018 | 0.010 | H90 (O13) | +0.205 | 0.013 |
| H77 (C28) | +0.020 | 0.010 | H92 (O6) | +0.220 | 0.012 |
| C28 (O11, C29) | +0.021 | 0.006 | Ti2 | +2.171 | 0.058 |
| H19 (C19) | +0.030 | 0.012 | Ti1 | +2.485 | 0.067 |

*Note:* Global parameters were $\langle EN \rangle = 13.70$ V, $\langle GH \rangle = 2.4$ eV, $\langle EB \rangle = -14{,}732.0$ kJ mol$^{-1}$, and $\langle GI \rangle = 24.7\%$. The symbol in parentheses refers to the immediate neighborhood.

dioxane molecule being hydrogen bonded to the hydroxy moiety of a Ph(Me)(O)(CH$_2$O)(CH$_2$OH) ligand (d$_{O6\cdots O12} = 271$ pm), we get for each molecule (H bond plus van der Waals interactions) $E_{int}(C_4H_8O_2) = -53.4$ kJ mol$^{-1}$. This is a strong value showing that this molecule should remain inside the cavity even after dissolution of the crystal, in agreement with $^1$H-NMR measurement [87]. For the other H-bonded molecule $\{C_2H_5OH \subset [Ti_4O_2(BHMPC)_6]\}$, we get $\langle EB_2 \rangle = -14{,}455.4$ kJ mol$^{-1}$, leading to $E_{tot}(C_2H_5OH) = \langle EB_{cal} \rangle + 2 \times \langle EB_{EtOH} \rangle - \langle EB_2 \rangle = -42.5$ kJ mol$^{-1}$. Here each ethanol molecule

is hydrogen bonded to one of the two OH moieties of Ph(Me)(O)(CH$_2$OH)$_2$ ligands (d$_{O4\cdots O13} = 292$ pm). The interaction energy (H bond plus van der Waals) is thus much lower than before, $E_{int}(C_2H_5OH) = -21.3$ kJ mol$^{-1}$, in good agreement with the longer H-bond length observed. But one may also compare the $\langle EB \rangle$ values of the two inclusion complexes $\{C_4H_8O_2 \subset [Ti_4O_2(BHMPC)_6]\}$ and $\{C_2H_5OH \subset [Ti_4O_2(BHMPC)_6]\}$ to that of a fully filled free tetramer $\{(C_4H_8O_2, C_2H_5OH) \subset [Ti_4O_2(BHMPC)_6]\}$ characterized by $\langle EB_{full} \rangle = -14{,}718.5$ kJ mol$^{-1}$. Now, we get $E_{int}(C_4H_8O_2) = (\langle EB_2 \rangle + 2 \times \langle EB_{diox} \rangle - \langle EB_{full} \rangle)/2 =$

−60.7 kJ mol$^{-1}$ and $E_{int}(C_2H_5OH) = (\langle EB_1 \rangle + 2 \times \langle EB_{EtOH} \rangle - \langle EB_{full} \rangle)/2 = -28.5$ kJ mol$^{-1}$. The common difference observed between the two interactions energies (7.2 kJ mol$^{-1}$) should then correspond to the mutual polarization existing between ethanol and dioxane molecules within the cavities.

For the four intramolecular H bonds existing in the empty double-calix shape, we can no longer use the above approach. Instead, we may rotate the OH bridges and plot how the hydrogen-bond energy changes with the rotation angle. Figure 46a displays the H-bond energy profile for the uncoordinated CH$_2$OH arm of the HBHMPC involved in intermolecular H bonding with the dioxane molecule ($d_{OH}$ = 169 pm, $d_{OO}$ = 271 pm). As the dioxane molecules have been removed for the computation, the rather flat minimum of about 80 kJ mol$^{-1}$ observed between 100 and 200° may be attributed to the electrostatic interaction with the neighboring phenolic Ti-bonded O atom ($d_{OO}$ = 299 pm). Such a large value is coherent with the possible formation of a six-membered ring. This is what should be expected for a ligand in a free state, that is, not bonded to a Ti atom and not already engaged in a strong H bond with a dioxane molecule. Figure 46b shows the very different H-bond energy profile obtained for the uncoordinated CH$_2$OH arm of a H$_2$BHMPC ligand. Recall that this arm forms an intermolecular acceptor H bond ($d_{OH}$ = 197 pm, $d_{OO}$ = 292 pm) with an ethanol molecule and an intramolecular donor H bond ($d_{OH}$ = 192 pm, $d_{OO}$ = 277 pm) inside the cavity. Two favorable positions are clearly evidenced, the deepest and sharpest one corresponding to the interaction shown as a dotted line and involving one of the two coordinated CH$_2$O–Ti arms of a fully deprotonated BHMPC



**Figure 46.** Quantification of intramolecular H-bond energies in the molecular structure of [Ti$_4$O$_2$(BHPMC)$_2$(HBHMPC)$_2$(H$_2$BHMPC)$_2$]. Each H atom was rotated independently along its C—O axis. (a) Variation of the outer H atom of the uncoordinated CH$_2$OH arm of a HBHMPC ligand not involved in the intramolecular H-bond pattern. (b) Variation of the uncoordinated CH$_2$OH arm of a H$_2$BHMPC ligand involved in the longest H···O interaction ($d_{OH}$ = 192 pm). (c) Variation of the other coordinated CH$_2$OH arm of a H$_2$BHMPC ligand involved in the shortest H···O interaction ($d_{OH}$ = 169 pm).

ligand. The corresponding minimum (about −20 kJ mol$^{-1}$) is well in line with what could be found in ice polymorphs displaying very similar O···O distances [90]. In contrast, the other less favorable minimum (about −10 kJ mol$^{-1}$) appears rather flat and has exactly the same origin as that shown in Figure 46a. It occurs owing to the electrostatic interaction with the neighboring phenolic Ti-bonded O atom ($d_{OO}$ = 336 pm) found within the same ligand. The interesting point is the drastic reduction in energy observed when the O···O distance is increased from 299 pm (Fig. 46a) to 336 pm (Fig. 46c). The last curve is obtained by rotating the OH group that belongs to the other Ti-bonded CH$_2$OH arm of the same H$_2$BHMPC ligand. Here a single very deep and steep minimum (about −120 kJ mol$^{-1}$) is evidenced. The origin of the rather large H-bond energy obviously lies in the very short O···O distance ($d_{OO}$ = 252 pm, $d_{OH}$ = 170 pm) existing between this arm and the uncoordinated CH$_2$OH arm of a HBHMPC ligand.

This nice example of a full *ab initio* quantification of all molecular and crystalline interactions in a quite complex hybrid organic–inorganic building block demonstrates the current capabilities of the PACHA model [(4)–(8)] in this field. However, owing to its very recent achievement and publication [87–90] during the writing of this chapter, it was not materially possible to review here all the calculations already done with this model.

## 3.4. Coordination Chemistry of Ti$^{IV}$ with O, N Donors

In this section, we will present a comprehensive overview of molecular complexes related to the synthesis of hybrid organic–inorganic materials without applying our full molecular tectonics approach. This section is thus devoted to a comprehensive description of all Ti$^{IV}$ complexes involving monodentate and/or multidentate ligands that have been characterized by X-ray diffraction for sol–gel, homogeneous catalytic, or supramolecular purposes. To keep this review to a reasonable length, complexes involving Ti—Cl or Ti—C bonds have been discarded.

### 3.4.1. Complexes Involving Monodentate Ligands

Nonhydrolyzed titanium alkoxides have been first used as catalysts in the Meerwein–Ponndorf–Verley–Oppenauer oxidation–reduction involving carbonyl compounds [292]:

$$R'C(O)R'' + Ti(OR)_4 \leftrightharpoons R'R''C=O$$
$$\rightarrow Ti(OR)_4 \leftrightharpoons R'R''CHO—Ti(OR)_3 + R—C(O)—R$$

The first addition step seems to be most favorable when R = Pr$^i$ owing to the monomeric nature of Ti(OPr$^i$)$_4$ and the high affinity of Ti$^{IV}$ for the fivefold coordination. Moreover, the formation of a six-membered ring in the transition state is a stabilizing factor favoring the reaction (Fig. 47) [293]. As far as homogeneous catalysis is concerned, the main point is to avoid the formation of Ti—O—Ti bonds, which generally results in some loss of catalytic activity. Moreover, knowledge of the molecular structure of the catalyst is of

**Figure 47.** Six-membered ring formation in the transition state for oxidation–reduction of carbonyl and alcohol compounds in the presence of titanium(IV) alkoxides.

the utmost importance for inferring the underlying molecular mechanisms responsible for the catalytic activity. In this respect, titanium isopropoxide is not a good candidate, as its crystalline molecular structure remains unknown.

This fact has led to the research of highly soluble homoleptic titanium alkoxide complexes and to the characterization of the highly soluble and volatile dimer $[Ti(OCH_2CMe_3)_4]_2$ (Fig. 48a) after alcoholysis exchange between $Ti(OPr^i)_4$ and neopentylic alcohol HONp [294]. Briefly stated, the electronic signature of this compound is $\langle EN \rangle = 13.3$ V, $\langle GI \rangle = 1.6$ eV, $\langle GI \rangle = 16.5\%$, $\langle EB \rangle = -7948.1$ kJ mol$^{-1}$, $q(Ti) = 2.527 \pm 0.006$, $Q(\mu_2\text{-ONp}) = -0.79$ (p$K_a = 9.4$), and $\langle Q(ONp) \rangle = -0.58 \pm 0.03$ ($4.9 <$ p$K_a < 5.7$). As the detailed crystalline molecular structures of $Ti(OEt)_4$, $Ti(OPr^n)_4$, $Ti(OPr^i)_4$, $Ti(OBu^n)_4$, $Ti(OBu^s)_4$, and $Ti(OBu^t)_4$ are still not available, our unique reference should be the values found previously for $Ti(OMe)_4$
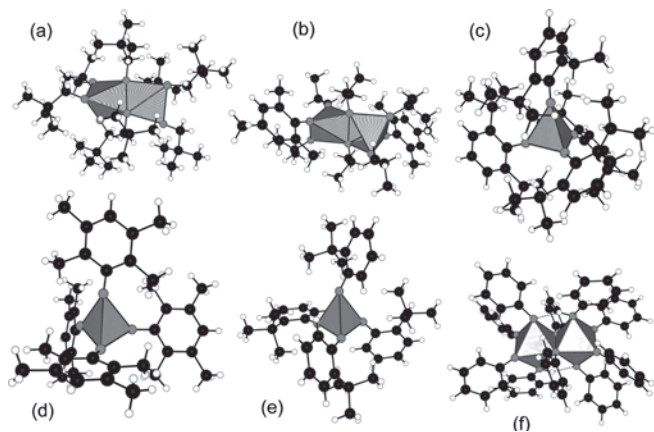


**Figure 48.** Molecular structures of some homoleptic titanium(IV) alkoxides and aryloxides. (a) Edge sharing between two distorted trigonal bipyramids in bis($\mu_2$-neopentoxo)-hexakis(neopentoxy)- di-titanium. (b) Edge sharing between two distorted trigonal bipyramids in bis[($\mu_2$-isopropoxo)-bis(isopropoxy)-(2,4,6-trimethylphenolato)-titanium(IV)]. (c) Single tetrahedron in the crystal structure of tetrakis(2,6-di-isopropylphenolato)-titanium(IV). (d) Single tetrahedron in the crystal structure of tetrakis(2,3,5,6-tetramethylphenoxy)-titanium(IV). (e) Single tetrahedron in the crystal structure of tetrakis(2-tert-butylphenoxy)-titanium(IV). (f) Edge-sharing octahedral dimer in the crystal structure of sym-trans-di-$\mu$-phenoxy-hexaphenoxy-diphenol-di- titanium(IV). The dotted lines show the intramolecular H bond between axial phenol molecules and axial phenoxy ligands.

(Table 4). The dramatic decrease in global ionicity and the much reduced HOMO–LUMO gap are coherent with the high volatility and lower stability of $Ti(ONp)_4$ relative to $Ti(OMe)_4$. Even if the $\mu_2$-ONp groups display a reduced basicity, the fivefold coordination for Ti$^{IV}$ (strongly distorted trigonal bipyramid), leading to a more electrophilic Ti atom, points to a high reactivity toward water. Finally, it is noteworthy that the $^{47,49}$Ti-NMR spectra in solution are virtually indistinguishable from those of $Ti(OPr^i)_4$, while no signals were detected in the solid state [294]. This is strong evidence of a reduction in coordination number from TBP-5 to T-4 (strongly reduced electric field gradients under tetrahedral symmetry) upon dissolution. Moreover, it was not possible even with an excess of alcohol to adopt an octahedral geometry as in the crystal structure of $[Ti(OC_6H_5)_4 \cdot HOC_6H_5]_2$ (Fig. 48f) [295]. For such a compound, it was found that $\langle EN \rangle = 13.8$ V, $\langle GI \rangle = 3.8$ eV, $\langle GI \rangle = 27.8\%$, $\langle EB \rangle = -4406.5$ kJ mol$^{-1}$, $q(Ti) = 2.723$, $Q(\mu_2\text{-OPh}) = -0.74$ (p$K_a = 9.3$), $\langle Q(OPh) \rangle = -0.55 \pm 0.03$ ($4.6 <$ p$K_a < 5.7$), and $Q(PhOH) \rangle = -0.35$ (p$K_a = 2.6$). One may notice the very large increase in $q(Ti)$ relative to the saturated compounds and the very similar basicity of $\mu_2$-OPh groups and $\mu_2$-OMe groups. By providing some steric crowding on the phenyl ring, a dimer compound $[Ti_2(\mu\text{-OPr}^i)_2(OPr^i)_4(TMP)_2]$ was obtained by reacting $Ti(OPr^i)_4$ with 2,4,6-trimethylphenol (TMP) in THF (Fig. 48b) [296]. Here again, Ti atoms are found in a distorted fivefold coordination with the following electronic signature: $\langle EN \rangle = 13.5$ V, $\langle GI \rangle = 1.6$ eV, $\langle GI \rangle = 18.9\%$, $\langle EB \rangle = -4010.2$ kJ mol$^{-1}$, $q(Ti) = 2.569$, $Q(\mu_2\text{-OPr}^i) = -0.77$ (p$K_a = 10.0$), $\langle Q(OPr^i) \rangle = -0.56 \pm 0.02$ (p$K_a = 5.6$), and $Q(OPh) = -0.68$ (p$K_a = 5.3$). One may notice the ability of the phenoxy group to draw electronic density from the terminal isopropoxy groups while keeping rather low basicity on the O atom. As before, one also observes a strong decrease in global ionicity on going from sixfold to fivefold coordination. Changing the methyl groups in the 2,6-positions to isopropoxy groups (DIPP = 2,6-di-isopropylphenoxy ligand) puts enough pressure on the Ti atom to force it to adopt a tetrahedral coordination as in $Ti(DIPP)_4$ (Fig. 48c) [297]. For this kind of molecular structure, the electronic signature was found to be $\langle EN \rangle = 13.7$ V, $\langle GI \rangle = 2.5$ eV, $\langle GI \rangle = 15.5\%$, $\langle EB \rangle = -4341.9$ kJ mol$^{-1}$, $q(Ti) = 2.718$, and $\langle Q(OPr^i) \rangle = -0.68 \pm 0.03$ (p$K_a = 6.5$). As expected, even if the Ti atom becomes very electrophilic, the global ionicity is nevertheless very low, owing to the dominant contributions of the phenyl rings bearing strong electron-donating isopropoxy groups. The same reduction in coordination number is observed with the TEMP ligand (TEMP = 2,3,5,6-tetramethylphenoxy) in the complex $Ti(TEMP)_4$ (Fig. 48d) [298]. An electronic signature very similar to the previous one was found for this tetrahedral molecule: $\langle EN \rangle = 13.6$ V, $\langle GI \rangle = 1.9$ eV, $\langle GI \rangle = 15.5\%$, $\langle EB \rangle = -4637.0$ kJ mol$^{-1}$, $q(Ti) = 2.726$, and $\langle Q(OPr^i) \rangle = -0.68 \pm 0.02$ ($6.4 <$ p$K_a 7.1$). A last tetra-coordinated species $[Ti(TBP)_4]$ (Fig. 48e) was identified using the TBP ligand (TBP = 2-tert-butylphenoxy) [296]. This complex is characterized by the following electronic signature: $\langle EN \rangle = 13.6$ V, $\langle GI \rangle = 1.4$ eV, $\langle GI \rangle = 16.5\%$, $\langle EB \rangle = -4485.5$ kJ mol$^{-1}$, $q(Ti) = 2.703$, and $\langle Q(OPr^i) \rangle = -0.68$ (p$K_a = 6.6$).

Consequently, and as expected, all these tetrahedral species are highly covalent molecules displaying a well-defined geometry from which catalytic activity may be modeled under the best conditions, particularly in the field of polymerization of ethylene through Ziegler–Natta catalysis [297–299]. They also have been used to study the origin of strong metal-support interactions (SMSIs) in heterogeneous catalyst systems [298]. Bulky aryloxy ligands such as 2,6-di-isopropylphenoxo (DIPP) have also proven to be very useful for the isolation and characterization of interesting oxo and imido complexes (Fig. 49). For example, after selective hydrolysis of the imine compound $Ti(DIPP)_2[\eta^2\text{-}t\text{-}BuNC(CH_2Ph)_2](py)$ [300] in the presence of 4-pyrrolidinopyridine (4PDP), one may obtain a mononuclear aryl oxide complex $[TiO(DIPP)_2(4PDP)_2]$ solvated by one benzene molecule and containing a rare terminal oxo group characterized by $d_{TiO} = 165.7(6)$ pm [301] (Fig. 49a). Its electronic signature was found to be $Ti^{+2.58}O^{-0.64}(DIPP)_2^{-0.55}(4PDP)^{-0.40}(C_6H_6)^{-0.03}$ with $\langle EN \rangle =$ 13.8 V, $e^2\langle GH \rangle = 4.1$ eV, $\langle GI \rangle = 15.6\%$, and $\langle EB \rangle = -3956.6$ kJ mol$^{-1}$. One may notice that by considering the entity [TiO] as a whole we get $Q(TiO) = +1.94$, a value very close to the formal charge for a titanyl $TiO^{2+}$ ion. Interestingly enough, performing the same hydrolysis reaction with $Ti(DIPP)_2[\eta^2\text{-}t\text{-}BuNC\text{-}(CH_2Ph)_2](4PDP)$ leads to the bridged oxygen dimer $[Ti(\mu\text{-}O)(DIPP)_2(4PDP)_2]_2$ (Fig. 49b) [302]. If one uses aniline instead of water, the result is a terminal phenylimido complex $[Ti(DIPP)_2(4PDP)_2(=N-Ph)]$ (Fig. 49c) with a very short Ti—N bond [165.8(1) pm] relative to a similar bis(phenylamido) complex $[Ti(DIPP)_2 \cdot (NHPh)_2]$ (Fig. 49d) characterized by $d_{TiN} = 188$–189 pm [303, 304]. Such $Ti(DPP)_2$ templates have proven to be use-

ful for catalytic C—C coupling reactions as they may be considered as $Cp_2Ti$ analogs with a predetermined steric pressure.

It is noteworthy that from a sol–gel viewpoint the molecules displayed in Figure 48 are still reactive toward hydrolysis, owing to their high Ti charge or to the occurrence of OR groups that are basic enough (more particularly the bridging ones). This is an interesting feature of such compounds. When the Ti coordination number is equal to four, all OR groups are found in the terminal position. Consequently, they should display their maximum resistance to proton addition. However, the Ti atom is rather depleted in electronic density and thus highly prone to nucleophilic attack by the O atoms of water molecules. Increasing the coordination number up to five reduces the titanium charge, but highly basic OR bridges should then be formed, rendering them highly prone to proton addition by water molecules. The worst case is encountered with titanium tetraphenoxide displaying both basic OPh bridges and highly nucleophilic Ti atoms. Consequently, switching to aryloxides instead of alkoxides is not a good strategy in order to get $Ti^{IV}$ complexes that are stable enough toward the hydrolysis reaction. A very well known and pretty old strategy to increase the hydrolytic stability of titanium(IV) alkoxides was to switch to chelating or multidentate ligands [305]. Numerous possibilities are possible, which, to the best of our current knowledge, have never been extensively reviewed.

### 3.4.2. Complexes Involving Bidendate Ligands

***Sevenfold and Eightfold Coordination*** The most simple carbon-based bidentate ligand is obviously the carbonate ion $[CO_3]^{2-}$. As relatively few carbonato complexes of high-valence metals are currently known, it was fortuitous that, upon mixing $TiCl_4$ with guanidinium carbonate, it was possible to isolate a tris(carbonato) titanyl complex [306]. This complex $[TiO(CO_3)_3]^{4-}$ is characterized by a Ti atom in sevenfold coordination (pentagonal bipyramid) with a very short $[d_{TiO} = 168.0(2)$ pm] Ti—O axial bond (Fig. 50a). The electronic signature of this complex was $[C(NH_2)_3]_2^{+0.21}[C(NH_2)_3]^{+0.26}[C(NH_2)_3]^{+0.33}[Ti^{+2.81}O^{-0.65}(CO_3)_3^{-1.06}]$ $(H_2O)^{-0.02}(H_2O)^{+0.04}$ with $\langle EN \rangle = 14.4$ V, $\langle GH \rangle = 2.7$ eV, $\langle GI \rangle = 16.7\%$, and $\langle EB \rangle = -6826.5$ kJ mol$^{-1}$. Consequently, despite the sevenfold coordination for the Ti atom, the charge on the terminal oxo group does not differ very much from that found for the fivefold coordinated complex $[TiO(DIPP)_2(4PDP)_2]$. At a local scale, the $pK_a$ values of the O atoms are found to be 8.2 (oxo group), 1.6 (short Ti—O—$CO_2$), 0.5 (long Ti—O—$CO_2$), $-0.8$ ($H_2O$), and $-5.5$ (C=O end). The considerable decrease in $pK_a$ values in going from the free state ($pK_a = 10.3$ for $HCO_3^-/CO_3^{2-}$) to the complex points to the stability of this species under neutral or moderate acid conditions. Note also that by considering the entity [TiO] as a whole we get $Q(TiO) = +2.2$, a value rather close to the formal charge for a titanyl $TiO^{2+}$ ion.

Higher coordination numbers for $Ti^{IV}$ (bidisphenoid or triangular dodecahedron) are also attained in the case of hydroxylamides such as $Ti(ONMe_2)_4$ (Fig. 50b) [307] or $Ti(ONEt_2)_4$ (Fig. 50c) [308]. The network electronic signature for the methyl derivative is $[Ti^{+2.74}(ONMe_2)_2^{-0.65}$
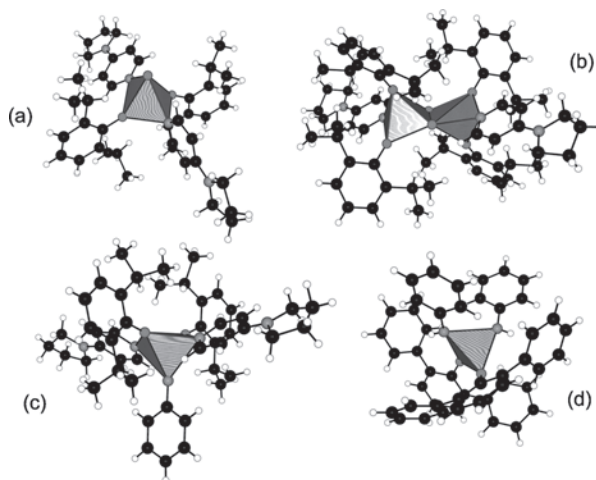


**Figure 49.** Coordination chemistry of the $Ti(DIPP)_2$ fragment (DIPP = 2,6-di-isopropylphenolato) with monodentate ligands. (a) Square pyramidal aryl oxide complex in the crystal structure of bis(2,6-di-isopropylphenoxy-$O$)-oxo-bis(4-pyrrolidinopyridine)-titanium(IV) benzene solvate. (b) Dimeric polymerization isomer of (a) in the crystal structure of bis($\mu_2$-oxo)-bis[bis(2,6-di-isopropylphenolato-$O$)-(4-pyrrolidinylpyridine-$N$)-titanium(IV)]. (c) Phenylimido analog of (a) in the crystal structure of bis(2,6-di-isopropylphenolato)-(phenylimido)-bis(4-pyrrolidinopyridine)-titanium. (d) Bis(phenylamido) analog of (c) in the crystal structure of bis(2,6-di-isopropylphenolato)-(phenylimido)-bis(4-pyrrolidinopyridine)-titanium.
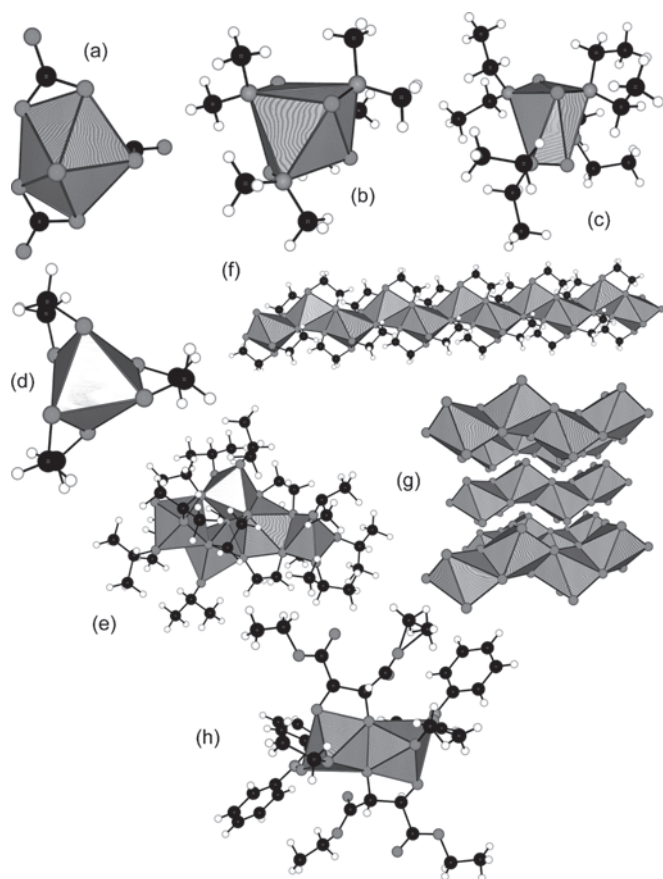
**Figure 50.** Complexation of Ti$^{IV}$ centers by simple bidentate ligands. (a) Pentagonal bipyramidal coordination of Ti$^{IV}$ atoms in the molecular structure of tetraguanidinium tris(carbonato-$O,O'$)-oxo-titanium(IV) dihydrate. (b) Bidisphenoid in the molecular structure of tetrakis($N,N$-dimethylhydroxylamido-$O$, $N$)-titanium(IV). (c) Bidisphenoid in the molecular structure of tetrakis($N,N$-diethylhydroxylamido-$O$, $N$)-titanium(IV) [Ti(ONEt$_2$)$_4$]. (d) Single octahedron in the crystal structures of aqueous tris(glycolate) complexes such as sodium or potassium tris(ethylene glycolato-$O,O'$)-titanium(IV) ethylene glycol solvate, [Na(C$_2$H$_6$O$_2$)$_2$]$_2$ · [Ti(C$_2$H$_4$O$_2$)$_3$] or [K(C$_2$H$_6$O$_2$)$_2$][K(C$_2$H$_6$O$_2$)$_3$][Ti(C$_2$H$_4$O$_2$)$_3$]$_2$, and aqua-tetrakis(ethylene glycol)-barium tris (ethylene glycolato)-titanium(IV) [(H$_2$O)Ba(C$_2$H$_6$O$_2$)$_4$][Ti(C$_2$H$_4$O$_2$)$_3$]. (e) Fivefold, sixfold, and sevenfold coordinated Ti atoms in the molecular structure of ($\mu_2$-ethanediolato)-($\mu_4$-ethanediolato)-tris($\mu_3$-ethanediolato)-($\mu_2$-isopropoxo)-nonakis(isopropoxy)-penta-titanium [Ti$_5$(OPr$^i$)$_{10}$ · (OC$_2$H$_4$O)$_5$]. (f) Crystal structure of *catena*-(bis($\mu_2$-ethylene glycolato-$O,O,O'$)-titanium) [Ti(O$_2$C$_2$H$_4$)$_2$] displaying chain of edge-sharing TiO$_6$ octahedra with mixed ($\eta_1$, $\mu_2$)-bridging coordination mode for the glycolato ligands. (g) van der Waals stacking of the chains displayed in (f) and characterized by $E_{vdw}$ = −16.8 kJ mol$^{-1}$. (h) Dimeric octahedral coordination with ($\mu$, $\eta^2$) diolate bridges in the crystal structure of bis{($\mu_2$-diethyl-tartrato-$O,O'$)-ethoxy-(diphenylhydroxamato-$O,O'$)-titanium(IV)}.

(ONMe$_2$)$_2^{-0.72}$] with ⟨EN⟩ = 13.5 V, ⟨GH⟩ = 2.3 eV, ⟨GI⟩ = 25.0%, and ⟨EB⟩ = −3915.4 kJ mol$^{-1}$. By comparing this last ⟨EB⟩ value with that of a free molecule (⟨EB⟩ = −3911.2 kJ mol$^{-1}$), one may anticipate a very low lattice energy (−4.2 kJ mol$^{-1}$) well in line with the high volatility of these compounds [307]. Consequently, these complexes

are attractive molecular precursors for a wide range of oxide materials synthesized through the MOCVD technique.

***Ethylene Glycol Derivatives*** Another quite simple bidentate ligand may be derived from ethylene glycol (HOCH$_2$–CH$_2$OH; EG). The remarkable feature of this molecule lies in its ability to dissolve hydrous titanium oxide or even anatase or rutile crystals [309]. Figure 50d shows that the complex responsible for this solubility is a tris(chelate) [Ti(OCH$_2$CH$_2$O)$_3$]$^{2-}$ entity. Such complexes have been characterized in the solid state with Na$^+$, K$^+$ [309], and Ba$^{2+}$ [259] as countercations. It was thus interesting to see if such stabilization of Ti$^{IV}$ centers in aqueous solutions could be understood in terms of charge distributions. Applying our PACHA model to the sodium compound leads to [Na$^{(+1.0)}$(C$_2$H$_6$O$_2$)$_2^{(-0.28)}$] [Na$^{(+1.0)}$(C$_2$H$_6$O$_2$)$_2^{(-0.32)}$][Ti$^{(+2.61)}$ {(C$_2$H$_4$O$_2$)$^{(-1.13)}$}$_3$] (3.3 < p$K_a$ < 5.8) with ⟨EN⟩ = 13.0 V, ⟨GH⟩ = 3.3 eV, ⟨GI⟩ = 31.8%, and ⟨EB⟩ = −15,988.6 kJ mol$^{-1}$. Obviously, the rather high ionicity is linked to the occurrence of mineral countercations. The interesting point lies in the quite low basicity (⟨p$K_a$⟩ = 4.6) found for a doubly negative species [Ti(O$_2$C$_2$H$_4$)$_3$]$^{2-}$. This rather low value associated with the well-known entropic chelate effect ensures these tris(glycolate) complexes sufficient stability under weakly acid or neutral conditions.

It has, however, long been known [310] that the coordination mode of the ethylene glycolato ligand could be much more complex than just $\eta^2$. For example, by mixing titanium alkoxides with ethylene glycol in a 1:2 ratio, it was possible to obtain a titanium bis(glycolate) [Ti(O$_2$C$_2$H$_4$)$_2$] compound completely insoluble in benzene and other common organic solvents [311]. Fortunately, during an investigation of the reaction between 2-hydroxy-ethylmethacrylate [HOC$_2$H$_4$OC(O)CMe=CH$_2$] and titanium isopropoxide, a cleavage of the ester bond was observed, leading to a pentanuclear complex [Ti$_5$(OPr$^i$)$_{10}$(OC$_2$H$_4$O)$_5$] with five-, six-, and sevenfold coordinated Ti atoms (Fig. 50e) [312]. Moreover, in this compound no more than three different kinds of coordination modes for the ethylene glycolate ligand were observed: ($\mu$,$\eta^2$-OC$_2$H$_4$O), ($\mu_3$,$\eta^2$-OC$_2$H$_4$O), and ($\mu_4$,$\eta^2$-OC$_2$H$_4$O). This sheds some light on the reticular chemistry possible with such a versatile ligand. Concerning the bis(glycolate) compound, it was possible to get single crystals when a mixture of Ti(OEt)$_4$, *n*-butylamine, and ethylene glycol was autoclaved at 160–180 °C for 5 days [313]. The resulting structure may be described as parallel chains built up from edge-sharing TiO$_6$ octahedra (Fig. 50f). The topology of this chain may be written as Ti($\mu_2$-OCH$_2$CH$_2$O)$_{4×1/2}$ with the following charge distribution: Ti$^{+2.50}$(O$_2$C$_2$H$_4$)$_2^{-1.25}$ and ⟨EN⟩ = 11.9 V, ⟨GH⟩ = 7.0 eV, ⟨GI⟩ = 38.6%, and ⟨EB⟩ = −3720.0 kJ mol$^{-1}$. At a local scale, one finds p$K_a$ values typical of neutral metal alkoxides p$K_a$($\mu_2$-Ti) = 9.5 and p$K_a$($\eta_1$-Ti) = 4.2. The van der Waals stacking interaction between these chains (Fig. 50g) is found to be quite strong −16.8 kJ mol$^{-1}$ (same order of magnitude as hydrogen bond), explaining the low solubility of this compound. This kind of ($\mu$,$\eta^2$) coordination for a diol group was also identified in a tartrate complex [Ti(OEt){$\mu_2$-OCH(COOEt)–CH(COOEt)O}{PhC(O)N(Ph)O}]$_2$ obtained after reacting

Ti(OEt)$_4$ with ($R$,$R$)-diethyltartrate and PhC(O)N(OH)Ph in dichloromethane (Fig. 50h) [314]. Such chiral transition metal complexes are commonly used in the enantioselective synthesis of organic compounds and more particularly in the asymmetric epoxidation of allylic alcohols by alkylperoxides [315].

***Derivatives Involving Amino Ligands*** The chelating $\eta^2$ coordination mode of diols toward Ti$^{IV}$ centers has very recently been used to synthesize unsymmetrical vicinal diols, R$_1$R$_2$C(OH)–C(OH)R$_3$R$_4$, or unsymmetrical carbonyl compounds, R$_1$COR$_2$, from carbon monoxide CO and titanium aminotroponiminate (ATI) alkyl complexes [Ti(Me$_2$ATI)$_2$R$_3$R$_4$] [316, 317]. As shown in Figure 51a, using benzaldehyde (R$_1$ = Ph, R$_2$ = H) and [Ti(Me)$_2$(Me$_2$ATI)$_2$], it was possible to form the [Ti(PhHCOCOCMe$_2$)(Me$_2$ATI)$_2$] complex, leading, after hydrolysis, to the unsymmetrical diol HPhC(OH) C(OH)Me$_2$. Similarly (Fig. 51b), starting from acetone (R$_1$ = R$_2$ = Me) and [Ti(Ph)$_2$(Me$_2$ATI)$_2$], the complex [Ti(Ph$_2$COCOCMe$_2$)(Me$_2$ATI)$_2$], precursor of the Ph$_2$C(OH)C(OH)Me$_2$ diol, was obtained. If isocyanides R—NC are used instead of carbon monoxide, $\eta^2$-imine complexes may first be obtained, leading, after treatment with a carbonyl compound R$_1$COR$_2$ and elimination of the Me$_2$C=N—R imine, to titanium diolate complexes such as [Ti(HPhCOCOPhH)(Me$_2$ATI)$_2$] (*anti*-pinacol coupling between two benzaldehyde molecules; Fig. 51c). Similar couplings between benzophenone Ph$_2$C=O and N-tosylbenzaldimine PhHC=N-(SO$_2$tol) or between thiobenzophenone Ph$_2$C=S and acetone Me$_2$C=O leads to diolates [Ti{Ph$_2$COCN(SO$_2$tol)PhH}(Me$_2$ATI)$_2$] (Fig. 51d) and [Ti(Ph$_2$CSCOMe$_2$)(Me$_2$ATI)$_2$] (Fig. 51e), respectively.

Amino alcohols are also known to coordinate to Ti$^{IV}$ centers with a chelating $\eta^2$ mode, while chiral Ti$^{IV}$–amino alcohols are known to stereo-specifically catalyze the Diels–Alder reaction, the kinetic resolution of epoxy alcohols, and the alkylation of aldehydes [318]. Such complexes have been recently characterized in the solid state and were obtained via ligand exchange/methathesis of titanium isopropoxide with chiral N-substituted amino alcohols derived from (1$S$, 2$R$)-(+)2-amino-1,2-diphenylethanol Tf—NH—C(Ph)—C(Ph)(OH) (Tf = SO$_2$CF$_3$) [318]. Figure 51f shows the trigonal bipyramidal coordination of Ti atoms by the chiral amino alcohol and the ligand DMAP = ($N$,$N$-dimethyl-4-aminopyridine) in the complex Ti(OPr$^i$)$_2${Tf—NCH(Ph)CH(Ph)O}(DMAP)]. This DMAP complex was found to be in equilibrium with a dimeric form [Ti(OPr$^i$)$_2${Tf—NCH(Ph)CH(Ph)O}]$_2$ (Fig. 51h) with a preference for a bridge involving the amino alcohol O atoms rather than the OPr$^i$ ligands.

***Pyridine Alkoxides and Aryloxides*** Bidentate pyridine-alkoxide ligands have also been studied in relation to the ability of [Ti(pyCAr$_2$O)$_2$(NMe$_2$)$_2$] complexes to act as catalysts for the polymerization of ethylene and, in some cases, of $\alpha$-olefins [319]. Figure 52a and b shows the $C_2$-symmetric structure adopted by these complexes with ligands 9-(2-pyridyl)-9-fluorenolato and 2-pyridyl[bis(4-diethylaminophenyl)]methanolato, respectively. In both cases, the distorted octahedral structure was characterized by *trans*-alkoxide, *cis*-pyridine, and *cis*-amide ligand arrangement [319]. Complexes [Ti(DIPP)$_2$L$_2$]
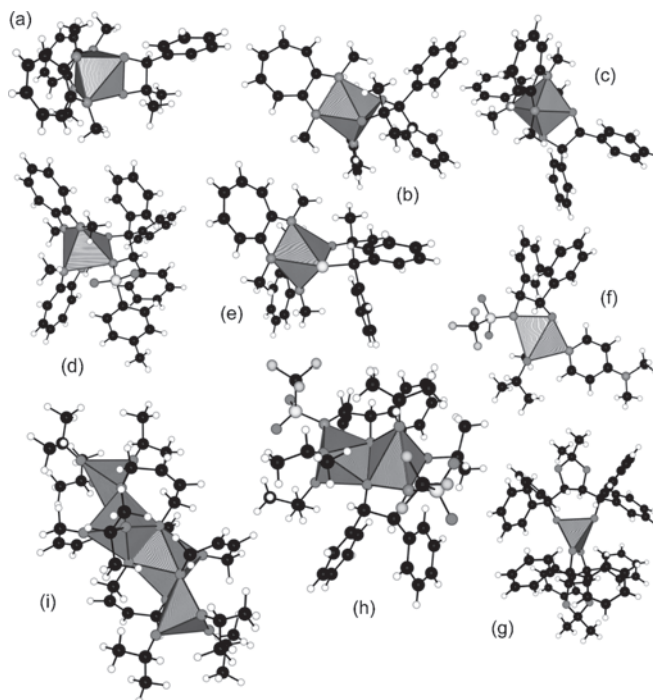


**Figure 51.** Some titanium diolate complexes. (a) Monomeric octahedral coordination in the crystal structure of bis($N$,$N'$-dimethylaminotroponiminato)-(1,1-dimethyl-2-phenylethane-1,2-diolato)- titanium. (b) Monomeric octahedral coordination in the crystal structure of bis(1-methylamino-7-methyliminocyclohepta-1,3,5-triene)-(1,1-dimethyl2,2-diphenylethane-diolato)-titanium. (c) Monomeric octahedral coordination in the crystal structure of bis($N$,$N'$-dimethylaminotroponiminato)-(1,2-diphenylethane-1,2-diolato)-titanium. (d) Monomeric octahedral coordination in the crystal structure of bis($N$,$N'$-dimethylaminotroponiminato)- (1,1,2-triphenyl- 2-$p$-tosylaminoethanolato)-titanium benzene solvate. (e) Monomeric octahedral coordination in the crystal structure of bis($N$,$N'$-dimethylaminotroponiminato)-(1, 1-dimethyl-2,2-diphenylethane-2-thiolato-1-olato)-titanium benzene solvate. (f) Monomeric trigonal bipyramidal in the crystal structure of [2-($N$-trifluoromethylsulfonyl)amido-3,4-diphenylethanolato]-bis(isopropoxy)-(4-dimethylamino-pyridine)-titanium(IV). (g) Dimeric and highly distorted trigonal bipyramidal in the crystal structure of bis{($\mu_2$-2-[$N$-trifluoromethylsulfonyl]amido-3,4-diphenylethanolato)-bis(isopropoxy)-titanium(IV)} perdeuterodichloromethane solvate. (h) Air-stable spiro-titanate [T-4-(4$R$-*trans*),(4$R$-*trans*)]-bis(2,2-dimethyl-$\alpha$,$\alpha$,$\alpha'$,$\alpha'$-tetraphenyl-1,3-dioxolane-4,5-dimethanolato)-titanium diethyl ether solvate. (i) Fivefold and sixfold coordinated Ti atoms in the crystal structure of bis($\mu_3$-but-2-ene-1,4-diolato)-bis($\mu_2$-but-2-ene-1,4-diolato)-octakis(isopropoxy)-tetra-titanium.

derived from bidentate pyridine-phenoxide and 2,6-diisopropylphenoxo ligands are also known [320]. As shown in Figures 52c (L = 8-quinolinolate or oxinate) and 51d (L = 2-methyl-8-quinolinolate = quinaldinate), they display a very similar *trans*-phenoxide, *cis*-pyridine, and *cis*-alkoxide ligand arrangement as with pyridine alcohols. Also notice that pyridine acids have been used to obtain unusually stable and extremely soft peroxides of Ti$^{IV}$. Figure 52e shows the pentagonal bipyramidal arrangement of ligands [Ti(O$_2$)(C$_6$H$_4$NO$_2$){OP(NMe$_2$)$_3$}] obtained with picolinic acid [321], while Figure 52f shows the molecular structure of the complex [Ti(O$_2$)(acac){pz(COO)(COOH){OP(NMe$_2$)$_3$}] obtained with
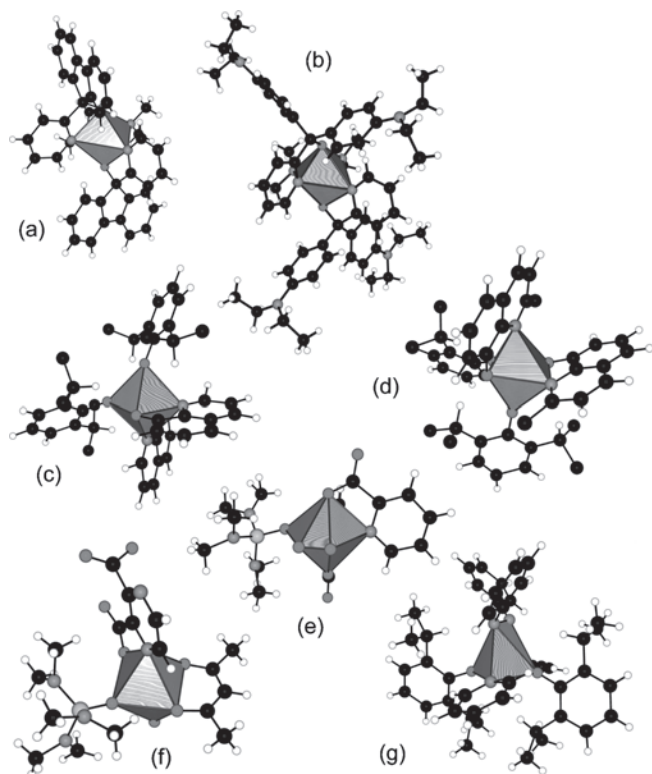
**Figure 52.** Monomeric Ti$^{IV}$ complexes involving pyridine-based ligands. (a) Molecular structure of bis[(9-(2-pyridyl)-9-fluorenolato)-dimethylamido]-titanium(IV). (b) Molecular structure of bis[(2-pyridyl(bis(4-diethylaminophenyl))methanolato)-dimethylamido]-titanium(IV). (c) Molecular structure of bis(8-quinolinolato)-bis(2,6-di-isopropylphenoxo)-titanium(IV). (d) Molecular structure of bis(2-methyl-8-quinolinolato)-bis(2,6-di-isopropylphenoxo)-titanium(IV). (e) Molecular structure of peroxo-bis(picolinato)-(hexamethylphosphoric-triamide)-titanium(IV). (f) Molecular structure of acetylacetonato- hexamethylphosphortriamide-peroxo-(pyrazine-2-carboxylato-3-carboxylic acid)-titanium(IV). (g) Molecular structure of (azobenzene-bis(2,6-di-isopropylphenoxy-*O*))-dipyridine-titanium(IV).

2,3-pyrazine dicarboxylic acid [322]. The existence of these complexes illustrates the ability of titanium to transfer oxygen in the asymmetric transformation of allylic alcohols into epoxyalcohols by *t*-BuOOH in the presence of Ti(OPr$^i$)$_4$ as a catalyst. Closely related to these peroxo complexes is the ability of the Ti(DIPP)$_2$ fragment to react with pyridine and azobenzene PhN=NPh to form a [Ti(DIPP)$_2$(PhNNPh)(py)$_2$] (Fig. 52g) having a square pyramidal arrangement of aryloxide and pyridine ligands as basal sites with an $\eta^2$-azobenzene group occupying the axial position [323]. The rather long N—N bond observed within the complex (142 pm) relative to the free ligand (125.3 pm) is good evidence for a bonding picture involving a [PhNNPh]$^{2-}$ ligand bound to Ti$^{IV}$ and not a PhN=NPh molecule bound to Ti$^{II}$ centers. Moreover, the fact that the N—N distance in Cp$_2$Ti($\eta^2$-PhNNPh) was found to be 134 pm points out the higher reducing power of the Ti(DIPP)$_2$ fragment relative to the bent titanocene unit Cp$_2$Ti [322].

Titanium chelate complexes are not limited to 1,2-derivatives leading to five-membered rings. Two seven-

membered rings may thus be identified in the molecular structure of an air-stable spiro-titanate [Ti(TADDOL)$_2$] (Fig. 51g) derived from TADDOL (2,2-dimethyl-$\alpha$,$\alpha$,$\alpha'$,$\alpha'$-tetraphenyl-1,3-dioxolane-4,5-dimethanolato) ligands, which can act as catalysts for enantioselective additions of dialkylzinc compounds to aldehydes [323]. Another example of seven-membered rings is provided by the molecular structure of [Ti$_4$(OPr$^i$)$_8$(OCH$_2$CH=CHCH$_2$O)$_4$], but with two kinds of coordination modes ($\mu$,$\eta^2$ and $\mu_3$,$\eta^2$) for the but-2-ene-1,4-diolato ligand (Fig. 51i) [324]. The occurrence of such a polymerizable ligand within the titanium coordination sphere has proven to be useful for the elaboration of hybrid organic–inorganic materials.

***Pyrocatechol Derivatives*** Another powerful way of coordinating Ti$^{IV}$ centers is to use pyrocatechol (1,2-dihydroxybenzene), which shares with ethylene glycol the ability to dissolve hydrous titanium oxide [325]. Applying our PACHA model to the crystal structure of [Et$_3$NH]$_2$[Ti(cat)$_3$] (Fig. 53a) [325] leads to the following global charge distribution: [Et$_3$NH]$_2^{(+0.165)}$[Ti$^{(+2.81)}$\{cat$^{(-1.05)}$\}$_3$] (2.5 < p$K_a$ < 3.4) with $\langle$EN$\rangle$ = 13.8 V, $\langle$GH$\rangle$ = 4.0 eV, $\langle$GI$\rangle$ = 19.3%, and $\langle$EB$\rangle$ = −4659.6 kJ mol$^{-1}$. This electronic signature is remarkably different from those previously encountered with neutral metal alkoxides or aryloxides. The rather high acidic character of O atoms, despite their location in a formally dianionic species [Ti(cat)$_3$]$^{2-}$, is remarkable and offers a pretty good explanation of the stability of such species toward water. This charge distribution tends to demonstrate that a high positive charge on the Ti atom does not necessarily mean that the complex will be unstable toward hydrolysis. The basic character of the O atoms that should accept a proton to favor elimination of the ligand also plays a major role. This original charge distribution could help to explain the power of catechol molecules when they act as bidentate chelating agents. Accordingly, protonation of catecholate complexes does not result in dissociation but rather in catechol bridging as evidenced in the complex [Ti$_2$(DTBC)$_4$(HDTBC)$_2$]$^{2-}$, where DTBC stands for 3,5-di-*tert*-butylcatechol [325]. Here, the singly protonated catechol coordinates as a monodentate phenolate anion, while one of the catecholate dianion O atoms makes a bridge to complete the coordination spheres (Fig. 53d). On the other hand, increasing the pH above 12 leads to the bis($\mu$-oxo) dimer [TiO(cat)$_2$]$^{4-}$ (Fig. 53b) [325]. Also notice that the reaction between titanium alkoxides and catechol leads to insoluble reaction products. It was recently possible to understand the origin of this insolubility by isolating the bowtie-shaped decamer [Ti$_{10}$O$_6$(OBu$^n$)$_{12}$(HOBu$^n$)$_2$(cat)$_8$] under careful hydrolysis of solutions having cat/Ti ratios lower than 1 (Fig. 53c) [89]. In this complex, a doubly bridging $\mu_3$-(O,O,O',O') coordination mode was evidenced for the catechol ligand, explaining the highly reticulated nature of the products obtained above cat/Ti = 1. Notice that quite recently a dimeric catecholate [Ti$_2$(OBu$^t$)$_4$(O$_2$C$_6$H$_4$)$_2$] has been characterized [326], but its molecular structure has not been determined. Closely related compounds are *o*-mercaptophenolates, which also lead to tris(chelate) [Ti(*o*-SC$_6$H$_4$O)$_3$]$^{2-}$ (Fig. 53e) and bridged bis(chelate) [Ti$_2$(OMe)$_2$(*o*-SC$_6$H$_4$O)$_4$]$^{2-}$ (Fig. 53f) structures [327]. Such titanium thiolates have potential
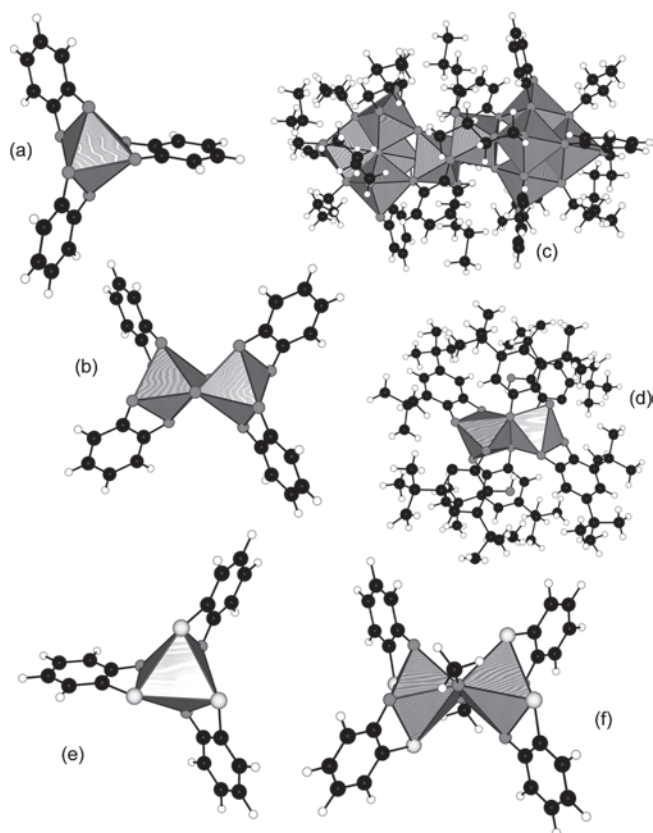
**Figure 53.** Complexes of Ti$^{IV}$ involving catecholate and mercapto-phenolate ligands. (a) Single octahedron (Λ form) in the crystal structure of bis(triethylammonium) tris(catecholato-$O,O'$)-titanium. (b) Edge-sharing octahedral oxo-dimer in the crystal structure of tetrapotassium bis($\mu_2$-oxo)-tetrakis(catecholato-$O,O'$)-di-titanium nonahydrate. (c) Bowtie-shaped decamer in the crystal structure of bis[($\mu_4$-oxo)-{$\mu_3$-($O,O,O',O'$)-pyrocatecholato}-(1-butanol)-bis($\mu_2$-oxo)-bis($\mu$-1-butoxo)-tris{$\mu_2$-($O,O,O'$)-pyrocatecholato}-tetrakis(1-butoxy)-penta-titanium]. (d) Edge-sharing octahedral dimer in the crystal structure of bis(triethylammonium) bis[($\mu_2$-3,5-di-*tert*-butylcatecholato-$O,O'$)-(3,5-di-*tert*-butylcatecholato-$O,O'$)-(3,5-di-*tert*-butyl-catecholato-$O$)-titanium] chloroform solvate. (e) Single octahedron in the crystal structure of bis(benzyltrimethylammonium) tris(*o*-mercaptophenolato)-titanium(IV). (f) Dimeric structure of bis(tetraethylammonium) bis[($\mu_2$-methoxy)- bis(*o*-mercaptophenolato)-titanium] dihydrate.

applications as antitumor agents, nonlinear optical devices, and polymer materials and in chemical sensor technology.

***Polymeric 1D, 2D, and 3D Networks*** Mixing titanium(IV) alkoxides with ligands displaying two reactive hydroxo groups leads very often to microcrystalline or highly polymeric compounds, as already shown in the case of catechol or ethylene glycol ligands. Fortunately, with the growing development of synchrotron radiation and of hydrothermal synthesis, it is sometimes possible to have a better knowledge of these hybrid organic–inorganic polymeric networks. An example of the formation of a 3D network is provided by the reaction at 100 °C of Ti(OPr$^i$)$_4$ with hydroquinone (Fig. 54a) [328]. This network may be derived from a body-centered arrangement of bioctahedral building blocks displaying a $\mu$-hydroxyphenolato bridge. On the

other hand, treatment of the reaction mixture with pyridine (py) afforded the pleated sheet structure shown in Figure 54b and built up from [*cis*-Ti(OC$_6$H$_4$O)$_2$py]$_n$ units and $\mu$-hydroquinato bridges. Switching to acetonitrile leads again to a 3D structure (Fig. 54c) but now with a pseudo-hexagonal arrangement of the bioctahedral building blocks [329].

These examples clearly show the versatility and importance of the solvent under hydrothermal conditions and apply to other elements related to titanium such as zirconium and vanadium [330]. A very similar example is provided by 2,7-hydroxynaphthalene, which affords in Et$_2$O the 3D network [Ti$_2$($\mu$-OC$_{10}$H$_6$O)$_2$($\mu$-OC$_{10}$H$_6$OH)$_2$(OPr$^i$)$_2$] (Fig. 55a), while a 1D ladder [*cis*-Ti($\mu$-OC$_{10}$H$_6$O)$_2$py$_2$]$_n$ is obtained in pyridine (Fig. 55b) [331]. Finally, by treating Ti(OPr$^i$)$_4$ with resorcinol or 4,4′-biphenol, one may switch from a 2D network {[Ti($\mu$-OC$_6$H$_4$O)($\mu$-OC$_6$H$_4$OH) (OC$_6$H$_4$OH)(HOPr$^i$)]$_2$}$_n$ (Fig. 56a) derived from a rectangular arrangement of bioctahedral building blocks (resorcinol derivative) to a 3D network {[Ti($\mu$-OC$_{12}$H$_8$O)$_{1.5}$(OPr$^i$)(HOPr$^i$)]$_2$.THF}$_n$ (Fig. 56b) derived from a base-centered arrangement of similar bioctahedral units (4,4′-biphenol derivative) [332]. It is worth noticing that, owing to the small crystallite size, it would not have been possible to resolve these structures using conventional X-ray equipment. All the results presented above were thus mainly obtained using a high-energy synchrotron source.

To check that the formation of a 3D network with the 4,4′-biphenol ligand was linked to its linear geometry, we have investigated the reaction between titanium isopropoxide and 2,2′-biphenol [89]. As expected, a molecular complex [Ti$_6$O$_4$(OPr$^i$)$_4$(HOPr$^i$)$_2$(*o*-OPhPhO)$_6$] with seven-membered rings was formed displaying a quasi-planar
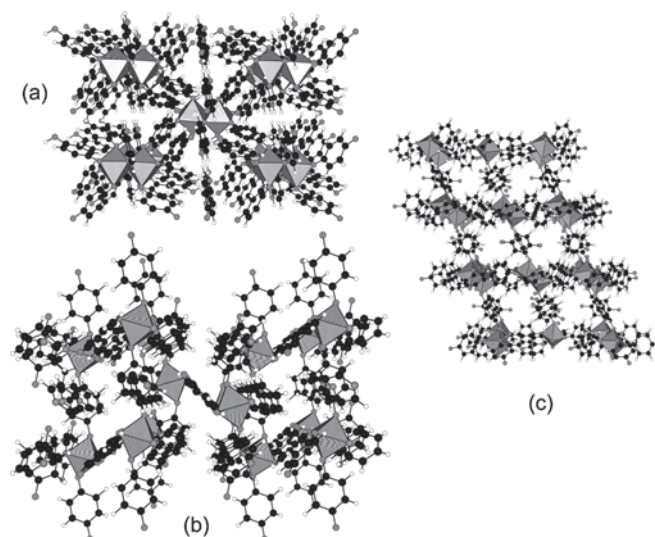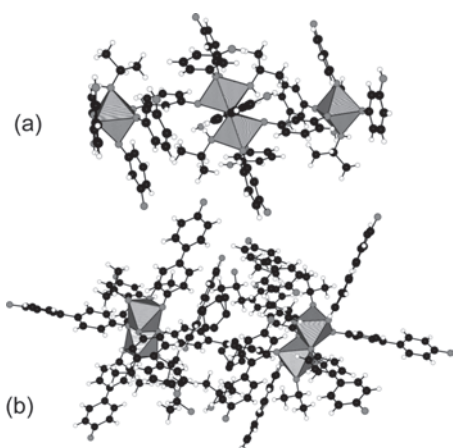


**Figure 54.** Polymeric 3D and 2D networks obtained by treating titanium isopropoxide with hydroquinone. (a) Crystal structure of *catena*-[bis($\mu_2$-4-hydroxyphenoxo-$O,O'$)-bis($\mu_2$-4-oxyphenoxo-$O,O'$)-bis($\mu_2$-4-hydroxyphenoxo-$O,O$)-di-titanium(IV)]. (b) Pleated sheet structure in *catena*(*cis*-tetrakis($\mu_2$-1,4-diphenoxo)-dipyridyl-titanium) 2D network. (c) Crystal structure of *catena*(tetra-aqua-tetrakis($\mu_3$-4-oxyphenoxo-$O,O,O'$)-tetrakis($\mu_2$-4-oxyphenoxy-$O,O'$)-tetra-titanium(IV) 4-hydroxy-phenol acetonitrile clathrate tetrahydrate).
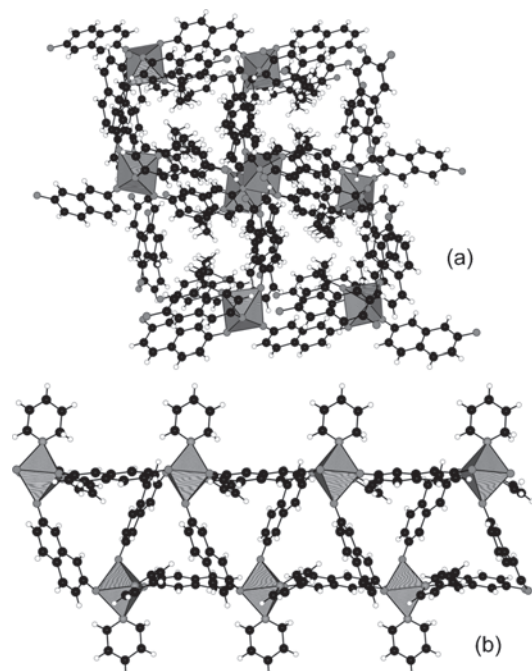
**Figure 55.** Polymeric 3D and 1D networks obtained by treating titanium isopropoxide with 2,7-hydroxynaphthalene. (a) Crystal structure of *catena*[($\mu_3$-2,7-dioxynaphthalene-*O,O,O'*)-($\mu_2$-2-hydroxy-7-oxynaphthalene-*O,O'*)-isopropoxy-titanium(IV)]. (b) 1D ladder found in the crystal structure of *catena*+[bis($\mu_2$-2,7-dioxynaphthalene-*O,O'*)-*cis*-bis(pyridine)-titanium(IV)].

ladder-like $Ti_6O_4$ hexameric core (Fig. 57a) based on four $\mu_3$-oxo groups. For this complex, one could identify two $\mu_2$-(O,O') bridging and four $\mu_2$-(O,O,O') chelating–bridging 2,2'-biphenol groups. This structure is also characterized by the existence of an intramolecular hydrogen bridge between an isopropanol molecule and a neighboring $\mu_2$-(O,O')-



**Figure 56.** Polymeric 2D and 3D networks obtained by treating titanium isopropoxide with resorcinol and 4, 4'-biphenol. (a) Crystal structure for the $\{[Ti(\mu\text{-}OC_6H_4O)(\mu\text{-}OC_6H_4OH)(OC_6H_4OH)(HOPr^i)]_2\}_n$ 2D network derived from a rectangular arrangement of bioctahedral dititanium building blocks. (b) Crystal structure for the $\{[Ti(\mu\text{-}OC_{12}H_8O)_{1.5}(OPr^i)(HOPr^i)]_2 \cdot THF\}_n$ 3D network derived from a base-centered arrangement of bioctahedral dititanium building blocks.
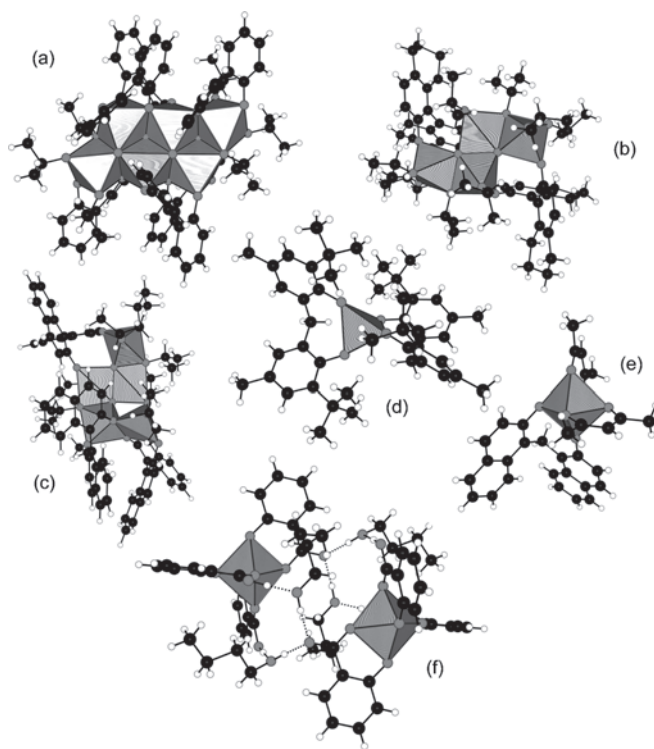


**Figure 57.** Molecular structures of some titanium bisphenolate and salicylate complexes. (a) Ladder-like hexamer in the crystal structure of bis{[($\mu_2$-2,2'-biphenolato(*O,O'*)]-($\mu_2$-isopropoxy)-isopropoxy-isopropanol-bis($\mu_3$-oxo)-bis[$\mu_3$-2,2'-biphenolato(*O,O,O'*)]-trititanium} chloroform solvate. (b) Ladder-like tetramer built from highly distorted $TiO_5$ trigonal bipyramids in the crystal structure of bis($\mu_3$-oxo)-bis($\mu_2$-isopropoxo)-bis($\mu_2$-5, 5', 6, 6', 7, 7', 8, 8'-octahydro-naphthalato-*O,O'*)-hexakis(isopropoxy)-tetra-titanium(IV). (c) Ladder-like pentamer in the crystal structure of bis($\mu_3$-oxo)-($\mu_2$-oxo)-bis($\mu_2$-isopropoxo)-hexakis(isopropoxy)-tris($\mu_2$-1, 1'-binaphthyl-2, 2'-diolato)-penta-titanium diethyl ether solvate. (d) Monomeric tetrahedron found in the crystal structure of bis[2, 2'-methylene- bis(6-*t*-butyl-4-methylphenolato)]-titanium hexane solvate. (e) Monomeric octahedron found in the crystal structure of (acetylacetonato)-chloro-[2-hydroxy-1-(3-hydroxy-2-methylprop-2-yliminomethyl)naphthalene]-titanium(IV). (f) Dimeric and racemic association for the reaction product (salicylato-*O,O'*)-bis[(2- carboxylato)-phenolato]-titanium(IV) 1-butanol solvate between salicylic acid (salH2) and titanium tetra-*n*-butoxide.

biphenol bridge. The formation of a ladder-like titanium-oxo core seems to be characteristic of bisphenolate ligands. Accordingly, a tetrameric ladder-like $Ti_4O_2$ core with two nine-membered rings has been identified in the molecular structure of $Ti_4O_2(OPr^i)_8(BINOH)_2$, where BINOH is the 5,5',6,6',7,7',8,8'-octahydrobinaphtholato-*O,O'* ligand (Fig. 57b) [333]. However, in contrast with 2,2'-biphenol where all Ti atoms are found in sixfold coordination, only highly distorted trigonal bipyramidal coordination is found in the BINOH derivative. A rather similar pentamer $[Ti_5O_3(OPr^i)_8(BINOL)_3]$ (Fig. 57c) was also obtained during the purification of a complex $[Ti(OPr^i)_2(BINOL)]$ involving the binaphtholato ligand (BINOL) and which provides an efficient asymmetric catalyst for the carbonylene reaction [334]. Two coordination modes may be identified for the BINOL ligands. The first one involves the formation of

a bridge spanning a Ti—O—Ti bond and defining a nine-membered ring as before. The second one corresponds to a very common dihapto bridging–chelating mode, leading to two seven-membered rings. BINOL-derived titanium complexes have also been widely used as efficient asymmetric Lewis acid catalysts [333, 334]. An alternative to the direct connection between two phenolate moieties is to use a methylene connector, allowing the formation of eight-membered rings. Using a sterically crowded phenolate, such as 6-*tert*-butyl-4-methyl-phenoxide (MBTMP ligand), it was possible to synthesize the tetrahedral monomeric spirotitanate [Ti(MBTMP)$_2$] displayed in Figure 57d [335]. An octahedral monomeric complex [Ti(acac)$_2$(MBN)] may also be obtained by reacting *cis*-[Ti(acac)$_2$Cl$_2$] with the MBN ligand [1,1'-methylene-bis(2-naphthol)] (Fig. 57e) [336].

***Salicylate Derivatives*** Up to now, we have mainly considered chelate compounds with five-membered rings (diolates, aminolates, pyridinolates, picolinates, quinolinates, catecholates) or compounds with seven- membered rings or more (taddolates, butenediolates, binolates). Six-membered rings are also known that may involve acetylacetonate or salicylate derivatives. Surprisingly enough, we have been the first group to synthesize quite recently a neutral tris(salicylate) titanium complex, $(\Lambda, \Delta)$-[Ti(sal)(salH)$_2$]($^n$BuOH)$_2$, by reacting titanium tetrabutoxide with salicylic acid (sal $= o$-O$_2$CC$_6$H$_4$O) [89]. As shown in Figure 57f, strong intermolecular H bonds exist between salicylate ligands and butanol molecules, leading to the formation of a dimer characterized by an H-bond energy, $E_{HB} = -23.2(1)$ kJ mol$^{-1}$ [90]. The charge distribution is very similar to that found in tris(catecholate) and tris(glycolate) complexes: [Ti$^{+2.94}$(sal)$^{-1.20}$(salH)$^{-1.02}$ (salH)$^{-0.97}$] (Bu$^n$OH)$^{+0.09}$(Bu$^n$OH)$^{+0.15}$ with $\langle EN \rangle = 14.1$ V, $\langle GH \rangle = 3.8$ eV, $\langle GI \rangle = 21.8\%$, and $\langle EB \rangle = -5599.6$ kJ mol$^{-1}$. The p$K_a$ distribution found among salicylate ligands is instructive. For the formal (sal)$^{2-}$ species, we get p$K_a = 5.2$ (phenol O atom), 2.3 (carboxy single-bond O atom), and $-5.1$ (carbonyl O atom). For the two other formal (salH)$^{-1}$ ligands, we have p$K_a = 5.2$ (phenol O atom), 2.3 (C—O bond), and $-3.3$ (C—OH bond). This species should then behave as a strong diacid in aqueous solutions, leading, as expected, to the tri(salicylate) complex [Ti(sal)$_3$]$^{2-}$.

***Acetylacetonate Derivatives*** In stark contrast with salicylates, a much higher number of titanium acetylacetonates have been synthesized and characterized by X-ray diffraction (Fig. 58). Simple monomeric octahedral coordination for Ti$^{IV}$ has been observed in Ti(DIPP)$_2$(acac)$_2$ with bulky DIPP = 2,6-di-isopropylphenolato ligand (Fig. 58a) [319]. This kind of coordination seems to be the rule for disubstituted *cis* titanium alkoxides [Ti(OR)$_2$(acac)$_2$] that have proved to have a nonrigid structure in solution through $^1$H-NMR [337, 338]. More detailed studies subsequently provided evidence for an intramolecular structural rearrangement via a twist mechanism [339]. The case of monosubstituted compounds, Ti(OR)$_3$(acac) (R = Me, Et, Pr$^i$, Bu$^t$), was less clear.

Thus, EXAFS studies of Ti(OR)$_4$/acac mixtures (R = Pr$^i$, Et) were interpreted in terms of monomeric five-coordinate species for R = Pr$^i$ and a mixture of monomers and dimers
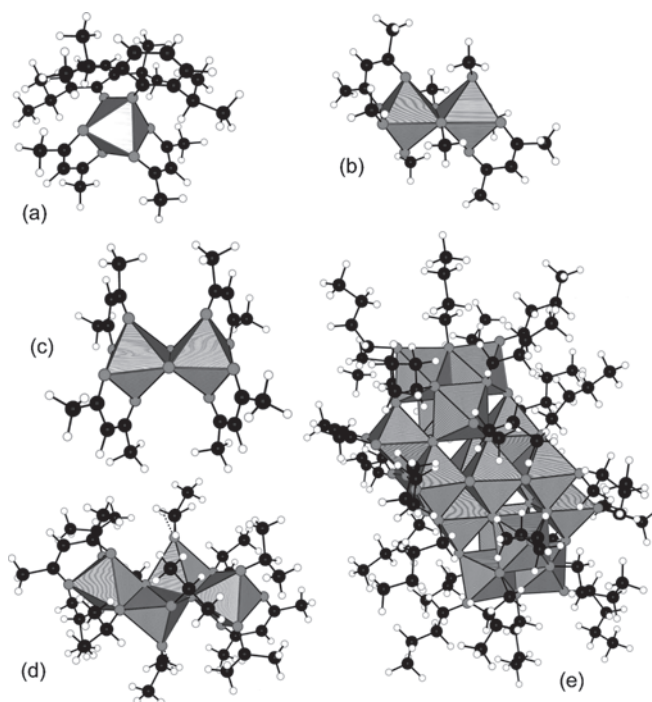


**Figure 58.** Molecular structures of titanium(IV) acetylacetonates (acac). (a) Monomeric octahedral coordination in the crystal structure of bis(2-methyl-8-quinolinolato)-bis(2,6-di-isopropylphenoxo) titanium(IV). (b) Dimeric octahedral coordination in the crystal structure of bis[($\mu_2$-methoxo)-bis(methoxy)-(acetylacetonato)-titanium]. (c) Dimeric octahedral coordination in bis[($\mu_2$-oxo)-bis(acetylacetonato)-titanium] and in bis[($\mu_2$-oxo)-bis(acetylacetonato)-titanium] dioxane solvate. (d) Tetrameric association of three distorted square pyramids and one distorted octahedron in the crystal structure of bis($\mu_3$-oxo)-bis($\mu_2$-isopropoxo)-bis(acetylacetonato)-octakis(isopropoxy)-tetra-titanium. (e) Octadecameric octahedral coordination in the crystal structure of bis($\mu_5$-oxo)-bis($\mu_4$-oxo)-decakis($\mu_3$-oxo)-octakis($\mu_2$-oxo)-tetradecakis($\mu_2$-$n$-butoxo)-dodeca-$n$-butoxy-bis(acetylacetonato)-octadeca-titanium [Ti$_{18}$O$_{22}$(OBu$^n$)$_{26}$(acac)$_2$] characterized by a Ti$_{18}$($\mu_5$-O)$_2$($\mu_4$-O)$_2$($\mu_3$-O)$_{10}$($\mu_2$-O)$_8$($\mu_2$-OBu$^n$)$_{14}$ core.

for R = Et [212, 340]. Later, a systematic study by X-ray diffraction showed that in the solid state primary and secondary alkoxide derivatives were all centrosymmetric binuclear compounds [Ti(OR)$_3$(acac)]$_2$ (R = Me, Et, OPr$^i$) (Fig. 58b) [341]. In this study, it was also shown by using $^1$H- and $^{13}$C-NMR spectroscopy that the secondary and tertiary derivatives were completely disproportionated into Ti(OR)$_4$ and Ti(OR)$_2$(acac)$_2$ in solution and that the octahedral dimer, [Ti(OR)$_3$(acac)]$_2$, was the major species in solution for R=Me and Et. If a titanium alkoxide is treated with an excess of acetylacetone, the remaining OR groups are not substituted, and an octahedral dimer, [TiO(acac)$_2$]$_2$, is obtained (Fig. 58c) that can be crystallized with or without dioxane solvent molecules [342]. The same structure could also be obtained after hydrolysis of Ti(OR)$_2$(acac)$_2$ [343]. On the other hand, water vapor hydrolysis of a 2:1 mixture of Ti(OPr$^i$)$_4$ and acetylacetone leads to a tetrameric association [Ti$_4$O$_2$(OPr$^i$)$_{10}$(acac)$_2$] of three distorted square pyramids and one distorted octahedron displaying a ladder-like Ti$_4$($\mu_3$-O)$_2$($\mu_2$-OPr$^i$)$_2$ core (Fig. 58d) [344]. Such a structure is quite reminiscent of that obtained with the BINOL or BINOH derivative [333, 334]. Finally, after hydrolysis

at $h = H_2O/Ti = 1$ of a $3:1$ mixture of $Ti(OBu^n)_4$ and acetylacetone, it was possible to isolate an octadecameric octahedral complex $[Ti_{18}O_{22}(OBu^n)_{26}(acac)_2]$ characterized by a very unusual $Ti_{18}(\mu_5\text{-}O)_2(\mu_4\text{-}O)_2(\mu_3\text{-}O)_{10}(\mu_2\text{-}O)_8(\mu_2\text{-}OBu^n)_{14}$ core (Fig. 58e) [345].

As acetylacetone is a widely used chemical additive in the sol–gel synthesis of titanium-containing materials, it was hoped that a better understanding of the underlying complexation chemistry could be reached by trying to synthesize new polynuclear compounds. A possible method of investigation is to keep the $C_3O_2$ core and replace the methyl groups by other organic groups (Fig. 59). As expected, monomeric octahedral coordination has been evidenced in the crystal structures of $Ti(OBu^t)_2(bzac)_2$ with bzac = benzoylacetonato-$O,O'$ ligand (Fig. 59a) [346] and $Ti(OEt)_2(tfpbd)_2$ with tfpbd = 4,4,4-trifluoro-1-phenyl-1,3-butanedionato ligand (Fig. 59b) [347]. However, if derivatives of the 2,2,6,6-tetramethyl-heptane-3,5-dionato ligand (tmhd) $[Ti(OR)_3(tmhd)]_2$ (R = Me, Et, $Pr^n$, $Pr^i$, $Bu^t$) were found to be isostructural of $[Ti(OR)_3(acac)]_2$ compounds (Fig. 59c) [341], this was not the case for the $TiO(tmhd)_2$



**Figure 59.** Molecular structures of substituted titanium(IV) acetylacetonates. (a) Monomeric octahedral coordination in the crystal structure of bis(benzoylacetonato-$O,O'$)-di-*tert*-butoxy-titanium. (b) Monomeric octahedral coordination in the crystal structure of diethoxy-bis(4,4,4-trifluoro-1-phenyl-1,3-butanedionato)-titanium(IV). (c) Dimeric octahedral coordination in the crystal structure of bis[($\mu_2$-methoxo)-bis(methoxy)-(2,2,6,6-tetramethylheptane-3,5-dionato)-titanium]. (d) Tetrameric octahedral coordination in the crystal structure of *cyclo*-{tetrakis[($\mu_2$-oxo)-bis(2,2,6,6-tetramethylheptan-3,5-dionato)titanium(IV)]} pentane solvate. (e) Dimeric octahedral coordination in the crystal structure of bis($\mu_2$isopropoxo)bis{di-isopropoxy-[bis(trifluoromethylsulfone)methylene-$O,O'$]-titanium}.

complex prepared by hydrolysis of $Ti(OR)_2(tmhd)_2$ or $TiCl_2(tmhd)_2$. In this case, an octahedral corner-sharing cyclic tetramer, $[TiO(tmhd)_2]_4$, was observed (Fig. 59d) owing to the steric hindrance that would occur for an edge-sharing found in the corresponding acac derivative [348]. In this case, the lower volatility of the $TiO(tmhd)_2$ derivative associated with this higher nuclearity relative to $Ti(OPr^i)_4$ or $Ti(OPr^i)_2(tmhd)_2$ was of crucial importance for the growth of ferroelectric phases such as $(Ba, Sr)TiO_3$ or $PbZr_{1-x}Ti_xO_3$ through CVD techniques. Finally, in attempts to develop new organometallic chemistry based on the fluorocarbon acids, the edge-sharing octahedral dimer $[Ti_2(OPr^i)_6\{HC(SO_2CF_3)_2\}]$ (Fig. 59e) was isolated during the reaction between $Ti(OPr^i)_3Cl$ and bis(trifluoromethylsulfone)methylene-silver(I) [349]. The remarkable feature of this structure lies in the semichelating behavior of the sulfone ligand, evidenced by the large asymmetry observed for the $HC(SO_2CF_3)$ binding with a difference in Ti—O bond lengths between axial and equatorial positions of about 10 pm.

### 3.4.3. Complexes Involving Tridendate Ligands

After this comprehensive review of titanium(IV) complexes displaying bidentate ligands, we now turn our attention to the more limited family of tridentate ligands. To be systematic, structures have been classified here according to the chemical nature of the donor atoms present on the ligand. Four main classes have thus been identified after a comprehensive search of the available literature: O,O',O'' donors, O,N,O' donors, N,N',N'' donors, and O,S,O' donors.
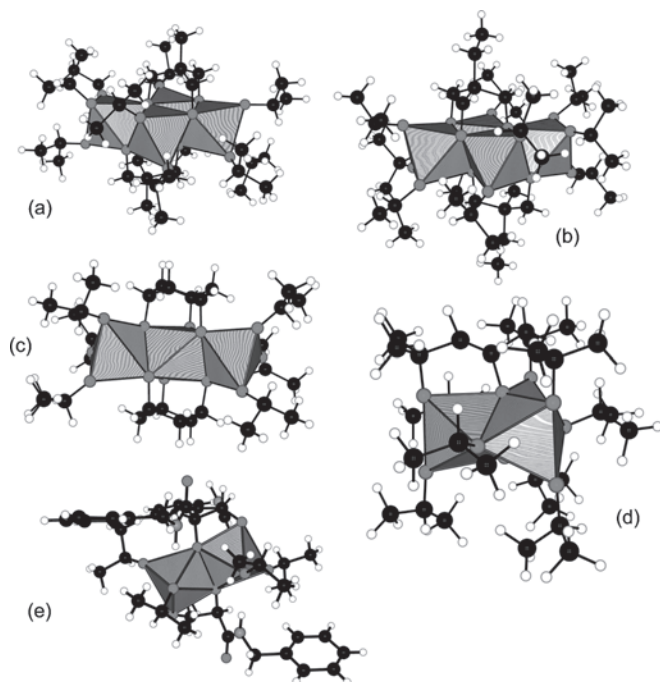
**Complexes with O,O',O'' Donors** Tridentate ligands involving only O-atom donors linked to $Ti^{IV}$ centers are not very common. Besides the case of the tris(hydroxymethyl)methane derivatives $[Ti_4(OPr^i)_{10}(THME)_2]$ (Fig. 60a) and $[Ti_4(OPr^i)_{10}(THMP)_2]$ (Fig. 60b) [290] already studied in the crystal engineering section, only three other examples have been found in the literature. The first compound is an open-chain trinuclear titanium(IV) complex $[Ti_3(OPr^i)_6(CCCT)_2]$ formed with the tridentate CCCT ligand (CCCT = *cis,cis*-cyclohexane-1,3,5-trialkoxide) (Fig. 60c) [350]. Here, two strongly distorted trigonal bipyramidal units flank one central octahedral unit capped by two CCCT ligands. The second example (Fig. 60d) is a complex $[Ti_3O(OPr^i)_7\{Me_2C(O)CH=C(O)CH_2C(O)Me_2\}]$ isolated during the reaction of titanium isopropoxide with acetone [285, 351]. In this case, a remarkable condensation of three acetone molecules occurs around the $Ti^{IV}$ center according to the following scheme: $3Me_2C=O + 3Ti(OPr^i)_4 \rightarrow [Ti_3O(OPr^i)_7(C_9H_{15}O_3)] + 3Pr^iOH + Pr^i_2O$ leads to the *in-situ* formation of the 2,6-dimethylhept-3-en-2,4,6-triolato ligand. The last example is a tartrate complex, $[Ti(OPr^i)_2\{\mu_2\text{-}OCH(CONHCH_2Ph)CH(CONHCH_2Ph)O\}]_2$ (Fig. 60e), that is obtained by reacting $Ti(OPr^i)_4$ with $(R,R)$-$N,N'$-dibenzyltartramide in dichloromethane and that can be used in the asymmetric epoxidation of allylic alcohols by alkylperoxides [314].

**Complexes with O,N,O' Donors** The vast majority of tridentate $Ti^{IV}$ complexes occurs with ligands having the

**Figure 60.** Molecular structures of titanium(IV) complexes involving $O,O',O''$ tridentate ligands. (a) Tetrameric octahedral coordination in the crystal structure of bis($\mu_4$-tris(hydroxymethyl)ethane)-deca-kis(isopropoxy)-tetra-titanium. (b) Tetrameric octahedral coordination in the crystal structure of bis($\mu_4$-tris(hydroxymethyl)propane)-decakis(isopropoxy)-tetra- titanium [Ti$_4$(OPr$^i$)$_{10}$(THMP)$_2$]. (c) Trimeric octahedral coordination in the crystal structure of bis[($\mu_3$-$cis$,$cis$-cyclohexane-1,3,5-triolato)-tris(isopropoxo)-titanium(IV)]-titanium [Ti$_3$(OPr$^i$)$_6$(CCCT)$_2$]. (d) Trimeric octahedral coordination with ($\mu_3$-O)Ti$_3$ core in the crystal structure of ($\mu_3$-2,6-dimethylhept-3-en-2,4,6-trionato)-($\mu_3$-oxo)-tris($\mu_2$-isopropoxo)-tetrakis(isopropoxy)-tri-tit-anium. (e) Dimeric octahedral coordination in the crystal structure of bis{($\mu_2$-$N$,$N'$-dibenzyltartramide)-disopropoxy-titanium(IV)}.

O,N,O$'$ sequence of donor atoms. The only known example of an amino alcoholate occurs after a controlled hydrolysis of a mixture of titanium isopropoxide with two equiva-lents of MDEAH$_2$ (MDEA = $N$-methyldiethoxoamine). This hexameric complex [Ti$_6$O$_6$(MDEA)$_6$] is built up by a ring of six edge-sharing [TiO$_5$N] octahedra with mixed ($\mu_2$-oxo, $\mu_2$-alkoxo) bridges (Fig. 61a) [352]. Notice that the parent [Ti(MDEA)$_2$] complex is highly hygro-scopic and cannot be crystallized. A different result is obtained when titanium isopropoxide is mixed with two equivalents of a $N$-hydroxyalkyl $\beta$-ketoimine. The product is now a monomeric distorted octahedral complex [Ti{MeC(O)CHC(NCH$_2$CH$_2$O)CH$_3$}$_2$] that should be described as a $\beta$-imino enolate rather than a $\beta$-ketoamide (Fig. 61b) [353]. Very similar complexes, Ti(aabh)$_2$ (Fig. 61c) and Ti(babh)$_2$ (Fig. 61d), may be formed when Ti(OPr$^i$)$_2$(acac)$_2$ is refluxed in the presence of ben-zoylhydrazine (aabh derivative) or 4-phenylbutane-2,4-dione-benzoylhydrazone (babh complex) [354]. The ubiquitous nature of this kind of coordination is further demonstrated by the reaction products, Ti(HHMYN)$_2$ (Fig. 61e) and Ti(HDTBPI)$_2$ (Fig. 61f), of 2-hydroxy-1-(3-hyd roxy-2-methylprop-2-yliminomethyl)naphthalene
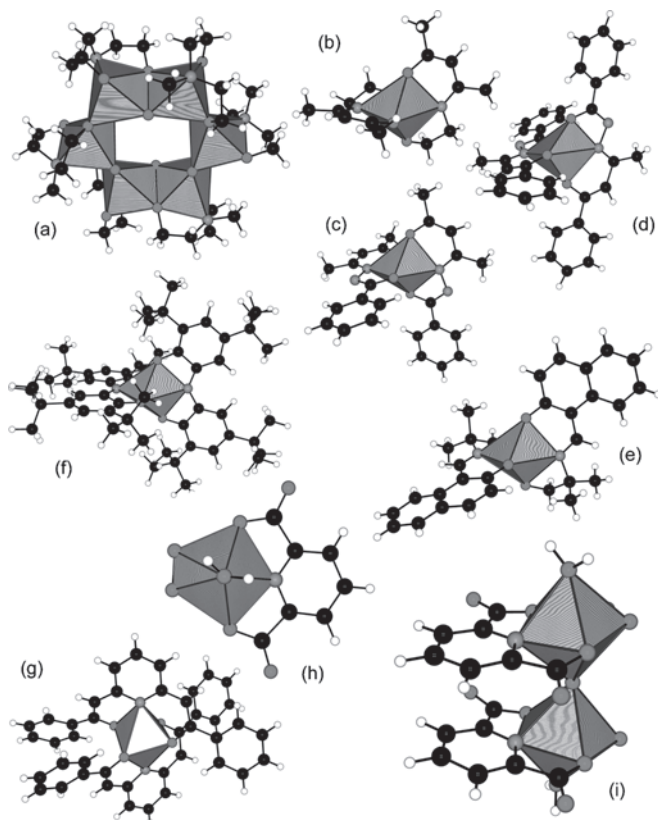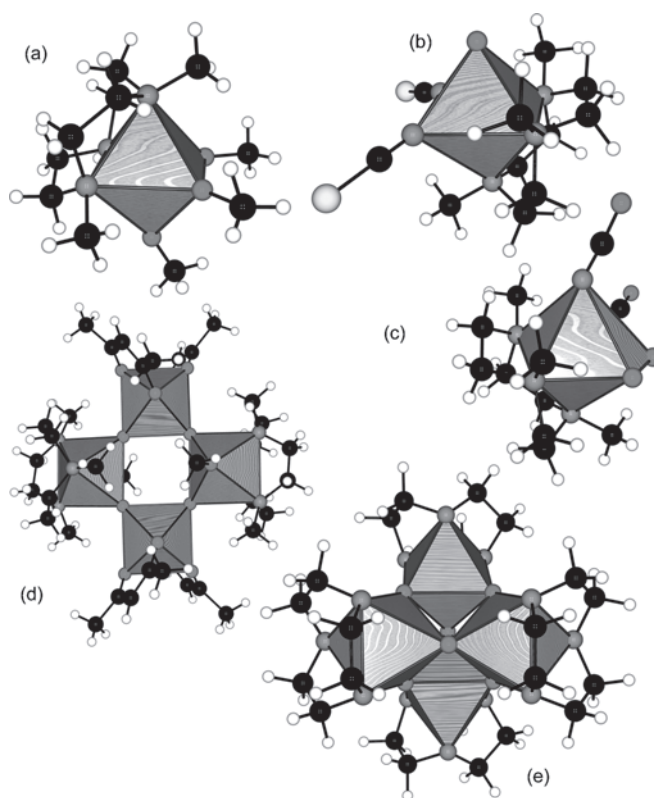


**Figure 61.** Molecular structures of titanium(IV) complexes involving O,N,O$'$ tridentate ligands. (a) Hexameric octahedral coordination in the crystal structure of hexakis[($\mu_2$-$N$-methyldiethoxoamine)-($\mu_2$-oxo)-titanium] dichloromethane solvate. (b) Monomeric distorted octahedral coordination in the crystal structure of bis(7-oxy-4-methyl-5-aza-hept-3-en-2-onato)-titanium dichloromethane solvate. (c) Monomeric distorted octahedral coordination in the crystal structure of bis(pentane-2,4-dione benzoylhydrazonato-$N$,$O$,$O'$)-titanium(IV). (d) Monomeric distorted octahedral coordination in the crystal structure of bis(4-phenylbutane-2,4-dione benzoylhydrazonato-$N$,$O$,$O'$)-titanium(IV). (e) Monomeric distorted octahedral coordination in the crystal structure of bis[2-hydroxy-1-(3-hydroxy-2-methylprop-2-yliminomethyl)naphthalene]-tita-nium(IV). (f) Monomeric distorted octahedral coordination in the crystal structure of bis[3,5-di-$tert$-butyl-1,2-quinone-1-(2-hydroxy-3,5-di-$tert$-butyl-phenyl)imine-$N$,$O$,$O'$]-titanium(IV). (g) Monomeric regular octahedral coordination in the crystal structure of bis[2,6-bis(phenylacyl)pyridinato]-titanium(IV). (h) Monomeric pentagonal bipyramidal coordination in the crystal structure of two polymorphs of diaqua-peroxo-(pyridine-2,6-dicarboxylato-$N$,$O$,$O'$)-titanium dihydrate. (i) Corner-sharing dimer formed by two pentagonal bipyramids in the crystal structure of potassium ($\mu_2$-oxo)-bis[(dipicolinato-$N$,$O$,$O'$)-aqua-peroxo-titanium(IV)] trihydrate.

(HHMYN) with TiCl$_2$(acac)$_2$ [335] or of TiCl$_3$ with 3,5-di-$t$-butyl-1,2-quinone-1-(2-hydroxy-3,5-di-$t$-butyl-phenyl)imine (HDTBPI) [355]. The characteristic distortion of the Ti(ONO)$_2$ octahedra in all the previous examples is obvi-ously linked to the formation of at least one five-membered ring. As shown in Figure 61g, a much more regular octahe-dron, Ti(DPAP)$_2$, is obtained when titanium isopropoxide is reacted with two equivalents of 2,6-diphenylacylpyridine (DPAP) [356].

The last example of a tridentate (O,N,O′) coordination mode toward Ti$^{IV}$ is provided by the dipicolinate ligand (dipic = pyridine-2,6-dicarboxylato). Thus, by adding dipicolinic acid to an aqueous solution containing the peroxo aquo complex TiO$_{2aq}^{2+}$ at pH 1, it was possible to isolate two deep-red polymorphic forms (one pleochroic triclinic and one nonpleochroic orthorhombic modification) [Ti(O$_2$)(dipic)(H$_2$O)$_2$]·2H$_2$O [357, 358]. Figure 61h shows the pentagonal bipyramidal structure of this complex with the basal plane occupied by the peroxo and dipic ligand, leaving the axial position for the two water molecules. Notice that a similar complex with two fluoride ions replacing the water molecules was evidenced in the crystal structure of K$_2$[TiO$_2$(dipic)F$_2$]·2H$_2$O [357]. Owing to the existence of an equilibrium between TiO$_{2aq}^{2+}$ and TiO$_2$(OH)$_{aq}^+$, it was also possible to isolate below pH 1 and pH 3 a dinuclear oxo-complex (Fig. 61i) characterized by two pentagonal bipyramid units sharing an apical μ-oxygen [359].

***Complexes with N,N′,N′ Donors*** We now turn our attention toward some molecular structures involving the facially coordinated tridentate (N,N′,N″) cyclic amine 1,4,7-trimethyl-1,4,7-triazacyclononane, (Me$_3$tacn)Ti$^{IV}$. Figure 62a shows the monomeric octahedral structure evidenced in [(Me$_3$tacn)–Ti(OMe)$_3$][BPh$_4$] obtained after oxidation of [(Me$_3$tacn)–Ti$^{III}$(NCS)$_3$] in the presence of NaOMe and NaBPh$_4$ [360]. If the same complex [(Me$_3$tacn)–Ti$^{III}$(NCS)$_3$] is oxidized by air at 55 °C, the monomeric octahedral [(Me$_3$tacn)Ti(O)(NCS)$_2$] complex (Fig. 62b), characterized by a very short Ti—O bond, d$_{TiO}$ = 163.8(3) pm, is obtained [361]. Notice that in the case of the isocyanate ligand the same complex [(Me$_3$tacn)Ti(O)(NCO)$_2$] may be formed, but it is rather difficult to separate it from the η$^2$-peroxotitanium(IV) complex [(Me$_3$tacn)Ti(O$_2$)(NCO)$_2$] (Fig. 62c) [360]. Finally, two interesting tetrameric species have been synthesized in this system. The first one was obtained upon reaction of [(Me$_3$tacn)–Ti$^{III}$Cl$_3$] and sodium acetylacetonate in a water/methanol mixture [362]. This leads to a co-crystallization of two different isomers with (Λ, Δ) configuration at the Ti(acac)$_2$(μ-O)$_2$ fragment and (δδδ) or (λλλ) conformation at the (Me$_3$tacn)Ti(OMe)(μ-O) fragment (Fig. 62d). The other one was obtained by treating titanyl-bis(acetylacetonate), TiO(acac)$_2$, with 1,4,7-triazacyclononane in an aqueous solution of sodium bromide [363]. In this case, an adamantane-like [Ti$_4$(μ-O)$_6$]$^{4+}$ octahedral core was identified together with a statistical disorder of δδδ- or λλλ-conformed rings attached to Ti centers (Fig. 62e).

***Complexes with O,S,O′ Donors*** We will finish this overview of complexation of Ti$^{IV}$ by tridentate ligands by considering two cases involving the (O,S,O′) coordination mode (Fig. 63). In comparison with methylene-bridged compounds, the presence of a sulfide bridge in [Ti(μ$_2$-OPr$^i$)(OPr$^i$)(S{C$_6$H$_2$(Me)(Bu$^t$)O}$_2$)]$_2$ (Fig. 63a) [364] or a disulfide bridge in [Ti(μ$_2$-OBu$^n$)(OBu$^n$)(S$_2${C$_6$H$_2$(Me)(Bu$^t$)O}$_2$)]$_2$ (Fig. 63b) [365] leads to a much higher catalytic activity in the polymerization of α-olefin such as ethylene, propylene, styrene, and some dienes [364]. These complexes thus provide good alternatives for both the *ansa*-metallocenes and the chelating diamido complexes [365].
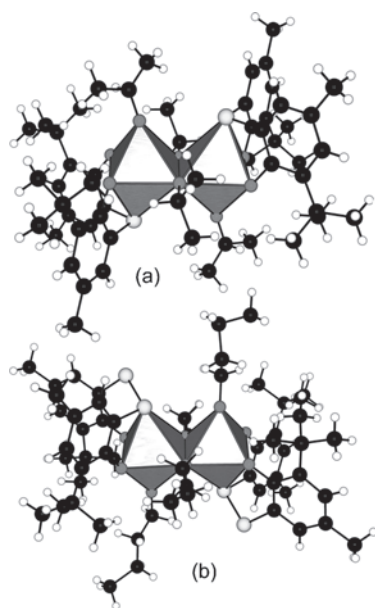


**Figure 62.** Molecular structures of some Ti$^{IV}$ complexes with N,N′,N″ tridentate ligands. (a) Monomeric octahedral structure in the crystal structure of trimethoxy-(1,4,7-trimethyl-1,4,7-triazacyclonane)-titanium(IV) tetraphenylborate. (b) Monomeric octahedral coordination in the crystal structure of di-isothiocyanato-oxo-(1,4,7-trimethyl-1,4,7-triazacyclononane)-titanium(IV). (c) Monomeric octahedral coordination in the crystal structure of di-isocyanato-peroxo-(1,4,7-trimethyl-1,4,7-triazacyclononane)-titanium(IV). (d) Corner-sharing octahedral tetramer in the crystal structure of tetrakis(μ$_2$-oxo)-bis(acetylacetonato)-dimethyl-bis(1,4,7-trimethyl-1,4,7-triazacyclonanane)-tetra-titanium diperchlorate dihydrate. (e) Adamantane-like corner-sharing octahedral tetramer in the crystal structure of hexakis(μ$_2$-oxo)-tetrakis[(1,4,7-triazacyclononane-*N,N′,N″*)-titanium(IV)] tetrabromide tetrahydrate.

### 3.4.4. Complexes Involving Tetradentate Ligands

As with tridentate ligands, structures have been classified here according to the chemical nature of the donor atoms present on the ligand. Five main classes have thus been identified after a comprehensive search of the available literature: O,O′,O″,O‴ donors, N,O,O′,O″ donors, O,N,N′,O′ donors, N,N′,N″,N‴ donors, and O,S,S′,O′ donors.

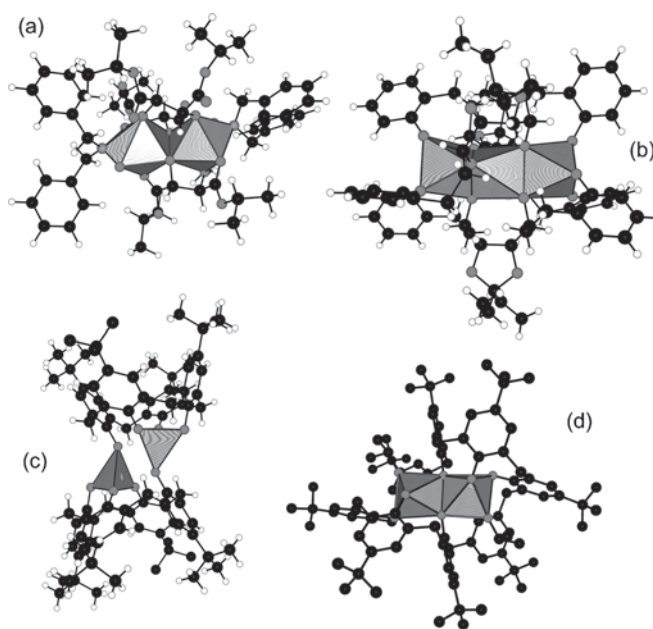***Complexes with O,O′,O″,O‴ Donors*** Tetradentate ligands involving only O-atom donors linked to Ti$^{IV}$ centers are quite common. Tartrate anions are here quite remarkable, owing to their ability to behave as bi-, tri-, or tetradentate ligands. Figure 64a shows the dimeric pentagonal bipyramidal coordination observed for the [Ti$_2$(DIPT)$_3${ON(CH$_2$Ph)$_2$}$_2$] complex, which may be prepared by reaction of Ti(OPr$^i$)$_4$, (*R,R*)-diisopropyltartrate (DIPT), and *N,N*-dibenzylhydroxylamine HON(CH$_2$Ph)$_2$ [366]. In this structure, one of the three DIPT ligands

**Figure 63.** Dimeric octahedral structures of some Ti$^{IV}$ complexes with O,S,O′ tridentate ligands. (a) Molecular structure of bis{($\mu_2$-isopropoxo)-(isopropoxy)-[2, 2′-thiobis(4-methyl-6-*tert*-butylphenoxy)]-titanium(IV)}. (b) Molecular structure of bis{($\mu_2$-*n*-butoxo)-(*n*-butoxy)-[2, 2′-dithiobis(6-*tert*-butyl-4-methylphenolato)]-titanium(IV)}. Sulfur atoms are shown in the axial position.

displays a $\mu$-(O,O′,O″,O‴) coordination mode, while the other two bind to Ti$^{IV}$ in a ($\mu$,$\eta^2$) chelating–bridging fashion. A more complex example is provided by the complex [Ti(HPPDEDO)]$_3$ (Fig. 64b) obtained by reacting the chiral tetraol 4,5-bis(1-hydroxy-3-(2′-phenoxy)propyl)-2,2-diethyl-1,3-dioxalane (HPPDEDO) with titanium tetra(1,1,1,3,3,3-hexafluoro-isopropoxide) [367]. This trimer contains a unique core of three face-sharing TiO$_6$ octahedra tied in a helical fashion to which is attached bridging alkoxides and terminal phenoxides. The potential of such titanates as chiral Lewis acids has been demonstrated by their use as catalysts for the addition of diethylzinc to aldehydes and for Diels–Alder reactions [367]. Another interesting class of supramolecular coordination complexes may be obtained by reacting TiCl$_4$ or titanium alkoxides with oxacalix[*n*]arene (*n* = 3–8) ligands [368–370]. Among the derivatives free of chloro ligands, two complexes are noteworthy. The first one [Ti$_2$(calix[4])$_2$] is formed by two calix[4]arene molecules encapsulating two Ti atoms in fourfold coordination, yielding a divergent association of two cavities (Fig. 64c) [371]. The second one, [Ti$_2$(OPr$^i$)$_2$(calix[8])]$^-$, involves again two Ti atoms but just one calix[8]arene ligand, leading to the encapsulation of an edge-sharing octahedral dimer (Fig. 64d) [372].

Bis(catecholates) are another class of tetradentate chelating units ideally suited for the spontaneous self-assembly of double- or triple-helical oligonuclear coordination compounds. Figure 65a shows the result, Na$_4$[Ti$_2$(BDHPP)$_3$], of reacting titanyl bis(acetylacetonate) with a $C_3$-bridged bis(catechol) ligand BDHPP (1,3-bis[2,3-dihydroxyphenyl]propane) in the presence of sodium carbonate. The binuclear complex formed involving three bis(catecholate) units can be described as a *meso*-helicate ($\Lambda$,$\Delta$) configuration for



**Figure 64.** Molecular structures of some Ti$^{IV}$ complexes with O,O′, O″,O‴ tetradentate ligands. (a) Dimeric pentagonal bipyramidal coordination in the crystal structure of bis($\mu_2$-*R*,*R*-di-isopropyltartrato-*O*,*O*′)-($\mu_2$-*R*,*R*-di-isopropyltartrato-*O*,*O*′,*O*″,*O*‴)-bis(*N*,*N*-dibenzylhydroxylamino-*N*,*O*)-di-titanium(IV) dichloromethane solvate. (b) Trimeric octahedral helix made of three face-sharing octahedra in the crystal structure of tris{[$\mu_3$-4,5-bis(1-hydroxy-3-(2′-phenoxy)propyl)-2,2-diethyl-1,3-dioxalane]-titanium} dichloromethane solvate. (c) Dimeric tetrahedral coordination in the crystal structure of bis{($\mu_2$-5,11,17,23-tetra-*tert*-butyl-25,26,27,28-tetrahydroxycalix[4]arene)-titanium(IV)} toluene solvate. (d) Encapsulation of an edge-sharing octahedral dimer in the crystal structure of sodium ($\mu_2$-5,11,17,23,29,35,41,47-octa-*tert*-butyl-49-hydroxy-50,51,52,53,54,55,56-heptaoxycalix[8]arene)-bis[isopropoxy-titanium(IV)] acetonitrile 1,2-dimethoxyethane solvate.

the two associated octahedra [373]. Figure 65b shows the ($\Delta$,$\Delta$) form, Li$_4$[Ti$_2$(BDHPE)$_3$], obtained with the dimethylene spacer (BDHPE = 1,3-bis[2,3-dihydroxyphenyl]ethane) [374]. By contrast, a single methylene spacer (BDHPM = 1,3-bis[2,3-dihydroxyphenyl]methane) leads again to the Li$_4$[Ti$_2$(BDHPM)$_3$] *meso* form (Fig. 65c) [375]. Finally, switching to a hexamethylene spacer (BDHPH = 1,3-bis[2,3-dihydroxyphenyl]hexane) leads again to a chiral helicate K$_4$[Ti$_2$(BDHPH)$_3$] (Fig. 65d) [376]. These results clearly show that the stereochemistry of helicate versus *meso*-helicate is governed by the zigzag conformation of the alkyl spacer [374]. An even number of methylene units should favor the helicate form, while an odd number leads to the *meso* structure. All these cryptand-type helicates and *meso*-helicates display a central cavity that can encapsulate one or two metal cations such as Li$^+$, Na$^+$, and K$^+$. However, owing to the flexibility of the spacer, the cavity of these metalla-cryptands can adopt different sizes and thus shows only low selectivity toward binding of different cations [373–376]. By using a rigid *p*-phenylene bridge (BBCAT = benzene-1,4-bis[catechol]), it was possible to get a triple-stranded helicate, K$_4$[Ti$_2$(BBCAT)$_3$], with a well-defined cavity size (Fig. 65e) and displaying a 21-nm helix pitch [377]. Interestingly enough, when the spacer was 2,6-bis(2,3-dihydroxy-benzamido)anthracene (BDHBA), it was shown
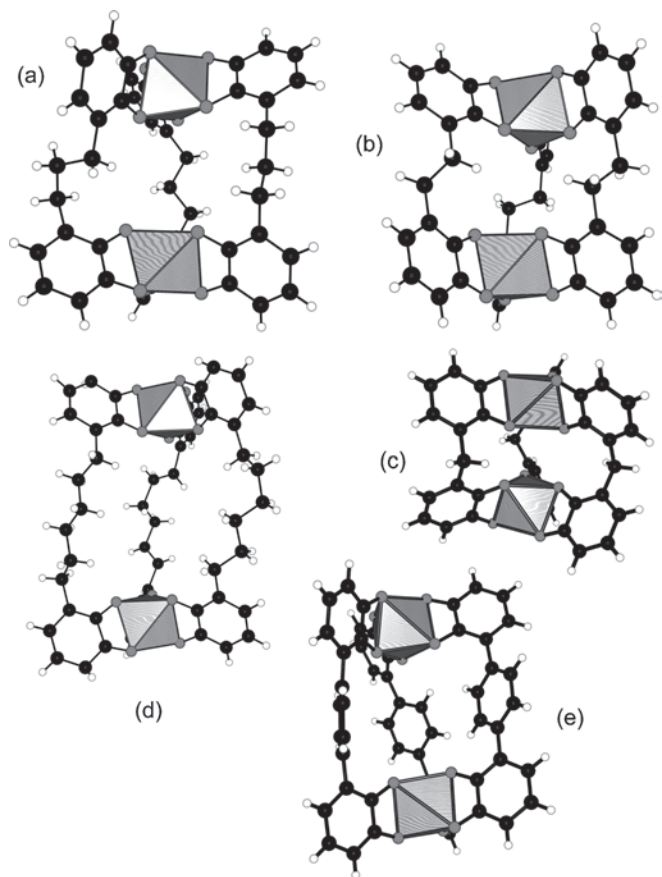
**Figure 65.** Molecular structures of some triple-stranded helicates and *meso*-helicates built from alkyl-bridged bis(catechol) ligands and able to behave as cation acceptors within their central cavity. (a) *meso*-Helicate in the crystal structure of tetra-sodium tris[$\mu_2$-1,3-bis(2, 3-dihydroxyphenyl)propane-*O*,*O'*,*O''*,*O'''*]-di-titanium dimethylformamide solvate pentahydrate. (b) ($\Delta$,$\Delta$)-Helicate in the crystal structure of tetrakis(dimethylformamide)-lithium bis[$\mu_5$-1,2-bis(2,3-dihydroxyphenyl)ethane]-[$\mu_3$-1,2-bis(2,3-dihydroxyphenyl)ethane]-bis(dimethylformamido)-diaqua-tri-lithium-di-titanium. (c) *meso*- Helicate in the crystal structure of bis{tris[$\mu_4$-bis(2,3- dihydroxyphenyl)methane]-tris(dimethylformamide)-di-titanium-tri-lithium} bis($\mu_2$-dimethylformamide)-tetrakis(dimethylformamide)- di-lithium. (d) Flexible helicate in the crystal structure of tetrapotassium tris[$\mu_2$-hexane-1,6-bis(phenyl-2,3-diolato)]-dititanium dimethylformamide solvate trihydrate. (e) Rigid helicate in the crystal structure of tetra-potassium tris[$\mu_2$-benzene-1,4-bis(catecholato)]- di-titanium dimethylformamide methanol solvate monohydrate.

[378] that the helicate form, $K_4[Ti_2(BDHBA)_3]$ (Fig. 66a), can be transformed into the more symmetric tetrahedron, $(NMe_4)_8[Ti_4(BDHBA)_6]$ (Fig. 66b), by simple addition of tetramethylammonium countercations. The rational design of these self-assemblies from geometrical considerations has been reviewed [379].

***Complexes with N,O,O′,O′ Donors*** $Ti^{IV}$ complexes with tetradentate ligands exhibiting a (N,O,O′,O″) coordination mode can be separated into two classes. The first one includes triethanolamine (TEA) derivatives and leads to the important family of titanatranes. Figure 67a shows the characteristic coordination mode of the TEA ligand, able to
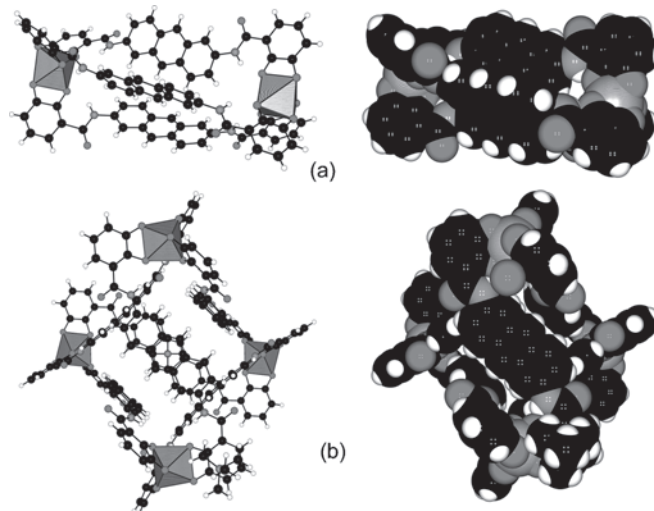


**Figure 66.** Triple-helicate tetrahedral cluster interconversion controlled by host–guest interactions. (a) Triple helicate in the crystal structure of tetra-potassium tris[$\mu_2$-2,6-bis(2,3-dihydroxy-benzamido)anthracene]-di-titanium dimethylformamide solvate. (b) $Ti_4L_4$ tetrahedron in the crystal structure of octakis(tetramethylammonium) hexakis[$\mu_2$-2,6-bis(2,3-dioxybenzamido)anthracene]-tetra-titanium dimethylformamide ethyl acetate solvate tetrahydrate.

span over the three equatorial positions of a trigonal bipyramid and with nitrogen occupying one of the two axial positions. When a bulky ligand occupies the remaining axial position, a monomeric complex is usually formed. Such is the case of [Ti(TEA)(OSiPh_3)], which may be synthesized by mixing equimolar quantities of $Ti(OBu^t)_4$, TEA, and triphenylsilanol ($Ph_3SiOH$) in THF [380]. As shown in Figure 67b, releasing the steric pressure, for example, by mixing $Ti(OPr^i)_4$ with TEA, leads to a highly distorted octahedral dimer, $[Ti(TEA)(OPr^i)]_2$, with one alkoxide arm of the TEA ligand found in the bridging position [380]. A very similar configuration, $[Ti(TEA)(OOCH_3)]_2$, is reached after mixing TEA with $Ti(OBu^t)_4$ in the presence of acetic acid (Fig. 67c) [24]. Another example is provided by the reaction of $Ti(NMe_2)_4$ and TEA, leading to $[Ti(TEA)(NMe_2)]_2$ (Fig. 67d) [381]. Owing to the lability of the terminal $NMe_2$ group in this last complex, other titanatranes may be readily synthesized such as $[Ti(TEA)(SPr^i)]_2$ (Fig. 67e) or the interesting pinacol derivative [(TEA)Ti($\mu$-OCMe_2CMe_2O)Ti(TEA)] (Fig. 67f) [382]. Another interesting aspect of the titanatrane fragment is its ability to trap reactive intermediates. For example, in the catalytic enantioselective oxidation of allylic alcohols by alkyl hydroperoxides in the presence of $Ti(OPr^i)_4$ and a chiral tartrate diester (Sharpless oxidation), the formation of a titanium peroxide intermediate was suspected. Figure 67g shows the dimeric edge-sharing pentagonal bipyramidal coordination and the $\eta^2$ coordination of the peroxide ligand evidenced for such a complex $[Ti(TEA)(OOBu^t)]_2$ obtained by mixing $[Ti(TEA)(NMe_2)]_2$ with *tert*-butyl hydroperoxide in dichloromethane at $-78$ °C [383].

The other class of N,O,O′,O″ donors involves acetate groups linked together by a nitrogen atom (nitrilotriacetate = NTA) or by a nitrosyl group (oxyiminodicarboxylate). NTA ligands bind to $Ti^{IV}$ in a very similar
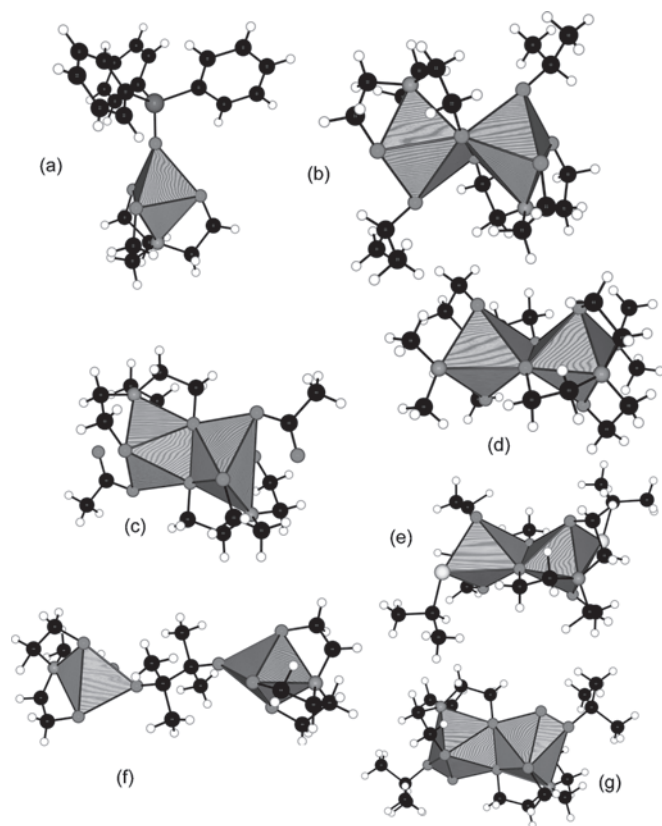
**Figure 67.** Titanatrane family of complexes involving triethanolaminato (TEA) ligands. (a) Monomeric trigonal bipyramidal coordination in the crystal structure of (2,2′,2″-nitrilotriethanolato)-(triphenylsilanolato)-titanium(IV). (b) Highly distorted octahedral dimer in the crystal structure of bis[(μ₂-2,2′,2″-nitrilotriethanolato)-(2-propanolato)-titanium(IV)]. (c) Highly distorted octahedral dimer in the crystal structure of (acetato)titanatrane chloroform solvate. (d) Highly distorted octahedral dimer in the crystal structure of bis[dimethylamido-(μ₂-titanatrane-$N,O,O,O′,O″$)]. (e) Highly distorted octahedral dimer in the crystal structure of bis[μ₂-tris(oxyethyl)amine]-isopropylthiolato-titanium. (f) Association of two [Ti(TEA)] trigonal bipyramids through a picanolate ligand in the crystal structure of bis(titanatranyl)pinacolate. (g) Dimeric edge-sharing pentagonal bipyramidal coordination in the crystal structure of bis[μ₂-$N,N,N$-tris(2-oxoethyl)amine]-bis(*tert*-butylperoxo-$O,O′$)-di-titanium dichloromethane solvate.

fashion as TEA as evidenced in the tetrameric oxidation product, [TiO(NTA)]₄⁴⁻, of a TiCl₃/NTA mixture by hydroxylammonium chloride (Fig. 68a) [384]. In addition, similar to TEA or dipicolinates, these ligands are able to stabilize Ti$^{IV}$ peroxo complexes as evidenced in the molecular structure of Na[Ti(μ₂-O)(η²-O₂)(NTA)]₂ (Fig. 68b) [384]. Hydroxyiminodicarboxylic acids, HON[CH(R)CO₂H]₂, may also react with TiO(acac)₂, leading to a monomeric eight-coordinate complex with a coordination polyhedron considered to be an octahedron in which a pair of *trans* vertices are occupied by η²-N,O groups [386, 387]. The relative orientation of the two η²-N,O groups define the Λ and Δ isomers of the stereogenic metal center. Figure 68c shows the geometry observed for the hida (hydroxyiminodiacetate) derivative, [Ca(H₂O)₄][(Λ,Δ)-Ti(hida)₂] · 2H₂O [386]. Similarly, Figure 68d shows the Δ-helical form, [Ca(H₂O)₄][Ca(H₂O)₅][Δ-Ti($R,R$-hidpa)₂]₂ · 2H₂O, obtained
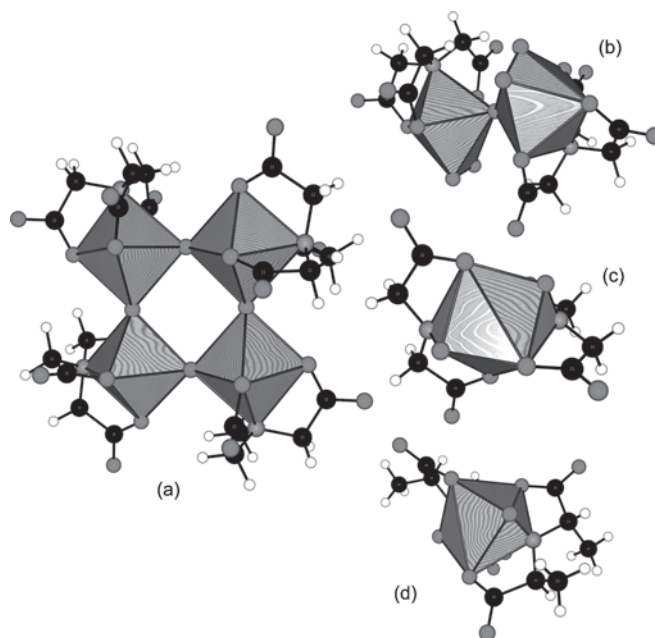


**Figure 68.** Some Ti$^{IV}$ complexes involving nitrilotriacetato (NTA) or oxyiminodicarboxylato ligands. (a) Cyclic octahedral tetramer with μ-oxo bridges in the crystal structure of cesium tetrakis(μ-oxo)-tetrakis[(nitrilotriacetato)-titanium(IV)] hexahydrate. (b) Corner-sharing between two pentagonal bipyramids in the crystal structure of sodium (μ-oxo)-bis[peroxo-(nitrilotriacetate) titanium] undecahydrate. (c) Eightfold coordination observed in the crystal structure of *catena*[(μ₃-oxyiminodiacetato)-(μ₂-oxyiminodiacetato)-tetra-aqua-calcium-titanium dihydrate]. (d) Similar coordination observed in the crystal structure of *catena*{tetrakis[η²-($R,R$)-2,2′-(hydroxyimino) dipropionato]-nona-aqua-di-calcium-di-titanium monohydrate}.

with the hidpa (oxyimino-$R,R$-2,2′-dipropionate) ligand [387]. This last complex is interesting in relation with the fact that vanadium is accumulated in mushrooms of the genus *Amanita* as amadavin, [V(S,S-hidpa)₂]²⁻.

**Complexes with O,N,N′,O′ Donors** The tetradentate (O,N,N′,O′) family is well exemplified by the salen [$N,N′$-ethylenebis(salicylideniminate)] dianions. This ligand is able to bind octahedral metal ions in a *mer*, pseudo-planar configuration, leaving two axial positions available for other ligands that are forced to adopt a *trans* geometry about the metal. Figure 69a shows such a complex [Ti(*mer*-salen)($^t$BuPhO)₂] obtained by reacting Ti(OPr$^i$)₄ with 4-*tert*-butylphenol and H₂salen in dichloromethane [388]. Interestingly enough, treating the readily available [Ti(NBu$^t$)Cl₂(py)₃] complex with a Na₂[Et₂salen] leads to the monomeric [Ti(NBu$^t$)(Et₂salen)] derivative (Fig. 69b) displaying a square pyramidal coordination [389]. Another example of such a monomeric imido complex (Fig. 69c) is provided by the salophen [$N,N′$-phenylene-bis(salicylideniminate) dianion] derivative [Ti(salophen)(NCPh₃)], which has proven to be useful for the realization of molecular batteries based on C—C bond formation [390]. Notice that such imido complexes may also be dimeric species if methoxy groups replace ethyl groups on the salen ligand. Figure 69d shows the resulting octahedral dimers [Ti(NBu$^t$){μ-(MeO)₂salen}]₂ with their
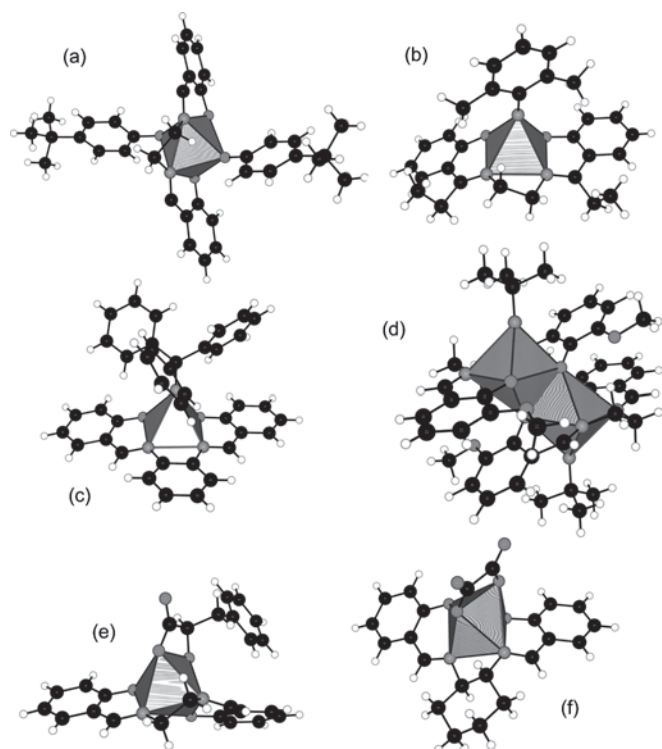
**Figure 69.** Titanium(IV) $N,N'$-ethylenebis(salicylideniminate) (salen) complexes. (a) Monomeric octahedral coordination in the crystal structure of bis(*tert*-butylphenolato)-($N,N'$- bis(salicylidene)ethylenediamine)-titanium(IV). Monomeric square pyramidal coordination in the crystal structure of bis{(*tert*-butylimido)-[$\mu_2$-bis(3-methoxysalicylidene)ethylenediamine]-titanium} dichloromethane solvate (b) and $N,N'$-phenylene-bis(salicylideneiminato)-triphenylmethylimidotitanium (c). (d) Dimeric octahedral coordination in the crystal structure of bis{(*tert*-butylimido)-[$\mu_2$-bis(3-methoxysalicylidene)ethylenediamine]-titanium} dichloromethane solvate. Monomeric octahedral coordination for the salen ligand in the crystal structure of [$N,N'$-ethylene-bis(salicylidenaminato)]-($\alpha$-hydroxybenzylcarboxylato)-titanium (e) and [($R,R$)-1,2-diaminocyclohexane-$N,N'$-bis(salicylidenaminato)]-(oxalato)-titanium dichloromethane solvate (f).

two *mer*-$\mu$-(MeO)$_2$salen bridges [389]. A very similar complex was also obtained by substituting the NBu$^t$ ligand by $N$-2,6-C$_6$H$_3$Me$_2$ [389]. Nevertheless, salen ligands may also be forced into *fac*-geometry for an octahedral complex, leading to an interesting helical conformation. This situation can be realized by reacting *trans*-(salen)TiCl$_2$ with a ($R$)- or ($S$)-$\alpha$-hydroxy carboxylic acid in the presence of a base such as aniline [391]. Figure 69e shows such a distorted octahedral geometry, $\Delta$-[(*fac*-salen)Ti{O$_2$CCH(O)(CH$_2$Ph)}], with the two O atoms of the 3-phenyllactato ligand occupying *cis* positions about the metal. The fact that the $R$-isomer should lead to the $\Delta$ conformation has also been nicely proven by replacing the ethylenediamine bridge by a chiral diamine such as ($R,R$)-1,2-diaminocyclohexane. Thus, by treating the chiral ($R,R$-salchxn)TiCl$_2$ complex (with salchxn = 1,2-diaminocyclohexane-$N,N'$-bis(salicylidenaminato) ligand) by oxalic acid, it was possible to obtain the $\Delta-$[(*fac-R,R*-salchxn)Ti(C$_2$O$_4$)] stereoisomer (Fig. 69c) [391].

One may notice that although monomeric imino [Ti(NR)(salen)] complexes have been characterized, similar

oxo complexes [TiO(salen)] remain unknown. For example, the result of oxidizing [Ti(acacen)Cl] or [Ti(salen)Cl] by dioxygen in THF [acacen = $N,N'$-ethylenebis (acetylacetoniminato) dianion] leads to an oxo-bridged dimer [Cl(acacen)Ti—O—TiCl(acacen)] or [Cl(salen)Ti—O—TiCl(salen)] and not to the expected [TiO(salen)] complex [392]. Figure 70a shows the $\delta$ conformation for the five-membered ring and the capping protective action of BPh$_3$ in the case of the acacen derivative [(acacen)Ti(O=BPh$_3$)] obtained after the removal of chloride ions by NaBPh$_4$. The square pyramidal coordination of titanium is probably due to the *trans* influence of the very short Ti—O bond [168.2(3) pm]. The structure of another product of this reaction is shown in Figure 70b. It is a linear centrosymmetric octahedral tetramer [{Ti(acacen)}$_4$($\mu_2$-O)$_3$(THF)$_2$]$^{2+}$ displaying three oxo bridges with alternating Ti—O distances [169.9(7) pm, 200.6(7) pm, and 181.0(2) pm]. When AgNO$_3$ was used in place of NaBPh$_4$, the result was an oxo dimer [{Ti(acacen)(h$^1$-ONO$_2$)}$_2$($\mu_2$-O)]
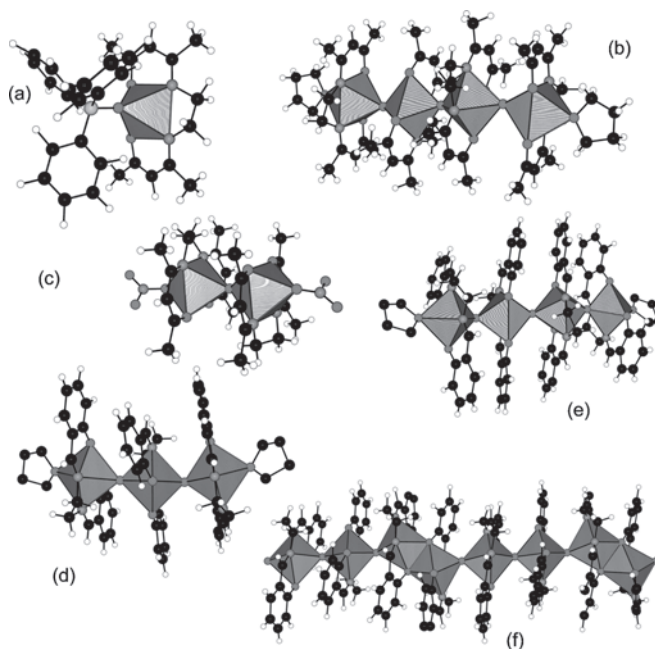


**Figure 70.** Linear titanoxane chemistry induced by the square planar bonding mode of a tetradentate Schiff base ligand. (a) Monomeric square pyramidal coordination in the crystal structure of [$N,N'$-ethylene-bis(acetylacetoneiminato)]-triphenylboryloxy-titanium(IV). (b) Tetrameric octahedral coordination in the crystal structure of tris($\mu_2$-oxo)-tetrakis($N,N'$-ethylenebis(acetylacetoneiminato))-bis(tetrahydrofuran)-tetra-titanium bis(tetraphenylborate). (c) Dimeric octahedral coordination in the crystal structure of ($\mu_2$-oxo)-bis[$N,N'$-ethylene-bis(acetylacetoneiminato)]-bis(nitrato)-di-titanium(IV). (d) Trimeric octahedral coordination in the crystal structure of bis($\mu_2$-oxo)-tris[$N,N'$-ethylene-bis(salicylideneiminato)]-bis(tetrahydrofuran)-tri-titanium(IV) bis(tetraphenylborate) tetrahydrofuran solvate. (e) Tetrameric octahedral coordination in the crystal structure of tris($\mu_2$-oxo)-tetrakis[$N,N'$-ethylene-bis(salicylideneiminato)]-bis(tetrahydrofuran)-tetra-titanium(IV) bis(tetraphenyl-borate) hexadeuteroacetone solvate. (f) Linear octahedral tetramers linked in zigzag chains by bridging salen units in the crystal structure of *catena*-{tris($\mu_2$-oxo)-bis[$\mu_2$-$N,N'$-ethylene-bis(salicylideneiminato)]-bis[$N,N'$-ethylene-bis(salicylideneiminato)]-tetra-titanium(IV) bis(tetraphenylborate) perdeuteroacetone solvate}.

(Fig. 70c) displaying a $(\lambda,\lambda)$ conformation for both aca-cen rings. Following the same synthetic procedure with [Cl(salen)Ti—O—Ti(salen)Cl] and $NaBPh_4$ leads to a mixture of trimers $[\{Ti(salen)\}_3(\mu_2\text{-}O)_2(THF)_2]^{2+}$ (Fig. 70d) and tetramers (Fig. 70e) [392]. However, in the presence of an excess of $NaBPh_4$, a polymeric species, $[\{Ti_2(\mu_2\text{-}salen)(salen)\}_2(\mu_2\text{-}O)_3]^{2+}$, consisting of linear tetramers linked in zigzag chains by bridging salen units, was also obtained (Fig. 70f) [393]. All these examples are coherent with the high nucleophilicity of the titanyl fragment, while the *trans* disposition of vacant coordination sites in Ti(salen) or Ti(acacen) derivatives orient the catenation process toward linear titanoxanes via this original push–pull mechanism [392, 393].

Very recently, there has been a renewed interest in asymmetric catalysis for titanium-salen derivatives acting as catalysts for the enantioselective formation of C—C bonds. To understand the relationship between active and inactive catalysts, several $Ti^{IV}$ complexes have been synthesized. It was thus demonstrated that, at least in two cases, inactivation of the catalysts may involve a reduction in the imine function —HC=N— to a secondary amine —HC(R)—NH—. Figure 71a shows the product $[Ti(flusal)_2\{(OPh)CH(CH_2Ph)(NHflu)\}_2]$ isolated from the reaction between *N*-2-fluorenyl(salicylidenimine) (flusal) and $Ti(CH_2Ph)_4$ [394]. In the same spirit, Figure 71b shows the dimeric complex $[Ti(\mu_2\text{-}O)(tbsaldmbp)]_2$ obtained after hydrolysis of the trigonal bipyramidal complex $[Ti(tbsaldmbp)(CH_2Ph)]$ with tbsaldmbp = *N*-(2′-[1-{4,6-bis(*tert*-butyl)-2-phenol}-2-phenylethyl]-6,6′-dimethyl-1,1′-biphenyl-2-yl)-3,5-bis(*tert*-butyl)salicylideneiminato ligand [395]. Similarly, to elucidate the role of water in the formation of trimethylsilyl ethers of cyanohydrins with up to 90% enantiomeric excess at ambient temperature, the dimeric octahedral complex $[(R,R\text{-}salchxn)Ti(\mu\text{-}O)]_2$ [salchxn = 1,2-diaminocyclohexane-*N*,*N*′-bis(salicylidenaminato) ligand] shown in Figure 71c was isolated from a mixture of $Ti(OPr^i)_4$ and $(R,R\text{-}salchxn)H_2$ in dichloromethane [396]. Another interesting case is provided by the synthesis of bis(sulfonamide) complexes of $Ti^{IV}$ $[Ti(OPr^i)_2\{c\text{-}C_6H_{10}(NHSO_2Ar)\}]$ displaying a very unusual rigid $C_2$ symmetry at the Ti atom. Figure 71d (Ar = *p*-tolyl) and e(Ar = 2,4,6-$Me_3$Ph) shows the geometry of these complexes supposedly responsible for the excellent enantioselectivity observed in the addition of dialkylzinc reagents to aldehydes [397]. To finish, Figure 71f shows the molecular structure of the $C_2$-symmetric dinuclear octahedral complex $[Ti_2(OPr^i)_2(\mu_2\text{-}OPr^i)_2(dtbmp)]$ obtained by treating titanium isopropoxide with 2,2′-dithiobis(5-*tert*-butyl-methylphenol) (dtbmp) [365]. Such complexes are known to be precursors for homogeneous $\alpha$-olefin polymerization catalysts and, more particularly, for the copolymerization of ethylene with bulky styrene monomers.

***Complexes with N,N′,N′,N″ Donors***  To conclude this section devoted to tetradentate ligands, we turn our attention toward some tetraaza-macrocycles. The first obvious class is composed of titanium porphyrin complexes that are able to stabilize either titanyl species [with $d_{TiO}$ = 161.3(5) pm] as evidenced in the crystal structure of 2,3,7,8,12,13,17,18-octaethyl-porphyrinatooxo-titanium(IV) [TiO(OEP)] (Fig. 72a) or to form dioxygen
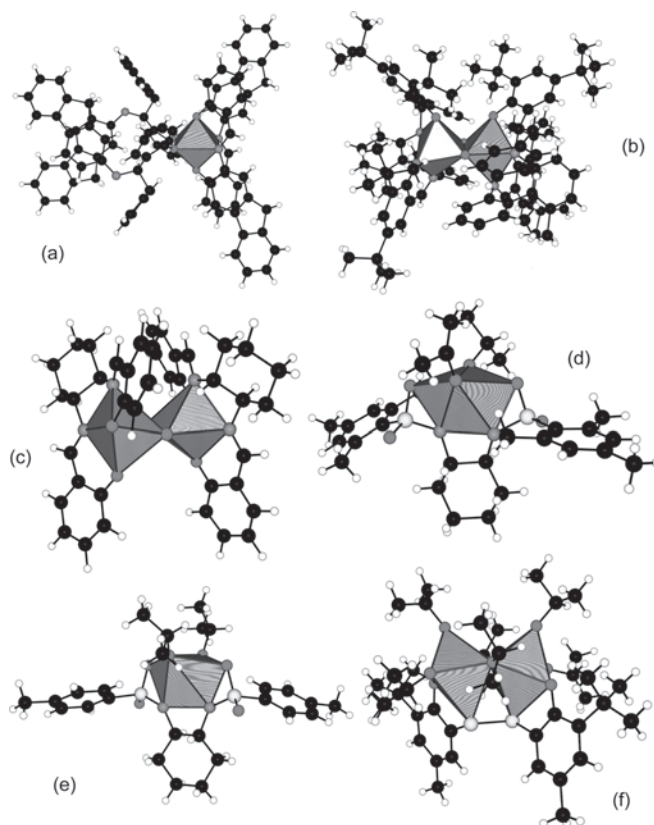


**Figure 71.** Molecular structures of some titanium complexes synthesized for understanding their activity as asymmetric catalysts in the enantioselective formation of C—C bonds. (a) Monomeric octahedral coordination in the crystal structure of bis{[2-(fluorenylamino) benzylmethyl]phenolato}-bis[(*N*-fluorenyl)salicylideneimino]-titanium(IV) toluene solvate. (b) Dimeric octahedral coordination in the crystal structure of bis($\mu_2$-oxo)-bis{*N*-[2′-(1-[4,6-bis(*tert*-butyl)-2-phenol]-2-phenylethyl)-6, 6′-dimethyl-1, 1′-biphenyl-2-yl]-3,5-bis(*tert*-butyl)salicylideneiminato-*N*,*N*′,*O*,*O*′}-di-titanium(IV). (c) Dimeric octahedral coordination in the crystal structure of bis{($\mu_2$-oxo)-[*N*,*N*′-(cyclohexane-1,2-diyl)-bis(salicylaldiminato)]-titanium} chloroform solvate. (d) Sixfold coordination with unusual rigid $C_2$ symmetry for the Ti atom in the crystal structure of bis(isopropoxy)-[1,2-bis(*p*-tolylsulfonamido)cyclohexane]-titanium. (e) Similar coordination as in (d) in the crystal structure of bis(isopropoxy)-{1,2-bis[(2,4,6-trimethylphenyl)sulfonamido]cyclohexane}-titanium. (f) Dimeric octahedral coordination with $\mu$, $\eta^1$-$S_2$ coordination mode for the disulfide function in the crystal structure of bis($\mu_2$-isopropoxo)- [$\mu_2$-2, 2′-dithiobis(6-*tert*-butyl-4-methylphenolato)]-tetra(isopropoxy)-di-titanium.

adducts as in the crystal structure of 2,3,7,8,12,13,17,18-octaethyl-porphyrinatoperoxo-titanium(IV) $[Ti(O_2)(OEP)]$ (Fig. 72b) [398]. In contrast, a monomeric octahedral coordination has been reported in the molecular structure of $[Ti(meso\text{-}OEP)(THF)_2]$ with *meso*-OEP = 2,2,7,7,12,12,17,17-octaethylporphyrinogen (Fig. 72c) [399]. Interest in this complex comes from its ability to stabilize $C_2$ bridges upon reduction with lithium in THF [399].

The other class includes dibenzotetraaza[14]annulene systems that are related to porphyrins, but are characterized by nonplanar geometries with a 10-pm smaller cavity size [400–402]. As with salen derivatives and in contrast to porphyrinato ligands, the titanyl complex [(tmtaa)Ti=O], where tmtaa stands for the dianion
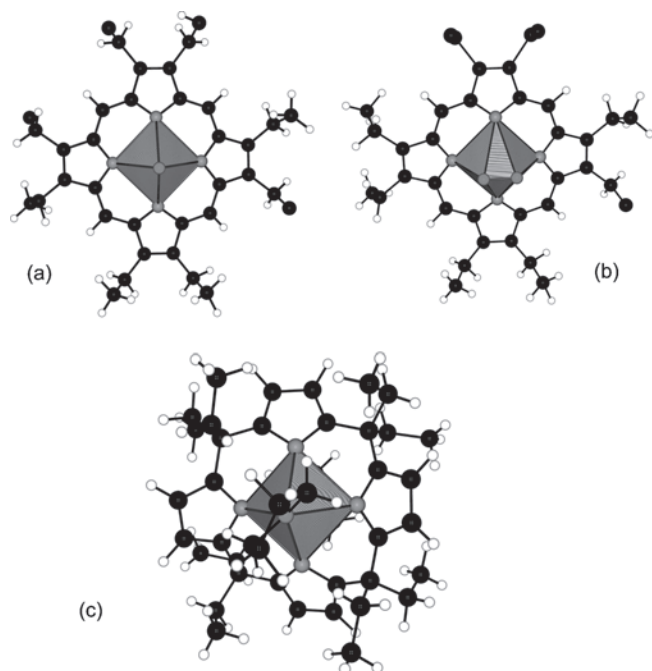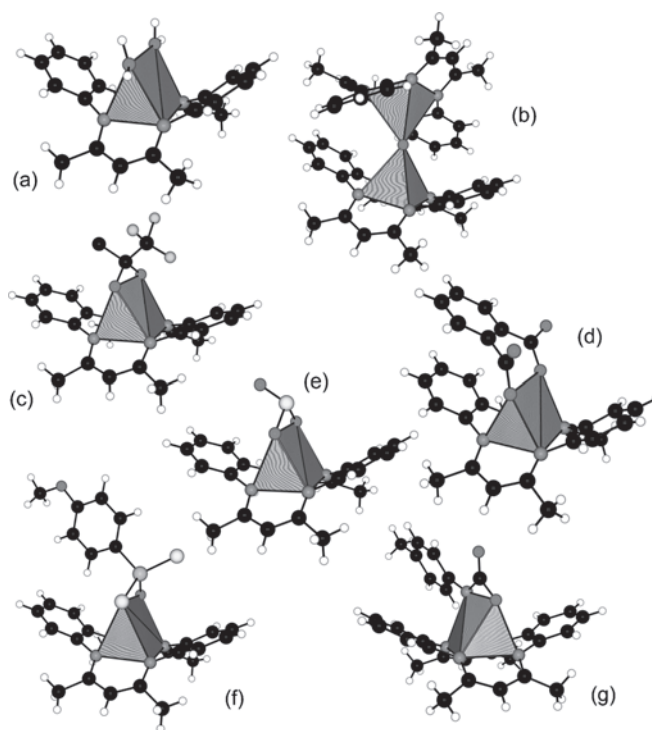
**Figure 72.** Some Ti$^{IV}$ complexes involving porphyrinato ligands. (a) Monomeric square pyramidal coordination in the crystal structure of 2,3,7,8,12,13,17,18-octaethylporphyrinato-(oxo)-titanium(IV). (b) Monomeric $C_{2v}$ sixfold coordination in the crystal structure of 2,3,7,8,12, 13,17,18-octaethylporphyrinato-(peroxo)-titanium(IV). (c) Monomeric octahedral coordination in the crystal structure of *meso*-bis(tetrahydrofuran)-(2,2,7,7,12,12,17,17-octaethylporphyrinogen)-titanium benzene solvate.

of 7,16-dihydro-6,8,15,17-tetramethyldibenzo[*b,i*][1,4,8,11]-tetraazacyclotetradecine, can be synthesized by reacting TiCl$_4$ with tmtaaH$_2$ in the presence of triethylamine. However, it cannot be isolated in the solid state. Instead, treating [(tmtaa)Ti=O] with triflic acid (HO$_3$SCF$_3$) leads either to a monomeric trigonal prismatic diaqua ion, [(tmtaa)Ti(OH$_2$)$_2$]$^{2+}$ (Fig. 73a), or to a dimeric square pyramidal oxo-cation, [(tmtaa)Ti—O—Ti(tmtaa)]$^{2+}$ (Fig. 73b) [401]. Alternatively, this titanyl complex may also be involved in various cycloaddition reactions across the Ti=O bond, leading to monomeric trigonal prismatic complexes [(tmtaa)Ti(X)] by reaction with CF$_3$(Me)C=O (Fig. 73c), phthalic anhydride (Fig. 73d), SO$_2$ (Fig. 73e) [400, 401], and also with Lawesson's reagent, OSP(=S)(C$_6$H$_4$OMe) (Fig. 73f) [401]. Corresponding imido complexes such as [(tmtaa)Ti(NR)] are also known and are able to react with carbon dioxide, yielding [(tmtaa)Ti{N(Tol)C(O)O}] complexes (Fig. 73g) [402].

### 3.4.5. Complexes Involving Hexadentate Ligands

Polycatecholates are important ligands found in siderophores (microbial iron-chelating agents), owing to their ability to dissolve highly polymeric metal oxides. This property has led to the development of the siderophore-like tripace ligand [(*N,N,N*-tripropyl)amine-3,3′,3″-trioxytris(3-catechol)], and the corresponding Ti$^{IV}$ anion [Ti(tripace)]$^{−}$ has been synthesized (Fig. 74a) in order to model



**Figure 73.** Molecular structures of Ti$^{IV}$ complexes involving the tetradentate tmtaa ligand with tmtaa = 7,16-dihydro-6,8,15,17-tetramethyldibenzo[*b, i*][1,4,8,11]-tetraazacyclotetradecinato ligand. (a) Monomeric trigonal prismatic coordination in the crystal structure of [(tmtaa)Ti(OH$_2$)$_2$][CF$_3$SO$_3$]$_2$. (b) Dimeric square pyramidal coordination in the crystal structure of [(tmtaa)Ti—O—Ti(tmtaa)][CF$_3$SO$_3$]$_2$. Other complexes are all monomeric trigonal prismatic species [(tmtaa)Ti(X)] with $X = \eta^2(O,O')$ -O$_2$C(Me)(CF$_3$) (1,1,1-trifluoropropane-2,2-diolato ligand) (c), $X = o$-C$_6$H$_4$(CO$_2$)$_2$ (phthalato ligand) (d), X = $\eta^2(O,O')$-SO$_3$ (sulfito ligand) (e), X = $\eta^2(O, S)$-OSP(=S)($p$-C$_6$H$_4$OMe) ($p$-methoxyphenyldithiophosphonato ligand) (f), and X = $N$(Tol)C(O)O ($N$-$p$-tolylcarbamato ligand) (g).

the ability of tripace to reduce the nuclide generator [$^{99m}$TcO$_4$]$^{−}$ and bind the reduced $^{99m}$Tc form [403]. One may also design special macrobicyclic tris(catecholate) ligands such as H$_6$BCT [BCT = tris($N,N'$-diethyl-2,3-dihydroxyterephthalamide)diamine] (Fig. 74b) for the stabilization of the rather unusual trigonal prismatic [Ti(BCT)]$^{2−}$ coordination around Ti$^{IV}$ centers [404]. To understand what algorithms control the formation of single clusters of defined stoichiometry and high symmetry, rather than the construction of a variety of shapes or random polymers, the hexadentate TDHBB = 1,3,5-tris(2,3-dihydroxybenzoylamino)benzene ligand was synthesized. As shown in Figure 74c, when this ligand was mixed with [Ti(OBu$^n$)$_4$] a spontaneous association into a [Ti$_4$(TDHBB)$_4$]$^{8−}$ tetrahedron was observed as predicted by the imposed threefold ligand symmetry [405]. Such a behavior could explain why nature provides numerous examples of noncovalently linked molecular clusters of high symmetry, which spontaneously self-assemble from their subunits. Typical examples are the 24-*mer* apoferritin or the 60-*mer* human rhinovirus protein coat [404].

Another well-known way to design hexadentate ligands is to use ethylenediamine derivatives. As expected, adding
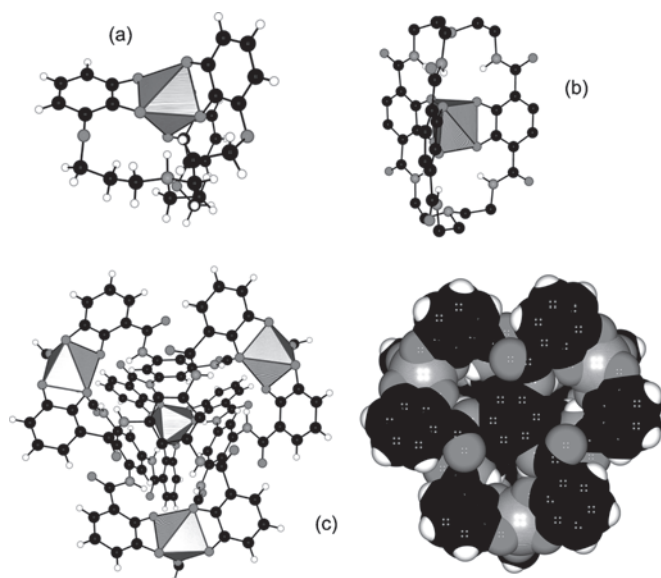
**Figure 74.** Molecular structures of some Ti$^{IV}$ tris(catecholate) complexes. (a) Monomeric octahedral coordination in the crystal structure of triethylammonium ($N,N,N$-tripropyl)amine-3, 3′, 3″-trioxytris(3-catecholato-$O,O'$)-titanium(IV) acetonitrile solvate. (b) Trigonal prismatic coordination reached with a macrobicyclic tris(catecholate) ligand in the crystal structure of dipotassium [tris($N,N'$-diethyl-2,3-dihydroxoterephthalamide)diamine]-titanium(IV) dimethylformamide solvate dihydrate. (c) Tetrameric octahedral coordination of a Ti$_4$L$_4$ tetrahedron in the crystal structure of octakis(triethylammonium) tetrakis-[$\mu_3$-benzene-1,3,5-tris(2,3-dihydroxybenzoylamino)]-tetra-titanium(IV).

ethylenediaminetetracetate (edta) to an aqueous solution at pH<1.0 has allowed for the isolation of a [Ti(edta)(H$_2$O)] complex displaying a pentagonal bipyramidal structure (Fig. 75a) [406]. In this structure, the pentagonal plane is formed by the two nitrogen atoms, two carboxylato ligands, and one aquo ligand. Reacting titanocene dichloride Cp$_2$TiCl$_2$ with Na$_2$H$_2$edta in aqueous methanol formed the same complex [407].

The same coordination polyhedron for Ti$^{IV}$ was evidenced in the thped = $N,N,N',N'$-tetrakis-(2-hydroxypropyl)ethylenediamine (quadrol) [408] and ehpg = $N,N'$-ethylenebis(o-hydroxyphenylglycine) [409] ligands. The [Ti(thped)]$_2$ complex (Fig. 75b), readily formed by reacting Ti(OPr$^i$)$_4$ with H$_4$thped, is a dimeric species with each titanium atom chelating to a N$_2$O$_5$ donor set and with one arm of each thped ligand found in the bridging position between the two titanium centers [408]. Things are more complicated with the ehpg ligand, which contains two chiral carbon atoms and two prochiral nitrogen atoms. When Cp$_2$TiCl$_2$ is reacted with the racemic ligand C($S,S$) or C($R,R$) in water, a monomeric pentagonal bipyramid [Ti(ehpg)(H$_2$O)] complex is obtained (Fig. 75c), displaying the unusual $\Lambda SS = $ N($S,S$)C($S,S$) or $\Delta RR = $ N($R,R$)C($R,R$) form [409]. In stark contrast, if the *meso* ligand C($R,S$) is used, the result is the selective formation of a dimeric oxo complex [{Ti(Hehpg)(H$_2$O)}$_2$O] (Fig. 75d) with both N($R,R$)C($R,S$) and N($S,S$)C($S,R$) isomers in the unit cell. Finally, monomeric octahedral coordination for the Ti atom implying hexadentate ligands is possible and has been evidenced with tben = $N,N,N',N'$-tetrakis(2-
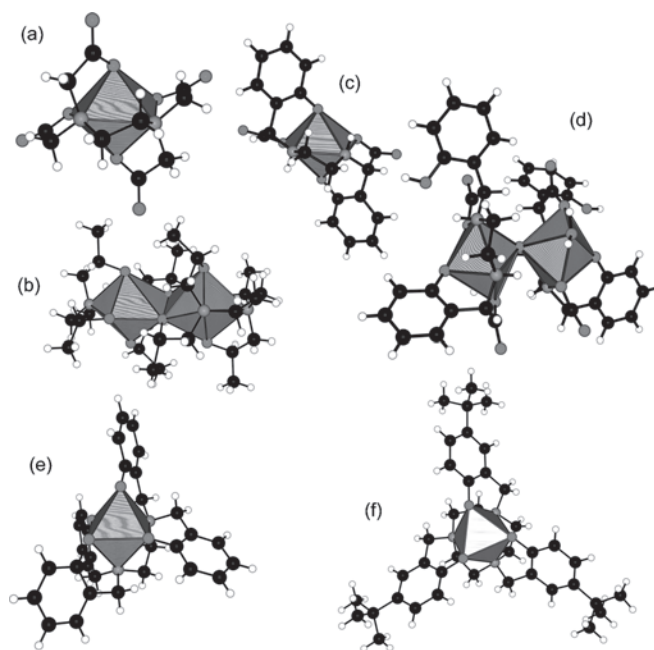


**Figure 75.** Molecular structures of Ti$^{IV}$ complexes involving hexadentate ligands derived from polyamines. (a) Monomeric pentagonal bipyramidal coordination in the crystal structure of aqua-($N,N,N',N'$-ethylenediamine-tetra-acetato)-titanium(IV). (b) Dimeric pentagonal bipyramidal coordination with oxypropyl bridges in the crystal structure of bis[$N,N,N',N'$-tetrakis(2-hydroxypropyl)ethylenediamine]-titanium(IV) toluene solvate. (c) Monomeric pentagonal bipyramidal coordination in the crystal structure of aqua-{rac-$N,N'$-ethylene-bis[(2-oxyphenyl)glycine]}-titanium(IV) hydrate. (d) Dimeric pentagonal bipyramidal coordination in the crystal structure of ($\mu_2$-oxo)-bis{aqua-[meso-$N,N'$-ethylene-([2-oxyphenyl]glycine)([2-hydroxyphenyl]glycine)]-titanium(IV)} tridecahydrate. (e) Monomeric octahedral coordination in the crystal structure of [$N,N,N',N'$-tetrakis(2-hydroxybenzyl)ethylenediamine]-titanium(IV) dichloromethane solvate. (f) Monomeric octahedral coordination in the crystal structure of [1,4,7-tris(5-*tert*-butyl-2-hydroxybenzyl)-1,4,7-triazacyclononane]-titanium(IV) tetraphenylborate.

hydroxybenzyl)ethylenediamine and tbtacn = 1,4,7-tris(5-tert-butyl-2-hydroxybenzyl)-1,4,7-triazacyclononane ligands. The first one [Ti(tben)] (Fig. 75e) was obtained by reacting titanium isopropoxide with H$_4$tben in methanol [410]. The second one [Ti(tbtacn)]$^+$ (Fig. 75f) involved oxidation of a TiCl$_3$/K$_3$tbtacn mixture in acetonitrile in the presence of triethylamine [411].

# 4. HYBRID ORGANIC–INORGANIC TiO$_2$-BASED MATERIALS

Interest in the titanium alkoxides and allied derivatives just reviewed stems from their possible use in the design of completely new organic–inorganic hybrid materials. Accordingly, the combination into a single phase of important properties such as high transparency (glasslike), low-temperature processing (polymer-like), and sufficient thermal stability (ceramic-like) [412] characterize all these new materials.

## 4.1. Hybrid Materials with Si—O—Ti Bonds

One of the very first reports in this field was the realization of hard contact lenses using a mixture of epoxide and methacryloxy-substituted alkoxysilanes and Ti alkoxides [413]. In this case, the linear cross-linking between the siliceous network and the polymethacrylate chains confers sufficient tensile strength to the hybrid material. Moreover, the incorporation of titania led to dense, high-refraction-index ($n_D = 1.533$) monolithic products displaying minor shrinkage during curing and good abrasion resistance [412]. Finally, the $O_2$ permeabilities were ensured by silicon-like O—Si—R structure elements, while glycol residues formed from epoxide radicals provided good wettability (contact angles with water of $25° \pm 5°$). Another interesting more recent example is provided by the use of 3-(glycidoxypropyl)-trimethoxysilane (GTPMS) and $Ti(OBu^n)_4$ or $TiCl_4$ for the sol–gel design of a hybrid host matrix for optical limiting applications [414]. Organic guest molecules displaying nonlinear optical properties such triethoxysilane-fulleropyrrolidine derivatives can be easily trapped in the host matrix, avoiding clustering of the active molecules.

### 4.1.1. Hybrids Based on TiO₄ Tetrahedra

To get a better understanding of the hydrolytic stability of the Si—O—Ti bonds in these hybrid materials, titanodiphenylsiloxane complexes have been synthesized by reacting diphenyldisiloxanediol (DPSD) with $Ti(OPr^i)_4$ and acetylacetone (acac) [415]. Figure 76a shows the dimeric octahedral coordination in the complex $[\{Ti(acac)(THF)\}_2\{\mu_2\text{-}(O,O')\text{-}O_2SiPh_2\}_3]$ displaying an 11-membered bicyclic $Ti_2O_6Si_3$ cage as the central unit. When THF was replaced by dioxane, a chain compound based on these cages bridged by dioxane molecules was characterized (Fig. 76b). Simple eight-membered $Si_2O_4Ti_2$ rings were also evidenced in $[\{(acac)_2Ti\}_2(\mu_2\text{-}O_2SiPh_2)_2]$ (Fig. 76c) as well as in $[(acac)_2Ti\{O(SiPh_2O)_3\}]_2$ [416]. Another kind of eight-membered $Si_3O_4Ti$ ring was identified in $[\{(acac)_2Ti\}_2(\mu_2\text{-}O_2SiPh_2)_2]$ (Fig. 76d). For such titanasiloxanes, the hydrolytic stability of the Si—O—Ti bond was found to decrease in the order cyclodimer > spirocyclomonomer > bicyclodimer [415]. If two monodentate pyridine molecules replace one bidentate acac ligand, a spiro[7.7]titanaheptasiloxane may be obtained (Fig. 76e) by reaction of $TiCl_4$ with $[Ph_4Si_2O(OLi)_2]$ in pyridine [418, 419]. In deep contrast, a similar reaction performed with $[Ph_4Si_2O(ONa)_2]$ gave the tris(tetraphenyldisiloxanediolato) complex $[Ti\{O(SiPh_2O)_2\}_3]^{2-}$ (Fig. 76f) displaying a six-membered titanasiloxane ring [419]. Finally, a monomeric octahedral complex $[Ti(OSiPh_3)_2\{O_2CN(Pr^i)_2\}_2]$ may be obtained by treating the hydrocarbon soluble $N,N$-diisopropylcarbamato derivative $[Ti(OOCNPr^i_2)_4]$ by triphenylsilanol (Fig. 76g) [420].

Tetrahedral coordination of Ti atoms has also been characterized for such mixed Si—O—Ti species. The development of this kind of chemistry was motivated by the remarkable properties of titanium silicalite-1 (TS-1). In the presence of hydrogen peroxide as the oxidant, this zeolitic material was active for a wide range of reactions. Catalyzed reactions involve epoxidation of alkenes,
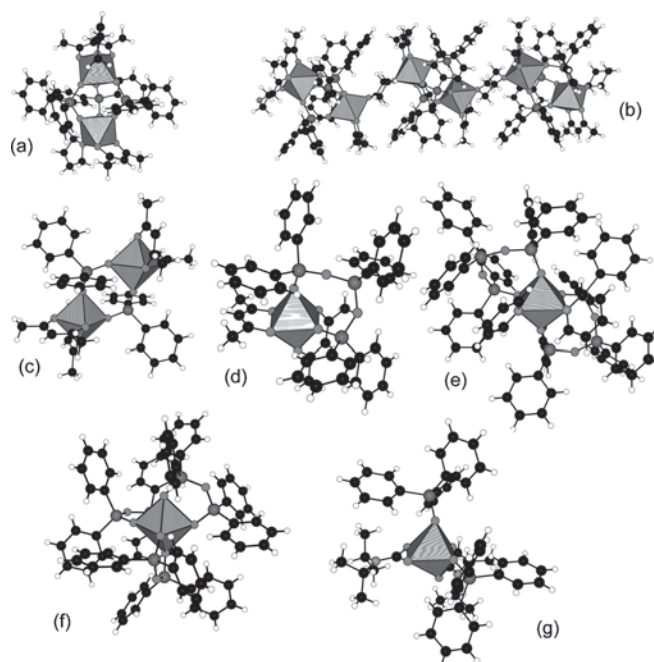


**Figure 76.** Molecular structures of some octahedral Ti$^{IV}$ complexes involving Si—O—Ti bonds. (a) Dimeric octahedral coordination in the crystal structure of tris($\mu_2$-diphenylsiloxa)-bis[(acetylacetonato)-tetrahydrofuran-titanium]. (b) Octahedral chain based on previous dimeric species in the crystal structure of *catena*-{tris($\mu_2$-diphenyl-siloxa)-($\mu_2$-dioxane)-bis[(acetylacetonato)-titanium] dioxane solvate}. (c) Dimeric octahedral coordination in the crystal structure of bis($\mu_2$-diphenylsiloxa)-bis[bis(acetylacetonato)-titanium] dioxane solvate. (d) Monomeric octahedral coordination in the crystal structure of bis(acetylacetonato)-(hexaphenyltrisiloxa-$O,O'$)-titanium. (e) Monomeric octahedral coordination in the crystal structure of cis-bis(pyridine)-bis(hexaphenyl-trisiloxanediolato-$O,O'$)-titanium(IV) toluene solvate. (f) Monomeric octahedral coordination in the crystal structure of sodium tris(tetraphenyldisiloxanediolato)-titanium pyridine solvate $[Ti\{O(SiPh_2O)_2\}_3\{Na(py)\}_2] \cdot py$. (g) Monomeric octahedral coordination in the crystal structure of bis-($N,N$-diisopropylcarbamato)-bis(triphenylsilanolato)-titanium(IV).

oxidation of alcohols into aldehydes or ketones, hydroxylation of aromatics, ammoxidation of ketones, and oxidation of alkanes to alcohol–ketone mixtures [421]. The most simple tetrahedral species is the $[Ti(OSiPh_3)_4]$ complex (Fig. 77a) readily synthesized by treating $Ti(OBu^n)_4$ or $[Ti(OOCNPr^i_2)_4]$ by an excess of triphenylsilanol [420, 422]. A spiro[9.9] bicyclic compound $[TiO_2(OSiPh_2)_8]$ (Fig. 77b) was obtained upon mixing $Ti(OBu^n)_4$ with diphenyldisiloxanediol [415, 423]. By reacting incompletely condensed silsesquioxanes $R_7Si_7O_9(OH)_3$ (R = $c$-$C_5H_9$, c-$C_6H_{11}$, c-$C_7H_{13}$) with homoleptic $TiL_4$ complexes (L = $CH_2Ph$, $NMe_2$, $OSiMe_3$, $OPr^i$, $OBu^t$), it was possible to form a cubane-like $[TiL\{(c\text{-}C_6H_{11})_7Si_7O_{12}\}]$ silsesquioxane complex involving a tripodal Ti atom (Fig. 77c) [421, 424]. When $(c\text{-}C_6H_{11})_7Si_7O_9(OSiMe_3)(OH)_2$ was reacted with $Ti(OPr^i)_4$, a $[Ti\{(c\text{-}C_6H_{11})_7Si_7O_{11}(OSiMe_3)\}_2]$ complex with a tetrapodal Ti atom was obtained (Fig. 77d) [421]. Using both compounds as catalysts in the epoxidation of oct-1-ene with *tert*-BuOOH showed that the tripodal form was much more active than the tetrapodal form [421]. Attempts to
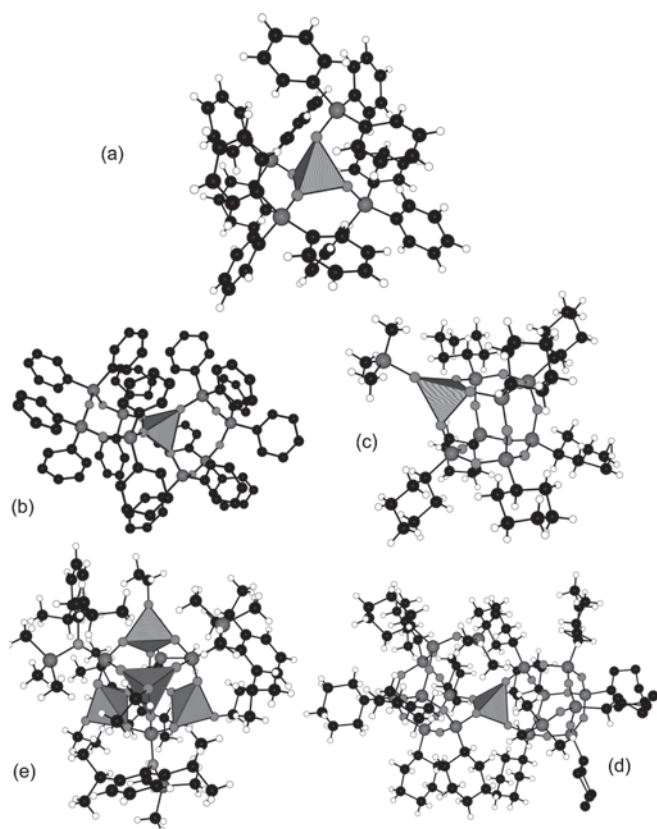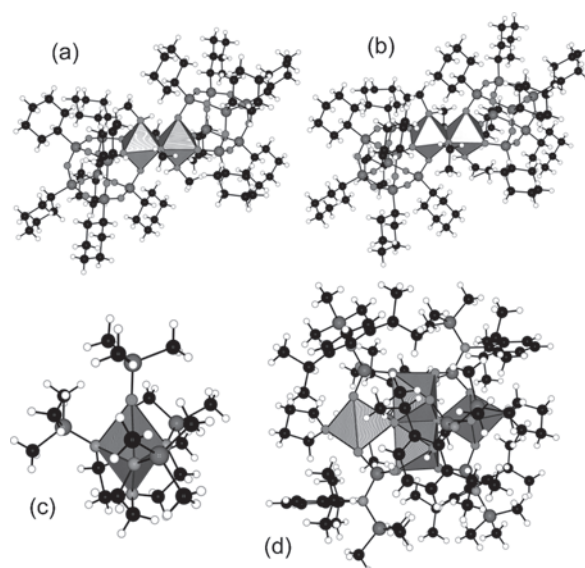
**Figure 77.** Molecular structures of some tetrahedral Ti<sup>IV</sup> complexes involving Si—O—Ti bonds. (a) Single tetrahedron in the crystal structure of tetrakis(triphenylsiloxy)-titanium(IV). (b) Single tetrahedron in the crystal structure of hexadecaphenyl-octasiloxy-spiro(9.9) titanium(IV). (c) Single tetrahedron in the crystal structure of heptakis-(cyclohexyl)-(trimethylsiloxy)-titanaheptasilasesquioxane dodecakis($\mu_2$-oxo)-heptakis(cyclohexyl)-trimethylsiloxy-hepta-silicon-titanium(IV). (d) Single tetrahedron in the crystal structure of bis{heptakis(cyclohexyl)-(trimethylsiloxy)-heptasilasesquioxane}. (e) Tetrameric cubic-like titanasiloxane in the crystal structure of dodecakis($\mu_2$-oxo)-tetrakis-{[(2,6-di-isopropylphenyl)(trimethylsilyl)amino]-silicon}-tetrakis(ethoxy-titanium) ethanol solvate.

increase the Ti/Si ratio required the use of better synthons such as aminosilanetriols RN(SiMe$_3$)[Si(OH)$_3$], yielding cubane-like [RN(SiMe$_3$SiO$_3$Ti(OR′)]$_4$ titanasiloxanes (R = 2,6-Me$_2$C$_6$H$_3$, 2,6-Pr$^i_2$C$_6$H$_3$, 2,4,6-Me$_3$C$_6$H$_3$; R′ = Et, Pr$^i$) (Fig. 77e) [425].

## 4.1.2. Hybrids Based on TiO$_5$ and/or TiO$_6$ Polyhedra

The last kind of problem that may be addressed in these titanasiloxane complexes is the transformation of tetrahedral to octahedral coordination for Ti<sup>IV</sup> centers and the characterization of fivefold coordinated complexes. For example, it was shown using $^{13}$C-NMR that in CDCl$_3$ solutions the complex [Ti(OPr$^i$){($c$-C$_6$H$_{11}$)$_7$Si$_7$O$_{12}$}] was engaged in an equilibrium between the four-coordinate monomer, whose molecular structure is depicted in Figure 77c, and a five-coordinate dimer [426]. Addition of methanol then led to fast ligand exchange and to the almost exclusive formation of the six-coordinate dimer (Fig. 78a)



**Figure 78.** Molecular structures of some octahedral and pentacoordinated Ti<sup>IV</sup> complexes involving Si—O—Ti bonds. (a) Dimeric octahedral coordination in the crystal structure of bis[($\mu_2$-methoxo)-(methanol)-heptakis(cyclohexyl)-titanosilsesquioxane]. (b) Dimeric octahedral coordination in the crystal structure of bis($\mu_2$-ethoxo)-bis[dodecakis($\mu_2$-oxo)-(ethanol)-heptakis(cyclohexyl)-heptasilicontitanium] diethyl ether solvate. (c) Tetrameric mixed octahedral and trigonal bipyramidal coordination in the crystal structure of bis($\mu_3$-oxo)-bis{$\mu_3$-[(2,6-di-isopropylphenyl)(trimethylsilyl)amino]-silanetriolato}-tetrakis{$\mu_2$-[(2,6-di-isopropylphenyl)(trimethylsilyl)amino]-silanetriolato}-bis(tetrahydrofuran)-tetra-titanium $n$-hexane solvate. (d) Monomeric trigonal bipyramidal coordination in the crystal structure of (trimethylsiloxy)-($N,N′,N″$-tris[(trimethylsilyl)-(2-aminoethyl)]amine)-titanium(IV).

[Ti($\mu$-OMe)(MeOH){($c$-C$_6$H$_{11}$)$_7$Si$_7$O$_{12}$}]$_2$. A very similar [Ti($\mu$-OEt)(EtOH){($c$-C$_6$H$_{11}$)$_7$Si$_7$O$_{12}$}]$_2$ molecular structure has also been reported (Fig. 78b) [427]. Interestingly, in the epoxidation of cyclohexene by *tert*-BuOOH, the catalytic activity of the isopropoxide monomer was much lower than that of the methoxy dimer [426]. This suggests that accessibility to the tetrahedral Ti<sup>IV</sup> center was the main parameter controlling the reactivity of the growing family of titanosilicates (titano-zeolite $\beta$, TS-1, TS-2, ETS-4, ETS-10, JDF-L1, and Ti-MCM41) [426]. Another interesting tetrameric complex [Ti$_4$($\mu_3$-O)$_2${$\mu_3$-(dipptmsa) SiO$_2$(OH)}$_2${$\mu_2$-(dipptmsa)SiO$_2$(OH)}$_4$(THF)$_2$] showing both trigonal bipyramidal and octahedral coordination (Fig. 78c) was also obtained by reaction of [Cp*TiCl$_3$] with (dipptmsa)Si(OH)$_3$ ={(2,6-di-isopropylphenyl) (trimethylsilyl)amino}-silanetriol in the presence of THF and NEt$_3$ [428]. Finally, a last case of fivefold coordination was evidenced in the molecular structure of an azatitanatrane complex [Ti(OSiMe$_3$){N(CH$_2$CH$_2$NSiMe$_3$)$_3$}] (Fig. 78d) obtained by reacting NaOSiMe$_3$ with [TiCl {N(CH$_2$CH$_2$NSiMe$_3$)$_3$}] in THF [429].

## 4.1.3. General Classification

The case of well-defined crystalline titanasiloxanes studied just above exemplified the good and rational approach for understanding the behavior of complex materials such as

titanosilicates. Nevertheless, as far as ill-defined and amorphous structures are concerned, hybrid organic–inorganic materials can be grossly divided into two major classes [430, 431].

Class I is characterized by organic molecules or polymers embedded in an organic matrix. Synthetic methods involve formation of the inorganic network in the presence of the organic compound or polymerization of organic monomers inside porous inorganic hosts. Therefore, interactions between both phases can occur only through rather weak van der Waals or hydrogen bonds.

Class II involves materials displaying strong covalent interactions between the inorganic and organic components. Here a new molecular precursor is first synthesized and characterized using conventional methods of organic chemistry and then used in a conventional sol–gel process to get the hybrid material. Here, the occurrence of a strong M—R chemical link between the two components overcomes the problem of phase separation and allows using synthetic strategies derived from block copolymer chemistry.

## 4.2. Hybrid Materials Based on Carboxylate Derivatives

A first limiting factor for the synthesis of class II hybrids using conventional sol–gel processing is the stability toward hydrolysis of the M—R bond linking the organic and inorganic parts. Another important problem is the choice of an inert solvent for performing the hydrolysis reaction under homogeneous conditions. These problems may be particularly awkward in the case of transition metal oxide–based hybrids. The nonhydrolytic solvent-free sol–gel process can be of considerable help. Its application to the design of hybrid organic–inorganic materials has been very recently reviewed [432].

### 4.2.1. Materials with RCOOH/Ti ≥ 2

One of the very first reports of a solvent-free sol–gel process concerned the spontaneous *in-situ* formation of amorphous titanium oxo-acetate fibers $TiO(OAc)_2$ upon mixing titanium alkoxides with pure acetic acid [433]. In contrast, crystalline phases displaying the same $TiO(OOCR)_2$ stoichiometry were obtained by reacting $TiCl_4$ with various fluoroaryl acids RCOOH ($R = C_6F_5$, $CH_2C_6F_5$) in toluene [434]. Their X-ray molecular structures reveal an octameric unit ("octacyclane" shape) with a unique 16-membered $Ti_8O_8$ ring (Fig. 79a). More recently, a closely related cyclic oligomer $Ti_9O_8(OPr^i)_4(CH_2C(Me)COO)_{16}$ has been characterized ("nonacyclane" shape) by reacting $Ti(OPr^i)_4$ with an excess of methacrylic acid [435] (Fig. 79b). Notice that fully tetrasubstituted $Ti(O_2CR)_4$ derivatives seem to be unstable, except for carbamato species ($R = NR_2$) that have been characterized in the solid state as a distorted dodecahedron with $R = Pr^i$ (Fig. 79c) [420].

### 4.2.2. Materials with RCOOH/Ti < 2

When the carboxylic derivative is not in excess, hexameric octahedral species are usually obtained, displaying no more than five different topologies (Fig. 80). The
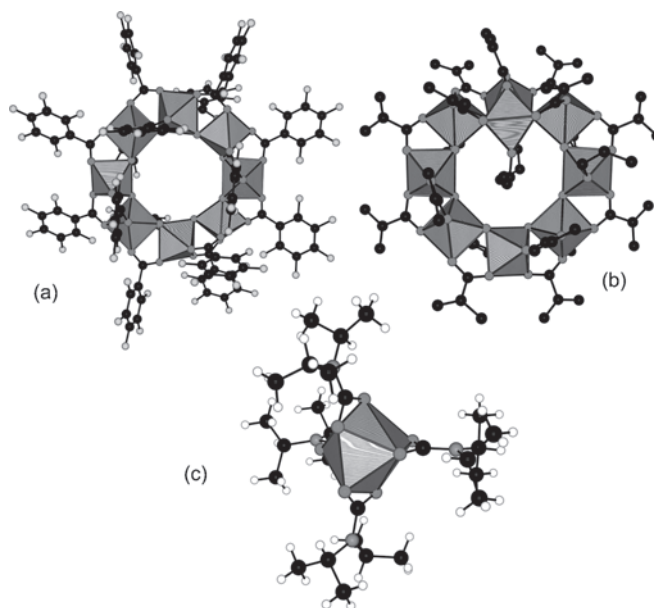


**Figure 79.** Molecular structures of some $Ti^{IV}$ complexes involving carboxylate derivatives. (a) Sixteen-membered ring in the molecular structure of octakis[($\mu_2$-oxo)-hexadecakis($\mu_2$-perfluorobenzoato-$O,O'$)-titanium] toluene solvate. (b) Ring of nine [$TiO_6$] octahedra in the molecular structure of bis($\mu_3$-oxo)-hexakis($\mu_2$-oxo)-hexadecakis($\mu_2$-methacrylato)-tetrapropoxy-nona-titanium. (c) Eightfold coordination with slightly asymmetric carbamato ligands in a distorted dodecahedral geometry in the crystal structure of tetrakis($N,N$-di- isopropylcarbamato) titanium(IV).

first structurally characterized hexamer was [$Ti_6(\mu_3$-O)$_2(\mu_2$-O)$_2(\mu_2$-OEt)$_2(\mu$-CH$_3$COO)$_8$(OEt)$_6$], which was obtained by reacting $Ti(OEt)_4$ with glacial acetic acid and ethanol in 1/4/5 molar ratios [436]. Its structure being reminiscent of the topology of the rutile structure, this shape (Fig. 80c) is referred to as "rutilane" [216]. Another topology (Fig. 80b) made of two corner-sharing trimers ("bitricyclane" shape) was evidenced in [$Ti_6(\mu_3$-O)$_2(\mu_2$-O)$_2(\mu_2$-OPr$^i)_6(\mu$-CH$_3$COO)$_4$(OPr$^i)_6$] obtained by mixing $Ti(OPr^i)_4$ with glacial acetic acid in a 1 : 2 ratio [285, 437]. Replacing $Ti(OPr^i)_4$ by $Ti(OBu^n)_4$ led to the already known rutilane shape [$Ti_6(\mu_3$-O)$_2(\mu_2$-O)$_2(\mu_2$-OBu$^n)_2(\mu$-CH$_3$COO)$_8$(OBu$^n)_6$] [438]. Initially, it was thought that this change in topology was induced by the different molecular structures of the parent titanium alkoxides $Ti(OR)_4$ (monomeric for $R = OPr^i$ and trimeric for $R = Et$ or $Bu^n$) [437]. However, the characterization of the rutilane shape [$Ti_6(\mu_3$-O)$_2(\mu_2$-O)$_2(\mu_2$-OPr$^i)_2(\mu$-CH$_3$COO)$_8$(OPr$^i)_6$] by mixing $Ti(OPr^i)_4$, acetic acid, and isopropanol [439] invalidates this view. Unfortunately, detailed experimental conditions were not reported in this last case. Consequently, it is not possible to conclude if the change in topology observed with $R = Pr^i$ was due to the introduction of the parent alcohol or to a different $CH_3COOH/Ti$ ratio. Interestingly, the rutilane shape may also be obtained by reacting $Ti(OEt)_4$ with methacrylic acid [440] or $Ti(OPr^i)_4$ with 2-phenylpropionic acid [441]. Attempts to find new molecular shapes were quite successful with the use of a cobalt carbonyl cluster carboxylic acid $(CO)_9Co_3(\mu_3$-CCOOH) displaying reduced acidity relative to acetic acid
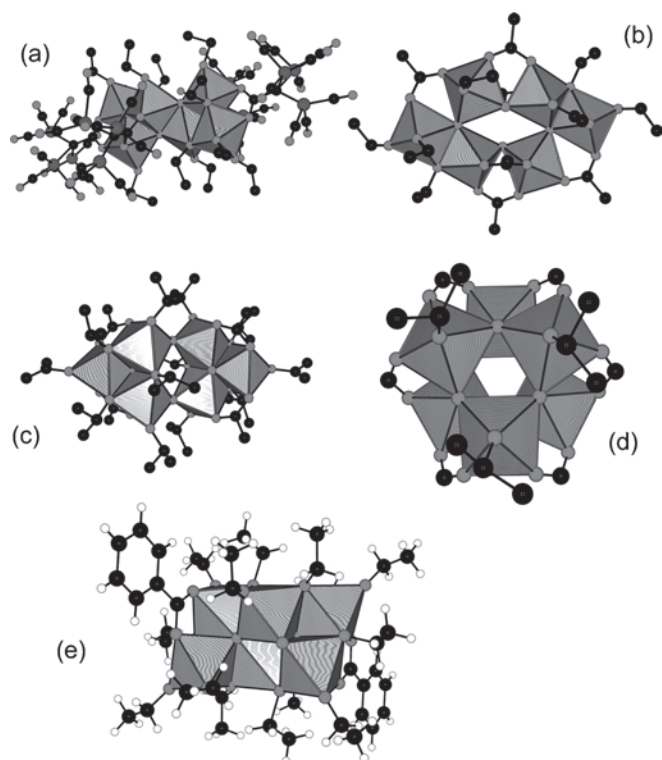
**Figure 80.** Hexameric titanium(IV) oxo-carboxylates formed under hydrolytic conditions. (a) Edge sharing between compact octahedral trimers in the crystal structure of tetrakis[($\mu_5$-methylidynecarboxylato)-($\mu_3$-oxo)-($\mu_2$-ethoxy)]-hexatriacontacarbonyl-octakis(ethoxy)-dodeca-cobalt-hexa-titanium. (b) Corner sharing between compact octahedral trimers in the crystal structure of bis[($\mu_3$-oxo)-($\mu_2$-oxo)-bis($\mu_2$-acetato-$O,O'$)-tris($\mu_2$-isopropoxo)-tris(isopropoxy)-tri-titanium]. (c) Corner sharing between linear octahedral trimers in the crystal structure of bis[($\mu_3$-oxo)-($\mu_2$-oxo)-tetrakis($\mu_2$-acetato-$O,O'$)-($\mu_2$-ethoxo)-tris(ethoxy)-tri-titanium]. Similar complexes $Ti_6O_4(OR)_8(O_2CCH_3)_8$ are known with R = $Pr^i, Bu^n$. (d) Edge sharing between cyclic octahedral trimers in the crystal structure of hexakis[($\mu_3$-oxo)-($\mu_2$-2-phenoxyphenyl)-ethoxy-titanium] toluene solvate. (e) Full edge sharing between cyclic octahedral trimers in the crystal structure of bis{($\mu_4$-oxo)($\mu_2$-oxo)-($\mu_2$-benzoato)-tris($\mu_2$-ethoxo)-tetrakis(ethoxy)-tri-titanium}.

[216]. Consequently, reacting $Ti(OEt)_4$ with the above cluster acid in a 1:2 ratio using THF as a solvent led to the compound $[Ti_6(\mu_3\text{-}O)_4\{\mu\text{-}(CO)_9Co_3(\mu_3\text{-}CCOOH)\}_4(\mu_2\text{-}OEt)_4(OEt)_8]$ displaying a new shape (Fig. 80a) [442] quite reminiscent of the topology of the anatase structure ("anatasane" shape) [216]. A similar structure was reported for the compound $[Ti_6O_4(O_2CCH_2CMe_3)_4(OPr^i)_{12}]$ isolated from the reaction between $Ti(OPr^i)_4$ and *tert*-butyl acetic acid [443]. Soon after, during the study of the reaction between $Ti(OEt)_4$ and 2-phenoxybenzoic acid in a 1 : 2 ratio in refluxing dichloromethane, the "hexaprismane" shape (Fig. 80d) was characterized in the molecular structure of $[Ti_6(\mu_3\text{-}O)_6\{\mu\text{-}(O_2C\text{—}C_6H_4\text{—}OPh)\}_6(OEt)_6]$ [444]. It was also realized using ^{1}H and IR spectroscopy that, under similar conditions, this hexaprismane shape $[Ti_6(\mu_3\text{-}O)_6(\mu\text{-}O_2CR)_6(OR')_6]$ was systematically obtained with other substituents R = Me, $C_6H_4OPh$ and R' = Et, $Pr^i$, but also from the rutilane shape after refluxing in toluene. In

fact, increasing the temperature is not necessary to get the hexaprismane shape. Reacting $Ti(OPr^i)_4$ with formic acid (1:2 ratio) in toluene directly led to $[Ti_6(\mu_3\text{-}O)_6(\mu\text{-}O_2CH)_6(OPr^i)_6]$ [445]. Similar compounds $[Ti_6(\mu_3\text{-}O)_6(\mu\text{-}O_2CR)_6(OPr^i)_6]$ were also obtained with dichloroacetic acid (1:1 ratio) in toluene (R = $CHCl_2$) [446] or with phenylacetic acid (3:2 ratio) in acetone/isopropanol mixtures [216]. Finally, a "bicrossane" shape $[Ti_6(\mu_4\text{-}O)_2(\mu_2\text{-}O)_2(\mu_2\text{-}O_2CC_6H_5)_2(\mu_2\text{-}OEt)_6(OEt)_8]$ was very recently characterized (Fig. 80e) by reacting $[Ti_7O_4(OEt)_{20}]$ with a 1.5 M excess of benzoic acid in benzene solution at ambient temperature [447].

The hydrolytic behavior of these carboxylate derivatives was investigated using the partial charge model [433, 448]. It was shown that alkoxide ligands were preferentially hydrolyzed. Nevertheless, it remains that, under an excess of water, some carboxylate groups may also be removed [449]. Here, switching to amino carboxylate ligands such as $Ti_2(OEt)_6(H_2NCH_2COO)_2$ (Fig. 81a) may be interesting as it has been reported that they should be considerably more stable toward hydrolytic cleavage than acetate ligands [450]. Notice that between monomeric and hexameric species other small oligomers have also been characterized. For example, reacting $Ti(OPr^i)_4$ with trichloroacetic acid (1:2 ratio) in toluene led to the octahedral dimer $[Ti_2(\mu\text{-}O)(\mu\text{-}O_2CCl_3)_2(O_2CCl_3)_2(OPr^i)_2(HO^iPr)_2]$ (Fig. 81b). For a 1:1
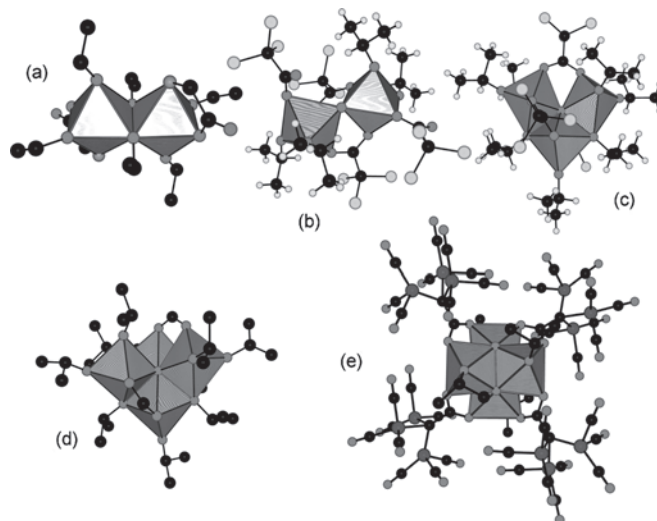


**Figure 81.** Molecular structures of some reaction products obtained by mixing titanium(IV) alkoxides with substituted acetic acid derivatives. (a) Reaction with glycine $H_2NCH_2COOH$ leading to an edge-sharing dimer bis($\mu_2$-ethoxo)-tetrakis(ethoxy)-bis(glycinato-$N,O$)-di-titanium. (b) Reaction with trichloroacetic acid $Cl_3CCOOH$ in 1 : 2 ratio leading to a corner-sharing dimer bis($\mu_2$-trichloroacetato-$O,O'$)-($\mu_2$-oxo)-bis(trichloroacetato-$O$)-bis(2-propanol)-bis(isopropoxy)-di-titanium(IV). (c) Reaction with trichloroacetic acid $Cl_3CCOOH$ in 1 : 1 ratio leading to a trimer ($\mu_3$-oxo)-tris($\mu_2$-trichloroacetato-$O,O'$)-bis($\mu_2$-isopropoxo)-pentakis(isopropoxy)-tri-titanium(IV). (d) Reaction with formic acid $HCOOH$ leading to a cross-shaped tetramer ($\mu_4$-oxo)-bis($\mu_2$-formato)-tetrakis($\mu_2$-isopropoxo)-($\mu_2$-oxo)-hexakis(isopropoxy)-tetra-titanium. (e) Reaction with tricobalt nonacarbonyl acetic acid $[(CO)_3Co]_3CCOOH$ leading to a cubane-shaped tetramer tetrakis[($\mu_5$-methylidynecarboxylato)-($\mu_3$-oxo)-isopropoxy]-hexatriacontacarbonyl-dodeca-cobalt-tetra-titanium.

ratio, it was rather an octahedral trimer [Ti$_3$($\mu_3$-O)($\mu$-O$_2$CCl$_3$)$_3$($\mu_3$-OPr$^i$)$_2$(OPr$^i$)$_5$] (Fig. 81c) that was formed [446]. With Ti(OPr$^i$)$_4$ and formic acid HCOOH (1 : 1 ratio) in toluene, an octahedral tetramer [Ti$_4$($\mu_4$-O)($\mu$-O)($\mu$-OOCH)$_2$($\mu_3$-OPr$^i$)$_4$(OPr$^i$)$_6$] displaying a "crossane" shape (Fig. 81d) was characterized [445]. Finally, reaction between Ti(OR)$_4$ (R = Pr$^i$, Bu$^n$) and nonacarbonyl-tricobalt-acetic acid (CO)$_9$Co$_3$($\mu_3$-CCOOH) (1 : 2 ratio) in THF led to a cubane-shaped tetramer [Ti$_4$($\mu_4$-O)$_4${$\mu$-(CO)$_9$Co$_3$($\mu_3$-CCOOH)}$_4$(OR)$_4$] (Fig. 81e) [442, 451]. In the presence of phenol or 2,6-dimethylphenol, the corresponding derivatives (R = Ph or Me$_2$—C$_6$H$_3$) could also be synthesized [451].

## 4.3. Hybrid Materials with Si—O—P Bonds

Nonhydrolytic sol–gel methods for hybrid materials involving new metal oxide phosphonates have recently been developed [452].

### 4.3.1. Molecular Complexes

Figure 82a and b shows the molecular structure of these new titanium oxide alkoxide phosphonates [Ti$_4$O(OPr$^i$)$_8$(RPO$_3$)$_3$(DMSO)] (R = Ph, Me, $^t$Bu, 4-CNPh) [453, 454] and [Ti$_4$O(OPr$^i$)$_8$(PhPO$_3$)$_3$(THF)] [455] obtained by reacting Ti(OPr$^i$)$_4$ with a solution of RP(O)(OH)$_2$. When R = Bu$^t$, another cyclic octahedral tetramer [Ti(OPr$^i$)$_2$($^t$BuPO$_3$)]$_4$ displaying $\mu_3$-$t$-butyl-phosphonato bridges and 5 + 1 coordination for the Ti atoms may be isolated (Fig. 82c) [454]. A different result was obtained when Ti(OMe)$_4$ was reacted with (Bu$_4^n$N)[PhPO$_2$(OH)] in acetonitrile [456]. In this case (Fig. 82e), an octahedral edge-sharing dimeric anion [Ti(OMe)$_3$(O$_3$PPh)]$_2^{2-}$ displaying both $\mu_2$-methoxo and $\mu_2$-phenylphosphonato bridges was characterized. In a very similar way, by mixing Ti(OPr$^i$)$_4$ with phosphinic acids such as Ph$_2$P(O)OH, a cubelike octahedral tetramer [Ti(OPr$^i$)($\mu_2$-O$_2$PPh$_2$)($\mu_3$-O)$_4$]$_4$ may be obtained displaying $\mu_3$-oxo and $\mu_2$-phenylphosphinato bridges (Fig. 82d) [453]. A big difference with carboxylic acids is the absence of esterification between the liberated alcohols and the phosphonic or phosphinic acids. Hybrid organic–inorganic materials displaying a homogeneous distribution of phosphonate groups in a TiO$_2$ network have been obtained after hydrolysis condensation of these new titanium phosphonate precursors [452]. Finally, during attempts to prepare an alkoxide KTP precursor containing titanium, phosphorus, and potassium in a 1 : 1 : 1 stoichiometry, two phosphato complexes were isolated. The first one was a dimeric trigonal bipyramidal complex [Ti(OPr$^i$)$_3${O$_2$P(OBu$^t$)$_2$}]$_2$ displaying $\mu_2$-di-*tert*-butylphosphato bridges (Fig. 82f) [457]. The other one was a face-sharing octahedral dimer K[Ti$_2$(OEt)$_8${O$_2$P(OBu$^t$)$_2$}$_2$] with three $\mu_2$-ethoxo bridges (Fig. 82g) [457]. Other phosphato complexes such as a dimeric [$^t$BuN=Ti{$\mu_2$-O$_2$P(OSiMe$_3$)$_2$}$_2$]$_2$ and a tetrameric [Ti($\mu_3$-O)(OSiMe$_3$){$\mu_2$-O$_2$P(OBu$_2^t$)$_2$}]$_4$ cubane-like complexes have also been synthesized [458], but are much too disordered to be drawn here.
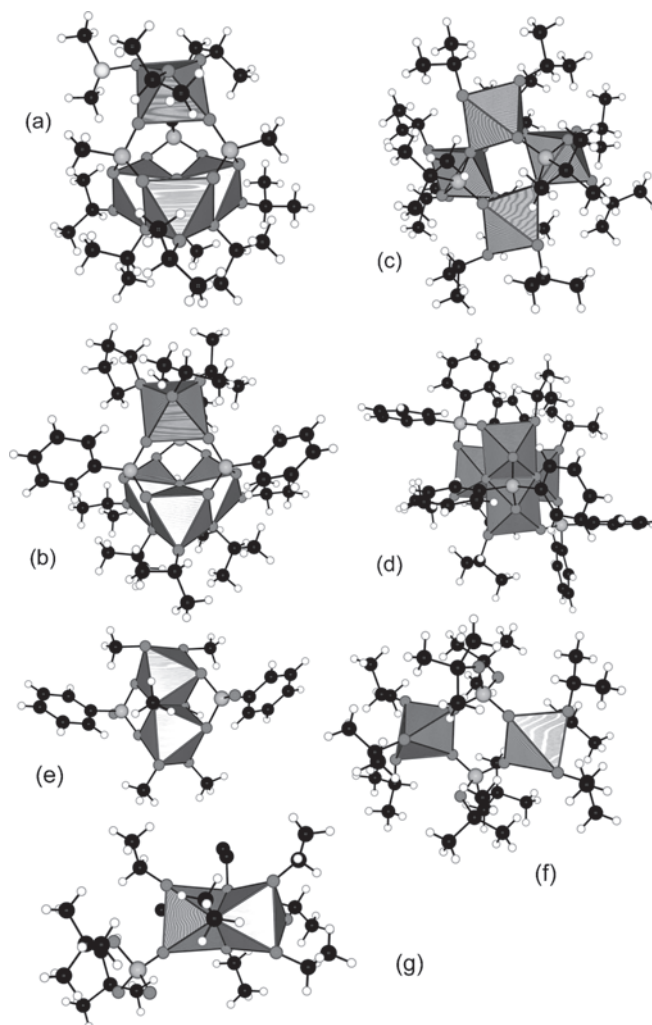


**Figure 82.** Molecular structures of some new titanium oxide alkoxide phosphonates and phosphates. (a) Tetrameric octahedral coordination in the crystal structure of ($\mu_3$-oxo)-tris($\mu_3$-methylphosphonato)-tris($\mu_2$-isopropoxo)-(dimethylsulfoxide)-pentakis(isopropoxy)-tetra-titanium. (b) Tetrameric octahedral coordination in the crystal structure of ($\mu_3$-oxo)-tris($\mu_3$-phenylphosphonato)-tris($\mu_2$-isopropoxo)-pentakis-(isopropoxy)-(tetrahydrofuran)-tetra-titanium tetrahydrofuran solvate. (c) Cyclic octahedral tetramer in the crystal structure of tetrakis[($\mu_3$-*tert*-butylphosphato)-bis(isopropoxy)-titanium]. (d) Cubane-like octahedral tetramer in the crystal structure of tetrakis[($\mu_3$-oxo)-($\mu_2$-diphenyl-phosphinato)-isopropoxy-titanium] dimethylsulfoxide solvate. (e) Edge-sharing octahedral dimer found in the crystal structure of bis(tetrabutylammonium) bis[($\mu_2$-methoxo)-($\mu_2$-phenylphosphonato)-dimethoxy-titanium] toluene solvate. (f) Dimeric trigonal bipyramidal coordination in the crystal structure of bis($\mu_2$-di-$t$-butylphosphato)-hexakis(isopropoxy)-di-titanium. (g) Face-sharing octahedral dimer in the crystal structure of bis($\mu_3$-di-$t$-butylphosphato)-tetrakis($\mu_3$-ethoxo)-tetrakis($\mu_2$-ethoxo)-octakis(ethoxy)-di-potassium-tetra-titanium.

### 4.3.2. Three-Dimensional Networks

Hydrothermal synthesis is yet another way of yielding new organic–inorganic hybrid phases with Ti atoms linked through phosphate or phosphonate bridges. The basic strategy here is to heat an aqueous mixture of hydrous TiO$_2$, H$_3$PO$_4$, and HF in the presence of an organic amine at high temperature ($T > 100°C$) under

autogeneous pressure. Thus, using ethylenediamine or 1,3-diaminopropane, it was possible to prepare two new layered oxyfluorinated titanium(IV) phosphates, $Ti_2(PO_4)_2F_4 \cdot H_3NCH_2CH_2NH_3$ and $Ti_2(PO_4)_2F_4 \cdot H_3NCH_2CH_2CH_2NH_3 \cdot H_2O$ [459]. Using a similar procedure, a layered phase $[H_3NCH_2CH_2NH_2][TiOPO_4]$ free of halogen atoms may be obtained [460]. As shown in Figure 83a, chains of *trans* corner-sharing $TiO_5N$ octahedra linked through $\mu_3$-phosphato bridges form these layers. The protonated amino group points to the interlayer space interacting with terminal P—O groups by strong hydrogen bonds. A similar structure was also obtained starting from a mixture of $Ti(OBu^n)_4$, $H_3PO_4$, and ethylenediamine [461] in the presence of hydrogen peroxide [462]. Increasing the phosphoric acid concentration in this system leads to two titanium phosphates, $[TiO(HPO_4)_2][H_3NCH_2CH_2NH_3]$ and $[(TiO)_3(PO_4)_6] \cdot 5[H_3NCH_2CH_2NH_3] \cdot 2[H_3O]$ [463]. Figure 83b shows the one-dimensional chiral chains found in this last compound. They are built up from *cis* corner-sharing $[TiO_6]$ octahedra running along a $2_1$-screw axis and stabilized by $\mu_2$-phosphato bridges.

Another kind of monodimensional chain is encountered in the crystal structure of $[TiO(O_3PCH_2PO_3)]$ $(NH_4)_2$ obtained from a mixture of hydrous $TiO_2$, methylenediphosphonic acid, and ammonia [464]. The chain is built up of *trans* corner-sharing $TiO_6$ octahedra with (di-$\mu_2$)-methylenediphosphonato bridges (Fig. 84a). If HF replaces ammonia in this system, a quite different structure, $[(Ti_3O_2)(H_2O)_2(O_3PCH_2PO_3)_2] \cdot 2H_2O$, was obtained [465]. In this new titanium(IV) diphosphonate, *trans* corner-shared trimeric units of $TiO_6$ octahedra are linked together via (di-$\mu_3$)-methylenediphosphonato bridges (Fig. 84b). This delimits a three-dimensional hybrid network with cross-linked 10-, 7-, and 6-membered ring tunnels along *a*, *b*, and *c*, respectively.



(a)

(b)

**Figure 84.** Crystalline structures of some hybrid organic–inorganic titanium(IV) diphosphonates. (a) Linear *trans* corner-sharing hybrid chain of $TiO_6$ octahedra with (di-$\mu_2$)-methylenediphosphonato bridges and H-bonded ammonium ions in the crystal structure of *catena*[diammonium ($\mu_2$-oxo)-(methylenediphosphonato-$O,O''$)-titanium(IV)]. (b) Hybrid three-dimensional framework based on *trans* corner-shared trimeric units of $TiO_6$ octahedra linked together via (di-$\mu_3$)-methylenediphosphonato bridges in the crystal structure of *catena*-[bis($\mu_4$-methylenediphosphonato)-bis($\mu_2$-oxo)-diaqua-tri-titanium(IV) dihydrate].

## 4.4. Hybrid Materials Obtained in the Presence of Organic Templates

Used in conjunction with surfactants or polymers, titanium compounds may yield very interesting new materials.

### 4.4.1. Sol–Gel Syntheses Using Surfactant Templates

The most well known application of these hybrid materials was the elaboration of mesoporous molecular sieves assisted by the self-organization of surfactant molecules.

***Mesoporous Titania*** The first example was the elaboration of Ti-MCM-41, a titanium-substituted derivative of hexagonal mesoporous silica MCM-41, from the basic hydrolysis of a mixture of $Ti(OPr^i)_4$, $Si(OEt)_4$, and CTAB, that is, cetyltrimethylammonium bromide, under hydrothermal conditions [466, 467]. A very similar material displaying a hexagonal arrangement of mesopores, Ti-HMS, may be obtained after gelation at room temperature of a $Ti(OPr^i)_4$, $Si(OEt)_4$, DDA (dodecylamine) mixture by alcoholic HCl solutions [467]. Such mesoporous phases were able to perform the selective catalytic oxidation of benzene



(a)

(b)

**Figure 83.** Crystalline structures of some hybrid organic–inorganic titanium phosphates. (a) Hybrid layer based on *trans* corner-sharing chain of $TiO_5N$ octahedra linked together through $\mu_3$-phosphato bridges in the crystal structure of *catena*[($\mu_3$-phosphato)-($\mu_2$-oxo)-(2-ammonio-ethylamino)-titanium(IV)]. (b) Hybrid helix based on *cis* corner-sharing chain of $TiO_6$ octahedra with $\mu_2$-phosphato bridges and H-bonded ethylenediamine molecules in the crystal structure of *catena*-[pentakis(ethane-1,2-diammonium)-bis(hydroxonium)-bis($\mu_2$-oxo)-hexakis($\mu_2$-phosphato-$O,O'$)-tri-titanium].

into phenol by $H_2O_2$. They were also active in the transformation of a much larger substrate such as 2,6-di-*tert*-butylphenol into quinone, a reaction not possible within the micropore structure of TS-1 (titanium silicatite). Soon after, using tetradecyl phosphate, a hexagonally packed mesoporous $TiO_2$ called Ti-TMS1 was reported [468]. Later, it was shown [469] that this material may well be lamellar and better described as titanium oxo-phosphate. A new synthetic approach using DDA was then tried, leading to a rather unstable material [470]. Several other approaches have been described to get a thermally stable mesoporous $TiO_2$, such as the use of $CTA[Ti(OCH_2CH_2O)_3]$ [471], CTA mixed with soluble peroxytitanates [472], and the atrane route using triethanolamine complexes and CTAB [473]. The preparation of a titanium oxo-phosphate displaying a high surface area using a nonionic surfactant (polyethyleneoxide dodecanol + 5EO) has also been described [474]. The detailed mechanisms involved in the formation of these mesoporous phases from solute species remain unclear. Possible identified pathways involve the metallate rod assembly, the metallate layer puckering, the charge density matching, the folding of sheets around intercalated surfactant molecules, the metallatropic liquid crystal route, and the metallate rod clusters [475]. Among the catalytic applications of these Ti-containing mesoporous materials, one may cite oxidation of olefins, conversion of linalool into cyclic furan and pyran hydroxyl ethers, and hydroxylation of benzene derivatives [475].

***Hollow Titania Fibers*** The use of surfactant molecules in the elaboration of porous materials is not limited to mesoporous phases. Thus, $Ti(OPr^i)_4$ may be gelled through hydrogen-bonding interactions with the amine group of *N*-carbobenzyloxy-L-isoleucylaminooctadecane molecules [476]. After drying, a three-dimensional hybrid network was formed, displaying fibers 300–1500 nm in diameter. After calcination at 450 °C, hollow $TiO_2$ fibers 15–150 nm in diameter of both anatase and rutile structure (particle size, 15–30 nm) were obtained. $TiO_2$ hollow fibers could also be prepared using supramolecular self-assemblies based on the sol–gel polymerization of $Ti(OPr^i)_4$ with the surfactant *trans*-(1*R*,2*R*)-1,2-cyclohexane-di-(11-aminocarbonylundecylpyridinium) hexafluorophosphate by ammonium hydroxide or HCl aqueous solutions [477]. In both cases, fibrous aggregates with diameters of 150–600 nm were obtained. However, owing to the positive charge present on the surfactant molecule, the fibrous structure could be preserved after calcination at 450 °C only for the material synthesized under basic conditions.

## 4.4.2. Sol–Gel Syntheses Using Organic Polymers

Mixing titanium alkoxides with polymeric materials is a very old idea that was used to produce water-repellent fabrics [478] or to promote rapid drying of oils, paints, and inks [293]. Titanium alkoxides have also been used as adhesion promoters in cellophane–polyethylene, mylar–polyethylene, and aluminum–polyethylene laminates [305].

***Mesoporous Titania*** Most recent applications involve the use of amphiphilic block copolymers for the templating

syntheses of mesoporous metal oxides with large ordering lengths and semicrystalline framework. The main advantage in using block copolymers instead of low-molecular-weight surfactants lies in the fine-tuning of the interactions between the inorganic and organic species. Such a control is obtained through variation of the chemical composition and/or variation of the chain lengths of the various blocks. For example, using triblock poly(alkylene) oxide polymers such as $EO_{20}PO_{70}EO_{20}$ [EO = $CH_2CH_2O$, PO = $CH_2CH(Me)O$] as structure-directing agents, it was possible to obtain a 2D hexagonal mesophase of $TiO_2$ by aerial hydrolysis of $TiCl_4$/EtOH mixtures [479]. A similar experiment performed with diblock polymers such as $EO_{75}BO_{45}$ [BO = $CH_2CH(Et)O$] yielded instead a cubic *Im3m* mesophase of $TiO_2$. The mesoscopic order present in these hybrid materials is preserved after calcination at 400 °C in air, yielding mesoporous titania with mean pore sizes of 65–70 Å and walls made of anatase nanocrystals of about 3 nm in size. The interactions between these PEO-based templates and metallic centers have been studied in some detail [480]. Briefly, in low-water-content media, strong chelation between metal centers and nonionic polar heads allows polymer unfolding, leading to wormlike phases. Larger quantities of water and acid seem to weaken the coordination bonds, leading to enhanced folding of the polymer and thus to more ordered mesophases. Another interesting aspect of these PEO-based systems lies in the possibility of using nano building blocks such as $[Ti_{12}O_{16}(OPr^i)_{16}]$ (Fig. 39c), $[Ti_{16}O_{16}(OEt)_{32}]$ (Fig. 38c), and $[Ti_{18}O_{22}(OBu^n)_{26}(acac)_2]$ (Fig. 58c) whose core structures can be preserved in the hybrid phase [481]. Another related strategy for assembling titanium oxo clusters into mesostructured hybrid materials is to use dendrimers as demonstrated by the reaction between $[Ti_{16}O_{16}(OEt)_{32}]$ and $S=P(p-OC_6H_4—X)_3$, where X stands for $CH=N—N(Me)P(S)(p-OC_6H_4-R)_3$ and R for $CH_2OH$ or $CH_2CH=COOH$ [482]. Extensions of this nano-building-block approach to other systems have recently been reviewed [483].

***Polymerization of Nano Building Blocks*** Another strategy that has been used to obtain transition metal–based hybrid organic–inorganic materials was to use prefunctionalized metal oxo-alkoxides containing a polymerizable coordinating ligand located at the periphery. The radical-initiated polymerization of the ligand usually performed in nonprotic solvents then allows the assembly of nano building blocks into a coherent material [483–486]. In this case, two different synthetic routes have been investigated. The first one (surface modification method) involves grafting a multidentate ligand (usually carboxylate or β-diketonate derivative) to a preformed oxo-alkoxide. An obvious drawback of this method is the possible occurrence of molecular rearrangements during the grafting process, as evidenced in the case of the reaction between $[Ti_7O_4(OEt)_{20}]$ and benzoic acid [447]. The other route (*in-situ* assembly) involves the formation of the oxo-alkoxide in the presence of the polymerizable ligands. For example, polymerization of the oxo-titanate oligomers $[Ti_6O_4(OEt)_8(OMc)_8]$ (Mc = $C(O)—C(Me)=CH_2$) or $[Ti_4O_2(OPr^i)_6(OAcr)_6]$ (Acr = $C(O)—CH=CH_2$) with methylmethacrylate (MMA) or methacrylic acid (MA)

co-monomers (1 : 50–1 : 200 molar ratio) in benzene or toluene resulted in polymers in which the polymer chains are efficiently cross-linked by the oxo-titanate complex [484]. A good way to check the integrity of the titanium-oxo core in this kind of polymerization is to rely on $^{17}$O-NMR solid-state measurements [483]. Such hybrid polymeric materials generally display higher glass transition, improved mechanical properties, and insolubility in organic solvents, but are nevertheless able to undergo swelling, with a solvent uptake dependent on the proportion of oxo-metallate complexes [484]. Sometimes, the polymerizable ligand may be formed as a result of an aldol condensation as was observed by reacting $Ti(OPr^i)_4$ with acetone, yielding the enolate derivative $[Ti_3(\mu_3\text{-}O)_2(OPr^i)_5(OCMe{=}CH_2)_3(^iPrOH)]$ [485]. As the crystallographic data of this compound were never published, the differences with the closely related and well-characterized trinuclear complex $[Ti_3(\mu_3\text{-}O)(OPr^i)_7\{Me_2C(O)CH{=}C(O)CH_2C(O)Me_2\}]$ obtained under similar conditions [285, 350] cannot be pointed out. Another side reaction is the possible cleavage of the C—O bond by the alkoxide, leading to the loss of the polymerizable site as was observed in the reaction of titanium isopropoxide with 2-hydroxyethylmethacrylate (HEMA) [312]. A good solution was provided by the use of butenediol derivatives such as $[Ti_4(OPr^i)_8(OCH_2CH{=}CHCH_2O)_4]$ that have been used for the synthesis of doped microcellular materials via copolymerization of polystyrene and divinylbenzene mixtures in biphasic media [324]. Such low-density microcellular foams have proven to be useful as deuterium and tritium sponges in direct-drive target designs for internal confinement fusion experiments. They may also be obtained using $[Ti(OPr^i)_2(AAEMA)_2]$ (HAAEMA = 2-(methacryloyl)oxyethyl acetoacetate) or $[Ti(APO_2)_2]$ ($APO_2H_2$ = 3-allyloxypropane-1,2-diol) derivatives [324].

### 4.4.3. Nanocoating and Nanocasting Processes

Another powerful way to make hybrid organic–inorganic materials is the nanocoating or nanocasting approach. This involves using the sol–gel process to cover a material (template) with a layer on the nanometer scale or to cover a nanoscale entity [487]. If the template is of an organic nature (emulsion droplets, polymer spheres, or gels), a truly organic–inorganic material is obtained, which, after calcination, may lead to three-dimensional structures displaying elaborate pore architectures. If the template is of an inorganic nature, a core–shell structure or a nanocomposite is obtained that may display optimized physical properties.

***Macroporous Titania*** The formation of ordered macroporous materials with periodicity in three dimensions and pore diameters comparable to optical wavelengths is an experimental challenge for catalysis, large-molecule separation processes, and elaboration of thermal, acoustic, or electrical insulators. The simplest synthetic route for such a $TiO_2$-based material involved the deposition, under vacuum, of millimeter-thick layers of latex spheres on filter paper in a Buchner funnel. Dropwise addition of titanium tetraethoxide while suction is being applied, followed by drying and calcination at 575 °C, leads to anatase particles

(20–35 nm in diameter) [488]. These particles display highly ordered hexagonal packing with 320- to 360-nm voids over a range of hundreds of micrometers. Such a simple process is, however, not well suited for the preparation of photonic crystals made of air spheres in titania. Such materials are useful for creating photonic band gaps or optical stop bands (frequency ranges that will not propagate light owing to multiple Bragg reflections). A first route able to generate photonic band-gap materials involved the formation of a stable nonaqueous monodisperse emulsion. This emulsion may be obtained by mixing formamide and iso-octane in the presence of a symmetric triblock copolymer, poly(ethylene glycol)$_{20}$–poly(propylene glycol)$_{70}$–poly(ethylene glycol)$_{20}$, as a surfactant with silicone oil to prevent Ostwald ripening [489, 490]. Above a volume fraction of about 50%, such monodisperse emulsion droplets spontaneously order to form a close-packed structure. This droplet structure can then be permanently captured by gelation of the liquid in which the droplets are suspended. For $TiO_2$, the gelling agent may be ammonia. It was added to a sol obtained after hydrolysis by aqueous formamide of a titanium isopropoxide/acetylacetone mixture with all the isopropanol removed by a double extraction with a fivefold excess of hexanes [489]. The complete removal of the alcohol produced by the hydrolysis reaction was mandatory to avoid destabilization upon mixing this sol with the emulsion. After heat treatment at 1000 °C of the hybrid gel, a macroporous rutile phase was obtained displaying highly uniform, spherical pores with sizes in the 50-nm to 10-$\mu$m range and lattice porosities up to approximately 90%. Another route to large macroporous photonic titania crystals involved the growth of a colloidal crystal (opal-like material) by controlled sedimentation and drying of a 10 vol% colloidal suspension of polystyrene latex spheres in water [491, 492]. Then, the interstitial space present in these synthetic opals was infiltrated from 1 to 8 times with an ethanolic solution of titanium alkoxides, $Ti(OR)_4$ (R = Et, $Pr^n$, $Pr^i$), followed by hydrolysis with water from air. Calcination at 450 °C yielded inverse opals made of anatase crystals with an average grain size of $20.2 \pm 1.2$ nm. The resulting material displays a nearly perfect hexagonal arrangement of macropores of radius between $322 \pm 3$ nm and $177 \pm 2$ nm and with a volume fraction between 5 and 12 vol% $TiO_2$ [492]. A further refinement of this infiltration technique involved the use of polystyrene colloidal spheres coated with polyelectrolyte multilayers [493]. In this case, the pore morphology and the resulting macroporous structures depend on the nature of the multilayers deposited on the colloidal spheres, while the wall thickness of the pores can be tuned by altering the number of multilayers. One important limitation of this two-step procedure is, however, the quality of the colloidal crystal template before infiltration. Consequently, a simpler method involving the fabrication of the template and the infiltration at the same time has recently been described [494]. The basic idea was to infill ultrafine $TiO_2$ particles into the voids of an ordered template directly by means of a local sucking capillary pressure. This could be easily realized by dipping a vertical substrate (glass, ITO, quartz slides) into a slurry containing polystyrene spheres and the ultrafine particles. Owing to the small size of the $TiO_2$ particles (around 10 nm) compared with that of the polystyrene particles (several

hundred nanometers), the voids can be completely filled during the assembly. Consequently, most defects within the template can be immediately mended by the capillary pressure. Highly ordered three-dimensional porous $TiO_2$ structures with macropores in the range of 300 to 600 nm were obtained using this cooperative method of assembly [494].

***Polymer Gel Templates***    Another way to obtain highly porous oxide networks is to use a polymer gel template such as acrylamide/glycidyl methacrylate made of cross-linked thin fibers [495]. After exchange of the water contained within the gel by isopropanol, a titanium(IV) isopropoxide solution was permeated and further hydrolyzed by an isopropanol/water mixture (1 : 1 by volume). Drying of the gel followed by calcination up to 1000 °C then yielded coral-like $TiO_2$ networks. Depending on the calcination temperature, anatase or rutile phases are formed displaying pore sizes ranging from 100 nm to micrometers in diameter and with wall thickness of about 100–150 nm [495]. By playing with the chemical nature of the polymer template, $TiO_2$ networks displaying porosities as high as 99% and surface areas from 5 to 100 $m^2\ g^{-1}$ could be easily produced [496]. A closely related process concerns the use of a cellulose acetate (CA) membrane as the polymeric template [497]. It involves dipping the CA membrane in a closed vessel containing the titanium alkoxide, followed by hydrolysis with an isopropanol/water solution (50 : 50 v/v). As before, drying and heating at 450 °C produce a $TiO_2$ material (particle size between 45 and 150 nm) with a thickness of about 80 $\mu$m. This material closely resembles the tricontinuous pore structure of the initial CA membrane. A quicker process involves placing the membrane on a glass frit filter and applying vacuum. The metal alkoxide is then dripped onto the membrane, followed by the alcohol/water mixture [498].

***Hollow Titania Spheres***    An alternative to the coating of a 1D, 2D, or 3D polymeric template by hydrolyzing titanium alkoxides is to use 0D templates such as polystyrene lattices in order to produce hollow spheres of $TiO_2$. Accordingly, mesoscale hollow spheres of ceramic materials are useful in many areas: encapsulation of drugs or biologically active agents, artificial cells, low-weight fillers, and so on [497]. Thus, submicrometer-sized anionic polystyrene lattices have been coated with uniform layers of amorphous $TiO_2$ by hydrolysis of ethanolic solutions of $Ti(OBu^n)_4$ containing the polymer cores and poly(vinylpyrrolidone) to prevent aggregation [499]. Calcination of these core–shell materials between 250 and 900 °C led to hollow $TiO_2$ particles of about 0.5 $\mu$m in diameter. In such a simple method, it may, however, be difficult to control the homogeneity and thickness of the coating. Further refinements were then achieved following two different routes. In the first one, a crystalline array of polystyrene beads was fabricated between two glass substrates and infiltrated after drying by a solution of titanium isopropoxide in isopropanol (1 : 19 v/v) through capillary action [497]. After gelation by moisture in air and partial drying, the cell is immersed in toluene to dissolve the polystyrene template, and the hollow spheres are released after sonication in a water bath of the disassembled cell. The voids of the resulting $TiO_2$ hollow spheres were between 190 and 380 nm in diameter with a wall thickness of about 30–100 nm, depending

on the concentration of the sol–gel solution [497]. The second route is based on the remarkable layer-by-layer (LbL) self-assembly technique [500]. It is based on the alternate adsorption of polycation and polyanion layers from their aqueous solutions, leading to multilayer films displaying a thickness controlled with a nanometer-scale precision [500]. This method has been very recently applied to the elaboration of titania nanosheet/polydiallyldimethylammonium composite films, where titania nanosheets were prepared from exfoliation of an acid-exchanged layered titanate [500]. Preparation of the template with this technique involved alternate deposition on negatively charged polystyrene (PS) spheres of a positively charged polymer such as poly(diallyldimethylammonium chloride) (PDAD-MAC) or poly(allylaminehydrochloride) (PAH) and of a negative polymer such as poly(sodium-4-styrenesulfonate) (PSS) [501]. Consequently, for a three-layer template (PS/PDADMAC/PSS/PDADMAC; $PE_3$), one gets positively charged polymer particles, while for a $PE_4$ structure (PS/PDADMAC/PSS/PDADMAC/PSS), the surface charge becomes negative. The role of these initial electrolyte layers is to produce a uniform and homogeneous surface for subsequent nanoparticle adsorption. Negatively charged $TiO_2$ nanoparticles may be produced after a hydrothermal treatment of a titanium(IV) bis(ammonium lactato)dihydroxide solution, leading to a milky-white sol of $TiO_2$ anatase nanoparticles ($\zeta$ potential of $-40$ mV for a diameter of about 5 nm) stabilized by lactate ions. On the other hand, a positively charged $TiO_2$ anatase colloid ($\zeta$ potential of $+42$ mV for a diameter of about 6 nm) may be obtained by ammonia hydrolysis of $TiCl_4$ after washing and redispersion by nitric acid under ultrasonic treatment [501]. When the negatively and positively charged sols are mixed with solutions containing $PE_3$- or $PE_4$-precoated PS spheres (diameter 200–700 nm), respectively, adsorption occurs, leading, on average, to a coating of about 1–3 monolayers of $TiO_2$ nanoparticles. After washing by centrifugation, further deposition of three PE layers (PSS/PDADMAC/PSS for positively charged nanoparticles and PDADMAC/PSS/PDADMAC for a negatively charged sol) makes the surface available for a new deposition cycle. At least three $TiO_2$ nanoparticles/$PE_3$ layers are needed to get $TiO_2$ hollow spheres that do not collapse after removal of the template by calcination at 500 °C.

## 4.4.4. Core–Shell Structures

The formation of core–shell structures is obviously not limited to polymeric materials. By using an inorganic template, other interesting materials could be obtained.

***Hybrids with Titania Shells***    First attempts in this domain involved the coating of ZnO [502] and copper(II) basic carbonate [503] monodisperse particles by the controlled hydrolysis of titanium butoxide in ethanol solutions. Moreover, owing to the considerable interest in catalytic, pigment, and photonic crystal applications, $TiO_2$-coated silica spheres were obtained using either titanium *tert*-butoxide in tetrahydrofuran [504] or $TiOSO_4$ in sulfuric acid [505]. Later on, the process was optimized by hydrolyzing titanium *n*-butoxide in ethanol solutions, yielding titania coatings, ranging from sub-monolayer to 7 nm ($\sim$20 monolayers) thick, on monodisperse silica spheres 270 nm in diameter [506].

A further improvement of the method with silica spheres 550 nm in diameter allowed for an increase in the thickness of the $TiO_2$ coating up to 46 nm (~125 monolayers of titania) [507]. Metallic core–shell systems have also been investigated. For example, silver cores coated by a 1- to 2-nm layer of titanium oxide can be readily obtained by reduction of $Ag^+$ ions by a DMF/ethanol mixture in the presence of $Ti(OBu^n)_4$ and acetylacetone [508]. These positively charged core–shell nanoparticles can then be further assembled by the layer-by-layer assembly technique to form closely packed layers interlaced with polyelectrolytes [poly(acrylic acid) and poly(diallyldimethylammonium chloride) as negatively and positively charged polymers]. This stratified core–shell hybrid material was shown to display unique structure and catalytic properties associated with the original electron-transport properties [508]. Similarly, gold-titania core–shell nanoparticles have been obtained by treating gold particles with a surfactant such as sodium 10-mercaptodecane sulfonate, followed by the electrostatic layer-by-layer self-assembly of poly(diallyldimethylammonium chloride), poly(sodium-4-styrenesulfonate), and a negatively charged sol of $TiO_2$ particles made from thermohydrolysis of titanium(IV) bis(ammonium lactato)dihydroxide solutions [509]. Anatase particles forming a shell thickness of about 10 nm around gold particles were evidenced in transmission electron micrographs of these organic–inorganic hybrid systems.

A last original example of the templating process involves the use of an anodically grown aluminum oxide displaying a nanostructure consisting of long and narrow holes with diameters in the range of 10–200 nm according to the anodizing voltage used and subsequent etching treatments [510]. Using this template, an array of $TiO_2$ nanotubes with inner diameter between 70 and 100 nm could be prepared by electrochemical deposition onto a poly(methyl methacrylate) (PMMA) replicated negatype of the porous alumina membranes. A much simpler method allowing for the synthesis of $TiO_2$ tubules and fibrils from these membranes involved the dipping of the template into a milky-white $TiO_2$ sol made after acid hydrolysis (HCl) of $Ti(OPr^i)_4$/EtOH solutions [511, 512]. Bundles of single-crystal anatase $TiO_2$ nanofibrils with diameters of 22 nm were obtained after drying and calcination at 400 °C of these membranes.

***Hybrids with Titania Cores*** Another class of hybrid materials is obtained when the surface of titania particles is modified by an organic or inorganic layer. For example, smart methods for polymerizing methylmethacrylate at the surface of nanometric titania particles have been developed in the paint and polymer industries [513]. In the domain of solar-energy conversion, nanocrystalline $TiO_2$–$(MoO_3)_x$ core–shell materials may be readily synthesized by a co-nucleation of polyoxometallates at the surface of surfactant micelles [514]. The synthesis involved mixing of aqueous solutions containing titanium(IV) bis(ammonium lactato)dihydroxide $(NH_4)_2Ti(OH)_2(C_3H_4O_3)_2$, cetyltrimethylammonium chloride, and $Na_4Mo_8O_{26}$ at 70 °C. The nanocrystalline core–shell material is obtained after washing, drying, and calcination at 450 °C and displays a photoabsorption energy (PE) correlated with the nanoparticle size that can be readily adjusted from 8 nm down to 4

nm. Such core–shell particles showed a PE redshift from 2.88 to 2.60 eV with decreasing particle size [514]. This is in deep contrast with bulk $TiO_2$ characterized by a mismatch between the band-gap energy (3.2 eV) and the most intense region of the solar spectrum centered at 2.6 eV. Still, in photovoltaic applications, electrochromic compounds are materials that change in color on application of a potential and are very interesting for large-segment static displays. $TiO_2$, being transparent to visible light and displaying electronic conductivity with a good affinity for defined ligands (bipyridinium salts, Prussian blue), is thus perfectly suited for these applications. Consequently, nanocrystalline electrodes derivatized by phosphonated triarylamines [515], mono-, di-, and trimeric $N,N'$-dialkyl- or diphenyl-4,4'-bipyridinium salts [516, 517], and bis(2-phosphonoethyl)-4,4'-bipyridinium dichloride [518] have been synthesized. These hybrid nanocrystalline $TiO_2$ layers can then be used for the elaboration of ultrafast electrochromic windows and displays. In this domain, nanocrystalline materials offer the opportunity to have fast interfacial electron transfer between the nanocrystal and the adsorbed modifier. They also provide high surface area of the support that amplifies optical phenomena by 2 or 3 orders of magnitude [516]. One then benefits from the long-term stability of solid-state devices as well as the sharp colors and fast switching of organic devices.

## 4.5. Hybrid Materials Involving Biological Matter

Interactions between titanium alkoxides and biological matter have a quite old history. In this field, interest in titania mainly arises from its nontoxicity, high insolubility in the whole range of pH, and strong chemical inertness.

### 4.5.1. Cellulose Gelation and Enzyme Immobilization

First applications in the textile industries include the gelation of cellulosics or proteinaceous materials such as wool or silk [519]. Since cellulose is a polymer of $\beta$-1,4-linked D-glucopyranose units, the 2- and 3-hydroxy vicinal diol groups are expected to be involved in chelate formation only. Consequently, the cross-linking of cellulose chains by Ti atoms should occur for steric reasons with the remaining 6-hydroxy group. On the other hand, for proteinaceous molecules, groups that may act as ligands toward Ti atoms are the free carboxy groups from the C terminus and acidic amino acids, the phenolic hydroxy groups from tyrosyl residues, the alcoholic hydroxy groups of seryl and threonyl residues, free sulfhydryl groups from any cysteinyl residues, and amino groups from the N terminus of $\varepsilon$-amino groups of lysyl residues [520]. For enzymes carrying —SH groups, one may also use $Sn^{2+}$ as a chemical linking agent [512]. Enzymes are also protein-based materials. They have been used by man for hundreds of years in the preparation of food, drink, and clothing. Consequently, there is a considerable interest in immobilizing these enzymes onto an insoluble carrier for industrial purposes. Among the obvious advantages of insolubilized enzymes, one may cite: easy separation between the substrate and soluble products by filtration or centrifugation, packing into columns for continuous conversion processes,

and changes in stability and kinetic properties upon immobilization [520]. Table 12 summarizes some bioencapsulates based on aqueous titania [520]. A very recent review of biodoped nanocomposite polymers involving sol–gel bioencapsulates is also available [521].

### 4.5.2. Blood and Hydroxyapatite Compatibility

In the domain of titanium-based metallic implants, it was reported that the rutile form of $TiO_2$ could be used to improve the blood compatibility of these materials [522]. On the contrary, the anatase form is characterized by low blood compatibility [523]. On the other hand, titania gels made from acid hydrolysis of $Ti(OEt)_4$ and further treated by hydrogen peroxide were reported to display the highest blood compatibility [523]. Another important aspect of titanium-based metallic implants is their compatibility with hydroxyapatite (HAP) $[Ca_{10}(PO_4)_6(OH)_2]$ that have been widely used as bioceramics for clinical applications [524]. The preparation of functionally graded $TiO_2$/HAP coatings for $Ti_6Al_4V$ implants, allowing the heterogeneous nucleation of HAP, was described starting from $Ca(NO_3)_2 \cdot 4H_2O$, $H_3PO_4$, $CH_3OCH_2CH_2OH$, $Ti(OPr^i)_4$, acetylacetone, and $^iPrOH$ was recently described [524].

### 4.5.3. Antitumor and Antiviral Agents

Finally, one may also notice the low toxicity and high antitumor activities of biscyclopentadienyl- and bis($\beta$-diketonato)-$Ti^{IV}$ complexes against a wide range of murine and human tumors [525]. Moreover, $Cp_2TiCl_2$ is known to exhibit pronounced antiviral, anti-inflammatory, and insecticidal activities [526]. Among such complexes, two of them, titanocene dichloride $(Cp_2TiCl_2)$ and budotitane $[Ti(bzac)_2(OEt)_2]$ (bzac = 1-phenylbutane-1,3-dionato ligand), are currently undergoing clinical trials [409]. An additional medical interest arises from the use of $^{45}Ti$ isotopes in radiopharmaceuticals [409]. In contrast with cisplatin-based drugs, the detailed mechanism of inhibition of DNA synthesis and mitotic activity by these complexes remains largely unknown.

**Table 12.** Biological materials (antibiotics, enzymes, bacteria) that have been used for immobilization on various organic or inorganic substrates.

| Biological material | Support |
|---|---|
| Antibiotics[a] | Cellulosics, paper, cotton, $TiO_2$, $ZrO_2$ |
| D-glucose oxidase | Chitin, alginic acid, glass, $TiO_2$ |
| Papain | Polypropylene, $ZrO_2$, glass, $TiO_2$ |
| $\alpha$-Amylase, glucoamylase | Poly(4- and 5-acrylomidosalicylic acids), $TiO_2$ |
| Dextranase | $TiO_2$, $ZrO_2$ |
| *Escherichia coli, Lactobacillus, Acetobacter* | $TiO_2$, $ZrO_2$ |

[a]Ampicillin, chloramphenicol, gentamycin, kanamycin, neomycin, paromomycin, polymixin B, penicillin G, streptomycin, amphotericin B, natamycin.
*Note:* Data gathered from [520]. For organic supports, coupling via hydrous titanium oxide was used.

## 5. CONCLUSION AND PERSPECTIVES

Several conclusions may be drawn after this comprehensive review of titanium-based compounds and materials.

(i) At a molecular scale, a large choice of monomeric complexes based on Ti—O or Ti—N bonds is already available. Most of these complexes have been characterized both in solution and in the solid state and display coordination numbers ranging from 4 to 8. The knowledge of their molecular structure is obviously of the utmost importance for mechanistic considerations particularly in the field of homogeneous catalysis. Surprisingly enough, their use in sol–gel syntheses was largely limited to titanium alkoxides. One may then hope that in the near future new $TiO_2$-based materials would be elaborated using the whole palette of $Ti^{IV}$ coordination compounds and not only titanium alkoxides. Another neglected aspect of these complexes concerns their use in crystal engineering. With the considerable help provided by the PACHA formalism, it should be easier to set out the basic molecular interactions responsible for network formation in the solid state. This point is obviously of the utmost importance for a rational development of sol–gel syntheses and molecular tectonics approaches.

(ii) At a nanometer scale, there have been considerable efforts to synthesize and characterize polynuclear titanium-based complexes. The amount of well-characterized oxo complexes is, however, too limited as most of them are obtained through completely blind shake-and-bake processes. Worse, the detailed mechanistic pathways leading to their formation or to rearrangements of their core remain largely unknown. Unveiling these mechanisms would be of the utmost importance for a rational design of hybrid materials, and we think that titanium compounds should be used as a benchmark for the elucidation of nucleation and growth processes from solution. At this same scale, most $TiO_2$ nanocrystals are elaborated after hydrolysis and condensation of titanium alkoxides. Here also, using the whole palette of $Ti^{IV}$ complexes instead of just $Ti(OR)_4$ derivatives would be of deep interest. The possible surface complexation, particularly by multidentate ligands, should be systematically studied and the resulting effect on size, shape, and morphology of the nanocrystals should be systematically investigated. Yet another largely neglected field concerns the mesostructure and mechanisms of formation of titania gels. If most past studies have focused on xerogels, the systematic use of atomic force microscopy should be particularly rewarding for the study of wet gels.

(iii) At a macroscopic scale, eight $TiO_2$ polymorphs have been isolated and characterized by X-ray diffraction. This observation raises the fascinating question of the possible existence of microporous $TiO_2$ networks. Obviously, the problem of their stability relative to rutile or anatase phases for enthalpic and/or entropic reasons should be carefully studied. On the other hand, the meso- or macrostructuring of titania has been intensively developed in the past few years, but again only for rutile or anatase polymorphs. More effort is thus needed to apply these new techniques to other polymorphs.

(iv) The lack of systematic studies devoted to the mesostructure of titania gels is probably responsible for the paucity of data concerning the biological applications of

titania. This is rather surprising, as this oxide is perfectly suited (nontoxicity, insolubility in the full pH range, chemical inertness, etc.) to the elaboration of biocompatible materials. Consequently, it is anticipated that studies devoted to biomineralization processes involving titania will grow in importance in the next few years.

# GLOSSARY

**Aquo cations** Soluble cationic hydrated species $[M(H_2O)_N]^{z+}$ displaying low electrical charge ($z < 3$) and stable at low pH.

**Aquo ligand** Formation of a coordination chemical bond between a water molecule and a cation ($M—OH_2$ type).

**Basic salt** Crystalline phases containing hydrolyzed cationic species (see normal salt).

**Colloidal solution or sol** Dispersion of solid particles (diameter 1–100 nm) in a liquid.

**Convergence parameter $G$** Adjustable value in the reciprocal space ($Å^{-1}$ unit) allowing to get the fastest convergence of a Madelung summation process for a given accuracy.

**Crystal** Solid matter characterized by a well ordered atomic structure allowing X-ray diffraction.

**Crystal engineering** Understanding of intermolecular interactions in the context of crystal packing and the use of this understanding in the design of new solids with desired physical and chemical properties.

**Density functional theory (DFT)** Theoretical frame using the whole electronic density $\rho(r)$ as basic variable instead of wave-functions $\Psi(r)$.

**Electric field gradient (efg)** Second partial derivatives of a classical electrostatic potential $V$ evaluated at a nuclear site.

**Electronegativity** According to L. Pauling, "*the power of an atom in a molecule to attract electrons to itself.*" According to density functional theory, "*the chemical potential of electrons in an atom or a molecule.*"

**Electronic signature** Set of parameters: mean electronegativity $\langle EN \rangle$, global hardness $\langle GH \rangle$, electrostatic balance $\langle EB \rangle$, global ionicity $\langle GI \rangle$, partial charges $q_i$ and frontier indexed $f_i$ computed using the PACHA formalism.

**Electrostatic balance $\langle EB \rangle$** Summation over all possible atomic pairs (charges $eq_i$ and $eq_j$ at distance $R_{ij}$) of purely Coulombic contributions $e^2 q_i q_j / (4\pi\varepsilon_0 R_{ij})$.

**Extended X-ray absorption fine structure (EXAFS)** A spectroscopic technique for studying local order (first and second neighbors) in condensed matter.

**Frontier index** Number $f$ attached to an atomic site and ruling its chemical reactivity according to HSAB (hard and soft acids and bases) principle. The larger $f$, the higher the atomic polarizability of the site.

**Gel** Dispersion of liquid droplets (diameter 1–100 nm) in a solid.

**Glass** Solid matter displaying no crystalline order showing only X-ray diffusion.

**Global ionicity $\langle GI \rangle$** Overall ionicity (ranging from 0 to 100%) of a given chemical compound in the PACHA formalism.

**Global softness $\langle GH \rangle$** Approximation of the HOMO–LUMO gap (I–A) in the PACHA formalism.

**Hardness** Parameter inversely proportional to the polarizability (size) of the electronic cloud of an atom or a molecule (see softness).

**Hydrothermal synthesis** Formation of crystalline phases from aqueous solutions at pressure higher than 1 atm.

**Hydroxo ligand** Formation of a coordination chemical bond between a hydroxide ion $OH^-$ and a cation ($M—OH$ type).

**ICSD database** Database located in Karlsruhe (Germany) gathering all published inorganic crystal structures displaying no C—H bonds.

**LCAO-MO theory** Theoretical frame using wave-functions based on linear combination of atomic orbitals (named molecular orbitals) and satisfying the time-independent Schrödinger equation $H|\Psi\rangle = E|\Psi\rangle$.

**$\mu_n$-coordination mode** Formation of $n$ chemical bonds (bridges) between one single ligand and $n$ cationic centers.

**Macroporous material** Porous structure with pore diameters comparable to or larger than optical wavelengths.

**Madelung matrix** A $n \times n$ square matrix whose non-diagonal elements are equal to $1/R_{ij}$ (reciprocal of distance between atoms $i$ and $j$) and whose diagonal elements are all equal to zero. This matrix may be contracted using strict mathematical rules for taking account the existence of symmetry elements and/or of periodic constraints.

**Mean electronegativity $\langle EN \rangle$** Average common value for the electronic chemical potential reached by all atoms after addition ($q < 0$) or removal ($q > 0$) of electrons after atomic orbitals overlaps.

**Metal alkoxides** Organometallic complexes of general formula $M(OR)_z$ ($R = C_nH_{2n+1}$) leading after hydrolysis and condensation to metallic oxides $MO_{z/2}$: $M(OR)_z + z/2\ H_2O \rightarrow MO_{z/2}: + z\ ROH$.

**Mesoporous material** Porous structure with pore diameters larger than 2 nm but smaller than optical wavelengths (less than *ca* 200 nm).

**Microporous material** Porous structure with pore diameters smaller than 2 nm.

**Molecular tectonics** Molecular-scale building of hybrid organic-inorganic materials using constructional processes based on supramolecular pre-organization, molecular recognition (templating) or cellular processing.

**Monodentate coordination mode** Formation of a single chemical bond between a cation and an anion.

**Normal salt** Crystalline phases containing non-hydrolyzed $[M(H_2O)_N]^{z+}$ aquo-cations (see basic salt).

**Ostwald ripening** Change upon aging of the size distribution of a collection of particles owing to the occurrence of redissolution/precipitation phenomena.

**Outer-sphere complex** Stable association between a cation $C^+$ and an anion $A^-$ mediated by a solvent molecule S: $[C^+–S–A^-]$.

**Oxo anions** Soluble anionic species $[MO_N]^{(2N-z)-}$ displaying high electrical charge ($z > 4$) and stable at high pH.

**Oxo ligand** Formation of a coordination chemical bond between an oxide ion $O^{2-}$ and a cation ($M=O$ type).

**PACHA model**   Non-empirical theoretical frame that uses Allen spectroscopic electronegativity scale and *ab initio* atomic radii for a fast and reliable evaluation of atomic partial charges from the sole knowledge of molecular or crystalline structures. Formally, it corresponds to a spherical-charge approximation of density functional equations.

**Partial charge**   Number $q$ attached to an atomic site in a chemical species equal to the difference between the atomic number $Z$ and the actual total number of electrons $N$ surrounding (on a time-average) this atom.

**Partial charge model (PCM)**   Empirical theoretical frame that uses the Allred-Rochow electronegativity scale for an ultra-fast evaluation of atomic partial charges from the sole knowledge of stoichiometry. It is particularly well suited for predicting chemical reactivity of solute chemical species whose detailed molecular structure remains unknown.

**Polyanions**   Small oligomeric species formed after adding an acid to oxo-anions.

**Polycations**   Small oligomeric species formed after adding a base to aquo-cations.

**Retrosynthetic index**   Number attached to an atomic site showing which parts of a molecular fragment are deeply involved in the building of a larger unit. This index may be obtained by comparing the partial charges computed when the fragment is embedded in its container and those computed for the same fragment isolated from its container.

**Softness**   Parameter proportional to the polarizability (size) of the electronic cloud of an atom or a molecule (see hardness).

**Sol**   See colloidal solution.

**Sternheimer anti-shielding factor**   Correction that should be applied to electric field gradients (efg) originating from sources external to an electron shell in order to account for the polarization of the charge distribution in the atomic core.

**THF**   Tetrahydrofurane.

**X-ray absorption near edge structure (XANES)**   A spectroscopic technique for studying nearest neighbors of an absorbing center in condensed matter.

# REFERENCES

1. S. Mann, *Nature* 365, 499 (1993).
2. H. Dislich, *Angew. Chem., Int. Ed. Engl.* 10, 363 (1971).
3. K. S. Mazdiyasni, *Ceram. Int.* 8, 42 (1982).
4. M. Henry, J. P. Jolivet, and J. Livage, *Struct. Bonding* 77, 153 (1992).
5. J. P. Jolivet, M. Henry, and J. Livage, "Metal Oxide Chemistry and Synthesis." Wiley, New York, 2000.
6. H. Schmidt, *J. Non-Cryst. Solids* 100, 51 (1988).
7. J. Livage, M. Henry, and C. Sanchez, *Prog. Solid State Chem.* 18, 259 (1988).
8. C. J. Brinker and G. W. Scherer, "Sol–Gel Science." Academic Press, San Diego, 1990.
9. T. J. Barton, L. M. Bull, W. G. Klemperer, D. A. Loy, B. McEnaney, M. Misono, P. A. Monson, G. Pez, G. W. Scherer, J. C. Vartuli, and O. M. Yaghi, *Chem. Mater.* 11, 2633 (1999).
10. M. Eddaoudi, D. B. Moler, H. Li, B. Chen, T. M. Reineke, M. O'Keefe, and O. M. Yaghi, *Acc. Chem. Res.* 34, 319 (2001).
11. G. Férey, *Chem. Mater.* 13, 3084 (2001).
12. J. Livage and M. Henry, in "Ultrastructure Processing of Advanced Ceramics" (J. D. Mackenzie and D. R. Ulrich, Eds.), p. 183. Wiley, New York, 1988.
13. B. M. Gatehouse, S. N. Platts, and T. B. Williams, *Acta Crystallogr., Sect. B* 49, 428 (1993).
14. K. K. Wu and I. D. Brown, *Acta Crystallogr., Sect. B* 29, 2009 (1973).
15. C. F. Baes Jr. and R. E. Mesmer, "The Hydrolysis of Cations," p. 148. Wiley, New York, 1976.
16. J. Kragten, "Atlas of Metal–Ligand Equilibria in Aqueous Solution," p. 660. Ellis Horwood, Chichester, 1978.
17. I. A. Sheka and T. V. Pevzner, *Russ. J. Inorg. Chem.* 5, 1119 (1960).
18. T. C. W. Mak, *Can. J. Chem.* 46, 3491 (1968).
19. M. G. Reichmann, F. J. Hollander, and A. T. Bell, *Acta Crystallogr., Sect. C* 43, 1681 (1987).
20. W. Haase and H. Hoppe, *Acta Crystallogr., Sect. B* 24, 282 (1968).
21. J. Patarin, F. Marcuccilli-Hoffner, H. Kessler, and P. Daniels, *Eur. J. Solid State Inorg. Chem.* 31, 501 (1994).
22. S. Cohen, H. Selig, and R. Gut, *J. Fluorine Chem.* 20, 349 (1982).
23. D. Mootz, E. J. Oellers, and M. Wiebcke, *Z. Anorg. Allg. Chem.* 564, 17 (1988).
24. W. M. P. B. Menge and J. G. Verkade, *Inorg. Chem.* 30, 4628 (1991).
25. M. Fourati, M. Chaabouni, C. H. Belin, M. Charbonnel, J. L. Pascal, and J. Potier, *Inorg. Chem.* 25, 1386 (1986).
26. C. D. Garner and S. C. Wallwork, *J. Chem. Soc. A* 1496 (1966).
27. G. M. H. van de Velde, S. Harkema, and P. J. Gellings, *Inorg. Chim. Acta* 11, 243 (1974).
28. M. Haddad and F. Brisse, *Can. Mineral.* 16, 379 (1978).
29. A. Fester, W. Bensch, and M. Tromel, *Acta Crystallogr., Sect. C* 50, 850 (1994).
30. A. Fester, W. Bensch, and M. Tromel, *Inorg. Chim. Acta* 193, 99 (1992).
31. G. Lundgren, *Ark. Kemi* 10, 397 (1956).
32. M. A. K. Ahmed, H. Fjellvag, and A. Kjekshus, *Acta Chem. Scand.* 50, 275 (1996).
33. I. E. Grey and R. Stranger, *J. Solid State Chem.* 101, 331 (1992).
34. S. Krimi, I. Mansouri, A. El Jazouli, J. P. Chaminade, P. Gravereau, and G. Le Flem, *J. Solid State Chem.* 105, 561 (1993).
35. Yu. A. Ivanov, E. L. Belokoneva, Yu. K. Egorov-Tismenko, N. V. Simonov, and Yu. A. Ivanov, *Dokl. Akad. Nauk SSSR* 252, 1122 (1980).
36. J. L. Rodrigo, P. Carrasco, and J. Alamo, *Mater. Res. Bull.* 24, 611 (1989).
37. E. S. Lunezheva, B. A. Maksimov, and O. K. Mel'nikov, *Kristallografiya* 34, 674 (1989).
38. R. Duhlev, *Acta Crystallogr., Sect. C* 50, 1525 (1994).
39. R. M. Hazen, D. C. Palmer, L. W. Finger, G. D. Stucky, W. T. A. Harrison, and T. E. Gier, *J. Phys.: Condens. Matter* 6, 1333 (1994).
40. A. N. Christensen, E. K. Andersen, I. G. K. Andersen, G. Alberti, M. Nielsen, and M. S. Lehmann, *Acta Chem. Scand.* 44, 865 (1990).
41. S. Bruque, M. A. G. Aranda, E. R. Losilla, P. Olivera-Pastor, and P. Maireles-Torres, *Inorg. Chem.* 34, 893 (1995).
42. M. A. Salvado, P. Pertierra, S. Garcia-Granda, J. R. Garcia, J. Rodriguez, and M. T. Fernandez-Diaz, *Acta Crystallogr., Sect. B* 52, 896 (1996).
43. E. R. Losilla, M. A. G. Aranda, and S. Bruque, *J. Solid State Chem.* 125, 261 (1996).
44. A. M. K. Andersen, P. Norby, and T. Vogt, *J. Solid State Chem.* 140, 266 (1998).
45. D. M. Poojary, A. I. Bortun, L. N. Bortun, and A. Clearfield, *J. Solid State Chem.* 132, 213 (1997).
46. M. A. Salvado, P. Pertierra, S. Garcia-Granda, J. R. Garcia, M. T. Fernandez-Diaz, and E. Dooryhee, *Eur. J. Solid State Inorg. Chem.* 34, 1237 (1997).

47. C. Serre and G. Férey, *C. R. Acad. Sci. Paris, Sér. IIc* 2, 85 (1999).
48. W. T. A. Harrison, T. E. Gier, J. C. Calabrese, and G. D. Stucky, *J. Solid State Chem.* 111, 257 (1994).
49. B. A. Maximov, N. E. Klokova, I. A. Verin, and V. A. Timofeeva, *Kristallografiya* 35, 847 (1990).
50. P. G. Nagornyi, A. A. Kapshuk, N. V. Stus', N. S. Slobodyanik, and A. N. Chernega, *Zh. Neorg. Khim.* 36, 2766 (1991).
51. A. Robertson, J. G. Fletcher, J. M. S. Skakle, and A. R. West, *J. Solid State Chem.* 109, 53 (1994).
52. I. N. Geifman, N. G. Furmanova, P. G. Nagornyi, Li Don Yun, and M. V. Rotenfel'd, *Kristallografiya* 38, 88 (1993).
53. P. G. Nagornyi, A. A. Kapshuk, N. V. Stus', and N. S. Slobodyanik, *Russ. J. Inorg. Chem.* 34, 1731 (1989).
54. M. L. F. Phillips, W. T. A. Harrison, G. D. Stucky, E. M. McCarron, J. C. Calabrese, and T. E. Gier, *Chem. Mater.* 4, 222 (1992).
55. P. G. Nagornyi, A. A. Kapshuk, N. V. Stus', and N. S. Slobodyanik, *Kristallografiya* 35, 634 (1990).
56. I. Tordjman, R. Masse, and J. C. Guitel, *Z. Kristallogr.* 139, 103 (1974).
57. I. V. Voloshina, R. G. Gerr, M. Yu. Antipin, V. G. Tsirel'son, N. I. Pavlova, Yu. T. Struchkov, R. P. Ozerov, and I. S. Rez, *Kristallografiya* 30, 668 (1985).
58. P. A. Thomas, A. M. Glazer, and B. E. Watts, *Acta Crystallogr., Sect. B* 46, 333 (1990).
59. N. K. Hansen, J. Protas, and G. Marnier, *Acta Crystallogr., Sect. B* 47, 660 (1991).
60. E. L. Belokoneva, O. L. Slovokhotova, M. Yu. Antipin, V. G. Tsirel'son, and Yu. T. Struchkov, *Dokl. Akad. Nauk SSSR* 322, 520 (1992).
61. S. Dahaoui, N. K. Hansen, and B. Menaert, *Acta Crystallogr., Sect. C* 53, 1173 (1997).
62. P. A. Thomas, S. C. Mayo, and B. E. Watts, *Acta Crystallogr., Sect. B* 48, 401 (1992).
63. J. A. Kaduk and R. H. Jarman, *Z. Kristallogr.* 204, 285 (1993).
64. A. S. Lyakhov, A. F. Selevich, and A. I. Verenich, *Zh. Neorg. Khim.* 38, 1121 (1993).
65. H. Nyman, M. O'Keeffe, and J. O. Bovin, *Acta Crystallogr., Sect. B* 34, 905 (1978).
66. Y. K. Egorov-Tismenko, M. A. Simonov, and N. V. Belov, *Dokl. Akad. Nauk SSSR* 240, 78 (1978).
67. A. Ziadi, G. Thiele, and B. Elouadi, *J. Solid State Chem.* 109, 112 (1994).
68. A. Ziadi, H. Hillebrecht, G. Thiele, and B. Elouadi, *J. Solid State Chem.* 123, 324 (1996).
69. W. H. Zachariasen, *Z. Kristallogr.* 73, 7 (1930).
70. R. Mongiorgi and L. Riva di Sanseverino, *Mineral. Petrol. Acta* 14, 123 (1968).
71. J. A. Speer and G. V. Gibbs, *Am. Mineral.* 61, 238 (1976).
72. M. Taylor and G. E. Brown, *Am. Mineral.* 61, 435 (1976).
73. C. L. Hollabaugh and F. F. Foit Jr., *Am. Mineral.* 69, 725 (1984).
74. V. S. Urusov, N. N. Eremin, and O. V. Yakubovich, *Kristallografiya* 40, 485 (1995).
75. S. Kek, M. Aroyo, U. Bismayer, C. Schmidt, K. Eichhorn, and H. G. Krane, *Z. Kristallogr.* 212, 9 (1997).
76. W. T. A. Harrison, T. E. Gier, and G. D. Stucky, *Zeolites* 15, 408 (1995).
77. E. A. Behrens, D. M. Poojary, and A. Clearfield, *Chem. Mater.* 8, 1236 (1996).
78. M. S. Dadachov and W. T. A. Harrison, *J. Solid State Chem.* 134, 409 (1997).
79. D. M. Poojary, A. I. Bortun, L. N. Bortun, and A. Clearfield, *Inorg. Chem.* 35, 6131 (1996).
80. P. Pertierra, M. A. Salvado, S. Garcia-Granda, A. I. Bortun, and A. Clearfield, *Inorg. Chem.* 38, 2563 (1999).
81. M. Henry, C. Gérardin, and F. Taulelle, *Mater. Res. Soc. Symp. Proc.* 271, 243 (1992).
82. M. Henry, *Mater. Sci. Forum* 152–153, 355 (1994).
83. M. Henry, *Top. Mol. Org. Eng.* 15, 273 (1997).
84. M. Henry, *Coord. Chem. Rev.* 180, 1109 (1998).
85. M. Henry, *Am. Chem. Soc. Symp. Ser.* 732, 277 (1999).
86. T. M. Alam and M. Henry, *Phys. Chem. Chem. Phys.* 2, 23 (2000).
87. A. Rammal, F. Brisach, and M. Henry, *J. Am. Chem. Soc.* 123, 5612 (2001).
88. S. Weymann-Schildknecht and M. Henry, *J. Chem. Soc., Dalton Trans.* 2425 (2001).
89. K. Gigant, A. Rammal, and M. Henry, *J. Am. Chem. Soc.* 123, 11632 (2001).
90. M. Henry, *Chem. Phys. Chem.*, 3, 561 (2002).
91. J. Dubuc and M. Henry, *Inorg. Chem.*, submitted.
92. F. Biechel and M. Henry, *Inorg. Chem.*, submitted.
93. R. P. Feynman, *Phys. Rev.* 56, 340 (1939).
94. P. Hohenberg and W. Kohn, *Phys. Rev. B* 136, 864 (1964).
95. J. B. Mann, T. L. Meek, and L. C. Allen, *J. Am. Chem. Soc.* 122, 2780 (2000).
96. J. B. Mann, T. L. Meek, E. T. Knight, J. F. Capitani, and L. C. Allen, *J. Am. Chem. Soc.* 122, 5132 (2000).
97. J. T. Waber and D. T. Cromer, *J. Chem. Phys.* 42, 4116 (1965).
98. L. Vegard, *Z. Phys.* 61, 185 (1930).
99. R. Fischer and H. Ludwiczek, *Monatsh. Chem.* 106, 223 (1975).
100. F. Schossberger, *Z. Kristallogr.* 104, 358 (1942).
101. W. H. Baur, *Naturwissenschaften* 42, 295 (1955).
102. S. Andersson, B. Collen, U. Kuylenstierna, and A. Magneli, *Acta Chem. Scand.* 11, 1641 (1957).
103. W. H. Baur, *Acta Crystallogr.* 14, 493 (1961).
104. W. H. Baur and A. A. Khan, *Acta Crystallogr., Sect. B* 27, 2133 (1971).
105. S. C. Abrahams and J. L. Bernstein, *J. Chem. Phys.* 55, 3206 (1971).
106. V. I. Khitrova, M. F. Bundule, and Z. G. Pinsker, *Kristallografiya* 22, 1253 (1977).
107. E. P. Meagher and G. A. Lager, *Can. Mineral.* 17, 77 (1979).
108. T. M. Sabine and C. J. Howard, *Acta Crystallogr., Sect. B* 38, 701 (1982).
109. W. Gonschorek, *Z. Kristallogr.* 160, 187 (1982).
110. W. Gonschorek and R. Feld, *Z. Kristallogr.* 161, 1 (1982).
111. H. Seki, N. Ishizawa, N. Mizutani, and M. Kato, *J. Ceram. Assoc. Jpn.* 92, 219 (1984).
112. R. Restori, D. Schwarzenbach, and J. R. Schneider, *Acta Crystallogr., Sect. B* 43, 251 (1987).
113. J. K. Burdett, T. Hughbanks, G. J. Miller, J. W. Richardson, and J. V. Smith, *J. Am. Chem. Soc.* 109, 3639 (1987).
114. K. Sugiyama and Y. Takeuchi, *Z. Kristallogr.* 194, 305 (1991).
115. C. J. Howard, T. M. Sabine, and F. Dickson, *Acta Crystallogr., Sect. B* 47, 462 (1991).
116. R. J. Swope, J. R. Smyth, and A. C. Larson, *Am. Mineral.* 80, 448 (1995).
117. I. E. Grey, C. Li, C. M. MacRae, and L. A. Bursill, *J. Solid State Chem.* 127, 240 (1996).
118. M. Henry, *Solid State Sci.*, submitted.
119. J. Pascual, J. Camassel, and H. Mathieu, *Phys. Rev. B* 18, 5606 (1978).
120. L. Pauling, *J. Phys. Chem.* 56, 361 (1952).
121. J. H. Binks and J. A. Duffy, *J. Chem. Soc., Faraday Trans. 2* 81, 473 (1985).
122. F. Gervais, personal communication.
123. L. A. Grunes, R. D. Leapman, C. N. Wilker, R. Hoffmann, and A. B. Kunz, *Phys. Rev. B* 25, 7157 (1982).
124. B. Poumellec, P. J. Durham, and G. Y. Guo, *J. Phys.: Condens. Matter* 3, 8195 (1991).
125. A. Stashans, S. Lunell, and R. W. Grimes, *J. Phys. Chem. Solids* 57, 1293 (1996).
126. A. Fahmi, C. Minot, B. Silvi, and M. Causa, *Phys. Rev. B* 47, 11717 (1993).
127. H. Shintani, S. Sato, and Y. Saito, *Acta Crystallogr., Sect. B* 31, 1981 (1975).

128. O. Kanert and H. Kolem, *J. Phys. C: Solid State Phys.* 21, 3909 (1988).
129. Y. Kudoh and H. Takeda, *Physica B and C* 139, 333 (1986).
130. D. C. Allan and M. P. Teter, *J. Am. Ceram. Soc.* 73, 3247 (1990).
131. D. J. Lacks and R. G. Gordon, *Phys. Rev. B* 48, 2889 (1993).
132. K. M. Glassford and J. R. Chelikowsky, *Phys. Rev. B* 46, 1284 (1992).
133. K. M. Glassford, N. Troullier, J. L. Martins, and J. R. Chelikowsky, *Solid State Commun.* 76, 635 (1990).
134. F. Schossberger, *Philos. Mag.* 32, 505 (1916).
135. R. L. Parker, *Z. Kristallogr.* 59, 1 (1924).
136. M. Horn, C. F. Schwerdtfeger, and E. P. Meagher, *J. Am. Ceram. Soc.* 53, 124 (1970).
137. V. I. Khitrova, M. F. Bundule, and Z. G. Pinsker, *Kristallografiya* 22, 1253 (1977).
138. M. Sakata, M. Takagi, M. Takata, and C. J. Howard, *Physica B* 213–214, 384 (1995).
139. D.-D. Mo and W. Y. Ching, *Phys. Rev. B* 51, 13023 (1995).
140. H. Tang, H. Berger, P. E. Schmid, and F. Lévy, *Solid State Commun.* 87, 847 (1993).
141. N. Hosaka, T. Sekiya, M. Fujisawa, C. Sakoto, and S. Kurita, *J. Electron Spectrosc. Relat. Phenom.* 78, 75 (1996).
142. J. K. Burdett, *Inorg. Chem.* 24, 2244 (1985).
143. T. J. Bastow, M. A. Gibson, and C. T. Forwood, *Solid State Magn. Reson.* 12, 201 (1998).
144. T. J. Bastow and S. N. Stuart, *Chem. Phys.* 143, 459 (1990).
145. C. J. Jameson and H. S. Gutowsky, *J. Chem. Phys.* 40, 1714 (1964).
146. J. Vaara, J. Lounila, K. Ruud, and T. Helgaker, *J. Chem. Phys.* 109, 8388 (1998).
147. W. H. Flygare and J. Goodisman, *J. Chem. Phys.* 49, 3122 (1968).
148. K. M. S. Saxena and P. T. Narasimhan, *Int. J. Quantum. Chem.* 1, 731 (1967).
149. G. Malli and S. Fraga, *Theor. Chim. Acta* 6, 54 (1966).
150. C. F. Bunge, J. A. Barrientos, and A. V. Bunge, *Atomic Data and Nuclear Data Tables* 53, 113 (1993).
151. P. Blaha, D. J. Singh, P. I. Sorantin, and K. Schwarz, *Phys. Rev. B* 46, 1321 (1992).
152. E. N. Kaufmann and R. J. Vianden, *Rev. Mod. Phys.* 51, 161 (1979).
153. R. Weyl, *Z. Kristallogr.* 68, 239 (1928).
154. W. H. Baur, *Acta Crystallogr.* 14, 214 (1961).
155. T. J. Bastow, G. Doran, and H. J. Whitfield, *Chem. Mater.* 12, 436 (2000).
156. C. Gervais, M. E. Smith, A. Pottier, J.-P. Jolivet, and F. Babonneau, *Chem. Mater.* 13, 462 (2001).
157. T. P. Feist and P. K. Davies, *J. Solid State Chem.* 101, 275 (1992).
158. L. Brohan, A. Verbaere, M. Tournoux, and G. Demazeau, *Mater. Res. Bull.* 17, 355 (1982).
159. J. Akimoto, Y. Gotoh, Y. Oosawa, N. Nonose, T. Kumagai, K. Aoki, and H. Takei, *J. Solid State Chem.* 113, 27 (1994).
160. M. Latroche, L. Brohan, R. Marchand, and M. Tournoux, *J. Solid State Chem.* 81, 78 (1989).
161. P. Y. Simons and F. Dachille, *Acta Crystallogr.* 23, 334 (1967).
162. I. E. Grey, C. Li, I. C. Madsen, and G. Braunshausen, *Mater. Res. Bull.* 23, 743 (1988).
163. J. S. Olsen, L. Gerward, and J. Z. Jiang, *J. Phys. Chem. Solids* 60, 229 (1999).
164. H. Sato, S. Endo, M. Sugiyama, T. Kikegawa, O. Shimomura, and K. Kusaba, *Science* 251, 786 (1991).
165. C. J. Howard, R. J. Hill, and B. E. Reichert, *Acta Crystallogr., Sect. B* 44, 116 (1988).
166. K. Lagarec and S. Desgreniers, *Solid State Commun.* 94, 519 (1995).
167. S. Shankar and R. G. Parr, *Proc. Natl. Acad. Sci. U.S.A.* 82, 264 (1985).
168. R. Ruus, A. Kikas, A. Saar, A. Ausmees, E. Nommiste, J. Aarik, A. Aidla, T. Uustare, and I. Martinson, *Solid State Commun.* 104, 199 (1997).
169. P. I. Sorantin and K. Schwarz, *Inorg. Chem.* 31, 567 (1992).
170. S.-K. Lin, *J. Chem. Inf. Comput. Sci.* 36, 367 (1996).
171. S.-K. Lin, *Int. J. Mol. Sci.* 2, 10 (2001).
172. E. T. Jaynes in "Maximum Entropy and Bayesian Methods" (C. R. Smith, G. J. Erickson, and P. O. Neudorfer, Eds.), p. 1. Kluwer Academic, Dordrecht, 1992.
173. T. Nagase, T. Ebina, T. Iwasaki, H. Hayashi, Y. Onodera, and M. Chatterjee, *Chem. Lett.* 9, 911 (1999).
174. Y. Zheng, E. Shi, S. Cui, W. Li, and X. Hu, *J. Am. Ceram. Soc.* 83, 2634 (2000).
175. A. Pottier, C. Chanéac, E. Tronc, L. Mazerolles, and J.-P. Jolivet, *J. Mater. Chem.* 11, 1116 (2001).
176. S. Komarneni, E. Breval, and R. Roy, *J. Non-Cryst. Solids* 79, 195 (1986).
177. I. P. Saraswat, S. K. Srivasta, G. Bhattacharjee, and Sharadanand, *J. Mater. Sci. Lett.* 5, 795 (1986).
178. P. Arnal, R. J. P. Corriu, D. Leclercq, P. H. Mutin, and A. Vioux, *J. Mater. Chem.* 6, 1925 (1996).
179. H. Kominami, M. Khono, and Y. Kera, *J. Mater. Chem.* 10, 1151 (2000).
180. C. Ligorio and L. T. Work, *Ind. Eng. Chem.* 29, 213 (1937).
181. H. B. Weiser and W. O. Milligan, *J. Phys. Chem.* 38, 513 (1934).
182. H. B. Weiser, W. O. Milligan, and E. L. Cook, *J. Phys. Chem.* 45, 1227 (1941).
183. Z. Jerman, *Collect. Czech. Chem. Commun.* 31, 3180 (1966).
184. O. Sönhel, *Collect. Czech. Chem. Commun.* 40, 2560 (1975).
185. J. F. Duncan and R. G. Richards, *New Zealand J. Sci.* 19, 171 (1976).
186. E. Matijevic, M. Budnik, and L. Meites, *J. Colloid Interface Sci.* 61, 302 (1977).
187. L. I. Bekkerman, I. P. Dobrovol'skii, and A. A. Ivakin, *Russ. J. Inorg. Chem.* 21, 223 (1976).
188. E. Narita, H. Tajeuchi, N. Horiguchi, and T. Okabe, *Bull. Chem. Soc. Jpn.* 57, 1388 (1984).
189. H. Schroeder, in "Physics of Thin Films," Vol. 5, p. 87. Academic Press, New York, 1969.
190. B. E. Yoldas, *J. Mater. Sci.* 21, 1087 (1986).
191. Y. Takahashi and Y. Matsuoka, *J. Mater. Sci.* 23, 2259 (1988).
192. R. Janes, M. Edge, J. Rigby, D. Mourelatou, and N. S. Allen, *Dyes Pigments* 48, 29 (2001).
193. M. Grätzel, *Nature* 414, 338 (2001).
194. A. Fujishima and K. Honda, *Nature* 238, 37 (1972).
195. N. Negishi and T. Takeuchi, *J. Sol–Gel Sci. Technol.* 22, 23 (2001).
196. M. Zaharescu, M. Crisan, A. Szatvanyi, and M. Gartner, *J. Optoelectron. Adv. Mater.* 2, 618 (2000).
197. J. Ovenstone and K. Yanagisawa, *Chem. Mater.* 11, 2770 (1999).
198. L. Kavan, M. Grätzel, S. E. Gilbert, C. Klemenz, and H. J. Scheel, *J. Am. Chem. Soc.* 118, 6716 (1996).
199. M. Ferroni, V. Guidi, G. Martinelli, G. Faglia, P. Nelli, and G. Sberveglieri, *Nanostruct. Mater.* 7, 709 (1996).
200. H. Tang, K. Prasad, S. Sanjinés, and F. Lévy, *Sens. Actuators, B* 26, 71 (1995).
201. E. Traversa, M. L. Di Vona, S. Licoccia, M. Sacerdoti, M. C. Carotta, L. Crema, and G. Martinelli, *J. Sol–Gel Sci. Technol.* 22, 167 (2001).
202. J. Aarik, A. Aida, V. Sammelselg, T. Uustare, M. Ritala, and M. Leskelä, *Thin Solid Films* 370, 163 (2000).
203. A. Rahtu, K. Kukli, and M. Ritala, *Chem. Mater.* 13, 817 (2001).
204. R. Matero, A. Rahtu, and M. Ritala, *Chem. Mater.* 13, 4506 (2001).
205. I. Moriguchi, H. Maeda, Y. Teraoka, and S. Kagawa, *J. Am. Chem. Soc.* 117, 1139 (1995).
206. S. Monticone, R. Tufeu, A. V. Kanaev, E. Scolan, and C. Sanchez, *Appl. Surf. Sci.* 162–163, 565 (2000).
207. R. Wang, K. Hashimoto, A. Fujishima, M. Chikuni, E. Kojima, A. Kitamura, M. Shimohigoshi, and T. Watanabe, *Nature* 388, 431 (1997).
208. B. O'Regan and M. Grätzel, *Nature* 353, 737 (1991).

209. A. Hagfeldt and M. Grätzel, *Acc. Chem. Res.* 33, 269 (2000).
210. M. Grätzel, *J. Sol–Gel Sci. Technol.* 22, 7 (2001).
211. D. Duonghong, J. Ramsden, and M. Grätzel, *J. Am. Chem. Soc.* 104, 2977 (1982).
212. A. Leaustic, F. Babonneau, and J. Livage, *Chem. Mater.* 1, 248 (1989).
213. E. Scolan and C. Sanchez, *Chem. Mater.* 10, 3217 (1998).
214. T. Moritz, J. Reiss, K. Diesner, D. Su, and A. Chemseddine, *J. Phys. Chem. B* 101, 8052 (1997).
215. A. Chemseddine and T. Moritz, *Eur. J. Inorg. Chem.* 235 (1999).
216. A. Rammal, F. Brisach, and M. Henry, *C. R. Acad. Sci. Paris, Sér IIc* 5, 59 (2002).
217. T. J. Bastow and H. J. Whitfield, *Chem. Mater.* 11, 3518 (1999).
218. E. Scolan, C. Magnenet, D. Massiot, and C. Sanchez, *J. Mater. Chem.* 9, 2467 (1999).
219. V. Luca, S. Djajanti, and R. F. Howe, *J. Phys. Chem. B* 102, 10650 (1998).
220. T. J. Trentler, T. E. Denler, J. F. Bertone, A. Agrawal, and V. L. Colvin, *J. Am. Chem. Soc.* 121, 1613 (1999).
221. A. Vioux, *Chem. Mater.* 9, 2292 (1997).
222. P. Krtil, D. Fattakhova, L. Kavan, S. Burnside, and M. Grätzel, *Solid State Ionics* 135, 101 (2000).
223. A. Hagfeldt, N. Vlachopoulos, and M. Grätzel, *J. Electrochem. Soc.* 142, L82 (1994).
224. S. Y. Huang, L. Kavan, I. Exnar, and M. Grätzel, *J. Electrochem. Soc.* 142, L142 (1995).
225. Q. Xu and M. A. Anderson, *J. Am. Ceram. Soc.* 77, 1939 (1994).
226. M. Visca and E. Matijevic, *J. Colloid Interface Sci.* 68, 308 (1979).
227. E. A. Barringer and H. K. Bowen, *J. Am. Ceram. Soc.* 65, C199 (1982).
228. T. A. Ring, *Mater. Res. Soc. Bull.* 15, 34 (1990).
229. E. A. Barringer and H. K. Bowen, *Langmuir* 1, 414 (1985).
230. A. Soloviev, R. Tufeu, C. Sanchez, and A. V. Kanaev, *J. Phys. Chem. B* 105, 4175 (2001).
231. J. Livage, M. Henry, J.-P. Jolivet, and C. Sanchez, *Mater. Res. Soc. Bull.* 15, 16 (1990).
232. S. J. Teichner, G. A. Nicolaon, M. A. Vicarini, and G. E. E. Gardes, *Adv. Colloid Interface Sci.* 5, 245 (1976).
233. O. Masson, V. Rieux, R. Guinebretière, and A. Dauger, *Nanostruct. Mater.* 7, 725 (1996).
234. F. Meng, J. R. Schlup, and L. T. Fan, *Chem. Mater.* 9, 2459 (1997).
235. I. Kraitzer, K. McTaggart, and G. Winter, *J. Oil Colour Chem. Assoc.* 31, 405 (1948).
236. K. Kamiya, K. Tanimoto, and T. Yoko, *J. Mater. Sci. Lett.* 5, 402 (1986).
237. T. Hayashi, T. Yamada, and H. Saito, *J. Mater. Sci.* 18, 3137 (1983).
238. K. Kamiya, S. Sakka, and S. Ito, *J. Ceram. Soc. Jpn.* 85, 599 (1977).
239. C. J. Brinker and M. S. Harrington, *Sol. Energy Mater.* 5, 159 (1981).
240. R. J. Davis and Z. Liu, *Chem. Mater.* 9, 2311 (1997).
241. S. Diré and F. Babonneau, *J. Non-Cryst. Solids* 167, 29 (1994).
242. P. E. Dirken, M. E. Smith, and H. J. Whitfield, *J. Phys. Chem.* 99, 395 (1995).
243. L. Delattre and F. Babonneau, *Chem. Mater.* 9, 2385 (1997).
244. C. Gervais, F. Babonneau, D. Hoebbel, and M. E. Smith, *Solid State NMR* 17, 2 (2000).
245. C. Gervais, F. Babonneau, and M. E. Smith, *J. Phys. Chem. B* 105, 1971 (2001).
246. R. Anderson, G. Mountjoy, M. E. Smith, and R. J. Newport, *J. Non-Cryst. Solids* 232–234, 72 (1998).
247. S. F. Dec, M. F. Davis, G. E. Maciel, C. E. Bronnimann, J. J. Fitzgerald, and S.-S. Han, *Inorg. Chem.* 32, 955 (1993).
248. D. Hennings, M. Klee, and R. Waser, *Adv. Mater.* 3, 334 (1991).
249. K. S. Mazdiyasni, *Ceram. Int.* 8, 42 (1982).
250. A. I. Yanovsky, M. I. Yanovskaya, V. K. Limar, V. G. Kessler, N. Ya. Turova, and Yu. T. Struchkov, *J. Chem., Soc. Chem. Commun.* 1605 (1991).
251. A. I. Yanovsky, E. P. Turevskaya, M. I. Yanovskaya, V. G. Kessler, N. Ya. Turova, A. P. Pisarevskii, and Yu. T. Struchkov, *Zh. Neorg. Khim.* 40, 355 (1995).
252. B. Gaskins, J. J. Lannutti, D. C. Finnen, and A. A. Pinkerton, *Acta Crystallogr., Sect. C* 50, 1387 (1994).
253. E. P. Turevskaya, V. G. Kessler, N. Ya. Turova, A. P. Pisarevsky, A. I. Yanovsky, and Yu. T. Struchkov, *J. Chem. Soc., Chem. Commun.* 2303 (1994).
254. M. Veith, S. Mathur, and V. Huch, *Inorg. Chem.* 36, 2391 (1997).
255. Z. A. Starikova, A. I. Yanovsky, N. M. Kotova, M. I. Yanovskaya, N. Y. Turova, and D. Benlian, *Polyhedron* 16, 4347 (1997).
256. M. Veith, S. Mathur, and V. Huch, *Inorg. Chem.* 35, 7295 (1995).
257. W. E. Rhine, R. B. Hallcock, W. R. Davis, and W. Wong-Ng, *Chem. Mater.* 4, 1208 (1992).
258. V. W. Day, T. A. Eberspacher, M. H. Frey, W. G. Klemperer, S. Liang, and D. A. Payne, *Chem. Mater.* 8, 330 (1996).
259. V. W. Day, T. A. Eberspacher, W. G. Klemperer, and S. Liang, *Chem. Mater.* 7, 1607 (1995).
260. V. G. Kessler, L. G. Hubert-Pfalzgraf, S. Daniele, and A. Gleizes, *Chem. Mater.* 6, 2336 (1994).
261. W.-F. Zhang, Q. Xing, and Ya.-B. Huang, *Mod. Phys. Letts. B* 14, 709 (2000).
262. I. Baxter, S. R. Drake, M. B. Hursthouse, K. M. A. Malik, D. M. P. Mingos, J. C. Plakatouras, and D. J. Otway, *Polyhedron* 17, 625 (1998).
263. C. D. Chandler and M. J. Hampden-Smith, *Chem. Mater.* 4, 1137 (1992).
264. M. Lencka and R. E. Riman, *J. Am. Ceram. Soc.* 76, 2649 (1993).
265. M. M. Lencka and R. E. Riman, *Ferroelectrics* 151, 159 (1994).
266. H. K. Chae, D. A. Payne, Z. Xu, and L. Ma, *Chem. Mater.* 6, 1589 (1994).
267. S. Daniele, R. Papiernik, L. G. Hubert-Pfalzgraf, S. Jagner, and M. Hakansson, *Inorg. Chem.* 34, 628 (1995).
268. L. G. Hubert-Pfalzgraf, S. Daniele, R. Papiernik, M.-C. Massiani, B. Septe, J. Vaissermann, and J.-C. Daran, *J. Mater. Chem.* 7, 753 (1997).
269. R. Papiernik, L. Hubert-Pfalzgraf, M. Veith, and V. Huch, *Chem. Ber.* 130, 1361 (1997).
270. S. Daniele, L. G. Hubert-Pfalzgraf, J.-C. Daran, and S. Halut, *Polyhedron* 13, 927 (1994).
271. R. Kuhlman, B. A. Vaartstra, W. E. Streib, J. C. Huffman, and K. G. Caulton, *Inorg. Chem.* 32, 1272 (1993).
272. C. D. Chandler, C. Roger, and M. J. Hampden-Smith, *Chem. Rev.* 93, 1205 (1993).
273. K. van Werde, G. Vanhoyland, D. Nelis, D. Mondelaers, M. K. Van Bael, J. Mullens, and L. C. van Poucke, *J. Mater. Chem.* 11, 1192 (2001).
274. J. A. Ibers, *Nature* 197, 686 (1963).
275. R. D. Witters and C. N. Caughlan, *Nature* 205, 1312 (1965).
276. D. A. Wright and D. A. Williams, *Acta Crystallogr., Sect. B* 24, 1107 (1968).
277. R. W. Adams and G. Winter, *Aust. J. Chem.* 20, 171 (1967).
278. K. Watenpaugh and C. N. Caughlan, *J. Chem. Soc., Chem. Commun.* 76 (1967).
279. V. W. Day, T. A. Eberspacher, W. G. Klemperer, C. W. Park, and F. S. Rosenberg, *J. Am. Chem. Soc.* 113, 8190 (1991).
280. R. Schmid, A. Mosset, and J. Galy, *J. Chem. Soc., Dalton Trans.* 1999 (1991).
281. A. Mosset and J. Galy, *C. R. Acad. Sci. Paris, Sér. II* 307, 1747 (1988).
282. F. Babonneau, S. Doeuff, A. Leaustic, C. Sanchez, C. Cartier, and M. Verdaguer, *Inorg. Chem.* 27, 3166 (1988).
283. N. Hao, B. G. Sayer, G. Denes, D. G. Bickley, C. Detellier, and M. J. McGlinchey, *J. Magn. Reson.* 50, 50 (1982).
284. V. W. Day, T. A. Eberspacher, Y. Chen, J. Hao, and W. G. Klemperer, *Inorg. Chim. Acta* 229, 391 (1995).

285. N. Steunou, F. Ribot, K. Boubekeur, J. Maquet, and C. Sanchez, *New J. Chem.* 23, 1079 (1999).

286. V. W. Day, T. A. Eberspacher, W. G. Klemperer, and C. W. Park, *J. Am. Chem. Soc.* 115, 8469 (1993).

287. N. Steunou, F. Robert, K. Boubekeur, F. Ribot, and C. Sanchez, *Inorg. Chim. Acta* 279, 144 (1998).

288. N. Steunou, G. Kickelbick, K. Boubekeur, and C. Sanchez, *J. Chem. Soc., Dalton Trans.* 3653 (1999).

289. C. F. Campana, Y. Chen, V. W. Day, W. G. Klemperer, and R. A. Sparks, *J. Chem. Soc., Dalton Trans.* 691 (1996).

290. T. J. Boyle, R. W. Schwartz, R. J. Doedens, and J. W. Ziller, *Inorg. Chem.* 34, 1110 (1995).

291. G. R. Desiraju, "Crystal Engineering." Elsevier, Amsterdam, 1989.

292. H. Meerwein, B. von Bock, B. Kirschnick, W. Lenz, and A. Migge, *J. Prakt. Chem.* 147, 113 (1937).

293. D. C. Bradley, *Adv. Chem. Ser.* 23, 10 (1959).

294. T. J. Boyle, T. M. Alam, E. R. Mechenbier, B. L. Scott, and J. W. Ziller, *Inorg. Chem.* 36, 3293 (1997).

295. G. W. Svetich and A. A. Voge, *Acta Crystallogr., Sect. B* 28, 1760 (1972).

296. S. C. James, N. C. Norman, and A. G. Orpen, *Acta Crystallogr., Sect. C* 54, 1261 (1998).

297. L. D. Durfee, S. F. Latesky, I. P. Rothwell, J. C. Huffman, and K. Folting, *Inorg. Chem.* 24, 4569 (1985).

298. R. T. Toth and D. W. Stephan, *Can. J. Chem.* 69, 172 (1991).

299. A. V. Firth, J. C. Stewart, A. J. Hoskin, and D. W. Stephan, *J. Organomet. Chem.* 591, 185 (1999).

300. L. D. Durfee, P. E. Fanwick, I. P. Rothwell, K. Folting, and J. C. Huffman, *J. Am. Chem. Soc.* 109, 4720 (1987).

301. J. E. Hill, P. E. Fanwick, and I. P. Rothwell, *Inorg. Chem.* 28, 3602 (1989).

302. J. E. Hill, P. E. Fanwick, and I. P. Rothwell, *Acta Crystallogr., Sect. C* 47, 541 (1991).

303. J. E. Hill, R. D. Profilet, P. E. Fanwick, and I. P. Rothwell, *Angew. Chem., Int. Ed. Engl.* 29, 664 (1990).

304. C. H. Zambrano, R. D. Profilet, J. E. Hill, P. E. Fanwick, and I. P. Rothwell, *Polyhedron* 12, 689 (1993).

305. J. H. Haslam, *Adv. Chem. Ser.* 23, 272 (1959).

306. L. Peng-Ju, H. Sheng-Hua, H. Kun-Yao, W. Ru-Ji, and T. C. W. Mak, *Inorg. Chim. Acta* 175, 105 (1990).

307. N. W. Mitzel, S. Parsons, A. J. Blake, and D. W. H. Rankin, *J. Chem. Soc., Dalton Trans.* 2089 (1996).

308. K. Wieghardt, I. Tolksdorf, J. Weiss, and W. Swiridoff, *Z. Anorg. Allg. Chem.* 490, 182 (1982).

309. G. J. Gainsford, T. Kemmitt, C. Lensik, and N. B. Milestone, *Inorg. Chem.* 34, 746 (1995).

310. R. E. Reeves and L. W. Mazzeno, *J. Am. Chem. Soc.* 76, 2533 (1954).

311. D. M. Puri and R. C. Mehrotra, *Indian J. Chem.* 5, 448 (1967).

312. N. Pajot, R. Papiernik, L. G. Hubert-Pfalzgraf, J. Vaisserman, and S. Paraud, *J. Chem. Soc., Chem. Commun.* 1817 (1995).

313. D. Wang, R. Yu, N. Kumada, and N. Kinomura, *Chem. Mater.* 11, 2008 (1999).

314. I. D. Williams, S. F. Pedersen, K. B. Sharpless, and S. J. Lippard, *J. Am. Chem. Soc.* 106, 6430 (1984).

315. D. P. Steinhuebel and S. J. Lippard, *Organometallics* 18, 109 (1999).

316. D. P. Steinhuebel and S. J. Lippard, *J. Am. Chem. Soc.* 121, 11762 (1999).

317. L. T. Armistead, P. S. White, and M. R. Gagné, *Organometallics* 17, 4232 (1998).

318. I. Kim, Y. Nishihara, R. F. Jordan, R. D. Rogers, A. L. Rheingold, and G. P. A. Yap, *Organometallics* 16, 3314 (1997).

319. P. H. Bird, A. R. Fraser, and C. F. Lau, *Inorg. Chem.* 12, 1322 (1973).

320. H. Mimoun, M. Postel, F. Casabianca, J. Fischer, and A. Mitschler, *Inorg. Chem.* 21, 1303 (1982).

321. M. Postel, F. Casabianca, Y. Gauffreteau, and J. Fischer, *Inorg. Chim. Acta* 113, 173 (1986).

322. L. D. Durfee, J. E. Hill, P. E. Fanwick, and I. P. Rothwell, *Organometallics* 9, 75 (1990).

323. D. Seebach, D. A. Plattner, A. K. Beck, Y. M. Wang, D. Hunziker, and W. Petter, *Helv. Chim. Acta* 75, 2171 (1992).

324. N. Miele-Pajot, L. G. Hubert-Pfalzgraf, R. Papiernik, J. Vaissermann, and R. Collier, *J. Mater. Chem.* 9, 3027 (1999).

325. B. A. Borgias, S. R. Cooper, Y. B. Koh, and K. N. Raymond, *Inorg. Chem.* 23, 1009 (1984).

326. H. Honda, K. Suzaki, and Y. Sugahara, *J. Sol–Gel Sci. Technol.* 22, 133 (2001).

327. T.-B. Wen, B.-S. Sheng, C.-Y. Su, D. X. Wu, L.-G. Wang, S. Liao, and H.-Q. Liu, *Bull. Chem. Soc. Jpn.* 71, 2339 (1998).

328. T. P. Vaid, E. B. Lobkovsky, and P. T. Wolczanski, *J. Am. Chem. Soc.* 119, 8742 (1997).

329. T. P. Vaid, J. M. Tanski, J. M. Pette, E. B. Lobkovsky, and P. T. Wolczanski, *Inorg. Chem.* 38, 3394 (1999).

330. J. M. Tanski, T. P. Vaid, E. B. Lobkovsky, and P. T. Wolczanski, *Inorg. Chem.* 39, 4756 (2000).

331. J. M. Tanski and P. T. Wolczanski, *Inorg. Chem.* 40, 2026 (2001).

332. J. M. Tanski, E. B. Lobkovsky, and P. T. Wolczanski, *J. Solid State Chem.* 152, 130 (2000).

333. N. W. Eilerts, J. A. Heppert, M. L. Kennedy, and F. Takusagawa, *Inorg. Chem.* 33, 4813 (1994).

334. M. Terada, Y. Matsumoto, Y. Nakamura, and K. Mikami, *Inorg. Chim. Acta* 296, 267 (1999).

335. M. H. Chisholm, J. H. Huang, J. C. Huffman, W. E. Streib, and D. Tiedtke, *Polyhedron* 16, 2941 (1997).

336. P. V. Rao, C. P. Rao, E. K. Wegelius, E. Kolehmainen, and K. Rissanen, *J. Chem. Soc., Dalton Trans.* 4469 (1999).

337. D. C. Bradley and C. E. Holloway, *J. Chem. Soc., Chem. Commun.* 284 (1965).

338. D. C. Bradley and C. E. Holloway, *J. Chem. Soc. A* 282 (1969).

339. R. C. Fay and A. F. Lindmark, *J. Am. Chem. Soc.* 105, 2118 (1983).

340. A. Leaustic, F. Babonneau, and J. Livage, *Chem. Mater.* 1, 240 (1989).

341. R. J. Errington, J. Ridland, W. Clegg, R. A. Coxall, and J. M. Sherwood, *Polyhedron* 17, 659 (1998).

342. G. D. Smith, C. N. Caughlan, and J. A. Campbell, *Inorg. Chem.* 11, 2989 (1972).

343. A. Yamamoto and S. Kambara, *J. Am. Chem. Soc.* 79, 4344 (1957).

344. P. D. Moran, C. E. F. Rickard, G. A. Bowmaker, R. P. Cooney, J. R. Bartlett, and J. L. Woolfrey, *Inorg. Chem.* 37, 1417 (1998).

345. P. Toledano, M. In, and C. Sanchez, *C. R. Acad. Sci. Paris, Ser. II* 313, 1247 (1991).

346. U. Schubert, H. Buhler, and B. Hirle, *Chem. Ber.* 125, 999 (1992).

347. J. L. Wang, F. M. Miao, X. J. Fan, X. Feng, and J. T. Wang, *Acta Crystallogr., Sect. C* 46, 1633 (1990).

348. S. I. Troyanov and O. Yu. Gorbenko, *Polyhedron* 16, 777 (1997).

349. A. R. Siedle and J. C. Huffman, *Inorg. Chem.* 29, 3131 (1990).

350. J. P. Corden, W. Errington, P. Moore, M. G. Partridge, and M. G. H. Wallbridge, *J. Chem. Soc., Dalton Trans.* 2647 (1999).

351. J. V. Barkley, J. C. Cannadine, I. Hannaford, M. M. Harding, A. Steiner, J. Tallon, and R. Whyman, *J. Chem. Soc., Chem. Commun.* 1653 (1997).

352. T. Kemmit, N. I. Al-Salim, and G. J. Gainsford, *Eur. J. Inorg. Chem.* 1847 (1999).

353. S. Doherty, R. J. Errington, N. Housley, J. Ridland, W. Clegg, and M. J. Elsegood, *Organometallics* 18, 1018 (1999).

354. A. A. Diamantis, M. Manikas, M. A. Salam, M. R. Snow, and R. T. Tiekink, *Aust. J. Chem.* 41, 453 (1988).

355. A. Caneschi, A. Dei, and D. Gatteschi, *J. Chem. Soc., Chem. Commun.* 630 (1992).

356. H. Hefele, E. Ludwig, E. Uhlemann, and H. Nöth, *Z. Anorg. Allg. Chem.* 621, 1431 (1995).

357. D. Schwartzenbach, *Helv. Chim. Acta* 55, 2990 (1972).

358. H. Manohar and D. Schwartzenbach, *Helv. Chim. Acta* 57, 1086 (1974).

359. D. Schwartzenbach, *Inorg. Chem.* 9, 2391 (1970).

360. P. Jeske, G. Haselhorst, T. Weyermüller, K. Wieghardt, and B. Nuber, *Inorg. Chem.* 33, 2462 (1994).

361. A. Bodner, P. Jeske, T. Weyhermüller, K. Wieghardt, E. Dubler, H. Schmalle, and B. Nuber, *Inorg. Chem.* 31, 3737 (1992).

362. P. Jeske, K. Wieghardt, and B. Nuber, *Z. Naturforsch., B*: Chem. Sci. 47, 1621 (1992).

363. K. Wieghardt, D. Ventur, Y. H. Tsai, and C. Krüger, *Inorg. Chim. Acta* 99, L25 (1985).

364. L. Porri, A. Ripa, P. Colombo, E. Miano, S. Capelli, and S. V. Meille, *J. Organomet. Chem.* 514, 213 (1996).

365. J. Okuda, S. Fokken, T. Kleinhenn, and T. P. Spaniol, *Eur. J. Inorg. Chem.* 1321 (2000).

366. S. F. Pedersen, J. C. Dewan, R. E. Eckman, and K. B. Sharpless, *J. Am. Chem. Soc.* 109, 1279 (1987).

367. E. J. Corey, C. L. Cywin, and M. C. Noe, *Tetrahedron Lett.* 35, 69 (1994).

368. S. Bott, A. W. Colman, and J. L. Atwood, *J. Chem. Soc., Chem. Commun.* 610 (1986).

369. P. D. Hampton, C. E. Daitch, T. M. Alam, Z. Bencze, and M. Rosay, *Inorg. Chem.* 33, 4750 (1994).

370. W. Clegg, M. R. J. Elsegood, S. J. Teat, C. Redshaw, and V. C. Gibson, *J. Chem. Soc., Dalton Trans.* 3037 (1998).

371. M. M. Olmstead, G. Sigel, H. Hope, X. J. Hu, and P. P. Power, *J. Am. Chem. Soc.* 107, 8087 (1985).

372. G. E. Hofmeister, F. E. Hahn, and S. F. Pedersen, *J. Am. Chem. Soc.* 111, 2318 (1989).

373. M. Albrecht and S. Kotila, *Angew. Chem., Int. Ed. Engl.* 34, 2134 (1995).

374. M. Albrecht and S. Kotila, *Angew. Chem., Int. Ed. Engl.* 35, 1208 (1996).

375. M. Albrecht and S. Kotila, *J. Chem. Soc., Chem. Commun.* 2309 (1996).

376. M. Albrecht, H. Rötteleand, and P. Burger, *Chem. Eur. J.* 2, 1264 (1996).

377. M. Albrecht, M. Schneider, and R. Fröhlich, *New J. Chem.* 753 (1998).

378. M. Scherer, D. L. Caulder, D. W. Johnson, and K. N. Raymond, *Angew. Chem., Int. Ed. Engl.* 38, 1588 (1999).

379. D. L. Caulder and K. N. Raymond, *J. Chem. Soc., Dalton Trans.* 1185 (1999).

380. R. L. Harlow, *Acta Crystallogr., Sect. C* 39, 1344 (1983).

381. A. A. Naiini, W. M. P. B. Menge, and J. G. Verkade, *Inorg. Chem.* 30, 5009 (1991).

382. A. A. Naiini, S. L. Ringrose, Y. Su, R. A. Jacobson, and J. G. Verkade, *Inorg. Chem.* 32, 1290 (1993).

383. G. Boche, K. Möbus, K. Harms, and M. Marsch, *J. Am. Chem. Soc.* 118, 2770 (1996).

384. K. Wieghardt, U. Quilitzsch, J. Weiss, and B. Nuber, *Inorg. Chem.* 19, 2514 (1980).

385. D. Schwartzenbach and K. Girgis, *Helv. Chim. Acta* 58, 2391 (1975).

386. S. M. Harben, P. D. Smith, R. L. Beddoes, D. Collison, and C. D. Garner, *Angew. Chem., Int. Ed. Engl.* 36, 1897 (1997).

387. S. M. Harben, P. D. Smith, M. Helliwell, D. Collison, and C. D. Garner, *J. Chem. Soc., Dalton Trans.* 4517 (1997).

388. H. Chen, P. S. White, and M. R. Gagné, *Organometallics* 17, 5358 (1998).

389. J. M. McInnes, D. Swallow, A. J. Blake, and P. Mountford, *Inorg. Chem.* 37, 5970 (1998).

390. F. Franceschi, E. Solari, C. Floriani, M. Rosi, A. Chiesi-Villa, and C. Rizzoli, *Chem. Eur. J.* 5, 708 (1999).

391. K. M. Carroll, J. Schwartz, and D. M. Ho, *Inorg. Chem.* 33, 2707 (1994).

392. F. Franceschi, E. Gallo, E. Solari, C. Floriani, A. Chiesi-Villa, C. Rizzoli, N. Re, and A. Sgamellotti, *Chem. Eur. J.* 2, 1466 (1996).

393. E. Gallo, E. Solari, F. Franceschi, C. Floriani, A. Chiesi-Villa, and C. Rizzoli, *Inorg. Chem.* 34, 2495 (1995).

394. S. J. Coles, M. B. Hursthouse, D. G. Kelly, A. J. Toner, and N. M. Walker, *Can. J. Chem.* 77, 2095 (1999).

395. P. R. Woodman, N. W. Alcock, I. J. Munslow, C. J. Sanders, and P. Scott, *J. Chem. Soc., Dalton Trans.* 3340 (2000).

396. Y. N. Belokon, S. Caveda-Cepas, B. Green, N. S. Ikonnikov, V. N. Khrustalev, V. S. Larichev, M. A. Moscalenko, M. Morth, C. Orizu, V. I. Tararov, M. Tasinazzo, G. I. Timofeeva, and L. V. Yashkina, *J. Am. Chem. Soc.* 121, 3968 (1999).

397. S. Pritchett, D. H. Woodmansee, P. Gantzel, and P. J. Walsh, *J. Am. Chem. Soc.* 120, 6423 (1998).

398. R. Guilard, J.-M. Latour, C. Lecomte, J.-C. Marchon, J. Protas, and D. Ripoll, *Inorg. Chem.* 17, 1228 (1978).

399. S. De Angelis, E. Solari, C. Floriani, A. Chiesi-Villa, and C. Rizzoli, *Angew. Chem., Int. Ed. Engl.* 34, 1092 (1995).

400. C. E. Housmekerides, R. S. Pilato, G. L. Geoffroy, and A. L. Rheingold, *J. Chem. Soc., Chem. Commun.* 563 (1991).

401. C. E. Housmekerides, D. L. Ramage, C. M. Kretz, J. T. Shontz, R. S. Pilato, G. L. Geoffroy, A. L. Rheingold, and B. S. Haggerty, *Inorg. Chem.* 31, 4453 (1992).

402. A. J. Blake, J. M. McInnes, P. Mountford, G. I. Nikonov, D. Swallow, and D. J. Watkin, *J. Chem. Soc., Dalton Trans.* 379 (1999).

403. F. E. Hahn, S. Rupprecht, and K. H. Moock, *J. Chem. Soc., Chem. Commun.* 224 (1991).

404. T. B. Karpishin, T. D. P. Stack, and K. N. Raymond, *J. Am. Chem. Soc.* 115, 182 (1993).

405. C. Brückner, R. E. Powers, and K. N. Raymond, *Angew. Chem., Int. Ed. Engl.* 37, 1837 (1998).

406. J. P. Fackler Jr., F. J. Kristine, A. M. Mazany, T. M. Moyer, and R. E. Shepherd, *Inorg. Chem.* 24, 1857 (1985).

407. N. Klouras, N. Tzavellas, and C. P. Raptopoulou, *Monatsh. Chem.* 128, 1201 (1997).

408. D. F. Evans, J. Parr, S. Rahman, A. M. Z. Slawin, D. J. Williams, C. Y. Wong, and J. D. Woollins, *Polyhedron* 12, 337 (1993).

409. M. Guo, H. Sun, S. Bihari, J. A. Parkinson, R. O. Gould, S. Parsons, and P. J. Sadler, *Inorg. Chem.* 39, 206 (2000).

410. H. Hefele, E. Ludwig, W. Bansse, E. Uhlemann, Th. Lügger, E. Hahn, and H. Mehner, *Z. Anorg. Allg. Chem.* 621, 671 (1995).

411. U. Auerbach, T. Weyhermüller, K. Wieghardt, B. Nuber, E. Bill, C. Butzlaff, and A. X. Trautwein, *Inorg. Chem.* 32, 508 (1993).

412. G. Schottner, *Chem. Mater.* 13, 3422 (2001).

413. G. Philipp and H. Schmidt, *J. Non-Cryst. Solids* 63, 283 (1984).

414. P. Innocenzi, G. Brusatin, M. Guglielmi, R. Signorini, R. Bozio, and M. Maggini, *J. Non-Cryst. Solids* 265, 68 (2000).

415. D. Hoebbel, M. Nacken, H. Schmidt, V. Huch, and M. Veith, *J. Mater. Chem.* 8, 171 (1998).

416. T. Gunji, T. Kasahara, A. Fujii, Y. Abe, and M. Kawano, *Bull. Chem. Soc. Jpn.* 68, 2975 (1995).

417. M. A. Hossain, M. B. Hursthouse, M. A. Mazid, and A. C. Sullivan, *J. Chem. Soc., Chem. Commun.* 1305 (1988).

418. M. A. Hossain, M. B. Hursthouse, A. Ibrahim, M. Mazid, and A. C. Sullivan, *J. Chem. Soc., Dalton Trans.* 2347 (1989).

419. M. Lazell, M. Motevalli, S. A. A. Shah, C. K. S. Simon, and A. C. Sullivan, *J. Chem. Soc., Dalton Trans.* 1449 (1996).

420. D. B. Dell'Amico, F. Calderazzo, S. Ianelli, L. Labella, F. Marchetti, and G. Pelizzi, *J. Chem. Soc., Dalton Trans.* 4339 (2000).

421. M. Crocker, R. H. M. Herold, A. G. Orpen, and T. A. Overgaag, *J. Chem. Soc., Dalton Trans.* 3791 (1999).

422. B. F. G. Johnson, M. C. Klunduk, C. M. Martin, G. Sankar, S. J. Teate, and J. M. Thomas, *J. Organomet. Chem.* 596, 221 (2000).

423. M. B. Hursthouse and M. A. Hossain, *Polyhedron* 3, 95 (1984).

424. M. Crocker, R. H. M. Herold, and A. G. Orpen, *J. Chem. Soc., Chem. Commun.* 2411 (1997).
425. A. Voigt, R. Murugavel, V. Chandrasekar, N. Winkhofer, H. W. Roesky, H.-G. Schmidt, and I. Uson, *Organometallics* 15, 1610 (1996).
426. T. Mashmeyer, M. C. Klunduk, C. M. Martin, D. S. Shepard, J. M. Thomas, and B. F. G. Johnson, *J. Chem. Soc., Chem. Commun.* 1847 (1997).
427. F. T. Edelmann, S. Giessmann, and A. Fischer, *J. Organomet. Chem.* 620, 80 (2001).
428. A. Voigt, R. Murugavel, M. L. Montero, H. Wessel, F.-Q. Liu, H. W. Roesky, I. Uson, T. Albers, and E. Parisini, *Angew. Chem., Int. Ed. Engl.* 36, 1001 (1997).
429. Z. Duan, A. A. Naiini, J.-H. Lee, and J. G. Verkade, *Inorg. Chem.* 34, 5477 (1995).
430. C. Sanchez and F. Ribot, *New J. Chem.* 18, 1007 (1994).
431. P. Judenstein and C. Sanchez, *J. Mater. Chem.* 6, 511 (1996).
432. J. N. Hay and H. M. Raval, *Chem. Mater.* 13, 3396 (2001).
433. S. Doeuff, M. Henry, and C. Sanchez, *Mater. Res. Bull.* 25, 1519 (1990).
434. H. Barrow, D. A. Brown, N. W. Alcock, H. J. Clase, and M. H. Wallbridge, *J. Chem. Soc., Chem. Commun.* 1231 (1995).
435. G. Kickelbick and U. Schubert, *Eur. J. Inorg. Chem.* 159 (1998).
436. I. Gautier-Luneau, A. Mosset, and J. Galy, *Z. Kristallogr.* 180, 83 (1987).
437. S. Doeuff, Y. Dromzee, and C. Sanchez, *C. R. Acad. Sci. Paris, Ser. II* 308, 1409 (1989).
438. S. Doeuff, Y. Dromzee, F. Taulelle, and C. Sanchez, *Inorg. Chem.* 28, 4439 (1989).
439. I. Laaziz, A. Larbot, C. Guizard, J. Durand, L. Cot, and J. Joffre, *Acta Crystallogr., Sect. C* 46, 2332 (1990).
440. U. Schubert, E. Arpac, W. Glaubitt, A. Helmeric, and C. Chau, *Chem. Mater.* 4, 291 (1992).
441. A. Rammal and M. Henry, to be published.
442. X. Lei, M. Shang, and M. Fehlner, *Organometallics* 15, 3779 (1996).
443. T. J. Boyle, C. J. Tafoya, and B. L. Scott, *Abstr. Pap.-Am. Chem. Soc.* 211, 62-INOR (1996).
444. R. Papiernik, L. G. Hubert-Pfalzgraf, J. Vaissermann, and M. C. H. B. Goncalves, *J. Chem. Soc., Dalton Trans.* 2285 (1998).
445. T. J. Boyle, T. M. Alam, C. J. Tafoya, and B. L. Scott, *Inorg. Chem.* 37, 5588 (1998).
446. A. Pandey, V. D. Gupta, and H. Nöth, *Eur. J. Inorg. Chem.* 1351 (2000).
447. I. Mijatovic, G. Kickelbick, and U. Schubert, *Eur. J. Inorg. Chem.* 1933 (2001).
448. C. Sanchez, J. Livage, M. Henry, and F. Babonneau, *J. Non-Cryst. Solids* 100, 65 (1988).
449. S. Doeuff, M. Henry, C. Sanchez, and J. Livage, *J. Non-Cryst. Solids* 89, 206 (1987).
450. U. Schubert, S. Tewinkel, and F. Möller, *Inorg. Chem.* 34, 995 (1995).
451. X. Lei, M. Shang, and M. Fehlner, *Organometallics* 16, 5289 (1996).
452. C. Guerrero, P. H. Mutin, and A. Vioux, *Chem. Mater.* 12, 1268 (2000).
453. C. Guerrero, M. Mehring, P. H. Mutin, F. Dahan, and A. Vioux, *J. Chem. Soc., Dalton Trans.* 1537 (1999).
454. M. Mehring, G. Guerrero, F. Dahan, P. H. Mutin, and A. Vioux, *Inorg. Chem.* 39, 3325 (2000).
455. M. Mehring, M. Schurmann, P. H. Mutin, and A. Vioux, *Z. Kristallogr.* 215, 591 (2000).
456. R. J. Errington, J. Ridland, K. J. Willett, W. Clegg, R. A. Coxall, and S. L. Heath, *J. Organomet. Chem.* 550, 473 (1998).
457. C. G. Lugmair and T. D. Tilley, *Inorg. Chem.* 37, 1821 (1998).
458. D. L. Thorn and R. L. Harlow, *Inorg. Chem.* 31, 3917 (1992).
459. C. Serre and G. Férey, *J. Mater. Chem.* 9, 579 (1999).
460. M. Riou-cavellec, C. Serre, and G. Férey, *C. R. Acad. Sci. Paris, Sér IIc* 2, 147 (1999).
461. K. O. Kongshaug, H. Fjellvag, and K. P. Lillerud, *J. Chem. Soc., Dalton Trans.* 551 (2000).
462. Y. Zhao, G. Zhu, X. Jiao, W. Liu, and W. Pang, *J. Mater. Chem.* 10, 463 (2000).
463. Y. Guo, Z. Shi, J. Yu, J. Wang, Y. Liu, N. Bai, and W. Pang, *Chem. Mater.* 13, 203 (2001).
464. C. Ninclaus, C. Serre, D. Riou, and G. Férey, *C. R. Acad. Sci. Paris, Sér. IIc* 1, 551 (1998).
465. C. Serre and G. Férey, *Inorg. Chem.* 38, 5370 (1999).
466. P. T. Tanev, M. Chibwe, and T. J. Pinnavaia, *Nature* 368, 321 (1994).
467. A. Corma, M. T. Navarro, and J. Perez-Pariente, *J. Chem. Soc., Chem. Commun.* 147 (1994).
468. D. M. Antonelli and J. Y. Ying, *Angew. Chem., Int. Ed. Engl.* 34, 2014 (1995).
469. R. L. Putnam, N. Nakagawa, K. M. McGrath, N. Yao, I. A. Aksay, S. M. Gruner, and A. Navrotsky, *Chem. Mater.* 9, 2690 (1997).
470. D. M. Antonelli, *Micropor. Mesopor. Mater.* 30, 315 (1999).
471. D. Khushalani, G. A. Ozin, and A. Kuperman, *J. Mater. Chem.* 9, 1491 (1999).
472. D. T. On, *Langmuir* 15, 8561 (1999).
473. S. Cabrera, J. E. Askouri, C. Guillem, J. Latorre, A. Beltran-Porter, D. Beltran-Porter, M. D. Marcos, and P. Amoros, *Solid State Sci.* 2, 405 (2000).
474. M. Thieme and F. Schüth, *Micropor. Mesopor. Mater.* 27, 193 (1999).
475. J. Y. Ying, C. P. Mehnert, and M. S. Wong, *Angew. Chem., Int. Ed. Engl.* 38, 57 (1999).
476. S. Kobayashi, K. Hanabusa, M. Suzuki, M. Kimura, and H. Shirai, *Chem. Lett.* 1077 (1999).
477. S. Kobayashi, H. Hanabusa, N. Hamasaki, M. Kimura, and H. Shirai, *Chem. Mater.* 12, 1523 (2000).
478. J. K. Speer and D. R. Carmody, *Ind. Eng. Chem.* 42, 251 (1950).
479. P. Yang, D. Zhao, D. I. Margolese, B. F. Chmelka, and G. D. Stucky, *Chem. Mater.* 11, 2813 (1999).
480. G. J. A. A. Soler-Illia and C. Sanchez, *New J. Chem.* 24, 493 (2000).
481. G. J. A. A. Soler-Illia, E. Scolan, A. Louis, P. A. Albouy, and C. Sanchez, *New J. Chem.* 25, 156 (2001).
482. G. J. A. A. Soler-Illia, L. Rozes, M. K. Boggiano, C. Sanchez, C. O. Turrin, A. M. Caminade, and J. P. Majoral, *Angew. Chem., Int. Ed. Engl.* 39, 4250 (2000).
483. C. Sanchez, G. J. A. A. Soler-Illia, F. Ribot, T. Lalot, C. R. Mayer, and V. Cabuil, *Chem. Mater.* 13, 3061 (2001).
484. U. Schubert, *Chem. Mater.* 13, 3487 (2001).
485. L. G. Hubert-Pfalzgraf, *Coor. Chem. Rev.* 178–180, 967 (1998).
486. U. Schubert, N. Hüsing, and A. Lorenz, *Chem. Mater.* 7, 2010 (1995).
487. R. A. Caruso and M. Antionetti, *Chem. Mater.* 13, 3272 (2001).
488. B. T. Holland, C. F. Blanford, and A. Stein, *Science* 281, 538 (1998).
489. A. Imhof and D. J. Pine, *Nature* 389, 948 (1997).
490. A. Imhof and D. J. Pine, *Adv. Mater.* 10, 697 (1998).
491. J. E. G. Wijnhoven and W. L. Vos, *Science* 281, 802 (1998).
492. J. E. G. Wijnhoven, L. Bechger, and W. L. Vos, *Chem. Mater.* 13, 4486 (2001).
493. D. Wang, R. A. Caruso, and F. Caruso, *Chem. Mater.* 13, 364 (2001).
494. Q.-B. Meng, C.-H. Fu, Y. Einaga, Z.-Z. Gu, A. Fujishima, and O. Sato, *Chem. Mater.* 14, 83 (2002).
495. R. A. Caruso, M. Giersig, F. Willig, and M. Antonietti, *Langmuir* 14, 6333 (1998).
496. R. A. Caruso, M. Antonietti, M. Giersig, H.-S. Hentze, and J. Jia, *Chem. Mater.* 13, 1114 (2001).
497. Z. Zhong, Y. Yin, B. Gates, and Y. Xia, *Adv. Mater.* 12, 206 (2000).
498. R. A. Caruso and J. H. Schattka, *Adv. Mater.* 12, 1921 (2000).
499. H. Shiho and N. Kawahashi, *Colloid Polym. Sci.* 278, 270 (2000).
500. T. Sasaki, Y. Ebina, T. Tanaka, M. Harada, M. Watanabe, and G. Decher, *Chem. Mater.* 13, 4661 (2001).

501. R. A. Caruso, A. Susha, and F. Caruso, *Chem. Mater.* 13, 400 (2001).

502. M. Ocana, W. P. Hsu, and E. Matijevic, *Langmuir* 7, 2911 (1991).

503. I. Haq and E. Matijevic, *Colloids Surf., A* 81, 153 (1993).

504. S. Srinivasan, A. K. Datye, M. Hampden-Smith, I. E. Wachs, G. Deo, J. M. Jehng, A. M. Turek, and C. F. H. Peden, *J. Catal.* 131, 260 (1991).

505. W. P. Hsu, R. Yu, and E. Matijevic, *J. Colloid Interface Sci.* 156, 56 (1993).

506. A. Hanprasopwattana, S. Srinivasan, A. G. Sault, and A. K. Datye, *Langmuir* 12, 3173 (1996).

507. X.-C. Guo and P. Dong, *Langmuir* 15, 5535 (1999).

508. I. Pastoriza-Santos, D. S. Koktysh, A. A. Mamedov, M. Giersig, N. A. Kotov, and L. M. Liz-Marzan, *Langmuir* 16, 2731 (2000).

509. K. S. Mayya, D. I. Gittins, and F. Caruso, *Chem. Mater.* 13, 3833 (2001).

510. P. Hoyer, *Langmuir* 12, 1411 (1996).

511. B. B. Lakshmi, P. K. Dorhout, and C. R. Martin, *Chem. Mater.* 9, 857 (1997).

512. B. B. Lakshmi, C. J. Patrissi, and C. R. Martin, *Chem. Mater.* 9, 2544 (1997).

513. C. H. M. Hoffman-Caris, *New J. Chem.* 18, 1087 (1994).

514. S. H. Elder, F. M. Cot, Y. Su, S. M. Heald, A. M. Tyryshkin, M. K. Bowman, Y. Gao, A. G. Joly, M. L. Balmer, A. C. Kolwaite, K. A. Magrini, and D. M. Blake, *J. Am. Chem. Soc.* 122, 5138 (2000).

515. P. Bonhôte, E. Gogniat, M. Grätzel, and P. V. Ashrit, *Thin Solid Films* 350, 269 (1999).

516. F. Campus, P. Bonhôte, M. Grätzel, S. Heinen, and L. Walder, *Sol. Energy Mater. Sol. Cells* 56, 281 (1999).

517. P. Bonhôte, E. Gogniat, F. Campus, L. Walder, and M. Grätzel, *Displays* 20, 137 (1999).

518. D. Cummins, G. Boschloo, M. Ryan, D. Corr, N. Rao, and D. Fitzmaurice, *J. Phys. Chem B* 104, 11449 (2000).

519. H. H. Beacham, *Adv. Chem. Ser.* 23, 282 (1959).

520. J. K. Kennedy, *Chem. Soc. Rev.* 8, 221 (1982).

521. I. Gill, *Chem. Mater.* 13, 3404 (2001).

522. H. Nan, C. Y. Ru, L. J. Ming, Y. J. Lu Rong, X. Z. Nan, and L. X. Huai, *J. Biomater. Appl.* 8, 404 (1994).

523. S. Takemoto, K. Tsuru, S. Hayakawa, A. Osaka, and S. Takashima, *J. Sol–Gel Sci. Technol.* 21, 97 (2001).

524. Y.-M. Lim, K.-S. Hwang, and Y.-J. Park, *J. Sol–Gel Sci. Technol.* 21, 123 (2001).

525. P. J. Sadler, *Adv. Inorg. Chem.* 36, 1 (1991).

526. P. Köpf-Maier and H. Köpf, *Struct. Bonding* 70, 105 (1988).

# Molecular Wires and Switches

Chen Wang, Chunli Bai

*The Chinese Academy of Sciences, Beijing, People's Republic of China*

## CONTENTS

## 1. INTRODUCTION

Molecular nanostructures with dimensions below 100 nm are considered important constituents in the pursuit of nanotechnology. The advances in supramolecular chemistry, self-assembly, and microlithography technology have laid the foundation for nanotechnology. It is reasoned that the structures at nanometer scale can introduce novel functions leading to new devices, and the assembling can improve the stringent demands on lithographic techniques at this scale. With the wealth of knowledge acquired in past decades in the field of supramolecular chemistry and self-assembly [1–3], as well as synthetic chemistry, molecular nanostructures can produce vast diversity in device functionality and enhanced performance [4–6]. The molecular structures can function either in the form of an individual unit, such as single molecules, or in a coherent way through self-assembling. The understanding of self-assembling at various scales has enriched the study of molecular crystallization, as well as new lithographic venues.

This work aims at providing a summary of the widely reported molecular wires and switches, with experimental evidence on their device applications. There have been numerous research reports and review articles as well as books on this fast-evolving front. Owing to the enormous literature in the relevant fields, some of the excellent advances in this work may have been overlooked. We intend to limit the scope of discussion of this work to the areas that are more relevant to nanometer-scale devices, such as molecular wires and switches [4, 5], although there are also structures with great importance in fields such as catalysis, materials sciences, and biological sciences, where nanometer-scale effects have also been extensively studied. The pursuit of device applications of the molecular wires and switches also can be reflected in the design considerations for molecular memory designs, as well as molecular motors. These latter aspects are briefly discussed at the end of this work.

## 2. MOLECULAR WIRES

Molecular wires are one-dimensional electrical conductive molecular structures. The effort in constructing molecular wires can be one of the representatives in combining chemistry with proposed nanodevices. Motivated by the conceptual inspiration of molecular electronics and other devices, the design and synthesis of electrical conductive one-dimensional molecular structures attract extensive interest. This effort, together with the effort in nanolithography techniques, is aimed at obtaining functional structures with electronic functions in the length scale below 100 nm. A chemical approach to this scale regime has its uniqueness owing to the diverse molecular functions.

The consideration for transportation processes in molecular wires can be described in electron transfer formalism:

$$K_{ET} = k_0 \exp(-\beta d) \quad \text{or} \quad R = R_0 \exp(\beta d)$$

where $K_{ET}$ represents the efficiency for electron transfer, $k_0$ is the preexponential factor, and $\beta$ is the decay length of the transfer that describes the electronic coupling between the donor and acceptor. The formalism was developed and tested in a solution, and applied successfully in solid junction studies [7–9].

So far, only limited species have been subjected to direct characterizations on a single molecular level. The development of self-assembling and the Langmuir–Blodget technique, scanning probe microscopy (SPM), and so on, has enabled the experimental realization of direct characterization of single molecules, greatly enhancing the feasibility of constructing molecular devices based on carrier transportation processes.

The other approach in designing molecular wires is derived from conjugated molecules, generally represented by the family of conductive polymers. Polymeric molecules have demonstrated appreciable carrier mobility when properly doped with donors or acceptors, and have already attained commercial device applications. The effort in studying this category of molecules can lead to improved mobility at a single molecular level and a larger carrier transportation range.

The third family of wires can be seen in the columnar structure of discotic liquid crystal molecules connected by ligands. The columns are formed by a stacking of molecules, leading to a conductive core with a typical diameter of a few nanometers, separated by a less conductive sheath of similar dimension. The coherence length of the columns can be in the range of a few tens of nanometers. This category of one-dimensional columns can be either electronic or ionic conductive. Some of the species have also demonstrated photoelectric responses.

Carbon nanotubes (CNTs) and other nanotube structures are also pursued as candidates for molecular wires. By controlling the tube structure and composition, we demonstrate properties from semiconducting to metallic, and the rectifying behavior of hybrid tubes. In particular, single-walled carbon nanotubes (SWCNTs) can be a promising component of future molecular electronic devices.

Probably one of the most interesting wire structures of natural existence is DNA molecules. The abundance and accessibility are highly attractive when it comes to applications. There have been uncertainties in characterizing the electron conductivity of this category of molecules. However, interest still remains in pursuing highly desirable molecular wire structures.

## 2.1. Linear Alkane Derivatives

Studies on this group of aliphatic molecules (exemplified by alkanethiols) are focused on constructing devices directly based on single molecule conductivity. The pursuit spanned nearly three decades, from the early study on stearic acetate [10], which was recently revisited by several groups [11–16]. The SPM method also contributed to the study [17]. The results revealed the effects of tunneling barriers, terminal groups, and so on, and helped examine the electron transfer mechanism.

The resistance of chemically bonded octanedithiol is determined at $900 \pm 50$ M$\Omega$, while nonbonded molecules have a resistance at least four orders of magnitude higher [17]. This value is significantly higher than the molecules containing phenylene groups (for example, the resistance of benzene–1,4–dithiol is about 22 M$\Omega$ [18]).

Recent studies obtained the tunneling characteristics of alkane derivatives formed on indium oxide [19], indicating the possible effect of functional groups on the tunneling behavior as theoretically predicted [20].

Typical values of the decay length of the transfer $\beta$ for alkanethiolate obtained on gold and mercury surfaces are in the range of 0.8–1.5 Å$^{-1}$ [21–28], and 0.4–0.6 Å$^{-1}$, respectively, for the phenyl group [21–28]. The decay lengths for nitro-based molecules were found to depend on the tip bias [28].

## 2.2. Conjugated Molecules

As mentioned previously, the conjugated molecules have a higher carrier mobility than aliphatic molecules due to the nature of the delocalized electronic states. There are a large number of one-dimensional molecules that have been vigorously studied [29, 30], and that can be considered as potential candidates for conductive wires.

The resistance of a number of different-sized molecules (monomers, oligomers) with aromatic components was measured. The resistance of double-ended aryl dithiols (xylyldithiol) was estimated as $18 \pm 12$ M$\Omega$ [31], and benzene–1,4–dithiol as about 22 M$\Omega$ [32].

One should note that the resistance measurements include the metal–molecule–metal junction, and the contact between the molecule and metal electrode could greatly affect the measured resistance [20].

Oligomers with linearly conjugated double and triple bonds are also typical for conductive molecules, as illustrated in Schemes 1 and 2. The effective conjugation length for poly (triacetylenes) 1 was determined in the range of 7–10 monomer units [34, 35]. There have been extensive studies on thiophene–ethynylene and phenylene–ethynylene oligomer-based molecular wires 2–5 [36], substituted with $\pi$-active groups. In addition, molecules with ferrocene as terminal groups were also studied for oligo (phenylethynyl) 6–10 [37] and oligo (phenylvinylene) 11 [38].

The wire structure was further expanded to branched structures of three-terminal and four-terminal systems 12–14, as shown in Scheme 3, intended for molecular transistor designs [39].

The oligomers of oligothiophenes and porphyrins have also been widely studied [40]. In the case of fused porphyrins



**Scheme 1.** Molecular wire structures. The molecular structure (1) is reprinted with permission from [35], R. E. Martin et al., *Angew. Chem. Int. Ed.* 38, 817 (1999). © 1999, Wiley-VCH. The molecular structures (2–5) are reprinted with permission from [36], J. M. Tour, *Acc. Chem. Res.* 33, 791 (2000). © 2000, American Chemical Society.

Scheme 2. Ferrocene-terminated molecular wire structures. The molecular structures (6–10) are reprinted with permission from [37], S. Creager et al., *J. Am. Chem. Soc.* 121, 1059 (1999). © 1999, American Chemical Society. The molecular structure (11) is reprinted with permission from [38], S. P. Dudek et al., *J. Am. Chem. Soc.* 123, 8033 (2001). © 2001, American Chemical Society.

15 [41, 42] (Scheme 4), the UV absorption results prove enhanced delocalization of electrons with increased porphyrin units (up to 128-mer), while direct measurements on electrical conductivity are yet to be performed.

A different wire-like structure formed by unsaturated elemental carbon chains was also studied as carbon-based polyynediyl molecular wires 16 [43] (Scheme 4).

Polymerization of the diacetylene compound R–C≡C–C≡C–R'(R=CH$_3$(CH$_2$)$_{11}$, R'=(CH$_2$)$_8$COOH) with high spatial precision was realized by using a scanning tunneling microscope (STM) [44]. The as-generated conjugated polymeric nanowires are in the range of 5–300 nm.



Scheme 3. Branched molecular wire structure [39]. The molecular structures (12–14) are reprinted with permission from [36], J. M. Tour, *Acc. Chem. Res.* 33, 791 (2000). © 2000, American Chemical Society.



Scheme 4. Molecular wire structures. The molecular structure (15) is reprinted with permission from [41], N. Aratani et al., *Angew. Chem. Int. Ed.* 39, 1458 (2000). © 2000, Wiley-VCH. The molecular structure (16) is reprinted with permission from [43], R. Dembinski et al., *J. Am. Chem. Soc.* 122, 810 (2000). © 2000, American Chemical Society.

## 2.3. Conductive Polymers

It is of natural interest to expand the achievements of conductive polymers such as oligothiophenes 17 (Scheme 5) to the pursuit of conductive wires [40, 45–47]. In particular, with the realization of single molecule manipulation with the SPM method, it is now feasible to measure the properties of single molecules, such as elasticity [48, 49].

The delocalized electronic states are also shown to enhance the chemosensory sensitivity. An example of such



Scheme 5. Polymeric molecular wire structures. The molecular structures (18–21) are reprinted with permission from [47], Q. Zhou and T. M. Swager, *J. Am. Chem. Soc.* 117, 12593 (1995). © 1995, American Chemical Society.

enhancement can be found in both polythiophenes and poly (phenyleneethynylene) 18–21 [47] (Scheme 5). This is beneficial in realizing high-sensitivity polyreceptor fluorescent chemosensors.

## 2.4. Rectification Molecular Wires

The concept of an electronic rectification wire was first explored with the donor–spacer–acceptor (D–S–A) model in the early 1970s, and became extensively tested in the study of molecular wire structures [50]. The study can be considered in a broader scope of research in electron transfer within molecules.

The characteristic linear molecular structures of D–S–A are studied for conductive wires. These molecules formed ideal examples to test the electron transfer formalism. A number of the wire structures manifested appreciable rectifying behavior which could be utilized for transistors.

The well-documented molecular wire structure with rectification behavior is represented by $\gamma$–hexadecylquinolinium tricyanoquinomethanide 22 ($C_{16}H_{33}Q$–3CNQ) [51–53] (Scheme 6). The rectification behavior of the molecule is demonstrated in the asymmetric current–voltage characteristic measurements shown in Figure 1.

## 2.5. Carbon Nanotubes

Carbon nanotubes can be thought of as graphite sheets with a hexagonal lattice that have been wrapped up into a seamless cylinder. Both single-walled and multiwalled carbon nanotubes have been examined for electron and hole transportation. The substitutional doping of boron and nitrogen in multiwalled carbon nanotubes (MWCNTs) has shown to change the electric conductive behavior in the range from semiconducting to metallic [54]. The inclusion of alkali and halogen in single-walled carbon nanotubes enhances the electrical conductivity [55, 56]. Hybrid carbon nanotubes have been shown to possess excellent rectifying behavior [57].

The conductance of the SWCNT was shown to be affected by the chemical environment, such as $NH_3$ and $NO_2$ [58], which could be applicable to chemical sensing.

In addition, it has been found that nanotubes can be made from a variety of materials, including carbon, ceramics, metals, and organic polymers. The control of size, especially the diameter, is a key factor in the success of nanotube synthesis. $C_{60}$ nanotubes with a monodisperse size distribution and uniform orientation can be directly made by evaporating
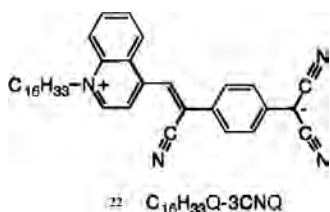


**Scheme 6.** Rectification molecular wire structures. The molecular structure (22) is reprinted with permission from [51], R. M. Metzger et al., *J. Am. Chem. Soc.* 119, 10455 (1997). © 1997, American Chemical Society.
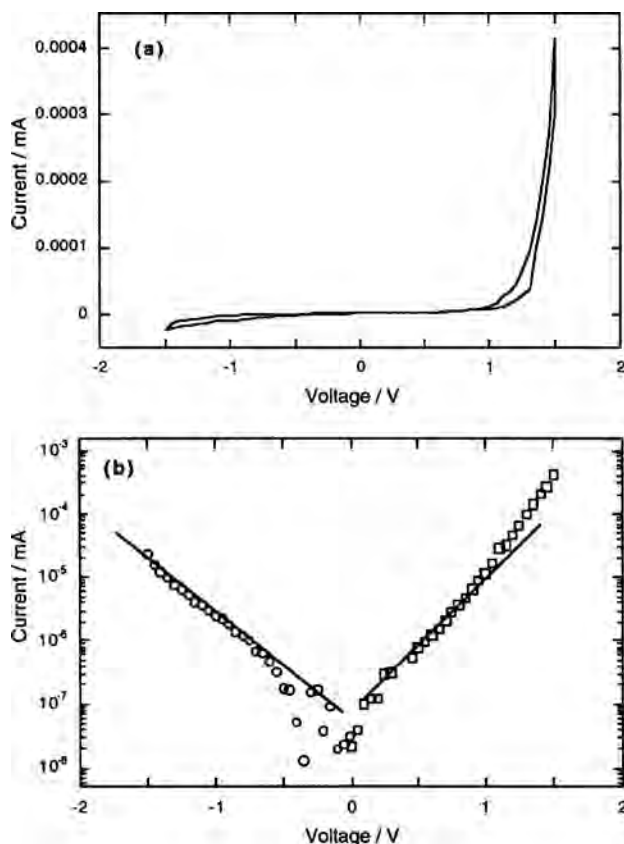


**Figure 1.** Schematic and *I–V* curve of ($C_{16}H_{33}Q$–3CNQ). Both (a) a linear plot and (b) a logarithmic plot are presented. Reprinted with permission from [51], R. M. Metzger et al., *J. Am. Chem. Soc.* 119, 10455 (1997). © 1997, American Chemical Society.

a toluene solution of $C_{60}$ from an ordered porous alumina template with a narrow pore size distribution [59].

## 2.6. Columnar Molecular Structures

In the columnar phase of discotic liquid crystals, the molecules form stacks, via ligand bonding or $\pi-\pi$ interaction, extending tens of nanometers in coherence length. Such structures have been studied for the potential of one-dimensional electron transportation [60]. For the species with alkyl substituents, the side chains interdigitate to form a separating region between molecular cores. The STM observation revealed various assembling behaviors of alkyl-substituted phthalocyanines 23 and porphyrins 24 on a graphite surface [61] (Scheme 7 and Fig. 2).

Alongwith the effort in transferring electrons or holes using low-dimensional molecular nanostructures, there have also been studies on ionic transportation which is important for both biological and chemical processes [62–65]. An example is illustrated by the columnar structure consisting of cyclic D,L–$\alpha$–peptides 25 [63] (Scheme 8).

Low-generation dendrimers are also known to form columnar structures via nonbonding interactions [66–68]. The assemblies of low-generation dendrimers with nanometer diameter cavity channels were directly observed by an STM [69].
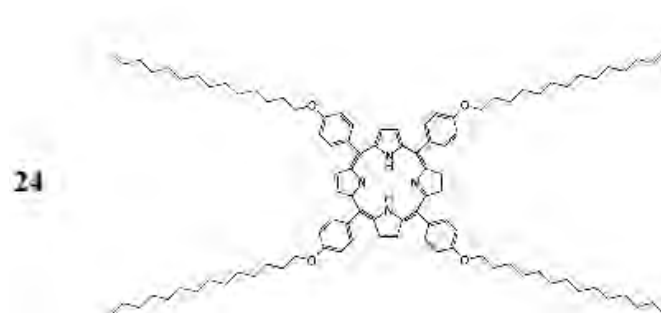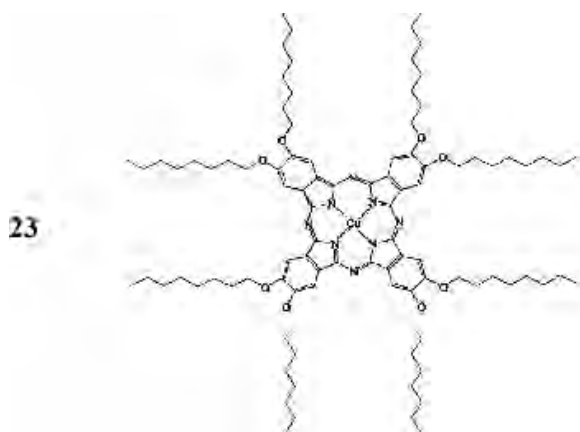
**Scheme 7.** Molecular structures of alkyl-substituted phthalocyanine and porphyrin.

## 2.7. DNA Molecules

The quest to use DNA as an electron conducting wire has been pursued in the past decade. The quest is rooted in the one-dimensional and well-defined helical structure that is composed of uniformly spaced base pairs which is $\pi$-electron rich. The range for electron transfer was proposed
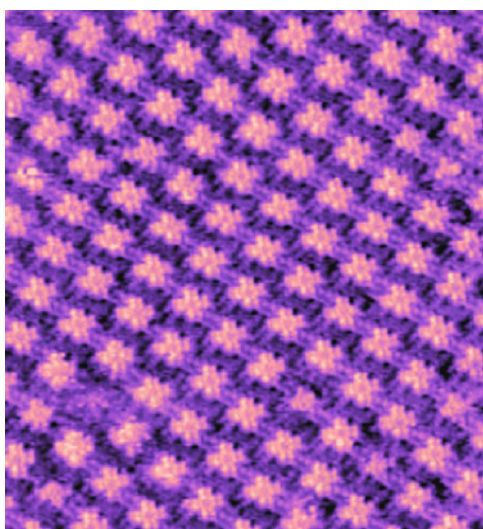


**Figure 2.** 2-D assembly of CuPcOC$_8$ on a graphite surface. Reprinted with permission from [61], X. H. Qiu et al., *J. Am. Chem. Soc.* 122, 5550 (2000). © 2000, American Chemical Society.
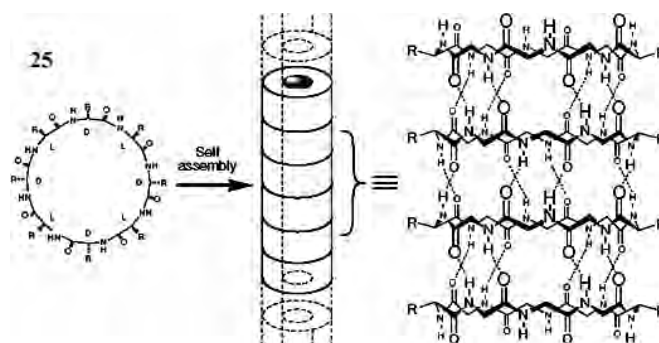


**Scheme 8.** Columnar molecular structure. The molecular structure (25) is reprinted with permission from [63], S. Fernandez-Lopez et al., *Nature* 412, 452 (2001). © 2001, Macmillan Magazines Limited.

to be as long as 40 Å, with the aid of covalently linked donor and acceptor intercalators [70]. A number of mechanisms have been pursued to understand the charge-transfer pathways under various conditions [71, 72].

The ongoing extensive exploration will help to clarify the nature of the charge migration process in DNA with respect to intercalators, sequence, and so on [70–74].

Apart from one-dimensional molecular wires, attaching specific sticky ends to a DNA-branched junction enables the construction of stick figures, whose edges are double-stranded DNA. This approach has been used to assemble a cube, a truncated octahedron, specific 2-D structural features on the nanometer scale, and nanomechanical devices by self-assembly techniques [75].

## 3. MOLECULAR SWITCHES

There is a large variety of molecules that can be effectively and reversibly affected by chemical, optical, and electrical means [1, 76]. Such behavior has been extensively exploited as molecular switches for various applications.

### 3.1. Molecular Switches Based on Interlocked Supramolecules

The family of cantenane-based interlocked molecules 26 (Scheme 9) has shown drastic UV–vis spectrum changes in the redox process [77] (Fig. 3). As an example, an electrochemical cell formed by a molecular monolayer of [2]–cantenane displayed bistable behavior [78, 79]. The behavior led to the design of current-driven molecular logic circuits and addressable memory [80–82]. It was further pointed out that the molecular domains, rather than individual molecules, are responsible for the observed switching behavior [83].

In addition, it has been known that pseudorotaxanes can dissociate into rotaxanes at elevated temperatures or light irradiation, leading to thermal or photomediated molecular switches [84].

The lifetime of the light-triggered excitation state is shown to be as long as a few hundred microseconds for [2]–catenane consisting of a bipyridium cyclophane and a dioxybenzene [85].
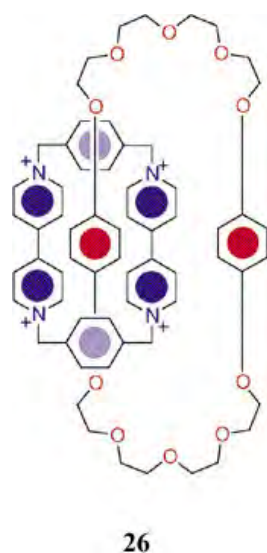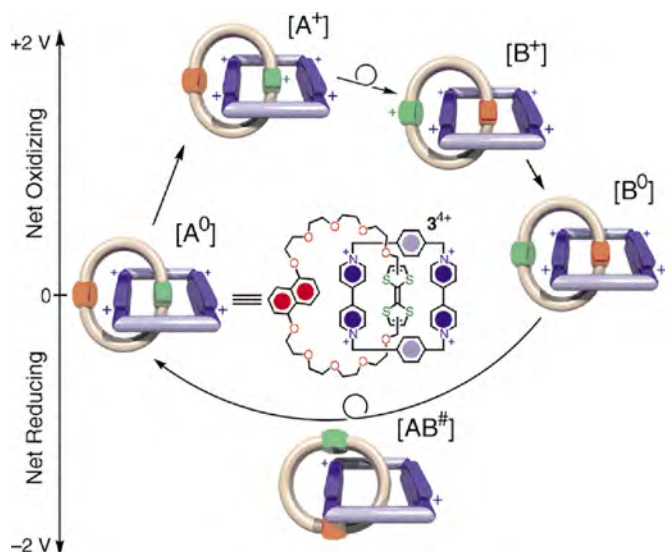
**Scheme 9.** Molecular structure of [2]–cantenane. The molecular structure (26) is reprinted with permission from [82], A. R. Pease et al., *Acc. Chem. Res.* 34, 433 (2001). © 2001, American Chemical Society.
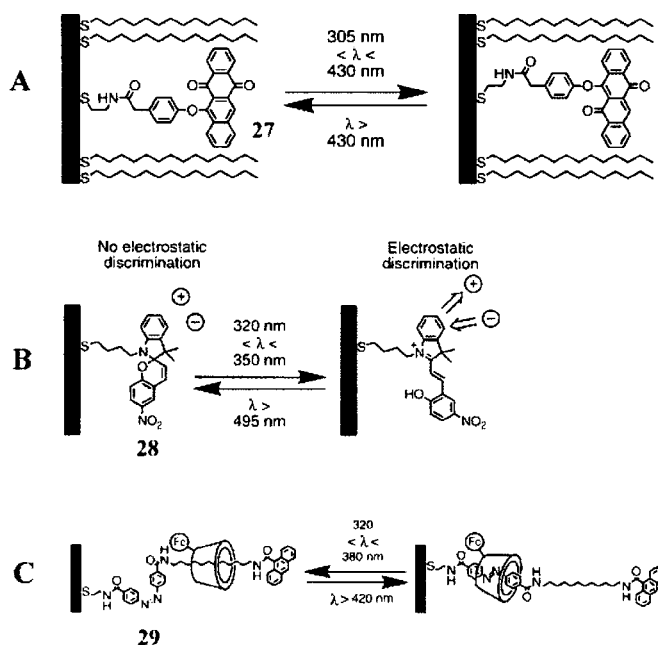
## 3.2. Conjugated Aromatic Molecular Switches

This category of molecular structures possesses rich functions in response to external conditions. The redox activity of a number of electrode-bound species, such as phenoxynaphthacene quinone 27, nitrospiropyran 28, rotaxane 29, and so on, were shown to be reversibly switched through photoisomerization [86]. The molecule 30, consisting of anthracene and acylated diaminopyridin as receptors, can undergo a redox process under electrochemical conditions [87] (Fig. 4).

The electrochromic effect in macrocyclic derivatives can be exploited for molecular switches. A recent example can be found in the octamethoxytetraphenylene compound 31



**Figure 3.** Schematic of switching behavior of a [2]–cantenane-based switch. Reprinted with permission from [82], A. R. Pease et al., *Acc. Chem. Res.* 34, 433 (2001). © 2001, American Chemical Society.



**Figure 4.** Molecular switches based on the photoisomerization process. Reprinted with permission from [86], A. N. Shipway and I. Willner, *Acc. Chem. Res.* 34, 421 (2001). © 2001, American Chemical Society.

[88] (Scheme 10). The dimerization of the conjugated aromatic species 1,3,5–tripyrrolidinobenzene 32 was also suggested as a venue for realizing molecular switching [89].

Anthracene-based molecules can be fluorescent in the presence of a proton [90]. These switches lead to a novel design of logic circuits based on supramolecular structures, especially interlocked molecules [91].

The concept of (D–S–A) has been widely utilized to design various photosensitive as well as electrical-induced molecular switches, as shown in a series of systems exemplified by D = zinc 5–phenyl–10,15,20–tri($n$–pentyl)porphyrin, S = perylene–3,4–dicarboimide, and A = 1,8:4,5–naphthalenediimide 33, 34 [92, 93] (Scheme 11). A comparison of the conformation dynamics and charge-transfer effect was analyzed in detail using phenothiazine–(phenyl)$_n$–pyrene ($n$ = 0, 1) dyads 35–40 [94] (Scheme 12).

It is also shown that, under electrode potential control, the molecular orientation of adsorbed 4,4′–bipyridine 41 changes reversibly from perpendicular to the electrode surface to nearly parallel [95, 96] (Fig. 5).

## 3.3. Oligomer-Based Switches

Direct measurement of conductive polymers using microfabricated electrodes revealed a much faster switching behavior compared with bulk material under electrochemical control (polyaniline) [97].

The oligophenylenevinylenes (OPVs) 42 (Scheme 13) having a protonable phenanthroline group can also be tuned by acidition [98].

Photochromic oligothiophene-substituted chromenes 43–46 (Scheme 14) displayed a structural change that can be associated with a change in electrical polarization [99].
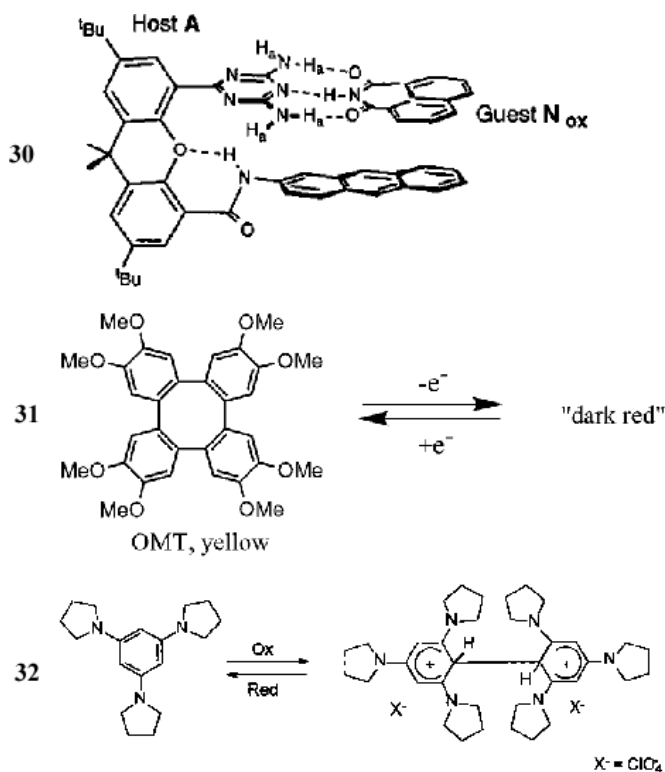
**Scheme 10.** Molecular switches. The molecular structure (30) is reprinted with permission from [87], R. Deans et al., *J. Am. Chem. Soc.* 119, 10863 (1997). © 1997, American Chemical Society. The molecular structure (31) is reprinted with permission from [38], R. Rathore et al., *Angew. Chem. Int. Ed.* 39, 809 (2000). © 2000, Wiley-VCH. The molecular structure (32) is reprinted with permission from [84], J. Heinze et al., *Angew. Chem. Int. Ed.* 40, 2861 (2001). © 2001, Wiley-VCH.

## 3.4. Nuclear-Compound-Based Molecular Switches

A series of mononuclear, dinuclear, and heteronuclear ruthenium complexes of 4,4′–azo–(2,2′–bipyridine)(L) 47–50 (Scheme 15) is shown to be redox responsive [100, 101]. The redox-driven translocation of copper cations was shown in double-stranded mononuclear cupric and cuprous complexes 51 [102] (Scheme 15).

The photoirradiation is also shown to induce structural changes in iron (II) molecular complexes, [Fe(phen)$_2$ (NCS)$_2$](phen = 1,10-phenanthroline) 52 (Scheme 16), leading to a transition between high-spin and low-spin states [103].

The concept of a molecular switch has been applied to control chemical reactions. It was shown that a molecule 53 (Scheme 17) consisted of aluminum porphyrin, and an olefin could be reversibly tuned by UV and visible light through photoisomerization of the olefin, and thus used to control the reaction of carbondioxide and epoxide [104].

## 3.5. Chiral-Molecule-Based Switches

In a recent review, the switching behavior of chiral molecules was also described [105]. The representative examples of chiral optical molecular switches can be
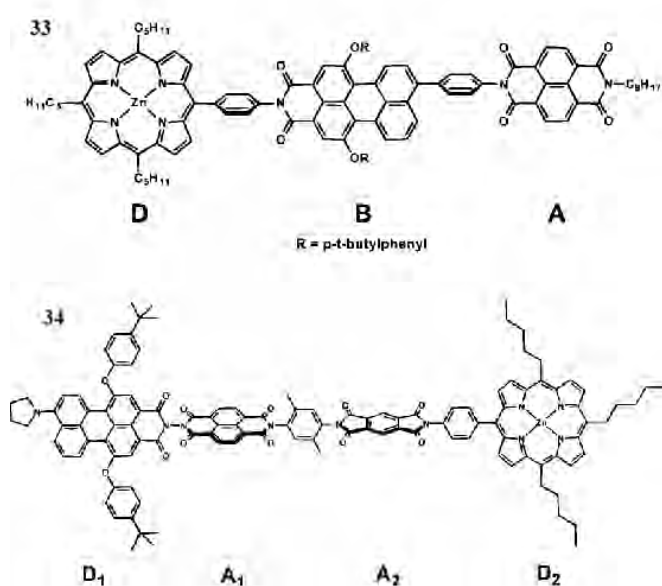


**Scheme 11.** D–S–A type of molecular switches. The molecular structure (33) is reprinted with permission from [92], R. T. Hayes et al., *J. Am. Chem. Soc.* 122, 5563 (2000). © 2000, American Chemical Society. The molecular structure (34) is reprinted with permission from [93], D. Gosztola et al., *J. Am. Chem. Soc.* 120, 5118 (1998). © 1998, American Chemical Society.
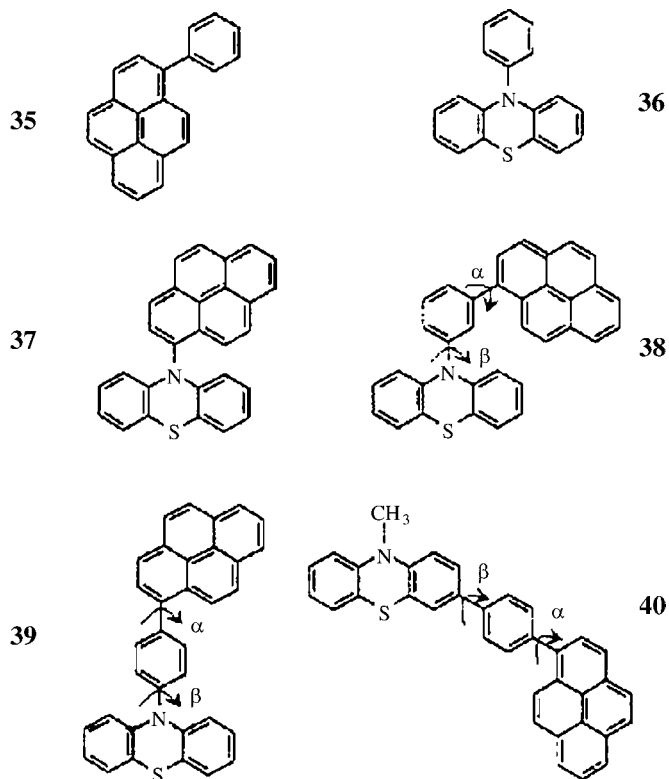


**Scheme 12.** Molecular switches. The molecular structures (35–40) are reprinted with permission from [94], J. Daub et al., *J. Phys. Chem. A* 105, 5655 (2001). © 2001, American Chemical Society.
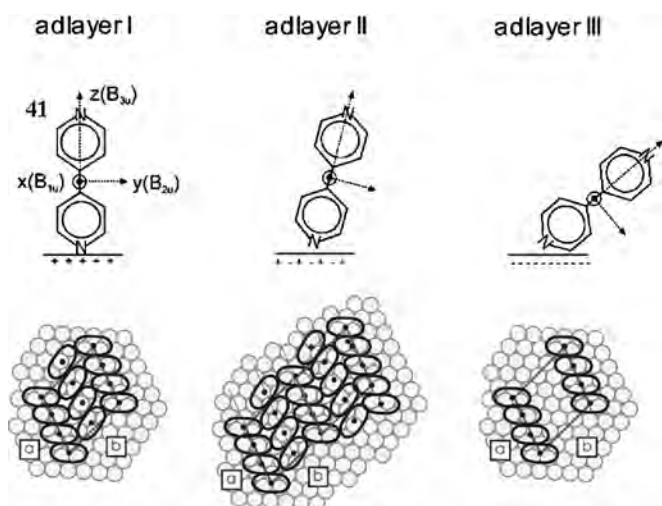
**Figure 5.** Orientation of bpy under electrochemical control. Reprinted with permission from [96], Th. Wandlowski et al., *Langmuir* 18, 4331 (2002). © 2002, American Chemical Society.

illustrated by a compound of unsymmetrically sterically over-crowded thiolxan-thenes 54–56 [105] (Scheme 18). These molecules consist of a static part and a rotary part that can be turned under light irradiation. Their potential applications in molecular motor designs were also explored. In a separate work, the effect of molecular chirality was demonstrated on the directional motion of rotaxane-based molecular motors [106].

## 3.6. Fullerene-Based Molecular Switches

A conformation change of fullerene molecules can lead to drastically different responses in electronic behavior, such as $C_{60}$ under deformation by an STM tip [107, 108] or by controlling the gate potential in a three-terminal geometry [109].

A significant negative differential resistance (NDR) effect can be observed in a junction formed by two $C_{60}$ molecules, due to the local density distribution at the Fermi level of $C_{60}$ molecules [110] (Fig. 6).

## 3.7. Multifunction Molecular Switches

In addition to the above-discussed single-function molecular-switched structures, others that consist of different functional groups have also been studied. By combining
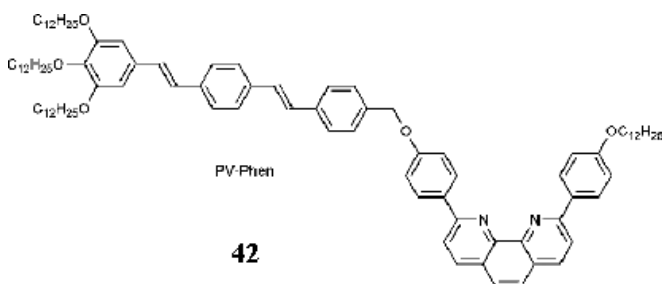


**Scheme 13.** Polymeric molecular switch. The molecular structure (42) is reprinted with permission from [98], N. Armaroli et al., *Chem. Commun.* 2105 (2000). © 2000, Royal Society of Chemistry.
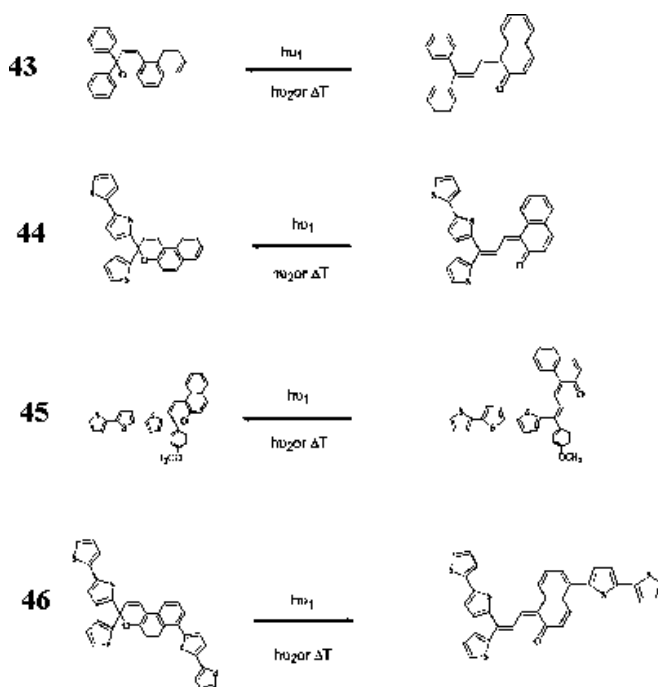


**Scheme 14.** Molecular switches. The molecular structures (43–46) are reprinted with permission from [99], A.Yassar et al., *Eur. Phys. J. AP* 18, 3 (2002). © 2002, EDP Sciences.

components that are photoisomerized and proton sensitive, respectively, a molecular switch 57 (Scheme 19) was realized that can be controlled by both pH and light [111]. A scheme for an optical communication network was proposed based on the photoisomerization of a spiropyran derivative 58 [112]. The spiropyran derivative was shown to be tunable (by ultraviolet light, visible light, and pH) to three distinctive states, namely, the colorless spiropyran state (SP) and two types of colored merocyanine forms (ME and MEH, respectively), as shown in Figure 7.

## 3.8. Biological Switches

A vital aspect of biological activities is regulation at all levels. There are numerous examples in biological systems where the regulation or switching functions involve individual protein molecules. A comprehensive summary is beyond the scope of this work, and dedicated literature [113–119] would be appropriate for interested investigators.

## 4. MOLECULES FOR DATA STORAGE

Along with the effort to develop nanostructures to construct prototype electronic circuits, there are studies to develop molecule-based storage structures. This is also an essential part of integrated nanometer-scale devices. The molecular species reported in this category can be triggered by an external field consisting of an electric field, light, and a magnetic field.
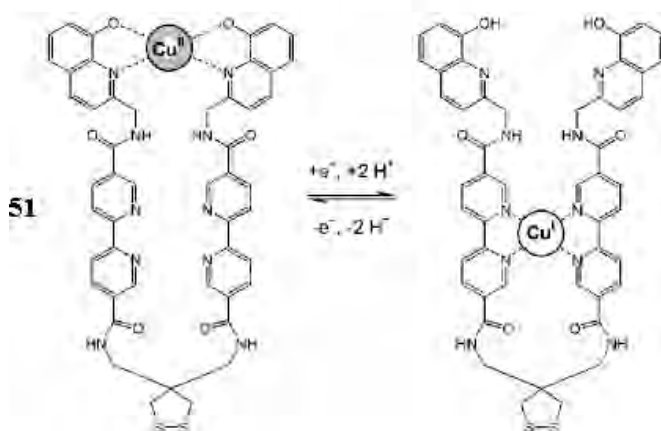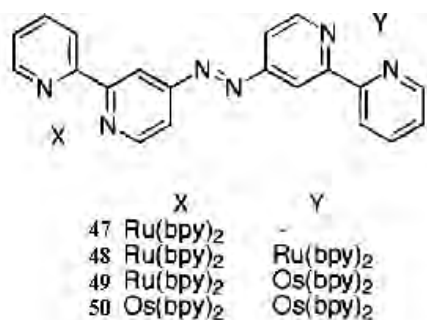
Scheme 15. Molecular switches. The molecular structures (47–50) are reprinted with permission from [101], J. Otsuki et al., *J. Am. Chem. Soc.* 119, 7895 (1997). © 1997, American Chemical Society. The molecular structure (51) is reprinted with permission from [102], D. Kalny et al., *Chem. Commun.* 1426 (2002). © 2002, Royal Society of Chemistry.
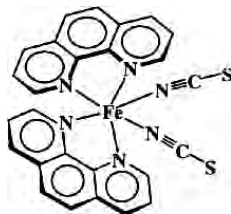


Scheme 16. Molecular switch. The molecular structure (52) is reprinted with permission from [103], M. Marchivie et al., *J. Am. Chem. Soc.* 124, 194 (2002). © 2002, American Chemical Society.
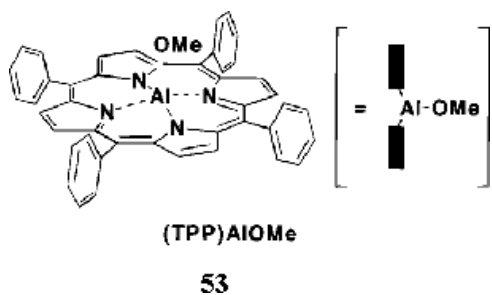


Scheme 17. Molecular switch. The molecular structure (53) is reprinted with permission from [104], H. Sugimoto et al., *J. Am. Chem. Soc.* 121, 2325 (1999). © 1999, American Chemical Society.

Scheme 18. Chiral molecular switches. The molecular structures (54–56) are reprinted with permission from [105], B. L. Feringa, *Acc. Chem. Res.* 34, 504 (2001). © 2001, American Chemical Society.
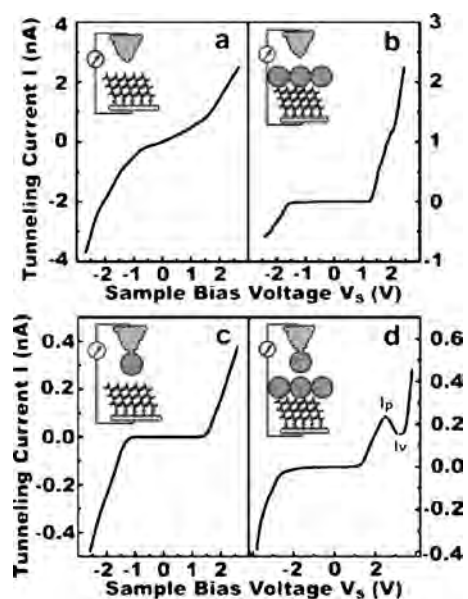


Figure 6. Negative differential resistance of C$_{60}$. Reprinted with permission from [110], C. G. Zeng et al., *Appl. Phys. Lett.* 77, 3595 (2000). © 2000, American Institute of Physics.
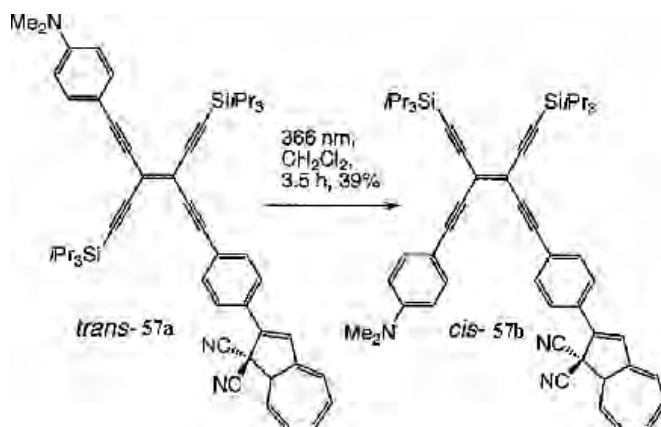


Scheme 19. Multifunction molecular switch. The molecular structure (57) is reprinted with permission from [111], L. Gobbi et al., *Angew. Chem. Int. Ed.* 38, 674 (1999). © 1999, Wiley-VCH.
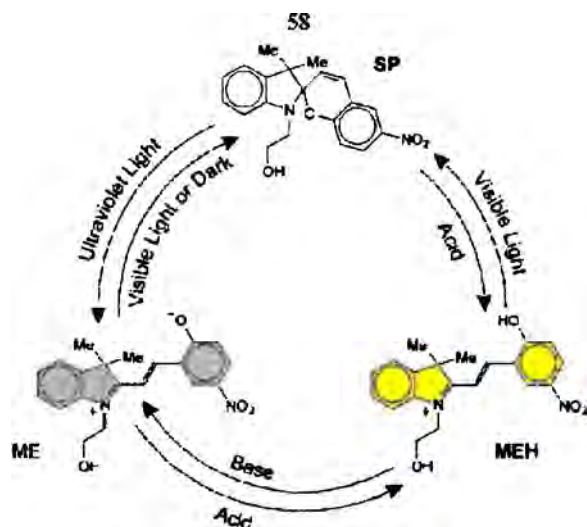
**Figure 7.** Schematic of optical communication system based on a molecular switch. Reprinted with permission from [112], F. M. Raymo and S. Giordani, *J. Am. Chem. Soc.* 124, 2004 (2002). © 2002, American Chemical Society.

## 4.1. Electric-Driven Molecular Storage

The switching behavior of a number of molecules that lead to different resistance states are important candidates for molecular memory designs.

The nanopore experiments [120, 121] indicated that the nitroamino compound 59 (Scheme 20) has two distinct conduction states (conducting and non conducting). It was also suggested that the charged state of dinitro compounds, 2′–nitro–4–ethynylphenyl–4′ethynylphenyl–5′-nitro–1–benzene thiolate 60 (Scheme 20), can also be considered for a type of molecular switch [122]. The switching behavior is associated with the ensemble of approximately 1000 molecules in the nanopore junction region.

Another study on the complex of 3–nitrobenzal malononitril and 1,4–phenylenediamine(NBMN–*p*DA), *p*–nitrobenzonitrile (PNBN) demonstrated distinctively different conductive states which could be reversibly controlled by an electric field [123–125].
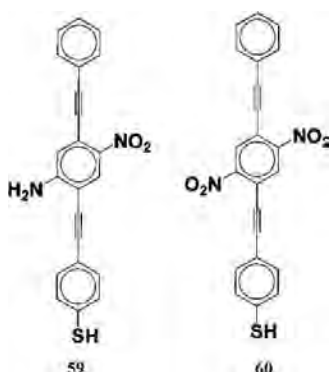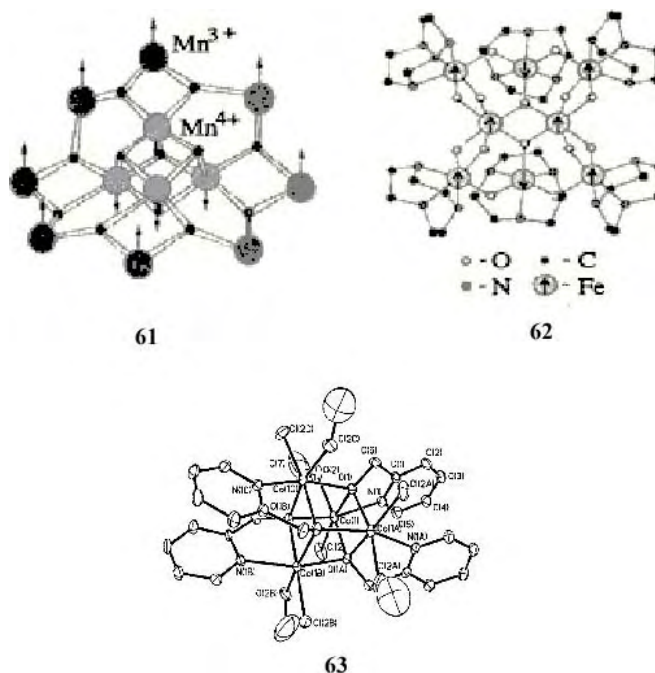


**Scheme 20.** Molecules for molecular memory device. The molecular structures (59, 60) are reprinted with permission from [122], J. M. Seminario et al., *J. Chem. Phys.* 116, 1671 (2002). © 2002, American Institute of Physics.



**Scheme 21.** Examples of single molecular magnetic molecules. The molecular structures (61, 62) are reprinted with permission from [121], K. Park et al., *J. Appl. Phys.* 91, 7167 (2002). © 2002, American Institute of Physics. The molecular structure (63) is reprinted with permission from [132], E.-C. Yang et al., *J. Appl. Phys.* 91, 7382 (2002). © 2002, American Institute of Physics.

## 4.2. Molecular Magnets for Data Storage

Molecules with paramagnetic transition metal centers have been pursued as magnetic materials. These species could provide potentials for designing data storage strategies on a single molecular level.

A family of molecules exemplified by $Mn_{12}$ $[Mn_{12}O_{12}(O_2CMe)_{16}(H_2O)_4] \cdot 4H_2O \cdot 2MeCOOH$ [126–129] 61 (Scheme 21) and $Fe_8$ $[Fe_8O_2(OH)_{12}(tacn)_6]^{+8}$ 62 [129–131] (Scheme 21) has been studied. Due to the weak intermolecular interactions between magnetic centers (12 Mn atoms), these species are widely pursued as single molecular magnets (SMMs).

Other examples of molecular magnets include $Co_4$ $[Co_4(hmp)_4(MeOH)_4Cl_4$ 63 (Scheme 21), where hmp− = anion of hydroxymethylpyridine] [132], $Fe_4$ $[Fe_4(OCH_3)(dmp)_6$, dpm = dipivaloylmethane] [133, 134]. Organic radicals (such as tetracyanoethylene (TCNE), nitroxide derivatives) provide another category of molecular magnets. The examples are $M(TCNE)_x \cdot y(solvent)$ ($M$ = V, Fe, Mn, Co, Ni; TCNE = tetracyanoethylene) [135], together with the family of radical-based molecular magnets [136]. $M(L) \times (4, 4′$–bipyridine) ($M$ = Fe, Co, Ni, Zn; $L = C_2O_4^{2-}$ or $Cl_2$) [137–139]. $V_{15}$ ($K_6[V^{IV}_{15}As_6O_{42}(H_2O)] \cdot 8H_2O$) [140–142].

## 4.3. Molecular Memory in Biological Systems

The understanding of the memory function of the brain has a profound impact on all aspects of life. Memory function is exhibited by storing and retrieving information for both long and short periods of time.

The extensive studies in the past several decades have remarkably advanced the knowledge of molecular memory in biological systems [143–145]. The proposition and confirmation of long-term potentiation is one of the major achievements in this field [146, 147]. This process is characterized by the sustained increase in synaptic strength generated by an action potential in the presynaptic axon [148, 149]. The mechanism of the information encoding process is identified by molecules such as $Ca^{2+}$/calmodulin-dependent protein kinase II (CaMKII) and the NMDA (N–methyl–D–aspartate) subtype of the glutamate receptor [150].

# 5. MOLECULAR MACHINES

## 5.1. Supramolecule-Based Molecular Motor

The interest in constructing nanometer-scale machines with dynamic functions has led to extensive efforts evidenced by the diverse designs of molecular nanostructures stemming from supramolecular chemistry. The function-oriented synthesis and assembling have provided rich options for mechanical parts, such as brakes, shuttles, and so on. The advances are summarized in a special issue of *Accounts of Chemical Research*, volume 34, issue 6 (2001).

The fascinating results shed light on the possibility of conversion of the photo and chemical potential difference into mechanical motion of various artificially designed molecular machines. The illustrated examples include triptycene 61-based molecular brakes and ratchet [151] (Fig. 8).

A number of cyclic components, such as rotaxane and cyclodextrin, could display rotational or translational motion, once threaded through a rigid rod-like structure (such as a polymer chain). The general principle of the driving force is based on the redox activity of the electroactive parts of the assembly. Rotational motion was shown in a
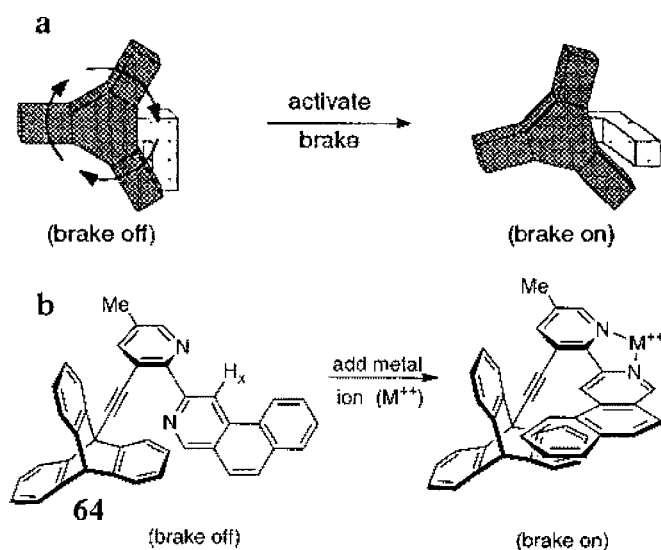


**Figure 8.** Examples of motions performed by molecular motor parts. (a) Schematic of the braking motion. (b) Corresponding molecular structures. Reprinted with permission from [151], T. R. Kelly, *Acc. Chem. Res.* 34, 514 (2001). © 2001, American Chemical Society.

chiral, helical alkene with the irradiation of ultraviolet light [152].

## 5.2. Biological Molecular Motors

Proteins that function as molecular motors are important parts of biological activities, typically driven by energy via the hydrolysis of adenosine triphosphate (ATP). With the characteristic size in the range of nanometers, these proteins can function either in single molecules or in large ensembles. A number of protein families have been extensively studied in this category, including actin-based myosins with more than ten different family types [153, 154], the microtubule-based kinesin family [155, 156], dyneins [157], and the membrane motor protein of prestin [158]. Prototype artificial molecular machines were proposed and explored based on a single molecule configuration [159–162].

# 6. SUMMARY

The surge of interest in nanoscience and technology has generated a vast expansion in research activities. The outcome of the endeavor may go much beyond the goal of device miniaturizations, to new perspectives and novel properties which are not prevalent in bulk materials. Studies of molecular nanostructures can contribute as well as benefit greatly during the process.

The interface between nanometer-scale molecular structures with a macroscopic environment is another field that needs to be explored. The interaction between molecules and the solid support, a combination of the assembling process with state-of-art lithography technology, are important issues that need to be vigorously addressed in future research.

The advances in self-assembly, especially the assembly processes involving multiple components and directional assembly, will have an important impact on the fabrication routes for devices.

Extensive explorations of the molecular properties (conductivity, etc.) on a single molecular level are also essential to the realization of high-performance molecular devices. As the major body of current knowledge is based on the results obtained on the molecular assemblies, progress in the detection techniques would greatly facilitate the understanding of single molecules in various environments.

## GLOSSARY

**Aliphatic molecule** Molecule that can be generally regarded as a methane derivative.

**Chiral molecules** Molecules containing asymmetric components that are mirror images of each other. They are also defined optically as right- and left-handed structures.

**Conjugated polymer** Polymer containing sequential double bonds.

**Dendrimer** Highly branched polymer of controlled branching structure.

**Ionic transportation** Movement of charged particles under the influence of an electric field.

**Liquid crystal** Anisotropic liquid state that possesses crystalline structures.

**Oligomer** Polymer with a degree of polymerization up to a value of 10–20.

**Rectification** Switching behavior of abrupt discontinuity in electrical resistance.

# REFERENCES

1. J.-M. Lehn, "Supramolecular Chemistry: Concepts and Perspectives." VCH, Weinheim, Germany, 1995.
2. G. M. Whitesides and B. Grzybowski, *Science* 295, 2418 (2002).
3. G. M. Whitesides, J. P. Mathias, and C. T. Seto, *Science* 254, 1312 (1991).
4. F. L. Carter (Ed.), "Molecular Electronic Designs I." Marcel Dekker, New York, 1987.
5. F. L. Carter (Ed.), "Molecular Electronic Designs II," Marcel Dekker, New York, 1987.
6. A. J. Bard, "Integrated Chemical Systems: A Chemical Approach to Nanotechnology." Wiley, New York, 1994.
7. M. A. Fox, *Acc. Chem. Res.* 32, 201 (1999).
8. M. N. Paddon-Row, *Acc. Chem. Res.* 27, 18 (1994).
9. S. N. Yalikari, A. E. Roitberg, C. Gonzalez, V. Mujica, and M. Ratner, *J. Chem. Phys.* 111, 6997 (1999).
10. B. Mann and H. Kuhn, *J. Appl. Phys.* 42, 4398 (1971).
11. M. A. Rampi, O. J. A. Schueller, and G. M. Whitesides, *Appl. Phys. Lett.* 72, 1781 (1998).
12. R. Haag, M. A. Rampi, R. E. Holmlin, and G. M. Whitesides, *J. Am. Chem. Soc.* 121, 7895 (1999).
13. R. E. Holmlin, R. Haag, M. L. Chabinyc, R. F. Ismagilov, A. E. Cohen, A. Terfort, M. A. Rampi, and G. M. Whitesides, *J. Am. Chem. Soc.* 123, 5075 (2001).
14. K. Slowinski, H. K. Y. Fong, and M. Majda, *J. Am. Chem. Soc.* 121, 7257 (1999).
15. K. Slowinski, K. U. Slowinski, and M. Majda, *J. Phys. Chem. B* 103, 8544 (1999).
16. K. Slowinski and M. Majda, *J. Electroanal. Chem.* 491, 139 (2000).
17. X. D. Cui, A. Primak, X. Zarate, J. Tomfohr, O. F. Sankey, A. L. Moore, T. A. Moore, D. Gust, G. Harris, and S. M. Lindsay, *Science* 294, 571 (2001).
18. M. A. Reed, C. Zhou, C. J. Muller, T. P. Burgin, and J. M. Tour, *Science* 278, 252 (1997).
19. X. L. Fan, C. Wang, D. L. Yang, L. J. Wan, and C. L. Bai, *Chem. Phys. Lett.* 361, 465 (2002).
20. S. N. Yaliraki, M. Kemp, and M. A. Ratner, *J. Am. Chem. Soc.* 121, 3428 (1999).
21. M. A. Rampi, O. J. A. Schueller, and G. M. Whitesides, *Appl. Phys. Lett.* 72, 1781 (1998).
22. K. Slowinski, H. K. Y. Fong, and M. Majda, *J. Am. Chem. Soc.* 121, 7257 (1999).
23. D. J. Wold and C. D. Frisbie, *J. Am. Chem. Soc.* 123, 5549 (2001).
24. D. J. Wold and C. D. Frisbie, *J. Am. Chem. Soc.* 122, 2970 (2000).
25. L. A. Bumm, J. J. Arnold, T. D. Dunbar, D. L. Allara, and P. S. Weiss, *J. Phys. Chem. B* 103, 8122 (1999).
26. D. J. Wold, R. Haag, M. A. Rampi, and C. D. Frisbie, *J. Phys. Chem. B* 106, 2813 (2002).
27. R. E. Holmlin, R. Haag, M. L. Chabinyc, R. F. Ismagilov, A. E. Cohen, A. Terfort, M. A. Rampi, and G. M. Whitesides, *J. Am. Chem. Soc.* 123, 5075 (2001).
28. F. R. F. Fan, J. P. Yang, L. T. Cai, D. W. Price, Jr., S. M. Dirk, D. V. Kosynkin, Y. X. Yao, A. M. Rawlett, J. M. Tour, and A. J. Bard, *J. Am. Chem. Soc.* 124, 5550 (2002).
29. C. K. Chiang, C. R. Fincher, Y. W. Park, A. J. Heeger, H. Shirakawa, E. J. Louis, S. C. Gau, and A. G. MacDiarmid, *Phys. Rev. Lett.* 39, 1098 (1977).
30. T. A. Skotheim, J. R. Reynolds, and R. L. Elsenbaumer (Eds.), "Handbook of Conducting Polymers," 2nd ed. Marcel Dekker, New York, 1997.
31. R. P. Andres, T. Bein, M. Dorogi, S. Feng, J. I. Henderson, C. P. Kubiak, W. Mahoney, R. G. Osifchin, and R. Reifenberger, *Science* 272, 1323 (1996).
32. M. A. Reed, C. Zhou, C. J. Muller, T. P. Burgin, and J. M. Tour, *Science* 278, 252 (1997).
33. C. Joachim, J. K. Gimzewski, and A. Aviram, *Nature* 408, 541 (2000).
34. R. E. Martin, U. Gubler, C. Boudon, V. Gramlich, C. Bosshard, J. P. Gisselbrecht, P. Gunter, M. Gruss, and F. Diederich, *Chem. Eur. J.* 3, 1505 (1997).
35. R. M. Martin, T. Mader, and F. Diederich, *Angew. Chem. Int. Ed.* 38, 817 (1999).
36. J. M. Tour, *Acc. Chem. Res.* 33, 791 (2000).
37. S. Creager, C. J. Yu, C. Bamdad, S. O'Connor, T. MacLean, E. Lam, Y. Chong, G. T. Olsen, J. Y. Luo, M. Gozin, and J. F. Kayyem, *J. Am. Chem. Soc.* 121, 1059 (1999).
38. S. P. Dudek, H. D. Sikes, and C. E. D. Chidsey, *J. Am. Chem. Soc.* 123, 8033 (2001).
39. J. M. Tour, M. Kozaki, and J. M. Seminario, *J. Am. Chem. Soc.* 120, 8486 (1998).
40. D. Fichou (Ed.), "Handbook of Oligo- and Polythiophenes," Wiley-VCH, Weiheim, Germany, 1999.
41. N. Aratani, A. Osuka, Y. H. Kim, D. H. Jeong, and D. Kim, *Angew. Chem. Int. Ed.* 39, 1458 (2000).
42. A. Tsuda and A. Osuka, *Science* 293, 79 (2001).
43. R. Dembinski, T. Bartik, B. Bartik, M. Jaeger, and J. A. Gladysz, *J. Am. Chem. Soc.* 122, 810 (2000), and references therein.
44. Y. Okawa and M. Aono, *J. Chem. Phys.* 115, 2317 (2001).
45. R. D. McCullough, *Adv. Mater.* 10, 93 (1998).
46. D. O. Cowan and F. M. Wiygyl, *Chem. Eng. News* 29, (1986).
47. Q. Zhou and T. M. Swager, *J. Am. Chem. Soc.* 117, 12593 (1995).
48. M. Rief, F. Oesterhelt, B. Heymann, and H. E. Gaub, *Science* 275, 1295 (1997).
49. R. M. Overney, D. P. Leta, C. F. Pictroski, M. H. Rafailovich, Y. Liu, J. Quinn, J. Sokolov, A. Eisenberg, and G. Overney, *Phys. Rev. Lett.* 76, 1272 (1996).
50. A. Aviram and M. A. Ratner, *Chem. Phys. Lett.* 29, 277 (1974).
51. R. M. Metzger, B. Chen, U. Hopfner, M. V. Lakshmikantham, T. V. Hughes, H. Sakurai, J. W. Baldwin, C. Hosch, M. P. Cava, L. Brehmer, and G. J. Ashwell, *J. Am. Chem. Soc.* 119, 10455 (1997).
52. R. M. Metzger, *Acc. Chem. Res.* 32, 950 (1999).
53. T. Xu, I. R. Peterson, M. V. Lakshmikatham, and R. M. Metzger, *Angew. Chem. Int. Ed.* 40, 1749 (2001).
54. D. L. Carroll, X. Blase, J.-C. Charlier, S. Curran, Ph. Redlich, P. M. Ajayan, S. Roth, and M. Ruhle, *Phys. Rev. Lett.* 81, 2332 (1998).
55. A. M. Rao, P. C. Eklund, S. Bandow, A. Thess, and R. E. Smalley, *Nature* 388, 257 (1997).
56. R. S. Lee, H. J. Kim, J. E. Fischer, A. Thess, and R. E. Smalley, *Nature* 388, 255 (1997).
57. C. W. Zhou, J. King, W. Yenilmez, and H. J. Dai, *Science* 290, 1552 (2000).
58. J. Kong, N. R. Franklin, C. W. Zhou, M. G. Chapline, S. Peng, K. Cho, and H. J. Dai, *Science* 287, 622 (2000).
59. H. B. Liu, Y. L. Li, H. Y. Luo, S. Q. Xiao, H. J. Fang, H. M. Li, D. B. Zhu, D. P. Yu, J. Xu, and B. Xiang, *J. Am. Chem. Soc.* 124, 13370 (2002).
60. S. Roth, "One-Dimensional Metals: Physics and Materials Science." Wiley, New York, 1995.
61. X. H. Qiu, C. Wang, Q. D. Zeng, B. Xu, S. X. Yin, H. N. Wang, S. D. Xu, and C. L. Bai, *J. Am. Chem. Soc.* 122, 5550 (2000).
62. T. Kato, *Science* 295, 2414 (2002).

63. S. Fernandez-Lopez, H. S. Kim, E. C. Choi, M. Delgado, J. R. Granja, A. Khasanov, K. Kraehenbuehl, G. Long, D. A. Weinberger, K. M. Wilcoxen, and M. R. Ghadiri, *Nature* 412, 452 (2001).

64. O. Ikkala and G. ten Brinke, *Science* 295, 2407 (2002).

65. G. W. Gokel and O. Murillo, *Acc. Chem. Res.* 29, 425 (1996).

66. G. R. Newkome, C. N. Moorefield, and F. Vögtl, "Dendritic Molecules. Concepts, Synthesis, Perspectives." VCH, Weinhem, 1996.

67. S. M. Grayson and J. M. J. Fréchet, *Chem. Rev.* 101, 3819 (2001).

68. A. W. Bosman, H. W. Janssen, and E. W. Meijer, *Chem. Rev.* 99, 1665 (1999).

69. P. Wu, Q. D. Zeng, S. L. Xu, C. Wang, S. X. Yin, and C. L. Bai, *Chem. Phys. Chem.* 12, 751 (2001).

70. C. J. Murphy, M. R. Arkin, Y. Jenkins, N. D. Ghatlia, S. H. Bossmann, N. J. Turro, and J. K. Barton, *Science* 262, 1025 (1993).

71. For example, A. Harriman, *Angew. Chem. Int. Ed.* 38, 945 (1998).

72. G. B. Schuster, *Acc. Chem. Res.* 33, 253 (2000); B. Giese, *Acc. Chem. Res.* 33, 631 (2000); M. Bixon and J. Jortner, *J. Am. Chem. Soc.* 123, 12556 (2001) and references.

73. U. Diederichsen, *Angew. Chem. Int. Ed.* 36, 2317 (1997).

74. M. W. Grinstaff, *Angew. Chem. Int. Ed.* 38, 3629 (1999).

75. N. C. Seeman, *Annu. Rev. Biophys. Biomol. Struct.* 27, 225 (1998).

76. J. F. Stoddart, *Acc. Chem. Res.* 34, 433 (2001).

77. For example, B. L. Feringa, "Molecular Switches." Wiley-VCH, Weinheim, 2001.

78. C. P. Collier, G. Mattresteig, E. W. Wong, Y. Luo, K. Beverly, J. Sampaio, F. M. Raymo, J. F. Stoddart, and J. R. Heath, *Science* 289, 1172 (2000).

79. C. P. Collier, E. W. Wong, M. Belohradsky, F. M. Raymo, J. F. Stoddart, P. J. Kuekes, R. S. Williams, and J. R. Heath, *Science* 285, 391 (1999).

80. C. L. Brown, U. Jonas, J. A. Preece, H. Ringsdorf, M. Seitz, and J. F. Stoddart, *Langmuir* 16, 1924 (2000).

81. C. P. Collier, J. O. Jeppesen, Y. Luo, J. Perkins, E. W. Wong, J. R. Heath, and J. F. Stoddart, *J. Am. Chem. Soc.* 123, 12632 (2001).

82. A. R. Pease, J. O. Jeppesen, J. F. Stoddart, Y. Luo, C. P. Collier, and J. R. Heath, *Acc. Chem. Res.* 34, 433 (2001).

83. Y. Luo, C. P. Collier, J. O. Jeppesen, K. A. Nielsen, E. Delonno, G. Ho, J. Perkins, H. R. Tseng, T. Yamamoto, J. F. Stoddart, and J. R. Heath, *Chem. Phys. Chem.* 3, 519 (2002).

84. F. M. Raymo and J. F. Stoddart, *Chem. Rev.* 99, 1643 (1999).

85. M. Alvaro, M. N. Chretien, B. Ferrer, V. Fornes, H. Garcia, and J. C. Scaiano, *Chem. Commun.* 2106 (2001).

86. A. N. Shipway and I. Willner, *Acc. Chem. Res.* 34, 421 (2001).

87. R. Deans, A. Niemz, E. C. Breinlinger, and V. M. Rotello, *J. Am. Chem. Soc.* 119, 10863 (1997).

88. R. Rathore, P. Le Maguere s, S. V. Lindeman, and J. K. Kochi, *Angew. Chem. Int. Ed.* 39, 809 (2000).

89. J. Heinze, C. Willmann, and P. Bauerle, *Angew. Chem. Int. Ed.* 40, 2861 (2001).

90. A. P. de Silva, *Nature* 364, 42 (1993).

91. F. M. Raymo, *Adv. Mater.* 14, 401 (2002).

92. R. T. Hayes, M. R. Wasielewski, and D. Gosztola, *J. Am. Chem. Soc.* 122, 5563 (2000).

93. D. Gosztola, M. P. Niemczyk, and M. R. Wasielewski, *J. Am. Chem. Soc.* 120, 5118 (1998).

94. J. Daub, R. Engl, J. Kurzawa, S. E. Miller, S. Schneider, A. Stockmann, and M. R. Wasielewski, *J. Phys. Chem. A* 105, 5655 (2001).

95. L. J. Wan, H. Noda, C. Wang, C. L. Bai, and M. Osawa, *Chem. Phys. Chem.* 10, 617 (2001).

96. Th. Wandlowski, K. Ataka, and D. Mayer, *Langmuir* 18, 4331 (2002).

97. H. X. He, J. S. Zhu, N. J. Tao, L. A. Nagahara, I. Amlani, and R. Tsui, *J. Am. Chem. Soc.* 123, 7730 (2001).

98. N. Armaroli, J. F. Eckert, and J. F. Nierengarten, *Chem. Commun.* 2105 (2000).

99. A. Yassar, H. Jaafari, N. Rebiere-Galy, M. Frigoli, C. Moustrou, A. Samat, and R. Gugliemetti, *Eur. Phys. J. AP* 18, 3 (2002).

100. J. Otsuki, K. Sato, M. Tsujino, N. Okuda, K. Araki, and M. Seno, *Chem. Lett.* 847 (1996).

101. J. Ostuki, M. Tsujino, T. Iizaki, K. Araki, M. Seno, K. Takatera, and T. Watanabe, *J. Am. Chem. Soc.* 119, 7895 (1997).

102. D. Kalny, M. Elhabiri, T. Moav, A. Vaskevich, I. Rubinstein, A. Shanzer, and A. M. Albrecht-Gary, *Chem. Commun.* 1426 (2002).

103. M. Marchive, P. Guionneau, J. A. K. Howard, G. Chastanet, J. F. Letard, A. E. Goeta, and D. Chasseau, *J. Am. Chem. Soc.* 124, 194 (2002).

104. H. Sugimoto, T. Kimura, and S. Inoue, *J. Am. Chem. Soc.* 121, 2325 (1999).

105. B. L. Feringa, *Acc. Chem. Res.* 34, 504 (2001).

106. C. A. Schalley, K. Beizai, and F. Vogtle, *Acc. Chem. Res.* 34, 465 (2001).

107. C. Joachim, J. K. Gimzewski, R. R. Schlittler, and C. Chavy, *Phys. Rev. Lett.* 74, 2102 (1995).

108. C. Joachim, J. K. Gimzewski, and H. Tang, *Phys. Rev. B* 58, 16407 (1998).

109. J. Taylor, H. Guo, and J. Wang, *Phys. Rev. B* 63, 121104 (2001).

110. C. G. Zeng, H. Q. Wang, B. Wang, J. L. Yang, and J. G. Hou, *Appl. Phys. Lett.* 77, 3595 (2000).

111. L. Gobbi, P. Seiler, and F. Diederich, *Angew. Chem. Int. Ed.* 38, 674 (1999).

112. F. M. Raymo and S. Giordani, *J. Am. Chem. Soc.* 124, 2004 (2002).

113. M. Yan, L. C. Wang, S. G. Hymowitz, S. Schilbach, J. Lee, A. Goddard, A. M. de Vos, W. Q. Gao, and V. M. Dixit, *Science* 290, 523 (2000).

114. H. T. Kao, H. J. Song, B. Porton, G. L. Ming, J. Hoh, M. Abraham, A. J. Czernik, V. A. Pieribone, M. M. Poo, and P. Greengard, *Nature Neurosci.* 5, 431 (2002).

115. J. Lisman, H. Schulman, and H. Cline, *Nat. Rev. Neurosci.* 3, 175 (2002).

116. T. Cheng, N. Rodrigues, H. M. Shen, Y. G. Yang, D. Dombkowski, M. Sykes, and D. T. Scadden, *Science* 287, 1804 (2000).

117. S. E. Ross, N. Hemati, K. A. Longo, C. N. Bennett, P. C. Lucas, R. L. Erickson, and O. A. MacDougald, *Science* 289, 950 (2000).

118. J. P. Zha, S. Weiler, K. J. Oh, M. C. Wei, and S. J. Korsmeyer, *Science* 290, 1761 (2000).

119. A. Wittinghofer and H. Waldmann, *Angew. Chem. Int. Engl.* 39, 4192 (2000).

120. J. Chen, M. A. Reed, A. M. Rawlett, and J. M. Tour, *Science* 286, 1550 (1999).

121. J. Chen, W. Wang, M. A. Reed, A. M. Rawlett, D. W. Price, and J. M. Tour, *Appl. Phys. Lett.* 77, 1224 (2000).

122. J. M. Seminario, A. G. Zacarias, and P. A. Derosa, *J. Chem. Phys.* 116, 1671 (2002).

123. H. J. Gao, K. Sohlberg, Z. Q. Xue, H. Y. Chen, S. M. Hou, L. P. Ma, X. W. Fang, S. J. Pang, and S. J. Pennycook, *Phys. Rev. Lett.* 84, 1780 (2000).

124. D. X. Shi, Y. L. Song, D. B. Zhu, H. X. Zhang, S. S. Xie, S. J. Pang, and H. J. Gao, *Adv. Mater.* 13, 1103 (2001).

125. D. X. Shi, Y. L. Song, H. X. Zhang, P. Jiang, S. T. He, S. S. Xie, S. J. Pang, and H. J. Gao, *Appl. Phys. Lett.* 77, 3203 (2000).

126. R. Sessoli, D. Gatteschi, and M. Novak, *Nature* 365, 149 (1993).

127. R. Sessoli, H. L. Tsai, A. R. Schake, S. Wang, J. B. Vincent, K. Folting, D. Gatteschi, G. Christou, and D. N. Hendrickson, *J. Am. Chem. Soc.* 115, 1804 (1993).

128. T. Lis, *Acta Crystall. Sect. B: Struct. Crystall. Cryst. Chem.* 36, 2042 (1980).

129. K. Park, M. A. Novotny, N. S. Dalal, S. Hill, and P. A. Rikvold, *J. Appl. Phys.* 91, 7167 (2002).

130. K. Wieghart, K. Pohl, I. Jibril, and G. Huttner, *Angew. Chem. Int. Ed.* 23, 77 (1984).
131. A. Caneschi, D. Gatteschi, C. Sangregorio, R. Sessoli, L. Sorace, A. Cornia, M. A. Novak, C. Paulsen, and W. Wernsdorfer, *J. Magn. Magn. Mater.* 200, 182 (1999).
132. E. C. Yang, D. N. Hendrickson, W. Wernsdorfer, M. Nakano, L. N. Zakharov, R. D. Sommer, A. L. Rheingold, M. L. Gairaud, and G. Christou, *J. Appl. Phys.* 91, 7382 (2002).
133. A. Barra, A. Caneschi, A. Cornia, F. F. de Biani, D. Gatteschi, C. Sangregorio, R. Sessoli, and L. Sorace, *J. Am. Chem. Soc.* 121, 5302 (1999).
134. A. Bouwen, A. Caneschi, D. Gatteschi, E. Goovaerts, D. Schoemaker, L. Sorace, and M. Stefan, *J. Phys. Chem. B* 105, 2658 (2000).
135. K. R. Dunbar (Ed.), "Proceedings of the 7th International Conference on Molecular-Based Magnets," San Antonio, TX; *Polyhedron* 20 (2001).
136. J. S. Miller and A. J. Epstein, *Angew. Chem. Int. Ed.* 33, 385 (1994).
137. J. Y. Lu, M. A. Lawandy, J. Li, T. Yuen, and C. L. Lin, *Inorg. Chem.* 38, 2695 (1999).
138. M. A. Lawandy, X. Huang, R. Wang, J. Li, J. Y. Lu, T. Yuen, and C. Lin, *Inorg. Chem.* 38, 5410 (1999).
139. T. Yuen, C. L. Lin, T. W. Milhalisin, M. A. Lawandy, and J. Li, *J. Appl. Phys.* 87, 6001 (2000).
140. A. Muller and J. Doring, *Angew. Chem. Int. Ed.* 27, 1721 (1991).
141. D. Gatteschi, L. Pardi, A. L. Barra, and A. Muller, *Mol. Eng.* 3, 157 (1993).
142. D. Gatteschi, L. Pardi, A. L. Barra, A. Muller, and J. Doring, *Nature* 354, 465 (1991).
143. J. E. Lisman and J. R. Fallon, *Science* 283, 339 (1999).
144. R. C. Malenka and R. A. Nicoll, *Science* 285, 1870 (1999).
145. T. V. Bliss and G. L. Collingridge, *Nature* 361, 31 (1993).
146. D. O. Hebb, "The Organization of Behavior." Wiley, New York, 1949.
147. T. V. Bliss and T. Lomo, *J. Physiol.* 232, 331 (1973).
148. For example, see J. E. Lisman and C. C. McIntyre, *Curr. Biol.* 11, R788 (2001).
149. D. G. Wells and J. R. Fallon, *Cell. Mol. Life Sci.* 57, 1335 (2000).
150. F. Gardoni, A. Caputi, M. Cimino, L. Patorino, F. Cattabeni, and M. Di Luca, *J. Neurochem.* 71, 1733 (1998).
151. T. R. Kelly, *Acc. Chem. Res.* 34, 514 (2001).
152. N. Koumura, R. W. J. Zijlstra, R. A. van Delden, N. Harada, and B. L. Feringa, *Nature* 401, 152 (1999).
153. J. A. Spudich and R. S. Rock, *Nature Cell Biol.* 4, E8 (2001).
154. M. Schliwa, *Nature* 401, 431 (1999).
155. G. Bloom and S. Endow, *Prot. Profiles* 1059 (1994).
156. S. A. Endow, *Nature Cell Biol.* 1, E163 (1999).
157. N. Hirokawa, *Science* 279, 519 (1998).
158. P. Dallos and B. Fakler, *Nat. Rev. Mol. Cell. Biol.* 3, 104 (2002).
159. J. T. Finer, R. M. Simmons, and J. A. Spudich, *Nature* 368, 113 (1994).
160. J. E. Molloy, J. E. Burns, J. Kendrick-Jones, R. T. Tregear, and D. S. C. White, *Nature* 378, 209 (1995).
161. A. Ishijima, H. Kojima, T. Funatsu, M. Tokunaga, H. Higuchi, and T. Yanagida, *Cell* 92, 161 (1998).
162. K. Visscher, M. J. Schnitzer, and S. M. Block, *Nature* 400, 184 (1999); A. E. Knight and J. E. Molloy, *Nature Cell Biol.* 1, E87 (1999).

# Monolayer-Assisted Electrochemical Nanopatterning

O. Azzaroni, P. L. Schilardi, R. C. Salvarezza

*INIFTA, UNLP—CONICET, La Plata, Argentina*

## CONTENTS

## 1. INTRODUCTION

Self-assembled monolayers (SAMs) consist in a single layer of molecules adsorbed on a substrate, with the particularity of being highly oriented, ordered, and packed. In particular, SAMs of thiols on metals have attracted considerable scientific interest because they provide a method for creating well-defined surfaces with controllable chemical functionality [1, 2]. The possible application of SAMs ranges from nanotechnology to fundamental surface science. Self-assembled monolayers can be used to prevent corrosion [3–5], modify wetting and wear properties [6–8] of solid surfaces, develop nano-devices for electronics [9], and for pattern formation [10–12]. In particular, by anchoring specific chemical groups to these molecular self-assemblies, well-ordered structures with controlled chemical features can be achieved in order to be employed in molecular recognition [13], protein adsorption [14], and templates for crystallization of inorganic salts [15]. Otherwise, the fabrication of nanostructures is one of the most relevant topics in modern technologies. Nanofabrication has been defined as a technique capable of generating structures with at least one lateral dimension between 1–100 nm [16, 17]. Nano- and micro-fabrication is based mainly on photolithography [18] and its immediate implications are related to the fabrication of microelectronic devices that have new architectures [19], biomimetic structures [20], fiber optic communications [21], and microfluidic systems [22]. The development of novel methods, in particular to build three-dimensional patterned microstructures, enables new options for microfabrication and creates the possibility of choosing the most convenient method considering several factors such as complexity, cost, and elapsed time of fabrication.

Several strategies have been developed for fabricating micrometer- and nanometer- scale patterns [23–25]. The method of fabrication often involves several steps of various degrees of complexity depending on the desired structure. In the case of patterned organic polymer surfaces using elastomeric masters [26], intermediate steps include elastomer curing, peeling off, organic polymer curing, compressing, bending, and stretching. In the case of patterned metallic nano-microstructures, common intermediate stages are electroplating [24], etching [26], surface pretreatment and electroless deposition [27]. In particular, micropatterned metal surfaces are considered very interesting in the electronic materials research field due to potential applications on printed wiring boards (PWB), magnetic recordings materials, microwave conductors, contact materials, display devices, and optical disks [28]. In some cases nano and microfabrication has been made by patterning the substrate with self-assembled monolayers (SAMs) of thiol by using contact printing or photopatterning [29]. The printed pattern can protect the underlying substrate acting as a mask against etchants [12] or for metal deposition. Recently, Ag films covered by patterned SAMs formed by microcontact printing have been used to fabricate thin film transistors [30].

Electrodeposition is used to produce materials and architectures that cannot be built by traditional techniques. By means of this method, different materials, such as nanometer-scale crystallites [31], nanocomposites [32], epitaxially deposited metal films [33], compositional superlattices [34], and ceramic materials [35] have been prepared. Electrodeposition is an intrinsically fast technique that is compatible with patterning and large scale production.

Here the electrodeposition of metals on self-assembled alkanethiol monolayers (alkanethiol SAMs) is reviewed in relation to nano/microtechnology applications. Based on

recent results, it can be concluded that electrodeposition on these surface-modified substrates is a powerful tool not only in producing standing-free thin metal and alloy films but also results in an easy way to fabricate nano/micro patterned masters, molds, and replicas in different materials. In contrast to other methods, which requires contact printing, masking, or photopatterning, the substrate treatment needed before electrodeposition on alkanethiol-covered surfaces involves only a simple immersion of the masters on the alkanethiol "ink."

This review is organized in the following order. First, we review SAM preparation, SAM quality (surface structural, defects), and SAM stability (interaction forces acting at SAMs). Second, underpotential and overpotential deposition of metals on SAM-covered metal substrates is reviewed. In a third part, the applicability of electrodeposition to prepare standing-free films of different metals and alloys, and the possibility of transferring nano/microstructures to the thin metallic films is presented. Finally, the fabrication of masters, molds, and replicas by electrodeposition techniques is described.

## 2. ALKANETHIOL SELF-ASSEMBLED MONOLAYERS (SAMs) ON METALS

Schemes showing the structure of typical alkanethiol molecules that self-assemble on metal surfaces are shown in Figure 1. All these molecules exhibit an active sulfur head that anchors the molecules on the substrate and long hydrocarbon chains consisting of $n$ methylene ($CH_2$) units. The terminal group could be a hydrophobic group such as methyl groups ($CH_3$), or a hydrophilic group such as $H_2N$, OH, or COOH. The number of $CH_2$ units and the nature of the terminal group (hydrophobic or hydrophilic) determine the solubility of the alkanethiol molecules in a given solvent. The introduction of conjugated bonds in the hydrocarbon chain increases markedly the electronic conduction of these molecules [36]. When dealing with oxide-covered surfaces other kind of molecules, different from alkanethiols, are used in order to build up self-assembled molecular films. That is the case of the hydrolysis and polymerization of alkyltrichlorosilanes on hydrated surfaces such as $SiO_2/Si$ or $Al_2O_3$ surfaces or the adsorption of carboxilic, hydroxamic, or phosphonic acids on native oxides like CuO/Cu, AgO/Ag, or $TiO_2/Ti$ [37–43].
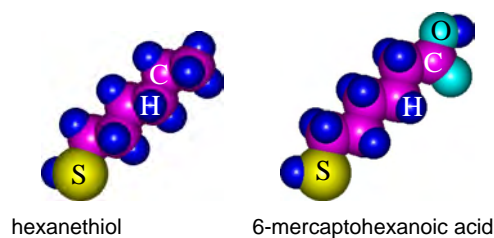
### 2.1. SAMs Preparation

Self-assembly of alkanethiol molecules on clean metal surfaces takes place through a redox process that can be represented by the following reaction [44]

$$X(CH_2)_nSH + Me = [X(CH_2)_nS\text{-}Me] + 1/2H_2 + e \quad (1)$$
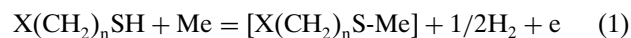
where Me stands for the metal substrate, X represents the terminal group, brackets stand for the adsorbed alkanethiolate-Me species. This reaction implies the formation of a strong thiolate bond similar to that formed for adsorbed S as revealed by XPS measurements (Fig. 2) and the formation of molecular hydrogen [45]. The self-assembly process represented by Eq. (1) can be made in both gas-phase and liquids environments (for methyl terminated alkanethiols usually ethanolic or toluenic solutions, pure alkanethiols, etc.). Self-assembled alkanethiol monolayers preparation from alkanethiol-containing solution is the most popular because it is extremely simple, and accordingly, accessible to all laboratories. In this case, the self-assembly process is made by immersion of the clean metal substrate in an alkanethiolate-containing ethanolic or toluene solution during a time $t_i$ as schematically shown in Figure 3. The SAMs quality strongly depends on $t_i$ values and hydrocarbon chain lengths. A scheme showing possible mechanisms for alkanethiol self-assembly is shown in Figure 4. In mechanism A, disordered phases are formed before islands of vertically oriented molecules nucleate and grow on the substrate. This mechanism has been observed in liquids media. In fact, for short alkanethiol ($n < 6$), self-assembly on Au(111) immersion times in the order of 24 hr result in a mixture of unstable ordered phases (the so-called $p(n \times 1)$ phases) and disordered domains (Fig. 5). On the other hand, for alkanethiols with $n > 6$, good quality SAMs (Fig. 6) have been obtained for immersion times in the 1–24 hr range. A scheme showing the temporal evolution of alkanethiol surface structures in liquids is shown in Figure 7. The size of the ordered domains can be increased and defect density decreased after annealing of the self-assembled monolayer for 4–6 hr at 60 °C in the alkanethiol containing solution [46]. On the other hand, mechanism B (Fig. 5) involves the formation of
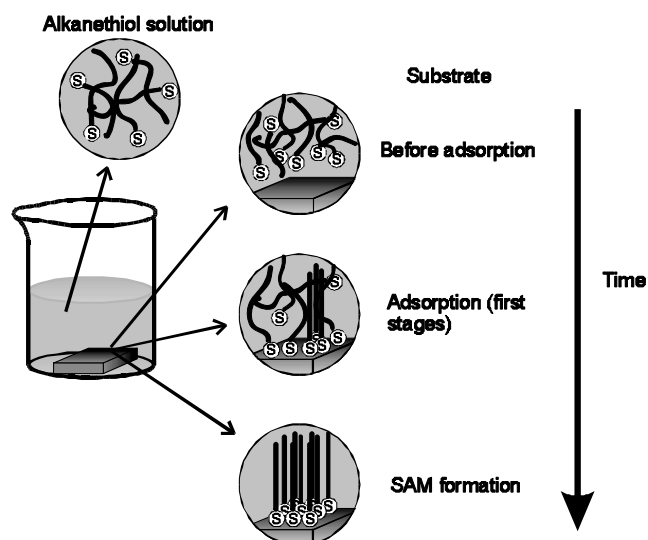


**Figure 1.** Schemes of the molecular structure of (a) hexanethiol and (b) 6-mercaptohexanoic acid.
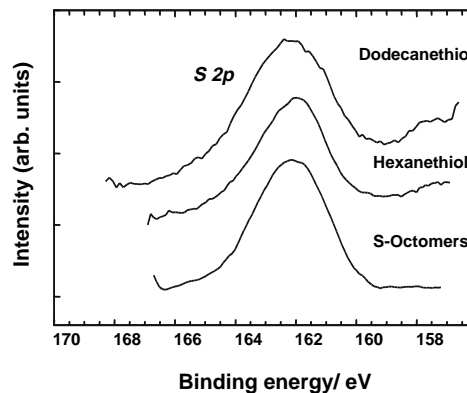


**Figure 2.** X-ray photoelectron spectroscopy (XPS) spectra (S 2p) for sulfur, hexanethiolate, and dodecanethiolate monolayers on Au(111). Reprinted with permission from [50], C. Vericat et al., *Langmuir* 17, 4919 (2001). © 2001, American Chemical Society.

**Figure 3.** Scheme showing self-assembling of alkanethiol molecules on a metallic substrate from liquid solution.

ordered domains of lying flat alkanethiol molecules before the formation of the ordered islands of vertically oriented molecules takes place. This mechanism has been observed by *in-situ* scanning tunneling microscopy (STM) in gas phase preparation [47].

## 2.2. Stable Surface Structures

Alkanethiolates adsorbed on Au(111) have been taken as a model system for SAM studies. Because of this possible use in many interesting technological applications, SAMs have been characterized by using different techniques as shown in Table 1. It is well known that the surface structure consists of monoatomic high vacancy islands and ordered domains (Fig. 6) of the $\sqrt{3} \times \sqrt{3}$ R30 ° lattice and its related $c(4 \times 2)$ superlattice in both gas phase [48] and liquid environments [49], irrespective of the X-terminal group and hydrocarbon chain length as shown in Figure 6 for hexadecanethiol and
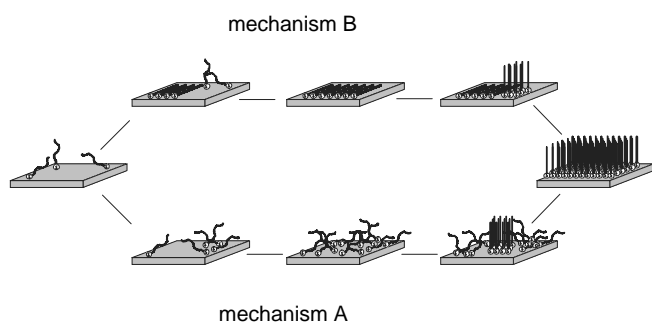


**Figure 4.** Two mechanisms for alkanethiol self-assembly. In mechanism A, islands of vertically oriented molecules are formed from a disordered phase; this mechanism has been observed in SAMs prepared from liquid media. Mechanism B involves the formation of ordered domains with alkanethiol molecules lying parallel to the surface before the formation of vertically oriented molecule domains.
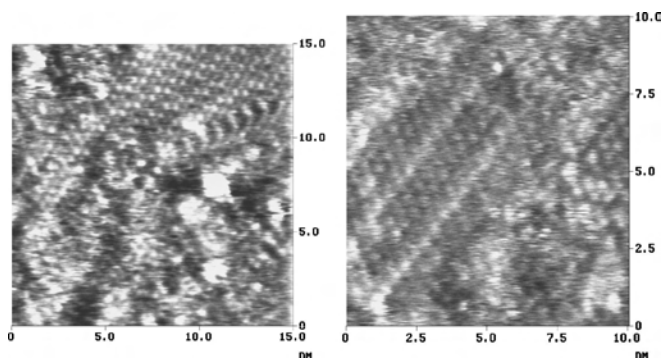


**Figure 5.** Self-assembly of butanethiol on Au(111) after 24 hr of immersion time. Ordered and disordered domains coexit on the Au(111) surface.

mercaptoundecanoic acid (MUA). In these lattices, the alkanethiolate molecules are chemisorbed on the Au surface by the S-heads forming the thiolate bond [50] and they are tilted 20–40 ° with respect to the substrate normal [51]. The $\sqrt{3} \times \sqrt{3}$ R30 ° lattice exhibits nearest neighbor distances $d \approx 0.5$ nm (Fig. 8a crosssection), while the $c(4 \times 2)$ lattice exhibits some pairing of the S atoms as revealed by GIXD data [52]. Besides, STM measurements have shown $d = 0.45$ nm between the bright and dark spots (interrows distance) (Fig. 8b) and $d = 0.5$ nm inside the row (intrarow distance) of the $c(4 \times 2)$ superlattices [48]. Recent density functional theory calculations have shown that the best sites for alkanethiol adsorption on the Au(111) surface is at fcc-bridge and hcp-bridge sites (Fig. 9). Lower adsorption energies are involved for fcc, hcp, bridge, and top sites. Reports
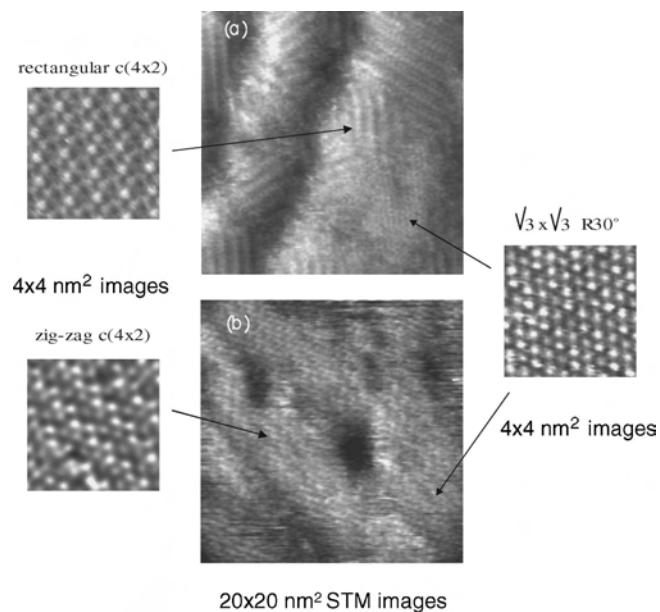


**Figure 6.** STM images of ordered alkanethiol domains produced on Au(111) after 24 hr of immersion in alkanethiol containing solutions. (a) hexanethiol (b) mercaptoundecanoic acid. The typical stable phases $\sqrt{3} \times \sqrt{3}$ R30 ° and $c(4 \times 2)$ (rectangular and zig-zag) are shown as insets. Reprinted with permission from [141], O. Azzaroni et al., *Langmuir* 17, 6647 (2001). © 2001, American Chemical Society.
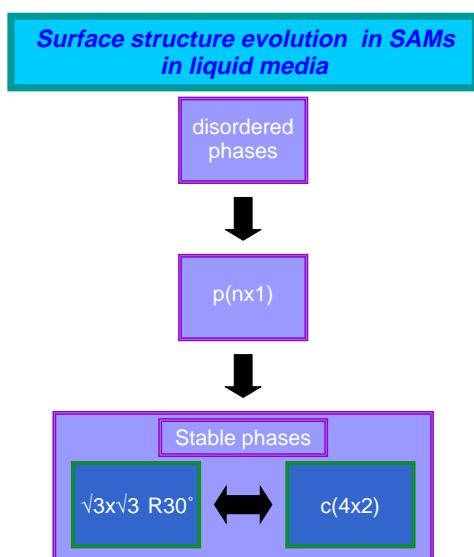
**Figure 7.** Scheme showing the possible temporal evolution of the surface structure of SAMs produced in liquid media.

on alkanethiol adsorption on the other faces of Au are scarcely found in the literature [53]. In the case of Au(100) $c(10 \times 10)$ (large hydrocarbon chain length) and $c(2 \times 2)$ (small hydrocarbon chain length), surface structures [54] have been reported [55].

In the case of alkanethiolate adsorption on Ag(111), chemisorbed molecules are also bonded by the S head to the Ag surface through a thiolate bond, although their tilt with respect to the substrate normal ranges from 0° to 15° [56]. Scanning tunneling microscopy studies have shown that alkanethiolates with large hydrocarbon chains ($n > 8$)

**Table 1.** Techniques used to characterize self-assembled monolayers.

Diffraction-based techniques

    Low energy electron diffraction (LEED)
    Grazing incidence X-ray diffraction (GIXD)
    Low-energy atom diffraction (LEAD)
    X-ray reflectivity (XR)
    Helium atom reflectivity (HAR)

Spectroscopy-based techniques

    Infrared spectroscopy (IR)
    Second harmonic generation (SHG)
    Sum frequency generation (SFG)
    Surface-enhanced Raman scattering (SERS)
    High-resolution electron energy loss spectroscopy (HREELS)
    Near-edge X-ray absorption fine structure spectroscopy (NEXAFS)
    X-ray photoelectron spectroscopy (XPS)

Microscopy-based techniques

    Scanning tunneling microscopy (STM)
    Atomic force microscopy (AFM)

Other techniques

    Thermally-programmed desorption (TPD)
    Ellipsometry
    Quartz crystal microbalance (QCM)
    Electrodesorption curves
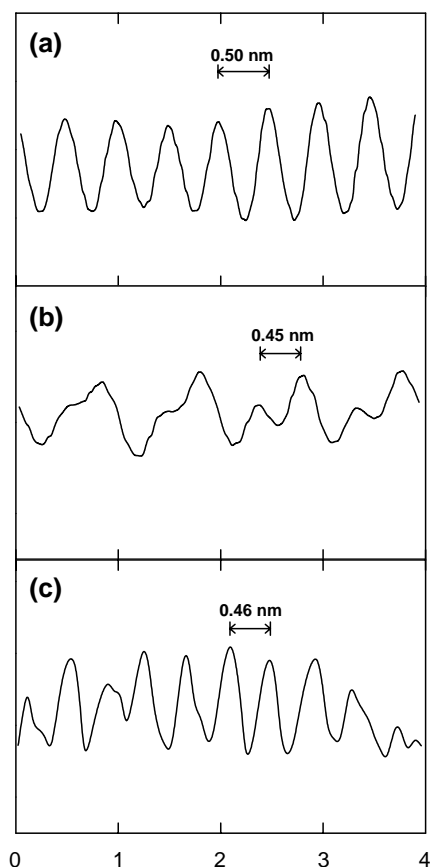


**Figure 8.** Cross-sections corresponding to dodecanethiolate SAMs adsorbed on (a) Au(111), $\sqrt{3} \times \sqrt{3}$ R30°, (b) Au(111), $c(4 \times 2)$, and (c) Ag(111), $\sqrt{7} \times \sqrt{7}$ R19°.

organize on Ag(111) forming an incommensurate hexagonal layer (Fig. 8) with $d = 0.46$ nm (Fig. 8c) [57], which is a value slightly greater than $d = 0.44$ nm found in the distorted $\sqrt{7} \times \sqrt{7}$ R19.1° lattice observed for S on Ag(111) at a high surface coverage, and for short alkanethiols on the same substrate [58]. In this lattice, the S atom is bonded at hollow and top sites, the unit cell involving one fcc, one hcp, and one top site. It should be noted that the value $d = 0.46$ nm has been observed in close-packed bulk alkanes, because this distance optimizes hydrocarbon chain interactions. Also note that the atomic size of the methyl group is 0.45 nm. Vibrational spectroscopic data (Raman, Fourier transform infrared spectroscopy (FTIR), and sum frequency
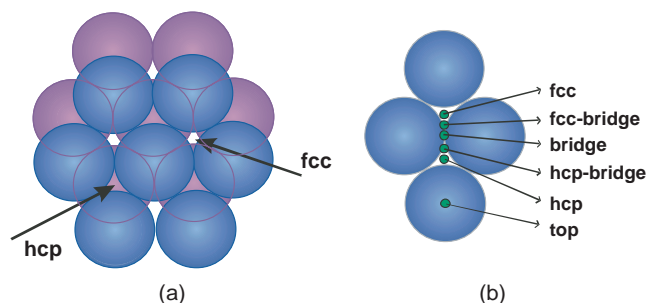


**Figure 9.** (a) fcc and hcp hollow sites on a (111) face. (b) Possible sites for alkanethiol adsorption on a (111) surface.

generation (SFG)) for alkanethiol monolayers on Au and Ag have also shown that the molecular chains are in a mostly trans configuration [59].

Alkanethiols strongly adsorb on Cu(111) at hollow site surfaces promoting a surface layer reconstruction [60]. Ultra high vacuum (UHV) X-ray standing wave (NIXSW) and near edge X-ray adsorption fine structure (NEXAFS) recent studies have shown that the alkanethiol molecules are almost normal (tilt angle 12 °) to the substrate surface, similar to alkanethiols on Ag(111) [61]. During adsorption of methanethiol on the Cu(111) face at room temperature, certain amounts of S atoms have been also produced [62]. In aqueous media, no surface structural data for alkanethiol adsorption on Cu have been reported [63].

Self-assembled alkanethiol monolayers can be also formed on Pt surfaces as judged from surface-sensitive techniques [64]. In addition, self-assembly of alkanetiols molecules have been recently reported on Pd [65, 66], although, in relation to Au, Ag, and Cu, little information is available. Using vibrational spectroscopy, ordered/disordered transitions in aqueous solutions have been observed. Other more reactive metals, such as Ni and Fe, have also been investigated in relation to the alkanethiol self-assembly in the frame of corrosion prevention [67–70]. However, for these metals, even small amounts of oxides result in poor quality SAMs. Therefore, they can be handled in ultra-high vacuum conditions reducing considerably their potential use for technological applications.

## 2.3. Stabilizing Forces at SAMs

The self-assembly and stability of these two-dimensional structures implies alkanethiolate-metal, alkanethiolate-alkanethiolate, alkanethiolate-environment, and metal-environment interactions. Previous studies for the alkanethiolate electrodesorption from Au surfaces in hexadecane have reported activation energies that increase 0.84 kJ/mol per C unit [71]. Stabilization energies in the order of 1.5 kJ/mol per C unit have also been proposed from the analysis of different adsorption/desorption data [72]. In the case of electrolyte solutions, the most important environment for nano/microtechnology applications, reductive electrodesorption curves have been used to estimate the magnitude of these interactions [73]. In aqueous 0.1 M NaOH $\sqrt{3} \times \sqrt{3}$ R30 ° and $c(4 \times 2)$, alkanethiolate lattices on Au(111) are desorbed in sharp voltammetric peaks (Fig. 10) according to the reaction

$$(CH_3)(CH_2)_nS\text{-}Au + solvent + e$$
$$= [(CH_3)(CH_2)_nS^-]_{solv} + Au_{solv}. \qquad (2)$$
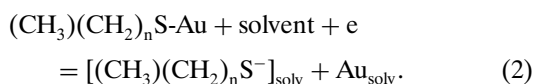
where solv indicates solvated species.

In fact, at potential values more positive than those related to the electrodesorption peak, the $c(4 \times 2)$ and the $\sqrt{3} \times \sqrt{3}$ R30 ° surface structures are stable although they exhibit potential-independent transitions and defect fluctuations, that is, they are repaired and reformed in the time range of a few seconds (Fig. 11a–f). It has also been shown [74] that in the potential range of the electrodesorption peak, the ordered surface structures are completely removed from the Au(111) terraces although
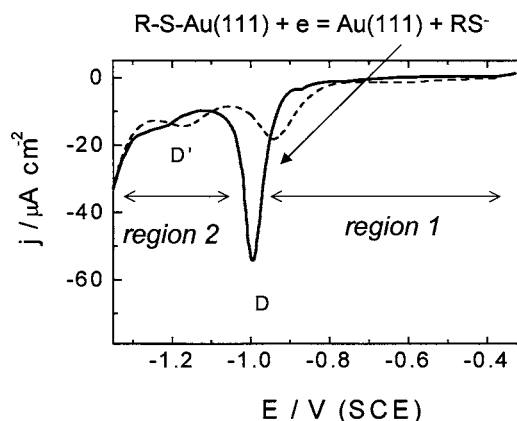


**Figure 10.** Typical electrodesorption curve for hexanethiolate electrodesorption from Au(111) in 0.1 M NaOH recorded at 0.05 V s$^{-1}$. (solid line) first scan; (dashed line) second scan. Region 1 corresponds to the potential region were the $\sqrt{3} \times \sqrt{3}$ R30° and $c(4 \times 2)$ surface structure at terraces are stable. Peak D corresponds to the electrodesorption of these surface structures from terraces. Region 2 corresponds to the potential region where Au(111) and hexanethiol molecules adsorbed at step edges coexits. Peak D corresponds to the electrodesorption of hexanethiol molecules from step edges. Reprinted with permission from [76], C. Vericat et al., *J. Chem. Phys.* 115, 6672 (2001). © 2001, American Institute of Physics.

alkanethiolate molecules remain adsorbed at step edges (Fig. 12). Complete desorption of these molecules takes place in the potential region where the hydrogen evolution reaction (her) takes place. However, in aqueous solutions for $n > 6$, micelle formation have been also reported (Fig. 13) [75, 76]. The peak potential ($E_p$) related the electrodesorption peak shifts in the negative potential ($E$) direction as the number of C units in the hydrocarbon chain ($n$) of alkanethiolate molecules increases (Fig. 14). From the slopes of peak potential ($E_p$) versus $n$ plots
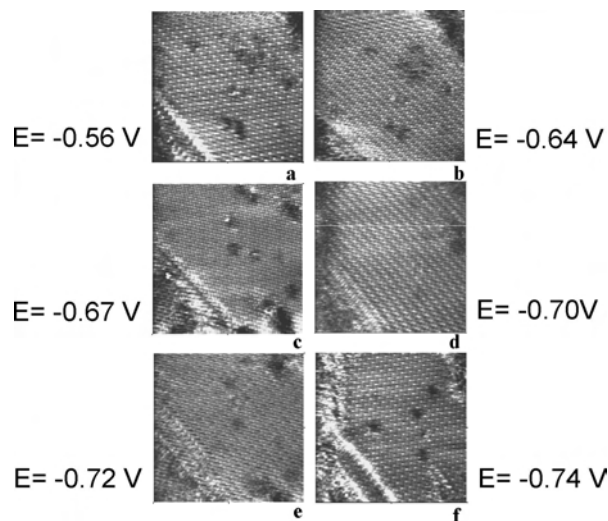


**Figure 11.** ($20 \times 20$ nm$^2$) STM images (raw data) of hexanethiolate covered Au(111) surface in 0.1 M NaOH taken at $E$ values within region 1. $\sqrt{3} \times \sqrt{3}$ R30 ° and $c(4 \times 2)$ reversible transitions and nanometer-sized defects are observed. Defects are continously created and repaired. Reprinted with permission from [76], C. Vericat et al., *J. Chem. Phys.* 115, 6672 (2001). © 2001, American Institute of Physics.
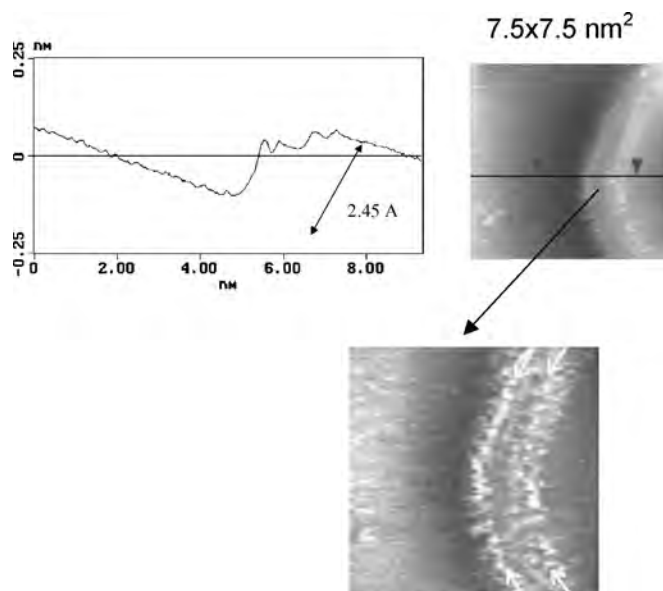
**Figure 12.** $(9 \times 9 \text{ nm}^2)$ STM image (raw data) and crosssection (upper) taken in region 2 (before the potential reached peak D′) showing a monoatomic high Au(111) step. $(6.5 \times 6.5 \text{ nm}^2)$ STM image. Bright spots at the step edges correspond to hexanethiol molecules.

the stabilizing interactions, van der Waals and hydrophobic forces have been estimated in 3–4 kJ/mol per C unit [77]. The use of methanol reduces interactions forces to 1.8–2 kJ/mol per C unit, then indicating the important role



Vertical distance: 0.29 nm
Horizontal distance: 2.13 nm
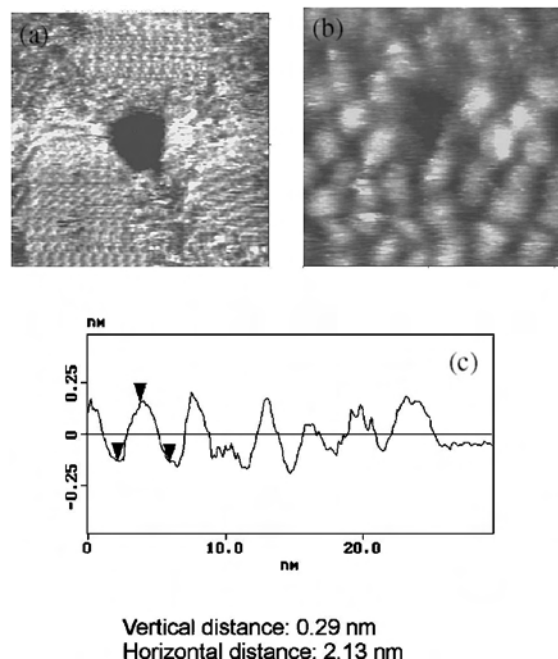
**Figure 13.** $(12.5 \times 12.5 \text{ nm}^2)$ STM images (raw data). (a) Au(111) surface in 0.1 M NaOH covered by an ordered hexanethiolate lattice, $E = -0.90$ (region 1). (b) physisorbed micelles resulting from the fast electrodesorption of the hexanethiol lattice, $E = -0.99$ V (region 2). The central hole observed in (a) and (b) indicate that the same region was imaged before and after electrodesorption. Reprinted with permission from [76], C. Vericat et al., *J. Chem. Phys.* 115, 6672 (2001). © 2001, American Institute of Physics.



**Figure 14.** $E_p$ versus $n$ plots for different alkanethiolates adsorbed on Au(111) and Ag(111) derived from the electrodesorption curves recorded at 0.1 V s$^{-1}$. (■) Au(111), aqueous 0.1 M NaOH, (▲) Au(111), 0.1 M NaOH 95% methanol + 5% H$_2$O, (●) Ag(111), 0.1 M NaOH 95% methanol + 5% H$_2$O.

of the hydrophobic forces on SAMs stability. All the above-mentioned data have been obtained in alkaline solutions. Conversely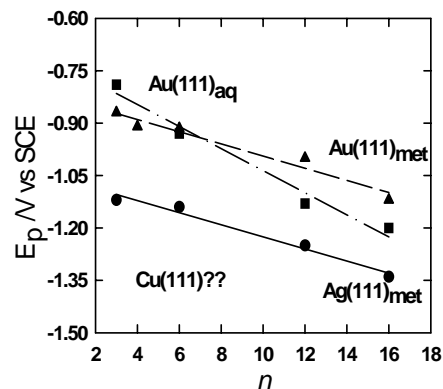, little information has been reported for alkanethiol electrodesorption from metal surfaces in acid solutions. For etanethiol-covered Au(111) in H$_2$SO$_4$ solutions, the $E_p$ value is strongly shifted in the positive direction with respect to that observed in the alkaline media, then reducing the stability range of the alkanethiol layer [78]. Similar results have been obtained for dodecanethiol-covered Au(111). In the case of ethanethiolate-covered Au(100) in 0.1 M H$_2$SO$_4$, potential-dependent reversible structural transitions have been reported [79]. It should be noted that polycrystalline Au exhibits the same electrodesorption behavior than those described for the single crystalline Au surfaces.

A detailed study on the reductive electrodesorption of SAMs on Ag(111) in aqueous and methanolic solutions has also been performed (Fig. 15a) [80, 81]. In aqueous solutions, the $E_p$ versus $n$ plots (Fig. 14) gives similar results for hydrocarbon chain-chain and hydrocarbon chain-solvent interactions than those found for alkanethiolates on Au(111). It has also been shown that for a constant $n$, the alkanethiolate molecules are desorbed from Ag (111) at more negative potential values than those corresponding to the desorption from Au(111). This difference has been explained by the smaller work function value of Ag than Au (12a) or to the stronger Lewis acid behavior of Ag than Au [82]. However, all electrochemical STM data and quantum density functional theory calculations have shown that the difference in peak potentials experimentally observed for the reductive desorption of a given alkanethiolate from the Ag(111) and Au(111) surfaces is determined by the energy to introduce an electron into the adsorbed alkanethiolate-metal species, the desorption energy of the alkanethiolate anion, and the solvent/metal interaction energy [83].

In the case of alkanethiolate covered-Cu, no voltammetric peaks related to the electrodesorption process can be observed in alkaline media (Fig. 15b). In fact, the alkanethiol-Cu interaction is so strong that the hydrogen evolution reaction takes place (probably at SAM defects) before the alkanethiolate electrodesorption takes place. The same behavior is observed in acid media (Fig. 15b) so that
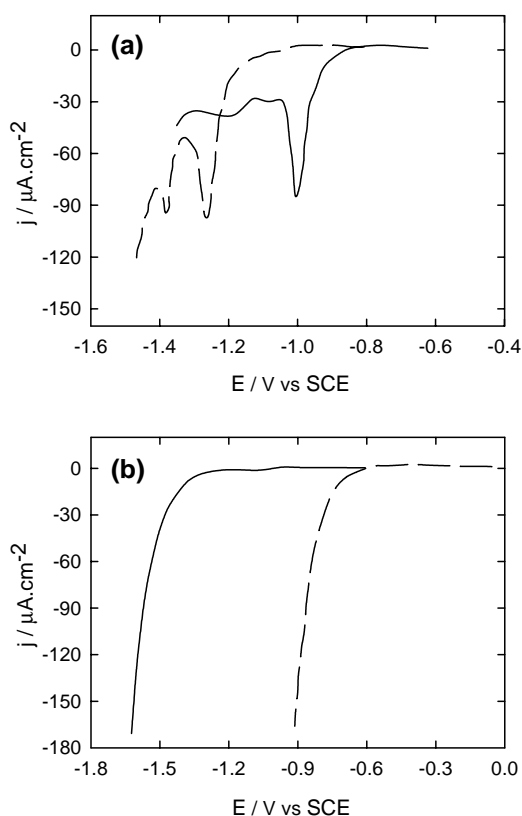
**Figure 15.** (a) Electrodesorption curves recorded at 0.1 V s$^{-1}$ in 0.1 M NaOH for dodecanethiolate on: (solid line) Au(111), (dashed line) Ag(111). (b) Electrodesorption curves at 0.1 V s$^{-1}$ for dodecanethiolate on Cu(111) in: (solid line) 0.1 M NaOH, (dashed line) 0.5 M H$_2$SO$_4$.

alkanethiolates on Cu form more stable SAMs than those formed on Ag(111) and Au(111). In the case of SAMs on Cu, the quality can be markedly improved by SAMs preparation on toluene solutions rather than ethanolic solutions [84].

Finally, the importance of the peak potential values should be stressed because alkanethiol electrodesorption determines the stability range of SAMs when they are used for modifying the physical chemistry of metal surfaces for metal electrodeposition. Thus, alkanethiolate SAMs on Cu appear as the best candidate for technological applications due to the high stability and low cost. In addition, long hydrocarbon chain alkanethiols and aqueous media should also be preferred due to the stabilizing effect of van der Waals and hydrophobic forces.

In the next section, the information about metal electrodeposition (from the submonolayer to the multilayer level) on alkanethiolate-covered substrates is reviewed.

# 3. METAL ELECTRODEPOSITION ON ALKANETHIOLATE SAMs

The key role played by metal/metal and metal/organic interfaces in several technological fields is well known, ranging from molecular electronics to industrial electroplating. From this aspect, alkanethiolate self-assembled monolayers were taken as model systems to study the metallization of organic surfaces under different experimental conditions.

## 3.1. Bulk Metal Electrodeposition

Bulk metal electrodeposition on self-assembled monolayers has been studied under galvanostatic (constant current) conditions [85, 86]. It has been observed that bulk electrodeposition is strongly affected by the presence of the self-assembled layer. The alkanethiolate self-assembled monolayer introduces an additional resistance to charge transfer from solution; thus the chain length determines the overpotential for copper electrodeposition Figure 16. The electrodeposit morphology is markedly influenced by the monolayer; in some cases the formation of low-adherence hemispherical copper deposits has been reported, in contrast to the uniform deposits electroformed on monolayer-free electrodes. Otherwise, it has been suggested that defects and pinholes play a determining role in the early stages of electrodeposition because they act as electro-crystallization nuclei [87]. When long-chain thiolates ($n <$ 12) are used at low current density, a few large crystallites are generated, but at higher current densities a high number of small crystallites are obtained. These facts indicate that large defects in the thiolate layer act as preferred sites for electrocrystallization at low-current densities, whereas at high-current densities, crystallites nucleate at minor defects. This fact is consistent with potential induced defects on self-assembled monolayers recently reported [88], considering that higher cathodic galvanic conditions require more negative electrode potentials.

The mechanism to describe the electrodeposition on SAMs is a matter of apparent controversy. Two different mechanisms of electrodeposition on thiolates SAMs have been suggested [85], depending on the length of the thiol chain. In the case of short chains, the charge transfer occurs on top of the monolayer by tunneling through the hydrocarbon chain. On the other hand, if a long chain thiolates monolayer is assembled on the electrode, the charge transfer takes place mainly at defects of the SAM. Despite this, a monolayer-defect-mediated mechanism has been proposed in which electrodeposition is done through defects on the monolayer making no differences between short and
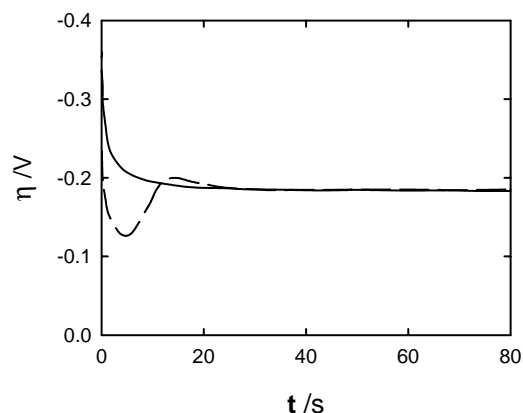


**Figure 16.** Overpotential ($\eta = E - E_r$) versus electrodeposition time for Cu electrodeposition on: (solid line) dodecanethiolate-covered polycrystalline Cu; (dashed line) polycrystalline Cu. $E$: applied potential; $E_r$: reversible potential for the Cu$^{2+}$/Cu reaction. Note that larger 3 are needed to deposit Cu on the SAM. Electrolyte: 0.6 M CuSO$_4 \cdot$5H$_2$O + 0.5 M H$_2$SO$_4$ + 0.025 mM thiourea.

long-chain thiols [86]. At late stages of metal electrodeposition, the deposit morphology is independent of surface hydrophilicity (i.e., independent of the terminal group of the alkanethiol chain) of the tailored electrodes.

Metal electrodeposition on alkanethiolate-covered metal substrates has also been studied under potentiostatic conditions at potential values slightly negative than the reversible potential of the $Me^{+z}/Me$ redox couple (overpotential deposition, (OPD) conditions). While three-dimensional growth takes place on a bare Au(111) substrate, a two-dimensional growth (layer-by-layer) is observed for short alkanethiolate covered-Au(111) [89]. However, for long-chain alkanethiols ($n > 12$), no further growth of initially deposited nanoclusters is observed at room temperature. At higher temperatures, the SAM act as a surfactant, even for long-chain alkanethiolates showing layer-by-layer growing in the OPD regime. This interesting behavior has been assigned to thermal-induced defects in the SAM, which allow rapid copper electroreduction due to an enhanced copper penetration in the disordered monolayer and surface diffusion [90]. Concerning defects, a recent Second Harmonic Generation (SHG) study showed that copper deposition is not accompanied by a strong conformational disorder of the SAM, but it can induce structural changes that differ from the well-known gauche defects [91].

## 3.2. Underpotential Deposition

Underpotential deposition (UPD) takes place when metal ions ($Me^{+z}$) can be deposited at potentials more positive than the equilibrium potential of the $Me^{+z}/Me$ redox couple. The combination of metal UPD and alkanethiolate self-assembled monolayers has brought useful routes for building up metal surfaces with well-defined physicochemical properties on the nanometer range or even at the molecular scale [92].

Metal UPD on alkanethiolate self-assembled monolayers has been performed in order to image individual defect structures contained on the SAM. By imaging the metal nanoislands underpotentially deposited at SAM defects, it has been possible to obtain information about self-assembly kinetics [93]. In the case of Cu UPD on alkanethiolate SAMs, it has been shown that the self-assembled layer has a striking influence on the growth morphology. In contrast to Cu UPD on bare Au(111), in the presence of decanethiolate self-assembled monolayers, Cu underpotential deposition proceeds by homogeneous and instantaneous nucleation of nanosized clusters on flat terraces, with no preferences for step edges or other sorts of surface defects [87]. The morphological evolution of the metal nanoclusters to dendritic-shape nanoislands resembles the metal epitaxy in UHV environments. *In-situ* STM and electrochemical measurements have shown that the absence of a clear UPD signal on the electrochemical response does not imply the absence of underpotentially deposited metal [87]. This finding has been attributed to kinetic effects introduced by the self-assembled film even for short-chain alkanethiolates. Several electrochemical studies have shown that the SAM acts as surfactants in the UPD regime, the metal is underpotentially deposited through the defects, and the deposited nanoisland is then covered by alkanethiolates

diffusing from surroundings. This mechanism is quite similar to place-exchange reactions used to describe the surfactant action of metal monolayers in UHV experiments [94]. This place-exchange reaction can be associated to a well-defined voltammetric signal in the case of Cu UPD on ethanethiolate-modified Au(111) electrodes [95]. In spite of the chain length of the SAM as a relevant factor in different SAM-related processes, it has been observed that the growth of nanoislands in the UPD region is a chain length independent phenomena in contrast to results reported for Cu OPD on SAM-modified Au(111) [96].

Silver UPD has also been performed on different thiolates-covered Au [97, 98]. It has been observed that short-chain alkanethiolates introduce changes in the UPD behavior of Ag, but this effect is considerably lower than in the case of Cu UPD. This can be explained considering that blocking effects of the SAM in electrochemical reactions increase with increasing Stokes radius of metal ions. Otherwise, it should be noted that Ag UPD on short-chain alkanethiolates may be affected by the electrochemical stability of these adsorbates, since anodic potentials could induce oxidative desorption of alkanethiolates. The mechanism proposed for Ag UPD on Au involves Ag deposition at defects of SAM, crawl under the SAM and lateral grow, which induces further defects at which Ag UPD can proceed, resulting in a preferential lateral growth of Ag monolayers [99, 100]. At present, metal electrodeposition involving SAMs is a very active research field [101–106] due to their potential applications in several technological areas.

# 4. APPLICATIONS

## 4.1. Patterning Alkanethiol-Masked Substrates

The viability of patterning SAMs by photo-oxidation [107–109], contact printing [110–112], pen writing [113–115], electron beam lithography [116], and SPM-based [117, 118] methods have recently been reported in the literature.

A simple way to patterning an alkanethiolate monolayer on a metal surface by STM consist in repetitive scanning on a desired surface area (Fig. 17) at a high tip-sample interaction (high tunneling current, low bias voltage). The patterned film on the metal surface can be used as a resist for subsequent etching or metal electrodeposition.
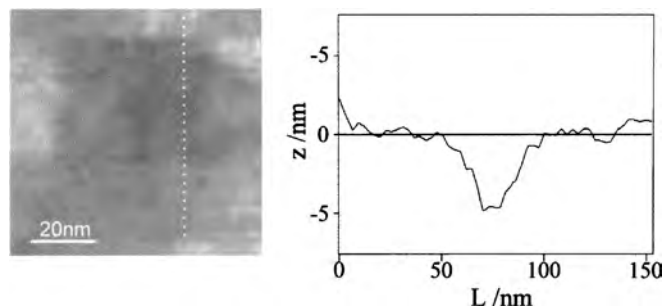


**Figure 17.** Scanning tunneling microscopy image and crosssection showing a square region "written" by repetitive scanning of a STM tip on a dodecanethiolate-covered Cu substrate. Reprinted with permission from [140], O. Azzaroni et al., *Langmuir* 17, 1483 (2001). © 2001, American Chemical Society.

25 μm
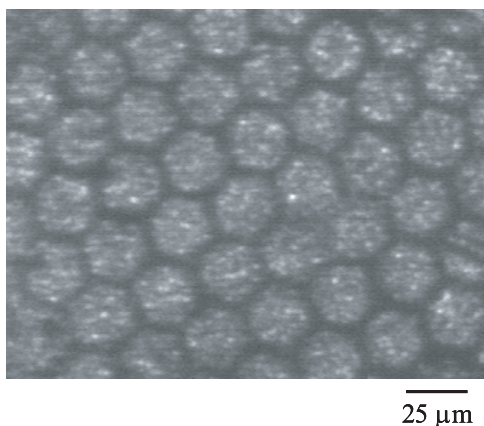
**Figure 18.** Patterned surface consisting in a Ag plate with Pd hexagonal features. An alkanethiolate-covered Ag surface was marked with a metal grid and exposed to UV radiation. The photo-oxidized alkanethiolate areas are chemically reactive and Pd is deposited by a redox reaction involving $Pd^{+2}$ ion reduction and Ag oxidation.

Patterning can also be performed by photo-oxidation by applying a short-time (20 min) UV exposure of SAM-covered metal masked with a metallic grid. The nonexposed areas to the UV act as a resist for subsequent deposition as shown in Figure 18. Ultraviolet radiation produces $O_3$ that rapidly oxides alkanethiol molecules to alkylsulfonates [119].

It has been shown that patterning Au or Cu substrates by contact printing with a long-chain alkanethiol ($n = 16$) as a resist material allows selective electrodeposition of iron group metals [120]. In this way, ordered Ni microstructures can be electrodeposited on these metals. The size of the structures that can be prepared by this technique depends on the resolution limit of the contact printing method due to the diffusion of the alkanethiol "ink" [121], and in this case, it results in the micrometer range. Other problems associated with metal electrodeposition on patterned alkanethiol monolayer is related to the lateral growth of the deposited island films when the thickness of the metal electrodeposit exceeds the length of the hydrocarbon chain.

Monolayer-covered metals can also be patterned by using electron beam nanolithography [122]. Well-defined regions of the self-assembled monolayer are removed selectively by dosing them with electron beams, and then copper nanostructures can be deposited on the exposed areas. With this approach, it is possible to nanofabricate metallic patterns as small as 75 nm.

## 4.2. Nanocrystal Preparation

Metallic nanoparticles supported on conducting substrates are of interest due to their unique physical chemistry properties, which result from the perturbations introduced by the large area/volume atom ratio in relation to bulk metals. These nanoparticles are important in dealing with heterogeneous catalysis and electrocatalysis. They also exhibit interesting properties such as giant magneto resistances and high saturation moments [123]. Metal electrodeposition on alkanethiolate SAMs can be used to prepare nanometer-sized metallic crystals. This method is based on the fact

that metal electrodeposition on alkanethiolate SAMs takes place at the nanometer-sized defects present in the monolayer (Fig. 11), that is, it results in the nucleation and growth of nanoparticles confined in the alkanethiolate layer. After deposition, the SAM can be easily removed by UV. Nickel nanocrystales (6 nm average size and 0.7–1 nm height) on Au(111) have been prepared using this method (Fig. 19).

## 4.3. Preparation of Nanocrystalline Standing-Free Films

Other interesting properties of adsorbed alkanethiols is dramatically increasing the antiadherent properties of the solid surface [124]. This property and the enhanced lateral growth when the deposit thickness exceeds the length of the hydrocarbon chain length [120], have been exploited for the fabrication of standing-free thin metal and alloy films by electrodeposition. Standing-free films have many technological uses and several methods have been developed in order to obtain metal thin films [125].

The method that uses SAMs to fabricate standing-free films has the advantages of simplicity and low cost, in contrast to other techniques previously developed, such as chemical vapor deposition, physical vapor deposition, sputtering, etc., which involve complicated and expensive equipment and need other methods to eliminate the substrate.

Figure 20(upper) shows STM images of a polished Cu substrate derivatized with a dodecanethiol monolayer for an immersion time $t_a = 1$ h and a Cu electrodeposit grown on it from 0.6 M $CuSO_4 \cdot 5H_2O$ + 0.5 M $H_2SO_4$ aqueous solution (Fig. 20 left). The electrodeposit surface consists of micrometer-sized Cu grains that form an irregular surface. Following the time ($t$) dependence of the root mean square roughness ($W$), the growth mode of the deposit can be elucidated [126]. $W$ increases with time as $W \propto t^\beta$ with $\beta = 0.7$, as it has been reported for Cu electrodeposition on nonderivatized Cu substrates [127]. It means that the growth
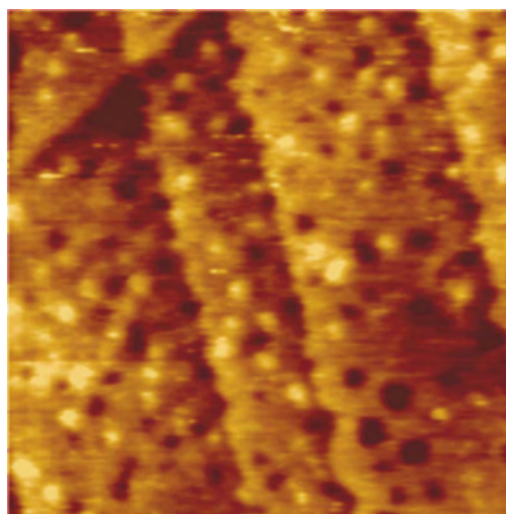


**Figure 19.** ($100 \times 100$ nm$^2$) STM image of Ni nanoclusters grown by electrodepositon on a hexanethiolate-covered Au(111). Electrolyte: 1 M $NiSO_4 \cdot 7H_2O$ + 0.25 M $NiCl_2 6H_2O$ + 0.61 M $H_3BO_3$, $E = -0.6$ V (vs SCE).
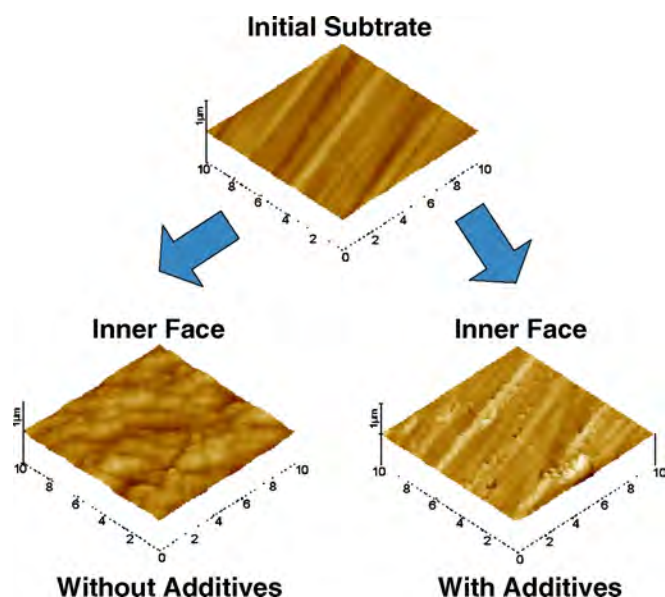
**Figure 20.** STM image of copper substrate (upper). STM images of Cu electrodeposits grown at 20 mA cm$^{-2}$ from 0.6 M CuSO$_4$·5H$_2$O + 0.5 M H$_2$SO$_4$ (left). The same electrolyte but containing 0.025 M thiourea (right). Reprinted with permission from [131], P. L. Schilardi et al., *Langmuir* 17, 2748 (2001). © 2001, American Chemical Society.

mode of the Cu deposit does not change under the presence of the SAM. However, the electrodeposited Cu samples detach spontaneously or they are easily removed from the Cu substrate with tweezers without deformations. The easy detachment of the Cu deposits is not observed when electrodeposition is made on nonderivatized Cu substrates, indicating that it is related to the presence of the dodecanethiol SAM. Similar results were obtained from the same plating bath using a derivatized Au(111) as substrate.

On the other hand, when Cu electrodeposition is made from the plating bath containing 0.025 mM thiourea, the growth mode of the Cu deposits is changed leading to smoother Cu films (Fig. 20 right) formed by nanometer-sized grains (20 nm in average size). In the presence of thiourea, Cu is preferentially deposited at valleys rather than at protrusions [128]. In this case, after detachment, the inner face of the electrodeposit resembles the morphology of the derivatized Cu substrate reproducing its polishing lines (Fig. 20 upper). These facts—substrate replication and easy detachment from the substrate—indicate the possible use for pattern transfer. This fact arises from the nanostructured nature of the deposited material that could replicate nano/microstructures larger than the 20 nm average grain size.

The possibility of using this method to fabricate standing-free films with complex chemical composition, such as magnetic alloys, have been recently explored. In principle, electrodeposition on alkanethiolate-covered substrates would be inadequate when alkanethiol adsorption is stronger on the surface of the metal to be deposited than on the surface of the metal used as the template. For example, when Ag is electrodeposited on a alkanethiolate-covered Au electrode, a place exchange process between the adsorbed alkanethiolate and the depositing Ag atom takes place [100].

Place exchange occurs because the adsorption energy of alkanethiolates on the Ag surface is greater than on the Au surface. Thus, the adsorbed layer floats on the surface of the deposited metal film proving the method inapplicable. On the other hand, chemical reactions among the alkanethiolates adsorbed on the template (used as the cathode in the electrochemical cell) and the ionic metal species of the plating bath could produce partial oxidation of the alkanethiolate layer [129]. Finally, and more important, the alkanethiolate layer could be electrodesorbed from the template at the high negative potential values required to electrodeposit active metals such as Fe, Co, and Ni for which $E < -1.2$ V are needed. However, recent experimental results have demonstrated that alkanethiol-assisted electrodeposition can be used to produce standing-free films of CoNiFe alloys (these films have an interesting low coercivity $Hc \approx 3$ Oe) by simple electrodeposition on a dodecanethiolate-covered Cu substrate [130]. The easy detachment and good quality of the alloy film show that neither flotation, nor desorption, nor damage of the dodecanethiolate layer, take place during the thiol-assisted electrodeposition. Therefore, this method has also been used to prepare Ni, Bi, Co standing-free films from different plating baths (Table 2) in an easy and simple way.

## 4.4. Patterning Metallic Films: Molding and Replication

The best route for serial fabrication of nano/micrometer-sized structures is molding and replication. Electrodeposition on alkanethiolate-covered metal substrates has been successfully used for both mold and replica fabrication in the nano/micrometer range. The method consists of metal electrodeposition onto a conducting patterned master which is previously derivatized with an alkanethiol self-assembled monolayer. In this procedure, the inner face of the electrodeposited sample is the mold of the master. By changing the electrodeposition time, the thickness of the mold can vary from micrometer to millimeter range in order to obtain a desired mechanical stability. After the preset thickness has been reached, the mold spontaneously detaches or it is easily removed from the master. Once the metallic mold is obtained, it is derivatized again with a SAM and a new metal electrodeposit is grown on it. After detaching the metal film, a replica of the master is obtained on the inner face of the electrodeposit. A scheme showing the steps to fabricate a mold and a replica of a given pattern by using

**Table 2.** Different plating baths used to prepare metallic standing-free films by electrodeposition.

| Metal | Plating bath | j (mA·cm$^{-1}$) | T (K) |
|---|---|---|---|
| Cu | 0.6 M CuSO$_4$·5H$_2$O + 0.5 M g/l H$_2$SO$_4$ + 2.5 × 10$^{-5}$ M thiourea | 10 | 298 |
| Ni | 1.1 M NiSO$_4$·7H$_2$O + 0.25 M NiCl$_2$·6H$_2$O + 0.6 M H$_3$BO$_3$ | 40 | 327 |
| Bi | 0.14 M Bi(NO$_3$)$_3$ + 1.3 M glycerol + 0.33 M tartaric acid + HNO$_3$ (pH = 2) | 5 | 298 |
| Co | 0.42 M CoCl$_2$·6H$_2$O + 0.9 M NH$_4$F·HF + 0.7 M H$_3$BO$_3$ | 20 | 298 |

metal electrodeposition on alkanethiol-covered masters is shown in Figure 21. Figure 22 shows a Cu mold and a Cu replica obtained from a dodecanethiol-covered Cu master by using this procedure. The master is a grid of 500 nm wide Cu rows separated by 900 nm wide and 90 nm deep channels as shown in the STM image and crosssection (Fig. 22a–b). The master was then subjected to the procedure indicated in Figure 21. After depositing a 7 $\mu$m thick Cu film from 0.6 M $CuSO_4 \cdot 5H_2O$ + 0.5 M $H_2SO_4$ + 0.025 mM thiourea, the copper sample was easily removed from the Cu master with tweezers. The STM image of the inner face of the 7 $\mu$m thick electrodeposited Cu film now shows a pattern consisting of 900 nm wide Cu rows separated by 500 nm wide and 90 nm in depth channels (Fig. 22c–d), that is, this face is a mold of the original Cu master. In order to obtain replicas, this mold is again derivatized with the SAM, and then a Cu electrodeposit is grown following the same procedure described above. After removing the electrodeposited film from the mold, STM imaging of the inner face shows a replica of the original gridmaster (Fig. 22e–f).



**Figure 22.** 10 $\mu$m $\times$ 10 $\mu$m STM image of the micropatterned Cu master grid (a) and crosssection (b). 10 $\mu$m $\times$ 10 $\mu$m STM image of the Cu mold obtained after electrodeposition and detachment from the derivatized Cu master grid (c) and crosssection (d). 10 $\mu$m $\times$ 10 $\mu$m STM image of the micropatterned Cu replica after electrodeposition and detachment (e) and crosssection (f). Reprinted with permission from [131], Schilardi et al., *Langmuir* 17, 2748 (2001). © 2001, American Chemical Society.



**Figure 21.** Scheme showing the different steps involved in molding and replication: a) micropatterned conducting master, b) micropatterned conducting master derivatized with an alkanethiolate monolayer (black, not in scale), c) electrodeposit grown on the derivatized conducting master, d) detachment of the electrodeposit, the inner face is a mold of the master, e) derivatized mold with an alkanethiol monolayer (black, not in scale), f) electrodeposition on the derivatized mold, the inner face is a replica of the master. Reprinted with permission from [131], P. L. Schilardi et al., *Langmuir* 17, 2748 (2001). © 2001, American Chemical Society.

The mechanical stability of the metallic molds is good. In fact, many (more than 20) Cu, Ni, CoNiFe, and polymer-made replicas (the polymer replicas prepared by the procedure described next) can be been fabricated by using the same derivatized-Cu mold without modification of the mold architecture [131]. This means that the wear of master caused by replica removal is not significant possibly due to the high mechanical stability of the Cu mold.

Another route for patterning metallic films has been recently proposed using triglyceride as an intermedium layer of resistant molecules [132]. In this method, a macromolecular membrane is used as an antiadherent layer and, like techniques using dodecanethol SAMs, allows the fabrication of metal thin films with bendable properties. Its main disadvantage is that it does not permit the reusage of molds because part of the membrane is left on the thin film.

The physical properties of the patterned sample depend markedly on the morphology and size of the grains that

constitute the building blocks of the system. Therefore, the study of possible routes for modifying grain size without changing the nano/micropattern is a crucial point for the fabrication of metallic samples with specific structural and physical properties. It has been shown that controlled post-deposition thermal annealing of nano/micropatterned standing free copper samples at temperatures $T < 0.5T_m$, $T_m$ the melting temperature, increases grain size and improves the electric conductivity of the sample by Otswald ripening without changing the nano/micro pattern [133].

## 4.5. Patterning Polymeric Films with Alkanethiolate-Covered Metallic Molds

The derivatized molds can be used directly for microtransfer molding ($\mu$TM) to polymeric materials. The use of metallic rigid molds improves the resolution limit of the conventional $\mu$TM method and eliminates the restrictions present on the other modified versions of this technique [134]. By using rigid dodecanethiolate-covered metallic mold patterns with ratio $l/d$, $l$ being the lateral size and $d$ the depth of the feature equal to 7, can be prepared and the resolution limit could move from 1 $\mu$m to sub-100 nm. The alkanethiolate layer modifying the metallic-made mold enables a complete release of the mold from the polymeric film producing defect-free patterns irrespective of the adhesive properties of the polymer; thus this method eliminates the severe restrictions present in $\mu$TM [135]. The versatility of the method is demonstrated by the fabrication of glass-supported gratings of polymer materials having very different adhesive and mechanical properties and with architecture similar to those fabricated by laser ablation. The method for fabricating the polymer-made grating involves a few very simple steps (Fig. 23). The dodecanethiol-modified mold is placed about 30 min in pure toluene to remove the physisorbed molecules forming multilayers. Then, the liquid polymer is poured on the glass support (Fig. 23c), and the thiol-modified copper mold is immediately pressed on the glass-supported liquid polymer film (Fig. 23d), controlling the applied pressure by using a micrometer screw. The use of metallic molds, in contrast to polydymethylsiloxane (PDMS) molds, allows the application of high pressures without introducing significant deformations. Once the polymer is cured, the thiol-modified mold is easily released from the polymeric film (Fig. 23e). In this method, the release procedure requires only a minimum mechanical effort producing no damages to the polymer-made grating or to the copper-made mold. The low adherence properties of methyl-terminated self-assembled monolayers have been previously exploited for micropatterning-conducting polymers on gold surfaces [136]. Atomic force microscopy (AFM) images of the copper-made master (Fig. 24a), the copper-made mold (Fig. 24b), and high impact polystyrene (HIPS)-made (Fig. 24c) and poly(isobutylcyanoacrylate)-made (Fig. 24d) replicas show the accurate form in which track periodicity and channel depth were reproduced in the polymeric gratings. Therefore, this method allows the fabrication of ordered gratings irrespective of the adhesive and mechanical properties of the polymers. In fact, HIPS exhibits a relatively poor adherence and is an easily deformed material,
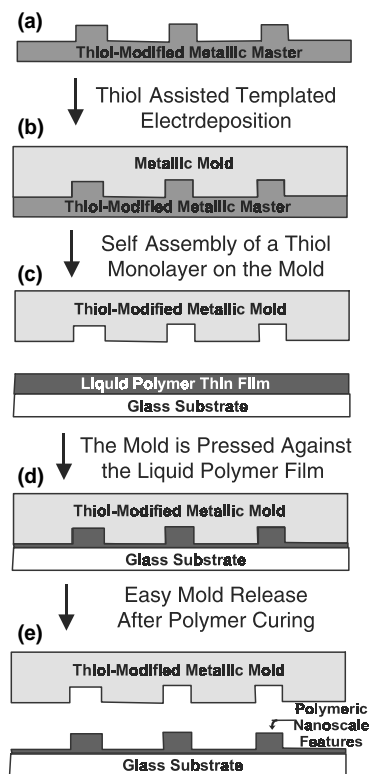


**Figure 23.** Schematic illustration of the complete procedure for fabrication of polymeric nanostructures by the microtransfer molding method. a) thiol-modified metallic master; b) mold fabrication by thiol-assisted templated electrodeposition, followed by mold modification by thiol adsorption; c) polymer film on the glass substrate; d) the thiol-modified mold is pressed on the liquid polymer film supported on the glass substrate; e) after casting, high impact polystyrene, or polymerization, poly(isobutylcyanoacrylate), the mold is easily released from the polymer-made film. The polymer face in contact with the mold is a replica of the template.
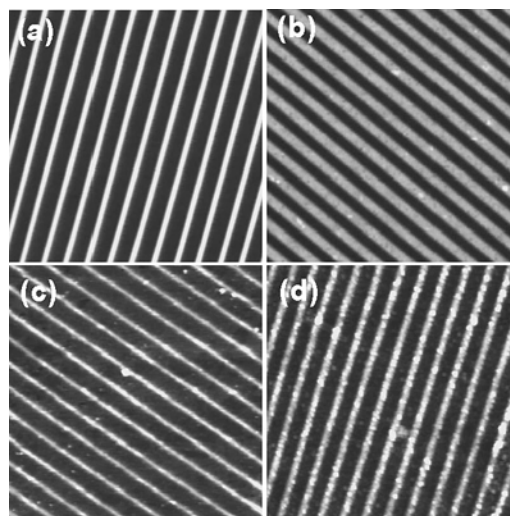


**Figure 24.** 20 × 20 $\mu$m$^2$ AFM images. (a) copper-made master, (b) copper made mold, (c) high impact polystyrene-made replica, and (d) poly(isobutylcyanoacrylate)-made replica.

whereas poly(isobutylcyanoacrylate) is an extremely adhesive and rigid polymer. The importance of the surface chemistry modification introduced by the alkanethiol layer is clearly revealed by performing control experiments, where the polymer deposition was directly made onto a bare Cu mold. In these cases the polymer films cannot be released from the Cu mold.

The resolution of the method was also explored by using an dodecanethiolate-modified Au(111) surface as template for poly(isobutylcyanoacrylate) embossing [134]. After the template was released, AFM imaging of the polymer inner face shows triangular terraces and steps that intersect forming 60° angles, that is, the typical pattern of the Au(111) surface. The crosssection analysis shows steps 0.6 nm in height. Typical monoatomic high steps with 0.24 nm have been lost in the transfer process. The smallest terraces that have been transferred are 40 nm in width. Therefore, considering the smallest features replicated from the Au(111) surface, it is believed that the method allows 40 nm lateral and 0.6 nm vertical resolutions.

## 4.6. Fundamental Aspects of Electrodeposition on SAMs

Now we focus on the mechanism involved in monolayer-assisted electrodeposition. Recently, it has been shown that when metal electrodeposition is made on a Cu electrode covered by a dodecanethiolate SAM, nucleation of the depositing material takes places only at defective sites allowing the growth of isolated crystals outwards [131]. This is clearly demonstrated in Figure 19, where Ni has been electrodeposited on a hexanethiol covered Au. The number of small Ni clusters (6 nm in size) observed in the STM image is $10^{11}$ cm$^{-2}$ in agreement with the defect density calculated from the STM image shown in Figure 11. Therefore, it is proposed that the initial step (Fig. 25a and b) is the nucleation of metal particles at defect sites. These particles grow outwards forming nanometer-sized columns Figure 25c. The column width should be close to defect size in the SAM, which is in the nanometer range, and its maximum height close to the molecular length, that is, $\approx 1.7$ nm for dodecanethiol monolayers [137]. After the column tips reach the outer limit of the SAM, they can coarsen closely following the substrate morphology as schematically shown in Figures 25d–e. The presence of organic additives such as thiourea (TU) in the plating bath plays a key role in this method. In fact, TU molecules adsorb at the tip of the growing columns enhancing lateral growth [138]. This results in smooth films required for molding and replication. As shown in Figure 20, the average grain size ($d$) in the presence of TU is $d = 20$ nm, much smaller than $d = 500$ nm, produced in the plating bath without TU. The value of $d$ of the Cu deposit grown in the presence of TU allows the replication of nanometer-sized features. The decrease in grain size has been assigned to a decrease in the diffusion length of metal adatoms due to the adsorption of the organic additive at the electrodeposit surface [139]. Detailed studies on the effect of TU in Cu deposit morphology have been reported
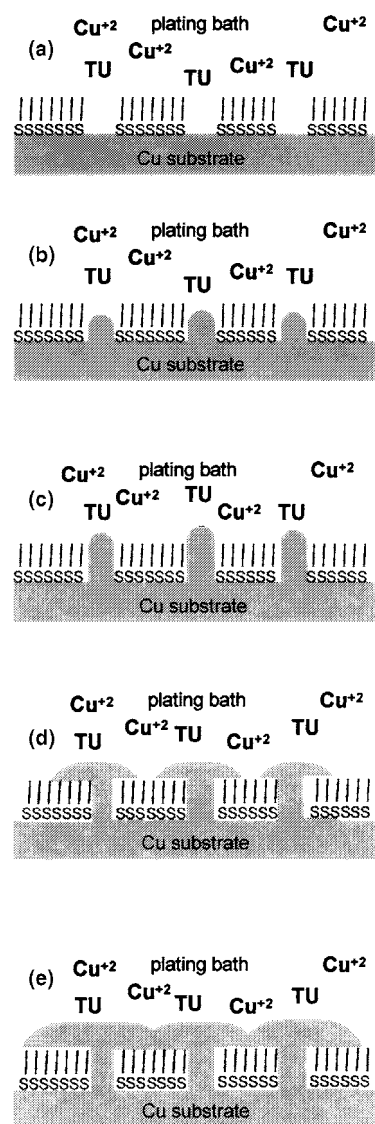


**Figure 25.** Scheme showing the steps involved in Cu electrodeposition on a derivatized Cu substrate: (a) The derivatized substrate in contact with the plating bath. Defects of the SAM are shown. (b) Cu crystals are formed at the defective sites of the SAM. The crystals grow outwards. (c–e) The presence of thiourea (TU) molecules in the bath enhances lateral growth leading to smooth and flat metal films. Reprinted with permission from [131], P. L. Schilardi et al., *Langmuir* 17, 2748 (2001). © 2001, American Chemical Society.

[127, 138]. The experimental conditions indicated in this work can be considered as the optimum conditions for molding and replication of Cu nanostructures in the case of SAM-modified Cu electrode.

The deposited sample is connected to the substrate only by the nanometer-sized columns. They can be easily broken allowing the detachment of the deposit, that is, the deposit adherence has been dramatically decreased. This poor adherence is an interesting interfacial property of metal electrodeposits on SAMs which is exploited in this method for molding and replication purposes. This phenomenon is not unexpected since SAMs act as

lubricant/antistick layer. Contact angle measurements show that the SAM remains on the derivatized electrode surface (the master or the mold) due to the strong binding energy that exists between the S atom of the alkanethiol head and the Cu surface. Also, it has been verified by derivatizing the Cu master for $t_a = 2$ days. In this case a multilayer is formed on the metal surface. After Cu electrodeposition and film detachment, the master surface was imaged with STM. Repetitive STM scanning over a given area of the master results in window formation due to the removal of the alkanethiol multilayer by the tip. When the inner face of the electrodeposited metal film in contact with the master was subjected to the same procedure, no window formation was observed. These results also demonstrate that the alkanethiol layer remains absorbed on the derivatized metal surface. In principle, it should be expected that multilayer formation should frustrate the plating process. However, the fraction of the surface covered by defects, that is, a fraction of the Cu surface exposed to the plating bath, decreases only from $1.7 \times 10^{-2}$ to $4.8 \times 10^{-3}$ as $t_a$ increases from 1 hr to 16 h [140]. Then, the defect density decreases very slowly with the adsorption time. Therefore, even for a long adsorption time, there are enough defects in the dodecanethiol multilayer to allow Cu electrodeposition. As previously mentioned, electrodeposition from the plating bath is possible even on derivatized Au(111) substrates, where the density of defects is expected to be much lower than that present on Cu. As expected, the decrease in the defect number favors the sample detachment but hinders the replication process because the growth centers are very separated. Note that the best conditions for molding and replication involves $t_a = 1$ hs, that is, the fraction of Cu substrate noncovered by dodecanethiol is $\approx 2\%$.

## 5. CONCLUSIONS

Electrodeposition of different metals on alkanethiolate-covered metallic substrates have been reviewed under a wide range of experimental conditions. The information available at present strongly suggests that this procedure can be used as a fast and inexpensive route to produce thin metallic standing-free films and/or to fabricate nano/micropatterned masters, molds, and replicas of different materials including a variety of polymers. The elapsed time of fabrication is about 2 hr and no hazardous reagents are involved in the preparation. This procedure is easily carried out using basic electrochemical instrumentation and facilities disposable at any laboratory.

## GLOSSARY

**Alkanes** Organic molecules with general formulae $C_nH_{n+2}$.

**Electrodeposition** Deposition of substances on a conducting substrate from an electrolyte by applying an electric potential or current.

**Electrodesorption** Desorption of species from a conducting substrate by applying an electric potential or current.

**Nanofabrication** Technique capable of generating structures with at least one lateral dimension less than 100 nm.

**Overpotential deposition (OPD)** Electrodeposition process carried out at potentials more negative than the equilibrium potential of the electrochemical reaction.

**Self-assembled monolayer (SAM)** Single layer of molecules that self-assembles on a substrate.

**Standing-free films** Self-supported deposited films that remain stable after removal from the substrate.

**Thiol** Organic molecules containing a -SH group.

**Underpotential deposition (UPD)** Electrodeposition of substances carried out at potentials more positive than the equilibrium potential of the electrochemical reaction.

## REFERENCES

1. H. O. Flinkea, in "Electroanalytical Chemistry" (A. J. Bard and I. Rubinstein, Eds.), Vol. 19, pp. 109–335. Marcel Dekker, New York, 1996.
2. H. O. Finklea, in "Encyclopedia of Analytical Chemistry: Theory and Instrumentation" (R. A. Meyers, Ed.), John Wiley & Sons, Chichester, 2000.
3. G. K Jennings, J. C. Munro, T.-H. Yong, and P. E. Laibinis, *Langmuir* 14, 6130 (1998).
4. F. P. Zamborini and R. M. Crooks, *Langmuir* 14, 3779 (1998).
5. E. Boubour and R. B. Lennox, *Langmuir* 16, 4222 (2000).
6. R. Maboudian and R. T. Howe, *J. Vac. Sci. Technol. B* 15, 1 (1997).
7. T. M. Mayer, M. P. de Boer, N. D. Shin, P. J. Clews, and T. A. Michalske, *J. Vac. Sci. Technol. B* 18, 2433 (2000).
8. R. Maboudian, W. R. Ashurst, and C. Carraro, *Sensors and Actuators A* 82, 219 (2000).
9. R. Haag, M. A. Rampi, R. E. Holmlin, and G. M. Whitesides, *J. Am. Chem. Soc.* 121, 7895 (1999).
10. M. Geissler, A. Bernard, A. Bietsch, H. Schmid, B. Michel, and E. Delamarche, *J. Am. Chem. Soc.* 122, 6303 (2000).
11. C. S. Chen, M. Mrksich, S. Huang, G. M. Whitesides, and D. E. Ingber, *Biotechnol. Prog.* 14, 356 (1998).
12. Y. Xia, E. Kim, M. Mrksich, and G. M. Whitesides, *Chem. Mater.* 8, 601 (1996).
13. O. Chailapakul and R. M. Crooks, *Langmuir* 9, 884 (1993).
14. S. Kidoaki and T. Matsuda, *Langmuir* 15, 7639 (1999).
15. J. Küther, R. Seshadri, G. Nelles, W. Assenmacher, H.-J. Butt, W. Mader, and W. Tremel, *Chem. Mater.* 11, 1317 (1999).
16. Y. Xia, J. A. Rogers, K. Paul, and G. M. Whitesides, *Chem. Rev.* 99, 1823 (1999).
17. H. I. Smith and H. G. Craighead, *Phys. Today* 24 (1990).
18. W. M. Moreau, in "Semiconductor Lithography," Plenum Press, New York, 1988.
19. C. S. Lent, P. D. Tougaw, W. Porod, and G. H. Bernstein, *Nanotechnology* 4, 49 (1993).
20. W. Gopel, *Biosens. Bioelectron.* 10, 35 (1995).
21. L. Y. Lin, E. L. Goldstein, and R. W. Tkach, *IEEE J. Selected Top. Quantum Electron.* 5, 4 (1999).
22. M. A. Unger, H.-P. Chou, T. Thorsen, A. Scherer, and S. R. Quake, *Science* 288, 113 (2000).
23. Y. Xia, E. Kim, X.-M. Zhao, J. A. Rogers, M. Prentiss, and G. M. Whitesides, *Science* 273, 347 (1996).

24. R. J. Jackman, S. T. Brittain, A. Adams, M. G. Prentiss, and G. M. Whitesides, *Science* 280, 2089 (1998).

25. W. T. S. Huck, J. Tien, and G. M. Whitesides, *J. Am. Chem. Soc.* 120, 8267 (1998).

26. A. Kumar, H. A. Biebuyck, and G. M. Whitesides, *Langmuir* 10, 1498 (1994).

27. P. C. Hidber, W. H. Helbig, E. Kim, and G. M. Whitesides, *Langmuir* 12, 1375 (1996); C. S. Dulcey, J. H. Georger Jr., V. Krauthamer, D. A. Stenger, T. L. Fare, and J. M. Calvert, *Science*, 252, 551 (1991); W. J. Dressick and J. M. Calvert, *Jpn. J. Appl. Phys.* 32, 5829 (1993).

28. M. Masuko, T. Osaka, and Y. Ito (Eds.) "Electrochemical Technology-Innovations and New Developments." Gordon and Breach Publishers, Amsterdam 1996.

29. M. J. Tarlov, D. R. F. Burguess, and G. Gillen, *J. Am. Chem. Soc.* 15, 5305 (1993).

30. J. A. Rogers, J. Tate, W. Li, Z. Bao, and A. Dodabalapur, *Isr. J. Chem.* 40, 139 (2000).

31. L. Lu, M. L. Sui, and K. Lu, *Science* 287, 1463 (2000).

32. J. A. Switzer, H.-J. Hung, E. W. Bohannan, M. G. Shumsky, and D. C. Van Aken, *Adv. Mat.* 9, 334 (1997).

33. F. Y. Yang, K. Liu, K. Hong, D. H. Reich, P. C. Searson, and C. L. Chien, *Science* 284, 1335 (1999).

34. J. A. Switzer, M. J. Shane, and R. P. Phillips, *Science* 247, 444 (1990).

35. J. A. Switzer, M. G. Shumsky, and E. W. Bohanna, *Science* 284, 293 (1999).

36. J. H. Schön, H. Meng, and Z. Bao, *Adv. Mater.* 14, 323 (2002).

37. A. Kumar, H. Biebuyck, and G. M. Whitesides, *Langmuir* 10, 1498 (1994).

38. J. P. Folkers, C. B. Gorman, P. E. Laibinis, S. Buchholz, G. M. Whitesides, and R. G. Nuzzo, *Langmuir* 11, 813 (1995).

39. J. Sagiv, *J. Am. Chem. Soc.* 102, 92 (1980).

40. R. Maoz and J. Sagiv, *J. Colloid. Interface. Sci.* 100, 465 (1984).

41. S. R. Wasserman, Y.-T. Tao, and G. M. Whitesides, *Langmuir* 5, 1074 (1989).

42. H. Lee, L. J. Kepley, H. G. Hong, S. Akhter, and T. E. Mallouk, *J. Phys. Chem.* 92, 2597 (1988).

43. B. L. Frey, D. G. Hanken, and R. M. Corn, *Langmuir* 9, 1815 (1993).

44. C. A Widrig, C. Chung and M. D. Porter, *J. Electroanal. Chem.* 310, 335 (1991).

45. C.-J. Zhong, N. T. Woods, G. B. Dawson, and M. C. Porter, *Electrochem. Comm.* 1, 17 (1999).

46. L. A. Bumm, J. J. Arnold, L. F. Charles, T. D. Dunbar, D. L. Allara, and P. S. Weiss, *J. Am. Chem. Soc.* 121, 8017 (1999).

47. G. Poirier, *Chem. Rev.* 97, 1117 (1997).

48. D. Anselmetti, A. Baratoff, H. J. Guntherodt, E. Delamarche, B. Michel, Ch. Gerber, H. Kang, H. Wolf, and H. Ringsdorf, *Europhys. Lett.* 27, 365 (1994).

49. F. Terán, M. E. Vela, R. C. Salvarezza, A. J. Arvia, *J. Chem. Phys.* 109, 5703 (1998).

50. C.-J. Zhong, R. C. Brush, J. Anderegg, M. D. Porter, *Langmuir* 15, 518 (1999); C. Vericat, M. E. Vela, G. Andreasen, R. C. Salvarezza, L. Vázquez, and J. A. Martín-Gago, *Langmuir* 17, 4919 (2001).

51. A. Ulman, *Chem. Rev.* 96, 1533 (1996).

52. F. Schreiber, *Prog. Surf. Sci.* 65, 151 (2000).

53. Y. Akinaga, T. Najajima, and K. Hirao, *J. Chem. Phys.* 114, 8555 (2001); J. Gottschalck and B. Hammer, *J. Chem. Phys.* 116, 784 (2002).

54. L. Strong and G. M Whitesides, *Langmuir* 4, 546 (1988).

55. L. H. Dubois, B. R. Zegarski, and R. G. Nuzzo, *J. Phys. Chem.* 98, 678 (1993).

56. A. Nemetz, T. Fischer, A. Ulman, and W. Knoll, *J. Chem. Phys.* 98, 5912 (1993).

57. K. S. Dhirani, M. A. Hines, A. J. Fischer, O. Ismail, and P. Guyot-Sionnest, *Langmuir* 11, 2609 (1995).

58. G. D. Aloisi, M. Cavallini, M. Innocenti, M. L. Foresti, G. Pezzatini, and R. Guidelli, *J. Phys. Chem. B* 101, 4774 (1997); H. Rieley, G. K. Kendall, R. G. Jones, and D. P. Woodruff, *Langmuir* 15, 8856 (1999).

59. M. A. Hines, J. A. Todd, and P. Guyot-Sionnest, *Langmuir* 11, 493 (1995).

60. G. J. Jackson, D. P. Woodruff, R. G. Jones, N. K. Singh, A. S. Y. Chan, B. C. C. Cowie, and V. Formoso, *Phys. Rev. Lett.* 84, 119 (1999).

61. H. Rieley, G. K. Kendall, R. G. Jones, and D. P. Woodruff, *Langmuir* 15, 8856 (1999).

62. S. Volmer, G. White, and C. Wöll, *Langmuir* 17, 7560 (2001).

63. J. Scherer, M. R. Vogt, O. M. Magnussen, and R. J. Behm, *Langmuir* 13, 7045 (1997).

64. L. Dreseen, C. Humbert, M. Celebi, J. J. Lemaire, A. A. Mani, P. A. Thiry, and A. Peremans, *Appl. Phys. B* 74, 621 (2002).

65. A. Carvalho, M. Geissler, H. Schmid, B. Michel, and E. Delamarche, *Langmuir* 18, 2406 (2002).

66. J. C. Love, D. B. Wolfe, M. L. Chabinyc, K. E. Paul, and G. M. Whitesides, *J. Am. Chem. Soc.* 124, 1576 (2002).

67. Z. Mekhalif, J. Delhalle, J.-J. Pireaux, S. Noël, F. Houze, and L. Boyer, *Surf. Coat. Technol.* 100–101, 463 (1998).

68. Z. Mekhalif, J. Riga, J.-J. Pireaux, and J. Delhalle, *Langmuir* 13, 2285 (1997).

69. M. Volmer-Uebing and M. Stratmann, *Appl. Surf. Sci.* 55, 19 (1992).

70. M. Volmer, B. Czodrowski, and M. Stratmann, *Ber. Bunsenges. Phys. Chem.* 92, 1335 (1988).

71. C. D. Bain, E. B. Troughton, Y. Tao, J. Evall, G. M. Whitesides, and R. G. Nuzzo, *J. Am. Chem. Soc.* 111, 321 (1989).

72. D. Schwartz, *Annu. Rev. Phys. Chem.* 52, 107 (2001).

73. M. Walczak, C. A. Alves, B. D. Lamp, and M. D. Porter, *J. Electroanal. Chem.* 396, 103 (1995).

74. H. Martín, C. Vericat, G. Andreasen, M. E. Vela, and R. C. Salvarezza, *J. Chem. Phys.* 117, 2293 (2002).

75. D. Hobara, K. Miyake, S. Imabayashi, K. Niki, and T. Kakiuchi, *Langmuir* 14, 2293 (1998).

76. C. Vericat, G. Andreasen, M. E. Vela, H. Martín, and R. C. Salvarezza, *J. Chem. Phys.* 115, 6672 (2001).

77. M. E. Vela, H. Martín, C. Vericat, G. Andreasen, A. Hernández-Creus, and R. C. Salvarezza, *J. Phys. Chem. B* 104, 11878 (2000).

78. H. Hagenström, M. A. Schneeweiss, and D. M. Kolb, *Langmuir* 15, 2435 (1999).

79. M. Schweizer, H. Hagenström, and D. M. Kolb, *Surf. Sci.* 490, L627 (2001).

80. D. W. Hatchett, K. J. Stevenson, W. B. Lacy, J. M. Harris, and H. S. White, *J. Am. Chem. Soc.* 119, 6596 (1997).

81. D. W. Hatchett, R. H. Uibel, K. J. Stevenson, J. M. Harris, and H. S. White, *J. Am. Chem. Soc.* 120, 1062 (1998).

82. N. Mohtat, M. Byloos, M. Soucy, S. Morin, and M. Morin, *J. Electroanal. Chem.* 484, 120 (2000).

83. O. Azzaroni, M. E. Vela, G. Andreasen, P. Carro, and R. C. Salvarezza, *J. Phys. Chem. B* 106, 12267 (2002).

84. H. Ron, H. Cohen, S. Matlis, M. Rappaport, and I. Rubinstein, *J. Phys. Chem. B.* 102, 9861 (1998).

85. J. A. M. Sondag-Huethorst, and L. G. J. Fokkink, *Langmuir* 11, 4823 (1995).

86. E. D. Eliadis, R. G. Nuzzo, A. A. Gewirth, and R. C. Alkire, *J. Electrochem. Soc.* 144, 96 (1997).

87. S. E. Gilbert, O. Cavalleri, and K. Kern, *J. Phys. Chem.* 100, 12123 (1996).

88. E. Boubour and R. B. Lennox, *J. Phys. Chem. B* 104, 9004 (2000).

89. O. Cavalleri, S. E. Gilbert, and K. Kern, *Chem. Phys. Lett.* 269, 479 (1997).

90. O. Cavalleri, H. Kind, A. M. Bittner, and K. Kern, *Langmuir* 14, 7292 (1998).

*91.* M. Epple, A. M. Bittner, K. Kuhnke, K. Kern, W.-Q. Zheng, and A. Tadjeddine, *Langmuir* 18, 773 (2002).

*92.* K. Shimazu, T. Kawaguchi, and T. Isomura, *J. Am. Chem. Soc.* 124, 652 (2002).

*93.* L. Sun and R. M. Crooks, *J. Electrochem. Soc.* 138, L23 (1991).

*94.* J. Camarero, J. Ferrón, V. Cros, L. Gómez, A. L. Angel de Parga, J. M. Gallego, J. E. Prieto, J. J. de Miguel, and R. Miranda, *Phys. Rev. Lett.* 81, 850 (1998).

*95.* H. Hagenström, M. A. Schneweiss, and D. M. Kolb, *Langmuir* 15, 7802 (1999).

*96.* O. Cavalleri, A. M. Bittner, H. Kind, K. Kern, and T. Greber, *Z. Phys. Chem.* 208, 107 (1999).

*97.* H. Hagenström, M. J. Esplandiú, and D. M. Kolb, *Langmuir* 17, 839 (2001).

*98.* M. J. Esplandiú and H. Hagenström, *Solid State Ionics* 150, 39 (2002).

*99.* D. Oyamatsu, S. Kubawata, and H. Yoneyama, *J. Electroanal. Chem.* 473, 59 (1999).

*100.* D. Oyamatsu, M. Nishizawa, S. Kubawata, and H. Yoneyama, *Langmuir* 14, 3298 (1998).

*101.* M. Nishizawa, T. Sunagawa, and H. Yoneyama, *Langmuir* 13, 5215 (1997).

*102.* C. M. Whelan, M. R. Smyth, and C. J. Barnes, *J. Electroanal. Chem.* 441, 109 (1998).

*103.* H. Hagenström, M. A. Schneweiss, and D. M. Kolb, *Electrochim. Acta* 45, 1141 (1999).

*104.* C. M. Whelan, M. R. Smyth, and C. R. Barnes, *Langmuir* 15, 116 (1999).

*105.* M. A. Scheneweiss and D. M. Kolb, *Phys. Stat. Sol. (A)* 173, 51 (1999).

*106.* X. G. Zhang, X. H. Li, and H. L. Li, *J. Colloid. Interface. Sci.* 234, 68 (2001).

*107.* M. J. Tarlov, D. R. F. Burguess, and G. Guillen, *J. Am. Chem. Soc.* 115, 5305 (1993).

*108.* G. Gillen, J. Bennett, M. J. Tarlov, and D. R. F. Burguess, *Anal. Chem.* 66, 2170 (1994).

*109.* J. Huang and J. C. Hemminger, *J. Am. Chem. Soc.* 115, 3342 (1993).

*110.* Y. Xia, E. Kim, M. Mrksich, and G. M. Whitesides, *Chem. Mater.* 8, 601 (1996).

*111.* A. Kumar, H. A. Biebuyck, and G. M. Whitesides, *Langmuir* 10, 1498 (1994).

*112.* Y. Xia, X.-M. Zhao, and G. M. Whitesides, *Microelectron. Eng.* 32, 255 (1996).

*113.* R. D. Piner, J. Zhu, F. Xu, S. Hong, and C. A. Mirkin, *Science* 283, 661 (1999).

*114.* S. Hong, J. Zhu, and C. A. Mirkin, *Science* 286, 523 (1999).

*115.* S. Hong and C. A. Mirkin, *Science* 288, 1808 (2000).

*116.* C. S. Whelan, M. J. Lercel, H. G. Craighead, K. Seshadri, and D. L. Allara, *Appl. Phys. Lett.* 69, 4245 (1996).

*117.* G. Y. Liu, S. Xu, and Y. Qian, *Acc. Chem. Res.* 33, 457 (2000).

*118.* J. K. Schoer and R. M. Crooks, *Langmuir* 13, 2323 (1997).

*119.* D. A. Hutt and G. J. Leggett, *J. Phys. Chem.* 100, 6657 (1996).

*120.* T. P. Moffatt and H. Yang, 142, L220 (1995).

*121.* Y. Xia and G. M. Whitesides, *J. Am. Chem. Soc.* 117, 3274 (1995).

*122.* J. A. M. Sondag-Huethorst, H. R. J. van Helleputte, and L. G. J. Fokkink, *Appl. Phys. Lett.* 63, 285 (1994).

*123.* C. Binns, *Surf. Sci. Rep.* 44, 1 (2001).

*124.* O. Azzaroni, P. L. Schilardi, and R. C. Salvarezza, *Nano Lett.* 1, 291 (2001).

*125.* A. Nobuyoshi, K. Toshio, M. Katsuyuki, K. Oku, and H. Akihiko, JP Patent JP10321621, 1998; T. P. Howard, US Patent US6171712, 2001.

*126.* R. C. Salvarezza and A. J. Arvia, in "Electrochemical Nanotechnology: *In-Situ* Local Techniques at Electrochemical Interfaces," (W. J. Lorenz and W. Plieth, Eds.) p. 57. Wiley-VCH, Weinheim, 1998.

*127.* S. Méndez, G. Andreasen, P. L. Schilardi, M. Figueroa, L. Vázquez, R. C. Salvarezza, and A. J. Arvia, *Langmuir* 14, 2515 (1998).

*128.* P. L. Schilardi, O. Azzaroni, and R. C. Salvarezza, *Phys. Rev. B* 62, 13098 (2000).

*129.* G. Capozzi and G. Modena, in "The Chemistry of the Thiol Group" (S. Patai, Ed.), John Wiley & Sons, New York, 1974.

*130.* O. Azzaroni, P. L. Schilardi, and R. C. Salvarezza, *Appl. Phys. Lett.* 80, 1061 (2002).

*131.* P. L. Schilardi, O. Azzaroni, and R. C. Salvarezza, *Langmuir* 17, 2748 (2001).

*132.* J. Feng, B. Cui, Y. Zhan, and S. Y. Chou, *Electrochem. Comm.* 4, 102 (2002).

*133.* G. Andreasen, P. L. Schilardi, O. Azzaroni, and R. C. Salvarezza, *Langmuir* 18, 10430 (2002).

*134.* M. Cavallini, M. Murgia, and F. Biscarini, *Nano Lett.* 1, 193, (2001).

*135.* E. Delamarche, H. Schmid, H. A. Biebuyck, and B. Michel, *Adv. Mater.* 9, 741 (1997).

*136.* Z. Huang, P.-C. Wang, A. G. MacDiarmid, Y. Xia, and G. M. Whitesides, *Langmuir* 13, 6480 (1997).

*137.* T. Kondo, M. Yanagida, K. Shimazu, and K. Uosaki, *Langmuir* 14, 5656 (1998).

*138.* P. L. Schilardi, S. Méndez, R. C. Salvarezza, and A. J. Arvia, *Langmuir* 14, 4308 (1998).

*139.* L. Vázquez, R. C. Salvarezza, and A. J. Arvia, *Phys. Rev. Lett.* 79, 709 (1997).

*140.* O. Azzaroni, M. Cipollone, M. E. Vela, and R. C. Salvarezza, *Langmuir* 17, 1483 (2001).

*141.* O. Azzaroni, M. E. Vela, H. Martin, A. Hernandez Creus, R. C. Salvarezza, *Langmuir* 17, 6647 (2001).

ENN
*Encyclopedia of Nanoscience and Nanotechnology*
www.aspbs.com/enn

# Monolayer-Based Scanning Probe Lithography

Ryan R. Fuierer, Christopher B. Gorman

*North Carolina State University, Raleigh, North Carolina, USA*

**CONTENTS**

## 1. INTRODUCTION

The requirement to fabricate at the meso- and nanometer ($10^{-7}$ to $10^{-9}$ m) length scales will be essential for the future miniaturization of electronic and sensing devices. With that, the spatial arrangement of functional materials on solid surfaces with artificial control has attracted attention for the construction of novel surface bound chemical systems. Potential applications range from fundamental scientific research in micro- and nanoscale surface chemistry, to practical applications, such as chemical sensors and electronic or optical devices.

One very promising candidate material for the further miniaturization of electronics is the use of molecules that self-assemble. Molecular self-assembly is a chemical process in which amphiphilic precursor molecules chemisorb to surfaces, producing films of monomolecular thickness, that are chemically bonded to those substrates. These materials are often organic in nature and are frequently termed soft materials.

### 1.1. Self-Assembled Monolayers

Self-assembled monolayers (SAMs) have attracted considerable attention as patterning materials because of their spontaneous adsorption on certain substrates, their excellent uniformity in molecular order, and their resistivity to various types of chemical etching. Self-assembling monomers can be considered bifunctional molecules that can bond to the substrate at one end (head) and an organic group (R) that imparts the desired functionality to the modified surface at the other end (tail) [1]. The surface reactions are thermodynamically driven to completion, lowering the free energy of the system when chemisorbed to the surface. Organothiol molecules (R-SH) self-assemble on coinage metal surfaces (Au, Ag, Cu, Pt) through the formation of chemisorbed bonds [2, 3]. Any surface that has exposed hydroxyl (—OH) groups can react with organosilanes (R—$SiX_3$, X = Cl, $OCH_3$, $OCH_2CH_3$) to form siloxane (Si—O—Si substrate) linkages. The amphiphilic nature of these self-assembling molecules has allowed them to be chemically tailored to perform specific functions on a variety of substrates.

Self-assembled monolayers are excellent candidates for preparing template architectures at the molecular scale or as resist layers; however, spatial resolution and rational placement at the molecular scale is often considered very challenging. Speculation exists that photolithography will not be able to create patterned features cheaply at the nanoscale (1 to 100 nm). Electron beam lithography is an alternative but does not permit definition of chemistry without subsequent processing steps. Microcontact printing [4] offers a promising alternative to parallel lithography of self-assembling materials; however, it has only begun to reach sub-50-nm length scales at the present day. Probe microscopy techniques appear particularly well suited for surface nanopatterning.

### 1.2. Scanning Probe Microscopy

Scanning probe microscopy (SPM) is a family of surface-based interface techniques for investigating and manipulating these materials (SAMs) at the molecular and nanometer scales. SPM techniques have emerged as a premier surface analysis methodology, and have been employed in many surface and materials modification studies. Surface science on the submicro-to-atomic scale has certainly been driven forward because of these tools. It was not long after

their initial development that microscope probe tips were used for lithographic applications on the atomic scale [5], which was one of the earliest demonstrations of scanning probe lithography (SPL).

The patriarch of the SPM family is the scanning tunneling microscope (STM) [6] (Fig. 1A). A sharp metal probe tip is attached to a computer-controlled piezo-positioning element, which allows the tip to be moved independently in three dimensions with atomic scale precision. The metal probe, typically made of tungsten or platinum/iridium alloy, is brought within several angstroms (Å, $1 \times 10^{-10}$ m) of a conducting or semiconducting sample. As a voltage is applied between the tip and sample, a small electrical current is measured between the two electrodes (tip and substrate). The current flow is a result of electrons tunneling through the tip–substrate gap, called the tunneling current. The feedback loop adjusts the height of the tip (in z-direction) by monitoring the tunneling current. If the measured current is smaller than a user set reference current, the tip is moved closer to the sample, to reestablish the set point current. Likewise, if the measured tunneling current is too large, the tip is moved away from the sample. To generate an image of the surface, the tip is scanned in a raster pattern across the sample in the x- and y-dimensions, systematically recording how much the tip was moved (in the z-direction) to maintain a constant set point current value along the scan pattern. A three-dimensional surface relief map is generated representing a convolution of the topography and electronic properties of the surface. Background material can be found in [7–13].



**Figure 1.** Schematics showing the operation of (A) the scanning tunneling microscope (STM), (B) the atomic force microscope (AFM).

Shortly after the invention of the STM, the atomic force microscope (AFM) was conceived [14]. In this new class of SPMs, the surface morphology is tracked by monitoring the forces imparted on a probe tip attached at the end of a flexible cantilever, rather than a current detection motif. Height information is deduced from the deflection of the cantilever as the tip scans the sample surface in a raster pattern (parallel to the length of the beam), while maintaining contact with the surface (Fig. 1B). The deflection of the cantilever is monitored by reflecting a laser beam off the back side of the cantilever, to a positron sensitive diode (PSD), which monitors the laser beam's coordinates to produce a three-dimensional relief of the surface morphology. Because of this optical detection scheme, cantilever-force-based SPM techniques are commonly referred to as scanning force microscopy (SFM).

There are two basic AFM modes that make SFM techniques so versatile for imaging and manipulation purposes: contact mode, and noncontact mode. Operation in contact mode involves tracking surface morphology by rastering the tip across the sample in its scan pattern, analogous to how a record player needle is dragged along its grooved track. A noncontact imaging mode is termed tapping mode AFM (TMAFM™), in which the cantilever is oscillated close to its resonant frequency, intermittently "tapping" the surface as it scans the surface. Differences in surface morphology cause damping in these oscillations detected by the PSD to generate a topographical image. This mode is very good at imaging softer surfaces that may normally be damaged by the forces applied to a cantilever in contact mode imaging. This mode was a common technique reported in the papers described within to survey the chemical pattern structures generated, or subsequent chemical binding event.

Many of the SPLs described within employed other popular SFM techniques and image the lithography generated. Lateral force microscopy (LFM) is a useful contact mode technique that can detect the friction (stickiness) between multiple chemical functionalities or components on a surface [15]. In this mode, the torsion that is imparted on the tip when scanning perpendicularly to the length of the cantilever beam is monitored by the left and right PSD segments, concomitantly monitoring the z-deflection in the cantilever, to give a morphological representation of a surface, viewed in two separate data images (friction and topography). SFM can also detect currents, or apply bias, when equipped with a potentiostat and conductive cantilever. The commonly termed "conducting AFM" (cAFM) measures surface morphology with conventional AFM optical detection, with the added ability to measure current similar to the two-electrode configuration used in STM, which makes this technique well suited for current–voltage measurements.

In all the AFM techniques briefly described above, there are cantilever force ranges with specific properties for different modes that are commercially available for optimal imaging results. It is also noted that STM was often employed in the fabrication for smaller studies ($<3$–5 $\mu$m), while AFM was suited to do work on larger scales; however, AFM had been used for some of the smallest lithography described within. Background SFM material can be found in [8–10, 13, 16, 17].
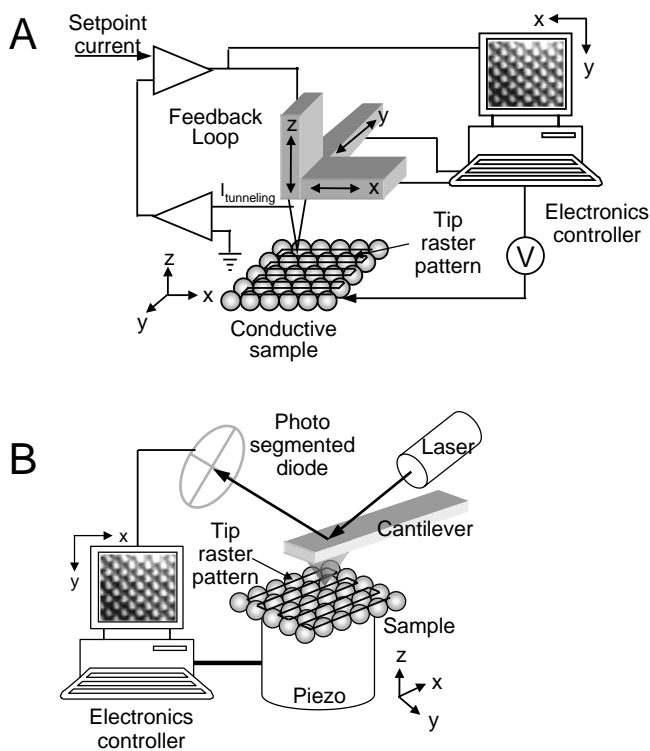
The SPL techniques described in this work have been used to fabricate chemical patterns in SAMs by mechanical or electrical approaches [12]. Mechanical lithography is the result of the probe tip being used as a contact tool that can push or scrape, and in some cases, use its material properties to induce chemical catalysis with a chemically functionalized surface. Electrical lithography involves the application of an electrical field to desorb the SAM, or induce a localized electrochemical event to an ultrathin film, changing its properties in some fashion. Under these two physical approaches, there are three general lithography pattern categories. *Positive* SPL is when the self-assembly ink is directly written to the substrate, as opposed to *negative* lithography where the first step is electrical or mechanical removal of an existing ultrathin film. A third type of SPL on SAMs is that in which the chemical functional group at the terminus of the SAM is locally modified with tip allowing subsequent multilayer construction of various self-assembly materials, while maintaining the structural integrity of the underlying and surrounding SAM.

The intent of this chapter is to report on the significant advancements that have occurred in SPL using SAM materials since the first demonstrations in the early 1990s. Working with soft materials at the molecular scale with a variety of SPMs has seen significant refinement in approach and technique over the past ten years. Many variations of SPL techniques exist. The basic configurations of these techniques will be illustrated and the novelty of the subsequent lithographic architectures fabricated will be highlighted with appropriate referenced material.

# 2. NEGATIVE PATTERN SCANNING PROBE LITHOGRAPHY (SPL)

## 2.1. STM-Based Negative SPL

There have been many reports of negative-based SPL utilizing STM and SFM techniques. Early work described degrading organothiol resists by repeated scanning in the same area, or through "voltage excursions" with STM bias and set point current parameters [18]. Other groups reported organosilane resist layers negatively patterned with STM, then performed *ex-situ* processes on the substrate, such as metallization or wet chemical etching, to prepare nano- and mesostructures within the patterned area surrounded by initial SAM resist.

### 2.1.1. Ambient Conditions Applications

Crooks and co-workers contributed some seminal work in this emerging field, observing that by applying elevated voltages to the tip, the SAM thiolates could be intentionally desorbed from Au⟨111⟩ surfaces with control, creating negative patterns within resist layers [19, 20]. The nature of this desorption was suggested to be electrochemical because of dependence of trace amounts of water present to facilitate the displacement of organothiols from the SAM matrix. Relative humidity (RH) studies revealed that desorption did not occur in dry environments (RH $\sim$ 6%) at the tip–substrate interface [21].

Similar work with organosilanes on Si⟨100⟩ substrates was demonstrated, in which negative patterns in tetramethylsilane resists were fabricated to serve as etching windows for the pattern transfer to the substrate below with wet chemical etchants (aqueous $NH_4F/H_2O_2$). Silicon features with ultimate resolutions of 80 nm were fabricated [22]. The authors noted that the etching proceeded isotropically (i.e., both laterally and vertically), which resulted in etched grooves widening as etch time increased, possibly decreasing the resolution of the initial SPL pattern. Similar experiments were performed in a later study using a conducting AFM (cAFM), in which patterning dependence on relative humidity, applied bias, and lithographic scan rate was investigated [23]. Using the same approach, Sugimura and co-workers also demonstrated the *ex-situ* replacement of amino terminated silane SAMs that were subsequently exposed to aldehyde (RCHO) functionalized latex microspheres ($\sim$30 nm) tagged with fluorescent markers [24]. Optical fluorescent microscopy images and TMAFM confirmed the immobilization of the spheres. The evaporation of Au films confined to the patterned regions was demonstrated in a later study [25].

### 2.1.2. High Vacuum Applications

Marrian, Calvert, Perkins and co-workers patterned organosilane resists on Si substrates with STM in ultrahigh vacuum (UHV was defined as $10^{-7}$–$10^{-8}$ torr) by using an STM tip as a low-energy electron beam lithography technique. The contention was that the STM was an attractive alternative to conventional electron beam lithography because it could be used as a localized source of low-energy ($<50$ eV) electrons, comparable to resist transformation threshold energies [26]. Amino-terminated SAMs were used as patterning resists because they did not promote electroless deposition of nickel after local exposure to the electrons from the STM tip. The lithographic effort afforded Ni structures as small as $\sim$30 nm wide after metallization [27]. Other UHV STM work has reported patterning negative patterns in alkylthiolate SAMs on gold substrates [28, 29]. The UHV patterning environments has the advantage of not inducing electrical breakdown of the SAM resists at low voltages (1–5 V), and are less likely to have surface contaminants found in ambient SPL systems.

### 2.1.3. SPL with Subsequent In-Situ Thiolate Replacement

Inspired by the demonstrations from Crooks (thiolate replacement into patterned areas on gold substrates, described in Section 2.1.1), Gorman et al. developed a low-current STM-based "replacement lithography" technique in which alkylthiolate SAMs were selectively removed from Au⟨111⟩ surfaces (similar to the Crooks method), but performed the lithography in an inert fluid [dodecane ($C_{12}H_{26}$), or mesitylene ($C_6H_3(CH_3)_3$)]. The low dielectric solvent chosen effectively insulated the tip from electron leak current into the fluid, and also solvated a second replacement organothiol molecule to chemisorb in the patterned area. The technique is illustrated in Figure 2. Figure 2A depicts the STM tip identifying a SAM region free of terraces or defects for patterning, just as one would avoid a torn area when writing on a piece of paper. Elevating the tip bias
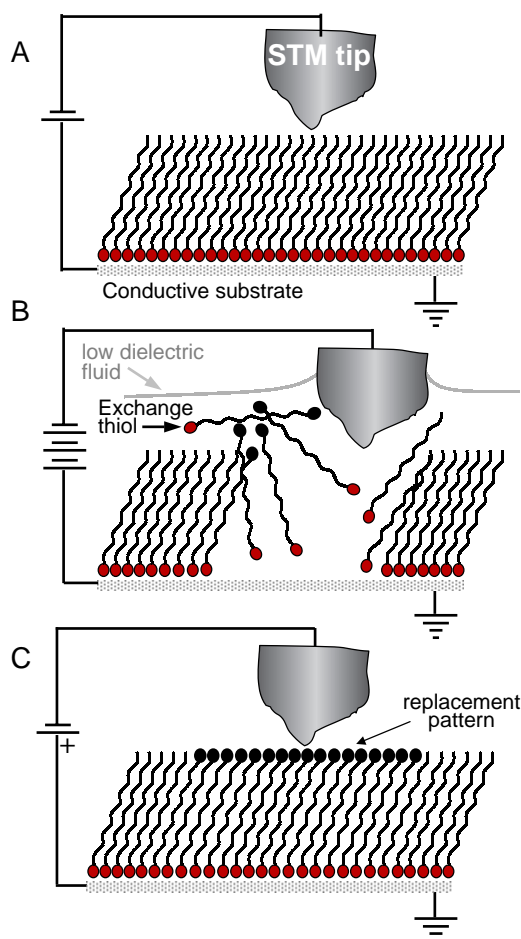
**Figure 2.** Schematic illustrating the process of STM-based negative lithography. (A) SAM is imaged at nonperturbative bias and setpoint current. (B) Upon parameter change, SAM thiolates desorbed in proximity of tip, resulting in removal of SAM resist. (C) Optional/further replacement of different thiol in solution to substrate.

(to ~3 V) removed the SAM thiolates in proximity of the tip (Fig. 2B), which allowed chemisorption of replacement thiol molecules in solution to the patterned areas. In Figure 2C, the STM parameters were returned to imaging conditions to ascertain the nanostructure fabricated. From this platform, demonstrations such as reverse STM image contrast of differing length alkylthiols in fluids with multiple thiolate ink patterning [30], and current–voltage ($I–V$) measurements of electroactive thiols displaying negative differential resistance were reported [31]. Novel SPL generated architectures such as fabrication of mesoscale chemical gradients [32] and host–guest recognition exchange through hydrogen bonded mediated assemblies were also demonstrated [33]. Figure 3 shows a 400 × 400 nm scan area image of a quarterfoil pattern written with ferrocenylundecanethiolate in a dodecanethiolate SAM (C12S-SAM), with line width resolution ca. 10 nm.

Similar to the "replacement lithography" technique developed by Gorman, Zhao, and Uosaki employed a cAFM tip to selectively remove octadecanethiolate (C18S-) SAMs on Au⟨111⟩ with elevated substrate bias excursions under an inert, low dielectric solvent (toluene, $C_6CH_5CH_3$).
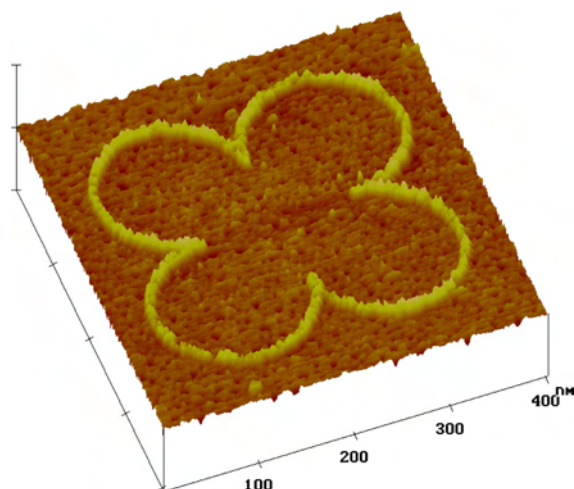


**Figure 3.** Example of quarterfoil pattern written with ferrocenylundecanethiolate in a C12S-SAM on Au⟨111⟩ fabricated with STM-based replacement lithography technique. (Image parameters: 400 nm × 400 nm scan area, 1.2 V, 8 pA, 1 Hz, z-scale: 3 nm.)

Investigation of patterning dependence on the applied bias, applied force, and relative humidity was the focus [34]. A more recent report described a series of shorter chain alkylthiolates (hexanethiolate, C6S-; octanethiolate, C8S-; decanethiolate, C10S-) replaced into C18S-SAMs using the cAFM technique described, and monitored by topographic and current cAFM images, as well as $I–V$ measurements of the replaced thiols within the pattern [35].

## 2.2. AFM-based Negative SPL Applications

A mechanical approach to negative SPL developed by Liu and co-workers used an AFM cantilever to scrape/shave SAM thiolates from an Au⟨111⟩ surface, done in a fluid medium solvating a differing thiol molecule, which could effectively adsorb onto the freshly exposed surface [36–38]. The technique was termed "nanoshaving" when only removing the SAM resist, or "nanografting" when a replacement thiol is exchanged to the patterned area, and is illustrated in Figure 4. Figure 4A depicts an AFM tip in contact mode under low nonperturbative imaging forces (0.3–0.5 nN) to locate an area suitable for patterning. An increased force imparted upon the cantilever (slightly larger than the threshold force needed to displace SAM thiolates from the surface) desorbed the SAM from the surface mechanically (Fig. 4B). Performing the lithography in a fluid medium (2-butanol) allowed solvation of a replacement thiol, which adsorbed to the freshly exposed gold surface, creating a SAM structure of a different organothiolate. Once the lithographic operation was complete, the applied force on the tip was reduced to imaging conditions to ascertain the nanostructure (Fig. 4C). The line width and spatial resolution between lines of alkylthiols is reported to be ~2 nm with this technique; however, it is ultimately dependent on tip shape and applied force. A series of AFM topography images (Fig. 5) demonstrated the systematic ability to change nanostructures written in a decanethiolate (C10S-) SAM *in-situ* using multiple-thiol inks. Figure 5A shows the unmodified C10S-SAM on Au(111) evaporated onto a mica substrate.
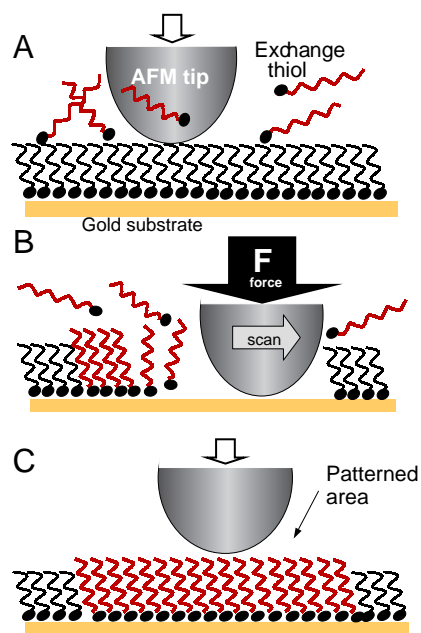
**Figure 4.** Schematic illustrating the process of "nanografting." (A) Identify area for SAM patterning under (low) force imaging, in replacement thiol in 2-butanol solution. (B) Under specific increased applied force, SAM mechanically desorbs in proximity of the AFM tip, with replacement exchange thiolate adsorbing to freshly exposed gold. (C) Ascertain pattern with contact AFM under lower imaging force.

The authors noted the slightly raised structure in the center of the image was an island of gold atoms (2.4 Å high) on the atomically flat substrate, which was used as a spatial reference in the images. Figure 5B shows two 10 nm × 50 nm parallel lines spaced 30 nm apart, nanografted with C18SH
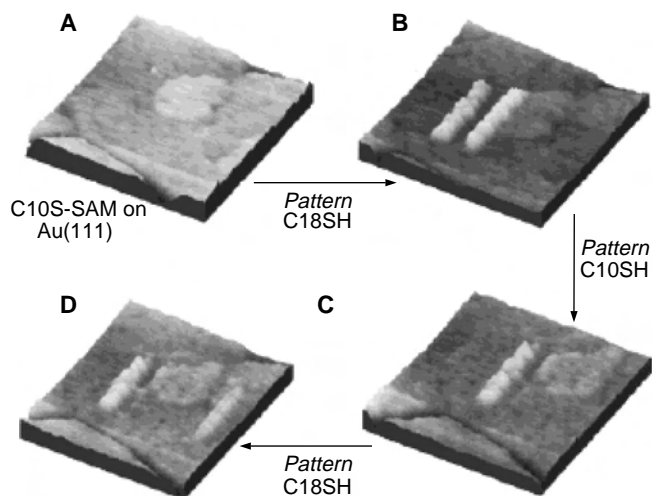


**Figure 5.** Nanografting to create multiple chemical patterns in a SAM. (A) A blank C10S-SAM on Au⟨111⟩ to which, (B) two 10 × 50 nm lines patterned 30 nm apart with ODT. (C) The line on right was erased by rewriting over structure under C10SH solution. (D) New line written 65 nm from first line with C18S-. Reprinted with permission from [36], G. Y. Liu et al., *Acc. Chem. Res.* 33, 457 (2000). © 2000, American Chemical Society.

in solution. The line on the right is "erased" by nanografting a 10 nm × 50 nm line over the original in the presence of C10SH solution, seen in Figure 5C. After replacing the solution with C18SH again, a new 10 nm × 50 nm line is fabricated, increasing the interline spacing to 65 nm, Figure 5D. It has been reported that the nanografted SAMs were highly ordered within the patterns. The kinetics of adsorption of the replacement thiolates into the confined regions between the matrix SAM and tip was suggested to occur more quickly and was more enthalpically favorable than SAMs formed on an unconfined substrate [39].

Patterning applications of biological entities with the nanografting technique has been reported at near physiological conditions (pH ∼ 7). Protein attachment to artificially SPL-engineered surface patterns was first reported by Liu and co-workers, who demonstrated that a carboxylic acid terminated pattern nanografted into an methyl terminated SAM matrix could electrostatically bind the enzyme lysozyme through the amino (—NH$_2$) groups in the protein [40]. In the same report, immunoglobin G (IgG) was covalently bonded to an aldehyde (RCHO) terminated thiol pattern through imine (R—CH=NR′) linkages. In both examples described above, it was reported that subsequent aqueous washings after exposure to the biological target of interest yielded little nonspecific binding to unpatterned methyl terminated regions of the SAM matrix. Further work demonstrated the specific antigen binding to the complementary patterned antibody IgG [41]. Liu and co-workers later demonstrated sub-10 nm patterns consisting of single stranded DNA oligonucleotide-tethered thiolates inserted into alkylthiolate SAMs [42].

Porter and co-workers used multiple negative SPL techniques to bind various proteins to submicrometer surface patterns, and addressed issues related to nonspecific binding using multiple SAM matrices on gold [43]. The first experiment described binding rabbit IgG to a carboxylate (—COOH) terminated pattern that was nanografted into a methyl terminated octanethiolate SAM matrix under buffer solution. The binding event was supported by AFM measured topographic height differences (4–6 nm) between IgG protein and the SAM matrix. A second binding event was performed to the same structure with the complementary anti rabbit IgG exposure to the existing IgG structure, supported by an even larger height difference (11–12 nm) between SAM matrix and structure. Ethylene-glycol terminated thiolate SAM matrices were also investigated as patterning substrates because of their inherent resistance to nonspecific protein binding, which can interfere with the topographic detection of the immunoassay with AFM.

## 3. POSITIVE PATTERN SPL—"DIP-PEN NANOLITHOGRAPHY"

The most prolific development of positive pattern SPL fabrication has been with a technique termed "dip-pen nanolithography" (DPN) [44], in which an AFM tip acts like a pen to draw patterns with various chemical inks of monomolecular thickness to a variety of solid substrates. Illustrated in Figure 6A, a contact mode AFM tip is coated with a material that can self-assemble on a surface, which
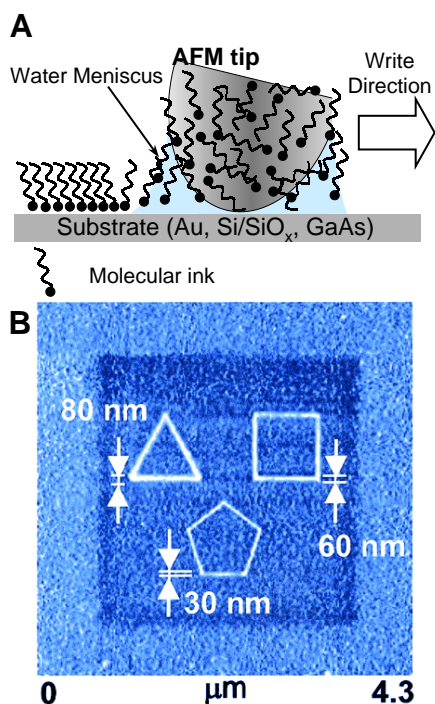
**Figure 6.** "Dip-pen nanolithography." (A) An AFM tip is coated with a molecular "ink" (organo- thiol or silane, metal salt precursor, conducting polymer). When tip is in contact with substrate, a water meniscus formed through capillary forces from inherent atmosphere moisture facilitates ink transport from tip to surface, which promptly self-assemble. (B) LFM image of multiple ink "overwriting" in which MHA (bright polygon shapes) was backfilled with ODT (dark) on a gold substrate. (Image parameters: ~0.1 nN, 5 Hz, RH: 35%.) Reprinted with permission from [48], S. Hong et al., *Science* 286, 523 (1999). © 1999, American Association for the Advancement of Science.

was transported to the surface, facilitated by the inherent water meniscus formed at the interface under atmospheric moisture. A chemical or electrochemical event subsequently immobilized the material on the substrate in a region confined to the dimensions of the meniscus's path. By choosing the appropriate chemistry that is compatible within the water meniscus in DPN experiments, many different organic and inorganic structures could be conceived.

An advantage of DPN was the pattern could be written, and imaged (read) *in-situ* using the same tip in LFM mode. Writing the molecular-based pattern was done at slow scan rates (<1 Hz) to facilitate adequate diffusion time for the ink species to arrive at the substrate. The structure could be imaged immediately after the lithographic operation with the same tip at higher (three- to fourfold) scan rates, without transferring more ink, presumably because the tip was moving at a fast enough rate that could not sustain an adequate meniscus.

Two critical parameters for successful DPN patterning were the tip–substrate contact time and the relative humidity, which limited the area of deposition through size/volume of the meniscus. Typically, increased tip substrate contact times resulted in larger chemical pattern features. Large RH created larger pattern sizes, presumably due to the size of the meniscus formed, while low moisture

content (a RH < 20%) did not form any patterns. The precise "ink" transport mechanism of meniscus and effect of RH have been the subject of some controversy [45–47].

One novel DPN demonstration was the ability to "overwrite" a nanostructure by rastering a tip modified with a different alkylthiol ink over the initial pattern, to effectively backfill around the first ink pattern with no apparent exchange between inks (detectable with LFM) [48]. Figure 6B shows an LFM image of three DPN-generated geometric structures written with mercaptohexadecanethiol (MHA, $HS(CH_2)_{15}COOH$, carboxylate terminated alkylthiol), that showed the lithographic scan rate dependency of DPN on the line resolution (triangle, 30 s writing per side, 80 nm line width; square, 20 s write per side, 60 nm line width; pentagon, 8 s write per side, 30 nm line width; RH: ~35%). The polygons were "overwritten" by a tip inked with ODT raster scanned over an area encompassing the three structures. The final pattern (imaged with an unmodified tip to prevent further thiol exchange) showed good LFM contrast between the MHA patterned polygons (light in the LFM image, indicating high tip friction) and the octadecanethiol (ODT, $H_3C(CH_2)_{17}SH$) backfilled area (dark indicating low tip friction). The ability to passivate the surface between functional patterns with "overwriting" could prove useful in the development of array architectures.

Advancements in DPN have included the ability to pattern lines or dots with multiple inks with high registry (5 nm spatial resolution) [44, 48], multiple tip arrays to fabricate multiple pattern single ink architectures *or* multiple ink single pattern architectures [49], and patterning long tail alkylthiols as resists to fabricate Si structures through wet chemical etchant protocols [50]. Organosilanes on semiconductor surfaces [51], metal oxides on semiconductors [52], metals on Si⟨100⟩ by utilizing a chemical reaction between substrate and metal salts on the tip [53] have all been recently reported.

Other groups have modified the dip-pen AFM lithography technique to directly fabricate metal nanostructures on silicon-based surfaces using cAFM. The methodology, termed electrochemical-DPN (EDPN) [54], inked the tip with a metal salt, and used the meniscus at the tip–substrate interface as an electrochemical "reaction vessel." By applying an appropriate bias to the substrate, the cationic metal ions dissolved within the meniscus were reduced at the substrate in the proximity of the meniscus, creating metallic structures. By coating a conductive AFM tip with a monomer reactant (3,4-ethylenedioxythiophene, EDOT, which was soluble in the water meniscus), a structure consisting of the analogous conducting polymer (poly-EDOT) was immobilized on the substrate by applying cathodic voltages between the tip and substrate [55].

DPN has been employed for patterning templates for the organization of modified metal nanoparticles or oligonucleotide chemical inks in predefined architectures. Typical approaches have involved the fabrication of dot arrays with some 'sticky' chemical ink, followed by the passivation of the nonpatterned surface with a self-assembling material that prevented nonspecific binding of the target assembly. In this way, nanoparticle assemblies could be fabricated by incubation in functionalized nanoparticle solution that

resulted in chemical or physical immobilization of the particles exclusively on the patterned areas of interest [56–59]. In a similar architecture patterning application, biological immunoassays were fabricated that demonstrated the exclusive binding between antibody and complementary antigen [60], or patterning of single stranded oligonucleotides on gold and SiO$_x$ substrates with subsequent binding of the complementary single stranded oligonucleotide [61]. Patterning demonstrations like this could prove useful in developing immunoassays with target pattern features well below 100 nm.

# 4. SPL ON SELF-ASSEMBLED MONOLAYERS (SAMs) VIA MODIFICATION OF TERMINAL CHEMICAL FUNCTIONALITY

This type of SPL involves locally inducing some kind of chemical reaction at the terminal functional groups of well-ordered SAMs, while maintaining the structural integrity of the SAM below. The induced chemical modification to the SAM is performed through a catalytic or nanoelectrochemical event provoked by an AFM tip.

## 4.1. Mechanical SAM Modification

An early example of an AFM-based chemical modification SPL report from Schultz and co-workers demonstrated that an azide terminated monolayer (N=N=N—R—Si—O—) on glass could be locally hydrogenated to amino groups (-NH$_2$) using a Pt-coated AFM tip as a catalytic source [62]. The reaction occurred as the tip was dragged along the surface, creating a pattern terminated with amino groups. By exploiting the attractive nature between aldehydes (RCHO) and amino groups, aldehyde functionalized latex microspheres were immobilized in the patterned areas of the SAM, with little nonspecific binding to nonpatterned areas reported.

## 4.2. Electrical SAM Modification

Another promising AFM-based SPL technique was developed by Sagiv and co-workers, termed "constructive nanolithography" [63]. A schematic illustration is seen in Figure 7. Figure 7A depicts a highly ordered, long tail silane SAM (terminated with methyl (—CH$_3$) or vinyl (—CH=CH$_2$)) prepared on $p$-type Si⟨100⟩ The technique utilized a conducting AFM tip to selectively induce localized nanoscale electrochemical modifications to the functional groups (Fig. 7B). Subsequent *in-situ* chemistry allowed for construction of organic multilayer architectures (or fabrication of inorganic nanostructures) that were immediately imaged to ascertain the patterned structure (Fig. 7C). The novelty of the experiments was the fabrication of chemical patterns at the sub-10-nm length scale, without damaging the underlying or surrounding SAM. The locally modified surfaces have been routinely demonstrated to induce site selective self-assembly of a number of different organic, metal, and semiconducting materials.
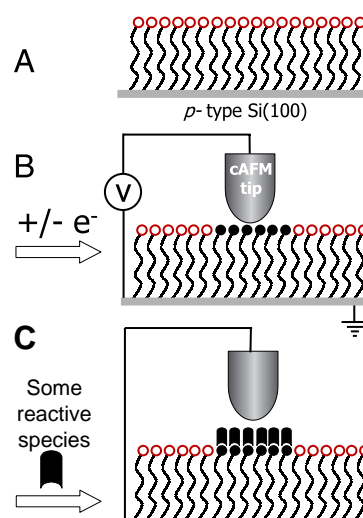


**Figure 7.** "Constructive lithography." (A) Well-ordered organosilane monolayer (functionalized with terminal —CH$_3$ or —CH=CH$_2$ groups) on $p$-type Si⟨100⟩ served as inert background. (B) cAFM induced localized electrochemical event at terminus of SAM, modifying functionality, while fully preserving SAM below. (C) Subsequent site selective self-assembly with a variety of organic, metal, or semiconducting materials.

An early implementation of constructive nanolithography can be seen in Figure 8A and B. Figure 8A shows an image set of a square pattern immediately after the local tip oxidation of nonadecenyltrichlorosilane (NTS, H$_2$C=CH(CH$_2$)$_{17}$Si(OCl)$_3$), imaged with LFM. The topography (height, left) data showed no significant change in height; however, the friction data (right) suggested a different (higher friction) functionality in the patterned area relative to surrounding unmodified NTS SAM. This was
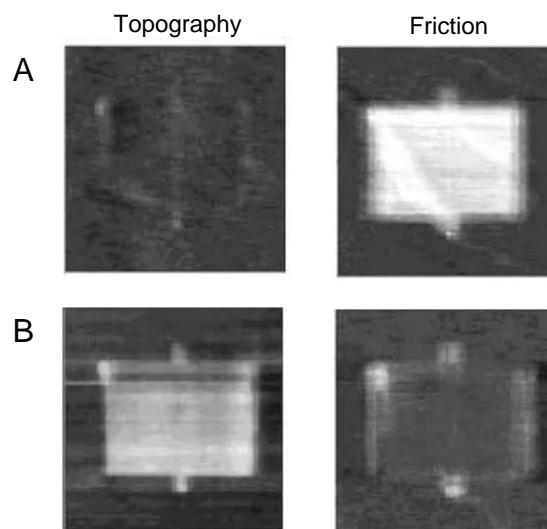


**Figure 8.** "Constructive nanolithography." (A) Topography (left) and friction (right) images after oxidation of NTS layer. (B) Same structure after fabrication of OTS bilayer. Topographical height in (B) between structure and surrounding SAM is ~2 nm. Panels A and B reprinted with permission from [63], R. Maoz et. al., *Adv. Mater.* 11, 55 (1999). © 1999, Wiley-VCH.

consistent with a hydrophilic patterned area surrounded by a hydrophobic SAM. Figure 8B shows the pattern immediately after the *in-situ* addition of octadecyltrichlorosilane (OTS), which reacts with the hydroxyl (—OH) groups of the oxidized NTS pattern area. Here, the topography data show an area of higher apparent height (~2 nm) relative to the surrounding SAM, consistent with expected height of the bilayer fabricated. The low contrast in the friction data of the patterned area and the surrounding SAM suggests each is composed of similar low-friction hydrophobic surfaces. This observation supported the conclusion that the patterned area contained methyl head groups, just as the SAM encompassing the pattern.

An advantage of this patterning technique is that once a reaction site template is created by the localized nanoelectrochemical event by the tip, many different chemical strategies with the reactive patterned sites could be employed, with the surrounding unpatterned SAM impermeable to *in-situ* wet chemical treatments. Localized tip-induced reduction of chemisorbed silver ions atop thiol terminated SAMs generated surface bound elemental silver nanoparticles at the tip inscribed sites [64]. Metal-organic hybrid architectures were realized following a hierarchical synthetic scheme [65] to fabricate an organic bilayer terminated with top thiol functionality, which (upon exposure) selectively immobilized triphenyl phosphine ligand-stabilized $Au_{55}$ nanoparticles through ligand exchange [66]. Gold nanoparticles were grown via wet chemical processes from CdS nanoparticles formed on top thiolated bilayers with a $Au^{(III)}$ salt ($HAuCl_4$) [67]. These latter two references demonstrated the ability to fabricate nanoscale "wires" connected to larger metallated areas that could potentially serve as contact pads to the macroscopic world.

## 5. CLOSING REMARKS

While physical lithography is adequate at micrometer scales, at nanometer scales, chemical lithography—that is, a lithographic process that defines the chemical identity of the regions upon the surface—is desirable. This is so because the lithographically defined features are approaching the length scale of the chemical functional groups that make them up. These examples illustrate that scanning probe lithography on a chemically well-defined substrate (e.g., a self-assembled monolayer) can be used to create nanometer-scale patterns defined by chemical functional groups. The ability to use SPL techniques in manufacturing processes remains to be seen. With the pace of engineering advancements that have occurred with SPL techniques, someday the development of high throughput parallel SPL techniques may yet occur [17, 49]. At a minimum, however, these tools offer a first glimpse of the patterning and interaction of molecular-scale features.

## GLOSSARY

**Atomic force microscopy (AFM)** A scanning probe microscopy technique that interprets surface morphology from monitoring the deflection of a probe tip attached to a flexible cantilever which is systematically scanned across a surface.

**Au $\langle 111 \rangle$** The specific crystal face of gold with Miller indices of $\langle 111 \rangle$; the close-packed orientation of the gold atoms at the surface is used as an atomically flat substrate in scanning probe microscopy.

**Cadmium sulfide (CdS)** A yellow-brown poisonous salt used especially in electronic parts, in photoelectric cells, and in medicine.

**Conducting atomic force microscopy (cAFM)** AFM technique that employs a conducting cantilever to measure current or apply bias, in addition to the force measurements that can be measured with conventional AFM cantilever deflection sensing.

**Decanethiol C10SH** Analogous to hexanethiol but with molecualr formula $CH_3(CH_2)_9SH$.

**Dodecanethiol C12SH** Analogous to hexanethiol but with molecular formula $CH_3(CH_2)_{11}SH$.

**Hexanethiol $CH_3(CH_2)_5SH$** (*abbreviated in text as* C6SH) Saturated linear hydrocarbon alkyl chain consisting of six consecutive carbons atoms, terminated with a sulfur headgroup, known to self-assemble on certain coinage metals.

**Lateral force microscopy (LFM)** SFM technique that detects surface chemical heterogeneities from monitoring the torsion imparted on an AFM tip by raster scanning perpendicular to the length of the cantilever.

**Mercaptohexadecanethiol (MHA)** The molecule $HS(CH_2)_{15}COOH$.

**Nonadecenyltrichlorosilane (NTS)** The molecule $H_2C=CH(CH_2)_{17}Si(OCl)_3$.

**Octadecanethiol (ODT)** The molecule $H_3C(CH_2)_{17}SH$.

**Octadecyltrichlorosilane (OTS)** The molecule $H_3C(CH_2)_{17}SiCl_3$.

**Relative humidity (RH)** A measure (in percent) of the amount of water moisture in an atmosphere.

**Scanning force microscopy (SFM)** Scanning probe microscopy techniques that rely on the detection of force imparted on a scanning tip by a surface.

**Scanning probe lithography (SPL)** The use of SPM to deliver, modify, or move molecular/atomic matter on a surface with high spatial resolution on the nanometer scale.

**Scanning probe microscopy (SPM)** Microscopy techniques that employ a sharp stylus probe to systematically scan a surface generating a three-dimensional relief of the surface morphology.

**Scanning tunneling microscopy (STM)** A microscope that makes use of the phenomenon of electron tunneling to map the positions of individual atoms in a surface or to move atoms around on a surface.

**Self-assembled monolayer (SAM)** Ultrathin organic film composed of amphiphilic molecules that spontaneously self-assemble at the surface of certain materials. These materials can be chemically tailored to incorporate a specific property for application in tribology, corrosion, electronics processing, and sensing applications.

**Si$\langle 100 \rangle$** The specific crystal face of silicon with Miller indices of $\langle 100 \rangle$.

**Single stranded deoxyribonucleic acid (ssDNA)** A macro-molecule consisting of one strand of linked deoxyribonu-cleotides.

## ACKNOWLEDGMENT

## REFERENCES

1. A. Ulman, "An Introduction to Ultrathin Organic Films: From Langmuir–Blodgett to self-assembly." 1991.
2. E. Delamarche, B. Michel, H. Biebuyck, and C. Gerber, *Adv. Mater.* 8, 719 (1996).
3. G. E. Poirier, *Chem. Rev.* 97, 1117 (1997).
4. Y. Xia and G. M. Whitesides, *Angew. Chem. Int. Ed. Engl.* 37, 550 (1998).
5. D. M. Eigler and E. K. Schweizer, *Nature* 344, 524 (1990).
6. G. Binnig, R. Roher, C. Gerber, and E. Weibel, *Phys. Rev. Lett.* 49, 57 (1982).
7. L. A. Bottomley, J. E. Coury, and P. N. First, *Anal. Chem.* 68, 185R (1996).
8. S. N. Magonov and M.-H. Whangbo, "Surface Analysis with STM and AFM—Experimental and Theoretical Aspects of Image Analysis." 1996.
9. Y. Martin, in *SPIE Milestones Series* (1995), Vol. MS 107.
10. G. E. McGuire, M. A. Ray, S. J. Simko, F. K. Perkins, S. L. Brandow, E. A. Dobisz, R. J. Nemanich, A. R. Chourasia, and D. R. Chopra, *Anal. Chem.* 65, 311R (1993).
11. M. Miles, *Science* 277, 1845 (1997).
12. R. M. Nyffenegger and R. M. Penner, *Chem. Rev.* 97, 1195 (1997).
13. M. A. Poggi, L. A. Bottomley, and P. T. Lillehei, *Anal. Chem.* 74, 2851 (2002).
14. G. Binnig, C. F. Quate, and C. Gerber, *Phys. Rev. Lett.* 56, 930 (1986).
15. C. M. Mate, G. M. McCelland, R. Erlandsson, and S. Chiang, *Phys. Rev. Lett.* 59, 1942 (1987).
16. R. W. Carpick and M. Salmeron, *Chem. Rev.* 97, 1163 (1997).
17. C. F. Quate, *Surf. Sci.* 386, 259 (1997).
18. Y.-T. Kim and A. J. Bard, *Langmuir* 8, 1096 (1992).
19. C. B. Ross, L. Sun, and R. M. Crooks, *Langmuir* 9, 632 (1993).
20. J. K. Schoer, C. B. Ross, R. M. Crooks, T. S. Corbitt, and M. J. Hampden-Smith, *Langmuir* 10, 615 (1994).
21. J. K. Schoer, F. P. Zamborini, and R. M. Crooks, *J. Phys. Chem.* 100, 11086 (1996).
22. H. Sugimura and N. Nakagiri, *Langmuir* 11, 3623 (1995).
23. H. Sugimura, K. Okiguchi, N. Nakagiri, and M. Miyashita, *J. Vac. Sci. Technol. B.* 14, 4140 (1996).
24. H. Sugimura and N. Nakagiri, *J. Am. Chem. Soc.* 119, 9226 (1997).
25. H. Sugimura, O. Takai, and N. Nakagiri, *J. Electroanal. Chem.* 473, 230 (1999).
26. C. R. K. Marrian, F. K. Perkins, S. L. Brandow, T. S. Koloski, E. A. Dobisz, and J. M. Calvert, *App. Phys. Lett.* 64, 390 (1994).
27. F. K. Perkins, E. A. Dobisz, S. L. Brandow, T. S. Koloski, J. M. Calvert, K. W. Rhee, J. E. Kosakowski, and C. R. K. Marrian, *J. Vac. Sci. Technol. B.* 12, 3725 (1994).
28. U. Kleineberg, A. Brechling, M. Sundermann, and U. Heinzmann, *Adv. Funct. Mater.* 11, 208 (2001).
29. J. M Keel, J. Yin, Q. Guo, and R. E. Palmer, *J. Chem. Phys.* 116, 7151 (2002).
30. C. B. Gorman, R. L. Carroll, Y. F. He, F. Tian, and R. R. Fuierer, *Langmuir* 16, 6312 (2000).
31. C. B Gorman, R. L. Carroll, and R. R. Fuierer, *Langmuir* 17, 6923 (2001).
32. R. R. Fuierer, R. L. Carroll, D. L. Feldheim, and C. B. Gorman, *Adv. Mater.* 14, 154 (2001).
33. G. M. Credo, A. K. Boal, K. Das, T. H. Galow, V. M. Rotello, D. L. Feldheim, and C. B. Gorman, *J. Am. Chem. Soc.* 124, 9036 (2002).
34. J. Zhao and K. Uosaki, *Langmuir* 17, 7784 (2001).
35. J. Zhao and K. Uosaki, *Nano Lett.* 2, 137 (2002).
36. G. Y. Liu, S. Xu, and Y. Qian, *Acc. Chem. Res.* 33, 457 (2000).
37. S. Xu, S. Miller, P. E. Laibinis, and G. Y. Liu, *Langmuir* 15, 7244 (1999).
38. S. Xu and G. Y. Liu, *Langmuir* 13, 127 (1997).
39. S. Xu, P. E. Laibinis, and G. Y. Liu, *J. Am. Chem. Soc.* 120, 9356 (1998).
40. K. Wadu-Mesthrige, S. Xu, N. A. Amro, and G. Y. Liu, *Langmuir* 15, 8580 (1999).
41. K. Wadu-Mesthrige, N. A. Amro, J. C. Garno, S. Xu, and G. Y. Liu, *Biophys. J.* 80, 1891 (2001).
42. M. Liu, N. A. Amro, C. S. Chow, and G. Y. Liu, *Nano Lett.* 2, 863 (2002).
43. J. R. Kenseth, J. A. Harnisch, V. W. Jones, and M. D. Porter, *Langmuir* 17, 4105 (2001).
44. R. D. Piner, J. Zhu, F. Xu, S. Hong, and C. A. Mirkin, *Science* 283, 661 (1999).
45. J. Jang, S. Hong, G. C. Schatz, and M. A. Ratner, *J. Chem. Phys.* 115, 2721 (2001).
46. P. V. Schwartz, *Langmuir* 18, 4041 (2002).
47. B. L. Weeks, A. Noy, A. E. Miller, and J. J. De Yoreo, *Phys. Rev. Lett.* 88, 255505 (2002).
48. S. Hong, J. Zhu, and C. A. Mirkin, *Science* 286, 523 (1999).
49. S. Hong and C. A. Mirkin, *Science* 288, 1808 (2000).
50. D. A. Weinberger, S. Hong, C. A. Mirkin, B. W. Wessels, and T. B. Higgins, *Adv. Mater.* 12, 1600 (2000).
51. A. Ivanisevic and C. A. Mirkin, *J. Am. Chem. Soc.* 123, 7887 (2001).
52. M. Su, X. Liu, S.-Y. Li, V. P. Dravid, and C. A. Mirkin, *J. Am. Chem. Soc.* 124, 1560 (2002).
53. B. W. Maynor, Y. Li, and J. Liu, *Langmuir* 17, 2575 (2001).
54. Y. Li, B. W. Maynor, and J. Liu, *J. Am. Chem. Soc.* 123, 2105 (2001).
55. B. W. Maynor, S. F. Filocamo, M. W. Grinstaff, and J. Liu, *J. Am. Chem. Soc.* 124, 522 (2002).
56. L. M. Demers and C. A. Mirkin, *Angew. Chem., Int. Ed.* 40, 3069 (2001).
57. L. M. Demers, S.-J. Park, T. A. Taton, Z. Li, and C. A. Mirkin, *Angew. Chem., Int. Ed.* 40, 3071 (2001).
58. A. Ivanisevic, J.-H. Im, K.-B. Lee, S.-J. Park, L. M. Demers, K. J. Watson, and C. A. Mirkin, *J. Am. Chem. Soc.* 123, 12424 (2001).
59. X. Liu, L. Fu, S. Hong, V. P. Dravid, and C. A. Mirkin, *Adv. Mater.* 14, 231 (2002).
60. K.-B. Lee, S.-J. Park, C. A. Mirkin, J. C. Smith, and M. Mrksich, *Science* 295, 1702 (2002).
61. L. M. Demers, D. S. Ginger, S.-J. Park, Z. Li, S.-W. Chung, and C. A. Mirkin, *Science* 296, 1836 (2002).
62. W. T. Müller, D. L. Klein, T. Lee, J. Clarke, P. L. McEuen, and P. G. Schultz, *Science* 268, 272 (1995).
63. R. Maoz, S. Cohen, and J. Sagiv, *Adv. Mater.* 11, 55 (1999).
64. R. Maoz, E. Frydman, S. R. Cohen, and J. Sagiv, *Adv. Mater.* 12, 424 (2000).
65. R. Maoz, E. Frydman, S. R. Cohen, and J. Sagiv, *Adv. Mater.* 12, 725 (2000).
66. S. Liu, R. Maoz, G. Schmid, and J. Sagiv, *Nano Lett.* 2, 1055 (2002).
67. S. Hoeppener, R. Maoz, S. R. Cohen, L. F. Chi, H. Fuchs, and J. Sagiv, *Adv. Mater.* 14, 1036 (2002).

# Monolayer-Coated Au and Ag Nanoclusters

## Nirmalya K. Chaki, T. G. Gopakumar, M. Aslam, K. Vijayamohanan

*National Chemical Laboratory, Pune, India*

## CONTENTS

## 1. INTRODUCTION

Since the introduction of the Brust method for synthesizing gold clusters in 1994, the emerging area of monolayer coated nanoclusters has rapidly became a topic of intense activity in the field of nanotechnology. This is mainly because of the simplicity of chemically preparing size and shape controlled nanoclusters of several metals and semiconductors to suit different applications [1]. The characteristic features of such nanoscale architectures include size and shape dependent quantum effects, collective behavior due to the control of interparticle distance, and the directional electron transfer arising from the multifunctional nature of organic capping ligands—all contributing to the unique behavior, which is vastly different from that of either the single molecule or the bulk phase [2–13]. The unusual interest also arises partly due to the possibility of modulating their physicochemical behavior, by controlling the spatial confinement of electrons within particles of dimensions smaller than the bulk electron delocalization length [14–16]. Despite challenges involved in the organization of ordered arrays of these clusters (idealized as quantum dots) the opportunities associated with their precise placement using nanofabrication protocols have kindled extensive attention in diverse fields due to their fundamental and technological implications. Consequently, several new applications including single electron transistors, resonant tunneling diodes, light emitting diodes, chemical sensors, and other quantum devices have been made recently using these materials [17–25].

The primary objective of this chapter is to summarize the basic aspects of metallic nanoparticles especially those of gold and silver with their relevant characterization data. General features of monolayer-protected clusters, however, are not discussed due to the availability of excellent recent reviews [4, 5, 26]. One of the principal objectives is to focus on the design of broadly applicable synthetic schemes that produce superlattices of nanoparticles of Au and Ag where the particle size as well as the interparticle coupling can be controlled using suitable monolayer forming molecules. Finally the problem and challenges of making interlinked heterostructures of Au and Ag are briefly mentioned along with the exciting promises in this direction.

### 1.1. Brief History

Although nanoclusters coated with various biological and other macromolecules have been known for several centuries especially for the application of stained glass windows and ceramic tiles and later by the celebrated colloidal formulation of Michael Faraday and colleagues [27], a simple chemical method to form hydrophobic powder of Au and Ag clusters started with the Brust reduction method, where spontaneous self-assembly of alkanethiols on colloidal gold particles occurs [1, 28, 29]. This capping of nanoparticles with surfactant was called three-dimensional self-assembled monolayer (3D SAM) formation to differentiate from the more thoroughly studied 2D SAM of alkanethiols on gold [30, 31], alkylsilane on silica surfaces, etc. [32, 33].

Soon after, several groups used Brust's method for the preparation of 3D SAMs of alkanethiols [34–37], aromatic thiols [38–40], and alkylamines [41] on Au, Ag, and Cu particles and the importance of curvature on controlling

the packing of organic molecules was realized. Terminally functionalized thiol molecules were also self-assembled on nanoparticle surfaces [42–46], thus enabling facile surface modification of the nanoparticles with exciting application potentials. However, the main technological challenge in exploring the potential applications is due to the lack of efficient methods to assemble these nanoparticles into well-ordered macroscopic systems. In the last five years, there has been a great deal of research devoted to develop new methodologies for the construction of ordered nano-assemblies [47–59], which has helped to resolve some of the key issues. Nevertheless, some of the clusters especially after organizations are very subtle and researchers are endeavoring to improve the stability of these superstructures with respect to change in preparation conditions such as temperature, pH, ionic strength, etc.

## 1.2. Theoretical Significance

The fascinating properties due to the quantum size effect can be understood in terms of the theoretical formulation of the problem of electron movement in a restricted environment. Since nanosize dimension causes the energy levels to become discrete compared to the bulk form of metal, the change in the spacing between the energy levels as a function of the number of atoms can be used to understand the electronic and optical properties [6, 60–62]. The confinement of electronic wave function causes discreteness of energy levels and, more importantly, the average spacing of successive quantum levels (Kubo gap, $\delta$) can be controlled to make a system metallic or nonmetallic. Since $\delta$ is given by $4E_f/3n$, where $E_f$ is the Fermi energy of bulk metal and $n$ is the number of valence electrons in the nanoclusters, a change in $n$ by size tuning can lead to the control of $\delta$ compared to the value of thermal energy. For example, $\delta$ can vary with $r^{-3}$ for spherical particles, as their density of states is proportional to volume. The low temperature behavior of these systems will be more interesting as the spacing $\delta$ may become larger than $k_B T$, and the lifetime, $\tau$, of the electronic states will be much larger than $\hbar/\delta$, thus making the system insulating. At the same time, disorder in the monolayer can create localization and this can be responsible for the temperature dependence as explained by variable range hopping theory [59].

A few theoretical attempts have been made to study the electronic structure of monolayer-protected clusters (MPCs) in the simultaneous presence of interaction and disorder [63–66]. When there is large interparticle separation ($D > 2r$), the clusters behave like a Mott insulator with a Coulomb gap described by the charging energies of individual nanoparticle sites (Fig. 1). On the other hand, when the distance between the adjacent clusters is very small ($D \ll 2r$) compared to their size, strong quantum mechanical exchange coupling can cause the disappearance of Coulomb gap, causing the insulator-to-metal transition (IMT) demonstrated in Figure 2 [67–69]. Since the charging energy scales inversely with particle size, the IMT is experimentally easier to observe in superlattices composed of larger clusters. This is to be contrasted with transition metal oxides, where IMT is normally accomplished by the
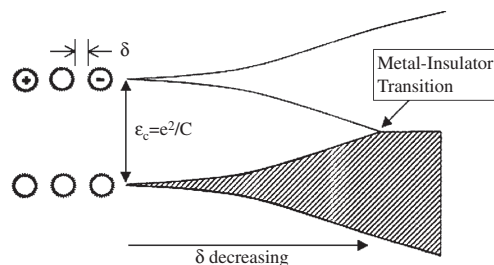


**Figure 1.** Representation of the effects of interparticle separation distance on the electronic structure of the QD superlattice. The energy to separate a positive and a negative charge barrier is the width of the Coulomb gap for a single particle and is equal to $e^2/C$. As interparticle separation is reduced, exchange interactions lead to the development of energy bands, and eventually the formation of a metallic solid. Adapted from [168], M. Aslam's thesis, Pune University, INDIA (2002).

variation of charge carrier density through alteration of the composition using substitution chemistry.

The low temperature properties appear to be determined by Coulomb Blockade effects, where, in order to tunnel onto the cluster, electrons should overcome the cluster charging energy ($E_c = e^2/2C(r)$, where $C(r)$ is the capacitance of the individual cluster) with an integral number of electrons on it, in contrast to the previous experiments on various transition metal oxide systems. Although several theoretical suggestions and preliminary experimental data have been made recently about interlinked nanoclusters using organic molecules as model systems to study Mott–Hubbard IMT [59, 60], there is little experimental evidence based on low temperature resistivity measurements. More refined preparation methods to get highly monodispersed clusters are essential to observe these electronic effects at room temperature.

## 2. MONOLAYER PROTECTED GOLD CLUSTERS

Gold nanoparticles are important because of their stability, change in structural characteristics with size variation, ease of preparation, etc. After the successful preparation of 3D gold nanoparticles by Brust and others, more attention has been paid to improve the size dispersion. Size dispersity often causes irreproducibility of cluster properties and necessitates complex methods for size sieving
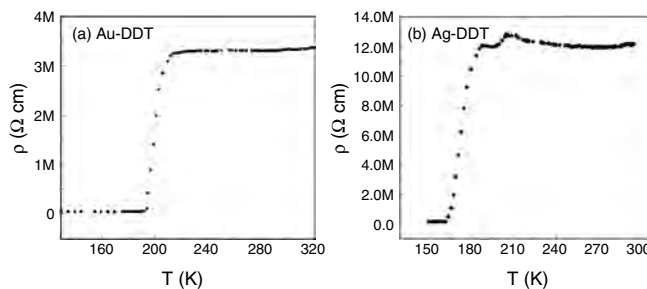


**Figure 2.** Low temperature resistivity measurements for (a) Au (10–12 nm) and (b) Ag (10–15 nm) nanoclusters protected with dodecane thiol showing insulator-to-metallic transition. Adapted from [68], M. Aslam, I. S. Mulla, and K. Vijayamohanan, *Appl. Phys. Lett.* 79, 689 (2001).

including solubility fractionation, chromatography, capillary electrophoresis, and mass spectrometry. Thus one of the principal objectives of various synthetic strategies is to achieve precise control over the size, shape, and dispersion. This section discusses different methods of preparation, structural features with size, properties, and application of different monolayer protected gold nanoparticles.

## 2.1. Preparation

Metallic nanoclusters have been prepared by different methods including the reduction of precursors, thermal decomposition, photolysis, etc. However, the simplest method for the preparation of monolayer protected nanoparticle is the Burst reduction method. In brief, Au salt in aqueous medium is reduced by a standard reducing agent such as $NaBH_4$ and $N_2H_4$, in an aqueous–nonaqueous interface, in presence of a surface-passivating agent in the nonaqueous medium. Vigorous stirring causes instantaneous transfer of the clusters to the organic phase through SAM formation with long chain organic thiols, amines, acids, etc. present in the organic phase [70–76]. Despite the success of the Brust method and its other variants, new methods for the synthesis and stabilization are being continuously tried due to the need for making stable clusters with as narrow a size distribution as possible along with shape control, which causes structural peculiarities [38, 54–56]. A systematic variation of parameters like strength of reducing agent, capping agent, temperature, pH, and ionic strength can be used to control the size and shape. For example, Yin and Wang have achieved [58] long-range order due to the narrow size distribution of Au particles, while Terril et al. have discussed the problems during the array formation using thiols as the capping agents [34]. In another interesting study Hostetler has shown that short chain length thiols, cause the formation of substantially disordered clusters compared to the case using longer chain thiols [77]. Some of these experimental results have been theoretically confirmed by Luedtke and Landman [78, 79] after performing molecular dynamic simulations, which corroborates the 3D-superlattice formation of Au nanoparticles. According to these studies longer chain length ($\geq$ C12 thiol) capped Au nanoparticles get bundled to cause tetragonal distortion of the face centered cubic (fcc) structure at room temperature in comparison with clusters using shorter chain length thiols forming a body centered cubic (bcc) type of superstructure. Some of these data for gold nanoparticles with their size, shape, and nature of capping agents are summarized in Table 1. The data clearly indicate that interesting nanocluster to nanorod transformations can be effected by changing the nature and amount of capping agent. In favorable cases even control of the aspect ratio of these nanorods can be possible by controlling the preparation chemistry.

## 2.2. Characterization

The characterization of nanoparticles aims to quantify the particle size, shape, distribution, overall composition, and impurity content. A variety of techniques have been applied to get valuable information about the structure, kinetic and thermodynamic stability, and mechanistic aspects of the

**Table 1.** Summary of different gold nanoparticles with size and shape distribution.

| Size of cluster (nm) | Capping agent | Structure | UV absorption (nm) | Ref. |
|---|---|---|---|---|
| 1.5–3.5 | alkyl thiolate | fcc | 515–518 | [70] |
| 2–3.2 | 2,6-bis(1′-(8-thiooctyl) benzimidazole-2-yl)pyridine | hexagonal network | 520–523 | [71] |
| 2–4 | dodecane | fcc | 520–525 | [72] |
| 3.5–4 | S-dodecyl thiosulphate in THF and water | | 516–527 | [73] |
| 8–9 | tris-$n$-octyl phosphine oxide | fcc | 525–530 | [74] |
| 10 | hexadecyl trimethyl ammonium bromide | nanorod | 520 + 600–700 | [75] |
| 40–50 | hexadecyl trimethyl ammonium bromide | nanorod | 520 + 800–850 | [76] |

monolayers on the cluster surface. These techniques useful to characterize various parts of MPCs are shown in Figure 3. Surface composition is also probed although this is a formidable task. The technique used for characterization should have no damaging interaction and must reveal subtle features like the conformation and orientation with respect to different functional groups on the nanocluster surface. Also, some of the techniques require a specific environment like MPC/solution, MPC/ultrahigh vacuum interface, and hence the possibility of reorganization of organic molecule due to change in the environment has to be considered during analysis. In brief, no single method of characterization provides complete insight and hence the application of various techniques is essential; some of them we will discuss.

### 2.2.1. Ultraviolet-Visible Spectroscopy

Ultraviolet-visible (UV-vis) spectroscopy is a commonly used technique to qualitatively determine the size and degree of aggregation of Au MPCs because of its characteristic surface plasmon resonance in the visible region. More specifically, surface plasmon absorption maximum ($\lambda_{max}$) and bandwidth can give valuable qualitative information about the size, shape, and the interparticle separation depending on the capping molecule. For example, Figure 4 shows the characteristic UV-vis absorbance spectra of Au MPCs (2.6–5 nm) in toluene, revealing a strong plasmon band at around 520 nm, which decays exponentially into the visible region.
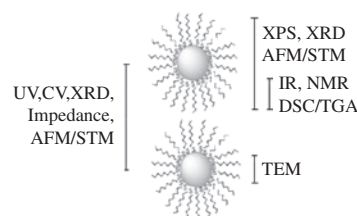


**Figure 3.** The scheme indicating the various techniques to be used to characterize various parts of monolayer-protected nanoclusters. Adapted from [168], M. Aslam's thesis, Pune University, INDIA (2002).
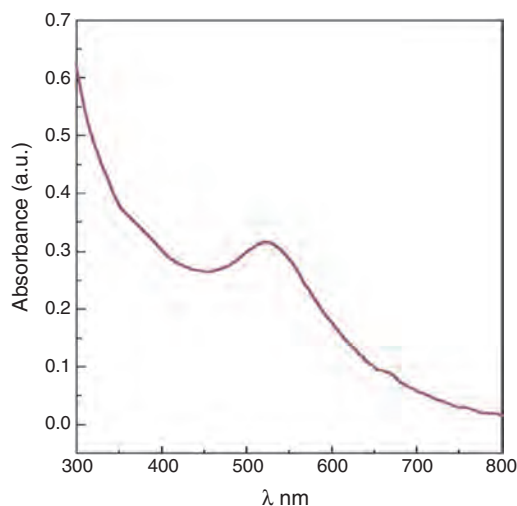
**Figure 4.** Characteristic surface plasmon absorption at 520 nm of Au nanoclusters protected by dodecane thiol in toluene.

This surface plasmon absorbance peak is redshifted with increasing size with a concomitant increase in their peak full width of half maximum (FWHM) [80]. Both the peak shape and position are affected by the nature of surface capping agent, as the nature of the dielectric environment changes around the nanoparticle surroundings.

### 2.2.2. X-Ray Diffraction

X-ray diffraction (XRD) is an important method to characterize crystalline nanoclusters. For example, XRD indicates that the alkanethiolate–gold nanocrystal has a fcc lattice with a mean lattice constant within 2% of the bulk value ($a = 0.409$ nm). In a recent study Zanchet et al. [72] have shown that in addition to bulk fcc structure (particle size 2.6–3.2 nm), some particles reveal decahedral (1.7 nm) and icosahedral ($\leq 1.3$ nm) structures depending on the particle size. More interestingly, few of these sample fractions condense reversibly to form ordered crystals or superlattices with long-range translational and orientational order.

The X-ray studies of several cases of ordered nanocrystals have also suggested that the image arises from a bcc superlattice viewed along a (101) axis. The model for this shows orientation of 54.7° with respect to (010) rows of the superlattice in which nine (111) gold planes (0.235 nm interplane spacing) are evident [70]. The (111) plane in such ordered lattices corresponds to diffraction from Au lattice planes within the nanocrystal. Further structural information can be obtained from the small-angle and long-angle region of diffraction studies. The long-range $2\theta$ values show broadened peaks, whose shapes and intensities arise from the diffraction of the finite number of atomic planes indexed to fcc Au, in individual Au nanoparticles. The clear sequence of diffraction peaks in the small-angle region reveals the structure of 3D superlattice, into which the fractionated samples of passivated nanoclusters crystallize [26]. Despite such useful information from X-ray studies, a complete determination of the structure and composition of nanoclusters in particular, the exact interaction between the metal nanocluster surface and "stabilizing ligands" is still a daunting task.

### 2.2.3. Transmission Electron Microscopy

The most widely used technique for characterizing nanoclusters is high-resolution transmission electron microscopy (HRTEM), which provides direct visual information on the size, shape, dispersion, and structure. TEM studies have shown that casting of dilute alkanethiolate Au MPC solution leads to a semiordered islands and chains of clusters with uniform core–core spacing of about two alkanethiolate chain lengths [70]. Such different morphology of the TEM samples probably reflects a complex amalgamation of differing, polarity-based level of adhesion of MPCs to one another and to the substrate surface during evaporation of the solvent and thus is tenuous to interpret in simple structural terms.

Most of the core sizes of the alkanethiol MPCs from TEM images appear to be relatively small ($<3$ nm) and they do have a nearly uniform size distribution. For example, Figure 5a shows typical TEM pictures of dodecane thiol protected Au MPCs, while Figure 5b indicates the selected area diffraction patterns, revealing fcc structures of the clusters. HRTEM studies can be particularly useful to study the faceting, crystallinity, and ordering in these nanocrystals. Spherical to rodlike transformation and chain melting can be studied *in-situ* in a TEM chamber if suitable capping agents are selected. For example, Au nanoclusters films are known to be sintered at temperatures far below the bulk melting point of the metal by this type of study [81].

Potential drawbacks of this techniques include: (a) electron-beam-induced structural rearrangements, aggregation, or decomposition; (b) the inherent problem in interpreting two-dimensional images of 3D samples, and (c) problems with sampling (only a small number of clusters can be analyzed and counted, which may not be representative of the sample as a whole). Despite these limitations, TEM has been the technique of choice due to atomic-level resolution and the attendant benefits of a possible selected area electron diffraction.

### 2.2.4. Fourier Transform Infrared Spectroscopy

Infrared spectroscopy is a general tool to study monolayers, especially their orientation, packing, and density. Detailed information about the packing and the functional groups can, in principle, be obtained with polarized light, since the adsorption in the vicinity of a molecular vibration frequency



(a)                                                    (b)
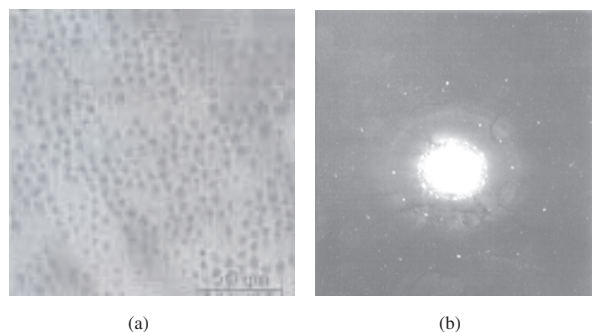
**Figure 5.** (a) TEM micrographs of Au nanoclusters protected with dodecane thiol. (b) The selected area diffraction pattern corresponding to the fcc structure of the same nanoclusters.

is dictated in general by the relative orientation of the electric field and the dipole transition moment. In comparison to a 2D SAM which has ca. $10^{13}$ molecules/cm$^2$, the density of monolayers will be more in 3D SAMs and hence the use of attenuated total reflection and grazing angle becomes proximate.

Comparative vibrational spectroscopic studies have shown that [82] alkanethiolate chains of 2D SAMs are typically in an all-*trans*, zigzag configuration, while chain conformations in solid-state MPC films are mostly all-*trans* containing significant (5.25%) gauche defect concentration at both inner and terminal chain ends, especially for longer chain lengths and above the chain melting temperature. Monolayer ordering in solid-state MPC samples is also associated with interdigitation of chain domains (or bundles) or neighboring cluster molecules [83, 84]. Also hydrogen bonding becomes an important structural component in MPCs with polar monolayers [85]. In contrast, monolayers of dissolved alkanethiolate MPCs exhibit disorder comparable to that of liquid alkanes. These MPCs have proved to be only rough analogies of 2D SAMs due to the high proportion of classically defined MPC core surface defect sites [45].

### 2.2.5. X-Ray Photoelectron Spectroscopy

X-ray photoelectron spectroscopy (XPS) is one of the most powerful tools to study monolayers on MPCs (3D SAMs) as it can give significant information about the nature of the chemical state of elements at the surface of MPCs, and the average number of ligands per core can be derived from combined analysis of XPS and thermogravimetry analysis (TGA) studies [34].

Although SAMs of alkylthiols on planar gold (2D SAMs) and on gold MPCs (3D SAMs) have been intensely studied (by Hostetler et al. and Terrill et al.), the actual nature of the Au–S bonding remains ambiguous. Comparison of the XPS spectra of 2D and 3D SAMs and a "reference" Au(I) complex, sometimes referred to as Au(I) thiolate polymers, provides detailed insight into this problem. High-resolution XP spectra with Au $4f_{7/2}$ and S $2p_{3/2}$ binding energies (B.E.) in 2D SAMs, 3D SAMs, and the Au(I) thiolate complexes reveal that the S atom in the SAM systems bears a charge of about $0.2e$. The 2D and 3D SAMs exhibit similar XPS characteristics and are both distinguishable from the Au(I) complex [86]. In brief, Au $4f_{7/2}$ B.E. appears very near to Au(0) (83.9 eV) and S $2p_{3/2}$ B.E. is consistent with a RS$^-$ ligand (161.9 eV). Like 2D SAMs, 3D SAMs give energies distinctive of Au(0) and a surface thiolate indicating that the bond is somewhere between RS–M and RS$^-$–M$^+$ [87]. These results also indicate that as many as one-third of the Au atoms in the MPC bear alkanethiolate ligand and for the smallest cores only an increased B.E. is seen [88].

This technique is also useful for analyzing mixed monolayers on MPC surfaces. The angle-dependent studies can give valuable information about the atomic distributions in the MPC surface. Nevertheless, in all these applications the limitations such as beam-induced damage on the monolayer and carbon contamination from XPS chamber are to be kept in mind during the XPS analysis. For example, several higher binding energy components for the S $2p$ signal like 163 and 164 eV have been reported for oxidized species like sulphate, sulphoxides, etc.

### 2.2.6. Thermogravimetry/Differential Scanning Calorimetry

Thermogravimetry is an important tool to study the stability of MPCs along with useful information about the Au core–thiol ratio. Thermal decomposition of Au MPCs leads to the loss of the organic part [34, 88] finally leading to a residue of Au powder. Considering the average core size of Au MPCs, the TGA results give average number of ligands per MPC as 4.7 ligands/nm$^2$. TG results confirm that MPC ligand coverage is more than 50%. This is greater than the ligand/Au surface atoms in the 2D Au(111) surface ($\sim$33%). Theoretical calculations also indicate that this high coverage results from larger ligand/Au binding ratios on core edges and vertexes [78, 79]. The alkanethiolate MPC decomposes at around 260 °C [88]. The mass loss occurs in a single step beginning at 230, 266, and 310 °C for $C_8$, $C_{12}$, and $C_{16}$–thiolate–Au MPCs, respectively, corresponding to the quantitative loss of the alkanethiolate chains. The temperature dependence of the mass loss indicates that the thermal stability of Au MPCs increases with increasing chain length [34].

A related technique, differential scanning calorimetry (DSC), is very useful to study the phase transitions in alkanethiolate–MPC monolayers. Phases of Au MPCs studied in the temperature range of −100 to 100 °C show that for smaller chains ($\leq C_8$–thiolate MPCs) no phase transition is observed, while for $C_{12}$ and $C_{16}$–thiolate MPCs a broad endotherm is seen corresponding to enthalpies of 6.5 kJ/mol for $C_{12}$ and 14 kJ/mol for $C_{16}$–thiolate monolayers respectively. The melting heats of pure $C_{12}$ and $C_{16}$–thiolate are smaller (37 and 50 kJ/mol, respectively) so that these melting transitions involve only a portion, not the entire hydrocarbon chain. The temperature dependence studies reveal that as the chain length of capping organic molecule increases the phase transition temperature increases [88].

### 2.2.7. Nuclear Magnetic Resonance

Nuclear magnetic resonance (NMR) spectroscopy is particularly useful to determine the structure and dynamics of monolayers on MPCs. Studies of order–disorder transitions are possible in MPCs using NMR and infrared. $^1$H and $^{13}$C NMR resonances of MPCs are characteristically broad relative to those of free alkanethiols [83, 84, 88]; the factors include spin–spin relaxation ($T_2$) broadening, a distribution in chemical shifts due to differences in Au–SR binding sites, and a gradient in monolayer packing density from near core to chain terminus with associated dipolar broadening [84]. For example, $^{13}$C NMR studies show that in both solution and solid state, the resonance of the first three C next to the sulfur headgroup disappears upon binding to gold, indicating a strong interaction with the surface. For $C_{12}$–thiolate MPC a broad resonance appears at 4.2 ppm for the C next to the sulfur headgroup. For $C_8$–thiolate MPCs the $^{13}$C resonance in solution and solid state is same while $C_{18}$–thiolate MPCs show a downfield shift by 4.5 ppm in solid state. This indicates that chains crystallize into an extended all-*trans* conformation, while the high conformational order, along with reduced methylene proton linewidth in $C_{18}$–thiolate MPCs, indicates that the chains are undergoing large amplitude

motion about their large axes. Molecular mobility increases toward the unbound ends, which have higher populations of gauche conformation [83]. In a variable temperature dependent $^1H$ NMR study of $C_{18}$–thiolate, it has been shown that as the temperature increases, disorder (increase in gauche bond population) propagates from the chain terminus to the middle of the chains leading to eventual chain melting.

### 2.2.8. Scanning Probe Microscopies

While standard methods of measurement and characterization are routinely employed for investigation, the increasing use of scanning probe microscopy (spatial resolution 0.1 nm), combined with high-resolution electron microscopy, has enabled direct images of the structure to be obtained. Scanning probe microscopies are now employed at low temperature, under vacuum, or in a magnetic field to image nanoparticles. In a scanning tunneling microscopy (STM) measurement, an atomically sharp tip is brought very close ($\leq 10$ Å) to the surface and on application of a small potential difference ($\sim 1$ V) between the surface and the tip, the generated tunneling current is monitored during scanning of the tip on the surface. The STM experiments can be done either in (a) constant current or (b) constant height mode. The samples for STM should have few desirable criteria such as (1) good electrical conductivity, (2) an atomically flat surface, and (3) limited surface mobility. Compared to STM, atomic force microscopy (AFM) is purely mechanical; a cantilever tip attached to a spring is dragged across the sample. The increase or decrease in the height of the tip is measured yielding the surface height profile as a function of distance. The advantage is that one can carry out measurements on nonconducting samples. AFM is good at determining the particle height but is poor at determining its diameter [89]. Likewise, AFM cannot differentiate shape differences or images of particles that are spatially close. Although limitations like tip-induced artifacts and the possibility of monolayer damage can complicate the interpretation, the added advantage of $I–V$ measurements to provide local density of states can be a powerful benefit.

The STM measurements performed on $C_{12}$–thiolate Au MPCs on a highly oriented pyrolitic graphite (HOPG) surface show clusters as spherical protrusions lying along the step edges. Clusters are not seen on the smooth HOPG surface and are pushed aside by the scanning tip. For different chain lengths no such big corresponding difference in size is observed. The average size lies in the range 3.9 to 4.5 nm and the percentage for $C_8$, $C_{12}$, and $C_{16}$ falls in the regime of 52%, 58%, and 68% respectively [34]. The advantage of using STM over TEM data is that TEM measures only core diameter, while STM measures the overall cluster dimension (organic molecule and core diameter). Convolution of the particle size with the STM tip dimension may cause the STM image to overestimate the true cluster size, while AFM measurements indicate slightly smaller particles. The images of $C_{12}$–thiolate MPCs on flat mica surfaces show that the aggregates have more width than their height and no significant difference in height is observed for small and large aggregates indicating that the groups consist of a single layer of clusters.

### 2.2.9. Other Characterization Methods

One of the important properties of Au MPCs is their room temperature conductivity. Solid-state electronic conductivity measurement on dry powders of MPCs using a four-probe method reveals that they are electronically conducting presumably due to the electron tunneling through the intervening monolayers. Besides the techniques described previously, several special characterization techniques such as He, electron, and neutron diffraction [90, 91], surface plasmon spectroscopy [92], magnetoelectrochemistry, [93] secondary ion mass spectroscopy [94], etc. have been applied for investigation of nanoparticles to get valuable information.

## 2.3. Properties

The main objective of controlling the architecture of nanoclusters is the potential to regulate their electrical, optical, and magnetic properties. For example, since the arrays of Au nanoparticles display unique optical properties quite distinct from their respective bulk properties it is easy to systematically vary preparation conditions to cause distinct changes in the shape, size, and chemical composition to tune the optical properties with the help of appropriate ligands. When particles are organized into an array, the plasmon absorption is redshifted due to the coupling of plasmon frequencies of the neighboring nanoclusters as illustrated by the shift of the characteristic plasmon absorption from 500 to 650 nm depending on the size and shape of Au clusters (Table 1). Interestingly, for smaller particles (core size), the intensity of the band is also found to decrease [88]. In addition, for very small particles (1–2 nm), moleculelike properties and transitions to discrete lowest unoccupied molecular orbitals (LUMOs) could be used to estimate the highest occupied molecular orbital–LUMO "gap" energies as a function of size [95].

The electrical properties of gold nanoclusters are very important since their use is considered to be one of the possible alternatives to semiconductor based integrated circuits, information storage devices, etc. [2–12] due to their unique electronic properties. Although their typical resistivity value suggests semiconductor behavior, if the size is below 3 nm, the $I–V$ curves show Coulomb blockade behavior that manifests single electron tunneling at room temperature. This has been recognized as one of the fundamental requirements for the development of quantum electronics. Several investigations have confirmed this phenomenon using STM/STS [96], although the use of atomic resolution is not essential to get staircase $I–V$ behavior. Even for bigger clusters, the $I–V$ behavior is strongly affected by the nature of the capping organic molecule as indicated in Figure 6. The nonlinearity progressively increases with the chain length of the capping agent when 5 nm gold monolayer coated clusters are organized on an Au(111) surface using $C_5$, $C_8$, $C_{12}$, PhC$_2$, and PhC thiols respectively for monolayer formation. The Kubo gap estimated from this $I–V$ curve increases as the length of the organic capping molecule increases.

Apart from the unique optical and electrical properties, gold nanoparticles also have interesting electrochemical behavior. For example, electrode reactions of redox-functionalized nanoclusters (e.g., ferrocene, anthraquinone) are unusual, in that many equivalents of redox charge per
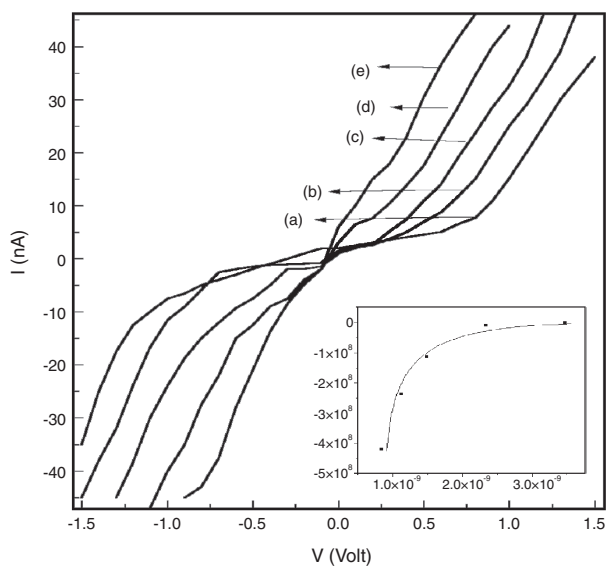
**Figure 6.** *I–V* behavior of 5 nm Au clusters passivated with different organic molecules such as, (a) dodecane ($C_{12}$), (b) octane ($C_8$), (c) pentane ($C_5$), (d) ethyl phenyl ($PhC_2$), and (e) phenyl ($PhC$) thiol, hydrophobically organized on Au/SAM surfaces showing a linear decrease in Kubo gap with chain length. Inset shows the exponential relationship between transmission probability and passivating molecular chain length, which limits for the chain lengths of $C_8$ and $C_{12}$ thiols.

MPC can be delivered, under diffusion control, to the electrode/solution interface. MPCs functionalized with two different redox groups exhibit voltammetry of two different groups occurring independently of each other [97, 98]. The electrochemical studies at high resolution also have shown quantized double layer charging in MPCs (diffusing nanoelectrodes). The capacitance is associated with the ionic space charge formed around an MPC dissolved in the electrolyte solution, upon electronic charging of the core. Because of the small subattofarad (aF) capacitance ($C_{CLU}$) of an MPC, charging of a tiny capacitor by a single electron occurs in the potential interval ($\Delta V = e/C_{CLU}$) that exceeds $k_B T$ [95, 99]. These potential intervals are seen sometime in voltammetry of MPC solution depending on the size. The quantized double layer charging is analogous to STM based "Coulomb staircase" experiments using MPC. The spacing of these current peaks on the potential axis reflects the nature of the MPC core charging process. Even peak spacing indicates a metallike core whose charging is controlled by electrostatic (i.e., double layer) principles. These studies reveal that the MPC properties can be tuned as a function of surface coverage, core size, etc. and are also helpful in understanding the electron transfer between clusters through the organic layer [27] when redox active groups like bipyridinium (Viologen) or ferocene containing dithiol molecules are used between the Au electrode and Au nanoparticles [7].

## 2.4. Stability and Reactivity

The stability of Au nanoclusters depends on the nature of the capping agents and can be controlled by taking care of the concentration of Au solution, capping agents, pH, etc.

during the time of preparation. Thermogravimetric analysis of thiol coated gold nanoparticles shows the thermal stability up to only 300 °C depending on the capping agent. The thermal stability can be increased by organizing/incorporating nanoparticles in suitable polymer matrixes.

Monolayer coated gold nanoparticles are known for their chemical reactivity; they undergo different types of chemical reactions like substitution, polymerization, coupling, etc. depending on the functional groups of the monolayer. This reactivity plays an important role in the organization of nanoparticles to form arraylike structures due to the secondary interactions (hydrophobic) as recently reported for gold nanoparticles [27].

## 2.5. Applications

Gold nanoclusters compared to other systems offer more potential applications in the field of electronics, optics, and information storage. They offer greatly decreased voltage and power requirements for all types of optical sources, from high performance communications lasers to general illumination. In order to deliver these benefits, functional nanostructures will have to be fabricated in huge quantities with extremely uniform and controlled size, shape, and composition distributions to optimize their properties for a particular application. A novel molecular electronic component devised this year is a nanoscale transistor that can be switched between "on" and "off" states with a single electron, which works efficiently at room temperature leading to the manufacturing of field-effect transistors (FETs), room-temperature single electron transistors (SET), etc. [17, 18]. Another important application of a resonant tunneling diode using gold nanoparticles has been recently reported using *N*,*N*-di-(10-mercaptodecyl)-4,4′-bypyridinium dibromide molecule, where the redox reaction of the bypyridinium molecule controls the current flow, thus acting as a molecular switch [7].

Au nanoparticles have been proven to be highly useful for designing biosensors. For example, gold nanoparticles capped with enzymes like cytochrome C, where the redox enzymes act as a sensor element and the nanoparticle array acts as a conductive matrix, are well known [100]. In yet another example, D-fructose has been sensed by gold nanoparticles encapsulated by D-fructose dehydrogenase on glassy carbon electrodes [101]. More interesting is the array constructed using biocatalytic enzymes and nanoparticles on thiol modified Au (111) surfaces as this shows the electron transfer process in the presence of a mediator like catechol or a conductive spacer [102, 103]. Similarly sensors built with multilayers of horseradish peroxide and gold nanoparticles are found to be electrocatalytically active for hydrogen peroxide reduction [104].

Apart from the previous applications of Au nanoparticles, there are several other interesting applications in catalysis although the clusters have often been prepared in oxide matrix. For example Au clusters prepared in $ZrO_2$ and $TiO_2$ matrix have shown remarkable catalytic activity for hydrocarbon oxidation [105]. Similarly, Au clusters prepared in the range of 1–6 nm have shown unique size dependent low temperature catalytic oxidation of CO due to quantum size

effects [106]. Also, $Au_{55}(PPh_3)_{12}Cl_6$ shows enhanced heterogeneous catalytic activity in hydrogenation, hydrosilysation, etc., and more reactions are being extensively investigated [51]. Monolayer coated clusters may also act in highly useful selective catalysis, especially if monolayer stability is ensured during the reaction condition. Further studies are desired in this direction to correlate their size dependent behavior with matrix effects.

# 3. MONOLAYER PROTECTED SILVER CLUSTERS

Monolayer protected silver nanoparticles have been investigated widely due to their ease of reduction and also the historical importance due to the photographic process. From the consideration of the electronegativity difference among Ag, Au, and S it can be inferred that the Ag–S bond should be more ionic than the Au–S bond [107, 108]. Therefore, SAMs on Ag can affect the charge distribution at the adsorption site to a larger extent than the case of gold (i.e., the dielectric function of Ag is much more affected than Au). Just like Au particles, Ag nanoparticles have also received significant interest during the last decade, because of their ease of monolayer formation to control the size, shape, and distribution. However, compared to Au nanoclusters these are less studied due to their inferior stability and easy agglomeration tendency. In this section we illustrate the different methods of preparation, properties, and applications of Ag nanoclusters.

## 3.1. Preparation

Methods of preparation of monolayer coated silver clusters are similar to that of gold except for few special methods (e.g., the photochemical method). Different preparation methods available for the synthesis of size selective clusters and their salient features are summarized in Table 2. Although special methods are available for the preparation of silver nanoparticles, especially in zeolitic and glassy matrices, their general method of preparation includes the use of surfactants either using inverse micelles or an aqueous–nonaqueous route using the standard Brust reduction. The easiest way for the preparation of silver nanoclusters is the Brust reduction, where a silver salt in aqueous medium is reduced by $NaBH_4$ and $N_2H_4$, in the aqueous–nonaqueous interface, in the presence of a surface-passivating agent in the nonaqueous medium [1, 60, 61]. Vigorous stirring causes instantaneous transfer of the clusters to the organic phase through SAM formation with long chain organic thiols, amines, acids, etc. present in the organic phase. An alternative radiolysis method also gives fine distributions where the evolution of size and preparation with time has been investigated [109, 110]. More recently a single phase preparation of Ag clusters has been reported by using triethyl amine as an electron transfer agent, where dodecane thiol has been used for surface passivation [111].

## 3.2. Characterizations

Several techniques are available to characterize monolayers of protected silver clusters and the principles of most of these techniques were already given in Section 2.2 with respect to the gold nanocluster. Nevertheless, the salient features of the characterization of Ag monolayer protected clusters and their structural nuances will be given for reference.

### 3.2.1. UV-vis Spectroscopy

Silver MPCs have a characteristic surface plasmon absorption at 420–430 nm as shown in Figure 7. The plasmon peak position and shape strongly depend on several factors such as size, shape, capping agent, and solvent dielectric constant. A recent study by Wlcoxon et al. [80] suggests that unlike gold plasmon peaks of silver MPCs are blueshifted with increase in size with a concomitant broadening of their FWHM.

**Table 2.** Summary of different silver nanoparticles with their size and shape.

| Size of cluster (nm) | Capping agent | Structure and properties | UV absorption (nm) | Ref. |
|---|---|---|---|---|
| 2–3 | 3-aminopropyltrimethoxy silane, boron nitride | fcc, hcp[a] | 400–410 | [117, 118] |
| 5–6 | dicotyl sulfosuccinate sodium salt, organo sulphur compounds, alkyl thiolate | fcc, hcp | 375–380 | [119] |
| 6 | alkane thiolate | hcp | | [113–120] |
| 7.8 | perfluropolyether carboxylic acid and aqueous ammonium hydrooxide, $N$-hexadecylethylenediamine | hexagonal array | 410–415 | [121, 122] |
| 7.7–8 | dodecane thiol, S $N,N$-dimethyl 2,6 pyridinediylbis[undecamide] | hcp | 415–420 | [123, 124] |
| 10–15 | poly(2,6-dimethyl-1,4-phenylene oxide), dodecane thiols | colloidal | 425–435 (doublet) | [125, 126] |

[a] Hcp = hexagonal close packed.
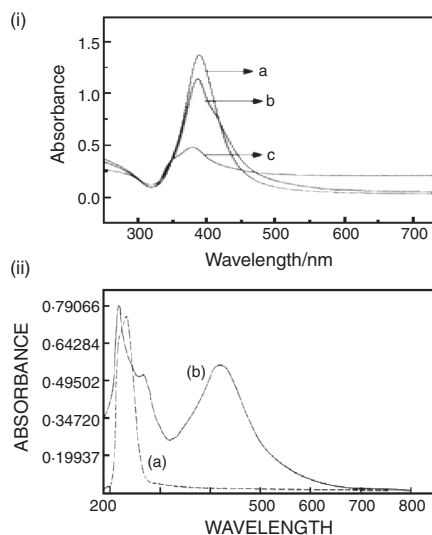
Figure 7. UV-vis absorption spectra of Ag nanoclusters. (i) Time dependent optical absorption spectra of uncapped silver clusters prepared by NaBH$_4$ reduction in aqueous solution: (a) as prepared, (b) after 150 min, (c) after 270 min. Adapted from [154], (i) S. Pethkar, M. Aslam, I. S. Mulla, P. Ganeshan, and K. Vijayamohanan, *J. Mater. Chem.* 11, 1710 (2001). (ii) Stability increase as capping agent dodecane thiol is used: (a) absorption spectra of Dodecane thiols, (b) UV-vis spectra of Ag nanoclusters protected with dodecane thiol (AgDDT) in hexane. (Position and shape do not change after storing for 6 months.) Adapted from [126], (ii) A. Manna, B. D. Kulkarni, K. Bandyopadhyay, and K. Vijayamohanan, *Chem. Mater.* 9, 3032 (1997).

### 3.2.2. X-Ray Diffraction

A x-ray diffraction study indicates that the alkane thiolate–silver nanocrystal has a fcc lattice. In a recent study, Sandhyarani and Pradeep have shown that silver MPCs with different chain length alkane thiolate molecules can form ordered crystals or superlattices with long-range translational and orientational order [112]. This study also reveals that shorter chain alkane thiol capped Ag MPCs show only bulk silver metal peaks corresponding to (111), (200), and (220) planes, but the higher alkane thiols show characteristic low angle peaks corresponding to larger unit cells. These types of odd lattices of silver clusters only result from the periodic arrangements of these clusters. Figure 8 schematically shows such an ordered superlattice structure.

### 3.2.3. Transmission Electron Microscopy

TEM studies along with selected area diffraction of dilute alkanethiolate Ag MPC solution dropcasted on carbon coated Cu grids are capable of getting detailed information about their shape, size, and crystallinity. Unlike Au MPCs, images of silver nanoclusters are comparatively less intense due to their lower electron density. Nevertheless, the use of TEM images has now become routine to study the superlattice structure. For example, Figure 9 shows typical TEM pictures of dodecane thiol-protected Ag MPCs, where Ag nanoclusters (a) prepared with triethyl amine (no capping agent is used) indicate polydispersed clusters and (b) Ag clusters prepared with simultaneous use of triethyl amine and dodecane thiols show monodispersity. In addition their
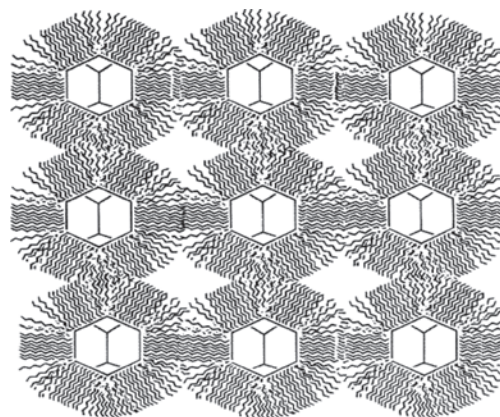


Figure 8. Schematic representation of a monolayer protected cluster and the cluster superlattice. (Interdegetation of aliphatic chain is also seen from the drawing.) Adapted from [169] S. Mitra, B. Nair, T. Pradeep, P. S. Goyal, and R. Mukhopadhyay, *J. Phys. Chem.* 106, 3960 (2002).

stability is increased for the latter case due to the presence of mixed ligands.

### 3.2.4. Fourier Transform Infrared Spectroscopy

In order to understand the surface passivation of Ag clusters Fourier transform infrared (FTIR) spectroscopy has been found to be very useful, for example, to understand the passivation of the Ag surface by dodacane thiol, where several clearly resolved peaks indicate ordered and dense crystalline bulk alkane, especially for all the C–H stretching regions (Fig. 10). The high degree of conformational order is best evidenced by the position of the symmetric ($d^+$) and antisymmetric ($d^-$) CH$_2$ stretching peaks, indicating an extremely high percentage of all-*trans* conformations. More importantly, the alkyl chain dynamics can be investigated from the variable temperature IR measurements. For example, at phase transition temperature, the melting of the alkyl chains is visible and the mechanism of chain motion can be studied in detail [112].

### 3.2.5. X-Ray Photoelectron Spectroscopy

The X-ray photoelectron spectroscopic analysis helps one to understand the surface passivation as well as the oxidation state of Ag. For example, XPS analyses of DDT capped
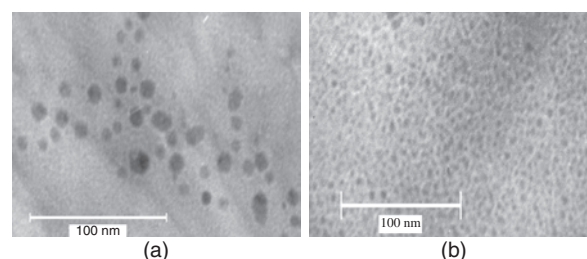


Figure 9. (a) TEM image of Ag nanoclusters prepared with triethyl amine; no capping agent is used and polydispersed clusters are seen. (b) TEM image of Ag clusters prepared with simultaneous use of triethyl amine and dodecane thiol; monodispersity is achieved.
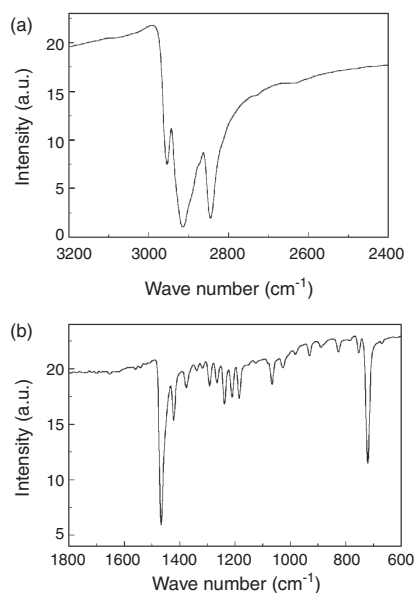
**Figure 10.** In order to understand the surface passivation of clusters prepared using DDT, FTIR has been found to be very useful. The modified surface due to dodecane thiol passivation shows several clearly resolved peaks indicating ordered and dense crystalline bulk alkane; especially for all the C–H stretching regions (a). All the other bands were assigned on the basis of *n*-alkane vibration (b).

Ag MPCs are given in Figure 11 for Ag 3*d* and S 2*p*. The peak position, line shape, and peak to peak separation of $6 \pm 0.1$ eV are the standard measure of the Ag oxidation state. (Fig. 11a) The B.E. values for Ag 3*d* doublets (368.2 and 374.2 eV) are consistent with the Ag° oxidation state. In addition, there is no asymmetry in the peak shape, indicating that all the silver atoms are in their zero oxidation state within the escape depth investigated. The S 2*p* doublet



**Figure 11.** XP spectra of Ag DDT nanoclusters; (a) Ag 3*d* core level spectra evident for Ag⁰ state, (b) S 2*p* spectra depicted that sulfur is present on the surface of Ag as a thioleted species.

B.E. appears at 161.9 and 163.2 eV (Fig. 11b), which is in agreement with those of the previously reported values for chemically bound thiolet sulphur species. The shift in B.E. is neither due to the presence of free alkylthiol, disulfide, nor thiolate moiety, as their B.E.'s are expected much larger than 163 eV.

### 3.2.6. Thermogravimetry/Differential Scanning Calorimetry

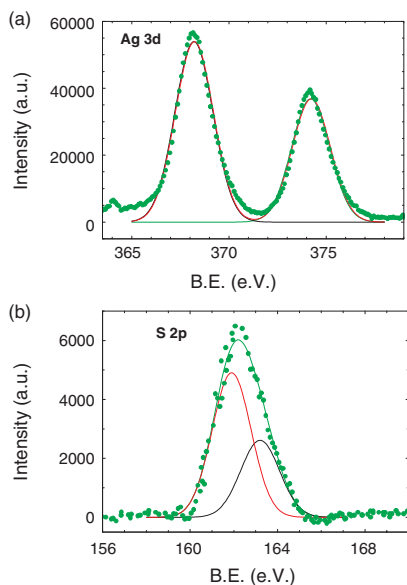Thermogravimetric analysis provides useful data on the thermal stability of DDT and similar monolayer capped Ag MPCs. The detailed analysis of the AgDDT thermogram shows that desorption starts at around 493 K and is complete around 589 K. The loss is attributed to the decomposition of alkanethiol chain (wt loss 55%). The increase in the boiling temperature of the thiol chains further confirms the surface passivation of DDT. The desorption temperature is also dependent on the length of the molecule as mentioned by Sandhyarani et al. [112]. In case of lower chain thiols desorption starts early compared to longer chains. The phase transitions of alkane chains in these MPCs studied by DSC show that Ag MPCs have a higher melting enthalpy compared to Au MPCs, perhaps due to the high degree of superlattice formation.

### 3.2.7. Scanning Probe Microscopes

Both STM and AFM have been used by several investigators to characterize monolayer coated Ag clusters [113, 114]. For example, Wen et al. used STM to show that large, two-dimensional Ag clusters undergo observable diffusion on Ag(100) [115]. In principle, chemical information is obtainable from metal surfaces by photon emission from the scanning tunneling microscope. However, the photon emission varies significantly with topography and choice of the tip. Downes and Welland addressed the important issue of geometry by studying the emission characteristics of Ag and Au spheres. First, photon maps of Ag clusters, consisting in some cases of just a few atoms, demonstrate that they can be uniquely identified from other nonmetallic particles. Then, the bias at which there is an onset of photon emission for 1 nm Ag and Au clusters is measured and is u3.3 and u2.1 V, resp. [116]. This allows for the demonstration of the ability of STM to distinguish different metal particles by their photon emission. However, the scanning probe microscopy data are to be interpreted carefully, because of the possibility of monolayer damage by the tip.

### 3.3. Properties

In recent years there has been a large effort to understand the structure and properties of silver quantum dots due to their attractive properties useful for application in the emerging field of nanotechnology. Silver nanoparticles show a characteristic UV-vis absorption in the range of 380–430 nm due to the surface plasmons although the exact absorption maximum varies with the size and shape of nanoparticles depending also on the interaction with the passivating agent [117–126]. Some of the silver nanoclusters also show interesting luminescent behavior as a function of size

and cluster–cluster spacing. A comparative study of the optical properties is helpful in understanding the real nature and mechanism of the charge transfer (metal to ligand and ligand to metal) in nanoparticles and their periodic arrays. The structural variations along with their optical properties with different capping agents prepared during last few years are summarized in Table 2.

The individual and collective electronic properties of both bare as well as protected silver nanoparticles are important due to their size/carrier confinement and this has been illustrated by several important devices for molecular electronics such as SETs [13]. Silver has an enhanced degree of supperlattice formation due to its size and shape selective organization, and the stability and crystallinity of the clusters are better than that of gold. Impedance measurements of Ag nanoarrays [127] reveal change in electronic properties as a function of the interparticle separation. For example, inductive behavior is clearly seen at smaller interparticle separation, while the array becomes an insulator as the particle separation increases. Interestingly, once the separation decreases, the *RC*-type tunneling transport switches to coherent long-range transport.

The electrochemical properties of silver clusters are interesting due to its variation with size and nature of capping agents. For example, the electrochemical behavior of ca 3 nm Ag clusters prepared with both triethyl amine and dodecane thiol shows a remarkable difference with similar electrochemical behavior of Ag clusters prepared only using triethyl amine as illustrated in Figure 12 [111]. The variation of Ag/Ag$^+$ redox potential with size has not been clearly demonstrated despite several cyclic voltammetric studies. The exception to this is a time dependent study of radiolytically prepared silver clusters (Ag$_n$) where the potential varies drastically with the value of $n$. For example, when $n$ is 1 (i.e., free atom) the potential is $-1.8$ V, reaching 0.799 V, on the other hand, corresponding to $n$ tending to infinity [109, 110]. While understanding the behavior of monolayer protected clusters we must also keep in mind the limitations like the potential induced reorganization, reductive desorption of organic molecules, changes due to solvent entrapment and etching of the nanoparticles due to cycling, etc.
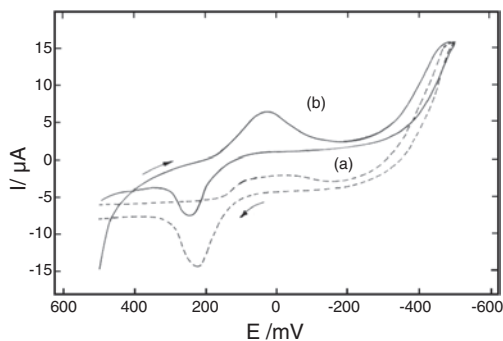


**Figure 12.** Superimposed cyclic voltammograms of silver nanoclusters prepared (a) without and (b) with DDT. Cyclic voltammograms were recorded on an EG&G pontentiostat using Pt wire as working electrode along with Pt foil as counterelectrode and an Ag/AgCl reference electrode in aqueous acetonitrile solution of LiClO$_4$ (0.1 M); (CH$_3$CN: H$_2$O, 100:10 v/v, 10 ml) at the scan rate of 10 mV/s.

## 3.4. Stability and Reactivity

Stability is an important parameter to control the fabrication of devices with Ag nanoclusters. Stability of nanoparticles of silver is less compared to that of gold because of its tendency to agglomerate and get oxidized. The stability of clusters can be improved during preparation itself by controlling parameters like concentration of silver solution, pH, and the chemical nature of the protecting ligands. According to the type of functional group, chain length, and branching nature of the ligand molecule, silver nanoparticles have chemical reactivity like substitution, coupling, etc. Interestingly, thiol protected silver nanoparticles show an enhanced rate of nucleophilic substitution reaction with other thiols. This reactivity can be controlled/enhanced by the selection of monolayers (functional groups containing branched chains can stop the substitution reaction). Moreover, this reactivity of Ag nanoparticles can be used for the preparation of interlinked mixed clusters with other metals like Au, Pt, etc.

## 3.5. Applications

Nanoparticles prepared by self-assembly are attractive for several exciting applications due to the possibility of engineering the surfaces at the molecular level. One of the important applications of Ag nanoclusters in the area of nanotechnology is the organization of quantum dot superlattices. For example, several nanocluster assemblies organized in different length scales have been found to be promising due to their potential applications in many diverse areas such as optoelectronic devices, single electron transistors, and chemical sensors.

The tiny FETs recently reported using Au clusters can also be designed with silver, which can be individually controlled after integration on a single chip. Similarly, when an aqueous suspension of silver nanoparticles is held in an alternating field between two planar electrodes, the particles assemble into conducting microwires that grow from one electrode to the other [107, 108]. These wires are not in nm diameter (actually in $\mu$m), but the method represents an easy way to create electrical connections in liquid environments. These wires could be used in wet electronic and bioelectronic circuits, including chemical sensors. In another key step toward single-molecule electronic devices, researchers wired a single molecule into an electrical circuit by chemically bonding the two molecular ends to metal conductors [108], so that their current–voltage characteristics could be studied. Thus it is possible to tether Ag nanoclusters to the ends of an octanedithiol molecular wire and using a conducting tip of an atomic force microscope; we can study the suitability of individual molecules for electronic applications.

## 4. Au–Ag CORE–SHELL CLUSTERS, ALLOY NANOCLUSTERS, AND Au–Ag INTERLINKED NANOCLUSTERS

The progress of nanotechnology necessitates different types of building blocks with unique structure and composition, which can be self-assembled to form functional materials.

In this regard, nanoparticles with core–shell morphologies represent a new type of constructional unit, consisting of two dissimilar compositional and structural domains. For example, several nanoclusters of silver with zirconium oxide, titanium oxide, and tin oxide shells represented as Ag@ZrO2, Ag@TiO$_2$, and Ag@SnO$_2$ have been recently demonstrated to possess unusual catalytic properties [128, 129]. The aim of such modification is augmented chemical and physical properties and a broad spectrum of applications, which are not possible with their single counterparts. Many types of nanoparticles could fit into the core–shell category, which was recently defined [130, 131] as cores and shells of different matter in close interaction, including inorganic–organic, inorganic–inorganic, organic–organic, or inorganic–biological core–shell combinations [26, 73, 130–137].

The electronic properties of individual Au and Ag clusters discussed earlier could be modulated by putting a thiol molecular interconnector between the Au and Ag clusters, although extensive precautions are necessary to prevent alloy formation even at room temperature [112, 138]. Recently, Hutter and Fendler showed a simple method to interconnect thiocyanate ion capped Au nanoclusters (3.5 nm) to ethylene di-ammine tetra acetic acid covered Ag nanoclusters (22 nm). Their study also reveals that when smaller Au nanoparticles (<3.5 nm) are used robust gold encased silver nanoparticles form, while chained structures are observed when larger (>11 nm) Au particles are used [139]. In another interesting study Fullam et al. used systematic molecular recognition chemistry to assemble both homo- and heterometallic (Au and Ag) nanocluster organizations [140–142].

### 4.1. Preparation

The core–shell synthesis typically involves tailoring the surface properties of particles, often accomplished by coating or encapsulating them within a shell of a preferred material. This coating can alter the charge, functionality, and reactivity of the surface as well as enhance the stability and dispersibility of the core. Also such compositions are reported to show enhanced optical, catalytic, and magnetic properties [143, 144]. For example, a Au–SiO$_2$ core–shell structure prepared through citrate reduction of Au salt initially followed by aminosilane moiety for the silica coating shows enhanced optical properties, which may be exploited further for device applications [128]. More recently, the synthesis of Au@TiO$_2$, Au@ZrO$_2$, Ag@TiO$_2$, and Ag@ZrO$_2$ particles in nanometer dimensions with controllable shell thickness in a single-step process has been demonstrated along with remarkable optical behavior [129]. Similarly the preparation of Au$_{core}$Ag$_{shell}$ nanorods using different types of surfactants has been reported recently [73].

Interconnected nanoclusters can be formed either by direct covalent attachment on terminally modified (such as by thiol, amine, acids on terminal end) nanoclusters or by noncovalent assembly of two different terminal functionally modified nanoclusters. Though homometallic assembly by direct covalent attachment is known, heterometallic assembly by this method is still missing in the literature [145].

Fullam et al. used noncovalent interaction to form programmed self-assembly of both homo- and heterometallic arrays of Au and Ag nanoclusters. More specifically, they first prepared individual Au and Ag nanoclusters protected by mixed monolayers of dodecane thiol with $N,N$,-2,6-pyridine-di-ylbis(mercaptoundecamide) and with 1,2-mercaptododecyl-1-uracil respectively. The programmed assembly is based on the interactions of the two complementary functional groups uracil and diaminopyridine, as the diaminopyridine moeity recognizes and selectively binds the uracil moiety in chloroform, through the formation of three complementary hydrogen bonds.

### 4.2. Properties

The chemical properties of core–shell structure can be fine tuned by selecting different types of terminal functional groups using their ease of formation and their flexibility in structure can be utilized to study wetting, tribology, adhesion, molecular recognition, and related phenomena. In certain core–shell structures like Ag$_{core}$CdS$_{shell}$, the thin semiconducting shell around small metal particles may lead to composite behavior with high electronic capacitance and low leakage rate. Due to the large difference between the intrinsic Fermi levels of heterostructures such core–shell structures with semiconducting clusters or interconnected heterometallic structures have potential applications both as information storage elements and as electronic circuit components. Moreover, these structures may prove to be usefull in optical applications such as second harmonic generation. Similarly, trimetallic clusters, Pd$_{core}$Au$_{shell}$Ag$_{shell}$, prepared radiolytically have been found to possess unusual optical properties [135].

## 5. ORGANIZATION OF MONOLAYER COATED Au AND Ag NANOCLUSTERS

To achieve predecided properties, one can design/tune solid surfaces accordingly via control over their surface properties, because the electron transport through devices depends critically on the properties of surfaces and interfaces through which an electron passes. By the methods of chemisorption and self-assembly we can glue molecules to metal, semiconductor, or insulator surfaces to yield a hybrid system, a combination of molecular and nonmolecular worlds [146]. The assembly of nanoclusters through molecules will lead to transfer of all quantum effects to the bulk substrate. The organization of these clusters can be accomplished in several ways [6, 7, 14–16, 19, 20]. Among them, one general strategy utilizes a bifunctional ligand, where a self-assembled monolayer is formed with one end adsorbed on the substrate while the other end is used to anchor the particles. Different alternative strategies to organize nanoclusters on self-assembled monolayer coated substrates are illustrated.

### 5.1. Electrostatic

Electrostatic interactions have long been known to play an important role in many biological and chemical processes [147–149]. Recently it has been shown that nanoparticle

arrays can be constructed from the interaction of charged nanoparticles with oppositely charged ligand molecules that can bind the nanoparticles (e.g., a quaternary amine to bind anionic monolayers coated particles) [3, 8]. The formation of a colloidal layer is achieved by placing the surface functionalized substrate in a solution of nanoparticles which adsorbs onto the surface and assembles into a saturated monolayer with time. The density of the nanoparticle depends on factors such as size, charge of the particle, attachment method, and the substrate [150–153]. The feasibility of the technique has been demonstrated recently and ultrathin films can be tailored by the variation of particle size, pH of the colloidal solution, etc. to control the distribution.

## 5.2. Covalent

The layer-by-layer self-assembly of organic molecules and nanoparticles onto substrates using covalent control is very simple. A well-cleaned substrate is primed by adsorbing a layer of bifunctional organic molecule onto its surface. This substrate is then immersed into a dilute aqueous solution of metallic nanoparticles for a time, optimized for adsorption of a monolayer, rinsed, and dried. These operations repeatedly complete the self-assembly of metallic nanoparticles sandwiched onto the functionalized substrate. For example, the scheme given in Figure 13 illustrates self-assembly of pentane dithiol and Ag nanoclusters onto Au (111) substrate. In this case (i.e., dithiol molecules), covalent bond formation between Au, Ag nanoparticles and the thiol group is one of the important driving forces [154]. The properties of the self-assembled multilayers depend primarily on the choice of the building block used, their rate of organization, and the integration along the axis perpendicular to the substrate. An advantage of this technique is that it can be potentially useful to prepare complex patterns of various types of nanocrystals [155]. For example, Figure 14 shows
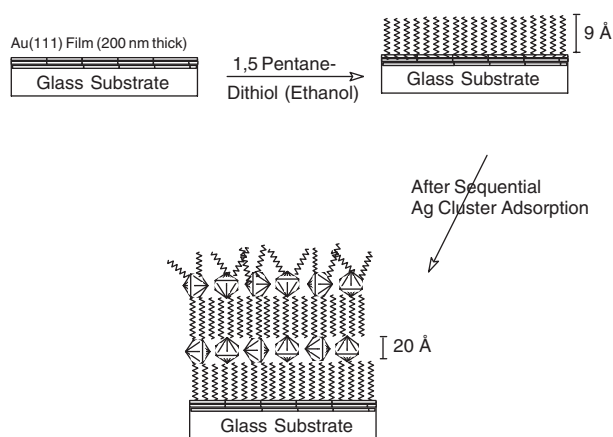


**Figure 13.** Schematic representation of layer-by-layer organization of 2 nm Ag nanoparticles sequentially on pentane dithiol SAM coated Au(111) substrate. Adapted from [154], S. Pethkar, M. Aslam, I. S. Mulla, P. Ganeshan, and K. Vijayamohanan, *J. Mater. Chem.* 11, 1710 (2001).
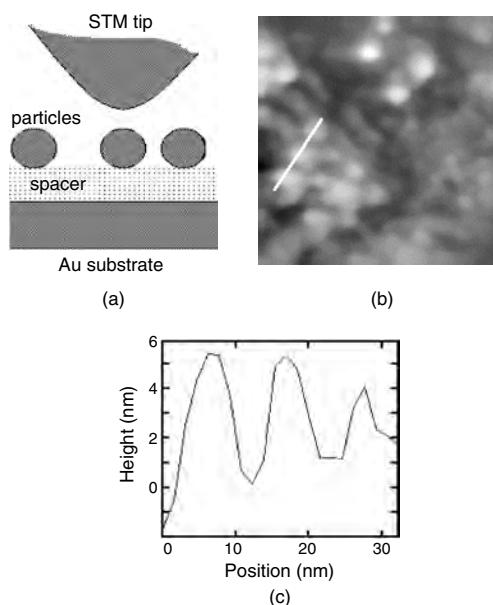


**Figure 14.** (a) Schematic of serial capacitive nanojunctions found by STM tip, Ag nanoparticle, and SAM covered Au substrate. (b) Constant current STM image (94 × 94 nm) obtained at 3.1 pA tunnelling current and 375 mV sample bias. (c) Line profile of three particles marked in (b), showing average particle size of 5 nm.

schematic representations of such Ag clusters on a SAM covered Au surface, where the nanojunction formation can be unravelled using an STM tip.

## 5.3. Hydrophobic

Various interactions between nanoparticles and molecular layers (dithiol) governs the spontaneous layer-by-layer self-assembly of ultrathin films. These forces are primarily covalent or electrostatic (for SAMs of dithiol onto metallic substrate) in nature, but they can also involve hydrogen bonding and van der Waals, hydrophobic, or $\pi$–$\pi$ types of interactions. Apart from the important role played in biological self-assembly, the hydrophobic forces are crucial in phenomena such as mineral floatation, wetting, coagulation, and surfactant aggregation. These forces are found to decrease exponentially (1.4 nm decay length) between the two hydrophobic neutral surfaces and are 10 to 100 times stronger than van der Waals forces on a very short length scale (i.e., 0 to 10 nm) [156]. Recently, we have reported 2D organization of Au MPCs on SAM functionalized substrate using weak van der Waals interactions between the methyl terminal ends of thiol molecules of 2D and 3D SAMs onto Au(111) substrate and nanoparticle surfaces, respectively [25]. (A schematic representation of these types of organizations is illustrated in Figure 15.) For this type of organization of monolayer coated clusters, attractive double-layer force between the surfaces of unequal charges, curvature of the nanocluster surface, dimension, and geometry of the substrate surfaces were found to play important roles [157]. This type of organization is extremely important in molecular electronics as demonstrated in the $I$–$V$ characteristics of 5 nm gold clusters protected with $C_5$, $C_8$, $C_{12}$, $PhC_2$, and PhC thiols respectively in Figure 6.
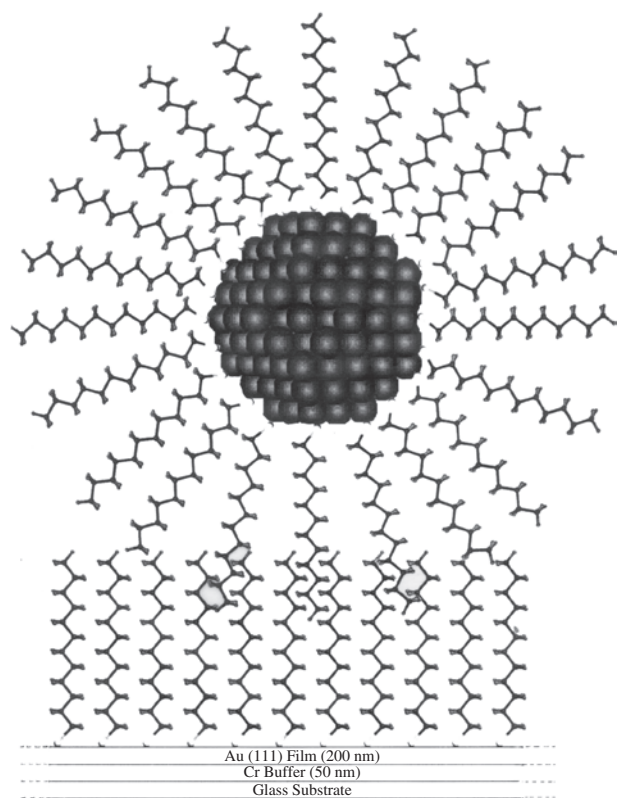
**Figure 15.** Schematic representation of hydrophobic organization of Au MPCs on Au(111) aliphatic thiol SAM surface. Adapted from [25], M. Aslam, I. S. Mulla, and K. Vijayamohanan, *Langmuir* 17, 7487 (2001).

## 5.4. Other Modes of Organization

Some of the other methods for the nanoparticle film formation involves (1) self-assembly by simple solvent evaporation [29, 35, 158–160] and (2) organization at the air–water or water–organic solvent interface (LB) [161–163]. For example, Bentzon and Tholen [164] have reported a 3D ordered superlattice formation through the solvent evaporation of iron oxide colloids. Similarly Geirsig and Mulvaney used a 14 nm Au nanoparticles to form an ordered hexagonal array through electrophoretic deposition [165]. Furthermores, Murray and co-workers showed 2D ordering for semiconducting nanoparticles, while Ohara et al. [166] reported that for metallic nanoparticles even with broad size distribution, size dependent interparticle dispersion attraction was sufficient to drive size aggregation and superlattice formation. In comparison to covalently bound particles, which forms irreversible cross-linkages, the assembly is not so stable, driven by the weak dispersion interaction. The narrower the particle size distribution, the easier the long-range order. Presently several groups are working on comparative organization of size selected Au and Ag clusters using covalent and hydrophobic assemblies since these methods have not been studied in detail. Efforts to enhance the stability of both clusters and ordered arrays also need urgent further investigation to improve the application prospects.

Anchoring them on suitable polymeric or carbon nanotube structures has been found to be useful in enhancing the stability [167].

## 6. SUMMARY

This chapter has presented most of the recent developments in the area of monolayer coated gold and silver nanoclusters with particular emphasis on their preparation, characterization, size-dependent electronic structure, and precise molecular organization. An array of such clusters can be considered as the closest experimental systems resembling ideal metallic quantum dots and their preparation with a variety of sizes and monolayer compositions enabling material scientists to "create" designer materials for the rapidly emerging applications in molecular electronics. Strategies aimed at controlling monodispersion as well as cluster–cluster spacing are outlined in a view to harness their collective behavior for device applications. Core–shell types of heterometallic nanoclusters using both silver and gold are also mentioned due to their unusual behavior. In the end, some interesting issues related to their potential applications and their future prospects in the next two to three decade are addressed along with suggestions to improve the order beheld during the organization of such superstructures.

How can soft and subtle organic molecules help to form order in inorganic nanomaterials like metallic and semiconducting clusters? The answer to the question mainly lies in their ability to form self-assembled monolayers on selected structures by their adsorption characteristics. This gives remarkable stability to monolayer protected nanoclusters of many noble metals, and semiconductors facilitating their use in real device applications. A unified understanding of the electromagnetic interaction of nanoclusters with tuneable size scales will unravel several fundamental questions of photon–solid interactions within a fully quantum electrodynamics framework. In addition, investigations of resonant absorption phenomena as a function of material dimensionality, symmetry, and excitonic structure would give several surprises for applications in the field of photonics and electronics. With such new nanostructures containing artificially designed ligands acting as molecular interconnectors, even supplementing some of the cluster property, the prospect for the field should continue to be bright in the next decade, leading eventually to more and more applications of monolayer protected clusters.

## GLOSSARY

**Brust synthesis** Well known methods for synthesizing metal monolayers protected nanoclusters. In brief, metal salt in aqueous medium is reduced by a standard reducing agent such as $NaBH_4$ and $N_2H_4$, in the aqueous–nonaqueous interface, in the presence of a surface-passivating agent in the nonaqueous medium under vigorous stirring.

**Kubo gap** The confinement of electronic wave function causes discreteness of energy levels, and more importantly, the average spacing of successive quantum levels are known

as Kubo gap ($\delta = 4E_f/3n$), where $E_f$ is the Fermi energy of bulk metal and $n$ is the number of valence electrons in the nanoclusters).

## REFERENCES

1. M. Brust, M. Walker, D. Bethell, D. J. Schiffrin, and R. Whyman, *J. Chem. Soc. Chem. Commun.* 801 (1994).
2. S. J. Chen, *Phys. Chem. B* 104, 663 (2001).
3. M. P. Pileni, *J. Phys. Chem. B* 104, 3358 (2001).
4. R. L. Whetten, M. N. Shafigullin, J. T. Khoury, T. G. Schaaff, I. Vezmar, M. M. Alvarez, and A. Wilkinson, *Acc. Chem. Res.* 32, 397 (1999).
5. G. Schmid, M. Baumle, M. Greekens, I. Heim, C. Osemann, and T. Sawitwoski, *Chem. Soc. Rev.* 28, 179 (1999).
6. D. L. Feldheim, *Nature* 408, 45 (2000).
7. D. I. Gittins, D. Bethell, D. J. Schiffrin, and R. J. Nichols, *Nature* 408, 67 (2000).
8. A. N. Shipway, E. Katz, and I. Willner, *Chem. Phys. Chem.* 1, 18 (2000).
9. C. N. R. Rao, G. U. Kulkarni, P. J. Thomas, and P. P. Edwards, *Chem. Soc. Rev.* 29, 27 (2000).
10. C. A. Mirkin, *Inorg. Chem.* 39, 2258 (2000).
11. V. L. Colvin, M. C. Schlamp, and A. P. Allvisatos, *Nature* 354, 370 (1994).
12. C. B. Murray, C. R. Kagan, and M. G. Bawendi, *Science* 270, 1335 (1995).
13. A. N. Shipway, M. Lahav, and I. Willner, *Adv. Mater.* 12, 993 (2000).
14. G. Markovich, D. V. Leff, S. W. Chung, H. M. Soyez, B. Dunn, and J. R. Heath, *Appl. Phys. Lett.* 70, 3107 (1997).
15. S. Peschel and G. Schmid, *Angew. Chem. Int. Ed. Engl.* 34, 1442 (1995).
16. E. Robert, J. S. James, C. M. Robert, L. L. Robert, and A. M. Chad, *Science* 277, 1078 (1997).
17. L. E. Harrell, T. P. Bigioni, W. G. Cullen, R. L. Whetten, and P. N. First, *J. Vac. Sci. Technol. B* 17, 2411 (1999).
18. R. P. Andres, T. Bein, M. Dorogi, S. Feng, J. I. Henderson, C. P. Kubiak, W. Mahoney, R. G. Osifchin, and R. Reinfenberger, *Science* 272, 1323 (1996).
19. J. H. Fendler, *Chem. Mater.* 8, 1616 (1996).
20. M. A. Hayat, "Colloidal Gold: Principles, Methods and Applications," Vol. 1. Academic Press, New York, 1989.
21. H. Haberland, "Clusters of Atoms and Molecules" Springer, New York, 1994.
22. U. Kreibig, H. Bonnenmann, and J. Hormes, Nanostructured metal clusters and colloids, in "Handbook of Surfaces and Interfaces of Materials," Vol. 3. Academic Press, San Diego, 2001.
23. A. P. Alivisatos, *Science* 271, 933 (1996).
24. C. P. Collier, R. J. Saykally, J. J. Shiang, S. E. Henrichs, and J. R. Heath, *Science* 277, 1978 (1997).
25. M. Aslam, I. S. Mulla, and K. Vijayamohanan, *Langmuir* 17, 7487 (2001).
26. A. C. Templeton, W. P. Wuelfing, and R. W. Murray, *Acc. Chem. Res.* 33, 27 (2000).
27. M. Faraday, *Philos. Trans. Roy. Soc. London* 147, 145 (1857).
28. R. Araujo (Corning Inc., USA), in "Physics of Non-crystalline Solids" (L. D. Pye, W. C. La Course, Stevens, and J. Harrie, Eds.), pp. 591–596. Taylor & Francis, London, 1992.
29. T. Gacoin, F. Chaput, J. P. Boilot, and G. Jaskierowicz, *Chem. Mater.* 5, 1150 (1993).
30. R. G. Nuzzo and D. L. Allara, *J. Am. Chem. Soc.* 105, 4481 (1983).
31. T. L. Freeman, S. D. Evans, and A. Ulman, *Langmuir* 11, 4411 (1995).
32. J. Sagiv, *J. Am. Chem. Soc.* 102, 92 (1980).
33. R. Maoz and J. J. Sagiv, *Colloid Interf. Sci.* 100, 465 (1984).
34. R. H. Terril, T. A. Postlethwaite, C. H. Chen, C. D. Poon, A. Terzis, A. Chen, J. E. Hutchison, M. R. Clark, G. Wignall, J. D. Londono, R. Superfine, M. Falvo, C. S. Johnson, Jr., E. T. Samulski, and R. W. Murray, *J. Am. Chem. Soc.* 117, 12537 (1995).
35. D. V. Leff, P. C. Ohara, J. C. Heath, and W. M. Gelbart, *J. Phys. Chem.* 99, 7036 (1995).
36. K. V. Sarathy, G. Raina, R. T. Yadav, G. U. Kulkarni, and C. N. R. Rao, *J. Phys. Chem. B* 101, 9876 (1997).
37. L. A. Porter, D. Ji, S. L. Westcott, M. Graupe, R. S. Czernuszewicz, N. J. Halas, and T. R. Lee, *Langmuir* 14, 7378 (1998).
38. M. Brust, J. Fink, D. Bethell, D. J. Shiffrin, and C. J. Kiely, *J. Chem. Soc. Chem. Commun.* 1655 (1995).
39. S. R. Johnson, S. D. Evans, S. W. Mahon, and A. Ulman, *Langmuir* 13, 51 (1997).
40. S. Chen and R. W. Murray, *Langmuir* 15, 682 (1999).
41. D. V. Leff, L. Brandt, and J. R. Heath, *Langmuir* 12, 4723 (1996).
42. C. S. Weisbecker, M. V. Merritt, and G. M. Whitesides, *Langmuir* 12, 3763 (1996).
43. S. D. Evans, S. R. Johnson, H. Ringsdorf, L. M. Williams, and H. Wolf, *Langmuir* 14, 6436 (1998).
44. R. S. Ingram, J. M. Hostetler, and R. W. Murray, *J. Am. Chem. Soc.* 119, 9175 (1997).
45. A. C. Templeton, M. J. Hostetler, C. T. Kraft, and R. W. Murray, *J. Am. Chem. Soc.* 120, 1906 (1998).
46. A. C. Templeton, M. J. Hostetler, E. K. Warmoth, S. Chen, C. M. Hartshorn, V. M. Krishnamurthy, D. F. Forbes, and R. W. Murray, *J. Am. Chem. Soc.* 120, 4845 (1998).
47. G. Markovich, D. V. Leff, S. W. Chung, H. M. Soyez, B. Dunn, and J. R. Heath, *Appl. Phys. Lett.* 70, 3107 (1997).
48. R. G. Freeman, K. C. Grabar, K. J. Allison, R. M. Bright, J. A. Davis, A. P. Guthrie, M. B. Hommer, M. A. Jackson, P. C. Smith, D. G. Walter, and M. J. Natan, *Science* 267, 1629 (1995).
49. K. C. Grabar, P. C. Smith, M. D. Musick, J. A. Davis, D. G. Walter, M. A. Jackson, A. P. Guthrie, and M. J. Natan, *J. Am. Chem. Soc.* 118, 1148 (1996).
50. L. A. Lyon, D. J. Pena, and M. J. Natan, *J. Phys. Chem.* 103, 5826 (1999).
51. G. Schmid, S. Peschel, and Th. Z. Sawitowski, *Anorg. Allg. Chem.* 623, 719 (1997).
52. R. P. Andres, T. Bein, M. Dorogi, S. Feng, J. I. Henderson, C. P. Kubiak, W. Mahoney, R. G. Osifchin, and R. Reinfenberger, *Science* 272, 1323 (1996).
53. R. P. Andres, V. R. Kolagunta, C. P. Kubiak, W. J. Mahoney, and R. G. Osifchin, *Science* 273, 1690 (1996).
54. T. Baum, D. Bethell, M. Brust, and D. J. Schiffrin, *Langmuir* 15, 866 (1999).
55. M. Brust, C. J. Kiely, D. Bethell, and D. J. Schiffrin, *J. Am. Chem. Soc.* 120, 12367 (1998).
56. C. J. Kiely, J. Fink, M. Brust, D. Bethell, and D. J. Shiffrin, *Nature* 396, 444 (1998).
57. K. S. Mayya and M. Sastry, *Langmuir* 15, 1902 (1999).
58. J. S. Yin and Z. L. Wang, *Adv. Mater.* 11, 469 (1999).
59. N. F. Mott and E. A. Davis, "Electronic Processes in Noncrystalline Materials." Clarendon, Oxford, UK, 1971.
60. S. Henrichs, C. P. Collier, R. J. Saykally, Y. Shen, and J. R. Heath, *J. Am. Chem. Soc.* 122, 4077 (2000).

61. W. P. McConnel, J. P. Novak, L. C. Brousseau III, R. R. Fuierer, R. C. Tenent, and D. L. Feldheim, *J. Phys. Chem. B* 104, 8925 (2000).
62. G. Schmid and L. F. Chi, *Adv. Mater.* 10, 515 (1998).
63. J. Hubbard, *Proc. Roy. Soc. London* 276, 238 (1963).
64. F. Remacle and R. Levine, *J. Am. Chem. Soc.* 122, 4084 (2000).
65. J. Lambe and R. C. Jaklevic, *Phys. Rev. Lett.* 22, 1371 (1969).
66. R. E. Cavicchi and R. H. Silsbee, *Phys. Rev. B* 37, 706 (1988).
67. J. J. Shiang, J. R. Heath, C. P. Collier, and R. J. Saykally, *J. Phys. Chem. B* 102, 3425 (1998).
68. M. Aslam, I. S. Mulla, and K. Vijayamohanan, *Appl. Phys. Lett.* 79, 689 (2001).
69. M. Aslam, N. K. Chaki, I. S. Mulla, and K. Vijayamohanan, *Appl. Surf. Sci.* 182, 338 (2001).
70. R. L. Whetten, J. T. Khoury, M. M. Alvarez, S. Murthy, I. Vezmar, Z. L. Wang, P. W. Stephenes, C. L. Cleveland, W. D. Luedtke, and U. Landman, *Adv. Mater.* 8, 428 (1996).
71. T. Teranishi, M. Haga, Y. Shiozawa, and M. Miyake, *J. Am. Chem. Soc.* 122, 4237 (2000).
72. D. Zanchet, B. D. Hall, and D. Ugarte, *J. Phys. Chem. B* 104, 11013 (2000).
73. Y.-S. Shon, S. M. Gross, B. Dawson, M. Porter, and R. Murray, *Langmuir* 16, 6555 (2000).
74. M. Green and P. O'Brien, *Chem. Commun.* 183 (2000).
75. Y.-Y. Yu, S.-S Chang, C.-L Lee, and C. R. C. Wang, *J. Phys. Chem. B* 101, 6661 (1997).
76. E. Dujardin, L. Hsin, C. R. C. Wang, and S. Mann, *Chem. Commun.* 1264 (2001).
77. M. J. Hostetler, J. J. Stokes, and R. W. Murray, *Langmuir* 12, 3604 (1996).
78. W. D. Luedtke and U. Landman, *J. Phys. Chem.* 100, 13323 (1996).
79. W. D. Luedtke and U. Landman, *J. Phys. Chem. B* 102, 6566 (1998).
80. J. P. Wilcoxon, J. E. Martin, and P. Provencio, *J. Chem. Phys.* 115, 998 (2001).
81. J. E. Martin et al., *J. Phys. Chem. B*, DIN: 10.1021/jpo20489ϕ (2002).
82. A. Ulman, *Chem. Rev.* 96, 1533 (1996).
83. A. Badia, W. Gao, L. Singh, L. Demers, L. Cuccia, and L. Reven, *Langmuir* 12, 1262 (1996).
84. A. Badia, L. Cuccia, L. Demers, F. Morin, and R. B. Lennox, *J. Am. Chem. Soc.* 119, 2682 (1997).
85. A. C. Templeton, S. Chen, S. M. Gross, and R. W. Murray, *Langmuir* 15, 66 (1999).
86. M. Bourg, A. Badia, and R. B. Lennox, *J. Phys. Chem. B* 104, 6562 (2000).
87. P. E. Laibinis, G. M. Whitesides, D. L. Allara, Y.-T. Tao, A. N. Parikh, and R. G. Nuzzo, *J. Am. Chem. Soc.* 113, 7152 (1991).
88. M. J. Hostetler, J. E. Wingate, C. J. Zhong, J. E. Harris, R. W. Vachet, M. R. Clark, J. D. Londono, S. J. Green, J. J. Stokes, G. D. Wignall, G. L. Glish, M. D. Porter, N. D. Evans, and R. W. Murray, *Langmuir* 14, 17 (1998) and references therein.
89. P. Mulvaney and M. Giersig, *J. Chem. Soc. Faraday Trans.* 92, 3137 (1996).
90. L. O. Brown and J. E. Hutchison, *J. Phys. Chem. B* 105, 8911 (2001).
91. F. Bodkev, M. F. Hansen, C. B. Koch, K. Leffman, and M. Steen, *Phys. Rev. B* 61, 6826 (2000).
92. E. Hutter, J. H. Fendler, and D. Roy, *J. Phys. Chem. B* 105, 11159 (2001).
93. S. Chen and Y. Yang, *J. Am. Chem. Soc.* 124, 5280 (2002).
94. L. Armelao, P. Colombo, M. Fabrizio, S. Gross, and T. E. Silvia, *J. Mater. Chem.* 9, 2893 (1999).
95. S. Chen, R. S. Ingram, M. J. Hostetler, J. J. Pietron, R. W. Murray, T. G. Schaaff, J. T. Khoury, M. M. Alvarez, and R. L. Whetten, *Science* 280, 2098 (1998).
96. M. Dorogi, J. Gomez, R. Osifchin, R. P. Andres, and R. Reinfenberger, *Phys. Rev. B* 52, 9071 (1995).
97. J. J. Pietron and R. W. Murray, *J. Phys. Chem. B* 103, 4440 (1999).
98. R. S. Ingram and R. W. Murray, *Langmuir* 14, 4115 (1998).
99. R. S. Ingram, M. J. Hostetler, R. W. Murray, T. G. Schaaff, J. T. Khoury, R. L. Whetten, T. P. Bigioni, D. K. Guthrie, and P. N. First, *J. Am. Chem. Soc.* 119, 9279 (1997).
100. K. J. Brown, A. P. Fox, and M. J. Natan, *J. Am. Chem. Soc.* 118, 1154 (1996).
101. S. Yabuki and F. Mitzutani, *Electroanalysis* 9, 23 (1997).
102. Y. Xiao, X. H. Ju, and H. Y. Chen, *Anal. Chim. Acta* 391, 73 (1999).
103. E. Katz and H. L. Schmid, *J. Electroanal. Chem.* 360, 337 (1993).
104. J. Zhao, R. W. Henkens, J. Stonehuerner, J. P. O'Daly, and A. L. Crumbliss, *J. Electroanal. Chem.* 327, 109 (1992).
105. P. Claus, A. Bruckner, C. Mohr, and H. Hofmeister, *J. Am. Chem. Soc.* 122, 11430 (2000).
106. M. Valden et al., *Science* 281, 1647 (1998).
107. M. A. Bryant and J. E. Pemberton, *J. Am. Chem. Soc.* 113, 8284 (1991).
108. M. H. Schoenfisch and J. E. Pemberton, *J. Am. Chem. Soc.* 120, 4502 (1998).
109. A. Henglein and D. Meisel, *J. Phys. Chem. B* 102, 8364 (1998).
110. A. Henglein, *Chem. Rev.* 89, 1861 (1989).
111. N. K. Chaki, S. G. Sudrik, H. R. Sonawane, and K. Vijayamohanan, *Chem. Commun.* 76 (2002).
112. N. Sandhyarani and T. Pradeep, *Chem. Mater.* 12, 1755 (2000).
113. M. C. Chen, S. D. Tsai, M. R. Chen, S. Y. Ou, W. H. Li, and K. C. Lee, *Phys. Rev. B* 51, 4507 (1995).
114. S. Remita, J. M. Orts, J. M. Feliu, M. Mostafavi, and M. O. Delcourt, *Chem. Phys. Lett.* 218, 115 (1994).
115. J. M. Wen, J. W. Evans, S. L. Chang, J. W. Burnett, and P. A. Thiel, *Mater. Res. Soc. Symp. Proc.* 355, 15 (1995).
116. A. Downes and M. E. Welland, *Appl. Phys. Lett.* 72, 2671 (1998).
117. J. B. Jackson and N. J. Halas, *J. Phys. Chem. B* 105, 2743 (2001).
118. T. Oku, T. Kusunose, K. Niihara, and K. Suganuma, *J. Mater. Chem.* 10, 255 (2000).
119. R. P. Bagwe and K. C. Khilar, *Langmuir* 16, 905 (2000).
120. S. A. Harfenist, Z. L. Wang, M. M. Alvarez, I. Vezmar, and R. L. Whetten, *J. Phys. Chem.* 100, 13904 (1996).
121. Y.-P. Sun, P. Atorngitjawat, and M. J. Meziani, *Langmuir* 17, 5707 (2001).
122. A. Manna, T. Imae, M. Iida, and N. Hisamatsu, *Langmuir* 17, 6000 (2001).
123. S. Y. Kang and K. Kim, *Langmuir* 14, 226 (1998).
124. S. Fullam, S. N. Rao, and D. Fitzmaurice, *J. Phys. Chem. B* 104, 6164 (2000).
125. H. S. Kim, J. H. Ryu, B. Jose, B. G. Lee, B. S. Ahn, and Y. S. Kang, *Langmuir* 17, 5817 (2001).
126. A. Manna, B. D. Kulkarni, K. Bandyopadhyay, and K. Vijayamohanan, *Chem. Mater.* 9, 3032 (1997).
127. J. R. Heath, T. Vossmeyer, E. DeIonno, and G. Markovich, in "Nanostructures Materials: Clusters, Composites and Thin Films" (V. M. Shalaev and M. Moskovits, Eds.), ACS Symp. Ser. 670, pp. 1–6. Am. Chem. Soc., Washington, DC, 1997.
128. G. Oldfield, T. Ung, and P. Mulvaney, *Adv. Mater.* 12, 1519 (2000).
129. R. T. Tom, A. S. Nair, N. Singh, M. Aslam, C. L. Nagendra, R. Philip, K. Vijayamohanan, and T. Pradeep, *Langmuir*, in press.
130. J. J. Schneider, *Adv. Mater.* 13, 529 (2001).
131. F. Caruso, *Adv. Mater.* 13, 11 (2001).
132. C. S. Ah, S. D. Hong, and D. Jang, *J. Phys. Chem. B* 105, 7871 (2001).
133. M. L. Steigerwald, A. P. Alivisatos, J. M. Gibson, D. T. Harris, R. Kortan, A. J. Muller, A. M. Thayer, T. M. Duncan, D. C. Douglass, and L. E. Brus, *J. Am. Chem. Soc.* 110, 3046 (1998).
134. A. Henglein, *J. Phys. Chem. B* 104, 2201 (2000).
135. A. Henglein, *J. Phys. Chem. B* 104, 6683 (2000).
136. J. H. Fendler, *Chem. Rev.* 87, 877 (1987).
137. V. T. Liveri, M. Rossi, G. D'Arrigo, D. Manno, and G. Micocci, *Appl. Phys. A* 69, 369 (1999).

138. L. Rivas, S. Sanchez-Cortes, J. V. García-Ramos, and G. Morcillo, *Langmuir* 16, 9722 (2000).

139. E. Hutter and H. Fendler, *Chem. Commun.* 378 (2002).

140. S. Fullam, H. Rensmo, S. N. Rao, and D. Fitzmaurice, *Chem. Mater.* 10.1021/cm011182e (2002).

141. S. Fullam, S. N. Rao, and D. Fitzmaurice, *J. Phys. Chem. B* 104, 6164 (2000).

142. D. Ahern, S. N. Rao, and D. Fitzmaurice, *J. Phys. Chem. B* 103, 1821 (1999).

143. M. Giersig, T. Ung, L. M. Liz-Marzan, and P. Mulvaney, *Adv. Mater.* 9, 570 (1997).

144. T. Ung, L. M. Liz-Marzan, and P. Mulvaney, *J. Phys. Chem. B* 103, 6770 (1999).

145. R. P. Andres, J. D. Bielefeld, J. I. Henderson, D. B. Janes, V. R. Kolagunta, C. P. Kubiak, W. J. Mahoney, and R. G. Osifchin, *Science* 273, 1690 (1996).

146. F. Seker, K. Meeker, T. F. Kuech, and A. B. Ellis, *Chem. Rev.* 100, 2505 (2000).

147. B. Honig and A. Nicholls, *Science* 268, 1144 (1995).

148. F. Caruso, H. Lichtenfield, M. Giersig, and H. Mohwald, *J. Am. Chem. Soc.* 120, 8523 (1998).

149. J. Tien, A. Terfort, and G. M. Whitesides, *Langmuir* 13, 5349 (1997).

150. J. Schmitt, P. Machtle, D. Eck, H. Mohwald, and C. A. Helm, *Langmuir* 15, 3256 (1999).

151. S. W. Keller, S. A. Johnson, E. S. Brigham, E. H. Yonemoto, and T. E. Mallouk, *J. Am. Chem. Soc.* 117, 12879 (1995).

152. V. Patil and M. Sastry, *Langmuir* 14, 2707 (1998).

153. A. Gole, C. Sathivel, A. Lachke, and M. Sastry, *J. Chromatogr. A* 848, 485 (1999).

154. S. Pethkar, M. Aslam, I. S. Mulla, P. Ganeshan, and K. Vijaya-mohanan, *J. Mater. Chem.* 11, 1710 (2001).

155. C. P. Collier, T. Vossmeyer, and J. R. Heath, *Annu. Rev. Phys. Chem.* 49, 371 (1998).

156. R. M. Pashley, P. M. McGuiggan, B. W. Ninham, and D. F. Evans, *Science* 229, 1088 (1985).

157. J. N. Israelachvili and R. M. Pashley, *Nature* 300, 341 (1982).

158. Z. L. Wang, *Adv. Mater.* 10, 13 (1998).

159. C. J. Brinker, Y. Lu, A. Sellinger, and H. Fan, *Adv. Mater.* 11, 579 (1999).

160. S. Connolly, S. Fullam, B. Korgel, and D. Fitzamurice, *J. Am. Chem. Soc.* 120, 2969 (1998).

161. J. H. Fendler and F. Meldrum, *Adv. Mater.* 7, 607 (1995) and references therein.

162. M. Sastry, V. Patil, K. S. Mayya, D. V. Paranjape, P. Singh, and S. R. Sainkar, *Thin Solid Films* 324, 239 (1998).

163. M. Li, K. K. W. Wong, and S. Mann, *Chem. Mater.* 11, 23 (1999).

164. M. D. Bentzon and A. Tholen, *Ultramicroscopy* 38, 105 (1990).

165. M. Geirsig and P. Mulvaney, *J. Phys. Chem.* 97, 6334 (1993).

166. P. C. Ohara, D. V. Leff, J. R. Heath, and W. M. Gelbart, *Phys. Rev. Lett.* 75, 3466 (1995).

167. A. Ellis et al., *Nano. Lett.*, in press.

168. M. Aslam, Thesis, Pune University, India, 2002.

169. S. Mitra, B. Nair, T. Pradeep, P. S. Goyal, and R. Mukhopadhyay, *J. Phys. Chem.* 106, 3960 (2002).

# Multiwall Carbon Nanotubes

## Dojin Kim

*Chungnam National University, Daejon, South Korea*

## CONTENTS

## 1. INTRODUCTION

A carbon nanotube (CNT) is a hollow tube formed by the roll up of graphite sheet(s) into a cylinder. It can be classified as a single-wall carbon nanotube (SWNT) or a multiwall carbon nanotube (MWNT), depending on the number of graphite sheets forming the tube wall. The CNT was disclosed for the first time by Iijima [1] in 1991 as an MWNT type. The distance between the atomic graphitic sheets of the wall in the MWNT is ∼0.34 nm, which is similar to the interplanar spacing in graphite. The diameter of the MWNT ranges from a few to tens of nanometers, and its length from micrometers to millimeters, showing its one-dimensional nature. In addition to this one-dimensional quantum geometry with very high aspect ratios, other properties originating from the characteristics of the atomic carbon and nanostructure, such as good electrical conductivity, stubborn mechanical property, nano-size cavity, and so on, have motivated its use in various applications.

The SWNT may have definite advantages over the MWNT in discussing the intrinsic properties of carbon nanotubes. Searching for the intrinsic properties of the carbon nanotube with MWNTs would not be a good idea because they usually contain a high density of defects, and the atomic registry between the graphene sheets has not been well identified. Therefore, the scientific studies on carbon nanotubes mostly have been carried out with SWNTs. Since the discovery of carbon nanotubes, extensive and intensive research has been done on the physical and chemical properties, synthesis methods, and applications, and already appear in several books [2–6] and review articles [7, 8]. On the other hand, the MWNT has a higher potential in diverse applications. Not only the abundance and low-cost production with various synthesis methods, but also a few unique synthesis morphologies can further expand the use of MWNTs. Distinguished examples may be the selective growth on patterned catalysts and vertically aligned growth morphology. These advantageous morphological features can be combined with the well-developed microelectronics technology for device application. This integration capability is an extremely important ingredient for practical applications because nanomanipulation technology on an individual structure will have very limited application. Furthermore, obtaining reduced cost for MWNTs along with the development of various production technologies will further expand the application, particularly to bulk amount usage. In the course of this, understanding and controlling the growth morphology of MWNTs is a prerequisite for their proper implementation. Since the growth mode is still an insufficiently explained issue, the author will focus on the status of the synthesis methods and relevant mechanisms/modes in the catalytic growth with the chemical vapor deposition (CVD) method. This is because gaining control over challenging growth issues is critical to the future advancement of nanotube science and technology. Furthermore, as the research with MWNTs is rather oriented toward application, the properties of the MWNT will be very restrictively summarized at a minimum, and the status of the MWNT applications will be surveyed by spotlighting the central principles and ideas. There are research fields derived from carbon nanotubes, such as nanorods, filling, and so on, but those derived areas, other than multiwall carbon nanotubes themselves, will not be covered in this review.

## 2. SYNTHESIS OF MULTIWALL CARBON NANOTUBES

Mainly two methods have been developed for MWNT synthesis: arc discharge and chemical vapor deposition. The arc-discharge method produces tubes of high quality with a thin wall, but the yield is low. On the other hand, the tubes synthesized by CVD methods are, in general, thicker and show many defects, but the yield is much higher. If high-quality tubes are in demand for an application, it would be better to use an SWNT or MWNT produced by arc discharge. MWNTs grown with the CVD method, however, in spite of their inferior quality, have unique advantages for applications where bulk quantity is necessary or integration is of practical importance. CVD is traditionally a favorable method for synthesis on large substrates, and therefore, becomes increasingly important method for MWNT production. MWNTs might have been synthesized by CVD before their disclosure by Iijima. Even though the old studies of the synthesis and growth mechanisms on carbon nanofibers may still explain many important issues for carbon nanotubes today, the diversely expanding growth technologies may require new aspects for consideration.
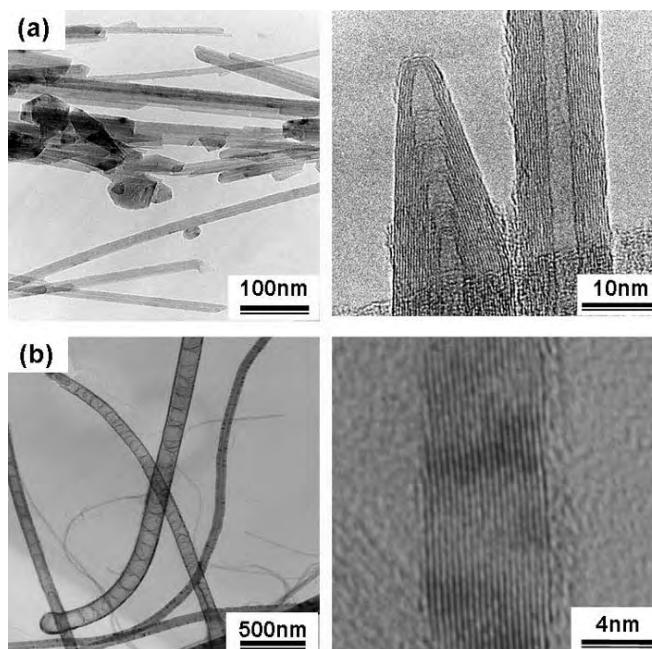
### 2.1. Arc-Discharge Method

The arc-discharge method has been in use for a long time for the production of carbon fibers. In the dc arc discharge, which has been the method favored over the ac arc discharge in the yield [9], direct current is applied between the graphite cathode and the anode in an inert gas such as He. This leads to the formation of a nanotube-containing deposit on the cathode. A schematic of the apparatus is shown in Figure 1(a). Arc discharge can produce both an SWNT and an MWNT. Unlike the arc discharge for SWNT synthesis, there is no need for mixing catalytic metal in the anode for an MWNT. The arc-discharge tubes are thin and straight, showing a high-quality wall structure owing to the high synthesis temperature of ~3000 °C [10, 11], but the production yield is generally as low as 10%. The quality and yield of the tubes depend on the arc-discharge process parameters, including inert gas and pressure [9, 12–15], plasma stability [12], the geometry of the electrodes [16], and so on. A breakthrough in the large-scale synthesis in gram quantity was first made by Ebbensen and Ajayan [9] by optimizing the process parameters. By modifying the cathode part into water-cooled copper, tens of micrometer length tubes
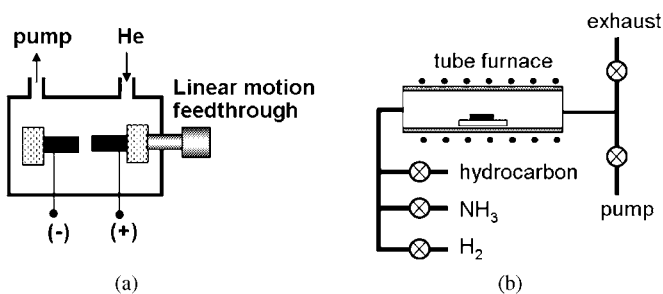
of high quality could be obtained [16]. Since the deposit on the cathode contains many various carboneous byproducts other than nanotubes, it needs to go through a purification process. A typical purification technique is to remove the graphitic products by oxidation either in air [17–19] or in chemicals [20–23]. A high-temperature treatment was shown to be effective in the purification as well as in the graphitization of the tubes [24]. A purification process is also necessary for CVD-grown tubes [21–23].

The typical structure grown by the arc-discharge process is shown in Figure 2(a). The diameter of the tubes is usually in the range of 2–20 nm, with the wall composed of double to a few tens of graphene sheets. The head tip is closed by a polyhedral cap [11]. The generation of a nonhexagonal network, pentagons and heptagons, is necessary for the closure of the cap. Experiments showed, however, that the end of the tube wall is kept open during the growth [25, 26]. This observation attracted great interest because, while a closed tip is energetically favored, the open tip should keep dangling bonds of high energy. The high electric field present at the tip during the process was proposed to explain the open tip during the growth, but was questioned by calculations [27–29]. Charlier et al. [30] proposed that a chemical bonding between the adjacent dangling bonds at the tip (called lip–lip interaction, which is mediated by a covalent bonding [31]) can reduce the energy, and thus stabilizes the open-tip state. On the other hand, this open end with strain exhibits high chemical activity for carbon absorption during the growth [30, 31]. Lip–lip interaction was also proposed as the mechanism for cap closure [32]. The growth models for the MWNT synthesis in the arc-discharge process are reviewed in detail in [6] and [7].

**Figure 2.** TEM images for MWNTs grown by (a) arc-discharge method and (b) thermal CVD method. Right side figures at high resolution. [(a) Courtesy of Iljin Nanotech Co.]

**Figure 1.** Schematic drawing of the apparatus for (a) arc-discharge method and (b) thermal CVD method.

## 2.2. Chemical Vapor Deposition

CVD now becomes a key production technology for solid-state materials via chemical reactions of the incoming source gases at an appropriate temperature. Since CVD has advantages in synthesizing or growing thin films uniformly over large-area substrates, it becomes a more and more attractive method in MWNT growth for ensemble-type applications such as field-emitter and microelectronic devices. A schematic of a thermal CVD equipment is shown in Figure 1(b). MWNT growth is done by decomposition of hydrocarbon over catalyst material in the reactor maintained at an appropriate temperature. The main process parameters are the hydrocarbon source, catalyst, and temperature. Most of the CVD methods employ ethylene or acetylene as the carbon source, often mixed with $H_2$, $N_2$, Ar, $NH_3$, and so on. Other carbon sources, such as $CH_4$, CO, benzene, polyethylene, and so on, were sometimes used [33]. The hydrocarbon gases supply carbon for graphitic carbon nanotube growth through reaction with the catalyst at moderately low temperatures [34]. The synthesis temperature is typically in the range of 700–900 °C, which is much lower than the temperature employed in the arc discharge. The graphitization level of the tubes is less with higher defect densities than those synthesized by the arc discharge [35]. The catalytic materials are typically transition metals such as Ni, Co, Fe, and their alloys. The presence of the catalyst material is essential to the nanotube synthesis with CVD, and thus the process is inherently a selective growth process. Namely, the nanotubes grow only where the catalytic particles are present. However, this presence is not sufficient for tube growth. The catalyst metals need to distribute in particulates with an appropriate size typically of tens of nanometers. Actually, the catalyst nanoparticles are in the center of the CVD growth of multiwall carbon nanotubes, and therefore, most of the discussions to understand the growth behavior in CVD have been made in relation to the catalyst particles. The CVD-synthesized MWNTs also reveal a larger diameter (20–100 nm) and a thicker wall than the arc-discharge tubes. Microstructures of typical MWNTs grown via thermal CVD are shown in Figure 2(b).

Thick MWNTs or carbon filaments have been grown before the disclosure of the MWNT by Iijima. Once the nanotube and filament were distinguished by the diameter [36], but they do not seem to be critically classified these days. In that period and after, powder-type support materials distributed with nanosize metal particles have been frequently used for the synthesis of an MWNT or filament [37]. This catalyst–support powder was made by impregnation or ion-exchange precipitation of a metallic catalyst into support materials of graphite, $SiO_2$, $Al_2O_3$, and so on, and subsequent treatment in an appropriate atmosphere [38, 39]. The catalytic property of the catalyst particles in the support depends on the interaction between the support and the metal particles during the preparation [40]. Recently, this traditional method with support materials of silica and zeolite has been considered for mass production [41–43]. Very long (∼2 mm) MWNTs are grown on a mesoporous silica substrate [44]. An advantage of this method is that the productivity is not limited by the substrate area as in the CVD synthesis on plain substrates, as described in the following.

The second CVD method uses thin metal films deposited on plain substrates (Si, alumina, glass, metals, etc. [45, 46]) for the catalyst, and has been very frequently employed in recent years. Thin films of a few to tens of nanometer thickness are deposited on a substrate by evaporation or the sputtering method. Subsequent heating of the thin films makes the thin film agglomerate into nanosize metal particles having a diameter of a few to ten times the thickness [47]. Since the particle agglomeration is a self-assembling process, the particles distribute in size, and consequently, the diameter of the grown MWNTs does too. The average size of the nanoparticles is proportional to the film thickness, and it was shown that nanotubes can be grown on particles of size 2–100 nm [38]. Figure 3 shows typical morphologies of Ni particles formed on an Si wafer and of the MWNTs grown upon it. The inset shows the macroscopic view of the grown vertically aligned MWNTs. For the growth on plain substrates, several kinds of CVD techniques (thermal, plasma- or microwave-enhanced, plasma-enhanced hot-filament CVD) have been used. The employed gas pressures typically range from atmospheric pressure to ∼100 torr. The low-pressure processes of the plasma-enhanced CVD (PECVD) and microwave-enhanced CVD (MECVD) methods have been frequently used to decrease the synthesis temperatures [48]. The use of plain substrates with extremely smooth surfaces such as Si has unique advantages for applications to nanodevices, along with the microelectronics fabrication technology. In this regard, CVD synthesis on plain substrates has attracted great attention in recent years.

The third CVD method is vapor phase synthesis, which is done by pyrolyzing source gases that contain both elements of carbon and catalyst. Metal organics [49–51] or their mixture with xylene or benzene [49, 52–54] have been used for the source gases. Sen et al. [49] carried out the pyrolysis of metallocenes (ferrocene, cobaltocene, and nickelocene) in an inert atmosphere at 900 °C to synthesize MWNTs. The production of low-cost CNTs is essential for applications involving bulk quantity use, such as hydrogen storage, composites, batteries, and so on. This method has definite advantages in development toward a continuous process for mass production. At present, the major stream for mass production may be vapor or gas phase synthesis, although the source gases are expensive. The arc-discharge process has limitations for mass production due to its low yield, although it can be modified to higher productivity by employing a continuous production scheme [55].
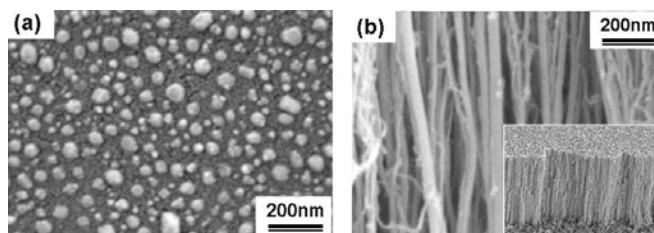


**Figure 3.** Morphology of (a) Ni nanoparticles agglomerated under $NH_3$ heat treatment and (b) carbon nanotubes grown upon with $C_2H_2$. Inset shows the macroscopic view.

Regarding the issue of mass production, CVD using catalyst–support powder material can also be considered as a method for mass production. Yield could be significantly increased by using zeolite as the support material [56]. Although it consumes support materials and involves complex chemistry, inexpensive powder can make it a plausible candidate. The CVD synthesis on substrates has not been considered as a method for mass production. The deposition of catalyst metal films being carried out in vacuum equipment is an expensive process. It is also apt to become a bottleneck step in the synthesis process because of the batch-type processing involved, and consequently, of the limited synthesis area. However, the barriers to mass production in the method can be overcome [57]. The key to the improvement is to eliminate the metal deposition process, and instead, use a liquid-type catalyst that can be applied on substrates by a simple spin-coating method. Magnetic fluid, which is iron–oxide nanoparticles floating in liquid, is used for the catalyst. Magnetic fluid is mixed with polyvinyl alcohol to have the appropriate viscosity, and the mixture is spin coated on substrates. A spinner designed to be heavy duty can handle the batch of many substrate plates, and thus eliminate the limitation in the area. The MWNTs grown on Si and alumina showed densely aligned morphology similar to that shown in Figure 3 [57].

The morphology of MWNTs grown in CVD is very different from that in the arc discharge (Fig. 2), mainly because the growth temperatures are remarkably lowered with the involvement of catalysts. The payment for using low temperature is less straight tubes with a high density of defects and greater diameter [35]. Among the different CVD methods, different growth morphologies have been observed due to differences in equipment and detailed process conditions, such as types of metals and substrate, catalyst particle size and distribution, type and ratio of the source and mixing gases, temperature, and other process parameters. Basically, two different growth modes have been observed, while the fundamental mechanism for the catalytic CVD growth of MWNTs has not yet been firmly established. The early searches for the growth mechanism in catalyst–support growth were reviewed by Laurent et al. [37].

Rodriguez and Baker [36, 38] established a diffusion model for carbon filament growth based upon the vapor–liquid–solid mechanism, where they proposed that the filament growth in CVD involves: (1) the dissociation of hydrocarbon molecules through catalysis by transition metals of nanoparticle form, (2) the dissolution and saturation of carbon in the catalyst nanoparticles, and (3) the subsequent segregation of carbon out of the catalyst for filament growth. It was found that the activation energy for the diffusion of carbon through the metal has a strong correlation with that for the growth [58]. This diffusion model has also been accepted in general for the growth of catalytic MWNTs.

It has been empirically shown that the growth temperature and catalyst particle size have specific ranges for the synthesis of carbon nanotubes as well as carbon filament [38, 47]. The ranges are 400–1000 °C and 2–100 nm, respectively. Since the CNT synthesis and the catalyst particle formation usually occur at the same temperature, the temperature influences both the decomposition rate of hydrocarbons and the activity of the catalyst. Mo et al. [59] showed, in a quadrupole mass spectroscopy analysis, that $C_2H_2$ does not decompose up to 600 °C while CNTs are grown. This observation suggests that the growth at the temperature was induced not by thermal decomposition of the gas, but indeed by the catalytic dissociation of acetylene on the Ni surface. This indicates that the catalytic reaction of the metal particle with hydrocarbon determines the low-temperature limit. The upper limit of the synthesis temperature has not been systematically studied, but various parameters may affect it in combination. Possible causes may be the changes in morphology of the catalyst and the process kinetics. The metal particles spread further with a smaller wetting angle at a higher temperature, forming a larger diameter particle with unclear particle boundaries. Now, the chance to nucleate large-diameter tubules decreases, while the decomposition of hydrocarbon into amorphous carbon in the reactor accelerates. If the rate of amorphous carbon formation overrides that of the nanotube nucleation and growth, the amorphous carbon depositing quickly on the catalyst will passivate the catalyst and stop the nanotube growth [60]. Note that the upper temperature limit then may vary with the metal–substrate system, film thickness, source gas, and so on. The chemical form of carbon in or at the surface of the metal particles is controversial between pure carbon and carbide [38, 61], while the microscopic mass transport has to be further explored.

The diffusion model also explains the dependence of the nanotube diameter on the size of the metal particles [38]. The strain energy of the tube becomes too large to grow on too small particles [62]. There are no clear explanations on the upper limit of the particle size for tube growth, but it may be difficult for the diffusing flux of carbon to define tubular nucleation sites of large diameter. The growth rate of nanotubes also depends on the particle size. This is shown in an MWNT growth on Si where Ni particles are distributed in size (Fig. 4). In the photo of an initial stage of the growth, one can see that small-diameter tubes on small Ni particles outgrow the large-diameter tubes on larger Ni particles. The diffusion flux of carbon into a catalyst particle is proportional to the surface area of the particle (two dimensional), while the tube growth occurs by segregation from the particles saturated with carbon (three dimensional). A smaller ratio of the volume-to-surface area will result in a shorter growth incubation time, and the thinner wall with a smaller diameter will show a relatively higher
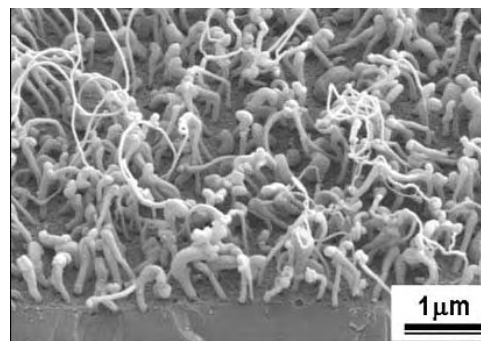


**Figure 4.** Morphology of carbon nanotubes in the initial stage of the growth.

growth rate in smaller particles. The wall thickness change with the tube diameter [39] can be understood by the diffusion model of Tibbetts [62].

The size of the catalyst metal particles has been controlled in various ways. In a catalyst–support powder system, the detailed chemical process to produce the catalyst–support mixture influences the metal particle size [63]. The physical and chemical interaction between the support and catalyst, physical and electronic structure of the support, catalyst coalescence, and so on, were shown to influence the behavior of the catalyst, and consequently, of the nanotube morphology. In catalyst-on-plain substrate systems, the catalyst size is controlled basically by the catalyst film thickness. The thicker film makes larger particles, and vice versa. The particle size can be correlated with the grain size since the grain size of the films increases with thickness [64, 65]. However, the grain boundary may not directly determine the particle's boundary because the grain size is much larger than the particle size [45]. The particle size also could be controlled by chemical or plasma etching of the deposited films [45, 64–68]. In PECVD or MECVD methods, etching of the metal films by plasma occurs regardless of the used gases ($NH_3$, $H_2$, $N_2$). However, the direct factor in determining the particle size is the thickness of the film at the time of thermal agglomeration, whether the additional etching control is made or not. The particle diameter is then determined by the surface, interface, and volume energies [38] involved in the given metal–substrate system at a given temperature.

The nanotubes grow either with a tip-growth mode or a base-growth mode on substrates, as schematically compared in Figure 5. In the tip-growth mode, catalyst particles are detached from the substrate, and move upward at the top of the growing tubes, while in the base-growth mode, they are stuck on the substrate during the growth, and push the tube upward. The tip-growth mechanism for a filament by Tibbetts [62] may also apply for the tip growth of an MWNT. Although the tip-growth mode was universally claimed in MECVD [69], thermal [70], and gas-phase growth [50], it was mostly observed with plasma CVD and thermal CVD using catalyst–support powder [44, 59, 64, 66, 71]. In the meantime, the base-growth mode was mainly proposed with thermal CVD on plain substrate and template [60, 72–74]. Such a distinction among the growth methods, however, may be simultaneously explained by the term of contact force between the catalyst particle and the substrate [38, 75].
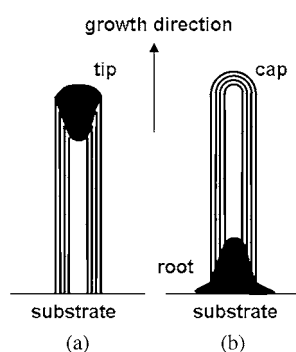
Namely, weak catalyst–substrate adhesion promotes the tip-growth mode, and vice versa. It, however, has not been discovered how the process parameters operate to result in the specific growth mode.

Examination of the growth modes usually has been done by transmission electron microscopy (TEM) observation of the tubes detached from the substrate. There is no sure way, however, to differentiate the root and the head of a tube with this method. The shapes of the tube head grown by the tip growth and the root grown by the base growth are sometimes very similar; the tube wall becomes thinner toward the end for both cases, when containing a bell-shaped catalyst. The ambiguity can be avoided by cross-sectional TEM examination of the tubes as attached to the substrate [76]. Figure 6 shows an example of the growth on Fe particles on Si substrate, revealing that the tubes are growing out of Fe particles at the roots in the base-growth mode. Catalyst particles enclosed by a thin graphite or amorphous carbon layer have been observed in both growth modes [50, 66, 71]. The thin graphene or amorphous layers covering the catalyst metal might be produced in the cooling cycle of the synthesis process [76].

The cap grown with the base-growth mode often contains metal in it. Whether or not the cap takes metal in it depends on the local geometry of the catalyst–substrate contact and the shape of the cap [60]. In order to discuss the metal capture into the cap in the base-growth mode, we may need to invoke the phase of the metal particles during the synthesis, as well as the shape of the cap. Solid and liquid phases of the metal particles have been proposed for both the tip- and base-growth modes [58, 59, 77–82]. The metal inclusion in the middle of the tube canal that is observable only for some particular tubes in a growth, however, suggests a liquid state of the particle during growth [76]. Since the wetting angle of the metal droplet with respect to the substrate changes with temperature [38], the shape of the metal particle determines the shape of the cap at the initial stage of the growth. At lower temperatures, the sphere-like cap synthesized following the shape of the metal droplet having a higher wetting angle can easily capture metals in it [60]. On the other hand, empty bell-shaped caps can be made with fluent and flatter metal particles at higher temperatures.

The same growth mechanism, diffusion and segregation, may operate in both the tip- and base-growth modes [83],



**Figure 5.** Schematic drawing of the tip- and base-growth modes.
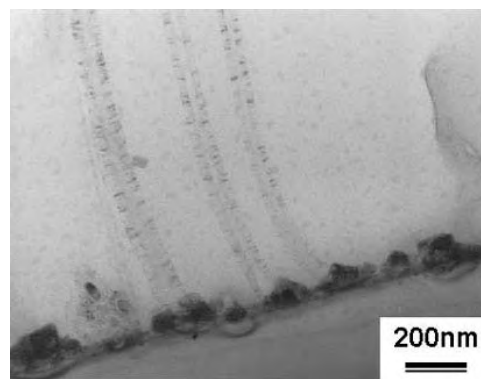


**Figure 6.** Cross-sectional TEM image of MWNTs grown on Fe nanoparticles.

but the route and direction of the carbon flow are different. In the tip growth, carbon diffuses in from the front face of the catalyst particle, and segregates out toward the back face [62]. However, in the base growth, carbon diffuses through the front face, and segregates back to the same face to form the cap at the beginning. The diffusion-in path will then be limited to the circumference of the particle at the interface between the cap and the substrate. For tubular growth extending from underneath the cap, therefore, diffusion-in of carbon through the circumference and its accumulation and/or segregation back to the circumference is necessary. When the tubule growth continues and pushes up the cap, the expanding space in the tube canal is to inhale the liquid metal droplet via vacuum sucking and/or capillary. The inhaling will continue until exhaustion of the droplet-forming liquid metal rod. The resisting force against this inhaling will be the metal-to-substrate contact force, which is assumed large in the base-growth mode. When the metal-to-substrate adhesion force overrides the vacuum sucking and/or the capillary, the metal rod is suddenly pulled back, and the initial particle shape is recovered. The tube growth process in the base-growth mode is schematically shown in Figure 7. In this procedure, a part of the metal droplet can be snatched by the cap or left in the tube canal as inclusion. The spherical shape of the cap with a neck made at a lower temperature can more easily snatch a metal droplet to form a filled cap than a cap of bell shape made at high temperatures [60, 68]. When the pull-back force operates continuously with the rod in the canal, a bamboo structure feature would not appear, as is sometimes observed at lower temperatures.

The bamboo structure (Fig. 2b) has been observed in all of the MWNTs, regardless of the employed growth techniques, arc discharge [84], and CVD [50, 74, 85, 86]. The morphology of the bamboo structure reveals repeated compartments in the tube canal, and can be explained by the repetition of the cap formation process (Fig. 7). However, the carbon to form the compartment has to be supplied through the circumference path, and diffuses toward the top of the metal rod. At high temperatures, regular bamboo compartments are formed, due possibly to the highly fluidized metal particle, but the morphology of irregular compartments or no compartment is revealed at low temperatures due to the higher viscosity of the metal particles [60]. In due course,
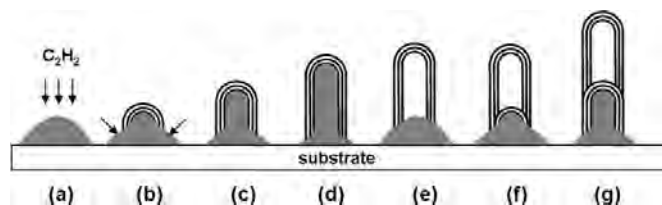


**Figure 7.** Growth process of MWNTs in the base-growth mode forming the cap and bamboo structure. (a) Nanometal particle formation and hydrocarbon diffusion. (b) Cap of graphene sheet formation. (c) Tubular growth and liquid metal inhaling. (d) Maximum of inhaling and operation of metal–substrate contact force to (e) pull down the metal rod, and the metal rod recovers to the particulate shape. (f) Bamboo compartment formation. (g) Tubular growth and liquid metal inhaling.

the metal rod needs to be pulled back suddenly to form the empty space between the compartments. In the tip-growth mode, there is no such pull-back force of the metal-to-substrate contact force as in the base-growth mode. Stress of the wall [84] and vapor pressure of the catalyst [87] have been proposed. Recently, Zhang et al. [86] proposed a model for the tip-growth mode based upon the liquid metal suction and pulling-back procedure similar to what the authors have proposed for the base-growth mode. The surface tension of the metal and the stress of the tube were suggested for the pull-back force.

## 2.3. Aligned Growth

Aligned carbon nanotubes have attracted great attention, particularly motivated by ensemble use for such areas as field-emission display (FED) and vacuum microelectronics. Although the tubes also may be aligned in the arc discharge [88], the alignment on plain substrates has definite advantages in pursuing application to electronic device structures, particularly in relation to the microelectronic fabrication process. Therefore, thermal and plasma-enhanced CVD methods on substrates are the first candidates for aligned growth due to the capability of uniform growth on a large area. Furthermore, patterning of the aligned CNTs for device fabrication can be achieved by selective growth on a patterned catalyst in the methods [89–91]. The substrates that are used to support the aligned CNTs can be divided into two categories: porous templates (mesoporous silica [44, 75, 89], nanochannel alumina [73, 92–94], etc.) and plain plates (quartz glass [64, 71], Si [72, 95], metal plate [45], etc.).

Li et al. [75] reported aligned CNTs in CVD growth with acetylene/nitrogen on Fe particles embedded in the pores of mesoporous silica. It was proposed that the alignment is made by the template effect in which the vertical direction of the pores constrains the CNT growth direction toward alignment. The macroscopically aligned nanotubes are bent and entangled with neighboring tubes in a microscopic view due to nonaligned mesopores. In the meantime, perfectly ordered arrays of nanotubes could be synthesized when nanochannel alumina templates are used [73, 92–94, 96, 97]. An alumina nanochannel template is made by anodizing high-purity aluminum to form periodic array of straight, deep, and uniform channels of nanometer scale diameter. Catalytic metal can be electrochemically deposited at the bottom of the channels, and hydrocarbon is flown over the template to synthesize carbon nanotubes along the channel. This method has produced two-dimensional arrays of densely packed aligned CNTs of uniform diameter, length, and orientation. The grown nanotubes are open ended and isolated from each other, forming a periodic hexagonal array.

Nanotubes can also be grown vertically aligned on plain substrates using CVD without relying on the templates. Ren et al. [64] grew aligned MWNTs by employing plasma-enhanced hot-filament CVD (PEHF–CVD) on Ni-coated glass with flowing acetylene and ammonia. Two distinctive methods have been employed thereafter: one is to grow on catalytic metal films using hydrocarbon, and the other is using a single metal-organic source containing both the

catalyst and carbon sources (so-called vapor phase CVD) [50–54, 98]. The former method can be further divided into thermal [60, 85, 90, 91, 99, 100] and PECVD/MECVD [45, 64–68, 101–104]. Growth at temperatures lower than the glass transition temperature of glass, ~650 °C, was sometimes stressed for flat-panel display application [64, 66, 68, 100]. The alignment on patterned substrates was also realized in all CVD growth methods of PECVD [101–103], thermal CVD [90, 99], and vapor phase CVD [50–54, 98]. It has been shown that the alignment morphology depends on various process parameters, such as catalytic metal film thickness and grain size [65], the chemical condition of the substrates [67, 68], source gas composition [45, 64, 67, 104], plasma condition [45, 64, 69], etching by gas or plasma [64, 66, 69], substrate bias [68, 69], and so on.

Although many of the alignments have been better achieved using plasma-assisted processes, the author will begin with thermal CVD where the alignment can be explained rather straightforwardly. The tubes would have a general tendency to grow perpendicular to the substrate in the base-growth mode when carbon diffuses and segregates uniformly at the circumference of the catalyst. However, the circumferential interface is also a place vulnerable to defect generation, and therefore, MWNTs growing alone on substrates are apt to reveal a wormy or crooked morphology. However, if the nucleation and growth occur all over the densely distributing catalyst particles, even such bending tubes lean on each other in the crowd, and grow upward from the substrate [50, 72]. Consequently, the macroscopic morphology reveals vertical alignment while each tube is microscopically curly growing (Fig. 3). Therefore, in order to obtain better alignment on plain substrates, as many as possible catalyst particles need to act as nucleation sites. The narrow distribution of the particle size will definitely help the alignment. For broader particle distribution, only a portion of the particles may offer nucleation sites due to the deactivation by amorphous carbon coating. The broader particle distribution condition can, however, to some extent, be relaxed by the atmosphere control in the reactor. $NH_3$ has been shown to be effective in etching away amorphous carbon from the surfaces of the catalyst particles and the tubes [60, 68, 103, 104]. The direct component for the etching seems to be atomic hydrogen decomposed from $NH_3$ [60, 104]. This environment can keep the surface of metal particles catalytically active, and make every particle act as a nucleation site, and consequently, dense tube growth is allowed. Tube alignment, which is directly related to dense tube growth, was achieved with both an $NH_3$ [45, 64, 66, 68, 101, 103, 104] and an $H_2$ [65, 67, 102] atmosphere in plasma-assisted CVD, but only with $NH_3$ in thermal CVD [60]. Plasma assistance may naturally offer higher efficiency in generating atomic hydrogen than a pure thermal process does. Therefore, vertical alignment in CVD growth on substrates is achieved, whatever the employed growth technique, basically by satisfying both the requirements of: (1) a dense distribution of nanoparticles of appropriate diameters, and (2) a process condition, including temperature, gas, plasma condition, and so on, that keeps the catalyst active during the growth.

## 3. SPECTROSCOPIC CHARACTERIZATION

It has been shown that the physical properties of the CNTs are closely related to their structure. For example, a CNT exhibits metallic or semiconducting behavior, depending upon its diameter and helicity [105]. There have also been controversial observations regarding the arrangement of the graphene sheets in the wall of an MWNT. Experimental observations supporting both concentric and scroll structures have been reported [6]. From the disclosure of MWNT by Iijima, the structural characterization of CNTs has been routinely made by TEM and high-resolution (HR) TEM observations. Information about the number of tubes, diameter, atomic configuration, and defects can be obtained. A study of the cross-section TEM observation of an MWNT reveals that both concentric and scroll-type structures coexist [106]. TEM has also been very useful in the direct observation of crystalline defects in the tubes [76, 106].

Other structural investigation methods used are scanning tunneling microscopy (STM), atomic force microscopy (AFM), field ion microscopy (FIM), and so on. STM and scanning tunneling spectroscopy (STS) have been used mostly to characterize SWNTs in the atomic structure and tunneling density of states [6]. SWNT is simpler in structure and far more defect free than MWNTs, but STM was also used to characterize the atomic and electronic structure of the surface shells in MWNTs [107]. The helicity of the surface shells can be determined by atomically resolved STM and AFM images [107, 108]. The distortion of the images in the measurement, however, needs to be considered in determining the tube diameter and chiral angles [109], which are closely related to the electrical properties of an MWNT [110]. A combined study of atomically resolved STM and STS on MWNTs revealed that there are interwall interactions, which depend on the registry of the atomic stacking between the walls [111]. The elastic modulus and radial deformation in MWNTs were examined by STM and AFM [112–113]. FIM was employed to investigate the atomic configuration at the tip [114]. A recent review on the characterization of the atomic structure is available [115].

A spectroscopic method for structural characterization is X-ray diffraction (XRD), with which a powder-like diffraction profile or a statistical structural property of the CNTs is obtained [115]. The technique has often been employed to reveal the radial stacking of the graphene sheets (concentric or scrolled) in MWNTs [116] by analyzing the peaks for (002), (004), and so on. Many now seem to accept the concentric cylinder model of the MWNT [117], although mixing with a small fraction of scroll-type tubes is very probable [118]. The MWNTs with high purity and graphitization exhibited a smaller (002) interlayer spacing and a higher (002) intensity [119]. Figure 8 shows an XRD pattern from purified arc discharge from MWNTs. A comparison is made with that from SWNTs. The (004)-like peak for the SWNT is due to bundle formation of the SWNTs. Neutron diffraction was also used for the structural study of MWNTs [120].

Optical techniques have been employed in investigating MWNTs. The most frequently used method is Raman scattering, which measures the normal modes of vibration in the CNT, particularly of $sp^2$ carbons [121]. The most prominent
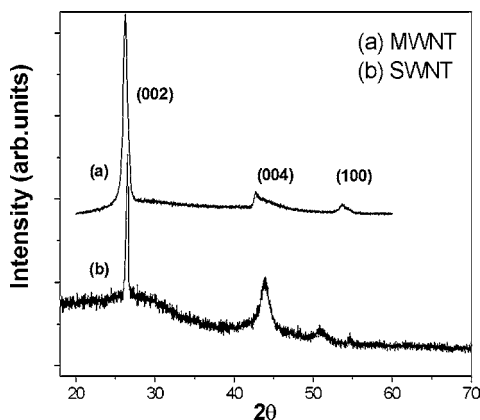
**Figure 8.** XRD patterns of arc discharge MWNT (purified) compared with that of SWNT. (Courtesy of Iljin Nanotech Co.)

peak is the first-order line at $\sim$1580 cm$^{-1}$, the so-called G-line, observed for CNTs, as well as for highly oriented pyrolytic graphite (HOPG). This vibration mode, which is also observable in single-crystal graphite, is usually quoted to determine the crystallinity of the CNTs [121]. However, a peak induced by disorder is observed most prominently at $\sim$1350 cm$^{-1}$ (called a D-line) for MWNTs, as well as for doped HOPG, glassy carbon, carbon nanoparticles, and so on [121, 122]. With a high degree of disorder, the intensity of the D-line increases with broadening, while that of the G-line decreases with broadening [121]. The CVD-grown MWNTs revealed inferior quality in comparison to SWNT and arc-discharge MWNTs [122, 123]. Raman peaks at a lower region <500 cm$^{-1}$ (radial breathing mode: RBM) induced by the thin central canal were observed [122], and those at a high region due to higher order scattering were examined [124]. Figure 9 shows typical Raman spectra for CVD and arc-discharge-grown MWNTs compared with that for SWNTs. The relative crystalline quality can be compared with the G- and D-line peaks. Note there are no D-line peaks for purified arc-discharge MWNTs and SWNTs. The dielectric function of the MWNT measured by ellipsometry was similar to that of HOPG [88], and an influence of
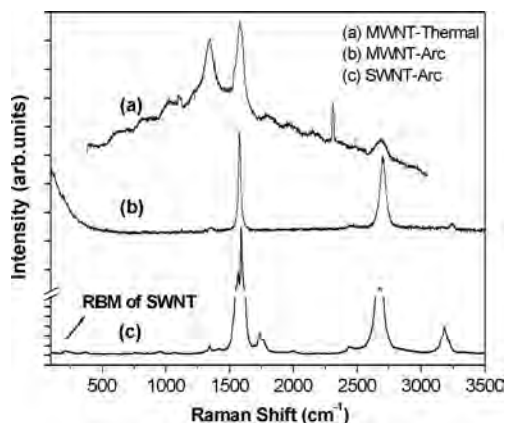
electromagnetic coupling between the tubes on the dielectric function was proposed [125]. Other optical investigations of infrared absorption, photoluminescence, reflectivity, optical conductivity, and photoemission of MWNTs have been also made [126–129]. An Auger electron spectroscopy study can also distinguish the ordered and disordered $sp^2$ bonds in the nanotube wall and head [130]. Electron spin resonance (ESR) studies indicated the existence of quasi-two-dimensional conduction carriers in the MWNTs [131, 132], and revealed a temperature-dependent ESR intensity of the MWNT similar to that for graphite.

# 4. PROPERTIES OF MULTIWALL CARBON NANOTUBES

Understanding the properties and exploring their potential applications have been a main driving force to recent intense research on carbon nanotubes. Theoretical and experimental works have been focused on understanding the atomic structures of carbon nanotubes in relation to the electronic structures, transport properties, chemical properties, optical properties, and so on. Thus far, CNTs have been utilized with either an individual or ensemble form. The individual use of the CNTs has been rather limited to demonstrations of field-emitter sources, tips for scanning probe microscopy, nanotweezers, chemical sensors, and so on, due to immaturity in the nanomanipulation technology. However, ensemble use of CNTs has been extensively studied under the present microfabrication technology for field-emission-based flat-panel displays. Bulk quantity applications also have been extensively studied for high-capacity hydrogen storage, supercapacitors, Li batteries, and so on.

## 4.1. Field-Emitting Properties

A field emitter is an electron source that emits electrons at an electric field. Bonard et al. have reviewed the progress in field emission from carbon nanotubes [133, 134]. The emitter tip for the field emitter requires thin conductors with a high aspect ratio, mechanical strength, and heat resistance. In this regard, carbon nanotube tips have shown better performance, particularly in turn-on voltage and current density, than Spindt-type tips made of refractory metal or Si.

There are intrinsic and extrinsic effects influencing the emitter performances. Since the emission of electrons from the tip of the emitter is controlled by the local electric field at the tip under a Fowler–Nordheim tunneling model, the work function of the MWNT, known usually as $\sim$5 eV, is an intrinsic factor that determines the emission properties. It was also shown that the electric field governing the emission is the local field at the tip of the emitter rather than the average field. This point has been addressed with various conditions of the tip: SWNT or MWNT [133], synthesis method [133], shape of the emitter and/or chemical status of the tip surface [134], nanotube diameter [134], density and height [134–136], physical and chemical surface modification [137, 138], open and closed tips [139], size of the patterns [140], substrates [141, 142], emission measurement area [133], and so on. Those various physical factors have often been summarized and described by an engineering



**Figure 9.** Raman scattering peaks of arc of CVD-grown MWNTs and arc discharge MWNTs (purified) compared with that of SWNTs. [(b) and (c) courtesy of Iljin Nanotech Co.]

fudge parameter $\beta$, called the geometric field enhancement factor, in evaluating the emission performance of the tips.

Both the SWNT and MWNT have been used for field emitters, and all types of nanotubes have revealed excellence in emission properties. Independent of the tube synthesis method and nanotube type (single wall or multiwall), the emitters revealed threshold fields of $\sim$1 V/$\mu$m and turn-on fields of $\sim$5 V/$\mu$m. The maximum emission current was varied by 0.1–1 A/cm$^2$ [133]. Bonard et al. [134, 143] compared the emission properties among films having different emitter densities, and found that a medium emitter density film revealed homogeneous and the strongest emission current with the lowest turn-on field. The actual number of emitting tubes was shown to be very small, or $10^3$–$10^4$ among $10^7$–$10^8$ emitters/cm$^2$ [133, 144, 145].

Applications of the carbon nanotube field emitter thus far have been applied to flat-panel displays [144, 146–150], X-ray tubes [151], lithography systems [152], microwave devices [153], luminescence tubes [154–156], and so on. It would be far better if the emitters could be processed easily and economically for practical application. Field emitters for display have been fabricated by either screen printing with purified tubes or patterned growth of MWNTs by CVD. De Heer et al. [144] made a field-emitter gun from nanotube films where MWNTs grown by arc discharge were aligned by drawing colloidal suspension of the tubes through a ceramic filter. An alternative film preparation method was dispersion of the tubes in a matrix of epoxy [146, 147], and Wang et al. [147] realized the first nanotube display by pasting nanotubes mixed in epoxy on patterned glass. This technology now became mature enough to fabricate a large-area field-emission display (FED) panel [148–150]. Recently, Lee et al. [148] demonstrated a 9 in full-color carbon nanotube FED using a similar screen-printing method. This was realized with SWNTs, but there are no particular reasons for it not to be realized with MWNTs.

Actually, selective CVD growth using a catalyst for emitter structures is actively being studied these days. For device fabrication using this method, patterning of the catalyst film is necessary. Several methods have been developed and employed, including lithography and etching or lift off [95, 157–160], shadow masking [89, 161], and soft lithography or stamping [162]. The aligned feature in the selectively grown MWNTs is considered favorable to enhance the emission properties. Figure 10 shows vertically aligned and selectively grown MWNTs on a patterned plane and in a trench. Emission properties have been examined for various MWNTs grown with thermal [135, 140, 163], plasma-assisted [142, 155, 159], template [89, 136, 164–166], and vapor
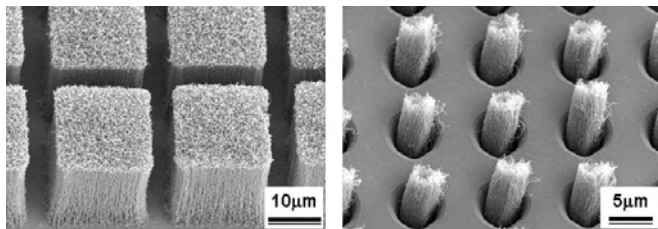
phase [141, 167, 168] CVDs. No demonstration of FED using CVD-grown nanotubes, however, has been made yet, although this method can have definite advantages in the application to the integration of emitter devices in small scales.

In the stage of commercial use as electronic devices, the stability and reliability of the emitters become important concerns. In the emission experiments, it has been shown that the nanotubes degrade by damages caused by the electric field during operation. Gas molecule bombardment [133, 145, 169] is shown to be a direct cause of damage related to the electric field. Nanotubes were shown to align along the field direction, and became permanently deformed at a high field [170, 171]. This failure may occur by resistive heating at the nanotube–substrate interface due to poor adhesion [172] or stripping/burning under the field [173]. MWNTs revealed less degradation than SWNTs [174]. The poor adhesion and/or shaking of the tubes in the electric field also caused current fluctuation and arcing in the $I$–$V$ measurements [171, 173]. In this regard, we have developed a process that dramatically improves the adhesion of the tubes to the substrate. The process utilizes the selective growth of the catalytic CVD method and planarization process using spin-on glass (SOG). SOG is a liquid type of silicon dioxide that hardens in air. Spin coating of SOG over the MWNTs selectively grown in trenches of the pixel on Si substrate greatly improves the adhesion of the tubes to the substrate after hardening. The schematic of the processing is shown in Figure 11. Furthermore, the planarization process trims the outgrown tubes and levels the tips at the height of the substrate plane. The emission measurements with processed CNTs as such actually revealed extremely stable $I$–$V$ curves without current fluctuation. This will not require an aging process to stabilize the emission characteristics [134].
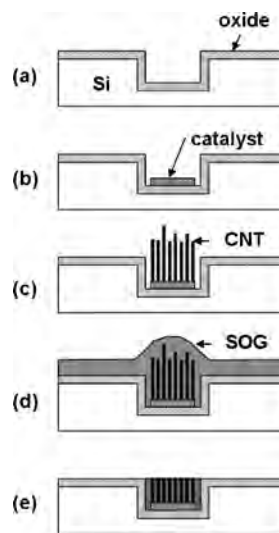


**Figure 11.** Process flow of SOG planarization to improve the adhesion of MWNTs to the substrate and trim the uneven CNTs. (a) Trench formation and oxidation. (b) Catalyst film formation selectively in trench by lift off. (c) CNT growth. (d) SOG spin coating and drying. (e) Planarization by mechanical polishing.



**Figure 10.** MWNTs selectively grown on plane and in trench with vertically aligned morphology.

## 4.2. Mechanical Properties

A carbon nanotube is mechanically the strongest and most resilient among the materials known to exist in nature. Young's modulus is ~1 TPa, and the tensile strength is about tens of gigapascals for MWNTs [175–177]. CNTs are also very flexible in bending, and resistant to failure [176, 178–181]. The mechanical properties are, however, in reality sensitive to the detail of the structure, such as chirality, diameter, defects, and so on [177, 178, 182, 183], although the elastic properties should be insensitive to such parameters according to the calculations [184, 185]. The van der Waals forces between adjacent graphene sheets may degrade the mechanical properties of MWNTs compared to SWNTs [176, 181]. It was also shown that the elastic modulus of the catalytically CVD grown MWNTs is an order of magnitude lower than that of arc-discharge-grown MWNTs due to the higher density of the structural defects [177, 186, 187].

MWNTs have been proposed as mechanical probes for nanoscale manipulation and nanoelectromechanical systems. Nanomanipulation is one of the key issues in nanoscience, and technology and is being applied for scanning probe microscopy (SPM), biology, and materials science samples [188]. The most extensive study was made on nanoprobe tips, which have been made either by attaching CNTs to a conventional probe [189, 190] or AFM/STM tips [145, 191, 192], or by directly growing CNTs on the probe [193, 194]. The superiority of the CNT tips in the applications comes from the small diameter, high aspect ratio, high mechanical strength, and unique chemical properties [195]. Stable atomic images of the Si surface were obtained by scanning tunneling microscope with an MWNT tip [196]. The CNT tips, when applied for SPM and nanolithography, revealed better resolution and a longer lifetime than conventional Si probe tips [197], suggesting their potential use in nanolithography [198, 199]. Hafner et al. [195] thoroughly reviewed the use of CNTs for a probe tip. Nanotweezers for nanoscale manipulation [179, 200, 201] and nanobearings for nanomechanical systems [180] were also proposed. Their use as a lubricant and reinforcements in composite materials may also have great potential [188].

The outstanding mechanical properties of CNTs also led to the development of CNT-reinforced composite materials that can be applied in the electronics and automotive industries. Composites of nanotubes in polymer are used for dissipating static charges in a semiconductor field. The dissipation is attained via interconnected carbon nanotubes of high conductivity in the polymer. The effect can be obtained at a relatively low concentration of carbon nanotubes compared to carbon blacks [202]. In the automotive industry, CNTs are used as a conducting agent for electrostatic painting. For this purpose and high mechanical strength, the uniform dispersion of nanotubes and their wetting to the polymer matrix are very important [203]. Polymerization, solution mixing, and melt mechanical mixing methods have been used in producing the composites [202, 203]. It was shown that the wear properties of the carbon composites have been greatly improved by introducing CNTs [204].

## 4.3. Electronic Properties

The unique electronic properties of the CNT come from the one-dimensionality of the material, the crystallographic ordering of carbon atoms (chirality) in graphene sheets, and the nature of atomic bonding. The complex structure of MWNTs, however, has discouraged theoretical and experimental studies on them, and thus most of the electronic properties have been intensively and extensively studied using SWNTs. Nevertheless, many of the properties of the MWNT may be able to be drawn from those of the SWNT. The first concern among electrical properties is conductance, and metal contact to the CNT is necessary for this measurement. Band structure calculations showed that CNTs exist as metal or a semiconductor, depending on the tube diameter and chirality [205]. The energy gap varies inversely with the tube diameter. For an MWNT, in principle, the chirality may differ among the shells, and thus may show complex conducting behavior. However, only the outermost shell was shown to be responsible for electrical transport [206–208], while a coupling between the shells and a contribution from all shells to ac conduction were also claimed [209, 210]. The metallic CNT can carry extremely high electron density up to $10^{10}$ A/cm$^2$ [211]. This metallic MWNT is highly stable, but the shells can be thermally destroyed by a high current [208]. Ballistic [212] to diffusive [213, 214] transport modes in MWNTs have been claimed. A geometric incommensurability between the shells was proposed for the nonballistic transport [215]. Various quantum phenomena have also been observed in MWNTs [206, 212, 216].

The carriers for the conduction in the as-grown MWNT were shown to be holes [210, 214]. The carrier type can be varied by doping or annealing [210, 217], which enables fabrication of carbon nanotube p–n junctions. For better performance of the fabricated transistors as well as for the accuracy in all of the characterizations, the property and quality of the contact between the electrode metal and CNTs are critical issues. The conductance measured on CNTs may contain a significant contribution from the very high resistance contacts [218–220], and methods for fabricating low-resistance contacts to CNTs and their reliability have been discussed [211, 218, 221, 222]. Transistors based upon the metallic and semiconducting CNTs have been demonstrated [223]. Recently, a logic gate with attractive transistor characteristics of high gain (>10) and a large on–off ratio (>10$^5$) and complementary NOT gate were also demonstrated [224, 225]. However, since the usefulness of the discrete nanotransistor is extremely limited, the ultimate goal must be large-scale integration of the transistors for logic and memory circuit applications [224, 226, 227]. Direct assembly of the CNTs [228, 229] and of a regular array of an aluminum oxide template [230] have been demonstrated as methodologies for large-scale integration, but on a primitive level, far from realistic. So many challenging tasks still remain in realizing practical CNT device and circuits [226].

The possibilities of electrochemical energy conversion using CNTs have been studied with lithium batteries, supercapacitors, hydrogen storage, fuel cells, and so on. This topic was reviewed in recent articles [7, 231–234]. Research focus has been on the use of anodic carbon materials for

better performance of Li-ion batteries. The material for an anode electrode has been carbon or graphite, through which insertion (intercalation) and extraction (deintercalation) of Li ions occur during the charging–discharging processes [234]. CNTs may be naturally used as carbon for the electrode material, where Li penetrates the graphene layers accompanying the charge transfer to carbon in the intercalation process. Electrochemical interactions with MWNTs during the process have been investigated [235–239], but the results seemed not promising. The potential difference between the insertion and extraction cycles showed hysteresis, and furthermore, the lack of a potential plateau during the extraction process precluded CNTs from this application of an Li-ion battery [231]. On the other hand, CNTs may be suitable for application to electrochemical capacitors, often called supercapacitors, which have potential advantages through their large capacitance, high power, high-frequency response, and long lifetime [240, 241]. The application naturally requires a large surface area of the electrodes for large capacitance. The mesoporous character of the hollow CNT, which provides high-density sites for charge accumulation at the electrode/electrolyte interface, is favorable for this purpose [242, 243]. The efficiency was further enhanced with uniform distribution, an open-end structure, and chemical treatment of the CNTs [231, 243]. In addition, modification of the carbon electrode by the addition of an electrically conducting polymer could enhance the performance [244].

Another important application thrust is hydrogen storage, which has been a long-term issue in energy and the environment. The storage materials in general need high capacity and stability, and carbon was well known as a good adsorbent for gases due to its porosity and interaction with gas molecules [232]. The capture of hydrogen by CNT at the exterior and interior of the tube is established by physical adsorption. However, incomplete desorption of the adsorbed hydrogen has been observed, and it suggested that a part of the hydrogen is captured by chemical adsorption [245, 246]. The hydrogen adsorption properties are shown to be pressure and temperature dependent [232, 247]. The opening of the CNTs is shown to be essential for hydrogen molecule adsorption [248–250], and aggregated pores in MWNTs created by aggregation of the CNTs were claimed as efficient sites for the storage [251]. The defective structure in MWNTs by heat and chemical treatments was also claimed to improve the storage capacity [248, 252]. The alkali-doped MWNTs showed a higher storage capacitance than undoped CNTs, probably due to increased hydrogen adsorption sites [253], but adsorption due to moisture contamination should be avoided [254, 255]. While the use of CNTs for hydrogen storage was motivated by a high capacity of ∼70% [256], most of the experimental adsorption data for hydrogen capture was highly scattered from 0.1 to 10 wt% [232, 234, 257]. Note that many of those experimental results for adsorption capacity are far more than the calculations; a calculation showed a maximum of ∼1%, even with the inclusion of chemical adsorption [246]. Experiments for further microscopic clarification of the phenomena to solve the difference are required. Excellence between the SWNT and MWNT in hydrogen storage is not obvious either.

## 4.4. Magnetic Properties

Magnetic susceptibility measurements showed that CNTs reveal diamagnetic behavior [258, 259]. The large diamagnetism of MWNT is due to the anisotropy of the tube and the large susceptibility component normal to the graphite layer [260, 261]. MWNTs were investigated for use in spintronics. An experiment of spin-polarized electron injection from ferromagnetic metal into CNT revealed that the transport of electron spins in MWNT is coherent [262]. Hysteretic switching of an MWNT device with a ferromagnetic metal contact was realized at 4.2 K using a magnetoresistance phenomenon caused by the coherent spin transport [263]. Negative magnetoresistance with conductance oscillation as a function of magnetic flux parallel to the MWNT was observed [206, 213]. A semiconducting MWNT showed a magnetic-field-induced metal–insulator transition behavior [264].

## 4.5. Optical Properties

Optical properties of CNTs have also been investigated. The most noticeable property of the CNT investigated is a strong nonlinear optical property in suspension–polymer composites of MWNTs [265–269]. The optical limiting property induced by this nonlinearity ranges from the visible to the infrared region, and can be applied to a device to protect optical sensors from high-intensity laser beam radiation [267]. The luminescence of CNT composites may be applied to an electroluminescence device [270].

## 5. SUMMARY

In spite of its divergence in the morphology, quality, synthesis methods, and ambiguity in properties in comparison with a single-wall carbon nanotube, a multiwall carbon nanotube becomes a progressively important type of carbon nanotube in applications. MWNTs by arc discharge will have definite application areas where they require rather high-quality nanotubes, and the production cost will also be progressively reduced. At the same time, MWNTs by CVD will expand the application by utilizing their unique advantages. CVD nanotubes may replace the applications made by the arc-discharge tubes by making good use of the low production cost if the quality can be further improved. It is necessary, then, to fully recognize the synthesis mechanisms to control the growth. It may not be completed until the catalytic role of the catalyst particles is clearly elucidated, but the surface and interface studies in nanoscale may expose the yet insufficiently explained issues such as the growth mode and the effects of the relevant parameters. Nevertheless, research on the application will proceed actively in parallel to the basic research. With the growth of information and biotechnologies, association with these technological areas will further expand the application of the nanotubes. At present, the applications are distributed in the areas of field-emission devices, electronic devices, nanoprobes and manipulators, energy storage, and so on. The scope of the application can be further expanded if the bulk-scale length of the tube can be synthesized. Recently, Zhu et al. [271] reported tens of centimeters length single-wall carbon nanotubes using vapor

phase CVD. This is an important step toward the bulk-type application of carbon nanotubes. To provide economic hardware for information technology, the integration processing capability with the nanotubes is still extremely important, while the developments of economical and fast nanomanipulation technologies are mandatory for highly value-added nanopiece products.

## GLOSSARY

**CVD** Chemical vapor deposition: a method of depositing thin solid films via chemical reaction of gases in a reactor.

**MWNT** Carbon nanotube made of multiple rolls of graphite sheets.

## ACKNOWLEDGMENTS

## REFERENCES

1. S. Iijima, *Nature* 354, 56 (1991).
2. T. W. Ebbenson, Ed., "Carbon Nanotubes—Preparation and Properties." CRC Press, New York, 1997.
3. R. Saito, G. Dresselhaus, and M. S. Dresselhaus, "Physical Properties of Carbon Nanotubes." ICP, London, 1998.
4. P. J. F. Harris, "Carbon Nanotubes and Related Structures." Cambridge University Press, Cambridge, 1999.
5. D. Tomanek and R. J. Enbody, Eds., "Science and Application of Nanotubes." Kluwer Academic/Plenum, New York, 2000.
6. M. S. Dresselhaus, G. Dresselhaus, and Ph. Avouris, Eds., "Carbon Nanotubes: Synthesis, Structure, Properties, and Applications," Topics in Applied Physics, Vol. 80. Springer-Verlag, Berlin, 2000.
7. C. N. R. Rao, B. C. Satishkumar, A. Govindaraj, and M. Nath, *Chemphyschem* 2, 78 (2001).
8. H. Dai, *Surf. Sci.* 500, 218 (2002).
9. T. W. Ebbensen and P. M. Ajayan, *Nature* 358, 220 (1992).
10. T. W. Ebbensen, *Phys. Today* 49, 26 (1996).
11. S. Iijima, T. Ichihashi, and Y. Ando, *Nature* 356, 776 (1992).
12. H. Zhang, X. Xue, D. Wang, Y. He, and S. Peng, *Mater. Chem. Phys.* 58, 1 (1999).
13. M. Cadek, R. Murphy, B. McCarthy, A. Drury, B. Lahr, R. C. Barklie, M. in het Panhuis, J. N. Coleman, and W. J. Blau, *Carbon* 40, 923 (2002).
14. Y. Ando, X. Zhao, H. Kataura, Y. Achiba, K. Kaneto, M. Tsuruta, S. Uemura, and S. Iijima, *Diamond Rel. Mater.* 9, 847 (2000).
15. Y. Ando, X. Zhao, S. Inoue, and S. Iijima, *J. Cryst. Growth* (2002).
16. D. T. Colbert, J. Zhang, S. M. McClure, P. Nikolaev, Z. Chen, J. H. Hafner, D. W. Owens, P. G. Kotula, C. B. Carter, J. H. Weaver, A. G. Rinzler, and R. E. Smalley, *Nature* 266, 1218 (1994).
17. S. C. Tsang, P. J. F. Harris, and M. L. H. Green, *Nature* 362, 520 (1993).
18. P. M. Ajayan, T. W. Ebbesen, T. Ichihashi, S. Iijima, K. Tanigaki, and H. Hiura, *Nature* 362, 522 (1993).
19. Y. S. Park, Y. C. Choi, K. S. Kim, D. Chung, D. J. Bae, K. H. An, S. C. Lim, X. Y. Zhu, and Y. H. Lee, *Carbon* 39, 655 (2001).
20. Y. K. Chen, M. L. H. Green, J. L. Griffin, J. Hammer, R. M. Rago, and S. C. Tsang, *Adv. Mater.* 8, 1012 (1996).
21. K. Hernadi, A. Siska, L. Thien-Nga, L. Forro, and I. Kiricsi, *Solid State Ionics* 141–142, 203 (2001).
22. P. X. Hou, S. Bai, Q. H. Yang, C. Liu, and H. M. Cheng, *Carbon* 40, 81 (2002).
23. L. P. Biro, N. Q. Khanh, Z. Vertesy, Z. E. Horvath, Z. Osvath, A. Koos, J. Gyulai, A. Kocsonya, Z. Konya, X. B. Zhang, G. Van Tendeloo, A. Fonseca, and J. B. Nagy, *Mater. Sci. Eng.* C19, 9 (2002).
24. R. Andrews, D. Jacques, D. Qian, and E. C. Dickey, *Carbon* 39, 1681 (2001).
25. S. Iijima, P. M. Ajayan, and T. Ichihashi, *Phys. Rev. Lett.* 69, 3100 (1992).
26. D. S. Tang, S. S. Xie, W. Liu, B. H. Chang, L. F. Sun, Z. Q. Liu, G. Wan, and W. Y. Zhou, *Carbon* 38, 475 (2000).
27. R. E. Smalley, *Mater. Sci. Eng.* B19, 1 (1993).
28. A. Maiti, C. J. Brabec, C. Roland, and J. Bernholc, *Phys. Rev. Lett.* 73, 2468 (1994).
29. A. Maiti, C. J. Brabec, C. Roland, and J. Bernholc, *Phys. Rev.* B52, 14850 (1995) and references therein.
30. J. C. Charlier, A. de Vita, X. Blasé, and R. Car, *Science* 275, 647 (1997).
31. Y. K. Kwon, Y. H. Lee, S. G. Kim, P. Jund, D. Tomanek, and R. E. Smalley, *Phys. Rev. Lett.* 79, 2065 (1997).
32. M. B. Nardelli, C. Brabec, A. Maiti, C. Roland, and J. Bernholc, *Phys. Rev. Lett.* 80, 313 (1998).
33. Q. Liang, L. Z. Gao, Q. Li, S. H. Tang, B. C. Liu, and Z. L. Yu, *Carbon* 39, 897 (2001).
34. N. I. Maksomova, O. P. Krivoruchko, G. Mestl, V. I. Zaikovskii, A. L. Chuvilin, A. N. Salanov, and E. B. Burgina, *J. Mol. Catal. A: Chem.* 158, 301 (2000).
35. L. Thien-Nga, J. M. Bonard, R. Gaal, L. Forro, and K. Hernadi, *Appl. Phys. Lett.* 80, 850 (2002).
36. R. T. K. Baker and N. M. Rodriguez, *Mater. Res. Soc. Symp. Proc.* 349, 251 (1994).
37. C. Laurent, E. Flahaut, A. Peigney, and A. Rousset, *New J. Chem.* 1229 (1998).
38. N. M. Rodriguez, *J. Mater. Res.* 8, 3233 (1993).
39. V. Ivanov, J. B. Nagy, P. Lambin, A. Lucas, X. B. Zhang, X. F. Zhang, D. Bernaerts, G. Van Tendeloo, S. Amelinckx, and J. Van Landuyt, *Chem. Phys. Lett.* 223, 329 (1994).
40. N. Nagaraju, A. Fonseca, Z. Konya, and J. B. Nagy, *J. Mol. Catal. A: Chem.* 181, 57 (2002).
41. A. Peigney, C. Laurent, O. Dumortier, and A. Rousset, *J. Eur. Ceram. Soc.* 18, 1995 (1998).
42. K. Mukhopadhyay, A. Koshio, T. Sugai, N. Tanaka, H. Shinohara, Z. Konya, and J. B. Nagy, *Chem. Phys. Lett.* 303, 117 (1999).
43. L. F. Sun, J. M. Mao, Z. W. Pan, B. H. Chang, W. Y. Zhou, G. Wang, L. X. Qian, and S. S. Xie, *Appl. Phys. Lett.* 74, 644 (1999).
44. S. Xie, W. Li, Z. Pan, B. Chang, and L. Sun, *Mater. Sci. Eng.* A286, 11 (2000).
45. Z. P. Huang, J. W. Xu, Z. F. Ren, J. H. Wang, M. P. Siegel, and P. N. Provencio, *Appl. Phys. Lett.* 73, 3845 (1998).
46. E. F. Kukovitskii, L. A. Chernozatonskii, S. L. L'vov, and N. N. Mel'nik, *Chem. Phys. Lett.* 266, 323 (1997).
47. M. Yudasaka, R. Kikuchi, T. Matsui, Y. Ohki, S. Yoshimura, and E. Ota, *Appl. Phys. Lett.* 67, 2477 (1995).
48. Y. Chen, D. T. Shaw, and L. Guo, *Appl. Phys. Lett.* 76, 2469 (2000).
49. R. Sen, A. Govindaraj, and C. N. R. Rao, *Chem. Phys. Lett.* 267, 276 (1997).
50. D. C. Li, L. Dai, S. Huang, A. W. H. Mau, and Z. L. Wang, *Chem. Phys. Lett.* 316, 349 (2000).
51. Q. Chen and L. Dai, *Appl. Phys. Lett.* 76, 2719 (2000).

52. A. Andrews, D. Jacques, A. M. Rao, F. Derbyshire, D. Qian, X. Fan, E. C. Dickey, and J. Chen, *Chem. Phys. Lett.* 303, 467 (1999).

53. Z. J. Zhang, B. Q. Wei, G. Ramanath, and P. M. Ajayan, *Appl. Phys. Lett.* 77, 3764 (2000).

54. B. Q. Wei, Z. J. Zhang, P. M. Ajayan, and G. Ramanath, *Carbon* 40, 47 (2002).

55. M. Ishigami, J. Cumings, A. Zettl, and S. Chen, *Chem. Phys. Lett.* 319, 457 (2000).

56. A. Fonseca, K. Hernadi, P. Piedigrosso, J. F. Colomer, K. Mukhopadhyay, R. Doome, S. Lazarescu, L. P. Biro, P. Lambin, P. A. Thiry, D. Bernaerts, and J. B. Nagy, *Appl. Phys.* A67, 11 (1998).

57. Y. S. Cho, G. S. Choi, S. Y. Hong, and D. J. Kim, *J. Cryst. Growth* 243, 224 (2002).

58. R. T. K. Baker, M. A. Barber, P. S. Barber, P. S. Harris, F. S. Feates, and R. J. Waite, *J. Catal.* 30, 86 (1973).

59. Y. H. Mo, A. K. M. F. Kibria, and K. S. Nahm, *Synth. Met.* 122, 443 (2001).

60. G. S. Choi, Y. S. Cho, S. Y. Hong, J. B. Park, K. H. Son, and D. J. Kim, *J. Appl. Phys.* 91, 3847 (2002).

61. A. Sacco, P. Thacker, T. N. Chang, and A. T. S. Chiang, *J. Catal.* 85, 224 (1984).

62. G. G. Tibbetts, *J. Cryst. Growth* 66, 632 (1984).

63. R. L. Vander Wal, T. M. Ticich, and V. E. Curtis, *Carbon* 39, 2277 (2001) and references therein.

64. R. F. Ren., Z. P. Huang, J. W. Xu, J. H. Wang, P. Bush, M. P. Siegel, and P. N. Provencio, *Science* 282, 1105 (1998).

65. Y. C. Choi, Y. M. Shin, Y. H. Lee, B. S. Lee, G. S. Park, W. B. Choi, N. S. Lee, and J. M. Kim, *Appl. Phys. Lett.* 76, 2367 (2000).

66. J. H. Han, B. S. Moon, W. S. Yang, J. B. Yoo, and C. Y. Park, *Surf. Coat. Technol.* 131, 93 (2000).

67. U. Kim, R. Pcionek, D. M. Aslam, and D. Tomanek, *Diamond Rel. Mater.* 10, 1947 (2001).

68. H. S. Kang, H. J. Yoon, C. O. Kim, J. P. Hong, I. T. Han, S. N. Cha, B. K. Song, J. E. Jung, N. S. Lee, and J. M. Kim, *Chem. Phys. Lett.* 349, 196 (2001).

69. S. H. Tsai, C. W. Chao, C. L. Lee, and H. C. Shih, *Appl. Phys. Lett.* 74, 3462 (1999).

70. Y. C. Choi, D. W. Kim, T. J. Lee, C. J. Lee, and Y. H. Lee, *Synth. Met.* 117, 81 (2001).

71. Z. W. Pan, S. S. Xie, B. H. Chang, L. F. Sun, W. Y. Zhou, and G. Wang, *Chem. Phys. Lett.* 299, 97 (1999).

72. C. J. Lee, D. W. Kim, T. J. Lee, Y. C. Choi, Y. S. Park, Y. H. Lee, W. B. Choi, N. S. Lee, G. S. Park, and J. M. Kim, *Chem. Phys. Lett.* 312, 461 (1999).

73. J. Li, C. Papadopoulos, J. M. Xu, and M. Moskovits, *Appl. Phys. Lett.* 75, 367 (1999).

74. C. J. Lee and J. Park, *Appl. Phys. Lett.* 77, 3397 (2002).

75. W. Z. Li, S. S. Xie, L. X. Qian, B. H. Chang, B. S. Zou, W. Y. Zhou, R. A. Zhao, and G. Wang., *Science* 274, 1701 (1996).

76. J. B. Park, G. S. Choi, Y. S. Cho, S. Y. Hong, D. J. Kim, S. Y. Choi, J. H. Lee, and K. I. Cho, *Thin Solid Films* 415, 78 (2002).

77. P. E. Anderson and N. M. Rodriguez, *J. Mater. Res.* 14, 2912 (1999).

78. A. Oberlin, M. Endo, and T. Koyama, *J. Cryst. Growth* 32, 335 (1976).

79. F. Benissard, P. Gadelle, M. Coulon, and L. Bonnetain, *Carbon* 26, 61 (1988).

80. E. F. Kukovitsky, S. G. L'vov, and N. A. Sainov, *Chem. Phys. Lett.* 317, 65 (2000).

81. X. Wang, W. Hu, Y. Liu, C. Long, Y. Xu, S. Zhou, D. Zhu, and L. Dai, *Carbon* 39, 1533 (2001) and references therein.

82. Z. Li, J. Chen, X. Zhang, Y. Li, and K. K. Fung, *Carbon* 40, 409 (2002).

83. S. Amelinckx, X. B. Zhang, D. Bernaerts, X. F. Zhang, V. Ivanov, and J. B. Nagy, *Science* 267, 635 (1995).

84. Y. Saito and T. Yoshikawa, *J. Cryst. Growth* 134, 154 (1993).

85. W. D. Zhang, Y. Wen, S. M. Liu, W. C. Tjiu, Q. X. Guo, and M. G. Leong, *Carbon* (2002).

86. X. X. Zhang, Z. Q. Li, G. H. Wen, K. K. Fung, J. Chen, and Y. Li, *Chem. Phys. Lett.* 333, 509 (2001).

87. V. V. Kovalevski and A. N. Safronov, *Carbon* 36, 963 (1998).

88. W. A. de Heer, W. S. Bacsa, A. Chatelain, T. Gerfin, R. Humphrey-Baker, L. Forro, and D. Ugarte, *Science* 268, 845 (1995).

89. S. Fan, M. Chapline, N. Franklin, T. Tombler, A. Cassell, and H. Dai, *Science* 283, 512 (1999).

90. H. Kind and J. M. Bonard, *Adv. Mater.* 11, 1285 (1999).

91. Y. Avigal and R. Kalish, *Appl. Phys. Lett.* 78, 2291 (2001).

92. T. Kyotani, L. Tsai, and A. Tomita, *Chem. Mater.* 7, 1427 (1995).

93. T. Iwasaki, T. Motoi, and T. Den, *Appl. Phys. Lett.* 75, 2044 (1999).

94. J. S. Suh and J. S. Lee, *Appl. Phys. Lett.* 75, 2047 (1999).

95. M. Terrones, N. Grobert, J. Olivares, J. P. Zhang, H. Terrones, K. Kordatos, W. K. Hsu, J. P. Hare, P. D. Townsend, K. Prassides, A. K. Cheetham, H. W. Kroto, and D. R. M. Walton, *Nature* 388, 52 (1997).

96. C. R. Martin, *Science* 266, 1961 (1994).

97. G. Che, B. B. Lakshmi, E. R. Fisher, and C. R. Martin, *Nature* 393, 346 (1998).

98. F. Rohmund, L. K. L. Falk, and E. E. B. Campbell, *Chem. Phys. Lett.* 328, 369 (2000).

99. A. Cao, X. Zhang, C. Xu, J. Liang, D. Wu, and B. Wei, *Appl. Surf. Sci.* 181, 234 (2001).

100. Y. M. Shyu and F. C. N. Hong, *Mater. Chem. Phys.* 72, 223 (2001).

101. Z. F. Ren, Z. P. Huang, D. Z. Wang, G. Wen, J. W. Xu, J. H. Wang, L. E. Calvet, J. Chen, J. F. Klemic, and M. A. Reed, *Appl. Phys. Lett.* 75, 1086 (1999).

102. H. Wang, J. Lin, C. H. A. Huan, P. Dong, J. He, S. H. Tang, W. K. Eng, and T. L. J. Thong, *Appl. Surf. Sci.* 181, 248 (2001).

103. K. B. K. Teo, M. Chhowalla, G. A. J. Amaratunga, W. I. Milne, D. G. Hasko, G. Pirio, P. Legagneux, F. Wyczisk, and D. Pribat, *Appl. Phys. Lett.* 79, 1534 (2001).

104. Y. S. Woo, D. Y. Jeon, I. T. Han, N. S. Lee, J. E. Jung, and J. M. Kim, *Diamond Rel. Mater.* 11, 59 (2002).

105. M. S. Dresselhaus, G. Dresselhaus, and R. Saito, *Phys. Rev.* B45, 6234 (1992).

106. S. Q. Feng, D. P. Yu, G. Hu, X. F. Zhang, and Z. Zhang, *J. Phys. Chem. Solids* 58, 1887 (1997).

107. K. Sattler, *Carbon* 33, 915 (1995).

108. S. C. Tsang, P. de Oliveira, J. J. Davis, M. L. H. Green, and H. A. O. Hill, *Chem. Phys. Lett.* 249, 413 (1996).

109. L. P. Biro, J. Gyulai, Ph. Lambin, J. B. Nagy, S. Lazarescu, and G. I. Mark, *Carbon* 36, 689 (1998).

110. A. Hassanien, M. Tokumoto, S. Ohshima, Y. Kuriki, F. Ikazaki, K. Uchida, and M. Yumura, *Appl. Phys. Lett.* 75, 2755 (1999).

111. A. Hassanien, A. Mrzel, M. Tokumoto, and D. Tomanek, *Appl. Phys. Lett.* 79, 4210 (2001).

112. V. Meunier and Ph. Lambin, *Carbon* 38, 1729 (2000).

113. M. F. Yu, T. Kowalewski, and R. S. Ruoff, *Phys. Rev. Lett.* 86, 87 (2001).

114. Y. Saito, R. Mizushima, and K. Hata, *Surf. Sci.* 499, L119 (2002).

115. Ph. Lambin, A. Loiseau, C. Culot, and L. P. Biro, *Carbon* (in press) and references therein.

116. D. Reznik, C. H. Olk, D. A. Neumann, and J. R. D. Copley, *Phys. Rev.* B52, 116 (1995).

117. G. Xu, Z. C. Feng, Z. Popovic, J. Y. Lin, and J. J. Vittal, *Adv. Mater.* 13, 264 (2001).

118. Y. Maniwa, R. Fujiwara, H. Kira, H. Tou, E. Nishibori, M. Takata, and M. Sakata, *Phys. Rev.* B64, 73105 (2001).

119. R. Andrews, D. Jacques, D. Qian, and E. C. Dickey, *Carbon* 39, 1681 (2001).

120. A. Burian, J. C. Dore, H. E. Fischer, and J. Sloan, *Phys. Rev.* B59, 1665 (1999).

121. P. C. Eklund, J. M. Holden, and R. A. Jishi, *Carbon* 33, 959 (1995) and references therein.

*122.* W. Li, H. Zhang, C. Wang, Y. Zhang, L. Xu, K. Zhu, and S. Xie, *Appl. Phys. Lett.* 70, 2684 (1997).

*123.* C. J. Lee, D. W. Kim, T. J. Lee, Y. C. Choi, Y. S. Park, W. S. Kim, Y. H. Lee, W. B. Choi, N. S. Lee, J. M. Kim, Y. G. Choi, and S. C. Yu, *Appl. Phys. Lett.* 75, 1721 (1999).

*124.* Y. Ando, X. Zhao, and H. Shimoyama, *Carbon* 39, 569 (2001).

*125.* J. M. Pitarke and J. Garcia-Vidal, *Phys. Rev.* B63, 73404 (2001).

*126.* A. V. Bazhenov, V. V. Kveder, A. A. Maksimov, I. I. Tartakovskii, R. A. Oganyan, Y. A. Ossipyan, and A. I. Shalynin, *J. Exp. Theor. Phys.* 86, 1030 (1998).

*127.* M. E. Brennan, J. N. Coleman, M. in het Panhuis, L. Marty, H. J. Byrne, and W. J. Blau, *Synth. Met.* 119, 641 (2001).

*128.* F. Bommeli, L. Degiorgi, P. Wachter, W. S. Bacsa, W. A. de Heer, and L. Forro, *Synth. Met.* 86, 2307 (1997).

*129.* J. Choi, S. M. Lee, Y. C. Choi, Y. H. Lee, and J. C. Jiang, *Chem. Phys. Lett.* 349, 185 (2001).

*130.* K. B. K. Teo, M. Chhowalla, G. A. J. Amaratunga, W. I. Milne, G. Pirio, P. Legagneux, F. Wyczisk, J. Olivier, and D. Pribat, *J. Vac. Sci. Technol.* B20, 116 (2002).

*131.* S. Bandow, *J. Appl. Phys.* 80, 1020 (1996).

*132.* A. S. Kotosonov and D. V. Shilo, *Carbon* 36, 1649 (1998).

*133.* J. M. Bonard, H. Kind, T. Stockli, and L. O. Nilsson, *Solid-State Electron.* 45, 893 (2001).

*134.* J. M. Bonard, M. Corci, C. Klinke, R. Kurt, O. Noury, and N. Weiss, *Carbon* (2002) and references therein.

*135.* A. L. Musatov, N. A. Kiselev, D. N. Zakharov, E. F. Kukovitskii, A. I. Zhbanov, K. R. Izrael'yants, and E. G. Chirkova, *Appl. Surf. Sci.* 183, 111 (2001).

*136.* D. N. Davydov, P. A. Sattari, D. Almawlawi, A. Osika, T. L. Haslett, and M. Moskovits, *J. Appl. Phys.* 86, 3983 (1999).

*137.* S. Dimitrijevic, J. C. Withers, V. P. Mammana, O. R. Moteiro, J. W. Ager, III, and I. G. Brown, *Appl. Phys. Lett.* 75, 2680 (1999).

*138.* D. H. Kim, H. R. Lee, M. W. Lee, J. H. Lee, Y. H. Song, J. G. Jee, and S. Y. Lee, *Chem. Phys. Lett.* 355, 53 (2002).

*139.* J. M. Bonard, J. P. Salvetat, T. Stockli, L. Forro, and A. Chatelain, *Appl. Phys.* A69, 245 (1999).

*140.* T. Ikuno, T. Yamamoto, M. Kamizono, S. Takahashi, H. Furuta, S. Honda, S. Ohkura, M. Katayama, T. Hirao, and K. Oura, *Physica B* (2002).

*141.* A. M. Rao, D. Jacques, R. C. Haddon, W. Zhu, C. Bower, and S. Jin, *Appl. Phys. Lett.* 76, 3813 (2000).

*142.* J. Han, H. J. Kim, M. Yang, C. W. Yang, J. Yoo, C. Park, Y. Song, and K. Nam, *Mater. Sci. Eng.* C16, 65 (2001).

*143.* J. M. Bonard, N. Weiss, H. Kind, T. Stockli, L. Forro, K. Kern, and A. Chatelain, *Adv. Mater.* 13, 184 (2001).

*144.* W. A. De Heer, A. Chatelain, and D. Ugarte, *Science* 270, 1179 (1995).

*145.* J. M. Bonard, F. Maier, T. Stockli, A. Chatelain, W. A. de Heer, J. P. Salvetat, and L. Forro, *Ultramicroscopy* 73, 7 (1998).

*146.* P. G. Collins and A. Zettl, *Appl. Phys. Lett.* 69, 1969 (1996).

*147.* Q. H. Wang, A. A. Setlur, J. M. Lauerhaas, J. Y. Dai, E. W. Seeling, and R. P. H. Chang, *Appl. Phys. Lett.* 72, 2912 (1998).

*148.* N. S. Lee, D. S. Chung, I. T. Han, J. H. Kang, Y. S. Choi, H. Y. Kim, S. H. Park, Y. W. Jin, W. K. Yi, M. J. Yun, J. E. Jung, C. J. Lee, J. H. You, S. H. Jo, C. G. Lee, and J. M. Kim, *Diamond Rel. Mater.* 10, 265 (2001).

*149.* W. B. Choi, D. S. Chung, J. H. Kang, H. Y. Kim, Y. W. Jin, I. T. Han, Y. H. Lee, J. E. Jung, N. S. Lee, G. S. Park, and J. M. Kim, *Appl. Phys. Lett.* 75, 3129 (1999).

*150.* J. L. Kwo, M. Yokoyama, W. C. Wang, F. Y. Chuang, and I. N. Lin, *Diamond Rel. Mater.* 9, 1270 (2000).

*151.* H. Sugie, M. Tanemura, V. Filip, K. Iwata, K. Takahashi, and F. Okuyama, *Appl. Phys. Lett.* 78, 2578 (2001).

*152.* W. I. Milne, K. B. T. Teo, M. Chhowalla, G. A. J. Amaratunga, J. Yuan, J. Robertson, P. Legagneux, G. Pirio, K. Bouzehouane, D. Pribat, W. Bruenger, and C. Trautmann, *Curr. Appl. Phys.* 1, 317 (2001).

*153.* K. L. Jensen, *Phys. Plasma* 6, 2241 (1999).

*154.* M. Yumura, S. Ohshima, K. Uchida, Y. Tasaka, Y. Kuriki, F. Ikazaki, Y. Saito, and S. Uemura, *Diamond Rel. Mater.* 8, 785 (1999).

*155.* H. Murakami, M. Hirakawa, C. Tanaka, and H. Yamakawa, *Appl. Phys. Lett.* 76, 1776 (2001).

*156.* J. M. Bonard, T. Stockli, O. Noury, and A. Chatelain, *Appl. Phys. Lett.* 78, 2775 (2001).

*157.* X. Xu and G. R. Brandes, *Appl. Phys. Lett.* 74, 2549 (1999).

*158.* J. Kong, A. M. Cassel, and H. Dai, *Chem. Phys. Lett.* 292, 567 (1998).

*159.* J. Yu, Q. Zhang, J. Ahn, S. F. Yoon, Rusli, Y. J. Li, B. Gan, K. Chew, and K. H. Tan, *Diamond Rel. Mater.* 10, 2157 (2001).

*160.* Y. R. Cho, J. H. Lee, Y. H. Song, S. Y. Kang, C. S. Hwang, M. Y. Jung, D. H. Kim, S. K. Lee, H. S. Uhm, and K. I. Cho, *Mater. Sci. Eng.* B79, 128 (2001).

*161.* Y. Yang, S. Huang, H. He, A. W. H. Mau, and L. Dai, *J. Am. Chem. Soc.* 121, 10832 (1999).

*162.* H. Kind, J. M. Bonard, C. Emmenegger, L. O. Nilsson, K. Hernadi, E. Maillard-Schaller, L. Schlapbach, L. Forro, and K. Kern, *Adv. Mater.* 11, 1285 (1999).

*163.* J. T. L. Thong, C. H. Oon, W. K. Eng, W. D. Zhang, and L. M. Gan, *Appl. Phys. Lett.* 79, 2811 (2001).

*164.* D. Xu, G. Guo, L. Gui, Y. Tang, Z. Shi, Z. Jin, Z. Gu, W. Liu, X. Li, and G. Zhang, *Appl. Phys. Lett.* 75, 481 (1999).

*165.* J. I. Sohn, S. Lee, Y. H. Song, S. Y. Choi, K. I. Cho, and K. S. Nam, *Curr. Appl. Phys.* 1, 65 (2001).

*166.* Z. H. Yuan, H. Huang, H. Y. Dang, J. E. Cao, B. H. Hu, and S. S. Fan, *Appl. Phys. Lett.* 78, 3127 (2001).

*167.* H. Araki, T. Katayama, and K. Yoshino, *Appl. Phys. Lett.* 79, 2636 (2001).

*168.* R. B. Sharma, V. N. Tondare, D. S. Joag, A. Govindaraj, and C. N. R. Rao, *Chem. Phys. Lett.* 344, 283 (2001).

*169.* A. Wadhawan, R. E. Stallcup, II, K. F. Stephens, II, and J. M. Perez, *Appl. Phys. Lett.* 79, 1867 (2001).

*170.* Y. Wei, C. Xie, K. A. Dean, and B. F. Coll, *Appl. Phys. Lett.* 79, 4527 (2001).

*171.* Y. H. Wang, J. Lin, and C. H. A. Huan, *Thin Solid Films* 405, 243 (2002).

*172.* L. Nilsson, O. Groening, P. Groening, and L. Schlapbach, *Appl. Phys. Lett.* 79, 1036 (2001).

*173.* Z. L. Wang, R. P. Gao, W. A. de Heer, and P. Poncharal, *Appl. Phys. Lett.* 80, 856 (2002).

*174.* P. J. De Pablo, S. Howell, S. Crittenden, B. Walsh, E. Graugnard, and R. Reifenberger, *Appl. Phys. Lett.* 75, 3941 (1999).

*175.* M. M. J. Treacy, T. W. Ebbensen, and J. M. Gibson, *Nature* 381, 678 (1996).

*176.* E. W. Wong, P. E. Sheehan, and C. M. Lieber, *Science* 277, 1971 (1997).

*177.* J. P. Salvetat, A. J. Kulik, J. M. Bonard, G. A. D. Briggs, T. Stockli, K. Metenier, S. Bonnamy, F. Beguin, N. A. Burnham, and L. Forro, *Adv. Mater.* 111, 161 (1999).

*178.* M. R. Falvo, G. J. Clary, R. M. Taylor, II, V. Chi, F. P. Brooks, Jr., S. Washburn, and R. Superfine, *Nature* 389, 582 (1997).

*179.* P. Kim and C. M. Lieber, *Science* 286, 2148 (1999).

*180.* J. Cummings and A. Zettl, *Science* 289, 602 (2000).

*181.* C. Q. Ru, *J. Appl. Phys.* 89, 3426 (2001) and references therein.

*182.* M. F. Yu, O. L. Lourie, M. J. Dyer, K. Moloni, T. F. Kelly, and R. S. Ruoff, *Science* 287, 637 (2000) and references therein.

*183.* P. Poncharal, Z. L. Wang, D. Ugarte, and W. A. de Heer, *Science* 283, 1513 (1999).

*184.* J. P. Lu, *J. Phys. Chem. Solids* 58, 1649 (1997).

*185.* E. T. Thostenson, Z. Ren, and T. W. Chou, *Composites Sci. Technol.* 61, 1899 (2001).

*186.* Z. W. Pan, S. S. Xie, L. Lu, B. H. Chang, L. F. Sun, W. Y. Zhou, G. Wang, and D. L. Zhang, *Appl. Phys. Lett.* 74, 3152 (1999).

187. S. Xie, W. Li, Z. Pan, B. Chang, and L. Sun, *J. Phys. Chem. Solids* 61, 1153 (2000).
188. M. Guthold, M. Falvo, W. G. Matthews, S. Paulson, J. Mullin, S. Lord, D. Erie, S. Washburn, R. Superfine, F. P. Brooks, Jr., and R. M. Taylor, II, *J. Mol. Graph. Model.* 17, 187 (1999).
189. H. Dai, J. H. Hafner, A. G. Rinzler, D. T. Colbert, and R. E. Smalley, *Nature* 384, 147 (1996).
190. S. S. Wong, E. Joselevich, A. T. Woolley, C. L. Cheung, and C. M. Lieber, *Nature* 394, 52 (1998).
191. A. G. Rinzler, J. H. Hafner, P. Nikolaev, L. Lou, S. G. Kim, D. Tomanek, P. Nordlander, D. T. Cobert, and R. E. Smalley, *Science* 269, 1550 (1995).
192. M. J. Fansen, T. L. Van Rooy, and P. Kruit, *Appl. Surf. Sci.* 146, 312 (1999).
193. J. H. Hafner, C. L. Cheung, and C. M. Liever, *Nature* 398, 761 (1999).
194. E. Yenilmez, Q. Wang, R. J. Chen, D. Wang, and H. Dai, *Appl. Phys. Lett.* 80, 2225 (2002).
195. J. H. Hafner, C. L. Cheung, A. T. Woolley, and C. M. Lieber, *Prog. Biophys. Mol. Biol.* 77, 73 (2001).
196. T. Shimizu, H. Tokumoto, S. Akita, and Y. Nakayama, *Surf. Sci.* 486, L455 (2001).
197. T. Larsen, K. Moloni, F. Flack, M. A. Eriksson, M. G. Lagally, and C. T. Black, *Appl. Phys. Lett.* 80, 1996 (2002).
198. H. Dai, N. Franklin, and J. Han, *Appl. Phys. Lett.* 73, 1508 (1998).
199. A. Okazaki, S. Akita, and Y. Nakayama, *Physica B* (in press).
200. S. Akita, Y. Nakayama, S. Mizooka, Y. Takano, T. Okawa, Y. Miyatake, S. Yamanaka, M. Tsuji, and T. Nosaka, *Appl. Phys. Lett.* 79, 1691 (2001).
201. H. Watanabe, C. Manabe, T. Shigematsu, and M. Shimizu, *Appl. Phys. Lett.* 78, 2928 (2001).
202. P. Potschke, T. D. Fornes, and D. R. Paul, *Polymer* 43, 3247 (2002).
203. Z. Jin, K. P. Pramoda, S. H. Goh, and G. Xu, *Mater. Res. Bull.* 37, 271 (2002).
204. D. Lim, J. An, and H. J. Lee, *Wear* 252, 512 (2002) and references therein.
205. J. P. Issi, L. Langer, J. Heremans, and C. H. Olk, *Carbon* 33, 941 (1995).
206. A. Bachtold, C. Strunk, J. Salvetat, J. Bonard, L. Forro, T. Nussbaumer, and C. Schronenberger, *Nature* 397, 673 (1999).
207. P. Delaney, M. Di Ventra, and S. Pantelides, *Appl. Phys. Lett.* 75, 3787 (1999).
208. P. G. Collins, M. S. Arnold, and P. Avouris, *Science* 292, 706 (2001).
209. R. Tarkianen, M. Ahlskog, J. Penttila, L. Roschier, P. Hakonen, M. Paalanen, and E. Sonin, *Phys. Rev.* B64, 195412 (2001).
210. P. Avouris, *Chem. Phys.* (in press) and references therein.
211. B. Q. Wei, R. Vajtai, and P. M. Ajayan, *Appl. Phys. Lett.* 79, 1172 (2001) and references therein.
212. S. Frank, P. Poncharal, Z. L. Wang, and W. A. de Heer, *Science* 280, 1744 (1988).
213. L. Langer, V. Bayot, E. Grivei, J. P. Issi, J. P. Heremans, C. H. Olk, L. Stockman, C. Van Haesendonck, and Y. Bruynseraede, *Phys. Rev. Lett.* 76, 479 (1996).
214. R. Martel, T. Schmidt, H. R. Shea, T. Hertel, and Ph. Avouris, *Appl. Phys. Lett.* 73, 2447 (1998).
215. S. Roche, F. Triozon, A. Rubio, and D. Mayou, *Phys. Lett.* A285, 94 (2001).
216. S. Roth, V. Krstic, G. L. J. A. Rikken, *Curr. Appl. Phys.* 2, 155 (2002).
217. L. Duclaux, *Carbon* (in press) and references therein.
218. A. Bachtold, M. Henny, C. Terrier, C. Strunk, C. Schonenberger, J. P. Salvetat, J. M. Bonard, and L. Forro, *Appl. Phys. Lett.* 73, 274 (1998).
219. J. Tersoff, *Appl. Phys. Lett.* 74, 2122 (1999).
220. E. Graugnard, P. J. de Pablo, B. Walsh, A. W. Ghosh, S. Datta, and R. Reifenberger, *Phys. Rev.* B64, 125407 (2001).
221. L. Langer, L. Stockman, J. P. Heremans, V. Bayot, C. H. Olk, C. Van Haesendonck, Y. Bruynseraede, and J. P. Issi, *Synthetic Metals* 70, 1393 (1995).
222. P. J. de Pablo, E. Graugnard, B. Walsh, R. P. Andres, S. Datta, and R. Reifenberger, *Appl. Phys. Lett.* 74, 323 (1999).
223. P. L. McEuen, *Nature* 393, 15 (1998) and references therein.
224. A. Bachtold, P. Hadley, T. Nakanishi, and C. Dekker, *Science* 294, 1317 (2001).
225. Ph. Avouris, R. Martel, V. Derycke, and J. Appenzeller, *Physica B* (in press).
226. G. Y. Tseng and J. C. Ellenbogen, *Science* 294, 1293 (2001).
227. T. Rueckes, K. Kim, E. Joselevich, G. Y. Tseng, C. L. Cheung, and C. M. Lieber, *Science* 289, 94 (2000).
228. Y. Y. Wei, X. Fan, and G. Eres, *J. Vac. Sci. Technol.* B18, 3586 (2000).
229. Y. Lee, Y. Jang, C. Choi, D. Kim, C. Lee, J. Lee, Y. Han, S. Yoon, J. Shin, S. Kim, E. Kim, and B. Ju, *Adv. Mater.* 13, 1371 (2001).
230. W. B. Choi, J. U. Chu, K. S. Jeong, E. J. Bae, J. W. Lee, J. Kim, and J. Lee, *Appl. Phys. Lett.* 79, 3696 (2001).
231. E. Frackowiak and F. Beguin, *Carbon* 39, 937 (2001).
232. F. L. Darkrim, P. Malbrunot, and G. P. Tartaglia, *Int. J. Hydrogen Energy* 27, 193 (2002).
233. V. V. Simonyan and J. K. Johnson, *J. Alloys Comp.* 330–332, 659 (2002).
234. E. Frackowiak and F. Beguin, *Carbon* (in press).
235. V. A. Nalimova, D. E. Sklovsky, G. N. Bondarenko, H. Alvergnat-Gaucher, S. Bonnamy, and F. Beguin, *Synthetic Metals* 88, 89 (1997).
236. G. Maurin, Ch. Bousquet, F. Henn, P. Bernier, R. Almairac, and B. Simon, *Chem. Phys. Lett.* 312, 14 (1999).
237. E. Frackowiak, S. Gautier, H. Gaucher, S. Bonnamy, and F. Beguin, *Carbon* 37, 61 (1999).
238. Z. Yang and H. Wu, *Solid State Ionics* 143, 173 (2001).
239. T. Ishihara, A. Kawahara, H. Nishiguchi, M. Yoshio, and Y. Takita, *J. Power Sources* 97–98, 129 (2001).
240. C. Niu, E. K. Sichel, R. Hoch, D. Moy, and H. Tennent, *Appl. Phys. Lett.* 70, 1480 (1997).
241. R. Z. Ma, J. Liang, B. Q. Wei, B. Zhang, C. L. Xu, and D. H. Wu, *J. Power Sources* 84, 126 (1999).
242. E. Frackowiak, K. Metenier, V. Bertagna, and F. Beguin, *Appl. Phys. Lett.* 77, 2421 (2000).
243. E. Frackowiak, K. Jurewicz, S. Delpeux, and F. Beguin, *J. Power Sources* 97–98, 822 (2001).
244. K. Jurenwicz, S. Delpeux, V. Bertagna, F. Beguin, and E. Frackowiak, *Chem. Phys. Lett.* 347, 36 (2001).
245. F. H. Yang and R. T. Yang, *Carbon* 40, 437 (2002) and references therein.
246. V. V. Simonyan and J. K. Jhonson, *J. Alloys Comp.* 330–332, 659 (2002).
247. A. Zuttel, Ch. Nutzenadel, P. Sudan, Ph. Mauron, Ch. Emmenegger, S. Rentsch, L. Schlapbach, A. Weidenkaff, and T. Kiyobayashi, *J. Alloys Comp.* 330–332, 676 (2002).
248. H. W. Zhu, A. Chen, Z. Q. Mao, C. L. Xu, X. Xiao, B. Q. Wei, J. Liang, and D. H. Wu, *J. Mater. Sci. Lett.* 29, 1237 (2000).
249. H. Lee, Y. Kang, S. Kim, and J. Lee, *Appl. Phys. Lett.* 80, 577 (2002).
250. M. Hirscher, M. Becher, M. Haluska, A. Quintel, V. Skakalova, Y. Choi, U. Dettlaff-Weglikowska, S. Roth, I. Epanek, P. Bernier, A. Leonhardt, and J. Fink, *J. Alloys Comp.* 330–332, 654 (2002).
251. Q. Yang, P. Hou, S. Bai, M. Wang, and H. Cheng, *Chem. Phys. Lett.* 345, 18 (2001).
252. X. Li, H. Zhu, L. Ci, C. Xu, Z. Mao, B. Wei, J. Liang, and D. Wu, *Carbon* 39, 2077 (2001).
253. A. K. M. Fazle Kibria, Y. H. Mo, K. S. Park, K. S. Nahm, and M. H. Yun, *Int. J. Hydrogen Energy* 26, 823 (2001).
254. P. Chen, X. Wu, J. Lin, and K. L. Tan, *Science* 285, 91 (1999).

*255.* R. T. Yang, *Carbon* 38, 623 (2000).
*256.* A. Chambers, C. Park, R. T. K. Baker, and N. M. Rodriguez, *J. Phys. Chem.* B102, 4253 (1998).
*257.* G. G. Tribetts, G. P. Meisner, and C. H. Olk, *Carbon* 39, 2291 (2001).
*258.* J. Heremans, C. H. Olk, and D. T. Morelli, *Phys. Rev.* B49, 15122 (1994).
*259.* A. S. Kotosonov and S. V. Kuvshinnikov, *Phys. Lett.* A229, 377 (1997).
*260.* A. S. Kotosonov, *JETP Lett.* 70, 476 (1999).
*261.* F. Tsui, L. Jin, and O. Zhou, *Appl. Phys. Lett.* 76, 1452 (2000).
*262.* K. Tsukagoshi, B. W. Alphenaar, and H. Ago, *Nature* 401, 572 (1999).
*263.* B. W. Alphenaar, K. Tsukagoshi, and M. Wagner, *Physica* E10, 499 (2001).
*264.* A. Fujiwara, K. Tomiyama, H. Suematsu, K. Uchida, and M. Yumura, *Physica* B298, 541 (2001).

*265.* P. Chen, X. Wu, X. Sun, J. Lin, W. Ji, and K. L. Tan, *Phys. Rev. Lett.* 82, 2548 (1999).
*266.* S. Curran, A. P. Davey, J. Coleman, A. Dalton, B. McCarthy, S. Maier, A. Drury, D. Gray, M. Brennan, K. Ryder, M. Lamy de la Chapelle, C. Journet, P. Bernier, H. J. Byrne, D. Carroll, P. M. Ajayan, S. Lefrant, and W. Blau, *Synthetic Metals* 103, 2559 (1999).
*267.* Z. Jin, X. Sun, G. Xu, S. H. Goh, and W. Ji, *Chem. Phys. Lett.* 318, 505 (2000).
*268.* Y. Sun, B. Zhou, K. Henbest, K. Fu, W. Huang, Y. Lin, S. Taylor, and D. Carroll, *Chem. Phys. Lett.* 351, 349 (2002).
*269.* Z. Jin, L. Huang, S. H. Goh, G. Xu, and W. Ji, *Chem. Phys. Lett.* 352, 328 (2002).
*270.* P. Fournet, D. F. O'Brien, J. N. Coleman, H. H. Horhold, and W. J. Blau, *Synthetic Metals* 121, 1683 (2001).
*271.* H. W. Zhu, C. L. Xu, D. H. Wu, B. Q. Wei, R. Vajtai, and P. M. Ajayan, *Science* 296, 884 (2002).